SECOND EDITION

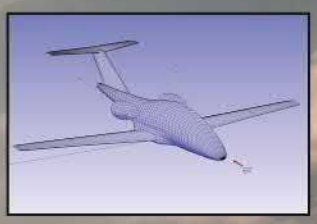
GENERAL AVIATION AIRCRAFT DESIGN

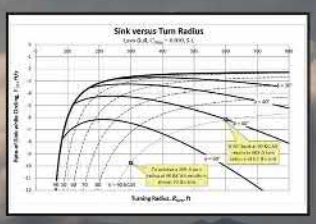
APPLIED METHODS AND PROCEDURES

SNORRI GUDMUNDSSON











B/H

GENERAL AVIATION AIRCRAFT DESIGN

This page intentionally left blank

GENERAL AVIATION AIRCRAFT DESIGN

Applied Methods and Procedures

SECOND EDITION

SNORRI GUDMUNDSSON, BSCAE, MSCAE, PH.D., FAA DER (ret.)
Associate Professor of Aerospace Engineering,
Embry-Riddle Aeronautical University, Daytona Beach, FL, United States

ELSEVIER
Butterworth-Heinemann
An imprint of Elsevier

Butterworth-Heinemann is an imprint of Elsevier
The Boulevard, Langford Lane, Kidlington, Oxford OX5 1GB, United Kingdom
50 Hampshire Street, 5th Floor, Cambridge, MA 02139, United States

Copyright © 2022 Elsevier Inc. All rights reserved.

No part of this publication may be reproduced or transmitted in any form or by any means, electronic or mechanical, including photocopying, recording, or any information storage and retrieval system, without permission in writing from the publisher. Details on how to seek permission, further information about the Publisher's permissions policies and our arrangements with organizations such as the Copyright Clearance Center and the Copyright Licensing Agency, can be found at our website: www.elsevier.com/permissions.

This book and the individual contributions contained in it are protected under copyright by the Publisher (other than as may be noted herein).

Notices
Knowledge and best practice in this field are constantly changing. As new research and experience broaden our understanding, changes in research methods, professional practices, or medical treatment may become necessary.

Practitioners and researchers must always rely on their own experience and knowledge in evaluating and using any information, methods, compounds, or experiments described herein. In using such information or methods they should be mindful of their own safety and the safety of others, including parties for whom they have a professional responsibility.

To the fullest extent of the law, neither the Publisher nor the authors, contributors, or editors, assume any liability for any injury and/or damage to persons or property as a matter of products liability, negligence or otherwise, or from any use or operation of any methods, products, instructions, or ideas contained in the material herein.

Library of Congress Cataloging-in-Publication Data
A catalog record for this book is available from the Library of Congress

British Library Cataloguing-in-Publication Data
A catalogue record for this book is available from the British Library

ISBN: 978-0-12-818465-3

For information on all Butterworth-Heinemann publications
visit our website at https://www.elsevier.com/books-and-journals

Publisher: Matthew Deans
Acquisitions Editor: Carrie Bolger
Editorial Project Manager: Isabella C. Silva
Production Project Manager: Sreejith Viswanathan
Cover Designer: Mark Rogers

Typeset by STRAIVE, India



Dedication

I dedicate this book to my five furry feline companions, Baxter, Boo, Oliver, Oskar, and Leo. You have tolerated my shortcomings, yet never expressed judgment or dismay. A better company on this journey I cannot imagine. Thank you for the wonderful memories. You reside in my heart, forever.

This page intentionally left blank

Contents

Preface to the 1st Edition **xi**
Preface to the 2nd Edition **xiii**
Acknowledgments for the 1st Edition **xv**
Acknowledgments for the 2nd Edition **xvii**
Helpful Notes **xix**

1. The Aircraft Design Process

1.1 Introduction 1
1.2 General Process of Aircraft Design and Development 2
1.3 Introduction to Aviation Regulations and Certification 10
1.4 How to Design a New Aircraft 15
1.5 Elements of Project Engineering 18
1.6 Presenting the Design Project 27
References 32

2. Aircraft Cost Analysis

2.1 Introduction 33
2.2 The Estimation of Project Development Costs 38
2.3 Estimating Aircraft Operational Costs 50
Exercises 55
References 55

3. Initial Sizing

3.1 Introduction 57
3.2 Constraint Analysis 58
3.3 Introduction to Trade Studies 69
3.4 Introduction to Design Optimization 73
Exercises 89
References 91

4. Aircraft Configuration Layout

4.1 Introduction 93
4.2 The Fundamentals of the Configuration Layout 100
References 111

5. Aircraft Structural Layout

5.1 Introduction 113
5.2 Aircraft Fabrication and Materials 114
5.3 Airframe Structural Layout 130
References 145

6. Aircraft Weight Analysis

6.1 Introduction 147
6.2 Initial Weight Analysis Methods 149
6.3 Secondary Weight Analysis Methods 159
6.4 Statistical Weight Estimation Methods 160
6.5 Direct Weight Estimation Methods 167
6.6 Inertia Properties 176
6.7 The Center-of-Gravity Envelope 183
Exercises 194
References 195

7. Selecting the Powerplant

7.1 Introduction 197
7.2 Piston Engines 202
7.3 Gas Turbine Engines 225
7.4 Electric Motors and Battery Technology 239
Exercises 253
References 253

8. The Anatomy of the Airfoil

8.1 Introduction 257
8.2 The Geometry of the Airfoil 282
8.3 The Force and Moment Characteristics of the Airfoil 299
Exercises 317
References 317

9. The Anatomy of the Wing

9.1 Introduction 322
9.2 The Trapezoidal Wing Planform 322
9.3 The Geometric Layout of the Wing 330
9.4 Planform Selection 350
9.5 Lift and Moment Characteristics of Wings 363
9.6 Wing Stall Characteristics 388
9.7 Prandtl's Lifting-Line Theory 399
Exercises 412
References 412

10. The Anatomy of Lift Enhancement

10.1 Introduction 415
10.2 Leading-Edge High-Lift Devices 416
10.3 Trailing-Edge High-Lift Devices 432
10.4 Effect of Deploying High-Lift Devices on Wings 456
10.5 Wingtip Design 461
References 477

11. The Anatomy of the Tail

11.1 Introduction 481
11.2 The Geometry of the Tail 483
11.3 On the Pros and Cons of Tail Configurations 491
11.4 Initial Tail Sizing Methods 505
Exercises 516
References 516

12. The Anatomy of the Fuselage

12.1 Introduction 517
12.2 Fundamentals of Fuselage Shapes 519
12.3 Sizing the Fuselage 521
12.4 Estimating the Geometric Properties of the Fuselage 529
12.5 Additional Information 535
References 539

13. The Anatomy of the Landing Gear

13.1 Introduction 541
13.2 Tires, Wheels, and Brakes 544
13.3 Geometric Layout of the Landing Gear 559
References 571

14. Thrust Modeling for Gas Turbines

14.1 Introduction 573
14.2 Theory of Reactive Thrust 581
14.3 General Thrust Modeling for Gas Turbines 588
Exercises 595
References 595

15. Thrust Modeling for Propellers

15.1 Introduction 597
15.2 Propeller Effects 608
15.3 Properties and Selection of the Propeller 620
15.4 Determination of Propeller Thrust 630
15.5 Rankine-Froude Momentum Theory 638
15.6 Blade Element Theory 646
References 656

16. Aircraft Drag Analysis

16.1 Introduction 658
16.2 The Basics of Drag Modeling 659
16.3 Estimating the Drag of a Complete Aircraft 678
16.4 Miscellaneous or Additive Drag 712
16.5 Special Topics Involving Drag 736
16.6 Additional Information—Drag of Selected Aircraft 744
Exercises 745
References 750

17. Performance—Introduction

17.1 Introduction 753
17.2 Atmospheric Modeling 756
17.3 Airspeed Theory 760
17.4 The Structural Envelope 769
17.5 Sample Aircraft 778
Exercises 783
References 784

18. Performance—Take-Off

18.1 Introduction 785
18.2 Fundamental Relations for the Take-Off Run 790
18.3 Conducting the Take-Off Analysis 795
18.4 Database—T-O Performance of Selected Aircraft 808
Exercises 809
References 810

19. Performance—Climb

19.1 Introduction 811
19.2 Fundamental Relations for the Climb Maneuver 812
19.3 General Climb Analysis Methods 815
19.4 Aircraft Database—Rate-of-Climb of Selected Aircraft 830
References 832

20. Performance—Cruise

20.1 Introduction 833
20.2 Fundamental Relations for the Cruise Maneuver 834
20.3 General Cruise Analysis Methods for Steady Flight 839
20.4 General Analysis Methods for Accelerated Flight 859
References 866

21. Performance—Range and Endurance

21.1 Introduction 867
21.2 Fundamental Relations for Range and Endurance 868
21.3 Range Analysis 873
21.4 Endurance Analysis 884
21.5 Analysis of Mission Profile 886
Exercises 890
References 890

22. Performance—Descent

22.1 Introduction 893
22.2 Fundamental Relations for the Descent Maneuver 894

22.3 General Descent Analysis Methods 895
22.4 Sailplane Glide Performance 900
References 914

23. Performance—Landing

23.1 Introduction 915
23.2 Fundamental Relations for the Landing Phase 917
23.3 Database—Landing Performance of Selected Aircraft 923
References 924

24. Longitudinal Stability and Control

24.1 Introduction 925
24.2 Static Longitudinal Stability and Control 931
24.3 Refined Horizontal Tail Sizing 957
24.4 Introduction to Hinge Moments 966
References 973

25. LAT-DIR Stability and Control

25.1 Introduction 975
25.2 Lateral-Directional Stability and Control 975
25.3 Directional Stability and Control 979
25.4 Lateral Stability and Control 988
25.5 Basics of Roll and Yaw Control 999
References 1005

26. Miscellaneous Design Notes

26.1 Introduction 1007
26.2 General Aviation Aircraft Design Checklist 1007
26.3 Faults and Fixes 1017
References 1029

Appendix A: Atmospheric Modeling 1031
Appendix B: The Aerospace Engineer's Formula Sheet 1039
Appendix C: Design of Biplanes and Seaplanes 1049
Appendix D: Derivation of Landing Side-Constraint 1075
Index 1079

This page intentionally left blank

Preface to the 1st Edition

The purpose of this book is to gather in a single place a diverse set of information and procedures that are particularly helpful to the designer of General Aviation aircraft. Additionally, it provides step-by-step derivations of many mathematical methods, as well as easy to follow examples that help illustrate their application. The procedures range from useful project management tools to practical geometric layout methods, as well as sophisticated aerodynamics, performance, and stability and control analysis methods.

The design of an airplane generally begins with the introduction of specific requirements: how fast, how far, how many, what amenities, what mission. Once introduced to such requirements, the entry-level designer often asks: "What's next? Where do I even begin?" This document provides step-by-step procedures that lead the reader through the entire process: from a clean sheet of paper to the proof-of-concept aircraft. They were selected and developed by the author's 15-year experience in the aircraft industry, initially as a flight test engineer, then structural engineer, aerodynamicist, and eventually an aircraft designer. Subsequent 4-year experience in academia and in various consulting projects allowed the presentation of methods to be polished based on student and client feedback. In the author's own design experience, such a book would have been extremely helpful in the form presented here, both as a resource and guide. This book *is* written with that in mind.

An effective design process answers not only whether the proposed design will meet the desired requirements, but also what remedies are viable in case it does not. During this phase, the speed of analysis is almost always of the utmost, and the competent designer should be able to predict differences between variations of the desired vehicle. However, the design process is multifaceted—it is more than just solving equations—managing the process is also imperative. It is necessary not only to wield the proper tools, but also to know when to apply them. This is particularly important for the manager of the design team; he should always know what step follows the current one and what tools and resources are required.

The book is intended to provide the experienced as well as the aspiring designer with clear and effective analysis procedures. There is already a good collection of well-written college textbooks on aerodynamics, structures, flight dynamics, and airplane design available for the engineering student. Many are mostly written with the student of aerospace engineering in mind and, consequently, often present simple problems inspired more by mathematical convenience than practical situations. Such conveniences are usually absent in industry environment, where problems involve natural processes that do not always accommodate "equation friendly" shortcuts. The book also offers a large chapter on propellers, a topic many textbooks, sadly, ignore. The propeller is here to stay for the foreseeable future, and this warrants the large space dedicated to it.

This book differs from such textbooks as it is solely written with the analysis of real airplanes in mind. Most of the examples presented involve actual production aircraft, allowing results to be directly compared to published data. This gives the reader a great sense for the accuracy of the various analysis methods. It also provides a number of numerical methodologies that take advantage of the power of the modern desktop or laptop computer. This comes in the form of powerful program snippets and spreadsheet setups intended for analysis work with Microsoft Excel. The book offers the student a thorough introduction to practical and industry-proven methods, and the practicing engineer with a great go-to text. I am certain you will find it a very helpful book and that it will increase your productivity.

This page intentionally left blank

Preface to the 2nd Edition

The second edition of this book adheres to the ideals of the original preface. None of these have changed. The book's primary purpose remains to support the aircraft designer by providing practical and effective scientific methods and procedures. However, as much as I, the author, cherish the first edition, it is indisputable that this edition offers several significant improvements. Some are discussed below.

- I combed through every single paragraph in the first edition to polish the writing. Where possible, I rewrote sentences using more concise language. In other places, I removed text I considered redundant or repeated. This made space for new material.
- The first edition was received favorably by readers and my aircraft design students. End-of-semester class evaluations revealed that some considered the book the best part of the class. However, while observing how the students used the book I discovered there was room for organizational improvements. For instance, Chapter 7 in the first edition, introduced piston engines, gas turbines, and electric motors. The presentation of the gas turbines included thrust modeling, while thrust modeling for piston- and electroprops was presented in Chapter 14, *The Anatomy of the Propeller* (now Chapter 15, *Thrust Modeling for Propellers*). This was followed by a discussion about engine installation. In contrast, this edition has each engine-class contained in a separate section. Thrust modeling for gas turbines is now presented in a new chapter, Chapter 14, *Thrust Modeling for Gas Turbines*. Additionally, the discussion of electric motors in Chapter 7 has been significantly increased. It now includes electric motors, battery technology, and electric system design. This change is driven by the increased popularity of electric fixed wing aircraft and eVTOLs.
- The book is now printed in color. I consider this a significant improvement. Some customers had expressed disappointment that the printed version of the first edition did not offer illustrations in color like the electronic version. I am excited that this option is now available for readers.
- The book now contains a good set of design formulation for electric aircraft. Formulation for initial weight estimation appears in Chapter 6, *Aircraft Weight Analysis*. As stated earlier, formulation for batteries, electric motors, and system design is given in Chapter 7. Formulation for range and endurance of electric aircraft is presented in Chapter 21, *Performance—Range and Endurance.*.
- Three new chapters have been added. Chapter 14 presents thrust modeling methods for gas turbines. A basic introduction to fluid mechanics and the "general thrust equation" is also presented in the chapter. Chapters 24 and 25 present longitudinal and lateral-directional stability and control, respectively. The presentation is largely in a review format, which means it is intended for readers with background in stability and control. The chapters offer an assortment of formulas that I have digitized using various graphs in the literature. This offers great advantages for design work that relies on spreadsheets or computer coding. Few things break up the smoothness of the design process like having to read a graph to extract a number. It helps cement this book as a go-to reference for the professional aircraft designer.
- Two appendices have been added. Appendix C provides design information for biplanes and seaplanes. In the first edition, this material was offered online on the publisher's website. Now, it is a part of the book. Appendix D contains a derivation of a landing distance side constraint for constraint analysis.
- The number of illustrations and photos in the book has increased from 828 to 1011. A large percentage of images that appeared in the first edition were polished in one way or another. As with the first edition, unless otherwise specified in captions, all illustrations and diagrams are created by me.

Finally, this. It has taken close to 3 years of hard work and personal sacrifices to revise this book. I have tried to fix all errors and mistakes found in the first edition. Regardless, it is inevitable that errors and mistakes creep into a large book like this. Thus, I will maintain an erratum that will be made available to the public on Elsevier's website. Thank you for purchasing my book. I hope it will be helpful in your development work. Please do not participate in intellectual piracy by sharing electronic or any other illegally produced copies of the book. This harms me directly and discourages further improvements in future. Please notify Elsevier of any illegal book-sharing/selling activity by contacting them directly. Thank you for your cooperation.

This page intentionally left blank

Acknowledgments for the 1st Edition

A large book like this is a substantial undertaking. It can only become reality with contributions from many individuals and companies who, in one way or another, participated in its making. I want to use the opportunity and thank these individuals and companies for their help in providing various information and support so that I would be able to provide you, the reader, with material of greater depth than otherwise possible.

I want to begin by thanking my editors, Mr. Joe Hayton, Mrs. Chelsea Johnston, and Mrs. Pauline Wilkinson of Elsevier Publishing, for invaluable guidance during the development of the book. I'd also like to thank Dr. Howard Curtis, my fellow Professor of Aerospace Engineering at Embry-Riddle Aeronautical University, who believed strongly enough in the project to suggest it to Joe.

The following individuals and companies deserve an expression of my gratitude. I want to thank Mr. Don Pointer of the Dassault Falcon Jet Corporation for providing information about Dassault business jets. I also want to extend thanks to Flightglobal.com, Williams International, Price Induction, Hirth Engines, and Electraflyer for material provided by them. I want to thank Mr. Raymond Ore for providing cutaways of the Spitfire and Mosquito aircraft and the Ed Coates collection. I am indebted to my former student, Mr. Phil Rademacher, for the large number of photographs he supplied to the project. Mr. Rademacher is an expert in aircraft recognition and, as such, has won a number of intercollegiate competitions. Phil provided me with an enormous pool of aircraft photos, of which many can be found throughout this book. Another student of mine, Mr. Nick Candrella, also provided selected pictures. A former colleague of mine, Mr. Jake Turnquist, provided selected pictures as well and also deserves thanks. I also want to thank Nirmit Prabahkar, Manthan Joshi, Thomas Ford, Brian Smith, Teddy Li, Matthew Clark, and Fabio An for data collection. I also want to thank Dr. Laksh Narayanaswami for proofreading Chapter 7, *The Selection of the Powerplant*, and providing priceless guidance regarding turbomachinery and inlet design. I also want to thank Mr. Brian Meyer of Hartzell Propellers Inc. for his contribution to the book. Mr. Meyer provided priceless guidance and help in proofreading Chapter 14, *The Anatomy of the Propeller*, supplied material, and provided suggestions that made the section much better. I want to further extend thanks to Hartzell Propellers for their permission to use selected material on propellers. I want to thank Mr. Dale Klapmeier of Cirrus Aircraft for permitting detailed information about the SR20 and SR22 aircraft to be presented in the book. I also want to thank Mr. Paul Johnston, Cirrus' chief engineer, for initial proofreading and helpful suggestions. I want to thank Mr. Bruce Barrett for several anecdotal nuggets from his colorful career as a flight test pilot. Finally, I want to express my gratitude to Professor Emeritus Charles Eastlake who provided most of the material on the development cost analysis of Section 2 in this book, in addition for his proofreading effort and insightful comments.

Snorri Gudmundsson

This page intentionally left blank

Acknowledgments for the 2nd Edition

I want to begin by thanking my editors, Ms. Carrie Bolger and Ms. Isabella Silva of Elsevier Publishing, for their instrumental help with the development of the book. I would also like to thank Mr. Sreejith Viswanathan (and his team) for their fantastic work on the layout of the book.

The following individuals and companies deserve an expression of my gratitude. I want to thank Mr. Don Pointer of the Dassault Falcon Jet Corporation for providing information about Dassault business jets. I also want to extend thanks to Mr. Kristopher Holt of Lycoming Engines for his help regarding piston engine technology. I want to thank Mr. Curtis Landherr of Cirrus Aircraft, Mr. John Sordyl of Williams International, Mr. Jean-Sebastien Mayen of Akira Technologies (current owner of the business that used to be called Price Induction), Mr. Peter Lietz of Hirth Engines, Mr. Michael Korte of Hartzell Propellers, Mr. George Bye of Bye Aerospace, and Captain Gudbjartur Runarsson. I want to thank Mr. Raymond Ore for providing cutaways of the Spitfire and Mosquito aircraft and Mr. Eddie Coates of the Ed Coates collection. I am indebted to my former student, Mr. Phil Rademacher, for the continued access he has given me to his enormously large database of aircraft photographs. Another former student of mine, Mr. Nick Candrella, and a former colleague of mine, Mr. Jake Turnquist, provided selected pictures as well and also deserve thanks.

I want to mention several of my students for the assistance in various research efforts. I want to thank Ms. Shannon Sumpter for help with evaluating the accuracy of the Eastlake Cost Estimation method, Mr. Mahteme Desta for his research of propeller costs, Mr. Alexandru Lopazan for reconciling the abbreviations and equation terms, Mr. Juan Leon for checking the arithmetic of specific examples, Mr. Aldous George and Mr. Lucas Ferrando for helping with the validation of detail weight analysis methods, and Mr. Louis Spier for his research of multielement high-lift systems. I also extend thanks to my student Xinyu Yang for the detailed cutaway of a business jet in Chapter 1, which he created while taking my aircraft design class.

I want to thank Mr. Scott Olson of Northrop Grumman for reviewing regulatory issues in Chapter 1. I also want to thank Dr. Laksh Naraynaswami for proofreading the gas turbine section of Chapter 7, *Selecting the Powerplant*, and for providing priceless guidance regarding turbomachinery and inlet design. He also deserves thanks for proofreading Chapter 14, *Thrust Modeling for Gas Turbines*. I also extend thanks to Dr. Jinhuia Liu for proofreading the electric aircraft section in Chapter 7, *The Selection of the Powerplant*, and providing invaluable advice and guidance on the design of power systems for electric aircraft. I also want to thank my wife, Linda, for proofreading selected chapters.

Dr. Snorri Gudmundsson

Disclaimer

Every effort has been made to trace and acknowledge copyright. The author welcomes any information from people who believe their photos have been used without due credit. Note that the inclusion of material from commercial entities in the book does not imply an endorsement by the author. Similarly, inclusion of material by any commercial entity in the book does not imply an endorsement by said entities of any content or opinions expressed.

Inclusion of Cirrus copyrighted material in this work does not imply any endorsement by Cirrus or its Affiliates of the content or opinions expressed herein.

This page intentionally left blank

Helpful Notes

Helpful Websites for the Aircraft Designer

FAA regulations:	http://www.faa.gov/
NACA/NASA Report Server	https://ntrs.nasa.gov/search
Aircraft three-view drawing database:	http://richard.ferriere.free.fr/3vues/3vues.html
Aircraft picture database:	https://www.airliners.net/
Airfoil usage database:	https://m-selig.ae.illinois.edu/ads/aircraft.html

The Greek Alphabet

Αα	Alpha	**Νν**	*Nu*
Ββ	Beta	**Ξξ**	Xi
Γγ	Gamma	**Οο**	Omicron
Δδ	Delta	**Ππ**	Pi
Εε	Epsilon	**Ρρ**	Rho
Ζζ	Zeta	**Σσς**	Sigma
Ηη	Eta	**Ττ**	Tau
Θθ	Theta	**Υυ**	Upsilon
Ιι	Iota	**Φφ**	Phi
Κκ	Kappa	**Χχ**	Chi
Λλ	Lambda	**Ψψ**	Psi
Μμ	Mu	**Ωω**	Omega

Prefixes for SI Units

Prefix	Symbol	Numeric notation		Scientific notation
Yotta-	Y	1,000,000,000,000,000,000,000,000	(diameter of observable universe $\approx 4.4 \times 10^{23}$ km)	10^{24}
Zetta-	Z	1,000,000,000,000,000,000,000		10^{21}
Exa-	E	1,000,000,000,000,000,000	(diameter of Milky-Way Galaxy $\approx 1 \times 10^{18}$ km)	10^{18}
Peta-	P	1,000,000,000,000,000	(distance to α-Centauri 40,208,000,000,000 km)	10^{15}
Tera-	T	1,000,000,000,000	(distance to Pluto 7,500,000,000 km)	10^{12}
Giga-	G	1,000,000,000	(distance to Sun 149,597,870 km)	10^{9}
Mega-	M	1,000,000	(distance to Moon 384,402 km)	10^{6}
Kilo-	k	1000	(1 km)	10^{3}
Hecto-	h	100		10^{2}
Deka-	da	10		10^{1}
–	–	1		10^{0}
Deci-	d	0.1		10^{-1}
Centi-	c	0.01		10^{-2}
Milli-	m	(diameter of human hair $\approx 0.000\,1$ m)	0.001	10^{-3}
Micro-	μ	(diameter of human red blood cell ≈ 0.000007 m)	0.000 001	10^{-6}
Nano-	n		0.000 000 001	10^{-9}
Pico-	p	(diameter of atoms ≈ 0.000000000500 m)	0.000 000 000 001	10^{-12}
Femto-	f		0.000 000 000 000 001	10^{-15}
Atto-	a	(diameter of a proton $\approx 0.000\,000\,000\,000001$ m)	0.000 000 000 000 000 001	10^{-18}
Zepto-	z	(diameter of a quark $\approx 1 \times 10^{-19}$ m)	0.000 000 000 000 000 000 001	10^{-21}
Yocto-	y		0.000 000 000 000 000 000 000 001	10^{-24}

Prefixes for SI Units

1 ft	=	0.3048 m
1 m	=	3.28084 ft
1 mi (statute mile)	=	5280 ft
1 nm (nautical mile)	=	6076 ft
1 BHP	=	0.7457 kW
1 BHP	=	745.7 W
1 BHP	=	33,000 ft lb_f/min
1 BHP	=	550 ft lb_f/s
1 kW	=	1.340483 HP
1 W	=	0.001340483 HP
1 ft/s	=	0.59242 knots
1 ft/s	=	0.3048 m/s
1 mph	=	1.467 ft/s
1 knot	=	1.688 ft/s
1 US gal of Avgas	=	6.0 lb_f (2.718 kg)
1 US gal of Jet A	=	6.7 lb_f (3.035 kg)
1 US gal	=	3.785412 L
Fuel tank volume: 1 $in.^3$	=	0.004328704 US gal
Fuel tank volume: 1 US gal	=	231.02 $in.^3$
1 GPa (giga-pascal)	=	145,037.73773 psi
1 MPa (mega-pascal)	=	145.03773773 psi

A Note About Format

This document is organized in a fashion designed to be useful to the reader. For this reason, the background of the document appears in three colors that have specific meaning:

1. The main topic of a section is discussed in a region of white background.
2. The derivation of specific formulae is presented in a region of a **gray background**.
3. Examples are presented in regions of a **light-blue background**.

The book is broken down further into sections as follows:

4. The book is broken down into *chapters* and *appendices*. An appendix contains supplemental material that is not essential to the chapters, but provides an improved insight.
5. Each chapter (and some appendices) is split into *sections*. Thus, the third section of Chapter 11 is denoted by 11.3.
6. Each section is split into *subsections*. Thus, the third subsection of Section 11.3 is denoted by 11.3.3.
7. Some subsections are split into focus areas. These are called *bullets*. Thus, the second focus area in Section 11.3.3 is denoted by 11.3.3(2).
8. Fitting large equations in a two-column layout can be challenging. At times, this is only possible by presenting the equation in a single-column format. In this case, the text flows from the 1st column to the 2nd column above said equation. It then continues to flow in the 1st column below the single-column equation.

A Note About Mass and Force

Often several forms of units of force are presented in the UK system. Examples include lbs (mass or force), lb_m (mass), lb_f (force), lb_{st} (engine static thrust), lb_t (engine thrust), and so on. Usually this is done to distinguish between mechanical and other kinds of forces, but ultimately it is confusing. In this document, the intention is to keep everything as simple as possible. Therefore, the following holds for all units of mass and force:

	UK system	SI system
Mass	slugs	kg
Force	lb_f	Newton, N

List of Abbreviations and Common Terms

Abbreviation	Description	Remarks
A&P	Airframe and Powerplant	
AC	Aircraft; Standard Airworthiness Certificate; Advisory Circular	(context dependent)
ACO	Aircraft Certification Office	
AD	Airworthiness Directives	
ADT	Actuator Disk Theory	
AF	Activity Factor	
AFTI	Advanced Fighter Technology Integration	
AIAA	American Institute of Aeronautics and Astronautics	
AISI	American Iron and Steel Institute	
aka	Also known as	
ALF	Artificial Laminar Flow	
AMM	Aircraft Maintenance Manual	
AMST	Advanced Medium STOL Transport	
AOA	Angle-of-Attack	degrees or rad
AOC	Angle-of-Climb	
AOD	Angle-of-Descent	degrees or rad
AOG	Angle-of-Glide	degrees or rad
AOI	Angle-of-Incidence	degrees or rad
AOL	Aircraft Operating Limitations	
AOY	Angle-of-Yaw	degrees or rad

Continued

Abbreviation	Description	Remarks
APU	Auxiliary Power Unit	
AR	Aspect Ratio	
ASI	Airspeed Indicator	
ASTM	American Society for Testing and Materials	
AWACS	Early Warning and Control Systems	
BCS	Body Coordinate System	
BET	Blade Element Theory	
BFL	Balanced Field Length	
BHP	Brake Horsepower	
BL	Boundary Layer	
BL	Butt line (or buttock line)	
BLT	Boundary Layer Theory	
BPR	Bypass Ratio	
CAA	Civil Aviation Authority	
CAD	Computer-Aided Design	
CAR	Civil Aviation Regulations	
CAT	Clear Air Turbulence	
CDBM	Component Drag Build-up Method	
CER	Cost Estimating Relationship	
CET	Compressor Exit Temperature	
CFD	Computational Fluid Dynamics	
CFR	Code of Federal Regulations	
CG	Center-of-Gravity	
CM	Center-of-Mass	
COM	Electronic communication	
CP	Center-of-Pressure	
CPI	Consumer Price Index	
CPM	Critical Path Method	
CRP	Carbon Reinforced Plastics	
CRUD	Cumulative Result of Undesirable Drag	
CS	Certification Specifications	
CV	Control volume	
CV	Centroid-of-Volume	
DAPCA	Development and Procurement Cost of Aircraft	
DAR	Dry Adiabatic Rate	
DOE	Design of Experiments	
DOF	Degree of Freedom	
dp/dx	Pressure gradient (change in p along direction x)	
EASA	European Aviation Safety Agency	
ELOS	Equivalent Level of Safety	
EOM	Equations-of-Motion	
ESDU	Engineering Sciences Data Unit (formerly)	
FAA	Federal Aviation Administration	
FAI	Federation Aeronautique Internationale	
FAR	Federal Aviation Regulations	
FEA	Finite Element Analysis	
FES	Fixed Earth Coordinate System	
FF	Form Factor	
FIKI	Flight Into Known Icing	
FOD	Foreign Object Damage	
FOV	Field-of-View	
FRP	Fiberglass Reinforced Plastics	
FS	Fuselage Station	
GA	General Aviation, Genetic Algorithm (context dependent)	
GAMA	General Aviation Manufacturers Association	
GDT	Geometric Dimensioning and Tolerancing	
GRP	Graphite Reinforced Plastic	
GS	Ground Speed	
HBPR	High Bypass Ratio	
HFDG	Human Factors Design Guide	
HLFC	Hybrid Laminar Flow Control	
HOP	Horizontally Opposed piston engine	
HQ	House of Quality	
HS	Horizontal Station	
HT	Horizontal tail	
ICTS	Ice Contaminated Tailplane Stall	
IF	Interference Factor	
IFR	Instrument Flight Rules	
IGE	In Ground Effects	
IPT	Integrated Product Team	
ISA	International Standard Atmosphere	
JAA	Joint Aviation Authorities	
JAR	Joint Aviation Regulations	
KCAS	Knots, Calibrated airspeed	
KEAS	Knots, Equivalent airspeed	
KGS	Knots, Ground speed	
KIAS	Knots indicated airspeed	
KTAS	Knots, True Airspeed	
LCO	Life-Cycle Oscillations	
LE	Leading Edge	
LFC	Laminar Flow Control	
LP	Linear Programming	
LSA	Light Sport Aircraft	
MAC	Mean aerodynamic chord	
MAP	Manifold Pressure	
MAV	Micro Air Vehicle	
MCP	Maximum Continuous Power	
MDO	Multidisciplinary Optimization	

Continued

Abbreviation	Description	Remarks
MFTS	Master Flight Test Schedule	
MGC	Mean Geometric Chord	
MIDO	Manufacturing Inspection District Offices	
MLG	Main Landing Gear	
MMPDS	Metallic Materials Properties Development and Standardization	
MNCF	Mach Number Correction Factor	
MOC	Means-of-Compliance	
NACA	National Advisory Committee for Aeronautics	
NAR	Normal Adiabatic Rate	
NASA	National Aeronautics and Space Administration	
NAV	Electronic navigation	
NBAA	National Business Aviation Association	
NLF	Natural Laminar Flow	
NLG	Nose Landing Gear	
NLP	Neihouse-Lichtenstein-Pepoon's criterion	
NOAA	National Oceanic & Atmospheric Administration	
NPA	Notice of Proposed Amendment	
NPRM	Notice of Proposed Rulemaking	
NSCFD	Navier-Stokes Computation Fluid Dynamics	
NSE	Navier-Stokes equations	
NURBS	Nonuniform Rational Basis Spline	
OAT	Outside Air Temperature	
OEI	One Engine Inoperative	
OGE	Out of Ground Effects	
OML	Outside Mold Line	
OPR	Overall Pressure Ratio (aka Compressor Pressure Ratio)	
PERT	Program Evaluation and Review Technique	
PFD	Primary Flight Display	
PFM	Pilots Flight Manual	
PFT	Potential Flow Theory	
PIO	Pilot-Induced Oscillation	
PMA	Parts Manufacturer Approval	
POC	Proof-of-Concept (aircraft)	
POH	Pilot's Operating Handbook	
QFD	Quality Function Deployment	
RC	Radio-Controlled	
RDT&E	Research, Development, Testing, & Evaluation	
RFP	Request for Proposal	
ROC	Rate of Climb	
ROD	Rate of Descent	
RTM	Resin Transfer Molding	
S&C	Stability and Control	
S-AC	Special Airworthiness Certificate	
SAE	Society of Automotive Engineers	
SAR	Saturated Adiabatic Rate	
SAS	Stability Augmentation System	
SB	Service Bulletin	
SCS	Stability Coordinate System	
SCS	Stability Coordinate System	
SFC	Specific Fuel Consumption	
SFF	Side Force Factor	
SHP	Shaft Horse Power	
S-L	Sea Level	
SM	Static Margin	
SOC	Statement of Compliance	
STC	Supplemental Type Certificate	
STOL	Short Takeoff and Landing	
TC	Type Certificate	
TCDS	Type Certificate Data Sheet	
TDPF	Tail-Damping Power Factor	
TE	Trailing Edge	
TED	Trailing Edge Down	
TEL	Trailing Edge Left	
TER	Trailing Edge Right	
TET	Turbine Entry Temperature	
TEU	Trailing Edge Up	
T-O	Takeoff	
TR	Taper Ratio, Throttle ratio (context dependent)	
TRA	Tire and Rim Association	
TSFC	Thrust-specific fuel consumption	
TSO	Technical Standard Order	
TSOA	Technical Standard Order Authorization	
UAV	Unmanned Aerial Vehicle	
US	United States of America	
USA	United States Army	
USAF	United States Air Force	
VASIS	Visual Approach Slope Indicator System	
VBA	Visual Basic for Applications	
VCS	Vehicle Coordinate System	
VDT	Variable Density Tunnel	
VFR	Visual Flight Rules	
VG	Vortex Generator	
VLM	Vortex Lattice Method	

Continued

Abbreviation	Description	Remarks
VS	Vertical Station	
VSC	Vendor Supplied Components	
VSI	Vertical Speed Indicator	
VT	Vertical tail	
WAS	Wind Axis Coordinate System	
WL	Water Line	
WS	Wing Station	

List of Variables

Note: The term *context dependent* means there are multiple definitions and further clarification requires additional information presented in the text.

Variable	Description	Typical units (UK and SI)
A	$\rho C_{L_{max}}$ (context dependent)	slugs/ft^3, kg/m^3
A	Cross-sectional area (context dependent)	ft^2 or m^2
A	Engine-dependent constant (for piston engines) (context dependent)	
A	Inflow angle (context dependent)	degrees or rad
A	Mannequin stature (context dependent)	ft or m
A	Constant in cruise range equation (context dependent)	
A, B, C	Constants (context dependent)	
A_B	Reference area of the baffle (radiator)	ft^2 or m^2
A_{cap}	Spar cap area	ft^2 or m^2
A_{cell}	Area of idealized cell	ft^2 or m^2
A_e	Exit cross-sectional area	ft^2 or m^2
AF	Activity factor	
AF_{TOT}	Total Activity factor	
$A_{halfweb}$	Area of half of the spar web	ft^2 or m^2
A_i	Inlet cross-sectional area	ft^2 or m^2
A_{IN}	Inlet area of a diffuser	ft^2 or m^2
$A_{\max}$	Maximum fuselage cross-sectional area	ft^2 or m^2
AOA	Angle-of-Attack	degrees or rad
AOC	Angle-of-Climb	degrees or rad
A_P	Propeller disk area	ft^2 or m^2
AR	Aspect ratio	
AR_{corr}	Corrected Aspect Ratio	
AR_e	Effective aspect ratio ($AR \bullet e$)	
AR_{HT}	Horizontal Tail Aspect Ratio	
AR_{lim}	Aspect Ratio limit	
AR_R	Reduced Aspect Ratio	
AR_{VT}	Vertical Tail Aspect Ratio	
AR_W	Wing Aspect Ratio	
A_{side}	Side area of fuselage	ft^2 or m^2
A_{top}	Top area of fuselage	ft^2 or m^2
A_{tube}	Cross-sectional area of stream tube	ft^2 or m^2
A_0	Cross-sectional area at station 0 (far-field)	ft^2 or m^2
A_1	Cross-sectional area at station 1 (inlet)	ft^2 or m^2
A_2	Cross-sectional area at station 2 (compressor)	ft^2 or m^2
A_π	Equivalent parasite area	ft^2 or m^2
a	Speed of sound (context dependent)	knots, ft/s, m/s, etc.
a	Mean line designation for NACA 6-series airfoils (context dependent)	
a	Major axis length of an ellipse (context dependent)	ft or m
a	Lapse rate (context dependent)	1/ft or 1/m
a	Instantaneous acceleration (context dependent)	ft/s^2 or m/s^2
a	Constant in altitude endurance equation (context dependent)	
a_{avg}	Average acceleration	ft/s^2 or m/s^2
a_o	Speed of sound at S-L on a standard day	knots, ft/s, m/s, etc.
BFL	Balanced field length	ft or m
BHP/W	Brake Horsepower-to-Weight ratio	BHP/lb$_f$, BHP/N
b	Wingspan (context dependent)	ft or m
b	Minor axis length of an ellipse (context dependent)	ft or m
b_a	Aileron span	ft or m
b_f	Flap span	ft or m
b_{HT}	Horizontal tail span	ft or m
$bore$	Diameter of each cylinder	ft or m
b_R	Reduced wingspan	ft or m
b_s	Slat span	ft or m
b_{VT}	Vertical tail span	ft or m
b_1	Spanwise station for the inboard edge of the aileron	ft or m

Continued

Variable	Description	Typical units (UK and SI)
b_2	Spanwise station for the outboard edge of the aileron	ft or m
C_{AC}	Insured valued of aircraft	$
C_{AP}	Yearly maintenance cost	$/year
$CASM$	Cost of Available Seat-Mile	$/seat
C_{CERT}	Total cost for certification	$
C_{CREW}	Crew Cost	$/h
C_{CSP}	Cost of a constant speed propeller	$
$C_{CSTPROP}$	Cost of constant speed propellers	$
C_d	Total drag coefficient for a 2-dimensional shape (e.g., airfoil)	
C_D	Total drag coefficient for a 3-dimensional body (e.g., aircraft)	
C_{DEV}	Total development support cost	$
C_{Df}	Skin friction drag coefficient	
C_{Dfo}	Incompressible skin friction drag coefficient	
C_{D_i}	Lift-induced drag coefficient	
$(C_{D_i})_{IGE}$	Induced drag coefficient, in ground effect	
$C_{Dincompressible}$	Incompressible drag coefficient at some condition	
$C_{D\ LDG}$	Drag coefficient after touchdown	
C_{DM}	Compressibility drag coefficient	
$C_{d_{\min}}$	Minimum 2-D drag coefficient	
$C_{D_{\min}}$	Minimum drag coefficient	
$C_{D\text{misc}}$	Miscellaneous drag coefficient	
$C_{D\text{mod}}$	Modified drag coefficient	
$C_{D_{TO}}$	Takeoff drag coefficient	
C_{D_w}	Wave drag coefficient	
C_{Dwng}	Drag coefficient for wing alone	
C_{Dx}	Drag coefficient for complete aircraft minus wing	
C_{D_α}	Change in drag coefficient due to AOA	/degrees or /rad
C_{D_β}	Change in drag coefficient due to sideslip angle	/degrees or /rad
$C_{D_{\delta_e}}$	Change in drag coefficient due to elevator deflection	/degrees or /rad
$C_{D_{\delta_f}}$	Change in drag coefficient due to flap deflection	/degrees or /rad
$C_{D_{\delta spoiler}}$	Change in drag coefficient due to spoiler deflection	/degrees or /rad
$C_{D\pi}$	Component equivalent drag coefficient	
C_{ENGR}	Total cost of engineering	$
C_f	Skin friction coefficient	
$C_{f\ \text{lam}}$	Skin friction coefficient for laminar boundary layer	
$C_{f\ \text{turb}}$	Skin friction coefficient for turbulent boundary layer	
C_{fix}	Fixed cost	$
C_{fixop}	Fixed operational cost per period (e.g., a year)	$
$C_{FIXPROP}$	Cost of pitch fixed propellers	$
C_{flight}	An estimate of all other costs associated with flight testing per month	$/months
C_{fo}	Reference skin friction coefficient	
C_{FT}	Total cost for flight test operations	$
C_{FUEL}	Annual fuel cost	$/year
C_{FXD}	Cost of a fixed pitch propeller	$
CG	Center of gravity	ft, m, or % MAC
C_h	Hinge moment coefficient	
C_{h0}	Zero AOA hinge moment coefficient	
C_{HR}	Cost per flight hour	$/h
C_{h_α}	Hinge moment coefficient curve slope	/degrees or /rad
C_{h_δ}	Hinge moment coefficient caused by flap deflection	/degrees or /rad
$C_{h_{\delta t}}$	Hinge moment coefficient caused by tab deflection	/degrees or /rad
C_{INS}	Annual cost for insurance	$/year
C_{INSP}	Annual inspection cost	$/year
C_l	2-dimensional lift coefficient (section lift coefficient)	
C_L	3-dimensional lift coefficient	
$\boldsymbol{C_L}$	Rolling moment coefficient	
C_{L_C}	Average cruise lift coefficient	
$C_{L\ HT}$	3-D lift coefficient of the horizontal tail	
$C_{L\ LDG}$	Lift coefficient after touchdown	
$C_{L\ ROC\max}$	3-D lift coefficient at maximum rate of climb	

Continued

Variable	Description	Typical units (UK and SI)
$C_{L\ TO}$	Lift coefficient during T-O run	
C_{lclimb}	2-D lift coefficient during climb	
$C_{lcruise}$	2-D lift coefficient during cruise	
C_{li}	Average C_l of the unflapped wing segments at stall AOA of flapped segments	
$C_{l_{max}}$	Maximum 2-D lift coefficient	
$C_{L_{max}}$	Maximum 3-D lift coefficient	
$C_{l_{max\ a}}$	Maximum lift coefficient at the inboard end of the segment	
$C_{l_{max\ avg}}$	Average of $C_{l\max\ a}$ and $C_{l\max\ b}$	
$C_{l_{max\ b}}$	Maximum lift coefficient at the outboard end of the segment	
$C_{l_{max\ i}}$	Maximum lift coefficient of the flapped wing segment	
$C_{l_{min}}$	Minimum 2-D lift coefficient	
$C_{L_{min}}$	Minimum 3-D lift coefficient	
$C_{l_{mind}}$	2-D lift coefficient at minimum drag	
$C_{L_{minD}}$	3-D lift coefficient at minimum drag	
C_{L0}	3-D lift coefficient at $\alpha = 0$ (context dependent)	
C_{l0}	2-D lift coefficient at $\alpha = 0$ (context dependent)	
C_{LOAN}	Monthly loan payment	$/year
C_{LoHT}	Horizontal tail lift coefficient at zero AOA	
C_{LoW}	Wing lift coefficient	
$\boldsymbol{C_{Lp}}$	Roll damping derivative	/degrees or /rad
C_{LW}	Wing lift coefficient	
C_{L0}	Lift coefficient at zero AOA	
C_{L2}	Magnitude of lift coefficient at V_2 (context dependent)	
C_{L2}	Lift coefficient at start of cruise segment (context dependent)	
C_{L3}	Lift coefficient at end of cruise segment	
$C_{L\alpha HT}$	Change in horizontal tail lift coefficient due to AOA	/degrees or /rad
$\boldsymbol{C_{L_\beta}}$	Dihedral effect	/degrees or /rad
$\boldsymbol{C_{L_{\beta VT}}}$	Vertical tail lift curve slope	/degrees or /rad
C_{l_α}	2-dimensional lift curve slope	/degrees or /rad
C_{L_α}	3-dimensional lift curve slope	/degrees or /rad
$C_{L_{\alpha HT}}$	3-dimensional lift curve slope of the horizontal tail	/degrees or /rad
C_{l_α}	Incompressible 2-dimensional lift curve slope	/degrees or /rad
C_{L_β}	Change in lift coefficient due to sideslip angle	/degrees or /rad
$\boldsymbol{C_{L_{\delta_a}}}$	Aileron authority derivative	/degrees or /rad
$C_{l_{\delta_a}}$	Change in lift coefficient with aileron deflection	
$C_{L_{\delta_e}}$	3-D coefficient of lift generated by elevator deflection	
$C_{L_{\delta f}}$	Change in lift coefficient due to flap deflection	/degrees or /rad
$C_{L\delta spoiler}$	Change in lift coefficient due to spoiler deflection	/degrees or /rad
$\boldsymbol{C_M}$	Pitching moment coefficient	
$\boldsymbol{C_{M_0}}$	Incompressible pitching moment coefficient	
C_{MAT}	Total material cost	$
C_{MFG}	Total manufacturing cost	$
C_{Mo}	3-D zero AOA pitching moment coefficient	
C_m	2-dimensional pitching moment coefficient	
$C_{m\ ac}$	2-D Coefficient of moment about aerodynamic center	
$C_{m\ avg}$	Average 2-D coefficient of moment	
$C_{m\ i}$	Average pitching moment coefficient of each wing segment	
$C_{mc/4}$	Airfoil pitching moment coefficient about the quarter-chord	
C_{misc}	Miscellaneous costs per month	$
C_{mo}	2-D coefficient of moment at $\alpha = 0$ (context dependent)	/degrees or /rad
C_{month}	Monthly load payment	$
C_{mROOT}	Pitching moment coefficient of the root airfoil	
C_{mTIP}	Pitching moment coefficient of the tip airfoil	

Continued

Variable	Description	Typical units (UK and SI)
C_{M_q}	Change in coefficient of pitching moment due to pitch rate	
C_{M_W}	Moment coefficient of the wing	
$C_{m\alpha}$	2-dimenstional pitching moment curve slope	/degrees or /rad
C_{M_α}	3-dimensional pitching moment curve slope	/degrees or /rad
C_{M_β}	Change in coefficient of pitching moment due to sideslip angle	/degrees or /rad
$C_{M_{\delta e}}$	Change in coefficient of pitching moment due to elevator deflection	/degrees or /rad
$C_{M_{\delta f}}$	Change in drag coefficient of pitching moment due to flap deflection	/degrees or /rad
C_N	Yawing moment coefficient	
C_{N_r}	Change in coefficient of yawing moment due to yaw rate	
C_{N_β}	Directional stability derivative	/degrees or /rad
$C_{N_{\delta r}}$	Change in coefficient of yawing moment due to rudder deflection	
C_{op}	All-inclusive operational cost per flight hour	$
C_{OVER}	Engine overhaul fund	$/year
C_p	Specific heat of constant pressure (context dependent)	BTU/(sl°R) or J/(kgK)
C_p	Pressure coefficient (context dependent)	
C_v	Specific heat of constant volume (context dependent)	BTU/(sl°R) or J/(kgK)
C_P	Estimated monthly operating cost for a prototype (context dependent)	$/mo
C_P	Power coefficient (context dependent)	
$\overline{C}_p$	Canonical pressure coefficient	
$C_{p\ crit}$	Pressure coefficient at critical Mach	
$C_{P1\rightarrow 2}$	Ideal pressure coefficient (for turbine inlet design)	
CPI_{2012}	Consumer price index relative to the year 2012	
CPI_{YYYY}	Consumer Price Index using YYYY as reference year	
C_{po}	Reference pressure coefficient	
C_{Po}	Incompressible pressure coefficient	
C_{PP}	Cost of engine	$
C_Q	Torque coefficient	
C_{QC}	Total cost of Quality control	$
C_r	Wing chord, root (context dependent)	
C_r	Nondimensional coefficient the relates AOA to force (context dependent)	
C_{STOR}	Cost for storage	$
C_T	Thrust coefficient	
C_{TOOL}	Total tooling cost	$
C_{var}	Variable cost	$
C_{VSC}	Cost of vendor supplied components	$
C_{ws}	SFC of a piston engine in terms of Watt Seconds	
C_y	Side force coefficient	
C_{YEAR}	Yearly operational cost	$/year
$C_{y\beta}$	Change in coefficient of side force due to sideslip angle	/degrees or /rad
c	Airfoil or propeller blade chord length (context dependent)	ft or m
c	Size of the gap at outlet of the slot (context dependent)	ft or m
c	Length of tire footprint (context dependent)	ft or m
$c/4$	Quarter-chord	ft or m
c_{avg} *or* $\bar{c}$	Average chord length	ft or m
c_{bhp}	Specific fuel consumption of a piston engine	$(lb_f/h)/BHP$ or g/J
c_{cell}	Chord length of idealized cell	ft or m
c_{do}	Zero AOA drag coefficient	
c_f	Flap chord (aft of hingeline)	ft or m
c_{fe}	Combined flap chord length when extended	ft or m
c_{fs}	Combined flap chord length when stowed	ft or m
c_{HT}	Chord length of horizontal tail	ft or m
c_{jet}	Specific fuel consumption for jet engines	1/h or g/(Ns)
c_{MGC}	Mean geometric chord	ft or m
c_{main}	Chord length of airfoil without flap	ft or m
c_r	Root chord length	ft or m
c_{rR}	Reduced root chord length	ft or m

Continued

Variable	Description	Typical units (UK and SI)
c_s	Slat chord length (context dependent)	ft or m
c_s	Split flap chord length (context dependent)	ft or m
c_t	Thrust specific fuel consumption (context dependent)	1/s
c_t	Tip chord length (context dependent)	ft or m
c_v	Vane chord length	ft or m
c_{VT}	Chord length of vertical tail	ft or m
D	Drag (context dependent)	lb_f or N
D	Diameter of geometric shape (context dependent)	ft or m
D	Diameter of tire (context dependent)	ft or m
D_P	Propeller diameter (context dependent)	ft or m
D_C	Cooling drag force	lb_f or N
D_f	Skin friction drag force	lb_f or N
D_{FUS}	Drag due to fuselage	lb_f or N
D_{HT}	Drag due to horizontal tail	lb_f or N
D_i	Lift-induced drag force	lb_f or N
DI	Directivity correction	dB
D_{LDG}	Drag due to landing gear	lb_f or N
D_{ldg}	Drag in landing configuration	lb_f or N
$D_{\min}$	Zero-lift drag force	lb_f or N
D_{NAC}	Drag due to nacelle	lb_f or N
DOC	Direct Operating Cost	$
D_{old}	Diameter of old propeller	ft or m
D_P	Propeller diameter	in., ft, or m
D_{trim}	Drag at trim condition	lb_f or N
D_{VT}	Drag due to vertical tail	lb_f or N
D_W	Drag due to the wing	lb_f or N
D_0	Basic drag force	lb_f or N
D_1	Inlet lip diameter (context dependent)	ft or m
D_1, D_2	Major and minor diameters of an ellipsis (context dependent)	ft or m
D_2	Drag at V_2 (context dependent)	lb_f or N
d	Airfoil drag force (context dependent)	lb_f or N
d	Diameter of circular cylinder (context dependent)	ft or m
d	Deflection of gear (context dependent)	ft or m
d	Diameter of wheel (context dependent)	ft or m
d	Difference between unloaded and loaded tire radius (context dependent)	ft or m
d_F	Maximum fuselage depth	ft or m
d_{fus}	Maximum diameter of the fuselage	ft or m
$d_i(y)$	Lift-induced drag per unit span	lb_f/ft or N/m
dl	Infinitesimally small vector length	ft or m
d_L	Distance from center of thrust of left propeller to the CG along y-axis	ft or m
d_{NAC}	Distance from nacelle to the CG along y-axis	ft or m
d_R	Distance from center of thrust of right propeller to the CG along y-axis	ft or m
dR	Rate of change of distance	knots, ft/s, m/s, etc.
dt	Infinitesimal change in time	s
dV	Infinitesimal change in velocity	ft/s or m/s
dw	Velocity induced at arbitrary point P by dl	knots, ft/s, m/s, etc.
dW	Rate of change of weight	lb_f/s or N/s
d_1, d_2	Diameters of frustum ends	ft or m
E	Endurance (context dependent)	h
E	Young's (elastic) modulus (context dependent)	ksi or MPa
E	Energy (context dependent)	ft lb_f; N m or J
E_{batt}	Energy density (of a battery)	(W h)/kg (SI only)
E_∞	Kinetic energy at some specific condition	ft lb_f; N m or J
E^*	Mass-Specific Energy	
E_0	Kinetic energy at some specific condition	ft lb_f; N m or J
e	Internal energy (context dependent)	ft lb_f; N m or J
e	Oswald efficiency (context dependent)	
F	Force or thrust at condition (context dependent)	lb_f or N
F	Actuation force (context dependent)	lb_f or N
$F()$	Objective function (context dependent)	

Continued

Variable	Description	Typical units (UK and SI)
F_{bend}	Bending force	lb_f or N
F_{bru}	Ultimate bearing stress (per MIL-HDBK)	ksi or MPa
F_{CERT}	Certification factor (context dependent)	
F_{CF}	Complex flap system factor (context dependent)	
F_{COMP}	Fraction of composites in an airframe (context dependent)	
F_{drag}	Drag landing force	lb_f or N
F_{EXP}	Experience effectiveness adjustment factor	
FF	Form-Factor (context dependent)	
FF	Total Fuel Flow of all engines (context dependent)	gal/h, kg/h
FF_C	Fuel Flow of all engines during cruise	gal/h, kg/h
F_H	Horizontal component of lift on a V-tail	lb_f or N
F_{hub}	Hub correction factor	
F_L	Left landing gear friction force	lb_f or N
FL_1–FL_3	Loudness levels 1 through 3	dB
F_{land}	Vertical landing force	lb_f or N
F_{MF}	Required maintenance workhours for every flight hour	
F_N	Nose gear friction force (context dependent)	lb_f or N
F_N	Normal force from propeller (context dependent)	lb_f or N
F_{net}	Net thrust	lb_f or N
F_{new}	Drag force of new propeller blade	lb_f or N
F_{old}	Drag force of old propeller blade	lb_f or N
F_P	Common correction factor for propeller tip and hub	
F_{press}	Pressure force	lb_f or N
F_{PRESS}	Pressurization factor (context dependent)	
F_R	Right landing gear friction force	lb_f or N
F_S	Side force due to propeller	lb_f or N
F_{side}	Side landing force	lb_f or N
F_{SL}	Rated thrust at S-L	lb_f or N
F_{su}	Ultimate shear stress (per MILD-HDBK-5)	ksi or MPa
F_{tail}	Vertical tail weight factor	
F_{TAPER}	Chord taper factor (context dependent)	
F_{tip}	Tip correction factor	
F_{tu}	Ultimate tensile stress (per MILD-HDBK-5)	ksi or MPa
F_{ty}	Yield tensile stress (per MIL-HDBK-5)	ksi or MPa
F_V	Vertical component of lift on a V-tail	lb_f or N
F_1	Force produced by gearwheel 1	lb_f or N
F_2	Force produced by gearwheel 2	lb_f or N
f	Equivalent flat plate (parasite) area (context dependent)	ft^2 or m^2
f	Friction force (context dependent)	lb_f or N
f	Fineness ratio (context dependent)	
f_c	Airfoil chord-wise force	lb_f or N
f_{comp}	Fraction of airframe made from composites (context dependent)	
f_n	Airfoil normal force	lb_f or N
f_Ω	Frequency of rotation	Hz
G	Shear modulus	ksi or MPa
GR	Gear ratio	
g	Acceleration due to gravity	ft/s^2 or m/s^2
g_i	Inequality constraint with index i	
H	Radial distance from outside of wheel to outside of tire (context dependent)	ft or m
H, h	Altitude (context dependent)	ft or m
H_C	Cruise altitude?	ft or m
H_E	Specific energy/Energy height	ft or m
H_{ENGR}	Number of engineering workhours	h
HM	Hinge moment	ft lb_f or N m
H_{MFG}	Number of manufacturing labor hours	h
H_{ref}	Reference altitude	ft or m
H_{TOOL}	Number of tooling workhours	h
h	Double-amplitude wave height (context dependent)	ft or m
h	Structural depth at MGC (context dependent)	ft or m

Continued

Variable	Description	Typical units (UK and SI)
h	Distance to point P perpendicular to velocity (context dependent)	ft or m
h	Height-to-chord fraction (Gurney flap) (context dependent)	
h	Height of winglets (context dependent)	ft or m
h	Winglet height (context dependent)	ft or m
h	Height of a fuselage (context dependent)	ft or m
h	Distance to turning center (context dependent)	ft or m
h	Distance from airfoil leading edge to CG (context dependent)	ft or m
h_{AC}	x-distance from LE of MGC to aircraft aerodynamic center	ft or m
h_{crit}	Critical altitude	ft or m
h_F	Flare height	ft or m
h_i	Equality constraint with index i	
h_n	Stick-fixed neutral point	
h_{obst}	Obstacle height	ft or m
h_P	Pressure altitude	ft or m
h_{SR}	Angular momentum of a spinning about an axis of rotation	$\text{slugs}\,\text{ft}^2/\text{s}$ or $\text{kg}\,\text{m}^2/\text{s}$
h_{SRx}	Angular momentum of a spinning about the x-axis	$\text{slugs}\,\text{ft}^2/\text{s}$ or $\text{kg}\,\text{m}^2/\text{s}$
h_{SRy}	Angular momentum of a spinning about the y-axis	$\text{slugs}\,\text{ft}^2/\text{s}$ or $\text{kg}\,\text{m}^2/\text{s}$
h_{SRz}	Angular momentum of a spinning about the z-axis	$\text{slugs}\,\text{ft}^2/\text{s}$ or $\text{kg}\,\text{m}^2/\text{s}$
h_{to}	Takeoff obstacle height	ft or m
h_{TR}	Takeoff transition height	ft or m
h_ρ	Density altitude	ft or m
h_0	Reference altitude	ft or m
h_2	Altitude at beginning of cruise segment	ft or m
h_3	Altitude at end of cruise segment	ft or m
I	Current (context dependent)	A (Amperes) (SI only)
I	Moment of inertia (context dependent)	ft^4 or m^4
I_{CG}	Moment of inertia of a body about its own CG	$\text{slugs}\,\text{ft}^2$ or $\text{kg}\,\text{m}^2$
IF	Interference Factor	
IOC	Indirect Operating Cost	$

Variable	Description	Typical units (UK and SI)
I_{prop}	Moment of inertia of propeller	$\text{slugs}\,\text{ft}^2$ or $\text{kg}\,\text{m}^2$
I_{xx}, I_{yy}, …	Moments of inertia about x-, y-, and z-axes	$\text{slugs}\,\text{ft}^2$, $\text{kg}\,\text{m}^2$
I_{XX_p}	Moment of inertia of propeller about the axis of rotation	$\text{slugs}\,\text{ft}^2$ or $\text{kg}\,\text{m}^2$
I_{xy}, I_{xz}, …	Products of inertia	$\text{slugs}\,\text{ft}^2$, $\text{kg}\,\text{m}^2$
i	Index, monthly interest rate (context dependent)	
i	Node index for mission segment (context dependent)	
$\mathbf{i}$, $\mathbf{j}$, $\mathbf{k}$	Unit vectors along the x-, y-, and z-axes, respectively	
i_{HT}	Horizontal tail angle-of-incidence	degrees or rad
i_{root}	Wing root airfoil angle-of-incidence	degrees or rad
i_W	Wing angle-of-incidence	degrees or rad
J	Advance ratio	
j	Mission segment index	
$KCAS$	Knots calibrated airspeed	knots
KE	Kinetic energy	BTU or J
K_g	Gust alleviation factor	
$KIAS$	Knots indicated airspeed	knots
K_p	Constant used for required propeller diameter	
K_S	Spring constant	$\text{lb}_\text{f}/\text{ft}$ or N/m
K_{SM}	Fraction design static margin	
$KTAS$	Knots true airspeed	knots
k	Lift-induced drag constant (context dependent)	
k	Pressure recovery coefficient (context dependent)	
k	Unknown constant of proportionality (context dependent)	
k	Smeaton's coefficient (context dependent)	
k	Fraction spanwise location of blade center of pressure (context dependent)	
k_1	Constant used with NACA five-digit airfoils	
k_2	Constant used with NACA five-digit airfoils	
L	Reference Length (context dependent)	ft or m
L	Lift force (context dependent)	lb_f or N

Continued

Variable	Description	Typical units (UK and SI)
L	Length of geometric shape (context dependent)	ft or m
$\boldsymbol{L}$	Rolling moment (context dependent)	ft lb$_f$ or N m
L/D	Lift-to-drag ratio	
LCC	Life-Cycle Cost	$
LD_c	Lift-to-drag ratio during cruise	
$LD_{\max}$	Maximum lift-to-drag ratio	
$LE\ Sweep$	Wing leading-edge sweep	degrees or rad
L_{HT}	Lift of horizontal tail	lb$_f$ or N
L_{LDG}	Lift due to landing gear	lb$_f$ or N
L_m	Length of main landing gear strut	in.
L_n	Length of nose landing gear strut	in.
$\boldsymbol{L}_p$	Rolling moment (due to change in roll rate)	ft lb$_f$ or N m
LR	Lift ratio	
L_{VT}	Vertical tail lift force	lb$_f$ or N
L_W	Lift force of wing	lb$_f$ or N
L_1, L_2, L_3, L_4	Fuselage segment lengths	ft or m
l	Characteristic length (context dependent)	ft or m
l	Airfoil lift force (context dependent)	lb$_f$ or N
l_{cabin}	Length of the cabin	ft or m
l_{emp}	Length of the empennage	ft or m
l_{FS}	Length of fuselage structure (forward bulkhead to aft frame)	ft or m
l_{fus}	Total length of the fuselage	ft or m
l_{fus}/d_{fus}	Fineness ratio	
l_{fwd}	Length of the forward section	ft or m
l_{HT}	Horizontal tail arm (distance of HT $c_{MGC}/4$ to wing $c_{MGC}/4$ along the x-axis)	ft or m
l_{LER}	Leading-edge radius	ft
l_T	Distance of HT and VT $c_{MGC}/4$ to wing $c_{MGC}/4$ along the x-axis	ft or m
l_{VT}	Vertical tail arm (distance of VT $c_{MGC}/4$ to wing $c_{MGC}/4$ along the x-axis)	ft or m
l_0	Basic length of a tail arm (to leading edge of tail root)	ft or m
$\boldsymbol{M}$	Moment (context-dependent)	ft lb$_f$ or N m
M	Mach number (context dependent)	
M	Bending moment (context dependent)	lb$_f$ ft or N m
M	Moment about CG along z-axis due to unbalanced thrust (context dependent)	ft lb$_f$ or N m
M_0	Mach number at station 0 (far-field)	
M_1	Mach number at station 1 (inlet)	
M_1, M_2	Landing gear reaction moments	lb$_f$ ft or N m
M_2	Mach number at station 2 (compressor)	
M_A	Mach number at some point A on an airfoil	ft lb$_f$ or N m
MAC	Mean aerodynamic chord	ft or m
M_{after}	Pitching moment after thrustline change	ft lb$_f$ or N m
MAP	Manifold pressure	in. Hg
MAP_{max}	Maximum manifold pressure as a function of RPM	in. Hg
M_{before}	Pitching moment before thrustline change	ft lb$_f$ or N m
M_C	Cruising Mach number	
M_{crit}	2-D critical Mach number	
M_D	Diving Mach number	
M_{DD}	Drag divergence Mach number	
$\boldsymbol{M}_{FUS}$	Pitching moment due to fuselage	ft lb$_f$ or N m
$\boldsymbol{M}_{HT}$	Pitching moment due to horizontal tail	ft lb$_f$ or N m
$\boldsymbol{M}_{LDG}$	Pitching moment due to landing gear	ft lb$_f$ or N m
$M_{\max}$	Maximum bending moment	ft lb$_f$ or N m
M_{MO}	Maximum operating Mach number	
$\boldsymbol{M}_T$	Pitching moment due to thrust	ft lb$_f$ or N m
M_{tip}	Mach at propeller tip	
$\boldsymbol{M}_{VT}$	Pitching moment due to vertical tail	ft lb$_f$ or N m
$\boldsymbol{M}_W$	Moment of wing about its aerodynamic center	lb$_f$ ft or N m
$\boldsymbol{M}_x$	Moment or gyroscopic couple about the X-axis	lb$_f$ ft or N m
$\boldsymbol{M}_y$	Moment or gyroscopic couple about the Y-axis	lb$_f$ ft or N m

Continued

Variable	Description	Typical units (UK and SI)
$\boldsymbol{M}_z$	Moment or gyroscopic couple about the Z-axis	lb_f ft or N m
M_∞	Far-field Mach number	
m	Mass (context dependent)	slugs or kg
m	Slope of the constant manifold pressure line (context dependent)	
m	Airfoil pitching moment (context dependent)	ft lb_f or N m
m	Constant for airfoil design (context dependent)	
$\dot{m}$	Mass flow rate of air through the engine compartment	slugs/s or kg/s
m_{batt}	Mass of battery	slugs or kg
$m_{c/4}$	Pitching moment about quarter-chord	ft lb_f or N m
$\dot{m}$	Mass flow rate	slugs/s or kg/s
$\dot{m}_e$	Exit mass flow rate	slugs/s or kg/s
$\dot{m}_{fuel}$	Fuel mass flow rate	slugs/s or kg/s
$\dot{m}_i$	Inlet mass flow rate	slugs/s or kg/s
m_o	Gross mass	slugs, kg
$\dot{m}_{propellant}$	Propellant mass flow rate	slugs/s or kg/s
$\dot{m}_{required}$	Required maximum mass flow rate (for turbine inlet)	slugs/s or kg/s
$\boldsymbol{N}$	Yawing moment	lb_f ft or N m
N	Number of planned aircraft to be produced (context dependent)	
N	Number of airfoil points (context dependent)	
N	Number of wing segments (context dependent)	
N	Number of main wheels featuring brakes (context dependent)	
N_B	Number of blades	
N_{BE}	Number of sold units to break even	
NC	Number of propellers correction	
N_{CREW}	Number of crew members to operate aircraft	
N_{ENG}	Number of engines (powerplant)	
N_{ENGR}	Number of engineers	
N_f	Number of flapped wing segments	
$N_{flgt\ hours}$	Number of expected flight hours over $N_{periods}$	h
N_{fte}	Number of flight test engineers involved in a flight test program	
N_{gc}	Number of ground crew members involved in a flight test program	
N_{month}	Number of months the flight test program is expected to last	
N_o	Stick-Fixed Neutral Point	
N_{OCC}	Number of occupants (crew and passengers)	
N_P	Number of prototypes	
$N_{periods}$	Number of years constituting a single life-cycle	years
N_{pilot}	Number of flight test pilots	
N_{rib}	Number of ribs	
N_{TANK}	Number of fuel tanks	
N_{uf}	Number of unflapped wing segments	
N_{VT}	Yawing moment developed by a vertical tail	ft lb_f, N m
n	Load factor (context dependent)	
n	Number of pay periods (context dependent)	
n	Engine-dependent constant (for piston engines) (context dependent)	
n	Revolutions per second (context dependent)	rps
n_-	Negative load factor	
n_+	Positive load factor	
n_g	Gust load factor	
n_l	Ultimate landing load factor	
n_{lim}	Structural limit load	
$n_{\max}$	Maximum sustainable load factor	
$n_{turn_{\min}}$	Load factor for minimum turning radius	
n_{ult}	Ultimate structural load	
n_z	Ultimate load factor	
P	Principal loan amount (context dependent)	$
P	Power at condition (context dependent)	ft lb_f/s, N m/s, hp, or W
P	Specific airfoil property (e.g., lift, drag, or moment coefficient)	ft or m
P_{AV}	Power available	ft lb_f/s or W

Continued

Variable	Description	Typical units (UK and SI)
P_{BHP}	Horsepower at condition	hp or W
$P_{BHP\ max}$	Maximum sea-level horsepower as a function of RPM	hp or W
PE	Potential energy	BTU or J
P_{ENG}	Engine power	ft lb$_f$/s or W
P_{EX}	Excess power	ft lb$_f$/s or W
P_{FHP}	Friction horsepower as a function of RPM	hp
P_G	Geometric pitch distance	ft or m
P_{HPa}	Power at altitude	
P_{HPC}	Typical engine horsepower during cruise	BHP or SHP
P_i	Induced power	ft lb$_f$/s or N m/s
PNL	Perceived noise level	dB
$P_{purchase}$	Purchase price (of an aircraft)	$
P_{rated}	Rated power of engine	BHP or SHP
P_{REQ}	Power required	ft lb$_f$/s or W
P_S	Specific excess energy	knots, ft/s, m/s, etc.
P_{SHP}	Rated shaft power	ft lb$_f$/s, N m/s
P_{SL}	Brake horsepower at sea-level	hp or W
P_{std}	Standard power at altitude and ISA	hp or W
P_{to}	Maximum engine power	BHP or kg m/s
P_U	Useful power	ft lb$_f$/s or N m/s
P_1	Power associated with gearwheel 1 (context dependent)	hp or W
P_1	Special parameter 1 (context dependent)	
P_2	Power associated with gearwheel 2 (context dependent)	hp or W
P_2	Special parameter 2 (context dependent)	
P_Ω	Period of rotation	s
p	Pressure (context dependent)	psi or Pa
p	Average pressure on tire (context dependent)	lb$_f$/ft^2 or N/m^2
p_0	Total pressure or reference S-L pressure	lb$_f$/ft^2 or N/m^2
p_∞	Far-field pressure	psi or psf; N/m^2 or Pa
p_A	Pressure at some point A on an airfoil	lb$_f$/ft^2 or Pa
p_{B1}	Pressure at the baffle forward face	lb$_f$/ft^2 or N/m^2
p_{B2}	Pressure at the baffle aft face	lb$_f$/ft^2 or N/m^2
p_{bottom}	Pressure with piston in bottom position	lb$_f$/ft^2 or N/m^2
p_e	Exit pressure	lb$_f$/ft^2 or N/m^2
p_{T0}	Total pressure at station 0 (far-field)	lb$_f$/ft^2 or N/m^2
p_{T1}	Total pressure at station 1 (inlet)	lb$_f$/ft^2 or N/m^2
p_{T2}	Total pressure at station 2 (compressor)	lb$_f$/ft^2 or N/m^2
p_{top}	Pressure with piston in top position	lb$_f$/ft^2 or N/m^2
p_{tot}	Total pressure at condition	lb$_f$/ft^2 or N/m^2
p_{00}	Total pressure at station 0 (far-field)	lb$_f$/ft^2 or N/m^2
p_{01}	Total pressure at station 1 (inlet)	lb$_f$/ft^2 or N/m^2
p_{02}	Total pressure at station 2 (compressor)	lb$_f$/ft^2 or N/m^2
$\hat{p},\hat{q},\hat{r}$	Rotation rates about x, y, and z axes, respectively	degrees/s or rad/s
$\dot{\hat{p}},\dot{\hat{q}},\dot{\hat{r}}$	Angular accelerations about x, y, and z axes, respectively	degrees/s^2 or rad/s^2
Q	First area moment (context dependent)	ft^3 or m^3
Q	Propeller torque (context dependent)	ft lb$_f$ or N m
Q	Volumetric flow (context dependent)	ft^3/s or m^3/s
Q_B	Heat flow into heat exchanger	BTU or J
QDF	Quality discount factor	
Q_f	Fuel quantity	US gal, L
Q_{FLGT}	Flight hours per year	h/year
Q_{int}	Quantity of fuel in integral tanks	US gal, L
Q_m	Aircraft production rate	aircraft/month
$\dot{Q}$	Heat transfer rate	ft lb$_f$/s or BTU/s or J/s
Q_{TOT}	Total fuel quantity	US gal, L
q	Dynamic pressure	lb$_f$/ft^2 or N/m^2
q_c	Compressible dynamic pressure	lb$_f$/ft^2 or Pa

Continued

Variable	Description	Typical units (UK and SI)
q_{stall}	Dynamic pressure at stall condition	lb_f/ft^2 or N/m^2
R	Resultant 3D aerodynamic force (context dependent)	
R	Range (context dependent)	Nautical miles (nm), km
R	Electric resistance (context dependent)	Ω (Ohms) (SI only)
R	Specific gas constant (context dependent)	$ft\,lb_f/(slug\,^\circ R)$, J/(kg K)
R	Leading-edge suction parameter (context dependent)	
R	Radius of takeoff or landing transition path (context dependent)	ft or m
$\overline{R}$	Universal gas constant	J/(K mol)
R_{AP}	Rate for certified Airframe and Power plant mechanic	$/h
$RASM$	Revenue per Available Seat-Mile	$/seat
R_{CREW}	Rate for crew	$/h
R_e	Reynolds number	
$R_{e\ cutoff}$	Cutoff Reynolds number	
R_{ENG}	Rate of engineering labor	$/h
R_f	Friction horsepower ratio	
R_{fin}	Final range	W
R_{FUEL}	Cost of fuel	$/gal
R_{glide}	Glide distance	ft or m
RH	Relative humidity	
R_{H_2O}	Specific gas constant for water vapor	$ft\,lb_f/(slug\,^\circ R)$, J/(kg K)
R_L	Loaded radius	ft or m
R_m	Manifold pressure ratio (context dependent)	
R_m	Main gear reaction force (context dependent)	lb_f or N
R_M	Main gear reaction force	lb_f or N
R_{MFG}	Rate of manufacturing labor	$/h
R_n	Nose gear reaction force	lb_f or N
R_N	Nose gear reaction force	lb_f or N
ROC	Rate of climb	ft/min of m/min
ROI	Return of Investment	$
R_P	Blade Radius	ft or m
RPM	Revolutions per minute of propeller	RPM
R_{STOR}	Rate for storage	$/year
R_T	Tailwheel reaction force	lb_f or N
R_{TOOL}	Rate of tooling labor	$/h
R_{turn}	Turning radius	ft or m
$R_{turn_{min}}$	Minimum sustainable turning radius	ft or m
$R_{\delta 1}$	Reynolds number of boundary layer	
R_1	Radius of gearwheel 1 (context dependent)	ft or m
R_1	Radius of frustum base (context dependent)	ft or m
R_1, R_2, R_3, R_4	Landing gear reaction forces (context dependent)	lb_f or N
R_2	Radius of gearwheel 2 (context dependent)	ft or m
R_2	Radius of frustum tip (context dependent)	ft or m
r	Resultant 2D aerodynamic force (context dependent)	lb_f or N
r	Distance to arbitrary point P (context dependent)	
r	Radius of arbitrary blade station (context dependent)	ft or m
r'	Distance from CG to an infinitesimal mass	ft or m
r_{CG}	Distance from CG to reference point	ft or m
S	Surface area (e.g., wing reference area) (context dependent)	ft^2 of m^2
S	Instantaneous position (context dependent)	ft or m
S_A	Approach distance	ft or m
S_{BR}	Braking distance	ft or m
S_C	Surface area of a cone (context dependent)	ft^2 or m^2
S_C	(Horizontal) Climb distance (context dependent)	ft or m
S_{cell}	Surface area of idealized cell	ft^2 or m^2
S_e	Elliptical area (of tire)	ft^2 or m^2
S_{EC}	Surface area of an elliptic cylinder	ft^2 or m^2
S_F	Surface area of a frustum	ft^2 or m^2
S_f	Flap area (aft of hingeline)	ft^2 or m^2
S_F	Distance traveled during flare	ft or m
SFC	Specific fuel consumption for a jet engine	$lb_f/(h\,lb_f)$ $=1/h$
SFC_C	Specific fuel consumption at cruise condition	Engine class depended
SFC_{hp}	Specific fuel consumption for a propeller aircraft based on power	$lb_f/(h\,BHP)$ or $lb_f/(h\,SHP)$

Continued

Variable	Description	Typical units (UK and SI)
S_{FR}	Free rolling distance	ft or m
S_{fte}	Average annual salary of a flight test engineer	$/year
S_{FUS}	Fuselage wetted (or surface) area	ft^2 or m^2
S_G	Ground run	ft of m
S_{gc}	Average annual salary of a ground crew member	$/year
S_{HT}	Horizontal tail area	ft^2 or m^2
S_i	Trapezoidal planform area of segment	ft^2 or m^2
S_{LDG}	Total distance for landing	ft or m
S_{obst}	Obstacle clearance distance	
S_P	Surface area of a paraboloid	ft^2 or m^2
S_{pilot}	Average annual salary of a flight test pilot	$/year
SPL	Overall sound pressure level	dB
SR	Specific range	nm/lb_f or km/kg
S_R	Reduced wing area	
S_{ROT}	Rotation distance	ft or m
S_{TAD}	Surface area of a tadpole fuselage	ft^2 or m^2
S_{TOT}	Total takeoff distance	ft or m
S_{TR}	Transition distance	ft or m
stroke	Total distance piston moves	ft or m
S_{UC}	Surface area of a uniform cylinder	ft^2 or m^2
S_{VT}	Vertical tail surface area	ft^2 or m^2
S_w	Wing planform area	ft^2 or m^2
S_{wet}	Total wetted surface area	ft^2 or m^2
$S_{wet\ WNG}$	Wetted area of a wing	ft^2 or m^2
T	Instantaneous Thrust (context dependent)	lb_f, N
T	Temperature (context dependent)	°R or K
$\overline{T}$	Average thrust during the T-O run	lb_f or N
T_{AV}	Available thrust	lb_f or N
T_{B1}	Temperature at the baffle forward face	°R or K
T_{B2}	Temperature at the baffle aft face	°R or K
T_G	Glass transition temperature	°R or K
THP	Total horsepower	hp
T/W	Thrust-to-weight ratio	
$T_{\max}$	Maximum engine thrust	lb_f or N
T_{net}	Net thrust	lb_f or N
T_{OAT}	Outside air temperature at condition	°R or K
T_{OEI}	Average thrust with one engine inoperative	lb_f or N
T_{opt}	Thrust at optimum propeller efficiency	lb_f or N
TR	Throttle ratio (context dependent)	
TR (or λ)	Wing Taper Ratio (context dependent)	
T_{rated}	Rated thrust of engine	lb_f or N
T_{REQ}	Required thrust for specified condition	lb_f or N
T_{SL}	Rated thrust	lb_f, N
T_{STATIC}	Static thrust	lb_f or N
T_{std}	Standard day temperature	°R or K
T_{TO}	Takeoff thrust	lb_f or N
T_{tot}	Total temperature at condition	°R or K
T_0	Total temperature (context dependent)	°R or K
T_0	Max thrust at sea level (context dependent)	lb_f or N
T_0	Standard S-L, reference, or far-field temperature (context dependent)	°R or K
T_{0des}	Design total temperature	°R or K
T_1	Temperature at station 1 (inlet)	°R or K
T_2	Temperature at station 2 (compressor)	°R or K
T_∞	Temperature in the streamtube behind the nozzle	°R or K
t	Time (context dependent)	s
t	Airfoil thickness (context dependent)	ft or m
t/c	Thickness-to-Chord ratio	
t_{AC}	Average time to manufacture a single unit	h
$t_{HT\ max}$	Maximum root chord thickness	in.
t_i	Time at node index	lb_f or N
t_{i-1}	Time at previous node index	lb_f or N
t_{LOF}	Time to liftoff	s
t_M	Mechanical trail	ft or m
t_{rib}	Thickness of rib	ft or m
t_{skin}	Skin thickness	ft or m
t_{tot}	Total time to run motor	s, min, or h
$t_{VT\ max}$	Maximum root chord thickness	in.
t_{web}	Thickness of spar web	ft or m
t_ψ	Time to turn ψ degrees	s
U	Vertical gust rate (context dependent)	ft/s or m/s
U	Voltage (context dependent)	V (SI only)

Continued

Variable	Description	Typical units (UK and SI)
U_{de}	Vertical gust velocity	ft/s or m/s
u	x-component of total velocity vector	knots, ft/s, m/s, etc.
$\forbidden{V}$	Volume	
V	Airspeed or velocity (context dependent)	knots, ft/s, m/s, etc.
V	Shear force (context dependent)	lb_f or N
V_∞	Far-field airspeed	knots, ft/s, m/s, etc.
V_A	Maneuvering speed or cornering speed	knots, ft/s, m/s, etc.
V_B	Design speed for maximum gust intensity	knots, ft/s, m/s, etc.
V_{B1}	Airspeed in front of the baffle	knots, ft/s, m/s, etc.
V_{B2}	Airspeed aft of the baffle	knots, ft/s, m/s, etc.
V_{BA}	Minimum rate-of-descent airspeed	knots, ft/s, m/s, etc.
V_{BG}	Airspeed for best glide ($LD_{\max}$)	knots, ft/s, m/s, etc.
V_{bottom}	Volume of the cylinder with piston at bottom position	ft^3 or m^3
V_{BR}	Airspeed when pilot begins to apply brakes after touch-down	knots, ft/s, m/s, etc.
$\forbidden{V}_C$	Cruise speed	knots, ft/s, m/s, etc.
V_C	Volume of a cone	ft^3 or m^3
V_C	Design cruising speed or maximum structural speed	ft/s or m/s
V_{cap}	Shear force in cap	lb_f or N
V_{CAR}	Carson's airspeed	ft/s or m/s
V_{CAS}	Calibrated airspeed	knots, ft/s, m/s, etc.
V_D	Dive speed	knots, ft/s, m/s, etc.
V_{disp}	Displacement of the piston engine	ft^3 or m^3
V_e	Exit velocity	knots, ft/s, m/s, etc.
V_E	Airspeed at the exit	ft/s or m/s
V_{EAS}	Equivalent airspeed	knots, ft/s, m/s, etc.
$\forbidden{V}_{EC}$	Volume of an elliptic cylinder	ft^3 or m^3
V_{EF}	Speed at which critical engine is assumed to fail during takeoff	knots, ft/s, m/s, etc.
$V_{E_{\max}}$	Best endurance speed	knots, ft/s, m/s, etc.
$\forbidden{V}_F$	Volume of a frustum	ft^3 or m^3
V_F	Design cruising speed for negative load factor	knots, ft/s, m/s, etc.
V_{FE}	Maximum flap extension speed	knots, ft/s, m/s, etc.
V_{FLR}	Airspeed for initiating flare maneuver	knots, ft/s, m/s, etc.
V_{fpm}	Airspeed in ft/min	ft/min
$V_{ft/s}$	Airspeed in ft/s	ft/s
V_{FTO}	Final takeoff speed	knots, ft/s, m/s, etc.
V_G	Negative maneuver speed	knots, ft/s, m/s, etc.
V_{GS}	Ground speed	knots, ft/s, m/s, etc.
V_H	Maximum level airspeed at S-L	KCAS, KEAS, KTAS
V_{HT}	Horizontal tail volume coefficient	
V_i	Inlet velocity	knots, ft/s, m/s, etc.
V_{IAS}	Indicated airspeed	knots, ft/s, m/s, etc.
V_{KTAS}	Airspeed in Knots, True Airspeed	knots, ft/s, m/s, etc.
V_{LDmax}	Airspeed for best glide ($LD_{\max}$)	knots, ft/s, m/s, etc.
V_{LE}	Maximum landing gear extended speed	knots, ft/s, m/s, etc.
V_{lim}	Maximum bank angle airspeed	knots, ft/s, m/s, etc.
V_{LO}	Maximum landing gear operating speed	knots, ft/s, m/s, etc.
V_{LOF}	Liftoff speed	knots, ft/s, m/s, etc.
$V_{\max}$	Maximum shear force (context dependent)	lb_f or N
$V_{\max}$	Maximum level airspeed (context dependent)	knots, ft/s, m/s, etc.
V_{MC}	Minimum control airspeed with critical engine inoperative	knots, ft/s, m/s, etc.
V_{MCA}	Minimum control speed while airborne	knots, ft/s, m/s, etc.
V_{MCG}	Minimum control speed on the ground	knots, ft/s, m/s, etc.
$V_{\min}$	Minimum airspeed	knots, ft/s, m/s, etc.

Continued

Variable	Description	Typical units (UK and SI)
V_{MO}	Maximum operating airspeed	knots, ft/s, m/s, etc.
V_{MU}	Minimum unstick speed	knots, ft/s, m/s, etc.
V_N	Airspeed normal to the line-of-sweep	knots, ft/s, m/s, etc.
V_n	Normal component of velocity	knots, ft/s, m/s, etc.
V_{NE}	Never-exceed speed	knots, ft/s, m/s, etc.
V_{NO}	Normal operating speed	knots, ft/s, m/s, etc.
V_O	Maximum operating maneuvering speed	knots, ft/s, m/s, etc.
V_{opt}	Airspeed of maximum propeller efficiency	
V_p	Parallel component of velocity	knots, ft/s, m/s, etc.
$\forbar{V}_P$	Volume of a paraboloid	ft^3 or m^3
$\forbar{V}_{PAX}$	Volume of aircraft (passenger cabin)	ft^3 or m^3
$V_{PR_{min}}$	Minimum power required airspeed	knots, ft/s, m/s, etc.
V_R	Resultant airspeed (context dependent)	knots, ft/s, m/s, etc.
V_R	Rotation speed (context dependent)	knots, ft/s, m/s, etc.
V_{REF}	Landing Reference airspeed	knots, ft/s, m/s, etc.
$V_{R_{max}}$	Best range airspeed	knots, ft/s, m/s, etc.
V_{RODmin}	Minimum descent speed	knots, ft/s, m/s, etc.
V_{ROT}	Propeller rotational speed	knots, ft/s, m/s, etc.
V_S	Stalling speed	knots, ft/s, m/s, etc.
V_{S_0}	Stalling speed in the landing configuration	knots, ft/s, m/s, etc.
V_{S1}	Stalling speed in a configuration other than landing (typ. T-O)	knots, ft/s, m/s, etc.
V_{SC}	Sink rate	m/s, ft/s, etc.
V_{Slevel}	Stalling speed with wings level	knots, ft/s, m/s, etc.
V_{SR}	Reference stalling speed	knots, ft/s, m/s, etc.
V_{SR0}	Reference stalling speed in landing configuration	knots, ft/s, m/s, etc.
V_{SW}	Speed at which stall warning occurs	knots, ft/s, m/s, etc.
$\forbar{V}_{t\ avail}$	Available volume in fuel tank	ft^3, m^3
$\forbar{V}_{t\ max}$	Max fuel volume required to complete mission	ft^3, m^3
$\forbar{V}_{TAD}$	Volume of a tadpole fuselage	ft^3 or m^3
V_{TAS}	True airspeed	knots, ft/s, m/s, etc.
V_{TD}	Velocity at touchdown	knots, ft/s, m/s, etc.
V_{tip}	Velocity at propeller tip	ft/s or m/s
$\forbar{V}_{top}$	Volume of the cylinder with piston at top position	ft^3 or m^3
V_{TR}	Transition airspeed	knots, ft/s, m/s, etc.
$V_{TR_{min}}$	Airspeed for minimum thrust required	knots, ft/s, m/s, etc.
$V_{turn_{min}}$	Minimum turning radius airspeed	knots, ft/s, m/s, etc.
$\forbar{V}_{UC}$	Volume of a uniform cylinder	ft^3 or m^3
V_V	Vertical Speed	ft/s m/s
V_{VT}	Vertical tail volume coefficient	
V_X	Airspeed for best (steepest) angle-of-climb	knots, ft/s, m/s, etc.
V_Y	Airspeed for best (maximum) rate-of-climb	knots, ft/s, m/s, etc.
V_{YSE}	Maximum rate of climb in OEI configuration	ft/s or m/s
V_0	Initial velocity in an iteration scheme or far-field airspeed	knots, ft/s, m/s, etc.
V_1	Maximum speed at which a multiengine aircraft can be stopped if critical engine fails during takeoff	knots, ft/s, m/s, etc.
V_2	Obstacle clearance speed (takeoff safety speed)	knots, ft/s, m/s, etc.
V_2	Velocity at beginning of cruise segment	knots, ft/s, m/s, etc.
V_{2min}	Minimum takeoff safety speed	knots, ft/s, m/s, etc.
V_3	Flap retraction speed	knots, ft/s, m/s, etc.
V_3	Velocity at end of cruise segment	knots, ft/s, m/s, etc.
v	y-component of total velocity vector	knots, ft/s, m/s, etc.
W	Weight, typically weight at condition (context dependent)	lb_f or N
W	Work (context dependent)	ft lb_f or J
W	Width of tire (context dependent)	ft or m

Continued

Variable	Description	Typical units (UK and SI)
W/S	Wing Loading	lb_f/ft^2, N/m^2
W_{AC}	Predicted weight of air conditioning and antiicing	lb_f or N
$W_{airframe}$	Weight of structural skeleton	lb_f or N
W_{AV}	Predicted weight of avionic systems	lb_f or N
W_{avg}	Average weight during cruise	lb_f or N
W_c	Weight of crew	lb_f or N
W_{caps}	Weight of spar caps	lb_f or N
W_{CTRL}	Predicted weight of flight control systems	lb_f or N
W_e	Empty weight	lb_f, kg
W_e/W_0	Empty weight ratio	
W_{EI}	Predicted weight of installed engine	lb_f or N
W_{EL}	Predicted weight of electrical systems	lb_f or N
W_{emp}	Combined weight of HT and VT	lb_f, kg
W_{emw}	Empty weight minus wing weight	lb_f, kg
W_{ENG}	Uninstalled (dry) engine weight	lb_f or N
W_f	Weight of fuel	lb_f or N
$W_{f\ avail}$	Weight of fuel in the available volume in fuel tank	lb_f, kg
$W_{f\ res}$	Reserve fuel weight	lb_f or N
W_f/W_0	Fuel weight ratio	
W_{fin}	Final weight at cruise	lb_f or N
W_{FS}	Predicted weight of fuel system	lb_f or N
W_{FURN}	Predicted weight of furnishing	lb_f or N
W_{FUS}	Predicted fuel weight of fuselage	lb_f or N
W_{FW}	Weight of fuel in wing	lb_f or N
W_{HT}	Predicted weight of horizontal tail	lb_f or N
W_{HYD}	Predicted weight of hydraulic system	lb_f or N
W_i	Aircraft weight at node index	lb_f or N
W_{i-1}	Aircraft weight at previous node index	lb_f or N
W_{ini}	Initial weight at cruise	lb_f or N
W_j/W_0	Segment fuel ratio	lb_f or N
W_l	Design landing weight	lb_f or N
W_{LDG}	Maximum landing weight	lb_f or N
W_{min}	Minimum aircraft weight	lb_f or N
W_{MLG}	Predicted weight of main landing gear	lb_f or N
W_{MNLG}	Predicted weight of entire landing gear	lb_f or N
W_{MZF}	Maximum zero fuel weight	lb_f or N
W_{NLG}	Predicted weight of nose landing gear	lb_f or N
W_p	Payload	lb_f or N
W_{prop}	Propeller weight	lb_f or N
W_R	Ramp weight	lb_f or N
W_{skin}	Wight of skin	lb_f or N
W_{to}	Takeoff weight	lb_f or N
W_{total}	Total weight of specified conditions	lb_f or N
W_u	Useful load	lb_f or N
W_{UAV}	Weight of uninstalled avionic systems	lb_f or N
W_{VT}	Predicted weight of vertical tail	lb_f or N
W_W	Wing weight	lb_f or N
W_{web}	Weight of shear web	lb_f or N
W_0	Gross weight of aircraft	lb_f or N
W_1	Aircraft weight at the beginning of the design mission	lb_f or N
W_2	Aircraft weight at the end of the design mission	lb_f or N
w	Total velocity induced at arbitrary point P (context dependent)	knots, ft/s, m/s, etc.
w	z-component of total velocity vector (context dependent)	knots, ft/s, m/s, etc.
w	Width of a fuselage (context dependent)	ft or m
w	Propeller-induced velocity (context dependent)	ft/s or m/s
w	Downwash (context dependent)	m/s, ft/s, etc.
w_F	Maximum fuselage width	ft or m
w_{fus}	Fuselage width	ft or m
w_t	Wheel track	ft or m
w_{y0}	Downwash velocity induced by vortices	knots, ft/s, m/s, etc.
$\dot{w}_{fuel}$	Fuel flow rate	lb_f/s or N/s
$\dot{w}_j$	Fuel flow rate during mission segment	lb_f/s or N/s
$\mathbf{X}$	Vector of design variables X_1, X_2, …	
X_{CG}	Lengthwise location of CG	ft or m or % MGC
X_{MGC}	x-distance to the leading edge of the MGC	ft or m

Continued

Variable	Description	Typical units (UK and SI)
x	Spatial variable, may or may not have context-dependent subscripts	ft or m
x	Humidity ratio (context dependent)	ft or m
x	Distance penetrated into gust (context dependent)	ft or m
$(x/c)_{\max}$	Location of maximum airfoil thickness	
x_{ac}	Location of aerodynamic center along x-axis	ft or m
x_{camber}	Location of camber line along x-axis	% chord
x_f	x-displacement of flap hinge line from TE of chord airfoil (Junkers flaps)	ft or m
x_f	x-displacement of flap hinge line from slot lip (Fowler flaps)	ft or m
x_h	x-distance from leading edge of airfoil to flap hinge	ft or m
x_l	Location of lower airfoil point along the x-axis	% chord
x_M	x-distance from CG to main gear	ft or m
x_N	x-distance from CG to nose gear	ft or m
x_{NM}	Distance between nose gear and main gear (wheelbase)	ft or m
x_n	Location of neutral along MGC	%MGC
x_T	x-distance from CG to tailwheel	ft or m
x_T	Distance of thrustline from CG along x-axis	ft or m
x_{tr}	Transition point	ft or m
x_{tr_lower}	Transition point on lower wing surface	ft or m
x_{tr_upper}	Transition point on upper wing surface	ft or m
x_u	Location of upper airfoil point along the x-axis	% chord
x_W	x-distance from CG to AC of wing	ft or m
x_0	Location where fictitious turbulent boundary layer starts	ft or m
y	Spatial variable, may or may not have context-dependent subscripts	ft, m
y_a	Distance of inboard end of segment from plane-of-symmetry	ft or m
y_b	Distance of outboard end of segment from plane-of-symmetry	ft or m
y_c	Mean-line function for NACA airfoils	ft or m
y_{camber}	Location of camber line along y-axis	% chord
Y_{CG}	Span-wise location of CG	ft or m
y_f	y-displacement of flap hinge from chord centerline (Junkers flap)	ft or m
y_f	y-displacement of flap hinge from slot lip (Fowler flap)	ft or m
y_h	y-distance from chord centerline to hinge	ft or m
y_l	Location of lower airfoil point along the y-axis	% chord
y_{MGC}	Span-wise location of MGC	ft or m
y_t	Thickness function for NACA airfoils	ft or m
y_T	y-distance between CG and thrust	ft or m
y_u	Location of upper airfoil point along the y-axis	% chord
y_1	y-distance from aircraft centerline to inboard flap chord	ft or m
y_2	y-distance from aircraft centerline to inboard slat chord	ft or m
y_3	y-distance from aircraft centerline to outboard flap chord	ft or m
y_4	y-distance from aircraft centerline to outboard slat chord	ft or m
Z	Simplification relating $LD_{\max}$ and T/W	
z	Spatial variable, may or may not have context-dependent subscripts	ft or m
z_{CG}	Height of center of gravity above ground	ft or m
z_{HT}	Distance of HT chordline to wing chordline along the z-axis	ft or m
z_T	Distance of thrustline from CG along z-axis	ft or m

Continued

Variable	Description	Typical units (UK and SI)
ΔAR	Addition of finite aspect ratio	
$\Delta C_{D\ flaps}$	Added drag due to flaps	
$\Delta C_{D\ OEI}$	Change in drag coefficient due to OEI	
ΔC_{Dcool}	Cooling drag	
$\Delta C_{D_{\min}}$	Change in 3-D drag coefficient	
$\Delta C_{d_{\min}}$	Change in 2-D drag coefficient	
ΔC_L	Change in lift coefficient	
$\Delta C_{L_{\max}}$	Mach number correction factor	
$\Delta C_{l_{\max}}$	Change in maximum 2-D lift coefficient	
ΔC_{lo}	Change in 2-D zero AOA lift coefficient	
ΔC_m	Change in 2-D pitching moment coefficient (context dependent)	
ΔC_m	Change in Spanwise moment coefficient (context dependent)	
$\Delta D_{windmill}$	Increase in drag due to windmill propeller	lb_f or N
ΔL_{VT}	Change in lift on vertical tail	lb_f or N
ΔM_x	Elemental rolling moment	ft lb_f or N m
Δp	Difference in pressure	lb_f/ft^2 or Pa
ΔQ	Change in flux between front and aft surface	ft^3/s or m^3/s
Δs	Change in entropy	
Δr	Change in radius of old propeller blade to new propeller blade	ft or m
ΔR	Change in distance	ft or m
ΔS	Area of elemental strip	ft^2 or m^2
ΔS_{to}	Inertia distance	ft or m
Δt	Change in time	s, min, or h
ΔT_{ISA}	Deviation from International Standard Atmosphere	°R or K
ΔV_{IAS}	Error in airspeed indicator	ft/s or m/s
ΔW	Rate at which work is being extracted	ft lb_f/s; N m/s or J/s
ΔU	Change in internal energy	ft lb_f/s; N m/s or J/s
Δw_L	Change in left wheel moment arm	ft or m
Δw_R	Change in right wheel moment arm	ft or m
Δx	Extension forward of slat from leading edge (context dependent)	ft or m
Δx	Displacement of rudder pedal (context dependent)	ft or m
Δx_1	Extension of first flap	ft or m
Δx_2	Extension of second flap	ft or m
Δx_3	Extension of third flap	ft or m
Δy	Leading-Edge Parameter (context dependent)	
Δy	Downward drop of slat below the leading edge (context dependent)	ft or m
Δy	Displacement of brake cylinder piston (context dependent)	ft or m
Δz	Vertical height of thrustline above (or below) CG (context dependent)	
$\Delta\Gamma$	Change in vortex strength	ft^2/s or m^2/s
$\Delta\alpha_{C_{L_{\max}}}$	Correction angle for stall AOA	degrees or rad
$\Delta\alpha_{stall}$	Change in stall angle-of-attack	degrees or rad
$\Delta\phi$	Angular Spacing	degrees or rad
$\Delta\phi_{MGC}$	Correction to account for wing twist	degrees or rad
$\Delta\gamma_2$	Change in climb angle	degrees or rad
$\partial\varepsilon/\partial\alpha$	Downwash gradient	/degrees or /rad
Φ_D	Ground influence coefficient for drag	
Φ_L	Ground influence coefficient for lift	
Γ	Dihedral angle (context dependent)	degrees or rad
Γ	2-D circulation (context dependent)	ft^2/s or m^2/s
Γ	Vortex filament strength (context dependent)	
$\Lambda_{c/2}$	Sweep of the mid-chord line	degrees or rad
$\Lambda_{c/4}$	Sweep of the quarter-chord line	degrees or rad
$\Lambda_{c/4\ \lim}$	Limit sweep of the quarter-chord line	degrees or rad
$\Lambda_{hingeline}$	Hingeline angle	degrees or rad
Λ_{HT}	Horizontal tail leading-edge sweep	degrees or rad
Λ_{LE}	Sweep of the leading edge	degrees or rad
$\Lambda_{t\ \max}$	Sweep of the maximum wing thickness line	degrees or rad
Λ_{VT}	Vertical tail leading-edge sweep	degrees or rad

Continued

Variable	Description	Typical units (UK and SI)
Ω	Angular speed of propeller	degrees or rad
Ω_1	Angular speed of gearwheel 1	RPM
Ω_2	Angular speed of gearwheel 2	RPM
Ω_x	Angular speed of propeller about the x-axis	rad/s or rad/min
α	Angle-of-attack	degrees or rad
α_0	Nonlinear lift angle-of-attack	degrees or rad
α_C	Cruise angle-of-attack	degrees or rad
α_e	Effective AOA	degrees or rad
$\alpha_{F\ opt}$	Optimum AOA for the fuselage	degrees or rad
α_i	Induced AOA	degrees or rad
α_{LDG}	AOA during landing after touchdown	degrees or rad
α_{stall}	Stall angle-of-attack	degrees or rad
$\alpha_{stall\ root}$	2-dimensional stall AOA for the root airfoil	degrees or rad
$\alpha_{stall\ tip}$	2-dimensional stall AOA for the tip airfoil	degrees or rad
α_{TO}	Takeoff angle-of-attack	degrees or rad
α_{trim}	Trim AOA	degrees or rad
α_{WB}	Wing-body AOA	degrees or rad
α_{ZL}	Angle-of-attack at zero-lift	degrees or rad
α_{ZLroot}	2-dimensional zero-lift AOA for the root airfoil	degrees or rad
α_{ZLtip}	2-dimensional zero-lift AOA for the tip airfoil	degrees or rad
α_{HT}	Horizontal tail AOA	degrees or rad
β	Yaw angle (context dependent)	degrees or rad
β	Prandtl-Glauert Mach number parameter (context dependent)	
β	Geometric pitch angle of a propeller blade (context dependent)	degrees or rad
δ	Thickness of boundary layer (context dependent)	in. or mm
δ	Lift-induced drag factor (context dependent)	
δ	Pressure ratio (context dependent)	
δ_a	Deflection angle of aileron	degrees or rad
δ_e	Elevator deflection angle	degrees or rad
δ_f	Flap deflection angle	degrees or rad
δ_{lam}	Thickness of laminar boundary layer	in. or mm
δ_r	Deflection angle of rudder	degrees or rad
$\delta_{r\ trim}$	Rudder deflection required for trim	degrees or rad
δ_s	Slat deflection angle	degrees or rad
δ_t	Deflection angle of tab	degrees or rad
δ_{turb}	Thickness of turbulent boundary layer	in. or mm
δ_v	Vane deflection angle	degrees or rad
δ^*	Displacement thickness	
ε	Normal strain (context dependent)	in./in. or mm/mm
ε	Downwash (context dependent)	
ε	Thrust angle (context dependent)	degrees or rad
ε_d	Diffuser expansion ratio	
ε_T	Thrust angle	degrees or rad
ε_o	Residual downwash angle	degrees or rad
ϕ	Bank angle, stall penalty function (context dependent)	degrees or rad
ϕ	Velocity potential (context dependent)	
ϕ	Washin/washout angle (context dependent)	degrees or rad
ϕ	Landing gear retraction angle (context dependent)	degrees or rad
ϕ	Tailwheel spindle axis angle/ Rake angle (context dependent)	degrees or rad
ϕ	Helix angle (context dependent)	degrees or rad
ϕ	Roll angle (context dependent)	degrees or rad
ϕ_A	Aerodynamic washout	degrees or rad
ϕ_D	Decalage angle	degrees or rad
ϕ_G	Geometric washout	degrees or rad
ϕ_{max}	Maximum bank angle	degrees or rad
γ	Shear strain (context dependent)	in./in. or mm/mm
γ	Ratio of specific heats (context dependent)	
γ	Specific heat ratio (context dependent)	
γ	Ratio of specific heats = 1.4 for air (context dependent)	
γ	Aircraft climb angle (relative to horizon) (context dependent)	degrees or rad
γ	Angle of uphill runway slope (context dependent)	degrees or rad
γ_2	Climb angle	degrees or rad
γ_{2min}	Angle dependent on aircraft configuration	degrees or rad

Continued

Variable	Description	Typical units (UK and SI)
γ_{app}	Approach angle	degrees or rad
γ_{climb}	Climb angle	degrees or rad
γ_{max}	Maximum climb angle	degrees or rad
η	Spanwise station (for b/2)	
η_i	Froude efficiency	
η_{opt}	Optimal propeller efficiency	
η_{prp}	Propulsive efficiency	
η_{prc}	Pressure recovery efficiency	
η_{th}	Thermal efficiency	
η_p	Propeller efficiency	
η_o	Overall efficiency	
η_v	Viscous profile efficiency	
κ	Lapse rate constant (context dependent)	1/ft or 1/m
κ	Ratio of 2-D lift curve slope to 2π (context dependent)	
κ	Skin roughness value (context dependent)	
λ	Mean-free path distance (context dependent)	
λ (or *BPR*)	Turbofan bypass ratio (context dependent)	
λ (or *TR*)	Taper ratio (context dependent)	
λ_{HT}	Horizontal tail taper ratio	
λ_R	Reduced taper ratio	
λ_{VT}	Vertical tail taper ratio	
λ_W	Wing taper ratio	
μ	Ground friction constant (context dependent)	
μ	Poisson's ratio (per MMPDS or MIL-HDBK-5) (context dependent)	
μ	Air viscosity (context dependent)	$lb_f s/ft^2$ or $N s/m^2$
μ'	$0.01C_{L_{max}}+0.02$	
μ_g	Aircraft mass ratio	
ν	Kinematic viscosity (context dependent)	$1/(ft^2\ s)$ or $1/(m^2\ s)$
ν	Poisson's ratio (context dependent)	
π_2	Pressure recovery ratio (turbines only)	
θ	Pitch angle (context dependent)	degrees or rad
θ	Included angle (context dependent)	degrees or rad
θ	Angle between tangent to mean-line and chordline (context dependent)	degrees or rad
θ	Caster angle (context dependent)	degrees or rad
θ	Overturn angle (context dependent)	degrees or rad
θ	Tip back angle (context dependent)	degrees or rad
θ	Turning angle of nose gear (context dependent)	degrees or rad
θ	Temperature ratio (context dependent)	
θ^*	Momentum thickness	
ρ	Density of air at altitude	$slugs/ft^3$ or kg/m^3
ρ_∞	Far-field density	$slugs/ft^3$ or kg/m^3
ρ_0	Density at station 0 (far-field)	$slugs/ft^3$ or kg/m^3
ρ_0	Reference S-L density	$slugs/ft^3$ or kg/m^3
ρ_1	Density at station 1 (inlet)	$slugs/ft^3$ or kg/m^3
ρ_2	Density at station 2 (compressor)	$slugs/ft^3$ or kg/m^3
ρ_{B1}	Air density at the baffle front face	$slugs/ft^3$ or kg/m^3
ρ_{B2}	Air density at the baffle aft face	$slugs/ft^3$ or kg/m^3
ρ_{caps}	Density of spar cap material	$slugs/ft^3$ or kg/m^3
ρ_E	Air density at the nozzle exit	$slugs/ft^3$ or kg/m^3
ρ_{prop}	Density of propeller material	$slugs/ft^3$ or kg/m^3
ρ_{skin}	Density of skin material	$slugs/ft^3$ or kg/m^3
ρ_{SL}	Sea-level density	$slugs/ft^3$ or kg/m^3
σ	Normal stress (context dependent)	psi or Pa
σ	Density ratio (context dependent)	
$\sigma_{bending}$	Normal stress due to bending	psi or Pa
σ_{std}	Standard day density ratio	
τ	Torque (context dependent)	in. lb_f or N m
τ	Time for free roll before braking begins (context dependent)	s
τ	Shear stress (context dependent)	psi or Pa

Continued

Variable	Description	Typical units (UK and SI)
τ	Lift curve slope correction factor (context dependent)	
τ	Control effectiveness parameter (context dependent)	
τ_1	Torque of gearwheel 1	in. lb_f or N m
τ_2	Torque of gearwheel 2	in. lb_f or N m
τ_{max}	Maximum shear stress in structure of interest (structural)	psi or Pa
τ_{skin}	Shear stress in skin (structural)	psi or Pa
$\tau_{torsion}$	Shear stress due to torsion (structural)	psi or Pa
ψ	Desired change in heading angle	degrees or rad
$\dot{\psi}$	Turn rate	rad/s
$\dot{\psi}_{max}$	Maximum sustainable turn rate	rad/s
∇	Nabla operator	

This page intentionally left blank

CHAPTER

1

The Aircraft Design Process

OUTLINE

1.1 **Introduction** 1
1.1.1 The Contents of This Chapter 2
1.1.2 Why Do We Need an Aircraft Design Process? 2

1.2 **General Process of Aircraft Design and Development** 2
1.2.1 Common Descriptions of the Design Process 2
1.2.2 Fundamental Phases of the Aircraft Design Process 4
1.2.3 Concepts of Importance to the Aircraft Design Process 6
1.2.4 Development Timeline for Typical GA Aircraft 9

1.3 **Introduction to Aviation Regulations and Certification** 10
1.3.1 Aviation Regulations That Apply to GA Aircraft 10
1.3.2 Important Regulatory Concepts 14

1.4 **How to Design a New Aircraft** 15
1.4.1 Conceptual Design Algorithm for a General Aviation Aircraft 16
1.4.2 Implementation of the Conceptual Design Algorithm 18

1.5 **Elements of Project Engineering** 18
1.5.1 Project Plan 18
1.5.2 Team Leadership 19
1.5.3 Task Management and the Task Matrix 20
1.5.4 Gantt Diagrams 20
1.5.5 PERT Charts 20
1.5.6 Fishbone Diagram for Preliminary Airplane Design 20
1.5.7 Documentation Standards and Drawing Organizing 22
1.5.8 Quality Function Deployment and a House of Quality 23

1.6 **Presenting the Design Project** 27

References 32

1.1 INTRODUCTION

This book focuses on the conceptual and preliminary design of General Aviation (GA) aircraft. The Federal Aviation Administration (FAA), which regulates aircraft in the United States, defines GA aircraft as one that is neither for commercial nor for military operations [1]. This definition classifies great many aircraft as GA, ranging from sailplanes and lighter-than-air vehicles to jet aircraft and even civilian supersonic aircraft (an emerging trend in contemporary business jet development). While GA includes many kinds of aircraft, commercial and military aircraft are discussed as well in the book, for there is much to be learned. The designer of GA aircraft should be well rounded in all types of aircraft, a point that will be made repeatedly.

Airplane design can be daunting even for veteran designers. Serious design projects demand multiple disciplines to join in perfect harmony to fashion a product that best suits an intended mission. The modern aircraft is subjected to many constraints demanded by concerns for safety, cost, maintainability, performance, and marketability, to name a few. The torrent of requirements calls for an effective process that systematically guarantees a balance between these constraints. This chapter presents elements of this process and introduces many topics for aspiring and professional designers alike. In this capacity, a thorough design algorithm is presented, helpful to anyone tackling a new design project. Additionally, important regulatory concepts and a few handy project management tools to help with the development of the new aircraft are discussed.

https://doi.org/10.1016/B978-0-12-818465-3.00001-X

Copyright © 2022 Elsevier Inc. All rights reserved.

The author is often asked what it takes to become an aircraft designer. The answer is not simple and requires *conceptual* design to be separated from *detail* design. In the opinion of this author, an effective *conceptual* designer possesses a wide-scope knowledge of aircraft as a collection of systems. It requires knowledge of not only aerodynamics, systems, structures, powerplant, electrics, and stability and control, but also regulations, certification, management, manufacturing, maintenance, and even marketing and financing. One does not have to be an expert in any of these fields but must know enough to make sound decisions. Ideally, some of these fields should be bolstered by industry experience—an effective conceptual designer must understand the consequences of a specific design direction, for this may dictate the success of the project. Sutter [2], pp. 76–79, gives a good example of this regarding the design of the wing and engine configuration of the Boeing 737. In contrast, an effective *detail* designer possesses a deep, but narrow-scope, knowledge of the system being designed. The detail designer should be considered an expert within that scope. While this book caters primarily to the conceptual aircraft designer, the detail designer, too, can find useful information in here.

1.1.1 The Contents of This Chapter

- Section 1.2 presents a general description of the aircraft design process, its fundamentals, and a typical timeline for the development and certification of General Aviation aircraft.
- Section 1.3 presents topics important to regulatory and certification of GA aircraft. Among those are recent changes made to 14 CFR Part 23, under which GA aircraft are certified.
- Section 1.4 presents a specific algorithm intended to guide the aircraft designer through the conceptual design process. If you are unsure of "what to do next," refer to it. It is based on actual industry experience and not academic "cookbook" approaches.
- Section 1.5 presents the responsibility of a team leader and an assortment of project management tools. Many beginning project leaders are often at a loss as to how to manage a project. If this is your predicament, you need to study these tools. Project management revolves around knowing what to do and when to do it.
- Section 1.6 presents helpful approaches to describing engineering ideas using graphics ranging from three-view drawings to composite photo images. These are extremely helpful when trying to "sell" an idea.

1.1.2 Why Do We Need an Aircraft Design Process?

New aircraft are designed for a variety of reasons. Most are designed to fulfill a specific role or a mission as dictated by prospective customers or perceived customer needs. The cost of developing new aircraft requires the design to be conducted in an organized fashion. No matter the type of aircraft or the reason for its design, several specific tasks must be completed before it can be built and flown. The order of these tasks is called the *design process*.

Aircraft manufacturers only fund projects for which probability of success is considered high. The design process helps by systematically evaluating critical aspects of the aircraft, allowing weaknesses to be identified and eliminated. During the conceptual design phase, this is done using mathematical procedures. Later, however, this involves specific testing of aerodynamic and structural configuration, materials, avionics, control system layout, and many more.

The order of the tasks comprising the design process may vary depending on the manufacturer involved. Usually, there is an overlap of tasks. For instance, the fuselage design may already be in progress before the sizing of the wing or stabilizing surfaces is completed. Additionally, the sophistication of the process is affected by the size and maturity of the company in which it takes place. Regardless, certain and identical steps must be completed in all of them; weight must be estimated, lifting surfaces and fuselage must be sized, performance must be assessed, and so forth.

1.2 GENERAL PROCESS OF AIRCRAFT DESIGN AND DEVELOPMENT

This section presents a general description of the airplane design process. Often, the process begins with the publication of a formal Request for Proposal (RFP), a release of a list of requirements, or similar documents. It may be considered completed once the delivery of a certified product begins, although another perspective would say once its development ceases. Many process-related topics of importance are also presented in this section. These are generalizations that also apply to other classes of aircraft.

1.2.1 Common Descriptions of the Design Process

(1) Elementary Outline of the Design Process

A general description of the aircraft design process is provided in several aircraft design textbooks intended for university students of aerospace engineering. Understanding this process is of great importance for design team leaders. An elementary, top-level depiction is presented in Figure 1-1. While the diagram correctly describes the chronological order of steps required to build the *Proof-of-Concept* (POC) aircraft, it omits the

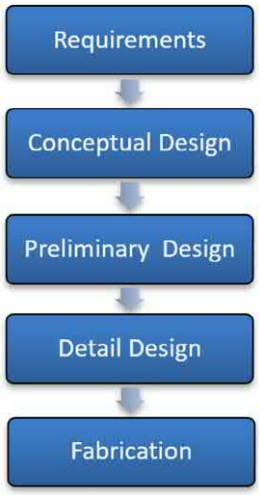


FIGURE 1-1 An elementary outline of the aircraft design process.

overlap between phases. In a real industry environment, there is not a set date at which conceptual design ends and preliminary design begins. Instead, there is a substantial overlap between the phases, which permits a more cost-effective use of the workforce.

(2) Design Process Per Torenbeek

In his classic text, Torenbeek [3], pp. 499 discusses the process in detail and presents a depiction reproduced in Figure 1-2. It demonstrates the process realistically by showing overlapping activities as well as several important milestones. *Configuration Freeze* is a set date after which no changes to the external geometry, called the *outside mold line* (OML), are allowed. This holds even if a better geometric shape is discovered. It marks the date for the aerodynamics group to cease geometric optimization, as the "frozen" configuration is adequate to meet the requirements. The *Go-ahead Approval* is the date at which upper management gives the green light for the design team to proceed with the selected configuration and develop an actual prototype. It marks the readiness of the organization to fund the project. The term *Type Certificate* is described in Section 1.3.2, *Important Regulatory Concepts*.

Torenbeek's depiction also shows that detail design begins during the preliminary design phase and that manufacturing tends to overlap preceding phases. The manufacturing phase includes the design and construction of production tooling, establishment of vendor relations, and other preparatory tasks.

(3) Typical Design Process for General Aviation Aircraft

Figure 1-3 presents the design process based on the author's experience. It parallels Torenbeek's depiction in many ways, but accounts for iteration cycles often required during this period. It differs in its focus on the fabrication of a *Proof-of-Concept* (POC) aircraft. It also reflects the fact that issues arise during preliminary design that require the OML of the configuration to be modified, in particular if the design is unorthodox. Such an issue might be a higher engine weight than expected, requiring it to be moved to a new location to maintain the original empty weight CG position. This, in turn, calls for a reshaping of the engine cowling or nacelle, and other modifications. Such changes are handled by numbering each version of the OML, as if it were the final version, because, eventually, the one with the highest number is "frozen." This allows the design team to proceed with work on structures and other internal features of the aircraft, rather than waiting for the configuration freeze.

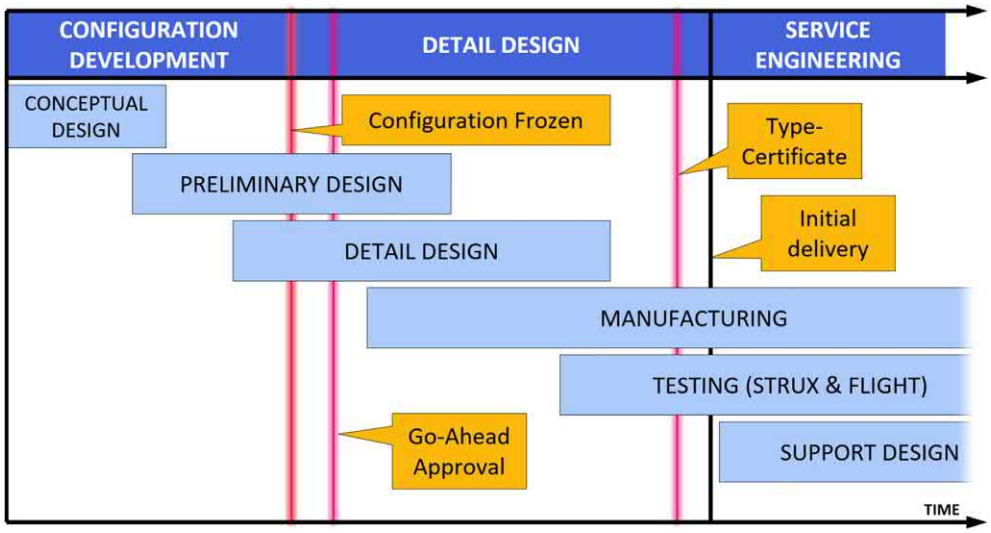


FIGURE 1-2 Aircraft design process per Torenbeek. *Reproduced from E. Torenbeek, Synthesis of Subsonic Aircraft Design, 3rd ed., Delft University Press, 1986.*

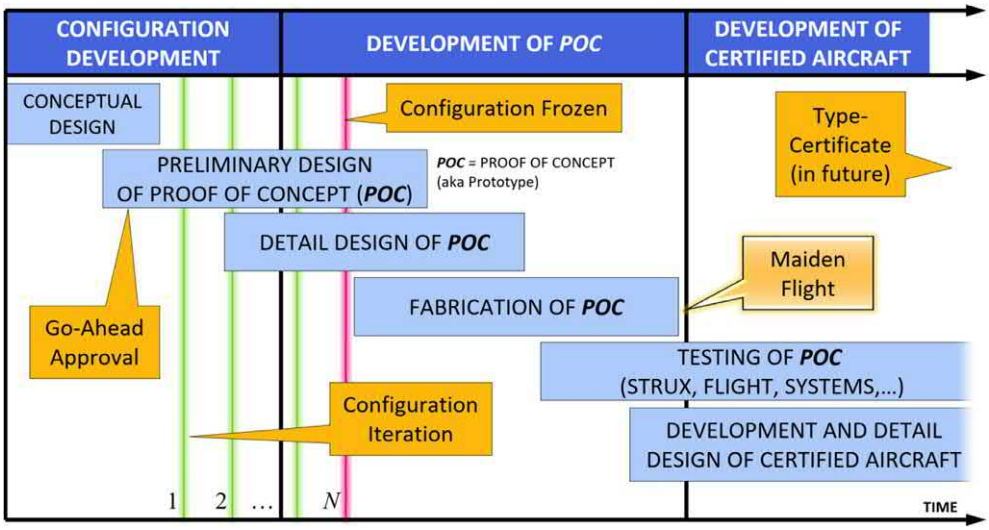


FIGURE 1-3 Aircraft design process for a typical GA aircraft.

1.2.2 Fundamental Phases of the Aircraft Design Process

(1) Requirements Phase

This is the initial phase, during which the required mission, capability, and regulatory constraints are formulated. *Requirements* are akin to a wish list. They express the capabilities the new design must deliver, such as how fast, how far, how high, how many occupants, what payload, and so on. The requirements may be as simple as a few lines of desired capabilities (e.g. range, cruising speed, and payload) or a complex document with thousands of pages, stipulating environmental impact, operating costs, maintainability, hardware, avionics, and ergonomics, just to name a few. It is the responsibility of the design lead to ensure the airplane has a fair chance of meeting the requirements, and this is demonstrated during the next phase, the Conceptual Design Phase.

(2) Conceptual Design Phase

This constitutes the initial sizing of the aircraft, estimation of cost, performance, stability, and evaluation of regulatory compliance issues, to name a few. It absorbs just enough engineering to provide management with a reliable assessment of desired performance, desired aesthetics, and basic understanding of the scope of the development effort, including marketability, labor requirements, and expected costs. Typically, the following characteristics are defined during this phase:

- Type of aircraft (piston, turboprop, turbojet/fan, fixed wing, rotorcraft).
- Special aerodynamic features (flaps/slats, wing sweep, etc.).
- Certification basis (LSA, Part 23, Part 25, Military).
- Mission (the purpose of the design).
- Technology (avionics, materials, engines, control system).
- Aesthetics (the importance of "good looks").
- Requirements for occupant comfort (pressurization, galleys, lavatories).
- Ergonomics (pilot and passenger ergonomics).
- Ease of manufacturing (how will it be produced).
- Maintainability (tools, labor, and methods required to maintain the aircraft).
- Initial cost estimation.
- Evaluation of marketability.

Deliverables: *Initial loft* and a *Conceptual Design Evaluation Report*, which allows management to make a well-reasoned call about whether to proceed to the preliminary design phase.

(3) Preliminary Design Phase

Interestingly, the definition of this phrase is unclear. For instance, Raymer states "*Preliminary design can be said to begin when the major changes are over*" [4], pp. 15. In contrast, Torenbeek considers this its *end*, stating: "*A characteristic of this phase is that modifications are made continuously until a decision can be taken to 'freeze' the configuration, and this marks the end of the preliminary design phase*" [3], p. 4. Nicolai states that various fine-tuning takes place and that many large decisions are made during this phase[1] [5], p. 25. To this author, the preliminary design phase simply refers to design work conducted on the POC and any *nonconforming prototype* intended for initial flight testing, evaluation, and demonstration. It confirms the viability of the idea, exposes potential problems, and offers opportunities to evaluate possible solutions. Thus, significant changes are actually

[1] To paraphrase the text in the reference.

considered (and sometimes implemented) on the prototype, regardless of whether it was already "frozen." Some of the specific tasks that are accomplished during this phase are:

- Detailed geometry development.
- Layout of major load paths.
- Detailed component weight estimation.
- Details of mission are polished.
- Detailed pre-maiden performance evaluation.
- Detailed pre-maiden stability and control analysis.
- Evaluation of special aerodynamic features.
- Evaluation of certifiability.
- Evaluation of mission capability.
- Refinement of producibility.
- Maintainability (including accessibility to implement repairs) is defined.
- Preliminary production cost estimation.

Deliverables: A *drawing package* and a *Preliminary Design Evaluation Report* that helps with the decision to go-ahead with the fabrication of the POC aircraft.

(4) Detail Design

This refers to any design effort that involves the detail design of the airframe and system integration (e.g. airframe design and engine installation). Detail design really needs to be considered from two perspectives: (1) During prototyping, when it refers to the design of the airframe and systems associated with the prototype aircraft. (2) During development of manufacturing, where it refers to the design of airframe and systems associated with production aircraft. Some of such design work is referred to as *sustaining engineering*. Of course, it is more complicated than that, and a limited description of the work that takes place is listed below.

- Detail design work (structures, systems, avionics, etc.).
- Study of technologies (vendors, company cooperation, etc.).
- Subcontractor and vendor negotiations.
- Prototype: Design of limited (one-time use) tooling (fixtures and jigs).
- Production: Design of multiuse tooling.
- Structural detail design.
- Mechanical detail design.
- Avionics and electronics detail design.
- Ergonomics detail design.
- Mockup fabrication.
- Iron-bird fabrication (for systems testing).
- Maintenance procedures planning.
- Material and equipment logistics.

Deliverables: Final *OML* and *internal structure for the POC or production aircraft*.

(5) Proof-of-Concept Aircraft and Testing

The construction of the POC begins during the detail design phase. This is a very involved process for established companies that intend to produce the design, as the production process, with all its paperwork and quality assurance protocols, is being prepared at the same time. Some of the tasks that are accomplished are listed below:

- Detail design revisions (structures, systems, avionics, etc.).
- Application of selected technologies.
- Tooling design and fabrication.
- Fabrication and assembly.
- Structural testing.
- Aeroelastic testing (Ground Vibration Testing).
- Mechanical testing.
- Avionics testing.
- Maintenance procedures and refinement of maintainability.

The culmination of this phase is *Maiden Flight of the POC*. This is followed by the development flight testing as discussed below.

(6) Development Program Phase

A development program follows a successful completion of the preliminary design. The development of this phase usually begins long before the Maiden Flight and is usually handled by flight test engineers, flight test pilots, and certification management.

- Establish Aircraft Operating Limitations (AOL).
- Establish Pilot's Operating Handbook (POH).
- Prepare Master Flight Test Schedule (MFTS).
- Envelope Expansion Schedule (or "Matrix").
- Test Equipment Acquisition.
- Flight Support Crew Training.
- Group roles must be trained prior to flight—not on the job.
- Establish emergency procedures.
- Establish group responsibilities.
- Revision of AOL, POH, and MFTS.
- Flight Readiness Review.

The conclusion of this phase is a *certifiable aircraft*. This means the organization understands the risks and scope of the required certification effort and should be convinced the certification program can be successfully completed.

(7) Postdevelopment Programs

A lot of work remains, even though the development program comes to a successful end. A viable aircraft design continues in development when customers begin its operation and discover features that would benefit the design. Then, there is the advancement of avionics. New equipment must be installed, and this must be engineered. A broad scope of various postdevelopment programs is listed below.

- Development flight test/structural/systems/avionics program.
- Certification flight test/structural/systems/avionics program.
- Aircraft is awarded a Type Certificate.
- Production process design.
- Production tooling design and fabrication.

- Delivery of produced aircraft.
- Eventual reception of Production Certificate.

1.2.3 Concepts of Importance to the Aircraft Design Process

(1) Definition of the Mission

The mission of the new aircraft must be clearly defined. How fast, far, and high shall it fly? Is it a cruiser? If so, at what cruising speed and altitude will it be operated? Is it a cargo transport aircraft? How much payload must it carry? Is it a fighter? What energy state or loitering capabilities are required? A clearly defined mission is important because the airplane will be sized to meet that mission: It will be most efficient when performing that mission. Clarity of this nature also has an unexpected redeeming power for the designer: It is common during aircraft development that changes to capabilities are suggested by outside agencies. Despite being well meant, some suggestions can be detrimental. A clearly defined mission allows the designer to turn down disadvantageous suggestions on the basis they compromise the primary mission.

(2) Performance Requirements and Sensitivity

Performance requirements must be a clearly defined subpart of the mission. Target take-off distance, time to cruise altitude, cruise range, and even environmental noise must be specified. It is also important to understand how deviations from the design conditions affect the performance. This is referred to as *performance sensitivity*. How does high altitude and high temperature impact the take-off distance? How about an upward slope of a runway? How will a routine operation of the airplane above or below design cruise altitude affect range and endurance? Rather than regarding this as a nuisance, the designer should turn it into a strength by making people in management and marketing aware of the deficiencies. And who knows? Perhaps the new aircraft is less sensitive to off-design flight conditions than the competition, and this could be spun into a marketing advantage.

(3) Handling Requirements (Stability and Control)

How important is the handling of the aircraft? Does it feature a manual control system, making stick forces and responsiveness imperative? Or does it use hydraulic or electric control system, so stick forces can be adjusted to acceptable levels? Has the design team considered responses to spoiler and flap deployment or changes in thrust?

The Lockheed SA-3 Viking, an antisubmarine warfare aircraft, features a high wing with two powerful pylon-mounted turbofans. The aircraft experiences commanding pitch changes with thrust, requiring a *Stability Augmentation System* (SAS) to suppress. It was not originally designed into the prototype, implying it was a fix. The Boeing B-52 Stratofortress uses spoilers for banking. When banking hard, the spoiler on the down-moving wing is deployed, reducing lift on the outboard portion. This, in turn, moves the center of lift forward, causing a nose pitch-up tendency, to which the pilot must respond by pushing the yoke forward (to bring the nose back down). Handling issues of this nature must be anticipated, and their severity assessed.

(4) Ease of Manufacturing

Ease of manufacture profoundly impacts the engineering of the product and its cost to the customer. While it is less expensive to manufacture a straight constant-chord wing than a tapered one, it is less efficient aerodynamically. Which is more important? The designer should justify on the merits why a particular geometry or raw material is required. It is simple to select composites for a new aircraft design on the grounds this makes it easier to manufacture compound surfaces. But are they really needed? For some aircraft, the answer is a resounding *yes*, but for others, the answer is simply *no*.

As an example, consider the De Havilland of Canada DHC-2 Beaver (see Figure 1-4). Manufacturing this



FIGURE 1-4 The De Havilland of Canada DHC-2 Beaver. *Photo by Phil Rademacher.*

otherwise sturdy airplane from composites is a questionable proposition: It would simply make it more expensive. First, it is hard to justify manufacturing an aerodynamically inefficient frustum-style fuselage[2] and constant-chord wing featuring a nonlaminar flow airfoil with composites. Composites are primarily justifiable for compound laminar flow surfaces. They require expensive molds to be built and maintained, and should the aircraft be produced in large numbers, these must be manufactured as well; each may only last for perhaps 30 to 50 units.

The interested reader is encouraged to jump to Section 2.2, *The Estimation of Project Development Costs*, for further information about manufacturing costs. For instance, see Example 2.3, which compares development cost for a composite and aluminum aircraft. Cost analysis methods, such as the widely used DAPCA-IV, predict work hours for the development of composite aircraft to be two times greater than that of comparable aluminum aircraft. They also predict tooling hours to double and manufacturing hours to be 25% greater than for aluminum aircraft. Thus, composite aircraft are more expensive to manufacture despite reduction in part count. There are numerous other complexities to contend with, some of which are presented in Section 5.2.6, *Composite Materials*. Composites offer great properties. However, just because they are right for one application does not mean they are appropriate for another.

(5) Certifiability

Will the aircraft be certified? If the answer is yes, then the designer must explore all stipulations this is likely to inflict. If no, the designer still bears a moral obligation to ensure the airplane is safe to operate. Since noncertified airplanes are destined to be small, this can be accomplished by designing it to prevailing certification standards, for instance, 14 CFR Part 23 or LSA standards such as ASTM F2245 [6]. Certification is a government quality stamp. It tells the customer the airplane conforms to strict safety standards.

(6) Features and Upgradability (Growth)

The weight of most civilian and military aircraft increases with time. It is not a question of if, but when and by how much. Requests for added capabilities and systems raise the weight and often require major changes such as a more powerful engine, and even wing enlargement. Additionally, it is often discovered during prototyping that the selected material and production methodology leads to a heavier aircraft than initially thought. The careful designer sizes the aircraft for a weight that is 5% to 10% higher than the projected gross weight.

(7) Maintainability and Accessibility

Maintainability is the ease by which an airplane can be kept airworthy by the operator. It refers to how easy it is to access critical components. The design team should spend an effort guaranteeing that inspecting and replacing critical components are easy. Such an effort is easy to spin into marketing advantage. Complicated manufacturing processes can result in an aircraft that is both hard and costly to maintain. One of the advantages of aluminum is how relatively easy it is to repair. Composites on the other hand can be hard to maintain. Maintainability also extends to the economics of repairing: Are expensive tools required? Accessibility extends to the ergonomics of repairing: Will the mechanic have to contort like a pretzel to replace the part? Will it take 10 h of labor to access a component that will take 5 min to replace? It cannot be emphasized enough that novice engineers should consult with Airframe and Powerplant (A&P) mechanics and try to understand their perspective. Many valuable lessons can be learned from people who perform fabrication, assembly, and maintenance.

(8) Aesthetics (Looks)

Looks may seem a secondary concern, but it should not be under-estimated. While beauty is in the eye of the beholder, it is a fact of business that aircraft that have a certain look appeal to a larger population of potential buyers. This may improve sales, even if their performance is less than that of the competition. The so-called Joint Strike Fighter program is a great example of such appeal. Its purpose was to introduce an aircraft for the US armed forces that simultaneously replaced the F-16, A-10, F/A-18, and AV-8B tactical fighter aircraft. Three versions of the aircraft were planned, and to keep down development, production, and operating costs, a common shape was proposed for which 80% of parts were interchangeable. There were two participants in the contract bid: Lockheed-Martin and Boeing. Lockheed's entry was the X-35 and Boeing's the X-32 (see Figure 1-5). Both aircraft were thought to be worthy candidates, but on October 26, 2001, Lockheed was announced as the winner. The reason cited by the Department of Defense, according to The Federation of American Scientists, an independent, nonpartisan think tank, was:

> The Lockheed Martin X-35 was chosen over the competing Boeing X-32 primarily because of Lockheed's lift-fan STOVL design, which proved superior to the Boeing vectored-thrust approach [7].

[2] A frustum style fuselage is a tapered structure that does not feature compound surfaces. It is discussed in Chapter 12, *The Anatomy of the Fuselage*.



FIGURE 1-5 Which aircraft looks better to you; the Boeing X-32 or the Lockheed X-35? *Left photo by Jake Turnquist; Right photo by Phil Rademacher.*

Apparently, in hover, the X-32's engine exhaust would return to the intake, reducing its thrust. However, soon thereafter, rumors began that the real reason was the looks of the two proposals, a claim denied by James Roche, the then secretary of the Air Force [8]. Rumor held that military pilots did not like the looks of the Boeing proposal. The two aircraft in Figure 1-5 allow the reader to opine on whether the looks of an airplane are of importance.

Another case in point is the Transavia PL-12 Airtruk, shown in Figure 1-6. It was originally developed in New Zealand as the Bennett Airtruck (later Waitomo Airtruk). It is a single-engine agricultural sesquiplane of all-metal construction. Among many unusual features is a cockpit mounted on top of the engine (for good forward visibility), twin tail-booms that are only connected at the wing to allow a fertilizer truck to back up and refill the airplane's hopper, and the sesquiplane configuration generates four wingtip vortices that help better spread fertilizer. It is a capable aircraft, with a 2000 lb. (900 kg) fertilizer capacity and can be used as a cargo, ambulance, or aerial survey aircraft as well. But a strange looking beast it is, at least to this author.

(9) Lean Engineering and Lean Manufacturing

The concepts *lean engineering* and *lean manufacturing* refer to design and production practices whose target is to minimize waste and unnecessary production steps. For instance, consider the production of a hypothetical wooden kitchen chair. Assume that pride has the manufacturer attach a gold-plated metal plaque to the lower surface of the seat that reads: "World's finest kitchen chairs, since 1889." Assume it takes five steps to attach the plaque and labor is required to order it from an outside vendor, transporting it to the manufacturer, keep it in stock, and so on. Strictly speaking, the purpose of a chair is to allow someone to sit on it and, then, said plaque is not visible. It can be argued the plaque is vain and as such brings no added value to the customer. In fact, it only brings up the cost of production; it certainly does not improve the seating experience. The plaque is



FIGURE 1-6 The Transavia PL-12 Airtruk agricultural aircraft. *Photo by Geoff Goodall - via Ed Coates collection.*

therefore wasteful and from the standpoint of a lean production should be eliminated from the process.

Lean manufacturing refines the production process to minimize waste, increasing the profitability of a business. The scope of lean manufacturing is large and covers topics such as optimizing the layout of templates for cutting fabric to minimize waste material, to minimizing the inventory of a stock room by ordering components just before they must be installed (so called *just-in-time* philosophy). The result is a production that is far less costly to the customer and Mother Earth.

The philosophy behind lean manufacturing is usually attributed to the car manufacturer Toyota, which is renowned for adhering to it in its production processes. Thus, it is also known as *Toyotism*. An important aspect of Toyotism is the identification of the Seven Wastes [9]; an approach attributed to Toyota's chief engineer Taiichi Ohno: (1) *Overproduction*, caused by the manufacturing of products before they are needed; (2) *waiting*, caused by parts that do not move smoothly in the production flow; (3) *transporting*, as in moving a product in between processes; (4) *unnecessary processing*, when expensive, high-precision methods are used where simpler methods suffice; (5) *unnecessary inventory*, which is the accumulation of vendor parts in stockrooms; (6) *excessive or unnecessary motion*, caused when the lack of ergonomics on the production floor increases production time; and (7) *production defects*, which are inflicted on the production floor and are costly due to the inspection and storage requirements. The above barely scratches the surface of lean manufacturing but is intended to whet the reader's appetite.

(10) Integrated Product Teams (IPT)

An *integrated product team* is a group of people with a wide range of skills who are responsible for the development of a product or some feature. The formations of IPTs are common in the aviation industry, as the modern airplane is a compromise of several disciplines. To better understand how IPTs work, consider the development of a pressurization system for an aircraft. An example IPT could consist of the following members:

(1) A structural analyst, who determines pressurization stresses in the airframe and suggests airframe modifications if necessary.
(2) A performance analyst, who evaluates the benefits of the higher cruise altitude and airspeed the pressurization will permit.
(3) A powerplant expert, who solves engine-side problems, such as those associated with bleed air, heat exchangers, and liaison duties between the engine and airframe manufacturers.
(4) An interior expert, who evaluates the impact of the pressurization system on the interior decoration, such as those that stem from the requirement of sealing and condensation.
(5) An electrical expert, who assesses the electrical work required to allow the pilot to operate the pressurization system.
(6) A systems expert, who works on the pressurization system ducting layout, interface issues with heat exchangers, cabin pressure relief valves, cabin sealing, and so on.

Such a group would meet, perhaps once a week, to discuss issues and come up with resolutions, often with the inclusion of representatives of the manufacturers of the various systems.

1.2.4 Development Timeline for Typical GA Aircraft

A flowchart showing a typical development timeline for GA aircraft is shown in Figure 1-7. The timeline lasts

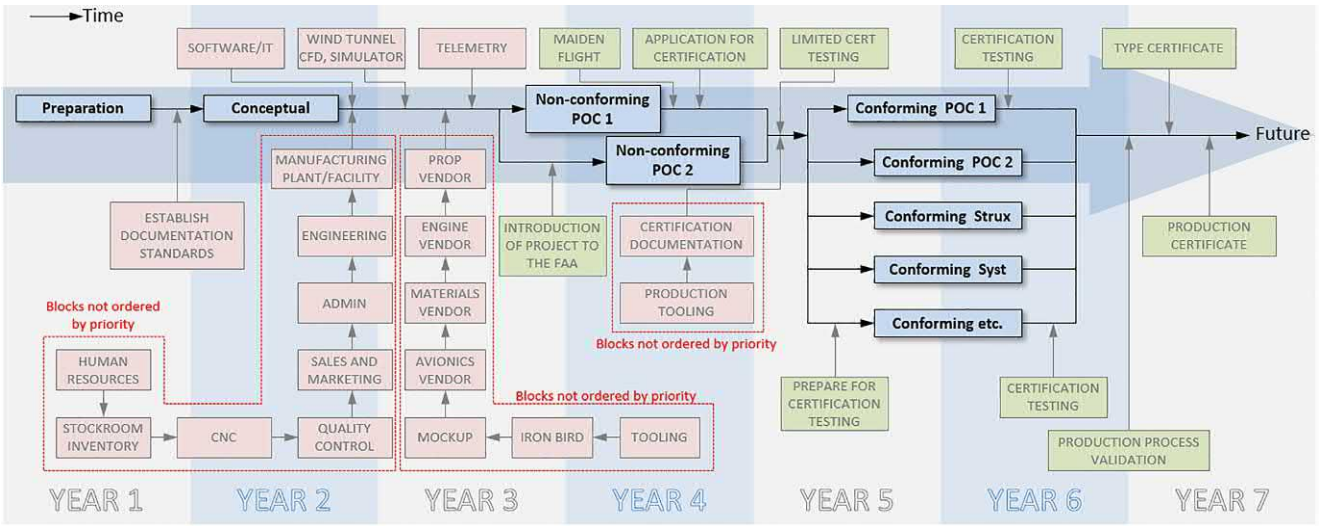


FIGURE 1-7 Typical development timeline for GA aircraft.

for 7 years and shows the approximate events comprising the entire development from the initial idea to reception of a type certificate. This timeline could be compressed with sound funding. Note that while the timeline assumes the construction of two nonconforming prototypes, this depends on the project. Expect 2 prototypes for LSA, and 4–6 for commuter class aircraft. Nonconforming prototypes are used for initial testing of the *proof-of-concept* aircraft and are usually built rapidly to save money. However, since they do not comply with (or conform to) airworthiness standards, they receive an airworthiness certificate in the so-called *Experimental* category. Once the conforming prototypes (the ones that *do* conform to the production aircraft) are fabricated and used for certification flight and systems testing, the nonconforming ones can come in handy as demonstration vehicles for marketing purposes.

1.3 INTRODUCTION TO AVIATION REGULATIONS AND CERTIFICATION

This section introduces aviation regulations and aircraft certification—specifically for GA aircraft. Aircraft are of substantial weight and can cause significant damage to property and death in event of a crash. A risk reduction is achieved, in part, by regulating their use, a task for which the FAA is responsible (in the United States). The regulatory scope includes design, manufacturing, maintenance, and operation of aircraft and requires manufacturers to comply with various *airworthiness regulations*. Depending on the class of aircraft, once compliance is shown, the applicant is awarded a certificate of the kind (and in the order) shown in Figure 1-8. The certification process itself is complex and beyond the scope this book. More information is provided in reference [10].

In the United States, aircraft are certified to regulations called the *Federal Aviation Regulations* (FAR). Enacted in 1965, they superseded the *Civil Aviation Regulations* (CAR). Today, thousands of aircraft operate that were certified to the CAR. The government agency that enforces these regulations is the *Federal Aviation Administration* (FAA). It superseded the *Civil Aeronautics Administration* (CAA) in 1958. FAA order 1320.46C prohibits FAA employees from using the acronym "FAR," to avoid confusion with the so-called "Federal Acquisitions Regulations." Instead, they are referred to as Title 14 of the *Code of Federal Regulations*, or simply 14 CFR. This is noted when citing regulations, e.g., 14 CFR Part 23.

In Europe, the regulations are called *Certification Specifications* (CS) [11]. These superseded the *Joint Aviation Regulations* (JAR) in 2003. The CS are enforced by the *European Aviation Safety Agency* (EASA). That year, EASA replaced the *Joint Aviation Authorities* (JAA), which had been formed in 1970. International harmonization of certification standards is on-going and allows compliance demonstrated in one country to be accepted in another. A prime example of this is 14 CFR Part 23 and the corresponding European CS-23 standards.

Adherence to the airworthiness regulations is enforced by the government of a country in which an aircraft is manufactured. An aircraft built in one country but certified in another must comply with airworthiness regulations in the latter country. Manufacturers and operators of aircraft that fail to comply with these standards are subject to severe penalties (typically financial). From a certain point of view, regulations can be considered a collection of standards. A standard stipulates a specific merit that must be met.

1.3.1 Aviation Regulations That Apply to GA Aircraft

As stated at the beginning of this chapter, the FAA defines General Aviation as aircraft other than airliners and military aircraft [1]. In the United States (US), GA aircraft must comply with a set of regulations contained under title 14 of the Code of Federal Regulations. For instance, typical small GA aircraft are certified under 14 CFR Part 23, whereas business jets (which are also considered GA) are certified under 14 CFR Part 25 (like commercial jetliners). This breakdown is illustrated in Figure 1-9 (note that lighter-than-air vehicles are omitted).

Regulations are either *prescriptive* or *performance based*. The advantage of the former is that it specifies what is required to meet a standard (e.g., "use a safety factor of 1.5 no matter what"). This reduces the level of sophistication required by a manufacturer to show compliance. In contrast, performance based allows flexibility that

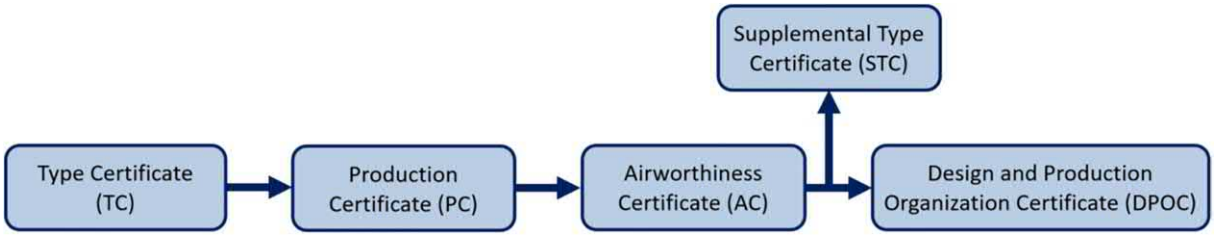


FIGURE 1-8 Classification of certificates related to aircraft development and manufacturing (per 49 US Code § 44,704).

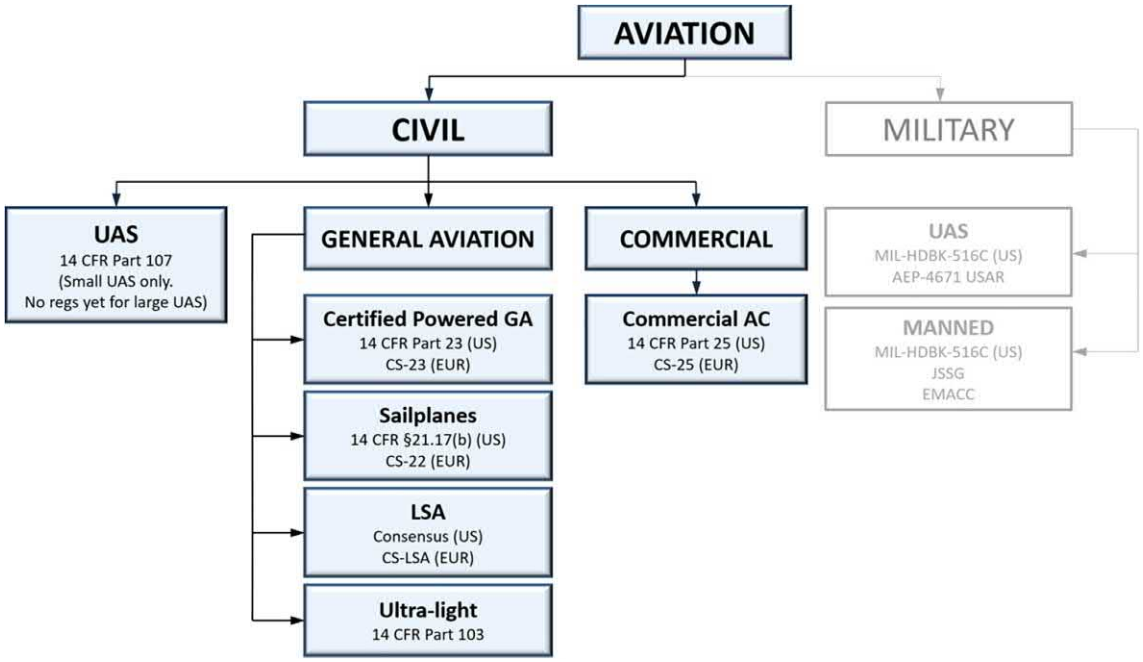


FIGURE 1-9 Classification of aircraft and associated regulations.

accommodates nonstandard design solutions. However, greater analytical sophistication is required (e.g., "my envelope protection will never allow the aircraft to reach limit loads, so why bother with a safety factor of 1.5.").

Table 1-1 lists a few regulations for selected classes of aircraft. Two frequently mentioned classes involving GA aircraft are 14 CFR Part 23 and LSA. Part 23 aircraft are awarded a Type Certificate (TC), while LSA receive a Special Airworthiness Certificate (S-AC). More information about the certification of aircraft is provided in Ref. [12].

On August 31, 2017, the FAA adopted a significant modification of 14 CFR Part 23 by releasing its 64th amendment. The change is recognized by many as the "New Part 23" or "Part 23 NPRM" (Notice of Proposed Rulemaking). The change introduced *performance based* rather than *prescriptive* certification. Additionally, the use of consensus standards, such as those issued by the American Society for Testing and Materials (ASTM), was introduced. Applicants (individuals or organizations) can also propose their own means of compliance (subject to FAA approval). However, it remains possible to certify per preamendment 64 standards. On March 14th, 2016, the FAA published the NPRM, entitled "Revision of Airworthiness Standards for Normal, Utility, Acrobatic, and Commuter Category Airplanes." In it, the FAA stated that it "*…proposes to amend its airworthiness standards for normal, utility, acrobatic, and commuter category airplanes by removing current prescriptive design requirements and replacing*

TABLE 1-1 Certification basis for several classes of aircraft.

Class	Regulations	Comments
General Aviation	14 CFR Part 23 (USA) CS-23 (Europe)	On August 31st, 2017, the FAA adopted a modified version of 14 CFR Part 23, commonly referred to as the "New Part 23."
Commercial Aviation	14 CFR Part 25 (USA) CS-25 (Europe)	
Sailplanes	14 CFR 21.17(b) (USA) CS-22 (Europe)	14 CFR 21.17(b) allows the FAA to tailor the certification on a need-to-basis to sailplanes. Then, by referring to AC 21.17-2A, the FAA accepts the former JAR-22 as a certification basis, which have now been superseded by CS-22.
Airships	14 CFR 21.17(b) (USA) CS-30 and CS-31HA	14 CFR 21.17(b) allows the FAA to tailor the certification on a need-to-basis to airships.
Nonconventional Aircraft	14 CFR 21.17(b) (USA) CS-22 (Europe)	14 CFR 21.17(b) allows the FAA to tailor the certification on a need-to-basis to nonconventional aircraft.
Light Sport Aircraft (LSA)	Consensus (USA) CS-LSA (Europe)	See discussion below regarding LSA acceptance in the US.

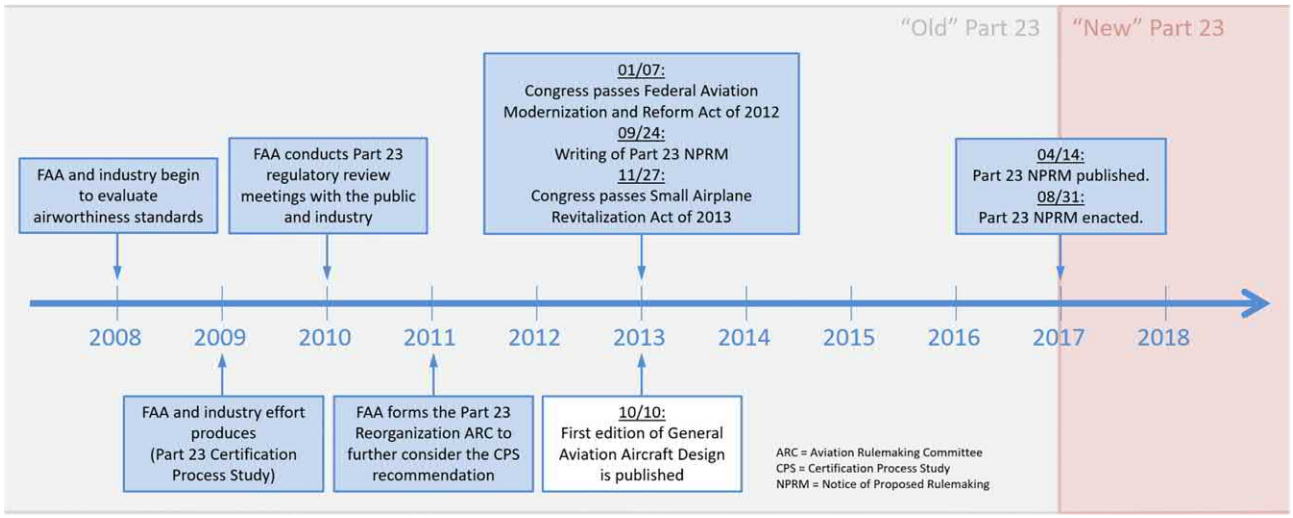


FIGURE 1-10 A brief timeline depiction of the rulemaking change.

them with performance-based airworthiness standards [13]." This rulemaking change is significant and constitutes one reason for the release of the second edition of this book. A timeline of events preceding the adoption of the modified standards is shown in Figure 1-10. A corresponding Notice of Proposed Amendment (NPA 2016–2005) was published by EASA on June 23rd, 2016 [14].

In the words of the FAA, not only are the (older) airworthiness standards of 14 CFR Part 23 based on dated design technology from the 1950s and 1960s, they are also *prescriptive* [13]. This means they prescribe the requirements with which the product must comply. An example of such prescription is paragraph §23.49 (c), which regulated stalling speed, stating that

> (c) Except as provided in paragraph (d) of this section, V_{SO} and V_{S1} at maximum weight must not exceed 61 knots for—
>
> **(1)** Single-engine airplanes; and
> **(2)** Multiengine airplanes of 6000 pounds or less maximum weight that cannot meet the minimum rate of climb specified in § 23.67(a) (1) with the critical engine inoperative.

Without going into too much detail, the paragraph *prescribes* that single-engine aircraft *must* have a stalling speed of no more than 61 KCAS in the landing configuration (V_{S_0}). It dictates so without ever justifying why the stalling speed *must* be 61 KCAS and not some other speed. For one, why should a large single-engine aircraft such as the Pilatus PC-12 be required to stall at 61 knots or less, like a small Cessna 152? The former typically cruises around 270+ KTAS [15] and is operated by skilled pilots; the latter cruises at 100+ KTAS and is operated by student pilots. It is in this capacity that prescriptive regulations can potentially drive a design in an undesirable direction. It may force the designers to feature large and complex high-lift system where a simpler system would suffice. The issuance of such exemptions requires extra cost and documentation for the manufacturer and the FAA. Thus, it constitutes an impediment to the certification process.

In contrast, performance-based standards are intended to conform the certification of an airplane to its actual capabilities. A case in point is the "new" paragraph §23.2110, *Stall speed*, which states.

> **§23.2110 Stall speed**
>
> The applicant must determine the airplane stall speed or the minimum steady flight speed for each flight configuration used in normal operations, including takeoff, climb, cruise, descent, approach, and landing. The stall speed or minimum steady flight speed determination must account for the most adverse conditions for each flight configuration with power set at—
>
> **(a)** Idle or zero thrust for propulsion systems that are used primarily for thrust; and
> **(b)** A nominal thrust for propulsion systems that are used for thrust, flight control, and/or high-lift systems.

There is no prescribed minimum stalling speed. Instead, a stalling speed appropriate to the size of the aircraft is selected. It is to be expected that the stalling speed of larger and faster aircraft will be higher than those which are smaller and slower. However, what differs is the demonstration of compliance for a large versus small aircraft, for both must demonstrate safe operation. This is harder to show for higher stalling speed (higher kinetic energy dissipated in case of emergency is but one aspect of the certification). The FAA (and industry) hopes that this will reduce the cost and time required to certify new aircraft and encourage applicants to bring new

and innovative technology to the market, without compromising safety. Time will tell.

Another aspect of Part 23 NPRM is the classification of aircraft. The "old" and "new" versions can be compared in Tables 1-2 and 1-3, respectively. Before August 31st, 2018, GA aircraft were certified under 14 CFR §23.3, *Airplane Categories*, under four categories: *Normal*, *Utility*, *Aerobatic*, and *Commuter*. These categories were subjected to the restrictions listed in Table 1-2. Except for the Commuter category, an aircraft may be certified in more than one category provided the requirements of each are met.

In contrast, in Part 23 NPRM, the classification is now accomplished per Table 1-3. All aircraft are now certified under a *normal category* but are separated in subcategories using *Certification Levels* (1 through 4) and *Performance Levels* (low and high). Additional requirements must be complied with if the new aircraft is aerobatic. Thus, a Cessna 172 class aircraft would be certified as a *Level 2*, *Low-Performance*, *Nonaerobatic* aircraft, while an Eclipse 550 would be certified as a *Level 3*, *High-Performance*, *Nonaerobatic* aircraft.

Guidance for the new 14 CFR Part 23 can be found on the FAA website (www.faa.gov) under FAA Home > Aircraft > Aircraft Certification > Design Approvals (retrieved in 2018). The webpage presents a document listing Means-of-Compliance (MOC) [17]. This listing presents numerous ASTM standards, the primary of which is ASTM 3264–18. Note that the applicant must pay upward of $60 (in 2018) for each ASTM standard.

The certification of Light Sport Aircraft (LSA) differs in important ways from aircraft certified under 14 CFR Parts 23 and 25. As stated earlier, LSA receives an S-AC, not a TC. Second, LSA must meet the definition 14 CFR Part §1.1 (General definitions) and §21.190 (Issue of a special

TABLE 1-2 Restrictions for aircraft classes certified under the "Old" 14 CFR Part 23.

Restriction	Commuter	Normal	Utility	Aerobatic
Number of pilots	1–2	1	1	1
Max number of occupants	19	9	9	9
Max T-O weight	19,000 lb_f	12,500 lb_f	12,500 lb_f	12,500 lb_f
Aerobatics allowed?	No	No	Limited	Yes
Nonaerobatic operations permitted	Normal flying Stalls (no whip stalls) Steep turns ($\phi < 60°$)	Normal flying Stalls (no whip stalls) Lazy eights Chandelles Steep turns ($\phi < 60°$)	Normal flying Stalls (no whip stalls) Lazy eights Chandelles Steep turns ($\phi < 90°$) Spins (if approved)	N/A
Max maneuvering g-loading, n_+	$2.1 + \frac{24000}{W + 10000} < n_+ \leq 3.8$		4.4	6.0
Min maneuvering g-loading, n_-	$-0.4n_+ < n_- \leq -1.52$		-1.76	-3.0

W = Maximum T-O weight. Maneuvering loads are based on 14 CFR §23.337.
A whip stall occurs when an airplane is pitched to a near vertical attitude, after which it falls on its nose such that the wing is subjected to AOA close to 90°. This can demand a dangerous recovery procedure [16].

TABLE 1-3 Restrictions for aircraft classes certified under the "New" 14 CFR Part 23.

	Aircraft certification level			
	1	**2**	**3**	**4**
Max seating capacity	0–1	2–6	7–9	10–19
	Aircraft performance level			
	Low		**High**	
Max normal operating and max operating airspeeds	V_{NO} and $V_{MO} \leq 250$ KCAS		V_{NO} or $V_{MO} > 250$ KCAS	
Max operating Mach number	$M_{MO} \leq 0.6$		$M_{MO} > 0.6$	
	Aerobatic capability?			
Certify for aerobatics (if YES, then also consider limitations of Subpart G)	YES		NO	

airworthiness certificate for a light-sport category aircraft). Eligibility requires a manufacturer's Statement of Compliance (SOC) (per §1.190(b)(1)(iii)), the details of which are listed in §21.190(c). Note that there are important differences between certifying manufactured LSA and those assembled from kits (see Chapter 9 of reference [12]). The system is a form of "self-regulation" and reduces FAA oversight. The LSA industry recognizes that responsible compliance is the only way to avoid more burdensome regulations. According to FAA officials in 2012, this system has been mostly problem free, excluding one instance [18]. The matrix of ASTM standards accepted by the FAA can be obtained from the FAA online website [19] for LSA and [17] for 14 CFR Part 23 for aircraft.

1.3.2 Important Regulatory Concepts

(1) Advisory Circular (AC)

An *advisory circular* is a means for the FAA to share information with the aviation community regarding specific regulations and recommended operational practices. This information is sometimes detailed enough to be presented in the form of a textbook (e.g., AC36-3H—Estimated Airplane Noise Levels in A-Weighted Decibels) or as simple as a few pages (e.g., AC 11–2A—Notice of Proposed Rulemaking Distribution System). A complete list of ACs is provided on the FAA website [20].

(2) Airworthiness

Airworthiness refers to activities required to support the safe operation of aircraft. The term comprises a complex set of actions that include the establishment of rules to enforce best engineering and maintenance practices, description of the legal and physical state of the aircraft, and provides evidence the aircraft meets design specifications and the applicable certification criteria. Airworthiness is a field of specialization too involved to permit appropriate presentation in this book.

(3) Airworthiness Directives (AD)

Sometimes the operation of a specific aircraft develops unanticipated issues that may compromise its safety. This requires the manufacturer to notify the aviation authorities. The authorities will issue an Airworthiness Directive (AD) to the manufacturer and to all operators worldwide. The AD is a document that stipulates redesign effort or maintenance actions to prevent the issue from developing into a catastrophic event. Compliance with the AD is required or the airworthiness certificate (AC, see Bullet (8)) for the specific aircraft may be cancelled. ADs for different aircraft types can be viewed on the FAA website [21].

(4) Maintenance Requirements

The use of an aircraft subjects it to wear and tear that eventually calls for repairs. Such repairs can be of a *preventive* type (e.g. replacement of a component expected to fail within a given period of time) or the *restorative* type (e.g. an addition of a doubler to improve the integrity of a structure beginning to show signs of fatigue). The manufacturer is required to specify frequency and rigor of preventive maintenance in a maintenance program. It instructs when such tasks must be accomplished. If the owner or operator of the aircraft does not comply with this satisfactorily, the aircraft may lose its AC and is then said to be "grounded."

(5) Parts Manufacturer Approval (PMA)

Parts manufacturer approval authorizes a manufacturer to produce and sell replacement or modification parts for a given aircraft. Thus, the manufacturer can produce airworthy parts even if it is not the original manufacturer.

(6) Service Bulletin (SB)

In due course of time, the manufacturer inevitably learns new things about the operation of its aircraft. This experience results from dealing with customers as well as the manufacturer's sustaining engineering effort. It usually improves the aircraft and its operation and is of great value to other operators. Such experience is shared by publishing *service bulletins* (SB). Although the recommendations in an SB are most often discretionary (optional), they will sometimes relay information required to comply with an AD.

(7) Special Airworthiness Certificate (S-AC)

A *special airworthiness certificate* can be issued for airplanes that, for some reason, must be operated in a specialized fashion (e.g., ferry flying, agricultural use, experimental, marketing, etc.). This precludes it from being used for commercial transportation of people or freight. LSA aircraft also receive an S-AC. It is issued in accordance with 14 CFR 21.175 in the following subclasses: primary, restricted, limited, light-sport, provisional, special flight permits, and experimental. Of these, the prototypes of new aircraft designs typically receive an experimental permit while they are being flight tested or used for market surveys.

Once the manufacturer is nearing the end of the certification process, the authorities may allow early delivery of the aircraft by issuing provisional permits. This helps the manufacturer begin to recover the extreme development costs. The provisional permit subjects the operation of the aircraft to limitations that are lifted once the manufacturer finally receives the TC. An example of this is a GA airplane designed for an airframe lifetime of, say, 12,000 h.[3] Since fatigue testing is one of the last

[3] General Aviation aircraft often specify airframe lifetime in terms or flight hours rather than cycles because they are operated in a much less rigorous environment than commercial aircraft.

compliances to be demonstrated, it is possible the aircraft would receive a provisional S-AC with a 2000-h airframe limitation. Since GA aircraft usually operate some 200 to 300 flight hours per year, the 2000-h limitation will not affect the operator for several years, allowing the manufacturer to complete the certification while being able to deliver aircraft. Once the 12,000-h lifetime is demonstrated, the 2000-h limitation on already delivered aircraft is lifted.

(8) Standard Airworthiness Certificate (AC)

Once the type certificate (TC) has been approved, each unit of the now mass-produced aircraft will receive a *standard airworthiness certificate*. This is only issued once each aircraft has been demonstrated to conform to the TC and has been assembled in accordance with industry practice; is ready for safe operation; and has been registered (given a tail number). Each aircraft produced is tracked using serial numbers. The AC allows the aircraft to be operated, provided its maintenance is performed in accordance with regulations.

(9) Supplemental Type Certificate (STC)

Many operators of airplanes request new features to be offered. An example of a common change is when a piston propeller is replaced with a turboprop. Another example is to convert an airplane to transport patients, something for which it was unlikely originally designed. Such changes require the approval of the aviation authorities. Once it is demonstrated that the change does not compromise the continued airworthiness of the aircraft, a *supplemental type certificate* is issued. The STC lists what changes were made to the aircraft, details how it affects the TC, specifies new or revised operational limitations, and stipulates the affected serial numbers (*effectivity*).

(10) Technical Standard Order (TSO)

A *technical standard order* is a minimum performance standard to which materials, parts, processes, and appliances used in civil aircraft are subjected. Effectively, a TSO is a letter to the manufacturer of a given product stating that in order to get the product TSOd, specific performance requirements must be met and a list of engineering documentations (drawings, specifications, diagrams, etc.) must be submitted. The TSO is an official certificate that confirms the part is safe for use in a specific aircraft—it is airworthy. This puts the manufacturer at a significant advantage over another one whose product is not TSOd. It is also essential for pilots to know that the equipment they are using is airworthy.

(11) Technical Standard Order Authorization (TSOA)

A *technical standard order authorization* is a document that authorizes the manufacturer to produce parts and components in accordance with a TSO. An example is a battery manufacturer who wants to produce a battery for use in a specific aircraft. The TSO tells the manufacturer the capability of the battery (e.g. amp-hours, temperature tolerance, etc.). The TSOA tells the manufacturer that, in the eyes of the FAA, the product is qualified and can now be produced.

(12) Type Certificate (TC)

Once the manufacturer of a civilian aircraft, engine, or propeller has demonstrated its product meets or exceeds the airworthiness standards, it is awarded a *Type Certificate*. This is done by publishing a Type Certificate Data Sheet (TCDS). The TCDS lists important information about operating limitations, applicable regulations, and other restrictions. This means the aircraft is now "officially defined" by the TC. TCDS for all civilian aircraft is available online on the FAA website [22].

While obtaining the TC is very costly for the manufacturer, it helps market the product. It can be stated with a high level of certainty that a product without a TC (i.e. "experimental") is unlikely to sell in the same quantity or at the same price it would with a TC. The TC is a quality stamp: It makes the product "trustworthy." The reason why a TC is so costly is that it requires the product to undergo strenuous demonstration of safe operation, quality of material, and construction. Additionally, the TC serves as a basis for producing the aircraft.

1.4 HOW TO DESIGN A NEW AIRCRAFT

This section presents a step-by-step method intended to help the novice designer begin the conceptual design of an aircraft and bring it to the preliminary phase. The *conceptual design phase* formally transforms the initial specifications into an external geometry and assesses its capabilities. Reliable analysis methods are required during this phase, as it is an opportunity to design as many problems out of the airplane as possible.

Another word for algorithm is process; it is a list of tasks arranged in a logical order. The design algorithm presented is an enhanced version of that attributed to Frank Barnwell (1880–1938, 57), a prolific designer of many aircraft, including the Bristol F·2B fighter [23]. It is a process of iteration, so the selected analysis methods must be *conducive to iteration* as well. During the design phase, discoveries are made that call for repeated calculations. For instance, if it is discovered that the wingspan must be increased, it will not just affect the wing geometry, but weight, drag, and performance, to name a few. Thus, all parameters that depend on wingspan, explicitly or implicitly, must be updated, from the most elementary to the most complex.

The modern spreadsheet is ideal for this analysis approach. This book provides the designer with methods

to simplify the implementation of the design process using spreadsheet analysis. As an example, many graphs in the book have no other data available besides the graphs themselves. These have been painstakingly digitized for the reader. Additionally, many methods are presented using computer codes written in Visual Basic for Applications (VBA), native to Microsoft Excel.

1.4.1 Conceptual Design Algorithm for a General Aviation Aircraft

The design algorithm is presented in Table 1-4 and illustrated in Figure 1-11. It covers the complete conceptual design process and presents several tasks that help bring the design into the preliminary design phase. Where appropriate, the reader is directed toward a section in this book that provides the needed analysis method. The algorithm treats the design process as a computer program: First, several initialization tasks are performed, followed by a set of iterative tasks.

Note that sketching the airplane is not suggested until Step 10. While this may appear strange to some, the reason is simple: Not enough information exists for an effective sketch until Step 10. Of course, this does not mean a sketch cannot be or should not be drawn before that—just that an accurate depiction of the airplane is not possible. For one, the wing and tail geometry are determined in Steps 8 and 9, so an earlier sketch is unlikely to represent

TABLE 1-4 Conceptual design algorithm for a GA aircraft.

Step	Task	Section
1	Understand requirements, mission definition, and the implications of the regulations to which the airplane will be certified.	–
2	Study aircraft that fall into the same class as the one to be designed. These may present you with great design ideas and solutions. They can also show you what to steer away from—which is priceless! • Qualitatively evaluate what configuration layout may best suit the mission. • Decide on a propulsion methodology (propeller, turbofan, others?).	–
3	If the target weight and maximum level airspeed are known, estimate the development and manufacturing costs for a projected 5-year production run. If the target weight is not known, perform this task once it is known (see STEP 6 or 12). Evaluate how many units must be produced to break-even and the required retail prices. Evaluate operational costs and labor force as well. How do these compare to the competition?	2.2 2.3
4	Create a *Constraint Diagram* based on the requirements of STEP 1 (target performance).	3.2
5	Select critical performance parameters (T/W or BHP/W and W/S) from the Constraint Diagram. Once T/W and W/S are known, the next step is to estimate the gross weight so that wing area and required engine thrust (or power) can be extracted.	3.2
6	Estimate initial empty and gross weight using W-ratios with historical relations and conduct a thorough mission analysis.	6.2
7	Using the results from the Constraint Diagram of STEP 4 and the initial gross weight of STEP 6 estimate the initial wing area and thrust required. This calls for a guess for an expected $C_{L_{max}}$. Thrust will reveal what sort of an engine is required for the airplane. Keep in mind the requirements for stall speeds (e.g. LSA limit is 45 KCAS, "old" 14 CFR Part 23 is 61 KCAS, etc.) to ensure the selected W/S and T/W (or BHP/W) will allow the design to simultaneously meet all performance requirements and stall speeds.	3.2
8	Estimate initial tail surface area and special position using V_{HT} and V_{VT} methodology.	11.4
9	Propose a wing layout that suits the mission by establishing initial AR, TR, airfoils, planform shape, dihedral, washout, etc. Note that many of these parameters are likely to change in the next iteration. For the airfoil selection, use a method like the one shown in Section 8.3.9, *Decision Matrix for Airfoil Selection*.	8 9
10	If not already done, sketch several initial configurations and methodically evaluate their pros and cons. Select a candidate configuration.	4
11	Based on the selected propulsion methodology (see STEP 2), select the engine type and layout (number of, types, properties of, location of) to be evaluated.	7
12	Using the candidate configuration, estimate empty, gross, and fuel weight using the appropriate combination of *Statistical*, *Direct*, and/or *Known Weights* methods.	6.3 6.4 6.5
13	Determine the empty weight CG, develop a CG loading cloud, gross weight CG, movement due to fuel burn, and inertia properties (I_{xx}, I_{yy}, …).	6.6
14	Determine a candidate CG envelope based on results from STEP 13. Expect this to change once STEP 16 will be completed.	6.7
15	Layout fuselage (space claims, occupant location, baggage, cargo) using a method similar to that of Section 12.3, *Sizing the Fuselage*.	12.3

TABLE 1-4 Conceptual design algorithm for a GA aircraft—cont'd

Step	Task	Section
16	Perform a detailed static and dynamic stability analysis of the candidate configuration.	Various
17	Modify the tail surface geometry in accordance with the results from the static and dynamic stability analysis of STEP 13. Note that dynamic stability modes should be converging, and the geometry will likely have to be "morphed" to eliminate any diverging dynamic modes.	11 24 25
18	Evaluate the following layout design modifications as needed based on the above analyses: • Structural load paths (wing, HT, VT, fuselage, etc.) • Control system layout (manual, hydraulic, fly-by-wire/light) • Flight control layout (geometry, aerodynamic balancing, trim tabs) • High lift systems and layout (flap types, LE devices) • Landing gear layout (tricycle, taildragger, fixed, retractable, etc.)	Various
19	Modify the design for benign stall characteristics (via washout, airfoils, slats, flaps).	9 10
20	Perform a detailed drag analysis of the candidate configuration. Design for minimum drag by polishing the geometry for elimination of flow separation areas, including the addition of wing fairings.	16
21	Perform a detailed performance analysis (T-O, climb, cruise, range, descent, and landing). Perform sensitivity analyses of T-O, climb, cruise, range, and landing. Create a payload-versus-range plot.	17–23
22	Optimize and refine where possible.	Various
23	Perform a regulatory evaluation and answer the following questions: **(1)** Will the candidate configuration meet the applicable aviation regulations? **(2)** Does it meet all requirements of STEP 1? **(3)** Does it satisfy the mission of STEP 1? If the answer to any of the three questions is NO, then go back to STEP 10 and modify the candidate configuration. If all can be answered with a YES, then continue to the next step.	14 CFR Part 23
24	Freeze OML. Do this by the release of an electronic solid model of the vehicle that is document controlled.	N/A
25	Create a *V-n* Diagram.	17.4
26	Detailed load analysis.	–
27	Move into the Preliminary Design Phase.	–

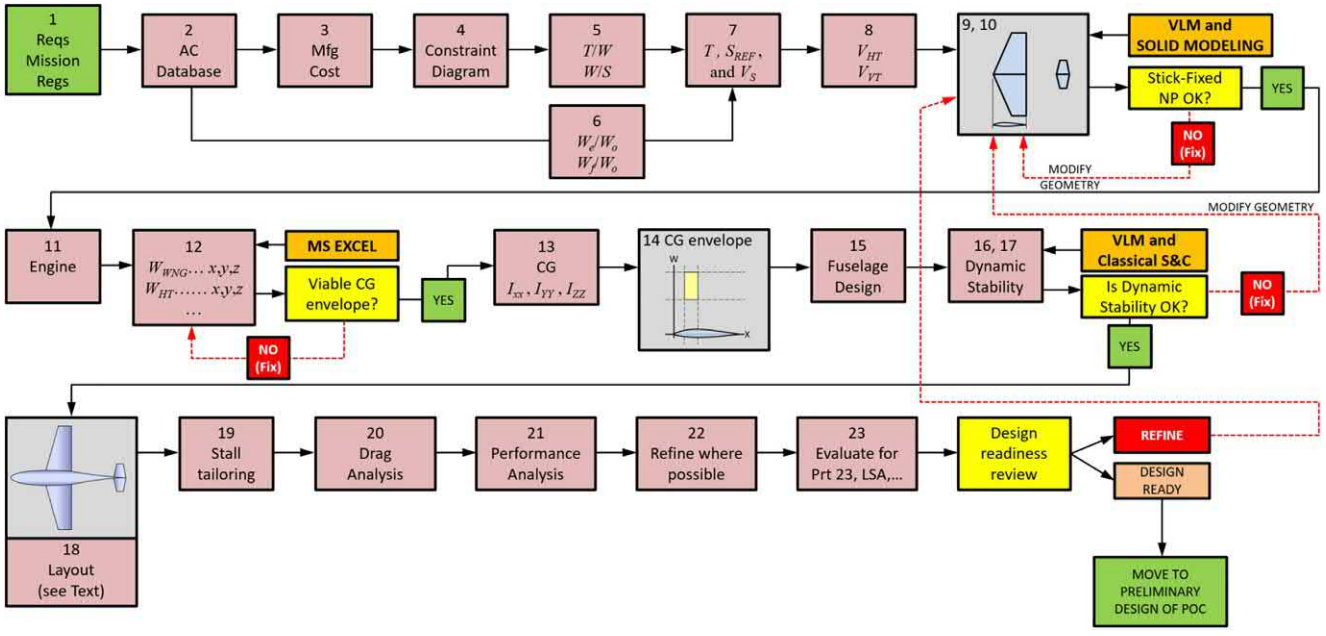


FIGURE 1-11 The aircraft design algorithm shown as a flow chart. AC stands for aircraft, VLM for Vortex-Lattice Method, S&C for Stability and Control, NP for Neutral Point and CG for Center of Gravity.

those with any precision. For this reason, and in the humble view of this author, an earlier sketch is a bit like a shot in the dark. That said, adhering to this algorithm is not the law of the land. It merely represents how this author does things. The reader can bend the algorithm to his or her own style. What works best for the reader is of greater importance.

As stated earlier, the algorithm is conveniently implemented in a spreadsheet. It is important to meticulously prepare it such that when any parameter changes, all dependent parameters are automatically updated. Do not leave this to the last minute; do it correctly from the start. This saves time. Where possible, enter formulas rather than numbers in the cells in the spreadsheet. Two common mistakes made by engineering students working on spreadsheets are (1) hardcoding numbers rather than formulas and (2) wait to the end of a semester to make the spreadsheets conducive to iteration. By then it is too late.

1.4.2 Implementation of the Conceptual Design Algorithm

The design algorithm is conveniently implemented using a 3-dimensional spreadsheet software. Such a spreadsheet allows multiple *worksheets*. It assigns one worksheet (called the "General" worksheet) as an information hub, while all remaining worksheets are organized in the hierarchy shown in Figure 1-12. All parameters that affect multiple worksheets are entered in the "General Tab". This ensures that changing multiuse parameters (e.g. wingspan) is automatically reflected in all codependent analyses in the other worksheets. A spreadsheet that requires the user to visit all affected worksheets to change the wingspan is poorly designed. It invites mistakes.

The power of the spreadsheet is further enhanced by writing VBA functions. For instance, it is highly recommended that the drag model (C_D) be developed as a VBA function, using appropriate arguments. For instance, such a function could be called `CD(Href, Vtas, df, ldg)`, where `Href` is the reference altitude (e.g., 25,000 ft), `Vtas` is the true airspeed in knots, `df` is the deflection of the flaps, and `ldg` the status of the landing gear for an aircraft with retractable landing gear. It is essential in teamwork that all members use the same lift, drag, and thrust models. Specific members can be tasked with developing these for the team. The use of such in-house functions reduces the risk of members "accidentally" using incorrect values, thus reducing chances of "late development surprises."

An example of an implementation in a real spreadsheet is shown in Figure 1-13. Note that two easily identifiable colors have been chosen for cells to indicate where the user shall enter information and where a formula has been entered. This reduces the risk of the user accidentally deleting important formulas and helps make the spreadsheet appear better organized and more professional.

1.5 ELEMENTS OF PROJECT ENGINEERING

This section introduces a few tools at the disposal of the project engineer. This is not a complete listing; there is a multitude of ways to conduct business. Readers interested in deeper understanding of each topic are directed toward a host of available texts on project engineering. Experienced project engineers may not find anything helpful in this section, but that is okay. This section is not intended for them, but the novice engineer who is not sure where to begin or how to proceed.

1.5.1 Project Plan

The successful development of a new aircraft requires a *project plan*. A project plan is a chronological listing of

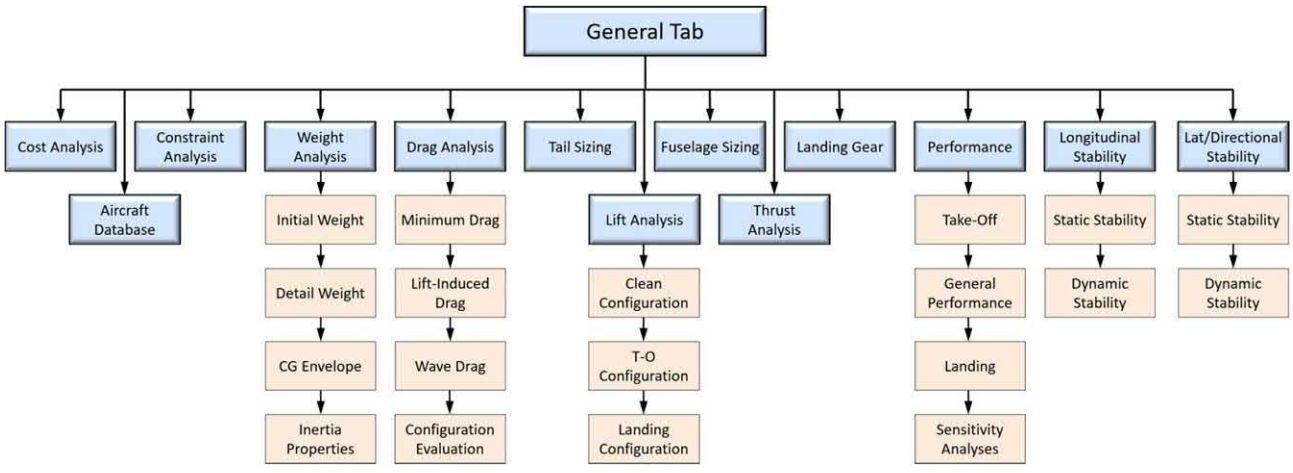
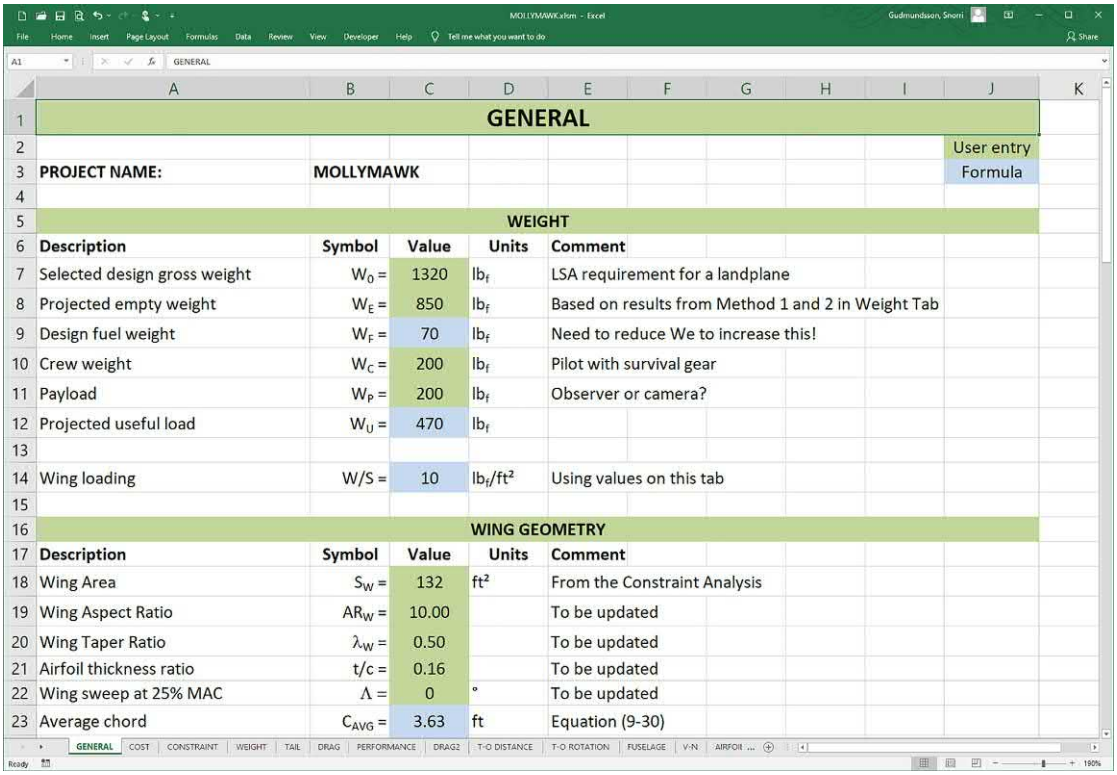


FIGURE 1-12 Organizational hierarchy for a spreadsheet (see text for explanation).



	A	B	C	D	E	F	G	H	I	J	K
1	GENERAL										
2										User entry	
3	PROJECT NAME:	MOLLYMAWK								Formula	
4											
5	WEIGHT										
6	Description	Symbol	Value	Units	Comment						
7	Selected design gross weight	W_0 =	1320	lb_f	LSA requirement for a landplane						
8	Projected empty weight	W_E =	850	lb_f	Based on results from Method 1 and 2 in Weight Tab						
9	Design fuel weight	W_F =	70	lb_f	Need to reduce We to increase this!						
10	Crew weight	W_C =	200	lb_f	Pilot with survival gear						
11	Payload	W_P =	200	lb_f	Observer or camera?						
12	Projected useful load	W_U =	470	lb_f							
13											
14	Wing loading	W/S =	10	lb_f/ft^2	Using values on this tab						
15											
16	WING GEOMETRY										
17	Description	Symbol	Value	Units	Comment						
18	Wing Area	S_W =	132	ft^2	From the Constraint Analysis						
19	Wing Aspect Ratio	AR_W =	10.00		To be updated						
20	Wing Taper Ratio	λ_W =	0.50		To be updated						
21	Airfoil thickness ratio	t/c =	0.16		To be updated						
22	Wing sweep at 25% MAC	Λ =	0	°	To be updated						
23	Average chord	C_{AVG} =	3.63	ft	Equation (9-30)						

FIGURE 1-13 Organizational hierarchy implemented in an actual spreadsheet (see text for explanation).

tasks to be executed and an associated time-stamp. The trick is to devise a balanced plan. A plan with little detail is useless. Too complex a plan is ineffective because it requires a considerable effort to create and maintain. A balanced plan resides somewhere between the two extremes.

A project plan can be developed by (1) defining milestones that stretch from the start of the project to its completion, (2) by assigning dates to the milestones, and (3) by assigning tasks that must be completed before each milestone. Sometimes it helps to create a project plan by first defining the initial and final milestones (e.g. "start design" and "first flight") and then place intermediary milestones between those (e.g. "design freeze" and "wind tunnel testing").

1.5.2 Team Leadership

Serious engineering projects need an effective *leader* who ensures the necessary tasks are executed in a proper order. Ordinarily, this position suits an experienced engineer, who is titled as the *project engineer* or *project manager*. This individual must understand the "big picture." In short, the project engineer delegates tasks to the design team. She (or he) also deals with multiple other tasks, such as scheduling, communication, hiring, conflict resolution, coordination, and interaction between groups of specialists, vendor negotiations, and development of working relationships, to name a few. The project engineer serves as a liaison between management of the company and the engineering workforce. Some of these are duties the project engineer never even heard mentioned while a student.

Six important skills are often attributed to good project managers: communication, organization, team building, leadership, coping, and technological skills. A *communication skill* is the ability to listen to people and being able to persuade them to act in a manner that favors the goals of the project. An *organizational skill* is the ability to plan, set goals, and analyze difficult situations. *Team building* involves being able to empathize and relate to people's personal issues. It leads to team loyalty and motivates it to succeed. *Leadership* is setting a good example and exercise professionalism. It is the display of enthusiasm and positive outlook, and it results in an effective delegation of tasks. A good leader sees the "big picture" and can communicate it to the team members. A *coping skill* involves flexibility, patience, persistence, and openness to suggestions from others. It makes the leader resolute and able to adjust to changing conditions. A *technological skill* involves the use of prior experience, knowledge of the project, and the exercise of good judgment. Additional characteristics of a good leader are integrity (strong morals), truthfulness (speak facts not subjective truths), and responsibility (do not blame others for own mistakes).

1.5.3 Task Management and the Task Matrix

To better manage the project, it helps to create a list of tasks to be completed. Figure 1-14 illustrates how a conceptual aircraft design project can be broken down into a 2-dimensional *task matrix*. For some, it offers greater clarity than the Gantt chart to be discussed next. However, it lacks the date-stamp. The matrix consists of a horizontal list of *subprojects* (Preliminaries—Cost—Weight—etc.), further broken down into vertical columns of *tasks*. Note that the numbers above each column refer to the chapters in this book providing the required information. Each task can be given a designation number to help keep track of its progress. Thus, the tasks under the subproject "Weight Modeling" could be enumerated as *W*1—*Weight of Rival AC*, *W*2—*Initial Weight*, and so on. Adding new tasks to the matrix and removing unnecessary ones is easy. Each task is assigned a starting and completion date and engineer(s) to which it is assigned. This not only helps the project engineer comprehend the project status and its individual subprojects but also allows it to be used as a basis for a Gantt diagram and PERT chart. Note that the shaded region at the bottom implies the target information (or knowledge) gained at the completion of each subproject. Thus, the subproject "Drag Modeling" yields a Drag Model, the subproject "Thrust Modeling" yields a Thrust Model, and so on. The Task Matrix can be expanded to include additional subprojects, e.g., "Mechanical Systems," "Electric System," "Avionics," "Flight Testing," and "Regulatory Compliance Review," to name a few. These are omitted from Figure 1-14 in interest of space.

1.5.4 Gantt Diagrams

A Gantt diagram depicts the chronological flow of a project. It is named after its inventor, Henry Gantt (1861–1919) [24]. The diagram breaks the project down into individual major tasks and associated subtasks, each with a start and an end date. Ordinarily, a multitude of other information is associated with these tasks, such as human resources and equipment (see the horizontal bars in Figure 1-15). Important project completion dates, called *milestones*, are displayed as well. Software, such as Microsoft Project, allows the generation of Gantt diagrams to be completed more effectively.

1.5.5 PERT Charts

A PERT chart displays the sequence of events that constitute a project as a network of nodes and arrows (see Figure 1-16). It offers the project manager several tools to help manage the project, including an estimate of duration and resource planning. It does so by arranging a series of events (tasks) and their duration in a network that represents the lifetime of the project. This allows the *critical path schedule*, which is the longest duration a project is expected to last, to be determined.

The method was developed in the late 1950s for the US Navy's Special Projects Office for the Polaris Fleet Missile Program as project *Program Evaluation and Review Task* (PERT) [25]. This name stuck, although the term *Task* was replaced with *Technique*. PERT is related to an older method called *Critical Path Method* (CPM) but has superseded it.

PERT breaks the project into a network of nodes that are connected with lines (arrows). The lines represent the length the tasks (or set of tasks) are expected to take. The nodes represent a break between separate tasks. The arrangement forms a network of activities and allows for a depiction of multiple tasks in progress at any time. Ordinarily, PERT uses three estimates for the time it takes to complete a task (e.g., 14 days most likely, 21 days pessimistic, 10 days optimistic). Then, the shortest and longest duration of the project is assessed by tracing the path from the initial to the final task. The reader is encouraged to further investigate the numerous pros and cons of the method as presented in the literature.

1.5.6 Fishbone Diagram for Preliminary Airplane Design

The *Fishbone Diagram*, more formally known as an *Ishikawa Diagram* or a *Cause-and-Effect Diagram*, is named after Kaoru Ishikawa (1915–1989), a Japanese quality control statistician. At its core, the diagram focuses on effects and their causes. The "causes" are drawn enclosed in a box around a horizontal arrow. Then, arrows pointing toward the "effect" (or consequence), are marked along the horizontal arrow. The resulting graph is reminiscent of a fish skeleton, which explains its nickname.

While the diagram is intended for *root-cause analysis*, it is also helpful to illustrate top-level (or big-picture) status of a design project (see Figure 1-17). In this application, the horizontal arrow is a timeline. It starts at the initiation of the project and terminates at its completion. It can represent the entire development program or subprojects. The "causes" can be thought of as major tasks that are broken down into subtasks, which are listed along the arrow pointing at the timeline. The arrows point to a milestone or a representative time location on the timeline, as shown in the figure. The advantage of this diagram is that it helps the project manager to (1) demonstrate the status of the project to upper management, (2) to anticipate when to ramp up for specific subprojects, and (3) to understand the "big-picture" of the project.

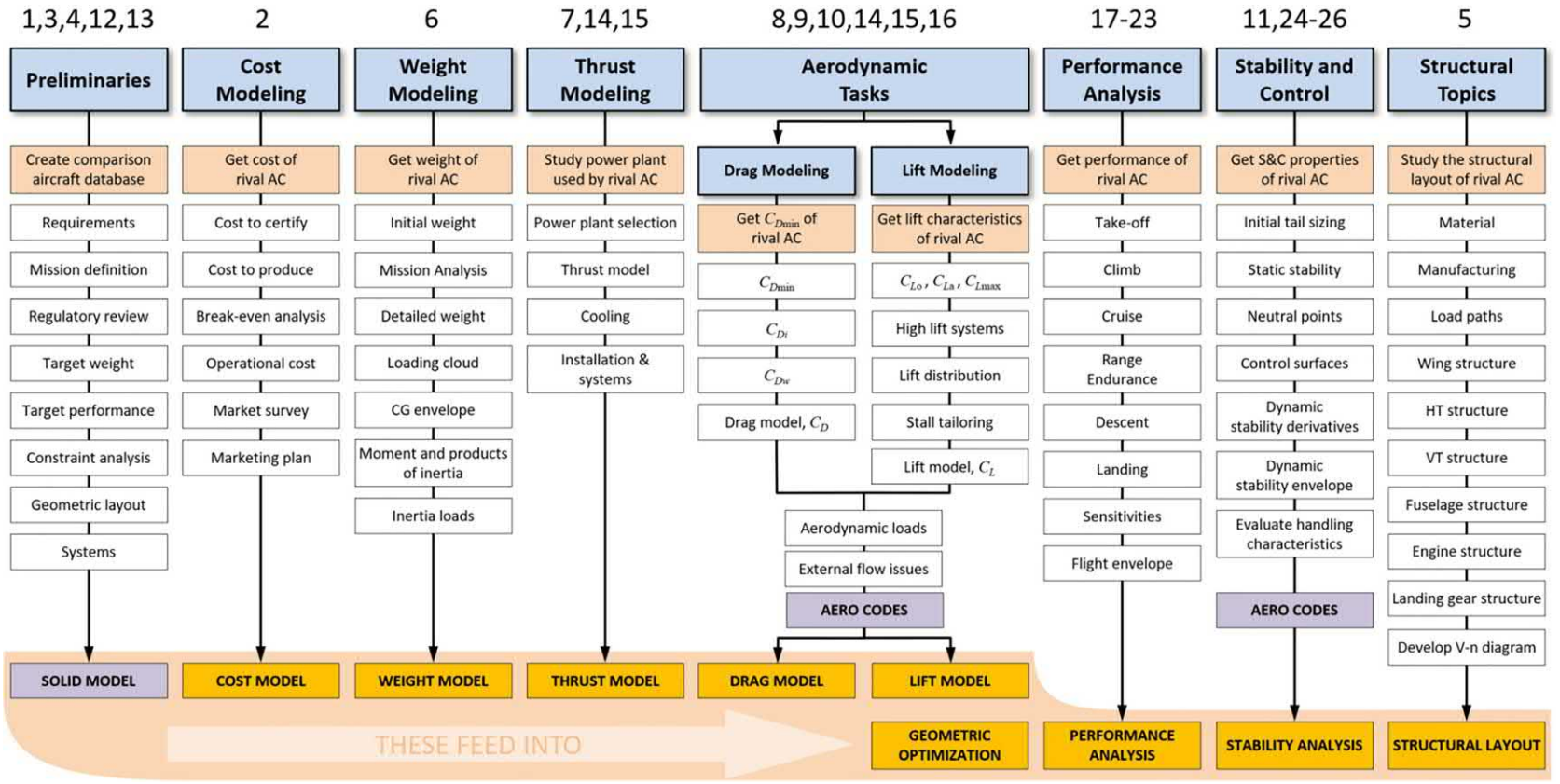


FIGURE 1-14 A *Task Matrix* breakdown of a conceptual design project into bite-sized tasks. The numbers above each column refer to chapters in this book that will help you complete said tasks.

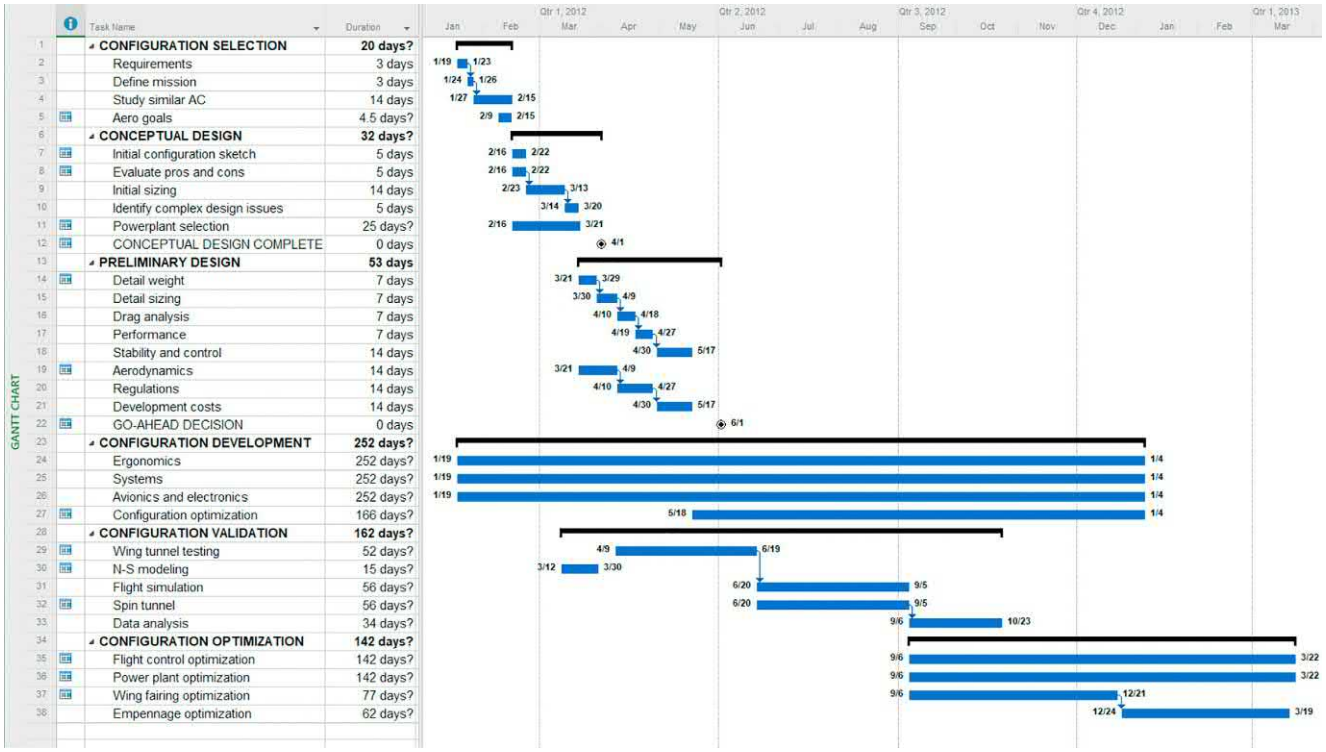


FIGURE 1-15 A Gantt diagram, showing a hypothetical conceptual design of a simple aircraft.

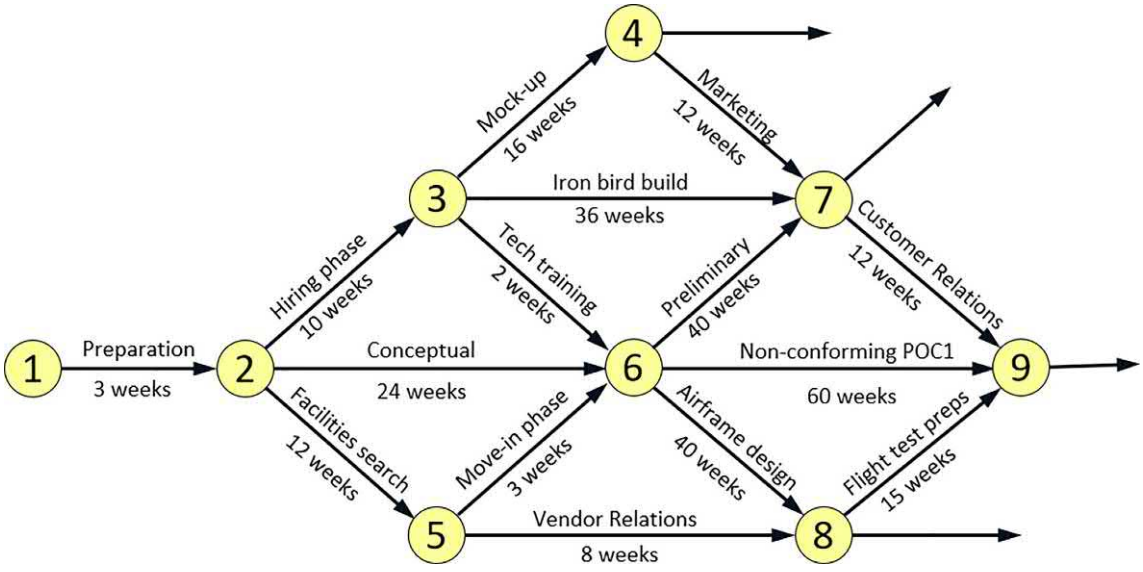


FIGURE 1-16 A simplified PERT chart with example task durations.

1.5.7 Documentation Standards and Drawing Organizing

Document standards refer to rules controlling how documents are to be formatted and stored. This ranges from the selection of font styles and layout for reports, to the way technical drawings are labeled and numbered. The project manager should establish document standards early. This should include a numbering system for drawings, bill-of-materials, reports, and design notes. The documents required to design an aircraft grow exponentially in scope and quantity with time. Storing the resulting deluge of data using a simple and effective

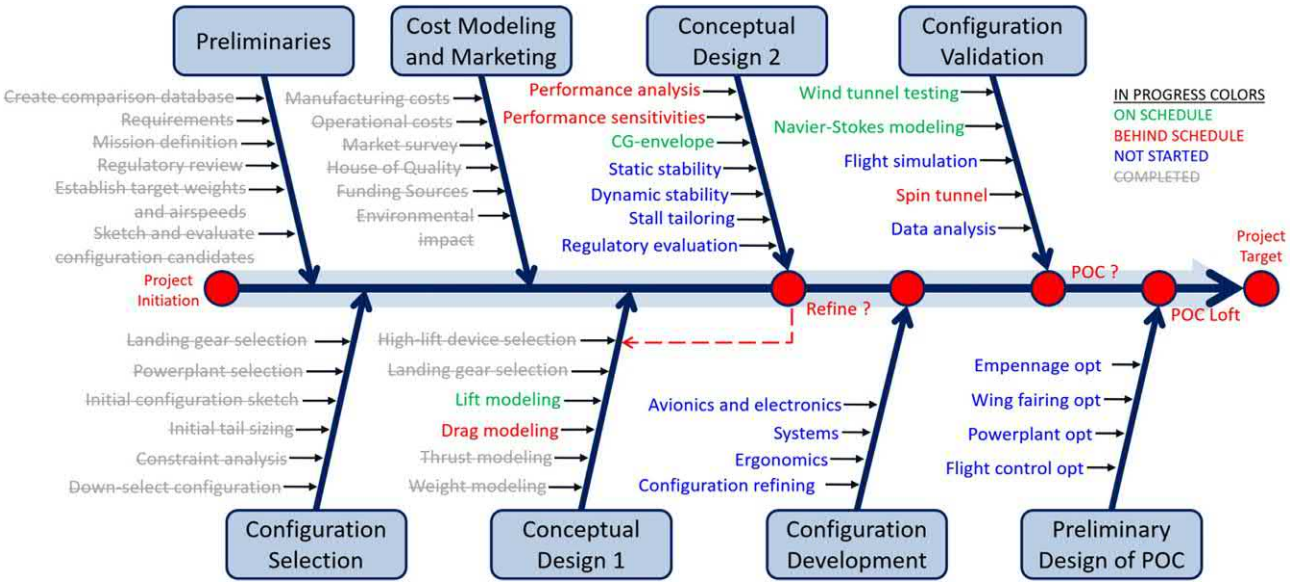


FIGURE 1-17 A typical Fishbone Diagram adapted to the design process. Completed tasks have been stricken through, and color coding can be used to further illustrate project progress.

document numbering system pays off quickly in time saved when searching and referencing this work. As an example, poor organization of documents can easily translate into a 30-min search for a specific part or assembly drawing when conducting stress analysis—5 min wasted here, and 10 min there quickly become a drag on productivity.

An example of a simple and practical drawing tree is shown in Figure 1-18. The same approach can be extended to any document involving the conceptual and preliminary design. For instance, regular *Design Notes* (which contain design calculations) can be given prefixed sequential numbers. Thus, design notes involving structural analysis could be called "DN-S-053-A," where S refers to Structures, 053 is the 53rd such document, and A is a revision letter. The design notes can incorporate similar denotation standards for Aerodynamics (A), Power plant (P), Mechanical systems (M), and so forth. Regardless, caution must be exercised in breakdown as there are extremes here, as in so many other areas of the development.

1.5.8 Quality Function Deployment and a House of Quality

Sophisticated products must simultaneously satisfy many requirements, including customer and engineering requirements. To improve the likelihood the product will satisfy the needs of the customer, it may be necessary to survey what it is they know (or think) they need. Unfortunately, survey responses can often be vague and, thus, it is necessary to convert them to statements that allow them to be measured. For instance, a statement like "I don't want to pay a lot of money for maintenance" can be translated to "reliability." This, in turn, can be measured in terms of how frequently parts fail and require repairs. It is inevitable that some of these requirements conflict with each other, in addition to depending on each other. For instance, the weight of an aircraft will have a great impact on its rate of climb, but none on its reliability.

Quality Function Deployment (QFD) is a method intended to help in this capacity by taking various customer wishes into account. This is accomplished using a multifaceted selection matrix to help evaluate the impact of various customer wishes on areas such as engineering development. This shows the designer which customer-wishes to focus on. It was developed by the Japanese specialists Dr. Yoji Akao and Shigero Mizuno. It is widely used in many industries. One of the method's best-known tools is the so-called *House of Quality* (HQ) (aka *Quality Functional Deployment Matrix*), a specialized matrix, resembling a sketch of a house, designed to convert customer requirements into a numeric score that helps defining areas for the designer to focus on. The primary drawback is that it can take considerable effort to develop, and it suffers from being highly dependent on the perspectives of the design team members.

Preparing a House of Quality

The HQ consists of several matrixes that focus on different facets of the product development (see Figure 1-19). The impact of desired (or customer) requirements on the technical requirements and their interrelation is identified, helping the designer understand which requirements are of greater importance than others and how this complicates the development of the product. The

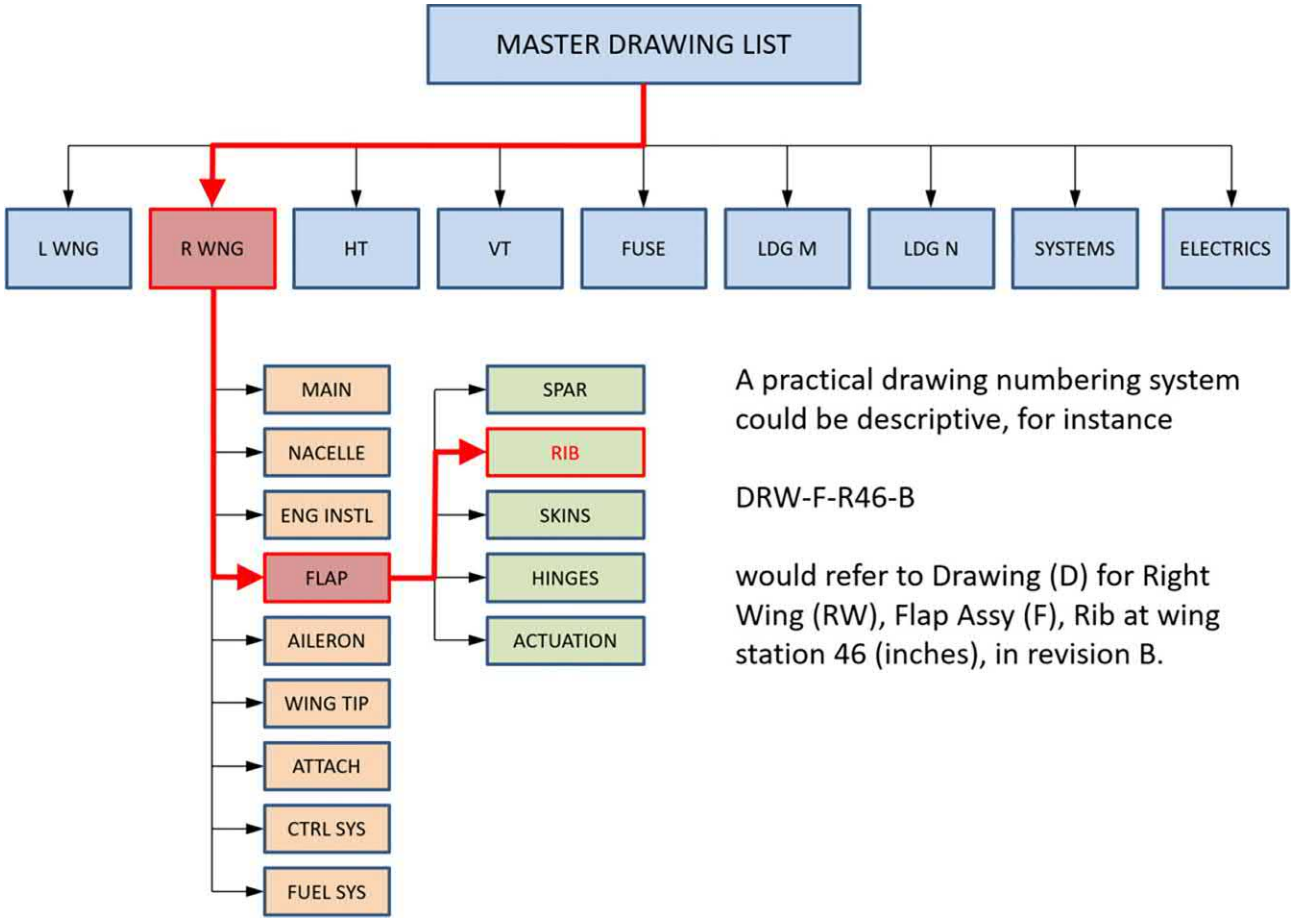


FIGURE 1-18 Example of a practical drawing numbering system.

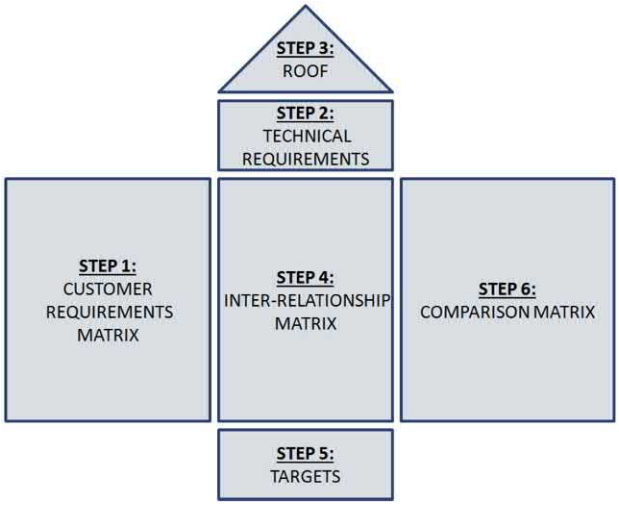


FIGURE 1-19 A basic *House of Quality*.

preparation of an HQ is best explained through an example. Below, a simplified version of the HQ, tackling the development of a small GA airplane, is presented. The reader is reminded that the HQ can be implemented in several ways—and a form that suits, say, the textile industry does not necessarily apply directly to the aviation industry.

From customer surveys

Customer Requirements	Importance 1 (not) – 5 (very)	
FAST	3.0	16.2%
EFFICIENT	5.0	27.0%
RELIABLE	4.5	24.3%
SPACIOUS	4.0	21.6%
INEXPENSIVE	2.0	10.8%
SUM =	18.5	100%

FIGURE 1-20 Customer requirements matrix.

Step 1: Customer Requirements

Assume that customer surveys have been collected for the design of a simple aircraft and the desired requirements are *fast*, *efficient*, *reliable*, *spacious*, and *inexpensive* (see Figure 1-20). An actual HQ would certainly have

more than five requirements, but, again, this demonstration will be kept simple.

The survey has requested that potential customers rate the requirements using values between 1 (something considered unimportant) and 5 (something very important). This is placed in a matrix shown in Figure 1-20. Here, let us assume the requirement FAST received an average rating of 3.0 (moderately important), EFFICIENT a rating of 5.0 (very important), etc. Then, the ratings are added and the sum (18.5) is entered as shown. The column to the right shows the percentages of the ratings. For instance, the percentage associated with the requirement "fast' is $100 \times 3.0/18.5 = 16.2\%$.

Step 2: Technical Requirements

The next step requires the designing team to list several engineering challenges that relate to the customer requirements. For instance, the requirement for "efficiency" calls for special attention to the lift and drag characteristics of the aircraft. These have been listed in Figure 1-21 with some other engineering challenges, such as "size of aircraft," "drag," "weight," and so on. These will be revisited in STEP 4.

Step 3: Roof

The roof (see Figure 1-21) is used to indicate interrelationships between the various engineering challenges. It must be kept in mind the roof sits on top of the technical requirements matrix and the diagonals enclose the columns of engineering challenges. This arrangement must be kept in mind for the following discussion.

The roof consists of two parts: the roof itself and, for lack of a better term, the fascia. The fascia is used to indicate whether the challenge listed below (e.g., "drag or "weight") has a favorable effect on the product. Thus, more "power" has a favorable effect (more power is good) and this is indicated using the arrowhead that points up. "Production cost," on the other hand, has negative effects on it, so the arrow points down.

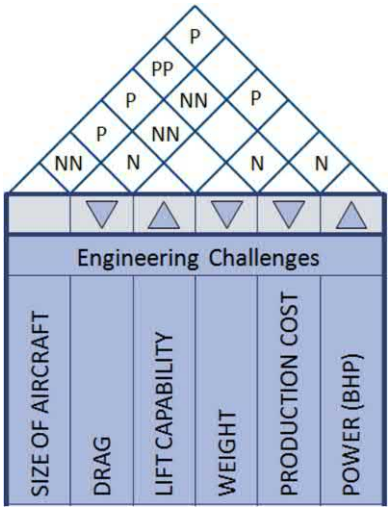


FIGURE 1-21 Technical requirements matrix.

The other challenges have been identified in a similar manner, except the first one (SIZE OF AIRCRAFT). It is not clear whether a larger or a smaller version of the aircraft is beneficial to the customer, so it is left without an arrow. Naturally, this may change if the team decides this is important; all parts of the HQ are decided by the design team and its consensus may differ from what is being shown here.

Next consider the roof itself, shown as the diagonal lines in Figure 1-21. It is used to indicate positive and negative relationships between the challenges. These are typically denoted with symbols (e.g., + for positive and—for negative), but here the following letters are used:

NN—Means there is a strong negative relationship between the two engineering challenges.
N—Means there is a negative relationship.
P—Means there is a positive relationship.
PP—Means there is a strong positive relationship between the two engineering challenges.

The term *relationship* in this context refers to how one challenge affects another. Consider the columns containing SIZE OF AIRCRAFT and DRAG. It can be argued that there is a strong negative relationship between the SIZE OF AIRCRAFT and DRAG (large aircraft = high drag). This is indicated by entering NN at the intersection of their diagonals. Similarly, there is a positive relation between SIZE OF AIRCRAFT and LIFT, indicated by the P at the intersection. Some might argue there should be a strong positive relationship; however, if the size refers to the volume of the fuselage rather than the wings, then the relationship is arguably only positive. This shows how the buildup of these relationships is highly subject to interpretation, requiring the design team to reach a consensus. Once complete, the example letter combinations are entered as shown in Figure 1-21.

Step 4: Interrelationship matrix

The next step is to try to place weight on the engineering challenges as they relate to the customer requirements. This is accomplished using the interrelationship matrix (see Figure 1-22). The design team must come up with a scale that can be used to indicate the severity of such associations. It is not uncommon to use a scale such as the one shown below:

9—Means the customer requirement has great influence.
3—Means the customer requirement has moderate influence.
1—Means the customer requirement has weak influence.

Engineering Challenges					
SIZE OF AIRCRAFT	DRAG	LIFT CAPABILITY	WEIGHT	PRODUCTION COST	POWER (BHP)
9	9	3	9	9	9
1	9	9		9	3
1				1	3
9	3			3	1
3	3	3	9	9	9
4.24	4.86	3.24	2.43	5.76	4.19
17.2	19.7	13.1	9.8	23.3	16.9

FIGURE 1-22 The interrelationship matrix.

This is employed as follows: Consider the customer requirement FAST (see Figure 1-20). It will have a strong influence on the engineering challenge DRAG. Thus, enter 9 in the intersection cell. However, LIFT will be less affected by FAST; enter 3 in the intersection cell. Similarly, the customer requirement RELIABLE will not have any effect on the WEIGHT, and so on.

For clarity, omit entering numbers in cells where no influence exists. Some people prefer to enter special symbols in such cells, but in this author's view, it only adds an extra layer of confusion. Note that these numbers will be used as multipliers in the next step.

Step 5: Targets

The target matrix (see Figure 1-23) represents the results of a cross-multiplication and summation that is used to determine where to place the most effort during the development of the product. The operation takes place as follows.

Consider the percentage column of the customer requirements matrix (16.2%, 27.0%, etc.) and the first column of the technical requirements column (SIZE OF AIRCRAFT, 9, 1, 1, etc.). These are multiplied and summed as follows:

$$0.162 \times 9 + 0.270 \times 1 + 0.243 \times 1 + 0.216 \times 9 + 0.108 \times 3 = 4.24$$

The remaining columns are multiplied in this fashion, always using the percentage column, yielding 4.86, 3.24, 2.43, and so on.

The next step is to convert the results into percentages. First, add all the results ($4.24 + 4.86 + \ldots$) to get 24.73. Second, for the first column, the percentage of the total is $100 \times 4.24/24.73 = 17.2\%$, $100 \times 4.86/24.73 = 19.7\%$ for the second one, and so forth. These numbers are the most important part of the HQ, as the highest one indicates where most of the development effort should be spent. The results and the entire House of Quality can be seen in Figure 1-24. We conclude that, in this case, the PRODUCTION COST and DRAG are the two areas that should receive the greatest attention.

Step 6: Comparison matrix

It is often helpful to create a matrix to compare an existing company product to that of the competition. This helps to identify shortcomings in the company products and to improve those. A comparison matrix is shown in

	From customer surveys		Engineering Challenges						
Customer Requirements	Importance 1 (not) – 5 (very)		SIZE OF AIRCRAFT	DRAG	LIFT CAPABILITY	WEIGHT	PRODUCTION COST	POWER (BHP)
FAST	3.0	16.2%	9	9	3	9	9	9
EFFICIENT	5.0	27.0%	1	9	9		9	3
RELIABLE	4.5	24.3%	1				1	3
SPACIOUS	4.0	21.6%	9	3			3	1
INEXPENSIVE	2.0	10.8%	3	3	3	9	9	9
SUM =	18.5	100%	4.24	4.86	3.24	2.43	5.76	4.19
			17.2	19.7	13.1	9.8	23.3	16.9

FIGURE 1-23 The target matrix.

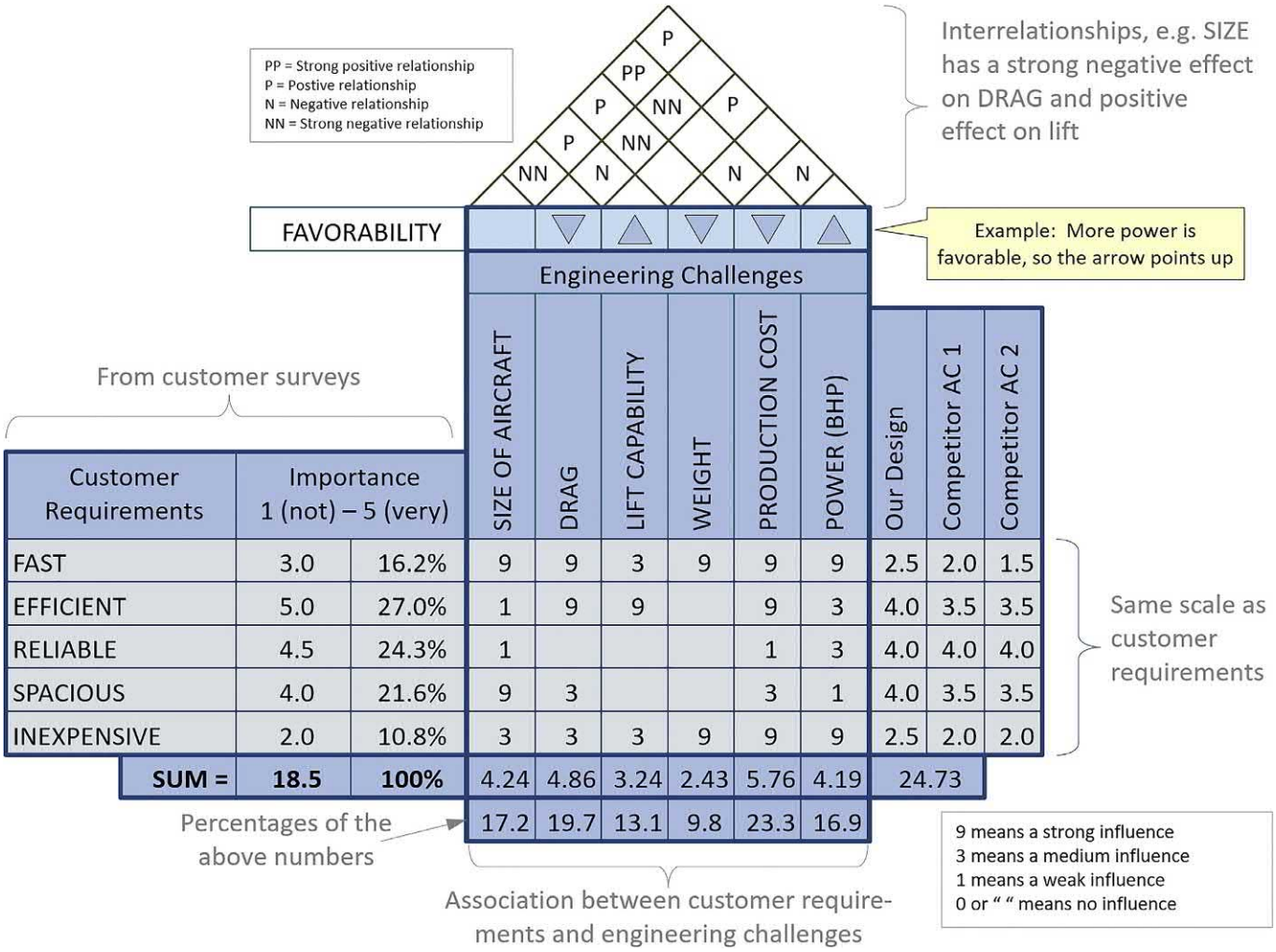


FIGURE 1-24 The completed house of quality.

Figure 1-24, where they have been "graded" in light of the customer requirements, allowing differences to be highlighted. Thus, while the customer requirement FAST has a score of 3.0, it is possible the design team values it a tad lower, or at 2.5. However, the team may also opine that competitor aircraft 1 and 2 appear to emphasize it even less. Such a conclusion should be based on hard numbers, such as drag coefficients or cruising speed, and not subjective opinions.

The purpose of this section was to introduce the reader to the HQ as a tool to help with the development of a new product (or the redesign of an existing one). The interested reader is directed toward the multitude of online resources that add greater depth to this topic.

1.6 PRESENTING THE DESIGN PROJECT

A picture is worth a thousand words. This adage is particularly true in the world of engineering, where detailed information about complicated mechanisms, machinery, and vehicles, must be communicated clearly and effectively. While the topic of geometric dimensioning and tolerancing (GDT) and industry standards in technical drafting is beyond the scope of this book, saying a few words about the presentation of images is not. The practicing engineer will participate in many meetings and design reviews, where often many experts in various fields gather and try to constructively criticize a new design. The process is often both exhausting and humbling but is invaluable as a character-builder. Being able to describe the functionality of one's design is priceless, and no tool is better for that purpose than a figure, an image, or a schematic. Three-dimensional depictions are particularly effective. The modern aircraft designer benefits from computer-aided design (CAD) tools such as solid modelers (Solidworks, CATIA, and others), which allow complex 3D geometry to be depicted with a photo-realistic quality. Highly specialized software, for instance, finite element analysis (FEA) and computational fluid dynamics (CFD) programs, allow the engineer to describe the pros and cons of very complicated

structural concepts and 3D flow fields, and even add a fourth dimension by performing time-dependent analyses. It cannot be overemphasized to the entry-level engineer to get up to speed on this technology. It not only helps with communication, but also develops a strong 3- and 4-dimensional insight into engineering problems.

(1) Three-View Drawings

The three-view drawing is a fundamental presentation tool the engineer should never omit. Airplane types are commonly displayed using three-view drawings, showing their top-, side-, and frontal views. Such drawings are an essential part of the complete submittal proposal package for any aircraft. Although such presentation images date back to the beginning of aviation, they are vital for any design proposal. Figure 1-25 shows a typical such drawing, with the added modern flare in the form of a 3D perspective rendering.

(2) Images Using Solid Modelers

The modern solid modeler software (CAD) has revolutionized aircraft design. Long gone are the large sloped drafting tables and the special architectural pens that deliver uniform line thicknesses and other tools of the past. These began to disappear in the late 1980s and early 1990s. Today, drafters equipped with personal computers or workstations, model complicated parts and assemblies in virtual space. At the time of writing, programs such as Solidworks, and CATIA are common packages for this purpose and pack an enormous sophistication in their geometric engines. Besides allowing photorealistic renderings of complex 3-dimensional geometry, some even offer limited FEA and CFD capabilities. They provide perfect mathematical definitions of complicated compound surfaces and allow curvature perfect OML to be created using NURBS surfaces. Images from such programs can be quite persuasive and informative. Figure 1-26 shows an image of a twin-engine regional jet design from one such package, superimposed on a background image taken at some 18,000 ft. The resulting image can be of great help in engineering and marketing meetings.

(3) Images Using Finite Element Modelers

The modern structural analysis often includes sophisticated Finite Element Analyzers, capable of producing compelling images. While such images should be used with care (as their compelling nature tricks many into thinking they *always* represent reality, which may be far off the mark), they can give even a novice an excellent understanding of load paths as well as where stress concentrations reside. While such images are usually available only after detailed design work has begun, images from previous design exercises can sometimes be helpful in making a point about possible structural concepts.

Figure 1-27 shows stress concentrations in a forward shear-web of the wing attachment/spar carry-through structure of a small General Aviation aircraft, subject to an asymmetric ultimate load. The elongated diamonds in the center of the spar carry-through are corrugations

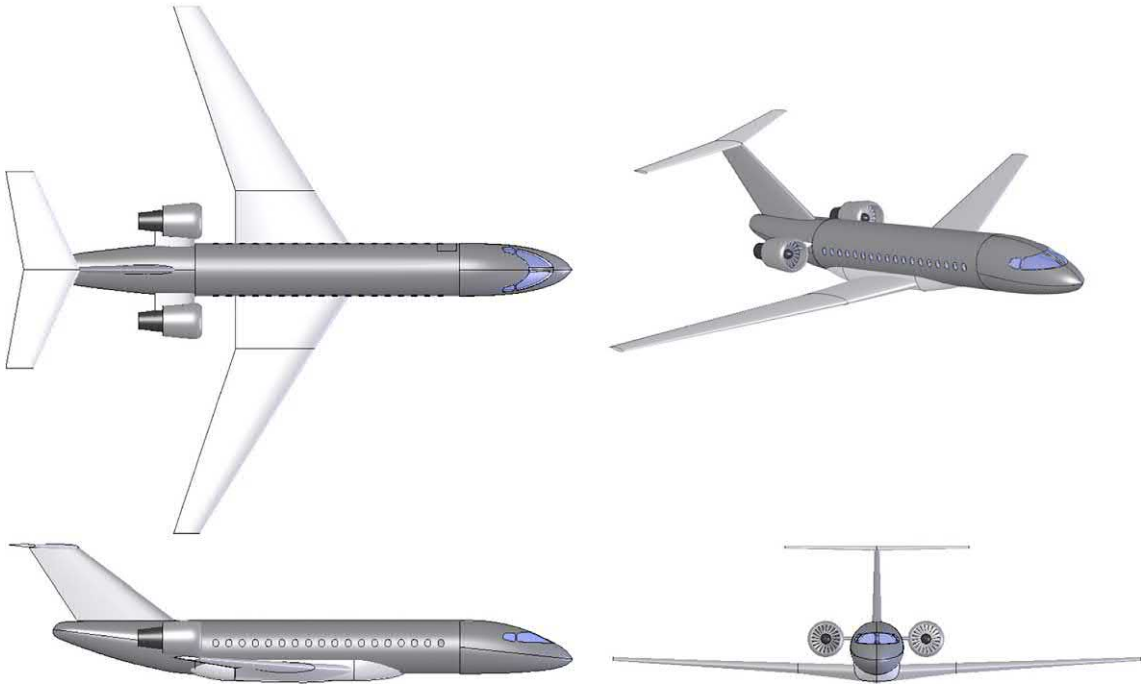


FIGURE 1-25 A nonstandard three-view drawing, made using modern solid modeling software.



FIGURE 1-26 A solid model of a modern regional jet superimposed on a photographic background, showing the capability of modern Computer Aided Design software.

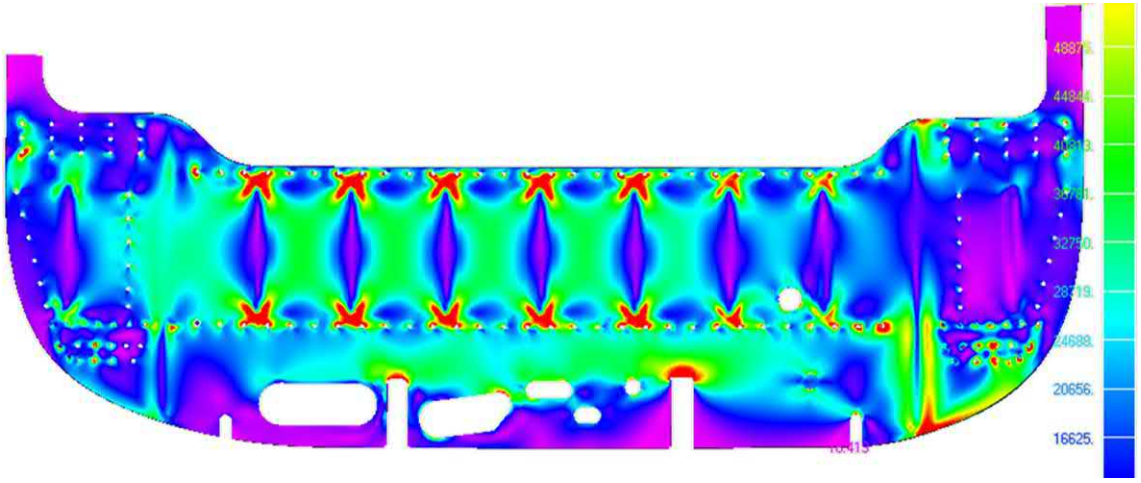


FIGURE 1-27 An image of a stress field in the spar carry-through of a small General Aviation aircraft due to asymmetric wing loads, generated by a popular Finite Element analysis software.

intended to stiffen the shear-web, but these cause high stress concentrations on their own.

(4) Images Using Computational Fluid Dynamics Software

Computational Fluid Dynamics (CFD) is a vibrant field within the science of Fluid Mechanics. Spurred by a need to predict and investigate aerodynamic flow around 3-dimensional bodies, this computational technology has become the stalwart of the modern aerodynamics group. Similar advice as above should be given to the entry-level aircraft designer. The images generated by the modern CFD packages are often mindboggling in their sophistication (Figure 1-28). It is therefore easy to be lulled into trusting them blindly—but they may not necessarily show what happens in real flow. This is not to say they never resemble reality, only that they do not always.

(5) Cutaway Drawings

Few visual representations are as capable of illustrating the complexity of an airplane as the cutaway drawing. Such images are normally extremely detailed and require a great depth of knowledge of the internal structure of an airplane to prepare correctly. A case in point is Figure 1-29, which shows a cutaway of a business jet designed by a student design team in the author's aircraft design class. Slated to be certified to 14 CFR Part 25 (Commercial Aviation) rather than 14 CFR Part 23

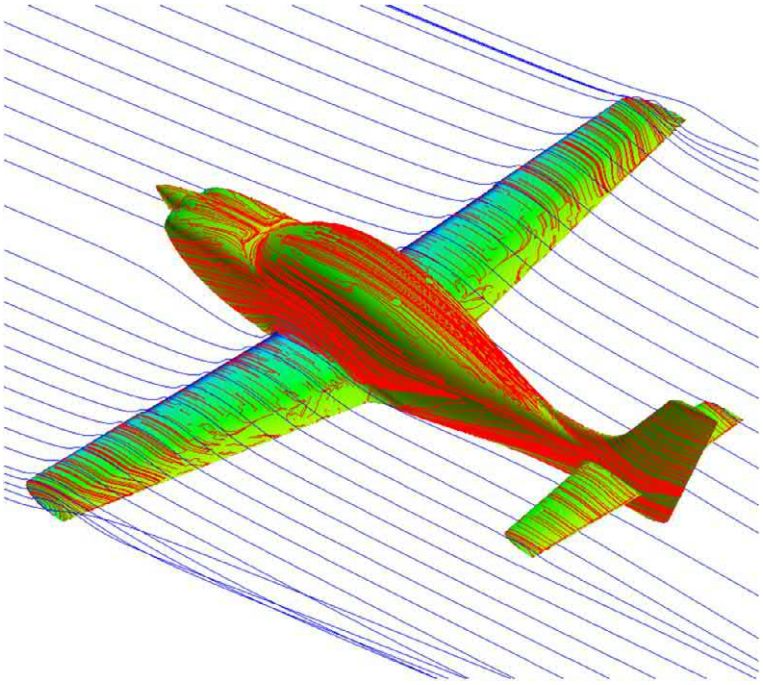


FIGURE 1-28 Streamlines and "oil flow" plots speak volumes about the nature of airflow around this SR22, showing the strength of Navier-Stokes CFD software. *Copyright 2021 Cirrus Aircraft or its Affiliates. All Rights Reserved. Image reproduced with the permission of Cirrus.*

(General Aviation) the figure depicts details about the structure, systems, aerodynamic features, and accommodation that is impossible to express in words.

(6) Engineering Reports

The work of the engineer is primarily of the "mental" kind; it involves the process of thinking. This poses an interesting challenge for anyone hiring an engineer—how can this intangible product be captured so it does not have to be recreated continually? The answer is the engineering report and engineering drawing.

An engineering report is a document that describes the details of a specific idea. Engineering reports encompass a large scope of activities. It can be a mathematical derivation of some formula, listing of test setup, analysis of test results, a justification for a way to fabricate a given product, evaluation of manufacturing cost, or geometric optimization, just to name a few. Regardless of its purpose, the report must always be written with completeness and detail on the forefront. Such technical reports are how a company retains the thinking of the engineer, so it does not have to be "re-thought" next time around—it turns the intangible into something physical.

The organization and format of reports varies greatly. It is not practical to present any given method here on how to write a report. However, what all reports share is that they should be objective, concise, and detailed. A common mistake made by rookie engineers is to ignore documenting what "appears trivial." The author is certainly guilty of making such mistakes. While working on a specific assignment, one effectively becomes an expert on that topic. Weeks of grueling work on such a project blurs the judgment for what needs to be included in the engineering report. The expertise, surprisingly, skews one's perspective; complex concepts become so trivial in the mind of the engineer that their definitions and other related details get omitted from the documentation. Then, several months or even a few years later, one has become an expert on a different topic. The previous work is a distant memory, securely archived in the digital vaults of the organization. At that moment, something happens that warrants a review of that work. This is when one realizes how many important concepts were omitted and these, now, call for extra effort and time for reacquaintance. Additionally, detail and careful documentation is priceless when you have to defend your work in a legal deposition. It is what US companies use every day to defend themselves against accusations of negligence, saving billions of dollars.

(7) Engineering Drawings

The modern engineering drawing has become a very sophisticated method of relaying information about the geometry of parts and assemblies. The details of what is called an "industry standard drawing" will not be discussed here, other than mentioning that such drawings must explain tolerance stack-ups and feature a bill of materials and parts to be dimensioned. Today, engineering drawings are exclusively created using computers by a specialized and important member of the engineering team—the drafter. A competent drafter knows the

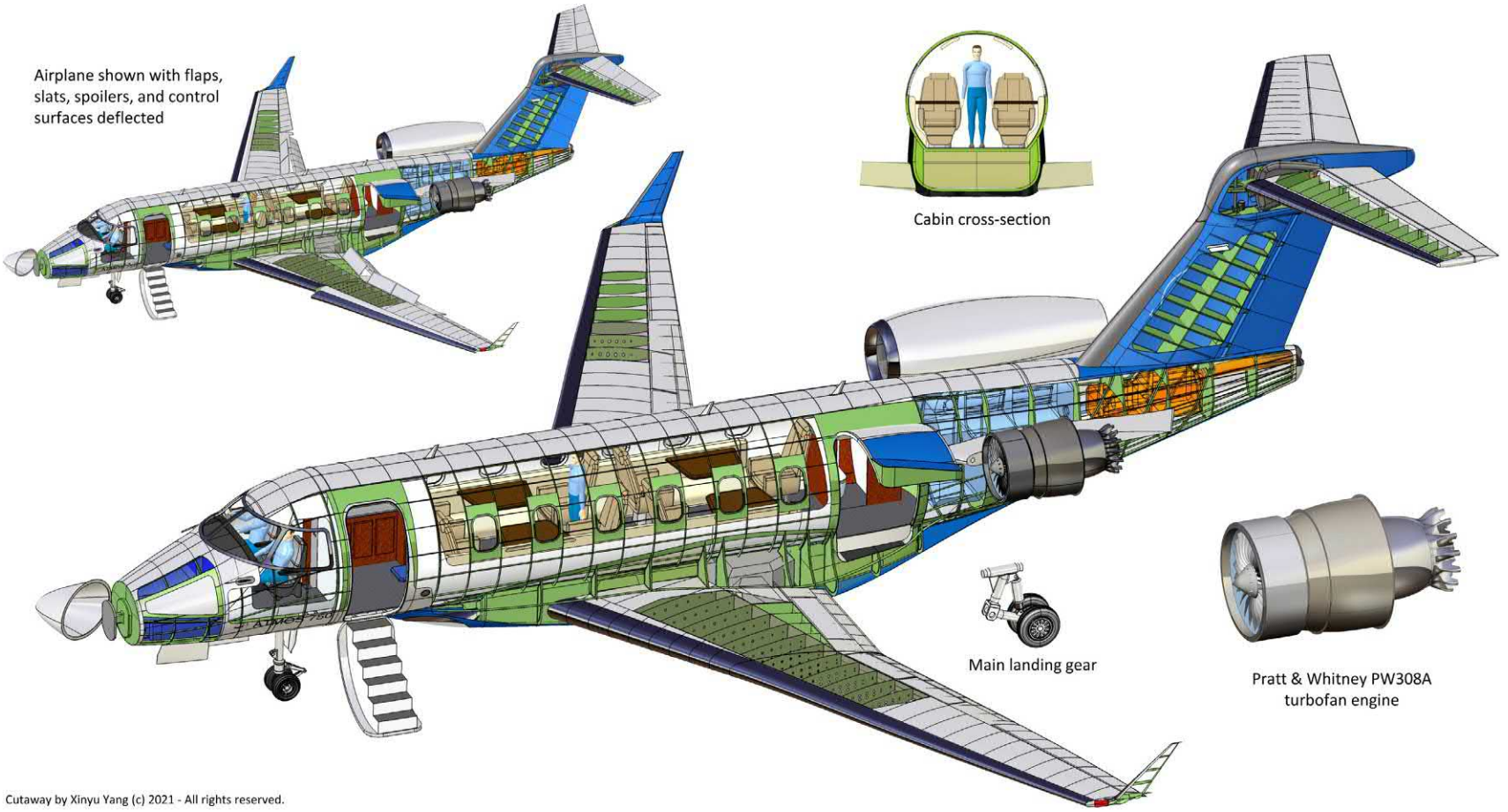


FIGURE 1-29 A cutaway of the Atmos 750, a business jet designed by the author's aircraft design students. It reveals details about the structure, systems, aerodynamic features, and accommodation, to name a few. *Cutaway by Xinyu Yang.*

ins-and-outs of the drafting standards and ensures these do not become a burden to the engineer.

The engineering drawings are typically of two kinds: a *part drawing* and an *assembly drawing*. The part drawing shows the dimensions of individual parts (a bracket, an extrusion, a tube, a bent aluminum sheet, etc.), while the assembly drawing shows how these are to be attached in relation to each other. A kit plane may require 100 to 200 drawings, a GA aircraft may require 10,000, and a fighter or a commercial jetliner 50,000 to over 100,000 drawings—according to Sutter [2], the original Boeing 747 required 75,000 drawings. For this reason, a logical numbering system that allows parts and assemblies to be quickly located is strongly recommended.

References

[1] Anonymous, FAA, December 12, 2003. http://faa.custhelp.com/app/answers/detail/a_id/154/kw/%22general%20aviation%22/session/L3RpbWUvMTMzNTgwOTk4MS9zaWQvSkxqTW9ZV2s%3D. (Accessed 1 June 2018).

[2] J. Sutter, *747 – Creating the World's First Jumbo Jet and Other Adventures from a Life in Aviation*, Smithsonian Books, New York, 2006.

[3] E. Torenbeek, *Synthesis of Subsonic Aircraft Design*, third ed., Delft University Press, 1986.

[4] D. Raymer, *Aircraft Design: A Conceptual Approach*, fifth ed., AIAA Education Series, 2012.

[5] L. Nicolai, G. Carichner, *Fundamentals of Aircraft and Airship Design, Vol. 1*, AIAA Education Series, 2010.

[6] Anonymous, *Standard Specification for Design and Performance of a Light Sport Airplane*, ASTM F2245-18, ASTM, 2018.

[7] R. Sherman, M.X. Hardiman, Federation of American Scientists, 2 November 2016. https://fas.org/man/dod-101/sys/ac/f-35.htm. (Accessed 1 June 2018).

[8] E.C. Aldridge, *Briefing on the Joint Strike Fighter Contract Announcement*, US Department of Defence, 26 October 2001. http://archive.defense.gov/Transcripts/Transcript.aspx?TranscriptID=2186. (Accessed 1 June 2018).

[9] D. McBride, *The 7 Wastes in Manufacturing*, EMS Consulting Group, 29 August 2003. http://www.emsstrategies.com/dm090203article2.html. (Accessed 1 June 2018).

[10] Anonymous, *The FAA and Industry Guide to Product Certification*, third ed., Prepared by Aerospace Industries Association (AIA), Aircraft Electronics Association (AEA), General Aviation Manufacturers Association (GAMA), and the FAA, May 2017.

[11] Anonymous, Certification Specifications (CSs), EASA, http://www.easa.europa.eu/agency-measures/certification-specifications.php [Accessed 06/14/2018].

[12] Anonymous, *FAA ORDER 8130.2J: Airworthiness Certification of Aircraft*, FAA, 2017.

[13] Anonymous, Federal Register, FAA, 14 March 2016. http://federalregister.gov/a/2016-05493. (Accessed 1 June 2018).

[14] Anonymous, *Notice of Proposed Amendment 2016-05*, EASA, 2016.

[15] Anonymous, Pilatus Aircraft, 12 July 2017. https://www.pilatus-aircraft.com/en/customer-support/publications#pc-12/flightmanuals. (Accessed 9 June 2018).

[16] Anonymous, *Weight-Shift Control Aircraft Flying Handbook*, FAA-H-8083-5, FAA, 2008.

[17] Anonymous, FAA Accepted Means of Compliance for Part 23 Airplanes (Amendment 23-64), 2018. https://www.faa.gov/aircraft/air_cert/design_approvals/small_airplanes/small_airplanes_regs/media/part_23_moc.pdf. (Accessed 5 October 2018).

[18] Anonymous, *Zodiac CH 601 XL Airplane*, Special Review Team Report, FAA, January 2010.

[19] Anonymous, FAA Accepted ASTM Consensus Standards - LSA, 3 October 2017. http://www.faa.gov/aircraft/gen_av/light_sport/media/StandardsChart.pdf. (Accessed 14 June 2018).

[20] Anonymous, n.d. Advisory Circulars. https://www.faa.gov/regulations_policies/advisory_circulars/ [Accessed 10/25/2018].

[21] Webpage for Airworthiness Directives. http://rgl.faa.gov/Regulatory_and_Guidance_Library/rgAD.nsf/Frameset?OpenPage. (Accessed 24 August 2019).

[22] Anonymous n.d., Type Certificate Data Sheets (Make Model), FAA, [Online]. Available: http://www.airweb.faa.gov/Regulatory_and_Guidance_Library/rgMakeModel.nsf/MainFrame?OpenFrameSet [Accessed 06/14/2018].

[23] J.D. Anderson, *The Grand Designers: The Evolution of the Airplane in the 20th Century*, Cambridge University Press, 2018, https://doi.org/10.1017/9780511977565.

[24] J.M. Nicholas, H. Steyn, *Project Management for Engineering, Business and Technology*, fifth ed., Routledge, 2017.

[25] D.G. Malcolm, J.H. Roseboom, C.E. Clark, W. Fazar, *Application of a Technique for Research and Development Program Evaluation*, Oper. Res. 7 (5) (1959) 646–669.

CHAPTER

2

Aircraft Cost Analysis

OUTLINE

2.1 **Introduction** 33
- *2.1.1 The Content of This Chapter* 34
- *2.1.2 A Review of the State of the General Aviation Industry* 34
- *2.1.3 The Basics of Development Cost Analysis* 35
- *2.1.4 Important Concepts in Air Transport Economics* 36

2.2 **The Estimation of Project Development Costs** 38
- *2.2.1 Development Cost of a GA Aircraft* 38
- *2.2.2 Development Cost of a Business Aircraft* 47
- *2.2.3 A Word About the Accuracy of the Eastlake Model* 48

2.3 **Estimating Aircraft Operational Costs** 50
- *2.3.1 Direct Operational Cost of a GA Aircraft* 50
- *2.3.2 Direct Operational Cost of a Business Aircraft* 52
- *2.3.3 A Word About Aircraft Operational Cost* 54

Exercises 55

References 55

2.1 INTRODUCTION

An estimation of the cost associated with developing a new aircraft is an essential part of the design process. We may have conceived of the world's most interesting airplane, but is it worth the cost and effort to manufacture? If we are convinced it is, how many airplanes do we plan to manufacture? How much will each cost to acquire and operate? How many must be delivered before we break-even financially? How many engineers and technicians will be needed? All of these are important questions, and this chapter presents tools that provide answers.

The estimation of acquisition costs is involved, but it provides a comprehensive insight into what affects the selling price of new aircraft. In this book, this cost is modeled using special *cost estimating relationships* (CER) originally derived by the RAND Corporation to estimate the development cost of new military aircraft. The CERs constitute a method commonly referred to as DAPCA-IV[1] (*development and procurement costs of aircraft*). It is described in a paper by Hess and Romanoff [1], available on the company's website [2]. The CERs are a set of statistical equations based on most US military aircraft in production and service at the time of its inception. They allow the cost of developing aircraft to be estimated using only basic information like empty weight, maximum airspeed, and expected production volume. Costs associated with research, development, testing, and evaluation (RDT&E), and even workforce size can be estimated as well.

The DAPCA-IV is biased toward US military aircraft, so it grossly overestimates manufacturing hours for GA aircraft. Professor Emeritus Charles Eastlake of Embry-Riddle Aeronautical University modified the original formulation to better reflect the development and operational cost of GA aircraft [3]. In this text, this modification is referred to as the *Eastlake Model*. Two cost models are provided: one for propeller aircraft and the other for executive aircraft.

Astute students often question the precision of CERs and ask: *How is it possible to estimate so much with so little*? This can be answered using an analogy. Suppose you plan to open a grocery store in your neighborhood. To secure funding by your bank, you are required to estimate the total cost of the adventure. This includes employee salaries, overhead, inventory, utilities, and so forth.

[1] The DAPCA-IV is preceded by the now obsolete DAPCA-III (R-1854-PR from 1976).

https://doi.org/10.1016/B978-0-12-818465-3.00003-3

Copyright © 2022 Elsevier Inc. All rights reserved.

There are at least two ways to do this. First, you can scout grocery stores in the area and try and estimate the number of workers, value of equipment, and inventory. While one might expect the approach to yield an accurate estimate, it would require an exorbitant amount of effort. The second method assumes you can sway willing store owners to disclose how much it cost them to launch their grocery stores. A further disclosure of monthly cost of utilities, salaries, inventory, and, of course, store floor area, would offer a treasure trove of information: It would permit the creation of statistical relations that depend on floor area. Knowing the expected floor area of the brand-new store, such relations could be used to predict the associated costs. The CERs work in this fashion.

2.1.1 The Content of This Chapter

- Section 2.1 presents a review of the state of general aviation and provides the basics of cost analysis for aircraft design and air transport economics.
- Section 2.2 presents methods to estimate the acquisition cost of a new GA aircraft. The method, which is based on the DAPCA-IV aircraft procurement cost analysis method, has been especially tailored for GA aircraft. In the process, detailed model of development and certification costs are determined. Two methods are provided; one aimed at propeller powered aircraft, the other at business jets.
- Section 2.3 presents methods to help estimate the operational cost for GA aircraft. Such methods are essential when trying to demonstrate whether the new aircraft will be more expensive to operate than competitor aircraft. Furthermore, a simple depreciation model is provided.

2.1.2 A Review of the State of the General Aviation Industry

First, a word of caution for overenthusiastic cost estimators: all cost analysis methods have limitations. They only yield "ballpark" values. In this context, it is sobering to consult manufacturer's data compiled by the General Aviation Manufacturers Association (GAMA) [4, 5], available from the organization's website [6]. It lists deliveries of all GA aircraft over a range of decades, giving an important understanding of the state of the industry. Some of these data are depicted in Figure 2-1, where it is broken down by classes of aircraft. It is important for the newcomer to the industry to realize it is hard to grab market share from recognized players, who already have a head start in the establishment of worldwide networks of support structure that provide spares and maintenance service.

References [4, 5] shed a needed light on the nature of the industry since 1946. Figure 2-2 Shows that, overall, there has been an enormous drop in aircraft deliveries, albeit with spurts of growth. The first drop takes place

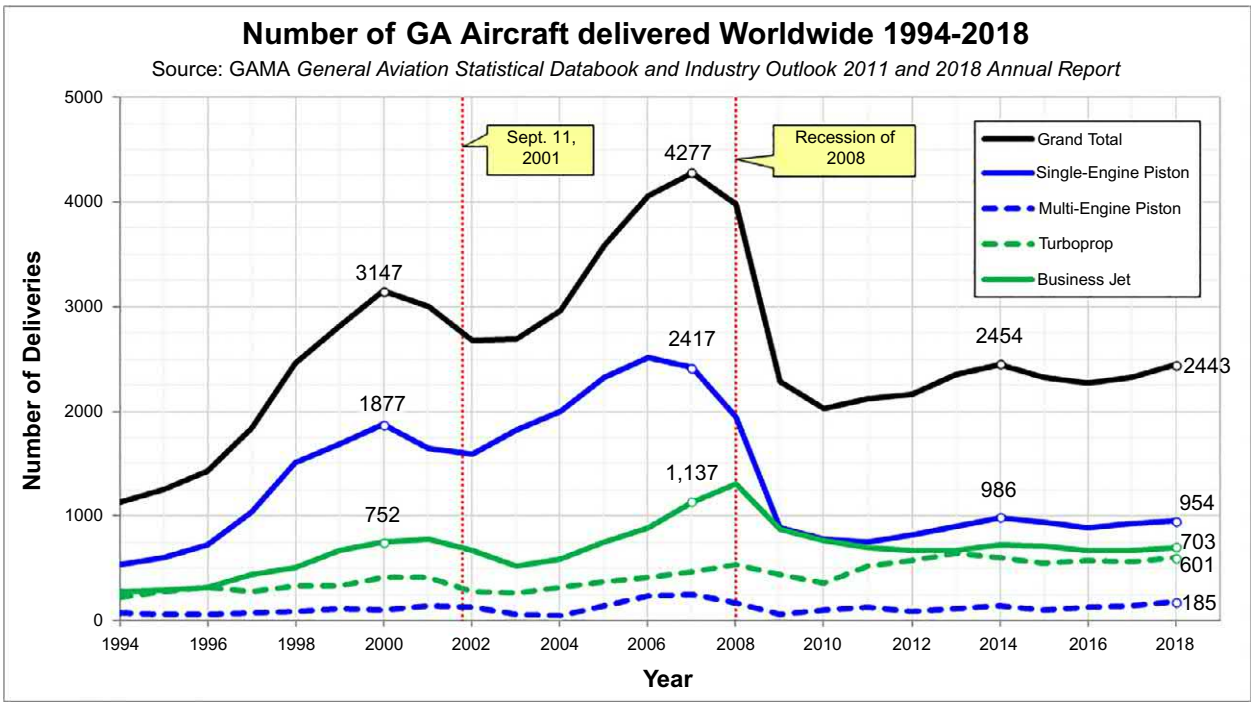


FIGURE 2-1 Sales prospects for GA aircraft from 1994 to 2018. *Based on references Anonymous, General Aviation Statistical Databook and Industry Outlook 2016, General Aviation Manufacturers Association, 2017; Anonymous, 2018 Annual Report, General Aviation Manufacturers Association, 2019.*

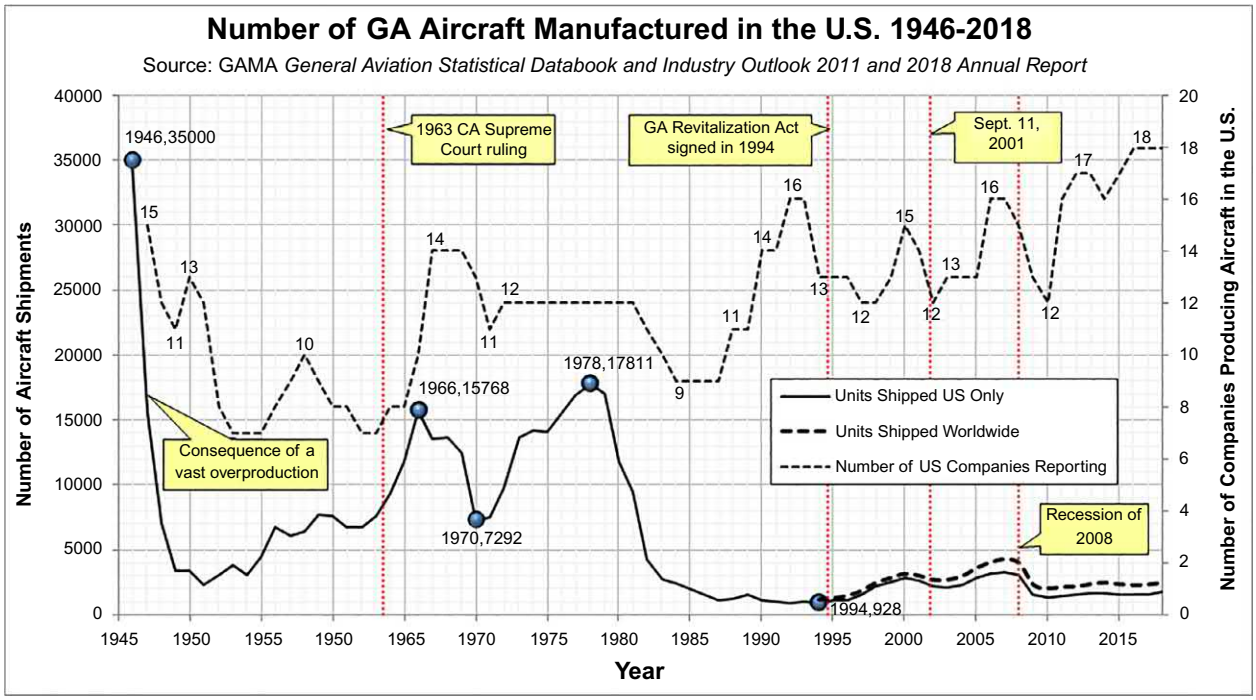


FIGURE 2-2 Number of aircraft produced in the United States has been dropping since 1946, with intermittent periods of growth. *Based on Anonymous, General Aviation Statistical Databook and Industry Outlook 2016, General Aviation Manufacturers Association, 2017; Anonymous, 2018 Annual Report, General Aviation Manufacturers Association, 2019.*

following the end of WWII. Over a 5-year period from 1946 to 1951, aircraft production plummeted from 35,000 to 2302. The thought at the time was that owning a private airplane would become the norm after the war, not unlike what happened to the ownership of the automobile after WWI. This view did not materialize, and a large surplus of aircraft was generated that took more than 5 years to unload. This was followed by a period of steady growth that peaked in 1966, when 15,768 aircraft were delivered

In 1963, the California Supreme Court made a decision that adopted the rule of "strict liability" with respect to negligence [7]. This meant that companies can be held liable for harm caused by their products even if there is no evidence of negligence. Other states in the United States soon followed suit, shifting the liability burden from the public onto industry. This caused a sharp rise in liability suits against manufacturers. The response of the aviation industry was to purchase protection in the form of a liability insurance and add it to the price tag of new aircraft. This, in turn, increased the price of new aircraft, causing demand to fall. This explains the reduction in aircraft deliveries between 1978, when production reached a high since 1946, with 17,811 deliveries; and the low of 928 units in 1994, which is the year that then-President Bill Clinton signed into law the General Aviation Revitalization Act (sometimes called the *tort reform*), whose purpose was to limit the extent of liabilities. This appears to have spurred a modest growth in deliveries, with a subsequent drop when the economic recession of 2008 began. Both graphs present data up to the year 2018. This drop has not yet recovered to prerecession levels at the time of this writing.

The point of this discussion is to emphasize that even though cost estimation models, like the DAPCA-IV, make reasonable predictions, the reader must be mindful that it is the economy that is unpredictable. What may seem like a viable business model today may not be so tomorrow—and vice versa.

2.1.3 The Basics of Development Cost Analysis

In its most basic form, development costs are estimated to help the manufacturer understand the financing required to develop a new aircraft, as well as revenue. The analysis also provides answers to questions by potential investors regarding return of investment. The effort, in part, is accomplished by determining two functions: one describes the total cost associated with producing N airplanes. The other describes the revenue associated with selling those airplanes. These will now be discussed in more detail.

(1) Fixed and Variable Cost

The total cost of producing N aircraft, denoted by, C, is a linear equation of the form

$$C(N) = C_{fix} + C_{var} \times N \tag{2-1}$$

where N is the number of aircraft to be produced within some time period (often called *volume*), C_{fix} is the *fixed cost*, and C_{var} is the *unit variable cost*. C_{fix} refers to all costs that remain constant regardless of quantity produced (e.g., facilities and utilities), while C_{var} is additional cost associated with each unit produced (e.g., material and engines). Each is determined using a *cost-model*, like the ones presented in this chapter. Note that the formulation presented is a step function since N is an integer.

(2) Cost-per-Unit

Cost-per-unit, C_{unit}, is the total cost divided by the number of units produced:

$$C_{unit} = \frac{C_{fix}}{N} + C_{var} \tag{2-2}$$

It is helpful to study how the cost-per-unit changes with the number of units produced (e.g., see Figure 2-6).

(3) Price-per-Unit and Revenue Function

The price-per-unit (P_{unit}) is selected as a compromise between one that is low enough to encourage sales and high enough to render the manufacturing profitable. In contrast, the revenue function, R, is the total income earned by the sales of N units. In its simplest form, it is given by

$$R(N) = P_{unit} \times N \tag{2-3}$$

Equations (2-1) and (2-3) allow the aircraft's marketability to be evaluated by estimating how many must be sold before the production breaks even.

(4) Break-Even Analysis

Break-Even Analysis is used to determine how many units must be produced before revenue equals the cost incurred in producing them. Using the standard *cost-volume-profit-analysis* the following expression is used to determine this:

Number of units to break-even:

$$N_{BE} = \frac{C_{fix}}{P_{unit} - C_{var}} \tag{2-4}$$

Example 2-4 shows the application of this approach.

DERIVATION OF EQUATION (2-4)

The total cost of developing N units is given by: $C_{fix} + C_{var} \times N$

The total revenue from selling N units is: $P_{unit} \times N$

When the two are equal, we have broken even, i.e.,

$$C_{fix} + C_{var} \times N = P_{unit} \times N \tag{i}$$

If we designate the number of units to break-even by the variable NBE, we can rearrange Equation (i) to get:

$$N_{BE} = \frac{C_{fix}}{P_{unit} - C_{var}}$$

2.1.4 Important Concepts in Air Transport Economics

It should not be surprising that the field of *air transport economics* is beyond the scope of this book. However, it develops several important concepts that are of interest to the aircraft designer.

(1) Cash Flow

It refers to the net amount of money transferred into and out of a business over some period. Consider a bank account with an initial balance of $1000 and 3 months later the balance is $700. Thus, the cash flow over the 3 months amounts to –$300 (or –$100 per month). A simplified cash flow history for the development of a new aircraft, based on [8], is shown in Figure 2-3. It is of importance to understand the role cash flow plays in the development of a new aircraft. Compiling such a graph may help the design team realize the need for capital investment during the critical development-phase, when revenue is limited or non-existent.

(2) Depreciation

It refers to the reduction in the value of an asset with time. The asset is some property such as a computer, a car, or an aircraft. The simplest approach to estimating

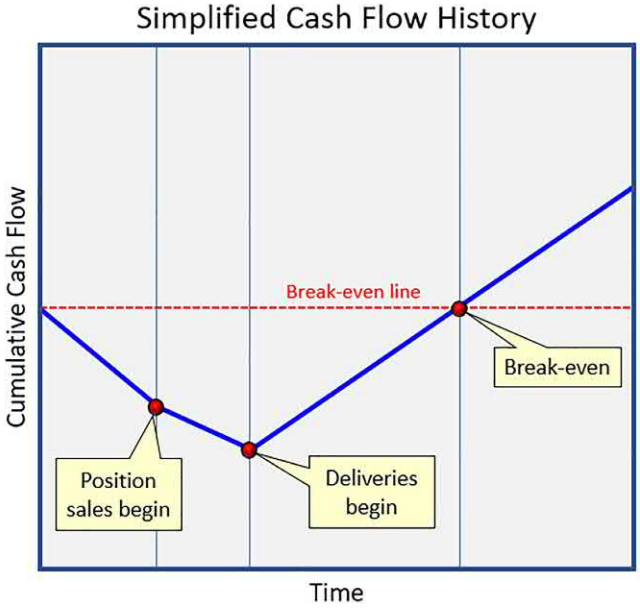


FIGURE 2-3 An idealized cash flow history for a development project. *Based on reference A. Jacobson, C. Tsubaki, Economics in New Commercial Aircraft Design, Aircraft Systems, Design and Technology Meeting, 1986. https://doi-org.ezproxy.libproxy.db.erau.edu/10.2514/6.1986-2667.*

depreciation is the *straight-line depreciation*. This model uses the initial value of an asset (C_{ini}) and a salvage value (C_{end}), which is the value of the asset at some later time. Generally, this time is considered in terms of periods (e.g., number of years) ($N_{periods}$). Then, the periodic depreciation is calculated from

$$P_{depreciation} = \frac{C_{ini} - C_{end}}{N_{periods}} \tag{2-5}$$

For instance, consider a car initially valued at \$30,000 (C_{ini}), but after 5 years ($N_{periods}$) it may be valued at \$15,000 (C_{end}). Thus, the annual depreciation is \$3000 per year. There are other methods to evaluate depreciation (e.g., double-declining balance and units-of-production), but the straight-line method suffices in this text.

Some students get confused by the nuances of depreciation. Depreciation works in the following way: (1) A person has X amount of money. (2) The person exchanges that money for a product valued X amount. (3) In its simplest terms, had the person kept the money, its value would have remained constant. In contrast, since the value of the product depreciates with time from its original value to some lesser value, depreciation equals loss of money.

(3) Business Capital and Equity

Business capital refers to the financial assets owned by a company. This includes funds in bank accounts, debt owed by customers, inventory, perceived value of equipment (e.g., computers, manufacturing tools, etc.), and facilities in which the business resides, to name a few. It can even include the perceived value of a brand and the workforce. In effect, it denotes anything the business can convert into money. In its simplest terms, *equity* refers to the value of all assets minus liabilities (e.g., debt owed by company). To use a simple analogy, suppose a business has only one asset; a car valued at \$10,000. Further assume it still owes \$7000 in a bank loan used to purchase it. In this case, the capital is \$10,000, liability is \$7000, and the equity is \$3000.

(4) Direct Operating Cost (DOC)

Refers to costs that arise directly from operating a product. In the operation of aircraft, these include the purchase price (airframe, spares, insurance, loan interest, and depreciation), maintenance, and flight operation (crew, fuel, fees). The minimization of DOC is frequently used in various optimization schemes in aircraft design—in particular commercial aircraft. DOC consists of a *fixed cost* (e.g., purchase price) and *variable cost* (e.g., maintenance and flight operation).

(5) Indirect Operating Cost (IOC)

Refers to costs associated with the operation of a product that are not directly attributed to the use of the product (e.g., all costs other than DOC). These include purchase of facilities, equipment, administration, training, customer services, and so forth.

(6) Return of Investment (ROI)

It refers to the ratio of the *net profit* to *cost-of-investment* associated with the acquisition of some product. If one pays \$100 for a box of cookies and then sells it for \$150, then the ROI = (\$150 – \$100)/\$100 = 0.5 (50%).

(7) Cost of Available Seat-Mile (CASM) and Revenue per Available Seat-Mile (RASM)

Used in commercial aviation, the term seat-mile is the product of total seats available (occupied or not) in the fleet of aircraft of an airline and the total number of miles flown. A 100-seat airliner that flies 300 nm generates 30,000 available seat-miles. The term *cost of available seat-mile* is determined by dividing the total operating expenses of the airline by the number of available seat-miles. The term *revenue per available seat-mile* is determined by dividing the total revenue by the number of available seat-miles.

(8) Life-Cycle Cost (LCC)

In the world of aviation, the term *life-cycle cost* (LCC) refers to the total cost associated with the operation of an airplane from its invention to its eventual desertion. The use of life-cycle costing dates to the 1960s when the Department of Defense began awarding bids for weapon systems using LCC rather than acquisition costs only [9]. It can be calculated from the perspective of the manufacturer or the operator of the product. For the latter, it refers to the cost of acquiring and operating an airplane from its delivery to its last day of service. For instance, the LCC for business jets is frequently based on a period of 10 years. This approach considers the combination of the cost-to-purchase, cost-to-operate, and the aircraft's salvage value at the end of its life span (or operational period). Thus, it helps make sound business decisions. For instance, an inexpensive product may come with a hefty maintenance cost, whereas a more expensive product may require less maintenance and, thus, cost less to operate over its service life. In this context, estimates of direct operating cost (DOC), cost per available seat-mile (CASM), in addition to the acquisition cost, are crucially important parameters.

In its simplest terms, LCC can be estimated as the sum of the purchase price, fixed operational cost, and variable operational cost.

$$LCC = P_{purchase} + \overbrace{N_{periods} C_{fixop}}^{\text{fixed operational cost}} + \overbrace{N_{\text{flgt hours}} C_{op}}^{\text{variable operational cost}} \tag{2-6}$$

where $P_{purchase}$ is the purchase price, $N_{\text{flgt hours}}$ is the number of expected flight hours over $N_{periods}$, C_{fixop} is the fixed operational cost per period (e.g., year), and C_{op} is the all-inclusive operational cost per flight hour (fuel, spares, maintenance, etc.).

2.2 THE ESTIMATION OF PROJECT DEVELOPMENT COSTS

Two versions of the Eastlake cost model for GA aircraft are presented in this section. One is aimed at typical propeller driven aircraft, the other at business (or executive) aircraft. Both rely on the expected weight of the bare airframe (without engines, tires, controls, and so on) and maximum level airspeed. Special correction factors are used to account for aircraft that require more complicated manufacturing technologies associated with tapered wings, complex flap systems, pressurization, and material selection (aluminum or composites). To keep up with the times, the author has revised several of the equations presented in the 1st edition.

2.2.1 Development Cost of a GA Aircraft

A general flow chart of the Eastlake model is presented in Figure 2-4. Moving from left to right, the first step involves calculating workhours (using CERs 1 through 3), followed by costs (CERs 4 through 11). The cost of vendor supplied components must be determined and the price adjusted for "buying in bulk." This is done by applying the *quantity discount factor* (*QDF*), to be discussed later. The costs obtained using the CERs are separated as fixed and variable costs (see Figure 2-4). The minimum selling price must include the cost of the manufacturer's liability insurance, added at the end of the process. Naturally, the actual selling price must be marked up to ensure profits.

The *Eastlake model* was developed in 1986. However, as presented here, the costs are calculated assuming the cost of living in the year 2012. For this reason, the model has been adjusted through the application of the *Consumer Price Index* (CPI), known informally as the cost-of-living index. The *CPI* for the years 1986 to 2012 is 2.0969. All appropriate constants (excluding exponentials) have been updated to reflect this by multiplying the original constants by this value. Thus, if the reader is applying this method, say in 2022, the CPI (denoted by the term CPI_{2012} in the following formulation) must be updated relative to the year 2012. The required value for the CPI_{2012} is easily obtained using the *CPI Inflation Calculator* provided at the website of the Bureau of Labor Statistics.[2] Also, note that the term workhour refers to the time it takes to complete a given task. For instance, if it takes 20 workhours to complete a given task, it could be completed by two people in 10 h.

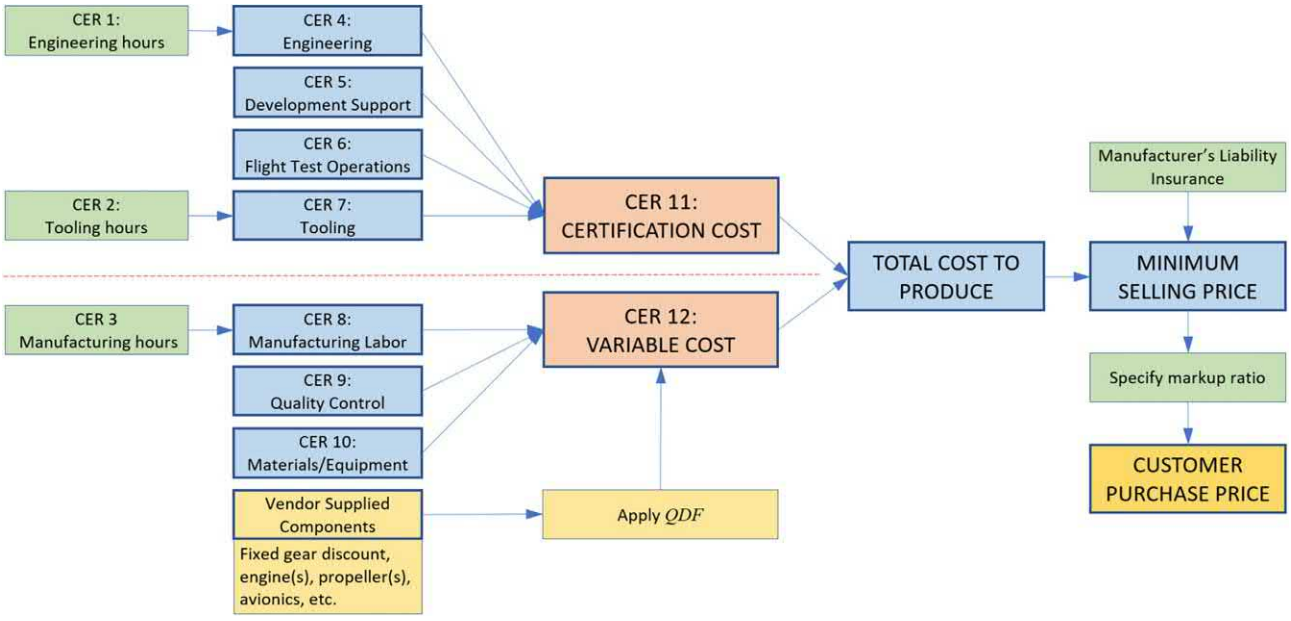


FIGURE 2-4 A flow chart describing the application of the Eastlake Cost Model.

[2] Website is www.bls.gov. In particular, see https://www.bls.gov/data/inflation_calculator.htm, which is a calculator that returns the index using simple user inputs. Also, explanations on how the CPI is calculated can be seen on https://www.bls.gov/cpi/cpifaq.htm#Question_11.

(1) Quantity Discount Factor

Just like the DAPCA-IV, the Eastlake model does not account for components such as propulsive devices and avionics. Such components are referred to as *vendor supplied components* (VSC). These are purchased separately and simply added to the results obtained using the CERs. The price-per-component of VSC is ordinarily negotiated with the vendor and can be expected to drop with the quantity purchased.[3] This is accounted for in the cost estimation by multiplying the price-per-component (assuming the purchase-price of a single unit) by a special factor called the *quantity discount factor* (QDF). The value of the *QDF* depends on the quantity of components purchased and requires the selection of an *experience effectiveness*, which is a measure of the vendor's potential price reduction. The resulting price reduction is of the same nature as that which occurs for the mass-produced airplane, exemplified in Figure 2-6.

Figure 2-5 shows the *QDF* for four values of experience effectiveness—80%, 85%, 90%, and 95%. The *QDF* is calculated using the expression:

Quantity Discount Factor:

$$QDF = (F_{EXP})^{1.4427 \cdot \ln N} \tag{2-7}$$

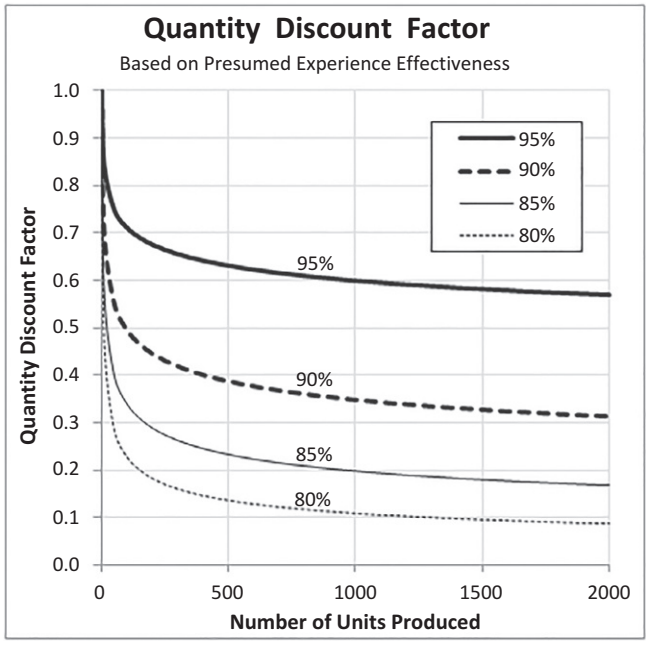


FIGURE 2-5 Quantity Discount Factor depends on presumed experience effectiveness.

where

F_{EXP} = Experience effectiveness (= 0.8 for 80%, 0.9 for 90%, and so on)
N = Number of units produced

The author recommends a value of F_{EXP} of 95%, as this results in costs that more closely match real world applications. Note that it is also acceptable to assign a unique *QDF* to each VSC. Note that getting a discount may also depend on the scope of airframes produced. A small-scale production may not receive *any* discounts when purchasing VSC.

(2) Incorporation of Product Liability Costs

An important addition to the minimum selling price is the manufacturer's product liability cost. It forces" *students to think about this reality of being in business in the US.*" [3] According to information from the insurance industry, the product liability cost for any particular manufacturer depends on the number of aircraft sold and their accident rate. It is next to impossible to predict how a product will fare once in production. Therefore, account for product liability per airplane by assuming it is 12%–17% of the *selling price*. The lower percentage applies to aircraft expected to have a low accident rate (e.g., passenger transport), while a high value applies to ones intended for riskier operation (e.g., trainers and aerobatic aircraft).

(3) CER 1—Engineering Workhours (H_{ENGR}):

The number of workhours of engineering time required to design the aircraft and perform the necessary RDT&E can be estimated from the following expression:

$$H_{ENGR} = 0.0396 \cdot W_{airframe}^{0.791} \cdot V_H^{1.526} \cdot N^{0.183} \cdot F_{CERT_1} \cdot F_{CF_1} \cdot F_{COMP_1} \cdot F_{PRESS_1} \tag{2-8}$$

where

$W_{airframe}$ = Weight of the structural skeleton
V_H = Maximum level airspeed in KTAS
N = Number of planned aircraft to be produced over a 5-year period
$F_{CERT\ 1}$ = 0.67 if certified as LSA, =1 if certified as a 14 CFR Part 23 aircraft
$F_{CF\ 1}$ = 1.03 for a complex flap system,[4] =1 if a simple flap system
$F_{COMP\ 1} = 1 + f_{comp}$ a factor to account for the use of composites in the airframe
f_{comp} = Fraction of airframe made from composites that range from 0 to 1 (=0 for aluminum aircraft, =1 for a complete composite aircraft)
$F_{PRESS\ 1}$ = 1.03 for a pressurized aircraft, =1 if unpressurized

[3] E.g., the price-per-unit for avionics is lower if purchased in bulk.

[4] What constitutes a complex flap system is subject to engineering judgment. In this context a fixed hinge flaps are considered simple, whereas ones with translating hinges are complex. An exception to this distinction would be the "paralift" flap system on single engine Cessna aircraft, which this author would consider simple (albeit clever).

Note that the structural skeleton weighs far less than the empty weight of the aircraft. This weight can be approximated by considering the empty weight less engines, avionics, seats, furnishing, control system, and other components. In the absence of such information, assume it is about 65% of empty weight.

(4) CER 2—Tooling Workhours (H_{TOOL}):

The number of workhours required to design and build tools, fixtures, jigs, molds, and so on.

$$H_{TOOL} = 1.0032 \cdot W_{airframe}^{0.764} \cdot V_H^{0.899} \cdot N^{0.178} \cdot Q_m^{0.066} \cdot F_{CF_2} \cdot F_{COMP_2} \cdot F_{PRESS_2} \cdot F_{TAPER_2} \quad (2\text{-}9)$$

where

Q_m = Estimated production rate in number of aircraft per month (= $N/60$ for 60 months/5 years)
$F_{CF\ 2} = 1.02$ for a complex flap system, =1 if a simple flap system
$F_{COMP\ 2} = 1 + f_{comp}$ a factor to account for the use of composites in the airframe
$F_{PRESS\ 2} = 1.01$ for a pressurized aircraft, =1 if unpressurized
$F_{TAPER\ 2} = 0.95$ for a constant chord wing, =1 for a tapered wing

(5) CER 3—Manufacturing Labor Workhours (H_{MFG}):

The number of workhours required to build the aircraft.

$$H_{MFG} = 9.6613 \cdot W_{airframe}^{0.74} \cdot V_H^{0.543} \cdot N^{0.524} \cdot F_{CERT_3} \cdot F_{CF_3} \cdot F_{COMP_3} \quad (2\text{-}10)$$

where

$F_{CERT\ 3} = 0.75$ if certified as LSA, =1 if certified as a 14 CFR Part 23 aircraft
$F_{CF\ 3} = 1.01$ for a complex flap system, =1 if a simple flap system
$F_{COMP\ 3} = 1 + 0.25 \cdot f_{comp}$ a factor to account for the use of composites in the airframe

EXAMPLE 2-1

(a) Estimate the workhours required to produce a single engine, piston powered composite aircraft certified if it is expected its airframe will weigh 1100 lb_f ($W_{airframe}$) and it is designed for a maximum level airspeed of 185 KTAS (V_H). It is expected that 1000 aircraft (N) will be produced in the first 5 years (Q_m = 1000 units/60 months ≈ 17 units per month since we do not sell airplanes as fractions). The non-pressurized aircraft will be certified per 14 CFR Part 23 and will feature a tapered wing with a simple flap system.
(b) If it is assumed the engineering staff works 40 h a week for 48 weeks a year, how many engineers are required to accomplish the development over a period of 5 years?
(c) What is the average time to manufacture a single unit?
(d) Determine and compare the corresponding values if the airplane is made from aluminum (i.e., only change the factor f_{comp}).

SOLUTION

Refer to description of equations for variables. Note that the following problems were solved using a spreadsheet, which retains a double-floating point accuracy. Thus, the reader attempting to repeat the calculations should expect minor differences.

(a) Number of workhours of engineering time:

$$H_{ENGR} = 0.0396 \cdot W_{airframe}^{0.791} \cdot V_H^{1.526} \cdot N^{0.183} \cdot F_{CERT_1} \cdot F_{CF_1} \cdot F_{COMP_1} \cdot F_{PRESS_1}$$
$$= 0.0396 \cdot (1100)^{0.791} \cdot (185)^{1.526} \cdot (1000)^{0.183} \cdot 1 \cdot 1 \cdot 2 \cdot 1$$
$$= 205\ 670 \text{ h}$$

Number of workhours to construct tooling:

$$H_{TOOL} = 1.0032 \cdot W_{airframe}^{0.764} \cdot V_H^{0.899} \cdot N^{0.178} \cdot Q_m^{0.066} \cdot F_{TAPER_2} \cdot F_{CF_2} \cdot F_{COMP_2} \cdot F_{PRESS_2}$$
$$= 1.0032 \cdot (1100)^{0.764} \cdot (185)^{0.899} \cdot (1000)^{0.178} \cdot (17)^{0.066} \cdot 1 \cdot 1 \cdot 2 \cdot 1 = 190\ 300 \text{ h}$$

Number of workhours to manufacture 1000 airplanes:

$$H_{MFG} = 9.6613 \cdot W_{airframe}^{0.74} \cdot V_H^{0.543} \cdot N^{0.524} \cdot F_{CERT_3} \cdot F_{CF_3} \cdot F_{COMP_3}$$
$$= 9.6613 \cdot (1100)^{0.74} \cdot (185)^{0.543} \cdot (1000)^{0.524} \cdot 1 \cdot 1 \cdot (1.25)$$
$$= 1\ 366\ 628 \text{ h}$$

(b) Number of engineers needed to develop the aircraft over a period of 5 years:

EXAMPLE 2-1 *(cont'd)*

$$N_{ENGR} = \frac{205\ 670 \text{ hrs}}{(5 \text{ years})(48 \text{ weeks})(40 \text{ hrs/week})} \approx 21 \text{ engineers}$$

(c) Average time to manufacture a single unit:

$$t_{AC} = \frac{1\ 366\ 628 \text{ hrs}}{1000 \text{ units}} = 1\ 367 \text{ h}$$

(d) Performing the same calculations for aluminum aircraft and comparing to the composite aircraft yielded the results shown in Table 2-1:

TABLE 2-1 Comparing workhours required for the development of an Aluminum and Composite Aircraft.

	Workhours	
	Composite AC	**Aluminum AC**
Engineering workhours	205670	102835
Tooling	190300	95150
Manufacturing labor	1366628	1093303
	Other	
Number of engineers	21	11
Number of tooling technicians	20	10
Number of mfg technicians	142	114
Time to manufacture each unit	1367	1093

The results from parts (b) and (c) in Example 2-1 need further explanation. The number of engineers indicates the average over the development period. Most projects have few engineers at first and then, as the project moves into the preliminary design phase, additional engineers are hired. There might be six engineers working on the project at first and 60 toward the end, with an annual average of 21 over the development period. The average number of hours to build each unit appears reasonable considering a fully optimized manufacturing process for a small airplane. However, it takes a while to polish the process to that level. The reader should be careful in trusting such numbers as they may mislead. It may take 5 to 20 times longer to manufacture the first few aircraft, so revenues are limited. Some businesses fail during this period due to limited financial capacity.

(6) Cost Analysis

Once the number of workhours has been determined, the next step is to estimate costs by multiplying these by the appropriate hourly rates. This is done below. In June 2012, a typical rate for engineering was $92 per hour, tooling labor was $61 per hour, and manufacturing labor was $53 per hour. Note that it is a common tendency among newcomers to reduce these values: Do not. They include cost of overhead, benefits, and so forth: the engineer will not receive the full $92. As an example, according to www.engineersalary.com, an engineer with a M.Sc. and 10 years of experience on the west coast of the United States should be making about $100,000 a year. This amounts to about $48 per hour. Thus, overhead cost associated with that engineer would be $44 per hour. A technician in a typical aircraft plant could make anywhere from $12 to $25 per hour.

(7) CER 4—Total Cost of Engineering (C_{ENGR}):

Total cost of engineering the aircraft:

$$C_{ENGR} = H_{ENGR} \cdot R_{ENGR} \cdot CPI_{2012} \tag{2-11}$$

where

R_{ENGR} = Rate of engineering labor in $ per hour (e.g., $92/h)
CPI_{2012} = Consumer Price Index relative to June 2012

Note that if the reader has up to date rates of engineering labor, then the value of $CPI_{2012} = 1$. In that case, we would simply write Equation (2-11) as $C_{ENGR} = H_{ENGR} \cdot R_{ENGR}$. On the other hand, if the reader chooses to use the $92/h reference-rate from June 2012, then the *CPI* must be accounted for, using 2012 as a reference year. For instance, the value of the constant CPI_{2012} for June 2012 relative to April 2019 amounts to 1.10 using the inflation calculator at www.bls.gov (see Footnote 2).

(8) CER 5—Total Cost of Development Support (C_{DEV}):

The cost of overhead, administration, logistics, human resources, facilities maintenance personnel and similar entities required to support the development effort, calculate and pay salaries, and other necessary tasks.

$$C_{DEV} = 0.06458 \cdot W_{airframe}^{0.873} \cdot V_H^{1.89} \cdot N_P^{0.346} \cdot CPI_{2012} \cdot F_{CERT_5} \cdot F_{CF_5} \cdot F_{COMP_5} \cdot F_{PRESS_5} \tag{2-12}$$

where

N_P = Number of prototypes
$F_{CERT\ 5}$ = 0.5 if certified as LSA, =1 if certified as a 14 CFR Part 23 aircraft
$F_{CF\ 5}$ = 1.01 for a complex flap system, =1 if a simple flap system
$F_{COMP\ 5} = 1 + 0.5 \cdot f_{comp}$ a factor to account for the use of composites in the airframe
$F_{PRESS\ 5}$ = 1.03 for a pressurized aircraft, =1 if unpressurized

(9) CER 6—Total Cost of Flight Test Operations (C_{FT}):

Total cost of completing the development and certification flight-test program[5]:

$$C_{FT} = 0.009646 \cdot W_{airframe}^{1.16} \cdot V_H^{1.3718} \cdot N_P^{1.281} \cdot CPI_{2012} \cdot F_{CERT_6} \tag{2-13}$$

where

$F_{CERT\ 6}$ = 10 if certified as LSA, =5 if a 14 CFR Part 23 aircraft

An alternative expression, based on the logistics, is suggested when more is known about the cost breakdown for the development and certification flight-test program[6]:

$$C_{FT} = \left(12N_P C_P + 12C_{flight} + N_{gc}S_{gc} + N_{pilot}S_{pilot} + N_{fte}S_{fte} + C_{misc}\right) \frac{N_{month}}{12} \tag{2-14}$$

where

C_P = An estimate of monthly operating cost for each prototype (parts, fuel, oil, etc.)
C_{flight} = An estimate of all other costs associated with flight testing on a monthly basis (hangar, telemetry, computers, utilities, flight test operations other than flying, etc.)
C_{misc} = Miscellaneous costs on a monthly basis (e.g., chase plane)
N_{fte} = Number of flight test engineers involved in the flight-testing program
N_{gc} = Number of ground crew members maintaining and preparing prototypes for flight testing missions
N_{pilot} = Number of flight test pilots
S_{fte} = Average annual salary of flight test engineers
S_{gc} = Average annual salary of ground crew members
S_{pilot} = Average annual salary of flight test pilots
N_{month} = Number of months the flight test program is expected to last (e.g., 24 months)

(10) CER 7—Total Cost of Tooling (C_{TOOL}):

This entails the cost of designing, fabricating, and maintaining jigs, fixtures, molds, and other tools required to build the airplane. The tooling requires industrial and manufacturing engineers for the design work and technicians to fabricate and maintain.

$$C_{TOOL} = H_{TOOL} \cdot R_{TOOL} \cdot CPI_{2012} \tag{2-15}$$

where

R_{TOOL} = Rate of tooling labor in $ per hour (e.g., $61/h)

(11) CER 8—Total Cost of Manufacturing (C_{MFG}):

This entails the cost of manufacturing labor required to produce the aircraft.

$$C_{MFG} = H_{MFG} \cdot R_{MFG} \cdot CPI_{2012} \tag{2-16}$$

where

R_{MFG} = Rate of manufacturing labor in $ per hour (e.g., $53/h)

(12) CER 9—Total Cost of Quality Control (C_{QC}):

This entails the cost of technicians and the equipment required to demonstrate that the product being manufactured is indeed the airplane shown in the drawing package.

$$C_{QC} = 0.13 \cdot C_{MFG} \cdot F_{CERT_9} \cdot F_{COMP_9} \tag{2-17}$$

where

$F_{CERT\ 9}$ = 0.5 if certified as LSA, =1 if certified as a 14 CFR Part 23 aircraft
$F_{COMP\ 9} = 1 + 0.5 \cdot f_{comp}$ a factor to account for use of composites in the airframe

(13) CER 10—Total Cost of Materials (C_{MAT}):

This is the cost of raw material (aluminum sheets, preimpregnated composites, landing gear, avionics, etc.) required to fabricate the airplane.

$$C_{MAT} = 24.896 \cdot W_{airframe}^{0.689} \cdot V_H^{0.624} \cdot N^{0.792} \cdot CPI_{2012} \cdot F_{CERT_{10}} \cdot F_{CF_{10}} \cdot F_{PRESS_{10}} \tag{2-18}$$

where

$F_{CERT\ 10}$ = 0.75 if certified as LSA, =1 if certified as a 14 CFR Part 23 aircraft
$F_{CF\ 10}$ = 1.02 for a complex flap system, =1 if a simple flap system
$F_{PRESS\ 10}$ = 1.01 for a pressurized aircraft, =1 if unpressurized

[5] The author has updated this expression to ensure it better matches real applications.

[6] The development and certification flight testing of a typical 4- to 6-seat high-performance propeller-powered GA aircraft might cost around 2 to 3 million dollars, give or take, while the cost for an LSA might be around $250,000.

(14) CER 11—Fixed Cost (or Total Cost to Certify) (C_{fix}):

The total cost to certify is the cost of engineering, development support, flight test, and tooling (assuming production tooling is used to produce at least some of the prototypes.

$$C_{fix} = C_{ENGR} + C_{DEV} + C_{FT} + C_{TOOL} \tag{2-19}$$

EXAMPLE 2-2

Estimate the total cost to certify (fixed cost) the airplane of Example 2-1, assuming engineering, tooling, and manufacturing rates are \$92, \$61, and \$53 per hour, respectively. The planned number of prototypes is 4. In April 2019, the $CPI_{2012} \approx 1.10$.

SOLUTION:

Total cost of engineering:

$$C_{ENGR} = H_{ENGR} \cdot R_{ENGR} \cdot CPI_{2012} = (205670) \cdot (92) \cdot (1.10) = \$20\ 813\ 804$$

Total cost of development support:

$$C_{DEV} = 0.06458 \cdot W_{airframe}^{0.873} \cdot V_H^{1.89} \cdot N_P^{0.346} \cdot CPI_{2012} \cdot F_{CERT_5} \cdot F_{CF_5} \cdot F_{COMP_5} \cdot F_{PRESS_5}$$
$$= 0.06458 \cdot (1100)^{0.873} \cdot (185)^{1.89} \cdot (4)^{0.346} \cdot (1.10) \cdot 1 \cdot 1 \cdot (1.5) \cdot 1 = \$1\ 499\ 633$$

Total cost of flight test operations:

$$C_{FT} = 0.009646 \cdot W_{airframe}^{1.16} \cdot V_H^{1.3718} \cdot N_P^{1.281} \cdot CPI_{2012} \cdot F_{CERT_6}$$
$$= 0.009646 \cdot (1100)^{1.16} \cdot (185)^{1.3718} \cdot (4)^{1.281} \cdot (1.10) \cdot 5 = \$1\ 361\ 666$$

Total cost of tooling:

$$C_{TOOL} = H_{TOOL} \cdot R_{TOOL} \cdot CPI_{2012} = (190\ 300) \cdot (61) \cdot (1.10) = \$12\ 769\ 130$$

Total cost of manufacturing;

$$C_{MFG} = H_{MFG} \cdot R_{MFG} \cdot CPI_{2012} = (1\ 366\ 628) \cdot (53) \cdot (1.10) = \$79\ 674\ 412$$

Total cost of quality control:

$$C_{QC} = 0.13 \cdot C_{MFG} \cdot F_{CERT_9} \cdot F_{COMP_9} = 0.13 \cdot (79\ 674\ 412) \cdot 1 \cdot (1.5) = \$15\ 536\ 510$$

Total cost of materials:

$$C_{MAT} = 24.896 \cdot W_{airframe}^{0.689} \cdot V_H^{0.624} \cdot N^{0.792} \cdot CPI_{2012} \cdot F_{CERT_{10}} \cdot F_{CF_{10}} \cdot F_{PRESS_{10}}$$
$$= 24.896 \cdot (1100)^{0.689} \cdot (185)^{0.624} \cdot (1000)^{0.792} \cdot (1.10) \cdot 1 \cdot 1 \cdot 1 = \$21\ 074\ 485$$

The fixed cost (which is also the total cost to certify) is:

$$C_{fix} = C_{ENGR} + C_{DEV} + C_{FT} + C_{TOOL} = \$20\ 813\ 804 + \$1\ 499\ 633 + \$1\ 361\ 666 + \$12\ 769\ 130 = \$36\ 444\ 233$$

(15) CER 12—Variable Cost (C_{var}):

The variable cost comprises the cost of manufacturing labor, quality control, material and vendor supplied components (VSC), divided by the number of airplanes we expect to produce.

$$C_{\text{var}} = \frac{C_{MFG} + C_{QC} + C_{MAT}}{N} + C_{VSC} + C_{INS} \tag{2-20}$$

where

C_{VSC} = Cost of all vendor supplied components that includes the appropriate *QDF*. Calculated on a unit basis as shown below.

C_{INS} = Manufacturer's liability insurance per unit. Estimate as 12% to 17% of the selling price in lieu of better estimates.

Cost of VSC 1—Fixed versus Retractable Landing Gear

The cost of retractable landing gear is already assumed in the DAPCA-IV formulation, so an adjustment is made only if the airplane has fixed landing gear. If so, *subtract* \$17,500 per airplane[7] (*QDF* not assumed). Note that this value drops if a *QDF* is assumed, because, if the landing gear is bought in bulk, each unit will cost less, resulting in reduced discount per unit.

Cost of VSC 2—Avionics

Information about the cost of avionics changes rapidly, making it necessary to visit vendor websites to obtain a current price of avionics packages. In 2019, manufacturers of avionics include companies such as Aspen Avionics, Avidyne, Bendix/King, and Garmin. In 2019, such sources include companies such as sarasotaavionics.com, www.pacificcoastavionics.com, and www.gulfcoastavionics.com. In the absence of more accurate information, likely prices in 2019 are tabulated in Table 2-2. They are based on prices scouted from the above sources.

Cost of VSC 3—Cost of Engines (C_{PP})

The cost of the engine depends on the number of engines (N_{ENG})[8] and the type (piston, turboprop, turbojet, or turbofan). For piston and turboprop engines the cost depends on the rated Brake-Horsepower (P_{BHP}) and Shaft-Horsepower (P_{SHP}), respectively. For turbojets

[7] Note that in the first edition of this book (published in 2013), this value was \$7500. This value was modified and rounded using the CPI between June 1986 and April 2019.

[8] Note that N_{ENG} is the number of engines, while N_{ENGR} is the number of engineers.

TABLE 2-2 Prices for avionics packages for several classes of aircraft (around 2019).

Class of aircraft	Price range
Ultralight	≈$2000
Light-sport aircraft	$4000 to $8000
Single engine piston	$6000 to $35,000
Single engine turboprop and twin-piston	$35,000 to $60,000
Multiengine turboprop	$40,000 to $100,000
Business jets—smaller avionics system	$200,000 to $300,000
Business jets—high end avionics system	$1,200,000 to $2,500,000

and turbofans, it is based on the rated thrust (T_o). Note that the application of QDF to engine purchases should not be taken as a given—there is no guarantee that engine manufacturers will offer bulk discounts.

Piston Engines[9]:

$$C_{PP} = N_{ENG} \cdot CPI_{2019} \cdot \left(1007N_{cyl}^3 - 22620N_{cyl}^2 + 155800N_{cyl} - 0.01447P_{BHP}^3 + 8.654P_{BHP}^2 - 1394P_{BHP} - 203900\right) \quad (2\text{-}21)$$

Turboprop Engines:

$$C_{PP} = 377.4 \cdot N_{ENG} \cdot P_{SHP} \cdot CPI_{2012} \quad (2\text{-}22)$$

Turbojet Engines:

$$C_{PP} = 868.1 \cdot N_{ENG} \cdot T_o^{0.8356} \cdot CPI_{2012} \quad (2\text{-}23)$$

Turbofan Engines:

$$C_{PP} = 1035.9 \cdot N_{ENG} \cdot T_o^{0.8356} \cdot CPI_{2012} \quad (2\text{-}24)$$

Cost of VSC 4—Cost of Propellers

Since piston and turboprop engines also require propellers, this cost must be accounted for as well. The two most common types are the fixed pitch and constant speed propellers. Constant speed propellers are more expensive and heavier. Note that the following expressions are based on price survey made in April 2019 and pertain to a single propeller only. The designer using these values must correct for *CPI* using 2019 as a reference year AND account for the number of power plant. Values using inequalities show price ranges, as relations to engine power, diameter, and RPM had negligible correlation.

Composite Propellers for LSA and Ultralight Aircraft (C_{FXP}):

Fixed or adjustable pitch—2 bladed[10]:

$$\$1\,500 < C_{FXP} < \$2\,000 \quad (2\text{-}25)$$

Fixed or adjustable pitch—3 bladed[10]:

$$\$1\,800 < C_{FXP} < \$2\,400 \quad (2\text{-}26)$$

Fixed Pitch Aluminum Propellers for 14 CFR Part 23 Class Aircraft (single engine only) (C_{FXP}):

Sample aircraft include Piper Pa-28, Beech A23, Cessna 172, and Grumman AA-1. Note that D_p is the propeller diameter in inches.

Fixed pitch—2 bladed[10]:

$$C_{FXP} = \left(17489 - 371D_p + 2.762D_p^2\right) \cdot CPI_{2019} \quad (2\text{-}27)$$

Aluminum Constant Speed Propellers for 14 CFR Part 23 Class Aircraft (single and multiengine) (C_{CSP}):

Sample aircraft (2-bladed) include Beech F35 and Cessna 182T, (3-bladed) Beech B55 and Cirrus SR22, and (4-bladed) Beech B90, DHC-6, and Jetstream 31.

Constant Speed Propellers—2 bladed[10]:

$$\$9\,500 < C_{CSP} < \$12\,500 \quad (2\text{-}28)$$

Constant Speed Propellers—3 bladed[10]:

$$\$11\,500 < C_{CSP} < \$19\,000 \quad (2\text{-}29)$$

Constant Speed Propellers—4 bladed[10]:

$$C_{CSP} = 1593D_p - 104323 \ (\text{valid for } 90'' < D_p < 106'') \quad (2\text{-}30)$$

EXAMPLE 2-3

(a) Create a cost summary for the airplane in Examples 2-1 and 2-2), assuming a production run of 1000 units over a 5-year period. The airplane is powered by a single 6-cylinder, 310 BHP piston engine driving a 3-bladed constant speed propeller priced at $14,000. Assume a $35,000 avionics suite. $CPI_{2012} = 1.10$ and

[9] The author has updated this equation since the first edition of this book. Add approximately $50,000 for turbocharged versions. Also note the CPI uses 2019 (and not 2012) as a reference year. Prices for piston engine may also be gleaned from http://www.airpowerinc.com/.

[10] The author has updated the cost of propeller equations since first edition of this book. Note that these costs should be updated using CPI based on 2019 as a reference year (i.e., CPI2019).

EXAMPLE 2-3 *(cont'd)*

$CPI_{2019} = 1.00$. Estimate fixed, variable, and total cost per unit, with and without QDF, as well as number of aircraft to break-even, if the unit retail price is \$350,000. Assume a manufacturer's liability insurance of 15% of the retail value (which amounts to \$52,500 per airplane).

(b) Plot how the number of units produced affects the minimum selling price.

(c) Perform the preceding analysis for an aluminum aircraft and compare to the composite airplane, by only changing the factor f_{comp} (=0 for aluminum, =1 for fully composite). Assume no QDF applies.

SOLUTION:

(a) First, we must estimate the engine cost:

$$C_{PP} = N_{ENG} \cdot CPI_{2019} \cdot \left(-203900 + 155800N_{cyl} - 22620N_{cyl}^2 + 1007N_{cyl}^3 + -1394P_{BHP} + 8.654P_{BHP}^2 - 0.01447P_{BHP}^3\right) = \$102\ 526$$

The entire cost estimation is tabulated in Table 2-3, indicating a minimum selling price of \$285,617. A reader repeating these calculations should expect minor numerical discrepancies due to round-off errors. An interpretation of the resulting costs is left to the reader. This evaluation is aimed at airplanes like the Cirrus SR22 and Cessna 400 TTx. Further insight may be gleaned from Section 2.2.3.

(b) The graph shown in Figure 2-6 was created by evaluating the minimum selling price considering a number of production scenarios with differing number of units produced. It shows how the price drops rapidly with the number of units produced and then becomes more asymptotic with higher production rates.

(c) A comparison of the cost of development and manufacturing between a composite and aluminum aircraft is shown in Table 2-4. It reveals that the DAPCA-IV type statistical analyses predict composite aircraft to be of the order of 25%–30% more expensive to manufacture than a comparable aluminum aircraft.

TABLE 2-3 Project cost analysis.

FIXED COST		Workhours		Total Cost	Cost per Unit
Engineering (\$92/hr)	H_{ENGR} =	205670	C_{ENGR} =	\$20,813,804	\$20,814
Development support			C_{DEV} =	\$1,499,633	\$1,500
Flight test operations			C_{FT} =	\$1,361,666	\$1,362
Tooling (\$61/hr)	H_{TOOL} =	190300	C_{TOOL} =	\$12,769,130	\$12,769
Fixed Cost			C_{fix} =	**\$36,444,233**	**\$36,444**

VARIABLE COST		Workhours		Total Cost	Cost per Unit
Manufacturing labor (\$53/hr)	H_{MFG} =	1366628	C_{MFG} =	\$79,674,412	\$79,674
Quality control			C_{QC} =	\$15,536,510	\$15,537
Materials/equipment			C_{MAT} =	\$21,074,485	\$21,074
Units produced in 5 years					1000
Quantity Discount Factor					0.5998
				Without QDF	**With QDF**
Fixed landing gear discount			VSC_1 =	-\$17,500	-\$10,496
Avionics			VSC_2 =	\$35,000	\$20,993
Engine(s)			VSC_3 =	\$102,526	\$61,494
Propeller(s)			VSC_4 =	\$14,000	\$8,397
Variable Cost (per unit)			C_{var} =	**\$250,311**	**\$196,672**
Total Cost per Unit			C_{unit} =	**\$286,755**	**\$233,117**
Manufacturers liability insurance				\$52,500	\$52,500
MINIMUM SELLING PRICE				**\$339,255**	**\$285,617**
Target Price per Unit			P_{unit} =	**\$350,000**	
Units to Break-Even			N_{BE} =	**366**	**238**

EXAMPLE 2-3 (*cont'd*)



FIGURE 2-6 The selling price in millions of $ as a function of units produced shows a rapid drop in price at first.

TABLE 2-4 Project cost comparison between a composite and aluminum aircraft.

	Costs per Unit (without QDF)		
	Composite AC	Aluminum AC	Ratio Comp/Al
Engineering	$20,814	$10,407	2.00
Development support	$1,500	$1,000	1.50
Flight test operations	$1,362	$1,362	1.00
Tooling	$12,769	$6,385	2.00
Certification Cost	**$36,444**	**$19,153**	**1.90**
Manufacturing labor	$79,674	$63,740	1.25
Quality control	$15,537	$8,286	1.87
Materials/equipment	$21,074	$21,074	1.00
Fixed landing gear discount	-$17,500	-$17,500	1.00
Engine(s)	$102,526	$102,526	1.00
Propeller(s)	$14,000	$14,000	1.00
Avionics	$35,000	$35,000	1.00
Manufacturers liability insurance	$52,500	$52,500	1.00
Minimum Selling Price	**$339,255**	**$298,779**	**1.14**

EXAMPLE 2-4

Estimate how many airplanes must be produced before the manufacturer can expect to break-even if the price is set at $350,000. Plot the production cost and revenue versus number of units produced assuming a retail price of $233,000, $300,000, and $350,000. Plot total production cost and revenue versus number of units produced. Indicate break-even points on the plot (Figure 2-7).

SOLUTION:
Total fixed costs from Table 2-3: C_{fix} = $36, 444, 233
Variable cost per unit from Table 2-3: C_{var} = $196, 672
Break-even point:

$$N_{BE} = \frac{C_{fix}}{P_{\text{unit}} - C_{\text{var}}} = \frac{36444233}{350000 - 196672} = 238 \text{ units}$$

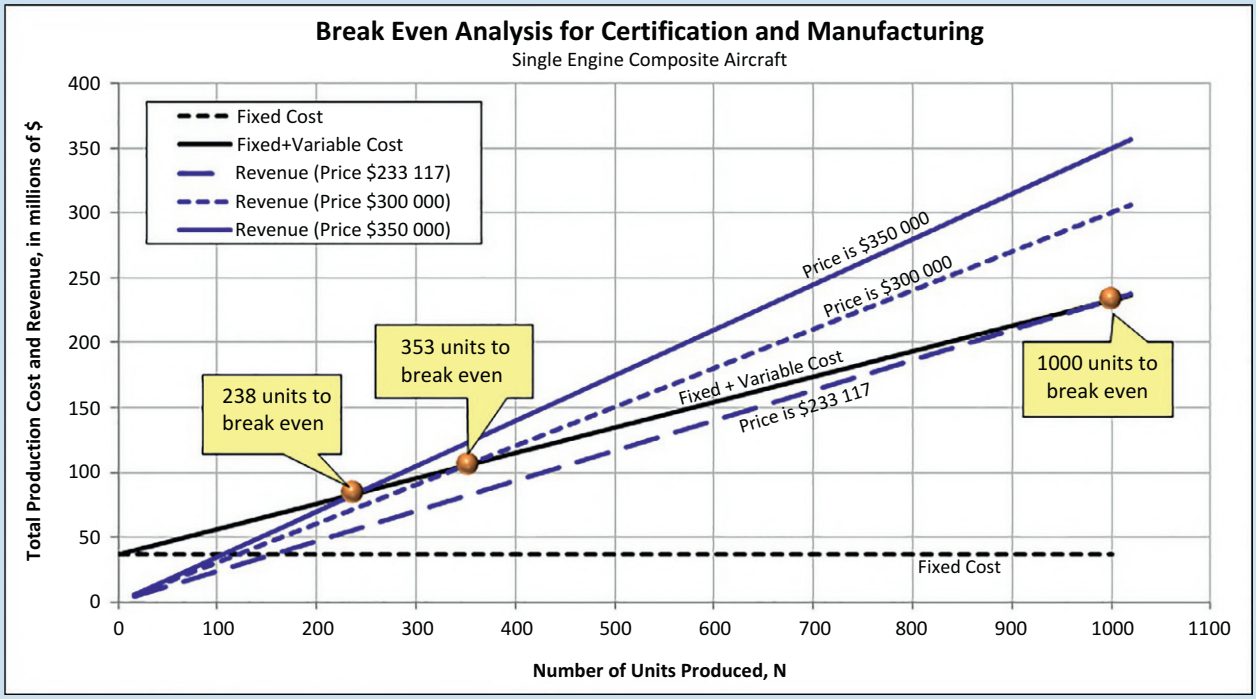


FIGURE 2-7 Break-even analysis assuming three difference prices.

2.2.2 Development Cost of a Business Aircraft

The Eastlake model has been adapted to the development of business (executive) aircraft. While the methodology parallels that of GA aircraft, the model is much closer to the original DAPCA-IV model. Certification per 14 CFR Part 23 or Part 25 is assumed. The latter category will be more expensive due to the stricter requirements. The factors denoted by the common variable F_{CERT} are best guesses for the cost difference—the reader can modify those values per own experience.

(1) CER 1—Engineering Workhours (H_{ENGR}):

$$H_{ENGR} = 4.86 \cdot W_{airframe}^{0.777} \cdot V_H^{0.894} \cdot N^{0.163} \cdot F_{CERT1} \cdot F_{CF1} \cdot F_{COMP1} \cdot F_{PRESS1} \quad (2\text{-}31)$$

where

$W_{airframe}$ = Weight of the structural skeleton
V_H = Maximum level airspeed in KTAS
N = Number of planned aircraft to be produced over a 5-year period.
$F_{CERT\ 1}$ = 1 if certified as a 14 CFR Part 23, =1.15 if certified as a 14 CFR Part 25
$F_{CF\ 1}$ = 1.03 for a complex flap system, =1 if a simple flap system
$F_{COMP\ 1} = 1 + f_{comp}$ a factor to account for the use of composites in the airframe
f_{comp} = Fraction of airframe made from composites (=1 for a complete composite aircraft)
$F_{PRESS\ 1}$ = 1.03 for a pressurized aircraft, =1 if unpressurized

(2) CER 2—Tooling Workhours (H_{TOOL}):

$$H_{TOOL} = 5.99 \cdot W_{airframe}^{0.777} \cdot V_H^{0.696} \cdot N^{0.263} \cdot F_{CERT2} \cdot F_{TAPER2} \cdot F_{CF2} \cdot F_{COMP2} \cdot F_{PRESS2} \quad (2\text{-}32)$$

where

$F_{CERT\ 2} = 1$ if certified as a 14 CFR Part 23, $=1.05$ if certified as a 14 CFR Part 25
$F_{TAPER\ 2} = 0.95$ for a constant chord wing, $=1$ for a tapered wing
$F_{CF\ 2} = 1.02$ for a complex flap system, $=1$ if a simple flap system
$F_{COMP\ 2} = 1 + f_{comp}$ a factor to account for the use of composites in the airframe
$F_{PRESS\ 2} = 1.01$ for a pressurized aircraft, $=1$ if unpressurized

(3) CER 3—Manufacturing Labor Workhours (H_{MFG}):

$$H_{MFG} = 7.37 \cdot W_{airframe}^{0.82} \cdot V_H^{0.484} \cdot N^{0.641} \cdot F_{CERT3} \cdot F_{CF3} \cdot F_{COMP3} \quad (2\text{-}33)$$

where

$F_{CF\ 3} = 1.01$ for a complex flap system, $=1$ if a simple flap system
$F_{CERT\ 3} = 1$ if certified as a 14 CFR Part 23, $=1.05$ if certified as a 14 CFR Part 25
$F_{COMP\ 3} = 1 + 0.25 \cdot f_{comp}$, a factor to account for the use of composites in the airframe

(4) CER 4—Total Cost of Engineering (C_{ENGR}):

Use Equation (2-11).

(5) CER 5—Total Cost of Development Support (C_{DEV}):

$$C_{DEV} = 95.24 \cdot W_{airframe}^{0.63} \cdot V_H^{1.3} \cdot CPI_{2012} \cdot F_{CERT5} \cdot F_{CF5} \cdot F_{COMP5} \cdot F_{PRESS5} \quad (2\text{-}34)$$

where

$F_{CERT\ 5} = 1$ if certified as a 14 CFR Part 23, $=1.10$ if certified as a 14 CFR Part 25
$F_{CF\ 5} = 1.01$ for a complex flap system, $=1$ if a simple flap system
$F_{COMP\ 5} = 1 + 0.5 \cdot f_{comp}$ a factor to account for the use of composites in the airframe
$F_{PRESS\ 5} = 1.03$ for a pressurized aircraft, $=1$ if unpressurized

(6) CER 6—Total Cost of Flight Test Operations (C_{FT}):

$$C_{FT} = 2606.51 \cdot W_{airframe}^{0.325} \cdot V_H^{0.822} \cdot N_P^{1.21} \cdot CPI_{2012} \cdot F_{CERT6} \quad (2\text{-}35)$$

where

$F_{CERT\ 6} = 1$ if certified as a 14 CFR Part 23, $=1.50$ if certified as a 14 CFR Part 25

(7) CER 7—Total Cost of Tooling (C_{TOOL}):

Use Equation (2-15).

(8) CER 8—Total Cost of Manufacturing (C_{QC}):

Use Equation (2-16).

(9) CER 9—Total Cost of Quality Control:

$$C_{QC} = 0.133 \cdot C_{MFG} \cdot F_{CERT9} \cdot F_{COMP9} \quad (2\text{-}36)$$

where

$F_{CERT\ 9} = 1$ if certified as a 14 CFR Part 23, $=1.50$ if certified as a 14 CFR Part 25
$F_{COMP\ 9} = 1 + 0.5 \cdot f_{comp}$ a factor to account for use of composites in the airframe

(10) CER 10—Total Cost of Materials (C_{MAT}):

$$C_{MAT} = 23.066 \cdot W_{airframe}^{0.921} \cdot V_H^{0.621} \cdot N^{0.799} \cdot CPI_{2012} \cdot F_{CERT} \cdot F_{CF} \cdot F_{PRESS} \quad (2\text{-}37)$$

where

$F_{CERT} = 1$ if certified as a 14 CFR Part 23, $=1.15$ if certified as a 14 CFR Part 25
$F_{CF} = 1.02$ for a complex flap system, $=1$ if a simple flap system
$F_{PRESS} = 1.01$ for a pressurized aircraft, $=1$ if unpressurized

(11) CER 11—Fixed Cost (or Total Cost to Certify) (C_{fix}):

Use Equation (2-19).

(12) CER 12—Variable Cost (C_{var}):

Use Equation (2-20).

Follow the same procedures as presented in Section 2.2.1.

2.2.3 A Word About the Accuracy of the Eastlake Model

Questions regarding the accuracy of the Eastlake method are common. Some words of caution have already been uttered in the text, but it stands to shed more light on this important question. Table 2-5 was prepared for this purpose. It lists a number of GA aircraft for which the minimum selling price was estimated using best information in the public domain, including number of units manufactured over the years 2014–2018 per

TABLE 2-5 Comparison between predicted and actual aircraft prices.

Aircraft Make and Model	Units Manufactured in Past 5 Yrs	① Minimum Selling Price per Method	② 2018 Retail Price per [10]	①/② Predicted/Actual
SINGLE-ENGINE PISTON				
Cessna C-172	633	$ 320,819	$ 425,000	0.755
Cessna C-182	160	$ 538,610	$ 480,000	1.122
Cessna T206H	202	$ 603,393	$ 665,000	0.907
Cessna TTx	121	$ 1,018,588	$ 715,000	1.425
Aviat Husky A1C-180	181	$ 313,069	$ 257,278	1.217
Aviat Husky A1C-200	181	$ 332,075	$ 314,064	1.057
Beechcraft Bonanza G36	108	$ 903,681	$ 815,000	1.109
Cirrus SR20	208	$ 669,860	$ 439,000	1.526
Cirrus SR22	648	$ 528,012	$ 609,900	0.866
Cirrus SR22T	805	$ 551,810	$ 709,900	0.777
Diamond DA20-C1	69	$ 657,541	$ 234,800	2.800
Diamond DA40 XLT	364	$ 433,516	$ 389,800	1.112
Diamond DA40 Tundra	364	$ 468,554	$ 455,000	1.030
Diamond DA40 NG	364	$ 481,681	$ 429,890	1.120
Mahindra Airvan 8	56	$ 968,573	$ 798,256	1.213
Mahindra Airvan 8 Turbo	56	$ 998,224	$ 827,133	1.207
Piper Warrior	50	$ 641,177	$ 340,000	1.886
Piper Archer LX	291	$ 338,101	$ 372,400	0.908
Piper Archer DX	291	$ 340,952	$ 412,000	0.828
Piper Arrow	36	$ 1,009,712	$ 467,000	2.162
Piper Matrix	13	$ 4,194,726	$ 916,680	4.576
Piper M350	126	$ 1,114,711	$ 1,178,000	0.946
Tecnam P2010	80	$ 572,458	$ 344,160	1.663
Tecnam P2010 IO-390	100	$ 566,270	$ 399,360	1.418
TWIN-ENGINE PISTON				
Beechcraft Baron G58	120	$ 1,671,978	$ 1,400,000	1.194
Diamond DA42-VI	214	$ 969,797	$ 739,800	1.311
Diamond DA62	101	$ 1,459,803	$ 1,100,000	1.327
Piper PA-44-180	103	$ 1,093,653	$ 699,990	1.562
Piper PA-34-220T	24	$ 3,156,045	$ 999,900	3.156
Tecnam P2006T	154	$ 698,467	$ 443,900	1.573

reference [5]. It assumes 15% liability. This is then compared to the actual retail price of said aircraft per reference [10].

The pricing of a new aircraft is complex. It involves the history of the manufacturer, the spread of its tentacles, how long said aircraft has been in production, whether it is a derivative or a clean sheet of paper aircraft, lifetime deliveries, sales network, just to name a few. It is important to recognize these complexities. Table 2-5 lists the minimum selling price per the Eastlake model (see Figure 2-4) in the column labeled ①. This price is divided by the actual retail price listed in column ②, yielding the fractions in the last column. Ordinarily, the minimum selling price is less than the retail price, so this fraction should be <1. The fractions shown range between 0.8 and 1.2, with some notable exceptions. Thus, the fraction 0.907 means the minimum selling price is 90.7% of the actual retail price and is arguably a reasonable estimate. In contrast, the fraction 4.576 is wildly off base and indicates erroneous result. This value pertains to the Piper Matrix, a variant of the Piper Pa-46, of which only 13 units were delivered between 2014 and 2018. As a rule of thumb, the lower the number of manufactured units, the greater is the deviation from the actual retail price (Figure 2-6 sheds light on an important contributor). In short, as Table 2-5 shows, the Eastlake

model returns reasonable approximation, although care must be applied when interpreting the results.

2.3 ESTIMATING AIRCRAFT OPERATIONAL COSTS

A part of marketing airplanes involves persuading potential customers to purchase your airplane rather than someone else's. To develop a convincing argument, manufacturers run sales departments whose purpose is to provide a realistic comparison of cost-of-ownership between comparable aircraft. One of the most important figures-of-merit used for this is the *cost-of-ownership*; the amount of money required to own and operate the aircraft per hour flown. This section presents two methods to assess direct operational cost per flight hour for GA aircraft; one applies to privately owned and operated GA aircraft, the other to a business aircraft.

2.3.1 Direct Operational Cost of a GA Aircraft

The following model is based on experience of actual aircraft ownership. It comprises basic book-keeping of costs associated with privately owned aircraft. The primary inputs are flight hours per year, cost of fuel, amount of money borrowed to purchase the aircraft, and the cost of insurance. Storage cost, annual inspections, and "contributions" to an "engine overhaul bank" are also included in the model. The cost is presented in dollars per flight hour, allowing a convenient comparison to rental cost for similar aircraft. The number of flight hours per year (Q_{FLGT}) for normal GA aircraft varies from around 100 h a year for an underutilized aircraft, to 1000 h[11] or more for a student trainer aircraft. Personal aircraft are flown in the ballpark of 100 to 500 h per year, with 300 h (5.75 h per week) being a reasonable average.

(1) Assumptions

The model assumes a single-engine, fixed gear, fixed pitch prop aircraft certified as 14 CFR Part 23 that requires 0.3 maintenance-workhours per flight-hour (denoted by the term F_{MF}). This number is adjusted for characteristics that affect the maintenance effort, such as difficult engine access, retractable landing gear, wet wings, complex avionics equipment, and complex high lift devices. Furthermore, the method assumes no cost for crew, as the owner is the pilot.

(2) Maintenance Cost

The cost of preventative and restorative maintenance is estimated as follows. The cost savings achievable when owners perform maintenance (to the extent of that permitted by FAA regulations) and for aircraft certified as LSA are accounted for in this formulation. Aircraft certified as 14 CFR Part 23 or 25 require qualified A&P mechanics. Small aircraft may require one mechanic, while large (e.g., twin engine, business aircraft) could have multiple mechanics.

$$\text{Maintenance Cost}\,(\$\,\text{per year}): C_{AP} = F_{MF} \cdot R_{AP} \cdot Q_{FLGT} \tag{2-38}$$

where

F_{MF} = Ratio of maintenance-workhours to flight-hours (see below)
R_{AP} = Hourly rate for a certified Airframe and Powerplant (A&P) mechanic (typ. \$53–67 per hour)
Q_{FLGT} = Number of flight hours per year.

$$\text{Maintenance}-\text{to}-\text{flight}-\text{hour ratio}: F_{MF} = 0.30 + F_1 + F_2 + F_3 + F_4 + F_5 + F_6 + F_7 + F_8 \tag{2-39}$$

where

F_1 = –0.15 if maintenance is performed by owner and 0 if performed by an A&P mechanic
F_2 = 0 for an easy engine access, =0.02 for a difficult access
F_3 = 0 for a fixed landing gear, =0.02 for a retractable landing gear
F_4 = 0 if no VFR radios are installed, =0.02 if VFR radios are installed
F_5 = 0 if no IFR radios are installed, =0.04 if IFR radios are installed
F_6 = 0 if no integral fuel tanks are installed, =0.01 if such tanks are installed
F_7 = 0 for a simple flap system, =0.02 for a complex flap system
F_8 = 0 for 14 CFR Part 23 certification, = − 0.10 for LSA certification

(3) Storage Cost

Airplane owners usually must pay for storage at a main base. Assume the rate per month is \$250 to 300.

$$\text{Storage Cost}\,(\$\,\text{per year}): C_{STOR} = 12 \cdot R_{STOR} \tag{2-40}$$

where

R_{STOR} = Storage rate (≈ \$250–300 per month)

(4) Fuel Cost

Fuel prices are volatile, so expect variation here.

$$\text{Annual Fuel Cost}\,(\$\,\text{per year}): C_{FUEL} = \frac{P_{HPC} \cdot SFC_C \cdot Q_{FLGT} \cdot R_{FUEL}}{6.5} = FF_C \cdot Q_{FLGT} \cdot R_{FUEL} \tag{2-41}$$

[11] A primary trainer operated 4 h, 5 days a week, flies $4 \times 5 \times 52 = 1040$ h per year. There are 8760 h/year.

where

P_{HPC} = Typical horsepower (BHP or SHP) during cruise (e.g., 75% of rated max engine power)
SFC_C = Typical specific fuel consumption during cruise (e.g., 0.5 per hour)
FF_C = Total *fuel flow* in gallons per hour (e.g., 12 gal/h)
R_{FUEL} = Price of fuel in $/gallon (e.g., $5.21 per gallon)

(5) Insurance Cost

The insurance cost is a nebulous value, disclosed by insurance companies on a plane-to-plane basis. It considers factors like pilot experience, price, class, and use of aircraft, to name a few. Low-time pilots pay a higher premium than high-time ones. Agricultural aircraft engage in high-risk operations and this increases the premium. In 2012, the premium for a Cessna 172 might be around $1000 to $1500 a year. The policy includes a hull value of $50,000 and a standard liability of $100,000 per passenger, with a maximum liability of $1,000,000. In contrast, the premium for a modern Cirrus SR22 aircraft, valued at $600,000, owned and operated by a low-time pilot, might be $20,000 a year, while a high-time pilot owning a less expensive Cirrus might only pay $3000. The following cost model is simple and does not account for such variations. If necessary, the reader can improve accuracy through research.

Annual Insurance Cost ($ per year):

$$C_{INS} = 500 + 0.015 \cdot C_{AC} \tag{2-42}$$

where

C_{AC} = Insured value of the aircraft.

If estimating the operational cost of a new design, the CAC amounts to the purchase price of the aircraft.

(6) Annual Inspection Cost

It accounts for an A&P mechanic inspecting the airplane for maintenance items.

Annual Inspection Cost ($ per year): $C_{INSP} = \$500$ (2-43)

(7) Engine Overhaul

The airplane's engine(s) is regularly overhauled per the engine's required *time-between-overhaul* (TBO—given in hours). This costly requirement is amortized over the total flight hours of the airplane over that period. If the cost is known in advance, an hourly rate can be obtained by dividing it by the engine's TBO. For instance, Lycoming and Continental engines usually have a TBO around 2000 h. If the cost of the overhaul is expected to be $10,000, it follows that it is reasonable to charge $5 per flight hour. This is reflected in the expression below:

Engine Overhaul Fund ($ per year):

$$C_{OVER} = 5 \cdot N_{ENG} \cdot Q_{FLGT} \tag{2-44}$$

where

N_{ENG} = Number of engines

(8) Cost of Loan Payments

If the airplane was fully or partially funded through financial institutions, the annual cost of paying back those loans should be included as well. This is accounted for as shown below, using the standard mortgage formula:

Monthly loan payment: $C_{month} = \dfrac{Pi}{1 - 1/(1+i)^n}$ (2-45)

where

P = The principal or amount of money originally borrowed
i = Monthly interest rate
n = Number of pay periods in months. This way 15 years would be $12 \cdot 15 = 180$ pay periods

Annual Loan Payment ($ per year):

$$C_{LOAN} = \frac{12 \cdot Pi}{1 - 1/(1+i)^n} \tag{2-46}$$

(9) Total Annual Operational Cost

This cost is obtained by summing all the contributions.

Total Yearly Cost:

$$C_{YEAR} = C_{AP} + C_{STOR} + C_{FUEL} + C_{INS} + C_{INSP} + C_{OVER} + C_{LOAN} \tag{2-47}$$

And finally, the cost per each hour flown should be:

Cost per Flight Hour: $C_{HR} = \dfrac{C_{YEAR}}{Q_{FLGT}}$ (2-48)

EXAMPLE 2-5

Estimate the operational cost for the airplane of Example 2-1, assuming the following scenario.

(1) The airplane is certified to 14 CFR Part 23.
(2) It is maintained by an A&P mechanic who charges $60 per hour.
(3) It has an easy engine access, fixed landing gear, IFR radios only, integral fuel tanks, and simple flap system.

EXAMPLE 2-5 (*cont'd*)

(4) It is flown 300 h per year. Its 310 BHP engine consumes 16 gal/h of fuel on the average at $5/gal.
(5) Storage cost is $250 per month.
(6) Use the given insurance model and the price of the airplane is that of Example 2-3, or $350,000.
(7) The airplane is fully paid by a 15-year loan with an APR of 9%.

SOLUTION:

Start by estimating the maintenance to flight hour ratio:

$$F_{MF} = 0.30 + F_1 + F_2 + F_3 + F_4 + F_5 + F_6 + F_7 + F_8$$
$$= 0.30 + 0 + 0 + 0 + 0 + 0.04 + 0.01 + 0 + 0 = 0.35$$

Annual maintenance cost:

$$C_{AP} = F_{MF} \cdot R_{AP} \cdot Q_{FLGT} = 0.35 \cdot 60 \cdot 300 = \$6300$$

Annual storage cost:

$$C_{STOR} = 12 \cdot R_{STOR} = 12 \cdot 250 = \$3000$$

Annual fuel cost:

$$C_{FUEL} = FF_{CRUISE} \cdot Q_{FLGT} \cdot R_{FUEL} = 16 \cdot 300 \cdot 5 = \$24000$$

Annual insurance cost:

$$C_{INS} = 500 + 0.015 \cdot C_{AC} = 500 + 0.015 \cdot (350000) = \$5750$$

Annual inspection cost:

$$C_{INSP} = \$500$$

Engine overhaul fund:

$$C_{OVER} = 5 \cdot 1 \cdot 300 = \$1500$$

Annual loan payment:

$$C_{LOAN} = \frac{12 \cdot Pi}{1 - 1/(1+i)^n} = \frac{12 \cdot (350000)(0.09/12)}{1 - 1/(1 + (0.09/12))^{(12 \times 15)}} = \$42\ 599$$

The monthly payment is $42,599/12 = $3550. The total annual cost of owning and operating the airplane amount to the sum of these, or:

$$C_{YEAR} = C_{AP} + C_{STOR} + C_{FUEL} + C_{INS} + C_{INSP} + C_{OVER} + C_{LOAN}$$
$$= \$6300 + \$3000 + \$24000 + \$5750 + \$500 + \$1500 + \$42599 = \$83649$$

Cost per flight hour assuming 300 h/year:

$$C_{HR} = \frac{\$83649}{300\ \text{h}} \approx \$279\ \text{per hour}$$

2.3.2 Direct Operational Cost of a Business Aircraft

This presentation is intended to help estimate costs associated with GA business aircraft. It assumes a professionally flown aircraft supported by a high-quality maintenance and that is subject to other costs that have already been detailed in Section 2.3.1. For business jets, certified to 14 CFR Part 25, the reader can seek more precise information from companies such as Conklin and de Decker,[12] which collects such data in detail for all aircraft currently in service. A listing of cost-related items for such aircraft is provided in Table 2-6 and is based on the approach by Conklin and de Decker.

The number of flight hours per year (Q_{FLGT}) for normal business aircraft varies from around 100 h a year for an underutilized aircraft, to perhaps 600 h or more. Business aircraft are certified as 14 CFR Part 23 or 25 and require qualified A&P mechanics: Most would have multiple mechanics.

(1) Maintenance Cost ($ per year):

$$C_{AP} = F_{MF} \cdot R_{AP} \cdot Q_{FLGT} \tag{2-49}$$

where

F_{MF} = Ratio of maintenance workhours to flight hours (see below)
R_{AP} = An hourly rate for a certified Airframe and Powerplant (A&P) mechanic (typ. $53–67 per hour)
Q_{FLGT} = Number of flight hours per year.

Maintenance to flight hour ratio :

$$F_{MF} = 2.00 + F_1 + F_2 + F_3 + F_4 + F_5 + F_6 \tag{2-50}$$

where

$F_1 = 0$ for an easy engine access, =0.2 for difficult access
$F_2 = 0$ for fixed landing gear, =0.2 for retractable landing gear
$F_3 = 0$ if simple avionics are installed, =0.2 if complex avionics are installed
$F_4 = 0$ if no integral fuel tanks are installed, =0.1 if such tanks are installed
$F_5 = 0$ for a simple flap system, =0.2 for a complex flap system
$F_6 = 0$ for 14 CFR Part 23 certification, =0.5 for 14 CFR Part 25 certification

(2) Storage Cost ($ per year):

Use Equation (2-40), but assume R_{STOR} = Storage rate ≈ $500 to $3000 per month, depending on size of hangar space needed.

(3) Annual Fuel Cost ($ per year):

$$C_{FUEL} = \frac{FF_{CRZ} \cdot Q_{FLGT} \cdot R_{FUEL}}{6.7} \tag{2-51}$$

[12] See http://www.conklindd.com.

TABLE 2-6 A variable and fixed cost analysis for typical business jet aircraft (valid for year 2019).

	Small Jet	Medium Jet	Large Jet
ESTIMATED HOURLY VARIABLE COSTS			
FUEL COSTS PER FLIGHT HOUR			
Fuel (typical jet fuel costs $4.73/gal in 2018)	$1,200	$1,400	$1,800
Fuel Additives	-	-	-
Lubricants	-	-	-
MAINTENANCE LABOR COSTS PER FLIGHT HOUR			
Maintenance Labor Cost per Hour	$110	$110	$110
Maintenance Hours/Flight Hour	4	4	4
Maintenance Labor	$440	$440	$440
Parts Airframe/Eng/Avionics	$200	$200	$200
POWERPLANT OVERHAUL FUND PER FLIGHT HOUR			
Engine Restoration	$350	$400	$600
Thrust Reverser Allowance	$14	$26	$45
APU Allowance	$14	$60	$60
MISCELLANEOUS EXPENSES PER FLIGHT HOUR			
Landing/Parking	$20	$45	$75
Crew Expenses	$70	$280	$280
Supplies/Catering	$35	$150	$150
Carbon Offset	-	-	-
Other	-	-	-
TOTALS			
Total Variable Cost/Hour	**$2,343**	**$3,001**	**$3,650**
ANNUAL FIXED COST			
CREW AND OPERATIONAL COSTS			
Crew salaries - Captain (NBAA rates)	$95,000	$135,000	$161,000
- Co Pilot	$60,000	$90,000	$94,000
- Flight Attendant	-	$84,000	$89,000
- Flight Eng/Other	-	-	-
- Benefits	$47,000	$93,000	$104,000
Hangar - Typical	$25,700	$61,300	$82,500
INSURANCE COSTS			
Insurance - Hull	$7,735	$32,300	$41,760
Single Limit Liability	$10,500	$16,500	$16,500
OTHER COSTS			
Recurrent Training	$27,200	$58,200	$85,600
Aircraft Modernization (?)	$45,000	$33,333	$33,333
Navigation Chart Service	$4,800	$18,500	$18,500
Refurbishing (?)	$16,800	$78,500	$117,500
Computer Mx. Program (?)	$9,750	$12,000	$12,000
Weather Service	$700	$700	$700
Other Fixed Costs	-	-	-
Mgmt Fee/Yr	-	-	-
TOTALS			
Total Fixed Cost/Year	**$350,185**	**$713,333**	**$856,393**

where

FF_{CRZ} = Total *fuel flow* in gallons per hour (e.g., 600 lb_f/h)
R_{FUEL} = Price of fuel in $/gallon (e.g., $6.32 per gallon)

(4) Annual Insurance Cost ($ per year):

Use Equation (2-42) in the absence of better information.

(5) Annual Inspection Cost ($ per year):

$$C_{INSP} = \$1000 - \$15000 \tag{2-52}$$

(6) Engine Overhaul

The same rules regarding a TBO for propeller engines holds for jet engines. For instance, Williams International FJ44 engines usually have TBO around 4000 h, Pratt & Whitney PW306 are around 6000 h. If the cost of the overhaul is expected to be $30,000 to $40,000, it follows that it is reasonable to charge $6.7 to $7.5 per flight hour per engine. The higher value is reflected in the expression below:

$$\text{Engine overhaul fund } (\$\,\text{per year}): \quad C_{OVER} = 7.5 \cdot N_{ENG} \cdot Q_{FLGT} \tag{2-53}$$

where

N_{ENG} = Number of engines

(7) Crew Cost

Some business aircraft are operated by flight hours only. The associated crew cost is then based on the number of hours flown annually. In the absence of better information, the following expression can be used to estimate this cost:

$$\text{Hourly crew}: C_{CREW} = N_{CREW} \cdot R_{CREW} \cdot Q_{FLGT} \tag{2-54}$$

where

N_{CREW} = Number of crew members required to operate the airplane.
R_{CREW} = Hourly rate of crew per hour—business dependent.

The term R_{CREW} depends on the business involved and can range from $50 to $150 per hour. Other business aircraft have full-time pilots and even a flight attendant, with the associated annual salary and benefit costs (see Table 2-6). Yet other businesses may keep only one full-time pilot on board and hire a co-pilot and a flight attendant on a need-to-basis. In this case, Equation (2-54) may be used to account for the additional crew and its value added to that of the full-time pilot.

(8) Annual Loan Payment ($ per year):

Use Equations (2-45) and (2-46).

$$\text{Total yearly cost}: C_{YEAR} = C_{AP} + C_{STOR} + C_{FUEL} + C_{INS} + C_{INSP} + C_{OVER} + C_{LOAN} + C_{CREW} \tag{2-55}$$

Follow the same procedures as presented in Section 2.3.1.

2.3.3 A Word About Aircraft Operational Cost

Operational cost of business aircraft is of great importance to the operator. The designer should estimate three kinds of costs for the customer to allow comparison to existing and rival aircraft: (a) Total annual fixed cost, (b) total variable cost per flight hour, and (c) cost per nautical mile (or km) flown. Example costs for specific aircraft are presented in Table 2-7. While dated, they can be updated using CPI based on the date when they appeared in print.

TABLE 2-7 Operational costs for specific business aircraft.

Aircraft	Total Annual Fixed Cost	Total Variable Cost per Flight Hour	Cost per Nautical Mile	Reference - Date
Pilatus PC-12 (1/8 share)	$174 354	$1 743.54	$8.07	[11] – 01/21/2010
Pilatus PC-12 (private)	$275 774	$2 757.74	$12.74	
Cessna Citation X (1/8 share)	$537 540	$5 375.40	$11.41	
Cessna Citation X (private)	$876 608	$8 766.08	$18.61	
Cessna Citation CJ3	$336 951	$1 607.52	$4.02	[12] – 11/12/2012
Hawker 850XP	$430 570	$2 695.24	$6.61	
Challenger 300	$703 552	$2 894.25	$6.91	
Falcon 2000EX	$715 545	$3 137.12	$7.04	
Gulfstream 550	$958 478	$4 272.14	$10.08	
Gulfstream 450	$878 884	$9 980.00	-	[13] – 05/10/2016

EXERCISES

(1) An LSA aircraft is being designed by a new startup business and you have been hired to evaluate the business case. It is planned that the lifting surfaces of the new aircraft will be composite, but the fuselage will be made from aluminum. Thus, it is estimated that 50% of the aircraft will be composite and 50% aluminum. The estimated airframe weight is 530 lb_f and the maximum level airspeed in 120 KTAS (V_H). It is estimated that 250 airplanes will be manufactured over a 5-year period. The airplane features a tapered wing with a simple flap system and, as required for LSA aircraft, the fuselage is unpressurized, and it has a 69-in. diameter fixed pitch propeller driven by a piston engine. Estimate the following:
- **(a)** Number of workhours of engineering time.
- **(b)** Number of workhours for construction tooling.
- **(c)** Number of workhours to produce 250 airplanes.
- **(d)** Estimate number of persons required for each of the above, assuming 40 h per week for 48 weeks per year and production run over 5 years (as stated above). In other words, how many engineers, tooling, and technicians will be required over the period?
- **(e)** Estimate the average number of hours required to produce each airframe.

(2) Using the airplane of Exercise (1), estimate the total cost to certify and manufacture 250 units over the 5-year period assuming 95% experience effectiveness, engineering, tooling, and manufacturing rates are \$95, \$65, and \$55 per hour, respectively. Assume 15% product liability cost. The planned number of prototypes is 2. Use the consumer price index for the year 2012 (i.e., $CPI_{2012}=1$). Solve the problem using spreadsheet software and prepare an estimate like that of Table 2-2 and validate using standard hand calculations. Determine:
- **(a)** Cost to certify.
- **(b)** *Total cost per unit* to produce.
- **(c)** Break-even analysis for retail prices at \$15,000, \$30,000, and \$45,000 above *total cost per unit*, assuming the sales agent is paid \$7000 for each airplane sold (i.e., add \$7000 on top of the three retail prices).
- **(d)** Determine the price of three LSA aircraft by researching manufacturer's websites (for instance go to: http://www.lightsportaircrafthq.com/ for a listing of manufacturers).

(3) Estimate the hourly operational cost for the airplane of Exercise (1) for the three retail price options, assuming it is maintained by an A&P mechanic who charges \$50 per hour. It has easy engine access, fixed landing gear; IFR radios only, integral fuel tanks, and a simple flap system. It is flown 150 h per year. Its 100 BHP engine consumes 6 gal/h of fuel on the average, at \$5/gal. Storage cost is \$50 per month. The engine *Time-between-Overhaul* (TBO) is 1500 h, and the cost to overhaul is \$4500. Include the acquisition cost for the airplane by assuming it is purchased using a 20% down-payment with the remainder borrowed at 9% APR for 15 years. Note that C_{AC} is the sum of the total cost per unit, the markup, and the sales commission, i.e., the total paid by the customer as a Fly-Away Price.

(4) **(a)** The total cost of developing a brand-new airplane can be expressed as the sum of the fixed cost (constant), denoted by FC, and the variable cost, which can be expressed as $U{\cdot}N$, where U is the unit variable cost and N is the number of units produced. Consider a scenario in which the retail price of the product is variable rather than constant in order to help initially market the airplane. As an example of such a variable retail price structure, consider a situation where the unit sales price (call it P_1) is low at first to help market the airplane, but is then raised to P_2 after a specific number of units, N_1, has been produced. Derive an expression for the break-even point, i.e., the total number of units, N, required to break-even.

(b) Calculate the number of units that must be produced to break-even for a scenario in which $FC=50$ million \$, $U=0.285$ million \$/unit, $P_1=0.350$ million \$, $P_2=0.450$ million \$, and $N_1=300$. How many units does it take if the price is not increased and it is offered a P_1?

References

[1] R. Hess, H. Romanoff, *Aircraft Airframe Cost Estimating Relationships*, R-3255-AF, RAND Corporation, December 1987.

[2] http://www.rand.org. (Accessed 18 December 2018).

[3] C.N. Eastlake, H.W. Blackwell, *Cost estimating software for general aviation aircraft design*, Proceedings of the ASEE National Conference, St. Louis, MO, 2000.

[4] Anonymous, *General Aviation Statistical Databook and Industry Outlook 2016*, General Aviation Manufacturers Association, 2017.

[5] Anonymous, *2018 Annual Report*, General Aviation Manufacturers Association, 2019.

[6] http://www.gama.aero. (Accessed 18 December 2018).

[7] Anonymous, *General Aviation: Status of the Industry, Related Infrastructure, and Safety Issues*, Report to Congressional Requesters, GAO-01-916, U.S. General Accounting Office, August 2001, p. 18.

[8] A. Jacobson, C. Tsubaki, *Economics in new commercial aircraft design*, Aircraft Systems, Design and Technology Meeting, 1986. https://doi-org.ezproxy.libproxy.db.erau.edu/10.2514/6.1986-2667.

[9] https://www.conklindd.com/t-Articleaircraftlifecyclecosting.aspx. (Accessed 18 December 2018).

[10] S. Pope (Ed.), *Flying Magazine 2018 Buyer's Guide*, Flying Magazine, January 2018. www.flyingmag.com.
[11] Cox, Jeremy, *What Your Own Business Jet Really Costs – The Formula Explained*, Forbes Business Magazine online, 2010. [Accessed 02/29/2019].
[12] Whyte, Alasdair, *How Much Does it Cost to Own a Business Jet?*, The Corporate Jet Investor online, 2012. [Accessed 01/03/2019].
[13] Young-Brown, Fiona, *The Cost to Own and Operate a Gulfstream G450*, Sherpa Report online, 2016. [Accessed 02/27/2020].

CHAPTER

3

Initial Sizing

OUTLINE

3.1 **Introduction** 57
3.1.1 The Content of This Chapter 57
3.1.2 Fundamental Concepts 57
3.2 **Constraint Analysis** 58
3.2.1 General Methodology 59
3.2.2 Methodology to Accommodate Normally Aspirated Piston Engines 64
3.2.3 Additional Helpful Tools for Initial Sizing 67
3.3 **Introduction to Trade Studies** 69
3.3.1 Parametric Analysis 69
3.3.2 Stall Speed–Cruise Speed Carpet Plot 71
3.3.3 Design of Experiments 72
3.4 **Introduction to Design Optimization** 73
3.4.1 Fundamental Concepts 75
3.4.2 More on Objective Functions 78
3.4.3 Linear Programming 80
3.4.4 Nonlinear Surfaces and Lagrange Multipliers 82
3.4.5 Wing Sizing Optimization by Example 86
Exercises 89
References 91

3.1 INTRODUCTION

A successful aircraft development program requires a satisfactory solution of many dissimilar problems. Ideally, we want airplanes to offer low empty weight, good performance, easy handling, a strong and light structure, and to be inexpensive to manufacture, maintain, and operate, to name a few. All present different problems to the design, and each requires a specific solution. However, the best solution to each individual problem is ordinarily not the best solution from a synergistic standpoint. Ultimately, the goal is to bring to market a useful product that reduces acquisition and operational costs while improving performance beyond previous technology. Achieving this requires *compromise* and *balance* of conflicting capabilities. Airplanes designed for just one requirement tend to satisfy that requirement only.

A correct sizing of an airplane depends on numerous important variables, such as those discussed in Section 1.2.3. A clearly stated mission plays a paramount role in this respect and allows the sizing to be accomplished using mathematical tools. This section presents a few optimization methods that focus on the initial sizing of the aircraft's external geometry. The chapter also introduces several methods to conduct trade studies.

3.1.1 The Content of This Chapter

- Section 3.2 presents a powerful method, called Constraint Analysis that helps the designer determine the W/S and T/W (or P/W) for the new design, such that it will meet all prescribed performance requirements.
- Section 3.3 presents several trade study methods, which are powerful tools for the solution of various engineering problems.
- Section 3.4 introduces design optimization and provides a few practical examples of its use.

3.1.2 Fundamental Concepts

This section introduces several concepts important in aircraft sizing, presented in alphabetical order.

(1) "At Condition"

The term appears in various places in the book. It refers to the flight condition of an airplane at the instant of

https://doi.org/10.1016/B978-0-12-818465-3.00027-6

Copyright © 2022 Elsevier Inc. All rights reserved.

inquiry and pins down current weight, position, altitude, airspeed, time, outside air temperature, and so forth.

(2) Constraint Analysis

Constraint analysis is used to assess the relative significance of selected aircraft performance parameters on the design. It allows one to understand which combinations of wing- and thrust-loadings permit the aircraft to simultaneously meet dissimilar performance requirements, such as rate of climb, take-off distance, and others. The method is presented in Section 3.2.

(3) Design of Experiments (DOE)

Refers to a method used to determine which variable(s) among a collection of variables is the most effective contributor to some process. These are presented in Section 3.3.3.

(4) Effectiveness

The *effectiveness* of an aircraft refers to a quantitative measure of how well it achieves its mission. This typically involves the performance of the aircraft. For instance, the effectiveness of a long-range transport aircraft can be defined as the distance flown per unit mass of fuel.

(5) Mathematical Optimization

Refers to the multitude of methods used to solve optimization problems. Such problems involve the determination of the maximum or minimum of multivariable objective functions and its position inside the design space. A simple example is the determination of wing area. Given a fixed $C_{L_{max}}$, a large wing area is an optimized solution to the design problem: "low stalling speed." Conversely, a small wing area is an optimized solution to the design problem: "high cruising speed." These exemplify conflicted solutions. Thus, if the design problem is "low stalling speed and high cruising speed," the optimized solution is a compromise in wing area, somewhere between the two extremes. A basic introduction to aircraft optimization is given in Section 3.4.

(6) Operational Efficiency

In terms of aircraft, the *operational efficiency* refers to the costs associated with acquiring, maintaining, and operating the vehicle. It addresses discrepancies between the three. For instance, an airplane can be affordable to purchase, while requiring high maintenance and operational costs. More information is given in Section 2.1.4.

(7) Parametric Analysis

Is a method that provides insight into how an analysis model responds to the variation of its constituent parameters (or variables). This is accomplished by selecting one or more focus-parameters and vary them while observing the changes in the model. It is discussed in Section 3.3.1.

(8) Performance Efficiency

For aircraft, the term refers to the magnitude of the maximum lift-to-drag ratio. However, it is more descriptive when performance parameters are transformed in terms of fuel consumption and payload. As is evident from the performance chapters in this book, this ratio is a key parameter for range and endurance. High fuel costs make this figure of merit even more important. High performance efficiency calls for aerodynamically sleek aircraft.

(9) Trade Study

The term *trade study* (aka *trade-off*) refers to methods used to select the best solution among a set of proposed viable solutions. Trade studies evaluate competing solutions in terms of factors such as cost, performance, effectiveness, safety, availability, impact on schedule, and so forth. See more in Section 3.3.

3.2 CONSTRAINT ANALYSIS

One of the first tasks in any new aircraft design is the creation of a constraint diagram. The graph allows the aircraft's required wing area and power plant needs to be assessed such that all performance requirements included will be met.

The constraint diagram is developed by plotting *constraints* on a special two-dimensional graph called *design space* (see Figure 3-1). It is the set of all possible solutions in terms of the chosen variables. A constraint is a specific design requirement that must be met (e.g., rate of climb of 2500 fpm). It is represented using an *isopleth.*[1] It is normally represented using thrust loading (T/W) as a

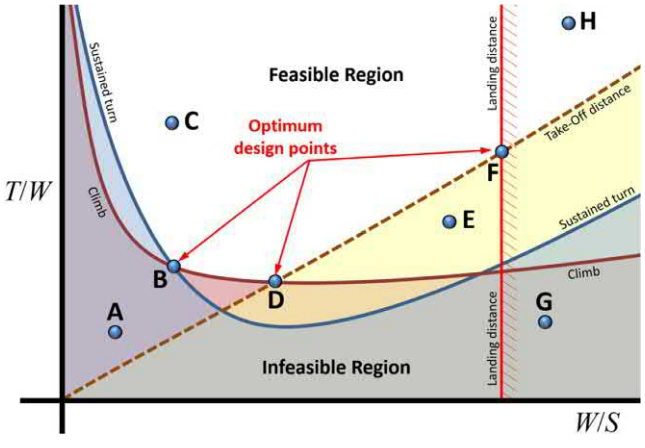


FIGURE 3-1 Typical design space. Only a combination of T/W and W/S that lie in the white (feasible) region constitute a viable design.

[1] An isopleth is a curve of some constant value. Arguably, the best-known isopleth is the isobar – a curve of constant pressure.

function of the form $T/W = f(W/S)$, where T is thrust, W is weight, and S is wing area. In this form, the wing loading (W/S) is plotted along the x-axis and the thrust-to-weight ratio (T/W) along the y-axis; thus, think of W/S as x and T/W as y. The graph is read by noting that any combinations of W/S and T/W above the constraint curves indicate the design surpasses the required values.

The white region in Figure 3-1 is the set of *feasible* (acceptable) solutions, while the shaded regions represent *infeasible* solutions. The landing distance constraint is a vertical line (a side constraint). The graph shows three *optimum design points* (B, D, and F) where the least amount of thrust loading is required to meet all the design requirements, given the associated wing loadings. Designs A, E, and G fail to meet all requirements simultaneously. Designs C and H exceed all; however, H exceeds the maximum landing distance. The graph displays the combinations of W/S and T/W that allows all the requirements to be met. If the weight of the vehicle has been assessed, the designer can extract the required wing area and thrust, allowing engine selection to be undertaken.

Of the three optimum points in Figure 3-1, the one that offers the lowest W/S and T/W should be pursued. It yields the least demanding power plant for the aircraft, given fixed weight. Here, points B or D would have to be evaluated: Point B may require a larger engine but offers lower stalling speed. The opposite holds for Point D. The method is extended to allow the designer to consider the stalling speed of the aircraft. For instance, the 14 CFR Part 1.1 requires Light Sport Aircraft (LSA) to stall at 45 KCAS or less. As discussed in Chapter 1, while 14 CFR Part 23 no longer requires a prescribed stall speed for single-engine aircraft, your design must still specify one.[2] Section 3.2.3 introduces how to incorporate this important limit into the constraint diagram.

3.2.1 General Methodology

The general methodology of constraint analysis requires performance characteristics of interests to be described using mathematical expressions. To be useful, the expressions are converted into the form $T/W = f(W/S)$. Criteria other than T/W and W/S may also be considered. The following formulation applies to all aircraft. It assumes the simplified drag model (See Chapter 16). This is acceptable because little is known about the design when the method is used. Note that this methodology has been expanded to include hybrid electric (e.g. see [1]), fully electric aircraft (e.g. see [2]), and eVTOL urban mobility vehicles (e.g. see [3]).

(1) T/W for a Desired T-O Ground Run Distance

The following expression is used to determine the T/W required to achieve a given ground run distance during T-O. The ground run is the phase of the take-off during which the airplane is level with the ground, i.e. its AOA is small. It does not include the subsequent lift-off and initial climb. An example of its use would be the extraction of T/W for a design required to have a ground run not exceeding 1000 ft.

$$\frac{T}{W} = \frac{1.21}{g\rho C_{L_{\max}} \cdot S_G}\left(\frac{W}{S}\right) + \frac{0.605}{C_{L_{\max}}}(C_{D\ TO} - \mu C_{L\ TO}) + \mu \quad (3\text{-}1)$$

where

$C_{L\ TO}$ = Lift coefficient during T-O run
$C_{D\ TO}$ = Drag coefficient during T-O run
q = Dynamic pressure at $V_{LOF}/\sqrt{2}$ and alt
$C_{L_{\max}}$ = Max lift coefficient in T-O config.
S_G = Ground run (ft or m)
μ = Ground friction constant (typ. 0.04)
g = Acceleration due to gravity (ft/s^2 or m/s^2)

(2) T/W for a Desired Rate of Climb

The following expression is used to determine the T/W required to achieve a given steady rate of climb. An example is the extraction of T/W for an aircraft required to climb at 2000 fpm at S-L or 1000 fpm at 10,000 ft.

$$\frac{T}{W} = \frac{V_V}{V_\infty} + \frac{q}{(W/S)}C_{D_{\min}} + \frac{k}{q}\cdot\left(\frac{W}{S}\right) \quad (3\text{-}2)$$

where

q = Dynamic pressure at the selected airspeed and altitude (lb$_f$/ft^2 or N/m^2)
V_∞ = Airspeed (ft/s or m/s), typically V_Y
V_V = Vertical speed (ft/s or m/s)

Ideally, the airspeed, V_∞, used should be an estimate of the best rate-of-climb airspeed (V_Y – see Section 19.3). Since this requires far more information than typically available at this stage of the design, use historical trends for V_Y. Also note that V_Y changes with wing loading and *this change must be incorporated*. In the absence of better information, the expressions in Table 3-1 can be used to relate V_Y to W/S:

These equations were developed by the author using historical data. They represent sea-level trends based on a mixture of piston and turboprops for 10 typical singles and 12 twins. Additionally, Equation (3-5) was developed using 3 business jets (constituting 13 cases). Note the range of valid wing loadings. Readers with better

[2] While the applicant may suggest a stalling speed, the FAA will have to approve it – do not abandon the 61 KCAS rule yet.

TABLE 3-1 Trends in best rate-of-climb speeds (CAS) of selected classes of aircraft.

Class of aircraft	Climb speed (KCAS)	Valid range of W/S (lb_f/ft^2)	
Single-engine piston and turboprop:	$V_Y = 43.591 + 2.2452(W/S)$	$10 < W/S < 40$	(3-3)
Twin-engine piston and turboprop:	$V_Y = 69.952 + 1.3402(W/S)$	$10 < W/S < 70$	(3-4)
Business jets:	$V_Y = 79.016 + 1.2722(W/S)$	$30 < W/S < 100$	(3-5)

data should develop own relations. Note that the units of V_∞ and V_V must be consistent and the calibrated airspeed must be converted to true airspeed at altitudes above S-L. Also note that V_Y (in CAS) for jets often changes with altitude—so, use it with care.

(3) T/W for a Desired Maximum Angle of Climb

The following expression is used to determine the T/W required to achieve a desired maximum angle of climb. This can be important for airplanes expected to have difficulties meeting noise regulations or to ensure it beats its rivals in this capability. An example of its use would be the extraction of T/W for an aircraft intended to exceed a climb angle of 10 degrees.

$$\frac{T}{W} = \sin\gamma + \frac{1}{LD_{\max}} = \sin\gamma + \sqrt{4kC_{D_{\min}}} \tag{3-6}$$

where

$LD_{\max}$ = Expected maximum L/D
γ = Desired climb angle

This expression is obtained directly from Equation (19-27) (see Section 19.3.2). It is a (horizontal) side constraint (independent of W/S), like the L/D-constraint of Equation (3-12). It may also be helpful to coplot it for specific values (e.g., 5 degrees, 10 degrees, etc.).

(4) T/W for a Level Constant Velocity Turn

The following expression is used to determine the T/W required to maintain a specific load factor (n), while banking at constant airspeed and altitude. For instance, consider a project where the design is required to maintain a 45 degrees bank angle at some airspeed. The first step would convert the angle into n using Equation (20-62). The second step would determine the required T/W using the following expression

$$\frac{T}{W} = q\left[\frac{C_{D_{\min}}}{(W/S)} + k\left(\frac{n}{q}\right)^2\left(\frac{W}{S}\right)\right] \tag{3-7}$$

where

$C_{D_{\min}}$ = Minimum drag coefficient
q = Dynamic pressure at the selected airspeed and altitude (lb_f/ft^2 or N/m^2)
k = Lift-induced drag constant
n = Load factor = $1/\cos\phi$

Note that Equation (3-7) corresponds to *specific excess power* $P_S = 0$ (ft/s or m/s) (see Section 20.4.4). If $n = 1$ (level flight), the expression returns the T/W required for level flight at the selected q. Also note this function is of the form $y = A/x + Bx$ (a specific *Laurent polynomial*), for which the optimal value[3] is $x_{opt} = \sqrt{A/B}$. Using the given parameters, this means the optimal wing loading (in the absence of any other constraint) is

$$\left(\frac{W}{S}\right)_{opt} = \frac{q}{n}\sqrt{\frac{C_{D_{\min}}}{k}} \tag{3-8}$$

The value under the radical is the lift coefficient for the best glide ratio ($L_{D\max}$) for an airplane whose drag can be modeled using the *simplified drag model* (see Section 20.3.5)—a direct consequence of using the simplified drag model.

(5) T/W for a Climbing Constant Velocity Turn

Equation (3-7) represents a flight condition for which altitude is constant (i.e. $P_S = 0$). However, the following expression is used to evaluate the T/W required for a climbing turn, requiring the desired rate of climb (or specific excess power) to be specified. For instance, consider the development of an aerobatic airplane that must climb 1000 fpm ($P_S = 1000/60 = 16.67$ ft/s) while banking 60 degrees. Similar considerations are used for fighter aircraft design.

$$\frac{T}{W} = q\left[\frac{C_{D_{\min}}}{(W/S)} + k\left(\frac{n}{q}\right)^2\left(\frac{W}{S}\right)\right] + \frac{P_S}{V_\infty} \tag{3-9}$$

where

q = Dynamic pressure at the selected airspeed and altitude (alt) (lb_f/ft^2 or N/m^2)
P_S = Specific excess power at the condition

(6) T/W for a Desired Cruise Airspeed

The following expression is used to determine the T/W required to achieve a given cruising speed at some desired altitude. An example of its use would be the extraction of T/W for a design required to cruise at 250 KTAS at 25,000 ft. Astute readers will note it is Equation (3-7) with $n = 1$. However, it is justified as a constraint at higher altitudes than Equation (3-7).

[3] Proof: $y = Ax^{-1} + Bx \;\Rightarrow\; y' = -Ax^{-2} + B = 0 \;\Rightarrow\; B = Ax^{-2} \;\Rightarrow\; x_{opt} = \sqrt{A/B}$.

$$\frac{T}{W} = qC_{D_{\min}}\left(\frac{1}{W/S}\right) + k\left(\frac{1}{q}\right)\left(\frac{W}{S}\right) \tag{3-10}$$

where

q = Dynamic pressure at the selected airspeed and altitude (lb_f/ft^2 or N/m^2)
S = Wing area (ft^2 or m^2)

(7) T/W for a Desired Service Ceiling

The following expression is used to determine the T/W required to achieve a given service ceiling, assuming it is where the best rate of climb of the airplane has dropped to 100 fpm (1.667 ft/s or 0.508 m/s). An example of its use would be the extraction of T/W for a design required to have a service ceiling of 25,000 ft.

$$\frac{T}{W} = \frac{1.667}{V_Y} + \frac{q}{(W/S)}C_{D_{\min}} + \frac{k}{q}\cdot\left(\frac{W}{S}\right) \tag{3-11}$$

where

ρ = Air density at the desired altitude ($slugs/ft^3$ or kg/m^3)
V_Y = Expected best rate-of-climb airspeed (in ft/s or m/s)

If using the SI-system, replace the value 1.667 ft/s with 0.508 m/s. Note that the term service ceiling implies V_Y, as this yields the maximum ROC. This is important to keep in mind when converting the T/W to thrust and then to power for propeller aircraft (as demonstrated later). Use Equation (3-3) to vary V_Y with wing loading (remember to convert to true airspeed and ft/s or m/s).

(8) T/W for a Desired Cruise Lift-to-Drag Ratio

Consider a situation in which a specific lift-to-drag ratio (L/D) during cruise is desired, as is common for commercial and other long range/endurance aircraft. This can be converted into constant T/W that is helpful to coplot with the other constraints (will result in horizontal lines only), as this gives an idea about the required "cleanliness" of the design with respect to drag.

$$\frac{T}{W} = \frac{1}{L/D} \tag{3-12}$$

(9) W/S for a Target Total Landing Distance

Since thrust is reduced to idle during landing, the landing constraint is unaffected by thrust and, instead, is treated as a side constraint (see Section 3.4) for wing loading, W/S. It is prepared by writing the total landing distance in terms of W/S and, assuming an approach glide angle of 3 degrees. Note that given a target landing distance, the equation is solved iteratively for the W/S (see Example 3-1). Also note that the derivation of the following equations is too long to fit conveniently inside this section and is provided separately in Appendix D. Requirements for total landing distance (S_{LDG}) is given by:

$$S_{LDG} = 19.08h_{obst} + \left[0.007923 + 1.556\tau\sqrt{\frac{A}{W/S}} + \frac{1.21}{g\left[\frac{0.605}{C_{L_{\max}}}(C_{D\ LDG} - \mu C_{L\ LDG}) + \mu - \frac{T_{gr}}{W}\right]}\right]\frac{W/S}{A} \tag{3-13}$$

Requirements for the landing ground roll distance (S_{LGR}) only is given by:

$$S_{LGR} = \left[0.01583 + 1.556\tau\sqrt{\frac{A}{(W/S)}} + \frac{1.21}{g\left[\frac{0.605}{C_{L_{\max_0}}}(C_{D\ LDG} - \mu C_{L\ LDG}) + \mu - \frac{T_{gr}}{W}\right]}\right]\frac{(W/S)}{A} \tag{3-14}$$

where

h_{obst} = Obstacle height (typ. 50 ft for GA, 35 ft for commercial)
$A = \rho C_{L_{\max}}$ (in $slugs/ft^3$ or kg/m^3)
ρ = Air density at the desired altitude ($slugs/ft^3$ or kg/m^3)
$C_{L_{\max}}$ = Max lift coefficient in the landing configuration
$C_{L\ LDG}$ = Lift coefficient during ground roll
$C_{D\ LDG}$ = Drag coefficient during ground roll
μ = Ground friction coefficient during ground braking (typ. 0.3, see Table 23.3)
τ = Time for free roll before braking begins (typ. 1–5 s)
T_{gr}/W = Thrust loading during ground roll, where T is idle or reverse thrust (see Table 23.5)

Note that the term μ here is NOT the same as the μ for the T-O constraint of Equation (3-1).

(10) Additional Notes

Note that the dynamic pressure, q, is always calculated at the specific condition to which it refers. This way, the following rules apply to q:

Equation (3-1): q is calculated at $V_{LOF}/\sqrt{2}$ in accordance with Section 18.3.1 and the associated altitude.

TABLE 3-2 Typical aerodynamic characteristics of selected classes of aircraft.

Class	$C_{D_{min}}$	C_{DTO}	C_{LTO}	Assumptions
Amphibious	0.040–0.055	0.050–0.065	≈0.7	Flaps in T-O position
Agricultural	0.035–0.045	0.045–0.055	≈0.7	Flaps in T-O position
Biplane	0.045–0.050	0.045–0.050	≈0.4	No flaps
Powered sailplane	0.010–0.015	0.010–0.015	≈0.4	No flaps
GA Trainer	0.030–0.035	0.040–0.045	≈0.7	Flaps in T-O position
GA High performance single	0.025–0.027	0.035–0.037	≈0.7	Flaps in T-O position
GA typical single, fixed gear	0.028–0.035	0.038–0.045	≈0.7	Flaps in T-O position
Turboprop commuter	0.025–0.035	0.035–0.045	≈0.8	Flaps in T-O position
Turboprop military trainer	0.022–0.027	0.032–0.037	≈0.7	Flaps in T-O position
Turbofan business jet	0.020–0.025	0.030–0.035	≈0.8	Flaps in T-O position
Modern passenger jetliner	0.020–0.028	0.030–0.038	≈0.8	Flaps in T-O position
1960s–70s passenger jetliner	0.022–0.027	0.032–0.037	≈0.6	Flaps in T-O position
World War II bomber	0.035–0.045	0.045–0.055	≈0.7	Flaps in T-O position
World War II Fighter	0.020–0.025	0.030–0.035	≈0.5	Flaps in T-O position

Equation (3-2): q is calculated at the climb airspeed and the associated altitude.
Equation (3-7): q is calculated at the turning airspeed and the associated altitude.
Equation (3-10): q is calculated at the desired cruising speed and the associated altitude.
Equation (3-11): ρ is at the desired service ceiling and q is calculated at V_Y.

A common problem encountered when using this method is that since the geometry of the airplane is unknown, important parameters such as $C_{D_{min}}$, C_{DTO}, C_{LTO}, and k are not known either. To resolve this issue, the designer must look to existing aircraft in the same class as the one being designed. Table 3-2 gives a range of typical values, in lieu of such a study. The table assumes ground-run $\alpha = 0$ degrees. Also, consider Table 16.22, which lists $C_{D_{min}}$ for a few aircraft.

DERIVATION OF EQUATION (3-1)

Assuming the ground run to start from rest, the kinematic relations between acceleration, speed, and distance can be written as shown below:

$$S - S_0 = \frac{V^2 - V_0^2}{2a} \quad \Leftrightarrow \quad S_G = \frac{V_{LOF}^2}{2a}$$

where a is the average acceleration during the T-O run, calculated at $V_{LOF}/\sqrt{2}$ using Equation (18-3), with $\gamma = 0$:

$$a = g\left[\frac{T}{W} - \frac{D}{W} - \mu\left(1 - \frac{L}{W}\right)\right]$$
$$= g\left[\frac{T}{W} - \frac{qSC_{D\ TO}}{W} - \mu\left(1 - \frac{qSC_{L\ TO}}{W}\right)\right]$$

Substituting this into the expression for S_G leads to:

$$S_G = \frac{V_{LOF}^2}{2a} = \frac{V_{LOF}^2}{2g\left[\frac{T}{W} - \frac{qSC_{D\ TO}}{W} - \mu\left(1 - \frac{qSC_{L\ TO}}{W}\right)\right]}$$

Solving for T/W by algebraic manipulations results in:

$$\frac{T}{W} = \frac{V_{LOF}^2}{2g \cdot S_G} + \frac{qSC_{D\ TO}}{W} + \mu\left(1 - \frac{qSC_{L\ TO}}{W}\right) \qquad \text{(i)}$$

where

$$V_{LOF} = 1.1V_{S1} = 1.1\sqrt{\frac{2}{\rho C_{L_{max}}}\frac{W}{S}}$$

where $C_{L_{max}}$ is the maximum lift coefficient in the take-off configuration. Therefore, the dynamic pressure used in Equation (i) is found using

$$q = \frac{1}{2}\rho\left(\frac{V_{LOF}}{\sqrt{2}}\right)^2 = \frac{1}{4}\rho\left(1.1\sqrt{\frac{2}{\rho C_{Lmax1}}\frac{W}{S}}\right)^2 = \frac{0.605}{C_{Lmax1}}\left(\frac{W}{S}\right)$$

Substitute this into Equation (i) and manipulate algebraically to get:

$$\frac{T}{W} = \frac{1.21}{g\rho C_{L_{max}} \cdot S_G}\left(\frac{W}{S}\right) + \frac{0.605}{C_{Lmax1}}(C_{D\ TO} - \mu C_{L\ TO}) + \mu \qquad \text{(ii)}$$

The above equation is a revised version of the one in the first edition of the book. While both are in fact one and the same, the previous presentation of the equation presumed the user would modify V_{LOF} with W/S, which unfortunately led to some confusion. Also, note that the argument for the equation is $V_{LOF}/\sqrt{2}$ (and not V_{LOF}), as this is used to calculate the acceleration. Therefore, when extracting power for a propeller powered aircraft, use $P_{BHP} = T \cdot (V_{LOF}/\sqrt{2})/(\eta_p \cdot 550)$, where η_p is the propeller efficiency at $V_{LOF}/\sqrt{2}$.

DERIVATION OF EQUATION (3-2)

Consider Equation (19-22) for rate of climb, also repeated for convenience:

$$V_V = V_\infty\left(\frac{T}{W} - \frac{qC_{D_{min}}}{(W/S)} - \frac{k}{q}\left(\frac{W}{S}\right)\right)$$

Solving for T/W yields Equation (3-2).

DERIVATION OF EQUATIONS (3-7)–(3-9)

Consider Equation (20-66) for thrust required in a sustained turn at a load factor n, here repeated for convenience (ignoring the trim drag):

$$T_{REQ} = qS\left[C_{D_{\min}} + k(nW/qS)^2\right]$$

This equation can be put into the desired form by dividing both sides by W (writing T instead of T_{REQ}):

$$T = qS\left[C_{D_{\min}} + k\left(\frac{nW}{qS}\right)^2\right] \quad \Leftrightarrow$$

$$\frac{T}{W} = \frac{qS}{W}\left[C_{D_{\min}} + k\left(\frac{nW}{qS}\right)^2\right]$$

$$= \frac{q}{(W/S)}\left[C_{D_{\min}} + k\left(\frac{n}{q}\right)^2\left(\frac{W}{S}\right)^2\right]$$

Bring W/S in the denominator inside the bracket to obtain Equation (3-7). Note that this formulation features the simplified drag model (see Chapter 16, specifically Equation (16-2)). Equation (3-8) uses the optimum for the specific Laurent equation presented, where $A = C_{D_{\min}}$ and $B = k\,(n/q)^2$:

$$x_{opt} = \sqrt{\frac{A}{B}} \;\Rightarrow\; \frac{W}{S} = \frac{q}{n}\sqrt{\frac{C_{D_{\min}}}{k}}$$

To derive Equation (3-9), consider a situation where there is more thrust available than the required thrust, T_{REQ}. Calling this thrust T_{AVAIL}, we can write this as the thrust required plus additional thrust, ΔT, i.e., $T_{AVAIL} = T_{REQ} + \Delta T$. Then, substitute Equation (3-7) and note that since the power associated with ΔT is $\Delta P = \Delta T \cdot V_\infty$, we can write:

$$T_{AVAIL} = T_{REQ} + \Delta T = qS\left[C_{D_{\min}} + k\left(\frac{nW}{qS}\right)^2\right] + \Delta T$$

$$= qS\left[C_{D_{\min}} + k\left(\frac{nW}{qS}\right)^2\right] + \frac{\Delta P}{V_\infty}$$

Then, multiply the additional term by 1 or W/W and note that $P_S = \Delta P/W$. This comes from the fact that ROC is power divided by weight (see Chapter 19). Therefore, we get:

$$T_{AVAIL} = qS\left[C_{D_{\min}} + k\left(\frac{nW}{qS}\right)^2\right] + \frac{\Delta P}{V_\infty}\frac{W}{W}$$

$$= qS\left[C_{D_{\min}} + k\left(\frac{nW}{qS}\right)^2\right] + \frac{P_S}{V_\infty}W$$

Then dividing both sides of the equal sign by W similar to what was done for Equation (3-7) yields Equation (3-9).

DERIVATION OF EQUATION (3-10)

Thrust equals drag in cruise. Thus, we can write:

$$T = D = \frac{1}{2}\rho V_\infty^2 S C_D = \frac{1}{2}\rho V_\infty^2 S\left(C_{D_{\min}} + \frac{C_L^2}{\pi \cdot AR \cdot e}\right)$$

Expand the above expression and substitute the definition for the lift coefficient, $C_L = 2W/(\rho V_\infty^2 S)$

$$T = \frac{1}{2}\rho V_\infty^2 S C_{D_{\min}} + \frac{\frac{1}{2}\rho V_\infty^2 S}{\pi \cdot AR \cdot e} C_L^2$$

$$= \frac{1}{2}\rho V_\infty^2 S C_{D_{\min}} + \frac{\frac{1}{2}\rho V_\infty^2 S}{\pi \cdot AR \cdot e}\left(\frac{2W}{\rho V_\infty^2 S}\right)^2$$

Manipulate algebraically by isolating the term W/S:

$$T = \frac{1}{2}\rho V_\infty^2 S C_{D_{\min}} + \frac{2\rho V_\infty^2 S}{\pi \cdot AR \cdot e \cdot \rho^2 \cdot V_\infty^4}\left(\frac{W}{S}\right)^2$$

$$= \frac{1}{2}\rho V^2 S C_{D_{\min}} + \frac{2S}{\pi \cdot AR \cdot e \cdot \rho \cdot V_\infty^2}\left(\frac{W}{S}\right)^2$$

Divide through by the weight W and manipulate:

$$\frac{T}{W} = \frac{\frac{1}{2}\rho V_\infty^2 S C_{D_{\min}} + \frac{2S}{\pi \cdot AR \cdot e \cdot \rho \cdot V_\infty^2}\left(\frac{W}{S}\right)^2}{W}$$

$$= \frac{\frac{1}{2}\rho V_\infty^2 S C_{D_{\min}}}{W} + \frac{2S}{\pi \cdot AR \cdot e \cdot \rho \cdot V_\infty^2 \cdot W}\left(\frac{W}{S}\right)^2$$

Rearrange in terms of W/S:

$$\frac{T}{W} = \frac{1}{2}\rho V_\infty^2 C_{D_{\min}}\left(\frac{1}{W/S}\right) + \frac{2}{\pi \cdot AR \cdot e \cdot \rho \cdot V_\infty^2}\left(\frac{W}{S}\right)$$

Since the dynamic pressure is $q = \frac{1}{2}\rho V_\infty^2$ and the lift-induced drag constant is $k = 1/(\pi \cdot AR \cdot e)$, these can be substituted into the above expression to yield Equation (3-10).

DERIVATION OF EQUATION (3-11)

It is assumed that the service ceiling is where the best rate of climb has dropped to 100 fpm ($V_V = 1.667$ ft/s). Therefore, using Equation (3-2), we can write:

$$\frac{T}{W} = \frac{V_V}{V_\infty} + \frac{q}{(W/S)}C_{D_{\min}} + \frac{k}{q}\cdot\left(\frac{W}{S}\right)$$

$$= \frac{1.667}{V_Y} + \frac{q}{(W/S)}C_{D_{\min}} + \frac{k}{q}\cdot\left(\frac{W}{S}\right)$$

3.2.2 Methodology to Accommodate Normally Aspirated Piston Engines

Normally aspirated piston engines require a special treatment due to their characteristic power reduction with altitude. A piston engine delivering 100 BHP at S-L on a standard day, delivers 75 BHP at some 8300 ft (assuming fixed throttle position). Conversely, to develop 75 BHP at 8300 ft, an engine must be capable of at least 100 BHP at S-L. This information is vital when the engine is purchased because it is always rated at S-L power. *This requires the T/W-versus-W/S constraint diagram to be converted to P_{BHP}-versus-W/S and normalized to sea level*. Note that transforming T/W-versus-W/S to P_{BHP}-versus-W/S requires correct propeller efficiency. Inevitably, this shifts the optimum W/S. The conversion is accomplished using the following procedure. Note that this is not needed for airplanes featuring electroprops, as their power is independent of altitude. The same holds for turboprops, provided the operating altitude is below the engine's flat-rating altitude.

STEP 1: Convert T/W into Thrust

The thrust (T) that the engine must develop at the flight condition of interest is obtained by multiplying the resulting T/W by the weight at condition, W.

$$T = W\left(\frac{T}{W}\right) \tag{3-15}$$

STEP 2: Convert T into Power at Altitude

This conversion is accomplished using Equation (15-51) or (15-52), repeated here for convenience (where η_p is propeller efficiency and V_∞ is true airspeed in ft/s or m/s):

$$\begin{aligned} P_{HP} &= \frac{TV_\infty}{\eta_p \times 550} \quad \text{(UK-system)} \\ P_{kW} &= \frac{TV_\infty}{\eta_p \times 1000} \quad \text{(SI-system)} \end{aligned} \tag{3-16}$$

STEP 3: Normalize P into Power at Altitude

Finally, if the above power refers to a flight condition above S-L, convert it to its corresponding S-L value using the Gagg-Ferrar model, presented in Equation (7-8) and repeated below for convenience:

$$\begin{aligned} P_{HP_{S-L}} &= P_{HP}/(1.132\sigma - 0.132) \quad \text{(UK-system)} \\ P_{kW_{S-L}} &= P_{kW}/(1.132\sigma - 0.132) \quad \text{(SI-system)} \end{aligned} \tag{3-17}$$

The use of this approach is shown in Example 3-1. Use Table 3-3 to select typical propeller efficiencies:

TABLE 3-3 Typical values for propeller efficiency, η_p.

Activity	Fixed pitch "climb"	Fixed pitch "cruise"	Constant speed prop
At rest	0	0	0
$V_{LOF}/\sqrt{2}$	0.45–0.50	0.40–0.45	0.50
Liftoff speed, V_{LOF}	0.60–0.65	0.55–0.60	0.65
Climb speed, V_Y	0.75	0.60–0.65	0.75–0.80
Cruising speed, V_C	0.65–0.70	0.75	0.85

EXAMPLE 3-1

To evaluate the effectiveness of the constraint analysis method, apply it to an existing aircraft; the Cessna 162 Skycatcher. As detailed in its Pilot's Operating Handbook [4], its aspect ratio (AR) is 8 and wing area (S) is 120 ft^2. As an LSA, its gross weight (W_0) is 1320 lb$_f$. Assume its $C_{D_{min}} = 0.0333$. Subject it to the following requirements:

(1) Ground run (S_G) must be less than 640 ft at W_0. Assume $C_{L_{max}}$ equals that of the C-162 during T-O, $\mu = 0.04$, $C_{L\ TO} = 0.5$, and $C_{D\ TO} = 0.038$.
(2) Best rate of climb of 880 fpm at the best climb speed (V_Y) at S-L.
(3) Must sustain $n = 1.155$ g (30 degrees bank) constant velocity turn while cruising at 108 KTAS at 8000 ft.
(4) Cruising speed of 108 KTAS at 8000 ft.
(5) Service ceiling of 15,000 ft.
(6) Landing distance over a 50 ft obstacle shall be less than 1369 ft at S-L (standard 3 degrees glide path). Assume $h_{obst} = 50$ ft, $C_{L_{max}} = 2.029$, $C_{L\ LDG} = 0.5$, $C_{D\ LDG} = 0.07$, $\mu = 0.3$, $T_{gr}/W = 0.0$, $A = \rho C_{L_{max}} = 0.004825$, and $\tau = 1$ s.

Plot a constraint diagram for these requirements for W/S ranging between $5 \le W/S \le 35$ lb$_f$/ft^2. In creating the constraint diagram, calculate a sample T/W for all constraints using $W/S = 10$ lb$_f$/ft^2. Then evaluate the required wing area and horsepower for the airplane assuming a propeller efficiency (η_p) or 0.60 at V_{lof}, 0.65 during climb, and 0.75 for cruise maneuvers, respectively.

SOLUTION:

***STEP* 1:** Calculate span efficiency per Section 9.5.12(4) (Method 1):

EXAMPLE 3-1 *(cont'd)*

$$e = 1.78\left(1 - 0.045AR^{0.68}\right) - 0.64$$
$$= 1.78\left(1 - 0.045(8)^{0.68}\right) - 0.64 = 0.8106$$

***STEP* 2:** Calculate the lift-induced drag constant, k per Equation (16-6):

$$k = 1/(\pi \cdot AR \cdot e) = 1/(\pi \cdot (8) \cdot (0.8106)) = 0.04909$$

***STEP* 3:** The T/W for the T-O ground-roll is calculated per Equation (3-1). First, calculate the $C_{L_{max}}$ for the C-162 in its T-O configuration (with flaps deployed at 10 degrees). Its pilot's operating handbook (POH) states it stalls at 43 KCAS at wing loading of 11 lb_f/ft^2. Assuming these numbers are accurate, we calculate its $C_{L_{max}}$ as follows:

$$C_{L_{max}} = \frac{2W}{\rho V_S^2 S} = \frac{2(11)}{(0.002378)(43 \times 1.688)^2} = 1.756$$

In comparison, its actual, clean-configuration $C_{L_{max}}$ for the C-162 is 1.68. Recalling that $\mu = 0.04$, $C_{L\ TO} = 0.5$, and $C_{D\ TO} = 0.038$ (to account for flaps), we get the following value of T/W (note that our sample calculation uses $W/S = 10$ lb_f/ft^2):

$$\left(\frac{T}{W}\right)_1 = \frac{1.21}{g\rho C_{L_{max}} \cdot S_G}\left(\frac{W}{S}\right) + \frac{0.605}{C_{L_{max}}}(C_{D\ TO} - \mu C_{L\ TO})$$
$$+ \mu = \frac{1.21(10)}{(32.174)(0.002378)(1.756)(640)}$$
$$+ \frac{0.605}{1.756}(0.038 - (0.04)(0.5)) + 0.04 = 0.1869$$

***STEP* 4:** Calculate the T/W for a desired ROC of 880 fpm (14.67 ft/s) using Equation (3-2). For this, we need the climb speed, V_Y, which we calculate using Equation (3-3). For $W/S = 10$ lb_f/ft^2, we get $V_Y = 43.591 + 2.2452(10) = 66.04$ KCAS (or 111.5 ft/s). Note that V_Y of the C-162 (per the POH) is 63 KCAS; the estimate is 3 KCAS off. Next, let us calculate the dynamic pressure:

$$q_2 = \frac{1}{2}\rho V_\infty^2 = \frac{1}{2}(0.002378)(111.5)^2 = 14.78\ lb_f/ft^2$$

Thus, we get the following value of T/W for $W/S = 10$ lb_f/ft^2:

$$\left(\frac{T}{W}\right)_2 = \frac{V_V}{V_\infty} + \frac{q_2}{(W/S)}C_{D_{min}} + \frac{k}{q_2} \cdot \left(\frac{W}{S}\right)$$
$$= \frac{14.67}{111.5} + \frac{14.78}{(10)}(0.0333) + \frac{0.04909}{14.78} \cdot (10) = 0.2140$$

***STEP* 5:** For the constant velocity turn, calculate the T/W per Equation (3-7). Begin by computing the dynamic pressure at 8000 ft:

$$\rho = 0.002378\ (1 - 0.0000068756 \times 8000)^{4.2561}$$
$$= 0.001869\ slugs/ft^3$$

Then, calculate the dynamic pressure at 108 KTAS (note that subscripts are used to indicate that q changes from constraint to constraint—this is the third curve):

$$q_3 = \frac{1}{2}\rho V_\infty^2 = \frac{1}{2}(0.001869)(108 \times 1.688)^2 = 31.06\ lb_f/ft^2$$

Then, calculate the T/W for the sample value of $W/S = 10$ lb_f/ft^2:

$$\left(\frac{T}{W}\right)_3 = q_3\left[\frac{C_{D_{min}}}{(W/S)} + k\left(\frac{n}{q_3}\right)^2\left(\frac{W}{S}\right)\right]$$
$$= (31.06)\left[\frac{0.0333}{(10)} + (0.04909)\left(\frac{1.155}{31.06}\right)^2(10)\right]$$
$$= 0.1245$$

***STEP* 6:** Of course, we recognize that since the cruise constraint assumes equal airspeed and altitude as the previous constraint, its value must be less. Regardless, let us calculate it too. We do this using Equation (3-10) with the values of ρ and q from ***STEP* 5**:

$$\left(\frac{T}{W}\right)_4 = q_4 C_{D_{min}}\left(\frac{1}{W/S}\right) + k\left(\frac{1}{q_4}\right)\left(\frac{W}{S}\right)$$
$$= (31.06)(0.0333)\left(\frac{1}{10}\right) + 0.04909\left(\frac{1}{31.06}\right)(10)$$
$$= 0.1192$$

***STEP* 7:** For the service ceiling constraint, calculate T/W per Equation (3-11), using $V_Y = 66.04$ KCAS from STEP 4. Since this is calibrated airspeed, we can use the dynamic pressure calculated in that step:

$$q_5 = q_2 = 14.78\ lb_f/ft^2$$

This assumes (1) V_Y is independent of altitude (which may not hold for some jet aircraft) and (2) low subsonic speed (better to include compressibility). That said, we must convert V_Y to true airspeed, as this is required by the formulation. Since this airspeed is less than Mach 0.3, let us choose the incompressible conversion methodology in Chapter 17. The density ratio at 17000 ft is $\sigma = 0.6292$, so $V_{Y\ TAS} = V_Y/\sqrt{\sigma} = 83.26$ KTAS (140.5 ft/s).

$$\left(\frac{T}{W}\right)_5 = \frac{1.667}{V_Y} + \frac{q_5}{(W/S)}C_{D_{min}} + \frac{k}{q_5} \cdot \left(\frac{W}{S}\right) = \frac{1.667}{140.5}$$
$$+ \frac{(14.78)}{(10)}(0.0333) + \frac{0.04909}{14.78} \cdot (10) = 0.09429$$

Continued

EXAMPLE 3-1 (*cont'd*)

***STEP* 8:** To evaluate the value of W/S for which the landing distance of 1369 ft can be met, assume we can achieve the same $C_{L_{max_0}}$ in the landing configuration as the C-162, at airspeed of 40 KCAS [4]:

$$C_{L_{max_0}} = \frac{2W}{\rho V_S^2 S} = \frac{2}{\rho V_S^2}\left(\frac{W}{S}\right)$$

$$= \frac{2}{(0.002378)(40 \times 1.688)^2}(11) = 2.029$$

Additionally, as stated earlier, other parameters equal $h_{obst} = 50$ ft, $\rho = 0.002378$ slugs/ft^3, $C_{L_{max_0}} = 2.029$, $C_{L\ LDG} = 0.5$, $C_{D\ LDG} = 0.07$, $\mu = 0.3$, $T_{gr}/W = 0.0$, $A = \rho C_{L_{max_0}} = 0.004825$ slugs/ft^3, and $\tau = 1$ s. These are substituted into Equation (3-13), transforming it into the arithmetic format below, which then is solved using iteration:

$$S_{LDG} = 954 + \left[0.1441 + \frac{0.1081}{\sqrt{W/S}}\right]\frac{W/S}{0.004825} \le 1369 \text{ ft}$$

$$\Leftrightarrow \quad \frac{W}{S} \le 11.37 \text{ lb}_f/\text{ft}^2$$

This indicates that the 1369 ft total landing distance is met for wing loading less than 11.37 lb$_f$/ft^2.

***STEP* 9:** Of course, these calculations must be repeated multiple times to build the constraint diagram. This is shown in the *left* graph of Figure 3-2. *Note that the region above the curves is the feasible region.*

***STEP* 10:** To convert the T/W into power, follow the procedure outlined in Section 3.2.2. Although neglected in this example, one should account for reduced weight at various altitudes (unless an electric vehicle). Applying Equations (3-15)–(3-17) to the cruise constraint at $W/S = 10$ lb$_f$/ft^2, where $T/W = 0.1192$ gives the required thrust for a cruising speed of 108 KTAS at 8000 ft.

$$T = W\left(\frac{T}{W}\right) = (1320)(0.1192) = 157.4 \text{ lb}_f$$

This thrust can be achieved using a propeller with an η_p of 0.75 at 108 KTAS and engine power per Equation (3-16), as shown below

$$P_{HP} = \frac{TV_\infty}{\eta_p \times 550} = \frac{(157.4)(108 \times 1.688)}{(0.75) \times 550} = 69.56 \text{ BHP}$$

However, to develop some 70 BHP at 8000 ft requires a minimum S-L rating of 92 BHP per Equation (3-17) (where $\sigma = 0.7860$). Note that the normalized power for all the constraints is plotted in the *right* graph of Figure 3-2.

Additional Remarks: This demonstration shows that, based on power, the optimum wing loading (11.2 lb$_f$/ft^2) is close to the gross weight wing loading of the Skycatcher ($W/S = 11$ lb$_f$/ft^2). It supports the viability of the method. Note that the position of the optimum in the two graphs of Figure 3-2 is not a mistake—when the T/W is converted to engine power, the optimum shifts due to propeller efficiency and altitude effects. The shift is ordinarily much greater than resulted for this aircraft.

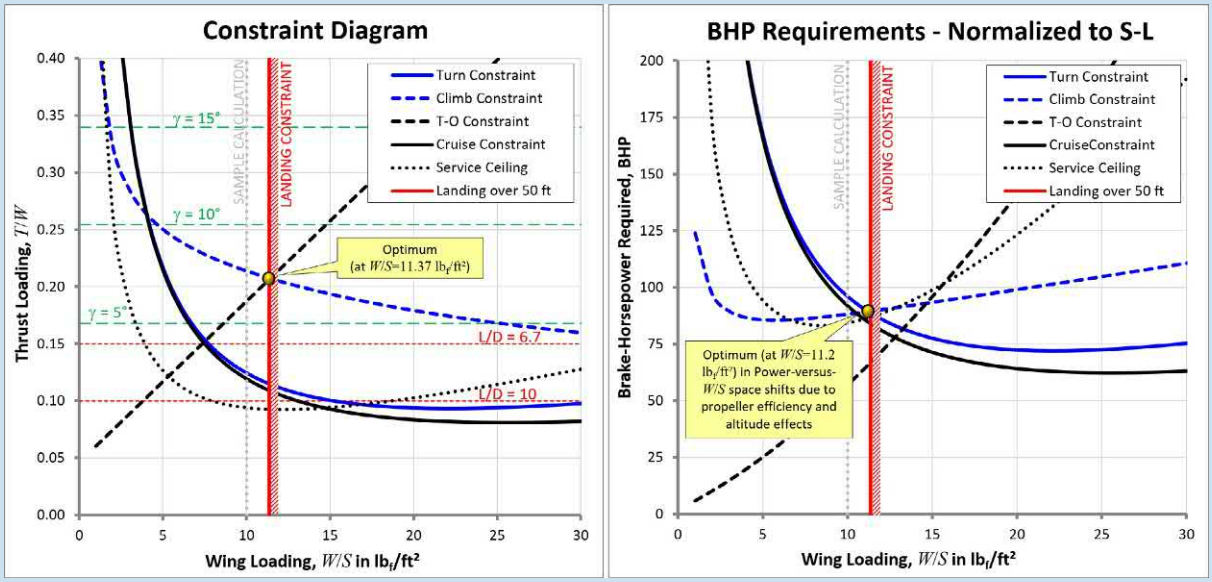


FIGURE 3-2 Constraint diagram. The left graph shows T/W versus W/S, while the right one shows the engine power requirements. Note that the L/D-isopleths show T/W associated with specific cruise L/D, while the γ-isopleths show T/W required to achieve a given climb angle.

3.2.3 Additional Helpful Tools for Initial Sizing

(1) $C_{L_{max}}$ for a Desired Stalling Speed

Stall speed limitations imposed by aviation authorities or operational preferences are of crucial importance when constructing the constraint diagram. This easily overlooked constraint must be considered, because the optimum W/S may easily yield an unacceptably high stalling speed. In effect, the optimum shown in the right graph of Figure 3-2 is a *constrained optimum* (see Section 3.4); however, the stall-speed constraint is missing.

The incorporation of the stalling speed is accomplished by coplotting the maximum lift coefficient, $C_{L_{max}}$, on the constraint diagram of Figure 3-2, using a second vertical axis (see Figure 3-3). To do this, the $C_{L_{max}}$ required for stall to occur at a constant dynamic pressure, q_{stall} is evaluated as a function of the wing loading, W/S:

$$C_{L_{max}} = \frac{1}{q_{stall}}\left(\frac{W}{S}\right) = \frac{2}{\rho V_S^2}\left(\frac{W}{S}\right) \tag{3-18}$$

To use this technique, select one or more target stalling speeds and calculate q_{stall} for each. Next, calculate the maximum lift coefficient for a range of wing loadings, W/S. Superimpose these on the constraint diagram as isopleths of q_{stall} using a secondary vertical axis for the $C_{L_{max}}$. This is shown in Figure 3-3 for the airplane of Example 3-1. In the example, $W/S = 11.2$ lb$_f$/ft^2 was shown to be an optimum in terms of power. The plot is interpreted as follows: *We* start at $W/S = 11.2$ lb$_f$/ft^2 and follow arrow ① to the optimum point. Then continue along arrow ② and read 89.4 BHP using the left vertical axis. Then, we go back to the optimum point and move vertically up to the diagonal isopleth–labeled "$V_S = 45$ KCAS." Then, move horizontally along arrow ③ to the right vertical axis and read $C_{L_{max}} = 1.62$. Note that the Cessna C-162 is coplotted for reference.

DERIVATION OF EQUATION (3-18)

The expression is simply obtained from the standard equation for lift, $L = \frac{1}{2}\rho V_\infty^2 S C_L$. At stall, we may write:

$$W \approx L = \frac{1}{2}\rho V_S^2 S C_{L_{max}} = q_{stall} S C_{L_{max}}$$
$$\Leftrightarrow \quad C_{L_{max}} = \frac{1}{q_{stall}}\left(\frac{W}{S}\right)$$

(2) Initial Estimation of Cruise Thrust and Fuel Requirements

An important early step in many design projects is to understand the thrust or power required for the new design. Consider an airplane designed for a given range (R) or endurance (E) and cruising speed (V_C) while operating at some specified cruise L/D (LD_C). If the weight (W) of the airplane is known at this condition (ideally midrange), we can estimate the thrust (T) and required fuel weight (W_f) for a short mission. However, for long range or endurance flight, we must resort to the Breguet equation. It requires the weight of the aircraft at start-of-cruise, W_{ini}. These expressions are presented below.

Thrust for a jet aircraft:
$$T = \frac{W}{LD_C} \tag{3-19}$$

Fuel weight for short flight (< 1h):
$$W_f = \frac{R}{V_C} \times SFC \times T = \frac{R}{V_C} \times SFC \times \frac{W}{LD_C} \tag{3-20}$$

Fuel weight for long range flight (jet):
$$W_f = W_{ini}\left(1 - e^{-\frac{R \times SFC}{V_\infty \times LD_C}}\right) \tag{3-21}$$

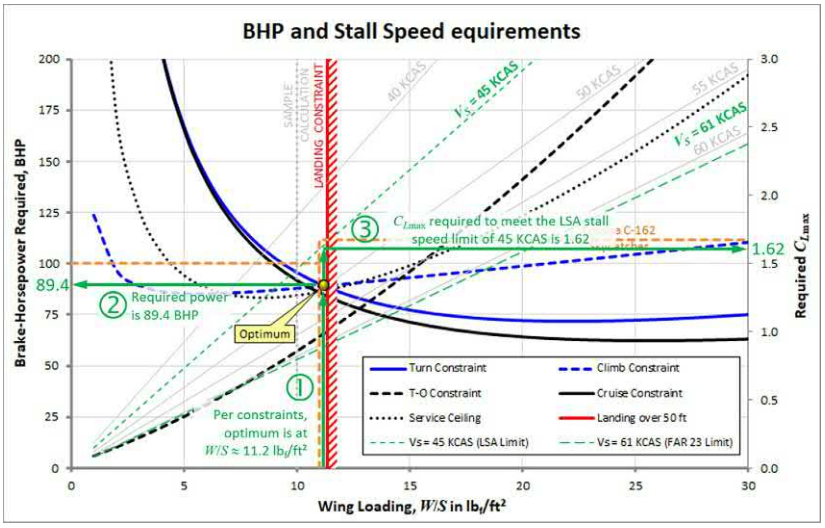


FIGURE 3-3 Constraint diagram with stall speed limits superimposed.

Fuel weight for long range flight (prop):

$$W_f = W_{ini}\left(1 - e^{-\frac{R \times SFC_{hp}}{325.9\eta_p \times (L/D)}}\right) \tag{3-22}$$

Fuel weight for long endurance flight (jet):

$$W_f = W_{ini}\left(1 - e^{-\frac{E \times SFC}{LD_C}}\right) \tag{3-23}$$

Fuel weight for long endurance flight (prop):

$$W_f = W_{ini}\left(1 - e^{-\frac{E \times SFC_{hp} V_\infty}{325.9\eta_p (L/D)}}\right) \tag{3-24}$$

Mass of fuel consumed:

$$m_f = W_f / g \tag{3-25}$$

Proper use of the equations requires unit consistency. For instance, if using Equation (3-21) with the SI-system, R should be in km, E is in h, V_C in km/h, T in N, and SFC in 1/h, yielding fuel weight in N. Divide by $g = 9.807\,\text{m/s}^2$ to get fuel mass in kg. In the UK-system, R should be in nm, E is in h, V_C in KTAS, T in lb_f, SFC in 1/h, and SFC_{hp} in $\text{lb}_\text{f}/(\text{hp}\cdot\text{h})$, yielding fuel weight in lb_f.

(3) Initial Estimation of Required Power for a Propeller Aircraft

Similarly, consider a propeller airplane intended to operate at speed V_C and LD_C. Again, assuming an estimated weight (W) at the condition is known, the power (P_{BHP}) required can be estimated from

Propeller powered aircraft (UK):

$$P_{BHP} = \left(\frac{1}{r}\right)\left(\frac{V_C}{550\eta_p}\right)\left(\frac{W}{LD_C}\right) \tag{3-26}$$

Propeller powered aircraft (SI):

$$P_{kW} = \left(\frac{1}{r}\right)\left(\frac{V_C}{1000\eta_p}\right)\left(\frac{W}{LD_C}\right) \tag{3-27}$$

Where r is the fraction of the rated maximum power. As an example, consider the development of a propeller aircraft, designed to cruise at 200 KTAS ($V_C = 337.6\,\text{ft/s}$) at 65% power ($r = 0.65$) and weight of 5000 lb_f, during which the target L/D at cruise is 15 and propeller efficiency is 0.85. The resulting airplane would require a minimum engine rating of 370 BHP at S-L. If this is our target at some altitude, we can normalize a normally aspirating engine using the Gagg-Ferrar model. Additionally, achieving an LD_C of 15 will require an efficient design. If using the SI-system, V_C must be in m/s and W in N: A corresponding airplane would cruise at 102.9 m/s and weigh 22,241 N, requiring a 275-kW engine.

Note that this can be inverted for a situation in which the designer has a specific engine in mind and needs to understand the impact on required cruise. For instance, consider a target engine slated to be operated at 65% power during cruise. This implies the selected geometry must develop a cruise L/D no worse than that presented below (and simply obtained by solving Equation (3-26) for the L/D):

$$LD_C = \frac{V_C W}{r P_{BHP} 550 \eta_p} \tag{3-28}$$

(4) Initial Estimation of Minimum Drag Coefficient

Estimation of $C_{D_{\min}}$ at this early stage is also of importance, as it helps the design team realize its implications for the external geometry and manufacturing quality. This can be estimated using the expression below.

$$C_{D_{\min}} = \frac{C_{L_C}}{LD_C} - kC_{L_C}^2 \tag{3-29}$$

where C_{L_C} is the lift coefficient during cruise. Note that the above expression tells you what $C_{D_{\min}}$ your airplane MUST NOT EXCEED to achieve said airspeeds and glide ratio. It does NOT guarantee your airplane will do so—that is where your design skills take over. As an example of its use, consider the previous airplane with an intended AR of 10 and expected to cruise at $C_{L_C} = 0.35$. The resulting Oswald span efficiency coefficient is estimated at 0.7566 (see Equation (9-129)) and lift-induced drag constant of $k = 0.04207$. Thus, the minimum drag coefficient must not exceed 182 dragcounts ($C_{D_{\min}} < 0.0182$). This implies the airplane should feature a retractable landing gear and smooth NLF surfaces, probably requiring composite airframe.

DERIVATION OF EQUATIONS (3-19) AND (3-29)

Expressions (3-19) and (3-26) can be obtained as follows:

$$\frac{T}{W} = \frac{D}{L} \Rightarrow T = \overbrace{\frac{W}{LD_C}}^{\text{sufficient for a jet}} = \overbrace{\frac{550 P_{BHP}\eta_p}{V_C}}^{\text{required for a prop aircraft}}$$

$$\Rightarrow \frac{W}{LD_C} = \frac{550 P_{BHP}\eta_p}{V_C} \Rightarrow P_{BHP} = \left(\frac{V_C}{550\eta_p}\right)\left(\frac{W}{LD_C}\right)$$

Equation (3-27) in the SI-system that returns required power in kilowatts is obtained from

$$T = \frac{W}{LD_C} = \frac{1000 P_{kW}\eta_p}{V_C} \Rightarrow P_{kW} = \left(\frac{V_C}{1000\eta_p}\right)\left(\frac{W}{LD_C}\right)$$

Expression (3-29) is obtained as follows:

$$LD_C = \frac{C_{L_C}}{C_{D_C}} = \frac{C_{L_C}}{C_{D_{\min}} + kC_{L_C}^2} \Rightarrow C_{D_{\min}} = \frac{C_{L_C}}{LD_C} - kC_{L_C}^2$$

3.3 INTRODUCTION TO TRADE STUDIES

Trade studies refer to methods used to find balanced solutions to technical problems. An understanding of such methods helps the design engineer make sound and objective decisions. Trade studies evaluate competing solutions in terms of cost, performance, effectiveness, safety, availability, impact on schedule, and so forth. Some trade studies are a form of "what-if" analyses: they allow us to evaluate which parameters will affect the characteristics of some baseline model the most and in which way.

3.3.1 Parametric Analysis

As stated in Section 3.1.2, parametric analysis provides insight into how an analysis model responds to changes in its constituent parameters (or independent variables). This is accomplished by selecting one or more *independent variables* and vary them within a given range while observing how one or more *dependent variables* react. A simple example considers the lift equation, applied at stall, as an analysis model: $W \approx L = \frac{1}{2}\rho V_\infty^2 S C_{L_{max}}$. Analyzing this expression parametrically provides insight into what sort of high-lift devices may be needed for the new design. One way of accomplishing this is to combine W and S into a single parameter (wing loading, W/S) and select it and $C_{L_{max}}$ as the two independent variables, while V_S (stalling speed) serves as the dependent one; the objective function. Thus, $V_S = [2(W/S)/(\rho C_{L_{max}})]^{1/2}$. Two examples of such analysis are presented in Figure 3-4. The left graph plots the W/S horizontally and V_S vertically for several fixed values of $C_{L_{max}}$. In contrast, the right graph plots the $C_{L_{max}}$ horizontally and V_S vertically for several fixed values of W/S. Both reveal the same answer, e.g., a wing loading of 40 lb_f/ft^2 and $C_{L_{max}}$ of 2.0 results in a stalling speed of 77 KCAS.

(1) Carpet Plots

Refers to a class of plots that result from parametric analysis in which the interaction of two or more parameters on an objective function is presented as a 2-dimensional plot. The details of the construction of these graphs are outside of the scope of this book, but interested readers can glean more from refs. [5–7].

(2) Baseline Parametric Analyses

Constitutes a method to evaluate how key variables affect a baseline model using a carpet plot. In aircraft design, the term baseline normally refers to the configuration at some known iterative step. A prime example of this is the so-called *nine-point parametric analysis*. It begins with the selection of an objective function, such as range, fuel mileage, payload, or direct operating cost, to name a few. Then, two (or three) parameters that are known to strongly affect the objective function are chosen. The number of parameters is kept low to reduce complexity. Example parameters could be W/S, T/W, and, perhaps, engine model. Next, the two specific values around the baseline are chosen for both parameters. For instance, they could

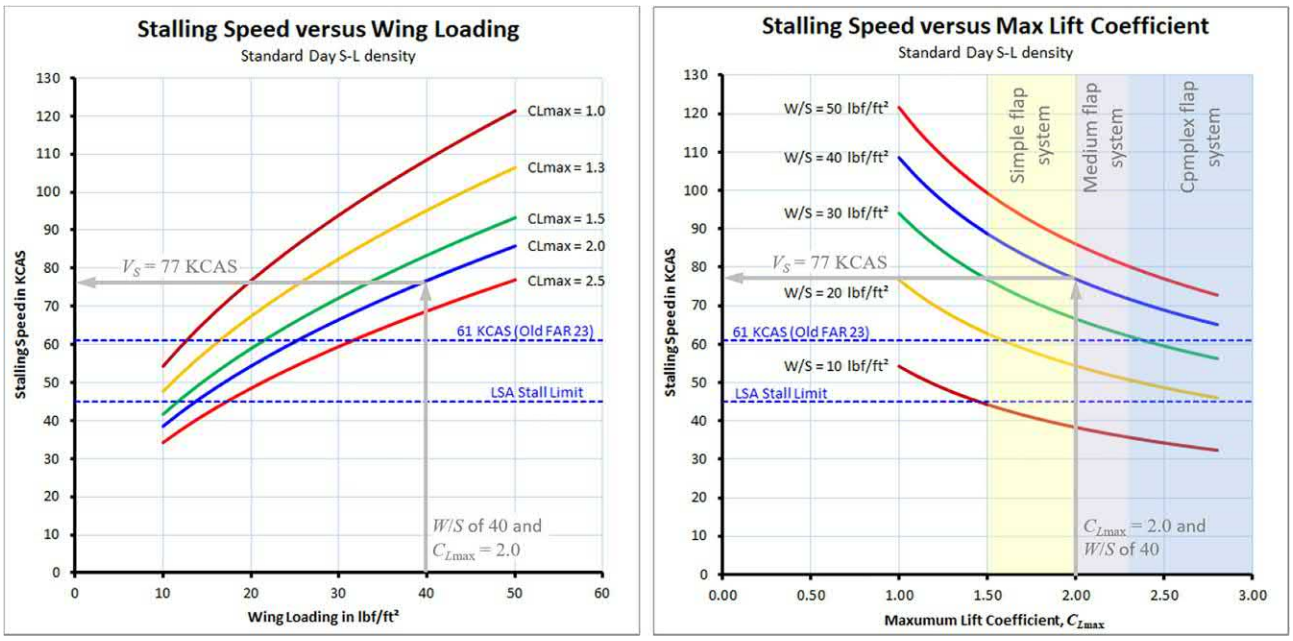


FIGURE 3-4 A sample parametric study of the effect of W/S and $C_{L_{max}}$ on V_S.

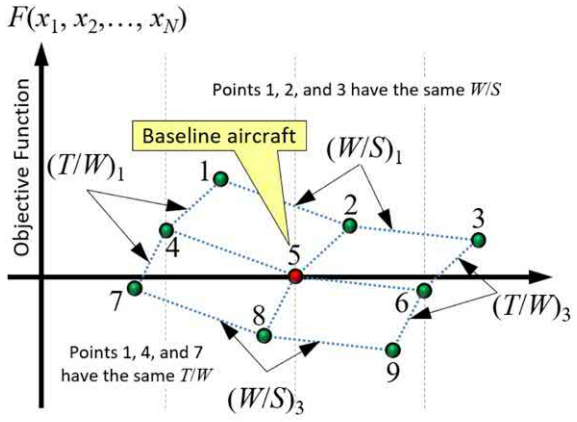


FIGURE 3-5 A setup of a sample nine-point parametric study, involving two parameters.

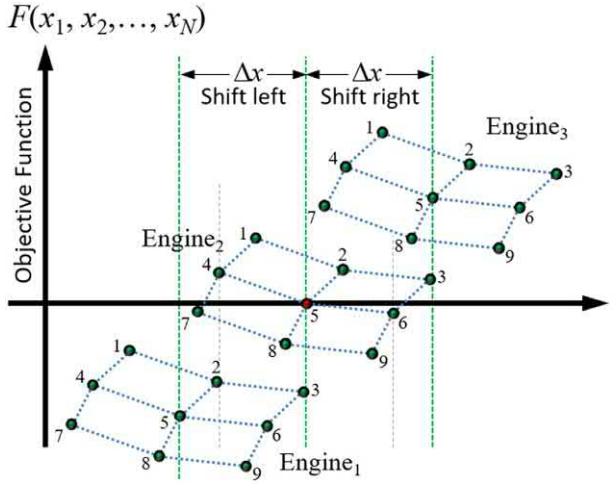


FIGURE 3-6 A setup of nine-point matrices when studying three parameters.

be varied by ±10% from that of the baseline value. This gives us three values for each parameter, yielding nine values of the objective function (a nine-point matrix). These nine are then plotted with the baseline represented as Point 5 (whose values are already known at the beginning of the study). This is illustrated in Figure 3-5. Thus, Point 1 would involve the combination $(W/S)_1$ and $(T/W)_1$, Point 2 involves $(W/S)_1$ and $(T/W)_2$, and so forth.

When a third parameter is included (e.g., engine model), nine-point matrices are set up as show in Figure 3-6. Note that the vertical scale is the objective function. Here, the horizontal axis is drawn through the baseline point for clarity. The horizontal axis may or may not have any direct coordinates. The illustration shows matrices for engines 1 and 3 shifted left and right, respectively, for clarity.

EXAMPLE 3-2

Conduct a nine-point parametric study of the T-O ground roll of the aircraft in Example 3-1 by evaluating a ±10% change in W/S and T/W.

SOLUTION:

To conduct this study, we solve Equation (3-1) for the ground run:

$$S_G = \frac{1.21}{g\rho C_{L_{max}}\left[\left(\frac{T}{W}\right) - \frac{0.605}{C_{L_{max}}}(C_{D\ TO} - \mu C_{L\ TO}) - \mu\right]}\left(\frac{W}{S}\right)$$

Recalling that $\rho = 0.002378$ slugs/ft^3, $\mu = 0.04$, $C_{L_{max}} = 1.756$, $C_{L\ TO} = 0.5$, and $C_{D\ TO} = 0.038$, we substitute these and rewrite it in a parametric form as a function of W/S and T/W:

$$S_G \approx \frac{9.006}{(T/W) - 0.04620}\left(\frac{W}{S}\right)$$

Thus, when using the values in Example 3-1, i.e. $W/S = 10$ lb$_f$/ft^2 and $T/W = 0.1869$, we get $S_G \approx 640$ ft, which we designate as the center point (Point 5). The remaining eight points are obtained using various combinations of $W/S = 9$, 10, and 11 lb$_f$/ft^2 and $T/W = 0.1682$, 0.1869, and 0.2056. This allows the construction of the graph in Figure 3-7. Note that the X-values are only used to separate the points, while the Y-values are the actual ground run distances. The X-values for the leftmost points are 0.8, 1.0, and 1.2. The X-values for the center row are 1.8, 2.0, and 2.2, and so forth. The result helps quantify the consequence of deviating from the design W/S of 10 lb$_f$/ft^2 and T/W of 0.1869.

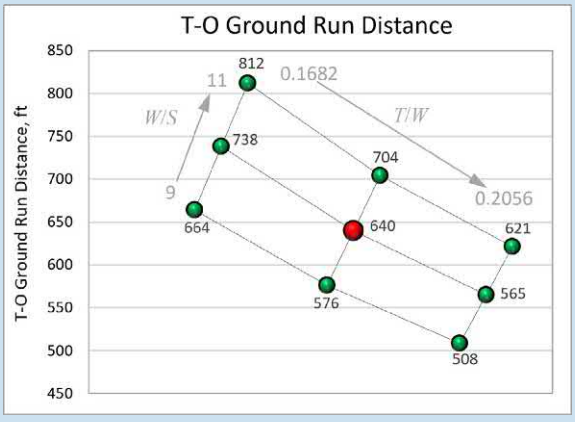


FIGURE 3-7 Example nine-point parametric analysis.

3.3.2 Stall Speed–Cruise Speed Carpet Plot

The *stall speed–cruise speed* carpet plot is another way to help the designer select wing area that simultaneously satisfies the desired stalling and cruising speed targets. More details on how to create this plot are given in the first edition of the book. The graph requires several key parameters to be known, unlike the constraint diagram, which requires much less initial knowledge. This renders the method a tool to use *after* the constraint diagram has been prepared. It is also ideal when considering the modification (growth) of existing airplane types.

In its simplest form, the method revolves around developing two tables; stalling speed versus wing area for a range of expected values of $C_{L_{max}}$ and cruise speed versus wing area (see Table 3-4). These speeds are called maximum speeds, as they truly are the maximums for the specified cruise power setting. Then, the information in the tables is coplotted in the carpet form shown in Figure 3-8.

TABLE 3-4 Stalling and maximum speeds as a function of $C_{L_{max}}$ and wing area.

Stalling Speed KCAS		WING AREA, ft²						
		120	130	140	150	160	170	180
Maximum Lift Coefficient	1.7	70	67	65	63	61	59	57
	1.8	68	65	63	61	59	57	56
	1.9	66	64	61	59	57	56	54
	2.0	65	62	60	**58**	56	54	53
	2.1	63	61	58	56	55	53	52
	2.2	62	59	57	55	53	52	50
	2.3	60	58	56	54	52	51	49

S, ft²	V_{max}, KTAS						
120	191	186	182	178	174	171	168
130	191	186	182	178	174	171	168
140	191	186	182	178	174	171	168
150	191	186	182	178	174	171	168
160	191	186	182	178	174	171	168
170	191	186	182	178	174	171	168
180	191	186	182	178	174	171	168

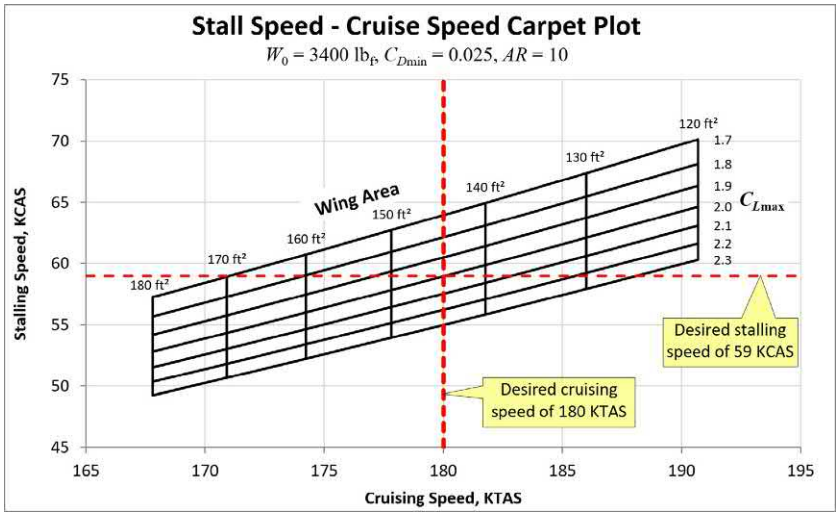


FIGURE 3-8 The resulting carpet plot.

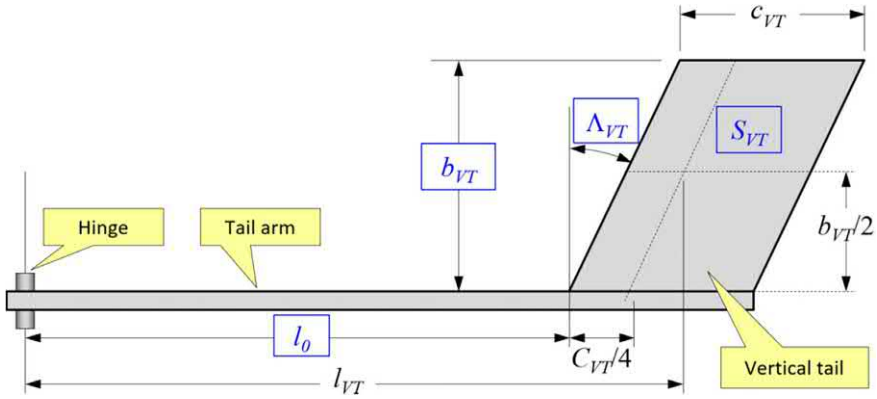


FIGURE 3-9 The geometric relations of a simple tail. The boxed variables will be evaluated.

The upper matrix in Table 3-4 can be recreated for the range of S and $C_{L_{max}}$ shown using Equation (20-29). The lower matrix in Table 3-4 requires a max speed performance analysis at 8000 ft with a $C_{D_{min}} = 0.025$, $AR = 10$, $W = 3400$ lb$_f$, max power at altitude is 235 BHP, and assumed propeller efficiency of $\eta_p = 0.85$. As stated before, more details are given in the first edition of this book.

3.3.3 Design of Experiments

The effectiveness of a given variable (of a collection of variables) on some process can be assessed using *Design of Experiments* (DOE). The method is best explained using an example.

Consider the development of a Vertical Tail (VT) for an airplane and that we seek to understand which properties contribute to its directional stability derivative, $\boldsymbol{C_{N\beta}}$. To keep things manageable, we will analyze the simple constant chord VT configuration shown in Figure 3-9. The tail is mounted to the hinged tail arm, which allows it to rotate freely. The hinge represents the location of the airplane's center of gravity with respect to the vertical surface. Aerodynamic theory dictates that the derivative is affected by the tail arm (l_{VT}), tail planform area (S_{VT}), tail span (b_{VT}), and leading-edge sweep (Λ_{VT}). Other contributions, such as that of taper ratio or airfoil type, will be ignored.

The following question can now be asked: Which of the above variables affect the $\boldsymbol{C_{N\beta}}$ the most? For instance, if any of the variables is changed by, say, ±10% of its initial value, which will change $\boldsymbol{C_{N\beta}}$ the most? The answer is important because if we want to change $\boldsymbol{C_{N\beta}}$, the result helps us understand where to focus our effort.

Before these questions can be answered, the appropriate formulation must be developed. First, the yawing moment, $\boldsymbol{N_{VT}}$, is the product of the lift force acting on the tail, L_{VT}, and its distance from the hinge or tail arm, denoted by l_{VT}. Dividing this by the dynamic pressure, reference area, and span yields the yawing moment coefficient, $\boldsymbol{C_N}$:

Directional moment coefficient:

$$\boldsymbol{C_N} = \frac{\boldsymbol{N_{VT}}}{qSb} = \frac{L_{VT} \times l_{VT}}{qSb} = \frac{qS\left(C_{L_\beta\ VT} \times \beta\right) \times l_{VT}}{qSb}$$
$$= \left(\frac{l_{VT}}{b}\right)\left(C_{L_\beta\ VT} \times \beta\right) \tag{3-30}$$

where

$\boldsymbol{N_{VT}}$ = Yawing moment
L_{VT} = Lift force generated by the tail
l_{VT} = Tail arm
β = Yaw angle
q = Dynamic pressure
S = Wing reference area
b = Wing reference span
$C_{L_\beta VT}$ = 3-dimensional lift curve slope of the tail

Then, the directional stability, $\boldsymbol{C_{N\beta}}$, at a low yaw angles can be approximated from:

$$\text{Directional stability:} \quad \boldsymbol{C_{N_\beta}} = \frac{\partial \boldsymbol{C_N}}{\partial \beta} \approx \left(\frac{l_{VT}}{b}\right) C_{L_\beta\ VT} \tag{3-31}$$

The tail arm, $l_{VT,}$ is based on the dimensions in Figure 3-9 and is calculated from (see the dimensions in the figure):

$$\text{Tail arm:} \quad l_{VT} = l_0 + \frac{c_{VT}}{4} + \frac{b_{VT}}{2}\tan\Lambda_{VT} \tag{3-32}$$

where

l_0 = A tail arm basic length (to the LE of the root)
c_{VT} = Average chord of the VT
b_{VT} = The span of the VT

In this analysis, it is better to use the term l_0 to control the length of the tail arm. The lift curve slope of the tail, $C_{L_\beta VT}$, can be calculated using Equation (9-72), but this is directly dependent on Λ_{VT} since the configuration features a constant chord. By varying each of the four variables (l_0, b_{VT}, S_{VT}, and Λ_{VT}) over a range of ±10%, using some representative numbers for the variables q, S, and b,

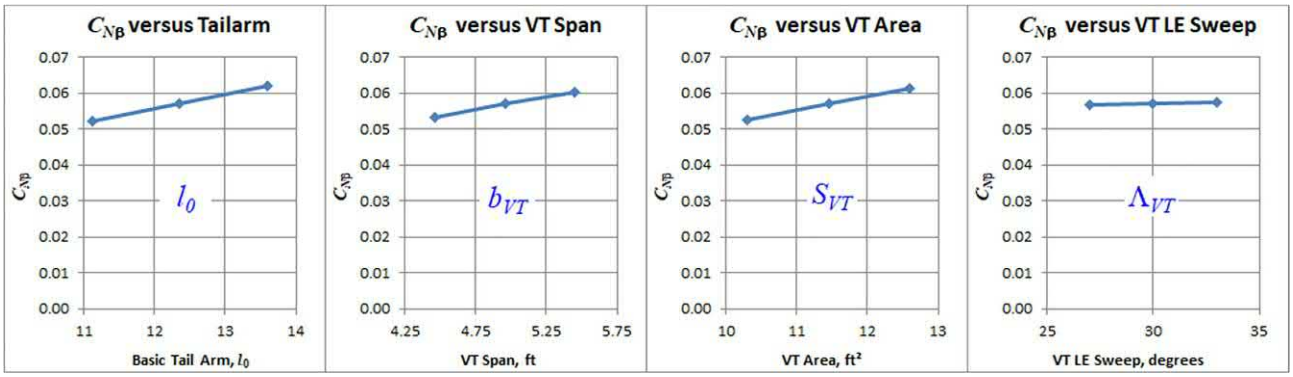


FIGURE 3-10 The results from a DOE analysis.

the graphs of Figure 3-10 were created. The results will now be discussed.

We specify lower and upper bounds for each focus variable as ±10% of its baseline value and calculate $C_{N\beta}$ inside this range. For instance, consider the VT span, b_{VT}. The lower bound would be calculated as $0.9 \cdot b_{VT}$ and the upper as $1.1 \cdot b_{VT}$. Figure 3-10 reveals the impact of these variations on the $C_{N\beta}$ and shows it is significantly affected by the variables l_0, b_{VT}, and S_{VT}, while Λ_{VT} has negligible effect. The effect of l_0, b_{VT}, and S_{VT} appear mostly equal. If we discovered our airplane had insufficient directional stability, it would be wise to focus attention on those three and ignore the leading-edge sweep.

Results such as these can help keep project research costs down; for instance, when planning wind tunnel testing. Here, the number of research variables is reduced from 4 to 3 and the time required to complete the wind tunnel testing should be reduced as well.

3.4 INTRODUCTION TO DESIGN OPTIMIZATION

This section is intended for the newcomer to design optimization. To most, the term *optimization* refers to people's innate inclination to improve a situation; even an already good one. In mathematics, it refers to the numerous computational techniques that allow the minimum or maximum value of some function to be determined (and located). These methods constitute a very important tool for the modern engineer. This section presents important fundamentals and culminates with an example of a wing sizing optimization.

Undergraduate students of engineering are exposed to mathematical optimization through calculus, primarily through the application of gradient methods such as a single-variable differentiation. For some, the exposure extends to the determination of optima through multivariable partial differentiation (using the gradient operator ∇). However, such methods are but the tip of an enormous iceberg of optimization techniques in a highly specialized field within mathematics. Only a selection of these methods is practical for aircraft design problems. You have already seen one such method used; the constraint diagram (which falls into a class of pattern search methods). Regardless, the scope of the field is too broad to allow but an elementary introduction—to whet the appetite. Interested readers are encouraged to seek further knowledge in academic literature.

(1) Classification of Optimization Methods

Optimization problems are generally classified as (1) *continuous-smooth* or *continuous-discrete*, (2) *linear* or *nonlinear*, (3) *constrained* and *unconstrained*, (4) *convex* or *nonconvex*, (5) *deterministic* or *stochastic* (random nature), and (6) *static* or *dynamic*. A specific optimization problem may involve a mixture of the above characteristics. The set of characteristics dictates the most effective method for solution. For instance, linear methods will not return a correct solution for nonlinear problems. Unfortunately, space prevents a detailed treatise of each class; for this, the reader can consult the literature. However, the problems discussed in this section are continuous-smooth, linear and nonlinear, unconstrained and constrained, deterministic (all data known with certainty), and static (independent of time).

Optimization methods are sometimes classified by fidelity, as listed below.

Fidelity	Pros	Cons
Zero-order	Require only the value of the objective function. Reliable, easy to understand and code, and can also deal with discontinuous functions.	In some ways constitute "brute-force" methods that may require the objective to be evaluated thousands of times. Thus, better for computationally lean objective functions.

First-order	Uses the gradient (e.g., the Jacobian matrix) of the objective function and, thus, is more efficient than zero-order methods (i.e., optimum is determined using fewer evaluations of the objective).	The Jacobian of the objective must be evaluated. The methods perform poorly if the gradient is discontinuous.
Second-order	Uses the second derivative (e.g., the Hessian matrix) of the objective to improve efficiency beyond that of first-order methods.	The Hessian of the objective must be evaluated. The methods perform poorly if the gradient is discontinuous.

(2) Grid Search, Pattern Search, and Random Search

Refers to zero-order methods in which the optimum is determined by calculating the value of the objective function at specific points in a grid defined in the design space. The advantage is simplicity; the drawback is excessive solution time if the number of design variables (dimensionality) is large. One way of improving the time-to-solve is to compute each grid point randomly, as this increases the chance of finding the optimum without having to calculate all points (e.g., see Bergstra and Bengio [8]). This is also referred to as a Monte Carlo approach. Another way involves calculating the objective using a low number of grid points, to determine the region in which the optimum is contained. Then, a second, refined distribution of grid points in that region is used to find the optimum with a greater accuracy. This scheme is faster but does not handle multiple optima well.

(3) Gradient Methods

Refers to first- and second-order methods that use the gradient and the second derivative of a multidimensional surface to find the optimum. Efficient for multiple design variables, provided the objective and constraint functions are continuous in the design space. It is important to remember that some optimization problems involve so many variables (hyperdimensions) that it is impossible to envision the shape of the objective function. This is akin to expecting a blind-folded person to identify the optimum of a 3-dimensional surface. Hyperdimensional problems require first- and second-order methods.

(4) Multidisciplinary Optimization (MDO)

Refers to the solution of optimization problems that simultaneously involve multiple disciplines, such as aerodynamics, structures, systems, finances, operation, and so forth. A standard MDO problem simultaneously minimizes/maximizes two or more objective functions, which differs from classical methods, which treat just one. The solution of an MDO problem leads to a set of solutions of the objective functions, forming a so-called a *Pareto front*. It represents the set of solutions for which an improvement in any objective function degrades at least one of the others.

Among a multitude of methods used to solve MDO problems are various forms of *genetic algorithms* (GA); a digitized version of biological evolution. These are also called *evolutionary algorithms*. In aircraft design, such algorithms will often affect many design variables that control the geometry of the vehicle, down to the shape of airfoils and fuselage cross section. Its implementation requires the use of geometric parametrization of the aircraft, including airfoils and fuselage shape. Ref. [9] details many techniques for this purpose. MDO remains a vibrant field of active research. Unfortunately, its scope precludes it from further treatise in a book that focuses on aircraft design in general terms.

EXAMPLE 3-3

The purpose of this example is to illustrate the benefit of optimization, rather than to focus on a specific optimization method. Here, we are interested in structural weight. Consider the clamped cantilevered beam shown in Figure 3-11. The 4.34-m beam is a hollow, constant diameter aluminum tube (6061-T6) of 60 mm diameter ($D=2R$) and wall thickness (t) of 7 mm. Assume we have demonstrated it can support a maximum load (P) of 750 N before yielding. Assume its limit normal stress (σ_{lim}) is 2.344×10^8 Pa (neglect shear stress). (a) Estimate the mass of this beam. (b) Estimate the mass of the beam if it is optimized for constant *bending stress* along its length, such that the wall thickness along the beam is constant (7 mm) and the minimum outside diameter is no less than 14 mm. Density (ρ) of 6061-T6 is 2713 kg/m^3.

SOLUTION:

(a) Mass of the original beam:

$$m=\rho\mathcal{V}=\rho\left[l\pi\left(R^2-r^2\right)\right]$$
$$=(2713)\left[(4.34)\pi\left(0.030^2-0.023^2\right)\right]=13.72\text{ kg}$$

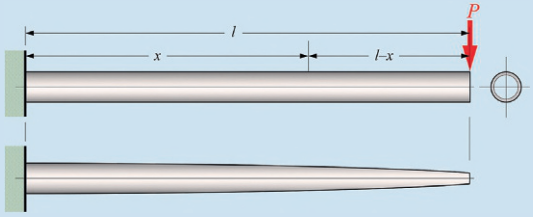


FIGURE 3-11 Original beam (upper) and optimized beam (lower).

EXAMPLE 3-3 (*cont'd*)

Note that the horizontal line through V (i.e., $\not{V}$) is used to distinguish volume from velocity or airspeed.

(b) This is a single-variable optimization problem that is relatively easy to solve analytically. To optimize the beam for constant bending stress, we set up the appropriate formulation at any point along the beam as follows:

$$\sigma = \frac{M \cdot R}{I} = \frac{P(l-x)\cdot R}{\frac{1}{4}\pi\left(R^4 - (R-t)^4\right)} \leq \sigma_{\text{lim}}$$

where M is the moment, I is the area moment of inertia of the cross section (for a hollow tube), and R and $(R–t)$ are the outside and inside radii, respectively. An expansion of the denominator, followed by a few steps of algebra, will yield the following cubic polynomial that describes the required beam radius as a function of position:

$$R^3 - \frac{3}{2}R^2 t + \left(t^2 - \frac{P(l-x)}{\pi\sigma_{\text{lim}}\, t}\right)R - \frac{1}{4}t^3 = 0 \qquad \text{(i)}$$

Solving this equation for R leads to the optimized shape shown in Figure 3-11 (lower beam). While this expression can be solved analytically for R, e.g., using the method presented in Ref. [10], it is unwieldy. A faster way approximates the solution for $R(x)$ using a least-squares regression analysis. Thus, we solve Equation (i) directly at several, evenly spaced intervals and then fit a cubic polynomial through those results. This leads to the following formulas for the outside (R) and inside radii (r), respectively:

$$\begin{aligned} R(x) &= 0.03 - 3.728616\times10^{-3}x \\ &\quad + 6.301147\times10^{-4}x^2 - 2.287553\times10^{-4}x^3 \\ r(x) &= 0.023 - 3.728616\times10^{-3}x \\ &\quad + 6.301147\times10^{-4}x^2 - 2.287553\times10^{-4}x^3 \end{aligned}$$

Note that these expressions are only valid for this problem. To determine the mass of the new beam, we must estimate its volume. The cross-sectional geometry is represented by two concentric circles, whose radius changes as a function of x; so $A(x) = \pi(R^2–r^2)$. Integrating this from 0 to l and multiplying by the density leads to (showing all steps is impractical, since this problem is simply making a point):

$$m_{opt} = \rho\not{V}_{opt} = \rho\int_0^{4.34}\pi\left(R^2 - r^2\right)dx = 9.360 \text{ kg}$$

The mass of the optimized beam is 68% of the original one. Of course, there is always a drawback: it is much harder to fabricate.

3.4.1 Fundamental Concepts

An aircraft is a collection of systems that can be optimized separately. However, the order of what is optimized first may be an issue. For instance, it is logical to optimize the airframe *after* the aerodynamic outside mold-line (OML), because the OML is a geometric constraint for the airframe. Regardless, before beginning the optimization, we must familiarize ourselves with the fundamentals. The discussion that follows is largely based on Vanderplaatz [11], Reklaitis et al. [12], Rardin [13], and Kochenderfer and Wheeler [14] but is adapted to aviation when possible.

(1) General Optimization Problem Statement

Optimization problems are stated in the following format:

Minimize/ maximize	$F(\mathbf{X})$		← Objective function
Subject to:	$g_i(\mathbf{X}) \leq 0$	$i = 1, l$	← Inequality constraints
	$h_j(\mathbf{X}) = 0$	$j = 1, m$	← Equality constraints
	$X_k^{lower} \leq X_k \leq X_k^{uppper}$	$k = 1, n$	← Side constraints
Where	$\mathbf{X} = \{X_1\ X_2\ \ldots\ X_n\}^T$		← Vector of design variables

In this form, the objective function might be payload, useful load, range, or other parameters of interest. The inequality constraint might be structural loading (e.g., stress), while the equality constraint might be lift or maximum lift coefficient. Note that the equality and inequality constraints are sometimes written with nonzero values on the right side.

(2) Design Variables

Refers to any variable the designer can use to modify a design. Common design variables for aircraft design include wing area, aspect ratio, and taper ratio. However, realistic problems include far more design variables, e.g., sweep, washout, dihedral, various geometric-scaling, and structural parameters, to name a few.

(3) Objective Function, $F(\mathbf{X})$

Is a linear or nonlinear function of the design variables and is the focus of the optimization; we seek to find the minimum or maximum of this function. The objective function can be a logical construct (e.g. useful load, range, or endurance) or a multiparameter function compiled to allow design configurations to be compared quantitatively (e.g. range per unit weight of fuel). Note that minimizing $F(\mathbf{X})$ is equivalent to maximizing $–F(\mathbf{X})$. Objective functions are sometimes referred to as *cost functions* or *loss functions*.

(4) Constraints

Constraints are limits to which the objective function, F**(X)**, is subjected. For instance, if the maximum weight (W_0) of an airplane is a constraint, then *any* value of F**(X)** associated with weight greater than W_0 must be rejected. Constraints that require design variables to be equal to some value are called *equality constraints*. Constraints that require design variables to be smaller or greater than some value are called *inequality constraints*. Constraints that require a given design variable to be inside a specific range (e.g., $0 \leq x \leq 5$ or $x \geq 0$) are called *side constraints*. Note that the constraint formulation is generally presented in a so-called *residual form*, with all terms moved to one side of an equality or inequality sign.

(5) Feasible and Infeasible Region

Simply, a *feasible region* is the region of the design space for which no constraint is violated. An *infeasible region* is the portion of the design space where one or more constraints are violated.

(6) Convex and Concave Functions

A function is *convex* on a segment if a line drawn between two points on the segment lies above the function. The segment around the point x_c in Figure 3-12 is convex. A function is *concave* if such a line lies below the function, as would be the case for the segment around the point x_a in Figure 3-12.

(7) Convex and Nonconvex Sets

A set (of points) is defined as *convex* if a line drawn between any two points inside the set results in a line that is fully contained inside it. Otherwise, it is *nonconvex*. A sphere is a convex set, while a doughnut is nonconvex.

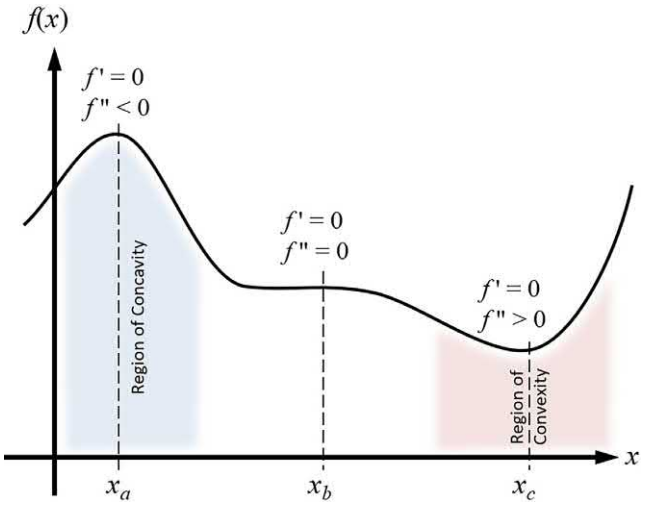


FIGURE 3-12 Requirements for stationary points.

A convex set makes optimization easier as it ensures the local minimum is also the global minimum. Therefore, only the gradient (and not curvature) suffices to determine the minimum.

(8) Unconstrained and Constrained Optimization Problems

Optimization problems come in two forms: *constrained* and *unconstrained*. An optimization problem is unconstrained if the range of the independent variables is unlimited (e.g., $-\infty < x < +\infty$). Thus, provided a global minimum or maximum exists, these can (theoretically) be determined. In contrast, an optimization problem is constrained if subjected to constraints. These may easily render the global (or local) optimum infeasible. This is illustrated in Figure 3-13, where the contours are

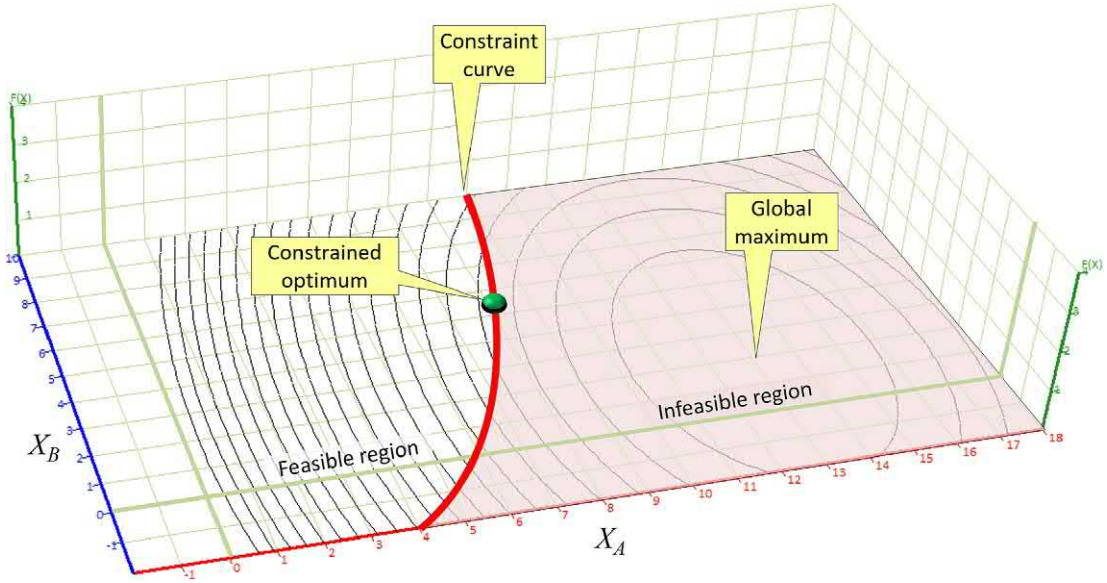


FIGURE 3-13 Contour plot of an objective function, showing global and constrained optimums.

isopleths representing the value of the objective function. Thus, the constrained optimum becomes the point inside the feasible region that is closest in value to the global (or local) optimum. Not all optimization problems have a well-defined optimum. For instance, an increase in wing aspect ratio (AR) reduces lift-induced drag. Considering only lift-induced drag as an objective function and AR as the only design variable, an unconstrained design problem has a simple solution: $AR \rightarrow \infty$. The problem is that the resulting wing weight would trend toward ∞ (heavier structure), and fuel volume (given a fixed wing area) would trend toward 0. The incorporation of other considerations necessarily demands that only a limited range of AR be considered, as dictated by the constraints.

(9) Optimum—Necessary Condition for Unconstrained Minima or Maxima

An optimum (pl. optima) refers to the minimum (pl. minima) or the maximum (pl. maxima) value of a function. Such a point is often referred to as an extremum (pl. extrema). If the minimum of the continuous function $f(x)$ is located at the point x^*, then the following conditions must be satisfied for any unconstrained minima:

$$\left.\frac{df}{dx}\right|_{x=x*} = 0 \qquad \text{and} \qquad \left.\frac{d^2f}{dx^2}\right|_{x=x*} \geq 0$$

The maximum is defined identically, but with the inequality symbol reversed. This is shown in Figure 3-12. Note that this only guarantees the minimum (or maximum) is *local* and not *global*. The minimums and maximums are referred to as *stationary points* (or *critical points*). Stationary points can be a local optimum (i.e. a min or max) or a point of *inflection*. If the first derivative at point x^* is zero and the first higher-order derivative (e.g. f', f'', etc.) of order n is not 0, then it can be proven (e.g. see [12]) that

(i) if n is odd, then x^* is a point of inflection.
(ii) if n is even, then x^* is a local optimum and if $f^n > 0$ then x^* is a local minimum and if $f^n < 0$ then x^* is a local maximum.

The above is valid for single-variable functions. For multivariable functions, we must up the complexity and use a vector-calculus approach. Thus, for multivariable functions, the gradient of the objective function, $\nabla F(\mathbf{X})$, must vanish and the Hessian, $\mathbf{H}$, must be *positive definite* (i.e. its eigenvalues must be positive), where

$$\nabla F(\mathbf{X}) = \begin{Bmatrix} \partial F(\mathbf{X})/\partial X_1 \\ \partial F(\mathbf{X})/\partial X_2 \\ \vdots \\ \partial F(\mathbf{X})/\partial X_n \end{Bmatrix} = 0$$

and

$$\mathbf{H} = \begin{bmatrix} \dfrac{\partial^2 F(\mathbf{X})}{\partial X_1^2} & \dfrac{\partial^2 F(\mathbf{X})}{\partial X_1 \partial X_2} & \cdots & \dfrac{\partial^2 F(\mathbf{X})}{\partial X_1 \partial X_n} \\ \dfrac{\partial^2 F(\mathbf{X})}{\partial X_2 \partial X_1} & \dfrac{\partial^2 F(\mathbf{X})}{\partial X_2^2} & \cdots & \dfrac{\partial^2 F(\mathbf{X})}{\partial X_2 \partial X_n} \\ \vdots & \vdots & \ddots & \vdots \\ \dfrac{\partial^2 F(\mathbf{X})}{\partial X_n \partial X_1} & \dfrac{\partial^2 F(\mathbf{X})}{\partial X_n \partial X_2} & \cdots & \dfrac{\partial^2 F(\mathbf{X})}{\partial X_n^2} \end{bmatrix}$$

(10) Local versus Global Optimum

The optimum may be *local* or *global* (see Figs. 3.14 and 3.15). A global minimum of a function $f(x)$ is the smallest

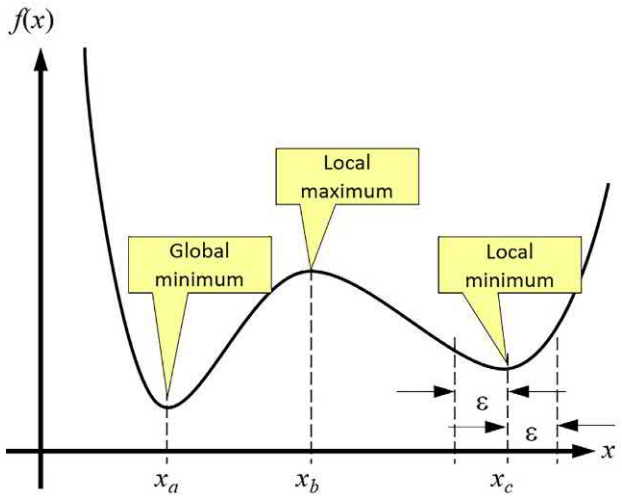


FIGURE 3-14 Global and local minimum and local maximum.

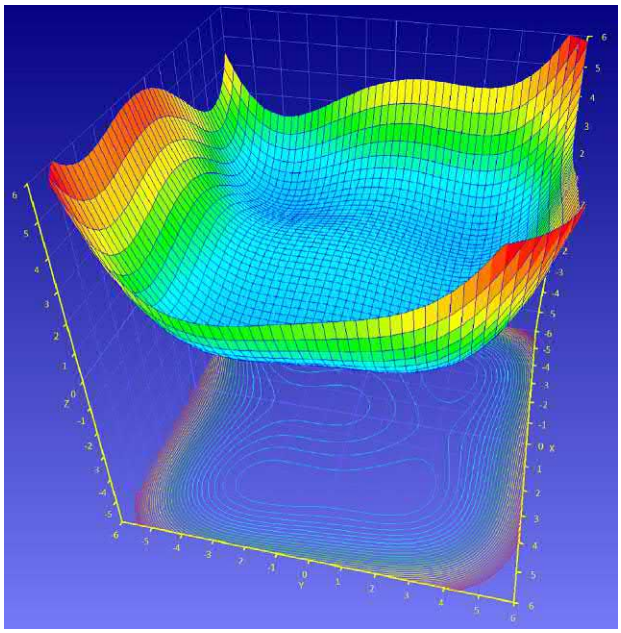


FIGURE 3-15 Himmelblau's function exemplifies a 3D surface with multiple stationary points.

value it returns. Mathematically, if $f(x)$ is defined on set S, it attains its global minimum at a point $x^* \in S$, if and only if $f(x^*) \le f(x)\ \forall x^* \in S$. In contrast, $f(x)$ has local minimum at point $x^* \in S$, if and only if $f(x^*) \le f(x)\ \forall x – \varepsilon \le x^* \le x + \varepsilon$. In words, $f(x^*)$ is the smallest value of $f(x)$ inside the interval $[x–\varepsilon,\ x + \varepsilon]$. The global and local maximum is defined identically, but with the inequality symbols reversed.

3.4.2 More on Objective Functions

As stated earlier, the objective function may represent some physical aspect of an optimization problem. At other times, the problem involves so many disparate parameters that a different approach must be applied. One such approach is presented here: The objective function is compiled as the sum of ratios of parameter-products. For instance, if we want to maximize the sum of three parameters, F_1, F_2, and F_3, we might simply define $F = F_1 + F_2 + F_3$. However, parameter F_1 might be the ratio of two other parameters, say, P_1 and Q_1. Thus, the objective function would be written as $F = P_1/Q_1 + F_2 + F_3$. Since we want to maximize favorable and minimize unfavorable characteristics of our design, we would select P_1 to be a favorable and Q_1 unfavorable. A large P_1 divided by a small Q_1 results in a larger P_1/Q_1. If we are interested in increasing the importance of parameter P_1 over that of Q_1, we could raise it to some power, using a weighing factor w_1, for instance: $F = P_1^{w_1}/Q_1 + F_2 + F_3$. This form of an objective function can be written in the generalized, albeit, unwieldy form shown below

$$F(\mathbf{X}) = \sum_{k=1}^{K} \left(\prod_{i=1}^{N_k} P_i^{w_i}(\mathbf{X}) \Big/ \prod_{j=1}^{N_k} Q_j^{v_j}(\mathbf{X}) \right)_k \tag{3-33}$$

where P_i is some property that is favorable when maximized (e.g., a large $LD_{\max}$ or payload is favored), Q_i is some property that is favorable when minimized (e.g., low weight or direct operating cost), and w_i and v_j are weighing factors. If P or Q is not used, they are represented as 1. Examples of use are shown in Examples 3.3 and 3.4.

EXAMPLE 3-3

Consider the functions $f = x \cdot (1 + \sin x)$ and $g = x/2$ that represent some properties of interest. Write the product $f \cdot g$ in terms of Equation (3-33). Plot these functions on the interval [0,3.5], as well as the product $f \cdot g$ and the quotients f/g and g/f. Determine the value of x^* inside the interval for each of the derivative function.

SOLUTION:

In using Equation (3-33) to express $f \bullet g$, we get $\mathbf{X} = x$, $K = 1$, $N_k = 2$, $P_1 = f$, $P_2 = g$, $Q_1 = Q_2 = 1$, and $w_1 = w_2 = 1$. Thus, we write

$$F(\mathbf{X}) = \sum_{k=1}^{K} \left(\prod_{i=1}^{N_k} P_i^{w_i}(\mathbf{X}) \Big/ \prod_{j=1}^{N_k} Q_j^{v_j}(\mathbf{X}) \right)_k$$

$$\Rightarrow \quad F(x) = (x(1 + \sin x)) \cdot (x/2) = \frac{x^2(1 + \sin x)}{2}$$

These functions and derivative functions are plotted over the stated interval in Figure 3-16. The approximate location of the optimums is shown in the figure.

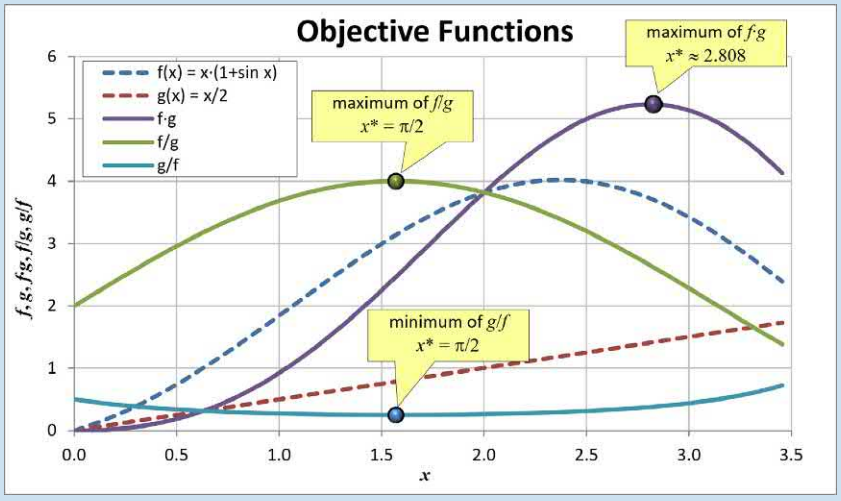


FIGURE 3-16 Stationary points for the derivative functions.

EXAMPLE 3-4

Five engine models are being considered for an airplane (see table below). It has been determined that all five will function well in the airplane, but we want to find out which engine is the best choice based on weight (W), price (C), power (P), and specific fuel consumption (SFC), as listed below. Suggest objective functions to help in this capacity.

Type	Weight lb_f	Cost $	Power BHP	SFC $lb_f/(hr \cdot BHP)$
Engine 1	125	3500	97	0.48
Engine 2	115	4700	120	0.46
Engine 3	135	4250	115	0.47
Engine 4	142	4260	105	0.48
Engine 5	126	3950	117	0.47

SOLUTION:

The approach is to maximize favorable properties and minimize unfavorable ones. For instance, we want a low weight (W), inexpensive (C) engine with low fuel consumption (SFC). Assuming we put equal weight on all three, the engine with the lowest value of $W \times C \times SFC$ is a potential winner. However, we also want the highest power (P) possible. Therefore, a more suitable objective function (which we want to maximize) is given below:

$$F(\mathbf{X}) = F(P, W, C, SFC) = \frac{P}{W \times C \times SFC}$$

This ratio is highest for an engine with high power, low weight, low price, and low SFC. It may not have the highest power or the lightest weight, but the most favorable combination of the selected characteristics. Calculated for the example engines, this would result in the following objective values, which indicates Engine 5 is the best option:

Type	Weight lb_f	Cost $	Power BHP	SFC $lb_f/(hr \cdot BHP)$	Cost $hr \cdot BHP^2/(lb_f \cdot \$)$
Engine 1	125	3500	97	0.48	0.000462
Engine 2	115	4700	120	0.46	0.000483
Engine 3	135	4250	115	0.47	0.000426
Engine 4	142	4260	105	0.48	0.000362
Engine 5	126	3950	117	0.47	0.000500

Objective functions can be defined in other ways too. For instance, we could evaluate ratios such as Power/Weight [BHP/lb_f], Power/Price [BHP/$], and Power/SFC [$BHP^2 \cdot h/lb_f$]. Since the high values of P/W, P/C, and P/SFC are desirable, a suitable objective function could be defined as the sum of these, i.e.

$$F(P, W, C, SFC) = \frac{P}{W} + \frac{P}{C} + \frac{P}{SFC}$$

This would result in the following values of the objective function:

Type	P/W BHP/lb_f	P/C BHP/$	P/SFC $hr \cdot BHP^2/lb_f$	Cost $hr \cdot BHP^3/(lb_f^2 \cdot \$)$
Engine 1	0.776	0.028	202	202.9
Engine 2	1.043	0.026	261	261.9
Engine 3	0.852	0.027	245	245.6
Engine 4	0.739	0.025	219	219.5
Engine 5	0.929	0.030	249	249.9

Engine 2 has the highest power to weight ratio, but the power-to-price ratio of Engine 5 is the best. Overall, according to this scheme, Engine 2 is the best choice.

Sometimes it is desirable to emphasize one ratio above others. In other words, it is possible the power/weight ratio is of greater importance to the designer than, say, the power/cost ratio. This can be handled by introducing weighing fractions in a variety of ways. As an example, if the importance of P/W is considered 4 times more important than P/C and 10 times more important than P/SFC, we could introduce this as shown below:

$$F(P, W, C, SFC) = \frac{P}{W} + \frac{1}{4}\frac{P}{C} + \frac{1}{10}\frac{P}{SFC}$$

Implementing these yields the following table and, again, Engine 2 comes out on top.

Type	P/W BHP/lb_f	0.25·P/C BHP/$	0.1·P/SFC $hr \cdot BHP^2/lb_f$	Cost $hr \cdot BHP^3/(lb_f^2 \cdot \$)$
Engine 1	0.776	0.006929	20.21	20.991
Engine 2	1.043	0.006383	26.09	27.137
Engine 3	0.852	0.006765	24.47	25.327
Engine 4	0.739	0.006162	21.88	22.621
Engine 5	0.929	0.007405	24.89	25.830

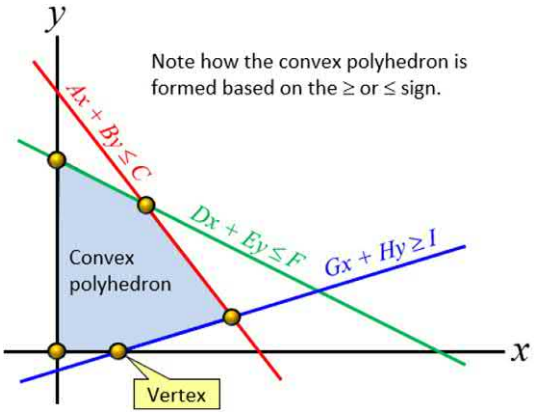


FIGURE 3-17 LP defines a (convex) polyhedron, whose vertexes are used to determine the optimum value of the objective function.

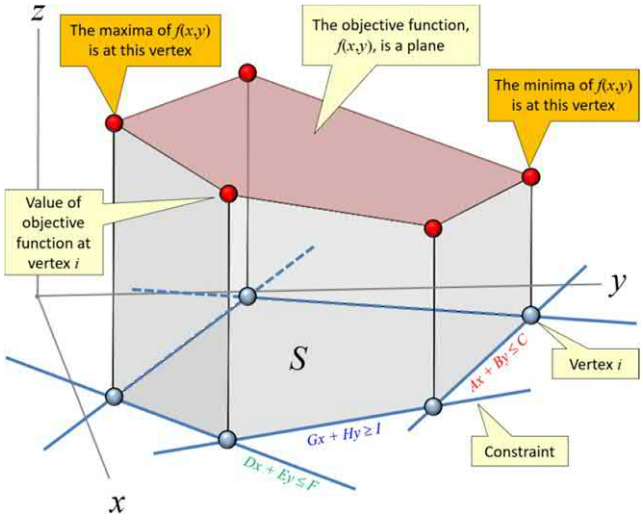


FIGURE 3-18 Graphical presentation of why an optimum occurs at a vertex in LP problems.

3.4.3 Linear Programming

Linear Programming (often abbreviated LP) is an optimization method that assumes a linear objective function subjected to linear constraints. Thus, it is not suitable for geometric sizing of an airplane, which have nonlinear objective function and constraints. However, the method is practical for various financial optimizing involving manufacturing, where it can be used to maximize profits and minimize costs. A well-known example of linear programming is the so-called salesman transit problem, in which a salesman must plan a driving route between farms such that the cost of fuel consumed is minimized.

Presenting the LP Problem

The linear programming problem is typically presented using the following mathematical terminology:

Minimize (or maximize)	$F(x_1, x_2, \ldots, x_N) = a_0 + a_1x_1 + a_2x_2 + \ldots + a_Nx_N$
subject to the constraints:	$C_{10} + C_{11}x_1 + C_{12}x_2 + \ldots + C_{1N}x_N \le D_1$
	$C_{20} + C_{21}x_1 + C_{22}x_2 + \ldots + C_{2N}x_N \le D_2$
	$\vdots$
	$C_{M0} + C_{M1}x_1 + C_{M2}x_2 + \ldots + C_{MN}x_N \le D_M$

where F is the objective function, x_i represents design variables, C_{ij} and D_i are constants. Note that $\ge$can also be used with the constraints. The constraints form a convex polyhedron in N-dimensional space, which constitutes the feasible region (see Figure 3-17).

LP problems can be solved in several ways. One way is to coplot the constraints. This is primarily practical for 2- and 3-dimensional problems. It allows the feasible region to be identified, enclosed by the constraints. This splits the region into two half-spaces, defined by the expressions $Ax + By \le C$, $Dx + Ey \le F$, and $Gx + Hy \ge I$. The feasible region is below the first two lines (because of $\le$) and above the last one (because of $\ge$). Furthermore, we stipulate that $x,y \ge 0$ (side constraints).

The intersection of two constraints is called a *vertex*. The region is convex, because a line stretched between any two points in the region is entirely inside the region. We can show that the max and min of the objective function resides at one of the vertices. This is illustrated for a 2-dimensional problem in Figure 3-18 (the objective function has two variables). For problems with dimensions greater than 2, the plane is called a *hyperplane*. For such problems, we need specialized methods.

One such method is the so-called *simplex method*. Its detail is beyond the scope of this book but interested readers can find an assortment of supplemental information online. Instead, in this text, a practical, 2-dimensional, aircraft manufacturing problem will be solved using the graphical method in Example 3-5.

EXAMPLE 3-5

An aircraft manufacturer is considering manufacturing and marketing two aircraft models and is evaluating how many of either one to produce each year. Aircraft Model A sells for $650,000 a unit and Model B sells for $550,000. The fabrication of Model A requires 700 lb_f of Alclad 2024-T4, 1500 lb_f of Alclad 6061-T6, and 900 lb_f of Reinforced Plastics (RFP or composites). In contrast, Model B requires 1200 lb_f of Alclad 2024-T4, 600 lb_f of

EXAMPLE 3-5 (*cont'd*)

Alclad 6061-T6, and 700 lb_f of RFP. This year, the manufacturer has secured 84,000 lb_f of 2024-T4, 90,000 lb_f of 6061-T6, and 63,000 lb_f of RFP for manufacturing. If all the aircraft manufactured will eventually be sold, how many units of A and B should be produced to maximize revenue.

SOLUTION:

The first step is to create an objective function, which should represent revenue from sold aircraft. Thus, if we denote the number of units of models A and B sold as X_A and X_B, respectively, the objective function is simply $F(X_A, X_B) = 650{,}000X_A + 550{,}000X_B$.

The next step is to apply constraints. In this example, these are the restrictions on material availability; we can only produce airplanes provided sufficient raw material is available. Also, we require that $X_A, X_B \geq 0$. This suffices to create constraint equations. First let us tabulate the material requirements for clarity:

	Unit Price, $	2024-T4, lb_f	6061-T6, lb_f	RFP, lb_f
Model A	650000	700	1500	900
Model B	550000	1200	600	700
Available quantity		84000	90000	63000

$$\text{Alclad } 2024-\text{T4}: \quad 0 \leq 700X_A + 1200X_B \leq 84000$$

$$\Rightarrow \quad 0 \leq X_B \leq \frac{84000 - 700X_A}{1200}$$

$$\text{Alclad } 6061-\text{T6}: \quad 0 \leq 1500X_A + 600X_B \leq 90000$$

$$\Rightarrow \quad 0 \leq X_B \leq \frac{90000 - 1500X_A}{600}$$

$$\text{RFP}: \quad 0 \leq 900X_A + 700X_B \leq 63000$$

$$\Rightarrow \quad 0 \leq X_B \leq \frac{63000 - 900X_A}{700}$$

We can now coplot the constraints (by plotting X_B versus X_A) and shade the enclosed feasible region, as shown in Figure 3-19. Then, determine the intersection for each vertex and substitute into the objective function. The resulting vertex values and accompanying revenue is shown in the figure. The plot shows that manufacturing 28 units of Model A and 53 of Model B maximizes the revenue. Note that the maximum revenue of $50,364,407 is almost $5,000,000 higher than the nearest vertex. The realism of this problem can be improved by assigning a price per lb_f of material and subtract this in the objective function. The cost of material per unit aircraft could then be subtracted from the basic objective function.

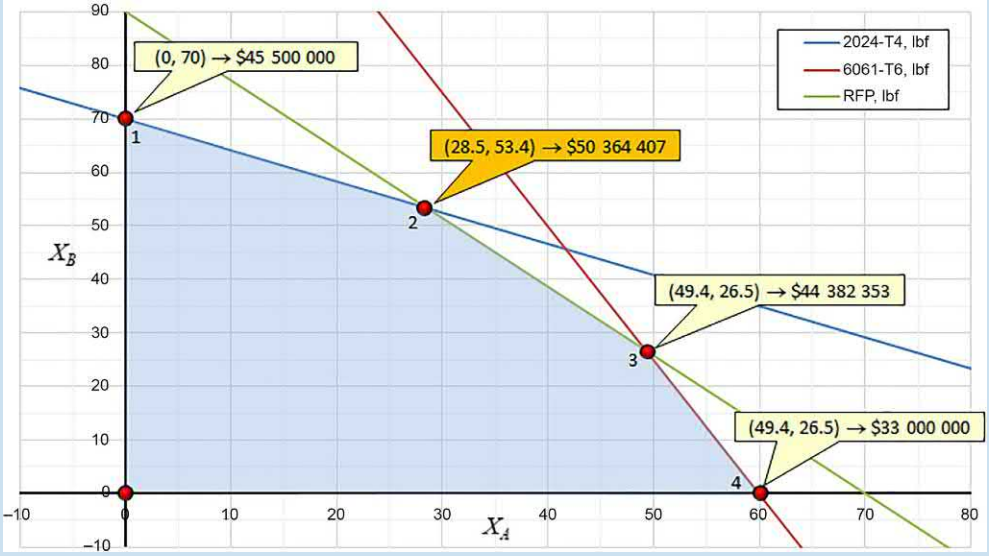


FIGURE 3-19 The resulting polyhedron shows the maximum revenue occurs at Vertex 2.

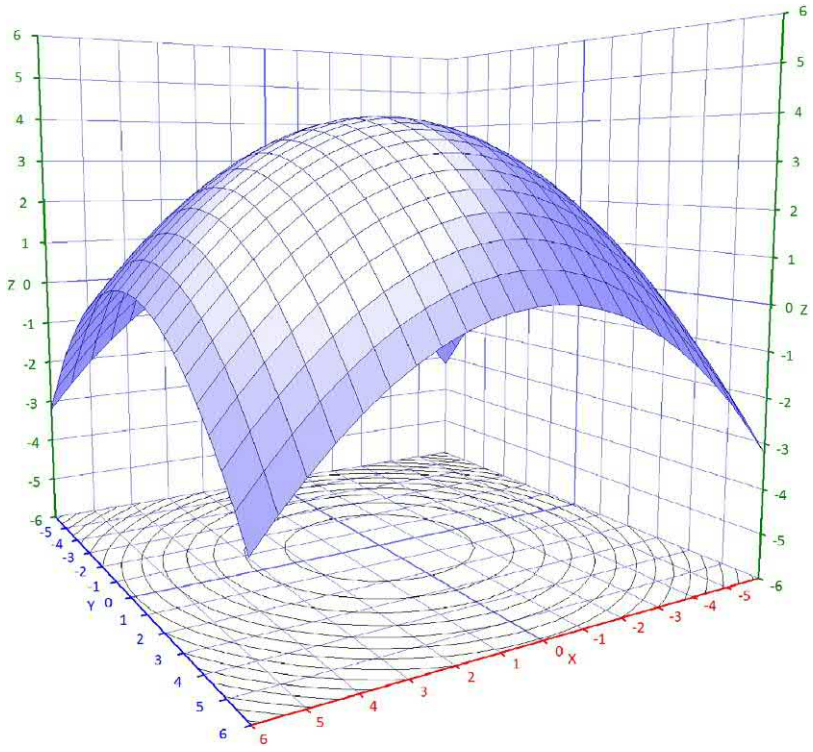


FIGURE 3-20 A parabolic surface in 3D space.

3.4.4 Nonlinear Surfaces and Lagrange Multipliers

Having seen a linear optimization problem solved begs the question; how are nonlinear problems solved? One way to determine the optima of a smooth, *unconstrained*, nonlinear surface is to use its gradient. This does not guarantee that the stationary point found is the global optimum. For smooth, *constrained*, nonlinear surfaces, a widely used method involves *Lagrange multipliers*. However, first the following prologue is offered to help the newcomer to optimization get familiar with the difference between unconstrained and constrained optimization problems.

(1) Unconstrained, Nonlinear Surfaces

The extremum of the parabolic surface in Figure 3-20 is relatively easy to find. The surface has the general form $z(x,y)=a(x-x_o)^2+b(y-y_o)^2+c$, where a, b, c, x_o, and y_o are constants. The stationary point is a minimum if $a,b>0$, a maximum if $a,b<0$, and a *saddle point* if the sign of a differs from that of b. It is determined by evaluating its gradient using the *del*-operator (∇) and setting it equal to zero. The operation converts the scalar function into a vector and is analogous to the differentiation of a single-variable function. The *del*-operator is given by

$$\nabla=\frac{\partial}{\partial x}\mathbf{i}+\frac{\partial}{\partial y}\mathbf{j}+\frac{\partial}{\partial z}\mathbf{k}$$

It follows that $\nabla z=2a(x-x_o)\mathbf{i}+2b(y-y_o)\mathbf{j}$. The position of the maximum for this surface is obtained by setting the gradient to zero and solving for x and y, i.e.,

$$\nabla z=2a(x-x_o)\mathbf{i}+2b(y-y_o)\mathbf{j}=0\mathbf{i}+0\mathbf{j}=\mathbf{0}$$

Thus, the extremum occurs at the point $(x, y)=(x_o, y_o)$, something evident from observation.

Solving the above problem is easy because it involves a single stationary point for a two-dimensional objective function. This is rarely so simple. Thus, we need methods that can deal with surfaces with multiple extrema, such as the mountain peaks function shown in Figure 3-21 or Himmelblau's function in Figure 3-15. Both feature multiple minima and maxima that make the task of determining the extrema that much harder. Various gradient methods have been developed to deal with this challenge. A common method is an iterative procedure that takes advantage of the fact that the gradient operator changes the function into a vector that points in a direction of the greatest change of the surface [11]. The process begins with a specific initial point (i.e. values of the design variables). Then, we move to a new point, which is calculated as shown below

$$\mathbf{X}^i=\mathbf{X}^{i-1}+\alpha\mathbf{S}^i \tag{3-34}$$

where i is an iteration index (not power) and $\mathbf{S}$ is a vector that indicates the direction in which we want to move in iteration i. It can be thought of as a unit vector. The term α is a scalar that represents the distance we want to move in

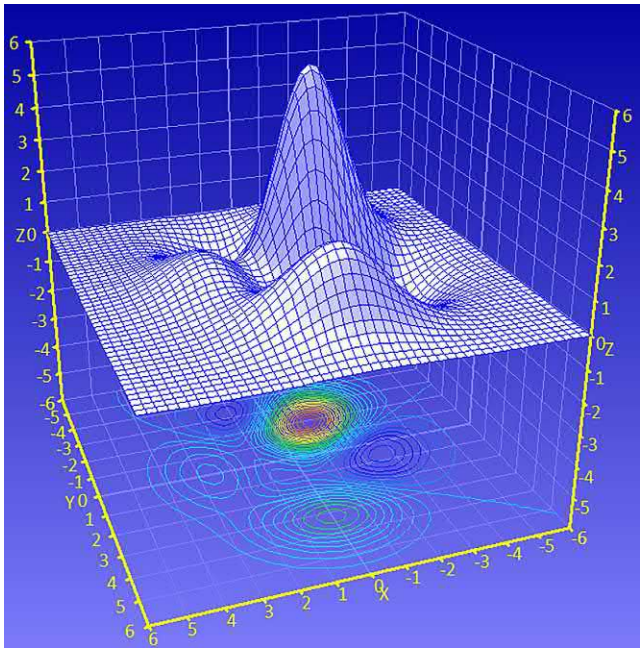


FIGURE 3-21 The mountain peaks function.

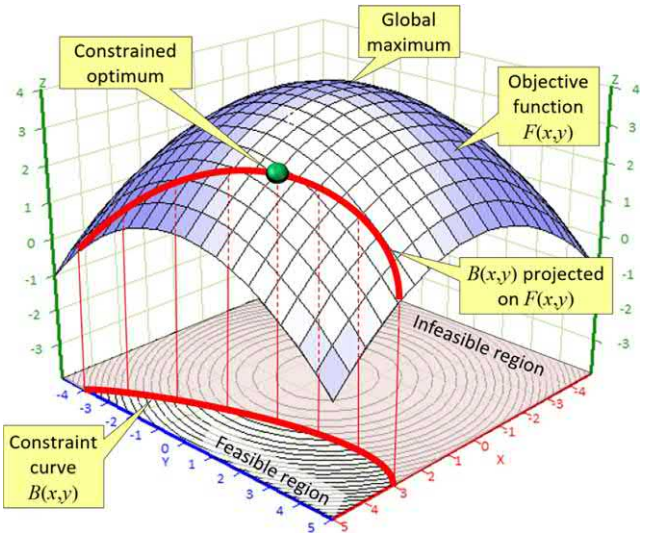


FIGURE 3-22 A parabolic surface subject to a single constraint (projected on surface).

this step. The direction vector is calculated using the gradient of the surface. It is necessary to evaluate if the destination **X** violates any constraints. It is a drawback that the result depends on the initial point—a different initial point can result in a different minimum (or maximum). Due to space constraints, it is impractical to present an example of the method, but interested readers are directed toward refs. [11, 12].

(2) Constrained, Nonlinear Surfaces

Now consider a situation in which we subject the objective function to a constraint, as shown in Figure 3-22. The constraint curve in the *x-y* plane has been projected onto the surface to help with the explanation. It is evident that the global optimum of the parabolic surface resides outside the feasible region of the design space. Since we are restricted to the feasible region, our goal is to determine the maximum value of the surface along the projection of the constraint curve, as this gets us as *close* to the global optimum as possible. To determine this constrained optimum, we must introduce *Lagrange multipliers*.

(3) Lagrange Multipliers

Consider the constraint curve (red) depicted in the *x-y* plane in Figure 3-23. It is superimposed on the contour plot of the parabolic objective function. Let's denote the objective by $F(x,y)$ and the constraint by $B(x,y)$. The gradient of the constraint, $\nabla B(x,y)$, is depicted along the curve using blue arrows. At some point, the gradients of the objective function ($\nabla F(x,y)$) and the constraint curve ($\nabla B(x,y)$) are parallel, although of unequal lengths and possibly opposite directions. This is the optimum. However, the determination of this point requires the two gradients to be related using a constant, λ, as follows:

$$\nabla F(x,y) = \lambda \nabla B(x,y) \tag{3-35}$$

The constant λ is called a *Lagrange multiplier* and its value makes the gradient of B equal to that of F. This is a necessary condition for the existence of a stationary point on the constraint curve and ∇B cannot get closer than this to the optimum of F. We now define a new function, called the *Lagrangian*, written as follows:

$$\mathbf{L}(x,y,\lambda) \equiv F(x,y) - \lambda B(x,y) \tag{3-36}$$

This function has an additional variable besides x and y; the Lagrange multiplier. It allows the extremum of the projected curve to be found by evaluating the gradient of the Lagrangian and set it equal to zero. A typical form of the constraint is $B(x,y) = b(x,y) - c = 0$, where c is a constant. Let us write the Lagrangian in terms of it, as shown below:

$$\mathbf{L}(x,y,\lambda) = F(x,y) - \lambda(b(x,y) - c) \tag{3-37}$$

The extrema can now be determined by solving

$$\nabla \mathbf{L}(x,y,\lambda) = \nabla[F(x,y) - \lambda(b(x,y) - c)] = \mathbf{0} \tag{3-38}$$

Note that we are primarily interested in the coordinates x and y. The Lagrange multiplier is only of temporary use and is only needed to determine the coordinates where $\nabla F(x,y)$ is parallel to $\nabla B(x,y)$. The solution process is presented in Example 3-7.

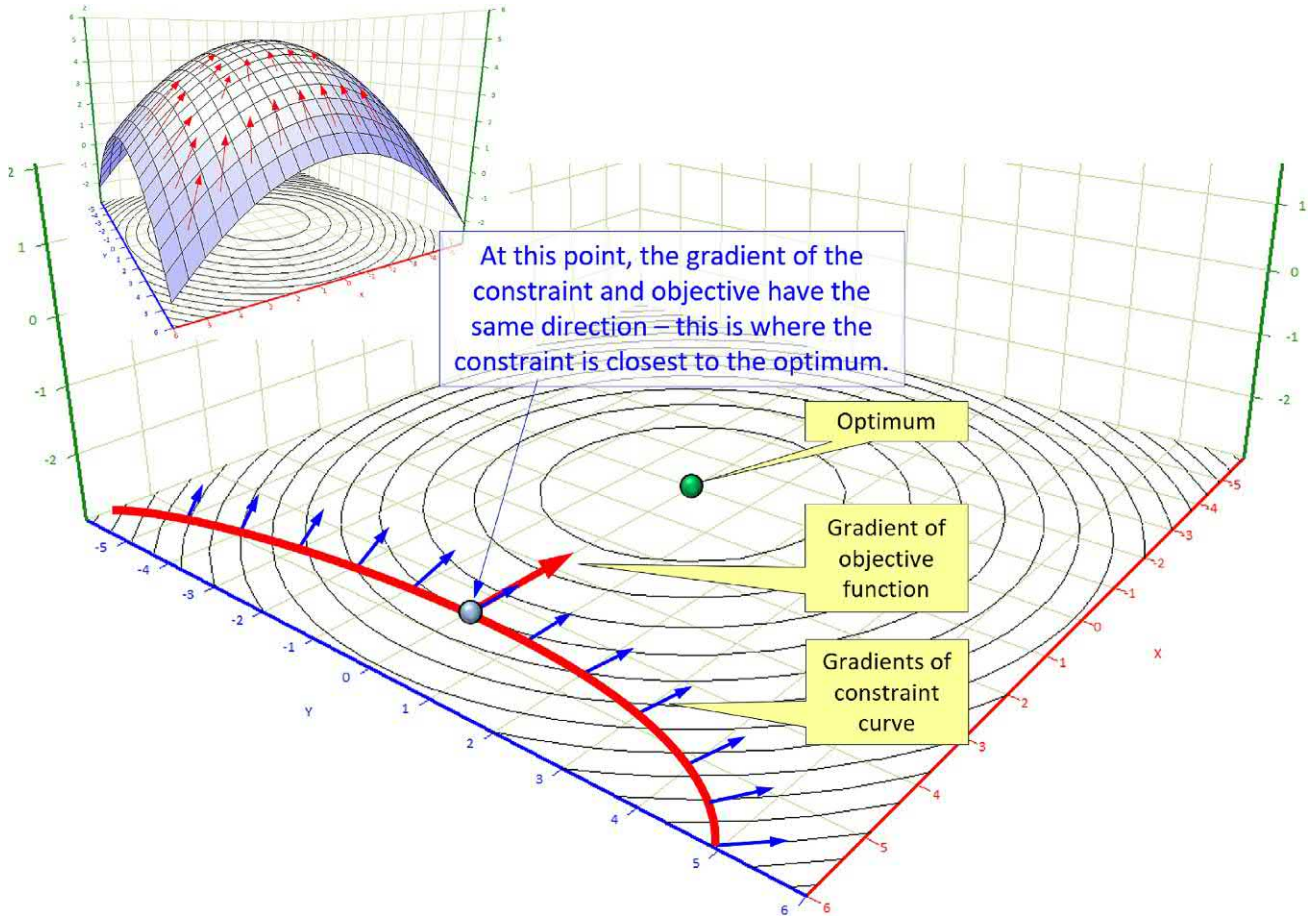


FIGURE 3-23 Subjecting an objective function to a constraint.

EXAMPLE 3-6

Determine the gradient of the constraint curve given by $y=2x^2$.

SOLUTION:

$$y=2x^2 \;\Rightarrow\; z=2x^2-y=0 \;\Rightarrow\; \nabla z=4x\mathbf{i}-\mathbf{j}$$

EXAMPLE 3-7

Determine the maximum of the objective function $z(x,y)=4–0.1x^2–0.1y^2$, subject to the constraint $B(x,y)=x+y–1$.

SOLUTION:

Start by writing the Lagrangian: $\mathbf{L}(x,y,\lambda)=z(x,y)-\lambda(B(x,y)-b)=4-0.1x^2-0.1y^2-\lambda(x+y-1)$

Then, take the gradient of $\mathbf{L}$ with respect to all its variables and set to zero:

$$\nabla\mathbf{L}=\begin{Bmatrix}\partial\mathbf{L}/\partial x\\ \partial\mathbf{L}/\partial y\\ \partial\mathbf{L}/\partial\lambda\end{Bmatrix}=\begin{Bmatrix}-0.2x-\lambda\\ -0.2y-\lambda\\ -x-y+1\end{Bmatrix}=\begin{Bmatrix}0\\0\\0\end{Bmatrix}$$

This gives three equations with three unknowns, x, y, and λ.

$$\Rightarrow\quad -0.2x-\lambda=0 \;\Rightarrow\; x=-5\lambda$$

$$\Rightarrow\quad -0.2y-\lambda=0 \;\Rightarrow\; y=-5\lambda$$

$$\Rightarrow\quad -\overbrace{x}^{-5\lambda}-\overbrace{y}^{-5\lambda}+1=0 \;\Leftrightarrow\; \lambda=-\frac{1}{10}$$

$$\Rightarrow\; x=0.5, y=0.5$$

Thus, the maximum of z is:

$$z_{\max}=4-0.1(0.5)^2-0.1(0.5)^2=3.95$$

See solution plotted in Figure 3-24.

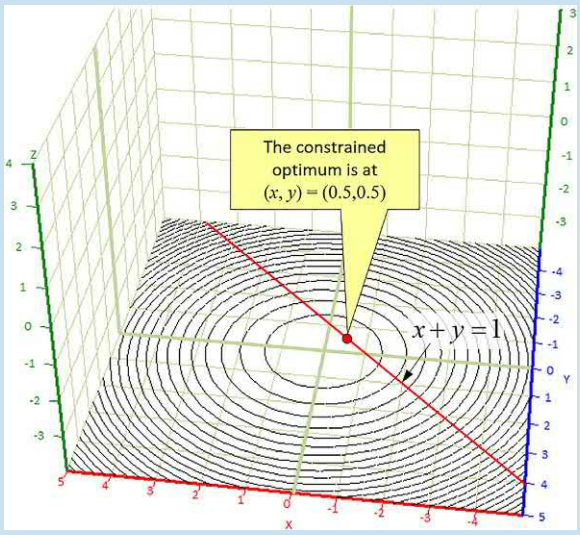


FIGURE 3-24 Position of optimum.

As alluded to earlier, realistic optimization problems involve multiple constraints (see Figure 3-25) and require an expanded version of the Lagrangian. The complete Lagrangian of an objective function subjected to multiple inequality and equality constraints is given by the following expression:

$$\mathbf{L}(\mathbf{X}, \lambda) \equiv F(\mathbf{X}) + \sum_{j=1}^{m} \lambda_j g_j(\mathbf{X}) + \sum_{k=1}^{n} \lambda_{m+k} h_k(\mathbf{X}) \qquad (3\text{-}39)$$

where $g_j(\mathbf{X})$ represents the inequality constraints and h_k the equality constraints. The determination of the optimum is defined mathematically using what is called the Kuhn–Tucker conditions (also called Karush-Kuhn-Tucker conditions). These conditions state that the design variables listed in $\mathbf{X}^*$ represent the optimum design if [11, 12]:

(1) $\mathbf{X}^*$ is feasible (i.e. it is in the feasible region).
(2) The $\lambda_j\, g_j\,(\mathbf{X}^*) = 0 \quad j = 1, \ldots, m \quad \lambda_j \geq 0.$
(3) The gradient of $\mathbf{L}(\mathbf{X}, \lambda)$ is given by

$$\nabla F(\mathbf{X}) + \sum_{j=1}^{m} \lambda_j \nabla g_j(\mathbf{X}) + \sum_{k=1}^{n} \lambda_{m+k} \nabla h_k(\mathbf{X}) = 0$$

where $\lambda_j \geq 0$, while there are no restrictions on the sign of λ_{m+k}.

This yields a set of equations that must be solved simultaneously. It is evident that when $m = n = 0$, the gradient reduces to that of the unconstrained objective function. Also note that the gradients of constraint curves 1 and 2 in Figure 3-25 are not parallel with the gradient of the objective function. However, the resultant vector formed when the two gradients (vectors) are multiplied by their corresponding Lagrange multipliers will indeed be parallel. This is illustrated in Figure 3-25. It should be evident that solving for multiple Lagrange multipliers is a task that requires far more space than possible here. And this marks the limits of what is practical for this introduction.

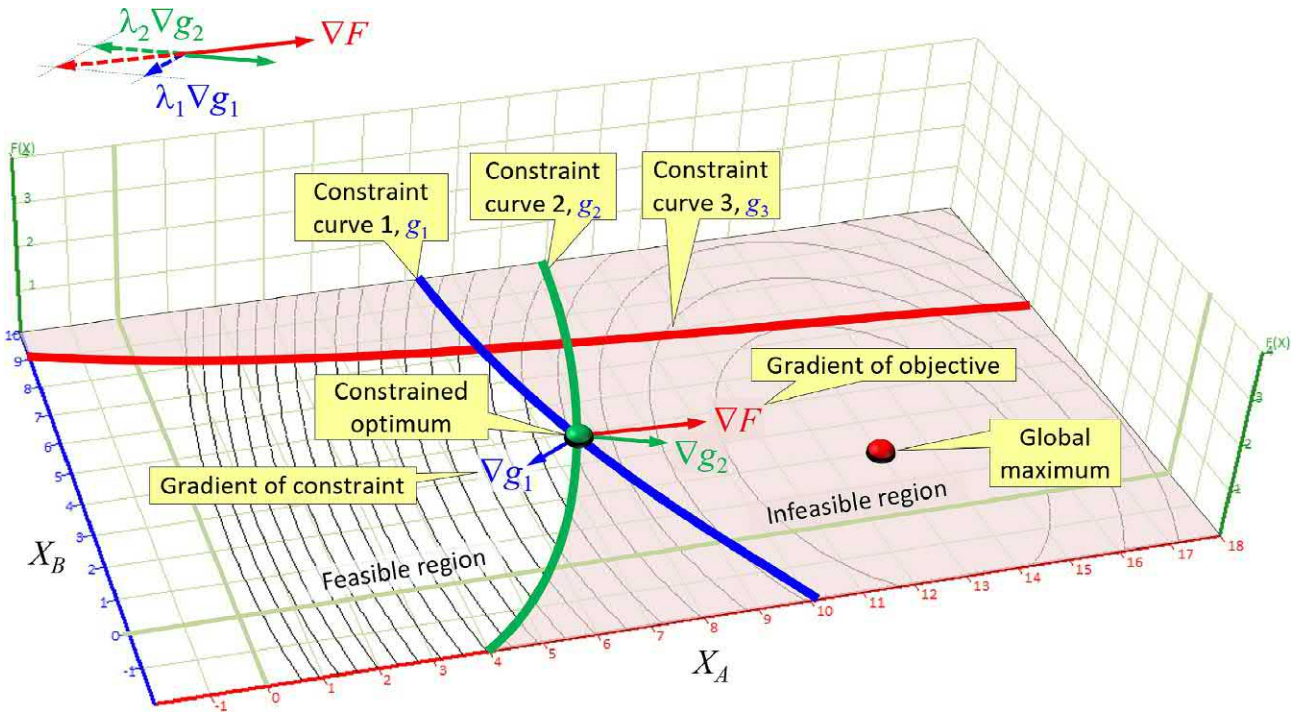


FIGURE 3-25 A contour plot of an objective function subject to multiple constraints.

3.4.5 Wing Sizing Optimization by Example

This section presents an elementary wing optimization for a small aircraft for which we want to maximize range, given some fixed gross weight, payload, and target cruising speed. We will also inflict a requirement to promote good stall characteristics and a simple high-lift system. The scheme that follows should only be considered a starting point slated for increased sophistication. For instance, influence of various aerodynamic effect of structures, stability and control, and so forth, are absent. In fact, this problem is simple enough to permit solution using a zero-order method and, thus, is easy to code. The discussion is presented in an algorithmic form to help interested readers write own code. The author implemented this by placing a loop for AR, inside a loop for S, inside a loop for λ. The solution will only return wing area (S), aspect ratio (AR), and taper ratio (λ) for the ideal wing configuration.

(1) Preparation

Before we begin this analysis, the empty and gross weight estimates should be available (e.g., see Section 6.2). Furthermore, the approach requires the airframe weight and drag coefficient *without* the wing, as well as handy formulation for expected wing weight and drag coefficient based on geometry (see Section 6.4 and Chapter 16). The following targets and constraints have been provided.

- Target gross weight $W_0 = 2500$ lb$_f$ (assume this is driven by rival aircraft in same class). For wing weight estimation, assume an ultimate load factor (n_z) of 6 and maximum horizontal airspeed (V_H) of 140 KEAS.
- Weight at top-of-climb to cruise altitude of $W = 0.95\,W_0$.
- Weight of the wing must meet $W_W \le 0.10\,W_0$.
- Mission payload $W_p = 650$ lb$_f$. Assume the empty weight without the wing is $W_{emw} = 1250$ lb$_f$.
- Range > 535 nm at $V_C = 130$ KTAS at $H_C = 10{,}000$ ft using a normally aspirated piston engine, with engine power as $P_{max} \le 180$ BHP at sea level. Assume a propeller efficiency at cruise of $\eta_p = 0.85$ and $SFC_{hp} = 0.5$ lb$_f$/(BHP·h). The range is calculated per Equation (21-38).
- All fuel for cruise must fit in wing fuel tanks between 25% and 65% chord (see Figure 3-26), from wing station 15% to 55% of half-span.
- Same airfoil is used from root to tip, with $t/c = 0.12$.
- Assume turbulent boundary layer over wings.
- $C_{L_{max}} \le 2.0$ at gross weight in landing configuration (to meet $V_{S_0} \le 46$ KCAS).
- To ensure "decent" glide characteristics, the objective function is subject to $LD_{max} \ge 13$.
- Penalize poor stall quality due to small taper ratio (λ) using the penalty function $\phi = \sqrt[n]{\sin\left(\frac{\pi}{2}\lambda\right)}$

The problem can be formally stated as follows:

$$\text{Maximize } F(\mathbf{X}) = \frac{325.9\eta_p}{SFC_{hp}}\frac{C_L}{C_D}\ln\left(\frac{W_{ini}}{W_{fin}}\right)\times\phi$$

where $\mathbf{X} = \{S \;\; AR \;\; \lambda\}^T$
Subject to:

Inequality Constraints		
Max allowable wing weight	g_1	$W_W - 0.10W_0 \le 0$
Fuel for range must fit into wing	g_2	$W_{t\ req} - W_{t\ avail} \le 0$
Range requirement	g_3	$535 - R \le 0$
Max lift requirement	g_4	$C_{L_{max}} - 2.0 \le 0$
LD_{max} requirement	g_5	$13 - LD_{max} \le 0$
Max stall speed requirement	g_6	$V_{S_0} - 46 \le 0$
Equality Constraints		
Gross weight	h_1	$W_0 - 2500 = 0$
Payload	h_2	$W_p - 650 = 0$
Side Constraints		
Wing area	X_1	$130 \le S \le 200$
Wing aspect ratio	X_2	$5 \le AR \le 14$
Wing taper ratio	X_3	$0.1 \le \lambda \le 1$

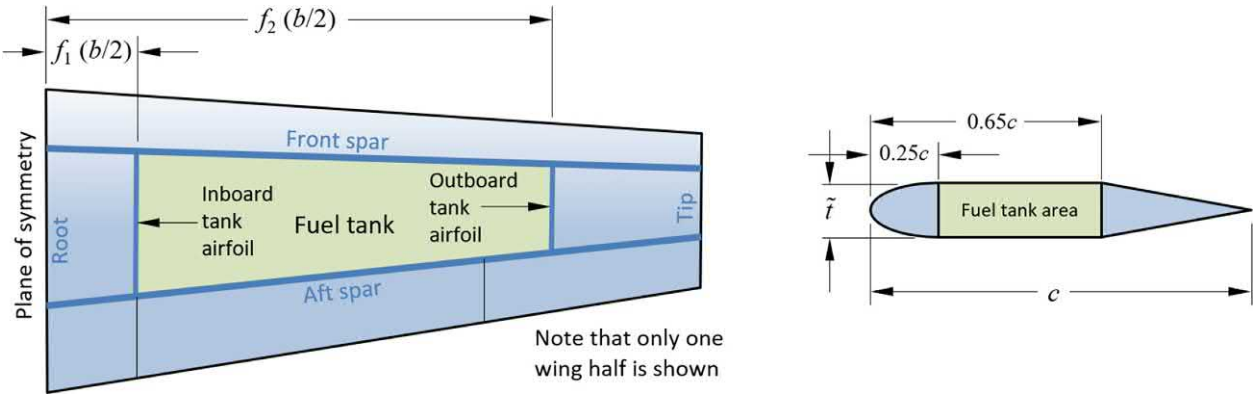


FIGURE 3-26 Fuel tank definition.

STEP 1: Calculate Wing Geometry

As stated earlier, we will consider three design variables: wing area (S), wing aspect ratio (AR), and wing taper ratio (λ). Using the formulation of Section 9.2, the wingspan (b) and the root and tip chords (c_r and c_t) are related to S, AR, and λ as follows:

$$b = \sqrt{AR \cdot S} \tag{9-28}$$

$$c_r = \frac{2S}{(1+\lambda)b} \tag{9-32}$$

$$c_t = \lambda c_r \tag{9-10}$$

As an example, if $S = 150\,\text{ft}^2$, $AR = 5$, and $\lambda = 0.5$, then $b = 27.39\,\text{ft}$, $c_r = 7.303\,\text{ft}$, and $c_t = 3.651\,\text{ft}$.

STEP 2: Calculate Volume of Wing Fuel Tanks, $\forall_{t\ avail}$

We must derive an expression for *available fuel volume*. The fuel tank is limited to that between the front and aft spars of the wing (at 25% and 65% chord, respectively), between wing stations 15% ($f_1 = 0.15$) and 55% ($f_2 = 0.55$) of wing half-span. We approximate this using the idealized wing and airfoil shown in Figure 3-26. Note that $\tilde{t}$ is the *average* or *effective thickness* of the airfoil between its forward and aft extremes. To simplify analysis, we will consider the chordwise shape of the fuel tank rectangular, as shown in Figure 3-26. Since the airfoil is curved, we cannot take full credit for the thickness and, thus, assume that only 85% of the thickness between 25% and 65% chord is available. This is what is done here, i.e. $\tilde{t}$ is 85% of the airfoil's maximum thickness. To derive an expression for $V_{t\ avail}$, we write the wing chord in a parametric form:

$$c(y) = c_r + (c_t - c_r)\left(\frac{2y}{b}\right) \tag{3-40}$$

Thus, the area of the inboard tank airfoil (A_{tr}) is ($y = f_1(b/2)$):

$$c_{ib} = c_r + (c_t - c_r)f_1 \quad \Rightarrow \quad A_{tr} = \overbrace{\tilde{t}}^{=0.85\left(c_{ib}\times\frac{t}{c}\right)} \times \overbrace{c_{ib}\underbrace{(0.65-0.25)}_{=0.4}}^{\text{airfoil's fuel tank width}}$$

$$= 0.34\left(\frac{t}{c}\right)c_{ib}^2$$

Similarly, the area of the outboard tank airfoil (A_{tt}) is ($y = f_2(b/2)$):

$$c_{ob} = c_r + (c_t - c_r)f_2 \quad \Rightarrow \quad A_{tt} = 0.34\left(\frac{t}{c}\right)c_{ob}^2$$

Average area of tank:

$$A_t = \frac{1}{2}(A_{tr} + A_{tt}) = 0.17\left(\frac{t}{c}\right)\left(c_{ib}^2 + c_{ob}^2\right)$$

The volume of the *available* fuel tank is estimated as a prism, extending from the inboard to outboard wing stations ($f_1(b/2)$ and $f_2(b/2)$, respectively). Also note that we have two tanks: one on each side of the plane of symmetry. Note that this is a crude approximation and Equation (9-36) is more accurate.

$$\forall_{t\ avail} = \overbrace{2}^{\text{Two fuel tanks}} A_t \overbrace{(f_2 - f_1)\frac{b}{2}}^{\text{Length of prism for each wing}} = 0.17\left(\frac{t}{c}\right)\left(c_{ib}^2 + c_{ob}^2\right)(f_2 - f_1)b \tag{3-41}$$

Using the previous values of S, AR, and λ, we get $c_{ib} = 6.755\,\text{ft}$, $c_{ob} = 5.295\,\text{ft}$, and $\forall_{t\ avail} = 16.46\,\text{ft}^3$. This means, we can fit $44.9 \times \forall_{t\ avail} = 739.2$ lb_f of fuel in the two-wing tanks.

STEP 3: Calculate Wing Weight, W_W

Use an appropriate choice of Equations (6-43)–(6-47). Make sure the parameters required by these equations are properly calculated. Note that W_W must be less or equal to $0.1W_0$, per constraint g_1. Equation (6-47), with $n_z = 6$ and $V_H = 140$ KEAS returns $W_W = 198.1$ lb_f.

STEP 4: Calculate Maximum Fuel Weight, W_f

In this step, it is important to recognize that even though we can theoretically fit 739.2 lb_f in the wings, the weight of the airplane and payload may not permit this due to the gross weight constraint. We must check if this is the case. As stated earlier, the weight of the airplane at top-of-climb (or start of cruise range) is denoted by W. At that moment, this weight is the sum of the empty weight without the wing ($W_{emw} = 1250$ lb_f), wing weight (W_W), payload (W_p), and fuel weight (W_f). Thus, we can calculate the *maximum* amount of fuel that can be carried without exceeding the gross weight (W_0) at start of mission.

$$W_f = 0.95W_0 - W_{emw} - W_W - W_p \tag{3-42}$$

Using the previous values of S, AR, and λ, we get $W_f = 2375–1250–198.1–650 = 276.8$ lb_f. This means we are weight limited. Since W_f is smaller than the available fuel weight, this is what we must use for the range calculation later.

STEP 5: Calculate Maximum Fuel Volume, $\forall_{t\ \max}$

The volume of this fuel is found by dividing W_f by the fuel density. If using the SI-system, the density of Avgas (ρ_{fuel}) is 0.715 kg/liter (715 kg/m^3) [15]. If using the UK-system, this corresponds to 6 lb_f/US gal (44.9 $\text{lb}_\text{f}/\text{ft}^3$). Thus, we can convert W_f into volume as follows (call it *maximum volume*, $\forall_{t\ \max}$):

$$\forall_{t\ \max} = \begin{cases} W_f/715 & \text{m}^3 \quad \text{if using SI} \\ W_f/44.9 & \text{ft}^3 \quad \text{if using UK} \end{cases} \tag{3-43}$$

Using the previous values of S, AR, and λ, we get that $\forall_{t\ \max} = 6.17\,\text{ft}^3$. In contrast to what is stated in STEP 4, it is also possible this volume will not fit inside the wing,

i.e. $\forbidden{V}_{t\ max} > \forbidden{V}_{t\ avail}$. Recall that it *is* required that all the fuel must fit inside the available wing volume. If $\forbidden{V}_{t\ max}$ is greater than $\forbidden{V}_{t\ avail}$, then the fuel for the mission is reduced to $\forbidden{V}_{t\ avail}$. Then, we calculate the fuel weight for the mission as follows:

$$W_{f\ avail} = \begin{cases} W_f & \text{if } \forbidden{V}_{t\ avail} \geq \forbidden{V}_{t\ max} \\ \rho_{fuel}\forbidden{V}_{t\ avail} & \text{if } \forbidden{V}_{t\ avail} < \forbidden{V}_{t\ max} \end{cases} \tag{3-44}$$

STEP 6: Aerodynamic Analysis

In this step, we calculate the lift coefficient (C_{L_C}) and drag coefficients (C_{D_C}) at cruise. The former is simply calculated using Equation (9-64); $C_{L_C} = L/(qS) = W/(qS)$. The drag coefficient, on the other hand, is more complex and must be calculated for each combination of S, AR, and λ. Consider the total drag coefficient as the sum of wing drag, C_{Dwng}, lift-induced drag, C_{D_i}, and drag of everything except wing drag, C_{Dx}, i.e.

$$C_{D_C} = \overbrace{C_{Dx} + C_{Dwng}}^{C_{D_{\min}}} + C_{D_i} \tag{3-45}$$

To implement this, an estimate for C_{Dx} must be provided. For this example, it will be assumed that $C_{Dx} = 0.020$. It can be obtained either by conducting a drag analysis of the aircraft or by extracting the minimum drag coefficient ($C_{D_{\min}}$) of a "similar" existing airplane and then subtract the drag contribution of its wing (using the method of Section 16.5). Possessing the $C_{D_{\min}}$ for said airplane, one can estimate the drag of the wing alone and subtract from this value. The aforementioned value of C_{Dx} is estimated in this fashion. The drag of the wing (C_{Dwng}) is estimated using

$$C_{Dwng} = \frac{S_{wet\ WNG}}{S} \times C_f \times FF \times IF \tag{3-46}$$

where $S_{wet\ WNG}$ is the wetted area of the wing, C_f is the expected average skin friction coefficient of the wing, FF is the wing's average form factor, and IF its interference factor (see methodologies for all of these in Chapter 16). Here, assume $IF = 1$. The skin friction coefficient is estimated using the Reynolds number (R_e) for fully turbulent boundary layer using Equation (16-41), or

$$R_e = \frac{\rho V_C c_{avg}}{\mu} = \frac{\rho V_C}{\mu}\sqrt{\frac{S}{AR}} \Rightarrow \overline{C}_{f_{turb}} = \frac{0.455}{(\log_{10} R_e)^{2.58}} \tag{16-41}$$

The form factor can be estimated using the methods of Section 16.3.6. Here, Equation (16-122) is used.

$$FF = 1 + 1.2\left(\frac{t}{c}\right) + 70\left(\frac{t}{c}\right)^4 \tag{16-122}$$

Then, we must estimate the lift-induced drag. Using standard formulation (i.e. $C_{D_i} = kC_L^2$) will not work well as it is invariant to taper ratio: it predicts the same C_{D_i} for all values of λ for a fixed AR. We must resort to greater computational sophistication; for instance, the lifting-line or vortex lattice method. In this example, the method of Section 9.7, was used (implemented using the VBA code of Section 9.7.4). A proper use of the routine requires the user to specify the AOA that returns the same C_L as C_{L_C}. The reader attempting to replicate this study can accomplish this by calculating the C_L for two separate AOAs and interpolate to get the AOA associated with C_{L_C}. This is necessary to extract the correct lift-induced drag (C_{D_i}) and span-efficiency (e) for the wing. We need e to estimate the maximum lift-to-drag ratio ($LD_{\max}$), which is one of the constraints in this example (g_5). This assumes that the drag of the airplane is estimated using the simplified drag model (see Chapter 16), which allows $LD_{\max}$ to be calculated using Equation (20-33).

Using the previous values of S, AR, and λ, it was found that $C_{L_C} = 0.3744$. This was used to find other aerodynamic properties using the Lifting Line Theory. This returned: AOA = 4.841 degrees, $C_{D_i} = 0.003160$, $e = 0.9911$. Using an average chord $c_{avg} = 5.477$ ft, other values are $C_f = 0.003267$, $C_{Dwng} = 0.007569$, $C_{D_{\min}} = 0.02757$, $C_{DC} = 0.03658$, $LD_C = 10.24$, and $LD_{\max} = 11.88$. Note that e is the inviscid span efficiency (see Section 9.5.12).

STEP 7: Estimate Range

Once we have the available fuel ($W_{f\ avail}$), we can determine the range of the aircraft using Breguet's range Equation (21-38) (see Section 21.3.4)

$$R = \frac{325.9\eta_p}{SFC_{hp}}\frac{C_{L_C}}{C_{D_C}}\ln\left(\frac{W}{W - W_{f\ avail}}\right) \tag{21-38}$$

For this problem, the range is our objective function. However, there is an additional step we must take to select a wing that is likely to have benign stall characteristics.

Using the previous values of S, AR, and λ, and noting that $W = 2375$ lb$_f$ and $W_{f\ avail} = 276.8$ lb$_f$ we find that $R = 703$ nm.

STEP 8: Penalty Function Range

To bias the solution toward acceptable stall characteristics, we want to (1) feature a simple high-lift system and (2) penalize low taper ratios, even if these return a greater range. This is necessary because low λ has a very detrimental effect on the quality of stall. We can enforce the former through a $C_{L_{\max}}$ constraint, as has been done as inequality constraint g_4. Thus, in this example, all solutions that require $C_{L_{\max}}$ greater than 2.0 will be rejected. This is checked by calculating the $C_{L_{\max}}$ required for each S and compare to the desired maximum. Enforcing this will result in wing area that will not require a complex high-lift system.

The stall quality can be enforced through the objective function, by penalizing range values associated with low taper ratios. See more about penalty functions in ref. [16]. One way of accomplishing this is the penalty function ϕ

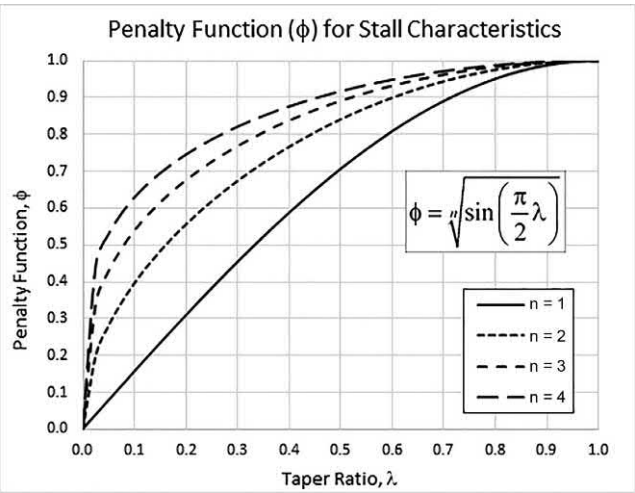


FIGURE 3-27 Penalty function.

presented in Figure 3-27. By multiplying the range estimation in Equation (21-38) by this function, we reduce the product, disfavoring low taper ratios. Thus, the objective function for this example is given by

$$R = \frac{325.9\eta_p}{SFC_{hp}}\frac{C_{L_C}}{C_{D_C}}\ln\left(\frac{W}{W - W_{f\ avail}}\right) \times \sqrt[n]{\sin\left(\frac{\pi}{2}\lambda\right)} \quad (3\text{-}47)$$

Where n is the severity factor. The larger the n, the less is the penalty inflicted by low taper ratio. It can be argued that $\lambda = 1$ yields the most benign stall characteristics. Therefore, there is no penalty ($\phi = 1$). If $n = 4$ yields, the stall quality of a wing with $\lambda = 0.3$ is about 80% of that expected for a constant chord wing. In this example, n was selected as 3.

Using the previous values of S, AR, and λ, we find that $\phi = 0.8919$ and $F(\mathbf{X}) = 627.0$ nm.

(2) Results

These steps were implemented in a computer code. Additional parameters (e.g. endurance, cruise power, etc.) were calculated as well, allowing these as potential objective functions as well. It should be stated that the *rival* aircraft used for this problem is the Cessna 177 Cardinal. For this reason, many parameters (e.g. V_C, H_C, f_1, f_2, etc.) were based on that airplane. The results are presented in Table 3-5.

It should be stressed that these results in *no way* imply the example aircraft is superior to the Cardinal. For one, the drag model may be underestimated. The author does not know if the wing sizing of the Cardinal involved any optimization in the first place. Regardless, it can be argued that even a simple optimization of this nature returns reasonable results. As expected, the wing areas are similar since the $C_{L_{max}}$ and V_{SO} used are those of the Cardinal. However, the optimized AR and λ are only related to theory and are close to the reference aircraft.

TABLE 3-5 Optimized versus reference aircraft.

Parameter	Symbol	Example aircraft	Cessna 177 [17]
Wing area	S	175 ft^2	174 ft^2
Wing aspect ratio	AR	6.00	7.24
Taper ratio	λ	0.6	0.7
Cruising speed	V_C	130 KTAS	130 KTAS
Cruising altitude	H_C	10,000 ft	10,000 ft
Range	R	674 nm	535 nm
Endurance	E	5.19 h	4.2 h
Cruise power required for V_C	P_C	114 BHP (64%)	135 BHP (75%)
Fuel quantity required for R	Q_f	46.3 US gal	42 US gal
Miles per gallon	mpg	14.56	12.74

(3) Final Notes

It is not hard to incorporate other characteristics of the airplane into the formulation. For instance, steady-state roll rate (see Equation (25-83)), wing washout, wing sweep, and even horizontal and vertical tail sizing (see Section 11.4) can all be included. The trick is to properly modify the objective function. It should be noted that adding these to the batch will increase the solution time. This level of detail to the optimization should push the interested programmer to greater sophistication for the solution; at minimum a scheme that would utilize Equation (3-34). The reader is encouraged to endeavor into the world of specialized optimization techniques that have been developed.

EXERCISES

(1) A single-engine piston-engine propeller airplane is being designed to meet the following requirements:
- **(a)** The design shall comply with LSA requirements as stipulated by ASTM F2245.
- **(b)** Design gross weight shall be 1320 lb_f in accordance with LSA requirements.
- **(c)** It must sustain a 1.5 g constant velocity turn while cruising at 100 KCAS.
- **(d)** It must be capable of climbing at least 1000 fpm at 70 KCAS at S-L.
- **(e)** It must be capable of operating from short runways in which the ground run is no greater than 500 ft and liftoff speed of 55 KCAS at design gross weight.
- **(f)** It must be capable of a cruising speed of at least 110 KTAS at 8000 ft.

(g) It must be capable of a service ceiling of at least 14,000 ft.

The designer's initial target is a minimum drag coefficient of 0.035 and an aspect ratio of 7. Furthermore, it is assumed the ground friction coefficient for the T-O requirement is 0.04, the T-O lift and drag coefficients are $C_{L\ TO}=0.5$ and $C_{D\ TO}=0.04$, respectively. Plot a constraint diagram for these requirements in terms of W/S and T/W for values of W/S ranging from 10 to 40 lb_f/ft^2. Then, determine the required wing area and horsepower for the airplane if its propeller efficiency at cruise is 0.80, 0.7 during climb, and 0.6 at other low-speed operations.

(2) A twin piston-engine propeller airplane is being designed to meet the following requirements:

(a) Design gross weight shall be 5000 lb_f.

(b) It must sustain a 1.5 g constant velocity turn while cruising at 180 KTAS at 12,000 ft.

(c) It must be capable of climbing at least 1800 fpm at 100 KCAS at S-L.

(d) It must be capable of operating from short runways in which the ground run is no greater than 1200 ft and liftoff speed of 75 KCAS at design gross weight.

(e) It must be capable of a cruising speed of at least 180 KTAS at 12,000 ft.

(f) It must be capable of a service ceiling of at least 25,000 ft.

The designer's initial target is a minimum drag coefficient of 0.035 and an aspect ratio of 7. Furthermore, it is assumed the ground friction coefficient for the T-O requirement is 0.04, the T-O lift and drag coefficients are $C_{L\ TO}=0.5$ and $C_{D\ TO}=0.04$, respectively. Plot a constraint diagram for these requirements in terms of W/S and T/W for values of W/S ranging from 10 to 40 lb_f/ft^2. Then, determine the required wing area and horsepower for the airplane if its propeller efficiency at cruise is 0.80, 0.7 during climb, and 0.6 at other low-speed operations.

(3) Prepare a stall speed–cruise speed carpet plot for a small twin-engine jet aircraft for which the following parameters are given:

Parameter	Symbol	Value	Units
Desired stalling speed	V_S	90	KCAS
Desired cruising speed	V_C	475	KTAS
Desired cruise altitude	H_C	41000	ft
Target gross weight	W	8000	lb_f
Expected minimum drag coefficient	$C_{D\min}$	0.020	
Expected LE sweep angle (to estimate e)	Λ_{LE}	20°	
Expected aspect ratio (to estimate e)	AR	8	
Expected taper ratio (to estimate e)	λ	0.5	
Max thrust at S-L	T_0	2000	lb_f

(4) Four avionics suites are being considered for a new small airplane (see table below) and you have been tasked with recommending one over the others. Using weight (W), cost (C), voltage (U), IFR rating (R), number of software features (F), screen width (S), and screen resolution area ($w \cdot h$) as variables, suggest a cost function that can be used to indicate the most suitable avionics suite. (Hint: use the min or max of each column as a reference value, noting that low weight, cost, and voltage, IFR rating, high number of software features, large screen width, and resolution are favorable.)

Type	Weight lb_f	Cost $	Voltage Volts	IFR rated? 0-no, 1-yes	Software features	Screen width, in	Resolution $w \times h$
Avionics Suite 1	9.8	8900	12	1	35	10	800x600
Avionics Suite 2	11.2	13500	12	1	82	12	1024x726
Avionics Suite 3	10.9	9100	18	1	36	10	800x600
Avionics Suite 4	8.8	6000	12	0	24	7	480x386

References

[1] D.F. Finger, C. Braun, C. Bil, *An initial sizing methodology for hybrid-electric light aircraft*, in: 2018 Aviation Technology, Integration, and Operations Conference, AIAA Aviation Forum, AIAA, 2018, https://doi.org/10.2514/6.2018-4229.

[2] C.E.D. Riboldi, F. Gualdoni, *An integrated approach to the preliminary weight sizing of small electric aircraft*, Aerosp. Sci. Technol. 58 (2016) 134–149. ISSN 1270-9638 https://doi.org/10.1016/j.ast.2016.07.014.

[3] M. Tyan, N. Van Nguyen, S. Kim, J.-W. Lee, *Comprehensive preliminary sizing/resizing method for a fixed wing – VTOL electric UAV*, Aerosp. Sci. Technol. 71 (2017) 30–41. ISSN 1270-9638 https://doi.org/10.1016/j.ast.2017.09.008.

[4] Anonymous, *Cessna 162 Skycatcher Pilot's Operating Handbook and Flight Training Supplement*, Rev.2, Cessna Aircraft Company, April 26, 2010.

[5] M. Oberhauser, *Carpet Plots in Parametric Trade Studies: Development of a Matlab Tool to Create Carpet Plots*, Technische Universität München, 2013.

[6] S. Powers, *The Generation of Carpet Plots*, Personal notes, 1997.

[7] J. O'Hara, G. Stump, M. Yukish, E. Harris, G. Hanowski, A. Carty, *Advanced visualization techniques for trade space exploration*, in: 48th AIAA/ASME/ASCE/AHS/ASC Structures, Structural Dynamics, and Materials Conference, 23–26 April 2007, Honolulu, HI, 2007.

[8] J. Bergstra, Y. Bengio, *Random search for hyper-parameter optimization*, J. Mach. Learn. Res. 13 (2012) 281–305.

[9] A. Sóbester, A. Forrester, *Aircraft Aerodynamic Design: Geometry and Optimization*, John Wiley and Sons, 2015.

[10] J.J. Tuma, *Handbook of Numerical Calculations in Engineering*, McGraw-Hill, 1989.

[11] G.N. Vanderplaats, *Numerical Optimization Techniques for Engineering Design: With Applications*, McGraw-Hill Book Company, 1984.

[12] G.V. Reklaitis, A. Ravindran, K.M. Ragsdell, *Engineering Optimization – Methods and Applications*, John Wiley and Sons, 1983.

[13] R.L. Rardin, *Optimization in Operations Research*, first ed., Pearson, 1997.

[14] M.J. Kochenderfer, T.A. Wheeler, *Algorithms for Optimization*, MIT Press, 2019.

[15] Anonymous, *Material Safety Data Sheet AVGAS 100LL*, SDS 800001008388 (Rev. 8.0, 04/30/2019), Shell.

[16] A.E. Smith, D.W. Coit, *Penalty Functions, Section C 5.2 of Handbook of Evolutionary Computation*, Oxford University Press and Institute of Physics Publishing, January 1996.

[17] Anonymous, *Cessna Model 177B Cardinal Pilot's Operating Handbook*, Cessna Aircraft, 1976.

This page intentionally left blank

CHAPTER

4

Aircraft Configuration Layout

OUTLINE

4.1 **Introduction** 93
- *4.1.1 The Content of This Chapter* 93
- *4.1.2 Requirements, Mission, and Applicable Regulations* 93
- *4.1.3 How to Design a Good Aircraft* 94
- *4.1.4 Summary of Common Configuration Targets* 95
- *4.1.5 Past and Present Directions in Aircraft Design* 96
- *4.1.6 Aircraft Component Recognition* 96

4.2 **The Fundamentals of the Configuration Layout** 100
- *4.2.1 Vertical Wing Location* 100
- *4.2.2 Wing Configuration* 102
- *4.2.3 Wing Dihedral* 103
- *4.2.4 Wing Structural Configuration* 104
- *4.2.5 Cabin Configuration* 104
- *4.2.6 Propeller Configuration* 106
- *4.2.7 Engine Placement* 106
- *4.2.8 Landing Gear Configuration* 108
- *4.2.9 Tail Configuration* 109
- *4.2.10 Configuration Decision Matrix* 109

References 111

4.1 INTRODUCTION

The selection of the configuration layout is one the earliest decisions made during the conceptual design phase. It involves choosing desired features of the airplane, more through qualitative than quantitative evaluation. Since this happens so early in the development, there is usually limited detail available about the final product. Thus, unless the design belongs to a *family* of aircraft for which operational experience exists, the designer must rely heavily on history; how have aircraft of similar configurations fared in the past? This chapter presents the pros and cons of various aircraft configurations and helps the designer understand the implications of the layout of the new airplane.

Today's aircraft designer has access to an enormous database of possible configurations. Many of those have a long operational history that gives the designer a realistic insight into advantages and shortcomings. It is no exaggeration that when it comes to positioning of wings, landing gear, and engines, or the shape and size of stabilizing surfaces, and even aesthetics, the modern designer can practically go window-shopping for ideas using this vast database.

Besides training the novice designer in evaluating the pros and cons of existing configurations, this chapter presents various examples of past and contemporary aircraft. This will be followed by the introduction of numerous aircraft configurations to provide the aspiring aircraft designer with ideas as to what shape suits the mission. Discussing advantages and disadvantages of each configuration is an imperative part of this process.

4.1.1 The Content of This Chapter

- Section 4.2 presents several important design considerations and discusses their advantages and disadvantages. This is intended to help the designer to develop a keener eye for the implications of the configuration selection. This awareness can avoid costly mistakes for any company designing a new aircraft.

4.1.2 Requirements, Mission, and Applicable Regulations

As stated in STEP 1 of Section 1.4.1, the design process begins by the execution of the statement: "Understand requirements, mission definition, and the implications of the regulations to which the airplane will be certified." This means:

https://doi.org/10.1016/B978-0-12-818465-3.00004-5

Copyright © 2022 Elsevier Inc. All rights reserved.

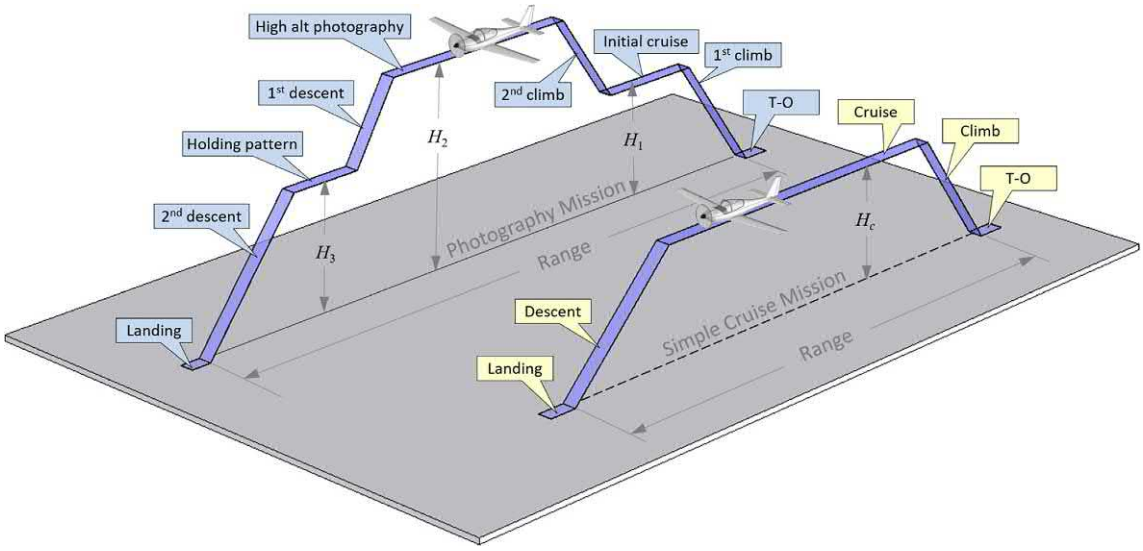


FIGURE 4-1 Two example missions: a simple cruise and a high-altitude photography mission.

(1) Requirements refer to the capability of the aircraft in terms of how far, how fast, how high, how heavy, how long a take-off and landing distance, and so on.
(2) The mission simply refers to how the airplane will generally operate. Is it a passenger transport that takes-off, climbs to some altitude where it cruises for a while before descending for landing? Or is the mission more complicated (see Figure 4-1)? Whatever the mission, its details should be clearly defined for the reasons stated in Section 1.2.3.
(3) Implications of regulations mean the designer must understand in what capacity aviation regulations will affect the airplane. For instance, will it be pressurized; will it need large entry doors; or will emergency fuel jettison be required?

4.1.3 How to Design a Good Aircraft

A brochure with the above title was published in 1954 by the McDonnell Aircraft Corporation.[1] It was written by Kendall Perkins, the company's VP of Engineering [1]. The brochure listed the company's aircraft design policy. The following is a condensed version of its message (italics are taken verbatim from the reference):

(1) ***Requirements***: When specifying functional and structural requirements, be equally ready to omit nonessential ones as you are including essential ones. *When in doubt, leave it out*.
(2) ***Efficiency***: Adding weight and drag comes at the cost of performance. *Efficiency leads to efficiency*.
(3) ***Simplicity***: The mark of a good design is simplicity. Simplicity leads to reduced weight, lower cost, greater reliability, less development time and cost, to name a few. *If it isn't as simple as it can be, it isn't as good as it can be*.
(4) ***Certainty***: Poor design must either be tolerated or changed. When an operator is forced to tolerate the quirks of a poor design, the airplane acquires a poor reputation. Avoid depending heavily on intuition—this leads to a poor design. Analyze. *Before you decide, be sure*.
(5) ***Reliability***: Most aircraft are less reliable than they could be. Complexity reduces reliability and requires far greater effort and cost. Schedule enough time for a thorough development. *Don't fail to forestall failure*.
(6) ***Weight***: The difference between a well and poorly designed aircraft is the difference in empty weight. Ensure direct load paths. Combine load paths and avoid redundant structures. *If it isn't light, it isn't good aircraft design*.
(7) ***Drag***: Pay close attention to anything that dirties up the airplane. *To get performance make it smooth*.
(8) ***Cost***: Minimizing cost takes effort. Better design reduces cost more than better manufacturing techniques and efficiency. *The best aircraft give the most performance per dollar*.
(9) ***Maintenance***: The reputation of an aircraft, in part, depends on the effort required to keep it flying. Keep the structure and access to it simple, rugged, and easy to repair. *There are too few mechanics who are experienced, conscientious and resourceful—design it to keep flying anyway*.

[1] McDonnell Aircraft Corporation merged with the famous aircraft manufacturer Douglas Aircraft in 1967 and became McDonnell-Douglas. In 1997, McDonnell-Douglas merged with Boeing.

(10) ***Scheduling***: Unrealistic scheduling can have important negative impact on aircraft. *In importance, time equals performance*.

(11) ***Newness***: Be open-minded about your own ideas and those of others. However, also be critical. Remember that an idea is not better just because it is new or different. *If it isn't necessary to change, it's necessary not to change*.

(12) ***Progressiveness***: Our goals can be progressive or conservative depending on the nature of a development project. It is important to achieve a balance of the two. *Be progressive, but do it conservatively*.

(13) ***Integration***: Each of the above bullets should be weighed when making the thousands of decisions required in the development of a new aircraft. Not only may the simplest design be the cheapest, most reliable, and easiest to develop, it may also be of equal weight and capability of the most complicated one. *The best designer finds the best solutions*.

4.1.4 Summary of Common Configuration Targets

The following lists common desirable targets for typical aircraft and are collected here with the rookie aircraft designer in mind. Note that in actual development environment, there are a number of factors that drive design decisions: (1) concerns about market needs and timing, (2) government actions and priorities, (3) competitor actions, (4) technology readiness, and (5) fiscal considerations [2].

Accessibility	Make all entry and exit doors easy for all occupants. Access to systems that must be "preflighted" must be easy. This includes checking oil, hydraulic fluid, and fuel. Make access to systems that require routine maintenance easy.
Aesthetics	Beauty is in the eyes of the beholder, but it is also a matter of probabilities. Not convinced? Survey a pool of people about what they consider appealing aircraft configuration. For instance, have participants rate tail configurations by aesthetics. The results are eye-opening. That said, strive to make your airplane look good. Airplanes cost a lot of money and customers want to show off sleek, attractive lines and not something resembling a shoebox with wings. If you're not sure what looks good, seek the opinion of others.
Cabin and cockpit	Unless constrained by other requirements, design the airplane with a roomy, uncluttered cabin, with plenty of legroom. This provides comfort and lowers anxiety in people who fear flying. Avoid having any wing structure inside the cabin. Design the cockpit to accommodate the 5th to 95th percentile of people. Offer adjustable cockpit seats. However, be mindful that too large a fuselage frontal area increases drag.
Certifiability	While bringing novelties to the market is to be encouraged, be careful. Novelties can make a product much more expensive to certify. Make sure the novelty is really needed, for instance for marketing advantage or as a safety feature. Refer to bullet (12) of Section 4.1.3.
Field of view (FOV)	Maximize FOV for pilots and passengers. It is important for pilots because it enhances safety by reducing risk of mid-air collisions. It also helps with situational awareness during ground and low altitude operations. Passengers, generally, appreciate the view as well. Of course, there is a drawback—excessive sunlight may lead to discomfort, so provide visors for occupants.
Ground operations	Provide a wide wheel track to promote pleasant, stable ground maneuvering (cornering). Provide wheelbase with high enough ground friction for nose or tailwheel to ensure safe, skid-free turns on the ground. Provide responsive braking and control system.
Low drag	For high-performance aircraft, pay special attention to external geometry, specifically components that "dirty up" the airplane. Pay attention to all intersections, as these can develop separation bubbles that increase drag. Do not trust your intuition regarding where this can happen. It can develop in surprising places. Soft curve surfaces are less likely; sharp, discontinuous breaks in surfaces are more likely. Separation results from flow deceleration and where this happens is not obvious, even on smooth surfaces.
Maintainability	Make access to systems easy. Do not hide one system behind another one. Having to remove a system to access another one for maintenance is a serious detriment. Plan early where to place access panels. Will a mechanic have to contort into a pretzel to fix that component? Consult an A&P mechanic when designing for maintenance.
Manufacturability	Refers to difficulties involved in manufacturing a product. A simple airframe is easier to manufacture than a complex one: its manufacturability is greater. Manufacturability is increased by choosing simplicity over complexity. A constant chord wing has higher manufacturability than a tapered one. So is fixed versus retractable landing gear, or gravity-fed fuel system. Of course, it is important to recognize that simplicity begets low performance, while complexity is the companion of high performance. Complexity is justified only based on performance.
Reliability	Reliability is the companion of safety. Reliability is achieved by simplicity and by using tried technology. An important wisdom of engineering posits that the *simplest solution that does the job* should always be pursued. Simplicity leads to reliability and reliability leads to safety.

Continued

Safety	The airplane must be safe. This should be the overbearing priority of all aircraft design projects. It requires the designer to carefully evaluate the state of technology. This means, avoid unproven technology. An adage of aircraft design says: "Mate a new engine to an old aircraft or an old engine to a new aircraft. But never mate a new engine to a new aircraft." Design the airplane for benign stall characteristics. Evaluate what-if situations: Multiengine aircraft must be controllable and capable of climbing above the highest mountains with one engine inoperative. Does this apply to your design? Besides standard emergency features consider emergency egress, airframe parachute system (if practical), airbags for occupants, and so forth. Remember: aggressively pushing a poorly designed schedule is detrimental to safety.
System complexity	The use of complex systems must be justified. It is easy to justify the selection of retractable landing gear based on competitive performance goals. However, justifying this for a slow aircraft because of aesthetics is altogether different. The history of engineering is wrought with examples of *parent*-systems that required *child*-systems to overcome shortcomings. There are the countless aircraft that feature stability augmentation systems to repair stability and control shortcomings resulting from other design requirements. Of course, demanding requirements associated with many aircraft are often only realized through system complexity. Regardless, select simplicity first.
Weight	Maximize useful load (difference between gross and empty weight). In aircraft design, it is a commodity. The best way to improve it is to reduce the empty weight. The best way to reduce empty weight is to stick with simple systems and efficient structure. Avoid redundant structure—stick with what this author calls *dual utility design*: try and combine the utility of two or more items.

4.1.5 Past and Present Directions in Aircraft Design

It may strike many as a surprise that aircraft design would be affected by fashion. Something as vain as style should be beyond engineering, but a review of the history of aviation reveals this is not the case. It is vibrant with shapes and components that were popular at one time, but later became a part of history, while others stuck around and became the norm. Table 4-1 lists a few fads that are clearly visible by observing the evolution of the aircraft from early times to modernity.

TABLE 4-1 Selected fads in aircraft design.

Era	Fashion
1910s	Rotary engines, biplanes, engine-synchronized machine guns (necessity more than fashion).
1920s	Corrugated aluminum aircraft, wheel fairings for fixed landing gear, open cockpits-closed passenger cabins.
1930s	Engines inside the wing, the birth of scheduled passenger transportation, closed cockpits-closed cabins, retractable landing gear, variable-pitch propellers, round wingtips, taildraggers, seaplanes, streamlining.
1940s	Elliptical wings, engine supercharging, sliding canopies (Malcolm hood) for fighters, tricycle landing gear, pressurized bombers.
1950s	Pressurized passenger piston- and turboprops, Jetson's style jet geometry,[a] supersonic aircraft.
1960s	VTOL aircraft, supersonic passenger transport, Yehudi flaps for commercial jet aircraft, multi-slotted Fowler flaps for jetliners, low bypass ratio jet engines, delta wings for fighters. Fuselage podded and wing-mounted jet engines.
1970s	Reduced Field-of-View (FOV) cockpits in fighters, "Walk-about-cabin" for business jets, STOL aircraft.
1980s	Composites, NLF airfoils, wide-body jets, increased FOV fighter cockpits, and T-tails, more simplified high-lift system for jetliners resulting from reduction in LE-sweep angles, which was a consequence of the development of airfoils using computers, kit planes.
1990s	Propfans, joined wing design, high bypass ratio turbofans, ETOPS certified commercial jetliners, glass cockpits for commercial jetliners, Hush-kits for older jetliners.
2000s	Winglets, glass cockpits for GA aircraft, LSA aircraft.
2010s	Chevrons for jet engines, raked wingtips, electric aircraft.

[a] *Generally, this means fuselages with a bullet shaped nose with a Pitot sticking out of it. The term is really the author's preference and is admittedly used to give name to something very hard to describe.*

4.1.6 Aircraft Component Recognition

Figures 4-2–4-4 are intended to familiarize the reader with the external parts of typical aircraft. All aircraft feature components exposed to the airflow. These not only affect performance and operation, but also cost of manufacturing and maintenance. The location of most of these components (e.g., Pitot-tubes, static sources, antennas, fairings, etc.) usually results from of hard work by various design groups. For instance, static ports must be installed in an area where surface pressure remains relatively constant with angle-of-attack. This area, on the other hand, may be prime real estate for an antenna or an inlet scoop. Understanding where specific components must be placed helps the designer anticipate and avoid possible detail-design conflicts (Figure 4-5).

Aircraft consist of major components: wings, fuselage, nacelle, empennage, horizontal tail (HT) and vertical tail (VT), power plant, and landing gear, to name a few. Of these, three need a further definition:

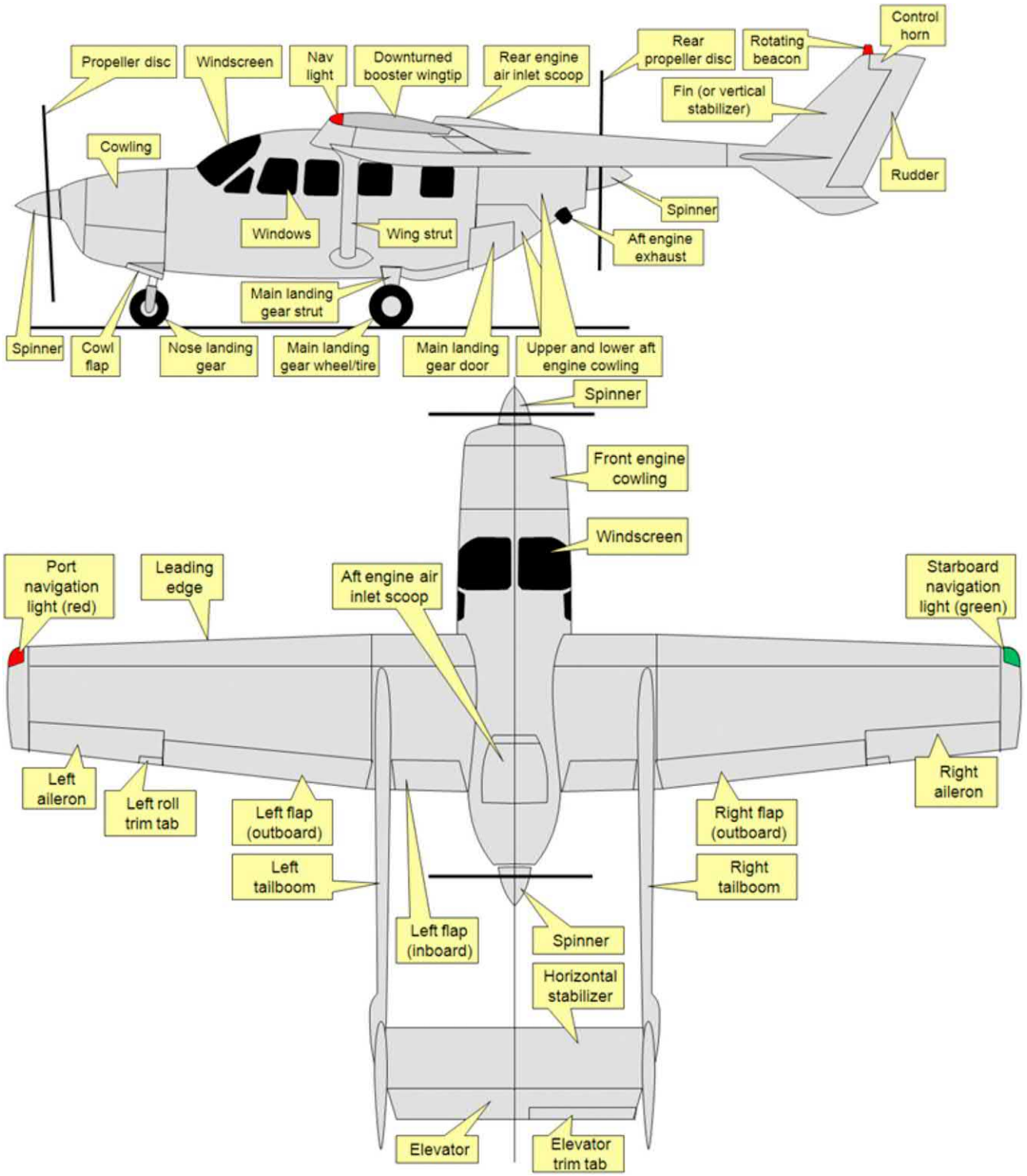


FIGURE 4-2 Cessna 337 Skymaster.

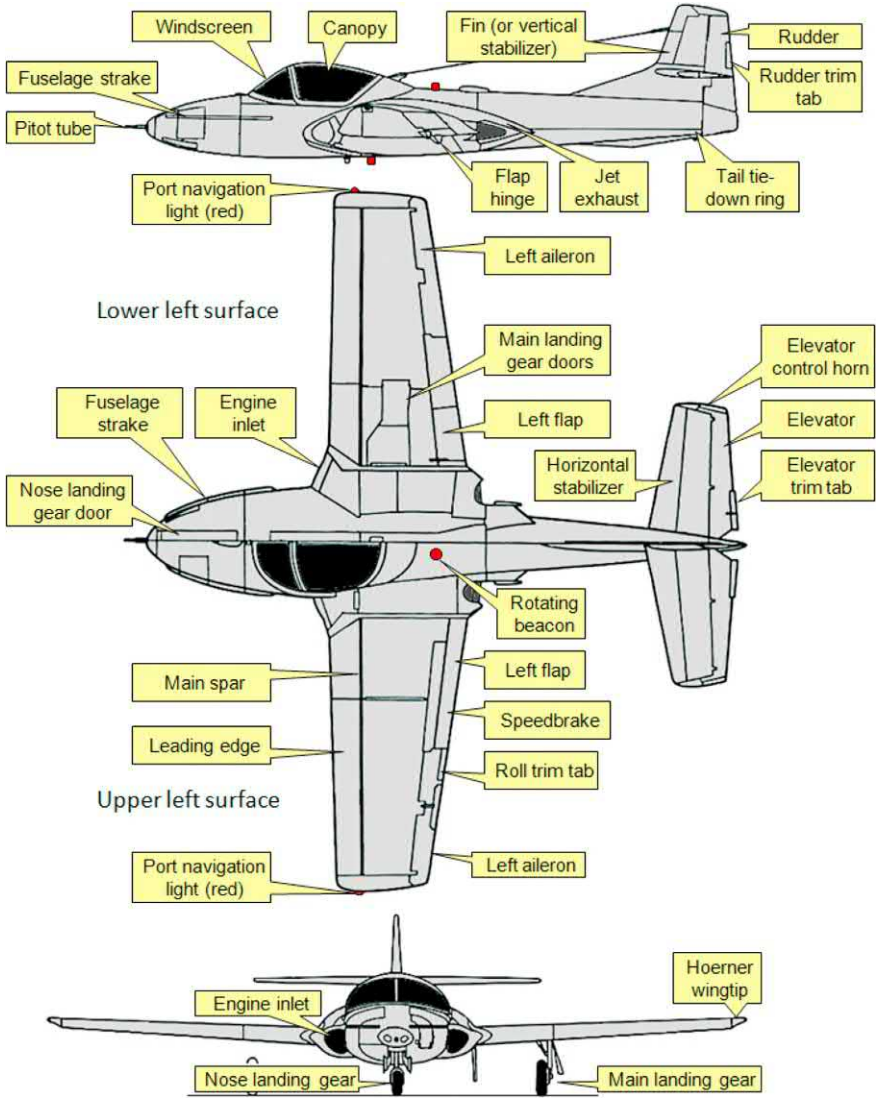


FIGURE 4-3 Cessna T-37 Dragonfly (also known as the "Tweety Bird").

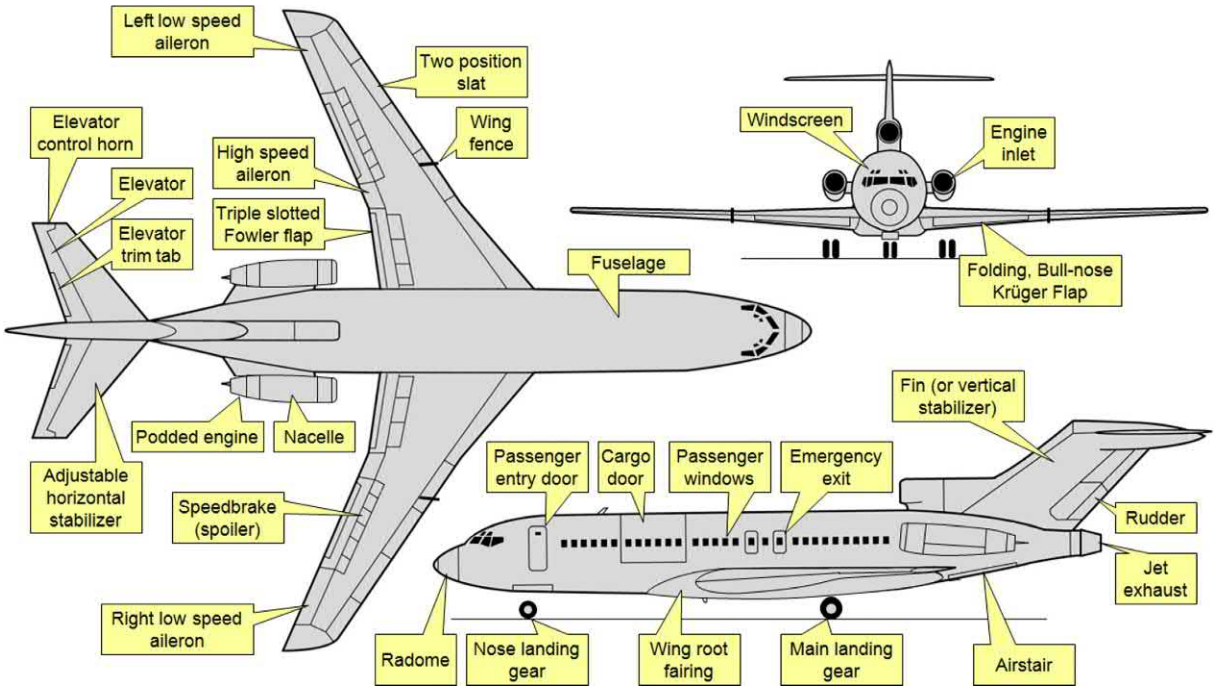


FIGURE 4-4 Boeing B-727 commercial jetliner.

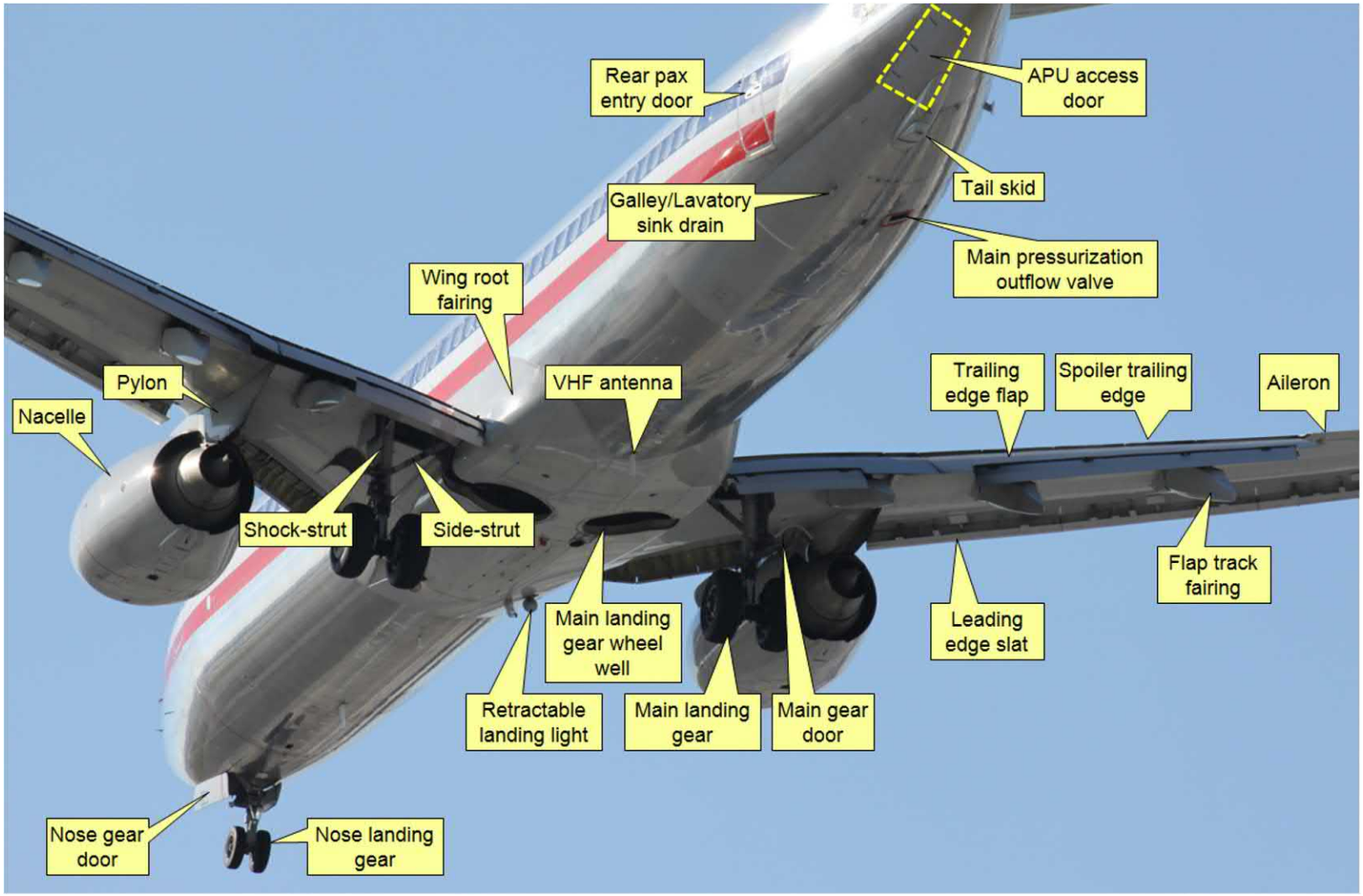


FIGURE 4-5 A Boeing 737-800 in landing configuration. *Photo by Phil Rademacher.*

A *fuselage* is a structural body not intended to generate lift (although it may) whose purpose is to contain engine, fuel, occupants, baggage, and mission-related equipment. A fuselage is always mounted to lifting and stabilizing surfaces. An *empennage* refers to the HT and VT of a conventional aircraft configuration. The word is of French origin where it refers to the tail feathers of an arrow. Sometimes it is taken to mean the general region or assembly of the fuselage that contains both the HT and VT. A *nacelle* is a fuselage that does not carry an empennage. Nacelles usually carry an engine but may or may not house occupants. Nacelles can be mounted to a lifting surface, such as a wing, or to a nonlifting geometry like a fuselage.

4.2 THE FUNDAMENTALS OF THE CONFIGURATION LAYOUT

This section presents important concepts regarding the configuration selection, as well as arguments for and against their selection. Pros or cons of features should not be equally weighed. Propwash over the horizontal tail increases drag (con) and elevator authority (pro). If the increased elevator authority shortens short-field take-off by 100 ft, but increases drag by 0.5 lb_f (0.2%), which should weigh more? When the design team struggles to select specific layout options, it is a good idea to use a decision matrix with proper weighing to help settle configuration disagreements (see Section 4.2.10).

Before starting a new airplane design, the novice designer should familiarize him/herself with Table 4-2, which shows typical dimensions for some selected classes of aircraft. Students of aircraft design, who have yet to develop a keen sense for dimensions and weights of airplanes, are encouraged to study the table in detail. Beginners frequently devise configurations that are either way too big or small, considering power plant. Yes, a new design *can* be outside the shown limits, however, most aircraft fall somewhere between the extremes cited. If your aircraft is outside of these limits, you are encouraged to take a second look at the numbers.

4.2.1 Vertical Wing Location

The vertical wing location is selected based on factors such as:

Accessibility (freight, passengers, fuel)	Field-of-view
Length of landing gear legs	Manufacturing issues
Stability and control	Structural issues
Protection of occupants	Interference with passenger cabin
Operation (amphibians, land only)	Aerodynamic drag
Aesthetics	Manufacturer's (or designer's) preference

Avoid succumbing to biases such as "low-wing airplanes are always faster," "mid-wing aircraft generate less drag," or "high-wing airplanes have better stall characteristics." These are aphorisms. There is no law of nature that says that one or the other is superior. It all depends on other details such as overall drag, engine

TABLE 4-2 Typical properties of aircraft based on class [3].

	LSA[a]	Single-prop GA aircraft[b]	Sailplanes[c]	Commuter propliners[d]	Bizjets	Commercial jetliners[e]
Wingspan, ft	17–35	30–45	35–101	45–100	44–70	90–290
Wing area, ft^2	75–160	150–400	120–250	300–860	200–1400	900–10,000
Wing aspect ratio	5–12	6–11	10–51	6–13	5–12.8	7–10
Wing taper ratio	0.5–1.0	0.3–1.0	0.4–0.5	0.35–1.0	0.3–0.5	0.20–0.5
HT aspect ratio	3–5	3–5	5–7.7	3–6	4.5–6.5	3–4
HT taper ratio	0.5–1.0	0.5–1.0	0.5–1.0	0.5–1.0	0.4–0.7	0.3–0.7
VT aspect ratio	0.7–3	1–2	1–3	1–3	1–3	1–3
VT taper ratio	0.3–1.0	0.5–1.0	0.5–1.0	0.5–0.9	0.4–0.9	0.5–1.0
Empty weight, lb_f	200–880	800–6800	100–1100	7000–26,000	7000–50,000	40,000–550,000
Gross weight, lb_f	400–1430	1500–12,500	280–1700	12,000–55,000	20,000–100,000	75,000–1,300,000
Wing loading, lb_f/ft^2	6–12	10–40	4–10	25–80	75–120	80–120

[a] *Light Sport Aircraft: Includes typical homebuilt and other experimental category aircraft.*
[b] *Refers to 14 CFR Part 23 or EASA CS-23 certified aircraft.*
[c] *Includes motorgliders.*
[d] *Refers to the typical turboprop powered domestic aircraft and a handful of piston aircraft.*
[e] *Refers to 14 CFR Part 25 passenger jetliners for both domestic and international operation.*

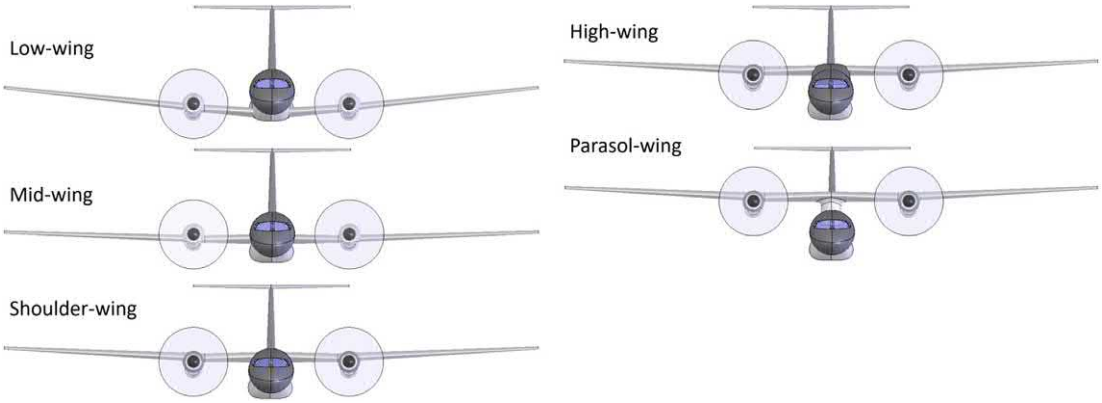


FIGURE 4-6 Vertical wing location nomenclature.

power, airfoil selection, geometry of the airplane, surface qualities, and so on. It is the interaction of the complete aircraft that matters. Case in point: Cessna 152 (high-wing with wing struts, 110 BHP Lycoming O-235) cruises at 103 KTAS at 4000 ft at 75% power [4]), Piper Tomahawk (low-wing, 112 BHP Lycoming O-235) cruises at 104 KTAS at 4000 ft at 75% power [5]), and Beech Skipper (low-wing, 115 BHP Lycoming 0–235) cruises at 105 KTAS at 4000 ft at 75% power [6]). The three pretty much cruise at the same airspeed regardless of wing position—the minor speed difference can be attributed to difference in engine power. The most common vertical wing placements are shown in Figure 4-6. The designer is urged to consider the consequences of the selection that are detailed below.

(1) Field-of-View (FOV)

The general goal is to maximize the FOV. Pilots of small aircraft usually sit in the wing area, which obstructs the FOV. High-wing configurations offer better FOV downward but obstruct pilot view when banking (turning). This arguably increases the risk of midair collision. The designer should consider transparencies in the roof to remedy this shortcoming. The opposite holds true for a low-wing configuration: downward visibility is reduced and improved in the direction of the turn. A compromise is struck for the shoulder wing configuration, although a forward swept wing may be required for proper placement of the Center of Gravity (CG). An example of such an aircraft is the SAAB MFI-15 Safari. None of this applies to large aircraft, as the pilot is located far ahead of the wing. There are other factors to consider. Among a host of issues plaguing the hapless Bell XP-77, one was poor visibility over its long nose [7]. Also, FOV is frequently reduced by large and poorly positioned window frames—something that justifies constructing a mockup to help designing it out of the vehicle.

(2) Impact on Airframe Design

In small aircraft, the high-wing configuration permits gravity-fed fuel system, whereas a low wing requires a fuel pump (an added system—e.g., see Section 7.2.6). Fueling high-wing aircraft with fuel tanks in the wing can be challenging. This requires a step ladder, which may not be available at all airfields. Larger airplanes solve this issue by featuring fueling points in the fuselage, where fuel is pumped under pressure. That option is impractical for GA aircraft that operate from airfields without such equipment.

Entry into a high-wing configuration is often as simple as opening a door and stepping into the cabin. Small, low-wing aircraft often feature reinforced walkways on the wing and an external step that usually remains exposed to the airstream.[2] This usually means a walkway with sandpaper texture that is known to detrimentally affect flight characteristics of some aircraft [8]. None of this applies to larger aircraft, which have doors outside of wing region.

Many high-wing airplanes use wing-struts, which substantially reduce the shear and bending moments (see Section 4.2.4). This leads to lighter wing structure than if built using cantilevered beam principles. Such struts are subjected to tension forces in normal flight, whereas struts on low-wing aircraft would be in compression exposing them to a buckling failure.[3]

Low-wing configuration permits shorter and lighter landing gear. In small aircraft, the low configuration also allows the occupant seats to be attached to the main spar and the fuselage structure necessitated by the aft spar (or shear web). Both result in a more efficient structure.

The low-, high-, and parasol-wing configurations open the passenger volume as the wing structure does not pass through the cabin. This is very important in the design of passenger aircraft. There are notable

[2] The Cessna 310 is an example of an aircraft that features a retractable step.

[3] Compression struts exist, but are rare. Examples include the homebuilt Evans VP-1 Volksplane and the De Havilland DH-53.

exceptions though. The Fokker F-27 Friendship has lowered ceiling around its high wing. Not really a problem, except for very tall people. The Tupolev Tu-104B features a raised floor segment to accommodate its low wing. This step tripped passengers and turned out to be a major nuisance [9]. This step explains the raised windows in this region. In contrast, the shoulder and mid-wing configurations accommodate the wing spar inside the cabin. While it is possible to use hoop-style structural frames to react the load, this is inefficient, heavy, and costly. Designers of small aerobatic aircraft solve this by placing the main spar well ahead of the occupant, typically in front of the instrument panel. This allows the legs of the pilot to pass comfortably below the structure. The mid-wing configuration was widely used in aircraft design during World War II. The configuration is never used in large passenger aircraft, but there are examples of smaller passenger transports; for instance, the 15-seat Hamburger Flugzeugbau HFB-320 Hansa Jet, the 10-seat IAI-1124 Westwind business jet, 9-seat Piaggio P-180 Avanti, and the 6-seat Piper Aerostar (formerly Ted Smith Aerostar). Although not a GA aircraft, the General Dynamics F-16 is an example of a mid-wing aircraft that solves the problem with stout machined hoop-frames around its single engine. These are justified by the engine placement.

(3) Impact on Flight and Operational Characteristics

High-wing aircraft are less affected by ground effect and, thus, float less than low-wing aircraft when landing. This may be an important consideration in the design of bush-planes, where accuracy in making a landing spot of a short unprepared runway is imperative. Additionally, a low position of the wing increases the risk of an accidental ground strike when operating from unprepared fields. High wings are more common in bush-planes than low wings.

The configuration increases roll stability (or dihedral effect—C_{l_β}), which may be detrimental for heavy transport (e.g., cargo) aircraft, requiring anhedral to remedy. The mid-wing configuration is common in aerobatic airplanes as it provides neutral roll stability. Examples include the Slick series of aerobatic aircraft (Slick Evolution, Slick 360, etc.), Laser Z-300, Sukhoi Su-31, and Extra 300. This allows rapid roll maneuvers with minimum yaw coupling, something very desirable for precision aerobatic maneuvers. A low-wing position has limited lateral stability, requiring wing dihedral to remedy it.

The high- and low-wing configurations often present some challenges in the geometry of the wing/fuselage fairing. Mid wings usually need smaller wing root fairings, although this may not hold for the aft part of the wing.

(4) Parasol Wings

Parasol wings are not common in modern aircraft design. The configuration has the wing separate from and placed above the fuselage; the fuselage hangs from below the wing. The best-known aircraft to feature such a wing is undoubtedly the Consolidated PBY-5 Catalina (designed in the 1930s) in Figure 4-7. Other examples include a series of aircraft built by Dornier, such as the Do J Wal (designed in the 1920s), Dornier Libelle (1920s), Do-18 (1930s), Do-24 (1930s), Dornier Seastar (1980s), and the Dornier S-Ray 007 (2000s), an amphibious sport aircraft. The configuration is beneficial for propeller powered amphibians as it protects the propeller from water spray. The parasol wing is arguably aerodynamically "cleaner" and, thus, more efficient. The absence of a fuselage restores the lift potential of the wing, yielding a lower lift-induced drag. However, it also results in two sources of interference drag: one at the fuselage side and the other at the wing side. For wing-mounted engines, the configuration lowers flutter speed due to the engine mass mounted to a relatively flexible wing structure. This is compounded as the fuselage is separated from the wing. The high thrustline of the configuration results in noticeable power effects. Dihedral effect may be excessive and may require added vertical tail area to increase directional stability to counteract its effect on dynamic stability modes such as Dutch roll.

4.2.2 Wing Configuration

Wing configuration refers to properties such as planform geometry, airfoils, sweep, and others. It also refers to the number of wings the airplane features (see



FIGURE 4-7 The Consolidated PBY-5 Catalina is an example of an airplane featuring a parasol wing. *Photo by Phil Rademacher.*

Figure 4-8). The *monoplane* is by far the most common configuration, due to its aerodynamic efficiency. The primary advantage of the *biplane* or *triplane* configuration is the large wing area packed into a small wingspan. This allows for very maneuverable airplanes with relatively low stalling speed without flaps. The drawback of the configuration is aerodynamic inefficiency that stems from placing the low-pressure region of the lower wing close to the high-pressure region of the upper wing. This requires higher AOA to generate the same lift coefficient and, consequently, increases lift-induced drag.

The *sesquiplane* is a biplane with a shorter span of the lower wing. This improves the efficiency of the outboard part of the upper wing by enabling higher pressure to be generated on its lower surface. It also results in a phenomenon that makes the configuration ideal for agricultural aircraft; the generation of four distinct wingtip vortices that help spread fertilizer or insecticide more effectively. This book primarily focuses on monoplanes, but details of biplane design are provided in Appendix C.1.

The difference between a canard and a tandem plane is in the size of the forward wing. Generally, the elevator is installed in the forward lifting surface. Both lifting surfaces generate upward pointing lift vectors in level flight and both forward surfaces are highly destabilizing, longitudinally.

4.2.3 Wing Dihedral

The dihedral angle is the angle the wing plane makes to the horizontal. It is a major contributor to the stability derivative C_{l_β} (dihedral effect). It affects the airplane's roll stability and the damping of dynamic modes such as Dutch Roll. C_{l_β} also depends on the wing's vertical location and sweep angle. Ultimately, the designer must predict the dynamic stability characteristics of the airplane design to evaluate the appropriate dihedral angle.

Figure 4-9 shows an airplane at airspeed V, banking through an angle ϕ. The banking causes a sideslip, whose manifestation is the yaw angle β. The yaw angle produces a side flow component $V \bullet \tan \beta$, which when combined with the change in vertical flow due to the roll causes a net change in AOA, $\Delta\alpha$, on each wing. The subsequent change in lift (ΔL) on each wing causes a restoring rolling moment (one that tends to rotate the aircraft back to level flight), here denoted by the letter M.

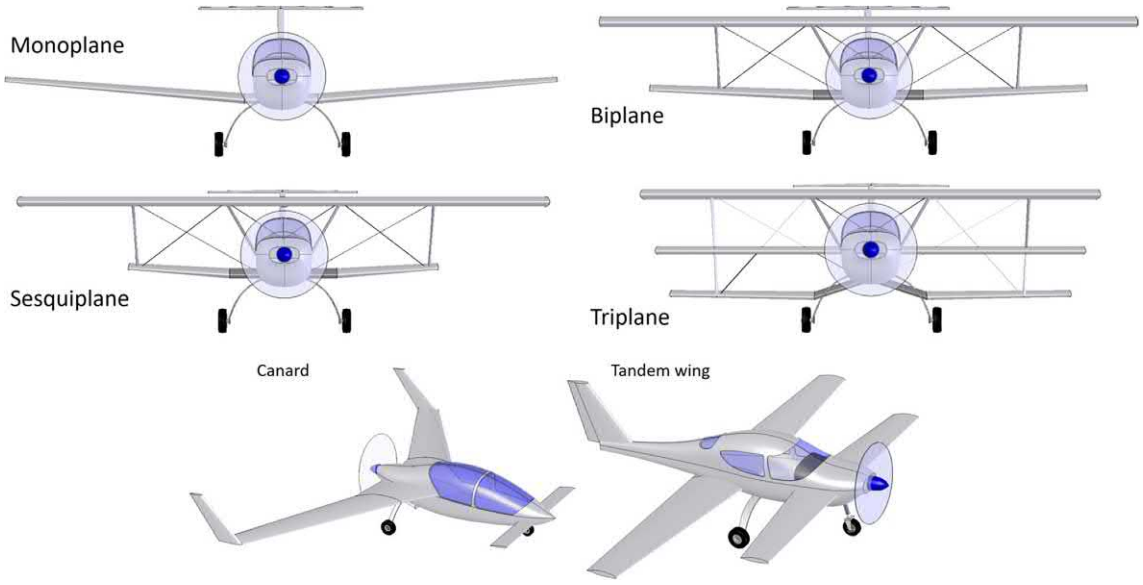


FIGURE 4-8 Common wing configurations.

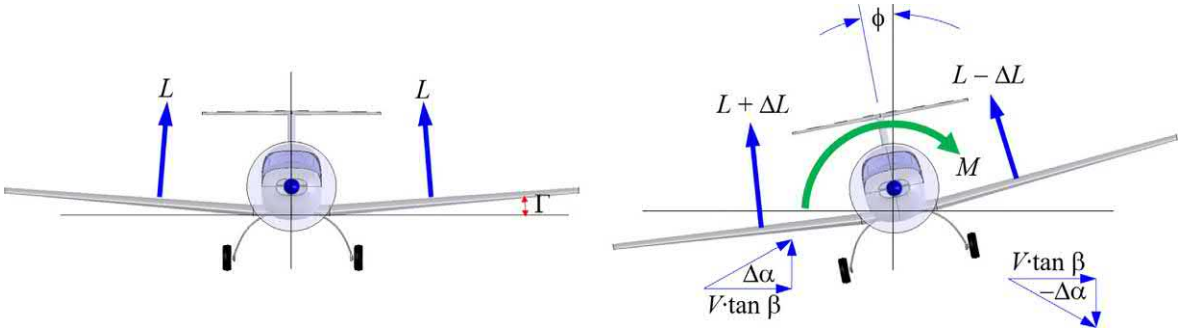


FIGURE 4-9 Dihedral effect explained.

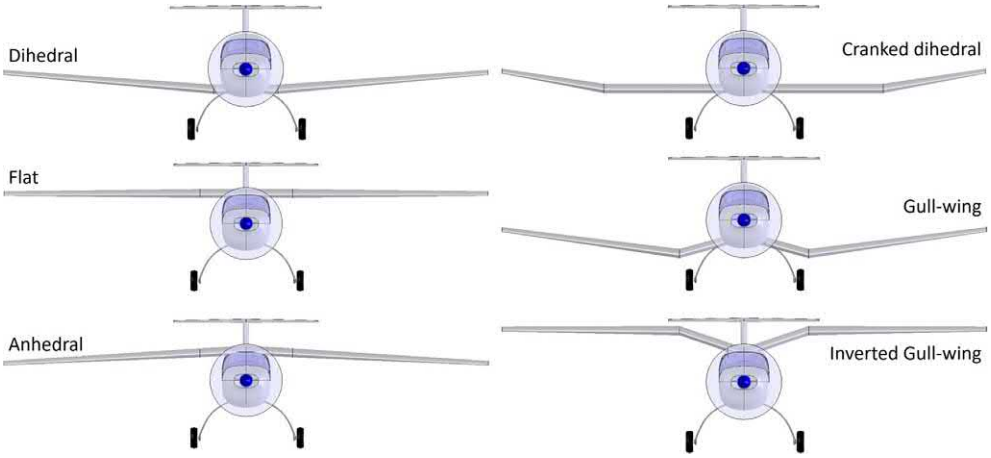


FIGURE 4-10 Wing dihedral nomenclature.

Common dihedral configurations are shown in Figure 4-10. Of these, the three leftmost are most common. The cranked dihedral is used extensively on the French Jodel and selected Robin aircraft, as well as on some sailplanes. However, it is also featured on the Argentinian FMA IA-58 Pucará twin turboprop ground attack aircraft and the McDonnell-Douglas F-4 Phantom.

The gull-wing configuration is rare, being most famously used on the Vought F4U Corsair, where its purpose was to increase the propeller clearance for carrier operations. It was also used for various reasons on the Blohm und Voss BV-137, Caproni Ca-331b Raffica, Dewoitine HD-780, Fairey AS-1 Gannet, Heinkel He-112 B, and Junkers Ju-87 Stuka.

The inverted gull-wing configuration is often used for twin engine seaplanes, where it helps bring wing-mounted engines and propellers away from the spray of water. It is featured on the Beriev Be-6, Be-12, Cetverikov MDR-6, and Moskalev 16 amphibians and seaplanes. It is also used on the Göppingen Gö-3 Minimoa sailplane, the PZL P-1, PZL P-11, Piaggio P-166, and Supermarine 224 landplanes. The B-25 Mitchell featured an inverted gull wing to fix to an unacceptable Dutch roll damping [10]. The Stinson SR-10 is an example of an aircraft that could fit into this class, featuring a wing whose upper surface has a distinct gull-wing break. However, the lower surface forms a straight line and the spar does not have a break, rendering it more of a transitional form.

4.2.4 Wing Structural Configuration

The structural layout of the wing is either cantilevered or strut-braced (see Figure 4-11). Cantilevered is less draggy, but heavier. The opposite holds true for strut-braced configurations. Strut-braced wings substantially reduce both shear and bending loads. This is illustrated in Figure 4-12, which shows a strut-braced (top) and cantilevered wing (bottom) subject to an equal aerodynamic load, represented by the simplified trapezoidal lift distribution. The lift distribution of real wings is not trapezoidal, but the accuracy of its shape is not important to the point being made.

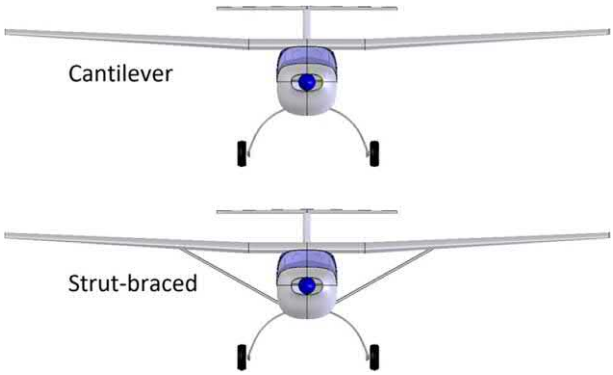


FIGURE 4-11 Wings are typically either cantilever or braced with struts.

The upper part of Figure 4-11 shows where the maximum shear and bending moment occurs on the strut-braced configuration. Their corresponding magnitudes are given by V_{max} and M_{max}, respectively. The lower image shows shear and moment diagrams for the cantilever configuration. It shows the maximum shear is 2.3× greater than that of the strut-braced wing and the moment is 4× greater. Although not shown, a substantial compression load develops between the wing-to-fuselage and strut-to-fuselage attachment points. It follows that the structural weight of the strut-braced wing will by much lighter and should be given a serious consideration if aerodynamic efficiency is not a factor.

4.2.5 Cabin Configuration

Here, the discussion of cabin configuration will be limited to light aircraft only, as cabins for passenger aircraft are presented in more detail in Chapter 12. Typically, there are two kinds of cabin styles; canopy and roofed

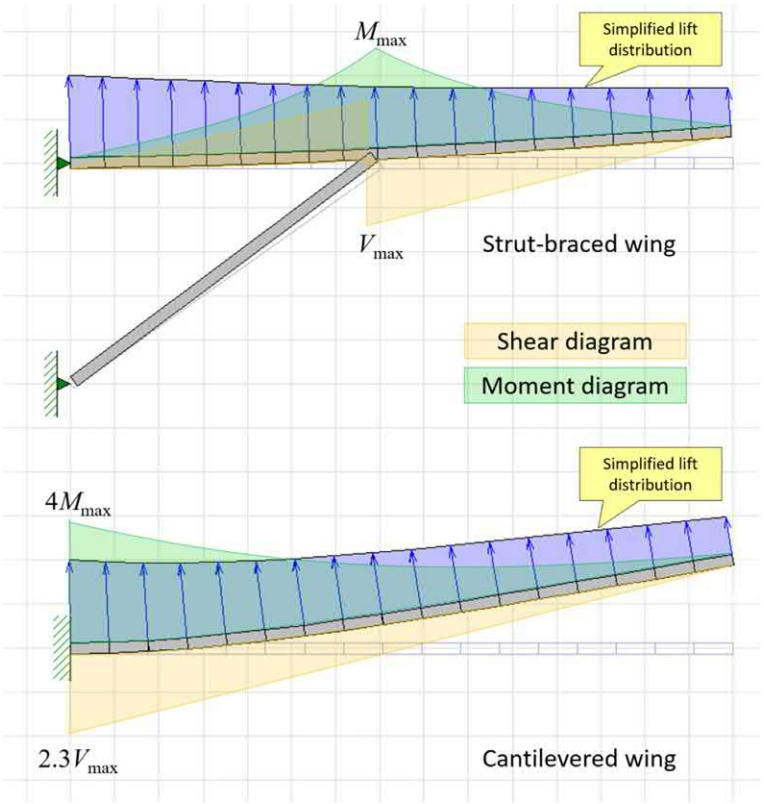


FIGURE 4-12 Shear and moment diagrams expose the structural implications of selecting a strut-braced versus cantilevered wing configuration.

(Figure 4-13). One advantage of the roofed cabin is an increased protection in case of a turnover accident. Another one is shadow from the sun on hot days. The configuration requires an entry door to be added, preferably one on each side. These may present some fit and function issues in production, although similar arguments can be made against the canopy. The roof also limits the FOV.

A canopy offers exceptional FOV, which is very desirable for many travelers. It also reduces the risk of a mid-air collision. However, turnover mishaps are of considerable concern for such aircraft. This is reflected in the previous version of 14 CFR §23.561, *General*. The applicant must demonstrate compliance by a reinforcing the window frame to which the windscreen is attached to prevent a harmful collapse. Often called the A-pillar, this frame is a rollover cage.

Excessively high cabin temperatures due to greenhouse effects are a drawback of the canopy. The configuration should allow the canopy to be left open during ground operations (while taxiing) for cabin cooling. This is important if the airplane does not have air conditioning (not common in small aircraft). Reduction in greenhouse effect makes the roofed cabin configuration a viable candidate.

The acrylic canopy must be installed and operated with care (if flexible), as cracks may develop around

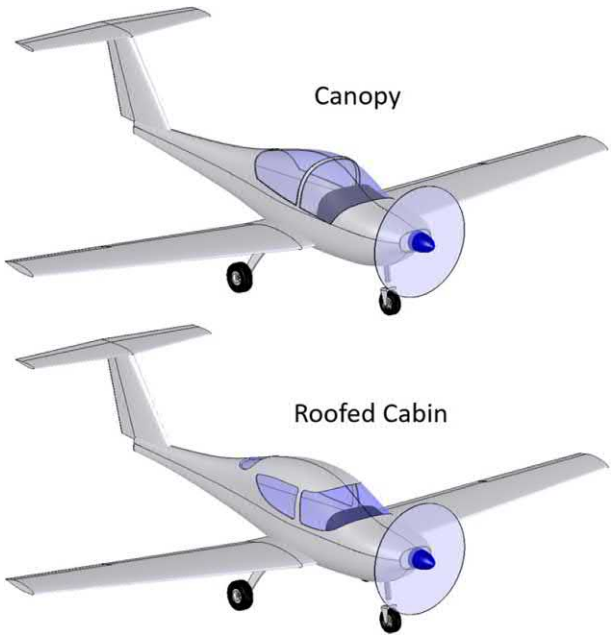


FIGURE 4-13 Typical cabin configurations for small aircraft.

fastener holes. The canopy should feature appropriate mechanism to prevent it from opening in flight due to aerodynamic forces. For instance, should the latching mechanism fail in flight, an aft hinged or side hinged canopy can be flung open by aerodynamic forces. If the

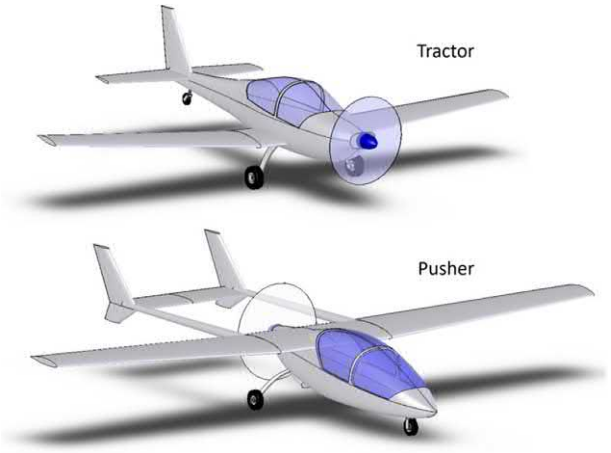


FIGURE 4-14 The two propeller configurations.

canopy departs the aircraft, it might damage the HT or VT, possibly rendering the vehicle uncontrollable. If the open canopy stays with the vehicle, a substantial asymmetry in loads could render the aircraft uncontrollable as well. A forward hinged canopy is better candidate for this reason. Ease of boarding the airplane should be considered for both cabin styles.

4.2.6 Propeller Configuration

Propellers are mounted to engines in two ways: as a *tractor* or a *pusher* (see Figure 4-14). Either configuration is practical for piston engines, gas turbines, and electric motors. The pros and cons of these configurations are discussed in detail in Section 15.1.2.

The tractor configuration is suitable for most applications. It provides undisturbed air for the propeller although the higher airspeed of turbulent flow increases the drag of the body immersed in the propwash. The pusher propeller is a good solution to some specialized mission requirements, for instance for single-engine reconnaissance or observation missions. Removing the propeller and engine from the FOV facilitates high-visibility cockpits.

Propeller manufacturers are sometimes apprehensive about the pusher configuration as it introduces unexpected problems. Some of those are detailed in Section 15.1.2. Regardless, the aspiring designer should not let this preclude pushers from consideration. Propeller manufacturers are happy to work on any such project. They only want the designer to anticipate the shortcomings.

4.2.7 Engine Placement

Any significant source of force on an aircraft is of great concern. Engine thrust is an example and, in magnitude, is second only to that of the wing lift. The moment generated by this force must be arrested by the stabilizing surfaces. If the thrust source is placed above the airplane's CG, a nose pitch-down moment will be generated that must be trimmed out using elevator Trailing Edge Up (TEU) deflection (see Figure 4-15). In contrast, a low thrustline destabilizes the airplane, reducing the required TEU deflection. The HT must be sized with this additional moment in mind.

Naturally, once the airplane is trimmed for level flight and power is changed, there is a very noticeable and undesirable response for both configurations. The larger the magnitude of Δz (or larger the thrust for a given Δz) in Figure 4-15, the less pleasant is the response. As a rule of thumb, we want Δz to be as close to zero as possible. If this is not possible, it helps to align the thrust vector to the CG, as shown in Figure 4-16. While the alignment shown might be ideal to eliminate the pitch effect, it reduces forward thrust and increases effective weight. The designer can determine a suitable alignment angle without incurring too great a penalty.

There are other noticeable effects associated with engine placement, specifically propellers (e.g., see Section 15.2). While not necessarily dangerous, such effects can be a nuisance. For example, some seaplanes resort to a high thrustline to protect propellers from water spray. For such airplanes, pitch changes with power settings are accepted because it saves the propeller; it is just something the pilot must get used to. Some models, e.g., the Lake LA-4 Buccaneer, feature a large horizontal trimtab to help reduce elevator stick forces at high-power settings and low airspeed.

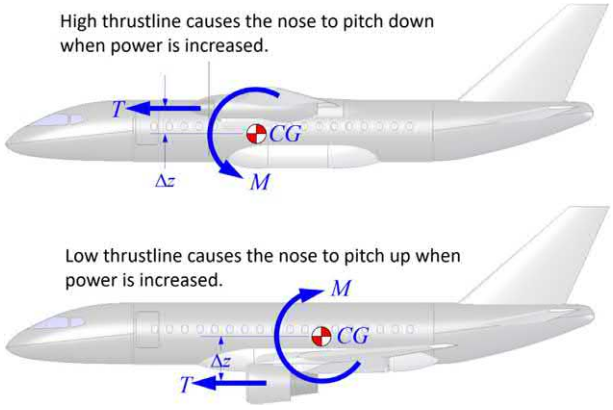


FIGURE 4-15 The effect of a high or low thrustline is a nose pitch-down or pitch-up tendency.

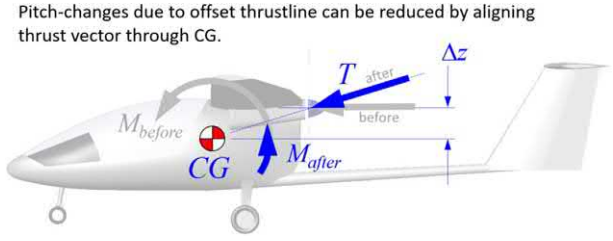


FIGURE 4-16 Thrust vector aligned to the CG.

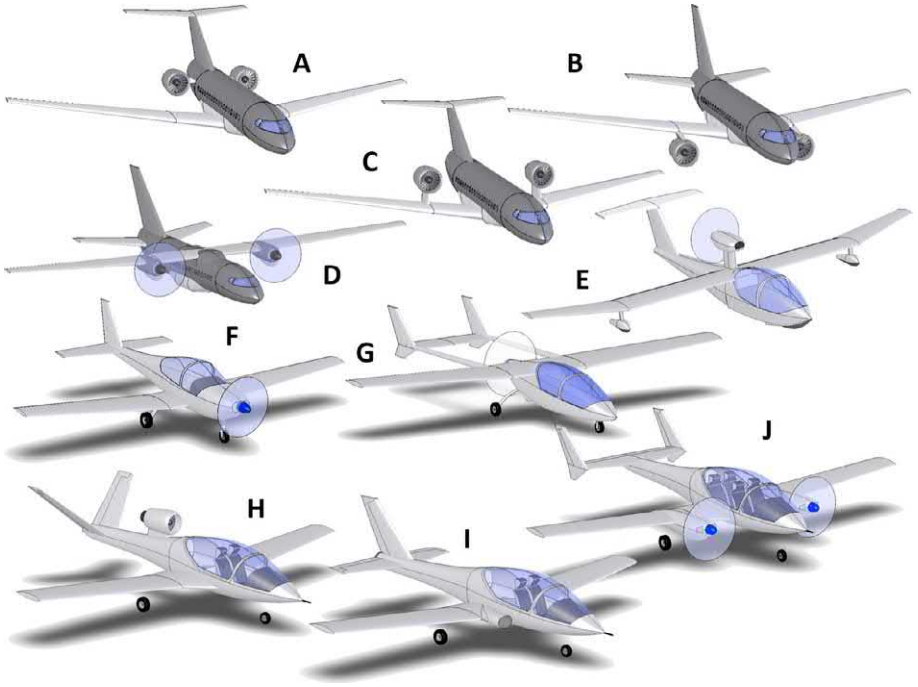


FIGURE 4-17 Common engine placements.

Another important consideration for the layout of propeller aircraft is the effect of propwash. If it flows over a control surface like the horizontal and vertical tail, control authority at high-power settings is improved. This is very noticeable at low airspeeds. However, it modestly increases the drag of the surface. Propwash flowing over the HT is favorable for T-O rotation, but in cruise causes pitch changes with change in power—thus, increasing power causes a nose-up pitch.

Figure 4-17 shows a few common engine placement methods. **Configuration A** features jet engines in pods (or nacelles) mounted to the aft part of the fuselage. This configuration was first introduced in the 1955 in the French Sud-Est Caravelle passenger jetliner [11]. The placement results in modest pitch effects and is intended to reduce engine noise in the cabin, although noise in the aft most part of the cabin is increased.

Configuration B mounts the engines on pylons below the wing. As stated earlier, this causes substantial pitch response with thrust changes. Many passenger aircraft feature *Stability Augmentation Systems* (SAS) to reduce the effect. While this configuration is vulnerable to *Foreign Object Damage* (FOD), it is the most common engine placement found on passenger jetliners. In part, because the engine weight provides bending moment relief, reducing airframe weight, and makes engine line maintenance easier. Additionally, positioning the engine forward of the wing's elastic axis has favorable effect on its flutter characteristics.

Configuration C features engines above the wing that generates nose pitch-down moment at high thrust settings. The configuration was first introduced in the 1970s on the German WFV-Fokker 614 jet, but later adopted on the Hondajet, where the intent is to avoid the ground clearance problem of underwing nacelles. It opens the aft part of the fuselage (like other wing-mounted engine configurations). It can introduce interesting aerodynamic and flutter issues [12, 13].

Configuration D is a twin-engine turboprop commuter with engines mounted on the wing. This is the most common engine installation in such aircraft. However, a *One-Engine-Inoperative* (OEI) situation causes large asymmetric thrust, calling for a large vertical tail. The wing must be stiff to prevent propeller *whirl-flutter* and avoid fatigue through *Life-Cycle-Oscillations* (LCO).

Configuration E is a pusher configuration amphibian. It features a high-mounted engine to protect the propeller from sea spray. This causes substantial pitch-due-to-power changes, although this detriment is accepted as it protects the prop.

Configuration F is a *tractor* propeller configuration is the most common arrangement for single engine propellers. It has relatively limited adverse thrust effects.

Configuration G is a pusher configuration with a relatively elevated thrustline. Propwash over the horizontal tail will cause pitch-due-to-power changes. The propeller helps keeping the flow attached on the aft part of the fuselage. However, a power-off glide may engulf this region in separated flow. This can be reduced through carefully shaped geometry and using vortex generators. The twin-boom configuration improves safety by making it hard to accidentally walk into a rotating propeller.

Configuration H is a single-engine jet that features a turbofan engine on a pylon on top of the fuselage. It is subject to pitch-due-to-thrust effect, although this can

be reduced by deflecting the nozzle a few degrees up. The engine placement results in high-pressure recovery, even at high AOAs.

Configuration I features a buried engine with minimal pitch-due-to-power effect. The bifurcated inlet reduces pressure recovery at the front face of the compressor, reducing maximum available thrust. The bifurcated duct is also problematic if operated in icing conditions as ice will accrete in the bend of the inlet.

Configuration J is a small four-seat, twin-engine propeller aircraft, suitable for reconnaissance or as a light VIP transport. Its wing-mounted piston engines are at risk of being nicked by small rocks thrown by the nose landing gear, unless placed forward enough. A flat-tire on any of the landing gear may risk prop-strike. The nacelles are designed to accommodate the retractable landing gear. Its H-tail helps generate restoring yawing moment in an OEI situation, if immersed in the propwash of the working engine.

4.2.8 Landing Gear Configuration

Great many landing gear configurations have been developed for use in aircraft. Six examples are shown in Figure 4-18. These cover approximately 99.99% of all GA aircraft. The most common configuration is the tricycle, followed by the taildragger. Taildragger landing gear is lighter and generates less drag than a tricycle. An example of improvements attained by a small aircraft involves a Cessna 150. It is claimed that converting a tricycle version of the aircraft to a taildragger gave it nearly 8-knot increase in cruising speed [14]. The improvements depend on the airplane and its overall drag, but a 4 to 10 knot increase in cruising speed is reasonable.

The monowheel with outriggers is a popular design for sailplanes and motor gliders like the British-designed Europa XS and the German Scheibe Tandem-Falke. The monowheel reduces the landing gear drag and weight. It was selected for the high-flying Lockheed U2 to keep down weight [15]. The same holds for the tandem wheel, although it is rarely used in GA aircraft. The British Hawker Harrier and the American B-52 Stratofortress are the best-known examples of tandem wheel configurations (some refer to the latter as a *quadricycle* configuration).

All landing gear configurations (except floats) can be retractable. Fixed landing gear is simpler and more reliable but increases the airplane's drag. The designer should strongly consider wheel fairings to reduce drag of fixed landing gear. Floats increase drag substantially but allow operation on land and water. They are popular among pilots who fancy access to obscure wilderness retreats over high airspeeds. Floats and amphibious airplanes are presented in Appendix C.2.

The tricycle landing gear makes the vehicle dynamically stable on the ground and reduces the risk of a ground loop. This makes it better for inexperienced pilots and, thus, trainer aircraft. Similarly, the taildragger configuration is dynamically unstable and more prone to ground looping [16]. Taildraggers are favored for operation off un-improved runways ("bush-plane" operations). Among advantages is high AOA at low airspeed. This helps the airplane lift off in ground effect, permitting markedly shorter take-off distances. However, this is not always reflected in the data. For instance, the Cessna Model 180 (taildragger) and 182 (tricycle) are effectively identical, excluding the landing gear. Nevertheless, reference [17] reports each having the same T-O and landing distances at the same weight. Taildraggers are harder to

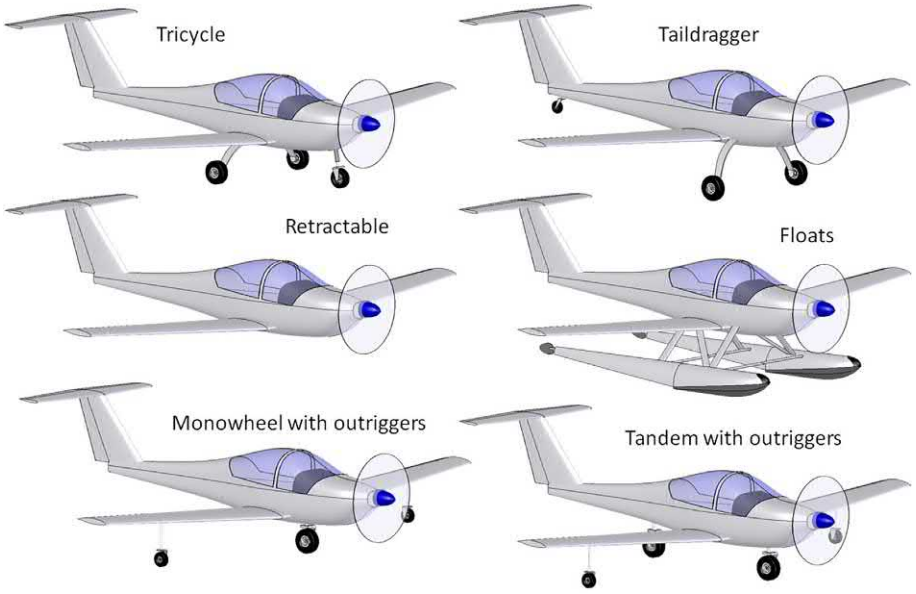


FIGURE 4-18 Selected landing gear configurations.

land and maneuver on the ground due to a high deck angle, which degrades visibility over the nose of the airplane. Today, the configuration is primarily seen in small aircraft, although it used to be common in large aircraft. The largest taildragger ever built is the eight-engine Soviet Tupolev ANT-20 Maxim Gorky, with a gross weight of 116,600 lb_f. The Curtiss C-46 Commando is another large taildragger, although its gross weight of 48,000 lb_f is dwarfed by the ANT-20. The pros and cons of and the conceptual design of the landing gear are presented in more detail in Chapter 13.

The total structural weight of the float is the highest, but least for the monowheel. The structure required to react the main landing gear impact load will weigh less than the structure required to react the impact loads of both tricycle and taildragger. The monowheel is also the least expensive to manufacture. It is a drawback that it is more vulnerable to crosswinds while taxiing on the ground. The same holds for the tandem wheel.

4.2.9 Tail Configuration

Several tail configurations are shown in Figure 4-19. Configuration **A** is a conventional tail, **B** is a cruciform tail, **C** is a T-tail, **D** is a V-tail, **E** is an H-tail, **F** a Y-tail, **G** an inverted Y-tail, and configuration **H** is an inverted V-tail. The pros and cons of these tails are detailed in Chapter 11, and will not be further addressed here.

4.2.10 Configuration Decision Matrix

Many aircraft manufacturers know up front what configuration is to be designed. Regardless of internal debates that may take place, and to which we are not privy, the history of aviation shows certain themes appear in these designs. All single-engine Cessna pistonprops are high-wing (except the Ag Wagon and Ag Cat agricultural aircraft). All Beech, Mooney, and Piper aircraft are low wing (except the Piper Cub and Tri-pacer). Mooney also features a signature straight LE lifting surfaces. However, other situations render the resulting configuration a result of internal debate. This section provides help for the configuration selection using a decision matrix (see Table 4-3).

The configuration selection is compounded when all candidate designs meet the performance and operational requirements. An observation of modern-day regional jets reveals that several dissimilar configurations can

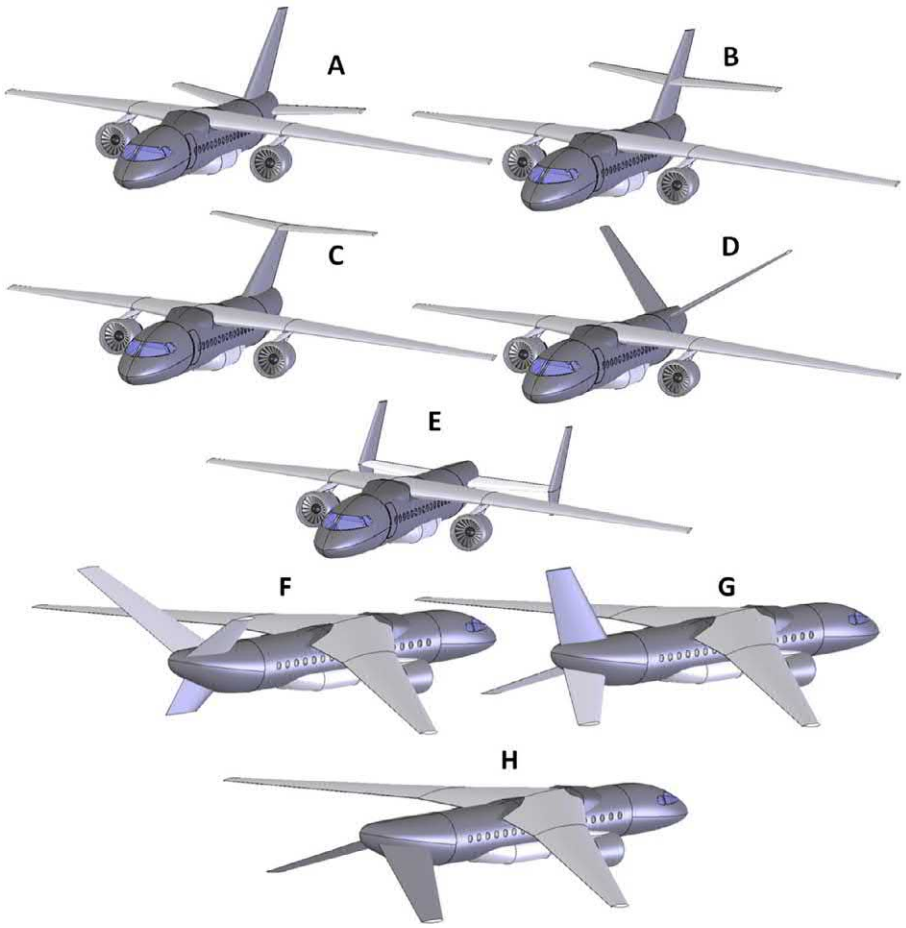


FIGURE 4-19 Eight-tail configurations.

TABLE 4-3 Decision matrix for a two-seat single-engine GA aircraft configuration.

Feature	Weight	Configuration Score 1 – Good, 2 – Better, 3 – Best		
		A	B	C
CONFIGURATIONS TO BE EVALUATED →				
Does the design allow for the desired side-by-side seating arrangement?	1	3	3	3
Is 360° field-of-view (practically) possible?	1	3	3	1
Suitability for bush-plane operation	2	1	3	3
Expected cost of developing canopy and windscreen (less cost is best)	1	1	1	2
Cabin susceptibility to greenhouse effects and uncomfortable sun exposure (low is best)	0.5	1	1	3
Does design offer the desired tricycle landing gear configuration?	1	3	1	1
Can retractable landing gear be accommodated?	0.25	1	1	1
Propeller configuration (tractor is less costly)	1	3	3	3
Propeller configuration (enclosed prop is safest)	2	1	1	1
Low drag – is LD_{max} >14 achievable?	0.75	1	2	1
Low drag – can NLF lifting surfaces be employed?	0.5	3	3	3
Low drag – are winglets necessary (no is best)	0.25	3	3	3
Low drag – does configuration allow the inclusion of smooth fillets and clean wing?	0.25	3	3	2
Fuel system – Is large fuel volume in wing possible?	0.5	2	2	2
Fuel system – is simple fuel system possible?	0.5	1	1	3
Can the design handle a large CG envelope?	1	3	3	3
Potentially the best spin recovery	3	3	3	2
Aesthetics – does design look unconventional?	0.5	1	2	3
Aesthetics – Stylish fin	0.5	2	3	1
Aesthetics – Stylish wingtips	0.25	1	1	1
Manufacturing – Composite fuselage	1	3	3	3
Manufacturing – Composite wing	1	3	3	3
Maintenance – Composite wing	1	1	1	1
Maintenance – Engine access	1	1	1	1
Operation – Cabin entry (easy is best)	2	1	1	3
Operation – Refueling (low tank fill point is best)	2	3	3	1
Operation – Preflight oil check	1	3	3	3
SUM OF WEIGHT x SCORE:		**55.75**	**59.5**	**56.25**

perform similar design missions effectively. Aircraft as disparate as the Dornier 328 (high wing, engines on wing), Bombardier CRJ200 (low wing, aft podded engines), and Embraer 175 (low wing, engines on wing) confirm this. Granted there is a difference in fuel efficiency and the economics of each, however, why would three manufacturers select such different configurations?

If many different candidate configurations are being considered, each should be evaluated based on desirable and undesirable characteristics. The configuration selection baffles the student of aircraft design and the less experienced (some would say less opinionated) designer. The weighted decision matrix of Table 4-3, which considers the development of a two-seat trainer aircraft, can be very helpful in this capacity. The trick is to phrase features such that a beneficial one receives the high score and unfavorable one a low score and permit the same score to be given more than once.

The number and selection of "questions" and weighing factors should be the result of an internal evaluation, where people with stake in the outcome can incorporate their concerns and goals. Note that while Configuration B (in Table 4-3) beats configurations A and C, all score well, indicating they are all plausible candidates for the mission. The greatest drawback of the approach is biased weighing factors. An honest debate about each should take place prior to the evaluation.

References

[1] K. Perkins, *How to Design a Good Aircraft*, McDonnell Aircraft Corporation Brochure, 1954.

[2] J.E. Steiner, *How Decisions are Made – Major Considerations for Aircraft Programs*, Lecture, AIAA 1982 Lectureship in Aeronautics, Seattle, WA, 1982.

[3] Taylor, John W.R., *Jane's All the World's Aircraft*, Jane's Yearbooks, various years.

[4] Anonymous, *Cessna 152 Pilots Operating Handbook 1985*, Cessna Aircraft, 1985.

[5] Anonymous, *Piper Pa-38-112 Tomahawk Pilots Operating Handbook 1978*, Piper Aircraft, 1978.

[6] Anonymous, *Beechcraft Skipper 77 Pilots Operating Handbook 1982*, Beech Aircraft Corporation, 1982.

[7] J. Winchester, *The World's Worst Aircraft – From Pioneering Failures to Multimillion Dollar Disasters*, Metro Books, 2007.

[8] Anonymous, *AD/DA42/4, Wing Stub Safety Walkway*, issued in June 2008 by the Australian CASA. Applies to selected Diamond DA-42 aircraft.

[9] D. Komissarov, *Tupolev Tu-154 – The USSR's Medium-Range Jet Airliner*, Midland Publishing, 2007.

[10] Anonymous, *B-25 General History*, B-25 History project. https://b-25history.org/history/b25.htm. (Accessed 8 March 2019).

[11] Anonymous, *The SNCASE SE210 Caravelle – France's First Jet Airliner*, Flight, May 20, 1955.

[12] M. Fujino, Y. Kawamura, *Wave-drag characteristics of an over-the-wing nacelle business-jet configuration*, J. Aircr. 40 (6) (2003).

[13] M. Fujino, H. Oyama, H. Omotani, *Flutter Characteristics of an Over-the-Wing Engine Mount Business-Jet Configuration*, AIAA-2003-1942, 2003.

[14] B. Clarke, *The Cessna 150 & 152*, second ed., TAB Books, 1993, pp. 180–181.

[15] P.W. Merlin, *Unlimited Horizons - Design and Development of the U-2*, NASA Aeronautics Book Series, National Aeronautics and Space Administration, 2015.

[16] Anonymous, *Airplane Flying Handbook, FAA-H-8083-3A*, Federal Aviation Administration, 2004.

[17] J.W.R. Taylor (Ed.), *Jane's All the World's Aircraft 1970–71*, Jane's Yearbooks, 1971.

This page intentionally left blank

CHAPTER

5

Aircraft Structural Layout

OUTLINE

5.1 **Introduction** 113
- *5.1.1 The Content of This Chapter* 113
- *5.1.2 Notes on Aircraft Loads* 113

5.2 **Aircraft Fabrication and Materials** 114
- *5.2.1 The Basics of Material Properties* 114
- *5.2.2 Various Fabrication Methods* 115
- *5.2.3 Aluminum Alloys* 119
- *5.2.4 Steel Alloys* 121
- *5.2.5 Titanium Alloys* 123
- *5.2.6 Composite Materials* 124

5.3 **Airframe Structural Layout** 130
- *5.3.1 Important Structural Concepts* 130
- *5.3.2 Fundamental Layout of the Wing Structure* 134
- *5.3.3 Fundamental Layout of the Horizontal and Vertical Tail Structures* 140
- *5.3.4 Fundamental Layout of the Fuselage Structure* 142

References 145

5.1 INTRODUCTION

The structural layout of the airframe is the foundation on which other design requirements rest. A poorly laid out structure may seriously complicate an aircraft development program. For instance, poorly conceived load paths in a pressurized fuselage may cause detrimental structural deformation that can make it impossible to maintain an advertised pressure differential. How such a flaw would affect the development program would depend on how far along it would have progressed when discovered. The required fix could be a major redesign of the fuselage structure, and depending on program status, its financial stability could be compromised. In contrast, even the ideal airframe will not guarantee a success: It might be structurally optimized while hiding aerodynamic, power, or other inadequacies that could bring about the project's demise. While the structural layout cannot *make*, it can certainly *break* the viability of the program.

This chapter introduces the general layout of aircraft structures. The presentation can only be done qualitatively. The focus of this book is conceptual and preliminary design, leaving little room for structural analysis of the airframe—this is the focus of the detail design phase. The purpose of this chapter is to help the designer understand how various configuration choices affect the resulting structure.

Note that the material properties presented are in the UK system. Use the following factors to convert to the SI system.

To convert psi to GPa (giga-pascal), multiply by 145,037.73773
To convert psi to MPa (mega-pascal), multiply by 145.03773773
To convert lb_f/in^3 to specific density, multiply by 27.7334934
To convert lb_f/in^3 to g/cm^3, multiply by 27.7334934
1 ksi equals 1000 psi

5.1.1 The Content of This Chapter

- Section 5.2 presents characteristics and properties of typical materials used for the construction of the modern GA aircraft.
- Section 5.3 presents a description of the fabrication and installation of various aircraft structural components.

5.1.2 Notes on Aircraft Loads

Aircraft are designed to react several types of loads, aerodynamic, inertia, and operational loads, as discussed below:

Copyright © 2022 Elsevier Inc. All rights reserved.

(1) *Aerodynamic loads* (or *airloads* for short) refer to forces and moments caused by the asymmetry of pressure over the surface of the aircraft. Airloads include forces (e.g., wing lift and drag) and moments (e.g., wing torsion and bending). Their magnitude depends on the weight of the aircraft, the load factor, its geometry, and, again, dynamic pressure. The total magnitude is defined based on requirements set forth by the aviation authorities—for instance, 14 CFR Part 23 and 25. However, the local values depend on the geometry. Consider two aircraft, A and B, of equal weight and wing area that differ only by the wing Aspect Ratio (*AR*) and Taper Ratio (*TR*). Assume aircraft A has the higher *AR* and lower *TR*. For reasons that will be detailed in Chapter 9, *The Anatomy of the Wing*, it will generate higher bending moment than Aircraft B.

(2) *Inertia loads* refer to forces and moments caused by subjecting aircraft components to acceleration. An example is the battery, which does not experience any aerodynamic loads. Its support structure must be capable of reacting the forces that result from the applied load factors. Other components, such as engines, are simultaneously subjected to both aerodynamic and inertia loads.

(3) *Operational loads* refer to loads other than aerodynamics and inertia. These are simply caused by using the airplane. Examples of such loads include door hinge and locking loads, floor loading loads, wing step-on loads, to name a few. Such loads are often tricky to define, but are usually small compared to say, the wing loads. Operational loads usually lead to wear and tear.

Note that the term *limit load* refers to a limit below which the airplane may only deform elastically. This means that once the load is removed, the airplane springs back to its original shape. *Ultimate load* refers to a limit above which the airplane may fail. Between limit and ultimate load, the airplane may experience plastic deformation (permanent shape change), while still being safe to fly. Ultimate load is 1.5× the limit load.

The location and shape of all the major load paths has a major influence on weight. It is the responsibility of the structural engineer to design the structure, so it only reacts loads it is likely to encounter in operation. An airplane whose strength is greater than required is structurally *overdesigned*. During each flight, it will carry around material whose weight would better be a part of the useful load. Additionally, wings, stabilizing surfaces, engines, and landing gear have major effects on the weight and location of the airplane's Center of Gravity. This can bring about loading problems that may have to be resolved using heavy ballast, again, whose weight would better be a part of the useful load.

That said, zealotry toward weight is also to be avoided in structural design. It is said that old aircraft develop new problems. Issues associated with insufficient structural material often surface after years of operation—highlighting the importance of periodic inspection philosophies. Designing long-lasting aircraft is art as well as science.

5.2 AIRCRAFT FABRICATION AND MATERIALS

The selection of structural material for a new aircraft can be challenging. Its selection impacts manufacturing and maintenance of the aircraft. Established companies tend to stick with the material and fabrication processes they know best from past projects. They are unlikely to change a manufacturing process that may have taken decades and substantial investment to perfect. Manufacturers of aluminum aircraft are unlikely to invest in the development of a composite aircraft, and vice versa. This does not preclude new materials from being introduced incrementally. This approach is evident among manufacturers of commercial jet-aircraft, such as Boeing and Airbus. The introduction of a new material requires a careful evaluation of its characteristics. The following listing provides some areas the designer should understand before a new material is selected:

Commercial availability	Fatigue
Compatibility with other materials	Fracture toughness and crack growth
Corrosion and embrittlement	Maintainability
Cost of certification	Material costs
Electrical characteristics	Producibility
Environmental stability	Static strength/weight
Erosion and abrasion	Thermal characteristics
Fabrication characteristics	Wear characteristics

At the time of this writing, aluminum is the most common material used for aircraft. It has several important properties that are ideal for the construction of light and stiff vehicles. Regardless, use of composite materials is growing in the commercial aircraft industry. They are widely used in GA already. Several all-composite aircraft, including the Cirrus SR20, SR22, and SF50, Cessna Corvalis (out-of-production), and Diamond DA-40 Katana and DA-42 Twinstar are certified under 14 CFR Part 23. Composites are a recent introduction to the aircraft industry, although their history and use date to the early 1950s.

5.2.1 The Basics of Material Properties

The best source of data for alloys for aerospace vehicles is the *Metallic Materials Properties Development and*

Standardization (or the MMPDS[1]) [1]. The MMPDS is the FAA's effort to replace the well-known MIL-HDBK-5 handbook [2] and is recognized world-wide as the most reliable source available for statistically based allowables for the design of aircraft, repairs, alterations, and modifications. It contains detailed design information on the strength and fatigue properties of alloys.

The production of aircraft requires uniformity and repeatability. An aircraft model produced today must be equally strong as the one produced last week or next week, within some statistical limits. This can only be accomplished by a uniform and repeatable manufacturing process and material properties. The properties of material used by an aircraft manufacturer must be established. This is accomplished by an on-site testing unless a certificate of testing from a third-party lab is available. The statistical confidence of the material properties at room-temperature is classified using a special *data basis*,[2] as listed below:

- *Typical Basis*—It is a typical average value of a material property (e.g., yield stress in tension) and has no statistical assurance associated with it.
- *S-Basis*—It means that the value of the material property is based on industry specifications or federal or military standards. As an example, industry specifications can be those of the SAE or ASTM.
- *B-Basis*—It means that at least 90% of the test coupons are expected to equal or exceed a statistically calculated mechanical property value with a statistical confidence of 95%. For instance, consider the ultimate tensile strength of 2024-T3 sheet, which might be 64,000 psi for a specific sheet thickness. If we test the ultimate strength of 10 coupons of this material, at least nine must equal or exceed 64,000 psi, with 95% confidence.
- *A-Basis*—It means that at least 99% of the test coupons are expected to equal or exceed a statistically calculated mechanical property value with a statistical confidence of 95%.

Typically, structural analysis uses A-Basis allowables for structural members whose failure is considered catastrophic. B-Basis allowables are used for redundant structural members whose failure would result in the redistribution of loads without compromising safety of flight. The reader is directed toward MMPDS for more details.

5.2.2 Various Fabrication Methods

Awareness of the multitude of fabrication techniques available for aircraft construction is essential. This section introduces common manufacturing methodologies, intended to whet the interest of the aspiring engineer.

(1) Casting

Casting is one of the oldest manufacturing methods known to man, dating back to at least 4000 BCE [3, Table 1, p. 6]. The process entails the following steps:

(A) A mold is created from an already existing part, for instance, by making an imprint of the part in granular material like sand.
(B) The material for the part is heated until it becomes liquefied at which time it is poured into the mold. An example of this is molten aluminum.
(C) The part is then allowed to cool ("freeze") for a specific time, during which it solidifies.
(D) Once solid, the part is removed from the mold, which is typically destroyed in the process. This gives rise to the saying: *One part, one mold*, making the casting process very labor intensive.

It is an advantage of casting that the original model can be less strong than the material used in the casting. It is possible to use a model made from wood to make metal copies. Several different casting methods exist and depend on the material used or the desired shape. Casting takes considerable expertise to do well. Casting of aircraft metals (aluminum or steel) leaves the material fully annealed and thus lacking strength. Consequently, casting should never be used for critical aircraft structure.

(2) Molding

The difference between casting and molding is that the latter uses a heat tolerant mold to make multiple copies of the part. Molding is a very sophisticated manufacturing process that requires considerable expertise. Examples of such processes includes injection molding, in which a liquified material is injected under high pressure into the mold—an operation intended to eliminate air bubbles. These are a source of stress concentrations in the material that can render it less durable than otherwise.

(3) Sheet Metal Forming

The term *forming* refers to any process that forces material into a desired shape. Many forming methods exist, although presenting them all is beyond the scope of this book. Thus, only sheet metal forming and *forging* will be presented, as these are widely used to fabricate aircraft.

Sheet metal is usually bent along the edges to create flanges to stiffen it for use as stringers, ribs, and

[1] Available from the National Technical Reports Library at https://ntrl.ntis.gov/NTRL/dashboard/searchResults/titleDetail/PB2003106632.xhtml (accessed 08/07/2019).

[2] See Sections 1.4.1.1, *Basis* and 9.1.6, *Data Basis*, of the document MMPDS.

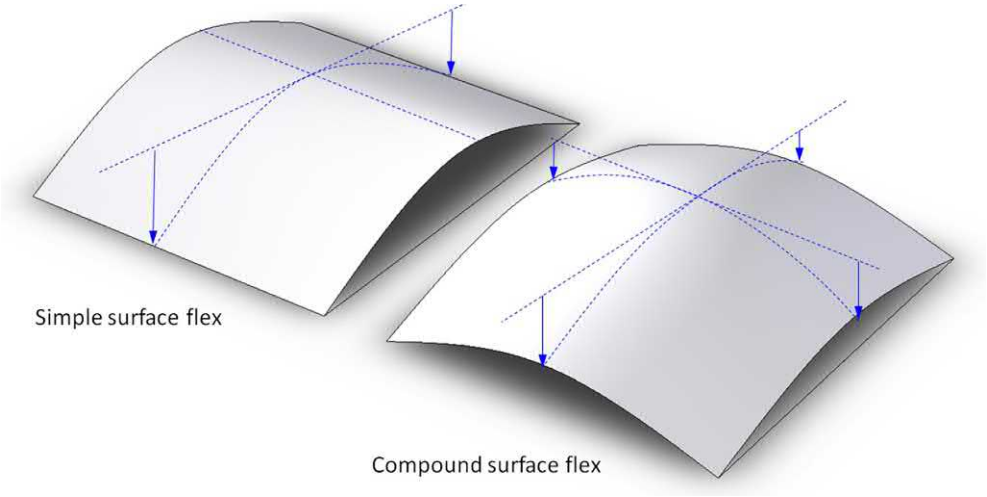


FIGURE 5-1 The difference between a simple and compound surface flex.

spars or for joining it with other sheet metal parts (see paragraph about Joining below). The bending involves a permanent plastic deformation. In contrast, sheet metals used for surface covering usually deforms elastically. This flexibility depends on the thickness, as well as the length and width of the sheet. Aluminum sheets used for smaller GA aircraft are between 0.020 and 0.100 in thick. They easily follow airfoil curvature, provided the surface flex is simple (see Figure 5-1). However, thicker sheets, such as those common in the inboard wing skin panels of commercial jetliners or military aircraft, must be bent using mechanical or hydraulic presses.

Sheet metal can flex in two ways: *simple* and *compound* (see Figure 5-1). The simple surface flex involves a simple plate bending. In contrast, compound flex requires bending about two axes and is accompanied by internal twist (shearing) of the material molecules. Metals resist this type of deformation, so it is near impossible to form the compound flex unless its internal molecular structure is stretched using specialized forming methods such as hydraulic pressing. Awareness of this fact is imperative when selecting material for aircraft. Simple flex suffices for the manufacturing of aircraft that feature frustum fuselages and simply tapered wings. For such aircraft consider using aluminum alloys. Efficient aerodynamic surfaces, such as those used in sailplanes and modern GA aircraft, require compound surfaces. This is where composite materials shine—but the manufacturing is more expensive.

It is an advantage of aluminum construction that it is easy to shape. It is cut to shape using hand- or hydraulically actuated *shears*. It is bent using a *sheet metal brake*. The bending operation requires some planning; there are limits to the bending radius—it requires allowances for extra material for the bend itself. The forming must also consider *spring-back*. It requires the operator to bend the sheet to a predetermined angle, which is slightly greater than the intended angle. Once removed from the metal brake, the sheet will spring back to the intended angle. Refs. [4, 5] provide details on these and other practices when working with aluminum.

(4) Extrusions

An *extrusion* is the process of forcing an ingot of near molten metal through a die with a specific geometric pattern. The process converts the half-molten ingot into a long and straight column featuring a constant cross-sectional shape. Aluminum extrusions are widely used as longerons or stringers in airframes. They feature cross-sections that resemble letters like "H," "L," "T," "U" (also called "C"), and "Z" are common. Of these, the L-extrusion, usually called an *angle extrusion*, is ideal as a stringer or a spar cap in aluminum spars. The C-extrusion, usually called a *C-channel*, is of great use for various brackets and hinges designed to react high structural loads. The use of extrusions in aircraft is extensive and not only includes stringers, but seat-tracks (see Figure 5-2), brackets, wing attachment fittings, and countless other applications. Extrusions have higher material strengths than plates, as the formation compresses its grain structure.

(5) Forging

The best known and probably the oldest forming operation is *forging*, dating perhaps back to 8000 BCE [3, p. 384]. Forging involves subjecting metal to large, local, compressive forces in the form of "hammering." The hammering is accomplished using various dies and tools. It can be done to cold and hot parts. It usually increases material strength, toughness, and durability through work hardening, which results from the deformation of the material's grain structure. Aircraft components that react large forces, such as landing gear struts, are usually made from forged metals [3, p. 384]. Most

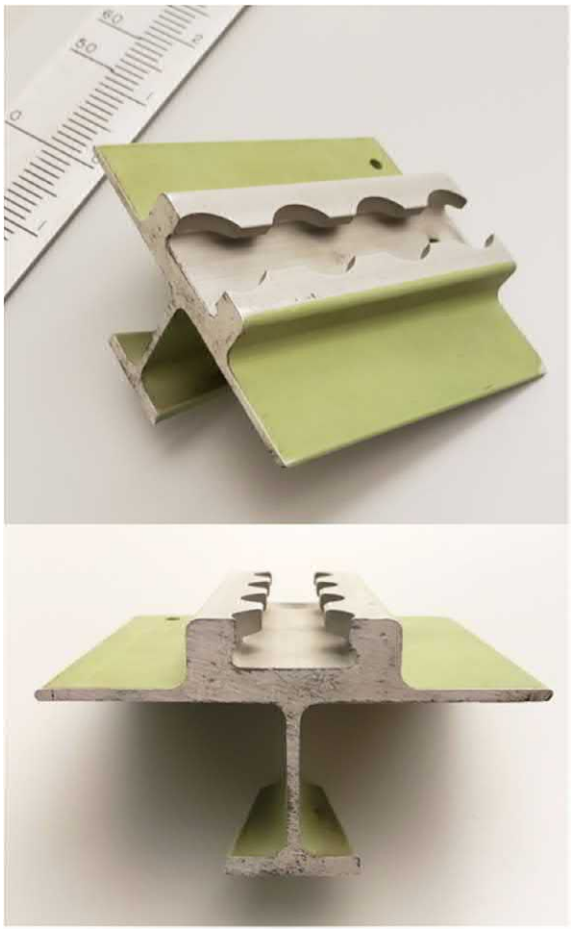


FIGURE 5-2 A seat-track extrusion. *Photo by author.*

forged parts are subjected to secondary machining operations to improve appearance (finishing), although the work hardening tends to complicate this task. Forging metals at elevated temperatures remedies this. Forging is more expensive than molding.

(6) Machining

Machining is the removal of excess material. It takes place in multiple ways. The most common include sawing, cutting, turning, and milling. Machining requires expertise and experience to do well, but an understanding of what can or cannot be machined is the key to success. Machining aluminum and low-carbon steels (e.g., AISI 1025) is easy but becomes gradually more difficult with increased carbon content. Hardened steels are difficult to machine and require sophisticated tools. This is easier to accomplish when the material is in annealed state. Afterward, heat treating is required to increase strength.

(7) Joining by Welding

Welding is the joining of parts made from identical metals by heating them to a point of melting while bringing them together to allow their molecules to *coalesce*. A filler material is often used to create a stronger joint. Welding forms a strong and durable bond between the parts. In contrast, *soldering* or *brazing* does not result in a strong bond, as neither melts the working parts. Welding is accomplished in multiple ways; most notable are a gas flame, an electric arc, a laser, and an electron beam. Low-carbon grade steels are easily welded or brazed by all techniques. Steels with higher carbon levels often require stress-relieving after the welding and even subsequent heat treating. Welding is commonly used to join parts making up engine mounts, landing gear, and fuselages, demonstrating it can take a beating if properly done. It is a drawback that the process may cause warping that changes the intended geometry. The welding of critical structural aircraft parts should always be done by a certified welder. Critical structural parts should not be made from welded aluminum due to a reduction in fatigue life.

(8) Joining by Riveting

Joining is the process of assembling small parts into a larger one. Joining by riveting is a prevalent method used to fabricate aluminum aircraft. The aspiring aircraft designer should understand the two most common riveting techniques used in the industry: *bucking* and *blind riveting*. Rivets primarily transfer shear.

Of the two, bucking is the primary method used in the industry. It is used when two (or more) aluminum sheets are joined or when joining a sheet and an extrusion. It requires ample access to either side of the parts to be joined. The standard procedure is illustrated in four steps in Figure 5-3. First, the sheets are aligned using carefully placed clamps (not shown). Then, holes are drilled at specific intervals depending on the shear stress to be transferred from one sheet to the next through the rivets. Since the drilling operation typically forms sharp edges (or burrs) on the opposite side, these must be removed prior to the insertion of the rivets. Otherwise, the joining will not develop full strength.

The technician usually inserts a special clamp, called a Cleco, through selected holes. This prevents the sheets from slipping during further drilling or bucking operations. The third step involves inserting the proper rivets into the hole. The fourth is the actual bucking operation. It often requires two technicians to accomplish, particularly when large sheets are joined. The technician on the head side of the rivet places an air hammer against the rivet, while the one on the opposite side places a heavy metal block (*bucking-bar*) against the rivet. When ready, the operator of the air hammer presses a trigger to generate a short burst of hammering to the rivet. The inertia of the bucking bar helps deform the rivet to form a strong joint. The hammering cold works the rivet. Bucking takes practice and careless handling of the tools may damage the sheets around the rivet.

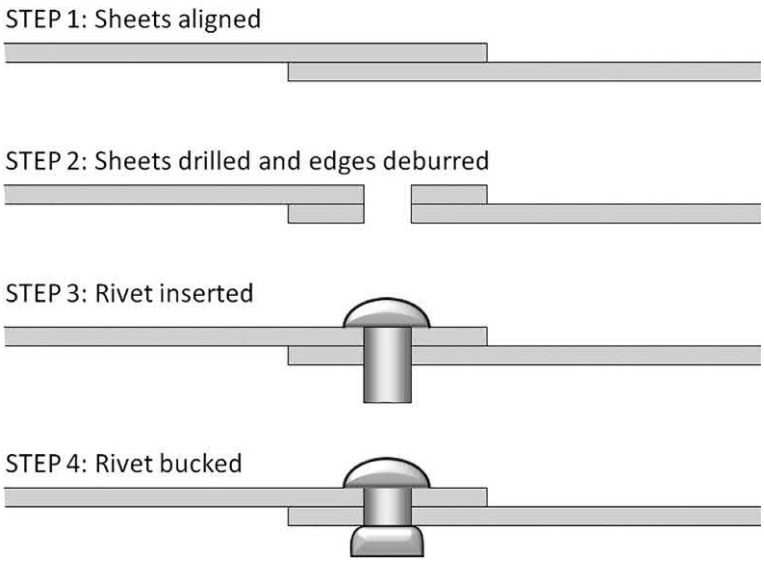


FIGURE 5-3 Standard procedure to join two aluminum sheets by bucking a rivet.

Blind-riveting is only used when access to the back side of the sheets prevents the use of bucking. It is also used for noncritical structural assembly. Driving a blind rivet is a simple two step operation (see Figure 5-4). A special tool (*rivet-gun*), is used to pull out the stem (or spindle) until it snaps. This pulls the stem up just enough to compress the opposite end of the rivet, locking it in place. Blind rivets are also available as structural rivets. Cherrymax is the best-known brand for such rivets. Blind riveting, while easier to accomplish than bucking, still requires care in installation to avoid tilting of the stem, which might misalign the rivet. It is also considerably more expensive that bucking.

Finally, there are several different types of rivet heads and presenting them all is beyond the scope of this text. Only the two most common types will be cited: *universal* and *counter-sunk* (see Figure 5-5). The universal head rivet

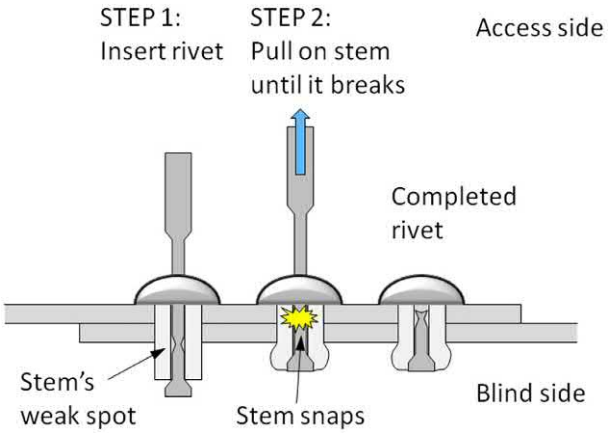


FIGURE 5-4 Standard procedure to join two aluminum sheets using a blind-rivet.

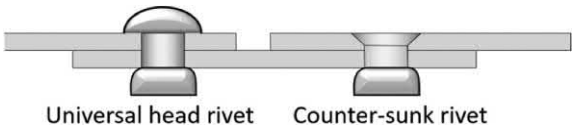


FIGURE 5-5 The two most common rivet head types: *Universal* and *Counter-sunk*.

is typically used for low-speed aircraft. It develops more drag and is less expensive than the counter-sunk rivet, whose head will be flush with respect to the surface of the sheet. This reduces the drag of high-speed aircraft, albeit at greater manufacturing cost. Counter-sunk rivets require an indentation to be made into the sheet metal to accommodate the rivet head. This is accomplished either by a special drilling operation or forming of a *dimple* using a special tool.

(9) Joining by Threaded Fasteners

Next to rivets, threaded fasteners (or bolts) are the most used fasteners in aircraft (see Figure 5-6). Such fasteners have superior tensile (and shear) strengths compared to rivets but are far more expensive. Like all aircraft hardware, threaded fasteners must be traceable

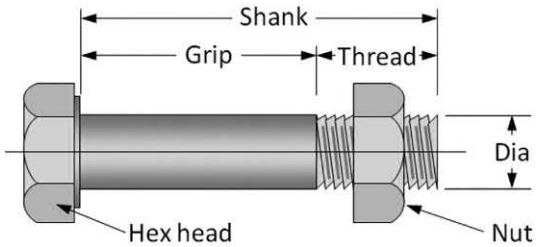


FIGURE 5-6 The nomenclature for a basic threaded fastener.

to an approved manufacturing process. Most bolts used for aircraft applications are general-purpose (e.g., AN-3 through AN-20 bolts), internal-wrenching (e.g., MS-20004 through MS-20024), and close tolerance (e.g., the hex-headed AN-173 through AN-186 or NAS-80 through NAS-86).

The shank of these bolts features a smooth section, called the *grip*, and a threaded section to which the nut is turned. The length of the grip must be equal to or slightly exceed the thickness of the material it is intended to join. The nut must be tightened or torqued to the right amount to preload the fastener. This ensures the joined parts do not slip during service, ensures a more uniform transfer of loads, and increases the fatigue life of the fastener. Nuts are usually *self-locking* or *nonself-locking*. Castellated nuts exemplify the latter. They are locked in place using special safety-pins called *cotter-pins*. Castellated nuts are required for all structurally critical parts, such as engine mounts, landing gear, and wing attachments. The installation of threaded fasteners should always use flat washers (e.g., AN960) so the torquing of the nut will not damage the surface of the joining materials.

TABLE 5-1 Basic designation for wrought and cast aluminum alloys.

Wrought alloys		Cast alloys	
Alloy group	**Major alloying elements**	**Alloy group**	**Major alloying elements**
1XXX	99.00% minimum aluminum	1XX.0	99.00% minimum aluminum
2XXX	Copper	2XX.0	Copper
3XXX	Manganese	3XX.0	Silicon with added Copper and/or Magnesium
4XXX	Silicon	4XX.0	Silicon
5XXX	Magnesium	5XX.0	Magnesium
6XXX	Magnesium and Silicon	6XX.0	Unused series
7XXX	Zinc	7XX.0	Zinc
8XXX	Other elements	8XX.0	Tin
9XXX	Unused series	9XX.0	Other elements

Based on Table 3.1 of Anonymous, Metallic Materials Properties Development and Standardization (MMPDS), DOT/FAA/AR-MMPDS-01, Federal Aviation Administration, 2003.

5.2.3 Aluminum Alloys

Aluminum is a lightweight structural material that can be strengthened further by chemical and mechanical means. Chemically, the strength is increased by adding specific elements to it (see Table 5-1). This process turns the aluminum into an alloy. Mechanically, the strength is increased via cold working and heat treatment. Aluminum has been the primary material for aircraft construction since before World War II.

Currently, aluminum accounts for about 75%–80% of commercial and military aircraft. According to data from the General Aviation Manufacturers Association (GAMA) from 2005,[3] some 65%–70% of GA aircraft delivered were made from aluminum. Three aluminum alloys are used more than others: 2024, 6061, and 7075. Table 5-1 lists the major alloying element for the different types of aluminum.

(1) Pros

The primary advantages of aluminum alloys are (A) low density; (B) high strength-to-weight ratio; (C) good corrosion resistance if alclad; (D) ease of fabrication and repair; (E) diversity of form; (F) electric conductivity; (G) isotropy; (H) abundance in the Earth's crust; and (I) repeatable properties.

(2) Cons

Aluminum alloys have at least three important flaws; (A) poorly defined *endurance limit*; (B) *stress corrosion*; and (C) *galvanic corrosion*. Additionally, it has (D) a low melting point and (E) poor bearing strength.

(3) Additional Comments

The properties of aluminum alloys depend on alloy content and method of fabrication. Besides strength, the designer must be aware of selected characteristics of aluminum, such as grain direction, dependency of strength on plate thickness, corrosion properties, and fatigue. These are beyond the scope of this discussion but interested readers can refer to Ref. [1].

Isotropy is one of the most important properties of aluminum. Theoretically, it offers omnidirectional strength and stiffness. Aluminum sheets used for aircraft construction are mostly isotropic, as there is a slight difference between the "rolled" and "transverse" directions. They are produced by first casting molten aluminum into a thick sheet, which is then hot rolled (at 260–343°C or 500–650°F) until a specific thickness is achieved. Then, the hot-rolled sheet is annealed and cold rolled until a desired "retail-ready" thickness is produced. This process gives the sheet its bidirectional properties.

[3] Some of 3580 aircraft delivered in 2005, some 2535 were made from conventional materials of which aluminum was by far the most common material. Some 1045 were composite aircraft.

Wrought alloys are rolled from an ingot or extruded into some specific shapes. The word "wrought" is the ancient past tense of the verb "to work." "Wrought alloy" means "worked alloy." *Cast alloys* are melted into a liquid form and poured into molds where they cool. These two methods lead to two different classes of alloys, in which wrought alloys are stronger because of special postprocesses such as cold working, heat treatment, and precipitation hardening.

Wrought and cast aluminum and aluminum alloys are identified by a special four-digit designation. First consider the alloys shown in the left part of Table 5-1. An example is the widely used 2024-T3 alloy. The first digit (2) indicates the alloy group. It indicates that 2024 contains copper (Cu) as the major alloying element. The second digit (0) indicates the kind of modifications made to the original alloy or impurity limits. This value is usually 0 for structural alloys used for GA aircraft (e.g., 2024, 6061, 7075). Then, consider the Cast Alloys in the right part of Table 5-1. The second and third digits identify the aluminum alloy, while the digit at the right of the decimal point indicates the product: XXX.0 means casting; XXX.1 and XXX.2 mean the metal is in ingot form.

The designation of wrought and cast aluminum alloys uses special suffixes to identify their temper properties and is based on the sequences of basic treatments used to produce the various tempers. Thus, 2024-T3 means the aluminum is solution heat-treated, cold worked, and naturally aged to a stable condition. The Basic Temper Designation System is listed in Table 5-2. The designation of the numerical codes, e.g., "3" in "-T3" is beyond the scope of this introduction, but interested readers can refer to Ref. [1] for more details.

Endurance limit (also called *fatigue limit*) is a property of many metals, for instance steel. It is indicative of its ability to resist cyclic stress loading. This means that if the amplitude of the cyclic stress during cyclic loading is below a certain value, the material can react the loading indefinitely. If the stress levels are higher, the material will eventually succumb to fatigue and fail. Some metals have very clear endurance limits, for instance steels. Aluminum, on the other hand, does not always have a clear endurance limit [3, p. 81]. Thus, even at very low stress levels, if the number of cycles is large enough it will fail (see Figure 5-7 for an example life cycle plot for 2024-T3 aluminum from Ref. [1]). Some engineers analyze aluminum structures assuming an endurance limit of some 10,000–12,000 psi, but such structures should still be subject to periodic inspection of crack growth.

Evaluating fatigue life of a structure is a challenging task, compounded by the randomness of loads during each flight. An airplane is subjected to greater gust loads on bumpy days. Frequency and magnitude of the loads also depends on the class of aircraft. Trainers experience hard landings more often than professionally flown transport aircraft. This variety of loads is accounted for in aircraft fatigue analyses using a so-called *load spectrum*. For instance, an ordinary Normal Category airplane (see Table 1.2) designed for a life of 12,000 h, might be expected to reach 3.8 g once or twice in its lifetime. It may experience 1.5 g several thousands of times.

Ref. [6] provides methods to estimate the *safe life* of aircraft structure—The first step toward determining the life expectancy of the airplane. It provides scatter factors and load spectra for various types of aircraft and operation (e.g., taxi loads, landing impact loads, gust and maneuver load, etc.). This information is used to develop the probability that structural components, such as wing or tail, could reach the end of their design life (in terms of ground-air-ground cycles) without developing detectable fatigue cracks.

Stress Corrosion is an affliction of ductile alloys exposed to high tensile stresses in a *corrosive environment*. Corrosive environment includes water vapor, aqueous solutions, organic liquids and liquid metals. The corrosion manifests itself as cracking along grain boundaries in the material. Research shows that aluminum alloys containing substantial amounts of soluble alloying elements, primarily copper (Cu), magnesium (Mg), silicon (Si), and zinc (Zn), are particularly susceptible to stress-corrosion cracking. Examples of such alloys include 7079-T6, 7075-T6, and 2024-T3, comprising more than 90% of the in-service failures of all high-strength aluminum alloys [7].

TABLE 5-2 Basic temper designation system for aluminum alloys.

Temper	Temper description
F	Fabricated. Indicates that no special control over thermal conditions or strain-hardening is employed.
O	Annealed. Used with wrought products that are annealed to obtain the lowest strength temper, and to cast products which are annealed to improve ductility and dimensional stability. The O may be followed by a digit other than zero.
H	Strain-hardened (wrought products only). Applies to products which have their strength increased by strain-hardening, with or without supplementary thermal treatments to produce some reduction in strength. The H is always followed by two or more digits.
W	Solution heat-treated. An unstable temper applicable only to alloys which spontaneously age at room temperature after solution heat treatment. This designation is specific only when the period of natural aging is indicated: for example, W ½ h.
T	T thermally treated to produce stable tempers other than F, O, or H. Applies to products which are thermally treated, with or without supplementary strain-hardening, to produce stable tempers. The T is always followed by one or more digits.

Based on Table 3.1.2 of Anonymous, Metallic Materials Properties Development and Standardization (MMPDS), DOT/FAA/AR-MMPDS-01, Federal Aviation Administration, 2003.

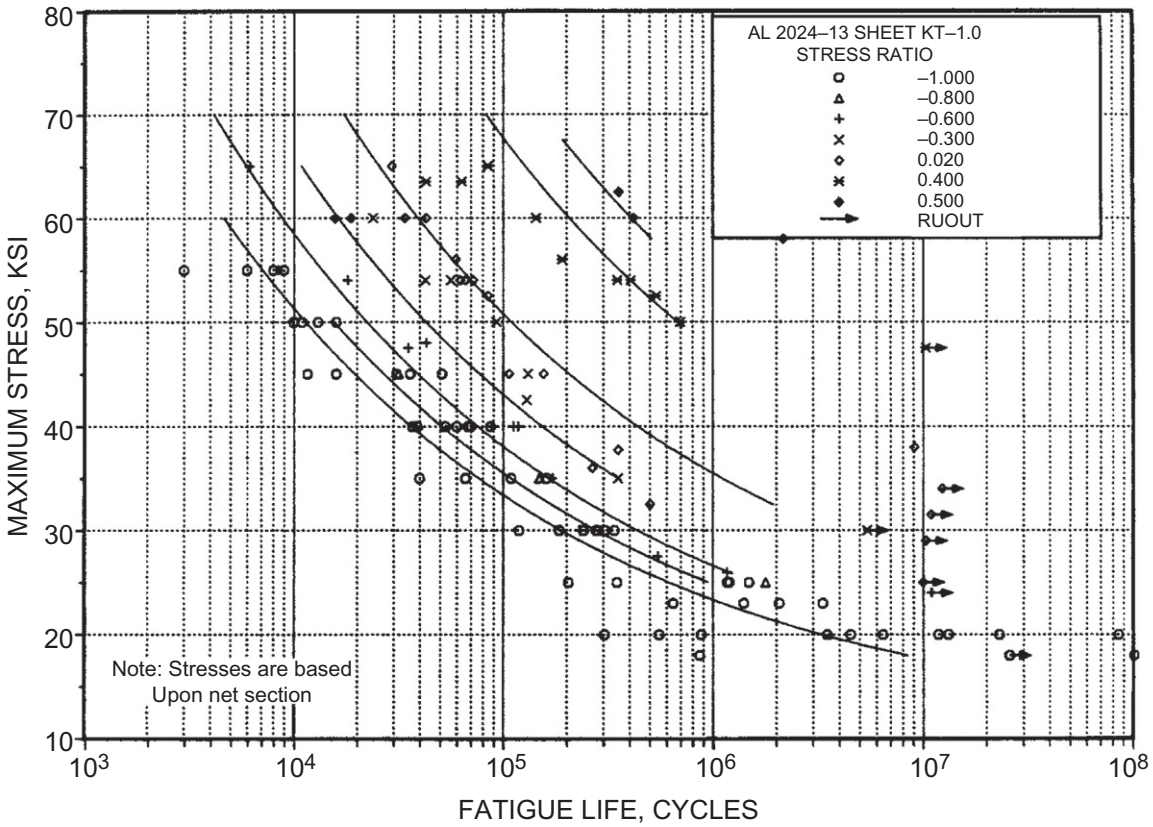


FIGURE 5-7 Figure 3.2.3.1.8(e) in Ref. [1], displays an important flaw—no clear endurance limit.

Galvanic Corrosion occurs when two electrochemically dissimilar metals are close to each other in a structure; for instance, when aluminum is joined to steel. Besides the electrochemical dissimilarity, an electrically conductive path between the two metals must exist to allow metal ions to move from the anodic to cathodic metal. While primarily an issue during detail design, potential issues stemming from insisting on dissimilar metals being joined in the airframe should be identified. While joining dissimilar metals is common in the aviation industry, it should be avoided when possible. The galvanic corrosion problem can be remedied by applying special plating or finishing to the metals as a protection.

Table 5-3 lists several aluminum alloys commonly used in General Aviation aircraft structures. The designer should regard these as alloys for primary and secondary structure. Table 5-4 shows selected properties for a few aluminum alloys that are frequently used in General Aviation aircraft. Table 5-5 shows common sheet thicknesses of commercially available aluminum alloys. Note that to save space, the sheet thicknesses are stacked in two columns for each unit.

5.2.4 Steel Alloys

By definition, Steel is Iron (Fe) that has been modified through the introduction of alloying elements, such as Nickel (Ni), Vanadium (V), Cobalt (Co), Chromium

TABLE 5-3 Typical applications of aluminum alloys in General Aviation aircraft.

Aluminum alloy	Typical application
2024-T3, 2024-T4	Used for high strength tension application such as wing-, fuselage-, and tail-structure. Has good fracture toughness (MMPDS [1] defines fracture toughness as *"The fracture toughness of a material is literally a measure of its resistance to fracture. As with other mechanical properties, fracture toughness is dependent upon alloy type, processing variables, product form, geometry, temperature, loading rate, and other environmental factors."*), slow crack growth, and good fatigue life compared to other aluminum alloys [8, p. 102].
6061-T6	Used for resilient secondary structure such as access panels, piston engine baffles, cockpit instrument panels, etc.
7075-T6, T651	Used for high stress applications like the 2024. It is stronger than 2024, but lower fracture toughness and fatigue resistance.

TABLE 5-4 Selected properties of common aluminum alloys (A-basis and longitudinal direction) [1].

Description Symbol Units	Density ρ lb_f/in^3	Tensile modulus E ksi	Shear modulus G ksi	Poisson's ratio μ	Yield tensile F_{ty} ksi	Ultimate tensile F_{tu} ksi	Ultimate shear F_{su} ksi	Ultimate bearing $e/D = 1.5$ F_{bru} ksi
2024-T3 Sheet 0.01–0.125″	0.100	10.5×10^3	4.0×10^3	0.33	47	64	39	104
2024-T4 Sheet 0.01–0.249″	0.100	10.5×10^3	4.0×10^3	0.33	40	62	37	93
6061-T4 Sheet 0.01–0.125″	0.098	9.9×10^3	3.8×10^3	0.33	16	30	20	48
6061-T6 Sheet 0.01–0.125″	0.098	9.9×10^3	3.8×10^3	0.33	36	42	36	67
7075-T6 Sheet 0.040–0.125″	0.101	10.3×10^3	3.9×10^3	0.33	70	78	47	121

TABLE 5-5 Common sheet metal thicknesses for aluminum alloys.

Inches		mm	
0.012	0.072	0.30	1.83
0.016	0.081	0.41	2.06
0.020	0.091	0.51	2.31
0.025	0.102	0.64	2.59
0.032	0.125	0.81	3.18
0.040	0.156	1.02	3.96
0.051	0.188	1.30	4.78
0.064	0.250	1.63	6.35

(Cr), Magnesium (Mg), Molybdenum (Mo), Carbon (C), and other elements. The introduction of these elements improves the properties of the iron, practically converting it into a new material.

(1) Pros

Steel is (A) strong; (B) stiff; (C) hard; and (D) durable. It has (E) a high melting point and (F) high endurance limit. Often, it is the only material for use in highly stressed regions of the airplane (e.g., landing gear, engine mounts, and high strength fasteners). These properties are enhanced further through the introduction of processes such as annealing, quenching, cold working, and heat treating.

(2) Cons

(A) Expensive; (B) heavier than aluminum; (C) harder to form; (D) causes galvanic corrosion when in direct contact with aluminum.

(3) Metallurgy

Properties or steel, such as hardness, ductility, and toughness, are controlled using various metallurgical processes. The branch of Materials Science that deals with such processes is called *Metallurgy* [9]. For instance, *annealing* is a process in which the metal is heated to a specific temperature, where it is kept for a given amount of time and after which it is cooled at a specific rate. This process relieves stresses that may be in the material and makes it more ductile (less hard), making it is easier to cut, stamp, or grind. *Quenching* is the rapid cooling of steel and produces grain structure that is particularly hard. Used for low-carbon and austenitic stainless steels, it improves durability and makes it ideal for highly loaded precision parts. *Cold working* is used to increase the yield strength of a metal. This is accomplished by cold rolling, cold extrusion, or cold drawing, to name a few. *Heat treating* involves heating the material, before cooling it at specific rates. It modifies the arrangement of the molecular structure and is used to strengthen steels other than low-carbon and austenitic stainless steels.

The properties of a selection of commonly used steels are presented in Table 5-6. Of these, AISI 1025 is a general-purpose steel used for various shop projects, such as to make jigs, fixtures, mockups, and similar. It is not used for aircraft, although it is possible to get it in aircraft quality. Steels such as AISI 4130 and 4340 are also known as "Chromoly," as it contains traces of both Cr and Mo. It is very common in aircraft due to reliable heat-treating practices and processing techniques, where it is used for engine mounts, landing gear, space-frame fuselages and other high stress components. It is readily available as sheet, plate, and tubing stock.

TABLE 5-6 Selected properties of common steels [1].

Description Symbol Units	Density ρ lb_f/in^3	Tensile modulus E ksi	Shear modulus G ksi	Poisson's ratio μ	Yield tensile F_{ty} ksi	Ultimate tensile F_{tu} ksi	Ultimate shear F_{su} ksi	Ultimate bearing $e/D = 1.5$ F_{bru} ksi
AISI 1025 Sheet, strip, and plate	0.284	29.0×10^3	11.0×10^3	0.32	36	55	35	90[a]
AISI 4130 ($t \leq 0.188''$) sheet Normalized, stress-relieved	0.283	29.0×10^3	11.0×10^3	0.32	75	95	57	200[a]
AISI 4130 ($t > 0.188''$) sheet Normalized, stress-relieved	0.283	29.0×10^3	11.0×10^3	0.32	70	90	54	190[a]
AISI 4130 ($t \leq 0.188''$) tubing Quenched and tempered	0.283	29.0×10^3	11.0×10^3	0.32	100	125	75	146 175[a]
AISI 4340 Bar, forging, tubing	0.283	29.0×10^3	11.0×10^3	0.32	217	260	156	347 440[a]
300M	0.283	29.0×10^3	11.0×10^3	0.32	220	270	162	414 506[a]

[a] *For* e/D = 2.0.

5.2.5 Titanium Alloys

Titanium is ideal for high-strength, light-weight applications in a demanding environment. It was discovered in 1791 by a British chemist, William Gregor (1761–1817) and rediscovered in 1793 by the German chemist Martin Heinrich Klaproth (1743–1817). Today, it is found in multiple applications, ranging from biomedical implants [10] to aircraft. The first large scale use of titanium was in the Lockheed SR-71 Blackbird. Its development and the ill-fated North American XB-70 solved many of the production problems accompanying its use, making it a suitable alternative to aluminum.

The properties of selected titanium alloys are presented in Table 5-7. Titanium is usually alloyed with aluminum for use in aircraft structures. Among several common titanium alloys are Ti-4Al-4Mo-2Sn-0.5Si or Ti-6Al-4 V, of which the latter is the most widely used [8, p. 109]. Besides Titanium (Ti), it contains 6% Aluminum (Al), 4% Vanadium (V), a trace of iron (Fe), and oxygen (O).

(1) Pros

(A) Greater strength, stiffness, competitive weight, and higher heat resistance than aluminum; (B) good strength-to-weight ratio; (C) low coefficient of thermal-expansion; (D) good toughness; and (E) good oxidation resistance. It melts at higher temperature than steel (1660°C versus 1650°C, respectively).

TABLE 5-7 Selected properties of titanium [1].

Description Symbol Units	Density ρ lb_f/in^3	Tensile modulus E ksi	Shear modulus G ksi	Poisson's ratio μ	Yield tensile F_{ty} ksi	Ultimate tensile F_{tu} ksi	Ultimate shear F_{su} ksi	Ultimate bearing $e/D = 1.5$ F_{bru} ksi
Pure Ti (sheet, plate) CP-1 (AMS 4901)	0.165	15.5×10^3	6.5×10^3	–	70	80	42	120
Ti-6Al-4V, $t \leq 0.1875$, B-basis	0.160	16.0×10^3	6.2×10^3	0.31	131	139	90	221
Ti-6Al-4V, $0.1875 < t \leq 2.000$, B-basis	0.160	16.0×10^3	6.2×10^3	0.31	125	135	84	214

(2) Cons

(A) While being one of the most abundant elements in nature, it is expensive to extract and isolate. (B) High cost (5–10-fold) limits its competitiveness in the GA industry.

5.2.6 Composite Materials

The term *composite* applies to structures that consist of more than one constituent material such the combination yields properties that are superior to those of the constituent materials. Composites are a large and disparate class of materials, ranging from steel reinforced concrete used for buildings to stiffened plywood-balsa-plywood sandwich panels used in airplanes. In aviation, the term refers exclusively to various fiber reinforced plastics that are used as primary, secondary, and tertiary structures (see Section 5.3.1, *Important Structural Concepts*). This section defines and explains most of the common terminology used by engineers and technicians alike.

In its most basic form, composites consist of layers of fiber cloth, impregnated with some type of *plastic matrix* (or resin) and then *cured* to form a rigid structure. An example is fiberglass or carbon cloth embedded in epoxy resin. The cloth typically comes in three forms: *unidirectional*, *bidirectional*, and *fiber mats*. The first two are shown in Figure 5-8. The third, fiber mats, are chopped strands of fibers that are randomly assembled into a cloth. They are commonly used for swimming pools, Jacuzzis, and boats (often called "boat glass"). They are not to be used for primary or secondary structures in aircraft as their strength and stiffness properties are unacceptably poor. They are acceptable as tertiary structure, provided it is light.

Each layer is a *ply*, and a stack of several plies constitutes a *laminate*. The act of creating such a laminate is called *lay-up*. Sometimes a third constituent material, called a *core*, is added to fabricate a *composite sandwich*. The core separates the plies by a given distance, increasing the stiffness of the structure. The resulting panels are light, stiff, and strong and are ideal for use as skin for wing, HT, VT, or fuselage structures. Such panels allow multiple ribs and frames to be eliminated from the structure, simplifying the airframe.

(1) Pros

Fiber-Reinforced Plastics (FRP) and *Carbon Reinforced Plastics* (CRP) offer many benefits over traditional materials, including (A) high strength-to-weight; (B) flexibility in design; (C) ease in the fabrication of compound surfaces; (D) part consolidation; (E) high dielectric strength; (F) dimensional stability; (G) corrosion resistance offers extended service life; (H) good thermal insulation; and (I) high impact resistance.

(2) Cons

FRPs and CRPs also come with disadvantages. (A) To work with it, special provisions must be made to keep moisture levels low and prevent dust from entering the production. (B) Protective clothing and respirators are required for all who work with it. (C) The resin is highly toxic. If not handled with care, it can easily cause serious dermatitis. (D) It is subject to storage limitations and strength variability. (E) The strength of the composite material depends on the soundness of the layup process, requiring the manufacturer to verify this through continuous strength testing. (F) While composites have high impact resistance (maintain its original shape), they also suffer from impact sensitivity that may cause *delamination*. This reduces strength, stiffness, and buckling resistance. (G) Composites tend to fail with limited warning. Metals, in contrast, fail after a plastic elongation. (H) Composites are vulnerable to fabrication flaws such as *wrinkling*, *bridging*, and *dry fibers* that compromise its strength. (I) In professional manufacturing environment, the structure is carefully inspected for such flaws, adding cost to the production. (J) Composites are notoriously poor in bearing and require careful attention to cleanliness during the construction process. (K) Additionally, they often require specific surface finish requirements. For instance, to minimize heat absorption, they require light-insensitive paint (preferably white) on surfaces exposed to sunlight. Heat is detrimental to the strength of the resin, so their operational temperature limits are well below that of aluminum (which is not that impressive to begin with). (L) The fact that FRPs are good electrical insulators makes them very vulnerable to catastrophic failure if struck by lightning. This is critical

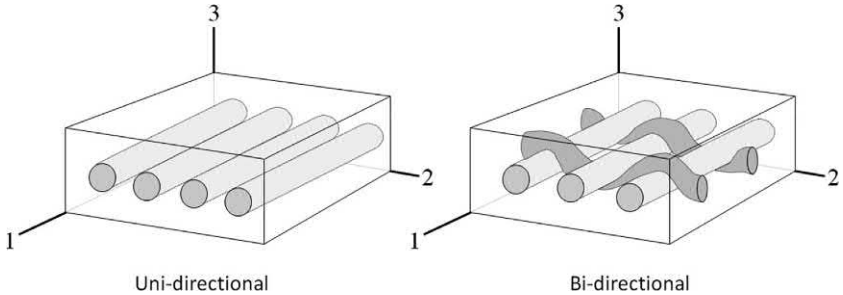


FIGURE 5-8 Difference between a unidirectional and bidirectional fiberglass cloth (a ply).

to airplanes and requires metal conductors to carry away the electrical surge to be co-cured with the composite. To add insult to injury, these conductors are typically a "one-shot deal." They must be replaced upon landing, unless of course a second lightning strikes first.

(3) Types of Composites

There are three common forms of composites used for industrial applications:

(A) ***Fibrous Composites*** consist of fibers embedded in a matrix (resin). Examples include FRPs and CRPs.

(B) ***Laminated Composites*** consists of layers of various materials. Composite sandwich panels are examples of a laminated composite. Such composites are simply referred to as *laminates* and the constituent layers are called *plies*.

(C) ***Particulate Composites*** which are composed of particles in a matrix. Steel reinforced concrete is an example of this. Particulate composites are not used in airplanes and, thus, is omitted from further discussion.

(4) Stiffness of Sandwich Laminates

To illustrate the stiffening effect of the core, consider the three 10″ long cantilevered composite beams in Figure 5-9. The top beam is a simple 4-ply laminate consisting of typical aircraft-grade fiberglass laid up using a $[+45\,\text{degrees}/-45\,\text{degrees}]_S$ layup (S stands for symmetrical). The center and bottom ones feature the same fiberglass layup, with the addition of a 0.375″ and 0.75″ cores, respectively. The resulting thicknesses and normalized densities (the density of the bottom beam is 1.69× that of the top one) are shown. Now, assume we apply force to the right end of the top beam, such it deflects 1″. Applying this same force to the end of the other beams causes them to deflect 1/110″ and 1/409″, respectively: The bending stiffness of these beams is 110× and 409× greater than the top laminate. This huge increase in stiffness only costs a very modest increase in weight.

(5) Structural Analysis of Composite Materials

Structural analysis of composite materials is conducted using micro- and macro-mechanics. *Micro-mechanics* examines the interaction of the constituent materials (i.e., fibers and matrix) on a microscopic level. It allows the "average" properties of the laminate (such as strength and stiffness) and stresses and strains in each constituent ply to be predicted. *Macro-mechanics* assumes the laminate can be approximated as if it were homogeneous and only uses the averaged properties of the combination of constituent materials. Thus, composite structural members are treated as if isotropic (except with different properties along each material axis). The approach permits a convenient workaround in Finite Element Analysis software:

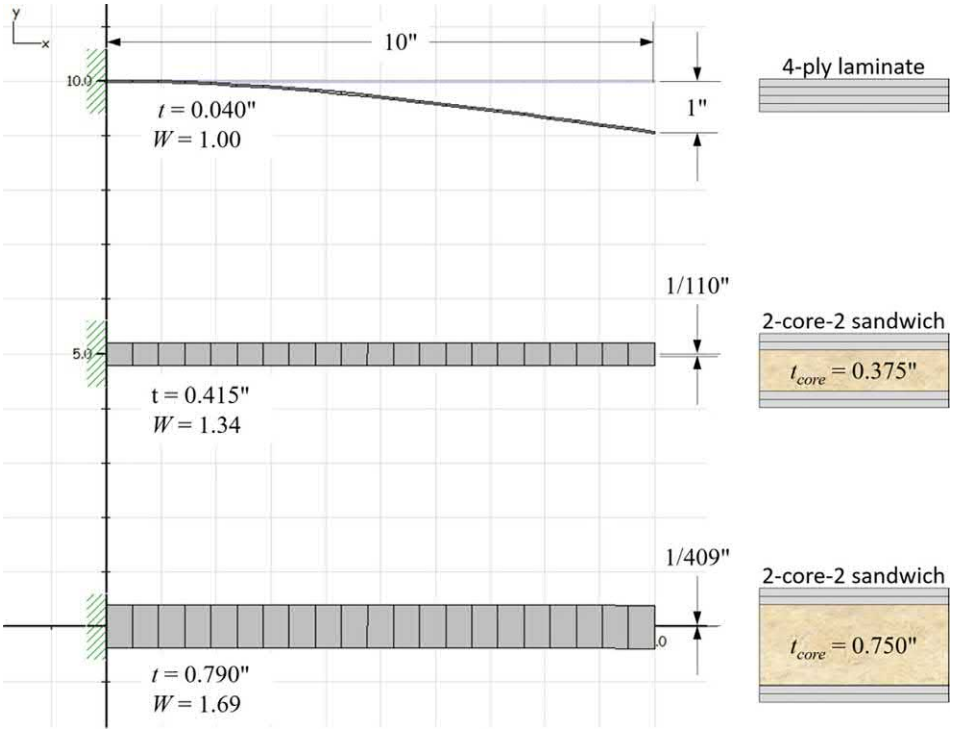


FIGURE 5-9 The effect of deflection of cantilevered beams under identical load is used here to compare the stiffness of a laminate and sandwich composite materials.

The loads reacted by the laminate are determined using macro-mechanics. Then, these loads are applied to the same laminate using micro-mechanics.

Stresses and strains in each ply are predicted using the *Classical Laminate Theory* (CLT). Among others, Tsai [11] and Jones [12] provide a good treatise of the theory. CLT assumes (1) orthotropic material properties, (2) ply properties are linearly elastic, and (3) no coupling between the normal and shear strains, ε and γ, or the normal and shear stresses, σ and τ. In the case of a unidirectional laminate, where the stress/strain coordinate axes are referred to as the principal material directions, the assumption is justified based on material symmetries.

General directions of the stress and strain axes are denoted as shown in Figure 5-8. Material properties in the principal material directions 1, 2, and 3 are as follows:

E_1, E_2, and E_3 = Young's (elastic) moduli in the principal material directions
G_{23}, G_{31}, and G_{21} = Shear moduli
ν_{ij} = Poisson's ratio for transverse strain in the j-direction, when stressed in the i-direction

The 1 and 2 directions may be oriented at some angle (e.g., 45 degrees) with respect to the x-y directions. Thus, the load the fibers pick up is misaligned when compared to the x-y directions. The examples presented in Figs. 5.9 and 5.10 were prepared using the theory.

An example of the capability of micromechanics is illustrated in Figure 5-10. A 6-core-6 sandwich with an unsymmetrical layup $[+45°/+45°/0°/+45°/0°/45°]_S$ using bidirectional weave is subjected to pure bending about the x-axis only. The three left columns show strains in a cross-section of the laminate, whereas the three right columns show strains in each of its constituent plies. The top and bottom of each column represents the fiberglass plies, while the lighter center region represents the thickness of the core (0.375″). The height of each layer is proportionally consistent. The strains in the left part of Figure 5-10, resemble that predicted by classical solid mechanics for isotropic materials. However, when transformed to the angular orientation of each ply (right part of Figure 5-10), the loading looks quite different. The largest ply strains are picked up by the four 0-degree plies and the core. The core has a very low modulus of elasticity (Young's modulus) so it can stretch quite a bit without the formation of large stresses. The plies, on the other hand, have a very high modulus of elasticity, so the four 0° plies will develop larger stresses than the +45° ones. Consequently, if the applied moment becomes large enough, they are the first plies to fail. Micro-mechanics further allows the structural analyst to answer; if this happens, will the remaining plies be capable of reacting the moment, or will they fail as well? This kind of study is called *residual strength analysis* and is a standard procedure in the structural analysis of composite aircraft.

(6) Fibers

Combining fiber with matrix gives composites its superior properties. It is helpful to consider these

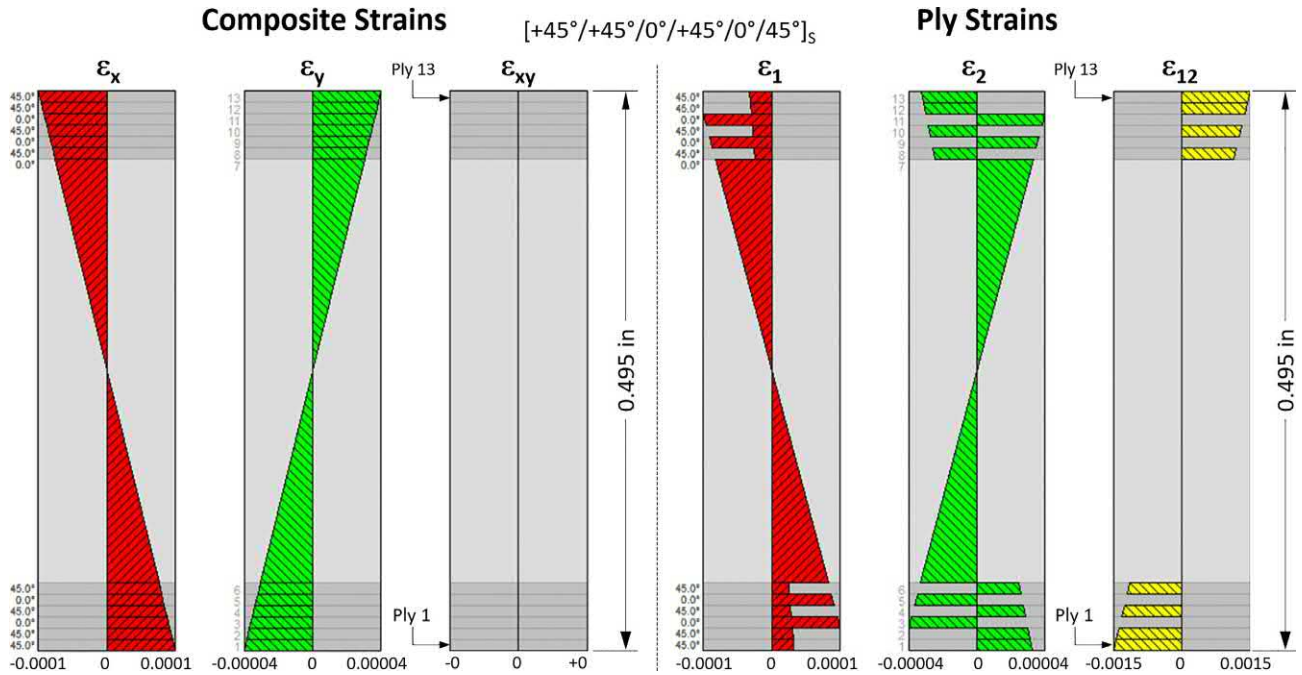


FIGURE 5-10 The effect of a pure bending moment on the strains (and therefore stresses) in a 6-core-6 laminate. The thicknesses of the core and plies is proportionally accurate.

elements separately. The presence of glass fibers in the matrix accounts for the strength advantage of FRPs. Since the fibers are much stiffer than the matrix, the load is inevitably reacted by the fibers. The resin matrix, in contrast, serves to distribute the load among the fibers, besides retaining the intended shape of the structure. Several types of fibers are available commercially. The most common are introduced below:

Aramid Fibers	Aramid are a class of very strong, lightweight, and heat-resistant multifilament fibers used for a myriad of applications ranging from bulletproof vests and helmets to parachute tethers. Introduced in 1961 by the DuPont Company, they are widely used in the aerospace industry, for instance under the name Nomex.
Boat Glass	Commonly used to identify fiberglass used for boat construction. It is also called *fiberglass mat* or, simply, *glass mat*. Consists of fiberglass chopped into short strands that are pressed into a mat. The mat offers far more uniform properties than unidirectional or bidirectional fiberglass, only much worse. The glass mat requires 1.5–2 times its own weight in resin to be fully saturated.
Boron Fibers	Boron is a class of sophisticated fibers that are high-strength and lightweight. They are widely used in various advanced aerospace structures, for instance in aircraft like the F-14, F-15, B-1 Lancer, and even the Space Shuttle. They are also found in bicycle frames, golf shafts, and fishing rods.
Carbon Fibers	Carbon-fibers is another advanced high-strength, high-stiffness, and lightweight fiber used in a variety of applications, ranging from baseball bats and bicycle frames to automotive and aerospace vehicles. It is used in Micro Air Vehicles (MAVs) as well as the fuselage of the Boeing 787 Dreamliner. Also known under the name *Graphite*. The primary drawback of laminates made from carbon fibers is their sensitivity to damage, compounded by difficulty in damage inspection due to their opaqueness.
C-glass	Specially developed to provide good corrosion resistance to hydrochloric and sulfuric acid. It gets its name for this property, which is short for ***Corrosion-Resistant Fiber***.
E-glass	The most popular type of fiberglass and is typically the baseline when comparing composites. It is inexpensive while offering good strength properties. It accounts for more than 90% of all glass fiber reinforcements. Named for its good electrical resistance, E-glass is well-suited to applications where radio-signal transparency is desired, such as aircraft radomes and antennas. It is also used extensively in computer circuit boards to provide stiffness and electrical resistance. Along with more than 50% silica oxide, this fiber also contains oxides of aluminum, boron and calcium, as well as other compounds.
Graphite Fibers	See Carbon Fibers.
Kevlar	Kevlar is the registered trademark of a version of aramid fibers developed by DuPont in 1965. The resulting fibers are extremely strong and resilient and are best known for their use in body armor and military helmets. Widely used in civilian aviation, for instance, as rotor-burst protection in jet engines, and even as the risers in the Cirrus Airframe Parachute System (CAPS) in the Cirrus SR20 and SR22 aircraft.
R-glass or S-glass or T-glass	Fiberglass that offers greater strength (~30%) and better temperature tolerance than E-glass. It is primarily used for aerospace applications. Also called ***High-Strength Glass Fiber***—When greater strength and lower weight are desired, S-glass is a candidate for other advanced fibers, such as Carbon. High-strength glass is known as S-type glass in the United States; it is often called R-glass in Europe and T-glass in Japan. It was originally developed for military applications in the 1960s. Later, a lower cost version, S-2 glass, was developed for commercial applications.
S-2 Glass	High-strength glass with greater amount of silica-, aluminum- and magnesium-oxide content than E-glass. S-2 glass has 40%–70% higher tensile and compressive strength than E-glass, besides being stiffer and offering improved impact resistance and toughness. In the aviation industry, S-2 Glass is used for helicopter blades, aircraft flooring and interiors, but it can be found in applications well beyond aviation as well. Like C-glass, it has good corrosion resistance to hydrochloric and sulfuric acid.

(7) Resin

The purpose of the resin is to bind the fibers together into a single structural unit and, in the process, distribute strains among them, while protecting them from the elements. There are two kinds of resins: *thermosets* and *thermoplastics*. The difference depends on the chemistry of the polymers, both of which contain highly complex molecular chains. When a thermoset resin cures, molecular chains *crosslink* to form a rigid structure that cannot be changed through the further application of heat; the final product is *irreversible*. Thermoplastics, on the other hand, can be reheated and reshaped more than once; the final product is *reversible*.

Thermosets—is the resin used for aircraft structures. They are inexpensive, simple to use, and offer good mechanical and electrical properties, as well as protection from the elements. It is a drawback that they usually cure during an exothermic chemical process. They have a stable shelf-life of several months, but when mixed with the proper catalyst ("hardener"), they cure within minutes. The most common thermosets are listed below.

Epoxies	The most common resin used for aerospace applications. The nickname "epoxy" comes from its chemical name "poly-epoxide." Epoxies are more expensive than the polyesters, but offer greater strength and stiffness, as well as less shrinkage. They are highly resistant to solvents, alkalis, and even some acids. They are easily incorporated into most composite manufacturing processes and allow chemical or electrical properties to be modified using a proper catalyst. Common types of epoxy resins for aircraft use are: (1) *Safe-T-Poxy* was developed to reduce the development of dermatitis, a common allergic reaction. It is no longer produced but has been replaced by a new resin called (2) *E-Z Poxy*, which offers the same handling and physical properties. (3) *MGS Epoxy* is used for certified aircraft applications. (4) *AlphaPoxy* is used for tertiary structures, (5) *Aeropoxy* is used for primary and secondary structures, to name a few. Also, well known are *Rutan Aircraft Epoxy* (RAE) systems.
Phenolic Resins	Used for a multitude of applications, some of which take advantage of its high temperature tolerance (brakes, rocket nozzles). Used to impregnate Nomex honeycomb floors and interior cabin liners in some aircraft, where it meets smoke, combustion, and toxicity requirements.
Polybutadienes	Have great electric properties and chemical resistance and as such are used for radomes as an alternative to E-glass/Epoxy laminates. Its high resilience renders it popular in the production of tires.
Polyesters	Used for a multitude of applications, such as boats, bathtubs, auto body parts, to name a few. Polyester resins are solvents for many types of synthetic foams (see below), so the user must make sure the proper core is used if making composite sandwiches.
Polyurethanes	Can be formed into either thermoset or thermoplastic resin. As a thermoset, it is primarily used for applications involving automotive bumpers.
Vinyl esters	Used for many of the same applications as polyesters but is more expensive. They are better than polyesters in applications exposed to high moisture environment, such as for boat manufacturing.

Thermoplastics—are less widely used for aviation applications than thermosets. Their best-known property is that when heated they become liquid and return to a solid state when cooled. This makes the material very practical for all sorts of applications, ranging from soda bottles, nylon garments, monofilament fishing lines, to engine fuel lines. Thermoplastics can be melted and frozen repeatedly, rendering them recyclable.

(8) Sandwich Core Materials

The sandwich core can be made from a multitude of materials, with some constraints though. First, the resin must not be a solvent for the core. Second, it must be resilient; their ultimate strain must be greater than that of the fiberglass. Otherwise, it will crack under load. The following materials are suitable for use in aircraft composite sandwiches, although some are not used for certified aircraft.

Urethane Foam	Costly, but easy to work with. It is impervious to most solvents and can thus be used with less expensive polyester resin. It is easy to cut and carve into shape and can even be sanded to shape with bits of itself [13]. It is useful for making wingtips and fairings in homebuilt aircraft, as well as compound surfaces. Readily available in sheets that are $24'' \times 48''$ in thicknesses from ½″ to 2″ at 2–4 lb_f/ft^3. It gives off toxic fumes when it melts and should not be used to hot-wire (see later). Not used for certified aircraft.
Clark Foam	A more expensive and denser (4.5 lb_f/ft^3) variety of urethane foam. Renowned for versatility and famous for use as core in surfboards. Not made since 2005. Not used for certified aircraft.
Styrofoam	Blue colored Styrofoam is the most popular material for use as core in wings of homebuilt aircraft. Used for insulation in homes. Readily available in sheets that are as large as $48'' \times 96''$ in thicknesses from ¾″ to 4″ at 2 lb_f/ft^3. Not used for certified aircraft.
Polystyrene	Commonly used for marine applications, it is also used as core in wings of several homebuilt aircraft. Widely used as insulation in homes and as packing material. Easily recognizable as the aggregate of small foam balls. Very susceptible to solvents and will dissolve in polyester resin. Available in blocks that are as large as $14'' \times 109''$ and 7″ thick at 1.6–2.0 lb_f/ft^3. Not used for certified aircraft.
Klegecell	Registered trademark for a PVC foam that meets all FAA regulations for fireproof aviation materials. Has been in production for over 50 years. Unaffected by UV rays and very stable with respect to resins. Extremely high strength-to-weight ratio, excellent thermal and acoustic insulation properties, low water absorption and good chemical resistance. Available in $48'' \times 96''$ sheets in thicknesses from ¼″ to 2″ at 3–6.25 lb_f/ft^3. Used for certified aircraft.
Divinycell	Registered trademark for a PVC foam that meets all FAA regulations for fireproof aviation materials. Unaffected by UV rays and very stable with respect to resins. Available in sheets as large as $48'' \times 96''$ in thicknesses from ¼″ to 2″ at 3–6 lb_f/ft^3. Used for certified aircraft.

Honeycomb	The term honeycomb refers to the hexagonal wax cells built by honeybees in their hives. It also refers to a class of materials used as sandwich cores, in which thin material, ranging from paper to alloys, is formed into hexagonal cells to use as core. Honeycomb is used for both flat and curved panels. It is a drawback that bonding fibers to the core is harder. There are three common types of honeycomb: (1) Aluminum honeycomb has one of the highest strength-to-weight ratio of any structural material, (2) Nomex honeycomb is made from Nomex paper dipped in phenolic resin and is widely used in the aviation industry, and (3) Thermoplastic honeycomb is used in multitude of transport applications. Used for certified aircraft.

(9) Glass-Transition Temperature

In terms of FRPs and GRPs, the *glass transition temperature*, T_G, refers to the temperature at which the resin transitions from a hard and brittle state into a molten (or soft) state. Reaching this temperature in operation could be catastrophic to primary structure as it renders the laminate incapable of reacting the applied loads. Most FRPs and GRPs used for aviation applications have a T_G in excess of 180°F.

(10) Gelcoat

Gelcoat provides the glossy, high-quality finish on the exposed surface of FRPs and GRPs. It is a polyester or epoxy resin specifically prepared with chemicals to control viscosity and cure time, as well as pigment with the desired color. Gelcoat is sprayed into the mold ahead of the plies being laid up.

(11) Precure

Precure refers to flat laminated plates that are cured prior to being used as a supplemental structural material. Think of it as a flat sheet of aluminum alloy, except it is made from an FRP. Having these at one's disposal is priceless, as one can cut them to a desired shape and then co-cure them with a laminate layup. Precures are frequently used to place hard points in a sandwich laminate, through which metal fasteners may be used. Their thickness is then equal to the thickness of the core. This forms a kind of an "island" of solid laminate in the sandwich panel, which is ideal to provide bearing strength and transfer fastener load into the sandwich.

(12) Aircraft Construction Methodologies

There are primarily two methods used to build composite airplanes. One is called *moldless composite sandwich construction*, the other is *molded composite construction*. The former is typically used for homebuilt or kit aircraft. It is thought to have been pioneered by the well-known Burt Rutan to permit customers to fabricate the experimental Rutan VariEze and Long-EZ kit planes [14]. The method is explained in detail in Refs. [13, 15], as well as in construction plans such as those of Refs. [16, 17].

Certified composite aircraft are built using molded composite construction. The method uses "female" or cavity molds that have been accurately shaped to form the Outside Mold Line (OML) of the part. Then fiberglass cloth is laid inside the mold. Once the layup has been completed, strands of sticky putty are laid around the part and a plastic sheet is draped over it and tacked to the putty. This encloses the part in a hermetically sealed environment (*vacuum-bagging*). Then a vacuum pump is connected to a hole in the plastic and turned on to form a vacuum. The mold is rolled into a warming room (some 150–180°F warm) where it can cure for some specific number of hours.

Pre-preg refers to fiberglass (or graphite) cloth impregnated with resin under controlled circumstances to improve property repeatability. The formation of low-pressure on the part side of the plastic veil, subjects the lay-up to substantial pressure difference. This squeezes air-bubbles out of the pre-preg and helps spread the resin uniformly in the laminate. Both improve its quality. The warming room ensures the resin cures at an optimum temperature, maximizing the laminate strength. It also lowers the viscosity of the resin, improving its flow under pressure. Some companies invest in a pressure vessel, called an *autoclave*, in which the composite part is cured. There it is subjected to higher pressure, as much as 5–10 times the atmospheric pressure. Autoclaves are not always necessary. Some composite fabricators even claim that vacuum "bagging" is equally effective [18, 19].

(13) Fabrication Methods

A few fabrication methods used to manufacture FRPs and GRPs are worthy of presenting and are listed below.

Hand Lay Up and Spray Up	The simplest and least expensive method to manufacture FRP or GRP parts. As stated before; a cloth of fibers is placed into a mold and impregnated with resin unless the cloth is a pre-preg.
Resin Transfer Molding—RTM	Consists of a rigid heated mold that contains Gelcoat, surfacing veil, and the fiberglass cloth, into which resin is pumped under pressure. The temperature of the mold is typically 100–120°F (40–50°C). The warm, pressurized resin flows through the tool and uniformly impregnates the laminate. The primary advantage of this method is superior surface quality, as well as dimensional tolerances and consistency of parts.

Continued

Compression Molding	Consists of placing the material (a thermoset) to be molded, preheated, in a heated open male-female mold. Then the mold halves are brought together, and the material is compressed, which forcefully spreads it uniformly over the entire mold surface. Compression molding is the oldest manufacturing method used by the plastic industry. Sometimes the mold is rotated to let centrifugal forces help spread the thermoset.
Injection Molding	The most common means of producing plastic parts. Melted plastic is forced under pressure into a mold of the desired part, where it cools and solidifies. The method is very versatile and most plastic parts commonly found in one's environment are made using this process.
Filament Winding	Filament winding is a process in which resin wet fibers are threaded through a roving delivery device called a feed-eye. The feed-eye moves back and forth along a rotating mandrel with the desired shape—a body of revolution. The fibers are wound helically in this fashion until a desired thickness is achieved. The method is used to create pipes, tanks (e.g., external fuel tanks), and even airplane fuselages. The fiber angle is controlled with the rotation speed of the mandrel and typically varies between 7 degrees and 90 degrees. The process compacts the laminate, making vacuum bagging unnecessary.
Pultrusion	Pultrusion consists of strands of fiber that are pulled through a die to form a column of some specific cross section. The operation involves prewetting the strands in liquid resin before they are pulled through a heated steel die. The process is analogous to forming metal extrusions, except the fibers are being pulled out of the die rather than being pressed through it. The fibers are pulled through the machine using two powerful pulling clamps, of which only one pulls at a time. When the active clamp reaches the end of its travel, the second one picks up the slack, allowing the first one to get back to its initial position where it resides until the process is repeated.

Selected properties of typical composite materials are shown in Table 5-8. Note that there is a large variation in properties between fiber brands, fiber volume, resin system, layup process, and other factors. The table should not be used for structural analyses—it is only presented to give ballpark values. Figure 5-11 compares the density, cost, strength, and stiffness of several composite materials (and polyethylene plastic), using E-glass as a baseline. Such a comparison matrix is helpful when selecting material for an application.

The reader wanting to learn more about composite materials and their use and certification in the aviation industry is directed to MIL-HDBK-17 [20], AC-20-107B [21], and AC-21-26 [22].

5.3 AIRFRAME STRUCTURAL LAYOUT

Detailed topics in structural analysis are beyond the scope of this book. However, a brief overview of structural layout is in order. In modern times, there are four common construction techniques used to fabricate aircraft: *wood construction*, *welded steel trusses*, *stiffened skin construction*, and *composites*. The last two are most widely used. Regardless, wood and welded trusses may be the best choice for specific projects. The pros and cons of the available fabrication methodologies must be understood to select the proper one. This section presents the application of these methods to real aircraft and introduces important structural concepts and challenges that are experienced in their development.

5.3.1 Important Structural Concepts

Several structural terms are introduced in the below discussion necessitating their brief definition [23]:

- The term *skin* refers to the material that covers lifting surfaces, fuselage, and so on.
- A *flange* is a longitudinal stiffener that runs along the edge of a flexible shell (or sheet) and whose purpose is to stiffen the shell structure and permit joining of other structural members.
- A *stringer* is a longitudinal stiffener that is not a flange. It carries axial loads resulting from bending loads. Stringers are also called *longerons*. Bruhn [24, p. C11.29] differentiates between the two by their number (if the number of the members is between 3 and 8, it is a longeron, otherwise a stringer). Ref. [25] states stoutness and number; longerons are thicker and fewer; and stringers are flimsier and more numerous.
- A *frame* is a transverse member in a closed shell (e.g., fuselage) that helps maintain its shape.
- A *bulkhead* is a transverse member in a closed shell to which other structures attach, for instance wing, horizontal tail, and engine, or reacts pressure loads. Bulkheads are always more substantial than frames.
- A *stiffener* is a longitudinal or transverse member intended to reinforce a structure by increasing its stiffness.
- A *boom* is a beam in the shape of a closed shell. Typical use is in twin tail-boom configurations.
- A *rib* is a transverse stiffener in an open shell, or the end of a closed shell. Typical use is in lifting surfaces.
- A *primary structure* is one that reacts flight, ground, or pressure loads [26, 27]. Fuselage and lifting surfaces constitute primary structure.
- A *secondary structure* carries only air or inertial loads generated on or within the secondary structure [27]. Such a structure is usually used for engine mounts,

TABLE 5-8 Selected properties of typical FRPs and CRPs.

Description Symbol Units	Density ρ lb_f/in^3	Tensile modulus E $\times 10^3$ ksi	Shear modulus G $\times 10^3$ ksi	Poisson's ratio μ	Yield tensile F_{ty} ksi	Ultimate tensile F_{tu} ksi	Ultimate shear F_{su} ksi
Epoxy (resin)	0.046	≈0.6	≈0.23	≈0.34	–	–	–
Polyester (resin)	0.042	≈0.47	≈0.17	≈0.38	–	–	–
Vinyl ester (resin)	0.046	≈0.5	≈0.17	≈0.38	–	–	–
E-glass	0.094	≈10	≈4	≈0.2	No yield	≈27	–
S-glass	0.092	≈7	≈0.6	≈0.26	No yield	≈50–90	10–12
High-Modulus Carbon	0.072	≈53	≈2.7	≈0.2	No yield	≈190	–
High-Strength Carbon	0.065	≈35	≈3.6	≈0.3	No yield	≈320	–
Boron	0.090	≈170	≈26	≈0.35	No yield	–	–
Aramid (Kevlar)	0.052	≈18	≈4	≈0.36	No yield	≈40	–

Based on B.C. Hoskin, A.A. Baker, Composite Materials for Aircraft Structures, AIAA Education Series, 1986 and other sources.

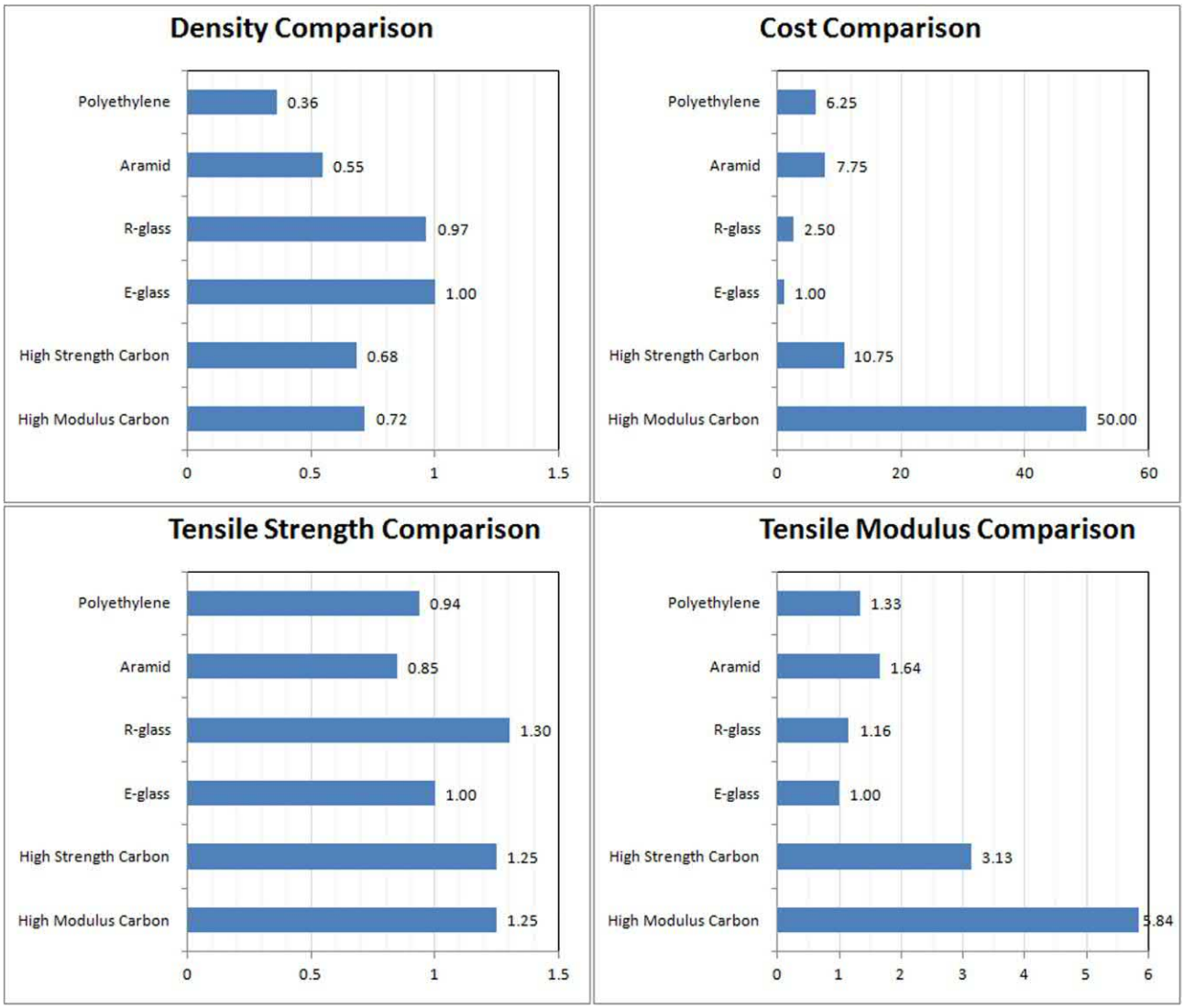


FIGURE 5-11 A comparison of several composite materials, normalized to E-glass. *Based on Anonymous, Various Datasheets From http://www.hexcel.com. (Accessed 15 March 2012).*

internal components, flight control surfaces, landing gear doors, to name a few.

- A *tertiary structure* refers to structure not subjected to any strength requirements [27]. Fairings and wingtips (excluding winglets or raked wingtips) fall into this category.
- An *allowable* is a maximum allowable stress value of some specific material property. For instance, the ultimate tensile stress allowable for 2024-T3 aluminum sheet of 0.125-in thickness is 64,000 psi.
- A *notched allowable* is an allowable assuming the material has some defects. This results in a reduction in the property, sometimes by as much as 50%.
- *Fail-safe* means that, should the primary load path in a structure fail during operation, an alternate load path exists that prevents a catastrophic failure of the structure.

(1) Monocoque and Semimonocoque Structure

The word *monocoque* comes from the Greek word *mono* (single) and the French word *coque* (shell). Monocoque is a structural technique in which stresses are reacted by a thin shell of material, rather than a collection of beams. Such structures are stiff in bending and light and, thus, ideal for weight sensitive vehicles such as airplanes. A good way to visualize a monocoque structure is to fold a sheet of paper into a cylinder and tape the free edge using Scotch tape. Although the resulting structure is stiff in bending, this reveals the structure's greatest weakness—structural instability. Monocoque structure tends to fail in buckling or crippling, something easily demonstrated by a person standing on top of an empty aluminum beverage can. The empty container can support the weight of a grown man, but (carefully) tap the side with a pencil and it will collapse in a blink of an eye. This instability necessitates the addition of an internal support structure that resists these failure modes. Such support structure is an assembly of frames, bulkheads, stringers, and longerons (Figure 5-12). The combination is called *semimonocoque* construction. Although the addition of the support structure adds to the overall weight of the configuration, it retains its light and stiff characteristics while reacting the applied loads. The advent of monocoque structure was a breakthrough in the development of aircraft structures. As stated earlier, such structures react large portion of the applied loads in the skin (hence the name "stressed-skin construction").

(2) Wood Construction

Today, wood is not widely used for aircraft construction. Nevertheless, a few models are still being operated. The most prominent is arguably the De Havilland DH-98 Mosquito, a twin-engine, multirole combat aircraft, made famous during World War II (see Figure 5-13). The fuselage of the Mosquito was made from a composite consisting of sheets of balsawood core, bonded to sheets of birch plywood. The wing was a one-piece all-wood construction. It featured two spars made from spruce and plywood, and the skin was a plywood sheet. A cutaway of the Mosquito can be seen in Figure 5-14, showing details of how ribs, spars, bulkheads, and skins were assembled to make this historical airplane.

The largest flying boat ever built, the Hughes H-4 Hercules (aka Spruce-Goose), was built from plywood. It boasted the largest wingspan (97.5 m or 320 ft) of any aircraft in the History of Aviation until April 2019, when the Scaled Composites Model 351 Stratolaunch flew for the first time (117 m or 385 ft). Well known examples of General Aviation aircraft made from wood are the Bellanca Viking (first flight 1967) and various types of aircraft made by Jodel (originated in 1946) and Robin DR400 (first flight in 1972). Additionally, several wooden kit planes for amateur builders are available.

Like everything else, constructing aircraft using wood has its pros and cons. Wood is abundant, inexpensive, comparatively strong, has good impact resistance, and is usually easy to work with. Among disadvantages are inconsistent material properties, crack growth (splitting), low Young's moduli, possibility of rotting and even termite infestation, flammability, water absorbability (moisture variation), reduction in strength if moisture content exceeds fiber-saturation, and sensitivity to grain direction (anisotropy).

Plywood is an excellent structural material for wooden aircraft. It is usually made from an odd number of thin

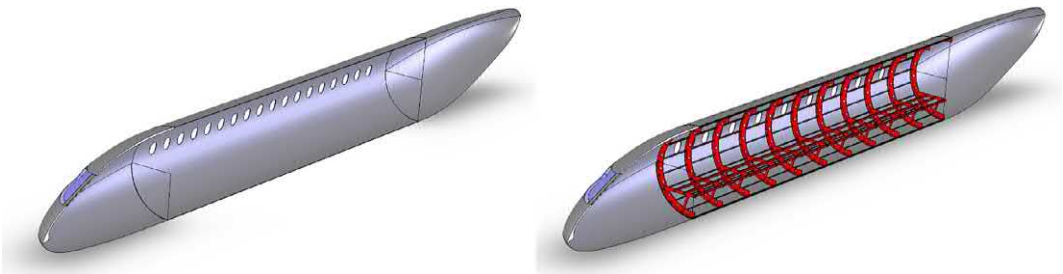


FIGURE 5-12 The difference between a pure *monocoque* (left) and *semimonocoque* (right) fuselage structure. The semimonocoque features internal structure to increase its buckling and crippling resistance.

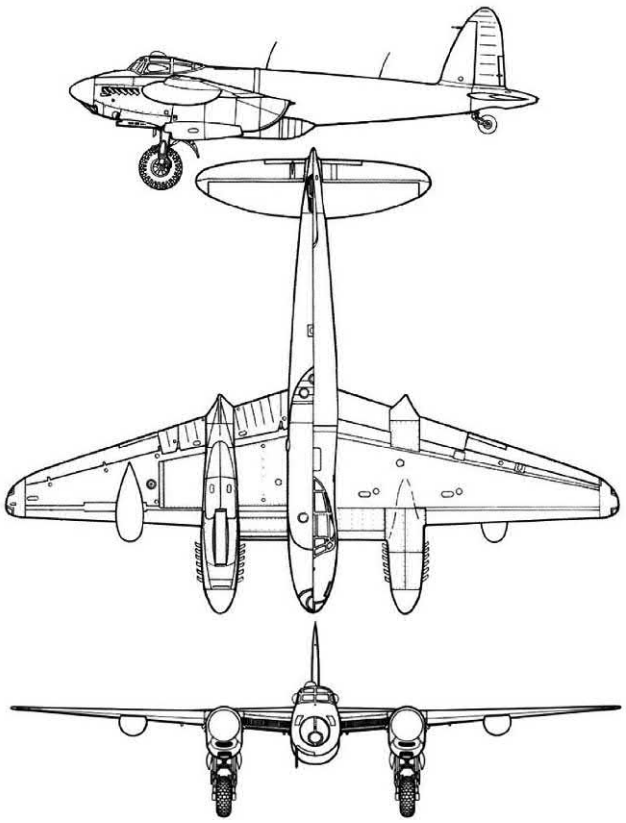


FIGURE 5-13 The De Havilland DH-98 Mosquito is the most sophisticated wooden aircraft in the History of Aviation.

sheets (plies), each oriented at a 90-degree angle with the adjacent ply. The primary advantage are bidirectional material properties, greater resistance to splitting, and much improved dimensional stability with moisture content. Plywood used in aircraft must comply with standards set by MIL-DTL-6070C [28], which requires it to be tested for dimensional discrepancies, glue strength, strength properties, and others. Plywood is typically used for wing skin, fuselage skin, ribs, and frames. Common types of plywood for use in aircraft are Birch, Poplar, Fir, Maple, and Mahogany.

Parts made from wood are primarily joined by two means: bonding and mechanical joints. The use of joining shapes (such as lap-joints, tongue and grooves, tenon and mortise, etc.) is not recommended as these invariably lead to stress concentrations that may lead to failure. Milling or routing parts is acceptable if corners are rounded. Wooden parts require special protection internally and externally. Adhesive bonding is typically conducted using Aerodux-500 Resorcinol Adhesive. It is water- and boil-proof resorcinol/formaldehyde adhesive designed for use in structural wood beams. It requires a hardener to cure, mixed in the ratio 1:1 and cures at temperatures as low as 7°C (45°F).

The reader interested in designing an aircraft from wood is directed toward the documents ANC-18 *Design of Wood Aircraft Structures* [29], a classic text on best practices and structural analysis of wooden structures, and

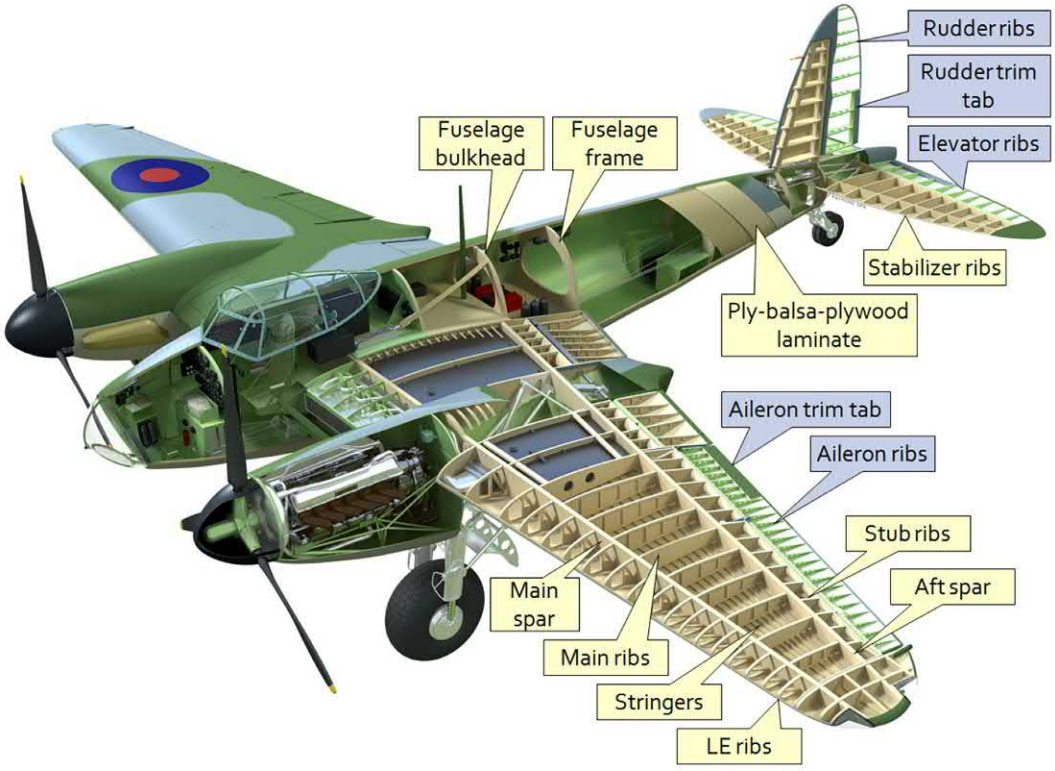


FIGURE 5-14 A cutaway of the De Havilland DH-98 Mosquito, showing important elements of its wooden construction. Dark labels indicate aluminum and light indicate wood. *Courtesy of Raymond Ore, www.raymondore.co.uk.*

NACA R-354 [30], a 34-page report with tips regarding selection and properties of wood.

(3) Steel Truss Covered with Fabric

Many aircraft feature fuselages consisting of space truss structures made from steel tubes welded to form a stiff, strong and light unit (see Figure 5-15). Normally, the truss is covered with fabric and dope (a paint-like compound that seals the fabric). The truss is usually made from straight-section steel tubing (nowadays from 4130 Chromoly) and, often, is rectangular in shape. While robust, such structure is not ideal for low drag fuselages. The German Scheibe SF-25 Motor Falke motor glider features such a fuselage and is an exception from the rule. The method is commonly used for aerobatic and agricultural airplanes, which take a beating operationally and for which the truss structure is a great choice.

(4) Aluminum Construction

Aluminum remains the most common aircraft construction method at the time of this writing. Stressed-skin construction is a very efficient means of producing aircraft, thanks to sheet metal skin riveted to sheet metal frames and bulkheads. The resulting structure is light and stiff, and industry has developed many impressive tools and techniques to assemble aircraft in a short time. As stated earlier, stressed skin reacts shear, torsion, and bending loads. The shell is made less susceptible to buckling and crippling using frames and stringers. Figure 5-16 shows a cutaway of the famous Supermarine Spitfire and reveals the many parts required to make the typical high-performance aluminum aircraft.

(5) Composite Sandwich Construction

Composites and composite sandwich construction have already been discussed. The advent of FAA certified aircraft such as the Cirrus SR20, SR22, Cessna Corvalis, and a series of aircraft produced by Diamond Aircraft reveals the advantage of such constructions. All feature modern tadpole fuselages and NLF airfoils, making them aerodynamically efficient. For instance, the SR22 and Corvalis, both of which have fixed landing gear and 50-in wide fuselages, offer cruising speeds close to that of rival aluminum aircraft, such as the Mooney M20R Ovation, which has a retractable landing gear and narrow fuselage (43.5 in per Ref. [31]).

The most obvious difference between composite and conventional wood or aluminum aircraft is the number of parts. For instance, a composite wing-spar is typically a one-piece component, tip-to-tip. Aluminum spar, in contrast, consists of multiple parts; spar caps, shear-webs, stiffeners, assembled using rivets. Composite wings also contain fewer ribs because the skins are stiffened. Also, they are void of stringers. The typical composite airplane is bonded together using adhesive, a commonality with wooden aircraft. From a certain point of view, assembling a modern composite (certified) aircraft is not unlike putting together a (large) plastic model. Shells of components are bonded (glued) together. Of course, the analogy ends there, but the process requires far fewer parts than aluminum aircraft. Regardless, composite airframe tends to be more expensive to manufacture and may even be a tad heavier than comparable aluminum structure.

5.3.2 Fundamental Layout of the Wing Structure

The wing is the most important structure of the airplane. It generates the largest aerodynamic load and often features complex mechanical systems that are subjected to substantial loads. In general, we want the wing to feature a thick airfoil. Such a wing offers (1) lighter structure and (2) larger volume for fuel and systems (e.g., landing gear and control system). To see why a thicker wing results in lighter structure, consider Figure 5-17. It shows an idealized spar that consists of a thin shear-web and circular spar caps of diameter D that are separated by distance $2h$. Assume this spar

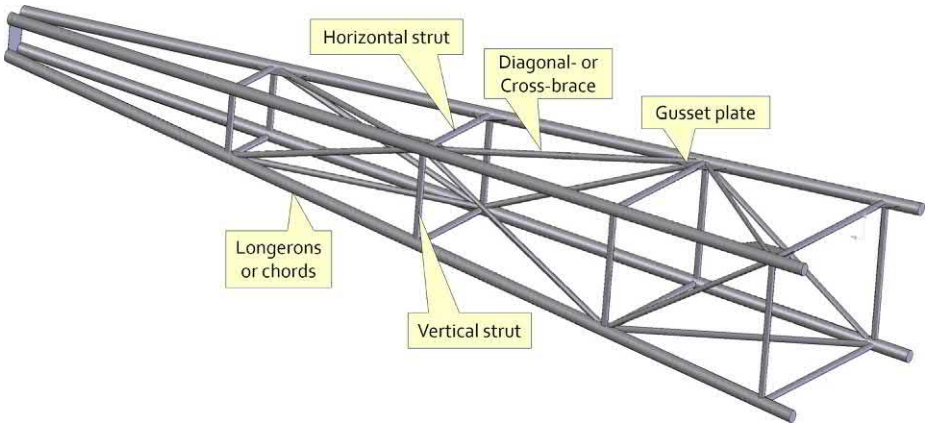


FIGURE 5-15 Example truss structure intended for an empennage of an airplane.

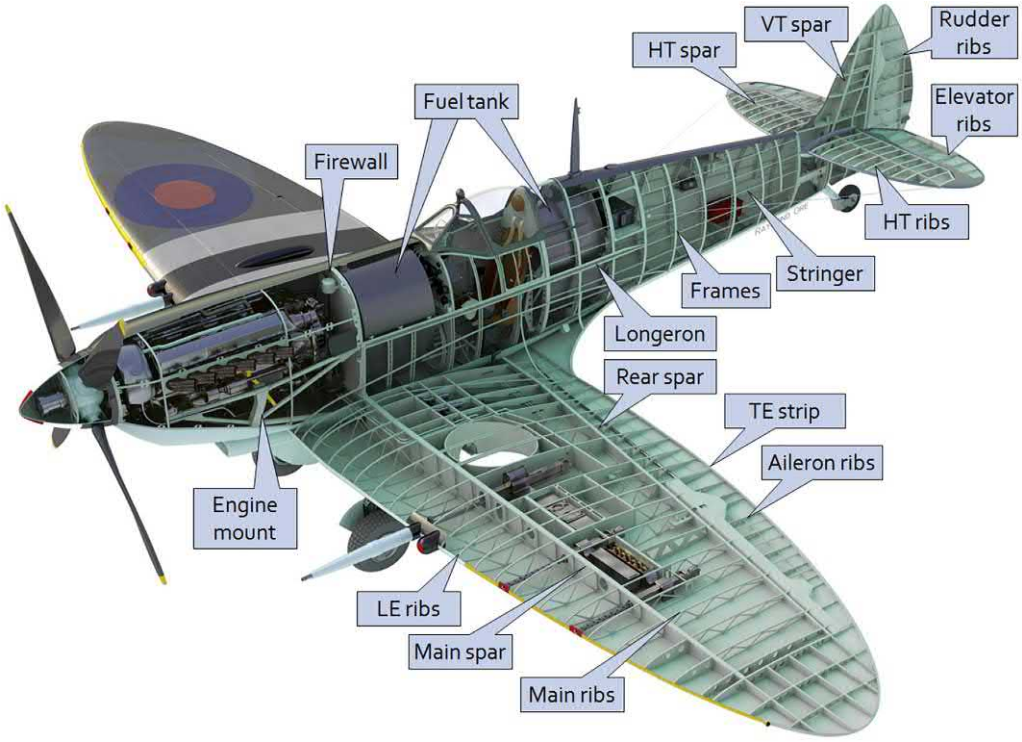


FIGURE 5-16 A cutaway of the Supermarine Spitfire, showing important elements of its aluminum construction. *Courtesy of Raymond Ore, www.raymondore.co.uk.*

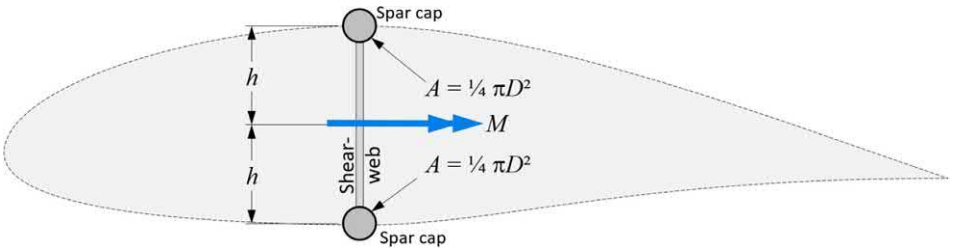


FIGURE 5-17 Idealized wing spar consisting of shear-web and spar caps.

is made from some material with tensile yield strength σ_y and is subjected to bending moment M. Using the expression for normal stress in a beam in bending, we can swiftly derive an expression to estimate the required spar cap diameter:

$$\sigma_y = \frac{Mh}{I} \approx \frac{Mh}{2Ah^2} = \frac{Mh}{2\left(\frac{1}{4}\pi D^2\right)h^2} = \frac{2M}{\pi D^2 h} \quad \Rightarrow \quad D = \sqrt{\frac{2M}{\pi h \sigma_y}} \tag{5-1}$$

Using this expression, we can investigate the effect of wing thickness on the spar cap diameter, assuming constant σ_y and M. Assume we are evaluating two wings; call them Wing 1 and 2, that are identical, except in thickness. Wing 1 has a spar-height of $2h_1$ and a spar cap diameter of D_1. It follows that if the spar-height of Wing 2 is double that of Wing 1 (i.e., $4h_1$) the required spar cap diameter drops to $D_2 \approx 0.707\ D_1$. The resulting mass will drop by one-half, as the spar cap volume depends on the square of the diameter. Furthermore, more mass reduction can be had by the reduction of shear flow in the skin and shear-webs because the wing torsion is reacted by a larger area. Of course, chances are the thicker wing will generate more aerodynamic drag, placing an upper limit on practical thickness. Regardless, we can establish a generalized engineering approach: *Select the thickest wing that does not compromise performance targets*.

The wing structure is designed to react shear forces and moments that result from the aerodynamic force. This is usually reacted as three mutually orthogonal forces (lift, drag, and a compressive inboard force if the wing has dihedral), and three mutually orthogonal moments (bending moment, drag moment, and wing

torsion). To react these loads, the wing features a number of load-carrying members that have to be carefully assembled so that that the wing will be (1) geometrically symmetrical (i.e., left- and right-wing halves are identical mirror image of each other) and (2) as close to the intended geometry as possible. A typical wing structure is shown in Figure 5-18. It consists of the following parts (note the labeling of A through N for easier identification).

The ***main spar*** **(A)** is the primary load path in the wing and is designed to react wing bending and shear loads. The idealized spar consists of a thin sheet of vertical structure called the ***main spar shear-web*** **(B)**. Two thicker members, called the ***main spar caps*** **(C)** are attached to the shear-web; one along the bottom and the other along the top edge. The shear load is the sum of the components of wing lift and drag normal to the wing plane. It is reacted by the main wing-spar and aft shear-web. This load also generates bending moment, which is reacted by the spar caps. The shear and moment are zero at the wingtip and reach a maximum at the root. The ideal wing spar would allow the thickness to change continuously from tip to root. However, this is difficult in practice, unless the spar is machined. Spars made from aluminum alloy, are designed with stepwise reduction in shear-web thickness from root to tip. This includes an increasing frequency of lightening holes and their radii.

Several typical main spar cross-sections are shown in Figure 5-19. Some of those feature dissimilar spar cap thicknesses on the top and bottom of the spar. This is indicative of the careful nature of aircraft structural analysis—material is used only where necessary. Aircraft are designed to react larger forces up than down. For this reason, the upper spar cap sees higher compressive loads than the lower cap and is made thicker.

The ***aft shear-web*** **(D)** is also a primary load path, although it reacts less lift than the front spar. The actual amount depends on the chordwise aerodynamic load distribution. Around 60%–70% is reacted by the main spar and 30%–40% by the aft shear-web. The aft shear-web also reacts the wing torsion generated by the airfoil's pitching moments and wing-sweep. It transfers wing torsion to the ribs and the aft attachment bracket, where it is reacted in shear. It also reacts the fore-aft chordwise force that results from the projection of the lift and drag on the chord plane. This force is peculiar in that, at high airspeed, it is mostly drag, which places the aft wing-attachment in compression. At low airspeed and high AOA, the projection of the wing lift onto the chord-plane becomes larger than that of the drag: It would force the wingtips forward were it not for the aft attachment.

The aft shear-web is called an ***aft spar*** if it reacts bending moments (like the main spar). This is rare in small aircraft. As a rule of thumb; an aft attachment with a single fastener hole is a simply supported joint and only resists shear; it is a shear-web. If it has two fastener holes it reacts bending moments in addition to shear; it is an aft spar. In this case, if it is designed to react the entire lift force, the structure can be called *fail-safe*. This means extra

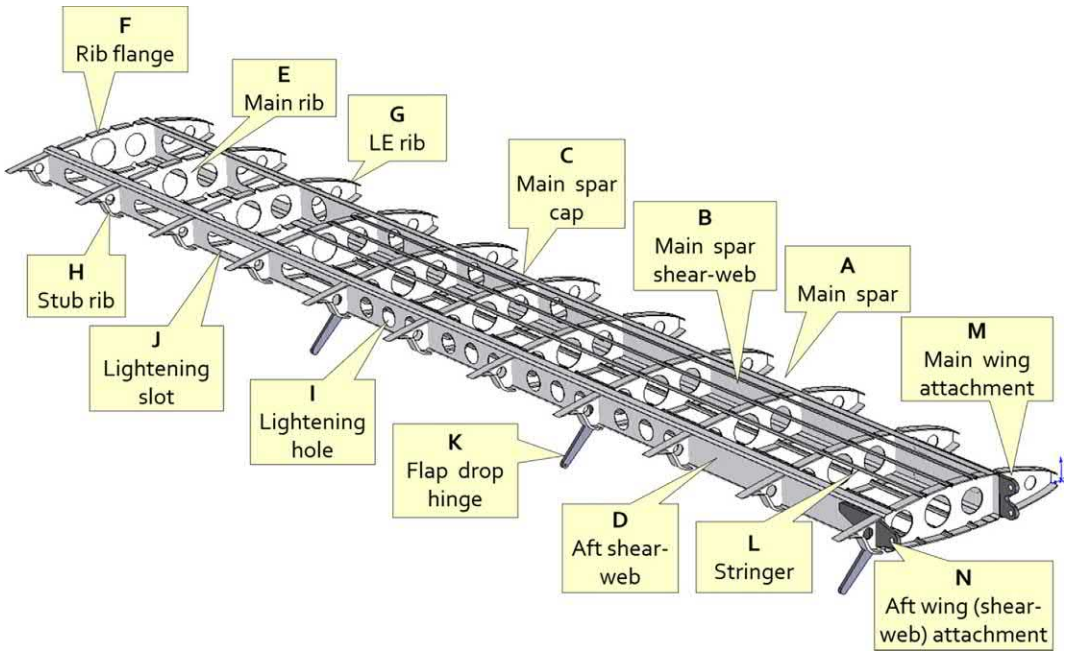


FIGURE 5-18 A simple schematic of a typical structural layout of a wing for General Aviation aircraft.

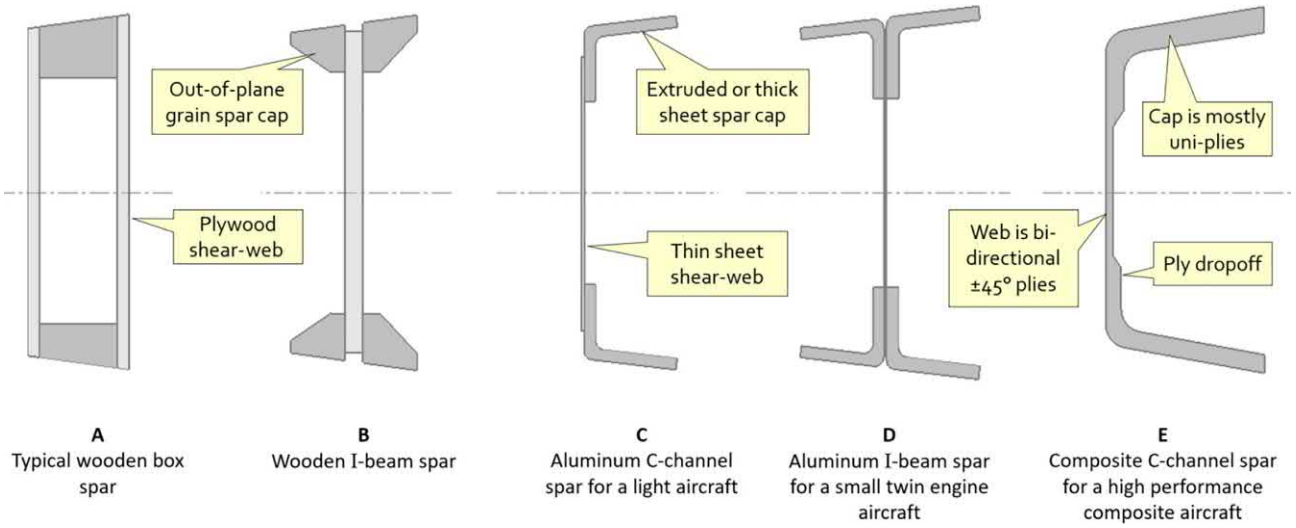


FIGURE 5-19 A schematic of typical main spar cross sections for General Aviation aircraft.

safety in case of structural failure of the main spar. This design philosophy is required in passenger aircraft per §25.571 *Damage—tolerance and fatigue evaluation of structure* (also see Ref. [32]). It is because statically indeterminate structure is inherently safer after being subjected to damage. The Rockwell 114 and 115 aircraft are examples of light 14 CFR Part 23 aircraft that feature a fail-safe wing structure.

The ***main ribs*** **(E)** are primary structural members that extend between the main spar and aft shear-web, tying them together. As such, the ribs serve several purposes [8, p. 278]. First, they stabilize the wing skin and prevent it from buckling while reacting wing torsion. This helps maintain the intended aerodynamic shape and the skin's ability to transfer torsional loads. Second, the ribs shorten the effective column length of the stringers (see later), making them more resistant to column buckling. Third, they transfer wing torsion to the spars and eventually to the wing attachments. Fourth, they react compression loads due to wing bending. Fifth, they redistribute concentrated loads, such as those due to the landing gear, flap deployment, and engine pylons. Sixth, they react diagonal tension loads from the skin if subjected to skin wrinkling.

Each rib is formed with a ***rib flange*** **(F)**, but these are used to rivet (aluminum wing) or bond (composite wing) the rib to the skins and spars, forming a solid structure. The rib-spacing is a task accomplished during the detail design phase. Ribs must be spaced close enough to prevent skin buckling and far enough to minimize weight.

An important question often asked during the layout of swept back wings is whether the ribs should be mounted normal to the main spar or parallel to the direction of flight (see Figure 5-20). At first, it would seem the

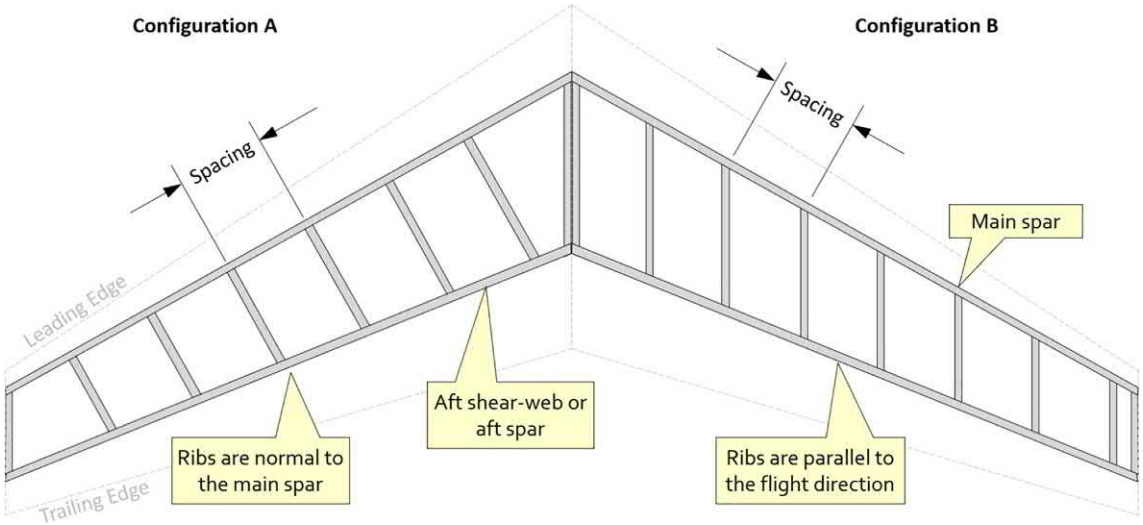


FIGURE 5-20 A schematic of two rib layouts for a swept back wing.

latter (Configuration B) is more reasonable because the rows of rivets along the skin (assuming aluminum construction) cause less disruption to the boundary layer. However, that argument is deflated by noting that the rows of spars and stringers (discussed later) extending spanwise from root to tip are also riveted to the skin—disrupting the boundary layer.

An important drawback of Configuration B is that, since the rib-spacing is the same as that of Configuration A, the rib-length is greater; the arrangement will be heavier. Another complication is that it is harder to install the ribs for Configuration B because they are not at a 90-degree angle with respect to the spar. Conversely, the ribs of Configuration A are normal to the main spar (although their aft parts are not) and this offers production advantages.

In practice, both configurations are used. One reason is that Configuration A is not practical next to the fuselage—mounting the ribs in parallel is simpler. Since the rib orientation is not usually changed immediately from B to A, it follows that several parallel ribs are installed first. Furthermore, it might be beneficial to use Configuration B in an airplane with wing mounted engines.

An inspection of aircraft with swept back wings reveals that most commercial jetliners feature all ribs that are normal to the main spar (Configuration A). However, there are many exceptions where a combination of the two approaches is used. For instance, all the inboard ribs of the Bombardier CRJ 1000 are parallel to the flight direction, while outside the flaps they are normal to the main spar. The Gulfstream G650 has the first six ribs parallel to the flight direction and the remaining normal to the main spar.

Another important question addresses how the rib-spacing is selected. This results from a labor-intensive structural analysis that is beyond the scope of this book—only an elementary explanation of the process is given. The procedure begins by assuming a specific rib spacing. Then, a structural analysis that determines the required material thicknesses is performed. This allows the weight of the ribs and skin to be estimated. The process is repeated for a few candidate rib-spacings. Eventually, a graph like the one shown in Figure 5-21 is created. It shows the weight of the skin, ribs, and their combination as a function of rib spacing. If a minimum exists, as shown in the figure, it is the selected for use in the wing design.

Two additional ribs of importance are mounted to the wing. The ***leading-edge rib*** **(G)** is vital as the forward shape of the airfoil. It transfers large pressure loads, generated by the leading edge at high AOAs, to the main spar. At high AOAs, most of the lift is generated by the forward part of the wing, calling for stout structure in this region. The other rib type of interest is the so-called ***stub rib*** **(H)**, which is attached to the aft shear-web. It maintains the aft shape of the wing airfoil, while allowing control cables and pulleys to be threaded through various openings. They also support various control system brackets and components. Aileron hinge brackets are typically attached to stub ribs, which transfer the air load to the aft shear-web.

In order to keep the weight of the wing structure to a minimum, ***lightening holes*** **(I)** and ***lightening slots*** **(J)** are cut where possible. Lightening holes and slots are more common in aluminum and wooden structures than in composites. Instead, composite spars allow for more uniform ply drop-off in the spanwise direction, rendering such holes unnecessary. Aluminum spars for light airplanes often resort to lightening slots at the wing outboard region, where the shear and torsion have reduced significantly. Examples of this are found in many Cessna propeller aircraft.

The deployment of flaps inflicts large torsion loads to the wing structure. This load is transferred directly to the

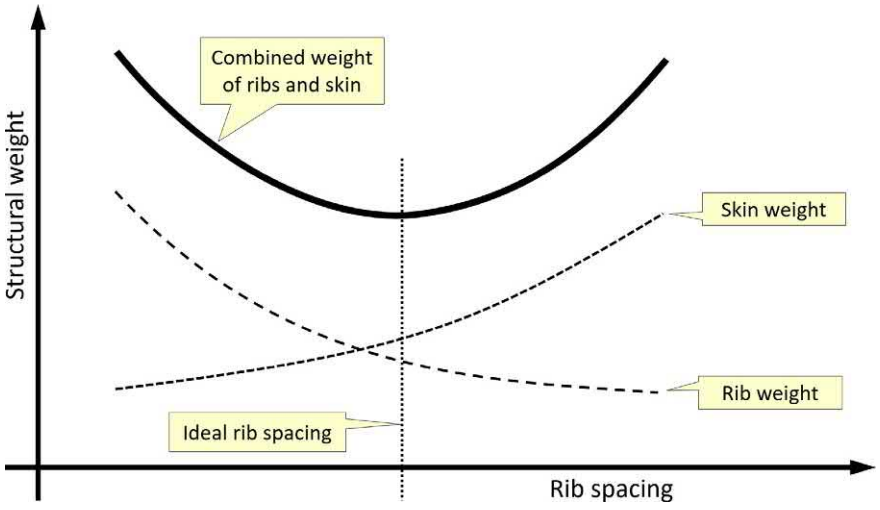


FIGURE 5-21 A schematic demonstrating the selection of rib-spacing. *Based on M.C.-Y. Niu, Airframe Structural Design, Conmilit Press, 1988.*

aft shear-web and main spar through the flap hinges, of which the ***dropped flap hinge*** **(K)** is an example. Such hinges are usually mounted right to the aft shear-web. This requires stout main ribs forward of them to provide load path to the main spar.

As discussed before, ***stringers*** **(L)** are long columns of comparatively small cross-section that stiffen the skins and prevent buckling under load. In small aircraft, the stringers are usually made from a folded strip of aluminum sheet, whereas larger aircraft feature extruded stringers. And even larger (and more expensive) aircraft often have machined integral stringers such that the stringers and skin form a single unit. This produces the lightest possible skin panel because the machining allows the stringers to be tapered smoothly along the span, as well as around holes and ribs [8, p. 258].

The ***main wing attachment*** **(M)** bracket is a primary load path and the most important hardpoint in the entire airplane. There are two common attachments types found in aircraft: *fixed* and *rotary*. The latter are primarily used for military aircraft with swiveling (F-14, F-111, Tornado, etc.) or folding wings (A-7, F-4, F-18, etc.) and are omitted from this text. A good discussion is given in Ref. [8]. Per Figure 5-18, the entire bending moment and most of the shear force is transferred to the fuselage by the main spar. This highlights that the main wing attachment must provide ample bearing area for reacting wing loads. This hardpoint reacts substantial loads, even during normal flight, rendering it very susceptible to fatigue. Not only should the wing attachments be designed with ample safety factors, it should also be accessible for inspection. Other concerns include the dissimilarity of metals. For instance, using steel fasteners with aluminum brackets or sheets risks galvanic corrosion and is a recipe for disaster unless proper precautions are in place [33].

Figure 5-22 shows several methods to mount the main spar to the fuselage of the fixed type. The detailed appearance of the layouts shown varies in practice and the figure should be regarded more from a stylistic perspective than a precise one. Configurations A, B, and C are used for high wing aircraft. A and B are used in some commuter aircraft, e.g., Fokker F-27. The wing bending moments are fully reacted by the wing and the fuselage is effectively hanging below it, using pinned joints. Thus the fuselage does not have to be reinforced to react the wing bending moments, although it must react internal moments due to the difference in the reaction forces between the two attachment points.

Configuration C is used by many Cessna aircraft that feature wing struts. The hard points on each wing form a structurally rigid triangle, although it is not fail-safe. The configuration, too, has pinned supports so bending moments put substantial compression load along a line going through the two hardpoints. Configuration D is used in many airplanes, e.g., Beech Bonanza and Eclipse 500. Tension fasteners are used in the Bonanza. This configuration uses a so-called *spar-carry through* to react the wing loads. The carry-through is by far the stiffest single structural member in the aircraft. It picks up the wing bending loads, bypassing the fuselage to which it is attached.

Configuration E is mostly used on mid wing fighter aircraft (e.g., F-104, F-16). The load carrying frame requires sophisticated and costly machining from solid

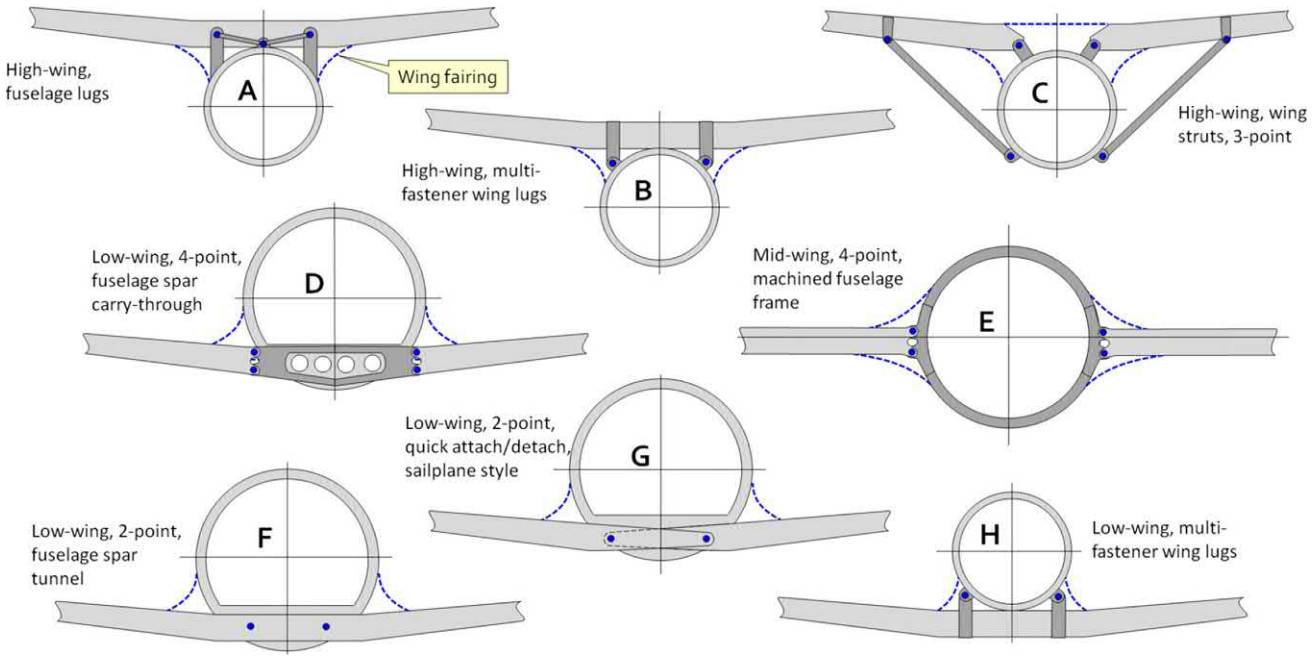


FIGURE 5-22 A schematic of common wing attachment methods.

ingot of alloy, making it very expensive to fabricate. Several such frames are required for the typical multispar fighter wing. Such aircraft feature the engine in the cavity between the wings, which is the reason for the selected configuration. The orientation of the fastener in the wing attachment is often normal to, rather than parallel to the fuselage, as shown here. Configuration F is used on the Cirrus SR20 and SR22 aircraft.

Configuration G is used in aircraft that must be quickly assembled and de-assembled for transportation purposes. Such airplanes include sailplanes and some homebuilt aircraft. Finally, Configuration H is used in many business jets, where the fuselage sits on top of the wing. Such airplanes feature much greater structural complexity than depicted and their attachments are statically indeterminate (fail-safe). The attachments transfer loads in a variety of ways. Some react bending moments as a force couple; others do not react them at all.

To give insight into the magnitude of wing loads consider Figure 5-23, which shows a simple cantilevered beam structure for a hypothetical aircraft. Assume it weighs 2000 lb_f (W_0), has a 40 ft wingspan (b), and is subject to a limit load of 3.8 g (n). When the airplane reacts this load symmetrically (both wing-halves generate equal load), each attachment point reacts a shear force of 3807 lb_f ($=½ \times 3.8 \times W_0$). However, when reacting asymmetric load per 14 CFR §23.349(a)(2) ("old" Part 23), in which one wing-halve reacts the full half-span load and the other 75%, things look a bit different. The attachment point on the fully loaded side reacts 5520 lb_f ($=2.76 \times W_0$). This is an unintuitive result for those seeing it for the first time. The purpose of the regulatory paragraph is to ensure this fact is not overlooked during the structural design of the aircraft.

The ***aft wing attachment*** **(N)** is a primary load path and the second most important hardpoint in the airplane. For the wing layout shown in Figure 5-18, it transfers a part of the shear force and reacts the wing torsion.

5.3.3 Fundamental Layout of the Horizontal and Vertical Tail Structures

The Horizontal Tail (HT) and Vertical Tail (VT) are aptly described as simplified versions of the wing. In comparison, the loads of the HT and VT are modest. In small aircraft, the structure often consists of a single spar to which a few ribs are riveted (or bonded), and then covered with skin. Sometimes, it suffices to stiffen the skin using corrugations. Such solutions are used by several manufacturers, including Beech, Cessna, and Piper.

The main spar of the HT and VT for light aircraft is usually placed at 60%–70% of the chord. This is driven by convenience as it allows the elevator and rudder hinges to be mounted directly to the spar. Selected Piper series of single and twin-engine aircraft feature simple all-movable stabilators consisting of two-spar-corrugated-skin construction, designed with the main spar along the hinge line and an auxiliary spar (stiffener) close to the trailing edge to support the installation of an antiservo tab.

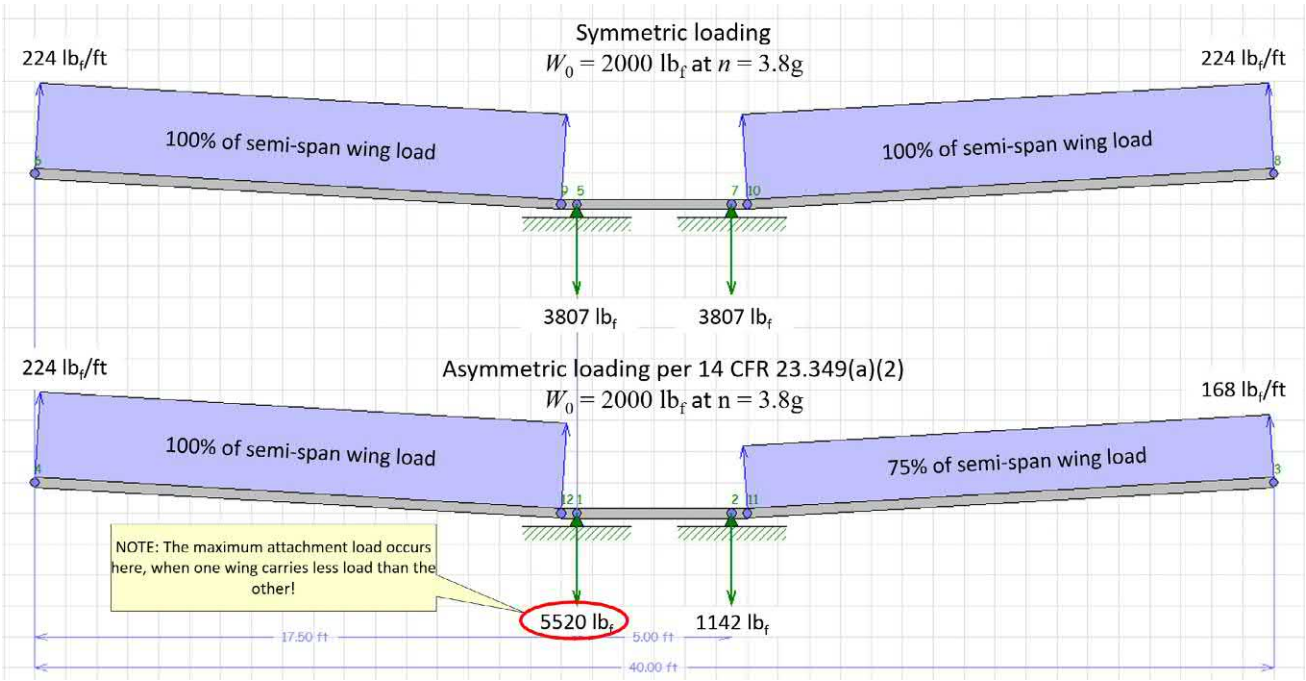


FIGURE 5-23 Reaction loads due to the aerodynamic lift generated by the left and right wing-halves of a 2000 lb_f hypothetical aircraft (erroneously assuming a uniform distribution of lift).

Larger airplanes feature a single main spar and a smaller auxiliary spar. Heavy aircraft have an HT and VT whose load paths are structurally superior to the wings of small aircraft. Such surfaces have two spars and statically indeterminate fail-safe structure. The incidence of the stabilizer of heavy aircraft is designed to be adjusted in flight, providing a means to trim the airplane over a wide CG range. The incidence of the stabilizer is typically changed using a powerful jackscrew drive. The stabilizer of the Boeing 727 commercial jetliner is an example (see Figure 5-24). The picture reveals many of the complexities inherent in any advanced aircraft; redundant rudders operated using independent hydraulic systems, antibalance tabs that deflect in the same direction as the rudders to increase rudder authority, elevator control tabs, vortex generators, and so on [34].

(1) Fabrication and Installation of Control Surfaces

The HT is usually attached to the fuselage using specific hardpoints, which are analogous to wing hardpoints, albeit simpler. The HT is bonded to a wide flange formed in the fuselage of many composite aircraft, while the VT is often integral to the fuselage. In aluminum aircraft, the VT spar is sometimes integral to the aft most bulkhead. This arrangement provides a load path for the stabilizing surfaces and means to anchor the control system hardware.

The stabilizing surfaces typically feature symmetric airfoils, such as NACA 0008 through 0012. These are low-drag airfoils that provide volume to accommodate control system cables, pushrods, pulleys, bellcranks, and trim motors. This thickness also results in a stiff structure that is free of flutter within the operating envelope of the aircraft. However, selecting a symmetric airfoil is not a rule. Cambered airfoils are used for HT and VT in several aircraft. Table 9-2 in Ref. [35] presents an array of examples for HT. Some propeller aircraft use either a cambered airfoil or a symmetrical airfoil at an angle of incidence with respect to the fuselage to reduce propeller effects (see Section 14.2, *Propeller Effects*). Many aircraft feature symmetric airfoils such as NACA 63-008 through NACA 63-012, whose maximum thickness is farther aft than that of the double-0 series, allowing the stabilizing surfaces to sustain NLF more extensively. When possible, the designer of efficient aircraft should consider such airfoils for stabilizing surfaces.

It is important to bring up two issues that cause difficulties in the production of control surfaces. The first is the selection of airfoils with narrow trailing edges. Often, this is associated with NLF airfoils that feature a cusp. This calls for ribs so small they cannot be installed without being shortened and this may lead to a partially unsupported trailing edge that is susceptible to flexing under loads. If built from aluminum, this may call for costly manufacturing methods for mass-produced aircraft. One solution is to ignore the cusp and replace it with a flat section (see Figure 5-25). Of course, the resulting airfoil is not the one the aerodynamicist intended. Awareness of such problems is important. The designer should avoid solutions that are impractical from a manufacturing standpoint and ensure the design analysis work represents production airfoils rather than the hard-to-fabricate theoretical airfoils.

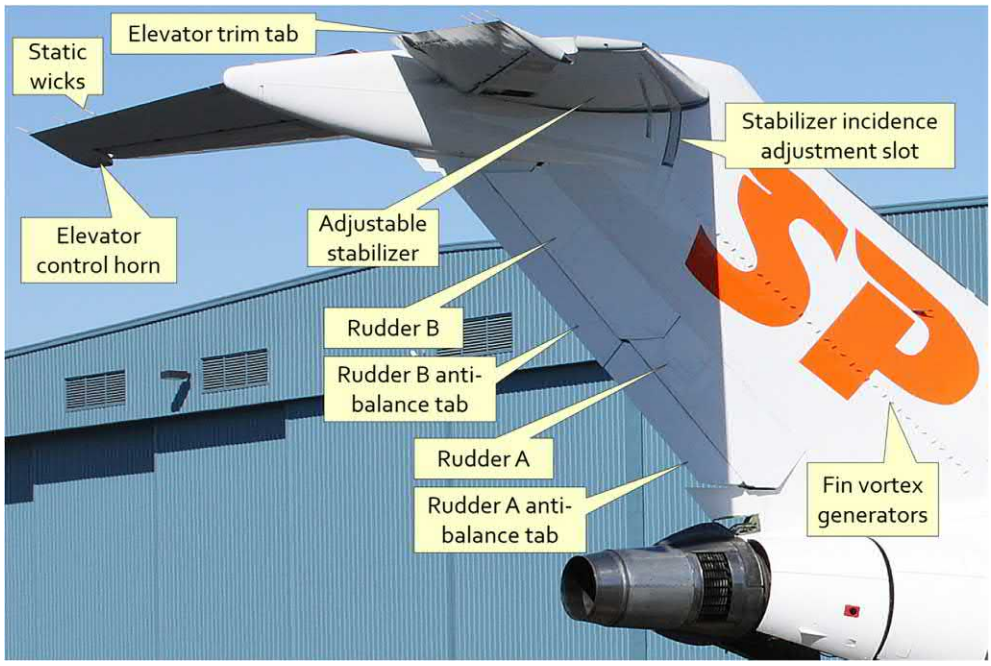


FIGURE 5-24 The T-tail assembly of a Boeing 727 commercial jetliner. *Photo by Phil Rademacher.*

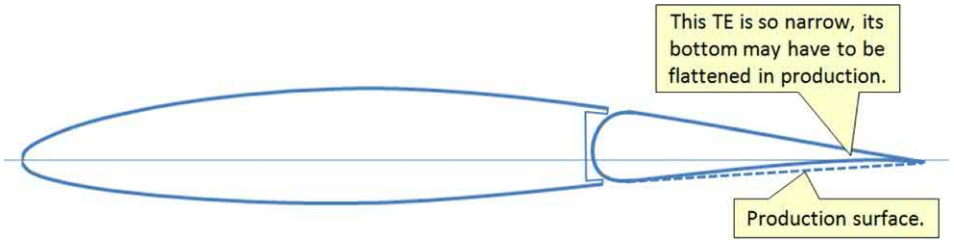


FIGURE 5-25 The manufacture of thin trailing edges is often solved by ignoring it and replacing it with a flat, rather than curved surface. Does this change invalidate the design analysis work?

The second issue also has to do with cusped NLF airfoils. The high pressure generated by the lower surface of the cusp results in hinge moments that deflect the surface trailing edge up at higher AOAs, for instance during climb (see Figure 5-26). This invalidates the drag coefficient, modifies the airfoil, and reduces the performance of the airfoil. The designer should insist that the engineers designing the flight control system are aware of such a detrimental tendency.

(2) Unconventional Tails: T-Tail, V-Tail, and H-Tail

Assuming equal size, a T-tail is subjected to higher asymmetric loads than a conventional tail. In yaw, a high-pressure region is generated on the windward side of the VT and low pressure on the leeward side. This loads the HT asymmetrically and the resulting torsion increases that generated by the VT alone. The structural reinforcement required to support this load renders both the fuselage and the VT heavier than a conventional tail. Aeroelastically, the mass of the HT at the tip of the VT reduces its natural frequency, lowering its flutter speed. The remedy is to stiffen the VT, which again adds weight to the airframe.

Similar concerns can be raised about the V-tail. Large surfaces are required for static and dynamic stability in V-tail aircraft. The rudder functionality requires the two ruddervators to deflect opposite to each other, like ailerons. The deflection generates substantial forces on the two tail surfaces—one directed up and the other down, developing a large torsion in the fuselage. Awareness of this effect is important. The designer should provide enough cross-sectional area of the fuselage in this region to help bring down the resulting shear flow.

The H-tail brings similar complications to the empennage loads as do the T- and V-tails. Additionally, as in the case of the T-tail, the two fins placed at the tip of the HT can be considered point masses at the end of a cantilevered beam, which brings down its natural frequency and, with it, the flutter speed. The designer must select thick enough airfoils to increase the stiffness of the HT.

The reader is directed to Section 11.3, *On the Pros and Cons of Tail Configurations*, for additional information about these and other tail configurations.

5.3.4 Fundamental Layout of the Fuselage Structure

(1) Fuselage Structural Assembly—Conventional Aluminum Construction

A conventional aluminum semimonocoque fuselage structure is shown in Figure 5-27. The figure illustrates an important feature of such structure: All cut-outs feature generously rounded corners or are elliptical or circular in some airplanes. This reduces stress concentrations, increasing the durability (and safety) of the structure. Figure 5-28 shows how this structure is assembled. It typically consists of numerous hoop-frames joined with stringers. Floor beams and frames are riveted, or metal bonded to the hoop-frames. Once the aluminum sheets comprising the fuselage skin are riveted to the frames and stringers, a very light and stiff structure results.

(2) Fuselage Structural Assembly—Composite Construction

A semimonocoque fuselage made from composites applies a different philosophy. Some companies wind

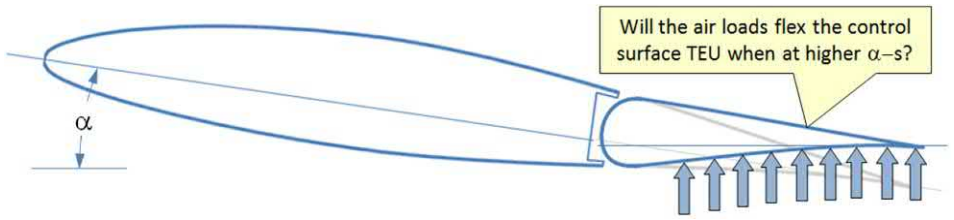


FIGURE 5-26 Cusped trailing edges may deflect at higher AOAs, unless the control system is very stiff. The actual aircraft will likely suffer from a reduced climb performance and reduced lift at stall.

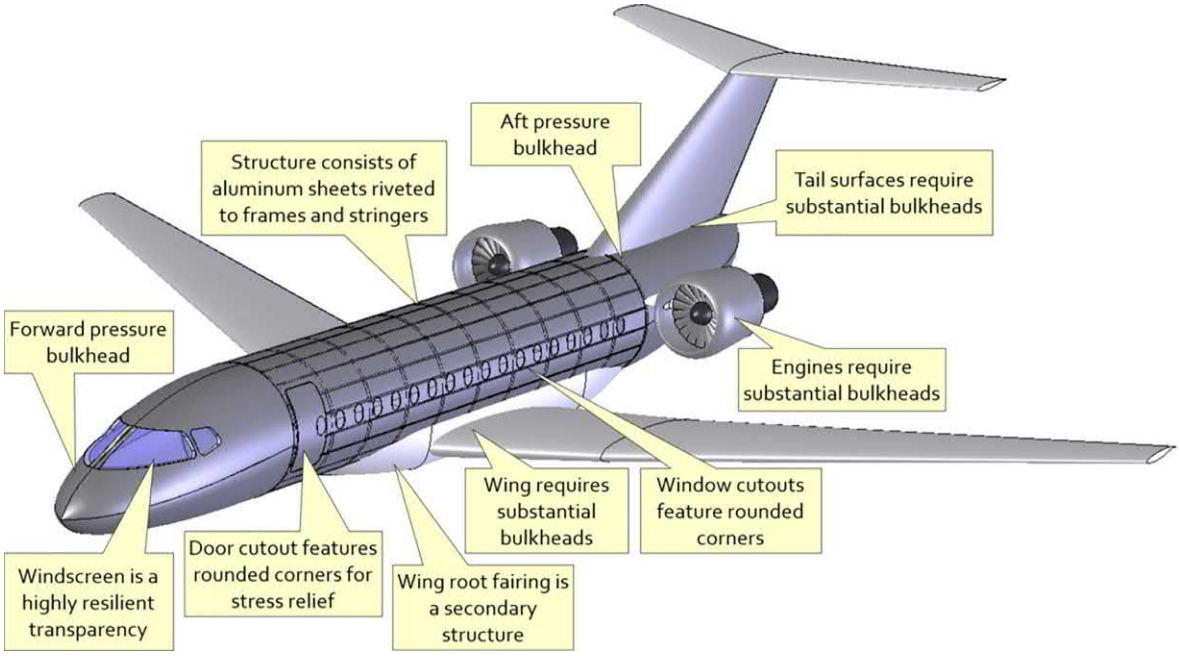


FIGURE 5-27 Typical fuselage for a passenger transportation aircraft consists of aluminum sheets riveted to an underlying rigid structure.

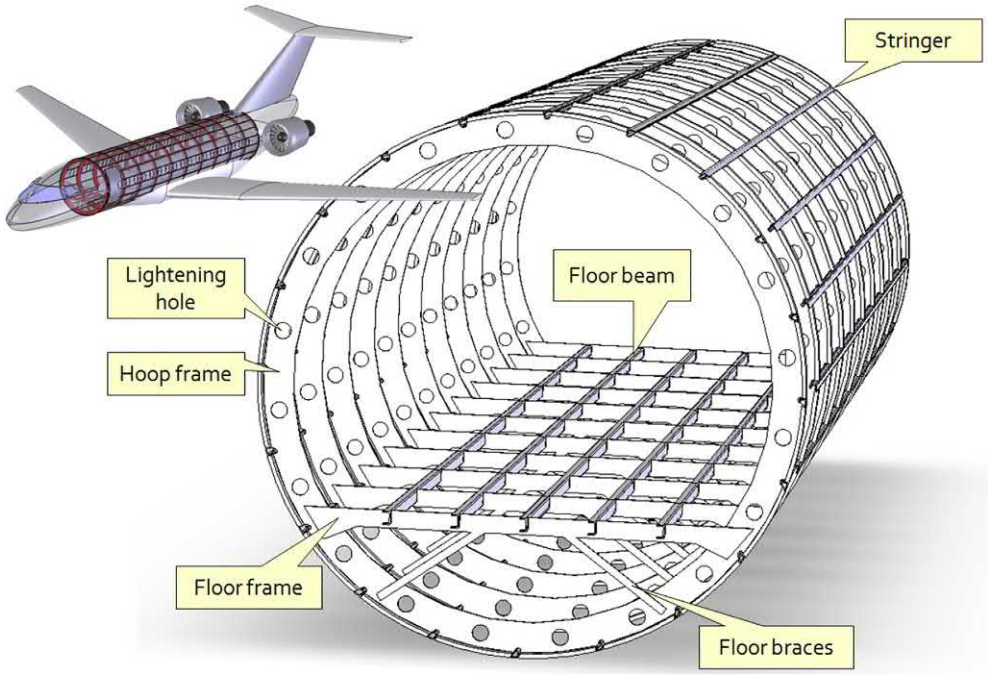


FIGURE 5-28 The underlying fuselage structure consists of hoop frames, stringers, floor frames, and floor beams (nose and tail structure is omitted).

the fuselage on a mandrel while others make them in molds in two halves. The former is beyond the scope of this book. In the latter, the skin is stiffened using a composite sandwich of the kind described earlier. Thus, the total number of frames can be reduced. Such fuselages are typically made by bonding the left and right halves together with the internal frames and bulkheads prebonded. The fuselages have joggles to which the adhesive is applied. It is easier said than done to properly join the two skin-halves together.

A common difficulty in the assembly of semimonocoque composite fuselages is to control the thickness of the

bonds (adhesive). Certified composite aircraft must demonstrate the repeatability of the bondline strengths. This is done by the manufacturer, which assesses a range of bondline thicknesses expected to be seen during production (e.g., from 0.040″ to 0.125″). Then, repeated strength tests of specimens using those thicknesses are performed to assess the bondline strength. During production, the bondline thickness of all bonds is inspected and if outside these limits, a repair in the form of a wet layup is performed.

(3) Special Considerations: Pressurization

Tens of thousands of passenger and business aircraft operate every day at altitudes ranging from 25,000 to 51,000 ft. At those altitudes, exposure to the outside atmosphere can lead to certain death. Aircraft operating at such altitudes must provide oxygen to the occupants. This is accomplished by pressurizing the fuselage, so it maintains cabin pressure higher than that of the ambient atmosphere. People begin to suffer from oxygen deficiency at altitudes as high as 14,000 ft. The individual capability varies, with some individuals capable of climbing mountains as high[4] as 28,600 ft, and as low as 6000–8000 ft for heavy smokers and people with heart problems.

Pressurization inflicts serious design, manufacturing, maintenance, and operational limitations on the aircraft. A study of these requirements exposes several challenges, ranging from fuselage deformation to system and equipment installation.

Pressurization was first successfully introduced to passenger flight on the Boeing 307 Stratoliner in 1938. It was accomplished using electric compressor, but this was later replaced by extracting bleed air from its turbosuperchargers. [36]. This technology advanced with the advent of the jet airliner. The Boeing 707 and DC-8, which were introduced to passenger service in the late 1950s, used turbo compressors, driven by engine bleed, to pressurize the cabins. Later airliners use bleed taken directly from the engine compressor for this purpose. A notable exception is the Boeing 787, which uses electric compressors [37].

Requirements from 14 CFR Part 121 to supply oxygen to the occupants when operating an aircraft are stipulated in the following paragraphs:

121.327—*Supplemental oxygen: Reciprocating engine powered airplanes.*
121.329—*Supplemental oxygen for sustenance: Turbine engine powered airplanes.*
121.331—*Supplemental oxygen requirements for pressurized cabin airplanes: Reciprocating engine powered airplanes.*
121.333—*Supplemental oxygen for emergency descent and for first aid; turbine engine powered airplanes with pressurized cabins.*

However, it is paragraphs 14 CFR §23.841 (in the old Part 23) and 14 CFR §25.841, *Pressurized cabins* that stipulate what capability the airframe must possess in order to sustain cabin pressure in case of a system failure. Design guidelines are also given in SAE ARP 1270, *Aircraft Cabin Pressurization Control Criteria* [38].

Figure 5-29 shows a cabin pressurization schedule for a typical commercial jetliner. The pressurizing begins immediately during climb. As it reaches the intended cruise altitude (here 39,000 ft) the pressure difference between the atmosphere at that altitude and the cabin pressure is about 8 psi (atmospheric pressure at S-L is 14.7 psi), but this is equivalent to an atmospheric pressure at 8000 ft, enough for all except the weakest of us to survive.

From a structural standpoint, the most efficient pressure vessel reacts *out-of-plane* stresses as tensile stresses [24, p. A16.1]. The spherical pressure vessel is the most efficient one (see Figure 5-30). However, when it comes to transporting passengers while providing acceptable performance and handling, this geometry is not practical. The next best shape is a cylinder, which is a sphere that has been split along a meridional and the two halves attached to a cylinder (again see Figure 5-30). This is the ideal shape for a pressurized aircraft and explains why this form prevails in the aviation industry.

As shown in Figure 5-30, the sphere reacts the out-of-plane pressure load as hoop stresses only, whereas the cylinder reacts it as hoop and tangential stresses. When used for fuselages, this requires especially reinforced structure to be placed at either end of the fuselage. This structure is called a *pressure bulkhead*, and it must react a substantial pressure force. The layperson is often oblivious to the forces the fuselage must support and which are solely attributed to the pressure differential. For instance, the typical passenger door in a commercial aircraft is 42×72 in (Type A door). When exposed to an 8-psi pressure differential (see Figure 5-29) the total out-of-plane force acting on it amounts to $42 \times 72 \times 8 = 24{,}192$ lb_f.

This number depicts the robustness of the reinforcement required to hold the doors in place. A common method is to use doors that are shaped like a plug (see

[4] For instance, in 1979, Reinhold Messner (1944–) and Michael Dacher (1933–94) ascended K2 without supplemental oxygen. This feat is well out of the norm of human capability and took immense training and preparation.

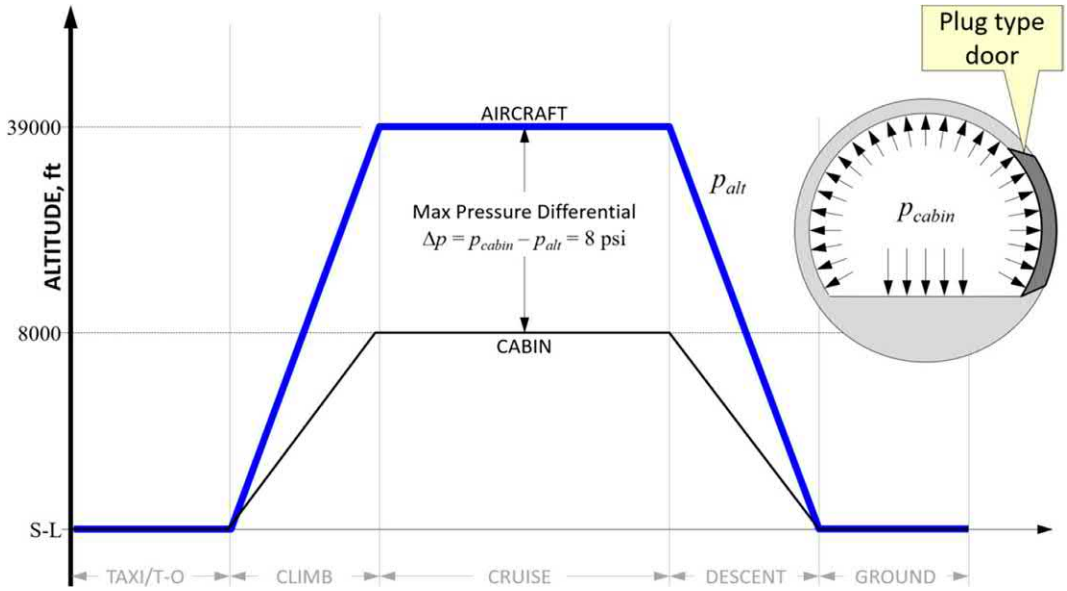


FIGURE 5-29 Cabin air pressure scheduling for a typical passenger jetliner.

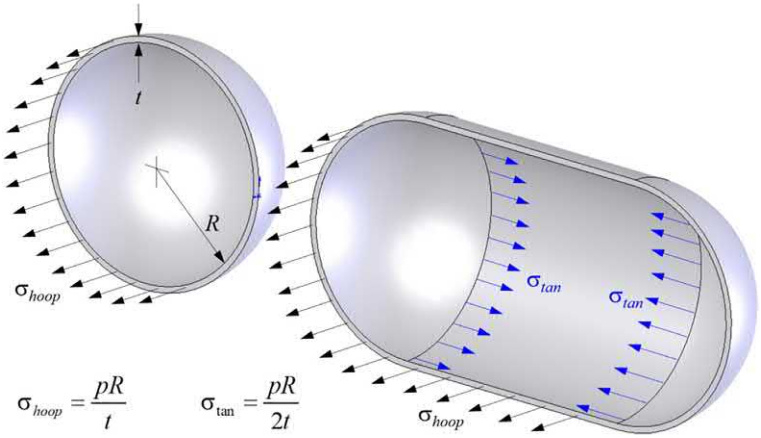


FIGURE 5-30 The difference between hoop and tangential stresses. The term p is the internal-external pressure difference. R and t are radius and wall thickness, respectively.

Figure 5-29). Such doors help distribute the pressure load around the door frame. These doors are truly a marvel of modern engineering. Not only do they have to react some 12 tons of load, when opened, many types swing to the outside of the airplane by a simply operated door handle. This feat is accomplished reliably thousands of times over the lifetime of the aircraft. In addition to the pressurization load, cutouts for windows and doors will further cause stress concentration requiring structural reinforcement. The aspiring designer insisting on superlarge doors and windows for a pressurized airplane should be aware of the structural challenges this may bring. While large openings can be implemented technically, these reinforcements will reduce the useful load of the aircraft.

References

[1] Anonymous, *Metallic Materials Properties Development and Standardization (MMPDS)*, DOT/FAA/AR-MMPDS-01, Federal Aviation Administration, 2003.

[2] Anonymous, *Metallic Materials and Elements for Aerospace Vehicle Structures*, MIL-HDBK-5J, Department of Defense, 2003.

[3] S. Kalpakjian, *Manufacturing Engineering and Technology*, Addison-Wesley Publishing, 1989.

[4] Anonymous, *NAVAIR 01-1A-1 Technical Manual—Engineering Handbook Series for Aircraft Repair/General Manual for Structural Repair*, US Air Force, November 15, 2006.

[5] Anonymous, *AC-43.13-1B Acceptable Methods, Techniques, and Practices—Aircraft Inspection and Repair*, FAA Flight Standard Service, September 8, 1998.

[6] Anonymous, *AFS-120-73-2, Fatigue Evaluation of Wing and Associated Structure on Small Airplanes*, FAA Engineering and Manufacturing Division, Airframe Branch, May, 1973.

[7] Anonymous, *Article 17, Stress Corrosion Cracking of Aluminum Alloys*. http://www.totalmateria.com/Article17.htm. (Accessed 08 August 2019).
[8] M.C.-Y. Niu, *Airframe Structural Design*, Conmilit Press, 1988.
[9] R.A. Flinn, P.K. Trojen, *Engineering Materials and Their Applications*, third ed., Houghton Mifflin Company, 1986.
[10] Anonymous, ASM Aerospace Specification Metals Inc., http://asm.matweb.com/search/SpecificMaterial.asp?bassnum=MTP641. (Accessed 08 August 2019).
[11] S.W. Tsai, *Composites Design*, fourth ed., Think Composites, 1987.
[12] R.M. Jones, *Mechanics of Composite Materials*, Hemisphere Publishing Corporation, 1975.
[13] J. Lambie, *Composite Construction for Homebuilt Aircraft*, Aviation Publishers, 1984.
[14] B. Rutan, *Moldless Composite Sandwich Aircraft Construction*, Aircraft Technical Book Company, 2005.
[15] B. Clarke, Building, *Owning, and Flying a Composite Homebuilt, TAB Books*, 1985.
[16] Anonymous, *Rutan Long-Ez Plans*, Rutan Aircraft Factory, March 1980.
[17] Anonymous, *Quickie Construction Plans*, Quickie Aircraft Corporation, 1978.
[18] Anonymous, Article on Autoclaves From. https://gmtcomposites.com/why/autoclave. (Accessed 13 November 2019).
[19] N. Barala, P. Davies, C. Baley, B. Bigourdan, Delamination behaviour of very high modulus carbon/epoxy marine composites, Compos. Sci. Technol. 68 (3-4) (2008) 995–1007, https://doi.org/10.1016/j.compscitech.2007.07.022.
[20] Anonymous, *MIL-HDBK-17F, Composite Materials Handbook*, Department of Defense, 2002.
[21] Anonymous, *AC-20-107B, Composite Aircraft Structures*, Federal Aviation Administration, 2009.
[22] Anonymous, *AC-21-26, Quality Control for the Manufacture of Composite Structures*, Federal Aviation Administration, 1989.
[23] P. Kuhn, *Stresses in Aircraft and Shell Structures*, McGraw-Hill, New York, 1956.
[24] E.F. Bruhn, *An Analysis and Design of Flight Vehicle Structures*, Jacobs Publishing, 1973.
[25] Anonymous, *Aviation Maintenance Technician Handbook—Airframe*, vol. 1, Federal Aviation Administration, 2012. FAA-H-8083-31.
[26] Anonymous, *AC 25.1529-1A, Instructions for Continued Airworthiness of Structural Repairs on Transport Airplanes*, Federal Aviation Administration, 2007.
[27] Anonymous, *GEN/B0500/04454, Airbus Stress Methods Manual*, Airbus, August 1997.
[28] Anonymous, *MIL-DTL-6070C, Detail Specification – Plywood and Veneer*, Department of Defense, February 24, 1997.
[29] Anonymous, *ANC-18, Design of Wood Aircraft Structures*, Army-Navy-Commerce Committee, 1944.
[30] L.J. Markwardt, NACA R-354, *Aircraft Woods: Their Properties, Selection and Characteristics*, 1930.
[31] Anonymous, *Mooney M20R Ovation Pilot's Operating Handbook*, Mooney Aviation Company, Inc., 1994.
[32] Anonymous, *AC-23-13A, Fatigue, Fail-Safe, and Damage Tolerance Evaluation of Metallic Structure for Normal, Utility, Acrobatic, and Commuter Category Airplanes*, Federal Aviation Administration, 2005.
[33] Anonymous, *Advisory Circular AC 43.13-1B, Acceptable Methods, Techniques, and Practices—Aircraft Inspection and Repair*, Federal Aviation Administration, 1998.
[34] D. Anderton, *727 Designed for Low Approach Speeds*, Article, Aviation News & Space Technology, December 10, 1962.
[35] E. Torenbeek, *Synthesis of Subsonic Airplane Design*, Delft University Press, 1976.
[36] L.R. Huber, *Super Highways*, Boeing Magazine (January 1945).
[37] J. Hale, Boeing 787 from the Ground Up, Boeing Commercial Aero Magazine (2006).
[38] SAE Committee AC-9, *SAE ARP1270B, Aircraft Cabin Pressurization Control Criteria*, Society of Automotive Engineers, 2010.

CHAPTER

6

Aircraft Weight Analysis

OUTLINE

6.1 **Introduction** 147
- 6.1.1 *The Content of This Chapter* 148
- 6.1.2 *Definitions* 148
- 6.1.3 *Fundamental Weight Relations* 149

6.2 **Initial Weight Analysis Methods** 149
- 6.2.1 *Method 1: Initial Gross Weight Estimation Using Historical Relations* 150
- 6.2.2 *Method 2: Historical Empty Weight Fractions* 152
- 6.2.3 *Method 3: Initial Gross Weight Estimation Using Mission Analysis* 153

6.3 **Secondary Weight Analysis Methods** 159

6.4 **Statistical Weight Estimation Methods** 160
- 6.4.1 *Weight of Aircraft Components—GA Aircraft* 160
- 6.4.2 *Estimating Engine Weight* 165

6.5 **Direct Weight Estimation Methods** 167
- 6.5.1 *Direct Weight Estimation for a Wing* 167
- 6.5.2 *Variation of Weight With AR* 170

6.6 **Inertia Properties** 176
- 6.6.1 *Fundamentals* 176
- 6.6.2 *Reference Locations* 177
- 6.6.3 *Total Weight* 177
- 6.6.4 *Moment About* (x_0, y_0, y_0) 178
- 6.6.5 *Center-of-Mass, Center-of-Gravity, Centroid of a Volume* 178
- 6.6.6 *Determination of CG Location by Aircraft Weighing* 180
- 6.6.7 *Mass Moment of Inertia* 180
- 6.6.8 *Mass Product of Inertia* 182
- 6.6.9 *Principal Moments of Inertia* 183
- 6.6.10 *Inertia Matrix* 183

6.7 **The Center-of-Gravity Envelope** 183
- 6.7.1 *Fundamentals* 183
- 6.7.2 *Creating the CG-Envelope* 186
- 6.7.3 *Loading Cloud* 189
- 6.7.4 *In-Flight Movement of the CG* 191
- 6.7.5 *Weight Budgeting* 191
- 6.7.6 *Weight Tolerancing* 191

Exercises 194

References 195

6.1 INTRODUCTION

Weight estimation is one of the most important tasks in the entire aircraft design process. While complicated mathematical tools are not needed, the task can be quite challenging. An excessive under- or overestimation of an airplane's empty weight has a serious impact on the development program. The history of aviation is wrought with overweight aircraft that led to serious developmental challenges. Difficulties in meeting weight targets of recent aircraft like the Lockheed-Martin F-35 [1], Boeing 787 Dreamliner [2], and Airbus 380 [3] were documented in the first edition of this book. If established manufacturers can make mistakes in their weight estimations, then certainly we can too.

This chapter introduces several methods to estimate the weight of new airplanes. Figure 6-1 provides guidance for this effort. These methods are classified either as *initial* or *detailed*. Several initial and detailed weight estimation methods are presented. The complexity and accuracy of these methods varies. The initial methods require a limited amount of information, yielding ballpark values. The detailed methods are more accurate but require more information about the aircraft's geometry and systems. They require the primary dimensions of the aircraft to be established.

https://doi.org/10.1016/B978-0-12-818465-3.00006-9

Copyright © 2022 Elsevier Inc. All rights reserved.

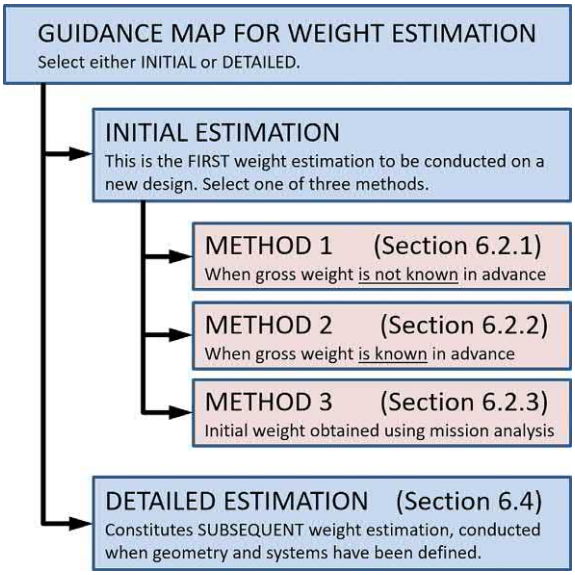


FIGURE 6-1 Guidance for selecting the appropriate weight estimation method.

As detailed in Section 1.4, a new estimate of the weight is required during each design iteration. The *first* iteration only gives a rudimentary idea about the weight of the airplane and is intended to allow basic sizing to take place (e.g., in conjunction with a constraint diagram). Subsequent methods are more detailed and usually include a mixture of known weights (such as of engines, landing gear components, etc.), statistical weights, and direct weight estimation (based on the geometry and density of materials chosen).

Note that weights engineering is an established discipline. An excellent resource for professional weights engineers is the Society of Allied Weight Engineers (SAWE) (www.sawe.org), an international organization that promotes best practices and expertise among its members. This includes the publication of industry standards and books.

(1) Weight Estimation Advice

Be realistic: Do not expect your design to weigh less than airplanes belonging to the same class—at least not for the first iteration. The aircraft you are comparing to have often gone through costly weight reduction programs and many can be considered weight optimized. Remember that the people who worked on these aircraft are smart people and spent a lot of time trying to get unnecessary weight out. Your design will not be weight optimized at first.

Be careful: If your airplane ends up weighing less than estimated, then great—it will have greater utility or growth capacity than planned and your boss may even pat you on the back. If it ends up heavier than expected, the project will be seriously compromised. Perhaps even canceled, although most likely, you would be asked to sharpen your pencil first.

(2) A Comment about Units of Weight

Weight is a force. Its unit in the UK-system (or US Customary system—USC) is lb_f, pronounced "pounds" or "pounds-force." In the SI-system, the correct unit is N, pronounced "Newtons." Most metric countries, while technically incorrect, specify weight using the unit of mass—kg (kilograms), rather than Newtons. Therefore, an airplane is specified to "weigh," say 906 kg (or kilos) and not 8885 N. When referring to the weight of aircraft using the metric system, this convention is adopted.

Also, this author strongly recommends that weight in the UK-system be written as lb_f and not lb. or lbs. in design documentation, to avoid the confusion that this is force and not mass.

6.1.1 The Content of This Chapter

- Section 6.2 presents three methods intended to assess the first estimate of the airplane's weight.
- Section 6.3 discusses detailed weight analysis methods a precursor to the Statistical and Direct Weight Estimation methods.
- Section 6.4 presents a method to estimate the weight of General Aviation aircraft.
- Section 6.5 presents Direct Weight Estimation methods.
- Section 6.6 discusses the various inertia properties, including numerical estimation of moments and products of inertia. The importance of weight budgeting in aircraft design is presented, as well as methods to evaluate uncertainty in the prediction of the CG and other inertia properties.

6.1.2 Definitions

The following are standard definitions for weight used in the aircraft industry.

(1) Empty Weight, W_e

Weight of an aircraft without useful load. Includes oil, unusable fuel, and hydraulic fluids. *Manufacturer's empty weight* refers to the sum of airframe, engines, systems, furnishing, and basic operational equipment weights. *Delivery empty weight* is the manufacturers' empty weight plus weight of operational items requested by customer (e.g., lavatories and galley structure). *Operating empty weight* is the delivery weight plus equipment installed by customer (e.g., galley, entertainment system, and life rafts) and crew required to operate the aircraft.

(2) Design Gross Weight, W_0

The maximum T-O weight for the mission for which the airplane is designed.

(3) Useful Load, W_u

Useful load is defined as the difference between the design gross weight and the empty weight. It is the weight of everything the aircraft will carry besides its own weight. This typically includes occupants, fuel, freight, etc.

(4) Payload, W_p

The part of the useful load that yields revenue for the operator (although it applies also to nonpaying passengers). Typically, it is the passengers, their baggage, and freight.

(5) Crew Weight, W_c

Weight of occupants required to operate the aircraft.

(6) Fuel Weight, W_f

Weight of the fuel needed to complete the design mission.

(7) Reserve Fuel Weight, $W_{f\ res}$

Weight of reserve fuel required for the operation of the aircraft. This is estimated by various means, although minimums are stipulated by 14 CFR 91.151 for *Visual Flight Rules* (VFR) and 91.167 for *Instrument Flight Rules* (IFR). Reserve fuel is also set by the *National Business Aviation Association* (NBAA), but these exceed the minimums set by these regulations.

(8) Ramp Weight, W_R

Design gross weight + small amount of fuel to accommodate warm-up and taxi into T-O position.

(9) Maximum Landing Weight, W_{LDG}

Maximum weight at which the aircraft may land without compromising airframe strength.

(10) Maximum Zero Fuel Weight, W_{MZF}

Max zero fuel weight is the maximum weight the airplane can carry with no fuel on board. Note that the maximum zero fuel weight implies that all weight above W_{MZF} must be fuel. It is a common occurrence in the aviation industry that gross weight must be increased. There are typically two underlying reasons: (1) the design team underestimated the gross weight and (2) it is desired the airplane be capable of being operated at a greater weight than initially anticipated. A hypothetical situation, in which a design team is confronted with an unexpected increase in empty weight and how W_{MZF} can be used to solve it, is presented in the first edition of this book. It has been eliminated here to make space for new material.

(11) Specific Fuel Consumption, *SFC*

A measure of the time-dependent consumption of fossil fuel in aircraft. For details refer to Section 21.2.4.

6.1.3 Fundamental Weight Relations

The following relations are fundamental expressions for an aircraft weight.

$$\text{Design gross weight:} \quad W_0 = W_e + W_u \tag{6-1}$$

$$\text{Useful load:} \quad W_u = W_c + W_f + W_p \tag{6-2}$$

$$\text{Design gross weight:} \quad W_0 = W_e + W_c + W_f + W_p \tag{6-3}$$

Note that Equation (6-1) gives the maximum or "official" W_u, while Equation (6-2) gives the "current" W_u. Thus, the former is a *primary* governing equation and (6-2) is an expression of what constitutes the useful load. It may or may not be equal to the "official" W_u. Weight ratios are imperative in estimating the weight during the first design iteration but are also necessary for mission analyses. The fundamental weight ratios are the empty weight and fuel weight ratios:

$$\text{Empty weight ratio:} \quad \frac{W_e}{W_0} \tag{6-4}$$

$$\text{Fuel weight ratio:} \quad \frac{W_f}{W_0} \tag{6-5}$$

EXAMPLE 6-1

Determine the useful load, empty weight ratio, and fuel weight ratio for a Cessna 150 aircraft, using the following information:

Gross weight: $W_0 = 1600\,\text{lb}_\text{f}$
Empty weight: $W_e = 1100\,\text{lb}_\text{f}$
Fuel weight: $W_f = (35\,\text{gal})(6\,\text{lb}_\text{f}/\text{gal}) = 210\,\text{lb}_\text{f}$

SOLUTION:

Useful load: $W_0 = W_0 - W_e = 1600 - 1100 = 500\,\text{lb}_\text{f}$

Empty weight ratio: $\dfrac{W_e}{W_0} = \dfrac{1100}{1600} = 0.6875$

Fuel weight ratio: $\dfrac{W_f}{W_0} = \dfrac{210}{1600} = 0.13125$

6.2 INITIAL WEIGHT ANALYSIS METHODS

This section details how to conduct the first weight estimation of your airplane. The analysis provides initial empty, fuel, and gross weights. Later, these weights are refined using secondary weight estimation methods (Section 6.3). However, this section gets the ball rolling. As evident in Figure 1-11, the initial weight estimate is completed by Step 7 and is used in Steps 8 through 11 to establish the *initial geometry*: it is a vital part of the design process.

Three methods are presented for this purpose. They are grounded in historical aircraft and, thus, are referred

to as *historical relations*. First, we determine the empty- and fuel-weight ratios of existing aircraft in the same class as the new one. Then, we argue that if the mission and certification basis of the new airplane is close to that of the reference aircraft, its empty- and fuel-weight ratios ought to be close to the historical values. An estimate of these ratios allows empty, fuel, and gross weight to be determined for the new aircraft. The accuracy of these methods depends on the number of reference aircraft and how closely they resemble the one being developed.

6.2.1 Method 1: Initial Gross Weight Estimation Using Historical Relations

***Guidance*: Use this method if the gross weight IS NOT KNOWN. Be careful—it is easy to under- or overestimate. Ensure that the reference aircraft database consists of aircraft in the same class and is not a mix of properties. For instance, if designing a piston-propeller aircraft, do not mix turboprop or turbofan aircraft in the database. Also, do not mix small two-place and large 19-place aircraft, or low performance VFR and high performance IFR aircraft, and so on.**

Consider the design of a new 6-seat, twin-engine piston propeller aircraft. Its reference database should *include* twin-engine aircraft such as the Piper PA-23 Apache, Beech Model 76 Duchess, Beech Model 58 Baron, Piper PA-31 Navajo, Cessna Model 303 and Cessna Model 421, to name a few. Their empty weight ranges from about 3200 to 4500 lb_f and the gross weight from 5200 to 7500 lb_f. All are powered by several makes of piston engines and carry 6 to 8 occupants, or so. In contrast, the database should *exclude* the Piper PA-42 Cheyenne or the Beech Model 100 King Air, and its larger relatives, the Model 200 and 300 Super King Air. These aircraft weigh some 6900 to 7800 lb_f empty, 11,200 to 12,500 lb_f loaded, are pressurized turboprops, and are *high-performance*. The point is that the selection of candidate aircraft must be refined enough to exclude aircraft that could skew the weight ratios that must be calculated. In the case of the above aircraft, we have major differences in properties such as pressurized versus unpressurized, piston engine versus turbine, and so forth.

Besides serving as a "sanity check" and, thus, preventing under- or overestimation of the weight, careful selection of candidate aircraft improves the reliability. It yields a more realistic "first stab" estimation of the airplane's gross weight. The fuel and empty weight can be written in terms of empty and fuel weight ratios as follows

$$\text{Fuel weight:} \qquad W_f = \left(\frac{W_f}{W_0}\right) W_0 \tag{6-6}$$

$$\text{Empty weight:} \qquad W_e = \left(\frac{W_e}{W_0}\right) W_0 \tag{6-7}$$

Substituting these into Equation (6-3) leads to

$$W_0 = \left(\frac{W_e}{W_0}\right) W_0 + W_c + \left(\frac{W_f}{W_0}\right) W_0 + W_p \tag{6-8}$$

This can be solved for W_0, yielding an expression that we use to estimate gross weight in terms of the weight ratios.

$$W_0 = \frac{W_c + W_p}{1 - \left(\frac{W_e}{W_0}\right) - \left(\frac{W_f}{W_0}\right)} \tag{6-9}$$

Then, the gross weight is estimated as follows: (1) Establish the desired payload, W_p, and crew weight, W_c. (2) Determine historical values for fuel and empty weight ratios of similar aircraft. (3) Calculate the gross weight using Equation (6-9).

The ratios W_e/W_0 and W_f/W_0 can be obtained from historical data, providing a solution to Equation (6-9). While relationships for W_e/W_0 are provided by refs. [4–6], it is recommended the designer compiles own database. Aircraft specifications in the public domain, such as those found in *Jane's All the World's Aircraft* or on Type Certificate Data Sheets, can be used to build such relationships. Table 6-1 shows an example of such analysis using several Light Sport Aircraft. Note that W_e stands for empty weight, W_0 is gross weight, Q_f is fuel quantity, W_f is fuel load, and W_u is useful load.

The statistical values in Table 6-1 shows the empty weight of the selected aircraft is 707 ± 79 lb_f and the gross weight is 1320 ± 1 lb_f. High standard deviation indicates large disparity in data—it suggests database contains outlier aircraft. Here, the resulting W_e/W_0, W_u/W_0, and W_f/W_0 are around 0.535, 0.465, and 0.093, respectively. This information is vital for the initial sizing, for instance when performing constraint analysis. Statistical equations for several classes of aircraft are presented in Section 6.2.2.

NOTE 1:
Equation (6-9) reveals an important scaling effect. To see this, define the *growth factor* $k \equiv 1/(1 - W_e/W_0 - W_f/W_0)$. We can now write Equation (6-9) as $W_0 = k(W_c + W_p)$. Next, consider a situation for which $k = 5$ and we want to increase $(W_c + W_p)$ from 900 lb_f to 1000 lb_f. This means the max gross weight must increase from 4500 lb_f to 5000 lb_f. This highlights that small change in payload has large impact on gross weight.

NOTE 2:
Most real airplanes exceed their gross weight with full passenger and fuel load. An airplane may be capable of a $W_f/W_0 = 0.20$, but only 0.10 if all seats are occupied. Using the former value with Equation (6-9) would thus yield gross weight that is unrealistically high. For this reason, the reader is urged to exercise caution and select the value of W_f/W_0 accordingly. For instance, adjust the historical

TABLE 6-1 Establishing weight ratios for light sport aircraft.[a]

Weight of selected LSA Aircraft							
	W_e lb$_f$	W_0 lb$_f$	Q_f US gals	W_f lb$_f$	W_e/W_0	W_u/W_0	W_f/W_0
Aerostar Festival LSA	848	1318	21	127	0.643	0.357	0.096
Allegro 2007	622	1320	13	79	0.471	0.529	0.060
Cessna C-162 Skycatcher	834	1320	24	144	0.632	0.368	0.109
ECO1 EXP (medium)	655	1322	13	79	0.495	0.505	0.060
ECO1 EXP (short)	655	1322	13	79	0.495	0.505	0.060
ECO1 LSA	655	1318	13	79	0.497	0.503	0.060
ECO1 UL	655	1318	13	79	0.497	0.503	0.060
ECO1 VLA(medium)	655	1322	13	79	0.495	0.505	0.060
ECO1 VLA(short)	655	1322	13	79	0.495	0.505	0.060
Flight Design CTLS	717	1320	34	204	0.543	0.457	0.155
Flight Design CTSW	693	1320	34	206	0.525	0.475	0.156
Flyfabriken LN-3 Seagull	639	1323	26	158	0.483	0.517	0.120
RANS S-19 Venterra	820	1320	24	144	0.621	0.379	0.109
RANS S-6 Coyote II	700	1320	18	108	0.530	0.470	0.082
RANS S-7 Courier	732	1320	26	156	0.555	0.445	0.118
Remos GX	639	1320	22	132	0.484	0.516	0.100
Sky Arrow 600 Sport	840	1320	26	155	0.636	0.364	0.117
Averages	**707**	**1320**	**20**	**123**	**0.535**	**0.465**	**0.093**
Standard deviations	**79**	**1**	**7**	**44**	**0.060**	**0.060**	**0.034**

[a] *Source of data are various manufacturer's websites. Data may contain erroneous weights.*

fuel weight ratio by simply calculating $W_f = W_0 - W_e - W_p - W_c$ and compute an adjusted W_f/W_0. Alternatively, the designer is at liberty to decide that when all seats are occupied, the airplanes can hold some specific quantity of fuel that may or may not refer to full fuel tanks.

EXAMPLE 6-2

A four-seat trainer is being designed and it is required to carry 300 lb$_f$ of baggage in addition to the occupants. Assume a crew of one, 200 lb$_f$/person, and use the ratios W_e/W_0 and W_f/W_0 obtained from the analysis of the Cessna 150 in Example 6-1. For the conceptual design estimate initial values for:

(1) Gross weight.
(2) Empty weight.
(3) Fuel weight.

SOLUTION:

Crew weight: $W_c = 200\,\text{lb}_f$

Payload:

$$W_p = (3\,\text{persons})\,(200\,\text{lb}_f/\text{person}) + 300 = 900\,\text{lb}_f$$

Empty weight and fuel weight ratios are:

$$W_e/W_0 = 0.6875 \text{ and } W_f/W_0 = 0.1313$$

(1) An initial gross weight is:

$$W_0 = \frac{W_c + W_p}{1 - (W_e/W_0) - (W_f/W_0)} = \frac{200 + 900}{1 - (0.6875) - (0.1313)} = 6069\ \text{lb}_f.$$

(2) An initial empty weight is:

$$W_e = \left(\frac{W_e}{W_0}\right) W_0 = (0.6875)(6069) = 4172\ \text{lb}_f.$$

(3) An initial fuel weight is:

$$W_f = \left(\frac{W_f}{W_0}\right) W_0 = (0.1313)(6069) = 797\ \text{lb}_f\,(132.8\,\text{US gal}).$$

Readers familiar with low speed aircraft probably notice these outrageously large weights (Cessna 172 has a gross weight of 2450 lbf). These highlight two lessons: (1) Use *compatible* aircraft for the weight ratios and (2) incorrectly accounting for fuel quantity per Note 2 above throws the estimate way off.

Initial Gross Weight for Electric Aircraft

In a widely cited paper [7], Hepperle derives formulation to estimate the range (R) of electric aircraft. It is detailed in Chapter 21, but the resulting expression is repeated below for convenience:

$$R = \frac{E^* \cdot \eta_{tot} \cdot LD_C}{g}\left(\frac{m_{batt}}{m}\right) \tag{6-10}$$

where E^* = mass energy density in Wh/kg (see Section 7.4.2), LD_C = expected lift-to-drag ratio during cruise, m_{batt} = battery mass in kg and m = total vehicle mass in kg, $\eta_{tot} = \eta_p \eta_{system}$ is the total power-system efficiency from battery-to-thrust (typ. 0.70–0.75). η_p is the propeller efficiency and η_{system} is the system efficiency (see Section 7.4.4 and Figure 7-56). Airspeed is included indirectly through L/D. Thus, for regular SI-units and range in km (noting that 1 km = 1000 m), Equation (6-10) can be rewritten as follows[1]

$$R = \frac{3.6E^* \cdot \eta_{tot} \cdot LD_C}{g}\left(\frac{m_{batt}}{m}\right) \quad [\text{km}] \tag{6-11}$$

In ref. [7], Equation (6-10) is rewritten to permit gross weight estimation for initial sizing by solving it for $m = m_0$. It is presented below, adapted to the discussion here and using the factor 3.6:

$$m_0 = \frac{m_c + m_p}{1 - \left(\frac{m_e}{m_0}\right) - \left(\frac{g \cdot R}{3.6E^* \cdot \eta_{tot} \cdot LD_C}\right)} \tag{6-12}$$

where m_e = empty mass, m_c = crew mass, m_p = payload mass, all in kg, and R = desired range in km. Note that the expression assumes the SI-system, in part, because the battery properties are metric. Electric formulae are SI by default (inferred by electric power being in Watts). Also, set $R = 0$ to obtain the empty weight (mass) ratio. The formulation reflects the altitude invariance of electric motor power. Hepperle's formulation allows the designer to evaluate other requirements to which the design will be exposed. For instance, given a desired range, R, the LD_C must amount to

$$LD_C > \frac{R \cdot g}{3.6[1 - (m_e/m_0)] \cdot E^* \cdot \eta_{tot}} \tag{6-13}$$

The mass-specific energy of the battery must exceed

$$E^* > \frac{R \cdot g}{3.6[1 - (m_e/m_0)] \cdot LD_C \cdot \eta_{tot}} \tag{6-14}$$

The empty weight ratio must be short of

$$\frac{W_e}{W_0} = \frac{m_e}{m_0} < 1 - \frac{R \cdot g}{3.6E^* \cdot \eta_{tot} \cdot LD_C} \tag{6-15}$$

EXAMPLE 6-3

Estimate the gross mass (in kg) for a 10-occupant commuter with a 500 km range. It is expected it will have an empty weight (mass) ratio of 0.5. Assume an occupant weight of 90 kg, $E^* = 180$ Wh/kg, and $\eta_{tot} = 0.70$.

SOLUTION:

First, we must determine what LD_C the airplane must achieve, using Equation (6-13):

$$LD_C > \frac{R \cdot g}{3.6[1 - (W_e/W_0)] \cdot E^* \cdot \eta_{tot}} = \frac{(500) \cdot (9.807)}{3.6[1 - 0.5] \cdot (180) \cdot (0.70)} = 21.62$$

It is not wise to select this value, because the resulting mass trends toward infinity. Instead, we should use it to select a reasonable target LD_C. For instance, if we aim for $LD_C = 30$, the resulting gross mass is obtained from Equation (6-12):

$$m_0 = \frac{m_c + m_p}{1 - \left(\frac{m_e}{m_0}\right) - \left(\frac{g \cdot R}{3.6E^* \cdot \eta_{tot} \cdot LD_C}\right)} = \frac{10 \times 90}{1 - (0.5) - \left(\frac{(9.807) \cdot (500)}{3.6(180) \cdot (0.70) \cdot (30)}\right)} = 6444 \text{ kg}$$

It is important for the designer to realize that achieving $LD_C = 30$ in cruise is easier said than done. It requires a very sleek, high AR, sailplane-like configuration.

6.2.2 Method 2: Historical Empty Weight Fractions

***Guidance*: Use this method if the gross weight IS KNOWN. In this case, we want to estimate this is the case for many types of aircraft, e.g., LSA, which should not weigh more than 1320 lb_f or 1430 lb_f if amphibious. There are also situations in which it is desired the aircraft does exceed a certain gross weight. Do not "back out" W_0 from a desired empty weight ratio using this method.**

The following set of equations was determined statistically by the author using historical data. The number in the parenthesis indicates the number of aircraft included. If we know the target gross weight for our new aircraft, the expressions allow us to estimate a "historical" empty-weight ratio. Thus, we can also estimate the empty weight, and then the useful load, and so forth.

Sailplanes (35):

$$\frac{W_e}{W_0} = \begin{cases} 0.2950 + 0.0386 \cdot \ln W_0 & \text{if } W_0 \text{ is in lb}_f \\ 0.3255 + 0.0386 \cdot \ln W_0 & \text{if } W_0 \text{ is in kg} \end{cases} \tag{6-16}$$

[1] This is demonstrated in Section 21.3.5. It also matches the range shown in Figure 15 in reference [7].

Powered sailplanes (13):

$$\frac{W_e}{W_0}=\begin{cases}0.3068+0.0510\cdot\ln W_0 & \text{if } W_0 \text{ is in lb}_f\\ 0.3471+0.0510\cdot\ln W_0 & \text{if } W_0 \text{ is in kg}\end{cases} \quad (6\text{-}17)$$

LSA (land) (35):

$$\frac{W_e}{W_0}=\begin{cases}1.5451-0.1402\cdot\ln W_0 & \text{if } W_0 \text{ is in lb}_f\\ 1.4343-0.1402\cdot\ln W_0 & \text{if } W_0 \text{ is in kg}\end{cases} \quad (6\text{-}18)$$

LSA (amphib) (adjusted from Equation (6-18)):

$$\frac{W_e}{W_0}=\begin{cases}1.6351-0.1402\cdot\ln W_0 & \text{if } W_0 \text{ is in lb}_f\\ 1.5243-0.1402\cdot\ln W_0 & \text{if } W_0 \text{ is in kg}\end{cases} \quad (6\text{-}19)$$

GA Single Engine (86):

$$\frac{W_e}{W_0}=\begin{cases}0.8841-0.0333\cdot\ln W_0 & \text{if } W_0 \text{ is in lb}_f\\ 0.8578-0.0333\cdot\ln W_0 & \text{if } W_0 \text{ is in kg}\end{cases} \quad (6\text{-}20)$$

GA Twin Piston (12):

$$\frac{W_e}{W_0}=\begin{cases}0.4074+0.0253\cdot\ln W_0 & \text{if } W_0 \text{ is in lb}_f\\ 0.4274+0.0253\cdot\ln W_0 & \text{if } W_0 \text{ is in kg}\end{cases} \quad (6\text{-}21)$$

GA Twin Turboprop (28):

$$\frac{W_e}{W_0}=\begin{cases}0.5319+0.0066\cdot\ln W_0 & \text{if } W_0 \text{ is in lb}_f\\ 0.5371+0.0066\cdot\ln W_0 & \text{if } W_0 \text{ is in kg}\end{cases} \quad (6\text{-}22)$$

Agricultural (5):

$$\frac{W_e}{W_0}=\begin{cases}1.4029-0.0995\cdot\ln W_0 & \text{if } W_0 \text{ is in lb}_f\\ 1.3242-0.0995\cdot\ln W_0 & \text{if } W_0 \text{ is in kg}\end{cases} \quad (6\text{-}23)$$

Business jets (72):

$$\frac{W_e}{W_0}=\begin{cases}0.9038-0.03163\cdot\ln W_0 & \text{if } W_0 \text{ is in lb}_f\\ 0.8788-0.03163\cdot\ln W_0 & \text{if } W_0 \text{ is in kg}\end{cases} \quad (6\text{-}24)$$

6.2.3 Method 3: Initial Gross Weight Estimation Using Mission Analysis

***Guidance*: Use this method when the gross weight IS NOT KNOWN and you are designing an aircraft to transport a given payload over a specific range (or endurance) in accordance with a dedicated *design mission* (including, but not limited to long range or long endurance aircraft). The method analyzes the intended mission profile and couples it with the empty weight ratios of Method 2 to determine the gross weight. Before using this approach, you may want to familiarize yourself with the mission analysis methodology presented in Section 21.5.1.**

This weight estimation is conducted using a fully defined design mission (exemplified in Figure 6-2). The mission consists of N–segments and $N+1$ nodes. These are indexed from 0 to N (see Figure 6-2). The weight of the aircraft at the initial and final nodes of segment i is denoted by W_{i-1} and W_i, respectively. The change in weight along a segment is defined as $\Delta W \equiv \dot{w}_{fuel}\Delta t$, where Δt is time to complete the segment and $\dot{w}_{fuel}$ is fuel-flow (e.g., in lb_f/h). Thus, $W_i = W_{i-1} - \Delta W$. Its value is calculated for each mission segment.

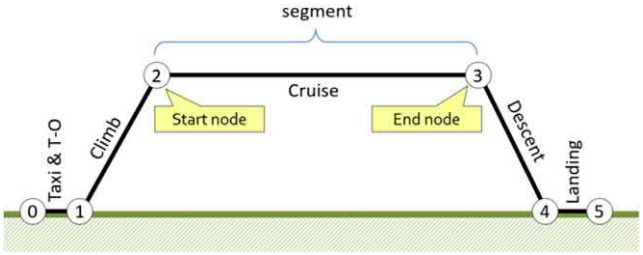


FIGURE 6-2 Elements of a mission definition.

The gross weight is obtained by tracing the flight of the aircraft, starting at Node 0, with engine startup at (design) gross weight (W_0), until engine shutdown at the end-of-mission (Node 5). The weight of the aircraft is estimated along each segment using $\dot{w}_{fuel}$ and flight-time. It is accomplished by relating the chain of weight fractions to the gross weight (W_0) in the following fashion:

Weight for mission segment $0 \rightarrow 1$:

$$W_1 = W_0\left(\frac{W_1}{W_0}\right)$$

Weight for mission segment $1 \rightarrow 2$:

$$W_2 = W_1\left(\frac{W_2}{W_1}\right) = W_0\left(\frac{W_1}{W_0}\right)\left(\frac{W_2}{W_1}\right)$$

Weight for mission segment $2 \rightarrow 3$:

$$W_3 = W_2\left(\frac{W_3}{W_2}\right) = W_0\left(\frac{W_1}{W_0}\right)\left(\frac{W_2}{W_1}\right)\left(\frac{W_3}{W_2}\right) \text{ etc.}$$

Using this approach, the weight of the aircraft at the end-of-mission can be written as follows

$$\begin{aligned}W_N &= W_0\left(\frac{W_1}{W_0}\right)\left(\frac{W_2}{W_1}\right)\cdots\left(\frac{W_i}{W_{i-1}}\right)\cdots\left(\frac{W_N}{W_{N-1}}\right)\\ &= W_0\prod_{i=1}^{N}\frac{W_i}{W_{i-1}}\end{aligned} \quad (6\text{-}25)$$

Thus, the weight fraction at the end-of-mission is

$$\frac{W_N}{W_0} = \prod_{i=1}^{N}\frac{W_i}{W_{i-1}} \quad (6\text{-}26)$$

It is best to account for **all** reserve fuel in terms of weight fractions as shown in Example 6-4. By assuming the aircraft consumes all its fuel at the *end-of-mission*, the final weight fraction can be related to the aircraft's empty weight, crew weight, and payload as follows:

$$\frac{W_N}{W_0} = \frac{W_e + W_c + W_p}{W_0} \quad \Leftrightarrow \quad \left(\frac{W_e}{W_0}\right)_{miss} = \frac{W_N}{W_0} - \frac{W_c + W_p}{W_0} \quad (6\text{-}27)$$

To close the formulation, we need another relation for W_e/W_0. We obtain this relation by associating our design to the class of aircraft to which it belongs. This is done using the methods of Section 6.2.2. These are expressions of the form

$$\left(\frac{W_e}{W_0}\right)_{hist} = A + B \ln W_0 \tag{6-28}$$

As stated in Section 6.2.2, such equations presume the gross weight is known a priori. This is not the case here. If we work from the premise that the historical weight fractions are accurate, it follows that the *end-of-mission* W_e/W_0 of Equation (6-27) must equal the *historical* W_e/W_0 of Equation (6-28). Equating the two yields the following form, which permits W_0 to be determined using an iterative scheme.

$$A + B \ln W_0 + \frac{W_c + W_p}{W_0} - \frac{W_N}{W_0} = 0 \tag{6-29}$$

It is also possible to solve $(W_e/W_0)_{\text{hist}} = (W_e/W_0)_{\text{miss}}$ by plotting both equations for a range of W_0 and note where the two intersect. Also note that readers should consider narrowing the range of aircraft used for the historical relations of Section 6.2.2. For instance, Equation (6-24) is based on 72 business aircraft. Some of them are large, while others are small. To make the expression more specific, narrow the range and determine own coefficient A and B.

(1) Formulation of Mission Weight Ratios

This weight estimation method is frequently used presuming a fixed maximum *thrust-to-weight ratio*, $T_{\max}/W$ for all segments (e.g., $T_{\max}/W = 0.3$). However, for some applications, it is necessary to account for the fact that $T_{\max}/W$ *increases* as fuel is consumed: It is *smaller at the beginning* of a mission than at its end. This may be important for aircraft that always climb at max thrust, as $T_{\max}$ does not depend on the quantity of remaining fuel.

This complication is treated here. For mathematical simplicity, we write the average thrust during a segment as a fraction of the aircraft's weight at the start node, e.g., rW_{i-1}, where r is a *thrust-to-weight ratio* (dimensionless). For propeller aircraft, we write this as pW_{i-1}, where p is a *power-to-weight ratio* (dimensions are HP/lb_f or kW/N).

Consider an aircraft for which $r = T_{\max}/W = 0.3$ during initial climb and 0.5 during climb to alternate airport. This implies faster rate-of-climb during the second climb than the initial one. This, in turn, implies less fuel is consumed because it takes less time to reach top-of-climb. While it is hard to accurately assess the value of r (or p) for an aircraft whose gross weight is unknown, we know precisely how it behaves as the fuel burn reduces the aircraft's weight.

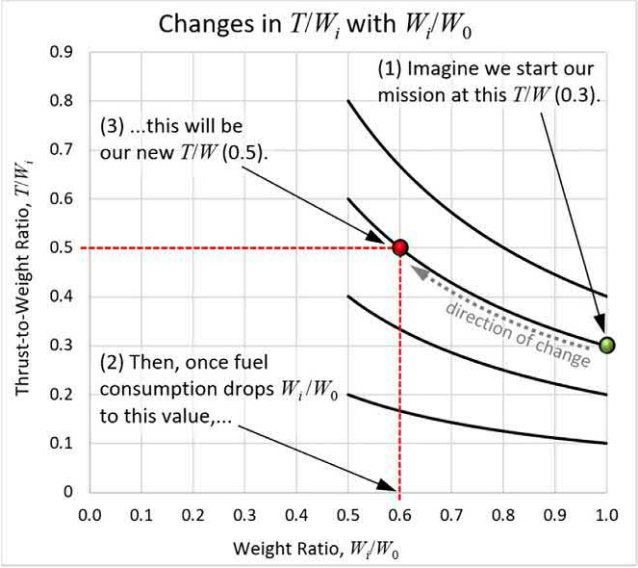


FIGURE 6-3 Elements of a mission definition.

This is shown in Figure 6-3. First, we guess an initial value of r (or p) based on existing aircraft. Then, we prepare calculations (e.g., in a spreadsheet) such that the initial guess for r and p can be revised in subsequent iterations. This is shown in Example 6-4. If we know the initial $T_{\max}/W$ (call it $T_{\max}/W_0$, where is W_0 gross weight), we can evaluate the ratio for any other weight using the following relations:

Thrust-to-weight ratio:

$$r_i = \frac{T_{\max}}{W_i} = \frac{T_{\max}}{W_0}\frac{W_0}{W_i} \tag{6-30}$$

Power-to-weight ratio:

$$p_i = \frac{P_{\max}}{W_i} = \frac{P_{\max}}{W_0}\frac{W_0}{W_i} \tag{6-31}$$

where i is a segment index (other subscripts can be used as well). For instance, if the expected $r_i = T_{\max}/W_0 = 0.3$ and, after first iteration, we find that W_0 is 10,000 lb_f, it follows that, at a node where $W_i = 8550$ lb_f, the ratio r_i should be $r_i = (0.3)(10{,}000/8550) = 0.3509$ (and not 0.3). For improved guidance, it is also wise to estimate T/W (or P/W) for aircraft in the same class. As an example, the $T_{\max}/W_0$ for the Gulfstream G450 is 0.371 at gross weight and 0.565 at its max-zero-fuel weight. These values assume static thrust and are reduced further at operational speeds. During regular operation, it is reasonable to expect the G450 has $r = 0.3$ for initial climb to cruise altitude and, perhaps, $r = 0.5$ for climb to alternate airport. In contrast, the $P_{\max}/W_0$ for propeller aircraft is about 0.060 to 0.10 BHP/lb_f for pistons and 0.10 to 0.20 SHP/lb_f for turboprops. Further details are shown in Example 6-4.

(2) Taxi and Take-off

This is used to estimate change in weight from engine start-up, taxi to take-off position, and take-off.

$$\frac{W_i}{W_{i-1}} = \begin{cases} 1-(\Delta t_{taxi}\times r_{idle}+\Delta t_{\max}\times r_{\max})\times SFC & \text{Jets} \\ 1-(\Delta t_{taxi}\times p_{idle}+\Delta t_{\max}\times p_{\max})\times SFC_{hp} & \text{Propellers} \end{cases} \tag{6-32}$$

where Δt_{taxi} is taxi time and $\Delta t_{\max}$ is max thrust time in hours, r_{idle} and $r_{\max}$ are thrust ratios for idle and max thrust, such that $T_{idle}=r_{idle}W_0$ and $T_{max}=r_{\max}W_0$. For propellers, p_{idle} and $p_{\max}$ are power ratios for idle and max power, such that $P_{idle}=p_{idle}W_0$ and $P_{\max}=p_{\max}W_0$.

(3) Typical Taxi and Take-off Weight Ratios

Uses previous formulae for typical engine start-up, taxi, and take-off, for typical jet and propeller aircraft. Assumes $\Delta t_{taxi}=20\,\text{min}=0.3333\,\text{h}$, $\Delta t_{\max}=1\,\text{min}=0.01667\,\text{h}$, and $T/W_0=0.30$. Study the derivation section for other situations (e.g., for standard *block-time* concepts, such as those presented for business and commercial aircraft in ref. [8]) and modify constants as needed.

$$\frac{W_i}{W_{i-1}} = \begin{cases} 1-0.015\times SFC & \text{Jets} \\ 1-0.004\times SFC_{hp} & \text{Propellers} \end{cases} \tag{6-33}$$

(4) Climb with Altitude change ΔH

Used to estimate change in weight during climb through an altitude band ΔH. r_{climb} and p_{climb} are the thrust and power ratios, while ROC_{avg} is the average rate-of-climb in fpm.

$$\frac{W_i}{W_{i-1}} = \begin{cases} 1-\dfrac{\Delta H\times SFC\times r_{\text{climb}}}{60\times ROC_{avg}} & \text{Jets} \\ 1-\dfrac{\Delta H\times SFC_{hp}\times p_{\text{climb}}}{60\times ROC_{avg}} & \text{Propellers} \end{cases} \tag{6-34}$$

(5) Range and Endurance for a Jet

Used to estimate change in weight during cruise of a jet, where R and V are in nm and KTAS (UK) or km and km/h (SI), respectively. E in hours (UK and SI).

Range:

$$\frac{W_i}{W_{i-1}} = e^{-\frac{R\times SFC}{V_{KTAS}\times(L/D)}} \tag{6-35}$$

Endurance:

$$\frac{W_i}{W_{i-1}} = e^{-\frac{E\times SFC}{(L/D)}} \tag{6-36}$$

(6) Range and Endurance for a Propeller Aircraft

Used to estimate change in weight during cruise of a propeller aircraft. Same rules hold for R and V as above. η_p is propeller efficiency in cruise, SFC_{hp} in $\text{lb}_\text{f}/(\text{hr}\cdot\text{BHP})$ or $\text{lb}_\text{f}/(\text{hr}\cdot\text{SHP})$.

Range:

$$\frac{W_i}{W_{i-1}} = e^{-\frac{R\times SFC_{hp}}{325.9\eta_p\times(L/D)}} \tag{6-37}$$

Endurance:

$$\frac{W_i}{W_{i-1}} = e^{-\frac{E\times SFC_{hp}V}{325.9\eta_p(L/D)}} \tag{6-38}$$

(7) Descent with Altitude Change ΔH

Used to estimate change in weight during descent through an altitude band ΔH. r_{descent} and p_{descent} are the thrust and power ratios, and ROD_{avg} is the average rate of descent in fpm.

$$\frac{W_i}{W_{i-1}} = \begin{cases} 1-\dfrac{\Delta H\times SFC\times r_{\text{descent}}}{60\times ROD_{avg}} & \text{Jets} \\ 1-\dfrac{\Delta H\times SFC_{hp}\times p_{\text{descent}}}{60\times ROD_{avg}} & \text{Propellers} \end{cases} \tag{6-39}$$

(8) Reserve Cruise

The operation of many classes of aircraft requires additional fuel to be available at the *end-of-mission*. Generally, this assumes cruising speed for a specific time. For instance, NBAA range profile requires 30 min while standard IFR profile calls for 45 min. This fuel can be conveniently accounted for by adding an extra segment at the end of the chain of weight-ratios. This is accomplished using Equation (6-35) and by estimating range as speed × time per the following expressions:

$$\frac{W_i}{W_{i-1}} = e^{-\frac{\Delta t\times SFC}{(L/D)}} \quad \text{Jets} \tag{6-40}$$

$$\frac{W_i}{W_{i-1}} = e^{-\frac{V_{KTAS}\times\Delta t\times SFC_{hp}}{325.9\eta_p\times(L/D)}} \quad \text{Propellers} \tag{6-41}$$

(9) End-of-Mission Landing at Alternate Airport

Used to estimate change in weight from landing to engine shutdown. It is reasonable to expect this ratio to range between 0.99 and 1.00.

$$\frac{W_N}{W_{N-1}} = \frac{W_e+W_c+W_p}{W_{N-1}} \tag{6-42}$$

DERIVATION OF EQUATIONS (6-32)–(6-42)

Equation (6-32): The taxi and take-off are often assumed to consist of several minutes taxiing at idle thrust, T_{idle}, followed by one minute at max thrust, $T_{\max}$. Note that the thrust is *always* the total thrust developed by all the engines, so there is no need to incorporate the number of engines in the formulation. Denoting the idle time (in hours) as Δt_{taxi} and max thrust time as $\Delta t_{\max}$, we can write the change in weight during the segment as

$$\Delta W = \begin{cases} (\Delta t_{taxi} \times T_{idle} + \Delta t_{\max} \times T_{\max}) \times SFC & \text{Jets} \\ (\Delta t_{taxi} \times P_{idle} + \Delta t_{\max} \times P_{\max}) \times SFC_{hp} & \text{Propellers} \end{cases} \quad \text{(i)}$$

Substitute $T_{idle} = r_{idle} W_{i-1}$ and $T_{\max} = r_{\max} W_{i-1}$ for jets or $P_{idle} = p_{idle} W_{i-1}$ and $P_{\max} = p_{\max} W_{i-1}$ for propeller aircraft into Equation (i) and rearrange as shown below

$$\Delta W = \begin{cases} (\Delta t_{taxi} \times r_{idle} + \Delta t_{\max} \times r_{\max}) \times SFC \times W_{i-1} & \text{Jets} \\ (\Delta t_{taxi} \times p_{idle} + \Delta t_{\max} \times p_{\max}) \times SFC_{hp} \times W_{i-1} & \text{Propellers} \end{cases}$$

Therefore, the weight W_i and the associated weight ratio can be determined as follows

$$W_i = W_{i-1} - \Delta W \quad \Rightarrow \quad \frac{W_i}{W_{i-1}} = \begin{cases} 1 - (\Delta t_{taxi} \times r_{idle} + \Delta t_{\max} \times r_{\max}) \times SFC & \text{Jets} \\ 1 - (\Delta t_{taxi} \times p_{idle} + \Delta t_{\max} \times p_{\max}) \times SFC_{hp} & \text{Propellers} \end{cases} \quad \text{(ii)}$$

Note that even though the ratio is written here in terms of indexes, it usually refers to the segment $0 \to 1$.

Equation (6-33): This is a special case of Equation (6-32) and represents typical business jet with $\Delta t_{taxi} = 20\,\text{min} = 0.3333\,\text{h}$ and $\Delta t_{\max} = 1\,\text{min} = 0.01667\,\text{h}$. If T_{idle} amounts to 10% of T_{max}, and T_{max} is 30% of W_0, then Equation (ii) becomes

$$\frac{W_1}{W_0} = 1 - (0.3333 \times (0.1 \times 0.30) + 0.01667 \times 0.30) \times SFC = 1 - 0.015 \times SFC$$

Similarly, for a propeller aircraft, if P_{idle} is $0.1P_{max}$, and $P_{max}/W_0 = 0.08$ HP/lb$_f$, then Equation (ii) becomes

$$\frac{W_1}{W_0} = 1 - (0.3333 \times (0.10 \times 0.08) + 0.01667 \times 0.08) \times SFC_{hp} = 1 - 0.004 \times SFC_{hp}$$

Equation (6-35): The climb covers some initial and final altitudes, denoted as H_{i-1} and H_i, respectively, during which we expect some average climb thrust (T_{climb}) or power (P_{climb}), rate-of-climb (ROC_{avg}), and total time, Δt_{climb}. Denoting the change in altitude as ΔH, we can write the change in weight as

$$\Delta W = \begin{cases} \Delta t_{\text{climb}} \times SFC \times T_{\text{climb}} = \dfrac{\Delta H}{ROC_{avg}} \times SFC \times r_{\text{climb}} W_{i-1} & \text{Jets} \\ \Delta t_{\text{climb}} \times SFC_{hp} \times P_{\text{climb}} = \dfrac{\Delta H}{ROC_{avg}} \times SFC_{hp} \times p_{\text{climb}} W_{i-1} & \text{Propellers} \end{cases} \quad \text{(iii)}$$

Since either form of SFC depends on 1/h, the value of ROC_{avg} (generally in ft/min or fpm) must be converted to ft/h. The preferred units are fpm, so let's convert it in the equation. Thus, we write

$$W_i = W_{i-1} - \Delta W \quad \Rightarrow \quad \frac{W_i}{W_{i-1}} = \begin{cases} 1 - \dfrac{\Delta H \times SFC \times r_{\text{climb}}}{60 \times ROC_{avg}} & \text{Jets} \\ 1 - \dfrac{\Delta H \times SFC_{hp} \times p_{\text{climb}}}{60 \times ROC_{avg}} & \text{Propellers} \end{cases} \quad \text{(iv)}$$

Equations (6-35)–(6-38): The range and endurance is derived by the Breguet range equation (see Chapter 21) and can be transformed as follows (where $W_{ini} = W_{i-1}$ and $W_{fin} = W_i$):

$$R = \frac{V_{KTAS}}{SFC}\frac{L}{D} \ln\left(\frac{W_{i-1}}{W_i}\right) \quad \Leftrightarrow \quad \frac{W_i}{W_{i-1}} = e^{-\frac{R \times SFC}{V_{KTAS} \times (L/D)}}$$

$$E = \frac{1}{SFC}\frac{L}{D} \ln\left(\frac{W_{i-1}}{W_i}\right) \quad \Leftrightarrow \quad \frac{W_i}{W_{i-1}} = e^{-\frac{E \times SFC}{(L/D)}}$$

These equations return range in nm and endurance in hours. For propeller aircraft, range and endurance become:

$$R = \frac{325.9\eta_p}{SFC_{hp}}\frac{L}{D} \ln\left(\frac{W_i}{W_{i-1}}\right) \quad \Rightarrow \quad \frac{W_i}{W_{i-1}} = e^{-\frac{R \times SFC_{hp}}{325.9\eta_p \times (L/D)}}$$

$$E = \frac{325.9\eta_p}{SFC_{hp} V}\frac{L}{D} \ln\left(\frac{W_{i-1}}{W_i}\right) \quad \Leftrightarrow \quad \frac{W_i}{W_{i-1}} = e^{-\frac{E \times SFC_{hp} V}{325.9\eta_p (L/D)}}$$

Equation (6-39): The descent covers some initial and final altitudes, denoted as H_i and H_{i-1}, respectively, during which we expect some average reduced thrust (T_{descent}) and rate-of-descent (ROD_{avg}) and total time, $\Delta t_{\text{descent}}$. Ensure that altitude effects on these parameters are properly accounted for. Denoting the change in altitude as ΔH, we can write the change in weight as

$$\Delta W = \begin{cases} \Delta t_{\text{descent}} \times SFC \times T_{\text{descent}} = \dfrac{\Delta H}{ROD_{avg}} \times SFC \times r_{\text{descent}} W_{i-1} & \text{Jets} \\ \Delta t_{\text{descent}} \times SFC_{hp} \times P_{\text{descent}} = \dfrac{\Delta H}{ROD_{avg}} \times SFC_{hp} \times p_{\text{descent}} W_{i-1} & \text{Propellers} \end{cases} \quad \text{(v)}$$

Therefore, the weight ratio for the segment is

$$W_i = W_{i-1} - \Delta W \Rightarrow$$

$$\frac{W_i}{W_{i-1}} = \begin{cases} 1 - \dfrac{\Delta H \times SFC \times r_{\text{descent}}}{60 \times ROD_{avg}} & \text{Jets} \\ 1 - \dfrac{\Delta H \times SFC_{hp} \times p_{\text{descent}}}{60 \times ROD_{avg}} & \text{Propellers} \end{cases} \quad \text{(vi)}$$

Equation (6-40): The operation of some aircraft requires fuel to be available for a specific time at cruise speed, for instance 30 or 45 min. To account for this fuel, we will add an extra segment representing this requirement at the end of the chain. This is best accomplished using Equation (6-35) and by noting that if we know the cruising speed, we can estimate range as speed × time as shown below:

$$\frac{W_i}{W_{i-1}} = e^{-\frac{R \times SFC}{V_{KTAS} \times (L/D)}} = e^{-\frac{V_{KTAS} \times \Delta t \times SFC}{V_{KTAS} \times (L/D)}} = e^{-\frac{\Delta t \times SFC}{(L/D)}}$$

Equation (6-41): For a propeller aircraft, this becomes

$$\frac{W_i}{W_{i-1}} = e^{-\frac{R \times SFC_{hp}}{325.9 \eta_p \times (L/D)}} = e^{-\frac{V_{KTAS} \times \Delta t \times SFC_{hp}}{325.9 \eta_p \times (L/D)}}$$

Equation (6-42): Assume we know the empty weight, W_e, of the airplane. This makes it possible to estimate the weight at the end-of-mission, W_N, as shown below

$$W_N = W_e + W_c + W_p$$

In terms of weight ratios, this becomes $\dfrac{W_N}{W_{N-1}} = \dfrac{W_e + W_c + W_p}{W_{N-1}}$

EXAMPLE 6-4

Determine the gross weight of a business jet, powered by two HBR turbofans, intended to fly 4000 nm at altitude of 36,000 ft and airspeed *M*0.85. The aircraft must carry enough reserve fuel to fly another 200 nm with nine occupants (including three crew). Figure 6-4 shows an idealized version of this mission, where $R_{2\text{–}3}$ represents 4000 nm and $R_{6\text{–}7}$ is the 200 nm range at *M*0.70 to the alternate. Assume each occupant weighs 170 lb_f and carries 35 lb_f of baggage. Thus, the payload is $W_p = 6 \times (170 + 35) = 1230\ \text{lb}_\text{f}$. The crew weight is $W_c = 3 \times (170 + 35) = 615\ \text{lb}_\text{f}$. Furthermore, assume a Specific Fuel Consumption (*SFC*) of 0.55 1/h. The mission segments are defined as follows:

Assumptions for Segments:

Segment ⓪–①: Engine startup, taxi, and take-off. Assume 20 min (Δt_{taxi}) with $r_{idle} = 0.03$, and 1 min ($\Delta t_{\max}$) at max thrust with $r_{\max} = 0.3$.
Segment ①–②: Climb from S-L to 36,000 ft. Assume $ROC_{avg} = 1500$ fpm and $r_{climb} = 0.3$.
Segment ②–③: Cruise-climb at *M*0.85 for 4000 nm range. Assume $L/D = 14$.
Segment ③–④: Descent at *M*0.85 from 36,000 ft. Assume descent from 36,000 to 5000 ft ($\Delta H = -31{,}000$ ft), $ROD_{avg} = -2000$ fpm, and $r_{descent} = 0.1$.

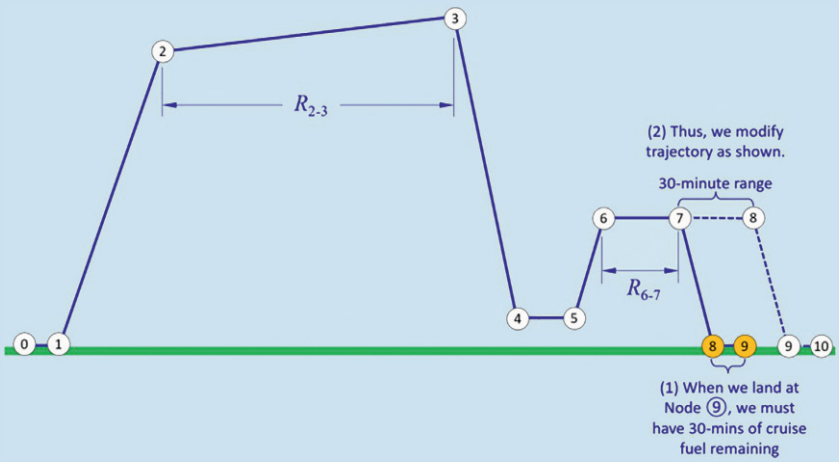


FIGURE 6-4 Mission profile based on the NBAA profile discussed in Chapter 21.

EXAMPLE 6-4 (*cont'd*)

Segment ④–⑤: Attempted IFR approach + ATC clearance to alternate. Assume a max endurance $L/D=10$ for 5 min.
Segment ⑤–⑥: Climb to cruise altitude (20,000 ft) toward alternate. Assume $ROC_{avg}=2000$ fpm and $r_{climb}=0.5$ (due to lighter weight).
Segment ⑥–⑦: Cruise-climb at $M0.70$ for 200 nm range. Assume $L/D=14$.
Segment ⑦–⑧: Rather than descending to alternate, continue for 30 min at $M0.70$ and $L/D=14$.
Segment ⑧–⑨: Descent at $M0.70$. Assume $ROD_{avg}=-2000$ fpm and $L/D=10$.
Segment ⑨–⑩: Landing and engine shutdown. For the final segment let's assume that $W_9/W_8\approx 1$.

Historical relation: $\left(\frac{W_e}{W_0}\right)_{hist}=0.9038-0.03163\cdot \ln W_0$

SOLUTION:

First, let's calculate the weight ratios for each mission segment using the above assumptions and by selecting the weight-ratio expressions for jets:

Segment 0–1: For engine startup, taxi, and take-off, use Equation (6-33);

$$\frac{W_1}{W_0}=1-0.015\times SFC=1-0.015\times(0.55)=0.9918$$

Segment 1–2: For climb, use Equation (6-34) with $\Delta H=36{,}000$ ft and $r_{climb}=0.3$ to get:

$$\frac{W_2}{W_1}=1-\frac{\Delta H\times SFC\times r_{\text{climb}}}{60\times ROC_{avg}}=1-\frac{36000\times 0.55\times 0.3}{60\times 1500}=0.9340$$

Segment 2–3: For cruise, use Equation (6-35). The cruising speed in KTAS is obtained from $V_{KTAS}=a_oM=(573.6)(0.85)=488$ KTAS, where a_o is the speed of sound in KTAS at 36,000 ft

$$\left(\frac{W_3}{W_2}\right)=e^{-\frac{R\times SFC}{V_{KTAS}\times(L/D)}}=e^{-\frac{4000\times 0.55}{488\times 14}}=0.7245$$

Segment 3–4: For descent, use Equation (6-39), $ROD_{avg}=-2000$ fpm, and $\Delta H=-31{,}000$ ft we get:

$$\left(\frac{W_4}{W_3}\right)=1-\frac{\Delta H\times SFC\times r_{\text{descent}}}{60\times ROD_{avg}}=1-\frac{-31000\times 0.55\times 0.1}{60\times(-2000)}=0.9858$$

Segment 4–5: For the 5-min hold, use Equation (6-36) with $L/D=10$;

$$\left(\frac{W_5}{W_4}\right)=e^{-\frac{E\times SFC}{(L/D)}}=e^{-\frac{(5/60)\times 0.55}{(10)}}=0.9954$$

Segment 5–6: For the climb to alternate, again use Equation (6-34) with $\Delta H=15{,}000$ ft, $ROC_{avg}=2000$ fpm and, now assume $r_{climb}=0.5$ (was 0.3 for Segment 1–2):

$$\frac{W_6}{W_5}=1-\frac{\Delta H\times SFC\times r_{\text{climb}}}{60\times ROC_{avg}}=1-\frac{15000\times 0.55\times 0.5}{60\times 2000}=0.9656$$

Segment 6–7: For the 200 nm cruise to alternate at 20,000 ft, again use Equation (6-35). The Mach number is 0.70, so $V_{KTAS}=a_oM=(614.1)(0.70)=430$ KTAS, and $L/D=14$;

$$\left(\frac{W_7}{W_6}\right)=e^{-\frac{R\times SFC}{V\times L/D}}=e^{-\frac{200\times 0.55}{430\times 14}}=0.9819$$

Segment 7–8: For descent, again use Equation (6-39), $ROD_{avg}=-2000$ fpm, and $\Delta H=-20{,}000$ ft we get:

$$\left(\frac{W_8}{W_7}\right)=1-\frac{\Delta H\times SFC\times r_{\text{descent}}}{60\times ROD_{avg}}=1-\frac{-20000\times 0.55\times 0.1}{60\times(-2000)}=0.9908$$

Segment 8–9: For the reserve cruise segment, we assume $M0.70$ at 20,000 ft with $L/D=14$ for $\Delta t=0.5$ h (30 min). Then use Equation (6-40) to get

$$\frac{W_i}{W_{i-1}}=e^{-\frac{\Delta t\times SFC}{(L/D)}}=e^{-\frac{0.5\times 0.55}{14}}=0.9805$$

Segment 9–10: For the final segment we assume $(W_9/W_8)\approx 1$. The complete mission is illustrated in Figure 6-5. We are now ready to determine the weight fraction W_{10}/W_0 using the weight fractions

$$\frac{W_{10}}{W_0}=\frac{W_1}{W_0}\frac{W_2}{W_1}\frac{W_3}{W_2}\frac{W_4}{W_3}\frac{W_5}{W_4}\frac{W_6}{W_5}\frac{W_7}{W_6}\frac{W_8}{W_7}\frac{W_9}{W_8}\frac{W_{10}}{W_9}=0.6066$$

Substitute into Equation (6-29) get

$$A+B\ln W_0+\frac{W_c+W_p}{W_0}-\frac{W_N}{W_0}=0$$

$$\Rightarrow\quad 0.9038-0.3163\ln W_0+\frac{615+1230}{W_0}-0.6066=0$$

This becomes: $\frac{1845}{W_0}-0.03163\ln W_0+0.2972=0$

This transcendental equation was solved through iteration and yielded $W_0\approx 44{,}556$ lb$_f$. It should be stated that parts of this problem were designed to resemble the performance of the Dassault Falcon 900, which has a range of 3995 nm with 7 passengers (and two crew). The estimated gross weight is about 2.1% less than its gross weight of 45,500 lb$_f$ [9]. Not bad considering a first stab.

EXAMPLE 6-4 (*cont'd*)

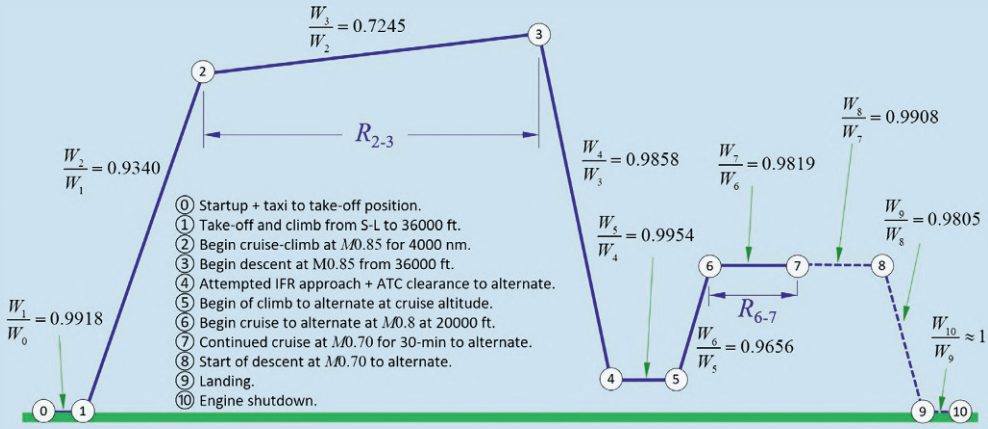


FIGURE 6-5 Mission profile based on the NBAA profile discussed in Chapter 21.

Further Analyses

(1) Once we know W_0, we can obtain the empty weight from either Equation (6-27) or (6-28). We find that $W_e/W_0 = 0.5652$, so $W_e = (W_e/W_0)\cdot W_0 = 25{,}184$ lb$_f$. This compares to approximately 23,400 lb$_f$ operating empty weight (7.6% difference) [9].

(2) We can also calculate the weight of the aircraft at every node. This is helpful to estimate various fuel weights. For instance, the complete mission requires $W_0 - (W_{10}/W_0)\cdot W_0 = 44{,}556 - 0.6066 \times 44{,}556 = 17{,}528$ lb$_f$ (2616 US gal). The Falcon 900's max fuel weight is 19,000 lb$_f$ [9].

(3) Additionally, we can adjust the values of r_{climb} for segments 1–2 and 5–6, using Equation (6-30). For segment 1–2, r_{climb} was 0.3, but should be 0.3025. For segment 5–6, r_{climb} was 0.5, but should be 0.4556. Using these in a second iteration changes the empty and gross weights to 24,684 and 43,619 lb$_f$, respectively.

6.3 SECONDARY WEIGHT ANALYSIS METHODS

Secondary weight analysis refers to all weight estimation methods that are used *after* the initial weight analysis has been completed. Per Figure 1-11, the initial weight is completed by Step 7 and is used in Steps 8 through 11 establish the initial geometry. Once established, it is possible to estimate the weight of numerous components constituting the aircraft, such as the wing, HT, VT, fuselage, and so forth. This is accomplished in Step 12 of the design algorithm: It returns a more refined estimate of the aircraft's empty weight.

The secondary weight analysis gives the designer deeper insight into the new aircraft. Of course, it is also far more laborious to accomplish—at least while it is being prepared in a spreadsheet or computer code. Since this step provides component weight, it allows target weights of subcomponents to be prepared and weight budget to be established. It is vital to introduce structural weight targets to the structural design team, as this helps drive the design toward a lighter weight. However, the most important questions that can be answered include the position of the center-of-gravity, as well as moments and products of inertia. These are essential parameters for the evaluation of the aircraft's certifiability via stability and control theory.

Typically, secondary weight estimation methods include:

Known weights	This section
Statistical weight estimation	see Section 6.4
Direct weight estimation	see Section 6.5

The concept "known weights" refers to parts and component that can either be weighed with reasonable accuracy or whose manufacturer (if the component is obtained from an outside vendor) can disclose the weight with reasonable confidence. Most of the time the weight analyst uses all three methods simultaneously, but known weights always supersede both the statistical and direct weight estimations. Engines, propellers, wheels, tires, brakes, landing gear struts, and standard

parts (electronics, avionics, antennas, instruments, fasteners, etc.) are examples of components that will likely have published weights. Statistical and direct weight estimations will now be treated in some detail.

6.4 STATISTICAL WEIGHT ESTIMATION METHODS

Statistical weight estimation methods are based on historical data derived from existing airplanes. For instance, if we know the weight of the wing structure for a population of aircraft that fall into a specific class (e.g., GA aircraft), it is possible to derive relationships based on geometric parameters such as wing area, aspect ratio, taper ratio, ultimate load factors, and so forth. The assumption is that the wing weight of two different aircraft in the same class that are certified to the same set of regulations and whose gross weight is similar, should be similar, even if made by different manufacturers. The statistical relationship established by the entire class of aircraft can thus be used to estimate the wing weight of any same class aircraft if it falls between the extremes of the aircraft in that class. Such estimation methods usually require some dimensions to have been established beforehand (e.g., AR, TR, sweep, S, etc.). Such methods are often developed in industry or in academia. Since many airplanes feature aluminum and composites alike, the user must use such statistical methods with care, as these may be solely based on aluminum aircraft.

Statistical weight estimations methods are always based on a specific class of aircraft, for instance, general aviation aircraft, commercial aircraft, fighters, and so on. Such classes share commonalities that improve the accuracy of the formulation. However, be mindful of some classes of aircraft have seen advances, such as an increased use of composites, that may skew the resulting weights.

6.4.1 Weight of Aircraft Components—GA Aircraft

***Guidance*: Generally, applies to single and multiengine propeller aircraft. Only use this method once you have more information about the geometry of the aircraft. This is not an initial weight estimation method like METHODS 1, 2, and 3, presented earlier; it requires a large amount of data that results from analysis that follows the use of those methods. It is to be used AFTER the initial weight has been determined. Also note that *this method yields the empty weight*, W_e, of the aircraft. To get the gross weight, W_0, occupants, freight, and fuel must be added.**

The set of equations has been expanded in this edition of the book. They are obtained from refs. [4, 5, 10–12]. All are intended for conventional GA aircraft. All assume aluminum aircraft, requiring a correction factor for composite aircraft. Note that the method presented by [10] is also presented by [11]. It was developed by Anderson of the Air Force Flight Dynamics Laboratory [13]. It is identified here as USAF. Also note that refs. [5, 11] present tables with component weights for several aircraft.

The reader may ask: "Which method should I select and why?" The short answer is that all the methods should be considered, provided they are inside the scope of their legitimacy (see Example 6-5 for guidance). Then, calculate the average. When justified, engineering judgment can be used to eliminate a specific equation from the batch. The reader is strongly urged to apply the methods to aircraft in the same class as the aircraft being designed and evaluate how "close" it matches their empty weight. If the results do not match well, then develop scaling factors. For instance, if the predicted weight is, say, 15% lighter than the actual empty weight of the reference aircraft, the results for the new aircraft can be multiplied by a factor of 1.18.

(1) Wing Weight

The following expressions estimate the weight of the wing structure and include ailerons, flaps, and wing tip fairings. Fuel tanks are not included. Equation (6-44) should be used with care because there is no reference to W_0. Upper value for t/c is 0.18. The Cessna equations are valid for $V_H \leq 200$ KTAS. USAF equations valid for $V_H \leq 300$ KTAS. Equation (6-47) valid for $W_0 \leq 12{,}500$ lb_f.

Cessna:

$$W_W = 0.04674 \cdot (n_z W_0)^{0.397} S_W^{0.360} AR_W^{1.712} \quad \text{(Cantilever)} \tag{6-43}$$

$$W_W = 0.002933 \cdot n_z^{0.611} S_W^{1.018} AR_W^{2.473} \quad \text{(Strut-braced)} \tag{6-44}$$

Raymer:

$$W_W = 0.036 \cdot S_W^{0.758} W_{FW}^{0.0035} \left(\frac{AR_W}{\cos^2 \Lambda_{c/4}}\right)^{0.6} \cdot q^{0.006} \lambda_W^{0.04} \left(\frac{100 \cdot t/c}{\cos \Lambda_{c/4}}\right)^{-0.3} (n_z W_0)^{0.49} \tag{6-45}$$

Torenbeek:

$$W_W = 0.00125 \cdot W_0 \left(\frac{b_W}{\cos \Lambda_{c/2}}\right)^{0.75} \cdot \left(1 + \sqrt{\frac{6.3 \cos \Lambda_{c/2}}{b_W}}\right) n_z^{0.55} \cdot \left(\frac{b_W S_W}{t_{W\max} W_0 \cos \Lambda_{c/2}}\right)^{0.30} \tag{6-46}$$

USAF:

$$W_W = 96.948 \cdot \left[\left(\frac{n_z W_0}{10^5} \right)^{0.65} \left(\frac{AR_W}{\cos^2 \Lambda_{c/4}} \right)^{0.57} \cdot \left(\frac{S_W}{100} \right)^{0.61} \left(\frac{1+\lambda_W}{2(t/c)} \right)^{0.36} \sqrt{1 + \frac{V_H}{500}} \right] 0.993 \qquad (6\text{-}47)$$

Where:

b_W = Wingspan in ft
S_W = Trapezoidal wing area in ft^2
AR_W = Aspect Ratio of wing
λ_W = Taper ratio of wing
$\Lambda_{c/4}$ = Wing sweep at 25% MGC
$\Lambda_{c/2}$ = Wing sweep at 50% MGC
t/c = Wing thickness-to-chord ratio (maximum)
$t_{W\ \max}$ = Max thickness of the wing root chord in ft
W_W = Predicted weight of wing in lb$_f$
W_{FW} = Weight of fuel in wing in lb$_f$. (If $W_{FW} = 0$ then let $W_{FW}^{0.0035} = 1$)
q = Dynamic pressure at cruise (lb$_f$/ft^2)
n_Z = Ultimate load factor (=1.5 × limit load factor)
W_0 = Design gross weight in lb$_f$
V_H = Maximum level airspeed at S-L in KEAS

(2) Horizontal Tail (HT) Weight

The expressions below predict the weight of the HT (stabilizer and elevator). They also apply to canards if they are lightly loaded (e.g., Cozy, Long EZ). Highly loaded canards (e.g., P-180 Avanti, Beech Starship) should use the Wing Weight equations. The Cessna equations are valid for $V_H \leq 200$ KTAS. Note that Equation (6-50) differs from the rest in that it predicts the combined weight of the HT and VT.

Cessna:
$$W_{HT} = \frac{3.184 W_0^{0.887} S_{HT}^{0.101} AR_{HT}^{0.138}}{174.04 t_{HT\max}^{0.223}} \qquad (6\text{-}48)$$

Raymer:
$$W_{HT} = 0.016 (n_z W_0)^{0.414} q^{0.168} S_{HT}^{0.896} \left(\frac{100 \cdot t/c}{\cos \Lambda_{c/4}} \right)^{-0.12} \cdot \left(\frac{AR_W}{\cos^2 \Lambda_{HT}} \right)^{0.043} \lambda_{HT}^{-0.02} \qquad (6\text{-}49)$$

Torenbeek:
$$W_{EMP} = 0.04 \left[n_z (S_{HT} + S_{VT})^2 \right]^{0.75} \qquad (6\text{-}50)$$

USAF:
$$W_{HT} = 71.927 \left[\left(\frac{n_z W_0}{10^5} \right)^{0.87} \left(\frac{S_{HT}}{100} \right)^{1.2} \left(\frac{l_{HT}}{10} \right)^{0.483} \cdot \sqrt{\frac{b_{HT}}{t_{HT\max}}} \right] 0.458 \qquad (6\text{-}51)$$

where

b_{HT} = HT span in ft
S_{HT} = Trapezoidal HT area in ft^2
AR_{HT} = Aspect Ratio of HT
λ_{HT} = HT taper ratio
Λ_{HT} = HT sweep at 25% MGC
W_{HT} = Predicted weight of HT in lb$_f$
$W_{EMP} = W_{HT} + W_{VT}$ = Combined weight of HT *and* VT in lb$_f$
l_{HT} = Horizontal tail arm, from wing $c/4$ to HT $c/4$ in ft
$t_{HT\ \max}$ = Max root chord thickness of HT in ft

(3) Vertical Tail (VT) Weight

The formulation below predicts the weight of the VT (fin and rudder) and applies to conventional and T-tail configurations. Other tail configurations can be treated with various modifications. For instance, the weight of a triple tail (e.g., L-1049 Constellation) can be treated by multiplying the weight of a single surface by 3. Weight boosting like that accomplished by F_{tail} for T-tails should be considered as well. The Cessna equations are valid for $V_H \leq 200$ KTAS.

Cessna:
$$W_{VT} = (1 + 0.2 F_{tail}) \frac{1.68 W_0^{0.567} S_{VT}^{0.1249} AR_{VT}^{0.482}}{639.95 t_{VT\max}^{0.747} (\cos \Lambda_{VT})^{0.882}} \qquad (6\text{-}52)$$

Raymer:
$$W_{VT} = 0.073 (1 + 0.2 F_{tail}) (n_z W_0)^{0.376} q^{0.122} \cdot S_{VT}^{0.873} \left(\frac{100 \cdot t/c}{\cos \Lambda_{VT}} \right)^{-0.49} \cdot \left(\frac{AR_W}{\cos^2 \Lambda_{VT}} \right)^{0.357} \lambda_{VT}^{0.039} \qquad (6\text{-}53)$$

Torenbeek: Weight of HT and VT combined in Equation (6-50)

USAF:
$$W_{VT} = 55.786 (1 + 0.2 F_{tail}) \left[\left(\frac{n_z W_0}{10^5} \right)^{0.87} \left(\frac{S_{VT}}{100} \right)^{1.2} \sqrt{\frac{b_{VT}}{t_{VT\max}}} \right]^{0.458} \qquad (6\text{-}54)$$

where

b_{VT} = VT span in ft
S_{VT} = Trapezoidal VT area in ft^2
AR_{VT} = Aspect Ratio of VT
λ_{VT} = VT taper ratio
Λ_{VT} = VT sweep at 25% MGC
$t_{VT\ \max}$ = Max root chord thickness of VT in ft
W_{VT} = Predicted weight of VT in lb$_f$
F_{tail} = 0 for conventional tail, =1 for T-tail

(4) Fuselage Weight

The below expressions predict the weight of the fuselage shell and the associated internal structure but

excludes furnishing. Cessna equations valid for $V_H \leq 200$ KTAS and unpressurized fuselages. Ref. [11] recommends multiplying W_{FUS} by 1.65 for seaplanes. To use Equation (6-56) with UAVs, set $N_{OCC} = 1$.

Cessna:

$$W_{FUS} = 0.04682 W_0^{0.692} R_{\max}^{0.374} l_{FS}^{0.590} \quad \text{(Low-wing)} \tag{6-55}$$

$$W_{FUS} = 14.86 W_0^{0.144} \left(\frac{l_{FS}}{R_{\max}}\right)^{0.778} l_{FS}^{0.383} N_{OCC}^{0.455} \quad \text{(High-wing)} \tag{6-56}$$

Raymer:

$$W_{FUS} = 0.052 \cdot S_{FUS}^{1.086} (n_z W_0)^{0.177} l_{HT}^{-0.051} \left(\frac{l_{FS}}{d_{FS}}\right)^{-0.072} \cdot q^{0.241} + 11.9 (V_P \Delta P)^{0.271} \tag{6-57}$$

Torenbeek: No expression given for GA aircraft

USAF:

$$W_{FUS} = 200 \left[\left(\frac{n_z W_0}{10^5}\right)^{0.286} \left(\frac{l_F}{10}\right)^{0.857} \left(\frac{w_F + d_F}{10}\right) \left(\frac{V_H}{100}\right)^{0.338} \right]^{1.1} \tag{6-58}$$

where

W_{FUS} = Predicted fuselage weight in lb_f
S_{FUS} = Fuselage wetted area in ft^2
w_F = Fuselage max width in ft
d_F = Fuselage max depth in ft
d_{FS} = Depth of fuselage structure in ft
V_P = Volume of pressurized cabin section in ft^3
l_F = Fuselage length in ft
l_{FS} = Length of fuselage structure (forward bulkhead to aft frame) in ft
$R_{\max}$ = Fuselage maximum perimeter in ft
N_{OCC} = Number of occupants (crew and passengers)
ΔP = Cabin pressure differential, in psi (typically 8 psi)

(5) Main Landing Gear Weight

The following expressions are used to estimate the weight of the main landing gear. Note that additional relations can be obtained from ref. [14]. The landing gear shock strut length is the distance between the upper attachment point and the center of the wheel axis. The Cessna equations are valid for $V_H \leq 200$ KTAS. USAF equation valid for $V_H \leq 300$ KTAS. Equations (6-62) and (6-63) are used to calculated the weight of each individual landing gear. The constants A, B, C, and D in those equations are given in Table 6-2. Equations (6-59), (6-60), and (6-64) predict the weight of the main and nose gears.

Cessna:

$$W_{MNLG} = 6.2 + 0.0143 W_0 + 0.362 W_l^{0.417} n_l^{0.950} L_m^{0.183} + 0.007157 W_l^{0.749} n_z L_n^{0.788} \tag{6-59}$$

$$W_{MNLG} = 6.2 + 0.0283 W_0 + 0.362 W_l^{0.417} n_l^{0.950} L_m^{0.183} + 0.007157 W_l^{0.749} n_z L_n^{0.788} \tag{6-60}$$

Raymer: $W_{MLG} = 0.095 (n_l W_l)^{0.768} L_m^{0.409}$ (6-61)

Torenbeek:

$$W_{LG} = A + B W_0^{0.75} + C W_0 + D W_0^{1.5} \quad \text{(Low wing)} \tag{6-62}$$

$$W_{LG} = 1.08 \left(A + B W_0^{0.75} + C W_0 + D W_0^{1.5}\right) \quad \text{(High wing)} \tag{6-63}$$

USAF: $W_{MNLG} = 0.054 (n_l W_l)^{0.684} L_m^{0.501}$ (6-64)

where

W_{MLG} = Predicted weight of the main landing gear in lb_f
W_{MNLG} = Predicted weight of the *entire* landing gear in lb_f
W_{LG} = Predicted weight of a specific landing gear (main, nose, or tail) in lb_f
n_l = Ultimate landing load factor (typical range 3.5–5.5)
W_l = Design landing weight in lb_f
L_m = Length of the main landing gear shock strut in ft

(6) Nose Landing Gear Weight

The following expressions are used to estimate the weight of the nose landing gear.

TABLE 6-2 Constants A, B, C, and D for Equations (6-62) and (6-63).

Class	Type of Landing Gear		A	B	C	D
Business and trainer jets	Retractable	Main	33	0.04	0.021	0
		Nose	12	0.06	0	0
All civil aircraft	Fixed	Main	20	0.10	0.019	0
		Nose	25	0	0.0024	0
		Tail	9	0	0.0024	0
	Retractable	Main	40	0.16	0.019	1.5×10^{-5}
		Nose	20	0.10	0	2.0×10^{-6}
		Tail	5	0	0.0031	0

Cessna: $W_{NLG} = 0$ (Included in W_{MNLG}) (6-65)

Raymer: $W_{NLG} = 0.125(n_l W_l)^{0.566} L_n^{0.845}$ (6-66)

Torenbeek: See Equations (6-62) and (6-63).

USAF: $W_{NLG} = 0$ (Included in W_{MNLG}) (6-67)

where

n_l = Ultimate landing load factor
W_l = Design landing weight in lb_f
W_{NLG} = Predicted weight of the nose landing gear in lb_f
L_n = Length of the nose landing gear strut in ft

(7) Nacelle/Cowling Weight

The set of equations below is used to estimate the weight of nacelles or cowlings. If used for podded engines (e.g., Learjet 35), they include the pylons and ducts. For buried engines (e.g., Aermacchi M-311), they include internal ducts, but not the inlet. For propeller engines, the weight includes engine mount and the cowlings. For the multiengine Torenbeek equations, add $0.04P_{max}N_{ENG}$ if main landing gear retracts into nacelle (e.g., Fokker F-27/F50 style). For Equation (6-73) add $0.11P_{max}N_{ENG}$ if engine exhaust is of "over-wing" style (e.g., Lockheed P-3C style). HOP is short for *horizontally opposed piston engine*. HBPR is short for *high-bypass ratio*.

Cessna: $W_{NAC} = 0.37P_{max}N_{ENG}$ (Radial piston engine) (6-68)

$W_{NAC} = 0.24P_{max}N_{ENG}$ (HOP engine) (6-69)

Raymer: Included in Equation (6-78)

Torenbeek:

$W_{NAC} = 2.5\sqrt{P_{max}}$ (Single-engine tractor propeller) (6-70)

$W_{NAC} = 0.32P_{max}N_{ENG}$ (Multi-engine HOP) (6-71)

$W_{NAC} = 0.045P_{max}^{1.25}N_{ENG}$ (Multi-engine radial piston) (6-72)

$W_{NAC} = 0.14P_{max}N_{ENG}$ (Multi-engine turboprop) (6-73)

$W_{NAC} = 0.055T_{max}$ (Podded turbojet or-fan) (6-74)

$W_{NAC} = 0.065T_{max}$ (HBPR turbofan on a pylon) (6-75)

USAF: Included in Eq.(6.80) (6-76)

where

W_{NAC} = Predicted weight of *all* engine nacelles in lb_f
N_{ENG} = Number of engines
P_{max} = Maximum rated power *per* engine in BHP or ESHP

(8) Uninstalled (Dry) Engine Weight

If engine weight (W_{ENG}) is unknown, use Equations (6-106), (6-107), and (6-108), for pistons, turboprops, and turbofans, respectively.

(9) Installed Engine Weight

The below equations predict the weight of the engine with nacelles or cowlings and propellers (if not a jet). Equations (6-78) and (6-80) do not need the weight of the nacelle/cowling, etc., as these are included. Propeller weight, $W_{PROP} = 0$ for jet engine configurations. It must be obtained directly from manufacturers (e.g., online).

Cessna: $W_{EI} = (1.3P_{max} + W_{PROP})N_{ENG} + W_{NAC}$ (6-77)

Raymer: $W_{EI} = 2.575\ W_{ENG}^{0.922}N_{ENG}$ (6-78)

Torenbeek:

$$W_{EI} = (W_{ENG} + W_{PROP})N_{ENG} + 1.03N_{ENG}^{0.3}P_{max}^{0.7} + W_{NAC} \quad (6\text{-}79)$$

USAF: $W_{EI} = 2.575\ W_{ENG}^{0.922}N_{ENG}$ (6-80)

where

W_{EI} = Predicted weight of *all* installed engines in lb_f
W_{ENG} = Weight of *each* uninstalled engine in lb_f (e.g., see Section 6.4.2)
W_{PROP} = Weight of a *single* propeller in lb_f

(10) Fuel System Weight

Fuel system consists of fuel tanks, pipes, pumps, vents, and other components required to deliver fuel to the engine(s). The following formulation estimates the weight of this system.

Cessna: $W_{FS} = 0.40Q_{tot}$ (Avgas – no tip-tanks) (6-81)

$W_{FS} = 0.4467Q_{tot}$ (Jet A – no tip-tanks) (6-82)

$W_{FS} = 0.70Q_{tot}$ (Avgas – tip-tanks) (6-83)

$W_{FS} = 0.7817Q_{tot}$ (Jet A – tip-tanks) (6-84)

Raymer: $W_{FS} = 2.49Q_{tot}^{0.726}\left(\frac{Q_{tot}}{Q_{tot}+Q_{int}}\right)^{0.363}N_{TANK}^{0.242}N_{ENG}^{0.157}$ (6-85)

Torenbeek: $W_{FS} = 2Q_{tot}^{0.667}$ (Single-engine piston) (6-86)

$W_{FS} = 4.5Q_{tot}^{0.60}$ (Multi-engine piston) (6-87)

$W_{FS} = 1.6Q_{tot}^{0.60}$ (Multi-engine piston) (6-88)

USAF: $W_{FS} = 2.49\left[Q_{tot}^{0.6}\left(\frac{Q_{tot}}{Q_{tot}+Q_{int}}\right)^{0.3}N_{TANK}^{0.2}N_{ENG}^{0.13}\right]^{1.21}$ (6-89)

where

Q_{tot} = Total fuel quantity in US gallons
Q_{int} = Fuel quantity in integral tanks in US gallons
N_{TANK} = Number of fuel tanks
W_{FS} = Predicted weight of the fuels system in lb_f
W_f = Maximum fuel quantity aircraft can carry in lb_f

(11) Flight Control System Weight

This system consists of everything needed to operate the flight controls (aileron, elevator, rudder, flaps). It consists of cables, pushrods, pulleys, bell-cranks, cockpit controls, and required structural reinforcements. It assumes dual cockpit controls, except as otherwise noted. Equation (6-90) valid for $W_0 \leq 8000$ lb_f.

Cessna:

$$W_{CTRL} = 0.0168 W_0 \quad \text{(Manual control system)} \tag{6-90}$$

Raymer:

$$W_{CTRL} = 0.053 l_{FS}^{1.536} b_W^{0.371} \left(n_z W_0 \times 10^{-4}\right)^{0.80} \tag{6-91}$$

Torenbeek:

$$W_{CTRL} = 0.23 W_0^{0.667} \quad \text{(Manual single control system)} \tag{6-92}$$

$$W_{CTRL} = 0.44 W_0^{0.667} \quad \text{(Manual transport aircraft)} \tag{6-93}$$

$$W_{CTRL} = 0.64 W_0^{0.667} \quad \text{(Powered transport aircraft)} \tag{6-94}$$

USAF:

$$W_{CTRL} = 1.066 W_0^{0.626} \quad \text{(Manual control system)} \tag{6-95}$$

$$W_{CTRL} = 1.08 W_0^{0.7} \quad \text{(Powered control system)} \tag{6-96}$$

where

W_{CTRL} = Predicted weight of the flight control system in lb_f,
b_W = Wingspan in ft

(12) Hydraulic System Weight

For small aircraft, hydraulic system is limited to brakes, retractable landing gear, and sometimes flaps. In larger aircraft, the flight controls, spoilers, and thrust reversers also use hydraulic boost. The weight of the hydraulic systems for the flight controls is usually included in the Flight Control System, so the following expression is for the other components.

$$\text{All:} \quad W_{HYD} = 0.001 W_0 \tag{6-97}$$

where

W_{HYD} = Predicted weight of the hydraulics system in lb_f.

(13) Avionics Systems Weight

Comprises the electronic navigation (NAV) and communication (COM) systems. The expression below assumes analog dials and overpredicts the weight of modern *electronic flight instrument system* (EFIS). Weights of various uninstalled avionics can be obtained from sources such as ref. [15]. Expect integrated avionics packages (e.g., Garmin G1000) for smaller aircraft to weigh 45 to 50 lb_f and as much as 1200 to 1500 lb_f for sophisticated business jets.

$$\text{All:} \quad W_{AV} = 2.11 W_{UAV}^{0.933} \tag{6-98}$$

where

W_{AV} = Predicted weight of the avionics installation in lb_f,
W_{UAV} = Weight of the uninstalled avionics in lb_f.

(14) Electrical System

Comprises all electric wiring for lights, instruments, avionics, fuel system, climate control, and so forth.

Cessna: $$W_{EL} = 0.0268 W_0 \tag{6-99}$$

Raymer/USAF: $$W_{EL} = 12.57 (W_{FS} + W_{AV})^{0.51} \tag{6-100}$$

Torenbeek: $$W_{EL} = 0.0078 (W_0 - W_u)^{1.2} - W_{HYD} \tag{6-101}$$

where

W_{EL} = Predicted weight of the electronics system in lb_f,
W_u = Target useful load in lb_f.

(15) Air Conditioning, Pressurization, and Antiicing

Air conditioning includes both cooling and heating of the cabin volume. Pressurization system usually consists of various equipment (outflow and relief valves, pressure regulators, compressors, heat exchangers, and ducting). Antiicing systems included are either pneumatic inflatable boots or bleed air heated elements.

$$\text{All:} \quad W_{\text{AC}} = 0.265 W_0^{0.52} N_{OCC}^{0.68} W_{AV}^{0.17} M^{0.08} \tag{6-102}$$

where

W_{AC} = Predicted weight of the AC and antiicing installation in lb_f,
N_{OCC} = Number of occupants (crew and passengers),
M = Mach number.

(16) Furnishings

Includes seats, insulation, sound proofing, lighting, galley, lavatory, overhead hat-racks, emergency equipment, and associated electric systems.

Cessna: $$W_{FURN} = 0.0412 N_{OCC}^{1.145} W_0^{0.489} \tag{6-103}$$

Raymer: $W_{FURN} = 0.0582 W_0 - 65$ (6-104)

USAF: $W_{FURN} = 34.5 N_{CREW} q_H^{0.25}$ (6-105)

where

W_{FURN} = Predicted weight of furnishings in lb_f,
N_{CREW} = Number of crew,
q_H = Dynamic pressure at max level airspeed, lb_f/ft^2.

EXAMPLE 6-5

Estimate the wing weight of a light airplane with the following specifications, using all appropriate methods:

S_W = Trapezoidal wing area = $130\,ft^2$
W_{fw} = Weight of fuel in wing = $100\ lb_f$
AR_W = Wing Aspect Ratio = 8
$\Lambda_{c/4}$ = Wing sweep at 25% MGC = 0 degree
$\Lambda_{c/2}$ = Wing sweep at 50% MGC = −2.386 degrees
q = Dynamic pressure at cruise (100 KCAS) = $33.9\ lb_f/ft^2$
λ_W = Wing Taper Ratio = 0.5
t/c = Wing thickness to chord ratio = 0.16
W_0 = Design gross weight = $1320\ lb_f$
n_Z = Ultimate load factor = $1.5 \times 4.0 = 6.0\,g$
c_r = Wing root chord = 5.375 ft
$t_{w\ max} = c_r \times t/c = 0.8600$ ft

SOLUTION:

An estimation using the Cessna formulation for a cantilever wing per Equation (6-43) gives:

$$W_W = 0.04674 \cdot (n_z W_0)^{0.397} S_W^{0.360} AR_W^{1.712} = 335\,lb_f$$

Using the Cessna formulation for a strut-braced wing per Equation (6-44) we get:

$$W_W = 0.002933 \cdot n_z^{0.611} S_W^{1.018} AR_W^{2.473} = 213\,lb_f$$

Using Raymer's formulation of Equation (6-45) we get

$$W_W = 0.036 \cdot S_W^{0.758} W_{FW}^{0.0035} \left(\frac{AR_W}{\cos^2 \Lambda_{c/4}}\right)^{0.6} q^{0.006} \lambda_W^{0.04} \left(\frac{100 \cdot t/c}{\cos \Lambda_{c/4}}\right)^{-0.3} (n_z W_0)^{0.49} = 180\,lb_f$$

Using Torenbeek's formulation of Equation (6-46) we get

$$W_W = 0.00125 \cdot W_0 \left(\frac{b_W}{\cos \Lambda_{c/2}}\right)^{0.75} \cdot \left(1 + \sqrt{\frac{6.3 \cos \Lambda_{c/2}}{b_W}}\right) n_z^{0.55} \left(\frac{b_W S_W}{t_{W\max} W_0 \cos \Lambda_{c/2}}\right)^{0.30} = 128\,lb_f$$

The USAF formulation of Equation (6-47) we get

$$W_W = 96.948 \cdot \left[\left(\frac{n_z W_0}{10^5}\right)^{0.65} \left(\frac{AR_W}{\cos^2 \Lambda_{c/4}}\right)^{0.57} \left(\frac{S_W}{100}\right)^{0.61} \cdot \left(\frac{1+\lambda_W}{2(t/c)}\right)^{0.36} \sqrt{1 + \frac{V_H}{500}}\right]^{0.993} = 139\,lb_f$$

Keeping in mind that typical wings of this class of aircraft range between 130 and 180 lb_f, this author would dismiss the two Cessna numbers as outliers and average the last three (149 lb_f).

6.4.2 Estimating Engine Weight

The following methods can be used to determine dry engine weight, W_{ENG}, used in several of the equations in the previous section. The formulas have been derived statistically, using multiple piston, turboprop, and turbofan engines. Regardless, always try and use manufacturer's data. In the absence of manufacturers' data, the following equations can be used.

(1) Weight of Piston Engines

Figure 6-6 shows the correlation between the uninstalled weight and rated maximum brake-horsepower (P_{max}) for a variety of contemporary piston engines that include models by Rotax, Limbach, Lycoming, and Continental. Power ranges from 48 to 400 BHP. All are normally aspirated, except the three square datapoints (orange), which are turbo-normalized. The diamond datapoints (green) are two-stroke engines. These data are coplotted with estimation using a model from ref. [12]. Given P_{max}, the engine weight is given by

Piston engines: $W_{ENG} = 50.56 + 1.352 P_{max}$ (6-106)

(2) Weight of Turboprop Engines

Figure 6-7 shows the correlation between the uninstalled weight and rated maximum shaft-horsepower (P_{max}) of a variety of current turboprop engines that include models by General Electric, Pratt & Whitney of Canada, Honeywell, Allison, and Rolls-Royce. Power of source-data ranges from 550 to 5823 SHP. Given P_{max}, the engine weight can be found from:

Turboprop engines: $W_{ENG} = 71.65 + 0.3658 P_{max}$ (6-107)

(3) Weight of Turbofan Engines

Figure 6-8 shows the correlation between the uninstalled weight and rated maximum static thrust (T_{max}) of a variety of current turbofan engines that include models by CFM, General Electric, Engine Alliance, SNECMA Turbomeca, Pratt & Whitney, and

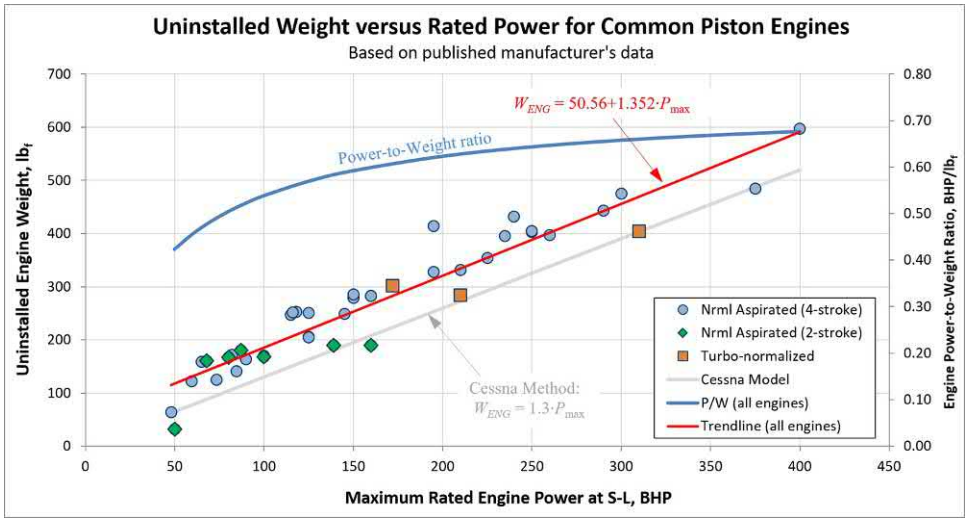


FIGURE 6-6 Correlation between the uninstalled weight of piston engines and their rated power.

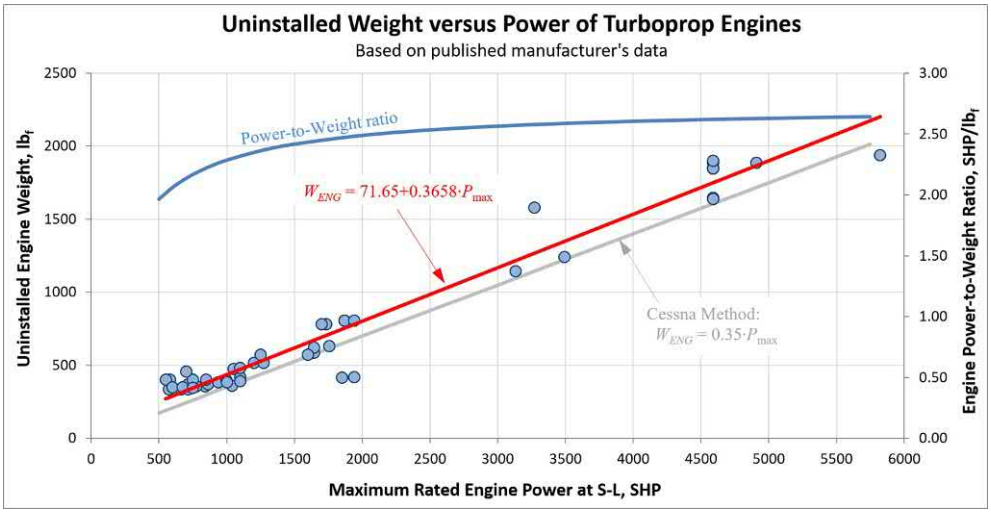


FIGURE 6-7 Correlation between the uninstalled weight of turboprops and their rated power.

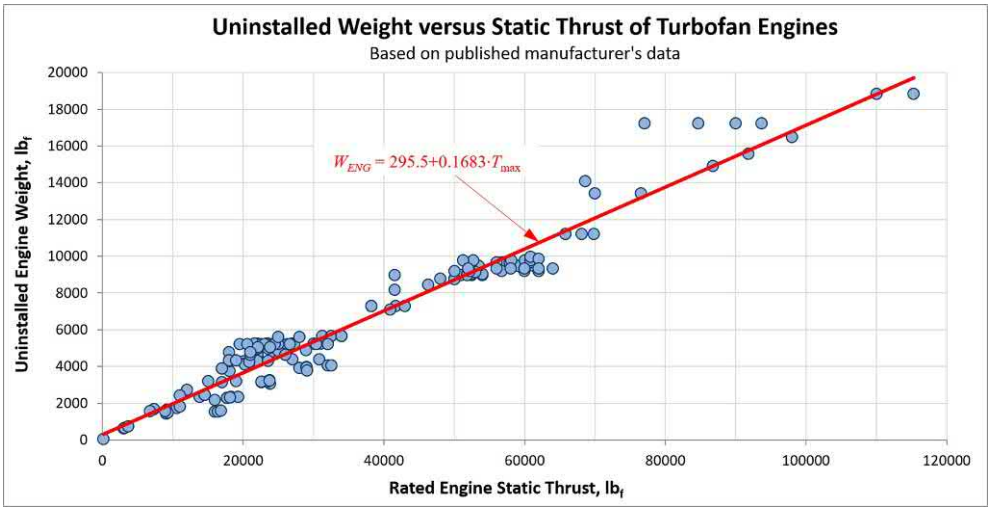


FIGURE 6-8 Correlation between the uninstalled weight of turbofan engines and their rated thrust.

Rolls-Royce. Thrust of the source-data ranges from 150 to 115,300 lb_f. Given T_{max}, the expected engine weight is obtained from:

Turbofan engines: $$W_{ENG} = 295.5 + 0.1683 T_{max} \quad (6\text{-}108)$$

6.5 DIRECT WEIGHT ESTIMATION METHODS

Components such as wings, fuselage, HT, VT, and control surfaces frequently require direct weight estimation, i.e., the estimation of component weight based on material volume and density. Nowadays, solid modeling software simplifies this effort considerably. When access to such software is not an option, one must resort to weight modeling via geometric analysis. A thorough treatise of such work is presented in ref. [16]. An introduction to how such an estimation is conducted is presented in this section. The method applies simplified structural analysis of an idealized aluminum wing. The method is easily adapted to other lifting surfaces as well.

6.5.1 Direct Weight Estimation for a Wing

First, the following method only gives a "ballpark" weight of the wing structure. *It is not a substitute for a detailed load and structural analysis and is intended only as a starting point for the weight analyst*. For one, it only considers simple failure modes: spar cap tension failure and shear web and skin shear failure. It ignores far more likely failure modes, such as buckling and crippling. Additionally, systems, attachment fittings, and control surfaces are not included. Although the following discusses wings, the method applies to any lifting surface that features spars, ribs, and skins, such as horizontal and vertical tail.

Consider the wing shown in Figure 6-9. If made from aluminum, it would normally feature a main spar, aft spar (or shear web), ribs, and skin riveted together to form a stiff but light structure. Note that for initial design purposes, it is common to break the wing structure into categories based on structural role:

(1) The shear web of the spar only reacts the vertical shear force (V).
(2) The spar caps only react the bending moment (M).
(3) The skin only reacts the wing torsion (T).

Assume this wing is designed to carry the entire weight (W_0) of the aircraft, while subjected to an *ultimate* inertia load factor of magnitude n_{ult}. This means the total force it must react amounts to $n_{ult}W_0$. To be cautious, let's assume this distributed load is symmetric and entirely carried by the wing. This means that each wing-halve must react a force of $n_{ult}W_0/2$. While this force is distributed along the span, we position it at the mean geometric chord (MGC) of the wing, as if it were a point force. This is shown in the front view of Figure 6-9. This allows the bending moment at the root to be estimated. The pitching moment coefficient (C_m) for the airfoil will be used to estimate torsion. If the wing is swept, the torsion associated with the sweep must be included. If the torsion with flaps deflected exceeds that for the clean wing at dive speed, it must be used.

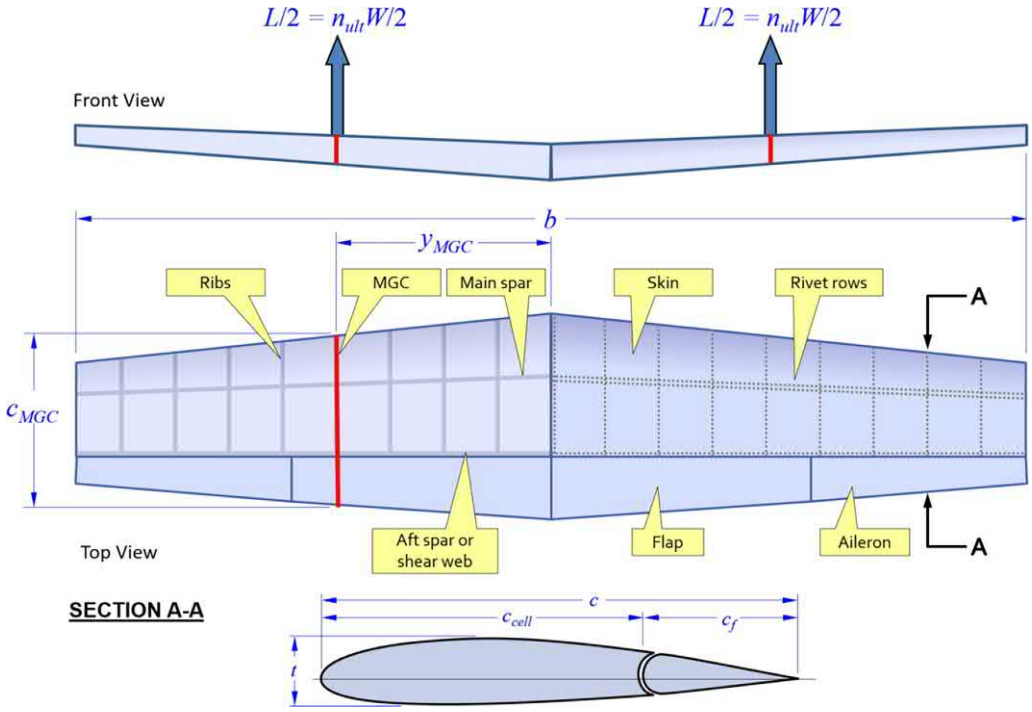


FIGURE 6-9 Lift is applied as a point load at the Mean Geometric Chord.

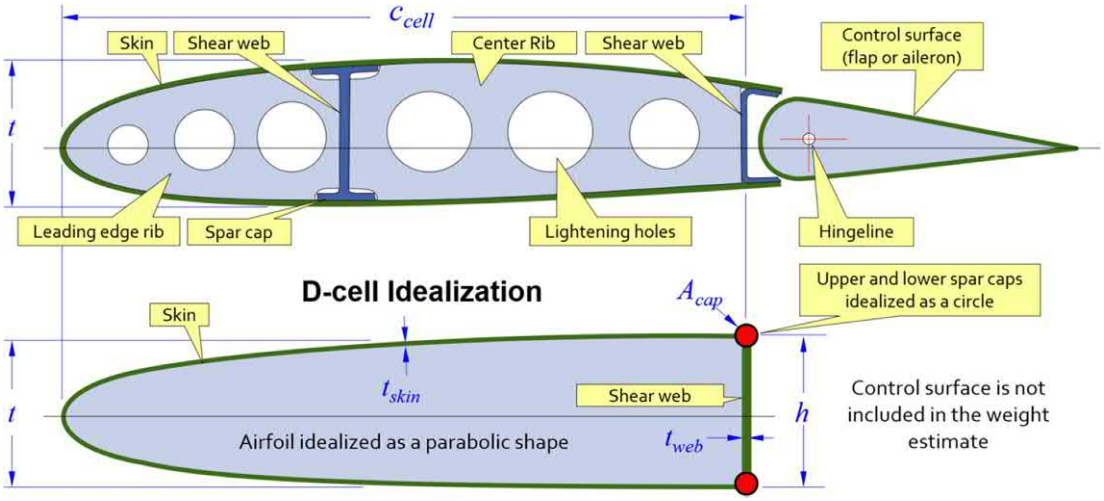


FIGURE 6-10 Section A-A showing structural detail.

Figure 6-10 shows an arbitrary cross-section of the wing. The upper image shows the extent of the control surface (e.g., flap or aileron), while the lower shows how it is idealized. The entire cross-sectional area of all spar caps[2] is idealized by concentrating it in the upper and lower spar caps. These are separated by distance h. This also applies to the maximum thickness (t) of the cross section. In case of a single spar, $h = t$. If multiple spars are used, h should be the average of all spar heights to avoid overestimating the structural depth. Similarly, the entire thickness of all shear webs is concentrated in the idealized shear web. A further idealization takes place by assuming the skin and airfoil to be represented by a parabolic D-cell section as shown in Figure 6-10. The parabolic shape is used because it has a simple formula for the cross-sectional area. It will be assumed that spacing between ribs is one-half the average cell length and that their thickness equals that of the skin. There are many limitations to this scheme. These include the omission of electrical harnesses, fuel and control system, hard points for landing gear or external ordnance, just to name a few.

The critical loads (V, M, and T) are applied to the wing as shown in Figure 6-11. They are defined mathematically as follows:

Shear force: $$V = n_{ult} W_0 / 2 \tag{6-109}$$

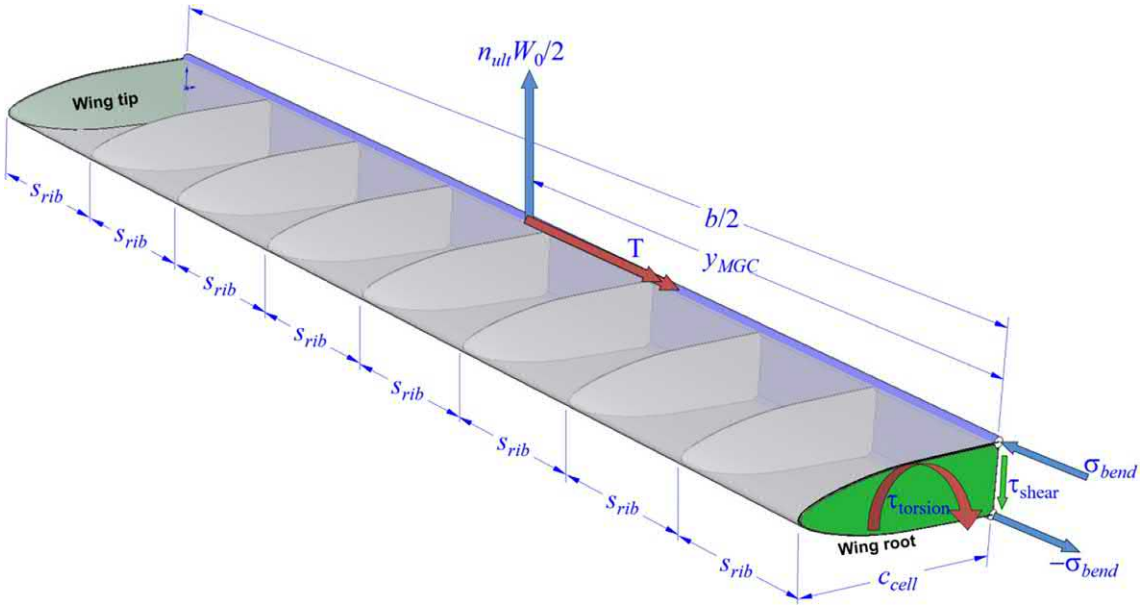


FIGURE 6-11 Loads reacted by the idealized wing segment.

[2] The term "…all spars" refers to wing structures that feature multiple spars.

Bending moment (at root):

$$M = \frac{n_{ult} W}{2} \times y_{MGC} = V \times y_{MGC} \tag{6-110}$$

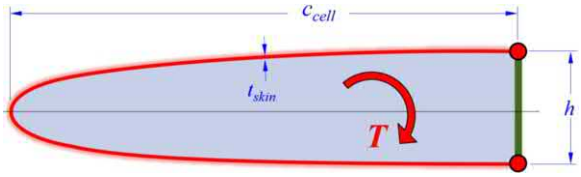
Wing torsion (at root):

$$T = \frac{1}{2}\rho V_\infty^2 \frac{S}{2} \cdot c_{MGC} \cdot C_m = \frac{1}{4}\rho V_\infty^2 S \cdot c_{MGC} \cdot C_m \tag{6-111}$$

where V_∞ is the relevant far-field airspeed (dive-speed for the clean wing or max flap extended speed if the torsion with flaps deflected is greater). These loads are applied to the wing as shown in Figure 6-11. Since they are really distributed loads and not point loads as indicated in Figure 6-11, all are zero at the wing tip and reach the maximum at the wing root, as approximated by Equations (6-109)–(6-111). Thus, the material geometry calculated is really that at the plane-of-symmetry (the root). If we used those thicknesses for the entire wing, we would be grossly overestimating its weight. Material thickness in real wings usually changes from root to tip. Thus, we will assume the material tapers in thickness from root to tip as follows. The area of the spar caps (A_{cap}) at the root reduces linearly to $0.05A_{cap}$ at the tip. Similarly, the wing skin and shear web thickness (t_{skin} and t_{web}, respectively) reduce to $0.15t_{skin}$ and $0.15t_{web}$, with a minimum aluminum sheet thickness of 0.020″ at the tip.

The following step-by-step procedure can be used to implement this method. See the list of variables for definition of terms. Note that Example 6-4 in the first edition of this book presents a numerical implementation of this method.

STEP 1: Weight of the wing skin



Assumption: The torsional moment of the wing-halve is reacted entirely by the wing skin. λ = wing taper ratio

Cell area at root: $A_{cell} = \frac{4c_{cell}h/2}{3} = \frac{2c_{cell}h}{3}$

Cell area at tip: $A_{cell_T} = \frac{2(\lambda c_{cell})(\lambda h)}{3} = \lambda^2 A_{cell}$

Cell arc length at root:
$$s_{cell} = \sqrt{(h/2)^2 + 4c_{cell}^2} + \frac{(h/2)^2}{4C_{cell}} \sinh^{-1}\left(\frac{2c_{cell}}{h/2}\right) = \sqrt{\frac{h^2}{4} + 4c_{cell}^2} + \frac{h^2}{16C_{cell}} \sinh^{-1}\left(\frac{4c_{cell}}{h}\right)$$

Cell arc length at tip: $S_{cell_T} = \lambda s_{cell}$

Continued

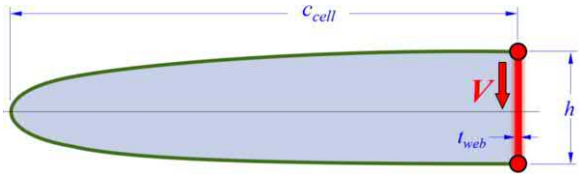
Skin shear stress at root: $\tau_{skin} = \frac{|T|}{2At} = \frac{\frac{1}{4}\rho V^2 S \cdot c_{MGC} \cdot |C_m|}{2A_{cell}t_{skin}} = \frac{\rho V^2 S \cdot c_{MGC} \cdot |C_m|}{8A_{cell}t_{skin}}$

Required minimum skin thickness at root: $\tau_{max} > \frac{\rho V^2 S \cdot c_{MGC} \cdot |C_m|}{8A_{cell}t_{skin}} \Rightarrow t_{skin} > \frac{\rho V^2 S \cdot c_{MGC} \cdot |C_m|}{8A_{cell}\tau_{max}}$
Don't select skin thickness less than 0.020″

Required minimum skin thickness at tip: $t_{skin_T} > 0.15 t_{skin}$
Don't select skin thickness less than 0.020″

Weight of skin: $W_{skin} = \rho_{skin} \frac{(t_{skin} + t_{skin_T})}{2} \frac{b}{2} \frac{(s_{cell} + s_{cell_T})}{2} = \rho_{skin} \frac{b(t_{skin} + t_{skin_T}) s_{cell}(1+\lambda)}{8}$

STEP 2: Weight of wing shear web



Assumption: The shear force of the wing half is reacted entirely by the shear web

Moment of inertia at root: $I = \frac{t_{web}h^3}{12}$

First area moment at root: $Q = A_{halfweb} \cdot \bar{y} = \left(\frac{h}{2}\right) t_{web} \left(\frac{h}{4}\right) = \frac{h^2 t_{web}}{8}$

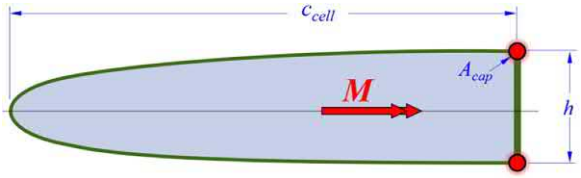
Shear web stress at root: $\tau_{web} = \frac{VQ}{It} = \frac{\left(\frac{n_{ult}W}{2}\right)\left(\frac{h^2 t_{web}}{8}\right)}{\left(\frac{t_{web}h^3}{12}\right)t_{web}} = \frac{12(n_{ult}W)(h^2 t_{web})}{16(t_{web}h^3)t_{web}} = \frac{3(n_{ult}W)}{4t_{web}h}$

Shear web thickness at root: $\tau_{max} > \frac{3(n_{ult}W)}{4t_{web}h} \Rightarrow t_{web} > \frac{3(n_{ult}W)}{4h\tau_{max}}$
Don't select web thickness less than 0.020″

Shear web thickness at tip: $t_{web_T} > 0.15 t_{web}$
Don't select web thickness less than 0.020″

Weight of shear web: $W_{web} = \rho_{web} \frac{(t_{web} + t_{web_T})}{2} \frac{b}{2} \frac{h(1+\lambda)}{2} = \rho_{web} \frac{b(t_{web} + t_{web_T})h(1+\lambda)}{8}$

STEP 3: Weight of wing spar caps



Assumption: The bending moment of the wing half is reacted entirely by the spar caps

"Bending force" at root (the couple that reacts M): $F_{bend} = \frac{M}{h} = \frac{n_{ult}W \times y_{MGC}}{2h}$

STEP 3: Weight of wing spar caps

Bending stress at root:	$\sigma_{bend} = \frac{F_{bend}}{A_{cap}} = \frac{\frac{n_{ult} W \times y_{MGC}}{2h}}{A_{cap}} = \frac{n_{ult} W \times y_{MGC}}{2h \cdot A_{cap}}$
Spar cap area at root:	$\sigma_{max} > \frac{n_{ult} W \times y_{MGC}}{2h \cdot A_{cap}} \Rightarrow A_{cap} > \frac{n_{ult} W \times y_{MGC}}{2h \cdot \sigma_{max}}$
Spar cap area at tip:	$A_{cap_T} > 0.05 A_{cap}$ Don't select cap area less than 0.010 in^2
Weight of spar caps:	$W_{caps} = 2 \times \rho_{caps} \frac{(A_{cap} + A_{cap_T})}{2} \frac{b}{2} = \rho_{caps} \frac{b(A_{cap} + A_{cap_T})}{2}$ Note that there are two spar caps (upper and lower) and therefore the weight is multiplied by 2.

STEP 4: Weight of ribs

Assumption:	**The spacing of ribs is approximately one-half of c_{cell}.**
Number of ribs:	$N_{rib} \approx INT\left(\frac{b}{c_{MGC}}\right) + 1 \approx INT\left(\frac{b}{c_{avg}}\right) + 1$ Where INT stands for the integer value of the ratio. It is possible to underestimate the number of ribs for highly loaded wings.
Thickness of ribs:	$t_{rib} = t_{skin}$ Don't select rib thickness less than 0.020″
Weight of ribs:	$W_{ribs} = \rho_{ribs} \frac{(A_{cell} + A_{cell_T})}{2} \frac{(t_{skin} + t_{skin_T})}{2} N_{ribs}$ $= N_{ribs} \rho_{ribs} \frac{A_{cell}(1 + \lambda^2)(t_{skin} + t_{skin_T})}{4}$

6.5.2 Variation of Weight with AR

The aspect ratio of the wing is of great importance in aircraft design. Long-range and high-endurance aircraft usually feature a high *AR* wing. The cost of such a wing is a greater weight, given constant wing area. It is prudent to evaluate the impact of the *AR* on empty weight using the parametric analysis introduced in Section 3.3.1. This section presents formulation to help in this capacity.

Consider the special case for which the wing area (S) and taper ratio (λ) are constant, but the *AR* is allowed to vary (see Figure 6-12). Assume we have a baseline wing and want to compare it to a modified wing of the same S and λ; the only change is in *AR* (and therefore wingspan, root chord, and tip chord). The weight of the modified *AR* wing can be approximated by the following assumptions:

(1) Changes do not include airfoils. Thus, the thickness ratio is constant. Given a constant S, a higher *AR* results in a "thinner" wing, whose chords are also shortened.

(2) Assume geometric changes are "small" so changes in the wing skin shear stress can be ignored. These are induced by wing torsion, which depends on the airfoil's pitching moment and torsion due to forward or aft swept wings. A large wing chord offers greater cross-sectional area to react this torsion but will also generate higher pitching moment. The designer should evaluate the validity of this assumption on a case-to-case basis, but, here, we assume that changes in shear stresses are small enough to permit a constant skin thickness.

(3) Assume the change in *AR* does not require other geometries to change (e.g., empennage geometry, etc.).

(4) Assume there is no change in vertical shear. Thus, the shear web thickness does not change. This is justified on the basis that changing the *AR* will not alter the airplane's gross weight, only its empty weight.

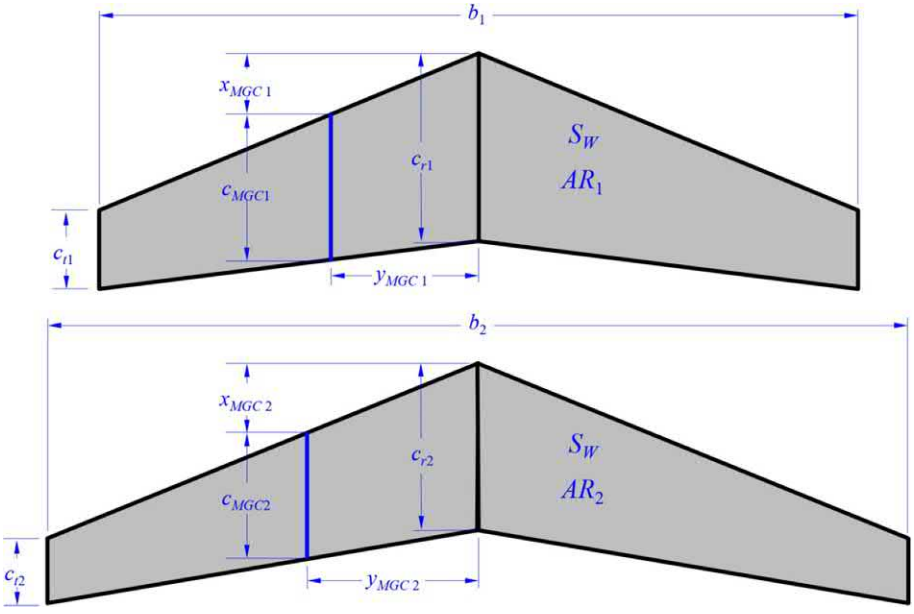


FIGURE 6-12 Two wings of equal areas but different Aspect Ratios.

(5) The maximum bending moment at the root is directly related to the location of the center of lift, which is assumed to act at the spanwise station for the MGC.
(6) The change in bending stresses is equal to the change in the bending moments. If the bending moments change by 25%, then so will the bending stresses.
(7) The change in material geometry required to react the bending moment is directly related to the change in stress levels—and, thus, our goal is to maintain similar stress levels in the spar caps before and after change.
(8) The material allowable, σ_{max}, is assumed the same for both wing geometries.
(9) Assume the structural depth of an airfoil to be based on its maximum thickness (see Figure 6-13).
(10) Assume the spar caps have a circular cross-section, separated by the structural depth, h (see Figure 6-13).
(11) Assume the cross-sectional area of the spar cap at tip to be 10% of that of the root.

These assumptions show that only the dimensions of the spar caps are changed. This implies that the only change in the weight of the structure will be associated with the change in the spar caps geometry. To estimate the magnitude of this change, we begin by establishing relationships between geometry and stress.

(1) Baseline Definitions for a Trapezoidal Wing

The following expressions are needed to begin the weight estimation and are all based on the parameters S, AR, and λ. For instance, they can be used to calculate the properties of the baseline wing.

Wingspan: $$b = \sqrt{AR \times S} \tag{9-28}$$

Mean Geometric Chord:

$$c_{MGC} = \frac{4}{3}\sqrt{\frac{S}{AR}}\left(\frac{1+\lambda+\lambda^2}{1+2\lambda+\lambda^2}\right) \tag{6-112}$$

Spanwise location of the center of lift:

$$y_{MGC} = \frac{\sqrt{AR \times S}}{6}\left(\frac{1+2\lambda}{1+\lambda}\right) \tag{6-113}$$

Structural depth at the MGC:

$$h = \frac{4}{3}\sqrt{\frac{S}{AR}}\left(\frac{1+\lambda+\lambda^2}{1+2\lambda+\lambda^2}\right)\left(\frac{t}{c}\right) \tag{6-114}$$

Maximum bending moment:

$$M_{max} = \frac{n_{ult} W \sqrt{AR \times S}}{12}\left(\frac{1+2\lambda}{1+\lambda}\right) \tag{6-115}$$

Moment of inertia:

$$I_{xx} = \frac{16 A_{cap}}{18}\left(\frac{S}{AR}\right)\left(\frac{1+\lambda+\lambda^2}{1+2\lambda+\lambda^2}\right)^2\left(\frac{t}{c}\right)^2 \tag{6-116}$$

Required spar cap area:

$$A_{cap} > \frac{n_{ult} W \times AR}{16\sigma_{max}}\left(\frac{1+3\lambda+2\lambda^2}{1+\lambda+\lambda^2}\right)\left(\frac{t}{c}\right) \tag{6-117}$$

Required spar cap weight:

$$W_{cap} = 1.1 \times \rho_{cap} \times A_{cap}\sqrt{AR \times S} \tag{6-118}$$

where

A_{cap} = Cross-sectional area of the upper or lower spar cap in m^2 or ft^2
AR = Aspect ratio
b = Wingspan in m or ft
n_{ult} = Ultimate flight load in g
S = Wing area in m^2 or ft^2 W = Airplane design gross weight in N or lb_f
λ = Wing taper ratio
ρ_{cap} = Weight density of spar cap material in N/m^3 or lb_f/ft^3
σ_{max} = Tensile stress allowable of spar cap material in Pa or lb_f/ft^2

With respect to the ultimate flight load, n_{ult}, the load must be the maneuvering or gust load, whichever is larger. Note that many of the derivations below refer to equations in Section 9.2.

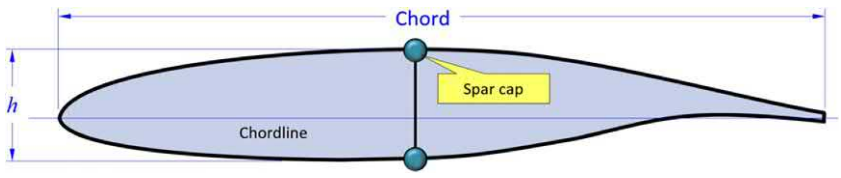


FIGURE 6-13 Structural depth, h, of an airfoil.

EXAMPLE 6-6

Let us evaluate these expressions by comparing them to an existing aircraft; the Beech Bonanza A36. The Bonanza's design gross weight is 3600 lb_f, wing area 181 ft^2, AR is 6.2, and λ is 0.538. Its airfoils are the NACA 23016.5 at the root ($t/c = 0.165$) and 23012 at the tip ($t/c = 0.12$). Use the root thickness ratio, 0.165, for the variable t/c. The airplane is certified under 14 CFR, Part 23, in the utility category. This means the ultimate load factor is $4.4\,g \times 1.5 = 6.6$ gs. Assume the spar caps are fabricated from 2024-T3 extrusion, whose density is 0.1 lb_f/in^3 and $\sigma_{max} = 65{,}000$ psi (or 9,360,000 psf). Evaluate the above parameters based on these numbers and compare to values that are in the public domain.

SOLUTION:

Wingspan is:

$$b = \sqrt{AR \times S} = \sqrt{6.2 \times 181} = 33.5 \text{ ft}$$

Mean Geometric Chord:

$$c_{MGC} = \frac{4}{3}\sqrt{\frac{S}{AR}}\left(\frac{1+\lambda+\lambda^2}{1+2\lambda+\lambda^2}\right) = \frac{4}{3}\sqrt{\frac{181}{6.2}}\left(\frac{1+0.538+0.538^2}{1+2\times0.538+0.538^2}\right) = 5.566 \text{ ft}$$

Spanwise location of the lift:

$$y_{MGC} = \frac{\sqrt{AR \times S}}{6}\left(\frac{1+2\lambda}{1+\lambda}\right) = \frac{\sqrt{6.2 \times 181}}{6}\left(\frac{1+2\times0.538}{1+0.538}\right) = 7.536 \text{ ft}$$

Structural depth at the MGC:

$$h = \frac{4}{3}\sqrt{\frac{S}{AR}}\left(\frac{1+\lambda+\lambda^2}{1+2\lambda+\lambda^2}\right)\left(\frac{t}{c}\right) = \frac{4}{3}\sqrt{\frac{181}{6.2}}\left(\frac{1+0.538+0.538^2}{1+2\times0.538+0.538^2}\right)(0.165) = 0.918 \text{ ft}$$

Maximum bending moment at the plane-of-symmetry:

$$M_{max} = \frac{n_{ult} W \sqrt{AR \times S}}{12}\left(\frac{1+2\lambda}{1+\lambda}\right) = \frac{6.6 \times 3600\sqrt{6.2 \times 181}}{12}\left(\frac{1+2\times0.538}{1+0.538}\right) = 89530 \text{ ft} \cdot \text{lb}_f$$

Required maximum spar cap area at the plane-of-symmetry:

$$A_{cap} > \frac{n_{ult} W \times AR}{16\sigma_{max}(t/c)}\left(\frac{1+3\lambda+2\lambda^2}{1+\lambda+\lambda^2}\right) = \frac{6.6 \times 3600 \times 6.2}{16 \times 9360000(0.165)}\left(\frac{1+3\times0.538+2\times0.538^2}{1+0.538+0.538^2}\right) = 0.01042 \text{ ft}^2 = 1.500 \text{ in}^2$$

Moment of inertia at the plane-of-symmetry:

$$I_{xx} = \frac{16A_{cap}}{18}\left(\frac{S}{AR}\right)\left(\frac{1+\lambda+\lambda^2}{1+2\lambda+\lambda^2}\right)^2\left(\frac{t}{c}\right)^2 = \frac{16 \times 0.01042}{18}\left(\frac{181}{6.2}\right)\left(\frac{1+0.538+0.538^2}{1+2\times0.538+0.538^2}\right)^2(0.165)^2 = 0.004394 \text{ ft}^4 = 91.1 \text{ in}^4$$

Spar cap weight:

$$W_{cap} = 1.1 \times \rho_{cap} \times A_{cap}\sqrt{AR \times S} = 1.1 \times (0.1 \times 12^3) \times 0.01042\sqrt{6.2 \times 181} = 66.3 \text{ lb}_f$$

Comparison of the approximated to "published" numbers are shown in Table 6-3. Note that the max bending moment in the "published" column is calculated using potential flow theory (and is not published by Beechcraft).

TABLE 6-3 Comparison of "official" to analysis for the beech bonanza.

Property	Symbol	"Published"	Analysis	Comment
Wingspan	b	33.5 ft	33.5 ft	Analysis values based on published data.
Mean Geometric Chord	c_{MGC}	5.441 ft	5.566 ft	Published value obtained from analysis of a 3-view drawing.
Spanwise location of center of lift	y_{MGC}	7.445 ft	7.536 ft	Published value obtained from a standard estimate based on a 3-view drawing.
Structural depth	h	0.941 ft	0.918 ft	Published value measured by author on the actual airplane.
Maximum bending moment	M_{max}	79,358 ft·lb_f	89,530 ft·lb_f	Published value based on Vortex-Lattice analysis of the aircraft, which accounts for lift on fuselage and horizontal tail, whereas this analysis assumes all lift is generated by the wings.
Required spar cap area	A	1.490 in^2	1.500 in^2	Published value measured by author on actual airplane.
Moment of inertia	I_{xx}	95.567 in^4	91.1 in^4	Published value calculated using parallel-axis theorem with A and h.
Weight of spar caps	W_{cap}	Unknown	66.3 lb_f	Published value is not known, but analysis value is considered reasonable.

These results show this method is in good agreement with the "published" values, lending support to its validity.

DERIVATION OF EQUATION (6-112)

Substitute Equation (6-6) into Equation (9-33) and manipulate:

$$c_{MGC} = \left(\frac{4b}{3AR}\right)\left(\frac{1+\lambda+\lambda^2}{1+2\lambda+\lambda^2}\right) = \left(\frac{4\sqrt{AR\times S}}{3AR}\right)\left(\frac{1+\lambda+\lambda^2}{1+2\lambda+\lambda^2}\right)$$
$$= \frac{4}{3}\sqrt{\frac{S}{AR}}\left(\frac{1+\lambda+\lambda^2}{1+2\lambda+\lambda^2}\right)$$

DERIVATION OF EQUATION (6-113)

Substitute Equation (6-6) into Equation (9-13) to determine the location of the center of lift:

$$y_{MGC} = \left(\frac{b}{6}\right)\left(\frac{1+2\lambda}{1+\lambda}\right) = \frac{\sqrt{AR\times S}}{6}\left(\frac{1+2\lambda}{1+\lambda}\right)$$

DERIVATION OF EQUATION (6-114)

Consider Figure 6-13, which defines the structural depth of the airfoil, h. At the MGC, this depth is given by:

$$h = c_{MGC}\left(\frac{t}{c}\right)$$

Then, substitute Equation (9-33) and manipulate algebraically:

$$h = \left(\frac{4b}{3AR}\right)\left(\frac{1+\lambda+\lambda^2}{1+2\lambda+\lambda^2}\right)\left(\frac{t}{c}\right) = \left(\frac{4\sqrt{AR\times S}}{3AR}\right)\left(\frac{1+\lambda+\lambda^2}{1+2\lambda+\lambda^2}\right)\left(\frac{t}{c}\right)$$
$$= \frac{4}{3}\sqrt{\frac{S}{AR}}\left(\frac{1+\lambda+\lambda^2}{1+2\lambda+\lambda^2}\right)\left(\frac{t}{c}\right)$$

DERIVATION OF EQUATION (6-115)

The maximum bending moment is given by[3]:

$$M_{\max} \approx \frac{L}{2}\times y_{MGC} = \frac{n_{ult}W}{2}\times y_{MGC}$$

where L is the lift, n_{ult} is the ultimate load factor, and W is the weight of the airplane. Inserting Equation (6-113) for y_{MGC} yields:

$$M_{\max} \approx \frac{n_{ult}W}{2}\times y_{MGC} = \frac{n_{ult}W}{2}\times\frac{\sqrt{AR\times S}}{6}\left(\frac{1+2\lambda}{1+\lambda}\right)$$
$$= \frac{n_{ult}W\sqrt{AR\times S}}{12}\left(\frac{1+2\lambda}{1+\lambda}\right)$$

DERIVATION OF EQUATION (6-116)

The moment of inertia can be calculated using the parallel-axis theorem, assuming the spar caps have an area A_{cap} and are separated by the structural depth h:

$$I_{xx} = 2\times A_{cap}\times\left(\frac{h}{2}\right)^2 = \frac{A_{cap}h^2}{2}$$

Inserting Equation (6-114) for structural height yields:

$$I_{xx} = \frac{A_{cap}h^2}{2} = \frac{A_{cap}}{2}\times\left(\frac{4b}{3AR}\right)^2\left(\frac{1+\lambda+\lambda^2}{1+2\lambda+\lambda^2}\right)^2\left(\frac{t}{c}\right)^2$$

Finally, yielding:

$$I_{xx} = \frac{16A_{cap}}{18}\left(\frac{\sqrt{AR\times S}}{AR}\right)^2\left(\frac{1+\lambda+\lambda^2}{1+2\lambda+\lambda^2}\right)^2\left(\frac{t}{c}\right)^2$$
$$= \frac{16A_{cap}}{18}\left(\frac{S}{AR}\right)\left(\frac{1+\lambda+\lambda^2}{1+2\lambda+\lambda^2}\right)^2\left(\frac{t}{c}\right)^2$$

DERIVATION OF EQUATION (6-117)

Maximum stress at the outer fibers may not exceed:

$$\sigma_{\max} > \frac{M_{\max}\times(h/2)}{I_{xx}} = \frac{M_{\max}\times h}{2I_{xx}} = \frac{M_{\max}\times h}{2\left(\frac{Ah^2}{2}\right)} = \frac{M_{\max}}{Ah}$$

We can use this expression to determine the minimum area A_{cap} required for the spar caps.

$$A_{cap} > \frac{M_{\max}}{\sigma_{\max}h}$$

Inserting the proper relations for $M_{\max}$ and h:

$$A_{cap} > \frac{M_{\max}}{\sigma_{\max}h} = \frac{\frac{n_{ult}W\sqrt{AR\times S}}{12}\left(\frac{1+2\lambda}{1+\lambda}\right)}{\sigma_{\max}\left(\frac{4b}{3AR}\right)\left(\frac{1+\lambda+\lambda^2}{1+2\lambda+\lambda^2}\right)\left(\frac{t}{c}\right)}$$
$$= \frac{n_{ult}W\sqrt{AR^3\times S}}{16b\sigma_{\max}\left(\frac{t}{c}\right)}\left(\frac{1+2\lambda}{1+\lambda}\right)\frac{(1+\lambda)^2}{1+\lambda+\lambda^2}$$
$$= \frac{n_{ult}W\sqrt{AR^3\times S}}{16\sqrt{AR\times S}\sigma_{\max}\left(\frac{t}{c}\right)}\frac{(1+2\lambda)(1+\lambda)}{1+\lambda+\lambda^2}$$
$$= \frac{n_{ult}W\times AR}{16\sigma_{\max}\left(\frac{t}{c}\right)}\left(\frac{1+3\lambda+2\lambda^2}{1+\lambda+\lambda^2}\right)$$

[3] Although the maximum bending moment is usually determined at the location of the wing attachments, for this method this is assumed at the plane of symmetry.

DERIVATION OF EQUATION (6-118)

The total volume of spar caps, assuming the thickness at the tip is 10% of that at the root:

$$V_{cap} = 2\frac{A_{cap}(1+0.1)}{2}b = 1.1A_{cap}\sqrt{AR \times S}$$

The spar cap weight is thus:

$$W_{cap} = \rho_{cap}V_{cap} = 2\frac{A_{cap}(1+0.1)}{2}b = 1.1 \times \rho_{cap} \times A_{cap}\sqrt{AR \times S}$$

(2) Method of Fractions

Once the baseline properties are known, it is possible to estimate the properties of a modified wing whose only geometric change is the AR (S and λ remain constant for both). Assume we have defined a baseline configuration, denoted by the subscript 1 and a comparison configuration, denoted by the subscript 2. Then, the following ratios hold between the two wings.

Wingspan: $$b_2 = b_1\sqrt{\frac{AR_2}{AR_1}} \quad (6\text{-}119)$$

Mean Geometric Chord:

$$c_{MGC_2} = c_{MGC_1}\sqrt{\frac{AR_1}{AR_2}} \quad (6\text{-}120)$$

Spanwise location of the center of lift

$$y_{MGC\ 2} = y_{MGC\ 1}\sqrt{\frac{AR_2}{AR_1}} \quad (6\text{-}121)$$

Structural depth: $$h_2 = h_1\sqrt{\frac{AR_1}{AR_2}} \quad (6\text{-}122)$$

Maximum bending moment:

$$M_{max2} = M_{max1}\sqrt{\frac{AR_2}{AR_1}} \quad (6\text{-}123)$$

Spar cap areas: $$A_{cap2} = A_{cap1}\frac{AR_2}{AR_1} \quad (6\text{-}124)$$

Moment of inertia: $$I_{xx_2} = I_{xx_1} \quad (6\text{-}125)$$

Required spar cap weight:

$$W_{cap2} = W_{cap1}\left(\frac{AR_2}{AR_1}\right)^{3/2} \quad (6\text{-}126)$$

Change in spar cap weight: $$\Delta W_{cap} = W_{cap2} - W_{cap1} \quad (6\text{-}127)$$

DERIVATION OF EQUATION (6-119)

Using Equation (9-28) with the two subscripts:

$$\frac{b_2}{b_1} = \sqrt{\frac{AR_2 \times S}{AR_1 \times S}} \Rightarrow b_2 = b_1\sqrt{\frac{AR_2}{AR_1}}.$$

DERIVATION OF EQUATION (6-120)

Using Equation (6-112) and applying the proper subscripts and dividing one MGC with the other leads to:

$$\frac{c_{MGC_2}}{c_{MGC_1}} = \frac{\frac{4}{3}\sqrt{\frac{S}{AR_2}}\left(\frac{1+\lambda+\lambda^2}{1+2\lambda+\lambda^2}\right)}{\frac{4}{3}\sqrt{\frac{S}{AR_1}}\left(\frac{1+\lambda+\lambda^2}{1+2\lambda+\lambda^2}\right)} = \frac{\sqrt{AR_1}}{\sqrt{AR_2}}$$

$$\Rightarrow c_{MGC_2} = c_{MGC_1}\sqrt{\frac{AR_1}{AR_2}}$$

DERIVATION OF EQUATION (6-121)

Using Equation (6-113) and applying the proper subscripts and dividing one y_{MGC} with the other leads to:

$$\frac{y_{MGC\ 2}}{y_{MGC\ 1}} = \frac{\frac{\sqrt{AR_2 \times S}}{6}\left(\frac{1+2\lambda}{1+\lambda}\right)}{\frac{\sqrt{AR_1 \times S}}{6}\left(\frac{1+2\lambda}{1+\lambda}\right)} = \frac{\sqrt{AR_2}}{\sqrt{AR_1}}$$

$$\Rightarrow y_{MGC\ 2} = y_{MGC\ 1}\sqrt{\frac{AR_2}{AR_1}}$$

DERIVATION OF EQUATION (6-122)

Using Equation (6-114) and applying the proper subscripts and dividing one h with the other leads to:

$$\frac{h_2}{h_1} = \frac{\frac{4}{3}\sqrt{\frac{S}{AR_2}}\left(\frac{1+\lambda+\lambda^2}{1+2\lambda+\lambda^2}\right)\left(\frac{t}{c}\right)}{\frac{4}{3}\sqrt{\frac{S}{AR_1}}\left(\frac{1+\lambda+\lambda^2}{1+2\lambda+\lambda^2}\right)\left(\frac{t}{c}\right)} = \frac{\sqrt{AR_1}}{\sqrt{AR_2}}$$

$$\Rightarrow h_2 = h_1\sqrt{\frac{AR_1}{AR_2}}$$

DERIVATION OF EQUATION (6-123)

Using Equation (6-115) and applying the proper subscripts and dividing one $M_{\max}$ with the other leads to:

$$\frac{M_{\max 2}}{M_{\max 1}}=\frac{\dfrac{n_{ult}W\sqrt{AR_2\times S}}{12}\left(\dfrac{1+2\lambda}{1+\lambda}\right)}{\dfrac{n_{ult}W\sqrt{AR_1\times S}}{12}\left(\dfrac{1+2\lambda}{1+\lambda}\right)}=\frac{\sqrt{AR_2}}{\sqrt{AR_1}}$$

$$\Rightarrow\quad M_{\max 2}=M_{\max 1}\sqrt{\frac{AR_2}{AR_1}}$$

DERIVATION OF EQUATION (6-124)

Using Equation (6-117) and applying the proper subscripts and dividing one A_{cap} with the other leads to:

$$\frac{A_{cap2}}{A_{cap1}}=\frac{\dfrac{n_{ult}W\times AR_2}{16\sigma_{\max}\left(\dfrac{t}{c}\right)}\left(\dfrac{1+3\lambda+2\lambda^2}{1+\lambda+\lambda^2}\right)}{\dfrac{n_{ult}W\times AR_1}{16\sigma_{\max}\left(\dfrac{t}{c}\right)}\left(\dfrac{1+3\lambda+2\lambda^2}{1+\lambda+\lambda^2}\right)}=\frac{AR_2}{AR_1}$$

$$\Rightarrow\quad A_{cap2}=A_{cap1}\frac{AR_2}{AR_1}$$

DERIVATION OF EQUATION (6-125)

Using Equation (6-18) and applying the proper subscripts and dividing one I_{xx} with the other leads to:

$$\frac{I_{xx_2}}{I_{xx_1}}=\frac{\dfrac{16A_{cap2}}{18}\left(\dfrac{S}{AR_2}\right)\left(\dfrac{1+\lambda+\lambda^2}{1+2\lambda+\lambda^2}\right)^2\left(\dfrac{t}{c}\right)^2}{\dfrac{16A_{cap1}}{18}\left(\dfrac{S}{AR_1}\right)\left(\dfrac{1+\lambda+\lambda^2}{1+2\lambda+\lambda^2}\right)^2\left(\dfrac{t}{c}\right)^2}=\left(\frac{A_{cap2}}{A_{cap1}}\right)\left(\frac{AR_1}{AR_2}\right)$$

$$\Rightarrow\quad I_{xx_2}=I_{xx_1}\left(\frac{A_{cap2}}{A_{cap1}}\right)\left(\frac{AR_1}{AR_2}\right)$$

Now, let's substitute Equation (6-124) and simplify:

$$I_{xx_2}=I_{xx_1}\left(\frac{A_{cap2}}{A_{cap1}}\right)\left(\frac{AR_1}{AR_2}\right)=I_{xx_1}\left(\frac{AR_2}{AR_1}\right)\left(\frac{AR_1}{AR_2}\right)=I_{xx_1}$$

DERIVATION OF EQUATION (6-126)

Using Equation (6-118) with the appropriate subscripts and dividing one W_{cap} by the other leads to:

$$\frac{W_{cap2}}{W_{cap1}}=\frac{1.1\times\rho_{cap}\times A_{cap2}\sqrt{AR_2\times S}}{1.1\times\rho_{cap}\times A_{cap1}\sqrt{AR_1\times S}}=\left(\frac{A_{cap2}}{A_{cap1}}\right)\frac{\sqrt{AR_2}}{\sqrt{AR_1}}$$

$$\Rightarrow\quad W_{cap2}=W_{cap1}\left(\frac{A_{cap2}}{A_{cap1}}\right)\sqrt{\frac{AR_2}{AR_1}}$$

Now, let's substitute Equation (6-124) and simplify:

$$W_{cap2}=W_{cap1}\left(\frac{A_{cap2}}{A_{cap1}}\right)\sqrt{\frac{AR_2}{AR_1}}=W_{cap1}\left(\frac{AR_2}{AR_1}\right)\sqrt{\frac{AR_2}{AR_1}}$$
$$=W_{cap1}\left(\frac{AR_2}{AR_1}\right)^{3/2}$$

EXAMPLE 6-7

Use the Method of Fraction to estimate the change in empty weight for the Beech Bonanza A36 aircraft of Example 6-6, for AR increasing from 6.2 to 14. This assumes the only change is in the weight of the spar caps. The standard empty weight is 2247 lb_f. Plot the change in empty weight and maximum bending moments.

SOLUTION:

All baseline values are calculated in Example 6-6, including the estimated baseline weight for the spar caps of 66.3 lb_f and maximum baseline bending moment is 89,530 $\text{ft}\cdot\text{lb}_\text{f}$. The baseline AR_1 is 6.2. Let's calculate a sample value using $AR_2=10$.

Maximum bending moment for $AR_2=10$: $M_{\max 2}=M_{\max 1}\sqrt{\frac{AR_2}{AR_1}}=89530\sqrt{\frac{10}{6.2}}=113703\ \text{ft}\cdot\text{lb}_\text{f}$

In order to estimate the empty weight, we first compute the spar cap weight for $AR_2=10$ and then use Equation (6-127) to determine the difference between the two. We then add this difference to the baseline empty weight.

$$W_{cap2}=W_{cap1}\left(\frac{AR_2}{AR_1}\right)^{3/2}=66.3\left(\frac{10}{6.2}\right)^{3/2}=135.9\ \text{lb}_\text{f}$$

Thus, the difference is:

$$\Delta W_{cap}=W_{cap2}-W_{cap1}=135.9-66.3=69.6\ \text{lb}_\text{f}$$

The empty weight is therefore:

$$W_{e_{AR=10}}=W_e+\Delta W_{cap}=2247+69.6=2317\ \text{lb}_\text{f}$$

The remaining values are plotted in Figure 6-14, which shows how AR can affect aircraft weight.

EXAMPLE 6-7 (*cont'd*)

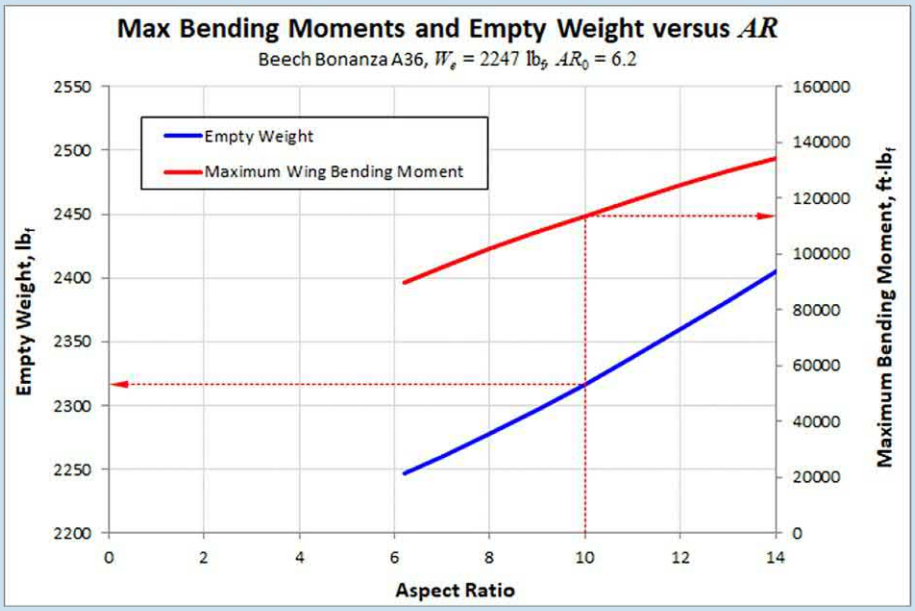


FIGURE 6-14 Predicted empty weight and maximum bending moments versus Aspect Ratio. The *red dashed lines* indicate the sample values calculated in the example.

6.6 INERTIA PROPERTIES

This section presents various formulae to determine properties such as the center-of-gravity (CG) and moments and products of inertia. The CG-position must accompany the construction of a CG-envelope to establish the most forward and aft position limits. This envelope must be designed such the CG remains within those limits regardless of fuel consumed or external stores dropped. Fuel for jets can constitute as much as 45% of their T-O weight and exceed 15% for piston engines. Consuming fuel can impart large changes in the inertia properties between T-O and landing. This may profoundly affect dynamic stability.

6.6.1 Fundamentals

The determination of aircraft inertia properties typically involves treating it as a collection of components. Thus, each component has a representative weight and position in space (see Figure 6-15). This permits the inertia properties to be determined using simple formulation.

This section presents methods to calculate the inertia properties listed in Table 6-4. The formulation presented assumes the airplane can be represented by a collection of point loads in 3-dimensional space, as

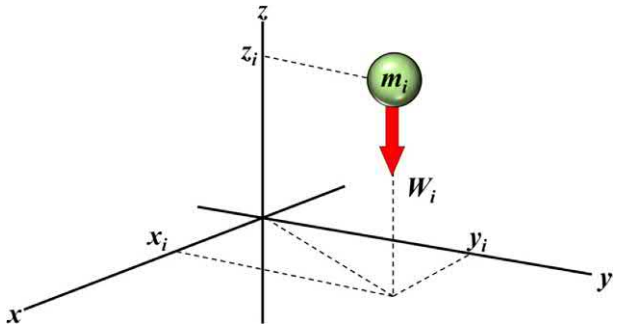


FIGURE 6-15 The definition of a point load in 3-dimensional space.

TABLE 6-4 Important inertia properties.

Property	Symbol	Section
Weight at a specific condition	W_{tot}	6.6.3
Center-of-gravity (CG) in terms of location	X_{CG}, Y_{CG}, Z_{CG}	6.6.5
CG is also given in terms of percentage of MGC	P_{CG}	6.6.5
Moment of inertia about the *x*-, *y*-, and *z*-axes	I_{xx}, I_{yy}, I_{zz}	6.6.7
Product of inertia in the *xy*-, *xz*-, and *yz*-planes	I_{xy}, I_{xz}, I_{yz}	6.6.7

shown in Figure 6-16. Note that each arbitrary point is denoted by the subscript *i*.

6.6.2 Reference Locations

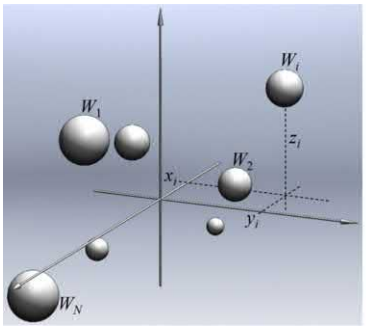
The aerospace engineer should use terminology commonly used in the aviation industry when referring to the position of components (such as avionics, engine CG, and occupants) in the aircraft. The physical location is referred to using terms such as:

FS—Fuselage Station
BL—Butt line (or buttock line)
WL—Water Line
WS—Wing Station
HS—Horizontal Station
VS—Vertical Station

Examples of these stations and their reference lines (datum) are shown in Figures 6-17 and 6-18. When an airplane features swept wings or tail, it is convenient to represent locations using a Wing, Horizontal, or Vertical Stations. These are effectively a BL aligned to something like the quarter-chord line or another conveniently selected datum.

6.6.3 Total Weight

To estimate the total weight of the aircraft, we break it into several subcomponents, e.g., engine, propeller, left wing, right wing, horizontal tail, fuselage, left main landing gear, right main gear, and so forth. Then, we estimate the weight of each subcomponent as discussed in Section 6.5. Denoting each by W_i, where the index i is



Item	Weight	x	y	z
Item 1	W_1	x_1	y_1	z_1
Item 2	W_2	x_2	y_2	z_2
Item 3	W_3	x_3	y_3	z_3
…	…	…	…	…
Item i	W_i	x_i	y_i	z_i
…	…	…	…	…
Item N	W_N	x_N	y_N	z_N

FIGURE 6-16 A collection of point loads in 3-dimensional space (left) and a tabular representation (right).

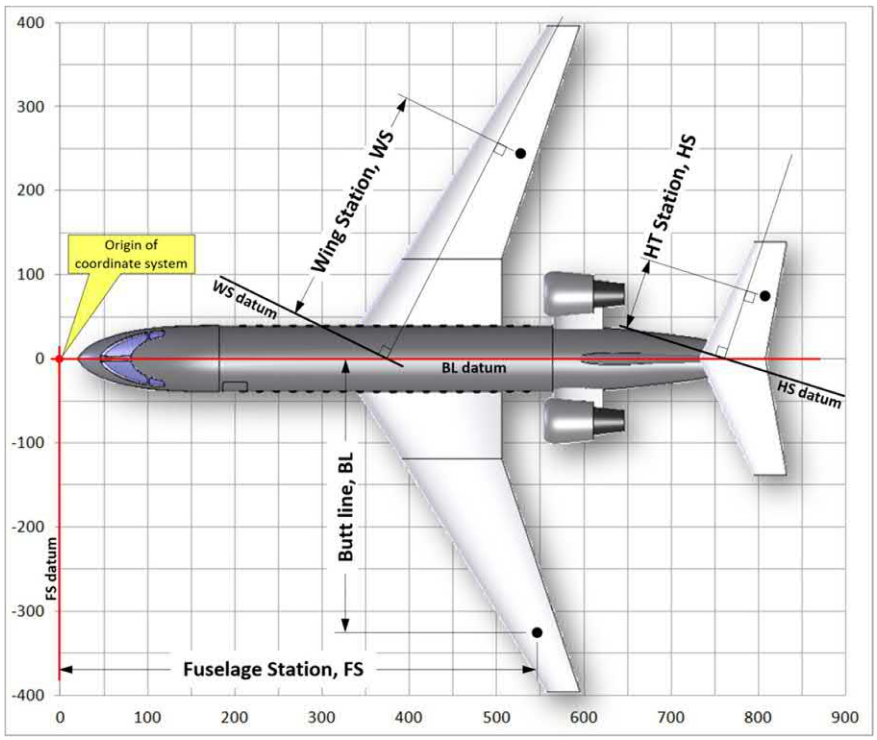


FIGURE 6-17 Reference locations seen from above.

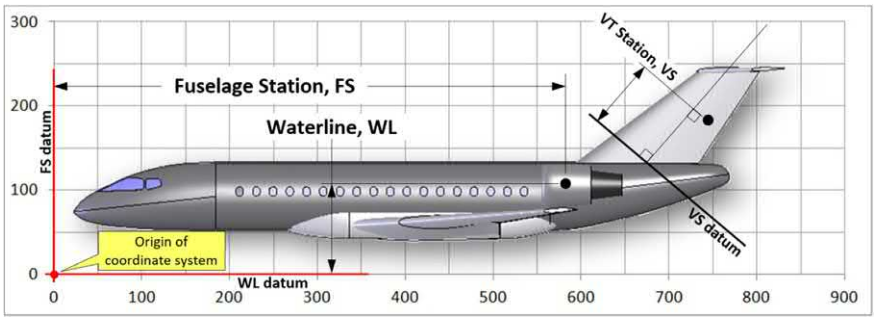


FIGURE 6-18 Reference locations seen from the left side.

assigned to identify each component, the total weight is calculated as follows:

$$\text{Total Weight:} \qquad W_{tot} = \sum_{i=1}^{N} W_i \tag{6-128}$$

6.6.4 Moment About (x_0, y_0, y_0)

Moments about an arbitrary reference point (x_0, y_0, y_0) are calculated using the expressions below. This is a necessary intermediary step before the center-of-gravity (CG) can be calculated:

$$M_x = \sum_{i=1}^{N} W_i \times (x_i - x_0) \qquad M_y = \sum_{i=1}^{N} W_i \times (y_i - y_0)$$
$$M_z = \sum_{i=1}^{N} W_i \times (z_i - z_0) \tag{6-129}$$

Unless otherwise specified, our reference point is always (0, 0, 0) and this is assumed in the following formulation. We rewrite Equation (6-129) by writing the moments about the point (0, 0, 0):

$$M_x = \sum_{i=1}^{N} W_i \times x_i \qquad M_y = \sum_{i=1}^{N} W_i \times y_i \qquad M_z = \sum_{i=1}^{N} W_i \times z_i \tag{6-130}$$

6.6.5 Center-of-Mass, Center-of-Gravity, Centroid of a Volume

The above properties are vitally important in aircraft design. Due to this significance, center-of-mass is capitalized as (X_{CM}, Y_{CM}, Z_{CM}), center-of-weight as (X_{CG}, Y_{CG}, Z_{CG}), and centroid as (X_C, Y_C, Z_C). More details of the integral presentation below can be found in Hibbeler [17] and similar sources.

(1) Center-of-Mass (CM)

Consider a system of matter (this could be a collection of solid objects, liquids, or gas, or any combination thereof) distributed in 3-dimensional space. We define *the Center-of-Mass (CM) of a system as the point in space at which its mass can be considered concentrated*. The CM for a continuous body in 3-dimensional Cartesian space is calculated as follows:

$$X_{CM} = \frac{\int x\, dm}{\int dm} \qquad Y_{CM} = \frac{\int y\, dm}{\int dm} \qquad Z_{CM} = \frac{\int z\, dm}{\int dm} \tag{6-131}$$

where

dm = Mass of an infinitesimal volume
x, y, z = Cartesian coordinates of the infinitesimal volume

The integration is performed over the entire body. The easiest way to determine the position of the CM with respect to the reference point (x_0, y_0, y_0) is by offsetting the coordinates (X_{CM}, Y_{CM}, Z_{CM}), i.e., ($X_{CM} - x_0$, $Y_{CM} - y_0$, $Z_{CM} - z_0$). The CM for a collection of finite masses is calculated as shown below:

$$\mathbf{R}_{CM} = \sum m_i \mathbf{r}_i / \sum m_i \tag{6-132}$$

where

$\mathbf{R}_{CM} = (X_{CM}, Y_{CM}, Z_{CM})$
i = Index from 1…N
m_i = Mass of a specific object within the collection of objects
$\mathbf{r}_i = (x_{CM}, y_{CM}, z_{CM})_i$ = Location of mass m_i

(2) Center-of-Gravity (CG)

We define *the Center-of-Gravity (CG) of a system as the point in space at which its weight can be considered concentrated*. For an aircraft, it is the point at which it is balanced and, so, has no tendency to drop on the nose or tail. The gravitational force acting on the system in a uniform gravitational field, such as that of Earth, also acts at the CM. In this case, we refer to it as the *center-of-gravity* (CG). While the CM and CG are often used

interchangeably, this does not hold true in a nonuniform gravitational field. In this book, the CM and CG are always the same point, unless otherwise specified. The CG of a continuous body in 3-dimensional Cartesian space is determined as follows:

$$X_{CG}=\frac{\int x\,dW}{\int dW} \qquad Y_{CG}=\frac{\int y\,dW}{\int dW} \qquad Z_{CG}=\frac{\int z\,dW}{\int dW} \tag{6-133}$$

where

dW = Weight of an infinitesimal volume

The location of the CG of the collection of components is estimated using the following expressions:

$$\mathbf{R}_{CG}=\sum W_i\mathbf{r}_i/\sum W_i \tag{6-134}$$

where

$\mathbf{R}_{CG}=(X_{CG}, Y_{CG}, Z_{CG})$
W_i = Weight of a specific object within the collection of objects
$\mathbf{r}_i=(x_{CG}, y_{CG}, z_{CG})_i$ = Location of weight W_i

This expression is commonly written in the following format

$$X_{CG}=\frac{M_x}{W_{tot}}=\frac{1}{W_{tot}}\sum_{i=1}^{N}W_i\times x_i$$
$$Y_{CG}=\frac{M_y}{W_{tot}}=\frac{1}{W_{tot}}\sum_{i=1}^{N}W_i\times y_i \tag{6-135}$$
$$Z_{CG}=\frac{M_z}{W_{tot}}=\frac{1}{W_{tot}}\sum_{i=1}^{N}W_i\times z_i$$

(3) Centroid-of-Volume (CV)

The centroid-of-volume of constant density can be determined using the formulation below:

$$X_C=\frac{\int x\,d\forall}{\int d\forall} \qquad Y_C=\frac{\int y\,d\forall}{\int d\forall} \qquad Z_C=\frac{\int z\,d\forall}{\int d\forall} \tag{6-136}$$

where

$d\forall$ = Infinitesimal volume

(4) CG-Location as a Percentage of MGC

In aviation, the x-location of the CG is commonly presented as a percentage of the MGC. This would be calculated as follows, where x_{MGC} is a reference distance to the leading edge of the MGC, as shown in Figure 6-19.

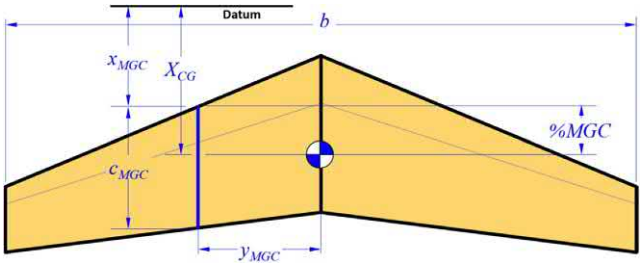


FIGURE 6-19 The location of the CG is commonly specified in terms of the %MGC.

$$P_{CG}=100\times\left(\frac{X_{CG}-x_{MGC}}{c_{MGC}}\right) \tag{6-137}$$

EXAMPLE 6-8

The CG of an airplane is reported to be at FS191.3 (in words: at Fuselage Station 191.3 in). If the LE of the MGC airfoil is at FS185 and the c_{MGC} is 6.32 ft, where is the CG as a percentage of c_{MGC}?

SOLUTION:

$$P_{CG}=100\left(\frac{X_{CG}-x_{MGC}}{c_{MGC}}\right)=100\left(\frac{191.3-185}{6.32\times 12}\right)$$
$$=8.31\%\text{MGC}$$

EXAMPLE 6-9

The following collection of point loads is given in Table 6-5. Determine the total weight, moments, and the location of the CG in 3-dimensional space.

TABLE 6-5 Collection of point loads.

i	W lb_f	x ft	y ft	z ft
1	3.25	5.0	3.0	1.0
2	7.50	3.5	-2.0	3.0
3	2.50	6.5	-2.5	-2.0
4	1.25	10.0	3.0	-2.5
5	5.00	12.0	-3.0	1.5
6	2.50	8.0	-1.0	-3.5
7	2.50	7.5	4.0	-4.0

SOLUTION:
Total weight:

$$W_{tot}=\sum_{i=1}^{N}W_i=3.25+7.50+2.50+1.25+\hookleft$$
$$5.00+2.50+2.50=24.50\,\text{lb}_\text{f}$$

EXAMPLE 6-9 *(cont'd)*

Moments about the origin of the coordinate system:

$$M_x = \sum_{i=1}^{N} W_i \times x_i = 3.25 \times 5.0 + 7.50 \times 3.5 + \cdots + 2.50 \times 7.5 = 170.0\,\text{ft} \cdot \text{lb}_\text{f}$$

$$M_y = \sum_{i=1}^{N} W_i \times y_i = 3.25 \times 3.0 + 7.50 \times (-2.5) + \cdots + 2.50 \times 4.0 = -15.25\,\text{ft} \cdot \text{lb}_\text{f}$$

$$M_z = \sum_{i=1}^{N} W_i \times z_i = 3.25 \times 1.0 + 7.50 \times 3.0 + \cdots + 2.50 \times (-4.0) = 6.38\,\text{ft} \cdot \text{lb}_\text{f}$$

CG with respect to the origin of the coordinate system:

$$X_{CG} = \frac{M_x}{W_{tot}} = \frac{170.0\,\text{ft} \cdot \text{lb}_\text{f}}{24.50\,\text{lb}_\text{f}} = 6.939\,\text{ft}$$

$$Y_{CG} = \frac{M_y}{W_{tot}} = \frac{-15.25\,\text{ft} \cdot \text{lb}_\text{f}}{24.50\,\text{lb}_\text{f}} = -0.622\,\text{ft}$$

$$Z_{CG} = \frac{M_z}{W_{tot}} = \frac{6.38\,\text{ft} \cdot \text{lb}_\text{f}}{24.50\,\text{lb}_\text{f}} = 0.260\,\text{ft}$$

6.6.6 Determination of CG Location by Aircraft Weighing

The CG location of actual aircraft is always determined by direct weighing. Small aircraft are parked on specially designed weighing kits, which consist of three separate electronic scales; one for the nose (or tail) gear and one for each of the two main gear (see Figure 6-20). A special computer simultaneously connects to all three, allowing the weight on each wheel and the total to be read. Larger aircraft are often equipped with special jacking points used for the same purpose. These aircraft are jacked-up and weighed using load cells. The advantage of such hard points is that their spatial location is known. This contrasts wheels-on-scales configurations, whose measurements are affected by structural flex that introduces inaccuracy. At any rate, once the distance between the weighing points is known, the measured weights can be used to calculate the location of the CG as shown below:

Location of CG from nose gear:

$$x_N = \left(\frac{R_M}{R_M + R_N}\right) x_{NM} = \left(\frac{R_M}{W}\right) x_{NM} \tag{6-138}$$

Location of CG from main gear:

$$x_M = \left(1 - \frac{R_M}{W}\right) x_{NM} \tag{6-139}$$

where

R_M = Main gear reaction, the sum of both main gear scales
R_N = Nose gear reaction
W = Total aircraft weight = $R_N + R_M$
x_N, x_M, and x_{NM} = Distances defined in Figure 6-20

Note that the CG location is usually determined with respect to some datum. Note that when weighing aircraft in this fashion, it is imperative that it is leveled as accurately as possible and that no wind conditions prevail where the weighing takes place. Additional methodologies and important hints for improved accuracy are provided by D'Estout [18], FAA staff [19], and Boynton [20, 21].

6.6.7 Mass Moment of Inertia

Mass moments and products of inertia are needed to evaluate the aircraft's flight dynamics. This section introduces computational methods for these properties. First, recall that a body of mass moving along a straight path tends to keep moving along that path. This tendency is called *linear momentum*. Similarly, a body that rotates about an axis tends to keep rotating. This is called *rotational momentum* (as in a flywheel). Unless acted on by some force (e.g. friction), both motions will continue indefinitely. Besides angular velocity, the rotational

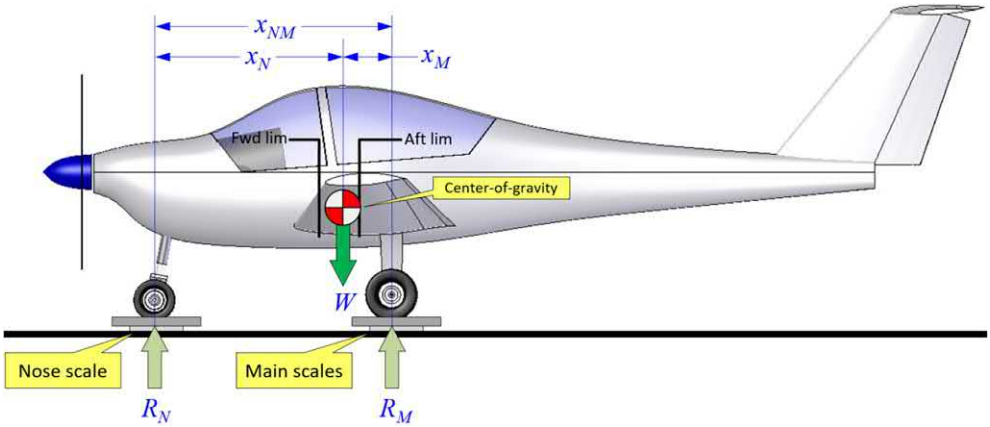


FIGURE 6-20 Typical setup of scales when weighing aircraft.

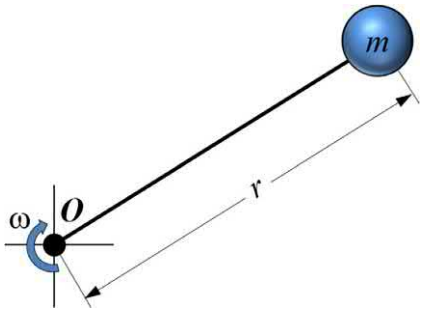


FIGURE 6-21 The definition of mass moment of inertia.

momentum depends on the mass and the distance of its CG from the axis of rotation. This gives rise to the property of *mass moment of inertia*. It is to rotational momentum what mass is to linear momentum.

(1) Moment of Inertia of a Continuous Mass

Figure 6-21 shows a pendulum of mass, m, placed at distance, r, from the point O. The moment of inertia of the mass about an axis going through point O is given by the following expression.

$$I = mr^2 = \frac{W}{g}r^2 \tag{6-140}$$

where W is the weight of the object and g is acceleration due to gravity. In aircraft stability and control theory, we are primarily interested in evaluating the moment of inertia about the x-, y-, and z-axes. Thus, Equation (6-140) is evaluated for each axis as follows:

$$I_{xx} = m(y^2 + z^2) \quad I_{yy} = m(x^2 + z^2) \quad I_{zz} = m(x^2 + y^2) \tag{6-141}$$

where the double-subscripts specify an axis of rotation. The value of the moment of inertia is always positive. The mass moment of inertia of an arbitrary body of constant density and continuous mass distribution can be determined by integrating the contribution of the infinitesimal mass, dm, over the volume of the body about an arbitrary axis of rotation, O (see Figure 6-22):

$$I = \int r^2 dm \tag{6-142}$$

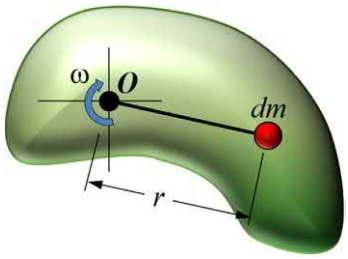


FIGURE 6-22 The mass moment of inertia of an arbitrary body about some arbitrary axis of rotation.

Again, the integration is performed over the entire body. The moment of inertia is a measure of the *distribution of matter about that axis*. Equation (6-142) is written about each axis by noting that r^2 about the x-axis is given by (y^2+z^2), r^2 about the y-axis is given by (x^2+z^2), and so on. Therefore, the moment of inertia about the point O is given by:

$$I_{xx} = \int (y^2 + z^2)dm \quad I_{yy} = \int (x^2 + z^2)dm$$
$$I_{zz} = \int (x^2 + y^2)dm \tag{6-143}$$

(2) Moment of Inertia of a System of Discrete Point Loads

The moment of inertia formulae for our analyses of the airplane are written in terms of a collection of discrete mass points; like the treatment in Section 6.6.5:

$$I_{xx} = \frac{1}{g}\sum_{i=1}^{N}\left(W_i\left[(y_i - Y_{CG})^2 + (z_i - Z_{CG})^2\right] + I_{xx_i}\right)$$
$$I_{yy} = \frac{1}{g}\sum_{i=1}^{N}\left(W_i\left[(x_i - X_{CG})^2 + (z_i - Z_{CG})^2\right] + I_{yy_i}\right) \tag{6-144}$$
$$I_{zz} = \frac{1}{g}\sum_{i=1}^{N}\left(W_i\left[(x_i - X_{CG})^2 + (y_i - Y_{CG})^2\right] + I_{zz_i}\right)$$

where

I_{xx_i}, I_{yy_i}, I_{zz_i} = Moment of inertia of component i about its own CG
x_i, y_i, z_i = Distance from the reference point O to the CG of the system of point loads

Note that the terms involving the product of the weight and distance from the CG represent the application of the parallel-axis theorem (see below). When referring to heavy objects, such as an engine or a wing, the moment of inertia of the body itself should be included. Such components can have significant moment of inertia about its own CG and this should be accounted for. The moment of inertia of a low mass item about its own CG is usually negligible and may be omitted.

(3) Parallel-Axis Theorem for Moments of Inertia

Consider Figure 6-23, which shows an arbitrary body rotating about a point other than its CG; point O. The distance between the CG and the axis of rotation, O, is denoted by r_{CG}. The distance between the CG and the infinitesimal mass dm is given by r'. The distance between O and dm is given by r. Thus, the moment of inertia about the point O is determined as follows using the *parallel-axis theorem*:

$$I_O = mr_{CG}^2 + \int r'dm = mr_{CG}^2 + I_{CG} \tag{6-145}$$

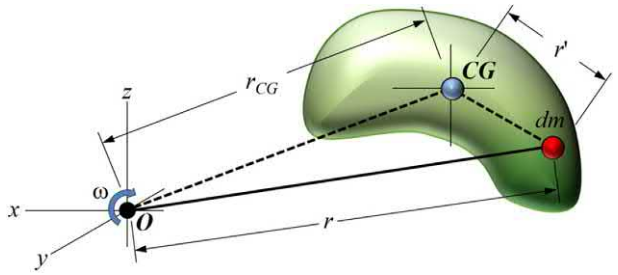


FIGURE 6-23 The parallel-axis theorem explained.

where

I_{CG} = Moment of inertia of the body about its own CG

A more practical form of the parallel-axis theorem is shown below:

$$\begin{aligned} I_{xx} &= I_{xx_{CG}} + m\left(y_{CG}^2 + z_{CG}^2\right) \\ I_{yy} &= I_{yy_{CG}} + m\left(x_{CG}^2 + z_{CG}^2\right) \\ I_{zz} &= I_{zz_{CG}} + m\left(x_{CG}^2 + y_{CG}^2\right) \end{aligned} \tag{6-146}$$

where

$I_{xx_{CG}}$, $I_{yy_{CG}}$, $I_{zz_{CG}}$ = Moment of inertia of the body about its own CG

x_{CG}, y_{CG}, z_{CG} = Distance from the reference point O to the CG of the body

DERIVATION OF EQUATION (6-145)

The moment of inertia about the arbitrary point in Figure 6-23 can be obtained from Equation (6-143):

$$\begin{aligned} I_O &= \int r^2 dm = \int (r_{CG} + r')^2 dm = \int \left(r_{CG}^2 + 2r_{CG}r' + r'^2\right) dm \\ &= \int r_{CG}^2 dm + \int 2r_{CG}r' dm + \int r'^2 dm \end{aligned}$$

Since r_{CG} is a constant, we can simplify this and write: $I_O = r_{CG}^2 \int dm + 2r_{CG} \int r'\, dm + \int r'^2 dm$.

By inspection, the first term is the moment of inertia of the mass, acting as a point mass, as it rotates about point O. It is given by (remember that r_{CG} is constant):

$$I_P = r_{CG}^2 \int dm = m r_{CG}^2$$

where the subscript P denotes the *parallel-axis term*. The second term is zero, because the origin of r 'is at the CG and the mass is distributed around it. To better see this, consider the coordinate system superimposed on the CG in Figure 6-23. The contribution of the mass above the x-axis will be canceled by the equal mass below it. In fact, the integral is effectively a moment integral analogous to Equation (6-129), where x_0 is the x_{CG}. Finally, the third term is the moment of inertia of the body about its own CG and is given by:

$$I_{CG} = \int r'^2 dm$$

From which we get Equation (6-145).

6.6.8 Mass Product of Inertia

The three orthogonal vectors that form the coordinate system about which the body rotates, necessarily form three separate and mutually orthogonal planes: the *xy*-, *xz*-, and *yz*-planes. The *products of inertia* are a measure of a body's asymmetric mass distribution in those planes.

(1) Product of Inertia of a Continuous Mass

$$\begin{aligned} I_{xy} = I_{yx} &= \int (xy) dm \quad I_{xz} = I_{zx} = \int (xz) dm \\ I_{yz} = I_{zy} &= \int (yz) dm \end{aligned} \tag{6-147}$$

The value of the product of inertia can be negative or positive. An airplane is often symmetrical about one of the planes—the *xz*-plane for a standard coordinate system. Thus, it is often called the *plane-of-symmetry*. The product of inertia about the *xz*-plane is often taken to be 0. However, this is false if the airplane has asymmetric mass loading, such as unbalanced fuel in the wing tanks, or a single pilot in a two-seat, side-by-side, cabin. Considering $I_{xz} = 0$ for such an asymmetric loading can only be justified if its magnitude is negligible compared to the other moments and products of inertia. It is not justifiable if one wing fuel tank is full and the other is empty.

(2) Product of Inertia of a System of Discrete Point Loads

The product of inertia for a collection of discrete mass points is estimated in a similar fashion as that of the moments of inertia. However, be careful as the position of component must include the proper sign. The products of inertia about own CG of large and heavy components objects (e.g., wings and engines) should be included in the total to improve accuracy.

$$\begin{aligned} I_{xy} &= \frac{1}{g}\sum_{i=1}^{N} \left(W_i (x_i - X_{CG})(y_i - Y_{CG}) + I_{xy_i}\right) \\ I_{xz} &= \frac{1}{g}\sum_{i=1}^{N} \left(W_i (x_i - X_{CG})(z_i - Z_{CG}) + I_{xz_i}\right) \\ I_{yz} &= \frac{1}{g}\sum_{i=1}^{N} \left(W_i (y_i - Y_{CG})(z_i - Z_{CG}) + I_{yz_i}\right) \end{aligned} \tag{6-148}$$

where

$I_{xy_{CG}}$, $I_{xz_{CG}}$, $I_{yz_{CG}}$ = Product of inertia of the body about its own CG.

(3) Parallel-Axis Theorem for Products of Inertia

The parallel-axis theorem for moment of inertia can be extended to the product of inertia:

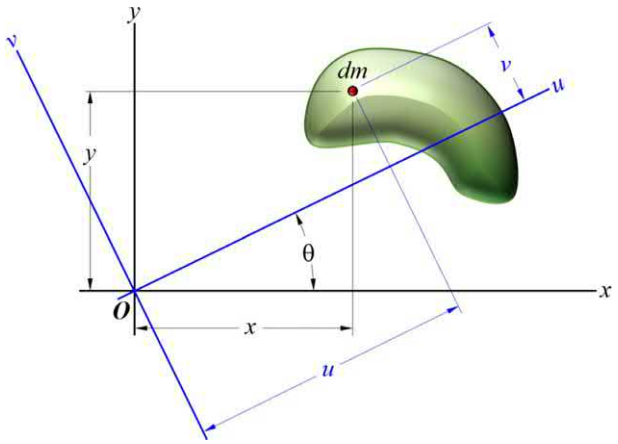


FIGURE 6-24 Rotation of original axes x–y to new axes u–v.

$$\begin{aligned} I_{xy} &= I_{xy_{CG}} + m\, x_{CG} y_{CG} \\ I_{xz} &= I_{xz_{CG}} + m\, x_{CG} z_{CG} \\ I_{yz} &= I_{yz_{CG}} + m\, y_{CG} z_{CG} \end{aligned} \tag{6-149}$$

where

$I_{xy_{CG}}$, $I_{xz_{CG}}$, $I_{yz_{CG}}$ = Product of inertia of the body about its own CG.

6.6.9 Principal Moments of Inertia

Consider the body in Figure 6-24, which is positioned in the x–y plane. Using our formulation so far, we should be able to estimate I_{xx}, I_{yy}, and I_{xy} for the body. However, this begs the question: is it possible to estimate the corresponding properties for the coordinate system u–v, if we know only the angle θ between the two systems, rotated about the point O? These properties would be denoted as I_{uu}, I_{vv}, and I_{uv}. It should not surprise the answer is yes. These are given by the following set of equations:

$$\begin{aligned} I_{uu} &= \frac{I_{xx}+I_{yy}}{2} + \frac{I_{xx}-I_{yy}}{2}\cos 2\theta - I_{xy}\sin 2\theta \\ I_{vv} &= \frac{I_{xx}+I_{yy}}{2} - \frac{I_{xx}-I_{yy}}{2}\cos 2\theta + I_{xy}\sin 2\theta \\ I_{uv} &= \frac{I_{xx}-I_{yy}}{2}\sin 2\theta + I_{xy}\cos 2\theta \end{aligned}$$

The magnitudes of I_{uu}, I_{vv}, and I_{uv} depend on the angle θ. The variation is periodic, which means that all three have a maximum and minimum value. It can be shown that the maximum and minimum values of I_{uu} and I_{vv} occur when θ takes the value of θ_P as shown below

$$\theta_P = \frac{1}{2}\tan^{-1}\left(\frac{-2I_{xy}}{I_{xx}-I_{yy}}\right) \tag{6-150}$$

Note that θ_P has two solutions, call them θ_{P1} and θ_{P2}, that are 90 degrees apart. Thus, the two specify the orientation of the u- and v-axes. When this happens, the value of $I_{uv}=0$. These values of I_{uu} and I_{vv} are called *principal moments of inertia*. Their significance is that they indicate where the mass of the body is symmetrically distributed. For instance, if the x-axis goes through the center of a circle, it is the *symmetrical* axis and the corresponding $I_{xy}=0$. The derivation of these equations is beyond the scope of this book, but interested readers are directed to ref. [17] and similar sources on engineering mechanics.

6.6.10 Inertia Matrix

The moments and products of inertia about a specific point are often represented in a matrix format, as this lends itself conveniently for various dynamic stability analyses. This matrix is called the *inertia matrix* and it is always symmetric. Here, it is shown in a format that assumes the axes of interest of go through the airplane's CG.

$$[I_{CG}] = \begin{bmatrix} I_{xx} & -I_{xy} & -I_{xz} \\ -I_{xy} & I_{yy} & -I_{yz} \\ -I_{xz} & -I_{yz} & I_{zz} \end{bmatrix}_{CG} \tag{6-151}$$

The inertia matrix depends on the orientation of the axes going through the CG of the body of interest. The matrix becomes diagonal for the principal moments of inertia. The principal axes depend on the location of the reference point; shifting it to a new location will change the orientation of the principal axes.

6.7 THE CENTER-OF-GRAVITY ENVELOPE

As stated earlier, the term CG refers to that point at which the weight of the airplane can be considered concentrated. It can also be considered the point about which the aircraft is balanced. Safe operation of aircraft requires the CG to remain inside a specific region in flight; too far forward and the airplane will be too "nose-heavy." Too far aft and it will be unstable. This region is constrained by the *forward* and *aft* CG-limits (see Figure 6-20) and constitutes the *CG-envelope*. The establishment of this envelope is a vital part of any aircraft design and is required by aviation regulations. It falls on the conceptual designer to create it and the flight test team to polish.

6.7.1 Fundamentals

An example of an actual CG-envelope for the Beech F33C Bonanza is plotted in Figure 6-25. It is based on its Type Certification Data Sheet [22]. Ordinarily, the vertical axis displays weight (in N or lb_f). The empty weight serves as a lower limit and a weight, slightly higher than gross weight, as upper limit. However, the horizontal axis may display position between the nose and tail in three ways: (1) as a Fuselage Station (FS—often in units of inches), (2) percentage of the MGC, and (3) moment (N•m or in•lb_f), often called *load moment*.

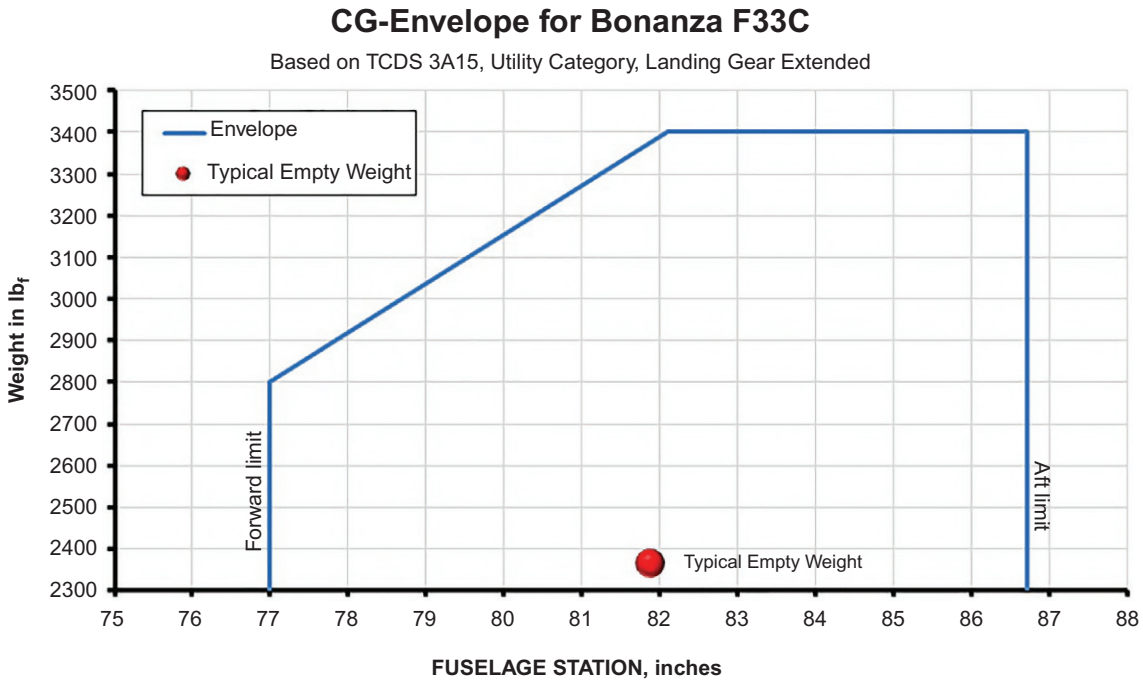


FIGURE 6-25 A typical CG-envelope for a light General Aviation aircraft.

Some manufacturers, e.g., Boeing, even present the CG-position using a specialized *universal index* system [23].

The reference point (FS0, WL0) is often placed far in front of and below the nose of the aircraft (see Figure 6-18). This ensures that when calculating moments due to the position of discrete weights, all spatial locations have a positive sign and not a combination of positive and negatives signs. This reduces the chance of summation error creeping into calculations and, thus, the chance of determining an erroneous CG-position. Regardless, FS0 is commonly placed at the front face of the firewall of single engine propeller aircraft.

(1) Regulations

Current aviation regulations dictate that all aircraft certified per 14 CFR Part 23 and 25 must be statically stable and, dynamically, the short period and Dutch roll modes must be convergent, while Spiral stability and Phugoid modes may be slightly divergent. ASTM F2245 for LSA (per 14 CFR Part §1.1) requires all oscillatory modes to be converging.

Establishment of CG-envelope: 14 CFR Part §23.27 (old), §23.2100 (new), §25.27, ASTM F2245 §4.2.3

Long/Lat/Dir stability: 14 CFR Part §23.171 (old), §23.2145, §25.171, ASTM F2245 §4.5.4.1

(2) Example Limits

Table 6-6 lists typical forward and aft CG-limits for several aircraft. All the limits reference the MGC of said airplanes, except as otherwise noted.

TABLE 6-6 CG-limits for selected aircraft.

		CG-envelope (% MGC)			
Make and model	**Class**	**Forward**	**Aft**	**Range**	**Reference**
Airbus A300 B2	C2	11.0	31.0	20.0	Torenbeek [5]
Airbus A310	C2	14.0	40.0	26.0	AIM
Airbus A330	C2	17.4	37.5	20.1	AIM
Airbus A340	C2	19.0	42.0	23.0	AIM
Antonov An-124-100	C4	26.5	42.5	16.5	AIM
Antonov An-148-100	C2	22.0	41.0	19.0	AIM

TABLE 6-6 CG-limits for selected aircraft—cont'd

Make and model	Class	CG-envelope (% MGC)			Reference
		Forward	Aft	Range	
ATR 72	TP2	10.0	39.0	29.0	AIM
BAC-111[a]	C2	14.0	41.0	27.0	Torenbeek [5]
Beech B-45 Mentor	PP1	19.0	28.0	9.0	Torenbeek [5]
Beech F33	PP1	3.2	18.1	14.9	POH
Boeing 707-120	C4	16.0	34.0	18.0	Torenbeek [5]
Boeing 720	C3	15.0	31.0	16.0	Torenbeek [5]
Boeing 737-100	C2	15.0	35.0	20.0	Torenbeek [5]
Boeing 737-400	C2	4.0	30.6	26.6	AIM
Boeing 747	C4	12.5	32.0	19.5	Torenbeek [5]
Boeing 757-200	C2	7.0	39.0	32.0	AIM
Caravelle 10	C2	25.0	41.5	16.5	Torenbeek [5]
Carbon Cub 11-160	P1	16.7	29.4	12.7	POH
Cessna 172 Skyhawk	PP1	15.6	36.5	20.9	POH
Cessna 177 Cardinal	PP1	5.1	28.1	23.0	POH
Cessna 182 Skylane	PP1	14.0	38.3	24.3	POH
Cessna 206 Skywagon	PP1	12.2	39.4	27.2	POH
Cessna 208 Caravan	TP1	3.1	40.3	37.2	POH
Cessna 337 Skymaster	PP2	17.3	30.9	13.6	POH
Cirrus SR22	PP1	10.2	31.5	21.3	POH
De Havilland DHC-2 Beaver	PP1	17.4	40.3	22.9	POH
De Havilland DHC-6	TP2	20.0	36.0	16.0	Torenbeek [5]
Dornier Do-28	PP2	10.7	30.8	20.1	Torenbeek [5]
Douglas DC-3	PP2	11.0	28.0	17.0	POH
Douglas DC-6	PP4	12.0	35.0	23.0	Torenbeek [5]
Douglas DC-8-21	C4	16.5	32.0	15.5	Torenbeek [5]
Douglas DC-9-10	C2	15.0	40.0	25.0	Torenbeek [5]
Douglas DC-9-33	C2	3.1	34.7	31.6	Torenbeek [5]
Extra EA-200	PP1	10.9	22.6	11.7	POH
Fokker F-27-200 Friendship	TP2	18.7	40.7	22.0	Torenbeek [5]
Fokker F-28 Fellowship	C2	17.0	37.0	20.0	Torenbeek [5]
Hawker-Siddeley HS-125[a]	B2	18.0	37.5	19.5	Torenbeek [5]
HFB-320 Hansa Jet	B2	11.7	21.7	10.0	Torenbeek [5]
Learjet 25	B2	9.0	30.0	21.0	Torenbeek [5]
Lockheed 1011 Tristar	C3	12.0	32.0	20.0	Torenbeek [5]
Lockheed 188 Electra	TP4	13.0	33.0	20.0	Torenbeek [5]
Lockheed C-130	TP4	15.0	30.0	15.0	Torenbeek [5]
Lockheed C-141A	MT4	19.0	32.0	13.0	Torenbeek [5]
Lockheed C-5A Galaxy	MT4	19.0	41.0	22.0	Torenbeek [5]

Continued

TABLE 6-6 CG-limits for selected aircraft—cont'd

Make and model	Class	CG-envelope (% MGC) Forward	Aft	Range	Reference
Lockheed L-1049	PP4	15.0	34.0	19.0	Torenbeek [5]
Pilatus PC-6 Porter	PP1	11.0	34.0	23.0	Torenbeek [5]
Piper Pa-30	PP2	12.0	27.8	15.8	POH

AIM, Airman's Information Manual; POH, Pilot's Operating Handbook; B, Business jet; C, Commercial; MT, Military transport; PP, Pistonprop; TP, Turboprop. Number following letter indicates number of engines.
[a] *References standard mean chord (SMC).*

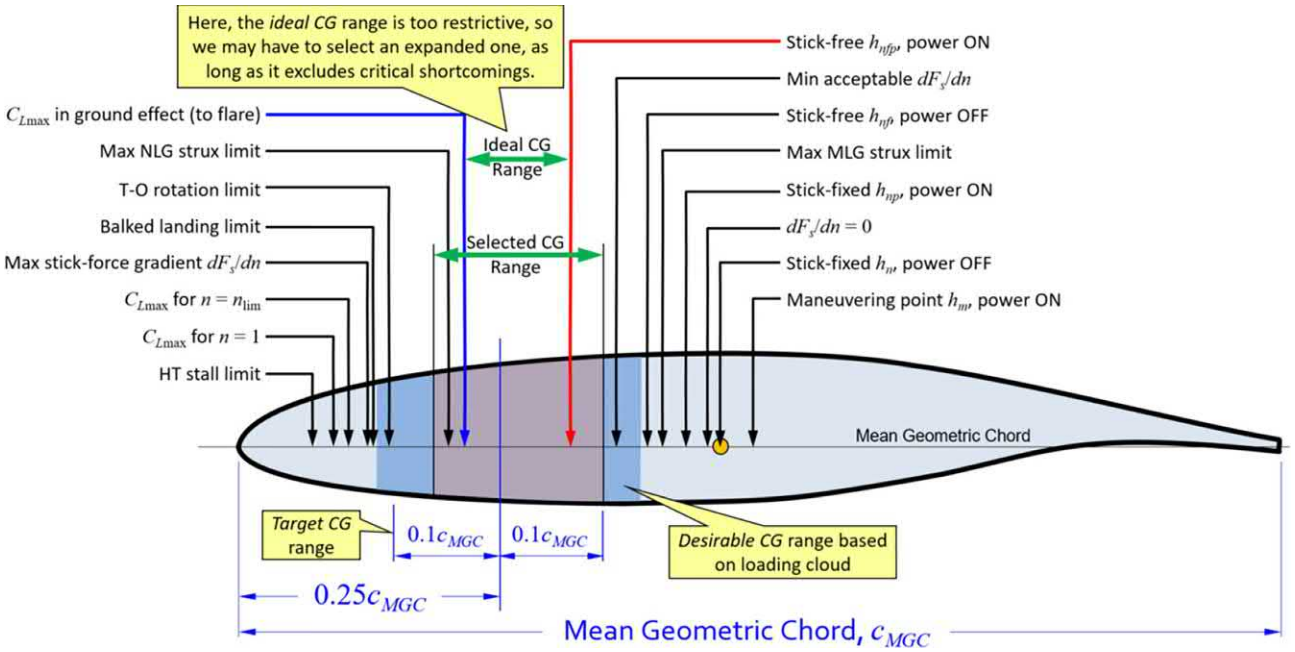


FIGURE 6-26 Typical factors affecting the creation of the CG-envelope.

6.7.2 Creating the CG-Envelope

This section details how the CG-envelope is created. It is a part of Step 12 in the aircraft design algorithm of Figure 1-11. The forward and aft limits depend on structural and aerodynamic parameters (through stability and control). The following listing presents most of the common parameters. They are also depicted in Figure 6-26. Note that stability and control (S&C) methods are presented in Chapters 24 and 25. Refer to the list of variables. Parameters marked with * should be considered critical or likely critical.

Parameters Affecting the Forward CG-Limit

Parameter	Description	How to determine during conceptual phase
Balked landing limit*	Required by 14 CFR Part §23.77 (old), §23.2120(c), §25.119, this condition is encountered when a landing must be aborted, and the aircraft is required to climb at full power in the landing configuration. This puts high loading demand on a horizontal tail operating at a low dynamic pressure and is compounded with forward CG.	S&C analysis with aircraft in landing configuration at $1.2V_{S_0}$.
T-O rotation limit*	Aircraft with high thrustline are susceptible to insufficient elevator authority when rotating for T-O, due to the added thrust moment. This is compounded with forward CG. Aircraft with nose gear should be able to rotate at $\leq 0.9V_{S1}$.	S&C analysis with aircraft in T-O configuration at $0.9V_{S1}$.

Parameter	Description	How to determine during conceptual phase
$C_{L_{max}}$ (or stall speed) limit*	We want enough elevator authority to stall the airplane. This guarantees our airplane achieves the advertised $C_{L_{max}}$. This has several side-benefits that include shorter T-O and landing distances and reduced kinetic energy in an emergency. Additionally, we want enough elevator authority to flare in ground effect (in the landing configuration). Moving the CG forward requires higher elevator deflection to stall and, eventually, the pilot will run out of elevator deflection. This causes the airplane to mush down, rather than break the stall.[a] The designer must establish the CG-position where this happens.	Use S&C analysis to evaluate elevator deflection to trim at V_S, V_{S1}, and V_{S_0}, with the aircraft in clean, T-O, and landing configurations, respectively. Do this for free flight at $n=1$ and $n=n_{lim}$, and ground effect at $n=1$.
HT (elevator) stall limit*	The airflow over the HT may separate if (1) it is subjected to high AOA, such as that caused by increased downwash due to flap deflection or (2) by too rapid a pitch rate. (3) This can also happen if the tailplane ices up in icing conditions (referred to as *Ice Contaminated Tailplane Stall* (ICTS)).	(1) Conduct HT flow analysis using VLM or CFD. (2) S&C analysis. (3) ICTS must be evaluated in flight testing for aircraft seeking certification to *fly into known icing* (FIKI))
Max Stick-force per g limit*	Also called the *stick-force gradient* (dF_s/dn), is used to evaluate handling characteristics (response) in maneuvering flight. An excessively high dF_s/dn is highly undesirable as it makes it difficult to maneuver the aircraft. In this case, high stick-forces are demanded even by modest maneuvers. Acceptable values for dF_s/dn are between 13 and 155 N/g or 3–35 lb_f/g. The low values are for aerobatic aircraft or fighters, while high are for large, heavy transports. Stick-force gradient helps the designer control the handling of the airplane.	S&C analysis to determine the CG-position for which the stick-force gradient approaches the acceptable maximum.
Nose landing gear structural limit*	Ideally, we want the static load on the nose landing gear to amount to 10%–20% of the airplane's weight. This is low enough to permit most airplanes to rotate for T-O, while low enough to create adequate ground friction to prevent nose-skidding when taxiing. This static load increases with forward CG-position. The actual strength of the nose gear is established once the design team selects the nose gear. Refer to Chapter 13 for more information.	Once the max load the nose gear may react is known, plot this load as an isopleth per the method discussed later in this section.
Tail wheel low load limit	Ideally, we want the load on the tail wheel to be 5%–10% of the weight of the airplane. The forward limit reduces the load on the tail wheel, increasing the likelihood of tail skidding when taxiing.	Evaluate CG-position that results in 5% weight on tailwheel using simple statics.

[a] *Mushing: A slow speed (albeit higher than stalling speed) descent in separated flow field (caused by aircraft) that renders the control surfaces marginally effective. Stall-break: Occurs when the airplane achieves a high enough AOA for drop in lift to take place, such it drops on the nose.*

Parameters Affecting Aft Limit

Parameter	Description	How to determine during conceptual phase
Stick-fixed neutral point, power off*	The *stick-fixed neutral point* (h_n) is the ultimate aft CG-limit. Forward of h_n, the airplane is statically stable. At h_n, it is neutrally stable, and aft of h_n, it is unstable. The conceptual designer is responsible for the level of stability of the aircraft. Note that power-off for propellers assumes windmilling. h_n is determined using elevator deflection as a function of CG-position.	S&C analysis
Stick-fixed neutral point, power on*	Power changes typically result in three responses: (1) pitch up, (2) no pitch, and (3) pitch down. This shows that the h_n is affected by power. At max power, this position is denoted as h_{np}. In terms of thrustline, we find that a low thrustline is destabilizing—it places h_{np} forward of h_n. The opposite holds true for a high thrustline—it places h_{np} aft of h_n. This is compounded by another contribution of propeller aircraft: propwash. When directed at the HT, the airplane is further destabilized.	S&C analysis

Parameter	Description	How to determine during conceptual phase
Stick-free neutral point, power off*	The difference between stick-fixed and *stick-free neutral points* (h_{nf}) is that the former assumes the elevator is fixed at $\delta_e = 0$ degree. In the latter, the elevator can float. The floating depends on the AOA and hinge moments. For typical elevators, this destabilizes the airplane and places the h_{nf} forward of h_n (assuming power off). This limit is considered critical here, although it is left to the flight test team to determine its severity. h_{nf} is determined using stick-force.	S&C analysis
Stick-free neutral point, power on	Same as the above limit, except it assumes power on. This point is not always critical because the pilot (or autopilot) close the control loop. It is left to the flight test team to determine its severity.	S&C analysis
Maneuvering point	The slope of the elevator-angle per g is reduced when the CG is shifted backwards and when airspeed is increased. The *maneuvering point*, $h_{m,}$ is where the slope becomes zero. It is always aft of the stick-fixed neutral point and, thus, not an issue.	S&C analysis
Main gear structural limit*	The main landing gear should carry 80%–90% of the weight of the airplane for a tricycle style, and 90%–95% if a taildragger. Moving the CG-position aft will place more weight on the main gear for tricycle models and less on taildraggers.	Once the max load the main gear may react is known, plot this load as an isopleth per the method discussed later in this section.
Tail wheel structural limit*	The position of the CG at which the structural integrity of the tail wheel is compromised.	Once the max load on tailwheel is known, plot similarly as for the nose gear structural limit.
Nose gear low load limit	Load on nose gear is 10% of the weight of the airplane or less (see text with Nose gear structural limit).	Using statics, estimate the CG-position that results in 10% weight on nose gear.
Min Stick-force per g limit*	An excessively low dF_s/dn is dangerous as it allows the pilot to pull high g with minimum effort. Besides subjecting the aircraft to high structural loads, this makes it difficult to maneuver the aircraft because of rapid response. It can cause pilot induced oscillation (PIO). Acceptable values for dF_s/dn are discussed above.	S&C analysis to determine the CG-position for which the stick-force gradient approaches the acceptable minimum.

These limits are illustrated in Figure 6-26. Note that their order and positions should be expected to differ from design to design. To create the CG-envelope, follow these steps:

***STEP 1*:** Define a *desirable CG-range*. This is obtained using the loading cloud analysis, discussed in Section 6.7.3. If this range is unrealistically large, you may have to review your design, which may require components (e.g., engine, equipment, lifting surfaces) to be moved around and, in extreme cases, changes to the geometry of the aircraft. Once this step is complete, the CG-envelope is a box-shaped region extending horizontally from the forward limit to the aft one and vertically from the empty weight to the gross weight. Subsequent steps typically reduce this region.

***STEP 2*:** Define a *target CG-range* based on Step 1. Typical medium target is $25\% \pm 10\%\ c_{MGC}$. Typical wide target is $25\% \pm 15\%\ c_{MGC}$. Compare this to the desirable CG-range. Note that while you may not be able to achieve the target CG-range, its purpose is to show you what a reasonable CG-envelope looks like. If your desirable CG-range extends well beyond this, you still have work to do shortening it.

***STEP 3*:** Estimate all applicable forward and aft limits per the listing presented earlier. Plot the results from Steps 1 through 3, like what is shown in Figure 6-28. This will help identify potential issues with the CG-envelope.

***STEP 4*:** Define the *ideal* CG-range as the region between the aft-most forward limit and forward-most aft limit, as shown in Figure 6-26. This range may be too narrow to be of practical use. Compare this range to typical values in Table 6-6 to better judge this possibility. If this is the case, the selection of a larger (and less than perfect) CG-range is necessitated. The selected limits may include some of the estimated limits. In the example shown in Figure 6-26, three such limits are inside the *selected CG-range*; the max NLG structural limit, $C_{L_{max}}$ in ground effect limit, and the limit for stick-free neutral point with power on. The first two may be remedied by reducing the forward limit with weight, as shown in Figure 6-28. This is a very common approach. The stick-free limit may result in worsening handling when CG-position is near the aft limit but may be tolerated. NOTE: CRITICAL LIMITS MUST BE OUTSIDE THE SELECTED CG-RANGE.

A Note on the MLG and NLG Isopleths

The main landing gear (MLG) and nose landing gear (NLG) structural limits are established during the detail (structural) design phase. One way to determine the landing gear loads is illustrated in Figure 6-27. This is

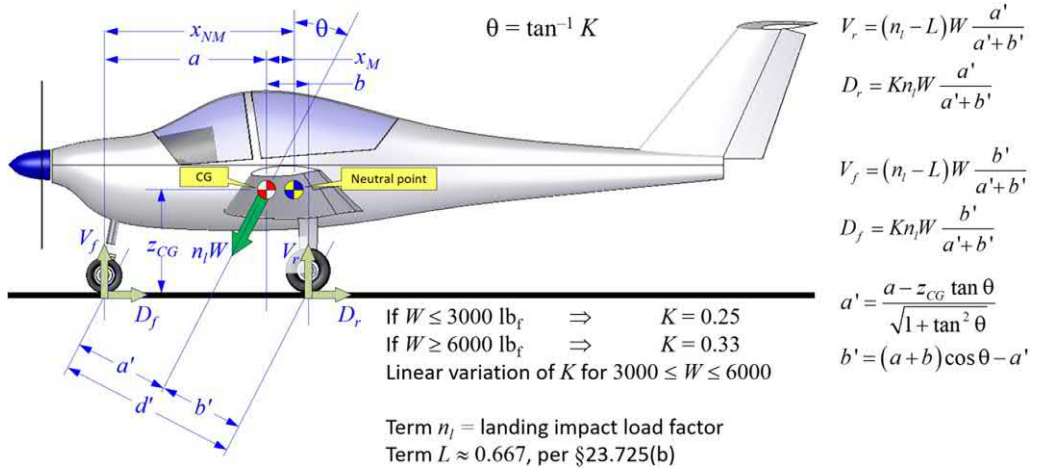


FIGURE 6-27 Main and nose landing gear loads per 14 CFR Part 23, Appendix C.

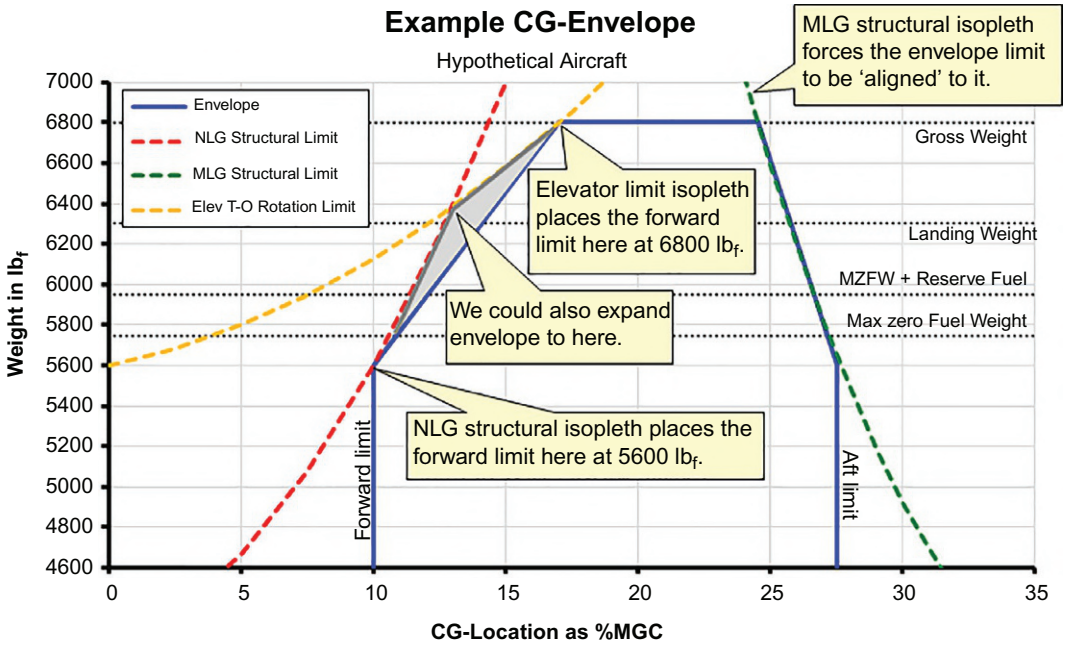


FIGURE 6-28 Example of how Nose or Main Landing Gear structural limits may affect CG-limits.

accomplished in accordance with 14 CFR Part 23 Appendix C. This is only a portion of the required loads. The landing impact load factor, n_l, is ordinarily determined by drop-testing. However, for conceptual design purposes, assume it ranges from 3.5 g (large deflection gear) to 5.5 g (short deflection gear). The hardest part of the analysis is the determination of the arms a' and b', which are aligned to the impact direction, even though the resulting reactions are horizontal and vertical. Luckily, expressions for these are provided in Figure 6-27. To create the isopleths shown in Figure 6-28, the designer selects three CG-positions and, for each, determines the weight such that V_f, D_f and V_r, D_r reach the structural limits of the landing gear. Armed with a set of three CG-positions and associated weights, fit a quadratic polynomial through the data and plot on the CG-envelope.

6.7.3 Loading Cloud

The generation of a *loading cloud* is an important step that should be completed for any aircraft that carries more than one occupant. It consists of plotting as many combinations of occupants + baggage + fuel as practical on the CG-envelope. While this is the first step in creating the CG-envelope, it also gives a powerful insight when plotted on CG-envelopes of rival aircraft. For existing design projects, the loading cloud reveals two important properties: (1) the most forward and aft CG-position the new aircraft must handle and (2) CG-travel due to fuel burn or jettisoning of stores. Additionally, when the loading cloud reveals our desired CG-envelope is seriously flawed, we can use it to plan how to fix.

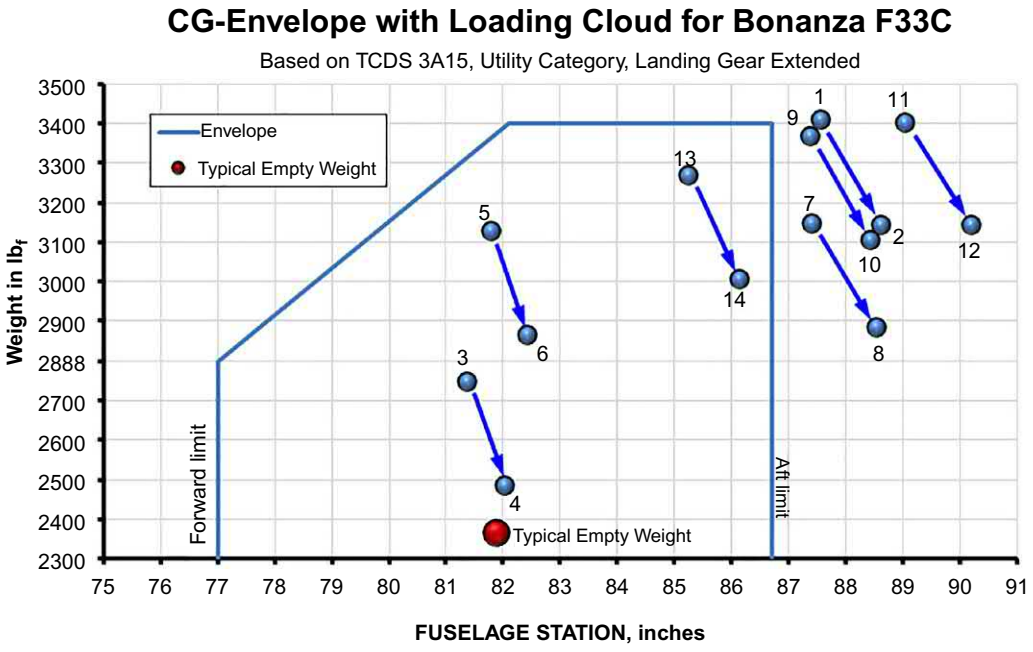


FIGURE 6-29 Example of a loading cloud exposing a serious problem. Here destined to render the aircraft "illegal" for a careless pilot. If this happens to your aircraft and the load combinations are "practical" (unlike the ones shown here), then DO something about it; move the wing, move heavy parts around to place the empty weight CG in a better location, so the envelope can accommodate most of the cloud. Just do something.

The *desirable CG-range* represents what would be oh-so lovely to have. However, this does not guarantee our current design can handle it. The desirable CG-envelope is often too wide (e.g., when compared to Table 6-6) or shifted too far forward or aft. It can even be surprisingly narrow. An example of a loading cloud shifted too far aft is shown in Figure 6-29 (note that some loading combinations are deliberately unrealistic). An example of a narrow loading cloud is shown in Figure 6-30. While this is less common, it is a possible scenario. Luckily, this is an easy problem to solve—simply reduce the proposed envelope. Too wide or too far forward or aft shifted loading clouds are harder to remedy. The solution may require a significant change in the position of components and the proposed loading combinations should be reviewed as well. Worst case scenarios call for geometric changes. Regardless, it is vital to deal with this early for the development of the new aircraft. Otherwise, a serious weight and balance problem will be designed into the aircraft.

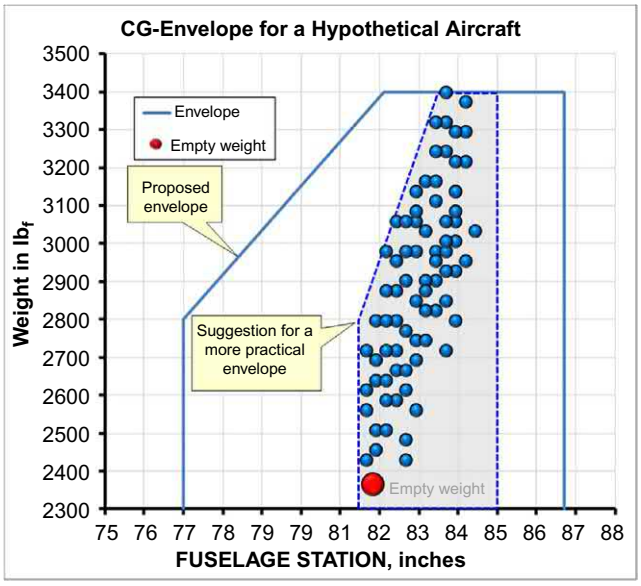


FIGURE 6-30 Sometimes the CG-envelope proposed turns out to be larger than needed.

Figure 6-29 is intended to help the reader visualize how loading combinations compare to an actual CG-envelope. The comparison uses the CG-envelope of the Beechcraft F33C Bonanza, presented in Figure 6-25. The source data are shown in Table 6-7. As can be seen, some of the combinations consist of various amounts of fuel, occupant, and baggage weights. The arrows indicate where the CG-position travels as fuel is fully consumed. The figure shows that the F33C hardly has a forward loading problem but is easily loaded outside the aft CG-limit. This results from the relative aft position of even the front seats. In defense of the F33C, some of the load combinations presented are admittedly "preposterous" or "unfair." However, they are presented to emphasize the importance of reviewing the rationale behind specific loading scenarios. For instance, Combo IDs 11 and 12 represent a wholly unrealistic loading: A competent pilot would not store 270 lb_f in the baggage area, with an empty seat farther forward, not to mention, 270 lb_f might exceed the allowable load in the baggage area.

Consider a scenario that sometimes comes up in practice; too large a CG-envelope is proposed. The initial

TABLE 6-7 Tabulated loading combinations used to create the loading cloud of Figure 6-29.

Combo	Empty Weight		Front Left Seat		Front Right Seat		Aft Left Seat		Aft Right Seat		Baggage Area		Fuel		Total	
ID	W_e	X_{CGe}	W	Arm	W	Arm	W	Arm	W	Arm	W	Arm	W	Arm	W	X_{CG}
1	2363	81.9	170	85.0	170	85.0	170	121.0	170	121.0	100	150.0	264	75.0	**3407**	**87.6**
2	2363	81.9	170	85.0	170	85.0	170	121.0	170	121.0	100	150.0	0	75.0	**3143**	**88.6**
3	2363	81.9	120	85.0	0	85.0	0	121.0	0	121.0	0	150.0	264	75.0	**2747**	**81.4**
4	2363	81.9	120	85.0	0	85.0	0	121.0	0	121.0	0	150.0	0	75.0	**2483**	**82.0**
5	2363	81.9	250	85.0	250	85.0	0	121.0	0	121.0	0	150.0	264	75.0	**3127**	**81.8**
6	2363	81.9	250	85.0	250	85.0	0	121.0	0	121.0	0	150.0	0	75.0	**2863**	**82.4**
7	2363	81.9	250	85.0	0	85.0	0	121.0	0	121.0	270	150.0	264	75.0	**3147**	**87.4**
8	2363	81.9	250	85.0	0	85.0	0	121.0	0	121.0	270	150.0	0	75.0	**2883**	**88.5**
9	2363	81.9	120	85.0	120	85.0	250	121.0	250	121.0	0	150.0	264	75.0	**3367**	**87.4**
10	2363	81.9	120	85.0	120	85.0	250	121.0	250	121.0	0	150.0	0	75.0	**3103**	**88.4**
11	2363	81.9	170	85.0	170	85.0	0	121.0	170	121.0	270	150.0	257	75.0	**3400**	**89.1**
12	2363	81.9	170	85.0	170	85.0	0	121.0	170	121.0	270	150.0	0	75.0	**3143**	**90.2**
13	2363	81.9	170	85.0	250	85.0	0	121.0	120	121.0	100	150.0	264	75.0	**3267**	**85.3**
14	2363	81.9	170	85.0	250	85.0	0	121.0	120	121.0	100	150.0	0	75.0	**3003**	**86.2**

Note that weights are in lb_f and arms in inches.

CG-envelope may have been based on analysis and even preliminary flight testing. However, it may be found to exceed what the airplane will ever be exposed to in operation. This may be the consequence of the loading possibilities of the aircraft; for instance, due to seating arrangement (e.g., side-by-side seating), limited travel with fuel consumption, and other factors. An unnecessarily large CG-envelope may bring about a serious headache for the flight test team because the airworthiness of the vehicle must be demonstrated at the extremes of the envelope. Our hypothetical aircraft would require heavy ballast to be mounted in awkward places to allow it to be flown at the extremes of the envelope. It might even require special temporary hard points to be designed, fabricated, and installed to carry the ballast. It is really a wasted effort, rendering it far more sensible to simply redraw a narrower envelope to resemble that of the shaded area in Figure 6-30. This will shave off certification cost and effort and the resulting airplane will be equally useful as the one featuring the wider envelope.

6.7.4 In-Flight Movement of the CG

All aircraft that burn fossil fuels are subject to weight reduction in flight. Additional weight reduction may be associated with activities such as dropping of parachutists or when military aircraft jettison empty fuel tanks or ordnance (missiles, bombs, etc.). This movement must be considered during the design phase of the aircraft and may not cause the CG to move out of the CG-envelope. Often this requires components to be relocated to ensure the airplane can contain the CG-location inside the CG-envelope regardless of such weight changes. Figure 6-31 shows an example of the Beech F33C Bonanza with two 200 lb_f people and full tanks of fuel (74 gals usable) as the fuel is completely consumed. It shows that while the CG moves back an inch or so, it fully resides inside the CG-envelope.

6.7.5 Weight Budgeting

The purpose of weight budgeting is to provide constraints for airframe designers and an impetus to design parts with strong emphasis on weight. It is a common problem in the aviation industry that components are overdesigned, which leads to unnecessarily stout and heavy components. This is one of the primary reasons for why empty weight targets get busted. Weight budgeting helps the weight reduction effort to stay where it belongs; with the cognizant designer (airframe, avionics, power plant, and so on). It also helps the engineer understand where to direct weight reduction efforts. This is important if empty weight targets have not been met. Remember the adage; "it is better to reduce 1000 lbs by 1% than 1 lb by 50%."

The weight budgeting process begins by breaking the complete aircraft into categories, such as Wings, Horizontal Tail, Vertical Tail, Fuselage, etc. Sometimes such categories are broken down further, e.g., Wings-Left Main for the main element of the left wing, Wings-Ailerons, Wings-Flaps, Wings-Electrics, and so forth. A hypothetical weight budget for use in weight management of a prototype is shown in Table 6-8. It shows that the projected weight of this aircraft is some 269 lb_f higher than planned. This might be acceptable for a test vehicle, although it could cause complications in a flight test program, if weight of available fuel for test flying is compromised. But it is unacceptable for the production airplane as it amounts to 10% over target.

6.7.6 Weight Tolerancing

During the preliminary design phase, a precise location for the CG or magnitudes of moments and products of inertia is impossible to pinpoint, because final weights and CG locations of individual components keep changing. For instance, the location of the engine's CG may be

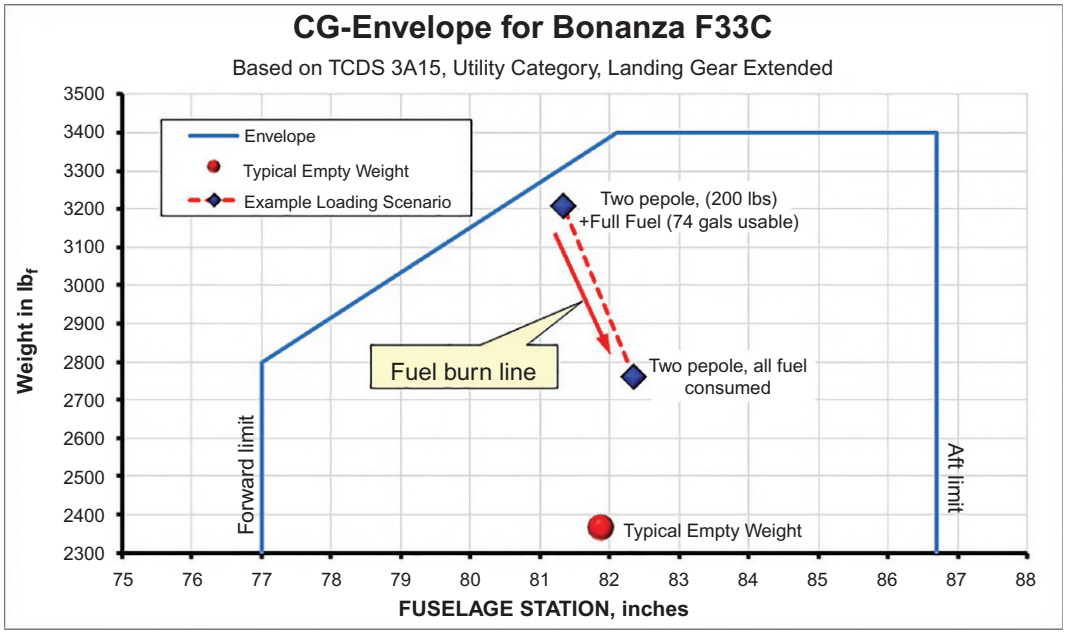


FIGURE 6-31 The CG-envelope with a CG movement due to fuel burn. For this airplane, the Bonanza F33C, it is clear the CG will remain inside the CG-envelope even if all the usable fuel were consumed.

TABLE 6-8 Example of a weight budget being compared to actual weights.

Category	Weight for category (budget) lb_f	Projected weight (actual) lb_f	Source
Wings	600	555	Direct
Horizontal/vertical tail	100	131	Direct
Fuselage	500	580	Direct
Weight penalty for pressurization	Included in Fuselage	35	Measured
Main Landing Gear	180	250	Measured
Nose Landing Gear	95	75	Measured
Nacelle	100	86	Direct
Fuel System	40	126	Statistical
Power Plant	450	485	Measured
Flight Control System	60	91	Statistical
Hydraulic System	40	24	Statistical
Electrical Systems	120	260	Statistical
HVAC	60	125	Statistical
Bleed Air System	15		Statistical
Pressurization System	15		Statistical
De-Icing System	65		Statistical
Oxygen System	30		Direct
Furnishings	200	216	Statistical
Other	100	0	Direct
Total	2770	3039	

specified as $x_{EI} \pm \Delta x$. It may be an engine in development and its installed weight may be given as $W_{EI} \pm \Delta W$. As an example, the engine manufacturer might specify the engine weight to be 356 ± 15 lb_f. Thus, the moment contribution of this engine to the total moment about the reference point (0, 0, 0) would be a range along the x-axis, rather than a specific point, computed as follows:

$$\begin{aligned} M_{EI} &= (x_{EI} \pm \Delta x)(W_{EI} \pm \Delta W) \\ &= x_{EI} W_{EI} \pm (x_{EI} \Delta W + \Delta x W_{EI} + \Delta x \Delta W) \end{aligned} \quad (6\text{-}152)$$

It is better to consider these as a "sphere" of possible values, rather than a single specific point. In the process, the designer can assess the probability of the CG being outside of the allowable limits. This section develops equations that allow the aircraft designer to keep track of these important parameters by assigning tolerances to them.

Consider a collection of point loads positioned in 3-dimensional space whose weight and position are known to a certain level of accuracy (tolerance) (see Table 6-9). Then, the inertia properties for such a collection are defined in the following formulation.

Total Weight:

$$W_{tot} = \sum_{i=1}^{N} W_i \pm \Delta W_i = \sum_{i=1}^{N} W_i \pm \sum_{i=1}^{N} \Delta W_i = \begin{cases} W_{TOT_{\min}} \\ W_{TOT_{nom}} \\ W_{TOT_{\max}} \end{cases} \quad (6\text{-}153)$$

X-moments about the point (0, 0, 0):

$$M_x = \begin{cases} \sum_{i=1}^{N} (W_i - \Delta W_i)(x_i - \Delta x_i) = M_{x_{\min}} \\ \sum_{i=1}^{N} W_i \times x_i = M_x \\ \sum_{i=1}^{N} (W_i + \Delta W_i)(x_i + \Delta x_i) = M_{x_{\max}} \end{cases} \quad (6\text{-}154)$$

TABLE 6-9 Point loads with tolerances.

Item	Weight	x	y	z
Item 1	$W_1 \pm \Delta W_1$	$x_1 \pm \Delta x_1$	$y_1 \pm \Delta y_1$	$z_1 \pm \Delta z_1$
Item 2	$W_2 \pm \Delta W_2$	$x_2 \pm \Delta x_2$	$y_2 \pm \Delta y_2$	$z_2 \pm \Delta z_2$
Item 3	$W_3 \pm \Delta W_3$	$x_3 \pm \Delta x_3$	$y_3 \pm \Delta y_3$	$z_3 \pm \Delta z_3$
...				
Item i	$W_i \pm \Delta W_i$	$x_i \pm \Delta x_i$	$y_i \pm \Delta y_i$	$z_i \pm \Delta z_i$
...				
Item N	$W_N \pm \Delta W_N$	$x_N \pm \Delta x_N$	$y_N \pm \Delta y_N$	$z_N \pm \Delta z_N$

Y-moments about the point (0, 0, 0):

$$M_y = \begin{cases} \sum_{i=1}^{N} (W_i - \Delta W_i)(y_i - \Delta y_i) = M_{y_{\min}} \\ \sum_{i=1}^{N} W_i \times y_i = M_y \\ \sum_{i=1}^{N} (W_i + \Delta W_i)(y_i + \Delta y_i) = M_{y_{\max}} \end{cases} \quad (6\text{-}155)$$

Z-moments about the point (0, 0, 0):

$$M_z = \begin{cases} \sum_{i=1}^{N} (W_i - \Delta W_i)(z_i - \Delta z_i) = M_{z_{\min}} \\ \sum_{i=1}^{N} W_i \times z_i = M_z \\ \sum_{i=1}^{N} (W_i + \Delta W_i)(z_i + \Delta z_i) = M_{z_{\max}} \end{cases} \quad (6\text{-}156)$$

Location of CG:

$$\begin{aligned} X_{CG_{\min}}, Y_{CG_{\min}}, Z_{CG_{\min}} &= \frac{M_{x_{\min}}}{W_{TOT_{\min}}}, \frac{M_{y_{\min}}}{W_{TOT_{\min}}}, \frac{M_{z_{\min}}}{W_{TOT_{\min}}} \\ X_{CG}, Y_{CG}, Z_{CG} &= \frac{M_x}{W_{TOT}}, \frac{M_y}{W_{TOT}}, \frac{M_z}{W_{TOT}} \\ X_{CG_{\max}}, Y_{CG_{\max}}, Z_{CG_{\max}} &= \frac{M_{x_{\max}}}{W_{TOT_{\max}}}, \frac{M_{y_{\max}}}{W_{TOT_{\max}}}, \frac{M_{z_{\max}}}{W_{TOT_{\max}}} \end{aligned} \quad (6\text{-}157)$$

where

W_i = Weight of item i
x_i = x-location of item i
y_i = y-location of item i
z_i = z-location of item i
ΔW_i = Tolerance assigned to the weight of item i
Δx_i = Tolerance assigned to the x-location of item i
Δy_i = Tolerance assigned to the y-location of item i
Δz_i = Tolerance assigned to the z-location of item i

EXAMPLE 6-10

A collection of point loads is given in Table 6-10. Determine a probable location of the CG along the x-axis by accounting for tolerances.

TABLE 6-10 Collection of point loads.

i	W lb_f	ΔW ft	x ft	Δx ft
1	10.0	2.0	5.0	0.5
2	20.0	1.0	3.5	0.5
3	30.0	2.0	8.5	0.5

EXAMPLE 6-10 (*cont'd*)

SOLUTION:

Total weight:

$$W_{tot}=\sum_{i=1}^{N}W_i\pm\sum_{i=1}^{N}\Delta W_i=60.0\pm5.0=\begin{cases}W_{TOT_{\min}}=55.0\,\text{lb}_\text{f}\\W_{TOT_{nom}}=60.0\,\text{lb}_\text{f}\\W_{TOT_{\max}}=65.0\,\text{lb}_\text{f}\end{cases}$$

X-moments about the point (0,0,0):

$$\begin{aligned}M_{x_{\min}}&=\sum_{i=1}^{N}(W_i-\Delta W_i)(x_i-\Delta x_i)\\&=(10.0-2.0)(5.0-0.5)+(20.0-1.0)(3.5-0.5)\\&\quad+(30.0-2.0)(8.5-0.5)\\&=317.0\,\text{ft}\cdot\text{lb}_\text{f}\end{aligned}$$

$$\begin{aligned}M_x&=\sum_{i=1}^{N}W_i\times x_i\ =10.0\times5.0+20.0\times3.5+30.0\times8.5\\&=375.0\,\text{ft}\cdot\text{lb}_\text{f}\end{aligned}$$

$$\begin{aligned}M_{x_{\max}}&=\sum_{i=1}^{N}(W_i+\Delta W_i)(x_i+\Delta x_i)\\&=(10.0+2.0)(5.0+0.5)+(20.0+1.0)(3.5+0.5)\\&\quad+(30.0+2.0)(8.5+0.5)\\&=438.0\,\text{ft}\cdot\text{lb}_\text{f}\end{aligned}$$

CG-range:

$$X_{CG_{\min}}=\frac{M_{x_{\min}}}{W_{TOT_{\min}}}=\frac{317.0\,\text{ft}\cdot\text{lb}_\text{f}}{55.0\,\text{lb}_\text{f}}=5.764\,\text{ft}$$

$$X_{CG}=\frac{M_x}{W_{TOT}}=\frac{375.0\,\text{ft}\cdot\text{lb}_\text{f}}{60.0\,\text{lb}_\text{f}}=6.250\,\text{ft}$$

$$X_{CG_{\max}}=\frac{M_{x_{\max}}}{W_{TOT_{\max}}}=\frac{438.0\,\text{ft}\cdot\text{lb}_\text{f}}{65.0\,\text{lb}_\text{f}}=6.738\,\text{ft}$$

Another way of presenting this would be:

$$X_{CG}=6.250\begin{cases}-0.483\\+0.486\end{cases}\ \text{ft}\ \approx6.25\pm0.48\ \text{ft}$$

EXERCISES

(1) Determine the useful load, empty weight ratio, and fuel weight ratio for an airplane whose gross weight is 1650 lbf, empty weight is 950 lbf, and can carry 33 gal of AvGas.

(2) You have been asked to design a twin-engine piston-powered GA aircraft that requires only one pilot for operation. The customer wants the airplane capable of taking off at the design gross weight with a useful load that consists of eight 200 lb_f individuals (which includes the pilot), 200 gal of avgas, and 350 lb_f of baggage on board. Additionally, he wants the design's empty weight to amount to no more than 65% of gross weight. Determine the empty weight (W_e), gross weight (W_o), useful load (W_u), payload (W_p), crew weight (W_c), fuel weight ratio (W_f/W_o), and empty weight ratio (W_e/W_o). Compare the empty weight ratio to the one obtained using the formulation of Section 6.2.2, for the same class of airplanes.

(3) (a) Estimate the empty and gross weight and the corresponding CG-positions using the data for the amphibious LSA aircraft depicted in Table 6-11:

(b) Also estimate the airplane's moment and products of inertia.

(4) This problem is intended to demonstrate a "typical" operational scenario for an airplane design using an actual aircraft. A CG-envelope for the Beech F33C Bonanza is shown in Figure 6-25. The empty weight of the airplane is 2363 lb_f and the empty weight CG location is at Fuselage Station (FS) 81.9 in. The gross weight of the airplane is 3400 lb_f. The airplane is to be loaded for a flight trip in accordance with the data of Table 6-12:

TABLE 6-11 Weight data for a hypothetical amphibious LSA.

Empty weight components				
Description	**Weight, lb_f**	**X, ft**	**Y, ft**	**Z, ft**
Wing	207	2.16	0.00	0.34
Horizontal Tail	17	15.82	0.00	0.00
Vertical Tail	24	16.83	0.00	0.00
Fuselage	84	-1.91	0.00	-0.77
Main gear	91	2.50	0.00	-2.50
Nose Gear	29	-5.50	0.00	-2.50
ROTAX 912	189	3.50	0.00	-0.50
Tail arm	20	9.52	0.00	0.00
Propeller	35	4.85	0.00	-0.25
BALLAST	75	-3.04	0.00	-1.00
Buffer weight (5%)	40	0.00	0.00	0.00

Operational items				
Description	**Weight, lb_f**	**X, ft**	**Y, ft**	**Z, ft**
Observer	200	-1.04	1.25	-1.00
Pilot	200	-1.04	-1.25	-1.00
Fuel tank	95	2.34	2.43	0.00
Fuel tank	95	2.34	-2.43	0.00
Baggage	25	0.00	0.00	0.00

TABLE 6-12 Weight data for a hypothetical amphibious LSA.

Item	FS (in)	Weight (lb_f)
Empty weight	81.9	2363
Pilot (front left seat)	85.0	180
Pax 1 (front right seat)	85.0	140
Pax 2 (aft left seat)	121	200
Pax 3 (aft right seat)	121	120
Baggage	150	50
Fuel	75.0	?

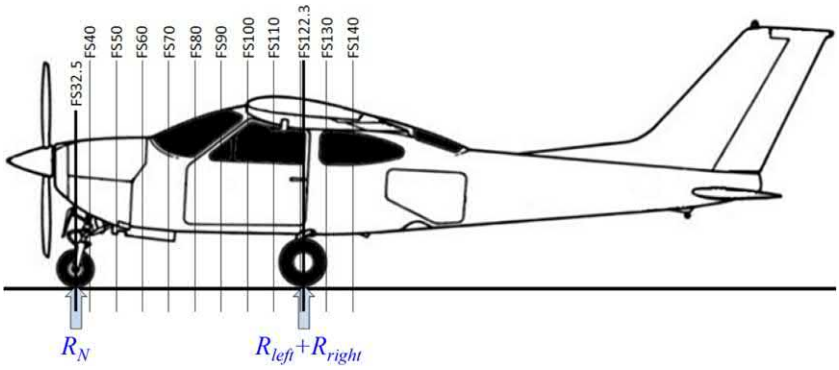


FIGURE 6-32 A side view of the Cessna 177 RG Cardinal.

Determine the following:

(a) The maximum fuel the pilot may take off with, in lb_f and US gallons.
(b) Determine the weight and FS with T-O fuel on board.
(c) Determine the weight and FS with all fuel consumed.
(d) *Plot the points representing the empty weight CG, as well as those from (b) and (c).*
(e) Is there a problem with the pilot's planned loading of this airplane? If so, what is it? Is there a simple solution to this problem? What is it? (Support with numbers where appropriate.)

(5) Consider the side view of the Cessna 177 RG Cardinal shown in Figure 6-32, as it is being weighed. This is done by placing scales under its nose wheel and the two main wheels. The airplane contains only unusable fuel and is otherwise empty. Determine the following for the airplane if the nose scale (R_N) reads 275 lb_f, the left main (R_{LEFT}) reads 725 lb_f, and the right main (R_{RIGHT}) reads 695 lb_f.

(a) Empty weight (Ans: 1695 lb_f).
(b) Fuselage Station of the CG (Ans: FS107.7).

References

[1] J. Pappalardo, *Weight Watchers. How a Team of Engineers and a Crash Diet Saved the Joint Strike Fighter*, Air and Space Magazine, 2006, pp. 66–73.

[2] G. Thomas, *Following Quantas Cuts, Attention Turns to 787*, Air Transport World, 2009 April 15.

[3] V. Moores, *Emirates Seeks A380 and 747-8 Weight Control*, Flightglobal, 2007 October 24.

[4] D. Raymer, *Aircraft Design: A Conceptual Approach*, AIAA Education Series, 1996.

[5] E. Torenbeek, *Synthesis of Subsonic Aircraft Design*, 3rd ed., Delft University Press, 1986.

[6] L. Nicolai, *Fundamentals of Aircraft and Airship Design*, Volume I, AIAA Education Series, 2010.

[7] M. Hepperle, *Electric Flight – Potential and Limitations, NATO Technical Paper STO-MP-AVT-209*, Energy Efficient Technologies and Concepts Operation, Lisbon, 2012 October 22–24.

[8] Anonymous, *Standard Method of Estimating Comparative Direct Operating Costs of Turbine Powered Transports*, Air Transport Association of America Report, December 1967.

[9] J.W.R. Taylor (Ed.), Jane's All the World's Aircraft 1987–88, Jane's Yearbooks, 1988.

[10] L. Nicolai, *Fundamentals of Aircraft Design*, 2nd ed., (1984).

[11] J. Roskam, *Airplane Design – Part V: Component Weight Estimation*, DAR Corporation, 1999.

[12] R.L. Schmitt, K.C. Foreman, W.M. Gertsen, P.H. Johnson, *Weight Estimation Handbook for Light Aircraft*, Cessna Aircraft Company, 1959.

[13] R. Anderson, *Weight Estimation Methods, Unpublished Notes*, Design Branch, Air Force Flight Dynamics Laboratory, Wright-Patterson AFB, Ohio, July 1973.

[14] N.S. Currey, *Aircraft Landing Gear Design: Principles and Practices*, AIAA Education Series, 1988.

[15] Anonymous, *Business and Commercial Aircraft 2018 Purchase Planning Handbook*, Aviation Week Network, May 2018.

[16] D.P. Wells, B.L. Horvath, *The Flight Optimiziation System Weights Estimation Method, NASA-TM-2017-219627*, Volume I, NASA, June 2017.

[17] R.C. Hibbeler, *Engineering Mechanics - Statics and Dynamics*, Pearson Prentice Hall, 2016.
[18] H.G. D'Estout, *Aircraft Weight and Balance Control*, 4th ed., Aero Publishers, 1967.
[19] Anonymous, *Weight and Balance Handbook, FAA Handbook H-8083-1B*, FAA, 2016.
[20] R. Boynton, *The seven secrets of accurate mass properties measurement*, in: 51st Annual Conference of the Society of Allied Weight Engineers, Hartford, Connecticut, 18–20 May, 1992.
[21] R. Boynton, K. Wiener, *How to Calculate Mass Properties (An Engineer's Practical Guide)*, Space Electronics, Inc, 2001.
[22] Anonymous, TCDS 3A15, Hawker Beechcraft Corporation, Revision 94, 02/25/2007, FAA.
[23] Anonymous, *Universal Index Loading System Substantiation, Report D043N321*, Boeing Commercial Aircraft, Seattle, WA, 1990 (nonproprietary).

CHAPTER

7

Selecting the Powerplant

OUTLINE

7.1 **Introduction** 197
- *7.1.1 The Content of This Chapter* 197
- *7.1.2 Factors Affecting the Selection of the Powerplant* 197
- *7.1.3 The Basics of Energy, Work, and Power* 199
- *7.1.4 Fundamental Definitions* 199
- *7.1.5 Fuel Basics* 200
- *7.1.6 On the Thermodynamics of the Powerplant* 201

7.2 **Piston Engines** 202
- *7.2.1 Fundamental Definitions* 202
- *7.2.2 Basic Theory of Internal Combustion Engines* 206
- *7.2.3 The Use of Gearboxes* 209
- *7.2.4 Extracting Piston Power From Engine Performance Charts* 210
- *7.2.5 Extracting Piston Power Using the Petty Equation* 211
- *7.2.6 Piston Engine Installation* 212
- *7.2.7 Piston Engine Inlet and Exit Sizing* 216

7.3 **Gas Turbine Engines** 225
- *7.3.1 Topics Specific to Turboprops* 225
- *7.3.2 Topics Specific to Turbojets* 228
- *7.3.3 Topics Specific to Turbofans* 230
- *7.3.4 Installation of Gas Turbines* 231
- *7.3.5 Subsonic Inlet Design* 234

7.4 **Electric Motors and Battery Technology** 239
- *7.4.1 Basic Formulas of Electricity* 239
- *7.4.2 Battery Basics* 241
- *7.4.3 Additional Sources of Electric Energy* 246
- *7.4.4 Electric Motor Basics* 248

Exercises 253

References 253

7.1 INTRODUCTION

The powerplant makes "heavier-than-air" flying possible. It generates the force that produces the airspeed needed to create lift. This chapter is intended to help the designer *select* a suitable powerplant for the aircraft design and provide understanding of its impact on the design. To keep the size of the chapter within limits, methods for thrust modeling are presented in Chapters 14 and 15. Readers interested in the history and evolution of aircraft engines are directed to references such as [1–3].

7.1.1 The Content of This Chapter

- Section 7.1 presents introduction to aircraft engines and fuels.
- Section 7.2 focuses on the piston engine and provides methods to estimate the effect of altitude, the use of gearboxes, and a method for estimating power as a function of pressure altitude and RPM.
- Section 7.3 introduces gas turbine engines (turboprops, turbojets, and turbofans). Basic tips for subsonic inlet design are provided.
- Section 7.4 presents the physics of the electric motor. Installation, wiring diagrams, and other information.

7.1.2 Factors Affecting the Selection of the Powerplant

Airplanes are either designed around a specific engine or the engine is selected once performance requirements are established. In the latter case, the selection process can be split into two steps:

(1) Target airspeed and operational altitude is used to identify a suitable engine class (pistonprop, turboprop, turbofan, etc.). Aircraft operational and efficiency maps, such as those in Figures 7-1 and 7-2, help in this capacity, as does the discussion about propulsive efficiency in Section 14.2.3.

https://doi.org/10.1016/B978-0-12-818465-3.00007-0

Copyright © 2022 Elsevier Inc. All rights reserved.

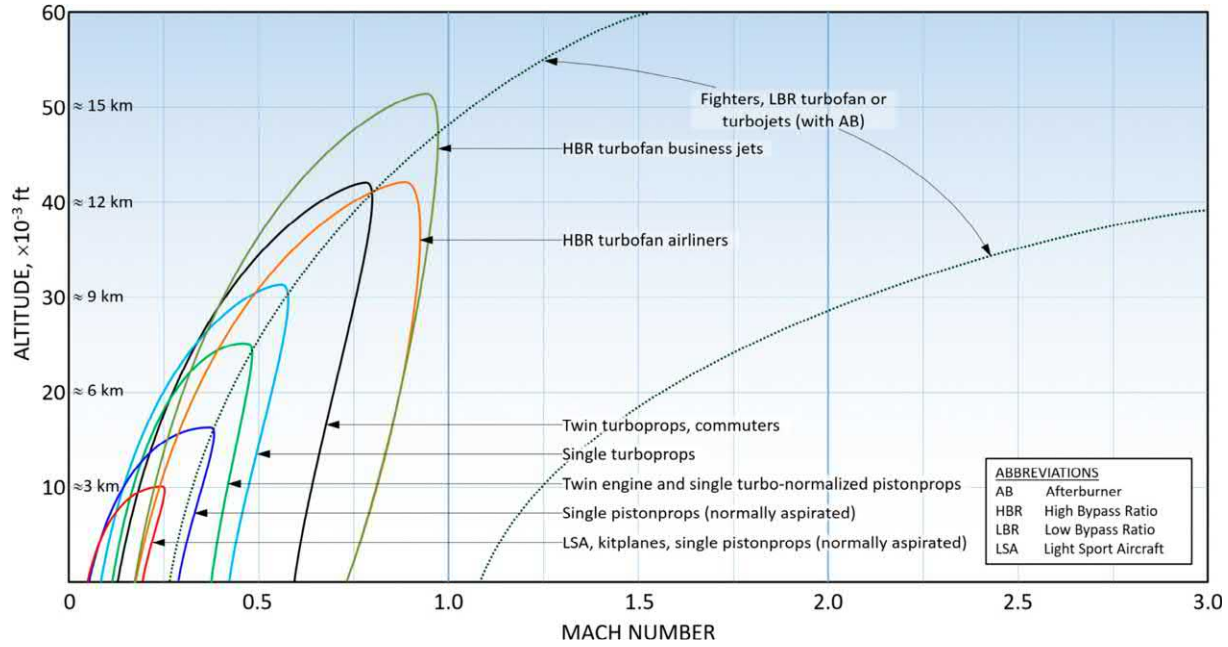


FIGURE 7-1 Aircraft operational map (inspired by refs. [4, 5]).

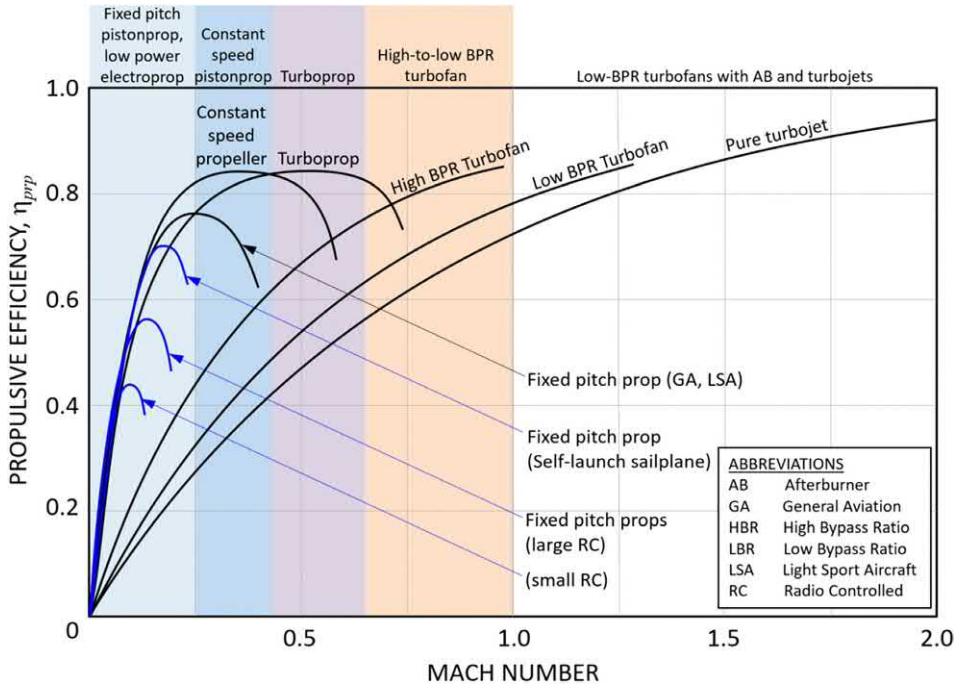


FIGURE 7-2 Efficiency map for an assortment of engine classes (inspired by refs. [6, 7]).

(2) Once the engine class is identified, a candidate engine is selected from available options in that class. The selection considers factors such as fuel consumption, thrust or power, engine weight, and price.

Additional issues considered during this process include cost and availability of the required fuel, environmental impact, mechanical complexity, maintainability, cooling, inlet and exhaust requirements, to name a few. The efficiency of jet engines is realized at high altitudes, whereas normally aspirated pistonprops are limited to around 15,000 ft (4572 m). Thus, selecting a jet engine causes secondary consequences; cabin pressurization is required for all aircraft operating above 25,000 ft (7620 m).[1] It has a major impact on the structure and system complexity. It exemplifies the impact of engine selection on the aircraft design.

[1] E.g. see §23.841, Pressurized cabins ("old" 14 CFR Part 23) and §25.841, Pressurized cabins. The language has been removed from the "new" 14 CFR Part 23, although the applicant may have to comply with the old Part 23 version.

TABLE 7-1 The basics of energy, work, and power.

Concept	Formulation	Units: SI system	Units: UK system
Energy The conservation of energy is one of the fundamental conservation laws of physics. It states that energy can neither be created nor destroyed, but it changes form. The form of energy refers to potential, kinetic, electrical, nuclear, chemical, and other forms of energy.	Kinetic energy: $KE = \frac{1}{2} mV^2$ Potential energy: $PE = mgh$ Pressure energy: $E_{press} = p\forall$ Electric energy: $E_{el} = UI \cdot \Delta t$	Joules (J) ($J = N \cdot m = kg \cdot m^2/s^2$) Wh or kWh 1 Wh = 3600 J	BTU (heat required to raise the temperature of 1 lb. of H_2O by 1°F) 1 BTU = 1055.06 J 1 BTU = 778.169 ft·lb$_f$
Work Work is defined as the product of force and distance. Work is also the same as *torque*.	Work ≡ Force × Distance	Joules N·m	ft·lb$_f$
Power Power is defined as the amount of work done in given time. It is also possible to define it as shown.	$\text{Power} \equiv \frac{\text{Work}}{\text{Time}} \equiv \frac{\text{Force} \times \text{Distance}}{\text{Time}} \equiv \text{Force} \times \text{Speed} \equiv \frac{\text{Torque}}{\text{Time}} \equiv \frac{dW}{dt} = \dot{W}$	W J/s N·m/s	hp ft·lb$_f$/s
One "Horsepower"		746 W 0.746 kW	33,000 ft·lb$_f$/min 550 ft·lb$_f$/s

Modern airplanes are typically propelled by any of the following classes of powerplant:

(1) Pistonprops (low subsonic speed, low altitudes)
(2) Electroprops (low to medium subsonic speed, low to high altitudes)
(3) Turboprops (medium subsonic speed, medium altitudes)
(4) High bypass ratio turbofan (medium to high subsonic speed, medium to high altitudes)
(5) Low bypass ratio turbofan (high subsonic to supersonic speed, high altitudes)
(6) Turbojet engines (high subsonic to supersonic speed, high altitudes)
(7) Pulsejets (very rare)
(8) Rockets (very rare, sometimes supplements other engines for T-O)

Piston engines and turboprops are the most common thrust generators in GA aircraft (14 CFR Part 23), followed by turbofan engines. Turboprops and turbofans are most common among commercial aircraft (14 CFR Part 25). Turboprops, turbojets, and low bypass ratio turbofans are most common for military applications. Electroprops are an emerging technology with promising potential. One is the prospect of reduced environmental impact (assuming batteries are charged with renewable energy) and the absence of power-sensitivity with altitude.

7.1.3 The Basics of Energy, Work, and Power

A review of the fundamentals of energy, power, and torque is presented for convenience, as familiarity with various energy and power concepts is essential for the discussion that follows. The basics are shown in Table 7-1: where m is mass, V is speed, g is acceleration due to gravity, h is elevation, I is current, U is voltage potential, $\forall$ is enclosed volume, and W is work.

A note on subscripts: In this text, properties such as temperature (T), pressure (p), and density (ρ) have supplemental subscripts. Thus, T is ambient temperature, while T_0 is total temperature. Ambient temperature in the far-field (far away from the aircraft) is denoted by T_∞, while the total temperature in the far-field is given by $T_{0\infty}$.

7.1.4 Fundamental Definitions

The following concepts are frequently used when specifying engine power and thrust ratings:

(1) Take-Off, Wet

Refers to (A) the thrust of a jet engine with afterburner or (B) the maximum available T-O thrust of an engine using water injection. The latter applies to GA aircraft. Water injection dates to early gas turbine technology, where it was used for engines such as the Rolls-Royce Dart (turboprop) and the Pratt & Whitney JT3D (turbofan).

Water injection mixes atomized water with air before it enters the combustion chamber. This lowers the *combustor inlet air temperature* (CET) and, thus, the *turbine entry temperature* (TET). The same effect is achieved by direct injection into the combustion chamber. Injecting water is a "trick" to get more thrust or power without exceeding TET limits. The injection is usually time limited to 5 min or so. Its use is constrained by altitude and ambient air- and water temperature. While water injection is no longer common, ref. [8] argues it can reduce NOx emissions and engine operating costs by lowering hot section temperatures and, thus, prolonging its operational life.

Water injection is related to *throttle ratio* (*TR*), discussed in Section 14.3.1. If $TR = 1$, the TET is at its maximum value for engine operation at standard S-L temperature. If the ambient temperature is above standard temperature, the engine power must be decreased to keep the CET and TET below limits. Newer engines have $TR > 1$, so at standard S-L temperature, the TET is below its maximum value. Thus, water injection is no longer necessary at higher ambient temperatures and, nowadays, often is associated with turbomachinery of the yesteryear.

(2) Take-Off, Dry

Refers either to thrust generation of a jet engine without an afterburner or the maximum thrust available for T-O without the use of water injection.

(3) Maximum Continuous Power/Thrust

Refers to the maximum power (thrust) setting that can be used continuously, although it is usually intended to be used in an emergency (e.g., in a *one engine inoperative* situation). It is abbreviated MCP or MCT. In pistonprops, maximum level airspeed (V_H) is obtained at MCP.

(4) Maximum Climb Power/Thrust

Refers to the power (thrust) setting used during normal climb operations. For pistonprops, this is often the same as the MCP or close to it.

(5) Maximum Cruise Power/Thrust

Refers to the power setting used for cruise. It is abbreviated as MCR.

(6) Flat Rating and De-Rating

An engine is *flat rated* if it generates constant power (or thrust) over a range of ambient temperatures. The power (thrust) of an engine varies inversely with temperature; its output is higher on a cold day than a hot one. The drawback is reduced available power (thrust) when taking off on a hot day, when other airplane characteristics are also deficient. Manufacturers offer engines with "published" power ratings that are lower than what the engine can generate. The fuel control system is used to control the maximum power available by metering the ambient temperature. Such an engine delivers the same engine power on a hot as it does on a cold day—it is *flat rated*. Consider a piston engine capable of delivering 300 BHP on a standard day ($T_\infty = 518.67°R$ or 288.15 K). Per Equation (7-12), on a day that is 30°C warmer, this power is reduced to 285 BHP. The engine manufacturer may market it as a 285 BHP flat-rated engine. Thus, as far as the pilot is concerned, the airplane is equipped with a 285 and not 300 BHP engine. Then, the fuel control computer adjusts the power based on the ambient temperature, providing a constant maximum power of 285 BHP for temperatures ranging from freezing to 45°C. Of course, thrust is still reduced with altitude because of lower density, but is greater than without the flat rating.

De-rating refers to a specific operation of a turbofan engine on a commercial jetliner. At low atmospheric temperatures, or when runway length is ample, or when the airplane is operated below gross weight, it is possible to take off at reduced engine thrust. This improves the operational life of the engine due to the reduced TET.

7.1.5 Fuel Basics

(1) Density of Aviation Gasoline (Avgas)

The density of Avgas is 0.71 kg/L. In the UK system, its weight is 5.9–6.0 lb_f/gallon. For analysis work in this text, a weight of 6.0 lb_f/gallon is always assumed. See more detail in Table 7-2.

TABLE 7-2 Common fuel grades for piston engine use [9].

Fuel grades	Color	Comment
80/87	Red	The first number (80) is the octane rating assuming a lean mixture. The second number (87) indicates the rating at a rich mixture. Used for aircraft engines with low compression ratios. No longer produced.
82UL	Purple	UL stands for Un-Leaded. Similar to Mogas, but without automotive additives. Intended for low compression engines such as those common in experimental aircraft and aircraft that have STCs permitting the use of Mogas. No longer in production.
91/96 91/96UL	Brown	UL stands for Un-Leaded. Avgas often intended for military use (e.g., UAVs). Produced today by the Swedish fuel manufacturer Hjelmco, who offers it in clear color.
100LL	Blue	LL stands for Low Lead. The most common avgas in use today. The fuel can be used with engines designed for 80/87.
100/130	Green	Also called Avgas 100. Superseded by 100LL, although still available in limited quantities.
115/145	Purple	Leaded fuel produced for warbirds and the supercharged radial engines used to power the passenger planes of the 1940s–1960s. Now produced in limited quantities for air races. This fuel is necessary in order to obtain rated power in such engines.

(2) Energy Content of Fuel for Piston Engines

Piston engine power is directly related to the amount of air mass flow into the intake manifold.

In the UK system: 1 hp ~ 620 × mass flow (in slugs/s).
In the SI system: 1 kW ~ 1019 × mass flow (in kg/s).

(3) Fuel Octane Rating and Fuel Grades for Piston Engines

Fuel octane rating is a measure of the fuel's resistance to spontaneous self-ignition during compression. This detrimental and premature self-ignition manifests itself as *knocking*. Fuel with a high-octane number withstands greater pressure inside the cylinder before self-igniting. This explains why such fuel is used in high-compression, high-performance engines. There are several different octane ratings (e.g., Research Octane Number—RON, Motor Octane Number—MON, etc.). These definitions are outside the scope of this book.

Fuel for piston engines aircraft is known as *Avgas* (aviation gasoline). This contrasts *Mogas* (motor gasoline), which is used in cars and some experimental and GA aircraft. The difference is that Avgas contains a toxic chemical called *tetraethyl lead* (TEL—formula $(CH_3CH_2)_4Pb$), which improves its combustion properties. It was banned for use in on-road vehicles in the United States in 1986 [10], and an effort is ongoing to phase it out of aviation. The fuel octane rating helps identify a few grades of fuel that are offered in different colors to prevent incorrect selection (see Table 7-2).

(4) Fuel Grades for Jet Fuel

There is a wide range of fuel grades intended for jet engines. Table 7-3 lists the most common one for civilian aircraft. A range of jet fuel with specifications for different countries is available too, but not presented. More details are available from ref. [11]. For analysis work in this text, a density of 6.7 lb_f/gallon is always assumed.

(5) Specific Fuel Consumption

Specific fuel consumption (SFC) is the quantity of fuel burned in unit time to produce a given engine output. *SFC is a technical figure of merit that indicates how efficiently the engine converts fuel into thrust or power*. It is among the most important metrics employed in aviation; it is as significant to the designer and operator as gas mileage is to car owners. It is used to estimate range and endurance. When selecting between engine makes and models, the engineer can convert SFC into *fuel consumption* (or *fuel-flow* (*FF*)—the quantity of fuel burned in unit time in lbs./h or kg/min) by multiplying it by thrust (or power) at condition. For details, refer to Section 21.2.4.

7.1.6 On the Thermodynamics of the Powerplant

The mechanism by which chemical energy is converted into mechanical energy in engines relies on air. The process changes its pressure and volume, allowing it to move a mechanical device, such as a piston or a turbine. This process is described using a *thermodynamic cycle*, represented on a graph such as that of Figure 7-3. The numbers in the left graph refer to the piston positions shown in Figure 7-5. The numbers in the right graph refer to engine stations in Figure 7-30.

(1) Piston Engines

The operation of piston engines is described using the four-stroke *Otto cycle* [12], named after Nicolas A. Otto (1832–1891). The first step in this cycle occurs as the piston reduces the volume inside the cylinder. This *compresses* the mixture of air and fuel (see Side 1-2 in Figure 7-3). Next, *combustion* rapidly releases chemical energy in the fuel/air mixture, which increases pressure without additional change in volume (Side 2-3). This forces the piston in the opposite direction, increasing the volume (Side 3-4). Once the piston reaches the position of maximum volume, a valve is opened allowing the gases to

TABLE 7-3 Common fuel grades for civilian jet engine use.

	Fuel grades			
Property	**Jet A**	**Jet A-1**	**Jet B**	**TS-1 (regular)**
Flash point	100 °F (38°C)	100°F (38°C)	–	82.4°F (28°C)
Freeze point	−40°F (−40°C)	−52.6°F (−47°C)	−59.8°F (−51°C)	< −76°F (−60°C)
Density at 15°C	6.48–7.02 lb_f/gal (0.775–0.840 kg/L)	6.48–7.02 lb_f/gal (0.775–0.840 kg/L)	6.27–6.69 lb_f/gal (0.750–0.801 kg/L)	6.48 lb_f/gal (0.775 kg/L)
Comment	Suitable for most gas turbines. Primarily available in the United States	Suitable for most gas turbines. Widely available.	An alternative to Jet A-1 but more flammable. A cold climate jet fuel.	Primarily used in Russia and the CIS states

Based on Anonymous, Shell Aviation Fuels, Article, Shell Corporation, publication year not cited; Anonymous, ExxonMobil: World Jet Fuel Specifications with Avgas Supplement, 2005.

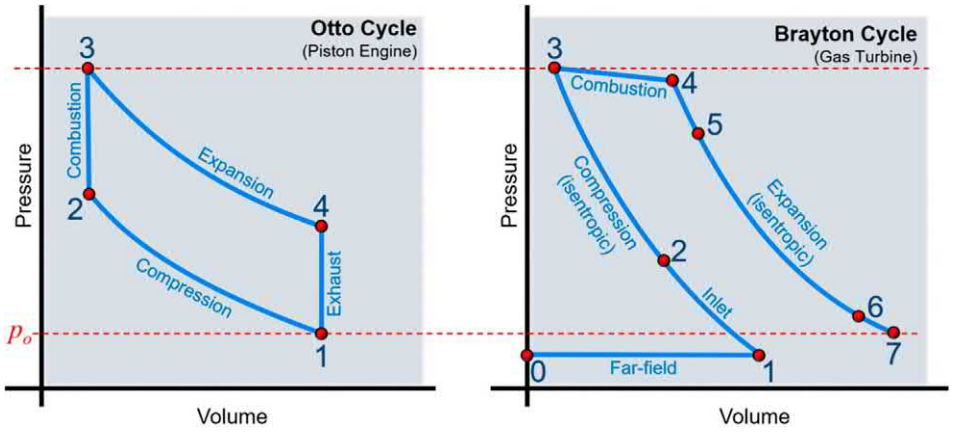


FIGURE 7-3 Thermodynamic cycles for a piston engine and a gas turbine.

escape (*exhaust*). This drops the pressure inside the cylinder without additional change in volume (Side 4-1). This operation is then repeated in the engine.

(2) Gas Turbines

A similar thermodynamic cycle for gas turbines is called the *Brayton cycle* (see Figure 7-3), named after George B. Brayton (1830–1892). In this cycle, air enters an intake to the engine at a specific pressure. It is compressed using a multibladed compressor after being forced through ducting that reduces its volume (Side 1-2-3). The air is directed into the combustion chamber where it is mixed with fuel and ignited. The geometry of the chamber forces volumetric expansion without change in pressure (Side 3-4). The fuel/air mixture rushes through an opening in the combustion chamber, impinges on a turbine wheel and is converted to mechanical energy. This drops the pressure and its volume increase (Side 4-5-6-7). This process is maintained continuously in the engine.

7.2 PISTON ENGINES

The piston engine has been a stalwart of the aviation industry since the Wright brothers flew their airplane on December 17, 1903. Aviation pistons come in multiple sizes, ranging from tiny single piston glow plug engines, such as the 0.010 in^3 Cox Tee Dee, which powers small model aircraft, to the giant, 36-cylinder, 5000 BHP Lycoming XR-7755 radial piston engine [13], intended to power huge airplanes like the early cold-war era Convair B-36 "Peacemaker." This section provides insight into piston engines. The reader interested in treatise of greater depth than possible here is directed to ref. [12].

7.2.1 Fundamental Definitions

(1) Pros of Piston Engines

(A) Widely available; (B) inexpensive; (C) simple to install in an airframe; (D) easy to maintain; (E) low operational cost; (F) uses widely available fuels; (G) adaptable to many fuel types; (H) more efficient at low airspeeds and altitudes than gas turbines; (I) develops maximum power at relatively low RPM; (J) low RPM enables engine installation without a gear-box.

(2) Cons of Piston Engines

(A) Relatively low power-to-weight ratio (see Figure 6-6); (B) mechanical complexity leads to a relatively low *time-between-overhaul* (TBO) between 1000 and 2000 h [14, 15]; (C) noisy; (D) high vibration levels; (E) relatively small power-to-volume; (F) emit contaminants harmful to the environment.

(3) Thrust Modeling for Propellers

Thrust modeling for propellers powered by various engines is presented in Chapter 15.

(4) Common Configurations

Piston engines come is several notable configurations of which the most common are presented in Figure 7-4. The modern piston engine for aircraft is air-cooled to

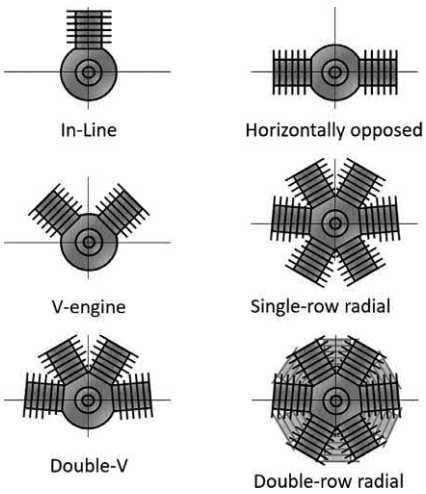


FIGURE 7-4 Common configurations of piston engines. *Based on Kroes, M.J., Wild, T.W., Bent, R.D., McKinley, J.L., Aircraft Powerplants, 6th ed., Glencoe as subsidiary of Macmillan/McGraw-Hill, 1992.*

reduce weight, with fins surrounding the cylinders to help dissipate the heat generated by the combustion.

(5) Manufacturers

Some modern manufacturers of piston engines for UAV and GA aircraft are listed in Table 7-4. At the time of this writing, all the manufacturers were still in business. This does *not* mean these are *all* the manufacturers; only those known to the author at the time of this writing. Out-of-business piston engine manufacturers are excluded.

All piston engines feature one or more pistons that rotate a common crankshaft. There are many variations of the concept, of which the so-called Wankel engine is the best known. However, all the engines dealt with here are conventional pistons. There are two kinds of such engines: two- and four-stroke. Several common types of piston engines are shown in Table 7-5.

TABLE 7-4 Power and weight of selected piston engines for GA and experimental aircraft.

Manufacturer	Type	Cylinders	Displacement (in^3)	TBO (h)	Weight (lb_f)	RPM	Rated power (BHP)	SFC $lb_f/(BHP \cdot h)$
Lycoming	O-235	4	235	2400	243–255	2800	115–125	0.6
	O-320	4	320	2000	268–299	2700	150–160	0.6
	O-360	4	360	2000	280–301	2700	168–180	0.6
	IO-390	4	390	2000	308	2700	210	0.6
	IO-580	6	580	–	444	2700	315	0.6
	IO-720	8	720	–	593–607	2650	400	0.6
Continental Motors	IO-360	6	360	–	327–331	2800	200	0.6
	IO-550	6	550	–	467–470	2700	300–310	0.6
Hirth Motoren	3003[a,b]	4	63.6	1000	93	6500	102	0.83–1.80
	3501[a,b]	2	38.1	1000	78	5500	60	
	3701[a,b]	3	57.3	1000	100	6000	100	
Rotax (Note: specific variants may be certified)	447 UL[a]	2	26.6	300	72	6800	40	–
	503 UL[a]	2	30.3	300	85	6800	49	–
	582 UL[a]	2	35.4	300	79	6800	65	–
	912 UL[a]	4	73.9	1500	122	5800	81	0.47
	912 ULS[a]	4	73.9	1500	125	5800	100	0.47
	914 UL[a]	4	73.9	1200	154	5800	115	–

[a] *Noncertified.*
[b] *Two-stroke.*
TBO, time-between-overhaul; RPM, *revolutions-per-minute;* SFC, *specific fuel consumption.*

TABLE 7-5 Selected manufacturers of piston engines for GA and UAV aircraft.

Maker	Country	Application	Horsepower range	Website
Continental Motors	USA	GA, LSA	75–360 BHP	www.genuinecontinental.aero
Limbach Engines	Germany	GA, LSA	20–167	www.limflug.de
Hirth Engines	Germany	GA, LSA	14.6–102	www.hirth-motoren.de
Rotax Engines	Austria	GA, LSA	40 – 115	www.flyrotax.com
SMA Engines	France	GA	227	www.smaengines.com
Textron Lycoming	USA	GA, LSA, UAV	115–400 BHP	www.lycoming.com
ULPower Aero Engines	Belgium	GA, LSA, UAV	97–130	www.ulpower.com
Zenoah	Japan	UAV, RC	1.68 – 5.82 BHP	www.zenoah.com
Jabiru Engines	Australia	GA, LSA, UAV	85–120	www.jabiru.net.au

GA, general aviation aircraft; *LSA*, light sport aircraft; *UAV*, unmanned aerial vehicles; *RC*, radio controlled aircraft.

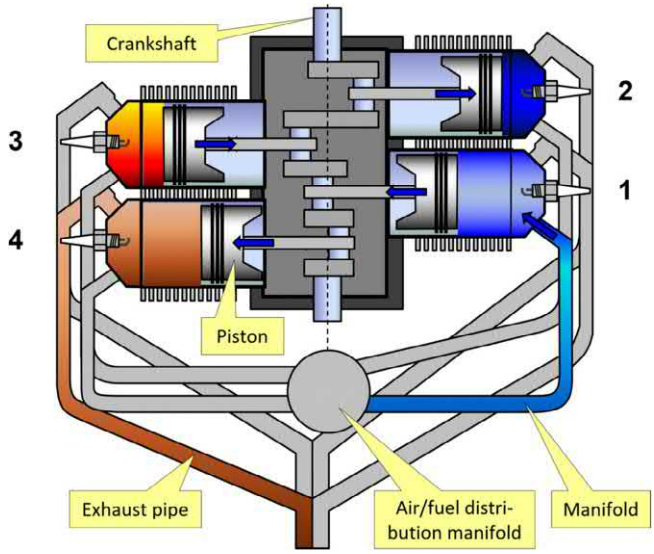


FIGURE 7-5 The workings of a four-cylinder piston engine.



FIGURE 7-6 A Hirth 3503, 70 BHP (52 kW) two-cylinder, two-stroke, water-cooled piston engine for ultralight and experimental (homebuilt) aircraft. *Courtesy of Hirth Engines. www.hirth-motoren.de.*

TABLE 7-6 Specific fuel consumption of typical piston engines for aircraft.

	Normally aspirated piston engines (conversion factor: 1 lb_f/h/BHP = 608.28 g/kW/h)	
	lb_f/h/BHP	**gr/kW/h**
Two-stroke	0.83–1.80	505–1095
Four-stroke	0.42–0.60	255–365

(6) Two-Stroke versus Four-Stroke Engines

The term *stroke* refers to the up- or downward-motion of a piston inside a cylinder. It is the distance between the piston's up- and down-positions. A two-stroke engine exhausts combustion gases and draws in a fresh mixture of fuel/air mixture during the downstroke. Compression and ignition take place during the up stroke. Figure 7.5 shows a schematic of a four-cylinder, four-stroke internal combustion engine. The piston and cylinders are labeled 1 through 4 to match the four stages of the Otto cycle in Figure 7-3. (1) *Injection:* Piston is at the end of its downstroke and has drawn in a fresh fuel/air mixture. (2) *Compression:* Piston is at the end of its upstroke and has compressed the fuel/air mixture just prior to ignition. (3) *Combustion:* Mixture has been ignited and the downstroke of the piston is beginning. (4) *Exhaust:* Piston is beginning its upstroke, forcing the combustion gases out and into the exhaust tube.

Ignition occurs once per revolution in a 2-stroke engine and once every other revolution in a 4-stroke. This gives the two-stroke engine a significant power boost and allows it, potentially, to double the power for the same displacement engine. A two-stroke engine manufactured by Hirth Engines is shown in Figure 7-6. Two-stroke engines are valve-less so they are simpler, lighter, and less expensive to manufacture. They are less durable than four-stroke engines because they lack a dedicated lubrication system. Instead, oil must be mixed with the gas (about 4 oz./gallon of gas). This increases oil burn compared to four-stroke engines. This does not apply to diesel engines.

The operation of a two-stroke engine is less efficient than that of a four-stroke. In part, this results from the use of cleaner, oil-free gasoline in a four-stroke engine. The two-stroke burning leaves remnants of combusted gases inside the cylinder during the compression and ignition. The incomplete combustion exhausts unburnt fuel, causing greater emission of environmentally harmful chemicals. In contrast, the combustion in a four-stroke engine is more complete and has higher temperature than the two-stroke; it is more efficient. A comparison between the SFC of two- and four-stroke engines is shown in Table 7-6.

(7) Indicated Horsepower (IHP, P_{IHP})

Refers to the amount of power that results when heat energy is converted to mechanical energy. In piston engines, this is estimated by the rise of pressure inside a cylinder due to the combustion of fuel. This is often done using a so-called *mean effective pressure* $\overline{p}$, which can be considered the mean pressure during the power stroke.

(8) Friction Horsepower (FHP, P_{FHP})

Refers to the amount of power required to overcome the internal friction of the engine's mechanical parts and components [16]. It can amount to 10% to 15% of the IHP.

(9) Brake Horsepower (BHP, P_{BHP})

Refers to the amount of power delivered at the output shaft of a piston engine. It is estimated by the expression $P_{BHP} = P_{IHP} - P_{FHP}$. If measured, it is obtained using an instrument called a *dynamometer* (aka *prony brake*), which is either a mechanical or electric braking device. In the UK system, the horsepower corresponds to the work required to raise a weight of 33,000 lb_f one foot in one minute. This also corresponds to the work required to

raise a weight of 550 lb_f one foot in one second. Thus, $1\,hp = 33{,}000\,ft{\cdot}lb_f/min = 550\,ft{\cdot}lb_f/s$. Horsepower can be converted to Watts (J/s) in the SI system by multiplying by a factor of 746, i.e., $1\,hp = 746\,W = 0.746\,kW$.

(10) Displacement Volume

Displacement is the total volume of the combustion chamber of all cylinders. The diameter of each cylinder is called a *bore*. The displacement of an engine with N cylinders is defined as follows:

$$\forall_d \equiv \frac{\pi}{4} N \left(bore^2 \times stroke \right) \tag{7-1}$$

(11) Mean Effective Pressure

Refers to the average pressure inside the cylinder during a cycle. Using the concept of pressure energy (or pressure work), it can be defined as follows:

$$\overline{p} = \frac{W}{\forall_d} \tag{7-2}$$

where W is the work done during one cycle (for all cylinders) and $\forall_d$ is the displacement volume. This pressure is usually estimated as *indicated*, *friction*, and *brake mean effective pressure*. See ref. [12] for more detail.

(12) Compression Ratio, Pressure Ratio

The *compression ratio* is the ratio between the cylinder volume with the piston in the bottom position, $\forall_{bot}$ (largest volume), and the top position, $\forall_{top}$ (smallest volume). The higher this ratio, the greater is the power delivered by the engine, but so is propensity of knocking. The compression ratio for typical piston engines ranges from 6:1 to 10:1.

Similarly, the *pressure ratio* is the ratio of the cylinder pressure with the piston in the top and bottom positions, denoted by p_{top} and p_{bot}, respectively. Assuming adiabatic compression inside the cylinder (no heat energy is added when compressing the gas), the relation between the pressure and volume is given by ($\gamma = 1.4$ for air):

$$p_{bot}\forall_{bot}^{\gamma} = p_{top}\forall_{top}^{\gamma} \quad \Leftrightarrow \quad \frac{p_{top}}{p_{bot}} = \left(\frac{\forall_{bot}}{\forall_{top}} \right)^{\gamma} \tag{7-3}$$

(13) Air-to-Fuel Ratio (AF)

The theoretically ideal stoichiometric ratio for piston engines is 1 kg of fuel per 14.7 kg of air ($AF = 14.7$). This ratio develops the highest temperature during combustion and, thus, is of concern when it comes to engine durability. Combustion is possible for $6 \le AF \le 19$ [12]. If the air-to-fuel mixture is less than 14.7 (e.g., 10:1), it is called *rich*. If greater (e.g., 16:1), it is called *lean*. These two concepts are of great importance to pilots.

The energy content of a 1 lb_f of Avgas is 14,800,000 $ft{\cdot}lb_f$ (20.07 MJ). Burning 1 lb_f of Avgas in 1 min with 100% efficiency would generate $(14{,}800{,}000\,ft{\cdot}lb_f)/(33{,}000\,ft{\cdot}lb_f/BHP) = 448$ BHP. As an example, a typical modern medium sized piston engine, such as the Continental IO-360, delivers 200 BHP at maximum power, while consuming 16 gal of Avgas per hour. This amounts to $16\,gal/h \times 6\,lb_f/gal = 96\,lb_f$ of fuel per hour, or $96\,lb_f/60 = 1.6\,lb_f/min$. The equivalent energy content of this fuel is $1.6 \times (14{,}800{,}000\,ft{\cdot}lb_f)/(33{,}000\,ft{\cdot}lb_f/BHP) = 716.8$ BHP:

However, only some 200 BHP is delivered as mechanical energy. The resulting efficiency is 200/716.8 or 27.9%. In a long-range cruise mode, the same engine delivers 55% of its rated power (110 BHP), while consuming some 8.4 gal/h. Applying the same calculation method we find the efficiency amounts to 29.2%.

TABLE 7-7 Energy wasted in a piston engine.

Cause	Percentage
Available in fuel	100%
Heat lost to oil	–2%
Heat lost to cooling air	–11%
Heat lost to radiation	–5%
Heat lost to exhaust	–52%
Mechanical losses	–5%
Sum	≈25%

Based on Stinton, D., The Design of the Aeroplane, Collins, 1983.

(14) Typical Specific Fuel Consumption for Piston Engines

The fuel consumption of piston engines varies by type as shown in Table 7-4. A typical breakdown of how energy is wasted in piston engines can be seen in Table 7-7.

(15) Operating "Square" and "Over Square"

The term operating "square" refers to a condition when an aircraft engine is operated at a manifold pressure (MAP) in inches-Hg that is equal to the RPM/100. An example of this is MAP of 25 in Hg and 2500 RPM. In contrast, the term operating "over square" refers to the engine being operated at MAP higher than RPM/100 (e.g., 29 inHg and 2500 RPM). It was once believed this was bad for the engine, but the pilot community has been pushing against this notion for a while now (e.g., see ref. [17]). The primary advantages of "over square" are improved fuel consumption during cruise, reduced wear of the engine, and reduced cabin noise. It is only to be used during cruise. This can be accomplished in normally aspirated engines at low altitudes and higher if the engine is turbocharged and features constant speed propeller. An analogy for "over square" is made with a car engine upshifted to the fifth gear while operating at high cruise speed.

(16) Aero- Diesel Engines

Diesel engines for aircraft are commonly referred to as *aero-diesels*. They should be strongly considered for

propeller aircraft. Such engines are already being used in aircraft such as the Diamond DA-42 Twin Star. The type of ignition is a significant difference between diesel and conventional gasoline engines: Gasoline uses *spark ignition* (SI), while diesels use *compression ignition* (CI). CI is the self-ignition of the air-fuel mixture that occurs when it is compressed beyond its *auto-ignition temperature*. The compression ratio for typical diesel engines ranges from 14:1 to 18:1.

Refs. [18, 19] are product brochures from two manufacturers who state multiple advantages of their aero-diesels. Among those is greater durability than gasoline engines, thanks to the lubricating nature of its fuel. They are more reliable and less expensive to maintain due to reduced part count, integral fuel, and lubrication systems, as well as absence of magnetos and spark plugs. Fuel injection eliminates risk of carburetor icing. Aero-diesels are more efficient than Avgas engines because diesel oil has approximately 6% higher energy content per unit volume than gasoline [20, App. A], which when combined with higher compression ratio and fuel injection results in more efficient use of fuel. This reduces the SFC by as much as 40%. Additionally, some diesels burn multiple fuels, including Jet A and A-1, so they benefit from greater fuel availability. The engines are lighter per unit power, have markedly smaller frontal area, and permit "cleaner" installation. They have lower CO_2 and NOx pollution, in part because substances such as lead, and benzene are absent in the fuel. Diesel fuel is also less volatile than Avgas, so it is safer.

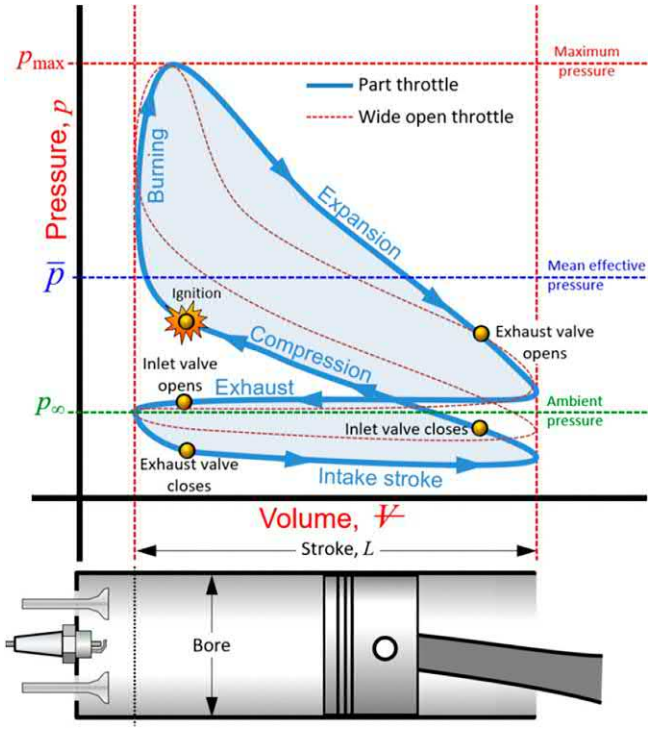


FIGURE 7-7 Pressure versus cylinder volume for a typical piston engine. *Adapted from Smil, V., Two Prime Movers of Globalization - The History and Impact of Diesel Engines and Gas Turbines, The MIT Press, Cambridge, MA, 2010; Pulkrabek, W.W., Engineering Fundamentals of the Internal Combustion Engine, 2nd ed., Pearson, 2003; Kroes, M.J., Wild, T. W., Bent, R.D., McKinley, J.L., Aircraft Powerplants, 6th ed., Glencoe as subsidiary of Macmillan/McGraw-Hill, 1992.*

7.2.2 Basic Theory of Internal Combustion Engines

Per Table 7-1, Work is the product of force and distance. Power is the time-rate-of-change of work. The pressure inside the cylinder of a piston engine varies markedly as the piston moves from the top-to-bottom of the power stroke (see Figure 7-7). The work accomplished during each combustion cycle is represented by the shaded area of the (closed) $p\forall$ curve. This work can be approximated as follows: (1) The *mean effective pressure* ($\overline{p}$, aka mep) and piston area (A) constitutes the pressure force. (2) The stroke (L) is the distance over which this force acts. Thus, the work done during each combustion cycle is $W = \overline{p}AL$. Each second, this means $n = RPM/60$ cycles for a two-stroke engine (combustion takes place each 360 degrees of rotation) and $n = RPM/120$ cycles for a four-stroke engine (combustion takes place each 720 degrees). Recall that 60 RPM means 360 degrees of rotation each second. Thus, the total work done by an engine with N_{cyl} cylinders is

$$W = \overline{p}ALnN_{cyl} \tag{7-4}$$

If using the SI system, this yields power in kW. If $\overline{p}$ is in N/m^2, A is in m^2, L is in m, n is in per second, and we have 1000 W per kW, the conversion looks as follows:

$$P_{IKW} = \frac{\overline{p}ALnN_{cyl}}{1000} \tag{7-5}$$

Note that the subscript *IKW* is used to designate this as *indicated kW*. If using the UK system, we would convert this power into *IHP* (*indicated horsepower*). If $\overline{p}$ is in lb_f/in^2, A is in in^2, L is in inches, and n is in per second, the following expression yields power in $ft{\cdot}lb_f/s$. Converting this to *indicated horsepower* requires:

$$P_{IHP} = \frac{\overline{p}A(L/12)nN_{cyl}}{550} = \frac{\overline{p}ALnN_{cyl}}{6600} \tag{7-6}$$

This remains to be converted into brake horsepower. This task is simple if we know the friction horsepower—and certainly not if we do not. The determination of this ratio is beyond the scope of this edition; interested readers are directed to ref. [12] as an excellent source.

EXAMPLE 7-1

Per ref. [21], a four-stroke, four-cylinder Rotax 912 UL has a bore of 79.5 mm (3.13″) and stroke of 61 mm (2.40″). If the mean effective pressure during the combustion stroke is 218 psi, calculate the indicated power

EXAMPLE 7-1 (*cont'd*)

at 5800 RPM ($n = 5800/120 = 48.3$ per second). If the friction horsepower is estimated as 15% of the indicated horsepower, estimate the brake horsepower.

SOLUTION:

The indicated horsepower is found from Equation (7-6):

$$P_{IHP} = \frac{\bar{p}ALnN_{cyl}}{6600} = \frac{(218)\left(\frac{\pi \times 3.13^2}{4}\right)(2.4)(48.3)(4)}{6600} = 117.8 \text{ IHP}$$

Thus, the brake horsepower is found to amount to $P_{BHP} = (1 - 0.15)P_{IHP} = 100.2$ IHP.

(1) Effect of Airspeed on Engine Power

The power generated by a piston engine is constant with airspeed, making it an *airspeed independent powerplant*. If a piston engine produces 100 BHP at a specific power setting, say, at stalling speed, it also generates 100 BHP at the same power setting at its maximum airspeed (assuming same altitude). In real applications, the power depends on the pressure recovery at the manifold. Engine power is airspeed dependent if pressure recovery changes with, say, angle-of-attack. However, during design work, piston engine power output can be considered independent of airspeed.

(2) Effect of Altitude on Engine Power

The power output of normally aspirated engines depends on how efficiently the fuel/air mixture burns during combustion. This depends on the quantity of oxygen molecules (O_2) inside the cylinder as the piston begins the compression stroke. This quantity depends on the density of air and it is directly related to the initial pressure in the cylinder. Pressure and density are fundamental variables in the operation of piston engines: normally aspirated engines are highly dependent on altitude.

The initial pressure in the cylinders can be increased by two means: (1) By recovering as much ram air pressure as possible in the engine manifold (pertains to normally aspirated engines) and (2) by artificially increasing the pressure in the manifold. The former is achieved by ensuring the intake is not blocked and is in an area where air can stagnate with minimum losses. The latter is done through the process of *turbocharging* or *turbo-normalizing*.

The impact of altitude on engine power is estimated using *altitude dependency models*. The simplest one, presented below, assumes that the engine power is directly dependent on the density ratio:

Simple altitude-dependency model:

$$P = P_{SL}\left(\frac{\rho}{\rho_{SL}}\right) = P_{SL}\sigma \tag{7-7}$$

where P, ρ and σ are power, density, and density ratio at altitude, respectively, and P_{SL} and ρ_{SL} correspond to S-L values. A more accurate model is the so-called Gagg and Ferrar model [22]. It is presented in its three most frequently encountered forms below:

Gagg-Ferrar model:

$$P = P_{SL}\left(\sigma - \frac{(1-\sigma)}{7.55}\right) = P_{SL}(1.132\sigma - 0.132) = P_{SL}\frac{(\sigma - 0.117)}{0.883} \tag{7-8}$$

where P_{SL} is power at S-L in terms of BHP and σ is density ratio. The above expressions are used with normally aspirated engines only. Figure 7-8 shows a comparison between the simple altitude-dependency model and the Gagg-Ferrar model. The Gagg-Ferrar model matches manufacturer's data far better than the simple altitude model and is recommended for design work. The horizontal axis shows the percentage power and the vertical altitude in ft. Consider an engine delivering 200 BHP at S-L at full-throttle. At 15,000 ft, the Gagg-Ferrar model predicts approximately 57.5% power, or 115 BHP at the same throttle setting.

Straight lines representing 55%, 65%, and 75% power have been plotted in Figure 7-8. They represent typical power settings reported by manufacturers of pistonprops. At 8283 ft, the maximum power of a normally aspirated engine is 75% of its rated S-L value. Corresponding altitudes for 65% and 55% are shown as 12,106 ft and 16,324 ft, respectively.

To prevent loss of power with altitude, the air flowing into the manifold must be introduced at a higher pressure; it must be *prepressurized*. The standard-day, sea-level manifold pressure for normally aspirated engines is 29.92 inHg (1013.25 mb). The prepressurization should maintain this pressure to the highest altitude possible. This is accomplished in three common ways: (1) *supercharging*, (2) *turbocharging*, and (3) *turbo-normalizing*. Space limits but a few introductory facts to be introduced here.

(3) Supercharging, Turbocharging, Turbo-Normalization

Supercharging is the oldest method for precompressing air before it enters the cylinder of a piston engine. A *supercharger* is a compressor, often of a centrifugal design, which is directly or indirectly connected to the engine. It operates at rotation rates as high as 120,000 RPM. While requiring extra engine power for operation, it boosts engine power far beyond this cost. The supercharger often generates manifold pressure in

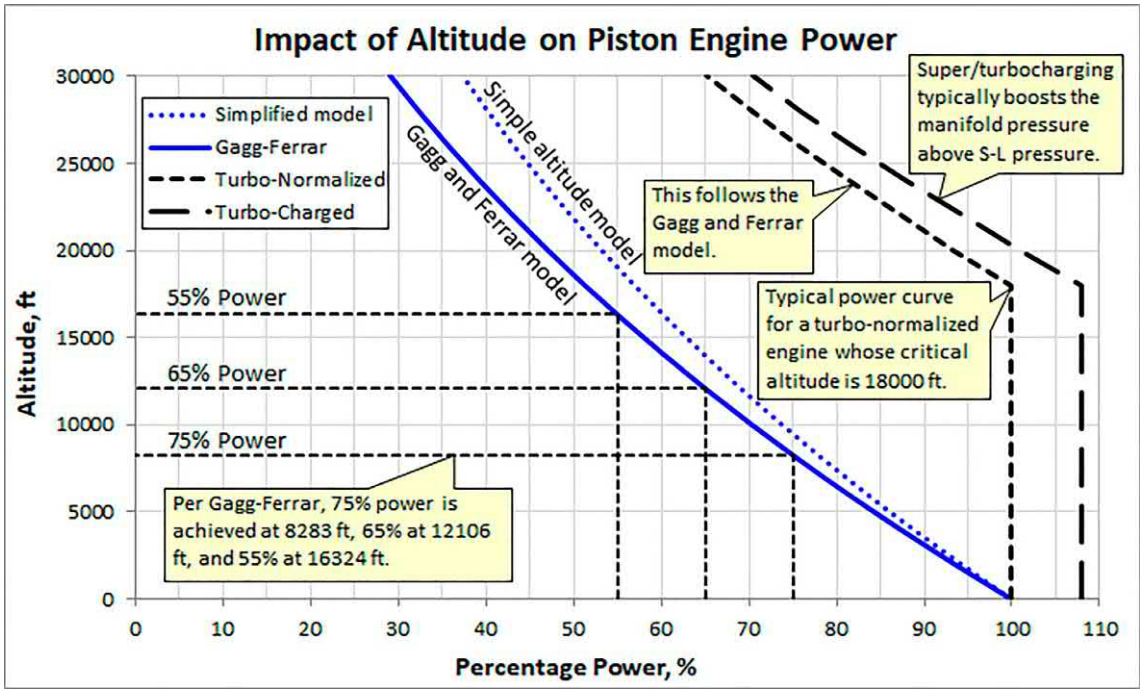


FIGURE 7-8 A comparison showing the difference between several models used to describe how piston engine power is affected by change in altitude.

the excess of 45 inHg. This was common for WWII aircraft. For instance, the maximum MAP of the Boeing B-29 was 48 inHg [23], 49 inHg for the Consolidated B-24 [24], and 52 inHg for the C-46 Commando [25] and P-47 Thunderbolt [26].

A *turbocharger* is a centrifugal compressor driven by the engine's exhaust gases. It utilizes thermal energy that otherwise would go unharnessed into the environment. The turbocharger inflicts minimal power penalty when operating at optimal conditions, making it more efficient than a supercharger. Regardless, its increases back-pressure in the exhaust manifold and reduces engine efficiency, despite increasing power. Back-pressure is the obstruction to free flow of the exhaust gases through the tailpipe. Its magnitude depends on a complex interaction of RPM, throttle setting, ambient pressure, and geometry of the inlet [27].

Turbo-normalization is a turbocharger designed to maintain (or normalize) S-L pressure in the manifold from S-L to a *critical altitude*. This is the altitude at which sea-level pressure can no longer be generated. Turbo-normalization is often introduced as a modification to normally aspirated engines, which are designed to S-L MAP. MAP above the S-L pressure risks engine knocking. Turbo-normalizing differs from turbocharging in the manifold pressure developed. A turbo-normalizer maintains S-L pressure to the critical altitude, whereas a turbocharger increases the manifold pressure above S-L pressure. The impact of altitude on turbocharged and turbo-normalized engines is shown in Figure 7-8. The critical altitude depends on installation. Some engines offer a critical altitude of 18,000 ft while others reach higher altitudes. The Cirrus SR22T features a turbo-normalized Continental IO-550, offering S-L power up to 25,000 ft. Of course, thrust reduces with altitude because of air density, although it far exceeds that of a normally aspirated engine.

Once the critical altitude is exceeded, engine power can be assumed to decrease per the Gagg-Ferrar model. Mathematically, if the S-L power is given by P_{SL} and critical altitude by h_{crit}, then power at other altitudes can be estimated using the following expression:

$$\text{If } h \le h_{crit} \text{ then } P = P_{SL} \tag{7-9}$$

$$\text{If } h > h_{crit} \text{ then } P = P_{SL}\left(1.132(1+\kappa(h-h_{crit}))^{4.2561} - 0.132\right) \tag{7-10}$$

where $\kappa = -0.0000068756$ 1/ft or -0.000022558 1/m. It is inevitable that increased compression of air increases its temperature. This calls for the use of *intercoolers* to cool the air exiting the centrifugal compressor. The cooling increases air density, improving the engine's combustion efficiency. The temperature rise can be approximated by assuming an isentropic process (adiabatic and reversible) as follows

$$p_2 = p_1(T_2/T_1)^{\gamma/(\gamma-1)} \Rightarrow T_2 = T_1\left(\frac{p_2}{p_1}\right)^{(\gamma-1)/\gamma} \tag{7-11}$$

(4) Effect of Temperature on Engine Power

Since power is affected by density and pressure, it follows it is also influenced by temperature. The following

expression is used in performance charts by one engine manufacturer to correct power at a nonstandard temperature condition:

$$\frac{P}{P_{std}} = \sqrt{\frac{T_{std}}{T_{OAT}}} = \sqrt{\frac{518.67(1+\kappa h)}{T_{OAT\ °R}}} = \sqrt{\frac{288.15(1+\kappa h)}{T_{OAT\ K}}} \tag{7-12}$$

where

P_{std} = Standard power at altitude and ISA
κ = Lapse rate constant (Table 17-3)
T_{std} = Standard day temperature
T_{OAT} = Outside air temperature (OAT) at condition
h = Pressure altitude at condition

Another manufacturer of engines for small aircraft suggests the following expression to correct for temperature:

$$\frac{P}{P_{std}} = \frac{T_{std}}{T_{OAT}} \tag{7-13}$$

A third way to correct for nonstandard temperature is through density ratio, using the Gagg-Ferrar model. The following example compares these three models. This author recommends the Gagg-Ferrar model for design work.

EXAMPLE 7-2

Estimate the power of a piston engine rated at 100 BHP while being operated at full power at 10,000 ft on a day on which the OAT is 30°F (or 30°R) higher than ISA.

SOLUTION:

Method 1: Equation (7-12)

Lapse rate factor:

$$(1+\kappa h) = (1–0.0000068756 \times 10{,}000) = 0.9312.$$

Standard day temperature at 10,000 ft:

$$T_{std} = 518.67 \times 0.9312 = 483.0°\text{R}.$$

Density ratio at 10,000 ft (standard day):

$$\sigma = 0.9312^{4.2561} = 0.7385.$$

Maximum power at 10,000 ft per Gagg–Ferrar:

$$P = P_{SL}\,(1.132\sigma - 0.132) = 100(1.132 \times 0.7385 - 0.132) = 70.4\ \text{BHP}$$

This is further reduced by the warmer than normal day using Equation (7-12) as follows:

$$P = P_{std}\sqrt{\frac{T_{std}}{T_{OAT}}} = 70.4\sqrt{\frac{483.0}{483.0+30}} = 68.3\ BHP$$

Method 2: Equation (7-13)

The procedure is identical to Method 1, up to the last:

EXAMPLE 7-2 *(cont'd)*

$$P = P_{std}\frac{T_{std}}{T_{OAT}} = 70.4\frac{483.0}{483.0+30} = 66.3\ BHP$$

Method 3: Ideal Gas Law with Gagg-Ferrar

The answer can also be estimated using the ideal gas equation as follows:

Pressure at 10,000 ft:

$$p = 2116(1 + \kappa h)^{5.2561} = 2116 \times 0.9312^{5.2561} = 1455\ \text{psf}$$

Density at 10,000 ft:

$$\rho = \frac{p}{RT} = \frac{1455}{1716 \times (483+30)} = 0.001653\ \text{slugs/ft}^3.$$

Density ratio at 10,000 ft:

$$\sigma = \frac{\rho}{\rho_0} = \frac{0.001653}{0.002378} = 0.6951.$$

Gagg and Ferrar:

$$P = 100(1.132 \times 0.6951 - 0.132) = 65.5\ \text{BHP}$$

(5) Effect of Manifold Pressure (MAP) and RPM on Engine Power

The relationship between the manifold pressure and RPM is complex and usually presented by the piston engine manufacturer in the form of an *engine performance chart*. An example is shown in Section 7.2.4. The primary drawback of this plot is that it lends itself poorly for use in spreadsheets. A remedy is found in a specialized formula, called the Petty Equation. This powerful tool is presented in Section 7.2.5.

7.2.3 The Use of Gearboxes

Aircraft engines deliver maximum power at a relatively low RPM, when compared to car or snow-mobile engines. For instance, Continental and Lycoming aircraft engines deliver their maximum power around 2700–2800 RPM, compared to 5000–6000 RPM for a car engine. Many airplane designers, specifically those designing homebuilt aircraft, often adapt automobile engines to their designs. If a propeller is connected directly to the crankshaft of such an engine, the high RPM would result in a supersonic tip speed. This would create unacceptable noise and associated propulsive losses. The remedy is to add a gearbox to bring down the rotation rate. Turboprops usually rotate at some 20,000–40,000 RPM, so a gearbox is a standard part of the engine unit.

The presence of a gearbox reduces the available engine power slightly due to internal friction. However, in the following discussion it is assumed such losses are negligible. Consider the gears in Figure 7-9. The radius of gearwheel 1 is R_1 and R_2 of gearwheel 2. Assume

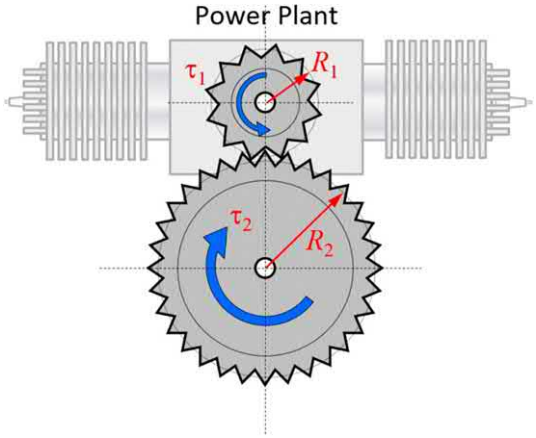


FIGURE 7-9 A schematic of a gearbox. R_1 is the gear wheel connected to the crankshaft. R_2 is the gear wheel connected to the output axle, e.g., the propeller axis.

gearwheel 1 rotates at a constant rate Ω_1 as it delivers torque τ_1. Then the following holds for gearwheel 2, where V_1 and V_2 are the linear speeds of a point on the perimeter of the wheels.

RPM of gearwheel 2:

$$\cancel{V_1 = V_2} \;\Rightarrow\; \Omega_1 R_1 = \Omega_2 R_2 \;\Leftrightarrow\; \Omega_2 = \Omega_1 \left(\frac{R_1}{R_2}\right) \qquad (7\text{-}14)$$

Torque of gearwheel 2:

$$\left.\begin{aligned} \tau_1 &= F_1 \times R_1 \\ \tau_2 &= F_2 \times R_2 \end{aligned}\right\} \;\Rightarrow\; \text{since } F_1 = F_2 \;\Rightarrow\; \tau_2 = \tau_1 \left(\frac{R_2}{R_1}\right) \qquad (7\text{-}15)$$

Power of gearwheel 1:

$$P_1 = F_1 \times \cancel{V_1} = \left(\frac{\tau_1}{R_1}\right) \times (\Omega_1 R_1) = T_1 \Omega_1 \qquad (7\text{-}16)$$

Power of gearwheel 2:

$$P_2 = \tau_2 \Omega_2 = \tau_1 \left(\frac{R_2}{R_1}\right) \times \Omega_1 \left(\frac{R_1}{R_2}\right) = \tau_1 \Omega_1 = P_1 \qquad (7\text{-}17)$$

From which we see that the gearwheels changes the RPM and torque, but power remains unchanged.

EXAMPLE 7-3

A 4-cylinder Rotax 912ULS engine generates a power of 100 BHP at 5800 RPM. If fitted with a 2.43:1 reduction drive, determine the reduced RPM and horsepower.

SOLUTION:

Rotation rate after gear reduction :

$$\Omega_2 = \Omega_1 \left(\frac{R_1}{R_2}\right) = 5800 \left(\frac{1}{2.43}\right) = 2387 \text{ RPM}$$

From Equation (7-17), horsepower after the reduction drive is the same as before, or 100 BHP.

7.2.4 Extracting Piston Power From Engine Performance Charts

Manufacturers of piston engines usually provide aircraft designers with engine performance charts like the one in Figure 7-10. Such charts are used to extract BHP for an engine based on RPM and MAP, which are parameters obtained from easily visible instruments in most piston-engine aircraft. Then, further corrections are made by accounting for the OAT at the condition. Note that the MAP is usually given in terms of inches Mercury (inHg).

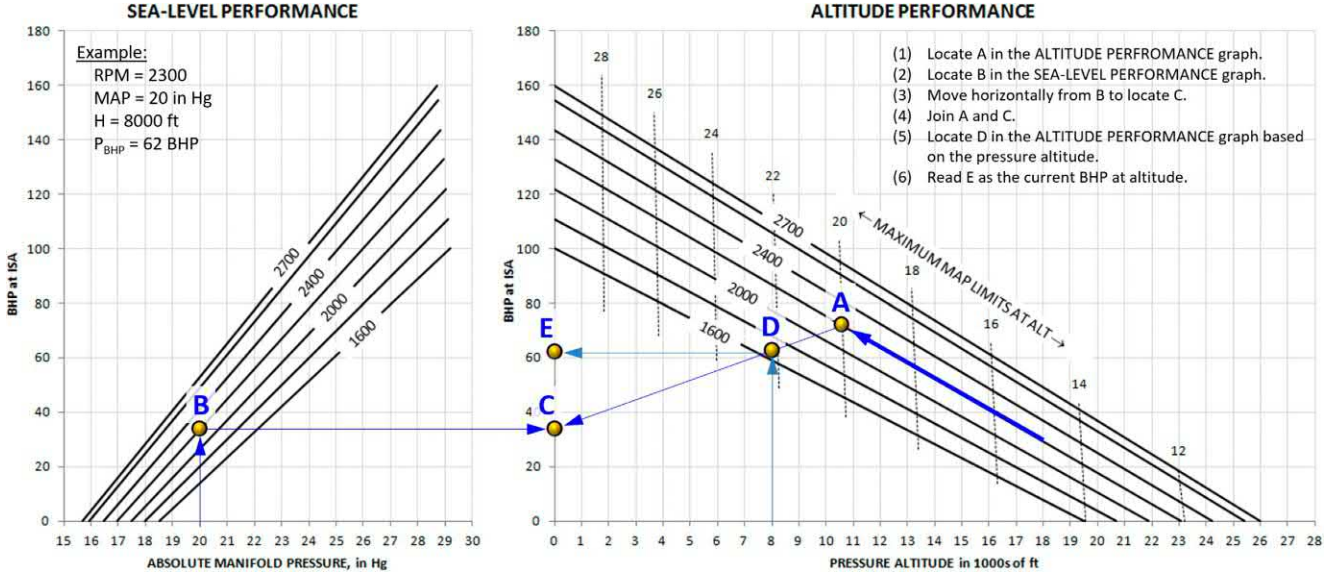


FIGURE 7-10 An example of a piston-engine performance chart for a typical certified 160 BHP aircraft engine. The chart is used to extract P_{BHP} for an engine based on its RPM and Manifold Pressure (MAP). See text for details on how to read it.

Such charts are read as explained below. This is easier to do using an example. Assume the performance chart in Figure 7-10 applies to an engine operating at 8000 ft at 2300 RPM and MAP of 20 inHg. Then the following steps are performed:

***STEP 1*:** Locate Point **A** in the ALTITUDE PERFORMANCE part of the graph by moving along the curve that indicates 2300 RPM.

***STEP 2*:** Locate Point **B** in the SEA-LEVEL PERFORMANCE graph.

***STEP 3*:** Move horizontally from **B** to locate Point **C**.

***STEP 4*:** Join **A** and **C**.

***STEP 5*:** Locate **D** in the ALTITUDE PERFORMANCE graph based on the pressure altitude.

***STEP 6*:** Read Point **E** as the current BHP at altitude.

***STEP 7*:** Correct for temperature deviation using Equation (7-12): $P_{BHP} = P_{BHPE}\sqrt{\frac{T_{std}}{T_{OAT}}}$ where T_{std} is standard day temperature at altitude and T_{OAT} is outside air temperature at condition.

7.2.5 Extracting Piston Power Using the Petty Equation

The extraction of engine power from the engine performance chart is a cumbersome and time-consuming effort. Section 7.2.4, reveals that reading such charts is not conducive to iterative analyses. The analytical equation below was developed by Dr. James S. Petty (1937) of the US Air Force Wright Aeronautical Laboratories (AFWAL) and first published in ref. [28]. It converts the performance chart into a handy equation that is easy to implement in a spreadsheet or a computer code. This equation is recognized as the *Petty equation*.

$$P_{BHP} = P_{BHP\max}\sqrt{\frac{T_{std}}{T_{OAT}}}\frac{\left[R_m - R_f(1-R_m)\right]\left(\sigma_{std} - R_m^{0.8097}\right) + \left(\frac{R_m^{0.8097} - 0.117}{0.883}\right)(1-\sigma_{std})}{1 - R_m^{0.8097}} \tag{7-18}$$

where P_{BHP} = horsepower at condition (specified MAP, RPM, and altitude), $P_{BHP\ max}$ = maximum S-L horsepower as a function of RPM (typically a polynomial), P_{FHP} = friction horsepower as a function of RPM (typically a polynomial, such that $P_{FHP} = P_{BHP}$ at $MAP = 0$), h = pressure altitude in feet, MAP = manifold pressure in inches Hg, $MAP_{\max}$ = maximum manifold pressure as function of RPM (typically a polynomial), R_m = manifold pressure ratio = $MAP/MAP_{\max}$, R_f = friction horsepower ratio = $|P_{FHP}|/P_{BHP\max}$ (always a positive value), and σ = density ratio for standard atmosphere = $(1+\kappa h)^{4.2561}$.

The equation is very helpful for the designer of piston powered aircraft, as it allows the power of a piston engine to be modeled using a spreadsheet or other computer software. Its worth far exceeds the effort of setting it up. The primary drawback in its use is the preparation of the two polynomials: for the $P_{BHP\ \max}$ and P_{FHP}. These must be determined using the original performance chart obtained from the engine manufacturer. Both are a function of RPM and can be determined as follows.

TABLE 7-8 Determining $P_{BHP\ \max}$ and P_{FHP} polynomials

①	②	③	④	⑤
RPM	$P_{BHP\ max}$	MAP	m	P_{FHP}
1600	100	18.50	9.524	-76.19
1800	110	18.00	10.000	-70.00
2000	122	17.50	10.609	-63.65
2200	133	17.00	11.083	-55.42
2400	145	16.50	11.600	-46.40
2600	156	16.00	12.000	-36.00
2700	163	15.75	12.302	-30.75

Determination of the Polynomials Describing $P_{BHP\max}$ and P_{FHP}

Consider the engine performance chart of Figure 7-10, in particular the **SEA-LEVEL PERFORMANCE** side. The trick to creating these polynomials is to tabulate the endpoints and then fit a curve through these (see Table 7-8). For instance, consider the generation of the polynomial for the values of $P_{BHP\max}$. Column ① contains the selected RPM values. Column ② contains the corresponding values of $P_{BHP\max}$, which have been obtained by extending all the curves to a MAP of 29.

The next three columns pertain to the determination of P_{FHP}. The easiest way to determine the values of P_{FHP} is to read the value of the MAP for $P_{BHP} = 0$, and then use the equation of a line to determine the values of P_{FHP} when MAP = 0. These values can be seen in Column ③. Column ④ contains the slope of the lines calculated from:

$$m = \frac{P_{BHP\max}}{29 - MAP_{P_{BHP}\ =\ 0}}$$

Then, the P_{FHP}, which is contained in Column ⑤, can be calculated as follows:

$$P_{BHP} = P_{FHP} + m \cdot P_{BHP\max}$$
$$\Leftrightarrow \quad P_{FHP} = P_{BHP} - m \cdot P_{BHP\max}$$

The points from Table 7-8 have been plotted in Figure 7-11. Then, it is an easy task to determine the best fit curve. Here, an equation of a line turned out to provide an acceptable fit, but this is not guaranteed. Commonly one must resort to quadratic and even cubic polynomials.

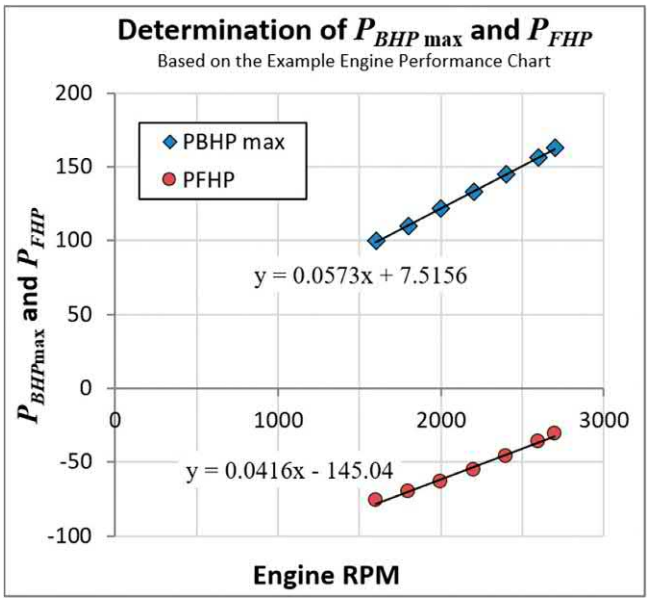


FIGURE 7-11 A simple curvefit is used to represent $P_{BHP\,max}$ and P_{FHP}.

7.2.6 Piston Engine Installation

(1) General Introduction to Engine Installation

The following applies to all aircraft engine installations: The installation of propeller engines (pistons or turboprops) requires a stout bulkhead (*firewall*) to which the engine mounts are attached. The firewall is frequently normal to the flight direction. The associated drag is reduced using an aerodynamically shaped *cowling*. In contrast, subsonic jet engines require inlets and exhaust that ideally should be short and without excessive bends. Turbojets and low bypass ratio turbofans for supersonic flight use long inlets. If mounted inside the fuselage (buried), a jet engine requires fire proofing and careful structural design in case of a rotor-burst. If outside the fuselage, bulkheads to which the engine pylon is mounted are still required.

In this section, typical engine installations for piston and jet engines are presented from the standpoint of impact on aesthetics, aerodynamics, and, to a limited extent, structures. While the structural design belongs

DERIVATION OF EQUATION (7-18)

Consider the simplified performance chart in Figure 7-12, on which only a single RPM is shown. The Sea-Level curve, in the **SEA-LEVEL PERFORMANCE** side, extends from a negative friction power (P_{FHP}), which is the norm at $MAP = 0$, to a maximum power, $P_{BHP\,max}$, at the maximum manifold pressure, MAP_{max}. The representative P_{BHP} versus Altitude curve is shown in the **ALTITUDE PERFORMANCE** side. It depends on σ and extends from the S-L P_{BHP} value to where MAP can no longer be maintained. The locus of these limit points results in a specific P_{BHP} versus Altitude curve for each RPM, starting at $\sigma = 1$ to $\sigma = 0.117$.

The **SEA-LEVEL PERFORMANCE** curve can be represented using the following parametric expression (noting that the MAP axis extends from 0 to MAP_{max} so the parameter can be defined as $R_m = MAP/MAP_{max}$):

$$P_{BHP\,SL} = P_{FHP}(1 - R_m) + P_{BHP\,max} R_m \qquad \text{(i)}$$

Now, let $R_f = P_{FHP}/P_{BHP\ max}$. Then, substitute R_f into Equation (i) and simplify.

$$\begin{aligned} P_{BHP\,SL} &= \frac{P_{BHP\,max}}{P_{BHP\,max}} P_{FHP}(1 - R_m) + P_{BHP\,max} R_m \\ &= P_{BHP\,max} R_f (1 - R_m) + P_{BHP\,max} R_m \\ &= P_{BHP\,max} \left(R_f (1 - R_m) + R_m \right) \end{aligned}$$

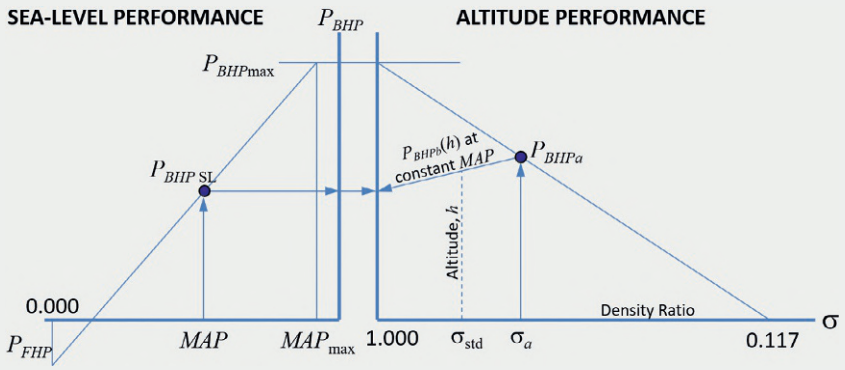


FIGURE 7-12 A simplified piston-engine performance chart that depicts only one value of the RPM.

In order to prevent sign errors, the value of R_f is considered positive. However, since P_{FHP} is always negative, writing the above result as follows preserves the sign:

$$P_{BHPSL} = P_{BHP\max}\left[R_m - R_f(1-R_m)\right] \quad \text{(ii)}$$

The **ALTITUDE PERFORMANCE** curve is based on the Gagg–Ferrar piston engine power correction of Equation (7-8), here repeated for convenience.

$$P_{BHPa} = P_{BHP\max}\left(\frac{\sigma_a - 0.117}{0.883}\right) \quad \text{(iii)}$$

where the subscript "*a*" indicates this is taken from the altitude side. The manifold pressure for each RPM varies linearly with the pressure ratio and, thus using Equation (17-10), can be written as follows:

$$\frac{MAP_a}{MAP_{\max}} = \frac{P}{P_{SL}} = \sigma_a^{1.235} \quad \text{(iv)}$$

$$\text{Or, conversely:} \quad \sigma_a = \left(\frac{MAP_a}{MAP_{\max}}\right)^{0.8097} = R_m{}^{0.8097} \quad \text{(v)}$$

Then, substituting Equation (v) into (iii) yields:

$$\begin{aligned} P_{BHPa} &= P_{BHP\max}\left(\frac{\sigma_a - 0.117}{0.883}\right) \\ &= P_{BHP\max}\left(\frac{R_m{}^{0.8097} - 0.117}{0.883}\right) \end{aligned} \quad \text{(vi)}$$

$P_{BHP\ a}$ is the power corrected for altitude effects only and it remains to be adjusted to standard day and corrected for temperature at the flight altitude, *h*. The adjustment takes place by locating the uncorrected power, denoted by $P_{BHP\ b}$, along the constant manifold pressure line on the altitude side of the performance chart using the equation:

$$P_{BHPb} = P_{BHPSL} + m(1-\sigma_{std}) \quad \text{(vii)}$$

where

σ_{std} = Standard day density ratio = $(1–0.0000068756h)^{4.2561}$
h = Altitude in ft
m = Slope of the constant manifold pressure line = $(P_{BHP\ a} - P_{FHP\ SL})/(1-\sigma_a)$

Inserting this into Equation (vii) yields:

$$\begin{aligned} P_{BHPb} &= P_{BHP\ SL} + m(1-\sigma_{std}) \\ &= P_{BHP\ SL} + \frac{P_{BHPa} - P_{BHP\ SL}}{1-\sigma_a}(1-\sigma_{std}) \end{aligned} \quad \text{(viii)}$$

Further algebraic manipulations:

$$\begin{aligned} P_{BHPb} &= P_{BHP\ SL} + (P_{BHPa} - P_{BHP\ SL})\frac{1-\sigma_{std}}{1-\sigma_a} \\ &= \frac{P_{BHP\ SL}(\sigma_{std} - \sigma_a) + P_{BHPa}(1-\sigma_{std})}{1-\sigma_a} \end{aligned} \quad \text{(ix)}$$

The uncorrected power must then be corrected for temperature and this is done using Equation (7-12):

$$P_{BHP} = P_{BHPb}\sqrt{\frac{T_{std}}{T_{OAT}}} \quad \text{(x)}$$

This represents the power used in performance calculations. Combining Equations (ii), (iii), (v), and (ix) with (x), leads to the following expression:

$$P_{BHP} = \sqrt{\frac{T_{std}}{T_{OAT}}}\frac{P_{BHP\max}\left[R_m - R_f(1-R_m)\right]\left(\sigma_{std} - R_m^{0.8097}\right) + P_{BHP\max}\left(\frac{R_m^{0.8097} - 0.117}{0.883}\right)(1-\sigma_{std})}{1-R_m^{0.8097}}$$

Further simplification yields:

$$P_{BHP} = P_{BHP\max}\sqrt{\frac{T_{std}}{T_{OAT}}}\frac{\left[R_m - R_f(1-R_m)\right]\left(\sigma_{std} - R_m^{0.8097}\right) + \left(\frac{R_m^{0.8097} - 0.117}{0.883}\right)(1-\sigma_{std})}{1-R_m^{0.8097}} \quad \text{(xi)}$$

to the detail design phase, the implications of an installation should be understood by the designer and regulatory aspects should be pondered. These can be found in Subpart E, under §23.901 through §23.1203 in the "old" 14 CFR Part 23 and under §23.2400 through §23.2440 in the "new" Part 23. GA aircraft certified under 14 CFR Part 25, must comply with §25.901 through §25.1207. Similar identification is used in the European CS framework. Further discussion about these and other pertinent paragraphs is omitted due to space constraints, but the interested reader should explore these regulations by visiting www.faa.gov or www.easa.europe.eu.

(2) Fire Proofing

Fire is a serious threat in all aircraft. Unlike a car, the inability to stop on a moment's notice makes fire particularly serious. *Fire Proofing* involves the addition of fire resisting material and the installation of fire suppression system. There are three regions in aircraft that are more susceptible to fire than others; the engine compartment, cabin area, and any place where electrical wiring is placed. Designing the fire proofing does not require much mathematics, but instead, compliance with applicable federal regulations requires a demonstration. The designer should scout the numerous paragraphs that call for fire proofing. These are required in all certification compliance plans.

(3) The Firewall

Piston and turboprop engine mounts comprise a truss structure made from welded Chrome-Molybdenum steel (SAE 4130) that is bolted to the firewall. The firewall

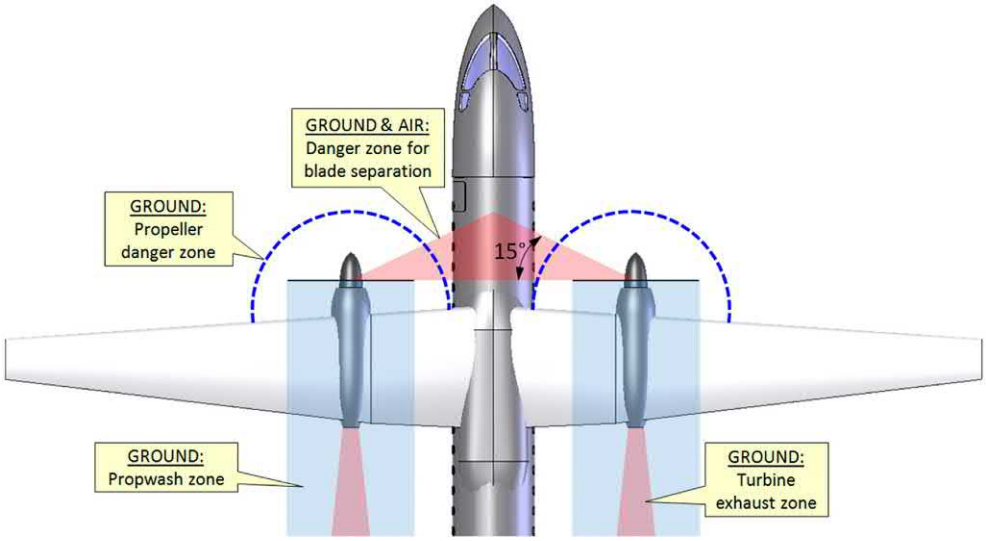


FIGURE 7-13 Danger zones around a typical turboprop.

prevents fire from spreading beyond the engine compartment. The firewall is usually made from stainless steel or other heat resistant material. As an example, 14 CFR §23.1191 exempts the following materials from fire retardation testing:

0.015-in. thick stainless-steel sheet
0.018-in. thick mild steel sheet (coated with aluminum or otherwise protected against corrosion)
0.018-in. thick Terne plate
0.018-in. thick Monel metal
0.016-in. thick Titanium sheet

Steel or copper base alloy firewall fittings are exempt as well. The fire resistance of other materials must be demonstrated, for instance, by showing that a $2000 \pm 150°F$ flame won't burn through it for at least 15 min. The material must also be protected against corrosion.

(4) Danger Zones around Propeller Aircraft

Awareness of engine related danger zones around the aircraft is important. There are two such danger zones; those associated with ground and air operations. These are due to (1) propwash, (2) turbine exhaust (applies to turboprops only), (3) prop strike (a person walking into the prop), and (4) blade separation. These are depicted in Figure 7-13.

Propwash can pick up and blow heavy objects at a person standing behind it. The exhaust zone contains dangerous fumes from the engine that can be harmful if inhaled and can burn a person standing close to the exhaust. Sadly, people walk into rotating propellers several times each year. Blades separating from propeller hubs are rare, but can happen both in flight and, sometimes, during emergency landings when landing gear has failed to extend or lock.

(5) Requirements for Piston Engine Installation

The piston engine installation must meet several requirements:

(1) Be structurally sound enough to react all loads generated by the engine.
(2) Allow for easy access for maintenance.
(3) Allow engine controls to be easily routed to and from the engine. This includes the electrical system, fuel lines, and engine controls.
(4) Must be fire resistant.
(5) Propeller must be type certified and be free of vibration.

The loads generated by the engine installation are primarily inertia loads and loads generated by the engine itself (due to thrust and gyroscopic moments). GA aircraft certified to the "old" 14 CFR Part 23 must react installation loads per 14 CFR §23.901(b) (thrust) and §23.361, *Engine torque*, and §23.363, *Side load on engine mount*. If certified to the "new" 14 CFR Part 23, paragraph §23.2225, *Component loading conditions*. In general, the engine installation must react the worst of the following loads:

(1) Simultaneous application of max T-O thrust, torque, and 75% of the limit load factor (see Table 1-2 for load factors).
(2) Simultaneous application of max continuous thrust, torque, and 100% of the limit load factor.
(3) For turboprops, to account for a sudden malfunction (e.g., quick feathering), the simultaneous application of max T-O thrust, torque, and 1 g load, multiplied by 1.6.
(4) For turbine engine installations, torque due to sudden engine stoppage (such as compressor jamming) or maximum acceleration of the engine.

(5) For all engine types, account for a lateral loading by multiplying engine weight by $n_1/3$, where n_1 is the limit load factor, with a minimum value of 1.33.

When determining the torque in (1) and (2), the appropriate mean torque must be multiplied by 1.25 for turboprops, 1.33 for pistons with 5 or more cylinders, and (6–$N_{cylinder}$) for pistons with less than five cylinders. These loads are applied at the CG of the engine, except propeller thrust (and normal force), which is applied at the hub, as shown in Figure 7-14.

(6) Systems Integration

Figure 7-15 shows a typical installation of a small piston engine and identifies several different systems required to operate the engine. Note the number of perforations that must be made through the firewall. For typical piston engine installations, provisions must be made for the following instruments:

(1) Oil pressure gage.
(2) Oil temperature gage.
(3) Tachometer (RPM indicator).

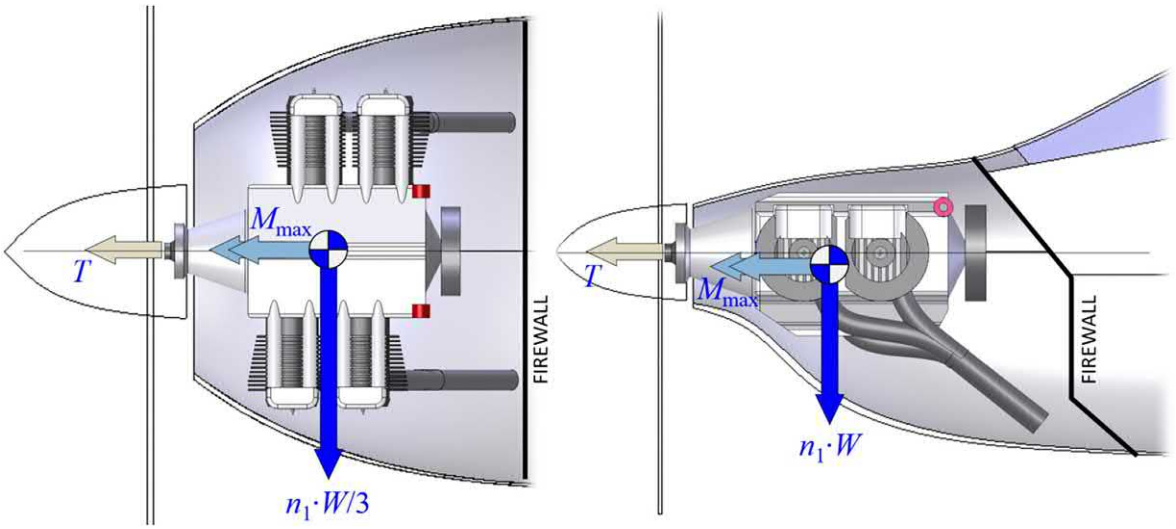


FIGURE 7-14 Application of engine loads to the CG and the propeller hub.

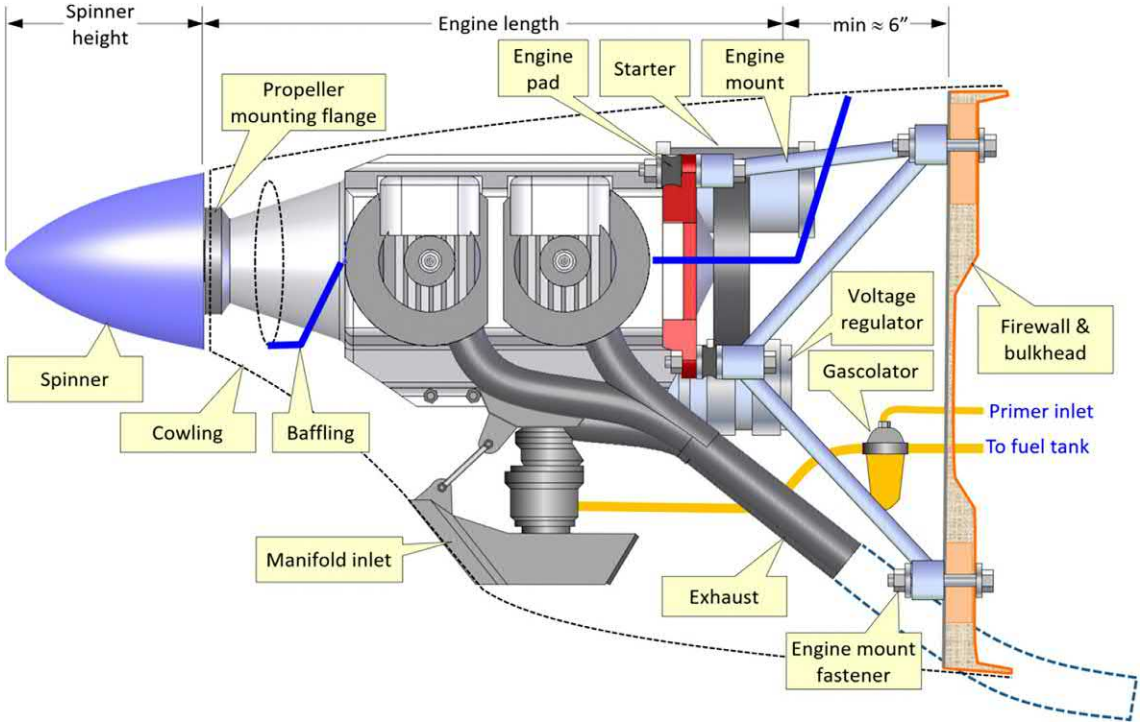


FIGURE 7-15 A typical piston engine installation.

(4) Manifold Pressure gage (MAP—often omitted for low powered engines).
(5) Fuel tank quantity gages.
(6) Fuel-flow indicator (omitted for low performance aircraft).
(7) Hobbs indicator (shows the number of hours on the engine).

These call for electrical connectors and instruments to be mounted on either side of the firewall. Additionally, the following electrical and fuel related equipment must be accounted for:

(1) Starter and ignition switch wiring.
(2) Battery, which is often inside the engine compartment, unless it serves a secondary purpose as ballast.
(3) Voltage regulator.
(4) Primer inlet and fuel lines.
(5) Mixture control.
(6) Throttle control.
(7) Carburetor heat control unless the engine features fuel-injection technology.

(7) Types of Engine Mounts

There are three common ways of mounting a piston engine to an airplane. *Dynafocal mounts* arrange the fastener pattern such that the fasteners point toward the CG of the engine. This reduces engine vibration but requires the engine mount and motor pads to be welded at an angle, making their fabrication harder. *Conical mounts* align the fasteners parallel to the crankshaft, while b*ed mounts* align the fasteners perpendicular to the crankshaft (see Figure 7-16).

(8) Fuel System

A typical fuel system layout for a low wing high performance pistonprop is shown in Figure 7-17. Normally, there are two fuel tanks, one in each wing. Float-type sensors in each tank detect remaining fuel quantity. The fuel is gravity fed from each tank into special *collector tanks*. They prevent drop in fuel pressure (fuel starvation) when the aircraft is maneuvered, as this might interrupt the engine operation.

Since the collector tank is below the engine, its content must be pumped to the engine's injector manifold, where it is delivered to individual cylinder. Two fuel pumps are used for this purpose—one is driven directly by the engine and the other is electric (called a *booster pump*) and is used when starting the engine and during critical operations, such as T-O and landing. It is also used for vapor suppression during climb and is left on for up to 30 min once the plane levels off for cruise. The pumps draw fuel from the collector tank selected by the pilot. Excess fuel not used in the manifold is returned to the selected fuel tank.

The operation of the fuel system in small aircraft requires proper venting. If venting were not provided, the pressure in the tank would reduce as the fuel is consumed. Eventually this would degrade fuel-flow and lead to fuel starvation and engine stoppage. Additionally, the tank might collapse due to the difference in tank and outside pressure. The fuel vents ensure ambient pressure is provided no matter the fuel quantity. This is often done by exposing a vent line to stagnation pressure port to help pressurize the tank to maintain suitable fuel-flow. Pressurized fuel systems are beyond the scope of this book and interested readers can refer to refs. [29, 30].

7.2.7 Piston Engine Inlet and Exit Sizing

The inlet and exit must promote enough engine cooling while minimizing cooling drag. In the spirit of ref. [31], *cooling drag* is defined as the difference in drag of the aircraft with and without the complete engine installation. The installation should permit the aircraft to achieve its maximum performance, while providing maximum service life [32]. The size of the inlet and exit depends on the engine's cooling requirements. The airflow into and out of the engine compartment is highly turbulent and is subject to loss in pressure recovery (see Section 14.2.3), heat transfer, and pressure drop as it is forced through the radiator (or cylinder cooling fins). Examples of typical inlets are shown in Figure 7-18.



FIGURE 7-16 Conical and bed mounts.

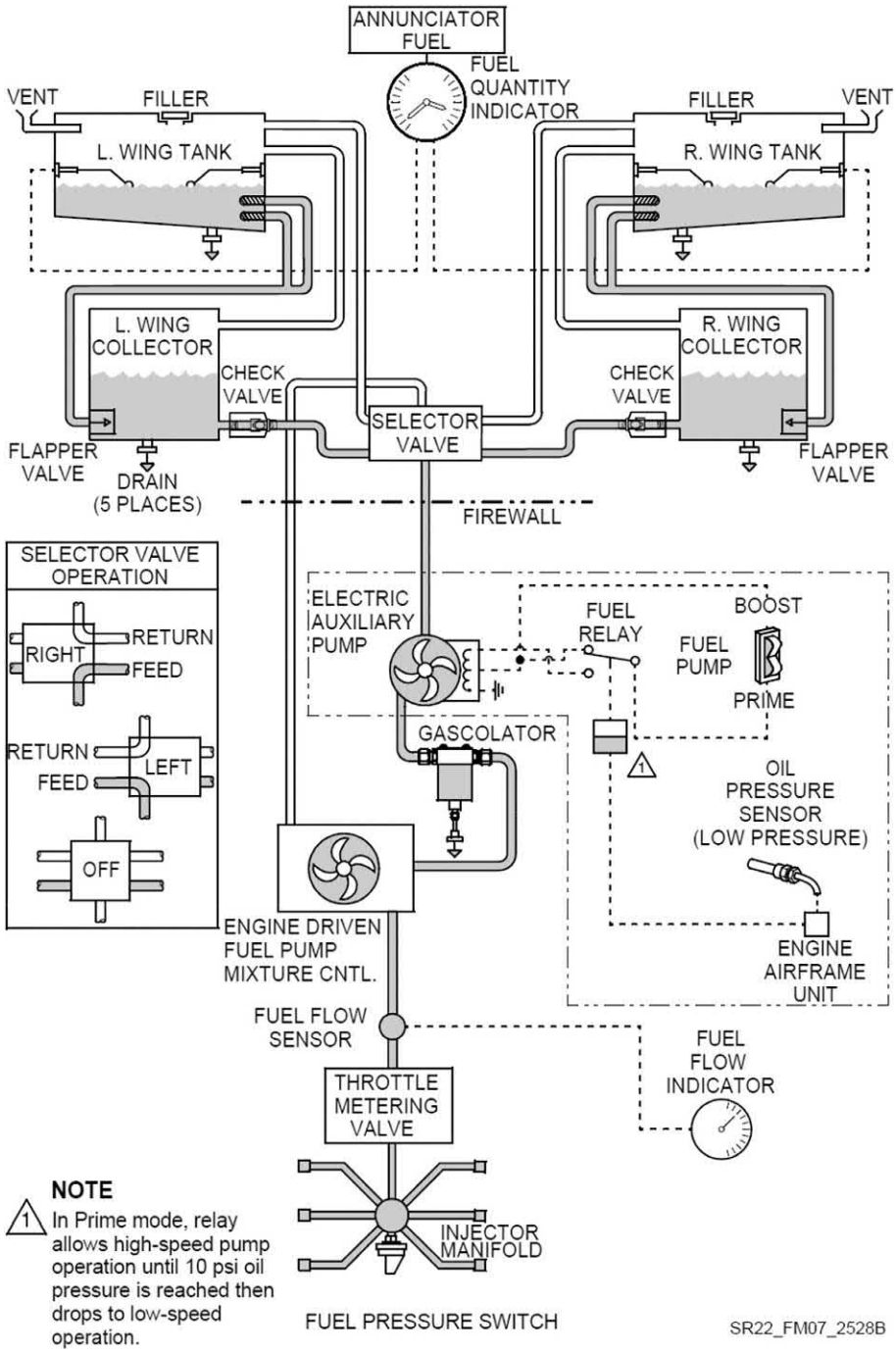


FIGURE 7-17 The fuel system for a single piston engine high performance aircraft. *Copyright 2021 Cirrus Aircraft or its Affiliates. All Rights Reserved. Image reproduced with the permission of Cirrus.*

(1) Basics of Operation

The cooling method introduces air through a front facing inlet and directs it around the cylinders using thin panels called *baffles*. The baffles ensure that the incoming air flows around the cylinder cooling fins by blocking other paths. The baffles split the compartment into an *upper* and *lower plenum*.

Refer to Figure 7-19. ① The cooling air in the far-field has pressure head that equals the dynamic pressure, q. ② The cooling air is captured by the inlet and directed into the upper plenum, usually with some loss in pressure recovery. A propeller operating in front of the inlet boosts the pressure head. ③ If the upper plenum was impermeable and pressure recovery was perfect, stagnation pressure would build up (and $V \rightarrow 0$). However, the loss in pressure recovery affects the magnitude of the pressure in the upper plenum. Throughflow requires higher pressure there than in the lower plenum.



FIGURE 7-18 Engine inlets for selected aircraft. *Photos by Phil Rademacher.*

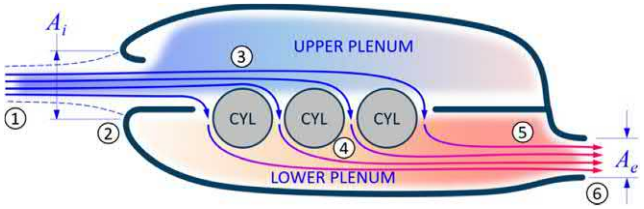


FIGURE 7-19 Operation of an inlet/exit. *Based on Miley, S.J., Cross, E.J., An Experimental Investigation of the Aerodynamics and Cooling of a Horizontally-Opposed Air-Cooled Aircraft Engine Installation, NASA CR-3405, National Aeronautics and Space Administration, 1981.*

④ Air flows between cylinder fins, heats up, and carries away thermal energy. In the process, its density is reduced. ⑤ The warmer air accelerates through the exit, such its static pressure equals that of the local external flow ⑥. If the pressure in this region is high, then throughflow slows and cooling suffers.

(2) Updraft and Downdraft Cooling

Tractor and pusher aircraft configurations predominantly cool engines using an *updraft* or *downdraft* methodology, illustrated in Figures 7-20 and 7-21, respectively. It is a drawback of updraft cooling for single engine tractor configurations, that if an engine failure is accompanied by oil leak, it may cover the windscreen (assuming the configuration in Figure 7-20). Updraft cooling invites an inlet placement that contains the cowling's stagnation front. This means an inlet below the propeller, which may require transposed upper and lower plenums. A wing mounted nacelle would permit the exit to be placed in the low-pressure region of the wing, which would help draw air through the engine compartment, improving cooling. This might eliminate the need for a cowl flap [33]. Flight Design's series of LSAs feature cooling inlets of this nature, although it adheres to the downdraft philosophy [34] (see lower left photo in Figure 7-18).

It is a drawback of downdraft cooling that if the exit is located in a high-pressure region on the bottom side of a fuselage or nacelle. This can be detrimental to the cooling. It is an advantage that it is a better fit for standard engine exhaust stacks. Modern piston engine design favors this philosophy. Several additional, detail-dependent pros and cons are provided in [35].

(3) Design Guidelines

Refs. [32, 33, 36–38] provide excellent guidance for the design of the inlet and exit of piston engine installations. The following summarizes these.

The design should reflect critical cooling conditions: (A) High engine power on a hot day, (B) during climb,

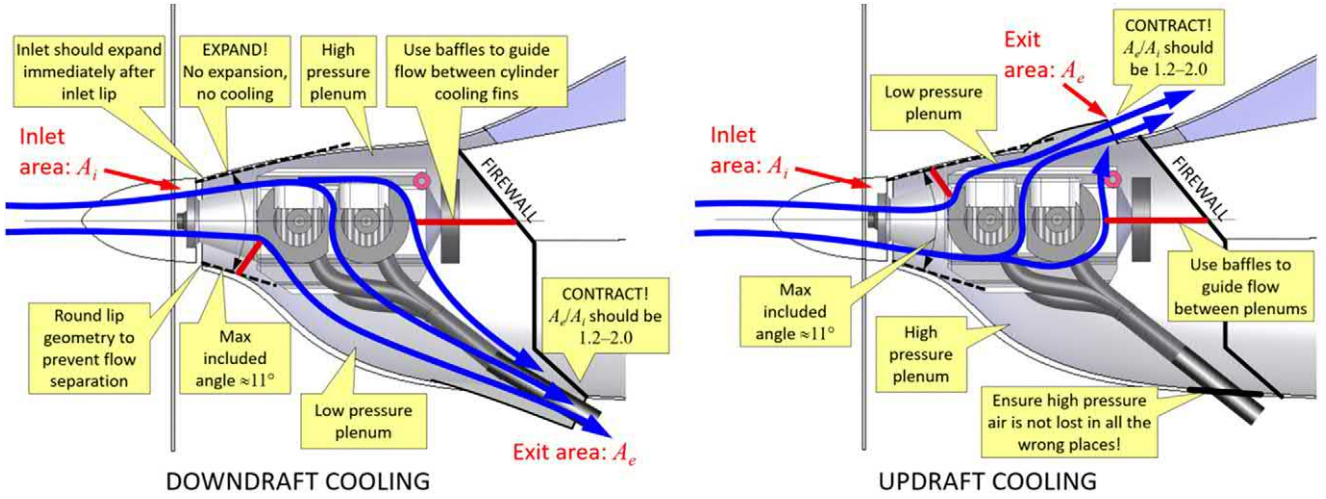


FIGURE 7-20 Airflow through a conventional tractor engine installation.

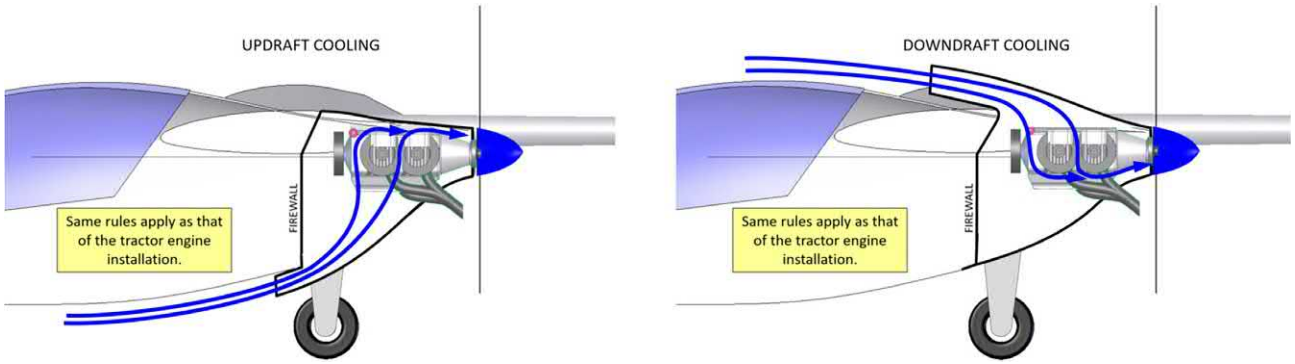


FIGURE 7-21 Airflow through a conventional pusher engine installation.

and (C) during cruise when leaning *rich-of-peak* or during cruise let-down. Cylinders farther from the inlets tend to get the warmest. The inlet must (A) function over the range of operational AOA, (B) recover the available dynamic pressure, and (C) convert it into upper plenum pressure [38]. The inlet size, which is usually fixed, should permit enough mass flow to satisfy the engine's cooling requirements. A common pressure recovery in airplane piston engine cowling inlets is of the order of 60% to 80%, based on airspeed.

A broad suggestion by Becker [39], states that the exit opening should be designed such the static pressure of the internal flow at the outlet should equal that of the external flow just outside the outlet. The variation in airspeeds and AOA makes this hard because it changes local pressures near typical exit locations. A common solution is a variable exit area using a *cowl-flap*. It allows the pilot to change the exit area on demand. Of course, there is a drawback—added system. Low-power engines usually get by with fixed inlets and exits. The exit-to-inlet area ratio (A_e/A_i) varies from one installation to another. An example in ref. [32] yields $A_e/A_i = 1.1$, while Example 7-5 yields about 2.03. Similar ratio (≈ 2) for a fixed A_e/A_i is suggested in ref. [35]. This range can justify a cowl-flap. When the airspeed is high, such as during cruise, the required exit area is small. When the airspeed is low, a larger area is required. The cost of incorrectly sized inlet and exit is higher cooling drag.

The cooling of pusher configurations can be problematic, as the fuselage geometry often requires cooling air to be introduced through curved ducts, besides ingesting air with reduced boundary layer energy. The designer should anticipate this possibility up front and consider scoop type inlets that maximize pressure recovery.

Consider the three extreme inlets in Figure 7-22. The leftmost is an engine without a cowling. It can be regarded as the largest possible "inlet." It results in excessive drag without any cooling benefits. The center inlet is tiny and would cause engine overheating because of insufficient mass flow through the engine compartment. The rightmost inlet is "practical" and provides adequate cooling at most operating conditions. While generating more drag than the center inlet, this is justifiable because of its cooling capability. A proper sizing of the cooling air exits should account for the presence of other heat exchangers, such as oil coolers, intercoolers, and cabin air heaters. Now, two methods to estimate engine cooling will be presented.

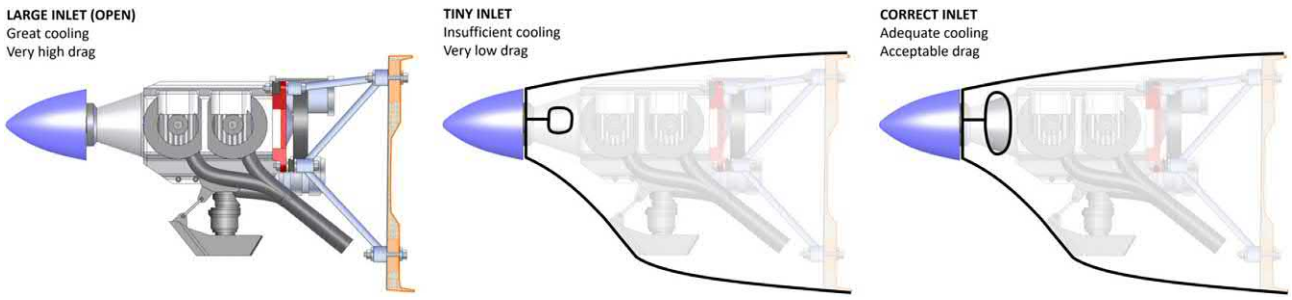


FIGURE 7-22 Extreme inlet sizing.

(4) Method 1: Inlet-Exit Dependent Heat Transfer

This method assumes that the heat transfer requirement of the engine is known and that the $A_e = 1.2$ to $2.0 \times A_i$. Furthermore, assume that mass is conserved in the flow. The heat carried away by the air flowing out of the engine compartment can be found from:

$$\dot{Q} = \dot{m} \cdot C_p \cdot \Delta T \tag{7-19}$$

where $\dot{m} = \rho V_\infty A_i$ = mass flow of air exiting the engine compartment, A_i = area of the inlet, C_p = specific heat of pressure for air (1000 J/(kg · K) for air), V_∞ = far-field airspeed, ΔT = rise in temperature as it flows through the engine compartment, ρ = density of air. The heat transfer through the exit is given by:

$$\dot{Q} = \dot{m} \cdot C_p \cdot \Delta T = \rho_e V_e A_e \cdot C_p \cdot \Delta T \tag{7-20}$$

where V_e is the engine compartment exit airspeed, A_e is exit area, and ρ_e is density of air at the exit. This can be used to solve for A_e, which then can be used as the inlet area, A_i:

$$A_e = 1.2A_i = \frac{\dot{Q}}{\rho_e V_e \cdot C_p \cdot \Delta T} \tag{7-21}$$

The resulting area depends on the exit airspeed, V_e. For initial work, this can be assumed to equal V_∞.

EXAMPLE 7-4

The installation manual for a Rotax 912 four-stroke aircraft piston engine states it recommends a radiator capable of transferring 28 kW of thermal energy. If air warms up by 50 K as it flows through the radiator, size the exit area as a function of the airspeed through it in m/s. How large must the exit area be for a cruising speed of 50 m/s and during climb at 30 m/s? Account for the density of the heated air and assume standard day at sea-level.

SOLUTION:

The heat to be carried away by air amounts to $\dot{Q} = 28000$ *W*. Thus, we can write:

$$\dot{Q} = \dot{m} \cdot C_p \cdot \Delta T = \rho_e V_e A_e \cdot C_p \cdot \Delta T$$

We determine density of the exit air using the ideal gas law:

$$\rho_e = \frac{p_o}{R(T_o + \Delta T)} = \frac{101325}{(287)(288.15 + 50)} = 1.044 \ \frac{\text{kg}}{\text{m}^3}$$

Solve for A_e:

$$A_e = \frac{\dot{Q}}{\rho V_e \cdot C_p \cdot \Delta T} = \frac{28000}{(1.044)V_e(1000)(50)} = \frac{0.5364}{V_e} \ \text{m}^2$$

At airspeed of 50 m/s the exit area must be 0.01073 m^2 (16.63 in^2).
At airspeed of 30 m/s the exit area must be 0.01788 m^2 (27.71 in^2).

(5) Method 2: Inlet-Radiator-Exit Method

The following method is attributed to Lycoming [32] and is also presented in ref. [40]. It is helpful when sizing inlet and exit areas. Its primary drawback is its reliance on engine manufacturer's data, which, unfortunately, is not always available. The piston engine (or a heat exchanger, such as a radiator) is analyzed based on the idealized configuration of Figure 7-23.

The engine is idealized as a system of *inlet-radiator-exit*. It is assumed that adiabatic compression and expansion of air takes place inside the inlet and exit, shown in Figure 7-24. The inlet and exit are idealized as a diffuser and nozzle, which correspond to the upper and lower plenums, respectively. However, the standard flow equations do not apply to the flow through the radiator itself. In fact, both pressure and airspeed drop through the radiator (whereas we would expect one to increase and the other to decrease using

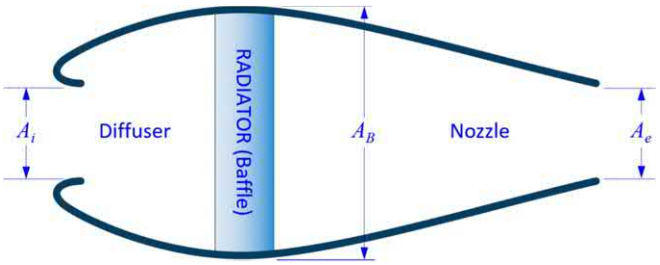


FIGURE 7-23 Idealization of a conventional engine installation.

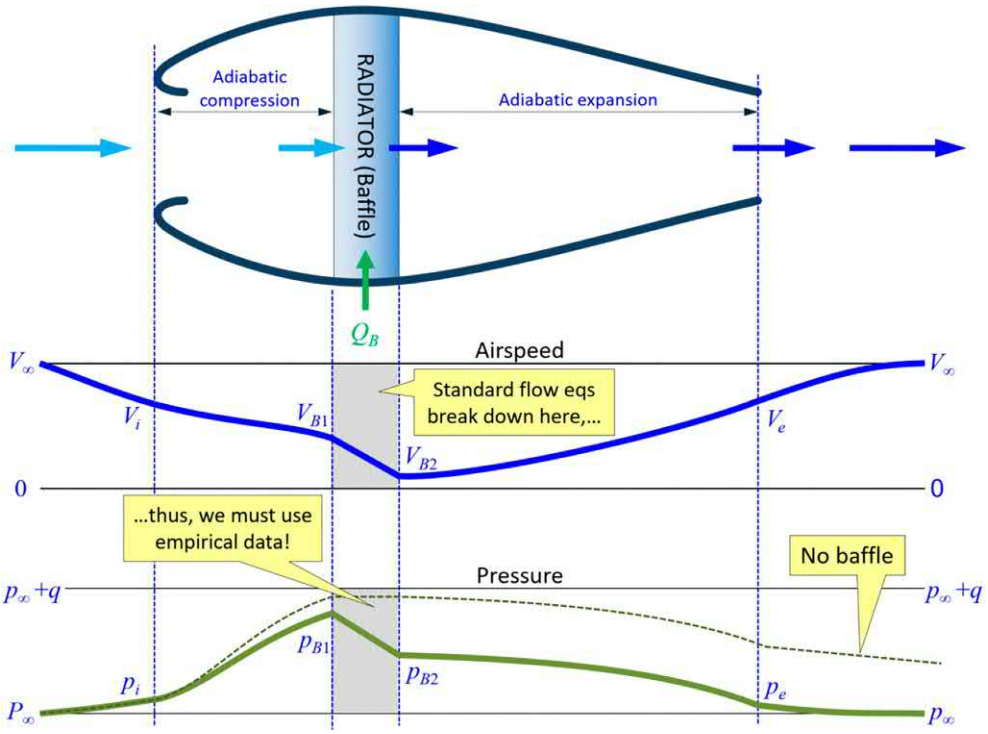


FIGURE 7-24 Changes in speed and pressure as air flows through engine installation (drop and rise in airspeed and pressure is not to scale).

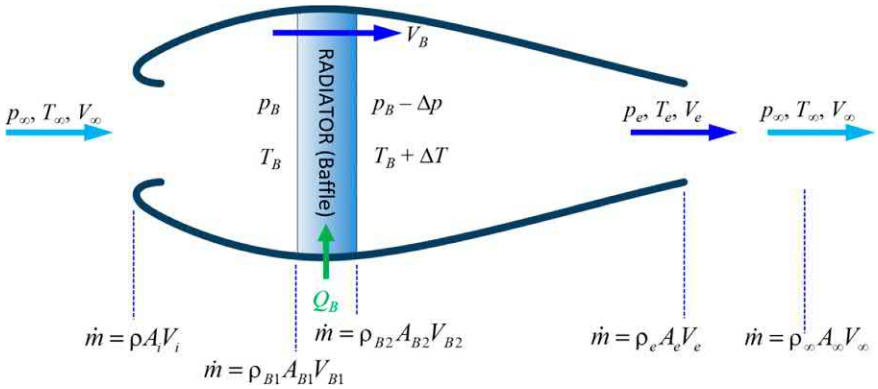


FIGURE 7-25 Flow requirements that must be met.

conventional flow equations). The flow through the radiator is highly turbulent, as it slows down and absorbs thermal energy. The flow condition at the aft face is estimated using empirical information provided by the engine manufacturer.

Figure 7-25 shows the model with the flow properties of interest identified at each station. The flow properties are estimated up to the front face of the radiator assuming an adiabatic compression and based on the flow conditions upstream. Flow properties up to the aft face of the radiator are estimated this way as well, using the downstream conditions. To tie the two together requires the change across the radiator to be known. This information must be provided by the engine manufacturer. The temperature and pressure in an adiabatic compression or expansion are estimated using isentropic flow relations:

$$\frac{p}{p_0}=\left(\frac{T}{T_0}\right)^{\frac{\gamma}{\gamma-1}} \quad \Rightarrow \quad \frac{p}{p_0}=\frac{p_0+kq}{p_0}=\left(\frac{T}{T_0}\right)^{\frac{\gamma}{\gamma-1}} \tag{7-22}$$

where

p and p_0 = Pressure at condition and reference, respectively
T and T_0 = Temperature at condition and reference, respectively
k = Pressure recovery coefficient (1 = complete recovery, 0.5 = 50% recovery, etc.)

The factor k indicates how much of the dynamic pressure is preserved as the speed of the airflow is slowed

down and is an indicator of the efficiency of the diffuser. If $k=0$, there is no recovery and the total pressure remains that of the ambient pressure in the far-field. If $k=1$, there is 100% recovery and all the dynamic pressure is converted into total air pressure without any losses. This is highly desirable.

With the pressure known, the airspeed at condition can be determined using the compressible Bernoulli equation:

$$V=\sqrt{V_0^2+\frac{2\gamma}{\gamma-1}\left(\frac{p_0}{\rho_0}-\frac{p}{\rho}\right)} \tag{7-23}$$

Determining the pressure drop through the radiator is not a simple task. Usually this is done by empirical methods (read "trial and error"). However, the pressure drop across baffle depends on:

$$\Delta p \propto \frac{1}{2}\rho V_{B1}^2 \tag{7-24}$$

The mass flow through the radiator is given by :

$$\dot{m}=\rho A_B V_B \tag{7-25}$$

This implies that the pressure drop is related to the mass flow rate and density as described by the following relationship, which is derived by substituting Equation (7-25) into (7-24):

$$\Delta p \propto \dot{m}^2/\rho \tag{7-26}$$

A_i = Inlet area
V_0 = Far-field airspeed
A_B = Reference area of the baffle (radiator)
V_{B1} = Airspeed in front of the baffle
A_e = Exit area
V_{B2} = Airspeed aft of the baffle
$\dot{m}$ = Mass (or weight) flow rate
V_e = Airspeed at the exit
ρ = Density of air
V_∞ = Airspeed in the streamtube behind the nozzle
T_0 = Far-field temperature
p_0 = Far-field pressure
T_{B1} = Temperature at the baffle forward face
p_{B1} = Pressure at the baffle (radiator) forward face
T_{B2} = Temperature at the baffle aft face
p_{B2} = Pressure at the baffle aft face
T_e = Temperature at the exit
P_e = Pressure at the exit
ΔT = Temperature increase through the baffle
Δp = Pressure-drop through the baffle
T_∞ = Temperature in the streamtube behind the nozzle
p_0 = Far-field pressure
Q_B = Heat flow into heat exchanger

EXAMPLE 7-5

A piston engine is being operated at 10,000 ft and airspeed of 185 KTAS where it delivers 230 BHP. OAT is 30°F above standard temperature. The manufacturer recommends a constant Cylinder Head Temperature (CHT) of 450°F for maximum engine life. Size the inlet and exit area assuming 75% pressure recovery at the radiator and that air temperature rises by 150°F across the cylinders. Estimate how much engine power is lost to cooling.

SOLUTION:

This problem assumes a typical piston engine installation. The pressure drop through the baffle is based on experimental measurements, and requires pressure, temperature, and airspeed to be evaluated at four stations through the inlet, radiator, and nozzle. These are denoted as stations 0, B_1, B_2, and E in Figure 7-26. Also, note that the problem was solved using a calculator with double-floating point accuracy. Therefore, if following along with a calculator, expect minor differences.

STEP 1: Determine conditions at Station 0

Calculate the far-field temperature using the information given in the problem:

$$T_0=518.69(1-0.0000068756\times 10000)+30=513.0\,^\circ\mathrm{R}$$

Calculate pressure at altitude using the hydrostatic gas equation:

$$p_0=2116(1-0.0000068756\times 10000)^{5.2561}=1455\,\mathrm{psf}$$

Calculate density using the ideal gas equation:

$$\rho=\frac{p_0}{RT_0}=\frac{1455}{(1716)(513.0)}=0.001653\ \mathrm{slugs/ft^3}$$

Airspeed: $V_0=185\times 1.688=312.3\,\mathrm{ft/s}$

Thus, we have completely defined p, T, and V in the far-field (Station 0).

STEP 2: Determine conditions at Station B_1

Determine the temperature at the radiator front-face using the adiabatic gas relation of Equation (7-22), assuming an adiabatic expansion inside the diffuser. This allows the flow characteristics at the forward face of the radiator to be determined based on the flight conditions Station 0. Thus, the temperature at the baffle is:

$$\frac{p_0+kq}{p_0}=\left(\frac{T_{B1}}{T_0}\right)^{\frac{\gamma}{\gamma-1}}\ \Rightarrow\ T_{B1}=T_0\left(\frac{p_0+kq}{p_0}\right)^{\frac{\gamma-1}{\gamma}}$$

EXAMPLE 7-5 (*cont'd*)

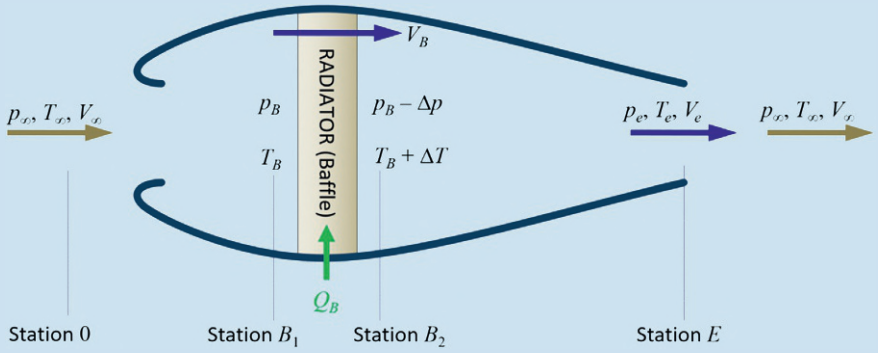


FIGURE 7-26 Definition of stations of interest.

where k is the pressure recovery factor. That said, let's calculate the far-field dynamic pressure to evaluate the impact of the pressure recovery:

$$q = \frac{1}{2}(0.001653)(312.3)^2 = 80.60 \text{ psf}$$

Substituting values (where $k = 0.75$ for 75% pressure recovery):

$$T_{B1} = T_0\left(\frac{p_0 + kq}{p_0}\right)^{\frac{\gamma-1}{\gamma}} = (513.0)\left(\frac{1455 + 0.75(80.60)}{1455}\right)^{\frac{0.4}{1.4}} = 519.0°R$$

This corresponds to 59.4°F. Pressure at the baffle (assuming 75% pressure recovery):

$$p_{B1} = p_0 + kq = 1455 + 0.75 \times 80.60 = 1516 \text{ psf}$$

Calculate density using the ideal gas equation:

$$\rho = \frac{p_{B1}}{RT_{B1}} = \frac{1516}{(1716)(519.0)} = 0.001702 \text{ slugs/ft}^3$$

The airspeed at the radiator can now be calculated from the compressible Bernoulli equation:

$$V_{B1} = \sqrt{V_0^2 + \frac{2\gamma}{\gamma - 1}\left(\frac{p_0}{\rho_0} - \frac{p_{B1}}{\rho_{B1}}\right)} = 159.5 \text{ ft/s}$$

This defines p, T, and V at Station B_1.

STEP 3: Determine conditions at Station B_2

This step relies on information that must be obtained from the engine manufacturer and this typically consists of two graphs similar to the ones shown in Figure 7-27. It is used to determine the conditions on the downstream side of the radiator. Since the temperature and pressure on the upstream side of the radiator has been determined (STEP 2), the pressure altitude must be determined because the graphs of Figure 7-27 depend on this value. The pressure altitude to which this corresponds can be estimated using Equation (16.8):

$$H_P = 145442\left(1 - \left(\frac{p}{p_0}\right)^{0.19026}\right) = 145442\left(1 - \left(\frac{1516}{2116}\right)^{0.19026}\right) = 8947 \text{ ft}$$

Next, determine the pressure loss through the radiator using the left graph of Figure 7-27. Locate 59.4°F on the horizontal axis and move along Arrow ① to the isopleth designated for a CHT = 450°F. Then move along Arrow ② to read 2.7 lb_f/s of required cooling airflow at this condition. This means that 2.7 lb_f of air must flow through the radiator every second to cool the engine. Then, extend the arrow to locate 8947 ft on the right graph (between the 5000 and 10,000 ft curves). Finally, follow Arrow ③ to locate 35 lb_f/ft^2 as the pressure drop across the radiator.

Required cooling airflow:

$$\dot{m} = \frac{2.7 \text{ lb}_f/\text{s}}{32.174 \text{ ft/s}^2} = 0.08392 \text{ slugs/s}$$

Resulting pressure drop:

$$\Delta p = 35 \text{ psf}$$

Pressure downstream of the baffle:

$$p_{B2} = p_{B1} - \Delta p = 1516 - 35 = 1481 \text{ psf}$$

Temperature (+150°F) rise downstream of the baffle:

$$T_{B2} = T_{B1} + \Delta T = 519.0 + 150.0 = 669.0°R$$

It is assumed the speed of air is near zero as it exits the aft face of the radiator. This is based on the speed already being accounted for in the value of the pressure loss, which was empirically determined (by the engine manufacturer). Therefore, we say that $V_{B2} = 0$ ft/s and, thus, claim we have completely defined p, T, and V at Station B_2.

STEP 4: Determine conditions at Station E

The properties at the exit are determined assuming an adiabatic expansion. This requires an additional property at the downstream face of the baffle; the density:

EXAMPLE 7-5 (*cont'd*)

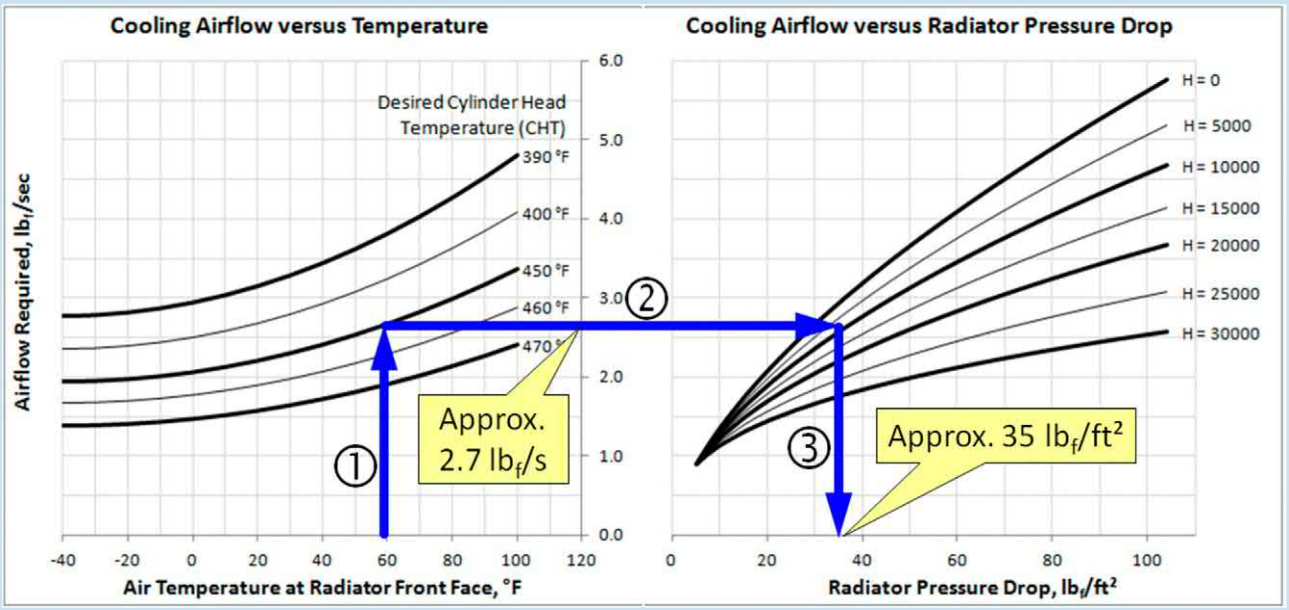


FIGURE 7-27 Special graphs supplied by the engine manufacturer are used to extract the required cooling airflow for the engine. The graphs do not represent any specific engine type.

$$\rho_{B2} = \frac{p_{B2}}{RT_{B2}} = \frac{1481}{(1716)(669.0)} = 0.001290 \text{ slugs/ft}^3$$

The pressure at the exit is assumed to be the atmospheric pressure in the far field. This may not hold for your aircraft. The pressure depends also on whether there is flow separation occurring at the exit, which would lower the pressure and affect our results. However, this is a reasonable first stab assumption if we are cognizant of its limitations and until we can measure it:

$$p_e = p_0$$

The density at the exit can be found from the adiabatic relation:

$$\frac{p_e}{p_{B2}} = \left(\frac{\rho_e}{\rho_{B2}}\right)^{\gamma} \quad \Rightarrow \quad \rho_e = \rho_{B2}\left(\frac{p_e}{p_{B2}}\right)^{\frac{1}{\gamma}}$$

$$\Rightarrow \quad \rho_e = 0.001290\left(\frac{1455}{1481}\right)^{\frac{1}{\gamma}} = 0.001274 \text{ slugs/ft}^3$$

And the airspeed at the exit can be found using the compressible Bernoulli equation:

$$\frac{V^2}{2} + \frac{\gamma}{\gamma - 1}\frac{p}{\rho} = \text{constant}$$

Substituting the above variables leads to:

$$\frac{V_{B2}^2}{2} + \frac{\gamma}{\gamma - 1}\frac{p_{B2}}{\rho_{B2}} = \frac{V_e^2}{2} + \frac{\gamma}{\gamma - 1}\frac{p_e}{\rho_e}.$$

Assuming speed V_{B2} through the baffle to be small:

$$0 + \frac{\gamma}{\gamma - 1}\frac{p_{B2}}{\rho_{B2}} = \frac{V_e^2}{2} + \frac{\gamma}{\gamma - 1}\frac{p_e}{\rho_e} \quad \Rightarrow \quad V_e = \sqrt{\frac{2\gamma}{\gamma - 1}\left(\frac{p_{B2}}{\rho_{B2}} - \frac{p_e}{\rho_e}\right)}$$

The airspeed at the exit comes to:

$$V_e = \sqrt{\frac{2\gamma}{\gamma - 1}\left(\frac{p_{B2}}{\rho_{B2}} - \frac{p_e}{\rho_e}\right)}$$

$$= \sqrt{\frac{2(1.4)}{1.4 - 1}\left(\frac{1487}{0.001295} - \frac{1455}{0.001275}\right)} = 199.3 \text{ ft/s}$$

Temperature at the exit:

$$T_E = T_{B2}\left(\frac{P_E}{P_{B2}}\right)^{\frac{\gamma - 1}{\gamma}} = (669.0)\left(\frac{1455}{1481}\right)^{\frac{0.4}{1.4}} = 665.7°\text{R}.$$

Now we have enough information to size the inlet area:

$$\dot{m} = \rho_0 V_0 A_{IN} \quad \Rightarrow \quad A_{IN} = \frac{\dot{m}}{\rho_0 V_0}$$

$$\Rightarrow \quad A_{IN} = \frac{2.7/32.174}{(0.001653)(312.3)} = 0.163 \text{ ft}^2$$

And the outlet area:

$$\dot{m} = \rho_e V_e A_e \quad \Rightarrow \quad A_e = \frac{\dot{m}}{\rho_e V_e}$$

$$\Rightarrow \quad A_e = \frac{2.7/32.174}{(0.001274)(199.3)} = 0.331 \text{ ft}^2.$$

EXAMPLE 7-5 *(cont'd)*

An area corresponding to about 5×5 in^2 suffices for an inlet and 6×6 in^2 for the exit at this airspeed. This flight condition does not dictate the final size of the inlet or exit and other flight conditions; ones involving low airspeed must be evaluated in this fashion as well. The results are shown graphically in Figure 7-28.

In this example it is assumed air temperature rises by 150°F across the cylinders. Let us see how much power this corresponds to (units for C_p are ft/lb$_f$/slug/°R):

$$\dot{Q} = \dot{m} c_p (\Delta T) = \left(\frac{2.7}{32.174}\right)(6000)(150) = 75527 \text{ ft} \cdot \text{lb}_f/\text{s}$$

In horsepower: $\dot{Q} = \dfrac{75527}{550} = 137.3$ *BHP*.

This is about 57% of the engine power. Generally, expect this to range between 40% and 50% (per ref. [40]). This example does not represent an existing engine model.

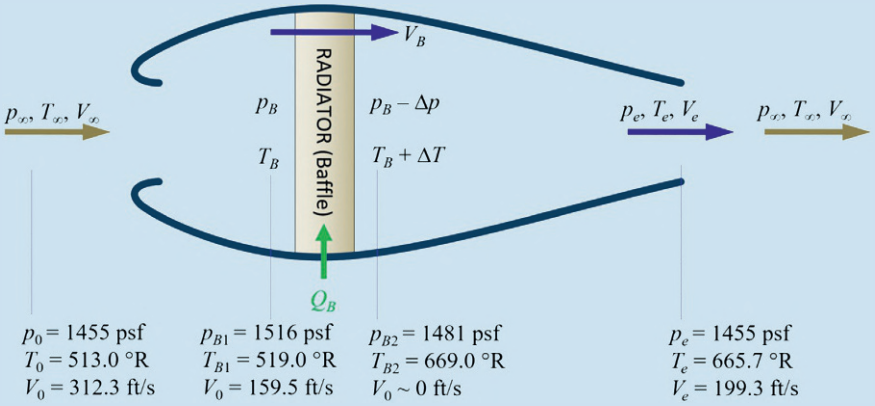


FIGURE 7-28 All properties are defined at the four stations of interest.

7.3 GAS TURBINE ENGINES

A gas turbine is an engine that develops propulsive thrust by compressing a gas (air) before mixing it with fuel and igniting it to increase its energy, directing it to rotate a turbine do drive the compressor. There are four types of gas turbines used to propel aircraft:

- *Turboshaft* is a gas turbine that delivers engine power through a shaft that is connected to an external machine. Turboshafts are commonly used in helicopters to drive the rotor and tail rotor. Turboshafts are omitted from this discussion.
- *Turboprop* can be considered a specialized turboshaft, on to which a special gearbox is mounted to power a propeller. Most of the thrust is developed by the propeller, however, there is a small contribution by the exhaust jet. Turboprops are discussed in Section 7.3.1.
- *Turbojet* is a gas turbine that develops thrust by ejecting the combusted mixture of air and fuel through a specially shaped nozzle that increases exit velocity. Turbojets are discussed in Section 7.3.2.
- *Turbofan* is a gas turbine that develops thrust by partially directing airflow through a combustion sequence (like a turbojet) and by bypassing the remaining airflow around the engine. Turbofans are discussed in Section 7.3.3.

7.3.1 Topics Specific to Turboprops

(1) Pros of Turboprop Engines

Compared to piston engines, the turboprop packs a lot of power per unit weight. Per Figure 6-7 the power-to-weight ratio of modern turboprops ranges between 2.3 and 2.7 SHP/lb$_f$ (1.5 and 1.7 SHP/lb$_f$ for engines developed between the 1950s and 1970s. This compares very favorably to the 0.45 to 0.7 BHP/lb$_f$ range for the typical piston engine (see Figure 6-6). The following advantages apply: (A) smooth, vibration-free operation; (B) very reliable with high *time-between-overhaul* (TBO) between 3000 and 6000 h [41]; (C) large power-to-volume ratio; (D) permit clean aerodynamic installation; (E) efficient at high altitudes, (F) permits high airspeed. Figure 7-29 shows a typical single-engine turboprop installation in an agricultural aircraft.

(2) Cons of Turboprop Engines

(A) Expensive to acquire, operate, and maintain, in part due to expensive heat tolerant alloys; (B) high fuel



FIGURE 7-29 A typical installation of a turboprop on an agricultural aircraft (Air Tractor AT-802). The comparative light weight of a gas turbine requires it to be mounted far ahead of the wing. *Photo by Phil Rademacher.*

consumption at low airspeeds and altitudes; (C) high RPM requires gear box for propellers; (D) noisy, albeit less so than the turbojet; (E) emit environmentally harmful contaminants; (F) sonic propeller-tip Mach number when flight speed approaches $M_\infty \approx 0.7$ [42].

(3) Thrust Modeling for Turboprops

A thrust model for turboprops, based on the method of Mattingly [43], is presented in Section 14.3.2. This model only requires a knowledge of static thrust and not propeller geometry. Thus, for consistency, it is appropriate to present it in Chapter 14. A separate thrust model is presented in Chapter 15. That method makes specific assumptions about the behavior of the propeller thrust and couples this with the static thrust per the Rankine–Froude momentum theory.

(4) Shaft Horsepower (SHP, P_{SHP})

Refers to the amount of power delivered at the propeller shaft of a gas turbine. When driving a propeller, a gear reduction drive is required to reduce the RPM to keep propeller tip airspeed subsonic. This drive is called *Propeller Speed Reduction Unit* (PSRU) and absorbs a small percentage of the available power due to losses in the mechanism.

(5) Equivalent Horsepower (EHP, P_{EHP})

Applies only to turboprops and refers to the combination of the SHP and the residual thrust available from its jet exhaust. The EHP is usually about 5% higher than the SHP.

(6) Typical Fuel Consumption

Table 7-9 shows the typical specific fuel consumption of selected turboprop engines.

(7) Thrust Horsepower (THP, P_{THP})

Sometimes it is helpful to convert the thrust into horsepower, for instance, to compare the effective power of a piston or a turboprop to that of a turbofan. This is done

TABLE 7-9 Typical T-O power and SFC of selected turboprop engines [44].

Engine type	Weight, dry	Prop RPM	T-O power rating[a]	SFC (T-O)
Garrett TPE331-10	380 lb_f 172 kg	–	1000 SHP 746 kW	0.560 lb_f/(SHP•h) 0.254 kg/(SHP•h)
Garrett TPE331-5/6	360 lb_f 163 kg	–	840 SHP 626 kW	0.626 lb_f/(SHP•h) 0.284 kg/(SHP•h)
Motorlet Walter M 601B	425.5 lb_f 193 kg	2450	691 SHP 515 kW	0.656 lb_f/(EHP•h) 0.298 (kg/(EHP•h)
Motorlet Walter M 601E	425.5 lb_f 193 kg	2450	751 SHP 560 kW	0.649 lb_f/(EHP•h) 0.294 (kg/(EHP•h)

TABLE 7-9 Typical T-O power and SFC of selected turboprop engines [44]—cont'd

Engine type	Weight, dry	Prop RPM	T-O power rating[a]	SFC (T-O)
Pratt & Whitney Canada PT6A-11	314 lb_f 142.4 kg	2200	528 EHP 373 kW	0.647 lb_f/(EHP•h) 0.293 (kg/(EHP•h)
Pratt & Whitney Canada PT6A-21	316 lb_f 143.3 kg	2200	580 EHP 410 kW	0.630 lb_f/(EHP•h) 0.286 (kg/(EHP•h)
Pratt & Whitney Canada PT6A-34	320 lb_f 145.1 kg	2200	783 EHP 559 kW	0.595 lb_f/(EHP•h) 0.270 (kg/(EHP•h)
Pratt & Whitney Canada PT6A-41	391 lb_f 177.3 kg	2000	903 EHP 634 kW	0.591 lb_f/(EHP•h) 0.268 (kg/(EHP•h)
Pratt & Whitney Canada PW118	861 lb_f 391 kg	1300	1892 EHP 1342 kW	0.498 lb_f/(EHP•h) 0.226 (kg/(EHP•h)
Pratt & Whitney Canada PW120	921 lb_f 417.8 kg	1200	2100 EHP 1491 kW	0.485 lb_f/(EHP•h) 0.220 (kg/(EHP•h)
Pratt & Whitney Canada PW123	992 lb_f 450 kg	1200	2502 EHP 1775 kW	0.470 lb_f/(EHP•h) 0.213 (kg/(EHP•h)
Pratt & Whitney Canada PW127	1060 lb_f 480 kg	1200	2880 EHP 2051 kW	0.459 lb_f/(EHP•h) 0.208 (kg/(EHP•h)
WSK-PZL TVD-10B	507 lb_f 230 kg	–	1011 SHP 754 kW	0.570 lb_f/(SHP•h) 0.258 (kg/(SHP•h)
Rolls-Royce Dart 535	1340 lb_f 607 kg	1395	2080 SHP 1551 kW	0.615 lb_f/(SHP•h) 0.279 (kg/(SHP•h)
Rolls-Royce Dart 536	1257 lb_f 569 kg	1395	2120 SHP 1580 kW	0.615 lb_f/(SHP•h) 0.279 (kg/(SHP•h)

[a] *EHP≈1.05•SHP.*

by multiplying the thrust (T) of the turbofan (or turbojet or pulsejet, etc.) with the airspeed (V_∞) at which it is flying. If working in the UK system, the thrust is given in lb_f and the airspeed in ft/s. Thus, the unit for power is ft·lb_f/s, which can be converted to horsepower (i.e., THP) by dividing the product by 550. In the SI system, thrust is in N and airspeed in m/s. The unit for power is watts (W), which is converted to SHP by dividing the product by 746:

UK system (T in lb_f, V_∞ in ft/s):

$$P_{THP} = TV_\infty/550 \text{ [THP]} \tag{7-27}$$

SI system (T in N, V_∞ in m/s):

$$P_{THP} = TV_\infty/746 \text{ [THP]} \tag{7-28}$$

The thrust of turbojets, turbofans, pulsejets, and rockets is generated by accelerating the fluid directly. Such engines are always rated in terms of the maximum thrust generated. This contrasts pistonprops, turboprops, and electroprops, whose mechanical work rotates a propeller, which then creates the thrust. Thus, it is more appropriate to rate such engines in terms of power: one can mount two different propellers on the same engine and generate two different levels of thrust at the same power level.

(8) Airspeed and Altitude Effect on Turboprop Power

Mair and Birdsall [45] present the effect of altitude and airspeed on turboprop power rather than thrust using the following expression:

$$\frac{P}{P_{SL}} = AM_\infty^n \tag{7-29}$$

where

A = Engine dependent constant,
P = Power at (the atmospheric) condition,
n = Engine dependent constant.
P_{SL} = Power setting at S-L,
M_∞ = Engine dependent constant.

The engine dependent constants A and n must be selected based on engine data provided by the engine manufacturer. The designer should request power output at specific altitudes and Mach Numbers and use this to determine both constants. The constant n is a fraction between 0 and 1, and it is often close to 0.5. It reflects

the fact that the available shaft power increases with ram pressure in the engine intake.

(9) Engine Torque and Turboprop Engines

The power output of turboprop aircraft is often represented using torque and RPM, rather than horsepower. Consequently, when considering performance data for turboprop aircraft, it is often helpful to convert the torque and RPM into horsepower.

Torque is equivalent to work (*force* × *distance*), whereas power is *force* × *speed*. Thus, torque is *power* × *time* (alternatively, power is torque divided by time). Consider an arm of length r rotating at rate RPM due to a force F. Thus, the work done each minute by the force F is the product of it and the distance over which it is applied. The distance covered during each rotation is $2\pi r$. For rotary motion, this can be written as $F \cdot 2\pi r \cdot RPM$. If we use the UK system of units, the units are in terms of $ft \cdot lb_f/min$. We can convert this to horsepower by dividing by $33{,}000\,ft \cdot lb_f/min$, yielding the following relationship:

To convert torque and RPM to SHP:

$$SHP = \frac{torque \times 2\pi \times RPM}{33000} = \frac{torque \times RPM}{5252} \qquad (7\text{-}30)$$

As an example, a turboprop operating at a torque of $1500\,ft \cdot lb_f$ and 2000 RPM delivers 571 SHP of power.

Since the gas turbine rotates at high rate (often in the 20–40,000 RPM), a gear reduction drive is required to reduce the rotation rate of the propeller. Turboprops are very reliable and generate ample power at high altitudes (where the fuel consumption is reduced). These qualities explain their great popularity among domestic and utility aircraft. Aircraft can fly into small and sometimes unimproved strips and then take-off and climb to altitudes above weather.

(10) Turboprop Inertial Separators

A rotating propeller can throw up a cloud of dust and particles on the ground. This can be sucked into the gas turbine and damage it. Many turboprops feature an inertial separator for maneuvering at low speeds on the ground. An inertial separator constitutes an inlet geometry that features a sharp turn that cannot be made by heavier particles. These get separated from the airstream and are ejected out of the inlet.

7.3.2 Topics Specific to Turbojets

There are four types of *jet engines*: the rocket, ramjet, pulsejet, and gas turbine jet. While the turbojet is rarely used for certified GA aircraft, there are a few such installations in experimental aircraft and UAVs. Turbojets were used up to and including third-generation fighters (1970s designs). Today, turbojets are primarily used for unmanned aircraft, military target aircraft, and experimental homebuilt aircraft.

(1) Characteristics of Flow through a Turbojet

Figure 7-30 shows the change in total pressure and Mach number of air flowing through a theoretical turbojet. The rise in total pressure of air flowing through the compressor is clearly visible, with the associated drop in Mach number. The speed of the air is constant, but the rise in temperature increases the speed-of-sound, causing the Mach number to drop. The flow through the diffuser between stations 3 and 4, further reduces the speed of the flow. This reduction in velocity is important to prevent flameout inside the combustion chamber. The total pressure drops rapidly between stations 5 and 6, as the combusted mixture of air flows out of the combustion chamber and loses energy to the turbine. If the aircraft travels at subsonic speeds, this air is ejected close to Mach 1 to maximize thrust. If the aircraft is to travel at supersonic speeds, this flow must be accelerated to an even higher speed. This is accomplished using a converging–diverging nozzle (aka ConDi nozzle).

(2) Pros of Turbojet Engines

(A) Thrust increases with Mach number, which makes them practical for operation at supersonic airspeeds; (B) generally, their small cross-sectional area helps with integration into small frontal area aircraft, making it the natural choice for high-speed supersonic aircraft ($M > 2.5$); (C) smooth and vibration-free operation; (D) thrust can be increased by afterburning, albeit at the cost of increased fuel consumption.

(3) Cons of Turbojet Engines

(A) Expensive to acquire, operate, and maintain; (B) high fuel consumption at low airspeeds and altitudes; (C) inefficient compared to turboprops and turbofans; (D) noisy; (E) emit environmentally harmful contaminants.

(4) Thrust Modeling for Turbojets

Methods for modeling the thrust of turbojets engines are provided in Chapter 14.

(5) Typical Fuel Consumption

Table 7-10 shows the typical specific fuel consumption of selected turbojet engines. Note that the reported values are all at a maximum T-O thrust.

(6) Engine Pressure Ratio (EPR)

EPR is the ratio of the total pressure at the turbine exit to the total pressure at the compressor-system entrance (fan entrance for a turbofan). Referring to Figure 7-30 (and Figure 7-33), it is the total pressure at Station 7 divided by that at Station 2. It is given by

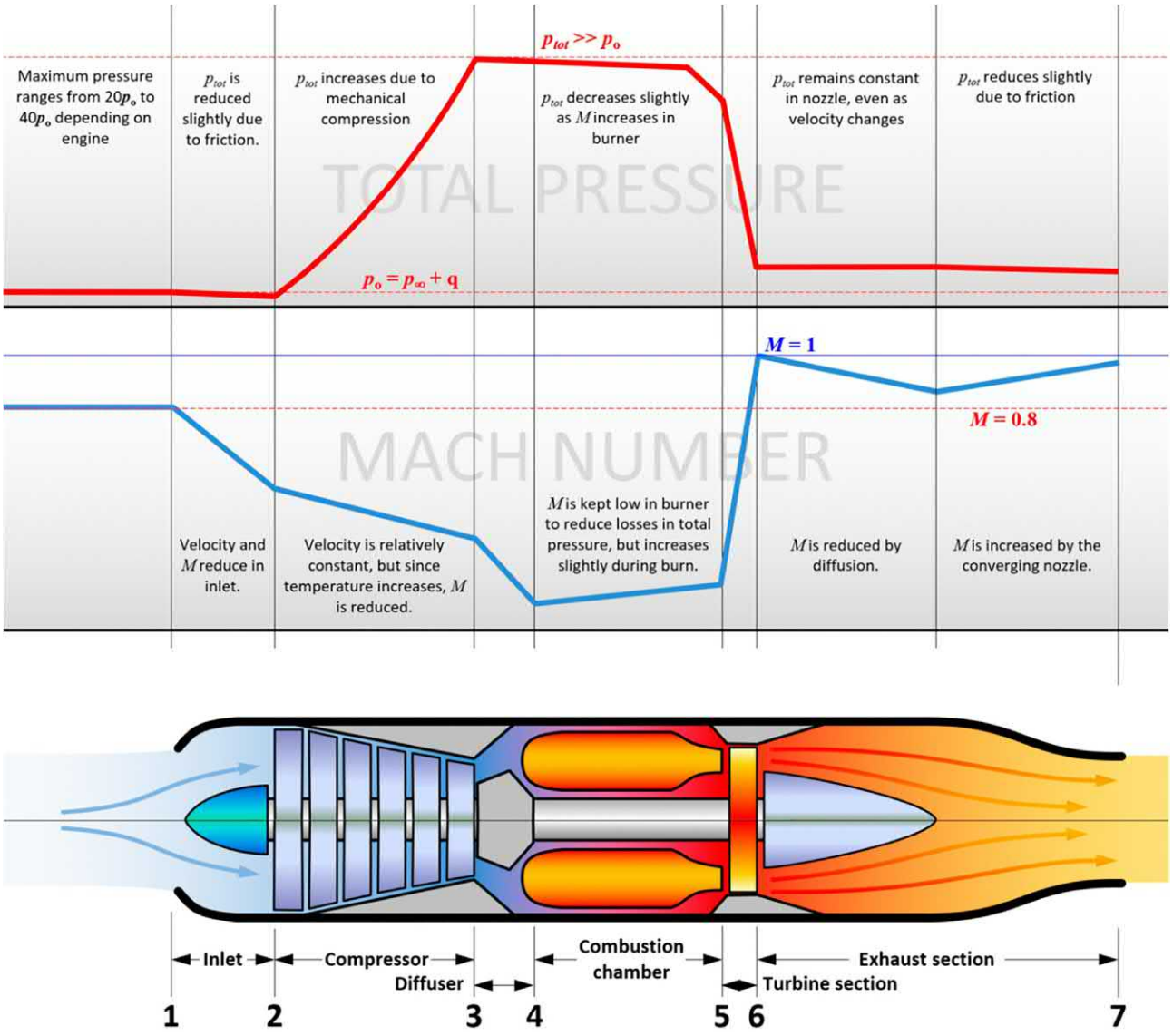


FIGURE 7-30 Variation of pressure and Mach number inside a theoretical turbojet.

TABLE 7-10 Typical T-O thrust and SFC of selected turbojet engines [44].

Engine type	T-O thrust rating	SFC (T-O)
Instytut Lotnictwa IL K-15	3305 lb_f 14.7 kN	1.006 1/h
LM WP6	6614 lb_f 29.42 kN	0.980 1/h
Microturbo TRS 18-046 (www.safran-power-units.com)	202 lb_f 0.898 kN	1.27 1/h
Microturbo TRS 18-056 (www.safran-power-units.com)	221 lb_f 0.982 kN	1.27 1/h
Microturbo TRI 60 (www.safran-power-units.com)	772 lb_f 3.430 kN	1.25 1/h
PBS VB TJ100 A (www.pbs.cz)	247 lb_f 1.097 kN	1.090 1/h
PBS VB TJ100 C (www.pbs.cz)	225 lb_f 1.000 kN	1.177 1/h

$$EPR = p_{07}/p_{02} \tag{7-31}$$

The pressures are measured using total pressure sensors. It applies to all gas turbines. The *EPR* is used by pilots for engine thrust management and is displayed using a dedicated cockpit instrument (an *EPR gauge*). For turbojets (and low *BPR* turbofans), in which the power required to drive the fan is small, it typically ranges from about 10 to 35, give or take. For high *BPR* turbofans, the large power required to drive the fan leads to a lower turbine exit pressure. For such engines, the *EPR* ranges between 1 and 3, give or take (a common range is 1–1.6).

(7) Overall Pressure Ratio (OPR)

OPR is the ratio of the total pressure at the aft and forward compressor faces. Referring to Figure 7-30, it is the total pressure at Station 3 divided by that at Station 2. It applies to all gas turbines. Typical *OPR* for early engines was around 3. *OPR* for modern turbofan engines is around 40–55. It is defined as follows

$$OPR = p_{03}/p_{02} \tag{7-32}$$

(8) Bleed Air

Refers to a fraction of the air flowing through the compressor of a turbojet (or turbofan or a turboprop) that is diverted before entering the combustion chamber. It is used for applications such as antiicing and pressurization. Considering Figure 7-30, air would be bled off between Stations 2 and 3, typically closer to Station 3. The hot and high-pressure bleed requires a pressure regulator and a heat exchanger for cooling.

7.3.3 Topics Specific to Turbofans

Turbofan engines are common in GA aircraft. While most of these are business jets, recently a few new small jets powered by turbofans have emerged. Among such jets is the emergence of the *personal jet*, a new class of aircraft designed to be owner-flown and operated, analogous to single engine piston aircraft. This trend has led to the development of small turbofans, such as the DGEN 380 in Figure 7-31. Examples of personal jets include the Eclipse 400, Diamond Jet, and the Cirrus SF50 Vision. These airplanes are made possible by the development of certified low thrust turbofans manufactured by Williams International and Pratt & Whitney Canada. One such engine (the Williams International FJ44 is shown in Figure 7-32).

(1) Characteristics of Flow through a Turbofan

Figure 7-33 shows the change in total pressure and Mach number of the airflow through a theoretical turbofan. The flow through the core is identical to that of



FIGURE 7-31 A cutaway of the Price Induction DGEN 380,730 lb_f thrust turbofan engine specifically designed for low and slow GA aircraft. *Courtesy of Akira Technologies (www.akira.pro).*

Figure 7-30; the flow of the bypass air presents the only difference. Note that both the bypass air and the air flowing through the core exit at speed near Mach 1. Both exits operate as choked nozzles. Since the exhaust temperature is higher than that of the bypass air, its velocity is higher. As an example, the temperature of the bypass air exiting the shroud may be 350 K, so the speed of sound is about 375 m/s (which also is the flow speed). In contrast, the temperature of the core flow exiting the nozzle may be 1400 K; the flow speed is 750 m/s.

(2) Pros of Turbofan Engines

(A) Efficient at high subsonic Mach numbers; (B) very reliable powerplant; (C) smooth and vibration-free operation; (D) noise levels can be suppressed.

(3) Cons of Turbofan Engines

(A) Expensive to acquire, operate, and maintain; (B) high fuel consumption at low airspeeds and altitudes; (C) inefficient compared to turboprops; (D) emit environmentally harmful contaminants; (E) large diameter fan makes them unsuitable for supersonic aircraft (unless low BPR).

(4) Difference between a Turbojet and Turbofan Engines

The turbofan differs from the turbojet in that a fraction of the air flowing through the fan flows through the *core* (the *hot section*), while the remainder is bypassed around it. The diameter of the forward compressor wheel is larger than that of the core.

(5) Bypass Ratio (BPR)

Refers to the ratio of the mass flow diverted to flow around the core of a jet engine to that going through the core. This is called *bypass flow*. If mass flow ingested by a turbofan amounts to 100 kg/s and 90 kg/s flows around the hot section and 10 kg/s flows through it, then the bypass ratio is 90/10 or 9 (often written as 9:1). This is defined mathematically as follows:

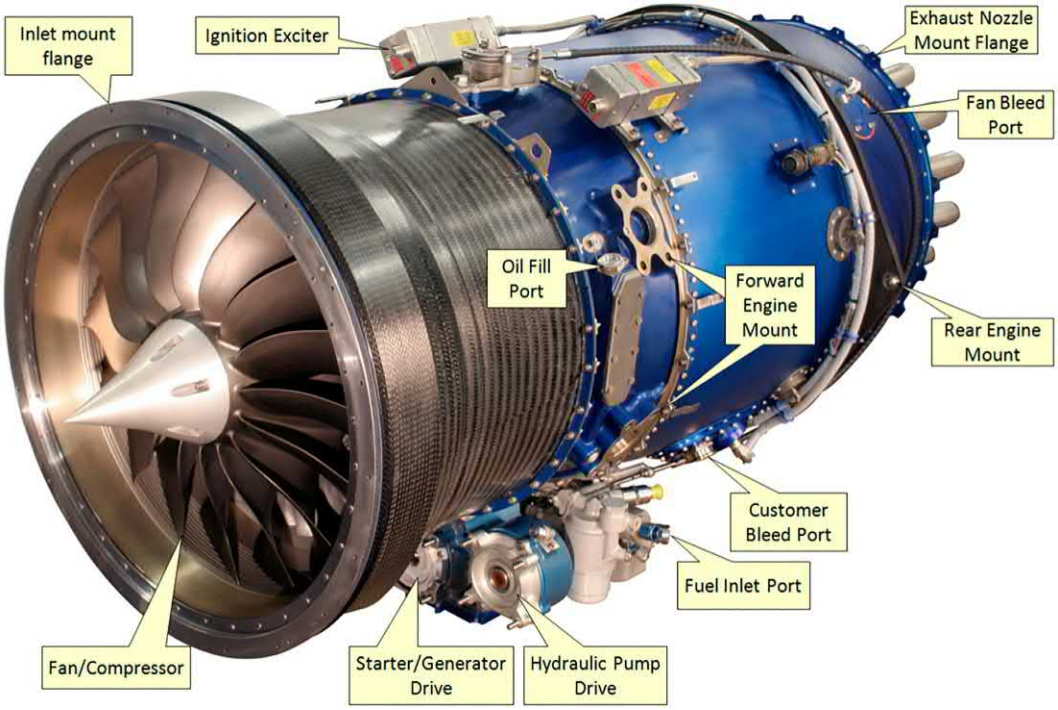


FIGURE 7-32 A Williams International FJ44 turbofan (1900–3600 lb_t class). *Courtesy of Williams International, www.williams-int.com.*

$$BPR = \dot{m}_{bypass}/\dot{m}_{core} \tag{7-33}$$

The mass flow entering the engine and fan ($\dot{m}_i$) is the sum of that going through the hot section ($\dot{m}_{core}$) and the bypass section ($\dot{m}_{bypass}$). Using the above definition for the *BPR*, we can write

$$\dot{m}_i = \dot{m}_{core} + \dot{m}_{bypass} = \dot{m}_i \frac{1}{BPR+1} + \dot{m}_i \left(1 - \frac{1}{BPR+1}\right)$$

Thus, the mass flow through the hot section and fan can be calculated as follows

$$\dot{m}_{core} = \frac{\dot{m}_i}{BPR+1} \qquad \dot{m}_{bypass} = \frac{\dot{m}_i BPR}{BPR+1} \tag{7-34}$$

As a rule of thumb, the higher the bypass ratio, the more fuel efficient is the engine. Turbofan engines fall into three classes: low, medium, and high bypass ratio engines [46]:

Low *BPR* turbofan:	$0.2 \le BPR \le 1.0$
Medium *BPR* turbofan:	$1.0 < BPR \le 5.0$
High *BPR* turbofan:	$BPR > 5.0$

The literature often defines only low and high BPR using the limits shown above. It seems logical to add a medium BPR to that classification. Note that *BPR* can also be defined for turboprops, which should be classified as ultra-high *BPR* engine (*BPR* ≈ 100:1 [42]). This would be estimated using the Froude–Rankine momentum theorem of Section 15.5. Engines in the ultra-high *BPR*-class, intended for commercial jetliners operating near *M* 0.8, were tested in the 1980s (e.g., the General Electric GE36, which had a *BPR* of 35 and PW-Allison 578-DX, which had a *BPR* of 56 [47]). These are also referred to as *propfans* or *unducted fans*.

(6) Specific Fuel Consumption (SFC)

Table 7-11 shows the typical *SFC* of selected turbofan engines. These are obtained from engine thermodynamic analysis and depend on airspeed (and not mass flow rates). The *SFC* for a turbofan at low speeds, such as that during T-O, is lower than in cruise; typically, in the 0.35–0.38 range versus around 0.55–0.70 in cruise. This results from low airspeed, when "ram drag" is small and net thrust equals the gross thrust (where $T \approx \dot{m}\cancel{V}_{jet}$).

7.3.4 Installation of Gas Turbines

Due to the complexity of gas turbine installation, design should be conducted with a direct involvement of the engine manufacturer. Polishing the inlet and exhaust design, fuel system layout, and bleed air and other systems requires expertise and experience only they wield. The reader is also directed to the available literature, including but not limited to refs. [42, 43, 46, 48, 49]. The following discussion should therefore only be considered introductory.

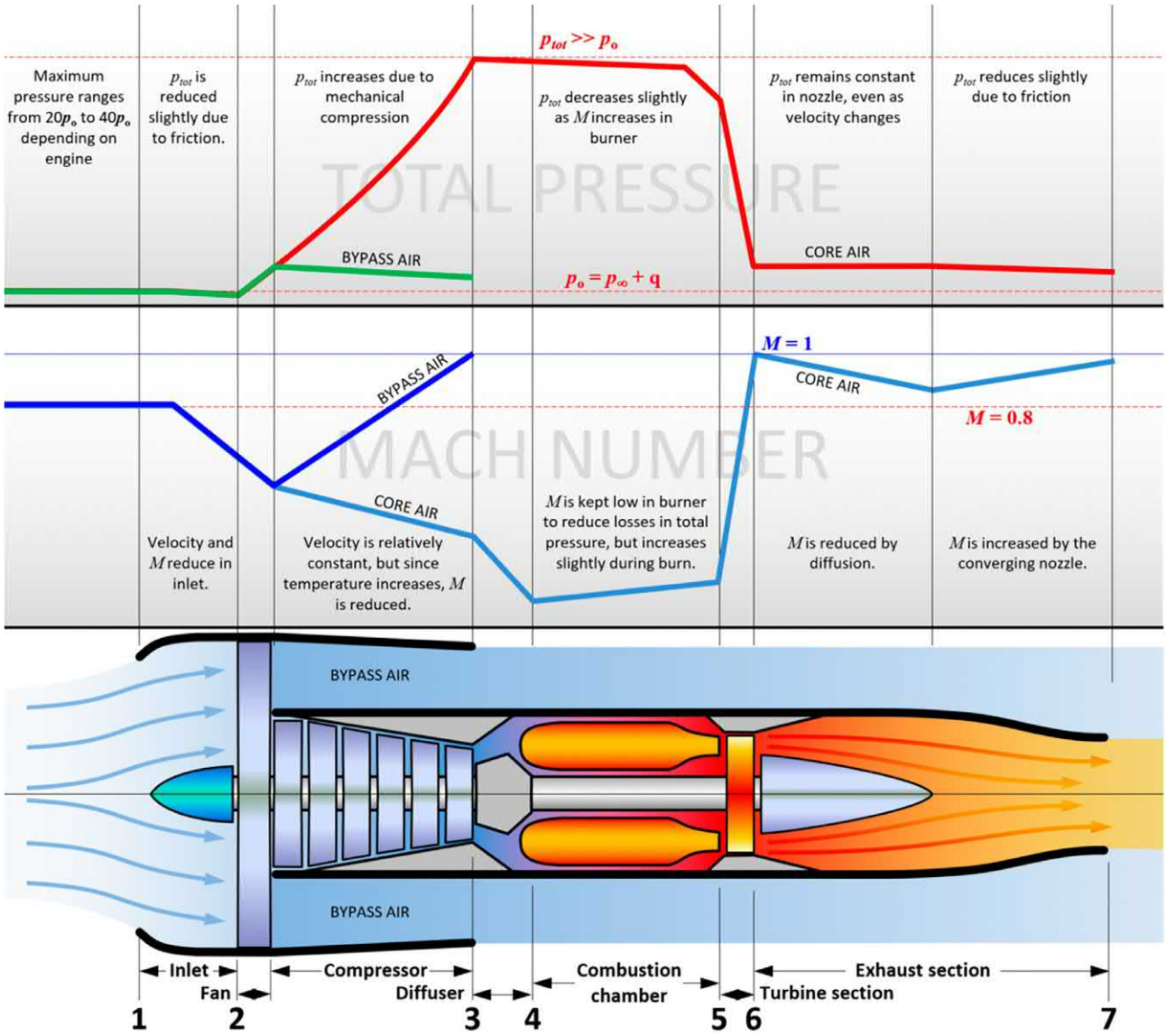


FIGURE 7-33 Variation of pressure and Mach number inside a theoretical turbofan.

TABLE 7-11 Typical T-O thrust and SFC of selected turbofan engines [44].

Engine type	Bypass ratio	T-O thrust rating	SFC (T-O)
Pratt & Whitney Canada JT15D-4B	3.3	2500 lb_f 11.12 kN	0.562 1/h
Pratt & Whitney Canada JT15D-5A	3.3	2900 lb_f 12.9 kN	0.551 1/h
Pratt & Whitney Canada P&WC530A	–	2887 lb_f 12.8 kN	–
Pratt & Whitney Canada P&WC910F	–	950 lb_f 4.22 kN	–
Turbomeca-SNECMA Larzac 04-C6	1.13	2966 lb_f 13.19 kN	0.71 1/h
CFM56-3B2	5.0	22,000 lb_f 97.90 kN	0.655 1/h

TABLE 7-11 Typical T-O thrust and SFC of selected turbofan engines [44]—cont'd

Engine type	Bypass ratio	T-O thrust rating	SFC (T-O)
CFM56-5C2	6.6	31,200 lb_f 138.8 kN	0.567 1/h
Williams International FJ33	–	1000–1900 lb_f 4.44–8.44 kN	–
Williams International FJ44-2A	4.1	2300 lb_f 10.23 kN	0.460 1/h
Price Induction DGEN 380[a]	7.6	574 lb_f 2.55 kN	0.439 1/h
Price Induction DGEN 390[a]	6.9	722 lb_f 3.21 kN	0.445 1/h

[a] *Still in development.*

(1) Installation of Gas Turbine Engines

The small diameter of gas turbines provides multiple installation options. Turbofans are frequently mounted on the aft fuselage or on pylons on the wings (podded configuration). They are also buried inside the wing or in the fuselage. There are usually good reasons that justify each type of installation. However, the buried installation poses a serious challenge in case of a fire. A fire in a podded engine may burn itself out without causing damage to the engine mounts or the nearby airframe. Conversely, a buried engine may present serious risks to the surrounding airframe and, thus, requires reliable fire proofing. Fire proofing even for small aircraft can weigh in excess of 100 lb_f, something easy to overlook during the design phase, but can easily shorten range by 50 to 200 nautical miles.

Installation of jet engines must comply with the same requirements as piston engines, with some exceptions. Figure 7-34 shows a schematic of a typical installation of a podded jet engine on a pylon. Internal and external engine installations need fire suppression systems, which increases the weight further. Additionally, if the aircraft is certified for *Flight Into Known Icing* (FIKI), the leading edge of the inlet (usually called *inlet lip*) must feature anti-ice capability, compounding the complexity.

(2) Installation of Turboprop Engines

Turboprop installations typically follow a similar process to that of piston engines. Turboprops are lighter than pistons of same power. While longer than pistons of comparable power, their girth (diameter) is more compact.

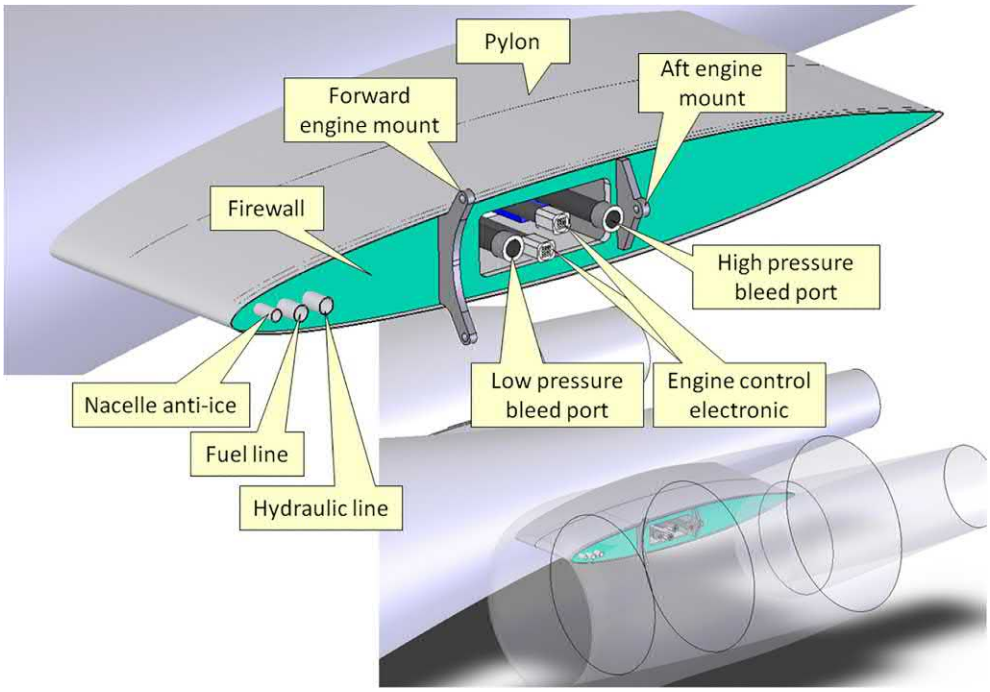


FIGURE 7-34 A typical external jet engine installation.

For instance, the 400 BHP Lycoming IO-720 weighs about 600 lb_f and its length × width × height is about 118 × 87 × 57 cm [50]. This contrasts the 600–1100 SHP Pratt & Whitney Canada PT6 weighs about 350–400 lb_f with length × diameter about 156 × 56 to 192 × 56 cm [51]. Thus, when a piston engine is replaced with a lighter weighing turboprop, the new installation must be mounted farther forward to ensure CG-limits are not violated. This gives the airplane a distinct appearance (e.g., see Figure 7-29). Increased propeller moments must be accounted for in such a modification (see Section 15.2).

(3) Turbo Machinery and Rotor-Burst

The compressor and turbine in a typical gas turbine rotate at very high rates when compared to a piston engine (20–40 thousand versus 2600–6000 RPM). While rare, compressor- and turbine-blades can fail in an event called *rotor-burst*. Ref. [52] identifies six types of rotor-burst events that range from a single blade separation to rotor failure. Since the blades are subject to substantial centripetal force, two things happen in a rotor-burst:

(1) The fragments turn into lethal projectiles that must be contained.
(2) The support structure needs to react oscillatory loading due to the imbalanced compressor or turbine rotors.

14 CFR §33.94 (Blade containment and rotor unbalance tests) requires engine casing and support to survive the damage. Although applicable during the detail design phase, ref. [53] provides guidance on compliance methods and design considerations for minimizing damage due to uncontained rotor-burst.

7.3.5 Subsonic Inlet Design

The purpose of an engine inlet is to (1) bring smooth, distortion-free air to the compressor and (2) slow it down with minimal loss in total pressure (high *pressure recovery*). Two installation methodologies are used for jet engines; *external* and *internal* (see Figure 7-35). Both are used in subsonic and supersonic aircraft. Note that reference [54] provides good inlet design information.

Inlet pressure recovery must be kept as high as possible because of the magnifying effect of the compressor. The pressure in the combustor is close to the total inlet pressure times the compressor pressure ratio. If the pressure drops by 1 psia in the inlet, it can fall by 25 psia in the combustor [57, pg. 209]. Pressure losses are caused by several external and internal sources. Flow inside the inlet can also experience unfavorable pressure gradients, promoting flow separation on the inside walls. These can have the following effects:

(1) Flow no longer slows down isentropically, lowering the total pressure inside the inlet.
(2) The flow separation region along the inside wall narrows the effective cross-sectional area, which leads to higher than desired airspeed (and thus lower total pressure) at the front face of the compressor.
(3) The separated flow is inherently unstable and loses "smoothness" as it enters the compressor, reducing its efficiency and stability of operation.

(1) External Inlet Types for Jet Engines

External subsonic inlets are usually of a *Pitot* style. It offers the best pressure recovery for the entire range of AOA and AOY the aircraft is likely to see in practice. There are examples of external Pitot inlets for supersonic aircraft, for instance, the B-58 Hustler and Tupolev Tu-22. The external installation allows easier access for maintenance and engine removal and replacement. However, the nacelle and pylon increase aerodynamic drag by adding wetted area and interference drag. When mounted on a wing, the Pitot inlet is indifferent to yaw. When mounted next to a fuselage (as common on commercial and business aircraft), the leeward engine may be subject to flow distortion in yaw, which can lead to surge and flameout.

(2) Internal Inlet Types for Jet Engines

The internal type, too, is selected for both subsonic and supersonic aircraft. It is primarily of three subtypes: the *NACA inlet*, the *single duct*, and the *bifurcated* inlet. These inlets have the following pros and cons.

The NACA inlet (see Figure 7-36) was invented in 1945 by Frick et al. [55] for internal-flow systems (such as jet

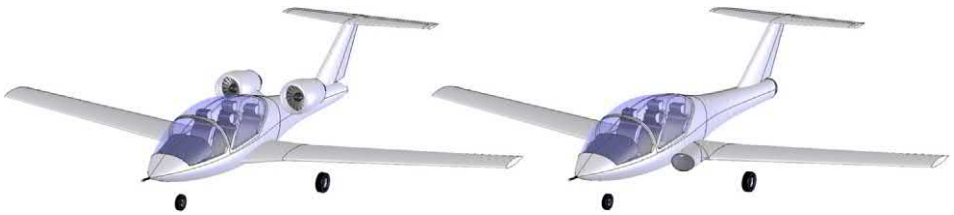


FIGURE 7-35 An external (left) and integrated (right) jet engine installation. The external one is also called a *pitot* inlet. The integrated inlet is of a *bifurcated* type.

engines) with small flow diffusion requirements. It is suitable for subsonic aircraft only and should be avoided if supersonic speed is expected at the inlet entry. The inlet entry is narrow but widens nonlinearly toward the submerged inlet opening. The inlet ramp has a shallow slope toward the opening; the optimum is ≈7 degrees [49]. In operation, each side edge develops a vortex, which helps turning the flow into the inlet. Some inlets feature small ridges along the edge to enhance the generation of this vortex. The submerged nature of the inlet should result in relatively low impact on aerodynamic drag. Refs. [55, 56] claim good pressure recovery, although actual installations in aircraft contradict this. Expect 80% pressure recovery, if that. Regardless, while it suitable for unique jet engine installations, it is more commonly used for component cooling. Examples of the NACA inlet for jet engines include the Caproni C-22J, Miles M100 Student, Microjet 200, and Bede BD-5J.

The shape of the NACA inlet edge can be approximated using the quartic polynomial below

$$w(x) = A + Bx + Cx^2 + Dx^3 + Ex^4 \tag{7-35}$$

where the coefficients A, B, C, D, and E are constants, obtained from the geometric definition of the inlet (see Figure 7-36), using Equation (7-36). This requires the square matrix to be inverted and multiplied by the vector on the right-hand side of the equal sign. Once computed, it is possible to approximate the edge with high accuracy.

$$\begin{bmatrix} 1 & 0 & 0 & 0 & 0 \\ 1 & x_{mid} & x_{mid}^2 & x_{mid}^3 & x_{mid}^4 \\ 1 & L & L^2 & L^3 & L^4 \\ 0 & 1 & 0 & 0 & 0 \\ 0 & 1 & 2L & 3L^2 & 4L^3 \end{bmatrix} \begin{Bmatrix} A \\ B \\ C \\ D \\ E \end{Bmatrix} = \begin{Bmatrix} w_o \\ \frac{1}{2}(w_o + w_e) \\ w_e \\ \tan\theta_o \\ \tan\theta_e \end{Bmatrix} \tag{7-36}$$

where w_o is the half-width of the inlet opening, w_e is the half-width of the inlet entry, L is the length of the inlet, x_{mid} is the x-position of a point midway between w_o and w_e. It is moved a short distance, left-or-right, to bias the edge shape and should be considered for fine-tuning the inlet only. The angles θ_o and θ_e are the edge slopes at the opening and entry of the inlet, respectively. Typical values are $\theta_o = 0$ degree and $\theta_e \approx -16$ degrees. The following values generate an inlet of unit length and width that resembles a typical NACA inlet of ref. [55]: $w_o = 0.5$, $w_e = 0.05$, $L = 1$, $x_{mid} = 0.45$, $\theta_o = 0$ degree, and $\theta_e = -16$ degrees. The resulting function is $w(x) = 0.5 + 0.2554x - 3.3743x^2 + 4.7353x^3 - 2.0774x^4$.

The single duct is used on modern fighter aircraft and numerous subsonic aircraft, e.g., De Havilland DH-106 Comet and, its derivative, the BAe Nimrod. Both feature inlets for engines that are buried in the wing root. The inlet is also used on many subsonic fighter and attack aircraft, including the single engine F-86 Sabre jet, the A-7 Corsair II, and early series MiG-fighters. It also shows up as an S-duct for several tri-jets, including the Boeing B727, Lockheed 1011, De Havilland Trident, Tupolev Tu-154, Yakovlev Yak-40 and 42, and selected Dassault Falcon jets. These aircraft have the inlet placed high above the fuselage, so it acts as a *boundary layer diverter*. At high AOA, such inlets may ingest separated flow from the fuselage, which may cause problems such as compressor stall or surge [49]. Furthermore, S-duct may accrete ice in the bend, calling for antiice remedies.

The internal bifurcated inlet is a good solution for single engine installations when the engine is placed behind the cabin. This is usually accomplished using wing root-inlets (e.g., see Figure 7-35). The internal installation avoids the wetted area increase of an external installation and, thus, of aerodynamic drag. The presence of the fuselage forward

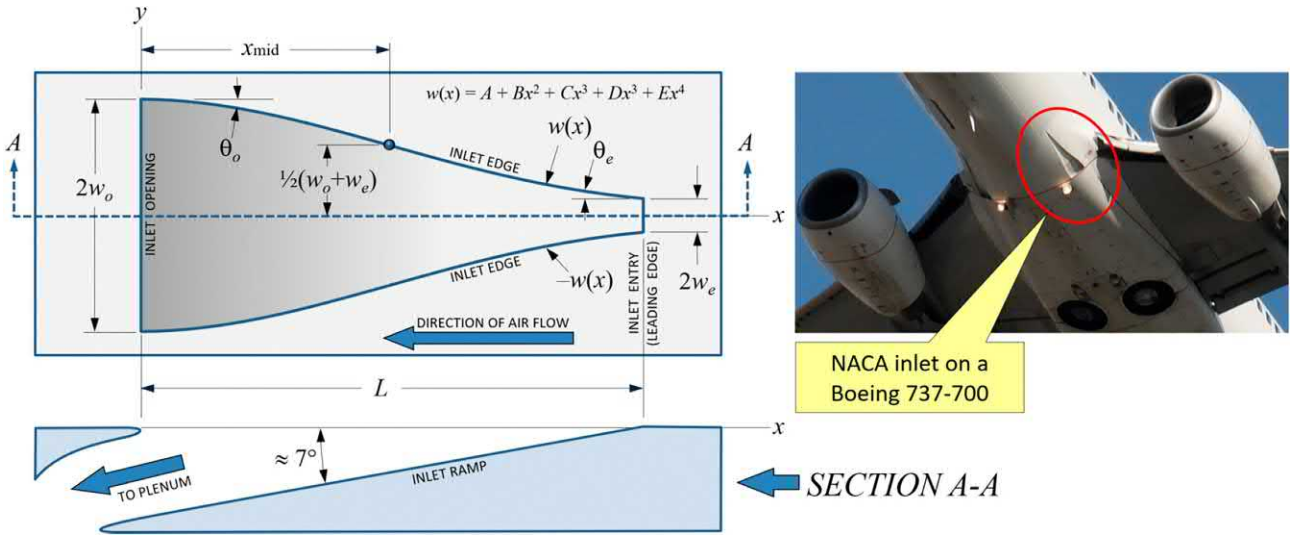


FIGURE 7-36 The basic NACA inlet. *Inserted photo by Phil Rademacher.*

of the inlet requires boundary layer growth to be considered. It can be ingested by the engine, calling for a boundary layer diverter. All internal configurations are at risk of ingesting flow-separated air in yaw. Additional problems associated with bifurcated ducts include pressure recovery losses due to inlet bending and problematic ice accretion in the forward-facing inlet turns. These require antiice remedies for aircraft certified for FIKI.

DERIVATION OF EQUATION (7-37)

We use forced curve-fitting by defining the values of Equation (7-36) at the opening, mid-point, and entry as follows:

$$w(0) = A + B(0) + C(0)^2 + D(0)^3 + E(0)^4 = w_o$$
$$w(x_{mid}) = A + Bx_{mid} + Cx_{mid}^2 + Dx_{mid}^3 + Ex_{mid}^4 = \frac{1}{2}(w_o + w_e)$$
$$w(L) = A + BL + CL^2 + DL^3 + EL^4 = w_e$$
$$w'(0) = B + 2C(0) + 3D(0)^2 + 4E(0)^3 = \tan\theta_o$$
$$w'(L) = B + 2CL + 3DL^2 + 4EL^3 = \tan\theta_e$$

Gathering terms into a matrix form to solve for the coefficients A, B, C, D, and E yields Equation (7-37).

(3) Design Guidance for a Diffuser Inlet

When the airplane is at rest, the inlet must admit enough mass flow for the engine to develop maximum thrust. In flight, the inlet must slow air from the far-field airspeed to the engine's most efficient inlet airspeed. For instance, the inlet of a jet cruising at high subsonic Mach number ($\approx M0.8$) must slow the air from M0.8 down to M0.5. The slowdown requires the cross-section to expand from the inlet lip to the compressor face; it is a *diffuser*. The internal shape of the inlet is designed based on mass conservation, assuming adiabatic expansion (see Section 14.1.3). The geometric expansion must take place over a given length to prevent flow separation (see Figure 7-37). A method for this is presented in Figure 7-40. Additional analyses should evaluate other contributors affecting pressure recovery. These are beyond the scope of this introduction, but methods are presented in references such as [42, 43, 48, 49].

The airspeed of an airplane impacts how the jet engine ingests air. Two extremes are shown in Figure 7-38. At rest, the jet engine ingests air from around and in front of the inlet; something very important for technicians to remember while working near such machines. The inflow can be tremendously powerful and, sadly, every year a person is sucked into large jet engines with fatal consequences. It also shows the engine can easily draw in debris off the ground and sustain considerable damage.

As the speed of the airplane increases, the streamlines shown in the upper diagram become more and more aligned with the engine axis and begin to form a distinct streamtube; only air inside of it is ingested by the engine. The lower diagram of Figure 7-38 shows this at cruising

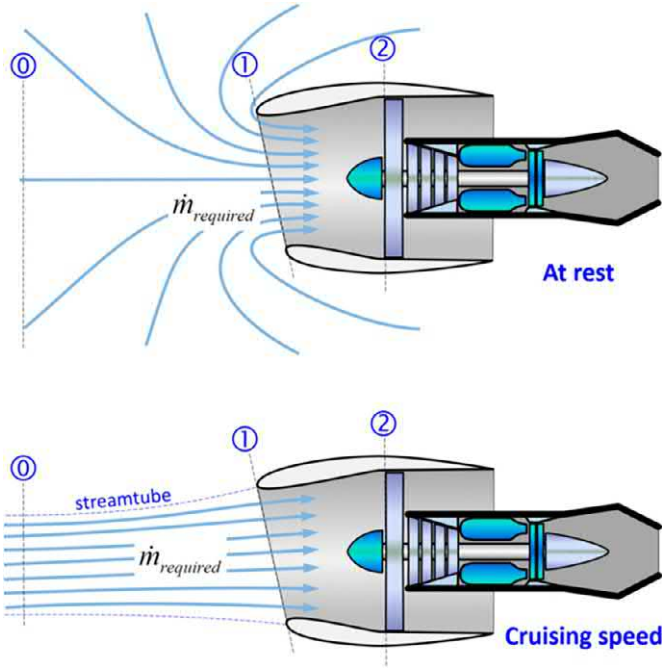


FIGURE 7-38 Shape of the flow field entering a jet engine at rest (top) and at cruise (bottom).

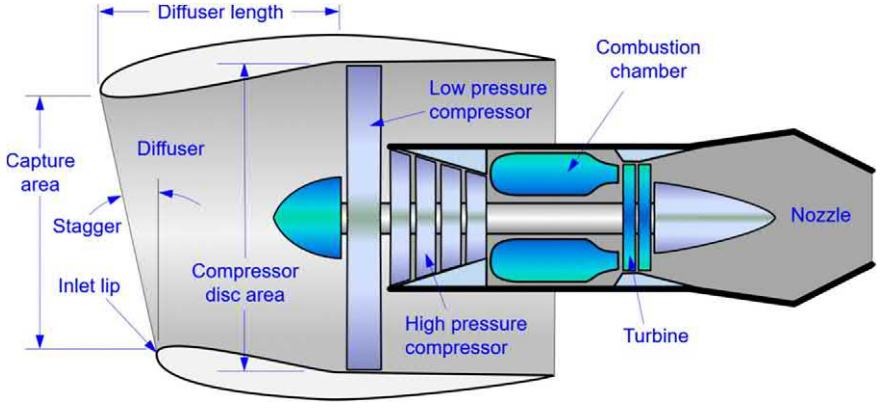


FIGURE 7-37 A typical external jet engine installation features an inlet designed to slow airspeed from the far-field airspeed to some target airspeed.

speed, during which much more air is available than required by the engine.

The following STEP-BY-STEP provides a method for the airframe designer to conduct a preliminary sizing of the inlet to support the layout of the airplane. Its design involves several important geometric parameters of interest. Three stations of interest have been superimposed on the engines of Figure 7-38, denoted by ⓪, ①, and ②. The inlet sizing requires pressure, density, temperature, airspeed, and cross-sectional area to be determined at each station. Station ⓪ represents the far-field. As it is infinite in size at rest, the Mach number is assumed zero. In cruise, the *capture area* at the inlet lip (denoted by ①) is smaller.

STEP 1: Required mass flow rate

Obtain the maximum mass flow rate required by the engine and call it $\dot{m}_{required}$. This information is usually provided by the engine manufacturer and is usually dictated by the engine performance at static T-O thrust, making it the critical flight condition for the design. This contrasts the cruise condition, in which the airspeed is so high that the inlet streamtube necks down in the far-field as shown in Figure 7-38, indicating plenty of air can enter the engine. The remaining steps assume this to be the case.

STEP 2: Determine airspeed limitations at the inlet lip and compressor

The airspeed at the inlet lip (Station ①) should not exceed Mach 0.8. Similarly, the airspeed at the front face of the compressor (Station ②) is limited to Mach 0.4 to 0.5 and is specified by the engine manufacturer. This is intended to prevent the airspeed at the tip of the fan becoming too high, resulting in decreased efficiency.

STEP 3: Establish known and unknown flow conditions

The known and unknowns can be established in a format like the one shown below. Question signs indicate the parameter is initially unknown. Recall that the total pressure is the sum of the ambient (p_∞) and dynamic pressure (q), i.e., $p_\infty + q$. However, as stated above, at this condition the engine is assumed to be at rest, so $q = 0$, so the total pressure is simply the ambient pressure.

Flow condition	Station ⓪ (far-field)	Station ① (inlet)	Station ② (compressor)
Area	$A_0 = \infty$	$A_1 = ?$	$A_2 =$ given
Mach number	$M_0 = 0$	$M_1 = 0.8$	$M_2 = 0.4$ to 0.5
Total pressure	$p_{T0} = p_0 = 0$	$p_{T1} = ?$	$p_{T2} = ?$
Temperature	$T_0 =$ given	$T_1 = ?$	$T_2 = ?$
Density	$\rho_0 =$ given	$\rho_1 = ?$	$\rho_2 = ?$
Pressure recovery ratio	–	–	$\pi_2 = p_{T2}/p_{T0}$

STEP 4: Determine conditions at Station ①

Even though the airspeed in the far-field is zero as the engine spools up to T-O thrust, air can easily accelerate to very high airspeeds at the inlet lip. Normally, the inlet lip radius is sized such that local airspeeds do not exceed $M0.8$. If it is assumed that isentropic flow relations hold between Stations ⓪ and ① and that the ratio of specific heats of air is $\gamma = 1.4$, it is possible to determine the flow variables P_T, T, and ρ, as follows (using $M_1 = 0.8$ and isentropic flow relations):

Total pressure:

$$p_{T1} = \frac{p_{T0}}{\left(1 + \frac{\gamma - 1}{2} M_1^2\right)^{\frac{\gamma}{\gamma - 1}}} = \frac{p_0}{\left(1 + \frac{\gamma - 1}{2} M_1^2\right)^{\frac{\gamma}{\gamma - 1}}} = 0.65602 p_0 \qquad (7-37)$$

Temperature:

$$T_1 = \frac{T_0}{\left(1 + \frac{\gamma - 1}{2} M_1^2\right)} = 0.88652 T_0 \qquad (7\text{-}38)$$

Density:

$$\rho_1 = \frac{p_{T1}}{RT_1} = \frac{0.65602 p_0}{(1716)(0.88652 T_0)} = 0.00043123 \frac{p_0}{T_0} \qquad (7\text{-}39)$$

Inlet area (capture area):

$$A_1 = \frac{\dot{m}_{required}}{M_1} \sqrt{\frac{1}{\gamma p_0} \left(\frac{\rho_0}{\rho_1}\right)} = 1.25 \dot{m}_{required} \sqrt{\frac{1}{\gamma p_0} \left(\frac{\rho_0}{\rho_1}\right)} \qquad (7-40)$$

STEP 5: Determine conditions at Station ②

Assuming the airspeed (M_2) at the front face of the compressor to be in the Mach 0.4 to 0.5 range, the remaining parameters are again determined using isentropic flow relations between Stations ① and ② in Figure 7-38:

Total pressure:

$$p_{T2} = \frac{p_{T0}}{\left(1 + \frac{\gamma - 1}{2} M_2^2\right)^{\frac{\gamma}{\gamma - 1}}} = \frac{p_0}{\left(1 + \frac{\gamma - 1}{2} M_2^2\right)^{\frac{\gamma}{\gamma - 1}}} \qquad (7\text{-}41)$$

Temperature:

$$T_2 = \frac{T_0}{\left(1 + \frac{\gamma - 1}{2} M_2^2\right)} \qquad (7\text{-}42)$$

Density:

$$\rho_2 = \frac{p_{T2}}{RT_2} \qquad (7\text{-}43)$$

Again, it is important to remember that the above equations reflect the assumption the engine is at rest.

(4) Pressure Recovery

For perfect inlets, the pressure recovery ratio, denoted by π_2, is 1. This yields the maximum thrust for a given flight condition. Short inlets common to podded jet

engines of the type shown in Figure 7-38 usually have π_2 close to 1. Integrated inlets (see below) have π_2 that are often well below 1.

(5) Inlet Lip Radius

It is imperative that the lip radius is carefully designed. A small radius can cause flow separation at high AOA or AOY. A large lip radius tends to reduce pressure distortion at high AOA or AOY and it also results in higher nacelle drag. A pressure distortion is a localized deviation of the expected average pressure at the front face of the compressor. It is usually less than the average pressure. This is very undesirable as it may cause oscillation in the airloads of the fan blades. Practical lip radii for subsonic aircraft range from about 6% to 10% of the inlet diameter.

(6) Diffuser Length

The length of the diffuser is of great importance as well. A schematic of a Pitot inlet is shown in Figure 7-39. The parameters of importance are the included angle, θ, the diffuser length, L, and the inlet lip diameter, D_1. The ratio L/D_1 is called the *inlet aspect ratio*. For a given L/D_1, too large an included angle θ indicates the diffuser is expanding too rapidly. This promotes detrimental flow separation on the inside wall. Conversely, for a given θ, too long a diffuser also promotes flow separation. The phenomenon is detailed by Schlichting [57, pp. 222–224], who demonstrates that no matter the included angle, if the diffuser length exceeds a certain distance, separation is inevitable. Additionally, such a diffuser is bound to have larger nacelle wetted area and, therefore, increases the aerodynamic drag of the installation in addition to being heavier. There is also a range of dimensions for which the formation of the flow separation is transitory, i.e., flow separation may fluctuate. The result may be compressor blade flutter and onset of early fatigue due to oscillatory loading of the blades. As indicated by Flack [48], the optimum pressure difference between Stations ① and ② in Figure 7-38 should comply with:

Ideal pressure coefficient:

$$C_{p\ 1\to 2} = \frac{2(p_{T2} - p_{T1})}{\rho V_1^2} < 0.6 \qquad (7\text{-}44)$$

The pressure between the stations must be allowed to rise over a suitable distance and this usually requires more sophisticated analysis methods that can account for the intricacies of the desired geometry. However, in the absence of such schemes, a convenient empirical method for simple diffusers is provided by Flack [48] to evaluate if the geometry is prone to separation. This way, separation is unlikely if the included angle θ is less than the minimum value obtained from the following expression:

Minimum angle:

$$\ln\theta_{\min} = 3.28 - 0.46 \ln\left(\frac{L}{D_1}\right) - 0.031\left(\ln\left(\frac{L}{D_1}\right)\right)^2 \qquad (7\text{-}45)$$

Conversely, separation is all but guaranteed if the included angle θ is greater than the maximum value obtained from the expression:

Maximum angle:

$$\ln\theta_{\max} = 3.39 - 0.38 \ln\left(\frac{L}{D_1}\right) - 0.020\left(\ln\left(\frac{L}{D_1}\right)\right)^2 \qquad (7\text{-}46)$$

where θ is in degrees. In between the two values is the transitory separation, in which there may or may not be separation. The trends based on this formulation are plotted in Figure 7-40. As an example, consider an inlet with an aspect ratio of 3. The graph shows that keeping

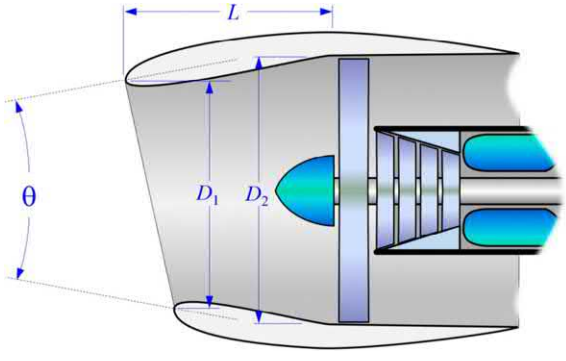


FIGURE 7-39 Dimensions for empirical diffuser length evaluation.

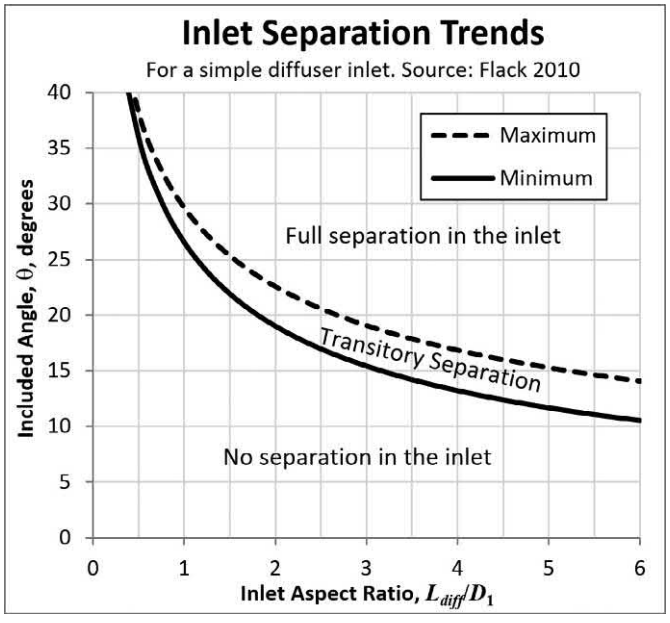


FIGURE 7-40 Flow separation trends for simple diffusers.

the included angle less than 15 degrees prevents flow separation inside the inlet.

(7) Stagger or Rake Angle

Stagger refers to lip geometry in which the upper lip is forward of the lower one (see Figure 7-37). The arrangement improves flow quality at higher AOAs, by reducing the airspeed at the lower lip and, thus, reduces tendency for flow separation [49]. Staggering is usually very modest in subsonic aircraft and ranges from 0 degree to 5 degrees.

DERIVATION OF EQUATION (7-40)

Of the set of equations, only Equation (7-40) needs to be derived. First, the required mass flow rate is given by:

$$\dot{m}_{required} = \rho_1 A_1 V_1 \tag{i}$$

The airspeed, V_1, is Mach number times the speed of sound, i.e., $V_1 = M_1 \cdot a_1$, where a_1 is the speed of sound at the inlet lip. The speed of sound can be calculated from the ideal gas expression:

$$a_1 = \sqrt{\frac{\gamma p_1}{\rho_1}}$$

Inserting this into Equation (i) and expanding and subsequently solving for the inlet area yields:

$$\dot{m}_{required} = \rho_1 A_1 V_1 = \rho_1 A_1 (M_1 a_1) = \rho_1 A_1 \left(M_1 \sqrt{\frac{\gamma p_1}{\rho_1}} \right)$$

$$\Leftrightarrow \quad A_1 = \frac{\dot{m}_{required}}{M_1} \sqrt{\frac{\rho_0}{\gamma p_0 \rho_1}}$$

7.4 ELECTRIC MOTORS AND BATTERY TECHNOLOGY

This section focuses on electric propulsion in aircraft. While aircraft powered by electric energy is an emerging technology, the electric motor dates to the 1840s. Its use in manned aircraft is made possible by the energy capacity of the modern Lithium-Ion (Li-Ion) battery; a class of batteries that use various Lithium-based chemistries: For instance, Lithium-Cobalt oxide ($LiCoO_2$) or Lithium-Manganese oxide ($LiMn_2O_4$), to name two. Operators of *radio controlled* (RC) aircraft are familiar with Lithium-Polymer batteries (often called *LiPos*). The technology is clean, low-weight, low-noise, smooth, reliable, and offers low operational cost. While battery technology already allows electric motors to power light aircraft, developers are working on its application in heavier aircraft. Figure 7-41 shows the clean installation of an electric motor in a twin-seat prototype aircraft.

The incorporation of electric propulsion in the aircraft calls for an understanding of the nature of electricity, batteries, electric motors, and associated limitations. This section provides a basic introduction to these topics.

7.4.1 Basic Formulas of Electricity

(1) Direct Current versus Alternating Current

Current in electric circuits flows either as *direct current* (DC) or *alternating current* (AC). DC can be generated from the release of electrons using chemical reaction, such as that which takes place inside a battery. The resulting current and voltage is uniform (considering time). In contrast, the current and voltage in an AC circuit varies with time. If generated by a mechanical generator (dynamo), it varies sinusoidally; it has a variable magnitude and reverses direction (see Figure 7-42). In electric motors, an *electronic speed controller* (ESC) is used to convert DC into AC. This is accomplished digitally using pulses in a so-called *pulse-width modulation* (PWM) technology. The resulting variation of current and voltage is not sinusoidal.

In this book, the letter *U* is used to represent electric potential (voltage). This is done to avoid confusion with

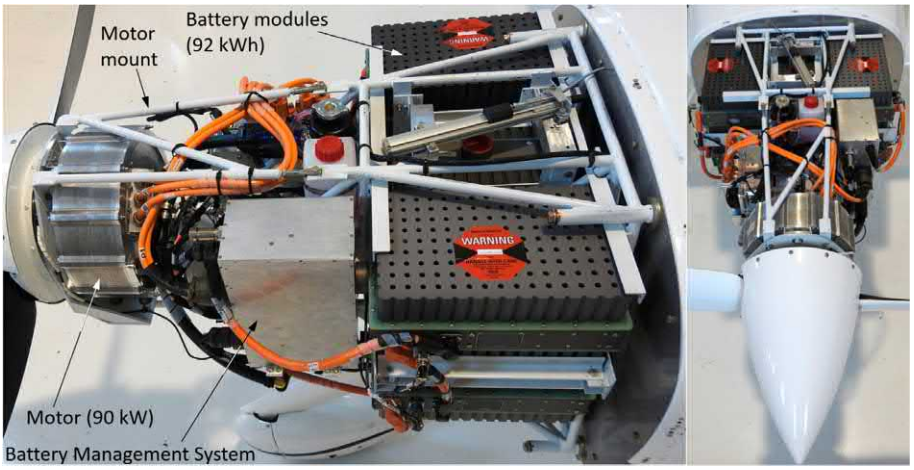


FIGURE 7-41 A side- and top-view of the electric propulsion system of the Bye Aerospace's eFlyer 2, a two-seat, all-electric airplane targeted for the pilot training market. *Courtesy of ByeAerospace.com.*

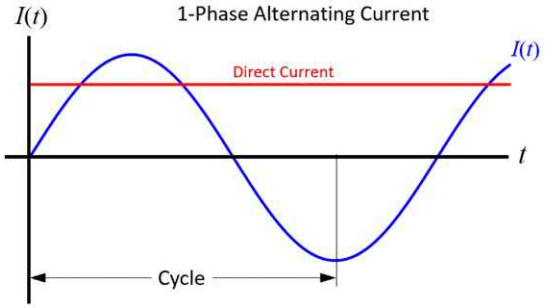


FIGURE 7-42 Comparison of DC and AC.

the letter V, which is used for airspeed or velocity. Regardless, the unit for voltage is represented using V. General information regarding batteries is widely available online, e.g., refs. [58–60]. Also, Hepperle [61] presents an excellent discussion of the potential of electric flight.

AC and DC both generate a magnetic field around the wire in which they flow. The difference is that the magnetic field generated by AC varies with time (50 or 60 Hz in a typical household current). This permits current and voltage to be transformed using *induction*. If using an *ideal transformer*, the conversion is lossless (e.g., 5 V and 2A can be transformed to 10 V and 1A, lossless). Consider the wire-transmission of fixed power, $P = UI$, over a long distance. The "resistance" (impedance) in the wire increases with distance. The current heats the wire, causing a power-loss of $\Delta P = I^2R$. Thus, the power at the receiving end is $P - \Delta P$. To minimize the loss, it is better to transmit the power as high voltage and low current. For instance, assuming fixed power, if voltage is increased by a factor of 10, the current drops by a factor of 10. Thus, ΔP is reduced by a factor of 100. The low loss transformation permitted by AC makes this more easily accomplished.

(2) Basic Formulas of Electricity for DC Circuits

The following basic equations of electric current (I), voltage (U), resistance (R), power (P), time (t), total time (T), and energy (E_{el}), are used when solving various problems involving DC circuits.

DIRECT CURRENT

Voltage (Volts):

$$U = \begin{cases} I \times R \\ P/I \\ \sqrt{P \times R} \end{cases}$$

Current (Amps):

$$I = \begin{cases} \sqrt{P/R} \\ P/U \\ U/R \end{cases}$$

Resistance (Ohms):

$$R = \begin{cases} U/I \\ U^2/P \\ P/I^2 \end{cases}$$

Power (Watts or Volt-Amps):

$$P = \begin{cases} U^2/R \\ I^2 \times R \\ U \times I \end{cases}$$

Electric energy (Watt-hours or Joules):

$$E_{el} = \int_0^T P \; dt = U \times I \times T$$

(3) Basic Formulas of Electricity for AC Circuits

AC circuits are common as single-phase (household current) or 3-phase (high-power equipment) sinusoidal waveforms. More phases are possible, but the added complexity and cost is considered impractical. The following basic equations are used when solving various problems involving AC circuits. If the wave amplitudes of $U(t)$ and $I(t)$ are known, the *instantaneous power* is defined as $P(t) = U(t)I(t)$. As shown with the single-phase AC circuit, the instantaneous power is time varying. This gives rise to the *mean power* ($\overline{P}$). It is of greater importance for electric motors, as this is delivered at the shaft. It corresponds to the power delivered by other types of engines.

The AC circuit may cause a phase difference between the current and voltage (see Figure 7-43). This is common for inductive or capacitive circuits, such as that of electric motors. The voltage is then said to *lead* or *lag* the current. This changes the instantaneous power, lowering the mean-power. This produces the term *power factor* (PF), which is defined as $PF = \cos\theta$. Power calculations for 3-phase circuits are beyond the scope of this text. In aircraft design, the mean power at the motor-shaft is evaluated using *system efficiency analysis*, as shown in Section 7.4.4. The following expressions are used when solving problems involving single- and 3-phase sinusoidal waveforms (see Figure 7-44). Note that the formulation for instantaneous

1-PHASE AC CIRCUIT

Voltage (volts) and Current (Amps):

$$U(t) = U_o \cos(\omega t)$$
$$I(t) = I_o \cos(\omega t + \theta)$$

Typical Cycles

Instantaneous power (Watts or Volt-Amps):

$$P(t) = U(t)I(t) = U_o I_o \cos(\omega t)\cos(\omega t + \theta) = \frac{U_o I_o}{2}\left[\cos(2\omega t + \theta) + \underbrace{\cos(\theta)}_{\equiv PF}\right]$$

Mean power (Watts or Volt-Amps):

$$\overline{P} = \frac{1}{T}\int_0^T P(t)dt = \frac{U_o I_o}{2}\cos\theta = \overline{UI}\cos\theta$$

3-PHASE AC CIRCUIT (BALANCED)

Voltage (Volts) and Current (Amps):

$$U_1 = U_o \cos(\omega t) \qquad I_1 = I_o \cos(\omega t + \theta)$$
$$U_2 = U_o \cos(\omega t + 2\pi/3) \qquad I_2 = I_o \cos(\omega t + 2\pi/3 + \theta)$$
$$U_3 = U_o \cos(\omega t + 4\pi/3) \qquad I_3 = I_o \cos(\omega t + 4\pi/3 + \theta)$$

Mean power (Watts or Volt-Amps):

$$P = \begin{cases} 3\left(U_o^2/R\right)\cos\theta \\ 3R \times I_o^2 \cos\theta \\ 3U_o \times I_o \cos\theta \end{cases}$$

Electric energy (Watt-hours or Joules):

$$E_{el} = \int_0^T P(t)\; dt = \overline{P}T$$

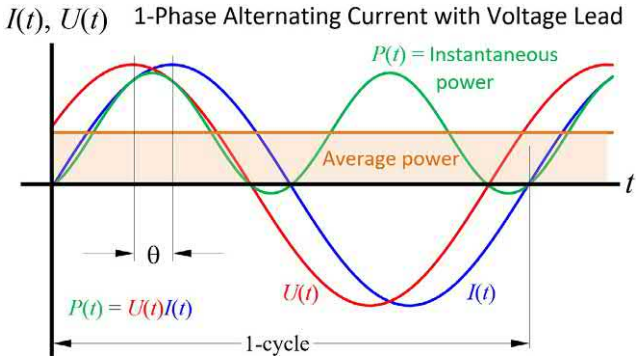


FIGURE 7-43 AC voltage leading the current.

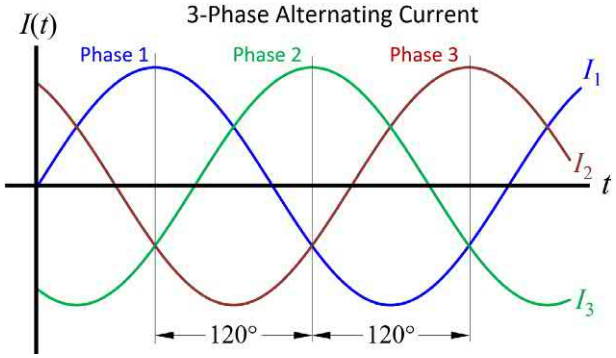


FIGURE 7-44 Variation of a 3-phase AC current.

power for a 3-phase waveform is more complex than that of the single-phase and, thus, is omitted.

where U_o = peak voltage (Volts), I_o = peak current (Amps), t = time (second), $\overline{U}$ and $\overline{I}$ are the root-mean-square (RMS) values of $U(t)$ and $I(t)$, respectively.

7.4.2 Battery Basics

(1) Cells, Modules, and Batteries

In electric aircraft, the motor is powered by a *battery* (aka *battery-pack* or *battery-system*). A battery consists of *cells* (e.g., 18650 Li-Ion-cells) arranged in *modules*. Thus, one or more cells constitute a module; one or more modules constitute a battery (see Figure 7-46).

A cell is a container of two chemicals, which when combined, undergo a chemical reaction of which an electric current is a primary byproduct. All cells have two terminals. One has a positive charge (lack of electrons) denoted by ⊕. The other has negative charge (abundance of electrons) denoted by ⊖. A *separator* is a component that isolates the two terminals.

Batteries fall into two classes: *primary* (disposable) and *secondary* (rechargeable). Primary cells permit discharge only because the constituent chemicals change permanently during the discharge process. In contrast, the chemical reaction in secondary cells is reversible; the original materials can be reconstituted using an electric potential between the terminals. Such batteries can be discharged and recharged multiple times. Properties of interest for a battery include its voltage, the maximum current it delivers, capacity, and mass.

(2) Historical Perspective

The complete history of the battery is long and interesting. Some claim the battery dates to the so-called Parthian batteries, at the beginning of the Common Era, some 2000 years ago. While contested, it is known with certainty that the modern battery was invented in the late 1700s by Alessandro Volta (1745–1827), although it dates to experiments by Luigi Galvani (1737–1798). Volta was the first to explain the phenomenon as the consequence of joining two dissimilar metals [62]. A brief history of the battery is compressed into the timeline in Figure 7-45. For a more detailed version see ref. [58]. The current state-of-the-art battery for transportation purposes is Li-Ion.

(3) Energy and Power Density of Batteries

The *energy density* of a substance refers to the amount of energy it stores per unit mass or volume: Thus, (1) *Mass specific energy* is the quantity of energy per unit mass (Watt·hours/kg or Wh/kg), while (2) *volume specific energy* is the quantity of energy per unit volume (Wh/L). *Mass specific power* is the quantity of power per unit mass (W/kg). Battery power is always rated in Watts (or Volt·Amps).

$$\text{Mass Specific Energy (Wh/kg):} \quad E^* \equiv \frac{UI\Delta t}{m_{batt}} \tag{7-47}$$

$$\text{Volume Specific Energy (Wh/liter):} \quad \forbidden{V}^* \equiv \frac{UI\Delta t}{\forbidden{V}_{batt}} \tag{7-48}$$

$$\text{Mass Specific Power (W/kg):} \quad P^* \equiv \frac{UI}{m_{batt}} \tag{7-49}$$

where Δt is time and m_{batt} is the mass of the battery. The E^* and $\forbidden{V}^*$ for a Li-Ion-battery is substantially lower than that of fossil fuels, about 60 and 18-times less, respectively [61, 64]. Energy densities for several batteries is listed in Table 7-12. Lithium-Sulfur batteries exemplify new technology on the horizon. Compared to Li-Ion, it doubles energy density to 500 Wh/kg.

(4) Battery Capacity and Energy Capacity

The battery *capacity* (C_{batt}) refers to the amount of Amp·hours (Ah or mAh for milli-amp-hours) of current contained in a battery. Multiplying this by the battery's *nominal voltage* (see later) yields its *energy capacity* (E_{batt}). This is rated in Watt-hours (Wh), kilowatt-hours (kWh), or Amp·Voltage·hours (AVh). Energy capacity can also be estimated if the mass and mass specific energy of a battery is known. Thus, it is commonly estimated using the two forms below:

$$E_{batt} = \begin{cases} C_{batt}\, U_{nom} \\ E^*\, m_{batt} \end{cases} \tag{7-50}$$

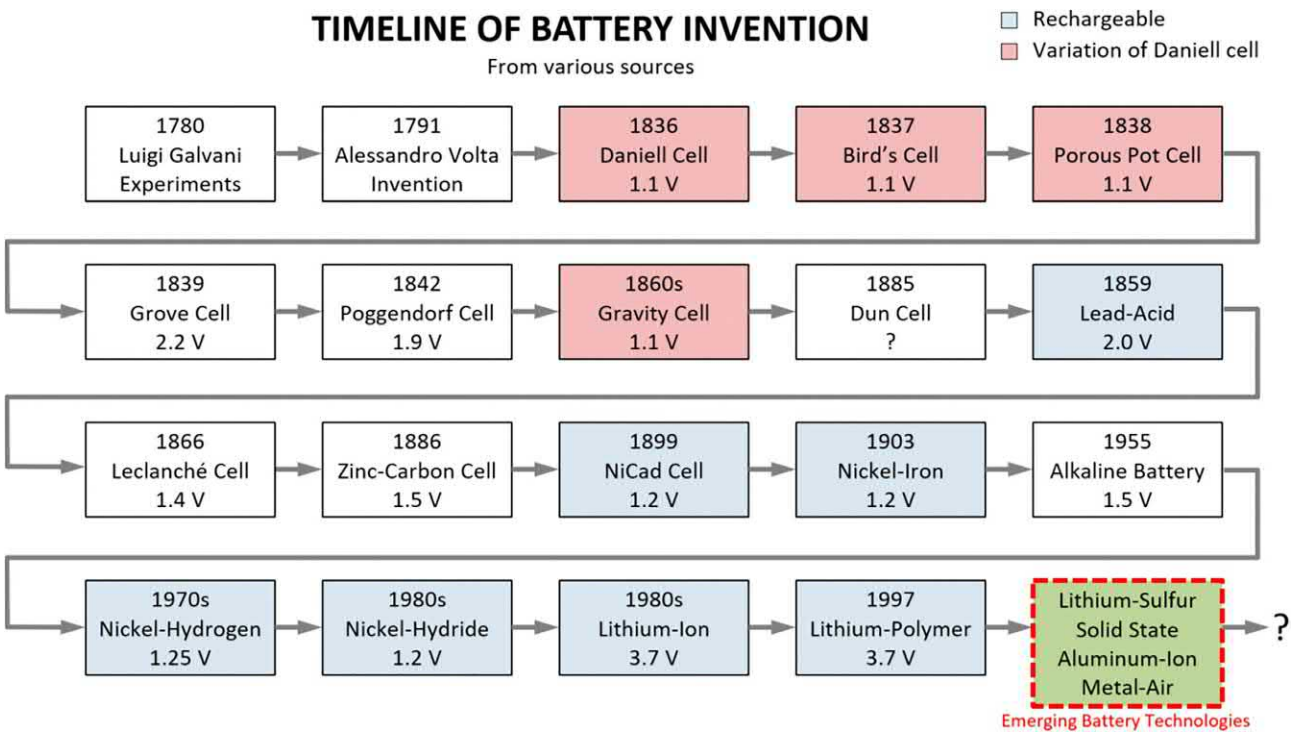


FIGURE 7-45 A basic timeline of battery development [63].

TABLE 7-12 Battery properties.

					Lithium-ion batteries		
Specifications	**Units**	**Lead-acid**	**Ni-Cad**	**Ni-MH**	**Cobalt**	**Manganese**	**Phosphate**
Mass specific energy, E^*	Wh/kg	30–50	45–80	60–120	150–250	100–150	90–120
Volume specific energy, ~~V^*~~	Wh/L	60–75	50–150	140–300	220–350	–	–
Mass specific power, P^*	W/kg	180	150	250–1000	760	–	–
Cycle life (80% DOD)	Cycles	200–300	1000	300–500	500–1000	500–1000	1000–2000
Charge time	Hours	8–16	1–2	2–4	2–4	1–2	1–2
Cell Nominal Voltage, U_{nom}	Volts	2.0	1.2	1.2	3.6	3.7	3.2–3.3
Peak load current	C	5	20	5	2	>30	>30
Ideal load current	C	0.2	1	0.5	<1	<10	<10

Based on http://www.batteryuniversity.com/ [Accessed 10/29/2019].

As an example, a 28 kg Li-Ion with $E^* = 200$ Wh/kg contains 5600 Wh (5.6 kWh) —it can deliver 5600 W over a period of 1 h. This would keep a 100-W lightbulb lit for 56 h (2.3 days) or a 1500 W microwave running for 3.7 h. The 2020 model of the Tesla Model S has a 100-kWh battery pack. In contrast, a 12 V lead-acid car battery rated at 50 Ah contains $12 \times 50 = 600$ Wh of energy and can provide a 10 Amp current for 5 h. On the battery side of the circuit, discharging the battery causes a voltage drop that, given a desired fixed power, requires increased current-draw. This further accelerates the reduction in the battery capacity. The battery capacity is also affected by temperature through the rate of the chemical reaction that takes place. Low temperature slows the chemical reaction, while high temperature reduces battery life.

(5) Serial and Parallel Battery Circuits

It is possible to build a high-voltage, high-capacity battery using multiple smaller cells. This is illustrated in Figure 7-46. If two cells are connected in *series* (⊕ terminal of one cell connects to the ⊖ of the other), the *total voltage* is the sum of the two. If the cells are connected in *parallel* (⊕ of one cell connects to the ⊕ of the other; same holds for the ⊖ terminals),

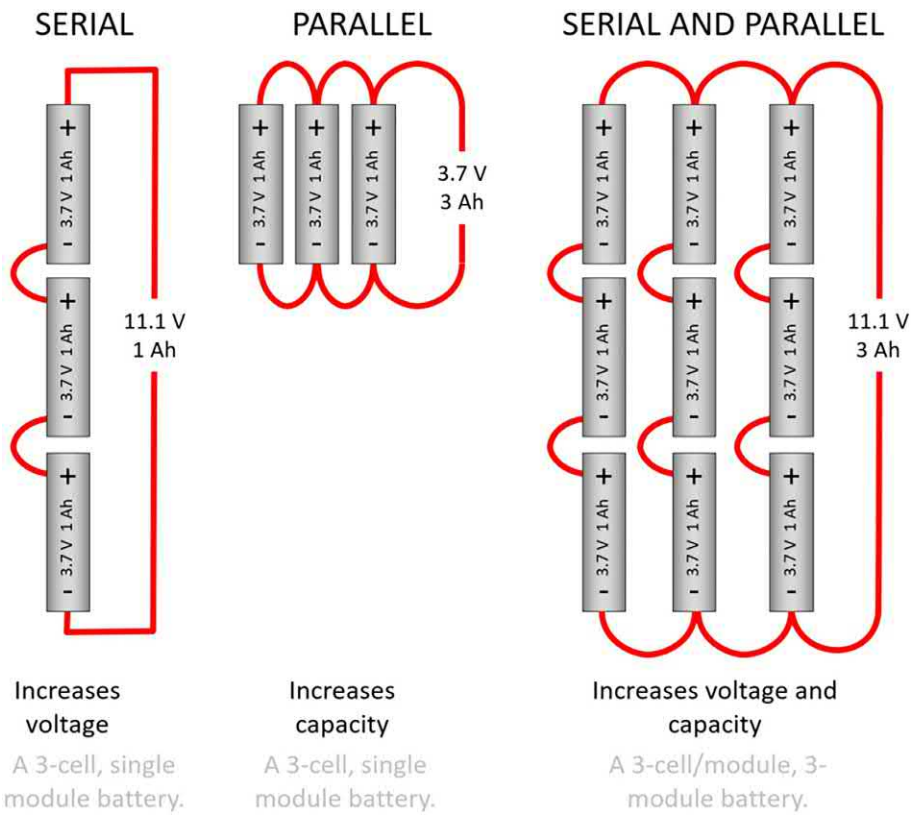


FIGURE 7-46 Serial and parallel battery circuits.

the *total capacity* is the sum of the two. Battery packs for electric aircraft are assembled in this fashion.

(6) Battery C-Rating

Indicates the maximum continuous current (I_{max}) a battery can deliver without damage. The higher the C-rating the better. It is defined mathematically as follows.

$$C_{rating} \equiv \frac{\text{max cont.current}}{\text{battery capacity}} = \frac{I_{max}}{C_{batt}} \qquad (7\text{-}51)$$

Since C_{batt} is in terms of Ah, the unit for C_{rating} is 1/h, usually written as "C." Consider the 5-Ah, 11.1 V, 25C, 3S-LiPo battery in Figure 7-58. Recharging at 1C takes 1 h, using a charging current of $I = C \times C_{batt} = 1 \times 5 = 5$A. Discharging it at 1C also takes 1 h, using the same 5A current. It delivers a maximum current of $I_{max} = C_{rating} \times C_{batt} = 25 \times 5 = 125$A. Of course, it can only do so for around 5 Ah/125 A = 0.04 h (=2.4 min). If one considers Peukert's law (see later) with a factor $k = 1.28$, this drops to about 37 s.

(7) Other Important Terms Regarding Batteries (ordered alphabetically)

Cold-Cranking Amps (CCA) is used for lead-acid batteries. Such batteries are typically marked with a CCA value, which indicates the current (in Amps) the battery can deliver at −18°C (0°F). Typical range is 200–1400 CCA.

Cycle life is how often a secondary battery can be charged and discharged. Depends on parameters such as chemical stability, environmental factors, operating temperatures, and typical DOD.

Depth-of-Discharge (DOD) and *State-of-Discharge* (SOC): DOD is the fraction (or percentage) of the capacity already consumed from a fully charged battery, while SOC is the remaining fraction (or percentage) of the capacity [65]. If 500 mAh have been consumed from a 1500 mAh battery, the DOD is 500/1500 = 0.333 and the SOC is 1–500/1500 = 0.667. A low value of DOD in secondary batteries results in greater cycle life of the battery [58].

Electrolyte is an ionic conductor inside the battery that serves as a medium to transfer electric charge as ions between the by ⊕ and ⊖ terminals.

Energy efficiency is the ratio of the energy contained in a source (gasoline, battery) to what can be harnessed. The charge and discharge efficiency of batteries is high compared to other sources. Charge-efficiency is close to 100% and discharge-efficiency is close to 95%. The discharge-efficiency of fuel cells is 20% to 60%. The energy efficiency of typical gas engines is about 25%.

Impedance is to AC current what resistance is to DC current. It is caused by the combination of Ohmic resistance and reactance.

Internal resistance within a battery is caused by the resistivity of the active materials in a cell and the quality of the contacts between the individual electrode particles.

Load is a device that uses electricity to do work.

Memory effect refers to a behavior in some batteries that progressively reduces their charge capacity. It only occurs in NiCad and to a lesser extent in NiMH batteries. It is caused by a growth of crystalline formation from a fine (desirable) to a large structure. Occurs when the cell is recharged before it is fully discharged.

Nominal voltage: Consider the two discharge curves in Figure 7-47, being discharged at constant current I over time T. We integrate the power (P) to obtain the electric energy (E_{el}) for both cells. Then, the nominal voltage, U_{nom}, is defined as E_{el} divided by the product $I \cdot T$. Even though both cells have the same voltage when $t=0$ and $t=T$, each has dissimilar U_{nom}. Of the two shown, U_{nom} for Curve 1 is higher.

Self-discharge is the inevitable and undesirable chemical reaction that takes place inside a battery due to current leakage through the electrolyte and reduces its charge when in storage. Self-discharge is temperature dependent.

Thermal runaway is a condition in which a battery overheats and destroys itself through internal heat generation. It is typically caused by overcharging or excessive current discharge and similar abuse.

(8) Battery Discharge Curves

The Voltage-Discharge plot in Figure 7-48 shows how the voltage reduces with state-of-discharge. Such curves are of great importance in the operation of battery powered vehicles. Most of the batteries shown, suffer from a rapid initial voltage drop, followed by a period of reduced drop. In fact, both Li-Ion (LiPo) and NiCad batteries maintain relatively constant voltage over 80% of their discharge capacity. Toward the end of their capacity, voltage drops rapidly and can destroy the battery if discharge continues. It is inadvisable to discharge

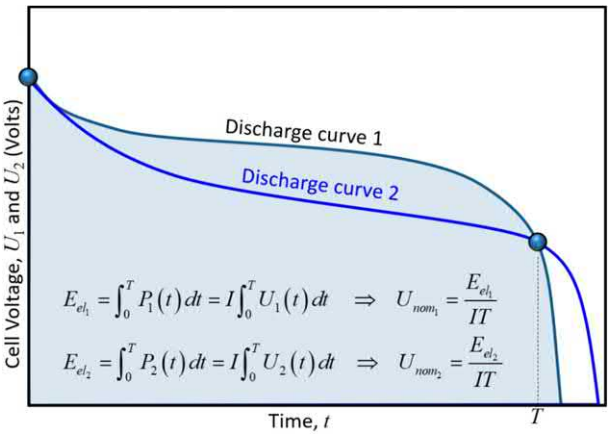


FIGURE 7-47 Example discharge curves for two cells.

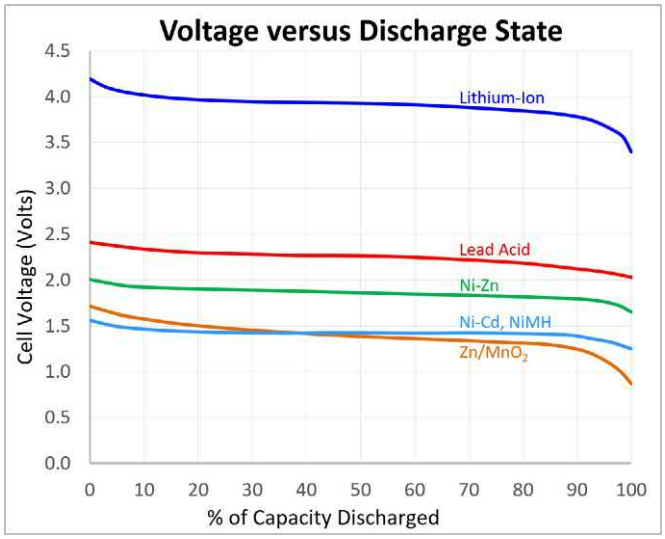


FIGURE 7-48 Discharge curves for several types of battery-cells. *Based on http://www.mpoweruk.com/index.htm [Accessed 10/29/2019].*

Li-Ion batteries below 2.5 V per cell, where 98% of the nominal charge capacity has been consumed. To simplify analysis, it can be assumed that voltage is constant at V_{nom} (3.7 V for Li-Ions).

(9) Tremblay's Method for Creating a Discharge Curve

Tremblay et al. [66] developed a simple model to estimate the open-circuit voltage of secondary (rechargeable) battery based on the state of charge. The approach makes several assumptions using the basic plot of Figure 7-49: No voltage recovery, constant internal resistance, discharge characteristics are the reverse of the charging characteristics, no self-discharge, and no Peukert, temperature, or memory effects. Tremblay's method is expressed as follows:

$$U_{OC}(C) = U_0 - \left(\frac{\kappa\, C_{cut}}{C_{cut} - C}\right) + Ae^{-B \cdot C} \tag{7-52}$$

where $A \equiv U_{full} - U_{exp}$ and $B \equiv 3/C_{exp}$ and

$$\kappa = \frac{\left(U_{full} - U_{nom} + A\left(e^{-B \cdot C_{nom}} - 1\right)\right)(C_{cut} - C_{nom})}{C_{nom}} = \left(U_{full} - U_{nom} + A\left(e^{-B \cdot Q_{nom}} - 1\right)\right)\left(\frac{C_{cut}}{C_{nom}} - 1\right) \tag{7-53}$$

and

$$U_0 = U_{\text{full}} + \kappa + (R_C\, I_0) - A \tag{7-54}$$

where

C = State of discharge (e.g., 345 mAh)
C_{exp} = Capacity discharged at the end of the exponential range (e.g., 220 mAh)
C_{nom} = Capacity discharged at the end of the nominal range (e.g., 1700 mAh)

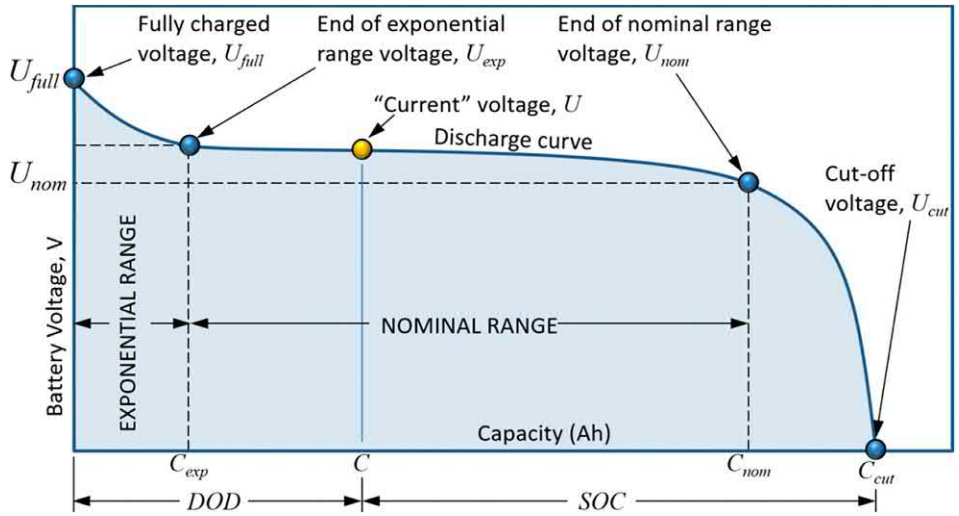


FIGURE 7-49 Nomenclature for a discharge curve per Tremblay's method. *Based on Tremblay, O., Dessaint, L.-A., Dekkiche, A.I., A Generic Battery Model for the Dynamic Simulation of Hybrid Electric Vehicles, IEEE, 2007.*

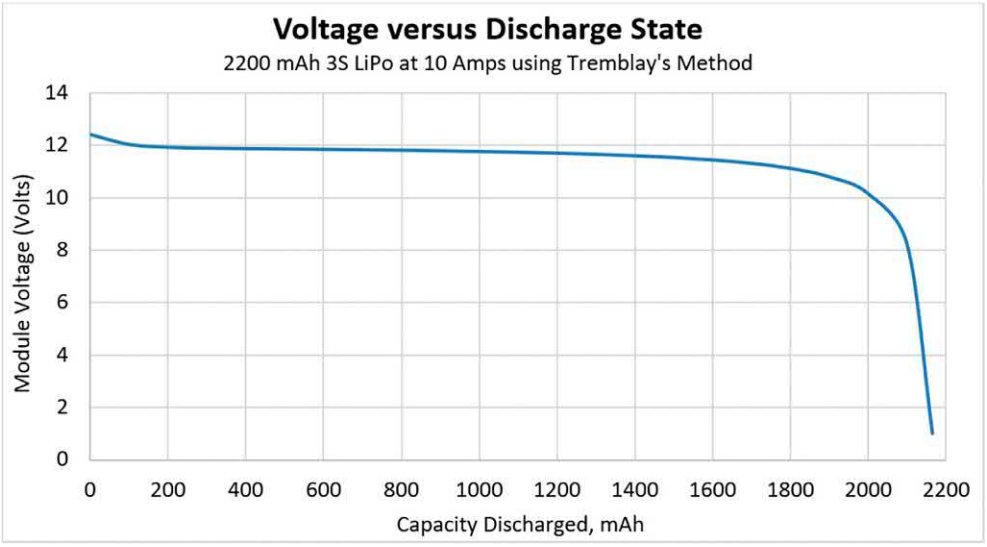


FIGURE 7-50 Discharge curve prediction for a typical 3-cell LiPo.

C_{cut} = Capacity discharged at cut-off (e.g., 2200 mAh)
U_{full} = Fully charged potential (e.g., 12.4 V)
U_{exp} = Potential at the end of the exponential range (e.g., 11.9 V)
U_{nom} = Potential at the end of the nominal range (e.g., 11.3 V)
U_{cut} = Cut-off potential (e.g., 9.8 V)
I_0 = Specified discharge current (e.g., 10 Amps)
R_C = Internal resistance (e.g., 2×10^{-3} Ohms)

An example of Tremblay's method for a typical 2200 mAh 3S LiPo battery for an RC aircraft is presented in Figure 7-50. The graph uses the data shown in the parenthesis next to the above variables.

(10) Discharge Effects-Peukert's Law

Additional effect must be considered when discharging batteries; a greater discharge rate leads to reduction in the available capacity. The discovery of this effect is attributed to the German scientist Wilhelm Peukert (1855–1932). It is important to the operation of electric vehicles, which periodically demand high current discharge. The effect can be phrased in the following fashion. Consider a 5 Ah battery being discharged at a constant 10-Amp draw. One would expect the battery to be fully drained in 5 Ah/10 A = 0.5 h. However, in practice the battery runs out in less time, about 0.4 h. The effect, which is called *Peukert's Law*, is expressed mathematically as shown below.

$$C = I^k \Delta t \tag{7-55}$$

where C is the discharge capacity (in Ah), I the current (in Amps), k is the *Peukert's constant*, and Δt the time (in hours) it takes to discharge the battery. The value of k depends on the type of battery and varies between 1 (ideal battery) and 2 (terrible battery). Typical values for lead-acid batteries are between 1.1 and 1.3 and for LiPo batteries it varies from 1.00 to 1.28 (see Omar et al. [67]). It is suggested that Peukert's law should be applied carefully and its reliability requires constant current draw and limited internal temperature rise due to discharge [68]. A rise in internal temperature increases charge capacity and counteracts Peukert's law. It is recommended that operators regard the battery as "a complex system, where the capacity is a function of current rate, depth of discharge and temperature." [67].

EXAMPLE 7-6

Powered paragliding is a popular sport. Some paragliders are powered by a propeller mounted to a compact electric power-pack strapped to the pilot's back. One seller offers a 15-kW power-pack with a 22-cell LiPo (81.4 V) and states it offers about 10-min flight. Determine an equivalent horsepower rating for the electric motor. Also compute the current to the motor and its equivalent load. If the battery pack capacity is 12 Ah, how long can the motor be run at peak force assuming a Peukert's constant of $k = 1.2$? How about a 50% power ($k = 1.0$)?

SOLUTION:

Power: $P = 15\,\text{kW} = 15000\,\text{W} = 15000\,\text{W}/(746\,\text{W/hp}) = 20.1\,\text{hp}$

Current: $I = P/U = 15000\,\text{W}/81.4\,\text{V} \approx 184\,\text{Amps}$

Equivalent load:

$$R = U/I = 81.4\,\text{V}/184\,\text{Amps} \approx 0.442\,\text{Ohms}$$

Duration:

$$\Delta t = C/I^k = \frac{12\,\text{Ah}}{(184\,\text{Amps})^{1.2}} \approx 0.023\,\text{hr} = 1.38\,\text{min}$$

Assuming 50% power (7.5 kW) and $k = 1.0$ yields 7.81 min.

(11) Temperature Effects—The Arrhenius Equation

The ideal operating temperature for most batteries is between 10°C and 35°C (50°F and 95°F). Intuitively, higher temperature speeds up the chemical reaction inside the battery, improving battery performance. An unfortunate side-effect is a reduction in battery-life. The relationship between temperature and the rate of the chemical reaction inside the battery is typically described using the Arrhenius equation [69], attributed to the Swedish scientist Svante Arrhenius (1859–1927, 68). The expression is omitted for space but is brought up for readers interested in deeper understanding of temperature effects on batteries. A common rule of thumb is that the rate of many chemical reactions at room temperature doubles with an increase of 10°C temperature.

7.4.3 Additional Sources of Electric Energy

(1) Solar Energy Basics

Solar powered flight dates to experiments conducted by Colonel H.J. Taplin of the UK in June 1957, who launched the first electrically powered (RC) aircraft, called the "Radio Queen" [70]. It demonstrated that flying using electric power was possible—a precursor to electric flight using solar power. The first truly solar powered aircraft, the Sunrise I, took place on November 4, 1974 [71, 72]. Then, there are the Swiss made *Solar Impulse 1* and 2. The latter completed circumnavigating the Earth in July 26, 2016, using only solar power [73], a remarkable achievement.

Solar power is usually harnessed either using lenses and mirrors through *concentrated solar power* (CSP) or *photo-voltaic* (PV), in which photons are directly converted to electricity. The voltage is produced between two dissimilar materials when their common junction is illuminated with photons [74]. Solar cells are rated by the power (Watts) and voltage between the by ⊕ and ⊖ terminals. Incorporating PV in aircraft increases weight, offsetting some of the benefits.

The efficiency of PV is a primary design variable for solar powered aircraft. Figure 7-51 shows a radiation spectrum for the Sun (*irradiance* is the flux of radiant energy per unit area normal to the direction of the light rays). A solar cell capable of utilizing the entire spectrum

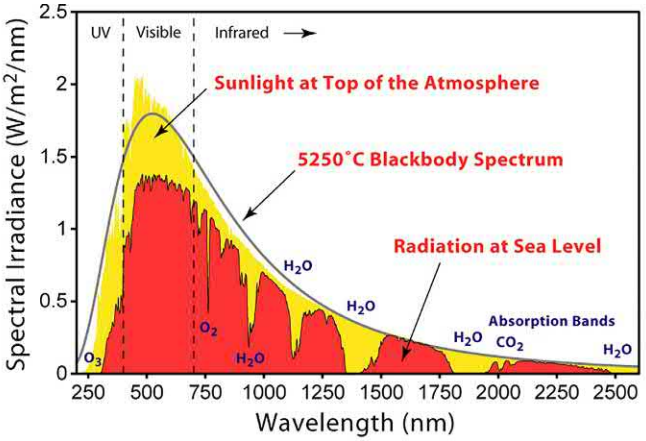


FIGURE 7-51 Solar radiation spectrum [75].

is 100% efficient. Current solar cells use semiconductors that only utilize selected range of wavelengths. The physics of the conversion is interesting (e.g., see [76, 77]), albeit beyond the scope of this text. The maximum theoretical radiative energy available on a sunny day is 1368 W/m^2 [78]. This quantity is called the *solar constant*. In industry setting, it is assumed 1000 W/m^2. This value varies with latitude, time of the day, season, and presence of clouds. The term *PV efficiency*, η_{PV}, is the amount of power that can be extracted from a unit area of a solar panel. It is defined as follows:

$$\eta_{PV} \equiv \frac{\text{Max power output}}{\text{Incident radiation flux} \times \text{Collector area}} = \frac{P_{max}}{E_i \times A_c} \tag{7-56}$$

where P_{max} is the maximum power output of the solar cell, E_i is the energy available per unit area (e.g., 1000 W/m^2) and A_c is the area usable for energy collection. Typical consumer solar panels are 21.5% efficient (e.g., see X-series Solar Panels [78]). There is annual deterioration, as efficiency typically reduces by 5% to 20% over 25 years of use. However, this technology is advancing. The maximum efficiency of solar panels has increased from about 15% in 1980 to 47% in 2019, although these are still in the research phase [79].

(2) Current and Voltage of a Solar Cell

Figure 7-52 shows a classical shape of the current versus voltage for a solar cell. When the cell pads are not connected the circuit is open (OC) and the voltage measured across pads amounts to U_{OC}. When short circuited (SC), the voltage drops to zero and the current flow reaches its maximum value, denoted by I_{SC}. At these extremes the power, $P = U \cdot I$, is zero. However, as shown in Figure 7-52, the power reaches a maximum between these values, when the voltage is U_{Pmax} and current is I_{Pmax}. This is where the solar cell should be operated. The current in Figure 7-52 is approximated using the following expression

$$I = \begin{cases} I_{SC} \cos\phi_{sun} & \text{if } U < U_{NL} \\ I_{SC} \cos^n\left(\frac{\pi}{2}\left(\frac{U - U_{NL}}{U_{OC} - U_{NL}}\right)\right) \cos\phi_{sun} & \text{if } U \geq U_{NL} \end{cases} \tag{7-57}$$

where I is the current from the circuit, I_{SC} is the short circuit current, ϕ_{sun} is the angle between the sun and a normal to the PV, U_{NL} is the voltage where curve becomes nonlinear, U_{OC} is the open circuit voltage (typical 0.62 V), U is the circuit voltage, and n is an exponential, which here varies linearly from 0.1 for 100% irradiance to 0.25 for 50% irradiance.

(3) Fuel Cells

A fuel cell produces electricity by combining hydrogen and oxygen, forming water and heat as byproducts (see Figure 7-53). The fuel cell is superior to batteries in many ways. Besides being a zero-emission device (assuming it is charged using renewable energy), its voltage remains constant with discharge. This means that maximum engine power is independent of the state of discharge. For electric aircraft to be truly compatible with conventional gas-powered aircraft, maximum power must be available regardless of the state of discharge. The primary drawback of fuel cells is low power density (W/kg), despite high energy density (Wh/kg). The first passenger carrying aircraft powered by a hydrogen fuel cell was the DLR HY4. Its maiden flight took place on September 29, 2016 [80].

There are several types of fuel cells, although, only one is considered here. This features a thin membrane, called a *proton exchange membrane* (PEM). One side of it is exposed to pure Hydrogen gas (H_2) and the other to Oxygen (O_2). The PEM catalytically strips the electrons off the Hydrogen, converting it into Hydrogen ions (H^+). Furthermore, the ions can only pass through it in one direction; to the side that is bathed in oxygen. The

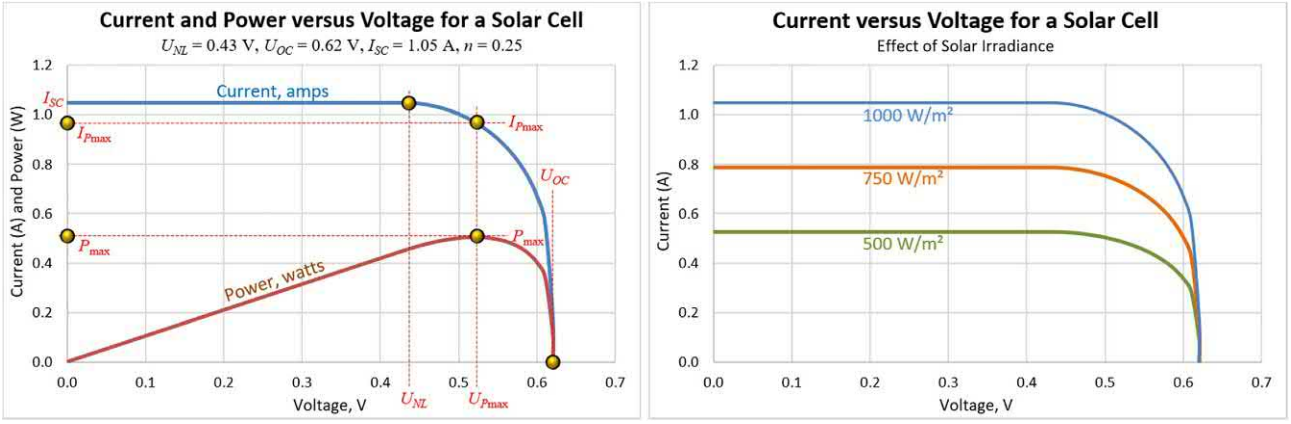


FIGURE 7-52 Current-versus-voltage for a typical solar cell (left) and effect of irradiance on ($\phi_{sun} = 90$ degrees).

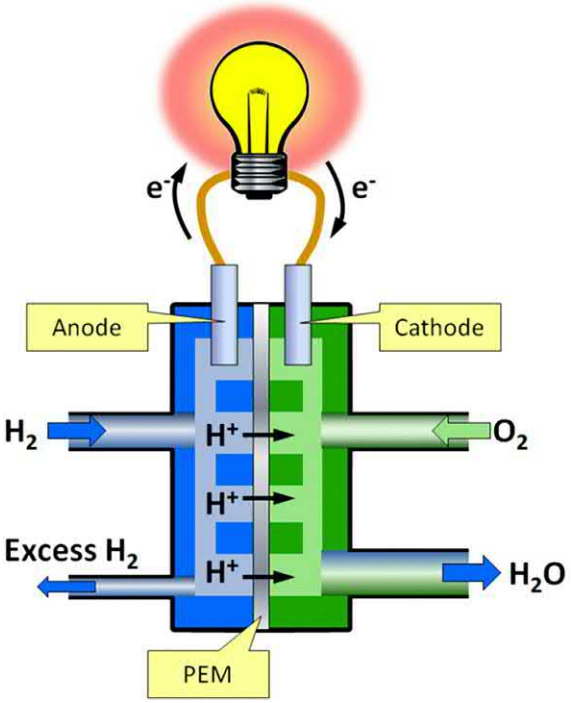


FIGURE 7-53 The workings of a fuel cell.

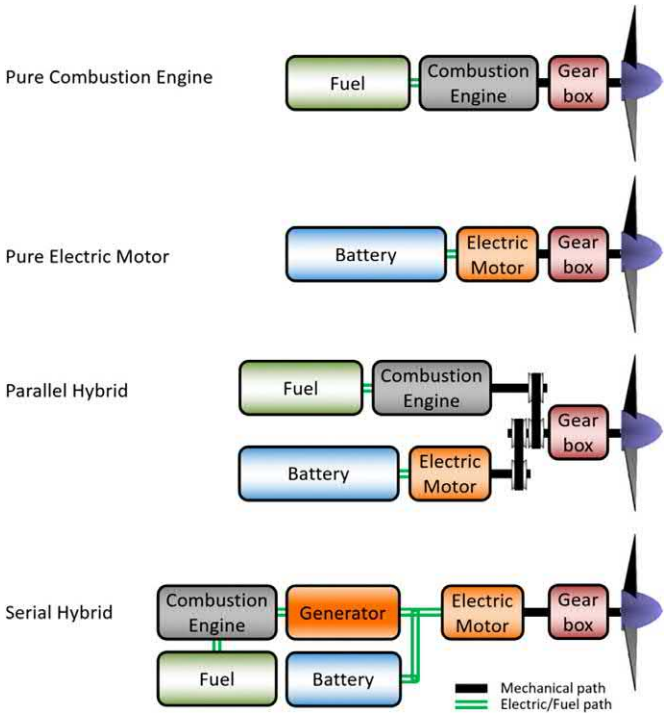


FIGURE 7-54 Basic aircraft powertrains (inspired by ref. [61].)

electrons that are stripped off take a different path and flow through the anode to the cathode, generating electric current. At the same time, H^+ pass through the PEM where they encounter O_2 and electrons flowing through the cathode. The three react to form H_2O, completing the process.

Anode reaction: $H_2 \rightarrow 2H^+ + 2e^-$

Cathode reaction: $\frac{1}{2}O_2 + 2H^+ + 2e^- \rightarrow H_2O$

7.4.4 Electric Motor Basics

Even though the energy density of the modern battery is much improved, it leaves a lot to be desired at the time of this writing. High power demand during take-off and climb of heavy aircraft may call for a work-around: hybrid power installations (powertrains). These combine a *pure combustion engine* and *pure electric motor* in the *parallel* and *serial* hybrid forms shown in Figure 7-54. These are not the only hybrid configurations. All have their pros and cons. Note that a gearbox is not always required.

(1) Electric Motors for Electric Aircraft

Electric motors differ from reciprocating engines in that their output is torque, not power. An electric motor only produces power when it turns. Regardless, it can develop its maximum torque without turning—which is why electric motors are used to start piston engines. This allows an electric motor to turn a propeller at lower RPM (at higher pitch and torque), while developing similar thrust. The propeller noise is reduced, so, even though its efficiency is compromised, it has a great potential for reduced operational noise while cruising above populated areas.

Electric motors are classified as AC or DC. There are subclasses within each. One such is *brushed* or *brushless*. Another is *inrunner* or *outrunner*. Electric motors for aircraft are usually driven by 3-phase alternating current to develop greater torque. This requires the DC from the battery to be converted to AC using an ESC (discussed below). Today, the most common DC motor is brushless, commonly referred to as *BLDC* (brushless, DC). The most common AC motor is the *synchronous AC motor*.

(2) Pros of Electric Motors

(A) Very high mechanical efficiency (electric-to-mechanical conversion); (B) power output independent of altitude; (C) very smooth operation of engines; (D) very simple and clean installation in aircraft; (E) very simple and light engines; (F) inexpensive technology; (G) very reliable stop-start characteristics; (H) very environmentally friendly (provided the electricity is not generated using fossil fuels).

(3) Cons of Electric Motors

(A) Low energy density of batteries is a major hurdle—currently. This precludes anything but high-efficiency aircraft designs to use the technology for long range/endurance; (B) limited to subsonic flight; (C) currently,

limited infrastructure is present to service electric aircraft; and (D) low energy density results in excessive battery weight.

(4) Thrust Modeling for Propellers Driven by Electric Motors

Thrust modeling for propellers driven by electric motors is presented in Chapter 15.

(5) Helpful Formulae when Analyzing Electric Motors

Cyclic function: $$y = A\sin(\omega t + \phi) = A\sin(2\pi f t + \phi) \tag{7-58}$$

where A = amplitude, ω = angular speed in rad/s, ϕ = phase angle, t = time in second, and f = frequency in Hertz.

Frequency (f) and period (T):
$$f = 1/T \quad [\text{cycles/sec or Hertz}] \tag{7-59}$$

Angular speed (ω): $$\omega = \frac{2\pi}{T} = 2\pi f \quad [\text{radians/sec}] \tag{7-60}$$

Convert RPM to ω: $$\omega = \frac{2\pi\ RPM}{60} \quad [\text{radians/sec}] \tag{7-61}$$

Convert RPS to ω: $$\omega = 2\pi\ RPS \quad [\text{radians/sec}] \tag{7-62}$$

Relationship between power (P), torque (τ), and rotation:

$$P = \overbrace{\text{work} = \overbrace{\text{force} \cdot \text{dist}}^{F\,2\pi r}}^{\text{work done each second}} \frac{RPM}{60} = \overbrace{F\,r}^{\tau = \text{torque}} \overbrace{\frac{2\pi\ RPM}{60}}^{\omega = \text{angular speed in radians/sec}} = \tau\omega = \tau\frac{2\pi}{T} = \tau(2\pi f) \tag{7-63}$$

Relationship between power (P), torque (τ), and RPM:

Power in Watts: $$P_W \approx 745.7 P_{HP} \approx \overbrace{0.1047}^{=2\pi/60}\ \tau_{[\text{Nm}]}$$

$$RPM \approx \overbrace{0.07734}^{=2\pi/(60\cdot 1.354)}\ \tau_{[\text{ft}\cdot\text{lb}_\text{f}]}\ RPM \tag{7-64}$$

Torque in Nm: $$\tau_{[\text{Nm}]} \approx \frac{9.549 P_W}{RPM} \approx \frac{9549 P_{kW}}{RPM} \approx \frac{7121 P_{HP}}{RPM} \tag{7-65}$$

Torque in ft · lb$_\text{f}$: $$\tau_{[\text{ft}\cdot\text{lb}_\text{f}]} \approx \frac{7.053 P_W}{RPM} \approx \frac{7053 P_{kW}}{RPM} \approx \frac{5259 P_{HP}}{RPM} \tag{7-66}$$

where

P_W = power in Watts
P_{kW} = power in kilo-Watts
P_{HP} = power in horse-power
$\tau_{[\text{Nm}]}$ = torque in Nm, and
$\tau_{[\text{ft}\cdot\text{lbf}]}$ = torque in ft·lb$_\text{f}$.

EXAMPLE 7-7

An electric motor rotates at 3000 RPM while consuming 5000 W. Calculate (a) angular frequency in rad/s and (b) the torque in Nm and ft·lb$_\text{f}$.

SOLUTION:

(a) $$\omega = \frac{2\pi\ RPM}{60} = \frac{2\pi\ (3000)}{60} = 314.2 \text{ rad/sec}$$

(b) $$\tau_{[\text{Nm}]} \approx \frac{9.549 P_W}{RPM} = \frac{9.549(5000)}{3000} = 15.92 \text{ Nm and } \tau_{[\text{ft}\cdot\text{lb}_\text{f}]} \approx \frac{7.053 P_W}{RPM} = \frac{7.053(5000)}{3000} = 11.76 \text{ ft}\cdot\text{lb}_\text{f}$$

(6) Brushed versus Brushless Motors

A *brushed* motor is one for which an electrical connection with the commutator (or slip-ring) inside the motor is made by a direct contact using brushes. Brushed motors are simpler and less expensive than brushless ones. However, they do not have permanent magnets and must generate their own magnetic field using a fraction of the current. This renders them less efficient than brushless motors (about 75%–80% versus 85%–98%) and reduces torque for a same-size brushless motor. Brushed motors are less reliable due to brush wear-out. Additionally, during operation, brush-arcing causes an ignition-risk in areas where fuel vapor may be present. Brushless motors do not arc. Given the same weight or volume, brushless motors rotate faster with greater torque: they deliver greater power. It is possible to increase or maintain torque at a given RPM. Their heat dissipation is better, their physical dimensions for same torque is less, and they develop less noise. Their biggest drawback is they are more expensive and complex to operate.

(7) Inrunner versus Outrunner Motors

An *inrunner* is a brushless electric motor for which the stators (to which the copper wire is wound) are *outside* a

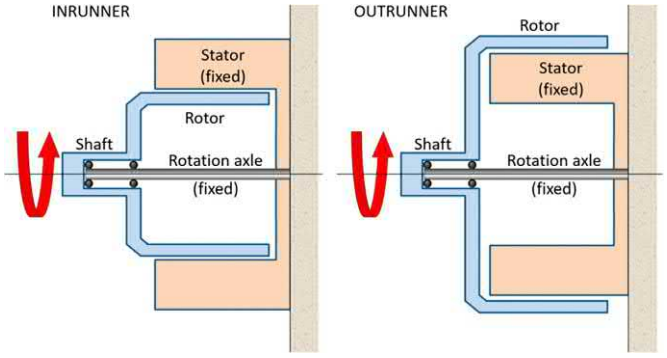


FIGURE 7-55 A schematic of the mechanical difference between an outrunner and inrunner electric motors.

rotating inner core (see Figure 7-55). In contrast, an *outrunner* is a brushless electric motor for which the stators are *inside* the rotating outer shell (with fixed magnets). Outrunners rotate at lower RPM but generate more torque than inrunners. The increased torque is attributed to the greater arm of the rotor. Outrunners are better suited for electric aircraft due to greater torque per unit weight and eliminate need for a reduction drive. However, their frontal area (diameter) is greater. In RC aircraft, outrunners are commonly used to drive propellers, while inrunners are chosen for small diameter ducted propellers, in part, because of higher RPM and, in part, because of smaller diameter.

(8) Electronic Speed Controller (ESC)

The ESC is an inverter that converts the battery's direct current into alternating current. Figure 7-56 illustrates its place the powertrain. The motor's power is controlled using battery current; the voltage on the battery-side remains relatively constant, albeit gradually dropping (it only alternates on the engine-side). In human-operated aircraft, this is accomplished using a *throttle*-control. In an unmanned aircraft (UAV or RC), it is controlled through the aircraft's remote-control system (receiver). The ESC uses between 5% and 20% of the battery energy to convert DC to AC. This energy is lost as heat. The designer should provide an escape path for this heat.

(9) Power Available and Efficiency of a Complete Drivetrain

Figure 7-56 shows a schematic of a typical drivetrain for an electric aircraft with typical component efficiencies. The propeller efficiency (η_p) is excluded; it depends on the RPM and airspeed and is dealt with in Chapter 15. The efficiency of the battery, ESC, motor, and gearbox are denoted by η_{batt}, η_{esc}, η_{em}, and η_{gb}, respectively. These constitute the system's total efficiency (η_{system}). The motor-efficiency (η_{em}) is usually provided by the manufacturer in an *efficiency map*, such as the one exemplified in Figure 7-57. It depicts how the motor's efficiency depends on the RPM and load (torque). Note that higher efficiencies are expected for higher quality components. When a gearbox is not needed, then $\eta_{gb}=1$. We can write the power delivered to the propeller in terms of the system efficiency as shown below. This power *is* the *available motor power* (P_{AVmot}), discussed later in Chapter 21. It is analogous to the power delivered to the shaft of a piston engine.

$$P_{AV_{mot}} = \eta_{system} UI \tag{7-67}$$

EXAMPLE 7-8

Consider the replacement of a 100 BHP piston engine (P_{ENG}) with an electric motor that maintains the same performance of the subject aircraft. Determine the required power rating of the motor (P_{MOT}) so it delivers the same power to the propeller, if the drivetrain efficiency (η_{system}) is 80%? What power must the battery deliver? If the battery circuit has a potential of 400 V, what is the current it must deliver?

SOLUTION:

$$P_{ENG} = 100\ BHP \Rightarrow P_{MOT} = 74.6\ kW$$

$$\Rightarrow P_{BATT} = \frac{P_{MOT}}{0.8} = 93.25\ kW$$

$$P_{BATT} = UI \Leftrightarrow I = \frac{P_{BATT}}{U} = \frac{93250}{400} = 310.8\ Amp$$

(10) Miscellaneous Terms for Small Electric Motors

Figure 7-58 shows a setup for a typical electric motor system for RC aircraft. Figure 7-59 show a basic setup for small human carrying aircraft.

Motor kV-rating refers to the increase in RPM associated with increase in voltage. 1000 kV means that increasing the potential by 1-V, increases the motor speed by 1000 RPM.

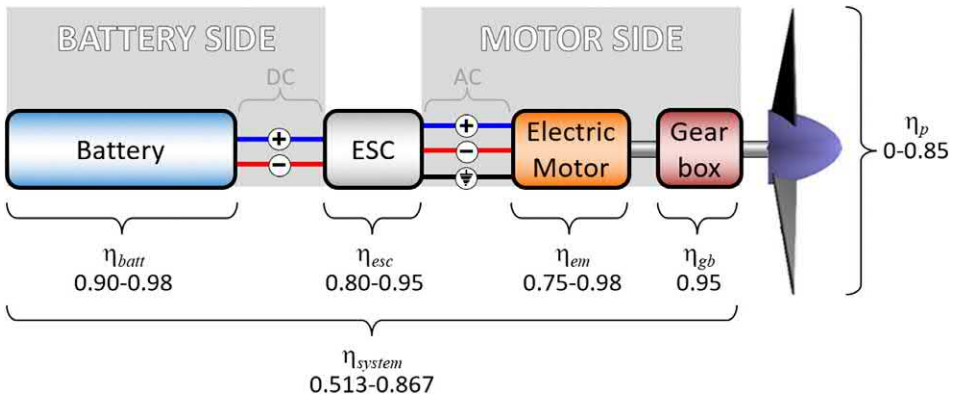


FIGURE 7-56 A schematic of a pure electric powertrain, with typical component efficiencies.

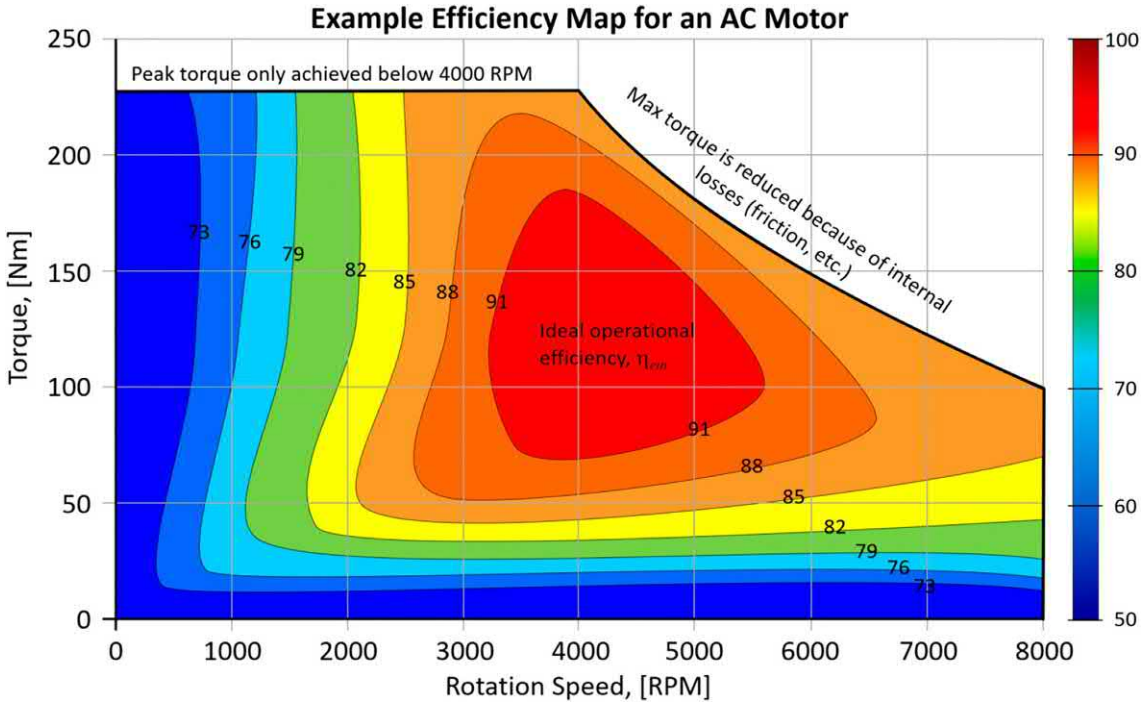


FIGURE 7-57 An example of an efficiency map for a hypothetical electric motor.

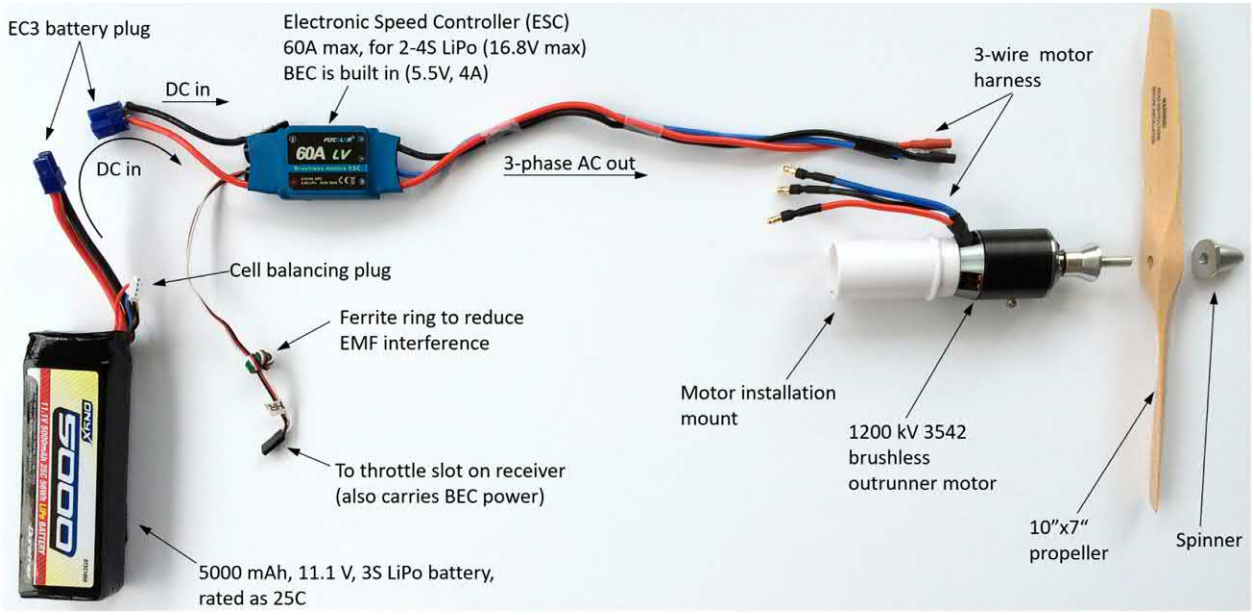


FIGURE 7-58 Typical electric motor setup for an RC aircraft. *Photo by author.*

The rating is the slope for the motor's RPM-versus-Volt graph. Motors for RC aircraft typically range between 400 and 3500 kV. Larger motors are around 15–100 kV.

Battery Eliminator Circuit (BEC) is an extra circuit provided in most ESCs to run the receiver using the battery that powers the motor. This permits the use of a single battery for the entire aircraft. The drawback is that if the electric connection is disrupted, power to the motor and servos is lost. When the BEC in RC aircraft detects voltage-drop associated with low battery-charge, it cuts off power to the motor, allowing for the possibility of a dead stick landing.

(11) Modeling Energy Consumption of Electric Motors

Consider a battery being used to power an electric motor with a total current draw of I_{tot} amps over a time

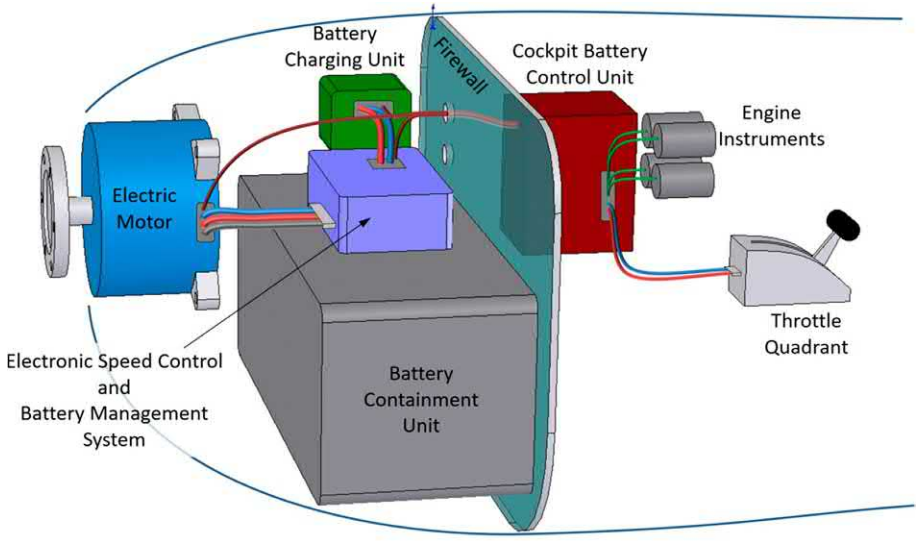


FIGURE 7-59 Typical electric motor setup for a manned aircraft.

segment Δt. This means the battery capacity is being reduced by amount

$$\Delta C = I_{tot}\ \Delta t \tag{7-68}$$

If the time segment is infinitesimal, the reduction in battery capacity can be written as

$$dC = I_{tot}\ dt \tag{7-69}$$

We can estimate the total battery capacity consumed as a function of the time-history of the current, through integration of Equation (7-69)

$$C_{used} = \int_0^{\Delta t} I_{tot}(t)\ dt \tag{7-70}$$

Figure 7-60 illustrates an actual operation of an electric motor in an RC aircraft, where the current and voltage

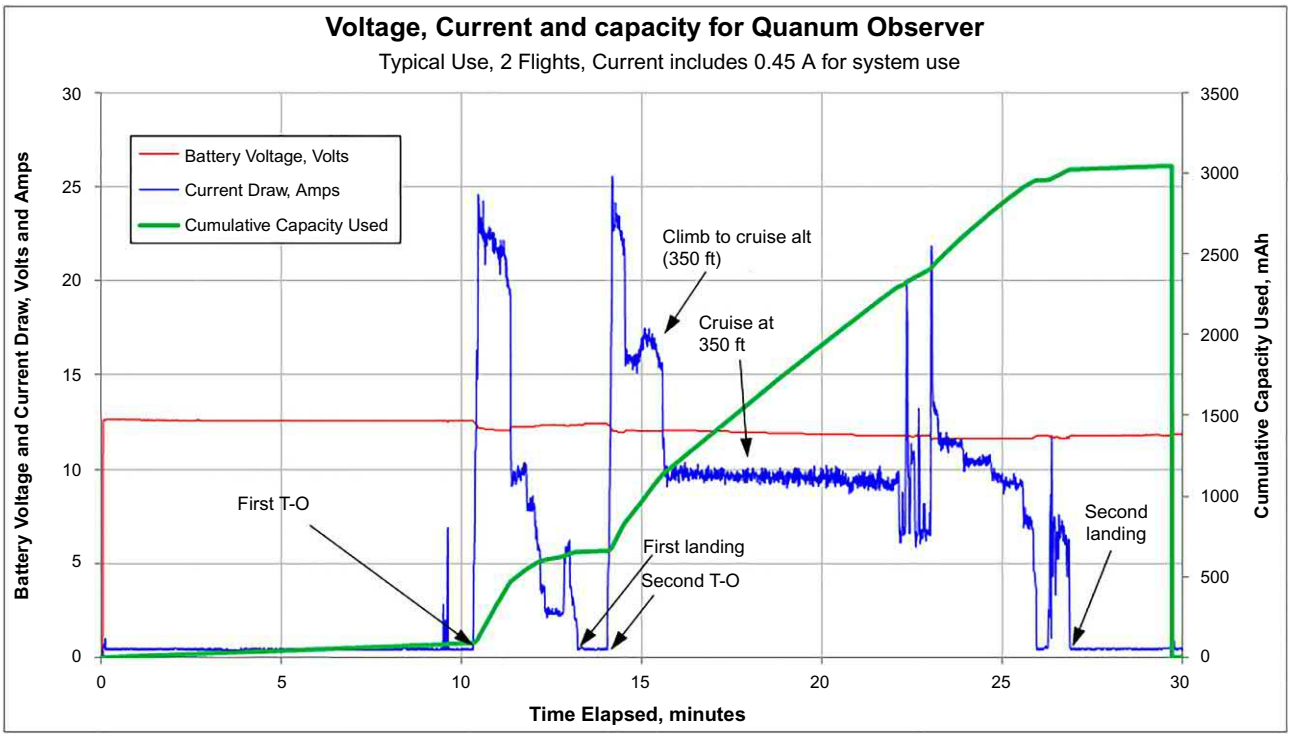


FIGURE 7-60 Typical consumption of electric power for a radio-controlled FPV aircraft.

from the battery was recorded. The first observation is that current to power systems is being drawn, even when the motor is not being used (the flat initial and final segments). It shows the voltage is relatively constant over the duration of a mission that included two T-Os and landings. What changes is the current. This is because the engine power is controlled by current draw, *not* voltage. However, the current draw includes the motor ($I(t)$) and systems (I_{sys}), required by avionics, lighting, etc. The total current draw, I_{tot}, is given by

$$I_{tot}(t) = I_{sys}(t) + I(t) \tag{7-71}$$

The total current draw dictates the total battery capacity consumed, C_{used}. Thus, we must rewrite Equation (7-70) in the following fashion

$$C_{used} = \int_0^{\Delta t} \left[I_{sys}(t) + I(t) \right] dt \tag{7-72}$$

Most of the time, the current directed to system operation is constant. It can, therefore, be integrated separately, yielding

$$C_{used} = I_{sys}\Delta t + \int_0^{\Delta t} I(t)\, dt \tag{7-73}$$

This expression can be converted to a discrete time format to keep track of battery capacity.

EXERCISES

(1) Determine the SFC for the following scenarios in the UK- and SI systems. (a) For a jet engine consuming 660 lb_f of fuel per hour while generating 990 lb_f of thrust. (b) For a piston engine consuming 21 gal while producing 275 BHP.

(2) Using the Gagg and Ferrar model tabulate the altitudes at which a normally aspirated piston engine generates 100%, 95%, 90%, …, 45% power for ISA, ISA–30°C, ISA, and ISA + 30°C.

(3) Using the Mattingly method (of Chapter 14) estimate the maximum power of a Garrett TPE331-10 at 30,000 ft and Mach 0.45, using the basic T-O data of Table 7-9 and assuming a Throttle Ratio of 1.072. Estimate the fuel consumption in gallons of Jet-A per hour. Assuming a cruise segment at that altitude, how far can the airplane fly on 500 gal if equipped with two TPE331s?

(4) Using the Mattingly method (of Chapter 14) to estimate the thrust of a Microturbo TRS 18-056 at 10,000 ft and Mach 0.39, using the basic T-O data of Table 7-10 and assuming a Throttle Ratio of 1.000. Estimate the fuel consumption in gallons of Jet-A per hour. How much fuel must this airplane carry to cover a 300 nm cruise segment at that altitude if equipped with only one TRS 18-056?

(5) Compare the thrust and fuel consumption of the two CFM56 engines in Table 7-11, at 35,000 ft and Mach 0.8 in terms of lb_f of Jet-A per hour, assuming it can be based off of the T-O data.

(6) A single engine electric aircraft is equipped with a 40-kW motor and battery packs that store 20 Ah of energy. Estimate its total endurance if it uses full power for 5 min, 65% power for 5 min, and 30% for the remaining charge (assuming no overheating and Peukert's constant $k = 1.08$)?

(7) A simple diffuser inlet is being designed for a specialized turbofan engine that requires the cruise speed Mach number of 0.65 to be reduced to Mach 0.3 at the front face of the compressor. The diameter of the compressor is 30 in. (a) Determine the required inlet lip diameter such the Mach number at the lip at T-O does not exceed 0.8. (b) If the included angle is expected to be 17 degrees, how long must the diffuser be in order to prevent flow separation?

(8) Estimate the power of the example engine in Section 7.2.5 at altitudes of 5000 ft, 10,000 ft, and 15,000 ft.

References

[1] J. Connors, *The Engines of Pratt & Whitney - A Technical History*, American Institute of Aeronautics and Astronautics, VA, 2010.

[2] C.F. Taylor, *Aircraft Propulsion – A Review of the Evolution of Aircraft Piston Engines*, Smithsonian Institution Press, 1971.

[3] V. Smil, *Two Prime Movers of Globalization - The History and Impact of Diesel Engines and Gas Turbines*, The MIT Press, Cambridge, MA, 2010.

[4] J. Roskam, *Airplane Design – Part II: Preliminary Configuration Design and Integration of the Propulsion System*, DARcorporation, 1997.

[5] A.K. Kundu, *Aircraft Design*, Cambridge University Press, 2010.

[6] P.G. Hill, C.R. Peterson, *Mechanics and Thermodynamics of Propulsion*, 2nd ed., Pearson Publishing, 1991.

[7] A. El-Sayed, *Aircraft Propulsion and Gas Turbine Engines*, 1st ed., CRC Press, 2008.

[8] D.L. Daggett, S. Ortanderl, D. Eames, J.J. Berton, C. A. Snyder, *Revisiting Water Injection for Commercial Aircraft*, SAE 2004-01-3108, 2004.

[9] Anonymous, Shell Aviation Fuels, Article, Shell Corporation, publication year not cited.

[10] J.L. Kitman, *The Secret History of Lead*, The Nation, 2000. March 2.

[11] Anonymous, *ExxonMobil: World Jet Fuel Specifications with Avgas Supplement*, 2005.

[12] W.W. Pulkrabek, *Engineering Fundamentals of the Internal Combustion Engine*, 2nd ed., Pearson, 2003.

[13] L. Bridgman, *Jane's all the World's Aircraft 1947*, Sampson Low, Marston & Co, London, 1947, 72d.

[14] Anonymous, *Lycoming Service Instructions*, Lycoming Engines, 2019 February 13.

[15] Anonymous, *Continental Motors Service Information Letter*, Continental Engines, 2013 July 17.

[16] M.J. Kroes, T.W. Wild, R.D. Bent, J.L. McKinley, *Aircraft Powerplants*, 6th ed., Glencoe as subsidiary of Macmillan/McGraw-Hill, 1992.

[17] M. Busch, *Why "Over Square" is Good*, July 30, AvWeb Onlinehttps://www.avweb.com/features_old/why-over-square-is-good/, 1995. Accessed 6 October 2019.

[18] Anonymous, *Zoche Aero-Diesels Brochure*, http://www.zoche.de/zoche_brochure.pdf. Accessed 22 November 2019.
[19] Anonymous, *DeltaHawk Jet Fuel Engines Brochure*, https://deltahawk.com/sites/default/files/DeltaHawk%20Brochure_2018.pdf. Accessed 22 November 2019.
[20] Anonymous, *Monthly Energy Review – October 2019, DOE/EIA-0035 (2019/10)*, U.S. Energy Information Administration, 2019.
[21] Anonymous, *Operator's Manual for all versions of Rotax 912*, Rotax Aircraft Engines, 1998.
[22] Anonymous, *Horsepower Correction Factors and Operating Techniques for Engine Development and Calibration*, Avco Lycoming Corporation Report 2268, August 1960.
[23] Anonymous, *The B-29: Airplane Commander Training Manual for the Superfortress*, AAF Manual No. 50-9, 1945.
[24] Anonymous, *Flight Manual B-24D Airplane*, Consolidated Aircraft, 1942.
[25] Anonymous, *Pilot Training Manual for the C-46 Commando, AAF Manual No. 50-16*, March 1945.
[26] Anonymous, *Pilot's Flight Operating Instructions Manual for the P-47B, -C, -D and -G Airplanes, Technical Order No. 01-65BC-1*, January 20, 1943.
[27] W.A. Benser, J.J. Moses, *An Investigation of Backflow Phenomenon in Centrifugal Compressors, NACA R-806*, 1945.
[28] A.P. Scott, *Benchmark – Aircraft Performance Testing Analysis for Single- and Multi-Engine Aircraft Using Constant-Speed Propellers*, Sequoia Aircraft Corporation, Richmond, VA, 1990.
[29] R. Langton, C. Clark, M. Hewitt, L. Richards, *Aircraft Fuel Systems*, John Wiley and Sons, 2009.
[30] I. Moir, A. Seabridge, *Aircraft Systems – Mechanical, Electrical, and Avionics Subsystems Integration*, 2nd ed., Professional Engineering Publishing Limited, UK, 2001.
[31] F.E. Weick, *Drag and Cooling with Various Forms of Cowling for a "Whirlwind" Radial Air-cooled Engine II, NACA TR-314*, January 1, 1930.
[32] F. Monts, *The development of reciprocating engine installation data for general aviation aircraft, SAE Paper 730325*, in: Business Aircraft Meeting, Wichita, Kansas, April 3-6, 1973.
[33] V.R. Corsiglia, J. Katz, R.A. Kroeger, *Full-scale wind-tunnel study of the effect of nacelle shape on cooling drag*. J. Aircr. 18 (2) 1981 82–88, https://doi.org/10.2514/3.57469.
[34] Anonymous, Flight Design CTSW LSA Maintenance and Inspection Procedures Manual, Rev. 6, 11/20/2008, Flight Design.
[35] Schubert, T. and Hertzler, G., Efficient pusher engine cooling and drag reduction, A Presentation for Rutan Longez kit-Builders,
[36] J. Katz, V.R. Corsiglia, P.R. Barlow, *Cooling air inlet and exit geometries on aircraft engine installations*. J. Aircr. 19 (7) 1982 525–530, https://doi.org/10.2514/3.57425.
[37] J. Katz, V.R. Corsiglia, P.R. Barlow, *Effect of propeller on engine cooling system drag and performance*. J. Aircr. 19 (3) 1982 193–197, https://doi.org/10.2514/3.57375.
[38] S.J. Miley, E.J. Cross, J.K. Owens, *An Investigation of the Aerodynamics and Cooling of a Horizontally-Opposed Engine Installation, SAE Technical Paper 770467*. 1977https://doi.org/10.4271/770467.
[39] J.V. Becker, *Wind Tunnel Tests of Air Inlet and Outlet Openings on a Streamline Body, NACA WR-L-300*, November 1940.
[40] B.W. McCormick, *Aerodynamics, Aeronautics, and Flight Mechanics*, John Wiley & Sons, 1979, 420.
[41] Anonymous, *Fashionably Late Doesn't Apply to Your Engine TBO. Here's Why*, online article by Pratt & Whitney Customer Service, Pratt & Whitney of Canada, 2018. February 9, https://www.pwc.ca/en/airtime-blog/articles/technical-tips/fashionably-late-does-not-apply-to-your-engine-tbo—here-is-why. Accessed 19 October 2019.
[42] G. Oates, *Aerothermodynamics of Gas Turbine and Rocket Propulsion*, AIAA Education Series, 1984.
[43] J.D. Mattingly, W.H. Heiser, D.T. Pratt, *Aircraft Engine Design*, 2nd ed., AIAA Education Series, 2002.
[44] Taylor, John W. R., Mark Lambert, Ed., Jane's All the World's Aircraft, Jane's Information Group, various years.
[45] Austyn-Mair, W. and Birdsall, David L., Aircraft Performance, Cambridge University Press, Cambridge, England, 1992, pg. 102–106.
[46] K. Huenecke, *Jet Engines – Fundamentals of Theory, Design, and Operation*, Motorbooks International Publishers & Wholesalers, 1997.
[47] Sutcliffe, Peter L., The Boeing 7J7-The Evolution of Technology and Design, Technical Paper 872405, 1987.11-13, SAE International. https://doi.org/10.4271/872405.
[48] R.D. Flack, *Fundamentals of Jet Propulsion with Applications, Cambridge Aerospace Series*, Cambridge University Press, 2010.
[49] J. Seddon, E.L. Goldsmith, *Intake Aerodynamics*, AIAA Education Series, 1985.
[50] Anonymous, *Lycoming IO-720 Operator's Manual*, 4th ed., Lycoming Engines, October 2006.
[51] Anonymous, *PT6 Description webpage*, https://www.pwc.ca/en/products-and-services/products/general-aviation-engines/pt6a. Accessed 6 December 2019.
[52] T.P. Collins, E.A. Witmer, *Application of the Collision-Imparted Velocity Method for Analyzing the Responses of Containment and Deflector Structures to Engine Rotor Fragment Impact, NASA CR-134494 (ASRL TR 154-8)*, Aeroelastic and Structures Research Laboratory, MIT, Cambridge, MA, August 1973.
[53] Anonymous, *Design Considerations for Minimizing Hazards Caused by Uncontained Turbine Engine and Auxiliary Power Unit Rotor Failure, AC20-128A*, FAA, 1997.
[54] Anonymous, *Drag and Pressure Recovery Characteristics of Auxiliary Air Inlets at Subsonic Speeds, ESDU-86002*, Engineering Sciences Data Unit, April 1986.
[55] C.W. Frick, W.F. Davis, L.M. Randall, E.A. Mossman, *An Experimental Investigation of NACA Submerged-Duct Entrances, NACA ACR 5I20*, October 1945.
[56] E.A. Mossman, D.E. Gault, *Development of NACA Submerged Inlets and a Comparison with Wing Leading-Edge Inlets for a ¼ – Scale Model, NACA RM A7A31*, August 7, 1947.
[57] H. Schlichting, *Boundary Layer Theory*, Pergamon Press Ltd, 1955.
[58] http://www.mpoweruk.com/index.htm [Accessed 10/29/2019]
[59] I. Buchmann, *Batteries in a Portable World: A Handbook on Rechargeable Batteries for Non-Engineers*, 3rd ed., Cadex Electronics, Inc, 2011.
[60] http://www.batteryuniversity.com/ [Accessed 10/29/2019]
[61] M. Hipperle, *Electric Flight – Potential and Limitations, NATO Technical Paper STO-MP-AVT-209*, Energy Efficient Technologies and Concepts Operation, Lisbon, 2012. October 22-24.
[62] B.S. Finn, *Origin of Electrical Power*, National Museum of American History, 2015. Retrieved 12/21/2015 from, http://americanhistory.si.edu/powering/past/prehist.htm. PDF available upon request.
[63] S. Gudmundsson, *A Biomimetic, Energy-Harvesting, Obstacle-Avoiding, Path-Planning Algorithm for UAVs*, 2016 306. Dissertations and Theses. https://commons.erau.edu/edt/306.
[64] J.J. Eberhardt, *Fuels of the Future for Cars and Trucks*, U.S. Department of Energy, 2002.
[65] A. McEvoy, T. Markvart, L. Castañer, *Practical Handbook of Photovoltaics – Fundamentals and Applications*, 2nd ed., Academic Press, 2012.
[66] O. Tremblay, L.-A. Dessaint, A.I. Dekkiche, *A Generic Battery Model for the Dynamic Simulation of Hybrid Electric Vehicles*, IEEE, 2007.
[67] N. Omar, P.V.d. Bossche, T. Coosemans, J. Van Mierlo, *Peukert revisited—critical appraisal and need for modification for lithium-ion batteries*. Energies 6 2013 5625–5641, https://doi.org/10.3390/en6115625.
[68] D. Doerfell, S.A. Sharkh, *A critical review of using the Peukert equation for determining the remaining capacity of Lead-acid and lithium-ion batteries*, J. Power Sources 155 2006 395–400.

[69] R.M. Noyes, R.G. Lerner, G.L. Trigg (Eds.), Encyclopedia of Physics, 2nd ed., VHC Publishers, Inc, 1991.
[70] A. Noth, *Design of Solar Powered Airplanes for Continuous Flight*, Ph. D Dissertation. Swiss Federal Inst. of Technology, Zurich, Switzerland, 2008.
[71] R.J. Boucher, *History of Solar Flight, AIAA-84-1429, 20th Joint Propulsion Conference, Joint Propulsion Conferences, Cincinnati, OH*, 1984.
[72] R.J. Boucher, *Sunrise, the World's first solar-powered airplane*, AIAA J. Aircraft 22 (10) 1985 840–846.
[73] https://aroundtheworld.solarimpulse.com/. [Accessed 12/31/2020]
[74] R.G. Lerner, G.L. Trigg, *Encyclopedia of Physics*, 2nd ed., article Photovoltaic Effect by John J. Hall, VCH Publishers, 1991.
[75] Image by Rohde, Robert A, *permission per GNU Free Documentation License, Version 1.2 or later. Source*, https://commons.wikimedia.org/wiki/File:Solar_Spectrum.png. Accessed 14 March 2020.
[76] K. Krane, *Modern Physics*, John Wiley and Sons, 1983.
[77] Huang, Huei-Ping, Notes for MAE 578, Arizona State University, School for Engineering of Matter, Transport, and Energy, retrieved on 07/07/2016 from http://www.public.asu.edu/~hhuang38/mae578_lecture_03.pdf.
[78] Anon, *X-Series Solar Panels, Datasheet for Commercially Available Solar Panels from SunPower Corporation, Document # 504828 Rev A*, Retrieved from, https://us.sunpower.com/sites/sunpower/files/media-library/data-sheets/ds-x21-series-335-345-residential-solar-panels-datasheet.pdf, April 2013.
[79] National Renewable Energy Laboratory, https://www.nrel.gov/pv/cell-efficiency.html. Accessed 22 December 2019.
[80] Boric, Marino, HY4: Maiden Flight of the Hydrogen Powered Aircraft, Aerospace Technology, online magazine: https://www.aerospace-technology.com/projects/hy4-aircraft/ [Accessed 01/16/2020].

This page intentionally left blank

CHAPTER

8

The Anatomy of the Airfoil

OUTLINE

8.1 **Introduction** 257
- 8.1.1 *The Content of This Chapter* 258
- 8.1.2 *Dimensional Analysis—Buckingham's Π–Theorem* 258
- 8.1.3 *Representation of Forces and Moments* 259
- 8.1.4 *Properties of Typical Airfoils* 260
- 8.1.5 *The Pressure Coefficient* 264
- 8.1.6 *Chordwise Pressure Distribution* 266
- 8.1.7 *Forces and Moment per Unit Span* 269
- 8.1.8 *Center of Pressure and Aerodynamic Center* 270
- 8.1.9 *The Generation of Lift* 271
- 8.1.10 *Boundary Layer Basics* 273
- 8.1.11 *Airfoil Stall Characteristics* 277
- 8.1.12 *Analysis of Ice Accretion on Airfoils* 279
- 8.1.13 *Designations of Common Airfoils* 280
- 8.1.14 *Airfoil Design* 280

8.2 **The Geometry of the Airfoil** 282
- 8.2.1 *Airfoil Terminology* 282
- 8.2.2 *NACA 4-Digit Airfoils* 284
- 8.2.3 *NACA 5-Digit Airfoils* 285
- 8.2.4 *NACA 1-Series Airfoils* 286
- 8.2.5 *NACA 6-Series Airfoils* 286
- 8.2.6 *NACA 7-Series Airfoils* 287
- 8.2.7 *NACA 8-Series Airfoils* 288
- 8.2.8 *Plotting NACA 4- and 5-Digit Airfoils* 288
- 8.2.9 *Summary of NACA Airfoils* 290
- 8.2.10 *Selected Famous Airfoils* 290

8.3 **The Force and Moment Characteristics of the Airfoil** 299
- 8.3.1 *The Effect of Camber* 299
- 8.3.2 *The Effect of Reynolds Number* 299
- 8.3.3 *The Effect of Early Flow Separation* 301
- 8.3.4 *The Effect of a Trailing-Edge Flap* 302
- 8.3.5 *The Effect of a Slot or Slats* 303
- 8.3.6 *The Effect of Deploying a Spoiler* 303
- 8.3.7 *The Effect of Leading-Edge Roughness and Surface Smoothness* 305
- 8.3.8 *The Effect of Compressibility* 306
- 8.3.9 *Decision Matrix for Airfoil Selection* 310

Exercises 317

References 317

8.1 INTRODUCTION

Any object moving through a fluid develops a force due to (1) *the pressure difference induced by its shape* and (2) *the friction to which it is subjected*. The pressure force is normal to its surface, while the friction is tangential and is generated by viscous shear stress (τ). The combination gives rise to a resultant force, R, which acts on the object (see Figure 8-1). Then, we define *lift*, L, as the component of R *normal* to the trajectory (or flight path). Similarly, *drag*, D, is defined as the component of R *tangent* to the trajectory. Applying the forces some distance from the center-of-gravity of an unconstrained body induces a *moment*, M. Since airfoils are usually physically constrained, it is more practical to consider the moment about specific points on the body. Typically, the one-fourth of the distance from the leading to trailing edge (i.e., quarter-chord) is selected. The orientation of M in Figure 8-1 has a negative value. The lift generated by 3-dimensional objects is treated in Chapter 9, while drag is treated in Chapter 16.

The airfoil differs from other geometry in that its resultant force approaches being normal to the tangent to the trajectory: Its lift force component is larger than the drag component. *It generates lift far more effectively than other shapes*. The lift component for modern day airfoils can exceed 200× the drag force.

https://doi.org/10.1016/B978-0-12-818465-3.00008-2

Copyright © 2022 Elsevier Inc. All rights reserved.

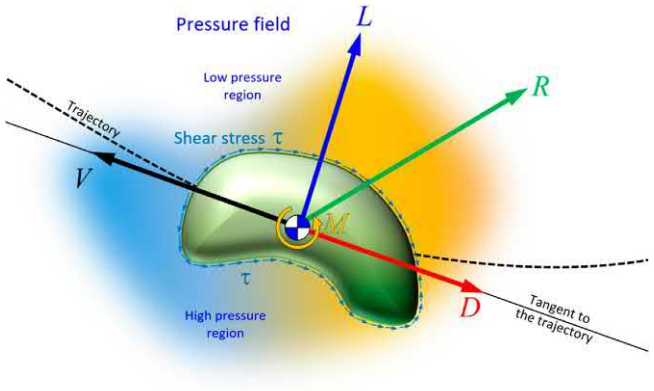


FIGURE 8-1 An object moving in fluid induces pressure field.

By convention, forces and moments for 2-dimensional geometry are denoted by a lower-case letter but are capitalized for 3-dimensional geometry. Thus, lift, drag, and moment for an airfoil would be denoted by l, d, and m, respectively, while L, D, and M would be used for a 3-dimensional wing. The difference between the two is that a wing has a finite *aspect ratio* (AR), whereas an airfoil can be considered a wing of infinite span (infinite AR). This convention will be adhered to in this text. The lift, drag, and moment coefficients for an airfoil are denoted as; C_l, C_d, C_m, respectively, while C_L, C_D, C_M are used for 3D wings or a complete aircraft.

8.1.1 The Content of This Chapter

- Section 8.1 presents fundamental concepts and theories regarding airfoil lift and drag generation. It contains very important definitions. Additionally, it introduces how pressure is distributed along the upper and lower surfaces of the airfoil and how it affects the growth of the boundary layer and, eventually, flow separation.
- Section 8.2 defines important geometric properties of airfoils. It also presents information intended to make the aircraft designer better rounded when comes to identifying various airfoil types, such as NACA airfoils, and understanding of their background. For this purpose, the section introduces several airfoils that have gained fame or notoriety in the history of aviation.
- Section 8.3 discusses the generation of forces and moments on the airfoil. It details how various outside agents, such as very high airspeeds, high angle-of-attack, deflection of control surfaces, and even contamination, affects their aerodynamic properties. Finally, it presents a decision matrix to help with airfoil selection for a new aircraft design.

TABLE 8-1 Selected base quantities of physics.

Base quantity	Symbol	SI-unit	UK-system
Mass	M	kg	slug
Length	L	m	ft
Time	T	s	s
Temperature	θ	Kelvin	°Rankine
Electric current	I	Ampère	Ampère

8.1.2 Dimensional Analysis—Buckingham's Π–Theorem

Dimensional Analysis refers to a method for evaluating relationships between parameters that contribute to some natural phenomenon. This is accomplished by enforcing unit consistency. In physics, the base quantities include those shown in Table 8-1.

All physical quantities, dimensionless or not, are based on these. An example is pressure (p), which is defined as force/area. Force is defined as mass × acceleration or $\mathrm{M}\cdot\mathrm{L}/\mathrm{T}^2$. Area ($A$) is L^2. Thus, it is possible to write pressure as $(\mathrm{M}\cdot\mathrm{L}/\mathrm{T}^2)/\mathrm{L}^2 = \mathrm{M}/(\mathrm{L}\cdot\mathrm{T}^2)$. In aerodynamics, pressure forces are denoted as follows:

$$F_{press} = pA = \underbrace{\frac{\mathrm{M}}{\mathrm{L}\cdot\mathrm{T}^2}}_{pressure}\ \underbrace{\mathrm{L}^2}_{area} = \underbrace{\frac{\mathrm{ML}}{\mathrm{T}^2}}_{force} \tag{8-1}$$

This matches the units for the force, showing its dimensional consistency. The primary tool of dimensional analysis is the Buckingham Π–Theorem, named after Edgar Buckingham (1867–1940). It is used to derive the familiar mathematical expression for aerodynamic forces. Observation shows that the force generated in a fluid flowing over a body depends on the density of the fluid (more density → larger force), the relative speed of the fluid with respect to the body (more speed → larger force), and the size of the body (larger body → larger force). It is possible to relate these using the following expression:

Force due to fluid flow:

$$F = k\rho^a V^b l^c \tag{8-2}$$

where

ρ = Density, M/L^3
V = Airspeed, L/T
l = Characteristic length, L
k = Unknown constant of proportionality
a, b, c = Exponents to be determined

Substituting the dimensions into Equation (8-2) yields:

$$\frac{\mathrm{ML}}{\mathrm{T}^2} = \mathrm{k}\left(\frac{\mathrm{M}}{\mathrm{L}^3}\right)^a\left(\frac{\mathrm{L}}{\mathrm{T}}\right)^b \mathrm{L}^c \tag{8-3}$$

Simplification on the right side leads to:

$$\frac{\mathrm{ML}}{\mathrm{T}^2}=\mathrm{k}\frac{\mathrm{M}^a\mathrm{L}^b}{\mathrm{L}^{3a}\mathrm{T}^b}\mathrm{L}^c=\mathrm{k}\times\frac{\mathrm{M}^a\times\mathrm{L}^{b+c-3a}}{\mathrm{T}^b}.$$

Since the dimensions on the left- and right-hand sides must be consistent, we can determine a, b, and c as follows:

$$\mathrm{M}^1=\mathrm{M}^a \;\Leftrightarrow\; a=1$$
$$\mathrm{T}^{-2}=\mathrm{T}^{-b} \;\Leftrightarrow\; b=2$$
$$\mathrm{L}^1=\mathrm{L}^{b+c-3a} \;\Rightarrow\; 1=b+c-3a=2+c-3 \;\Leftrightarrow\; c=2$$

Thus, we can rewrite Equation (8-2) as follows:

$$F=k\rho V^2 l^2 \tag{8-4}$$

This formulation is the basis for all forces used in aerodynamic theory. Applying it in Equation (8-6), the term $k=½$ is selected to match the notation for dynamic pressure [1]. The lift coefficient (C_l) accounts for the orientation of the body (whose effect we ignored above). A similar equation is obtained for moments, where the term l is cubed. Refer to standard texts on Fluid Mechanics for more detail.

8.1.3 Representation of Forces and Moments

The total (or resultant) force generated by a wing depends on several parameters; its geometry, density of air, airspeed, and the angle the chordline of the wing's airfoils make to the flow of air, the *angle-of-attack*. While the wing is 3-dimensional, it is usually treated as a set of two 2-dimensional geometric features; the airfoil (x–z plane as shown in Figure 8-2) and planform (x–y plane, see Section 9.4). Using Equation (8-4), the resultant force, r, is written as.

$$r=\frac{1}{2}\rho V_\infty^2 S C_r \tag{8-5}$$

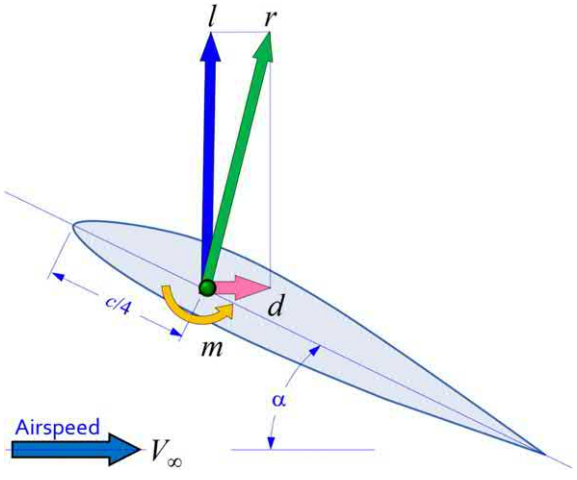


FIGURE 8-2 Forces and moments acting on an airfoil.

where

S = Reference wing area, in m^2 or ft^2.
C_r = Nondimensional coefficient that relates AOA to the force.

Figure 8-2 shows lift, drag, and pitching moment, assumed to act at the quarter chord. When dealing with airfoils, S is considered that of a *wing of unit span*, e.g., S = chord × 1 = chord. If we denote the chord as c, we can write these as follows:

$$l=\frac{1}{2}\rho V_\infty^2 c C_l=\frac{1}{2}\rho V_\infty^2 c C_r\cos\alpha$$
$$d=\frac{1}{2}\rho V_\infty^2 c C_d=\frac{1}{2}\rho V_\infty^2 c C_r\sin\alpha \tag{8-6}$$
$$m=\frac{1}{2}\rho V_\infty^2 c^2 C_m$$

For 3-dimensional objects like aircraft, lift, drag, and pitching moment are denoted by L, D, $\boldsymbol{M}$, respectively and are given by:

$$L=\frac{1}{2}\rho V_\infty^2 S C_L$$
$$D=\frac{1}{2}\rho V_\infty^2 S C_D \tag{8-7}$$
$$\boldsymbol{M}=\frac{1}{2}\rho V_\infty^2 S c_{MGC}\boldsymbol{C_M}$$

where C_L is the 3-dimensional lift coefficient, C_D the drag coefficient, and $\boldsymbol{C_M}$ the pitching moment coefficient of the complete aircraft. These will be treated in more detail in Chapters 9, 16, and 24. c_{MGC} is the wing's *mean geometric chord* (MGC) and S is the reference wing area. Both are presented in detail in Chapter 9.

The Smeaton Lift Equation (Obsolete)

The now obsolete Smeaton lift equation is of interest from a historical standpoint. It is attributed to the English civil engineer John Smeaton (1724–1792), often referred to as the "father of civil engineering." It was in use until the beginning of the 20th century. When the Wright brothers applied it to estimate the wing area required for their Flyer, they discovered its inaccuracy [2]. Smeaton's lift equation is given as follows:

$$L=\text{pressure factor}\times\text{velocity}^2\times\text{wing area}\times\text{lift factor}$$
$$=kV_\infty{}^2 S C_l \tag{8-8}$$

where

L = Lift force in lb_f,
k = Smeaton's coefficient,
V_∞ = Airspeed in ft/s
C_l = Lift coefficient

At the time, engineers considered the lift coefficient as the ratio of the object's lift force to its drag force, where

the drag was for a flat plate of area A mounted perpendicular to the airstream. Smeaton's coefficient, k, is the drag of a 1 ft^2 flat plate at 1 mph. Around 1900, the accepted value for this coefficient was 0.005 and this had been the value used by Otto Lilienthal in the design of his gliders. In fact, Smeaton himself came up with this value. Various sources claim it ranged from 0.0027 to 0.005. The Wright brothers concluded the coefficient was wrong and experimentally determined it to be closer to 0.0033. The "modern" value is 0.00326 [3].

8.1.4 Properties of Typical Airfoils

There are several classes of airfoils the aircraft designer should be aware of. Some are listed in Table 8-2. In addition to these, airfoils are sometimes classified as *front-*, *mid-*, and *aft-loaded*, based on the location of the camber. Thus, front-loaded airfoils have the camber between 20% and 40% of the chord, mid-loaded at 50%, and aft loaded at 60% to 70%. This affects the position of the low-pressure peak on the upper surface at low AOAs.

(1) Angle-of-Attack

The angle between the airfoil's chordline and the oncoming airflow, far ahead of the airfoil. In this book, it is denoted by the letter α (see Figure 8-4) or its abbreviation, AOA. Typical presentation of lift coefficients versus AOA is shown in Figure 8-5, with important properties labeled. The graph shows true wind tunnel test results for the NACA 4415 airfoil.

(2) Section Lift Coefficient, C_l

The 2-dimensional lift coefficient is commonly called the *section lift coefficient*. It is of great importance to the airplane designer and will be discussed at length later. One of its most useful properties is that it indicates the airfoil's effective AOA and how close to stall or optimum lift (C_{lopt}) it is.

(3) Stall and Maximum and Minimum Lift Coefficients, $C_{l_{max}}$ and $C_{l_{min}}$

The largest and smallest magnitudes of the lift coefficient are denoted by $C_{l_{max}}$ and $C_{l_{min}}$, respectively. The former always has a positive magnitude and the latter a negative one. These values dictate the aircraft's stalling speed (at positive and negative loading) and, thus, the required wing size given its weight. It also impacts other important characteristics such as maneuvering loads and spin behavior. The stall is defined as the flow condition that follows the first lift curve peak, which is where the $C_{l_{max}}$ (or $C_{l_{min}}$) occur [6].

(4) Maximum Theoretical Lift Coefficient

A question sometimes asked is "what is the maximum value of the lift coefficient?" and "what kind of shape yields that value?" Answers to these questions are addressed in a classic paper by A.M.O. Smith (1911–1997) [7]. The answer, in part, depends on *passive* (no system assistance) or *active* (driven by a system) approaches. Knowing such theoretical limits is helpful for airfoil comparison. It allows efficiency and potential for improvements to be quantified. Figure 8.3 shows an example of an active lifting system (it could represent a Flettner rotor). A cylinder of diameter d is rotating in uniform inviscid flow of velocity V, exposed to three values of the circulation, Γ. Since the flow is inviscid, it will not separate. While such a flow exists only in the imagination, it is still of considerable importance in aerodynamics. Not only does it show what could be if not for viscosity, it also allows one to assess theoretical limits.

Using *potential flow theory* (PFT), it is possible to simulate airflow around a rotating cylinder by adding the elementary flows of uniform, doublet, and vortex flow (see Figure 8-3). Figure 8-3(a) shows two stagnation points, A and B. In Figure 8-3(b), the circulation is strong enough to bring the two stagnation points together (D), and in Figure 8-3(c), it is strong enough to move one stagnation point off the surface (D) and (theoretically) the other one (E) inside. It can be shown using PFT that the circulation required to create the flow in Figure 8-3(b) amounts to $2\pi V_\infty d$ (e.g., see Anderson [9]). Using Equation (8-32), we can write:

$$l = \rho V_\infty \Gamma = \rho V_\infty (2\pi V_\infty d) = 2\pi\rho V_\infty^2 d \tag{8-9}$$

But it is also possible to write lift using Equation (8-55). Therefore, the lift coefficient, C_l, can be found to equal:

$$l = 2\pi\rho V_\infty^2 d = \frac{1}{2}\rho V_\infty^2 d C_l \quad \Rightarrow \quad C_l = 4\pi \tag{8-10}$$

The corresponding lift coefficients for values of the circulation on either side of $2\pi V_\infty d$ result in lift coefficients that are less than 4π. A passive lifting system that yields a larger lift coefficient is not known by this author. The value $C_{l_{max}} = 4\pi$ can therefore be considered a maximum theoretical lift coefficient. This puts in context current passive technology ($C_{L_{max}} \approx 3$) versus this limit, as shown in Figure 34 of ref. [10].

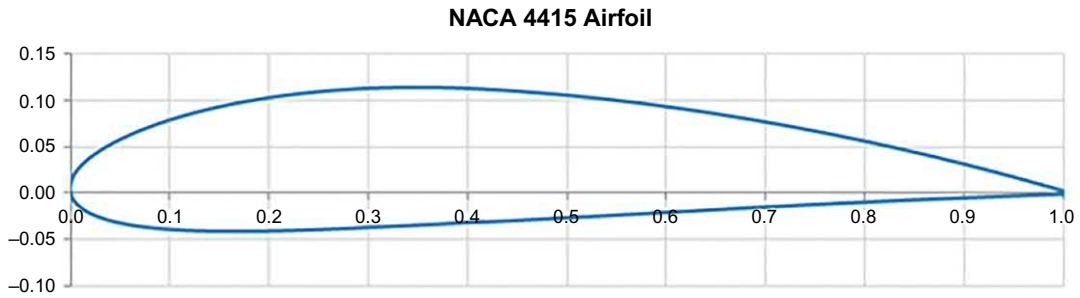
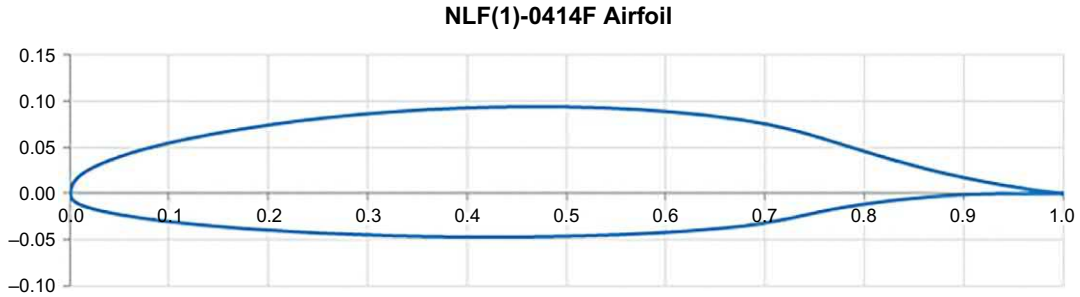
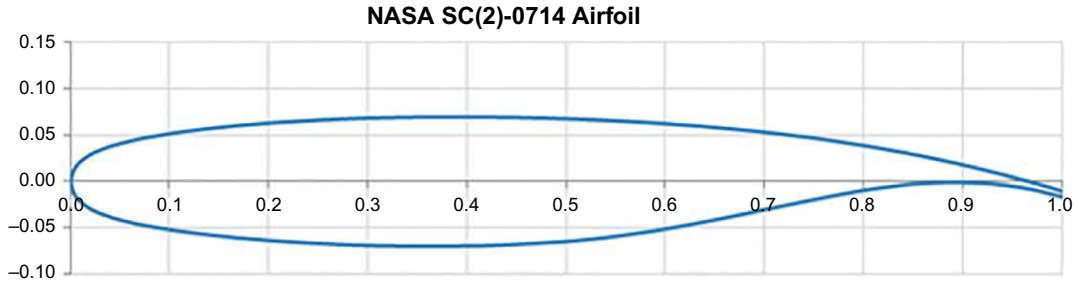
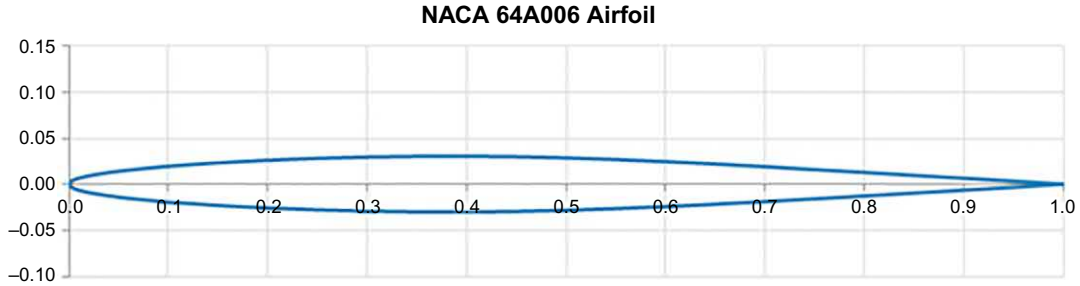
(5) Lift Curve Slope, $C_{l\alpha}$

$C_{l\alpha}$ indicates how rapidly lift changes with angle-of-attack. A maximum value of $C_{l\alpha}$ is 2π (≈ 6.283), as predicted by linear thin airfoil theory for incompressible flow. Most airfoils are close to that. For instance, the slope of the line representing the linear range in Figure 8-5 is ≈ 5.90. The lift curve slope is usually linear at low AOAs but is nonlinear outside of this range and can have a negative slope. A nonlinear lift curve slope indicates prevailing flow separation on the body.

(6) Angle-of-Attack at Zero Lift, α_{ZL}

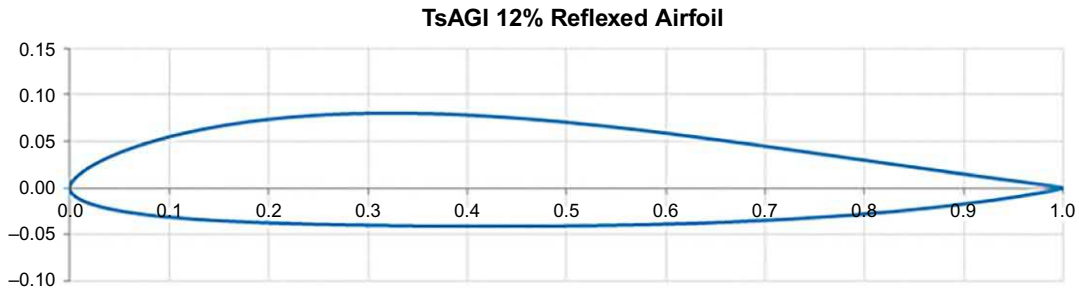
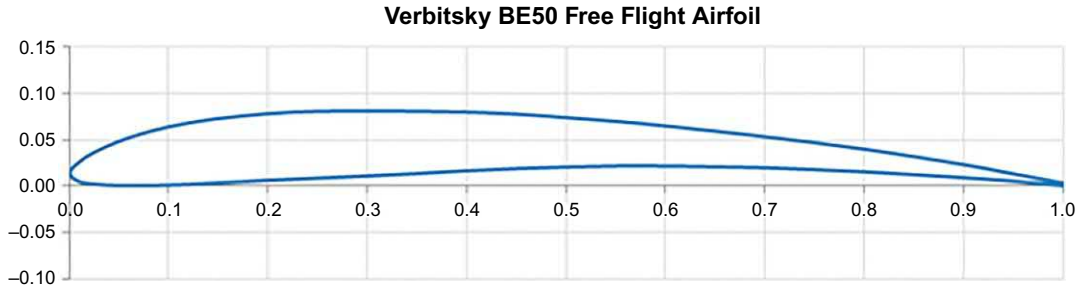
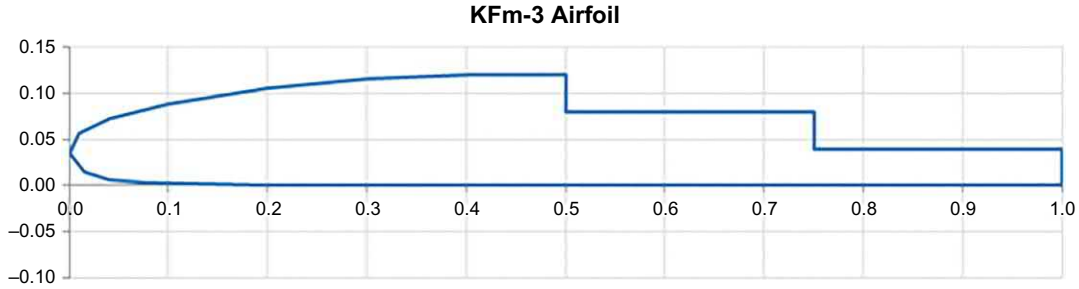
α_{ZL} is the AOA at which the airfoil produces no lift. It is important when considering wing washout

TABLE 8-2 Classes of airfoils.

Airfoil class	Description	Example
Conventional	Refers to airfoils that do not fall into any of the following classes.	
Natural Laminar Flow (NLF)	Refers to airfoils that employ pressure distribution with extensive favorable pressure gradient (dp/dx) to help sustain natural laminar boundary layer.	
Supercritical and Transonics	Refers to airfoils for high subsonic flight. Designed to operate at cruise with small C_p over most of the top surface (see 8.1.5, *The Pressure Coefficient*). This limits flow acceleration, shifting shock-formation to higher Mach numbers. An older generation of this class, called "peaky" airfoils, was used on early high subsonic aircraft.	
Supersonic	Refers to airfoils designed for flight above Mach 1. These are thin airfoils ($t/c \approx 0.030$–0.065) with sharp leading edges. It also includes diamond-shaped (ideal for theoretical analyses) and biconvex airfoils (used in limited aircraft, including the F-104 Starfighter).	

Continued

TABLE 8-2 Classes of airfoils—cont'd

Airfoil class	Description	Example
Reflexed	Refers to airfoils for flying wings and planks. The reflexed trailing edge reduces pitching moments and allows the wing to be trimmed without a dedicated stabilizer.	
Low Reynolds number	Refers to airfoils suitable for flight at very low R_e, such as those of birds, small RC, and hand-launched aircraft.	
Kline–Fogleman	Refers to simple stepped airfoils that form vortices behind the steps. Really a subgroup of low-*Re* airfoils. Not suitable for large aircraft due to poor aerodynamic properties [4,5] but may be practical for foam-board RC aircraft.	

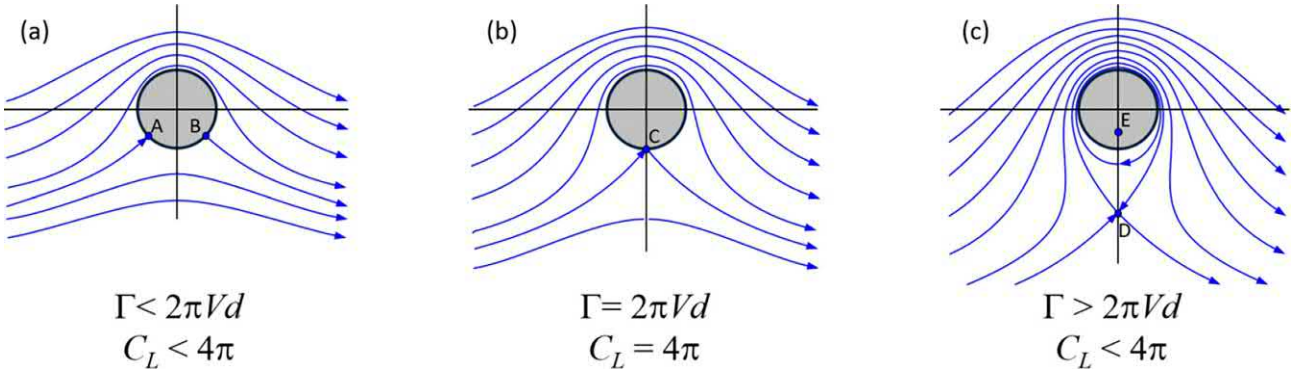


FIGURE 8-3 Potential flow past a circular cylinder for three values of circulation Γ. (Based on reference [8].)

(see Section 9.3.5) and when transforming the lift curve to 3-dimensions. The transformation is accomplished by rotating the lift curve around this point such the slope is reduced (see Section 9.5.3). The α_{ZL} is shown in Figure 8-4.

(7) Linear Range

The linear range (shown ranging from $\alpha = -12°$ through 8° in Figure 8-5) allows one to estimate the lift coefficient (or α for a given C_l) using simple linear expressions such as one below. The extent of this region depends on the geometry and operational airspeeds (via Reynolds numbers as discussed in Section 8.3.2).

$$C_l = C_{l_0} + C_{l_\alpha}\alpha = C_{l_\alpha}(\alpha - \alpha_{ZL}) \tag{8-11}$$

(8) C_l at Zero AOA, C_{lo}

C_{lo} is the value of the lift coefficient at $\alpha = 0$. It affects the wing's *angle-of-incidence*. This value ranges from 0 (for symmetric airfoils) to 0.6 (for highly cambered airfoils). An extreme example is the NACA 6716 used in the A-10 Warthog, which has $C_{lo} > 1.1$. $C_{lo} < 0$ for under-cambered airfoils (e.g., airfoils used near the root of high subsonic jet aircraft). Using Equation (8-11), it is easy to show that C_{lo} can be calculated from:

$$C_{l_0} = -C_{l_\alpha}\alpha_{ZL} \tag{8-12}$$

(9) Estimating Zero-Lift AOA for Selected NACA Airfoils

Ref. [[11], 4.1.1.1] presents a helpful expression to estimate a target α_{ZL}, based on Equation (16) in ref. [12]. If the airfoil's design AOA (α_{dg} in degrees) and lift coefficient (C_{ldg}) are known, the zero-lift AOA is given by

$$\alpha_{ZL} = K\left(\alpha_{dg} - \frac{90}{\pi^2}C_{l_{dg}}\right) \tag{8-13}$$

where $K = 0.93$ for NACA 4-digit airfoils, $K = 1.08$ for NACA 5-digit airfoils, and $K = 0.74$ for NACA 6-series airfoils.

As an example, consider a NACA 6-series airfoil for which $\alpha_{dg} = 3°$ and $C_{ldg} = 0.7$. Using Equation (8-13), we readily find the target α_{ZL} should be near −2.5°.

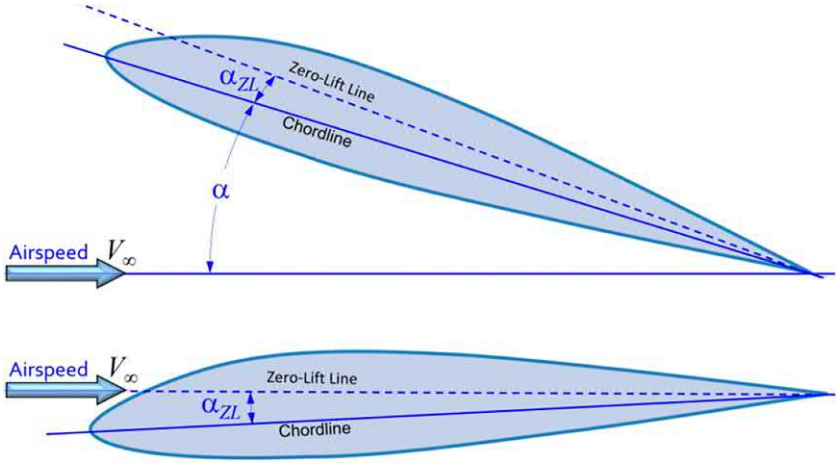


FIGURE 8-4 An airfoil at an angle-of-attack, α. The upper image depicts the zero-lift AOA, α_{ZL}. The lower figure shows the airfoil at α_{ZL}, as no lift is generated.

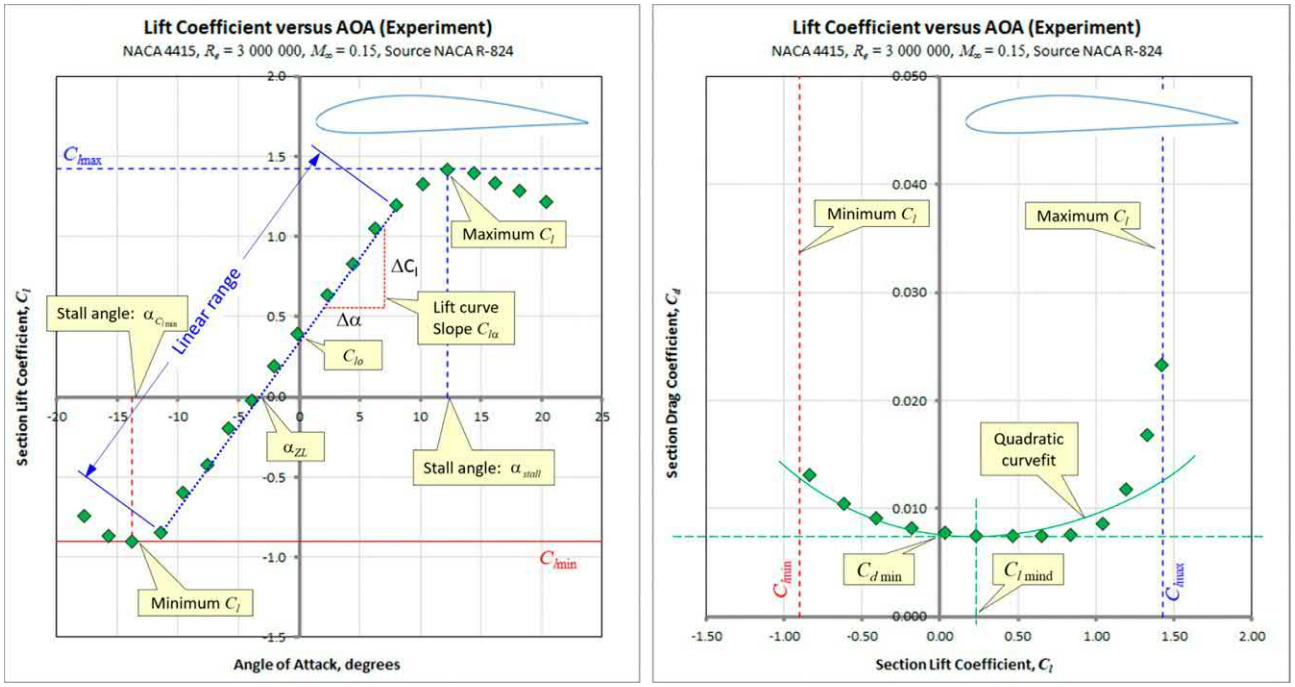


FIGURE 8-5 A typical experimental 2-dimensional lift curve and drag polar for an airfoil.

(10) Profile Drag, C_d

Profile drag refers to the drag of an airfoil. It is the sum of the pressure drag and skin friction acting on the airfoil. The profile drag varies with α, as exemplified in Figure 8-5.

(11) Minimum Drag Coefficient, $C_{d_{\min}}$

Is the lowest value of the drag coefficient found on the drag polar. Its magnitude is vital to the selection of the airfoil. Ideally, $C_{d_{\min}}$ should be a low as possible, but it must be low where it counts, in the region of intended lift coefficient of climb and cruise.

(12) Lift coefficient of Minimum Drag, $C_{l_{mind}}$

Is the lift coefficient where $C_{d_{\min}}$ occurs on the drag polar. It is sometimes called $C_{l\text{opt}}$. Its location impacts airfoil selection just like $C_{d_{\min}}$. Ordinarily, we prefer an airfoil whose section lift coefficient (C_l) in cruise is close to $C_{l_{mind}}$. Thus, a proper airfoil selection also depends on the planform shape (see Chapter 9), which dictates the distribution of C_l along the wing.

(13) Pitching Moment Coefficient, C_m

Refers to the magnitude of the moment generated by the airfoil. It is usually measured about its quarter-chord or aerodynamic center (see Section 8.1.8). In NACA literature, it is plotted against α or C_l (see Figure 8-6). The magnitude of the moment is a function of the airfoil's camber [12]. Larger camber leads to greater moment.

(14) Lift-to-Drag and Airfoil Efficiency Ratios

The *lift-to-drag ratio* is defined as C_l/C_d. It is vital for assessing airfoil efficiency. It is usually plotted against C_l (see Figure 8-7). Its maximum value is denoted by $ld_{\max}$ for airfoils and $LD_{\max}$ for 3D aircraft. Figure 8-7 compares the C_l/C_d for two 15% thick airfoils: the NACA 4415 and 65_2–415. The latter is an NLF airfoil (see Section 8.1.6). A sharp drop occurs in its C_l/C_d above $C_l = 0.75$ because of the airfoil's drag-bucket. Another important observation for the 65_2–415 airfoil is that its $ld_{\max}$ occurs at a lower C_l than that of the 4415. This means closer to typical cruise and climb lift-coefficient; it is a more efficient airfoil and is better for cruise and climb. However, its $C_{l_{\max}}$ is 1.30 versus 1.41 for the 4415.

Mentioning $C_{l_{\max}}$ is a segue for another term, *airfoil efficiency ratio*, defined as $C_{l_{\max}}/C_{d_{\min}}$. It is helpful for comparing airfoils.

8.1.5 The Pressure Coefficient

The *pressure coefficient* is important to the discussion that follows, so a brief review is warranted. It is very useful to represent pressure in terms of a dimensionless quantity, like that of lift and drag. The incompressible pressure coefficient is defined as follows:

$$C_p \equiv \frac{p - p_\infty}{\frac{1}{2}\rho_\infty V_\infty^2} = \frac{\Delta p}{q_\infty} \tag{8-14}$$

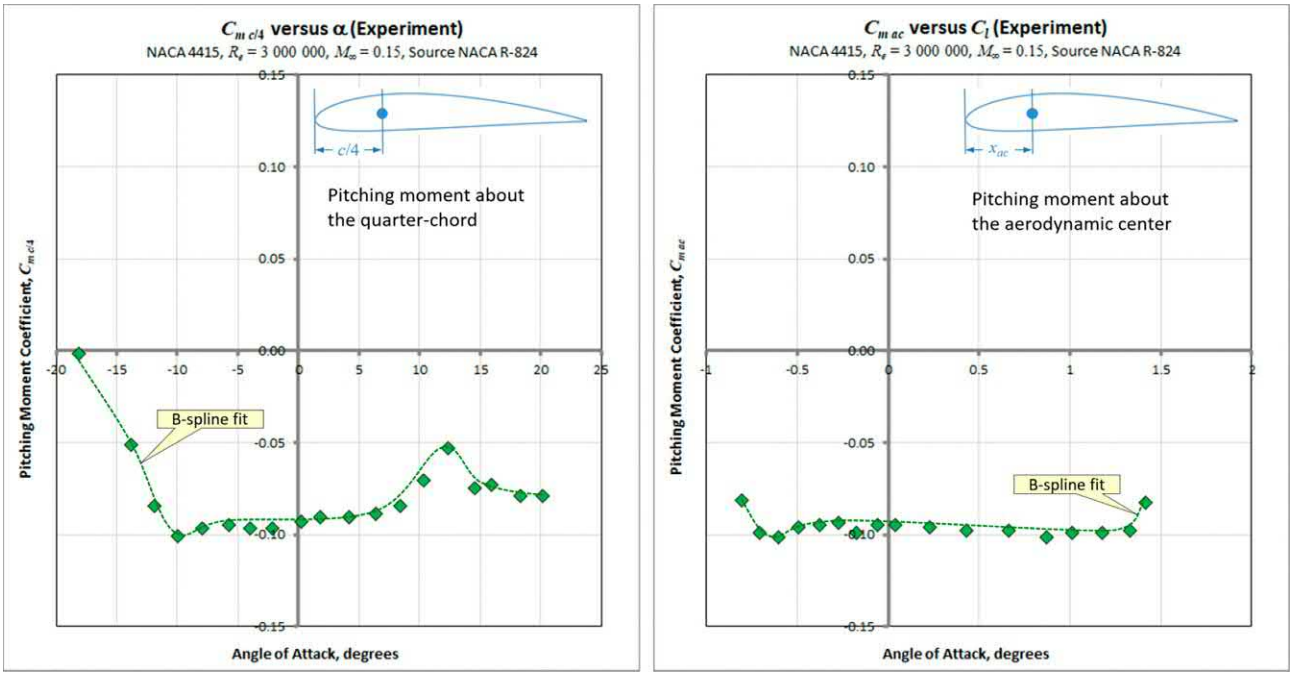


FIGURE 8-6 A typical experimental 2-dimensional pitching moment curves for an airfoil.

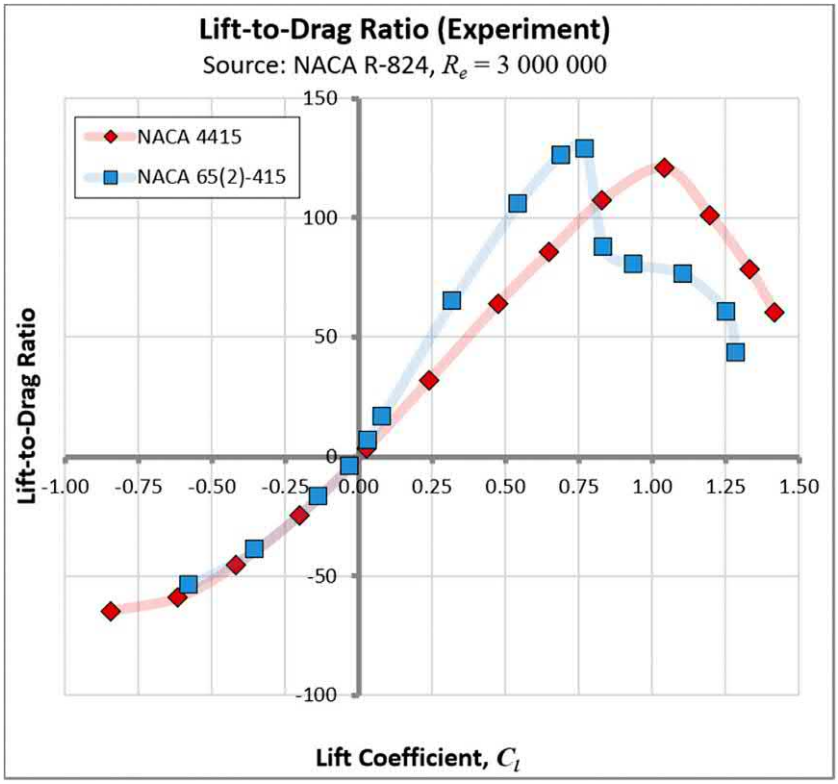


FIGURE 8-7 Lift-to-drag ratio for a conventional and NLF airfoil.

where

q_∞ = Dynamic pressure, in lb_f/ft^2 or N/m^2
p = Pressure, in lb_f/ft^2 or N/m^2
p_∞ = Far-field pressure, in lb_f/ft^2 or N/m^2
V = Local airspeed, in ft/s or m/s
V_∞ = Far-field airspeed, in ft/s or m/s
ρ_∞ = Far-field density, in slugs/ft^3 or kg/m^3

The incompressible pressure coefficient can also be written as follows:

$$C_p = 1 - \left(\frac{V}{V_\infty}\right)^2 \tag{8-15}$$

The maximum possible value of the C_p at the stagnation point in incompressible flow is 1. The C_p in compressible flow can become larger than 1 if the flow is supersonic. The compressible C_p is given by:

$$C_p = \frac{2}{\gamma M_\infty^2}\left(\frac{p}{p_\infty} - 1\right) \tag{8-16}$$

where

M_∞ = Far-field Mach number
γ = Ratio of specific heats = 1.4 at altitudes where aircraft typically operate

DERIVATION OF EQUATION (8-15)

From Bernoulli's equation:

$$p_\infty + \tfrac{1}{2}\rho_\infty V_\infty^2 = p + \tfrac{1}{2}\rho_\infty V^2 \quad \Rightarrow \quad p - p_\infty = \tfrac{1}{2}\rho_\infty\left(V_\infty^2 - V^2\right)$$

Inserting this into Equation (8-14):

$$C_p \equiv \frac{p - p_\infty}{\frac{1}{2}\rho_\infty V_\infty^2} = \frac{\frac{1}{2}\rho_\infty\left(V_\infty^2 - V^2\right)}{\frac{1}{2}\rho_\infty V_\infty^2} = \frac{V_\infty^2 - V^2}{V_\infty^2} = 1 - \left(\frac{V}{V_\infty}\right)^2.$$

DERIVATION OF EQUATION (8-16)

Using the equation of state ($p = \rho RT$), the speed of sound can be found from: $a_0 = \sqrt{\gamma RT_\infty} = \sqrt{\gamma p_\infty/\rho_\infty}$.

Thus, the dynamic pressure can be written as follows:

$$q_\infty = \frac{1}{2}\rho_\infty V_\infty^2 = \frac{1}{2}\frac{\gamma p_\infty}{\gamma p_\infty}\rho_\infty V_\infty^2 = \frac{\gamma p_\infty}{2}\left(\frac{\rho_\infty}{\gamma p_\infty}\right)V_\infty^2 = \frac{\gamma p_\infty}{2}\left(\frac{1}{a_0^2}\right)V_\infty^2 = \frac{\gamma p_\infty}{2}M_\infty^2$$

Substituting into Equation (8-14) yields:

$$C_p = \frac{p - p_\infty}{\frac{1}{2}\rho_\infty V_\infty^2} = \frac{p - p_\infty}{q_\infty} = \frac{p - p_\infty}{\frac{\gamma p_\infty}{2}M_\infty^2} = \frac{2}{\gamma M_\infty^2}\left(\frac{p}{p_\infty} - 1\right).$$

The Canonical Pressure Coefficient

The *canonical pressure coefficient* is regarded by many as a better way to represent airfoil pressure distribution. The concept was introduced by A.M.O. Smith [7] to evaluate the adverse pressure gradient (dp/dx) and help determine the onset of flow separation. The approach scales the pressure coefficient, such it varies between 0 and 1. This is done by selecting the airspeed (V_m) at the minimum pressure (at the start of the adverse dp/dx, where pressure begins to increase). The canonical pressure coefficient is defined as follows:

$$\overline{C}_p = 1 - \left(\frac{V}{V_m}\right)^2 \tag{8-17}$$

8.1.6 Chordwise Pressure Distribution

The distribution of surface pressure on an airfoil affects a host of properties. These range from structural loads to the magnitude of drag, lift, and pitching moment, shock formation, laminar-to-turbulent boundary layer transition, hinge moments, and many others. The pressure distribution is usually shown by plotting C_p for a given α along the upper and lower surfaces, as shown in Figure 8-8. For clarity, the pressure distribution for the upper surface is plotted above the one for the lower surfaces (with the vertical axis is inverted).

(1) Pressure Distribution around "Conventional" Airfoils

Figure 8-8 shows the pressure distribution generated around a NACA 4415 airfoil at subsonic airspeed and $\alpha = 2°$. The thick solid line represents the pressure along the upper surface while the dashed one denotes the lower surface. The red shade indicates accelerating flow (pressure drop), and the blue shade indicates deceleration (pressure rise). A favorable pressure gradient (dp/dx) for the formation of a laminar BL exists between the LE and $x = 0.2$, assuming a smooth surface. However, it is likely to transition to turbulent boundary layer near this point. Two software packages, Xfoil [13] and JavaFoil [14] predict this to occur at 41% and 29%, respectively. Figure 8-8 also shows the pressure differential (between the upper and lower surface pressure). It is negative along the chord, indicating the entire chord contributes to lift. The forward 50% of the chord contributes more to the total lift than the aft 50%.

Figure 8-9 shows how C_p changes with α. It illustrates how the leading edge carries more load as α increases. When the C_p reaches a low value, the distance required for proper pressure rise exceeds that available by the chord: The flow separates and the airfoil stalls. Figure 8-10 gives idea about the actual changes in airspeed and pressure over the airfoil. The pressure distribution along the lower surface starts with stagnation condition ($C_p = 1$ near $x = 0$). A low-pressure dip is developed on the lower surface, near $x = 0.10$, as the airflow accelerates around the curved the leading edge. This is followed by a steady rise in pressure. On the upper surfaces, the flow accelerates to some peak value, with

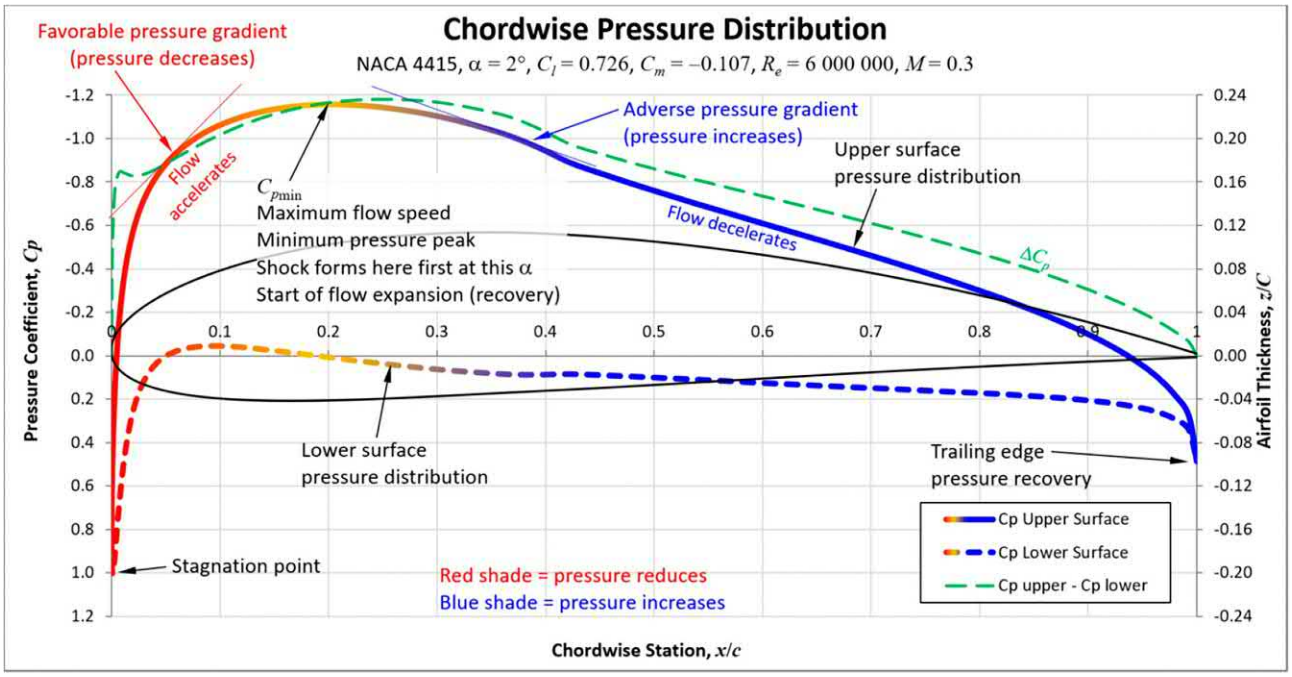


FIGURE 8-8 Important properties of a pressure distribution curves for a typical airfoil.

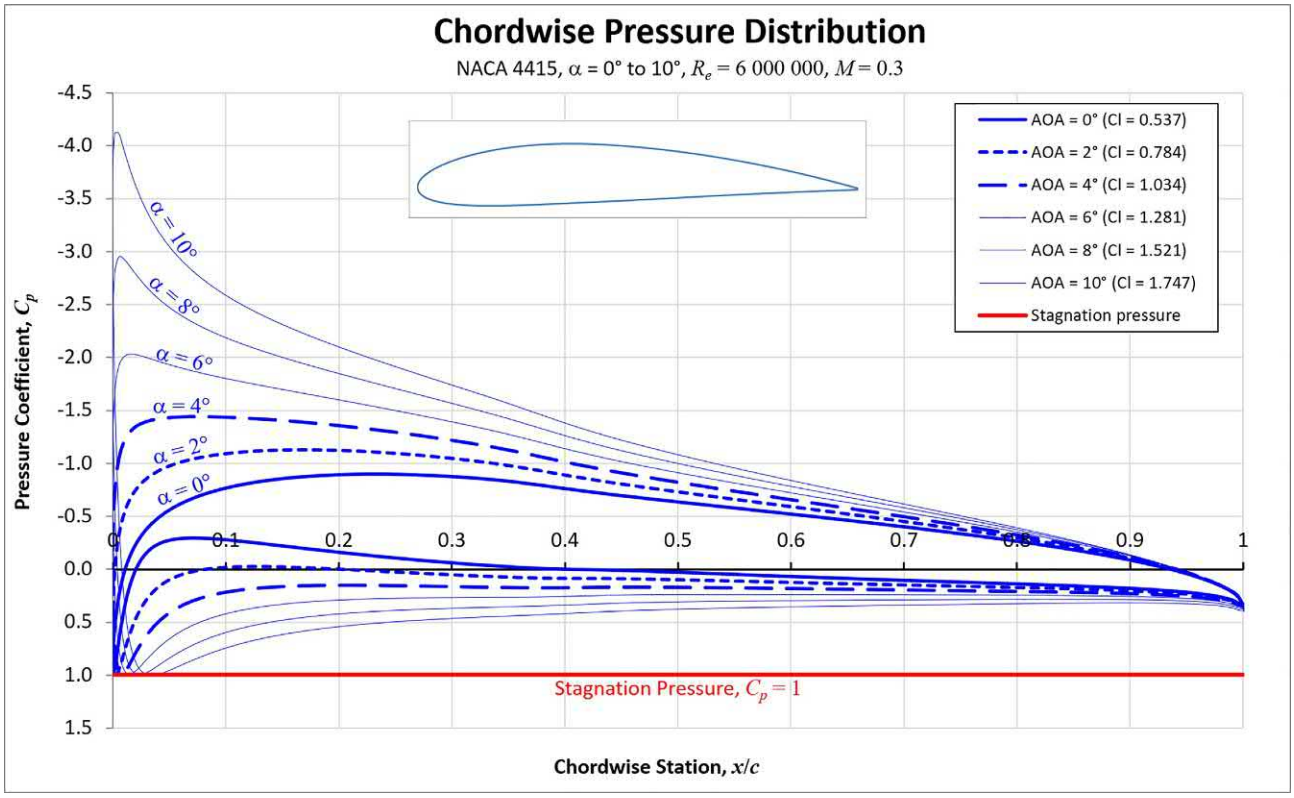


FIGURE 8-9 Change in C_p for NACA 4415 from α = 0° to 10°.

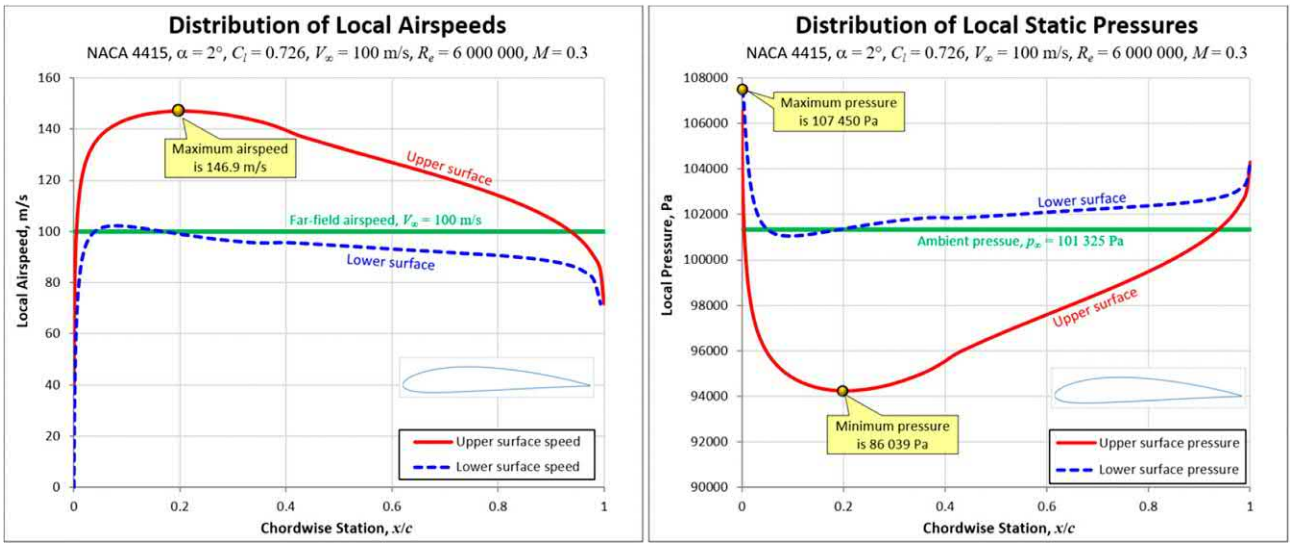


FIGURE 8-10 Example of the distribution of local airspeeds and static pressures over an airfoil at low AOA.

associated drop in pressure that depends on α and Mach number.

(2) Pressure Distribution around "NLF" Airfoils

The NLF(1)-0414F airfoil in Figure 8-11 exemplifies a class of airfoils called *natural laminar flow* (NLF) airfoils. The graph shows the chordwise distribution at the same α = 2° as above. It forms a distinct flat pressure contour on the upper surface, commonly referred to as a "rooftop" or Stratford pressure distribution. The absence of an unfavorable pressure gradient (dp/dx) over 70% of the chord promotes extensive laminar boundary layer provided the surface is sufficiently smooth. Since laminar skin friction is about 4× less than turbulent one, it will generate far

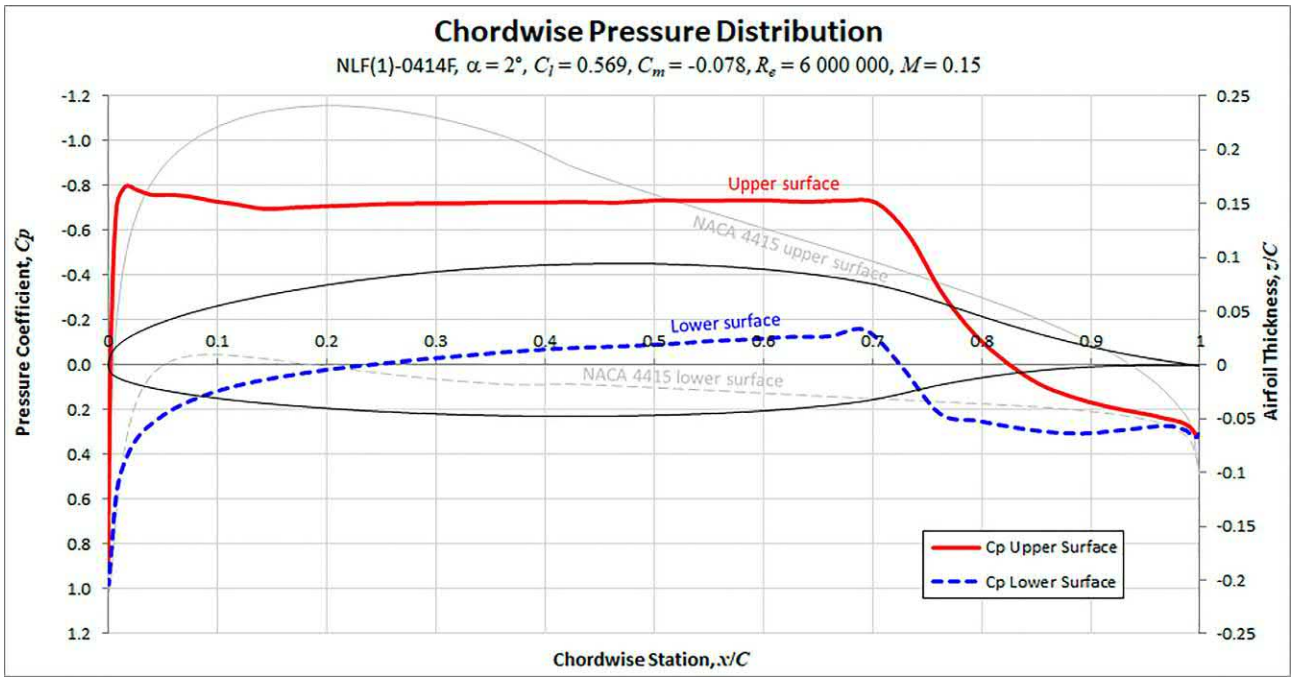


FIGURE 8-11 The chordwise distribution for an NLF airfoil at α = 2°, showing the so-called Stratford distribution. The distribution for a NACA 4415 at the same α is coplotted for comparison.

less drag than the NACA 4415 over the narrow range of AOAs where the rooftop forms.

Consider a hypothetical, uniform pressure distribution along the chord of the airfoil. It represents the most efficient means to generate lift, as each chordwise segment contributes equally to the total lift. However, it is physically impossible because it would require discontinuous pressure changes at the leading and trailing edges. In real applications, pressure changes over finite distances: flow must be allowed to decelerate over a given distance (increasing pressure, which eventually returns to ambient pressure). If the distance is too short, the flow will separate; too long, a full advantage is not taken of the benefits of laminar boundary layer. The distance is ideal if the flow is on the verge of separating and the flat rooftop extends as far aft as possible. This minimizes the airfoil's skin friction drag. NLF airfoils are designed to generate such a pressure distribution. However, this can only be achieved for a small range of specific AOAs (say 1°-3°).

8.1.7 Forces and Moment per Unit Span

The *normal* and *chordwise* forces *per unit span*, f_n and f_c, respectively, are of great importance to the structural engineer (see Figure 8-2). The normal force is perpendicular to the wing plane (the hypothetical plane formed by the span- and chordwise vectors) and generates the bending moment. The chordwise force, in contrast, is parallel to the chord plane. At low angles-of-attack, the magnitude of f_c points toward the trailing edge of the airfoil. At high angles-of-attack, f_c points forward, toward the leading edge. The effect tends to move the wing in a forward direction! This effect must be considered in structural analysis as it places aft spar attachment in tension, whereas at low angles-of-attack, it places the aft attachment in compression. Figure 8-2 shows that the normal and chordwise forces can be determined in terms of C_l and C_d as follows:

$$f_n = \frac{1}{2}\rho V_\infty^2 c(C_l \cos\alpha + C_d \sin\alpha)$$
$$f_c = \frac{1}{2}\rho V_\infty^2 c(C_d \cos\alpha - C_l \sin\alpha) \tag{8-18}$$

Lift and drag per unit span are related to f_n and f_c through the following transformations (Figure 8-12):

$$\begin{Bmatrix} l \\ d \end{Bmatrix} = \begin{bmatrix} \cos\alpha & -\sin\alpha \\ \sin\alpha & \cos\alpha \end{bmatrix} \begin{Bmatrix} f_n \\ f_c \end{Bmatrix} \quad \text{and}$$
$$\begin{Bmatrix} f_n \\ f_c \end{Bmatrix} = \begin{bmatrix} \cos\alpha & \sin\alpha \\ -\sin\alpha & \cos\alpha \end{bmatrix} \begin{Bmatrix} l \\ d \end{Bmatrix} \tag{8-19}$$

If the distribution of pressure and viscous shear stress along the upper and lower surfaces of an airfoil is available, the normal and chordwise forces and pitching moment about the leading edge *per unit span* can be estimated using the expressions below:

$$f_n = -\int_{LE}^{TE} (p_u \cos\theta_u + \tau_u \sin\theta_u) ds_u + \int_{LE}^{TE} (p_l \cos\theta_l - \tau_l \sin\theta_l) ds_l$$
$$f_c = -\int_{LE}^{TE} (p_u \sin\theta_u - \tau_u \cos\theta_u) ds_u + \int_{LE}^{TE} (p_l \sin\theta_l + \tau_l \cos\theta_l) ds_l$$
$$m_{LE} = \int_{LE}^{TE} [(p_u \cos\theta_u + \tau_u \sin\theta_u)x - (p_u \sin\theta_u - \tau_u \cos\theta_u)y] ds_u$$
$$+ \int_{LE}^{TE} [(-p_l \cos\theta_l + \tau_l \sin\theta_l)x + (p_l \sin\theta_l + \tau_l \cos\theta_l)y] ds_l \tag{8-20}$$

where p_u, τ_u and p_l, τ_l are the pressure and viscous shear stress along the upper and lower surfaces, respectively. θ_u and θ_l are the angles between the tangent and the coordinate system on the upper and lower surfaces,

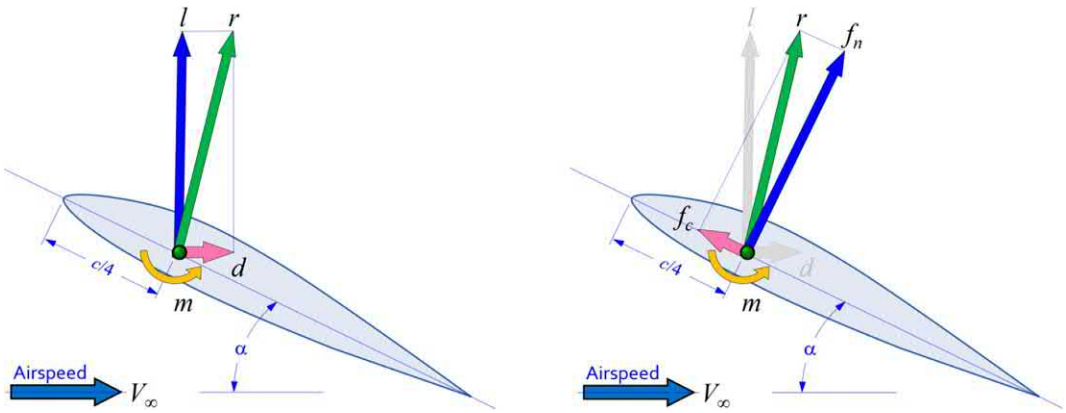


FIGURE 8-12 Forces and moments acting on an airfoil (left) and the definition of normal and chordwise force on an airfoil at a high AOA (right).

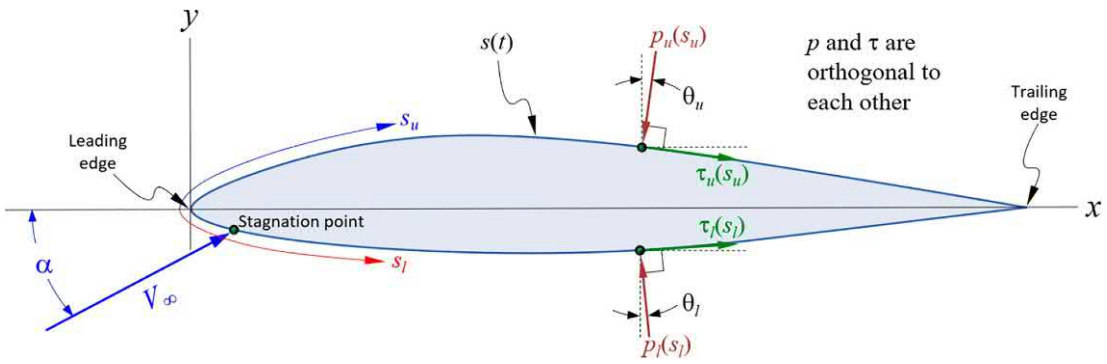


FIGURE 8-13 Distribution of pressure and viscous shear stress over an airfoil.

respectively (see Figure 8-13). A derivation for these equations is provided in ref. [9].

8.1.8 Center of Pressure and Aerodynamic Center

(1) Center of Pressure, x_{cp}

In addition to generating a resultant force, a body immersed in fluid flow generates a moment. The magnitude of the moment depends on the position on the body about which it is measured. Note that by convention, counter-clockwise moment is negative. Clockwise is positive. The *center of pressure* (CP) is defined as the point where the moment equals zero ($C_m = 0$).

To explain the concept, consider the airfoils in Figure 8-14, which are hinged in three places: (1) The top one is hinged at the leading edge: The normal force (f_n) generates a counter-clockwise moment about this point. (2) The bottom airfoil is hinged at the trailing edge, for which f_n generates a clockwise moment. It follows there must be a point between (1) and (2) about which no rotation takes place. This point is the CP (see center airfoil). Its location depends on the distribution of pressure along the airfoil and it changes with AOA. If we know the moment about the leading edge, m_{LE}, and f_n, we can calculate the <u>physical position</u> of the CP (x_{cp}) as follows:

$$m_{LE} = f_n \times x_{cp} \quad \Rightarrow \quad x_{cp} = m_{LE}/f_n \tag{8-21}$$

It is evident that x_{cp} varies with f_n and approaches ∞ when $f_n \to 0$.

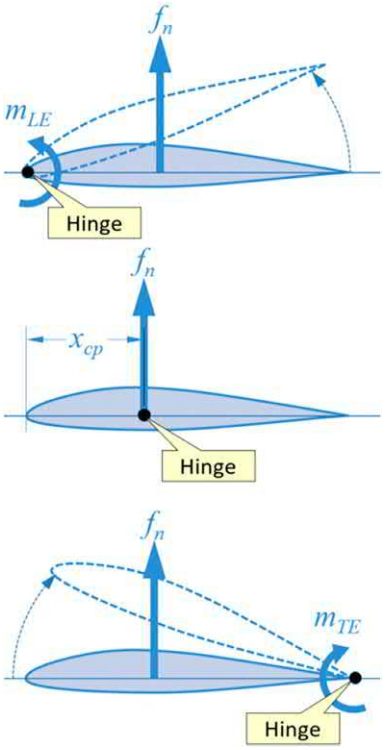


FIGURE 8-14 Center of pressure explained.

(2) Aerodynamic Center (x_{ac}) and Quarter-Chord Moment ($C_{mc/4}$)

The *aerodynamic center* is the point on a body about which the aerodynamic moment is independent of the AOA ($C_{m\alpha\ ac} = 0$). An experimental example is show in Figure 8-6. If the pitching moment about the quarter chord ($C_{m\alpha\ c/4}$) and $C_{l\alpha}$ are known, the <u>physical position</u> of the aerodynamic center (x_{ac}) can be computed from:

$$x_{ac} = \left(0.25 - \frac{C_{m_{\alpha\ c/4}}}{C_{l_\alpha}}\right)c \tag{8-22}$$

Pitching moment of airfoils is often reported at the aerodynamic center, although it is needed at the quarter-chord for many stability and control problems. The following expression can be used to transfer the moment from the aerodynamic center to the quarter chord:

$$C_{m_{c/4}} = C_{m_{ac}} + C_l\left(0.25 - \frac{x_{ac}}{c}\right) = C_{m_{ac}} + C_{l_\alpha}\alpha\left(0.25 - \frac{x_{ac}}{c}\right) \tag{8-23}$$

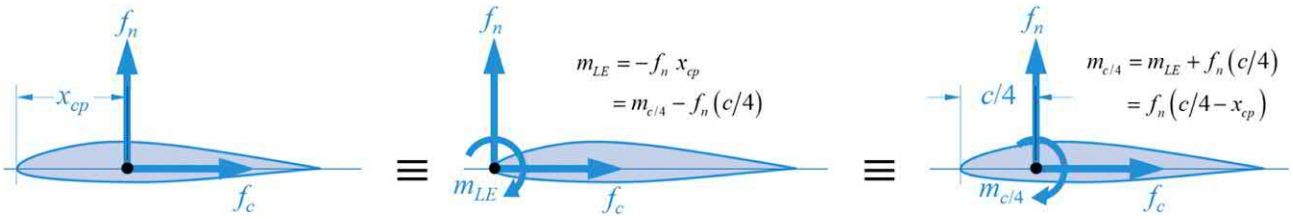


FIGURE 8-15 Equivalent force–moment combinations (inspired by ref. [9]).

Also note that the combination of forces and moments can be presented at any point by adjusting the magnitude of the moment. Three ways are presented in Figure 8-15.

DERIVATION OF EQUATIONS (8-22) AND (8-23)

Based on Figure 8-16, the moment about the aerodynamic center can be obtained by summing the forces (l) and moments (m) as follows:

$$m_{ac} = m_{c/4} + l(x_{ac} - c/4) = m_{c/4} + l\left(\frac{x_{ac}}{c} - 0.25\right)c$$

Dividing through by qSc, where $q = \frac{1}{2}\rho V^2$, and converting to coefficient form using Equation (8-6), we get

$$\frac{m_{ac}}{qSc} = \frac{m_{c/4}}{qSc} + \frac{l}{qSc}\left(\frac{x_{ac}}{c} - 0.25\right)c \quad \Rightarrow \quad C_{m_{ac}} = C_{m_{c/4}} + C_l\left(\frac{x_{ac}}{c} - 0.25\right)$$

Solving for $C_{mc/4}$ gives Equation (8-23). Then, differentiating with respect to α and setting to zero, this becomes

$$\frac{dC_{m_{ac}}}{d\alpha} = \frac{dC_{m_{c/4}}}{d\alpha} + \frac{dC_l}{d\alpha}\left(\frac{x_{ac}}{c} - 0.25\right) = 0$$

Using convention in writing the slopes and solving for x_{ac} yields Equation (8-22).

8.1.9 The Generation of Lift

The generation of lift can be explained in at least three ways. These are known by their casual names as *momentum theorem*, *Bernoulli theorem*, and the *circulation theorem*. Each is briefly introduced to provide clarity, as each is referred to in various places in the text. Each is a tool for the aerodynamicist that suits the right situation, just like carpenters pick different hammers for different jobs.

(1) Momentum Theorem

The *momentum theorem* explains lift as the consequence of a wing moving through a mass of air and giving it a downward motion (see Figure 8-17). The vertical speed of the mass of air changes, over some specific amount of time, from zero to some finite value. This, in turn, means that a force (lift) will be generated in the opposite direction in accordance with *Newton's Third Law of Motion*. The magnitude of this force is estimated using one of the conservation laws of fluid mechanics; the momentum theorem (see Chapter 14). A common analogy used to describe this phenomenon is the recoil of a firearm. The change in the momentum of a bullet generates a force that acts in the opposite direction of its motion. Lift is analogous to a continuous recoil.

The downward motion of the air is called *downwash*, here denoted by w. It represents the vertical speed of air behind the wing. It contrasts the horizontal speed of the wing moving through air. If we know the downwash and the mass flow of air being deflected, the magnitude of the lift can be estimated using momentum theorem:

$$L = \dot{m}w \tag{8-24}$$

where

$\dot{m}$ = mass flow rate inside the cylinder $= \rho V_\infty \cdot \pi b^2/4$

The mass flow rate in the stream tube is given by $\dot{m} = \rho A_{tube} V_\infty$, where A_{tube} is the cross-sectional area of the stream tube. The diameter of the stream tube in Figure 8-17 equals that of the wingspan (b). Thus, the rate of change of momentum (lift force) can be estimated from:

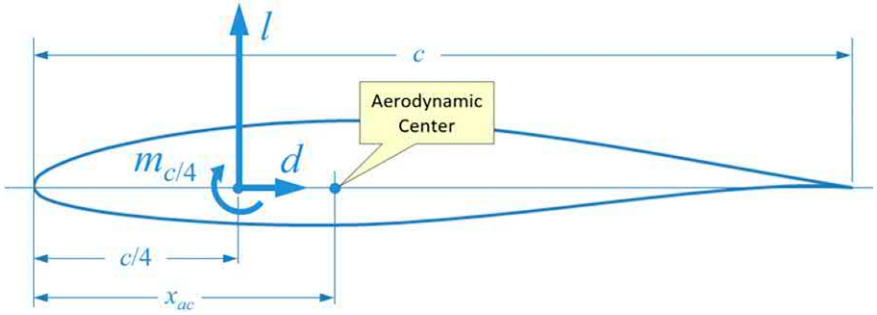


FIGURE 8-16 Location of the aerodynamic center.

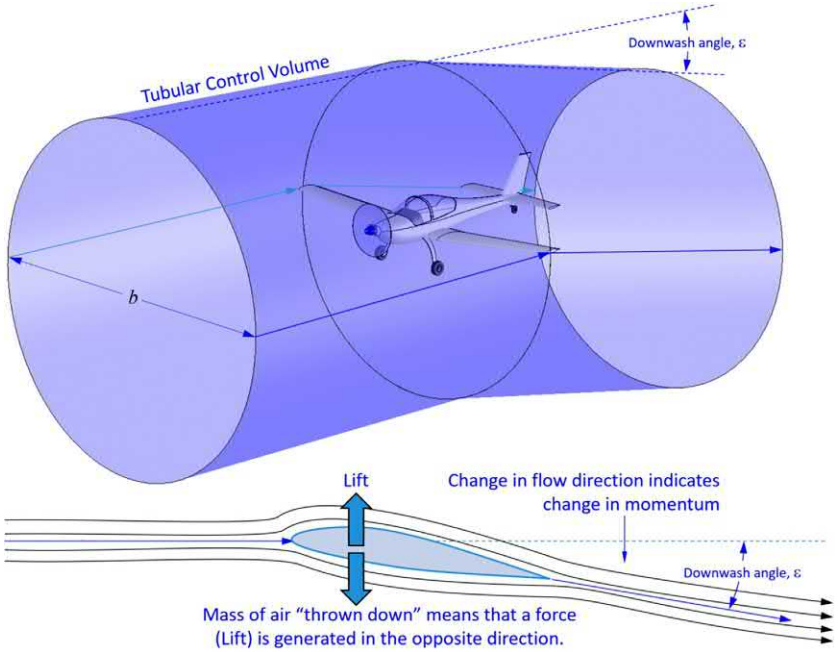


FIGURE 8-17 An airplane's motion causes a downward deflection of a tube of air. In accordance with Newton's second law of motion, its rate of change of vertical momentum generates a force in the opposite direction (lift).

$$L = \dot{m}w = \rho A_{tube} V_\infty w = \rho\left(\frac{\pi}{4}\right) b^2 V_\infty w \tag{8-25}$$

Equating this with the standard expression for lift (Equation (8-6)) allows the downwash speed to be estimated:

$$L = \rho\left(\frac{\pi}{4}\right) b^2 V_\infty w = \frac{1}{2}\rho V_\infty^2 S C_L \quad \Leftrightarrow \quad w = 2V_\infty \frac{S}{\pi b^2} C_L \tag{8-26}$$

Since the wing aspect ratio is $AR = b^2/S$, this can be rewritten as

$$w = \frac{2C_L}{\pi AR} V_\infty \tag{8-27}$$

Since the downwash speed can be approximated by $w = \varepsilon V_\infty$ (see Figure 8-17), we can write:

$$\varepsilon = \varepsilon_0 + \frac{\partial \varepsilon}{\partial \alpha}\alpha = \frac{2C_L}{\pi AR} \tag{8-28}$$

where ε_0 is the *residual downwash*. It is nonzero for cambered airfoils and deflected flaps. Noting that $C_L = C_{L0} + C_{L\alpha}\alpha$, this equation leads to another result, which as will be shown later, is very helpful in Stability and Control Theory:

$$\frac{\partial \varepsilon}{\partial \alpha} = \frac{2}{\pi AR}\frac{d}{d\alpha}(C_{L_0} + C_{L_\alpha}\alpha) = \frac{2C_{L_\alpha}}{\pi AR} \tag{8-29}$$

(2) Bernoulli Theorem

The *Bernoulli theorem* has been used to explain the formation of lift to generations of engineers and pilots. It postulates that lift is the consequence of the difference in pressure between the upper and lower surfaces of an airfoil, although this would more properly be explained as the resultant of integrating the pressure over the entire surface of a body (see Figure 8-10). Named after the Swiss mathematician Daniel Bernoulli (1700–1782), the theorem stipulates the following relationship between the pressure and speed of the fluid at a point and along a streamline that goes through that point:

Incompressible Bernoulli Equation

$$p_\infty + \frac{1}{2}\rho V_\infty^2 = \text{constant} \tag{8-30}$$

Compressible Bernoulli Equation

$$p_\infty + \frac{1}{2}\rho V_\infty^2 \left(\frac{\gamma - 1}{\gamma}\right) = \text{constant} \tag{8-31}$$

where

p = Pressure, in lb_f/ft^2 or N/m^2
V_∞ = Far-field airspeed, ft/s or m/s
ρ = Fluid density, in $slugs/ft^3$ or kg/m^3
γ = Ratio of specific heat for the fluid (1.4 for air at altitudes below 100 km)

Bernoulli's theorem is used daily by thousands of people in industry and academia to estimate the aerodynamic forces acting on a body. Computational Fluid Dynamics (CFD) software uses the theorem to estimate aerodynamic forces and moments acting on a body with great success.

(3) Kutta–Joukowski Circulation Theorem

The *Kutta–Joukowski Circulation Theorem* is more a mathematical method than an explanation. Named after the German mathematician Martin Wilhelm Kutta

(1867–1944) and the Russian scientist Nikolay Yegorovich Joukowski (often spelled Zhukovsky) (1847–1921), the theorem postulates that the lift generated by an airfoil can be considered the product of density, airspeed, and a mathematical concept called *circulation* (Γ). It is estimated *per unit span*. Thus, the lift of a wing with span b can be expressed as follows:

$$L = \rho V_\infty \, \Gamma b \tag{8-32}$$

The circulation is calculated using the expression [15]:

$$\Gamma = -\oint_C \vec{V} \cdot d\vec{s} \tag{8-33}$$

where $\vec{V}$ is velocity and C is a closed curve in a flow field (see Figure 8-18). In reality, the air does not flow in a circular motion. Rather, the term means that the path integral of Equation (8-33) is nonzero. Regardless, to better understand circulation, consider Figure 8-18, which shows the airflow around an airfoil. The top figure shows that the far-field airspeed, V_∞, and some representative airspeed, V_1 through V_6, positioned at selected locations in the flow-field, above and below the airfoil. The local airspeed over the top surface is greater than that over the bottom surface. If the far-field airspeed is subtracted from these local airspeeds, we get airspeeds ΔV_1 through ΔV_6 in the center figure. The airspeed differences along the upper surface are positive and point in the flow direction. They are negative along the lower surface and point in a direction opposite of the general airflow. As can be seen in the bottom figure, these differentials form a path around the airfoil: it *is* the circulation.

The Kutta–Joukowski theorem is very useful in several *Computational Fluid Dynamics* (CFD) methods, such as the Lifting Line method (see Section 9.7) and the vortex-lattice method, where it is directly used to estimate the lift and induced drag force generated by a lifting surface.

(4) Alternative Analogy

The following analogy is intended to help laypeople relate to why pressure decreases over the upper surface and rises on the lower one (see Figure 8-19). It is based in *kinetic theory* and uses the principle of pressure equalization, which holds that fluid molecules flow rapidly from a high- to a low-pressure region. A high-pressure region is rich of molecules (=more frequent molecule-to-surface collisions) while the opposite holds for a low-pressure region (=reduced collisions). Although the molecular motion "tends to even" the number of molecules per unit volume, the airfoil's motion forms a transient variation in pressure over its surface. The process is complicated by the presence of viscosity. It dictates how the flow leaves the trailing edge (*Kutta condition*) such that downwash forms [9]. Those details are beyond the scope of this text.

8.1.10 Boundary Layer Basics

An understanding of fluid mechanics is needed to explain important flow phenomena on aircraft, but also when interpreting results from wind tunnel testing. Much of this understanding is borrowed from *boundary layer theory* (BLT), which describes the nature of viscous flow near the surface of a body. The applicable formulae

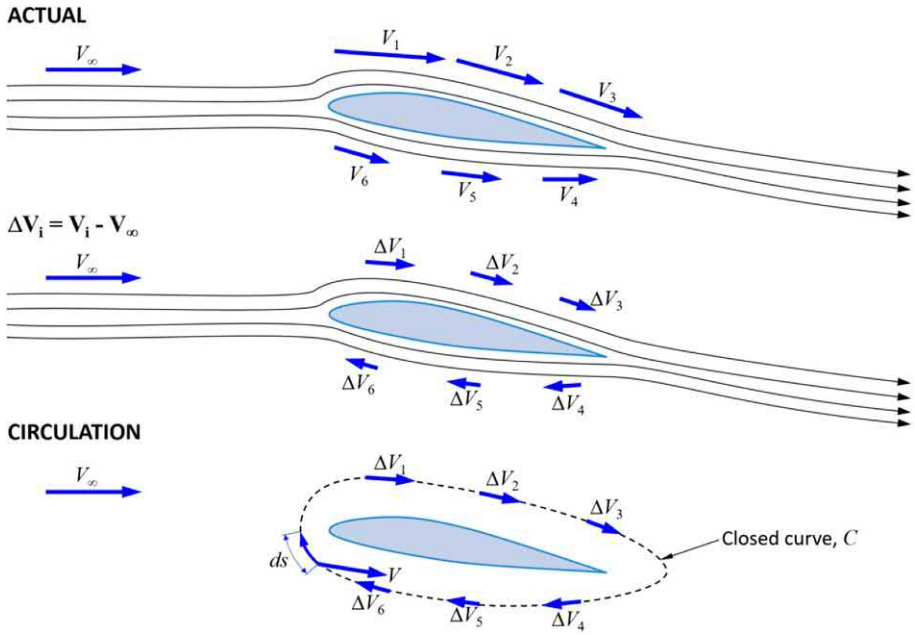


FIGURE 8-18 Circulation made easy. See text for explanation.

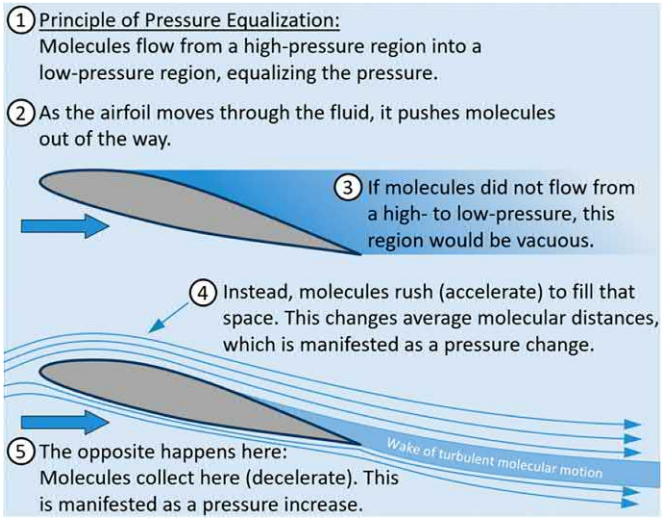


FIGURE 8-19 Explaining the pressure-field around an airfoil.

are developed using conservation laws and the Navier-Stokes equations. BLT is extensive and while essential to treatment of viscous flow, its scope is too large for this book. This discussion is placed here because of its impact on airfoils. The topic reemerges in Chapter 16, alongside multiple analysis methods. For theoretical derivations refer to texts such as those of Schlichting [16] and Young [17].

(1) Boundary Layer (BL)

Is a thin layer of fluid in direct contact with the surface of an object. At the surface, the fluid is at rest, but its speed increases with distance (y) from the surface until it equals the local speed outside of the BL. The thickness of the BL is denoted by δ. It is the distance between the surface and where the flow speed is 99% of that outside of it. This is illustrated in Figure 8-20, which shows two velocity profiles inside a BL. The shape of the velocity profile dictates the magnitude of the surface (or skin) friction through *viscous shear stress*. Note that while the speeds at $y=0$ and $y=\delta$ is identical for both, its variation is different between the two. The pressure through the BL, along the y-axis is constant, i.e., $\partial p/\partial y \cong 0$.

$$u(y)=\begin{cases} U\left(\frac{y}{\delta}\right) & \text{if } 0<y<\delta \\ U & \text{if } y\geq\delta \end{cases} \qquad u(y)=\begin{cases} U\sqrt{\frac{y}{\delta}} & \text{if } 0<y<\delta \\ U & \text{if } y\geq\delta \end{cases}$$

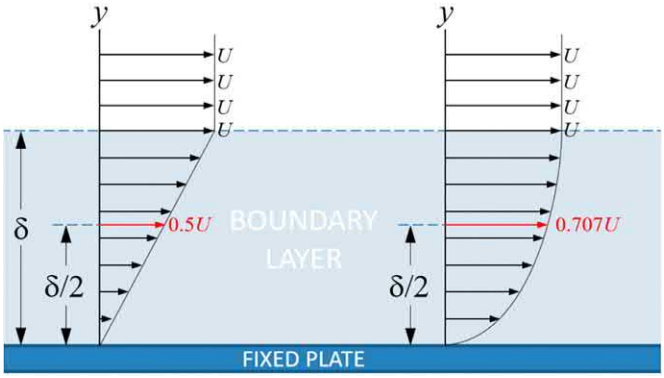


FIGURE 8-20 Two hypothetical velocity profiles inside a boundary layer.

(2) Viscosity

Refers to the resistance of fluids to change form and, thus, flowing. Syrup is more viscous than water; it flows slower down a ramp than water. Viscosity is caused by (A) transfer of *intermolecular momentum* between molecules, and (B) *bonding* between molecules. These cause liquids and gases to respond differently to changes in temperature. In liquids, molecules are packed tightly, so (B) plays a more prominent role than (A). Increased temperature reduces the bonding force, causing viscosity to drop. In gases, the molecules are sparser, so (A) plays a more prominent role than (B). Increasing temperature intensifies intermolecular momentum transfer and increases viscosity. See Section 16.3.1 for analyses methods.

(3) Types of Flow Inside the Boundary Layer

Fluid flow inside the boundary layer is either *laminar*, *turbulent*, or *separated* (see Figure 8-21). Flow inside a laminar BL is dominated by a smooth flow without vertical translation of fluid parcels. This contrasts turbulent BL, which is chaotic with horizontal and vertical translation. Laminar BL transforms into a turbulent one through a process called *transition*. This happens near the leading edge of bodies with poor surface qualities. However, smooth bodies (e.g., composites), sustain laminar BL until the R_{ex} approaches 5×10^5, after which the chances of transition increases (also see Section 16.3.1). This is referred to as the *transition Reynolds number*.

Transition can happen at R_e that is lower or higher than the transition-R_e [18]. If the R_e is lower, we talk about *early transition* and *delayed transition*, if it is higher. The transition is complicated by the following factors:

(A) *Surface roughness*. The transition depends on flow disturbances inside the boundary layer. The presence of small surface imperfections (roughness) excites disturbances and expedite the transition—even to very low values of the Reynolds number. Also see Section 8.3.7.

(B) *Surface temperature*. The thickness of the BL increases with temperature, as does the energy it contains. The increase in temperature and thickness promotes an earlier transition. A cold surface tends to delay transition.

(C) *Pressure gradient*. A *favorable* dp/dx (see Figure 8-8) stabilizes the laminar BL and delays transition. The opposite holds for an *adverse* dp/dx. Also see Section 8.1.6.

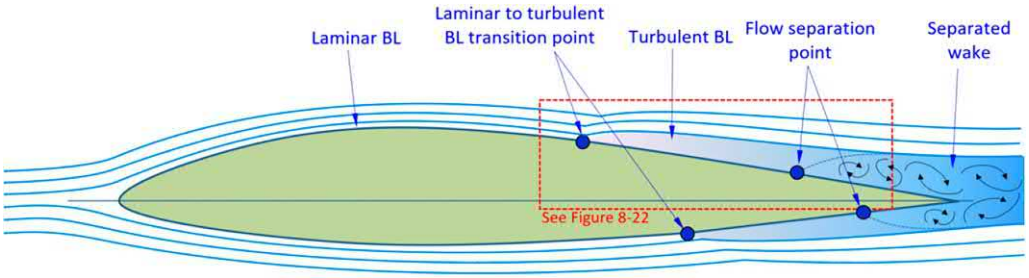


FIGURE 8-21 Three types of fluid regions; laminar, turbulent, and separated. Also see Figure 8-23.

(D) *Mach number*. The transition-R_e increases with Mach number (i.e., in compressible flow).

(4) Factors Affecting Laminar Flow

Laminar boundary layer is very sensitive to several factors. Some are out of control of the designer, while others depend on his awareness. Among those are (list partially based on Bertin [19]):

(A) Geometry (e.g., sweep and surface curvature).
(B) Surface smoothness (or lack thereof).
(C) Surface temperature.
(D) Compressibility effects (M, R_e).
(E) Atmospheric conditions (ice crystals, rain).
(F) Manufacturing quality (waviness, smoothness, steps and gaps in surface joints).
(G) Leading-edge quality (insects, dirt, erosion, icing).
(H) Suction or blowing at the surface (surface openings, distribution of boundary layer control).
(I) Noise (engine, propwash).

Favorable conditions for the formation of laminar boundary layer exist when the pressure is dropping (favorable dp/dx). The laminar BL tends to transition to a turbulent one near where pressure begins to rise (unfavorable dp/dx). This is depicted in Figure 8-22, for NACA 0018 (conventional) and 66–018 (NLF) airfoils. The favorable dp/dx extends much farther back for the latter.

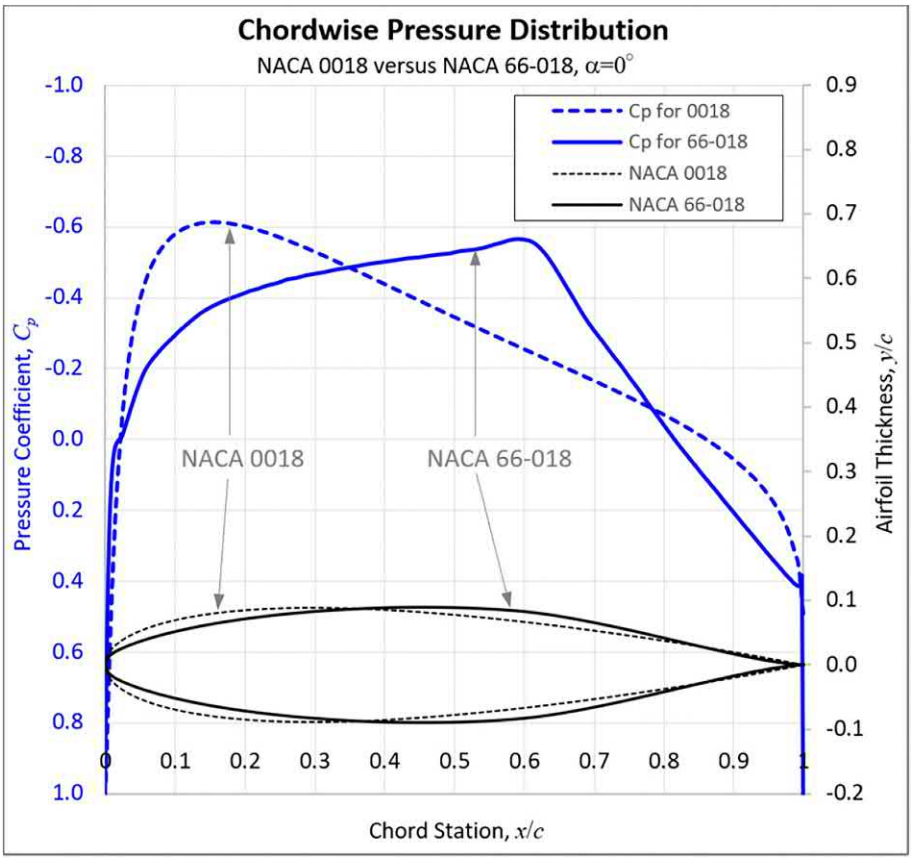


FIGURE 8-22 Pressure distributions for a conventional (0018) and an NLF airfoil (66–018) at $\alpha = 0°$.

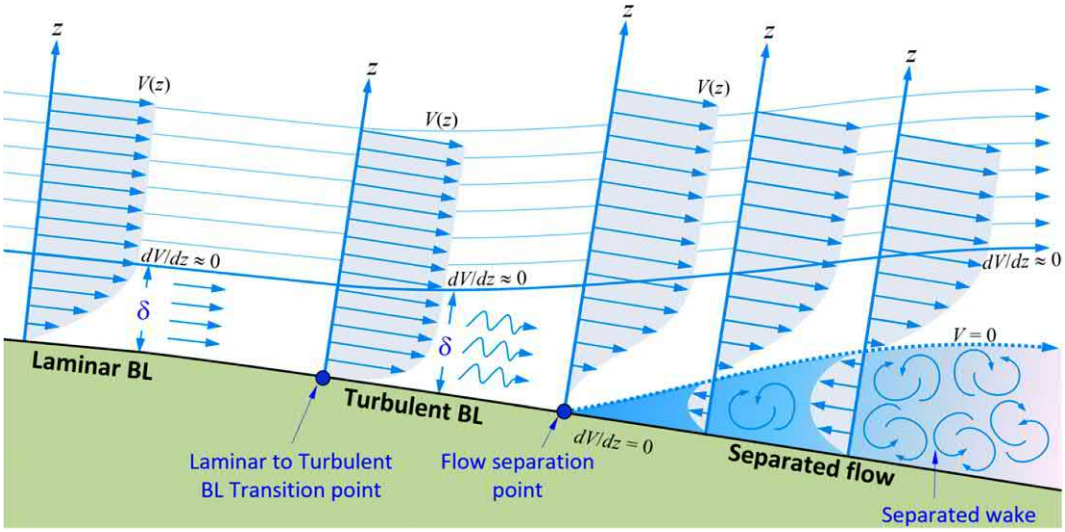


FIGURE 8-23 The nature of fluid flow inside laminar and turbulent boundary layers, and separated flow.

(5) Flow Separation

In *separated flow*, the streamlines are separated from the surface and is highly chaotic, with upstream flow. The flow separates where the gradient dV/dz equals zero on the surface (see Figure 8-23). The external geometry of an airplane should be shaped to minimize or eliminate areas of flow separation at the mission condition.

The three flow-types develop in the order shown in Figure 8-23. This typically occurs on bodies as shown in Figure 8-24. The upper image illustrates the flow over an object with a rounded, small radius Leading Edge (LE). The flow forms laminar boundary layer on the forward part of the object (the bow), followed by a transition to turbulent boundary layer, and, finally, by the flow separating into turbulent wake at the stern. The lower image shows an object with a blunt LE causing a flow separation on the LE that result in (highly) turbulent, circulatory flow inside the flow separation region. The laminar streamlines flow over this region attach aft of this region before separating into the turbulent wake at the stern. The forward flow separation region is usually referred to as a "separation bubble." Besides increasing drag, separation bubbles on airfoils are very detrimental to stall characteristics.

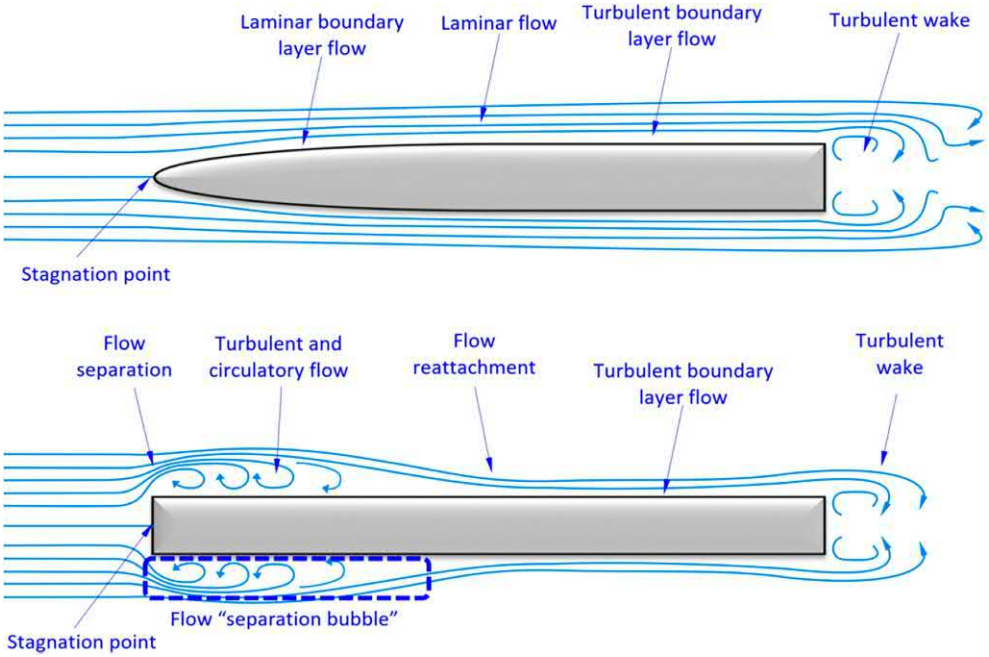


FIGURE 8-24 Flow over an object with a small leading-edge radius (upper) and a blunt LE object (lower).

Separation bubbles can form in the wing–fuselage juncture. However, the phenomenon also occurs on lifting surfaces, on small chords (or low Reynolds numbers). As discussed in Section 8.2.10, The NACA 23012 airfoil is used for many GA aircraft despite its abrupt stall characteristics, which is attributed to the formation of a separation bubble. But they are a prevalent problem for even smaller Reynolds numbers, such as those in which radio-controlled aircraft operate (50,000–500,000). In this region, a stable bubble may form in the laminar boundary layer along the leading edge of the wing, increasing the drag of the vehicle. This is called "bubble drag" [20]. This drag can be reduced by designing the airfoil such its transition ramp reduces the chance of a bubble formation. A *transition ramp* refers to the shape of the pressure coefficient curve aft of where it peaks. The ramp can be tailored to modify the adverse pressure gradient (dp/dx) to control the transition of the laminar into turbulent BL without promoting the formation of a large separation bubble (see Ref. [20] for more details). Another way is to place a transition strip (often called a "trip-strip") along the leading edge to force laminar boundary layer to transition into a turbulent one without forming the separation bubble. Currently, this is a trial and error approach and a trip-strip that is ideal for one Reynolds number may be detrimental for another one. Their effect is contingent upon the size of the bubble, its intensity, AOA, and geometry of the airfoil.

(6) The Effect of Flow Separation

Consider two identical aircraft that differ only in scale. Immersing these in airflow at some airspeed results in two dissimilar *Reynolds numbers*. Assume these are brought slowly through an alpha-sweep, from 0° to 90°, as their force and moment coefficients are collected. At first, while the flow is mostly attached, the linear force and moment coefficients for both aircraft will be identical. However, at some AOA (e.g., $\alpha = 8°$), flow separation begins on the smaller body, while it remains attached on the larger one. The resulting force and moment coefficients for the small body turn nonlinear, while remaining linear for the larger one. Eventually, the larger body too begins to experience the same effect (e.g., $\alpha = 12°$). The flow separation causes a large increase in drag and reduction in lift. The pitching moment may increase or reduce depending on the overall geometry. This calls for a distinction in the nature of the flow over the two bodies.

8.1.11 Airfoil Stall Characteristics

In this text, *stall* refers to the flow condition that follows the first peak of the lift curve. It results from the extensive separation between the leading and trailing edge of the airfoil. The thickness of the airfoil dictates how the flow separates on the airfoil. If the airfoil is thick, the separation tends to begin at the trailing edge and move forward with increasing AOA. If the airfoil is thin, the separation begins at the leading edge in the form of a separation bubble, with or without reattachment (see Figure 8-25). On a wing, the bubble is a spanwise vortex. Other parameters that affect the maximum lift ($C_{l_{max}}$) include the location of the airfoil's maximum thickness, camber and its chordwise location, Mach number, Reynolds number, free-stream turbulence, and surface qualities (roughness) [21]. The reference classifies the flow separation as *trailing-edge* and *leading-edge* stalls, as described below:

(1) Trailing-Edge (TE) Stall

The best known among the three types of stalls and typically occurs on thick airfoils, whose $t/c \geq 0.12$ [11, 4.1.1.3]. It is characterized by the flow separation point moving from the TE forward toward the LE. Such airfoils feature a smooth change in C_l and C_m between $C_{l_{min}}$ and $C_{l_{max}}$ (e.g., see Figure 8-5). The shape of the peak of the lift curve is rounded with a gentle drop in C_l. Growth in post-stall drag polar is gradual, and the pitching moment curve is without sharp breaks. The flow stays mostly attached to an $\alpha \approx 10°$, beyond which the separation region moves progressively forward. At $C_{l_{max}}$, the flow is separated from the TE to mid-chord. The late airfoil designer Harry Riblett (1929–2012) suggested that for an airfoil to provide gentle stall characteristics, the slope of the mean-line at $x = 0$ should be between 12° and 15° [22].

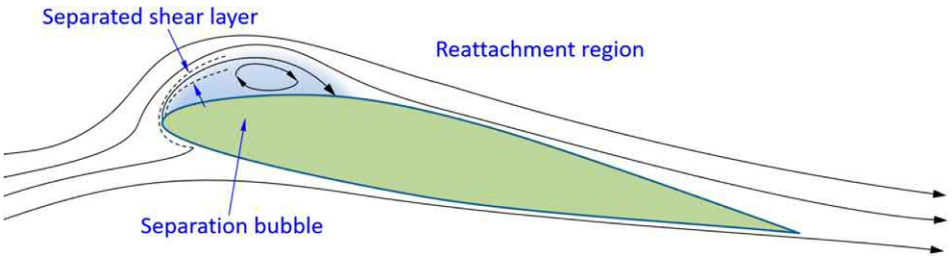


FIGURE 8-25 Formation of a separation bubble on a thin airfoil. *Based on Crabtree, L.F., The Formation of Regions of Separated Flow on Wing Surfaces, Aeronautical Research Council R.&M. No. 3122, 1959.*

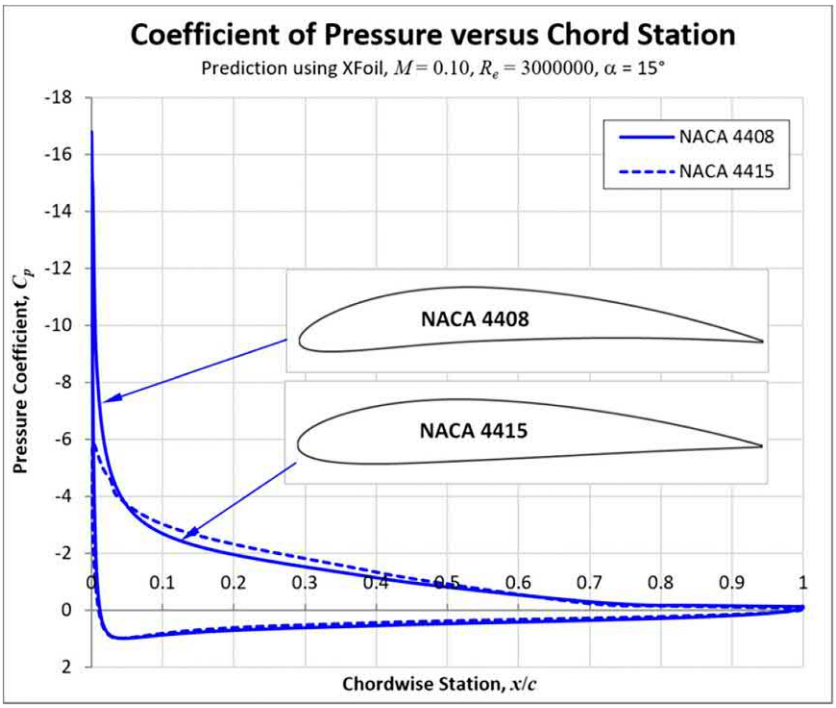


FIGURE 8-26 Pressure distribution for NACA 4408 and NACA 4415 airfoil shows a greater pressure peak for the 4408.

(2) Leading-Edge (LE) Stall

LE stalls are less familiar to the GA community than TE stalls. These come in two styles: Short and long leading-edge bubble. These form on thinner airfoils, whose small LE radius creates a larger pressure peak than airfoils with larger LE radius. This is evident in Figure 8-26, which shows the thinner NACA 4408 airfoil peaks at $C_p \approx -16$ versus $C_p \approx -6$ for the thicker NACA 4415. The steep pressure recovery (adverse dp/dx) for the thinner airfoil causes the laminar BL at the LE to separate. This happens well below the α_{stall}, when the laminar BL separates near the LE and forms a bubble of trapped low-energy air between the surface and the boundary layer [23].

The difference between the two bubble-styles is determined using *Owen's criterion*, which computes the Reynolds number of the displacement thickness of the boundary layer using the following expression [24]:

$$R_{\delta_1} = \frac{V}{\nu}\delta_1 \tag{8-34}$$

where V is the velocity at the edge of the BL, ν is the kinematic viscosity, and δ_1 is the displacement thickness. Ref. [24] states that this value is ≥ 500 for a short bubble and < 500 for a long one. The size of the bubble depends on the free stream R_e. If the R_e is large enough, chances are no bubble will form. The difference between the two is as follows:

(1) Short-Bubble Leading-Edge Stall: Occurs on airfoils of moderate thickness ($0.09 \leq t/c \leq 0.12$). The length of the bubble is about 1% of the chord at low AOAs but reduces in size with increased AOA. The bubble has limited effect on the pressure distribution and high-peak suction can continue to rise despite the bubble's presence up until some specific AOA, when the flow abruptly and finally separates from the airfoil's surface. This results in a violent stall, accompanied by large change in lift and pitching moment [11].

(2) Long-Bubble Leading-Edge Stall: Occurs on thin airfoils ($t/c \leq 0.09$). The length of the bubble is about 2% to 3% of the chord at a low AOA. However, this grows rapidly with AOA until a reattachment fails to take place, causing the bubble to combine with the full flow separation over the airfoil. A long bubble will affect the pressure distribution over the airfoil in profound ways and will cause a drop in peak suction. The maximum lift for the long bubble is less than that for the short one, but the stall is less abrupt [11].

The $C_{l_{max}}$ of thin airfoils that stall due to flow separation at the LE can be determined based on the leading-edge geometry. The *leading-edge parameter*, defined as the difference between the upper surface ordinates of the airfoil at the 0.15% and 6% chord stations, has been used for this purpose with good results [11, 4.1.1.4] (e.g., see Section 9.5.5, Bullet (6)). Additional correction is required for thicker airfoils. Compressibility effects are important on thick airfoils as it reduces $C_{l_{max}}$, starting at $M \approx 0.2$. Ref. [11] presents a method to estimate the maximum lift coefficient of airfoils. The three types of airfoil stalls are

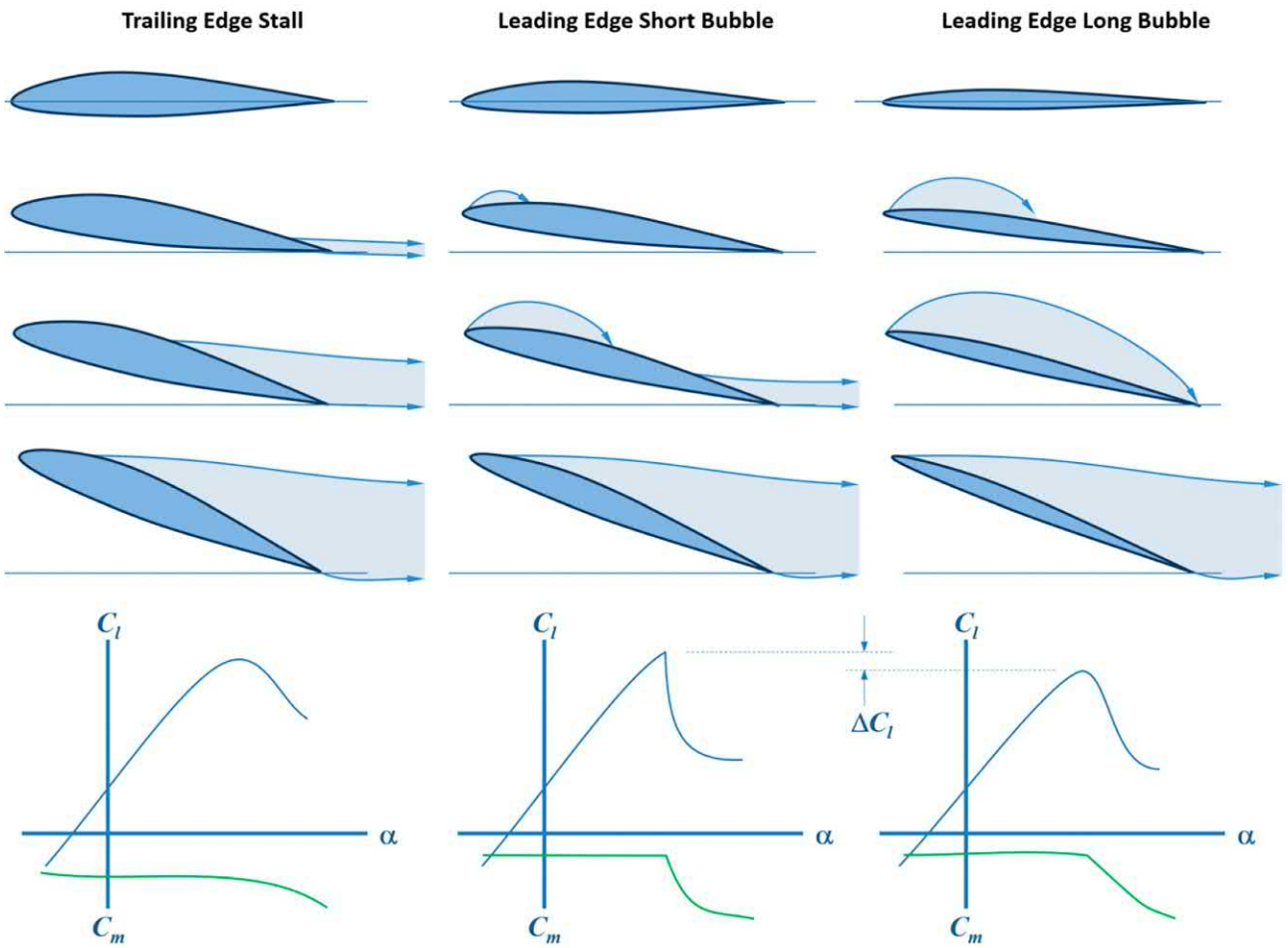


FIGURE 8-27 Types of stall and its effect on the lift and pitching moment. *Based on Crabtree, L.F., The Formation of Regions of Separated Flow on Wing Surfaces, Aeronautical Research Council R.&M. No. 3122, 1959; Kundu, A.K., Aircraft Design, Cambridge University Press, 2010.*

illustrated in Figure 8-27. Background on this phenomenon is provided in references such as [23–28], which complements more recent research.

8.1.12 Analysis of Ice Accretion on Airfoils

Flight into inclement weather is commonplace. However, certifying aircraft for *flight into known icing* (FIKI) represent one of the greatest challenges of its development. The aircraft designer should understand the challenges of ice accretion on airfoils.

NASA's Glenn Research Center has pioneered computational methods to estimate ice accretion on an airfoil's leading edge. This development included the implementation of these methods in a computer code called LEWICE (after the research center's former name Lewis Research Center). The code predicts the growth of ice under a range of meteorological conditions and, due to extensive validation by NASA scientists, is considered very reliable in industry.

Such codes work as follows. First, the geometric description of the airfoil (i.e., x- and y-coordinates) is read and analyzed using a panel-code solver. This yields the flow field around the airfoil, including the stagnation points. Then, the accretion of ice at the stagnation points is estimated for a given time-step. It is used to modify (grow) of the initial geometry, giving rise to a new geometry. It becomes the "input airfoil" for the next iteration. The process is then repeated for a specified amount of time. The user must specify various properties of the air at the flight condition, such as its relative humidity, liquid-water content, droplet size, temperature, airspeed, and other parameters. Figure 8-28 shows an example output from LEWICE for a common General Aviation airfoil, the NACA 64–215. It shows that ice accretion is a formidable foe to aircraft wings.

The software provides aircraft manufacturers with a reliable tool to estimate the *impingement limits* for the airfoil. The limit yields the region on the upper and lower surfaces inside which ice accretion takes place. It specifies how far aft of the leading-edge ice protection must wrap. Impingement limits are determined for a variety of flight conditions and atmospheric conditions and are based on the collectively aft-most limits.

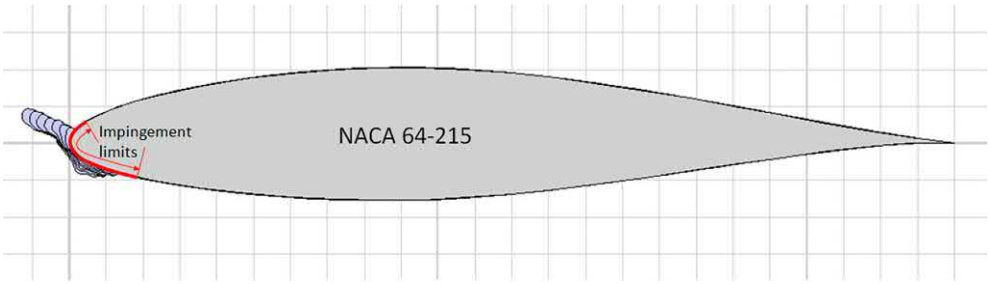


FIGURE 8-28 A LEWICE prediction showing ice accretion on an unprotected NACA 64-215 airfoil after a 45 min exposure to supercooled liquid-water at −4.75°C (23.4°F) at an airspeed of 90 m/s (295 ft/s) and AOA of 4°. The chord is 1.0 m (about 40 in.).

8.1.13 Designations of Common Airfoils

Many different airfoils have been designed since the dawn of flight, making airfoil selection a bit daunting. These offer a range of properties, some ideal, while others are less so. Table 8-3 lists designations of airfoils that are found in use on various airplanes.

8.1.14 Airfoil Design

During the history of aviation, thousands of different airfoils have been designed for applications ranging from aircraft, turbo machinery, wind turbines, propellers, and even ships (hydrofoils). Chances are that a suitable airfoil for your new design resides in that database, but suitable is not the same as ideal. Modern aircraft manufacturers usually opt to design airfoils tailored for the new

TABLE 8-3 Designations of common airfoils [29].

AG	Dr. Ashok Gopalarathnam, an independent airfoil designer
ARA	The Aircraft Research Association, Ltd. in Britain
Clark	Col. Virginius Clark of the NACA
Davis	David Davis, an independent airfoil designer
DESA	Douglas El Segundo Airfoil
DLBA	Douglas Long Beach Airfoil
Do	Dornier
DSMA	Douglas Santa Monica Airfoil
DFVLR	The German Research and Development Establishment for Air and Space Travel
DLR	The German Aerospace Center
Drela	Dr. Mark Drela of MIT
EC	The National Physical Laboratories in Britain
Eiffel	Gustave Eiffel, an early French aeronautical researcher
Eppler	Dr. Richard Eppler of the University of Stuttgart
FX	Dr. F.X. Wortmann of the University of Stuttgart
GU	University of Glasgow in Scotland
Gilchrist	Ian Gilchrist of Analytical Methods, Inc.
Gottingen	the AV Gottingen aerodynamics research center in Germany
Joukowsky	Nicolai Egorovich Joukowsky, an early Russian aeronautical researcher
K	Dr. Yasuzu Naito of Nakajima
LB	Dr. Ichiro Tani of Tokyo University
Liebeck	Dr. Robert Liebeck of McDonnell Douglas, now Boeing
Lissaman	Dr. Peter Lissaman of AeroVironment Inc.
MAC	Airfoils designed at Mitsubishi. During the 1940s, the designer was Tsutomu Fujino.
McWilliams	Rick McWilliams, an independent airfoil designer
Narramore	Jim Narramore of Bell Helicopter Textron
NACA	The US National Advisory Committee for Aeronautics
NASA	The US National Aeronautics and Space Administration
NN	Dr. Hideki Itokawa of Nakajima
NPL	The National Physical Laboratories in Britain
Navy	The US Navy, Philadelphia Navy Yard
Onera	The French National Aerospace Research Establishment
RAE	The Royal Aeronautical Establishment in Britain
RAF	The National Physical Laboratories in Britain
Riblett	Harry Riblett, an independent airfoil designer
Roncz	John Roncz, an independent airfoil designer
Selig	Dr. Michael Selig of the University of Illinois, Urbana-Champaign
Somers	Dan Somers of Airfoils, Inc.
TH	Dr. Tatsuo Hasegawa of Tachikawa
TsAGI	The Russian Central Aerodynamics and Hydrodynamics Institute
USA	The US Army
Viken	Jeff Viken of NASA Langley Research Center

aircraft—it is *mission designed*. Such airfoils are likely to improve the performance of the aircraft. In the scheme of things, the cost of designing airfoils is usually a minor expenditure of the complete development program.

Airfoils are typically designed by *direct analysis* or *inverse design*. Nowadays, this is always done using computer software. Airfoil codes such as Xfoil [13], XFLR5 [30], the Eppler Code [31], AeroFoil [32], and JavaFoil [14] are widely used and run on any Personal Computer (PC). Xfoil, XFLR5, and JavaFoil are shareware. All allow polars (C_l versus α, C_d versus C_l, etc.) to be plotted and airfoils to be designed using the *inverse design* method.

(1) Xfoil and XFLR5

Xfoil may be the best known of the above codes. It dates to 1986 and was written by Dr. Mark Drela, an aerodynamics professor at the Massachusetts Institute of Technology. It uses a high-order panel method and a fully coupled viscous/inviscid interaction method to evaluate drag, boundary layer transition, and separation. Xfoil was written in the era of MS-DOS. Its user interface has been updated in a program called XFLR5 [33], developed by Mr. André Deperrois (see Figure 8-29).

(2) PROFILE ("The Eppler Code")

The software PROFILE was written by Dr. Richard Eppler and Dan Somers, a consulting aerodynamicist. The program uses a conformal-mapping method to design airfoils for low-speed applications with prescribed velocity-distribution characteristics.

(3) AeroFoil

The software AeroFoil was developed by Mr. Donald Reid, a professional nuclear engineer who has a background in aerospace engineering, and is "*is intended to be the most "user-friendly" of its type*" [32]. The software uses a vortex-panel method coupled with integral boundary layer equations to calculate the aerodynamic properties of airfoils. It allows up to three airfoils to be compared simultaneously. Validation examples are provided on the website and show the predictions made by the program are in good agreement with experiment.

(4) JavaFoil

JavaFoil is simple and easy to use software developed by the German aerodynamicist Dr. Martin Hepperle. The program performs a potential flow analysis using a higher order panel method, in which the vorticity varies linearly along each panel representing the airfoil. Then, an integral boundary layer method is applied, using a separate boundary layer analysis module. Beginning at the stagnation point, the method solves the boundary layer equations. According to information on the developer's website, the equations and criteria for transition

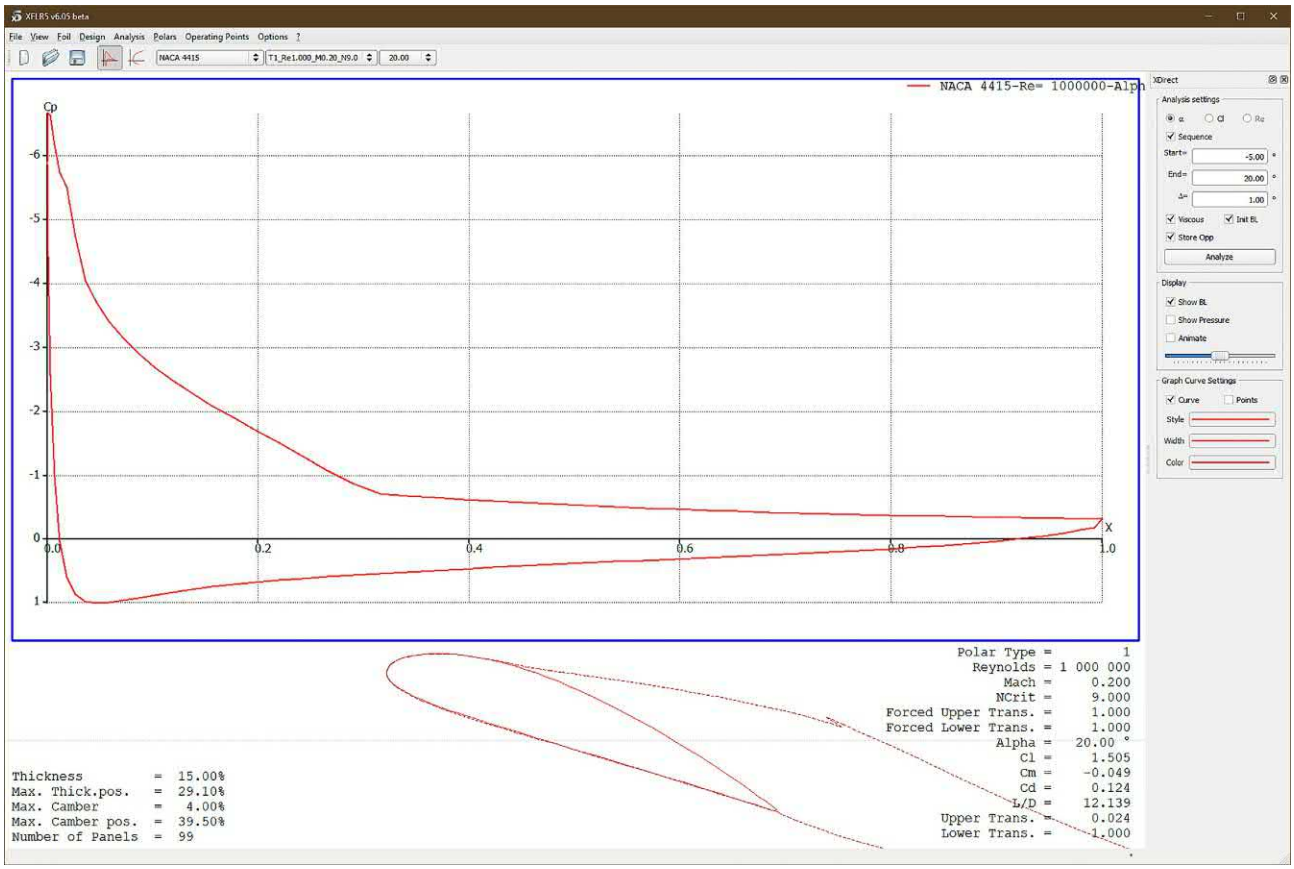


FIGURE 8-29 The XFLR5 user interface makes it easier to access the capabilities of Xfoil.

and separation were developed by Dr. Eppler. It provides a powerful airfoil generator.

(5) Design Process

The first step in airfoil design is to list the desired characteristics. This includes a range of operational lift coefficients and conditions (e.g., M and R_e), $C_{l_{max}}$, stall characteristics, C_l for $C_{d_{min}}$, extent of laminar flow, C_m, as well as desirable geometric characteristics such as thickness and its location along the chord. The next step is to decide on a methodology; direct or inverse method (see below). Some designers use existing airfoils as a baseline and modify it, applying both methods and trial-and-error to achieve the desired characteristics.

(6) Direct Analysis Method

Direct analysis evaluates the pressure field around an *already defined* airfoil. The airfoil ordinates are entered into the software to predict lift, drag, and pitching moment at the specified AOA. Accurate prediction of flow separation growth with AOA, subsequent stall, and width and depth of the drag bucket at lower AOA is vital for this work. The above software is capable of such predictions, although the accuracy must be validated by the user. This is a mandatory step and requires the predicted results to be compared with reliable wind tunnel tests.

(7) Inverse Airfoil Design Method

The *inverse airfoil design method* is a better approach to design an airfoil with a desired pressure distribution. It allows the airfoil designer to specify a desired velocity distribution along the surface. This is used to calculate a geometry that will generate such a distribution. The knowledgeable designer understands the consequences, including regions of laminar flow or early separation. Airfoil design is a field of specialization that requires multiple airfoils to be evaluated to help the designer build an experience-based understanding of airfoil behavior. Inverse methods were responsible for significant advances in airfoil design in the 1950s, when enough computational power was available to allow integral boundary-layer methods to be coupled with potential-flow solutions.

8.2 THE GEOMETRY OF THE AIRFOIL

This section presents important properties of the geometry of the airfoil and presents several famous airfoils the aircraft designer should be aware of as some offer interesting possibilities, while others should be avoided.

8.2.1 Airfoil Terminology

(1) Leading Edge, Trailing Edge, and Chordline

The *leading edge* (LE) is the most forward point of an airfoil. It is the origin of the coordinate system to which the airfoil geometry refers. The *trailing edge* (TE) is the aftmost point of the airfoil. A *chordline* is a line drawn between the LE and TE (see Figure 8-30). Then, *chord* is defined as the length of the chordline.

(2) Representation of Airfoils

Airfoils are typically represented in two ways: (1) As a table of (x, y) coordinates and (2) what can be referred to as *standard NACA-notation*. The former is a list of N ordered coordinates that describe the airfoil. This list typically arranges the coordinates in three ways: (a) It starts at the lower TE, flows toward and around the LE, and terminates at the upper TE (see the upper image of Figure 8-30). (b) It starts at the upper TE, flows toward and around the LE, terminating that the lower TE. (c) It is a dual list of upper and lower surfaces coordinates, both of which start at the LE and terminate at the TE. Typically, the spacing between points is smaller near the LE than the TE to better represent the curvature. The standard NACA-notation represents airfoils as mathematical functions of the ordinate x (see the lower image of Figure 8-30). Airfoil representations always assume $c = 1$. This makes it simple to scale the airfoil to fit the chord of interest.

(3) Thickness, Thickness-to-Chord Ratio, Mean-line, Camber, and LE Radius

Consider the vertical line in Figure 8-30 that intersects the upper airfoil's lower and upper surfaces at (x,y_a) and (x,y_b), respectively. The *thickness* (t) of the airfoil is the maximum of $(y_b – y_a)$ and is located at $x_{t\ max}$. The *thickness-to-chord ratio* is given by t/c. The *mean-line* is a curve defined by $\frac{1}{2}(y_a + y_b)$ inside the limit $0 \leq x \leq c$. The *camber* (y_{camber}) is the maximum of $\frac{1}{2}(y_a + y_b)$. It is located at x_{camber}. The distance between (x, y_a) or (x, y_b) and the mean-line point $(x, \frac{1}{2}(y_a + y_b))$ is $\frac{1}{2}(y_b – y_a)$. The *LE radius* is used to provide a mathematical shape for the LE. It is positioned as shown in Figure 8-30. Only a small arc of the circle is used, where the slope of the airfoil's upper and lower surfaces is equal to that of the circle. It impacts $C_{l_{max}}$ and $C_{d_{min}}$. A large radius delays flow separation near the LE, increasing lift at high AOA. This reduces the abruptness of the stall ("stall break"). However, this method causes cambered airfoils to protrude a hair forward of the LE [12]. Too large a radius results in the deformity shown in Figure 8-31.

(4) Important Airfoil Properties

Eastman N. Jacobs (1902–1987) and colleagues at the NACA Variable Density Tunnel (VDT) demonstrated around 1929 that airfoil characteristics depended on

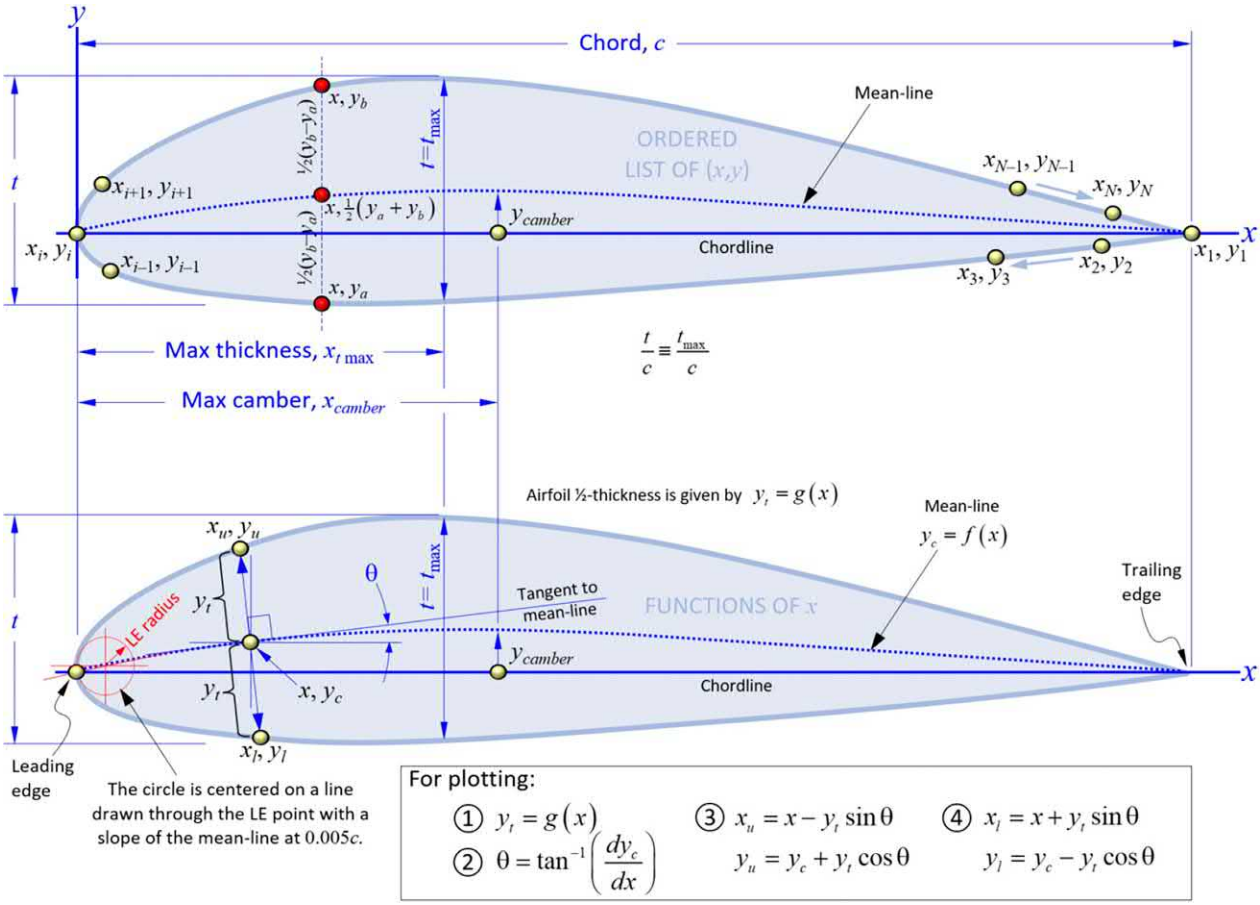


FIGURE 8-30 Airfoil nomenclature. The upper applies to an ordered list of coordinates; the lower applies to the classical NACA notation.

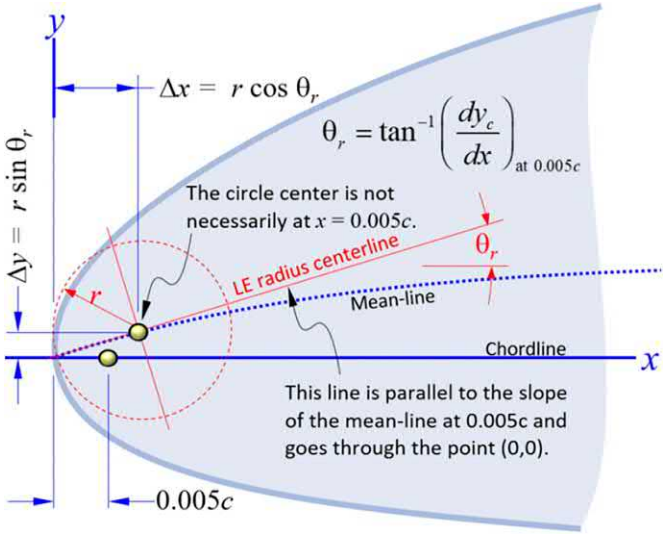


FIGURE 8-31 Standard NACA positioning of the LE radius. An exaggerated LE radius creates the conundrum shown.

thickness and mean-line [34]. An important byproduct of this work are airfoils known as the NACA *4-digit*, *5-digit*, *6-*, 7-, and *8-series*. A thorough treatise of Jacobs and his pioneering work at the VDT is presented in ref. [2]. Table 8-4 summarizes some of their findings.

(5) Cusp

The term "cusp" refers to the curved lower surface near the TE of an airfoil (see Figure 8-32). It is primarily used for NLF and supercritical airfoils to develop supplemental lift by forming a high-pressure region. The geometry of such airfoils revolves around controlling the extent and shape of the region of favorable $\partial p/\partial x$, typically by reducing the pressure peak on the upper surface at cruise. The resulting pressure distribution lacks lift, which is remedied by the cusp. An unfortunate by-product is higher pitching moment coefficient.

(6) Square Trailing Edges

Base drag is generated by the formation of "dead air" on the back side of blunt-base bodies (see Figure 8-32). The flow around the base insulates this air from replenishment and causes the pressure in the wake to drop below the ambient pressure [35,36], forming its pressure-drag. This also applies to airfoils or wings with blunt TE, called *Square-TE* or *flatbacks*.

There are two ways to make the TE square; by building up thickness of the TE (Type A) or cutting off a part of the TE (Type B). Type B shortens the chord without changing the geometry ahead of the cut. The longer the cut-off, the

TABLE 8-4 Summary of geometric effects on airfoils [34].

	Effect of t/c	Effect of x_{camber} and y_{camber}
1	$C_{l\alpha}$ decreases with increased t/c ($\approx 0.95 \times 2\pi$ for low t/c to $0.81 \times 2\pi$ for high).	$C_{l\alpha}$ not greatly affected by y_{camber}.
2	$\alpha_{ZL} \rightarrow 0$ with increased t/c (for $t/c \geq 0.09$–0.12).	α_{ZL} is around 75%–100% of that predicted by thin-airfoil theory.
3	Highest $C_{l_{max}}$ obtained for $0.09 \leq t/c \leq 0.15$.	$C_{l_{max}}$ increases with y_{camber}. $x_{camber} \approx 0.3c$ appears optimal.
4	Instability of airflow at $C_{l_{max}}$ worst for moderate t/c and low y_{camber}.	Airflow stability at $C_{l_{max}}$ best for $0.3c \leq x_{camber} \leq 0.5c$.
5	$\lvert C_{m\ cl=0} \rvert$ decreases with increased t/c.	$C_{m\ cl=0}$ proportional to y_{camber}.
6	x_{ac} is slightly forward of $c/4$ and moves forward with increased t/c.	x_{ac} moves forward with increased x_{camber}.
7	$C_{d_{min}} = k + 0.0056 + 0.01(t/c) + 0.1(t/c)^2$ Where k is obtained from Figure 92 in ref. [34].	$C_{d_{min}}$ increases with increased x_{camber} and y_{camber}.
8	$C_{l_{mind}} \rightarrow 0$ with increased t/c.	$C_{l_{mind}}$ increases with increased y_{camber} and x_{camber} (for highly cambered airfoils).
9	ld_{max} is highest for $0.09 \leq t/c \leq 0.12$.	ld_{max} decreases with increased y_{camber} and x_{camber} (for highly cambered airfoils).

greater the increase in drag and reduction in lift of the airfoil.

In contrast, Type A changes the airfoil by "filling up" the aft region without shortening the chord (see Figure 8-32). At high α, this region is immersed in flow separation and the associated low pressure. The fill-up improves the pressure recovery, effectively reducing the flow separation over the aft upper surface and, thus, improves lift generation. The above references state that both $C_{l_{max}}$ and ld_{max} of thick airfoils increase with the square-TE. While the drag of the airfoil increases slightly, there is an improvement in the airfoil efficiency ratio, $C_{l_{max}}/C_{d_{min}}$. Square-TE airfoils are ideal for propellers and wind turbines. Many NLF airfoils feature square-TE. Refs. [37,38] are recent treatise of flatback airfoils, with the latter presenting wind tunnel testing of a flatback airfoil for a wind turbine. Ref. [39] presents more detail about square-TE for supercritical airfoils.

8.2.2 NACA 4-Digit Airfoils

The NACA four-digit airfoils are described using a mathematical formulation and feature a designation system reflecting their geometric properties. These airfoils have designations like 2412, 3308, or 4415 (shown in Figure 8-33). Further development of these airfoils for propellers was made by Albert von Doenhoff [40]. The development of NACA 4-digit series airfoils is detailed in refs. [34,40]. A method to generate airfoil ordinates is provided in Section 8.2.8. A numerical example is provided in the first edition of the book.

(1) Applications

The airfoils are widely used in GA aircraft, with the best-known aircraft being a family of Cessna airplanes. Cambered versions are used for wings, while symmetric are used for HT and VT. Symmetric airfoils are also used for helicopter rotors, antennas, and even for some supersonic aircraft and missile fins.

(2) Numbering System

The numbering system is based on the geometry of the airfoil. The first digit indicates the camber as a fraction of the chord. The second digit indicates its distance from the LE as a fraction of the chord. The last two digits indicate the thickness as a fraction of the chord. Thus, the **NACA 4415** airfoil has a $0.04c$ camber, located at $0.40c$ and is

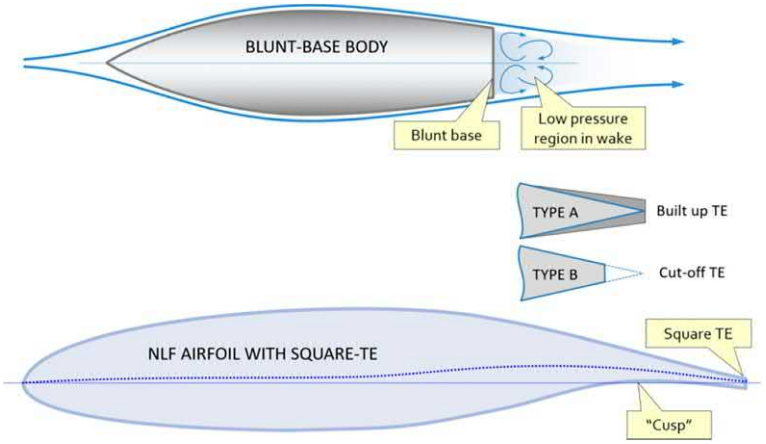


FIGURE 8-32 Flow around a blunt base projectile and an NLF airfoil with a square TE.

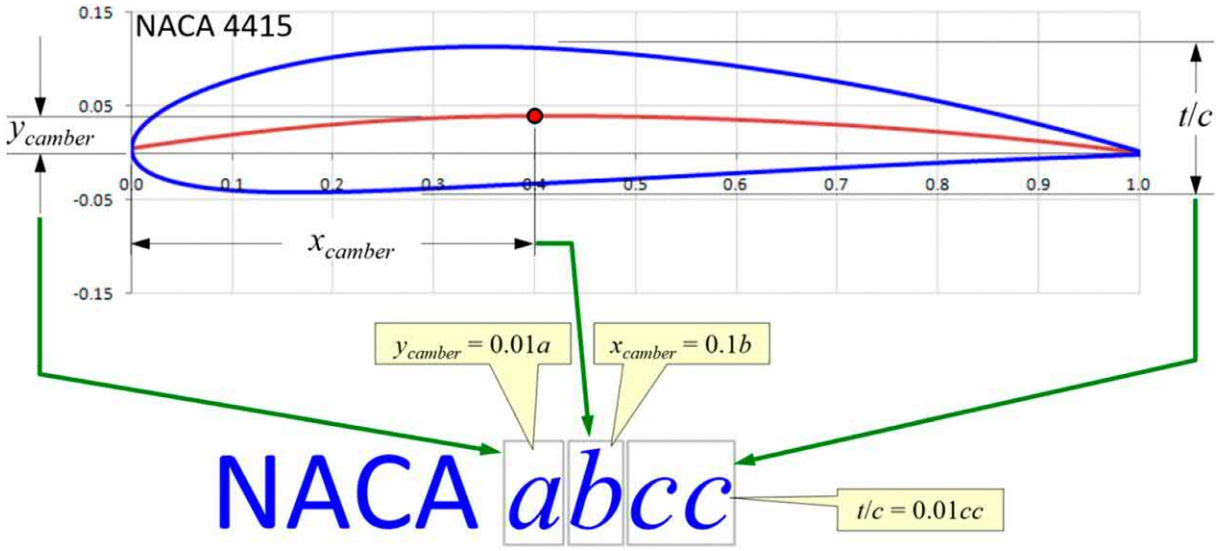


FIGURE 8-33 Interpretation of NACA 4-digit airfoil designation.

0.15c thick. Also, **NACA 0009** is a symmetrical airfoil as indicated by the first two digits 00 and is 0.09c thick.

8.2.3 NACA 5-Digit Airfoils

The NACA 5-digit airfoils were developed by Jacobs' team, following the development of the 4-digit airfoils. The thickness distribution is same as that of the 4-digit series; however, the mean-line was modified to place the "…Maximum Camber Unusually Far Forward," to quote the title of ref. [41], which details their investigation. The investigation followed the revelation that the forward position of the camber increased $C_{l_{max}}$ [42]. The 5-digit airfoils were designed to provide a high $C_{l_{max}}$, and low $C_{d_{min}}$ and C_m. A family of 5-digit airfoils features a reflexed camber to provide a zero C_m but have seen limited use. A NACA 23012 airfoil is shown in Figure 8-34 (see further discussion in Section 8.2.10). A method to generate airfoil ordinates is provided in Section 8.2.8. A numerical example is provided in the first edition of the book.

(1) Applications

The airfoils are widely used in GA aircraft, commuters, and business jets, where they are used for wings. Among aircraft using 5-digit airfoils are several models manufactured by Cessna and Beechcraft.

(2) Numbering System

Per ref. [41], "the first digit is used to designate the relative magnitude of the camber." Ref. [12] adds that "the

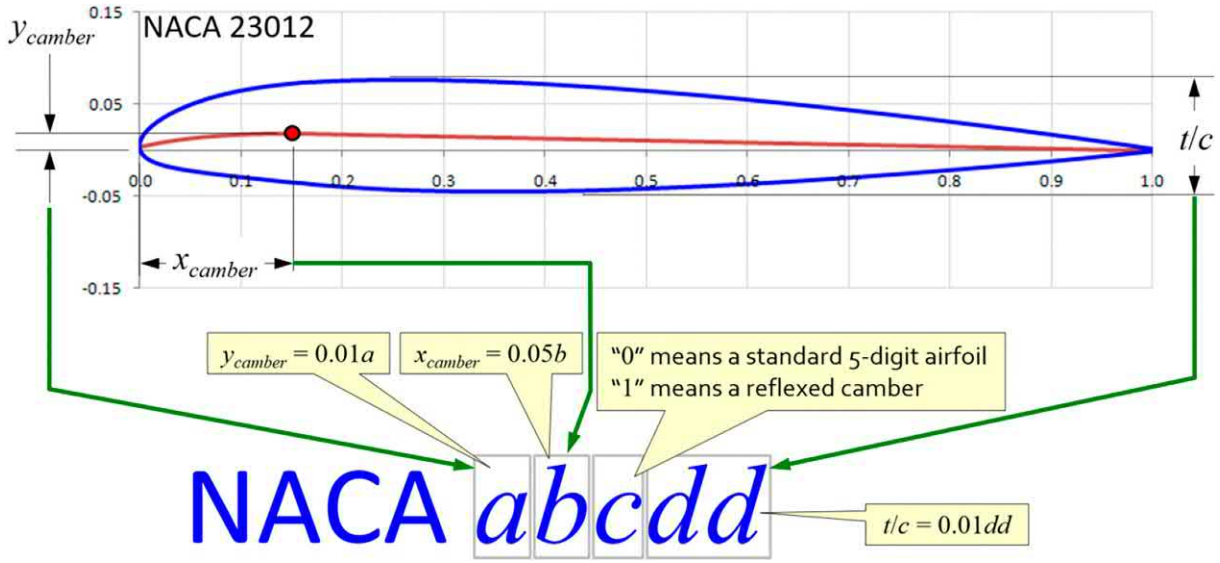


FIGURE 8-34 Interpretation of NACA 5-digit airfoil designation.

first digit indicates the amount of camber in terms of the relative magnitude of the design lift coefficient; the design lift coefficient in tenths is thus three-halves of the first integer." Thus, the **NACA 23012** airfoil has a $0.02c$ camber and a design lift coefficient of $0.2 \times (3/2) = 0.3$. The second digit, when divided by 20, places the maximum camber at $0.15c$. The third digit is "0" for normal camber and "1" for reflexed airfoils like those used for flying wings. The last two digits denote the airfoil is $0.12c$ thick. Using this nomenclature, the various members of the family of 5-digit airfoils would be represented as shown in Table 8-5.

8.2.4 NACA 1-Series Airfoils

The 1-series airfoils were designed in the late 1930s, after the 4- and 5-digit series (which explains the order of the airfoils in this presentation). The geometry was based on thin-airfoil theory rather than geometric properties, marking the first application of inverse airfoil design. The 1-series airfoils are primarily used for propellers, as they prevent large, detrimental pressure peaks near supersonic airspeeds. It is primarily the 16-version of the 1-series airfoils that have seen most use, so these are sometimes classified separately. Ref. [43] presents a computer code to help develop ordinates for NACA 16-series airfoils. A NACA 16–012 airfoil is shown in Figure 8-35.

(1) Applications

Widely used for aircraft and ship propellers.

(2) Numbering System

Typical 1-series airfoils are designated by a five-digit number such as NACA 16-212. The first integer "1" indicates the series. The second digit "6" denotes the distance in tenths to the chordwise location of the minimum pressure when the symmetrical airfoil is at zero lift (60%). The first number following the dash "2" is the amount of camber in terms of the design lift coefficient in tenths (0.2). The final two digits "12" represent the thickness of the airfoil ($0.12c$ or 12%).

8.2.5 NACA 6-Series Airfoils

The 6-series were designed to sustain laminar boundary layer over a larger portion of the chord by pushing the thickness of the airfoil as far back as possible. Their origin dates to

TABLE 8-5 Various members of the NACA 5-digit airfoil series.

Location of maximum camber	Camber position, x_{camber}	Conventional airfoil	Example	Reflexed airfoil	Example
5% or 0.05c	0.05	10	NACA 21012	11	NACA 21112
10% or 0.10c	0.10	20	NACA 22012	21	NACA 22112
15% or 0.15c	0.15	30	NACA 23012	31	NACA 23112
20% or 0.20c	0.20	40	NACA 24012	41	NACA 24112
25% or 0.25c	0.25	50	NACA 25012	51	NACA 25112

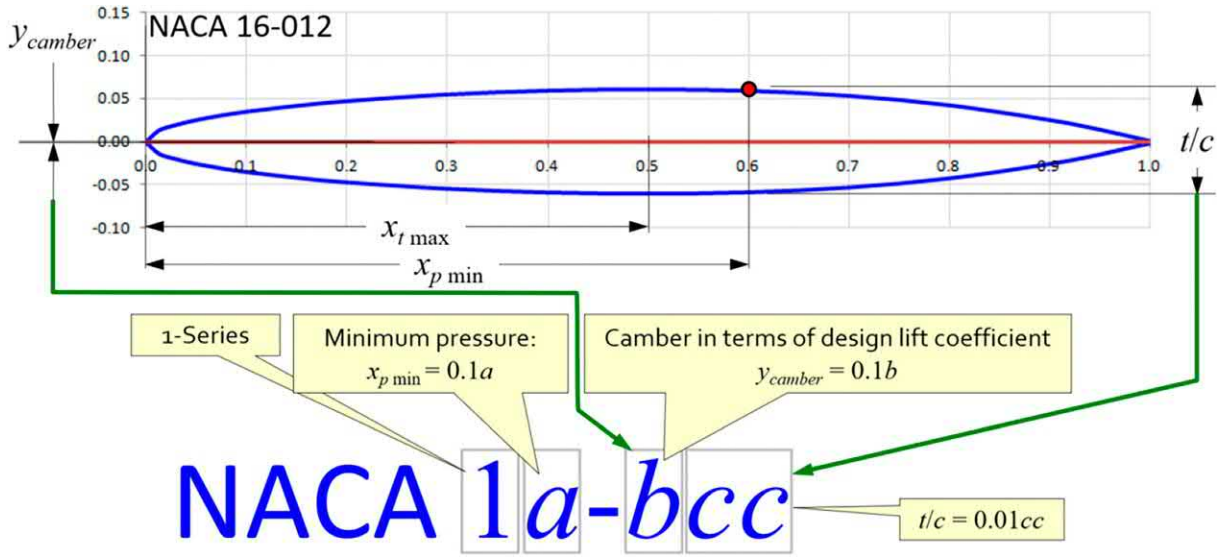


FIGURE 8-35 Interpretation of NACA 1-series airfoil designation.

a meeting Eastman Jacobs had with the British fluid dynamicists Geoffrey Taylor (1886–1975) and Melvill Jones (1887–1975). They shared with Jacobs that laminar BL can be sustained in regions of decreasing pressure (favorable pressure gradient, dp/dx) up to a point where pressure begins increasing (adverse dp/dx). It is a captivating tale of engineering curiosity, complicated by a feud between two colleagues; Eastman Jacobs and Theodore Theodorsen (1897–1978) [44]. The thickness of the 6-series airfoils was developed using Theodorsen's airfoil theory, while the camber is based on thin-airfoil theory, as described in ref. [12]. A typical NACA 6-series airfoil is shown in Figure 8-36.

A subfamily of the NACA 6-series is called the 6A-series airfoils. They were designed to eliminate the trailing-edge cusp associated with the former, which posed great difficulties in their fabrication [45]. For instance, conventional construction methods that require folding aluminum sheet to form such a trailing edge results in geometry far too tight to accommodate supporting ribs in the trailing edge. Therefore, the trailing edge is unsupported and at higher angles-of-attack it can flex, effectively modifying the airfoil. Ref. [46] presents a Fortran IV code to develop the ordinates of NACA 6-series airfoils. Note that ref. [47] presents an updated version of the code that is more portable between machines.

(1) Applications

The airfoils are widely used for aircraft ranging from WWII era fighters, high performance GA aircraft, business jets, and military trainers.

(2) Numbering System

The NACA 6-series airfoils feature a six-digit designation with an indicator of the mean-line used. For instance, the designation for the airfoil **NACA 65_3-415, a = 0.5**, the "6" refers to the 6-series airfoils, "5" denotes the chordwise location of the maximum camber in tenths of the chord (50%). The subscript "3" gives the range (ΔC_l) around the design lift coefficient (C_{ldg}) for which favorable pressure gradients exists on both surfaces (± 0.3). The "4" following the dash indicates the design lift coefficient in tenths ($C_{ldg} = 0.4$). This airfoil is expected to sustain laminar flow for lift coefficients ranging from 0.1 to 0.7 ($C_{ldg} \pm \Delta C_l = 0.4 \pm 0.3$). The last two digits indicate the airfoil thickness in percent of the chord (0.15% or 15%). The designation "a = 0.5" refers to the mean-line used, but the 6-, 7-, and 8-series airfoils are derived using conformal mapping that relies on a specific formulation of the mean-line and for which "a" is a parameter. When a mean-line designation is omitted the default value of a = 1.0 is used.

The airfoil designation has several variations. For instance, the above airfoil (NACA 65_3–415) is sometimes represented as NACA 65(3)-415 or 65,3-415. There are multiple other deviations from the above numbering system. The interested reader is directed to ref. [12].

8.2.6 NACA 7-Series Airfoils

The NACA 7-series airfoils were designed to maximize the extent of laminar flow on the upper and lower surfaces. A typical NACA 7-series airfoil is shown in Figure 8-37.

(1) Applications

Not widely used. The University of Illinois at Urbana-Champaign "Incomplete Guide to Airfoil Usage" [48] airfoil database indicates only 5 airplanes use such

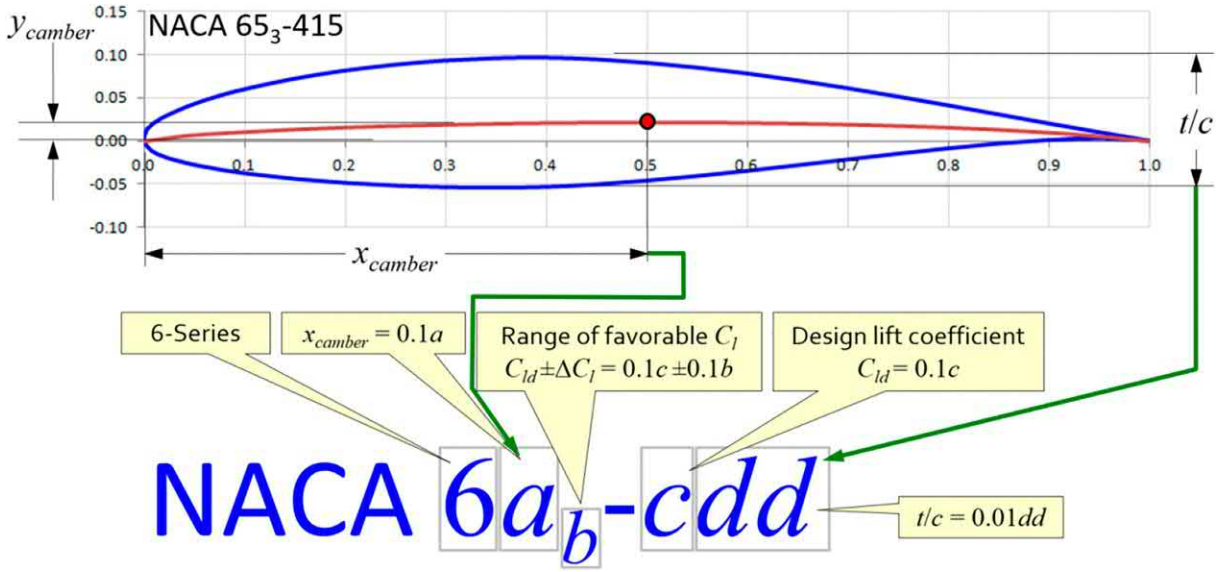


FIGURE 8-36 Interpretation of NACA 6-series airfoil designation.

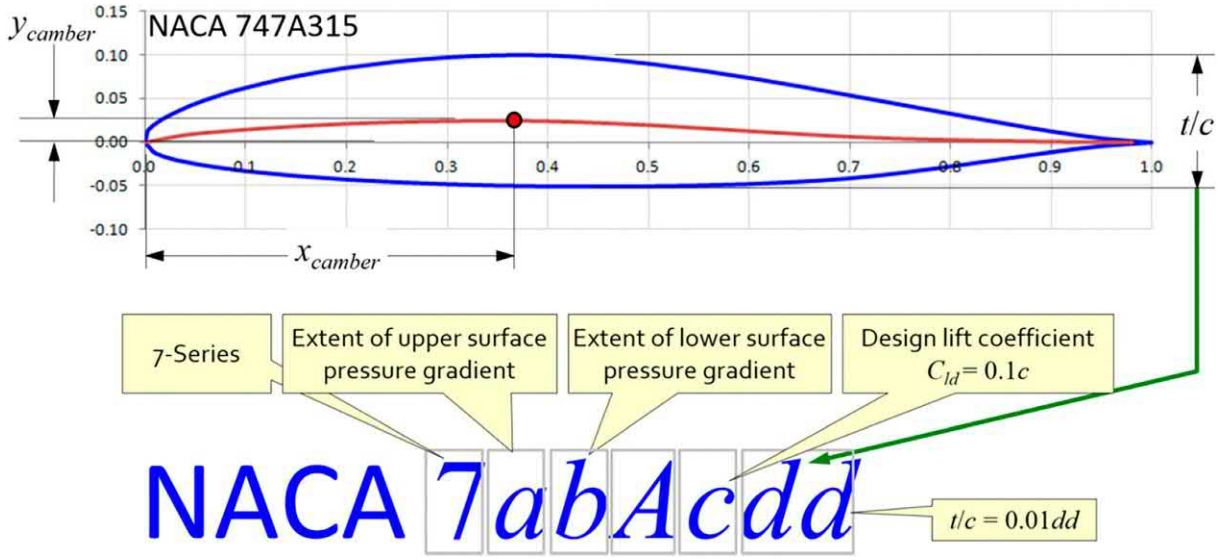


FIGURE 8-37 Interpretation of NACA 7-series airfoil designation.

airfoils. To this author, this appears more a consequence of (limited) awareness than aversion.

(2) Numbering System

The NACA 7-series have their own numbering system best explained by considering a typical type: **NACA 747A315**. The "7" indicates the series number. The "4" indicates the extent of favorable pressure gradient over the upper surface of the airfoil in tenths of the chord length (40%), while "7" indicates this over the lower surface (70%) (provided smooth surface). The three numbers, "315," following the letter "A," mean the same as that of the 6-series. The intent of the "A" is to distinguish between airfoils that have properties that would lead to identical digit but differ in camber or thickness distribution. For instance, another 7-series airfoil with an equal coverage of favorable pressure gradients, but with a different camber-line or thickness distribution, would be distinguished from the first one using the serial letter "B." As with the 6-series airfoils, the 7-series also feature mean-lines that are the combination of two or more lines.

8.2.7 NACA 8-Series Airfoils

In 1949, NACA developed a new family of airfoils, called the 8-series [49]. They were developed to prevent the abrupt loss of lift (exemplified in Figure 8-66) near the critical Mach number (see Section 8.3.8). These airfoils have not seen much use and, some 10 to 15 years later, were abandoned in favor of Peaky airfoils (see Section 8.2.10). They are really presented here in interest of completeness.

(1) Applications

No known application.

(2) Numbering System

The numbering system for typical NACA 8-series airfoils is best explained by considering a representative type, e.g., **NACA 835A216**. The first digit, "8," identifies the series. The next two, "3" and "5," denote the position of the minimum pressure on the upper and lower surfaces, respectively, in tenths (0.30 and 0.50). The letter "A" has an identical function as that of the 7-series airfoils, as do the remaining three digits.

8.2.8 Plotting NACA 4- and 5-Digit Airfoils

One of the primary advantages of NACA airfoils is their mathematical definition. This allows the designer to specify and plot the geometry to a desired accuracy. The "geometry" is a table containing the airfoil's x- and y-ordinates. The following STEP-BY-STEP illustrates how to generate the ordinate tables for these airfoils using a spreadsheet. The algorithm is based on refs. [34,41]. The procedure involves calculating the mean-line and airfoil thickness as functions of x and then add the two. The detail is disclosed in the STEP-BY-STEP.

(1) Preparation

The definition of airfoils always assumes the LE is located at $x=0$ and the TE at $x=1$ (a unit chord). This makes it easy to scale the desired airfoil by multiplying the ordinates by the chord. At the onset, we must decide how many points (N) to compute. The ordinate table lists the x-values distributed along the x-axis. While these are sometimes distributed uniformly, a more desirable distribution is based on the cosine-scheme as shown in Figure 8-38. It better defines the leading edge, where curvature is greater. This scheme

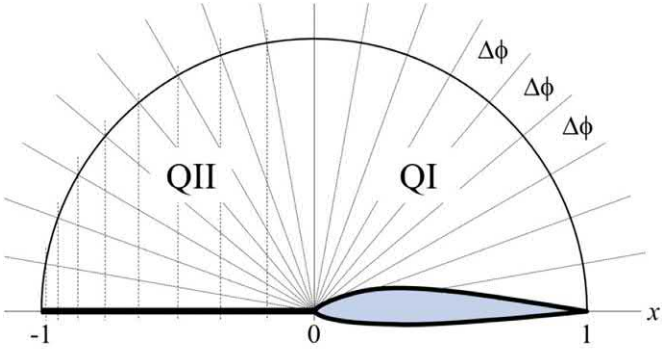


FIGURE 8-38 A preparation of the cosine-scheme.

uniformly sectors a unit circle at angle $\Delta\phi$. The value of $\Delta\phi$ is determined as follows:

$$\Delta\phi = \frac{90^\circ}{N-1} \quad or \quad \Delta\phi = \frac{\pi}{2(N-1)} \tag{8-35}$$

Now consider the thick dark line extending from $x=-1$ to 0 in Figure 8-38 (QII). The x-values of the intersection of the sector lines and the circle are projected vertically on to this line, revealing a tight separation of points close to $x=-1$. The vertical line spacing increases gradually as $x \to 0$. If we shift this pattern into QI (by adding 1 to each x), we achieve a tight separation close to $x=0$ (the leading edge of our airfoil) and sparser as $x \to 1$. We now specify each x using indexes ranging from 1 through N, where N is the number of points. Mathematically, we can write:

$$\begin{aligned} x_1 &= 0 \\ x_2 &= 1-\cos(\Delta\phi) \\ x_3 &= 1-\cos(2\Delta\phi) \\ &\vdots \\ x_i &= 1-\cos((i-1)\Delta\phi) \\ &\vdots \\ x_N &= 1-\cos((N-1)\Delta\phi) = 1 \end{aligned} \tag{8-36}$$

(2) Implementation

These definitions allow us to prepare the following STEP-BY-STEP to calculate the geometry of the most common NACA airfoils.

STEP 1: Preliminary Values (see Figure 8-30 for variables)

NACA 4-DIGIT: (Example 2412) The first digit is y_{camber} ($2 \to y_{\text{camber}} = 0.02$). Second digit is x_{camber} ($4 \to x_{\text{camber}} = 0.4$). Last two digits denote t ($12 \to t = 0.12$).

NACA 5-DIGIT: (Example 23012) The first digit is y_{camber} ($2 \to y_{\text{camber}} = 0.02$). Second digit is x_{camber} ($3 \to x_{\text{camber}} = 0.3$). Third digit is either 0 (specifies standard airfoil) or 1 (specifies reflexed camber). Last two digits denote t ($12 \to t = 0.12$).

STEP 2: Prepare Ordinate Table

NACA 4- AND 5-DIGIT: Decide how many points (N) to include in the analysis (e.g., $N=100$ for 100 points). Tabulate the x-ordinates along the unit chord using the cosine-scheme where $\Delta\phi$ is calculated using Equation (8-35), such that $0 \le x \le 1$. Index them such that $x_1 = 0$ (leading edge) and $x_N = 1$ (trailing edge).

STEP 3: Calculate Thickness

NACA 4- AND 5-DIGIT: For each x_i calculate the ½-thickness using the expression below

$$\pm y_t = 5t\left(0.29690\sqrt{x} - 0.12600x - 0.35160x^2 + 0.28430x^3 - 0.10150x^4\right) \tag{8-37}$$

STEP 4: Compute the y-value for the Mean-line

NACA 4-DIGIT: For each x_i calculate the y-value of the mean-line, y_{ci}, depending on whether x_i is larger or smaller than x_{camber}:

$$\text{If } x \le x_{\text{camber}} \text{ then} \quad y_c(x) = y_{camber}\frac{(2x_{camber} - x)x}{x_{camber}^2} \tag{8-38}$$

If $x > x_{\text{camber}}$ then

$$y_c(x) = y_{camber}\frac{(1-2x_{camber}) + 2x_{camber}x - x^2}{(1-x_{camber})^2} \tag{8-39}$$

NACA 5-DIGIT: Calculate y_{ci} for each x_i similar as above, except using the following polynomials, where the constants m and k_1 are obtained from Table 8-6. For standard 5-digit airfoils (e.g., 23012), calculate y_{ci} per the following relations:

If $x \le x_{\text{camber}}$ then

$$y_c = \frac{k_1}{6}\left[x^3 - 3mx^2 + m^2(3-m)x\right] \tag{8-40}$$

If $x > x_{\text{camber}}$ then

$$y_c = \frac{k_1 m^3}{6}(1-x) \tag{8-41}$$

For reflexed 5-digit airfoils (e.g., 23112), calculate y_{ci} using the relations:

If $x \le x_{\text{camber}}$ then

$$y_c = \frac{k_1}{6}\left[(x-m)^3 - \frac{k_2}{k_1}(1-m)^3 x - m^3 x + m^3\right] \tag{8-42}$$

TABLE 8-6 Mean-line designations for NACA 5-digit airfoils.

Mean-line designation	x_{camber}	m	k_1	k_2/k_1	Reference
210	0.05	0.0580	361.400	–	[34]
220	0.10	0.1260	51.640	–	
230	0.15	0.2025	15.957	–	
240	0.20	0.2900	6.643	–	
250	0.25	0.3910	3.230	–	
211	0.05	–	–	–	[41]
221	0.10	0.1300	51.99	7.64	
231	0.15	0.2170	15.793	67.70	
241	0.20	0.3180	6.520	303.0	
251	0.25	0.4410	3.191	1355	

If $x > x_{\text{camber}}$ then

$$y_c = \frac{k_1}{6}\left[\frac{k_2}{k_1}(x-m)^3 - \frac{k_2}{k_1}(1-m)^3 x - m^3 x + m^3\right] \quad (8\text{-}43)$$

where

$$\frac{k_2}{k_1} = \frac{3(m - x_{\text{camber}})^2 - m^3}{(1-m)^3} \quad (8\text{-}44)$$

STEP 5: Calculate the Slope of the Mean-line

NACA 4-DIGIT: A part of the procedure involves a rotation about the point (x, y_c) on the mean-line. This aligns the upper and lower coordinates to the slope. The angle-of-rotation, θ, is given by Equation (8-51). This requires an evaluation of the slope of the mean-line, (dy_c/dx), and as shown in Figure 8-30. Thus, the x-value of the upper surface point (x_u) differs from that of the lower surface (x_l). The slope of the mean-line is given by:

$$\text{If } x \le x_{\text{camber}} \text{ then} \quad \frac{dy_c}{dx} = y_{\text{camber}} \frac{2(x_{\text{camber}} - x)}{x_{\text{camber}}^2} \quad (8\text{-}45)$$

$$\text{If } x > x_{\text{camber}} \text{ then} \quad \frac{dy_c}{dx} = y_{\text{camber}} \frac{2(x_{\text{camber}} - x)}{(1 - x_{\text{camber}})^2} \quad (8\text{-}46)$$

NACA 5-DIGIT: The slope of the mean-line for standard airfoils (e.g., 23012) is given by:

$$\text{If } x \le x_{\text{camber}} \text{ then} \quad \frac{dy_c}{dx} = \frac{k_1}{6}\left[3x^2 - 6mx + m^2(3-m)\right] \quad (8\text{-}47)$$

$$\text{If } x > x_{\text{camber}} \text{ then} \quad \frac{dy_c}{dx} = -\frac{k_1 m^3}{6} \quad (8\text{-}48)$$

For reflexed 5-digit airfoils (e.g., 23112), the slope is given by:

$$\text{If } x \le x_{\text{camber}} \text{ then} \quad \frac{dy_c}{dx} = \frac{k_1}{6}\left[3(x-m)^2 - \frac{k_2}{k_1}(1-m)^3 - m^3\right] \quad (8\text{-}49)$$

If $x > x_{\text{camber}}$ then

$$\frac{dy_c}{dx} = \frac{k_1}{6}\left[3\frac{k_2}{k_1}(x-m)^2 - \frac{k_2}{k_1}(1-m)^3 - m^3\right] \quad (8\text{-}50)$$

STEP 6: Calculate the Ordinate Rotation Angle

Calculate the angle of the slope, θ, as follows:

$$\theta = \tan^{-1}(dy_c/dx) \quad (8\text{-}51)$$

STEP 7: Calculate the Upper and Lower Ordinates

Calculate the upper and lower surface ordinates as follows:

$$\begin{aligned} x_u &= x - y_t \sin\theta \quad & y_u &= y_c + y_t \cos\theta \\ x_l &= x + y_t \sin\theta \quad & y_l &= y_c - y_t \cos\theta \end{aligned} \quad (8\text{-}52)$$

8.2.9 Summary of NACA Airfoils

The general advantages and disadvantages of NACA airfoils are summarized in Table 8-7. Also note Figure 8-39, which shows typical differences in lift, pitching moment, and drag for the different classes of airfoils. Table 8-8 lists the top 10 of the best and worst of $C_{l_{\max}}$, $C_{d_{\min}}$, and airfoil efficiency, $C_{l_{\max}}/C_{d_{\min}}$. Table 8-9 lists the aerodynamic properties of numerous NACA airfoils. For convenience, Table 8-10 lists sources for aerodynamic data for multiple NACA (and two NASA) airfoils. It is mostly based on ref. [11].

TABLE 8-7 Pros and cons of the NACA airfoils presented.

	Pros	Cons
4-Digit	Generally thick airfoils with benign stall characteristics. Insensitive to nonsmooth surfaces. Center of pressure has limited movement over a wider range of AOA.	Relatively low $C_{l_{\max}}$ and high $C_{d_{\min}}$ and $\lvert C_m \rvert$.
5-Digit	High $C_{l_{\max}}$ and relatively low $C_{d_{\min}}$ and $\lvert C_m \rvert$. Insensitive to nonsmooth surfaces.	Abrupt stall characteristics.
16-Series	Prevent high-pressure peaks that lead to detrimental performances near $M = 1$.	Low $C_{l_{\max}}$
6-Series	Relatively high $C_{l_{\max}}$ and low $C_{d_{\min}}$. Sustains extensive laminar flow if surface is smooth and forms a drag bucket. Relatively thick airfoils.	Sensitive to nonsmooth surfaces. High $\lvert C_m \rvert$. Higher drag outside the drag bucket than that of the 4- and 5-digit airfoils. Some have poor stall characteristics.
7-Series	Low $C_{d_{\min}}$. Sustains extensive laminar flow if surface is smooth and forms a drag bucket. Lower $\lvert C_m \rvert$ than the 6-series. Some display good stall characteristics.	Sensitive to nonsmooth surfaces. Low $C_{l_{\max}}$.
8-Series	N/A	N/A

8.2.10 Selected Famous Airfoils

(1) Clark Y

The Clark Y airfoil (see Figure 8-40) is famous for being one of the most widely used airfoil in the history of aviation, although its use is mostly in airplanes designed before World War II. It was designed in 1922 by Colonel Virginius E. Clark (1886–1948), a prolific airfoil designer in the World-War I era [44]. A distinguishing feature of this airfoil is its flat lower surface, which extends from 30% chord to the trailing edge. Aerodynamic properties are provided in refs. [51,56,57]. Among famous aircraft using this airfoil are (1) Ryan NYP Spirit of *St*. Louis,

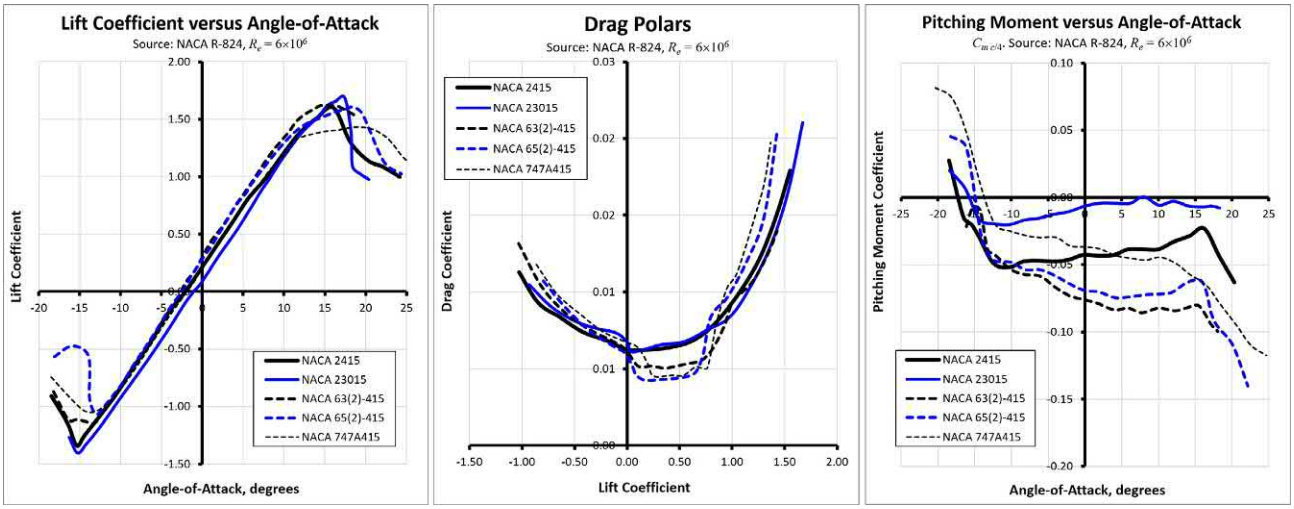


FIGURE 8-39 Lift, drag, and pitching moment characteristics of selected NACA series airfoils. *From Abbott, I.H., von Doenhoff, A.E., Stivers Jr., L. S., Summary of Airfoil Data, NACA R-824, 1945.*

TABLE 8-8 Top 10 best and worst of NACA airfoils (longer bars indicate larger magnitudes).

	TOP 10 BEST VALUES						TOP 10 WORST VALUES					
	Airfoil	MAX $C_{l_{max}}$	Airfoil	MIN $C_{d_{min}}$	Airfoil	MAX $C_{l_{max}}/C_{d_{min}}$	Airfoil	MIN $C_{l_{max}}$	Airfoil	MAX $C_{d_{min}}$	Airfoil	MIN $C_{l_{max}}/C_{d_{min}}$
1	23012	1.78	65_1-006	0.0035	65_1-412	431.6	64_1-006	0.83	0025	0.0143	0025	83.9
2	63_1-412	1.77	65_1-206	0.0036	66_3-418	424.3	0006	0.88	0021	0.0120	0021	115.0
3	23015	1.72	65_1-410	0.0037	65_1-410	410.8	65_1-006	0.93	0018	0.0108	0018	138.0
4	64_1-412	1.67	66_3-418	0.0037	63_1-412	402.3	64_1-206	1.03	0015	0.0093	0015	164.5
5	4412	1.66	64_1-006	0.0038	65_2-415	385.7	65_1-206	1.06	2412	0.0085	0006	169.2
6	64_2-415	1.66	64_1-206	0.0038	64_1-412	379.5	65_1-009	1.08	0012	0.0083	2424	173.3
7	2415	1.65	65_1-012	0.0038	65_1-212	370.0	64_1-009	1.17	2424	0.0075	0012	184.3
8	4415	1.64	65_1-209	0.0038	64_1-212	369.0	0025	1.20	4421	0.0072	2412	190.6
9	65_1-412	1.64	65_1-412	0.0038	64_2-415	360.9	2424	1.30	2421	0.0071	4421	202.8
10	23018	1.62	64_1-009	0.0040	65_3-418	360.5	65_1-209	1.30	23021	0.0070	2421	207.0

flown by Charles Lindbergh across the Atlantic in 1927 and (2) Lockheed Vega, made famous by Amelia Earhart's Atlantic crossing and Wiley Post's two flights around the globe. Ref. [48] cites this airfoil for 493 different aircraft out of 7420 models.

(2) USA-35B

The USA series of airfoils was designed by engineers of the US Army (USA) in the era before 1920. The USA35B (see Figure 8-41) is the best known. It is flat bottom airfoil is used in many well-known aircraft, especially in a line of aircraft made by Piper Aircraft, such as the Piper J-3 Cub, PA-25 Pawnee, PA-23 Apache, and Aztec twin engine aircraft. Like the Clark Y airfoil, it features a substantial camber and generates a high maximum lift coefficient and gentle entry into the poststall region, but also high drag. Aerodynamic properties are provided in ref. [51]. Ref. [48] cites this airfoil 74 times.

(3) NACA 23012

One of the best-known NACA 5-digit airfoils is the NACA 23012 (see Figure 8-42). Ref. [48] cites it 397 times. This includes multiple Beechcraft and Cessna models (including the Caravan and the Citation), military bombers such as the Avro Lancaster, and transport aircraft like Douglas' DC-4, −5, −6, and −7. Wind tunnel testing of symmetrical 4-digit NACA airfoils showed that while the $C_{d_{min}}$ was small, the same held for the $C_{l_{max}}$. It was proposed this could be improved by deflecting the forward part of the leading edge to form a camber (see Figure 8-43). This new airfoil showed great promise in wind tunnel testing; offering a low $C_{d_{min}}$, high $C_{l_{max}}$, and

TABLE 8-9 Properties of selected NACA airfoils (longer bars indicate larger magnitudes).

								C_d						
Airfoil	$C_{l\max}$	α_{stall}	α_{ZL}	$C_{l\alpha}$	$C_{l\,mind}$	$C_{d\min}$	$C_{l\max}/C_{d\min}$	$C_l = 0$	$C_l = 0.4$	$C_l = 0.8$	$C_{m\,ac}$	x_{ac}	M_{crit}	Reference
0006	0.88	13.0	0.0	0.102	0.00	0.0052	169.2	0.0052	0.0058	0.0090	-0.002	0.250	0.805	A and B
0009	1.33	14.0	0.0	0.101	0.00	0.0056	237.5	0.0056	0.0060	0.0084	-0.003	0.250	0.766	B and C
0012	1.53	17.0	0.0	0.101	0.00	0.0083	184.3				-0.002	0.250		B
0015	1.53	17.0	0.0	0.100	0.00	0.0093	164.5				0.000	0.240		B
0018	1.49	17.0	0.0	0.098	0.00	0.0108	138.0				-0.002	0.240		B
0021	1.38	17.0	0.0	0.094	0.00	0.0120	115.0				-0.001	0.230		B
0025	1.20	16.0	0.0	0.089	0.00	0.0143	83.9				-0.003	0.230		B
1408	1.35	14.0	-1.0	0.105	0.20	0.0052	259.6	0.0057	0.0057	0.0070	-0.024	0.250		A
1410	1.52	14.0	-1.0	0.109	0.20	0.0055	276.4	0.0057	0.0570	0.0070	-0.020	0.250		A
1412	1.57	15.0	-1.2	0.103	0.20	0.0057	275.4	0.0058	0.0061	0.0076	-0.023	0.252	0.720	A and C
23012	1.78	18.0	-1.2	0.104	0.10	0.0060	296.7	0.0068	0.0060	0.0068	-0.015	0.247	0.672	A and C
23015	1.72	18.0	-1.0	0.103	0.10	0.0062	277.4	0.0072	0.0064	0.0072	-0.008	0.243	0.663	A and C
23018	1.62	16.0	-1.2	0.104	0.30	0.0069	234.8	0.0069	0.0068	0.0078	-0.005	0.243	0.655	A and C
23021	1.51	15.5	-1.2	0.100	0.10	0.0070	215.7	0.0070	0.0073	0.0089	-0.004	0.238	0.623	A and C
2412	1.62	16.0	-1.8	0.101	0.20	0.0085	190.6	0.0060	0.0060	0.0072	-0.047	0.247	0.690	A and C
2415	1.65	16.0	-2.0	0.106	0.20	0.0063	261.9	0.0064	0.0064	0.0077	-0.045	0.246	0.677	A and C
2418	1.47	14.0	-2.1	0.099	0.25	0.0067	219.4	0.0068	0.0071	0.0081	-0.045	0.241	0.650	A and C
2421	1.47	16.0	-1.9	0.099	0.20	0.0071	207.0	0.0071	0.0072	0.0088	-0.040	0.241	0.630	A and C
2424	1.30	16.0	-1.9	0.093	0.10	0.0075	173.3	0.0075	0.0078	0.0099	-0.040	0.231	0.606	A and C
4412	1.66	14.0	-4.0	0.106	0.40	0.0060	276.7	0.0062	0.0060	0.0064	-0.092	0.247	0.647	A and C
4415	1.64	14.0	-4.0	0.106	0.40	0.0064	256.3	0.0066	0.0064	0.0070	-0.093	0.245	0.635	A and C
4418	1.54	14.0	-4.0	0.100	0.40	0.0066	233.3	0.0070	0.0066	0.0076	-0.088	0.242	0.620	A and C
4421	1.46	16.0	-4.0	0.096	0.27	0.0072	202.8	0.0075	0.0073	0.0081	-0.086	0.238	0.602	A and C
63_1-412	1.77	15.0	-3.0	0.110	0.35	0.0044	402.3	0.0062	0.0044	0.0075	-0.075	0.271		A
64_1-006	0.83	8.0-10.0	0.0	0.104	0.00	0.0038	218.4	0.0038	0.0057	-	0.000	0.256	0.836	A and C
64_1-009	1.17	11.0	0.0	0.108	0.00	0.0040	292.5	0.0040	0.0061	0.0082	0.000	0.262	0.785	A and C
64_1-012	1.44	15.0	0.0	0.110	0.00	0.0042	342.9	0.0042	0.0062	0.0081	0.000	0.262	0.744	A and C
64_1-206	1.03	12.0	-1.2	0.104	0.18	0.0038	271.1	0.0050	0.0057	0.0062	-0.040	0.253	0.793	A and C
64_1-209	1.40	13.0	-1.4	0.104	0.20	0.0040	350.0	0.0053	0.0060	0.0075	-0.040	0.261	0.760	A and C
64_1-212	1.55	15.0	-1.2	0.108	0.19	0.0042	369.0	0.0043	0.0050	0.0077	-0.028	0.262	0.728	A and C
64_1-412	1.67	15.0	-2.6	0.112	0.36	0.0044	379.5	0.0058	0.0046	0.0076	-0.070	0.267	0.700	A and C
64_2-215	1.57	15.0	-1.5	0.111	0.22	0.0045	348.9	0.0046	0.0048	0.0081	-0.030	0.265	0.700	A and C
64_2-415	1.66	16.0	-2.8	0.114	0.40	0.0046	360.9	0.0060	0.0049	0.0080	-0.070	0.264	0.678	A and C
64_3-418	1.56	14.0-20.0	-3.0	0.117	0.40	0.0050	312.0	0.0060	0.0050	0.0062	-0.065	0.273	0.655	A and C
64_3-421	1.48	18.0-24.0	-2.8	0.119	0.40	0.0050	296.0	0.0056	0.0050	0.0058	-0.065	0.276	0.642	A and C
65_1-006	0.93	12.0	0.0	0.105	0.00	0.0035	265.7	0.0035	0.0058	-	0.000	0.258	0.838	A and C
65_1-009	1.08	11.0	0.0	0.106	0.00	0.0041	263.4	0.0041	0.0060	0.0081	0.000	0.264	0.790	A and C
65_1-012	1.36	14.0	0.0	0.106	0.00	0.0038	357.9	0.0038	0.0061	0.0081	0.000	0.261	0.750	A and C
65_1-206	1.06	10.0-16.0	-1.2	0.106	0.20	0.0036	294.4	0.0050	0.0055	0.0071	-0.030	0.257	0.791	A and C
65_1-209	1.30	12.0	-1.2	0.108	0.20	0.0038	342.1	0.0052	0.0058	0.0075	-0.032	0.259	0.755	A and C
65_1-212	1.48	14.0	-1.2	0.108	0.20	0.0040	370.0	0.0047	0.0057	0.0082	-0.032	0.261	0.726	A and C
65_1-410	1.52	14.0	-2.6	0.110	0.36	0.0037	410.8	0.0058	0.0038	0.0072	-0.068	0.262	0.714	A and C
65_1-412	1.64	16.0	-3.0	0.109	0.38	0.0038	431.6	0.0056	0.0038	0.0075	-0.070	0.265	0.697	A and C
65_2-415	1.62	16.0	-2.6	0.107	0.38	0.0042	385.7	0.0060	0.0042	0.0084	-0.060	0.268	0.675	A and C
65_3-418	1.55	18.0	-2.6	0.106	0.40	0.0043	360.5	0.0062	0.0043	0.0072	-0.060	0.265	0.656	A and C
65_4-421	1.55	22.0	-3.2	0.111	0.42	0.0044	352.3	0.0048	0.0044	0.0053	-0.065	0.272	0.637	A and C
66_3-418	1.57	18.0	-3.0	0.100	0.40	0.0037	424.3	0.0065	0.0037	0.0110	-0.075	0.266		A

References: A is NACA R-824, B is NACA TN-460, C is Perkins & Hage $R_e \approx 9\times10^6$

TABLE 8-10 Sources of wind tunnel data for selected airfoils (in part based on ref. [11]).

REFERENCE A	REFERENCE C		REFERENCE D	REFERENCE F		REFERENCE G
NACA 67(1)-215	Boeing 103	Clark-Y	NACA 0012	NACA 2306	NACA 6318	NACA 16-009
NACA 747A315	Boeing 103A	Clark-Y-B	NACA 0015	NACA 2309	NACA 6321	NACA 16-106
NACA 747A415	Boeing 106	Clark-YM-15	NACA 0018	NACA 2312	NACA 6406	NACA 16-106
REFERENCE B	Boeing 106R	Clark-YM-18	NACA 0021	NACA 2315	NACA 6409	NACA 16-115
NACA 0012-63	Boeing 111	Clark-Y-6	NACA 0025	NACA 2406	NACA 6412	NACA 16-130
NACA 0012-64	Boeing 112	Clark-Y-8	NACA 0030	NACA 2506	NACA 6415	NACA 16-209
NACA 0012-65	Sikorsky GS-M	Clark-Y-10	NACA 2212	NACA 2509	NACA 6418	NACA 16-215
NACA 23012-33	Sikorsky GS-I	Clark-Y-14	NACA 2409	NACA 2512	NACA 6421	NACA 16-306
NACA 23012-34	S.T. Ae. 27A	Clark-Y-18	NACA 4406	NACA 2515	NACA 6506	NACA 16-309
NACA 23012-64	RAF 34	Clark-Y-22	NACA 4409	NACA 2518	NACA 6509	NACA 16-312
NACA 21012	USA 27	NACA CYH	NACA 23006	NACA 2521	NACA 6512	NACA 16-315
NACA 22012	USA 35A	NACA-M6	NACA 23009	NACA 2612	NACA 6515	NACA 16-321
NACA 24012	USA 35B	NACA 15	NACA 43012	NACA 2712	NACA 6518	NACA 16-409
NACA 25012	C-62	NACA 16	NACA 43015	NACA 4212	NACA 6521	NACA 16-506
NACA 32012	C-72	NACA 17	NACA 43018	NACA 4306	NACA 6612	NACA 16-509
NACA 33012	C-80	NACA 18	NACA 63012	NACA 4309	NACA 6712	NACA 16-512
NACA 34012	N-22	NACA 19	NACA 63018	NACA 4312	NACA 0006T	NACA 16-515
NACA 42012	N-60	NACA 20	**REFERENCE E**	NACA 4315	NACA 0006B	NACA 16-521
NACA 43009	N-60R	NACA 21	NACA 63A009	NACA 4318	NACA 0012T	NACA 16-515
NACA 43012A	N-68	NACA 23	NACA 64A004	NACA 4321	NACA 0012B	NACA 16-521
NACA 43021	N-69	NACA 24	NACA 64A006	NACA 4506	NACA 0018T	NACA 16-530
NACA 44012	N-71	NACA 25	NACA 64A206	NACA 4509	NACA 0018B	NACA 16-709
NACA 62021	N-75	NACA 26	NACA 64A506	NACA 4512	NACA $2R_1 12$	NACA 16-712
NACA 63009	N-76	NACA 27	NACA 64A009	NACA 4515	NACA $2R_2 12$	NACA 16-715
NACA 63015	N-80	NACA 22112	NACA 64A012	NACA 4518	NACA $0012F_0$	NACA 16-1009
NACA 63021	N-81	NACA 23112	NACA 65A009	NACA 4521	NACA $0012F_1$	NACA 16-1012
NACA 64021	Göttingen 387	NACA 24112		NACA 4612	T = Thin LE	**REFERENCE H**
	Göttingen 398	NACA 25112		NACA 4712	F = Modified TE	NASA GA(W)-1
	Göttingen 398-A	Göttingen 429-AG		NACA 6212	R = Reflexed mean-line	**REFERENCE I**
	Göttingen 398-B	Göttingen 429-J		NACA 6306		NASA GA(W)-2
	Göttingen 398-R	Göttingen 436		NACA 6309		
	Göttingen 413	Göttingen 532		NACA 6312		
	Göttingen 420			NACA 6315		

Reference A = NACA R-824 [12], B = NACA TR-610 [42], C = NACA R-628 [50], D = NACA TR-669 [51], E = NACA R-903 [45] and TN-3607 [52], F = NACA TR-460 [34], G = NACA TN-1546 [53], H = NASA TN D-7428 [54], and I = NASA CR-2948 [55].

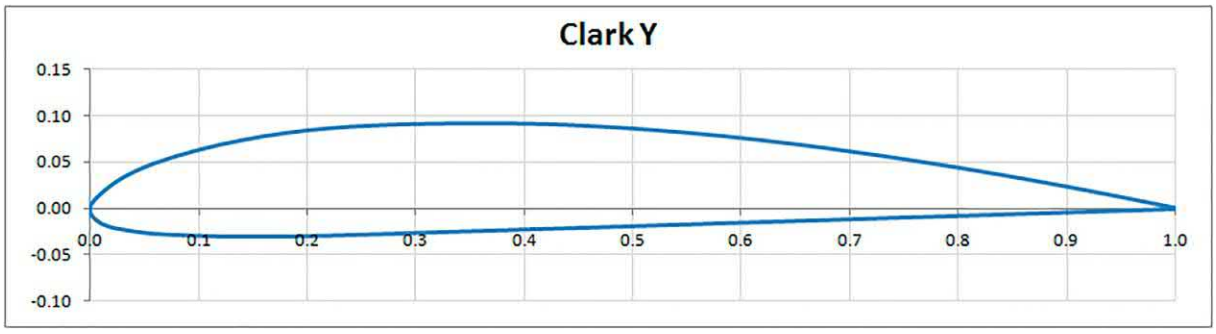


FIGURE 8-40 The Clark Y airfoil.

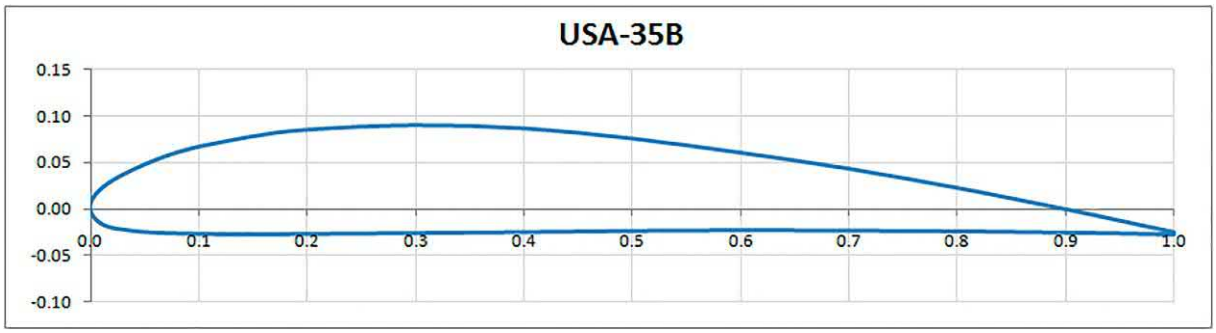


FIGURE 8-41 The USA-35B airfoil.

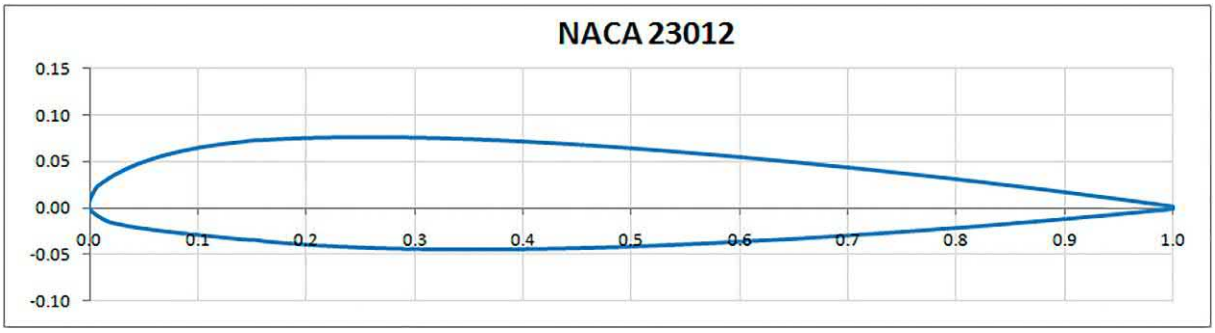


FIGURE 8-42 The NACA 23012 airfoil.

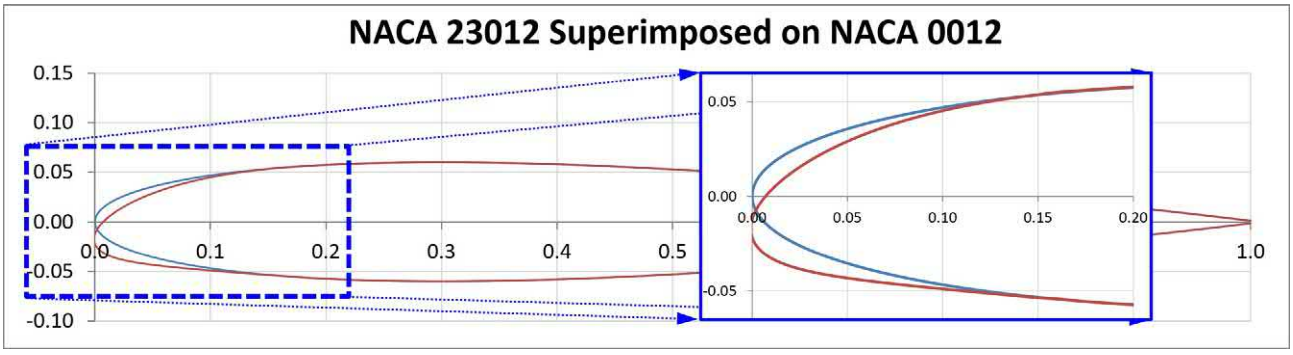


FIGURE 8-43 The NACA 23012 superimposed on the NACA 0012 airfoil reveals the only difference between the two is from the leading edge to 0.15C.

low C_m; everything the aircraft designer would ever want in an airfoil. However, what was less touted in the NACA literature was the abruptness of its stall. And this is a serious problem. This does not just apply to the NACA 23012, but a host of airplanes that feature a root/tip combination of 23015/23009. That said, there is more to a bad stall than just an abrupt drop in C_l; the planform geometry, surface quality, proximity of fuselage or nacelles to the wing, and others play a major role as well. Aerodynamic properties are provided in refs. [41,42].

As stated in Section 8.1.11, a leading-edge bubble of the short kind may form on airfoils whose t/c is 12% or less. Compounding this issue on the NACA 230XX series airfoil is the nature of its geometry; the leading-edge deflection at 15% chord. The mean-line discontinuity may contribute to the formation of the separation bubble [22]. As the AOA increases, the airflow will reattach behind the bubble (see schematic to the left in Figure 8-44) and separate again at the trailing edge. As AOA increases further, the TE separation moves forward. Eventually and suddenly, it combines with the LE separation bubble, causing an abrupt and large drop in the lift coefficient. This is clearly visible as the sharp drop in Figure 8-44, from the wind tunnel test data presented in ref. [41].

Once featured on a wing, manufacturing differences between the two wing halves on either side of the plane-of-symmetry raise the probability that one wing

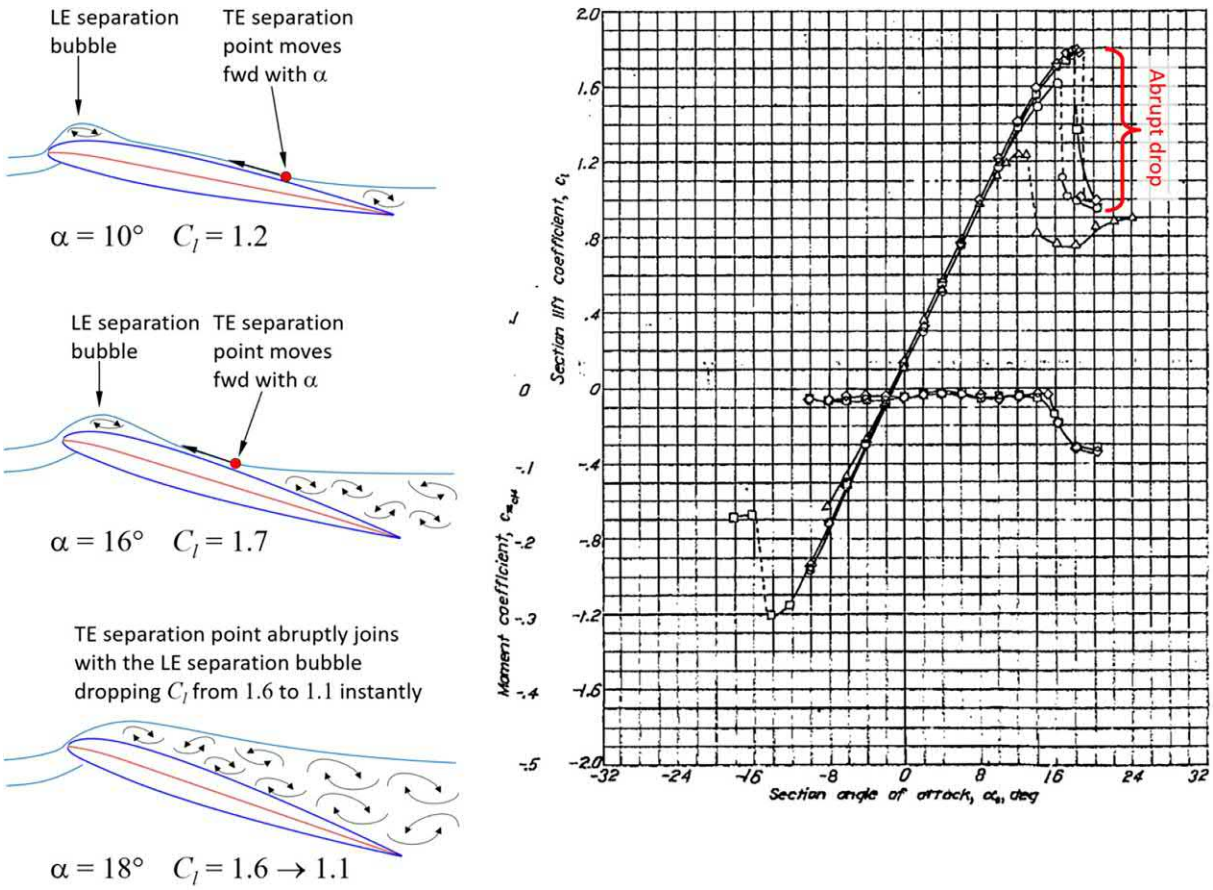


FIGURE 8-44 Data from ref. [41] for the NACA 23012 airfoil illustrate the sharp drop in the lift coefficient at stall.

will stall (abruptly) before the other. The consequence is an uncontrollable roll-off at stall, of which the designer should be strongly aware. While it is possible to "beat" such stall behavior into submission with adequate wing washout and stall strips, the cost is extra development time.

(4) GA(W)-1 or LS(1)-0417

The GA(W)-1 (see Figure 8-45) was designed in 1972 by Robert T. Whitcomb and associates at the NASA Langley Research Center using Computational Fluid Dynamics [58]. It is specifically developed for GA aircraft. It is also known as NASA/Langley/Whitcomb LS(1)-0417. Details of its characteristics are presented in refs. [54,59]. The airfoil was wind tunnel tested at Reynolds numbers between 2×10^6 and 20×10^6 and Mach numbers ranging from 0.15 to 0.28. Its $C_{l_{max}}$ was found to range from 1.64 to 2.12. A section C_l/C_d of 65 to 85 were obtained at a climb $C_l = 1.0$. Per ref. [48], it is used in 36 different models.

Besides aerodynamics, another favorable characteristic of the GA(W)-1 is the structural depth offered by its $t/c = 0.17$. This provides ample volume for fuel and should result in a lighter wing structure. However,

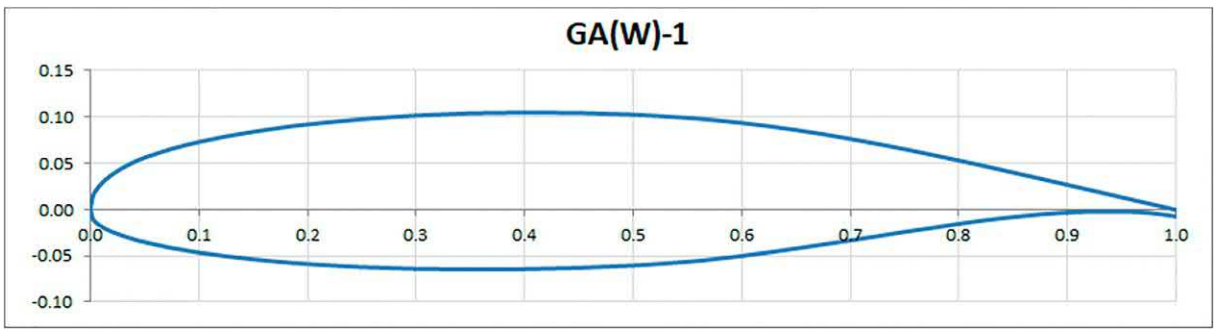


FIGURE 8-45 The GA(W)-1 airfoil.

fabricating ribs for its cusp (reflexed curvature) is destined to be a challenge. A discussion of is presented in Section 5.3.3. A flight test evaluation of the airfoil on a twin-engine Piper Seneca is provided in ref. [60]. It left a lot to be desired. There is also a GA(W)-2 airfoil.

(5) Davis Wing Airfoil

The Davis wing stood for a wing design philosophy used for many military aircraft, of which the Consolidated B-24 Liberator is probably the best known. The airfoil, which was inspired by what, at the time, was thought to be the shape of a teardrop (see Figure 8-46). The airfoil is evaluated in ref. [61], where it was found to offer low drag and high lift. An Xfoil analysis of the airfoil at Reynolds number of 9×10^6 agrees with the experimental data in places (except shape of stall). It has an ld_{max} in excess of 160, and a $C_{l_{mind}}$ of 0.65 (suitable for a lumbering heavy transport aircraft). Xfoil slightly underpredicts the $C_{l_{max}}$ of about 1.35 versus 1.4 from experiment.

(6) "Peaky" Airfoils

The term *Peaky airfoils* refers to transonic airfoils designed using a philosophy popular in the 1960s. As stated in Section 8.3.8 the flow around a body accelerates to $M=1$ well before the far-field speed does so. This causes a normal shock to form on the body, like the one shown in Figure 8-47. It shifts the airfoil's center of lift from (approximately) the quarter-chord to the mid-chord. Among effects is: (1) Increased stability that calls for increased pitch authority. (2) Shock-induced separation that thickens the wake behind the shock and increases drag (see Figure 8-67). (3) A drastic drop in

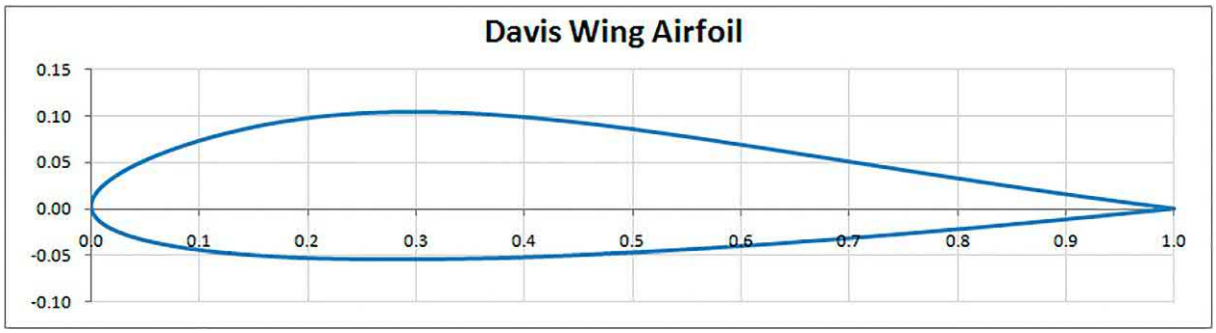


FIGURE 8-46 The basic Davis Wing airfoil for the B-24 Liberator.

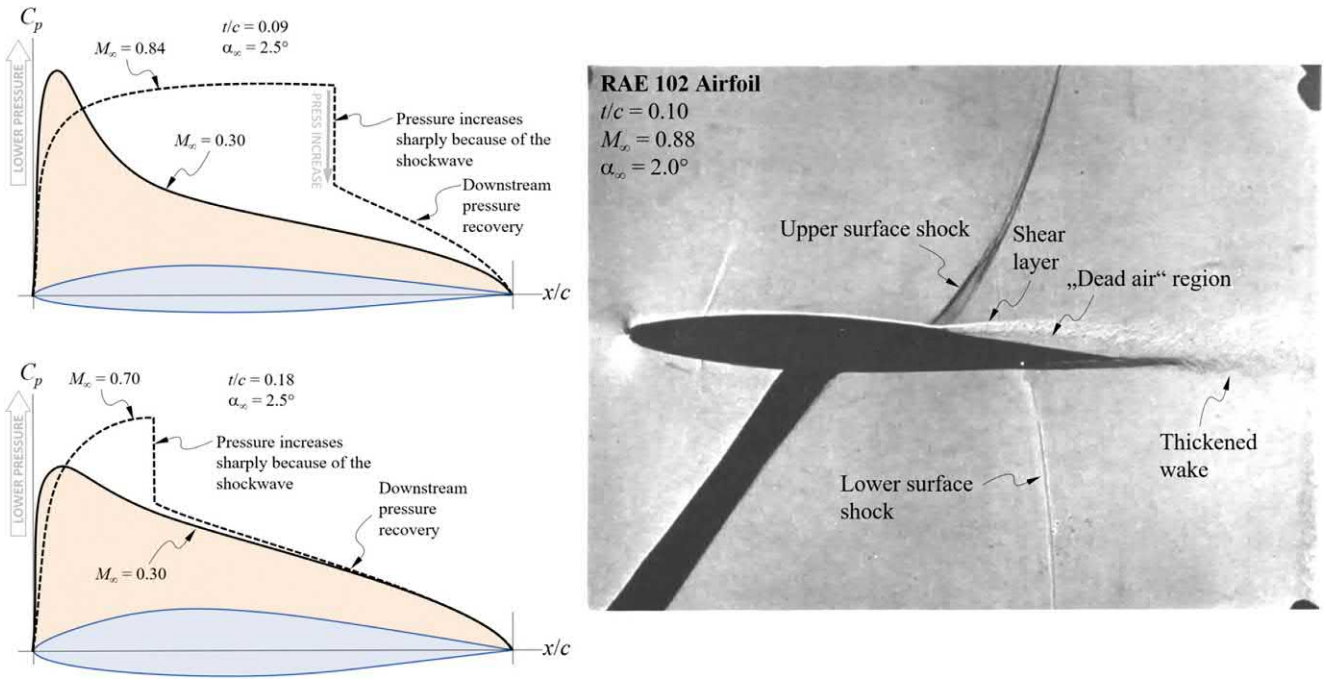


FIGURE 8-47 Difference in pressure coefficient for a thin and thick airfoil at low and high subsonic speeds. Illustration is based on [62]. The schlieren photograph shows the severe separation downstream of the upper surface shock (photograph from ref. [63]).

the lift coefficient, which gives rise to the term *shock-stall*. (4) Aeroelastic problems [64]. These effects can be delayed by increasing the sweep of the wing, but eventually they are inescapable. The thicker wake is clearly visible behind the upper surface shock in Figure 8-47 [63]. The far-field Mach number at which such shock appears on a body is called its *critical Mach number*, denoted by M_{crit}. The value of M_{crit} for typical NACA 4-digit or 5-digit airfoils at low AOA may be a hair over Mach 0.6, rendering them impractical for high-speed aircraft.

Research on such high-speed effects began in the 1930s, but serious work on airfoils began in 1955 with the pioneering work of H. H. Pearcey, who tried to experimentally obtain "an essentially shock-free flow" [65]. Pearcey showed it was possible to weaken the shock by reshaping the airfoil's leading edge. This allowed the flow to expand rapidly from the stagnation point and become supersonic in the leading-edge area. This formed a series of compression shock waves that reduced the local Mach number, weakening the final shock wave [66]. Less drag was an important benefit of this change. It was thought the modified airfoils would weaken the shock for maximum local Mach numbers as high as 1.4. The resulting pressure distribution has a prominent pressure peak near the leading edge and was describes as being *peaky* (see Figure 8-48). The airfoil has a flat upper surface, which necessitates a cusp in the trailing edge to improve its lift generation.

Experience in using peaky airfoils in combat aircraft has revealed that high-speed, high-g maneuvers (which call for high AOA) generate significant shock strengths that may cause sudden loss of lift (*shock-stall*). When introduced to the Hawker Siddeley Kestrel FGA.1, the prototype of the Hawker Siddeley Harrier, this shock would occur above Mach 0.8, causing a serious wing-rocking at an AOA where gentle buffet would be expected [66].

(7) Supercritical Airfoils

Supercritical airfoils are often referred to as one of the three major contributions to aviation made by the famous aerodynamicist Richard T. Whitcomb (1921–2009), which many historians of aviation call the most distinguished alumnus of the NASA Langley's Research Center. The other two contributions are the area-rule and the winglet. Ref. [39] details the development of supercritical airfoils by NASA.

Like peaky airfoils, supercritical airfoils are intended for high-speed aircraft. They feature a large radius (blunt) leading edge, considerably flatter upper surface than the peaky airfoils, and a significant cusp near the trailing edge (see Figure 8-49). The blunt leading edge softens the suction peak of the smaller radius peaky airfoil. The flatter upper surface keeps down the local Mach number and keeps down adverse pressure gradients. The cusp was introduced to help generate lift without lowering M_{crit} by forming a high-pressure region under the airfoil.

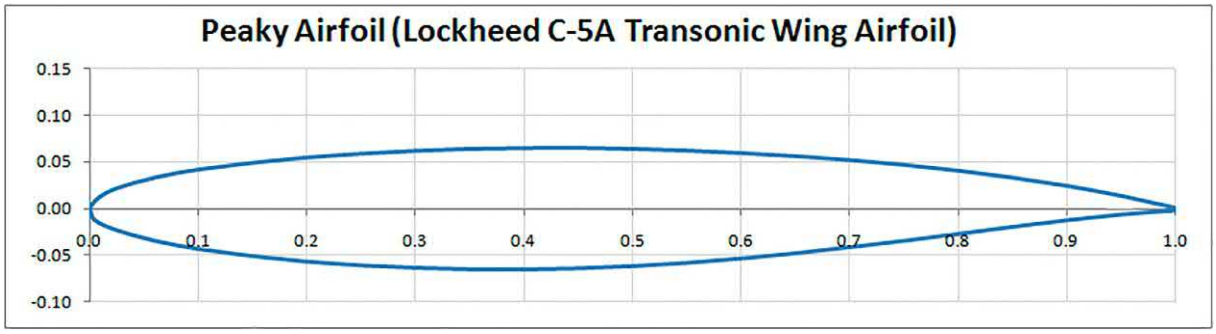


FIGURE 8-48 A typical "Peaky" airfoil. This one is the basic C-5A Galaxy airfoil.

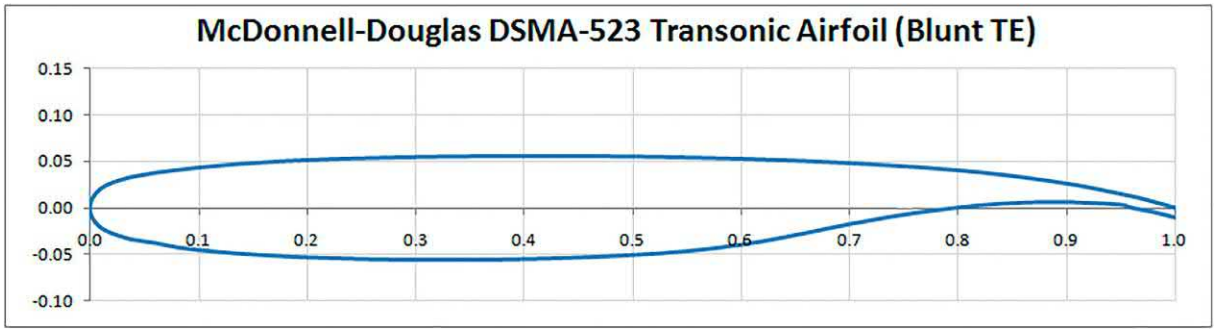


FIGURE 8-49 A transonic blunt TE airfoil developed by McDonnell Douglas under the designation DSMA-523.

The characteristics of supercritical airfoils can be summarized as follows: (1) The drag rise Mach number, M_{crit}, is higher than for more conventional airfoils. As an example, at $C_l = 0.65$, the M_{crit} of one such airfoil is 0.79, which compares very favorably to 0.67 of a NACA 64A-series airfoil of an equal thickness [67]. (2) Their section pitching moment coefficient (C_m) is more negative than for conventional airfoils. This is caused by the high-pressure region that forms at the lower surface of the cusp. (3) The supercritical airfoil has higher M_{crit} at off-design section lift coefficients. (4) The airfoil also increases $C_{l_{max}}$ at high subsonic Mach numbers.

Supercritical airfoils offer many advantages to high-speed aircraft: (1) They increase M_{crit} for a given thickness and wing sweep. (2) Their thickness offers structural depth and volume for fuel. (3) They allow reduced wing sweep, which offers a host of benefits, including improved low-speed characteristics and performance capabilities.

(8) Joukowski Airfoils

Joukowski airfoils are much more a clever mathematical tool to demonstrate aerodynamic theory than a practical solution to aircraft airfoil design. The airfoils are named after the Russian scientist Nikolay Zhukovsky (1847–1921), who also is the originator of the circulation theorem (see Section 8.1.9). The airfoils are generated by a conformal transformation of a circle on the complex plane, using the complex number ζ:

$$z = x + \mathbf{i}y = \zeta + \frac{1}{\zeta} \tag{8-53}$$

Consider the complex number ζ to be given by $\zeta = a + \mathbf{i}b$. Substituting this into Equation (8-53) and manipulating yields the two spatial variables x and y that are given by the following relation:

$$x = \frac{a\left(a^2 + b^2 + 1\right)}{\left(a^2 + b^2\right)} \quad \text{and} \quad y = \frac{b\left(a^2 + b^2 - 1\right)}{\left(a^2 + b^2\right)} \tag{8-54}$$

By varying the values of a and b between -1 and 1 (e.g., try $a = -0.1$ and $b = 0.1$), the shape of the airfoil can be modified (see Figure 8-50). Then, using elementary flow concepts, such as uniform flow, sources, sinks, and vortex flow, airflow around the resulting airfoil can be simulated. Joukowski airfoils are a subject of most texts on theoretical aerodynamics, although, they are rarely used on actual aircraft. In fact, ref. [48] indicates 5 instances, all of them sailplanes.

(9) Liebeck Airfoils

The unconventionally shaped airfoil shown in Figure 8-51 belongs to a class of airfoils named after Dr. Robert Liebeck. In ref. [68], he states: "Work on this problem originated as a response to a general question from A.M.O." Smith: "*What is the maximum lift which can be obtained from an airfoil, and what is the shape of that airfoil*?" This refers to the $C_{l_{max}}$ that can be passively generated using geometry that is physically possible

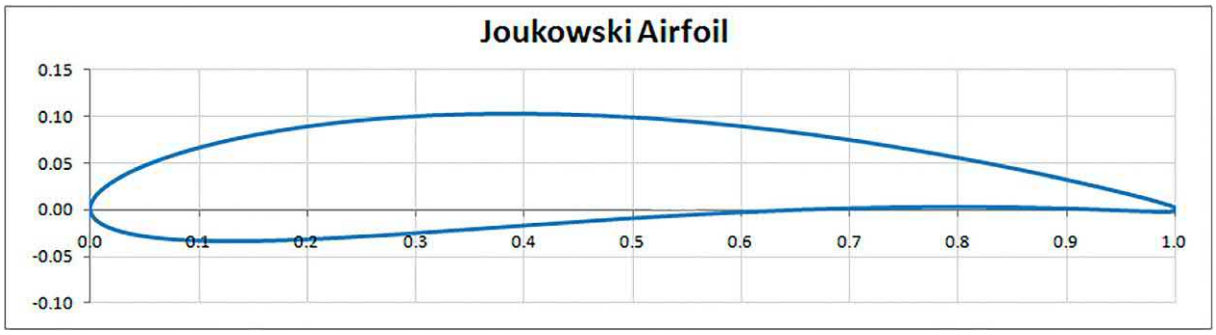


FIGURE 8-50 A Joukowski airfoil.

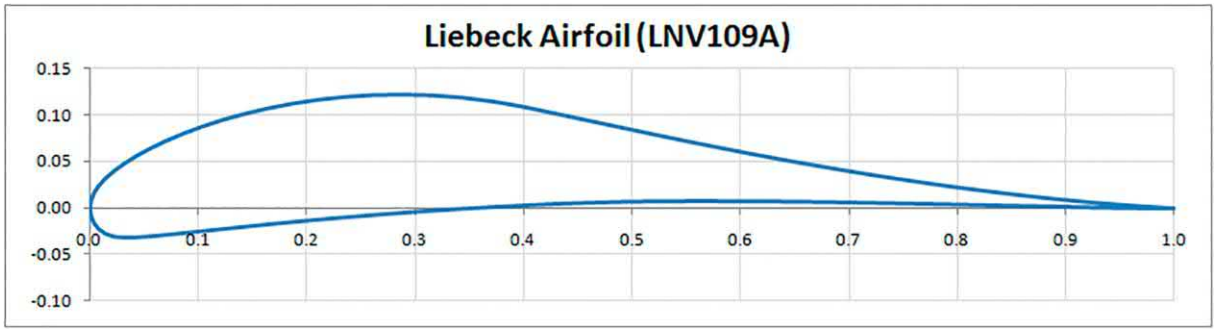


FIGURE 8-51 A Liebeck airfoil.

assuming subsonic and unseparated flow. The airfoils are designed to generate the Stratford distribution discussed in Section 8.1.6. The airfoils are intended for low Reynolds number applications, such as High-Altitude Long Endurance (HALE) aircraft, sailplanes, and propellers [68]. Some 12 applications are cited by ref. [48].

(10) Horten and Fauvel Flying Wing Airfoils

These two exemplify airfoils intended for tailless aircraft, such as flying wings and planks. The German brothers Walter Horten (1913–1998) and Reimar Horten (1915–1994) are among the best-known early developers of flying wings and whose personal story is presented in ref. [69]. The 13% Horten airfoil was used on the Horten Ho-II. The Fauvel airfoil was designed by the French sailplane designer Charles Fauvel (1904–1979) [70], best known for numerous tailless aircraft, powered and unpowered, which feature mostly straight wings (Figures 8-52 and 8-53).

8.3 THE FORCE AND MOMENT CHARACTERISTICS OF THE AIRFOIL

The airfoil's lift, drag, and pitching moment are usually converted to dimensionless coefficients. The primary advantage of this is *transferability*. It means that if the coefficients are known for some airfoil geometry, they can be used to extract forces and moments for any other size of the airfoil, airspeed, and atmospheric conditions. These coefficients can be defined in terms of Equation (8-6) as shown below

$$C_l \equiv \frac{2l}{\rho V_\infty^2 S}, \qquad C_d \equiv \frac{2d}{\rho V_\infty^2 S}, \qquad C_m \equiv \frac{2m}{\rho V_\infty^2 S c} \tag{8-55}$$

All variables have already been defined in this chapter. This assumes we know l, d, and m, for instance through wing tunnel testing. Refer to the variable list for other variables.

8.3.1 The Effect of Camber

Positive (or negative) camber affects an airfoil's lift curve and drag polar, as shown in Figure 8-54. A positive camber shifts the lift curve to the left and up, increasing $C_{l_{max}}$. This makes α_{ZL} "more" negative and C_{l_0} positive. The opposite happens if a negative camber is introduced. Camber also changes the drag polar. If the camber is modest, the change is primarily a shift up or down, as shown in Figure 8-54. Large change (e.g., associated with deflected flaps) also increases the airfoil's minimum drag coefficient, $C_{d_{min}}$. This introduces a new variable; $C_{l_{min_d}}$, which is the value of C_l where $C_{d_{min}}$ occurs. $C_{d_{min}}$ for a symmetrical airfoil is at $C_l = 0$.

8.3.2 The Effect of Reynolds Number

Figure 8-55 shows how the Reynolds number (R_e) affects the airfoil's lift curve and drag polar. The left

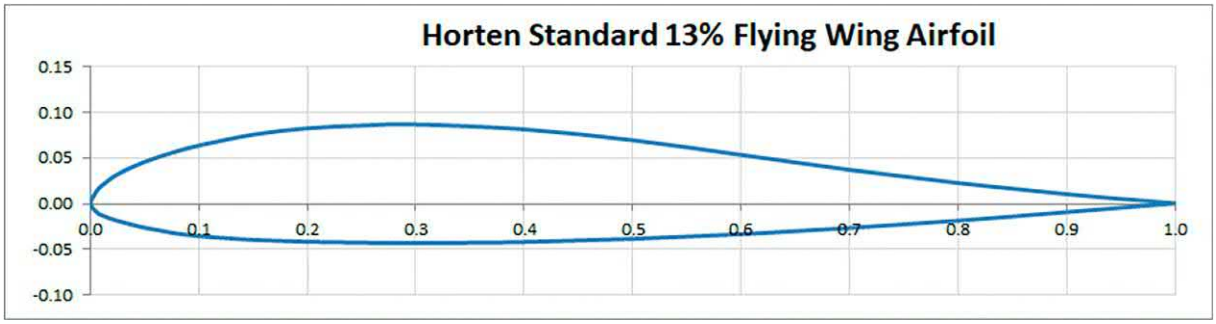


FIGURE 8-52 A 13% thick Horten airfoil.

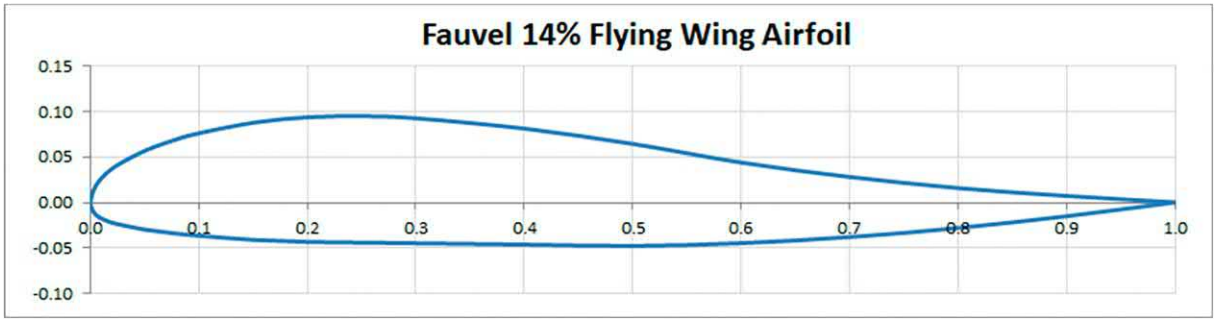


FIGURE 8-53 A 14% thick Fauvel airfoil.

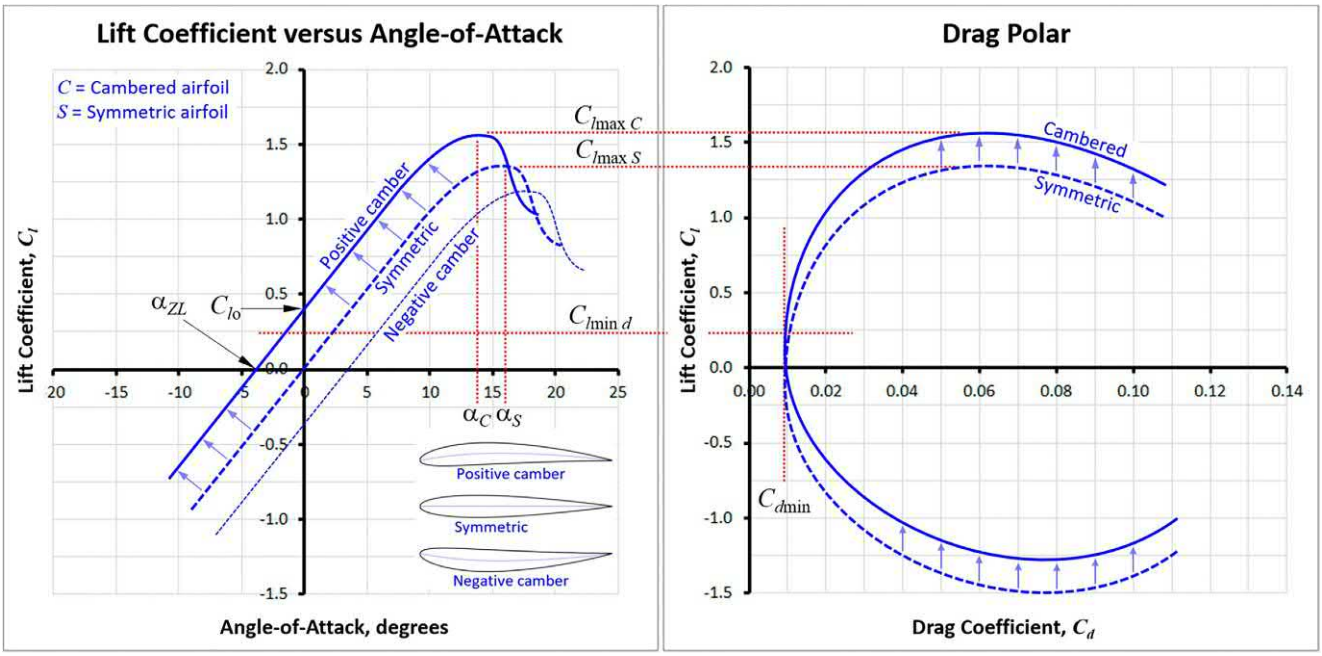


FIGURE 8-54 The effect of camber on the lift curve and drag polar.

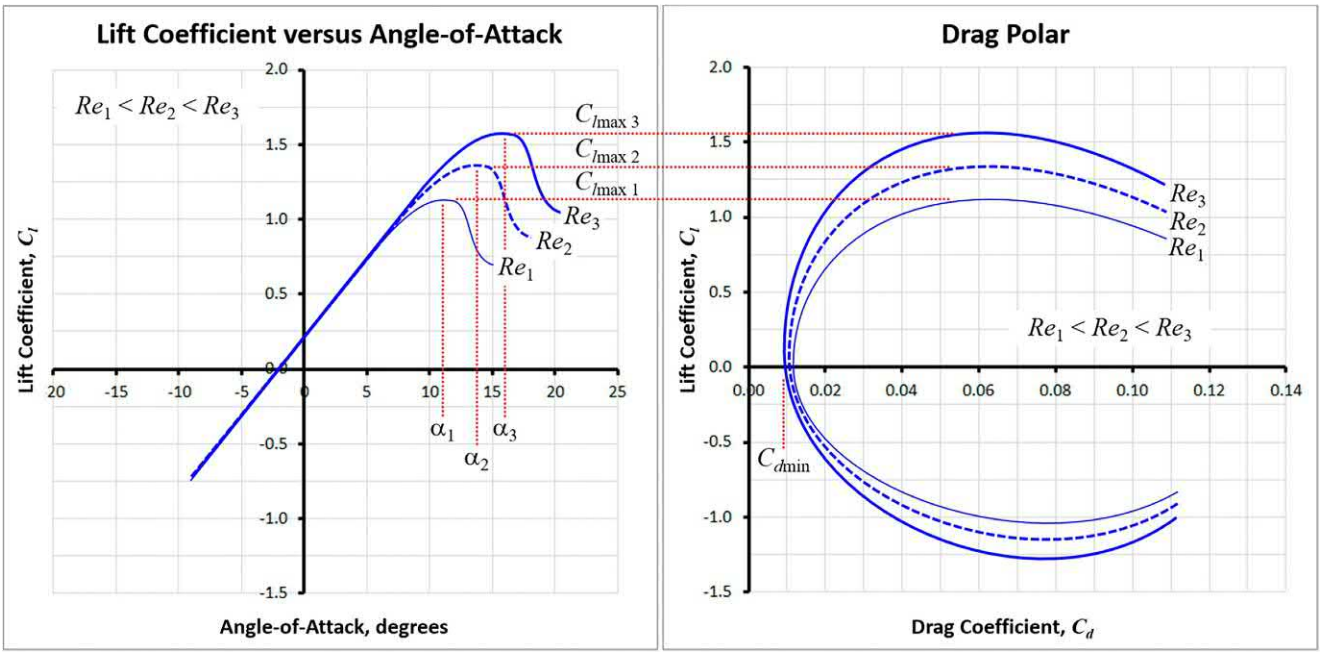


FIGURE 8-55 The effect of Reynolds number on the lift curve and drag polar.

graph shows the slope and intersection of the linear region is unaffected by the R_e. However, the higher the R_e, the higher is the stall AOA (denoted by α_1, α_2, and α_3), maximum lift coefficient (denoted by $C_{L\max 1}$, $C_{L\max 2}$, and $C_{L\max 3}$), and the point where the slope becomes non-linear. Note that the change shown is exaggerated – the change is diminished for very large R_e.

A typical change in the drag polar is illustrated in the right graph of Figure 8-55. Generally, $C_{d_{\min}}$ decreases gradually with increase in R_e, up to approximately 20×10^6, after which it remains constant up to 40×10^6 [12]. However, this is dependent on surface qualities (e.g., see Section 8.3.7). On the other hand, delayed tendency for flow-separation reduced the C_d elsewhere. Thick airfoils tend to suffer from a large flow separation in the trailing-edge region at low R_e. The gradual reduction of this region at higher R_e causes the drag polar to get wider.

8.3.3 The Effect of Early Flow Separation

Figures 8-56 and 8-57 show the consequence of early flow separation on an airfoil's lift curve and drag polar. This is easy to detect from the lift curve and, thus, the designer reviewing wind tunnel test results should recognize the symptoms: Slope change, followed by a stall AOA that may be slightly less than expected, and a substantially lower $C_{l_{max}}$. This holds for 2- and 3-dimensional lift curves. For aircraft, the shallower slope will require the airplane to operate at a higher AOA, with the associated increase in lift-induced drag.

The early separation on airfoils, can result from a too short a pressure recovery region, the trailing-edge region of the airfoil being too steep, or the discontinuity of a surface caused by the presence of a control surface. For efficiency the lift curve should be linear to as high a lift coefficient as possible.

The presence of such a flow separation is harder to detect from the drag polar. As shown in Figure 8-57,

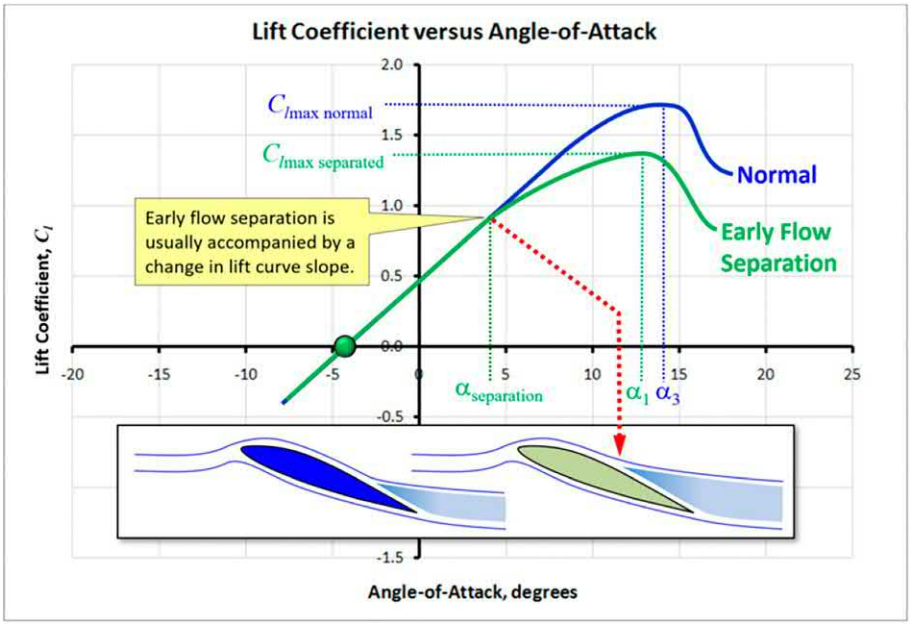


FIGURE 8-56 The effect of early flow separation on the lift curve.

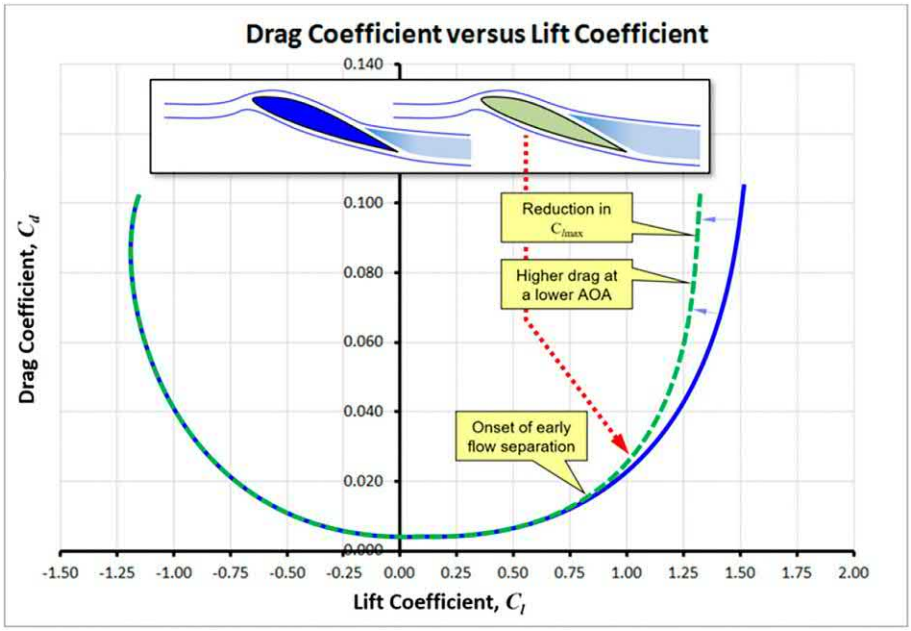


FIGURE 8-57 The effect of early flow separation on the drag polar.

the drag polar is narrowed and accompanied by an earlier deviation from a quadratic approximation. For aircraft, there is higher drag that lowers the rate of climb and detrimentally affects endurance and range. Thus, it is vital to determine what causes the early flow separation and fix it.

8.3.4 The Effect of a Trailing-Edge Flap

Deflecting TE flaps significantly increases the magnitudes of lift, drag, and pitching moment at the operational AOA. Figs. 8.58 and 8-59 illustrate the impact on an airfoil's lift and drag. In general, deflecting the flap *trailing edge down* (TED) increases the airfoil's camber, shifting the unflapped lift curve up and to the left. This increases $C_{l_{max}}$ and reduces the α_{stall}. The opposite takes place for *trailing edge up* (TEU) deflection. The airfoil's camber is reduced, shifting the lift curve downward and to the right, lowering the $C_{l_{max}}$ and increasing α_{stall}.

The deflection increases the drag, regardless of whether the flap is deflected TEU or TED. The drag polar is also shifted as shown in Figure 8-59. The magnitude

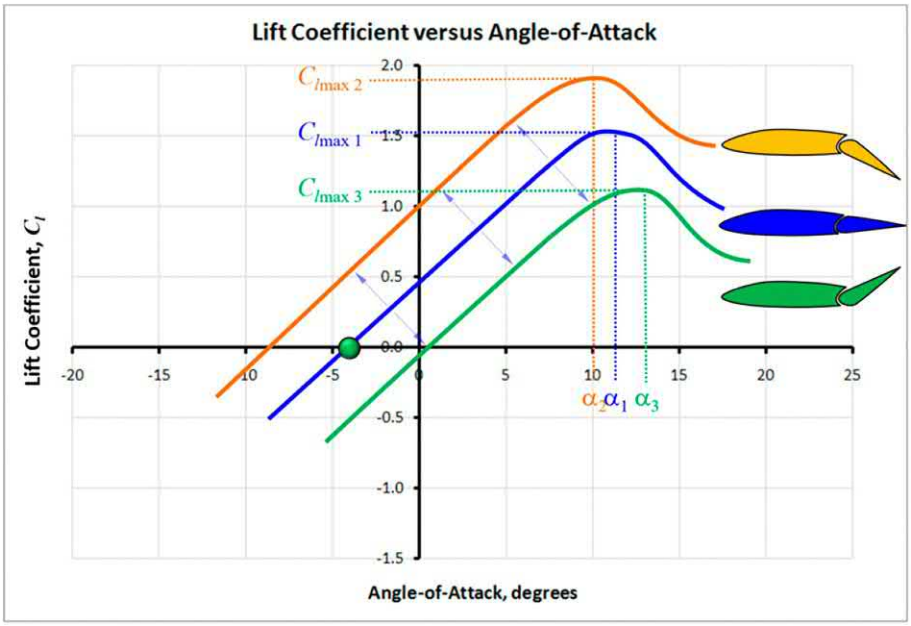


FIGURE 8-58 The effect of introducing flap to the airfoil on the lift curve.

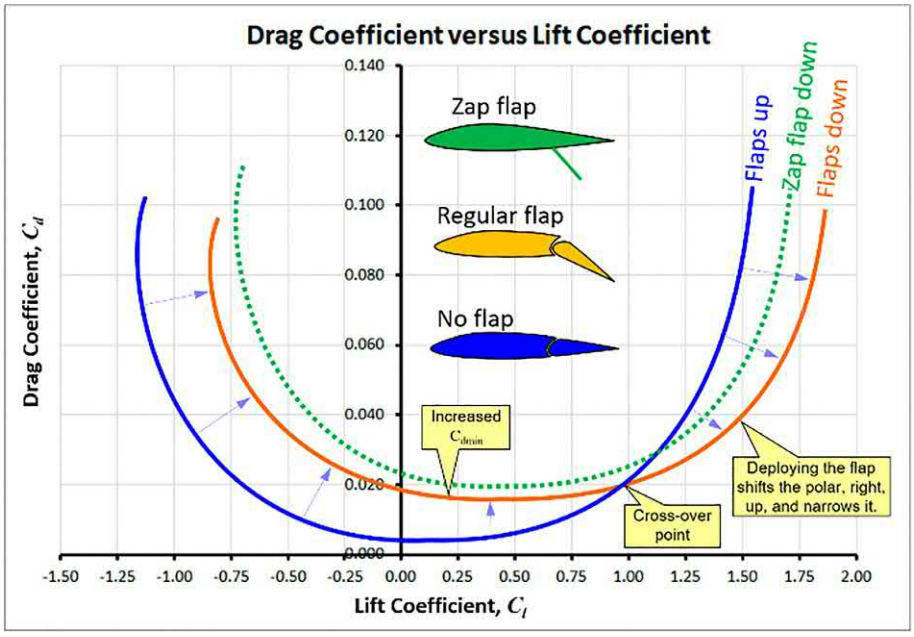


FIGURE 8-59 The effect of introducing a flap to the airfoil on the drag polar.

(and even the sign) of the airfoil's pitching moment changes significantly. Deflecting a flap TEU allows wings to be made statically stable without the use of stabilizing surfaces such as horizontal tails or canards. The magnitude of these changes depends on the flap geometry, as discussed in Section 10.3.

(1) Cruise Flaps

The term *cruise flap* refers to a wing flap deflected TEU at higher speeds. This contrasts the TED deflection of regular flaps at lower speeds. Cruise flap deflection ranges from 1° to 10°, For aircraft, this has twofold effect: (A) The drag polar is shifted the left, which moves the $LD_{\max}$ to a lower C_L and, thus, higher airspeed (see Figure 8-60). Expect the minimum drag coefficient, $C_{D_{\min}}$, to increase slightly. (B) Thick NLF airfoils designed for very low C_d tend to have a deep but narrow drag bucket. This can be increased by a cruise flap [71]. Also see [72]. (C) The overall C_m is reduced, which reduces trim drag.

Cruise flaps are common in sailplanes where they permit faster glide between thermals. They are an extension of the functionality of regular flaps. This allows a TEU deflection in addition to the normal downward deflection, using the same control handle. This reduces design complexity. Cruise flaps are harder to implement using flaps that translate (in addition to rotation) due to the upper wing surface extending farther aft (*slot lip*). Sailplane flaps are normally of the plain flap style.

(2) Climb Flaps

The term *climb flap* refers to a wing flap deflected slightly TED during climb. This functionality is implemented in some sailplanes, but also in modern commercial jetliners, such as the Airbus A350 and Boeing 787 [73]. In sailplanes, climb flaps are thought to permit tighter turning radii in thermals, while reducing drag (and, thus, improve climb performance) in the jetliners.

8.3.5 The Effect of a Slot or Slats

Figures 8-61 and 8-62 show the effect of introducing a leading-edge slot or slat to an airfoil. The primary effect on the airfoil's lift curve is that it "extends" to a higher $C_{l_{\max}}$ (or $C_{L_{\max}}$ for 3-dimensional geometry) and α_{stall}. However, two additional (minor) effects are sometimes manifested as well. (1) As the curvature of the mean-line increases, the lift curve may shift a hair to the left, like that of a flap deflection (see Section 8.3.4). (2) If the chord of the airfoil increases because of deployment, the lift curve slope increases a tad. Various leading-edge devices are presented in Section 10.2.

8.3.6 The Effect of Deploying a Spoiler

A *spoiler* is a device whose purpose is to reduce lift and increase the drag of the airfoil. It is a required control for low drag aircraft, such as sailplanes and jets. These tend to glide at shallow angles, which makes it surprisingly challenging to land. Without a spoiler, the airplane will float long distances before touching down, while "eating up" precious runway. It is also useful to "kill" or "dump" lift at touch-down, preventing bouncing touchdowns. Spoilers are also known as *airbrakes* or *speed-brakes*. Spoilers also allow rapid descents at cruise speeds and are used in many aircraft as a roll control.

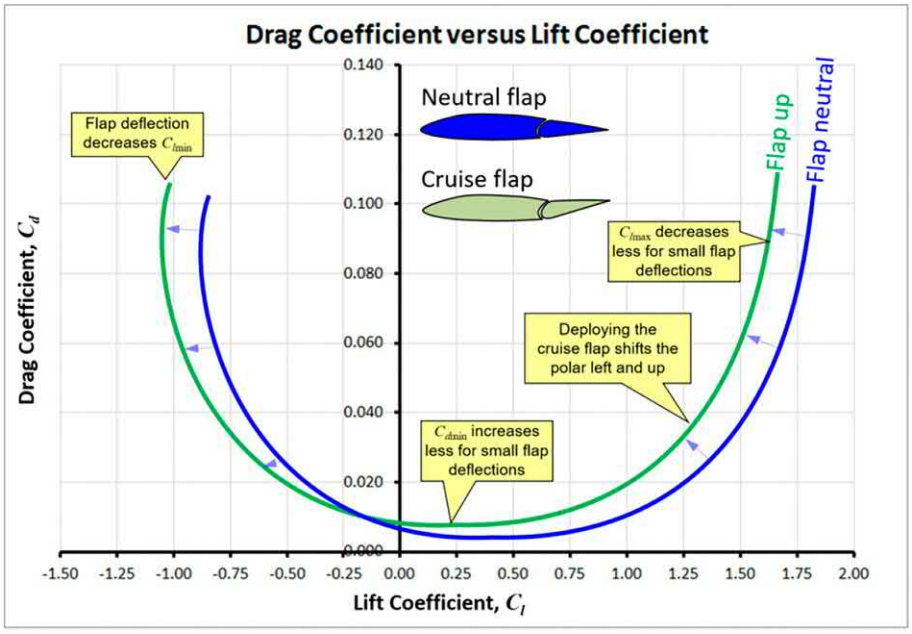


FIGURE 8-60 The effect of introducing a "cruise" flap to the airfoil on the drag polar.

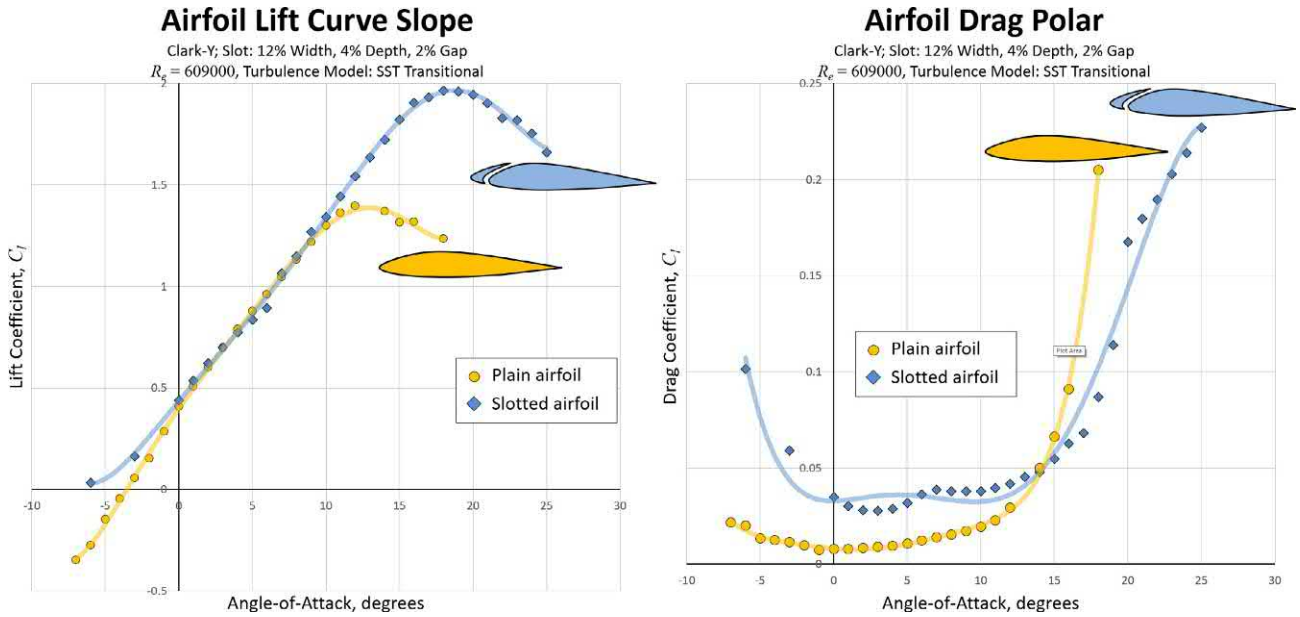


FIGURE 8-61 The effect of introducing a slot or slat on lift and drag [74].

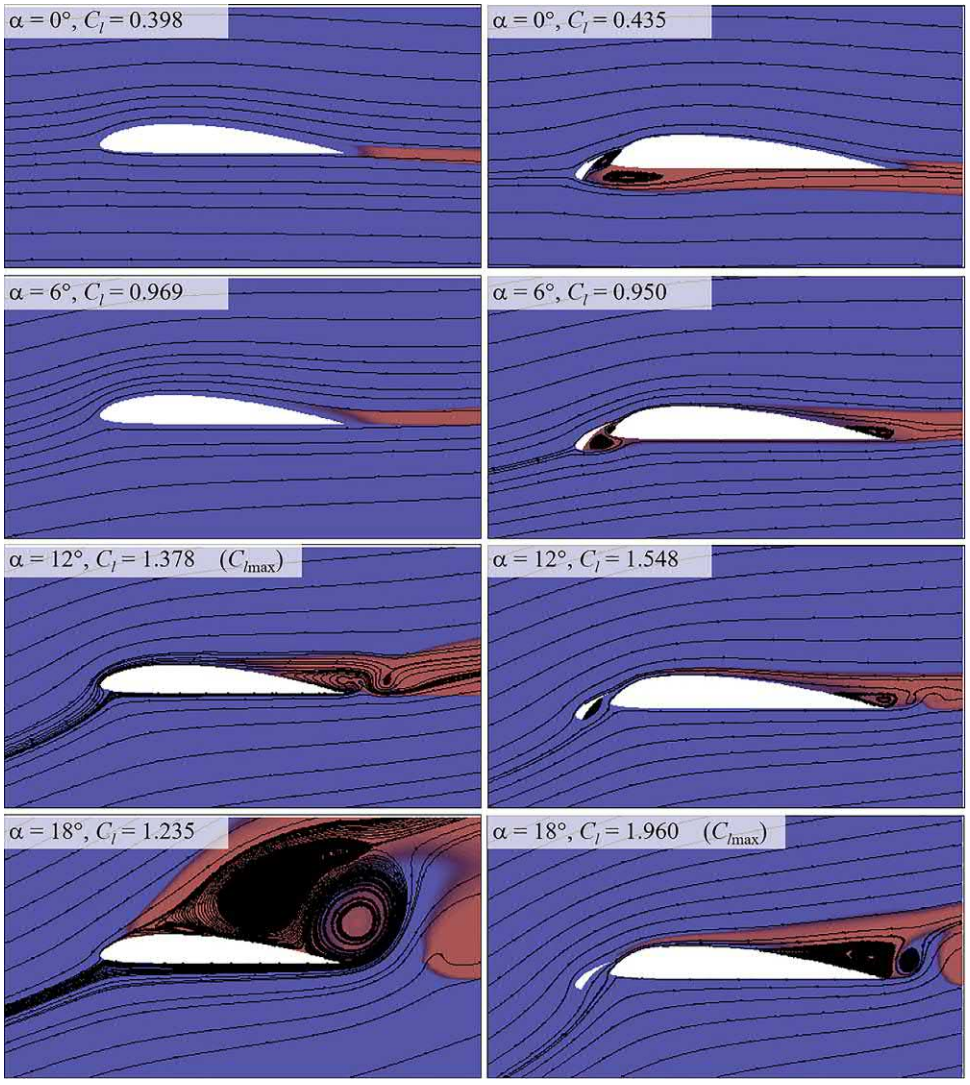


FIGURE 8-62 Predicted flow field around a Clark-Y airfoil, without and with a fixed slot [74].

Some people make a distinction between a spoiler and a speed brake. Thus, a spoiler is deployed from the wing where it "spoils" the lift and increases drag. In contrast, a speed brake is deployed from another part of the aircraft (e.g., the fuselage). It only generates drag and does so without changing the AOA.

In most cases, the effect of deploying a speed-brake can be approximated by shifting the drag polar upward to a higher $C_{d_{min}}$, while reducing $C_{l_{max}}$. This is illustrated in Figure 8-63. Note that while the $C_{l_{max}}$ of the airfoil decreases due to the accompanying flow separation, the magnitude of $C_{l_{min}}$ increases as well (and becomes more negative). The effect resembles a split flap on an inverted airfoil.

8.3.7 The Effect of Leading-Edge Roughness and Surface Smoothness

The impact of surface quality on airfoil properties was investigated by NACA as early as in the late 1930s [75]. It confirmed that surface roughness increases drag and that smooth surfaces are important even for non-NLF airfoils [12]. It also demonstrated that, while being smooth, surfaces do not have to be superbly polished. In fact, 320-grit sandpaper produces acceptable surface smoothness for all aerodynamically smooth surfaces. It is also shown that surface particles are more detrimental than surface scratches when comes to the transition of laminar to turbulent boundary layer.

Figure 8-64 shows the effect of surface finish on the section drag coefficient ($C_{d_{min}}$) of a NACA 64–420 airfoil with two kinds of surface finish: a smooth and unpolished camouflage paint. The camouflage paint nearly doubles the $C_{d_{min}}$ near a R_e of 20×10^6. It is essential to recognize such trends when estimating aircraft performance. The magnitude of the drag increase is as follows:

$$\text{If } R_e < 20 \times 10^6 : \Delta C_d = 0.000453$$

$$\text{If } R_e \geq 20 \times 10^6 : \Delta C_d = 0.00308$$

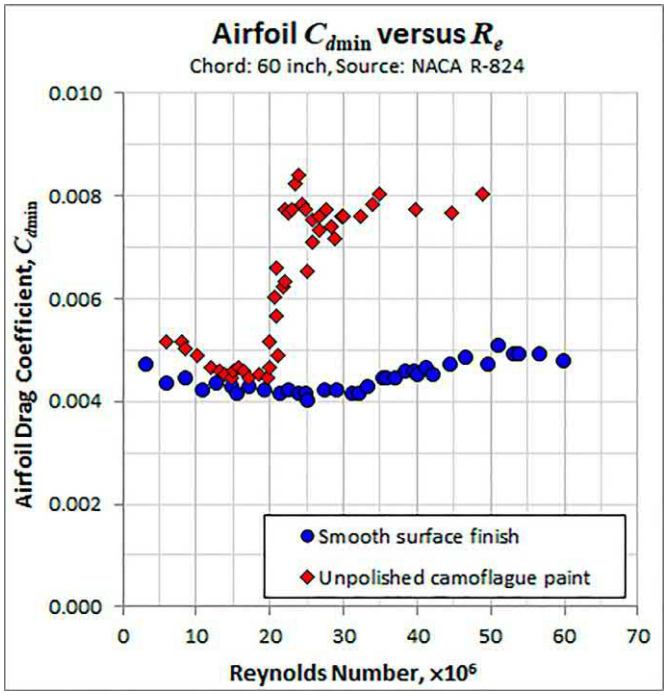


FIGURE 8-64 The effect of surface finish on the minimum drag of an airfoil. *Based on Abbott, I.H., von Doenhoff, A.E., Stivers Jr., L.S., Summary of Airfoil Data, NACA R-824, 1945.*

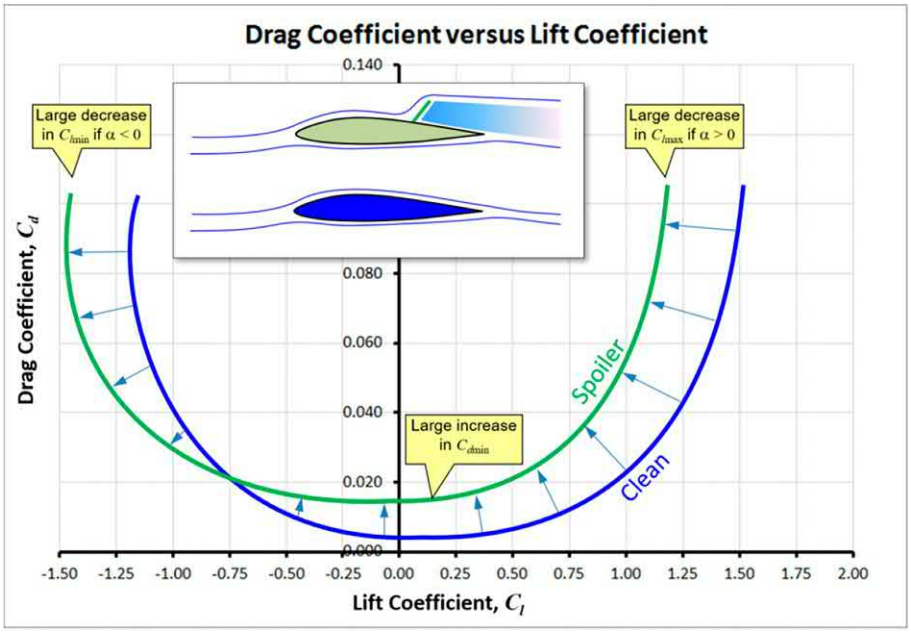


FIGURE 8-63 Increase in $C_{d_{min}}$ due to the deployment of a spoiler. Generally, the shape of the drag polar changes through a vertical upward shift and contraction, possibly shifting the $C_{l_{mind}}$.

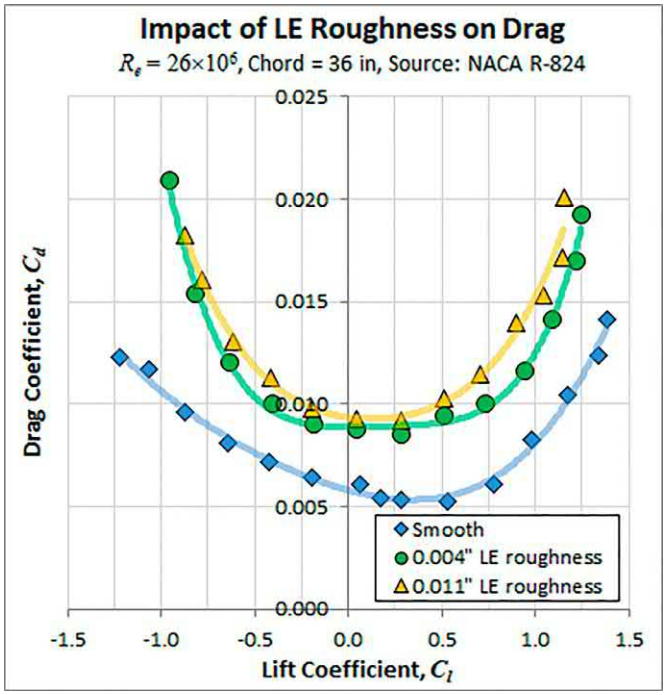


FIGURE 8-65 The effect of surface roughness on the drag polar. *Based on Abbott, I.H., von Doenhoff, A.E., Stivers Jr., L.S., Summary of Airfoil Data, NACA R-824, 1945.*

The effect of a contaminated leading edge is also presented in ref. [12] and is reflected in the drag polar in Figure 8-65. The drag polar, initially smooth, is shifted sharply upward because of grain contamination as small as 0.004 in. While the polar is shifted farther upward when the grain size grows to 0.011 in., the shift is less than that experienced by the initial contamination – the damage is already done. Ref. [12] also shows that LE roughness also reduces section lift curve slope and maximum lift coefficient (Figure 8-65).

8.3.8 The Effect of Compressibility

The term *compressibility* encompasses all effects associated with flight at transonic speeds. This causes complex changes in aerodynamic characteristics, particularly when shock begins to form on the aircraft. Figure 8-66 shows how the lift and drag of a NACA 2412 airfoil is affected by compressibility (at fixed AOAs). It also reveals the abrupt onset of these changes. Among others, references [76,77] contain experimental data on this topic. Flow can be considered incompressible up to *M*0.3 and in some cases up to *M*0.5. Compressibility requires the following considerations:

- The concept of *equivalent airspeed* must be adopted. This is treated in Section 17.3.2.
- Corrections must be made to pressure-, lift-, drag-, and pitching moment coefficients.
- The onset of these effects must be predicted.

(1) Compressibility Corrections for the Pressure Coefficient

The following methods are used to account for the impact of compressibility on the pressure coefficient.

Prandtl-Glauert [78]:

$$C_p = \frac{C_{p_{inc}}}{\sqrt{1-M_\infty^2}} \tag{8-56}$$

Kármán-Tsien [79]:

$$C_p = \frac{C_{p_{inc}}}{\sqrt{1-M_\infty^2} + \left(\frac{M_\infty^2}{1+\sqrt{1-M_\infty^2}}\right)\frac{C_{p_{inc}}}{2}} \tag{8-57}$$

Laitone [80]:

$$C_p = \frac{C_{p_{inc}}}{\sqrt{1-M_\infty^2} + \left(\frac{M_\infty^2\left(1+0.2M_\infty^2\right)}{2\sqrt{1-M_\infty^2}}\right)C_{p_{inc}}} \tag{8-58}$$

where C_{pinc} is the incompressible value. These corrections are applied to the C_p, such as that shown in Figures 8-8 and 8-9, allowing the lift and pitching moment coefficients to be corrected. All are unreliable when the body is subjected to extensive regions of shock, as indicated by the substantial changes in coefficients (see Figure 8-66).

(2) Compressibility Corrections for Lift

Figure 8-67 shows the effect of compressibility on the airfoil's lift and drag. The lift curve slope increases with Mach number, which means the AOA required to generate a specific lift coefficient is reduced (see the left graph in Figure 8-67). This trend continues up to a point. Eventually, a shock, like the one shown in Figure 8-47, begins to form on the airfoil. It causes the flow to separate, triggering a sharp reduction of the lift curve slope. The impact on pitching moment is even more chaotic. The consequence for conventional airfoils is shown in the left and center graphs of Figure 8-66. Prior to that, the compressible lift and pitching moment coefficients can be adjusted using the compressibility corrections discussed before. The simplicity of the Prandtl–Glauert correction allows a closed form solution for both [81] and is valid to an upper limit around *M*0.75.

$$C_l = C_{l_{inc}}/\sqrt{1-M_\infty^2} \tag{8-59}$$

$$C_m = C_{m_{inc}}/\sqrt{1-M_\infty^2} \tag{8-60}$$

where the subscript *inc* represents the incompressible value. Given a C_l in the linear range, the required AOA is

$$\alpha = \frac{C_l\sqrt{1-M_\infty^2} - C_{lo_{inc}}}{C_{l\alpha_{inc}}} \tag{8-61}$$

Generally, compressibility has negligible effect on C_{loinc} up to M_{crit} (see below), but large changes above it [[11], 4.1.1.1].

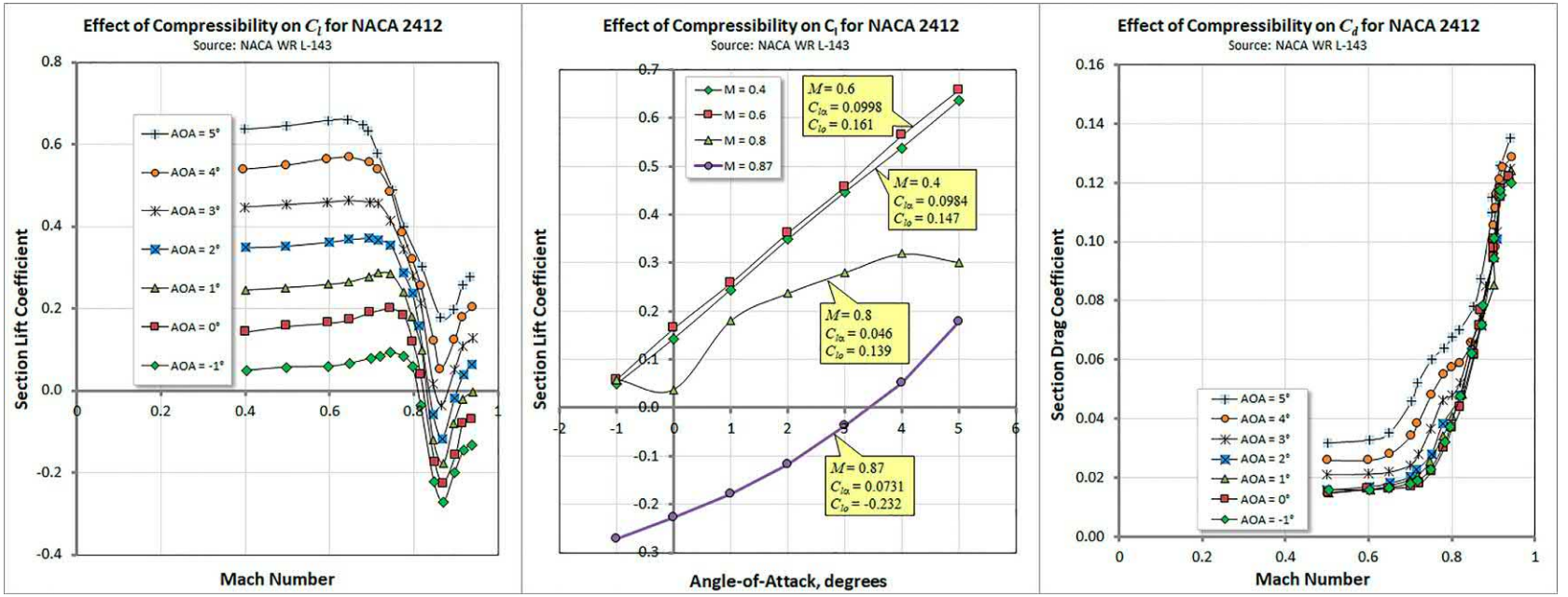


FIGURE 8-66 The effect of Mach number on the lift and drag coefficient of a NACA 2412 airfoil. *Reproduced from Ferri, A., Completed Tabulation in the United States of Tests of 24 Airfoils at Hhigh Mach Nnumbers, NACA WR L-143, 1945.*

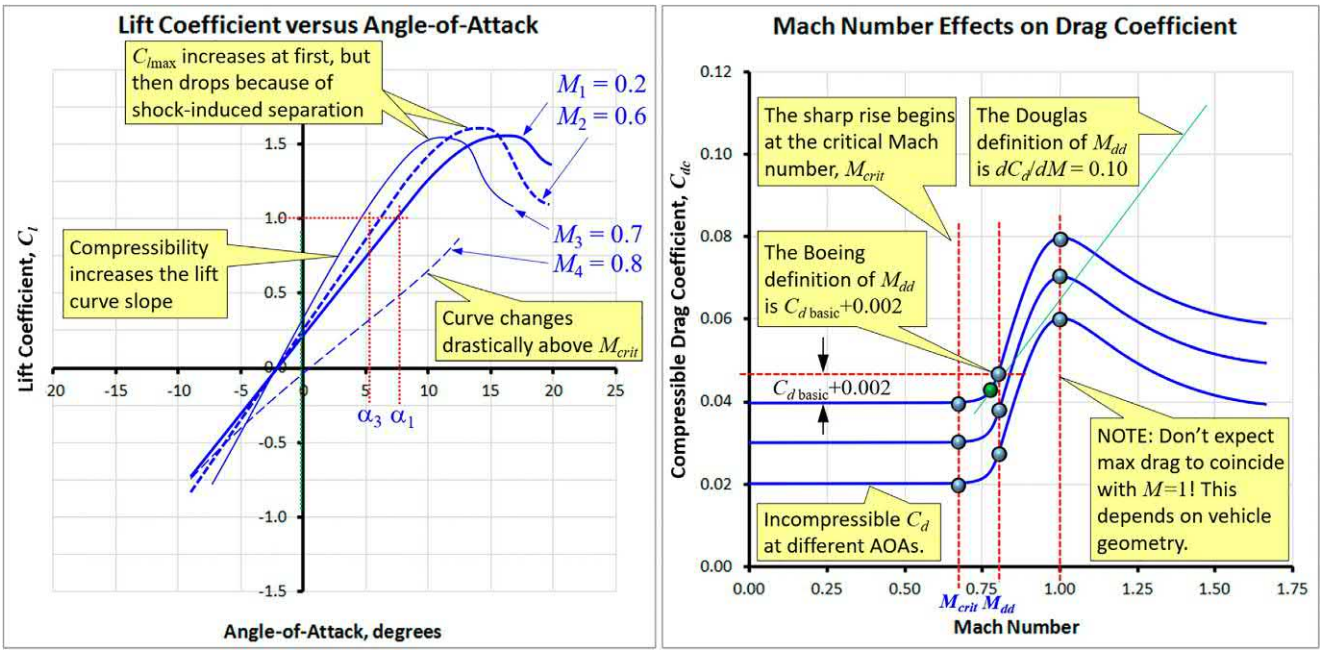


FIGURE 8-67 The effect of Mach number on lift and drag.

DERIVATION OF EQUATION (8-61)

In the linear range, the incompressible lift coefficient is given by $C_{linc} = C_{l\alpha inc}\alpha + C_{loinc}$. Thus, we write:

$$C_l = \frac{C_{l_{inc}}}{\sqrt{1-M_\infty^2}} = \frac{C_{l\alpha_{inc}}\alpha + C_{lo_{inc}}}{\sqrt{1-M_\infty^2}} = \frac{C_{l\alpha_{inc}}}{\sqrt{1-M_\infty^2}}\alpha + \frac{C_{lo_{inc}}}{\sqrt{1-M_\infty^2}}$$

$$\Rightarrow \quad \alpha = \frac{C_l\sqrt{1-M_\infty^2} - C_{lo_{inc}}}{C_{l\alpha_{inc}}}$$

(3) Airfoil Critical Mach Number, M_{crit}

Consider an airfoil (or other arbitrary body) accelerating from rest to some final Mach number, denoted by M_∞ (see Figure 8-68). The presence of the body accelerates (and decelerates) the flow locally on the body, causing associated changes in the local Mach number. Thus, there are regions on the body where flow speed exceeds that of the far-field speed, M_∞. Eventually, further increase in M_∞ causes the speed at some point on the body to reach $M_\infty = 1$ before M_∞ reaches unity. Such a point is denoted by A in Figure 8-68. The value of M_∞ when this happens is called the *critical Mach number* (M_{crit}). In part, this is manifested by the formation of a normal shock at A and a sharp decrease in lift and increase in the drag of the body.

Typical airfoils begin to experience this phenomenon when M_∞ exceeds 0.60 to 0.80. M_{crit} is a function of t/c and α. The thicker the airfoil, the lower the M_{crit} (e.g., see Table 8-9). The M_{crit} has a maximum value at a specific AOA; it is reduced at all other AOAs. M_{crit} for airfoils used for high-speed aircraft can be increased by sweeping the wing forward or aft (see Chapter 9).

(4) STEP-BY-STEP: Determining M_{crit} for a Body

The M_{crit} can be determined for a body, such as an airfoil or a fuselage, by the application of the following method, based on refs. [9,82,83]:

STEP 1: Establish the Minimum Pressure Coefficient

Through theory or experiment, determine the minimum incompressible pressure coefficient, $C_{p\min}$, on the body (e.g., see Figure 8-8). For airfoils, this can be done by any of the freely (and commercially) available

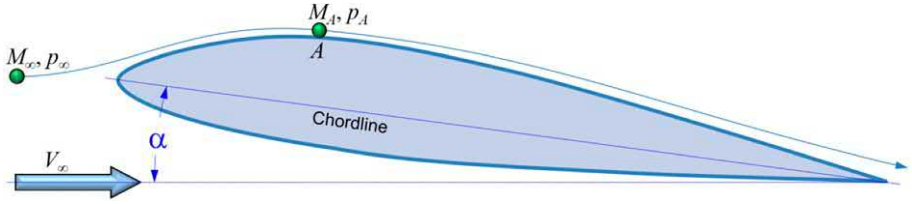


FIGURE 8-68 An airfoil immersed in airflow with the point of minimum pressure identified as Point A.

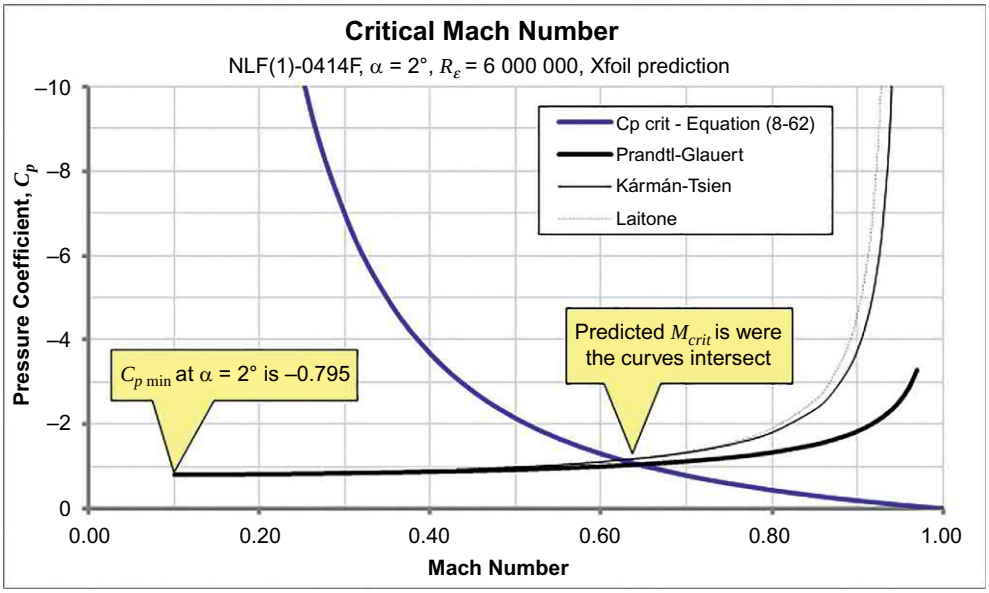


FIGURE 8-69 The critical Mach number of the NASA NLF(1)-0414F airfoil at an AOA of 2° is approximately at $M = 0.63$ to 0.65, depending on compressibility model.

computer codes cited in Section 8.1.14. Refs. [12,84] also list airspeed ratios for several NACA airfoils.

STEP 2: Select Compressibility Correction Method

Correct the $C_{p\min}$ using any of the methods presented with Equations (8-56) through (8-58). Note that Equations (8-57) and (8-58) are considered more precise than the Prandtl–Glauert method.

STEP 3: Solve to Determine M_{crit}

M_{crit} is found when the critical pressure coefficient, C_{pcrit}, calculated using the following expression equals that of the corrected $C_{p\min}$ [85,86]. C_{pcrit} is the pressure coefficient required for sonic conditions to prevail:

$$C_{p_{crit}} = \frac{2}{\gamma M_{crit}^2}\left\{\left[\frac{2}{1+\gamma}\left(1+\frac{(\gamma-1)}{2}M_{crit}^2\right)\right]^{\frac{\gamma}{\gamma-1}} - 1\right\} \quad (8\text{-}62)$$

An example of this procedure is illustrated in Figure 8-69, applied to the NASA NLF(1)-0414F airfoil in Figure 8-11.

DERIVATION OF EQUATION (8-62)

Consider the Point A on the airfoil in Figure 8-68. Denote the static pressure in the far field with p_∞ and at A using p_A. Assuming isentropic flow (adiabatic and irreversible), the pressure in the far-field and at A can be related to the total pressure as follows:

Total – to – far – field pressure ratio :

$$\frac{p_{tot}}{p_\infty} = \left[1+\frac{\gamma-1}{2}M_\infty^2\right]^{\frac{\gamma}{\gamma-1}} \quad \text{(i)}$$

Total – to – Point A pressure ratio :

$$\frac{p_{tot}}{p_A} = \left[1+\frac{\gamma-1}{2}M_A^2\right]^{\frac{\gamma}{\gamma-1}} \quad \text{(ii)}$$

Therefore, the pressure at Point A can be related to that in the far-field by dividing Equation (i) by (ii) as follows:

$$\frac{p_A}{p_\infty} = \frac{p_{tot}/p_\infty}{p_{tot}/p_A} = \frac{\left[1+\frac{\gamma-1}{2}M_\infty^2\right]^{\frac{\gamma}{\gamma-1}}}{\left[1+\frac{\gamma-1}{2}M_A^2\right]^{\frac{\gamma}{\gamma-1}}} = \left[\frac{1+\frac{\gamma-1}{2}M_\infty^2}{1+\frac{\gamma-1}{2}M_A^2}\right]^{\frac{\gamma}{\gamma-1}}$$
$$= \left[\frac{2+(\gamma-1)M_\infty^2}{2+(\gamma-1)M_A^2}\right]^{\frac{\gamma}{\gamma-1}} \quad \text{(iii)}$$

Of special interest is the case when the airspeed at Point A becomes sonic, i.e., $M_A = 1$. Then Equation (iii) can be rewritten as shown below:

$$\frac{p_A}{p_\infty} = \left[\frac{2+(\gamma-1)M_\infty^2}{2+(\gamma-1)M_A^2}\right]^{\frac{\gamma}{\gamma-1}} = \left[\frac{2+(\gamma-1)M_\infty^2}{1+\gamma}\right]^{\frac{\gamma}{\gamma-1}}$$
$$= \left[\frac{2}{1+\gamma}\left(1+\frac{(\gamma-1)}{2}M_\infty^2\right)\right]^{\frac{\gamma}{\gamma-1}} \quad \text{(iv)}$$

Inserting Equation (iii) into Equation (8-16) and renaming M_∞ as M_{crit} yields Equation (8-62).

Modern panel-codes and compressibility corrections make it easy to estimate M_{crit}. However, there are situations (e.g., early design studies) in which the airfoil is unknown. Then, one can resort to low fidelity methods to estimate a possible M_{crit}. Two examples of such methods are presented as Equations (8-63) and (8-64).

Section IV of ref. [12] provides graphs of M_{crit} for NACA airfoils. Of those, Sforza [87] presents a handy expression to estimate M_{crit} for NACA 6-series airfoils:

$$M_{crit} = 0.89 - 1.3(t/c) - kC_l \quad (8\text{-}63)$$

where k is a constant, given in Table 8-11 and C_l is a lift coefficient inside the range of design lift coefficients.

TABLE 8-11 Constant k for Equation (8-63) [87].

NACA 6-series airfoils	Constant k
NACA 63-209 to 215	0.095
NACA 63-412 to 415	0.080
NACA 64-208 to 215	0.080
NACA 64-412 to 415	0.068
NACA 65-209 to 215	0.071
NACA 65-410 to 415	0.066
NACA 66-209 to 215	0.050

Shevell [82] presents a graph of M_{crit} for peaky airfoils for t/c ranging from 0.06 to 0.16 and C_l ranging from 0 to 0.6. The graph can be approximated to within ±1% accuracy using the following expression (derived by author):

$$M_{crit} = 0.92748 - 0.24642C_l + (0.532C_l - 1.198)t/c \quad (8\text{-}64)$$

(5) Airfoil Drag Divergence Mach Number, M_{dd}

A discussion of compressibility effect on drag requires the introduction of *drag divergence* and *drag divergence Mach number*, M_{dd} (for airfoils). Generally, $M_{dd} \cong 1.02M_{crit}$. For wings, M_{dd} becomes M_{DD} and ranges from 1.02 to $1.04M_{crit}$, depending on wing sweep [82]. It is presented in Section 16.3.3. Drag divergence refers to the sudden rise of drag soon after M_{crit} is reached (see Figure 8-67). There are two common definitions used establish drag divergence: one is attributed to Boeing, the other to Douglas [88]:

Boeing definition:

$$M_{dd} = M_\infty \text{ when } C_{dw} = +0.002 \quad (8\text{-}65)$$

Douglas definition:

$$M_{dd} = M_\infty \text{ when } dC_{dw}/dM = 0.10 \quad (8\text{-}66)$$

where C_{dw} is the *wave drag coefficient*. When added to the airfoil's subsonic C_d at the same AOA, the sum constitutes the airfoil's *compressible drag coefficient*. The M_{dd} for a specific airfoil can also be estimated using *Korn's relation* [89–93],

$$M_{dd} = \kappa - t/c - 0.1C_{ldg} \quad (8\text{-}67)$$

where C_{ldg} = design lift coefficient, t/c = thickness ratio, and κ = airfoil class constant (obtained using airfoil specific CFD analyses). Refer to the above references for details. In the absence of such work, use $\kappa = 0.87$ for conventional airfoils and 0.95 for NASA-style supercritical airfoils. As an example, Korn's relation predicts $M_{dd} = 0.87 - 0.1(0.4) - 0.12 = 0.71$ for the NACA 65_1–412, while Table 8-9 states $M_{crit} = 0.697$, so $M_{dd}/M_{crit} = 1.019$. For the NACA 65_2–415, it predicts $M_{dd} = 0.68$, whereas Table 8-9 states $M_{crit} = 0.675$ (so $M_{dd}/M_{crit} = 1.007$). Note that M_{dd} for wings (referred to as M_{DD}) requires modifications of this expression, presented in Section 9.3.3.

(6) Compressibility Corrections for Drag

See Section 16.3.1.

8.3.9 Decision Matrix for Airfoil Selection

Airfoil design was introduced in Section 8.1.14. That option is not always available for low-cost design projects. Instead, the designer must resort to "catalog airfoils," such as those of refs. [12,94]. Selecting airfoils from such sources is often a challenging task, made harder when one recognizes their impact on performance, handling, structure, and weight. In some respects, the airfoil selection is a form of a multidisciplinary optimization where ideal properties conflict. For instance, thick airfoils provide structural depth and volume for fuel, but generate more drag and lower $C_{l_{max}}$. This section provides help by showing how to compile a decision matrix to help select a suitable airfoil. First, select a class of airfoils suited for the design, per Table 8-12.

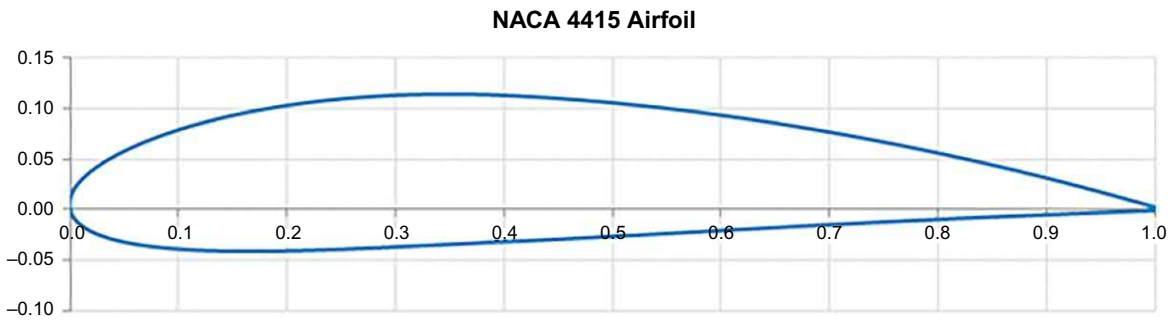
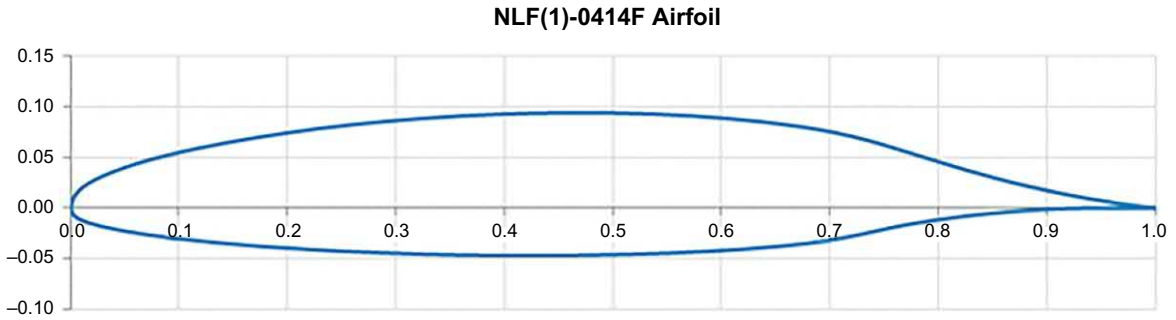
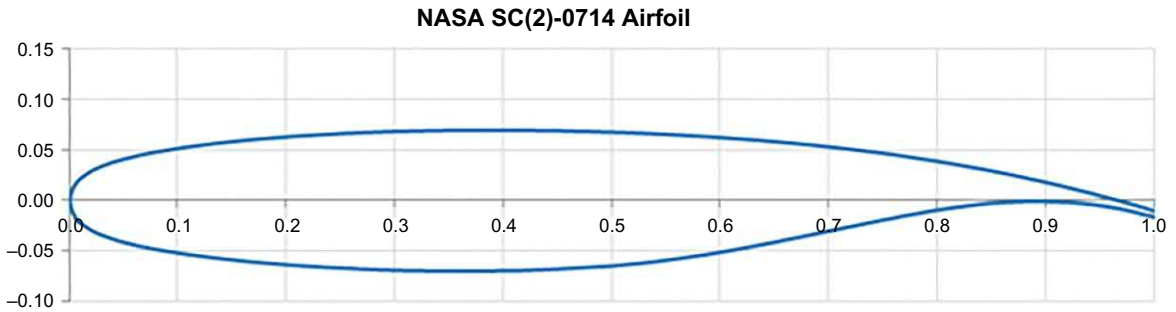
(1) Airfoil Drag

First, we must distinguish between NLF and non-NLF airfoils. We prefer an airfoil with a low $C_{d_{min}}$. However, we want that $C_{d_{min}}$ to be realized at some appropriate section lift coefficient, C_l. A more targeted selection is conducted when we know the spanwise distribution of section lift coefficients (C_l). This can be done using a panel method such as the vortex-lattice method. Consider the wing in Figure 8-70 operating in cruise at $C_L = 0.263$. We discover that, in a specific region of the wing, the range of C_l at the cruise condition is $0.27 < C_l < 0.29$. Thus, we want the $C_{d_{min}}$ of a non-NLF airfoil to occur at a C_l close to 0.28, i.e., $C_{l_{min_d}} \approx 0.28$. For an NLF airfoil, we want the C_l to be captured inside the drag bucket, preferably both during climb ($C_{l\ climb}$) and cruise ($C_{l\ cruise}$). This is illustrated in Figure 8-71. These targets must be captured by the decision matrix. A method to estimate the total drag of a wing during such studies is provided in Bullet (5) of Section 16.2.2.

(2) Airfoil Maximum Lift and Stall Characteristics

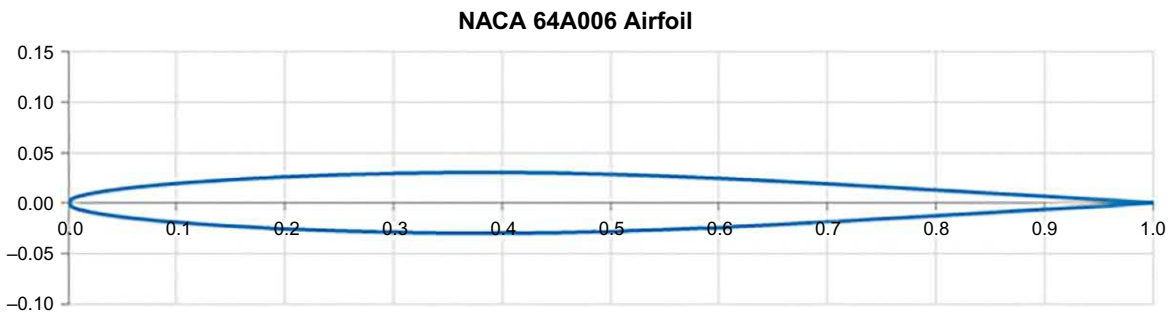
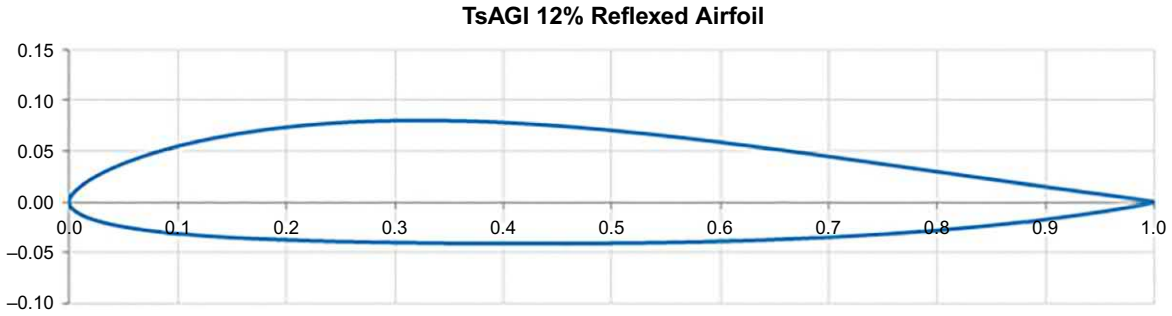
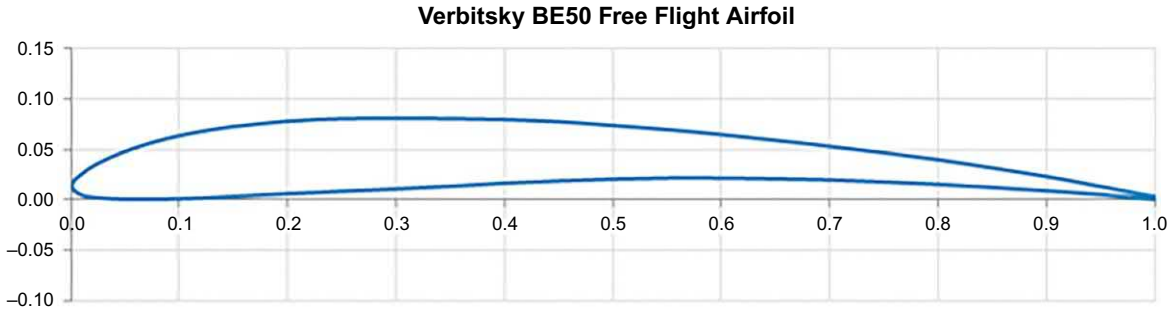
We want our airfoil to develop the highest possible $C_{l_{max}}$, while providing gentle stall behavior. However, avoid airfoils with sharp drop in C_l immediately after stall. Select lower $C_{l_{max}}$ and gentle stall over higher $C_{l_{max}}$ and abrupt stall. The sharp drop indicates a presence of a separation bubble near the leading edge on the upper surface of the airfoil, which causes a sudden drop in the C_l. This can have very serious consequences for real airplanes. Typically, it causes one wing to stall before the other, resulting in a powerful roll-off. Always place

TABLE 8-12 Match the airfoil class to the aircraft class.

Airfoil class	Aircraft class	Example
Conventional	Propeller driven aircraft, such as aerobatic aircraft, primary trainers, commuters, private, ultralights, and similar aircraft.	
Natural laminar flow (NLF)	Sailplanes, electric aircraft, medium to long range/endurance aircraft at low to medium subsonic airspeeds. Requires composite surfaces.	
Supercritical and transonics	Business jets, commercial jetliners, and similar high-subsonic jet aircraft.	

Continued

TABLE 8-12 Match the airfoil class to the aircraft class—cont'd

Airfoil class	Aircraft class	Example
Supersonic	High-speed military trainers and fighters, supersonic aircraft.	
Reflexed	Flying wings, flying planks.	
Low Reynolds number	Radio controlled and hand-launched aircraft.	

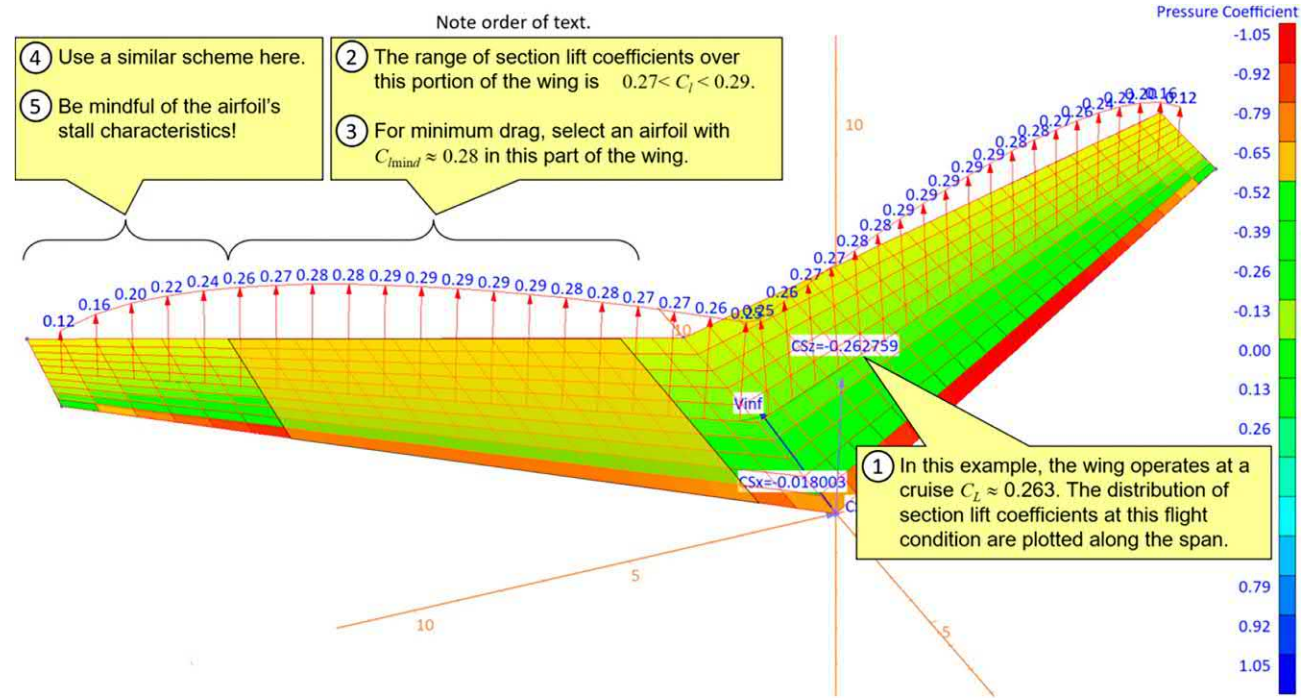


FIGURE 8-70 Selection of a region on a wing of relatively constant C_l.

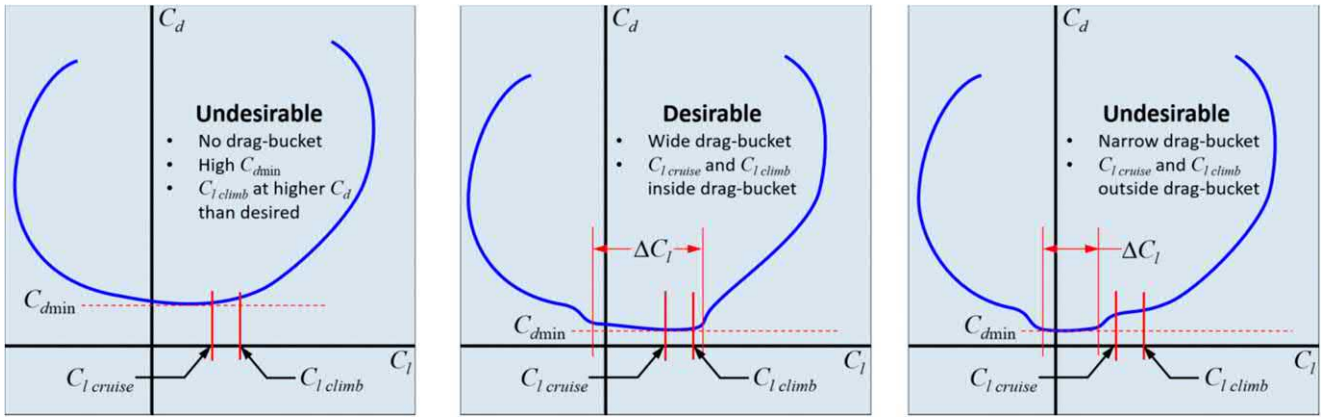


FIGURE 8-71 Characteristics of desirable and undesirable drag polars.

a great emphasis on good stall characteristics even if it means a loss of a few knots in cruise. In this capacity, it is helpful to classify airfoil stall behavior as shown in Figure 8-72. More information is presented in Section 8.1.11. The $C_{l_{max}}$ and stall characteristics must be captured by the decision matrix.

(3) Boundary Layer Transition and Flow Separation

We prefer airfoils that are insensitive to contamination and whose separation fronts are small at the trailing edge at low AOAs. The *separation front* is to a wing what a *separation point* is to an airfoil. It is a curve that forms between attached and detached flow. It grows with AOA, can extend from root to tip, and increases the drag. We want to identify airfoils that are poor in this regard in the decision matrix. *Contamination* refers to bugs and dirt that accumulates on the wing and its impact of the airfoil properties (e.g., see Figures 8-64 and 8-65.). It also trips laminar BL. NLF airfoils are sensitive to contamination.

(4) Pitching Moment

As a rule of thumb, we want our airfoil to have a low negative to zero $C_{mc/4}$ (pitching moment about the quarter chord). Our decision matrix must identify airfoils that have very negative C_m (see Figure 8-73). This is common for NLF and supercritical airfoils, whereas symmetric

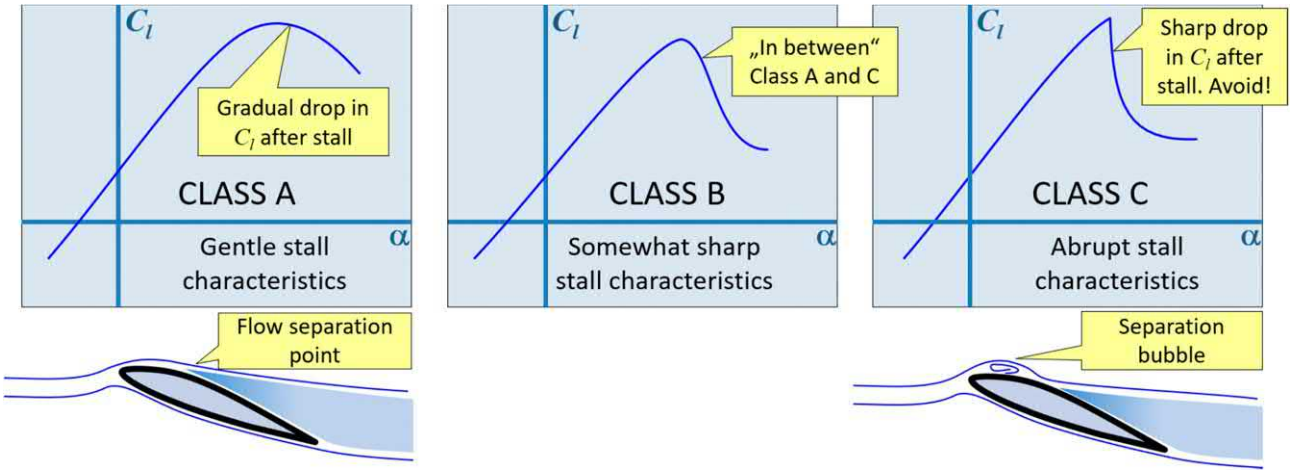


FIGURE 8-72 Classification of airfoil stall behavior.

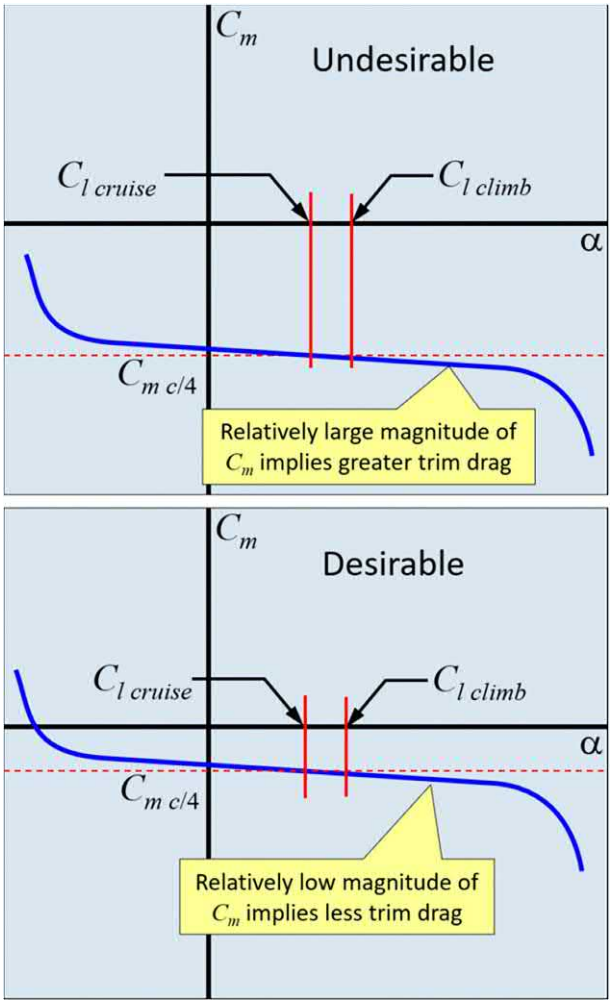


FIGURE 8-73 Characteristics of desirable and undesirable pitching moment curves.

airfoils have a zero C_m about their aerodynamic center. For airfoil selection, contribution of deployed flaps is ignored—instead, the C_m of the clean airfoil is of greater interest because this affects trim drag during cruise.

(5) Critical Mach Number

If designing an aircraft for high-subsonic airspeed, we prefer an airfoil with the highest possible M_{crit}. This falls under the umbrella of compressibility effects, discussed in Section 8.3.8. Recall that M_{crit} also varies with AOA, so comparison should be accomplished at appropriate AOA for each airfoil. Like drag, this puts an upper limit on airfoil thickness.

(6) Airfoil Thickness

A thick airfoil provides structural depth that accommodates a taller spar. Taller spar, in turn, brings down bending stresses in the spar caps and allows lighter structure with greater fuel volume. Thus, we should be biased toward a thick, rather than thin airfoils. However, $C_{d_{\min}}$ and M_{crit} put upper limit on practical thickness.

(7) Wing-Fuselage Juncture

Airflow acceleration in the wing–fuselage juncture presents challenges. The effect is twofold: (1) Acceleration to a higher airspeed means lower M_{crit}. (2) Acceleration to a higher airspeed implies air must undergo greater deceleration (pressure recovery). If the deceleration takes place over a short distance a flow separation will occur. This may even take place at a low AOA. The consequence is higher drag and impaired performance. This concern is captured in the decision matrix and is lumped in with airfoil thickness.

(8) Airfoil Efficiency Ratio

Introduced in Section 8.1.4 and is defined as $C_{l_{max}}/C_{d_{min}}$. It is used as a figure of merit in many NACA reports. The greater this ratio, the farther apart are the two parameters and, thus, one can argue, the better the airfoil. It is a worthy parameter to include in the decision matrix but should be prefaced with: *The greatest airfoil efficiency ratio that has benign stall characteristics*.

(9) Lift-to-Drag Ratio

Ideally, the maximum L/D ratio (LD_{max}) should be achieved close to the cruise AOA. Unfortunately, in practice the two AOAs are often far apart. Therefore, when considering two airfoils that offer the same LD_{max}, place a higher weight on the one whose AOA of LD_{max} is closer to the cruise AOA. A higher LD at cruise yields a more efficient aircraft.

As an example, the graphs of Figure 8-74 compare the aerodynamic properties of NACA 23015 and 65_2–415 airfoils. This allows convenient assessment of how the airfoils lift and drag curves match an assumed aircraft performance (using target cruise and climb lift coefficients). Keep in mind that the graphs superimpose C_L (3-dimensional) on C_l (2-dimensional). This is justified over selected regions of the wing, where the two are indeed close (e.g., see Figure 8-70). For instance, the cruising speed requires the lift coefficient to vary between $0.25 < C_{L_c} < 0.32$ (depending on weight) and climb lift coefficient is expected to be close to $C_{L\ climb} \approx 0.7$. Figure 8-74 shows that the cruise range resides inside the drag bucket of the NACA 65_2–415 airfoil and $C_{L\ climb}$ is much closer to its maximum l/d (ld_{max}) than that of the NACA 23015 airfoil. An airplane using the NACA 65_2–415 airfoil will be more efficient than a one using the 23015 airfoil. It can also be seen that a wing featuring the NACA 23015 airfoil must be installed at a higher angle-of-incidence than the NACA 65_2-415. Additionally, while the NACA 65_2–415 results in a slightly higher stalling speed, its stall characteristics are far more benign. The decision matrix must allow such nuances to be detected.

(10) Designing the Decision Matrix

The decision matrix is presented as Table 8-13. It contains three example airfoils whose pertinent properties have been tabulated to allow them to be scored. The data for the airfoils was obtained from ref. [12]. The designer can also add other criteria to the matrix. The airfoils may be scored by entering a "1" for a winning airfoil in the columns on the right-hand side. When a specific property of two or more airfoils are close, the user can score the worst "0," the best "1," and prorate the others. Consider if we have four airfoils with thickness ratios 0.10, 0.12, 0.14, and 0.16. Rather than scoring the first three a 0 and the last one 1, prorate the scores. Thus, t/c of 0.10 gives 0, 0.12 gives 0.333, 0.14 gives 0.667, and 0.16 gives 1. Also, use integer for lift-to-drag ratios. If ld_{max} for one airfoil is 99.6 and 100.4 for another, round-off these: both have ld_{max} of 100. It is also possible to score important properties higher than others, e.g., the max score for $C_{l_{max}}$ could be "3" while being "1" for the ideal C_m. Then, the total score for each airfoil is summed at the bottom of the table.

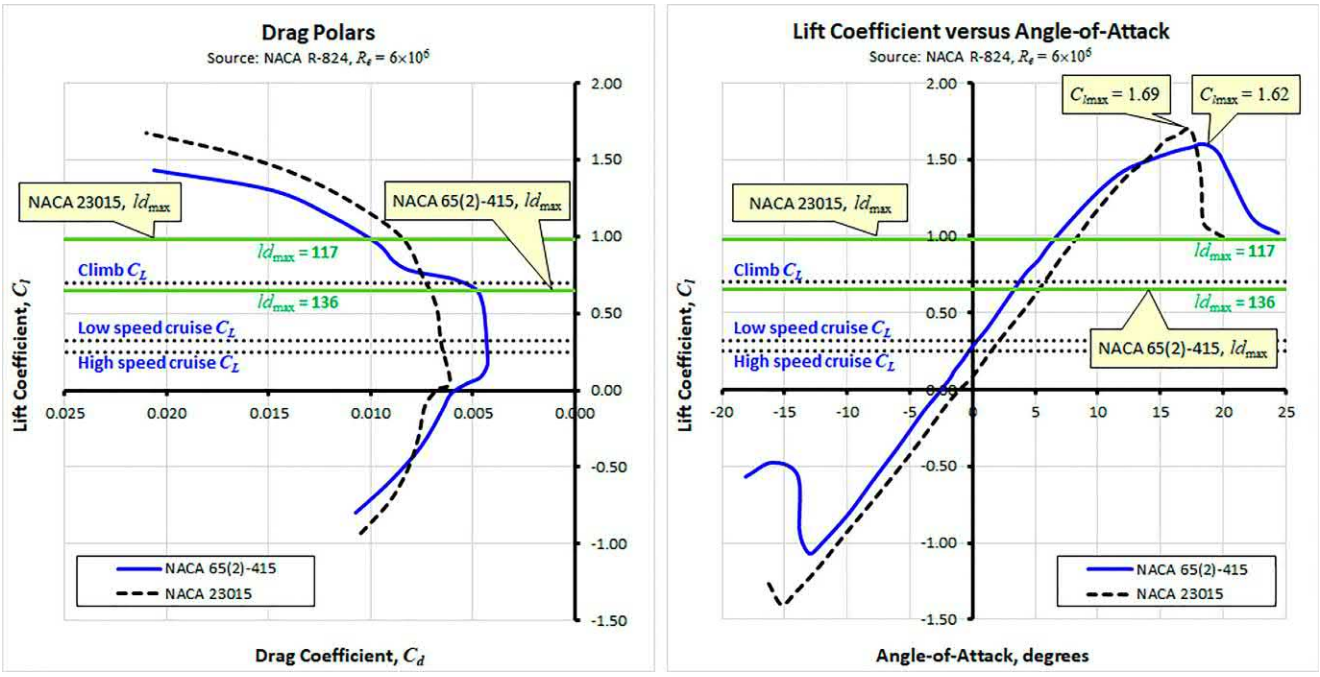


FIGURE 8-74 The aerodynamic comparison of NACA 23015 and 65_2-415 airfoils.

TABLE 8-13 Table used to down-select candidate airfoils.*

	ID	Parameter	Airfoil 1	Airfoil 2	Airfoil 3	SCORE		
	1	R_e for stall	≈ 2.4x10^6			Score of '1' indicates the top characteristic and '0' the lowest. Prorate airfoils between the two extremes. Add your own criterion and delete rows not needed. Also, modify the matrix and scoring on a need-to-basis. For instance, if high $C_{l_{max}}$ is more important than low $C_{d_{min}}$, the give it 2 or 3 points, rather than 1.		
	2	R_e for best ROC	≈ 4.1x10^6					
	3	R_e for cruise	≈ 7.5x10^6					
	4	Target $C_{L_{max}}$	1.45					
	5	C_L for best ROC, $C_{L\ ROC_{max}}$	≈ 0.70					
	6	C_L for target cruise, C_{LC}	≈ 0.3					
	7	Airfoil Name →	65_2-415	23015	747A415	1	2	3
MISC	8	Airfoil efficiency ratio ($C_{l_{max}}/C_{d_{min}}$) (high is best)	373	273	316	1	0	0.43
MISC	9	Thickness ratio (high is best)	0.15	0.15	0.15	1	1	1
STALL	10	R_e for data below →	3x10^6	3x10^6	3x10^6			
STALL	11	C_l for AOA = 0° (close to C_{LC} is best)	0.3	0.1	0.2	1	0	0.5
STALL	12	AOA for C_l = 0	-2.6°	-1.0°	-2.0°			
STALL	13	$C_{l_{max}}$ (highest is best)	1.58	1.69	1.43	0.58	1	0
STALL	14	AOA of $C_{l_{max}}$ (highest is best)	16.5°	17.4°	18.8°	0	0.39	1
STALL	15	Stall Characteristics (A, B, or C) (A is best)	A	C	A	1	0	1
CRUISE	16	R_e for data below →	6x10^6	6x10^6	6x10^6			
CRUISE	17	$C_{d_{min}}$ (lowest is best)	0.00424	0.0062	0.00453	1	0	0.85
CRUISE	18	Sensitive to surface quality? (N is better)	(Y)/N	Y/(N)	(Y)/N	0	1	0
CRUISE	19	C_l of $C_{d_{min}}$ (close to cruise is best)	0.4	0.1	0.5	1	0	0
CRUISE	20	$(C_l/C_d)_{max}$ (highest is best)	136	117	150	0.58	0	1
CRUISE	21	C_l of $(C_l/C_d)_{max}$ (low C_l is best)	0.65	0.98	0.77	1	0	0.64
CRUISE	22	Cruise C_m (low $\|C_m\|$ is best)	-0.084	-0.004	-0.038	0	1	0.575
CLIMB	23	R_e for data below →	6x10^6	6x10^6	6x10^6			
CLIMB	24	Drag bucket start at C_l	0.2	0	0.2			
CLIMB	25	Drag bucket ends at C_l	0.6	0.1	0.77			
CLIMB	26	Is $C_{L\ ROC_{max}}$ inside drag bucket?	(Y)/N	(Y)/N	(Y)/N	0	0	1
CLIMB	27	Is C_{LC} inside drag bucket?	(Y)/N	(Y)/N	(Y)/N	1	0	1
					Sum:	9.15	4.39	8.99

Stall Characteristics: A = gentle, B = between A and C, C = abrupt. *Shaded cells contain information not directly used for scoring.

The airfoil with the highest score is the one to consider, although the results may be more ambiguous than that.

(11) NACA Recommended Criteria

The conclusion section of ref. [12] lists several things to keep in mind when selecting airfoils. These are paraphrased below:

Airfoils permitting extensive laminar flow, such as the NACA 6- and 7-series, have less drag at typical cruise lift coefficients than other kinds of airfoils. However, these characteristics are realized only if the surface quality of the lifting surface is smooth. Wind tunnel tests have shown that extensive laminar flow is possible on smooth 3-dimensional wings if the surface quality is smooth and like that provided by sanding in the chordwise direction with No. 320 carborundum sandpaper.

Wings of moderate thickness ratios with such surface qualities can achieve a $C_{D_{\min}}$ of the order of 0.0080. In fact, the $C_{D_{\min}}$ depends more on the surface quality than the chosen airfoil. This way, at high Reynolds numbers where laminar flow is no longer achievable, drag can be kept low by ensuring smooth surface qualities.

The $C_{l_{max}}$ for moderately cambered 6-series airfoils are as high as those achieved using NACA 24- and 44-series airfoils. The NACA 230-series airfoils with thickness ratio less than 20% achieve the highest maximum lift coefficients. The $C_{l_{max}}$ with flaps is about the same for moderately thick 6-series airfoils as it is for the NACA 23012 with flaps. However, the thinner 6-series airfoils have substantially lower $C_{l_{max}}$ with flaps. The lift curve slope for smooth 6-series airfoils is slightly steeper than that

of the 24-, 44-, and 230-series airfoils. It exceeds the theoretical value (2π) for thin airfoils.

Leading-edge contamination (roughness) causes large reductions in $C_{l_{max}}$ for plain and flapped airfoils. The magnitude of the reduction is similar for both. The leading-edge contamination also reduces the lift curve slope, especially for thicker airfoils that have the location of minimum pressure farther aft than thinner ones. This lends support to the importance of understanding the impact of poor surface quality and leading-edge contamination on the overall characteristics of the airfoils and, thus, the performance of the aircraft when designing wings.

At typical cruise lift coefficients, NACA 6-series airfoils have higher M_{crit} than the earlier airfoil types. Conversely, their M_{crit} are lower at higher lift coefficients than are the same types of airfoils. The 6-series airfoils also offer better lift coefficients at higher Mach numbers than the earlier airfoils.

EXERCISES

(1) The purpose of this exercise is to train the student in retrieving information from available literature. Here, information from NACA R-824 will be used. It is available for download (free of charge) from the NASA Technical Report Server (http://ntrs.nasa.gov/search.jsp). Perform the following tasks for the NACA 23012 airfoil:

(a) Locate the *Station and Ordinate* table (pg. 359) and plot the airfoil assuming a wing chord of 39.4 in. (100 cm). This task can easily be accomplished using spreadsheet software like Microsoft Excel. More specifically, plot the upper, lower, and mean-lines. Also determine the x-locations of the airfoil's maximum thickness and camber.

(b) Using the graph of page 375, determine the critical Mach number (M_{crit}) of the airfoil at a lift coefficient $C_l = 0.30$.

(c) Using the graph of page 404, determine the following characteristics for a Reynolds numbers of 3 and 6 million. For the R_e of 6 million, use both the "clean" and "standard roughness" data. Determine $C_{l_{max}}$, $C_{l\alpha}$ of the linear range, "average" C_m for $\alpha < 14°$, $C_{d_{min}}$, and $C_{l_{mind}}$:

Ans: (b) 0.6, (c) for R_e of 3×10^6, $C_{l_{max}} = 1.62$, $C_{l\alpha} = 0.104$, $C_m = -0.05$, $C_{d_{min}} = 0.006$, and $C_{l_{mind}} = 0.1$.

(2) An airfoil is subjected to airspeed of 315 ft/s on a standard day at S-L, when the pressure at a specific point on it is found to be 13.3 psi. Determine the incompressible and compressible pressure coefficient, C_p using all three compressibility models of Section 8.3.8.

Ans: −1.702, −1.774, −1.840, and −1.918.

(3) Using the information about the critical Mach number obtained in Exercise (1), determine the critical pressure coefficient, $C_{p\ crit}$, of the NACA 23012 airfoil at the lift coefficient of 0.3.

Ans: −1.294.

References

[1] R.W. Fox, A.T. McDonald, P.J. Pritchard, *Introduction to Fluid Mechanics*, eighth ed., John Wiley and Sons, 2011.

[2] J.D. Anderson, *History of Aerodynamics: And Its Impact on Flying Machines*, Cambridge University Press, 1999. January 28.

[3] Source: http://wright.nasa.gov/airplane/liftold.html [Accessed on 12/29/2019].

[4] J. Delaurier, J. Harris, *An experimental investigation of the aerodynamic characteristics of stepped-wedge airfoils at low speeds*, in: 2nd International Symposium on the Technology and Science of Low Speed and Motorless Flight, AIAA, 1974, https://doi.org/10.2514/6.1974-1015.

[5] E. Lumsdaine, W.S. Johnson, L.M. Fletcher, J.E. Peach, *Investigation of the Kline-Fogleman Airfoil Section for Rotor Blade Applications*, Semi-Annual Report (AE-74-1054-1) May 1 to November 30, 1974, University of Tennessee, Knoxville, TN, 1974 (NASA CR-141282).

[6] G.B. McCullough, D.E. Gault, *Examples of Three Representative Types of Airfoil-Section Stall at Low Speed*, NACA-TN-2502, 1951, p. 1.

[7] A.M.O. Smith, High-lift aerodynamics, J. Aircr. 12 (6) (1975), https://doi.org/10.2514/3.59830.

[8] B. Thwaites, *Incompressible Aerodynamics*, Dover Publications, 1960.

[9] J.D. Anderson, Fundamentals of Aerodynamics, fourth ed., McGraw-Hill, 2007.

[10] F.A. Cleveland, *Size effects in conventional aircraft design*, J. Aircr. 7 (6) (1970), https://doi.org/10.2514/3.44204.

[11] D.E. Hoak, *USAF Stability and Control DATCOM*, Flight Control Division, Air Force Flight Dynamics Laboratory, 1978.

[12] I.H. Abbott, A.E. von Doenhoff, L.S. Stivers Jr., *Summary of Airfoil Data*, NACA R-824, 1945.

[13] Source: http://www.xflr5.tech/xflr5.htm. [Accessed on 12/29/2019].

[14] Source: https://www.mh-aerotools.de/airfoils/jf_applet.htm. [Accessed on 12/29/2019].

[15] J.D.,J. Anderson, *Introduction to Flight*, third ed., McGraw-Hill, 1989.

[16] H. Schlichting, *Boundary Layer Theory*, Pergamon Press, Ltd, 1955.

[17] A.D. Young, *Boundary Layers*, AIAA Education Series, 1989.

[18] J. Bertin, M.L. Smith, *Aerodynamics for Engineers*, Prentice-Hall, 1979, p. 95.

[19] J.J. Bertin, *Engineering Fluid Mechanics*, Prentice-Hall, 1984.

[20] A. Gopalarathnam, et al., *Design of low Reynolds number airfoils with trips*, J. Aircr. 40 (4) (2003).

[21] G.B. McCullough, D.E. Gault, *Examples of Three Representative Types of Airfoil-Section Stall at Low Speed*, NACA TN-2502, 1951.

[22] H. Riblett, *GA Airfoils – A Catalog of Airfoils for General Aviation Use*, fifth ed., 1988. Self-published.

[23] P.R. Owen, L. Klanfer, *On the Laminar Boundary Layer Separation from the Leading edge of a Thin Aerofoil*, Aeronautical Research Council C.P. No. 220, 1955.

[24] L.F. Crabtree, *The Formation of Regions of Separated Flow on Wing Surfaces*, Aeronautical Research Council R.&M. No. 3122, 1959.

[25] T. Maekawa, S. Atsumi, *Transition Caused by the Laminar-Flow Separation*, NACA TM-1352, 1952.

[26] H.P. Horton, *A Semi-Empirical Theory for the Growth and Bursting of Laminar Separation Bubbles*, Aeronautical Research Council C.P. No. 1073, 1969.

[27] M. Gaster, *The Structure and Behaviour of Laminar Separation Bubbles*, Aeronautical Research Council R.&M. No. 3595, 1969.
[28] A.K. Kundu, *Aircraft Design*, Cambridge University Press, 2010.
[29] Primarily based on. http://www.public.iastate.edu/~akmitra/aero361/design_web/airfoil_usage.htm.
[30] Source. http://www.xflr5.tech/xflr5.htm. (Accessed 20 January 2020).
[31] Source. http://www.airfoils.com/index.htm. (Accessed 20 January 2020).
[32] Source. http://aerofoilengineering.com/. (Accessed 20 January 2020).
[33] F. Meschia, *Model analysis with XFLR5*, Radio Controlled Soaring Digest 25 (2) (2008).
[34] E.N. Jacobs, K.E. Ward, R.M. Pinkerton, *The Characteristics of 78 Related Airfoil Sections from Tests in the Variable-Density Wind Tunnel*, NACA TR-460, 1933.
[35] S.F. Hoerner, *Base drag and thick trailing edges*, J. Aeronaut. Sci. 17 (10) (1950) 622–628, https://doi.org/10.2514/8.1750.
[36] S.F. Hoerner, *Fluid-Dynamic Drag*, Hoerner Fluid Dynamics, 1965.
[37] K.J. Standish, C.P. van Dam, *Aerodynamic analysis of blunt trailing edge airfoils*, ASME. J. Sol. Energy Eng. 125 (4) (2003) 479–487, https://doi.org/10.1115/1.1629103.
[38] J.P. Baker, C.P. van Dam, B.L. Gilbert, *Flatback Airfoil Wind Tunnel Experiment*, SANDIA Report, SAND2008.2008, April 2008.
[39] C.D. Harris, *NASA Supercritical Airfoils – A Matrix of Family-Related Airfoils*, NASA TP-2969, 1990.
[40] J. Stack, A.E. von Doenhoff, *Tests of 16 Related Airfoils at High Speed*, NACA TR-492, 1935.
[41] E.N. Jacobs, R.M. Pinkerton, *Tests in the Variable-Density Wind Tunnel of Related Airfoils Having the Maximum Camber Unusually Far Forward*, NACA TR-537, 1936.
[42] E.N. Jacobs, R.M. Pinkerton, H. Greenberg, *Tests of Related Forward-camber Airfoils in the Variable-density Wind Tunnel*, NACA TR-610, 1937.
[43] C.L. Ladson, C.W. Brooks Jr., *Development of a Computer Program to Obtain Ordinates for NACA 4-Digit, 4-Digit Modified, 5-Digit, and 16 Series Airfoils*, NASA TM-X-3284, 1975.
[44] J.D. Anderson Jr., *The Airplane – A History of Its Technology*, AIAA, 2002.
[45] L.K. Loftin Jr., *Theoretical and Experimental Data for a Number of NACA 6A-Series Airfoil Sections*, NACA TR-903, 1948.
[46] C.L. Ladson, C.W. Brooks Jr., *Development of a Computer Program to Obtain Ordinates for NACA-6 and 6A-Series Airfoils*, NASA TM-X-3069, 1974.
[47] C.L. Ladson, C.W. Brooks Jr., A.S. Hill, D.W. Sproles, *Computer Program to Obtain Ordinates for NACA Airfoils*, NASA TM-4741, 1996.
[48] Source. https://m-selig.ae.illinois.edu/ads/aircraft.html. (Accessed 2 February 2020).
[49] D.J. Graham, *The Development of Cambered Airfoil Sections Having Favorable Lift Characteristics at Supercritical Mach Numbers*, NACA TR-947, 1949.
[50] R.M. Pinkerton, H. Greenberg, *Aerodynamic Characteristics of a Large Number of Airfoils Tested in the Variable-Density Wind Tunnel*, NACA R-628, 1938.
[51] E.N. Jacobs, I.H. Abbott, *Airfoil Section Data Obtained in the NACA Variable-Density Tunnel as Affected by Support Interference and Other Corrections*, NACA TR-669, 1939.
[52] B.N. Daley, R.S. Dick, *Effect of Thickness, Camber, and Thickness Distribution on Airfoil Characteristics at Mach Numbers up to 1.0*, NACA TN-3607, 1956.
[53] W.F. Lindsey, D.B. Stevenson, B.N. Daley, *Aerodynamics Characteristics of 24 NACA 16-series Airfoils at Mach Numbers between 0.3 and 0.8*, NACA TN-1546, 1948.
[54] R.J. McGhee, W.D. Beasley, *Low-Speed Aerodynamic Characteristics of a 17-Percent-Thick Airfoil Section Designed for General Aviation Applications*, NASA TN D-7428, 1973.
[55] W.H. Wentz Jr., K.A. Fiscko, *Pressure Distributions for the GA(W)-2 Airfoil with 20% Aileron, 25% Slotted Flap and 30% Fowler Flap*, NASA CR-2948, 1978.
[56] M.M. Munk, E.W. Miller, *The Aerodynamic Characteristics of Seven Frequently Used Wing Sections at Full Reynolds Number*, NACA TR-233, 1927.
[57] A. Silverstein, *Scale Effect on Clark Y Airfoil Characteristics From NACA Full Scale Wind-Tunnel Tests*, NACA R-502, 1934.
[58] W.H. Wentz Jr., H.C. Seetharam, *Development of a Fowler Flap System for a High Performance General Aviation Airfoil*, NASA CR-2443, 1974.
[59] W.H. Wentz Jr., H.C. Seetharam, K.A. Fiscko, *Force and Pressure Tests of the GA(W)-1 Airfoil with a 20% Aileron and Pressure Tests with a 30% Fowler Flap*, NASA CR-2833, 1977.
[60] B.J. Holmes, *Flight Evaluation of an Advanced Technology Light Twin-Engine Airplane (ATLIT)*, NASA CR-2832, July 1977.
[61] H.R. Turner Jr., *Lift and Drag Tests of Three Airfoil Models with Fowler Flaps, Submitted by Consolidated Aircraft Corporation*, NACA WR-L-677, 1941.
[62] H.-U. Meier, *German Development of the Swept Wing 1935–1945*, AIAA, 2006.
[63] H.H. Pearcey, *Some Effects of Shock-induced Separation of Turbulent Boundary Layers in Transonic Flow past Aerofoils*, Aeronautical Research Council R.&M. No. 3108, 1955.
[64] J. Sato, *On Peaky Airfoil Sections*, NASA TT-F-749, 1973.
[65] H.H. Pearcey, *The aerodynamic design of section shapes for swept wings*, Advances Aero. Sci., Vol. 3, in: Proceedings of the 2nd International Congress on Aeronautical Science, 1962, pp. 277–322.
[66] R. Whitford, *Design for air Combat*, Jane's Publishing Company Limited, 1987.
[67] R.T. Whitcomb, L.R. Clark, *An Airfoil Shape for Efficient Flight at Supercritical Mach Numbers*, NASA TM-X-1109, 1965.
[68] Liebeck, Robert H., *Design of subsonic airfoils for high lift*, Journal of Aircraft, 1978/09/01, American Institute of Aeronautics and Astronautics. DOI:https://doi.org/10.2514/3.58406.
[69] D. Myhra, *The Horten Brothers and their all-Wing Aircraft*, Schiffer Military History Publishing, 1998.
[70] Source: http://www.nurflugel.com/Nurflugel/Fauvel/e_biograph.htm states 1904 as Charles' birthyear, while the year 1905 is stated in an article by Georges Jacquemin, which appeared in Sport Aviation, April 1962.
[71] B.H. Carmichael, *Summary of Past Experience in Natural Laminar Flow and Experimental Program for Resilient Leading Edge*, NASA CR-152276, May 1979.
[72] W. Pfenninger, *Investigations on Reduction of Friction on Wings, In Particular by Means of Boundary Layer Suction*, NACA TM-1181, 1946.
[73] R. Agarwal, F. Collier, A. Schäfer, A. Seabridge, *Green Aviation*, John Wiley & Sons, 2016.
[74] J. Granizo, *Effect of Slot Span on Wing Performance*, Master's Thesis, Embry-Riddle Aeronautical University, December 2016.
[75] M.J. Hood, *The Effects of Some Surface Irregularities on Wing Drag*, NACA TN-695, 1939.
[76] A. Ferri, *Completed Tabulation in the United States of Tests of 24 Airfoils at High Mach Numbers*, NACA WR L-143, 1945.
[77] D.J. Graham, *High-Speed Tests of an Airfoil Section Cambered to Have Critical Mach Numbers Higher Than Those Attainable With a Uniform-Load Mean Line*, NACA TN-1396, August 1947.
[78] H. Glauert, *The Effect of Compressibility on the Lift of an Aerofoil*, CXVIII, Proceedings of the Royal Society, London, 1928, pp. 113–119.
[79] D. Cohen, R.T. Jones, *High Speed Wing Theory*, Princeton University Press, 1960.
[80] E.V. Laitone, *New compressibility correction for two-dimensional subsonic flow*, J. Aeronaut. Sci. 18 (5) (1951) 350.
[81] H. Ashley, *Engineering Analysis of Flight Vehicles*, Dover Publications, 1974.

[82] R.S. Shevell, *Fundamentals of Flight*, Prentice Hall, 1983, p. 191.
[83] C.D. Perkins, R.E. Hage, *Airplane Performance, Stability, and Control*, John Wiley & Sons, 1949, pp. 59–63.
[84] H. Abbott Ira, E. Von Doenhoff Albert, *Theory of Wing Sections*, Dover, 1959.
[85] H.W. Liepmann, A. Roshko, *Elements of Gas Dynamics*, Dover Publications, 2002. January 11.
[86] J.D. Anderson Jr., *Modern Compressible Flow: With Historical Perspective*, third ed., McGraw-Hill, 2004.
[87] P.M. Sforza, *Commercial Airplane Design Principles*, Elsevier, 2014.
[88] J. Roskam, *Airplane Design, Part VI*, DARcorporation, 2000.
[89] C.W. Boppe, *Computational Aerodynamic Design: X-29, the Gulfstream Series and a Tactical Fighter*, SAE Technical Paper, SAE-851789, October 1985.
[90] C.W. Boppe, *CFD Drag Prediction for Aerodynamic Design, Technical Status Review on Drag Prediction and Analysis from Computational Fluid Dynamics: State of the Art*, AGARD AR 256, June 1989, pp. 8.1–8.27.
[91] W. Mason, *Analytic Models for Technology Integration in Aircraft Design*, AIAA 90-3262-CP, 1990, https://doi.org/10.2514/6.1990-3262.
[92] B. Malone, W. Mason, *Multidisciplinary Optimization in Aircraft Design using Analytic Technology Models*, AIAA 91-54093, 1991, https://doi.org/10.2514/6.1991-3187.
[93] S.S. Chauhan, J.R.R.A. Martins, *Low-fidelity aerostructural optimization of aircraft wings with a simplified Wingbox model using OpenAeroStruct*, in: Proceedings of the 6th International Conference on Engineering Optimization, EngOpt 2018, Springer, September 2018, https://doi.org/10.1007/978.3-319-97773-7_38.
[94] D. Althaus, *Stuttgarter Profilkatalog I*, F. Vieweg, 1981.

This page intentionally left blank

CHAPTER

9

The Anatomy of the Wing

OUTLINE

9.1 **Introduction** 322
- 9.1.1 *The Content of This Chapter* 322
- 9.1.2 *Definition of Reference Area* 322
- 9.1.3 *The Process of Wing Sizing* 322

9.2 **The Trapezoidal Wing Planform** 322
- 9.2.1 *Geometric Formulation of an Arbitrary Planform* 323
- 9.2.2 *Geometric Formulation of the Trapezoidal Planform* 324
- 9.2.3 *Geometric Formulation of a Cranked Planform* 326
- 9.2.4 *Poor Man's Determination of the MGC* 328
- 9.2.5 *Planform Dimensions in Terms of S, AR, and λ* 328
- 9.2.6 *Wing Volume Approximation* 329

9.3 **The Geometric Layout of the Wing** 330
- 9.3.1 *Wing Aspect Ratio* 331
- 9.3.2 *Wing Taper Ratio, TR or λ* 337
- 9.3.3 *Wing Sweep Angle, Λ* 338
- 9.3.4 *Dihedral and Anhedral, Γ* 340
- 9.3.5 *Wing Twist—Washout and Washin, ϕ* 340
- 9.3.6 *Wing Angle-of-Incidence, i_W* 348
- 9.3.7 *Wing Layout Properties of Selected Aircraft* 350

9.4 **Planform Selection** 350
- 9.4.1 *Methods to Present Spanwise Lift Distribution* 351
- 9.4.2 *The Optimum Lift Distribution* 352
- 9.4.3 *Constant Chord ("Hershey Bar") Planform* 354
- 9.4.4 *Elliptical Planforms* 355
- 9.4.5 *Straight-Tapered Planforms* 356
- 9.4.6 *Compound-Tapered Planforms* 357
- 9.4.7 *Swept Planforms* 357
- 9.4.8 *Cranked Planforms* 359
- 9.4.9 *Delta Planforms* 361
- 9.4.10 *Some Exotic Planform Shapes* 363

9.5 **Lift and Moment Characteristics of Wings** 363
- 9.5.1 *Properties of the 3-Dimensional Lift Curve* 364
- 9.5.2 *The Lift Model* 366
- 9.5.3 *The Zero-α Lift, C_{L_0}* 367
- 9.5.4 *The Lift Curve Slope, C_{L_α}* 367
- 9.5.5 *The Maximum Lift Coefficient, $C_{L_{max}}$* 370
- 9.5.6 *The Wing Pitching Moment Coefficient* 376
- 9.5.7 *The Lift Curve for a Delta Wing* 376
- 9.5.8 *Adding Nonlinearity to Lift Curve* 378
- 9.5.9 *The Law of Effectiveness* 379
- 9.5.10 *Flexible Wings* 379
- 9.5.11 *Ground Effect* 379
- 9.5.12 *Determination of Span Efficiency, e* 383

9.6 **Wing Stall Characteristics** 388
- 9.6.1 *Growth of Flow Separation on an Aircraft* 389
- 9.6.2 *Deviation From the Generic Stall Pattern* 389
- 9.6.3 *Tailoring the Stall Progression* 391
- 9.6.4 *Cause of Spanwise Flow for a Swept Back Wing Planform* 395
- 9.6.5 *Pitch-Up Stall Boundary for a Swept Back Wing Planform* 396
- 9.6.6 *Influence of Manufacturing Tolerances on Stall Characteristics* 398

9.7 **Prandtl's Lifting-Line Theory** 399
- 9.7.1 *Introduction* 400
- 9.7.2 *Prandtl's Lifting-Line Method—Special Case: The Elliptical Wing* 403
- 9.7.3 *Prandtl's Lifting-Line Method—Special Case: Arbitrary Wings* 405
- 9.7.4 *Computer Code: Prandtl's Lifting-Line Method* 410

Exercises 412

References 412

https://doi.org/10.1016/B978-0-12-818465-3.00009-4

Copyright © 2022 Elsevier Inc. All rights reserved.

9.1 INTRODUCTION

Now that the characteristics of airfoils have been discussed, it is time to evaluate their use in lifting surfaces. A *lifting surface* is any 3-dimensional body whose primary purpose is to generate aerodynamic lift. Of course, this is accompanied by aerodynamic drag, which is treated in Chapter 16, *Aircraft Drag Analysis*. The geometry of lifting surfaces is usually defined in terms of two 2-dimensional shapes, the *airfoil* and *planform*. This chapter focuses on the combination of the two and the resulting generation of lift. Note that even though the chapter title specifies wings, the methods presented apply equally to all lifting surfaces.

We have seen in Chapter 5, *Aircraft Structural Layout*, how the wing and stabilizing surfaces are typically constructed. A spar-rib-stringers-skin is always used for aluminum structures and spar-rib-stiffened-skin construction for composite structures. A planform shape that deviates from the shapes shown in Section 9.4, *Planform Selection*, can present serious structural challenges. If a challenging planform is chosen, it would be wise to lay out the structure early in the process and work out potential manufacturing problems, besides the aerodynamic ones. Such problems may range from limited fuel volume, space claims for retractable landing gear, high-lift system, and primary control system, curved spars, to unexpected aeroelastic issues.

The history of aviation shows that a great many combinations of airfoils and planform shapes have been devised, some with great success, others with much less so. The design team (the aerodynamics group) is responsible for ensuring that the selected airfoils and planform not only fulfill the aerodynamic goals, but also permits the requirements of other design groups to be met. Such requirements include safe handling, enough internal volume to accommodate systems, landing gear, fuel, and so on. The aero group must also recognize that any systems required to enhance lift increase manufacturing and maintenance cost, not to mention flight test risk. Of course, in the spirit of Section 4.1.3, *How to Design a Good Aircraft*, the goal should always be to select the simplest system that does the job.

9.1.1 The Content of This Chapter

- Section 9.2 presents handy geometric formulation for trapezoidal surfaces, which is the most common planform shape for lifting surfaces.
- Section 9.3 presents various concepts, topics, and methods for laying out the wing planform. These include Aspect Ratio, Taper Ratio, washout, and wing incidence angle.
- Section 9.4 is intended to help with the selection of a suitable planform shape. It introduces a variety of geometry and evaluates their pros and cons.
- Section 9.5 presents several methods to evaluate the lift and pitching moment characteristics of the wing.
- Section 9.6 presents several issues that have to do with wing stall characteristics and how to improve them.
- Section 9.7 presents Prandtl's lifting-line theory, which is a numerical method used to estimate the aerodynamic properties of the wing. A computer function, written in Visual Basic for Applications, intended for use with Microsoft Excel is presented as well.

9.1.2 Definition of Reference Area

One of the most important concepts in aircraft design (as well as in the entire discipline of aerodynamics) is the *Reference Area*. Characteristics such as lift, drag, and moment coefficients all require this area to be specified, as does performance, stability and control, and load analyses, just to name a few. The shaded areas in Figure 9-1 show how aircraft designers typically define the reference area.

Since the definition of this area takes place in the early stages of the airplane's design, it is defined in a simple manner. Thus, when the geometry gets modified later (for instance, a wingtip is reshaped), the reference area is not changed, because this would require countless documents to be revised, even certification documents. An added wingtip shape, strakes, or leading-edge extensions are typically omitted because they are often afterthoughts or added as a consequence of a wind tunnel or a flight test program (stall and spin recovery) or added features (wing tip tanks for greater range or modifications to the initial wing/fuselage fairing).

9.1.3 The Process of Wing Sizing

The concept *wing sizing* refers to the process required to determine the size, shape, and 3-dimensional positioning of the wing surfaces. This procedure is listed in Table 9-1 below.

The Establishment of a Basic Datum

It is convenient to use the leading-edge point of the wing at the plane-of-symmetry as a reference point (datum) for the rest of the aircraft. This applies to the conceptual definition of the aircraft. This datum is independent of other reference points.

9.2 THE TRAPEZOIDAL WING PLANFORM

The *trapezoidal* planform is the simplest planform shape selected for aircraft lifting surfaces. It comprises a range of geometries from the constant chord planform ("Hershey bar") to tapered planform shapes that may be

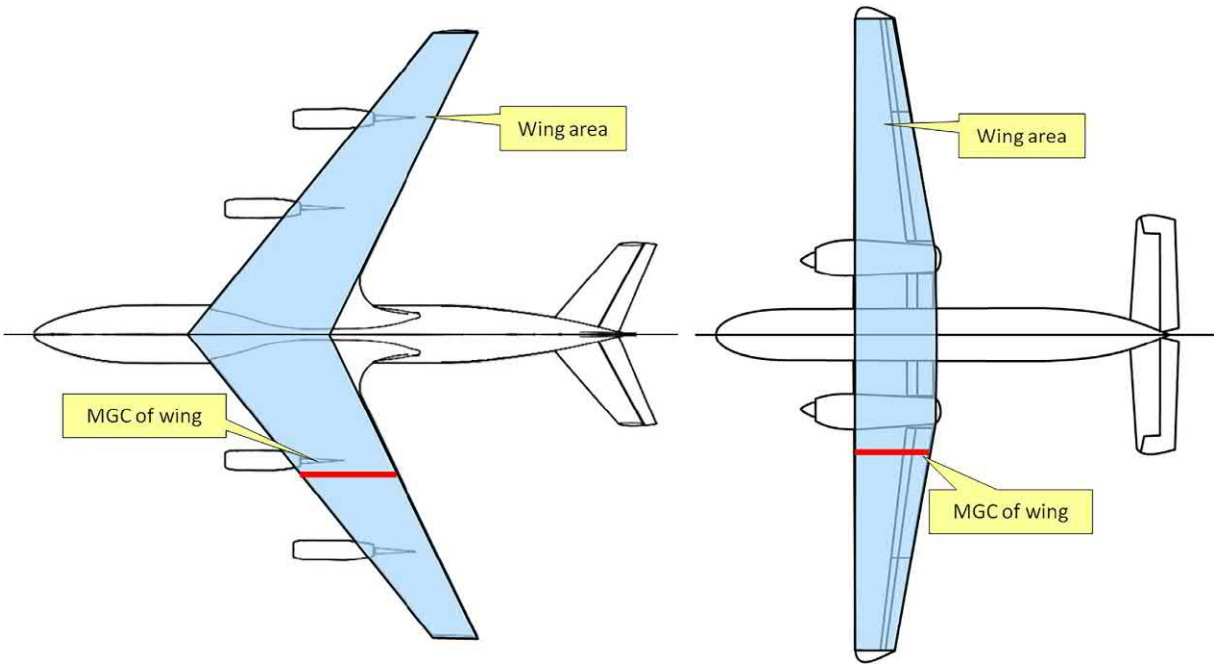


FIGURE 9-1 Reference area for the Boeing 707 and De Havilland of Canada DHC-7 Caribou (not to scale).

TABLE 9-1 Initial sizing and layout algorithm for a wing for a GA aircraft.

Step	Task	Section
1	It is assumed that the required wing area has already been determined using the constraint analysis method of Section 3.2, *Constraint Analysis*. Verify the predicted stalling speed is within regulatory margins before proceeding.	3.2
2	Select the wing planform geometry (see Section 9.4, *Planform Selection*). This may or may not be the final shape.	9.4
3	As a starting point, select a candidate *aspect ratio* (AR) and *taper ratio* (λ). This may require an optimization approach such as that presented in Section 3.4.5, *Wing Sizing Optimization by Example*. In the absence of specific target values, initial values can be selected by considering the class of aircraft being designed. For instance, refer to Table 4-2 regarding the specific class of airplanes and then Tables 9-3, and 9-4 for additional help. Alternatively, make use of Equation (9-37). These are initial values that are likely to change but are a reasonable starting point.	3.4 4.2 9.3.1 9.3.2
4	Select candidate airfoils for the root and tip. Do not assign a wing washout at this time.	Ch. 8
5	Evaluate the need for wing sweep. Will the aircraft operate at high subsonic airspeed? Is there a problem with CG location that calls for a wing sweep to solve?	9.3.3
6	Once the airplane takes shape, a more sophisticated reshaping is required, in accordance with the design algorithm of Section 1.4.1, *Conceptual Design Algorithm for a General Aviation Aircraft*. This reshaping considers performance, stability and control, structural, and systems considerations.	1.4.1

swept forward or aft. Although basic, it is important enough to warrant a specific discussion. One of the primary advantages of this geometry is the simple math that can be used to describe it. Absence of curvature or LE and TE discontinuities offers convenience when sizing the airplane and is extremely helpful when performing trade studies or during optimization.

9.2.1 Geometric Formulation of an Arbitrary Planform

Consider the arbitrary planform in Figure 9-2, confined between the *root*, *tip*, *leading edge* (LE), and *trailing edge* (TE). The x-axis is a vector in a reference plane we call the *plane-of-symmetry* (for symmetric wings). The y-axis is normal to the plane-of-symmetry. The distance between wingtips is called *wingspan* and is denoted by b. Note that Figure 9-2 only shows one halve of the complete wing. The LE and TE are defined using the functions $x_{LE}(y)=f(y)$ and $x_{TE}(y)=g(y)$, which do not have to be continuous. We define the chord per Section 8.2.1, *Airfoil Terminology*. Thus, $c(y)\equiv x_{LE}(y)-x_{TE}(y)=f(y)-g(y)$. The chord is parallel to the x-axis, while span positions are measured along the y-axis. We wish to develop formulae to calculate various properties of the planform.

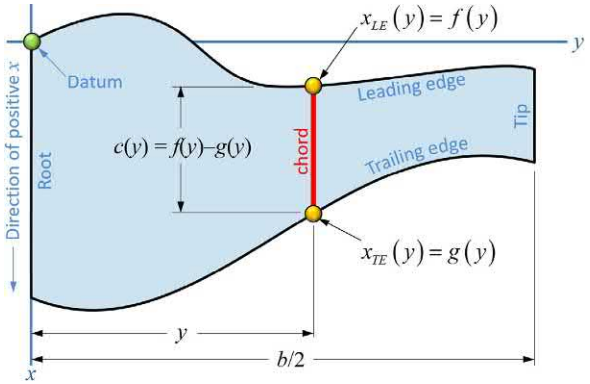


FIGURE 9-2 An arbitrary 2-dimensional planform.

The expressions that follow assume the wing is centered at the plane-of-symmetry.

Area of an asymmetric wing ($c(y)$ defined on $[-b/2, b/2]$):

$$S = \int_{-b/2}^{b/2} c(y)dy \tag{9-1}$$

Area of a symmetric wing ($c(y)$ defined on $[0, b/2]$):

$$S = 2\int_{0}^{b/2} c(y)dy \tag{9-2}$$

Aspect ratio (AR):

$$AR \equiv \frac{b^2}{S} \tag{9-3}$$

The *mean chord* is the average chord of the planform and is given by

$$\bar{c} \equiv \frac{area}{span} = \frac{2}{b}\int_{0}^{b/2} c(y)dy \tag{9-4}$$

The *mean geometric chord* (MGC or c_{MGC}) is the chord-length at the spanwise centroid of the wing.

$$c_{MGC} \equiv \frac{2}{b}\int_{0}^{b/2} c(y)dS = \frac{2}{b}\int_{0}^{b/2} c(y)^2 dy \tag{9-5}$$

The MGC is commonly referred to as *mean aerodynamic chord* (MAC). While used as a reference geometry in aerodynamics, it has NO direct relation with aerodynamics but is altogether a geometric construct. It is the chord-length at the geometric centroid of an area. For instance, if the wing is rectangular ($\lambda = 1$), then $c_{MGC} = \bar{c}$ and is located distance $b/4$ from the plane-of-symmetry—the centroid of the half-span rectangle. For a triangular wing ($\lambda = 0$) $c_{MGC} = \frac{4}{3}\bar{c}$ and is located distance $b/6$ from the plane-of-symmetry—the centroid of the half-span triangle. Figure 9-3 compares the spanwise position of the MGC and center-of-lift (which is genuinely aerodynamic in nature) with taper ratio and sweep. It shows that for $\Lambda_{c/2} = 0°$ they are not interchangeable. For $\Lambda_{c/2} = 35°$, while close over a range of λ, they are still not interchangeable. The term MAC is a legacy term and is not used in this book.

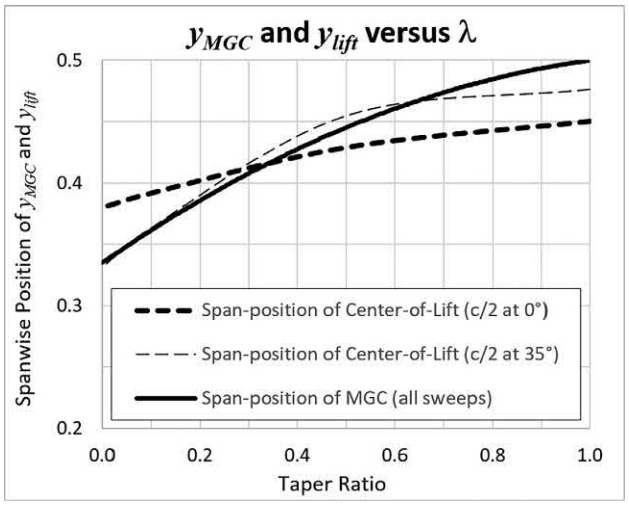


FIGURE 9-3 Do not expect to find the center-of-lift at the MGC.

The spanwise position of the MGC is denoted by y_{MGC} is given by.

$$y_{MGC} \equiv \frac{2}{S}\int_{0}^{b/2} ydS = \frac{2}{S}\int_{0}^{b/2} yc(y)dy \tag{9-6}$$

9.2.2 Geometric Formulation of the Trapezoidal Planform

Figure 9-4 shows general definitions for the trapezoidal planform. The span is denoted by b, root chord by c_r and tip chord by c_t. The term x_{MGC} is the chordwise distance from the datum to the leading edge of the MGC. The term y_{MGC} is the spanwise position of the MGC. The term *taper ratio* is a measure of the tapering of the wing and is defined as $\lambda = c_t/c_r$.

The *quarter-chord line* is drawn from a point one-fourth of the distance from the leading edge of the root-chord to a point one-fourth of the distance from the leading edge of the tip chord. It is important because 2-dimensional aerodynamic data, such as Ref. [1], frequently references the quarter-chord point for pitching moment. Additionally, this is often selected as the location of the main spar in lifting surfaces.

The *center-chord line* is obtained in a similar fashion as the quarter-chord line and is also used as a reference in scientific literature. Other important parameters are the sweep angles of the leading edge, quarter-chord, and mid-chord, denoted by Λ_{LE}, $\Lambda_{c/4}$, and $\Lambda_{c/2}$, respectively.

Considering Figure 9-4, we will now present mathematical expressions for important properties of the wing. These are derived using the formulation for arbitrary shapes:

Wing area: $$S = b\left(\frac{c_r + c_t}{2}\right) \tag{9-7}$$

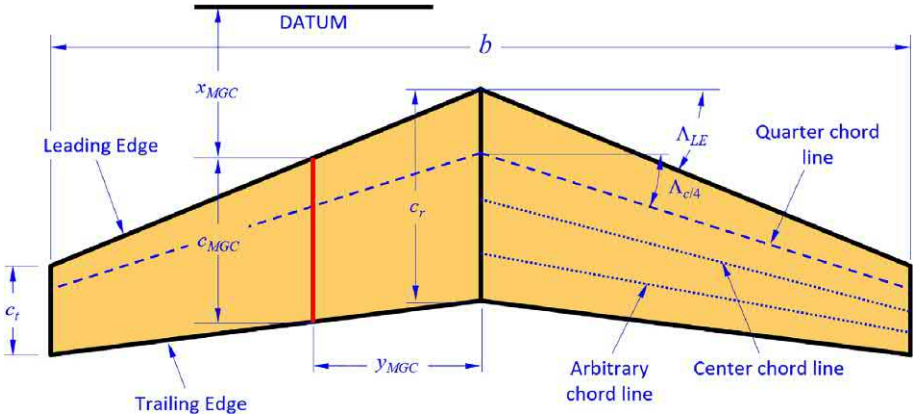


FIGURE 9-4 Fundamental definitions of a trapezoidal wing planform.

Aspect ratio — general: $AR = b^2/S$ (9-8)

Aspect ratio — constant chord: $AR = b/\bar{c}$ (9-9)

Taper ratio: $\lambda = c_t/c_r$ (9-10)

Average chord: $\bar{c} = \dfrac{c_r + c_t}{2} = \dfrac{c_r}{2}(1+\lambda)$ (9-11)

Mean Geometric Chord:

$$c_{MGC} = \left(\frac{2}{3}\right)c_r\left(\frac{1+\lambda+\lambda^2}{1+\lambda}\right) \quad (9\text{-}12)$$

Mean Aerodynamic Chord: Use expression for c_{MGC}

Y-location of MGC: $y_{MGC} = \left(\dfrac{b}{6}\right)\left(\dfrac{1+2\lambda}{1+\lambda}\right)$ (9-13)

X-location LE of MGC: $x_{MGC} = y_{MGC}\tan\Lambda_{LE}$ (9-14)

Angle of quarter-chord line:

$$\tan\Lambda_{c/4} = \tan\Lambda_{LE} + \frac{c_r}{2b}(\lambda - 1) \quad (9\text{-}15)$$

Angle of an arbitrary chord – line:

$$\tan\Lambda_n = \tan\Lambda_m - \frac{4}{AR}\left[(n-m)\frac{1-\lambda}{1+\lambda}\right] \quad (9\text{-}16)$$

Equation (9-16) is obtained from Ref. [1], where m and n are chordwise fractions of the chord line (0.25 for quarter-chord, 0.5 for the center-chord line, etc.) and m is the fraction for a known angle, and n for the unknown angle (see Example 9-1 for example of use).

(1) Aspect Ratio for HT and VT

The AR for a *horizontal tail* (HT) is calculated exactly as it is for the wing. The AR for the *vertical tail* (VT) is calculated using the following expression:

$$AR_{VT} = b_{VT}^2/S_{VT} \quad (9\text{-}17)$$

Where:

b_{VT} = Height of the VT from its base to tip, in ft or m.

S_{VT} = Area of the VT, in ft^2 or m^2.

The AR for a twin tail is calculated by applying Equation (9-17) to one tail only, where S_{VT} refers to one half the total area of the VT.

(2) Aspect Ratio for Multiwing Configurations

The AR for multiwing aircraft, such as biplanes and triplanes, is given by.

Aspect ratio for a biplane: $AR_{biplane} = \dfrac{2b^2_{\text{larger wing}}}{S}$ (9-18)

Aspect ratio for a triplane: $AR_{triplane} = \dfrac{3b^2_{\text{largest wing}}}{S}$ (9-19)

These approximate the AR of the largest wing. See more about the *equivalent monoplane aspect ratio* (EMAR) for biplanes in Appendix C.

DERIVATION OF EQUATIONS (9-12), (9-13), AND (9-15)

Equation (9-12): Obtained using Equations (9-5) and (9-34), where $c(y) = c_r(1+(\lambda-1)t) = c_r(1+2(\lambda-1)y/b)$.

Equation (9-13): Obtained using Equations (9-6), (9-7), and (9-34), where $c(y) = c_r(1+2(\lambda-1)y/b)$.

Equation (9-15): Refer to Figure 9-5 to define the dimensions a, $b/2$, c, d, and h.

$$\Rightarrow h = \underbrace{\frac{b}{2}\tan\Lambda_{LE}}_{d} + \underbrace{\frac{\lambda c_r}{4}}_{c} - \underbrace{\frac{c_r}{4}}_{a}$$

$$= \frac{1}{2}b\tan\Lambda_{LE} + \frac{1}{4}\lambda c_r - \frac{1}{4}c_r$$

$$\Rightarrow h = \frac{1}{2}\left[b\tan\Lambda_{LE} + \frac{1}{2}\lambda c_r - \frac{1}{2}c_r\right] = \frac{1}{2}\left[b\tan\Lambda_{LE} + \frac{1}{2}c_r(\lambda-1)\right]$$

$$\Rightarrow \tan\Lambda_{c/4} = \frac{h}{b/2} = \frac{\left[b\tan\Lambda_{LE} + \frac{1}{2}c_r(\lambda-1)\right]}{b}$$

$$= \tan\Lambda_{LE} + \frac{c_r}{2b}(\lambda-1)$$

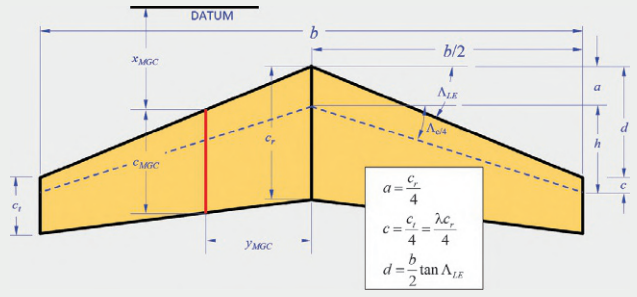


FIGURE 9-5 Deriving the quarter-chord angle.

9.2.3 Geometric Formulation of a Cranked Planform

In aviation, the term *cranked* refers to something broken or discontinuous. Thus, a cranked wing refers to a planform featuring a discontinuous leading and (or) trailing edge (see Figure 9-7). Such geometry is common in aircraft, as reflected in aircraft manufactured by Cessna and Piper, not to mention business and commercial jetliners. Here, a *simple leading and trailing-edge break* will be presented. A simple break means the LE and TE discontinuity occurs at the same span-station.

In addition to root chord (c_r) and tip chord (c_t), we define the chord at the break as c_b, the inboard chord as

EXAMPLE 9-1

Determine the primary characteristics of the trapezoidal wing shown in Figure 9-6. Also calculate the angle of the center-chord line using Equation (9-16).

SOLUTION:

Wing area: $S = b\left(\frac{C_r + C_t}{2}\right) = (10)\left(\frac{2+1}{2}\right) = 15\,\text{ft}^2$

Aspect ratio—general:

$$AR = b^2/S = 10^2/15 = 6^2/_3 \approx 6.667$$

Taper ratio: $\lambda = c_t/c_r = 0.5$

Mean Geometric Chord:

$$c_{MGC} = \left(\frac{2}{3}\right)c_r\left(\frac{1+\lambda+\lambda^2}{1+\lambda}\right) = \left(\frac{2}{3}\right)(2)\left(\frac{1+0.5+0.5^2}{1+0.5}\right)$$
$$= 1^5/_9\,\text{ft} \approx 1.556\,\text{ft}$$

y-location of MGC_{LE}:

$$y_{MGC} = \left(\frac{b}{6}\right)\left(\frac{1+2\lambda}{1+\lambda}\right) = \left(\frac{10}{6}\right)\left(\frac{1+2\times 0.5}{1+0.5}\right)$$
$$= 2^2/_9\,\text{ft} \approx 2.222\,\text{ft}$$

x-location of MGC_{LE}:

$$x_{MGC} = y_{MGC}\tan\Lambda_{LE} = \left(2^2/_9\right)\tan(30°) \approx 1.283\,\text{ft}$$

Angle of the quarter-chord line:

$$\tan\Lambda_{c/4} = \tan\Lambda_{LE} + \frac{c_r}{2b}(\lambda - 1) = \tan(30) + \frac{2}{2(10)}(0.5-1)$$
$$\approx 0.5274 \;\Rightarrow\; \Lambda_{C/4} \approx 27.8°$$

Angle of the center-chord line using the quarter-chord line ($m = 0.25$, $n = 0.50$) is obtained from Equation (9-16):

$$\tan\Lambda_n = \tan\Lambda_m - \frac{4}{AR}\left[(n-m)\frac{1-\lambda}{1+\lambda}\right]$$

Substituting the given values, we get:

$$\tan\Lambda_{0.50c} = \tan\Lambda_{0.25c} - \frac{4}{6.667}\left[(0.50-0.25)\frac{1-0.5}{1+0.5}\right]$$
$$= 0.4772 \;\Rightarrow\; \Lambda_{0.50C} = 25.5°$$

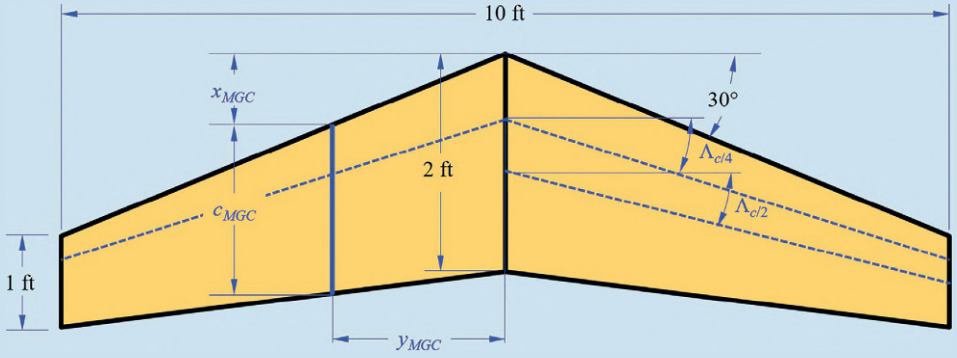


FIGURE 9-6 The wing geometry.

c_i, and outboard chord as c_o, both as functions of spanwise station (y). The break occurs at span-station y_b. Then, we present the following formulation for the wing geometry. It applies to any inboard and outboard taper ratios. Determine y_{MGC} first and use it to calculate c_{MGC}.

Wing area: $$S=(c_r-c_t)y_b+(c_b+c_t)b/2 \tag{9-20}$$

Aspect ratio — general: $$AR=\frac{2b^2}{2(c_r-c_t)y_b+(c_b+c_t)b} \tag{9-21}$$

Taper ratio: $$\lambda=c_t/c_r \tag{9-22}$$

Inboard chord: $$c_i(y)=c_r+\left(\frac{c_b-c_r}{y_b}\right)y \quad 0\le y\le y_b \tag{9-23}$$

Outboard chord: $$c_o(y)=c_b+\left(\frac{c_t-c_b}{b/2-y_b}\right)(y-y_b)$$

$$y_b<y\le\frac{b}{2} \tag{9-24}$$

$y-$location of MGC: $$y_{MGC}=\frac{2}{S}[A+B+C+D] \tag{9-25}$$

where

$$a=\frac{c_t-c_b}{b/2-y_b} \qquad A=\frac{1}{2}(c_r-c_b)y_b^2 \qquad B=\frac{1}{3}\left\{\frac{(c_b-c_r)}{y_b}+\frac{1}{2}a\right\}y_b^3$$
$$C=\frac{1}{2}\{c_b-ay_b\}\left(\frac{b}{2}\right)^2 \qquad D=\frac{1}{3}a\left(\frac{b}{2}\right)^3 \tag{9-26}$$

Mean Geometric Chord:

$$\text{if } y_{MGC}\le y_b \Rightarrow c_{MGC}=c_r+(c_b-c_r)\frac{y_{MGC}}{y_b}$$
$$\text{if } y_{MGC}>y_b \Rightarrow c_{MGC}=c_b+\left(\frac{c_t-c_b}{b/2-y_b}\right)(y_{MGC}-y_b) \tag{9-27}$$

DERIVATION OF EQUATION (9-25)

Refer to Figure 9-7 for all dimensions. Using the mathematical definition of a *centroid of an area*, we substitute the appropriate geometric parameters and get

$$\bar{y}=y_{MGC}=\frac{2}{S}\int y\,dS=\frac{2}{S}\left[\int y\,dS_i+\int y\,dS_o\right]$$
$$=\frac{2}{S}\left[\int yc_i(y)dy+\int yc_o(y)dy\right]$$
$$=\frac{2}{S}\left[\int_0^{y_b}\left(c_r y+\frac{(c_b-c_r)}{y_b}y^2\right)dy+\int_{y_b}^{b/2}\left(c_b y+\frac{(c_t-c_b)}{b/2-y_b}(y^2-y_b y)\right)dy\right]$$

Then, evaluating the integrals and substituting the integration limits, we get the spanwise position of the MGC:

$$\Rightarrow\ y_{MGC}=\frac{2}{S}\left[\left[\frac{1}{2}c_r y^2+\frac{(c_b-c_r)}{3y_b}y^3\right]_0^{y_b}+\left[\frac{1}{2}c_b y^2+\frac{(c_t-c_b)}{b/2-y_b}\left(\frac{1}{3}y^3-\frac{1}{2}y_b y^2\right)\right]_{y_b}^{b/2}\right]$$
$$=\frac{2}{S}\left[\frac{1}{2}(c_r-c_b)y_b^2+\frac{1}{3}\left\{\frac{(c_b-c_r)}{y_b}+\frac{1}{2}\frac{(c_t-c_b)}{b/2-y_b}\right\}y_b^3+\frac{1}{2}\left\{c_b-\frac{(c_t-c_b)}{b/2-y_b}y_b\right\}\left(\frac{b}{2}\right)^2+\frac{1}{3}\frac{(c_t-c_b)}{b/2-y_b}\left(\frac{b}{2}\right)^3\right]$$

An inspection of the coefficients allows further simplification:

$$a=\frac{c_t-c_b}{b/2-y_b}$$
$$A=\frac{1}{2}(c_r-c_b)y_b^2 \qquad B=\frac{1}{3}\left\{\frac{(c_b-c_r)}{y_b}+\frac{1}{2}a\right\}y_b^3$$
$$C=\frac{1}{2}\{c_b-ay_b\}\left(\frac{b}{2}\right)^2 \qquad D=\frac{1}{3}a\left(\frac{b}{2}\right)^3 \Rightarrow\ y_{MGC}=\frac{2}{S}[A+B+C+D]$$

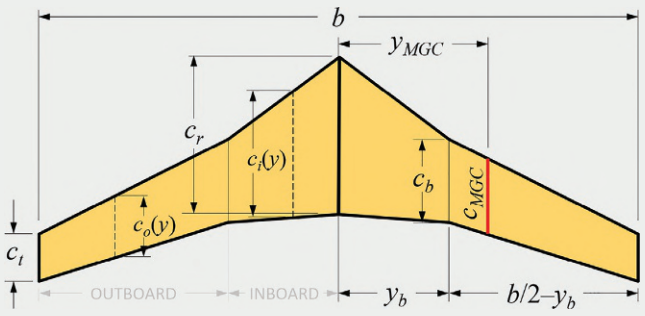


FIGURE 9-7 Fundamental definitions of a cranked wing planform.

EXAMPLE 9-2

Determine the y_{MGC} and c_{MGC} for the cranked wing in Figure 9-8.

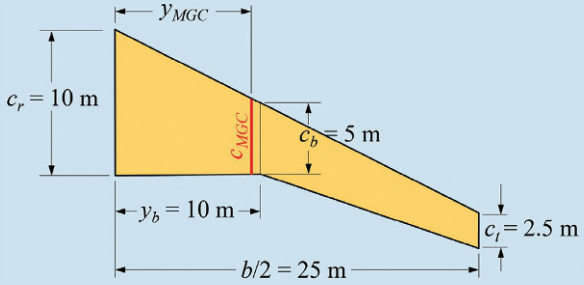


FIGURE 9-8 One half of a cranked wing planform.

SOLUTION:

First, calculate wing area:

$$S=(c_r-c_t)y_b+(c_b+c_t)b/2$$
$$=(10-2.5)(10)+(5+2.5)(25)=262.5\ \text{m}^2$$

Next, calculate parameters a, A, B, C, and D.

EXAMPLE 9-2 *(cont'd)*

$$a=\frac{c_t-c_b}{b/2-y_b}=\frac{2.5-5}{25-10}=-\frac{1}{6} \qquad A=\frac{1}{2}(c_r-c_b)y_b^2=250\ \text{m}^3$$

$$B=\frac{1}{3}\left\{\frac{(c_b-c_r)}{y_b}+\frac{1}{2}a\right\}y_b^3=-194.44\ \text{m}^3$$

$$C=\frac{1}{2}(c_b-ay_b)\left(\frac{b}{2}\right)^2=2083.3\ \text{m}^3 \qquad D=\frac{1}{3}a\left(\frac{b}{2}\right)^3=-868.06\ \text{m}^3$$

Substitute into Equation (9-25) to get:

$$y_{MGC}=\frac{2}{S}[A+B+C+D]=9.683\ \text{m}$$

Use Equation (9-27) to determine the c_{MGC} at that wing station:

$$y_{MGC}\le y_b \;\Rightarrow\; c_{MGC}=c_r+(c_b-c_r)y_{MGC}/y_b$$
$$=10+(5-10)(9.683/10)$$
$$=5.159\ \text{m}$$

9.2.4 Poor Man's Determination of the MGC

When a calculator is absent, the designer can determine the c_{MGC} and y_{MGC} using the graphical scheme in Figure 9-9. It is important to remember that such graphical tools are relics of a bygone era and, at best, are what the slide-rule is to the modern calculator—results from a digital calculator should always take precedence.

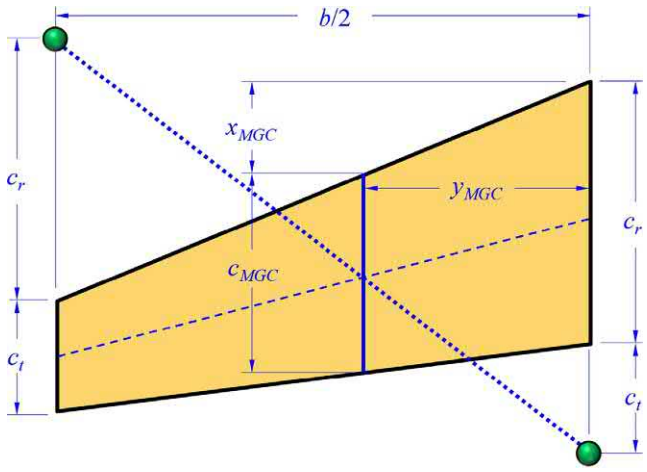


FIGURE 9-9 Graphical scheme to determine the MGC for a simple trapezoidal planform.

9.2.5 Planform Dimensions in Terms of S, AR, and λ

During the design phase, the basic dimensions of the wing (b, c_r, and c_t) are sometimes defined by S, AR, and λ as governing variables. This is convenient because these parameters can tell the designer a lot about the aerodynamic properties of the wing. With the wing parameters defined in this fashion, use the following formulation to determine the required wing span, root chord, and tip chord of a simple-tapered planform like the one in Figure 9-10. These are based on Equations (9-2), (9-3), and (9-10):

$$\text{From } AR=b^2/S \quad\Rightarrow\quad b=\sqrt{AR\cdot S} \tag{9-28}$$

$$\text{From } AR=b/\bar{c} \quad\Rightarrow\quad \bar{c}=\frac{1}{2}(c_r+c_t)=b/AR \tag{9-29}$$

$$\text{Average chord:}\quad \bar{c}=\frac{1}{2}(c_r+c_t)=\frac{1}{2}c_r(1+\lambda)=S/b \tag{9-30}$$

$$\text{From } 2\bar{c}=2b/AR=c_r(1+\lambda) \quad\Rightarrow\quad c_r=\frac{2b}{(1+\lambda)AR} \tag{9-31}$$

$$\text{From } 2\bar{c}=2S/b=c_r(1+\lambda) \quad\Rightarrow\quad c_r=\frac{2S}{(1+\lambda)b} \tag{9-32}$$

Mean Geometric Chord:

$$c_{MGC}=\left(\frac{4b}{3AR}\right)\left(\frac{1+\lambda+\lambda^2}{1+2\lambda+\lambda^2}\right) \tag{9-33}$$

Chord for a straight-tapered wing:

$$c(y)=c_r\left(1+\frac{2(\lambda-1)}{b}y\right) \tag{9-34}$$

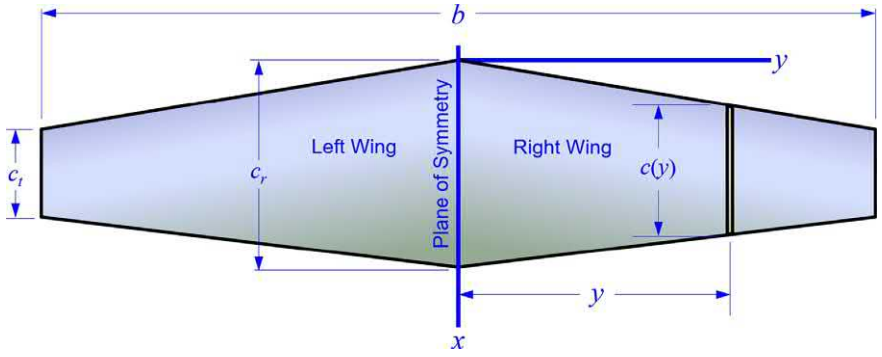


FIGURE 9-10 A simple-tapered planform.

DERIVATION OF EQUATION (9-33)

Using Equation (9-31), we can calculate the root chord, c_r, using any set of values for the wingspan, b, and AR:

$$C_r = \frac{2b}{(1+\lambda)AR}$$

We then insert this into Equation (9-12) and manipulate as follows:

$$\begin{aligned} C_{MGC} &= \left(\frac{2}{3}\right) C_r \left(\frac{1+\lambda+\lambda^2}{1+\lambda}\right) \\ &= \left(\frac{2}{3}\right)\left(\frac{2b}{(1+\lambda)AR}\right)\left(\frac{1+\lambda+\lambda^2}{1+\lambda}\right) \\ &= \left(\frac{4b}{3AR}\right)\left(\frac{1+\lambda+\lambda^2}{1+2\lambda+\lambda^2}\right) \end{aligned}$$

DERIVATION OF EQUATION (9-34)

Parametric formulation of $c(y)$ for a straight-tapered wing whose taper ratio is λ, root chord c_r, and span is b is obtained by inserting the geometric parameters as follows (where the parameter t is $2y/b$ and ranges from 0 to 1):

$$\begin{aligned} c(y) &= c_r(1-t) + \lambda c_r t = c_r\left(1 - \frac{2y}{b}\right) + \lambda c_r \frac{2y}{b} \\ &= c_r\left[1 - \frac{2y}{b} + \lambda\frac{2y}{b}\right] = c_r\left(1 + \frac{2(\lambda-1)}{b}y\right) \end{aligned}$$

9.2.6 Wing Volume Approximation

The internal volume of the wing is evaluated to assess available fuel volume. This requires the cross-sectional area of the airfoil ($A_{airfoil}$) to be determined. In the absence of precise airfoil data, the two following approximations can be used to approximate the internal area of an airfoil:

$$A_{airfoil} = \begin{cases} \frac{1}{6}(k+3)c \cdot t \\ \frac{1}{6}(k+3)(t/c)c^2 \end{cases} \qquad (9\text{-}35)$$

Where: k is the location of the airfoil's maximum thickness a fraction of c (e.g. 0.3) and t is the airfoil's physical thickness (e.g. 15 cm).

The upper equation assumes thickness is known, while the lower assumes the thickness-to-chord ratio (t/c) is known (using the product $(t/c)\cdot c$). Once the cross-sectional area is known, the volume of interest can be estimated by integration along the tapered wing, using the parameters shown in Figure 9-11. Note it may be handy to recall the conversion factors $1\,\text{US gal} = 231.02\,\text{in}^3$ or $1\,\text{US gal} = 3.785412\,\text{L} = 3785.412\,\text{cm}^3$.

$$\forall = \frac{(k+3)}{6}\left(\frac{t}{c}\right)\left[A(b_2-b_1) + \frac{1}{2}B(b_2-b_1)^2 + \frac{1}{3}C(b_2-b_1)^3\right] \qquad (9\text{-}36)$$

Where the constants A, B, and C are given by

$$A = c_1^2 - 2b_1\left(\frac{c_1c_2 - c_1^2}{b_2-b_1}\right) + b_1^2\left(\frac{c_2-c_1}{b_2-b_1}\right)^2,$$

$$B = 2\left[\left(\frac{c_1c_2-c_1^2}{b_2-b_1}\right) - b_1\left(\frac{c_2-c_1}{b_2-b_1}\right)^2\right], \qquad C = \left(\frac{c_2-c_1}{b_2-b_1}\right)^2$$

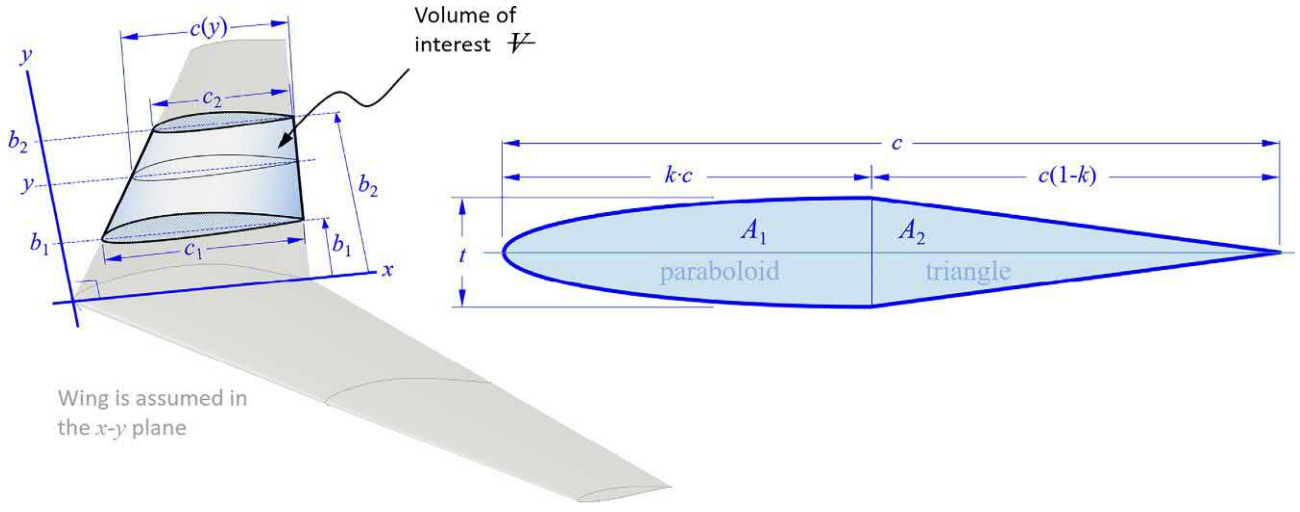


FIGURE 9-11 An approximation of a wing volume using elementary geometry.

DERIVATION OF EQUATIONS (9-35) AND (9-36)

Consider Figure 9-11, which shows an airfoil of chord c approximated by a parabolic D-cell and a triangular section. The two sections join at the location of maximum thickness (t). The chordwise position of t is given by $k \cdot c$, where k is a fraction of c (e.g., if t is at mid-chord, then $k = 0.5$). The cross-sectional areas of the two sections and the total area are given by the following expressions:

Parabolic section: $$A_1 = \frac{2}{3} k \cdot c \cdot t \quad \text{(i)}$$

Triangular section: $$A_2 = \frac{1}{2} c \cdot (1-k) t \quad \text{(ii)}$$

Therefore, the internal area of the airfoil can be approximated by adding the two as shown below:

$$A_{airfoil} = A_1 + A_2 = \frac{2k \cdot c \cdot t}{3} + \frac{c \cdot (1-k) t}{2} = \frac{(k+3) c \cdot t}{6}$$

This is the upper result shown. Then, multiply by c/c (=1) to get the lower expression. Equation (9-36) uses the lower expression of Equation (9-35) and assumes the chord variation along the span is expressed using the parametric form: $c(y) = c_1 + (c_2 - c_1)\frac{y-b_1}{b_2-b_1}$. This is integrated along the span as follows:

$$\forall = \int_{b_1}^{b_2} \frac{(k+3)}{6} \left(\frac{t}{c}\right) c^2 dy$$

$$= \frac{(k+3)}{6} \left(\frac{t}{c}\right) \int_{b_1}^{b_2} \left(c_1 + (c_2 - c_1)\frac{y-b_1}{b_2-b_1}\right)^2 dy$$

Expansion and integration, followed by some algebra leads to Equation (9-36) and the associated constants A, B, and C. It is easy to show that for a constant chord wing, these coefficients become $A = c^2$ and $B = C = 0$.

EXAMPLE 9-3 WING VOLUME

A wing is to be designed such that $S = 130\,\text{ft}^2$, $\lambda = 0.5$, and $AR = 8$. Determine the resulting wingspan, root chord, and tip chord. Also determine the total fuel we can fit between wing-stations $y = 5$ ft and 10 ft (in US gal). Assume the fuel tank is confined between the main-spar and shear-web, allowing about 30% of the available volume. Assume an airfoil with $t/c = 0.15$ and $k = 0.3$. How many lb_f will the fuel weigh if this is Avgas ($6\,\text{lb}_\text{f}$/US gal)?

SOLUTION:

Wingspan: $AR = b^2/S \Rightarrow b = \sqrt{AR \cdot S}$

$$= \sqrt{(8) \cdot (130)} = 32.25 \text{ ft}$$

Wing root chord:

$$c_r = 2S/b(1+\lambda) = 2(130)/(32.25)(1+0.5) = 5.375 \text{ ft}$$

Wing tip chord: $c_t = \lambda c_r = 0.5(5.375) = 2.687$ ft

Using the parameter notation in Figure 9-11 and Equation (9-34), we get $b_1 = 5$ ft and $b_2 = 10$ ft. Thus,

$$c_1 = c(5) = c_r\left(1 + \frac{2(\lambda-1)}{b} b_1\right) = 4.542 \text{ ft and}$$

$$c_2 = c(10) = c_r\left(1 + \frac{2(\lambda-1)}{b} b_2\right) = 3.708 \text{ ft}$$

Where the constants A, B, and C are given by

$$A = c_1^2 - 2b_1\left(\frac{c_1 c_2 - c_1^2}{b_2 - b_1}\right) + b_1^2\left(\frac{c_2 - c_1}{b_2 - b_1}\right)^2 = 28.89 \text{ ft}^2$$

$$B = 2\left[\left(\frac{c_1 c_2 - c_1^2}{b_2 - b_1}\right) - b_1\left(\frac{c_2 - c_1}{b_2 - b_1}\right)^2\right] = -1.792 \text{ ft}$$

$$C = \left(\frac{c_2 - c_1}{b_2 - b_1}\right)^2 = 0.02778$$

Thus, the total volume per wing is

$$\forall = \frac{(k+3)}{6}\left(\frac{t}{c}\right)\left[A(b_2-b_1) + \frac{1}{2}B(b_2-b_1)^2 + \frac{1}{3}C(b_2-b_1)^3\right]$$
$$= 10.16 \text{ ft}^3$$

Total volume in two wing-halves is $20.33\,\text{ft}^3 = 35{,}130\,\text{in}^3$. Since only 30% of this is available for fuel, the total fuel quantity and weight is (using the conversion factor given earlier)

$$Q_{fuel} = 0.3\frac{2\forall}{231.02} = 0.3\frac{2(10.16)}{231.02} = 45.62 \text{ US gal}$$

$$W_{fuel} = 273.7 \text{ lb}_\text{f}$$

9.3 THE GEOMETRIC LAYOUT OF THE WING

The geometric layout of the wing refers to properties such as the aspect ratio, taper ratio, wing sweep, dihedral, and others. It has a major impact on the design, affecting most areas of development: aerodynamics, performance, stability and control, structures, and systems layout, to name a few. The layout constitutes the establishment of the geometric properties presented in Table 9-2.

Of these, the AR, TR, and the LE sweep give the designer fundamental control over the aerodynamic characteristics of the wing. Other properties are important too but constitute "dials for fine-tuning." Recall that 3-dimensional lift, drag, and pitching moment coefficients are denoted by C_L, C_D, and C_M, respectively.

TABLE 9-2 Geometric properties of the wing.

Geometric property	Section
Planform shape	9.4
Aspect Ratio (AR)	9.3.1
Taper Ratio (TR or λ)	9.3.2
Leading edge (Λ_{LE}), quarter-chord ($\Lambda_{c/4}$), or mid-chord ($\Lambda_{c/2}$) sweep angle	9.3.3
Dihedral angle (Γ_W)	9.3.4
Washout (ϕ)	9.3.5
Angle-of-incidence (i_W)	9.3.6
Positioning of the wing on the fuselage	4.2.1
Partitioning of the wing into a roll control region (ailerons), high-lift region (flaps, slats), and lift suppression (spoilers)	10.4

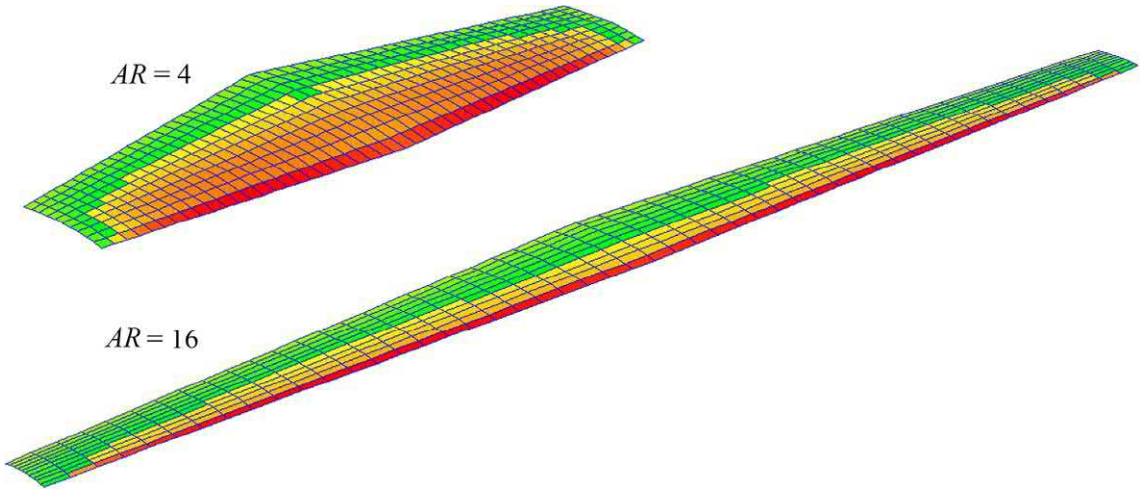


FIGURE 9-12 Two planform shapes of equal areas, but different Aspect Ratios.

9.3.1 Wing Aspect Ratio

The effect of the ratio of wingspan to the average chord on lift and drag is profound. It was identified as early as 1889 by Otto Lilienthal [2]. It is surprisingly easy to confirm. Hold a rectangular ruler against the wind. First, the short side against the wind, then the long side. Detect any difference in the force?

Figure 9-12 shows two planforms of equal area, but different *aspect ratio* (AR). This has important effect on their properties. The stubby configuration ($AR = 4$) has a low C_{L_α} and $C_{L_{max}}$, but higher stall AOA (α_{stall}) than the slender wing ($AR = 16$). Also, it has less roll damping than the high AR and, thus, provides better roll response. It is better for aerobatic aircraft. The high AR wing develops lower lift-induced drag (C_{D_i}) than the stubby one. It is better for efficient aircraft, such as sailplanes. But it has higher roll damping and will be structurally heavier because of larger bending moments.

This exemplifies the multifaceted effect the AR has on the aircraft. Table 9-3 gives general rules of thumb about its impact. Table 9-4 shows typical values of the AR for several classes of aircraft. The mathematical definition of the AR is given by Equations (9-8), (9-9), and (9-17) through (9-19).

(1) Illustrating the Difference between Low and High AR Wings

It is helpful to compare the difference between a low- and high AR wings of equal area and taper ratio using numbers. An example is given in Figure 9-13. Each is positioned at an AOA that generates 2000 lb_f of lift at airspeed of 100 KTAS (at S-L). To do this, the low AR wing requires an AOA of 1.55°, while the high AR one requires 0.66°. The low AR wing generates higher lift-induced drag: 71 lb_f versus 45 lb_f. Its flow field disruption is visible by the larger wingtip vortex. The low AR wing stalls at a higher AOA than the high AR wing and it is more responsive due to a lower roll damping coefficient, C_{L_p}.

TABLE 9-3 Typical impact of taper ratio on aerodynamic properties of the wing.

Aspect Ratio, *AR*	Pros	Cons
1.0	High stall angle-of-attack. High flutter speed. Low roll damping. Low structural weight. Great gust penetration capability (because of low C_{L_α}) Maximum wing volume for fixed area	Inefficient because of high-induced drag. Shallow C_{L_α} requires large changes in AOA with airspeed. Low $C_{L_{max}}$ (high stalling speed). Low LD_{max}. Awful low-speed properties.
5–7	Good roll response. Relatively high flutter speed. Limited adverse yaw. Reasonable gust penetration.	Inefficient to marginally efficient for long range design. Relatively high-induced drag.
7–12	Good balance between low-induced drag and roll response. Good glide characteristics for powered aircraft.	Some adverse yaw may be noticed toward the higher extreme of *AR*. Reasonable to marginal gust penetration capability (steep C_{L_α}).
20+	Low-induced drag. Great glide characteristics (high LD_{max}). Steep C_{L_α} (large change in lift with small changes in α). High $C_{L_{max}}$.	High structural weight. Low flutter speed. High roll damping. High adverse yaw. Steep C_{L_α} results in higher gust loads. Large wing flex. Minimum wing volume for fixed wing area.

TABLE 9-4 Typical values of AR for various classes of aircraft.

Type of vehicle or vehicle component	AR range
Missiles	0.5–1
Military fighters	2.5–4.0
General Aviation aircraft	6–11
Aerobatic airplanes	5–6
Twin engine commuters	10–14
Commercial Jetliners	7–10
Sailplanes	10–51

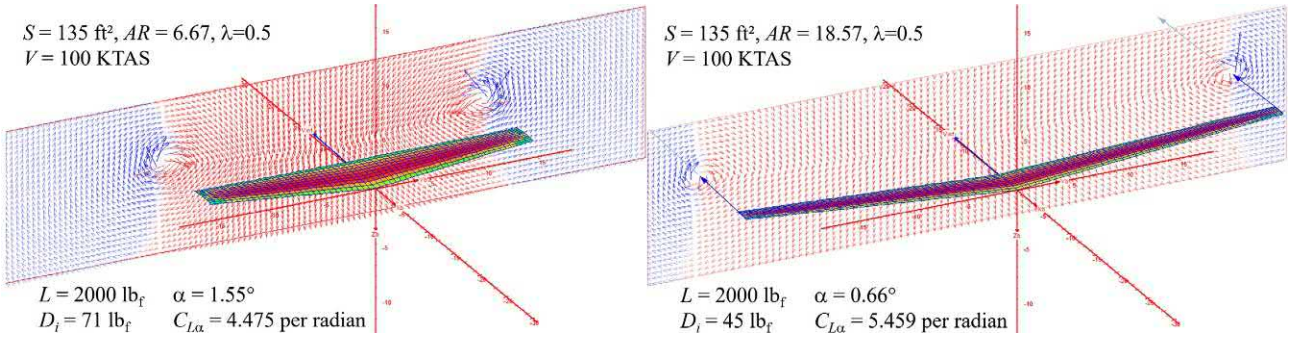


FIGURE 9-13 The difference between a Low AR (left) and high AR (right) is illustrated. Both wings are of equal area and each generates 2000 lb_f of lift at 100 KTAS.

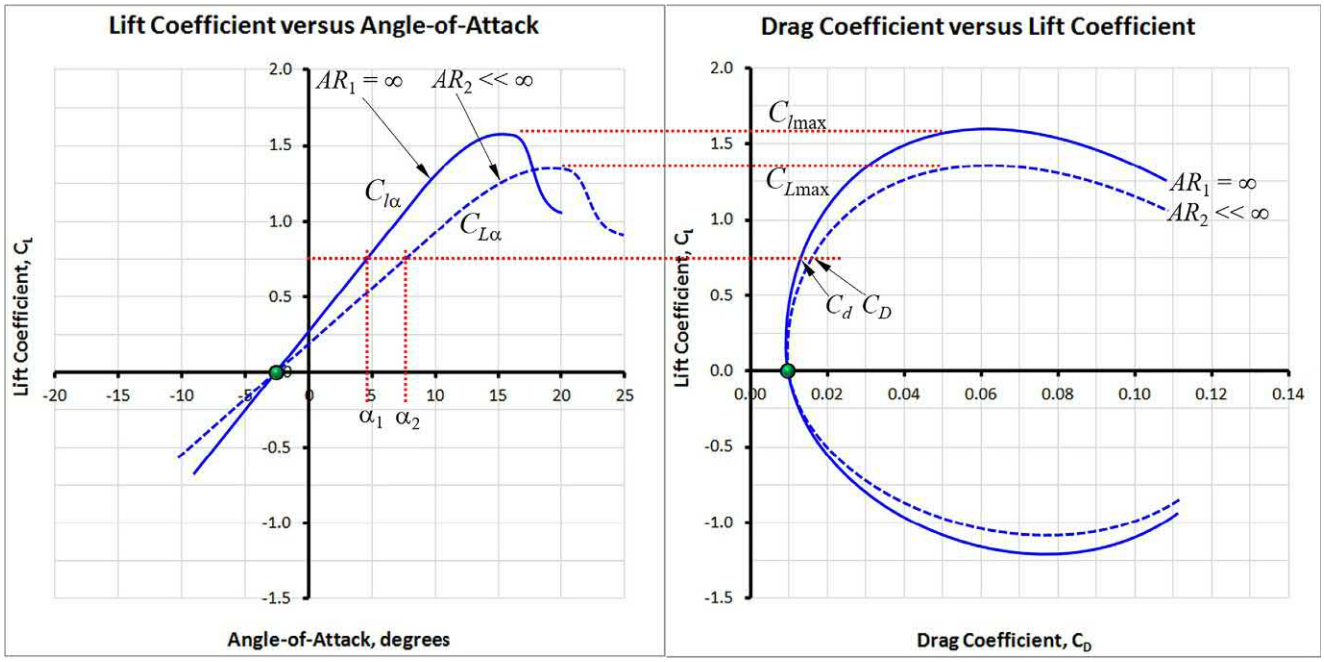


FIGURE 9-14 The effect of Aspect Ratio on a 3D lift curve and drag polar.

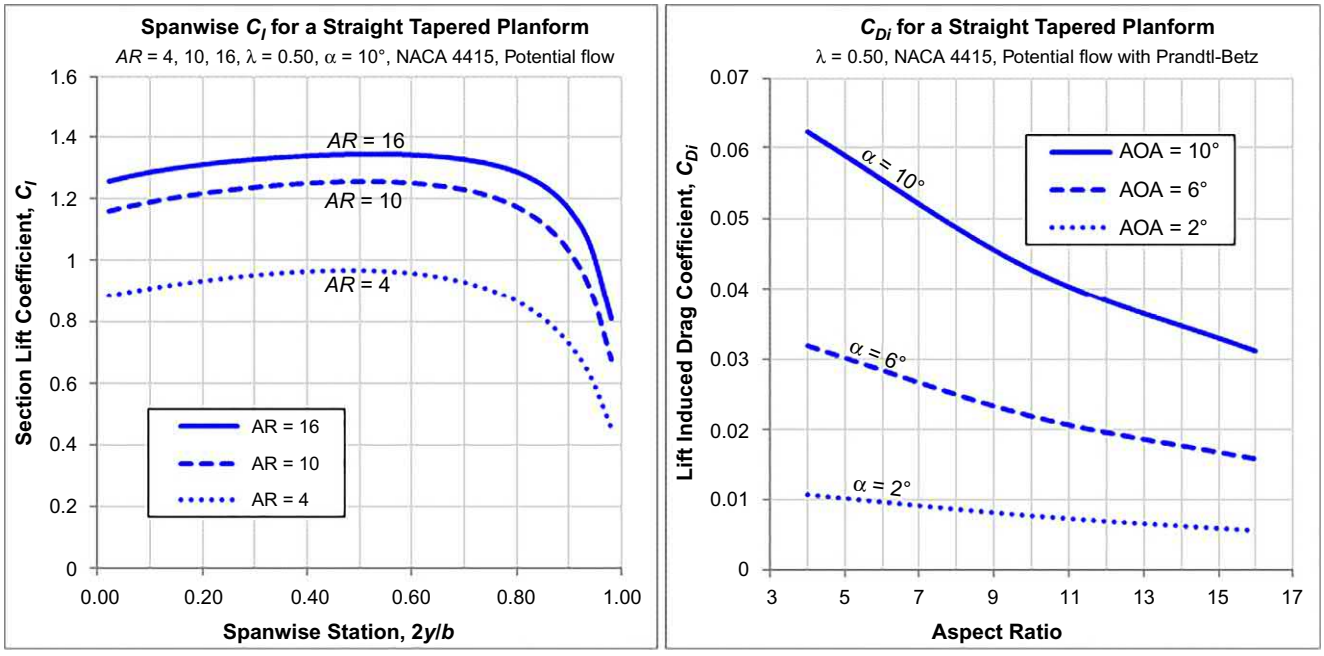


FIGURE 9-15 The left graphs shows the spanwise distribution of section lift coefficients for three different ARs, while the right one shows the effect of *AR* on the lift-induced drag coefficient.

Figure 9-14 shows how *AR* affects the wing's lift curve and drag polar. Consider an airfoil (for which AR_1 is treated as ∞) used in a 3-dimensional wing (whose AR_2 is much smaller). As the *AR* reduces, so does the lift curve slope (denoted by C_{l_α} for the airfoil and C_{L_α} for the wing) and maximum lift coefficient (denoted by $C_{l_{max}}$ for the airfoil and $C_{L_{max}}$ for the wing). If the airfoil generates a specific C_l at α_1, the wing will require a higher AOA, α_2, to generate C_L of equal magnitude. The drag coefficient for the airfoil, C_d, increases to C_D for the wing. This is caused by the wing's lift-induced drag and added pressure drag due to extensive growth in its flow separation region.

The impact of *AR* is further illustrated using potential flow theory in Figure 9-15. The left graph shows the spanwise distribution of section lift coefficients (C_l) at an AOA of 10° for three wings, each of identical taper ratio

($\lambda = 0.5$). The *tip-loading* (of C_l) that results from the λ (and will be discussed next) is evident. The high AR of 16 generates the highest C_l at the given AOA. This is to be expected since its C_{L_α} is the highest. Besides the magnitude of the C_l, the AR does not have large influence on the shape of the distribution.

The right graph in Figure 9-15 shows how the AR affects the lift-induced drag (C_{D_i}). This is illustrated for three AOAs; 2°, 6°, and 10°. The graph shows a substantial reduction in C_{D_i} with larger AR. Although the low AR surface is less efficient aerodynamically, it is better suited as a control surface for tail-aft configurations (i.e., as a horizontal and vertical tail) because it increases the stall AOA. This introduces a certain level of safety, demanding very high AOA or AOY before the stabilizing moments begin to drop.

Of course, the big question is: What is the best way to select a suitable AR for the new aircraft? The short answer is: Conduct an optimization of the sort presented in Section 3.4.5, *Wing Sizing Optimization by Example*. However, there are situations where low fidelity methods suffice. These range from "guessing" a suitable AR based on the class of aircraft, to estimating it using some of the following methods.

(2) Determining AR based on a Desired Range or Endurance

A suitable AR can be estimated based on (1) desired cruise range (R) or (2) desired endurance (E). The method estimates the *effective aspect ratio*, $AR_e = AR \cdot e$, rather than the *geometric AR*. The term e is the Oswald's span efficiency. With AR_e determined, the designer must ensure the planform geometry achieves this value. Also, if the airplane features a swept back planform the AR limits of Equation (9-139) should be considered as well.

The method requires a few parameters to be presumed: $C_{D_{min}}$, expected initial and final cruise weights, W_{ini} and W_{fin}, respectively, the expected cruise speed (V_C) and the average cruise lift coefficient (C_{L_C}) that corresponds to the average of W_{ini} and W_{fin}. Assuming the simplified drag model (see Chapter 16), we extract AR_e based on range using Equation (21.37) or endurance using Equation (21.63). The following equation is used for both range and endurance constraints:

$$AR_e = \frac{C_{L_C}^2}{\pi} \frac{1}{(A - C_{D_{min}})} \tag{9-37}$$

Where A for **range** is given by:

$$A = \begin{cases} \dfrac{V_{C_{KTAS}}}{R} \dfrac{C_{L_C}}{SFC} \ln(W_{ini}/W_{fin}) & \text{Jets} \\ \dfrac{325.9\eta_p}{SFC_{hp}} \dfrac{C_{L_C}}{R} \ln(W_{ini}/W_{fin}) & \text{Propellers} \end{cases} \tag{9-38}$$

and A for **endurance** is given by:

$$A = \begin{cases} \dfrac{1}{E} \dfrac{C_{L_C}}{SFC} \ln(W_{ini}/W_{fin}) & \text{Jets} \\ \dfrac{325.9\eta_p}{SFC_{hp} V_{C_{KTAS}}} \dfrac{C_{L_C}}{E} \ln(W_{ini}/W_{fin}) & \text{Propellers} \end{cases} \tag{9-39}$$

and

C_{L_C} = Cruise lift coefficient
R = Range in nm
E = Endurance in h
V_{CKTAS} = Average cruising speed in KTAS
SFC = Specific fuel consumption in 1/h
SFC_{hp} = Specific fuel consumption in $lb_f/(h \cdot HP)$
η_p = Propeller efficiency in cruise.

The denominator in Equation (9-37) results in singularity when $C_{D_{min}} = A$ and returns negative values if $C_{D_{min}} > A$. It is possible to derive restrictions for the value of V_C or C_{L_C}. For instance, for range, the following limits apply:

$$\begin{aligned} V_{C_{KTAS}} &> \frac{R \cdot SFC \cdot C_{D_{min}}}{C_{L_C} \ln(W_{ini}/W_{fin})} \quad \text{Jets} \\ C_{L_C} &> \frac{R \cdot SFC_{hp} \cdot C_{D_{min}}}{325.9\eta_p \ln(W_{ini}/W_{fin})} \quad \text{Propellers} \end{aligned} \tag{9-40}$$

Similar restrictions can be derived for endurance and are shown below.

$$\begin{aligned} C_{L_C} &> \frac{E \cdot SFC \cdot C_{D_{min}}}{\ln(W_{ini}/W_{fin})} \quad \text{Jets} \\ V_{C_{KTAS}} &< \frac{325.9\eta_p C_{L_C} \ln(W_{ini}/W_{fin})}{C_{D_{min}} SFC_{hp} E} \quad \text{Propellers} \end{aligned} \tag{9-41}$$

DERIVATION OF EQUATION (9-37)

Assuming the simplified drag model for a jet, Equation (21.37) can be solved for C_D as follows:

$$R = \frac{V_{C_{KTAS}}}{SFC} \frac{C_L}{C_D} \ln(W_{ini}/W_{fin}) \quad \Leftrightarrow$$

$$C_D = C_{D_{min}} + \frac{C_L^2}{\pi \cdot AR_e} = \frac{V_{C_{KTAS}}}{R} \frac{C_L}{SFC} \ln(W_{ini}/W_{fin}) \quad \text{(i)}$$

For propeller aircraft, this becomes:

$$R = \frac{325.9\eta_p}{SFC_{hp}} \frac{C_L}{C_D} \ln(W_{ini}/W_{fin}) \quad \Leftrightarrow$$

$$C_D = C_{D_{min}} + \frac{C_L^2}{\pi \cdot AR_e} = \frac{325.9\eta_p}{SFC_{hp}} \frac{C_L}{R} \ln(W_{ini}/W_{fin}) \quad \text{(ii)}$$

Solving for AR_e for each expression leads to Equations (9-37) and (9-38).

DERIVATION OF EQUATION (9-39)

Assuming the simplified drag model for a jet, Equation (21-63) can be solved for C_D as follows:

$$E = \frac{1}{SFC}\frac{C_L}{C_D}\ln\left(W_{ini}/W_{fin}\right) \Leftrightarrow$$

$$C_D = C_{D_{\min}} + \frac{C_L^2}{\pi \cdot AR_e} = \frac{1}{E}\frac{C_L}{SFC}\ln\left(W_{ini}/W_{fin}\right) \quad \text{(i)}$$

For propeller aircraft, this becomes:

$$E = \frac{325.9\eta_p}{SFC_{hp}V_{C_{KTAS}}}\frac{C_{L_C}}{C_D}\ln\left(\frac{W_{ini}}{W_{fin}}\right) \Leftrightarrow$$

$$C_D = C_{D_{\min}} + \frac{C_{L_C}^2}{\pi \cdot AR_e} = \frac{325.9\eta_p}{SFC_{hp}V_{C_{KTAS}}}\frac{C_{L_C}}{E}\ln\left(\frac{W_{ini}}{W_{fin}}\right) \quad \text{(ii)}$$

Solving for AR_e for each expression leads to Equations (9-37) and (9-39).

DERIVATION OF EQUATIONS (9-40) AND (9-41)

All four equations of (9-40) and (9-41) are derived in a similar fashion by stating that the denominator of Equation (9-37) requires $A - C_{D_{\min}} > 0$. Otherwise, AR_e will be negative or $\to\infty$. Here, only the second equation of Equation (9-41) will be derived.

$$A - C_{D_{\min}} > 0 \Leftrightarrow$$

$$\frac{325.9\eta_p}{SFC_{hp}V_{C_{KTAS}}}\frac{C_{L_C}}{E}\ln\left(W_{ini}/W_{fin}\right) - C_{D_{\min}} > 0$$

$$\Rightarrow \quad V_{C_{KTAS}} < \frac{325.9\eta_p C_{L_C}\ln\left(W_{ini}/W_{fin}\right)}{C_{D_{\min}}SFC_{hp}E}$$

EXAMPLE 9-4

The Cirrus SR22 Pilot Operating Handbook (POH) [3] reveals an 899 nm range at 65% power at 10,000 ft. It states the cruising speed at this condition is 174 KTAS and fuel consumption is 15.4 gal/h. Thus $SFC = 15.4\,\text{gal/h} \times (6\ \text{lb}_\text{f}/\text{gal})/(0.65 \times 310\ \text{BHP}) = 0.4586\ \text{lb}_\text{f}/\text{h/BHP}$. Evaluate Equation (9-37) assuming a hypothetical design of a SR22-class aircraft, which "happens" to share several parameters. This hypothetical airplane is designed for a range of 900 nm precisely at the same condition. Estimate AR_e for this airplane using Equation (9-37) and compare to that of the SR22. Assume the weight at the beginning of cruise is 3379 lb_f and 2910 lb_f at end of cruise. Assume the wing area is 145 ft^2 and $C_{D_{\min}} = 0.02541$ (per Example 16-24).

SOLUTION:

Average weight during cruise:

$$W_{avg} = \frac{W_{ini} + W_{fin}}{2} = \frac{3379 + 2910}{2} = 3145\ \text{lb}_\text{f}$$

Density at 10,000 ft:

$$\rho = 0.002378(1 - 0.0000068756 \times 10{,}000)^{4.2561}$$
$$= 0.001756\ \text{slugs/ft}^3$$

The airspeed is $174 \times 1.688 = 293.7$ ft/s, so the lift coefficient at cruise is:

$$C_{L_C} = \frac{2W_{avg}}{\rho V_C^2 S} = \frac{2 \times 3145}{(0.001756)(293.7)^2(145)} = 0.2864$$

Next, let's calculate the constant A:

$$A = \frac{325.9\eta_p}{SFC_{hp}}\frac{C_{L_C}}{R}\ln\left(W_{ini}/W_{fin}\right)$$
$$= \frac{325.9(0.85)}{0.4586}\frac{(0.2864)}{900}\ln(3379/2910) = 0.02872$$

Thus, AR_e is

$$AR_e = \frac{C_{L_C}^2}{\pi}\frac{1}{(A - C_{D_{\min}})} = \frac{(0.2864)^2}{\pi}\frac{1}{(0.02872 - 0.02541)}$$
$$= 7.893$$

Note that $AR = 10$ for the SR22. The answer implies a required Oswald efficiency of 0.7893. This compares favorably to Equation (9-129) as follows:

$$e = 1.78\left(1 - 0.045 \times 10^{0.68}\right) - 0.64 = 0.7566$$

Also, note that the C_{L_C} limit per Equation (9-40) is 0.2533. This compares to the actual $C_{L_C} = 0.2864$.

(3) Estimating AR based on Minimum Cruise Drag

The AR can also be extracted using a carpet plot of the total drag (C_D) and design lift coefficient (C_{L_C}) (e.g., see Equation 9.61). This is a simplified version of the optimization of Section 3.4.5, *Wing Sizing Optimization by Example*. Assuming a constant wing area (based on stalling speed), the C_D for the airplane is estimated for a range of AR. The estimation requires some sophistication using the methods of Chapter 16, *Aircraft Drag Analysis*. It evaluates the root and tip chords as a function of AR, conducts wing skin friction analysis to estimate the minimum drag ($C_{D_{\min}}$). The $C_{D_{\min}}$ is calculated as $C_{Dx} + C_{Dwng}$, where C_{Dx} is the drag of everything minus the wing and C_{Dwng} is the drag of the wing, including form and interference factors. C_{Dwng} is a function of AR. The lift-induced drag coefficient (C_{D_i}) is also calculated using an appropriate model of the Oswald's span efficiency. Then, $C_D = C_{D_{\min}} + C_{D_i}$ is plotted against AR for a range of C_{L_C}, as shown in Figure 9-16. The plot reveals the location of the optimum AR_{opt}. The upper and lower bounds are simply the optimum $AR_{opt} \pm 2$. Figure 9-16 illustrates that any AR between the two limits

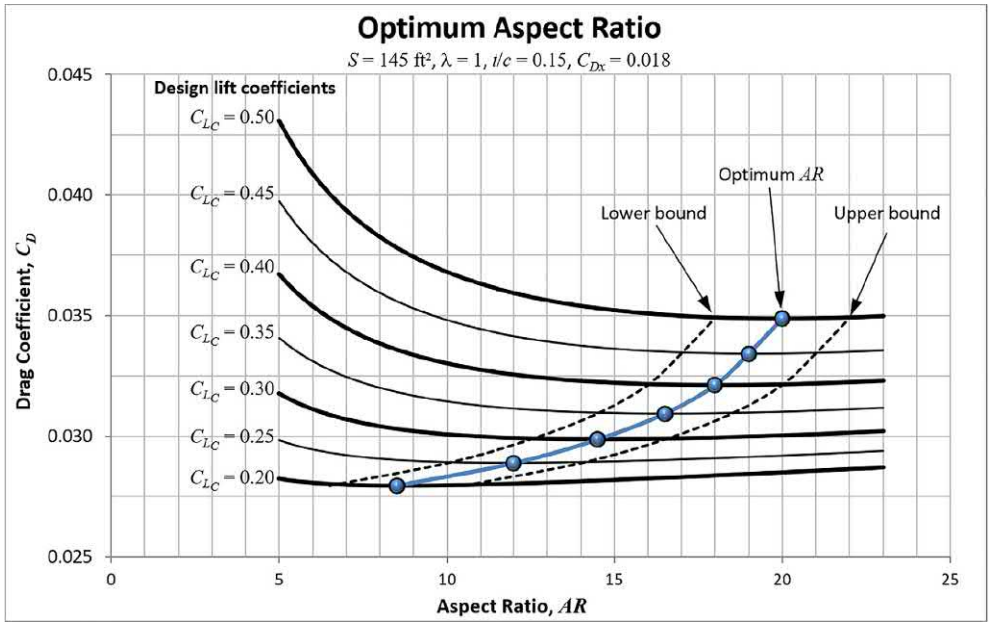


FIGURE 9-16 The effect of Aspect Ratio on the drag coefficient of a hypothetical aircraft.

yields the lowest value of the total drag coefficient. This gives the designer room to accommodate other concerns such as structural weight. Note that the simplicity of this approach ignores a host of other issues, such as taper ratio, internal wing volume, structural depth, wing weight, and others.

(4) Estimating AR for Sailplane Class Aircraft

A plausible AR for powered and unpowered sailplanes can be established using the historical data in Figure 9-17, collected from Ref. [6]. The maximum lift-to-drag ratios (LD_{max}) presented are for the complete

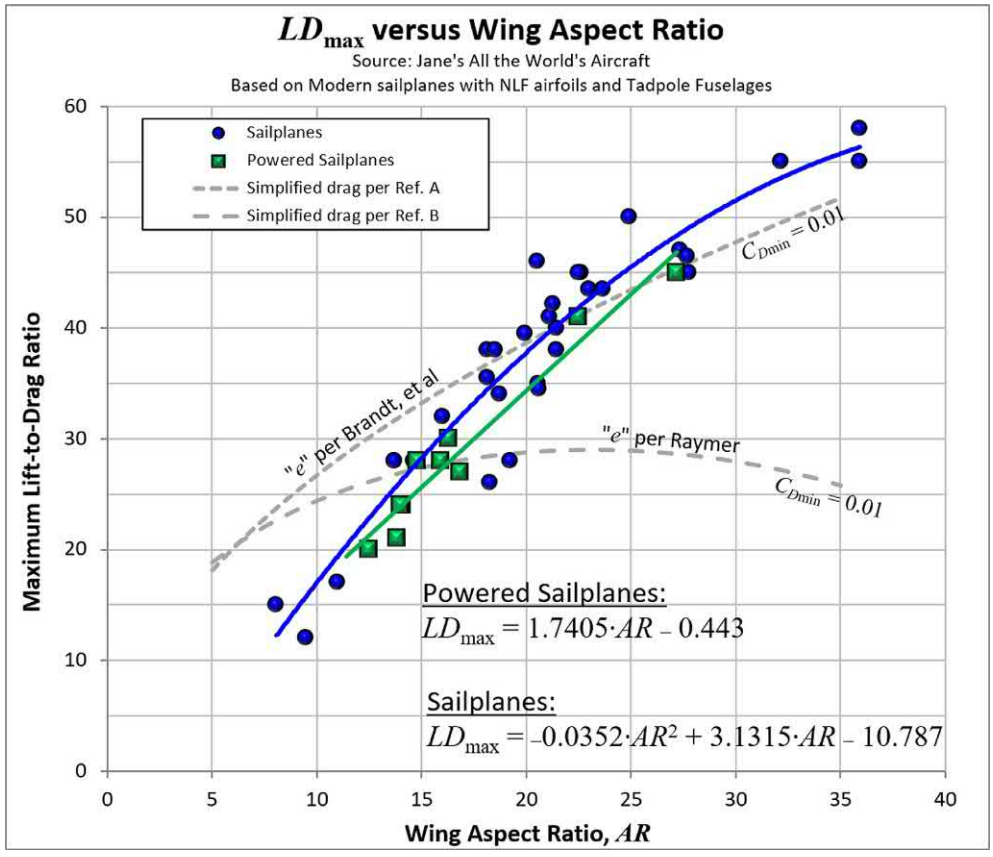


FIGURE 9-17 LD_{max} as a function of AR for modern sailplanes and powered sailplanes. Ref. A is [4]. Ref. B is [5].

aircraft and reveals the sophistication of the modern sailplane. The graph shows trends for both regular and powered sailplanes and presents accompanying least-squares curve fits. These estimates do not replace analyses such as that of Ref. [7], but provide initial estimates based on historical sailplanes (provided $AR < 36$).

Also plotted are theoretical predictions of the LD_{max} using the *simplified drag model* (see Chapter 16, *Aircraft Drag Analysis*) and assuming a $C_{D_{min}}$ of 0.01 (typical of many sailplanes). This model is often the first choice of the novice airplane designer, but it is inaccurate for sailplanes as it neither models NLF nor the offset position of $C_{D_{min}}$. The theoretical LD_{max} was calculated using Equation (20-33), where the Oswald's span efficiency was calculated per Equations (9-131) and (9-129). (Neither equation is intended for high AR wings.) The graph clearly shows the limitation of the simplified drag model.

$$\text{Sailplanes: } AR \approx 44.482 - \sqrt{1672.2 - 28.41 LD_{max}} \quad (9\text{-}42)$$

$$\text{Powered sailplanes: } AR \approx \frac{LD_{max} + 0.443}{1.7405} \quad (9\text{-}43)$$

Note that the calculated AR will not guarantee a desired LD_{max} will be achieved. Rather, it indicates that, historically, sailplanes with that AR have achieved the said LD_{max}. Achieving it requires utmost attention to any source of drag on the airplane.

9.3.2 Wing Taper Ratio, TR or λ

The *taper ratio* is the second of the three primary geometric properties of a wing. Figure 9-18 illustrates its profound impact on the distribution of lift along the wingspan. The left graph shows this in terms of section lift coefficients (C_l), while the right one show this in terms of unit lift[1] per unit span. λ also impacts C_{D_i} and this is discussed in Section 9.4, *Planform Selection*.

The influence of λ on the spanwise distribution of C_l (left graph) is very distinct. The tip-loading that results from a low taper ratio is noticeable. However, it also affected by the leading-edge sweep angle (to be discussed next). Forward sweep reduces tip-loading, while aft sweep intensifies it. The lifting surfaces in the graphs have the quarter-chord line normal to the plane-of-symmetry. The tip-loading results from the spanwise spread of upwash in front of the leading edge. This increases the effective AOA from root to tip and, thus, the C_l. The effect is very detrimental for the stall behavior but beneficial for bending loads (lower wing weight). The selection of λ should consider these in addition to issues like manufacturing cost. There is a golden medium between $\lambda = 0.3$ and $\lambda = 1$ for your airplane. Avoid $\lambda < 0.3$. Table 9-5 provides general rules of thumb regarding the impact of λ on selected aerodynamic properties.

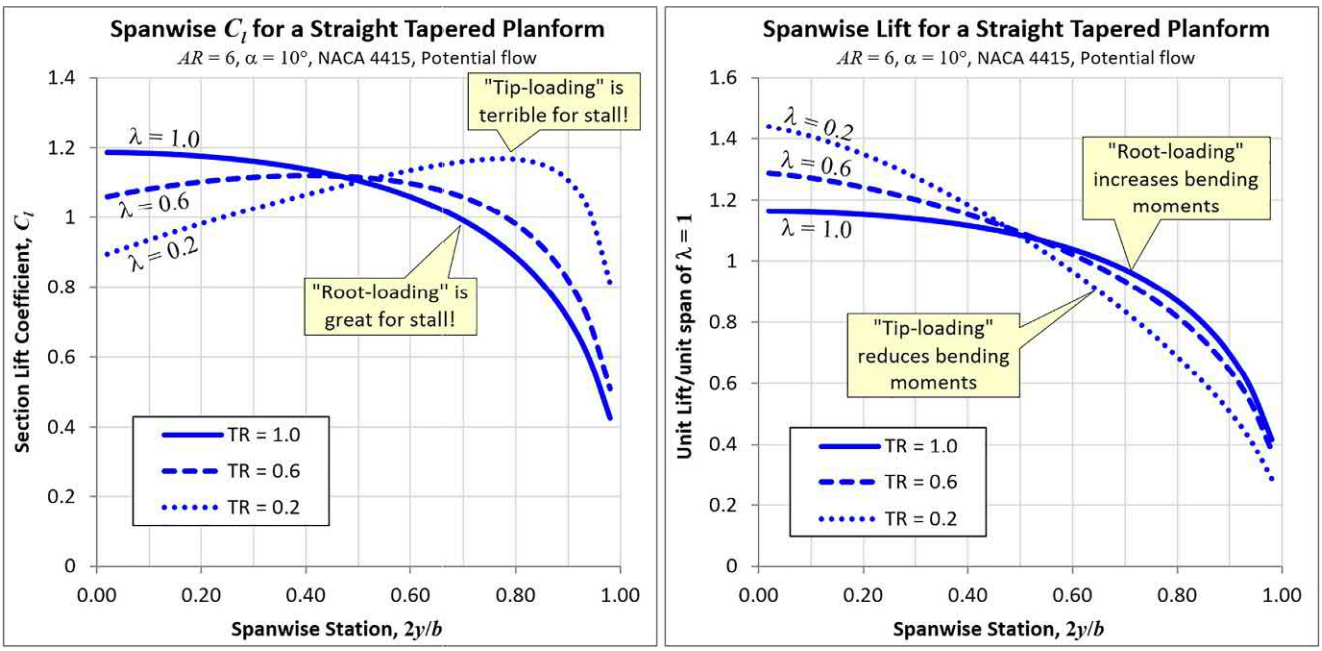


FIGURE 9-18 The effect of λ on the spanwise distribution of section lift coefficients (left) and lift force (right).

[1] Unit lift because it is divided by the average load per unit span. Thus, the area under the graphs is 1.

TABLE 9-5 Typical impact of taper ratio on aerodynamic properties of the wing.

Taper Ratio, λ	Pros	Cons
0.3	Induced drag is close to that of an elliptical wing planform but is much simpler to manufacture.	Poor stall characteristics. Tip loaded planform requires a large washout to delay tip stall. Consider this the minimum value of usable λ.
0.5	Good balance between low induced drag and good stall characteristics	Stall begins mid-span and spreads to tip and root. Usually requires moderate washout.
1.0	Good stall progression. Washout is usually not required. Simple to manufacture.	High-induced drag, higher bending moments.

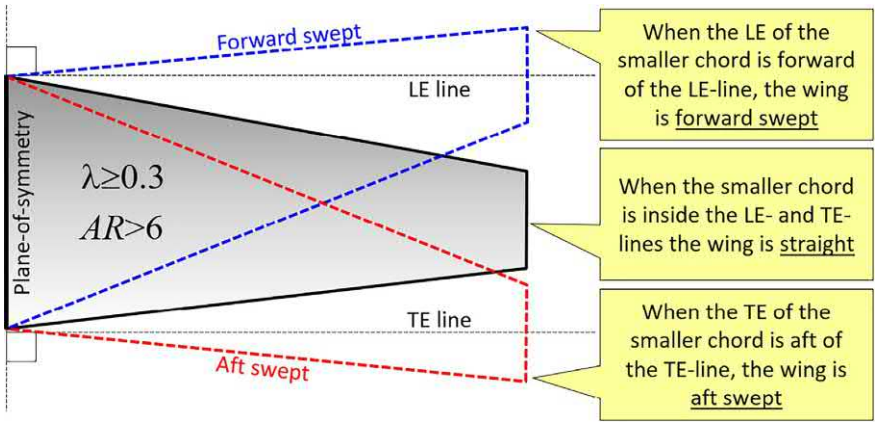


FIGURE 9-19 Definition of a straight-tapered wing planform.

9.3.3 Wing Sweep Angle, Λ

The *sweep angle* is the last of the three primary geometric properties of a wing. There are two reasons to sweep the wing: (1) to fix a CG problem or (2) high-speed flight ($M > 0.65$). Let us deal with them in that order. First let it be said that, in the absence of justifications (1) and (2), avoid wing sweep at all cost. It makes the wing less efficient aerodynamically, is detrimental to stall characteristics, causes serious aeroelastic problems, and requires a structurally inefficient discontinuous spar. In addition to the following discussion, also review Section 9.4.7, *Swept Planforms*.

First, let us define what constitutes a straight or swept wing in this book. Consider the tapered planform in Figure 9-19. If the smaller chord resides between the LE and TE lines of the large chord, it is called *straight* in this book. Wings for which $\lambda \geq 0.3$ and $AR > 6$ will have $|\Lambda_{c/4}| < 10°$ and $|\Lambda_{c/2}| < 5°$. This is a refined definition from the first edition that accommodates most GA aircraft, including Zlins and Mooneys.

If any portion of the LE or TE crosses the LE or TE lines, it is considered either *forward* or *aft swept*.

While wing sweep dates to the 1930s, it was preceded by the work of earlier scientists. Meier [8] takes this history to Isaac Newton (1643–1727), Pierre Simon Marquis de Laplace (1749–1827), Ernst Mach (1838–1916), and Adolf Busemann (1901–86), to name a few. Busemann is credited with the invention of the wing configuration. He belonged to a group of famous German scientists led by Ludwig Prandtl (1875–1953). The best known are Theodore von Kármán (1881–1963), Max M. Munk (1890–1986), and Jakob Ackeret (1898–1981) [9]. Busemann's work was first published at the fifth Volta conference in Rome in 1935 [10]. It was an annual conference of physics, mathematics, history, and philosophy, named in honor of Alessandro Volta (1745–1827). In the United States, Robert T. Jones (1910–1999) tested swept back wings toward the end of 1944. It was the first such work to be published in the United States [11]. In it, Jones cites Busemann's research from 1935 as one of his references.

(1) Sweep Associated with CG Issues

Figure 9-20 shows the secret of *tail-aft* aircraft configurations: To fly, place the CG close to the quarter-chord of the c_{MGC}. This holds for all three wing sweep styles. This is usually preferred for maiden flight as well. The only trick is to correctly identify the c_{MGC}—and then to place a properly sized balancing surface (HT) behind the wing. At any rate, should you discover that your airplane has the CG far from this spot, you have three solutions at your disposal: (1) Add ballast to move the CG to the c_{MGC} quarter-chord. This solution cuts into the useful load and, thus, is only feasible if the ballast weight is small. (2) Move the entire wing forward or aft as needed for

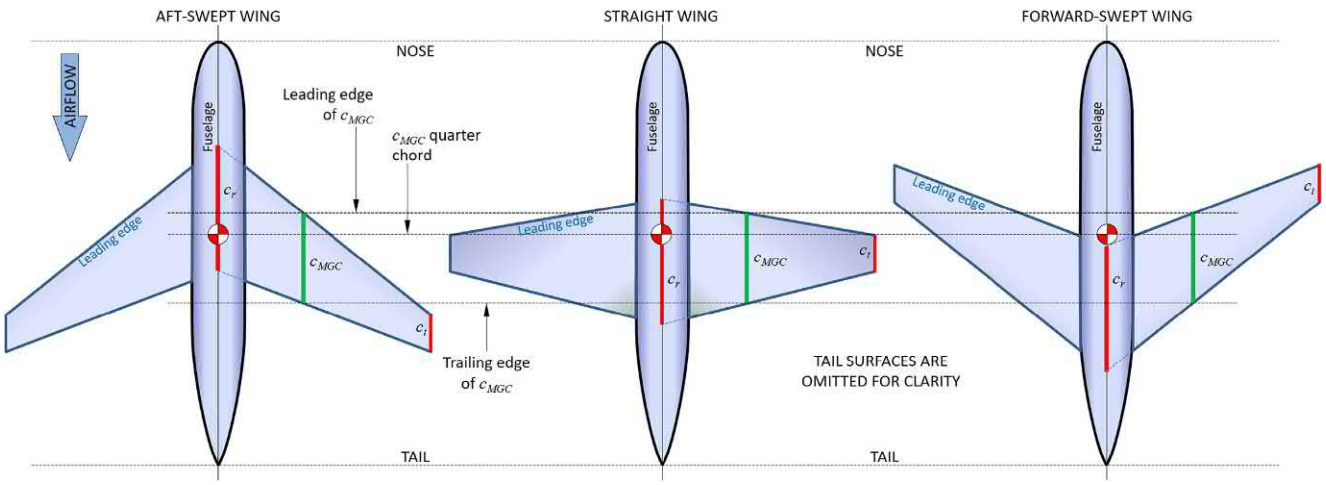


FIGURE 9-20 Where to locate the CG for various wing sweeps.

the same effect. There will be a small shift in the CG, but it is a fraction of the wing translation. (3) Sweep the wing forward or aft for the same effect. The last two need to be accomplished before conforming prototypes are built. The last one explains the aft swept wings of the venerable Douglas DC-3 Dakota (C-47) [12] and Messerschmidt Me-262 [13]. The Swedish SAAB MFI-15 Safari features a forward-swept, shoulder-mounted wing for the same reason.

(2) Sweep Associated with High-Speed Flight

High-speed flight is the most common reason for using wing sweep. The sweep increases the critical Mach number, M_{crit}, delaying the onset of *drag divergence*, where drag rises sharply at high subsonic airspeeds. That airspeed is called *drag-divergence Mach number*, denoted as M_{DD} (M_{dd} for airfoils). The associated drag is called *wave drag* and is treated in Chapter 16, *Aircraft Drag Analysis*. These concepts were introduced in Section 8.3.8, *The Effect of Compressibility*. Figures 16-37 and 16-38 illustrate the impact of sweep on drag divergence.

(3) Impact of Sweep on $C_{L_{max}}$

The maximum lift coefficient is reduced with an increase in wing sweep angle. This is discussed in Section 9.5.5, *The Maximum Lift Coefficient*.

(4) Impact of Sweep on Aerodynamic Characteristics

(1) Aft sweep increases dihedral effect, which reduces damping and magnifies roll tendency in Dutch roll. Additionally, it is very detrimental for stall characteristics. This is illustrated on the left wing in Figure 16-38: As AOA increases, a strong spanwise flow toward the tip forms, causing the tip to stall before the remainder of the wing. The reasons are detailed in Sections 9.6.4, *Cause of Spanwise Flow for a Swept Back Wing Planform* and 9.6.5, *Pitch-Up Stall Boundary for a Swept Back Wing Planform*. This causes two serious scenarios: (a) As AOA increases, reduced lift generation in the tip region shifts the wing's center-of-lift forward, resulting in a forceful nose pitch-up moment. The pitch-up also depends on the tail configuration. (b) This also reduces roll-authority, such that even a modest combination of yaw and roll may cause the airplane to drop uncontrollably on one wing at stall. If this happens near the ground, the results are disastrous. Note that modern swept-back aircraft use a combination of envelope protection and leading-edge slats to beat such wings into submission.

(2) Forward sweep decreases dihedral effect and reduces roll tendency in Dutch roll. It improves stall characteristics, thanks to a distribution of section lift coefficients resembling that of a Hershey-bar wing—its stall progresses from the root. However, it is subject to the detrimental aeroelastic deformation explained below.

(5) Impact of Sweep on Structural Loads

Sweep has two important effect on structural loads of the wing:

(1) Aft sweep increases wing torsion because the lift generation is behind the root airfoil. This increase is significant and must be accounted for during structural analysis. Figure 9-21 illustrates the difference between a forward and aft swept wing. It shows how the tip airfoils of an aft swept wing deform to reduce the *angle-of-incidence* (AOI). This is aggravated when ailerons are deflected, causing an aeroelastic effect called *roll-reversal*. If flying fast enough, a left-roll aileron input results in a right roll (and vice versa).

(2) Forward sweep reduces wing torsion as the lift generation is forward of the root airfoil up to a point, after which the resulting torsion is divergent: It increases the AOI of the outboard wing, which increases its lift, which increases the AOI further. The short story is that the wing must be very stiff structurally to prevent this *aeroelastic*

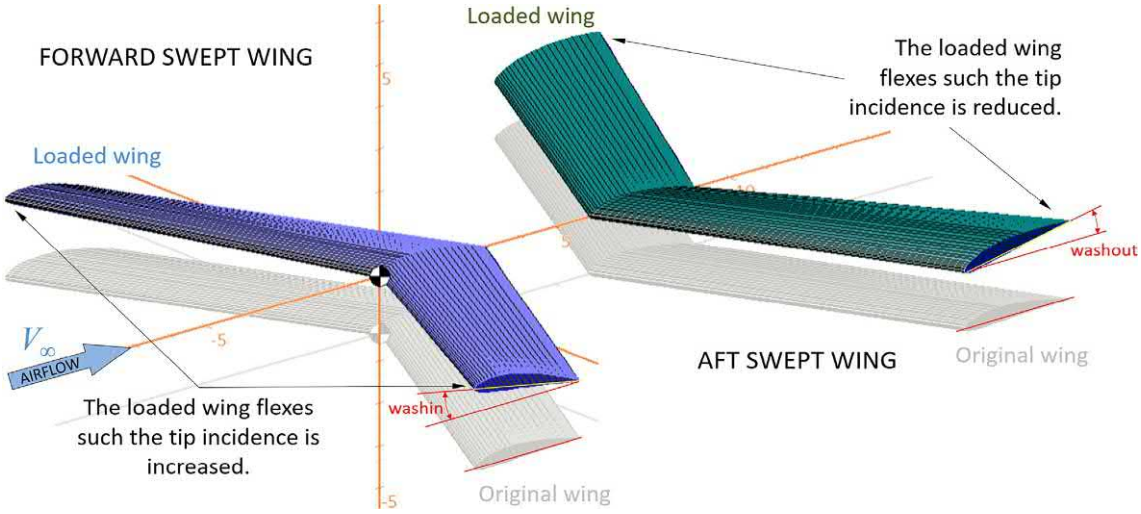


FIGURE 9-21 Aeroelastic consequences of wing sweep.

divergence. This is illustrated in Figure 9-21, which shows the tips deflected LE up compared to the original configuration.

9.3.4 Dihedral and Anhedral, Γ

The *dihedral* (or *anhedral*) is the angle the wing makes with respect to the ground plane (x–y plane) when viewing the airplane from the front (or back). Dihedral means the wingtip is higher (above the ground) than the wing root. The opposite holds true for anhedral (see Figure 4-10). The dihedral tilts the lift force (inboard) and changes the AOA of the wing. Thus, a wing with a dihedral (Γ) operating at an AOA given by α, is subjected to reduced AOA (α_N), by factor cos Γ. For instance, if $\Gamma = 0°$, then $\alpha_N = \alpha$. If $\Gamma = 90°$, then $\alpha_N = 0°$, regardless of α. Therefore, we can write:

$$\alpha_N = \alpha \cos\Gamma \tag{9-44}$$

The lift generated in the plane-of-symmetry is the product of the lift normal to the wing surface (L_N) and cos Γ.

$$L = L_N \cdot \cos\Gamma \tag{9-45}$$

Since L_N can be written as $L_N = qSC_{LN} = qSC_{L_\alpha}\alpha_N = qSC_{L_\alpha}\alpha$ cos Γ, the lift in the plane-of-symmetry is given by:

$$L = qSC_{L\alpha}\alpha\cos^2\Gamma \tag{9-46}$$

Where C_{L_α} = Lift curve slope of the wing for $\Gamma = 0°$. This result has been confirmed experimentally [14]. Furthermore, see discussion of V-tails in Section 11.3.4, *V-Tail or Butterfly Tail*. Dihedral for typical aircraft ranges from $4° < \Gamma < 7°$ (for which the term $\cos^2\Gamma$ amounts to 0.995–0.985). Thus, it can be ignored in the estimation of some stability derivatives. The impact of low dihedral on a typical wing is modest, as can be seen in Figure 9-22. Besides wing dihedral, other contributors to *dihedral effect* include location of wing above or below the center-of-gravity, wing sweep, and dihedral of the horizontal tail (also see Section 4.2.3, *Wing Dihedral*). Values for several classes of aircraft are given in Table 9-6.

9.3.5 Wing Twist—Washout and Washin, ϕ

Aircraft wings are frequently twisted along the span, such the *angle-of-incidence* (AOI) of the tip airfoil is different from the root airfoil. *Washout* refers to the AOI of the tip being less than that of the root (see Figure 9-24) and *washin* if the opposite holds true. In this context, the forward-swept wing in Figure 9-21 illustrates an (exaggerated) washin, while the aft swept wing illustrates washout. Washin is not used besides describing aeroelastic effects such as that shown in Figure 9-21. This section deals with the intentional twisting of the wing, where its purpose is usually twofold: stall improvement or change in lift distribution.

(1) Wing Twist for Stall Improvement

If the wing tip stalls before or concurrently with the root, an abrupt roll and loss of control results. This is a dangerous condition that may lead to spin. Roll tendency of this nature contributes to fatal accidents if it occurs at low altitudes [15]. A typical scenario involves a pilot executing a steep bank for final at low altitude and airspeed. This is followed by a sudden roll as the lower wing stalls (see Figure 11-11). While such accidents are usually classified as pilot-error, the aircraft designer can do the following to help: (1) Choose a high-lift, Class-A airfoil (per Figure 8-72) as a tip-airfoil, (2), if necessary, feature a 1–4° washout, or (3) consider a leading-edge extension per Ref. [16]. Figure 9-22 shows that twist has a major influence on the distribution of section lift coefficients (C_l). It illustrates how washout shifts *start-of-stall* inboard.

TABLE 9-6 Various wing layout properties for selected aircraft.

Aircraft	Aspect Ratio AR	Taper Ratio λ	Dihedral (degrees) Γ	Washout (degrees) ϕ_G	Incidence (root) (degrees) i_W	Leading edge sweep (degrees) Λ_{LE}
Experimental and Homebuilt						
Colomban MC 15 Cri Cri	7.75	1	4	1.5	1	0
Corby Starlet	5.00	1	6	3.5	2.5	0
Rutan Varieze	9.20	–	–	−3	–	–
Verilite Model 100 Sunbird	7.56	1	2	2	2	0
Sailplanes						
Rolladen-Schneider LS4	21.4	–	4	–	–	0
Schempp-Hirth Nimbus-3D	35.9	–	3	–	1.5	-2
Schleicher ASK 21	16.1	–	4	–	–	−1.5 ($c/4$)
Schweizer SGM 2-37	18.1	–	3.5	1	1	0
Commercial Jetliners						
Airbus A300-600	7.7	–	–	–	–	28 ($c/4$)
Airbus A310	8.8	0.260	11.13 (IB) 4.05 (OB)	–	5.05	28 ($c/4$)
Airbus A320-200	9.4	–	5.2	–		25 ($c/4$)
Boeing 707	7.056	0.275	7	–	2	35 ($c/4$)
Boeing 727	7.2	0.304	3	–	2	32 ($c/4$)
Boeing 737-100, -200	8.83	0.340	6	–	1	25 ($c/4$)
Boeing 747-100, -200	6.96	0.245	7	–	2	37.5 ($c/4$)
Boeing 757	7.77	0.211	5	–	3.2	25 ($c/4$)
Boeing 767	7.9	0.267	6	–	4.25	31.5 ($c/4$)
Fokker F28 Fellowship	8.4	0.239	2.5	–	–	17.4 ($c/4$)
McDonnell-Douglas DC-9/MD87	9.62	0.156	3	–	1.25	24.5 ($c/4$)
McDonnell-Douglas DC-10-30/40	7.5	0.252	5.24 (IB) 3.03 (OB)	–	–	35 ($c/4$)
Business Jets						
Cessna M550 Citation II	7.8	–	4	3	2.5	–
Cessna M650 Citation III	8.94	–	3	–	–	25 ($c/4$)
Dassault Falcon 20	6.4	–	2	–	1.5	30 ($c/4$)
Dassault Falcon 100	6.5	–	2	–	1.5	30 ($c/4$)
Gates Learjet 55	6.72	0.391	–	–	–	13 ($c/4$)
Turboprops, Commuter, and Military						
ATR 42	11.08	0.549	2.5	–	2	3.1 ($c/4$)
ATR 72	12.0	0.549	2.5	–	2	2.8 ($c/4$)
De Havilland DHC-6 Twin Otter	10.1	1	–	–	–	–
De Havilland DHC-7 Dash 7	10.1	0.441	4.5	–	3	3.2 ($c/4$)
De Havilland DHC-8 Dash 8	12.4	–	2.5	–	3	3.03 ($c/4$)
Dornier Do 28 Skyservant	8.3	1	1.5	–	4	0
Fokker F27 Friendship	12.0	0.404	2.5	2	3	0 ($c/4$)

Continued

TABLE 9-6 Various wing layout properties for selected aircraft—cont'd

Aircraft	Aspect Ratio AR	Taper Ratio λ	Dihedral (degrees) Γ	Washout (degrees) ϕ_G	Incidence (root) (degrees) i_W	Leading edge sweep (degrees) Λ_{LE}
IAI-101, 201 Arava	10	1	1.5	–	0.45	0
LET L-410	10.79	–	1.75	2.5	2	0 ($c/4$)
Lockheed C-130 Hercules	10.09	0.852	2.5	3	3	0 ($c/4$)
Mitsubishi MU-2	7.71	–	0	3	2	0.35 ($c/4$)
SAAB 340	11.0	0.375	7	–	2	3.6 ($c/4$)
Shorts SD3-30	12.3	1	3	–	–	0
Shorts Skyvan Series 3M	11	1	2.03	–	2.5	0
GA Single Engine, Piston, and Turboprop						
Beechcraft Sierra/Sundowner	7.5	1	6.5	2	3	0
Beechcraft T-34C Mentor	6.22	0.412	7	3	4	0 ($c/4$)
Beechcraft V35 Bonanza	6.2	0.5	6	3	4	0 ($c/4$)
Cessna 150/152	6.7	0.687	1	1	1	–
Cessna 172 Skyhawk	7.52	0.687	2.73	3	1.5	–
Cessna 177 Cardinal	7.31	0.726	1.5	3	3.5	0
Cessna 182 Skylane	7.37	0.669	1.73	3.62	0.78	0
Cessna 208 Caravan	9.61	0.616	3	3.22	2.62	–
Cessna 210 Centurion	7.66	0.726	1.5	3	1.5	–
Cirrus SR20/22	10	0.5	4.5	0	0.25	0 ($c/4$)
Pilatus PC-6 Turbo-Porter	8.4	1	1	–	2	0
Piper PA-28 Cherokee Arrow II	6.11	1	7	–	2	0
Piper PA-28 Cherokee Warrior	7.24	0.669	7	3	2	–
Piper PA-46 Malibu	10.57	–	4	–	–	–
SIAI-Marchetti SF260	6.3	0.49	6.33	2.75	2.75	0 ($c/4$)
Valmet L-70 Miltrainer	6.62	–	–	–	–	–
Valmet L-90 Redigo	7.25	0.6	6	3	3	–
Zlin 142	6.4	1	6	–	–	−4.33
GA Twin Engine						
Beechcraft B58 Baron	7.16	0.42	6	4	4	–
Beechcraft B60 Duke	7.243	0.32	6	4	4	–
Beechcraft B99 Airliner	7.51	0.5	7	4.8	4.8	–
Britten-Norman BN-2A (standard)	7.4	1	0	–	2	0
Cessna 310	7.3	0.674	5	3	2.5	–
Cessna 337 Skymaster	7.18	0.667	3	2	4.5	–
Partenavia P.68 Victor	7.7	1	1	–	1.5	0
Piaggio P.180 Avanti	11.8	0.352	2	–	0	0 (0.15c)
Piper PA-31 Cheyenne	7.22	–	5	2.5	1.5	0 (0.3c)
Piper PA-31-310 Navajo	7.22	–	–	1.0 (aero) 2.5 (geo)	–	–

Based on J.W.R. Taylor, Jane's All the World's Aircraft, Jane's Yearbooks, various years.

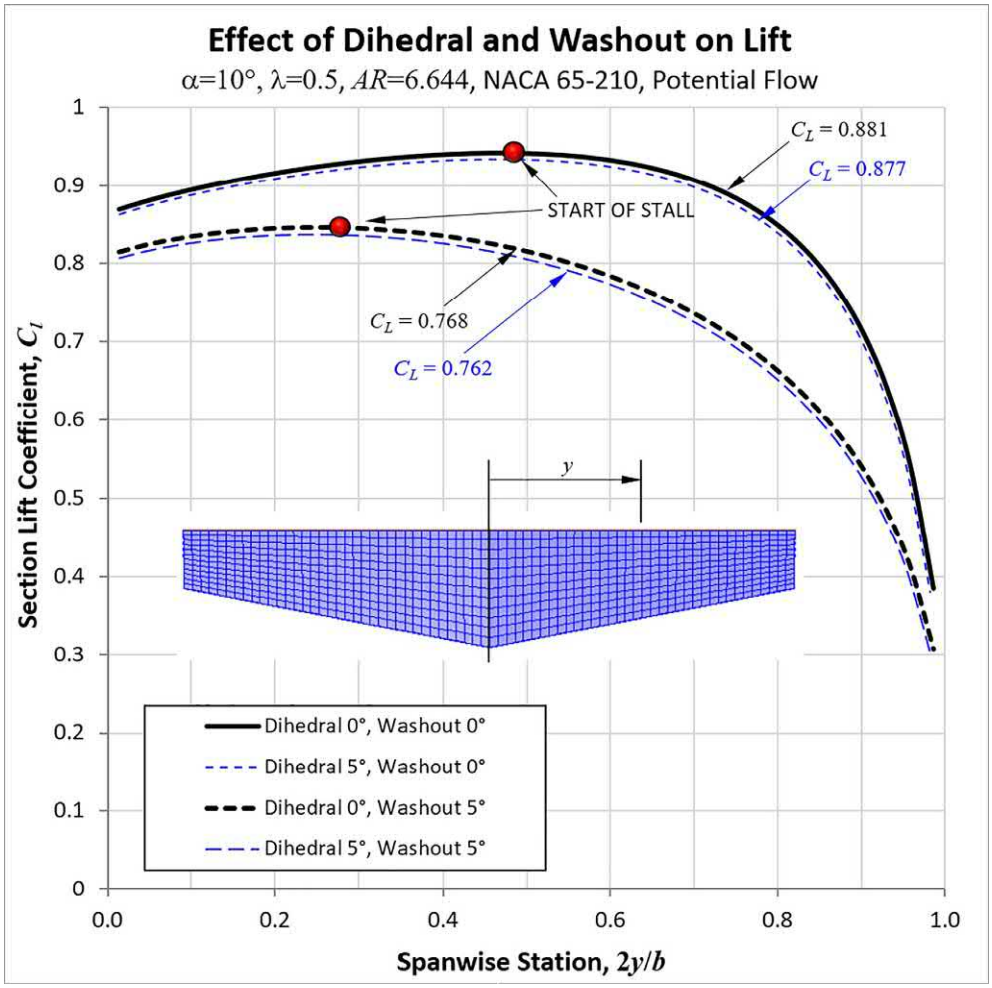


FIGURE 9-22 Impact of geometric washout and dihedral on the aerodynamics of a typical wing.

Also recognize that real-world manufacturing tolerances lead to airplanes that are not perfectly symmetrical. Loose tolerances and poor-quality control further increase the chances of such roll-offs. Items (1) through (3) above help the wingtips remain unstalled when the inboard wing stalls, improving roll stability.

(2) Wing Twist to Modify Lift Distribution

Wing twist is a tool to beneficially control lift distribution.

(1) Figure 8-70 shows that understanding the distribution of C_l over a wing can be utilized to minimize skin friction. Thus, washout can be used to modify the distribution to better suit the drag properties of a selected airfoil.

(2) Recall that a uniform distribution of C_l over the wing results in minimum lift-induced drag. Thus, washout can be used shape the distribution more uniformly. However, Figure 9-22 reveals some of the limitations of this approach (discussed below). Planform shape is a far more effective way of achieving uniform distribution of C_l.

(3) Wing twist changes the pressure distribution over the wing (a change in C_l implies change in C_p). Thus, it can be used to change the shock-formation on a transonic wing. An example of this is the McDonnell-Douglas AV-8B, whose twist varies in a segmented fashion to a maximum of −8° at the tip [17].

(4) Washout offers only a minor reduction in wing bending moments as the center of lift is brought closer to the plane-of-symmetry. This is illustrated in Figure 9-23. When evaluating improvements, the two wing configurations (with and without washout) must be compared at the same lift coefficient (not the same AOA).

(3) The Cost of Twist

Wing twist adds complexity to the design. Washout increases manufacturing cost through added tooling complexity (even for Hershey bar wings). It also costs more money in quality control to inspect. In Figure 9-22, the cost of the 5-degree washout is a 13% reduction in C_L. To make up for that loss, the wing must be placed at

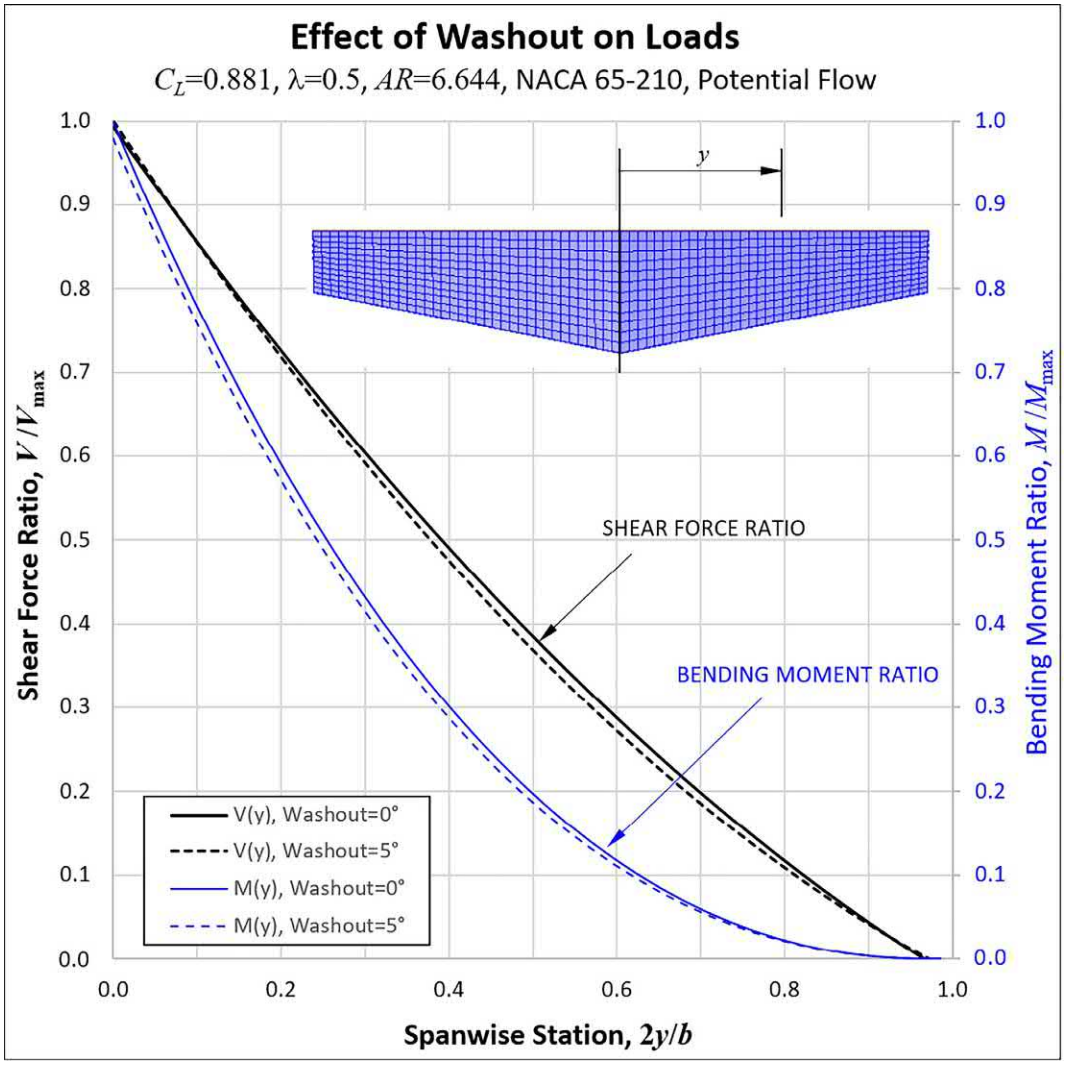


FIGURE 9-23 Impact of geometric washout on the shear and moment of a typical wing.

higher AOA in flight. In this example, to generate the same lift as the baseline does at $\alpha = 10°$ ($C_L = 0.881$), the wing with the 5-degree washout must operate at $\alpha = 11.5°$. Thus, expect washout to increase lift-induced drag. The increase depends on other factors, primarily wing planform.

(4) Estimation of Washout, ϕ

There are two kinds of washout: *geometric* (ϕ_G) and *aerodynamic* (ϕ_A). The washout for the wing must account for the combination:

$$\phi = \phi_A + \phi_G = \alpha_{stall_{root}} - \alpha_{stall_{tip}} + \phi_G \qquad (9\text{-}47)$$

(5) Geometric Washout, ϕ_G

Geometric washout refers to the difference in angles of incidence of the root and tip airfoils (see Figure 9-24). Typical washout ranges from −1° to −4° (the negative sign indicates the tip LE is less than that of the root). When we say the "washout is 3°," we mean that $\phi_G = -3°$. Thus, if "washin is 3°," we mean that $\phi_G = +3°$. If the twist is linear, the relative angle of twist at any spanwise station can be determined using the following expression:

$$\phi(y) = \frac{2y}{b}\phi_G \qquad (9\text{-}48)$$

The expression assumes the reference angle is 0 when $y = 0$ (the plane-of-symmetry) and becomes ϕ_G at the wing tip (where $y = b/2$).

(6) Aerodynamic Washout, ϕ_A

Aerodynamic washout differs from the geometric one in that the root and tip airfoils are selected based on their zero-lift AOA (α_{ZL}) and 2-dimensional stall AOA (α_{stall}). The determination of a "suitable" aerodynamic washout requires an understanding of (1) the relative

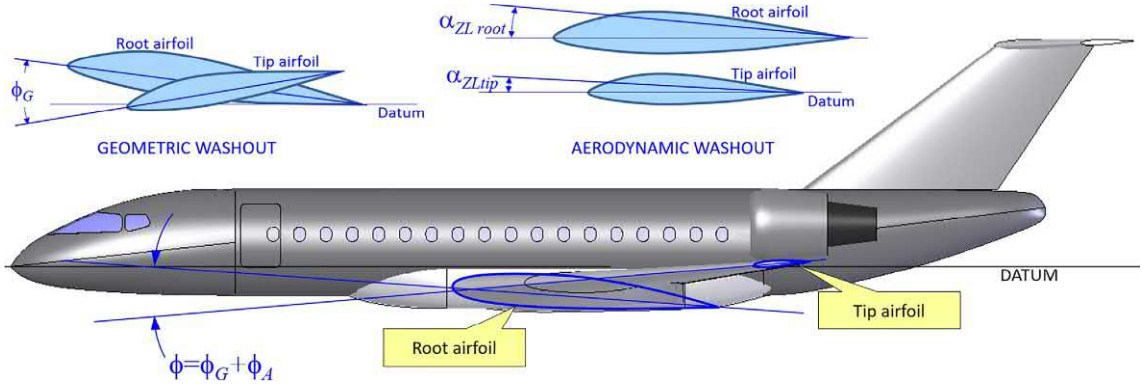


FIGURE 9-24 Definition of geometric washout.

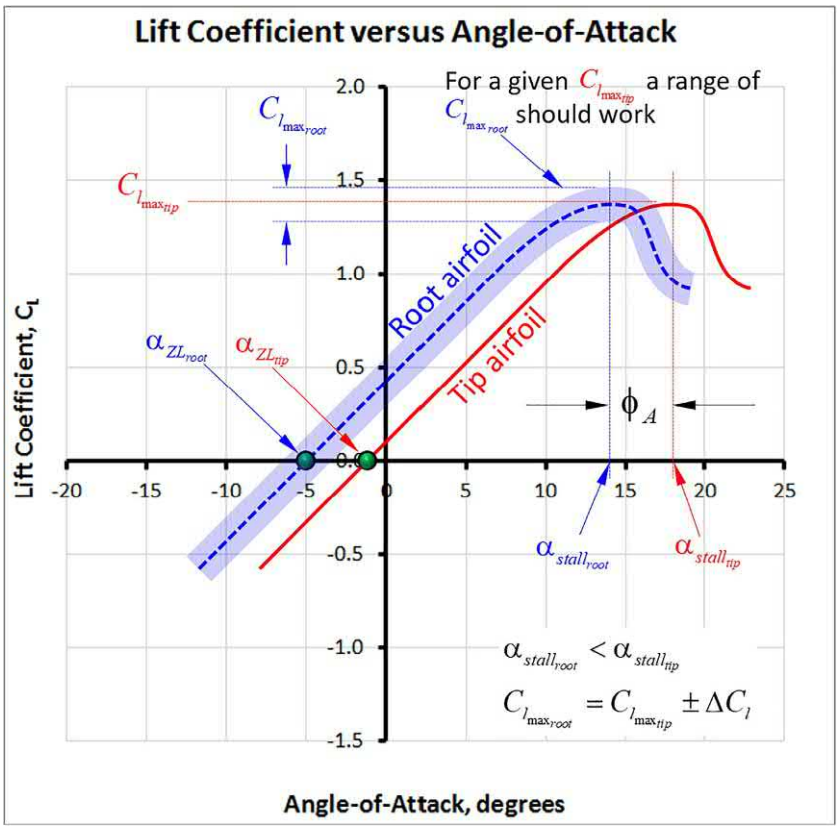


FIGURE 9-25 Requirements for aerodynamic washout.

$C_{l_{max}}$ of the airfoils used, (2) the distribution of C_l along the wing (planform), and (3) instabilities in the flow separation progress. Only rules of thumb can be given. The idea is illustrated in Figure 9-25. The root airfoil must have a lower α_{ZL} and α_{stall} than the tip airfoil. The value of the $C_{l_{max}}$ of the root is less important. In mathematical terms, this is

$$\alpha_{ZL_{root}} < \alpha_{ZL_{tip}}$$
$$\alpha_{stall_{root}} < \alpha_{stall_{tip}}$$
$$C_{l\max_{root}} = C_{l\max_{tip}} \pm \Delta C_l$$

Where the subscripts refer to the root and tip airfoils and ΔC_l defines the range of suitable values of $C_{l_{max}}$.

Aerodynamic washout allows rib chord lines to be aligned normal to the wing spar, simplifying assembly. It can be defined in two ways:

$$\text{Twist based on zero-lift AOA:} \quad \phi_A = \alpha_{ZL_{root}} - \alpha_{ZL_{tip}} \tag{9-49}$$

$$\text{Twist based on stall AOA:} \quad \phi_A = \alpha_{stall_{root}} - \alpha_{stall_{tip}} \tag{9-50}$$

That said, expect the aerodynamic washout to be less effective than geometric washout. Let it be said that the

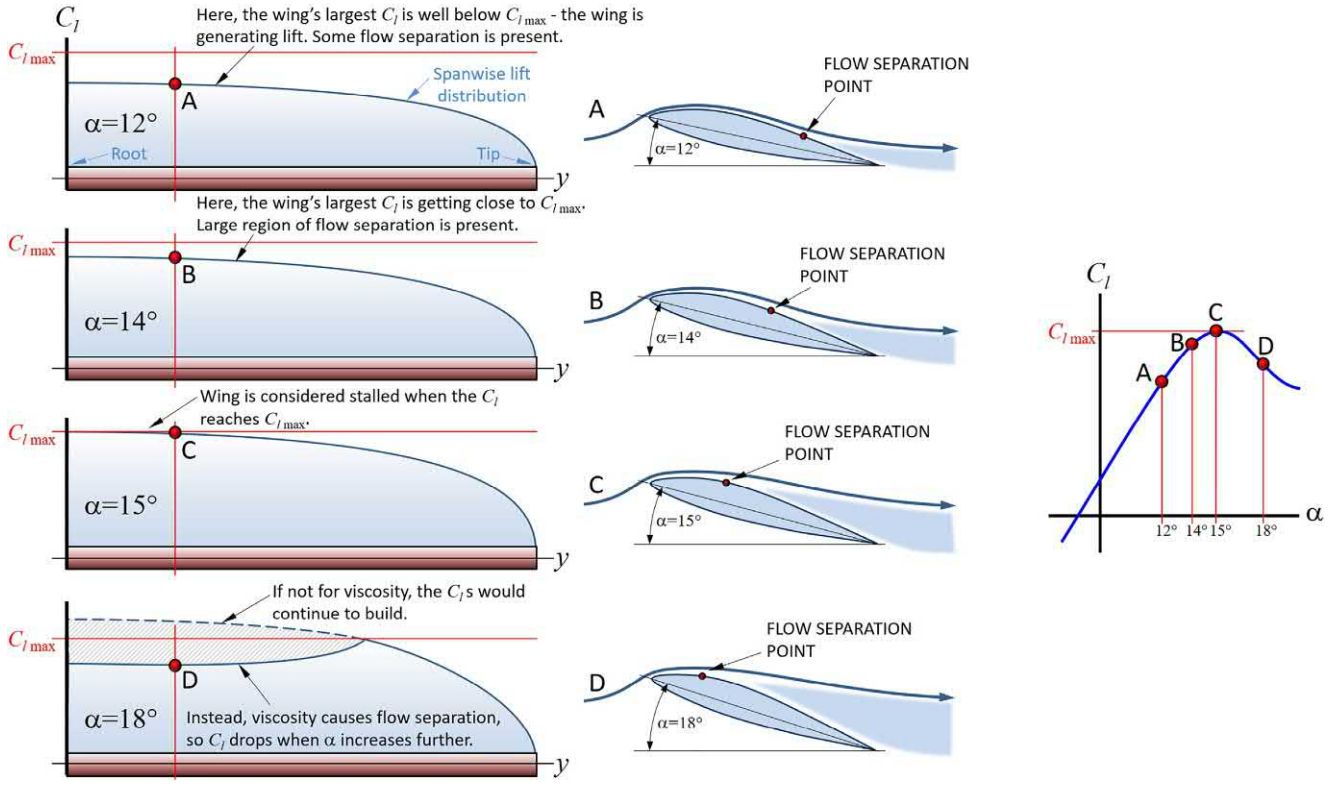


FIGURE 9-26 Change in spanwise lift distribution as wing stall progresses.

flow field over the wing near stall is too complicated for the simplicity of the approach. Figure 9-26 illustrates changes in the distribution of C_l for a simple, untwisted Hershey-bar wing in the pre- and poststall. Points A, B, C, and D refer to the flow at four AOAs at a specific wing station. During prestall, the C_l keeps increasing as AOA increases (A and B). At C, the C_l has reached $C_{l_{max}}$, after which it begins to drop with further increase in AOA (D). But do not be deceived by its clean appearance. The region of the wing under the dip is dynamic and, for high AR wings, tends to form multiple cells whose size and shape change rapidly (e.g., see Refs. [18–20]). The resulting separation and reattachment fronts oscillate such its effect reaches far beyond its extent shown in Figure 9-26. Since, aerodynamic washout tends to be a low value (as a large washout would require large difference in camber), it is more sensitive to deviations of this nature (also see Section 9.6.2, *Deviation from Generic Stall Patterns*). To this author, aerodynamic washout is to be used to supplement geometric washout and not to replace it.

EXAMPLE 9-5

An airplane features two dissimilar airfoils at the root and tip whose $\alpha_{stall_{root}} = 16.5°$ and $\alpha_{stall_{tip}} = 15.0°$. What is the combined washout for a geometric washout of $\phi_G = 0°$ and $\phi_G = 3°$?

SOLUTION:

Combined washout for $\phi_G = 0°$:

$$\phi = \alpha_{stall_{root}} - \alpha_{stall_{tip}} + \phi_G$$
$$= 16.5° - 15.0° + 0° = +1.5° \quad (\text{“washin”})$$

Combined washout for $\phi_G = 3°$:

$$\phi = \alpha_{stall_{root}} - \alpha_{stall_{tip}} + \phi_G$$
$$= 16.5° - 15.0° + (-3°) = -1.5° \quad (\text{“washout”})$$

Recall that a negative angle means the root is at a greater AOA than the tip.

(7) Panknin and Culver Wing Twist Formulas

The wing twist of a flying wing is a fundamental design variable that should be determined early in the design process. In the absence of other tools, the designer of tailless aircraft can determine the proper washout of the wing using one of two specialized formulas for such configurations. They are called the *Panknin* and *Culver twist formulas*. They are presented here without derivation for completeness of the discussion in this section.

The *Panknin Twist Formula* is attributed to Dr. Walter Panknin, who in 1989 presented it to help designers of Radio Controlled (RC) flying wings determine the

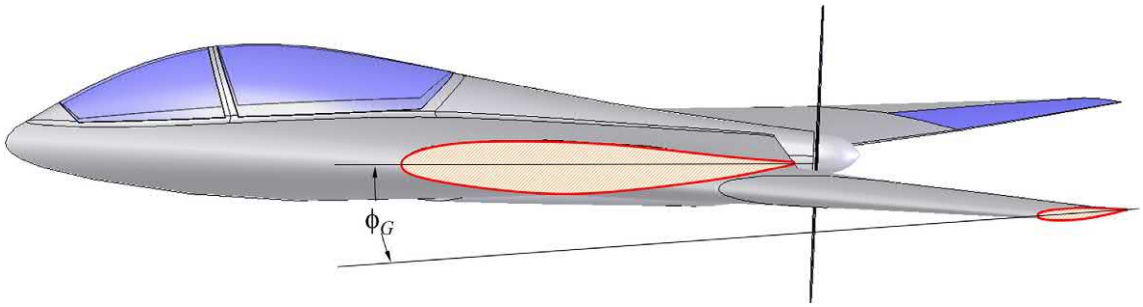


FIGURE 9-27 The Panknin and Culver formulas are used to set the geometric washout of tailless aircraft.

washout of such the elevons are in trail at cruise. The formula was originally derived by Schenk [21, 22]. It has been applied with great success to many RC flying wing designs [23]. It determines the required geometric washout ϕ_G between the inboard and outboard airfoils of the wing (see Figure 9-27) using the following expression:

$$\phi_G = 71429\frac{\left(K_1 C_{m_{root}} + K_2 C_{m_{tip}}\right) - C_{L_C}\cdot K_{SM}}{AR^{1.43}\times\Lambda_{c/4}} - \left(\alpha_{ZL_{root}} - \alpha_{ZL_{tip}}\right) \tag{9-51}$$

Where: $C_{m_{root}}$ = Pitching moment coefficient of the root airfoil

$C_{m_{tip}}$ = Pitching moment coefficient of the tip airfoil
C_{L_C} = Lift coefficient at cruise (for which the aircraft is designed)
K_{SM} = Fraction design *static margin* (e.g., if SM = 10% then $K_{SM} = 0.1$)
$K_1 = \frac{3+2\lambda+\lambda^2}{4\left(1+\lambda+\lambda^2\right)}$
$K_2 = 1 - K_1$
$\alpha_{ZL_{root}}$ = Zero-lift AOA for the root airfoil, in degrees
$\alpha_{ZL_{tip}}$ = Zero-lift AOA for the tip airfoil, in degrees
$\Lambda_{c/4}$ = Quarter-chord sweep angle, in degrees.

The formula allows the designer to determine ϕ_G based on desired static margin (difference between stick-fixed neutral point and center-of-gravity), airfoils, *AR*, and $\Lambda_{c/4}$. It is applicable to both forward and aft swept wings.

The *Culver Twist Formula* is attributed to Mr. Irv Culver (1912–99), a famous engineer at the Lockheed Skunk Works [24, 25]. Like the Panknin formula, it is popular by designers of small tailless RC aircraft. It is intended for flying wings of moderate sweep angles (typically ≈20°) and design lift coefficients of 0.9–1.2, where the lower value indicates a high-speed glider and the higher is for high-performance sailplanes [23]. Note that the presentation here differs slightly from that of Ref. [23] in the simplification of terms.

$$\phi_G = \pi\cdot\Lambda_{c/2}\left(\frac{AR}{AR+1}\right)\frac{C_{L_C}}{C_{L_\alpha}} \tag{9-52}$$

Where: C_{L_α} = Lift curve slope

$\Lambda_{c/2}$ = Center-chord sweep angle, in degrees or radians.

Once the washout is known, its distribution along the span can be found using the following expression:

$$\phi(y) = \phi_G(1-y)^{1+AR/2\pi} \tag{9-53}$$

EXAMPLE 9-6

A flying wing is being designed for operation at a $C_{L_C} = 0.5$ at a static margin of 10% ($K_{SM} = 0.1$). Its $AR = 10$, $\lambda = 0.5$, and $\Lambda_{c/4} = 30°$. Compare the use of a NACA 4415 airfoil (a conventional highly cambered airfoil, whose C_m is −0.1 and $\alpha_{ZL} = -4°$) and a NACA 0015 airfoil (whose C_m is 0.0 and $\alpha_{ZL} = 0°$). What is the required washout using each airfoil, in accordance with the Panknin formula?

SOLUTION:

The solution is effectively "plug and chug" into Equation (9-51). First, the parameters K_1 and K_2 must be determined.

$$K_1 = \frac{3+2\lambda+\lambda^2}{4\left(1+\lambda+\lambda^2\right)} = \frac{3+2(0.5)+(0.5)^2}{4\left(1+0.5+0.5^2\right)} = 0.6071$$
$$\Rightarrow\quad K_2 = 1 - K_1 = 0.3929$$

Using these with Equation (9-51) for the NACA 4415 airfoil leads to:

$$\phi_G = 71429\frac{\left(K_1 C_{m_{root}} + K_2 C_{m_{tip}}\right) - C_{L_{cruise}}\cdot K_{SM}}{AR^{1.43}\times\Lambda_{C/4}} - \left(\alpha_{ZL_{root}} - \alpha_{ZL_{tip}}\right)$$
$$= 71429\frac{(0.6071\times -0.1 + 0.3929\times -0.1) - 0.5\times 0.1}{10^{1.43}\times 30°} - (-4° + 4°) = -13.3°$$

EXAMPLE 9-6 (*cont'd*)

Using these with Equation (9-51) for the NACA 0015 airfoil leads to:

$$\phi_G = 71429\frac{\left(K_1 C_{m_{root}} + K_2 C_{m_{tip}}\right) - C_{L_{cruise}} \cdot K_{SM}}{AR^{1.43} \times \Lambda_{C/4}} - \left(\alpha_{ZL_{root}} - \alpha_{ZL_{tip}}\right)$$

$$= 71429\frac{(0+0) - 0.5 \times 0.1}{10^{1.43} \times 30^\circ} - (0^\circ + 0^\circ) = -4.42^\circ$$

The analysis shows that using a conventional cambered airfoil like the NACA 4415 is a bad choice, as it would require a 13.3° washout. Using a symmetrical airfoil like the NACA 0015 would bring this down to 4.42°. The right choice is a reflexed airfoil.

9.3.6 Wing Angle-of-Incidence, i_W

The wing *angle-of-incidence* (AOI), denoted by i_W, refers to the angle between the root wing chord and a horizontal reference line on the fuselage. Once the position of the wing and horizontal tail on the fuselage is known, their relative incidence angles are determined. The incidence of the horizontal tail is driven by stability and control, whereas the wing AOI is frequently driven by concerns about cruise drag. The goal is to ensure the airplane cruises as close as possible to its minimum drag AOA. This means keeping the fuselage near its minimum drag AOA. This requires the range of cruise AOAs for typical cruise missions to be evaluated.

Consider a commercial jet cruising at airspeed V_C at some altitude (e.g., $M = 0.8$ at 35,000 ft). Let us denote its weight at top-of-climb (or start-of-cruise) as W_1 and its weight at end-of-cruise as W_2. If the airplane operates on fossil fuel, then W_1 will be greater than W_2. Thus, the AOA at start-of-cruise will be higher than at end-of-cruise. It is better to use the mid-range AOA as a representative AOA for the cruise segment. Let us denote it as α_C. This AOA will be closer to both the initial and final AOAs, than if either the initial or final AOA were selected.

Once α_C is known, we can determine the ideal AOI. Consider Figure 9-28, which shows three orientations of a fuselage during the cruise. The two top configurations generate greater cruise drag than the bottom one, which places the fuselage in its minimum drag orientation at cruise. Note that all three fuselage placements show a representative root airfoil mounted at the same α_C—only the fuselage is mounted differently.

The optimum AOA for the fuselage may be based on the minimum drag AOA of the fuselage, its maximum lift-to-drag ratio, or its maximum lift contribution when joined with the wing. The following four steps procedure helps determine a suitable wing AOI.

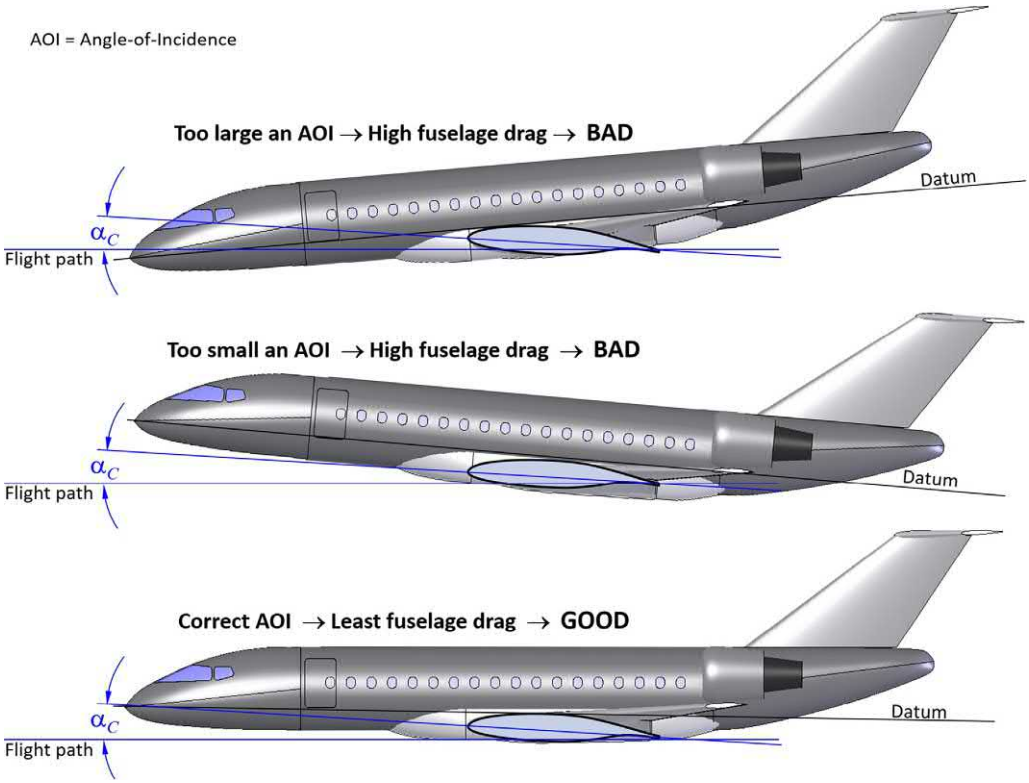


FIGURE 9-28 Determination of the wing AOI based on minimum fuselage drag.

Step 1: Determine the optimum AOA for the Fuselage

The ideal way to determine the optimum AOA for the fuselage (α_{Fopt}) is through wind tunnel testing or a CFD analysis. Such analysis should include the wing and fuselage, as the resulting 3-dimensional flow field is complicated. For computations that follow, we stipulate that.

(1) If α_{Fopt} requires a nose-down fuselage attitude, then let $\alpha_{Fopt} > 0$.
(2) If α_{Fopt} requires a nose-up fuselage attitude, then let $\alpha_{Fopt} < 0$.

Step 2: Determine the Representative AOA at Cruise

The value of α_C can be determined using the following expression:

$$\alpha_C = \left(\frac{1}{C_{L_\alpha}}\right)\frac{(W_1+W_2)}{\rho V_C^2 S} + \alpha_{ZL} \tag{9-54}$$

Where: C_{L_α} = Lift curve slope,

S = Reference wing area,
α_{ZL} = Zero lift angle-of-attack of the aircraft,
ρ = Density at cruise altitude.

Step 3: Determine the Recommended Wing Angle-of-Incidence

The AOI (see Figure 9-29) of the root airfoil (i_W) can now be determined from:

$$i_W = \alpha_C + \alpha_{Fopt} - \Delta\phi_{MGC} \tag{9-55}$$

Where $\Delta\phi_{MGC}$ = Correction to account for wing twist (see below).

Note that since the first two terms of the above expression really return the AOI of the MGC rather than the root, a correction must be introduced if the wing features a washout. This is denoted by the term $\Delta\phi_{MGC}$, which is the difference in angular incidences between the root and MGC airfoils. If the twist is linear, the value of $\Delta\phi_{MGC}$ can be determined by substituting the spanwise location of the MGC, y_{MGC}, of Equation (9-13) into Equation (9-48). Note that the minus sign in Equation (9-55) is required to ensure that this washout correction is added properly.

$$\Delta\phi_{MGC} = \left(\frac{1+2\lambda}{3+3\lambda}\right)\phi_G \tag{9-56}$$

Step 4: Determine the Recommended HT Angle-of-Incidence

Once a recommended wing AOI has been determined, the incidence of the HT can be determined. Again, using the representative cruise mission weight $(W_1+W_2)/2$ the horizontal tail should be mounted such the elevator deflection at this point will be neutral. This is called to "fly with the horizontal in trail" and simply means neutral deflection. This helps reduce trim drag.

DERIVATION OF EQUATION (9-54)

Assuming the general lift properties of the wing are known, the lift coefficient can be written as follows:

$$C_L = C_{L_0} + C_{L_\alpha}\alpha = \frac{2W}{\rho V_\infty^2 S} \tag{i}$$

The weight of the airplane at the midpoint during the cruise is the average of the initial cruise weight, W_1, and the weight at the end of cruise, W_2:

$$C_L = C_{L_0} + C_{L_\alpha}\alpha_C = \frac{2\left(\frac{W_1+W_2}{2}\right)}{\rho V_\infty^2 S} = \frac{(W_1+W_2)}{\rho V_\infty^2 S} \tag{ii}$$

Where α_C is the mid-range AOA. Solving for α_C leads to:

$$C_{L_\alpha}\alpha_C = \frac{(W_1+W_2)}{\rho V_\infty^2 S} - C_{L_0} \quad \Leftrightarrow \quad \alpha_C = \frac{(W_1+W_2)}{\rho V_\infty^2 S C_{L_\alpha}} - \frac{C_{L_0}}{C_{L_\alpha}}$$

The last term is simply the zero-lift AOA, α_{ZL}. Thus, we can write:

$$\alpha_C = \frac{(W_1+W_2)}{\rho V_\infty^2 S C_{L\alpha}} - \frac{C_{L_0}}{C_{L_\alpha}} = \left(\frac{1}{C_{L\alpha}}\right)\frac{(W_1+W_2)}{\rho V_\infty^2 S} + \alpha_{ZL}$$

DERIVATION OF EQUATION (9-56)

The wing washout correction is obtained by inserting Equation (9-13) into Equation (9-48). This leads to:

$$\Delta\phi_{MGC} = \phi(y_{MGC}) = \frac{2y_{MGC}}{b}\phi_G = \left(\frac{2}{b}\right)\left(\frac{b}{6}\right)\left(\frac{1+2\lambda}{1+\lambda}\right)\phi_G$$
$$= \left(\frac{1}{3}\right)\left(\frac{1+2\lambda}{1+\lambda}\right)\phi_G = \left(\frac{1+2\lambda}{3+3\lambda}\right)\phi_G$$

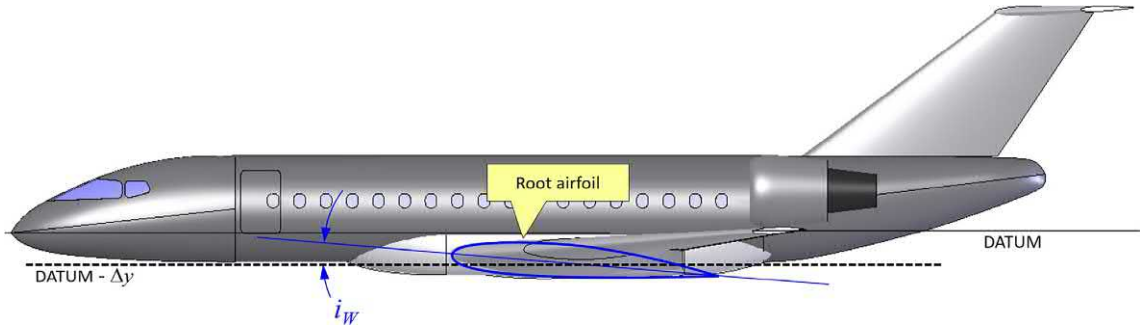


FIGURE 9-29 Definition of a wing incidence angle.

EXAMPLE 9-7

A reconnaissance aircraft is being designed and is expected to weigh 20,000 lb_f at start-of-cruise at a cruising speed $V_C = 250$ KTAS at 25,000 ft, and 11,650 lb_f at end-of-cruise. Determine a suitable AOI for its wing if the following parameters have been determined (ignore compressibility effects): $C_{L_\alpha} = 4.2$ per radian, $S = 350\,ft^2$, $\alpha_{ZL} = -2.5°$, $\alpha_{Fopt} = -2.0°$ (nose-up), taper ratio $\lambda = 0.5$, and $\phi_G = -2.25°$.

SOLUTION:

Step 1: The optimum AOA for the fuselage is 2° nose-up with respect to the **flight path**, so $\alpha_{Fopt} = -2.0°$.

Step 2: Determine the mid-range AOA (density at 25,000 ft is 0.001066 slugs/ft^3).

$$\alpha_C = \left(\frac{1}{C_{L_\alpha}}\right)\frac{(W_1 + W_2)}{\rho V_C^2 S} + \alpha_{ZL}$$
$$= \left(\frac{1}{4.2 \times \pi/180}\right)\frac{(20,000 + 11,650)}{(0.001066)(250 \times 1.688)^2(350)} - 2.5° = 4.0°$$

In other words, mid-range, the AOA of the MGC should be 4.0°.

Step 3: Determine the recommended AOI based on the minimum drag configuration of the fuselage at the cruise midpoint. First, calculate the correction angle since the wing has a 3-degree washout.

$$\Delta\phi_{MGC} = \phi(y_{MGC}) = \left(\frac{1 + 2\lambda}{3 + 3\lambda}\right)\phi_G$$
$$= \left(\frac{1 + 2(0.5)}{3 + 3(0.5)}\right)(-2.25°) = -1.0°$$

Second, calculate the recommended AOI for the wing root chord as follows:

$$i_W = \alpha_C + \alpha_{Fopt} - \Delta\phi_{MGC}$$
$$= 4.0° - 2.0° - (-1.0°) = 3.0°$$

i_W is measured from the **datum**. Recall the AOA of the MGC is given by α_C and is 4.0°. If the α_{Fopt} was 0° rather than −2.0°, the recommended AOI would be 4.0° − (−1.0°) = 5.0°. The resulting geometry is shown in Figure 9-30.

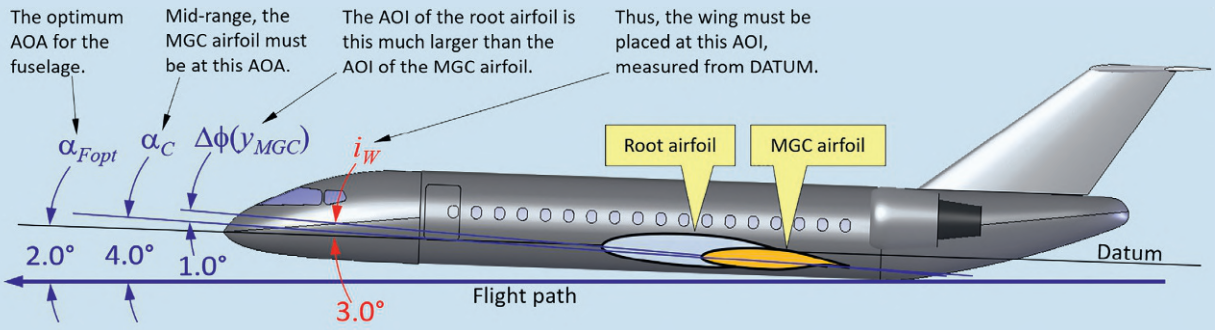


FIGURE 9-30 Wing incidence angle determined for the example aircraft.

Decalage Angle for a Monoplane, ϕ_D

For monoplanes, the *decalage angle* is the difference between the incidence angles of the wing and horizontal tail Figure 9-31. The angle is an important indicator of the stability of the aircraft and requires substantial stability analyses to determine. Strictly speaking, the AOI of the HT, i_{HT}, is determined based on the wing AOI, i_W, and then the decalage angle is calculated as follows:

$$\phi_D = i_W - i_{HT} \tag{9-57}$$

9.3.7 Wing Layout Properties of Selected Aircraft

The purpose of Table 9-6, is to present the reader with typical values of some of the wing parameters presented above to help assessing appropriate values.

9.4 PLANFORM SELECTION

As stated in the introduction of this chapter, great many wing configurations have been devised in the history of aviation. Some are successful (e.g., constant chord, tapered, swept back), while others are not (e.g., triplanes, disk-shaped, circular, channel wings). This section discusses the pros and cons of a variety of wing planforms.

To support the assessment, wing planforms are compared using the spanwise distribution of section lift coefficients (C_l). These are compared to that of a rectangular constant chord wing (baseline). Evaluation of $C_{L_{max}}$ or stall characteristics is not conducted in this elementary study. All the planforms feature a reference area of 10 ft^2, a NACA 4416 airfoil, and are subject to an $\alpha = 10°$. Wing dihedral and washout is 0° for all examples. Aircraft that use said

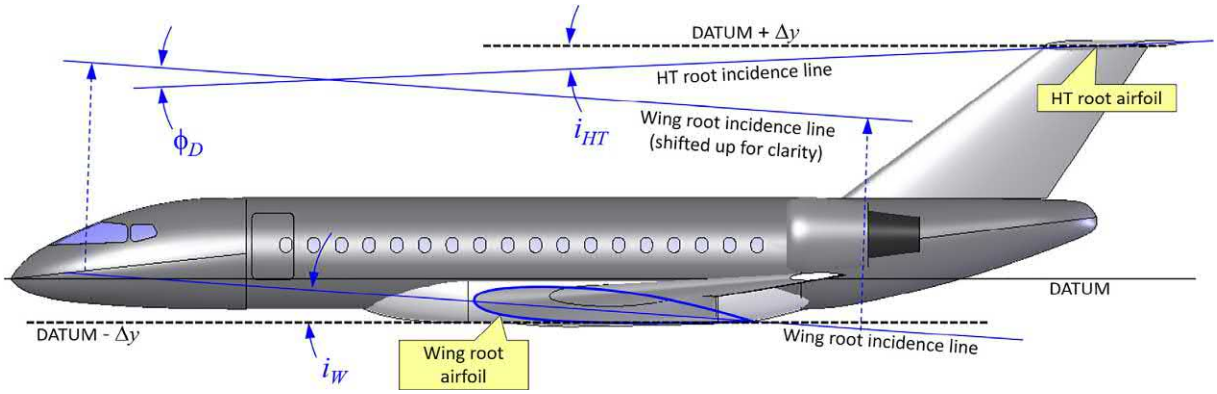


FIGURE 9-31 Definition of a decalage angle for a monoplane.

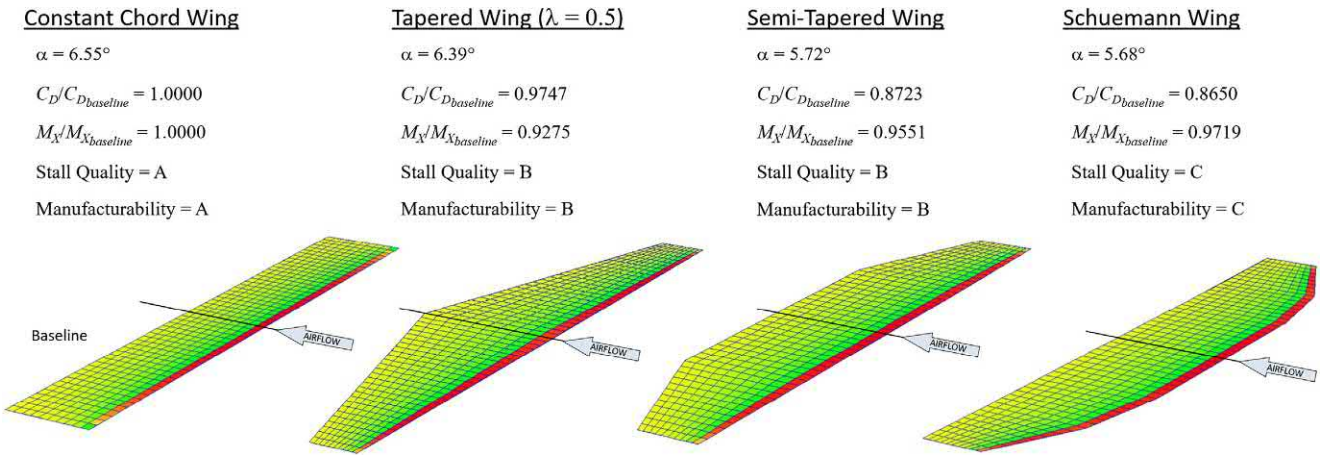


FIGURE 9-32 Comparison of four planform shapes reveals planform selection is multifaceted.

planforms are cited as well. This gives great insight into the lifting capabilities of each planform. However, it does not tell the whole story.

The planform selection is a nuanced process. A proper selection requires a multidisciplinary appraisal. Figure 9-32 compares important properties of four specific planform styles. All are of equal area and aspect ratio ($AR = 6.67$), and all develop $C_L = 0.5$. It is evident that the constant chord wing (the baseline) develops the highest drag (C_D) and bending moment (M_X), but scores the highest in stall quality and manufacturability. The Schuemann wing generates the least drag of the four, but has the worst stall characteristics (in its unmodified form). It is also the most complex to manufacture.

9.4.1 Methods to Present Spanwise Lift Distribution

The lift distribution is usually presented using (1) spanwise force, (2) section lift coefficients (C_l), and the ratio of C_l to the total lift coefficient generated by the wing. These are compared in Figures 9-33–9-35 using a rectangular and elliptic wing planform.

Figure 9-33 shows the distribution of lift as a force along the span. The graph is presented using the physical dimensions of the wingspan (e.g., $b = 35$ ft or similar). In this case, the units for the y-axis of the graph are more correctly represented as lb_f/ft or N/m. The area under the graph is the shear force along the span and, assuming a cantilevered wing, the progression of integration from tip inboard to root will provide a shear diagram. Then, integrating the shear diagram from tip to root will generate the moment diagram. Another important observation is the difference in the force generated by the elliptical wing planform when compared to the rectangular form.

Figure 9-34 shows the distribution of section lift coefficients along the span. The advantage of this presentation is that it can be used to evaluate the magnitude of geometric (or aerodynamic) twist required to help control stall progression or even bending moments. Since an airfoil stalls at a specific 2-dimensional lift coefficient and this format presents the current 2-dimensional lift coefficient (i.e., C_l) the graph can be used to design good stall characteristics into the airplane (see Section 9.6.3, *Tailoring the Stall Progression*).

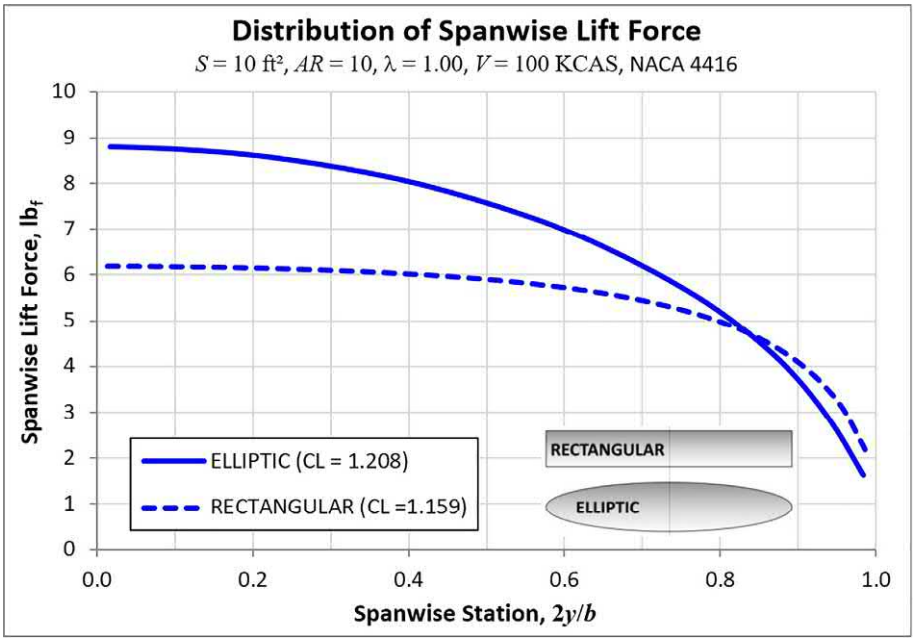


FIGURE 9-33 Comparison of spanwise lift generated by rectangular and elliptical planforms.

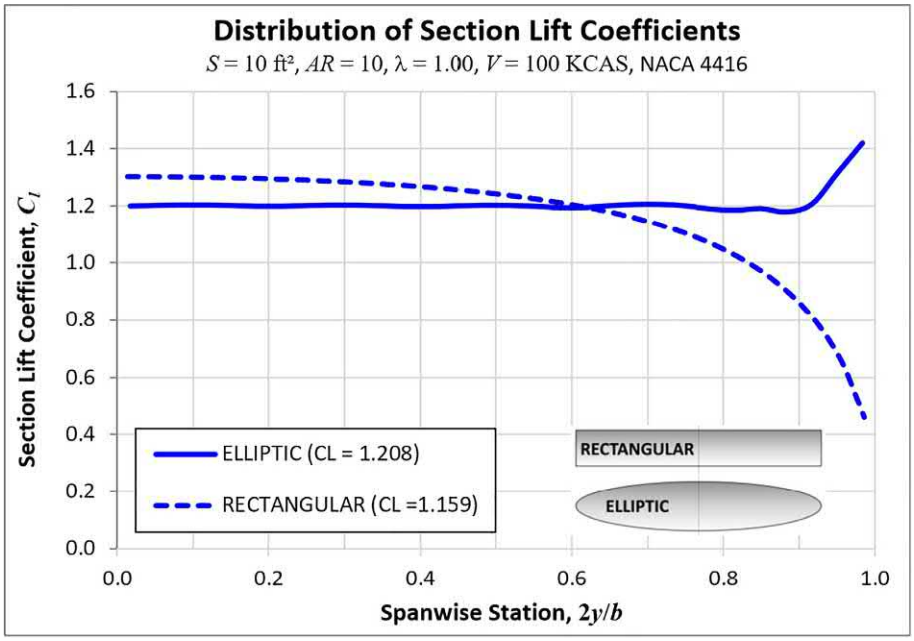


FIGURE 9-34 Comparison of section lift coefficient.

Figure 9-35 shows the distribution of the contribution of the section lift coefficient to the total lift generated by the geometry. It helps identify wing regions that contribute a lot or little to the overall lift.

9.4.2 The Optimum Lift Distribution

Planform selection goals typically include (1) an effective use of the available span for lift generation, (2) low bending moment, (3) docile stall characteristics, and (4) adequate roll responsiveness. Let us consider these in more detail.

Figure 9-36 shows the front view of a cantilevered wing of an arbitrary planform and the spanwise distribution of C_l. Two kinds of distribution of C_l are shown. The first can be considered an *ideal* distribution, which would be achieved if lift did not vanish at the wing tip. This would result in each spanwise station contributing uniformly to the total lift coefficient: When compared to

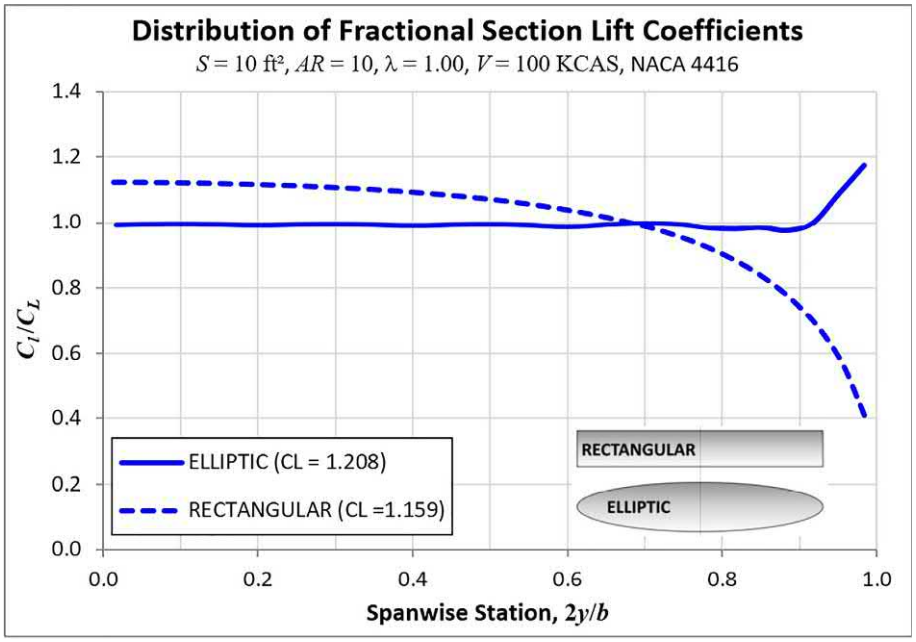


FIGURE 9-35 Comparison of fractional section lift coefficient.

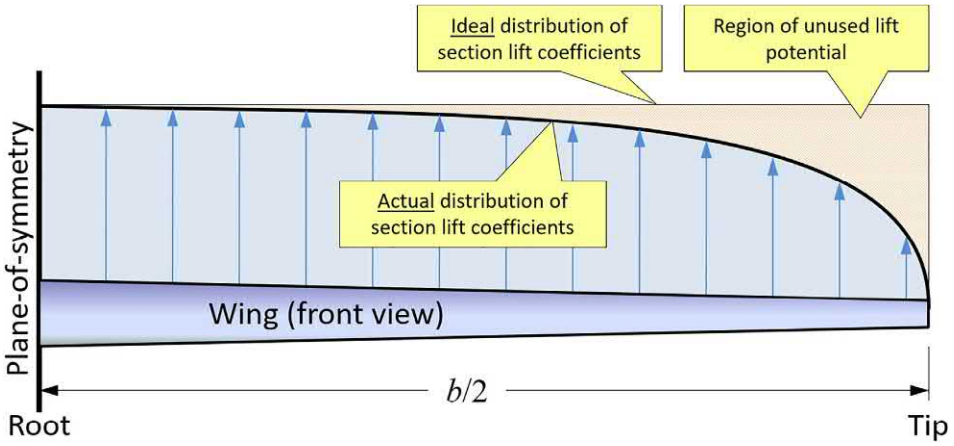


FIGURE 9-36 Ideal, actual, and wasted lift distributions.

other distributions, it requires the least AOA at any given airspeed to maintain altitude. From that perspective, it can be considered the most efficient distribution at our disposal.

The second kind of distribution is the *actual* distribution of C_l. It represents what said wing develops and it differs from the ideal distribution. The region outside the actual distribution represents *unused* lift potential. The smaller this area, the more efficient the wing. The larger this region, the larger the stalling speed and lift-induced drag in cruise. The stalling speed is larger because the missing lift must be made up for using higher dynamic pressure. The induced drag is larger because the missing lift must be made up by a larger AOA in cruise. An important design goal for lifting surfaces is to minimize the wasted lift distribution.

There is one well-known wing planform that, at least in theory, achieves the ideal lift distribution; the elliptical planform (see Figure 9-37). As luck would have it, things are more complicated than that though. Wings designed to generate a uniform a distribution of C_l have a serious side effect: poor stall characteristics. This is driven by the entire wing stalling at the same instant (assuming an identical airfoil from tip-to-tip). As stated in the previous section, this would cause a real airplane to roll abruptly and uncontrollably to one side—a dangerous scenario if the airplane is close to the ground. Thus, we sacrifice some of the efficiency for safety. This is accomplished in elliptic wing using a combination of high-lift airfoils in the tip region and washout.

Another important observation can be made from Figure 9-37: The difference between the distribution of

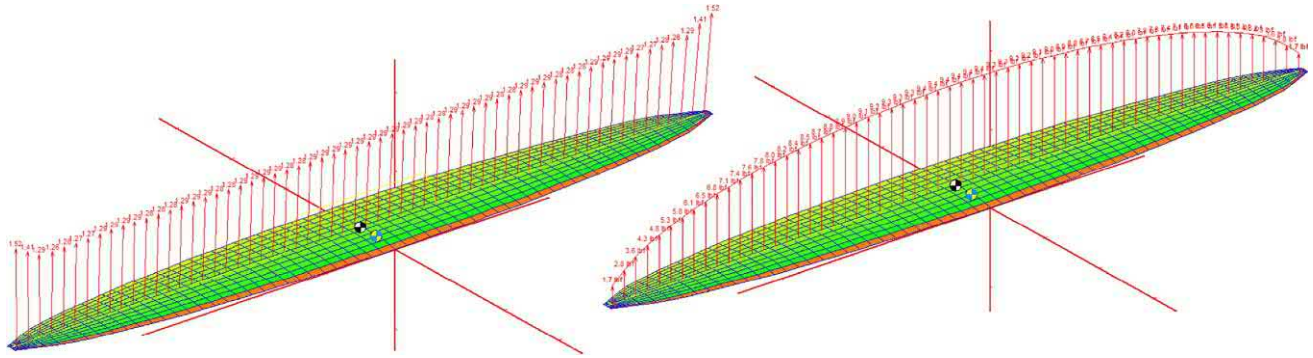


FIGURE 9-37 The difference between the distribution of section lift coefficients (left) and lift force (right). The distribution of section lift coefficients is indicative of stall tendency and induced drag coefficient. The lift force distribution is important for structural issues. The rise in section lift coefficients near the tips is due to imperfect shape approximation of the wing segments.

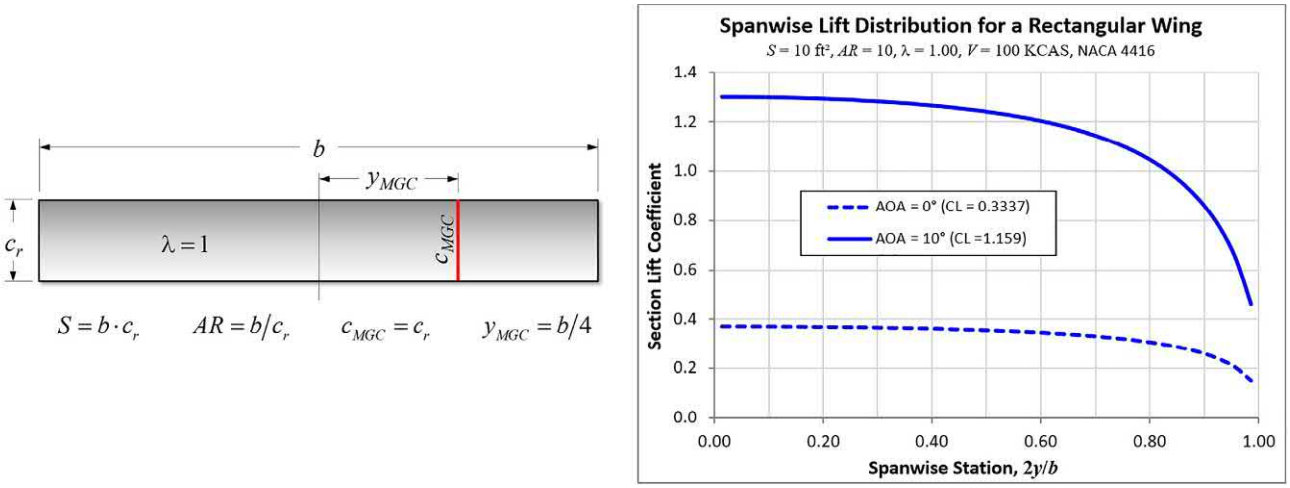


FIGURE 9-38 Basic geometry and lifting characteristics of the *constant chord* wing planform.

section lift coefficients and spanwise lift. While the distribution of C_l is an important indicator for stall tendency and induced drag coefficient, spanwise lift force distribution is imperative for structures. The vertical shear force is determined by integrating the distributed lift force along the span. Bending moments are obtained by integrating the shear along the span. With this in mind, the right graph of Figure 9-18 shows that low λ reduces the wing bending moments by moving the center of the lift inboard. Thus, tapered wings help reduce structural weight. Typical savings are that changing λ from 1 to 0.5 reduces root bending moment by 5%, while changing λ to 0.1 reduces the bending moment by 13%.

9.4.3 Constant Chord ("Hershey Bar") Planform

Nicknamed for its simple constant chord geometry, this planform is widely used. The distribution of spanwise section lift coefficients, C_l, for a Hershey bar wing is shown in Figure 9-38. This is done for two AOAs; 0° and 10°. For comparison, the latter curve is superimposed on all subsequent planform shapes to compare the lift distribution of other planforms to that of the constant chord wing. The Hershey-bar wing is ideal for trainers or airplanes for which manufacturing cost is imperative. The planform is a poor choice for efficient aircraft, such as sailplanes or long-range aircraft. Note that the following images assume the leading edge faces up and the trailing edge down, and simple expressions of wing area and *AR* are provided for convenience. This comparison is implemented via the Vortex-Lattice Method (VLM) using the commercially available code SURFACES [26]. All the models have 720 panels and are aligned along the mean line of the NACA 4416 airfoil.

(1) Pros

(A) Forgiving stall characteristics due to the reduction in section lift coefficients near the wingtip (see Figure 9-38). This promotes a favorable stall progression that begins at the root and progresses outboard, rendering the tip the last region of the wing to stall. This is very desirable as it provides important roll stability at stall. (B) Therefore, washout is usually not required. (C) Lower manufacturing costs because all ribs have

the same basic geometry and the spar is a constant thickness beam. This simplicity extends to the control surfaces.

(2) Cons

(A) The planform is aerodynamically inefficient and (B) develops higher lift-induced drag than tapered wings with $\lambda > 0.1$. (C) It is less efficient structurally because its bending moment is higher than that for tapered wings.

(3) Samples

Beech Model 77 Skipper, Piper PA-38 Tomahawk, Piper PA-28 Cherokee, Piper J-3 Cub, De Havilland of Canada DHC-6 Twin Otter, and Short 360.

9.4.4 Elliptical Planforms

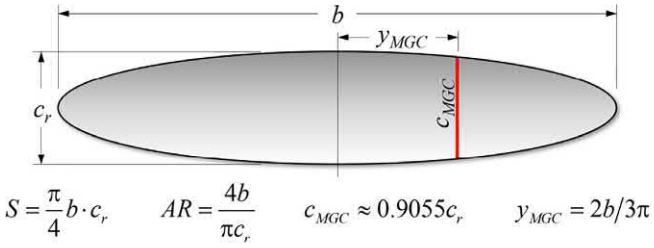
The elliptical wing planform (see Figure 9-39) is most famous for its use in the British Supermarine Spitfire, one of the most formidable fighters of the Second World War. Interestingly, the aerodynamic properties of the planform are widely recognized, even among laypeople. That said, the Spitfire did not feature an elliptical wing because of concerns about lift-induced drag, but because of how its root chord extends outboard. Initially, it tapers very slowly. This provided ample wing thickness to accommodate the landing gear and the outboard position of the machineguns, which were mounted outside the radius of the propeller [27].

The planform shown in Figure 9-39 is a pure ellipse, so the mid-chord line extends from tip-to-tip. There is no requirement that elliptic wings must comply exactly with that geometry. Instead, elliptical wings feature geometry consisting of two halves of dissimilar ellipses joined at positions between leading- and trailing edge—a configuration called *double-ellipse*. For instance, the Spitfire had this at 37% root chord and a straight spar at 27% root chord. Its LE ellipse was different from the TE ellipse.

Elliptical planforms with straight leading or trailing edges (see Figure 9-40) are common in RC aircraft and are sometimes referred to as crescent wings. The graph of Figure 9-40 shows that the distribution of C_l for the three planforms is the same, except at the tip. While all three planform shapes generate a similar C_L at $\alpha = 10°$, the one with the straight LE generates lower section lift coefficient at the tip than the others, implying a less severe means are required to improve stall characteristics. The sharp tip introduces important viscous effects at higher AOAs that render the linear predictions invalid. These are discussed in Section 9.6.2, *Deviation from Generic Stall Patterns*.

(1) Pros

(A) Uniform spanwise distribution of C_l results, which makes the planform very efficient aerodynamically (see Figure 9-39). (B) It produces the least amount of lift-induced drag of any planform.



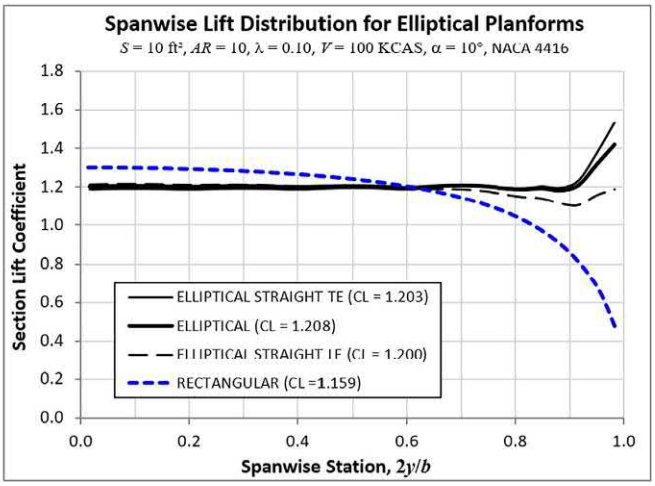


FIGURE 9-39 Basic geometry and lifting characteristics of the *elliptical* wing planform.

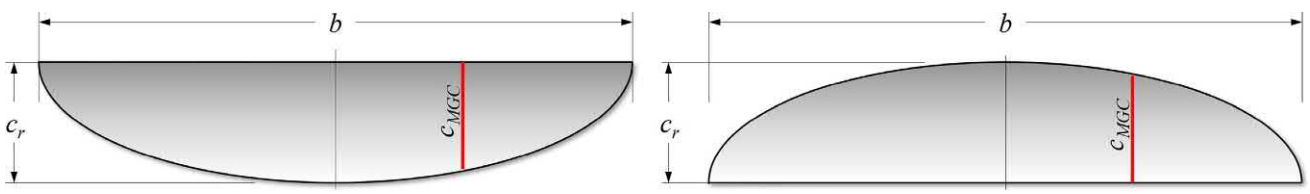


FIGURE 9-40 Basic geometry of *elliptical* planform with a *straight LE* and *TE*.

(2) Cons

(A) Difficult to manufacture due to its complex compound surfaces. Aluminum sheets must be stretched through hydroforming (or similar). However, it is easier to manufacture using modern composites. (B) Since the section lift coefficients are mostly uniform along the span, the entire wing will stall at once, unless measures are taken to improve this. This presents a serious problem for low speed (or high AOA) operations. Fixes include high-lift Class A airfoil in the tip region and washout. The Spitfire utilized a 2.5-degree washout [27].

(3) Samples

Supermarine Spitfire, American Republic P-47 Thunderbolt, Heinkel He-70, He-112B, Mudry CAP-10, and CAP-20.

9.4.5 Straight-Tapered Planforms

The list of airplane types that use this wing planform is very long. A generic-tapered planform and its spanwise distribution of section lift coefficient is shown in Figure 9-41. Note that swept version of this planform is discussed in Section 9.4.7, *Swept Planforms*.

(1) Pros

(A) The primary advantage of tapered wings over the Hershey-bar wing are reduced bending moments. As stated earlier, changing taper ratio $\lambda = 1$ to $\lambda = 0.5$ reduces root bending moment by 5%. Changing this to $\lambda = 0.1$ reduces it by 13%. Figure 15-22 shows how λ reduces lift-induced drag. (B) Compared to the elliptical planform, the linear taper is easier to manufacture, rendering it ideal for most airplanes.

(2) Cons

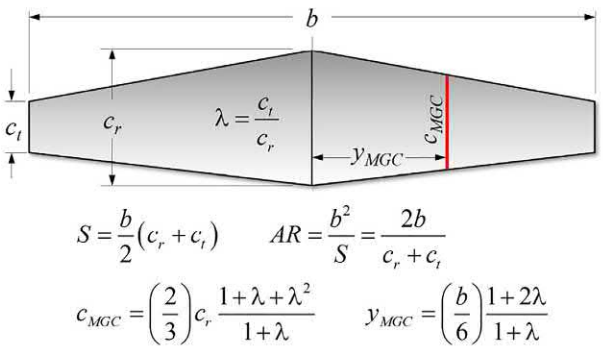
(A) The taper compromises stall characteristics and requires remedies of the kind discussed in Section 9.3.5, *Wing Twist—Washout and Washin*. (B) Manufacturing complications arise due to the different geometry of each rib.

(3) Straight Leading or Trailing Edges

Some airplanes feature straight-tapered wings whose leading or trailing edge is perpendicular to the plane-of-symmetry (see Figure 9-42). This means the quarter-chord line (often selected for main spar location) is swept forward or back.

(4) Pros

(A) Improved structural and aerodynamic efficiency over the constant chord configuration. (B) The straight LE planform may be advantageous if it is foreseen that the operational CG will be too far forward. The opposite holds for operational CG that turn out to be too far aft.



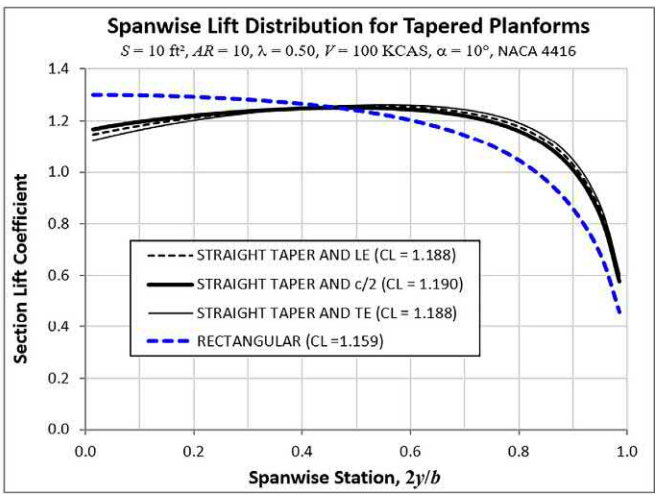


FIGURE 9-41 Basic geometry and lifting characteristics of *straight-tapered* wing planforms.

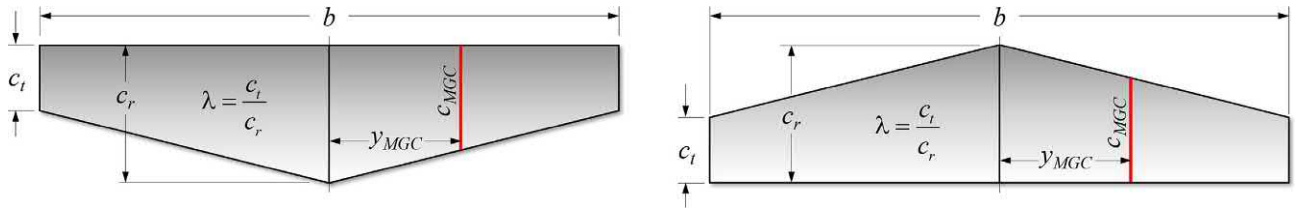


FIGURE 9-42 Basic geometry of the *straight-LE and -TE–tapered* wing planform.

(5) Cons

(A) Harder to manufacture than the constant chord wing. (B) A straight, unbroken spar that is perpendicular to the plane-of-symmetry will have curved spar-caps. If this remedied by sweeping the spar forward, then a single-piece straight spar is not possible. (C) Control surfaces hinge lines may inherit a significant sweep, making them less efficient aerodynamically and can complicate the design of the control system. A straight trailing-edge–tapered wing is shown in Figure 9-42. Many of the same arguments for or against hold for this planform.

(6) Samples

Straight LE: Arado Ar-79, Cessna 177 Cardinal, Commonwealth Ca-12 Boomerang, Fairey Barracuda, and a series of Mooney aircraft feature the planform shape for both the wing and stabilizing surfaces. Straight TE: Aermacchi MB-326 and MB-339, Bücker Bü-180 Student, Zlin Z-326, Z-526, Z-726, and Z-26.

9.4.6 Compound-Tapered Planforms

The compound-tapered wing planform consists of two tapered sections; the inboard section is an inverse taper and the outboard section has standard taper (see Figure 9-43). The lift distribution of this planform shows high-section lift coefficients peak inboard (where stall should begin). Adding a little washout to the outboard wing would not hurt. Without washout, one can argue the planform provides more lift at a given AOA than the Hershey-bar wing but begs the question if the complex structure is worth the effort. That said, it is possible the LE discontinuity improves stall handling by splitting the planform into low AR segments.

Samples

The best-known aircraft featuring this planform is the Westland Lysander, a British single-engine observation aircraft with Short Take-Off and Landing (STOL) characteristics designed in the 1930s. Its design was led by Teddy Petter, who also led the design of aircraft such as the Westland Whirlwind, Folland Gnat, English-Electric Canberra, and English-Electric Lightning [28]. The reason for this choice was pilot visibility—its STOL capability can be attributed to its high-lift system and not the planform itself.

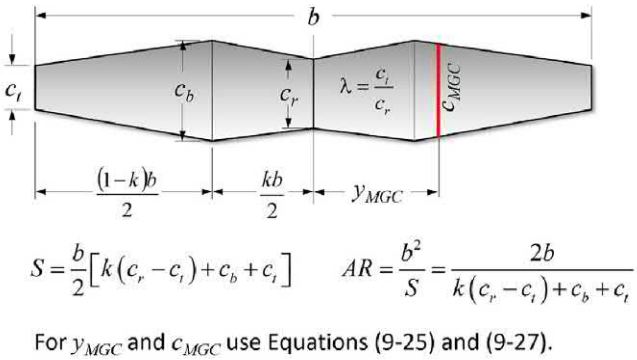
9.4.7 Swept Planforms

Like the tapered wing planform, the swept wing is one of the most used planforms in aviation. All commercial jets use swept wings, and many low airspeed aircraft use aft swept stabilizing surfaces. This warrants more detailed discussion.

(1) Classes of Swept Wing Planforms

It is helpful to classify swept wings based on Taper Ratio, λ. Let's define three classes; $\lambda<1$, $\lambda=1$, $\lambda>1$ (see Figure 9-44 and 9-45). Most swept wing aircraft fall into the first category. The majority of high-speed military and passenger transport aircraft feature tapered aft sweep.

The other two classes only contain a few examples. Examples of aircraft for which $\lambda=1$ include the Northrop Grumman B-2 Spirit, Dunne Monoplane and Biplane (designed in the 1910s by John W. Dunne (1875–1949)), English Electric Lightning, MiG-8 Outcka, MiG I-320, MiG-17, Sukhoï Su-15P, and Yakovlev Yak-25. To knowledge of this author, the only contender in the third category ($\lambda>1$) is the Republic XF-91 Thunderceptor. Its larger tip chord reduces C_l at the tip to improve low speed handling. It also delays shock formation at high subsonic speeds.



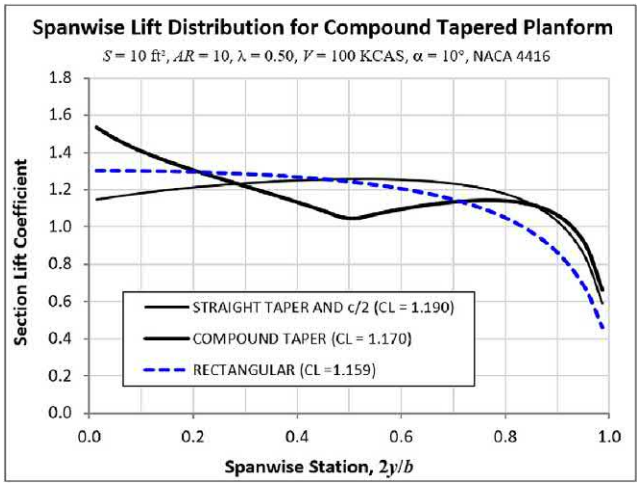


FIGURE 9-43 Basic geometry and lifting characteristics of the *compound-tapered* wing planform.

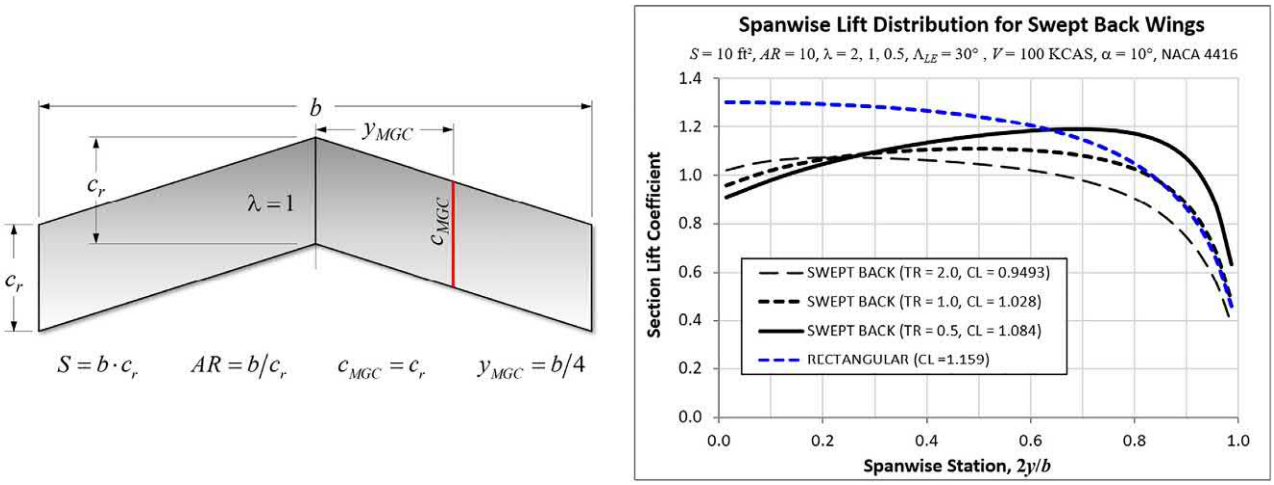


FIGURE 9-44 Basic geometry of the constant chord *sweptback* wing planform.

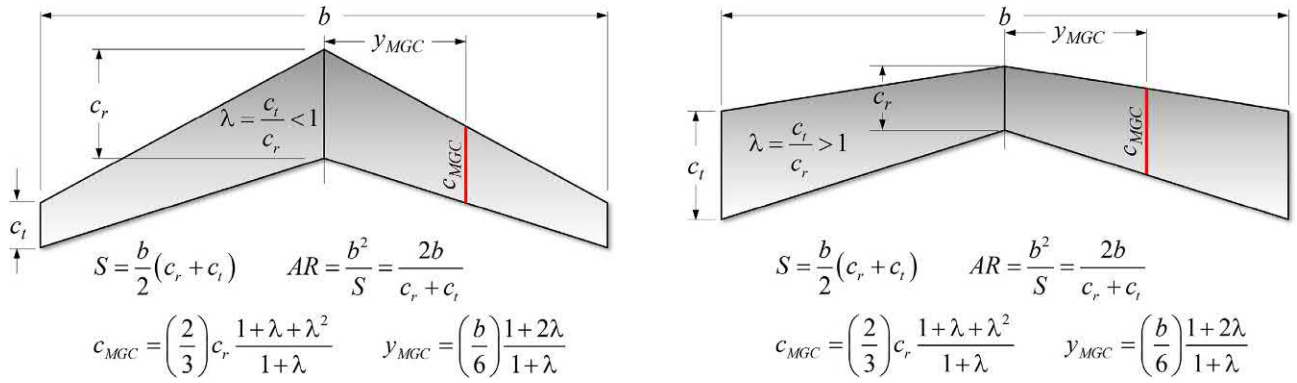


FIGURE 9-45 Basic geometry of the *tapered* and *inverse-tapered sweptback* wing planform.

(2) Aft Swept Planform—Pros

(A) Moves shock formation to a higher Mach number (see Section 9.3.3, *Wing Sweep Angle*). (B) Less susceptible to flutter than the straight- and forward-swept configurations. This results from an aeroelastic reduction in the wingtip AOA due to positive lift. (C) The aft (or forward) swept configuration can be used to solve minor CG-position issues. The Messerschmitt Me-262 Schwalbe was the first jet to feature a swept back wing. Its sweep angle of 18.5° was too modest to impact drag divergence. Rather, its Junkers Jumo jet engines were heavier than expected and moved its CG aft. The originally straight wings were swept aft to solve this issue [29]. (D) Reduces transonic and supersonic drag. (E) Increases buffeting speed (important for fighters) [13]. (F) Causes gradual reduction in C_L in transonic range, contrasting a sharp reduction of straight wings. (G) Reduces the shift of the aerodynamic center in transonic range compared to straight wings.

(3) Aft Swept Planform—Cons

(A) Reduced $C_{L_{max}}$ increases runway requirements. (B) Reduced C_{L_α} requires higher nose-up attitude at low airspeeds, limiting C_L during T-O. (C) Swept high AR wings are susceptible to roll-reversal. (E) Reduced control surface effectiveness. (D) Structural span is greater than actual wing span and, in combination with higher wing torsion, results in heavier structure. (E) Deterioration in airflow in the tip region as AOA increases (see Section 9.6.4, *Cause of Spanwise Flow for a Swept Back Wing Planform*). Near stall, this induces a strong nose pitch-up moment and an accompanying reduction in roll stability and aileron effectiveness. It also limits usable C_L-range. (F) Prone to asymmetric stalling due to early tip-stall. This causes terrible stall characteristics with violent roll-offs, calling for aggressive remedies such as slats (wing fences may be inadequate) and, sometimes, envelope protection. (G) Center-of-lift behind the wing root attachment increases wing torsion, increasing airframe weight. (H) More susceptible to aileron reversal because the lift force reduces the AOA of the tip through aeroelastic effects. This is aggravated by aileron deflection. (i) Issues with wing fuel tanks. For instance, as the airplane rotates to take-off and begins to climb, fuel will flow toward the tip and aft side of the tank, shifting the CG aft. This is solved using one-way flapper valves, called *baffle check valves*. These only allow fuel to flow

inboard [30]. Large transport aircraft, some carrying as much as 40% of their gross weight in fuel, can experience large changes in CG location as fuel is consumed. This often calls for a computer-controlled fuel management system that monitors and controls how fuel from the wing tanks is used.

(4) Forward Swept Planform—Pros

(A) Reduced section lift coefficients at the tip (see Figure 9-46). This is one of its primary aerodynamic advantages. It ensures the inboard wing stalls first, giving the configuration great roll stability at stall (also while pulling high g). (B) The reduced tip-loading improves aileron authority at high AOA (albeit offset by swept hinge-lines). (C) Spanwise flow is directed inboard rather than outboard, where the fuselage acts as an endplate, reducing its detrimental effect.

(5) Forward Swept Planform—Cons

(A) Divergent aeroelastic deformation. The AOA of the wingtip is increased due to the center-of-lift being forward of wing root. This increases the torsion, further raising the AOA and is conducive to divergent aeroelasticity. (B) This tendency requires stiffer wing, increasing its weight.

The first major development of a forward swept wing configuration was the German Junker Ju-287. An interesting discussion of its development is given in Ref. [8]. The configuration has been used in a few other designs, including the Grumman X-29, the HFB-340 Hansajet, and the Sukhoi Su-47. Ref. [31] provides a great insight into the development of the X-29. A modest forward sweep is common, for instance in sailplanes and a number of GA aircraft. However, it is always a CG fix and not associated with compressibility.

(6) Variable Swept Planform

The variable sweep planform (see schematic in Figure 9-47) dates back to the German Messerschmitt P.1101, whose incomplete prototype was discovered at the end of Second World War. It featured a swiveling wing design whose sweep angle was to be selected and set manually before each flight. Later, this innovative design led to fighter and bomber models, such as the General Dynamics F-111, Grumman F-14, Sukhoi Su-17, MiG-23, and Panavia Tornado. The configuration is not used in any GA aircraft, as it increases weight and control system complexity, to name a few. It is suited for supersonic aircraft, where it solves problems at the high and low speed extremes of the flight envelope. It is included here for the sake of completeness.

9.4.8 Cranked Planforms

The term *cranked* refers to a discontinuous leading or trailing edge of a wing. Such planforms are common.

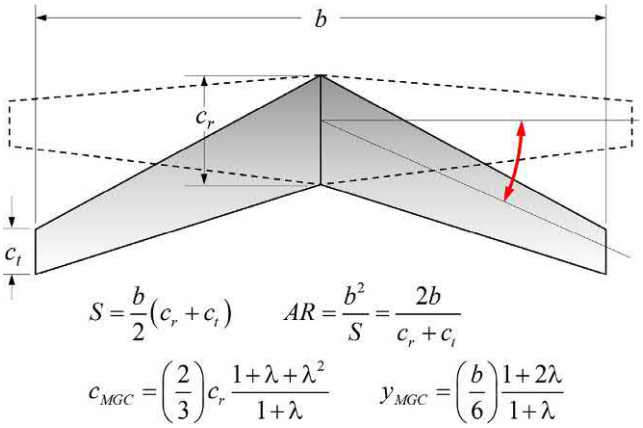
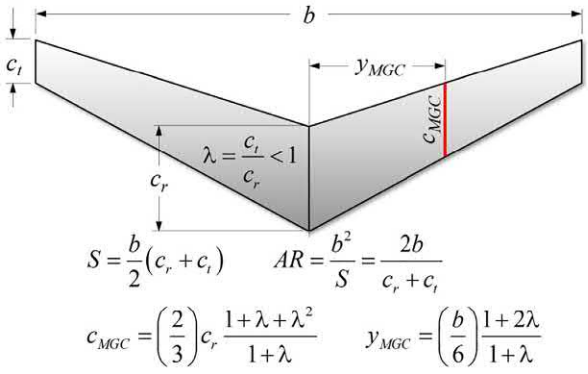


FIGURE 9-47 Basic geometry of the *variable sweep* wing planform.



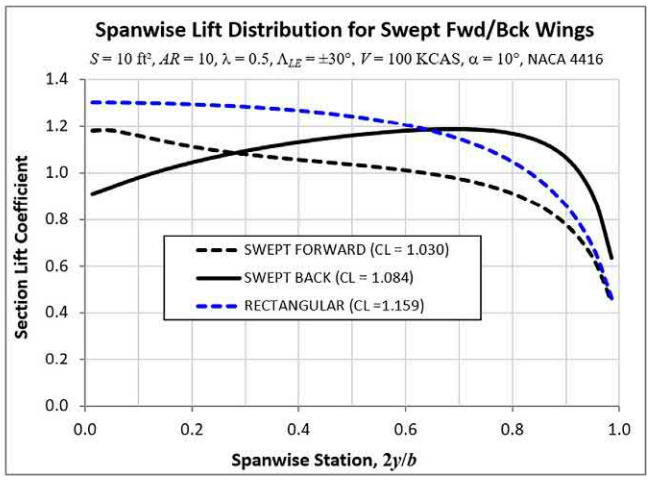


FIGURE 9-46 Basic geometry and basic lifting characteristics of the forward swept wing, compared to the constant chord and the tapered swept-back planform shapes.

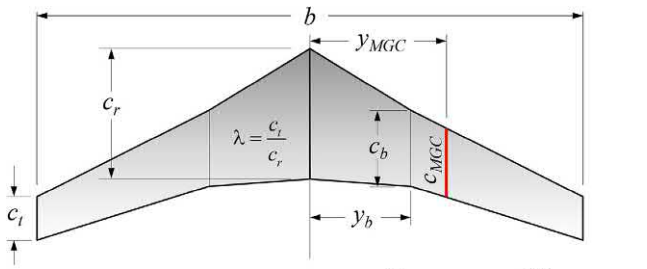
Many single-engine Cessna aircraft feature cranked wings, as do other popular aircraft like the Piper PA-28 Cherokee Archer or the Beechcraft Bonanza. Although considered a separate class, the double-delta planform is also a cranked planform. In fact, any aircraft that features a leading-edge extension falls into this category. However, by convention, double deltas are considered a member of the family of delta wings.

(1) General Cranked Planform

The cranked planform (see Figure 9-48) is discussed in Section 9.2.3, *Geometric Formulation of a Cranked Planform*. In addition to many GA aircraft, it is a common layout for commercial and business aircraft.

(2) Semitapered Planform

The semitapered planform has a constant chord inboard section and a tapered outboard section (see Figure 9-49). This increases the section lift coefficients on the outboard wing, improving its efficiency over that of the Hershey bar wing. A side benefit of this is improvement in aileron effectiveness. The drawback is the added complexity of construction, and reduction in the aileron effectiveness if its hinge line becomes highly swept. The configuration is best known on a family of single-engine Cessna aircraft; the 150, 152, 172, 182, 206, and many others. It is also used on Piper PA-28 Warrior and Cherokee Archer aircraft.



$$S = (c_r - c_t)\,y_b + (c_b + c_t)\,b/2 \qquad AR = \frac{b^2}{S} = \frac{2b^2}{2(c_r - c_t)\,y_b + (c_b + c_t)\,b}$$

For y_{MGC} and c_{MGC} use Equations (9-25) and (9-27).

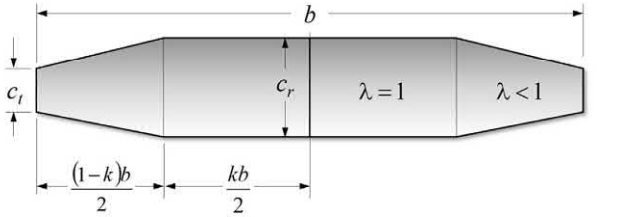
FIGURE 9-48 Basic geometry of the *cranked* wing planform.

(3) Crescent Planform

Despite being superbly imaginatively conceived, the *Crescent* wing planform (see Figure 9-50) has seen limited use. It is best known for its use on the British Handley-Page Victor. Its wing was split into three sections: inboard, center, and outboard. The inboard section houses two turbojet engines, the center section houses the landing gear, and the outboard section is clear from such duties. This arrangement called for a thick inboard airfoil ($t/c = 0.22$), moderately thick center airfoil, and thin outboard airfoil ($t/c = 0.04$). To keep wave-drag manageable (and this depends on t/c), the inboard wing has the highest sweep angle (53°) and the outboard the least (22°). This allowed a constant M_{crit} to be maintained along the wing and resulted in more efficient reaction of bending moments. An additional benefit of this design is enhanced aileron roll response, reduced tendency for tip stall and subsequent nose pitch-up [32].

(4) Schuemann Planform

Named after Wil Schuemann, who in a 1983 article [33] argued that a straight trailing edge and aft swept wingtip reduces spanwise pressure gradients and, thus, spanwise flow along the trailing edge at higher AOA. This suppresses the formation of a separation region extending from the wingtip to the root, reducing drag. It is found on several modern sailplanes, e.g., the Stemme S-10 and the DG-1000. The wing style has also been introduced on commuter aircraft such as the Dornier Do-228, Dornier



$$S = \frac{b}{2}\left[c_r(1+k) + c_t(1-k)\right] \qquad AR = \frac{b^2}{S} = \frac{2b}{c_r(1+k) + c_t(1-k)}$$

For y_{MGC} and c_{MGC} use Equations (9-25) and (9-27).

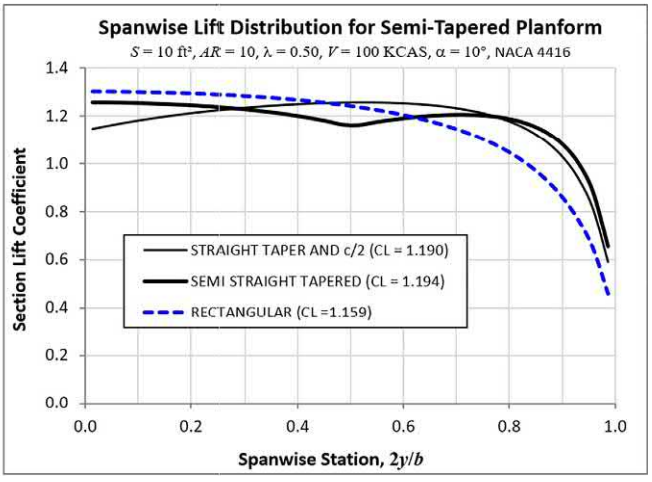
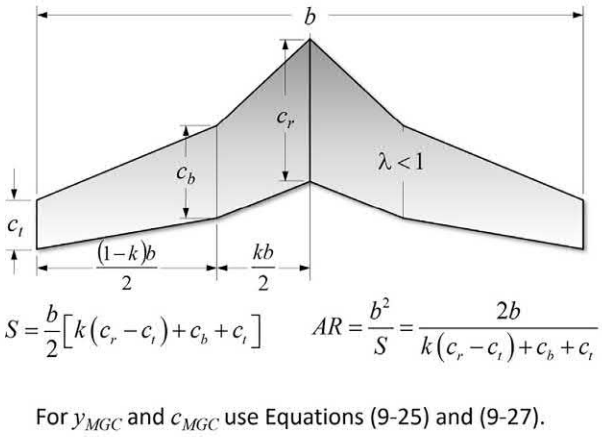


FIGURE 9-49 Basic geometry and lifting characteristics of the *semitapered* wing, compared to the constant chord and the tapered sweptback planform.



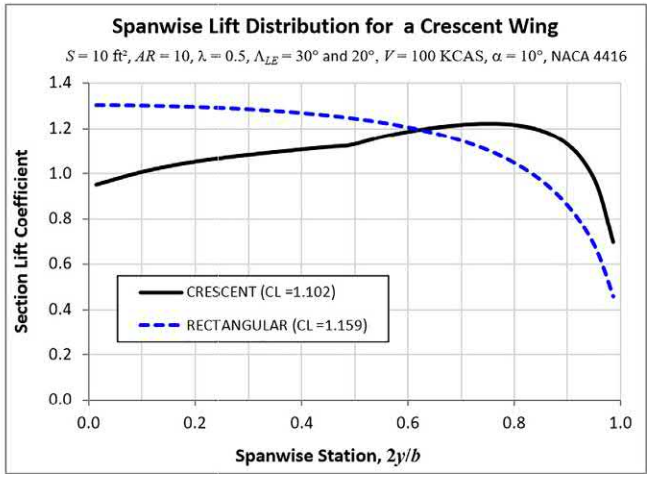
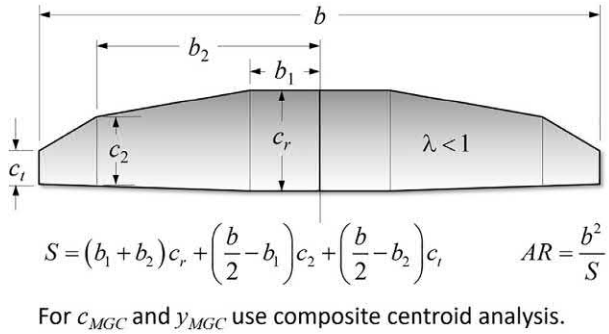


FIGURE 9-50 Basic geometry and lifting characteristics of the *crescent* wing planform.



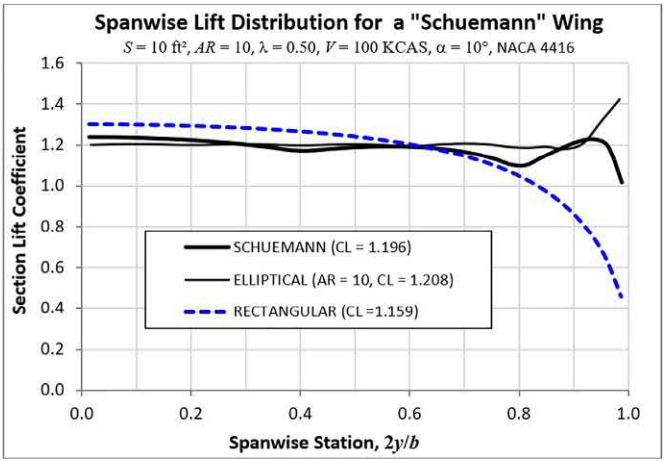


FIGURE 9-51 Basic geometry and lifting characteristics of *Schuemann* wing planform.

328, and Fairchild-Dornier 328JET. Additional information is presented in Refs. [34, 35].

Figure 9-51 shows the fundamental dimensions of the planform shape and the distribution of the section lift coefficients to that of a Hershey-bar and elliptical planform shapes. The distribution approximates that of the elliptical planform, leading to a reduction in lift-induced drag. Being simpler to fabricate than an elliptic wing explains the wing's popularity for sailplanes. The graph reveals an early tip stall as a potential problem due to its sharp outboard taper. Nevertheless, the wingtip of the Dornier 228 and 328 are touted to perform like *raked wingtips* (see Section 10.5.7, *Raked Wingtip*). Sailplane wingtips at a high AOA flex significantly due to aeroelastic effects. This unloads the wingtip and loads up the center portion of the wing, which then stalls before the wing tip. For this reason, sailplanes usually have good stall characteristics. Short, stiff wings for GA aircraft will not flex as much as the high AR wing. Thus, a decisive wing washout at the tip may have to be considered.

9.4.9 Delta Planforms

(1) The Delta Planform Shape

The delta wing is intended for high-subsonic or supersonic aircraft, not low-subsonic airplanes. While it is possible to use delta wings for that purpose (as evident by the Dyke Delta), the choice is hard to justify for reasons other than fun flying and reduced hangar space. Deltas stall at high AOA and low $C_{L_{max}}$ compared to straight wings. As an example, the 2000 lb_f Dyke JD-2 Delta reportedly stalls at about 61–65 KCAS [36]. This means its 173 ft^2 wing generates a $C_{L_{max}}$ around 0.8–0.9. This is 60%–65% of the capability of a conventional straight wing. Figure 9-52 shows typical lift curves for delta wings [37]. Figure 9-53 shows its basic geometry. Note that the two deltas being compared produce $C_L \approx 1.0$ at $\alpha \approx 25$–$28°$. Conventional wings develop this near 10°, give or take. This means the airplane must either land at an excessive deck angle or "come in hot." This drives their requirements for longer T-O and landing distances.

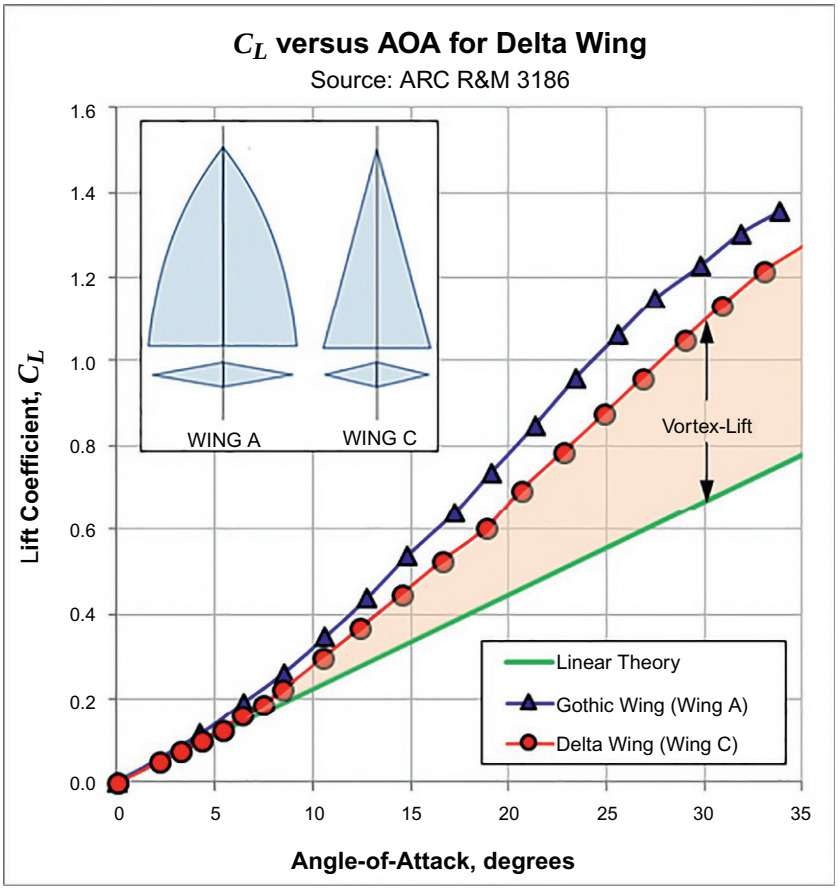


FIGURE 9-52 Lift curves for two types of delta wings. *Based on D.H. Peckham, Low-Speed Wind-Tunnel Tests on a Series of Uncambered Slender Pointed Wings With Sharp Edges, Aeronautical Research Council, R.&M. No. 3186, 1959.*

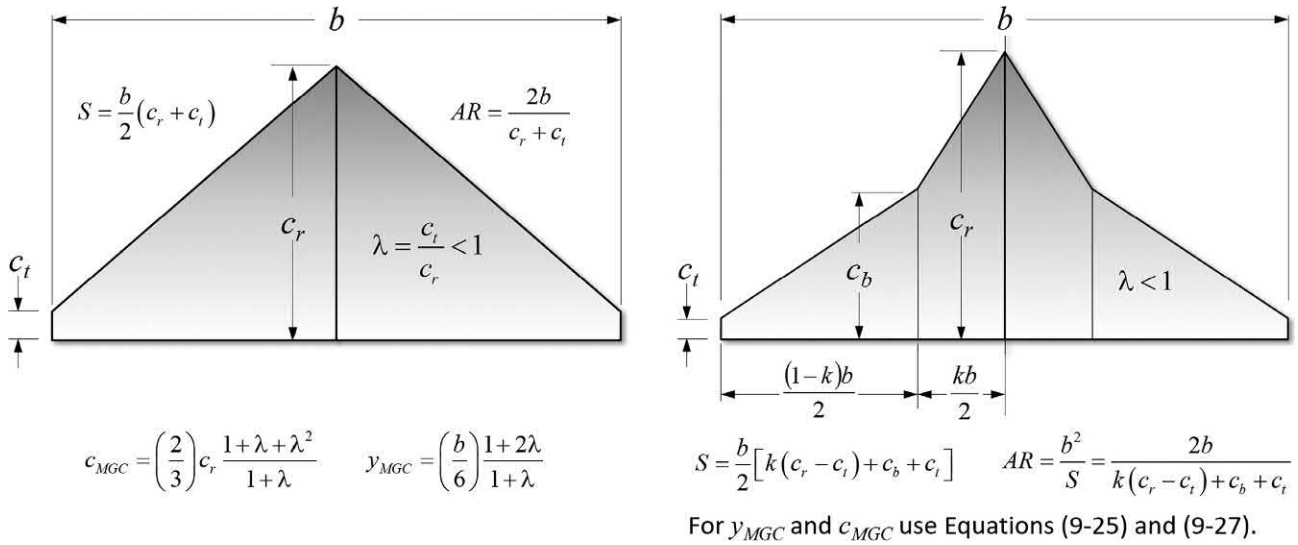


FIGURE 9-53 Basic geometry of the *delta* and *double-delta* wing planforms.

Furthermore, their low AR produces a poor LD_{max}, which is of concern for engine-out emergencies and range. The best-known aircraft that uses the configuration is the MiG-21 (has HT) and Dassault Mirage III (no HT) and its various derivative aircraft (e.g., Mirage IV, 2000, Rafale).

Despite this bleak introduction, delta wings are excellent for supersonic aircraft and high-speed fighters. Supersonic aircraft typically feature airfoils with t/c around 3%–6%. This poses multiple challenges for the wing structure. The delta wing's large root chord provides substantial structural thickness that allows landing

gear and fuel to be accommodated as well. It has another ace up its sleeve. The line in Figure 9-52 represents what potential flow theory predicts how lift should change with AOA. However, wind tunnel testing reveals that for AOA > 5°, actual lift exceeds this prediction. This is caused by a strong vortex that forms along its LE and whose low-pressure region provides a significant increase in lift. This extra lift is called *vortex-lift*. It is a viscous phenomenon not predicted by linear potential flow. It can be argued that if not for this lift, delta-wing aircraft would not be practical. A method to estimate the lift of delta wings is presented in Section 9.5.7.

(2) The Double-Delta Planform Shape

The Double-delta (see Figure 9-53) is also known as the *compound delta*. They produce a vortex pair over each wing, rather than a single vortex. These interfere with each other. The resulting system increases the lift of the double-delta over that of the conventional delta, rendering supersonic fighter aircraft far more maneuverable [13]. The configuration has been used on military aircraft like the SAAB J-35 Draken and General Dynamics F-16E "Cranked Arrow."

9.4.10 Some Exotic Planform Shapes

(1) Disk- or Circular-Shaped Planform

The disk-shaped planform in Figure 9-54 is something no self-respecting aircraft designer proposes as a primary lifting surface. Perhaps inspired by the fad of UFO sightings in the 1950s, the well-respected but long-defunct Avro Canada Ltd., a company that at one time employed some 50,000 people, dared to develop the AVRO Canada VZ-9A. It was nicknamed the "AVRO car" or "Project 1794" among UFO-philiacs. A secret military project, the UFO-like Avrocar employed the Coanda-effect to generate lift and thrust. The project was canceled in 1961 when it became clear insufficient thrust and stability issues would hamper its success.

Figure 9-54 compares spanwise lift distribution of the disk to an elliptical and a Hershey bar wing. Despite the uniform distribution of C_l (after all, what is a circle but an ellipse with equal minor and major axes), the graph underscores the inefficiency of this planform: it barely ekes out one-third of the lift at the selected AOA (10°). Its lift is beyond objectionable. Regardless, it is an ideal shape for a radar disk of the kind installed on a reconnaissance or Early Warning and Control System (AWACS) military aircraft such as the Boeing E-3 Sentry or Grumman E-2 Hawkeye. Knowing the disk's aerodynamic properties is essential for stability and control reasons.

(2) Other Configurations

Four other configurations are shown in Figure 9-55; an ogival, joined wing, blended wing-body, and a rhomboid planform. Lift distribution curves for these shapes will not be presented here since these planform shapes are highly specialized or experimental.

9.5 LIFT AND MOMENT CHARACTERISTICS OF WINGS

In this section, the 3-dimensional lift and moment characteristics of the wing will be evaluated. Drag is treated in Chapter 16, *Aircraft Drag Analysis*. Here, several important characteristics will be discussed, including construction of the 3-dimensional lift curve, estimation of span efficiency and the maximum 3-dimensional lift coefficient, and others. Lift, drag, and pitching moment

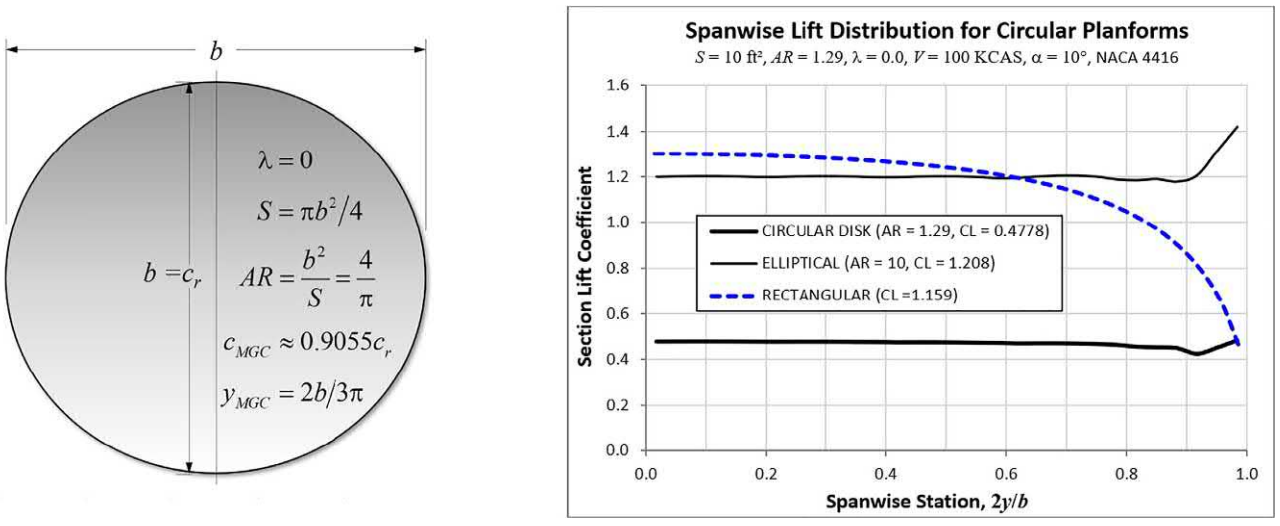


FIGURE 9-54 Basic geometry and lifting characteristics of the *Disk or Circular* wing planform.

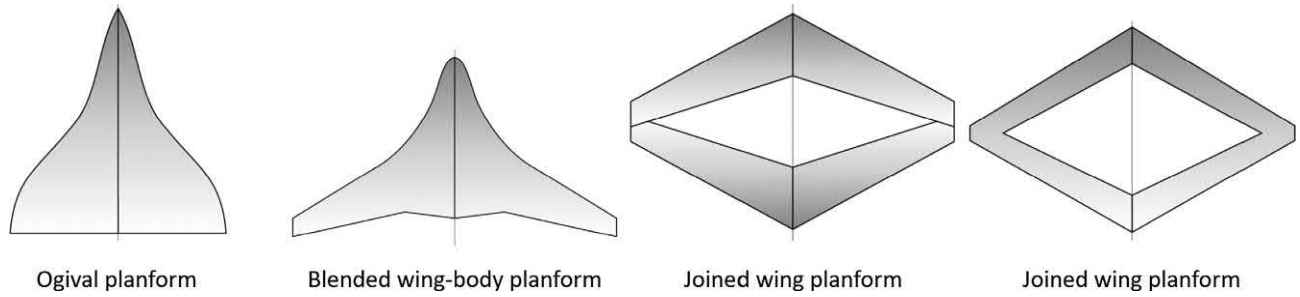


FIGURE 9-55 Selected unorthodox wing planform shapes.

is always converted into a dimensionless coefficient form to allow transferability (see Equations 8-6 and 8-7). The lift, drag, and pitching moment coefficients for a 3-dimensional body are repeated below:

$$L = \frac{1}{2}\rho V_\infty^2 S C_L$$
$$D = \frac{1}{2}\rho V_\infty^2 S C_D \qquad (8.7)$$
$$M = \frac{1}{2}\rho V_\infty^2 S c_{MGC} C_M$$

The variables were defined in Chapter 8. Figure 9-56 shows how lift, drag, and moment acts at a wing's *aerodynamic center* (ac), as indicated by the subscript "*W*." If the spanwise distribution of chord, $c(y)$, and coefficients of section lift (C_l), airfoil profile drag (C_d), and pitching moment (C_m) are known, the 3-dimensional lift coefficient (C_L), profile drag coefficient (C_{Dp}), and pitching moment (C_M) for a "clean" wing is estimated using

$$C_L = \frac{2}{S}\int_0^{b/2} C_l(y)\cdot c(y)dy \qquad (9\text{-}58)$$
$$C_{D_p} = \frac{2}{S}\int_0^{b/2} C_d(y)\cdot c(y)dy \qquad (9\text{-}59)$$
$$C_M = \frac{2}{S}\int_0^{b/2} C_m(y)\cdot c(y)dy \qquad (9\text{-}60)$$

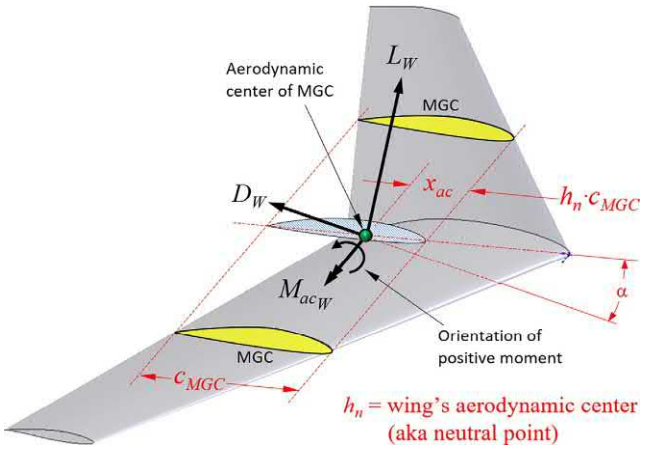


FIGURE 9-56 Wing lift, drag, and moment act at the wing's aerodynamic center.

Note that the complete drag coefficient requires the inclusion of the lift-induced drag coefficient.

9.5.1 Properties of the 3-Dimensional Lift Curve

Figure 9-57 shows a typical 3-dimensional lift curve for a complete aircraft (wings, fuselage, tail, etc.) for an AOA range of $-90° \le \alpha \le +90°$. It is based on actual wind tunnel test data. The geometry of the airplane shapes the curve and makes it different from the airfoils used for the lifting surfaces. Two important observations can be made. The first is the linear range at low AOA (here ranging $-7° \le \alpha \le +9°$). Its extent depends on geometry and operational airspeeds (via Reynolds numbers). The second observation is the surprisingly large values of C_L near $\alpha = -50°$ and $+50°$. These are driven by the high drag at those AOAs.

(1) C_L at Zero AOA, C_{L_0}

Is the value of the lift coefficient the wing produces at zero AOA. It is of great importance because it affects the angle-of-incidence (AOI) for the wing installation. This usually ranges from 0 (symmetric airfoils) to 0.6 (high-camber airfoils). It is negative for undercambered airfoils (e.g., flattop airfoils used near the root of high-subsonic jet aircraft - see Figure 26-32). When referring to the contribution from the wing only, we write $C_{L_{0W}}$.

(2) Lift Curve Slope, C_{L_α}

The lift curve slope is a measure of how rapidly the wing generates lift with change in AOA. As stated in Section 8.1.4(5), the theoretical maximum is 2π, although real airfoils deviate from it. The lift curve slope of a 3-dimensional wing is always less than that of the airfoils it features (see Section 9.5.4, *The Lift Curve Slope*). When referring to the contribution from the wing only, we sometimes write $C_{L_{\alpha W}}$.

(3) Maximum and Minimum Lift Coefficients, $C_{L_{max}}$ and $C_{L_{min}}$

Consider deepest valley and tallest peak in the lift curve in Figure 9-57. The region between the two represent the operational range for an aircraft. A *practical operational range* is that between the *zero-lift angle* and

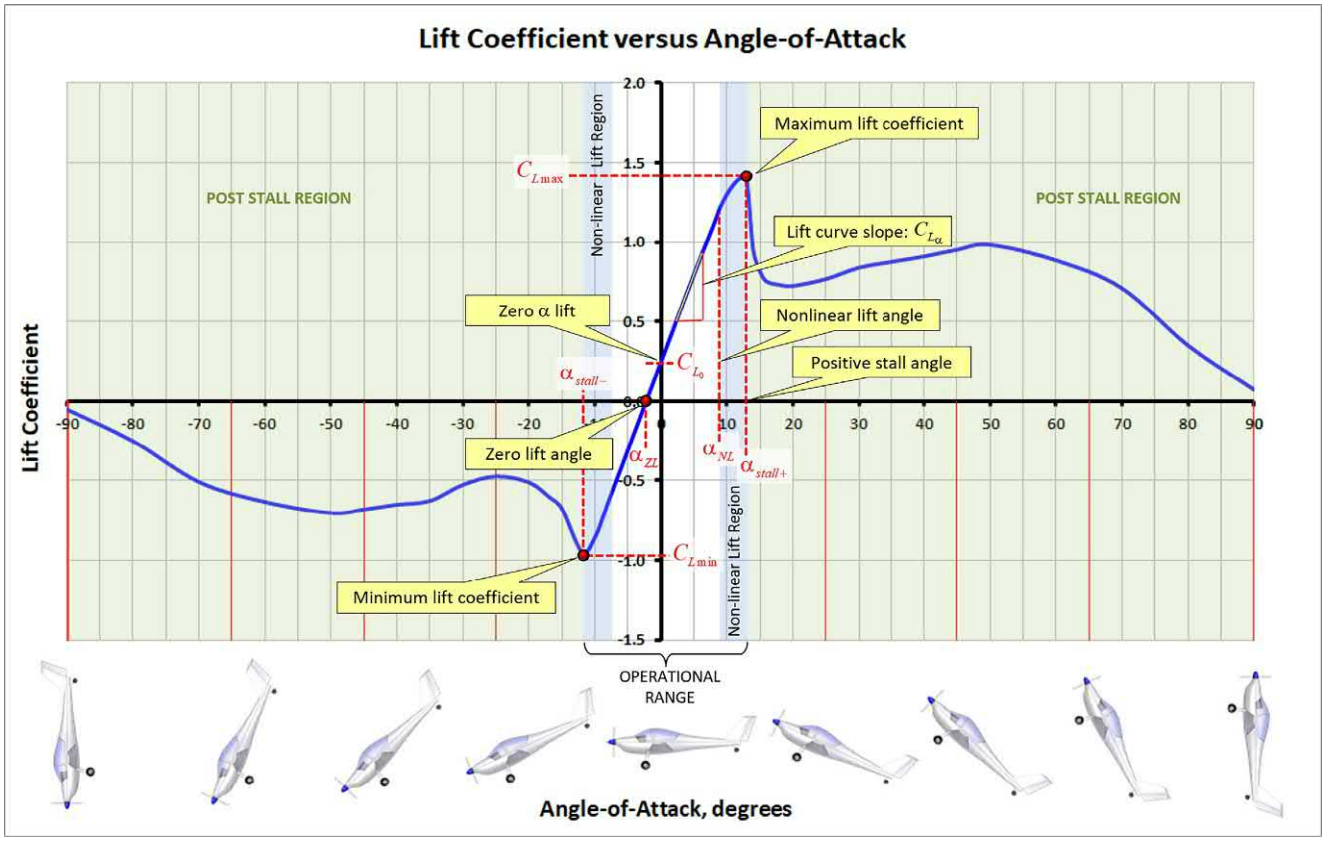


FIGURE 9-57 Important properties of the lift curve.

maximum lift coefficient. The valley is the *minimum lift coefficient* ($C_{L_{min}}$) and represents the AOA at which the airplane would stall if flying inverted. The peak is the *maximum lift coefficient* ($C_{L_{max}}$). It dictates the stalling speed of the airplane and, thus, how much wing area it requires. As for the airfoil, the stall is defined as the flow conditions that follows the first lift curve peak [38]. Both values are required when generating aerodynamic loads for the structures group.

(4) Angle-of-Attack at Zero-Lift, α_{ZL}

This is the angle at which the wing generates no lift. For positively cambered airfoils this angle is always negative unless some specific components (e.g., cambered fuselage) affect this. For symmetrical airfoils it is always 0°.

(5) Angle-of-Attack for Maximum Lift Coefficient, α_{stall}

Once a certain AOA is reached, a pronounced reduction in lift curve takes place; this is the stall.

(6) Angle-of-Attack where Lift Curve becomes Nonlinear, α_{NL}

Once a certain AOA is reached the wing begins to display a pronounced reduction in the lift curve slope. This always happens before the stall AOA is reached.

(7) Linear Range

The linear range is analogous to that of the airfoil (see Figure 8-5), except here it applies to the entire aircraft.

(8) Design Lift Coefficient, C_{L_C}

Is the value of C_L at which the aircraft is expected to operate during the mission for which it is designed. It is usually the lift coefficient during cruise (range-driven, although sometimes loiter-driven). It may be presented as a range to accommodate change in weight with fuel burn. If the target airspeed is known, it is possible to estimate C_{L_C} using the weight of the airplane at the *start-of-cruise* and *end-of-cruise* using the following expression:

$$C_{L_C} = C_{L_0} + \frac{(W_1 + W_2)}{\rho V_C^2 S} + C_{L_\alpha}\alpha_{ZL} \tag{9-61}$$

Where:

S = Reference wing area,
V_C = Expected cruising speed,
ρ = Density at cruise altitude,
α_{ZL} = Zero-lift angle-of-attack,
W_1, W_2 = Weight at the beginning (1) and end (2) of mission.

(9) Angle-of-Attack for Design Lift Coefficient, α_C

In cruise, the airplane should be flying at its minimum-drag AOA. In case of the design mission being a cruise or loiter mission, this AOA can be calculated from Equation (9-54).

DERIVATION OF EQUATION (9-61)

Substitute Equation (9-54) into Equation (9-63) (ignoring $C_{L_{\delta e}}$ and $C_{L_{\delta f}}$) and manipulate algebraically:

$$C_{L_C} = C_{L_0} + C_{L_\alpha}\alpha_C = C_{L_0} + C_{L_\alpha}\left(\left(\frac{1}{C_{L_\alpha}}\right)\frac{(W_1+W_2)}{\rho V_C^2 S} + \alpha_{ZL}\right)$$
$$= C_{L_0} + \frac{(W_1+W_2)}{\rho V_C^2 S} + C_{L_\alpha}\alpha_{ZL}$$

9.5.2 The Lift Model

The term refers to a mathematical description of the lift curve for the complete aircraft. It is presented below in a highly generalized form, where *f*() is a function of the *state* of the airplane:

$$C_L = C_{L_0} + f_\alpha(\alpha, \dot{\alpha}) + f_\beta(\beta, \dot{\beta}) + f_{\delta_e}(\delta_e) + f_{\delta_f}(\delta_f) + f_{\delta_s}(\delta_s) + \ldots \quad (9\text{-}62)$$

Where α is angle-of-attack, $\dot{\alpha}$ is time rate-of-change of α, β is angle-of-yaw, $\dot{\beta}$ is time rate-of-change of β, δ_e is elevator deflection, δ_f is flap deflection, δ_s is spoiler deflection, and so forth. To compile a complete lift model for a complete aircraft, see Section 24.2.5, *The Lift Model*. To give a brief insight, consider a simple form of the expression

$$C_L = C_{L_0} + C_{L_\alpha}\alpha + C_{L_{\delta_e}}\delta_e + C_{L_{\delta_f}}\delta_f \quad (9\text{-}63)$$

Where C_{L_0} is the zero-α lift, C_{L_α} is the lift curve slope, $C_{L_{\delta e}}$ is change in lift with δ_e, and $C_{L_{\delta f}}$ is change in lift with δ_f. This represents an aircraft with elevator and flaps. To estimate the derivatives requires knowledge of the airplane geometry, as shown in Chapter 24.

The lift coefficient must be considered from two perspectives: (1) As related to lift through dynamic pressure and (2) as related to lift through AOA and control surface deflections. If the lift force is known at some dynamic pressure, then C_L is calculated using Equation (8-7), repeated here for convenience

$$C_L = \frac{2L}{\rho V^2 S} \quad (9\text{-}64)$$

In contrast, if α, δ_e, and δ_f are known, we can calculate C_L using Equation (9-63). Alternatively, if we know C_L from Equation (9-64) and the state of δ_e and δ_f, then, theoretically, we could solve Equation (9-63) for α.

$$\alpha = \frac{C_L - C_{L_0} - C_{L_{\delta_e}}\delta_e - C_{L_f}\delta_f}{C_{L_\alpha}} \quad (9\text{-}65)$$

In flight simulation software, C_L is calculated using the form of Equation (9-63) (with more terms added). One way of interpreting these equations is that Equation (9-64) reveals *how much* C_L *is needed*. Equation (9-63) reveals how the airplane *must be contorted* to generate it. For steady flight, Equations (9-63) and (9-64) will be equal.

The Relationship between Airspeed, Lift Coefficient, and Angle-of-Attack

Figure 9-58 shows an airplane being operated in horizontal flight at different airspeeds. For generality, these are denoted by the ratio V/V_S, where V_S is its stalling speed. The upper left image shows the aircraft at high

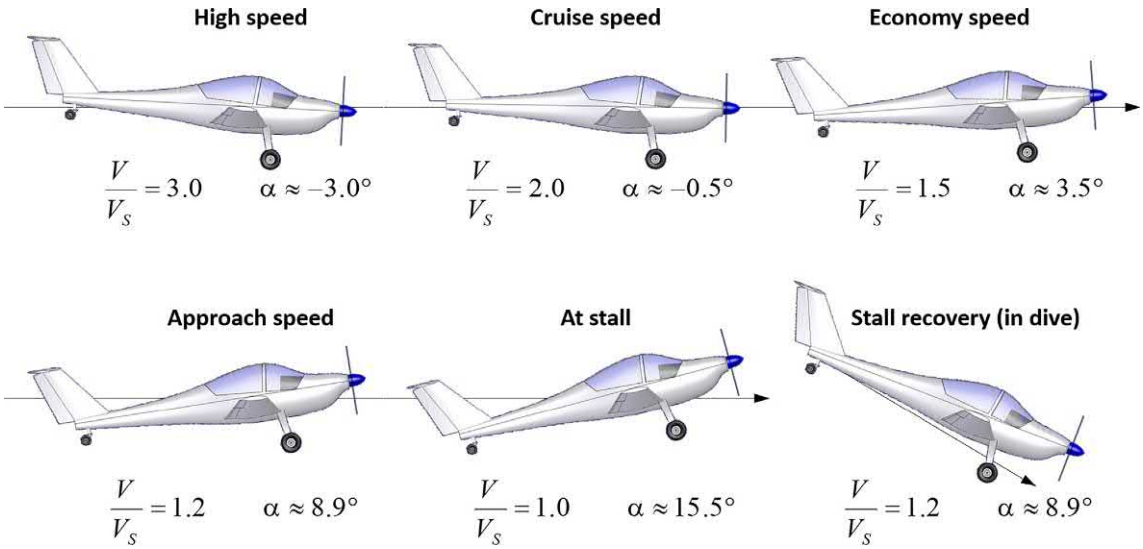


FIGURE 9-58 A schematic showing the attitude of an aircraft at different airspeed, *V*. Stalling speed is denoted by V_S. The AOA are typical values for light planes.

airspeed (e.g., if $V_S = 50$ KCAS, the figure shows it at $V = 3 \times 50 = 150$ KCAS). This results in a low C_L, which the airplane generates using a slightly nose-down attitude. As the aircraft slows down, it maintains altitude by exchanging less airspeed for a higher C_L. This calls for a higher α. Further slowdown requires a gradually higher nose-up attitude to generate the larger C_L. Eventually, a larger C_L can no longer be achieved: This is the $C_{L_{max}}$. This is followed by an immediate and forceful drop of the nose caused by the sudden loss of lift. The airplane begins a dive toward the ground, which increases its airspeed, making stall recovery possible. This is shown as the left bottom image, which shows the aircraft recovering and while in a nose-down attitude, its higher airspeed has already lowered the α.

EXAMPLE 9-8

Determine the AOA required for an aircraft flying at $V = 65$ KCAS without flaps and with flaps deflected to $\delta_f = 30°$. The airplane weighs 1320 lb_f, has wing area 130 ft^2, with aerodynamic properties $C_{L_0} = 0.15$, $C_{L_\alpha} = 4.5$/rad, and $C_{L_{\delta f}} = 1.43$/rad. Ignore contributions from $C_{L_{\delta e}}$ and $C_{L_{\delta s}}$.

SOLUTION:

Start by determining the lift coefficient that must be developed using Equation (9-64). This is equal for the flapped and unflapped configuration since the airspeed is equal in both cases.

$$C_L = \frac{2L}{\rho V_\infty^2 S} \approx \frac{2W}{\rho V^2 S} = \frac{2(1320)}{(0.002378)(65 \times 1.688)(130)} = 0.7094$$

Then, use Equation (9-65) to estimate the required AOA. First, without flaps:

$$\alpha = \frac{C_L - C_{L_0} - C_{L_f}\delta_f}{C_{L_\alpha}} = \frac{0.7094 - 0.15 - (1.43)(0)}{4.5} \times \frac{180}{\pi} = 7.12°$$

Then with flaps deflected at $\delta_f = 30°$:

$$\alpha = \frac{C_L - C_{L_0} - C_{L_f}\delta_f}{C_{L_\alpha}} = \frac{0.7094 - 0.15 - (1.43)\left(30 \times \frac{\pi}{180}\right)}{4.5} \times \frac{180}{\pi} = -2.41°$$

9.5.3 The Zero-α Lift, C_{L_0}

Figure 9-59 reveals how a 2-dimensional lift curve for an airfoil changes once it is introduced to a wing of finite AR. Among noticeable effects is (1) a reduction in the lift curve slope, (2) reduction in lift at $\alpha = 0$, (3) reduced $C_{L_{max}}$, and (4) increased α_{stall}. This section shows how to estimate the zero-α lift for a wing. The method assumes

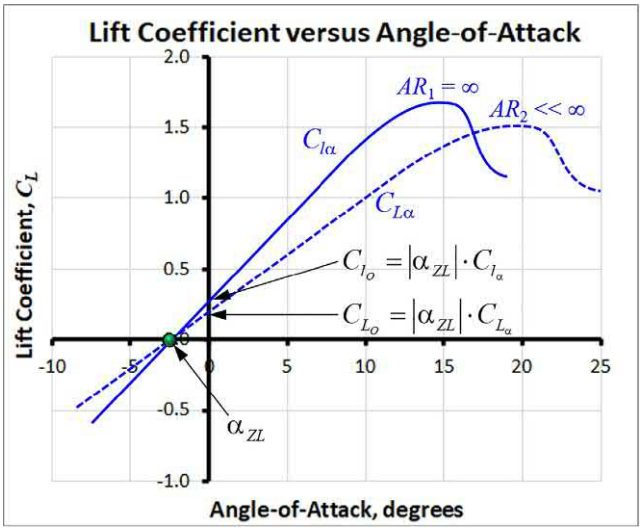


FIGURE 9-59 Determination of the lift coefficient at zero AOA for a 3-dimensional lift curve.

the same airfoil along the wing. For multiairfoil wings assume the properties of the airfoil at the MGC. Estimate these using the *law of effectiveness*, presented in Section 9.5.9.

Step 1: Compute a 3-dimensionl lift curve slope using Equation (9-72).

Step 2: Compute α_{ZL} for the 2-dimensional airfoil using the following expression, which is obtained by inspection of the curves in Figure 9-59:

$$C_{l_0} = -\alpha_{ZL} \cdot C_{l_\alpha} \Leftrightarrow \alpha_{ZL} = -C_{l_0}/C_{l_\alpha} \qquad (9\text{-}66)$$

Step 3: Compute zero-α lift for the 3D wing using:

$$C_{L_0} = |\alpha_{ZL}| \cdot C_{L_\alpha} \qquad (9\text{-}67)$$

Note that the C_{L_0} for a complete aircraft includes contributions from the fuselage, HT, nacelles, etc. This method only applies to the wing.

9.5.4 The Lift Curve Slope, C_{L_α}

Consider the lift curve slope of an airfoil used for a lifting surface (a wing, HT, or VT). As shown in Figure 9-97, the downwash behind the wing and corresponding upwash in front of it "tilt" the undisturbed air, reducing the geometric angle-of-attack, α, by amount α_i (called *induced* α). The resulting angle-of-attack is called the *effective* α (α_e). Thus, the wing must operate at a larger AOA to generate the same lift coefficient as the airfoil. This reduces the wing's lift curve slope compared to the airfoil. This is used to derive the following expressions that allow the airfoil's C_{l_α} to be converted to that of a wing (C_{L_α}).

(1) Lift Curve Slope for an Elliptical Wing

The transformation is usually derived using Prandtl's *lifting-line theory* (see Section 9.7.2, *Prandtl's Lifting-Line*

Method—Special Case: The Elliptical Wing). The following expression is used with elliptical wings only:

$$C_{L_\alpha} = \frac{C_{l_\alpha}}{1 + C_{l_\alpha}/(\pi \cdot AR)} \tag{9-68}$$

A common (but not necessarily correct) assumption is that the C_{l_α} of an airfoil is 2π. This yields the following expression for elliptical wing with $C_{l_\alpha} = 2\pi$:

$$C_{L_\alpha} = \frac{2\pi \cdot AR}{AR + 2} \tag{9-69}$$

Note that Refs. [39, 40] present methods to adapt Equation (9-69) for $AR < 4$, but these are generally unwieldy.

(2) Lift Curve Slope for Arbitrary Wings

The following expression is an attempt to extend Equation (9-68) to more arbitrary wing shapes and requires the correction factor, τ, to be determined:

$$C_{L_\alpha} = \frac{C_{l_\alpha}}{1 + C_{l_\alpha}(1+\tau)/(\pi \cdot AR)} \tag{9-70}$$

The factor τ is a function of the Fourier coefficients determined using the lifting-line theory and represents the following correction to α_i (mentioned earlier) as shown in Dommasch [41]. The actual value of τ is calculated and provided by Glauert [42].

$$\alpha_i = \frac{C_L(1+\tau)}{\pi \cdot AR}$$

By making some approximations and determining the downwash at the three-fourth chord station, Helmbold [43] derived the general expression shown below:

$$C_{L_\alpha} = \frac{2\pi \cdot AR}{2 + \sqrt{AR^2 + 4}} \tag{9-71}$$

It applies to straight wings of arbitrary planform. Finally, the following expression, called the *Polhamus equation*, is derived in [44]. It is based on a modification made to Helmbold's equation. It is also presented on pp. 4.1.3.2–49 in Ref. [1]. The expression accounts for compressibility, deviation from the 2π airfoil lift curve slope, and taper ratio. While λ does not appear explicitly in the equation, Ref. [44] demonstrates that if the mid-chord sweep angle ($\Lambda_{c/2}$) is used, λ can be eliminated. The resulting expression is only valid for noncurved planform shapes and $M \leq 0.8$:

$$C_{L_\alpha} = \frac{2\pi \cdot AR}{2 + \sqrt{\left(\frac{AR \cdot \beta}{\kappa}\right)^2 \left(1 + \frac{\tan^2 \Lambda_{c/2}}{\beta^2}\right) + 4}} \tag{9-72}$$

Where: β = Mach number parameter (Prandtl-Glauert) = $(1 - M^2)^{0.5}$,

κ = Ratio of 2-dimensional lift curve slope to 2π,
$\Lambda_{c/2}$ = Sweepback of mid-chord.

Note that Equation (9-71) can be corrected by replacing 2π by the airfoil's true C_{l_α}. Thus, Equation (9-71) becomes:

$$C_{L_\alpha} = \frac{C_{l_\alpha} \cdot AR}{2 + \sqrt{AR^2 + 4}} \tag{9-73}$$

Of the previously mentioned methods, Equation (9-72) compares well with experiment (and this author's experience). This can be assessed indirectly by comparing results to that of the *Vortex-Lattice Method* (VLM), which compares well with experiment. Such a comparison is made in Table 9-7. The general trend is that Equations (9-69) and (9-71) (intended for elliptical planform shapes) predict steeper lift curve slopes than Equation (9-72) and VLM. Also, note the insensitivity of Equations (9-69) and (9-71) to other characteristics, such as sweep and general planform shape of the wing.

TABLE 9-7 Comparing C_{L_α} calculated using three selected methods and VLM.

			C_{L_α} per radian			
Wing planform	***AR***	**$\Lambda_{c/2}$**	**Equation (9-69)**	**Equation (9-71)**	**Equation (9-72)**	**VLM**
Elliptical, $\Lambda_{c/2} = 0°$	10	0.00	5.24	5.15	4.90	5.02
Elliptical, $\Lambda_{LE} = 0°$	10	−6.60	5.24	5.15	4.87	4.99
Elliptical, $\Lambda_{TE} = 0°$	10	6.60	5.24	5.15	4.87	4.99
Schuemann	10	5.04	5.24	5.15	4.88	4.99
Semistraight taper	10	0.00	5.24	5.15	4.90	4.98
Straight taper, $\Lambda_{c/2} = 0°$	10	0.00	5.24	5.15	4.90	4.96
Straight taper, $\Lambda_{LE} = 0°$	10	−3.81	5.24	5.15	4.89	4.95
Straight taper, $\Lambda_{LE} = 0°$	10	3.81	5.24	5.15	4.89	4.95
Compound taper	10	0.00	5.24	5.15	4.90	4.88
Rectangular	10	0.00	5.24	5.15	4.90	4.82

TABLE 9-7 Comparing C_{L_α} calculated using three selected methods and VLM—cont'd

			C_{L_α} per radian			
Wing planform	***AR***	$\Lambda_{c/2}$	**Equation (9-69)**	**Equation (9-71)**	**Equation (9-72)**	**VLM**
Crescent	10	22.48	5.24	5.15	4.59	4.60
Swept back, $\lambda=0.5$, $\Lambda_{LE}=30°$	10	28.55	5.24	5.15	4.40	4.52
Swept forward, $\lambda=2.0$, $\Lambda_{LE}=30°$	10	−32.78	5.24	5.15	4.24	4.32
Swept back, $\lambda=1.0$, $\Lambda_{LE}=30°$	10	30.00	5.24	5.15	4.35	4.29
Swept back, $\lambda=2.0$, $\Lambda_{LE}=30°$	10	27.05	5.24	5.15	4.45	3.98
Delta	2.27	38.59	3.34	2.84	2.51	2.44
Double-delta	2.26	45.08	3.33	2.83	2.39	2.30
Disk	1.29	0.00	2.46	1.85	1.83	1.84

DERIVATION OF EQUATION (9-68)

The graph in Figure 9-60 shows the lift curve for two ARs; $AR=\infty$ (an airfoil) and an elliptical wing of an arbitrary AR. The lift coefficient for the airfoil can be written as follows:

$$C_L = \text{constant} + C_{l_\alpha} \cdot \alpha$$

The wing induces upwash that reduces the α by an amount denoted by α_i (induced AOA). Therefore, the lift coefficient for the wing is given by:

$$C_L = \text{constant} + C_{l_\alpha} \cdot (\alpha - \alpha_i)$$

Substitute the value of α_i given by Equation (16.75), yields:

$$C_L = \text{constant} + C_{l_\alpha} \cdot \left(\alpha - \frac{C_L}{\pi AR}\right)$$

The lift curve slope can now be found by differentiating this with respect to α:

$$\frac{dC_L}{d\alpha} = C_{l_\alpha} - C_{l_\alpha} \cdot \frac{1}{\pi AR}\frac{dC_L}{d\alpha} = C_{l_\alpha} - C_{l_\alpha} \cdot \frac{1}{\pi AR}\frac{dC_L}{d\alpha}$$

$$\Rightarrow \quad \frac{dC_L}{d\alpha} = C_{L\alpha} = \frac{C_{l_\alpha}}{1 + C_{l_\alpha}/(\pi AR)}$$

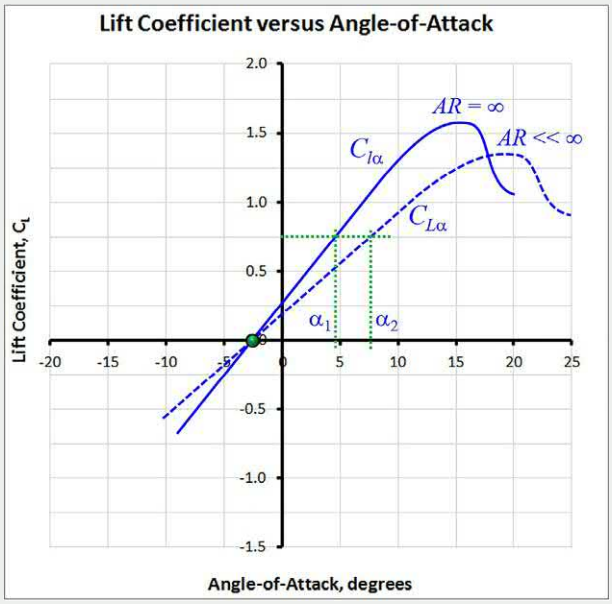


FIGURE 9-60 Lift curves for an airfoil and an elliptical wing.

DERIVATION OF EQUATION (9-69)

We begin with Equation (9-68) and replace the airfoil lift curve slope with 2π:

$$C_{L_\alpha} = \frac{C_{l_\alpha}}{1 + C_{l_\alpha}/(\pi AR)} = \frac{2\pi}{1 + 2\pi/(\pi AR)}$$

Then, manipulate algebraically:

$$C_{L_\alpha} = \frac{2\pi}{1 + 2\pi/(\pi AR)} = 2\pi \frac{\pi AR}{\pi AR + 2\pi} = \frac{2\pi \cdot AR}{AR + 2}$$

9.5.5 The Maximum Lift Coefficient, $C_{L_{max}}$

The maximum lift coefficient is one of the most important parameters in aircraft design. It stipulates how slowly the airplane can fly and impacts the extremes of maneuverability, as well as take-off and landing distances. This section presents several methods to estimate it.

(1) The Impact of $C_{L_{max}}$ and Wing Loading on Stalling Speed

Figure 9-61 presents a carpet plot that shows how wing loading (W/S) and maximum lift coefficient ($C_{L_{max}}$) affect stalling speed (here shown in KCAS). It shows two stall speed limits: The single-engine 61-KCAS limit per the "old" 14 CFR Part 23 and the 45-KCAS limit for Light Sport Aircraft (LSA). Selected aircraft are superimposed. As an example of use, consider a single engine airplane with $W/S = 25$ lb$_f$/ft^2 slated for Part-23 certification. To meet the 61-KCAS requirement, it must feature a high-lift system capable of $C_{L_{max}} \geq 2.0$. Alternatively, if it features a simple high-lift system capable only of $C_{L_{max}} = 1.8$, then it will comply with said requirement if $W/S < 25$ lb$_f$/ft^2. The carpet plot is drawn based on the following expression. The right-most approximation is only valid at S-L. The constants ($1/1.688 = 0.592$ and $29/1.688 = 17.18$) convert airspeed in ft/s to knots.

$$V_S = 0.592\sqrt{\frac{2W}{\rho S C_{L_{max}}}} \approx 17.18\sqrt{\frac{(W/S)}{C_{L_{max}}}} \qquad (9\text{-}74)$$

(2) A General Model for $C_{L_{max}}$

The airplane's maximum lift coefficient should account for leading- and trailing-edge high-lift devices, in addition to that developed by its clean (no high-lift) configuration. Such a model is presented below. This model may also be used for flying wings, although high-lift system is rarely used in such aircraft.

$$C_{L_{max}} = \left(C_{L_{max_0}} + \Delta C_{Lmax_{LE}} + \Delta C_{Lmax_{TE}}\right) K_\Lambda \qquad (9\text{-}75)$$

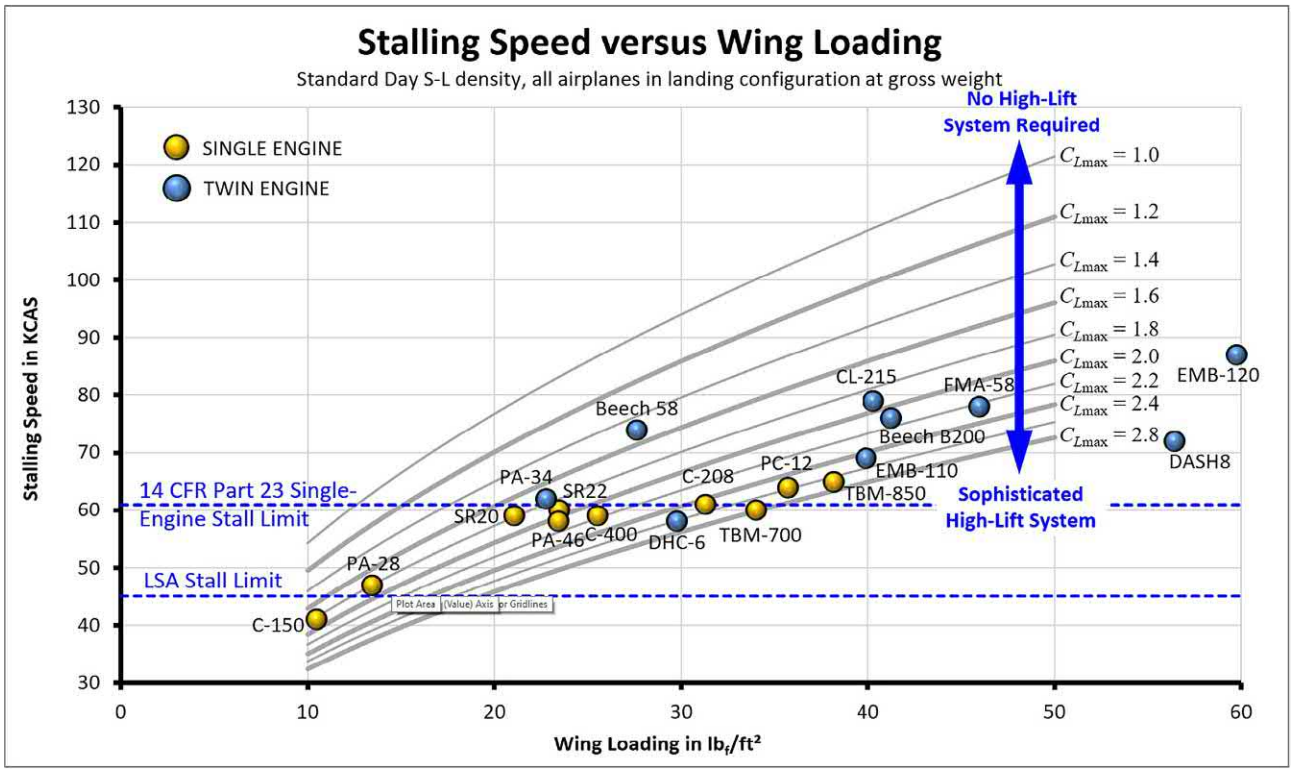


FIGURE 9-61 A carpet plot showing stalling speed as a function of wing loading and maximum lift coefficient.

Where: $C_{L_{max_0}}$ = Max lift coefficient of wing in its clean configuration,
$\Delta C_{Lmax_{LE}}$ = Contribution of leading-edge devices to max lift (see Section 10.2),
$\Delta C_{Lmax_{TE}}$ = Contribution of trailing-edge devices to max lift (see Section 10.3),
K_Λ = Correction of max lift due to wing sweep angle.

(3) Wing Sweep Correction, K_Λ

As shown above, wing sweep reduces the maximum lift. It is important to account for this reduction. A standard correction uses the cosine of the quarter-chord sweep [5, 45]:

$$K_\Lambda = \cos\Lambda_{c/4} \tag{9-76}$$

(4) Method 1: Rapid Estimation of $C_{L_{max_0}}$

Provided in multiple sources (e.g., Refs. [5, 45]), this method allows a fast estimation of a $C_{L_{max_0}}$. While its simplicity renders its accuracy suspect, it has a "fair chance" of providing a reasonable first estimate. It is acceptable only during initial studies and should be replaced with more accurate methods once the design matures.

Step 1: Determine a Representative $C_{l_{max}}$
Calculate a representative $C_{l_{max}}$ for the airfoil at the MGC using the *Law of Effectiveness*:

$$C_{l_{max}} = (C_{l_{max}})_{root} + \frac{2y_{MGC}}{b}\left[(C_{l_{max}})_{tip} - (C_{l_{max}})_{root}\right] \tag{9-77}$$

Step 2: Compute $C_{L_{max_0}}$
Calculate the 3-dimensional $C_{L_{max_0}}$ from the following expression (this is the $C_{L_{max}}$ for the unswept wing):

$$C_{L_{max_0}} = 0.9 \times C_{l_{max}} \tag{9-78}$$

Substitute this result into Equation (9-75) to complete the task.

EXAMPLE 9-9

Compare the calculated $C_{L_{max_0}}$ for the Cessna 172 using the METHOD 1 and compare to its POH value ($S = 174\,\text{ft}^2$, $b = 36\,\text{ft}$, $W = 2550\,\text{lb}_\text{f}$, and $V_S = 53\,\text{KCAS}$ ($M \cong 0.10$)). The 172 features a NACA 2412 airfoil for both the root and tip.

SOLUTION:

First estimate $C_{L_{max_0}}$ based on the POH information:

$$C_{L_{max_0}} = \frac{2W}{\rho V_\infty^2 S} = \frac{2 \cdot 2550}{0.002378 \cdot (53 \cdot 1.688)^2 \cdot 174} = 1.54$$

Next, compute the Reynolds number at stall to help determine the airfoil's $C_{l_{max}}$. Let us use the average chord in lieu of the MGC. The average chord can be found from Equation (9-30):

$$\bar{c} = S/b = (174\ \text{ft}^2)/(36\ \text{ft}) = 4.833\ \text{ft}$$

Use Equation (16.27) to estimate Reynolds number:

$$R_e \approx 6400VL = 6400 \times (53 \times 1.688) \times (4.833) \approx 2{,}770{,}000$$

Use this to extract the $C_{l_{max}}$ for the NACA 2412 airfoil using the wind tunnel data in NACA R-824 [46]. Using the data for $R_e = 3.1 \times 10^6$ (which is closest to 2.77×10^6), we extract and use a $C_{l_{max}} \approx 1.58$ with the average root. Therefore, the 3-dimensional maximum lift coefficient can be found to equal:

$$C_{L_{max_0}} = 0.9 \times C_{l_{max}} = 0.9 \times 1.58 = 1.422$$

The difference between this method and the POH is 8% less than the airplane's actual capability. Similar analysis conducted on the SR22 in the first edition of this book yielded a 10% underestimation. While the method gives an idea about the $C_{L_{max_0}}$, its level of accuracy could adversely affect the wing sizing of a brand-new aircraft.

(5) Method 2: $C_{L_{max_0}}$ Estimation per USAF DATCOM Method 1

The wing's maximum lift coefficient can be estimated using the following method from the USAF DATCOM (where it is called Method 1). This method requires software to estimate the spanwise distribution of C_l along the wing, such as the vortex-lattice or doublet-lattice methods. The method is limited to moderately swept planforms, where vortex-lift is not yet significant (delta wings). Furthermore, the spanwise location where stall is first detected should be limited within a band extending from one local chord-length away from the wing root and tip. The DATCOM considers this method superior to Method 2 (see next section).

Step 1: Determine the Spanwise Distribution of $C_{l_{max}}$
Determine the $C_{l_{max}}$ along the span for the wing, based on the appropriate Mach number and Reynolds number. Experimental data should always be used if available.

Step 2: Plot the Spanwise Distribution of $C_{l_{max}}$
Plot $C_{l_{max}}$ along a normalized spanwise station ($2y/b$, ranging from 0 to 1), shown as the dashed line in Figure 9-62.

Step 3: Determine the AOA at which Local C_l Intersect $C_{l_{max}}$

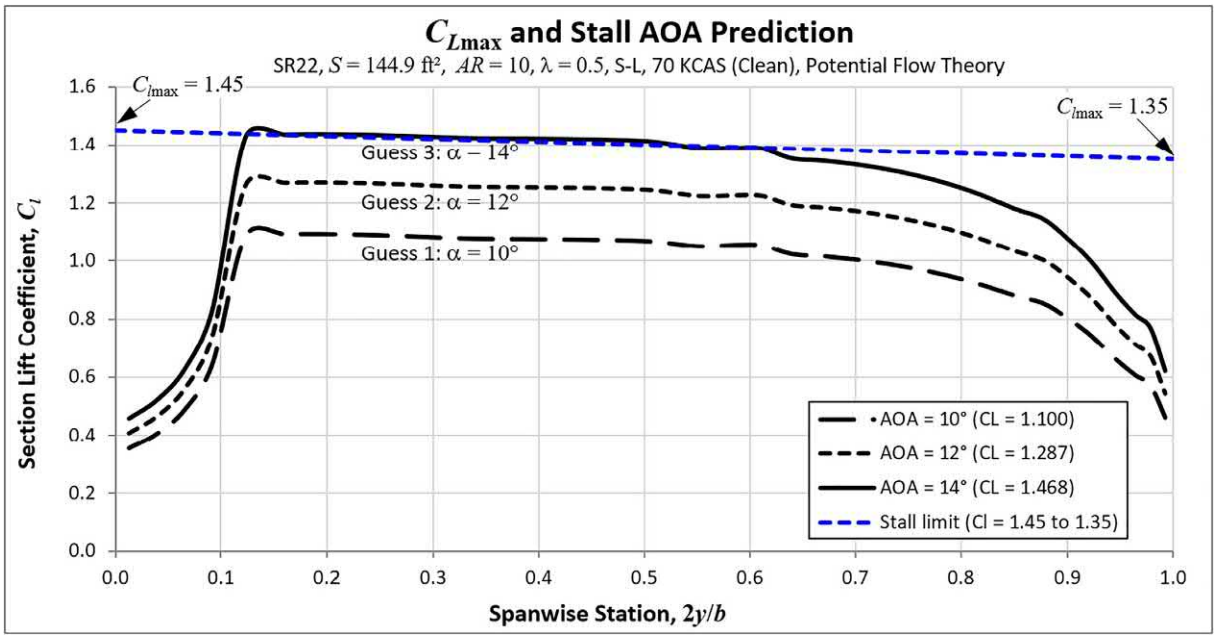


FIGURE 9-62 Lift distribution near stall predicted by potential flow. The waviness in places is due to the discontinuity in the segment of the wing, which features a leading-edge extension.

Evaluate and plot the spanwise distribution of C_l for a range of AOA until the maximum of a local C_l intersects the airfoil's $C_{l_{max}}$. This is where the stall will first occur. An approximate value of where this occurs can be estimated from Section 4.1.3.4 of Ref. [1] (λ = taper ratio):

$$\eta_{stall} = 1 - \lambda \tag{9-79}$$

Step 4: Compute $C_{L_{max_0}}$

Calculate the $C_{L_{max_0}}$ by integrating along the span:

$$C_{L_{max_0}} = \frac{1}{S}\int_0^{1.0} b \cdot C_l(\eta) \cdot c(\eta) d\eta \tag{9-80}$$

Where:

$C_l(\eta)\eta$ = Section lift coefficient as a function of spanwise station,
$c(\eta)$ = Wing chord as a function of spanwise station,
η = Spanwise station = $2y/b$. Ranges from 0 to 1 (for $b/2$).

EXAMPLE 9-10

Predict the maximum lift coefficient for the Cirrus SR22 using the Method 2 and compare to the "known" value of $C_{L_{max_0}}$ (=1.41), calculated using its POH. Assume the airplane has an airfoil in the NACA 65_2-415 class and account for the effect of Reynolds number on the $C_{l_{max}}$ at the root and tip.

SOLUTION:

The results in Figure 9-62 were obtained using the vortex-lattice solver SURFACES, but similar data are obtainable from other solvers. It allows this method to be implemented as trial and error (hence Guess 1, 2, 3 in the graph) until C_l begins to "contact" the stall limit (blue dashed line). This allows the stall AOA and the maximum lift coefficient to be estimated

$$C_{L_{max_0}} \approx 1.468 \quad \text{and} \quad \alpha_{stall} \approx 14°$$

The difference between the POH ($C_{L_{max_0}} = 1.41$) and the estimated value ($C_{L_{max_0}} = 1.468$) is some 4.1%, indeed a good agreement. This method agrees well with experiment and, generally, differs by approximately ±6%. The model is based on measurements taken from Figure 16-48 and included the wing's leading-edge extensions (called "cuffs"), fuselage, and horizontal tail. Note that the program calculates the total lift coefficient, C_L (shown in parentheses in the legend), which represent values that would be returned by Equation (9-80) if the shape of the lift distribution were to be presented as a function of the spanwise station.

(6) Method 3: Estimation of $C_{L_{max_0}}$ per USAF DATCOM Method 2

The wing's $C_{L_{max_0}}$ can be calculated using the following empirical method from the USAF DATCOM (where it is called Method 2). While involved, it predicts the subsonic $C_{L_{max_0}}$ and the associated α_{stall} for untwisted, high aspect ratio, single-airfoil wings. According to the

DATCOM, while the wing planform influences the $C_{L_{max0}}$, this effect is less important than the $C_{l_{max}}$ of the airfoil.

Step 1: Determine the Taper Ratio Correction Factor

First determine if the wing complies with the DATCOM's "definition" of a high aspect ratio wing. Do this by determining the *taper ratio correction factor* (TRCF), C_1, from Figure 9-63. Alternatively, the TRCF can be approximated using following empirical expression (derived by the author), based on the curve of Figure 9-63.

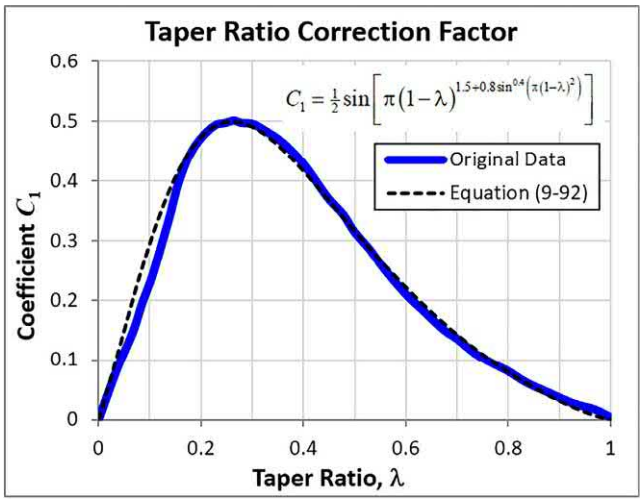


FIGURE 9-63 Taper ratio correction factor. *Based on D.E. Hoak, USAF Stability and Control DATCOM, Flight Control Division, Air Force Flight Dynamics Laboratory, 1978.*

$$C_1 = \frac{1}{2}\sin\left[\pi(1-\lambda)^{1.5+0.8\sin^{0.4}\left(\pi(1-\lambda)^2\right)}\right] \tag{9-81}$$

Step 2: Determine if Wing Qualifies as "High AR"

Determine if the wing complies with the DATCOM's "definition" of a high aspect ratio wing:

$$AR > \frac{4}{(C_1+1)\cos\Lambda_{LE}} \tag{9-82}$$

This procedure may be used as long as the airplane's AR is greater than the ratio of Equation (9-82).

Step 3: Determine the Leading-Edge Parameter

Determine the *leading-edge parameter* (LEP), denoted by Δy, which is used several steps later. The parameter Δy is the difference between the airfoil ordinate at 6% and 0.15% chord and is represented in terms of %. Thus, a value of 0.03 is written as 3.00. Since the method assumes a single airfoil wing, it is appropriate to approximate the leading-edge parameter based on the geometry of the airfoil at the MGC. Figure 9-64 illustrates the process. Note that this assumes an airfoil ordinate table that has been normalized to a chord of unity ($c=1$).

The below listing contains expressions for the LEP, Δy, for selected types of airfoils, based on their thickness-to-chord ratios (t/c). The expressions are based on Figure 2.2.1-8 of Ref. [1].

NACA 4/5-digit Airfoils: $\Delta y = 25(t/c)$ (9-83)

NACA 63-Series: $\Delta y = 22.132(t/c)$ (9-84)

NACA 64-Series: $\Delta y = 20.411(t/c)$ (9-85)

NACA 65-Series: $\Delta y = 19.091(t/c)$ (9-86)

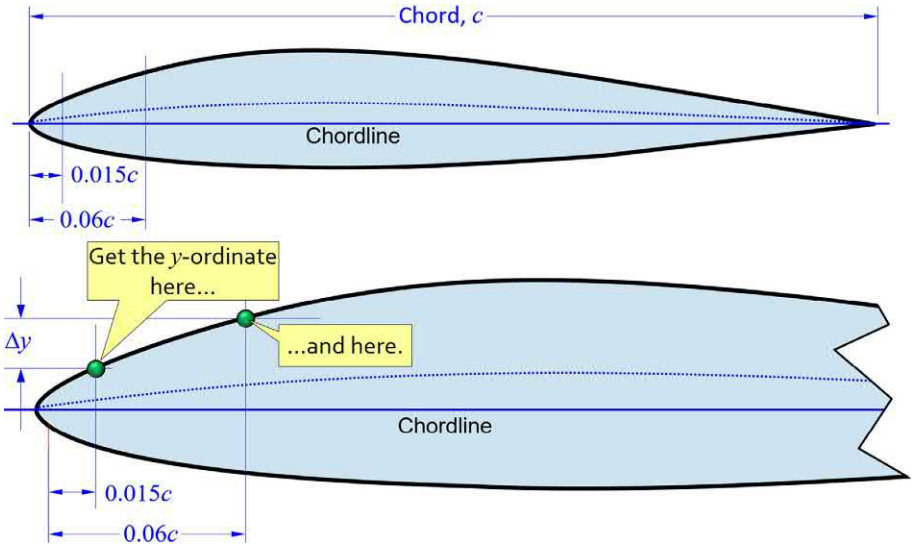


FIGURE 9-64 Determination of the LEP. *Based on D.E. Hoak, USAF Stability and Control DATCOM, Flight Control Division, Air Force Flight Dynamics Laboratory, 1978.*



FIGURE 9-65 $C_{L_{max_0}}/C_{l_{max}}$ ratio data plot. *Based on D.E. Hoak, USAF Stability and Control DATCOM, Flight Control Division, Air Force Flight Dynamics Laboratory, 1978.*

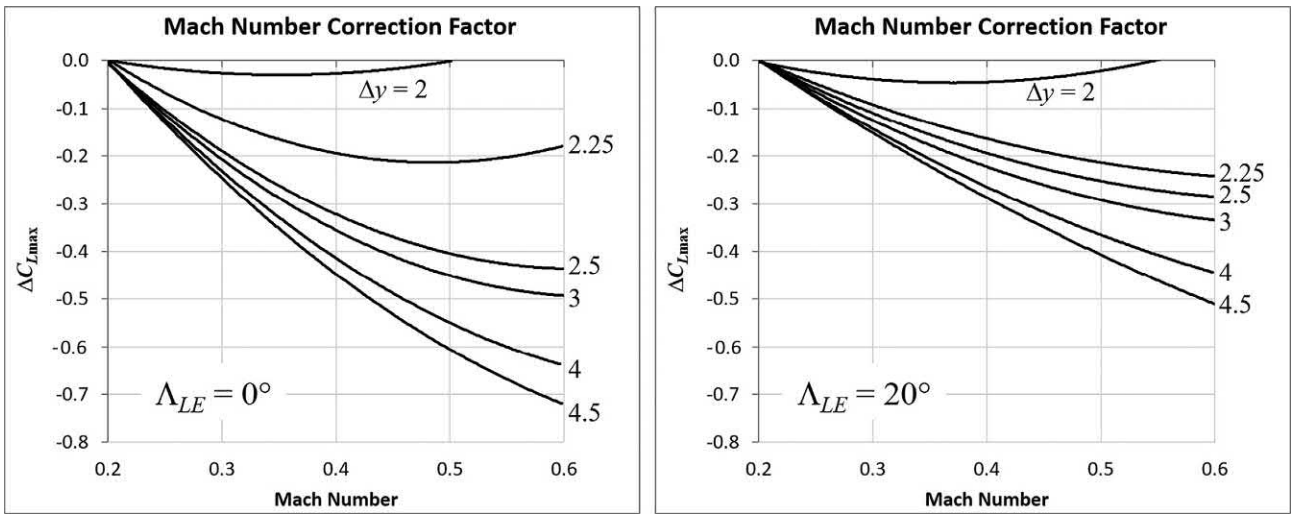


FIGURE 9-66 Determine $\Delta C_{L_{max}}$ using the above graphs. *Based on D.E. Hoak, USAF Stability and Control DATCOM, Flight Control Division, Air Force Flight Dynamics Laboratory, 1978.*

NACA 66-Series: $\Delta y = 18.182(t/c)$ (9-87)

Biconvex: $\Delta y = 11.667(t/c)$ (9-88)

Double Wedge: $\Delta y = 5.882(t/c)$ (9-89)

Step 4: Determine the Max Lift Ratio

Determine the *max lift ratio*, $(C_{L_{max}}/C_{l_{max}})$, using Figure 9-65. The figure establishes the variation of the ratio between the wing's $C_{L_{max}}$ and $C_{l_{max}}$ as a function of the leading-edge sweep and the LEP Δy.

Step 5: Mach Number Correction Factor

Determine the *Mach number correction factor* (MNCF), $\Delta C_{L_{max}}$, from Figure 9-66, using the LEP, the wing's leading-edge sweep (Λ_{LE}), and Mach number evaluated at the stalling speed. Note that the reference document also presents similar graphs for $\Lambda_{LE} = 40°$ and 60°, but such sweeps are rarely used on GA aircraft.

Step 6: Calculate the $C_{L_{max_0}}$

Calculate the wing's $C_{L_{max_0}}$ using the expression below:

$$C_{L_{max_0}} = \left(\frac{C_{L_{max}}}{C_{l_{max}}}\right) C_{l_{max}} + \Delta C_{L_{max}} \quad (9\text{-}90)$$

Step 7: Determine Zero-Lift Angle and Lift Curve Slope

Determine the wing's zero-lift angle, α_{ZL}, and lift curve slope, C_{L_α}. Both must be in terms of degrees.

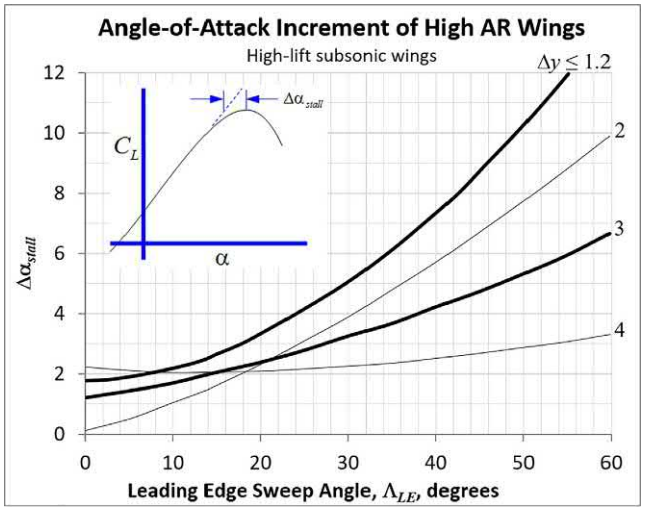


FIGURE 9-67 Determine $\Delta\alpha_{stall}$ using the above graphs. *Based on D. E. Hoak, USAF Stability and Control DATCOM, Flight Control Division, Air Force Flight Dynamics Laboratory, 1978.*

Step 8: Determine a Correction for the Stall Angle-of-Attack

Determine the stall angle correction, $\Delta\alpha_{stall}$, for the nonlinear effects of vortex flow from Figure 9-67. The curves have the basic form shown below:

For $\Delta y \le 1.2$:

$$\Delta\alpha_{stall} = 0.003020\Lambda_{LE}{}^2 + 0.01954\Lambda_{LE} + 1.729 \quad (9\text{-}91)$$

For $\Delta y = 2$:

$$\Delta\alpha_{stall} = 0.001256\Lambda_{LE}{}^2 + 0.09095\Lambda_{LE} + 0.02991 \quad (9\text{-}92)$$

For $\Delta y = 3$:

$$\Delta\alpha_{stall} = 0.0007883\Lambda_{LE}{}^2 + 0.04332\Lambda_{LE} + 1.212 \quad (9\text{-}93)$$

For $\Delta y = 4$:

$$\Delta\alpha_{stall} = 0.00057\Lambda_{LE}{}^2 - 0.01497\Lambda_{LE} + 2.179 \quad (9\text{-}94)$$

Step 9: Determine the Wing Stall Angle-of-Attack

The angle-of-attack of the wing a stall can be calculated from the following equation:

$$\alpha_{stall} = \frac{C_{L_{max}}}{C_{L_\alpha}} + \alpha_{ZL} + \Delta\alpha_{stall} \quad (9\text{-}95)$$

EXAMPLE 9-11

Compare the calculated maximum lift coefficient for the Cirrus SR22 using Method 3 and compare to the known value of $C_{L_{max_0}}$ (=1.41) for the airplane.

SOLUTION:

All values in this solution were obtained by scaling the 3-view drawing of the airplane (see Figure 16.48) using the indicated wingspan. Based on this scaling, the following geometry was extracted (note: a reader trying to reproduce the solution may come up with slightly different dimensions): $\Lambda_{LE} = 1.93°$, $AR = 10.12$, and $\lambda = 0.5$. Additionally, the leading-edge parameter Δy for its assumed NACA 65_2-415 airfoil is 2.86%, obtained using Equation (9-86). First, check if it complies with the DATCOM definition of a high AR wing. To do this, we calculate the taper ratio correction factor (TRCF) using Equation (9-81), which is $C_1 = 0.3064$. Thus, from Equation (9-82):

$$10.12 > \frac{4}{(C_1+1)\cos\Lambda_{LE}} = \frac{4}{(0.3064+1)\cos(1.93°)} = 3.064$$

The method is applicable to the SR22. Next read Figure 9-65 to determine the max lift ratio $C_{L_{max}}/C_{l_{max}}$. We find it close to $C_{L_{max}}/C_{l_{max}} = 0.89$. Note that a maximum section lift coefficient for its NACA 65_2-415 airfoil is $C_{l_{max}} = 1.40$, using wind tunnel data from Ref. [46]. Next estimate the Mach number correction factor (MNCF), $\Delta C_{L_{max}}$ using Figure 9-66 with $\Lambda_{LE} = 0°$ (since the LE sweep is only 1.93°), $M = 0.10$, and $\Delta y = 3.5$. Thus, $\Delta C_{L_{max}} = 0$.

We can now estimate the 3-dimensional maximum lift coefficient for the wing using Equation (9-90):

$$C_{L_{max_0}} = \left(\frac{C_{L_{max}}}{C_{l_{max}}}\right) C_{l_{max}} + \Delta C_{L_{max}} = (0.89)1.40 + 0 = 1.246$$

The difference between this and the POH value is 11.6%. Considering effort, this is not impressive. Anyway, let us move on to the stall AOA. First, estimate C_{L_α} for the SR22 using Equation (9-72), repeated for convenience.

$$C_{L_\alpha} = \frac{2\pi \cdot AR}{2 + \sqrt{\frac{AR^2\beta^2}{\kappa^2}\left(1 + \frac{\tan^2\Lambda_{C/2}}{\beta^2}\right) + 4}}$$

Where: β = Mach number parameter (Prandtl-Glauert) $= (1 - M^2)^{0.5} \approx 0.995$. Call it 1,

κ = Ratio of 2D lift curve slope to $2\pi = 0.107 \times (180/\pi)/(2\pi) = 0.9757$,

$\Lambda_{c/2}$ = Sweepback of mid-chord is close 0°.

$$C_{L_\alpha} = \frac{2\pi \cdot 10.12}{2 + \sqrt{\frac{10.12^2}{0.9757^2}(1) + 4}} = 5.061 \text{ per rad}$$

$$= 0.08834 \text{ per degree}$$

From Table 8-9, the zero-lift angle for the 65_2-415 airfoil is $\alpha_{ZL} = -2.6°$. Next, let's determine the nonlinear vortex flow-correction angle from Figure 9-67. Using the leading-edge sweep angle $\Lambda_{LE} = 1.93°$ and the leading-edge parameter (LEP) $\Delta y = 2.86\%$ the correction angle is $\Delta\alpha_{stall} = 1.3°$. This allows us to calculate α_{stall} using Equation (9-16):

EXAMPLE 9-11 *(cont'd)*

$$\alpha_{stall} = \frac{C_{L_{max}}}{C_{L_\alpha}} + \alpha_{ZL} + \Delta\alpha_{stall}$$

$$= \frac{1.291}{0.08834} - 2.6° + 1.3°$$

$$= 13.3°$$

The actual stall angle for the SR22 is not published, so a comparison cannot take place. However, it is thought that this angle may be 1° to 3° too low.

(7) $C_{L_{max}}$ for Selected Aircraft

Examples of the maximum lift coefficient for selected aircraft are shown in Table 9-8. The aspiring designer is encouraged to be realistic and careful when estimating this value. It has a profound impact on the capability of the aircraft; an overestimation inevitably results in an undersized wing area, which could have major impact on the stall and low-speed characteristics of the new design. Always compare your maximum lift coefficient to that of similar aircraft to avoid unrealistic overestimation.

9.5.6 The Wing Pitching Moment Coefficient

The pitching moment of an airfoil about its quarter-chord was presented as Equation (8.23) by the linear relation $C_{m_{c/4}} = C_{m_{ac}} + C_{m_\alpha}\alpha = C_{m_{ac}} + C_{l_\alpha}(0.25 - x_{ac}/c)\alpha$. Referencing Figure 9-56, this can be transformed for a 3-dimensional wing as follows. The complete moment coefficient for the wing is given by

$$\boldsymbol{C_{M_W}} = \boldsymbol{C_{M_{0_W}}} + \boldsymbol{C_{M_{\alpha_W}}}\alpha \tag{9-96}$$

Where $\boldsymbol{C_{M_{0_W}}}$ is simply $\boldsymbol{C_{M_{0_W}}} = C_{m_{ac}}$ (9-97)

Where $C_{m_{ac}}$ is that of the MGC airfoil. Recall it does not change with α. For multiairfoil wings, the *law of effectiveness* can be used to approximate the value of $C_{m_{ac}}$. In contrast to $C_{m_{ac}}$, the moment at $c/4$ changes with α. Thus, $C_{m_\alpha} = C_{l_\alpha}(0.25 - x_{ac}/c) = C_{l_\alpha}\cdot\Delta x$. We can write: $\Delta x = C_{m_\alpha}/C_{l_\alpha}$. It follows that $\boldsymbol{C_{M_\alpha}} = C_{L_\alpha}\cdot\Delta x \Leftrightarrow \boldsymbol{C_{M_\alpha}} = C_{L_\alpha}\cdot(C_{m_\alpha}/C_{l_\alpha})$. Therefore, we can write $\boldsymbol{C_{M_{\alpha W}}}$ as follows (refer to Figure 9-56 for variables):

$$\boldsymbol{C_{M_{\alpha_W}}} = C_{L_\alpha}\cdot(C_{m_\alpha}/C_{l_\alpha}) = C_{L_{\alpha_W}}(0.25 - h_n)$$

$$= C_{L_{\alpha_W}}\left(0.25 - \frac{x_{ac}}{c_{MGC}}\right) \tag{9-98}$$

Refer to Chapter 24, *Longitudinal Stability and Control* for more information about this coefficient.

EXAMPLE 9-12

A "Hershey bar" wing ($\lambda = 1$) with an $AR = 10$ is being evaluated for use in a low-speed vehicle ($M \approx 0$). One of the airfoils being considered is a NACA 23012. Convert the following 2-dimensional data for the airfoil (which have been extracted from the *Theory of Wing Sections*, by Abbott and Doenhoff) for the 3-dimensional:

Lift curve slope: $C_{l_\alpha} = 0.1051$ per degree

Lift at zero AOA: $C_{l_o} = 0.1233$

Slope of the pitching moment curve:

$$C_{m_\alpha} = 0.00020\alpha - 0.01198$$

The last expression is obtained from interpolation.

SOLUTION:

Step 1: Compute a 3D lift curve slope using Equation (9-71), where

$$C_{L_\alpha} = \frac{2\pi\cdot AR}{2 + \sqrt{AR^2 + 4}} = \frac{2\pi\cdot(10)}{2 + \sqrt{(10)^2 + 4}} = 5.151 \text{ per rad}$$

$$= 0.08990 \text{ per degree}$$

Step 2: Compute zero-lift angle for the 2-dimensional airfoil per Equation (9-66):

$$\alpha_{ZL} = -C_{l_o}/C_{l_\alpha} = -0.1233/0.1051 = -1.173°$$

Step 3: Compute zero α lift for the 3D wing per Equation (9-67):

$$C_{L_0} = |\alpha_{ZL}|\cdot C_{L_\alpha} = |-1.173°| \times 0.08990 = 0.1055$$

Step 4: Compute pitching moment for 3-dimensional wing per Equation (9-98):

$$\boldsymbol{C_{M_{\alpha_W}}} = C_{L_\alpha}\cdot(C_{m_\alpha}/C_{l_\alpha}) = (0.08990)\cdot(-0.01198/0.1051)$$

$$= -0.01025$$

9.5.7 The Lift Curve for a Delta Wing

The pros and cons of the delta wing were discussed in Section 9.4.9, *Delta Planforms*. The formation of a strong leading-edge vortex provides additional lift (called *vortex-lift*) not predicted by potential flow theory. Examples are shown in Figure 9-52 and 9-68. Several methods have been devised to predict lift for delta wings. Polhamus presents one such method for a sharp LE delta wing. It is supported by experimental data [47]. The essence of Polhamus' theory is presented below, using variables that better fit the standards in this book. Polhamus' variables are shown in parentheses.

Lift curve slope (K_p in Ref. [47]), valid for $AR \leq 4$:

$$C_{L_\alpha} = 1.595AR - 0.2845AR^2 + 0.02414AR^3 \tag{9-99}$$

TABLE 9-8 Maximum lift coefficients for selected aircraft.

	Name	Gross Weight	Wing Area	Stalling Speed, KCAS		Maximum Lift Coefficient		Source
		lb_f	ft^2	V_S (clean)	V_{S0} (flaps)	$C_{L\,max}$	$C_{L\,max0}$	
Single Engine	Aerotec A-135 Tangará II	2116	158	55	48	1.31	1.72	JAWA
	Bede BD-5A Micro	660	47	54	48	1.41	1.78	JAWA
	Cessna 162 Skycatcher	1320	120	44	40	1.68	2.03	POH
	Cessna 172 Skyhawk	2550	174	53	48	1.54	1.88	POH
	Cessna 182 Skylane	3100	174	56	50	1.68	2.10	POH
	Cessna 208B Grand Caravan	8750	279	78	61	1.52	2.48	POH
	Cirrus SR20	3050	145	67	59	1.38	1.79	POH
	Cirrus SR22	3400	145	70	60	1.41	1.92	POH
	Embraer EMB-201	3417	194	57	51	1.60	2.00	JAWA
	Let Z-37 Cmelak (Bumble-Bee)	3855	256	49	45	1.85	2.19	JAWA
	Neiva N621A	3306	185	64	57	1.31	1.65	JAWA
	Piper PA-46-350 Malibu	4340	175	69	58	1.56	2.18	JAWA
	Taylor J.T.1 Monoplane	610	76	40	33	1.48	2.18	JAWA
	Transavia PL-12 Airtruk	3800	256	55	52	1.45	1.62	JAWA
	XtremeAir Sbach 300	2205	121	-	57	-	1.65	POH
Twin Engine Propeller	Beechcraft Baron 55	5100	199	81	72	1.15	1.46	POH
	Beechcraft Duke B60	6775	213	86	76	1.27	1.63	JAWA
	Beechcraft Queenair B80	8800	294	85	71	1.22	1.75	JAWA
	Cessna 337 Skymaster	4630	201	70	61	1.39	1.83	JAWA
	Cessna 421 Golden Eagle	7450	215	83	74	1.49	1.87	POH
	Partenavia P.68	4327	200	64	56	1.56	2.03	JAWA
	Pilatus Britten-Norman BN-2B Islander	2993	325	50	40	1.09	1.70	JAWA
	Piper PA-34 Seneca	4200	209	66	60	1.36	1.65	POH
	Rockwell Commander 112A	3250	152	64	56	1.54	2.01	POH
	Vulcanair P.68 Observer	4594	200	68	57	1.47	2.09	JAWA
Commuter Turboprops	Beechcraft Kingair 100	10600	298	92	76	1.24	1.82	JAWA
	Beechcraft Kingair C90	9650	294	80	72	1.51	1.87	JAWA
	CASA C.212 Aviocar	13889	431	72	62	1.84 (T-O)	2.48	JAWA
	Frakes conversion Turbo-Mallard	14000	444	76	66	1.61	2.14	JAWA
	Let L-140 Turbolet	11905	354	83	64	1.44	2.43	JAWA
	Lockheed Model 85 Orion P-3	135000	1300	133	112	1.73	2.44	JAWA
	Nomad N22	8000	324	65	47	1.73	3.30	JAWA
	Piper PA-31P Pressurized Navajo	7800	229	80	72	1.57	1.94	JAWA
	Rockwell Commander 690A	10250	266	82	77	1.69	1.92	JAWA
	Shorts SD3-30	22000	453	92	74	1.69	2.62	JAWA
Business Jets	Beechjet 400A	16100	241	-	93	-	2.28	JAWA
	Cessna Citation CJ1	10700	240	82	77	1.96	2.22	JAWA
	Cessna Citation Mustang	8645	210	91	73	1.47	2.28	Estimate
	Dassault Falcon 2000X	41000	527	98	84	2.39	3.26	JAWA
	Dassault Falcon 900	45500	527	106	85	2.27	3.53	JAWA
	Dassault-Breguet Mystere-Falcon 900	20640	528	104	82	1.07	1.72	JAWA
	Embraer Phenom 100	10472	202	100	77	1.53	2.58	JAWA
	Gates Learjet 24D	13500	232	126	99	1.08	1.75	JAWA
	Gulfstream Aerospace IV	71700	950	120	108	1.55	1.91	JAWA
	Safire S-26	5130	143	92	69	1.26	2.23	JAWA
Commercial Jetliners	Airbus A300-B4	360000	2800	150	120	-	2.64	Estimate
	Airbus A310	361600	2357	178	122	1.42	3.02	FCOM
	Airbus A320-200	170000	1320	179	121	1.19	2.60	JAWA
	Airbus A330	520000	3892	170	128	1.37	2.40	FCOM
	Airbus A340-200	610000	3892	189	134	1.30	2.59	FCOM
	Boeing B727-200	160000	1700	171	106	1.10	2.47	JAWA
	Boeing B737-200	103000	1098	-	102	-	2.66	JAWA
	Boeing B737-400	150000	1135	150	120	-	2.71	Estimate
	Boeing B757-200	255000	1994	145	120	-	2.62	Estimate
	Boeing B777-200A	545000	4605	150	120	-	2.43	Estimate
	Fokker 100	95000	1006	160	109	1.09	2.35	JAWA
	Lockheed L-1011-1 Tristar	430000	3456	166	125	1.33	2.35	JAWA

Sources: JAWA = Jane's All the World's Aircraft, POH = Pilot's Operating Handbook, FCOM = Flight Crew Operating Manual

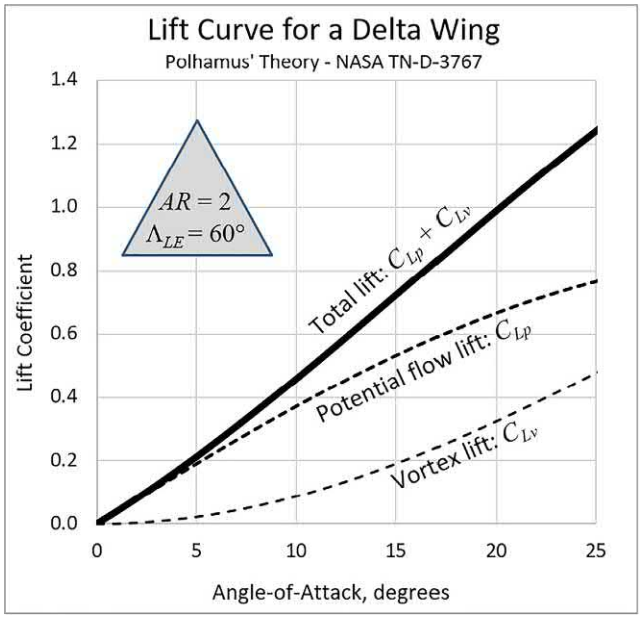


FIGURE 9-68 Potential and vortex-lift for a delta wing.

Lift-induced drag parameter[2] (K_i in Ref. [47]), valid for $AR \leq 4$:

$$k = 3.133 - 0.01123AR + 0.02510AR^2 \tag{9-100}$$

Constant of proportionality (K_v):

$$K_v = \left(C_{L_\alpha} - kC_{L_\alpha}^2\right)/\cos\Lambda_{LE} \tag{9-101}$$

Potential flow lift coefficient:

$$C_{L_p} = C_{L_\alpha} \sin\alpha \cos^2\alpha \tag{9-102}$$

Vortex lift coefficient: $C_{L_v} = K_V \cos\alpha \sin^2\alpha$ (9-103)

Total lift coefficient for a delta wing:

$$C_L = C_{L_p} + C_{L_v} \tag{9-104}$$

9.5.8 Adding Nonlinearity to Lift Curve

Sometimes, the nonlinearity in the lift curve near stall must be accounted for. One way of accomplishing this is to stitch a polynomial spline at the point where the lift curve becomes nonlinear (α_{NL}, $C_{L_{NL}}$). This is shown in Figure 9-69. To do this, we must have a reasonable estimate (or guess) for α_{NL}, α_{stall}, and $C_{L_{max}}$. Then, we establish boundary conditions: (1) same C_L and slope for line and spline at α_{NL}. (2) Spline goes through (α_{stall}, $C_{L_{max}}$) with zero slope. This is implemented by solving the matrix below for A through D.

$$\begin{bmatrix} \alpha_{NL}^3 & \alpha_{NL}^2 & \alpha_{NL} & 1 \\ 3\alpha_{NL}^2 & 2\alpha_{NL} & 1 & 0 \\ \alpha_{stall}^3 & \alpha_{stall}^2 & \alpha_{stall} & 1 \\ 3\alpha_{stall}^2 & 2\alpha_{stall} & 1 & 0 \end{bmatrix} \begin{Bmatrix} A \\ B \\ C \\ D \end{Bmatrix} = \begin{Bmatrix} C_{L_{NL}} \\ C_{L_\alpha} \\ C_{L_{max}} \\ 0 \end{Bmatrix}$$

Then, the lift curve can be written in the following form:

$$C_L = \begin{cases} C_{L_0} + C_{L_\alpha}\alpha & \text{if } \alpha < C_{L_{NL}} \\ A\alpha^3 + B\alpha^2 + C\alpha + D & \text{if } \alpha \geq C_{L_{NL}} \end{cases} \tag{9-105}$$

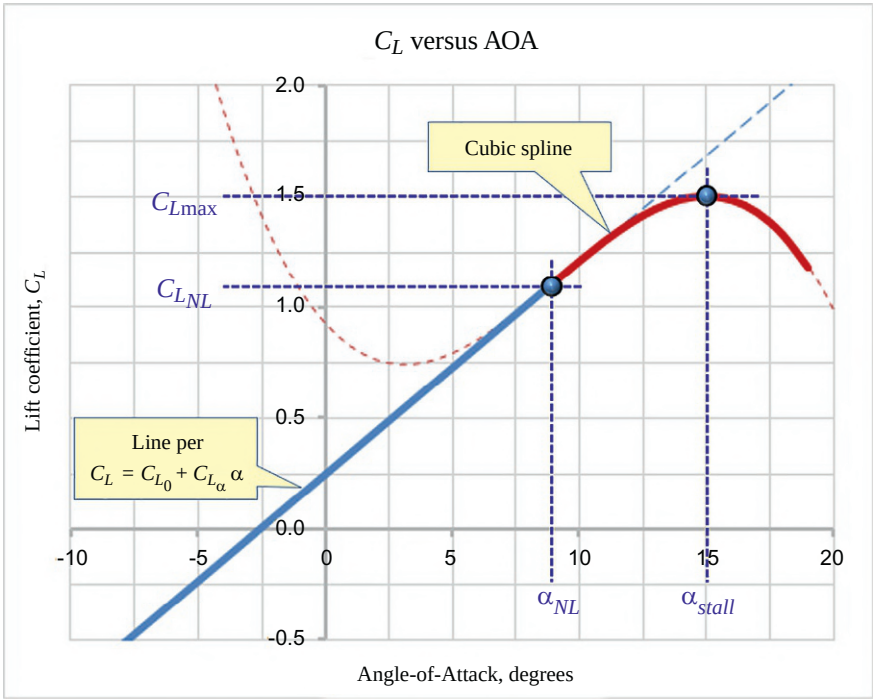


FIGURE 9-69 Stitching a cubic spline to the lift curve.

[2] Interpolation of Figure 9 in Ref. [47] by author.

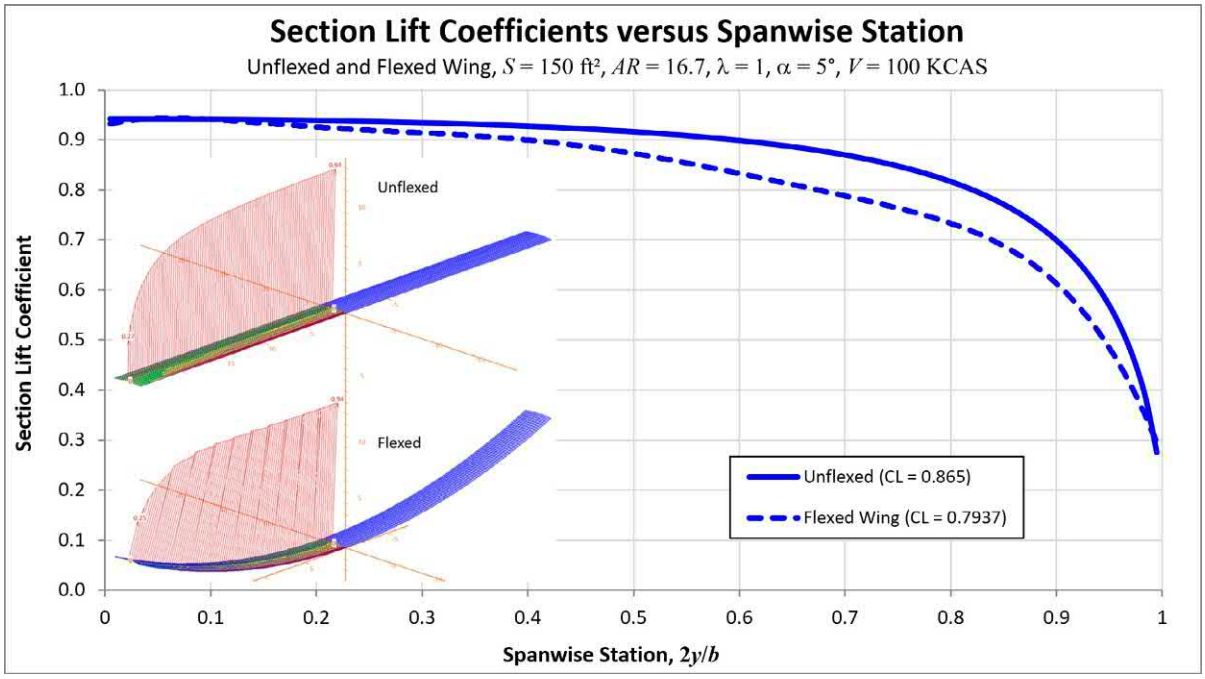


FIGURE 9-70 Lift distribution of a flexed and unflexed wings compared.

Note that this is an approximation and does not guarantee the actual shape of the lift curve is captured.

9.5.9 The Law of Effectiveness

Consider a wing with two distinct airfoils at the root and tip. Assume the root has $C_{d_{min}} = 0.002$ and the tip $C_{d_{min}} = 0.004$. What is a representative $C_{d_{min}}$ for this wing? One answer is the average of the two, i.e., $C_{d_{min}} = 0.003$. A better answer is obtained using the *law of effectiveness*. It contends an aerodynamic property along a multiairfoil wing changes linearly between airfoil stations. Thus, a better value for $C_{d_{min}}$ should be its value at the MGC. A handy way to estimate a property at the MGC is obtained using a parametric line:

The Law of Effectiveness:

$$P_{MGC} = P_{root} + \frac{2y_{MGC}}{b}\left(P_{tip} - P_{root}\right) \tag{9-106}$$

Where P stands for *airfoil property*. The P can be the C_{l_α}, $C_{l_{max}}$, $C_{d_{min}}$, C_m, and similar. For instance, when applied to $C_{d_{min}}$ for two airfoils, Equation (9-106) becomes:

$$(C_{d_{min}})_{MGC} = (C_{d_{min}})_{root} + \frac{2y_{MGC}}{b}\left[(C_{d_{min}})_{tip} - (C_{d_{min}})_{root}\right] \tag{9-107}$$

9.5.10 Flexible Wings

The high aspect ratio wings of sailplanes flex excessively during maneuvers and even in normal flight. Flex as large as 6 ft (2 m) is common. The same can be said of commercial aircraft like the Boeing 747, 787, Airbus A350, and A380. Regardless of aircraft class, if excessive wing flex is anticipated its effects on lift must be considered.

Figure 9-70 shows how wing flex affects the distribution of C_l. In this example, a wing with a 50 ft wingspan is deflected so its tips are 5 ft higher than the unflexed wing. At a given AOA, the center-of-lift moves inboard, reducing the bending moment (by 4.5%), less lift (in this case, some 3% less), and C_{L_α} is reduced by 3%. This calls for a higher operational AOA, which means higher operational lift-induced drag, a detriment to the wing's long-range efficiency. While this sounds negative, there are two sides to this topic; the other is discussed in Section 10.5.10, *The Polyhedral Wing(tip)*.

9.5.11 Ground Effect

Ground effect is the change in the aerodynamic forces due to a body's proximity to the ground. The ground gets in the way of the downwash, preventing its full development (see Figure 9-71). The modified flow field around the aircraft reduces drag and increases lift slightly [48]. Ground effect should be accounted for during take-off and landing analyses. It becomes noticeable when the wing-to-ground separation is less than 1 × wingspan.

Ground effect is modeled using vortex theories such as Prandtl's lifting-line theory, lumped vortices, or the vortex-lattice theory. By creating a mirror image of the wing (or airfoil) with bound vortices of equal strength but rotating in opposite directions (see Figures 9-71 and 9-72) the resulting flow field will feature a horizontal streamline. It represents the ground plane. As shown in Figure 9-71, this realigns streamlines compared to the flow field in the absence of the ground.

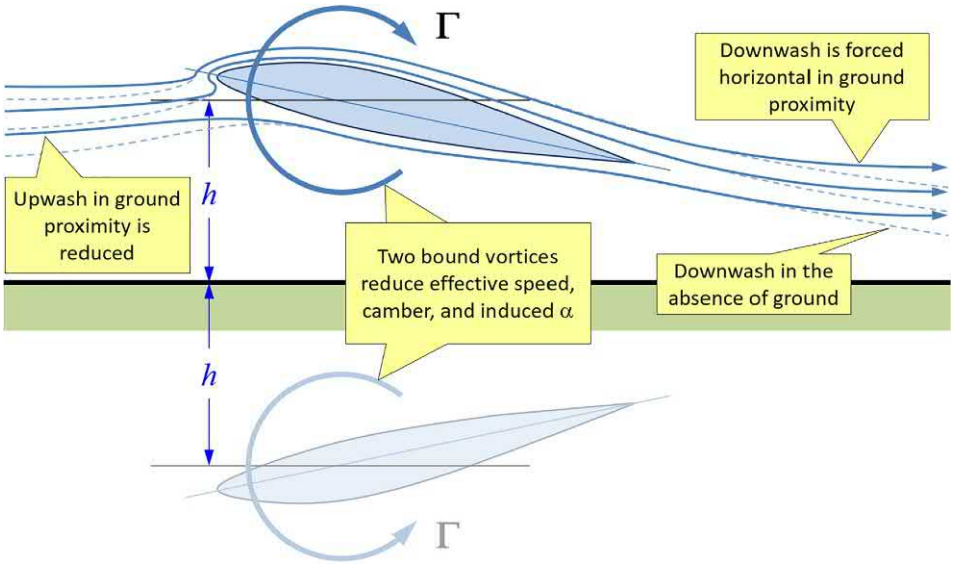


FIGURE 9-71 Modeling the ground effect is done using a mirror image airfoil (or wing).

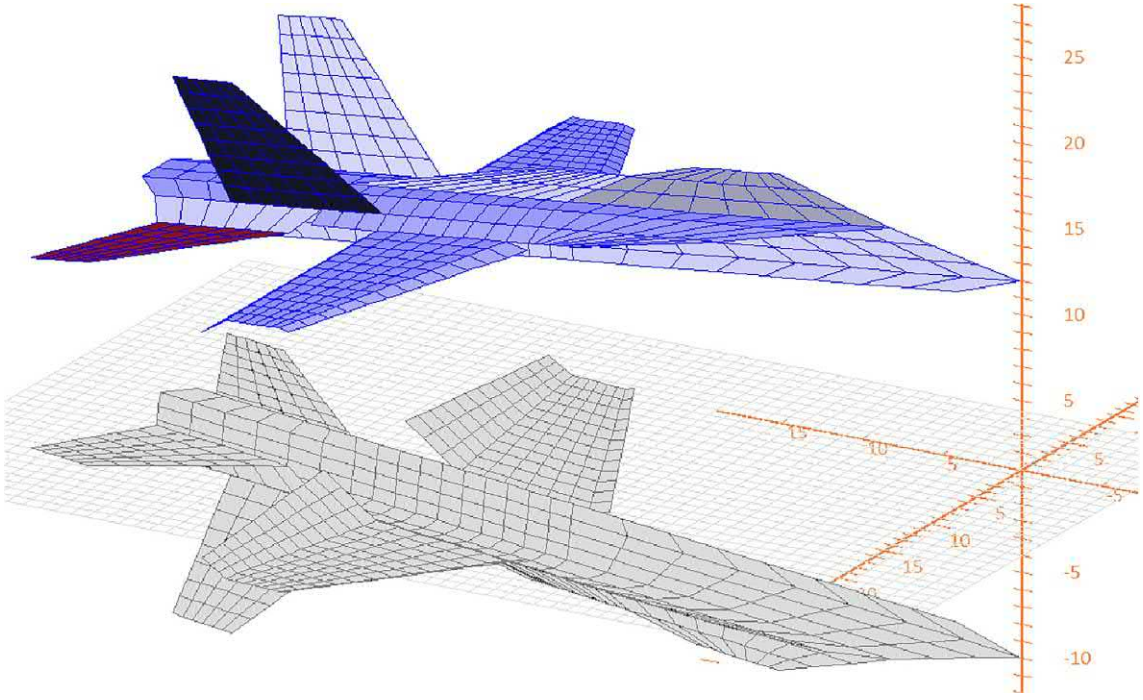


FIGURE 9-72 Setup for ground effect studies using a mirrored vortex-lattice model.

The problem of ground effect was studied as early as in 1912 by Albert Betz (1885–1968) [49]. Using Prandtl's lifting-line theory, Wieselberger [50] developed formulation to estimate the reduction in the lift-induced drag near the ground (translated in Ref. [48]). This requires the calculation of a special *ground influence coefficient*, here denoted by Φ. These are evaluated in terms of the *separation ratio*, h/b, in which h is the distance between the aerodynamic center of the c_{MGC} and the ground (see Figure 9-73) and b is wingspan.

Ground effect *increases* the C_L at a given geometric AOA. The flow field changes consist of *reduced* upwash and downwash (see Figure 9-71). This reduces (a) the effective airspeed, (b) effective camber, and (c) the induced AOA (α_i—see Section 9.5.4) [51]. The contribution of (a) increases static pressure in the vicinity of the wing's lower surface, increasing lift, while (b) reduces lift because of reduced camber. Thus, (a) and (b) tend to cancel each other. In contrast, (c) reduces induced α_i, increasing the effective α_e (where $\alpha_e = \alpha - \alpha_i$). This increases the

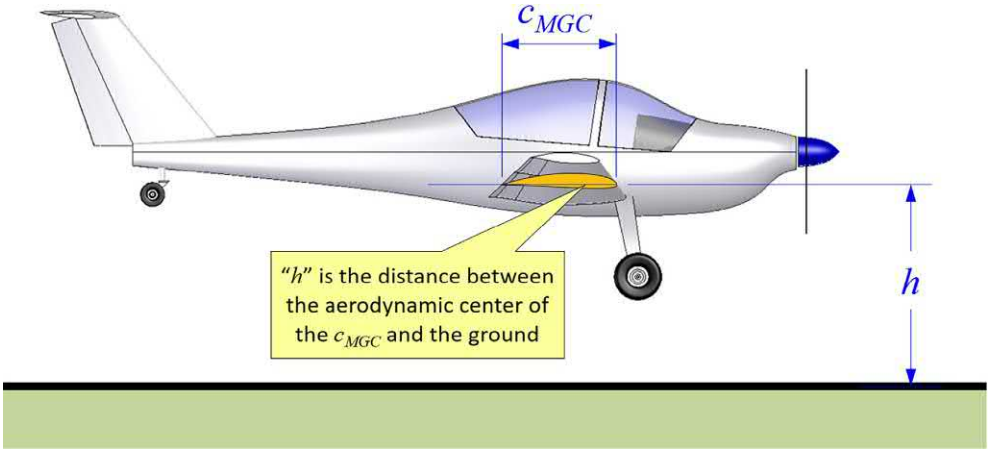


FIGURE 9-73 An airplane in ground effect.

lift. For tail-aft aircraft, this *increases* the AOA on the horizontal tail (recall that the free downwash *reduces* the AOA on the HT), although this change is less than the change in downwash angle [51]. The change in α is given by [51, 52]

$$\Delta\alpha_i = -\frac{C_L}{\pi \cdot AR}\sigma = -\frac{C_L}{\pi \cdot AR}e^{-2.48(2h/b)^{0.768}} \tag{9-108}$$

The expression returns the angle in radians. The term σ is called *Prandtl's interference coefficient* for multiplanes. The reduction in lift-induced drag increases the effective AR, AR_{IGE}. The accompanying increase in lift at a given AOA, increases the L/D ratio, causing a "floating" tendency. AR_{IGE} is given by

$$AR_{IGE} = \frac{AR}{1-\sigma} \tag{9-109}$$

The lift increase causes a small increase in the lift curve slope. Per Ref. [53], this tends to result in a small reduction in the zero-AOA lift. The trim AOA is reduced, so the airplane tends to go to a lower AOA. The elevator effectiveness of a conventional tail-aft configuration is reduced as the low-pressure region on the lower surface is counteracted by the formation of a high-pressure region like that of the wing. By the same token, the elevator effectiveness of a canard configuration increases.

(1) Ground Effect and Lift

The influence of ground effect on lift revolves around relating the lift coefficient at some AOA, *out-of-ground-effect*, $C_{L_{OGE}}(\alpha)$, to that *in-ground-effect*, $C_{L_{IGE}}(\alpha)$. Thus, the *ground influence coefficient for lift*, Φ_L, between the two is defined as

$$\Phi_L = \frac{C_{L_{IGE}}(\alpha)}{C_{L_{OGE}}(\alpha)} \Rightarrow C_{L_{IGE}} = \Phi_L \cdot C_{L_{OGE}} \tag{9-110}$$

Phillips and Hunsaker [54] present a practical method derived using Prandtl's lifting-line theory to evaluate this ratio for elliptic and tapered wings. This method includes a correction for high AOAs (β_L).

$$\text{Elliptic:}\quad \Phi_L = \frac{1}{\beta_L}\left[1 + \frac{288(h/b)^{0.787}}{AR^{0.882}}e^{-9.14(h/b)^{0.327}}\right] \tag{9-111}$$

$$\text{Tapered:}\quad \Phi_L = \frac{1}{\beta_L}\left[1 + \delta_L\frac{288(h/b)^{0.787}}{AR^{0.882}}e^{-9.14(h/b)^{0.327}}\right] \tag{9-112}$$

Where:

$$\delta_L = 1 - 2.25\left(\lambda^{0.00273} - 0.997\right)\left(AR^{0.717} + 13.6\right) \quad \text{and}$$

$$\beta_L = 1 + \frac{0.269C_L^{1.45}}{AR^{3.18}(h/b)^{1.12}}$$

(2) Ground Effect and Drag

The influence of ground effect on drag is evaluated in a fashion similar lift, by relating lift-induced drag at some AOA (and thus C_L) to that some distance above the ground. The minimum drag does not change. For untwisted wings with symmetric airfoils, $C_{D_i} = kC_L^2 \Rightarrow k = C_{D_i}/C_L^2$. Thus, it is convenient to compare the lift-induced drag constant (k) for the two conditions. Define the *ground influence coefficient for drag* between the two, Φ_D, as

$$\Phi_D = \frac{\left[C_{D_i}/C_L^2\right]_{IGE}}{\left[C_{D_i}/C_L^2\right]_{OGE}} \Rightarrow C_{Di_{IGE}} = \Phi_L^2 \cdot \Phi_D C_{Di_{OGE}} \tag{9-113}$$

In the absence of Φ_L, use 1.05 if $h/b < 0.5$ and 1 otherwise. The literature presents several methods to determine Φ_D. Wieselberger's approach has been adapted to this text. He used $h/2$ for height above the ground and a special coefficient σ (*Wieselberger's coefficient*) that is subtracted from 1, yielding:

$$\Phi_D \text{ per Wieselberger:}\quad \Phi_D = 1 - \frac{1 - 1.32(h/b)}{1.05 + 7.4(h/b)} \tag{9-114}$$

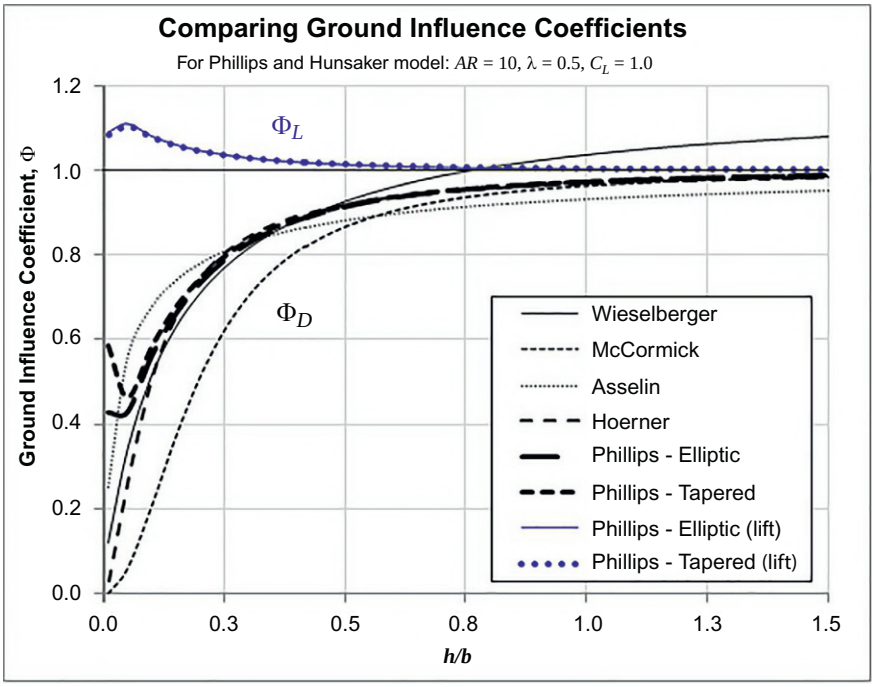


FIGURE 9-74 Comparing ground influence coefficients.

This approximation appears in good agreement with experiment for $0.033 \le h/b \le 0.25$ [53]. Using the Biot-Savart law applied to a horseshoe vortex whose span is $\pi b/4$, McCormick [54, 55] shows that the ground influence coefficient can be estimated from:

Φ_D per McCormick[3]:

$$\Phi_D = \frac{(16h/(\pi b))^2}{1+(16h/(\pi b))^2} \tag{9-115}$$

Using the lifting-line theory and assuming an elliptical lift distribution of a straight wing of $AR \approx 5$, Asselin [56] derives the following ground influence coefficient:

$$\Phi_D \text{ per Asselin:} \quad \Phi_D = 1 - \frac{2}{\pi^2}\ln\left(1+\frac{\pi}{8\cdot h/b}\right) \tag{9-116}$$

Phillips and Hunsaker [54] present the following expressions for elliptic and tapered wings

Elliptic:

$$\Phi_D = \beta_D\left[1 - e^{-4.74(h/b)^{0.814}} - (h/b)^2 e^{-3.88(h/b)^{0.758}}\right] \tag{9-117}$$

Tapered:

$$\Phi_D = \beta_D\left[1 - \delta_D e^{-4.74(h/b)^{0.814}} - (h/b)^2 e^{-3.88(h/b)^{0.758}}\right] \tag{9-118}$$

Where:

$$\delta_D = 1 - 0.157\left(\lambda^{0.775} - 0.373\right)\left(AR^{0.417} - 1.27\right) \quad \text{and}$$

$$\beta_D = 1 + \frac{0.0361 C_L^{1.21}}{AR^{1.19}(h/b)^{1.51}}$$

Hoerner and Borst [57] suggest the following ground influence coefficient:

$$\Phi_D \text{ per Hoerner:} \quad \Phi_D = \frac{33(h/b)^{1.5}}{1+33(h/b)^{1.5}} \tag{9-119}$$

The lift- and drag-related ground influences are plotted in Figure 9-74.

DERIVATION OF EQUATION (9-113)

From the definition of Φ_D we can write:

$$\Phi_D = \frac{\left[C_{D_i}/C_L^2\right]_{IGE}}{\left[C_{D_i}/C_L^2\right]_{OGE}} \quad \Rightarrow \quad \frac{C_{Di_{IGE}}}{C_{L_{IGE}}^2} = \Phi_D \frac{C_{Di_{OGE}}}{C_{L_{OGE}}^2}$$

Substitute $C_{L_{IGE}} = \Phi_L \cdot C_{L_{OGE}}$ and manipulate algebraically

$$\frac{C_{Di_{IGE}}}{\left(\Phi_L \cdot C_{L_{OGE}}\right)^2} = \Phi_D \frac{C_{Di_{OGE}}}{C_{L_{OGE}}^2}$$

$$\Rightarrow \quad C_{Di_{IGE}} = \left(\Phi_L^2 \cdot C_{L_{OGE}}^2\right)\Phi_D \frac{C_{Di_{OGE}}}{C_{L_{OGE}}^2}$$

$$= \Phi_L^2 \cdot \Phi_D C_{Di_{OGE}}$$

[3] Note that in the first edition of this book, McCormick's expression had a typographical error inherited from Ref. [55]. See discussion about its origin and correction in Ref. [54].

TABLE 9-9 Examples of Oswald's span efficiencies for selected aircraft.

SINGLE ENGINE PROPELLER						TWIN ENGINE PROPELLER					
Manufacturer	Model	S, ft²	b, ft	AR	e	Manufacturer	Model	S, ft²	b, ft	AR	e
Beechcraft	35	184	33.5	6.10	0.82	Beechcraft	AT-7	349	47.7	6.51	0.74
Boeing-Stearman	PT-18	298	32.2	6.94	0.75	Cessna	AT-8	295	41.9	5.96	0.61
Cessna	OE-2	174	36.0	7.45	0.7	Douglas	A-26B	540	70.0	9.07	0.79
Cessna	180	174	35.8	7.38	0.75	Curtiss	C-46A	1360	108.1	8.59	0.88
Cessna	150	160	33.3	6.94	0.77	Douglas	C-47B	987	95.5	9.24	0.89
Cessna	172	174	36.1	7.48	0.77	North American	B-25D	610	67.6	7.49	0.78
Cessna	182	174	36.0	7.45	0.84	Martin	B-26F	658	71.0	7.66	0.76
Cessna	185	174	35.8	7.38	0.86	Cessna	310	175	35.0	7.00	0.73
Cessna	177	174	35.5	7.24	0.57	Gulfstream	G-I	610.3	76.5	9.59	0.78
Douglas	O-46A	332	45.8	6.30	0.8	SAAB	SF340	450	70.3	10.99	0.8
Stinson	L-5	155	34.0	7.46	1.02						

Based on Roskam, Jan, Airplane Design, Part VI, DARcorporation, 2000.

9.5.12 Determination of Span Efficiency, *e*

Span efficiency is a parameter used to predict the lift-induced drag of aircraft. While drag is dealt with in Chapter 16, *Aircraft Drag Analysis*, it is appropriate to present span efficiency here because of its dependency on wing geometry.

The literature discusses two kinds of span efficiency: (1) That which is attributed to W. Bailey Oswald (1906–98) who first defined it in 1933[4] [58]. (2) That which is obtained from Prandtl's lifting-line theory, presented in Section 9.7, *Prandtl's Lifting-Line Theory*. The difference is that Oswald's efficiency applies to the entire aircraft, whereas Prandtl's span efficiency, which is based on inviscid potential flow theory, only applies to the wing. To complicate things, both kinds are usually represented using the letter *e*, which is easy to confuse with Euler's number ($e = 2.71828\ldots$). Table 9-9 lists the Oswald efficiency for selected single and twin-engine aircraft.

(1) Basic Definition

At most operational AOAs, the drag coefficient for a wing (or a complete aircraft) can be written as

$$C_D = C_{D_{\min}} + C_{D_i} = C_{D_{\min}} + k(C_L - C_{L_{\min D}})^2 \qquad (9\text{-}120)$$

Where $C_{D_{\min}}$ is the *minimum drag coefficient*, C_{D_i} is the *lift-induced drag coefficient*, k is the *lift-induced drag constant*, and $C_{L_{\min D}}$ is the *lift of minimum drag*. $C_{L_{\min D}}$ accounts for the fact that $C_{D_{\min}}$ does not occur at $C_L = 0$ for most aircraft. Per Prandtl's lifting-line theory for arbitrary wings, k is defined as:

$$k \equiv (1 + \delta)/(\pi \cdot AR) \qquad (9\text{-}121)$$

Where δ is the *lift-induced drag factor*. Frequently, k is written in terms of span efficiency (or Oswald's efficiency), e:

$$k = 1/(\pi \cdot AR \cdot e) = 1/(\pi \cdot AR_e) \qquad (9\text{-}122)$$

Where AR_e is the *effective aspect ratio*. Note that e is a variable but remains relatively constant over a range of practical lift coefficients—at low AOAs. The growth of flow separation at high AOAs changes its value. Using Equation (9-121), δ and e are related as shown below:

$$e = 1/(1 + \delta) \qquad (9\text{-}123)$$

The representation is altogether theoretical, requiring a redefinition in a moment. One way to obtain these parameters is through flight or wind tunnel testing. Section 16.5.5, *Determining Drag Characteristics from Wind Tunnel Data* presents a method for this purpose. Thus, we can calculate $C_{D_i} = C_D - C_{D_{\min}}$ and extract an "experimental" e using the expression:

$$C_{D_i} = \frac{(C_L - C_{L_{\min D}})^2}{\pi \cdot AR \cdot e} \quad \Leftrightarrow \quad e = \frac{(C_L - C_{L_{\min D}})^2}{\pi \cdot AR \cdot C_{D_i}} \qquad (9\text{-}124)$$

When $C_{L_{\min D}} = 0$, we get a more standard form of Oswald's efficiency factor.

$$e = \frac{C_L^2}{\pi \cdot AR \cdot C_{D_i}} \qquad (9\text{-}125)$$

Nita and Scholz present an excellent treatment of this topic in Ref. [59]. They argue that e should be defined using the general form below:

$$e = \frac{1}{Q + P \cdot \pi \cdot AR} \qquad (9\text{-}126)$$

Where: Q = Inviscid contribution to lift-induced drag,

P = Viscous contribution to lift-induced drag.

[4] Interestingly, Oswald called it the *airplane efficiency factor*.

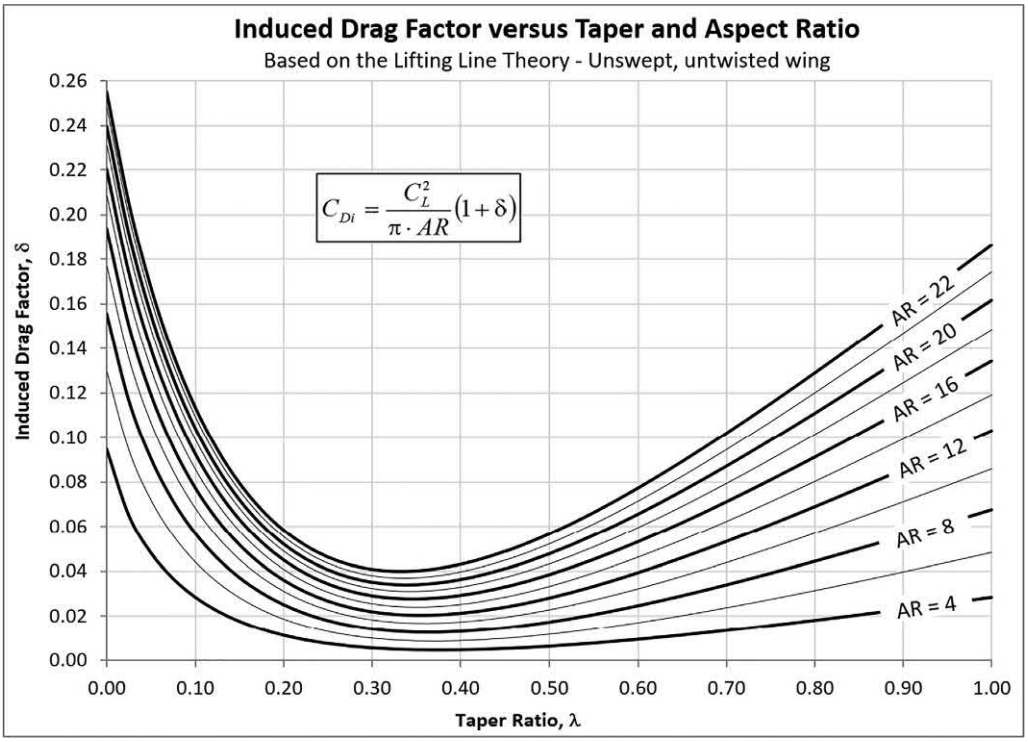


FIGURE 9-75 Induced drag factor for $0 \le \lambda \le 1$ and $4 \le AR \le 22$.

Q is caused by induced velocities in the wake, while P is caused by increase in skin-friction and pressure drag. The authors summarize P and Q for 13 methods for determining e.

(2) Theoretical Span Efficiency, e_{theo}

Ref. [59] asserts that not all methods to calculate e are created equal. Rather, these should be classified as *theoretical* (e_{theo}) and *effective span efficiencies* (e). The former represents the wing alone, whereas the latter represents the *whole aircraft*. This requires e_{theo} to be subjected to corrections. The span efficiency obtained by Prandtl's lifting-line theory using Equation (9-121) is theoretical. Thus

$$e_{theo} = \frac{1}{1+\delta} \tag{9-127}$$

The theoretical span efficiency can be calculated using the method shown in Section 9.7.4, *Computer Code: Prandtl's Lifting-Line Method*. It presents a code snippet allowing the factor to be determined using Microsoft Excel's *Visual Basic for Applications* (VBA). Figure 9-75 shows the variation of δ over a range of λ and AR. Note that $e_{theo} = 1$ is interpreted as the efficiency of an elliptical wing.

(3) Effective Span Efficiency, e

To maintain tradition, the effective span efficiency will be represented using the letter e. This is e_{theo} corrected for the presence of a fuselage, winglets, dihedral, compressibility, and others. There are two kinds of corrections: *intrinsic* and *factorial*. Intrinsic refers to a correction of a parameter used to estimate span efficiency. For example, we correct the regular AR for the presence of winglets, yielding a *corrected aspect ratio*, AR_{corr}. Then, as an example, AR_{corr} is used with Equation (9-129) in lieu of AR. Factorial corrections directly multiply the theoretical span efficiency as shown below:

$$e = e_{theo} \cdot k_{corr_1} \cdot k_{corr_2} \cdot \ldots \tag{9-128}$$

Where k_{corr_i} is a correction factor. Several methods to calculate effective span efficiency will now be presented, followed by correction methods.

(4) Method 1: Empirical Estimation for Straight Wings

Raymer [5] presents the following statistical expression to estimate Oswald's efficiency of straight wings. Note that it omits dependency on taper ratio (λ) and is limited to $AR_{corr} > 3$.

$$e = 1.78\left(1 - 0.045 AR_{corr}^{0.68}\right) - 0.64 \tag{9-129}$$

(5) Method 2: Empirical Estimation for Swept Wings

Raymer [5] also presents the following statistical expression to estimate the Oswald efficiency of swept wings. It has similar limitations as Equation (9-129) and is limited to $AR_{corr} < 10$ and $\Lambda_{LE} > 30°$:

$$e = 4.61\left(1 - 0.045 AR_{corr}^{0.68}\right)(\cos\Lambda_{LE})^{0.15} - 3.1 \tag{9-130}$$

(6) Method 3: Brandt's Method

Brandt et al. [4] present the following expression to estimate e. It is limited to $4 < AR_{corr} < 15$:

$$e = \frac{2}{2 - AR_{corr} + \sqrt{4 + AR_{corr}^2(1 + \tan^2\Lambda_{t\max})}} \tag{9-131}$$

Where: Λ_{LE} = Leading-edge sweep angle.

$\Lambda_{t\ \max}$ = Sweep angle of the maximum wing thickness line.

(7) Method 4: Douglas Method

Shevell [60] presents the following expression to calculate Oswald's efficiency. It is based on unpublished studies by the Douglas aircraft company. Its presentation has been adapted to the discussion in here.

$$e = \frac{1}{\pi \cdot AR_{corr} \cdot r \cdot C_{D_{\min}} + 1/\{(1 + 0.03t - 2t^2)u\}} \tag{9-132}$$

Where: t = Fuselage width to wingspan ratio = w_{fus}/b,

w_{fus} = Maximum width of the fuselage

b = wingspan,

u = Correction factor for nonelliptical wing planform, typically 0.98–1.00,

r = Parasitic correction factor and $r = 0.38 - \Lambda_{LE}/3000 + \Lambda_{LE}^2/15{,}000$ and Λ_{LE} is in degrees.

(8) Method 5: Howe's Method for Subsonic to Transonic Range

Howe [61] presents a statistical expression for subsonic to transonic aircraft (commercial and business jets) with moderate to high aspect ratios ($AR > 5$ and $M < 0.95$).

$$e = \frac{1}{(1 + 0.12M_\infty^6)\left\{1 + \dfrac{0.142 + f(\lambda)AR_{corr}(10t/c)^{0.33}}{\cos^2\Lambda_{c/4}} + \dfrac{0.1(3N_{PP} + 1)}{(4 + AR_{corr})^{0.8}}\right\}} \tag{9-133}$$

Where: M_∞ = Far-field Mach number,

N_{PP} = Number of power plants (engines) on wing.

$N_{PP} = 0$ if none,

$f(\lambda)$ = Wing's taper ratio function = $0.005(1 + 1.5(\lambda - 0.6)^2)$,

t/c = Wing's representative thickness-to-chord ratio,

$\Lambda_{c/4}$ = Wing's quarter-chord sweep.

(9) Method 6: USAF DATCOM Method for Swept Wings—Step-by-Step

This method comes from Section 4.1.5.2 of Ref. [1] and is based on a 1963 paper by Frost and Rutherford [62]. The paper suggests that the Oswald's efficiency depends on the factor R, which is the ratio between the actual drag force of a wing and that of an elliptical wing. It assumes both wing styles utilize a symmetrical airfoil. Using statistical analysis of multiple NACA reports, the authors devised a method to estimate the span efficiency over a range of AR. Per Ref. [60], the method is subject to the following limitations:

Aspect ratio:	$2 \le AR \le 10.7$
Taper ratio:	$0 \le \lambda \le 0.713$
Leading-edge sweep angle:	$19.1° \le \Lambda_{LE} \le 63.4°$
Leading-edge suction parameter:	$2 \le R_{rLE} \le 10$
Mach number:	$0.13 \le M \le 0.81$

This does not mean it is not applicable to other planforms. The method is used to estimate a special factor, called the *leading-edge suction parameter*, R, which is used with the following expression to estimate the span efficiency:

$$e = \frac{1.1(C_{L_\alpha}/AR_{corr})}{R(C_{L_\alpha}/AR_{corr}) + (1 - R)\pi} \tag{9-134}$$

This method requires several parameters to be determined, which are then used to extract the parameter R for use with Equation (9-134).

Step 1: Calculate the Lift Curve Slope

Lift curve slope can be calculated from Equation (9-72).

Step 2: Calculate the Leading-Edge Suction Parameter

The *leading-edge suction parameter* is really Reynolds number based on the LE radius and airspeed in ft/s. It is given by

$$R_{r_{LE}} = \rho V r_{LE}/\mu$$

Where: r_{LE} = Leading-edge radius (from airfoil data),

μ = Air viscosity, in $lb_f\ s/ft^2$,

ρ = Air density, $slugs/ft^3$.

Step 3: Calculate Special Parameter 1

$$P_1 = \frac{AR_{corr}\lambda}{\cos\Lambda_{LE}}$$

Step 4: Calculate Special Parameter 2

$$P_2 = R_{r_{LE}} \times \cot\Lambda_{LE}\sqrt{1 - M_\infty^2\cos^2\Lambda_{LE}}$$

Step 5: Read or Calculate the Leading-Edge Suction Parameter

Determine R from Figure 9-76 or calculate from the following expressions:

if $P_2 \le 1.3 \times 10^5 \Rightarrow$

$$R = \left(-4.728 + 2.185 \cdot \log_{10}(P_2) - 0.2131 \cdot \log_{10}(P_2)^2\right) + 0.095 \cdot \sin(0.05\pi P_1)$$

if $P_2 > 1.3 \times 10^5 \Rightarrow R = 0.86 + 0.1119 \cdot (0.1P_1)^{\frac{1}{1.8 + P_1}}$

Both equations were derived by the author using statistical analysis and result in acceptable fit to the graphs.

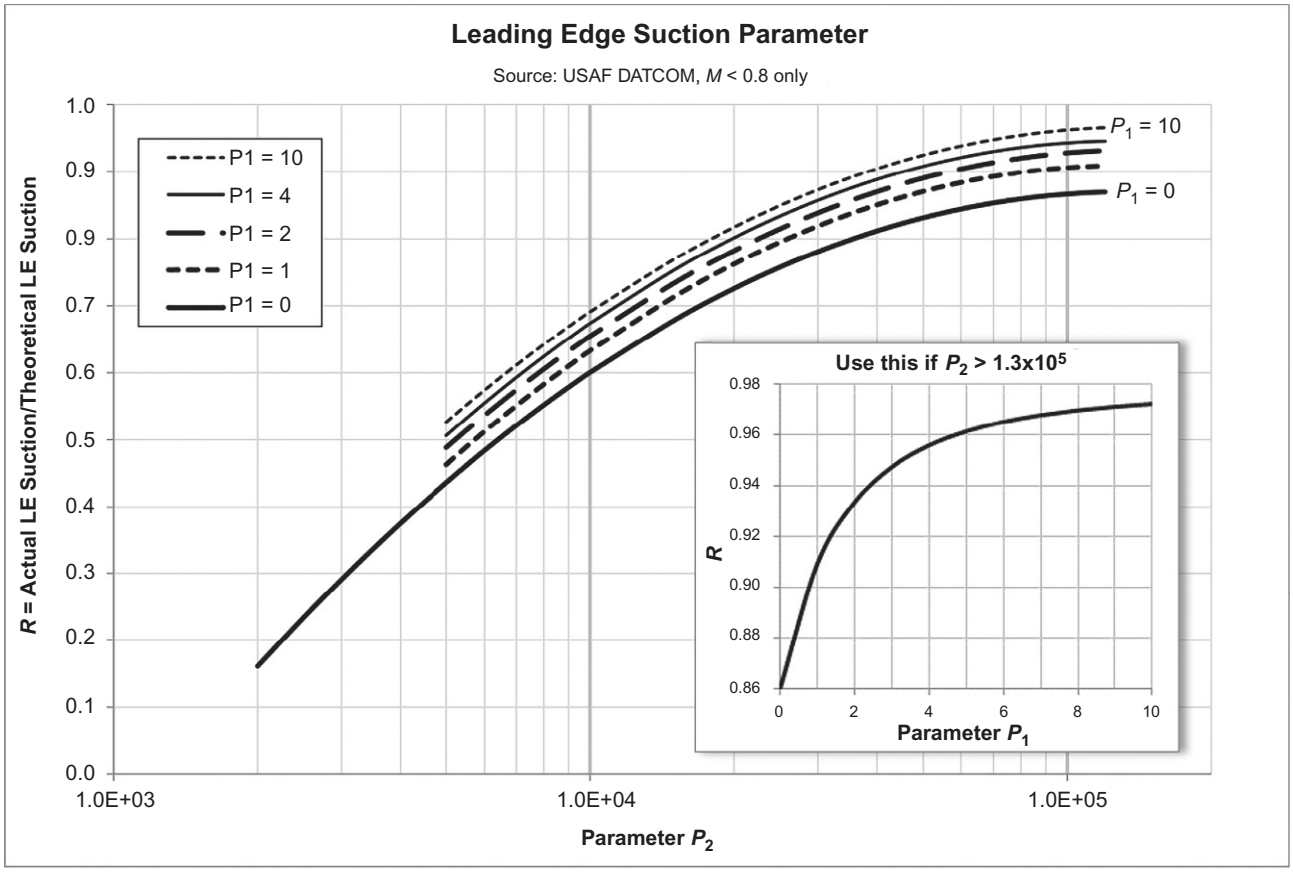


FIGURE 9-76 Leading-edge suction parameter. *Based on D.E. Hoak, USAF Stability and Control DATCOM, Flight Control Division, Air Force Flight Dynamics Laboratory, 1978.*

EXAMPLE 9-13

Determine the Oswald's span efficiency for the Learjet 45, whose $AR_{corr} = 7.33$ and $\lambda = 0.391$. Compare methods 3 and 6. Assume the airfoil has a section lift curve slope of 2π, a LE sweep of 17°, mid-chord sweep of 10.5°, and a LE radius of 0.1 ft. Assume the maximum thickness is at the mid-chord as well. Assume an airspeed of $M = 0.3$ at S-L on a standard day ($V = 335$ ft/s) and ignore the fact the airplane has winglets.

SOLUTION:

For Method 3 use Equation (9-131):

$$e = \frac{2}{2 - AR_{corr} + \sqrt{4 + AR_{corr}^2(1 + \tan^2\Lambda_{t\max})}} = 0.8374$$

For Method 4 follow the step-by-step:

Step 1: Mach number parameter:

$$\beta = \sqrt{1 - M_\infty^2} = \sqrt{1 - 0.3^2} = 0.9539$$

$$C_{L_\alpha} = \frac{2\pi \cdot AR_{corr}}{2 + \sqrt{\left(\frac{AR_{corr} \cdot \beta}{\kappa}\right)^2 \left(1 + \frac{\tan^2\Lambda_{C/2}}{\beta^2}\right) + 4}}$$

$$C_{L_\alpha} = \frac{2\pi \cdot 7.33}{2 + \sqrt{\left(\frac{7.33 \times 0.9539}{1}\right)^2 \left(1 + \frac{\tan^2 10.5°}{0.9539^2}\right) + 4}} = 4.90$$

Step 2: $R_{l_{LER}} = \frac{\rho V l_{LER}}{\mu} = \frac{(0.002378)(335)(0.1)}{3.745 \times 10^{-7}} = 212718$

Step 3: $P_1 = \frac{AR_{corr} \cdot \lambda}{\cos\Lambda_{LE}} = \frac{7.33 \times 0.391}{\cos 17°} = 2.997$

Step 4:

$$P_2 = R_{l_{LER}} \times \cot\Lambda_{LE} \sqrt{1 - M_\infty^2 \cos^2\Lambda_{LE}} = 6.67 \times 10^5$$

Step 5: Since $P_2 > 1.3 \times 10^5$, R can be determined as follows:

$$R = 0.86 + 0.1119 \cdot (0.1P_1)^{\frac{1}{1.8 + P_1}}$$

$$= 0.86 + 0.1119 \cdot (0.1 \cdot 2.997)^{\frac{1}{1.8 + 2.997}} = 0.947$$

Step 6:

$$e = \frac{1.1(C_{L_\alpha}/AR_{corr})}{R(C_{L_\alpha}/AR_{corr}) + (1 - R)\pi}$$

$$= \frac{1.1(4.90/7.33)}{0.947(4.90/7.33) + (1 - 0.947)\pi} = 0.919$$

The two numbers are slightly apart. Unless there is a confidence in a specific method, this author would take the average of the two (0.933).

(10) Correction Methods

Apply the following corrections to methods 1 through 6 on a need-to-basis. These are taken from Ref. [59].

Correction 1: Aspect Ratio Correction for Winglets

If the wing features winglets of height h, the aspect ratio should be corrected using the following expression. Note that since wings feature one-winglet per side, the total length of added lifting surface is $2h$. Where applicable, use AR_{corr} in lieu of AR:

$$AR_{corr} = AR\left(1 + \frac{2}{k_{WL}}\frac{h}{b}\right)^2 \tag{9-135}$$

Where:

AR = Original wing AR.
b = Wingspan.
AR_{corr} = Corrected AR.
h = Height of winglets.
k_{WL} = Effectiveness factor.

The factor k_{WL} is used to correct the effectiveness of the winglet. If the winglet is equally effective as a span increase of magnitude $2h$, then $k_{WL} = 1$. If the winglet is half as effective as a span increase of magnitude $2h$, then $k_{WL} = 2$. Ref. [59] lists k_{WL} for several aircraft, repeated in Table 9-10.

Correction 2: Correction for Dihedral

If the wing has winglets, the aspect ratio should be corrected using the following expression

$$AR_{corr} = AR\left(\frac{1}{k_{WL}\cos^2\Gamma}\right) \tag{9-136}$$

Correction 3: Correction for Fuselage

Correct for the presence of a fuselage of maximum diameter d_{fus} using the formula below. Do not apply to methods that already contain a fuselage correction.

$$k_{fus} = 1 - 2\left(d_{fus}/b\right)^2 \tag{9-137}$$

Correction 4: Correction for Compressibility

Correct for compressibility using the expression below. Do not apply to methods that already contain a compressibility correction.

$$k_M = \begin{cases} \text{if } M_\infty \le 0.3 \;\Rightarrow\; 1 \\ \text{if } M_\infty > 0.3 \;\Rightarrow\; 1 + a_e(3.333M_\infty - 1)^{b_e} \end{cases} \tag{9-138}$$

TABLE 9-10 Effectiveness factor for several aircraft [59].

Aircraft	k_{WL}
Airbus A320 NEO	3.29
Boeing KC-135 winglet	2.65
Boeing 737-800 blended winglet	3.08
Boeing 747-400 tip plus winglet	2.92
Boeing 767-400 raked tip	1.58
McDonnell-Douglas MD-11 extended winglet	3.62

Where a_e and b_e are statistical constants that may depend on class of aircraft. Ref. [59] gives numbers for commercial jetliners as $a_e = -0.001521$ and $b_e = 10.82$.

DERIVATION OF EQUATION (9-135)

Denote b as projected span and b_{eff} as effective span. Based on Figure 9-77, if the winglet height h is equivalent to a span increase, we can write:

$$b_{eff} = b + 2h \Rightarrow b_{eff}/b = 1 + 2h/b$$

Thus, the aspect ratio associated with b_{eff} is denoted by AR_{corr} and is related to the original wing as follows:

$$AR_{corr} = b_{eff}^2/S = b^2(1 + 2h/b)^2/S = AR(1 + 2h/b)^2$$

Since not all winglets are created equal, we want to adjust the AR_{corr} based on their effectiveness. This can be done by introducing the effectiveness factor k_{WL} as shown in Equation (9-135).

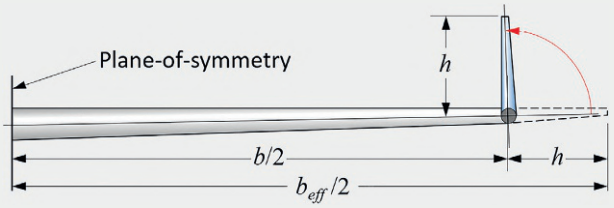


FIGURE 9-77 Winglet definition.

DERIVATION OF EQUATION (9-136)

The derivation assumes that dihedral increases span efficiency like a winglet. Thus, our goal is to determine a height ratio, h/b. Again, b and b_{eff} represent projected and effective span. Based on Figure 9-78, b_{eff} is larger than b by amount $2h$, so h is given by

$$b_{eff} = b + 2h \Rightarrow h = (b_{eff} - b)/2$$

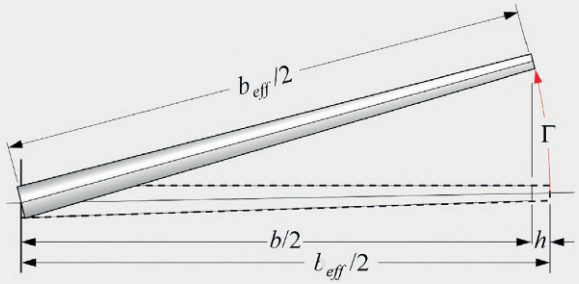


FIGURE 9-78 Dihedral definition.

However, since $b = b_{eff}\cos\Gamma$, we get

$$h = \frac{1}{2}\left(\frac{b}{\cos\Gamma} - b\right) = \frac{b}{2}\left(\frac{1}{\cos\Gamma} - 1\right) \Rightarrow \frac{h}{b} = \frac{1}{2}\left(\frac{1}{\cos\Gamma} - 1\right)$$

Substitute this into the expression for AR_{corr} to get

$$AR_{corr} = A(1+2h/b)^2 = AR\left(1+2\frac{1}{2}\left(\frac{1}{\cos\Gamma}-1\right)\right)^2$$
$$= AR\left(\frac{1}{\cos^2\Gamma}\right)$$

This too is subject to adjustment, again using the effectiveness factor k_{WL} as shown in Equation (9-136).

EXAMPLE 9-14

Estimate the reduction in drag counts for the Boeing 737 NG with and without its blended winglets as it operates at $C_L=0.6$. Assume that without winglets its $AR=10.3$ and $C_{D_{min}}=0.0210$. With winglets $C_{D_{min}}=0.0213$ and $h/b=0.071$. Use Method 3, assuming $\Lambda_{tmax}=20°$. (Note that these data are "guesses.")

SOLUTION:

Estimate drag without winglets:

$$e = \frac{2}{2-AR+\sqrt{4+AR^2(1+\tan^2\Lambda_{tmax})}}$$
$$\frac{2}{2-10.3+\sqrt{4+10.3^2(1+\tan^2 20°)}} = 0.7037$$

$$C_D = C_{D_{min}} + \frac{C_L^2}{\pi\cdot AR\cdot e} = 0.0210 + \frac{0.6^2}{\pi\times 10.3\times 0.7037}$$
$$= 0.03681$$

Estimate drag with winglets, by correcting AR and substitute in Method 3:

$$AR_{corr} = AR\left(1+\frac{2}{k_{WL}}\frac{h}{b}\right)^2 = 10.3\left(1+\frac{2}{3.08}0.071\right)^2 = 11.27$$

$$e_{corr} = \frac{2}{2-AR_{corr}+\sqrt{4+AR_{corr}^2(1+\tan^2\Lambda_{tmax})}}$$
$$= \frac{2}{2-11.27+\sqrt{4+11.27^2(1+\tan^2 20°)}} = 0.6923$$

$$C_D = C_{D_{min}} + \frac{C_L^2}{\pi\cdot AR_{corr}\cdot e_{corr}} = 0.0213 + \frac{0.6^2}{\pi\times 11.27\times 0.6923}$$
$$= 0.03599$$

Difference in drag counts:

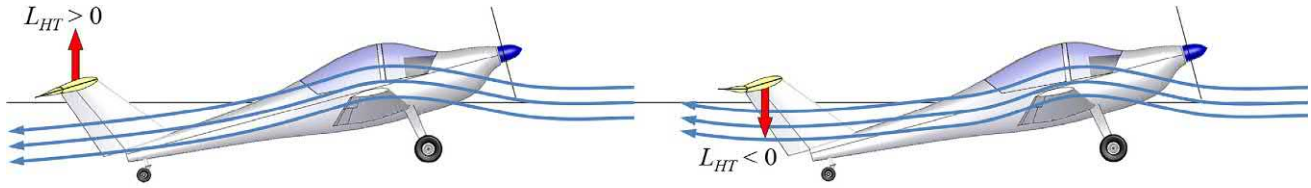
$$\Delta C_D = 0.03681 - 0.03599 = 0.0082 \rightarrow 8.2 \text{ drag counts}$$

This difference is reasonable in the view of the author. The reader is advised to treat these corrections with care to prevent overestimating the drag reduction. If the k_{WL} from Table 9-10 is ignored ($k_{WL}=1$) then $\Delta C_D=27$ drag counts and that would be unrealistic.

9.6 WING STALL CHARACTERISTICS

All fixed-wing airplanes must exceed a certain minimum airspeed before they become airborne. This airspeed is the *stalling speed*. It represents one of the most important design constraints for an airplane. This section is dedicated to the stall and attempts to provide important information about this phenomenon.

Figure 9-79 illustrates two kinds of stall, *basic* and *controlled*: (1) *Basic stall* is conducted during wind tunnel testing. In this case, the stabilizing surface is fixed, typically at zero elevator deflection. Then, the airplane is swung through an *alpha-sweep*. When the wing stalls, the HT is *contributing* to the aircraft's total lift. (2) *Controlled stall* occurs when a pilot stalls the airplane. To stall, the elevator is deflected trailing edge up, increasing α until the wing stalls. The balancing force opposes lift, so the HT *reduces* total lift at a given AOA (so the airplane requires higher airspeed for level flight). Since the wing's α_{stall} for (1) and (2) is equal, the $C_{L_{max}}$ for controlled stall is smaller than it is for basic stall (see Figure 24-37). This is important because controlled stall stipulates the stalling speed.



BASIC STALL (WIND TUNNEL)

Elevator deflection is fixed, typically at $\delta_e=0°$. The HT is subjected to reduced α because of downwash. For instance, if $\alpha=15°$ then $\alpha_{HT}\approx 7°$ (give or take). Thus, the HT generates upward lift. This adds to the total lift. So, when the wing stalls, the $C_{L_{max}}$ includes this additional lift.

⇒ **Stalling speed is lower than if elevator is deflected.**

CONTROLLED STALL (PILOT)

Elevator is deflected trailing edge up ($\delta_e<0°$). The HT is still subjected to reduced α, but because $\delta_e<0°$, the HT generates downward lift. This reduces the total lift. So, when the wing stalls, the $C_{L_{max}}$ is lower than for the basic stall. This lower $C_{L_{max}}$ dictates the stalling speed of the aircraft.

⇒ **Stalling speed is higher than if elevator is fixed.**

NOTE:

The above holds for forward CG positions. For aft CG, the HT-lift may be directed upward for trim (with reduced δ_e). Over the CG-range, the most critical $C_{L_{max}}$ occurs at the forward CG.

FIGURE 9-79 The difference between *basic* and *controlled* stall.

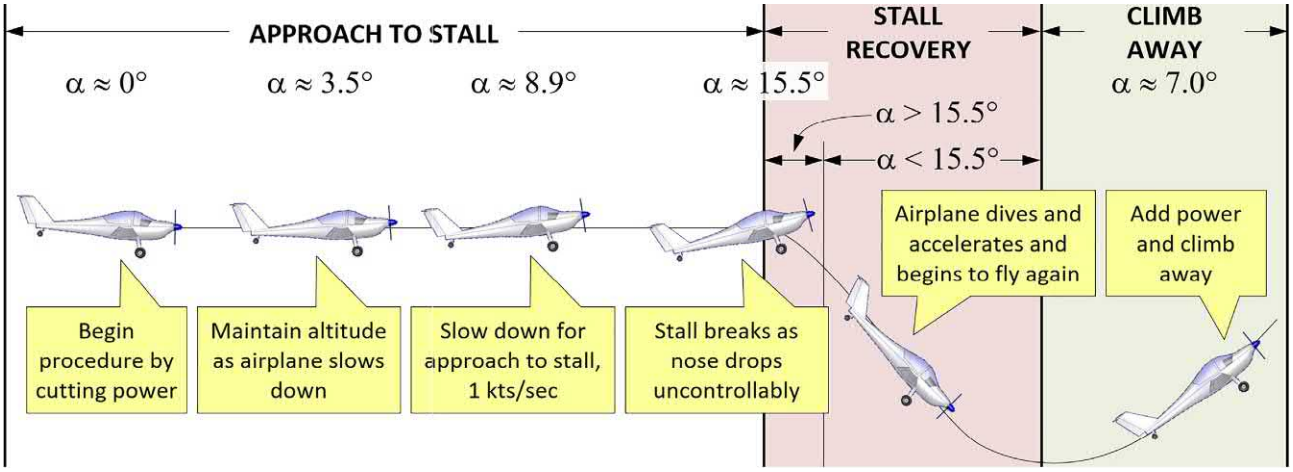


FIGURE 9-80 A schematic showing an approach to stall, stall recovery and subsequent climb away.

It is helpful to visualize the stall maneuver in terms of altitude as well as airspeed. A controlled stall maneuver is depicted in Figure 9-80. It begins with engine power being cut and a subsequent deceleration. For compliance with 14 CFR Part 23 regulations, this deceleration should be as close to 1 KCAS per second as possible.

As the airplane slows down, a larger α is required to maintain altitude and the *Approach to Stall* phase culminates in the stall itself, as the airplane approaches α_{stall} and then "breaks the stall" by a sudden drop of the nose. The drop leads to a dive, which results in altitude loss, as shown in the figure. The altitude loss depends on the size of the aircraft. It can be as small as 50 ft for an ultralight, to 2000 ft or more for a large commercial jetliner aircraft. The *Stall Recovery* phase ends with power being added and a subsequent climb to altitude.

9.6.1 Growth of Flow Separation on an Aircraft

A well-designed aircraft should be void of flow separation at cruising speed to minimize pressure drag. However, as the airplane slows down, the AOA increases and, unavoidably, flow separation regions begin to form and grow. Figure 9-81 shows an airplane with a tapered wing at different airspeeds. At cruise speed, it is void of flow separation. At economy cruising speed (or best rate-of-climb airspeed), a separation region has formed in two places: mid-span and at the wing/fuselage juncture. This is undesirable and unavoidable. As stated in Section 9.4, the development of flow separation regions depends on the wing planform. Section lift coefficients for the tapered wing shown in Figure 9-81, peak near the mid-span (see Section 9.4.5, *Straight-Tapered Planforms*). This initiates the flow separation mid-span. We prefer the separation to progress from the root toward the tip, as this provides roll stability at stall.

In addition to the mid-span flow separation, another region begins to form at this AOA—in the wing/fuselage juncture. While it complements the mid-span separation, it is unrelated to it. It is caused by poor geometry between the wing and fuselage. The shape of this separation is best described as a bubble that extends downstream behind the juncture. Hence the name *separation bubble*. It forms when air accelerates over the wing—and around the fuselage. Add the two to get an even greater increase in airspeed (lower pressure). The airspeed must reduce over the aft part of the wing because the low pressure must rise to ambient. If the distance allotted to this process is short, a rapid deceleration (adverse pressure gradient) is required. Too rapid and a separation develops. The pressure inside the bubble is less than the ambient pressure so it increases drag. It also reduces the airplane's lift curve slope, requiring a higher operational AOA and induced drag (e.g., see Figure 8-56). It falls on the aerodynamicist to suppress this formation. It is best achieved by a careful tailoring of a *wing root fairing*.

Further deceleration of the aircraft to, say, its *best angle-of-climb airspeed*, causes the two separation regions to join. The region extends from the fuselage to a specific span station. The separation bubble at the wing/fuselage juncture continues to grow into the flow field and this is represented as the volume aft of the wing root trailing edge. As the aircraft approaches stall, a larger and larger area of the wing is covered with flow separation. The direction of the progression of the separation should be away from the fuselage toward the wing tips. Eventually, at stall, the wing is mostly separated, but if well designed the wingtip should still be unstalled for roll stability.

General Stall Progression on Selected Wing Planforms

Figure 9-83 shows highly idealized stall progression schematics for common wing planforms. These are useful to build anticipation, but do not guarantee the implied stall progression.

9.6.2 Deviation From the Generic Stall Pattern

Figure 9-82 shows the stall progression over three separate straight-tapered planform shapes [63–65]. The

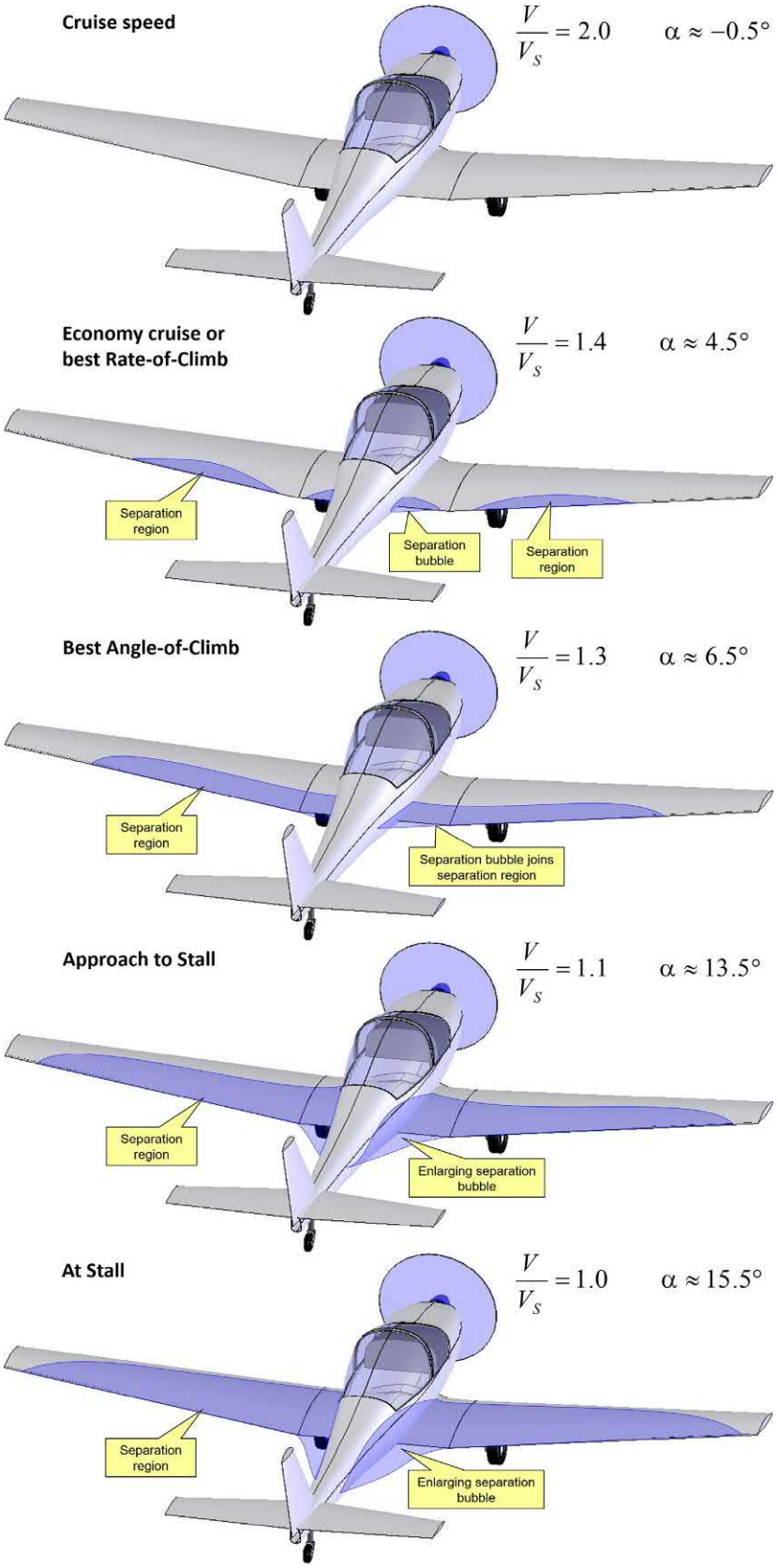


FIGURE 9-81 Growth of flow separation on an aircraft.

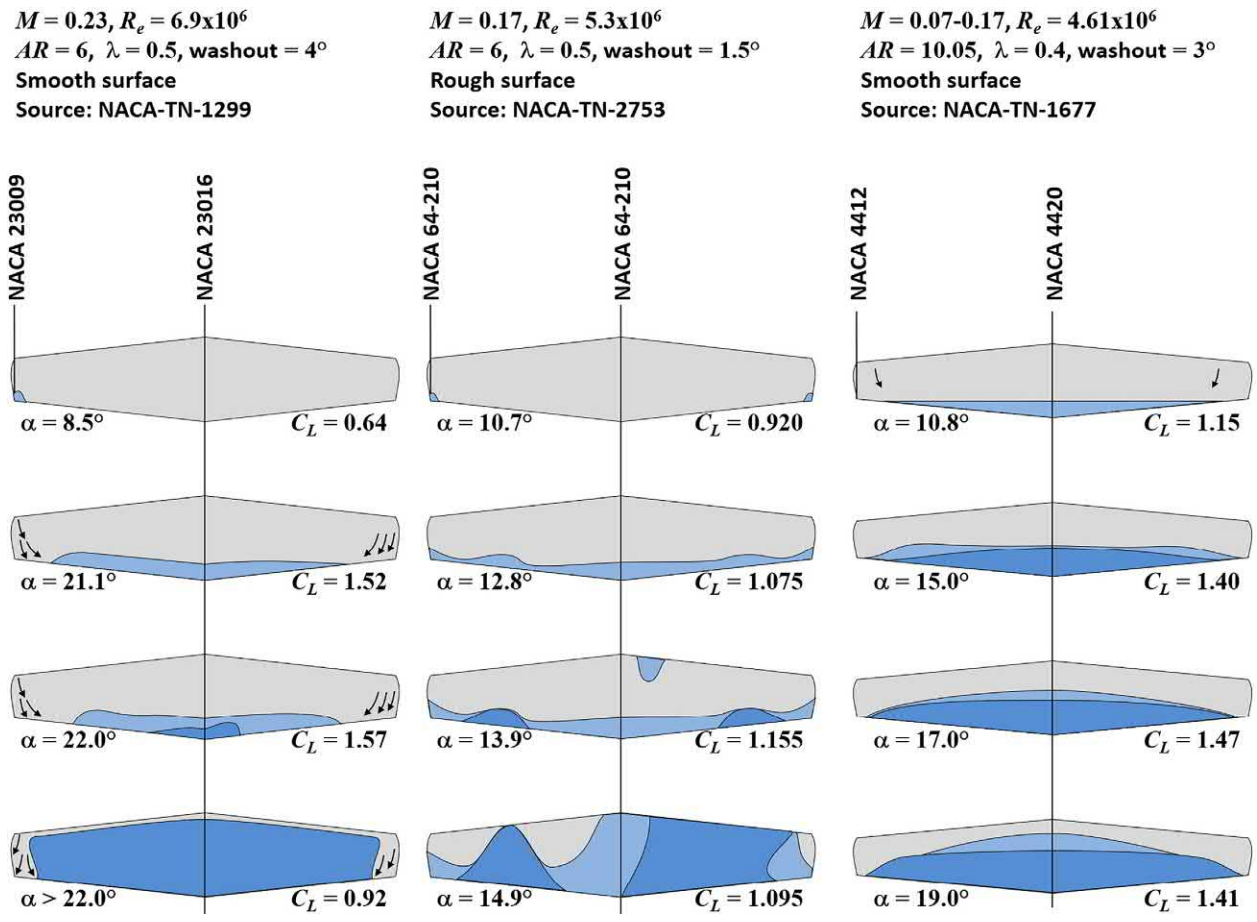


FIGURE 9-82 Stall progression on straight-tapered wing planforms differing in AR, λ, washout, and surface roughness. *Based on G.C. Furlong, J. E. Fitzpatrick, Effects of Mach Number and Reynolds Number on the Maximum Lift Coefficient of a Wing of NACA 230-Series Airfoil Sections, NACA TN-1299, 1947; J.E Fitzpatrick, W.C. Schneider, Effects of Mach Number Variation between 0.07 and 0.34 and Reynolds Number Variation between 0.97x106 and 8.10x106 on the Maximum Lift Coefficient of a Wing of NACA 64-210 Airfoil Sections, NACA TN-2753, 1952; T.V. Bollech, Experimental and Calculated Characteristics of Several High-Aspect-Ratio Tapered Wings Incorporating NACA 44-series, 230-series, and Low-Drag 64- Series Airfoil Sections, NACA TN-1677, 1948.*

figure shows that airfoils, *AR*, λ, R_e, and even surface roughness affects the stall progression. It can introduce asymmetry in the stall progression, as well as regions of initial flow separation, intermittent and complete stalling. Also see Refs. [18–20] for added insight. Each wing style must be evaluated on its own merit.

Figure 9-83 provides a basic insight into how the planform impacts stall progression. The actual progression is both dynamic and complex (see discussion in Section 9.3.5, *Wing Twist—Washout and Washin*).

9.6.3 Tailoring the Stall Progression

Good stall characteristics are a matter of safety. An airplane that constantly rolls left or right at stall is at an increased risk of entering spin. If it stalls close to the ground it cannot recover, regardless of spin recovery characteristics or proficiency of the pilot. The consequence is usually a fatal crash.

The designer has an ethical duty to design good stall characteristics into the airplane. Naturally, only flight testing will reveal if this is successful. However, the purpose of such a design philosophy is just to improve the odds. Nowadays, this is much easier using CFD solvers. CFD methods such as vortex-lattice, doublet-lattice, and other panel codes can be used to control the spanwise distribution of section lift coefficients. Navier-Stokes solvers multiply that power as long as the selected turbulence model does not misrepresent the extent and shape of the flow separation (see Section 26.2.13, *Miscellaneous Topics*). Then, select a combination of airfoil types and wing washout to control the stall progression along span of the wing.

(1) Design Guidelines

Standard design philosophy: (1) Use a high-lift, Class-A airfoil (per Figure 8-72) as a tip-airfoil. (2) Consider a 1–4° washout. (3) Consider a leading-edge extension per Ref. [26]. The target stall pattern should begin at

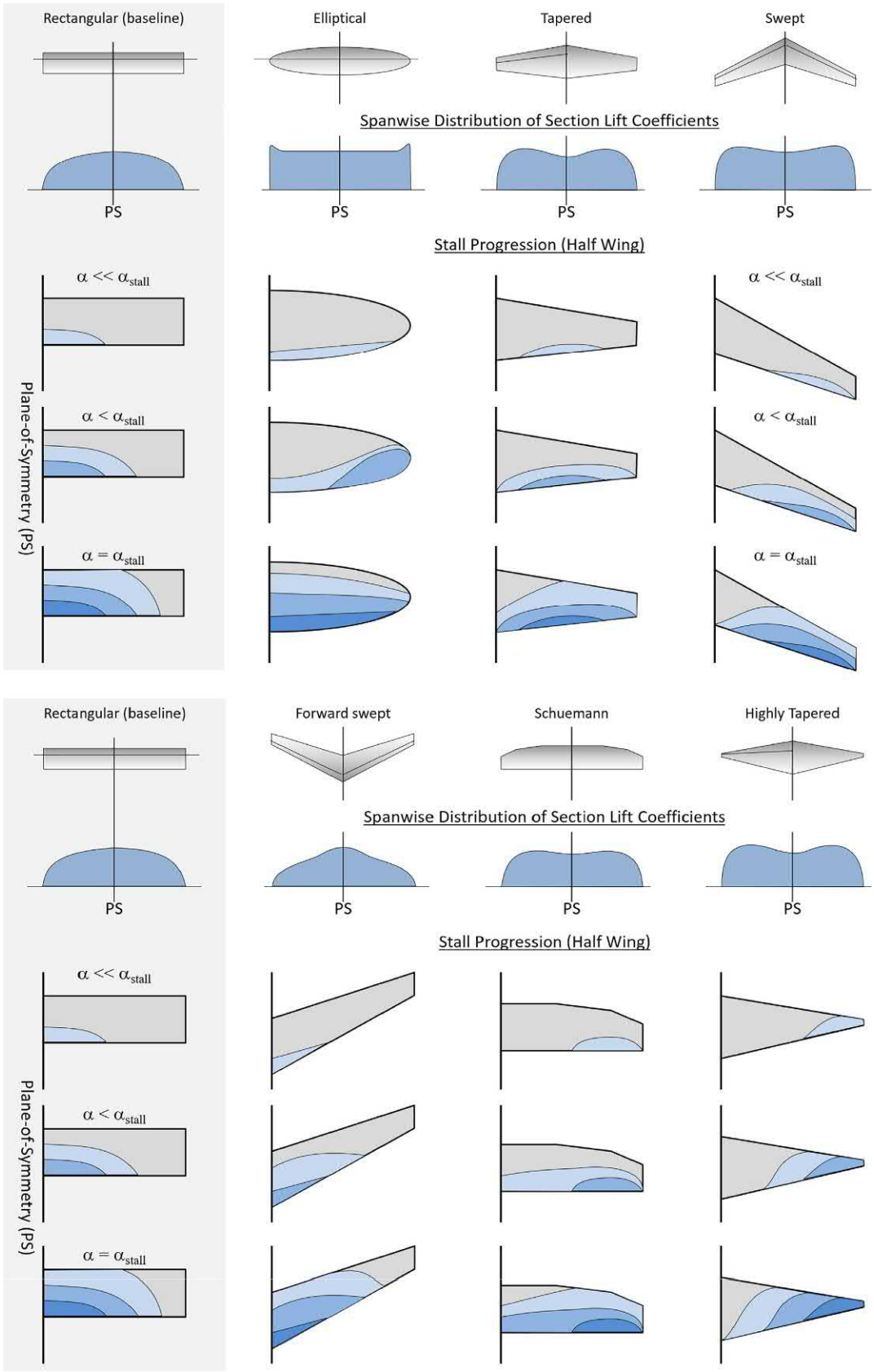


FIGURE 9-83 Basics of stall progression on selected wing planforms.

the root and progress toward the tip as the AOA is increased. This ensures the wingtip region will be the last to stall, providing vital roll stability and control throughout the maneuver. If using inviscid methodology to tailor the stall progression, the section lift coefficient (C_l) at the 70% span station should not exceed the airfoil's maximum lift coefficient ($C_{l_{max}}$) of the airfoil at that station. Furthermore, from 70% to 100%, C_l should gradually fall to zero. Some authors (e.g., Torenbeek [66]) go further and recommend ($C_{l_{max}} - 0.1$), although this may be hard to achieve in practice without excessive washout (also see Section 9.3.5, *Wing Twist—Washout and Washin*). Viscous analysis (i.e., Navier-Stokes solvers) provides a more pinpointed tailoring. For something as serious as stall tailoring, flow visualization of the separation region obtained from wind tunnel testing should always be used to validate the CFD model.

Figure 9-84 shows an example of typical linear analysis for a tapered wing ($\lambda = 0.5$) that features the same airfoil (NACA 65_2-415) throughout the wing. Since the Reynolds number at the tip is only one-half the root value, the $C_{l_{max}}$ is less at the tip and this should be considered for airplanes that feature tapered planform shapes. The baseline wing design (solid curve) has no washout, whereas the other three have a 2°, 4°, and 6° washout, respectively. The graph shows the distribution of C_l for these four models at AOA of 16°. The thick dashed line shows the distribution of the $C_{l_{max}}$ from root to tip.

The baseline curve in Figure 9-84 shows that the C_l exceeds the $C_{l_{max}}$ between spanwise stations 0 and 0.87. With barely 10% of the tip "unstalled," poor stall behavior should be expected. The proposals for 2°, 4°, and 6° washout all lead to improvements, especially the 6° one. However, as evident in Table 9-6, washout higher than 4° is rare. Excessive washout increases the lift-induced drag. A better solution is less washout, say, somewhere between 2° and 4°, and a high-lift Class-A tip airfoil. Such as solution is plotted in Figure 9-84.

(2) Issues Associated with Wings with Multiple Airfoils

Multiairfoil wings are the norm for high-performance aircraft but are also common in smaller and simpler GA aircraft. Wing design for high-performance aircraft is challenging because of the wide airspeed range demanded. These require complex high-lift system for operation at low airspeeds. This is particularly challenging in the production of wings made from alloys, as the difference in geometry inevitably requires the wing skin to be stretched to conform to the resulting compound surface.

A hypothetical multiairfoil wing is shown in Figures 9-85–9-87, based on the layout presented in Figure 9-85. The airfoils have only been selected to demonstrate possible aerodynamic, structural, and manufacturing complexities. The wing is defined using three airfoils: at the root, the intersection of the flap and aileron and the tip. Structurally, switching to a new airfoil at the intersection of the flap and aileron is a good choice, as it avoids complicating the geometry of the control surfaces.

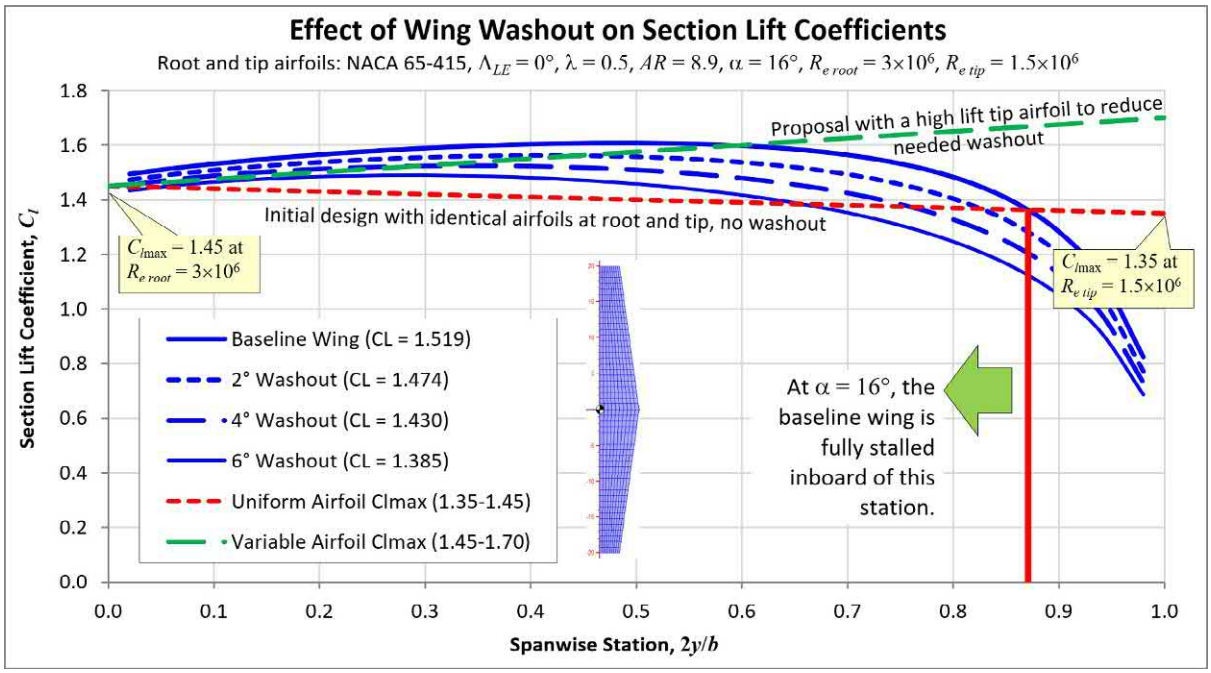


FIGURE 9-84 The effect of washout on probable stall progression. The baseline wing is more tip-loaded than the ones with washout and this will cause it to stall closer to the tip, which may cause roll-off problems.

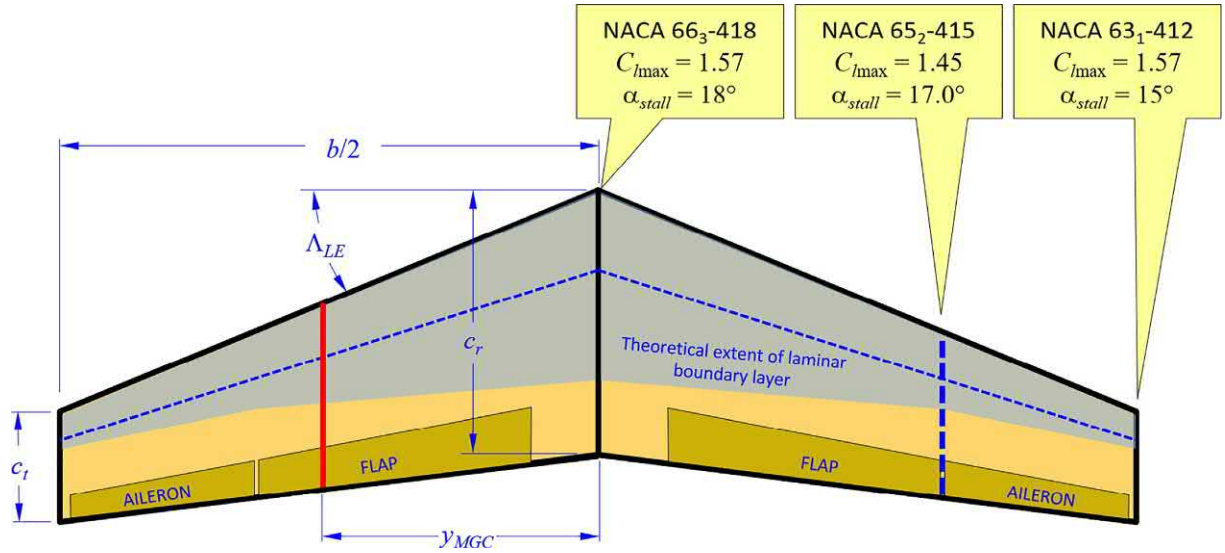


FIGURE 9-85 An example wing layout, showing the theoretical extent of laminar boundary layer and variation in its maximum lift capability.

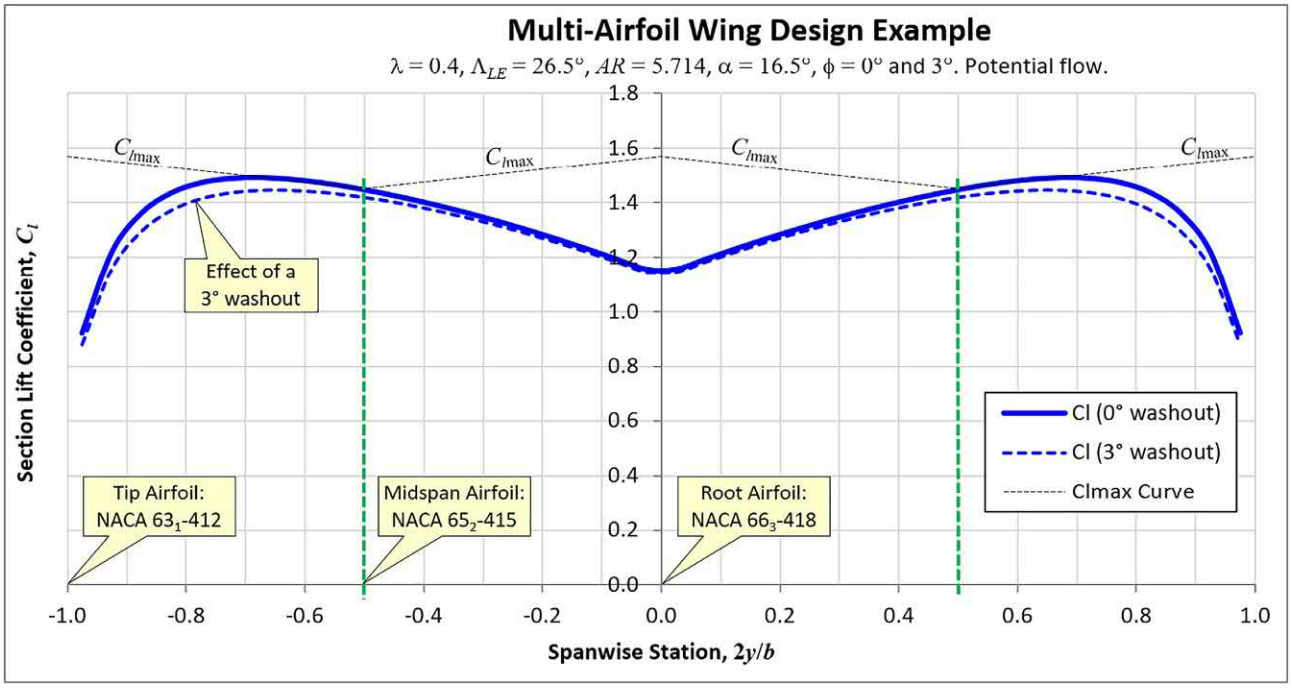


FIGURE 9-86 An example of a multiairfoil wing layout featuring 0-degree and 3-degree washout.

Figure 9-85 also shows an assumed extent of the laminar boundary layer on the wing's upper surface. Achieving laminar boundary layer is difficult, as has already been discussed in Chapter 8, *The Anatomy of the Airfoil*. Attempting this on the above wing will require careful and more expensive manufacturing tooling.

Figure 9-86 shows the spanwise distribution of C_l and $C_{l_{max}}$ along both wing halves at $\alpha = 16.5°$. It also shows that the progression of stall begins just outside of the 50% span station. Also plotted is the distribution of C_l with a 3° washout, showing improvements, albeit limited. There are limitations to this analysis: the linear method used does not capture flow separation due to spanwise flow over the swept wing. Regardless, it should raise concerns for the designer.

Figure 9-87 shows some structural and manufacturing issues that present themselves in wings with multiple airfoils. The resulting geometry may surprise the unsuspecting structural engineer. It results from the dissimilarity of the three chosen airfoils. This subjects the spar to a

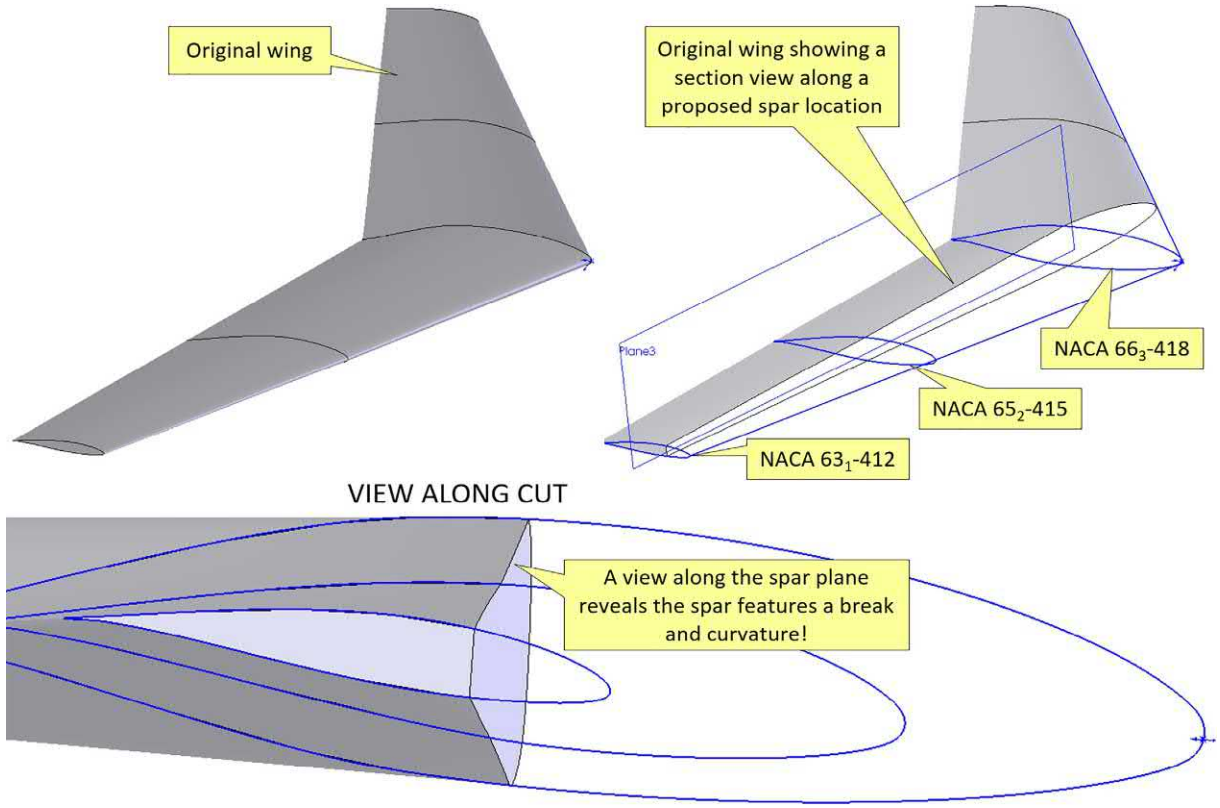


FIGURE 9-87 An example of the geometric complexities arising the multiairfoil wing layout.

geometric nonlinearity from root to tip; the skin surface is *compound*. A view along the cut shows two situations: (1) The spar's *outside mold line* (OML) at the mid-span station is discontinuous. (2) The spar cap features a slight curve, extending from root to mid-span and then to the tip. If the wing is made from aluminum and requires the skin to adhere perfectly to the compound surface, the skin will require hydraulic pressing. This will increase the production cost. In real aircraft, especially less expensive ones, the discontinuity is usually solved by sheets terminating along the discontinuity. The curvature issue is solved by straightening the spar cap and inserting shims between the spar and skin. The aerodynamics group must accept that the wing geometry no longer represents their intent. Additionally, if the intent is to promote natural laminar boundary layer, the resulting shape may no longer do so satisfactorily.

9.6.4 Cause of Spanwise Flow for a Swept Back Wing Planform

Swept back wings can experience a significant and uncontrollable pitch-up moment at high angles-of-attack. The reason for this is twofold:

(1) The aft swept planform induces local upwash near the tip which increases the local section lift coefficients. Thus, section lift coefficients in the tip region reach their $C_{l_{max}}$ sooner than the inboard airfoils.

(2) Airflow acquires a gradually increasing spanwise flow near the tip, leading to early flow separation.

The first cause is hard to explain in layman's terms, but we will try. Imagine the wing is cut into a finite number of small sections along the span of the wing. The sections extend from root-to-tip such the inboard section is always upstream of the adjacent outboard section. For this reason, the inboard section disturbs the flow field before the outboard section. This disturbance generates an upwash that extends spanwise into the flow field. Thus, when the outboard section begins to disturb the flow field, it already has an upwash component that was induced by the inboard section. This section induces additional upwash, which manifests itself as a slightly greater upwash for the section outboard of it, and so on. The upwash means a greater local AOA. A greater local AOA implies a higher C_l. section lift coefficient.

In contrast, the spanwise flow can be explained as follows. Consider the swept wing in Figure 9-88.

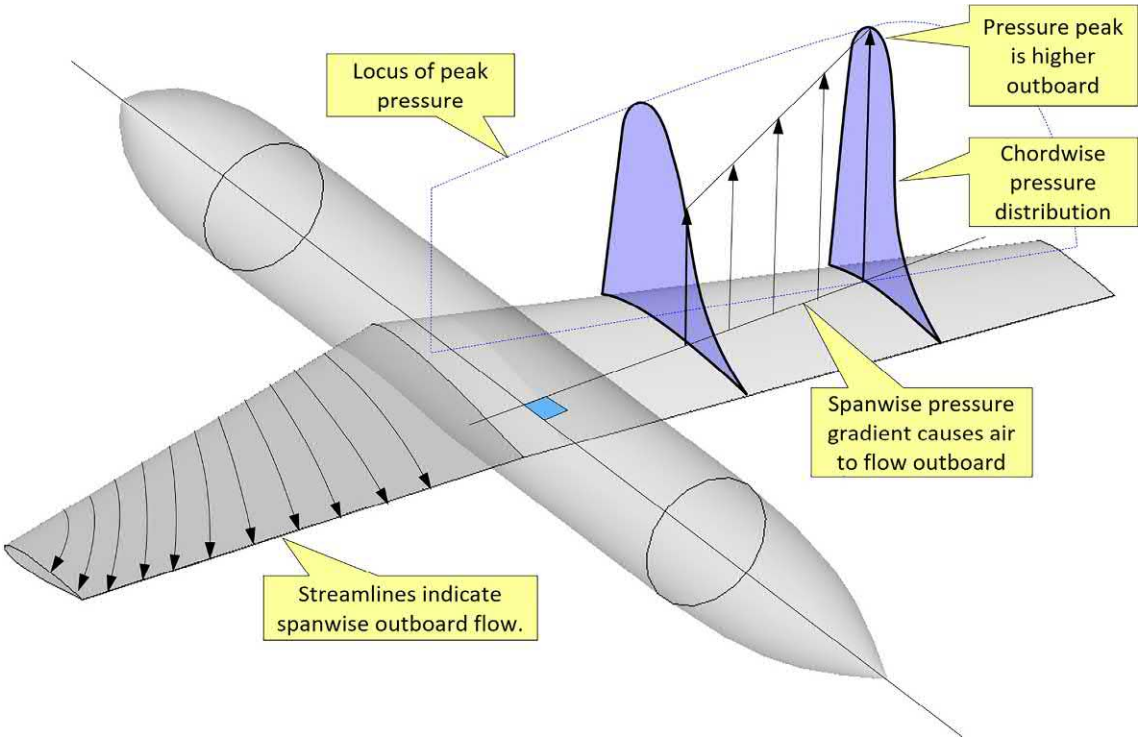


FIGURE 9-88 The spanwise pressure gradient on an aft swept wing causes outboard spanwise flow. The opposite holds true for a forward swept wing. *Based on R. Whitford, Design for Air Combat, Jane's Publishing Company Limited, 1987.*

Two chordwise pressure distributions are drawn on the right wing. The locus of the peak spanwise pressure is shown as a dashed curve. It shows the outboard pressure peak is higher than the inboard one. Now, consider a line perpendicular to the centerline of the fuselage at some arbitrary chord station. It cuts through the chordwise pressure distributions as indicated by the vertical arrows. The inboard arrow is shorter than the outboard one, indicating higher inboard pressure. Therefore, the higher pressure inboard forces the flow toward the outboard region. This is indicated by the streamlines on the left wing.

9.6.5 Pitch-Up Stall Boundary for a Swept Back Wing Planform

The pitch-up moment generated by sweptback wings near stall is investigated in Refs. [67, 68]. It is related to the quarter-chord sweep angle ($\Lambda_{c/4}$) and aspect ratio (AR) as shown in Figure 9-89. It shows that higher the AR, the less the $\Lambda_{c/4}$ at which the pitch-up is experienced. This is important for long-range high-subsonic aircraft as elevated AR favors long range and high $\Lambda_{c/4}$ high-airspeed: The two conflict. The modern airfoil has relaxed this constraint by offering greater critical Mach number. This has allowed aircraft with lower $\Lambda_{c/4}$ ($\approx$20–27°) to utilize higher AR and, thus, operate more efficiently at airspeeds near $M \approx 0.78$–0.82.

An empirical equation based on the data in Ref. [67] can now be developed. It relates the taper ratio (λ) and $\Lambda_{c/4}$ to calculate an AR limit for swept back wings. For a given $\Lambda_{c/4}$, the selected AR should be less than this limit:

$$AR_{\text{lim}} \leq 17.714(2-\lambda)e^{-0.04267\Lambda_{c/4}} \tag{9-139}$$

Conversely, given a target AR, the $\Lambda_{c/4}$ in degrees should not exceed the below value:

$$\Lambda_{c/4_{\text{lim}}} \leq 23.436[\ \ln(17.714(2-\lambda)) - \ \ln(AR)] \tag{9-140}$$

As shown in Figure 9-90, the combination of AR, λ, and $\Lambda_{c/4}$ can lead to desirable or undesirable pitch characteristics near stall. Aircraft that feature aft swept wings should always be wind tunnel tested for stability at stall, but the awareness of the data in Figure 9-89 provides guidance during conceptual design.

Ref. [69] presents results helpful to designers of swept-back wings. It investigated the effect of various high-lift devices and fences on their stall characteristics (see Figure 9-91). It concludes that half-span leading-edge slats eliminate tip stall and nose-up pitching moment. The flaps complicated the stall characteristics and formed a loop in the pitching moment curve (in the figure), although it is suggested it could be brought under control using a stabilizing surface.

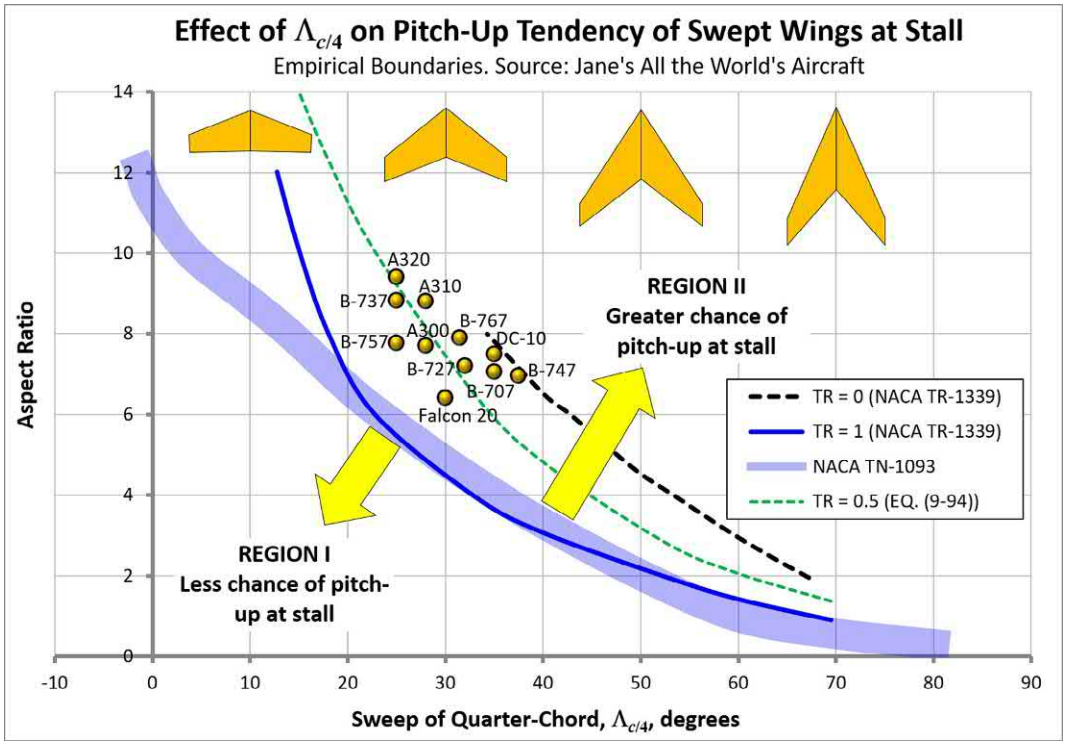


FIGURE 9-89 Empirical pitch-up boundary for a swept back wing. *Reproduced based on G.C. Furlong, J.G. McHugh, A Summary and Analysis of the Low-Speed Longitudinal Characteristics of Swept Wings at High Reynolds Numbers, NACA TR 1339, 1957 and J.A. Shortal, B. Maggin, Effect of Sweepback and Aspect Ratio on Longitudinal Stability Characteristics of Wings at Low Speeds, NACA TN 1093, 1946.*

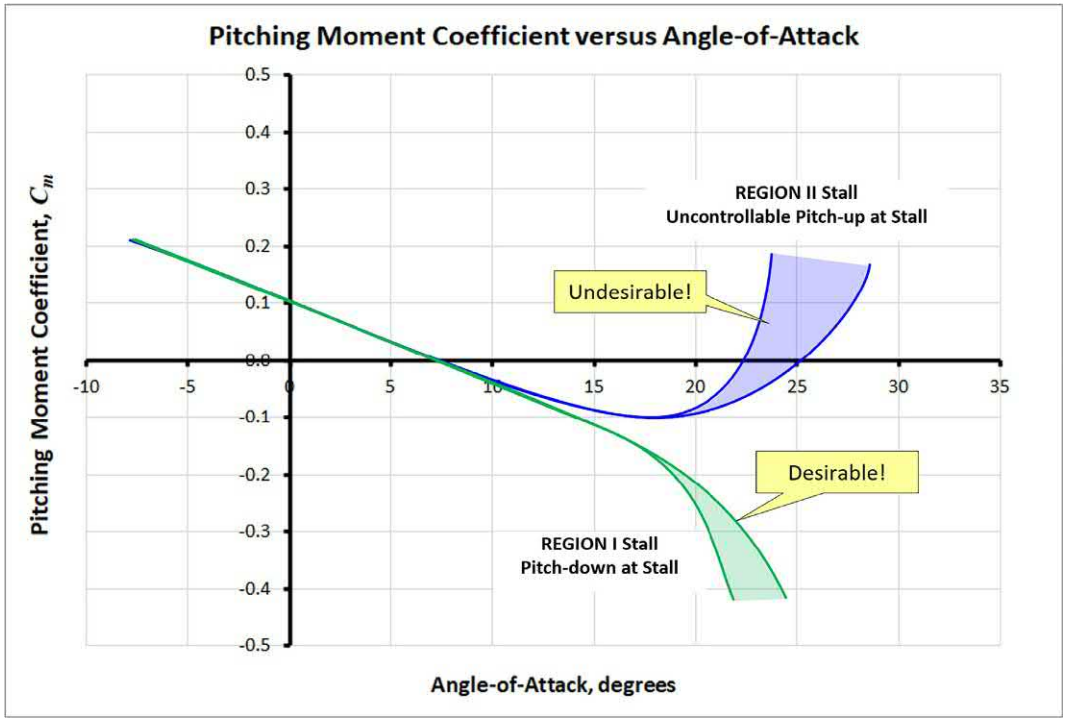


FIGURE 9-90 The combination of *AR*, λ, and $\Lambda_{c/4}$ can lead to desirable or undesirable pitch characteristics at stall.

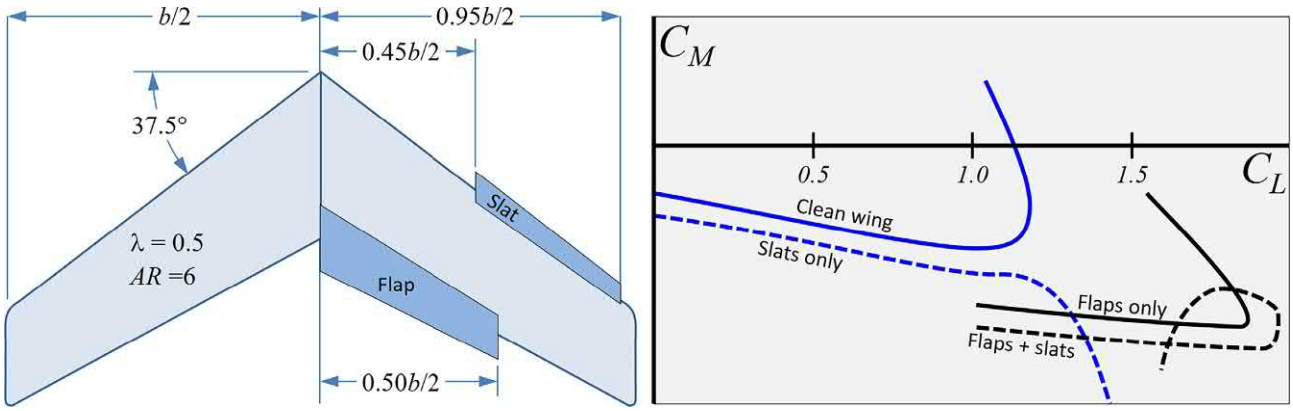


FIGURE 9-91 The effect of various combinations of a double-slotted flaps and slats on the pitching moment of a 37-degree swept wing. The loop is caused by the addition of a double-slotted flap. *Based on W. Koven, R.R. Graham, Wind-Tunnel Investigation of High-Lift and Stall-Control Devices on a 37 Degree Sweptback Wing of Aspect Ratio 6 at High Reynolds Numbers, NACA RM-L8D29, 1948.*

DERIVATION OF EQUATIONS (9-139) AND (9-140)

The derivation uses data obtained from Ref. [67]. It presents two curves that are functions of $\Lambda_{c/4}$: One for $\lambda = 0$ and the other for $\lambda = 1$. These are used to derive an empirical function of λ and $\Lambda_{c/4}$ that closely fits both expressions. Least-squares exponential fit to the two curves yields the two following expressions:

$$\text{For } \lambda = 0: \qquad AR = 35.885 \cdot e^{-0.04206\Lambda_{c/4}}$$
$$\text{For } \lambda = 1: \qquad AR = 18.171 \cdot e^{-0.04329\Lambda_{c/4}}$$

Since the two exponents are close to each other we deduce that λ impacts it and primarily affects the constant. Therefore, the average of the two (-0.04267) will be used. Assume a function of the form:

$$AR = f(\lambda) \cdot e^{-0.04267\Lambda_{c/4}} \tag{i}$$

The function $f(\lambda)$ can be approximated by noting that the constant changes from 35.885 for $\lambda = 0$ to 18.171 for $\lambda = 1$. It is convenient to employ a parametric representation for this variation, considering that λ can be used unmodified as the parameter. Thus, Equation (i) can be rewritten as follows:

$$\begin{aligned} AR &= (35.885(1-\lambda) + 18.171\lambda)e^{-0.04267\Lambda_{c/4}} \\ &= (35.885 - 35.885\lambda + 18.171\lambda)e^{-0.04267\Lambda_{c/4}} \\ &= 17.714(2-\lambda)e^{-0.04267\Lambda_{c/4}} \end{aligned} \tag{ii}$$

And this is Equation (9-139). Equation (9-140) is obtained by solving for $\Lambda_{c/4}$.

$$\begin{aligned} & AR = 17.714(2-\lambda)e^{-0.04267\Lambda_{c/4}} \\ \Rightarrow\ & \ln(AR) = \ln(17.714(2-\lambda)) - 0.04267\Lambda_{c/4} \\ \Rightarrow\ & \Lambda_{c/4} = 23.436[\ln(17.714(2-\lambda)) - \ln(AR)] \end{aligned}$$

9.6.6 Influence of Manufacturing Tolerances on Stall Characteristics

Inherent roll instability at stall is one of the most common handling deficiencies affecting aircraft. Most aircraft ever built display such tendencies, requiring "fixes" to remedy. The condition is manifested at stall when an aircraft rolls uncontrollably to the left or right side (see Figure 9-92). The root causes consist of a combination of factors.

It may sound strange, but all aircraft are inherently asymmetric, even though this is usually impossible to discern with the naked eye. Nevertheless, each serial number differs slightly from the previous or the following one in its deviation from the intended *outside mold line* (OML): The left wing is not a perfect mirror image of the right one. There are subtle differences in washout, thickness, waviness, and their corresponding locations on each wing; all which may contribute to roll instability at stall. A typical deviation from the OML in the aviation industry amounts to ± 0.125 in. Wings must usually meet tolerances ranging from ± 0.050 to ± 0.100 in. Manufacturers of GA aircraft featuring NLF lifting surfaces often maintain even tighter tolerances: sometimes as tight as ± 0.005 in along the leading edge.

Maintaining tolerances is imperative in aircraft manufacturing and certification. However, overly tight tolerances are detrimental. They call for costly and robust inspection procedures and should always be justified with research. There is a point of diminishing returns. For instance, near stall AOA, the flow is separated and, therefore, insensitive to minor deviation from the OML. The source of roll instability should be looked for elsewhere, such as in deviation in thickness, twist, dihedral, and components that are asymmetrically exposed to the airflow.

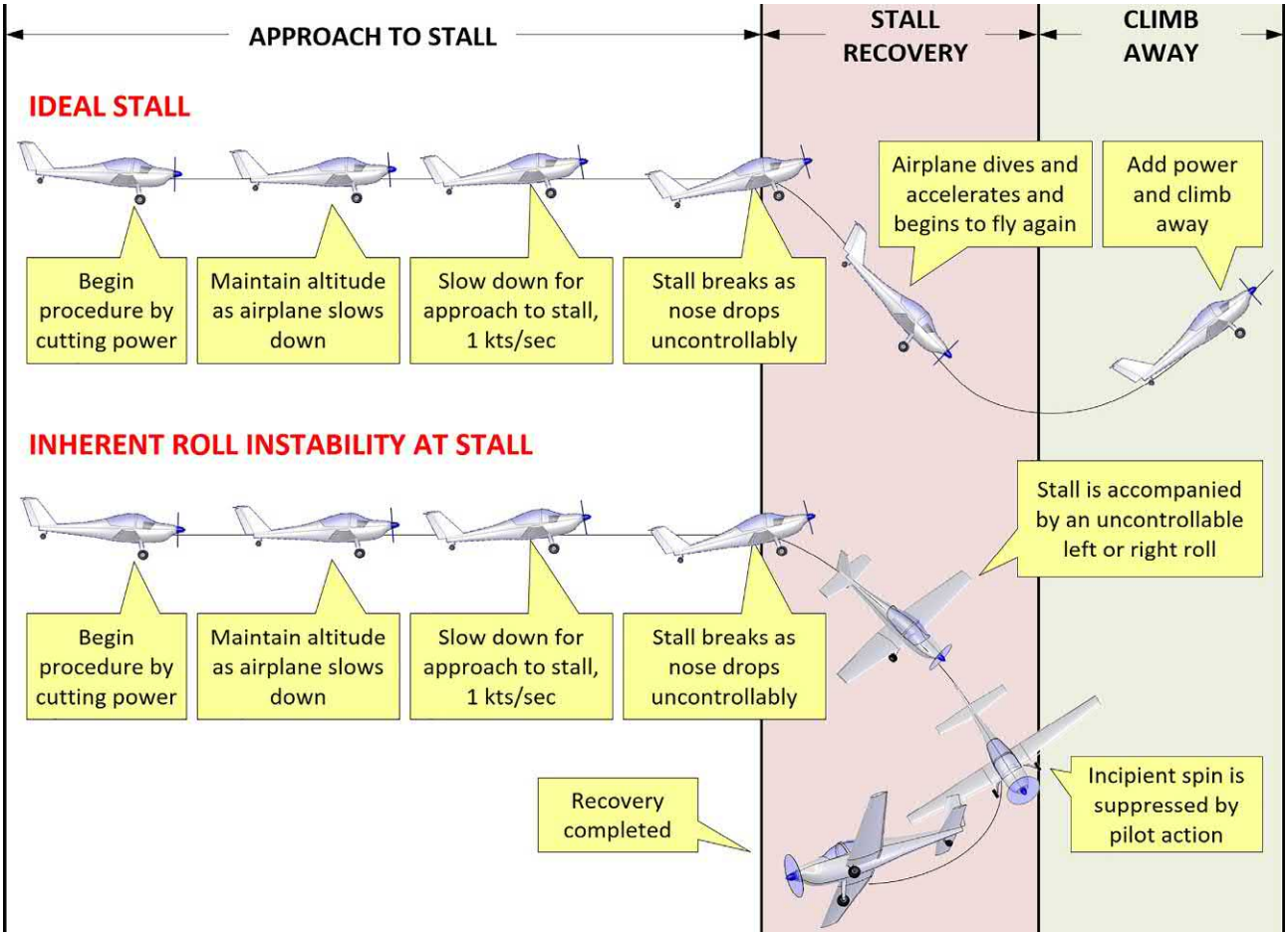


FIGURE 9-92 Comparing an "Ideal Stall" (top) to one with an inherent roll instability (bottom).

At the same time, loose tolerances are detrimental as well. They lead to excessively asymmetric aircraft that certainly can cause inherent roll instability. It is best to design sensitivity to small deviations out of the OML by providing assertive aerodynamic roll stability at high AOA. This can be done using the guidance of Section 9.6.3, *Tailoring the Stall Progression*. See Section 11.2.4, *Basics of Spin and Spin-Recovery* for more information on spin.

9.7 PRANDTL'S LIFTING-LINE THEORY

The advent of the digital computer has revolutionized science and engineering. Aircraft design has benefitted through more complicated and realistic analyses. Computer technology allows the full *Navier-Stokes equations* (NSE) to be solved for extremely complex situations ranging from a flying insect to that of a meteorite entering the Earth's atmosphere. At the present time, this fascinating technology remains time consuming and expensive. It requires a detailed digital geometry and a cluster of interconnected computers to solve. Meshing the model is more art than science and requires an experienced individual to complete. Improperly prepared mesh yields erroneous results. It can easily take a couple hours to couple of days to solve. For this reason, conceptual design using NSE solvers is impractical and should not even be considered. In the view of this author, NSE is a superb *postconceptual* design tool to be used *after* the concept has been designed and not to design it.

There are several practical numerical methods available to the designer that, in comparison, are lightning fast and, for attached flow, are equally accurate as solutions obtained using NSE. Among those are the *lifting-line method* and panel methods such as the vortex-lattice or doublet-lattice. While programmatically considerably older than NSE solvers, they are more practical during conceptual design and are simple enough to implement using a desktop computer. Due to space limitations, only the most basic of these methods will be demonstrated; *Prandtl's lifting-line method*. For other methods, the reader is directed toward excellent texts such as those by Katz and Plotkin [70], Pope [71], Bertin and Smith [72], and Moran [73].

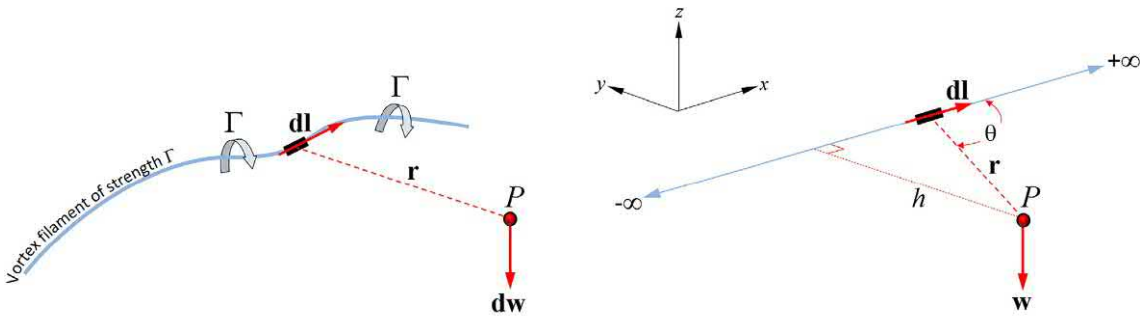


FIGURE 9-93 A curved vortex filament (left) and an infinite, straight vortex filament (right).

9.7.1 Introduction

Developed by Ludwig Prandtl (1875–1953) and his colleagues at the University of Göttingen during the period 1911–18, the lifting-line theory can be used to determine the aerodynamic characteristics of straight wings. The method does not treat dihedral or sweep but can account for arbitrary planform, washout, and dissimilar airfoils. It is reliable for wings whose $AR > 4$. The method replaces the wing with multiple constant-strength vortices, here denoted with the Greek symbol Γ. The problem revolves around determining their strength. However, once this has been accomplished, it allows several characteristics to be determined (e.g., lift, drag, downwash, and spanwise lift). It is useful for aerodynamic properties, structures, and stability. A derivation of the method will now be presented, but first the following mathematical concepts must be introduced.

(1) The Vortex Filament and the Biot-Savart Law

A *vortex filament* is a mathematical curve that positions rotary flow in space (see Figure 9-93). The best analogy is to think of it as the core of a tornado. The circulation around its core depends on its strength, denoted by Γ. Consider an infinitely small vector segment **dl** along the filament and some arbitrary point P in space. The small segment will induce a velocity **dw** at the point P, whose magnitude can be determined using the so-called *Biot-Savart Law*[5]:

$$\text{Biot-Savart Law:} \qquad \mathbf{dw} = \frac{\Gamma}{4\pi}\frac{\mathbf{dl}\times\mathbf{r}}{|\mathbf{r}|^3} \tag{9-141}$$

The Biot-Savart law is named after the French mathematician and physicist Jean-Baptiste Biot (1774–1862) and Félix Savart (1791–1841), a fellow Frenchman who trained for a career in medicine, although his mind was absorbed by natural philosophy.

The derivation of the law is beyond the scope of this book but interested readers can refer to almost any textbook on electrical engineering. The law was derived to relate a magnetic field induced by an electric current in a wire. However, it can also be used to estimate the circulation of flow around a wing. This is because the Biot-Savart law is one of multiple solutions of *Laplace's equation*, which is the governing equation for irrotational, incompressible fluid flow. It enforces mass conservation in the resulting flow field, which is as law of nature. It is shown below for convenience:

$$\nabla^2\phi = \frac{\partial^2\phi}{\partial x^2} + \frac{\partial^2\phi}{\partial y^2} + \frac{\partial^2\phi}{\partial z^2} = 0 \tag{9-142}$$

Where ϕ represents the *velocity potential*. Note that the direction of the velocity is imperative. In accordance with a right-handed coordinate system, assume the thumb of the right-hand points in a direction indicated by the filament **dl** in Figure 9-93. Then the other four fingers curl around the filament as if holding a rope. The direction of the velocity is always in the direction the four fingers make. This is an important concept to keep in mind for what follows.

In the lifting-line theory, the Biot-Savart law is applied to several infinitely long and straight vortex filaments (see right schematic in Figure 9-93). It stretches from -∞ to +∞. Knowing the contribution of each tiny segment **dl**, the total velocity induced at P can be determined by integrating the contribution along the entire filament, i.e.:

$$\mathbf{w} = \int_{-\infty}^{+\infty} \frac{\Gamma}{4\pi}\frac{\mathbf{dl}\times\mathbf{r}}{|\mathbf{r}|^3} \tag{9-143}$$

To constrain the discussion here to the essentials, the solution of the integral is omitted and only the result presented. Interested reader can, for instance, refer to Ref. [74] for the evaluation. The solution involves relating the parameters h, **r**, and θ in Figure 9-93, which are substituted into the integral prior to its evaluation. Thus, the fluid speed at the point P, induced by the straight vortex filament of strength Γ, is given by:

$$\text{Velocity induced a point } P\text{:} \qquad \mathbf{w} = \frac{\Gamma}{2\pi h} \tag{9-144}$$

[5] Pronounced bee-yo-suh-var.

(2) Helmholz's Vortex Theorems

In 1858, the German scientist Hermann von Helmholz (1821–94) made the next step by applying the vortex idea to analyze inviscid, incompressible fluid flow [74]. In doing so, he established what became known as *Helmholz's vortex theorems*. These state that

(1) the strength of the vortex filament is constant along its entire length, and
(2) a vortex filament cannot end in a fluid but must either extend to infinity or form a closed path.

These theorems are used to evaluate a special kind of a vortex called a *horseshoe vortex*. It has important properties that will be discussed shortly and allows it to represent the lift of a finite wing.

(3) Lifting-Line Formulation

Once established that a straight vortex positions the circulation around the vortex filament, it is possible to extend the idea to a 3-dimensional wing. An observation of real finite wings reveals two important facts:

(1) The wing induces circulation that extends from tip to tip and
(2) each wingtip sheds a vortex that extends far into the flow field behind the wing.

This fact can be approximated using three separate vortex filaments as shown in Figure 9-94: (1) A *trailing vortex* extends from infinity to the left wingtip. (2) A *bound vortex* extends from the left wingtip to the right wingtip. (3) A *trailing vortex* extends from the right wingtip back to infinity. The downwash along the bound vortex is only due to the trailing vortices. The system satisfies Helmholz's vortex theorems and represents flow field resembling that of real 3-dimensional wings. Additionally, the three vortices, all of constant strength Γ, have the same sign as can be observed using the right-handed rule (the right-hand thumb should point forward for the first vortex, to the right for the second, and backward for the third). This system allows us to calculate the velocity, $u\cdot\mathbf{i}+v\cdot\mathbf{j}+w\cdot\mathbf{k}$, at any point P in space—a prerequisite for analyzing the wing.

While promising, there is a problem. A single vortex of constant strength develops uniform lift from tip-to-tip. This is not what happens for real wings. Additionally, the trailing vortices cause the downwash at the wingtips to go to infinity. The solution to this problem is to add more horseshoe vortices to the system, each with its own constant circulation and of lesser span than the next (see Figure 9-95). The inboard vortices usually have greater strength than the outboard ones, but their interaction yields downwash and spanwise load distribution that resembles experiment.

The lifting-line method assumes that the vortex strength along the span is known. Consider that, at some spanwise wing station y, the vortex strength is given by the value $\Gamma(y)$. This means that if we move a distance Δy to another spanwise station, the change in the strength of the vortex, $\Delta\Gamma$, can be found from:

$$\Delta\Gamma = \frac{d\Gamma}{dy}\Delta y \tag{9-145}$$

Now consider the spanwise station at y_0 and the vortex at y, shown in Figure 9-95. It is possible to determine the contribution of the vortex at y to the downwash at y_0. We denote this contribution as δw_{y_0}. Since the trailing vortex extends from infinity to $x=0$ where it stops (because this is where we planted our vortex system, so it does not extend to $-\infty$ also), the influence will be half of that shown by Equation (9-144), or:

$$\delta w_{y_0} = \frac{1}{2}\left[+\frac{d\Gamma}{dy}dy\frac{1}{2\pi(y-y_0)}\right] \tag{9-146}$$

As depicted in Figures 9-95 and 9-96, the vortex at y also induces an upward contribution at y_0. This is emphasized

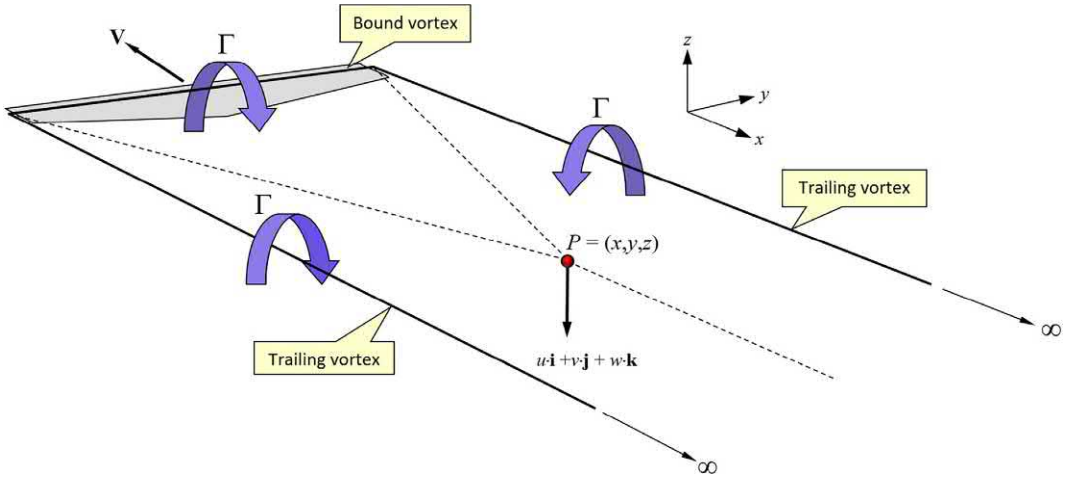


FIGURE 9-94 The flow field around a wing approximated by three connected constant strength vortex filaments.

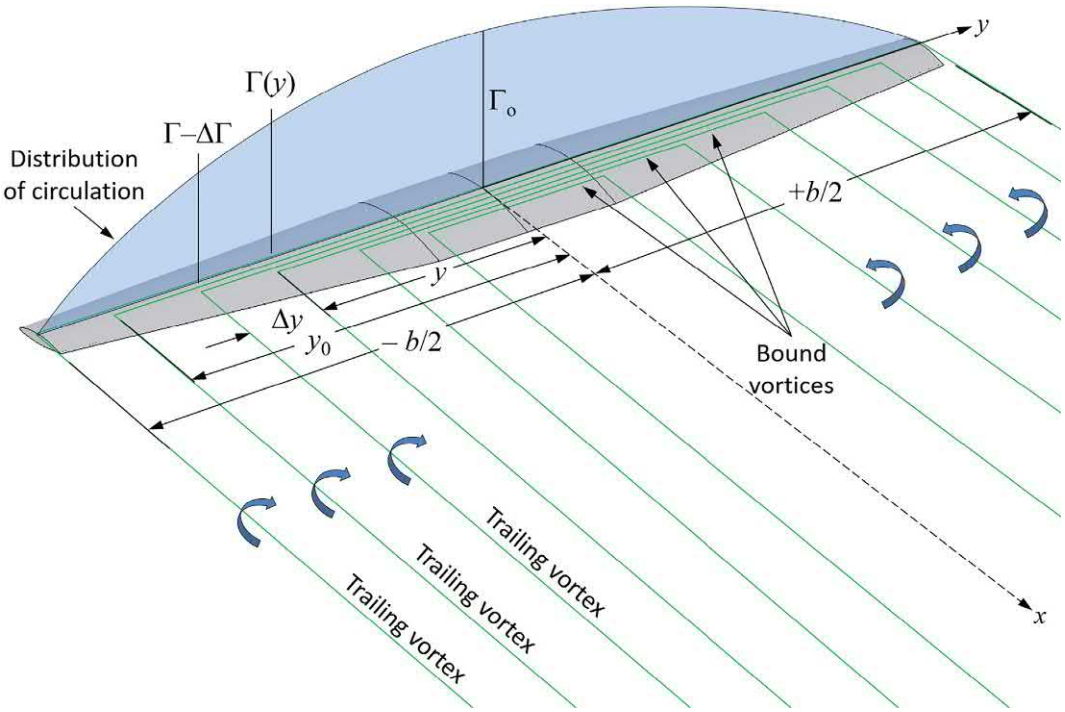


FIGURE 9-95 Airflow around a wing simulated with a system of vortices.

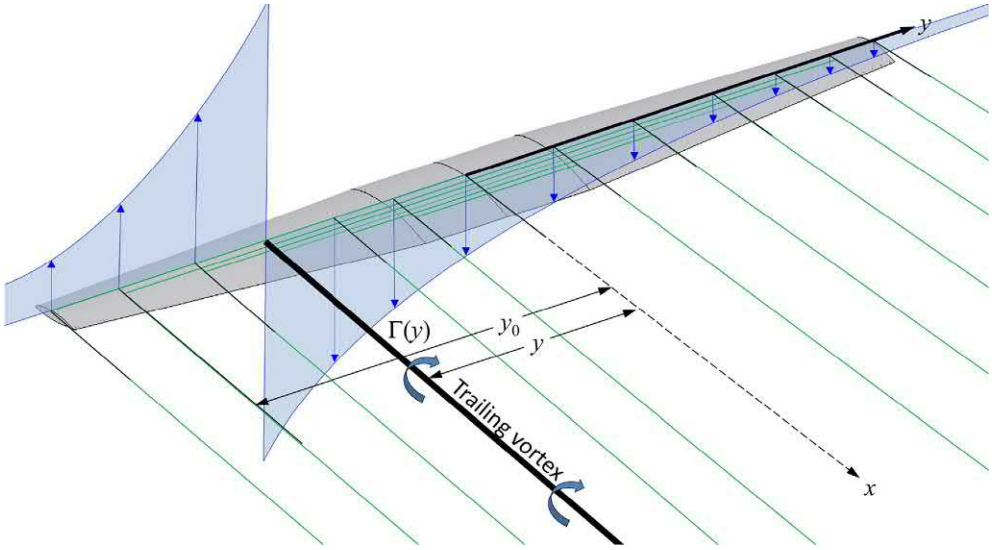


FIGURE 9-96 A depiction of how the trailing vortex at y influences the downwash at the other stations. The other trailing vortices affect the one at y in a similar fashion.

by the + sign in the equation. In order to calculate the total downwash at y_0 due to all the vortices distributed along the span, Equation (9-146) is integrated from the left wingtip ($y=-b/2$) to the right one ($y=+b/2$):

$$w_{y_0} = +\frac{1}{4\pi}\int_{-b/2}^{b/2} \frac{d\Gamma/dy}{(y-y_0)}dy \qquad (9\text{-}147)$$

As can be seen, the downwash depends on the strength of the circulation along the span. The contributions of other vortices in the system eventually yield a downward pointed velocity at y_0. With the downwash at y_0 known, the downwash angle α_{iy0} at y_0 can now be calculated as follows:

$$\alpha_{i_{y_0}} = \tan^{-1}\left(-w_{y_0}/V_\infty\right) \approx -w_{y_0}/V_\infty \qquad (9\text{-}148)$$

Where V_∞ denotes the far-field airspeed. As stated in Section 16.3.2, *Estimating Lift-Induced Drag*, the downwash behind the wing and corresponding upwash in front of it effectively "tilt" the undisturbed air through

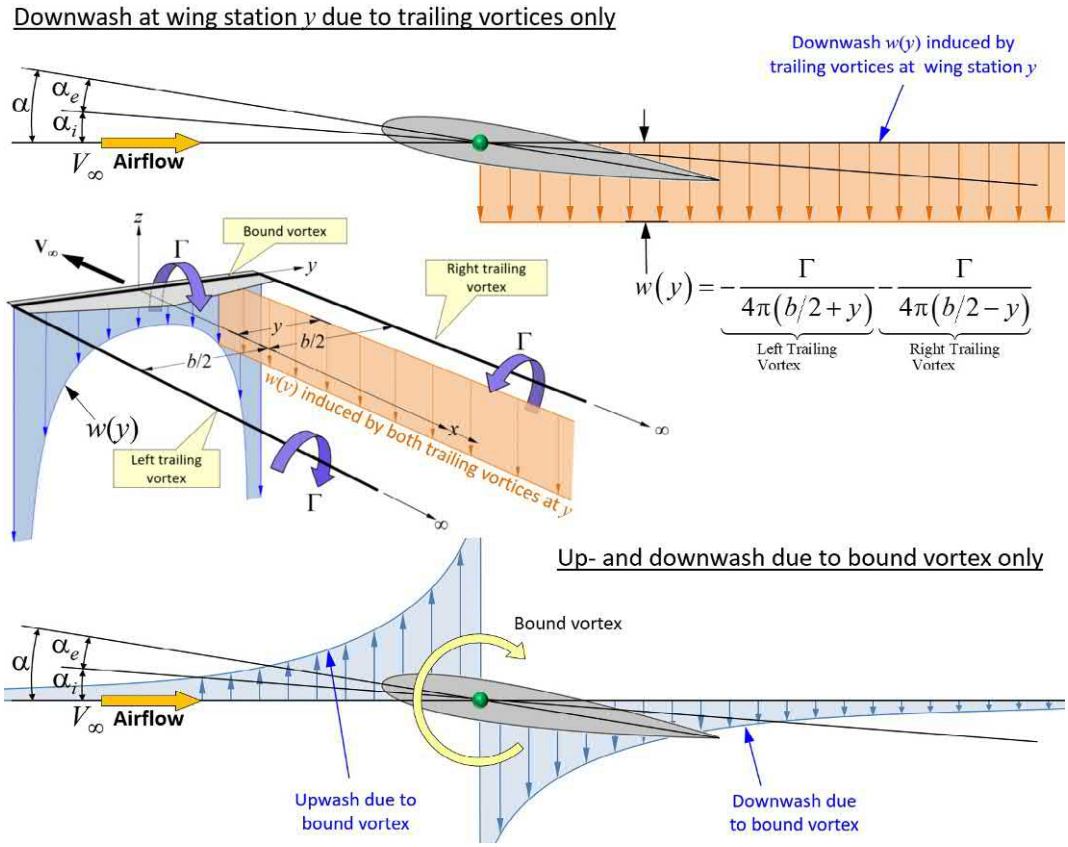


FIGURE 9-97 A side view of the bound vortex along the wing and the resulting up- and downwash.

an *induced AOA*, denoted by α_i, reducing the geometric AOA, α, at $c/4$ by what is called the *effective AOA*, α_e (see Figure 9-97):

Effective AOA: $$\alpha_e = \alpha - \alpha_i \tag{9-149}$$

If the wing features washout, α_i (and thus α_e) become functions of the spanwise station. Similarly, cambered airfoils are handled by subtracting their α_{ZL} from the geometric AOA. The presence of α_i tilts the lift force back by the angle ε (see Figure 16-32). Thus, the lift must be resolved into two force components: one normal to the flight path (lift) and the other parallel to the flight path (lift-induced drag). The Kutta-Joukowski theorem (see Section 8.1.9, *The Generation of Lift*) makes it possible to calculate these two forces per unit span using the following expressions:

Lift per unit span:
$$l(y) = \rho V_\infty \cdot \Gamma(y) \tag{9-150}$$

Lift-induced drag per unit span:
$$d_i(y) = -\rho w(y) \cdot \Gamma(y) \tag{9-151}$$

The minus sign is necessary to ensure the negative value of the downwash produces a positive drag force. The total lift and lift-induced drag forces can now be determined as shown below:

Lift: $$L = \rho V_\infty \int_{-b/2}^{b/2} \Gamma(y)dy \tag{9-152}$$

Drag: $$D_i = -\rho \int_{-b/2}^{b/2} w(y)\Gamma(y)dy \tag{9-153}$$

Consequently, the lift and lift-induced drag coefficient are given by:

Lift coefficient:
$$C_L = \frac{2L}{\rho V_\infty^2 S} = \frac{2}{V_\infty S}\int_{-b/2}^{b/2} \Gamma(y)dy \tag{9-154}$$

Lift-induced drag coefficient:
$$C_{D_i} = \frac{2D_i}{\rho V_\infty^2 S} = -\frac{2}{V_\infty^2 S}\int_{-b/2}^{b/2} w(y)\Gamma(y)dy \tag{9-155}$$

If there is a representative zero-lift AOA for the wing, the lift curve slope can be calculated from:

Lift curve slope: $$C_{L_\alpha} = \frac{C_L}{\alpha - \alpha_{ZL}} \tag{9-156}$$

The subsequent sections present several applications of this method.

9.7.2 Prandtl's Lifting-Line Method—Special Case: The Elliptical Wing

As discussed in Section 9.4.4, *Elliptical Planforms*, the elliptical wing planform is the most efficient and, thus,

of great interest to the aircraft designer. In this section, the lifting-line method is applied to an elliptical planform and several useful closed form solutions of selected aerodynamic characteristics are derived. These characteristics are helpful even if they are only used for comparison reasons. The solution assumes that the distribution of circulation is known and is given by:

Elliptical lift distribution: $$\Gamma(y)=\Gamma_0\sqrt{1-\left(\frac{2y}{b}\right)^2} \quad (9\text{-}157)$$

Using this distribution, the following aerodynamic characteristics for the elliptical planform can be derived (see derivation section that follows):

Vortex strength (constant): $$\Gamma_0=\frac{2C_LS}{\pi b}V_\infty \quad (9\text{-}158)$$

Downwash (constant): $$w=-\frac{\Gamma_0}{2b} \quad (9\text{-}159)$$

Induced AOA: $$\alpha_i\approx\frac{\Gamma_0}{2bV_\infty}=\frac{C_L}{\pi AR} \quad (9\text{-}160)$$

Lift force: $$L=\rho V_\infty\cdot\Gamma_0\frac{\pi b}{4} \quad (9\text{-}161)$$

Lift-induced drag force: $$D_i=\rho\Gamma_0^2\frac{\pi}{8} \quad (9\text{-}162)$$

Lift coefficient: $$C_L=\frac{\pi b\Gamma_0}{2V_\infty S} \quad (9\text{-}163)$$

Lift-induced drag coefficient: $$C_{D_i}=\frac{C_L^2}{\pi AR} \quad (9\text{-}164)$$

DERIVATION OF EQUATIONS (9-158) THROUGH (9-164)

First evaluate the derivative $d\Gamma/dy$ using the Chain-Rule of Differentiation:

$$\frac{d\Gamma}{dy}=\Gamma_0\frac{d}{dy}\left(1-\left(\frac{2}{b}\right)^2y^2\right)^{\frac{1}{2}}=\Gamma_0\frac{1}{2}\left(1-\left(\frac{2}{b}\right)^2y^2\right)^{-\frac{1}{2}}\left(-\frac{8}{b^2}y\right)$$
$$=-\frac{4\Gamma_0}{b^2}\frac{y}{\sqrt{1-(2y/b)^2}}$$

Substitute into Equation (9-147) to calculate the total downwash at any spanwise station, say y_0 (for sake of consistency):

$$w(y_0)=\frac{1}{4\pi}\int_{-b/2}^{b/2}\frac{d\Gamma/dy}{(y-y_0)}dy=\frac{1}{4\pi}\int_{-b/2}^{b/2}\frac{-\frac{4\Gamma_0}{b^2}\frac{y}{\sqrt{1-(2y/b)^2}}}{(y-y_0)}dy$$
$$=-\frac{\Gamma_0}{\pi b^2}\int_{-b/2}^{b/2}\frac{y}{\sqrt{1-(2y/b)^2}(y-y_0)}dy$$

It is helpful to evaluate the integral by transforming spanwise stations into an angular form as follows:

$$y=(b/2)\cos\phi\Rightarrow dy=-(b/2)\sin\phi\,d\phi \quad (9\text{-}165)$$

Using this transformation, we find the lower limit $(-b/2)$ becomes 0 and the upper one $(+b/2)$ becomes π. If we define $y_0=(b/2)\cos\phi_0$ the above integral can be rewritten as follows:

$$w(y_0)=$$
$$-\frac{\Gamma_0}{\pi b^2}\int_\pi^0\frac{(b/2)\cos\phi\times(-(b/2)\sin\phi\,d\phi)}{\sqrt{(b/2)^2-(b/2)^2\cos^2\phi}\times((b/2)\cos\phi-(b/2)\cos\phi_0)}$$

Simplifying further yields:

$$w(y_0)=\frac{\Gamma_0}{2\pi b}\int_\pi^0\frac{\cos\phi\sin\phi d\phi}{\sqrt{1-\cos^2\phi}\times(\cos\phi-\cos\phi_0)}$$
$$=\frac{\Gamma_0}{2\pi b}\int_\pi^0\frac{\cos\phi\sin\phi d\phi}{\sin\phi\times(\cos\phi-\cos\phi_0)}$$

Finally, this leads to:

$$w(y_0)=-\frac{\Gamma_0}{2\pi b}\int_0^\pi\frac{\cos\phi}{\cos\phi-\cos\phi_0}d\phi \quad (i)$$

The evaluation of this integral is beyond the scope of this text, but a solution is provided by Karamcheti [75]. An alternative solution method based on the original expression omitting the transformation is presented by Bertin and Smith [72]. In either case, the resulting expression reduces to:

$$w(y_0)=-\Gamma_0/2b \quad (ii)$$

This is Equation (9-159). Note that the distribution of downwash is constant along the span. The downwash angle can thus be obtained from Equation (9-148):

$$\alpha_i(y_0)\approx-w(y_0)/V_\infty=\Gamma_0/(2bV_\infty) \quad (iii)$$

This is Equation (9-160). Note that this angle is constant along the span as well. Substitute Equation (9-157) into (9-152) to calculate the total lift generated by the wing:

$$L=\rho V_\infty\int_{-b/2}^{b/2}\Gamma(y)dy=\rho V_\infty\int_{-b/2}^{b/2}\Gamma_0\sqrt{1-\left(\frac{2y}{b}\right)^2}dy \quad (iv)$$

Using the above angular transformations, Equation (iv) can be rewritten and simplified as follows:

$$L=\rho V_\infty\cdot\Gamma_0\int_0^\pi\sqrt{1-\cos^2\phi}(b/2)\sin\phi\,d\phi=\rho V_\infty\Gamma_0\frac{\pi b}{4} \quad (v)$$

This is Equation (9-161). The lift coefficient can now be determined from:

$$C_L = \frac{2L}{\rho V_\infty^2 S} = \frac{\pi b \Gamma_0}{2 V_\infty S} \tag{vi}$$

This is Equation (9-163). Alternatively, the vortex strength Γ_0 is readily obtained from Equation (vi) as follows:

$$\Gamma_0 = \frac{2SC_L}{\pi b} V_\infty \tag{vii}$$

This is Equation (9-158). Similarly, the lift-induced drag is computed from Equation (9-153):

$$D_i = -\rho \int_{-b/2}^{b/2} w(y)\Gamma(y)dy = -\rho \int_{-b/2}^{b/2} w(y)\Gamma_0 \sqrt{1-\left(\frac{2y}{b}\right)^2}\, dy \tag{viii}$$

Substituting Equation (9-159) and using the spanwise angular transformation of Equation (9-165), we get Equation (9-162):

$$D_i = -\rho \int_{-b/2}^{b/2} \frac{-\Gamma_0}{2b}\Gamma_0 \sqrt{1-\left(\frac{2y}{b}\right)^2}\, dy$$

$$= \frac{\rho\Gamma_0^2}{2b}\int_0^\pi \sqrt{1-\cos^2\phi}\,(b/2)\sin\phi\, d\phi = \rho\Gamma_0^2\frac{\pi}{8} \tag{ix}$$

The lift-induced drag coefficient can now be determined as follows, using Equation (vii):

$$C_{D_i} = \frac{2D_i}{\rho V_\infty^2 S} = \frac{2\left(\rho\Gamma_0^2\frac{\pi}{8}\right)}{\rho V_\infty^2 S} = \frac{\pi}{4V_\infty^2 S}\Gamma_0^2$$

$$= \frac{\pi}{4V_\infty^2 S}\left(\frac{2SC_L}{\pi b}V_\infty\right)^2 = \frac{SC_L^2}{\pi b^2} = \frac{C_L^2}{\pi AR} \tag{x}$$

This is Equation (9-164).

9.7.3 Prandtl's Lifting-Line Method—Special Case: Arbitrary Wings

Most aircraft do not feature elliptical wing planform. Hence, it is desirable to extend the lifting-line method to nonelliptical wings. One way of accomplishing this is to represent the spanwise distribution of vortex strengths using a Fourier sine series, consisting of N terms:

Fourier series lift distribution:

$$\Gamma(\phi) = 2bV_\infty \sum_{n=1}^{N} A_n \sin n\phi \tag{9-166}$$

Note that if the lift distribution is symmetric, all even values of n are omitted. The first equation of interest is the one that allows the coefficients A_1, A_2, A_3, …, A_N to be solved.

Monoplane equation:

$$\sum_{n=1}^{N} A_n \sin n\phi(\mu n + \sin\phi) = \mu(\alpha - \alpha_{ZL})\sin\phi \tag{9-167}$$

The monoplane equation is used to construct a system of simultaneous equations, as shown below. The left-hand side of this equation is called the *aerodynamic influence matrix*:

Where: α_{ZL_i} = Zero-lift angle for the airfoil at station ϕ_i.

ϕ_i = Angles (in radians) that correspond to the spanwise angular stations obtained from $y_i = (b/2)\cos\phi_i$ (i.e., Equation 9.165), in radians.
$\mu = c \cdot C_{l_\alpha}/4b$, dimensionless. The airfoil's lift curve slope, C_{l_α}, may be a function of ϕ.
b = Wingspan, in ft or m.
c = Chord at station ϕ_i, in ft or m.

Solving the system leads to several interesting results, some of which are presented below.

Lift force:

$$L = \frac{1}{2}\rho V_\infty \cdot S \cdot (\pi \cdot AR \cdot A_1) = \frac{1}{2}\rho V_\infty \cdot b^2 \cdot \pi \cdot A_1 \tag{9-169}$$

Lift-induced drag:

$$D_i = \frac{\rho V_\infty^2}{2} b^2 \pi \sum n A_n^2 \tag{9-170}$$

Lift coefficient:

$$C_L = \pi \cdot AR \cdot A_1 \tag{9-171}$$

The lift curve slope can thus be calculated from:

Lift curve slope:

$$C_{L_\alpha} = \frac{C_L}{\alpha - \alpha_{ZL}} = \frac{\pi \cdot AR \cdot A_1}{\alpha - \alpha_{ZL}} \tag{9-172}$$

$$\begin{bmatrix} \sin\phi_1(\mu+\sin\phi_1) & \sin 2\phi_1(2\mu+\sin\phi_1) & \cdots & \sin N\phi_1(N\mu+\sin\phi_1) \\ \sin\phi_2(\mu+\sin\phi_2) & \sin 2\phi_2(2\mu+\sin\phi_2) & \cdots & \sin N\phi_2(N\mu+\sin\phi_2) \\ \vdots & \vdots & \ddots & \vdots \\ \sin\phi_N(\mu+\sin\phi_N) & \sin 2\phi_N(2\mu+\sin\phi_N) & \cdots & \sin N\phi_N(N\mu+\sin\phi_N) \end{bmatrix} \begin{Bmatrix} A_1 \\ A_2 \\ \vdots \\ A_N \end{Bmatrix} = \begin{Bmatrix} \mu(\alpha-\alpha_{ZL_1})\sin\phi_1 \\ \mu(\alpha-\alpha_{ZL_2})\sin\phi_2 \\ \vdots \\ \mu(\alpha-\alpha_{ZL_N})\sin\phi_N \end{Bmatrix} \tag{9-168}$$

Lift-induced drag coefficient:

$$C_{D_i} = \frac{C_L^2}{\pi \cdot AR}(1+\delta) = \frac{C_L^2}{\pi \cdot AR \cdot e} \tag{9-173}$$

Where $\delta = \sum_{n=2}^{N} n\left(\frac{A_n}{A_1}\right)^2$ and $e_{theo} = \frac{1}{1+\delta}$.

As stated earlier, if the spanwise distribution of lift is symmetrical, all the even indexed constants (A_2, A_4, …) of the summation are set to zero. This can be written as follows:

$$\delta = \sum_{n=2}^{N} n\left(\frac{A_n}{A_1}\right)^2 = 3\left(\frac{A_3}{A_1}\right)^2 + 5\left(\frac{A_5}{A_1}\right)^2 + 7\left(\frac{A_7}{A_1}\right)^2 + \cdots \tag{9-174}$$

See Figure 9-75 for a graph plotting δ as a function of taper ratio and aspect ratio for straight-tapered wings.

Change in Induced Angle-of-Attack

The induced AOA on an arbitrary planform differs from that of an elliptical planform of an equal *AR* according to the following expression:

$$\alpha_{wing} - \alpha_{airfoil} = \frac{C_L}{\pi AR}(1+\tau) \tag{9-175}$$

Where τ is given by: $(1+\tau) = \frac{\alpha_{wing}}{A_1} - \frac{\pi AR}{C_{l_\alpha}}$ (9-176)

DERIVATION OF EQUATIONS (9-169) THROUGH (9-173)

To determine the coefficients A_1, A_2, A_3, …, A_N, the circulation for the *N* vortices must be determined. The procedure begins by relating the section lift coefficient at any angular station ϕ as follows:

$$C_l(\phi) = \frac{\text{lift per unit span}}{\frac{1}{2}\rho V_\infty^2 c} = \frac{\rho V_\infty \cdot \Gamma(\phi)}{\frac{1}{2}\rho V_\infty^2 c(\phi)} = \frac{2\Gamma(\phi)}{V_\infty c(\phi)} \tag{i}$$

Where $c(\phi)$ is the chord at a specific angular station ϕ. However, if the lift curve slope, $C_{l_\alpha} = dC_l/d\alpha$, of the airfoil at the angular station ϕ is known, the section lift coefficient can also be determined from:

$$C_l = \left(\frac{dC_l}{d\alpha}\right)(\alpha_e - \alpha_{ZL}) = C_{l_\alpha}(\alpha - \alpha_i - \alpha_{ZL}) \tag{ii}$$

Where α_{ZL} is the zero-lift AOA of the airfoil at the angular station ϕ. Note that α, α_{ZL}, and α_i are all functions of the angular station ϕ. By equating Equations (i) and (ii), we get:

$$\frac{2\Gamma(\phi)}{V_\infty c(\phi)} = C_{l_\alpha}(\alpha - \alpha_i - \alpha_{ZL}) \Rightarrow \frac{2\Gamma(\phi)}{C_{l_\alpha} c(\phi)}$$

$$= V_\infty(\alpha - \alpha_{ZL}) - V_\infty \alpha_i \tag{iii}$$

The product $V_\infty \alpha_i$ is given by Eq. (9.147):

$$V_\infty \alpha_i = -w = -\frac{1}{4\pi}\int_{-b/2}^{+b/2} \frac{d\Gamma/dy}{y - y_0} dy \tag{iv}$$

Where the minus sign indicates a downward flow of air. Using the definition of Γ(ϕ) given by Equation (9-166) this can be rewritten as follows:

$$-w(\phi) = -V_\infty \frac{\sum nA_n \sin n\phi}{\sin\phi} \tag{v}$$

Therefore, Equation (iii) can be rewritten as follows:

$$\frac{2\Gamma(\phi)}{c(\phi) \cdot C_{l_\alpha}} = V_\infty(\alpha - \alpha_{ZL}) - V_\infty \frac{\sum nA_n \sin n\phi}{\sin\phi} \tag{vi}$$

Expanding by substituting Γ(ϕ) per Equation (9-166) yields:

$$\frac{4b}{c \cdot C_{l_\alpha}} \sum A_n \sin n\phi = (\alpha - \alpha_{ZL}) - \frac{\sum nA_n \sin n\phi}{\sin\phi} \tag{vii}$$

Let $\mu = cC_{l_\alpha}/4b$ and substitute into Equation (vii). This leads to:

$$\sin\phi \sum A_n \sin n\phi = \mu(\alpha(\phi) - \alpha_{ZL}(\phi))\sin\phi - \mu \sum nA_n \sin n\phi$$

$$\Rightarrow \sin\phi \sum A_n \sin n\phi + \mu \sum nA_n \sin n\phi = \mu(\alpha(\phi) - \alpha_{ZL}(\phi))\sin\phi$$

Simplify terms in the summation sign to yields a governing equation that is called the *monoplane equation*.

$$\sum_{n=1}^{N} A_n \sin n\phi(\mu n + \sin\phi) = \mu(\alpha - \alpha_{ZL})\sin\phi \tag{9-167}$$

This equation yields a set of equations that must be solved simultaneously to obtain the constants A_1, A_2, A_3, …, A_N. The angle ϕ refers to a spanwise angle transformation of Equation (9-165). If the problem deals with symmetrical load distribution, all even terms ($n = 2, 4$, etc.) are omitted from the solution.

Next consider the lift coefficient generated by the wing, given by:

$$C_L = \frac{2L}{\rho V^2 S} = \frac{2}{VS}\int_{-b/2}^{b/2} \Gamma(y) dy \tag{viii}$$

Again, using the definition of Γ(ϕ) given by Equation (9-166), Equation (viii) becomes:

$$C_L = \frac{2}{V_\infty S}\int_{-b/2}^{b/2} \Gamma(y) dy$$

$$= \frac{2}{V_\infty S}\int_0^\pi \left[2bV_\infty \sum_{n=1}^{N} A_n \sin n\phi\right]\left(\left(\frac{b}{2}\right)\sin\phi d\phi\right)$$

$$= \frac{2b^2}{S}\int_0^\pi \left[\sum_{n=1}^{N} A_n \sin n\phi\right]\sin\phi d\phi$$

The integral can be solved noting that:

$$\int_0^{\pi} \sin n\phi \sin\phi d\phi = \begin{cases} \pi/2 & \text{if } n=1 \\ 0 & \text{if } n \neq 1 \end{cases}$$

This allows Equation (ix) to be rewritten as follows:

$$C_L = \frac{2b^2}{S}\int_0^{\pi}\left[\sum_{n=1}^{N} A_n \sin n\phi\right]\sin\phi d\phi = \frac{2b^2}{S}\frac{\pi}{2}A_1$$
$$= \frac{\pi b^2 A_1}{S} = \pi \cdot AR \cdot A_1 \qquad \text{(ix)}$$

This is Equation (9-171). Then consider the lift-induced drag coefficient generated by the wing. Equation (9-153) defines the lift-induced drag, D_i. Inserting Equation (v) for $w(y)$ and Equation (9-166) for $\Gamma(\phi)$ we get:

$$D_i = -\rho\int_{-b/2}^{b/2} w(y)\Gamma(y)dy$$
$$= -\rho\int_{-b/2}^{b/2}\left[-V_\infty \frac{\sum nA_n \sin n\phi}{\sin\phi}\right]$$
$$\left[2bV_\infty \sum A_n \sin n\phi\right]\left(\left(\frac{b}{2}\right)\sin\phi d\phi\right)$$
$$= \frac{\rho V_\infty 2bbV_\infty}{2}\int_0^{\pi}\left[\frac{\sum nA_n \sin n\phi}{\sin\phi}\right]\left[\sum A_n \sin n\phi\right](\sin\phi d\phi)$$

This reduces to:

$$D_i = \rho V_\infty{}^2 b^2 \int_0^{\pi} \sum nA_n \sin n\phi \sum A_n \sin n\phi d\phi$$

Where the evaluation of the integral yields:

$$\int_0^{\pi} \sum nA_n \sin n\phi \sum A_n \sin n\phi d\phi = \tfrac{\pi}{2}\sum nA_n^2$$

Therefore, the lift – induced drag is given by:

$$D_i = \frac{\rho V_\infty^2}{2} b^2 \pi \sum nA_n^2 \qquad \text{(x)}$$

Using Equation (9-155), it is now possible to determine the lift-induced drag coefficient:

$$C_{D_i} = \frac{2D_i}{\rho V_\infty^2 S} = \frac{2\left[\frac{\rho V_\infty^2}{2} b^2 \pi \sum nA_n^2\right]}{\rho V_\infty^2 S}$$
$$= \frac{b^2\pi}{S}\sum nA_n^2 = \pi \cdot AR \cdot \sum nA_n^2 \qquad \text{(xi)}$$

Since $C_L = \pi \cdot AR \cdot A_1 \Leftrightarrow A_1 = C_L/(\pi \cdot AR)$, it is possible to rewrite this as follows:

$$C_{D_i} = \pi \cdot AR \cdot \sum nA_n^2 = \pi \cdot AR \cdot \left(A_1^2 + \sum_{n=2}^{N} nA_n^2\right)$$
$$= \frac{C_L^2}{\pi \cdot AR}\left(1 + \sum_{n=2}^{N} n\left(\frac{A_n}{A_1}\right)^2\right) \qquad \text{(xii)}$$

This is a classic form of this equation, typically written in the following form, using the term δ to denote the lift-induced drag factor.

$$C_{D_i} = \frac{C_L^2}{\pi \cdot AR}(1+\delta) \qquad \text{(xiii)}$$

It is evident that the minimum C_{D_i} is obtained when $\delta = 0$, but this represents an elliptic lift distribution.

DERIVATION OF EQUATION (9-175)

Consider an airfoil and a wing whose cross section is that of said airfoil. The airfoil is akin to a 3-dimensional wing of infinite wingspan. Consider these at specific AOA such they both generate an equal lift coefficient, C_L. This allows the aerodynamic AOA[6] for each "wing" to be determined as follows:

Airfoil: $\alpha_{airfoil} = C_L/C_{l_\alpha}$

Wing: $\alpha_{wing} = C_L/C_{L_\alpha}$

Subtracting one from the other leads to:

$$\alpha_{wing} - \alpha_{airfoil} = \frac{C_L}{C_{L_\alpha}} - \frac{C_L}{C_{l_\alpha}} = C_L\left(\frac{1}{C_{L_\alpha}} - \frac{1}{C_{l_\alpha}}\right)$$

This represents the difference in AOA between the two geometries. Next, substitute $A_1 = C_L/\pi AR$ into the expression for the wing, i.e., $C_{L_\alpha} = C_L/\alpha_{wing}$. This yields the following relationship between C_{L_α} and A_1:

$$A_1 = C_L/\pi AR \;\Rightarrow\; C_L = A_1 \pi AR$$
$$\Rightarrow\; C_{L_\alpha} = C_L/\alpha_{wing} = A_1 \pi AR/\alpha_{wing}$$

Replacing the corresponding term in the above equation for the difference in AOA, leads to:

$$\alpha_{wing} - \alpha_{airfoil} = C_L\left(\frac{1}{C_{L_\alpha}} - \frac{1}{C_{l_\alpha}}\right) = C_L\left(1\Big/\left(\frac{C_L}{\alpha_{wing}}\right) - \frac{1}{C_{l_\alpha}}\right)$$
$$= \frac{C_L}{\pi AR}\left(\frac{\alpha_{wing}}{A_1} - \frac{\pi AR}{C_{l_\alpha}}\right)$$

[6] The aerodynamic AOA is measured with respect to zero lift; in other words: $\alpha - \alpha_{ZL}$.

EXAMPLE 9-15

Estimate the aerodynamic characteristics of the SR22 wing (ignoring the fuselage) using the lifting-line method. Determine this using 4 terms in the monoplane equation, assuming symmetrical lift distribution. Assume the aircraft is flying at $\alpha = 5°$ and a NACA 65-415 airfoil. Assume the airfoil's zero-lift AOA, α_{ZL}, is approximately $-2.7°$ and its lift curve slope, C_{l_α}, is 2π per radian. Note that the dimensions in Figure 9-98 are calculated based on the geometry shown and are not the "official" numbers (e.g., official $S = 144.9\,\text{ft}^2$ and $AR = 10$). Determine the airspeed the airplane must fly at S-L if it weighs $3400\,\text{lb}_\text{f}$.

SOLUTION:

Begin by creating the relationship between the physical and angular span stations (see Figure 9-99). Note that the physical stations are given by $y_i = (b/2)\cos\phi_i$ (Equation 9.165). For this reason, the cosine of ϕ is in effect a parameter that varies between 1 and 0 that can be used with a parametric representation for the chord. Since $c_r = 5.18\,\text{ft}$ and $c_t = 2.59\,\text{ft}$ we can calculate the chord at any spanwise station using the parametric equation:

$$c_i = c_t\cos\phi_i + c_r(1-\cos\phi_i) \;\Rightarrow$$
$$c_i = 2.59\cos\phi_i + 5.18(1-\cos\phi_i),$$

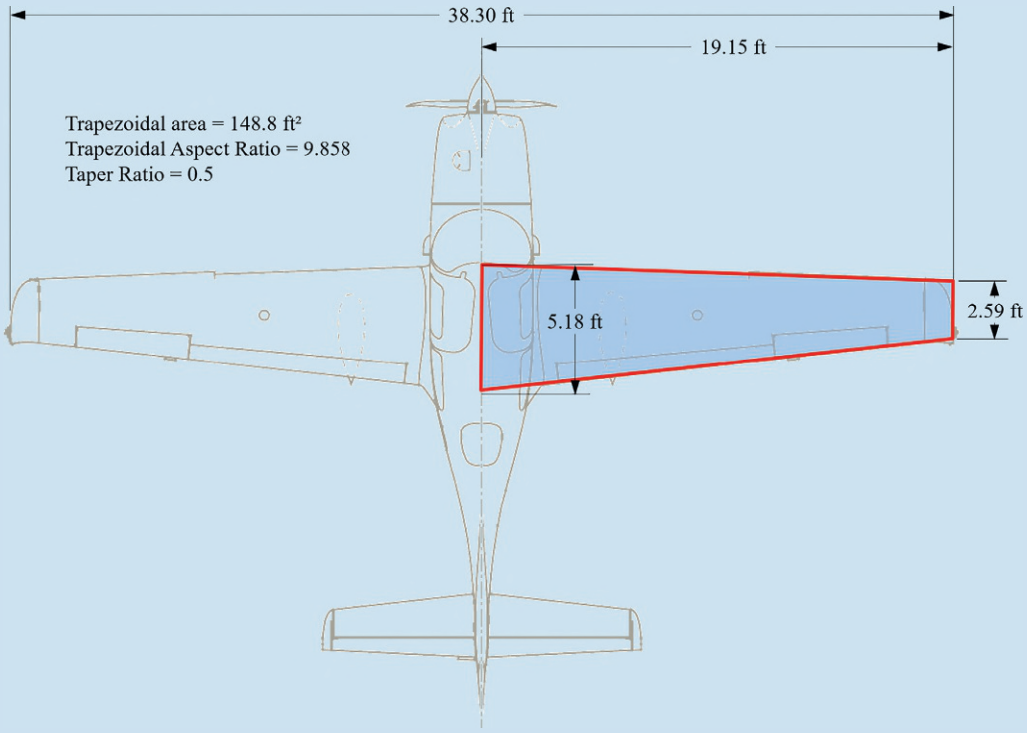


FIGURE 9-98 A top view of the SR-22 showing dimensions used for this example.

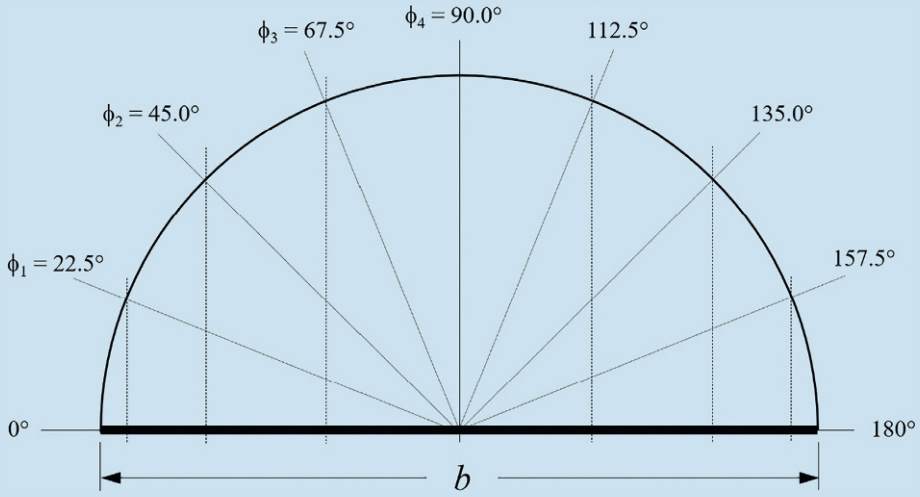


FIGURE 9-99 Relationship between physical and angular stations along the wingspan.

EXAMPLE 9-15 (*cont'd*)

Next tabulate the following values:

Columns ① and ②: Contain the spanwise angular stations from Figure 9-99 both in degrees and radians.

Column ③: Contains the cosine of the angular station.

Column ④: Contains the wing chord at the angular station. Calculated using $c_i = 2.59\cos\phi_i + 5.18(1-\cos\phi_i)$.

Columns ⑤ through ⑧: Contain the various sines of the angular stations. These are needed to properly set up the matrix as required by the monoplane equation.

Column ⑨: Is calculated as follows, using values from the first row (ID = 1):

$$\mu_1 = c_1 \cdot C_{l_\alpha}/4b = (2.79)\cdot(2\pi)/4(38.3) = 0.1143$$

	①	②	③	④	⑤	⑥	⑦	⑧	⑨
	Angular Station			$c(\phi)$					
ID	Deg	Rad	$\cos\phi$	ft	$\sin\phi$	$\sin 3\phi$	$\sin 5\phi$	$\sin 7\phi$	μ
1	22.5	0.3927	0.9239	2.79	0.3827	0.9239	0.9239	0.3827	0.1143
2	45.0	0.7854	0.7071	3.35	0.7071	0.7071	-0.7071	-0.7071	0.1373
3	67.5	1.1781	0.3827	4.19	0.9239	-0.3827	-0.3827	0.9239	0.1718
4	90.0	1.5708	0.0000	5.18	1.0000	-1.0000	1.0000	-1.0000	0.2124

Next prepare the aerodynamic influence matrix per Equation (9-168). Since the lift distribution is symmetrical, we are only concerned with the constants A_1, A_3, A_5, and A_7. This leads to the following setup.

$$\begin{bmatrix} 0.1902 & 0.6704 & 0.8816 & 0.4527 \\ 0.5971 & 0.7913 & -0.9856 & -1.1798 \\ 1.0123 & -0.5508 & -0.6823 & 1.9646 \\ 1.2124 & -1.6373 & 2.0622 & -2.4871 \end{bmatrix} \begin{Bmatrix} A_1 \\ A_3 \\ A_5 \\ A_7 \end{Bmatrix} = \begin{Bmatrix} 0.005879 \\ 0.001305 \\ 0.002133 \\ 0.028551 \end{Bmatrix}$$

For instance, the first row in the above matrix is calculated as follows, using the monoplane equation:

$$A_{11} = \sin\phi_1(\mu + \sin\phi_1) = (0.3827)(0.1143 + 0.3827) = 0.1902$$

$$A_{12} = \sin 3\phi_1(3\mu + \sin\phi_1) = (0.9239)(3\times 0.1143 + 0.3827) = 0.6704$$

$$A_{13} = \sin 5\phi_1(5\mu + \sin\phi_1) = (0.9239)(5\times 0.1143 + 0.3827) = 0.8816$$

$$A_{14} = \sin 7\phi_1(7\mu + \sin\phi_1) = (0.3827)(7\times 0.1143 + 0.3827) = 0.4527$$

$$B_1 = \mu(\alpha - \alpha_{ZL_1})\sin\phi_1 = (0.1143)(0.08727 - (-0.04712))(0.3827) = 0.005879$$

Solving requires the square matrix to be inverted and then multiplied by the column matrix on the right-hand side. This yields the following solution:

$$\begin{Bmatrix} A_1 \\ A_3 \\ A_5 \\ A_7 \end{Bmatrix} = \begin{Bmatrix} 2.251\times 10^{-2} \\ 8.674\times 10^{-4} \\ 1.195\times 10^{-3} \\ -8.441\times 10^{-5} \end{Bmatrix}$$

The aerodynamic parameters can now be determined. The lift coefficient can be calculated from Equation (9-171):

$$C_L = \pi ARA_1 = \pi\cdot(9.858)\cdot 2.251\times 10^{-2} = 0.6971$$

The lift-induced drag coefficient can be found by first determining the factor δ:

$$\delta = \sum_{n=2}^{N} n\left(\frac{A_n}{A_1}\right)^2 = 3\left(\frac{A_3}{A_1}\right)^2 + 5\left(\frac{A_5}{A_1}\right)^2 + 7\left(\frac{A_7}{A_1}\right)^2 = 0.01865$$

This yields the following drag coefficient per Equation (9-173):

$$C_{D_i} = \frac{C_L^2}{\pi\cdot AR}(1+\delta) = \frac{(0.6971)^2}{\pi\cdot(9.858)}(1+0.01865) = 0.01599$$

Span efficiency is:

$$e_{theo} = \frac{1}{1+\delta} = \frac{1}{1+0.01865} = 0.9817$$

Note that this value ignores the fuselage and dihedral as discussed in Section 9.5.12, *Determination of Span Efficiency*. Finally, the wing's lift curve slope can be determined as follows:

$$C_{L_\alpha} = \frac{C_L}{(\alpha - \alpha_{ZL})} = \frac{0.6971}{(0.08727 + 0.04712)} = 5.187 \text{ per radian}$$

Finally, the airspeed the airplane must fly at to generate 3400 lb_f of lift at 5-degree AOA can be determined as follows:

$$V_\infty = \sqrt{\frac{2W}{\rho S C_L}} = \sqrt{\frac{2(3400)}{(0.002378)(148.8)(0.6971)}} = 166 \text{ ft/s}$$

$$= 98.4 \text{ KCAS}$$

	AR					
λ	4	6	8	10	12	14
	=LiftingLine(U$76,$R77,B78, C10,D11,F16,50,2)					
0.025	0.0653	0.0940	0.1168	0.1352	0.1504	0.1632
0.050	0.0484	0.0717	0.0907	0.1064	0.1194	0.1305
0.075	0.0369	0.0558	0.0716	0.0848	0.0959	0.1054
0.100	0.0286	0.0440	0.0571	0.0682	0.0776	0.0858
0.125	0.0224	0.0350	0.0459	0.0553	0.0633	0.0703
0.150	0.0177	0.0281	0.0372	0.0451	0.0520	0.0580
0.175	0.0141	0.0227	0.0304	0.0371	0.0431	0.0484
0.200	0.0114	0.0185	0.0251	0.0309	0.0362	0.0409
0.225	0.0093	0.0153	0.0210	0.0262	0.0308	0.0351
0.250	0.0077	0.0129	0.0179	0.0226	0.0268	0.0308
0.275	0.0065	0.0111	0.0157	0.0199	0.0239	0.0277
0.300	0.0057	0.0099	0.0141	0.0182	0.0220	0.0256
0.325	0.0051	0.0091	0.0131	0.0171	0.0209	0.0245
0.350	0.0048	0.0087	0.0127	0.0166	0.0205	0.0241
0.375	0.0047	0.0086	0.0126	0.0167	0.0206	0.0244
0.400	0.0048	0.0088	0.0130	0.0172	0.0213	0.0253
0.425	0.0050	0.0092	0.0136	0.0181	0.0225	0.0267
0.450	0.0054	0.0099	0.0146	0.0193	0.0240	0.0286
0.475	0.0059	0.0107	0.0158	0.0209	0.0259	0.0308
0.500	0.0064	0.0117	0.0172	0.0227	0.0281	0.0334

FIGURE 9-100 An example of how calls can be made to the *Lifting-Line* function from within Microsoft Excel.

9.7.4 Computer Code: Prandtl's Lifting-Line Method

The following code implements the lifting-line method for an arbitrary wing covered in previous section. It is written using *Visual Basic for Applications* (VBA) for use in Microsoft Excel. It allows as many vortices as system resources can handle, represented by the variable N (see the commented variable definitions in the code). Regardless, a $N > 50$ is usually impractical. It is assumed the reader is familiar with how to operate Microsoft Excel and the VBA environment. If not, there are multiple tutorials available on video websites such as YouTube. In short, the code is entered in a special window, called *module*. The program is written as a *function*. It is then called from the spreadsheet itself as shown in Figure 9-100. Simple cell references are used to pass arguments to the routine. Here 50 vortices are being used, and the Mode is 2, which means the term δ is returned. Additionally, the reader can extract the spanwise distribution of lift and induced drag and use in many of the methods in this book.

```
Function LiftingLine(AR As Single, TR As Single, S As Single, Cla As Single, AOA As Single,
AOA_ZL As Single, N As Integer, Mode As Byte) As Single
'This function implements Prandtl's lifting-line theory
'
'Variables: AR     = Aspect Ratio
'           TR     = Taper Ratio
'           S      = Wing area (ft²)
'           Cla    = Average airfoil lift curve slope (per rad)
'           AOA    = Angle of attack (rad)
'           AOA_ZL = Average zero-lift AOA of airfoils (rad)
'           N      = Number of vortices
'
'Mode:      =0  Return CL
'           =1  Return CDi
'           =2  Return del
'           =3  Return e
'
'Initialize
    Dim i As Integer, j As Integer, m As Single
    Dim Pi As Single, Sum As Single
    Dim dPhi As Single, sinPhi As Single, t As Single, C_of_Phi As Single
    Dim Cr As Single, Ct As Single, b As Single
    Dim CL As Single, CDi As Single, CLalpha As Single, del As Single

'Dimension arrays
    ReDim Phi(N) As Single
    ReDim mu(N) As Single
    ReDim A(N, 1) As Double
    ReDim MatB(N, N) As Double
    ReDim MatC(N, 1) As Double

'Presets
    Pi = 3.14159265
    b = Sqr(S * AR)                             'Wing span
    Cr = 2 * S / (b + b * TR)                   'Root chord
    Ct = TR * Cr                                'Tip chord
'Create stations
    dPhi = 0.5 * Pi / CSng(N)                   'in Radians
    For i = 1 To N
        'Calculate station angle
        Phi(i) = Phi(i - 1) + dPhi

        'Calculate mu
        t = Cos(Phi(i))                         'Parameter t
        C_of_Phi = (1 - t) * Cr + t * Ct        'Chord determined using parametric formulation
        mu(i) = 0.25 * C_of_Phi * Cla / b
    Next i

'Prepare aerodynamic influence coefficients
    For i = 1 To N
        'Calculate the sine of the angle Phi(i) so it won't have to be calculated over and over
        sinPhi = Sin(Phi(i))

        'Calculate the vortex influence matrix
        For j = 1 To N
            m = 2 * j - 1
            MatB(i, j) = Sin(m * Phi(i)) * (m * mu(i) + sinPhi)
        Next j

        'Calculate the boundary conditions
        MatC(i, 1) = mu(i) * (AOA - AOA_ZL) * sinPhi
    Next i
'Invert matrix - NOTE: USER MUST WRITE OWN ROUTINE FOR THIS PURPOSE! Mine is called MAT_GaussP()
    i = MAT_GaussP(MatB(), MatC(), A())

'Calculate lift coefficient
    CL = A(1, 1) * Pi * AR
    CLalpha = CL / (AOA - AOA_ZL)

'Calculate lift induced drag coefficient
    Sum = 0
    For i = 2 To N
        m = 2 * i - 1
        Sum = Sum + m * A(i, 1) ^ 2
    Next i
    del = Sum / (A(1, 1) ^ 2)
    e = 1 / (1 + del)
    CDi = CL ^ 2 * (1 + del) / (Pi * AR)

'Return
    If Mode = 0 Then LiftingLine = CL
    If Mode = 1 Then LiftingLine = CDi
    If Mode = 2 Then LiftingLine = del
    If Mode = 3 Then LiftingLine = e
    If Mode = 4 Then LiftingLine = CLalpha

End Function
```

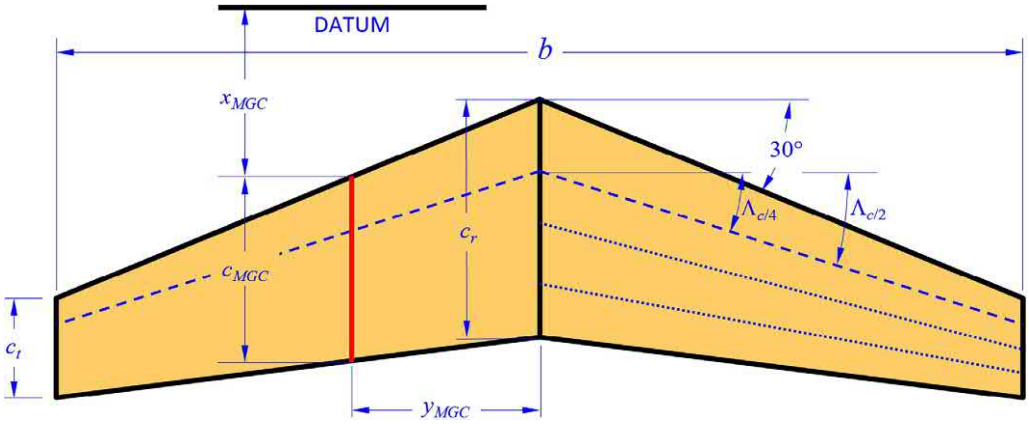


FIGURE 9-101 Wing used in Exercise (1).

EXERCISES

(1) Determine all the variables of the wing in Figure 9-101, if its planform area, S, is 200 ft^2, $AR = 7.5$, and $\lambda = 0.5$. Approximate its internal volume if it features a constant 15% thick airfoil, whose maximum thickness is at 50% chord. If 30% of this volume is to be used for the fuel tanks, how much fuel can the wing hold and how much will it weigh assuming Jet-A fuel (1 US gal = 231.02 in^3). Assume datum is at the leading edge of the root airfoil.

Ans: $b = 38.73$ ft, $c_r = 6.885$ ft, $C_{MGC} = 5.355$ ft, $y_{MGC} = 8.607$ ft, $x_{MGC} = 4.969$ ft, $\Lambda_{c/4} = 28.05°$, $\Lambda_{c/2} = 26.03°$, wing volume is approximately 94 ft^3; it can hold 210 US gal that weighs 1410 lb$_f$.

References

[1] D.E. Hoak, *USAF Stability and Control DATCOM*, Flight Control Division, Air Force Flight Dynamics Laboratory, 1978.

[2] O. Lilienthal, *Der Vogelflug als Grundlage der Fliegerkunst*, R. Gaertners Verlagsbuchhandlung, 1889.

[3] Anonymous, *Cirrus SR22 Pilot's Operating Handbook*, Cirrus Design Corporation, October 10, 2003.

[4] S.A. Brandt, R.J. Stiles, J.J. Bertin, R. Whitford, *Introduction to Aeronautics: A Design Perspective*, AIAA Education Series, American Institute of Aeronautics and Astronautics, 1997.

[5] D.P. Raymer, *Aircraft Design: A Conceptual Approach*, AIAA Education Series, American Institute of Aeronautics and Astronautics, 1996.

[6] John W.R. Taylor, Jane's All the World's Aircraft, Jane's Yearbooks, various years.

[7] F. Thomas, *Fundamentals of Sailplane Design*, College Park Press, 1999.

[8] H.-U. Meier, *German Development of the Swept Wing 1935–1945*, AIAA, 2006.

[9] R.T. Jones, A. Busemann, *1901-1986, Memorial Tributes*, vol. 3, National Academy of Engineering, 1989.

[10] A. Busemann, *Aerodynamischer Auftrieb bei Überschallgeschwindigkeit*, Luftfahrtforschung 12 (6) (1935) 210–220 (Title means: Aerodynamic Forces at Supersonic Airspeeds).

[11] R.T. Jones, *Wing Plan Forms for High-Speed Flight*, NACA TR-863, 1945.

[12] L.K. Loftin Jr., *Quest for Performance; The Evolution of Modern Aircraft*, NASA SP-468, 1985, p. 93.

[13] R. Whitford, *Design for Air Combat*, Jane's Publishing Company Limited, 1987.

[14] P.E. Purser, J.P. Campell, *Experimental Verification of a Simplified Vee-Tail Theory and Analysis for Available Data on Complete Model With Vee Tails*, NACA R-823, 1944.

[15] Nall Report. https://www.aopa.org/training-and-safety/air-safety-institute/accident-analysis/joseph-t-nall-report. (Accessed 28 March 2020).

[16] E.R. White, *Wind-Tunnel Investigation of Effects of Wing-Leading-Edge Modifications on the High Angle-of-Attack Characteristics of a T-tail Low-Wing General-Aviation Aircraft*, NASA CR-3636, 1982.

[17] I.R. Lacey, K. Miller, *The AV-8B Wing: Aerodynamic Concept and Design*, AIAA-1977-607-721, AIAA, 1977.

[18] D. Weihs, J. Katz, *Cellular patterns in poststall flow over unswept wings*, AIAA J. 21 (12) (1983) 1757–1759, https://doi.org/10.2514/3.8321.

[19] H. Dell'Orso, M. Amitay, *Parametric investigation of stall cell formation on a NACA 0015 airfoil*, AIAA J. 56 (8) (2018) 3216–3228,- https://doi.org/10.2514/1.J056850.

[20] D. Ragni, C.S. Ferreira, *3D stall-cell effects on the pressure field of a NACA64-418*, in: 53rd AIAA Aerospace Sciences Meeting, 5-9 January, 2015, https://doi.org/10.2514/6.2015-1033.

[21] B. Kuhlman, Bunny, *On the Wing…*, R/C Soaring Digest, May 1999.

[22] Helmut Schenk, Laengsmomentum-Rechnung Beim Nurflugel-Modell, Pforzheim, Germany. Self-published. Publishing year unknown.

[23] B. Kuhlman, Bunny, *On the Wing…*, R/C Soaring Digest, October 2003.

[24] E. Woo, *Skunk Works' Irven Culver Dies*, LA Times, September 17, 1999. https://www.latimes.com/archives/la-xpm-1999-sep-17-mn-11249-story.html. (Accessed 19 April 2020).

[25] S. Hall, Irv Culver—An Engineer's Engineer, Online article, Soaring Society of America, 09/01/1999. https://www.ssa.org/FinalGlide?show=blog&id=695 (Accessed 19 April 2020).

[26] Website for SURFACES is www.flightlevelengineering.com.

[27] J.A.D. Ackroyd, *The spitfire wing planform: a suggestion*, J. Aeronaut. Hist. (2013) 121–135. Paper No. 2013/02, Royal Aeronautical Society.

[28] G. Davies, *From Lysander to Lightning: Teddy Petter, Aircraft Designer*, The History Press, September 1, 2014.

[29] W.J. Boyne, *Messerschmitt Me 262: Arrow to the Future*, Schiffer Publishing, Ltd., 1992.

[30] R. Langton, et al., *Aircraft Fuel Systems*, John Wiley and Sons, Ltd., 2009.
[31] F.A. Johnsen, *Sweeping Forward: Developing and Flight Testing the Grumman X-29A Forward Swept Wing Research Aircraft*, NASA Aeronautics Book Series, NASA, 2013.
[32] R.R. Brooks, *The Handley Page Victor: The History and Development of a Classic Jet*, Pen and Sword Aviation, 21 Sept. 2006.
[33] W. Schuemann, *A new wing planform and improved low-speed performance*, Soaring 47 (2) (1983) 16–26.
[34] M.D. Maughmer, *The Evolution of Sailplane Wing Design*, 2003. AIAA 2003-2777.
[35] C.P. van Dam, *Induced-drag characteristics of crescent-moon-shaped wings*, J. Aircr. 24 (2) (1987) 115–119.
[36] S.B. Sargent, *A Dyke Delta Reborn*, EAA Sport Aviation Magazine (December, 2008).
[37] D.H. Peckham, *Low-Speed Wind-Tunnel Tests on a Series of Uncambered Slender Pointed Wings With Sharp Edges*, Aeronautical Research Council, 1959. R.&M. No. 3186.
[38] G.B. McCullough, D.E. Gault, *Examples of Three Representative Types of Airfoil-Section Stall at Low Speed*, NACA-TN-2502, 1951, p. 1.
[39] R.T. Jones, *Correction of the Lifting Line Theory for the Effect of the Chord*, NACA TN-817, 1941.
[40] R.S. Swanson, S.M. Crandall, *Lifting-Surface-Theory Aspect-Ratio Corrections to the Lift and Hinge-Moment Parameters for Full-Span Elevators on Horizontal Tail Surfaces*, NACA TN-1175, 1947.
[41] D.O. Dommasch, S.S. Sherby, T.F. Connolly, *Airplane Aerodynamics*, fourth ed., Pittman Publishing Corporation, 1967, pp. 154–160.
[42] H. Glauert, *The Elements of Aerofoil and Airscrew Theory*, Cambridge University Press, 1926.
[43] H.B. Helmbold, *Der unverwundene Ellipsenflügel als tragende Flache*, in: Jahrbuch 1942 der Deutschen Luftfahrtforschung, R. Oldenbourg, Munich, 1942, pp. I 111–I 113.
[44] J.G. Lowry, E.C. Polhamus, *A Method for Predicting Lift Increments Due to Flap Deflection at Low Angles of Attack in Incompressible Flow*, NACA TR-3911, 1957.
[45] L.R. Jenkinson, P. Simpkin, D. Rhodes, *Civil Jet Aircraft Design*, AIAA Education Series, 1999.
[46] I.H. Abbott, A.E. von Doenhoff, L.S. Stivers Jr., *Summary of Airfoil Data*, NACA R-824, 1945.
[47] E.C. Polhamus, *A Concept of the Vortex Lift of Sharp-Edge Delta Wings Based on a Leading-Edge-Suction Analogy*, NASA TN-D-3767, NASA, December 1966.
[48] C. Wieselberger, *Wing Resistance Near the Ground*, NACA TM-77, 1922.
[49] A. Betz, *Lift and Drag of a Wing Near a Horizontal Surface*, Zeitschrift für Flugtechnik und Motorluftschiffahrt, 1912, p. 212.
[50] C. Wieselberger, *Wing Resistance Near the Ground*, Zeitschrift für Flugtechnik und Motorluftschiffahrt, 1921. No. 10.
[51] S. Katzoff, H.H. Sweberg, *Ground Effect on Downwash Angles and Wake Location*, NACA TR-738, 1941.
[52] J.T. Wetmore, L.I. Turner Jr., *Determination of Ground Effect from Tests of a Glider in Towed Flight*, NACA TR-695, 1940.
[53] A.W. Carter, *Effect of Ground Proximity on the Aerodynamic Characteristics of Aspect-Ratio-1 Airfoils With and Without End Plates*, NASA TN-D-970, 1961.
[54] W.F. Phillips, D.F. Hunsaker, *Lifting-line predictions for induced drag and lift in ground effect*, AIAA J. Aircr. 50 (4) (2013), https://doi.org/10.2514/1.C032152.
[55] B.W. McCormick, *Aerodynamics, Aeronautics, and Flight Mechanics*, John Wiley & Sons, 1979, p. 420.
[56] M. Asselin, *An Introduction to Aircraft Performance*, AIAA Education Series, American Institute of Aeronautics and Astronautics, 1997.
[57] S.F. Hoerner, H.V. Borst, *Fluid-Dynamic Lift*, second ed., Mrs. Liselotte Hoerner, 1985.
[58] W.B. Oswald, *General Formulas and Charts for the Calculation of Airplane Performance*, NACA TR-408, 1933.
[59] M. Nita, D. Scholz, *Estimating the Oswald factor from basic aircraft geometrical parameters*, in: Deutcher Luft- und Raumfahrtkongress 2012, 2012. Doc ID 281424.
[60] R.S. Shevell, *Fundamentals of Flight*, Prentice Hall, 1983, pp. 181–183.
[61] D. Howe, *Aircraft Conceptual Design Synthesis*, Professional Engineering Publishing Limited, 2000.
[62] R.C. Frost, R. Rutherford, *Subsonic wing span efficiency*, AIAA J. 1 (4) (1963) 931–933.
[63] G.C. Furlong, J.E. Fitzpatrick, *Effects of Mach Number and Reynolds Number on the Maximum Lift Coefficient of a Wing of NACA 230-Series Airfoil Sections*, NACA TN-1299, 1947.
[64] J.E. Fitzpatrick, W.C. Schneider, *Effects of Mach Number Variation Between 0.07 and 0.34 and Reynolds Number Variation Between 0.97x106 and 8.10x106 on the Maximum Lift Coefficient of a Wing of NACA 64-210 Airfoil Sections*, NACA TN-2753, 1952.
[65] T.V. Bollech, *Experimental and Calculated Characteristics of Several High-Aspect-Ratio Tapered Wings Incorporating NACA 44-Series, 230-Series, and Low-Drag 64-Series Airfoil Sections*, NACA TN-1677, 1948.
[66] E. Torenbeek, *Synthesis of Subsonic Aircraft Design*, Delft University Press, 1986.
[67] G.C. Furlong, J.G. McHugh, *A Summary and Analysis of the Low-Speed Longitudinal Characteristics of Swept Wings at High Reynolds Numbers*, NACA TR 1339, 1957.
[68] J.A. Shortal, B. Maggin, *Effect of Sweepback and Aspect Ratio on Longitudinal Stability Characteristics of Wings at Low Speeds*, NACA TN 1093, 1946.
[69] W. Koven, R.R. Graham, *Wind-Tunnel Investigation of High-Lift and Stall-Control Devices on a 37 Degree Sweptback Wing of Aspect Ratio 6 at High Reynolds Numbers*, NACA RM-L8D29, 1948.
[70] J. Katz, A. Plotkin, *Low-Speed Aerodynamics*, Cambridge University Press, 2001.
[71] A. Pope, *Basic Wing and Airfoil Theory*, Dover Publications, 2009.
[72] J.J. Bertin, M.L. Smith, *Aerodynamics for Engineers*, Prentice-Hall, 1979, p. 171.
[73] J. Moran, *An Introduction to Theoretical and Computational Aerodynamics*, John Wiley and Sons, 1984.
[74] J.D. Anderson Jr., *Fundamentals of Aerodynamics*, fourth ed., McGraw-Hill, 2007.
[75] K. Karamcheti, *Principles of Ideal-Fluid Aerodynamics*, John Wiley & Sons, 1966, p. 624. Appendix E.

This page intentionally left blank

CHAPTER

10

The Anatomy of Lift Enhancement

OUTLINE

10.1 **Introduction** 415
10.1.1 The Content of This Chapter 416
10.1.2 How Do I Select a High-Lift System 416

10.2 **Leading-Edge High-Lift Devices** 416
10.2.1 Leading-Edge Device Quick-Guide 417
10.2.2 Hinged Leading Edge (Droop Nose) 420
10.2.3 Variable Camber Leading Edge 422
10.2.4 Fixed Slot 422
10.2.5 The Krüger Flap 424
10.2.6 The Leading-Edge Slat 427
10.2.7 Summary of Leading-Edge Device Data 432

10.3 **Trailing-Edge High-Lift Devices** 432
10.3.1 Trailing-Edge Device Quick-Guide 433
10.3.2 Plain Flap 433
10.3.3 Split Flap 442
10.3.4 Junkers Flap or External Flap 444
10.3.5 Single-Slotted Flap 445
10.3.6 Double-Slotted Flaps 446
10.3.7 Fowler Flaps 449
10.3.8 Gurney Flap 452
10.3.9 Summary of Trailing-Edge Device Data 454

10.4 **Effect of Deploying High-Lift Devices on Wings** 456
10.4.1 Lift Distribution on Wings With Flaps Deflected 456
10.4.2 Wing Partition Method 458

10.5 **Wingtip Design** 461
10.5.1 The Round Wingtip 462
10.5.2 The Spherical Wingtip 463
10.5.3 The Square Wingtip 464
10.5.4 Booster Wingtips 465
10.5.5 Hoerner Wingtip 466
10.5.6 Küchemann Wingtip 466
10.5.7 Raked Wingtip 467
10.5.8 Endplate Wingtip 469
10.5.9 The Winglet 470
10.5.10 The Polyhedral Wing(tip) 474
10.5.11 Comparison Based on Potential Flow Theory 476

References 477

10.1 INTRODUCTION

The airspeed range requires conflicted design objectives at its extremes. High airspeed calls for small wing area, while low speed demands a large one. The drag equation, $D = \frac{1}{2}\rho V^2 \cdot S \cdot C_D$, shows how the wing area affects drag—halve the area, halve the drag. In contrast, the lift equation, $L = \frac{1}{2}\rho V^2 \cdot S \cdot C_L$, favors a large wing area at low airspeed. A common solution to the problem is to keep S as low as practical, and then improve low-speed lift by increasing $C_{L_{max}}$. This is accomplished by installing special mechanical devices in the wing; *high-lift devices*.

The purpose of lift enhancement is to (1) permit operation at lower airspeeds, which translates into shorter runway requirements, (2) improve L/D in the T-O configuration to improve departure climb and help complying with noise requirements, (3) increase drag in the landing configuration to steepen the approach, (4) increase drag during landing to reduce floating in ground effect, and (5) reduce deck angle near maximum lift so the airplane is easier to land.

A great example of the sophistication of high-lift devices is shown in the venerable Boeing B-727 tri-jet (see Figure 10-1). Developed in the 1960s, it allowed operation from shorter runways than the jetliners of the day, all which required long runways. This was achieved using an impressive assortment of leading- and trailing-edge high-lift devices, giving it a very high $C_{L_{max}}$.

Copyright © 2022 Elsevier Inc. All rights reserved.



FIGURE 10-1 A Boeing B-727 airliner taxiing into T-O position. Visible are parts of its sophisticated wing high-lift system; the *folding, bullnose Krüger flap* on the inboard part of the wing, and the *three-position slats* on the outboard part of the wing. *Photo by Phil Rademacher.*

High-lift devices usually serve a dual purpose: (1) Change the camber of the wing's airfoils and (2) delay flow separation. There are two kinds of high-lift devices: *passive* and *active*. Passive high-lift devices do not require external energy to provide lift enhancement. Active ones do. Examples of active lift enhancement include the jet-blown flap and vectored thrust. They add substantial cost to the aircraft in terms of hardware and operation and are only used in specialized military aircraft. Therefore, only the passive kind is presented here. This chapter discusses how to enhance the lift generation of a wing using an assortment of leading-edge and trailing-edge high-lift devices. A method to estimate $C_{L_{max}}$ using high-lift devices is presented, followed by multiple wingtip designs.

10.1.1 The Content of This Chapter

- Section 10.2 presents helpful design information for the selection of leading-edge high-lift systems.
- Section 10.3 presents helpful design information for the selection of trailing-edge high-lift systems.
- Section 10.4 presents methods to estimate the impact of adding partial span high-lift devices.
- Section 10.5 introduces several different wingtip options and discusses their pros and cons.

10.1.2 How Do I Select a High-Lift System

Selecting a high-lift system is very consequential for any design. It adds system and structural complexity, increases drag, and affects handling. The decision is frequently a challenge for newcomers to aircraft design. Consider an important rule of thumb that has been thrown around elsewhere in this text: Select the simplest solution that does the job. The safest way to select a suitable high-lift system is by creating a decision matrix similar to those of Tables 4-3 and 8-13. Table 10-1 exemplifies such a matrix for selecting a high-lift system. The scores should be prorated as done for Table 8-13. Add any suitable constraints.

10.2 LEADING-EDGE HIGH-LIFT DEVICES

In general, leading-edge (LE) high-lift device increase the stall angle (α_{stall}) and maximum lift coefficient ($C_{L_{max}}$) of the airfoil without shifting the lift curve as common with trailing-edge devices. Therefore, an in-flight deployment of a leading-edge device has minor effect on trim compared to flaps (see Sections 8.3.4, *The Effect of a Trailing-Edge Flap* and 8.3.5, *The Effect of Addition of a Slot or Slats*). A summary of the aerodynamic properties of numerous leading-edge devices is given in Table 10-2. These data are helpful during the conceptual and preliminary design phases. Table 10-3 offers a more detailed listing of their properties.

It is important to keep in mind that LE devices increase the stall AOA so much that they, alone, are surprisingly impractical. For instance, a fixed slot increases α_{stall} by some 9°. An airplane normally stalling at $\alpha_{stall} = 15°$ would stall around 24° with a fixed slot. Thus, realizing the benefit of the higher $C_{L_{max}}$ requires a much larger deck angle. While this may not be a problem for a bush plane with Tundra tires, it is for other aircraft. The remedy is to mix them with trailing-edge (TE) flaps, which reduce α_{stall}. Thus, the 9° of stall AOA added by the leading-edge device is reduced to, say, an overall increase of 2°.

As stated earlier, an airfoil's maximum lift capability can be improved by two means: by increasing

TABLE 10-1 Example decision matrix for downselection of a suitable high-lift system (HLS).

					Score		
Feature	**Clean aircraft**	**HLS 1**	**HLS 2**	**HLS 3**	**HLS 1**	**HLS 2**	**HLS 3**
Leading-edge device	None	None	Fixed slot	Fixed slot			
Trailing-edge device	None	Single-slotted	Plain-flap	Single-slotted			
Airfoil Lift Coefficient							
Clean airfoil $C_{l\max}$	1.50	1.50	1.50	1.50			
$\Delta C_{l\max}$ due to LE	0	0	0.48	0.48			
$\Delta C_{l\max}$ due to TE	0	1.32	0.70	1.32			
Airfoil total $C_{l\max}$	1.50	2.82	2.68	3.30			
Total 3-D $C_{L\max}$	1.35	2.02	1.93	2.38			
Required $C_{L\max}$ with flap	2.00				2	0	3
Stall Angle-of-Attack							
$\Delta\alpha_{stall}$ due to LE	0°	0°	9°	9°			
$\Delta\alpha_{stall}$ due to TE	0°	–3°	–2°	–3°			
α_{stall}	15°	12°	22°	21°	3	1	2
Cruise Drag							
Additive cruise drag	0	+0.0005	+0.0080	+0.0013	3	2	1
System Complexity							
Weight ratio of W_0	1.00	1.03	1.05	1.05	3	2	2
Wing strux complexity	None	Nominal	Increased	Significant	3	2	1
Control system complexity	None	Nominal	Increased	Increased	3	2	1
Development cost	None	Nominal	Significant	Significant	3	1	1
Maintenance cost	None	Nominal	Significant	Significant	3	1	1
Add other constraints…	…	…	…	…	…	…	…
Total Score	–	–	–	–	**23**	**11**	**12**

curvature and delaying flow separation. This section presents multiple devices, some of which only increase curvature while others do both. Some devices are simple enough to be ideal for slow flying aircraft, e.g., bush planes. Others are far more complex and require sophisticated mechanism to deliver them into a proper position and shape. These are intended for commercial jetliners and business jets. Movable mechanical leading-edge devices are subjected to many challenges. They are fundamental to the operational safety of the airplane, so they must be reliable—while reacting substantial loads. Jamming is not an option.

The effectiveness of a leading-edge device is best described by the resulting change in $C_{l_{\max}}$ and α_{stall}. This is a direct measure of its ability to delay flow separation. This is an important capability, because while an airfoil's curvature can be increased geometrically, this alone does not guarantee the flow will follow that shape. The effectiveness depends on the *correct* geometry. Impact on drag and pitching moment is also of importance.

10.2.1 Leading-Edge Device Quick-Guide

See Table 10-2. Further detail can be seen in Table 10-3. Add the Δ-values to that of the airfoil. For instance, if the $C_{l_{\max}}$ and α_{stall} of the basic airfoil are 1.5 and 15°, respectively, then expect the *fixed slot* to change these to 1.95 and 24°.

TABLE 10-2 Quick-guide for selecting a leading-edge device.

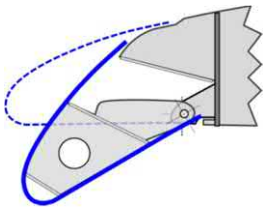
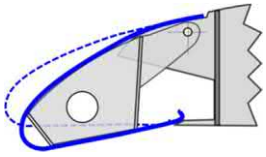
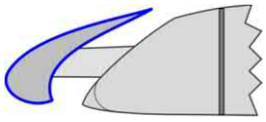
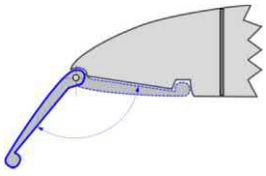
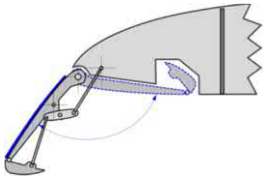
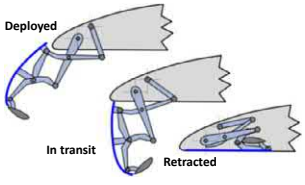
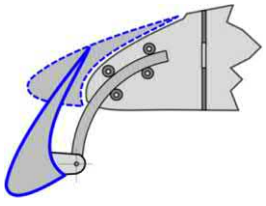
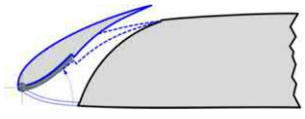
Name	Schematic	$\Delta C_{l_{max}}$	$\Delta\alpha_{stall}$ (degrees)	ΔC_{l_0}	$\Delta C_{d_{min}}$
Hinged LE (droop nose)		0.58	7.8	−0.15	–
Variable Camber LE		≈0.58	≈7.8	–	–
Fixed Slot		0.45	9.0	−0.08	0.0079
Simple Krüger Flap		0.30	5.0	−0.09	0.0149
Bullnose Krüger Flap		≈0.30	≈5.0	–	–
Variable Camber Krüger Flap		≈0.68	≈6.8	–	–
Leading-Edge Slat		0.84	11.0	−0.21	–
Maxwell Flap Type 1		0.55	9.0	−0.13	0.0156
Maxwell Flap Type 2		0.81	11.8	−0.17	0.0276

TABLE 10-3 Summary of the aerodynamic properties of leading-edge devices.

Description	Section	Basic Airfoil	$R_e \times 10^6$	Flap Type	c_S/c	$(c_f/c)_1$	$(c_f/c)_2$	δ_S	$(\delta_f)_1$	$(\delta_f)_2$	$C_{l\max}$	α_{stall}	C_{l_0}	$C_{d\min}$	C_{m_0}	$\Delta C_{l\max}$	$\Delta\alpha_{stall}$	ΔC_{l_0}	$\Delta C_{d\min}$	ΔC_m	Reference
HINGED LEADING EDGE																					
Airfoil only	10.2.2	NACA 64A010	6	-	0.15	-	-	0°	-	-	1.10	11.0	0.01	-	0.000	-	-	-	-	-	NACA TN-3007
Hinged LE			6	-	0.15	-	-	30°	-	-	1.66	18.8	-0.14	-	-0.048	0.56	7.8	-0.15	-	-0.0478	
Hinged LE + TE Flap			6	Split	0.15	0.0557	0.1723	30°	60°	-	2.58	15.8	1.27	-	-0.215	1.48	4.8	1.26	-	-0.2148	
Hinged LE + TE Flap			6	Dbl-Slotted	0.15	0.25	-	30°	30°	55°	3.09	10.5	2.23	-	-0.565	1.99	-0.5	2.22	-	-0.5649	
VARIABLE CAMBER LEADING EDGE																					
Variable Camber LE	10.2.3	-	-	-	-	-	-	-	-	-	-	-	-	-	-	-	-	-	-	-	-
FIXED SLOT																					
Airfoil only	10.2.4	Clark Y	0.63	-	0.1475	-	-	-	-	-	1.297	15.0	0.36	0.0150	-	-	-	-	-	-	NACA TR-407
Fixed Slot			0.63	-	0.1475	-	-	-	-	-	1.751	24.0	0.28	0.0229	-	0.45	9.0	-0.08	0.0079	-	
SIMPLE KRÜGER																					
Airfoil only	10.2.5	Mustang 2	2.14	-	0.1	-	-	0°	-	-	1.13	12.3	0.09	0.0082	-0.017	-	-	-	-	-	NACA TM-1177
Simple Krüger Flap			2.14	-	0.1	-	-	120°	-	-	1.43	17.3	0.00	0.0230	-0.044	0.30	5.0	-0.09	0.0149	-0.027	
Simple Krüger Flap + TE Flap			2.14	Split	0.1	0.2	-	120°	60°	-	2.25	13.0	1.15	0.1656	-0.194	1.12	0.7	1.06	0.1575	-0.177	
FOLDING BULL-NOSE KRÜGER																					
Folding, Bull-nose Krüger Flap	10.2.5	-	-	-	-	-	-	-	-	-	-	-	-	-	-	0.30	5.0	-	-	-	Estimated
VARIABLE CAMBER KRÜGER																					
Airfoil only	10.2.5	Supercritical	5.12	-	-	-	-	-	-	-	1.49	14.3	-	-	-	-	-	-	-	-	NASA CR-159389
Variable Camber Krüger Flap	10.2.5			-	-	-	-	-	-	-	2.17	21.1	-	-	-	0.68	6.80	-	-	-	
SLATS																					
Airfoil only	10.2.6	NACA 64A010	6	-	0.17	-	-	0°	-	-	1.10	11.0	0.01	-	0.000	-	-	-	-	-	NACA TN-3007
Slat (optimum deflection)			6	-	0.17	-	-	25.6°	-	-	1.94	22.0	-0.20	-	-0.115	0.84	11.0	-0.21	-	-0.1149	
Slat (opt. deflection) + TE Flap			6	Split	0.17	0.0557	0.1723	25.6°	60°	-	2.72	17.3	1.25	-	-0.283	1.62	6.3	1.24	-	-0.2825	
Slat (opt. deflection) + TE Flap			6	Dbl-Slotted	0.17	0.25	-	25.6°	30°	55°	3.00	9.0	2.26	-	-0.551	1.90	-2.0	2.25	-	-0.5506	
MAXWELL FLAP																					
Airfoil only	10.2.6	Clark Y	0.61	-	0.175	-	-	-	-	-	1.26	14.0	0.38	0.0201	-0.0767	-	-	-	-	-	NACA TN-598
Maxwell Flap 1 ($c_f = 0.175c$)			0.61	-	0.175	-	-	Open	-	-	1.81	23.0	0.25	0.0357	-0.0759	0.55	9.0	-0.13	0.0156	0.0008	
Maxwell Flap 1 + TE Flap			0.61	Split	0.175	0.211	-	Open	60°	-	2.31	16.7	1.31	0.2835	-0.1771	1.05	2.7	0.93	0.2634	-0.1004	
Maxwell Flap 2 ($c_f = 0.30c$)			0.61	-	0.3	-	-	Open	-	-	2.07	25.8	0.21	0.0477	-0.1131	0.81	11.8	-0.17	0.0276	-0.0365	
Maxwell Flap 2 + TE Flap			0.61	Split	0.3	0.211	-	Open	60°	-	2.53	21.6	1.27	0.2834	-0.2191	1.27	7.6	0.89	0.2633	-0.1424	
Handley Page slat			0.61	-	0.147	0.211	-	Open	-	-	1.83	25.0	1.27	0.2834	-	0.57	11.0	0.89	0.2633	-	

Abbreviations: LE, Leading Edge; TE, Trailing Edge; $R_{e\ test}$, Reynolds Number during test; c_S, Chord of LE device; c, Airfoil chord; Dbl, Double; δ_S, Deflection angle of LE device; $(\delta_f)_1$, Deflection of element 1 of a TE device; $(\delta_f)_2$, Deflection of element 2 of a TE device; $C_{l_{max}}$, Max section lift coefficient; α_{stall}, Stall AOA; C_{l_0}, Lift coefficient at $\alpha = 0°$; $C_{d_{min}}$, Minimum section drag coefficient; C_{m_0}, Pitching moment coefficient at $\alpha = 0°$. Specific references: [1–5].

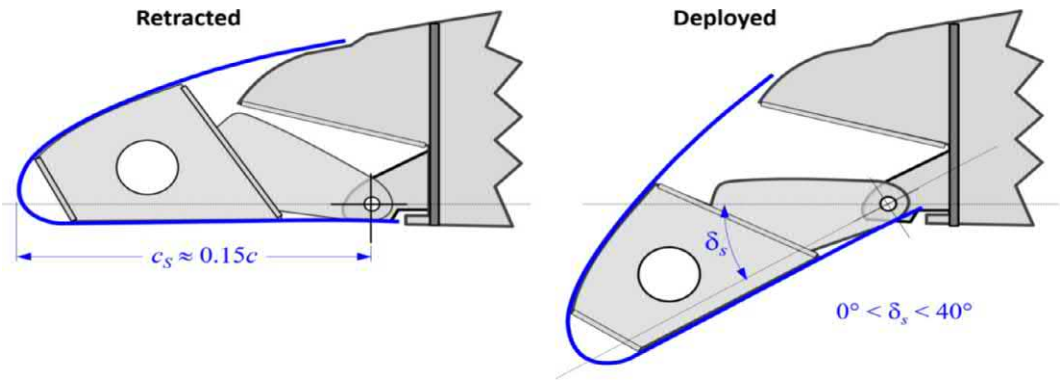


FIGURE 10-2 A schematic of the *hinged leading edge* (aka *droop nose*).

10.2.2 Hinged Leading Edge (Droop Nose)

The *hinged leading edge* (aka *droop nose* and *leading-edge flap*) increases the leading-edge camber and, thus, $C_{L_{max}}$ and α_{stall} (see Figure 10-2). This reduces stalling speed and roll instability at stall. It generates low drag when retracted, as it prevents air "leaking" from the lower to the upper surface. However, the resulting $C_{L_{max}}$ is limited by the small radius of curvature of its deflection. This is caused by an absence of a slot and discontinuous curvature that promotes flow separation. Typical deflection range is 15–40°. Its main strength is low cost, ease of manufacturing, and light weight. It is often the only option for thin, high-speed wings. Among aircraft that use the device is the Lockheed F-104 Starfighter. The increase in $C_{L_{max}}$ is too small for use in passenger aircraft.

Figure 10-3 shows flow visualization made of the hinged LE (and plain flap) and reveals issues detrimental to its effectiveness. Awareness of such issues helps justifying alternatives. In the pictures, the leading- and trailing-edge flaps, denoted by δ_s and δ_f, respectively, are deflected 33°. The pictures show the airfoil at an AOA of 4°, 13°, and 25°. The top picture reveals the stagnation point is located just above the nose radius of the leading edge. This requires air to flow downward around the nose. The boundary layer lacks the energy to fully flow around the nose radius and, instead, creates a separation bubble on the lower surface. This diminishes the circulation around the airfoil, causing additional drag and caps the lift of the device. Of course, reducing the angle of deflection at that AOA will help. Also note the flow separation behind the flap. While the flow is low Reynolds number (R_e), a flap deflection of 33° at large R_e also suffer such massive separation (e.g., see Section 10.3.3, *Plain Flap*).

The center picture in Figure 10-3 shows the airfoil at $\alpha = 13°$. The stagnation point is closer to the tip of the nose, eliminating the separation bubble seen in the top picture. However, another one has begun to form on the upper surface, right behind the discontinuity in the upper bend. The bottom picture shows the airfoil deep in the poststall region, at $\alpha = 25°$. The stagnation point is now below the nose tip and the separation bubble on the trailing edge of the drooped nose has increased substantially. It has become a part of the massive separation region behind the stalled airfoil.

(1) General Design Guidelines

Ref. [1] provides helpful guidelines for the initial design of a hinged leading edge. Using a symmetrical NACA 64A010 airfoil, the results of an investigation of combinations of a leading-edge slat and flap, and split flap and a double-slotted flap are presented. With respect to the leading-edge flap, the investigation showed that for $R_e \approx 2 \times 10^6$ a droop deflection $\delta_s = 40°$ resulted in the highest $C_{l_{max}}$. For higher R_e, $\delta_s = 30°$ was found to result in the highest $C_{l_{max}}$. The reference did not investigate drag.

(2) Aerodynamic Properties

Results for the hinged leading edge using a NACA 64A010 airfoil are given in Table 10-3 and are obtained from Ref. [1], for an $R_e = 6 \times 10^6$. Results for other airfoils and conditions are likely to be different. A maximum change in maximum section lift coefficient to be expected is $\Delta C_{l_{max}} \approx 0.56$. This increases the stall AOA by about $\Delta\alpha_{stall} \approx 7.8°$, and the change in pitching moment coefficient is $\Delta C_m \approx -0.048$.

As intuition tells, the maximum lift coefficient increases with the deflection of the hinged leading edge, up to a maximum around 30°. The variation of $C_{l_{max}}$ is plotted against the deflection in Figure 10-4. Higher deflections reduce this maximum and can be attributed to separation of effects caused by the sharp curvature around the hingeline.

(3) Summary:

$\Delta C_{l_{max}} \approx 0.56$	$\Delta C_{d_{min}}$ not specified
$\Delta\alpha_{max} \approx 7 - 8°$	$\Delta C_m \approx -0.048$

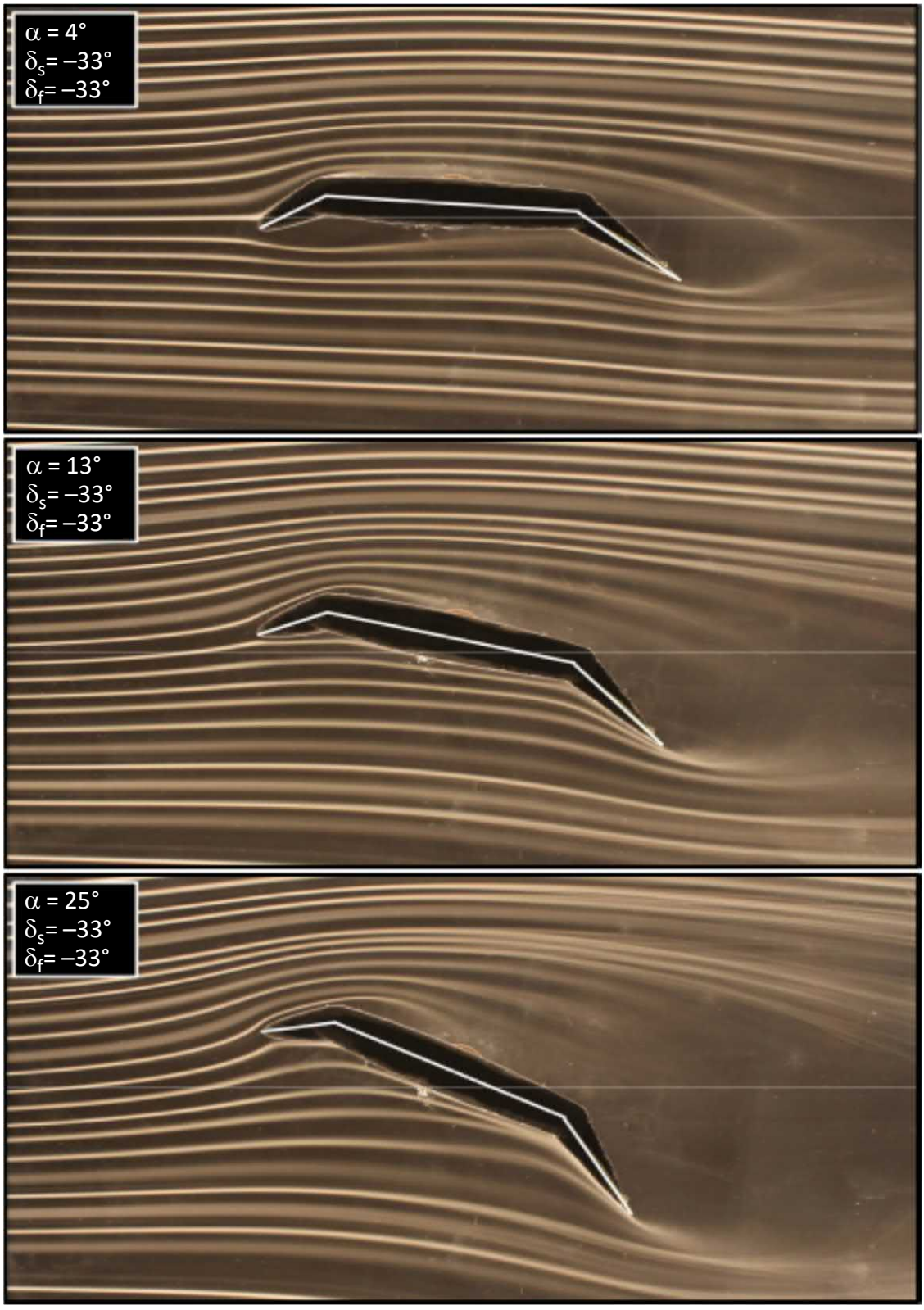


FIGURE 10-3 Flow visualization of the *hinged leading edge*. See discussion in text. *Photos by Phil Rademacher.*

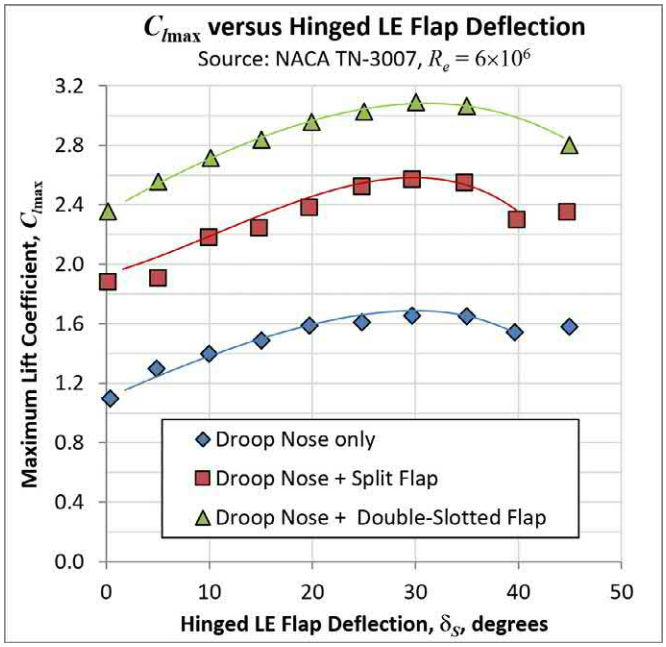


FIGURE 10-4 A schematic of the *hinged leading edge*.

10.2.3 Variable Camber Leading Edge

The *variable camber leading edge* (see Figure 10-5) increases the airfoil camber at the LE while minimizing impact on cruise drag. Like its droop-nose sibling, the device increases the low-pressure peak at higher AOAs and therefore $C_{L_{max}}$. However, it improves the continuity of the upper surface curvature, making it smoother than its hinged counterpart. This reduces the chance of separation bubble forming on the top surface. The continuous skin extending over the leading edge prevents leakage drag. When used with an active flight control system the device offers mission adaptability. This makes it ideal for aircraft that must maneuver at higher airspeeds, such as fighter aircraft.

It is a drawback that the device requires complicated mechanical linkage (not shown in schematic) to ensure a smooth skin curvature. This mechanism adds weight and complexity to the structure and increases design, development, and operational costs. The device requires flexible skin and movable linkages such it no longer contributes to the wing stiffness and flutter resistance. It gives a modest increase in $C_{L_{max}}$ due to the absence of slot flow. A typical deflection range is 15–30°. The F-111 AFTI (Advanced Fighter Technology Integration) Mission Adaptive Wing test program exemplifies an application of this concept [6]. Boeing also performed studies on a mission adaptive wing for a commercial jetliner [7]. The study assumed both the leading- and trailing-edge devices featured smooth variable camber mechanism and it was shown this allowed less sweep and improved aerodynamic efficiency below the design Mach number.

Aerodynamic Properties

Not available at this time. In the absence of better data, aerodynamic properties are expected to be similar to that of the droop nose leading-edge flap, which are presented in Table 10-3.

10.2.4 Fixed Slot

The *fixed slot* (see Figure 10-8) is a wing design philosophy and not a mechanical device, as it is immovable. Its invention is attributed to Gustav Lachmann and Sir Handley Page (see Section 10.2.6, *The Leading-Edge Slat*). It has been used with great success in many Short Take-Off and Landing (STOL) aircraft, which includes the Fieseler Fi-156 Storch (see Figure 10-6), Zenith STOL series CH701, CH750, CH801, and Heintz Zenith. The fixed slot is ideal for simple, slow flying aircraft designed to operate in and out of small patches of land most people would hardly dignify as an "airfield." A more sophisticated version of the fixed slot has been used in high speed aircraft too. The Douglas DC-8 commercial jetliner, widely used in the 1970s–1990s, features fixed slots near its engine pylons. These are closed during cruise, but are opened to improve low speed handling. Fixed slots are used on the horizontal stabilator of the Cessna 177 Cardinal to prevent inboard horizontal tail stall in sideslip with flaps deployed [8, 9].

The fixed slot is very simple in construction compared to other leading-edge devices. It is a very effective

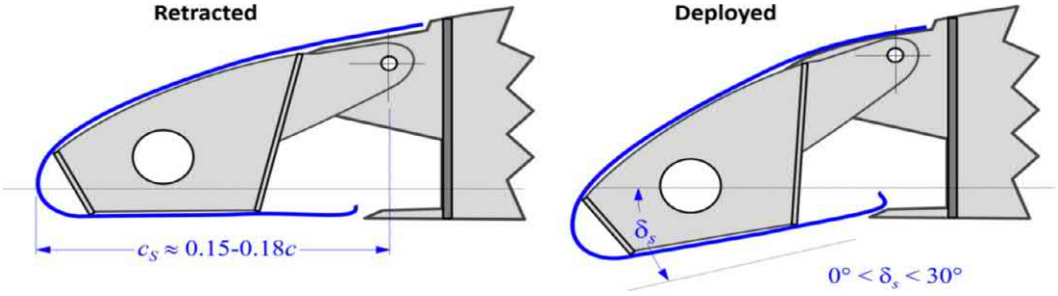


FIGURE 10-5 A schematic of the *variable camber leading edge*.



FIGURE 10-6 A German Fieseler Fi-156 Storch STOL aircraft boasting its *fixed slot*. *Photo by Phil Rademacher.*

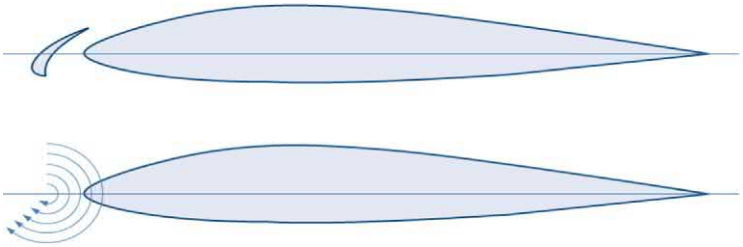


FIGURE 10-7 The workings of the slat explained using vortex flow. *Based on A.M.O. Smith, High-lift aerodynamics, J. Aircr. 12 (6) (1975).*

and inexpensive device that allows aircraft like the Fieseler Storch (Figure 10-6) to achieve a $C_{L_{max}}$ in excess of 4.2 (assuming $W_0 = 2920\,\text{lb}_\text{f}$, $S = 280\,\text{ft}^2$, and $V_S = 27\,\text{KCAS}$). While the fixed slot is ideal for STOL aircraft, it adds high drag, rendering it impractical for high speed aircraft.

The slot works through the so-called *slat-effect*. Conventional wisdom contends the slot provides an access for high-pressure air from the lower surface to flow to the upper surface. This accelerates the flow, somehow energizing it over the upper surface of the airfoil, yielding a higher $C_{l_{max}}$ and α_{stall}. On the other hand, in a famous paper, A.M.O. Smith [10], disputes this explanation and points out that the airflow through the slot is actually reduced. In fact, the slat works more like a small wing placed in front of the larger wing rather than a device that accelerates slot flow.

As shown by Liebeck [11], Smith's explanation can be realized by replacing the leading-edge element with a vortex (see Figure 10-7). The circulation caused by this vortex induces velocity on the larger airfoil that *reduces* the airspeed over its leading edge and through the slot and this drops the pressure peak on the leading edge of the airfoil, delaying stall. Thus, the airfoil generates higher $C_{l_{max}}$ than without it. This description is supported by wind tunnel tests and analyses performed using Computational Fluid Dynamics [10].

(1) General Design Guidelines

Ref. [2] provides helpful guidelines for the initial design of a fixed slot. It was spurred by the popularity of the Handley-Page slat, which increased drag by a factor of 3 when deployed. The reference investigated a series of fixed slot geometries to reduce the minimum drag coefficient without reducing $C_{l_{max}}$ and α_{stall} of a Clark Y airfoil. Of the configurations tested, the one in Figure 10-8 yielded the best results. It was found that reducing the drag coefficient of the auxiliary airfoil does not necessarily reduce the drag of the combination; it may even cause the opposite effect. Rounding the nose of the main airfoil was determined to be the most promising way to reduce the drag of the combination. It was also shown that moving the depth of the slot aft (to the right in Figure 10-8) did not have appreciable effect on the aerodynamic characteristics of the combination.

(2) Aerodynamic Properties

Results for the fixed slot using a Clark Y airfoil are given in Table 10-3 and are obtained from Ref. [2]. The test Reynolds Number was about 0.63×10^6. A maximum change in maximum section lift coefficient to be expected is $\Delta C_{l_{max}} \approx 0.45$, about 0.11 less than that of the hinged leading edge. This will increase the stall AOA by about

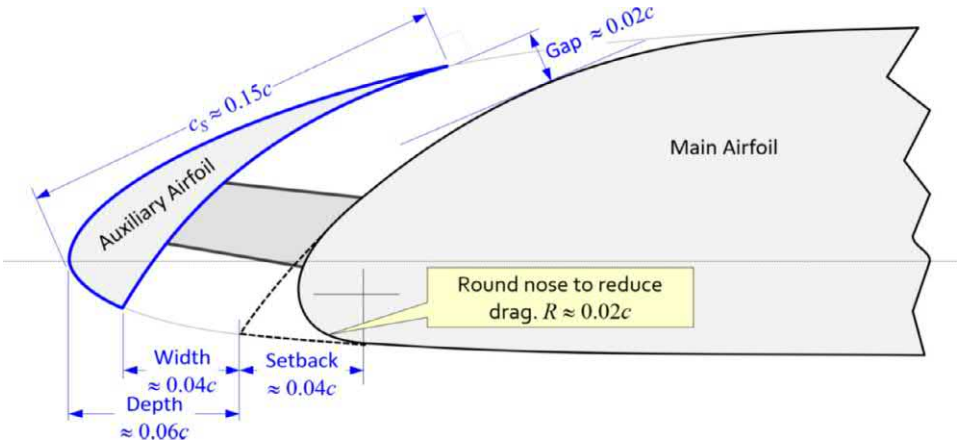


FIGURE 10-8 A schematic of a *fixed slot*. Airfoil (Clark Y) and dimensions show the optimum configuration determined by Ref. [2].

$\Delta\alpha_{stall} \approx 9°$, zero AOA lift coefficient will drop by about $\Delta C_{l_0} \approx -0.074$, and the minimum drag coefficient will increase by about $\Delta C_{d_{min}} \approx 0.0079$ (79 drag counts). Figure 10-9 shows typical changes in lift and drag for a low-speed airfoil with and without a fixed slot. Ultimately, the gain depends on the shape and the experimental setup does not represent an optimized geometry.

(3) Summary:

$\Delta C_{l_{max}} \approx 0.45$	$\Delta C_{d_{min}} \approx 0.0079$
$\Delta\alpha_{max} \approx 9°$	ΔC_m not specified

10.2.5 The Krüger Flap

The *Krüger Flap* was invented in 1943 by the German Werner Krüger (1910–2003), an aerodynamicist for Dornier, who worked with the noted aerodynamicist Hermann Schlichting (1907–82) [12, p. 200]. Krüger's career goal was to improve flight characteristics using boundary-layer control. He patented his invention in 1944 and it was first used in the Boeing 367-80, the prototype of the Boeing 707. The flap is a two position device (retracted-deployed) and, at first glance, a simple device mechanically (which at a closer scrutiny is not so). The deployed position is generally biased toward landing ($C_{L_{max}}$) and not take-off [13]. Optimizing it to other flight conditions requires a different deployment angle. This would require a more complex mechanism or improved geometry (e.g., bullnose Krüger). The Krüger flap is used for the inboard wing, where it delays flow separation to a lesser AOA than the outboard slats and, therefore, improves roll stability. Additionally, the top surface of the wing is free of misalignment and gaps that can accompany slats and, arguably, increases drag. Regardless, today, this role has been superseded by the use of slats, rendering the device obsolete.

(1) Simple Krüger Flap

The *simple Krüger flap* is the first version of this high-lift device. It increases the curvature of the airfoil. It delays flow separation tendency of the undercambered airfoil in the wing/fuselage juncture. The *outside mold line* (OML) of the device must be shaped like the lower surface of the airfoil's leading edge and this inflicts an aerodynamic limitation on its shape. The effectiveness of the simple Krüger flap with variations in AOA is considered poor and it is not used on any modern airplane. The flap rotates into a position that is approximately 110–140° with respect to the chord line (see Figure 10-10). Examples of aircraft that use the simple Krüger flap are the Boeing 707, Convair 880, and Convair 990, which featured it from root to tip.

(2) Folding, Bullnose Krüger Flap

The *folding, bullnose Krüger flap* improves the curvature of the airfoil camber over the simple Krüger flap. The round bullnose (see Figure 10-11) improves the ability of the flap to "capture" the stagnation point over a larger range of AOA. Like the simple Krüger flap, it is a two-position device whose deployed position is biased toward landing ($C_{L_{max}}$) and not take-off. It too has a limited increase in $C_{L_{max}}$. The rigid flap is highly dependent on the lower surface of the leading edge. The folding, bullnose Krüger flap sometimes requires a complex slaved mechanical linkage to fold the bullnose in the retracted position. The flap is used on the Boeing 727 (see Figures 10-1 and 10-11), 737, and 747 (see Figure 10-12) jetliners.

(3) Variable Camber Krüger Flap

The *variable camber Krüger flap* (VCK) develops far superior curvature than the simple and bullnose Krügers, greatly improving its aerodynamic properties. It is a two position device (retracted-deployed), with the deployed position is biased toward landing ($C_{L_{max}}$). Each flap panel must be flexible and is usually made from fiberglass and in short sections. Two hat sections are installed parallel to the leading edge for spanwise stiffening, while allowing chordwise flex only. Investigation of the device on a commercial jetliner is provided in Ref. [3].

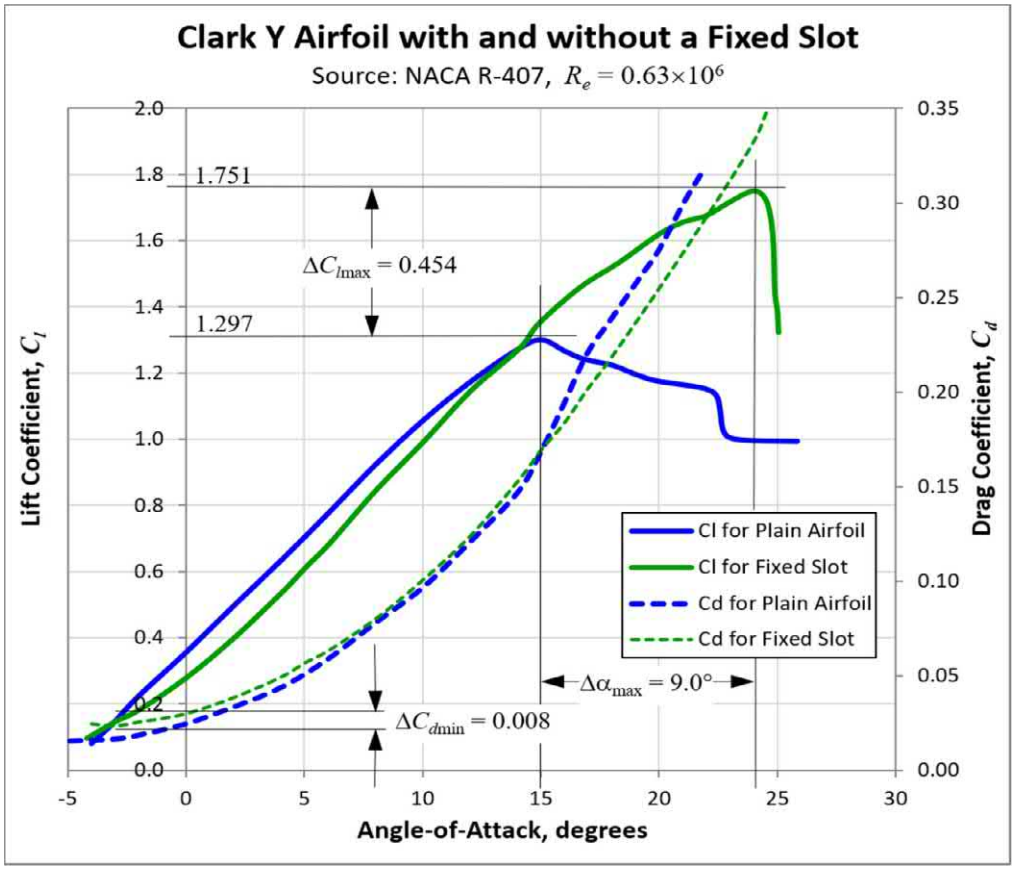


FIGURE 10-9 Effect of the *fixed slot* on the lift and drag characteristics of the Clark Y airfoil. *Reproduced from F.E. Weick, C.J. Wenzinger, The Characteristics of a Clark Y Wing Model Equipped With Several Forms of Low-Drag Fixed Slots, NACA TR-407, 1933.*

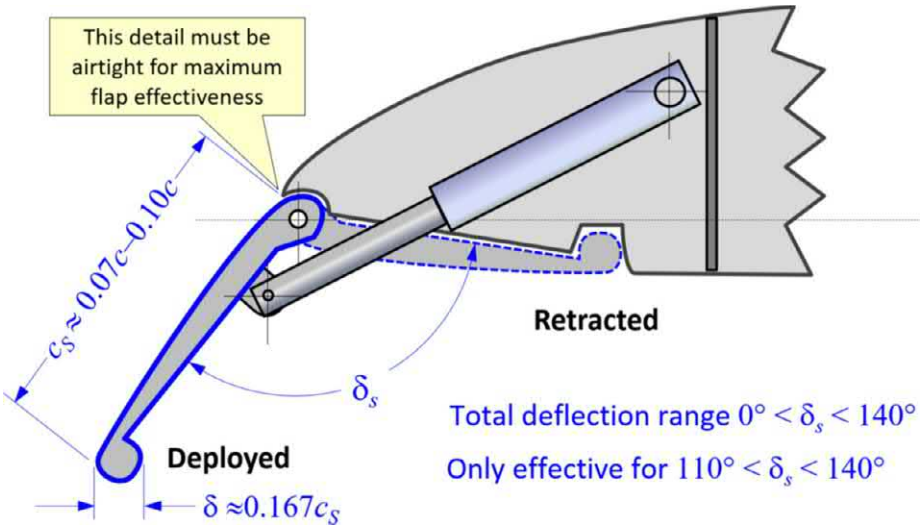


FIGURE 10-10 A schematic of the *simple Krüger flap*.

The flap deflects through approximately 120° from the stowed position. During transit, it transforms from a more or less a flat panel into a highly curved one. This feat requires a complex 4-bar linkage to guarantee the right shape and position (see schematic in Figure 10-12). It explains why the device only allows two positions. Figure 10-12 shows the combination of a bullnose and variable camber Krüger flaps on a Boeing 747-400 commercial jetliner.

The sophistication of the actuation mechanism of the flap system is impressive—it is a marvel of engineering. However, in order to make the system work reliably, it

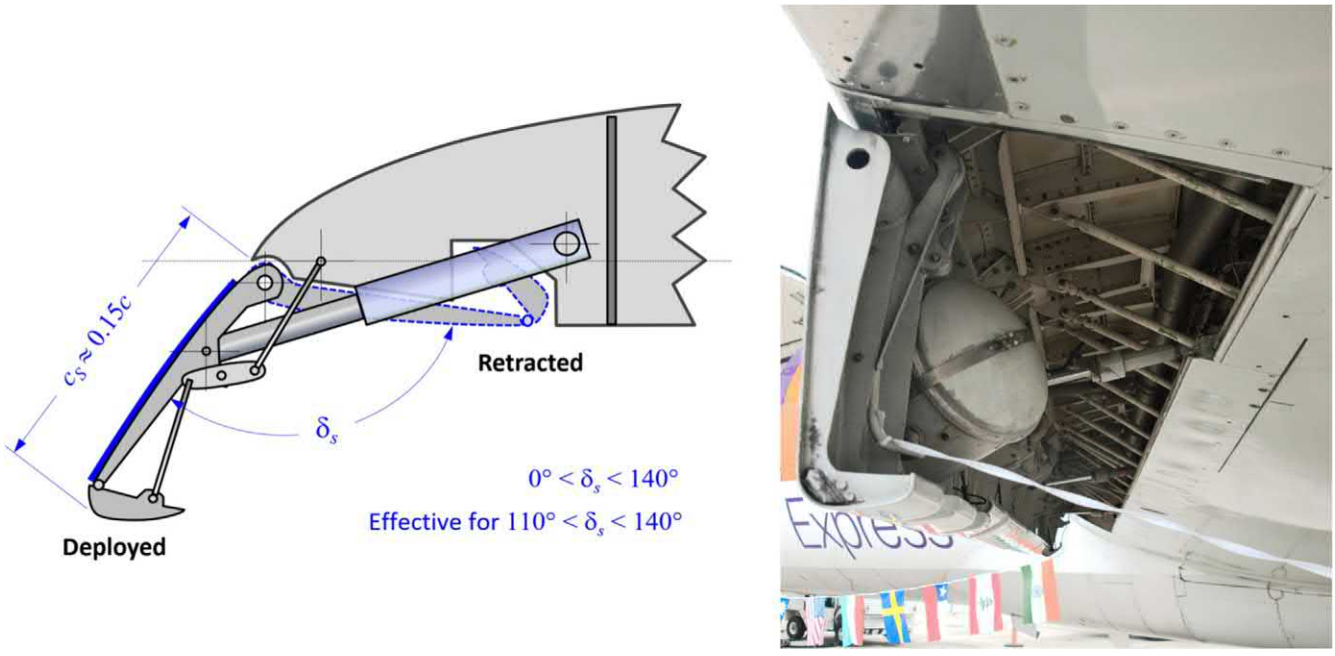


FIGURE 10-11 A schematic of the *folding, bullnose Krüger flap* (left). Implementation of the device in a Boeing 727 commercial jetliner (right). *(left) Based on P.K.C. Rudolph, High-Lift Systems on Commercial Subsonic Airliners, NASA CR-4746, 1996. (right) Photo insert by Nick Candrella.*



FIGURE 10-12 A schematic of the *variable camber Krüger flap* (left). Lower wing on a Boeing 747-400 reveals recesses into which the VCK retracts. The inboard wing features bullnose Krügers (right). *(left) Based on P.K.C. Rudolph, High-Lift Systems on Commercial Subsonic Airliners, NASA CR-4746, 1996. (right) Photo insert by Phil Rademacher.*

must be made to tight tolerances. Therefore, it is expensive to manufacture and maintain. The flap must be carefully rigged to prevent undesirable distortion of the panels under airloads and be preloaded to avoid panel bulging when retracted.

In spite of limitations, Krüger flaps can be considered a potential candidate for aircraft with laminar boundary layer wings. Since the flap is stowed on the lower surface, an opportunity exists to provide a smooth upper surface. To the author's best knowledge, the Boeing 747 is the only aircraft currently in production to use the variable camber Krüger flap. It was also featured on the proof-of-concept Boeing YC-14, a participant in the USAF Advanced Medium STOL Transport (AMST) project in the late 1970s.

(4) General Design Guidelines

The Krüger flap requires the stagnation point of the incoming airflow to be captured by its leading edge. This reduces the excessive airspeed over the leading edge of the airfoil and allows the airflow to accelerate over a

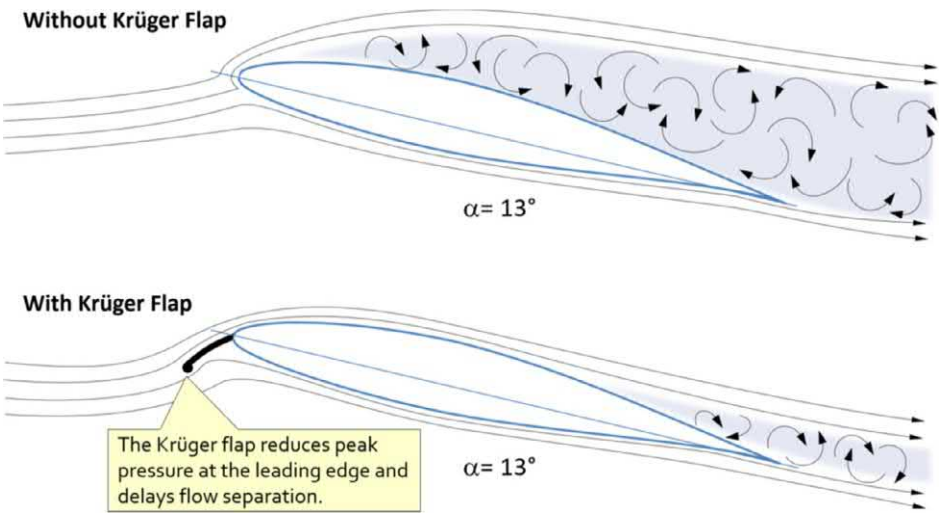


FIGURE 10-13 The *simple Krüger flap* in action. The upper figure shows an airfoil stalled at a given α. By repositioning the stagnation point, air can accelerate over greater distance, reducing the pressure peak. *Based on H.-U. Meier, German Development of the Swept Wing 1935-1945, AIAA, 2010.*

longer distance: Local airspeeds are reduced, as are the associated pressure peaks, delaying the formation of flow separation and pushes the stall to a higher α (see schematic in Figure 10-13). Consequently, the airfoil stalls at a higher AOA [12, pp. 170–171]. In short, the general design requires trial and error approach through extensive wind tunnel testing, although some basic design guidelines can be presented. Also note that Krügers are subjected to high loads when stowed at low AOA. During deployment (at low AOA), the actuation mechanism is subject to high loading. At high AOA the actuation force remains high, but is reversed. Thus, the installation requires powerful actuators [13].

Krüger investigated the device in Ref. [4], with and without the presence of a *split flap*. He found that the chord length of the flap, c_S, should be $0.07c$–$0.10c$, where c is the airfoil chord length. He tested two chord lengths; one that was $0.05c$ and the other $0.10c$, and found the shorter one actually reduced the maximum lift. From this he concluded that a minimum chord length should be $0.07c$, as shown in Figure 10-10. He suggests the leading edge of the flap should feature a rounded leading edge with a radius around $0.167c_S$, although increasing it to $0.334c_S$ showed no detriment. However, allowing air to flow through a gap between the flap and the leading edge of the wing reduced the increase in $\Delta C_{l_{max}}$, cited below, by about 50%–70%.

(5) Aerodynamic Properties

Results for a $0.01c$ Krüger flap using a Mustang 2 airfoil are given in Table 10-3. The test Reynolds Number was about 2.14×10^6. Per Ref. [4] the maximum increase in $\Delta C_{l_{max}}$ for the Krüger alone without trailing-edge flaps amounted to $\Delta C_{l_{max}} \approx 0.30$, at a deflection angle $\delta_S = 130°$. In fact, it must swing through approximately 90° before it even begins to increase the $C_{l_{max}}$. This gain is negatively affected by the presence of a deflected trailing-edge flap. The reference also tested a $0.2c$ Split flap at 60-degree deflection and found that with the flap $\Delta C_{l_{max}}$ increased only by 0.15, for δ_S ranging from 100 to 120°. It is also stated that there was a substantial reduction in the magnitude of the low-pressure region on the leading edge.

The Krüger flap increases α_{stall} by about 5°, C_{l_o} will drop by about −0.093, and $C_{d_{min}}$ increases by about 0.0149 (149 drag counts), so it add substantial drag to the airplane. Change in pitching moment coefficient is approximately $\Delta C_m \approx -0.027$. The combination of the Krüger flap and the $0.2c$ Split flap increased the stall AOA by some $\Delta\alpha \approx 0.7°$. While this may not seem like much, recall that practical high-lift devices increase the lift without changing the stall AOA excessively (i.e., making it too large or too small). In the absence of design data, assume the properties of the simple Krüger flap also apply to the bullnose and variable camber Krüger flaps, although both are superior. Results for the simple Krüger flap are given in Table 10-3.

(6) Summary:

$$\Delta C_{l_{max}} \approx 0.30 \qquad \Delta C_{d_{min}} \approx 0.0149$$
$$\Delta\alpha_{max} \approx 5° \qquad \Delta C_m \approx -0.027$$

10.2.6 The Leading-Edge Slat

The leading-edge slat dates to 1918, to work by the German aeronautical engineer Gustav Lachmann (1896–1966). Lachmann's original work has been translated to English in Ref. [14]. The slat was also developed independently by the British industrialist and aircraft manufacturer Sir Frederick Handley Page (1885–1962). In 1919, in order to avoid a patent conflict he came to

an agreement with Lachmann, who ended up working for Sir Page for the next 3 years [15]. The device was described publically in a lecture given by Sir Page before the British Royal Aeronautical Society in 1921 [10, 16]. Handley Page seems to have been among the first to try it out in practice, where it was tested on a De Havilland D.H. 9. The device later became known as the *Handley Page slot*. Initially, it was fixed (as discussed in Section 10.2.4, *Fixed Slot*), but later, the drag associated with it encouraged Handley-Page's chief engineer George Volkert and his assistant S. G. Ebel to develop a slot that was closed at low AOAs and automatically opened when the airplane slowed down and the AOA increased [15]—the *airload actuated slat* was born.

(1) Two-Position Slats

The *two-position slat* is a two-position device that increases $C_{l_{max}}$ through the *slat-effect*, explained in Section 10.2.4, *Fixed Slot*. Mechanically, it is moderately complex.

Important aerodynamic properties of slats are described in terms of the dimensions shown in Figures 10-14 and 10-15, but the motion is described in terms of:

(1) Extension forward of the leading edge (Δx or a),
(2) Downward drop below the leading edge (Δy or b),
(3) Size of the gap at the outlet of the slot (c),
(4) The rotation of the element (δ_S).

Generally, aerodynamic data are provided for the slat by referencing these parameters.

(2) The Airload Actuated Slat (or the Automated Handley-Page Slat)

As stated earlier, the *airload actuated slat* is the automated version of Handley-Page's fixed slot. It is an ingenious device designed to extract and retract by the pressure difference acting on the leading edge of the wing (see Figure 10-16). Its operation is completely passive; at low speed, the low pressure automatically pulls it out. At high speed the stagnation pressure automatically stows

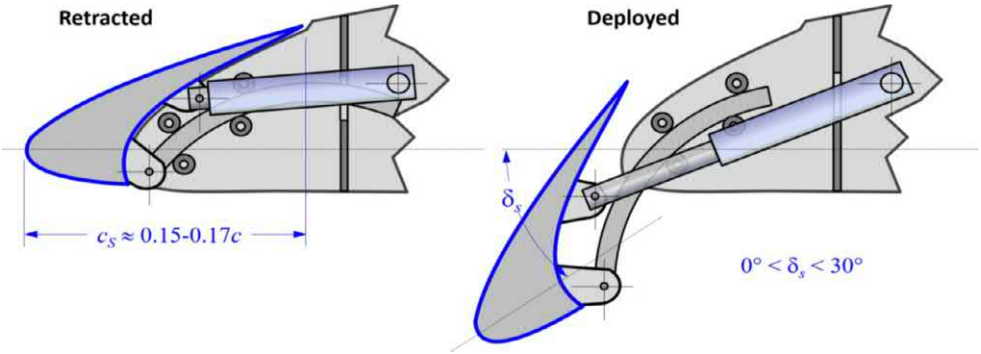
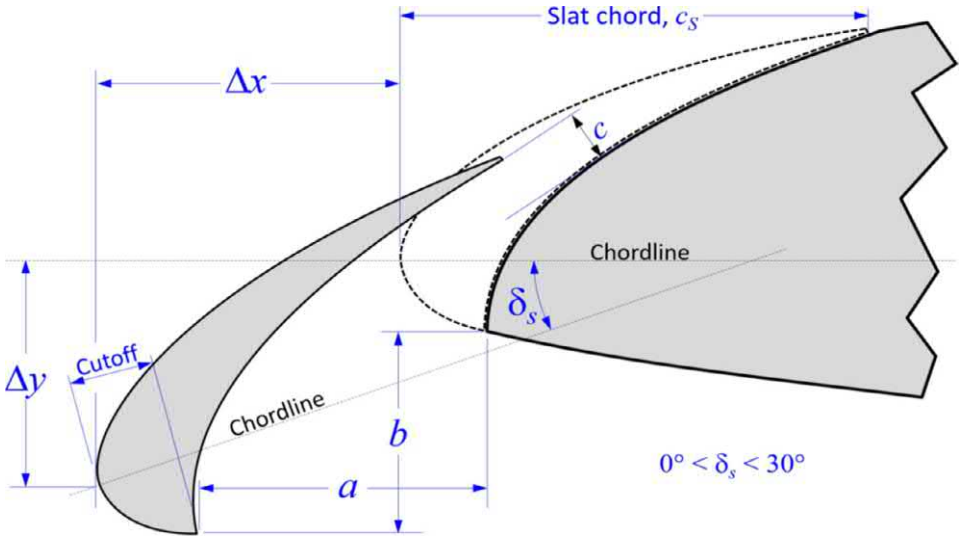


FIGURE 10-14 A schematic of the mechanical aspect of the *two-position slat*. *Based on Peter K.C. Rudolph, High-Lift Systems on Commercial Subsonic Airliners, NASA CR-4746, 1996.*

FIGURE 10-15 Definition of the geometric parameters pertaining to the deployment of the *two-position slat*.



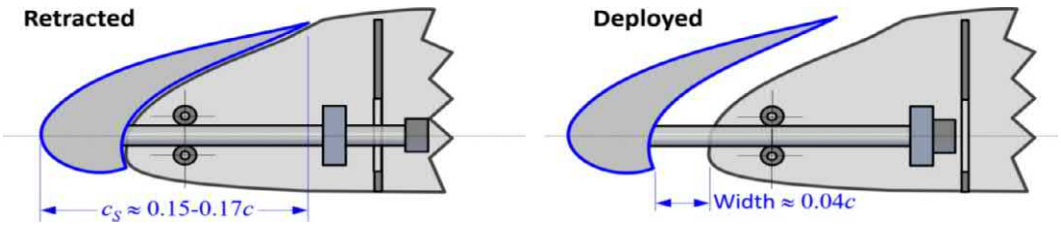


FIGURE 10-16 A schematic of the *airload actuated slat*.



FIGURE 10-17 The *airload actuated slats* on the McDonnell-Douglas A-4 Skyhawk do not need a mechanical actuation system. *Photos by Phil Rademacher.*

it. Some designs feature a spring to help retract the slat. The airload actuated slat can be found on aircraft like the Messerschmitt Me-262 Schwalbe, SOCATA Rallye 100, Westland Lysander, and McDonnell Douglas A-4 Skyhawk (see Figure 10-17).

The slat travels in or out of the leading edge and features slightly curved actuation. This is done to ensure the slat rotates during translation. The fact that the slat retracts when the airplane accelerates to higher airspeeds reduces its drag penalty compared to the fixed slot. Airplanes rolling rapidly at high speeds (fighter aircraft) have been known to occasionally have the slat on the downtraveling wing forced out, while the one on the up-traveling wing remains retracted. The resulting asymmetry may result in a violent roll departure.

(3) The Maxwell Leading-Edge Slot

The *Maxwell slot* is best described as an in-between the fixed slot and slat. Rather than translating and rotating like the standard (or Handley Page) slat, the device operates through rotation only about the leading edge, as shown in Figure 10-18. From that perspective, the slat is mechanically simple, although the addition of the hinged door adds complexity. However, the cruise configuration of the airfoil is relatively smooth, although it would almost certainly trip the laminar boundary layer on both the upper and lower surfaces if used with an NLF airfoil. The position of the slat is referred to in terms of the gap opening (e.g., 0.01c or 0.0175c, etc.) rather than rotation in degrees, as this will vary based on the airfoil geometry.

The Maxwell slot can also be used without the hinged door shown in Figure 10-18. This will make its installation mechanically simpler and at first glance it appears more like a fixed slot. However, with one important difference—in cruise, the gap size is zero, whereas it remains constant for the fixed slot. The device is investigated in Refs. [5, 17]. Ref. [5] concludes that the increase in $C_{l_{max}}$ of a Maxwell slot is similar to that achievable with a Handley Page slat. Ref. [17] found the optimum gap width to be 0.0175c. The investigation shows that the drag of the slat increases with gap size.

(4) Three-Position Slats

The *Three-Position Slat* is a version of the leading-edge slat that features the three following positions (see Figure 10-19): The first position is the retracted one. The second one is a take-off setting. In this position, the slat either rests against the leading edge of the main airfoil, preventing air from flowing from the lower to the upper surface, or a very narrow slot opens. In this configuration, it works more to increase the camber of the basic airfoil, as the closed slot does not permit circulation to develop around the slat. The ideal motion of the slat is

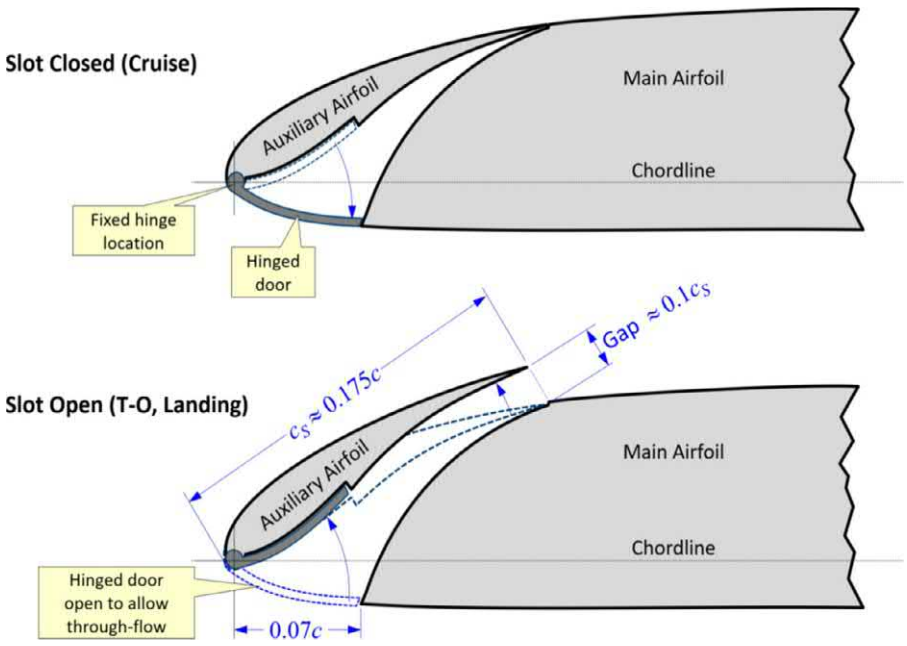


FIGURE 10-18 A schematic of the *Maxwell slot. Based on W.E. Gauvain, Wind Tunnel Tests of a Clark Y Wing With "Maxwell" Leading Edge Slots, NACA TN-598, 1937.*

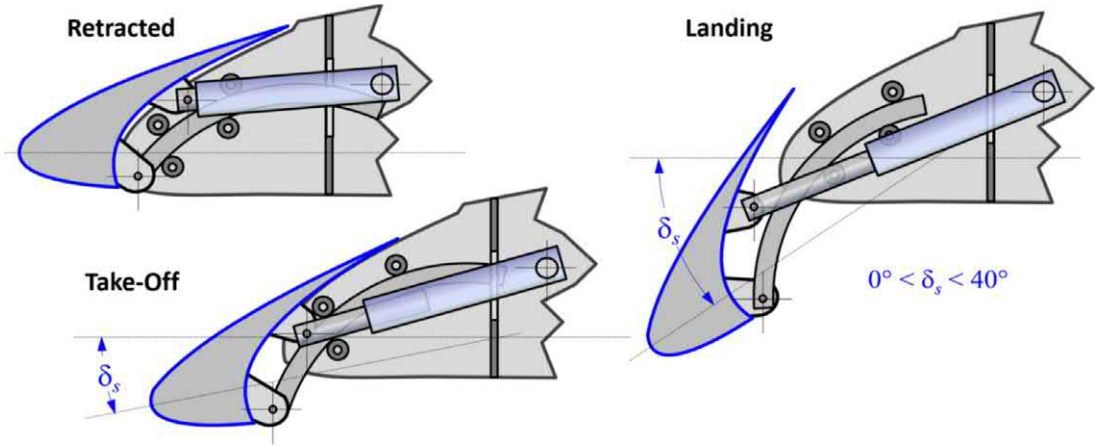


FIGURE 10-19 A schematic of the *three-position slat*.

one of forward and downward motion, with limited rotation. The resulting airfoil geometry offers higher L/D than the open slot configuration and this improves T-O and climb performance. The third setting is a landing setting. In this position, the slat rotates to open a slot, offering the maximum improvement in the wing's $C_{L_{max}}$.

The track and mechanism required to move the slat in the above fashion is more complicated than shown in Figure 10-19, as such a system is biased toward translation at first and rotation later. However, many modern aircraft simply feature a circular arc design and live with a narrow slot for the T-O setting. Other aircraft, such as the B-777, has the main airfoil leading edge shaped such that it forms a seal with the trailing edge of the slat. Figure 10-20 shows the three-position slat in action on the MD-80 jetliner. The difference in slot sizes between the second and third setting is clearly visible in the center and right pictures, respectively. The three-position slat is the most common leading-edge high-lift device in use today. Practically all commercial jetliners, except the B-747, use the device.

(5) General Design Guidelines

Besides the geometry as noted, the effectiveness of the slat depends on its position and deflection as defined in Figure 10-15. The key design parameters include the chord length, c_S, gap, slot width, a (which is equal to the forward translation, Δx), vertical translation, Δy, and deflection angle, δ_S.

Generally, the chord length should be of the order of 0.15–0.175c and gap around 0.001–0.002c. The optimum deflection is usually in the neighborhood of 25°.



FIGURE 10-20 *Three-position slat* in action on the MD-80 commercial jet liner. Cruise position (left), T-O and early descent position (center) with slot closed, and landing position (right) with slot open. *Photos by author.*

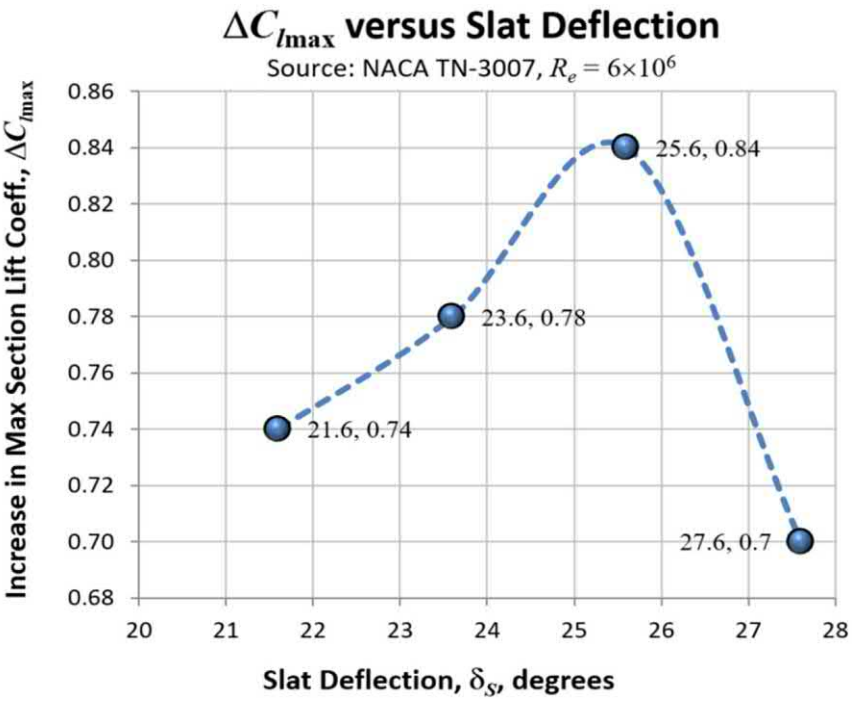


FIGURE 10-21 Change in $C_{l_{max}}$ with a slat deflection angle. *Based on N.-L.F. Hayter, J.A. Kelly, Lift and Pitching Moment at Low Speeds of The NACA 64A010 Airfoil Section Equipped with Various Combinations of a Leading-Edge Slat, Leading-Edge Flap, Split Flap, and Double-Slotted Flap, NACA TN-3007, 1953.*

Figure 10-21 shows how the slat deflection angle affects the increase in $C_{l_{max}}$. It is actually a combination of the deflection angle and the gap opening that yields the highest increase.

Note that there is a discrepancy in the literature as to how the chord length is defined. The two options can be seen in Figures 10-14 and 10-18. The interested reader should refer to the cited sources to determine out which one applies to the published data.

(6) Aerodynamic Properties

Properties for slats and Maxwell slots using a NACA 64A010 and Clark Y airfoils are given in Table 10-3, obtained from Refs. [1, 5]. Slats increase the maximum lift coefficient by some $\Delta C_{l_{max}} \approx 0.84$ for an optimized configuration. The slats increase the stall AOA by about $\Delta\alpha_{stall} \approx 11°$ while the zero AOA lift coefficient drops by about $\Delta C_{l_0} \approx -0.21$. This ignores the shift of the lift and

assumes the slat will only extend the lift curve upward as shown in Figure 8-61. The minimum drag coefficient increases by about $\Delta C_{d_{min}} \approx 0.008$ (80 drag counts).

(7) Summary for Slats:

$\Delta C_{l_{max}} \approx 0.84$ $\quad$ $\Delta C_{d_{min}}$ not specified
$\Delta\alpha_{max} \approx 11°$ $\quad$ $\Delta C_m \approx -0.115$

(8) Summary for Maxwell Flap:

$\Delta C_{l_{max}} \approx 0.55 - 0.81$ $\quad$ $\Delta C_{d_{min}} \approx 0.0156 - 0.0276$
$\Delta\alpha_{max} \approx 9 - 11.8°$ $\quad$ $\Delta C_m \approx 0.0008$ to -0.03656

10.2.7 Summary of Leading-Edge Device Data

Table 10-3 lists important aerodynamic characteristics for a number of leading-edge high-lift devices. The purpose is to provide the designer with answers to questions like—what is the change in lift, drag, and pitching moment when such devices are added to the aircraft. All data presented below are based on wind tunnel testing.

How to Use the Tables

Remember that the tables are intended to get you "in the ballpark" during the conceptual design phase. Begin by locating the part of the table containing the type of leading-edge flap. Make note of the airfoil and Reynolds number used during the wind tunnel testing, as well as the flap chord and deflection. These are important to keep in mind if the geometry and operational conditions of the target flap deviates significantly from these values. For values relatively close, it is acceptable to prorate the characteristics of interests (see Example 10-1). The values to be extracted are $\Delta C_{l_{max}}$, $\Delta\alpha_{stall}$, $\Delta C_{d_{min}}$, and ΔC_m.

EXAMPLE 10-1

A NACA 65_2-415 airfoil is to be used in a wing design and will feature a slat whose chord is 15% of the chord length and will be deflected to 22°. Determine the airfoil's $C_{l_{max}}$, α_{stall}, $C_{d_{min}}$, and C_m at a Reynolds number of 6 million.

SOLUTION:

Using Table 8-9, the baseline airfoil characteristics are given by (generally the data in the table are for $R_e = 9 \times 10^6$) $C_{l\max\ b} = 1.62$, $\alpha_{stall\ b} = 16°$, $C_{d\min\ b} = 0.0042$, and $C_{mb} = -0.060$.

Using Table 10-3 the following values are obtained for the slat as tested on a NACA 64A010 airfoil.

$$\Delta C_{l_{max}} = 0.84, \Delta\alpha_{stall} = 11°,$$
$$\Delta C_{d_{max}} = \text{not available, and } \Delta C_m = -0.115$$

Unfortunately, we are unable to determine the increase in the airfoil's minimum drag using the available data. We prorate the other properties as follows to account for differences in deflection and chord length:

$$C_{l_{max}} = C_{l\max b} + \Delta C_{l_{max}} \left(\frac{\delta_{Strue}}{\delta_S}\right)\left(\frac{c_{Strue}}{c_S}\right)$$
$$= 1.62 + 0.84\left(\frac{22°}{25.6°}\right)\left(\frac{0.15}{0.17}\right) = 2.26$$
$$\alpha_{stall} = \alpha_{stallb} + \Delta\alpha_{stall}\left(\frac{\delta_{Strue}}{\delta_S}\right)\left(\frac{c_{Strue}}{c_S}\right)$$
$$= 16° + 11°\left(\frac{22°}{25.6°}\right)\left(\frac{0.15}{0.17}\right) = 24.3°$$
$$C_m = C_{mb} + \Delta C_m\left(\frac{\delta_{Strue}}{\delta_S}\right)\left(\frac{c_{Strue}}{c_S}\right)$$
$$= -0.06 - 115\left(\frac{22°}{25.6°}\right)\left(\frac{0.15}{0.17}\right) = -0.147$$

10.3 TRAILING-EDGE HIGH-LIFT DEVICES

In this section we will look at a number of trailing-edge high-lift devices. Such devices are essential in reducing T-O and landing distances for aircraft. Not only do they make it possible to operate aircraft over a wide range of airspeeds; for commercial aircraft, they ultimately make or break their business case as they dictate the kind of airports from which the airplane can be operated.

The purpose of the trailing-edge high-lift device is to increase the maximum lift coefficient of the airfoil. Since this is accomplished by increasing the camber of the airfoil, this usually reduces the stall AOA as well. The effect is described in Section 8.3.4, *The Effect of a Trailing-Edge Flap*. Deploying a flap will affect not only $C_{l_{max}}$ and α_{stall} but also the pitching moment and is, thus, of great importance when sizing control surfaces. The pitching moment increases substantially and this must be arrested by an adequately sized stabilizer and elevator. From aircraft handling standpoint, deploying flaps has a major effect on the stall characteristics of the aircraft. It can also be problematic in the development of aircraft—an airplane may stall impeccably without flaps, and terribly with them deployed.

Flaps increase drag and require higher thrust to maintain straight and level flight. Naturally, this also means that the maximum level airspeed is reduced. Trailing-edge devices greatly influence the distribution of lift over the wing and have profound effect on the structural design. They develop large aerodynamic forces that must be reacted through the appropriate hard points in the wing. This also requires increase in skin thickness to react increased wing torsion. A few small aircraft feature manually operated flaps. For such aircraft the

deflection loads are of concern and must be kept low enough to enable pilots with limited upper body strength to actuate them.

The investigation of trailing-edge high-lift devices is made harder by the complexity of analysis methods. Their operation is affected by viscosity in major ways and this renders the wind tunnel as the primary methodology. Computational Fluid Dynamic (CFD) codes utilizing Navier-Stokes solvers are making such effort easier, although such codes should always be validated for each case using wind tunnel testing. Before the advent of such computational methods, flaps were analyzed using Glauert's extension of the thin airfoil theory. The theory allows lift, pitching moment and hinge moments to be estimate using closed form solutions [18].

The invention of the flap dates back to the early days of aviation. One of the earliest research can be found in Ref. [19], published in 1914. In spite of this, the flap did not become widely used until in the early 1930s, when aerodynamic efficiency and wing loading had reached a state where take-off and landing speeds presented serious challenges to the operation of aircraft [20]. The trailing-edge flap was a clear solution and it allowed fast aircraft to both reduce airspeed and increase the glide slope. Since then a substantial number of configurations has been devised and utilized in aircraft. The most common ones are presented here, but the reader should be aware of that more exist.

10.3.1 Trailing-Edge Device Quick-Guide

See Table 10-4. Further detail can be seen in Table 10-5. Add the Δ-values to that of the airfoil. For instance, if the $C_{l_{max}}$ and α_{stall} of the basic airfoil are 1.5 and 15°, respectively, then expect the *Zap flap* to change these to 2.58 and 14°.

10.3.2 Plain Flap

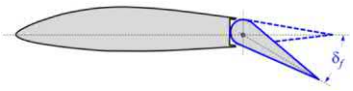
The *plain flap* is a simple high-lift surface that rotates (deflects) only. It is better suited as a control surface than a high-lift device. Its geometry is a semicircle joined at the base of a triangle (see Figure 10-22). The hingepoint is the center of the circle, but this ensures the gap between the control surface and the trailing edge of the skin remains constant. This yields a simple and reliable control system, although an overhang (the part of the flap ahead of the hingeline) larger than the circle radius introduces complications. Most aircraft, big and small, fast and slow, feature plain flap ailerons, elevators, and rudder control surfaces.

Among drawbacks is a relatively low $C_{l_{max}}$ compared to more sophisticated flap types. The small nose radius requires heavy ballast to mass balance. A common remedy is to install an arm to carry the ballast. However, it is challenging to hide from the airstream. The flap deflection increases drag only slightly for deflections in the ±10° range. Deflection increases the airfoil camber, yielding higher $C_{l_{max}}$ and reduced α_{stall}. If deflected beyond ±15°, expect separation to form, reducing its effectiveness (see Figure 10-23). At lower Reynolds numbers (small UAVs and RC aircraft), such separation begins at deflection as low as ±10°. The maximum deflection is usually limited to ±25–30°. In part, because further deflection has limited improvements of $C_{l_{max}}$, and, in part, because of control system gains.

(1) General Design Guidelines

The primary design variables for the plain flap are chord, deflection, hingeline location, and airfoil. The flap

TABLE 10-4 Quick-guide for selecting a trailing-edge device.

Name	δ_f (degrees)	Schematic	$\Delta C_{l_{max}}$	$\Delta\alpha_{stall}$ (degrees)	ΔC_{l_0}	$\Delta C_{d_{min}}$
Plain $c_f/c=0.1$	15		0.21	−1.1	0.309	–
	30		0.35	−2.2	0.405	–
	45		0.51	−1.6	0.539	–
Plain $c_f/c=0.2$	15		0.24	−1.1	0.453	–
	30		0.48	−2.1	0.608	–
	45		0.66	−1.9	0.794	–
Plain $c_f/c=0.3$	15		0.29	0.1	0.668	–
	30		0.60	−2.2	0.750	–
	45		0.71	−2.3	0.933	–

Continued

TABLE 10-4 Quick-guide for selecting a trailing-edge device—cont'd

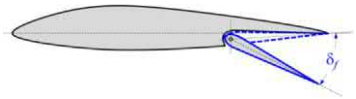
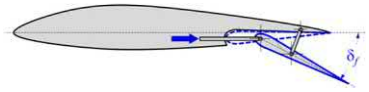
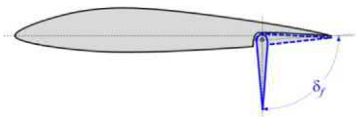
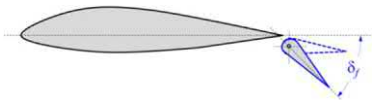
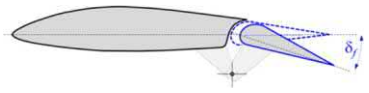
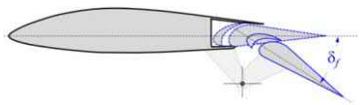
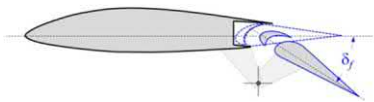
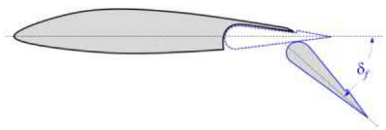
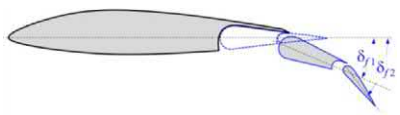
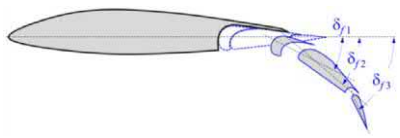
Name	δ_f (degrees)	Schematic	$\Delta C_{l_{max}}$	$\Delta\alpha_{stall}$ (degrees)	ΔC_{l_0}	$\Delta C_{d_{min}}$
Split $c_f/c=0.2$	15		0.35	−2.1	0.33	–
	30		0.62	−2.4	0.58	–
	45		0.82	−1.4	0.79	–
	60		0.89	−1.4	0.90	–
Zap $c_f/c=0.376$	43		1.08	−1.0	1.2	0.112
Schrenk $c_f/c=0.2$	67		0.98	−3.9	1.143	–
	97		0.87	−4.0	1.143	–
Junkers $c_f/c=0.2$	20		0.71	–	–	−0.0004
	30		0.84	–	–	−0.0004
	40		0.65	–	–	−0.0004
Junkers $c_f/c=0.3$	20		0.82	–	–	−0.0007
	30		0.96	–	–	−0.0007
	40		1.00	–	–	−0.0007
Single-Slotted $c_f/c=0.3$	30		1.10	−2.0	–	–
	40		1.32	−3.0	–	–
	50		1.37	−5.0	–	–
Double-Slotted (fixed-vane)	55–60		1.40	–	–	–
Double-Slotted (articulating)	55–60		1.40	–	–	–
Single-Element Fowler $c_f/c=0.3$	20		1.61	–	–	0.0015
	30		1.99	–	–	0.0040
	40		2.24	–	–	0.0355
Dual-Element Fowler Flap	12		1.00	−8.0	–	0.0120
	30		1.60	−12.0	–	0.0190
	44		2.00	−15.0	–	0.0370
Triple-Element Fowler Flap	16		1.88	−1.0	–	0.0170
	46		2.63	−10.5	–	0.0365
	53		2.72	−7.5	–	0.0730
Gurney Flap ($h=0.01c$)	–		0.27	≈1.2	0.15	0.005

TABLE 10-5 Summary of the aerodynamic properties of trailing-edge devices.

Description	Section	Basic Airfoil	$R_c \times 10^6$	Flap Type	c_{main}/c	c_f/c	δ_f	$C_{l\,max}$	α_{stall}	$C_{l\,o}$	$C_{d\,min}$	$C_{m\,o}$	$\Delta C_{l\,max}$	$\Delta\alpha_{stall}$	$\Delta C_{l\,o}$	$\Delta C_{d\,min}$	ΔC_m	Reference
PLAIN FLAPS																		
Airfoil only	10.3.2	Clark Y	0.609	-	1	-	0°	1.250	14.3	0.40	0.0150	-	-	-	-	-	-	NACA TR-554
Plain flap				Plain	0.9	0.1	15°	1.472	13.2	0.71	-	-	0.222	-1.07	0.309	-	-	NACA TR-938 and NACA TR-554
							30°	1.605	12.1	0.80	-	-	0.355	-2.19	0.405	-	-	
							45°	1.765	12.7	0.93	-	-	0.515	-1.63	0.539	-	-	
					0.8	0.2	15°	1.502	13.2	0.85	-	-	0.252	-1.07	0.453	-	-	
							30°	1.741	12.2	1.00	-	-	0.491	-2.11	0.608	-	-	
							45°	1.914	12.4	1.19	-	-	0.664	-1.87	0.794	-	-	
					0.7	0.3	15°	1.546	14.4	1.06	-	-	0.296	0.05	0.668	-	-	
							30°	1.853	12.1	1.15	-	-	0.603	-2.19	0.750	-	-	
							45°	1.965	12.0	1.33	-	-	0.715	-2.27	0.933	-	-	
SPLIT FLAPS																		
Airfoil only	10.3.3	Clark Y	0.609	-	1	-	0°	1.250	14.3	0.40	-	-	-	-	-	-	-	NACA TR-554
Airfoil+Split Flap				Split	1	0.2	15°	1.603	12.2	0.73	-	-	0.353	-2.07	0.328	-	-	
Airfoil+Split Flap				Split	1	0.2	30°	1.869	11.9	0.98	-	-	0.619	-2.39	0.584	-	-	
Airfoil+Split Flap				Split	1	0.2	45°	2.074	12.9	1.19	-	-	0.824	-1.36	0.790	-	-	
Airfoil+Split Flap				Split	1	0.2	60°	2.138	12.9	1.30	-	-	0.888	-1.44	0.898	-	-	
Airfoil only		NACA 64A010	6	-	1	-	-	1.10	11.0	0.01	-	0.00	-	-	-	-	-	NACA TN-3007
Airfoil+Split Flap			6	Split		0.2	60°	1.88	5.3	-	-	-	0.78	-5.7	-	-	-	
Airfoil only		Mustang 2	21.4	-	0.1	-	-	1.13	12.3	0.09	0.0082	-0.017	-	-	-	-	-	NACA TM-1177
Airfoil+Split Flap			21.4	Split	0.1	-	-	2.11	11.1	1.29	0.1594	-0.204	0.98	-1.2	1.20	0.1512	-0.19	
Airfoil only		NACA 66(215)-216	6	-	1	-	-	1.56	17.1	0.20	-	-0.045	-	-	-	-	-	NACA WR-L-140
Airfoil+Split Flap				Split		0.2	70°	2.61	11.0	1.73	-	-0.218	1.05	-6.10	1.53	-	-0.17	
Airfoil only		NACA 66_1-212		-		-	-	1.41	14.1	0.14	-	-0.039	-	-	-	-	-	
Airfoil+Split Flap				Split		0.2	70°	2.17	6.9	1.56	-	-0.212	0.76	-7.20	1.42	-	-0.17	
Airfoil only		NACA 65_1-212		-		-	-	1.49	14.7	0.15	-	-0.035	-	-	-	-	-	
Airfoil+Split Flap				Split		0.2	60°	2.15	7.65	1.49	-	-0.199	0.66	-7.05	1.34	-	-0.16	
ZAP FLAPS																		
Wing only (3D airplane)	10.3.3	N-22	3.12	-	1	-	-	1.29	13	0.4	0.053	-0.025	-	-	-	-	-	NACA WR-L-437
Wing + 0.947b Zap Flap				Zap		0.376	43°	2.37	12	1.6	0.165	-0.25	1.08	-1.0	1.20	0.11	-0.225	
Wing + 0.947b Zap Flap + Gap				Zap		0.376	43°	2.57	13	1.72	-	-	1.28	0.0	1.32	-	-	
SCHRENK FLAPS																		
Airfoil only	10.3.3	RAF 44	0.42	-	1	-	-	1.15	18.3	0	-	-	-	-	-	-	-	ARC RM-1698
Airfoil+SChrenk Flap				Schrenk		0.2	67°	2.13	14.3	1.14	-	-	0.976	-3.9	1.14	-	-	
Airfoil+SChrenk Flap				Schrenk		0.2	97°	2.02	14.3	1.14	-	-	0.872	-4.0	1.14	-	-	
JUNKERS FLAPS (ALL POSITIONS ARE OPTIMAL, BUT THE POSITION OF $C_{l\,max}$ DOES NOT NECESSARILY COINCIDE WITH THAT OF $C_{d\,min}$)																		
Airfoil only	10.3.4	Clark Y (main) NACA 0012 (flap)	0.609	-	1	-	-	1.250	18	-	0.0155	-	-	-	-	-	-	NACA TN-524
Airfoil + Junkers Flap				Junkers		0.15	45°	1.810	12	-	0.0146	-	0.56	-6.0	-	-0.0009	-	
Airfoil only		Clark Y (main) Clark Y (flap)	0.609	-	1	-	-	1.300	-	-	0.0145	-	-	-	-	-	-	NACA R-541
Airfoil + Junkers Flap				Junkers		0.2	30°	1.96	-	-	0.0123	-	0.66	-	-	-0.0022	-	
Airfoil + Junkers Flap				Junkers		0.2	40°	2.00	-	-	0.0123	-	0.70	-	-	-0.0022	-	
Airfoil only		NACA 23012 (main) Clark Y (flap)	0.609	-	1	-	-	1.145	-	-	0.0105	-	-	-	-	-	-	
Airfoil + Junkers Flap				Junkers		0.2	20°	1.85	-	-	0.0101	-	0.71	-	-	-0.0004	-	
Airfoil + Junkers Flap				Junkers		0.2	30°	1.98	-	-	0.0101	-	0.84	-	-	-0.0004	-	
Airfoil + Junkers Flap				Junkers		0.2	40°	1.79	-	-	0.0101	-	0.65	-	-	-0.0004	-	
Airfoil only		NACA 23012 (main) Clark Y (flap)	0.609	-	1	-	-	1.145	-	-	0.0105	-	-	-	-	-	-	
Airfoil + Junkers Flap				Junkers		0.3	20°	1.961	-	-	0.0098	-	0.82	-	-	-0.0007	-	
Airfoil + Junkers Flap				Junkers		0.3	30°	2.108	-	-	0.0098	-	0.96	-	-	-0.0007	-	
Airfoil + Junkers Flap				Junkers		0.3	40°	2.140	-	-	0.0098	-	1.00	-	-	-0.0007	-	
Airfoil + Junkers Flap				Junkers		1.3	60°	1.908	-	-	0.0098	-	0.76	-	-	-0.0007	-	

Continued

TABLE 10-5 Summary of the aerodynamic properties of trailing-edge devices—cont'd

SINGLE-SLOTTED FLAPS												
Airfoil Section	c_{main}/c	c_f/c	Slot Entry Config.	Flap Nose Shape	δ_f (deg)	$C_{l\max}$	$\Delta C_{l\max}$	x_f	y_f	Optimum position	$R_e \times 10^6$	Reference
NACA 23012 (airfoil only)	1.000	-	-	-	-	1.55	-	-	-	-		NACA R-679
NACA 23012 (flap)	0.930	0.100	a	A	50	2.25	0.70	0.004	0.005	YES		NACA R-679
	1.000	0.150	b	A	30	2.68	1.13	0	0.015	YES		NACA ACR, Nov 1940
	1.000	0.250	b	A	40	3.22	1.67	0	0.015	YES		
	0.800	0.257	a	B	50	2.76	1.21	0.005	0.018	YES		NACA R-664
	0.830	0.257	a	A	50	2.81	1.26	0.005	0.016	YES		
	0.830	0.257	a	A	40	2.83	1.28	0.013	0.024	YES		NACA R-679
	1.000	0.257	b	A	30	2.90	1.35	0	0.025	NO	3.5	NACA R-664
	0.900	0.300	c	A	30	2.40	1.10	0.002	0.010	NO		NACA TN 808
	0.900	0.300	c	A	40	2.88	1.32	0.002	0.020	NO		
	0.900	0.300	c	A	50	2.91	1.37	0.002	0.030	NO		
	0.900	0.300	b	A	40	2.88	1.33	0.002	0.020	NO		
	1.000	0.300	b	A	40	3.29	1.74	0	0.015	NO		
	0.715	0.400	b	A	50	2.87	1.32	0.015	0.015	YES		NACA TN 715
	0.715	0.400	a	A	50	2.90	1.35	0.015	0.015	YES		
NACA 23021 (airfoil only)	1.000	-	-	-	-	1.35	-	-	-	-		NACA R-677
NACA 23021 (flap)	1.000	0.150	b	A	60	2.59	1.24	0	0.015	YES		NACA TN 782
	1.000	0.150	b	A	60	2.66	1.31	0.050	0.030	YES		NACA ACR,Feb 1941
	1.000	0.250	b	A	40	3.17	1.82	0.025	0.015	YES		
	0.827	0.257	b	B	60	2.69	1.34	0	0.015	YES	3.5	NACA R-677
	0.827	0.257	a	B	60	2.74	1.39	0	0.015	YES		
	0.827	0.257	b	A	60	2.71	1.36	0.005	0.020	YES		
	0.827	0.257	a	A	50	2.82	1.47	0	0.025	YES		
	0.715	0.400	b	A	50	2.79	1.44	0.015	0.025	YES		NACA TN 728
	0.715	0.400	a	A	50	2.88	1.53	0.015	0.045	YES		

TABLE 10-5 Summary of the aerodynamic properties of trailing-edge devices—cont'd

SINGLE-SLOTTED FLAPS - Continued												
Airfoil Section	c_{main}/c	c_f/c	Slot Entry Config.	Flap Nose Shape	δ_f (deg)	$C_{l\max}$	$\Delta C_{l\max}$	x_f	y_f	Optimum position	$R_e \times 10^6$	Reference
NACA 23030 (airfoil only)	1.000	-	-	-	-	1.01	-	-	-	-	3.5	NACA TN 755
NACA 23030 (flap)	0.860	0.257	b	B	60	2.59	1.58	0.025	0.040	YES		
NACA 23030 (flap)	0.860	0.257	a	B	60	2.60	1.59	-0.005	0.040	YES		
NACA 23030 (flap)	0.775	0.400	b	B	50	2.82	1.81	0.025	0.060	YES		
NACA 23030 (flap)	0.775	0.400	a	B	50	2.90	1.89	0.025	0.060	YES		
63_4-420	0.880	0.250	b	B	35	3.00	1.58	0.018	0.045	NO	6	NACA R-824
63_4-421(approx)	0.835	0.243	a	A	40	3.21	-	0	0.027	YES	9	NACA MR, Jan 7, 1943
65-210	0.840	0.250	c	A	45	2.47	-	0.009	0.010	YES	6	NACA TN 1191
	0.900	0.250	c	A	41.3	2.48	-	0.014	0.009	YES		
	0.975	0.250	c	A	35	2.45	-	0.004	0.020	YES		
$65_{(112)}$-111 (approx.)	0.839	0.350	c	A	35	2.69	-	-0.020	0.032	YES	9	NACA TN 1463
65_1-213 (approx.)	0.889	0.336	c	A	40	2.63	1.45	0.019	0.046	NO	9	NACA MR L5L11
$65_{(215)}$-114	0.915	0.259	c	A	40	2.80	1.65	0.019	0.038	NO	9	
66(215)-216	-	0.250	-	-	40	2.34	0.92	-	-	-	6	NACA R-938
65_2-221	0.832	0.263	a	B	30	2.83	-	0.025	0.046	YES	9.95	NACA MR, June 4, 1942
$66_{(215)}$-116, a = 0.6	0.824	0.250	c	B	55	2.70	-	0	0.028	NO	6	NACA MR L4K21
66_2-116, a = 0.6	0.827	0.250	a	A	45	2.69	-	0.017	0.038	NO	6	NACA MR, May 23, 1942
66,2-216	0.900	0.300	c	A	37	2.92	-	0	0.016	NO	6	NACA R-824
	0.824	0.250	a	A	40	2.89	-	0.023	0.040	YES	5.1	NACA MR A4L28
	0.834	0.250	c	A	45	2.88	-	0.011	0.031	YES	5.1	
66_2-118	0.900	0.250	-	-	32.5	2.68	-	-	-	NO	6	NACA MR, Dec 2,1941
Davis (t/c = 0.18)	1.000	0.300	b	A	40	3.45	-	-	-	NO	6.2	NACA MR, Dec 29,1941
Davis (modified) (t/c = 0.18)	1.000	0.300	b	A	40	3.14	-	-	-	NO	6	
66-Series (approx) (t/c = 0.18)	1.000	0.300	b	A	30	3.34	-	-	-	NO	6.2	

Continued

TABLE 10-5 Summary of the aerodynamic properties of trailing-edge devices—cont'd

SINGLE-SLOTTED FOWLER FLAPS												
Airfoil Section	c_{main}/c	c_f/c	**Slot Entry Config.**	**Flap Nose Shape**	δ_f **(deg)**	$C_{l\max}$	$\Delta C_{l\max}$	x_f	y_f	**Optimum position**	$R_e \times 10^6$	**Reference**
Clark Y (airfoil only)	-	-	-	-	-	1.27	-	-	-	-	6	NACA TN-419
Clark Y (flap)	1.000	0.400	-	-	40	3.17	1.90	0	0.025	YES	6	
GA(W)-1 (airfoil only)	1.000	-	-	-	-	1.56	-	-	-	-	2.2	NASA CR-2443 *Flap x_f and y_f are absolute values that reference leading edge of airfoil
GA(W)-1 (flap)	0.960	0.290	-	-	15	2.72	1.16	0.900*	-0.055	YES		
		0.290	-	-	30	3.35	1.79	0.940*	-0.043	YES		
		0.290	-	-	40	3.48	1.92	0.950*	-0.040	YES		
GA(W)-1 (flap)	1.000	0.300	-	-	20	3.17	1.61	0.953*	-0.025	YES		
		0.300	-	-	30	3.55	1.99	0.978*	-0.025	YES		
		0.300	-	-	40	3.80	2.24	1.007*	-0.027	YES		
GA(W)-1 (flap)	1.000	1.290	-	-	40	3.71	2.15	-	-	YES	2.2	NASA CR-3687
Clark Y (airfoil only)	1.000	-	-	-	-	1.30	-	0	-0.025	YES	0.61	NACA TR-407
Clark Y (flap)		0.200	b	A	30	2.44	1.143	0	-0.025	YES		NACA R-534
		0.300	b	A	40	2.83	1.533	0	-0.025	YES		
		0.400	b	A	40	3.10	1.803	0	-0.025	YES		
Supercritical airfoil	1.000	-	-	-	0	1.73	-	-	-	-	2.83	NASA CR-2214
		-	-	-	20	2.54	1.243	-	-	-		
		-	-	-	30	2.77	1.473	-	-	-		
		-	-	-	40	2.80	1.503	-	-	-		

TABLE 10-5 Summary of the aerodynamic properties of trailing-edge devices—cont'd

DOUBLE SLOTTED FLAPS														
Airfoil Section	c_{main}/c	c_f/c	c_v/c	$C_{l\max}$	$\Delta C_{l\max}$	δ_v (deg)	δ_f (deg)	x_f	y_f	x_v	y_v	Optimum position	$R_e \times 10^6$	Reference
NACA 1410 (airfoil only)	1.000	-	-	1.50	-	-	-	-	-	-	-	-	6.0	NACA TN-1545
NACA 1410 (flap)	0.840	0.250	0.075	3.06	1.56	25	50	0.026	0.016	0.012	0.019	YES	6.0	
NACA 23012	0.830	0.100	0.189	2.99		40	70	0.009	0.009	0.014	0.024	YES	3.5	NACA R-679
	0.715	0.257	0.227	3.47		30	70	0.014	0.012	0.015	0.035	NO	3.5	NACA R-723
	0.826	0.257	0.117	3.30		25	60	-0.016	0.010	-0.004	0.017	YES	3.5	NACA ARR 3L10
NACA 23021	0.715	0.257	0.227	3.56		30	60	0.019	0.024	0.025	0.065	NO	3.5	NACA R-723
	0.827	0.257	0.147	3.32		30	70	0.017	0.027	0.007	0.024	YES	3.5	NACA ARR L4J05
NACA 23030	0.715	0.257	0.260	3.71		40	80	0.040	0.050	0.045	0.040	NO	3.5	NACA R-723
NACA 63_4-421(approx)	0.870	0.195	0.083	3.30		14	55	0.038	0.012	-0.009	0.016	NO	6.0	-
NACA 63-210 (airfoil only)	1.000	-	-	1.51	-	-	-	-	-	-	-	-	6.0	NACA TN-1545
NACA 63-210 (flap)	0.840	0.250	0.075	2.93	1.42	25	50	0.022	0.024	0.024	0.018	YES		
NACA 64-208 (airfoil only)	1.000	-	-	1.02	-	-	-	-	-	-	-	-		
NACA 64-208 (flap)	0.840	0.250	0.075	2.51	1.49	30	45	0.015	0.015	0.015	0.019	YES		
NACA 64-208 (flap)	0.840	0.250	0.056	2.40	1.38	25	50	0.018	0.014	0.015	0.024	YES		
NACA 64-210 (airfoil only)	1.000	-	-	1.45	-	-	-	-	-	-	-	-		
NACA 64-210 (flap)	0.840	0.250	0.075	2.82	1.37	30	55	0.023	0.006	0.012	0.018	YES		
NACA 64_1-212 (airfoil only)	1.000	-	-	1.53	-	-	-	-	-	-	-	-		
NACA 64_1-212 (flap)	0.840	0.250	0.075	3.03	1.50	30	50	0.021	0.020	0.010	0.019	YES		
NACA 64-A212	0.833	0.229	0.083	2.83		26	55	0.044	0.005	0.004	0.014	YES	6.0	NACA TN-1293
NACA $65_{(216)}$-215, a=0.8	0.820	0.248	0.096	3.38		12	70	0.024	0.010	0.025	0.032	NO	6.3	NACA RM L7A30
NACA 65-118	0.864	0.244	0.100	3.35	1.80	23	65	0.038	0.007	0.009	0.025	YES	6.0	NACA ACR 3120, R-824
NACA 65-121	0.850	0.236	0.109	3.08		20	51	0.029	0.017	0.012	0.024	YES	2.2	NACA TN-1395
NACA 65-210 (airfoil only)	1.000	-	-	1.40	-	-	-	-	-	-	-	-	6.0	NACA TN-1545
NACA 65-210 (flap)	0.840	0.250	0.075	2.72	1.32	25	50	0.025	0.011	0.009	0.024	YES		
NACA 65-418	0.851	0.236	0.106	3.50		21	65	0.027	0.007	0.012	0.028	YES	6.0	NACA TN-1071
NACA 66-210 (airfoil only)	1.000	-	-	1.25	-	-	-	-	-	-	-	-	6.0	NACA TN-1545
NACA 66-210 (flap)	0.840	0.250	0.075	2.64	1.39	25	55	0.029	0.023	0.012	0.022	YES		
NACA 66-210 (flap)	0.840	0.250	0.100	2.72	1.47	25	60	0.027	0.039	0.024	0.021	YES		
NACA 66-214(approx)	0.854	0.227	0.085	3.00		20	55	0.044	0.009	0.004	0.025	YES	9.0	NACA TN-1110
Douglas 7-series type t/c=0.154	0.820	0.250	0.056	3.15		19	50	0.017	0.016	0.012	0.024	NO	6.0	NACA MR L5C2a
Republic 6-series type t/c=0.17	0.880	0.238	0.092	3.55		25	60	0.015	0.020	-0.005	0.020	YES	8.5	NACA MR L6A08a
Republic 6-series type t/c=0.17	0.880	0.238	0.092	3.43		25	60	0.015	0.020	-0.005	0.020	YES	14.0	NACA MR L6A08a
Airfoil NACA 64A010 (airfoil only)	-	-	-	1.10		-	-	-	-	-	-	-	6	NACA TN-3007
Airfoil NACA 64A010 (flap)	0.823	0.25	0.075	2.36	1.26	30	52.7	-	-	-	-	-	6	

Continued

TABLE 10-5 Summary of the aerodynamic properties of trailing-edge devices—cont'd

TRIPLE SLOTTED FLAPS												
Airfoil Section	**Setup**	c_{main}/c	c_f/c	c_v/c	δ_f (deg)	$C_{l\max}$	$\Delta C_{l\max}$	$C_{d\min}$	$\Delta C_{d\min}$	**Optimum position**	$R_e \times 10^6$	**Reference**
Supercritical airfoil with slat Element deflection 20°/45°/65°	Airfoil only	1.000	-	-	-	1.73	-	0.0080	-	-	2.8	NASA CR-2214
	Slat only	-	-	-	-	2.82	1.10	0.0200	0.0120	-		
	Slat + 16°	-	-	-	16	4.70	2.98	0.0380	0.0300	-		
	Slat + 46°	-	-	-	46	5.45	3.73	0.0565	0.0485	-		
	Slat + 53°	-	-	-	53	5.54	3.82	0.0930	0.0850	-		

Abbreviations: LE, Leading Edge; TE, Trailing Edge; $R_{e\ test}$, Reynolds Number during test; c_S, Chord of LE device; c, Airfoil chord; Dbl, Double; δ_S, Deflection angle of LE device; $(\delta_f)_1$, Deflection of element 1 of a TE device; $(\delta_f)_1$, Deflection of element 2 of a TE device; $C_{l_{max}}$, Max section lift coefficient; α_{stall} = Stall AOA; C_{l_0}, Lift coefficient at $\alpha = 0$ °; $C_{d_{min}}$, Minimum section drag coefficient; C_{mo}, Pitching moment coefficient at $\alpha = 0$ °.
Specific references: [1, 4, 18, 21–27, 47–73].

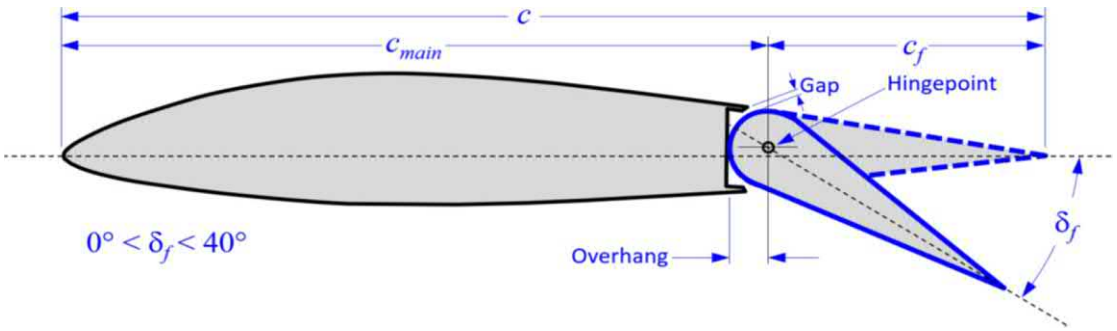


FIGURE 10-22 A schematic of the *Plain Flap*.

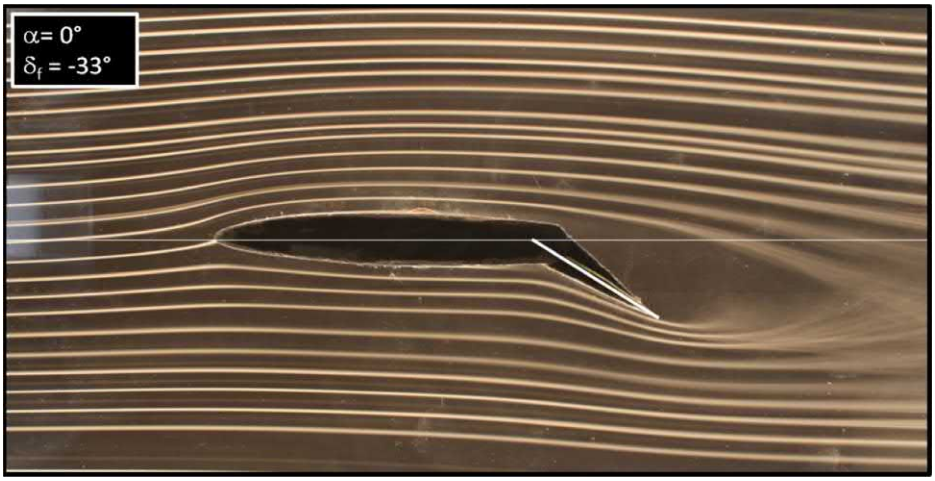


FIGURE 10-23 Streamlines show one of the drawbacks of the *plain flap*—a flow separation that forms at deflection angles over 15°. This flap is deflected at 33°. *Photo by Phil Rademacher.*

area is defined as the area behind the hingeline. The maximum lift of the plain flap depends on the flap chord, which varies between 20% and 30%. Some airplanes feature plain flaps for rudders with flap chords as large as 50%. The Boeing B-52 has a 10% chord for its rudder. The flap should be oversized by approximately 0.0003*c* to 0.0030*c*. If the chord is 3.28 ft (1.00 m), the oversizing should amount to 0.012″–0.120″ (0.3–3.0 mm) per side (see Figure 10-24). The oversizing re-energizes the boundary layer, helping it to remain attached. This improves the effectiveness of the surface at low deflections by preventing it from operating in "dead air."

Plain flaps sometimes feature offset hingelines to reduce hinge moments. This results in large overhang (see Figure 10-25). Deflecting the flap moves its leading edge up and down, requiring the skin on the upper and lower surfaces to be trimmed to accommodate this motion. Otherwise, the overlapping skin (or trailing-edge lip as it is commonly called) contacts the flap. This should be avoided at all cost, because in-flight wing flex can potentially lead to jamming. This opens a gap for air to flow through, increasing drag. For many applications, the small gap may range from 0.050″ to 0.125″ (1.3 to 3.2 mm). The presence of the lip may adversely affect stall characteristics and increase drag in cruise. The presence of this gap is remedied on the Cirrus SR22 by a flexible plastic strip that is bonded to the upper surface and greatly reduces the gap size. A special gap seal can also be used.

(2) Aerodynamic Properties

The $C_{l_{max}}$ depends on flap chord ratio, c_f/c. A comparison for three flap chords is provided in Ref. [18]. These

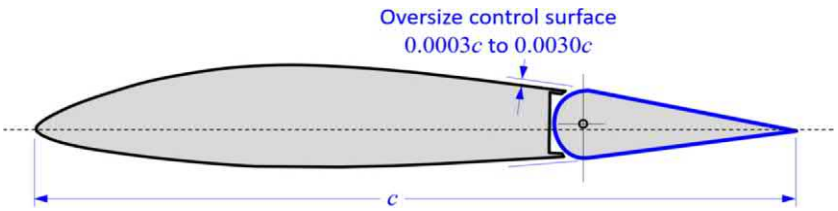


FIGURE 10-24 The *plain flap* should be slightly oversized to help re-energize the boundary layer.

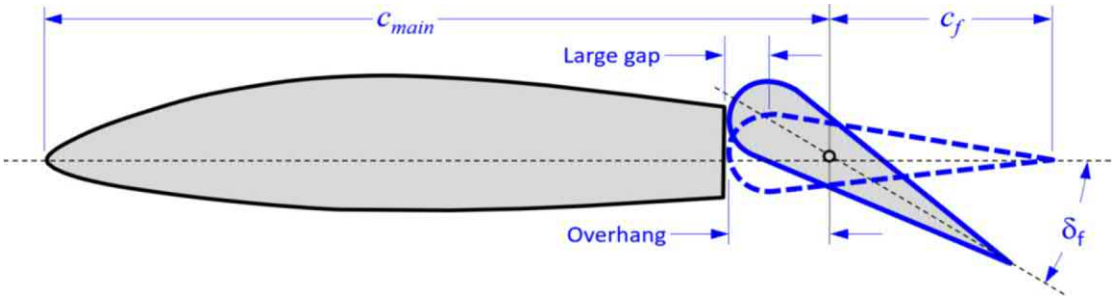


FIGURE 10-25 Enlarged overhang may cause geometric issues that may turn into aerodynamic issues.

are shown in Figure 10-26. Equation (10-1) is a least squares curve fit to the data for the three flaps.

$$C_{l\max 0.1C} = 1.262 + 0.01492\delta_f - 8.315\times10^{-5}\delta_f^2$$
$$C_{l\max 0.2C} = 1.234 + 0.02216\delta_f - 1.611\times10^{-4}\delta_f^2 \quad (10\text{-}1)$$
$$C_{l\max 0.3C} = 1.250 + 0.02418\delta_f - 2.093\times10^{-4}\delta_f^2$$

Where δ_f is in degrees. It can be seen that a flap chord ratio of 0.20c to 0.30c will yield the highest value of the maximum lift coefficient. Ref. [18] recommends 0.25c as the optimum flap chord. The highest $C_{l_{max}}$ of the flap is obtained when it is deflected 60°. The magnitude of the $C_{l_{max}}$ was not found to vary much within the range of Reynolds Numbers tested (0.6×10^6–3.5×10^6). Drag coefficients were shown to increase rapidly once the lift coefficient exceeds 1.2, which can be attributed to the increased flow separation behind the flap.

Another aerodynamic issue is the influence of a gap between the flap and the main wing. Such a gap allows air to flow from the higher pressure on the lower surface to the upper one. This reduces the effectiveness of the flap, as is clearly shown in Figure 10-27. At a deflection of 60°, the maximum lift coefficient drops from about 2.02 to 1.65 in the presence of a 0.0032c gap. Other data can be seen in Table 10-5.

10.3.3 Split Flap

The *Split Flap* is really a two member family of trailing-edge flaps that consist of deflecting a plate on the lower surface without any change in the geometry of the upper surface. The two family members are the *split flap* and the *Zap flap*.

(1) Split Flap

The *split flap* is a simple device that, like the plain flap, is deflected through rotation only (see Figure 10-28). It was invented in part by Orville Wright [28] and James M.H. Jacobs, who patented it jointly in 1924 under US Patent 1,504,663. Typical deflection angles range from 0 to 70°. The flap is very simple mechanically. When

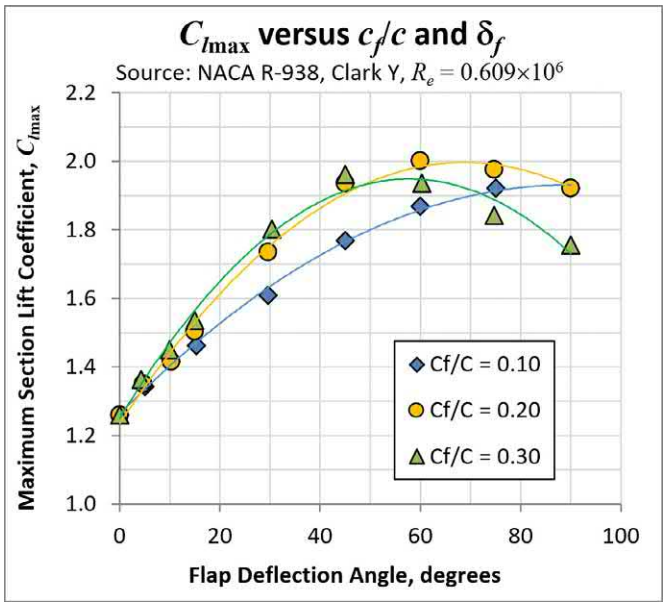


FIGURE 10-26 The maximum lift coefficient as a function of flap deflection angle and flap chord ratio.

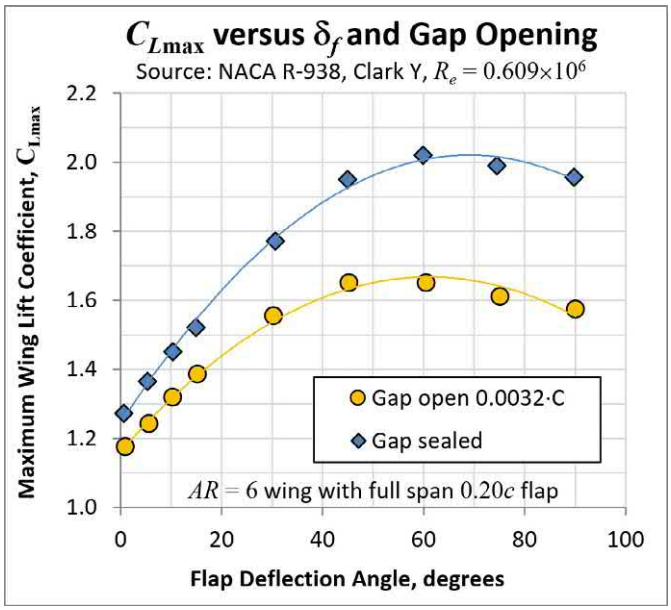


FIGURE 10-27 The effect of gap on the magnitude of the maximum lift coefficient.

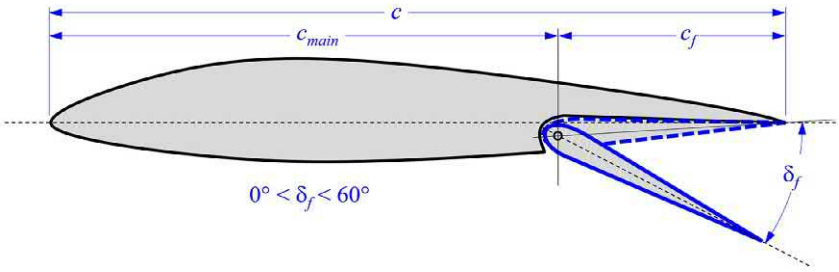


FIGURE 10-28 A schematic of the *split flap*.

deployed it enlarges and magnifies the high-pressure region on the lower surface, while generating a large separation behind it. The added drag provides attitude and glide-slope control for the pilot. As a speed brake, it is superior to a spoiler (which operates on the upper surface) because of reduced L/D ratio. Although surprisingly high, its $C_{l_{max}}$ is lower than that of more sophisticated flap types (not surprising). Thus, the flap is not used on any modern airliner. However, it is used on the Douglas DC-3 (C-47) and many fighter and bomber aircraft operated during WWII. For instance, the Curtiss SB2C Helldiver and Douglas SBD Dauntless dive bombers, both which featured split flaps with multiple perforations to reduce buffeting [29]. Among GA aircraft featuring the flap is the Cessna 310 and the Yakovlev Yak-18T.

(2) Zap Flap

The Zap flap is a variation of the split flap that introduces translation in addition to the rotation (see Figure 10-29). It gets its name from inventor Edward F. Zaparka, who patented it in 1933 as US Patent 2,147,360. In its simplest implementation, an actuator forces the leading edge of the flap backward while a special linkage simultaneously rotates it. Unlike the split flap, the chord is increased, generating higher lift than the split flap. The flap has not seen much use, but was tested in the late 1930s and early 1940s by NACA using Fairchild 22 [30] and Fairchild XR2X-1 [21] aircraft. It was also used in the first prototype of the Northrop P-61 Black Widow, but presented problems. It was replaced with conventional flaps in the production aircraft [31].

(3) Schrenk Flap

The *Schrenk flap* was invented by Oskar Schrenk, who is better known for the development of the simple spanwise wing-load method called *Schrenk's approximation* [32]. The flap is a simple split-flap style device, which bears close resemblance to the split-flap besides deflecting to 90° (see Figure 10-30) and being $0.05c < c_f < 0.20c$. The device was introduced in 1932 in Germany per Ref. [33]. Experimental data are provided in Refs. [22, 33]. The lift increase obtained by the flap is attributed, in part, to the high pressure on the lower surface and, in larger part, by the additional reduction in upper surface pressure due to the low-pressure field behind the flap [33].

(4) General Design Guidelines

Split flaps (of either kind) may cause severe buffeting if deployed at high airspeed, for instance, when used as dive brake. The solution is a perforated flap. The hinge moment of the Zap flap may reverse if there the gap between the wing and the leading edge of the flap as a consequence of the flap's translation and rotation.

(5) Aerodynamic Properties

The split flap increases $C_{l_{max}}$ by a value ranging from 0.66 to 1.05, depending on airfoil, chord, and deflection. Generally it is deflected to an angle of 60°. The references cited showed the stall AOA to change from −1.2 to −7.2°. The change in C_m is −0.16 to −0.19. The zero AOA drag coefficient changed by some 0.1512.

The Zap flap was tested on a full-scale aircraft in 1942. A deployment of both the split and Zap flap leads to a relatively small shift in the stall AOA, in particular

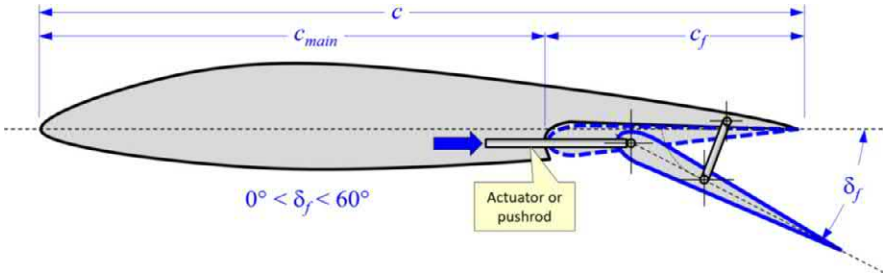


FIGURE 10-29 A schematic of the *Zap flap*.

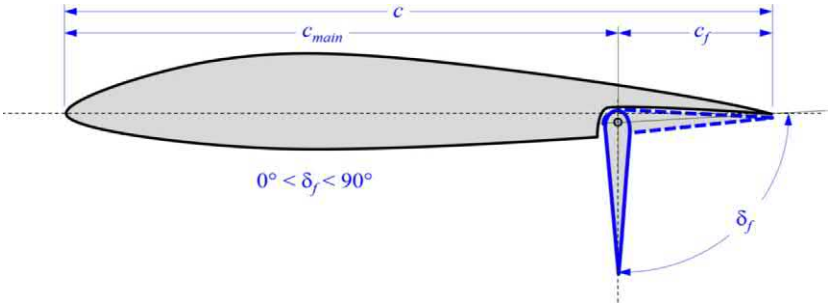


FIGURE 10-30 A schematic of the *Schrenk flap*.

the Zap flap, which had a marginal increase in the stall AOA (which is very unusual for trailing-edge high-lift devices) according to Refs. [21, 30].

Ref. [21] found the zap flap to increase maximum lift coefficient by 1.08 for a configuration that had a gap of 0.010*c* between the wing and the flap leading edge. The same flap with a gap of 0.037*c* increased this by 0.20. The minimum drag coefficient increased by 0.11 and the pitching moment coefficient decreased by −0.225. Other data can be seen in Table 10-5. Note that the data for the zap flap pertain to a wing rather than an airfoil, like the other devices in this chapter. The wing of the test vehicle had a constant chord of 4.34 ft, wingspan of 33.02 ft, and wing area of 141.5 ft^2, giving it an *AR* of 7.705.

10.3.4 Junkers Flap or External Flap

The *Junkers flap* (also called the *external flap*) is unorthodox in the sense it resides entirely outside of the wing. Mechanically, it is a simple design (see Figure 10-31) that results in a modest increase in $C_{l_{max}}$ compared to more modern devices. However, it generates low drag when neutrally deflected.

The external flap is most notable for its use on the German Junkers 52-3 tri-motor military (and commercial) transport aircraft designed around 1930 (see Figure 10-32) and for which it receives its name. It was also used on the Junkers Ju-87 Stuka dive bomber. A similar device was patented by Charles E. Wragg in the United States in 1930 (US Patent 1,756,272), although it is almost certain it was conceived earlier in Germany. The device was referred to as the *Wragg compound wing*. Among other notable aircraft featuring the flap is the Colomban MC-15 Cri Cri (often cited as the world's smallest twin-engine aircraft), the Miles Gemini, and Zenith CH 701, 750, and 801 STOL kitplanes.

The flap lends itself well as a flaperon (the flap combines the functionality of a flap and aileron), although it may create adverse yaw. One of its primary advantages is low zero-deflection drag. The installation may even reduce the drag of the airfoil in front of it by a few drag counts if properly located. Some of this is offset by the drag of the external hinges. The flap does not generate a large enough $C_{l_{max}}$ to be suited for modern GA aircraft (see below), but its simple installation may be the right choice for selected applications. The flap resides outside the boundary layer, making it more effective at low deflection angles than identically sized conventional ailerons.

(1) General Design Guidelines

Loads are reacted by external flap hinges, which should be aerodynamically faired (apparently not a concern in the Ju-52). The flap was investigated by NACA in 1935 and 1936. Ref. [23] found the ideal hinge location to be 0.0125*c* (1.25%) behind the trailing edge and 0.025*c* (2.5%) below the chord line. These dimensions are referred to as x_f and y_f in Figure 10-31. Ref. [24] also presents similar results, but remarked a correct position is critical. The flap must be neutrally balanced (or slightly nose-heavy) about the hingeline to prevent flutter. The flap may require a ballast arm, like the plan flap, further increasing the drag of the design.

(2) Aerodynamic Properties

Ref. [23] wind tunnel tested a Junkers flap featuring a Clark Y main-wing element and NACA 0012 flap

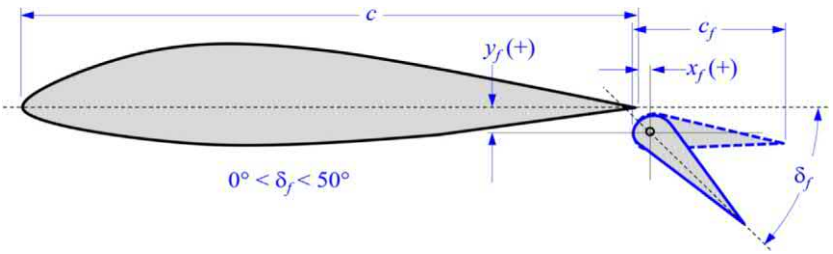


FIGURE 10-31 A schematic of the *Junkers flap*.



FIGURE 10-32 An airworthy example of a German Junkers Ju-52 military transport aircraft featuring *Junkers flap*. *Photo by Nick Candrella.*

element. The $C_{l_{max}}$ of the flap in the optimum location was 1.81, based on the area that included the combined area of the wing and flap. This compares to 1.250 for the basic Clark Y at the test R_e of 0.609×10^6. The increase in $C_{l_{max}}$ amounts to 0.56. The $C_{d_{min}}$ of the baseline airfoil was 0.0155, but reduced to 0.0146 by deflecting the flap −5° (TEU). Furthermore, a deflection angle of +5° (TED) is suggested for use during climb.

Ref. [24] investigated the use of a Junkers flap using NACA 23012, 23021, and Clark Y basic airfoils. The flap chord tested was 0.20*c* and 0.30*c*. The resulting aerodynamic effects are listed in Table 10-5. The optimum flap location was found to depend on the airfoil and optimum position was close to that of Ref. [23].

10.3.5 Single-Slotted Flap

The *Single-Slotted Flap* (see Figure 10-33) is an improved version of the plain flap. It consists of an airfoil mounted to a hinge that is offset from the main airfoil. The resulting motion combines rotation and translation, increasing the chord length by some 5%–10%. The motion opens a slot along the trailing edge that is imperative to the flap's functionality. Such a translation is often called *Fowler motion*, although the flap is not considered a Fowler flap (see Section 10.3.7, *Fowler Flaps*). It may deflect to an angle as large as 50°, although this results in mostly separated flow over the flap. The single-element slotted flap is the most common type of high-lift devices used for GA aircraft.

The flap develops higher $C_{l_{max}}$ than the plain flap and less drag than the Split and Zap flaps. The lower drag is attributed to the reduced flow separation over the flap. The higher lift is often explained as a consequence of energized airflow that delays flow separation to a higher flap deflection angle. The author prefers A.M.O. Smith's circulation analogy [10] of Figure 10-7. With respect to trailing-edge flaps, it considers the formation of two sources of circulation; one on the wing element and the other on the flap. The analogy helps explain the observed airspeed over the leading edge of the flap and the resulting low-pressure peak. This has been demonstrated experimentally in many of the references presented in this book. It explains the higher $C_{l_{max}}$ and shows that the presence of the slot is essential. This is important when designing variable cambered airfoils (e.g., see Section 10.2.3, *Variable Camber Leading Edge*)—such airfoils are usually

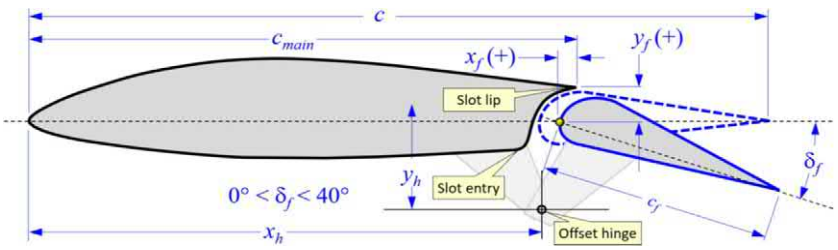


FIGURE 10-33 A schematic of the *single-element slotted flap*.

designed without slots—not separating the leading- or trailing-edge elements yields lower $C_{l_{max}}$ than their separated counterparts.

(1) General Design Guidelines

Some forethought must be exercised when laying out the hinge geometry. First, the flap system should be capable of deflecting to approximately 40°, as shown in Figure 10-34. Exceeding this has limited value and may actually aggravate stall characteristics. Figure 10-35 shows the capability of a slotted flap deflected to 40°. The $\Delta C_{l_{max}}$ gained is 0.926.

Second, if the highest point on the flap is ahead of the hingeline when stowed, it will travel to an even higher point during deployment. This is compounded by the upward flex of the flap when loaded. This may cause the flap to jam in flight, even if no such problems are evident on the ground. Therefore, the flight test team should try to emulate the flap flexing on the ground to avoid the problem during flight testing. The most likely scenario is a jammed flap that requires the airplane to return to base. However, it could also cause a serious flap asymmetry, if the control system is such the flap on one side can deploy fully with the other one partially deployed.

A frequently overlooked issue related to the above is *actuation binding*. It is caused by excessive friction in the flap actuation system that the actuation motor may lack power to overcome. It also flexes the structure and is a fatigue problem waiting to happen. It is usually a result of multiple hinges, whose hinge points are not perfectly concentric or mounted on poor foundations (e.g., flexible brackets mounted to plates rather than stiff frames and bulkheads).

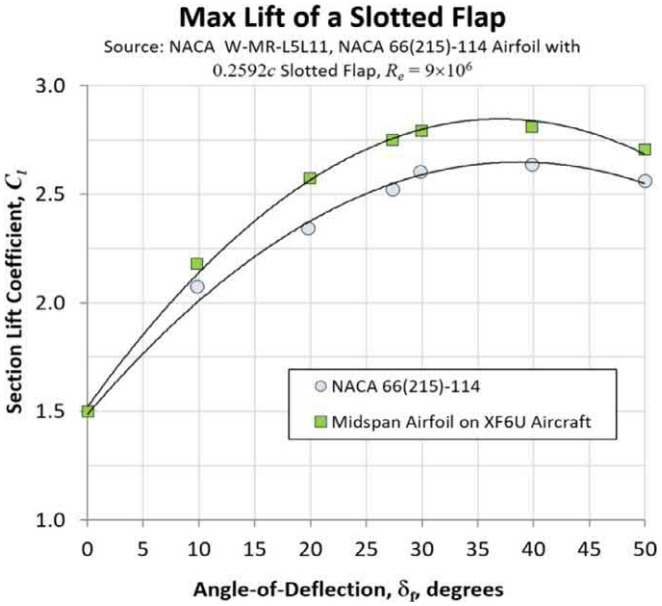


FIGURE 10-34 Typical *single element slotted flap* achieves its $C_{l_{max}}$ near a 40° flap deflection.

Since the presence of the slot entry (or cove entry) increases cruise drag, there are variations of this flap that feature a cove panel that opens and closes via special slave linkage. An example is shown in Figure 1.10 of Ref. [13]. For smaller airplanes such added complexity should be avoided. However, sealing the cove is recommended, as shown in Figure 10-36. It reduces drag considerably at typical cruise lift coefficients.

The flap requires at least two hinges. To minimize flap flex, three or more hinges should be considered. The hingeline must be a mathematically straight line through all the hinges—one must be able to simultaneously look through all the hinge-holes. This requires a tight tolerance must be associated with their location. Often the only way to mount the flap is through a high-precision match drilling once the flap-hinges are installed: Predrilling is destined to create a disappointment.

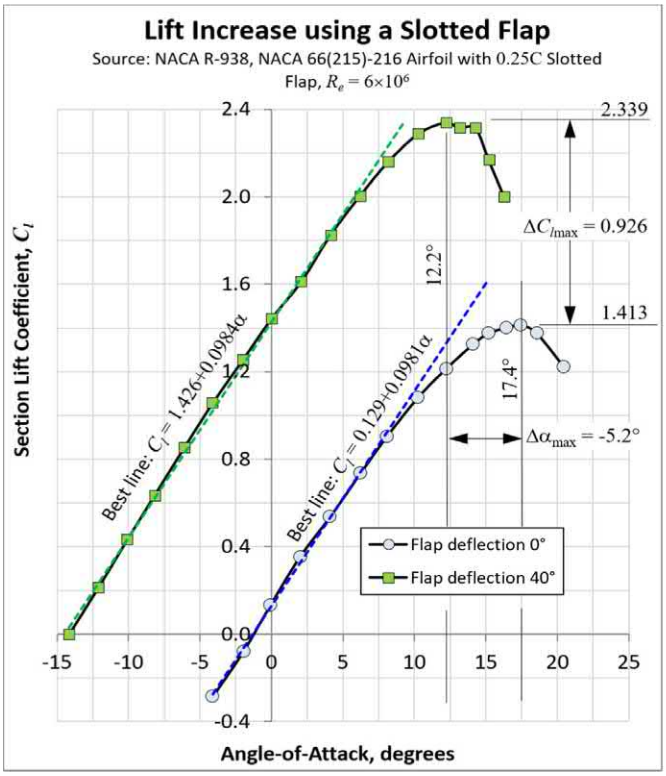
(2) Aerodynamic Properties

The presence of the slot entry is required on the lower surface of the airfoil. This increases the drag of the airfoil with the flap stowed (see Figure 10-36) by approximately 10 drag counts (i.e., 0.0010). The expected increase in lift, $\Delta C_{l_{max}}$, should be a fairly good 0.6–1.0, depending on geometry and Reynolds number.

A round slot entry is recommended, although it may be harder to manufacture. The drag can be kept down using a gap seal as indicated in Figure 10-36. A rubber seal is a good choice but should not obstruct the flow when flap is deployed or cause jamming if it holds water that freezes. A carefully sculpted wing trailing edge that contacts the upper surface of the flap without causing friction of movement can also work as a seal. However, the paint on the flap may be scraped off (can be solved with an Ultra-High Molecular Weight Polyethylene tape with high abrasion tolerance) and quality control issues may arise if the tight fit required in flight is not achieved.

10.3.6 Double-Slotted Flaps

The *double-slotted flap* increases the maximum lift coefficient in the same way as the single-slotted flap—by the formation of multiple sources of circulation. Alternative explanation: Smoother mean-line curvature helps delaying flow separation over the flap elements, increasing lift. The key difference is that the double-slotted flap adds a level of boundary-layer control not possible with the single-slotted one. The extra slot allows the flap to be deflected to an even higher angle before flow becomes excessively separated, boosting the $C_{l_{max}}$. Examples are shown in Figures 10-37 and 10-38. The forward of the two flap elements is called the *vane* and the other one is simply the *flap*.



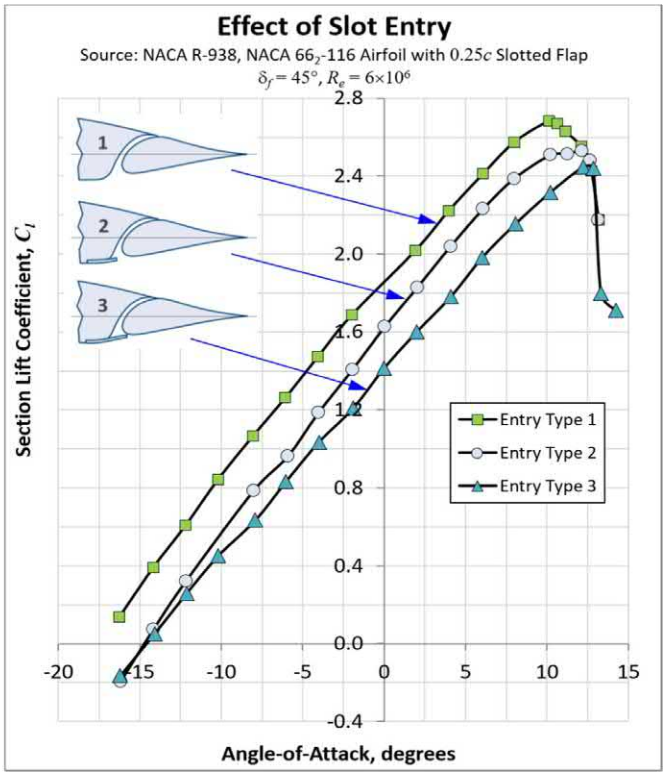


FIGURE 10-35 Typical lift gain obtained from a *single-element slotted flap* (left). The $C_{l_{max}}$ is highly dependent on the cove shape (right). Rounded slot entry yields the highest $C_{l_{max}}$. *Based on J.F. Cahill, Summary of Section Data on Trailing-Edge High-Lift Devices, NACA R-938, 1949.*

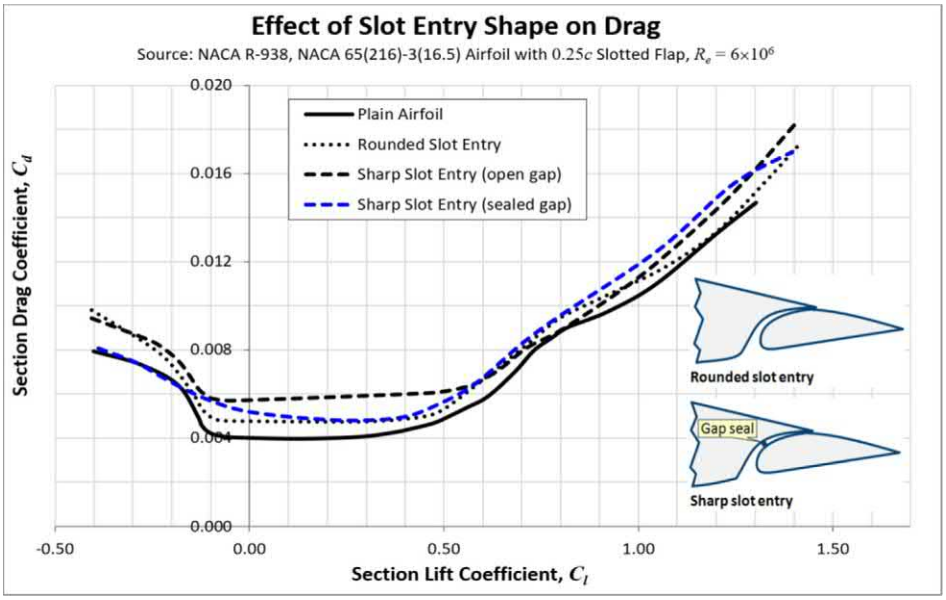


FIGURE 10-36 The effect of slot entry and slot gap seal are shown in the graph. *Based on J.F. Cahill, Summary of Section Data on Trailing-Edge High-Lift Devices, NACA R-938, 1949.*

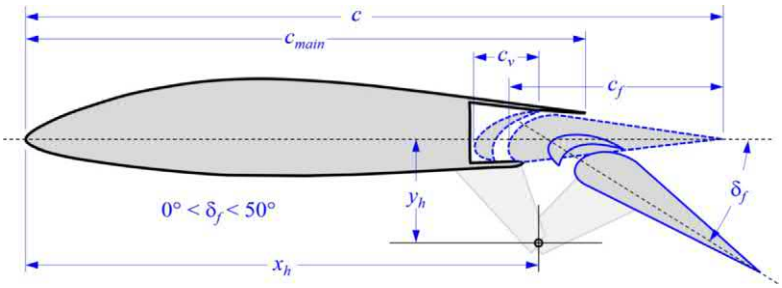


FIGURE 10-37 A schematic of the *fixed-vane double-slotted flap*. The position of the vane relative to the flap element does not change with the actuation.

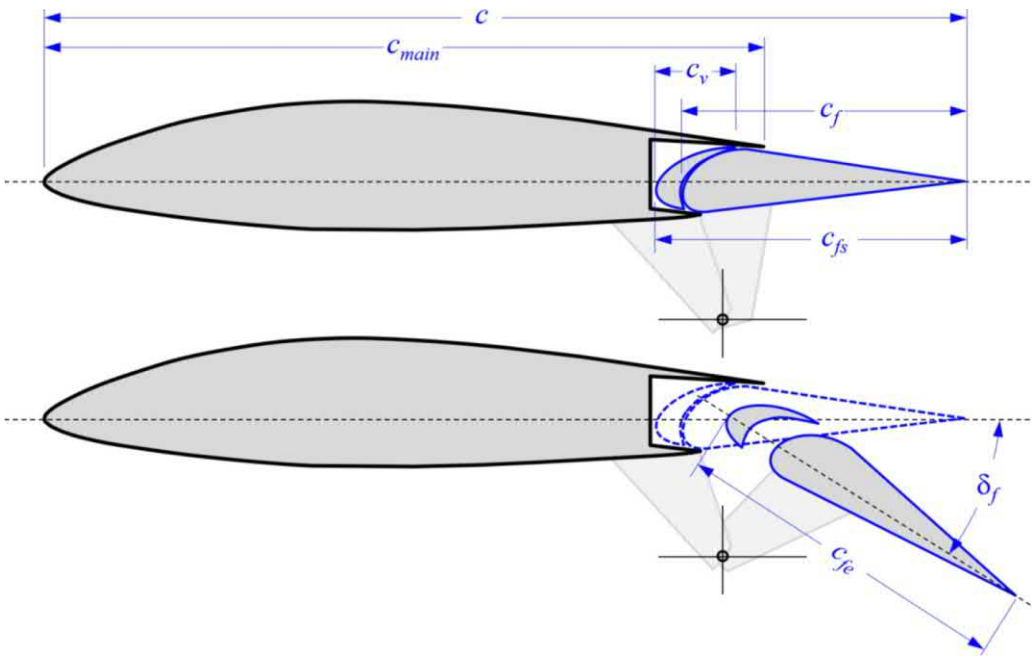


FIGURE 10-38 A schematic of the *articulating-vane double-slotted flap*.

The term double-slotted refers to a family of two-element flaps, just like there is a family of Krüger flaps. The primary difference between members is how the two elements interact. Generally the most important design parameters are flap deflection, flap size, flap extension, and the slot geometry, which dictates how efficiently air flows through the slot. The following listing cites the most common types of double-slotted flaps.

(1) Fixed-Vane Double-Slotted Flap

The *fixed-vane double-slotted flap* (see Figure 10-37), as the name implies, has the vane fixed in front of the flap. This means the separation of the two does not change, regardless of position. The advantage is mechanical simplicity, less cost and weight than its articulating cousin, to be discussed next. The disadvantage is greater chord length and requires larger wing volume than if the flap could be shortened when stowed. This may cut into the available wing fuel volume. The vane allows the main flap to be deflected to an angle as high as 55° before suffering reduced improvement in $C_{L_{max}}$. The wing skin on both surfaces should reach past the leading edge of the flap element to reduce. The fixed-vane is used on the McDonnell Douglas DC-9/MD-80 commercial jetliner, the Hondajet and the Cirrus SF50 Vision.

(2) Articulating-Vane Double-Slotted Flap

There are two primary advantages in using the articulating-vane double-slotted flap (see Figure 10-38). First, it is possible to close the slot between the vane and the flap. This reduces its drag when stowed. Second, the articulation reduces the total flap chord, potentially increasing wing fuel volume. However, when deployed, it generates the same $C_{l_{max}}$ as a fixed-vane flap of identical geometry, unless the flap-to-vane angle changes.

The primary drawback of the articulating vane is mechanical complexity and weight. The vanes are usually spring loaded and rest up against a stop [13]. Once the main element has transited backward a certain distance, the vane slot has opened fully and the vane now begins to transit aft with the main element of the flap. The vane is attached to the flap using straight or curved tracks that are hidden in the main element.

(3) General Design Guidelines

Designing a multielement flap system usually takes scores of engineers. The complexity of such flaps should not be underestimated. Mechanically sophisticated flaps, which require translation and rotation, can pose a number development issues in addition to those that have already been brought up. One is excessive play in the actuation mechanism that leads to a reduced deflection, not to mention possible flutter problems. Issues often arise with the overlap and gap between the flap and the wing that prevent the advertised lift from being generated. There are issues with the positioning of the flap with respect to the wing, when deployed. The optimum location of the flap for maximum lift as predicted by Navier-Stokes solvers often differs from that obtained in wind tunnel testing. If tight tolerances are not maintained, asymmetric flap deflection between the left and right sides may result, leading to roll-off when stalling. The flap motion must be such that the vane remains in contact with the upper slot lip (or upper cove) for the first

15°, reducing drag during T-O. Finally, the more sophisticated the flap, the more internal wing volume it tends to absorb. This will affect available fuel volume for selected applications and should be considered during the flap selection process.

Ideally, the flap should actuate reliably and repeatedly for many years without jamming, requiring only routine maintenance, such as regular lubrication. As usual, when comes to mechanical design, the simplest configuration that does the job is always the best.

10.3.7 Fowler Flaps

The term Fowler flap usually refers to a high-lift device that significantly increases the chord of an airfoil to complement the deflection. They are named after the American inventor and aeronautical engineer Harlan D. Fowler (1895–1982) [34]. Ref. [35] offers a fascinating insight into the development of this flap. It was invented in 1924 and was first used by the Glenn L. Martin Company, who hired Fowler to design flaps. In 1937, the flaps were introduced on the Lockheed L-14 and later on the Boeing B-29 Superfortress.

The most notable feature of Fowler flaps is the large increase in chord it provides. Since the section lift coefficient is based on the shorter stowed chord, this greatly boosts its value. It is regarded by many as the first modern high-lift mechanical flap (e.g., see Ref. [10]). Figure 10-39 compares the flow field around a single-element Fowler and fixed-vane double-slotted flaps. It shows many similarities, including similar $C_{l_{max}}$ and α_{stall}. However, the single element Fowler flap is simpler than the two-element fixed-vane flap. That said, both flaps pose structural and operational complexities that also have to be considered.

(1) Single-Slotted Fowler Flap

The *single-slotted Fowler flap* is generally deployed by a large translation first, followed by a rotation to as much as 40–45° (see Figure 10-40). The translation requires the upper skin to extend much farther aft than the single-slotted flap. This means the upper aft wing skin must be stiffened in order to prevent the trailing edge from deflecting upward, creating a structural challenge. A single-slotted Fowler flap is used on the Boeing B-52 bomber and 747-SP commercial jetliner. A derivative single-slotted Fowler flap is used on the Cessna 152, 172, and other models under the name *Para-Lift* flaps. These translate far enough aft to justifiably be considered single-slotted Fowler flaps.

(2) Double-Slotted Fowler Flap

The *double-slotted Fowler flap* differs from the fixed- and articulating-vane flaps discussed earlier in that the forward element is the larger of the two and is now referred to as the main element. The flap is more complex mechanically and both elements translate and rotate (see Figure 10-41). The resulting chord increase is also larger than the articulating vane, yielding a slightly higher $C_{l_{max}}$. The wing overlaps the forward element, which overlaps the aft element. The forward flap typically deflects 30–35° (δ_{f1}) and the aft one 28–30°, or through

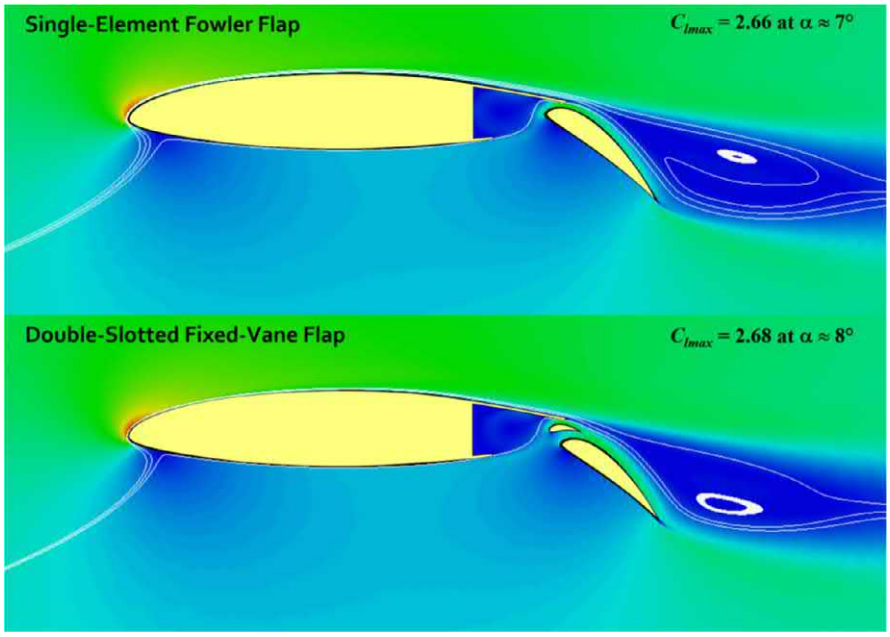


FIGURE 10-39 Comparing the flow-field around a single-element Fowler and a double-slotted fixed-vane flaps.

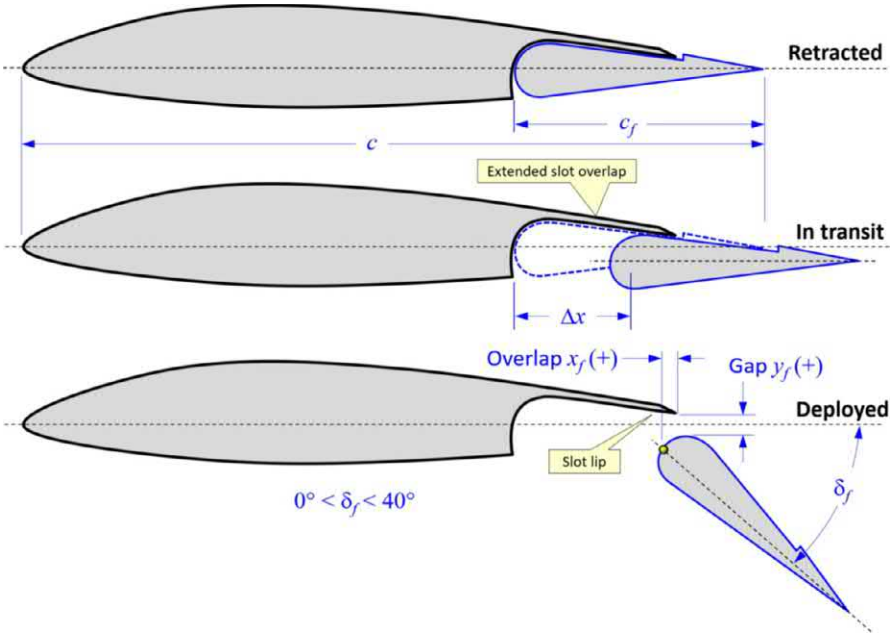


FIGURE 10-40 A schematic of the *single-slotted Fowler flap*.

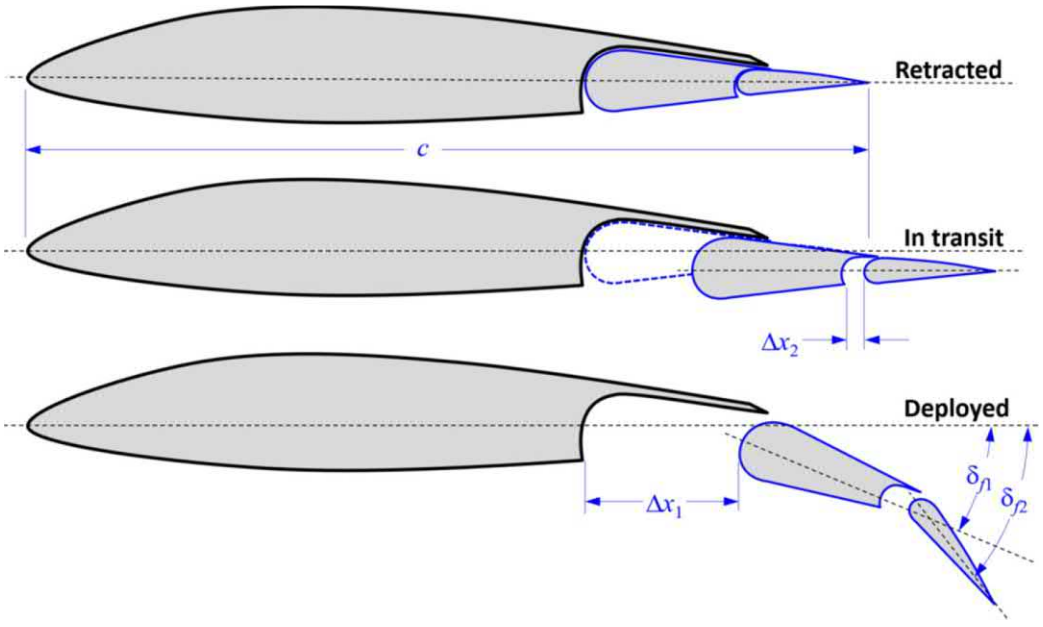


FIGURE 10-41 A schematic of the *double-slotted Fowler flap*.

a total deflection of 58–65° (δ_{f2}). This flap style is primarily used for commercial jetliners, such as the 757, 767, and those made by Airbus.

(3) Triple Slotted Fowler Flap

The *triple-slotted Fowler flap* an even more complex variation of the Fowler flap. It offers a large translation and rotation (see Figure 10-42). Typical deflection of the front element is 30°, center element 45°, and aft element 80°. The flap increases airfoil chord length and camber, yielding a large increase in $C_{L_{max}}$, C_D, and C_M. A very large increase in $C_{L_{max}}$ results in substantial reduction of the stalling speed of heavy aircraft. Using A.M.O. Smith's vortex analogy [10], there is a very complex interaction of gap jet airspeeds that combine to reduce flow separation over the elements, resulting in a high $C_{L_{max}}$. Triple-slotted flaps are primarily used for commercial jetliners. Among aircraft featuring the flap is the Boeing B-727, 737, and 747.

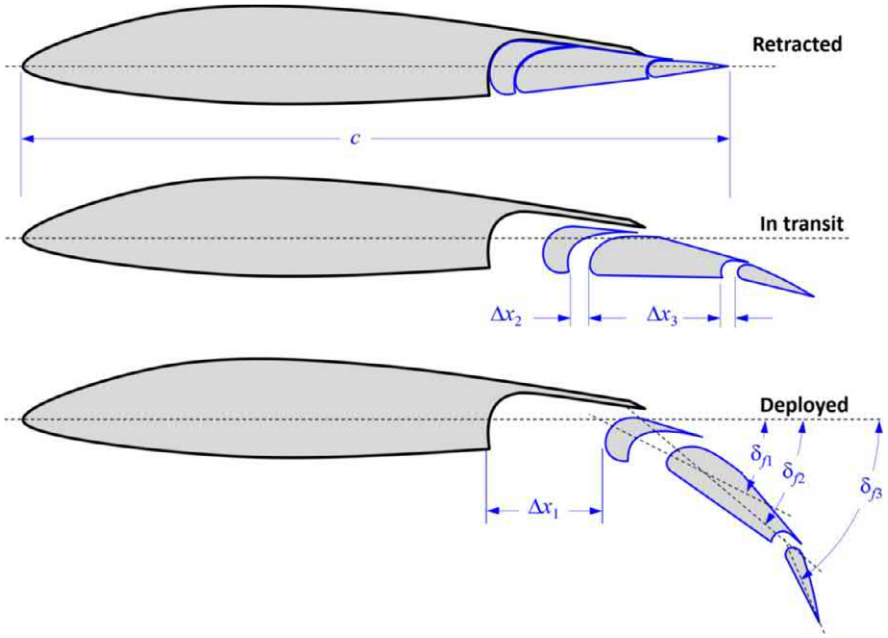


FIGURE 10-42 A schematic of the *triple-slotted Fowler flap*.

(4) General Design Guidelines

A Fowler flap may present unexpected challenges. As stated earlier the upper skin that covers the flap must be stiffened to ensure it will not flex outward due to the pressure differential between the upper and lower surfaces. This can be challenging if the flap is thick, as it will leave less thickness for structural reinforcement of the slot overlap. Play in the system can compromise such flaps, as can the bending stiffness of the flap itself. These are important pitfalls to recognize. If a single actuator is used per flap side, it should be placed near the mid-span station of the flap (ideally near the center of lift). This will minimize the flap moment that could to twist (or yaw) the flap around its vertical axis. Such a moment can jam the flap in the guide slots as one end moves forward (or aft), in the opposite direction to the other end. Lack of bending stiffness can flex the flap between the flap tracks such it puts undue load on the tracks or causes the flap to strike the upper surface of the wing between the tracks.

The double- and triple-slotted Fowlers require complicated and heavy mechanism to deliver each flap element to its intended position. The elements must move reliably on each side of the plane-of-symmetry to avoid flap asymmetry. The flaps generate high aerodynamic loads calling for substantial structure to support. This subjects the main wing to large torsion. The flaps generate high drag, which helps during landing but requires high power setting. This can cause handling complaints if engine spool-up time is slow. The flaps increase the pitching moment, which must be considered when sizing the horizontal tail. It also is more expensive to fabricate and maintain. Advances in CFD have led to a reduction in wing sweep that, in turn, has reduced the need for triple-slotted Fowler flaps.

Figure 10-43 shows one way to acquire a Fowler motion for a flap design. The flap has two guide pins that move inside specially shaped flap track slots. The motion requires an actuator to moves it forward and aft. That detail is left out, but can be accomplished using a linear actuator or jack-screws. The figure illustrates how the flap travels linearly about 60% of the total translation distance with merely 5° of deflection. The

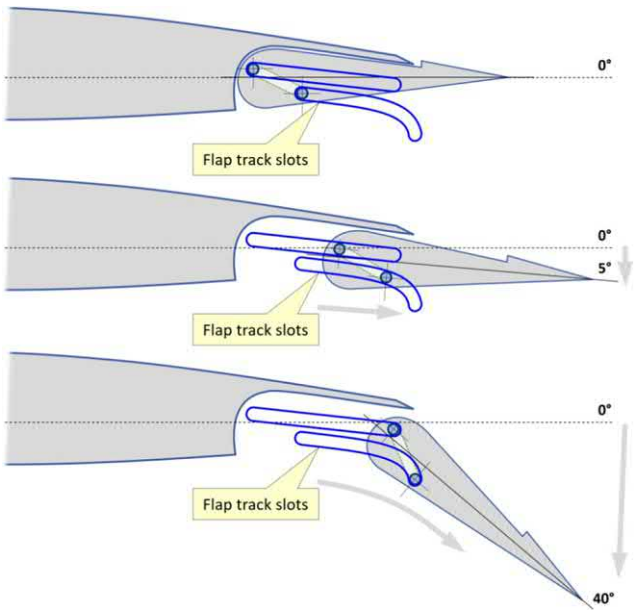


FIGURE 10-43 Fowler motion developed using double flap-track slots to force the flap to translate far back before rotation begins.

remaining 35° are accomplished over the remainder of the translation, resulting in substantial increase in the airfoil chord. This method is used in multiple Cessna aircraft models.

(5) Aerodynamic Properties

Ref. [36] tested two types of Fowler flaps intended for use on a GA(W)-1 airfoil; a 29% chord flap designed using computer method developed by Lockheed Aircraft, and a 30% chord flap designed by Robertson Aircraft, a company that specialized in the manufacture and installation of STOL STCs. The smaller flap achieved a $C_{l_{max}}$ of 3.48 on the airfoil, while a $C_{l_{max}}$ of 3.80 was achieved by the 30% chord flap. A range of optimized flap positions based on deflection angle is presented in the reference. The performance gain is highly dependent on the gap and overlap, with an optimum gap width of approximately 2.5%–3.0% chord for the GA(W)-1 airfoil tested.

The flap increases the pitching moment by a significant value, or $\Delta C_m = -0.75$. The increase in the minimum drag coefficient amounted to $\Delta C_{d_{min}} = 0.040$, and shifted it to a higher C_l.

Among other observations made in Ref. [36], the GA(W)-1 airfoil has a prominent cusp on the aft portion of the lower surface. It was found that straightening this, as is often necessary in a production environment, lead to a performance penalty at $C_l > 0.8$. It was also found that adding vortex generators increased $C_{l_{max}}$ by 0.2. The vortex generators increased drag at low AOAs, but decreased it at higher AOAs. Additionally, the vortex generators had a negligible effect on the stall AOA.

Observation indicates that a multielement airfoil experiences two kinds of poststall patterns referred to as an *airfoil stall* or a *flap stall* [37] (see Figure 10-44). The airfoil stall consists of the separation located mostly on the main element, whereas the flap stall resides mostly on the flap. The appearance of these is dependent on the gap between the cove and the flap, with a wide gap leading to a flap stall. The optimum gap will lead to an airfoil stall with a flow fully attached over the flap. This yields the highest maximum lift coefficient.

10.3.8 Gurney Flap

A *Gurney flap* (see Figure 10-45) is a small angle added to the trailing edge of the high-pressure side of an airfoil. It helps increase its $C_{l_{max}}$ similar to deflecting a flap. It also increases the wing drag and nose-down pitching moment. The device is nothing more than a strip of an extruded aluminum angle (or a folded sheet metal). It forms a circulation pool that modifies the shape of the overall circulation over the airfoil. Considering its small size, its lift increase is substantial. The magnitude depends on its *height-to-chord fraction*, h (see Figure 10-45). Typical values of h range from 1% to 5%.

The invention of the Gurney flap is attributed to Dan Sexton Gurney (1931–2018) an American race car legend, who in the early 1970s used it to help increase the down force on racecars [38]. Since then, the flap has found a variety of applications ranging from wings on race cars, wind-turbine blades, and helicopter stabilators. It can also be seen on the trailing edge of the Cessna 208 Caravan,

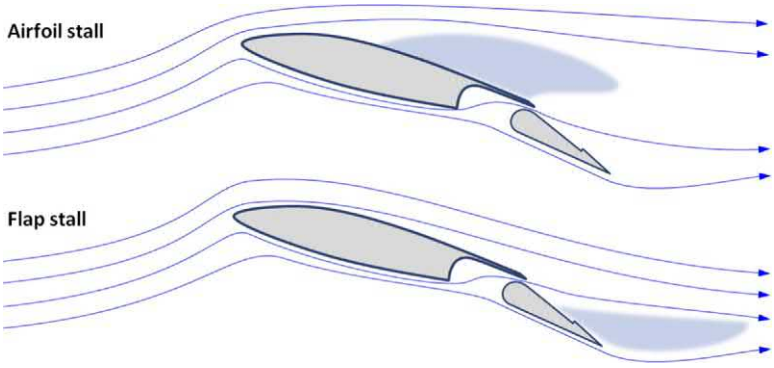


FIGURE 10-44 A flapped airfoil can stall in two ways; airfoil and flap stall. *Based on W.H. Wentz Jr., C. Ostowari, Additional Flow Field Studies of the GA(W)-1 Airfoil With 30-percent Chord Fowler Flap Including Slot-Gap Variations and Cove Shape Modifications, NASA-CR-3687, 1983.*

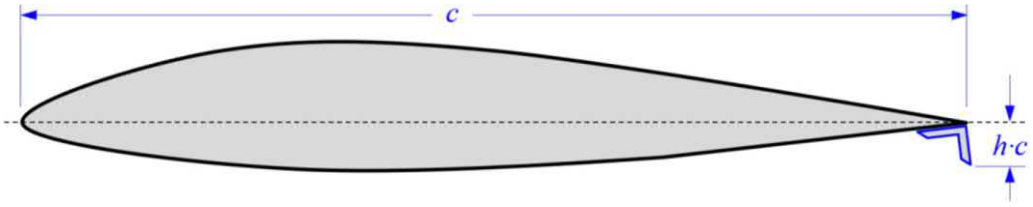


FIGURE 10-45 A schematic of the *Gurney flap*.

single-engine turboprop. However, the device could not be patented because it looks like a small Zap flap [39]. Some would say it looks more like a small Schrenk flap.

(1) General Design Guidelines

Select a suitable flap height using data from the literature, for instance Ref. [42]. Refer to Figures 10-46 and 10-47 for more details.

(2) Aerodynamic Properties

Several papers have been published on the Gurney flap. Liebeck [38] is probably the first to present information on the flap and attempting to explain its effect. The paper cites early testing performed by Douglas Aircraft that seemed to indicate drag reduction, primarily for thick airfoils. However, many later publications indicate that there is a drag increase for airfoil geometry useful in

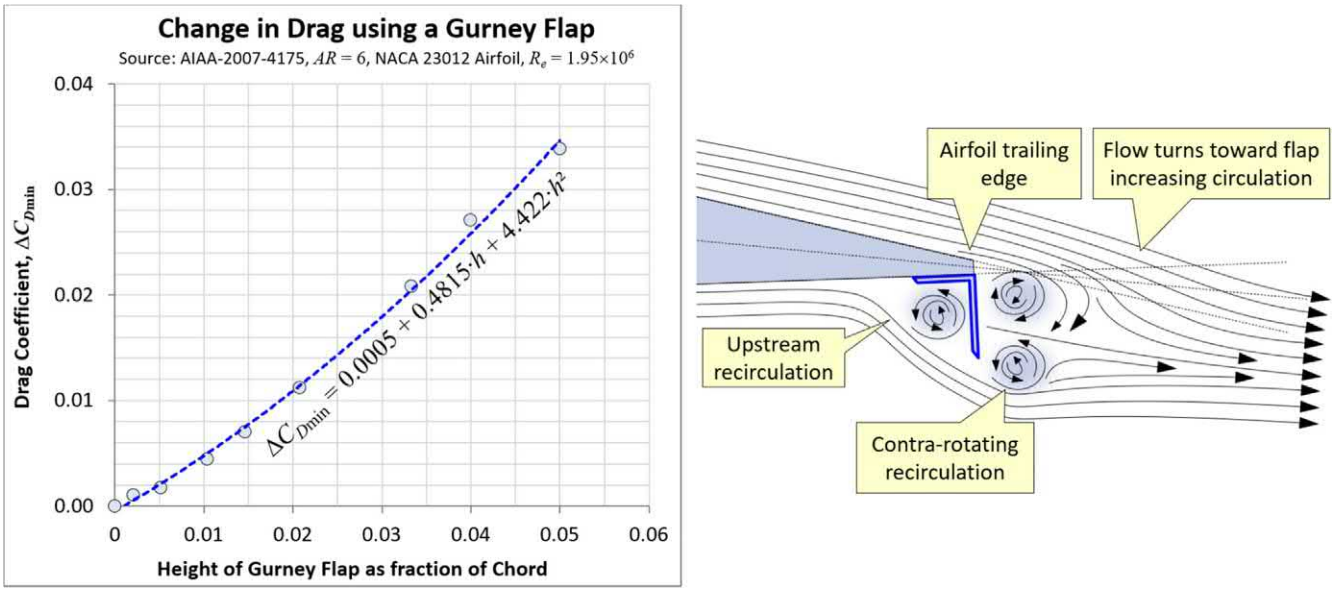


FIGURE 10-46 Drag characteristics of the *Gurney flap* as a function of its height (left) on a wing of $AR = 6$. A schematic of the flow field around a *Gurney flap* (right). *Both based on M.A. Cavanaugh, P. Robertson, W.H. Mason, Wind Tunnel Test of Gurney Flaps and T-Strips on an NACA 23012 Wing, AIAA 2007-4175, 2007.*

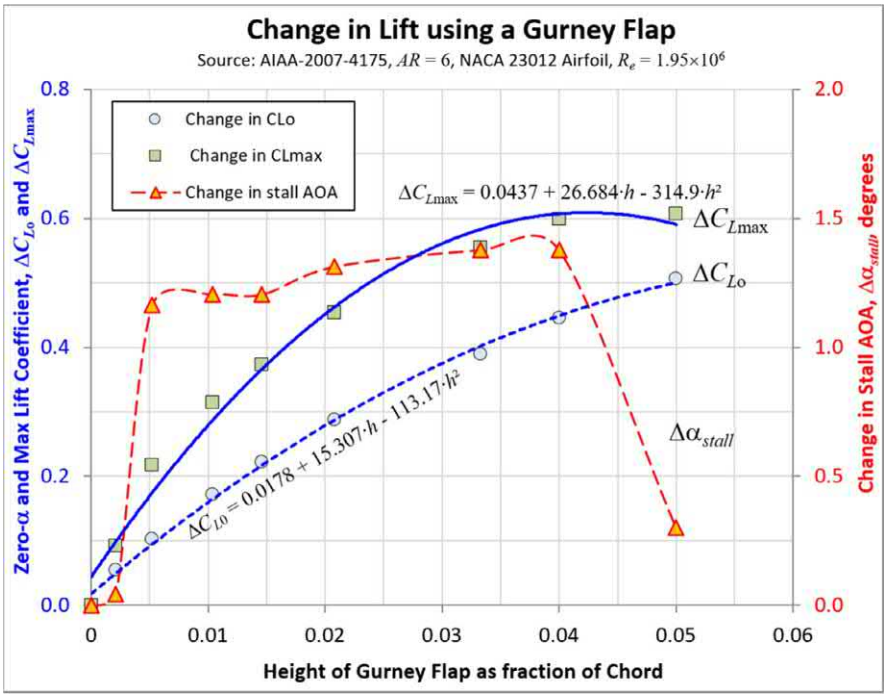


FIGURE 10-47 Lift characteristics of the *Gurney flap* as a function of its height. *Based on M.A. Cavanaugh, P. Robertson, W.H. Mason, Wind Tunnel Test of Gurney Flaps and T-Strips on an NACA 23012 Wing, AIAA 2007-4175, 2007.*

aircraft. Example are references [40–42], which demonstrate increase in $C_{L_{max}}$ and $C_{D_{min}}$. Neuhart [43] presents a Gurney flap that tripled the airfoil drag at low C_L. Similar results can be found in other papers.

Ref. [42] investigated how height affected the aerodynamics of a Gurney flap on a wing of $AR=6$ in a wind tunnel test. The impact on lift is presented in Figure 10-47. This research gives a good insight into its effectiveness. It supports that Gurney flaps increase $C_{d_{min}}$, C_{mo}, $C_{m\alpha}$, $C_{l_{max}}$, and C_{lo} (decreases α_{ZL}). Ref. [43] presents pressure measurements on the upper and lower surfaces of an airfoil with a Gurney flap. It found pressure decreased on the upper and increased on the lower surface, just like that discussed regarding the Schrenk flap.

The impact on lift and drag are shown in Figures 10-46 and 10-47. The former figure also shows a schematic of the flow field around the trailing edge, explaining how the flap changes the circulation around the airfoil by shifting the wake downward. The formulas shown in the graphs are quadratic least-squares fit to the published data. They can be used to get an idea about the effect of the Gurney flap for new aircraft designs. Note that these results are valid for $AR=6$ and $R_e=1.95\times10^6$ and should be used carefully for wing shapes and flight conditions that deviate greatly from those.

An effort has been made to reduce the drag of the Gurney flap. For instance, Vijgen et al. [44] patented a serrated trailing edge for this purpose. Mayda and van Dam [45] proposed a Gurney flap with slits. The common denominator in these attempts is reduced $C_{d_{min}}$ accompanied by a drop in $C_{l_{max}}$.

10.3.9 Summary of Trailing-Edge Device Data

Unless otherwise specified, the data in this chapter apply to airfoils and not wings. The data are obtained from multiple sources. It applies to various airfoils at various Reynolds numbers. The reader is urged to review the sources for deeper insight.

(1) Simplified Methodology

Ref. [46] presents a simple method to estimate $\Delta C_{l_{max}}$ for several styles of flapped airfoils (see Figure 10-48).

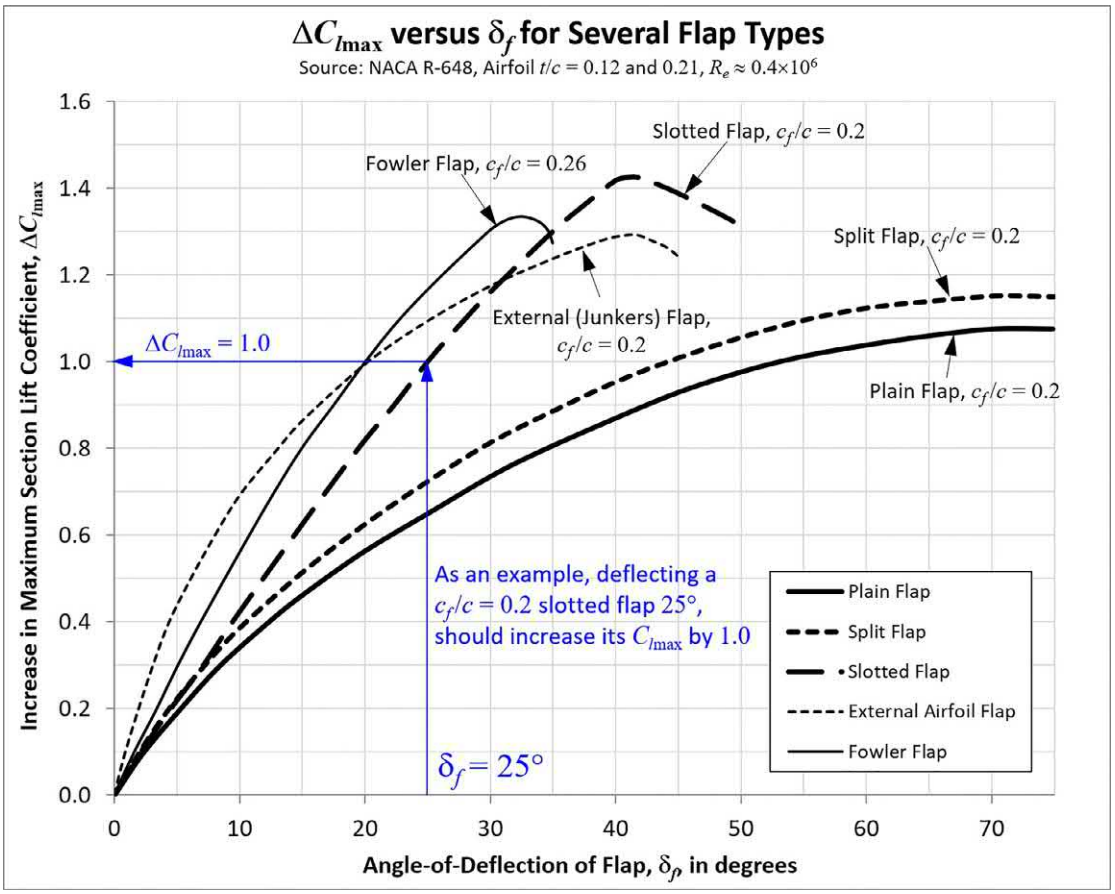


FIGURE 10-48 Increment in maximum lift coefficient, $\Delta C_{l_{max}}$, for several types of flaps. All curves are for an airfoil with $t/c=0.12$. The $c_f/c=0.20$ for all flaps, except the Fowler flap, whose $c_f/c=0.26$. *Based on M.A. Cavanaugh, P. Robertson, W.H. Mason, Wind Tunnel Test of Gurney Flaps and T-Strips on an NACA 23012 Wing, AIAA 2007-4175, 2007.*

(2) Properties of Various Types of Flaps Tabulated

Table 10-5 lists important aerodynamic characteristics for a number of trailing-edge high-lift devices. The purpose is to provide the designer with answers to questions like—what is the change in lift, drag, and pitching moment when such devices are added to the aircraft. All data presented below are based on wind tunnel testing.

(3) How to Use the Tables

First, consider using Table 10-4, which provides rudimentary guidance for selecting an appropriate high-lift system. Once the system is selected, review the following tables for further guidance. The tables only get you "in the ballpark" during the conceptual design phase. *When comes to multielement airfoils, proceed with care. The aerodynamics of such airfoils is highly dependent on viscosity—thus, adding the* $\Delta C_{l_{max}}$ *to the* $C_{l_{max}}$ *of the clean-airfoil only indicates potential lift capability. The actual values depend on factors like* R_e*, geometry, flap-chord-ratio, deflection, surface quality, and others.* Begin by locating the part of the table containing the selected type of trailing-edge flap. Make note of the airfoil and Reynolds number used during the wind tunnel testing, as well as the flap chord and deflection. These are important value to keep in mind if the geometry and operational conditions of the target flap deviates significantly from these values. For values relatively close, it is acceptable to prorate the characteristics of interests (see Example 10-1 or 10-2). The values to be extracted are $\Delta C_{l_{max}}$, $\Delta\alpha_{stall}$, $\Delta C_{d_{min}}$, and ΔC_m. Also, make note of the geometry details shown in Figures 10-49 and 10-50, which must be defined for proper referencing in Table 10-5.

EXAMPLE 10-2

A NACA 65_2-415 airfoil is to be used in a wing design and will feature a simple slotted flap whose chord is 30% of the chord length and will be deflected to 32°. Determine the airfoil's $C_{l_{max}}$ at a Reynolds number of 6 million.

SOLUTION:

Using Table 8-9, the baseline airfoil characteristics are given by (generally the data in the table are for $R_e = 6\times10^6$) $C_{lmaxb} = 1.62$, $\alpha_{stallb} = 16°$, $C_{dminb} = 0.0042$, and $C_{mb} = -0.060$. Then use Table 10-5 for data applicable to the selected flap style. Unfortunately, in this case, Table 10-5 only contains data to determine $C_{l_{max}}$. The other parameters will have to be determined by other means, e.g., the methods of Section 16.4.7, *Drag of Deployed Flaps*.

Looking through the data of Table 10-5, it can be seen there are two 65-series airfoils that feature a single-slotted flap and are "reasonably" similar to 65_2-415 airfoil (NACA 65_1-213 and $65_{(215)}$-114). Here, use the latter. However, the increase in $C_{l_{max}}$ is based on testing at $R_e = 9\times10^6$, which is one-third greater than our target R_e of 6×10^6. This exposes one of the problems with using test data for dissimilar airfoils exposed to dissimilar flight conditions; applicability. However, in the absence of more direct data, Table 10-5 is our best bet but calls for a sound engineering judgment. If possible, adjust the $C_{l_{max}}$ to the appropriate Reynolds number. Here assume the $C_{l_{max}}$ at 6 million to be 90% of that at 9 million.

Continued

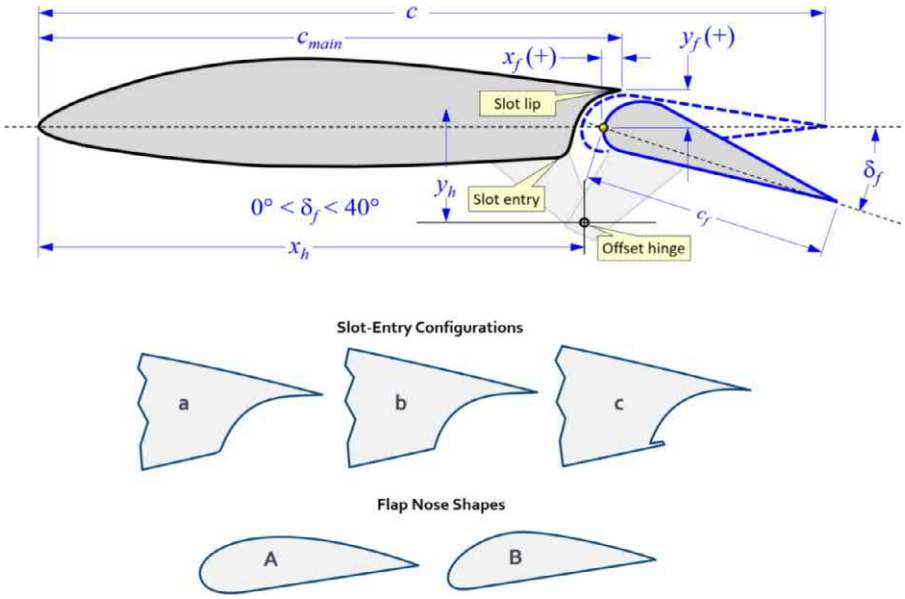


FIGURE 10-49 Reference geometry schematics for slotted flaps for Table 10-5.

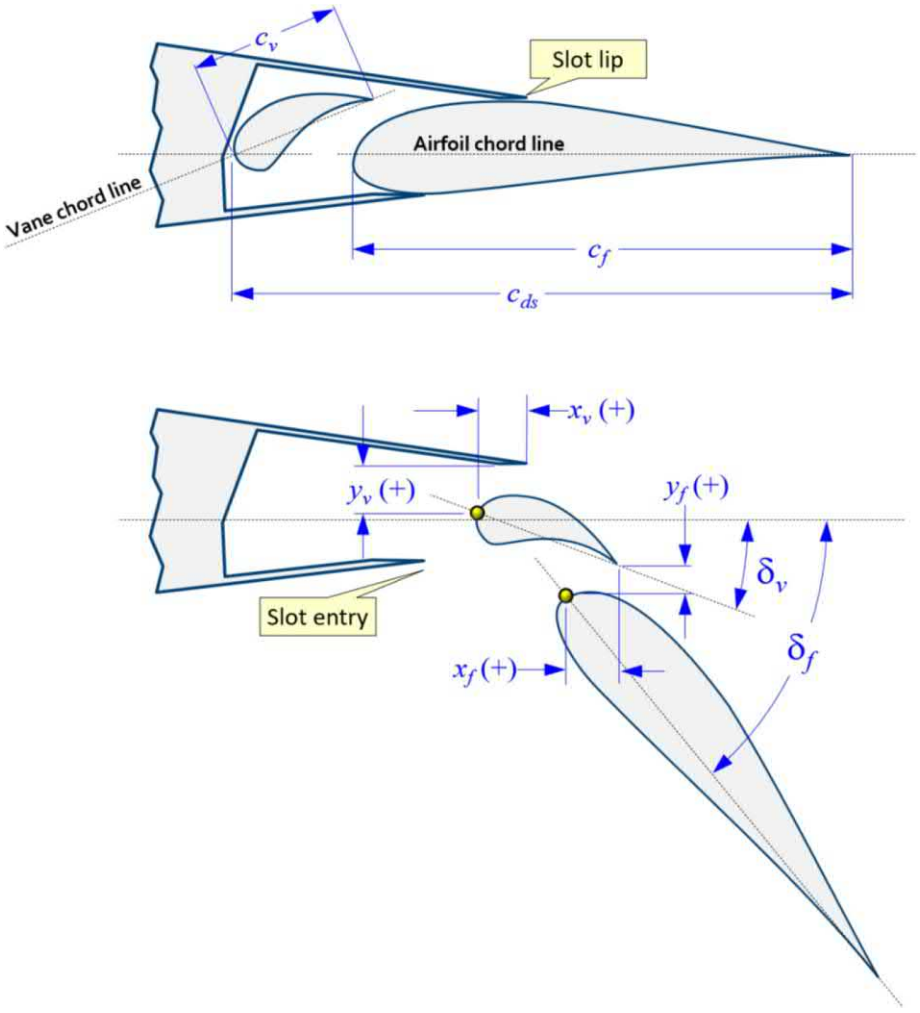


FIGURE 10-50 Reference geometry schematics for double-slotted flaps for Table 10-5.

EXAMPLE 10-2 (*cont'd*)

Using Table 10-5 the following values are obtained for the $65_{(215)}$-114 airfoil:

$$\Delta C_{l_{max}} = 1.65 \text{ for } \delta_f = 40° \text{ and } c_f/c = 0.256$$

Therefore, we can estimate the maximum section lift coefficient as follows:

$$C_{l_{max}} = C_{l\max b} + \Delta C_{l_{max}} \left(\frac{\delta_{f\ true}}{\delta_f}\right)\left(\frac{C_{f\ true}}{C_f}\right)$$

$$= 1.62 + (0.90 \times 1.65)\left(\frac{32°}{40°}\right)\left(\frac{0.30}{0.256}\right) = 3.01$$

10.4 EFFECT OF DEPLOYING HIGH-LIFT DEVICES ON WINGS

This section discusses how the distribution of lift changes when high-lift devices are deployed and presents a method to estimate resulting selected aerodynamic characteristics. The analysis methods use the dimensioning scheme shown in Figure 10-51. The subscripts "*a*," "*f*," and "*s*" stand for *aileron*, *flap*, and *slat*, respectively. Any kind of high-lift device is permitted.

10.4.1 Lift Distribution on Wings With Flaps Deflected

(1) Partial Span Flaps

Figure 10-52 shows the spanwise distribution of section lift coefficients at $\alpha = 2°$ with partial span flaps deflected 0°, 10°, 20°, and 30°. It shows how C_l changes gradually in the flapped/unflapped region. This is caused by the increased circulation in the flap region, which increases upwash outside of the flap ends. The figure also shows how the upwash complicates stall tailoring efforts, as the increase in section lift coefficients on the outboard wing may cause early flow separation in that area of the wing.

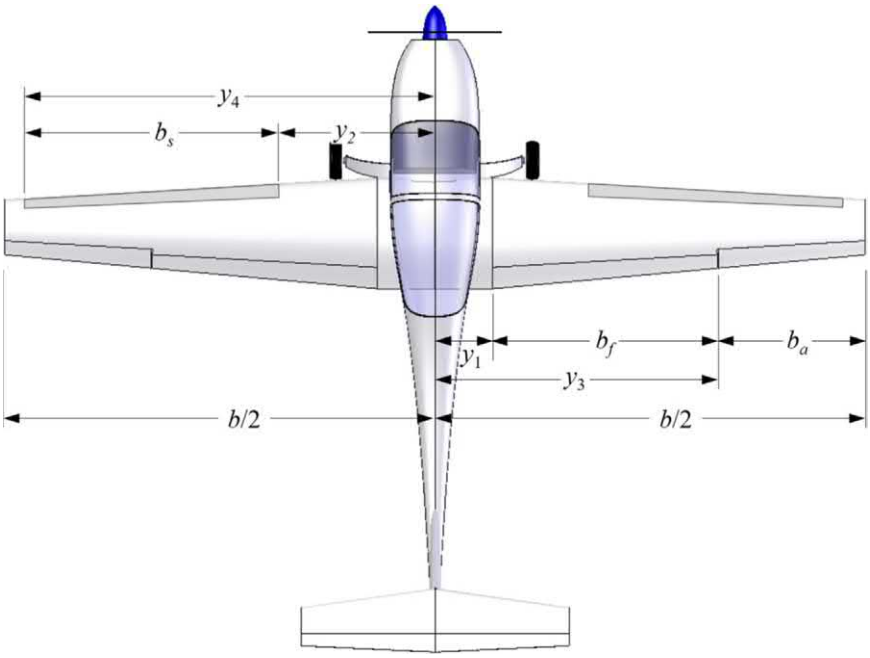


FIGURE 10-51 Layout and important dimensions of a typical aircraft with partial span flaps and slats.

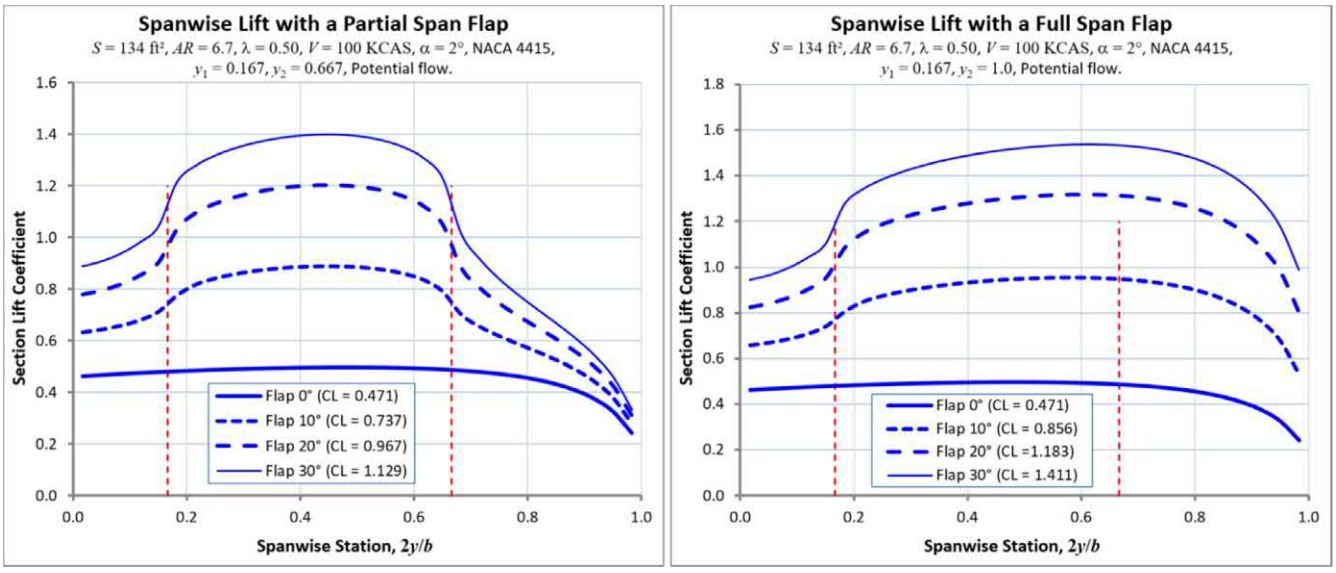


FIGURE 10-52 Spanwise distribution of section lift coefficients for a partial and full span flaps ($c_f/c = 0.30$).

(2) Full Span Flaps—Flaperons

Full span flaps, as the name implies, extend from the inboard wing to the tip. They increase the total wing lift substantially, but may introduce new problems not present with partial span flaps. First, in order to maintain roll control, aileron functionality is usually introduced by splitting the flap into inboard and outboard segments. The outboard segment functions both as a flap and aileron. Such a control system configuration is referred to as *flaperons*.

Second, when deployed, the overall spanwise distribution of C_l is modified such the stall progression is pushed outboard (see Figure 10-52). This may cause roll instability at stall for the flapped wing, even if there is none present for the unflapped configuration. The problem is compounded because roll control requires one flaperon to be deflected beyond that of the rest of the flap. This can cause premature aileron stall at low speeds and high AOA, just when they are needed the most. The De Havilland of Canada DHC-6 Twin Otter is an example of an aircraft that features such flaps and solves this by varying the deflection of the flaps. This is readily evident from its *Type Certificate Data Sheet* (TCDS) [74], the deflection of its double-slotted flaps varies as shown in Table 10-6.

TABLE 10-6 Deflection characteristics of the DHC-6 Twin Otter Flaperons.

Flap	Inboard element	Outboard element
Forward Element	0–40 degrees	0°–26 degrees
Aft (trailing) Element	0–62.5 degrees	Aileron (flaps up): Up 17.5 degrees/Down 16.0 degrees Aileron (flaps dn): Up 25.0 degrees/Down 17.5 degrees

Thus, while the inboard trailing element deflects to 62.5 degrees, the aileron (which is the trailing element of the outboard flap) is limited to 26 degrees + 17.5 degrees = 43.5 degrees. Helped by the presence of a slot in the flap, flow separation is kept to a minimum. Third, flaperons may cause adverse yaw. The downdeflected aileron element, which is associated with the high wing, adds substantial drag to the outboard wing. The opposite happens on the low wing; comparative reduction in drag. The combination may cause adverse yaw that must be countered with rudder deflection.

10.4.2 Wing Partition Method

In order to better estimate lift and pitching moments resulting from the deployment of various high-lift devices, it is common to use the *Wing Partition Method*. The method is more or less a derivative of the Blade Element Theory (BET) presented in Section 15.6. The method partitions the wing into the segments shown in Figure 10-53 and, then, the aerodynamic properties of the individual segments is estimated and used to calculate the total of the wing. The partitioning makes it is much easier to manage the change in aerodynamic properties. The scheme presented here is only for demonstration. Your airplane may be more or less complicated. A demonstration of the method is presented in Example 10-3.

The first step is to tabulate the geometric properties of each segment, using a table similar to the one shown in Table 10-7. These are then summed in accordance with the

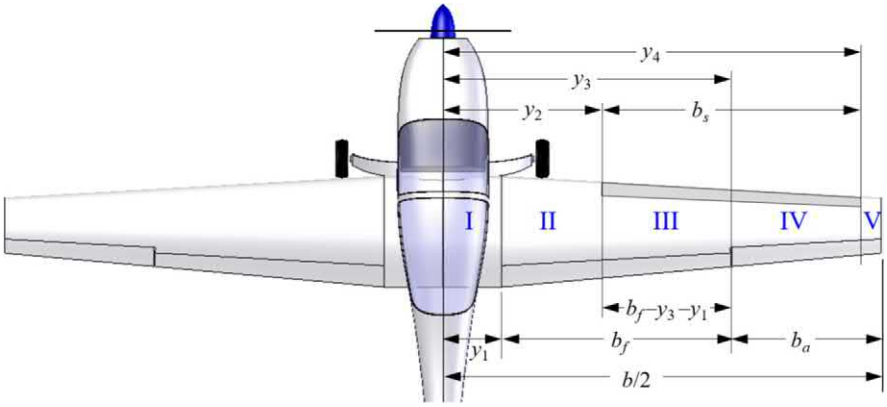


FIGURE 10-53 Partitioning of the wing into manageable segments helps with analysis.

TABLE 10-7 Wing geometric properties based on segment.

Segment	y_a	y_b	Area, S_i	$\Lambda_{hingeline}$	$C_{l\,max\,a}$	$C_{l\,max\,b}$	$\Delta C_{l\,max}$	$C_{l\,max\,avg}$	$C_{l\,max\,avg} \cdot S_i$
I									
II									
III									
IV									
								Sum =	

Where: y_a = Distance of the segment's inboard end from the plane-of-symmetry,
y_b = Distance of the segment's outboard end from the plane-of-symmetry,
S_i = Trapezoidal planform area of the segment,
$\Lambda_{hingeline}$ = Hingeline angle (with respect to a vector normal to the plane-of-symmetry),
$C_{l\max\,a}$ = Maximum lift coefficient at the inboard end of the segment,
$C_{l\max\,b}$ = Maximum lift coefficient at the outboard end of the segment,
$\Delta C_{l_{max}}$ = Increase in maximum lift coefficient due to a high-lift device,
$C_{l\max\,avg}$ = Average of $C_{l\max\,a}$ and $C_{l\max\,b}$.

formulation presented below (here assuming four segments). An example of its use is shown in Example 10-3.

(1) Estimation of the Maximum Lift Coefficient

The following expression, in effect, is the BET variation used to estimate the maximum lift coefficient:

$$C_{L_{\max}} \approx \frac{0.9}{S}\left[\sum_{i=1}^{N_f} C_{l\max i} \times S_i \times \cos\left(\Lambda_{hingeline}\right)_i + \sum_{i=1}^{N_{uf}} C_{li} \times S_i\right] \tag{10-2}$$

Where: N_f = Number of flapped wing segments

N_{uf} = Number of unflapped wing segments
$C_{l\max\, i}$ = Maximum lift coefficient of the flapped wing segment
C_{li} = Average lift coefficient of the unflapped wing segments at the stall AOA of the flapped one
$\Lambda_{hingeline}$ = Angle of the hingeline to a normal to the plane-of-symmetry

The factor 0.9 is used to account for 3-dimensional effect. The detrimental effects of hingeline sweep must be accounted for. Note that even straight tapered wings will be subject to it, unless of course the planform is laid out such that the hingeline is perpendicular to the plane-of-symmetry.

(2) Estimation of the Pitching Moment Coefficient

Since the pitching moment of an airfoil, effectively, is the product of the lift it generates and its location on the airfoil, it is possible to approximate the total pitching moment of the wing in a manner similar to that presented in Equation (10-2):

$$C_m = \frac{0.9}{S_{ref}}\sum_{i=1}^{N} C_{mi} \times S_i \tag{10-3}$$

Where: N = Total number of wing segments

C_{mi} = Average pitching moment coefficient of each wing segment, flapped and unflapped

EXAMPLE 10-3

Estimate the maximum lift coefficient for the SR22 using the wing partition method. The aircraft features single-slotted flaps that deflect to 32 degrees. Its reference area is 144.9 ft^2. Assume a NACA 65$_2$-415 airfoil for the entire wing (although this is not the case for the real aircraft). Use data from Table 8-9 for the airfoil. The pertinent dimensions for the wing are shown in Figure 10-54, where:

$y_1 = 3.00$ ft $\quad y_2 = 11.75$ ft $\quad y_3 = 16.42$ ft $\quad y_4 = b/2 = 19.15$ ft
$b_f = 8.75$ ft $\quad b_a = 4.67$ ft

Use the equation of the chord given for the SR22 in the Section 17.5.1, *Cirrus SR22*, given by 5.160–0.1342y (ft). Compare the value to the POH value, which is shown to be 1.99 in Table 17-7.

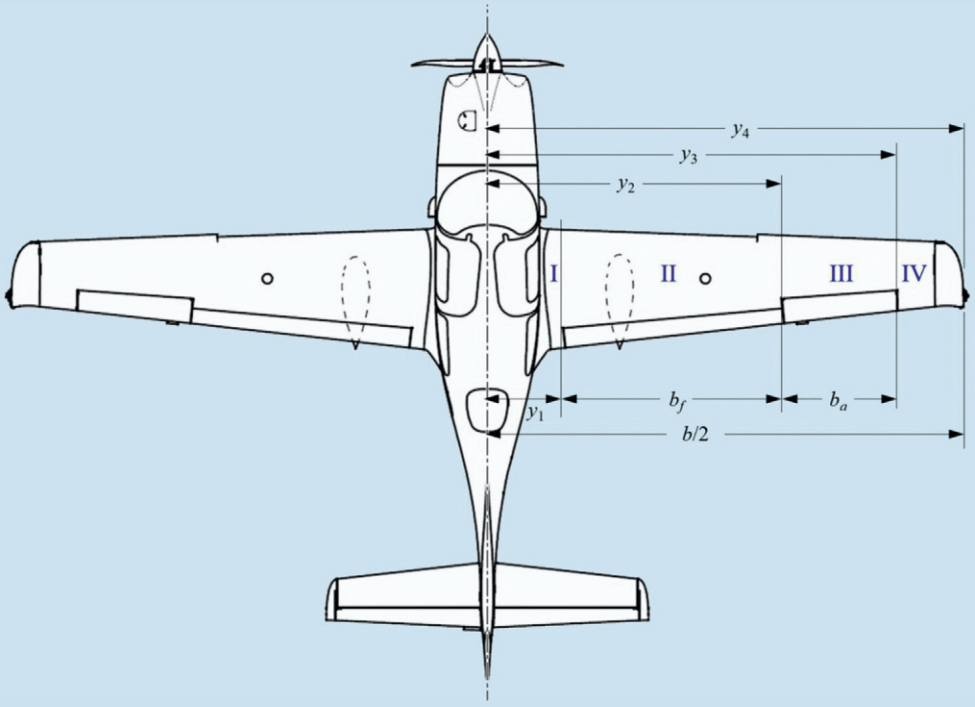


FIGURE 10-54 Partitioning of the wing of the SR22 for this example. *Copyright 2021 Cirrus Aircraft or its Affiliates. All Rights Reserved. Image reproduced with the permission of Cirrus.*

Continued

EXAMPLE 10-3 (*cont'd*)

SOLUTION:

It is a tad tricky to find data specifically using the NACA 65_2-415 airfoil. Ultimately, we will have to use "hybrid" data, i.e., splice together a data set using airfoils that "resemble" the 65_2-415. First retrieve information from Table 8-9, from which the stall AOA, zero lift AOA, and lift curve slope for the airfoil are found to be as follows:

$$\alpha_{stall} = 16.0^\circ \quad \alpha_{ZL} = -2.6^\circ$$
$$C_{l_\alpha} = 0.107 \quad C_{l_{max}} = 1.62$$

Next, resort to Table 10-5 for a single-slotted flap on airfoils similar to the 65_2-415. One of the airfoils is the NACA $65_{(215)}$-114, detailed in Ref. [57]. We will consider it "close enough" to use in this example. Researching the sources gives the following information. Figure 9 of the reference (i.e., Ref. [57]) shows a $C_{l_{max}}$ of about 2.80 for 32° of flap deflection at a $R_e = 9 \times 10^6$. Figure 10 shows that (fortunately) there is not a large reduction in $C_{l_{max}}$ by lowering the R_e to 3×10^6 (although there is a huge drop when one goes to 1×10^6). We will, thus, use the value of 2.80, however, to be conservative, we multiply it by 0.95. Therefore, consider $C_{l_{max}} = 0.95 \times 2.80 = 2.66$. Figure 8 of the reference document also shows the stall AOA changes by 4°, from 14° for the unflapped airfoil, to 10° for the flapped one. Using this data, we now rewrite the properties as follows:

Unflapped airfoil: $\alpha_{stall} = 16.0^\circ \quad \alpha_{ZL} = -2.6^\circ$
$C_{l_\alpha} = 0.107 \quad C_{l_{max}} = 1.62$

Flapped airfoil: $\alpha_{stall} = 12.0^\circ \quad \alpha_{ZL} = -2.6^\circ$
$C_{l_\alpha} = 0.107 \quad C_{l_{max}} = 2.66$

We do not need all of the above information, but it is good to have nevertheless. Next determine the AOA of the unflapped airfoil when the flapped one stalls. To do this we resort to Equations (8-11) and (8-12), i.e.:

$$C_l = C_{l_0} + C_{l_\alpha}\alpha = -C_{l_\alpha}\alpha_{ZL} + C_{l_\alpha}\alpha$$
$$= -(0.107)(-2.6^\circ) + (0.107)(12.0^\circ) = 1.562$$

We now have enough information to begin to populate Table 10-9. First, take care of the initial geometry as shown in Table 10-8. Columns ① and ② are the spanwise stations in units of ft (i.e., distance from the plane-of-symmetry) that enclose the corresponding wing segment. Columns ③ and ④ are the chords at those stations in ft. Column ⑤ is the average of the two chords and Column ⑥ is the planform area of the segment.

Table 10-9 presents the analysis necessary to determine the maximum lift coefficient. It is ideal to review Equation (10-2) to recall the variables that must be included. The first three columns correspond to Columns ①, ②, and ⑥ of Table 10-8 and are merely here for reference. Column ④ is the hingeline angle (assumed 4° for the flapped section). Columns ⑤ and ⑥ are the

TABLE 10-8 Geometry of the wing segments.

	①	②	③	④	⑤	⑥
Segment	y_a	y_b	$c(y_a)$	$c(y_b)$	c_{avg}	**Area,** S_i
I	0	3	5.16	4.76	4.959	14.88
II	3	11.75	4.76	3.58	4.170	36.49
III	11.75	16.42	3.58	2.96	3.270	15.27
IV	16.42	19.15	2.96	2.59	2.773	7.57

TABLE 10-9 Estimating the contribution of the wing segments to the total $C_{L_{max}}$.

	①	②	③	④	⑤	⑥	⑦	⑧	⑨
Segment	y_a	y_b	**Area,** S_i	$\Lambda_{hingeline}$	$C_{l\,max\,a}$	$C_{l\,max\,b}$	$\Delta C_{l\,max}$	$C_{l\,max\,avg}$	$C_{l\,max\,avg} \cdot S_i$
I	0	3	14.88	0	1.562	1.562	0.000	1.562	23.24
II	3	11.75	36.49	-4	1.562	1.562	1.100	2.662	96.90
III	11.75	16.42	15.27	0	1.562	1.562	0.000	1.562	23.85
IV	16.42	19.15	7.57	0	1.562	1.562	0.000	1.562	11.83
								Sum =	**155.81**

EXAMPLE 10-3 *(cont'd)*

maximum lift coefficients estimated at the two spanwise stations y_a and y_b. It is simply a linear interpolation of the $C_{l_{max}}$ for the unflapped airfoils at the root and tip. Column ⑦ is the increase in the $C_{l_{max}}$ of the segment due to the deflected flap. Here, it can be seen that only Segment II has an associated increase, as this is where the flap is. Column ⑧ is the average of the $C_{l_{max}}$ of the airfoils at stations y_a and y_b. Finally, Column ⑨ is the segment weighted value of the average $C_{l_{max}}$ of the segment; i.e., the larger the segment area, the greater is its contribution to the total $C_{L_{max}}$.

Then, the maximum lift for the airplane can be determined using Equation (10-2) as shown below:

$$C_{L_{max}} \approx \frac{0.9}{S_{ref}}\left[\sum_{i=1}^{N_f} C_{l\max i} \times S_i \times \cos\left(\Lambda_{hingeline}\right)_i + \sum_{i=1}^{N_{uf}} C_{li} \times S_i\right]$$

$$= \frac{0.9 \times 2 \times 155.81}{144.9} = 1.936$$

The factor "2" is there to account for both wing halves, but the formulation in Table 10-9 only treats one wing half. The result is about 97.3% of the POH value of 1.99 (see Table 17-7)—not too a bad an agreement at all.

10.5 WINGTIP DESIGN

Wingtips are among the most noticeable features of any aircraft. They come in many shapes and sizes, begging the question—are they aerodynamically important? Or are they just an expression of aesthetics? The answer to both questions is yes. Wingtips can modify efficiency and handling, and are sometimes selected for appearance. Only the most common wingtip styles will be presented here along with some detail about their aerodynamic effectiveness. The looks are left to the reader to judge.

Wingtips contribute to drag in at least three ways: (1) They affect wetted area and, therefore, viscous drag. (2) They affect the wingtip vortex similar to aspect ratio [75]. (3) They modify the spanwise distribution of pressure and can be shaped to delay the onset of wavedrag.

Hoerner [76] states that the separation of the wingtip vortices "does not coincide with the geometrical span," but depends on the shape of the wingtips. For instance, a square wingtip reduces lift-induced drag more than the spherical tip (both are discussed shortly). This is attributed to a flow-field distortion that either brings the wingtip vortices closer or farther from the plane-of-symmetry. The greater the separation, the greater will be the "apparent" AR of the wing and less will be the lift-induced drag. An example of this is shown in Figure 10-55. The round shaped wingtip (as seen when looking at the front) results in the highest drag. Although the difference at low lift coefficients is small, it grows

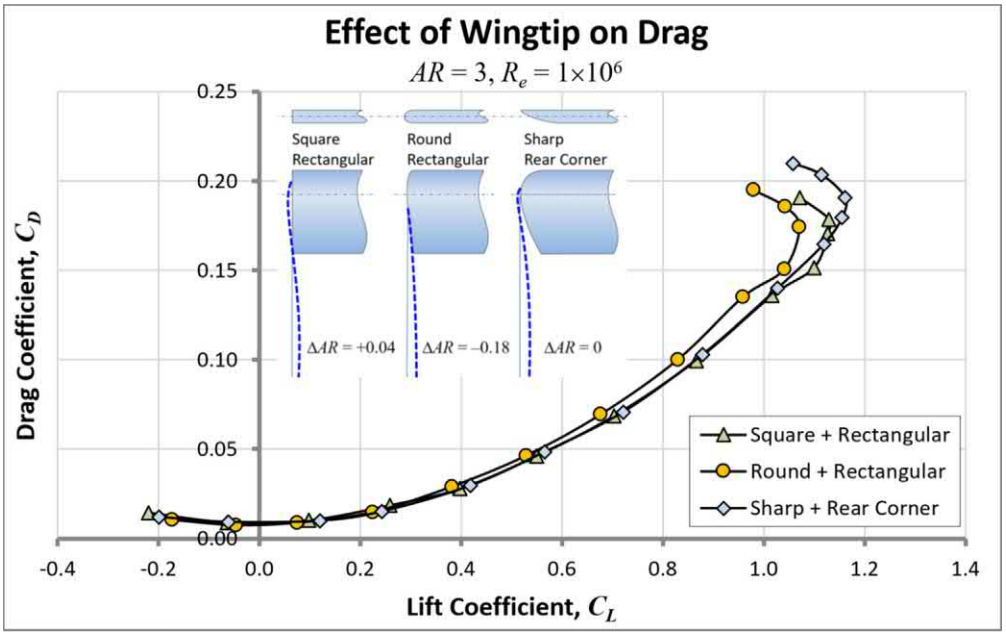


FIGURE 10-55 The effect of wingtip shape on the drag polar. The effect holds for higher AR wings as well. Note that the "Sharp, Rear Corner" wingtip is a "Hoerner" wingtip. *Based on S.F. Hoerner, Fluid-Dynamic Drag, L. Hoerner, 1965.*

rapidly enough to yield a measurable reduction in rate of climb and maximum lift-to-drag ratio.

Aerodynamic Effectiveness of Wingtips

Being able to evaluate the effectiveness of a wingtip is important to its selection. Anecdotal claims about wingtips are common. One such claim states that a specific wingtip "improves" the low speed handling of an airplane. All such assertions must be regarded with great skepticism, in particular if associated with the marketing of an aftermarket product. Low-speed effectiveness is hard to evaluate without wind tunnel or flight testing (e.g., see Ref. [78]). High-speed effectiveness can be measured in terms of impact on range and endurance. E.g., an airplane covers 100 nm at constant cruising speed using 10 gal of fuel on the average, before a new wingtip is installed and 9.8 gal after. If we can extract ΔC_{D_i} from this change, then we can say it appears the wing's aspect ratio has changed by value ΔAR. Thus, we can express this using an *apparent* or *corrected AR*, AR_{corr}, as follows:

$$AR_{corr} = AR + \Delta AR \tag{10-4}$$

To extract ΔC_{D_i} we can conduct a series of flight test, without and with the new wingtip. Then, we could use the *PIWVIW* method (e.g., see Ref. [79]) or a similar approach to extract the drag coefficient associated with each wing style. Even though the baseline wing is modified by the installation, we continue to use the original reference geometry. Additionally, we presume the difference in the efficiency of the two wing styles is solely caused by the addition of finite aspect ratio, ΔAR, to the baseline AR. To understand why, consider the expression for lift-induced drag of the two wing styles at some given lift coefficient, C_L:

$$\text{Original wing:}\quad (C_{D_i})_1 = \frac{C_L^2}{\pi \cdot AR \cdot e} \tag{10-5}$$

$$\text{Modified wing:}\quad (C_{D_i})_2 = \frac{C_L^2}{\pi \cdot (AR + \Delta AR) \cdot e} \tag{10-6}$$

As far as lift-induced drag is concerned, it is the product $AR \cdot e$ that matters and not AR or e on its own. Therefore, we can either modify AR or e or the product of the two. For convenience, we will attribute this change to AR only as it is easier to relate to. The change in AR can be calculated from:

$$\Delta AR = \left(\frac{C_L^2}{\pi \cdot AR \cdot e \cdot \Delta C_{D_i} + C_L^2} - 1 \right) AR \tag{10-7}$$

Where AR is the aspect ratio of the original wing, C_L is the lift coefficient at some reference flight condition, and e is the Oswald's span efficiency of the original wing.

There also are two other perspectives to consider. (1) *We* can ask—What wingspan corresponds to a specific ΔAR? Calling it b_{eff}, we can transform Equation (10-4) to get:

$$b_{eff} = \sqrt{AR_{corr} S} = \sqrt{(AR + \Delta AR) S} \tag{10-8}$$

(2) *We* can also ask—Given a specific increase in halfspan (Δb_t), what is the corresponding increase in AR (ΔAR)? Given a trapezoidal wing of span b, area S, and taper ratio λ, using basic geometry, the increase equals

$$\Delta AR = \frac{b(b + 2\Delta b_t)^2}{Sb + 2c_r[\lambda \Delta b_t b - (1+\lambda)\Delta b_t^2]} - \frac{b^2}{S} \tag{10-9}$$

DERIVATION OF EQUATION (10-7)

Using the above expressions for $(C_{D_i})_1$ and $(C_{D_i})_2$ we find the difference in lift-induced drag is given by:

$$\Delta C_{D_i} = (C_{D_i})_2 - (C_{D_i})_1 = \frac{C_L^2}{\pi \cdot (AR + \Delta AR) \cdot e} - \frac{C_L^2}{\pi \cdot AR \cdot e}$$

$$= \frac{C_L^2}{\pi \cdot e} \left(\frac{1}{AR + \Delta AR} - \frac{1}{AR} \right)$$

Solve for ΔAR:

$$\Delta AR = \frac{C_L^2 AR}{\pi \cdot AR \cdot e \cdot \Delta C_{D_i} + C_L^2} - AR$$

$$= \left(\frac{C_L^2}{\pi \cdot AR \cdot e \cdot \Delta C_{D_i} + C_L^2} - 1 \right) AR$$

EXAMPLE 10-4

An aircraft with straight wing of $AR = 7$ is found to develop a $\Delta C_{D_i} = -0.00055$ at $C_L = 0.5$ when tested with a new wingtip. Determine the corrected AR if $e = 0.84$.

SOLUTION:

$$\Delta AR = \left(\frac{C_L^2}{\pi \cdot AR \cdot e \cdot \Delta C_{D_i} + C_L^2} - 1 \right)$$

$$AR = \left(\frac{0.5^2}{\pi(7)(0.84)(-0.0005) + 0.5^2} - 1 \right)(7) = 0.2965$$

$$\Rightarrow \quad AR_{corr} = AR + \Delta AR = 7.297$$

10.5.1 The Round Wingtip

The *round wingtip*, shown in Figures 10-56 and 10-57, is one of the oldest and simplest ways to terminate the wing at the tip. It consists of a semicircular edge that extends from the leading to the trailing edge. The wingtip has been around since the 1920s. Hoerner [76] demonstrated it is less effective than once thought, as the wingtip vortex tends to move onto the upper surface. This reduces the apparent AR. This means that when working with a specific AR in drag or stability and control analyses, the AR must be reduced by as much as 0.20.

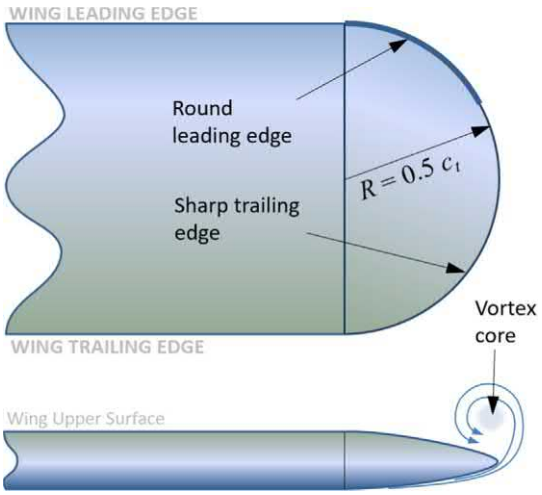


FIGURE 10-56 The *round wingtip*.

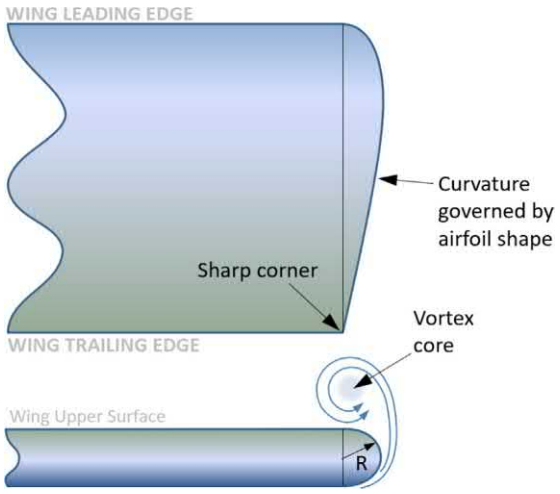


FIGURE 10-58 The *spherical wingtip*.

The effectiveness of the tip is overestimated by potential flow theory, which renders it more effective than either a square or the spherical wingtip (see Section 10.5.11, *Comparison Based on Potential Flow Theory*). This can be explained by increasing section lift coefficients near the rapidly tapering tip, which at cruise AOA makes the configuration more efficient. However, this is contradicted by the results of Ref. [76], which are based on wind tunnel testing.

AR correction: $\Delta AR = -0.19$

10.5.2 The Spherical Wingtip

The *spherical wingtip*, shown in Figures 10-58 and 10-59, is a simple and commonly used wingtip. It is simple to fabricate using composites and poses minimal challenges in the layout of its loft. Its planform view of the curvature is usually governed by the airfoil, as the geometry is a semicircle along the tip chord.

Zimmer [80] refers to the wingtip under the name *Goettinger* wingtip, but the author has been unable to confirm that name.

Aerodynamically, the spherical tip is an inefficient shape, as it causes the wingtip vortex to roll up and inboard, as shown in Figure 10-58. This reduces the separation between the two wingtip vortices, which leads to a reduction in the corrected *AR* (see Figure 16-34) and increased lift-induced drag.

The geometry has no influence on dihedral effect. However, it is thought to have detrimental effect on spin characteristics due to the formation of a low-pressure



FIGURE 10-57 A Beechcraft C-45 boasting its round wingtips. The twin vertical tail surfaces are endplates for the horizontal tail. *Photo by Phil Rademacher.*



FIGURE 10-59 A Piper PA-28 Cherokee four-seat, single-engine sport aircraft features round wingtips. *Photo by Phil Rademacher.*

region around the wingtip. This develops prospin moment, rendering spin recovery more difficult.

AR correction: $\Delta AR = -0.18$

10.5.3 The Square Wingtip

The *square wingtip* (see Figure 10-60) is the simplest geometry possible for a wingtip. The sharp termination forces the wingtip vortex to form and reside on the outboard side of the tip (rather than above like for the round tip). This pushes the wingtip vortices farther apart from the centerline of the aircraft and increases the apparent AR by a small amount. The tip has no influence on dihedral effect. An example of a square wingtip is shown in Figure 10-61.

AR correction: $\Delta AR = +0.04$

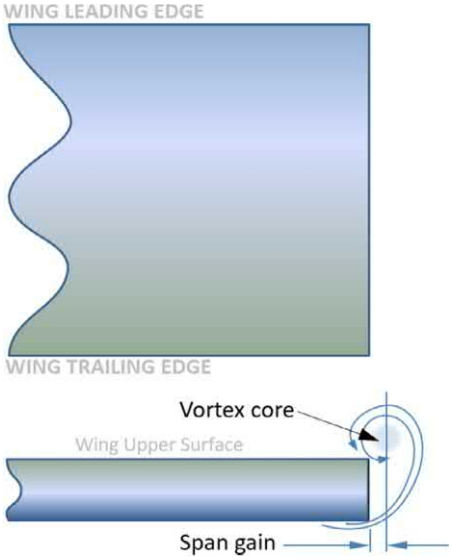


FIGURE 10-60 The *square wingtip.*



FIGURE 10-61 An Extra 300 single-seat, single-engine aerobatic aircraft and a Cessna CJ4 executive aircraft featuring square wingtips. *Photos by Phil Rademacher.*



FIGURE 10-62 Cirrus SR22 four-seat, single-engine high performance aircraft, featuring upturned booster wingtips. *Photo by Phil Rademacher.*



FIGURE 10-63 A Cessna 172F four-seat, single-engine sportsplane featuring downturned booster wingtips. *Photo by Phil Rademacher.*

10.5.4 Booster Wingtips

Booster wingtips are noticeable by a distinct trailing-edge curvature that comes in two forms; *upturned* and *downturned* (see Figures 10-62 and 10-63). Both are intended to bring the wingtip vortices farther outboard, increasing apparent *AR*. The true effect on drag is not well known, although some manufacturers of aftermarket booster wingtips claim benefits such as low speed roll stability and reduction in stalling speed. The author has been unable to locate any published papers the supports such claims. Characteristics of the booster wingtip will now be discussed.

(1) The Upturned Booster Wingtip

The upturned booster wingtip consists of geometry in which the lower and upper surfaces join in a sharp termination, or edge, that flares upward at the trailing edge (see Figures 10-64 and 10-62). The wingtip style is most

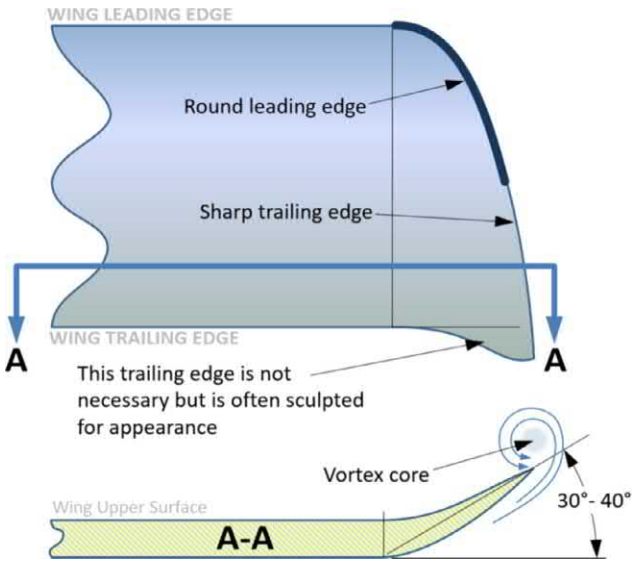


FIGURE 10-64 The *upturned booster wingtip.*



FIGURE 10-65 An American-Aviation AA-1 two-seat, single-engine sport aircraft featuring a Hoerner wingtip. *Photo by Phil Rademacher.*

easily made from composite materials, although the sharp edge sometimes requires fabrication techniques that minimize the formation of production nuisances such as dry fibers and "bridging."

Theoretically, the wingtip increases the separation of the wingtip vortices and, therefore, increases the apparent *AR*. In practice, the increase is probably negligible. It also *increases* dihedral effect by a small amount.

AR correction: $\Delta AR = 0.00$

(2) The Downturned Booster Wingtip

The downturned booster wingtip is an inversion of the upturned style. There is not much found in the literature regarding its effectiveness (e.g., see Rokhsaz [81]). Naik and Ostowari [82] present an experimental investigation of several nonplanar wingtip configurations, including a downturned droop. The results provided show limited to no benefit over the planar reference wing. In accordance with standard lateral stability theory, the downturned booster wingtip *decreases* dihedral effect, i.e., roll stability. However, there is perception they improve handling near stall and, thus, have been marketed as a part of Short T-O and Landing (STOL) STCs for low speed aircraft. Other schools of thought claim they have detrimental effect on spin characteristics as a low-pressure region is formed around the wingtip, which will help drive the autorotation and, thus, can render spin recovery more difficult.

AR correction: $\Delta AR = 0.00$

10.5.5 Hoerner Wingtip

The Hoerner wingtip is named after the German aerodynamicist Sighard Hoerner (1906–71) who showed its effectiveness to be superior to that of the round wingtip. Its primary advantage is neutral (rather than negative) impact on the corrected *AR* like that of the round wingtip (see Section 16.3.2, *Estimating Lift-Induced Drag*, bullet (7)).

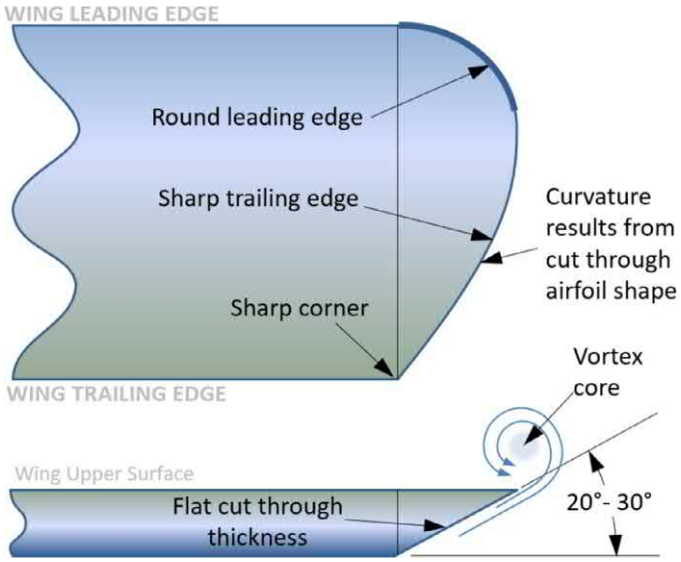


FIGURE 10-66 Typical geometric considerations for the layout of a *Hoerner wingtip.*

Hoerner wingtips are used in several aircraft; most notably the Grumman American AA-5 series of aircraft, produced during the timeframe 1971–2005 (see Figure 10-65).

The wingtip increases dihedral effect. Theoretically, it is intended to shift the wingtip vortex farther outboard, which requires a sharp edge separating the upper and lower surfaces along the aft trailing edge as shown in Figure 10-66. Normally, the first part of the leading edge features a round geometry to prevent the upper surface from stalling at low AOAs.

AR correction: $\Delta AR = 0.00$

10.5.6 Küchemann Wingtip

The *Küchemann wingtip* (see Figure 10-67) is intended for sweptback wings operating at transonic airspeeds. It is

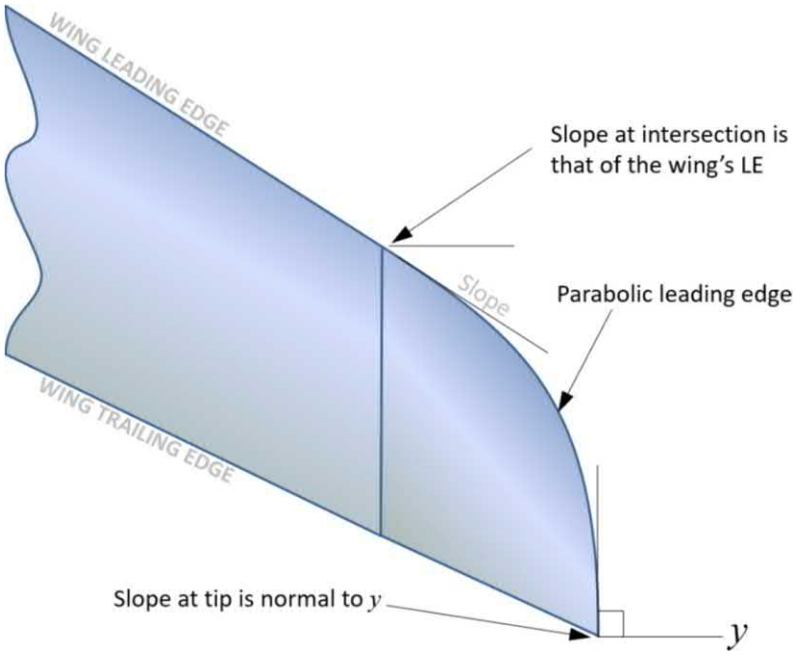


FIGURE 10-67 General shape of the *Küchemann wingtip*.

attributed to the German aerodynamicist Dietrich Küchemann (1911–76), famous for research in high-speed aerodynamics that included the development the Ogive delta wing used for the Concorde and of the so-called *Küchemann carrot*. The Küchemann wingtip smooths the distribution of pressure over the wing at transonic speeds (see Figure 10-68). This reduces low-pressure peaks (i.e., local airspeeds), delaying the formation of shocks and increases the drag-divergence Mach number. It is one of several tools at the disposal of the aerodynamicist to suppress early shock-formation (the others include airfoil selection, twist, and wing-fuselage fairing). While *AR* correction is given as 0, it reduces wave drag through means other than ΔAR. More information can be found in Refs. [83–85]. The Vickers VC10, McDonnell-Douglas DC-9, Airbus A320, and A380 are among aircraft featuring this wingtip.

AR correction: $\Delta AR = 0.00$

10.5.7 Raked Wingtip

Of the simple wingtip devices, nothing increases apparent AR like the *raked wingtip*. Its primary drawback is increased wingspan and wing bending moments. The wingspan increase may spur parking and hangar space challenges, whereas the increase in bending moments raises the airframe weight. It does not develop interference drag, although it increases skin friction if added to an existing baseline wing. An example of a raked wingtip is shown on the Boeing 777 commercial transport aircraft in Figure 10-69. Such wingtips have also been used in the Boeing 767 and 787 Dreamliner aircraft. Their use in GA aircraft, at this time, is rare. The best example is the Coast Guard surveillance version of the Schweizer SGM 2-37 motorglider, called the RG-8A.

Contrary to popular belief, the raked wingtip has a long history, having been first evaluated in 1921 in Ref. [86]. Both positive (forward sweep) and negative (aft sweep) rakes were studied and found the maximum L/D ratio at an AOA of 4° increased by 7%. Interestingly, the best result was that of a 20-degree positive rake. The report concluded, "*the effect of rake on the lift and drag are so small that considerations of strength and aileron efficiency should govern the wing tip form.*" This interesting conclusion highlights the difference in the airplane design of the 1920s and 2020s—today, 7% translates into substantial fuel savings—which was much less of a problem in the early 20th century.

The effectiveness of the raked wingtip depends on the *rake angle*, ϕ, *dihedral angle*, Γ, and *span increase*, Δb_t (see definitions in Figure 10-70). Potential flow theory indicates that Γ should be around 4–8°, depending on wing geometry. A very high or low dihedral (±10° and greater) increased the lift-induced drag. An example of this is shown in Figure 10-71. The graph compares three raked wingtip styles to a baseline Hersey bar wing of $AR = 6$. All the configurations have the same total wingspan and the raked tip span is $\Delta b_t = 0.125b$. For this reason, the wing and wetted area of the baseline wing is larger than that of the other configurations, called Tip A, Tip B, and Tip C. Tip A has a 5.71-degree dihedral, Tip B has a 26.57-degree dihedral, and Tip C has a 26.57-degree anhedral.

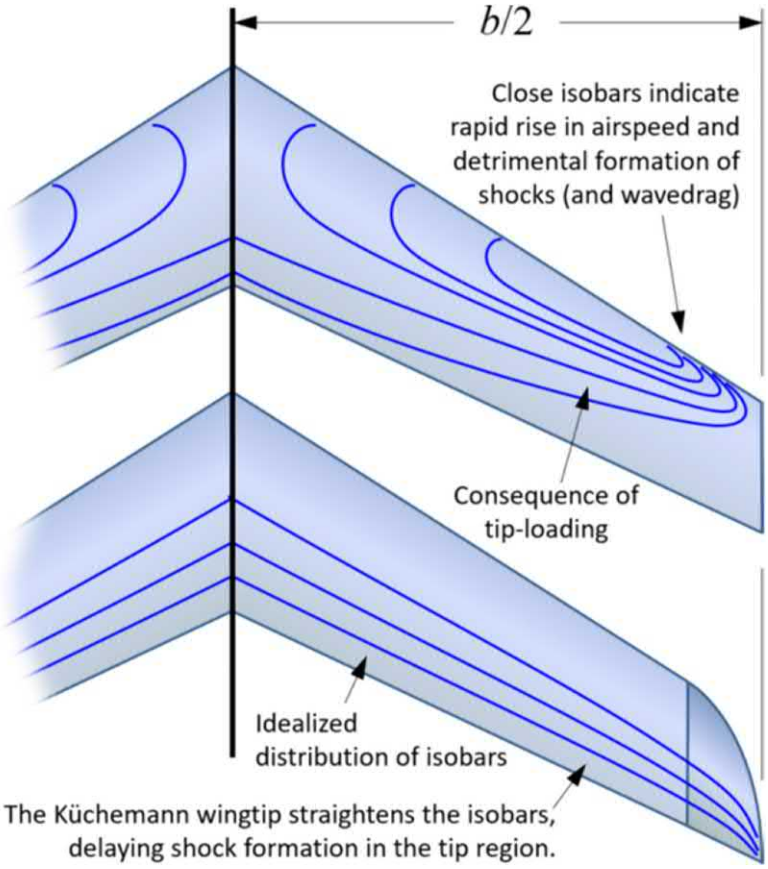


FIGURE 10-68 The Küchemann wingtip smooths isobars along the wing. *Based on D. Küchemann, The Aerodynamic Design of Aircraft, Pergamon Press Ltd., 1978.*



FIGURE 10-69 A Boeing 787-9 commercial transport and Cessna C680 Citation Latitude executive aircraft, featuring raked wingtips. *Photos by Phil Rademacher.*

It can be seen that Tip A (sometimes referred to as the Trilander wingtip, as in Britten-Norman Trislander) generates the least lift-induced drag of the four wing styles. It also has the least wetted area: It is the most efficient wing style of the four. Tips B and C generate equal lift-induced drag and are less efficient in cruise than either the baseline or Tip A. This result shows that designing a raked wingtip demands a careful evaluation of the geometry.

AR correction depends on the details of the geometry, but expect $\Delta AR = +0.5$ and possibly higher than +1.5 for well-optimized wingtips. For instance, Tip A in Figure 10-71 achieves a $\Delta AR \approx +0.88$ without any optimization.

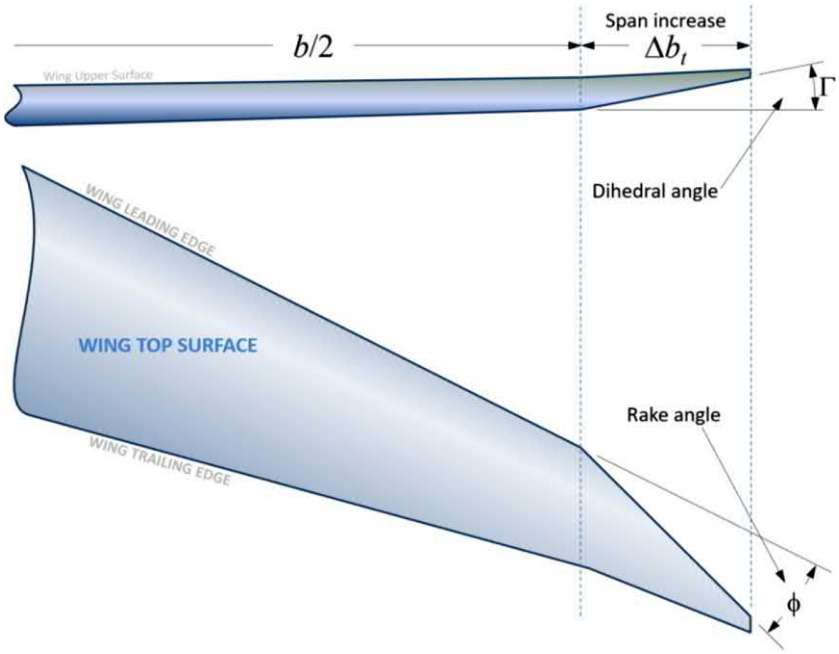


FIGURE 10-70 Basic geometry of the *raked wingtip*.

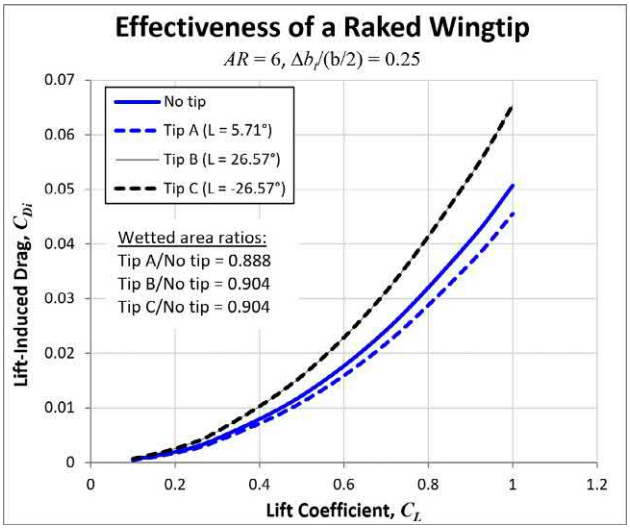


FIGURE 10-71 An example of a raked wingtip shows that a low dihedral decreases lift-induced drag, while larger dihedral increases it.

Rakelet

The *rakelet* is best described as a small winglet at the tip of a raked wingtip. It is considered a new wingtip device (US patent US8382041). It was investigated as a proposal for the KC-135 Stratotanker by Diaz et al. [87], where it is claimed to improve its best range by 7.5% over that of the baseline wing. The inventor is one of the paper's authors.

10.5.8 Endplate Wingtip

The invention of the endplate is attributed to the British scientist Frederick W. Lanchester (1868–1946) who showed that vertical plates positioned at the tip of a lifting surface greatly improved its lift. Other serious studies date back to the early 1920s with the work of Reid [88]. The endplate has a similar effect as placing a wing section from wall-to-wall in a wind tunnel—it makes it behave more like a 2-dimensional airfoil. This is referred to as *endplate effect*. It increases C_L, $C_{L\alpha}$, and $C_{L_{max}}$ [89] and reduces C_{D_i}. An example of theoretical treatment of lift and drag endplates is given in Refs. [90–92], respectively.

Endplates have a number of drawbacks. The surface adds parasitic drag through increased wetted area and interference drag where the plate joins the lifting surface. The combination cuts into the aerodynamic benefits and may exceed the reduction in lift-induced drag. Their inertia increases weight and reduces the natural frequency of the lifting surface, making it more susceptible to flutter. To solve this issue, the lifting surface must be stiffened, which adds more weight. If the endplates are used as a vertical tail and include two rudders, a more complicated control system is required. Additionally, using two vertical surfaces for a VT, rather than one, increases manufacturing complexity.

The magnitude of the endplate effect depends on its height, h (see Figure 10-72). When used on a horizontal tail, the endplate allows for a smaller horizontal tail surface, improved elevator effectiveness and the endplates serve as vertical tails.

In spite of these shortcomings, endplates are widely used in the aviation industry. Airplanes dating to the 1930s and later frequently featured the configuration as a horizontal and vertical tail surfaces. During WWII, many multiengine bombers and transport aircraft were designed with twin tail (H-tail), which was helpful in

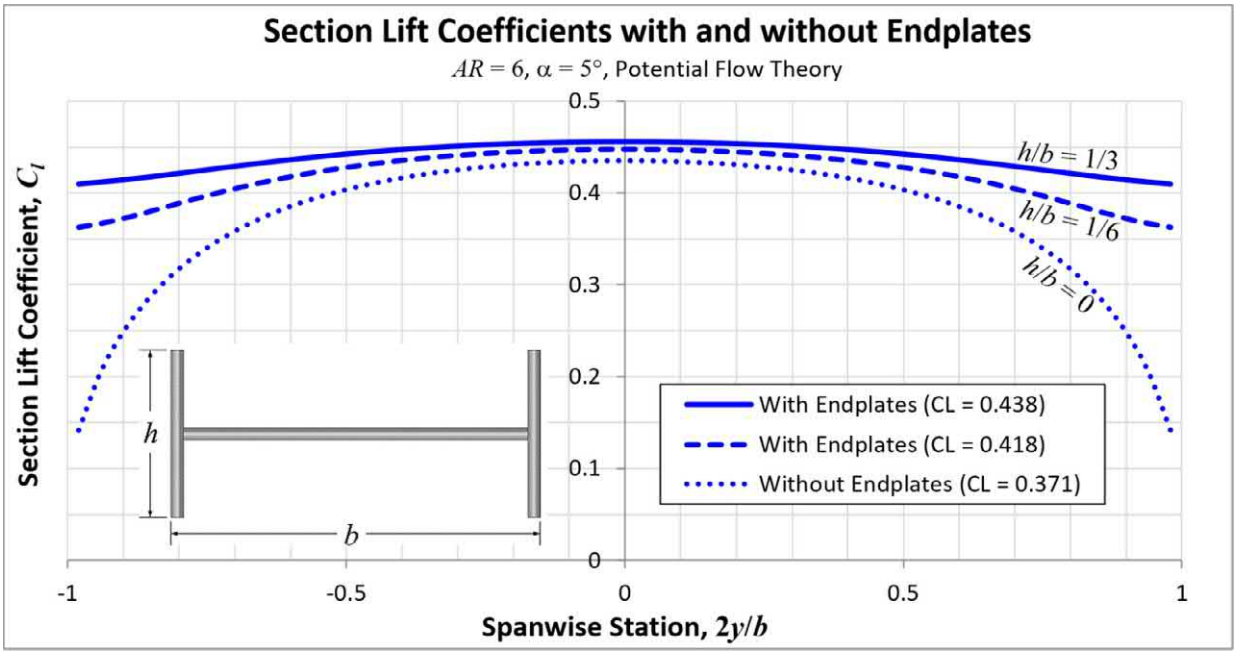


FIGURE 10-72 Comparing the distribution of section lift coefficients with and without endplates shows great improvement in surface lift effectiveness depending on endplate height.

an environment in which "losing" an engine (or a vertical tail) was a likely scenario. Immersing the two tails in the propwash of an operational engine improved controllability and survivability. A recent example of an H-tail surface is the Russian transport aircraft Antonov An-225 Mriya. It is currently the world's heaviest airplane with a 1.41 million lb_f (640,000 kg) gross weight. Originally designed to carry the Buran spacecraft on top of its wings, its H-tail opens a fly-off path where conventional vertical tail would be placed. Regardless, that solution also helps to keep the overall height of the aircraft down, allowing it to be stored in existing hangars for maintenance (its tail height is some 5 ft less than that of the Boeing 747 and 20 ft less than the Airbus A380). Endplates are also used in place of a winglet on the Airbus 320 family of commercial jetliners (see Figure 10-73).



FIGURE 10-73 The familiar Airbus "winglet" is actually an endplate. *Photo by Phil Rademacher.*

AR correction [93]:

$$\Delta AR = 1.9AR(h/b) = 1.9bh/S \qquad (10\text{-}10)$$

10.5.9 The Winglet

The *winglet* is arguably a sophisticated mutation of the endplate wingtip. It improves some of the drawbacks of the endplate, but exacerbates others. For one, while the wing integration is less draggy, the larger size and shape of the winglet increases the lateral stability derivative ($C_{L\beta}$ or dihedral effect) over that of the endplate. This aggravates Dutch roll damping. It also increases the side force derivative, $C_{Y\beta}$, to the detriment of cross-wind handling. Winglets also pose structural ramifications as add-ons: They increase the wing bending moments and lower the flutter speed beyond that of the endplate wingtip.

The true difference in drag between a "clean" wing and one with winglets is increased *parasitic drag*—a combination of skin friction, pressure, and interference drag. Winglets only reduce the lift-induced drag—when properly designed. To "pay off," the reduction in lift-induced drag must be greater than the increase in parasitic drag. This is illustrated in Figure 10-74. It compares the hypothetical installation of winglets on a Cirrus SR22 class aircraft to the original "clean" wing. While the numbers are "pulled out of thin air" (except the $C_{D_{min}}$ of the original configuration, which is calculated in Example 16-24),

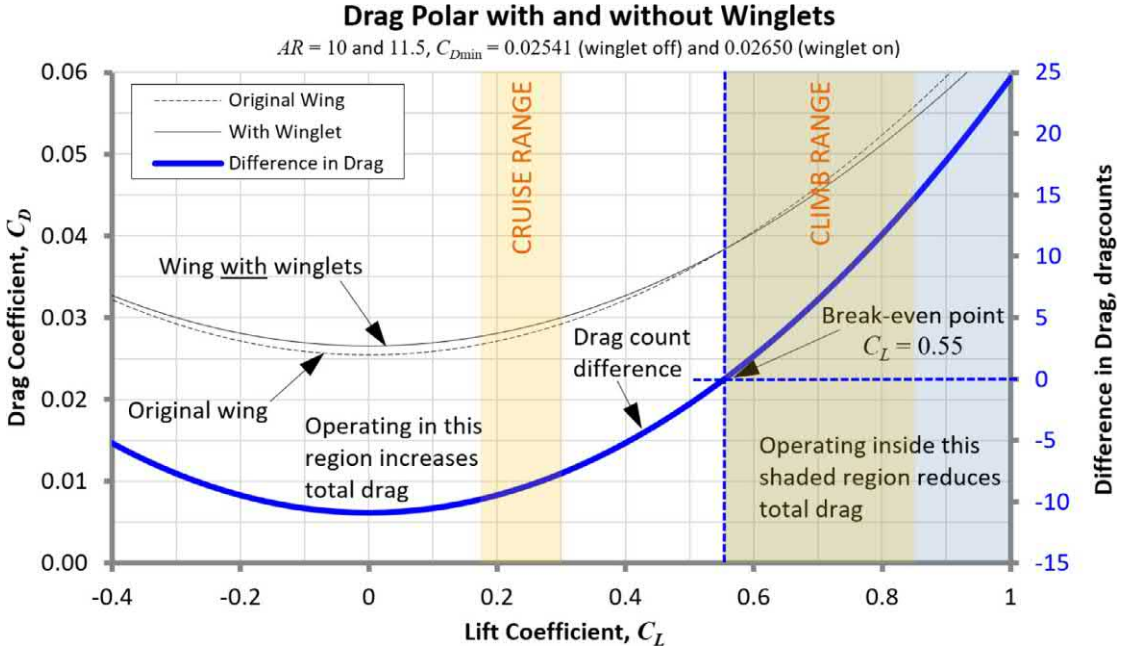


FIGURE 10-74 A comparison of drag polars before and after a winglet has been installed helps explaining their benefits. The thin dashed curve is the drag polar for the original wing, the solid thin curve represents the wing with the winglet, and the thick solid line is the difference between the two. The thin curves utilize the left vertical axis. The thick solid one utilizes the right vertical axis.

they still represent a realistic scenario. The presence of the winglet is treated as an increase in the original AR and $C_{D_{min}}$. Figure 10-74 shows that when operating at $C_L < 0.55$ (e.g., at cruise), the total C_D of the original airplane is actually lower than with the winglet. If operating at $C_L > 0.55$ (e.g., during climb) the total drag is reduced compared to the original wing. It is easy to determine from its POH, the SR22 cruises at C_L ranging from 0.17 to 0.30. Therefore, this installation would have to be justified on other merits, such as aesthetics or improved climb and T-O performance. It should be stated that the estimate uses the *simplified drag model* (see Chapter 16). If we assume $C_{L_{minD}} > 0$ and a different winglet geometry, the break-even point will move to a different location.

It comes as a surprise to many the winglets only shave off a few drag counts (see Figure 10-74). For instance, at $C_L = 0.8$, drag is reduced by 12 drag counts. Compare that to 254 drag counts of the original aircraft (4.7%). At $C_L = 0.3$ the opposite holds; the drag increases by 8 drag counts. This means the airplane must operate at higher altitude (where it would cruise at a higher C_L) to justify the winglets based on drag reduction. Cruising at low altitudes comes with drag penalty.

The workings of a winglet can be explained in a number of ways. The author's favorite explanation is that the magnitude of the section lift coefficients near the wingtip increases due to an expanded low-pressure region generated inboard of the winglet. The resulting lift distribution resembles that of a wing with a larger AR, which reduces C_{D_i} for the same C_L. This explains why the winglet has to be "loaded up" in order to function. "Loaded up" means it must be placed at a relative AOA large enough to generate lift and boost the low-pressure region near the wingtip. The *angle-of-incidence* of the winglet must be placed at a specific "toe-in" or "toe-out" angles, depending on geometry (see Figure 10-75).

Another explanation attributes the reduction in lift-induced drag to the distribution of the sheet of trailing vortices over greater distance, making it better resemble that of an elliptic planar wing (which has the minimum lift-induced drag). An insightful reasoning is provided by Hoerner [77] and McCormick [94] who explain it as the consequence of the lift force acting on the winglet surface, which is tilted forward due to the local AOA on the winglet. This way, the lift of the winglet, effectively, generates a forward force component—thrust—that can be subtracted from the drag. This perspective allows formulation to be derived to estimate the drag reduction. Regardless, all the explanations are different sides of the same box.

For effectiveness use Equation (9-135) and Table 9-9. The equation is repeated below for convenience:

$$AR_{corr} = AR\left(1 + \frac{2}{k_{WL}}\frac{h}{b}\right)^2 \tag{9-135}$$

Where k_{WL} = effectiveness factor per Table 9-9. The gain in AR is unlikely to exceed +1.5.

(1) The Whitcomb Winglet

The development of the *Whitcomb winglet* (see Figure 10-76) is attributed to Richard T. Whitcomb (1921–2009) who in the early 1970s conducted research

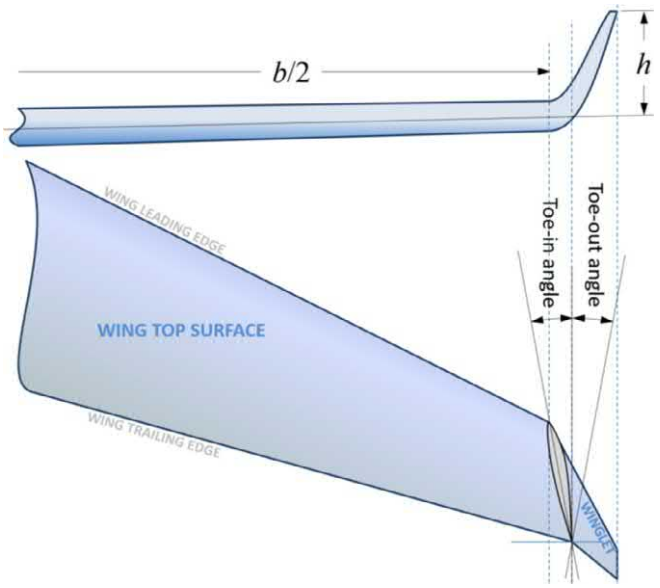


FIGURE 10-75 Definition of a toe-in and toe-out angles.

with his team of scientists in the Langley 8-ft Transonic Pressure Tunnel [95]. Part of this work was published in Ref. [96], published in 1976. It marks the first time a winglet was seriously considered for a large and heavy aircraft. Once this pioneering work demonstrated winglets were indeed effective, NASA began to conduct a substantial research on the topic. Ref. [97] was the first in a long line of technical papers evaluating its capabilities. In the late 1970s, Whitcomb developed a winglet for use on a Boeing KC-135 tanker aircraft. The research showed the winglet increased its cruise range by as much as 7% [98]. This work encouraged many manufacturers of commercial, business, and GA aircraft to offer winglets with their products. In 1977, the Gates Learjet Model 28/29 Longhorn became the first production airplane to feature winglets (although these had the lower winglet omitted) [99]. A Whitcomb winglet was also featured on the Rutan Varieze designed in 1974. The Boeing 747-400 was the first commercial jetliner produced with winglets.

A flight test evaluation of a Whitcomb winglet on the McDonnell-Douglas DC-10 commercial jetliner in the early 1980s revealed that the most efficient configuration consisted of a combination of a slight aileron droop with a reduced span winglet. The combination reduced fuel burn at cruise by 3%, increased range by 2%, and reduced T-O distance by 5% at maximum gross weight [100]. In 1990, McDonnell-Douglas began deliveries of MD-11s with such a winglet installed. The winglet differed from the basic Whitcomb type in that it had a lower AR and started much closer to the leading edge of the wing (see Figure 10-77).

Ref. [96] compared lift, drag, and pitching moment of a wind tunnel model of the KC-135 with three wingtip devices attached; a wingtip extension of 38% of the height of the upper winglet, the upper winglet only, and the upper and lower winglets combined. The results for drag are reproduced in Figure 10-78. It supports that the winglet generates less drag than a wing extension. It also shows the drag reduction obtained by the upper and lower combination is not any better than that with only the upper winglet. This has resulted in a modification to the general Whitcomb design, to be discussed next. Strictly speaking, the smaller winglet does not have to be smaller—it is just so to prevent it from striking the ground on low wing aircraft [96, p. 8].

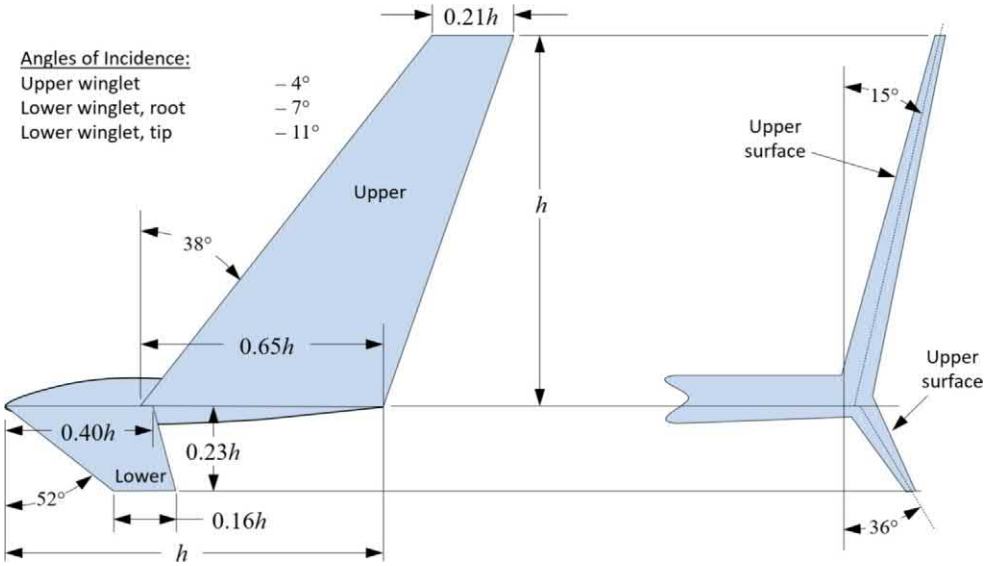


FIGURE 10-76 A general layout of the Whitcomb winglet. *Reproduced from R.T. Whitcomb, A Design Approach and Selected Wind-Tunnel Results at High Subsonic Speeds for Wing-Tip Mounted Winglets, NASA TN D-8260, 1976.*



FIGURE 10-77 A Whitcomb winglet on a McDonnell-Douglas MD-11 commercial jetliner. *Photo by Phil Rademacher.*

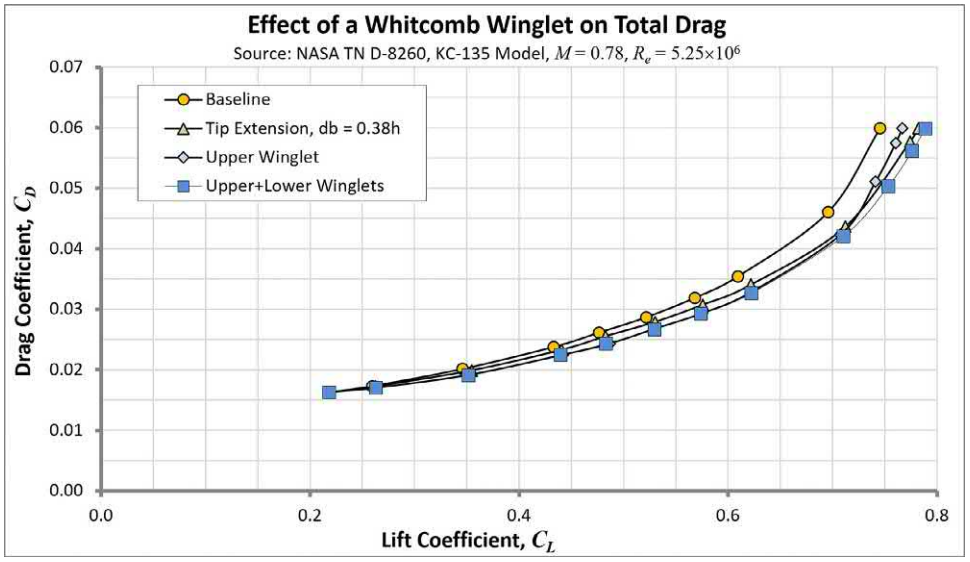


FIGURE 10-78 A drag polar comparing the basic KC-135 wing to one with a tip extension and Whitcomb winglet, one of which had the lower surface removed. *Reproduced from R.T. Whitcomb, A Design Approach and Selected Wind-Tunnel Results at High Subsonic Speeds for Wing-Tip Mounted Winglets, NASA TN D-8260, 1976.*

(2) The Blended Winglet

The *blended winglet* differs from the Whitcomb winglet in the absence of a lower winglet. As evident in Figure 10-78, the drag benefit of smaller winglet of Whitcomb's layout is marginal at cruise lift coefficients. Comparing its contribution to the manufacturing complexity and weight, it is reasonable to simply eliminate it. Another difference between the two is the generous arc (blending) of the intersection between the wing and the winglet. It allows the wing airfoils to transition smoothly to the winglet airfoils. It also replaces the sharp intersection of the Whitcomb winglet, reducing the pressure peak and, therefore, local airspeeds. This prevents flow separation at high AOA and shock formation at high Mach numbers (wave drag).

The blended winglet can be seen on many modern airliners. The most visible aircraft include aircraft such as the Boeing 737, Boeing 757 (see Figure 10-79), and many others.

The blended winglet was designed and patented by Louis B. Gratzer as US Patent 5,348,253. The patent states the theoretical background behind the design, where it is intended to solve a common deficiency of winglet installation—sharp discontinuities of intersections that results in departure from optimum loading. It was specifically selected by Boeing due to fewer changes required to the existing airframe [101]. Some pros and cons of winglets are presented in Table 10-10.

(3) Split Winglet

The *split winglet* (aka *split scimitar winglet*) is a variant of the Whitcomb winglet, primarily in the lower winglet being placed near the trailing edge. At the present time



FIGURE 10-79 A blended winglet on a Boeing 757 commercial jetliner. *Photo by Phil Rademacher.*

TABLE 10-10 Summary of pros and cons of winglets.

Pros	Cons
• Increases the wing's aerodynamic efficiency by reducing lift-induced drag. • This improves fuel consumption. • Reduced T-O distance and increased rate of climb. • Thought by many to bring ramp appeal to aircraft. • Increases effective wing *AR* with minimum increase in wingspan. • Can improve handling qualities (e.g., see Ref. [103]).	• Increases dihedral effect. • Can add adverse yaw (e.g., see Ref. [103]). • Moves center of lift outboard, increasing wing bending moments. • Increases wing weight due to the higher bending moments. • Reduction in the natural frequency of the wing, which lowers flutter speed. • Adds parasitic drag that must be overcome by the reduction in lift-induced drag. Thus, the winglets usually increase drag at low C_L. • The support structure for the winglet adds manufacturing complexity and cost.

it is seen on versions of the Boeing 737 aircraft (see Figure 10-80). Boeing markets one such as the 737 MAX AT (Advanced Technology) winglet [102]. It features natural laminar flow surface. It is not clear if the antiice leading-edges trip the boundary layer. To use this author's favorite explanation: the upper winglet expands the low-pressure region above the wing—the lower expands the high-pressure region below the wing. Thus, it improves the effective *AR*.

10.5.10 The Polyhedral Wing(tip)

The *polyhedral wingtip* is really a special wing shape. It is also known as the *cambered-span wing* or *nonplanar wing* (see Figures 10-81 and 10-82). It consists of gradually increasing dihedral at several wing stations along the wing. The idea originated with Cone [104] who showed that cambered-span wings can increase the apparent AR by as much as 50% compared to a flat elliptical wing of equal span, producing equal lift. Cone [105] also

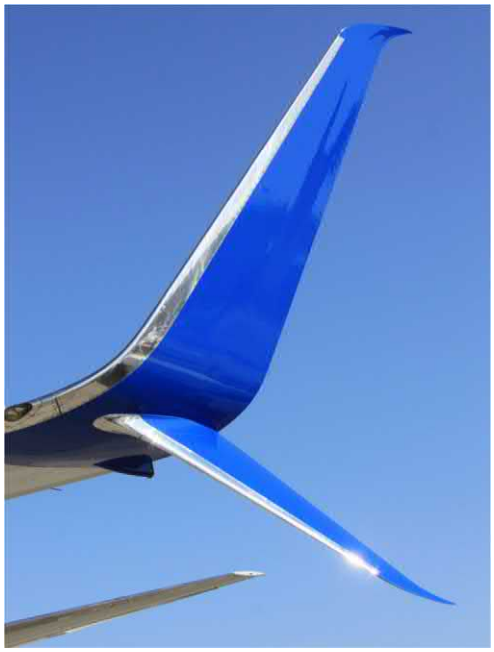


FIGURE 10-80 A split winglet on a Boeing 737-800 commercial jetliner. *Photo by Phil Rademacher.*

presented a method and an illustrative example to help with the design of cambered-spans and evaluate the reduction in lift-induced drag. A good description of Cone's theoretical work is presented by Jones [106].

The polyhedral wing increases manufacturing complexity due to the brake in the wing-spar and -skin. It also increases dihedral effect. The polyhedral wingtip is used on at least two sailplanes, the Schempp-Hirth Discus-2 and the DG Flugzeugbau DG-1000 (see Figure 10-81). From a conceptual design standpoint, nonplanar wings can be considered from at least two perspectives, each which leads to very different results. As explained below, this is important to keep in mind when designing such aircraft. For better understanding, refer to Figure 10-83.

First, consider a stiff straight wing design, denoted as Wing A in Figure 10-83. Assume this wing has a baseline wingspan b, wing area S, and is generating some lift coefficient, C_L. Then consider Wing B, which unloaded is geometrically identical to Wing A. However, assume it is structurally flexible enough to deform into the shape of Wing B in level 1g flight. As can be seen in Figure 10-83, the resulting wingspan will be shortened by the amount Δb and its effective wing area will be reduced by an amount ΔS. Therefore, to generate the same C_L as Wing A, Wing B requires a slightly higher AOA than Wing A. Thus, Wing B generates higher lift-induced drag than Wing A. An example of such as scenario is shown in Figure 9-70, which compares the lift of a flexed and straight wing at the same AOA.

Alternatively, consider the nonplanar Wing C in Figure 10-83. It is designed to *be* polyhedral while operating at the same wingspan (and area) as Wing A (flexed or



FIGURE 10-81 DG Flugzeugbau DG-1000 sailplane features a polyhedral wing. *Photo by Phil Rademacher.*

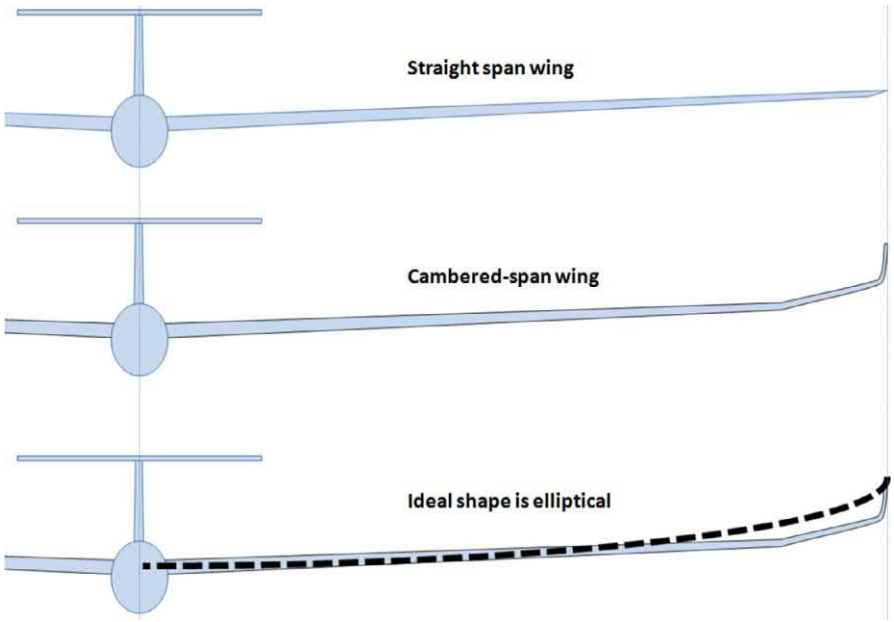


FIGURE 10-82 Comparison of the polyhedral wing, showing a straight wing, the polyhedral camber, and the ideal elliptical shape. *Based on F. Thomas, Fundamentals of Sailplane Design, College Park Press, 1999.*

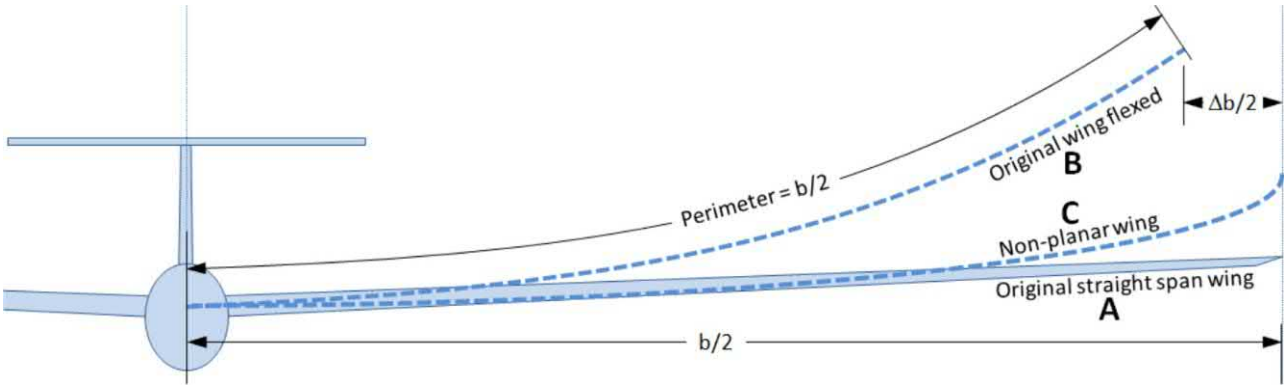


FIGURE 10-83 Comparison of a polyhedral wing to an actual wing flex. Wing A is the original straight wing of wingspan b and area S. Wing B is Wing A flexed due to airloads; it suffers a reduction in effective wing span and area. Wing C is a nonplanar wing is designed with wingspan b and S.

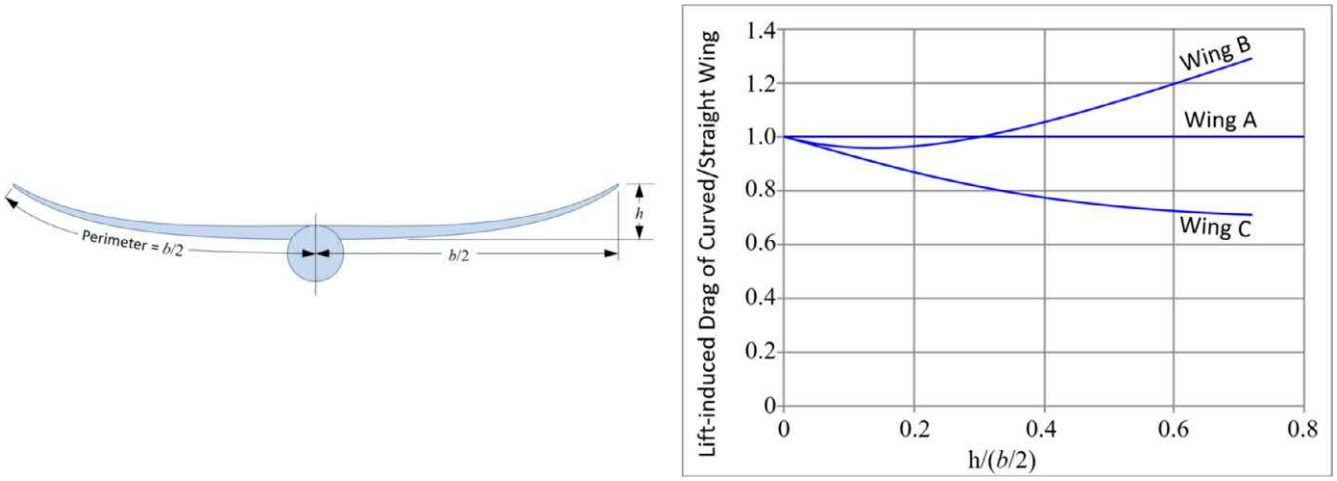


FIGURE 10-84 A comparison of the three wing styles discussed in the section. *Based on R.T. Jones, Minimizing induced drag, Soar. Motorglid. 43(10) (1979).*

TABLE 10-11 Summary of characteristics of several wingtip designs.

Wingtip Type	AR	$S_{wet}/S_{wet\,o}$	α	$C_{L\alpha}$	C_{Di}	e	$AR{\cdot}e$	LD_{max}	h_n	$\Delta C_{l\beta}$
			degrees	per radian						per degree
Spherical (baseline)	8.000	1.0000	8.00	4.564	0.0200	0.8099	6.48	22.6	0.250	0.00000
Upturned	8.076	1.0004	7.90	4.620	0.0198	0.8095	6.54	22.7	0.254	-0.00029
Downturned	8.076	1.0004	7.90	4.620	0.0198	0.8095	6.54	22.7	0.254	0.00031
Round tip	8.240	0.9708	7.82	4.671	0.0194	0.8078	6.66	23.2	0.254	0.00000
Trilander type	8.427	0.9509	7.79	4.685	0.0191	0.8012	6.75	23.6	0.270	-0.00032
Raked	9.014	0.9509	7.59	4.813	0.0180	0.7974	7.19	24.4	0.298	-0.00042

not). In contrast to Wing B, this wing develops the same lift coefficient as Wing A at a slightly lower AOA; its lift-induced drag will be less.

This peculiar result is attributed to a more efficient reduction of pressure on the upper surface due to a longer spanwise bound-vortex than that of the straight wing. This can be readily demonstrated using potential flow theory (e.g., Vortex-Lattice). Of course, Wing C has a greater wetted area than Wing A, it will be slightly heavier and this may offset the benefit some. A comparison between the three wing styles as a function of flex height is shown in Figure 10-84.

10.5.11 Comparison Based on Potential Flow Theory

Potential flow theory can be used to evaluate the effectiveness of various wingtip devices, primarily when they are designed for operation at C_L for which flow separation is limited. This section compares a few such designs for lift, drag, and contribution to lateral stability (see Table 10-11). It can be used for guidance when selecting the appropriate wingtip geometry. Note that the table does not feature the winglet or the polyhedral wing.

Of the wingtip types compared, it can be seen that the raked wingtip and the Trilander type yield the most efficient wings for cruising flight. Generally, the more efficient the wing style, the steeper is its lift curve slope. The explanation for this can be seen in Figure 10-85, which shows that the section lift coefficients for the more efficient wing styles remain high along the tip. While favorable for cruise, the wingtip region will stall before other wing regions. If the span of the wingtip is substantial, this can have detrimental effect on the roll stability of the wing at stall. This would be less of a concern for a relatively short span wingtip, such as the Trilander type, as it is subject to the formation of a leading-edge vortex, similar to that of a deltawing. However, it may pose concern for a long span raked wingtip, although the remedy is washout.

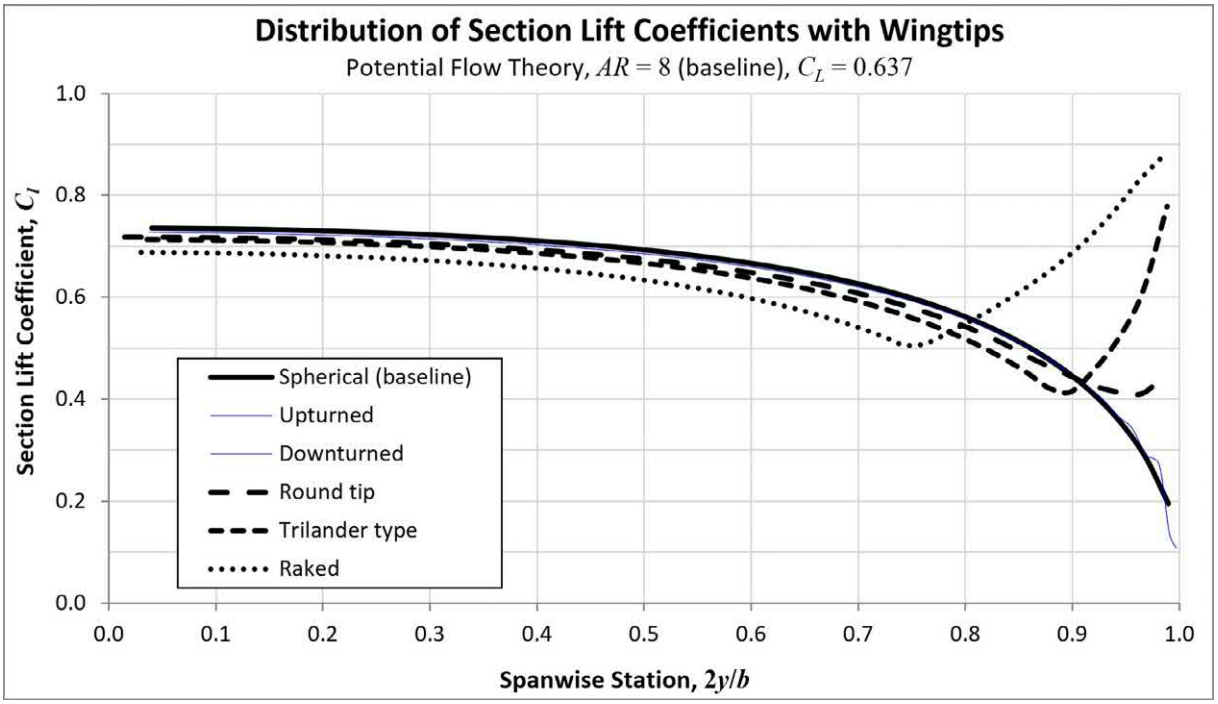


FIGURE 10-85 Distribution of section lift coefficients reveals how the Trilander type and Raked wingtips boost lift at the wingtip, which helps explain how they improve the overall wing efficiency by allowing operation at a lower AOA to generate the same C_L.

References

[1] N.-L.F. Hayter, J.A. Kelly, *Lift and Pitching Moment at Low Speeds of The NACA 64A010 Airfoil Section Equipped with Various Combinations of a Leading-Edge Slat, Leading-Edge Flap, Split Flap, and Double-Slotted Flap*, NACA TN-3007, 1953.

[2] F.E. Weick, C.J. Wenzinger, *The Characteristics of a Clark Y Wing Model Equipped With Several Forms of Low-Drag Fixed Slots*, NACA TR-407, 1933.

[3] W.R. Oliver, *Results of Design Studies and Wind Tunnel Tests of an Advanced High Lift System for an Energy Efficient Transport*, NASA CR-159389, December, 1980.

[4] W. Krüger, *Wind-Tunnel Investigations on a Changed Mustang Profile With Nose Flap Force and Pressure-Distribution Measurements*, NACA TM-1177, 1947.

[5] W.E. Gauvain, *Wind Tunnel Tests of a Clark Y Wing With "Maxwell" Leading Edge Slots*, NACA TN-598, 1937.

[6] J.W. Smith, W.P. Lock, G.A. Payne, *Variable-Camber Systems Integration and Operational Performance of the AFTI/F-111 Mission Adaptive Wing*, NASA TM-4370, 1992.

[7] Anonymous, *Assessment of Variable Camber for Application to Transport Aircraft*, NASA CR-158930, 1980.

[8] W.D. Thompson, *Cessna—Wings for the World—The Single-Engine Development Story*, Maverick Publications, 1992.

[9] J. Latas, *Aerodynamic Development of the Cessna 177*, SAE Technical Paper 680199, 1968.

[10] A.M.O. Smith, *High-lift aerodynamics*, J. Aircr. 12 (6) 1975, pp. 501–530.

[11] R.H. Liebeck, D.N. Smyth, *Study of slat-airfoil combinations using computer graphics*, J. Aircr. 20 (4) 1973, pp. 254–256.

[12] H.-U. Meier, *German Development of the Swept Wing 1935-1945*, AIAA, 2010.

[13] P.K.C. Rudolph, *High-Lift Systems on Commercial Subsonic Airliners*, NASA CR-4746, 1996.

[14] G. Lachmann, *Experiments With Slotted Wings*, NACA TN-71, 1921.

[15] C.H. Barnes, *Handley Page Aircraft Since 1907*, Putnam, 1976.

[16] F.H. Page, *The handley page wing*. Aeronaut. J. (London, England : 1897), 25 (126) 1921, 263–289, https://doi.org/10.1017/S2398187300139817.

[17] C.L. Gillis, J.W. McKee, *Wind-Tunnel Investigation of an NACA 23012 Airfoil With an 18.05-Percent-Chord Maxwell Slat and With Trailing Edge Flap*, NACA WR-L-574, 1941.

[18] J.F. Cahill, *Summary of Section Data on Trailing-Edge High-Lift Devices*, NACA R-938, 1949.

[19] Nayler, et al., *Experiments on Models of Aeroplane Wings at the National Physical Laboratory*, ARC R.&M. No. 110, March 1914.

[20] A.D. Young, *The Aerodynamic Characteristics of Flaps*, ARC R.&M. No. 2622, 1947.

[21] W.J. O'Sullivan, *Full-Scale Wind-Tunnel and Flight Tests of a Fairchild XR2K-1 Airplane With a Zap Flap and Upper-Surface Aileron-Wing Installation*, NACA WR-L-437, 1942.

[22] K.W. Clark, F.W. Kirkby, *Wind Tunnel Tests of the Characteristics of Wing Flaps and Their Wakes*, ARC R.&M. No. 1698, March 1935.

[23] R.W. Noyes, *Wind-Tunnel Tests of a Wing With a Trailing-Edge Auxiliary Airfoil Used as a Flap*, NACA TN-524, 1935.

[24] R.C. Platt, *Aerodynamic Characteristics of Wings With Cambered External Airfoil Flaps, Including Lateral Control, With a Full-Span Flap*, NACA R-541, 1935.

[25] C.J. Wenzinger, *Wind-Tunnel Investigation of Ordinary and Split Flaps on Airfoils of Different Profile*, NACA TR-554, 1937.

[26] F.F. Fullmer Jr., *Wind Tunnel Investigation of NACA 66(215)-216, 66,1-212, and 65(sub 1)-212 Airfoils With 0.20-airfoil-chord Split Flaps*, NACA WR-L-140, 1944.

[27] C.J. Wenzinger, W.E. Gauvain, *Wind-Tunnel Investigation of an N.A.C.A. 23012 Airfoil With a Slotted Flap and Three Types of Auxiliary Flap*, NACA-TR-679, 1939.
[28] R. Freedman, *The Wright Brothers: How They Invented the Airplane*, Holiday House, 1991, 116.
[29] P.E. Purser, T.R. Turner, *Wind-Tunnel Investigation of Perforated Split Flaps for Use as Dive Brakes on a Tapered NACA 23012 Airfoil*, NACA WR-L-373, 1941.
[30] C.H. Dearborn, H.A. Soule, *Full-Scale Wind-Tunnel and Flight Test of a Fairchild 22 Airplane Equipped With a Zap Flap and Zap Ailerons*, NACA TN-596, 1937.
[31] J. Rickard, *Northrop P-61 Black Widow—Introduction and Development*, http://www.historyofwar.org/articles/weapons_northrop_P-61_development.html, 1 July 2009 (Accessed 19 May 2020).
[32] O. Schrenk, *A Simple Approximation Method for Obtaining the Spanwise Lift Distribution*, NACA TM-948, 1940.
[33] E. Gruschwitz, O. Schrenk, *A Simple Method for Increasing the Lift of Airplane Wings by Means of Flaps*, NACA TM-714, 1933.
[34] S.C. Lott, *Guide to the Harlan D. Fowler Papers 1920-1980*, Collection number: MSS-1995-04, San José State University Library, 2009.
[35] J.R. Hansen, *The Wind and Beyond*, NASA SP-2007-4409, 2007.
[36] W.H. Wentz Jr., H.C. Seetharam, *Development of a Fowler Flap System for a High Performance General Aviation Airfoil*, NASA CR-2443, 1974.
[37] W.H. Wentz Jr., C. Ostowari, *Additional Flow Field Studies of the GA (W)-1 Airfoil With 30-percent Chord Fowler Flap Including Slot-Gap Variations and Cove Shape Modifications*, NASA-CR-3687, 1983.
[38] R.H. Liebeck, *Design of subsonic airfoils for high lift*, J. Aircr. 15 (9) 1978, 547–561.
[39] K. Howard, *Gurney Flap*, Motor Sport Magazine September 2000.
[40] J. Zerihan, X. Zhang, *Aerodynamics of gurney flaps on a wing in ground effect*. AIAA J. Aircr. 39 (5) 2001 772–780, https://doi.org/10.2514/2.1396.
[41] R. Myose, M. Papadakis, I. Heron, *Gurney flap experiments on airfoils, wings, and reflection plane model*, J. Aircr. 35 (2) 1998, pp. 206–211.
[42] M.A. Cavanaugh, P. Robertson, W.H. Mason, *Wind Tunnel Test of Gurney Flaps and T-Strips on an NACA 23012 Wing*, AIAA 2007-4175, 2007.
[43] D.H. Neuhart, O.C. Pendergraft Jr., *A Water Tunnel Study of Gurney Flaps*, NASA-TM-4071, 1988.
[44] Paul M.H.W. Vijgen, Floyd G. Howard, Dennis M. Bushnell, Bruce J. Holmes, Serrated Trailing Edges for Improving Lift and Drag Characteristics of Lifting Surfaces, US-PATENT-5,088,665, 1992.
[45] E.A. Mayda, C.P. van Dam, D. Nakafuji, *Computational Investigation of Finite Width Microtabs for Aerodynamic Load Control*, AIAA-2005-1185, 2005.
[46] A. Silverstein, S. Katzoff, *Design Charts for Predicting Downwash Angles and Wake Characteristics Behind Plain and Flapped Wings*, NACA R-648, 1925.
[47] C.J. Wenzinger, T.A. Harris, *Wind-Tunnel Investigation of an NACA 23012 Airfoil With Various Arrangements of Slotted Flaps*, NACA-TR-664, 1939.
[48] J.G. Lowry, *Wind-Tunnel Investigation of an NACA 23012 Airfoil With Several Arrangements of Slotted Flaps With Extended Lips*, NACA TN-808, 1941.
[49] T.A. Harris, *Wind-Tunnel Investigation of an N.A.C.A. 23012 Airfoil With Two Arrangements of a Wide-Chord Slotted Flap*, NACA-TN-715, 1939.
[50] C.J. Wenzinger, T.A. Harris, *Wind-Tunnel Investigation of NACA 23012 Airfoil With Various Arrangements of Slotted Flaps*, NACA-TR-677, 1939.
[51] R.S. Swanson, T.A. Harris, *Wind Tunnel Tests of an NACA 23021 Airfoil Equipped With a Slotted Extensible and a Plain Extensible Flap*, NACA-TN-782, 1940.
[52] F. Duschik, *Wind-Tunnel Investigation of an N.A.C.A. 23021 Airfoil With Two Arrangements of a 40-Percent-Chord Slotted Flap*, NACA-TN-728, 1939.
[53] I.G. Recant, *Wind-Tunnel Investigation of an NACA 23030 Airfoil With Various Arrangements of Slotted Flaps*, NACA-TN-755, 1940.
[54] I.H. Abbott, A.E. Von Doenhoff, L.S. Stivers Jr., *Summary of Airfoil Data*, NACA-TR-824, 1945.
[55] J.F. Cahill, *Two-Dimensional Wind-Tunnel Investigation of Four Types of High-Lift Flap on an NACA 65-210 Airfoil Section*, NACA-TN-1191, 1947.
[56] S.F. Racisz, *Investigation of NACA 65 (112) A111 (approx.) Airfoil With 0.35-chord Slotted Flap at Reynolds Numbers up to 25 Million*, NACA-TN-1463, 1947.
[57] F.J. Rice Jr., L.K. Loftin Jr., *Two-Dimensional Wind-Tunnel Investigation of Two NACA Low-Drag Airfoil Sections Equipped With Slotted Flaps and a Plain NACA Low-Drag Airfoil Section for XF6U-I Airplane*, NACA-MR-L5L11, 1946.
[58] J.F. Cahill, *Aerodynamic Tests of an NACA 66(215)-116, a=0.6 Airfoil With a 0.25c Slotted Flap for the Fleetwings XA-39 Airplane*, NACA-MR-L4K21, 1944.
[59] H.A. James, L.W. Hunton, *Estimation of Incremental Pitching Moments Due to Trailing-Edge Flaps on Swept and Triangular Wings*, NACA-MR-A4L28, 1955.
[60] F.E. Weick, R.C. Platt, *Wind-Tunnel Tests of the Fowler Variable-Area Wing*, NACA-TN-419, 1932.
[61] R.C. Platt, *Aerodynamic Characteristics of a Wing With Fowler Flaps Including Flap Loads, Downwash, and Calculated Effect on Take-Off*, NACA-TR-534, 1936.
[62] J.F. Cahill, S.F. Racisz, *Wind-Tunnel Investigation of Seven Thin NACA Airfoil Sections to Determine Optimum Double-Slotted-Flap Configurations*, NACA-TN-1545, 1948.
[63] T.A. Harris, I.G. Recant, *Wind-Tunnel Investigation of NACA 23012, 23021, and 23030 Airfoils Equipped with 40-Percent-Chord Double Slotted Flaps*, NACA-TR-723, 1941.
[64] J.M. Riebe, *Wind-Tunnel Investigation of an NACA 23012 Airfoil With a 0.30-Airfoil-Chord Double Slotted Flap*, NACA-ARR-3L10, 1943.
[65] J. Fischel, J.M. Riebe, *Wind-Tunnel Investigation of an NACA 23021 Airfoil With a 0.32-Airfoil-Chord Double Slotted Flap*, NACA-ARR-L4J05, 1944.
[66] J.H. Quinn Jr., *Tests of the NACA 64(SUB 1)A212 Airfoil Section With a Slat, a Double Slotted Flap, and Boundary-layer Control by Suction*, NACA-TN-1293, 1947.
[67] F. Visconti, *Wind-Tunnel Investigation of Air Loads Over a Double Slotted Flap on the NACA 65(216)-215, a = 0.8 Airfoil Section*, NACA-RM-L7A30, 1947.
[68] S.M. Bogdonoff, *Wind-Tunnel Investigation of a Low-Drag Airfoil Section With a Double Slotted Flap*, NACA-ACR-3I20, 1943.
[69] J.H. Quinn Jr., *Wind-Tunnel Investigation of the NACA 654-421 Airfoil Section With a Double Slotted Flap and Boundary Layer Control by Suction*, NACA-TN-1395, 1947.
[70] J.H. Quinn Jr., *Wind-Tunnel Investigation of Boundary-Layer Control by Suction on the NACA 653-418, a = 1.0 Airfoil Section With a 0.29-Airfoil-Chord Double Slotted Flap*, NACA-TN-1071, 1946.
[71] A.L. Braslow, L.K. Loftin Jr., *Two-Dimensional Wind-Tunnel Investigation of an Approximately 14-Percent-Thick NACA 66-Series-Type Airfoil Section With a Double Slotted Flap*, NACA-TN-1110, 1946.
[72] J.F. Cahill, *Aerodynamic Data for a Wing Section of the Republic XF-12 Airplane Equipped With a Double Slotted Flap*, NACA-MR-L6A08a, 1946.
[73] E. Zierten, T. Omar, A. Mahal, *Two-Dimensional Wind-Tunnel Tests of a NASA Supercritical Airfoil With Various High-Lift Systems*, Data Analysisvol. I, April 1973NASA-CR-2214.
[74] TCDS A9EA, Viking Air Limited, Revision 15, 06/11/2012, FAA.
[75] S.F. Hoerner, *Fluid-Dynamic Lift*, L. Hoerner, 1965.

[76] S. Hoerner, *Aerodynamic Shape of the Wing Tips*, Technical Report 5752, USAF, Air Material Command, Wright-Patterson Air Force Base, 1949.
[77] S.F. Hoerner, *Fluid-Dynamic Drag*, L. Hoerner, 1965.
[78] C.P. Van Dam, *Effects of Wingtip Modifications on Handling Qualities of Agricultural Aircraft*, SAE TP-810606, 1981.
[79] R.D. Kimberlin, *Flight Testing of Fixed-Wing Aircraft*, AIAA Education SeriesAIAA, 2003.
[80] H. Zimmer, *The Aerodynamic Optimization of Wings at Subsonic Speeds and the Influence of Wingtip Design*, 1987NASA TM-88534, (Dissertation 1983).
[81] K. Rokhsaz, *A Brief Survey of Wing Tip Devices for Drag Reduction*, SAE TP-932574, 1993.
[82] D.A. Naik, C. Ostowari, *Effects of nonplanar outboard wing forms on a wing*, J. Aircr. 27 1990 117–122.
[83] J. Weber, D. Küchemann, G.G. Brebner, *Low-Speed Tests on 45-Deg Swept-Back Wings Part I and II*, ARC R.&M. No. 2882, May 1951.
[84] D. Küchemann, J. Weber, *The Subsonic Flow Past Swept Wings at Zero Lift Without and With Body*, ARC R.&M. No. 2908, March 1953.
[85] D. Küchemann, *The Aerodynamic Design of Aircraft*, Pergamon Press Ltd., 1978.
[86] F.H. Norton, *An Investigation on the Effect of Raked Wing Tips*, NACA TN-69, 1921.
[87] M.R.A. Diaz, T.R. Yechout, E.M. Bryant, *'The Rakelet'—A Wingtip Modification Approach to Improve Endurance, Range and Fuel Savings*, AIAA 2012-0669, 2012.
[88] E.G. Reid, *The Effects of Shielding the Tips of Airfoils*, NACA TR-201, 1925.
[89] D.R. Riley, *Wind-Tunnel Investigation and Analysis of the Effects of End Plates on the Aerodynamic Characteristics of an Unswept Wing*, NACA TN-2440, 1951.
[90] W. Mangler, *The Lift Distribution of Wings With End Plates*, NACA TM-856, 1938.
[91] P.E. Hemke, *Drag of Wings With Endplates*, NACA R-267, 1927.
[92] J. Weber, *Theoretical Load Distribution on a Wing With Vertical Plates*, ARC R.&M. No. 2960, March 1956.
[93] D. Raymer, *Aircraft Design: A Conceptual Approach*, fifth ed., AIAA (American Institute of Aeronautics and Astronautics) Education Series, 2012.
[94] B.W. McCormick, *Aerodynamics, Aeronautics, and Flight Mechanics*, John Wiley & Sons, 1979.
[95] J.R. Chambers, *Concept to Reality*, NASA SP-2003-4529, 2003.
[96] R.T. Whitcomb, *A Design Approach and Selected Wind-Tunnel Results at High Subsonic Speeds for Wing-Tip Mounted Winglets*, NASA TN D-8260, 1976.
[97] R.T. Whitcomb, S.G. Flechner, P.F. Jacobs, *A High Subsonic Speed Wind Tunnel Investigation of Winglets on a Representative Second-Generation Jet Transport Wing*, NASA TN D-8264, 1976.
[98] R.P. Hallion, *On the Frontier—Flight Research at Dryden, 1946-1981*, NASA History Series1984NASA SP-4303.
[99] P.T. Reynolds, *The Learjet "Longhorn" Series—The First Jets With Winglets*. SAE Technical Paper 790581, SAE, 1979, https://doi.org/10.4271/790581.
[100] A.B. Taylor, *DC-10 Winglet Flight Evaluation—Summary Report*, NASA CR-3748, 1983.
[101] Anonymous, Blended Winglets for Improved Airplane Performance, Boeing Publication.
[102] Anonymous, 737 MAX AT Winglet. http://www.boeing.com/commercial/737max/737-max-winglets/ (Accessed 28 May 2020).
[103] B.J. Holmes, C.P. van Dam, P.W. Brown, P.L. Deal, *Flight Evaluation of the Effect of Winglets on Performance and Handling Qualities of a Single-Engine General Aviation Airplane*, NASA-TM-81892, NASA, December 1980.
[104] C.D. Cone Jr., *The Theory of Induced Lift and Minimum Induced Drag of Nonplanar Lifting Systems*, NASA TR-R-139, 1962.
[105] C.D. Cone Jr., *The Aerodynamic Design of Wings With Cambered Span Having Minimum Induced Drag*, NASA TR-R-152, 1960.
[106] Robert T Jones, *Minimizing induced Drag*, Soaring Magazine, October 1979, Soaring Society of America.

This page intentionally left blank

CHAPTER

11

The Anatomy of the Tail

OUTLINE

11.1 **Introduction** 481
11.1.1 The Content of This Chapter 481
11.1.2 The Process of Tail Sizing 482

11.2 **The Geometry of the Tail** 483
11.2.1 Definition of Reference Geometry 484
11.2.2 Horizontal and Vertical Tail Volumes 484
11.2.3 Various Tail Fixes 485
11.2.4 Basics of Spin and Spin Recovery 486

11.3 **On the Pros and Cons of Tail Configurations** 491
11.3.1 Conventional Tail 491
11.3.2 Cruciform Tail 493
11.3.3 T-Tail 494
11.3.4 V-Tail or Butterfly Tail 495
11.3.5 Inverted V-Tail 499
11.3.6 Y-Tail 499
11.3.7 Inverted Y-Tail 499
11.3.8 H-Tail 499
11.3.9 A-Tail 500
11.3.10 Twin Tail Boom or U-Tail Configuration 500
11.3.11 Three-Surface Configuration 501
11.3.12 Canard Configuration 501
11.3.13 Basic Design Guidelines for Selecting a Tail Configuration 503

11.4 **Initial Tail Sizing Methods** 505
11.4.1 Recommended Initial Values for V_{HT} and V_{VT} 505
11.4.2 Design Guidance for Initial Sizing of HT for Stick-Fixed Neutral Point 508
11.4.3 General Formulation of Initial Estimation of V_{HT} and V_{VT} 508
11.4.4 Method 1: Initial Tail Sizing Optimization Considering the Horizontal Tail Only 510
11.4.5 Method 2: Initial Tail Sizing Optimization Considering the Vertical Tail Only 511
11.4.6 Method 3: Initial Tail Sizing Optimization Considering Horizontal and Vertical Tail 511
11.4.7 Method 4: Initial Tail Sizing Optimization for an Arbitrary Fuselage 513

Exercises 516

References 516

11.1 INTRODUCTION

This chapter is intended to help with the design of the tail of the airplane. The tail provides means for stability and control and, after the wing, is the most important component of any fixed-wing aircraft. The task of the aircraft designer here is unambiguous: Select a configuration and then determine the required size, location, and type of controls to use (e.g., flapped or all-moving). Then, size these too. In this text, the term *tail* refers to any configuration of aft-mounted lifting surfaces used to balance an airplane. The tail usually includes both the horizontal and vertical stabilizing surfaces; however, a *horizontal tail* (HT) refers to a surface intended to control the pitch of the aircraft while *vertical tail* (VT) refers to one intended to control the yaw (and sometimes roll). The term *canard* refers to any configuration using a front-mounted lifting surface for this purpose. Such configurations still require an aft-mounted vertical tail for directional stability.

This chapter relies heavily on *stability and control theory*, presented in Chapters 24 and 25. The discussion in this chapter assumes the reader is familiar with the concepts in that chapter.

11.1.1 The Content of This Chapter

- Section 11.2 presents a general discussion of static stability and control. In addition to defining fundamental stability concepts, it discusses trends

Copyright © 2022 Elsevier Inc. All rights reserved.

in longitudinal and lateral/directional stability derivatives.
- Section 11.3 presents a general discussion of the pros and cons of different tail configurations.
- Section 11.4 provides general formulation applicable to the horizontal and vertical tail. The section presents four methods to size the optimal tail arm and planform areas of the horizontal and vertical tail in terms of minimum surface area. The first three methods use (1) the horizontal tail volume, (2) the vertical tail volume, and (3) a combination of the two. The fourth method is intended for arbitrary fuselage configurations, e.g. tadpole fuselages.

11.1.2 The Process of Tail Sizing

The concept *tail sizing* refers to the process required to determine the size, shape, and 3-dimensional positioning of the stabilizing surfaces. This procedure is listed in Table 11-1.

Design Requirements for the Horizontal and Vertical Tail

(1) The HT must allow the airplane to be stalled at its forward CG location. It is imperative that the stalling speed is the airplane's minimum airspeed. If this cannot be accomplished, e.g., because of limited elevator authority, the aircraft's minimum airspeed will be higher than the stalling speed. This calls for higher approach speed and longer runways. The higher kinetic energy may even compromise the certifiability of the aircraft if it cannot comply with emergency landing regulations.

(2) The HT must be capable of trimming the airplane at low airspeeds at forward CG location. This means airspeed at least as low as $1.2V_{S_0}$ (V_{S_0} = stalling speed in the landing configuration) with full thrust (balked landing).

(3) If tricycle landing gear, the HT must be capable of lifting the nose gear at no higher than $0.9V_{S1}$ (V_{S1} = stalling speed in the take-off configuration).

(4) The HT must be capable of trimming the airplane at high airspeeds at aft CG location. This means, at least for *cruise let-down*, i.e., maintain descent at airspeed as high as cruising speed plus 5 to 20 KTAS.

(5) The HT may not stall because of excessive pitch rate, $\hat{q}$.

(6) The VT must be capable of maintaining a yaw angle of at least 15 degrees for crosswind handling without excessive control surface deflections.

(7) The VT must provide means to prevent rudder locking. This usually means the addition of a dorsal fin (see Section 11.2.3).

(8) The HT and VT must be of a low AR to reduce the risk of tail stall and yet be of suitably large AR to make the stabilizing surfaces responsive to AOA or AOY changes. Typically, this means that the AR of the HT should be $3 < AR_{HT} < 5$ and the VT should be $0.9 < AR_{VT} < 2$.

(9) The HT and VT must develop stability derivatives such as $C_{y\beta}$, $\boldsymbol{C_{M\alpha}}$, $\boldsymbol{C_{M\delta e}}$, $\boldsymbol{C_{Mq}}$, $\boldsymbol{C_{N\beta}}$, $\boldsymbol{C_{N\delta r}}$, $\boldsymbol{C_{Nr}}$, and others that ensure the airplane is naturally stable, statically and dynamically. All 14 CFR Part 23 aircraft are required to be statically stable and demonstrate stable longitudinal short period and lateral directional oscillation (also known as Dutch roll) modes. However, the designer should strive to make the remaining dynamic modes convergent. Strictly speaking, GA aircraft do not need fly-by-wire control systems because, by law, they *must be stable*. This, however, does not preclude the development of such systems for GA aircraft as these may offer supplemental benefits such as envelope protection.

(10) The HT and VT should not have detrimental impact on the nonlinear behavior of the above stability derivatives at high AOAs and AOYs. For instance, the derivatives should not acquire values that render the airplane unrecoverable in spins or deep stall.

(11) The HT and VT must be designed for minimum structural weight, with the designer being cognizant of the manufacturability and aeroelastic consequences of a given design. This means only make the HT and VT as large as they need to do their job.

TABLE 11-1 Initial sizing and layout algorithm for a HT and VT for a GA aircraft.

Step	Task	Section
1	If unsure about what sort of tail configuration to use, begin by qualitatively evaluating the pros and cons of all applicable configurations per Section 11.3 specific to the aircraft being designed. Compile a decision matrix of the sort shown in Chapters 4 and 8 to help with the selection. Consider parameters like expected cost of implementation, weight, manufacturing and mechanical complexity, and effectiveness, to name a few.	11.3
2	Once the tail configuration is selected, conduct an initial sizing based on historical data, such as shown in Section 11.4. This is an initial estimate based on historical trends and should be expected to change in the next step.	11.4
3	The initial geometry of STEP 2 is only a starting point. It needs to be evaluated to confirm it has the necessary balancing power. The bulleted list in this section presents design requirements. Add any items specific to your airplane. Any requirements not met means the HT or VT must be reshaped, typically by increasing area or tail arm. If the HT or VT easily meets the requirements, consider reducing area.	

(12) The control system should be simple and reliable, and it should not require excessive control surface deflection to command the airplane, even in demanding maneuvers. Large control surface deflection usually causes control surface stall, which sharply lowers control authority.

(13) Manual control system should not require excessive stick forces inside the operating envelope of the aircraft. Consult 14 CFR §23.155, *Elevator control force in maneuvers* and §23.397, *Limit control forces and torques*, regarding regulatory limits.

(14) The designer must be cognizant of other operational limitations. For instance, excessive length of the tail arm may interfere with T-O rotation, subject the structure to high stresses, and lower the flutter speed of the airplane. Excessively short tail arms will require high deflection angles of control surfaces and may result in poor handling characteristics due to unacceptably low pitch damping.

Some of these bullets are not treated directly in this section. Among those are the evaluation of dynamic stability and compliance with the design checklist of Section 26.2. Also consider the design guidance in Chapters 24 and 25. Provided the designer does not violate other design requirements, drag should always be minimized. Section 11.4 provides initial tail sizing methods that minimize the wetted area of the empennage to reduce skin friction drag.

11.2 THE GEOMETRY OF THE TAIL

This section presents methods to estimate several geometric properties of the tail. Geometric properties such as span, planform area, aspect ratio, and taper ratio are identical to those of the wing (see Section 9.2). We will use the abbreviations HT and VT for the horizontal and vertical tail, respectively. Properties uniquely related to the HT or VT are specified using the simplified airplane in Figure 11-1. Note the section of the fuselage that extends from the wing's quarter-chord to that of the horizontal or vertical tail (denoted by the dashed lines). It has been approximated by a frustum. The stabilizing surfaces have been approximated by flat plates. Recall from Section 4.1.6 that the HT and VT of a conventional aircraft is called *empennage*, a French word for the tail feathers of an arrow. Correct or not, many take empennage to mean the general aft section of the fuselage that contains both the HT and VT.

The area of the HT, S_{HT}, is defined as the product of its average chord, c_{HT}, and span, b_{HT}. Similarly, the area of the VT, S_{VT}, is defined as the product of its average chord,

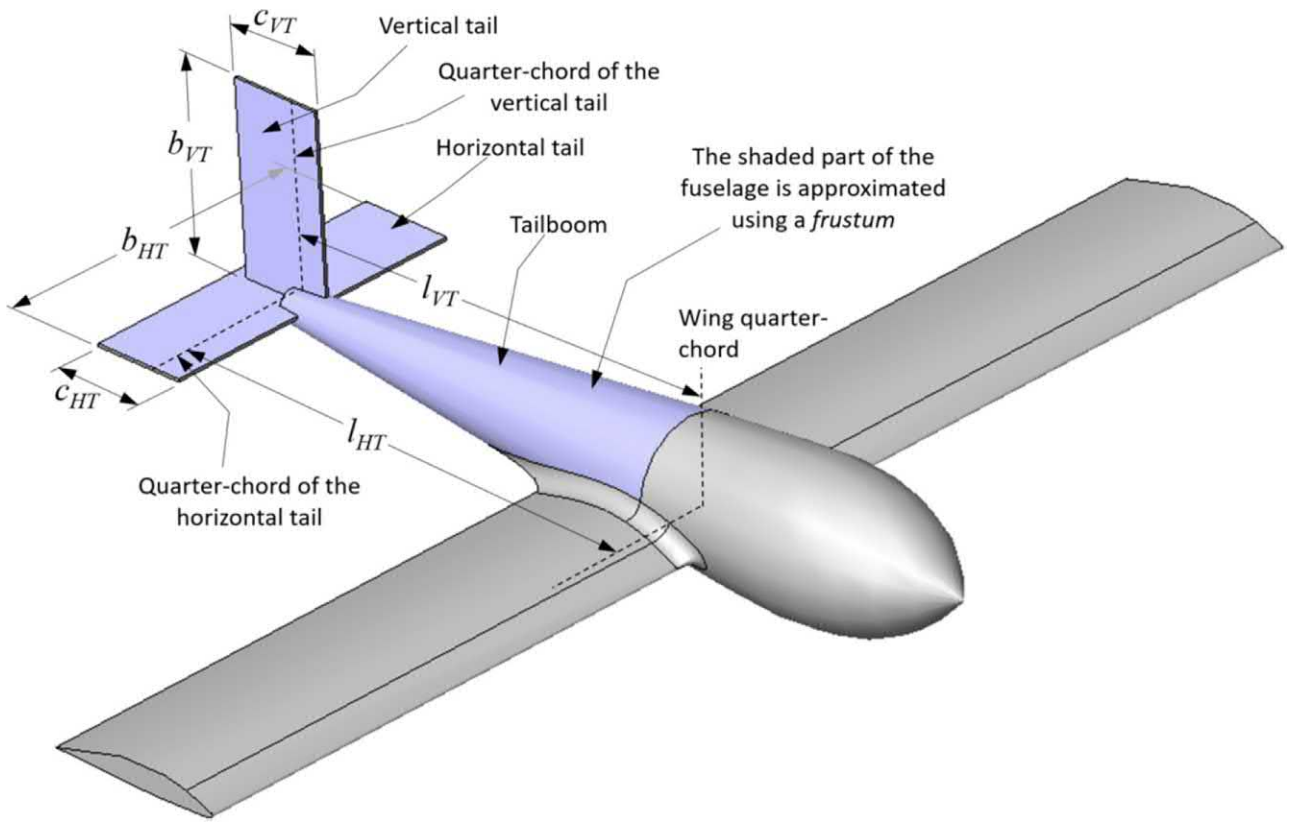


FIGURE 11-1 A simplified airplane layout.

c_{VT}, and span, b_{VT}. Then we define the *horizontal tail arm*, l_{HT}, as the distance from the quarter-chord of the wing's MGC to the quarter-chord of the MGC of the HT. The *vertical tail arm*, l_{VT}, is defined in a similar manner. These definitions are used for initial tail sizing. Similar definitions, referencing the *center-of-gravity* (CG), are also used for stability and control to account for CG-position.

11.2.1 Definition of Reference Geometry

Just like we define the reference wing area, we also define reference area for the horizontal and vertical lifting surfaces. Figure 11-2 shows how this is typically defined. The shaded regions simply show a likely approach.

The distances l_{HT} and l_{VT} were defined in Figure 11-1. The distances l_a and l_c, in Figure 11-2 are the distances from the wing-apex to the apex of the HT and VT, respectively. The distances l_b and l_d are the distances from the wing-apex to the quarter-chord of the MGC of the HT and VT, respectively. These distances are helpful as references when drawing the aircraft. Also, let us define the following angles: (1) Λ_{LE} is the angle between the wing-apex and the leading edge of the wing's *mean geometric chord* (c_{MGC}). It is often the wing's LE angle. (2) $\Lambda_{LE_{HT}}$ is the angle between the HT-apex and the leading edge of the HT's *mean geometric chord* ($c_{MGC_{HT}}$). (3) $\Lambda_{LE_{VT}}$ is the angle between the VT-apex and the leading edge of the VT's *mean geometric chord* ($c_{MGC_{VT}}$). The following formulae are used to estimate these parameters:

$$l_b = l_a + y_{MGC_{HT}} \tan\Lambda_{LE_{HT}} \tag{11-1}$$

$$l_d = l_c + z_{MGC_{VT}} \tan\Lambda_{LE_{VT}} \tag{11-2}$$

$$l_{HT} = l_a - \left(y_{MGC} \tan\Lambda_{LE} + \frac{1}{4}c_{MGC}\right) + \left(y_{MGC_{HT}} \tan\Lambda_{LE_{HT}} + \frac{1}{4}c_{MGC_{HT}}\right) \tag{11-3}$$

$$l_{VT} = l_c - \left(y_{MGC} \tan\Lambda_{LE} + \frac{1}{4}c_{MGC}\right) + \left(z_{MGC_{VT}} \tan\Lambda_{LE_{VT}} + \frac{1}{4}c_{MGC_{VT}}\right) \tag{11-4}$$

For convenience, the aspect ratio for the HT and VT are repeated below (see Section 9.2).

$$AR_{HT} = b_{HT}^2/S_{HT} \qquad AR_{VT} = b_{VT}^2/S_{VT}$$

11.2.2 Horizontal and Vertical Tail Volumes

The derivation of static pitch and directional stability leads to the occurrence of nondimensional ratios that are known as *horizontal* (V_{HT}) and *vertical tail volumes* (V_{VT}), shown below. This ratio correlates to classes of aircraft (see Section 11.4.1).

$$\text{Horizontal Tail Volume}: \quad V_{HT} = \frac{l_{HT} \cdot S_{HT}}{c_{MGC} \cdot S} \tag{11-5}$$

$$\text{Vertical Tail Volume}: \quad V_{VT} = \frac{l_{VT} \cdot S_{VT}}{b \cdot S} \tag{11-6}$$

where

c_{MGC} = Mean Geometric Chord
b = Reference span (e.g., wingspan)

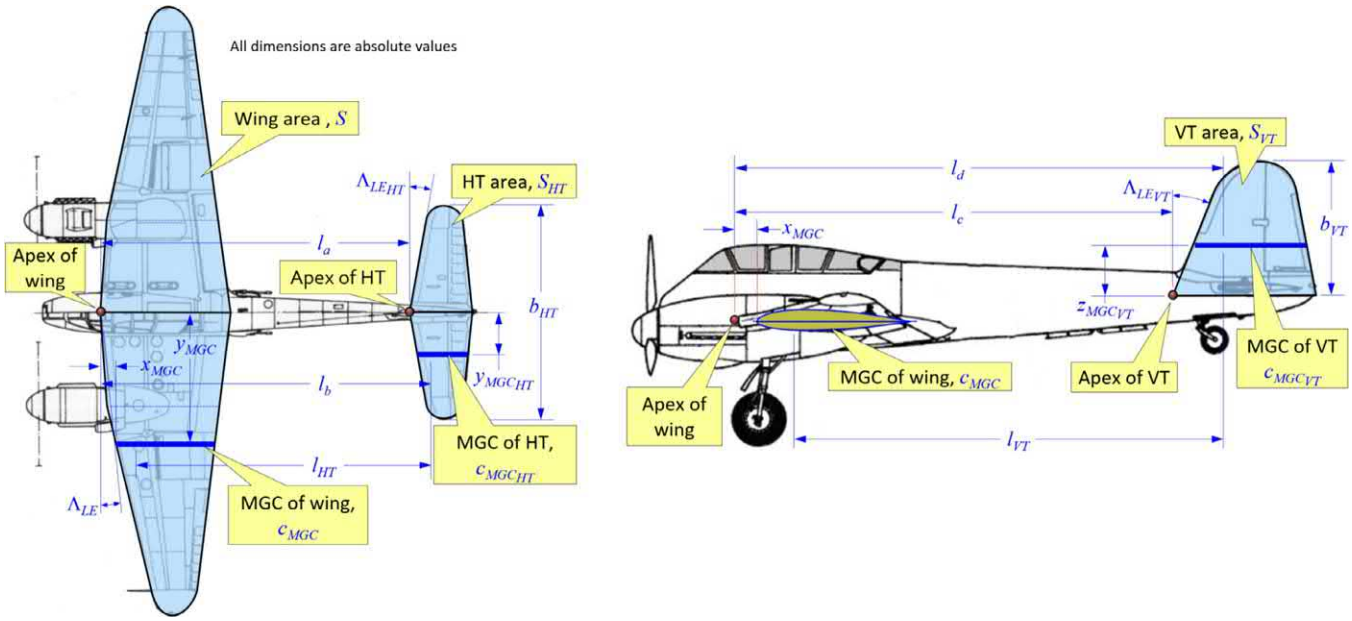


FIGURE 11-2 Definition of geometric terms for the HT. *Messerschmitt Me-210 Hornisse source: www.wikipedia.org.*

S = Reference area (e.g., wing area)
S_{HT} = Horizontal tail area
S_{VT} = Vertical tail area
l_{HT} = Horizontal tail arm
l_{VT} = Vertical tail arm

11.2.3 Various Tail Fixes

(1) The Dorsal Fin

A *dorsal fin* is a small surface extension installed at the leading edge of the root of the vertical tail (see Figures 11-3 and 11-4). It increases directional stability and helps prevents a serious condition known as *rudder lock*. The "dorsal" can be as simple as a thin flat plate or as complicated as a curved compound surface stamped aluminum fairing riveted to an existing fin. A sharp LE discontinuity between dorsal and fin is more effective.

Rudder locking occurs at high AOY (β) and results from insufficient directional stability ($C_{N\beta}$) and excessive *rudder floating*. Floating results as the side-flow forces the rudder to the leeward side. When the airplane is yawed at a low β (for instance in a side-slip maneuver), the rudder tends to display limited floating. To the pilot, the rudder pedal-force (which is the difference between deflection and floating moments) appears to increase linearly. As β increases further, so does side-flow. It begins to rise rapidly. To the pilot, the pedal-force appears to lighten. Eventually, at a specific β, the pedal-force equals that developed by the side-flow: To the pilot, the force required to deflect the rudder is zero. Should the sideslip increase beyond this point, a pedal-force reversal will take place. It forces the rudder against the stops (see Figure 11-5). This is *rudder lock*. A considerable pedal-force is required to bring the rudder back—it may exceed human strength.

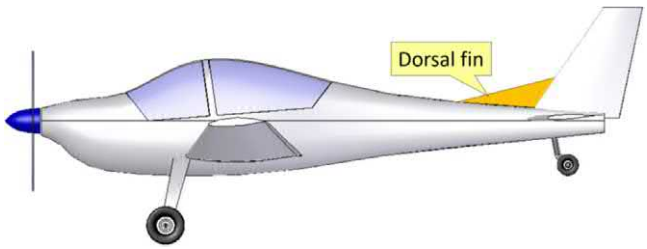


FIGURE 11-3 The dorsal fin is a surface extension between the VT and the fuselage.



FIGURE 11-4 A dorsal fin on a Dornier Do 228. *Photo by Phil Rademacher.*

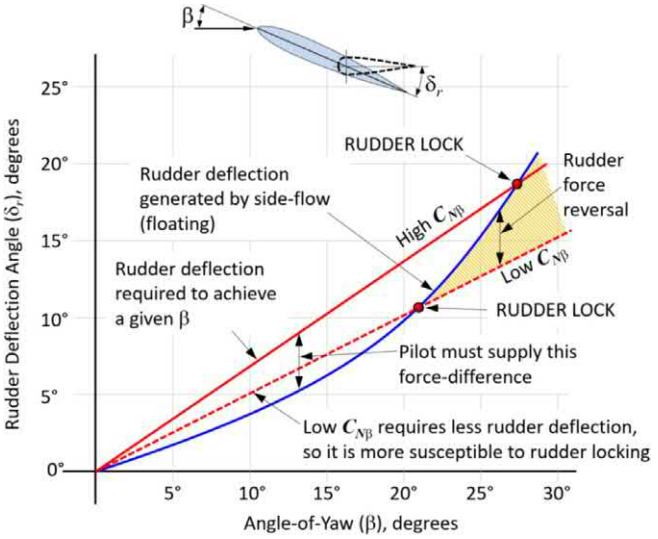


FIGURE 11-5 Rudder locking occurs at high β, when the side-flow pushes the rudder beyond what is required for deflection. *Based on Perkins, C.D., Hage, R.E., Airplane Performance, Stability, and Control, John Wiley & Sons, 1949.*

A classic example of the gravity of the rudder locking occurred on March 18, 1939, involving an early production version of the Boeing 307 Stratoliner. Officials of the Dutch airline KLM had expressed interest in the aircraft and sent a test pilot to evaluate it. The demonstration airplane was at 10,000 ft when the KLM pilot shut down two of its engines on the same wing to evaluate its asymmetric thrust characteristics. He brought it to maneuvering speed, where it stalled and entered spin. The rudder locked during the spin, making recovery attempts by its two pilots impossible [1]. It is thought these attempts caused the wing and empennage to separate from the airplane. The aircraft crashed, killing all 10 people on board [2]. Later wind tunnel testing showed the original tail was too small and rudder area too large. It revealed that adding a dorsal would remedy the problem [3].

A dorsal fin helps by partitioning the vertical into two low aspect ratio segments. This increases the stall AOA of both (because low *AR* surfaces stall at a higher AOA than high *AR* surfaces) and helps to maintain sufficient directional stability up to a higher β (see Figure 11-5). The recovery from rudder lock may require the airspeed to be reduced by a roll or a pull-up maneuver for the hinge moment drops to a magnitude that allows the pilot to neutralize the rudder [3, p. 221].

(2) The Ventral Fin

The ventral fin is a lifting surface used for two purposes; to improve stall or Dutch roll characteristics. Dorsal fins are rarely installed for other purposes, although the author of this book was involved in a project that featured one purely for looks. The installation of a ventral fin means two things: (1) There is insufficient nose pitch-down moment at stall or (2) insufficient Dutch roll damping. In either case, it is relatively easy to identify either case, as ventral fins installed for the former are usually substantially more horizontal than the latter (see Figure 11-6). Ventral fins should not be mistaken for an aft fuselage strake—a large chord short span fin seen on some aircraft (e.g., Aermacchi MB-326, Fiat G-91)—These are either a spin recovery fix or a tailskid fairing. Ventral fins would require a large cross flow of air to contribute to spin recovery. They should be aft-swept and feature a sharp leading edge.

The installation of ventral fins must consider the 3-dimensional flow-field around the aft fuselage. They are aligned such, in cruise, they produce no lift. Thus, they contribute no pitching moment and no lift-induced drag. Inevitably, they add skin friction. As the aircraft slows down and the AOA increases, the ventral begins to create vortex-lift and contribute to longitudinal stability. If large enough, they permit certification without a stick-shaker/pusher. Figure 11-7 depicts their impact for a hypothetical airplane. The nonlinearity in Figure 11-7 results in a trim point around 32 degrees. If this airplane reached that AOA, it may not have the elevator authority to recover (see Figure 11-21 for further insight). The ventral fin increases the nose pitch-down moment at this condition, deleting the trim point and allowing the modified aircraft to recover.

11.2.4 Basics of Spin and Spin Recovery

Spin entry and recovery is of major concern in GA aircraft. Spin is an autorotation that follows an aggravated stall [4]. Spin is a consequence of asymmetric wing stall that typically results in the wing rolling left or right. This initiates a dynamic mode called *autorotation*. It is caused as the lower/inside wing has a higher AOA than the higher/outside wing (recall both wings are stalled). This causes the outside lift to be larger than the inside lift, and the difference drives the rotation. The motion is a rapid vertical descent along a helical path. A break-down of the spinning motion is shown in Figure 11-8. Inadvertent spin is avoided by awareness and by focusing on aviating.

(1) Equations-of-Motion for Spinning Motion

The rigid body equations-of-motions are introduced in Section 24.1.4. They suffice to describe the 6-*degree-of-freedom* (DOF) spinning motion:

$$\dot{u} = \frac{V_\infty^2}{2\mu b} C_x - g\sin\theta + v\hat{r} - w\hat{q} \tag{11-7}$$

$$\dot{v} = \frac{V_\infty^2}{2\mu b} C_y + g\sin\phi\cos\theta + w\hat{p} - u\hat{r} \tag{11-8}$$

$$\dot{w} = \frac{V_\infty^2}{2\mu b} C_z + g\cos\phi\cos\theta + u\hat{q} - v\hat{p} \tag{11-9}$$

$$\dot{\hat{p}} = \overbrace{\frac{V_\infty^2}{2\mu k_x^2} C_L}^{\text{Aerodynamic moment}} + \overbrace{\frac{I_{yy} - I_{zz}}{I_{xx}}\hat{q}\hat{r} + \frac{I_{xz}}{I_{xx}}\left(\dot{\hat{r}} + \hat{p}\hat{q}\right)}^{\text{Inertia coupling}} \overbrace{- \frac{1}{I_{xx}}\left(\hat{q}h_{SRz} - \hat{r}h_{SRy}\right)}^{\text{Engine gyroscopic coupling moment}} \tag{11-10}$$

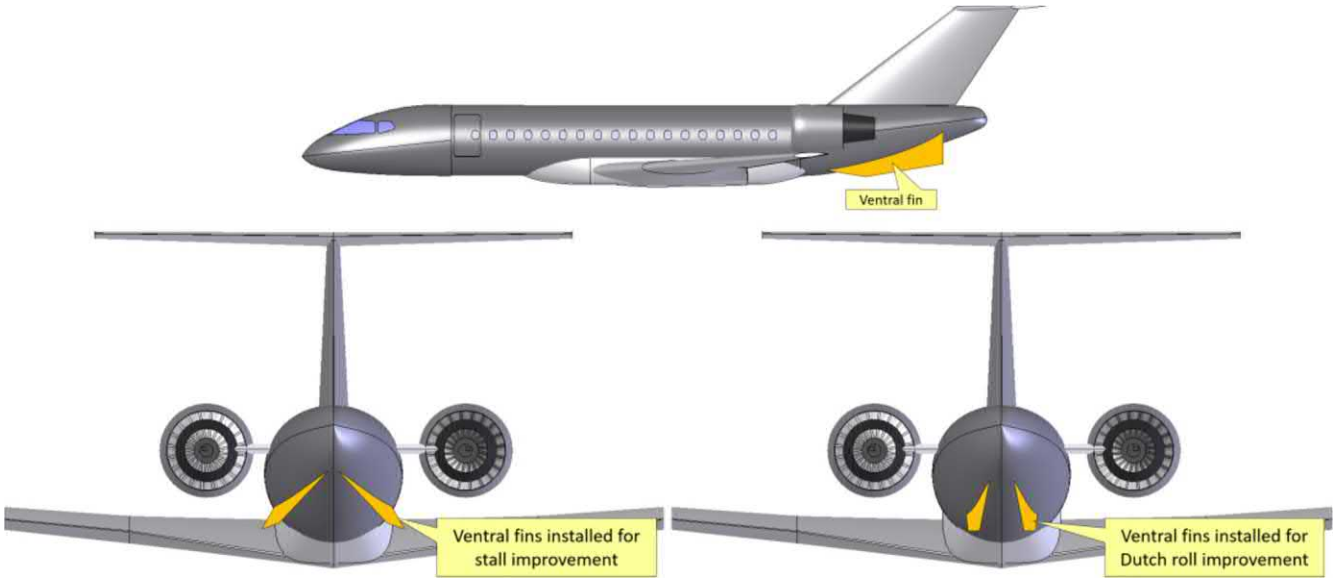


FIGURE 11-6 The purpose of installing ventral fins.

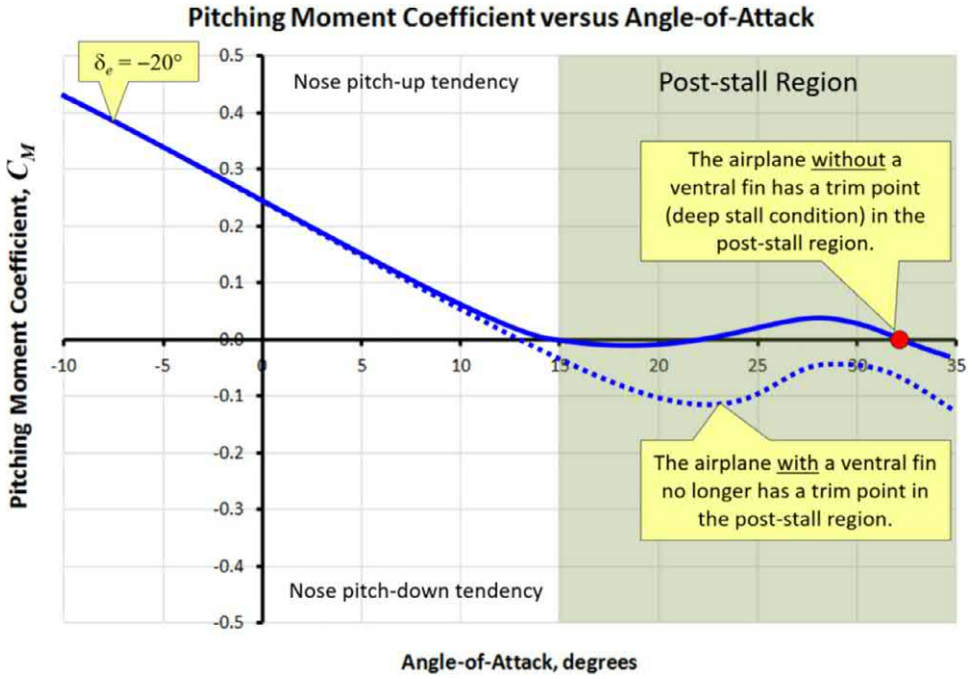


FIGURE 11-7 A ventral fin prevents deep stall by deleting the trim point in the poststall region.

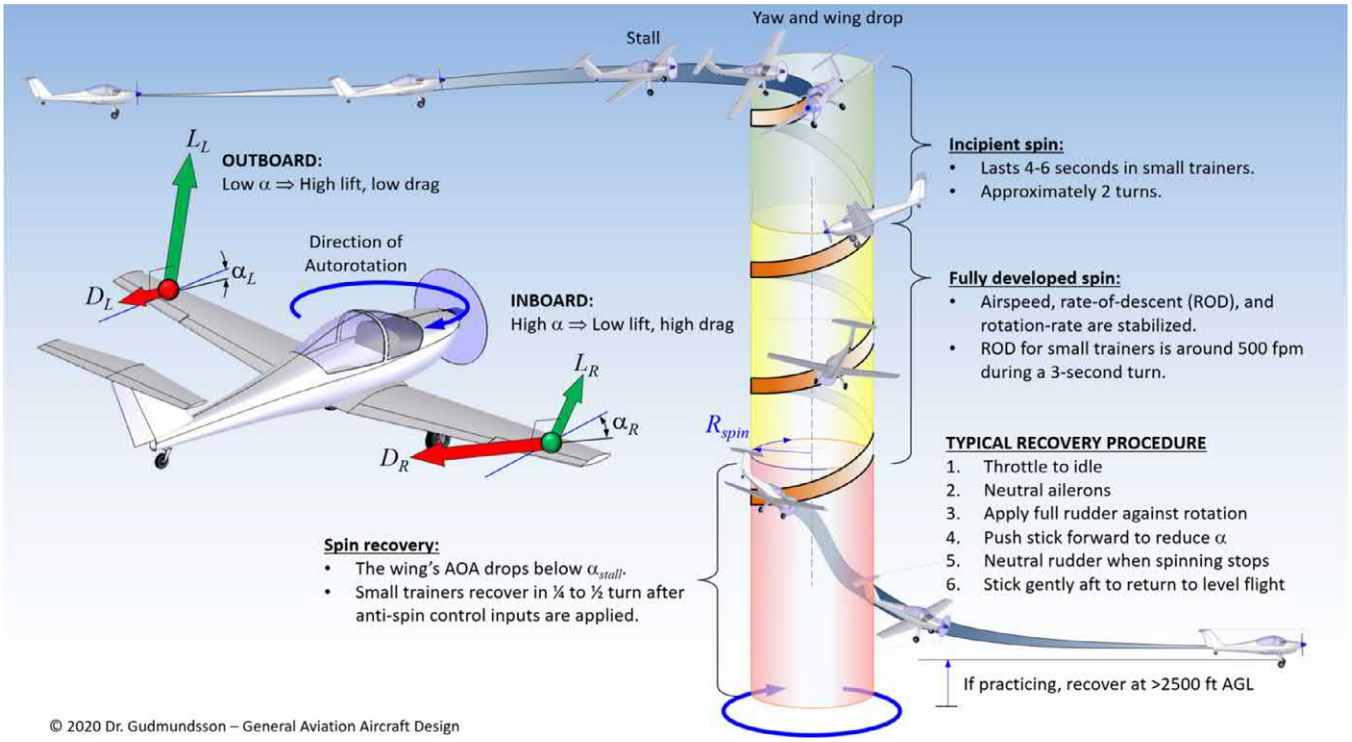


FIGURE 11-8 Spin entry, development, and recovery. *Based on Bowman, J.S. Jr, Summary of Spin Technology as Related to Light General-Aviation Airplanes, NASA TN-D-6575, December 1971; Anonymous, Airplane Flying Handbook, FAA-H-8083-3B, Federal Aviation Administration, 2016.*

$$\dot{\hat{q}} = \frac{V_\infty^2}{2\mu k_y^2} C_M + \frac{I_{zz} - I_{xx}}{I_{yy}} \hat{p}\hat{r} - \frac{I_{xz}}{I_{yy}} (\hat{p}^2 - \hat{r}^2) - \frac{1}{I_{yy}} (\hat{r} h_{SRx} - \hat{p} h_{SRz}) \tag{11-11}$$

$$\dot{\hat{r}} = \frac{V_\infty^2}{2\mu k_z^2} C_N + \frac{I_{xx} - I_{yy}}{I_{zz}} \hat{p}\hat{q} + \frac{I_{xz}}{I_{zz}} \left(\dot{\hat{p}} - \hat{q}\hat{r}\right) - \frac{1}{I_{zz}} (\hat{p} h_{SRy} - \hat{q} h_{SRx}) \tag{11-12}$$

where k_x, k_y, and k_z are the radii of gyration, e.g., $k_x = \sqrt{(I_{xx}/m)}$. The term μ is the *airplane relative-density coefficient*, given by $m/(\rho S b)$ [5]. ϕ,θ,ψ are roll, pitch, and yaw components of the Euler angles, respectively. They reference the so-called *body coordinate system* (see Figure 24-3). Other variables are defined in Chapter 24. Note that bold typeface denotes moment coefficients (e.g., $\boldsymbol{C_L}$ is the rolling moment coefficient). A spin prediction method is presented in ref. [6].

(2) Design Tools

There are two basic criteria the designer can use to help evaluate possible spin recovery characteristics: (1) *Kerr's criterion* of ref. [7] and (2) *Neihouse–Lichtenstein–Pepoon criterion* of refs. [8, 9].

Kerr's Criterion

Kerr's method stipulates that the most important parameters in spin are the unbalanced rolling moment coefficient ($\boldsymbol{C_L}$) about the wind-axis and the ratio I_{yy}/I_{xx}. By conducting spinning flight tests of 34 aircraft, Kerr developed an empirical assessment of their recovery characteristics using three classes: satisfactory, borderline, and unsatisfactory. This gave rise to a simple method to evaluate $\boldsymbol{C_L}$ and I_{yy}/I_{xx} for a new aircraft. Knowing its mass distribution, the method is used to assess into which class spin recovery characteristics fall.

Neihouse–Lichtenstein–Pepoon's (NLP) Criterion and Tail-Damping Power Factor (TDPF)

In contrast, the NLP criterion stipulates that the product of the tail-damping ratio and the unshielded rudder volume coefficient (called the *Tail-Damping Power Factor* or TDPF) is an indicator of the airplane's ability to recover from spin. A method to calculate TDPF is provided in refs. [8, 9]. Using a Grumman AA-1 Yankee test aircraft, ref. [10] tested four separate tail configurations for spin recovery. The reference concludes that "…the tail damping power factor (TDPF) as a parameter, cannot be used alone to predict airplane spin recovery characteristics."

Other Resources

Readers working on unconventional aircraft can resort to sophisticated experimental techniques. Bihrle Applied Research exemplifies a highly specialized research company that uses three-axis rotary balance wind tunnel to evaluate the spin recovery characteristics of aircraft [11]. Among others, this provides the test-pilot with priceless information about anti- and pro-spin control surface deflections.

(3) Factors Affecting Spin

Equations (11-7)–(11-12) indicate which and how physical parameters affect the spin. Ref. [12] summarizes various contributors.

Airplane Relative-Density Coefficient

The *relative-density factor* is a measure of the density of the aircraft compared to that of air. It is defined as $\mu = m/(\rho S b)$. An aircraft with a large μ calls for higher rudder and elevator authority for recovery than one with a low value of μ.

Mass Distribution

Mass distribution is the single most important factor in spinning because it dictates how the aircraft responds to control inputs for recovery. From the standpoint of inertia, the airplane can be considered a large gyroscope. However, unlike regular gyroscopes, it is subject to aerodynamic forces and moments. The mass distribution can be split into three categories based on the *inertia parameter* $(I_{xx}–I_{yy})/(mb^2)$. When the mass of the airplane is distributed mostly along the wing, its roll moment of inertia, I_{xx}, is larger than the pitch moment of inertia, I_{yy}. Thus, the parameter is positive, giving rise to what is called *wing-heavy loading*. If most of the mass is in the fuselage, the parameter is negative, or *fuselage-heavy loaded*. Most GA aircraft are *zero-loaded*, which means they fall between the other two categories. A small difference of $I_{xx}–I_{yy}$ indicates that the two inertias contribute little or nothing to the recovery control inputs [12]. The consequences of the three load-classes are listed in Table 11-2.

Tail Configuration

The arrangement of the HT and VT is of great importance in spin recovery. The rudder and elevators are primary controls for spin recovery. Since the recovery requires a large yawing moment, the rudder must be effective in the spin attitude. The wake from the HT may "blanket" the rudder, rendering it far less effective

TABLE 11-2 Primary recovery control inputs for spinning aircraft.

Inertia category	Inertia parameter values	Primary recovery control inputs
Negative or fuselage-heavy loaded	$(I_{xx}–I_{yy})/(mb^2) < -0.005$	Ailerons and Rudder against rotation
Zero-loaded	$-0.005 \le (I_{xx}–I_{yy})/(mb^2) \le +0.005$	Rudder against rotation followed by elevator down
Positive or wing-heavy loaded	$(I_{xx}–I_{yy})/(mb^2) > 0.005$	Elevator down followed by rudder against rotation

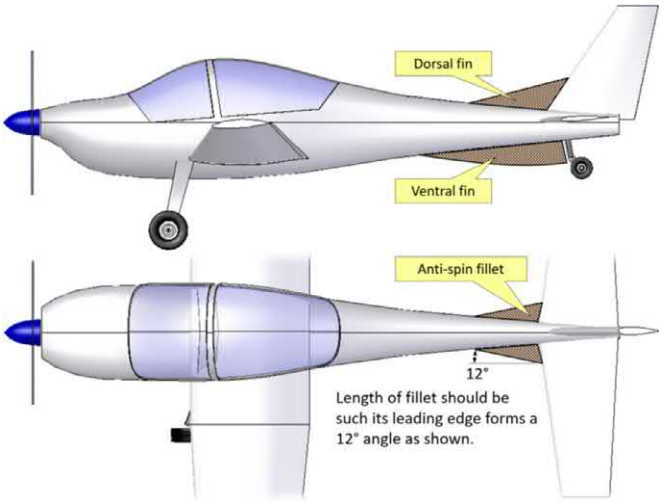


FIGURE 11-9 Geometric antispin modifications.

than otherwise. Figure 11-10 shows common HT/VT arrangements and idealized wakes emanating from the HT. The conventional tail is exposed to different levels of blanketing, whereas some of the other configurations are void of blanketing (e.g., V-tail, T-tail, and H-tail). These tails are better for spin recovery, although this alone is not a guarantee.

Ventral and Dorsal Fins

The ventral fin improves spin recovery by adding area below the HT (Figure 11-9). This steepens the spin. However, expect minor improvements only [13, 14]. The dorsal fin was declared ineffective in ref. [15].

Antispin Fillets

Increases the effectiveness of the fuselage area below the HT. This improves the tail damping and leads to a steeper spin from which it is easier to recover. However, as for the ventral fin, expect minor improvements only—they only help if the aircraft is borderline recoverable [15]. Their width must be such it does not increase the wake blanketing, while improving the tail-damping factor.

Wingtips

Spherical wingtips (see Section 10.5.2) generate asymmetric low-pressure regions in spin and, thus, tend to develop pro-spin moments. Effect of winglets on spin is not well known.

External Fuel Tanks

These have two important effects on spin: (1) *Aerodynamic Effect:* External fuel tanks, underwing or at the wing tip, develop pro-spin moment and are detrimental to spin characteristics. (2) *Inertia Effects:* The mass of fuel in external tanks, especially tip tanks, changes the mass distribution markedly (and the *inertia parameter* value). Per Table 11-2, it can change the primary recovery control from a rudder to elevator. It is possible this could change in flight due to fuel burn [12]. The designer of such aircraft should consider sizing both the rudder and elevator with spin recovery in mind.

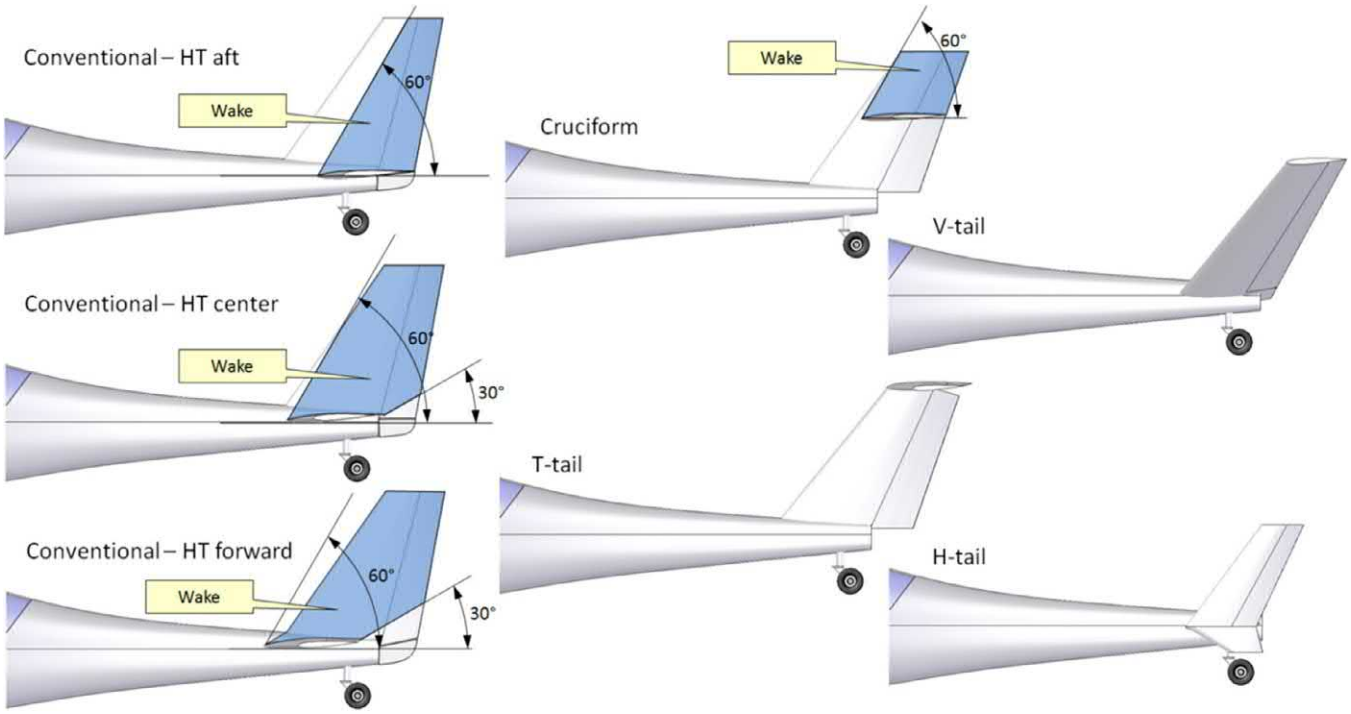


FIGURE 11-10 The blanketing of the rudder during spin is dependent on the tail configuration.

Wing Flaps and Landing Gear

Per refs. [16, 17], deployed wing flaps have detrimental effect on the spin by flattening the spin attitude and decrease in spin-rate due to increase in inward sideslip. This reduces the effectiveness of the rudder for recovery. It is recommended that if inadvertently entering spin with flaps down, these should be retracted immediately [16]. Landing gear has minor detrimental effect, albeit enough for retracted position to be recommended.

Wing Position

The high- or low-position of the wing is an underresearched topic when comes to spin. It is thought that high-wing aircraft have better spin and spin recovery characteristics than low wing aircraft [12]. This is attributed to their higher dihedral effect and the placement of the wing wake, which is thought to clear the tail.

Tail Length

Increased tail length improves spin recovery. It is a more effective means of improvement than adding side area and improves recovery beyond its impact on the TDPF [13]. Longer tail causes the aircraft to spin at reduced AOA (=steeper nose-down attitude) and higher spin-rate, making recovery easier. Ref. [17] shows that lower AOA during spin renders the rudder- and elevator-effectiveness greater than at higher AOA (flatter spin).

Center-of-Gravity

The CG-position has an important impact on spin and spin recovery. In general, aft CG flattens the spin attitude [14], reducing the effectiveness of the primary recovery controls. How much and how severely depends on the TDPF and other features of the aircraft and necessitates flight testing.

Power

Power effects is an underresearched topic when comes to spin, albeit rich of anecdotal uncontrolled evidence. Ref. [18] is an exception and found limited impact unless thrust was offset from the CG and, thus, produced moment. However, its subject is the F-104 Starfighter, so this hardly applies to GA aircraft. The general notion holds that the impact on spin of single-engine aircraft is limited, while it is considerable for asymmetric thrust of multiengine aircraft. This can be pro- or antispin depending on spin-rotation direction [12].

(4) Spin Regulations

Spin regulations for certified GA aircraft are presented in 14 CFR §23.221, Spinning ("old" Part 23). The paragraph states that a normal, utility, and aerobatic category aircraft, for which spin certification is sought "…must be able to recover from a one-turn spin or a three-second spin, whichever takes longer, in not more than one additional turn after initiation of the first control action for recovery, or demonstrate compliance with the optional spin resistant requirements of this section."

Spin Resistance and Aircraft Characteristically Incapable of Spinning

Paragraph 14 CFR §23.221, Spinning, stipulates requirements for *spin-resistant* aircraft and aircraft *characteristically incapable of spinning*. Spin resistance requires challenging capabilities to be demonstrated in flight testing. The most challenging of those is §23.221(a)(2)(ii), which requires pro-spin controls to be held for 7 s (or 360 degrees, whichever occurs first). The Icon A5 amphibian was certified with this capability.

The option to certify the aircraft as *characteristically incapable of spinning* was offered in §23.221(d) up to amendment 23–50. The ERCO Ercoupe was the first aircraft certified as such. This is achieved, in part, by limiting deflections of control surfaces. This prevents abused controls from bringing the aircraft to the edge of spin. The advantage of this option is that it is less challenging to certify than spin resistance. The drawback is the airplane cannot stall and thus requires longer take-off and landing distances than otherwise.

(5) Design Guidance

The above can be summarized as follows (see [12] for further guidance):

- Primary spin recovery control depends on whether the airplane is wing-heavy, fuselage-heavy, or zero-loaded (see Table 11-2). Ailerons against the spin tend to flatten the spin attitude [19].
- A full-length rudder is preferable. For conventional tails, the rudder should be extended below the plane of the HT. Place the HT forward of the rudder and high on the fuselage to minimize wake blanketing. The area below the HT has been shown to contribute to the damping of the spin [9]. Partial-span rudders call for the opposite approach—place the HT low and aft to minimize the wake blanketing [12].
- Keep rudder clear of the HT wake. Avoid arranging aft-swept VT such it resides fully inside the wake from the HT.
- High-wing configuration improves spin recovery [12].
- Longer tail improves spin recovery [13].
- Avoid external wing tanks, especially wingtip tanks [12].
- Ref. [19] advises that wing design needs to be included. It recommends a sharp inboard leading edge and drooped outboard leading edge separated by sharp discontinuity.
- Fixes like antispin fillets and ventral fin provide minor improvements. Dorsal fins provide none.

It is not possible to end this discussion without highlighting a serious consequence of spins—the

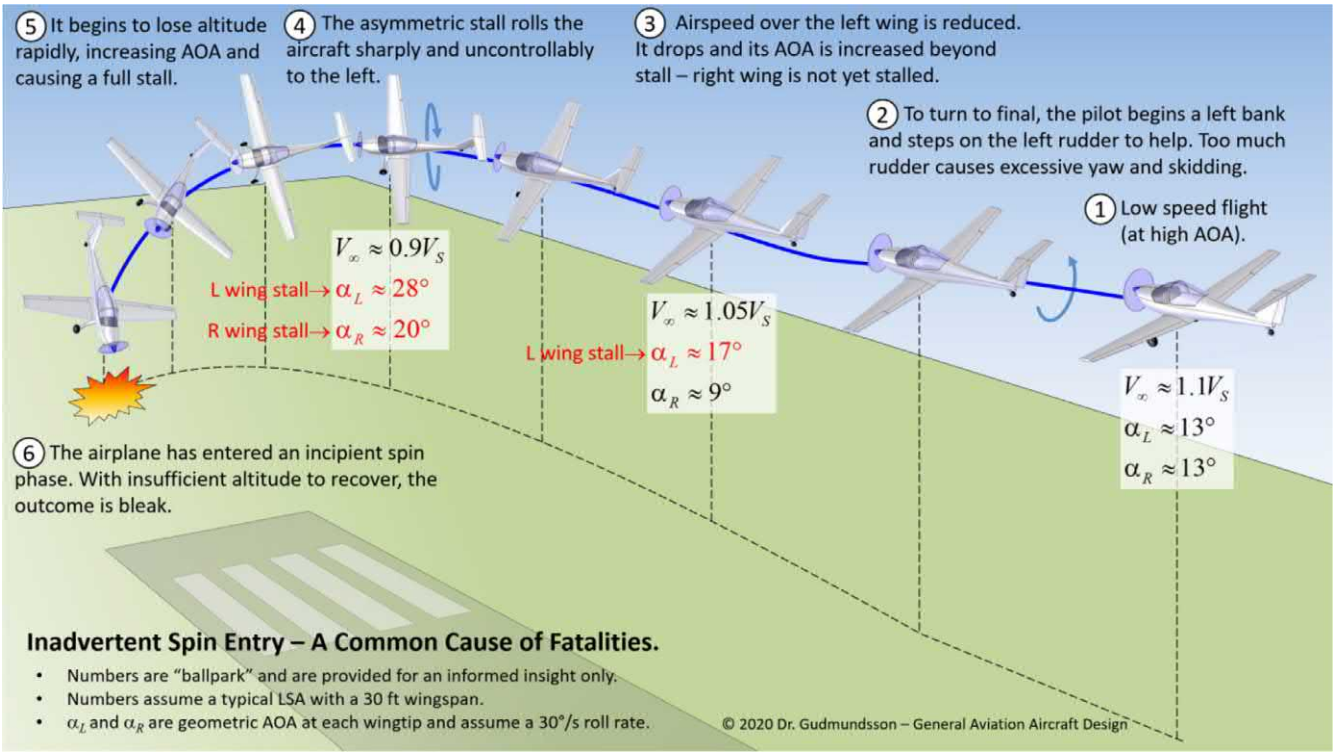


FIGURE 11-11 One consequence of careless piloting.

inadvertent spin entry. Figure 11-11 shows the steps involved with approximate values for a typical LSA. This kind of accident is common. As a former flight-test engineer, seeing first-hand how close the down-moving wing gets to stall when aggressively rolling was sobering. If you are a private pilot, establish a professional approach to the landing phase. Maintain $1.3V_S$ or greater while turning on final. Do not bank beyond 30 degrees at that airspeed. Use wide approaches. If turning on final requires steep banking, extend a wide final or go around. Steep banking before landing does not make a good pilot, but a dangerous one.

11.3 ON THE PROS AND CONS OF TAIL CONFIGURATIONS

This section introduces several tail configurations that have seen use throughout the History of Aviation. The selection itself can only be made easier if the designer is aware of the many advantages and disadvantages of each configuration, both in terms of aerodynamics, stability and control, structural layout, aeroelasticity and operational characteristics.

11.3.1 Conventional Tail

The *conventional tail* is so called because it is the most common of all tail configurations. Some 80% of aircraft ever built feature this tail configuration, ranging from ultra-light aircraft to the world's largest passenger transport aircraft, the Airbus A380 and Boeing 747. A large number of GA aircraft also feature the tail, such as the Cessna single-engine series aircraft (140, 150, 152, 172, and so on) as well as the latest entries, the all-composite Cirrus SR20, SR22, and Cessna Corvalis high performance aircraft. The configuration is often a "default" configuration unless some special requirements call for alternative solutions. *For the discussion that follows, this configuration is considered the baseline configuration (see Figure 11-12).*

(1) Pros

(A) A safe and tried configuration as evidenced by the fact that majority of airplanes feature it. (B) For single-engine propeller aircraft, the configuration takes



FIGURE 11-12 A conventional tail configuration.

advantage of the propwash, which gives it a boost during the T-O run. This helps during soft-field take-off, allowing early rotation at a lower airspeed, reducing the ground run (also see a discussion about drawbacks below). (C) The HT and VT are joined in the fuselage, where its girth is still large and, thus, is still effective in reacting torsional loads. This torsional rigidity also helps resisting empennage flutter. (D) The horizontal tail is sometimes positioned such the wing wake at high AOA hits the tail, causing it to oscillate (often violently) providing a natural feedback to the pilot of an imminent stall, and then exiting the wake in the poststall to allow for ready recovery (although often it remains inside the wake). This phenomenon is illustrated in Figure 11-13. Achieving this reliably and by design (as compared to "luck") requires a thorough understanding of the flow field behind the wing and calls for wind tunnel testing or Computational Fluid Dynamics (CFD) analysis. (E) It may be possible to position the HT such that as the flaps are deployed, the increased nose pitch-down moment may be canceled by an increase in downwash on the HT (which increases nose pitch-up moment). This would promote modest, if any need to change trim settings when the flaps are deployed. However, this is airspeed and weight dependent and, thus, cannot always be taken advantage of.

(2) Cons

(A) The wake from the HT may "blanket" the rudder for AOAs in the poststall range (see Figure 11-14). This compromises its ability to aid in spin recovery. Many aircraft are designed to ensure adequate rudder area is outside of the separated region. Aerobatic aircraft such as the Yakolev Yak-55 and the Extra 300 exemplify this. Regardless, multiple aircraft feature conventional tails with partially blanketed rudder that have excellent spin recoverability (e.g., aerobatic aircraft). As stated in previous section, spin is a complicated phenomenon and recoverability is affected by characteristics other than rudder blanketing. (B) The position of the HT prevents an "aft podded" engine configuration, in which the engines are mounted on the aft fuselage. This is a drawback because it pushes the designer away from this solution. (C) While placing the HT inside the propwash for single-engine propeller aircraft is helpful during the T-O run; this also has the following drawbacks: (i) Wake causes small amplitude *life-cycle oscillations* that may induce metal fatigue. (ii) Higher airspeed inside the propwash slightly increases the drag of the immersed portion of the HT. (iii) The propwash changes the pitching moment with power changes. For instance, if power is increased in steady straight flight, the increase in propwash will cause a nose pitch-up. The opposite happens when power is reduced. This may be significant enough on turboprops to resort to a different tail configuration.

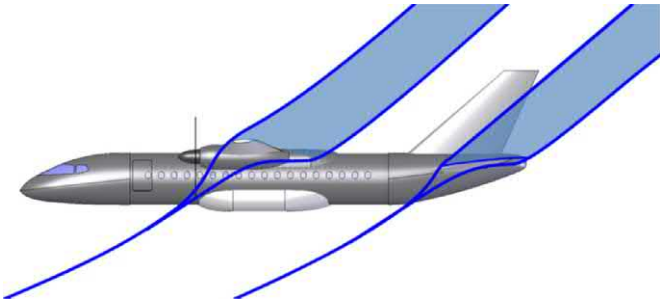


FIGURE 11-14 The same aircraft at a high AOA in a poststall condition. The shaded areas represent the highly separated wakes emanating from the wing and HT. The HT wake covers a substantial portion of the rudder, reducing the rudder authority. This is Point D in Figure 11-15.

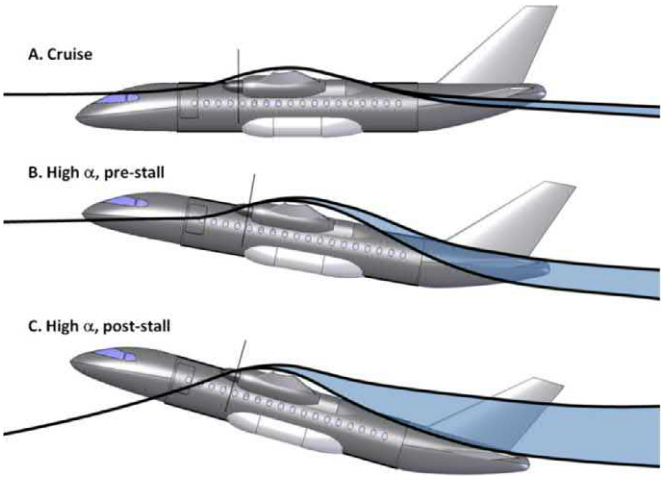


FIGURE 11-13 An aircraft at three different conditions. See text for details.

(3) Additional Comments

The designer should always convert specific drawbacks into numbers. This allows any flaw to be assessed on its merit. For instance, consider an aircraft configuration that requires 350 lb_f of thrust at cruise. Say we estimate that by placing the HT in the propwash drag increases by 1 lb_f, but the T-O run is reduced by 150 ft. Which is of greater importance? Such numbers provide insight that helps the designer decide.

Figure 11-13 shows an airplane at three specific elevator deflections and AOA. The top figure (A) shows it at a low AOA during cruise. The wing wake is thin and lies below the HT. The center figure (B) shows it at a high AOA, just before stall. The thickness of the wake has grown substantially and, now, the HT is inside of it. The turbulent airflow causes the HT to oscillate, which the pilot senses if using a mechanical control system. The oscillation can be significant enough for the pilot to detect it even if equipped with a digital control system. The bottom figure (C) shows the aircraft at a

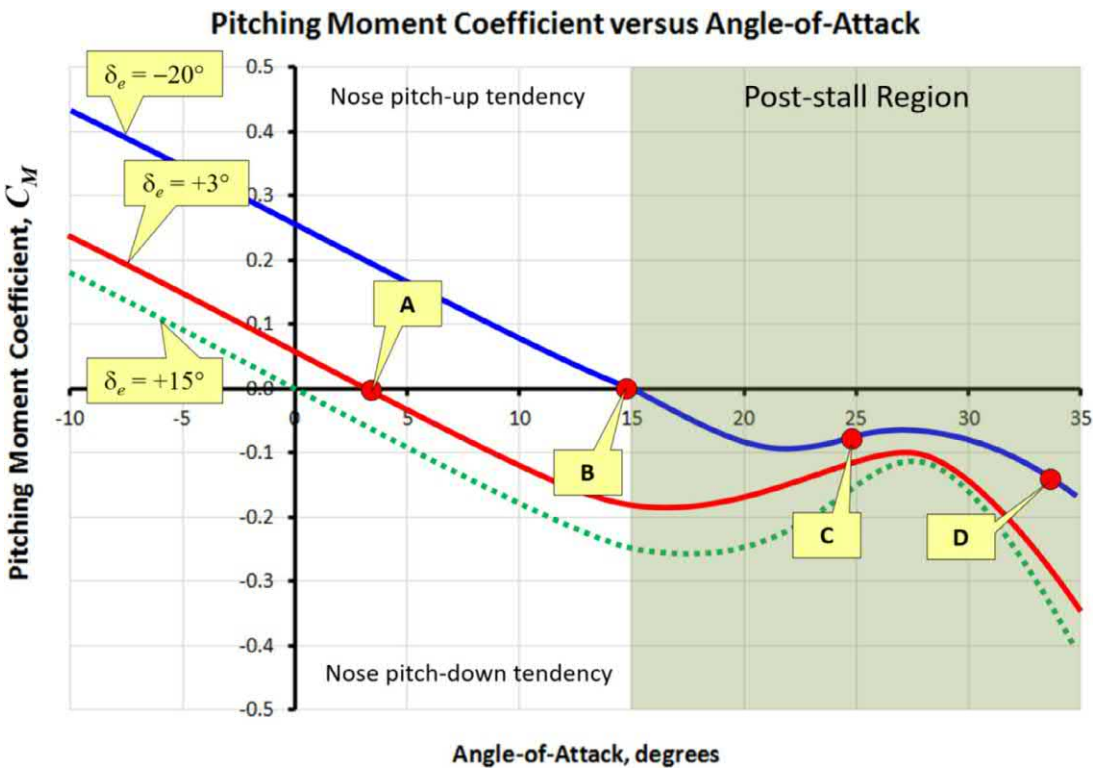


FIGURE 11-15 The conditions for the aircraft in Figures 11-13 and 11.14.

poststall condition, with a fully stalled wake. Depending on its thickness, the HT may or may not reside inside the wake. If inside the wake, the elevator authority is noticeably reduced.

Figure 11-15 shows the C_M versus AOA for the aircraft during the above events (labeled A through C). Point A is trim point for a condition where the elevator deflection might be 3 degrees TED. Point B represents an elevator deflection of 20 degrees TEU and the aircraft is close to stall. Point C represents the aircraft, still with the elevator deflected 20 degrees TEU, at an AOA of 25 degrees, inside the poststall region. Point D represents the condition of Figure 11-14, deep inside the poststall region. Some aircraft, for instance the Cirrus SR20 and SR22, are designed to be laterally controllable at this condition, as a part of their Equivalent Level of Safety (ELOS) certification. However, many others are not. Some of those would experience uncontrollable roll tendency to the left or right.

11.3.2 Cruciform Tail

The cruciform tail configuration is often resorted to if it is desirable to feature aft podded engines. A wide range of aircraft use this tail arrangement, ranging from bombers such as the B-1B Lancer, the twin turboprop passenger transport aircraft Handley Page HP-137 Jetstream, or the Sud-Est Caravelle, a classic early commercial jet



FIGURE 11-16 A cruciform tail configuration.

transport aircraft. The Dassault Falcon family of business jets also features this tail configuration. NACA research on cruciform tails can be found in NACA reports TN-2175 [20] and RM-L54I08 [21], among others. An example of a cruciform tail is shown in Figure 11-16.

(1) Pros

(A) The cruciform tail is a practical solution for an aft podded engine configuration and one that will result in lower structural loads than the T-tail (see later). (B) It is a practical solution for freight aircraft designed to allow the empennage to be swung open for loading and unloading through the rear fuselage (as is T-tail). Depending on the position of the break in the fuselage, the baseline HT might hit the wings when swung open and limit the allowable swing angle. Still, there are conventional tail airplanes (e.g., the four-engine Canadair

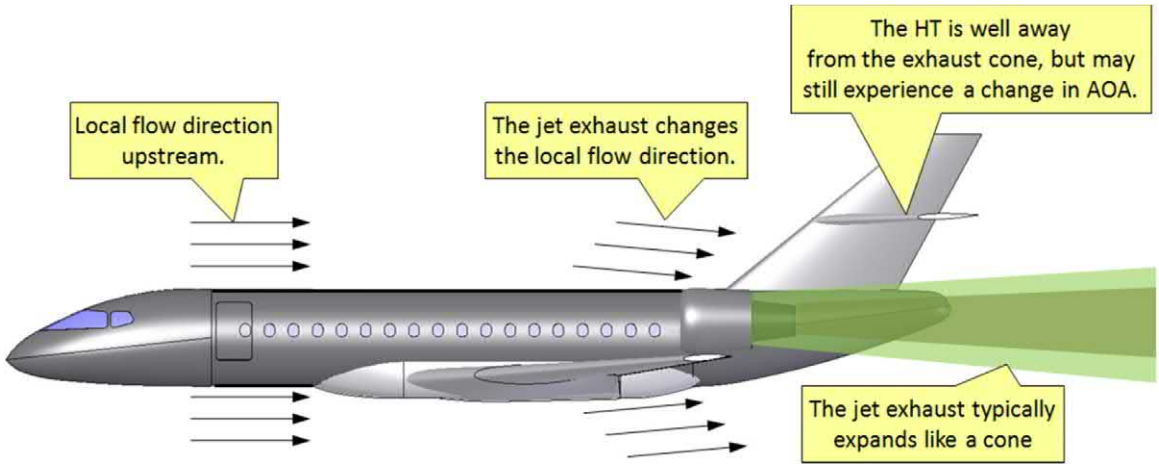


FIGURE 11-17 The cruciform tail configuration brings the HT out of the jet exhaust, although it may still be affected by a change in AOA on the tail with thrust setting.

CL-44) that show this depends on the location of the opening and length of the fuselage. (C) The HT sits above the exhaust from the aft-mounted jet engines shown in Figure 11-17. (D) The lower part of VT is exposed to "clean" airflow at high, poststall AOA, improving spin recoverability. The position of the HT creates limited endplate effect.

(2) Cons

(A) Higher torsional loads than for the conventional tail. This results in a heavier structure (albeit lighter than T-tail). (B) The VT must feature structural reinforcement to allow the HT to be mounted to it. Therefore, will be heavier than the baseline tail, assuming identical size and shape of the tail surfaces. (C) The upper part of the rudder is partially blanketed during spin recovery. (D) The configuration requires sectored elevator (i.e., a sector of the root of the elevator is removed) to allow the rudder to deflect freely, or the rudder must be split in the area of the HT for the same reason. This requires additional manufacturing steps that could increase the cost of producing the rudder (or elevator). (E) The configuration has higher interference drag.

11.3.3 T-Tail

T-tails have been common on aircraft since the mid-1960s when it appeared for the first time on a commercial passenger transport aircraft—the Boeing B-727. The concept was tested by NACA as early as 1954 [21, 22] but has since been studied by NASA and other researchers in multiple publications. The configuration is considered by many to be stylish, a feature of great importance to the marketability of aircraft. Besides commercial transports, T-tails are very common on business jets, where their popularity exceeds the conventional tail. Business jets ranging from the early Gates Learjet 25 through to the Gulfstream G650 features the configuration. In the GA industry, several aircraft feature the configuration. The best known among smaller such aircraft are the twin-seat, single-engine trainers Piper PA-38 Tomahawk and Beech Model 77 Skipper. T-tails can also be found on larger twin-engine turboprops, such as the Beech 1900 and 350 King Air. Additionally, T-tails can be found on a range of sailplanes, where they are mostly selected because of improved spin recovery [23]. An example of a T-tail is shown in Figure 11-18.

(1) Pros

(A) HT leaves the rudder wake-free at poststall AOA, improving spin recovery potential. Figure 11-19 shows an aircraft at an AOA beyond deep stall. Note that the figure has shortcomings: a simple representation of a highly complex flow phenomenon (see Section 11.2.4). (B) The configuration lends itself perfectly to aft podded engines, so common among business jets. (C) If the VT is swept aft, which is also the norm for high-speed aircraft, an additional tail arm is gained by the configuration. Consequently, the tail can be slightly smaller than the baseline tail. This reduces downward HT load for trim in cruise and, thus, trim drag. (D) Endplate-effect of the HT can be utilized to reduce the VT, reducing drag and



FIGURE 11-18 A T-tail configuration.

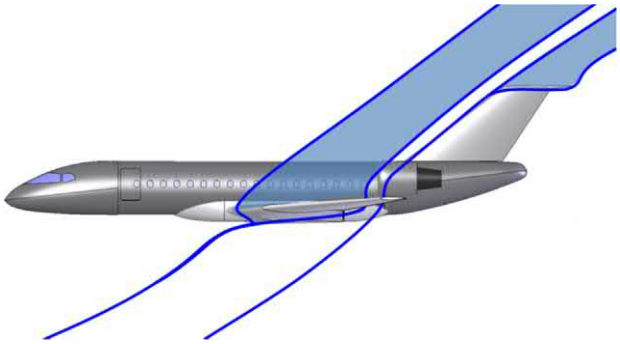


FIGURE 11-19 A schematic of a T-tail aircraft poststall at a very high AOA, showing the turbulent wing wake clears the VT (see text for more details).

weight (albeit modestly). (E) The HT resides in undisturbed air, although this primarily holds true at low AOA. On sailplanes, where low drag is of an utmost importance, this helps maintaining NLF on the HT. (F) For single-engine propeller aircraft, the configuration moves the HT out of the propwash, eliminating propwash-induced pitch changes.

(2) Cons

(A) The high-mounted HT, coupled with the presence of the VT, can generate substantial asymmetric lift in yaw. This results in high torsional loads that are reacted at the top of the fin and eventually by the fuselage. This torsion is compounded by the torsion from the VT caused by the yaw. (B) These higher loads cause an overall increase in weight. (C) The yaw also induces a rolling moment. The F-104 Starfighter featured main wing anhedral to suppresses such a tendency. (D) The mass of the HT mounted at the tip of the VT reduces the tail's natural frequency of oscillation, lowering its flutter speed. This can be remedied by increase the tail's stiffness, increasing its weight. (E) Maintenance is impacted as repair stations will have to accommodate technicians working on the tail high above the ground.

(F) One of the T-tail's primary disadvantages occurs if it is immersed in the wing wake at stall or poststall (see Figure 11-20). The figure shows how the HT may come to rest inside the highly separated wing wake. This severely reduces the elevator authority and can render the aircraft incapable of recovering from the stall. It is recognized as a "*deep stall*." It has caused multiple development and operational vehicles to crash with fatal consequences.

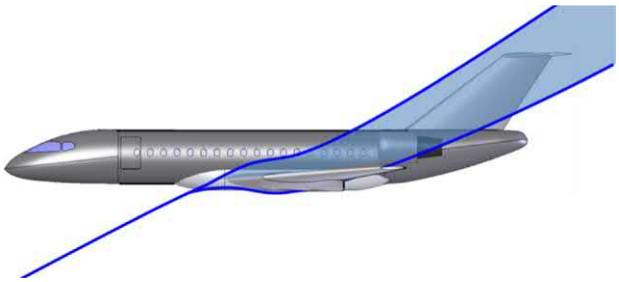


FIGURE 11-20 A T-tail aircraft at a high AOA, showing the HT inside the wing wake, causing the "deep stall" phenomenon.

The history of aviation is wrought with deep stall accidents in T-tail aircraft. A Gloster Javelin was lost on June 11, 1953 due to this phenomenon, killing the pilot [24]. On March 23, 1962, a Handley-Page Victor crashed killing two of the crew of five and two people on the ground [25]. On October 22, 1963, a BAC 1-11 crashed on a test flight due to deep stall killing all seven occupants [26]. On June 3, 1966, a Hawker-Siddeley HS-121 Trident crashed on a test flight, killing the crew of four [27]. These are but a few of a long list of accidents to which a T-tail is considered a contributing factor.

To understand how the deep stall affects an airplane consider Figure 11-21, which shows the C_M versus α for a typical T-tail aircraft. The three curves represent the C_M with different elevator deflections identical to Figure 11-15, with three trim points in the prestall region. However, Figure 11-21, has three additional trim-points in the "postall region." If the airplane stalled abruptly, it is possible the angular momentum about the pitch axis might drive it to an α greater than 15 degrees. If the angular momentum is high enough, the aircraft could be driven to an α large enough (here, around 30–32 degrees) to achieve trim equilibrium without being able to return into the prestall range. Modern commercial jetliners with T-tails always feature "stick-shakers" or "stick-limiters" for the elevator control yoke in the cockpit to prevent an inadvertent stall.

11.3.4 V-Tail or Butterfly Tail

Research on V-tail configurations dates to 1931 with the publication of an anonymous paper that discussed the so-called Rudlicki V-tail [28]. Jerzy Stanislaw Rudlicki (1893–1977) was a Polish aeronautical engineer who is considered the inventor of the V-tail. He acquired a Polish patent for it in 1930 (patent# 15938). The configuration combined the three surfaces of the conventional tail into two that form a distinct V (see Figure 11-22). It joined the functionality of the rudder and elevator into what is called *ruddervators*. The function of ruddervators is illustrated in Figure 11-23.

Considerable research into V-tails was conducted by NACA in the 1940s and multiple reports are available on the online NASA Technical Report Server. For instance, refs. [29–31] should be very helpful to the designers of V-tail aircraft. Note that a simplified theory of the V-tail is provided in Chapter 24.

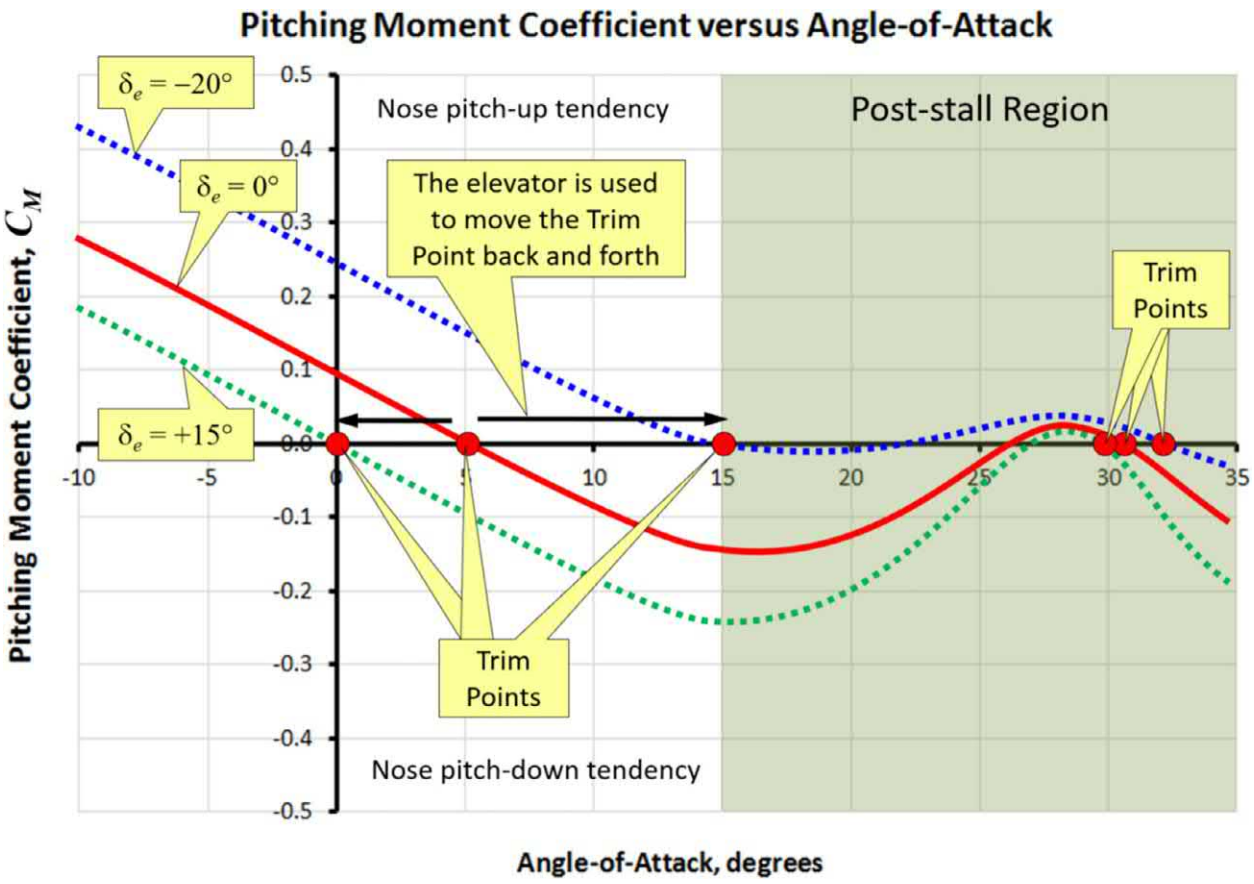


FIGURE 11-21 The physics of the "deep stall" phenomenon explained.



FIGURE 11-22 A V-Tail configuration.

V-tails can be found on a wide range of aircraft, ranging from sailplanes, to propeller- and jet aircraft. Some of these are listed in Table 11-3.

(1) Pros

The advantages of V-tails compared to conventional tail as stated by ref. [31]: (A) Less interference drag because the V-tail has fewer fuselage-tail junctures. (B) Less tendency for "rudder locking," a phenomenon discussed in Section 11.2.3. (C) The higher position of the tail surfaces improves elevator authority as the center of pressure is above the fuselage, contributing to the nose

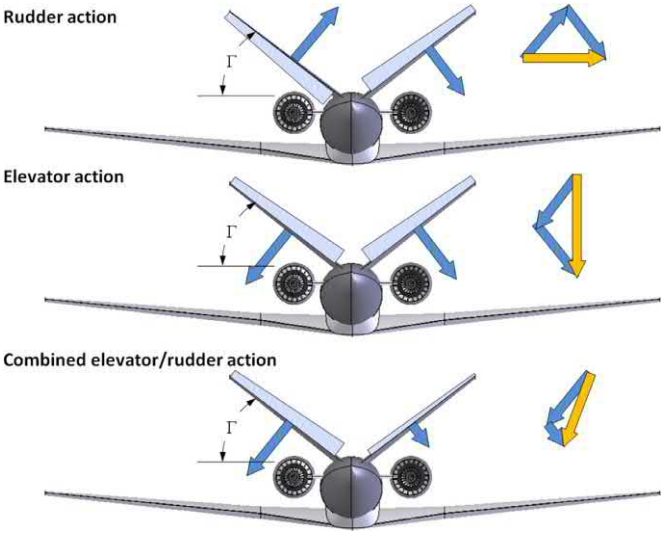


FIGURE 11-23 How ruddervators are used to generate the primary functionality of the conventional rudder, elevator, and combined action.

pitch-up moment (see Figure 11-24). This moment M can be written as: $M = F_V \cdot a + F_H \cdot b$, where F_V and F_H are the vertical and horizontal components of the resultant force acting on the V-tail, and a and b are the arms shown in the figure. The corresponding moment for a conventional tail

TABLE 11-3 Selected aircraft featuring V-Tails.

Aircraft type	Comment
Beechcraft V35 Bonanza	Single-engine, four-seat GA aircraft. Produced in large numbers
Fouga CM-170 Magister	Twin-engine, twin-seat military trainer (195 ×). Produced in large numbers
Potez-Heinkel C.M. 191	Based on the Fouga Magister. Prototypes only
The Zipper	Ill-fated aircraft
F-117 Night Hawk	Military fighter, stealth configuration, fly-by-wire
Northrop Grumman RQ-4 Global Hawk	UAV
Microjet	Twin-engine, twin-seat jet trainer candidate. Only prototypes built
Dale AE Weejet 800	Prototype only
P-63 King Cobra	A King Cobra fitted with a V-tail for testing purposes. Prototype only
Eclipse V-jet	Prototype GA personal jet. Single-engine jet. Prototype only
V-jet	Developed in participation with Williams International. Prototype only
Cirrus SF50 Vision	Prototype GA personal jet. Single-engine Williams FJ33 jet
Hütter 30 GFK	Sailplane
Musters HKS 1	Sailplane
Schleicher Ka 3	Sailplane
Greif 1a (FK 1)	Sailplane
Greif 2a (FK 2)	Sailplane
Schreder HP-12	Sailplane
Schreder HP-18	Sailplane
Start & Flug H101 Salto	Sailplane, aerobatic
Schempp-Hirth Standard Austria	Sailplane

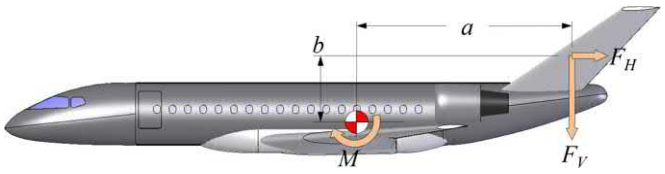


FIGURE 11-24 Increase in pitch authority explained.

would be closer to $F_V \cdot a$. (D) The surfaces extend farther out of ground effect than the conventional tail, making it more effective. (E) The tail of amphibious aircraft is clear of the spray during the T-O, making it more effective. (F) The tail is clear of the wake from the wing and canopy in high-speed flight, reducing tail buffeting. (G) There are fewer tail surfaces to manufacture. Besides these, the V-tail is a great configuration for aircraft equipped with single-jet engines, allowing installation on top of the fuselage, on the aircraft's centerline. Examples include the Cirrus SF50 Vision, Eclipse-jet, and RQ-4 Global Hawk.

(2) Cons

The following disadvantages are cited in ref. [31]: (A) Interaction of elevator and rudder control forces. For instance, during a crosswind landing the pilot might use the rudder pedals to sideslip the airplane on final. Since this would cause a TEU deflection in one of the ruddervators and TED in the other, the elevator stick-forces change compared to that of a conventional configuration. (B) Interaction of elevator and rudder trimming when trim tabs are deflected to large angles. (C) The control system requires a *control system mixer* (see Figure 11-25). (D) Greater loads on the tail and fuselage, which tends to increase structural weight. Since the V-tail serves as a HT and VT its size must be larger than if it only served one purpose. Consequently, during maneuvers, such as yawing, a larger force will be generated, which of course requires stouter and, thus, heavier airframe.

But there are other shortcomings not mentioned by ref. [31]. (E) The normal component of lift acting on the V-tail is less effective because of the dihedral. Thus, a larger tail is needed. (F) There is a control system interaction, such that stepping on the rudder pedals may cause a nose pitch-up or -down moment, depending on the geometry of the tail and the airfoil. This may require ruddervator deflection differentials to be provided by the control system (e.g., TED ruddervator deflects −6 degrees while the TEU ruddervator deflects +10 degrees). (G) The V-tail increases the dihedral effect of the aircraft. This reduces Dutch roll damping and makes it more of the "rolling" type. High-flying jets may require a yaw damper of the no-dispatch (if inoperative) kind. (H) At high AOA, the V-tail can enter the wing wake, and this may cause undesirable structural oscillation. This can be suppressed with a fuselage mounted vortex-generator. (I) The application of rudder induces roll in a direction opposite of the intended bank. For instance, a left turn rolls the left wing down and the right wing up. The heading change moves the right wing through a larger arc than the left wing. This makes it move faster through air than the left wing. It follows it generates higher drag than the left wing, causing the nose to point slightly to the right, out of the turn. This asymmetry is a manifestation of a yawing moment known as an *adverse yaw*. It can be canceled by applying force to the left rudder pedal. If we observed the aircraft from behind at this instant, we would see the corrective pilot action forcing the tail to the right and the nose left (the intended direction). This action would be

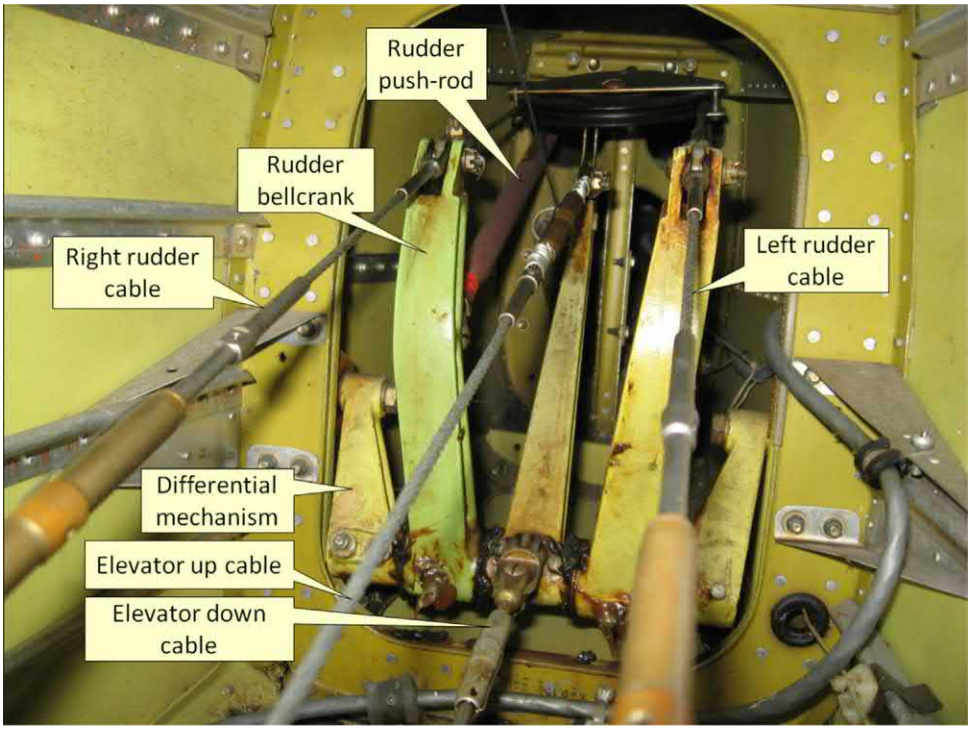


FIGURE 11-25 Rudder/Elevator control mixer in a Beech Bonanza. *Photo from author's collection.*

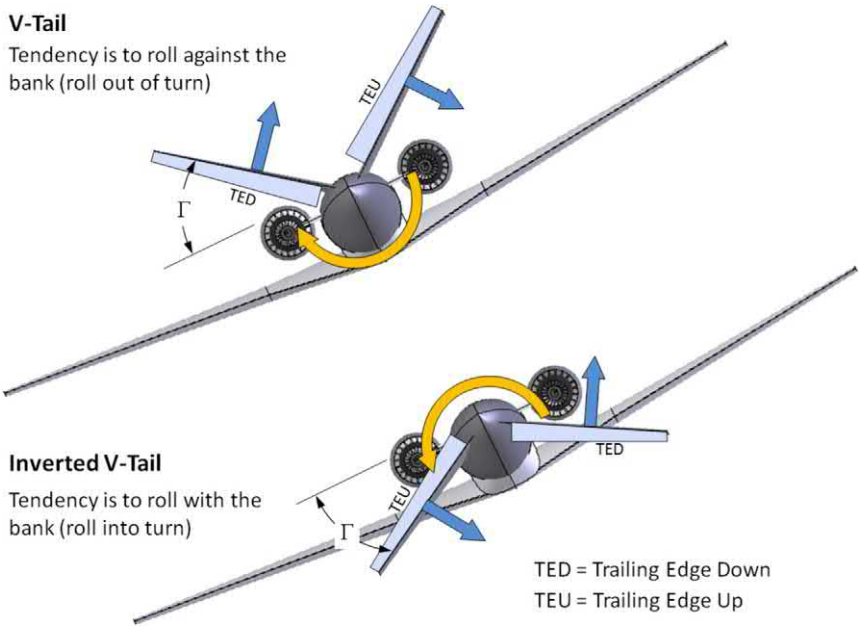


FIGURE 11-26 The difference in yaw response of a V-tail and an inverted V-tail (see text for detail).

accompanied by a roll out of the turn. Such a tendency is called *adverse roll* (see upper image in Figure 11-26). The pilot must compensate by adding aileron to the left.

Also consider the lower image in Figure 11-26. It shows the ruddervators on an inverted V-tail would have to be deflected for the same reason. The left ruddervator is deflected TEU and the right one TED. The resulting force vectors on the tail cause a tendency that induces a left roll—in the intended direction (*proverse roll*). This helps with the execution of the turn. In short: A V-tail rolls the airplane *out of* a turn. An inverted V-tail rolls the airplane *into* the turn. The latter is more desirable.

11.3.5 Inverted V-Tail

The inverted V-tail shares many of the pros and cons of the V-tail but has seen far less use in the industry. The best-known example of its use is the homebuilt single-seat monoplane Aerocar Mini IMP, although some versions featured a vertical tail addition resulting in an Inverted Y-tail (see later). The General Atomics Predator, an unmanned military aircraft, also has an inverted V-tail, although some would object to that definition as it also has a vertical fin between the two outboard tails—sort of like a "collapsed" inverted Y-tail. Additionally, the Elbit Hermes 90 UAV features an interesting inverted V-tail on an elevated tail boom.

An advantage of the inverted V-tail configuration is the proverse roll tendency discussed in the previous section. Its greatest drawback is that its tips reduce the T-O rotation and flare potential of the aircraft. For this reason, the tail must be mounted high on the fuselage and long main landing gear legs would be required to improve the rotation capability of the airplane (Figure 11-27).

11.3.6 Y-Tail

From a certain point of view, the Y-tail is a variation of the V-tail. One might say it is a V-tail with an additional vertical surface. Like the V-tail it requires a ruddervator control mixer (otherwise it is just an inverted conventional tail with the horizontal featuring large dihedral). However, sometimes a rudder is also mounted on the vertical ventral fin on the bottom, giving the aircraft increased rudder authority. The most notable aircraft that feature this tail is the General Atomics Predator B and the canceled LearAvia Lear Fan 2100 aircraft.

Among the tail's advantages is improved directional stability and Dutch roll damping over the conventional V-tail (thanks to the tail's vertical member). This allows a shorter span V-tail. Even a short span vertical element can provide substantial improvement in the Dutch roll damping. A major drawback is rotation limitation during T-O and flare during landing. This can put a cap on the span of the vertical surface, reducing its ability to improve directional stability and Dutch roll damping (Figure 11-28).



FIGURE 11-27 An inverted V-Tail configuration.

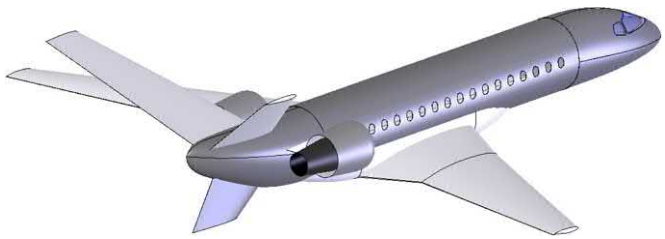


FIGURE 11-28 A Y-Tail configuration.

11.3.7 Inverted Y-Tail

Many of the pros and cons of the Y-tail apply to the inverted Y-tail. However, the tail improves stall recovery as the down-pointing tail feathers pitch into un-separated flow. This contrasts the Y-tail's tendency to rotate into the wing wake. By far the best know aircraft that features an inverted Y-tail is the cold-era fighter McDonnell Douglas F-4 Phantom, although its elevator functionality makes it a conventional tail whose HT has a large anhedral. The greatest detriment of the configuration is shown in Figure 11-29, in case of a conventional jetliner in which it would severely limit the ability of the aircraft to rotate for T-O or landing.

11.3.8 H-Tail

(1) Pros

(A) The H-tail is a good solution when the overall height of an airplane is an issue and a single VT is simply too tall. (B) It is a good configuration for multiengine propeller aircraft as well, providing means to supplement a restoring yawing moment to balance the asymmetric moment with *one engine inoperative* (OEI). Should one engine be lost, the VT behind the operative engine benefits from the higher dynamic pressure inside the propwash stream-tube. The resulting flow-field asymmetry also allows the propwash to better follow the fuselage shape. This bends it inward, placing the VT at an AOA such it produces a restoring yawing moment. (C) In military aircraft, it provides redundancy in case one VT is shot off. (D) The configuration increases the efficiency of the horizontal tail through endplate effects. This promotes a uniform lift distribution by reduced lift



FIGURE 11-29 An inverted Y-Tail configuration.

drop-off at the tip and allows as smaller HT (and thus lower weight and drag) (see Section 10.5.8). (E) On the A-10 Warthog, the tail helps shielding the exhaust heat.

(2) Cons

(A) Reduced flutter speed caused by the reduced natural frequency of the HT because of the mass of the VT being placed at its tip. This reduction in flutter speed must be improved by stiffening the HT, which increases the airframe weight. The Lockheed Model 14 Electra, a twin-engine, 10-passenger transport aircraft is a classic example of an aircraft featuring an H-tail that suffered fatal accident due to tail flutter[1] [32]. (B) The tail is subject to various asymmetric loading scenarios at high AOY that increase bending moment and torsion, increasing structural weight. (C) The configuration requires a split rudder control system so both rudders can move in harmony. This increases control system complexity. (D) Higher interference drag (Figure 11-30).

11.3.9 A-Tail

The A-tail is a variant of the inverted V-tail, so the reader is referred to Section 11.3.5 for discussion of pros and cons. The configuration is used in UAVs such as the AAI RQ-7 Shadow and UAV Factory Penguin B UAV, although it has seen very limited use in aircraft that carry people. The Vogt LO-120 ultralight is an example of a small experimental aircraft, as is the Advanced Aero LLC's Inverted V-tail Technology Demonstrator. The former is exceedingly rare, and the latter has not flown yet, although the configuration experienced limited flight testing on a heavily modified Sadler Vampire experimental light plane in 2010 (Figure 11-31).

11.3.10 Twin Tail Boom or U-Tail Configuration

The twin tail boom configuration has seen extensive use in the History of Aviation, in small and large aircraft.

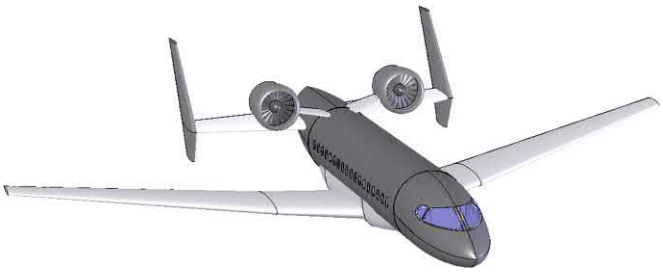


FIGURE 11-30 An H-Tail configuration.

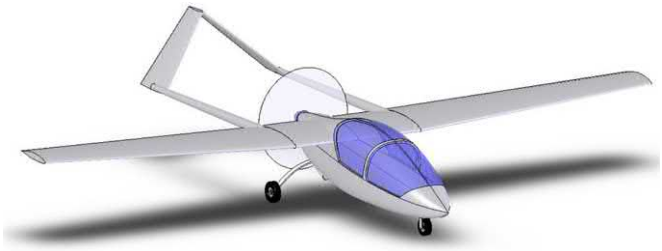


FIGURE 11-31 An A-Tail configuration.

Examples of GA aircraft include the Cessna 337, of which some 3000 aircraft were built: Adam A500 and A700, and others. Famous military aircraft include the Northrop P-61 Black Widow, Lockheed P-38 Lightning, and the North American OV-10 Bronco. The latest entry of such a configuration is the South African AHRLAC twin-seat, reconnaissance/close-air support aircraft. A typical GA implementation of this configuration is shown in Figure 11-32. Although the version shows extension on the lower VT, the tail forms an arrangement that can be described with the letter U (hence the U-tail name).

For propeller configurations, the HT is often placed in the propwash giving it boost for soft-field T-O maneuver and good responsiveness (also see drawbacks in Section 11.3.1). However, this is not always the case. A great advantage of the configuration for smaller aircraft is that the tail booms form an obstruction making it hard for people to accidentally walk into the prop. Pros and cons of the configuration are detailed in Section 11.3.8.

Inverted U-Tail

An inverted U-tail refers to a configuration in which the HT is placed on the top of the VT (see Figure 11-33). This configuration is used on the North American OV-10, Adam A500, and Adam A700. On propeller aircraft, it places the HT outside of the propwash, reducing its drag, but also eliminating a propwash boost over it (and the pitch-up, pitch-down associated with power changes).

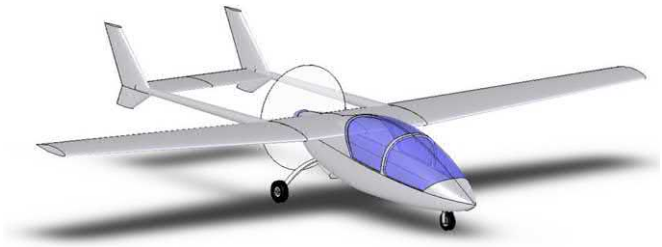


FIGURE 11-32 A Twin tail boom (U-tail) configuration.

[1] The airplane was operated by Northwest Airlines on October 1st, 1938. It is not clear whether this was due to the rudder flutter (e.g. due to incorrect balancing) or the HT/VT itself.

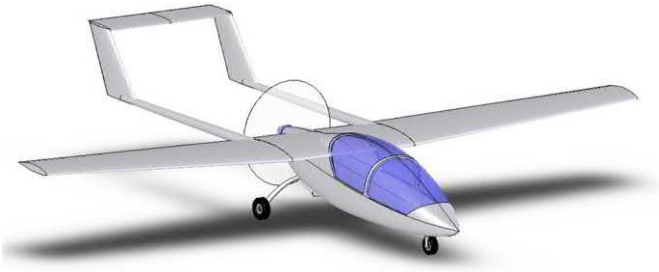


FIGURE 11-33 An inverted U-Tail configuration.

11.3.11 Three-Surface Configuration

In modern times, a three-surface configuration refers to aircraft with a main wing supplemented by a foreplane (ahead of the wing) and an aft horizontal tail. Examples of such aircraft include the Russian Molniya-1 and Sukhoi Su-33, the American Scaled Composites Triumph, and the Italian Piaggio P180 Avanti. Among earlier aircraft are at least three designed by Joseph Albessard. These were the Albessard 1911, Albessard 1912, and the Albessard Triavion [33], which flew for the first time in 1926. All are peculiar aircraft with the main wing in front, a smaller wing in the middle of the fuselage, and a smaller yet horizontal tail located aft. Of these, the Avanti is probably the best-known modern three-surface aircraft. It is a 10-seat, twin-turboprop business class transport aircraft. It is a unique airplane intended to compete with business jet aircraft. Piaggio claims 34% less drag than comparable turbofan aircraft, offering 40% reduction in fuel consumption. It is touted as the fastest twin turboprop ever built, capable of 402 KTAS at 38,000 ft ($M \approx 0.70$). Compare that to the four-engine Tupolev Tu-114 that holds the ultimate record with a maximum speed of 474 KTAS ($M \approx 0.82$), set on April 9, 1960 and would routinely cruise at 415 KTAS ($M \approx 0.72$). The foreplane has a flap that deflects *trailing edge down* (TED) when the wing flaps are deployed to counter the resulting pitch-down moment. The elevator is located on the aft surface. This arrangement helps keep control system complexity manageable.

(1) Pros

(A) The airplane can be trimmed such that all three lifting surfaces contribute to lift [34]. This allows the main wing to be smaller and lighter. (B) In cruise, the airplane trims such the HT develops a downward force while the canard develops upward force. The resultant force of these two means that trim drag can be made very small, theoretically zero. This, in turn, means small trim drag, making the configuration more efficient than either conventional or canard configurations [35].

(2) Cons

(A) Compared to two-surface configurations, three lifting surfaces are more expensive to manufacture. (B) They also have increased interference drag (even though this can be reduced using a mid-wing configuration as done for the P180 Avanti [34]). (C) Three surfaces require no less than three localized structural reinforcements. This is bound to be heavier than two-surface configurations. However, in the case of the Avanti, the wing and main landing gear attach to the aft pressure bulkhead, rendering the structure more efficient. (D) The foreplane places the inboard wing in downwash, reducing the wings effectiveness. (E) Furthermore, considering the aircraft in Figure 11-34, the foreplane tip vortices might cause a distortion in flow into engine and cause detrimental compressor distortion. (F) Deploying flaps on the Avanti increases pitching moment enough to require a flap on the foreplane to balance the airplane. This flap is connected mechanically to the main wing flaps—one more system to consider. (G) Reduced forward and downward visibility by the foreplane.

11.3.12 Canard Configuration

A canard configuration has the horizontal stabilizing surface placed in front of the main wing (see Figure 11-35). This placement generates a destabilizing pitching moment, which contrasts the stabilizing moment generated by tail-aft configuration. The configuration dates to the early days of aviation. As an example, the Wright Flyer, the first human-carrying airplane, was a canard. The configuration sporadically appeared in various experimental designs throughout history and got its greatest boost in the early 1970s with the Rutan VariEze and LongEze kitplanes.



FIGURE 11-34 A three-surface configuration.

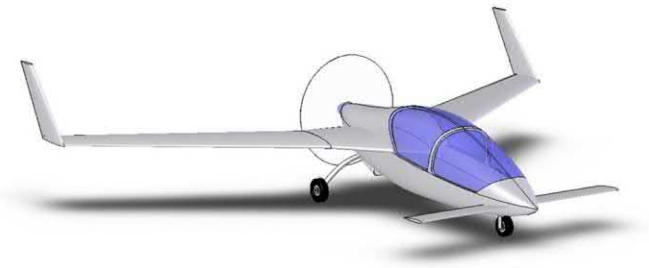


FIGURE 11-35 A canard configuration.

(1) Pros

(A) One of the most touted advantages of the canard configuration is the so-called *stall-proofing*. It refers to a characteristic in which the canard stalls before the main wing, lowering the nose and preventing a main wing stall. However, claiming this an inability to stall is inaccurate; it *is* possible to stall the main wing, e.g., by an abused stall entry. Using high rotational momentum, the airplane can be rotated to a high enough AOA to stall the main wing. The term stall-proofing is associated with a 1 knot/s deceleration to stall. If this deceleration is maintained, such airplanes are designed to drop the nose gently before the main wing stalls. Under those circumstances, the canard can be considered stall-proof. (B) In cruise, the canard lift points upward, contrasting the downward force generated by conventional tail-aft configurations. Thus, the canard contributes to the total lift of the aircraft, making the concept more efficient than conventional aircraft. This is offset by the canard downwash.

(2) Cons

(A) The stall-proofing feature must be deliberately designed into the airplane. If not, the main wing can stall before the canard. This results in a dangerous nose pitch-up at stall. (B) The configuration requires higher T-O airspeed than a tail-aft configuration and, thus, requires longer runway. This is a direct consequence of the stall-proofing. Since the main wing is not permitted to develop its $C_{L_{max}}$, the lift-off speed is higher than comparable tail-aft configuration: This requires higher rotation speed during which it covers greater distance. Its landing distance is longer for the same reason. (C) The compact size of canards results in a smaller tail arm than similarly sized conventional aircraft. This calls for a larger stabilizing surface or an increased arm by an aft sweep to further separate the MGC and canard. (D) While the flight characteristics of popular canard configurations (LongEze, Cozy, etc.) are considered good, their directional stability is often weak due to the short tail arm of the winglets that serve as VT (e.g., see [36]). Again, an aft swept wing improves this. (E) The stall may result in a large nose-drop, depending on how aggressively it is performed. As pointed out by Larrabee and Abzug [3, p. 252], the pitch rate following the stall *increases* the AOA on the canard and can delay stall recovery until a steep nose pitch-down attitude is achieved. An argument can be made that conventional tail-aft aircraft can also recover automatically with the appearance of sudden upwash on the HT as the wing's downwash disappears at stall. (F) Reduction of forward and downward visibility by the canard. (G) The canard-downwash reduces the effectiveness of the main wing (see Figure 11-36). This cuts

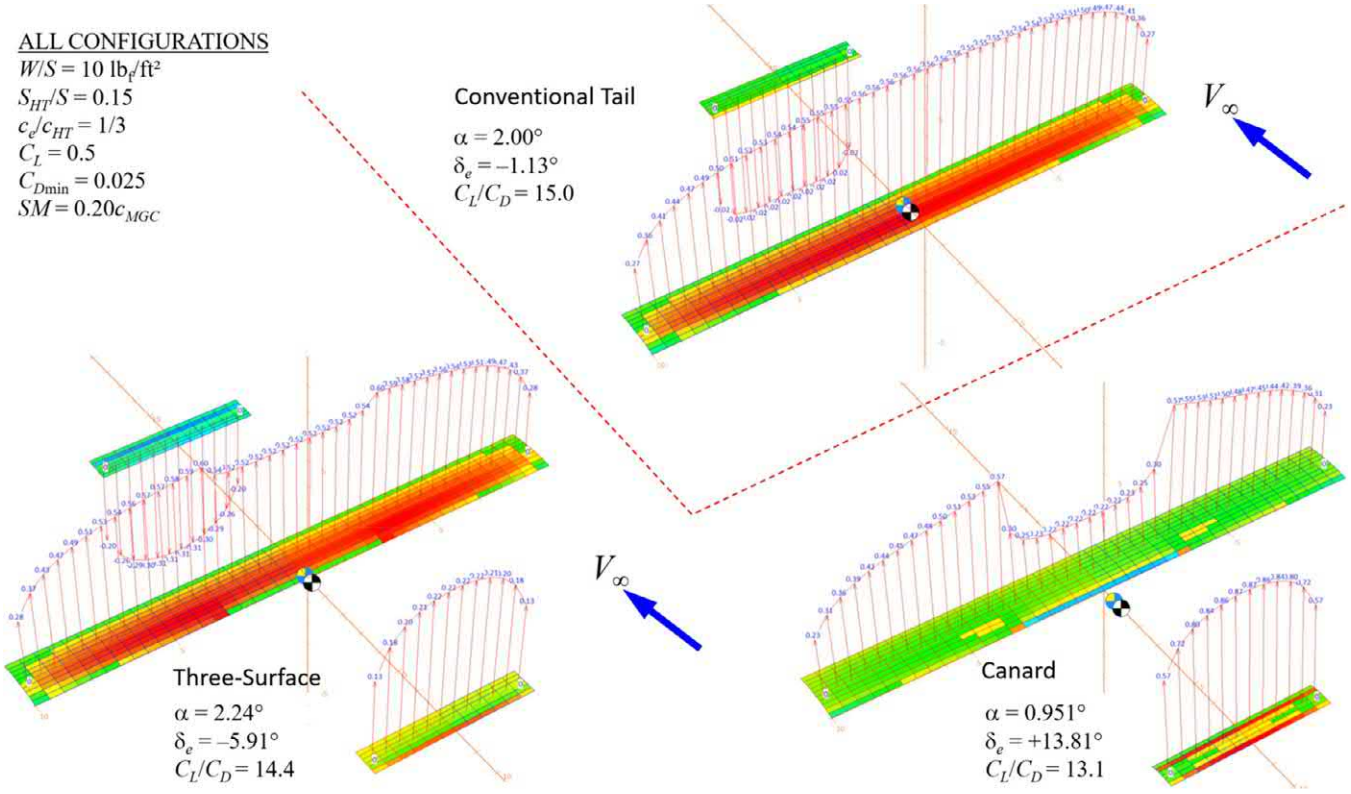


FIGURE 11-36 Comparing the spanwise section lift coefficients for a conventional, canard, and three-surface configuration. All are trimmed for level flight and operating at $C_L = 0.5$ (see captions).

into the advantage offered by the positive lift of the canard. (H) Reduced section lift coefficients of the main wing behind the canard increases the margin between the canard stall and the subsequent wing stall—which further increases the minimum speed of the vehicle. (I) The downwash moves the center-of-lift outboard, increasing the wing bending moments.

11.3.13 Basic Design Guidelines for Selecting a Tail Configuration

Figure 11-36 compares spanwise distribution of section lift coefficients (C_l) for three configurations that feature the same constant-chord main wing. These are a conventional, canard, and a three-surface configuration. None has been "optimized" and all feature identical stabilizing surfaces. The three-surface configuration has two such surfaces. That said, they are modeled to permit a fair comparison. The angle-of-incidence of all surfaces is 0 degree with respect to the x-axis (chord axis). All have the same wing area, wing loading, dynamic pressure, static margin (SM), and are trimmed at a design lift coefficient of $C_L = 0.5$.

Figure 11-36 allows multiple observations regarding these configurations. Note how the downwash of the foreplane/canard suppresses the C_l over the wing's center region. The conventional tail requires the least δ_e to trim. This is caused by the wing's downwash, which here places the HT at a suitable AOA so large deflection is not needed. The canard requires the largest δ_e. This is caused by the limited upwash where it is located and the high balancing-load demanded by the SM ($=0.2c_{MGC}$). It can be remedied by installing the canard at a larger angle-of-incidence or by a cambered airfoil. The lift generated by the foreplane and aft horizontal surface of the three-surface configuration nearly cancels each other, highlighting one of its benefits. Like the canard, this configuration would also benefit from further polishing. Also, note that, of the three configurations, the conventional one has the highest C_L/C_D at the cruise $C_L = 0.5$; the canard the lowest.

This is presented here as food-for-thought. Inexperienced designers often opt for canards or three-surface configurations as their first choice, justifying the selection on perceived "efficiency" or aesthetics. Figure 11-36 shows such configurations are not more efficient by default, but rather following considerable and laborious refinements. This requires access to the right analysis tools and a baseline for comparison. In Figure 11-36, the conventional configuration serves as the baseline. The other two configurations clearly require work to match or beat its efficiency when cruising at $C_L = 0.5$. Additionally, do the other configurations beat the conventional one in other areas? For instance, is their take-off or landing performance better? Are their empty weight ratios lower? Are they easier to manufacture? Will their unconventional appearance help or hinder sales? Such questions should be answered to justify the selection of a tail configuration. Review Section 4.1.3 for further insight. A further insight is gleaned by comparing the *We/Wo* of the Piaggio Avanti (three-surface), Beech Starship (canard), and Beech 350ER King Air (conventional).

Additional Guidelines for Positioning Tail-Aft Stabilizing Surfaces

The position of a horizontal tail behind the wing of conventional aircraft significantly affects its handling characteristics near or at stall. One region behind the wing leads to a pitch-up tendency while another leads to pitch-down. Swept wings compound this due to tip-stalling. The characteristics are driven by the turbulent wake emanating from the wing and fuselage at high AOAs (see Section 11.3.3). The designer must be aware of this shortcoming and its solution, for instance the ventral fin (see Section 11.2.3).

The pitch-up problem was studied in ref. [37] and showed that, near stall, Λ_{LE} of the wing has an important impact on the nonlinearity of the pitching moment curve. The presence and location of the HT plays a role too (see Figure 11-37). The figure illustrates the instability of a swept wing only (A). Adding a T-tail (B) stabilizes the combination but at high AOA, the curve crosses the horizontal axis and creates a deep stall trim point (here at $\alpha = 29$ degrees).

In contrast, straight wings with T-tails (C) may cause nonlinearities that are restricted to a smaller range of AOAs near stall (see Figure 11-37). Such aircraft may experience reduced stability but not detrimental instability like their swept wing counterparts. They are less likely to have a deep stall trim point. It suffices to size the HT to handle trim for its operational range only—not poststall. Regardless, this author recommends the designer evaluates possible deep stall tendency, either by wind tunnel testing or by a stall evaluation of a radio-controlled model. The former should be required for all aircraft intended to carry people for commercial purposes. Per ref. [37], the presence of the fuselage may be hard to predict otherwise and can easily devolve into a major design problem, in particular for low AR wings with thin airfoils. As discussed in Chapter 9, aft-swept wings suffer flow separation at C_L well below $C_{L_{max}}$ and are either unstable or marginally stable through stall. This requires aft-swept configurations to be treated more stringently than straight wing. They should be wind tunnel tested.

In addition to ref. [37], the pitch-up problem was also studied in refs. [38, 39]. It reaffirms that the wing's Λ_{LE}, λ and AR also impact the pitching moment nonlinearity near stall. To prevent instability, a large AR wing should have reduced Λ_{LE}. Low λ aggravates tip stall and is detrimental to stability. This impacts the selection of the HT location, because it must remedy the resulting instability. The combined effect of AR and leading-edge sweep from refs. [37, 38] are depicted in Figure 11-38.

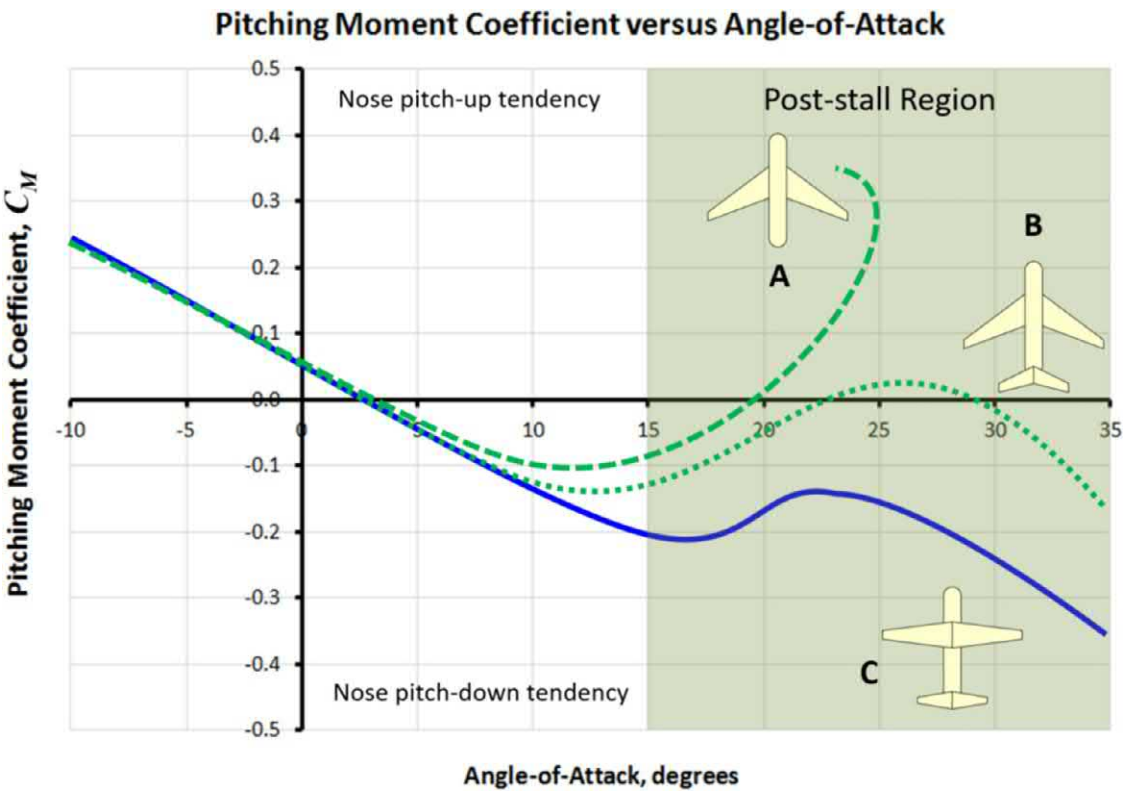


FIGURE 11-37 Pitching moment curves for an aft-swept and straight wing configuration. Configuration A (tailless + sweep) displays instability starting near $\alpha = 10$ degrees. Configuration B (T-tail + sweep) has a deep stall trim-point. Configuration C (T-tail + straight) has acceptable C_M-curve.

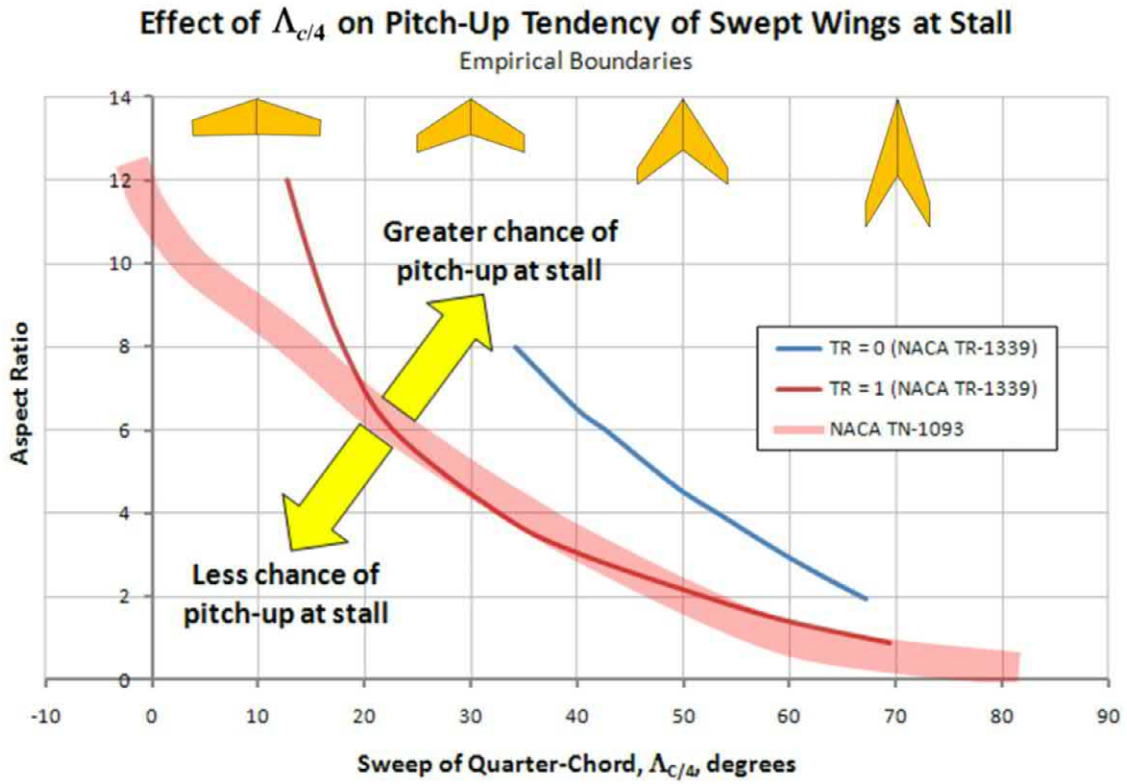


FIGURE 11-38 Empirical pitch-up boundary for a swept back wing. *Reproduction from Furlong, G.C., McHugh, J.G., A Summary and Analysis of the Low-Speed Longitudinal Characteristics of Swept Wings at High Reynolds Numbers, NACA TR-1339, 1957; Shortal, J.A., Maggin, B., Effect of Sweepback and Aspect Ratio on Longitudinal Stability Characteristics of Wings at Low Speeds, NACA TN-1093, 1946.*

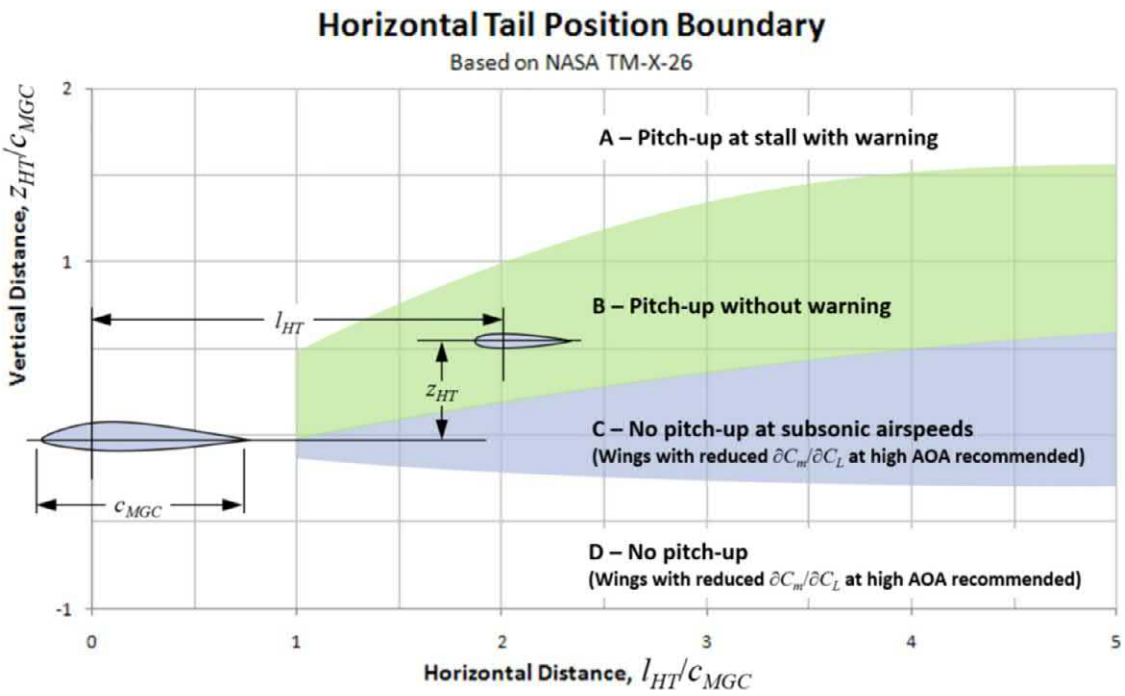


FIGURE 11-39 Recommended placement of the HT behind the wing. *Reproduction from Spreemann, K.P., Design Guide for Pitch-Up Evaluation and Investigation at High Subsonic Speeds of Possible Limitations due to Wing-Aspect-Ratio Variations, NASA TM-X-26, 1959.*

Ref. [39] considers wings of $1.55 < AR < 3.0$ with Λ_{LE} commonly associated with supersonic fighters. While the results, in general, apply only to aircraft with $2 < AR < 5$, they give important clues about trends involving the aft position of the HT (see Figure 11-39, which is a reproduction from ref. [39]). The designer of tail-aft aircraft should compare the intended location of the HT to assess the probability of an uncontrollable pitch-up at stall. An HT positioned in region A or B call for aerodynamic fixes in the form of ventral fins.

11.4 INITIAL TAIL SIZING METHODS

Unless other factors are of higher priority, the designer should always try to minimize drag. Since a bulk of the airplane's drag results from skin friction, reducing the wetted area of the empennage ekes us closer to that goal. This section shows how the horizontal and vertical tail can be sized and positioned in space such the resulting wetted area of the aft fuselage is minimized. Four methods are presented in this edition. The first method assumes that a specific horizontal tail volume, V_{HT}, is desired. The second method assumes a specific vertical tail volume, V_{VT}, is desired. The third method assumes V_{HT} and V_{VT} are desired. The fourth method permits nonlinear fuselages, such as tadpoles, to be considered.

11.4.1 Recommended Initial Values for V_{HT} and V_{VT}

The first task to be accomplished regarding initial tail sizing is to identify as suitable V_{HT} and V_{VT}. Thus, the V_{HT} and V_{VT} of existing classes of aircraft must be investigated. Table 11-4 presents V_{HT} and V_{VT} for different classes of aircraft. Regardless, each class consists of subgroups. Greater accuracy is achieved by collecting data for those. Table 11-5 exemplifies such data. All were evaluated by detail oriented graduate students (to whom we owe gratitude), using scaled-up three-view drawings.

TABLE 11-4 Candidate horizontal and vertical tail volumes per class of aircraft.

	V_{HT}	V_{VT}
Sailplanes	0.50	0.02
Homebuilt	0.50	0.04
General aviation - single engine	0.70	0.04
General aviation - twin engine	0.80	0.07
Agricultural aircraft	0.50	0.04
Twin turboprop	0.90	0.08
Flying boat	0.70	0.06
Jet trainer	0.70	0.06
Jet fighter	0.40	0.07
Military cargo/bomber	1.00	0.08
Jet transport	1.00	0.09

Based on Raymer, D., Aircraft Design: A Conceptual Approach, 5th ed., AIAA Education Series, 2012.

TABLE 11-5 Geometric properties of the horizontal and vertical tails of selected aircraft.

SAILPLANES						
Aircraft	AR_W	Taper Ratios			Tail Volumes	
		λ_W	λ_{HT}	λ_{VT}	V_{HT}	V_{VT}
PW-5	17.83	0.184	1.000	0.414	0.766	0.0192
Akaflieg D-36	24.73	0.264	0.514	0.537	0.456	0.0166
Avialsa A-60	20.56	0.409	0.527	0.441	0.515	0.0182
Caproni A-21	25.67	0.270	0.432	0.451	0.464	0.0095
Centrair 101 Pegase	21.47	0.413	0.664	0.590	0.625	0.0188
Centrair 201 Marianne	20.01	0.357	0.581	0.675	0.490	0.0157
EIRI PIK-20E	22.46	0.374	0.680	0.684	0.674	0.0177
Fournier RF-4D	11.22	0.420	0.437	0.312	0.549	0.0185
Grob Astir CS	18.24	0.392	0.820	0.594	0.594	0.0135
Grob G-109	15.94	0.443	0.617	0.574	0.517	0.0139
Max =	25.67	0.443	1.000	0.684	0.766	0.0192
Min =	11.22	0.184	0.432	0.312	0.456	0.0095
Average =	19.81	0.353	0.627	0.527	0.565	0.0162

GENERAL AVIATION SINGLE ENGINE - PISTON						
Aircraft	AR_W	Taper Ratios			Tail Volumes	
		λ_W	λ_{HT}	λ_{VT}	V_{HT}	V_{VT}
Aermacchi Al60	7.17	0.660	0.684	0.368	0.695	0.0413
Aeronca Champion	7.27	1.000	0.471	0.339	0.419	0.0240
Auster Autocrat	7.01	1.000	0.328	0.350	0.372	0.0224
Aviamilano F.14 Nibbio	6.99	0.520	0.475	0.377	0.668	0.0418
Beagle Pup	8.04	0.565	1.000	0.909	0.723	0.0523
Beechcraft Bonanza G36	6.13	0.500	0.667	0.467	0.628	0.0492
Beechcraft Sierra Be-24	7.35	1.000	1.000	0.357	0.581	0.0348
Bolkow 208 Junior	6.37	1.000	1.000	0.444	0.493	0.0378
Cessna 152	6.81	0.693	0.604	0.461	0.557	0.0337
Cessna 172	7.45	0.638	0.563	0.443	0.761	0.0419
Cessna 210	8.13	0.690	0.543	0.484	0.766	0.0378
Cessna 400	9.19	0.714	0.694	0.274	0.774	0.0418
Christen A-1 Huskey	6.89	1.010	0.111	0.304	0.362	0.0190
DA20	10.18	0.689	0.361	0.556	0.820	0.0351
DA40 (XLS)	10.76	0.622	0.554	0.660	0.721	0.0423
Janowski J-1 Przasniczka	7.50	1.000	1.000	0.738	0.471	0.0322
Lancair IV-P	6.46	0.495	0.630	0.373	1.000	0.0601
Lancair Legacy	7.88	0.533	0.727	0.445	0.568	0.0563
Mooney Ovation2 GX	8.05	0.476	0.540	0.483	0.606	0.0407
Piper J-3 Cub	6.96	1.000	0.636	0.272	0.479	0.0180
PZL Koliber 160	7.48	1.000	1.000	0.720	0.926	0.0520
SR-20	10.14	0.549	0.633	0.500	0.686	0.0323
SR-22	10.14	0.498	0.613	0.502	0.637	0.0333
Max =	10.76	1.010	1.000	0.909	1.000	0.0601
Min =	6.13	0.476	0.111	0.272	0.362	0.0180
Average =	7.84	0.733	0.645	0.471	0.640	0.0383

GENERAL AVIATION SINGLE ENGINE - PISTON - AEROBATIC						
Aircraft	AR_W	Taper Ratios			Tail Volumes	
		λ_W	λ_{HT}	λ_{VT}	V_{HT}	V_{VT}
ACS 100 Sora	7.07	0.500	0.534	0.313	0.607	0.0725
Blackshape Prime	6.55	0.371	0.404	0.297	0.538	0.0699
CAP 10	6.01	0.342	0.503	0.358	0.743	0.0710
CAP 232	5.38	0.479	0.522	0.327	0.499	0.0580
Extra EA-300	5.41	0.486	0.662	0.356	0.576	0.0753
Fournier RF-6b	8.85	0.494	0.562	0.318	0.694	0.0392
Slick 360	6.23	0.487	0.505	0.255	0.627	0.0626
Sukhoi SU-26	5.62	0.522	0.695	0.325	0.573	0.0615
Yakovlev Yak 3M	4.89	0.321	0.411	0.364	0.368	0.0468
XtremeAir Sbach 342 (XA42)	5.00	0.461	0.487	0.285	0.554	0.0601
Max =	8.85	0.522	0.695	0.364	0.743	0.0753
Min =	4.89	0.321	0.404	0.255	0.368	0.0392
Average =	6.10	0.446	0.528	0.320	0.578	0.0617

TABLE 11-5 Geometric properties of the horizontal and vertical tails of selected aircraft—cont'd

GENERAL AVIATION SINGLE ENGINE - TURBOPROP						
Aircraft	AR_W	Taper Ratios			Tail Volumes	
		λ_W	λ_{HT}	λ_{VT}	V_{HT}	V_{VT}
Cessna 206	7.48	0.603	0.646	0.646	0.738	0.0500
Cessna Caravan	9.72	0.615	0.603	0.397	0.982	0.0560
Embraer Super Tucano	6.52	0.408	0.612	0.612	0.841	0.1004
Epic LT	8.10	0.592	0.593	0.593	0.798	0.0761
FAdeA IA-73	7.40	0.509	0.584	0.584	0.648	0.0625
Pilatus PC-12	10.24	0.520	0.694	0.644	0.992	0.0495
Pilatus PC-6	8.36	1.000	1.000	1.000	0.592	0.0330
Pilatus PC-9	6.27	0.514	0.561	0.561	0.707	0.0609
Piper Meridian	10.38	0.559	0.561	0.461	0.983	0.0499
Piper Meridian	8.33	0.449	0.474	0.474	0.729	0.0517
SOCATA TBM700	8.17	0.607	0.817	0.817	0.911	0.0774
SOCATA TBM850	9.05	0.598	0.793	0.793	0.904	0.0768
Max =	10.38	1.000	1.000	1.000	0.992	0.1004
Min =	6.27	0.408	0.474	0.397	0.592	0.0330
Average =	8.33	0.581	0.661	0.632	0.819	0.0620

GENERAL AVIATION MULTI-ENGINE - PISTON						
Aircraft	AR_W	Taper Ratios			Tail Volumes	
		λ_W	λ_{HT}	λ_{VT}	V_{HT}	V_{VT}
Aero 45	8.78	0.394	0.580	0.338	0.369	0.0295
Beechcraft Baron G58	7.19	0.423	0.667	0.429	0.791	0.0464
Beechcraft Duchess	7.98	0.796	1.000	0.615	0.666	0.0477
Beechcraft Duke	7.24	0.327	0.545	0.386	0.821	0.0573
Britten-Norman BN-2 Islander	7.39	1.000	1.000	0.333	0.635	0.0489
Cessna 421	7.87	0.657	0.630	0.505	1.280	0.0782
Diamond DA42	10.11	0.545	0.481	0.511	0.500	0.0338
Partenavia P68	7.74	1.000	1.000	0.449	0.657	0.0488
Max =	10.11	1.000	1.000	0.615	1.280	0.0782
Min =	7.19	0.327	0.481	0.333	0.369	0.0295
Average =	8.04	0.643	0.738	0.446	0.715	0.0488

MULTI-ENGINE - TURBOPROP						
Aircraft	AR_W	Taper Ratios			Tail Volumes	
		λ_W	λ_{HT}	λ_{VT}	V_{HT}	V_{VT}
Antonov An-10	11.86	0.345	0.354	0.272	1.060	0.0639
Antonov An-24	11.20	0.268	0.438	0.348	1.097	0.0867
Beechcraft 1900	9.80	0.420	0.500	0.571	1.289	0.0796
Bombardier Dash 8 Q100	12.35	0.500	0.769	0.709	1.522	0.1157
Bombardier Dash 8 Q400	12.81	0.418	0.771	0.743	1.769	0.1252
Dassault MD-415 Communaute	7.50	0.361	0.629	0.344	0.579	0.0414
DHC-6 Twin Otter	10.06	0.988	0.990	0.519	0.918	0.0783
DHC-7 Dash 7	10.06	0.427	0.725	0.496	1.099	0.0888
Grumman G-159	10.10	0.379	0.470	0.275	0.869	0.0697
Ilyushin Il-114	10.99	0.375	0.417	0.398	1.140	0.0769
Ilyushin Il-14	12.73	0.368	0.484	0.539	0.847	0.0694
Ilyushin Il-18	9.99	0.333	0.467	0.342	0.869	0.0670
Let L-410 Turbolet	10.78	0.451	0.568	0.452	0.924	0.0773
Lockheed L-188 Electra	7.54	0.392	0.333	0.221	0.884	0.0694
NORD 262	9.15	0.580	0.517	0.543	1.182	0.0604
Max =	12.81	0.988	0.990	0.743	1.769	0.1252
Min =	7.50	0.268	0.333	0.221	0.579	0.0414
Average =	10.46	0.440	0.562	0.451	1.070	0.0780

Continued

TABLE 11-5 Geometric properties of the horizontal and vertical tails of selected aircraft—cont'd

BUSINESS JET AIRCRAFT						
Aircraft	AR_W	Taper Ratios			Tail Volumes	
		λ_W	λ_{HT}	λ_{VT}	V_{HT}	V_{VT}
Beechcraft Hawker 4000	6.70	0.330	0.467	0.652	0.916	0.0411
Bombardier Challenger 605	7.59	0.309	0.382	0.722	0.692	0.0419
Bombardier Learjet 23	5.46	0.509	0.500	0.512	0.639	0.0743
Bombardier Learjet 29	7.25	0.381	0.462	0.600	0.613	0.0549
Bombardier Learjet 45	7.32	0.376	0.435	0.735	0.652	0.0519
Cessna Citation II	8.02	0.323	0.530	0.429	0.599	0.0316
Dassault Falcon 7x	8.60	0.245	0.533	0.352	0.616	0.0262
Dassault Falcon 900	6.82	0.329	0.488	0.319	0.725	0.0398
Embraer Legacy 600	7.01	0.236	0.621	0.633	0.766	0.0457
Gulfstream G550	7.26	0.256	0.457	0.642	0.629	0.0212
IAI Westwind	6.04	0.335	0.429	0.333	0.698	0.0768
Lockheed JetStar	5.44	0.373	0.286	0.323	0.559	0.0597
Max =	8.60	0.509	0.621	0.735	0.916	0.0768
Min =	5.44	0.236	0.286	0.319	0.559	0.0212
Average =	6.96	0.333	0.466	0.521	0.675	0.0471

COMMERCIAL JET TRANSPORT AIRCRAFT						
Aircraft	AR_W	Taper Ratios			Tail Volumes	
		λ_W	λ_{HT}	λ_{VT}	V_{HT}	V_{VT}
Airbus A320	9.49	0.317	0.272	0.263	1.409	0.1148
Airbus A340	13.53	0.263	0.424	0.284	1.106	0.0810
Airbus A380	7.52	0.249	0.386	0.369	0.719	0.0518
BAe BAC-111 Series 475	8.48	0.322	0.641	0.737	0.851	0.0425
BAe-146	8.89	0.382	0.435	0.679	1.537	0.1128
Boeing 707-320B	6.96	0.275	0.412	0.346	0.545	0.0431
Boeing 727-200	6.86	0.304	0.342	0.607	0.688	0.0667
Boeing 737-100	7.88	0.344	0.391	0.264	1.379	0.0746
ERJ-145	7.90	0.272	0.643	0.505	0.908	0.0709
Tupolev Tu-154	7.00	0.252	0.492	0.533	0.552	0.0589
Max =	13.53	0.382	0.643	0.737	1.537	0.1148
Min =	6.86	0.249	0.272	0.263	0.545	0.0425
Average =	8.45	0.298	0.444	0.459	0.969	0.0717

11.4.2 Design Guidance for Initial Sizing of HT for Stick-Fixed Neutral Point

Tables 11-4 and 11-5 apply to specific classes of aircraft. If none of these apply, the reader can use Equation (24-131) as an initial guess to estimate horizontal tail volume (V_{HT}) based on desirable stick-fixed neutral point (h_n) and aspect ratio (AR). Note that once $AR > 4$, h_n is mostly independent of AR and mostly a function of V_{HT}. This is illustrated in Figure 11-40, which depicts how V_{HT} affects h_n. The graph assumes the wing and HT only and symmetric airfoils for both.

The graph in Figure 11-40 is read as follows. Assuming an airplane whose $V_{HT} = 0.70$, the h_n should be around 0.55. This may drop to 0.45 or so once a fuselage is added. The graph helps estimating V_{HT} for a desired stick-fixed neutral point. This is done the curve fit in Figure 11-40 for V_{HT}:

$$V_{HT} = 3.193 - 3.426\sqrt{1.084 - h_n} \tag{11-13}$$

This expression can be used to determine a "first stab" V_{HT}, assuming no fuselage. The fuselage may move the h_n some 0.05 to 0.10 forward, assuming $0.4 < V_{HT} < 1.0$. This estimation says nothing about handling—some aircraft may need smaller or greater V_{HT} depending on other operational requirements.

11.4.3 General Formulation of Initial Estimation of V_{HT} and V_{VT}

The following method for the estimation of initial tail geometry assumes V_{HT} and/or V_{VT} are known, perhaps, by studying Tables 11-4 and 11-5. The method returns the tail arm of the minimum wetted area of the combination of stabilizing surfaces and the part of the fuselage to which they are mounted. This corresponds to the shaded area in Figure 11-41. Once the arm is determined, the rest of the geometry can be calculated using the planform formulae of Section 9.2.2.

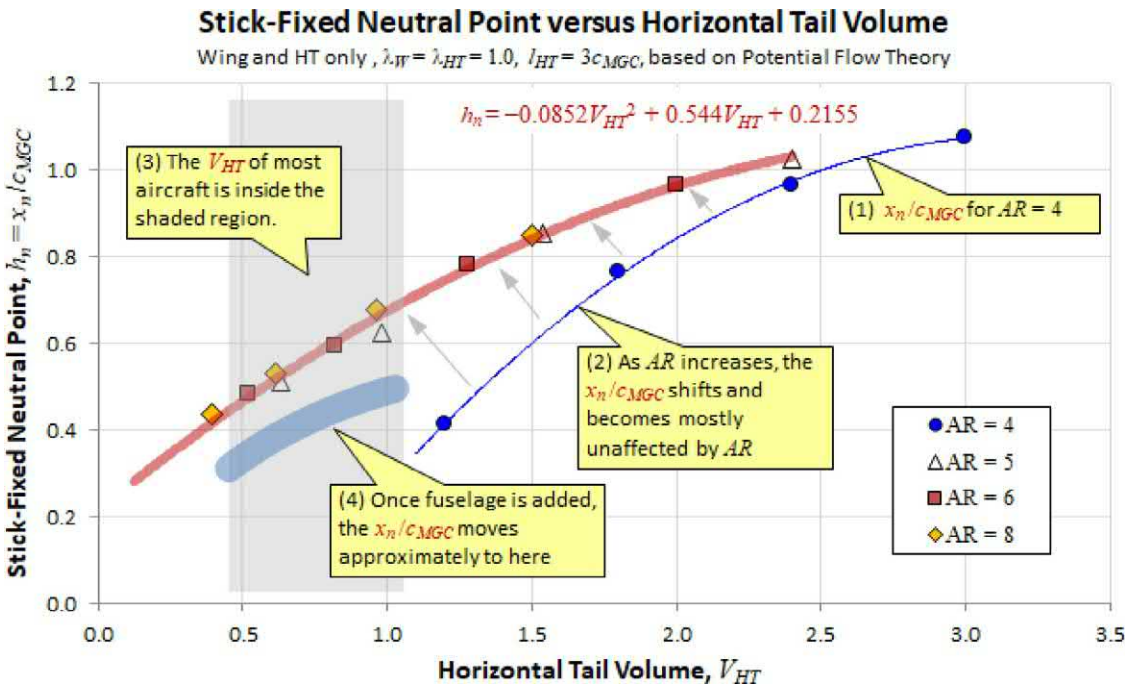


FIGURE 11-40 Impact of V_{HT} on the location of the stick-fixed neutral point. When $AR > 4$, the AR has minimal influence on the location of the neutral point.

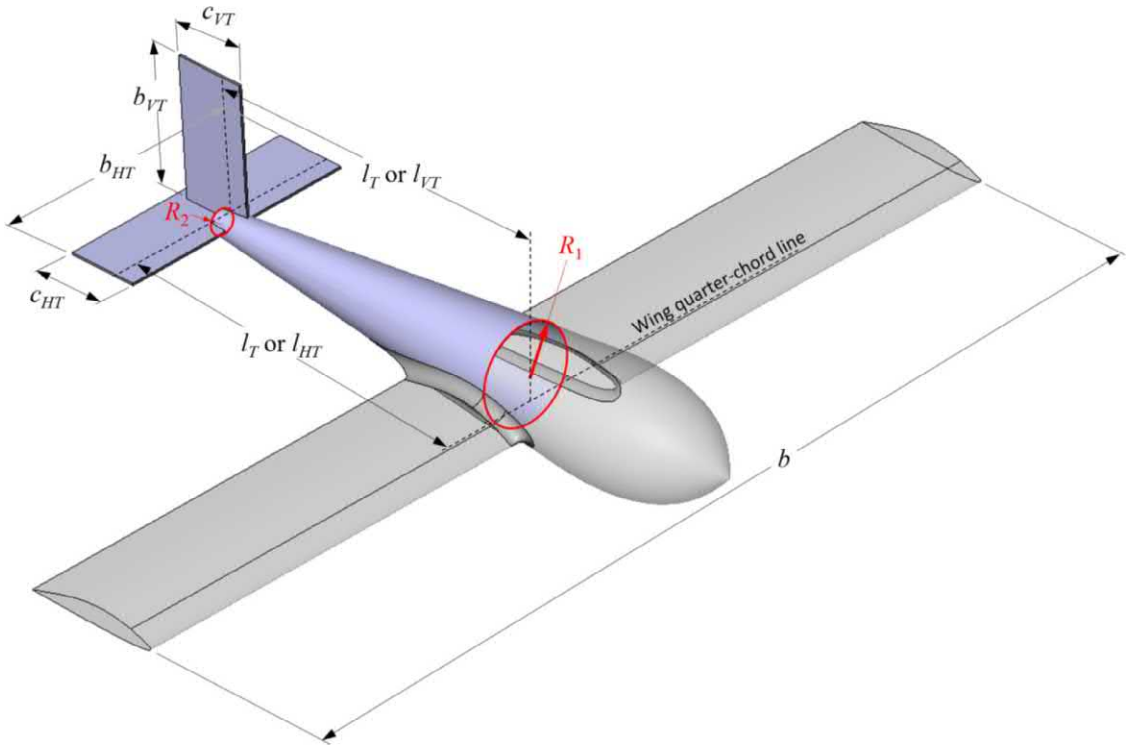


FIGURE 11-41 Definition of dimensions for the HT and VT.

The wetted area is the sum of the contributions of the fuselage, HT, and/or VT. We denote these wetted area contributions as S_{wetFUS}, S_{wetHT}, and S_{wetVT}. The fuselage tail arm is given by l_T and extends from the wing's $c_{MGC}/4$ to that of the HT and/or VT (see Figure 11-41). S_{wetFUS}, S_{wetHT}, and S_{wetVT} must be specified as functions of that tail arm. Thus, the wetted area is

$$S_{wet} = S_{wet\ FUS}(l_T) + S_{wet\ HT}(l_T) + S_{wet\ VT}(l_T) \tag{11-14}$$

The next step is to differentiate Equation (11-14) with respect to l_T and set equal to zero. This allows the resulting expression to be solved for l_T.

$$\frac{dS_{wet}}{dl_T} = \frac{d}{dl_T}S_{wet\ FUS}(l_T) + \frac{d}{dl_T}S_{wet\ HT}(l_T) + \frac{d}{dl_T}S_{wet\ VT}(l_T) = 0 \tag{11-15}$$

Typical formulae for S_{wetFUS}, S_{wetHT}, and S_{wetVT} are given below

Circular frustum fuselage:

$$S_{wet\ FUS}(l_T) = \pi(R_1 + R_2)\cdot l_T \tag{11-16}$$

Circular arbitrary fuselage:

$$S_{wet\ FUS}(l_T) = 2\pi\int_0^{l_T} y\sqrt{1+(dy/dx)^2}\,dx \tag{11-17}$$

Horizontal tail: $$S_{wet\ HT}(l_T) \approx 2\frac{V_{HT}\cdot S\cdot c_{MGC}}{l_T} \tag{11-18}$$

Vertical tail: $$S_{wet\ VT}(l_T) \approx 2\frac{V_{VT}\cdot S\cdot b}{l_T} \tag{11-19}$$

where Equations (11-18) and (11-19) are obtained from Equations (11-5) and (11-6), respectively. The function y is the curve describing the shape of the aft fuselage section (see Figure 11-42). Once l_T is known, other geometries can be evaluated using the following formulae:

Horizontal tail area: $$S_{HT} = \frac{V_{HT}\cdot S\cdot c_{MGC}}{l_T} \tag{11-20}$$

HT span: $$b_{HT} = \sqrt{AR_{HT}\times S_{HT}} \tag{11-21}$$

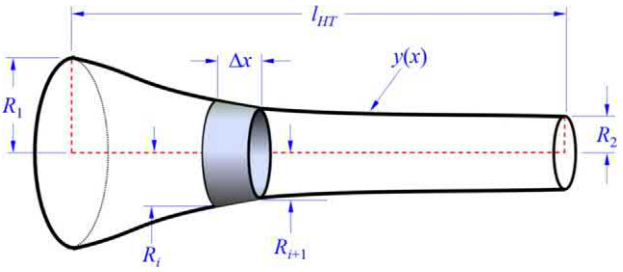


FIGURE 11-42 An arbitrary aft fuselage section can be generated by rotating curve $y(x)$ around the x-axis.

Average chord of the HT: $$c_{avg} = \frac{b_{HT}}{AR_{HT}} \tag{11-22}$$

Vertical tail area: $$S_{VT} = \frac{V_{VT}\cdot S\cdot b}{l_T} \tag{11-23}$$

VT span: $$b_{VT} = \sqrt{AR_{VT}\times S_{VT}} \tag{11-24}$$

Average chord of the VT: $$c_{avg_{VT}} = \frac{b_{VT}}{AR_{VT}} \tag{11-25}$$

11.4.4 Method 1: Initial Tail Sizing Optimization Considering the Horizontal Tail Only

***Guidance*: To use this method you need a *target value of* V_{HT}. This method only considers the HT *and* ignores the presence of the VT. It is assumed that either an alternative method will be used for the VT or it will be placed using the tail arm calculated in this section. See Section 11.4.6 for a method that considers both the horizontal and vertical tail volumes simultaneously.**

Determination of Tail Arm for a Desired V_{HT} such that Wetted Area is Minimized

The distance between the wing's MGC quarter-chord and the quarter-chord of the horizontal tail is calculated using the following expression. Since this arm is only associated with the HT, it is denoted by l_{HT}.

$$l_{HT} = \sqrt{\frac{2\cdot V_{HT}\cdot S\cdot c_{MGC}}{\pi(R_1+R_2)}} \tag{11-26}$$

DERIVATION OF EQUATION (11-26)

From Equation (11-14), we get:

$$\begin{aligned} S_{wet} &= S_{wet\ FUS}(l_{HT}) + S_{wet\ HT}(l_{HT}) \\ &\approx \pi(R_1+R_2)\cdot l_{HT} + 2\frac{V_{HT}\cdot S\cdot c_{MGC}}{l_{HT}} \end{aligned}$$

Then, differentiate this with respect to l_{HT}:

$$\begin{aligned} \frac{dS_{wet}}{dl_{HT}} &= \frac{d}{dl_{HT}}\left(\pi(R_1+R_2)\cdot l_{HT} + 2\frac{V_{HT}\cdot S\cdot c_{MGC}}{l_{HT}}\right) \\ &= \pi(R_1+R_2) - \frac{2\cdot V_{HT}\cdot S\cdot c_{MGC}}{l_{HT}^2} \end{aligned}$$

Set to zero and solve for l_{HT}:

$$\frac{dS_{wet}}{dl_{HT}} = 0 \;\Rightarrow\; l_{HT}^2 = \frac{2\cdot V_{HT}\cdot S\cdot c_{MGC}}{\pi(R_1+R_2)}$$

$$\Rightarrow\; l_{HT} = \sqrt{\frac{2\cdot V_{HT}\cdot S\cdot c_{MGC}}{\pi(R_1+R_2)}}$$

EXAMPLE 11-1

To help develop a feel for which prediction method suits, we will use the three methods to estimate the tail arm of the Cessna 172 Skyhawk. We will start with Method 1 in this example. The Skyhawk's actual $V_{HT}=0.761$. Its reference area is $S=174\,\text{ft}^2$ and we will use its average chord as the mean geometric chord $c_{MGC}=4.83\,\text{ft}$. Suitable values for R_1 and R_2 are $R_1=2.0\,\text{ft}$ and $R_2=0.5\,\text{ft}$. Also, estimate the wetted area of the tail section and HT, and the planform area and span of the horizontal tail assuming its $AR_{HT}=3.0$.

SOLUTION:

Determine the optimum tail arm using Equation (11-26) (actual is $l_{HT}=15.0\,\text{ft}$):

$$l_{HT}=\sqrt{\frac{2\cdot V_{HT}\cdot S\cdot c_{MGC}}{\pi(R_1+R_2)}}=\sqrt{\frac{2\cdot(0.761)\cdot(174)\cdot(4.83)}{\pi(2.0+0.5)}}=12.76ft$$

Use Equation (11-14) to calculate the wetted area (actual is $S_{wet}=200.5\,\text{ft}^2$):

$$S_{wet}\approx\pi(R_1+R_2)\cdot l_{HT}+2\frac{V_{HT}\cdot S\cdot c_{MGC}}{l_{HT}}$$
$$=\pi(2.0+0.5)\cdot(12.76)+2\frac{(0.761)\cdot(174)\cdot(4.83)}{(12.76)}$$
$$=200.5\ \text{ft}^2$$

Use Equation (11-20) to calculate the planform area (actual value $S_{HT}=41.4\,\text{ft}^2$):

$$S_{HT}=\frac{V_{HT}\cdot S\cdot c_{MGC}}{l_{HT}}=\frac{(0.761)\cdot(174)\cdot(4.83)}{(12.76)}=50.1\ \text{ft}^2$$

Use Equation (11-21) to calculate the span of the HT (actual value $b_{HT}=11.3\,\text{ft}$):

$$b_{HT}=\sqrt{AR_{HT}\times S_{HT}}=\sqrt{(3.0)\times(50.12)}=12.26\ \text{ft}$$

11.4.5 Method 2: Initial Tail Sizing Optimization Considering the Vertical Tail Only

***Guidance*: To use this method you need a *target value of* V_{VT}. This method only considers the VT *and* ignores the presence of the HT. It is assumed that either an alternative method will be used for the HT or it will be placed using the tail arm calculated in this section. See Section 11.4.6 for a method that considers both the horizontal and vertical tail volumes simultaneously.**

Determination of Tail Arm for a Desired V_{VT} such that Wetted Area is Minimized

The distance between the wing's MGC quarter-chord and the quarter-chord of the vertical tail is calculated using the following expression. Since this arm is only associated with the VT, it is denoted by l_{VT}.

$$l_{VT}=\sqrt{\frac{2\cdot V_{VT}\cdot S\cdot b}{\pi(R_1+R_2)}} \tag{11-27}$$

DERIVATION OF EQUATION (11-27)

From Equation (11-14), we get:

$$S_{wet}=S_{wet\ FUS}(l_{VT})+S_{wet\ VT}(l_{VT})\approx\pi(R_1+R_2)\cdot l_{VT}+2\frac{V_{VT}\cdot S\cdot b}{l_{VT}}.$$

Then, differentiate this with respect to l_{VT}:

$$\frac{dS_{wet}}{dl_{VT}}=\frac{d}{dl_{VT}}\left(\pi(R_1+R_2)\cdot l_{VT}+2\frac{V_{VT}\cdot S\cdot b}{l_{VT}}\right)$$
$$=\pi(R_1+R_2)-\frac{2\cdot V_{VT}\cdot S\cdot b}{l_{VT}^2}$$

Set to zero and solve for l_{VT}:

$$\frac{dS_{wet}}{dl_{VT}}=0\ \Rightarrow\ l_{VT}^2=\frac{2\cdot V_{VT}\cdot S\cdot b}{\pi(R_1+R_2)}\ \Rightarrow\ l_{HT}=\sqrt{\frac{2\cdot V_{VT}\cdot S\cdot b}{\pi(R_1+R_2)}}.$$

EXAMPLE 11-2

Continue Example 11-1 by estimating the tail arm of the Cessna 172 Skyhawk using Method 2. Use the geometric values specified in the example as needed. Its actual $V_{VT}=0.0419$ and wingspan is $b=36.0\,\text{ft}$. Also, estimate the planform area and span of the vertical tail assuming its $AR_{VT}=1.35$.

SOLUTION:

Determine the optimum tail arm using Equation (11-27) (actual is $l_{VT}=15.5\,\text{ft}$):

$$l_{VT}=\sqrt{\frac{2\cdot V_{VT}\cdot S\cdot b}{\pi(R_1+R_2)}}=\sqrt{\frac{2\cdot(0.0419)\cdot(174)\cdot(36.0)}{\pi(2.0+0.5)}}=8.18ft$$

Use Equation (11-23) to calculate the planform area (actual value $S_{VT}=20.2\,\text{ft}^2$):

$$S_{VT}=\frac{V_{VT}\cdot S\cdot b}{l_{VT}}=\frac{(0.0419)\cdot(174)\cdot(36.0)}{(8.18)}=32.1\ \text{ft}^2$$

Use Equation (11-24) to calculate the span of the VT (actual value $b_{VT}=5.22\,\text{ft}$):

$$b_{VT}=\sqrt{AR_{VT}\times S_{VT}}=\sqrt{(1.35)\times(32.1)}=6.58\ \text{ft}$$

11.4.6 Method 3: Initial Tail Sizing Optimization Considering Horizontal and Vertical Tail

Many airplane configurations feature a HT and VT whose center of lift is close to one another (along the longitudinal axis). Thus, we really have a single tail arm for both. This



FIGURE 11-43 Method 3 applies to the Cessna 172P Skyhawk (left), while Method 1 (or 2) applies to the SOCATA TB-20 Trinidad (right). *Photos by Phil Rademacher.*

justifies a simultaneous optimization for both. The Cessna 172 in Figure 11-43 (left) is such an aircraft, while the SOCATA Trinidad (right) is not.

***Guidance*: Use this method if the location of the centroids of the HT and VT are expected to be relatively close to one another along the *x*-axis.**

Determination of Tail Arm for a Desired V_{HT} and V_{VT}

The distance between the wing's MGC quarter-chord and the quarter-chord of the horizontal *and* vertical tail is calculated using the following expression. Since this arm is associated with the HT and VT, it is denoted by l_T.

$$l_T = \sqrt{\frac{2 \cdot S(V_{HT} \cdot c_{MGC} + V_{VT} \cdot b)}{\pi(R_1 + R_2)}} \tag{11-28}$$

DERIVATION OF EQUATION (11-28)

From Equation (11-14), we get:

$$\begin{aligned} S_{wet} &= S_{wet\ FUS}(l_T) + S_{wet\ HT}(l_T) + S_{wet\ VT}(l_T) \\ &\approx \pi(R_1 + R_2) \cdot l_T + 2\frac{V_{HT} \cdot S \cdot c_{MGC}}{l_T} + 2\frac{V_{VT} \cdot S \cdot b}{l_T} \end{aligned}$$

Then, differentiate this with respect to l_T:

$$\begin{aligned} \frac{dS_{wet}}{dl_T} &= \pi(R_1 + R_2) - \frac{2 \cdot V_{HT} \cdot S \cdot c_{MGC}}{l_T^2} - \frac{2 \cdot V_{VT} \cdot S \cdot b}{l_T^2} \\ &= \pi(R_1 + R_2) - \frac{2 \cdot S}{l_T^2}(V_{HT} \cdot c_{MGC} + V_{VT} \cdot b) \end{aligned}$$

Set to zero and solve for l_T:

$$\begin{aligned} \frac{dS_{wet}}{dl_T} = 0 \quad &\Rightarrow \quad l_{VT}^2 = \frac{2 \cdot S(V_{HT} \cdot c_{MGC} + V_{VT} \cdot b)}{\pi(R_1 + R_2)} \\ &\Rightarrow \quad l_T = \sqrt{\frac{2 \cdot S(V_{HT} \cdot c_{MGC} + V_{VT} \cdot b)}{\pi(R_1 + R_2)}} \end{aligned}$$

EXAMPLE 11-3

Continue Examples 11-1 and 11-2 by estimating the tail arm of the Cessna 172 Skyhawk using Method 3. Use the geometric values specified in the previous examples as needed.

SOLUTION:

Determine the optimum tail arm using Equation (11-28) (actual is $l_{VT} = 15.5$ ft):

$$\begin{aligned} l_T &= \sqrt{\frac{2 \cdot S(V_{HT} \cdot c_{MGC} + V_{VT} \cdot b)}{\pi(R_1 + R_2)}} \\ &= \sqrt{\frac{2 \cdot (174) \cdot [(0.761)(4.83) + (0.0419) \cdot (36.0)]}{\pi(2.0 + 0.5)}} = 15.2ft \end{aligned}$$

Use Equations (11-20) and (11-23) to calculate the planform areas (actual value $S_{HT} = 41.4\,\text{ft}^2$ and $S_{VT} = 20.2\,\text{ft}^2$):

$$\begin{aligned} S_{HT} &= \frac{V_{HT} \cdot S \cdot c_{MGC}}{l_{HT}} = \frac{(0.761) \cdot (174) \cdot (4.83)}{(15.2)} = 42.2\ \text{ft}^2 \\ S_{VT} &= \frac{V_{VT} \cdot S \cdot b}{l_{VT}} = \frac{(0.0419) \cdot (174) \cdot (36.0)}{(15.2)} = 17.3\ \text{ft}^2 \end{aligned}$$

Use Equations (11-21) and (11-24) to calculate the span of the HT (actual value $b_{HT} = 11.3$ ft and $b_{VT} = 5.22$ ft):

$$\begin{aligned} b_{HT} &= \sqrt{AR_{HT} \times S_{HT}} = \sqrt{(3.0) \times (41.4)} = 11.25\ \text{ft} \\ b_{VT} &= \sqrt{AR_{VT} \times S_{VT}} = \sqrt{(1.35) \times (17.3)} = 4.84\ \text{ft} \end{aligned}$$

Of the three methods, Method 3 is by far the most suitable for an aircraft like the Cessna 172.

EXAMPLE 11-4

A small airplane is being designed with a twin tail boom configuration (see Figure 11-44). Derive an expression similar to Equation (11-28) for the drag optimized tail arm. Use R_1 and R_2 to represent the base and top radii of each boom and assume S_{VT} to represent to total VT area.

SOLUTION:

Following the same procedure, we define the total wetted area as follows. Note that we have *two* tail booms and not one as before. Therefore, note the slight change to Equation (11-14):

$$S_{wet} = 2 \cdot \pi(R_1 + R_2) \cdot l_T + 2\frac{V_{HT} \cdot S \cdot c_{MGC}}{l_T} + 2\frac{V_{VT} \cdot S \cdot b}{l_T} \tag{i}$$

Differentiate Equation (i) with respect to l_T:

$$\frac{dS_{wet}}{dl_T}=\frac{d}{dl_T}\left(2\pi(R_1+R_2)\cdot l_T+2\frac{V_{HT}\cdot S\cdot c_{MGC}}{l_T}+2\frac{V_{VT}\cdot S\cdot b}{l_T}\right)$$
$$=2\pi(R_1+R_2)-\frac{2\cdot S}{l_T^2}(V_{HT}\cdot c_{MGC}+V_{VT}\cdot b)$$

Set to zero to determine the optimum tail arm:

$$\frac{dS_{wet}}{dl_T}=0 \;\Rightarrow\; l_T^2=\frac{S(V_{HT}\cdot c_{MGC}+V_{VT}\cdot b)}{\pi(R_1+R_2)}$$
$$\Rightarrow\; l_T=\sqrt{\frac{S(V_{HT}\cdot c_{MGC}+V_{VT}\cdot b)}{\pi(R_1+R_2)}}$$

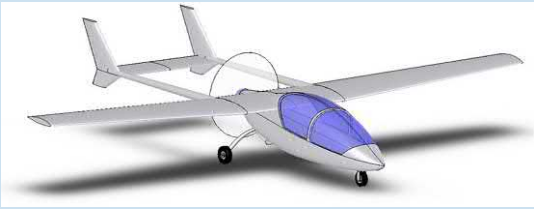


FIGURE 11-44 A small twin tail boom configuration.

11.4.7 Method 4: Initial Tail Sizing Optimization for an Arbitrary Fuselage

Fuselages featuring compound surfaces, e.g., low-drag tadpole fuselages, must be treated differently. Sailplane fuselages have a distinct contraction behind the cabin to reduce drag (see Figure 11-45). Thus, to calculate the wetted area of the fuselage, we must resort to Equation (11-17), repeated below for convenience.

$$S_{wet\ FUS}(l_T)=2\pi\int_0^{l_T} y\sqrt{1+(dy/dx)^2}\,dx \qquad (11\text{-}17)$$

It is to be expected that even shapes of simple geometry will result in unwieldy integrals. For instance, if we define the curve y in Figure 11-42 as $y=ax^2+bx+c$, the integral of Equation (11-17) becomes[2]

$$S_{wet\ FUS}(l_T)=2\pi\int_0^{l_T}(ax^2+bx+c)\sqrt{1+(2ax+b)^2}\,dx$$
$$=\frac{2\pi}{64a^2}\left[D\sqrt{1+D^2}\left(2D^2+16ac-4b^2+1\right)+\left(16ac-4b^2-1\right)\sinh^{-1}(D)\right]_0^{l_T}$$

where $D=2ax+b$. It is surely easier to use a numerical scheme to solve the integral. This is shown in the following step by step.



FIGURE 11-45 A Schleicher ASK-21 tandem seat sailplane in flight. *Photo by Phil Rademacher.*

STEP 1: Create a Curve to Describe Fuselage Tail boom Shape

As an example, a quadratic spline can be used to represent the curve y in Figure 11-42. It is of form

$$y=ax^2+bx+c \qquad (11\text{-}29)$$

To determine the coefficients a, b, and c, we need to specify the points $(0,R_1)$ and (l_T,R_2). We must also specify the slope, either at $x=0$ or $x=R_2$ (see Figure 11-46). If we want to specify the desired slope at $x=0$ using an angle θ_1, we can use the following matrix setup. The top equation captures $y=ax^2+bx+c=a(0)^2+b(0)+c=R_1$, the center one captures $y=ax^2+bx+c=a(l_T)^2+b(l_T)+c=R_2$, and the bottom one captures the slope, $y'=2ax+b=2a(0)+b=\tan(\theta_1)$:

$$\begin{bmatrix}0 & 0 & 1\\ l_T^2 & l_T & 1\\ 0 & 1 & 0\end{bmatrix}\begin{Bmatrix}a\\ b\\ c\end{Bmatrix}=\begin{Bmatrix}R_1\\ R_2\\ \tan\theta_1\end{Bmatrix} \qquad (11\text{-}30)$$

$$\text{Solving gives:}\quad y=\left(\frac{R_2-R_1-l_T\tan\theta_1}{l_T^2}\right)x^2+\tan\theta_1 x+R_1 \qquad (11\text{-}31)$$

Alternatively, if we want to specify the desired slope at $x=R_2$ using an angle θ_2, we can use the following matrix setup. It is created in a fashion like that of Equation (11-30). This form is better suited for tadpole fuselages, as setting $\theta_2=0$ gives a curve that is horizontal at $x=R_2$ (where the HT is located).

$$\begin{bmatrix}0 & 0 & 1\\ l_T^2 & l_T & 1\\ 2l_T & 1 & 0\end{bmatrix}\begin{Bmatrix}a\\ b\\ c\end{Bmatrix}=\begin{Bmatrix}R_1\\ R_2\\ \tan\theta_2\end{Bmatrix} \qquad (11\text{-}32)$$

$$\text{Solving gives:}\quad y=\left(\frac{R_1-R_2+l_T\tan\theta_2}{l_T^2}\right)x^2+\left(\frac{2R_2-2R_1-l_T\tan\theta_2}{l_T}\right)x+R_1 \qquad (11\text{-}33)$$

The designer should consider higher order polynomials (e.g., cubic or even quartic splines) for fuselages whose shapes are not captured with the quadratic spline.

[2] The integral was evaluated using the online integral solver by https://www.wolframalpha.com/.

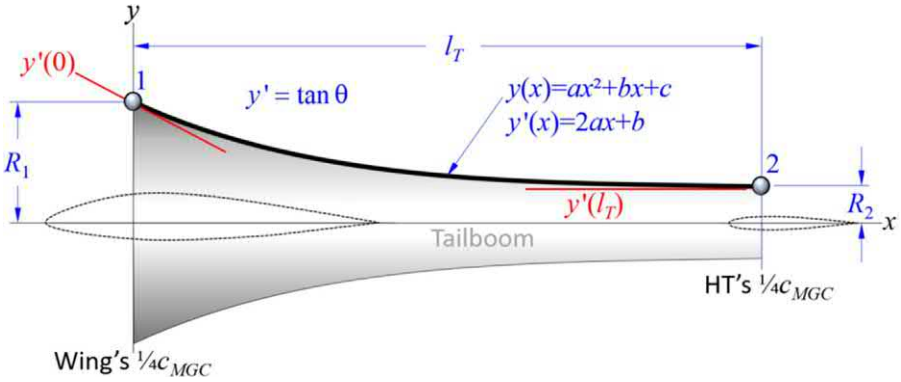


FIGURE 11-46 A quadratic spline used for curve y.

STEP 2: Create Spreadsheet and VBA Code

In this step, a spreadsheet is prepared where the optimum tail arm is determined. It is shown in Figure 11-47. A part of this step involves creating a VBA (*Visual Basic for Applications*) function to calculate the wetted area of the fuselage tail section. This is accomplished by transforming Equation (11-17) into a numerical form. This form breaks the fuselage into N–1 segment, whose

EXAMPLE 11-5

Estimate the optimum tail arm of the Cessna C-172 of Examples 11-1 through 11-3, using both the HT and VT volumes.

SOLUTION:

All geometric values used are those of Examples 11-1 through 11-3. The spreadsheet is prepared as shown in Figure 11-47 (left). Column l_T stores a range of tail arms to test. Column $S_{wet\ FUS}$ calculates the wetted area of tail section using the VBA function `AftFuselageSwet`. Columns $S_{wet\ HT}$ and $S_{wet\ VHT}$ calculates the wetted area of the HT and VT using Equations (11-18) and (11-19), respectively. Column S_{wet} sums up the three columns. The four columns are plotted in the graph of Figure 11-47 (right). This result suggests that if the C-172 were to feature a tadpole fuselage described by Equation (11-33), its minimum wetted area length should be 16 ft. Of course, this solution ignores the resulting fuselage neck-down would leave no space for the aft seats. The solution is interesting, nonetheless.

c_{MGC} =	4.83	ft	R_1 =	2	
b =	36	ft	R_2 =	0.5	
S =	174	ft²	θ_1 =	-10	
V_{HT} =	0.761		θ_2 =	0	
V_{VT} =	0.0419		Mode =	2	

l_T	S_{wet_FUS}	S_{wet_HT}	S_{wet_VT}	S_{wet}
ft	ft²	ft²	ft²	ft²
10.0	63.82	127.91	26.25	217.98
10.5	66.88	121.82	25.00	213.70
11.0	69.96	116.28	23.86	210.10
11.5	73.03	111.23	22.82	207.08
12.0	76.11	106.59	21.87	204.58
12.5	79.19	102.33	21.00	202.52
13.0	82.28	98.39	20.19	200.86
13.5	85.37	94.75	19.44	199.56
14.0	88.46	91.37	18.75	198.58
14.5	91.56	88.22	18.10	197.87
15.0	94.65	85.27	17.50	197.42
15.5	97.75	82.52	16.93	197.21
16.0	100.85	79.94	16.40	197.20
16.5	103.95	77.52	15.91	197.38
17.0	107.05	75.24	15.44	197.74
17.5	110.16	73.09	15.00	198.25
18.0	113.26	71.06	14.58	198.91

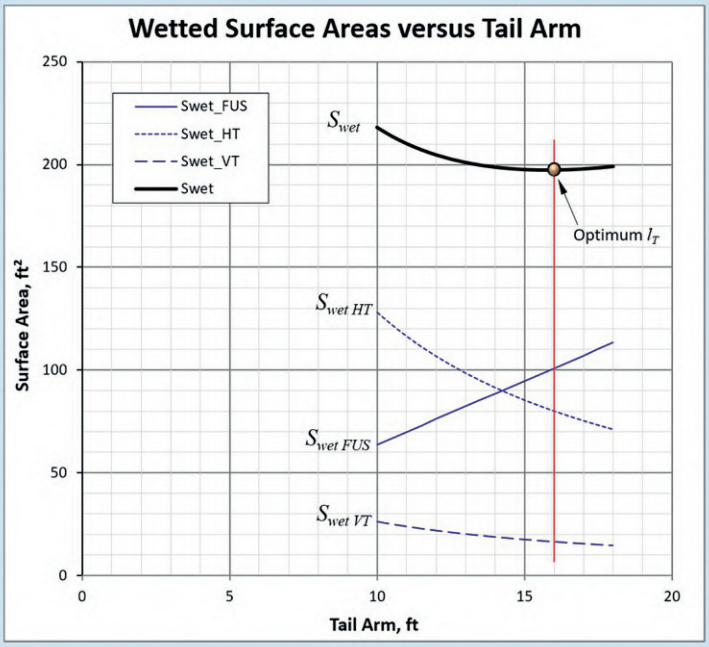


FIGURE 11-47 Frustum dimensions.

geometry is specified in Figure 11-42. Then, the surface area of each infinitesimal frustum is calculated by rotating the line segment ΔL around the x-axis. The radius of rotation is the average of the line-segment's endpoints above the x-axis, given by Y_i and Y_{i-1}:

$$\begin{aligned} S_{wet\ FUS} &= 2\pi \int_0^{l_T} y(x)\sqrt{1+\left(\frac{dy}{dx}\right)^2}\,dx \\ &\approx 2\pi \sum_{i=1}^{N-1} \frac{(Y_i + Y_{i+1})}{2}\Delta L \end{aligned} \tag{11-34}$$

where

$$\begin{aligned} \Delta X &= X_i - X_{i-1} \\ \Delta Y &= Y_i - Y_{i-1} \\ \Delta L &= \sqrt{\Delta X^2 + \Delta Y^2} \end{aligned} \tag{11-35}$$

The VBA function below accomplishes this work. It calculates the values in the spreadsheet of Figure 11-47 of Example 11-5. Details of its creation are presented in the example.

```
Function AftFuselageSwet(R1 As Single, R2 As Single, Theta_deg As Single, lt As Single, Mode As
Byte)
'This function calculates the surface area of a quadratic spline rotated about the x-axis.
'Its output is used to represent the surfaces area of a tadpole aft fuselage section.
'
'Initialize
    Dim a As Single, b As Single, c As Single
    Dim i As Integer, Pi As Single
    Dim deltaX As Single, deltaY As Single, deltaL As Single, deltaS As Single
    Dim X1 As Single, X2 As Single, Xstep As Single
    Dim Y1 As Single, Y2 As Single
    Dim Perimeter As Single, Swet As Single

'Presets
    Pi = 3.14159265358979
    Theta = Theta_deg * (Pi / 180)
    Select Case Mode
    Case 1 'Theta comes from point 1
        a = (R2 - R1 - lt * Tan(Theta)) / (lt ^ 2)
        b = Tan(Theta)
        c = R1
    Case 2 'Theta comes from point 2
        a = (R1 - R2 + lt * Tan(Theta)) / (lt ^ 2)
        b = (2 * R2 - 2 * R1 - lt * Tan(Theta)) / lt
        c = R1
    End Select

'Process
    X1 = 0
    Y1 = R1
    Xstep = 0.01 * lt
    For i = 2 To 100
        'Advance X
        X2 = X1 + Xstep

        'Compute Y2
        Y2 = a * X2 ^ 2 + b * X2 + c
        'Compute deltas
        deltaX = X2 - X1
        deltaY = Y2 - Y1
        deltaL = Sqr(deltaX * deltaX + deltaY * deltaY)      'Length of segment

        'Compute segment
        Perimeter = Pi * (Y1 + Y2)                           '=0.5*(Y1+Y2)*2*Pi
        deltaS = Perimeter * deltaL                          'Area of elemental frustum
        Swet = Swet + deltaS                                 'Add to the cumulative surface area

        'Exchange
        X1 = X2
        Y1 = Y2
    Next i

'Return
    AftFuselageSwet = Swet
End Function
```

EXERCISES

(1) You're working on a military jet trainer of $W_0 = 20{,}000$ lb_f, $S = 180\,ft^2$, $AR = 5.9$, and $\lambda = 0.5$. The width of the fuselage at the quarter-chord of the wing is 3.0 ft. The fuselage narrows in the back to a width of 1.0 ft. The horizontal tail is to be designed such its $AR_{HT} = 4$ and $\lambda_{HT} = 0.5$. Using the c_{MGC} as the reference chord, compute the tail arm that results in a minimum wetted area of the empennage structure (assuming a frustum shaped tail cone) by taking into account both vertical and horizontal tail volumes. (Hint: Consider Table 11-4.) Determine the optimized tail arm length (l_T), HT span (b_{HT}), HT root chord (c_{rHT}), and HT tip chord (c_{tHT}). (Ans: $l_T = 18.3$ ft, $b_{HT} = 12.3$ ft, $c_{rHT} = 4.12$ ft, and $c_{tHT} = 2.06$ ft)

References

[1] W.H. Cook, *Road to the 707: The Inside Story of Designing the 707*, William H. Cook, 1991.

[2] Source http://www.historylink.org/index.cfm?DisplayPage=output.cfm&file_id=2230. [Accessed 06/29/2020].

[3] M.J. Abzug, E.E. Larrabee, *Airplane Stability and Control: A History of the Technologies that Made Aviation Possible*, 2nd ed., Cambridge Aerospace Series, 2002.

[4] W.K. Kershner, *The Advanced Pilot's Flight Manual*, 6th ed., Iowa State University Press, 1994.

[5] Neihouse, Anshal I., Klinar, Walter J., and Scher, Stanley H., *Status of Spin Research for Recent Airplane Designs*, NASA TR R-57.

[6] W.J. Bihrle, B. Barnhart, *Spin prediction techniques*. AIAA J. Aircraft 20 (2), February 1983. https://doi.org/10.2514/3.44837.

[7] T.H. Kerr, *A Criterion for the Prediction of the Recovery Characteristics of Spinning Aircraft, A.R.C. CP-195*, 1955.

[8] A.I. Neihouse, J.H. Lichtenstein, P.W. Pepoon, *Tail-Design Requirements for Satisfactory Spin Recovery, NACA TN-1045*, 1946.

[9] A.I. Neihouse, *Tail-Design Requirements for Satisfactory Spin Recovery for Personal-Owner-Type Light Airplanes, NACA TN 1329*, 1947.

[10] I.I.I. Stough, H. Paul, J.M. Patton Jr., S.M. Sliwa, *Flight Investigation of the Effect of Tail Configuration on Stall, Spin, and Recovery Characteristics of a Low-Wing General Aviation Research Airplane, NASA TP-2644*, 1987.

[11] Source: https://bihrle.com/. [Accessed 07/01/2020].

[12] J.S. Bowman Jr., *Summary of Spin Technology as Related to Light General-Aviation Airplanes, NASA TN-D-6575*, December 1971.

[13] W.J. Klinar, T.L. Snyder, *Influence of Tail Length Upon the Spin-Recovery Characteristics of a Trainer -Type -Airplane Model, NACA TN-1764*, 1948.

[14] W.J. Klinar, J.H. Wilson, *Spin-Tunnel Investigation of the Effects of Mass and Dimensional Variations on the Spinning Characteristics of a Low-Wing Single-Vertical-Tail Model Typical of Personal-Owner Airplanes, NACA TN-2352*, 1951.

[15] L.J. Gale, I.P. Jones Jr., *Effects of Antispin Fillets and Dorsal Fins on the Spin and Recovery Characteristics of Airplanes as Determined from Free-Spinning-Tunnel Tests, NACA TN-1779*, 1948.

[16] L.J. Gale, *Effect of Landing Flaps and Landing Gear on the Spin and Recovery Characteristics of Airplanes, NACA TN-1643*, 1948.

[17] R.W. Stone Jr., S.M. Burk Jr., W. Bihrle Jr., *The Aerodynamic Forces and Moments on a l/lO-Scale Model of a Fighter Airplane in Spinning Attitudes as Measured on a Rotary Balance in the Langley 20-Foot Free-Spinning Tunnel, NACA TN-2181*, 1950.

[18] H.A. Lee, C.E. Libbey, *Incipient- and Developed-Spin and Recovery Characteristics of a Modern High-speed Fighter Design With Low Aspect Ratio as Determined From Dynamic-Model Tests, NASA TN D-956*, 1961.

[19] J.M. Patton Jr., H.P. Stough III, D.J. DiCarlo, *Spin Flight Research Summary, SAE-790565*, 1991.

[20] W. Letko, D. Riley, *Effect of an Unswept Wing on the Contribution of Unswept-Tail Configurations to the Low-Speed Static- and Rolling-Stability Derivatives of a Midwing Airplane Model, NACA TN-2175*, 1950.

[21] H.G. Wiley, W.C. Moseley Jr., *Investigation at High Subsonic Speeds of the Pressure Distribution on a 45° Sweptback Vertical Tail in Sideslip with a 45° Sweptback Horizontal Tail Mounted at 50-Percent and 100-Percent Vertical Tail Span, NACA RM-L54I08*, 1954.

[22] D.R. Riley, *Effect of Horizontal-Tail Span and Vertical Location on the Aerodynamic Characteristics of an Unswept Tail Assembly in Sideslip, NACA TR-1171*, 1954.

[23] V. Pajno, S. Design, *A Guide for Students and Designers*, IBN Editore, 2010.

[24] Source: http://aviation-safety.net/wikibase/wiki.php?id=20519 [Accessed 07/01/2020]

[25] Source: https://aviation-safety.net/wikibase/55302. [Accessed 07/01/2020].

[26] Source: http://aviation-safety.net/database/record.php?id=19631022-0. [Accessed 07/01/2020].

[27] Source: http://aviation-safety.net/database/record.php?id=19660603-1. [Accessed 07/01/2020].

[28] Anonymous, The Rudlicki Vee Tail, Aircr. Eng. IV (37) March 1932 63–64.

[29] R.O. Schade, *Effect of Geometric Dihedral on the Aerodynamic Characteristics of Two Isolated Vee-Tail Surfaces, NACA TN-1369*, 1947.

[30] E.C. Polhamus, R.J. Moss, *Wind Tunnel Investigation of the Stability and Control Characteristics of a Complete Model Equipped with a Vee Tail, NACA TN-1478*, 1947.

[31] P.E. Purser, J.P. Campell, *Experimental Verification of a Simplified Vee-Tail Theory and Analysis fo Available Data on Complete Model with Vee Tails, NACA R-823*, 1944.

[32] Source: http://www.airdisasters.co.uk/. [Accessed 07/01/2020].

[33] J. Serryer, *Albessard Triavion Aircraft, NACA AC-89*, 1929.

[34] D.J. Roskam, *Lessons Learned in Aircraft Design – The Devil is in the Details*, DARcorporation, 2018.

[35] E. Kendall, *The Aerodynamics of Three-Surface Airplanes, Aircraft Design and Operations Meetings*. AIAA, 1984. https://doi.org/10.2514/6.1984-2508.

[36] D.R. Satran, *Wind-Tunnel Investigation of the Flight Characteristics of a Canard General-Aviation Airplane Configuration, NASA TP-2623*, 1986.

[37] G.C. Furlong, J.G. McHugh, *A Summary and Analysis of the Low-Speed Longitudinal Characteristics of Swept Wings at High Reynolds Numbers, NACA TR-1339*, 1957.

[38] J.A. Shortal, B. Maggin, *Effect of Sweepback and Aspect Ratio on Longitudinal Stability Characteristics of Wings at Low Speeds, NACA TN-1093*, 1946.

[39] K.P. Spreemann, *Design Guide for Pitch-Up Evaluation and Investigation at High Subsonic Speeds of Possible Limitations due to Wing-Aspect-Ratio Variations, NASA TM-X-26*, 1959.

CHAPTER

12

The Anatomy of the Fuselage

OUTLINE

12.1 Introduction 517
12.1.1 The Content of This Chapter 517
12.1.2 The Function of the Fuselage 517

12.2 Fundamentals of Fuselage Shapes 519
12.2.1 The Frustum Shaped Fuselage 519
12.2.2 The Pressure Tube Fuselage 519
12.2.3 The Tadpole Fuselage 519

12.3 Sizing the Fuselage 521
12.3.1 Initial Design of the External Shape of the Fuselage 521
12.3.2 Refining the External Shape of the Fuselage 525
12.3.3 Internal Dimensions of the Fuselage 526
12.3.4 Cockpit Layout 527

12.4 Estimating the Geometric Properties of the Fuselage 529
12.4.1 Simple Estimation of the Surface Area of a Body of Revolution 530
12.4.2 Fundamental Properties of Selected Solids 531
12.4.3 Surface Areas and Volumes of a Typical Tubular Fuselage 533
12.4.4 Surface Areas and Volumes of a Tadpole Fuselage 534
12.4.5 Surface Areas and Volumes of a Pod-Style Fuselage 535

12.5 Additional Information 535

References 539

12.1 INTRODUCTION

The purpose of the fuselage is multifaceted. It provides volume for occupants and freight, it serves as an aerodynamically efficient protection from the elements, and it joins the wing and stabilizing surfaces. This chapter focuses on the design of the fuselage.

12.1.1 The Content of This Chapter

- Section 12.2 discusses three elementary fuselage shapes commonly used in aircraft design, the frustum, tubular, and tadpole. The section presents a range of information on the pros and cons of each that will help with the selection, although the tubular shape is usually default geometry for pressurized and nonpressurized passenger transport aircraft.
- Section 12.3 presents a simple method to sketch a fuselage for a GA aircraft. While there are many ways to accomplish initial fuselage sizing, this method forces the CG range and wing position to be considered from the beginning; an approach that quickly reveals unexpected problems with airplane passenger and payload combinations.
- Section 12.4 presents simple methods to estimate geometric properties of typical fuselage shapes.
- Section 12.5 presents typical dimensions for humans (male and female) that are helpful for the internal design of fuselages. It also tabulates the internal dimensions of several aircraft.

12.1.2 The Function of the Fuselage

The function of the fuselage is uniquely diverse. Among factors that affect the design of the fuselage are:

(1) The fuselage structure must provide adequate load paths for the attachment of lifting surfaces, engines, and landing gear and be able to react the large loads they generate.

https://doi.org/10.1016/B978-0-12-818465-3.00012-4

Copyright © 2022 Elsevier Inc. All rights reserved.

(2) Amenities (lavatories and galleys) must be provided for the occupants in large aircraft. Such aircraft should have at least 1 lavatory per 50 passengers and 1 galley per 100 passengers.

(3) Such aircraft should offer sufficient personal space to each person, enabling passengers and cabin crew members to move around with ease (e.g. access to lavatory, galley, and emergency egress).

(4) The cockpit should be ergonomically laid out, regardless of airplane size. Primary instruments and controls should be within reach of the pilot. The pilot should not have to lean or stretch when reaching for those.

(5) Windscreen shape and strength requirements dictate the forward part of the airplane. This depends on airplane geometry and operational requirements (e.g. pressurization, bird strike, etc.).

(6) Layout of emergency exits. 14 CFR Part 121.291 requires all manufacturers of passenger aircraft with seating capacity greater than 44 to demonstrate it can be completely evacuated in less than 90 s.

(7) Layout of control, electrical, and other important systems: The fuselage structure must accommodate control cables, pushrods, pulleys, and wiring harnesses. These must bypass critical structural members and not penetrate them. Control system should be anchored to stiff structural members.

(8) The fuselage should offer compartments to carry baggage and freight. These should be easily accessible. Such compartments must also be accessible from the outside in large aircraft. The fuselage must provide structure to allow baggage to be tied down to prevent it from shifting in flight, altering the CG. This structure must be stout enough to react emergency landing loads.

(9) The multiple openings required for easy access into and out of the fuselage create stress concentrations. Since doors are usually not intended to transfer axial and shear loads (except in pressurized vessels, where they transfer out-of-plane pressurization loads) the openings must be reinforced to reduce stress levels and minimize the structural deformation. Some pressurized aircraft feature pressurized baggage compartments that allow a safe transportation of animals. This increases the empty weight of the vehicle and forces the designer to objectively justify their presence: are they necessary or just desirable?

(10) If landing gear loads are reacted by the fuselage (in contrast to the wing) stout hoop frames around the landing gear are required. Such landing gear retracts into special aerodynamically shaped housing on the bottom of the fuselage. Volume must be provided in the forward fuselage for the nose landing gear. It is good practice to examine existing aircraft of similar configurations when evaluating the pros and cons of a design direction.

(11) The fuselage must also provide structure for wing attachment. Commuter aircraft usually feature high or low wing configurations. Mid-wing commuters are unknown in modern times—the most recent one was the HFB-340 Hansajet, designed in the 1960s and was operated until the early 1970s. Besides reduced drag, it is hard to justify mounting the wing in the middle of the passenger cabin of such aircraft. High wing aircraft typically feature hard points on the main and rear spars that allow the fuselage to be hung below them. Examples of such aircraft are the Shorts SD3–30, Fokker F-27, and F50 twin-turboprop commuter aircraft. The main spar of the last two penetrates the ceiling inside the cabin; a protective spar cover in the cabin ceiling is clearly noticeable upon entry. This is undesirable, although only very tall people must lower their head to avoid hitting the ceiling material that covers the spar.

(12) Low wing aircraft may have the fuselage mounted on top of the spar, although a reinforced spar box under the cabin floor is more common.

(13) Externally, the fuselage must accommodate an external wing root fairing to prevent separation of air flowing through the juncture. Depending on the aircraft, wing root fairings can be massive and require an internal support structure on its own.

(14) Some fuselages carry engines, typically in the front or back. This is very common for small single engine aircraft, but also for selected twin engine aircraft. Most small propeller aircraft utilize a tractor configuration, while there are also several pusher configurations (see Chapter 4). The Cessna 337 Skymaster and Adam A500, both feature two engines; as a tractor and pusher. Regardless of engine configuration, a *firewall* is required between the engine and the cabin (see Section 7.2.6 and 14 CFR Part §23.1191, *Firewalls*).

(15) Other fuselages carry jet engines internally or externally. An internally mounted engine must be surrounded by fireproofing and fail-safe structure. The fireproofing must protect the primary structure from engine fire. Requirements are given by 14 CFR Part §23.1195, *Fire extinguishing systems*. The failsafe structure is necessary in case fragments from a rotor-burst penetrate the primary structure. Primary systems in the aircraft must also be redundant, for instance, a rotor burst cannot take out the primary flight control system and if it does there should be a secondary control system to allow the aircraft to continue flying.

12.2 FUNDAMENTALS OF FUSELAGE SHAPES

This section discusses three fundamental shapes of the fuselage: frustum, tubular, and tadpole. The designer should recognize the pros and cons of each configuration.

12.2.1 The Frustum Shaped Fuselage

The *frustum fuselage* is used to describe a fuselage aft section that is shaped like a *frustum* (a *trapezoidal prism*). In geometry, a frustum is the portion of a cone that lies between two parallel planes cutting it. Here, in interest of simple classification, it is extended to any prism with walls of simple flex (see Figure 5-1). Such a fuselage is shown in Figure 12-1. It is also associated with welded space-frame fuselages. They are easily recognizable by their tapered box-like appearance (see Figure 12-24), although the term frustum refers to a tapered cylinder. Frustum fuselages are common to manufacturers like Beechcraft, Cessna, and Piper. They are inexpensive to produce because of structural simplicity. They are made from folded sheet metal (simple flex) riveted to frames, which produce a light and stiff structure. Their drawback is greater drag than tadpole fuselages. The configuration is the right choice for roomy, inexpensive, stiff, and strong fuselages, where drag is not an issue, but internal volume is. It is ideal for utility transport aircraft, for instance feeder aircraft for package services. However, if the goal is an aerodynamically efficient aircraft, a frustum-shaped fuselage is the wrong choice. Such fuselages are indicative of aircraft design philosophy of the yesteryear and, today, are primarily justified by reduced production costs.



FIGURE 12-1 A Piper PA-28 Cherokee featuring a conventional frustum style fuselage. *Photo by Phil Rademacher.*

12.2.2 The Pressure Tube Fuselage

The *pressure tube fuselage* is used to describe a cylindrical fuselage, with a tubular main section and capped ends (see Figure 12-2). The fuselage is ideal for passenger aircraft, small and large, pressurized or not, of any airspeed range. The circular cross-section is the most efficient structurally for reacting pressure loads (see Section 5.3.4). For typical dimensioning, the fuselage can be split into three regions: forward (nose), center cylinder (cabin), and aft (tail). If the diameter of the center cylinder is d_{fus}, then the forward section ranges from $1.45d_{fus}$ to $1.75d_{fus}$. The length of the empennage ranges from $3d_{fus}$ to $3.35d_{fus}$ for most airplanes. The tail fineness ratio (length/diameter) has the least drag, as shown in Section 16.3.6.

12.2.3 The Tadpole Fuselage

The term *tadpole fuselage* describes a fuselage whose empennage and forward portion resembles the shape of a *tadpole*, the larval stage of a frog (see Figure 12-3). If made from aluminum, tadpole fuselages are more expensive to produce than frustum fuselages. The reason



FIGURE 12-3 A Rolladen-Schneider LS4 sailplane boasts a tadpole style fuselage. *Photo by Phil Rademacher.*

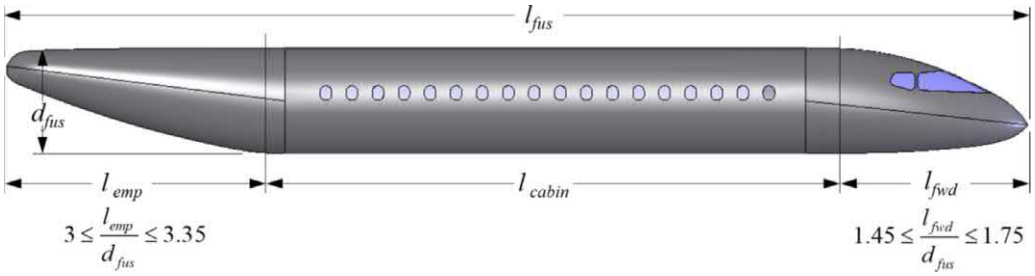


FIGURE 12-2 A schematic of a pressure tube fuselage, showing typical lengths of the forward and aft sections in terms of the fuselage diameter.

is the extent of compound surfaces that require expensive metal forming processes. It is less costly to produce tadpole fuselages using composites and this remains the primary method used for this purpose. All modern sailplanes feature a tadpole fuselage shape, as well as several modern GA aircraft. Among those are the Cirrus SR20 and SR22, the Diamond DA-20 Katana, DA-40 Diamond Star, and DA-42 TwinStar.

Galvao [1] pointed out the advantages of fuselages shaped like fish by citing examples from nature. He used the superposition of sources and sinks to represent and evaluate the aerodynamic properties of such fuselages. He used what is called the *three-halves power law* to determine the ratio between width and height of a fuselage and discussed means of converting an airfoil silhouette into a 3-dimensional fuselage. While not a tadpole shape, the resulting fuselage resembles a short tadpole.

Althaus [2] was one of the first to investigate the properties of the tadpole fuselage. Dodbele et al. [3] use a surface singularity analysis method to help design such fuselages. Radespiel [4] presents the effect of proper contraction geometry (called *waisting*) on the transition region and the drag of the fuselage, supported by wind tunnel testing. There is a plethora of literature on tadpole fuselages available for the interested reader, although presenting the details of it all is beyond the scope of this book.

Tadpole fuselages generate far less drag than the frustum kind for two primary reasons: (1) Their forward portion is shaped to sustain laminar boundary layer, and (2) their empennage shape results in as much as 30% –40% less wetted area. Per reference [2]:

1. Like laminar airfoils, the front part of the body should produce favorable pressure gradients in all meridians, even at incidences of about ±10 degrees. The whole surface should be smooth and leak free to avoid any disturbances to the laminar flow.
2. Behind the transition front, it is favorable to contract the cross-section. On one hand, this reduces the wetted surface; on the other hand, it shifts the unavoidable pressure rise to the thinner parts of the turbulent boundary layer, which is a well-known principle of favorable boundary layer control.

Althaus compared three tadpole style fuselages to a frustum fuselage of equal length and diameter, whose fineness ratio was 10. Both shapes were representative of those used for sailplanes (see Figure 12-4). The study revealed an important difference in the transition front (the curve along which laminar-to-turbulent transition takes place) and their drag characteristics. As shown in the figure, the minimum drag coefficient (based on the frontal area) of the fuselage at a Reynolds Number of 7.1×10^6 is 0.034 for the tadpole and 0.0505 for the frustum (at an AOA of 0 degree). This means the drag of the frustum is 48.5% greater than that of the tadpole, explaining why such fuselages have become the norm in modern sailplane design.

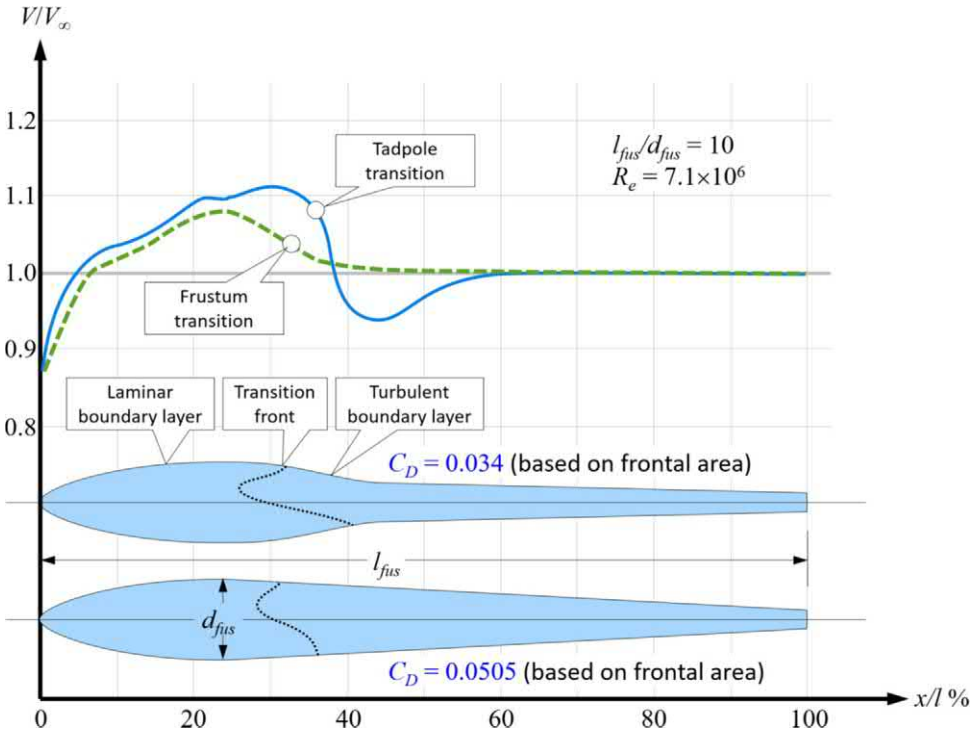


FIGURE 12-4 Difference in transition and total fuselage drag of a tadpole and frustum fuselages. The drag of the tadpole fuselage is 67% of that of the frustum fuselage. *Based on Althaus, D., NASA CR-2315, Motorless Flight Research, Edited by James L. Nash-Webber, 1972.*

The tadpole design requires careful attention to the curvature of the geometry aft of the maximum thickness. Too sharp a contraction separates the flow, increasing the fuselage drag. Too small a contraction does not reduce the wetted area enough to make a dent in the drag. The contraction in Figure 12-4 reduces the local airspeeds (relatively speaking) in an area where the turbulent boundary layer is still relatively thin. This helps to prevent an early separation. This region is analogous to the pressure recovery region of an NLF airfoil. The goal is to maintain laminar boundary layer as far aft as possible, but once the maximum thickness has been exceeded, give air enough distance to slow down without flow separation.

Another aspect of tadpole fuselage design is the downward tilt of the fuselage, shown in Figure 12-5. This is a response to the upwash caused in the airflow ahead of the wing. Before the tilt is implemented, the forward fuselage is subject to higher AOA than after, and this increases its drag. Some even tilt the tail boom down or reshape it to better match the flow field behind the wing as well. A flow-adaption design of this nature should only be performed using CFD technology or wind tunnel testing.

12.3 SIZING THE FUSELAGE

The initial design of the fuselage should be implemented once the wing and stabilizing surfaces have been sized. This is followed by the positioning of the most important components (such as engines and landing gear) payload (passengers and freight), considering any dimensional restriction. Finally, the *outside mold line* (OML) of the fuselage can be drawn to encompass the entire layout. This process allows for modifications and shifting of components to ensure the CG will remain within reasonable margins.

12.3.1 Initial Design of the External Shape of the Fuselage

This author refrains from using statistical methodologies to estimate the physical dimensions of the fuselage design, as these are limited to specific shapes and do not consider space claim conflicts. For instance, how will an engine's width × height × length affect the fuselage OML? What about the head of an occupant? Will it remain entirely inside of the airplane or be exposed to the airstream? Space claim problems must be tackled during the fuselage design to prevent them from surfacing later, when they are harder to solve. The following process helps.

A proper sizing of the complete aircraft requires awareness of the following axiom:

(1) To fly, an aircraft's *center-of-gravity position* (X_{CG}) must remain inside its CG-envelope. The actual CG-position depends on the *empty weight CG-position* (X_{CGe}).

(2) When the aircraft is loaded with fuel, freight, and occupants, X_{CG} is shifted to a new position. As the aircraft consumes fuel during flight, X_{CG} gradually shifts to a new position. These positions *must always remain inside the CG-envelope*.

(3) While X_{CG} must remain inside the CG-envelope during flight, X_{CGe} does not have to. However, it must move inside the CG-envelope as soon as *minimum*

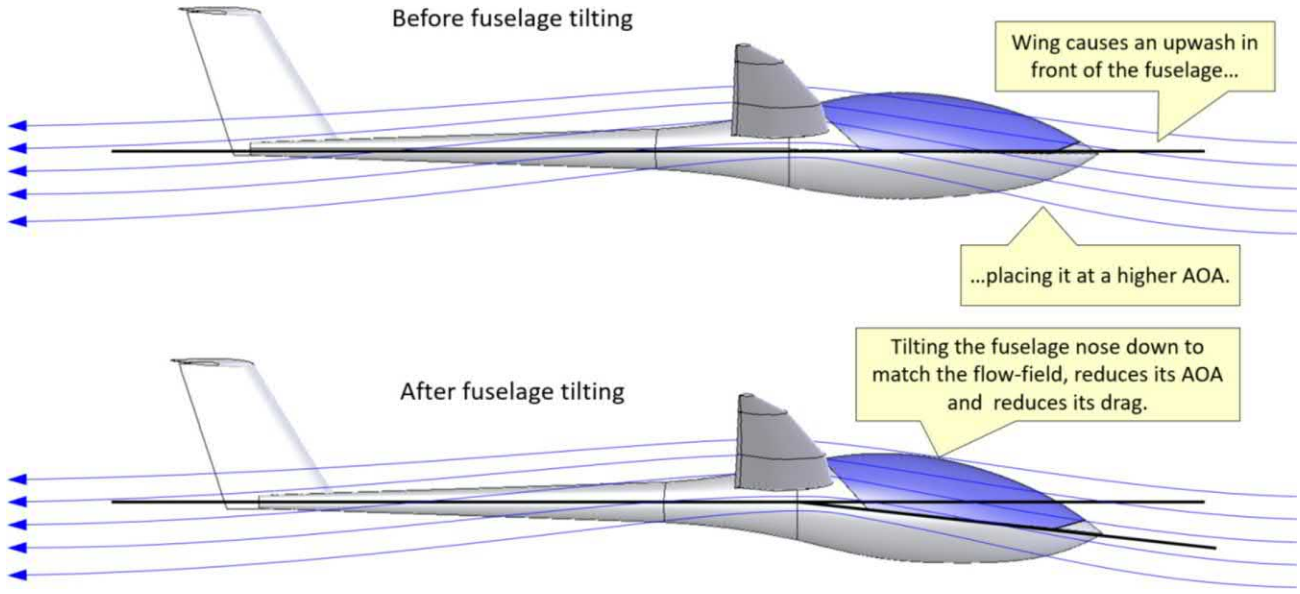


FIGURE 12-5 Reduction of drag by aligning the fuselage with the oncoming airflow. *Adapted from Thomas, F., Fundamentals of Sailplane Design, College Park Press, 1999.*

flying weight (W_{min}) is achieved. W_{min} for small aircraft is given by $W_{min} = W_e + W_{cmin}$, where W_e is empty weight and W_{cmin} is minimum crew weight (e.g. 100 lb_f).

STEP 1 – Establish Wing and HT Dimensions: Complete the sizing of the wing and HT using information gathered from Steps 1 through 9 in Table 1.4. These data should be detailed enough to provide the span and chords of the wing and stabilizing surfaces and their location with respect to the wing's $c_{MGC}/4$ (see Figure 12-6). Convert the resulting dimensions into a visual form. Figure 12-6 represents the aerodynamic requirement of the design.

STEP 2 – Coplot Desired CG-envelope: Indicate the desired CG envelope on the MGC (see Figure 12-7). The CG envelope for conventional aircraft may range from 15% to 35% MGC. At this point, the final CG envelope remains unknown because far more detailed analysis remains to be done. However, we must start somewhere, and this is a reasonable first step. Regard the wing as a fixed component.

STEP 3 – Establish X_{CGe}, W_e, and X_{CG},W: Estimate the weight of all known components constituting the airplane, e.g. using the methods of Section 6.4. Also include all fuel, freight, and occupants to account for gross weight (W). Tabulate the weights in your favorite spreadsheet software, by entering them in a column format. The next column should be the x-location of the expected CG-position of each of the components. The next column should list the product $x_i \cdot W_i$, where i is index. Then, sum these two columns to estimate W_e and X_{CGe} (e.g., per Example 6.9).

STEP 4 – Co-Plot Components: Plot symbols representing components and X_{CGe}, as shown in Figure 12-8. Note that we do not yet know if this CG location is viable—this is evaluated in STEP 5.

STEP 5 – Evaluate Component Positions: Using trial and error, moving selected components, occupants, and freight around, representing forward and aft CG limits are established. Either must be inside the desired CG limits (see Figure 12-9). This process should be supported by a *loading cloud*, like the one described in Section 6.7.3, ideally using the spreadsheet tabulation from the previous step. Plot the resulting CG-positions on the figure as shown in Figure 12-9. If most CG-locations fall outside the limits, try to modify X_{CGe} by moving selected components to a new location. However, the location of the wing must remain fixed.

HT and VT should not be changed unless necessary. If the HT or VT is moved to a different location, the resulting tail arm (l_T) will change as well: The *horizontal* and *vertical tail volumes* (denoted by V_{HT} and V_{VT}) change also. Therefore, the geometry of the HT and VT should be updated to ensure the V_{HT} and V_{VT} remain constant. This, in turn, affects their weight, which, again, affects the CG. (Welcome to the world of aircraft design.) The process is made much easier by using a spreadsheet that automatically updates the necessary variables.

Some components only require a small nudging, while others require a large relocation. It is more effective to move

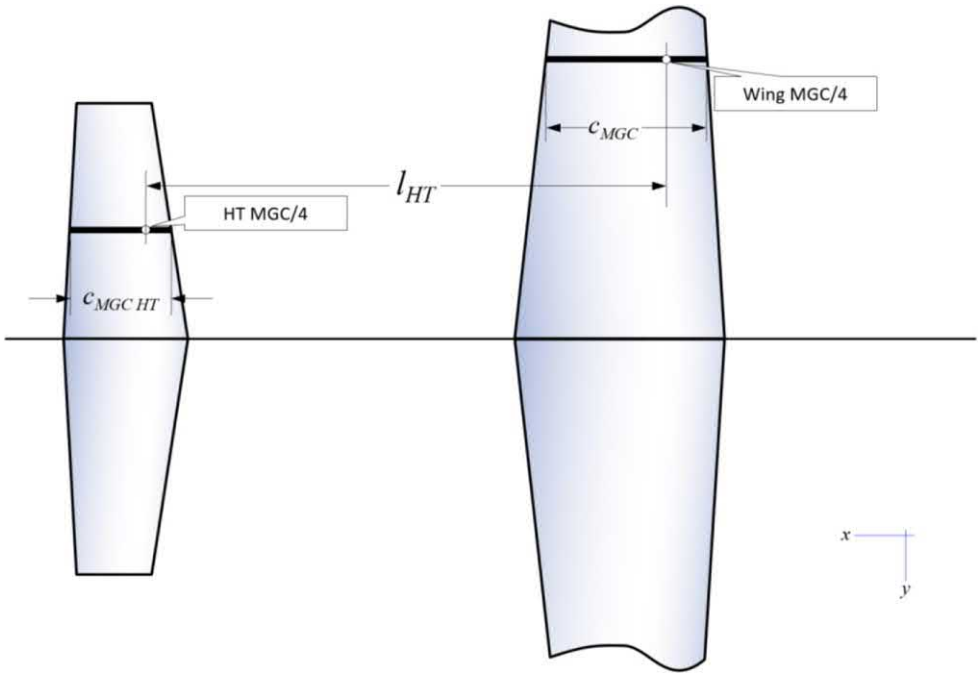


FIGURE 12-6 In STEP 1, the lifting surfaces are drawn to scale and separated by the correct tail arm *lT*.

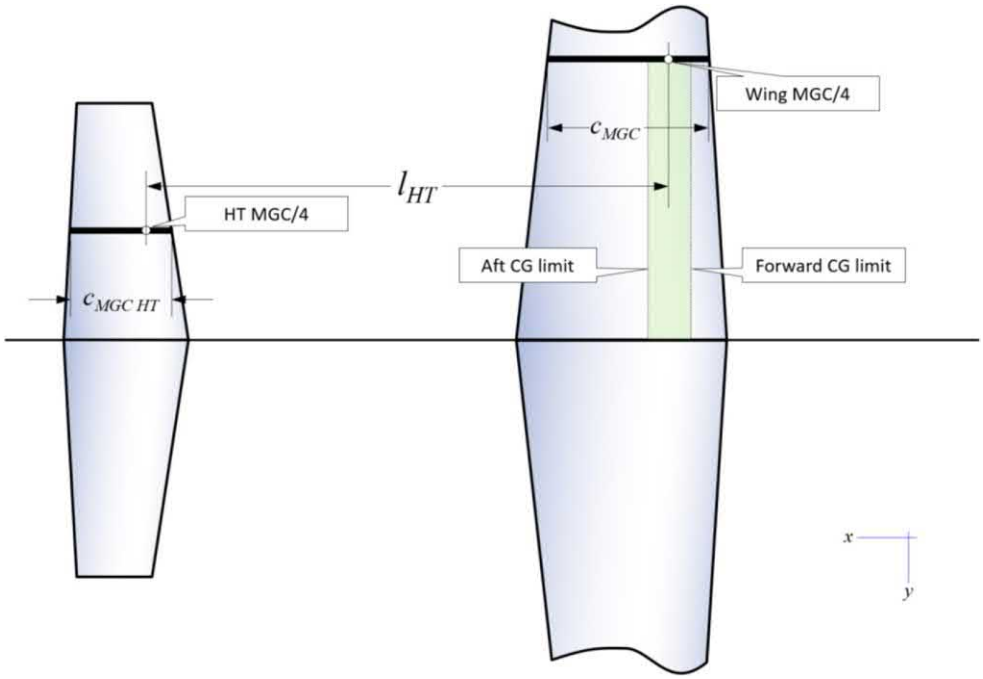


FIGURE 12-7 In STEP 2 the expected CG limit around the quarter-chord of the wing's MGC is labeled.

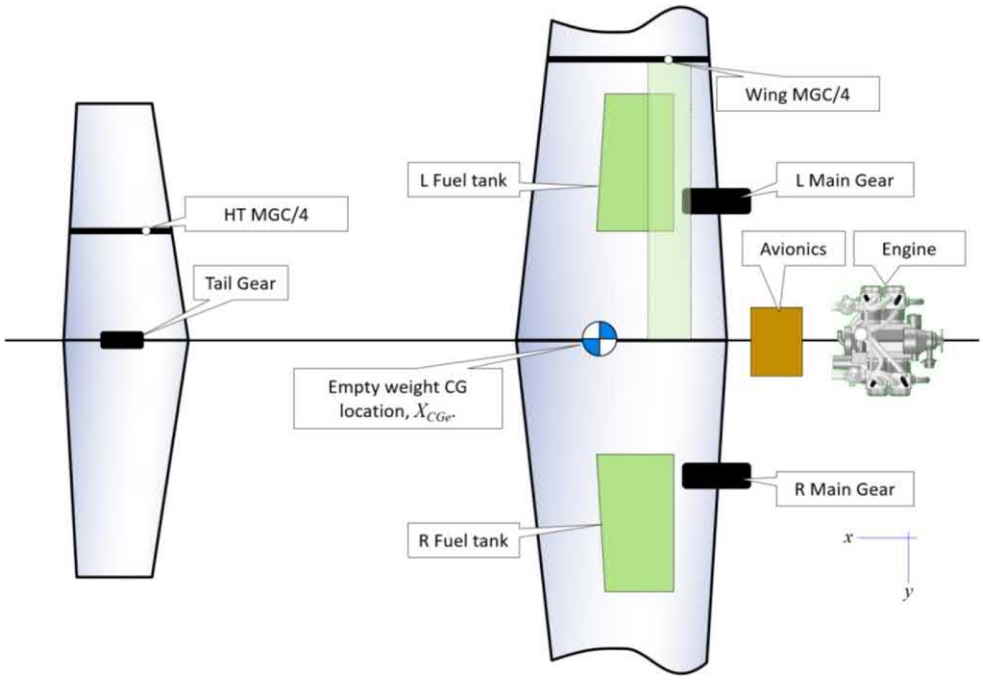


FIGURE 12-8 In STEP 4 all major components constituting the predicted empty weight of the aircraft are placed in their proper location. The *XCGe* is indicated on the drawing.

heavy components. While tedious, this process is necessary to prevent future "surprises" once the airplane has been developed further and making changes has become much harder. It is to be expected that components end up in "interesting" or "surprising" locations, necessitated by placing the CG loading cloud in its proper location.

STEP 6 – Dimension and Sketch Fuselage: Upon completion of STEP 5, indicate the positions of occupants and components on the diagram. Trace a rudimentary fuselage that encloses occupants and internal components, keeping in mind its aerodynamic and aesthetic appearance (see Figure 12-10). This effectively concludes the

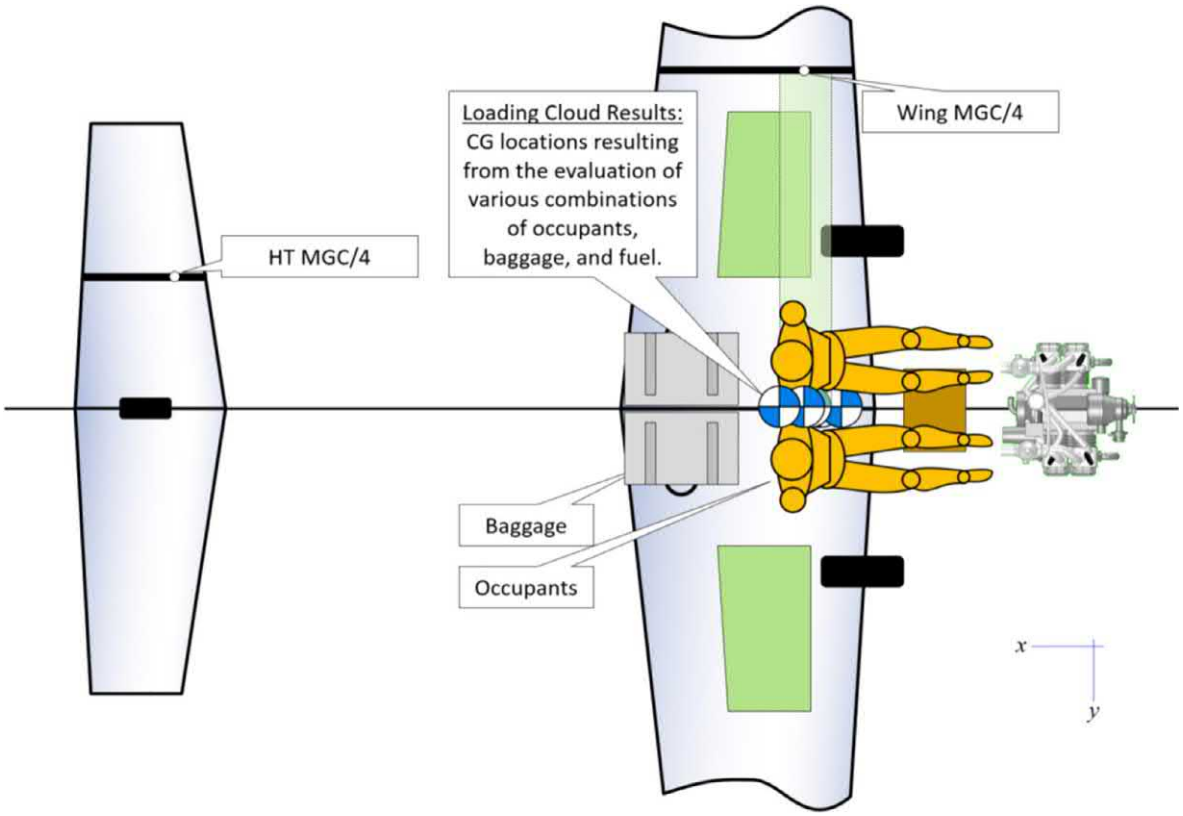


FIGURE 12-9 In STEP 4 occupants, baggage, engine, and other known "heavy" components are moved (or nudged) around until the CG loading cloud is mostly placed within the desired CG limits.

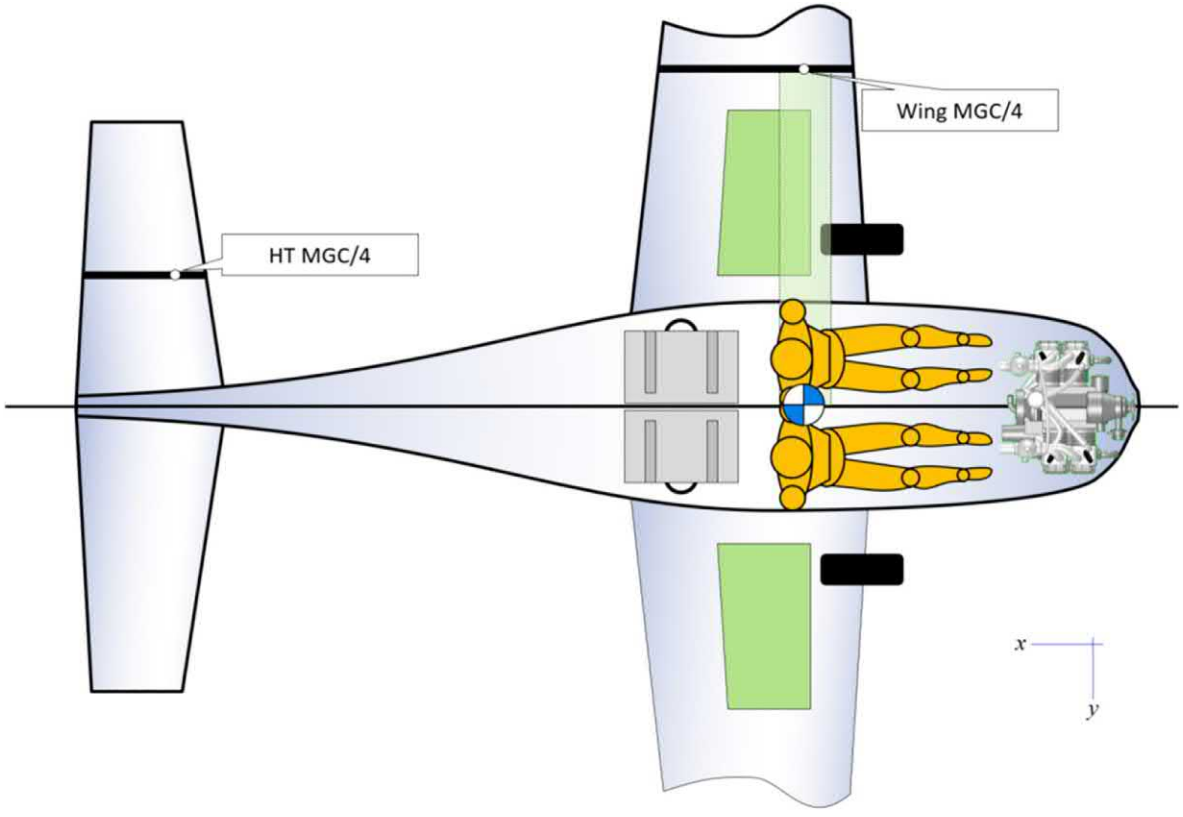


FIGURE 12-10 STEP 6 is the final step. With the approximate dimensions of internal parts known, trace the outline of the fuselage around, using a tadpole or other desired fuselage shape.

initial definition of the fuselage and it is now possible to begin refining it by considering other requirements it must satisfy.

12.3.2 Refining the External Shape of the Fuselage

Once the initial design of the fuselage is complete, consider these refinement steps.

(1) The fuselage should be made as streamlined as possible. It should feature an appropriate forward shape that minimizes stagnation regions. Consider the effect of fineness ratio (empennage length/diameter) on drag when shaping its aft geometry. The ideal fineness ratio is between 3 and 3.35 (see Figure 12-2).

(2) The tail upsweep angle must be considered to guarantee the airplane can rotate for T-O and flare for landing with the selected landing gear layout (see Figure 12-11). Assuming compressed landing gear at gross weight, aim for upsweep that allows rotation close to its clean stall AOA (see Figure 12-12). Designers of passenger aircraft consider growth potential: If future growth demands a fuselage enlargement, will a redesign effort be required to modify the empennage for ground clearance? The value of such forethought is shown in Figure 12-12.

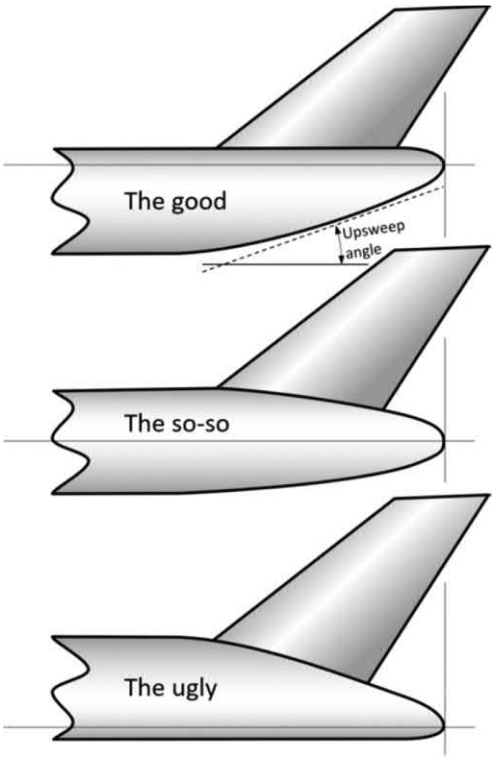


FIGURE 12-11 Upsweep is necessary.

(3) Designers of small composite airplanes should consider a tadpole shape as they generate less drag than conventional frustum type fuselages. Airplanes made from aluminum frequently use the frustum shape, as a tadpole fuselage requires compound surfaces. Larger aircraft normally do not feature tadpole shapes as it reduces the available internal volume.

(4) The external cabin area of the fuselage must consider the airframe thickness in addition to the desired internal dimensions. If pressurized, the designer should strongly consider a pressure tube fuselage, as it is structurally the most efficient for this purpose. Unpressurized fuselages are not subject to such constraints.

(5) Be cognizant of structural load paths when laying out openings for doors and windows. Consider the small aircraft in Figure 12-14. The frame to which the windscreen mounts (often called *A-pillar*) should be placed close to the expected position of the wing's main spar. This allows it to become a part of the airframe unit already required to react the wing loads. There is a caveat though: this position may restrict the pilot's field-of-view (FOV). Fuselage windows should provide convenient FOV for passengers. Windows should be distributed to fall between hoop frames. These are usually placed at even intervals.

(6) The location of the wing (high, mid, low, and parasol) must be considered when refining the external fuselage, as well as the possible shape of the wing root fairing. The maximum fuselage width tends to be where the wing joins the fuselage. Think about how this affects the geometry of the wing root fairing.

(7) Jet engines buried in the fuselage influence its external geometry in important ways. Space claims of inlet and exhaust must be clearly defined. The volume reserved for the engine is out of reach for other systems. It is a common mistake to locate equipment near such a volume, later to discover it penetrates engine volume.

(8) Consider the placement of avionics, battery, hydraulic system, control system, etc. Consider access for maintenance crews. Collector tanks are placed inside the fuselage, typically between the main spar and aft shear web.

(9) Finally, this food-for-thought advice: Many people find it appealing when an aircraft "leans a little" on the nose-gear on the ground. Of course, this is purely subjective—it is akin to people's views on the aesthetic of T-tails or winglets. Regardless, even if the designing team agrees with this view, this is not always practical. For instance, many tractor propeller aircraft must comply with prop-strike requirements and designing around this aesthetic view could

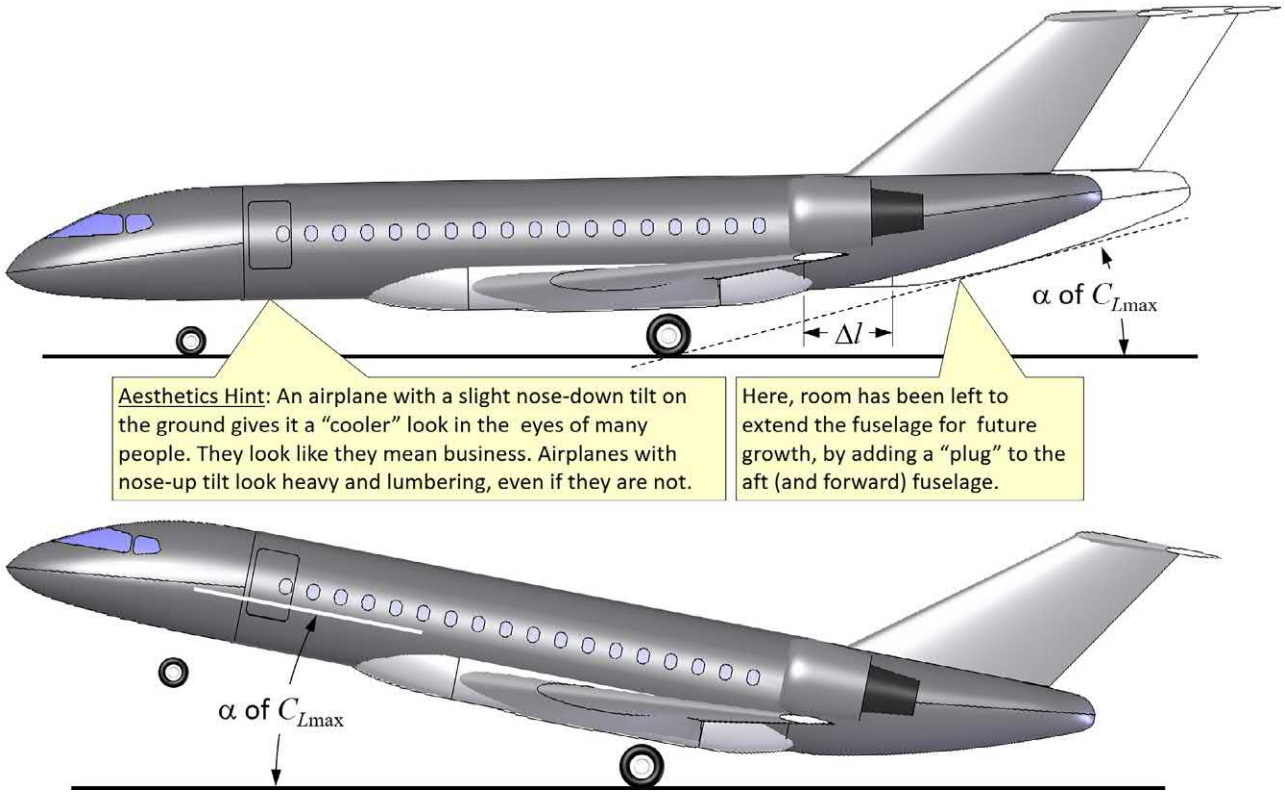


FIGURE 12-12 The fuselage should allow the airplane to rotate to an angle close to that of the AOA of its $C_{L_{max}}$, although it is also prudent to think about growth.

require excessively long main landing gear legs. Examples of aircraft that have an improved look (admittedly in the author's opinion) are the Rockwell OV-10 Bronco, the Lockheed P-3C Orion, and the Grumman Gulfstream II. Examples of the opposite are the Piper Cherokee Six and the Beech A36 Bonanza. Not surprisingly both are tractor propeller aircraft.

12.3.3 Internal Dimensions of the Fuselage

The designer must be aware of the constraints the human body places on the external shape. Figure 12-13 shows three cross-sections intended for a side-by-side seating. When comes to occupant comfort, the ones on the left and right provide ample headroom, whereas the center one does not. Added comfort requires increased diameter of the center fuselage, perhaps at least as what is indicated by the dashed circle.

For GA aircraft several regulations apply to the design of the crew and passenger areas. Prior to the "new Part 23" the following regulations (from the "old Part 23") considered the accommodation of occupants and cargo. They remain an acceptable means of compliance:

Personnel and Cargo Accommodations

§23.771 – *Pilot compartment.*
§23.773 – *Pilot compartment view.*
§23.775 – *Windshields and windows.*
§23.777 – *Cockpit controls.*
§23.779 – *Motion and effect of cockpit controls.*
§23.781 – *Cockpit control knob shape.*
§23.783 – *Doors.*
§23.785 – *Seats, berths, litters, safety belts, and shoulder harnesses.*
§23.787 – *Baggage and cargo compartments.*
§23.791 – *Passenger information signs.*
§23.803 – *Emergency evacuation.*
§23.805 – *Flightcrew emergency exits.*
§23.807 – *Emergency exits.*
§23.811 – *Emergency exit marking.*
§23.812 – *Emergency lighting.*
§23.813 – *Emergency exit access.*
§23.815 – *Width of aisle.*
§23.831 – *Ventilation.*

Pressurization
§23.841 – *Pressurized cabins.*
§23.843 – *Pressurization tests.*

Fire Protection
§23.851 – *Fire extinguishers.*
§23.853 – *Passenger and crew compartment interiors.*
§23.855 – *Cargo and baggage compartment fire protection.*

Among factors that should be considered during the design of the fuselage are:

(1) Typical passenger space (width × depth × height) is 22 × 43 × 65 in. (56 × 109 × 165 cm).
(2) A stand-up cabin featuring an aisle, should offer width × height of 20 × 76 in. (51 × 193 cm). This allows passengers to move around freely and for beverage

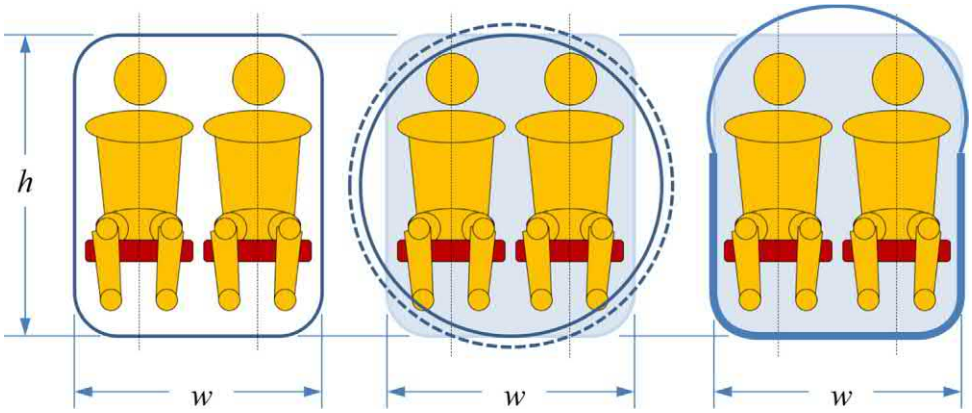


FIGURE 12-13 Cross-sections of a fuselage for a small airplane reveals headroom problems.

carts to fit comfortably. These aisle widths are minimums per 14 CFR §23.815, *Width of aisle*.

(3) Even though federal regulations assume an average of 170 lb_f per passenger, the modern passenger weighs closer to 200 lb_f.

(4) A lavatory and food provisions should be provided for missions that exceed 1 h. Assume one lavatory per 1–50 passengers and 1 galley per 50–100 passengers. A 50-passenger Fokker F-50 has a single lavatory and a ½-galley. A 150-passenger Boeing 737 typically has three lavatories (one in front, two in the back) and two galleys (front and back).

(5) The cockpit size depends on the aircraft. Primary and secondary controls should be within reach, although they should be separated from each other. Details of equipment layout in cockpit design are beyond the scope of this text.

(6) Passenger and crew emergency exits must be provided in accordance with 14 CFR 23.

12.3.4 Cockpit Layout

The term *accommodation* refers to both the passenger cabin and the cockpit (flight deck). General dimensions for the cabin of a small, side-by-side (or single) seat aircraft are shown in Figure 12-14. It is based on general internal dimensions of Cessna 150/152. It accommodates most people but should be considered a minimum by modern standards. Figure 12-15 shows the cabin with a 95th percentile mannequin. It offers very limited headroom for a tall individual. A design review should improve that detail.

Minimum recommended width and height for a small aircraft is shown in Figure 12-16. The height assumes upright seating. Sailplanes are exempted from the height requirement, as upright seating increases their frontal area and, thus, drag. The cabin width should allow at least 20″ (50 cm) per person. Less width can make a part of the population claustrophobic and is too narrow for the stout pilot. Cabin dimensions for several aircraft are provided in Table 12-5.

(1) Pilot Visibility

Pilot visibility is of paramount importance in manned aircraft design. Certified GA aircraft must comply with 14 CFR §23.773, *Pilot compartment view*. The recommended Field-of-View (FOV) for a typical GA aircraft is shown in Figure 12-17. The cost of good FOV is reduced structural integrity.

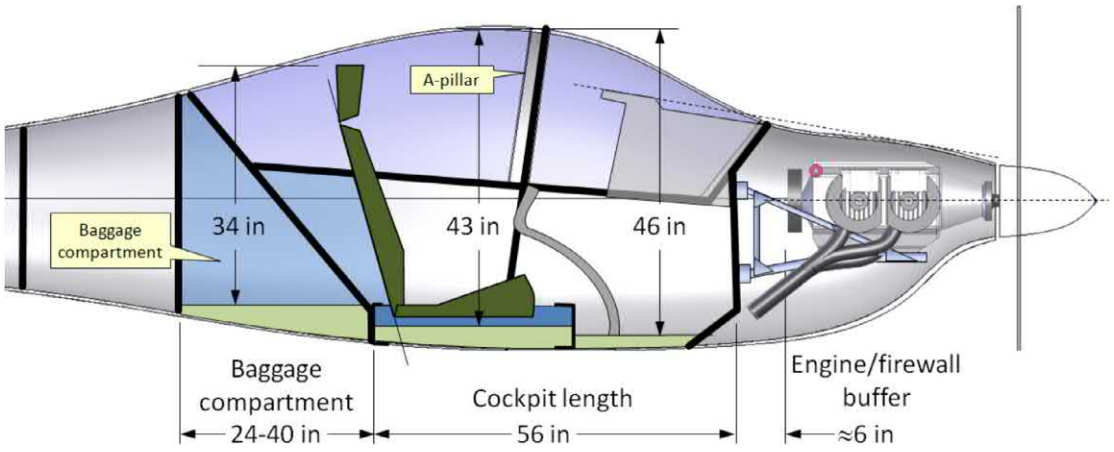


FIGURE 12-14 General cabin layout for a small airplane. The dimensions are typical.

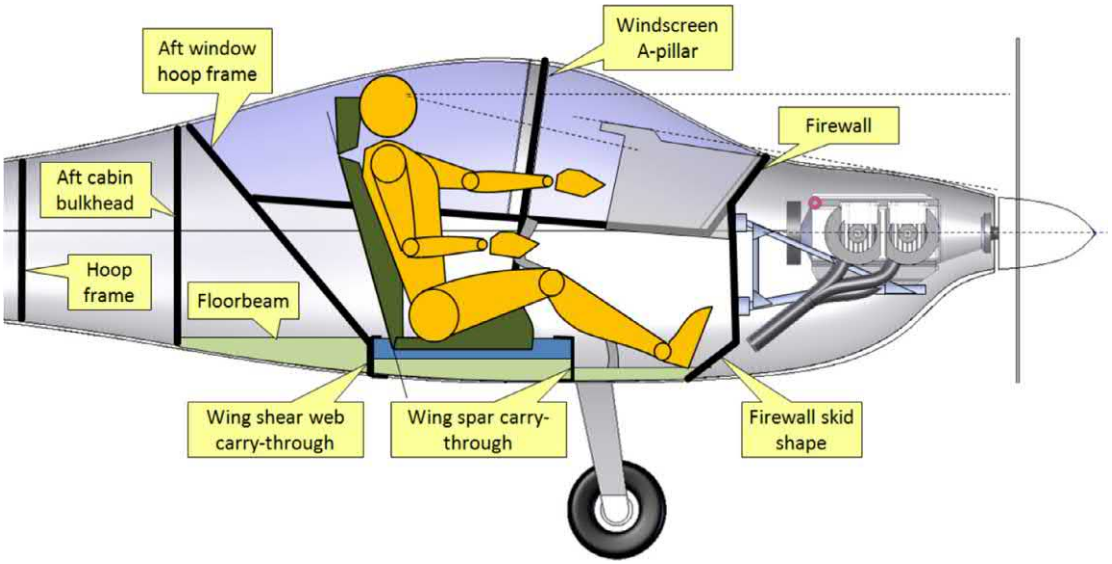


FIGURE 12-15 General accommodation of a large person (95th percentile) in the cabin of a small aircraft. A good fit that also accommodates smaller pilots is a challenge and should be studied in detail before the final loft for a Proof-of-Concept aircraft is released.

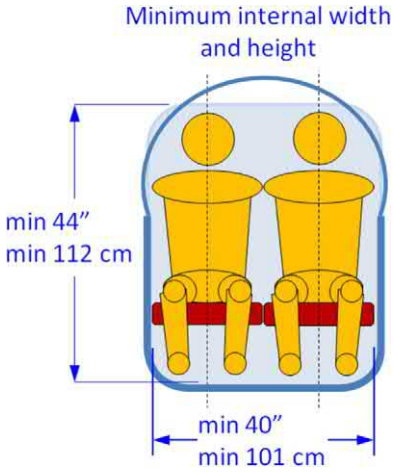


FIGURE 12-16 Minimum cabin dimensions.

(2) Transparencies

Transparencies are usually made from two kinds of plastics: acrylics or polycarbonate. Acrylics is a thermoplastic polymer and is both light and clear to look through. It allows more than 90% of external light to get through. It is the choice for nonpressurized aircraft. It allows complicate geometries to be formed with ease, by heating the material in molds. The primary drawback is cracking, which may start due to imperfections and, if left to its own devices, will continue to propagate.

Stretched acrylics refers to acrylics that is physically stretched using special machinery. This reorients the long polymer chains, improving the properties of the plastic. Among those are improved tensile stress (of the order of 10,000 psi) and reduced crack propagation. This makes the material suitable for bird proof windshields and enables its use in pressurized aircraft.

Polycarbonate is a specialized plastic considered the strongest transparent plastic available. It offers outstanding toughness, temperature tolerance, and impact resistance. It is ideal for windscreens subjected to bird strikes at high airspeeds, such as low flying fighter aircraft. Its primary drawback is the formation of a network of small cracks, called *crazing*. This requires the application of a protective coating. Polycarbonate is not used for GA aircraft. Typical dimensions for various cabin layouts are shown in Figure 12-18.

(3) Large Aircraft

It should not have to be stated that the design of the cockpit of a large aircraft is a monumental undertaking that requires volumes to present. While most of the cockpit design is really a task taken on during the detail design phase, it is imperative the external shape of the aircraft allows an ergonomically efficient cockpit to be designed. An example of a spacious cockpit is shown in Figure 12-19.

(4) General Passenger Cabin Layout

Jenkinson et al. [5] cite common separation (pitch) between seat rows in the passenger cabin of typical commuter or commercial aircraft. These are shown in Figure 12-20. An example of the luxurious spacing between passenger seats in a business jet is shown in Figure 12-21. While that comfort is out of reach for most people, it is presented here to contrast the opposite extreme presented in Figure 12-16.

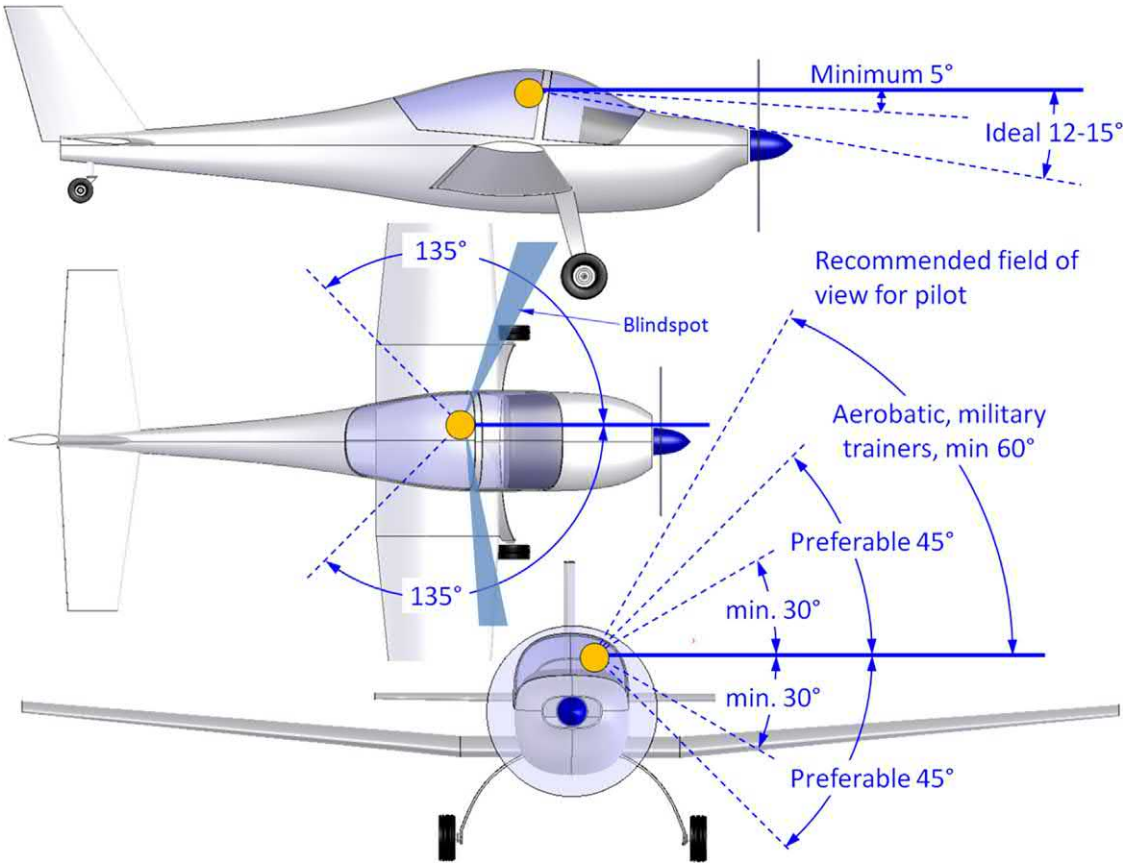


FIGURE 12-17 Recommended pilot's Field-of-View.

(5) Special Considerations: Galley Design

A galley is a kitchen in an aircraft. It is where food, liquids, ice-cubes, and beverage carts are stored. It allows hot beverages to be brewed and it contains ovens that are used to reheat chilled meals for passengers. Furthermore, it contains cabinets for dry goods and duty-free goods. The galley is usually purchased from a vendor. The production and installation of galleys is accomplished by numerous engineering companies. Several provisions must be made in the region of the fuselage where the galley is to be placed. First, it should always be next to a service door. Such doors allow a galley service truck to park outside the galley for a rapid removal and replenishing of food and beverage carts, as well as trash. Second, plumbing for a sink is needed. Third, electric outlets capable of powering several ovens simultaneously must be provided. Fourth, structural provisions to anchor the galley equipment must be present. These must react substantial inertia loads per 14 CFR §23.561(b)(3) (3.0 g upward, 18.0 g forward, and 4.5 g sideways). A galley is only offered in larger multiengine passenger aircraft.

(6) Special Considerations: Lavatory Design

Just like the galley, lavatory equipment is also engineered and produced by specialized vendors. Such equipment consists of a sink and a faucet, a counter, mirror, lighting, soap dispensers, amenity racks, and of course the toilet itself. The lavatory is a fully functional module that can be installed anywhere in the aircraft, provided some preparations have been made. The lavatory consists of a centralized waste tank that connects to the toilets using small pipes. It allows the waste tank to be emptied in a single place, rather than for each individual toilet. Modern toilets use a *vacuum flush* technology that does away with the recirculation of the blue-chemical flush liquid of the yesteryear. Such toilets are lighter and environmentally friendlier than the old generation toilet (Figure 12-22).

12.4 ESTIMATING THE GEOMETRIC PROPERTIES OF THE FUSELAGE

Early in the design process, details for a precise calculation of surface areas and volumes are not available.

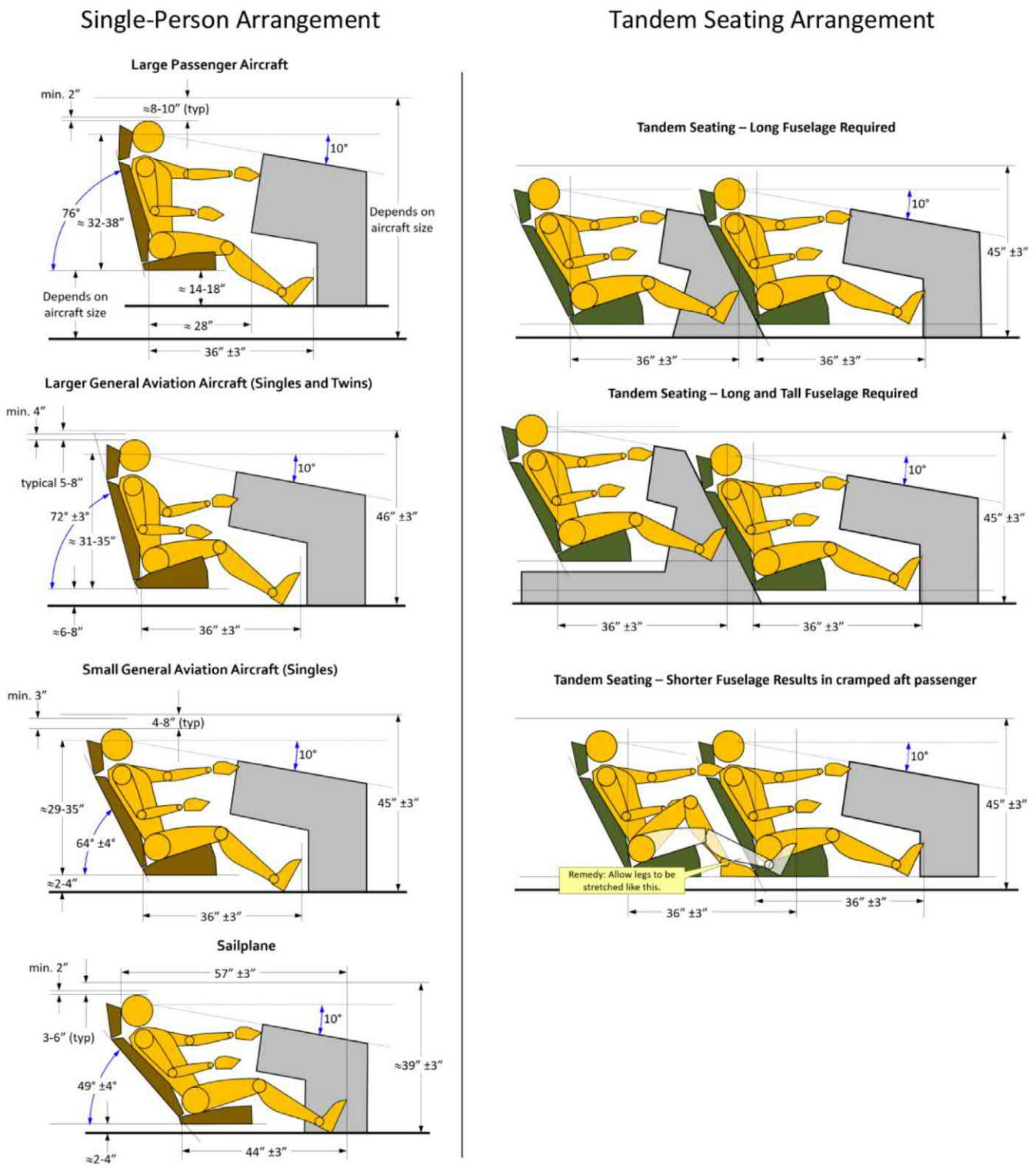


FIGURE 12-18 Typical seating for cockpit layout.

Thus, we must resort to approximations. If we know the fuselage length and average diameter, it is possible to estimate the basic geometric properties using simple shapes that are spliced to resemble the aircraft. This section presents several such shapes and handy formulas to estimate their surface area and volume.

12.4.1 Simple Estimation of the Surface Area of a Body of Revolution

The fastest way to estimate the wetted area of a fuselage uses the areas of the side- and top-silhouettes. This is based on the notion that the surface area of an elliptic

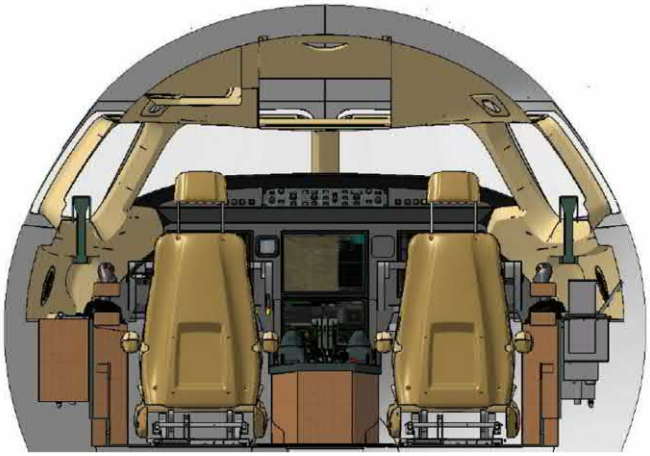


FIGURE 12-19 Cockpit layout in a large business jet, here the Dassault 7X. *Courtesy of Dassault Falcon Jet Corporation.*

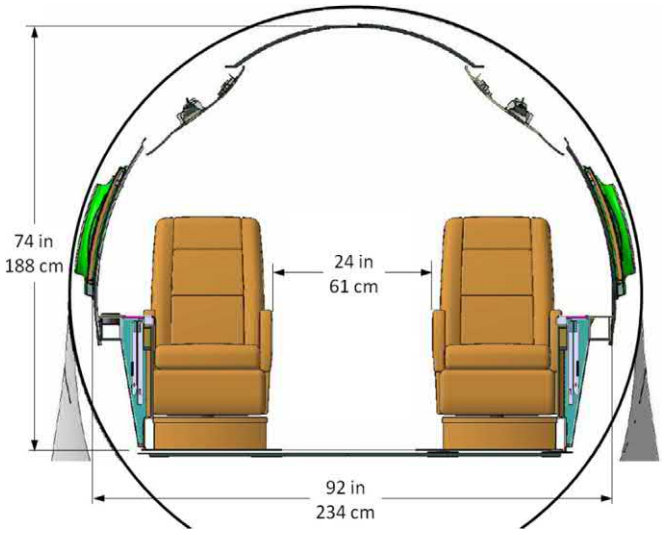


FIGURE 12-21 Cabin layout in a Dassault 7X business jet. *Courtesy of Dassault Falcon Jet Corporation.*

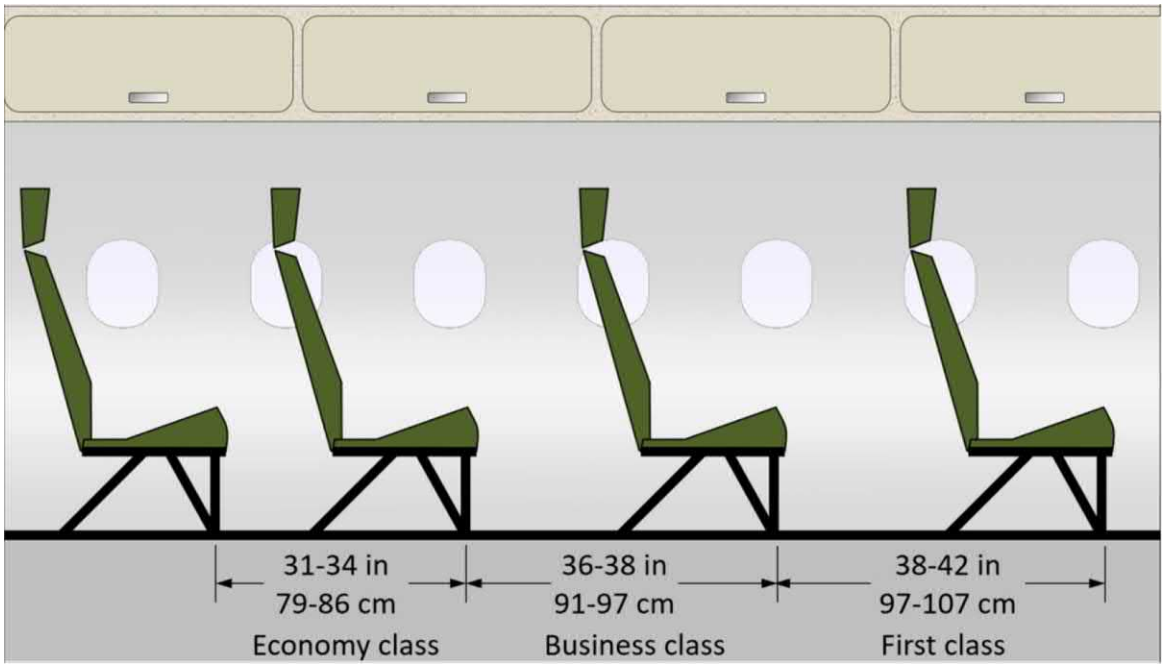


FIGURE 12-20 Typical pitch of seats in a commuter or commercial aircraft. *Based on Jenkinson, L.R., Paul, S., Rhodes, D., Civil Jet Aircraft Design, Arnold Publishers, 1999.*

cylinder can be estimated using the average of the major and minor widths times its length (Figure 12-23).

$$\text{Surface area}: \qquad S_{FUS} = \pi\left(\frac{A_{side} + A_{top}}{2}\right) \qquad (12\text{-}1)$$

12.4.2 Fundamental Properties of Selected Solids

A more complex formulation for typical aircraft fuselage is based on segmenting it into simple geometric shapes such as the ones shown in Figure 12-24. This section presents formulas to determine the properties of various fuselage geometric types.

The advantage of this method is acceptable accuracy for more geometrically complicated fuselages. However, its formulation is more complicated than that of the previous method. Note that volume is denoted using the symbol $\forall$ to avoid confusing it with V used for velocity.

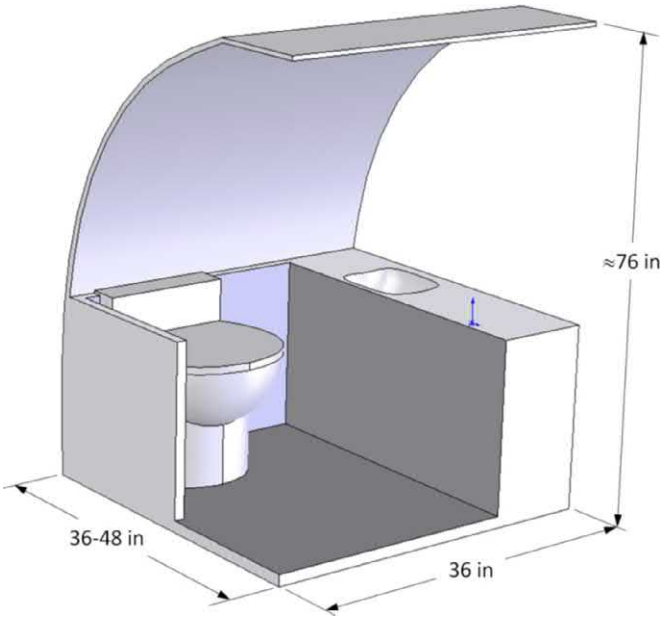


FIGURE 12-22 Space claims of a typical aircraft lavatory.

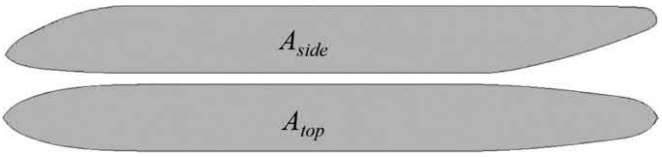


FIGURE 12-23 The wetted area of a body-of-revolution can be approximated using the areas of its side and top silhouettes.

(1) Elliptic Cylinder (excludes base and top)

Surface area: $$S_{EC} = \frac{\pi}{2}(D_1 + D_2)\left(1 + \frac{3h}{10 + \sqrt{4 - 3h}}\right)L$$

where $$h = \left(\frac{D_1 - D_2}{D_1 + D_2}\right)^2 \qquad (12.2)$$

Volume: $$\forall_{EC} = \frac{\pi}{4} D_1 \cdot D_2 \cdot L \qquad (12\text{-}3)$$

(2) Uniform Cylinder ($D = D_1 = D_2$) (excludes base and top)

Surface area: $$S_{UC} = \pi DL \qquad (12\text{-}4)$$

Volume: $$\forall_{UC} = \frac{\pi}{4} D^2 L \qquad (12\text{-}5)$$

(3) Paraboloid (excludes base)

Surface area: $$S_P = \frac{\pi D}{96L^2}\left[\left(D^2 + 16L^2\right)^{3/2} - D^3\right] \qquad (12\text{-}6)$$

Volume: $$\forall_P = \frac{\pi}{8} D^2 L \qquad (12\text{-}7)$$

(4) Cone (excludes base)

Surface area: $$S_C = \frac{\pi}{4} D\sqrt{D^2 + 4L^2} \qquad (12\text{-}8)$$

Volume: $$\forall_C = \frac{\pi}{12} D^2 L \qquad (12\text{-}9)$$

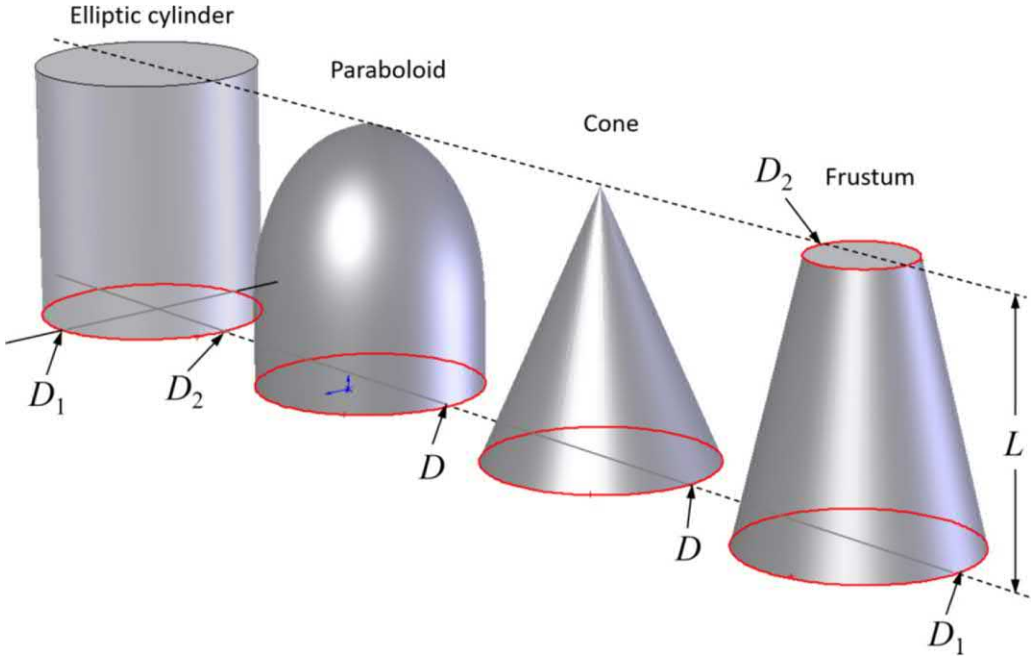


FIGURE 12-24 Elementary solids of equal height L.

(5) Frustum (excludes base and top)

$$\text{Surface area}: S_F = \frac{\pi}{2}\left(\frac{D_1 + D_2}{2}\right)\sqrt{D_1^2 - 2D_1D_2 + D_2^2 + L^2} \tag{12-10}$$

$$\text{Volume}: \quad \forall_F = \frac{\pi}{12}\left(D_1^2 + D_1D_2 + D_2^2\right)L \tag{12.11}$$

(6) Test Values

To minimize the risk of an error when entering these in a spreadsheet or other computer codes, the validation values in Table 12-1 are provided for the reader for comparing own calculations.

12.4.3 Surface Areas and Volumes of a Typical Tubular Fuselage

The following geometry can be used to estimate the geometric properties of a generic passenger transport aircraft. The geometry combines a paraboloid, cylinder, and cone, featuring the dimensions shown in Figure 12-25. Each section height, which here conveniently is described using the component length, is denoted by an appropriate subscript. The fundamental dimension D (diameter) is the same for all sections.

$$\text{Total length}: \quad L_{fuse} = L_1 + L_2 + L_3 \tag{12-12}$$

Surface area:

$$S_{fuse} = \pi D\left[\frac{\left(D^2 + 16L_1^2\right)^{3/2} - D^3}{96L_1^2} + L_2 + \frac{\sqrt{D^2 + 4L_3^2}}{4}\right] \tag{12-13}$$

$$\text{Volume}: \quad \forall_{fuse} = \frac{\pi D^2}{4}\left(\frac{L_1}{2} + L_2 + \frac{L_3}{3}\right) \tag{12-14}$$

TABLE 12-1 Validation sample.

THESE ENTRIES SHOULD YIELD		
Base diameter	D =	2
Diameter 1	D_1 =	2
Diameter 2	D_2 =	1
Height	L =	3

	h	S	V
Elliptic Cylinder	0.1111	14.533	4.712
Uniform Cylinder	-	18.850	9.425
Paraboloid	-	13.035	4.712
Cone	-	9.935	3.142
Frustum	-	14.902	5.498

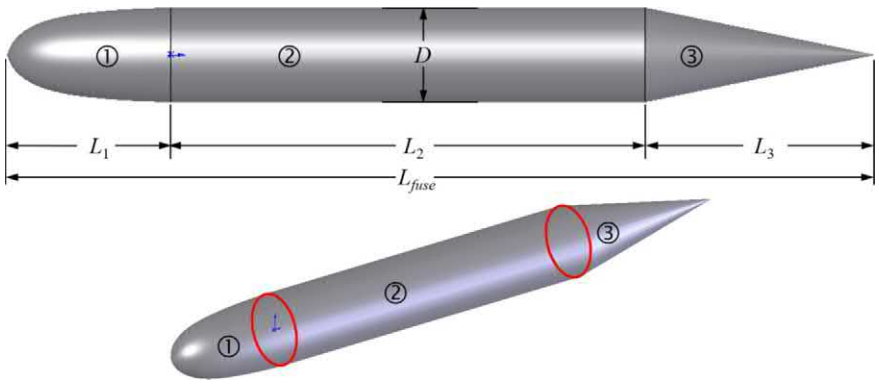


FIGURE 12-25 An approximation of a jet transport fuselage using elementary solids.

DERIVATION OF EQUATION (12.13)

$$S_{fuse} = \overbrace{\left\{\frac{\pi D}{96L_1^2}\left[\left(D^2+16L_1^2\right)^{3/2}-D^3\right]\right\}}^{Paraboloid} + \overbrace{\{\pi D L_2\}}^{Cylinder} + \overbrace{\left\{\frac{\pi}{4}D\sqrt{D^2+4L_3^2}\right\}}^{Cone}$$
$$= \pi D\left[\frac{\left(D^2+16L_1^2\right)^{3/2}-D^3}{96L_1^2} + L_2 + \frac{\sqrt{D^2+4L_3^2}}{4}\right]$$

DERIVATION OF EQUATION (12.14)

$$\cancel{V}_{fuse} = \frac{\pi D^2 L_1}{8} + \frac{\pi D^2 L_2}{4} + \frac{\pi D^2 L_3}{12} = \frac{\pi D^2}{4}\left(\frac{L_1}{2} + L_2 + \frac{L_3}{3}\right)$$

12.4.4 Surface Areas and Volumes of a Tadpole Fuselage

The following geometry can be used to estimate the geometric properties of the generic tadpole fuselage shown in Figure 12-26. This is handy when estimating wetted area of sailplanes and the modern GA aircraft. The geometry consists of a paraboloid, cylinder, and two sets of frusta, featuring the dimensions shown. Each section length is denoted by an appropriate subscript. The dimension D (diameter) is the same for the first three sections.

Total length: $$L_{fuse} = L_1 + L_2 + L_3 + L_4 \qquad (12\text{-}15)$$

Surface area:

$$S_{fuse} = \frac{\pi D}{96L_1^2}\left[\left(D^2+16L_1^2\right)^{3/2}-D^3\right] + \pi D L_2 + \frac{\pi}{2}\left(\frac{D+d_1}{2}\right)\sqrt{D^2-2Dd_1+d_1^2+L_3^2} + \hookleftarrow$$
$$+\frac{\pi}{2}\left(\frac{d_1+d_2}{2}\right)\sqrt{d_1^2-2d_1d_2+d_2^2+L_4^2} \qquad (12-16)$$

Volume: $$V_{fuse} = \frac{\pi}{4}\left[\frac{1}{2}D^2L_1 + D^2L_2 + \frac{1}{3}\left(D^2+Dd_1+d_1^2\right)L_3 + \frac{1}{3}\left(d_1^2+d_1d_2+d_2^2\right)L_4\right] \qquad (12\text{-}17)$$

DERIVATION OF EQUATION (12.16)

Begin by adding the contribution of all the elementary solids used, with tops and bases removed:

$$S_{fuse} = \overbrace{\left\{\frac{\pi D}{96L_1^2}\left[\left(D^2+16L_1^2\right)^{3/2}-D^3\right]\right\}}^{Paraboloid} + \overbrace{\{\pi D L_2\}}^{Cylinder} + \overbrace{\left\{\frac{\pi}{2}\left(\frac{D+d_1}{2}\right)\sqrt{D^2-2Dd_1+d_1^2+L_3^2}\right\}}^{Frustum} + \hookleftarrow$$
$$+\underbrace{\left\{\frac{\pi}{2}\left(\frac{d_1+d_2}{2}\right)\sqrt{d_1^2-2d_1d_2+d_2^2+L_4^2}\right\}}_{Frustum}$$

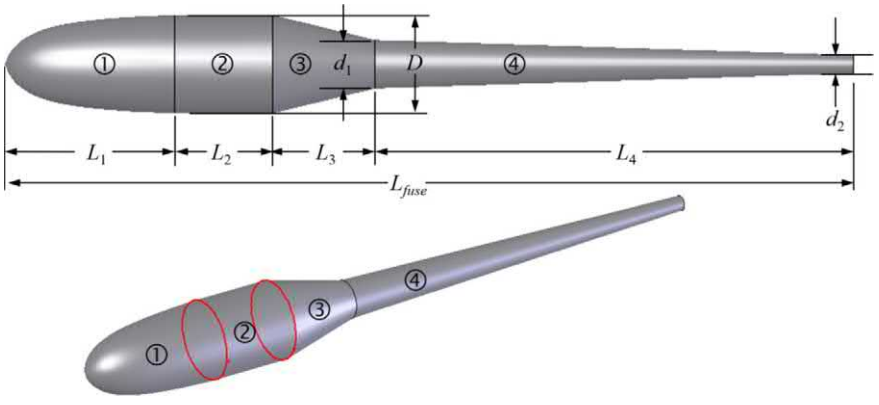


FIGURE 12-26 An approximation of a tadpole fuselage using elementary solids.

DERIVATION OF EQUATION (12.17)

$$V_{fuse} = \frac{\pi}{8}D^2L_1 + \frac{\pi}{4}D^2L_2 + \frac{\pi}{12}(D^2 + Dd_1 + d_1^2)L_3 + \frac{\pi}{12}(d_1^2 + d_1d_2 + d_2^2)L_4$$

$$= \frac{\pi}{4}\left[\frac{1}{2}D^2L_1 + D^2L_2 + \frac{1}{3}(D^2 + Dd_1 + d_1^2)L_3 + \frac{1}{3}(d_1^2 + d_1d_2 + d_2^2)L_4\right]$$

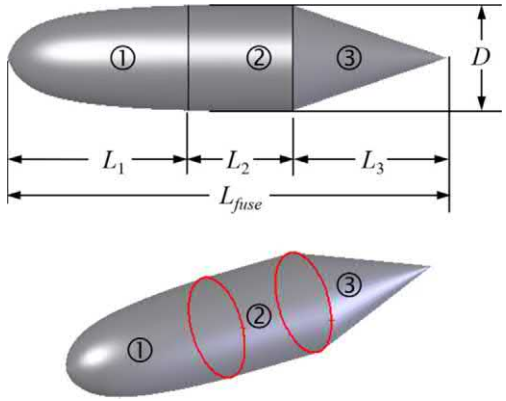


FIGURE 12-27 An approximation of a pod-style fuselage using elementary solids.

12.4.5 Surface Areas and Volumes of a Pod-Style Fuselage

The following geometry can be used to estimate the geometric properties of a generic pod-style fuselage shown in Figure 12-27, such as that of airplanes like the P-38 Lightning. The geometry consists of a paraboloid, cylinder, and a cone, featuring the dimensions shown. This effectively identical to the passenger transport fuselage, except the cylindrical segment is shorter. Use Eqs. (12.12), (12.13), and (12.14).

12.5 ADDITIONAL INFORMATION

A general mannequin is essential when claiming space for occupants during the layout of the cabin and cockpit. A simple mannequin can be made using elementary geometry such as circles for joints and head, and sticks for torso, stomach, arms, and legs. Such a figure should feature joints to allow limbs to bend to help assess space claims when standing, sitting down, or reaching out and so on. It should give a realistic representation of the size of buttocks and thighs so that, when folded into a sitting position, the distance from the head to the buttock is accurate. It is common in initial fuselage design to discover that the pilot's head penetrates the fuselage side.

An example of a mannequin is shown in Figure 12-28. The dimensions indicated by the letters A through L are published in documents such as *The Human Factors Design Guide* (HFDG) [6]. It is a great resource that provides a collection of dimensions of human physical data. The dimensions are listed in Tables 12.2 and 12.3 for both males and females, ranging from the 1st percentile to the 99th percentile. The concept of percentile refers the percentage of people are included in that class. For instance, the 50th percentile means that 50% of the general population does not surpass the cited physical dimensions. The stature (A) of the 95th percentile is 186.7 cm

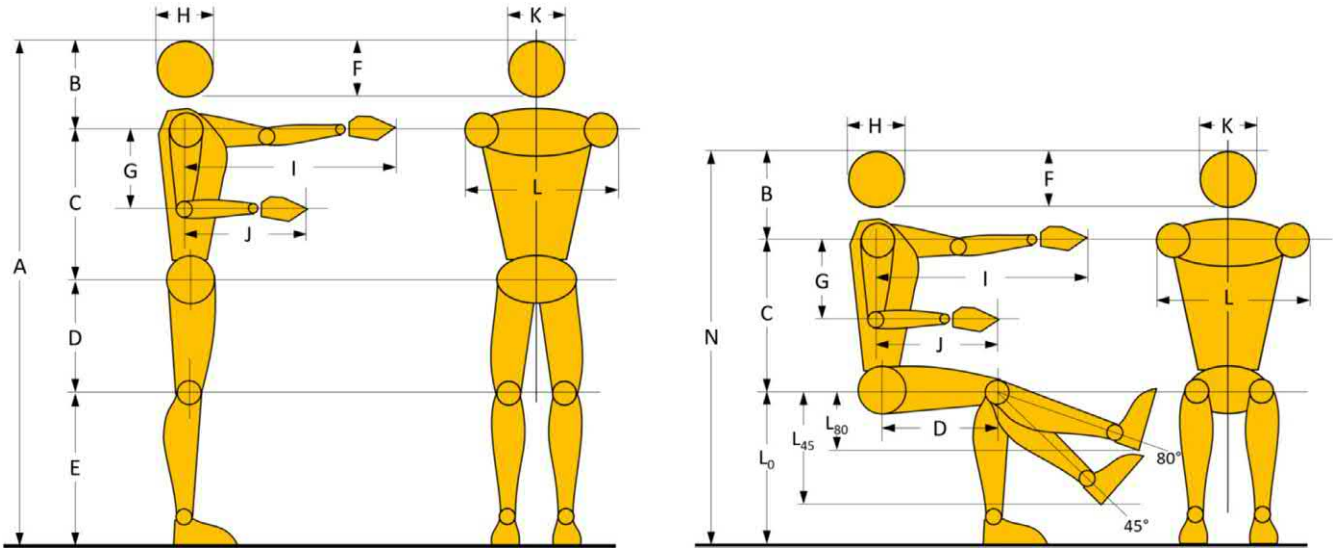


FIGURE 12-28 A standard erect mannequin used for space claims by occupants.

TABLE 12-2 Dimensions of the erect mannequin in Figure 12-28.

			MALE AND FEMALE PHYSICAL CHARACTERISTICS					
			1st	5th	50th	95th	99th	
Stature	A	Male	63.1	64.8	69.1	73.5	75.2	in
			160.3	164.6	175.5	186.7	191.0	cm
		Female	58.4	60.2	64.1	68.4	70.1	in
			148.3	152.9	162.8	173.7	178.1	cm
Shoulder-head	B	Male	11.8	11.9	12.5	13.0	13.2	in
			30.0	30.2	31.8	33.0	33.5	cm
		Female	10.9	11.3	11.8	12.3	12.5	in
			27.7	28.7	30.0	31.2	31.8	cm
Torso	C	Male	19	19.3	20.1	20.8	21.1	in
			48.3	49.0	51.1	52.8	53.6	cm
		Female	17.5	17.8	18.4	19.2	19.2	in
			44.5	45.2	46.7	48.8	48.8	cm
Hip height	D	Male	14.9	15.4	16.7	18.0	18.5	in
			37.8	39.1	42.4	45.7	47.0	cm
		Female	14.3	14.7	15.9	17.1	17.8	in
			36.3	37.3	40.4	43.4	45.2	cm
Knee height	E	Male	17.4	18.2	19.8	21.7	22.4	in
			44.2	46.2	50.3	55.1	56.9	cm
		Female	15.7	16.4	18.0	19.8	20.6	in
			39.9	41.7	45.7	50.3	52.3	cm
Head height	F	Male	8.4	8.6	8.6	9.1	9.4	in
			21.3	21.8	21.8	23.1	23.9	cm
		Female	7.8	8.3	8.6	9.1	9.4	in
			19.8	21.1	21.8	23.1	23.9	cm
Upper arm	G	Male	11.3	11.5	12.3	13.5	14	in
			28.7	29.2	31.2	34.3	35.6	cm
		Female	10.5	10.7	11.5	12.4	12.8	in
			26.7	27.2	29.2	31.5	32.5	cm
Head length	H	Male	7.1	7.3	7.8	8.2	8.4	in
			18.0	18.5	19.8	20.8	21.3	cm
		Female	6.8	7.0	7.4	7.8	8.0	in
			17.3	17.8	18.8	19.8	20.3	cm
Functional reach	I	Male	28.4	29.1	31.5	34.1	35.3	in
			72.1	73.9	80.0	86.6	89.7	cm
		Female	25.9	26.7	28.9	31.4	32.4	in
			65.8	67.8	73.4	79.8	82.3	cm
Elbow-fingertip	J	Male	17.1	17.6	19.2	20.6	21.3	in
			43.4	44.7	48.8	52.3	54.1	cm
		Female	15.4	16.0	17.4	19.0	19.6	in
			39.1	40.6	44.2	48.3	49.8	cm
Head width	K	Male	5.1	5.6	6.0	6.3	6.5	in
			13.0	14.2	15.2	16.0	16.5	cm
		Female	5.2	5.4	5.7	6.0	6.1	in
			13.2	13.7	14.5	15.2	15.5	cm
Shoulder breadth	L	Male	17.1	17.7	19.3	21.1	21.7	in
			43.4	45.0	49.0	53.6	55.1	cm
		Female	15	15.6	17.0	18.6	19.4	in
			38.1	39.6	43.2	47.2	49.3	cm

Based on Human Factors Design Guide (HFDG), DOT/FAA/CT-96/1.

TABLE 12-3 Dimensions of the sitting mannequin in Figure 12-28.

			MALE AND FEMALE PHYSICAL CHARACTERISTICS					
			1st	5th	50th	95th	99th	
Sitting stature	N	Male	48.2	49.4	52.4	55.5	56.7	in
			122.4	125.5	133.1	141.0	144.0	cm
		Female	44.1	45.5	48.2	51.3	52.3	in
			112.0	115.6	122.4	130.3	132.8	cm
Leg at 0°	L_0	Male	17.4	18.2	19.8	21.7	22.4	in
			44.2	46.2	50.3	55.1	56.9	cm
		Female	15.7	16.4	18	19.8	20.6	in
			39.9	41.7	45.7	50.3	52.3	cm
Leg at 45°	L_{45}	Male	12.3	12.9	14.0	15.3	15.8	in
			31.3	32.7	35.6	39.0	40.2	cm
		Female	11.1	11.6	12.7	14.0	14.6	in
			28.2	29.5	32.3	35.6	37.0	cm
Leg at 80°	L_{80}	Male	3.0	3.2	3.4	3.8	3.9	in
			7.7	8.0	8.7	9.6	9.9	cm
		Female	2.7	2.8	3.1	3.4	3.6	in
			6.9	7.2	7.9	8.7	9.1	cm

Based on Human Factors Design Guide (HFDG), DOT/FAA/CT-96/1.

(68.4 in.). This means that 95% of all people are equal to or below that. The modern aircraft should be designed to accommodate the 95th percentile male.

Table 12-4 details typical occupant weights used in the design of GA aircraft. Table 12-5 shows the cabin dimensions for selected aircraft.

TABLE 12-4 Typical occupant weights used in aircraft design.

STANDARD OCCUPANT WEIGHT		
	lb_f	kg
Standard weight per 14 CFR 23.25	170	77
Recommended for GA design	200	91
Typical zero/zero ejection seat	250-300	113-136

TABLE 12-5 Cabin dimension for selected aircraft.

SINGLE ENGINE PISTON					
Aircraft	Passengers	Length, in	Width, in	Height, in	Baggage, ft^3
Beechcraft V35 Bonanza	4	-	42	50	-
Cessna 152	2	-	39.75	42	-
Cessna 172 Skyhawk	4	142	39.5	48	-
Cessna 182 Skylane	4	-	42	48	-
Cessna 206 Skywagon	6	145	44	49.5	-
Cessna Corvalis	4	139.5	49	49	-
Cirrus SR20 and SR22	4	-	49	50	-
Mooney 201	4	-	43.5	44.5	-
Piper Arrow	4	-	41	45	-
Piper Cherokee PA-28-140	4	-	40	44	-

TURBOPROP AIRCRAFT					
Aircraft	Passengers	Length, in	Width, in	Height, in	Baggage, ft^3
Beechcraft 1900D	19	303	54	71	192
Beechcraft King Air 200	10	200	54	57	54
Beechcraft King Air 90	6	155	57	54	-
Dornier 328	32	407	87	75	222
Embraer Brasilia 120	30	378	64	68	226
Jetstream 31	18	291	73	71	52-65
Metroliner 23	19	305	64	58	143.5
Piaggio Avanti P180	8	170	74	69	51

Continued

TABLE 12-5 Cabin dimension for selected aircraft—cont'd

REGIONAL AND BUSINESS JETS					
Aircraft	**Passengers**	**Length, in**	**Width, in**	**Height, in**	**Baggage, ft^3**
Canadair Regional Jet	30	545	98	73	250
Cessna 525C Citation CJ4	-	268	58	57	-
Cessna 680 Citation Sovereign	-	369	66	68	-
Cessna Citation Bravo	8	192	58	56	74
Cessna Citation EXCEL	8	223	67	68	87
Cessna Citation Ultra	8	208	59	58	67
Cessna Citation X	9	282	67	68	82
Cessna Citationjet / CJ1	6	136	59	57	58
Challenger 300	16	343	86	73	131
Challenger 604	16	306	99	74	115
Challenger 800	30	581	98	73	250
Dassault Falcon 2000	13	315	92	74	134
Dassault Falcon 900	17	398	92	75	127
Dornier 328 Jet	32	408	88	75	277
Galaxy	10	293	87	76	150
Global Express	16	540	98	76	325
Gulfstream 100	7	206	58	67	51
Gulfstream IV/ SP	16	488	88	74	169
Gulfstream V	16	527	88	74	226
Hawker 125-700	9	256	71	69	40
Hawker 125-800	10	256	72	69	48
Hawker 450	-	250	59	57	-
Honda HA-420 Hondajet	-	214	60	59	-
LearJet 45	8	238	62	59	65
LearJet 60	7	212	71	68	59
Legacy	14	517	82	67	242

HOMEBUILT/KITPLANE AIRCRAFT					
Aircraft	**Passengers**	**Length, in**	**Width, in**	**Height, in**	**Baggage, ft^3**
Europa XS Monowheel	2	-	40	37.5	22.50
Hummel Hummelbird	-	-	20.5	36	-
Lancair Lancair ES	3	-	44	39	-
Robson-Rand KR-2 (Custom)	1	-	32	-	-
Rutan Long-EZ	1	-	22	38	-
Rutan Vari-Eze	1	-	-	36	-
Skystar Kitfox 4-1050			39.5	37	
Stoddard-Hamilton Glasair III	1	-	40.5	37	-
Thorp T-18 Tiger	1	-	36	35	-
Vans RV-3	-	-	22.5	34	-
Vans RV-4	1	-	22	41	-
Vans RV-6	1	-	38-40.5	36-39	-
Vans RV-8	1	-	24	40	-
Zenair CH-601HD	-	-	41	37	-
Zenair CH-801	-	-	44	37	-

Based on manufacturers data.

References

[1] F.L. Galvao, *A note on low drag bodies*, in: Paper Presented at the XI OSTIV Congress, Lesyno, Poland, 1968.

[2] D. Althaus, NASA CR-2315, *Motorless Flight Research*, 1972. Edited by James L. Nash-Webber.

[3] S.S. Dodbele, C.P. van Dam, P.M.H.W. Vijgent, B.J. Holmes, *Shaping of airplane fuselages for minimum drag*, AIAA J. Aircraft 24 (5) (May 1987).

[4] NASA TM-77014, *Wind Tunnel Investigations of Glider Fuselages with Different Waisting and Wing Arrangements*, Radespiel, R, 1983.

[5] L.R. Jenkinson, P. Simpkin, D. Rhodes, *Civil Jet Aircraft Design*, Arnold Publishers, 1999.

[6] *Human Factors Design Guide (HFDG)*, DOT/FAA/CT-96/1.

This page intentionally left blank

CHAPTER

13

The Anatomy of the Landing Gear

OUTLINE

13.1 Introduction 541
13.1.1 The Content of This Section 542
13.1.2 Landing Gear Arrangement 542
13.1.3 Landing Gear Design Checklist 543

13.2 Tires, Wheels, and Brakes 544
13.2.1 Important Dimensions and Concepts for Landing Gear Design 544
13.2.2 Retractable Landing Gear 547
13.2.3 Types and Sizes of Tires, Wheels, and Brakes 548
13.2.4 Types of Landing Gear Legs 554
13.2.5 Reaction of Landing Gear Forces 556
13.2.6 Comparing the Ground Characteristics of Taildragger and Tricycle Landing Gear 559

13.3 Geometric Layout of the Landing Gear 559
13.3.1 Geometric Layout of the Tricycle Landing Gear 559
13.3.2 Geometric Layout of the Taildragger Landing Gear 562
13.3.3 Geometric Layout of the Monowheel Landing Gear With Outriggers 564
13.3.4 Tricycle Landing Gear Reaction Loads 564
13.3.5 Taildragger Landing Gear Reaction Loads 568

References 571

13.1 INTRODUCTION

The purpose of the landing gear is obvious—to allow the aircraft to return to the ground without causing damage to the structure. The primary function of the landing gear is to react the substantial impact forces and moments (repeatedly) and transfer these safely into the airframe. Additionally, the landing gear must permit the secondary functions listed below:

(1) It must allow the airplane to maneuver easily on the ground, during taxi, take-off, and landing (steering).
(2) It must provide means to slow down after touchdown or when maneuvering on the ground (braking).
(3) Large aircraft must feature means for towing and pushing by airport vehicles.
(4) It must distribute the weight of the airplane such that it will not damage taxi- and runways (number of wheels).

Landing gear design is not trivial, let alone when the gear must be retractable as well. The challenges include the kinematics of the landing gear mechanism and space-claims inside the affected airframe (wing or fuselage). Before the design even begins, the following issues must be resolved:

(1) Desired landing gear configuration:
  a. What is the landing gear arrangement (tricycle, taildragger, etc.)?
  b. What is the location of the wheels and tires?
  c. What is the wheelbase and wheel track?
  d. Number and size of wheels and tires.
(2) Should the landing gear be fixed or retractable?
  a. If retractable, should there be hydraulic or electric actuation?
  b. If retractable, will doors cover landing gear fully, partially, or not at all?
(3) Landing gear details
  a. What kind of shock absorption (leaf spring, oleo-pneumatic, trailing link, etc.)?
  b. What kind of braking system (calipers, drogue chute)?
  c. What kind of floatation (ability of the airplane to operate on "soft" airfields)?

https://doi.org/10.1016/B978-0-12-818465-3.00013-6

Copyright © 2022 Elsevier Inc. All rights reserved.

13.1.1 The Content of This Section

- Section 13.2 presents important information about wheels, tires, and brakes used for aircraft, allowing the reader to size and select these landing gear components. Additionally, several important concepts regarding fixed and retractable landing gear are presented. It is recommended the reader is familiar with these before beginning the layout of the landing gear.
- Section 13.3 presents cookbook methods to place the nose, main, and tailwheels of the airplane, for a conventional, taildragger, and monowheel configurations. Additionally, methods to calculate the reaction loads for the landing gear and to evaluate the airspeed required to rotate the airplane during T-O are presented.

13.1.2 Landing Gear Arrangement

The first decision to make regarding the landing gear is arrangement. Many different types of landing gear have been employed during the history of aviation. Figure 13-1 shows the four most common. Among those, the most common are the tricycle and taildragger. While specialized projects may force the consideration of alternative options, the viability of these four should first be weighed carefully. There is a reason why the tricycle and taildragger configurations are used in 99.5% of all aircraft, and the four arrangements cover 99.9% of all aircraft ever built. Pazmany [1, p. 21] presents multiple pros and cons that apply to these configurations, some of which are presented in Table 13-1.

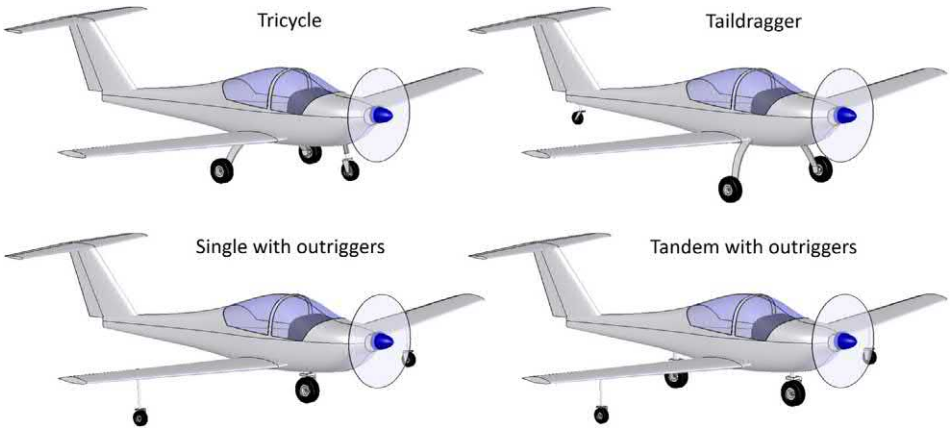


FIGURE 13-1 Examples of landing gear arrangement.

TABLE 13-1 Pros and cons of several landing gear arrangements.

	Advantages	Disadvantages
Tricycle	• Dynamically stable on the ground so it is easier to maneuver. • Good ground control in crosswinds. • Good forward visibility because of low deck angle. • Floor deck angle on the ground is closer to being horizontal, making passenger entry and exit easier. • Propeller better protected from ground strike. • Hard braking on main wheels cannot cause the airplane to nose over. • Airplane pitches nose-down upon main gear touch-down, reducing lift. • Less bounce after touch-down. • Good acceleration during T-O due to lower AOA. • Shorter wheelbase permits tight turning radius. • Easier to land and, thus, more forgiving for inexperienced pilots.	• Requires a minimum airspeed before the airplane can be rotated for T-O. • Higher structural weight due to three highly loaded landing gear legs. • More costly for the same reason (if fixed). • Higher cruise drag for fixed gear configuration. • Three landing gear legs make ground ride worse on uneven surfaces. • Susceptible to nose wheel shimmy that can be very damaging. • Nose wheel shimmy is a more common design problem than tailwheel shimmy for taildraggers. • Higher dynamic ground loads due to heavier load on nose gear, than on a tailwheel. • More complex steering mechanism. • Nose wheel retraction can often be challenging due to limited space in the nose of the airplane. • Low aero-drag due to the low AOA attitude during landing requires more braking effort. • Heavier braking unloads main wheels and may cause skidding.

TABLE 13-1 Pros and cons of several landing gear arrangements—cont'd

	Advantages	Disadvantages
Taildragger	• Allows the pilot to rotate at low speeds, reducing soft-field T-O distance. • Less structural weight due to only two highly loaded landing gear legs. • Less costly for the same reason. • Less cruise drag for fixed gear compared to tricycle. • Two landing gear legs improves ride on uneven surfaces. • Better adapted for rough fields (favored by bush pilots) • Structurally simpler fuselage or wing attachment. • High AOA for landing increases aero-drag and lessens demand on brakes. • Light weight of tailwheel due to low ground loads. • Simple steering mechanism. • When on all wheels, greater propeller clearance during taxiing increases safety on unprepared runways.	• Dynamically unstable on the ground so it is harder to maneuver on the ground. • Tendency to ground-loop. • Poor directional control with strong crosswinds. • Poor forward visibility because of high deck angle. • Harder to land for inexperienced pilots. • Prop strikes are possible because of heavy braking that may force nose down. • High AOA during landing may cause the airplane to bounce. • Slower initial acceleration due to the higher deck angle.
Monowheel	• Eliminates reinforcement for landing gear hardpoints on wing. • Low weight due to ground loads transferred directly to fuselage through a short load path. • Lower weight (single strut versus multiple). • Less costly for the same reason. • Less cruise drag for fixed gear compared to tricycle and taildraggers. • Wheel is close to CG reduces asymmetric moments (due to braking, mud, slush, flat tires, etc.) reducing need for large aerodynamic corrective deflections. • Ability to have one large tire improves ground ride.	• Requires outriggers or wing tip skids for ground stability. • Outriggers may require wider taxiways. • Since steering mechanism is absent, aerodynamic forces (e.g. propwash) are required. This means poor ground control, especially in crosswind. • Reduced propeller ground clearance. • Reduced AOA for flare. • Retraction of main gear forward of CG can be challenging because of space constraints. • Higher T-O speed to make up for the limited ability to rotate. • Not intended for extensive taxiing.
Tandem Wheel	• Eliminates reinforcement for landing gear hardpoints from the wing. • Reduced weight over tricycle. • Less costly for the same reason. • Less cruise drag for fixed gear compared to tricycle or taildraggers. • Low weight due to ground loads transferred directly to fuselage through a short load path.	• Requires outriggers or wing tip skids for ground stability. • Outriggers may require wider taxiways. • Poor ground control, especially in crosswind. • Reduced propeller ground clearance. • Reduced AOA for flare. • Gear retraction is challenging because of space constraints. • Higher T-O speed to make up for the limited ability to rotate. • Not intended for extensive taxiing.

13.1.3 Landing Gear Design Checklist

Consider the following items for a well-designed system.

(1) Positioning

The main and auxiliary landing gears (nose wheel, tailwheel, etc.) must be properly positioned with respect to the CG to reduce the risk of ground looping, overturning, crosswind canting, and tail angle, and allow the airplane to be maneuvered as needed during the T-O and landing ground run. Methods that address this are presented in Sections 13.3.1–13.3.3. Remember that weight-efficient structure places stout structural elements near the hardpoints for the landing gear so additional support structure will not be called for.

(2) Ground Clearance

A well-designed landing gear provides adequate ground clearance, even in the worst combination of flat tire and deflated oleo-pneumatic shock absorber. This protects propeller tips, nacelles, wing tips, deflected flaps, and so on. A tailskid or bumper should be installed to prevent damage to the airplane from a tail strike.

(3) Landing Gear Component Vendors

Table 13-2 lists a few companies that manufacture and sell components for landing gear:

(4) Tires and Tire Inflation Pressure

The inflation pressure should be selected based on the weight of the aircraft, number of tires, and the bearing capability of the airfield from which the airplane will be operated. The nose-wheel tire pressure should be based on the applicable dynamic loads. In the absence of such loads, estimate it by boosting the static load as follows:

Type III tires: $1.4\times$ static max vertical force
Type VII tires: $1.35\times$ static max vertical force

TABLE 13-2 Selected vendors of landing gear components.

Company	Website	Tires	Wheels	Brakes	Landing Gear	Comment
Aircraft Spruce	www.aircraftspruce.com	X	X	X	X	Retailer of gear for kitplanes. No manufacturing.
Azusa	www.azusaeng.com	X	X	X		Non-certified products, for kitplanes and ultralights
Bridgestone	www.bridgestone.com	X				Tires for most types of aircraft
Goodrich	www.goodrich.com		X	X	X	Large, business, and military aircraft
Goodyear	www.goodyearaviation.com	X				Tires for most types of aircraft
Grove	www.groveaircraft.com	X	X	X	X	Aluminum leaf spring, fixed, for certified and experimental aircraft.
Messier-Bugatti-Dowty	www.safranmbd.com		X	X	X	Large commercial, military, helicopter, business and regional aircraft
Michelin	www.airmichelin.com	X				Tires for most types of aircraft
Parker	www.parker.com		X	X		Business and GA aircraft
Triumph	www.triumphgroup.com				X	Contract design of landing gear
Wicks Aircraft	www.wicksaircraft.com	X	X	X	X	Retailer of gear for kitplanes. No manufacturing.
Desser Tire & Rubber Company	www.desser.com	X				Manufacturer of "Aero Classic" tires. Offers various other parts for landing gear
Dunlop	www.dunlopaircrafttyres.com	X				Tires for most types of aircraft
Specialty Tires of America	www.stausaonline.com	X				Formerly McCreary Tire

Main gear tire should allow for 25% growth in aircraft gross weight. The main gear tire load rating should be based on maximum gross weight and adverse CG location. Forged aluminum-alloy wheels are recommended.

(5) Landing Impact and Braking

The landing gear is required by applicable regulations to handle several landing scenarios. For GA aircraft, the applicable landing gear loads are stipulated by 14 CFR §23.471 to §23.511. For seaplanes, the hull landing loads are stipulated in 14 CFR §23.521 to §23.562. For landplanes, there are individual requirements for landing on the main gear only, three-point landing, and side impact loads. The magnitude of these loads is very high, and they are reacted as point loads in the airframe. In addition to the impact forces, the landing gear should provide good damping characteristics and should permit the aircraft to taxi over uneven ground without transmitting excessive shocks to the airframe. The airplane should possess a good, reliable, and safe braking system so that it can handle all braking conditions. It should offer a parking brake that can hold the airplane at gross weight on a 1:10 gradient slope or on a level runway with maximum T-O power applied on one engine. Antiskid brakes are recommended.

13.2 TIRES, WHEELS, AND BRAKES

This section presents important concepts when designing the landing gear layout, e.g. configuration, wheelbase, wheel track, and turning radius.

13.2.1 Important Dimensions and Concepts for Landing Gear Design

Figure 13-2 shows important concepts and dimensions used when discussing landing gear arrangement. The tailwheel spindle axis angle, ϕ, should be inclined forward by some 5 degrees. The tailwheel trail should be 1/10th of the wheel's diameter. When deflected, the tailwheel shock absorber should place the wheel axle inside the shaded area.

(1) Turning Radius

The *turning radius* is a very important feature in aircraft ground maneuvering; specifically, when "turning into position" on a narrow runway. Figure 13-3 shows how the turning radius for a given rotation of the nose landing gear can be determined. The distance h denotes the location of the center of turn and can be calculated using:

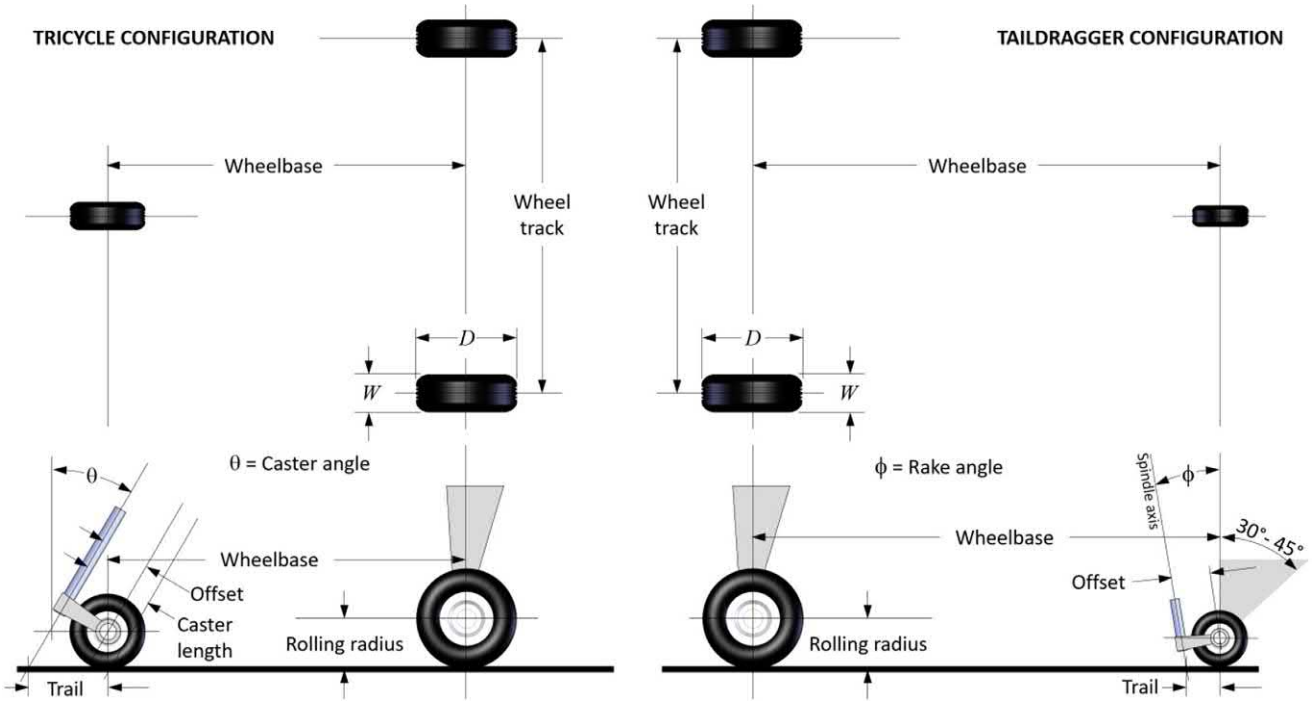


FIGURE 13-2 Important geometric definitions for tricycle and taildragger configurations. *Based on Pazmany, L., Landing Gear Design for Light Aircraft, Vol. 1, Ladislao Pazmany, 1986.*

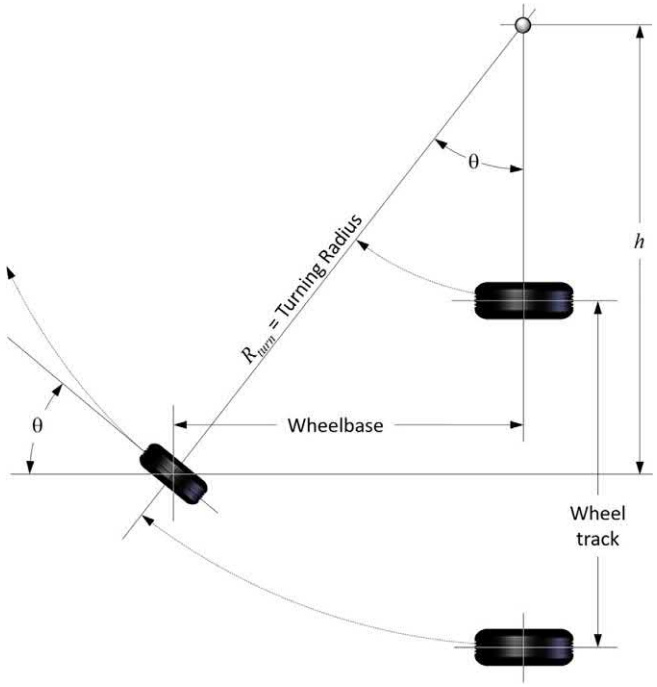


FIGURE 13-3 Important geometric definitions for determining turning radius.

Distance to turning center: $$h = \frac{\text{Wheel base}}{\tan\theta} \tag{13-1}$$

The turning radius is determined based on the *wheelbase* and the turning angle of the nose gear.

Turning radius:

$$R_{turn} = \sqrt{\text{Wheel base}^2 + h^2} = \text{Wheel base}\sqrt{1 + \frac{1}{\tan^2\theta}} \tag{13-2}$$

A large-enough nose gear turning angle allows some aircraft to "turn on a dime." The minimum nose gear turn angle to achieve this feat is

$$h = \frac{\text{Wheel base}}{\tan\theta} = \frac{\text{Wheel track}}{2} \quad \Rightarrow \quad \tan\theta = \frac{2 \times \text{Wheel base}}{\text{Wheel track}} \tag{13-3}$$

(2) Tire Footprint

A tire in contact with the ground flattens slightly on the bottom so its contact area resembles that of an ellipse (see Figure 13-4). The weight, F, supported by the tire is distributed over this area and generates an average pressure (p) on the area (S_e) which amounts to:

$$p = F/S_e = \frac{4F}{\pi \cdot a \cdot b} \tag{13-4}$$

where p is the internal tire pressure. The higher the pressure inside the tire, the less are the values of a and b. The dimension a is usually taken to be 85% of the distance c. High-pressure tires supporting large loads may cause

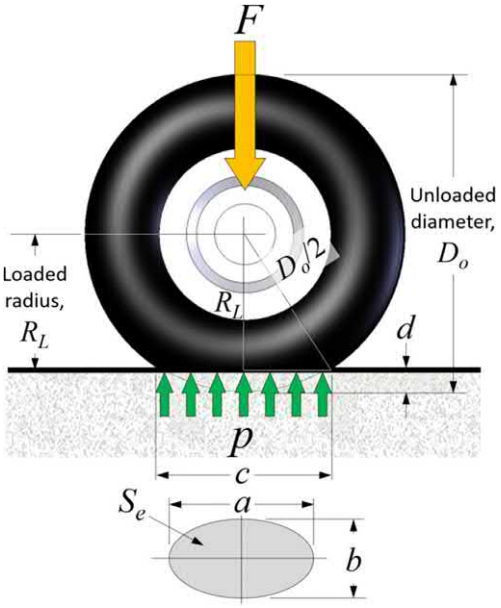


FIGURE 13-4 Tire footprint. *Based on Pazmany, L., Landing Gear Design for Light Aircraft, Vol. 1, Ladislao Pazmany, 1986.*

rutting damage to the runway. The tire may sink into soft ground, which explains why high floatation tires ("*Tundra tires*") have a large diameter and low internal pressure.

The compression of the tire increases the internal pressure due to the reduction of internal volume. Thus, the unloaded pressure is always lower than the loaded one. Inflation pressure reported by manufacturers refers to the unloaded tire at standard S-L temperature. When the tire is loaded to the rated load, the pressure will be some 4% higher than the rated pressure. Tires should always be allowed to cool for at least an hour before checking the pressure.

Equation (13-4) can be used to estimate the required internal pressure for a tire if the allowable ground pressure limits are known for a particular runway or taxiways.

Manufacturer's data, such as that of reference [2], tabulates the *loaded radius*, R_L, enabling the estimation of the dimension a in Figure 13-4. First, it must be related to the distance c as shown below:

$$\frac{D_0}{2}=\sqrt{R_L^2+\frac{c^2}{4}} \quad \Leftrightarrow \quad c=\sqrt{D_0^2-4R_L^2}$$

Thus, the dimension can be calculated as follows:

$$\Rightarrow \quad a=0.85c=0.85\sqrt{D_0^2-4R_L^2} \tag{13-5}$$

(3) Castering Nose and Tailwheels

The castering nose landing gear and tailwheels (in taildraggers) is a common solution for steerable landing gear in many light GA aircraft. The steering is usually implemented using differential braking, i.e., the pilot steps on the left or right rudder pedals to generate braking in the corresponding main wheel, which turns the aircraft on the ground.

The most common problem with castering landing gear is *shimmy*, which is a violent oscillation that is a function of speed and the inertia characteristics of the landing gear. Shimmy can begin when the aircraft moves over uneven ground and even due to worn tires or landing gear parts. It ranges from a simple wobble to oscillation so violent it breaks the landing gear off the airplane. To prevent this, castering landing gear is sometimes equipped with a small device called a *shimmy damper*. It is a small cylinder filled with hydraulic fluid that has a piston inside that connects to the movable (rotational) part of the landing gear. Several configurations are shown in Figure 13-5. Their properties are shown in Table 13-3.

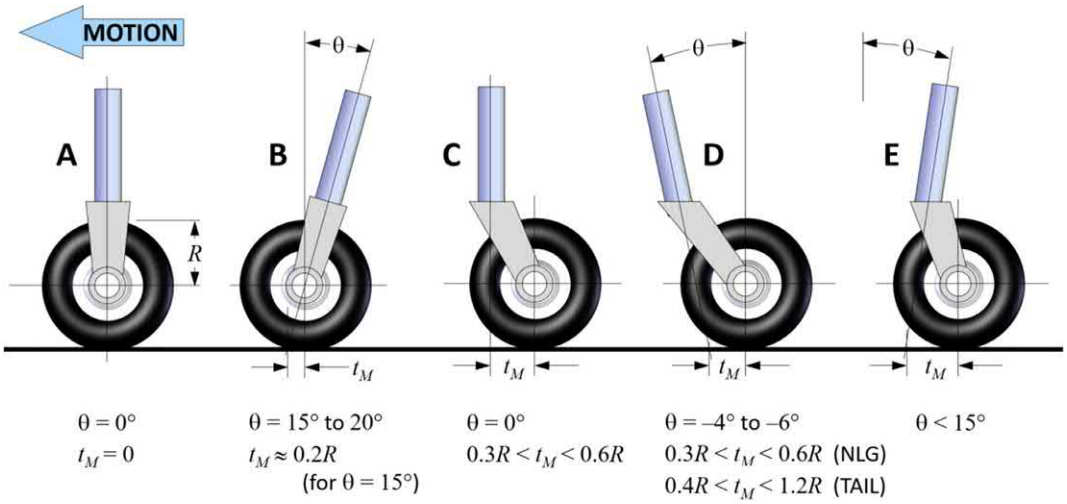


FIGURE 13-5 Five common styles of castering wheel configurations used for nose and tailwheels. NLG, nose landing gear; TAIL, taildragger; t_M, mechanical trail. *Based on Pazmany, L., Landing Gear Design for Light Aircraft, Vol. 1, Ladislao Pazmany, 1986.*

TABLE 13-3 Types of castering nose and tailwheels.

Style	Used for		Statically stable?	Dynamically stable?	Shimmy damper required?	Comment
	Nose wheel	Tailwheel				
A	YES	NO	Neutral	Neutral	–	Requires steered mounting.
B	YES	NO	NO	YES	–	Shimmy damper may be required.
C	YES	YES	Neutral	YES	YES	Shimmy damper not required if twin wheeled or one wheel with double treads.
D	NO	YES	YES	YES	YES	Shimmy damper may not be required when $t_M > R$.
E	YES		NO	YES	YES	When sideways, the nose of the aircraft is lowered, so it is statically unstable.

Based on Pazmany, L., Landing Gear Design for Light Aircraft, Vol. 1, Ladislao Pazmany, 1986.

13.2.2 Retractable Landing Gear

The advent of the retractable landing gear marked an important milestone in aircraft evolution. It allowed substantial reduction in drag and increase in cruising speed. However, there were drawbacks. The design is complicated by a braking system on the main landing gear and steering mechanism for the nose gear. In addition to challenges in reliability, a new type of accidents reared its ugly head; landings with perfectly operational landing gear retracted. Figure 13-6 shows a common landing gear retraction mechanism.

The actual retraction and extension of retractable landing gear constitutes the most critical phase in its operation. The reliability of locking and unlocking of the actuation mechanism is critical. The reliability is compounded by operation in environment that exposes it to mud or ice. The actuation mechanism, doors, and support structure should be designed to allow actuation at gross weight and 1.6 V_{S1} or higher. Some aircraft, like the high-flying Learjet business jets, allow the landing gear to be partially extended at high airspeeds to provide additional drag in an emergency descent [3]. Actuation air loads during retraction or extension remain a serious challenge. These can easily exceed the capacity of the actuation mechanism. If a partially extended retractable landing gear is not possible, it should be designed to withstand at least 0.67 V_C. The time to retract and extend should be less than 10 and 15 s respectively [4].

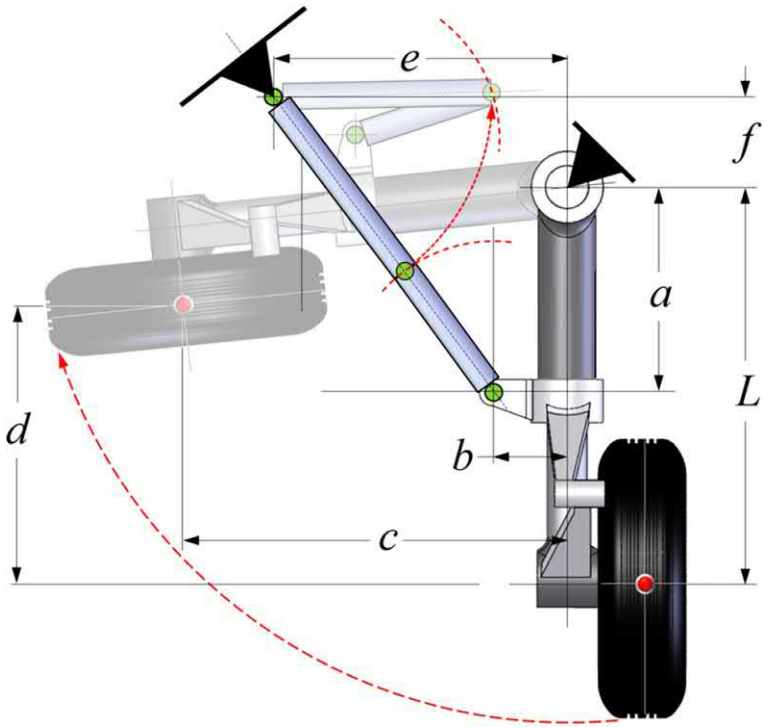


FIGURE 13-6 A common retractable landing gear mechanism for GA aircraft.

To reap the benefit of a retractable landing gear it should be stowed under aerodynamically smooth fairings. The development of retractable landing gear should be left to the experts. There are numerous pitfalls for the novice designer. For instance, airloads during retraction and deployment are hard to predict accurately. These can be surprisingly large, making it impossible for the specified hydraulic mechanism to perform this duty. One consequence is an impossibility to extend the landing gear fully after a successful retraction. This explains why maiden flights are made with the landing gear locked in its extended position. Not much needs to be said about the risk to a development program if the pilot must opt for a belly landing during the first flight.

The kinematics of landing gear retraction and extension is challenging. This is best appreciated by considering the massive landing loads that must be reacted by a compact frame that must repeatedly and effortlessly fold into and out of a small container (the wheel well). The complexity of the system becomes evident in the design of some aircraft, which feature landing gear doors that open temporarily, just to allow as the landing gear to pass through, and then close again—not once, but tens of thousands of times. It takes foresight and engineering experience to design a reliable system like that. While this section presents methods to allow the most important geometric details of the landing gear to be designed, the various retraction kinematics are beyond the scope of this text. References [1, 4, 5] are good resources for general design of landing gear.

The size of the internal volume required to house the retracted gear must be kept in mind when sizing the OML. A potential mistake is discovering, *after* substantial analysis has been completed, that the wheel wells penetrate the cabin or engine compartment. This imposes time consuming revisions. An emergency actuation system should be provided to allow manual deployment, should the normal actuation mechanism fail. The up locking of retractable landing gear shall not use gear door locks and allow an override emergency release. Failure of electric locking systems shall never prevent an emergency deployment of the landing gear. Mechanical sequencing (e.g. special landing gear door opening before the landing gear is retracted and the closing after retraction) should be minimized. Curry [4] and Niu [5] offer other good advice for the detail design of retractable landing gear.

Figure 13-7 shows several so-called "stick-diagrams." These are helpful for visualizing the kinematics of retractable landing gear. The images show the landing gear in its unloaded configuration (in the air) and do not reveal ground deflection. Black nodes represent *immovable joints*, while white ones are *movable joints*. An immovable joint only allows rotation about a fixed point. A movable joint allows rotation and translation. Note that an immovable joint that appears on top of a retracted wheel simply implies an offset hardpoint.

13.2.3 Types and Sizes of Tires, Wheels, and Brakes

The selection of tires for airplanes involves the determination of the *type of tire*, *tire size*, *wheel*, and *brakes*. This section presents information to help in this matter.

(1) Tire Types

Of the number of standard tire designations used for aircraft, the ones presented in this book are based on a definition by the Tire and Rim Association (TRA), which is the technical standardizing body of tires and rims in the United States. TRA designations for common tires are shown in Table 13-4. The Three-Part Type designation is the modern system. The designer of certified GA aircraft picks a *Three-Part Type* designation, whereas the designer of homebuilt aircraft can resort to other types of tires.

(2) Tire Geometry

The following parameters for tires are important (see Figure 13-8):

Tire Aspect Ratio : $AR = H/W$

Ensure there is no confusion with the AR of a wing. A low tire AR means it is wider than it is high. Such tires are intended for high speeds on smooth surfaces. High AR tires are meant for rough field operations that call for improved floatation [1].

Type III have AR ranging from	0.85–1.00
Type VII have AR ranging from	0.77–0.90
Type VIII have AR ranging from	0.65–0.77
Three Part Type have AR ranging from	0.73–0.92

Lift Ratio : $LR = D/d$

An LR of 1.5 to 2.0 is considered low, while 2.0 to 2.5 is desirable [1].

(3) Inflation Pressure

The tire maintains its shape because of the inflation pressure. Tires are flexible in bending but have very limited extension (or stretch). As the tire reacts the load, its cross-section flexes and a side force is generated on the rim flange. The tire deflects some 32% to 35% under static load, but this means it bottoms out at approximately 3 times the static load. Shock absorbers are designed to bottom out at 3 × the static loads as well, and are intended to do so before the tire bottoms out [1]. Table 13-5 shows range of pressure for various applications.

(4) Tire Sizes

Unfortunately, when comes to specifying tire sizes there is no one standard, but several that have evolved since the inception of tire standardization in 1903. This

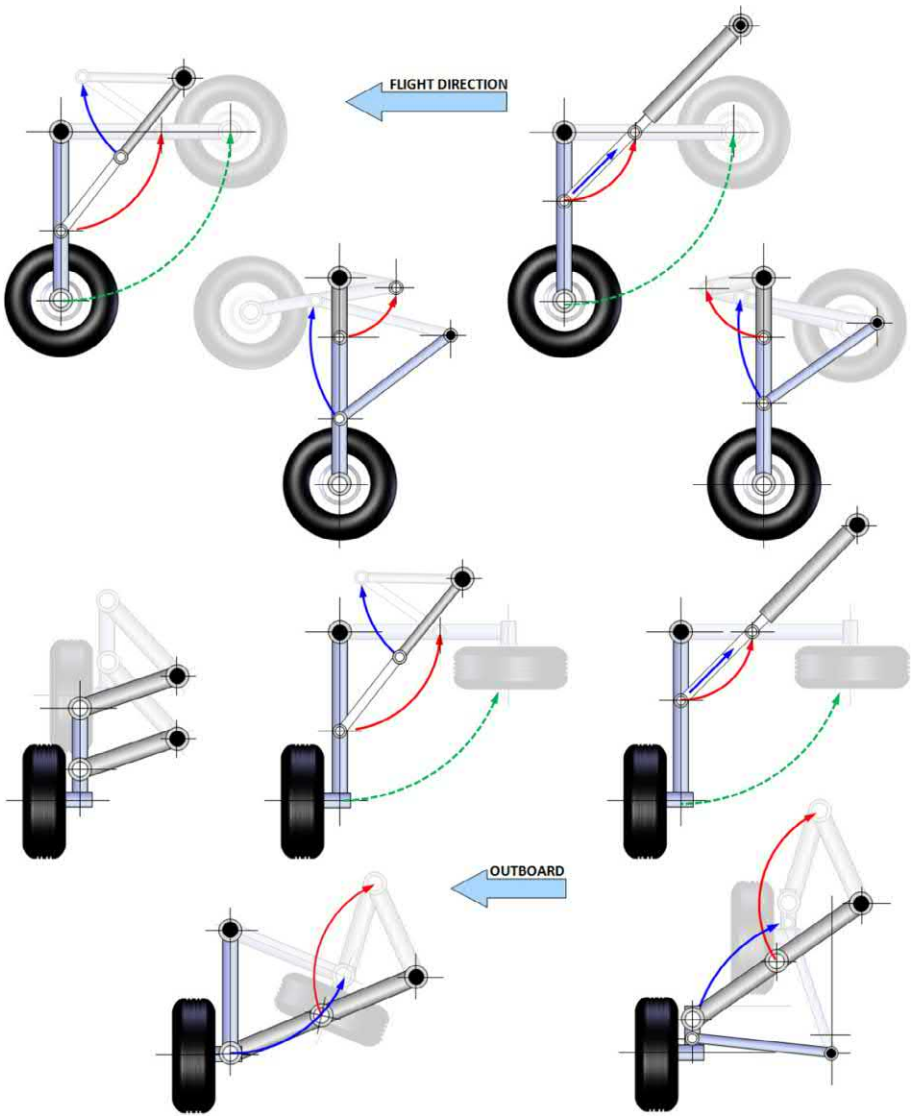


FIGURE 13-7 Some retraction methodologies for configurations that retract forward or aft with respect to flight direction (upper half) and some that retract inboard and extend outboard. *Based on Pazmany, L., Landing Gear Design for Light Aircraft, Vol. 1, Ladislao Pazmany, 1986; Curry, N.S., Aircraft Landing Gear Design: Principles and Practices, AIAA Education Series, 1988.*

TABLE 13-4 Contemporary types of tires for aircraft [2].

Type	Pressure	Used for	Speed limit [1], KGS[a]	Comment
I	Low	Piston aircraft	Low	This is the oldest size designations for tires and is based only on the outside diameter of the tire.
III	Low	Piston aircraft	<140	This is one of the earliest size designations and is used for early piston-prop type aircraft. It is a low-pressure tire intended to provide improved cushioning and flotation.
VII	100–250 psi	Jet aircraft	140–195	A more recent type than Type III. This type covers most of the older sizes and was designed for today's jet aircraft with its higher load capacity.
Three-Part Type	–	Piston and jet aircraft	183–204	All new tires follow this classification. This group was developed to meet the higher speeds and loads of today's aircraft. NOTE: Some sizes have a letter such as "H" in front of the diameter. This is to identify a tire that is designed for a higher percent deflection.
Radial	–	Piston and jet aircraft	183–204	Radial size nomenclature is the same as Three Part Type, except an "R" replaces the "-" (dash) before the wheel/rim diameter to indicate a radial tire.
Metric	–	Piston and jet aircraft	183–204	Same as Three Part Type, except the diameter and section width dimensions are in millimeters, and the wheel/rim diameter is in inches.

[a] *KGS stands for Knots, Ground Speed. See Chapter 17 for more details. Note that the ground speed shown is the maximum permitted.*

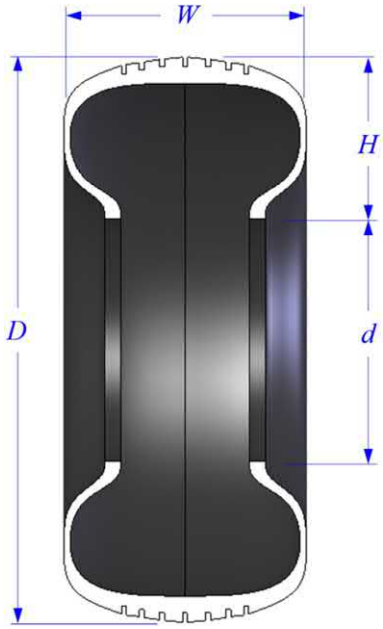


FIGURE 13-8 Important geometric definitions for a tire.

TABLE 13-5 Range of inflation pressures for typical aircraft.

Pressure, psi	Comment
<40	Recommended for unimproved, low strength and uneven runways. A high AR tire and low pressure offers great impact cushioning, minimizes surface rutting, improves the durability of the treads and tire in general. This is the pressure range for the typical automobile tire.
40–75	Used for tires expected to operate off improved runways.
75–125	Intended for high performance aircraft operating off asphalt and concrete runways only. The higher pressure allows for a smaller and lighter tire, which is helpful for reduced aerodynamic drag and stowing volume.
>125	Generally, not used for GA aircraft.

results in several choices at the disposal of the designer, although focusing on the Three-Part Type is recommended for modern aircraft design. The TRA type tires shown in Table 13-4 have the sizing designation shown in Table 13-6. Figure 13-9 shows schematics of the three most common types, Type III, VII, and the Three-Part Type. It is problematic that Type III does not explicitly specify the nominal diameter of the tire. This is important to estimate their drag. For specific dimensions, refer to reference [2].

(5) Selection of Tire Sizes

The first step is to download a document like reference [2], which features an excellent selection guide in *Section 4*

TABLE 13-6 Examples of dimension designation for various types of tires for aircraft.

Type	Tire size example	Nominal diameter	Nominal section width	Nominal wheel/rim diameter
I	27	27.0 in	–	–
III	8.50–10	–	8.50 in	10.0 in
VII	49 × 17	49.0 in	17.0 in	–
Three-part type	49 × 19.0–20	49.0 in	19.0 in	20.0 in
Radial	32 × 8.8R16	31.8 in	9.25 in	16.0 in
Metric	670 × 210–12	670 mm	210 mm	12.0 in

Based on Goodyear Aircraft Tire Data Book, Goodyear Tire and Rubber Company, 2002.

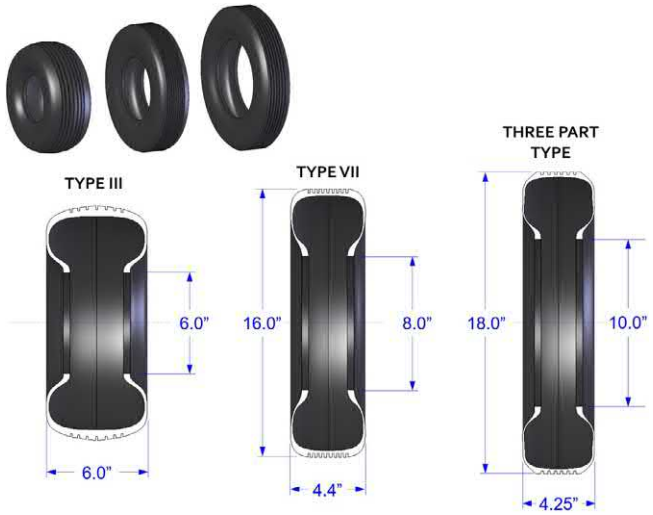


FIGURE 13-9 The three most common aircraft tire types. Left is Type III 6.00-6, center is Type VII 16 × 4.4 (with an 8-in. rim), and right is Three Part Type 18 × 4.25-10. Images are to scale.

(*Data Section—Tires*). The document lists tires by type and rated speed, load, inflation pressure, braking load, and bottoming load. It is an ideal resource to pick a potential tire during the conceptual and preliminary design phase. It can be downloaded free of charge from: http://www.goodyearaviation.com/resources/. Also, note that for the certification of GA aircraft, the tire selection is bound by 14 CFR §23.733 *Tires*.

Main Wheel Tires: Select main landing gear tires per these guidelines:

(1) Account for growth in the weight of the airplane (assuming it is successful). It is customary to assume a weight 25% greater than the initial gross weight. History shows that airplanes increase their weight as new models are introduced in response to a desire for

added capabilities. Selecting a larger tire now can avoid costly re-engineering later.

(2) Selection should be based on the load caused by the *aft-most* CG location for tricycle and *forward-most* CG location for taildraggers.

(3) Assume the most severe load-speed-time history during normal operation. This means determining the most adverse combination of high-elevation and high-ambient temperature take-off or landing. Low-density atmospheric conditions lead to higher ground speeds and this is critical to the tire selection process.

Nose Wheel Tires: Select nose landing gear tires per these guidelines:

(1) As with the main landing gear tire, account for growth in the weight of the airplane by assuming a 25% weight increase.

(2) Estimate static and dynamic braking load on the tire. Consider 14 CFR §23.493 *Braked Roll Conditions* in this matter.

(3) Base selection on the most forward CG location.

Tailwheel and Outrigger Wheels: The tailwheel and outrigger wheels for smaller aircraft are solid rubber. For larger aircraft, inflated tires are used and can be selected using the above approach. In the absence of rational analysis, if the outrigger wheels are intended to support landing loads, the attachment structure must support vertical and side loads amounting to ½ g. The wheel can then be selected based on the resulting load. For example, an airplane with an outrigger and 1000 lb_f gross weight would be reinforced to react 500 lb_f acting at the tire. This side load requirement is in accordance with 14 CFR §23.485 *Side Load Conditions*, although the regulations do not specifically address outrigger configuration. There is no set rule in outrigger structure. Aircraft like the Fournier RF-1 and RF-3 use outriggers not capable of reacting the above load, albeit sufficient to support taxi loads. The Fournier RF-2 does not even use wheels, but a wire loop, of which each end is attached to the wing structure.

(6) Wheels

The modern wheel is usually made from forged aluminum or magnesium alloy. Aluminum wheels are heavier but less expensive and offer better corrosion resistance. Both are equal in robustness and have the same performance rating.

Wheels usually consist of two halves that are joined by bolts (see Figure 13-10). Some modern designs are of a single piece configuration that is easier to maintain. They feature special lock-rings to provide the necessary lip for the tire. The wheel contains tapered roller bearings press-fit into a space called the *bearing housing*. They are kept in place by spring-fit snap rings. Brake discs are often attached to the wheels using the fastener that hold the two halves together.

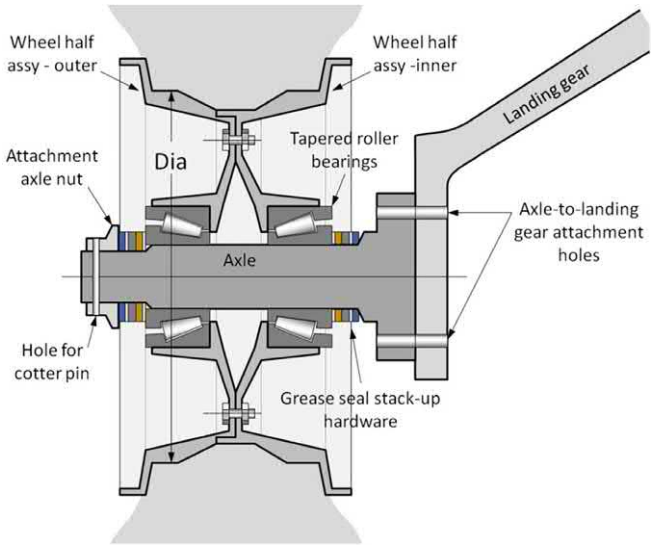


FIGURE 13-10 A schematic of a typical modern wheel made from joined halves.

There are three common sizes of wheels for small aircraft: 5″, 6″, and 7″ diameter. The diameter (Dia) is measured between the wheel shelves as shown in Figure 13-10.

(7) Brakes

The brakes must provide the airplane with means to (1) stop the aircraft after landing or an aborted take-off, (2) keep the airplane at rest at full power (this means the critical engine only for a multiengine aircraft), (3) allow the airplane to be steered via differential braking or appropriate slow-downs during taxiing, and (4) parking. The brakes are not expected to retain the aircraft with the wheels locked, should there be enough thrust to move the aircraft. A simplified schematic of the brake system in a light aircraft is shown in Figure 13-11.

There are two common kinds of brakes: *drum brakes* and *disc brakes*. Drum brakes reside inside the wheel, which reduces their frontal area. Thus, if used with retractable landing gear, they can help solving space-claims issues in thin wings. Disc brakes have superior performance, are lighter, and are easier to maintain.

Braking generates considerable heat through friction. The amount of heat depends on factors such as (1) the weight of the vehicle being stopped, (2) the speed at which braking is applied, (3) the effectiveness of the conversion of friction into heat, and (4) the friction area of the brakes. This is where the difference between drums and discs become apparent. The drum brakes dissipate heat

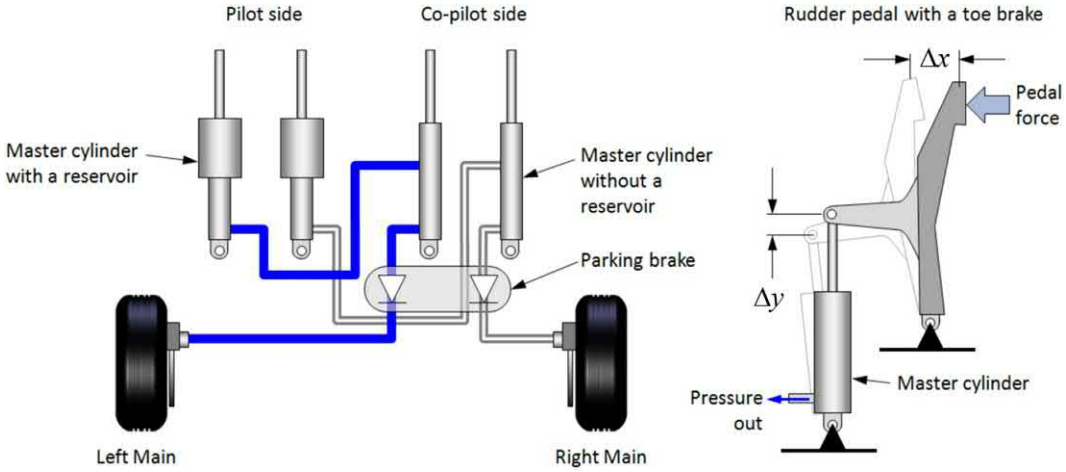


FIGURE 13-11 A schematic of a brake system for a small aircraft. It is recommended that $\Delta y = \frac{1}{2}\Delta x$. *Based on http://groveaircraft.com/brakedesign.html [Accessed 06/07/2020].*

less effectively than disc brakes. Since the drum brake is contained inside the wheel, the result is inferior heat transfer from the drum. If too much heat is generated, the braking capacity is lost ("fading") just when it is needed the most. In contrast, disc brakes reside on the outside of the wheel and are directly exposed to air, in addition to featuring calipers with two braking pads on each side of the disc (and sometimes multiple discs). Direct exposure to air leads to superior cooling and more effective braking under demanding conditions.

Manufacturers recommend that wheels and brakes be selected together. These should be selected in accordance with the following guidelines:

(1) Determine the static load on each wheel. Select wheels whose rating matches or exceeds this value.

(2) The selection of brakes for GA aircraft is bound by 14 CFR §23.735 *Brakes*. This requires the brakes to have the capacity to absorb the kinetic energy of the aircraft based on one of the two methods: (i) conservative rational analysis and, in the absence of such analysis, (ii) based on the following formula:

$$KE = \frac{0.0433 W V_{S_0}^2}{N} \tag{13-6}$$

Where

KE = Kinetic Energy in ft·lb$_f$,
V_{S_0} = Stalling speed in the landing configuration in KTAS,
N = number of main wheels featuring brakes,
W = aircraft weight in lb$_f$.

Equation (13-6) yields the kinetic energy per each brake and this value must be specified when contacting brake manufacturers.

DERIVATION OF EQUATION (13-6)

For V_{S_0} in ft/s (or m/s) and m in slugs (or kg), the kinetic energy is given by:

$$KE = \frac{1}{2} m V_{S_0}^2$$

The above regulatory paragraph assumed V_{S_0} in KTAS and W in lb$_f$. Therefore,

$$KE = \frac{1}{2} m V_{S_0}^2 \rightarrow \frac{KE}{N} = \frac{\frac{1}{2}\frac{W}{g}(1.688 V_{S_0})^2}{N} = \frac{0.0433 W V_{S_0}^2}{N}$$

(8) Other Useful Information

Aircraft tires are designed such that the internal tensile forces in the fabric layers are uniform when unloaded. When deflected, this force is higher in the outer plies than the inner ones. This variation generates shear stresses tire that must not be exceeded. Exceeding the allowable shear stress is possible for under-inflated or over-loaded tires. This causes large deflections that causes heat build-up, which can cause ply separation. The result is decreased durability of the tire. It also causes an uneven wearing of the tread and deterioration of the shoulder. This may damage the tire's sidewall during high impacts (landing). Excessive inflation pressure is detrimental due to uneven tread wear, reduced braking effectiveness, and by making the tire more susceptible to damage by foreign objects.

Tires can withstand reasonably high temperatures. Typical maximum operational limits of surface temperature is 225°F (107°C) or brake heat reaches 300°F (149°C). Such temperature results from excessive braking after a high-speed landing.

Finally, when selecting wheels and tires, it can be helpful to know the types of tires used for existing fleet of

TABLE 13-7 Examples of tires used by for various business jet aircraft.

BUSINESS AIRCRAFT					
Aircraft Maker	Model	Main Tire		Nose or Tail Tire	
		Size	Ply Rating	Size	Ply Rating
Aerospatiale	SN-600 Corvette	26x6.6	10 TL	17.5x6.25-6DDT	8 TL
BAe-Hawker	HS-125	23x7.00-12BR	12 TL	18x4.25-10 DT	6 TL
Bombardier	CL-600/601-Challenger	26x6.6	14TL	18x4.4 DT	12 TL
Cessna	500 Citation I	22x8.00-10	10 TL	18x4.4 DDT	10 TL
	550 Citation II	22x8.00-10	12 TL	18x4.4 DDT	10 TL
	650 Citation III	22x5.75-12	10 TL	18x4.4 DDT	10 TL
	560 Citation V	22x8.00-10	12 TL	18x4.4 DDT	10 TL
	650 Citation VI	22x5.75-12	10 TL PR	18x4.4 DDT	10 TL
	650 Citation VII	22x5.7512	10 TL PR	18x4.4 DDT	10 TL
	750 Citation X	26x6.6R14	14 TL PR	18x4.4 DT	10 TL
Dassault	10 Falcon	22x5.75-12	10TL	18x5.75-8	8TL
	20 Falcon	26x6.6 26x6.6R14	10TL	13x5.0-4 DT	14TL

Based on Goodyear Aircraft Tire Data Book, Goodyear Tire and Rubber Company, 2002.

TABLE 13-8 Examples of tires used by for various single engine propeller aircraft.

SINGLE ENGINE PROPELLER					
Aircraft Maker	Model	Main Tire		Nose or Tail Tire	
		Size	Ply Rating	Size	Ply Rating
American Champion	Decathlon/Super Decathlon	6.00-6/8.00-6	4 or 6	Scott	-
Commander	112/114 Commander	6.00-6/7.00-6	6	5.00-5	4 or 6
Beechcraft	C-17R Staggerwing	7.50-10	6	10.00SC	-
	BE-23 Musketeer, BE-A24 Sundowner	6.00-6	4	6.00-6	4
	BE-33A Bonanza	7.00-6	6	5.00-5	4
	BE-36 Bonanza	7.00-6	6	5.00-5	4
Bellanca	17-30A Viking, 17-31A Super-Viking	6.00-6	6	15x6.00-6	6/8
Cessna	150,-152 Commuter, Aerobat	6.00-6	4	5.00-5	4
	172 Skyhawk	6.00-6	4	5.00-5	4
	177RG Cardinal RG	15x6.00-6	6	5.00-5	4
	180 Skywagon	6.00-6	6	8.00" SC	6
	182RG, T182RG Skylane	15x6.00-6	6	5.00-5	4
	185 Skywagon	6.00-6	6	8.00" SC	8
	188 AG-Wagon	22x8.00-8	6	10.00" SC	6
	206 StationAir	6.00-6	6	5.00-5	6
	207 Skywagon	6.00-6	8	6.00-6	8
	208 (FLO) Caravan	8.50-10	8	22x8.00-8	6
	210 Centurion	6.00-6	8	5.00-5	6
Cirrus	SR20, SR22	15x6.00-6	6	5.00-5	6
Embraer	EMB-200 Ipanema	6.50-8	8TT	2.80/2.50-4	4TT
Mooney	MO-20 Ranger, MO-21C Super	6.00-6	6	5.00-5	4/6
	MO-22 Mustang	6.00-6	6	15x6.00-6	6
	MO-20E Chapparal	6.00-6	6	5.00-5	4
	MO-20F Executive	6.00-6	6	5.00-5	6
	MO-20J 201	6.00-6	6	5.00-5	6
	MO-20K Turbo 231	6.00-6	6	5.00-5	6
	M-20M Bravo, M-20S Eagle, M-20R Ovation	6.00-6	6	5.00-5	6
Piper	J3 Cub	8.00-4	4	8.00"SC	Solid
	PA18-135 Super Cub, PA18-150 Super Cub	6.00-6	4	8.00"SC	Solid
	PA25-150 Pawnee	7.00-6	4	8x3.00-4	4
	PA28-160 Cherokee	6.00-6	4	6.00-6	4
	PA28-161 Warrior II	6.00-6	4	5.00-5	4
	PA28-181 Archer II	6.00-6	4/6	6.00-6	4
	PA28R-201 Arrow	6.00-6	6	5.00-5	4
	PA32 6-300	6.00-6	6	6.00-6	6
	PA32R-301T Saratoga II TC	6.00-6	8	5.00-5	6
	PA36 Brave	8.50-10	6	10x3.5-4	6
	PA38 Tomahawk	6.00-6	6	5.00-5	6
	PA46-350P Malibu Mirage	6.00-6	8	5.00-5	6
Lake Aircraft	LA-4 Buccaneer, LA-250 Renegade/Seafury	6.00-6	4	5.00-4	4

Based on Goodyear Aircraft Tire Data Book, Goodyear Tire and Rubber Company, 2002.

TABLE 13-9 Examples of tires used by for various twin engine propeller aircraft.

TWIN ENGINE PROPELLER					
Aircraft Maker	Model	Main Tire		Nose or Tail Tire	
		Size	Ply Rating	Size	Ply Rating
Beechcraft	BE-18	11.00-12	8 TL	14.50SC	8 TL
	BE-50 Twin Bonanza	8.50-10	6	6.50-10	4
	BE-B55 Baron	6.50-8	8	5.00-5	6
	BE-60 Duke	19.5x6.75-8	10 TL	15x6.00-6	4
	BE-80 Queen Air	8.50-10	8 TL	6.50-10	6 TL
	BE-C90B King Air	8.50-10	8 TL	6.50-10	6 TL
	BE-200T Super King Air	22x6.75-10	8 TL	22x6.75-10	8 TL
	BE-99	18x5.5	8 TL	6.50-10	6 TL
	BE-300/350 Super King Air	22x6.75-10	8 TL	19.5x6.75-8	10 TL
	BE-1900 Airliner	22x6.75-10	8 TL	19.5x6.75-8	10 TL
Cessna	T303-Crusader	6.00-6	8	6.00-6	6
	310,-T310	6.50-10	6	6.00-6	4
	320,-340	6.50-10	6	6.00-6	4
	Model 336	6.00-6	6	15x6.00-6	6
	337-Super-Skymaster	18x5.5	8	15x6.00-6	6
	401,-402	6.50-10	8	6.00-6	6
	404-Titan	22x7.75-10	10 TL	6.00-6	6
	Model 411	6.50-10	8	6.00-6	6
	414-Chancellor	6.50-10	8	6.00-6	6
	421-Golden Eagle	6.50-10	8	6.00-6	6
	425-Conquest I	6.50-10	10	6.00-6	6
	441-Conquest II	22x7.75-10	10 TL	6.00-6	6
Piper	PA23,x160-235xApache	7.00-6	6	6.00-6	4
	PA23-250xAztec	7.00-6	8	6.00-6	4
	PA34-270T Seneca V	6.00-6	8	6.00-6	8
	PA44-180 Seminole	6.00-6	8	5.00-5	6
	PA42xCheyenne IIIA	6.50-10	12TL	17.5x6.25-6	10
	PA44-180xSeminole	6.00-6	6	6.00-6	6
	600/601Bx(PA60)xAerostar	6.50-8	TL	6.00-6	6
	PA30 Twin Commanche	6.00-6	4	6.00-6	6
	PA31 Chieftain	6.50-10	8	6.00-6	6
	PA31T Navajo	6.50-10	10	6.00-6	6
	PA34-220 Seneca	6.00-6	8	6.00-6	6

Based on Goodyear Aircraft Tire Data Book, Goodyear Tire and Rubber Company, 2002.

aircraft. Tables 13-7–13-9 provide such information for selected aircraft of various classes. The reader is directed toward reference [2] for more details.

13.2.4 Types of Landing Gear Legs

One of the most important capability of the landing gear is how it absorbs the landing impact. GA aircraft commonly use leaf-springs, rubber-doughnuts, rubber-bungees, coiled steel springs, and oleo-pneumatic shock absorbers. The first three are depicted in Figure 13-12, showing typical deflection at impact (denoted by "*d*"). The primary advantage of such landing gear is simplicity and light weight. However, their shock absorption efficiency is less than ideal. To understand why, consider the graphs of Figure 13-13. A few words about shock absorption are necessary.

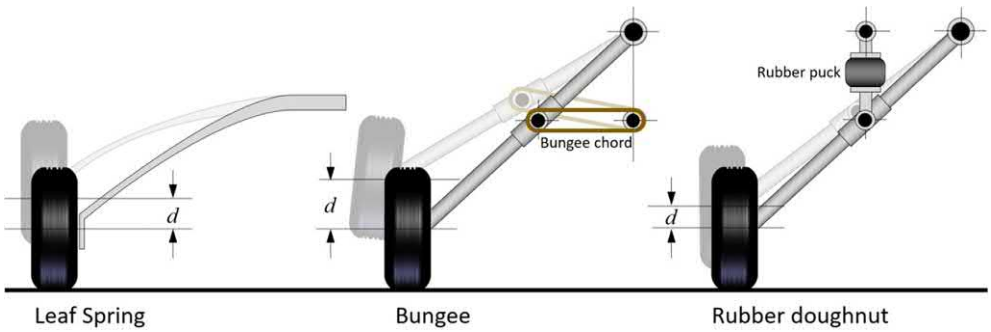


FIGURE 13-12 A schematic of a typical leaf spring, bungee, and rubber doughnut shock absorbers. The dimension *d* denotes the deflection of the gear, which is indicative of the efficiency of the landing gear shock absorption.

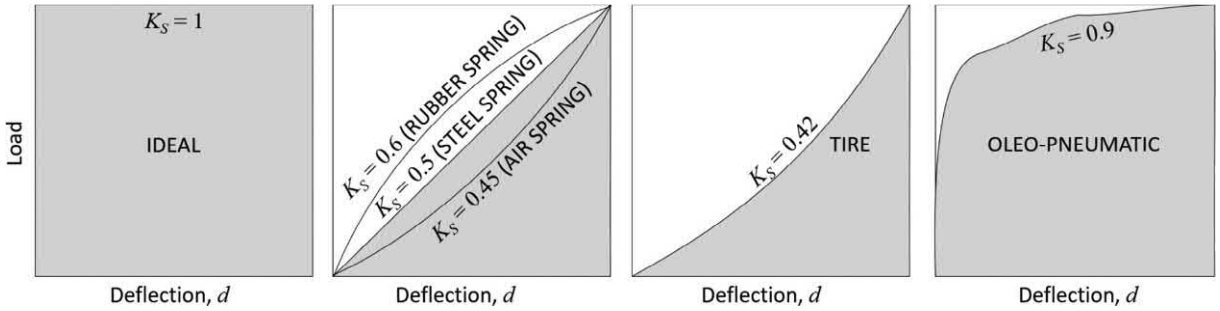


FIGURE 13-13 Load versus deflection highlights shock absorption efficiency. *Based on Pazmany, L., Landing Gear Design for Light Aircraft, Vol. 1, Ladislao Pazmany, 1986.*

First, consider the distance between the initial contact of the tire with the ground and its maximum deflection geometry a moment later (when it maxes out). This distance represents what is required to decelerate from the rate-of-descent to zero vertical speed. The efficiency of the deceleration is denoted by the constant K_S in Figure 13-13. The ideal shock absorber is 100% efficient because it achieves this in zero distance ($K_S = 1$). Efficient, yes, but not exactly comfortable. A steel spring obeys Hooke's law and can be sized to react the impact over the available distance with 50% efficiency ($K_S = 0.5$). It improves the ride but demands greater distance for the deceleration. A tire is even less efficient, with efficiency $K_S = 0.39$ to 0.47 [1]. The oleo-pneumatic strut is one of the most efficient means to absorb the impact energy. The graph shows that it reacts most of the landing load over a short distance, and the remainder is reacted while providing a much more comfortable ride for the occupants.

The landing gear comes in a variety of shapes and sizes, and much could be said about their pros and cons. In interest of space, only the four most common types are presented (see Figure 13-14). These are (A) the *leaf-spring* steel (or composite) main landing gear, (B) *oleo-pneumatic strut* retractable main landing gear, (C) oleo-pneumatic retractable *trailing-link* main landing gear, and (D) a *steerable* oleo-pneumatic strut nose landing gear.

It should be stressed that there are other ways to absorb the landing impact. Many are presented in references [1, 4, 5]. Reference [6] presents incredibly original landing gear designs devised by German engineers during World War II.

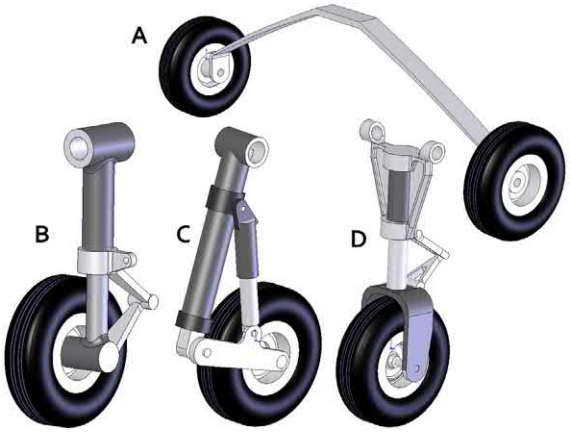


FIGURE 13-14 Common types of landing gear for small aircraft: A = Leaf-spring steel (or composite) MLG, B = Oleo-strut retractable MLG, C = Oleo-strut retractable trailing link MLG, and D = Steerable oleo-strut NLG.

(1) Leaf-Spring Landing Gear (A)

The leaf-spring landing gear consists of a flat but stiff cantilever beam that reacts landing loads in bending. Its primary advantages include low cost, stout, durable, and installation simplicity. It represents the simplest form of the landing gear. It is intended as a main landing gear. The low thickness-to-chord ratio of the strut (leg) generates low drag while the wheels, tires, and braking calipers generate high drag. This is remedied using a wheel fairing. Primary drawbacks include high reaction loads in the airframe, as the spring beam tends to have a large moment arm. This moment generates high bending stress, requiring high-strength material. The landing gear is hard to implement in a retractable configuration. Some Cessna aircraft feature retractable leaf-spring landing gear made from tubular geometry. The leaf-spring has limited structural damping but works well because of the damping provided by the scrubbing motion of the tires. To the best knowledge of this author, the largest aircraft to currently use a leaf-spring landing gear is the De Havilland of Canada DHC-6 Twin Otter, with a maximum gross weight of 12,500 lb_f.

(2) Oleo-Pneumatic Landing Gear (B, C, D)

The landing gear labeled B, C, and D, in Figure 13-14 uses a mechanical oleo-pneumatic shock absorber of the type shown in Figure 13-15. In simple terms, the shock energy is absorbed by forcing oil in a chamber (in the strut) through orifices, against a chamber of dry air or nitrogen (oil and gas are under very high pressure). This allows the shock from the landing impact to be reacted

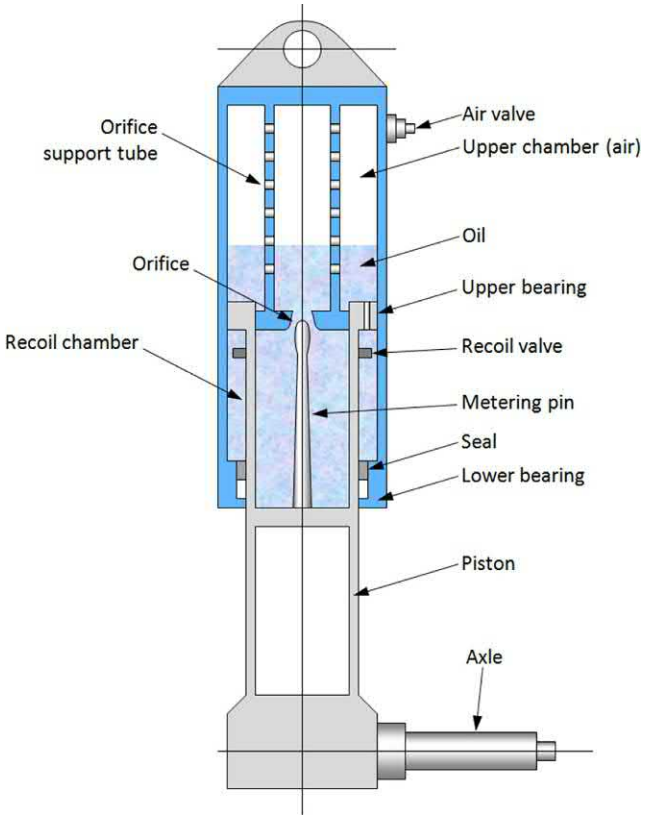


FIGURE 13-15 A schematic of a typical oleo-pneumatic cylinder.

initially with a short deflection, and then a larger one as the oil seeps back. The rebound is accomplished by the gas pushing the oil back into its chamber at a controlled rate, which expands the shock absorber. Reference [4] provides methods to size oleo-pneumatic struts.

(3) Oleo-Pneumatic Trailing Link Landing Gear (C)

The oleo-pneumatic trailing link landing gear has become a popular option in many aircraft due to the superior ride quality it offers. This is possible as the mechanism allows larger deflection of the wheel and tire assembly than possible when mounted directly to the strut. The drawback of the trailing link landing gear is greater weight and cost. It also requires larger internal volume to stow.

(4) Various Landing Gear Issues—Shimmy

Shimmy is a violent dynamic instability that occurs, primarily in free-castoring landing gear due to unbalancing of the forces that act on the members of the trailing link. This frequently happens to nose-landing gear and can be violent enough to break it off. The phenomenon is of great importance to manufacturers and operators alike. The aircraft designer should be aware of it and possible solutions (shimmy dampers, high friction castoring, geometric relations, mass balancing, and so on).

(5) Various Landing Gear Issues—Whistling

Whistling is a phenomenon in which the complex geometry of a landing gear exposed to the airflow in flight generates a high-pitch sound. An example is the Piper PA-28 Arrow with its retractable landing gear extended. There is not much that can be done to eliminate the whistling. The author is not aware of any studies addressing this issue.

(6) Various Landing Gear Issues—Nonlinear Loads during Retraction and Deployment

During the retraction or deployment of landing gear, the actuation system (linkages and hydraulic actuator) undergo variable loading. An actuator capable of brisk retraction or extension during ground tests (when airspeed in zero) may be grossly undersized when air loads compound the inertia loads. For instance, consider the retraction of a main landing gear into a wing, exemplified in Figure 13-16. As the gear rotates into the wheel well, the air loads acting on the landing gear door (whose effect is attenuated by the complex flow field around the landing gear leg and wheel) may overload the actuator unexpectedly, so the gear gets stuck in a partially-retracted position. It might get stuck at a ϕ ranging from 30 to 60 degrees. This may cause a serious problem in flight test if the actuator is undersized—it should be oversized to provide the power needed. The test pilot should be ready with a contingency plan—for instance, try retraction just above stalling speed.

13.2.5 Reaction of Landing Gear Forces

The landing gear force matrix consists of three force components; a vertical force (F_{land}), drag force (F_{drag}), and side force (F_{side}). The magnitude of these load is worked out by *regulatory* or *rational* analyses. The regulatory loads comprise "cookbook" style calculations designed to be overly conservative. Its primary advantage (some would say its only advantage) is that it reduces analysis time. However, it can be argued it increases the weight of the aircraft. For GA aircraft, 14 CFR §23.471 through §23.511 provides the necessary guidance to estimate all regulatory loads for land-and sea-based aircraft.

Figure 13-17 shows a balanced free-body diagram depicting how typical landing loads are reacted. These loads (R_1 through R_4 and M_1 and M_2) is reacted at specific hardpoints, either in the wing or the fuselage. These, in turn, require a proper local reinforcement for transfer into the airframe. Local reinforcement means "added structural weight." Of course, the only countermeasure is to try and minimize this weight through effective load paths.

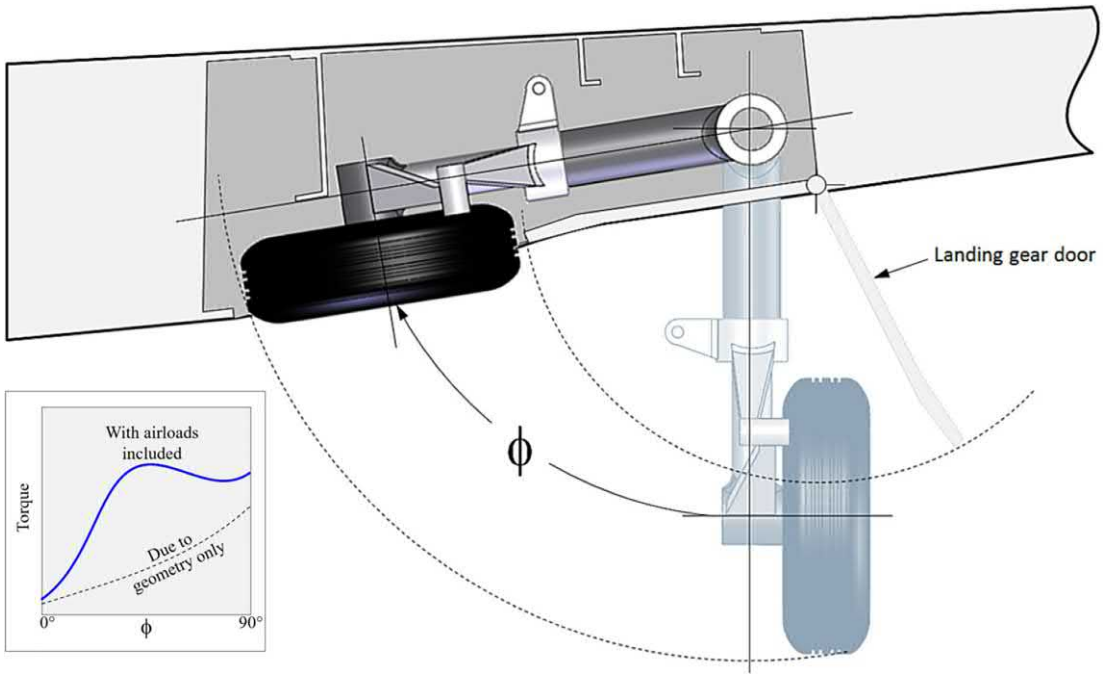


FIGURE 13-16 The retraction of the landing gear often causes unsuspected air loads to overload the actuator, with unforeseeable results.

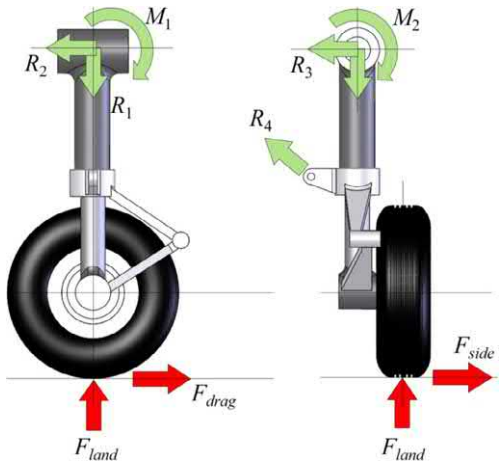


FIGURE 13-17 A free-body diagrams showing reaction forces on a typical landing gear strut.

(1) Sink Rate at Touchdown

Aircraft are subject to landing impact that depends on the sink rate at touchdown. Certification of GA aircraft for landing impact loads requires the applicant to demonstrate shock absorption by a drop test. Referencing the "old" 14 CFR Part 23, the required drop height (in inches) is estimated by an equation given per §23.725(a). Using elementary kinematics, we can convert this expression to give touchdown sink rate (w) as follows:

$$h_{inches} = 3.6(W/S)^{1/2} \quad \Rightarrow \quad w \approx 4.4(W/S)^{1/4} \qquad (13\text{-}7)$$

The same paragraph limits drop height between 9.2 and 18.7 in. This sets the sink rate between 7 and 10 ft/s.

(2) Landing Gear Impact Response

Spring action and shock absorption of a landing gear combine to bring a mass, at some initial vertical speed, to a complete stop. This is accomplished through a controlled deceleration over a given distance. Consider the landing gear making its first contact with the ground. Assume that at this instant, the rate-of-descent is w. Simple kinematics allows us to estimate the *average deceleration* required to bring w to zero.

$$a_z = -\frac{w^2}{2d} \qquad (13\text{-}8)$$

where d is the vertical distance the between the initial touchdown and the first "bottom out." The minus sign indicates deceleration. If d is large, then the landing will "appear" soft. Unfortunately, we do not have the luxury of a long deceleration distance. The sink rate, w, which can be as much as 10 ft/s (for GA) to 22 ft/s (for carrier-based aircraft) (3–6.7 m/s), must be brought to zero over a short distance—and therein lies the challenge. The solution is an initial rapid deceleration, followed by a reduced deceleration (see Figure 13-13).

When more detail about the dynamics of the landing gear is desired, its vertical motion can be studied by replacing it with the simple *mass-spring-damper* system shown in Figure 13-18. For simplicity, assume that (1) immediately after ground contact the tires remain on the ground, (2) the tires are stiff and provide no shock absorption, and (3) neglect lift. The *equation-of-motion* for this system can be written as

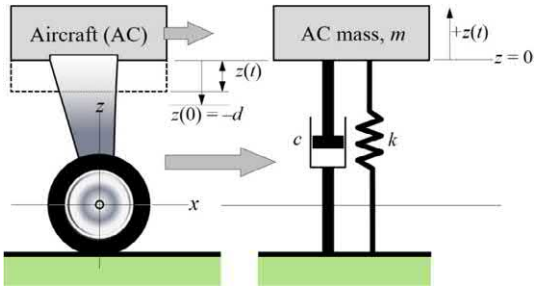


FIGURE 13-18 Approximating the landing gear dynamic response.

$$\sum F = m\ddot{z}$$
$$\Rightarrow \quad m\ddot{z} + F_{damper} + F_{spring} = 0 \qquad (13\text{-}9)$$
$$\Leftrightarrow \quad m\ddot{z} + c\dot{z} + kz = 0$$

where m is the mass of the aircraft, given by W/g. The landing strut constitutes a spring of *spring stiffness* k and damper with *damping coefficient* c. Both exert a force on the mass that slows it down. The spring force operates through *Hooke's law* ($F_{spring} = kz$). The damper force depends on the speed of the mass and is given by $F_{damper} = c\dot{z}$. The distance is a function of time (t), denoted by $z(t)$. We start the clock once the mass has bottomed out for the first time, when it has moved through distance $z(0) = -d$. We can identify Equation (13-9) as a *homogeneous, ordinary second-order differential equation*. Such equations come with packaged solutions.

First, rearrange to get $$\ddot{z} + \frac{c}{m}\dot{z} + \frac{k}{m}z = 0 \qquad (13\text{-}10)$$

To solve the second-order differential equation, we must identify its *characteristic equation*. This leads to three possible solutions, governed by the magnitude of m, c, and k. Since $m > 0$, $c > 0$, and $k > 0$, our solution requires $c < 2\sqrt{km}$ and has the form:

$$z(t) = e^{-\frac{c}{2m}t}[C_1 \cos(\omega t) + C_2 \sin(\omega t)] \qquad (13\text{-}11)$$

where $\omega = \frac{1}{2}\sqrt{4(k/m) - (c/m)^2}$ is the angular frequency. The speed and acceleration of the oscillation is given by the first and second time-derivative of Equation (13-11):

$$\dot{z}(t) = \left(\frac{c}{2m}\right)e^{-\frac{c}{2m}t}[\omega C_1 \sin(\omega t) - \omega C_2 \cos(\omega t)] \qquad (13\text{-}12)$$

$$\ddot{z}(t) = \left(-\frac{c^2\omega^2}{4m^2}\right)e^{-\frac{c}{2m}t}[C_1 \cos(\omega t) + C_2 \sin(\omega t)] \qquad (13\text{-}13)$$

To determine the coefficients C_1 and C_2 we substitute the initial conditions, $z(0) = -d$ and $\dot{z}(0) = 0$, into Equations (13-11) and (13-12).[1] This gives $C_1 = -d$ and $C_2 = 0$. Therefore, the oscillatory motion is fully described by

$$z(t) = -d \cdot e^{-\frac{c}{2m}t}\cos(\omega t) \qquad (13\text{-}14)$$

$$\dot{z}(t) = \left(-d\frac{c\omega}{2m}\right)e^{-\frac{c}{2m}t}\sin(\omega t) \qquad (13\text{-}15)$$

$$\ddot{z}(t) = \left(d\frac{c^2\omega^2}{4m^2}\right)e^{-\frac{c}{2m}t}\cos(\omega t) \qquad (13\text{-}16)$$

Example 13-1 illustrates the application of this method. Note the limitations in the procedure. For instance, shock absorption by scrubbing loads is absent, tire dynamics and lift are ignored. Regardless, it gives some insight.

EXAMPLE 13.1

A small 2500 lb_f aircraft features a steel leaf-spring landing gear of cross-section 8×0.75 in. and leg-length of 44 in. (see Figure 13-19). Evaluate the dynamic response of the airplane for a hard landing of 4 g. Assume steel has a *Young's modulus* of $E = 29 \times 10^6$ psi and structural damping of $c = 156$ slugs/s. This problem expects reader familiarity with elementary solid mechanics.

SOLUTION:

Assume the airplane lands with both tires simultaneously, with each leaf-spring acting as a cantilevered beam carrying ½ the load.

The load acting on the landing gear is $P = nW/2 = (4)(2500)/2 = 5000$ lb_f. The moment of inertia of the cross-section is $I = bh^3/12 = (8)(0.75)^3/12 = 0.2813$ in^4. Thus, the maximum deflection of the beam is

$$d = \frac{Pl^3}{3EI} = \frac{(5000)(44)}{3(29 \times 10^6)(0.2813)}$$
$$= 17.41 \text{ in} \quad (= 1.451 \text{ ft})$$

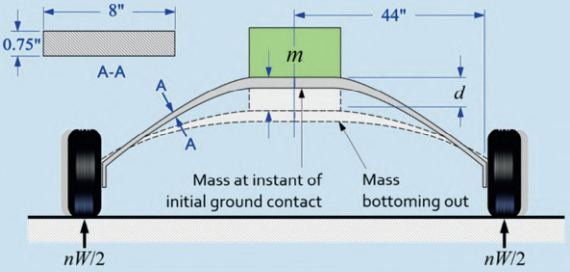


FIGURE 13-19 Landing gear at moment of impact.

[1] We may just as well start the clock at the moment of touchdown, which requires $z(0) = 0$ and $\dot{z}(0) = -w$.

EXAMPLE 13.1 (*cont'd*)

The mass is $m = W/g = (2500)/(32.174) = 77.70$ slugs. Since a total force of 2×5000 lb_f deflects the two legs 1.451 ft, our beam stiffness coefficient, $k = 2 \times 5000/1.451 = 6894$ lb_f/ft. The angular frequency is

$$\omega = \frac{1}{2}\sqrt{4(k/m) - (c/m)^2}$$

$$= \frac{1}{2}\sqrt{4(6894/77.7) - (156/77.7)^2} = 9.366 \text{ rad/s}$$

Note that a real landing gear would have to be thicker to withstand the bending stress, but this is ignored here. We can now determine the position (ft), speed (ft/s), and acceleration (ft/s^2) as a function of time (Figure 13-20).

$$z(t) = -d \cdot e^{-\frac{c}{2m}t}\cos(\omega t)$$
$$= -17.41e^{-1.004t}\cos(9.366t)$$
$$\dot{z}(t) = -d\frac{c\omega}{2m}e^{-\frac{c}{2m}t}\sin(\omega t)$$
$$= -17.85e^{-1.004t}\sin(9.366t)$$
$$\ddot{z}(t) = d\frac{c^2\omega^2}{4m^2}e^{-\frac{c}{2m}t}\cos(\omega t)$$
$$= 219.7e^{-1.004t}\cos(9.366t)$$

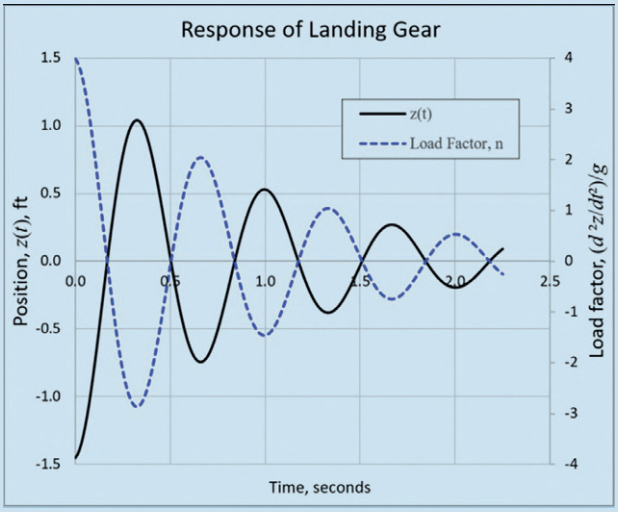


FIGURE 13-20 Landing gear response shows the damping leaves a lot to be desired.

13.2.6 Comparing the Ground Characteristics of Taildragger and Tricycle Landing Gear

An important difference between a taildragger and tricycle landing gear is ground handling. The taildragger is dynamically unstable while the tricycle is dynamically stable. To see why, consider Figure 13-21, which shows the bottom side of the airplane. It is a taildragger configuration, with a wheel-track w_t in a straight and yawed configuration. In this situation, the ground friction of each main gear (F_R and F_L) tire creates an equal and opposite moment about the CG.

In the right image the aircraft is yawing right. This changes the moment arms of the two ground reactions. The right one (F_R) is increased by a distance Δw_R, resulting in an increased *destabilizing moment*. The left reaction (F_L) is decreased by a distance Δw_L, yielding a reduced *stabilizing moment*. The sum of the two is a destabilizing moment that promotes an even greater yawing tendency. Consequently, the configuration will be inherently unstable.

The opposite holds for a tricycle landing gear (Figure 13-22). The left image shows the main-gear ground friction creates an equal and opposite moment about the CG, just like the taildragger. Note the addition of the reaction of the nose landing gear, F_N. The right image shows the aircraft yawing right. As before, the ground friction from the right main and nose tires generates a destabilizing moment. However, they act along a decreasing moment arm. The ground friction of the left tire, on the other hand, is stabilizing and it acts along a moment arm that increases with the yaw angle. The net sum is a stabilizing moment that increases with yaw angle, rendering the configuration stable.

When comes to ground-loop, the tricycle configuration is statistically safer than the taildragger. Ground-loop in taildraggers are about 6-times more common than tricycles (e.g. see statistics from [7] some of which is summarized in [8]). Primary trainers and commercial aircraft should always feature this configuration. However, as has already been discussed in Table 13-1, the taildragger configuration is a better choice for light aircraft that takeoff and land on poorly prepared runways (bushplanes).

13.3 GEOMETRIC LAYOUT OF THE LANDING GEAR

This section presents methods that help to accurately lay out the landing gear geometry for a tricycle, taildragger, and monowheel configurations. Additionally, methods to evaluate loads on the landing gear will be developed.

13.3.1 Geometric Layout of the Tricycle Landing Gear

If a decision is made to proceed with a tricycle landing gear, the next step is to define the layout of its geometry. The tricycle landing gear can be laid out as presented below *after* the following tasks have been completed:

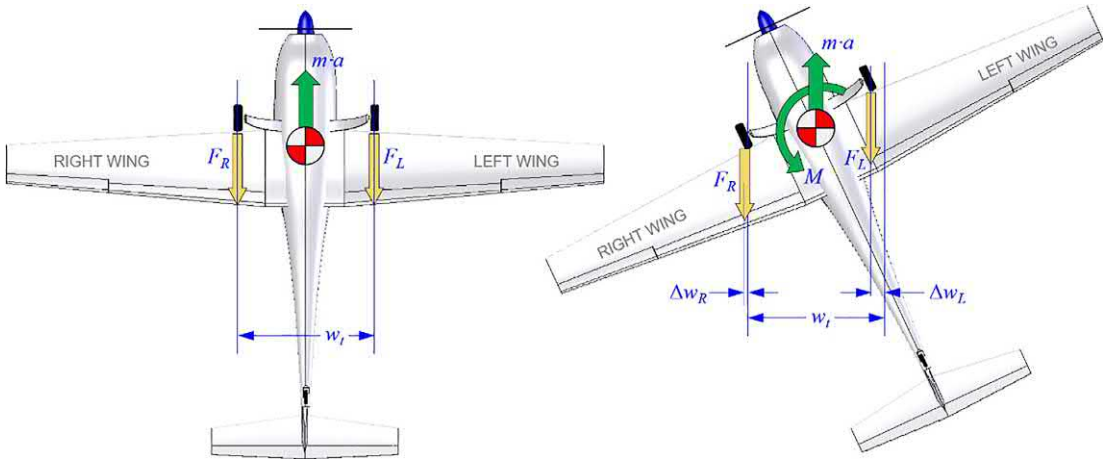


FIGURE 13-21 Ground instability of the taildragger configuration explained (bottom view.)

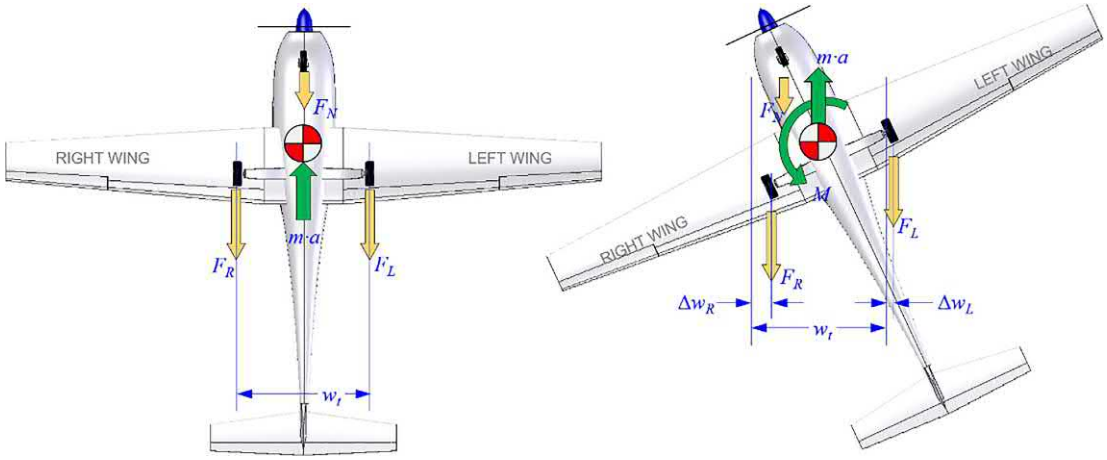


FIGURE 13-22 Ground stability of tricycle configuration explained (bottom view.)

(1) A side view of the design in a cruise attitude. Draw the mean geometric chord (MGC) on the side view.
(2) A top or bottom view of the airplane.
(3) A completed center-of-gravity (CG) envelope.

Refer to Figure 13-23 for STEPS 1 and 2.
STEP 1: Draw the forward CG-limit.
STEP 2: Draw the aft CG-limit.
Refer to Figure 13-24 for STEPS 3 through 5.

STEP 3: Determine the *highest* vertical position of the CG at the aft CG-limit and plot on the diagram as shown. This position is the most critical one. If it crosses the vertical line drawn in Step 7, the plane will fall on its tail.

STEP 4: Draw the prop-strike limit as shown, ensuring it is *parallel* to the ground plane. This is as close to the ground the propeller should get under most adverse conditions, such as a flat nose gear tire. The limit per 14 CFR §23.925(a) is 7-in.

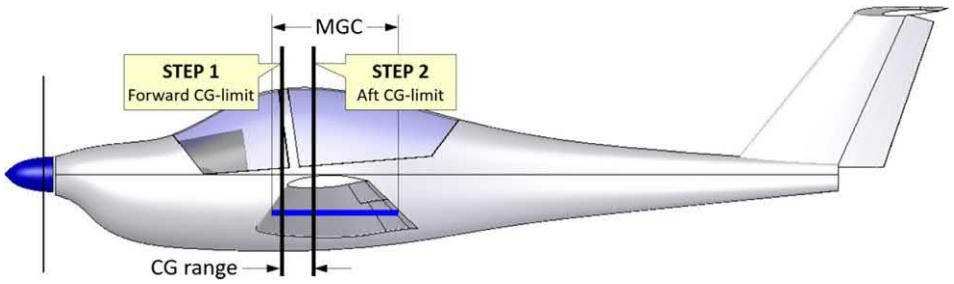


FIGURE 13-23 Steps 1 and 2 for the location of the tricycle landing gear.

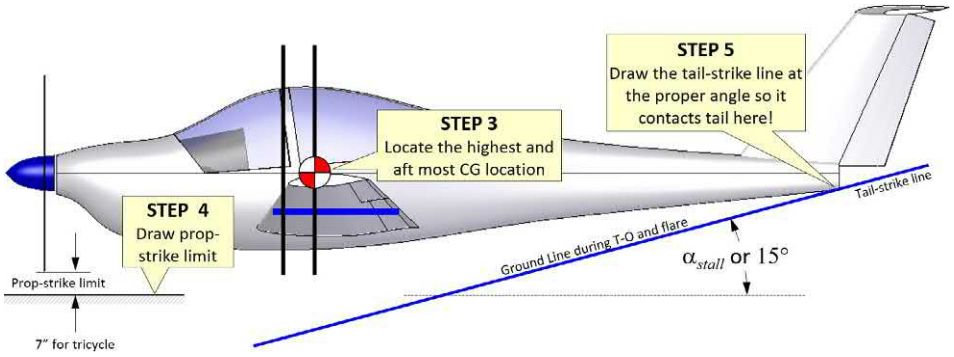


FIGURE 13-24 Steps 3 through 5 for the location of the tricycle landing gear.

STEP 5: Draw the tail-strike line shown, ensuring it is as close to α_{stall} in the clean configuration as practical, up to a maximum recommended value of 15 degrees. *The tail-strike line is also the ground line* for the airplane in tail-down position.

Refer to Figure 13-25 for STEPS 6 and 7.

STEP 6: Draw a line through the CG, *perpendicular* to the tail-strike line. It represents the contact point of the tire at a static deflection at 1 g load. *IMPORTANT: This is the static deflection of 1 g load. The landing gear drops below the tail-strike line once airborne.*

STEP 7: Draw a vertical line through the intersection of the tail-strike line *and normal to it*. It should form the same angle as the tail-strike line does to the horizontal. If done correctly, the three lines should all intersect at the same point.

Refer to Figure 13-26 for STEPS 8 and 9.

STEP 8: Position the main landing gear such the contact point of the wheel is at the intersection of the three lines as shown in Figure 13-26. If practical, align the main landing gear leg along the vertical line.

STEP 9: Position the nose landing gear such it carries no more than 20% of the aircraft weight when the CG is at

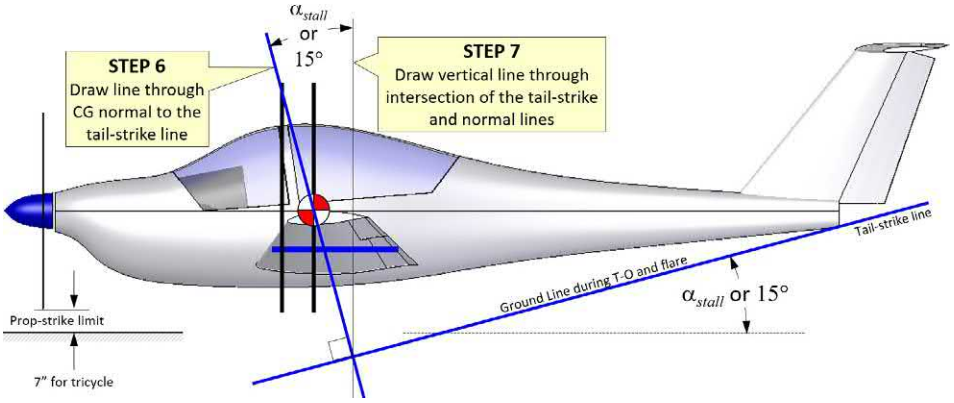


FIGURE 13-25 Steps 6 and 7 for the location of the tricycle landing gear.

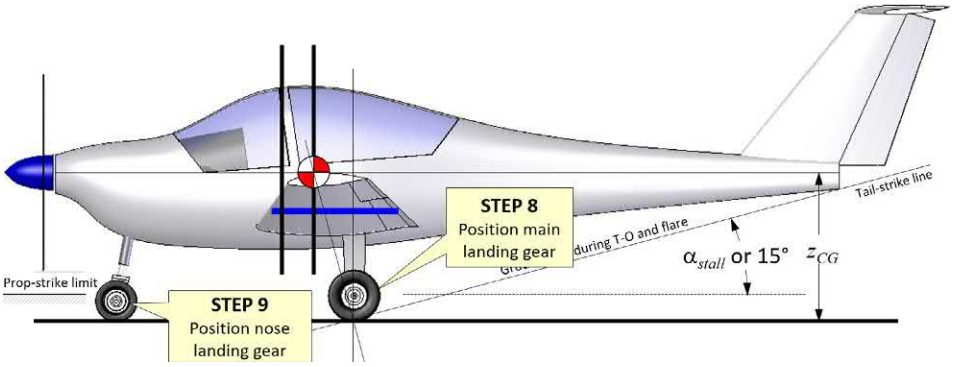


FIGURE 13-26 Steps 8 and 9 for the location of the tricycle landing gear.

the forward limit, and no less than 10% when the CG is at the aft limit. Too much nose gear load will simply make it harder to rotate the airplane for lift-off and will make the support structure heavier. Too light a load will make steering the aircraft harder because of reduced ground friction. Light nose gear load can also promote "porpoising," on the ground.

A few more steps are required to properly position the landing gear.

Overturn Angle

The following steps are intended to verify that the wheel track is wide enough to provide lateral stability when taxiing and turning around a corner. Since the CG is located distance z_{CG} above the ground, the centrifugal force it generates as the airplane turns will result in an overturning moment that can roll the airplane on the wing outside of the trajectory. To minimize the risk of this, the designer should check that the combination of wheel track and z_{CG} will not cause this to take place. As a rule of thumb, the closer to the ground the CG is, the better the lateral stability of the airplane. The farther forward the CG the less is the lateral stability.

Refer to Figure 13-27 for STEPS 10 through 14.

STEP 10: Draw a line through the center of the contact points of the nose and the left or right main landing gear as shown in Figure 13-27. Here, the right landing gear has been chosen (note that we are looking up at the bottom of the airplane, so the right wing appears to the left).

STEP 11: Draw a line through the CG that is *parallel* to the line drawn in STEP 10. For clarity, draw both lines far enough from the airplane to allow additional lines to be marked with ease.

STEP 12: Draw a line that is *perpendicular* to the lines drawn in STEP 10 and STEP 11. This line represents the ground.

STEP 13: Place the CG distance z_{CG} above the ground line, along the line drawn in STEP 11, as shown in Figure 13-27. Also refer to the definition of the z_{CG} in Figure 13-26.

STEP 14: Draw a line that extends from the intersection of the line drawn in STEP 10 and the ground line drawn in STEP 12, to the CG. This line represents the *overturn angle*, θ. This angle should be less than 63 degrees for general land-based aircraft and 54 degrees for carrier-based aircraft. If it is larger, then any of the following measures can be taken (provided preceding requirements are not violated):

1. The wheel track can be increased.
2. The height of the landing gear can be reduced.
3. The spacing between the nose and main landing gear can be increased.
4. A combination of the above three.

13.3.2 Geometric Layout of the Taildragger Landing Gear

If a taildragger configuration is to be designed, the next step is the layout of its geometry. The procedure is fundamentally similar, with a couple of exceptions. As before, the following must be completed:

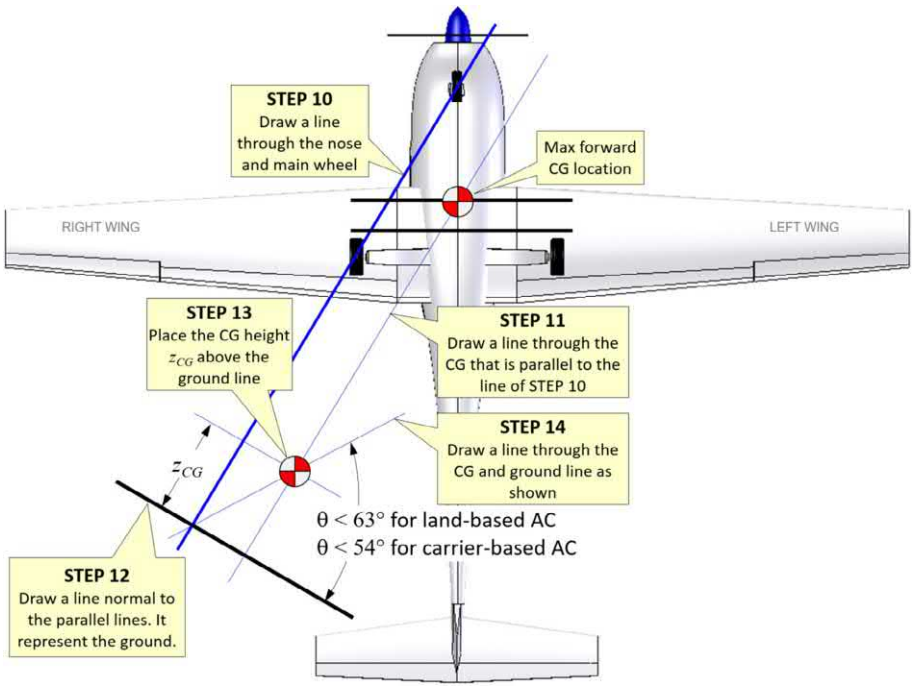


FIGURE 13-27 Steps 10 through 14 for the location of the landing gear.

(1) A side view of the design in a cruise attitude. Draw the mean geometric chord (MGC) on the side view.
(2) A top or bottom view of the airplane.
(3) A completed center-of-gravity (CG) envelope.

Refer back to Figure 13-23 for STEPS 1 and 2.

STEP 1 and 2 are identical to those for the tricycle landing gear.

Refer to Figure 13-28 for STEPS 3 through 7.

STEP 3: Determine the *highest* vertical CG location at the *forward and aft CG limits* and plot on the diagram as shown. These two locations are critical to the proper positioning of the main landing gear.

STEP 4: Draw the prop-strike limit as shown; ensuring it is *parallel* to the ground plane. This is as close to the ground the propeller should get under most adverse conditions. The limit per 14 CFR §23.925(a) is 9 in.

STEP 5: Draw a line at an incline of 15 degrees (with respect to the vertical) that goes through the forward CG location. Note that some references cite 16 degrees, but either one will work just fine.

STEP 6: Draw a line at an incline of 25 degrees that goes through the aft CG location. For most aircraft, the CG envelope is enclosed between these two lines.

STEP 7: Locate the intersection of the lines in STEP 5 and STEP 6. This is where the contact point of the tire should be, at a static deflection of 1 g load. Draw a line at an incline of 12 to 15 degrees that goes through this intersection, as shown in Figure 13-28. This line represents the ground and should be used to place the tailwheel. Note that the incline of the ground line shown is 12 degrees. Ideally, the angle-of-incidence made by the MGC with respect to the ground line should be that of α_{stall} up to a maximum value (recommended) of 15 degrees.

Refer to Figures 13-29 and 13-30 for STEPS 8 through 10.

STEP 8: Position the main landing gear such the contact point of the wheel is at the intersection of the three lines as shown in Figure 13-29.

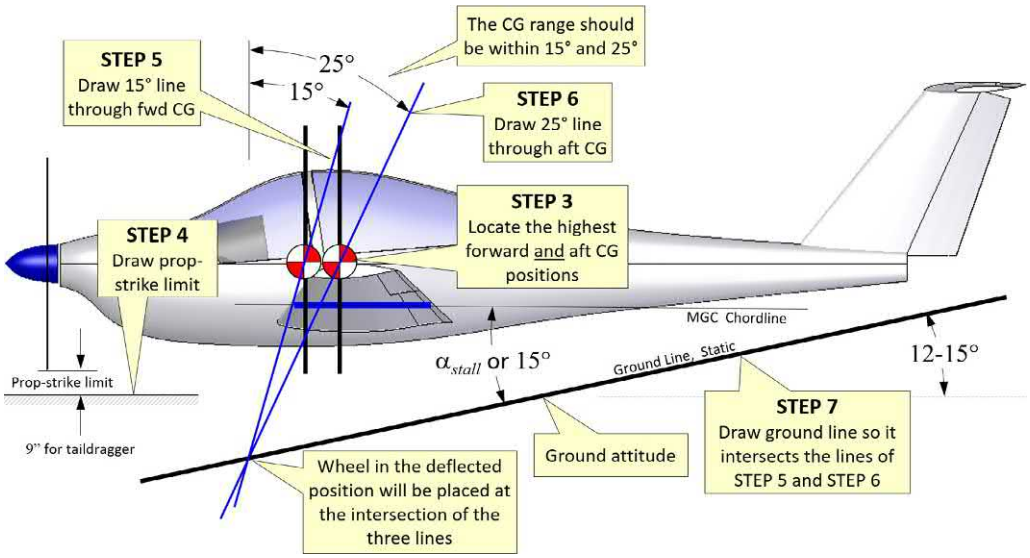


FIGURE 13-28 Steps 3 through 7 for the location of the taildragger landing gear.

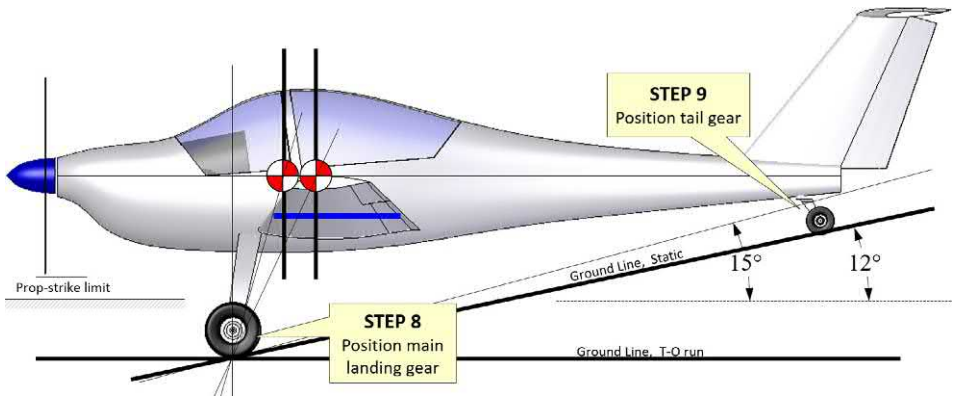


FIGURE 13-29 Steps 8 and 9 for the location of the taildragger landing gear.

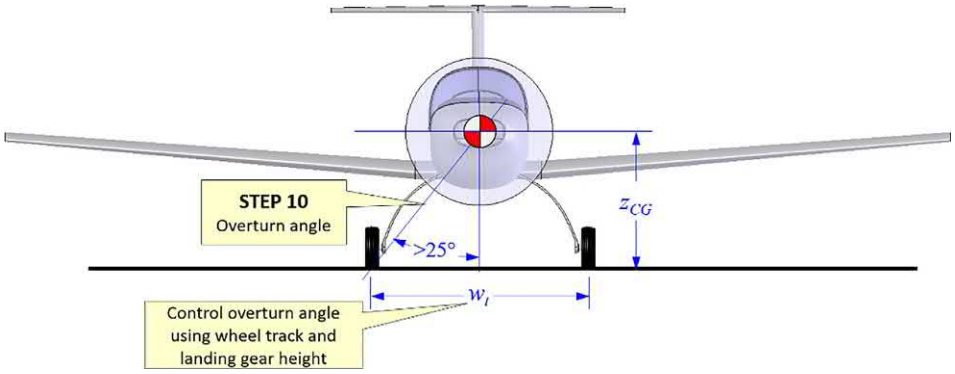


FIGURE 13-30 Step 10 ensures overturn angle is 25 degrees or greater.

STEP 9: Position the tailwheel landing gear such it carries no more than 5% of the aircraft weight when the CG is at the forward limit, and no greater than 10% when the CG is at the aft limit. Too much load on the tailwheel will make it harder to raise the airplane during the ground run. Too light a load will make steering and controlling the aircraft in crosswind harder because of reduced ground friction.

STEP 10: It is imperative that the main landing gear wheel track is wide enough to guarantee the airplane is stable while it corners on the ground. Ensure the width between the tires, w_t, is large enough such the overturn angle is 25 degrees or greater (see Figure 13-30).

13.3.3 Geometric Layout of the Monowheel Landing Gear With Outriggers

The monowheel landing gear with outriggers is primarily used in motor gliders. Examples of such aircraft include the Scheibe SF-25 Falke, SF-28 Tandem Falke, Fournier RF-1, RF-2, RF-3, RF-4, RF-5, and Europa XS, to name a few. The procedure to positioning the main wheel and the outriggers follows previous methods, with a couple of exceptions. Important design guidelines are shown in Figure 13-31 and 13-32.

Stinton [9] suggests the ideal spanwise position of the outrigger is at the rolling radius of gyration.[2] This minimizes the outrigger load in an "outrigger first" landing. Exploring a database of such aircraft shows this approach is not widely used in outrigger design. Pazmany [1, p. 20] shows that the outrigger distance (a) from the plane of symmetry generally ranges from 33% to 100% of the wing half-span ($b/2$). Placing the outriggers at the wing tip is not unheard of. For instance, the Rutan Solitaire and the Monnett Monerai both feature outriggers at the wing tip.

13.3.4 Tricycle Landing Gear Reaction Loads

Figure 13-33 shows loads acting on a tricycle landing gear configuration as it moves at a *constant* speed during

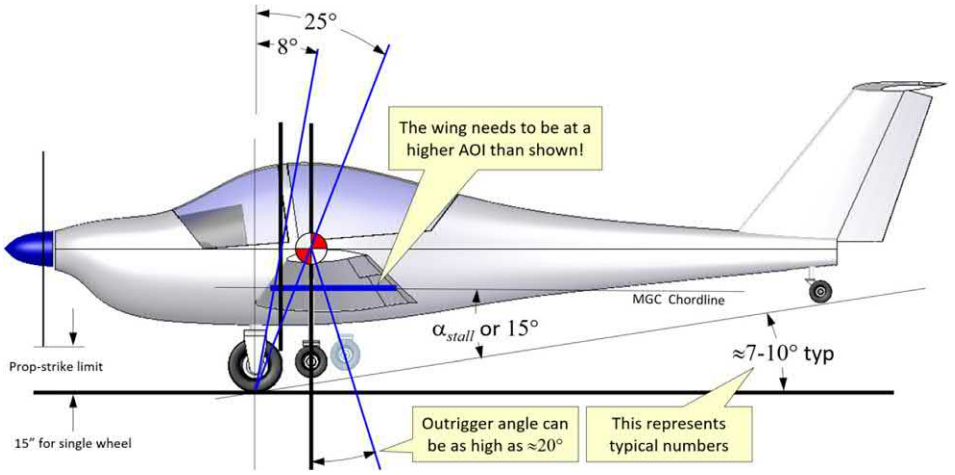


FIGURE 13-31 Design guidelines for a monowheel with outriggers.

[2] Which would be calculated using $r_x = \sqrt{I_{xx}/m}$, where I_{xx} is the mass moment of inertia about the roll axis, and m is the mass of the airplane.

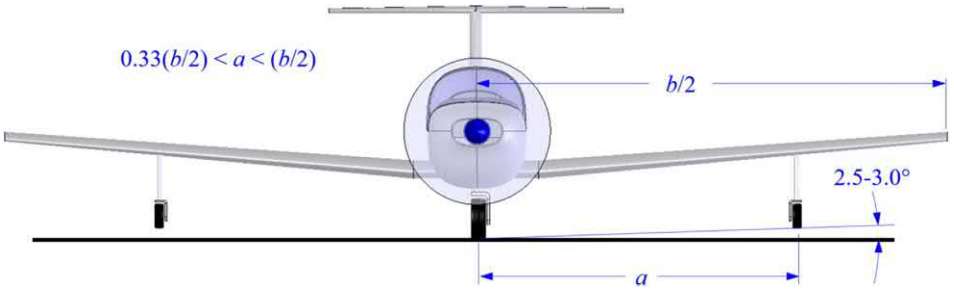


FIGURE 13-32 Design guidelines for positioning the outriggers.

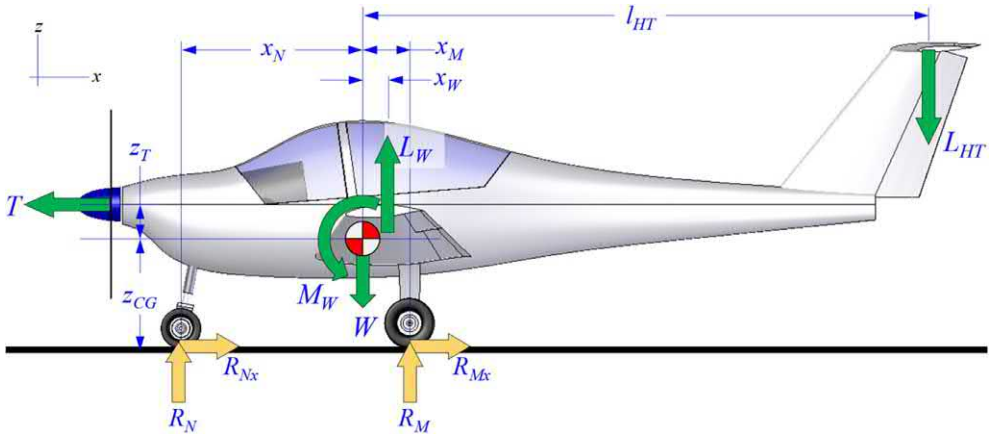


FIGURE 13-33 Balanced Force Diagram for a typical tricycle landing gear configuration.

the ground run. We want to determine the reaction loads on the nose and main landing gear, denoted by R_N and R_M, respectively. Note that all aerodynamic loads must include ground effect (see Section 9.5.11).

Nose gear reaction, R_N:

$$R_N = \frac{T \cdot z_T + (W + L_{HT} - L_W) \cdot (x_M + \mu \cdot z_{CG}) + L_W \cdot x_W - L_{HT} \cdot l_{HT} - M_W}{x_N + x_M} \tag{13-17}$$

Main gear reaction, R_M: $R_M = W + L_{HT} - L_W - R_N$ (13-18)

where

L_W = Wing lift, in lb_f or N.
L_{HT} = Horizontal tail lift, in lb_f or N
M_W = Pitching moment, in ft·lb_f or N·m.
T = Thrust, in lb_f or N.

(1) Special Case—Static Loads

For this case $V = 0$ and $T = 0$ (note that this makes friction irrelevant as it only affects the aircraft in motion), leading to the following results:

$$R_N = \frac{W \cdot x_M}{x_N + x_M} \quad \text{and} \quad R_M = W - R_N \tag{13-19}$$

The summation of moments in Figure 13-33 is taken about the CG, where positive forces point up and positive moments results in clockwise rotation. The formulation assumes absolute values of all dimensions and forces. Signs are taken care of in the formulation of both forces and moments. The only exception is the sign of M_W, which is typically negative (nose pitch-down). Its sign is the only one that must be accounted for when using the formulation.

(2) Definition of Aerodynamic Loads

The following formulation of the lift and thrust is convenient, as it permits an insight into how aerodynamic characteristics affect the landing gear reaction forces. For instance, if prepared in a spreadsheet, the designer can evaluate the airspeed when rotation to lift-off can be achieved and assess necessary modifications.

Thrust for a propeller: $T = \eta_p \cdot 550 \cdot BHP / V$.

Wing lift: $L_W = \frac{1}{2}\rho V^2 S C_L = \frac{1}{2}\rho V^2 S (C_{L_0} + C_{L_\alpha} \cdot \alpha_{TO})$.

HT lift:
$$L_{HT} = \frac{1}{2}\rho V^2 S_{HT} C_{L_{HT}} = \frac{1}{2}\rho V^2 S_{HT} \left(C_{L_{\alpha HT}} \cdot i_{HT} + C_{L_{\delta_e}} \cdot \delta_e\right).$$

DERIVATION OF EQUATION (13-17)

Assume the already stated orientation of forces and moments. Begin by defining the horizontal ground friction force:

$$R_{Nx} + R_{Mx} = \mu(R_N + R_M) \tag{i}$$

Sum forces in the vertical (z) direction, such that positive forces act upward:

$$\sum F_Z = 0 \;\Rightarrow\; R_N + R_M + L_W - W - L_{HT} = 0 \tag{ii}$$

This yields the main landing gear reaction force R_M:

$$\Rightarrow\; R_M = W + L_{HT} - L_W - R_N \tag{iii}$$

Sum moments about the CG, where the ground friction R_{Mx} and R_{Nx} are written explicitly as $\mu(R_N+R_M)\cdot h_{CG}$:

$$\begin{aligned}\sum M_{CG} = 0 \;\Rightarrow\; & -T\cdot z_T + R_N\cdot x_N - R_M\cdot x_M \\ & - L_W\cdot x_W + L_{HT}\cdot l_{HT} \\ & - \mu(R_N + R_M)\cdot z_{CG} + M_W = 0\end{aligned} \tag{iv}$$

Typical values of the wing pitching moment, M_W, is negative. Expand and rearrange the R_N and R_M terms:

$$\begin{aligned}&-T\cdot z_T + R_N\cdot x_N - \mu\cdot R_N\cdot z_{CG} - R_M\cdot x_M - \mu\cdot R_M\cdot z_{CG} \\ &- L_W\cdot x_W + L_{HT}\cdot l_{HT} + M_W \\ &= 0\end{aligned}$$

Simplify in terms of R_N and R_M:

$$\begin{aligned}&-T\cdot z_T + R_N\cdot(x_N - \mu\cdot z_{CG}) - R_M\cdot(x_M + \mu\cdot z_{CG}) \\ &- L_W\cdot x_W + L_{HT}\cdot l_{HT} + M_W \\ &= 0\end{aligned}$$

Inserting Equation (iii) for R_M yields:

$$\begin{aligned}&-T\cdot z_T + R_N\cdot(x_N - \mu\cdot z_{CG}) \\ &- (W + L_{HT} - L_W - R_N)\cdot(x_M + \mu\cdot z_{CG}) - L_W\cdot x_W \\ &+ L_{HT}\cdot l_{HT} + M_W = 0\end{aligned}$$

Rearrange to combine the term R_N yields:

$$\begin{aligned}&-T\cdot z_T + R_N\cdot(x_N - \mu\cdot z_{CG}) + R_N\cdot(x_M + \mu\cdot z_{CG}) \\ &-(W + L_{HT} - L_W)\cdot(x_M + \mu\cdot z_{CG}) + \hookleftarrow \\ &- L_W\cdot x_W + L_{HT}\cdot l_{HT} + M_W = 0\end{aligned}$$

Simplify further to yield:

$$\begin{aligned}&-T\cdot z_T + R_N\cdot(x_N + x_M) - (W + L_{HT} - L_W)\cdot(x_M + \mu\cdot z_{CG}) \\ &- L_W\cdot x_W + L_{HT}\cdot l_{HT} + M_W \\ &= 0\end{aligned}$$

Finally, solving for the nose gear reaction force, R_N yields

$$\Rightarrow\; R_N = \frac{T\cdot z_T + (W + L_{HT} - L_W)\cdot(x_M + \mu\cdot z_{CG}) + L_W\cdot x_W - L_{HT}\cdot l_{HT} - M_W}{x_N + x_M} \tag{v}$$

EXAMPLE 13-2

Consider the dimensions of the aircraft in Figure 13-34 and whose pertinent characteristics are listed below. Determine the following:

(a) The static ground reaction loads without engine power,
(b) Dynamic ground reaction loads on the NLG and MLG, assuming no rotation at V = 40 KTAS, and
(c) Determine the airspeed at which the pilot can rotate the nose of the aircraft to lift off, assuming the constant airspeed formulation.

For convenience, assume the propeller efficiency can be described using the function shown in Figure 14-45.

Wing area, $S_W = 110\,\text{ft}^2$	Propeller diameter, $D_P = 5.75\,\text{ft}$
Wing Mean Geometric Chord, $c_{MGC} = 3.25\,\text{ft}$	Propeller T-O rotation, $RPM = 2500$
Horizontal tail area, $S_{HT} = 25\,\text{ft}^2$	C_L of HT during T-O run, $C_{LHT} = -0.825$
Take-Off weight, $W = 1320\ \text{lb}_\text{f}$	Propeller efficiency, $\eta_p = 0.096574 + 1.703049\,J - 0.952281\,J^2$
Lift coefficient during T-O run, $C_{L\ TO} = 0.5$	Pitching moment coefficient about the CG, $C_M = -0.05$
Engine T-O power, $P_{TO} = 100$ BHP	

EXAMPLE 13-2 (*cont'd*)

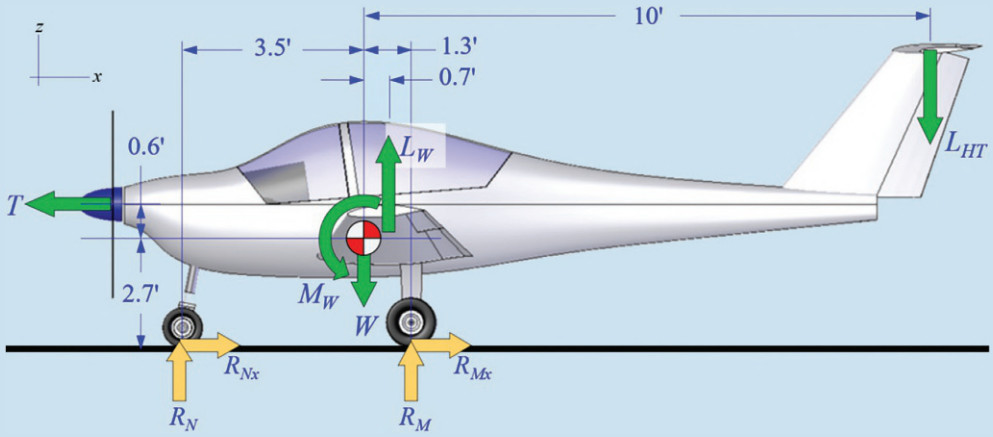


FIGURE 13-34 Example configuration.

SOLUTION:

(a) *Static Ground Reaction Loads without Power:*
Nose reaction from Equation (13-19):

$$R_N = \frac{W \cdot x_M}{x_N + x_M} = \frac{1320 \times 1.3}{3.5 + 1.3} = 357.5 \text{ lb}_\text{f}.$$

Main landing gear reaction:

$$R_M = W - R_N = 1320 - 357.5 = 962.5 \text{ lb}_\text{f}.$$

(b) *Dynamic Ground Reaction Loads at V = 40 KTAS:*
Airspeed in ft/s: $V = 40 \times 1.688 = 67.5$ ft/s.
Dynamic pressure:

$$q = \frac{1}{2}\rho V^2 = \frac{1}{2}(0.002378)(67.5)^2 = 5.42 \text{ lb}_\text{f}/\text{ft}^2.$$

Advance ratio: $J = \dfrac{60V}{RPM \times D} = \dfrac{60 \times 67.5}{2500(5.75)} = 0.2818.$

Propeller efficiency:

$$\eta_p = 0.096574 + 1.703049J - 0.952281J^2 = 0.5009$$

Thrust:

$$T = \frac{\eta_p \times 550 \times BHP}{V} = \frac{0.5009 \times 550 \times 100}{67.5} = 408 \text{ lb}_\text{f}$$

Wing lift: $L_W = qS_W C_{LTO} = (5.42)(110)(0.5) = 298.1$ lb$_\text{f}$.
HT lift: $L_{HT} = qS_{HT} C_{HT} = (5.42)(25)|-0.825| = 111.8$ lb$_\text{f}$.
Pitching moment:

$$M_W = qS_W C_{MGC} C_M = (5.42)(110)(3.25)(-0.05) = -96.9 \text{ ft} \cdot \text{lb}_\text{f}.$$

Nose landing gear reaction load:

$$R_N = \frac{T \cdot z_T + (W + L_{HT} - L_W) \cdot (x_M + \mu \cdot z_{CG}) + L_W \cdot x_W - L_{HT} \cdot l_{HT} - M_W}{x_N + x_M}$$
$$= \frac{408 \times 0.6 + (1320 + 111.8 - 298.1) \cdot (1.3 + 0.04 \times 2.7) + 298.1 \times 0.7 - 111.8 \times 10 + 96.9}{3.5 + 1.3}$$
$$= \frac{244.8 + 1133.7 \times 1.408 + 208.67 - 1118 + 96.9}{4.8} = 214.3 \text{ lb}_\text{f}$$

Main landing gear reaction loads (total for both wheels):

$$R_M = W + L_{HT} - L_W - R_N = 1320 + 111.8 - 298.1 - 214.3 = 919.4 \text{ lb}_\text{f}$$

(c) *Determine the Rotation Airspeed:*
The rotation airspeed can be determined by calculating the vertical NLG reaction load for a range of airspeeds and then identifying where it becomes zero. The calculations are easily implemented in a spreadsheet like Microsoft Excel. The calculations shown here were implemented for airspeeds ranging from 10 through 59 KTAS. The results have been plotted in Figure 13-35. It is imperative to check the rotation capability below V_{LOF}. It appears this airplane can rotate at 55.5 KTAS. For an LSA, this should be achievable at 40 KCAS. The solution indicates a problem with the design or the loading or both.

As soon as the NLG lifts off the runway the model is no longer valid because the rotation changes the AOA and, thus, the wing and HT lift coefficients. Regardless, the method returns a reliable value up to the rotation speed.

Continued

EXAMPLE 13-2 (*cont'd*)

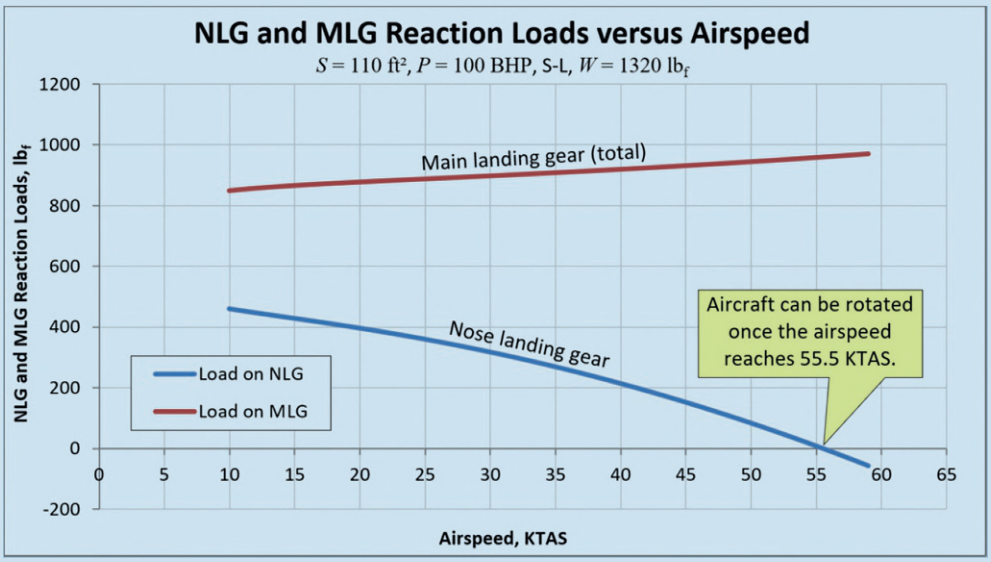


FIGURE 13-35 Nose and main landing gear reaction loads. Note that the NLG reaction load goes to zero at 55.5 KTAS. This means the aircraft must be accelerated to that airspeed before rotating the airplane is possible.

13.3.5 Taildragger Landing Gear Reaction Loads

Figure 13-36 shows loads acting on a taildragger landing gear configuration at a *constant* speed during the ground run, while the tail is still on the ground. We want to determine the reaction loads on the main and tail landing gear, denoted by R_M and R_T, respectively. Note that all aerodynamic loads must include ground effect (see Section 9.5.11).

Tailwheel reaction, R_T:

$$R_T = \frac{-T \cdot z_T + (W - L_{HT} - L_W) \cdot (x_M - \mu \cdot z_{CG}) - L_W \cdot x_W - L_{HT} \cdot l_{HT} + M_W}{x_M + x_T} \tag{13-20}$$

Main gear reaction, R_M:

$$R_M = W - L_{HT} - L_W - R_T \tag{13-21}$$

Variables are defined in Section 13.3.4.

Special Case—Static Loads:

For this case $V = 0$ and $T = 0$, leading to the following results:

$$R_T = \frac{W \cdot x_M}{x_M + x_T} \quad \text{and} \quad R_M = W - R_T \tag{13-22}$$

The formulation uses the same constraints and aerodynamic load formulation as discussed in Section 13.3.4.

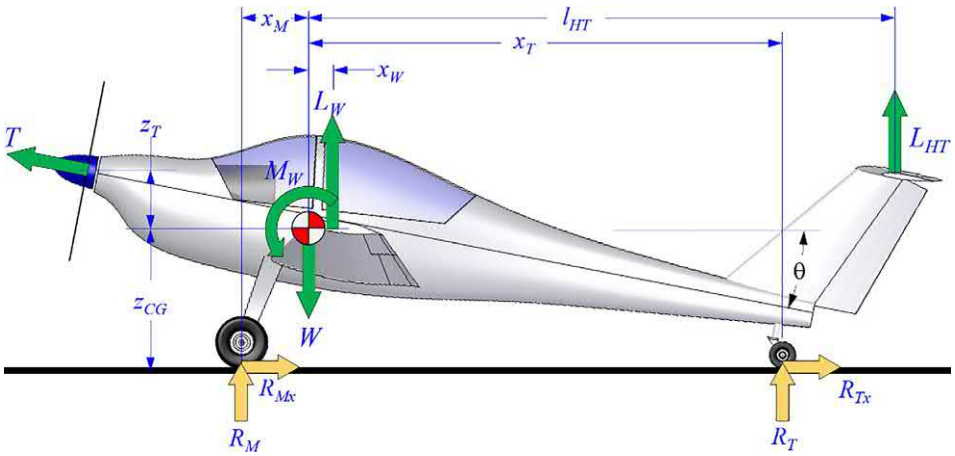


FIGURE 13-36 Balanced Force Diagram for a typical taildragger landing gear configuration.

DERIVATION OF EQUATION (13-20)

Begin by defining the horizontal ground friction force:

$$R_{Mx} + R_{Tx} = \mu(R_M + R_T) \qquad \text{(i)}$$

Sum forces in the vertical (z) direction, such that positive forces act upward:

$$\sum F_Z = 0 \quad \Rightarrow \quad R_M + R_T + L_W - W + L_{HT} = 0 \qquad \text{(ii)}$$

This yields the main landing gear reaction force R_M:

$$\Rightarrow \quad R_M = W - L_{HT} - L_W - R_T \qquad \text{(iii)}$$

For simplicity assume thrust is horizontal. Sum moments about the Center of Gravity (CG), such that nose pitch-up moments are positive:

$$\sum M_{CG} = 0 \quad \Rightarrow \quad -T \cdot z_T + R_M \cdot x_M - L_W \cdot x_W - R_T \cdot x_T - L_{HT} \cdot l_{HT} - \mu(R_M + R_T) \cdot z_{CG} + M_W = 0 \qquad \text{(iv)}$$

Note that typically the value of the wing pitching moment, M_W, is negative. Expand and rearrange the R_T and R_M terms:

$$-T \cdot z_T + R_M \cdot x_M - L_W \cdot x_W - R_T \cdot x_T - L_{HT} \cdot l_{HT} - \mu R_M \cdot z_{CG} - \mu R_T \cdot z_{CG} + M_W = 0$$

Simplify in terms of R_T and R_M:

$$-T \cdot z_T + R_M \cdot (x_M - \mu \cdot z_{CG}) - L_W \cdot x_W - R_T \cdot (x_T + \mu \cdot z_{CG}) - L_{HT} \cdot l_{HT} + M_W = 0$$

Substitute Equation (iii) for R_M yields:

$$-T \cdot z_T + (W - L_{HT} - L_W - R_T) \cdot (x_M - \mu \cdot z_{CG}) - L_W \cdot x_W - R_T \cdot (x_T + \mu \cdot z_{CG}) - L_{HT} \cdot l_{HT} + M_W = 0$$

Rearrange to combine the term R_T yields:

$$-T \cdot z_T + (W - L_{HT} - L_W) \cdot (x_M - \mu \cdot z_{CG}) - L_W \cdot x_W - R_T \cdot (x_M + x_T) - L_{HT} \cdot l_{HT} + M_W = 0$$

Finally, solving for the nose gear reaction force, R_T, yields

$$\Rightarrow \quad R_T = \frac{-T \cdot z_T + (W - L_{HT} - L_W) \cdot (x_M - \mu \cdot z_{CG}) - L_W \cdot x_W - L_{HT} \cdot l_{HT} + M_W}{x_M + x_T} \qquad \text{(v)}$$

EXAMPLE 13-3

Consider the dimensions of the aircraft in Figure 13-34 and whose pertinent characteristics are listed below. Determine the following:

(a) The static ground reaction loads without engine power,

(b) Determine the airspeed at which the tailwheel lifts off the ground for elevator deflection $\delta_e = -10$ degrees, 0 degrees, +10 degrees, assuming the constant airspeed formulation. Note that this method does not permit the complete take-off run to be analyzed.

For convenience, assume the propeller efficiency can be described using the function shown in Figure 15-40. Use the same set of variables used in Example 13-2, except $C_{LHT} = 0.72 + 0.055 \cdot \delta_e$.

SOLUTION:

(a) *Static Ground Reaction Loads without Power:*

Nose reaction from Equation (13-22):

$$R_T = \frac{W \cdot x_M}{x_M + x_{TW}} = \frac{1320 \times 1.3}{1.3 + 10} = 151.9 \text{ lb}_\text{f}.$$

Main landing gear reaction:

$$R_M = W - R_N = 1320 - 151.9 = 1168 \text{ lb}_\text{f}.$$

The tailwheel carries 11.5% of the weight of the aircraft in the static configuration. This is the upper limit of what is advisable for static load and the designer should consider moving the tailwheel aft unless other factors make it impossible.

(b) *Determine the airspeed at which the tailwheel lifts off the ground for elevator deflection $\delta_e = -10$ degrees, 0 degree, +10 degrees:*

Note that the HT lift coefficient is given by $C_{LHT} = 0.72 + 0.055 \cdot \delta_e$, where the value 0.72 reflects that while the tail is on the ground the HT generates lift that points upward. The elevator deflection (δ_e) increases the lift coefficient when the elevator is deflected Trailing Edge Down (TED) and decreases when it is deflected Trailing Edge Up (TEU).

Validation calculation for $V = 40$ KTAS and $\delta_e = 0$ degree (or $C_{LHT} = 0.72$):

Airspeed in ft/s: $V = 40 \times 1.688 = 67.5$ ft/s.

Continued

EXAMPLE 13-3 (*cont'd*)

Dynamic pressure:

$$q=\tfrac{1}{2}\rho V^2=\tfrac{1}{2}(0.002378)(67.5)^2=5.42\ \text{lb}_\text{f}/\text{ft}^2.$$

Advance ratio: $J=\dfrac{60V}{RPM\times D}=\dfrac{60\times 67.5}{2500(5.75)}=0.2818.$

Propeller efficiency:

$$\eta_p=0.096574+1.703049J-0.952281J^2=0.5009$$

Thrust:

$$T=\frac{\eta_p\times 550\times BHP}{V}=\frac{0.5009\times 550\times 100}{67.5}=408\ \text{lb}_\text{f}$$

Wing lift: $L_W=qS_WC_{LTO}=(5.42)(110)(0.5)=298.1\ \text{lb}_\text{f}.$
HT lift: $L_{HT}=qS_{HT}C_{HT}=(5.42)(25)|-0.825|=111.8\ \text{lb}_\text{f}.$
Pitching moment:

$$M_W=qS_WC_{MGC}C_M=(5.42)(110)(3.25)(-0.05)=-96.9\ \text{ft}\cdot\text{lb}_\text{f}.$$

Wing lift: $L_W=qS_WC_{LTO}=(5.42)(110)(1.4)=834.7\ \text{lb}_\text{f}.$
HT lift: $L_{HT}=qS_{HT}C_{HT}=(5.42)(25)(0.72)=97.6\ \text{lb}_\text{f}.$
Pitching moment:

$$M_W=qS_WC_{MGC}C_M=(5.42)(110)(3.25)(-0.05)=-96.9\ \text{ft}\cdot\text{lb}_\text{f}.$$

Tailwheel reaction load:

$$R_T=\frac{-T\cdot z_T+(W-L_{HT}-L_W)\cdot(x_M-\mu\cdot z_{CG})-L_W\cdot x_W-L_{HT}\cdot l_{HT}+M_W}{x_M+x_T}$$
$$=\frac{-(408)(1.2)+(1320-97.6-834.7)\cdot(1.3-0.04\cdot 3.5)-(834.7)(0.7)-(97.6)(12)-96.9}{1.3+10}$$
$$=-167.5\ \text{lb}_\text{f}$$

$$\Rightarrow\ R_M=W-L_{HT}-L_W-R_T=1320-97.6-834.7-(-167.5)=555.2\ \text{lb}_\text{f}$$

The negative sign for R_T indicates the tailwheel is already off the ground: These calculations are no longer valid for $R_T\geq 0$. Since $R_M>0$, there still is weight on wheels. To extend the approximation beyond $R_T\geq 0$, the lift coefficient should acquire its low AOA value as soon as R_T becomes negative (Figure 13-37). A better modeling of the take-off run is provided in Chapter 18.

By completing the same calculation for a range of airspeeds and the other elevator deflections, the graph in Figure 13-38 was prepared. It shows the various airspeeds at which the tail lifts off the runway.

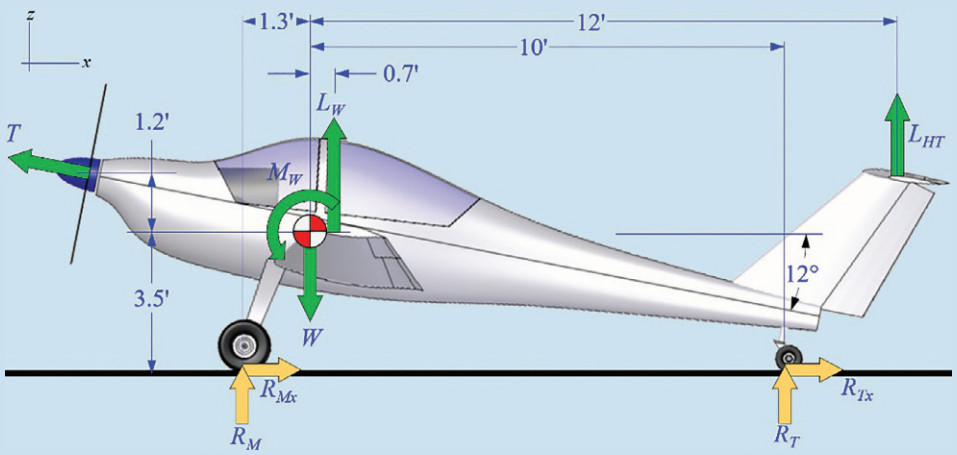


FIGURE 13-37 Example configuration.

EXAMPLE 13-3 (*cont'd*)

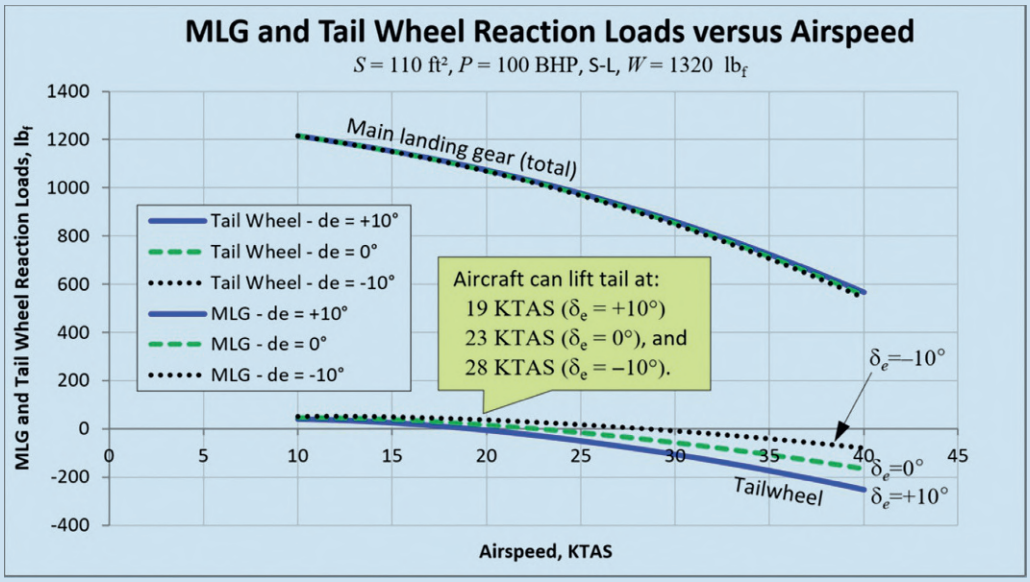


FIGURE 13-38 Main landing gear and tailwheel reaction loads. Note that the tailwheel reaction load goes to zero at 19, 23, and 28 KTAS, depending on elevator deflection ($\delta_e = -10$ degrees, 0 degree, +10 degrees).

References

[1] L. Pazmany, *Landing Gear Design for Light Aircraft, Volume 1*, Ladislao Pazmany, 1986.

[2] Anonymous, *Goodyear Aircraft Tire Data Book*, Goodyear Tire and Rubber Company, 2002.

[3] Anonymous, *Gates Learjet 35A/36A FAA Approved Airplane Flight Manual*, Gates Learjet Corporation, 1983.

[4] N.S. Curry, *Aircraft Landing Gear Design: Principles and Practices*, AIAA Education Series, 1988.

[5] M.C.-Y. Niu, *Airframe Structural Design*, Conmilit Press, 1988, pp. 439–441.

[6] G. Sengfelder, *German Aircraft Landing Gear*, Schiffer Publishing, 1993.

[7] Source. https://www.ntsb.gov/investigations/data/Pages/aviation_stats.aspx. (Accessed 9 June 2020).

[8] A. Meyer, *Weekend Pilots: Technology, Masculinity, and Private Aviation in Postwar America*, Johns Hopkins University Press, 2015. December 30.

[9] D. Stinton, *The Design of the Aeroplane*, Collins, 1983.

This page intentionally left blank

CHAPTER

14

Thrust Modeling for Gas Turbines

OUTLINE

14.1 **Introduction** 573
14.1.1 The Content of This Chapter 573
14.1.2 Introduction to Thrust Modeling 573
14.1.3 Fundamental Concepts of Fluid Mechanics 574
14.1.4 The Basic Equations of Thermodynamics 580

14.2 **Theory of Reactive Thrust** 581
14.2.1 Conservation Laws 581
14.2.2 The General Thrust Equation 583
14.2.3 Propulsive Efficiency 586

14.3 **General Thrust Modeling for Gas Turbines** 588
14.3.1 Definitions 588
14.3.2 Mattingly Model for a Turboprop Engine 590
14.3.3 Mattingly Model for a Turbojet Engine 591
14.3.4 Mattingly Model for a Turbofan Engine 592
14.3.5 Computer Code: Thrust as a Function of Altitude and Mach Number 592

Exercises 595

References 595

14.1 INTRODUCTION

The term *thrust model* refers to mathematical formulation used to predict the operational thrust of a given engine. Ideally, such models allow the effect of atmospheric condition and airspeed to be accounted for. This chapter develops the so-called *general thrust equation* and shows how it can be used to model thrust of a turbojet and turbofan engine. Additionally, a convenient thrust model for turboprop, turbojet, and turbofan engines is presented. Thrust modeling for propeller engines is presented in Chapter 15.

14.1.1 The Content of This Chapter

- Section 14.2 presents the theory of reactive thrust, in which a generalized thrust formula is derived using the conservation laws of fluid dynamics.
- Section 14.3 presents a convenient thrust model for turboprops, turbojets, and turbofans. Referred to as the "Mattingly model," its relative simplicity makes it very practical during conceptual design work.

14.1.2 Introduction to Thrust Modeling

Air-breathing mechanical engines operate by converting the chemical energy in fuel into mechanical energy. Typically, this is accomplished by an intermediary conversion to thermal energy via an exothermic chemical reaction. Adding this thermal energy to the air increases its pressure or volume rapidly. This change is used to move the machine's mechanical components.

Thrust models are either prepared by an engine manufacturer or the aircraft designer. Thrust models for jet engines are typically prepared by the engine manufacturer in the form of software. These are often called *engine decks*, where the term "deck" refers to times when computer programs were stored in a deck of paper cards. Fortunately, those days are behind us, but the term stuck. An engine deck returns the engine thrust at a specific power setting, altitude, and airspeed. Frequently, it accounts for deviations from standard atmosphere. Some even allow the effect of various aircraft systems to be included, for instance, the discharge of bleed air or a running generator.

In contrast, propeller thrust models are frequently prepared by the designer or performance analyst. This is a

https://doi.org/10.1016/B978-0-12-818465-3.00014-8

Copyright © 2022 Elsevier Inc. All rights reserved.

consequence of the engine and propeller being produced by different manufacturers: an engine can drive multiple propeller models—the engine maker does not know what propeller brand the end user chooses. This effort is made a little easier when the propeller manufacturer provides a map of propeller-efficiency versus advance ratio and thrust and power coefficients. But even this is not always the case. Many low-cost propeller manufacturers do not offer such conveniences, forcing the designer to perform this task. This is treated in Chapter 15.

Thrust models for conceptual design can be prepared in a computer code. This allows thrust and fuel consumption to be called as functions in the spreadsheet environment; priceless if performance and stability work is being accomplished in a spreadsheet. This author prefers Visual Basic for Applications (VBA) included with Microsoft Excel. Of course, there are other options. Some prefer to use MATLAB and even dedicated programming languages (Fortran, VB, C+, C#, Python, etc.). Regardless, such a code should at minimum return thrust and fuel consumption when the user passes arguments such as altitude, airspeed, and power setting. Figure 14-1 shows an example of what the output of such a code may look like.

14.1.3 Fundamental Concepts of Fluid Mechanics

This section presents the fundamentals required to develop and use the general thrust equation. Note that the discussion is deliberately concise and void of derivation to conserve space. Readers interested in further treatise of these concepts can consult references such as [1–5], to name a few.

Fluid Mechanics is the study of fluids (liquids and gases). It is split into *fluid statics* (study of fluids at rest) and *fluid dynamics* (study of fluids in motion). *Aerodynamics* and *hydrodynamics* are subdisciplines inside fluid dynamics. The fluid we seek to investigate is analyzed using the *continuum model*. This model assumes large quantities of fluid molecules per unit volume and that the average distance between molecular collision (called *mean-free path*, denoted by λ) is multiple orders of magnitude smaller than the physical dimensions being analyzed (denoted by δ). Table 14-1 details notations used in this chapter.

(1) Basic Properties of Fluids

Fluids are split into *liquids* and *gases*. The basic properties of interest for all fluids are *pressure*, *temperature*, *density*, *viscosity*, and *speed of sound*. All are *scalar fields*, which means they have spatial (x,y,z) and temporal (t) coordinates. An example of this is pressure, p, which can be written as $p=p(x,y,z,t)$.

Pressure ($p=p(x,y,z,t)$) is the ratio of a normal force to the area over which it is applied. Typical units are $[N/m^2]=[Pa]$ or $[lb_f/ft^2]$. If dF and dA are infinitesimal normal force and area, respectively, then the pressure is defined as

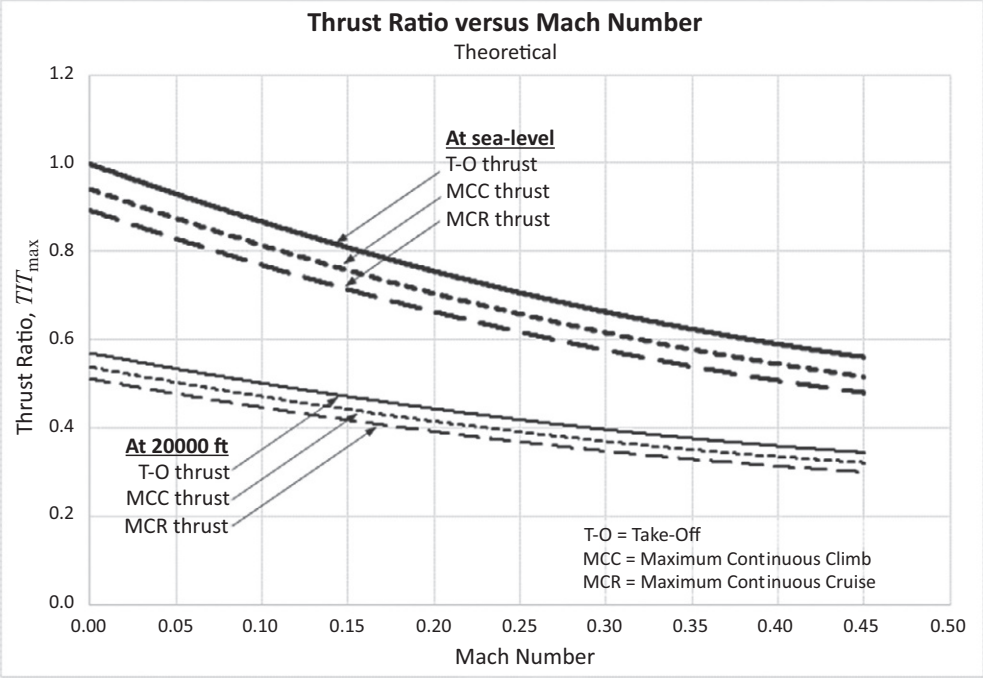


FIGURE 14-1 A thrust model example for a small turbofan engine.

TABLE 14-1 Notation for fluid properties.

Property	Symbol	Remark
Volume	$\not{V}$	Strike-through distinguishes it from velocity, V.
Local temperature, pressure, and density	T, p, and ρ	Static properties.
Standard day properties (ambient) at S-L	T_{std}, p_{std}, and ρ_{std}	Based on ISA. Always far-field values.
Temperature, pressure, and density in far-field	T_∞, p_∞, and ρ_∞	Ambient properties at condition.
Total temperature, pressure, and density	T_0, p_0, and ρ_0	Local properties.
Total temperature, pressure, and density in far field	$T_{0\infty}$, $p_{0\infty}$, and $\rho_{0\infty}$	

$$p = \lim_{dA \to \delta^2} \left[\frac{dF}{dA}\right] \quad \text{where } \delta \gg \lambda \tag{14-1}$$

Temperature ($T = T(x,y,z,t)$) in fluids is related to the average kinetic energy (KE_{avg}) of its molecules through the Boltzmann constant ($k \equiv 1.380649 \times 10^{-23}$ J/K) as shown below. Units are [°C], [K], [°F], or [°R]. Unless otherwise stated, T is static temperature.

$$T = \frac{2}{3}\frac{KE_{avg}}{k} \tag{14-2}$$

Density ($\rho = \rho(x,y,z,t)$) is the ratio of the mass (m) of matter to its volume ($\not{V}$). Units are [kg/m^3] or [slugs/ft^3].

$$\rho = \lim_{d\not{V} \to \delta^3} \left[\frac{dm}{d\not{V}}\right] \quad \text{where } \delta \gg \lambda \tag{14-3}$$

Viscosity is presented in Section 16.3.1. The *speed of sound* (a) is a function of the thermodynamic properties of the matter through which the sound wave travels. For calorically perfect gases,[1] it is possible to show that this leads to the following expression [2].

$$a = \sqrt{\gamma RT} \tag{14-4}$$

where R is the specific gas constant 286.7 J/(kg·K) in SI or 1716 ft·lb$_f$/(slug·°R) in the UK-system. γ is the ratio of specific heats.

(2) The Ideal Gas Law

Figure 14-2 illustrates the timeline of the discovery of the various gas laws. It reveals how the early gas laws were related. Using *Avogadro's law*, attributed to the Italian Amedeo Avogadro (1776–1856), the French naturalist Émile Clapeyron (1799–1864) combined the Boyle's, Charles', and Gay-Lussac's gas laws into one; the *ideal gas law* [6]. This law constitutes an important thermodynamic process, such as those listed in Table 14-3. The ideal gas law is also recognized as the *equation of state*.

The ideal gas law is stated as follows (note that R is the *specific gas constant* and applies only to a specific gas):

$$p = \rho RT \tag{14-5}$$

where $\overline{R} = 8.314 J/(K \cdot \text{mol}), M_{air} = 29 g/\text{mol} = 0.029 \text{kg/mol}$, $R_{air} = \overline{R}/M_{air} = 8.314/0.029 = 286.7 J/(\text{kg} \cdot K)$. In this book, R_{air} is simply denoted as R.

Other forms:

$$\frac{p\not{V}}{T} = \text{constant} \qquad p\not{V} = n\overline{R}T \qquad p\not{V} = mRT.$$

where n = mass/molar mass $= m/M$ and $\overline{R}$ is the *universal gas constant* (same for all gases). Note that $R_{gas} = \overline{R}/M_{gas}$.

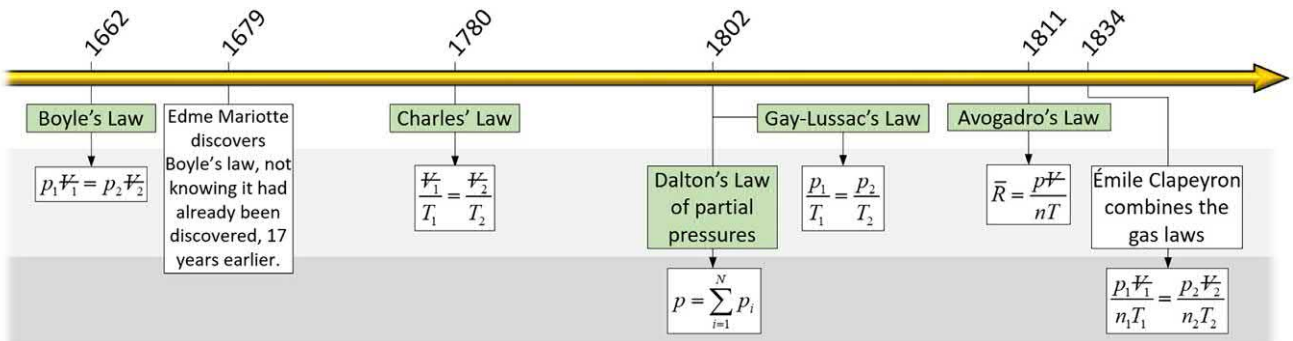


FIGURE 14-2 The timeline of discovery of gas laws.

[1] A calorically perfect gas is one for which the specific heat capacity is constant. Air is such a gas. If the specific heat capacity changes with temperature, the gas is called calorically imperfect.

DERIVATION OF EQUATION (14-5)

Avogadro's law can be written as:

$$\overline{R} \equiv \text{constant} = p\cancel{V}/(nT).$$

Thus, we write:

$$\Rightarrow \quad p\cancel{V} = n\overline{R}T = \frac{\overbrace{m}^{\text{mass}}}{\underbrace{M}_{\text{molar mass}}}\overline{R}T \quad \Rightarrow \quad \left(p\cancel{V} = \frac{m}{M}\overline{R}T\right)\frac{1}{m}$$

$$\Rightarrow \quad p\underbrace{\frac{\cancel{V}}{m}}_{\equiv 1/\rho} = \frac{1}{m}\frac{m}{M}\overline{R}T \quad \Rightarrow \quad \frac{p}{\rho} = \underbrace{\frac{\overline{R}}{M}}_{\substack{\equiv R \\ \text{specific to} \\ \text{each gas}}} T = RT \quad \Rightarrow \quad p = \rho RT$$

(3) Total Derivative

Is the *full* derivative of a multivariable function. It is frequently used in fluid mechanics. Consider the multivariable function $f(t,x(t),y(t),z(t))$. It is an *explicit* function of t, x, y, and z. However, since x, y, and z also depend on t, f is also *implicitly* dependent on t. Unlike a partial derivative, which assumes other arguments are constant while the focus-variable changes, the total derivative assumes all arguments that depend on the focus-variable (say t) change as well. Thus, the total derivative of $f(t,x(t),y(t),z(t))$ with respect to t is given by

$$\frac{df}{dt} = \frac{\partial f}{\partial t}\frac{dt}{dt} + \frac{\partial f}{\partial x}\frac{dx}{dt} + \frac{\partial f}{\partial y}\frac{dy}{dt} + \frac{\partial f}{\partial z}\frac{dz}{dt}$$

This reduces to $\frac{df}{dt} = \frac{\partial f}{\partial t} + \frac{\partial f}{\partial x}\frac{dx}{dt} + \frac{\partial f}{\partial y}\frac{dy}{dt} + \frac{\partial f}{\partial z}\frac{dz}{dt}$

Multiplying both sides by dt leads to

$$df = \frac{\partial f}{\partial t}dt + \frac{\partial f}{\partial x}dx + \frac{\partial f}{\partial y}dy + \frac{\partial f}{\partial z}dz \tag{14-6}$$

Its use is shown in Example 14-1.

(4) Fluid Statics

Fluid statics is the study of fluids at rest. One of its primary products is the *hydrostatic equation*, which allows pressure in incompressible fluids (liquids) and compressible fluids (gases) to be determined. Thus, it permits the design of balloons and blimps, dams and dykes, as well as floatplanes and fuel tanks. It is expressed as shown below

$$-\nabla p + \rho\, \mathbf{f_b} - \rho\, g\mathbf{k} = \mathbf{0} \tag{14-7}$$

where *nabla* (∇) is differential operator given by $\nabla = \partial/\partial x\mathbf{i} + \partial/\partial y\mathbf{j} + \partial/\partial z\mathbf{k}$, p is the pressure field, ρ is density, $\mathbf{f_b}$ is acceleration vector to which the fluid is subjected, g is the acceleration due to gravity, and $\mathbf{0}$ is the null vector. It can also be written in a component form, along the x-, y-, and z-axes as follows:

$$\frac{\partial p}{\partial x} = \rho f_x \qquad \frac{\partial p}{\partial y} = \rho f_y \qquad \frac{\partial p}{\partial z} = \rho f_z - \rho g \tag{14-8}$$

These differential equations yield dissimilar results depending on whether the fluid is incompressible (e.g., water) or compressible (e.g., atmosphere). They are solved by separating variables and integrating. Also note the reference system in Figure 14-3. For static conditions ($f_x = f_y = f_z = 0$), we are only left with the third equation of Equation (14-8). It gives

$$\frac{\partial p}{\partial z} = \rho \overbrace{f_z}^{=0} - \rho g \quad \Rightarrow \quad dp = -\rho g dz \quad \Rightarrow \quad p - p_o = -\int \rho g dz \tag{14-9}$$

For incompressible fluids, we substitute constant density (ρ = constant) and solve to give Equation (14-10). For compressible fluids, we represent density using the ideal gas law ($p = \rho RT$). In case of the atmosphere, the temperature is represented using the lapse rate formulation $T = T_0(1 + \kappa z)$. Here, R is the specific gas constant, T_0 is reference temperature, κ is lapse rate, and z is elevation. Substituting these into Equation (14-9) and, again using separation of variables, yields Equation (14-11), presented below.

Hydrostatic pressure in liquids:

$$\begin{matrix}\text{absolute} \\ \text{pressure}\end{matrix} \quad \begin{matrix}\text{reference} \\ \text{pressure}\end{matrix} \quad \begin{matrix}\text{gauge} \\ \text{pressure}\end{matrix}$$

$$\overbrace{p}^{\text{absolute pressure}} = \overbrace{p_0}^{\text{reference pressure}} - \overbrace{\rho g z}^{\text{gauge pressure}} \tag{14-10}$$

Hydrostatic pressure in atmosphere:

$$p = p_0(1 + \kappa h)^{-\frac{g}{RT_0\kappa}} \tag{14-11}$$

where p_0 is a reference pressure (e.g., absolute atmospheric pressure at sea level), z is depth in liquid and has a negative value, h is elevation or altitude and has a positive value. Both reference the point of the reference pressure. The term κ is the lapse rate constant (see Chapter 17), R is the specific gas constant, and T_0 is a reference temperature (e.g., absolute static atmospheric temperature at sea level). κ has a negative value (so pressure drops with altitude).

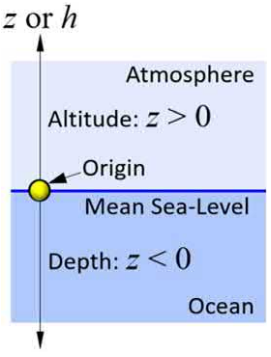


FIGURE 14-3 Reference system for variable z.

EXAMPLE 14-1: APPLICATION OF THE HYDROSTATIC EQUATION—ACCELERATING CONTAINER IN 3D

This example demonstrates the power of the hydrostatic equation. The container shown in Figure 14-4 is initially full of water ($\rho = 1000\,\text{kg/m}^3$) at sea level, where pressure is $p = 101{,}325\,\text{Pa}$. Then, it is accelerated at constant rate (a_x, a_y, a_z), where $a_z = 1\,\text{g}$ (where $g = 9.81\,\text{m/s}^2$), such the free surface becomes inclined as shown (note that the excess water spills over the sides). What acceleration is required (i.e., a_x and a_y)? Write the complete pressure function (as a function of x, y, and z). Find the location of maximum pressure and its magnitude.

SOLUTION:

Start with the hydrostatic Equation (14-7):

$$-\nabla p + \rho\ \mathbf{f_b} - \rho\ g\mathbf{k} = \mathbf{0}$$

Denoting $\mathbf{f_b} = a_x\mathbf{i} + a_y\mathbf{j} + a_z\mathbf{k}$ and write this in component form leads to

$$-\frac{\partial p}{\partial x} + \rho a_x = 0 \quad \Leftrightarrow \quad \frac{\partial p}{\partial x} = \rho a_x$$
$$-\frac{\partial p}{\partial y} + \rho a_y = 0 \quad \Leftrightarrow \quad \frac{\partial p}{\partial y} = \rho a_y$$
$$-\frac{\partial p}{\partial z} + \rho a_z - \rho g = 0 \quad \Leftrightarrow \quad \frac{\partial p}{\partial z} = \rho a_z - \rho g$$

NOTE 1: When the KINEMATIC value of the acceleration is POSITIVE (e.g., $9.81\,\text{m/s}^2$), the numerical value of a_x used in this formulation must be NEGATIVE (i.e., –9.81). In this problem, the pressure on the left side of the container *increases* when the value of x *decreases*.

NOTE 2: Use the absolute value of g (i.e., $+9.81\,\text{m/s}^2$ and not -9.81). The minus sign left of ρ indicates the water pressure increases with lower values of z (i.e., $z < 0$). This ensures the pressure correctly increases with depth.

Therefore, the total derivative is

$$dp = \overbrace{\frac{\partial p}{\partial x}}^{=\rho a_x} dx + \overbrace{\frac{\partial p}{\partial y}}^{=\rho a_y} dy + \overbrace{\frac{\partial p}{\partial z}}^{=\rho a_z - \rho g} dz$$
$$= \rho a_x dx + \rho a_y dy + (\rho a_z - \rho g) dz$$
$$\Rightarrow \int_{p_0}^{p} dp = \int_{x_o}^{x} \rho a_x dx + \int_{y_o}^{y} \rho a_y dy + \int_{z_o}^{z} (\rho a_z - \rho g) dz$$
$$\Rightarrow p - p_0 = \rho a_x (x - x_o) + \rho a_y (y - y_o) + (\rho a_z - \rho g)(z - z_o)$$

At the free surface, p must equal p_0 (the atmospheric pressure). Also, note where the origin is placed in Figure 14-4. While one can pick any location on the free surface as a reference point (because we know the pressure there is p_0), it is convenient to pick Point A in Figure 14-4, i.e.,

$$\Rightarrow \quad (x_o, y_o, z_o) = (0, 0, 3)$$

We know the acceleration along the z-axis ($1\,\text{g} = 9.81\,\text{m/s}^2$ upward—thus, substitute $-9.81\,\text{m/s}^2$). Also, substitute the reference values ($p = p_0, x_o = 0$, $y_o = 0$, $z_o = 3$) and g ($= 9.81\,\text{m/s}^2$) to get the equation of the free surface:

$$\Rightarrow \overbrace{p}^{p_0} - p_0 = \rho a_x \left(x - \overbrace{x_o}^{0} \right) + \rho a_y \left(y - \overbrace{y_o}^{0} \right) + (\rho a_z - \rho g) \left(z - \overbrace{z_o}^{3} \right)$$
$$\Rightarrow 0 = \rho a_x x + \rho a_y y + (\rho a_z - \rho g)(z - 3)$$
$$\Rightarrow z = 3 - \frac{a_x}{a_z - g} x - \frac{a_y}{a_z - g} y = 3 + \frac{a_x}{19.62} x + \frac{a_y}{19.62} y$$

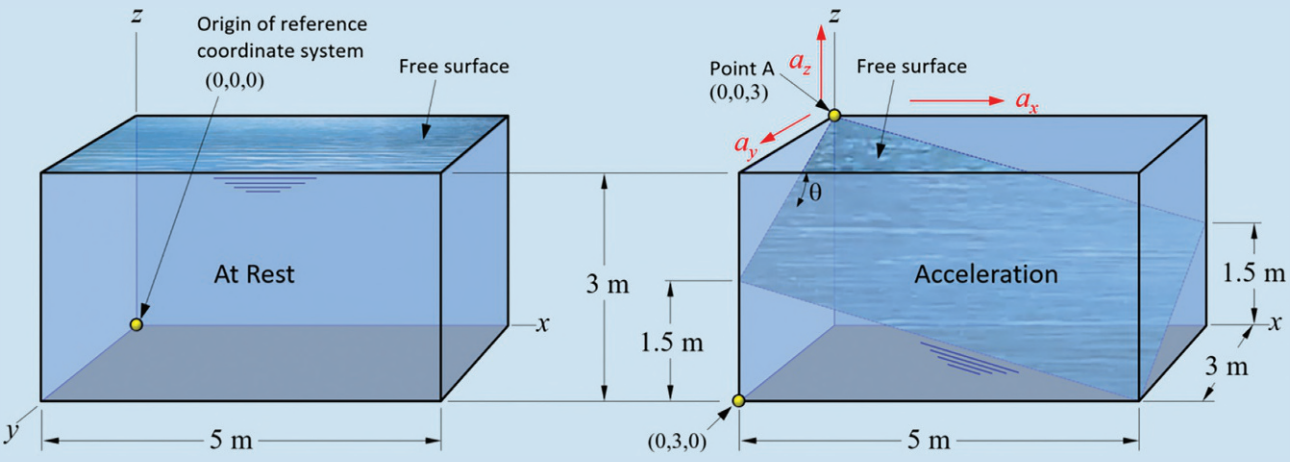


FIGURE 14-4 3-Dimensional acceleration of a container.

EXAMPLE 14-1: APPLICATION OF THE HYDROSTATIC EQUATION—ACCELERATING CONTAINER IN 3D (*cont'd*)

The accelerations (a_x and a_y) can be obtained by noting the geometry of the plane the free surface makes with respect to the container and by noting that the difference $p–p_0=0$ anywhere along it. For instance, when $(x,y,z)=(0,3,1.5)$ we get:

$$z=3+\frac{a_x}{19.62}x+\frac{a_y}{19.62}y \;\Leftrightarrow\; 1.5=3+\frac{a_x}{19.62}(0)+\frac{a_y}{19.62}(3)$$

$$\Rightarrow\; 1.5=3+\frac{3}{19.62}a_y \;\Leftrightarrow\; a_y=\frac{-1.5\times 19.62}{3}=-9.81\ m/s^2$$

Similarly, when $(x,y,z)=(5,0,1.5)$ we get:

$$z=3+\frac{a_x}{19.62}x-9.81y \;\Leftrightarrow\; 1.5=3+\frac{a_x}{19.62}(5)-9.81(0)$$

$$\Rightarrow\; -1.5=\frac{a_x}{19.62}(5) \;\Leftrightarrow\; a_x=\frac{-1.5\times 19.62}{5}=-5.886\ m/s^2$$

$$\Rightarrow\; z=3-5.886x-9.81y$$

Having determined the magnitudes of the accelerations a_x and a_y, we can now complete the pressure expression as follows:

$$p-p_0=\rho\, a_x(x-x_o)+\rho\, a_y(y-y_o)+(\rho\, a_z-\rho g)(z-z_o)$$

$$=(1000)\,(-5.886)(x-0)-(1000)(9.81)$$
$$(y-0)-(1000)(19.62)(z-3)$$
$$=-5886\,x-9810y-19620(z-3)\Rightarrow\; p=p(x,y,z)$$
$$=101325-5886\,x-9810y-19620(z-3)$$

By observation, the max pressure occurs at the point $(x,y,z)=(0,0,0)$ and amounts to

$$p=p(0,0,0)=101325-5886\,(0)-9810(0)-19620(0-3)$$
$$=160185\ Pa$$

(5) Newton's Laws of Motion

First law:
$$\sum \mathbf{F}=\mathbf{0} \;\Rightarrow\; \frac{d\mathbf{V}}{dt}=0 \qquad (14\text{-}12)$$

Second law — closed system:
$$\mathbf{F}=\frac{d(m\mathbf{V})}{dt}=m\frac{d\mathbf{V}}{dt} \quad (\text{no mass change}) \qquad (14\text{-}13)$$

Second law — open system:
$$\mathbf{F}+\mathbf{U}\frac{dm}{dt}=m\frac{d\mathbf{V}}{dt} \quad (\text{mass ejection at rate } \mathbf{U}) \qquad (14\text{-}14)$$

Third law: Any *action* results in an equal and opposite *reaction*.where **F** is force, **V** is velocity of the system, **U** is velocity of mass ejection or accretion, and m is mass.

(6) Two Approaches to Studying Fluid Flow

The formulation of fluid flow is derived using one of two observation approaches: *Eulerian* and *Lagrangian*. In the Eulerian approach, the properties of the fluid are observed as it enters and exits a volume that is fixed in space. In the Lagrangian framework, we observe the same properties changing inside a volume that moves with the fluid. This is illustrated in Figure 14-5. The two forms of observation lead to different formulation, although resulting properties match at the same position in space and time. Of the two approaches, the former is commonly used.

(7) Steady and Unsteady Fluid Flow

The difference between steady and unsteady fluid flow is illustrated in Figure 14-6. Imagine we regularly measure the speed of the flow in a river at two locations, A and B. If we tend to measure constant speeds at A (say 10 m/s) and B (say 20 m/s) as shown in the left image of Figure 14-6, the flow is considered *steady*. If we measure irregular speeds at those locations, the flow is *unsteady*.

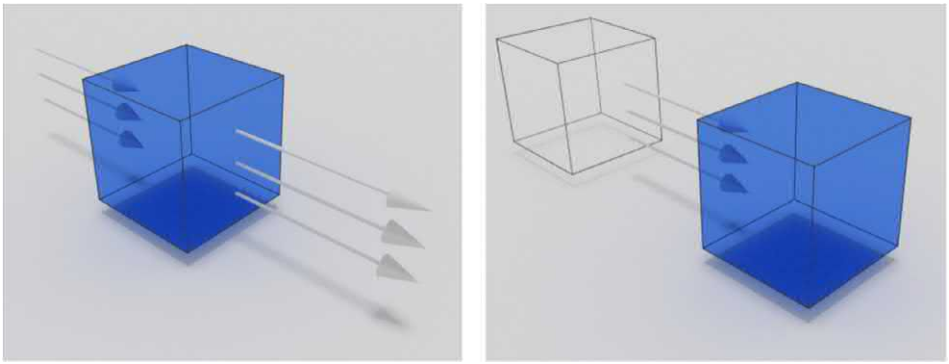


FIGURE 14-5 Eulerian (left) and Lagrangian (right) approach to formulation of fluid flow.

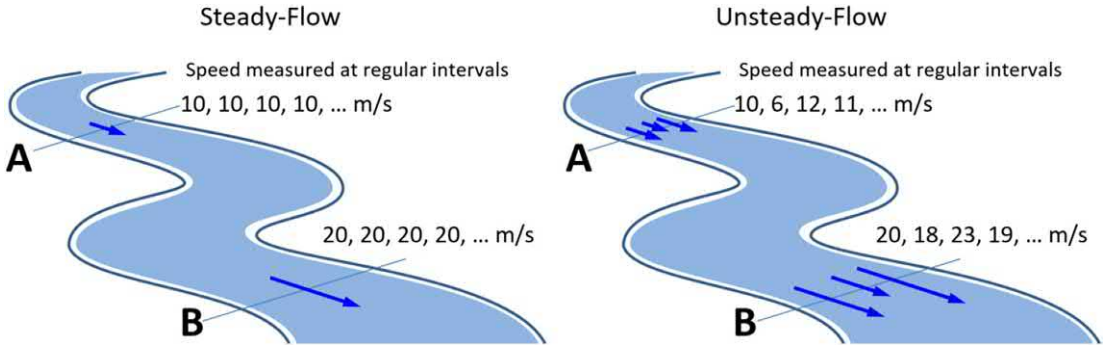


FIGURE 14-6 The difference between steady and unsteady flow.

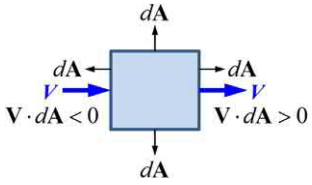


FIGURE 14-7 An infinitesimal element with fluid flowing through it.

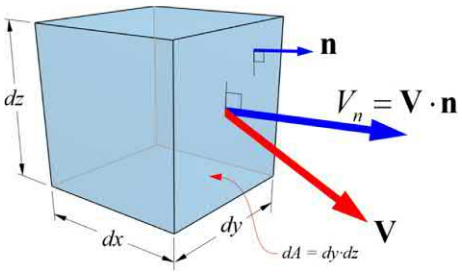


FIGURE 14-8 Normal velocity is the true velocity dotted with the surface normal.

(8) Elemental Vector Area, Volume, and Mass

An *infinitesimal vector area*, $d\mathbf{A}$, is the product of the elemental area dA and the unit normal to the area, $\mathbf{n}$ (see Figure 14-7). This is written as $d\mathbf{A} = \mathbf{n}dA$. It is also called the *unit normal vector area*. An *infinitesimal volume*, $d\forall$, is given by $d\forall = dxdydz$. Thus, an *infinitesimal mass* of that volume, given density ρ, amounts to $dm = \rho d\forall = \rho dxdydz$.

Note that $d\mathbf{A}$ points out and away from the element. This has important consequences: If the dot product of $\mathbf{V}$ and $d\mathbf{A}$ is negative, then $\mathbf{V}$ and $d\mathbf{A}$ have opposite directions, which means $\mathbf{V}$ is flowing INTO the volume. If positive, the opposite happens and $\mathbf{V}$ is flowing OUT of the volume (see Figure 14-7).

(9) Normal Velocity

Consider the velocity, $\mathbf{V}$, flowing through some volume as shown in Figure 14-8. Then, the velocity normal to a plane with a unit normal $\mathbf{n}$, is given by

$$V_n = \mathbf{V} \cdot \mathbf{n}$$

(10) Mass Flow, $\dot{m}$

Refers to the mass of fluid flowing through some area per *unit* time. An example of units is "kilograms of fluid per second." The mass flow through the infinitesimal area dA is written as

$$\frac{dm}{dt} = d\dot{m} = \rho V_n \, dA = \rho \underbrace{(\mathbf{V} \cdot \mathbf{n})}_{V_n} \, dA = \rho \mathbf{V} \underbrace{d\mathbf{A}}_{\substack{\text{unit normal} \\ \text{vector area}}}$$

Infinitesimal mass flow:

$$d\dot{m} = \rho V_n \, dA \qquad \left[\frac{kg}{m^3}\right]\left[\frac{m}{s}\right]\left[m^2\right] = \left[\frac{kg}{s}\right] \tag{14-15}$$

Average mass flow:

$$\dot{m} = \rho V_n A \tag{14-16}$$

(11) Volumetric Flow Rate

Refers to the volume of fluid flowing through an area per *unit* time. An example of units is "cubic meters of fluid per second."

$$\text{Volumetric Flow Rate} = \dot{\forall} = VA \qquad \left[\frac{m}{s}\right]\left[m^2\right] = \left[\frac{m^3}{s}\right] \tag{14-17}$$

(12) Mass Flux

Refers to the mass of fluid flowing through *unit* area per *unit* time. An example of units is "kilograms of fluid per m^2 each second."

Infinitesimal mass flux:

$$\frac{d\dot{m}}{dA} = \rho V_n \qquad \left[\frac{kg}{m^3}\right]\left[\frac{m}{s}\right] = \left[\frac{kg}{m^2 \cdot s}\right] \tag{14-18}$$

Average mass flux:

$$\frac{\dot{m}}{A} = \rho V_n \tag{14-19}$$

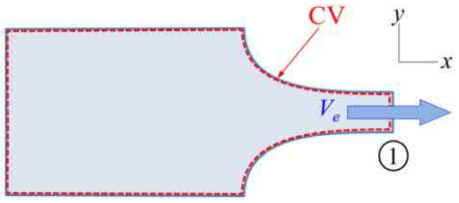


FIGURE 14-9 An example of a single-exit CV.

If $\mathbf{V} = u\mathbf{i} + v\mathbf{j} + w\mathbf{k}$, then terms like ρu, ρv, ρw are called *flux terms*.

(13) Momentum Flux

Momentum flux refers to the momentum of fluid passing through some area per unit time. Example units are "kilogram-meters-per-second, each second."

$$\text{Momentum Flux} = \rho V^2 A \qquad \left[\frac{kg}{m^3}\right]\left[\frac{m^2}{s^2}\right][m^2] = \left[\frac{kg \cdot m}{s^2}\right] \tag{14-20}$$

As can be seen, the unit for momentum flux is the unit of force, a Newton. It is in fact a force.

(14) Control Volumes and Control Surfaces

The solution of problems of fluid mechanics utilizes *control surfaces* or *control volumes* (CV). This isolates the extent of the problem into a manageable region. An example of a CV is shown in Figure 14-9, as the dashed shape.

(15) The Basics of Energy

The fundamental principle of energy states that "Energy can neither be created nor destroyed; it can only change in form." Traditional relations for energy are presented in Table 14-2.

(16) Isentropic Flow Relations

Isentropic flow applies to many flow phenomena, e.g., high speed and duct flow. Such flow is both *adiabatic*[2] and *reversible*.[3] The following set of equations is derived in standard texts on fluid mechanics (e.g., [1, 2, 4, 5]).

Total (stagnation) temperature:

$$T_0 = T\left[1 + \frac{\gamma - 1}{2} M_\infty^2\right] \tag{14-21}$$

Total (stagnation) pressure:

$$p_0 = p\left(1 + \frac{\gamma - 1}{2} M_\infty^2\right)^{\frac{\gamma}{\gamma - 1}} \tag{14-22}$$

Compressible dynamic pressure:

$$q_c = p_0 - p = p\left[\left(1 + \frac{\gamma - 1}{2} M_\infty^2\right)^{\frac{\gamma}{\gamma - 1}} - 1\right] \tag{14-23}$$

Total (stagnation) density:

$$\rho_0 = \rho\left(1 + \frac{\gamma - 1}{2} M_\infty^2\right)^{\frac{1}{\gamma - 1}} \tag{14-24}$$

where T, p, and ρ are the static temperature, pressure, and density, respectively, and M_∞ is Mach number.

14.1.4 The Basic Equations of Thermodynamics

Only basic equations of thermodynamics are presented here.

$$\text{First Law of Thermodynamics:} \quad \Delta U = Q - W \tag{14-25}$$

TABLE 14-2 Traditional energy relations.

Concept	Formula	Unit analysis
Kinetic energy:	$KE = \frac{1}{2} mV^2$	$[kg]\left[\frac{m^2}{s^2}\right] = \left[\frac{kg \cdot m}{s^2} \cdot m\right] = [N \cdot m] = [J]$
Potential energy:	$PE = mgh$	$[kg]\left[\frac{m}{s^2}\right][m] = \left[\frac{kg \cdot m}{s^2} \cdot m\right] = [N \cdot m] = [J]$
"Pressure" energy:	$pV = mRT$	$\left[\frac{N}{m^2}\right]\left[m^3\right] = [N \cdot m] = [J]$
Thermal energy:	$\Delta U =$ see Table 14-3.	$[kg]\left[\frac{J}{kg \cdot K}\right][K] = [J]$
Electric energy:	$EE =$ voltage $\cdot$ current $\cdot$ time $= UI \cdot \Delta t$	$[Wh]$ *or* $[J]$ $1000\ Wh = 1000\ W(3600\ s) = 3.6 \times 10^6\ J$

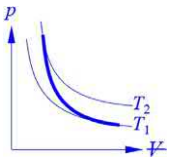
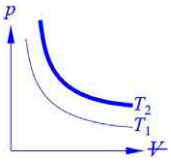
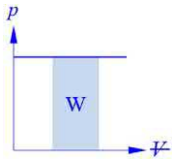
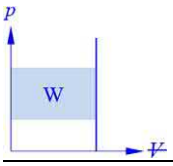
where

m = Mass	T = temperature
V = speed	R = specific gas constant
G = gravitational acceleration	ΔU = change in internal energy
h = elevation	U = voltage
p = pressure	I = current
V = volume	Δt is time.

[2] An adiabatic process is one in which no heat is transferred; only work is done.

[3] An example of a reversible process is the isothermal expansion (or compression) of an ideal gas by a piston inside a cylinder.

TABLE 14-3 Basic thermodynamic processes.

Process	General definition	W	Q	ΔU	Δs
Adiabatic 	$Q=0$ $\Delta U=-W$ $p\cancel{V}^k=\text{const}$ $p\cancel{V}^{k-1}=\text{const}$	$-\Delta U$ $-mC_v\,\Delta T$	0	$mC_v\,\Delta T$	0
Isothermal 	$T=\text{const}$ $\Delta U=0$ $W=Q$ $p\cancel{V}=\text{const}$	$mRT\ln\left(\frac{\cancel{V}_2}{\cancel{V}_1}\right)$ $mRT\ln\left(\frac{p_1}{p_2}\right)$	$mRT\ln\left(\frac{\cancel{V}_2}{\cancel{V}_1}\right)$ $mRT\ln\left(\frac{p_1}{p_2}\right)$	0	$mR\ln\left(\frac{\cancel{V}_2}{\cancel{V}_1}\right)$ $mR\ln\left(\frac{p_1}{p_2}\right)$
Isobaric 	$p=\text{const}$ $\Delta U=Q-p\Delta\cancel{V}$	$p\Delta V=mC_p\,\Delta T$	$mC_p\,\Delta T$	$mC_v\,\Delta T$	$mC_p\ln\left(\frac{T_2}{T_1}\right)$
Isovolumetric 	$\cancel{V}=\text{const}$ $\Delta U=Q$ $W=0$	0	ΔU $mC_v\,\Delta T$	$mC_v\,\Delta T$	$mC_v\ln\left(\frac{T_2}{T_1}\right)$
Free expansion	$Q=0$ $\Delta U=0$ $W=0$ $T=\text{const}$	0	0	0	$mR\ln\left(\frac{\cancel{V}_2}{\cancel{V}_1}\right)$
Isentropic	$Q=0$ $\Delta U=-W$ $T=\text{const}$				

where
Q = Heat added to a system
ΔU = change in internal energy
W = work
C_v = Specific heat for constant volume
C_p = Specific heat for constant pressure
Δs = Change in entropy.

Basic thermodynamic processes are shown in Table 14-3. All variables are defined above.

14.2 THEORY OF REACTIVE THRUST

This section presents the basics of the theory of reactive thrust. The general thrust equation is developed for a turbojet, turbofan, propellers, and a rocket. Reactive thrust refers to a force developed by the discharge of fluid that has been undergone mechanical or chemical acceleration. This changes its momentum, creating thrust as explained by Newton's 2nd and 3rd laws. A deeper insight is of importance to the aircraft designer and is gleaned through *fluid mechanics*. Here, only the basics are reviewed—readers interested in further treatise can consult references such as [1–5], to name a few.

14.2.1 Conservation Laws

Conservation laws refer to several principles of nature that prevail in fluid flow. Three principles are of great

interest within the context of this chapter: (1) *conservation of mass*, (2) *conservation of momentum*, and (3) *conservation of energy*. All three are referred to as continuity laws. The importance of these laws is listed below:

(1) Conservation of Mass returns flow speeds, mass flows, and flow areas.
(2) Conservation of Momentum returns forces.
(3) Conservation of Energy provides additional relations by ensuring kinetic, potential, and thermal energy is conserved.

These laws are presented in two forms: *integral* and *derivative* (or *differential*). The problem-solving flows as follows:

(1) Conservation of mass is used to determine parameters such as geometry, $\dot{m}$, and $\mathbf{V}$ (which are the primary flow-field variables) of the flow. It ensures that matter is properly accounted for.
(2) Conservation of momentum is used to determine forces that result from the interaction of p,ρ,$\mathbf{V}$, and the geometry involved in the flow. This allows forces and moments acting on the geometry to be estimated.
(3) Conservation of mass and momentum are *fundamental equations* that suffice for the analysis of incompressible flow (ρ = constant).
(4) For compressible flow (ρ = variable), we must add a new fundamental equation, the *energy equation*. We do this to obtain expressions that preserve the energy associated with the flow in terms of p, ρ, $\mathbf{V}$, etc. This also adds two new flow-field variables: e = internal energy and T = temperature. This calls for additional equations.

Some problems can be solved using only conservation of mass. Other problems require both conservation of mass and momentum. Then there are problems that require all three to be solved simultaneously.

(1) Conservation of Mass

While all the conservation theorems are continuity laws, the term *continuity equation* is often used synonymously with conservation of mass. It is formulated as shown in equations (14-26) and (14-27):

Integral form:

$$\overbrace{-\frac{\partial}{\partial t}\overbrace{\iiint_{\forall}\rho\, d\forall}^{\text{mass}}}^{=\frac{dm}{dt}=\Delta\dot{m}} = \overbrace{\oiint_{A}\overbrace{\rho\mathbf{V}\cdot d\mathbf{A}}^{\text{mass flow}}}^{\text{net mass flow out of CV}} \tag{14-26}$$

Derivative form:

$$\frac{\partial}{\partial t}\rho\, d\forall + \nabla\cdot\rho\mathbf{V} = 0 \tag{14-27}$$

Some Simplifications

(A) Continuity for steady, compressible flow:

$$\frac{\partial}{\partial t}=0,\quad \rho=\text{variable} \quad\Rightarrow\quad \oiint_{A}\rho\vec{V}\cdot d\vec{A}=0$$

(B) Continuity for steady, incompressible flow:

$$\frac{\partial}{\partial t}=0,\quad \rho=\text{constant} \quad\Rightarrow\quad \oiint_{A}\vec{V}\cdot d\vec{A}=0$$

(C) Continuity for steady, compressible, 1-D flow in the x-direction flow:

$$\vec{V}=u\,\hat{i} \;\Rightarrow\; \oiint_{A}\vec{V}\cdot d\vec{A}=0 \;\rightarrow\; \oint\rho\left(u\,\hat{i}\right)\cdot d\vec{l}=\rho u l=0$$

where l = area per unit depth.

(2) Conservation of Momentum

The momentum conservation yields forces. Momentum equation in integral form is presented below with notes explaining terms. Among those is the reaction force $\mathbf{R}$. When the equation is solved, it represents thrust.

$$\overbrace{\vec{\mathbf{R}}}^{\text{unbalanced reaction force}} + \overbrace{\overbrace{\iiint_{\forall}\rho\mathbf{f}\, d\forall}^{\text{body force due to acceleration}} - \overbrace{\oiint_{A}p\, d\mathbf{A}}^{\text{pressure force}} + \overbrace{\vec{F}_{\mu}}^{\text{friction}}}^{\text{analogous to } \vec{F}} = \overbrace{\oiint_{A}\overbrace{\left(\rho\mathbf{V}\cdot d\mathbf{A}\right)\mathbf{V}}^{\text{mass flow}}}^{\text{net flow of mass momentum}} + \overbrace{\frac{\partial}{\partial t}\overbrace{\iiint_{\forall}\rho\mathbf{V}\, d\forall}^{\text{momentum}}}^{\text{rate of change of momentum}}}^{\text{analogous to } \frac{d}{dt}\left(m\vec{V}\right)} \tag{14-28}$$

Momentum equation is also presented in a differential form. This form is utilized in *computational fluid mechanics* (CFD) in various finite difference schemes.

$$\begin{aligned}
\frac{\partial(\rho u)}{\partial t}+\nabla\cdot(\rho u\mathbf{V}) &= -\frac{\partial p}{\partial x}+\rho f_x+(F_x)_{viscous}\\
\frac{\partial(\rho v)}{\partial t}+\nabla\cdot(\rho v\mathbf{V}) &= -\frac{\partial p}{\partial y}+\rho f_y+(F_y)_{viscous}\\
\frac{\partial(\rho w)}{\partial t}+\nabla\cdot(\rho w\mathbf{V}) &= -\frac{\partial p}{\partial z}+\rho f_z+(F_z)_{viscous}
\end{aligned} \tag{14-29}$$

(3) Conservation of Energy

Here, the energy equation is only presented in integral form

$$\overbrace{\underbrace{\iiint_{\forall} \dot{q}\rho\, d\forall}_{\left[\frac{J}{s\cdot kg}\right]\left[\frac{kg}{m^3}\right]\left[m^3\right]} + \dot{Q}_{visc}}^{Q} \overbrace{- \underbrace{\oint_S p\mathbf{V}\cdot d\mathbf{A}}_{=(-pd\mathbf{A})\cdot\vec{V}\ =\text{Force}\times\text{Vel}} + \iiint_{\forall}\rho(\mathbf{f}\cdot\mathbf{V})\,d\forall + \dot{W}_{visc} + \dot{W}_{mech}}^{-W}$$

Heat added to fluid inside the CV from surroundings in J/s; Rate-of-work done on fluid inside CV by pressure force on S in J/s; Rate-of-work done on fluid inside the CV by body forces in J/s; Rate of viscous work inside the CV in J/s; Rate of mechanical work added to CV in J/s

$$= \underbrace{\frac{\partial}{\partial t}\iiint_{\forall}\rho\left(e+\frac{V^2}{2}+gz\right)d\forall}_{\text{Time rate of change of total energy inside CV due to transient variations of flow-field variables in J/s}} + \underbrace{\oint_S \rho\left(e+\frac{V^2}{2}+gz\right)\mathbf{V}\cdot d\mathbf{A}}_{\text{Net rate of flow of total energy across the control surface in J/s}} \qquad (14\text{-}30)$$

The total energy stored in the elemental volume $d\forall$ in J; Note that mass flow across $d\mathbf{A}$ is $p\mathbf{V}\cdot d\mathbf{A}$ so this is the elemental flow of total energy across $d\mathbf{A}$.

ΔE

Application of the Energy Equation

One of the best-known offspring of the energy equation is Bernoulli's equation (it can also be derived using the momentum equation). While the derivation is omitted to save space, interested readers can refer to references [1–5]. A general integral form of the equation is given by

$$\frac{dp}{\rho}+\frac{1}{2}d\left(V_\infty^2\right)+gz=0 \quad\Rightarrow\quad \int\frac{dp}{\rho}+\frac{1}{2}V_\infty^2+gz=\text{constant} \qquad (14\text{-}31)$$

This is used to derive two general solutions: incompressible and compressible. The incompressible form presumes constant density $\rho_1=\rho_2=\rho$ and, upon substituting this into Equation (14-31), is given by

$$p_1+\frac{1}{2}\rho V_1^2+\rho g z_1=p_2+\frac{1}{2}\rho V_2^2+\rho g z_2 \quad (=\text{constant}) \qquad (14\text{-}32)$$

The difference in elevation is usually negligible in problems involving aircraft. Thus, we drop the product gz and rewrite Equation (14-32) as

$$p_1+\frac{1}{2}\rho V_1^2=p_2+\frac{1}{2}\rho V_2^2 \qquad (14\text{-}33)$$

The compressible form presumes isentropic (reversible and adiabatic) flow. This substitutes the *isentropic equation of state*, given by $p=C\rho^\gamma$, for density. Substituting this into Equation (14-31) and manipulating leads to

$$\left(\frac{\gamma}{\gamma-1}\right)\frac{p}{\rho}+\frac{1}{2}V^2=\text{constant} \qquad (14\text{-}34)$$

14.2.2 The General Thrust Equation

The *general thrust equation* is usually presented in the following, 1-dimensional form. It is derived below.

$$F_{NET}=p_eA_e-p_iA_i+\dot{m}_eV_e-\dot{m}_iV_i \qquad (14\text{-}35)$$

where the variables as given in Figure 14-10. Note that, in this chapter, F is used for thrust

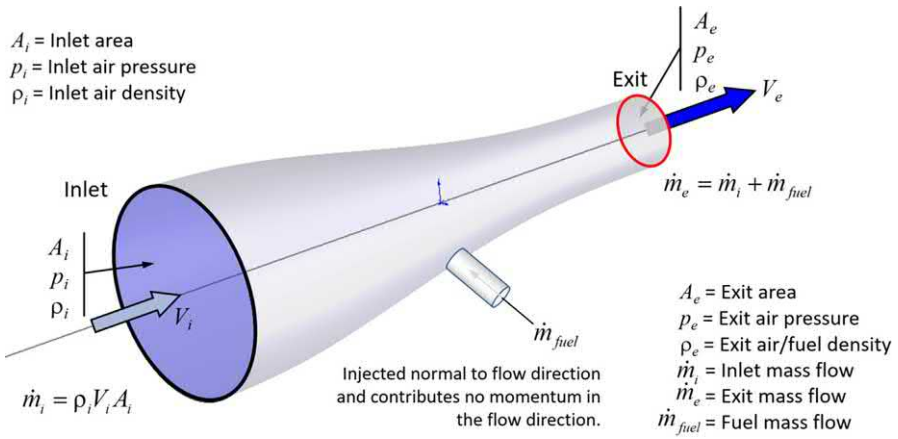


FIGURE 14-10 A theoretical representation of thrust generation.

instead of T to avoid confusion with temperature. If f is the fuel-to-air ratio, then the exit mass flow is given by

$$\dot{m}_e = \dot{m}_i + \dot{m}_f = \dot{m}_i(1+f) \tag{14-36}$$

$$F_{NET} = (p_e - p_i)A_e + \dot{m}_i(V_e - V_i) \tag{14-37}$$

When in motion, the pressure differential does not contribute as much to thrust as the mass flow term. Albeit old, the Rolls-Royce Viper, which powered aircraft such the

DERIVATION OF EQUATION (14-35)

Consider the 1-dimensional stream tube in Figure 14-10. Assume steady, inviscid flow that enters only through the air- and fuel-inlets and exits only through the exit. The parameters A, p, and ρ are the cross-sectional area, pressure, and density, respectively, where the inlet is denoted by the subscript i and the exit by e. The mass flow inside the stream tube is obtained from Equation (14-26). Since we assume steady flow, the time derivative is zero. Thus, simplifying Equation (14-26) leads to

$$\overbrace{-\frac{\partial}{\partial t}\iiint_V \rho\, d\forall}^{\Delta\dot{m}=0} = \overbrace{\oiint_A \rho\vec{V}\cdot d\vec{A}}^{\rho(A_eV_e - A_iV_i)} \quad\Rightarrow\quad 0 = \overbrace{\rho_e A_e V_e}^{\text{Plus because } \vec{V}\cdot d\vec{A}>0} - \overbrace{\rho_i A_i V_i}^{\text{Minus because } \vec{V}\cdot d\vec{A}<0} \quad\Rightarrow\quad \overbrace{\rho_e A_e V_e}^{\dot{m}_e} = \overbrace{\rho_i A_i V_i}^{\dot{m}_i}$$

Thus, the mass flow rate through the inlet is $\dot{m}_i = \rho_i V_i A_i$. The mass flow through the exit amounts to this plus the mass flow of fuel, i.e., $\dot{m}_e = \dot{m}_i + \dot{m}_{fuel}$. This relation ensures mass conservation and is important when we do not know all parameters. Next, we resort to Equation (14-28) to estimate the *net force* acting on the stream tube. It is the difference between the pressure at the inlet, p_i, and exit, p_e, times the area over which these act, plus the rate of change of momentum of the mixture. This is obtained as follows:

$$\overbrace{\mathbf{R}}^{\substack{\text{Imbalance between the left and right sides of the equation sign, gives rise to a residual force: "net thrust," } F_{NET}}} + \overbrace{\iiint_V \rho\mathbf{f}\, d\forall}^{\substack{\text{Neglect elevation change.}\\ \text{Neglect acceleration.}\\ =0}} - \oiint_A p\, d\mathbf{A} + \overbrace{\mathbf{F}_\mu}^{\substack{\text{No friction}\\ =0}} = \oiint_A (\rho\mathbf{V}\cdot d\mathbf{A})\mathbf{V} + \overbrace{\frac{\partial}{\partial t}\iiint_V \rho\mathbf{V}\, d\forall}^{\substack{\text{Steady flow}\\ =0}}$$

$$\Rightarrow\quad F_{NET} - \oiint_A p\, d\mathbf{A} = \oiint_A (\rho\mathbf{V}\cdot d\mathbf{A})\mathbf{V} \quad\Rightarrow\quad T_{NET} + \left[-\oiint_A p\, d\mathbf{A}\right] = \oiint_A (\rho\mathbf{V}\cdot d\mathbf{A})\mathbf{V}$$

$$\Rightarrow\quad F_{NET} + \overbrace{p_iA_i - p_eA_e}^{\substack{\text{Based on the direction of the pressure force } pA}} = \overbrace{(-\rho_iA_iV_i)}^{\substack{\text{Based on the sign of } \mathbf{V}\cdot\mathbf{A}}}V_i + (\rho_eA_eV_e)V_e = -\dot{m}_iV_i + \dot{m}_eV_e = -\dot{m}_iV_i + (\dot{m}_i + \dot{m}_f)V_e$$

$$\Rightarrow\quad \overbrace{F_{NET}}^{\substack{\text{In the absence of reaction we have net thrust in the opposite direction}}} = \overbrace{p_e}^{\substack{\text{This is static pressure}}}A_e - \overbrace{p_i}^{\substack{\text{This is static pressure}}}A_i + (\dot{m}_i + \dot{m}_f)V_e - \dot{m}_iV_i$$

(1) Application 1 – Turbojets

The following applications of the thrust equations require engine-specific simplifications. For a turbojet, we assume $\dot{m}_{fuel} << \dot{m}_i \;\Rightarrow\; \dot{m}_e \approx \dot{m}_i$ and $A_i \approx A_e$. Thus, Equation (14-35) becomes

Aermacchi MB-339 and BAC Strikemaster, exemplifies a turbojet engine for military trainers. Its mass flow during T-O is about 20 kg/s while delivering some 11,120 N (2500 lb_f) of thrust [7].

EXAMPLE 14-2

Determine net thrust for the theoretical turbojet in Figure 14-11 assuming the measured absolute inlet and exit pressures is $p_i = 95{,}000\,\text{Pa}$ and $p_e = 10{,}1325\,\text{Pa}$, inlet and exit speeds are $V_i = 57\,\text{m/s}$ and $V_e = 515\,\text{m/s}$, inlet and exit areas are $A_i = A_e = 0.305\,\text{m}^2$, and inlet temperature is $T_i = 288\,\text{K}$.

SOLUTION:

Density in inlet:

$$\rho_i = \frac{p_i}{RT_i} = \frac{95000}{(287)(288)} = 1.149\ \text{kg/m}^3.$$

Mass flow in inlet and exit:

$$\dot{m}_i = \rho_i A_i V_i = \dot{m}_e = (1.149)(0.305)(57) = 20.0\ \text{kg/s}.$$

Net thrust:

$$F_{NET} = (p_e - p_i)A_e + \dot{m}_i(V_e - V_i) = (101325 - 95000)(0.305) + (20.0)(515 - 57) = 11095\ \text{N}\ (= 2500\,\text{lb}_\text{f})$$



FIGURE 14-11 Estimating the thrust of a theoretical turbojet.

(2) Application 2 – Turbofans

For a turbofan, we assume $\dot{m}_{fuel} << \dot{m}_i \Rightarrow \dot{m}_e \approx \dot{m}_i$. Turbofans typically feature more than one inlet and exit (see Figure 14-12). There is one inlet for the bypass air, another for the core (although usually combined in one inlet). There are also two exits: one for the bypass air, the other for the core flow. In its simplest form, we can assume the pressure across the inlets and exits are uniform (e.g., see Figure 7-33). However, if the exit pressure for the core and bypass air differs, Equation (14-35) becomes:

$$F_{NET} = \left(p_{e_{core}} A_{e_{core}} + p_{e_{bypass}} A_{e_{bypass}}\right) - p_i A_i + \dot{m}_{e_{core}}(V_{e_{core}} - V_i) + \dot{m}_{e_{bypass}}\left(V_{e_{bypass}} - V_i\right) \quad (14\text{-}38)$$

See variables in Figure 14-12. The General Electric GE90 that powers the Boeing 777, exemplifies a turbofan engine for commercial aviation. Its mass flow during T-O is about 1350 kg/s. Its maximum diameter is 3.87 m and bypass ratio is 9.

(3) Application 3 – Propellers

For propellers, the magnitude of $\dot{m}_{fuel}$ is small enough to be neglected. If we consider the propeller an infinitesimally thin disc, it follows that (1) the inlet and exit speeds, V_i and V_e, and (2) the inlet and exit area, A_i and A_e, must be equal. Thus, we rewrite Equation (14-35) as follows:

$$\dot{m}_f \approx 0,\ \ A_e = A_i = A_{prop},\ \ V_e = V_i \ \Rightarrow$$
$$F_{NET} = (p_e - p_i)A_{prop} \quad (14\text{-}39)$$

This result is the so-called *actuator-disc* or *Rankine-Froude Momentum Theory*, presented in Chapter 15. It details more results.

(4) Application 4 – Rockets

For rockets the values of $\dot{m}_i$ and V_i are zero, since no air is introduced from the outside. Thus, $\dot{m}_{fuel}$ takes on a leading role and is more appropriately referred to as $\dot{m}_{propellant}$ where $\dot{m}_{propellant} = \dot{m}_{fuel} + \dot{m}_{oxidizer}$, which is carried like fuel. Additionally, A_e and A_i both refer to the area at the nozzle exit plane and p_i is the ambient pressure. Therefore, we rewrite Equation (14-35) as follows:

$$F_{NET} = (p_e - p_i)A_e + \dot{m}_{propellant} V_e \quad (14\text{-}40)$$

(5) Thrust-to-Weight Ratio

The Thrust-to-Weight ratio, denoted by T/W, is a very important figure of merit for aircraft. Note that here, by tradition, T is used instead of F. It ranges from a value of 0 for unpowered aircraft to values in the ballpark of 1.1 for many fighter aircraft (see Table 14-4). Of course,

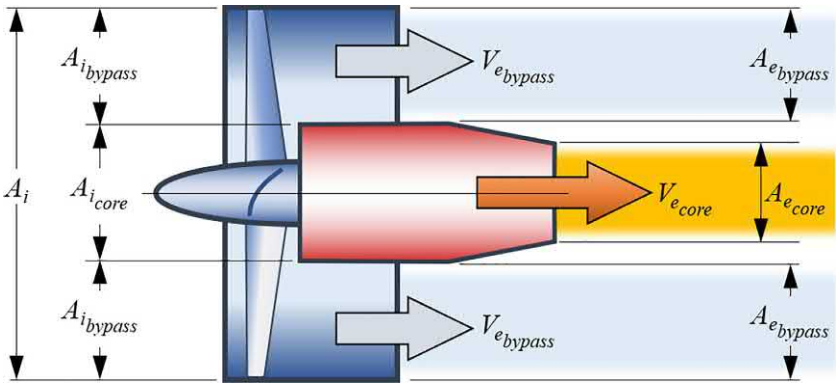


FIGURE 14-12 Schematic of a turbofan.

TABLE 14-4 Typical range of T/W for selected classes of aircraft.

Type of aircraft	T/W
Unpowered (sailplanes, hang gliders, etc.)	0
General aviation	0.20–0.45
Commercial jetliners of the 1950s–1960s	0.18–0.26
Commercial jetliners of the 1970s–present	0.20–0.35
Modern fighter aircraft	0.55–1.15

thrust varies with airspeed and weights with time aloft, so the true value of T/W changes in flight. Therefore, the stated T/W usually refers to a specific weight, such as maximum gross weight or some other specific weight, while the thrust refers to the maximum static thrust.

The importance of high enough T/W cannot be overemphasized. As an example, the De Havilland DH-106 Comet 1 suffered two hull losses, one with fatalities, both that were directly attributed to its low T/W of 0.18. The first one occurred on October 26, 1952 and the second one on March 3, 1953 [8]. Due to the low T/W, the airplane had to be rotated with utmost care to avoid a sharp rise in drag and a subsequent reduction of acceleration. In comparison, modern jetliners have a T/W of the order 0.3–0.35.

EXAMPLE 14-3

An aircraft of 15,000 kg mass is propelled by two turbojet engines. It is flying straight and level at altitude of 10,000 m and constant airspeed of 280 m/s. The volumetric flow into the engines is 140 m^3/s and is mixed with fuel added at a rate of 4.0 kg/s. The mixture is discharged from the engine at speed of 450 m/s. Determine the thrust developed by the engines and estimate the cruise L/D and T/W (note that $D=T$ in this steady-state condition). Assume the products p_iA_i and p_eA_e are equal. Density of air at 10,000 m is $\rho = 0.413\,kg/m^3$.

SOLUTION:

The inlet mass flow is found from

$$\dot{m}_i = \rho(V_iA_i) = (0.413)(140) = 57.8 \text{ kg/s}.$$

The exit mass flow is calculated using Equation (14-36)

$$\dot{m}_e = \dot{m}_i + \dot{m}_f = 57.8 + 4.0 = 61.8 \text{ kg/s}$$

Then, use Equation (14-35) to calculate the thrust:

$$F_{NET} = \overbrace{p_eA_e - p_iA_i}^{=0} + \dot{m}_eV_e - \dot{m}_iV_i = (61.8)(450) - (57.8)(280) = 11626 \text{ N}$$

This corresponds to 2614 lb_f. Thus, the L/D and $T/W = F_{NET}/W$ is given by

$$\frac{L}{D} = \frac{W}{T} = \frac{15000 \times 9.81}{11626} \approx 12.7 \quad \Rightarrow \quad \frac{T}{W} \approx \frac{1}{12.7} = 0.079$$

14.2.3 Propulsive Efficiency

Efficiency is a measure of the quality of some process. Below are definitions for several efficiencies, commonly used in aircraft design. Note that to follow tradition, the letter T will be used for thrust, rather than F.

(1) Propeller Efficiency, η_p

See Section 15.3.8.

(2) Pressure Recovery Efficiency, η_{prc}

Refers to how effectively air entering an inlet slows down. This is shown in Figure 14-13 assuming adiabatic expansion in a subsonic inlet. The goal of inlet design is to conserve the total pressure of the flow (p_0). Friction and possible flow separation in the inlet reduce the total pressure (p_{0f}) at the compressor face.

Compressible flow:

$$\eta_{prc} \equiv \frac{\text{Compressive Work}}{\text{Available Kinetic Energy}} = \frac{\left(p_f/p_\infty\right)^{\frac{\gamma-1}{\gamma}} - 1}{\frac{\gamma-1}{2}\left(M_\infty^2 - M_f^2\right)} \tag{14-41}$$

Incompressible flow:

$$\eta_{prc} \equiv \frac{p_{0f} - p_\infty}{q_\infty} \tag{14-42}$$

(3) Propulsive Efficiency for Single-Exit Thrust Device, η_{prp}

The generation of thrust by propellers and jet engines consumes more energy than it delivers. The thrust is developed when matter (air) is accelerated from some initial airspeed (V_∞) to the exit speed of the thrust device (V_e). The acceleration increases the kinetic energy of the propulsive mass flow ($\dot{m}$) going through the engine. A fraction of this kinetic energy is converted to thrust power and the rest is lost to the environment. This loss explains why the speed of the vehicle is less than that of the matter propelling it. The difference between V_e and V_∞ is indicative of the kinetic energy lost. For instance, if the speed of the vehicle is zero, all the kinetic energy of the propulsive mass flow is lost. If the speed of the vehicle is the same as the exit speed, no kinetic energy is lost. In real applications, this cannot be achieved because thrust drops to zero. The loss in kinetic energy of the propulsive mass flow is expressed as follows

$$K\dot{E}_{loss} = \frac{1}{2}\dot{m}(V_e - V_\infty)^2$$

Thus, the total power required for flight is

$$P_{req} = T_{NET}V_\infty + K\dot{E}_{loss} = T_{NET}V_\infty + \frac{1}{2}\dot{m}(V_e - V_\infty)^2 \tag{14-43}$$

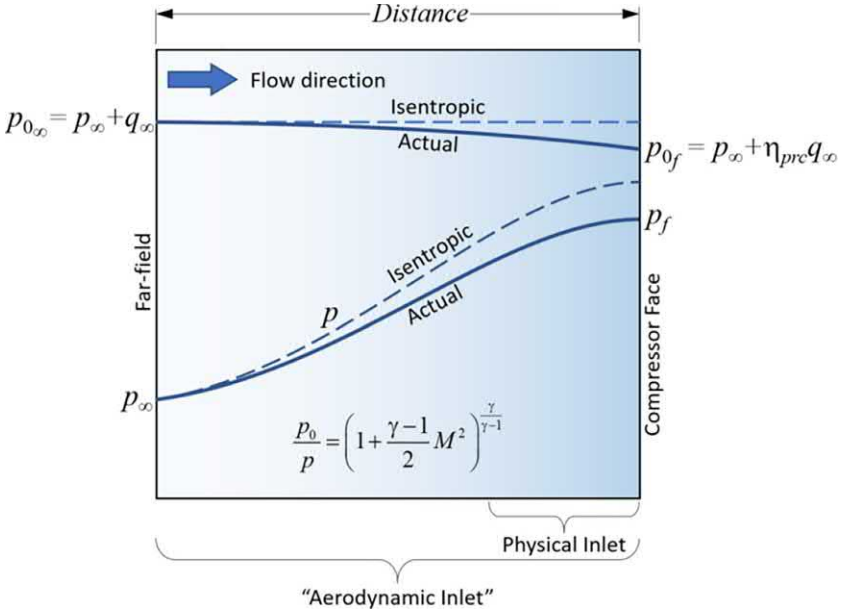


FIGURE 14-13 Changes in pressure in an inlet. *Based on Seddon, J., Goldsmith, E.L., Intake Aerodynamics, AIAA Education Series, 1985.*

If we assume the contribution of the pressure difference between the front and aft face of the engine is small, the thrust can be expressed as

$$T_{NET} = \dot{m}(V_e - V_\infty) \tag{14-44}$$

The propulsive efficiency can now be defined as follows

$$\eta_{prp} \equiv \frac{\text{Thrust Power}}{\text{Total Power for Flight}} = \frac{T_{NET} V_\infty}{T_{NET} V_\infty + \frac{1}{2}\dot{m}(V_e - V_\infty)^2} \tag{14-45}$$

Next, substitute Equation (14-44) into Equation (14-45) and manipulate algebraically to get

$$\eta_{prp} = \frac{2}{1 + V_e / V_\infty} \tag{14-46}$$

Per Equation (14-35), the generation of thrust requires $V_e > V_\infty$. Consider an imaginary situation in which $V_e = V_\infty$ and for which Equation (14-46) returns $\eta_{prp} = 1$. This also implies $T_{NET} = 0$. Since the drag of the vehicle increases with airspeed, it is impossible to achieve steady flight without $T_{NET} > 0$. Regardless, say we strive to get as close to $\eta_{prp} = 1$ as possible. For low values of V_e and V_∞, such as those associated with propeller aircraft, we get a high value of η_{prp}. For instance, if $V_e = 1.2 V_\infty$, then $\eta_{prp} = 0.91$. In contrast, a high value of V_e and low V_∞ results in a poor η_{prp}. This corresponds to a jet engine at low airspeed. As an example, if $V_e = 3 V_\infty$, then $\eta_{prp} = 0.5$. This shows that a propeller is the correct choice for low-speed aircraft. Jet propulsion is the right choice for high-speed aircraft.

(4) Propulsion Efficiency for Multiexit Thrust Device, η_{prp}

Equation (14-46) must be modified to treat jet engines, such as turbofans, which feature multiple jet exits (e.g., see Figure 14-12). Neglecting the contribution of the fuel to the mass flow rate, we can write the mass flow entering the engine in terms of the mass flow through the numerous exits, i.e.,

$$\dot{m}_i = \sum_{j=1}^{N} \dot{m}_{e_j} \tag{14-47}$$

where j is an index to identify an exit, N is the number of exits, and $\dot{m}_{e_j}$ is the mass flow through that exit. Thus, the thrust of the engine is given by (neglecting pressure difference across it and assuming $\dot{m}_i = \sum \dot{m}_{e_j}$)

$$T_{NET} = \sum_{j=1}^{N} \dot{m}_{e_j} \left(V_{e_j} - V_\infty\right) \tag{14-48}$$

where V_{e_j} is the speed of the flow through exit j. We can also represent the loss in kinetic energy for this multiexit thrust device as shown below

$$K\dot{E}_{loss} = \frac{1}{2} \sum_{j=1}^{N} \dot{m}_{e_j} \left(V_{e_j} - V_\infty\right)^2 \tag{14-49}$$

To calculate the propulsive efficiency, we modify Equation (14-46) as shown below

$$\eta_{prp} = \frac{2}{1 + \overline{V}_e / V_\infty} \tag{14-50}$$

where $\overline{V}_e$ is the weighted exit speed and is calculated as follows

$$\overline{V}_e = \frac{\sum_{j=1}^{N} \dot{m}_{e_j} V_{e_j}}{\sum_{j=1}^{N} \dot{m}_{e_j}} = \frac{1}{\dot{m}_i} \sum_{j=1}^{N} \dot{m}_{e_j} V_{e_j} \tag{14-51}$$

A common representation of the total thrust and the weighted exit speed for a typical turbofan with a bypass-ratio BPR per Equation (7-34) and total entry mass flow of $\dot{m}_i$, is given by.

Net thrust:

$$T_{NET} = \dot{m}_i \frac{1}{BPR+1}(V_{e_{core}} - V_\infty) + \dot{m}_i \left(1 - \frac{1}{BPR+1}\right)\left(V_{e_{bypass}} - V_\infty\right) \tag{14-52}$$

Substitute Equation (7-34) into Equation (14-51) to obtain the weighted exit speed:

$$\overline{V}_e = \frac{\dot{m}_i \frac{1}{1+BPR} V_{e_{core}} + \dot{m}_i \left(1 - \frac{1}{1+BPR}\right) V_{e_{bypass}}}{\dot{m}_i}$$

Thus,

$$\overline{V}_e = \frac{1}{1+BPR} V_{e_{core}} + \left(1 - \frac{1}{1+BPR}\right) V_{e_{bypass}} \tag{14-53}$$

(5) Thermal Efficiency, η_{th}

Thermal efficiency is a measure of how effectively the engine converts heat energy released by burning fuel in air, to mechanical engine power. It is defined as follows

$$\eta_{th} \equiv \frac{\text{Net engine power}}{\text{Rate of thermal energy released in fuel}} = \frac{\dot{W}_{ENG}}{\dot{Q}_{AF}} = \frac{V_e^2 - V_\infty^2}{2C_p(T_5 - T_3)} \tag{14-54}$$

where W_{ENG} is the mechanical energy produced by the engine, Q_{AF} is the heat energy of the mixture of air and fuel, C_p is the specific heat at constant pressure (in J/K or Btu/°F), T_3 and T_5 are the temperature at the compressor exit and turbine entry, respectively (see station numbers in Figure 7-30 or 7-33). The increase in temperature from T_3 and T_5 results from the addition of heat in the combustion chamber. It is evident that for fixed airspeed V_∞, higher exit speed V_e, improves the thermal efficiency.

(6) Overall Efficiency, η_o

Refers to the product $\eta_p \cdot \eta_{th}$ for propeller powered aircraft and $\eta_{prp} \cdot \eta_{th}$ for jet propelled ones [9]. Considering propulsive efficiency, we write

$$\eta_o \equiv \frac{\text{Useful Work done on Aircraft}}{\text{Heat Energy of Fuel}} = \frac{W_{AC}}{Q_{AF}} = \eta_{prp} \cdot \eta_{th} \tag{14-55}$$

where W_{AC} is the useful work the propulsion system does moving the aircraft. In particular, substituting Equations (14-46) and (14-54) into Equation (14-55), followed by some algebraic manipulations, we get

$$\eta_o = \frac{V_e V_\infty - V_\infty^2}{C_p(T_5 - T_3)}$$

Then, differentiate with respect to V_∞ and set to zero to find the requirement for ideal overall efficiency:

$$\frac{d\eta_o}{dV_\infty} = \frac{V_e - 2V_\infty}{C_p(T_5 - T_3)} = 0 \quad \Leftrightarrow \quad V_e = 2V_\infty$$

This shows that the best overall efficiency is obtained when the exit velocity, V_e, is twice the far-field airspeed.

14.3 GENERAL THRUST MODELING FOR GAS TURBINES

This section presents a convenient method for estimating the thrust for aerospace gas turbines during the conceptual design phase. It was developed by Mattingly, Heiser, and Pratt of reference [10]. The method permits thrust for turboprops, turbojets, and turbofans to be estimated as a function of altitude and Mach number. It is appropriate to present the method in this chapter, as it is an application of aerothermodynamics.

14.3.1 Definitions

(1) Specific Thrust

Refers to the thrust of an air breathing engine, divided by its mass flow rate. Mathematically:

$$F_s \equiv \frac{\text{Thrust}}{\text{mass flow}} = \frac{F}{\dot{m}} \quad \left[\frac{m}{s}\right] \tag{14-56}$$

(2) Theta Break and Throttle Ratio (TR)

Ambient air is the propellant in gas turbines. Air pressure affects mass flow rate and, thus, engine thrust. Since pressure and density reduce with altitude, so does engine thrust. However, the total temperature (T_0), which depends on flight Mach number and altitude (see Equation (14-21)), plays an even more important role than pressure and density because it affects material properties.

Engine materials and cooling methodologies limit permissible *compressor exit temperature* (CET) and *turbine entry temperature* (TET). The former is the temperature

of air as it leaves the last compressor stage. The latter is the temperature after combustion before it enters the first turbine stage. Practical compressor efficiencies require the engine to operate at its maximum TET and compressor pressure ratio. This implies a specific value of T_{05}, call it T_{05des} (for *design total temperature*). See Figure 7-30 or 7-33 for details on engine station numbers. The ratio of T_{05des} to standard S-L temperature (518.67°R or 288.15 K) is known as *theta break*. If the actual $T_0 < T_{0des}$ (e.g., due to lower M_∞ or higher altitude) then TET can be decreased to maintain efficiency. If the actual $T_0 > T_{0des}$ (due to higher M_∞ or lower altitude) then the power generated by the turbine is reduced, causing the *overall pressure ratio* (OPR, aka *compressor pressure ratio*, also see Section 7.3.2) to decline.

High OPR results in good *thrust-specific fuel consumption* (TSFC) and high TET yields a high-specific thrust F_s (see Equation (14-56)). This implies it is best to always operate the engine at its theta break. However, this is impossible to accomplish because the engine must operate over a range of Mach numbers and altitudes. As a compromise, an engine may be designed so its theta-break value is near its intended range of operational altitudes and Mach numbers. The engine is then said to have *Throttle Ratio* (*TR*) equal to the theta-break value. The *TR* is selected by the engine manufacturer and is required for an accurate prediction of engine thrust and, thus, aircraft performance analysis. As terms, "…throttle ratio and theta break are used interchangeably in the propulsion industry." [10].

A target *TR* can be calculated using Equation (14-21). For instance, if $M_\infty = 0$ and $h = 0$ (takeoff condition) is chosen as the desired combination, then the theta break (T_{05}/T_{std}) and *TR* will be 1. The TET, of such an engine, will be at its maximum on a standard day at S-L. When the ambient temperature is higher than standard, the engine control system reduces fuel flow to the engine, which decreases the TET. This, in turn, reduces the thrust. The consequence for the aircraft is reduced T-O and climb performance.

If the desired combination is, say, $M_\infty = 0.6$ at sea level, then the theta break is $(T_{05}/T_{std}) = 1.072$, and $TR = 1.072$. When $M_\infty = 0$ and $h = 0$, the engine operates at TET below its maximum. On a day when the ambient temperature is higher than standard, the TET may be raised, and allowing constant thrust to be maintained up to some specific altitude. In this case, the thrust may be maintained up to ambient temperature of $518.67 \times 1.072 = 556$°R (87°F or 35°C). This is favorable for the aircraft, as it permits a better performance on hot days.

The name "theta break" can be inferred from gas turbine performance graphs, which show a decisive break in each curve (e.g., see Figure 6.E8 of reference [10]). In the cited figure, the break occurs at $M_\infty = 0.6$ at S-L, but at $M_\infty = 1.45$ at 36,000 ft. The engine has a unique *TR* (1.07 in this case), but the break shifts to higher Mach numbers with increasing altitude due to decline in T_0. Beyond 36,000 ft the break remains at the same Mach number (stratosphere).

The concept of throttle ratio appears to have been first introduced by Mattingly et al in reference [10]. The fundamentals of the method were developed by Mattingly in reference [11]. It utilizes simple empirical algebraic equations, dependent on Mach number and altitude, to determine the change in thrust from some baseline thrust value. The method is ideal for use in spreadsheets or software routines during the conceptual and preliminary design stage of aircraft featuring such engines (for instance see the Microsoft Excel Visual Basic routine presented in the Section 14.3.5).

(3) Suitable Values of TR

(A) Turbojets and low-*BPR* turbofans: A suitable *TR*-range is between 0.8 and 1.1. Hot day take-off and super-cruise for military aircraft calls for a *TR* closer to 1.1. (B) High-*BPR* turbofans: Top-of-climb altitude is often selected as a design point. A suitable *TR*-range for such engines may range between 0.85 and 1.05. For instance, for $M_\infty = 0.84$ and top-of-climb of 33,000 ft (where $\theta = 0.7731$) the resulting $TR = 0.8822$. (C) Turboprops: Similar reasoning can be applied to estimate the *TR* for a turboprop. In general, for (B) and (C): Once a target cruise Mach number (M_∞) and cruise altitude (h) have been established, a reasonable *TR* can be estimated from

$$TR = \theta\left[1 + \frac{\gamma - 1}{2} M_\infty^2\right] \tag{14-57}$$

where $\theta = 1 + \kappa h$ is the temperature ratio per Equation (17-5).

DERIVATION OF EQUATION (14-57)

The ambient temperature at altitude is given by Equation (17-5) by $T = T_{std}\ \theta = T_{std}\ (1 + \kappa h)$. Thus, per Equation (14-21), the total temperature at airspeed M_∞ is

$$T_0 = T\left[1 + \frac{\gamma - 1}{2} M_\infty^2\right] = T_{std}\theta\left[1 + \frac{\gamma - 1}{2} M_\infty^2\right] \tag{14-58}$$

This leads to the following expression for the throttle ratio:

$$TR = \theta_0 \equiv \frac{T_0}{T_{std}} = \frac{T_0\left(1 + \frac{\gamma - 1}{2} M_\infty^2\right)}{T_{std}} = \frac{T_{std}\theta\left[1 + \frac{\gamma - 1}{2} M_\infty^2\right]}{T_{std}}$$
$$= \theta\left[1 + \frac{\gamma - 1}{2} M_\infty^2\right] \tag{14-59}$$

(4) Installed Thrust-Specific Fuel Consumption

The *thrust-specific fuel consumption* (TSFC) of installed engines is provided by the manufacturer. However, an engine manufacturer may not yet be selected in the early conceptual design phase. Reference [10] provides the

following set of equations to remedy this situation. These apply to engines developed after 2010. $\theta = T/T_{std}$ is the temperature ratio, where T is the ambient temperature and T_{std} is ambient temperature on a standard day.

Turboprop:

$$TSFC = (0.18 + 0.80M_\infty)\sqrt{\theta} \tag{14-60}$$

Turbojet (military power):

$$TSFC = (1.1 + 0.30M_\infty)\sqrt{\theta} \tag{14-61}$$

Turbojet (max w/AB):

$$TSFC = (1.5 + 0.23M_\infty)\sqrt{\theta} \tag{14-62}$$

Low bypass turbofan (military power):

$$TSFC = (0.9 + 0.30M_\infty)\sqrt{\theta} \tag{14-63}$$

Low bypass turbofan (max power w/AB):

$$TSFC = (1.6 + 0.27M_\infty)\sqrt{\theta} \tag{14-64}$$

High bypass turbofan ($M < 0.9$)

$$TSFC = (0.45 + 0.54M_\infty)\sqrt{\theta} \tag{14-65}$$

Units are 1/h (h^{-1}). Note that Equation (14-65) overestimates the *TSFC* for high-*BPR* turbofan engines. Typical values for modern turbofans are $0.68\,h^{-1}$ or lower.

14.3.2 Mattingly Model for a Turboprop Engine

The effect of altitude and airspeed on the thrust of turboprop engines can be modeled using the Mattingly method of reference [10]. Its implementation is accomplished using the step-by-step below.

STEP 1: Determine the baseline thrust to use at S-L, F_{SL}, for instance the maximum static thrust at ISA.

STEP 2: Calculate temperature ratio:

$$\theta_0 = \frac{T_0}{T_{std}} = \frac{T}{T_{std}}\left(1 + \frac{\gamma - 1}{2}M_\infty^2\right) \tag{14-66}$$

STEP 3: Calculate pressure ratio

$$\delta_0 = \frac{p_0}{p_{std}} = \frac{p}{p_{std}}\left(1 + \frac{\gamma - 1}{2}M_\infty^2\right)^{\frac{\gamma}{\gamma - 1}} \tag{14-67}$$

STEP 4:

If $M_\infty \le 0.1$ then $F = F_{SL}\delta_0$ (14-68)

If $M_\infty > 0.1$ and $\theta_0 \le TR$ then

$$F = F_{SL}\delta_0\left[1 - 0.96(M_\infty - 0.1)^{0.25}\right] \tag{14-69}$$

If $M_\infty > 0.1$ and $\theta_0 > TR$ then

$$F = F_{SL}\delta_0\left[1 - 0.96(M_\infty - 0.1)^{0.25} - \frac{3(\theta_0 - TR)}{8.13(M_\infty - 0.1)}\right] \tag{14-70}$$

where

F = Thrust at (the atmospheric) condition
p_0 = Total pressure at condition
F_{SL} = Thrust at a given power lever setting at S-L
T = Temperature at condition
p = Pressure at condition
T_{std} = Standard S-L temperature
p_{std} = Standard S-L pressure
T_0 = Total temperature at condition
M_∞ = Far-field Mach number.

The thrust of a generic turboprop engine is plotted for several altitudes as a *thrust ratio* (i.e., as F/F_{SL}) in Figure 14-14 using the above formulation and a

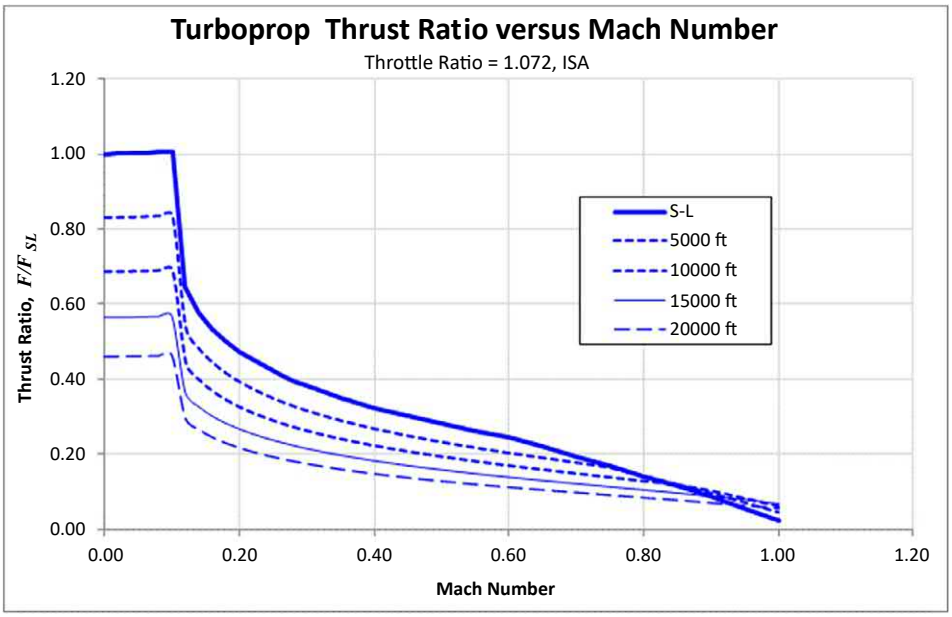


FIGURE 14-14 Thrust Ratio of a turboprop as a function of Mach number and altitude.

$TR = 1.072$. The sharp drop around $M = 0.1$ occurs when the TET reaches a maximum because of the increase in total air temperature. Until that point, it is possible to offer constant thrust—something that offers great performance improvements in the operation of turboprop aircraft. Plotting the thrust ratio, rather than for a specific rated S-L thrust, allows the curves to be applied to nonspecific turboprop engines. It can be shown using the formulation that at an altitude of approximately 7800 ft the maximum thrust has fallen to 75% of the rated S-L value.

14.3.3 Mattingly Model for a Turbojet Engine

While the turbojet is rarely used for certified GA aircraft, there are several such installations on experimental aircraft and UAVs. One of the best-known uses of a jet engine in such an aircraft was the installation of a Microturbo TRS-18 turbojet in a Bede BD-5J single-seat kit plane. A pair of those was used to power the Caproni C22J trainer aircraft. Microturbo (www.safran-power-units.com) is a well-known manufacturer of small turbojets for drones. PBS VB (www.pbsvb.com) is a company in the Czech Republic that manufactures small turbojets for experimental aircraft and even self-launching sailplanes. Its engines have been installed on a Sonex experimental aircraft and a Blanik, Salto, and TST-14J BonusJet sailplanes. The Blanik has been operated at altitudes as high as 32,000 ft using the engine.

Effect of Altitude and Airspeed on Turbojet Engine Thrust.

Reference [10] presents the following method to estimate the effect of altitude and airspeed on the thrust of turbojet engines. Turbojets are typically used in military applications and, thus, feature formulation for maximum and military thrust (with afterburner used). See more information of turbojets in Section 7.3.2.

STEP 1: Calculate temperature ratio:

$$\theta_0 = \frac{T_0}{T_{std}} = \frac{T}{T_{std}}\left(1 + \frac{\gamma - 1}{2} M_\infty^2\right) \tag{14-66}$$

STEP 2: Calculate pressure ratio

$$\delta_0 = \frac{p_0}{p_{std}} = \frac{p}{p_{std}}\left(1 + \frac{\gamma - 1}{2} M_\infty^2\right)^{\frac{\gamma}{\gamma - 1}} \tag{14-67}$$

STEP 3a: Maximum thrust (means afterburner is on).

If $\theta_0 \le TR$ then

$$F = F_{SL}\delta_0\left[1 - 0.3(\theta_0 - 1) - 0.1\sqrt{M_\infty}\right] \tag{14-71}$$

If $\theta_0 > TR$ then

$$F = F_{SL}\delta_0\left[1 - 0.3(\theta_0 - 1) - 0.1\sqrt{M_\infty} - \frac{1.5(\theta_0 - TR)}{\theta_0}\right] \tag{14-72}$$

STEP 3b: Military thrust (means afterburner is off)

If $\theta_0 \le TR$ then $\quad F = 0.8F_{SL}\delta_0\left[1 - 0.16\sqrt{M_\infty}\right]$ (14-73)

If $\theta_0 > TR$ then

$$F = 0.8F_{SL}\delta_0\left[1 - 0.16\sqrt{M_\infty} - \frac{24(\theta_0 - TR)}{(9 + M_\infty)\theta_0}\right] \tag{14-74}$$

The thrust of a generic turbojet engine is plotted for several altitudes as a thrust ratio (i.e., as T/T_{SL}) in Figure 14-15 using the above formulation and a $TR = 1.072$.

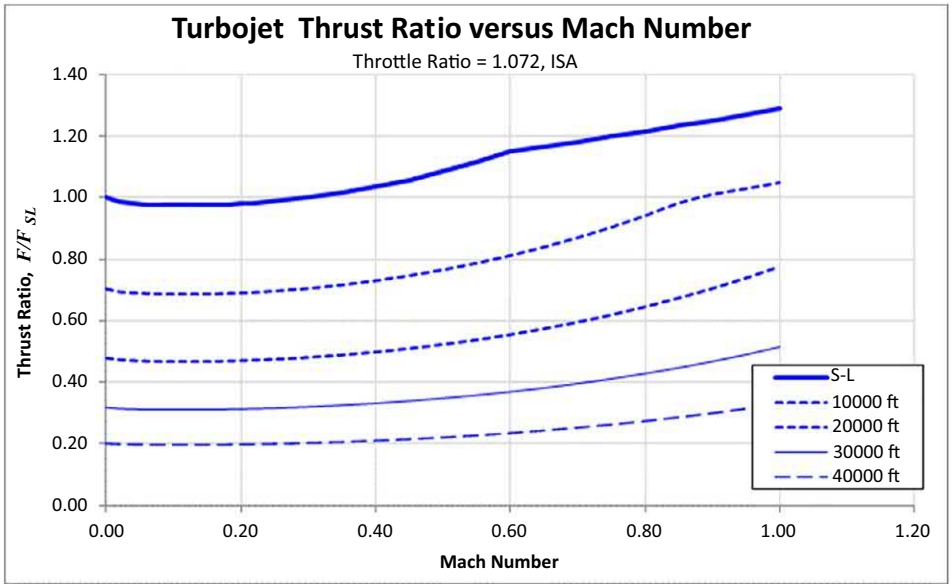


FIGURE 14-15 Thrust Ratio of a turbojet as a function of Mach number and altitude.

14.3.4 Mattingly Model for a Turbofan Engine

Turbofan engines are used in several GA aircraft. While most are business jets, recently a new class of turbofan-powered jets has emerged, the *Personal Jet*. These are designed to be owner flown and operated, analogous to the operation of single engine piston powered aircraft. This trend has led to the development of small turbofans, such as the DGEN 380 in Figure 7-31 and Williams International FJ44 in Figure 7-32. Examples of such jets are the Cirrus SF50 Vision and the Diamond Jet (both which actually use the FJ33).

The turbofan differs from the turbojet in that the diameter of the forward compressor (the fan) is larger than that of the engine behind it (the *core*). The core contains the remaining compressor, the combustion chamber, and the turbine wheels. See more about turbofans in Section 7.3.3.

Effect of Altitude and Airspeed on Turbofan Engine Thrust

Reference [10] presents the following method to estimate the effect of altitude and airspeed on the thrust of turbofan engines, like those presented above. As mentioned in Chapter 7, engines with bypass ratios less than 1 are classified as *low bypass ratio* engines and are intended for military applications. In contrast, high bypass ratio engines are typically used in civilian applications. For this reason, specific formulation is presented for each type.

STEP 1: Calculate temperature ratio:

$$\theta_0 = \frac{T_0}{T_{std}} = \frac{T}{T_{std}}\left(1 + \frac{\gamma - 1}{2} M_\infty^2\right) \tag{14-66}$$

STEP 2: Calculate pressure ratio

$$\delta_0 = \frac{p_0}{p_{std}} = \frac{p}{p_{std}}\left(1 + \frac{\gamma - 1}{2} M_\infty^2\right)^{\frac{\gamma}{\gamma - 1}} \tag{14-67}$$

STEP 3a: Maximum thrust of low bypass ratio turbofans.

$$\text{If } \theta_0 \le TR \text{ then} \qquad F = F_{SL}\delta_0 \tag{14-75}$$

$$\text{If } \theta_0 > TR \text{ then } F = F_{SL}\delta_0\left[1 - \frac{3.5(\theta_0 - TR)}{\theta_0}\right] \tag{14-76}$$

STEP 3b: Military thrust of low bypass ratio turbofans.

$$\text{If } \theta_0 \le TR \text{ then} \qquad F = 0.6F_{SL}\delta_0 \tag{14-77}$$

$$\text{If } \theta_0 > TR \text{ then} \qquad F = 0.6F_{SL}\delta_0\left[1 - \frac{3.8(\theta_0 - TR)}{\theta_0}\right] \tag{14-78}$$

STEP 3c: High bypass ratio turbofans

$$\text{If } \theta_0 \le TR \text{ then} \qquad F = F_{SL}\delta_0\left[1 - 0.49\sqrt{M_\infty}\right] \tag{14-79}$$

$$\text{If } \theta_0 > TR \text{ then} \quad F = F_{SL}\delta_0\left[1 - 0.49\sqrt{M_\infty} - \frac{3(\theta_0 - TR)}{1.5 + M_\infty}\right] \tag{14-80}$$

The thrust of a generic low bypass ratio turbofan engine is plotted for several altitudes as thrust ratio (i.e., as F/F_{SL}) in Figure 14-16 using the above formulation and a throttle ratio $TR = 1.072$. The thrust of a generic high bypass ratio turbofan engine is also plotted for several altitudes in Figure 14-17 in terms of thrust ratio using the above formulation and $TR = 1.072$.

14.3.5 Computer Code: Thrust as a Function of Altitude and Mach Number

One of the most important capabilities of the designer is the ability to predict the thrust of the selected engine as a function of altitude and airspeed. This is imperative for Performance and Stability and Control theories. The preceding methods can be coded in a function that can be called from analysis spreadsheets like Microsoft Excel. The following function incorporates all the preceding methods and allows piston engines as well as high bypass ratio turbofans to be evaluated. The input arguments are rated thrust at sea level (`F_SL`), throttle ratio (`TR`), altitude (`H`), Mach Number (`M`), and deviation from standard atmospheric ambient temperature at altitude. Note that the routine treats piston engines in a different manner than the other engines, since such engines are constant power devices whose power output is independent of airspeed.

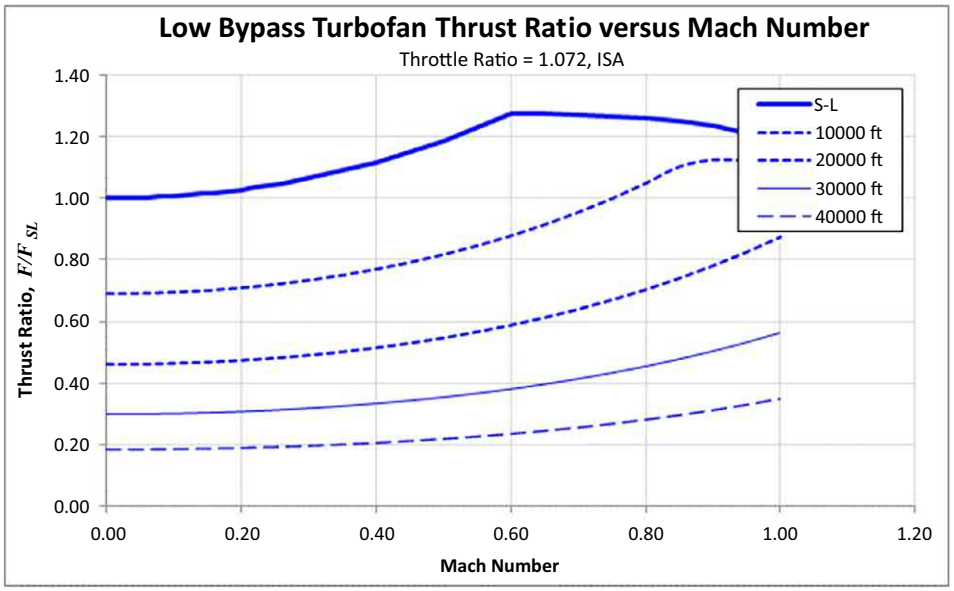


FIGURE 14-16 Thrust Ratio of a low bypass ratio turbofan as a function of Mach number and altitude.

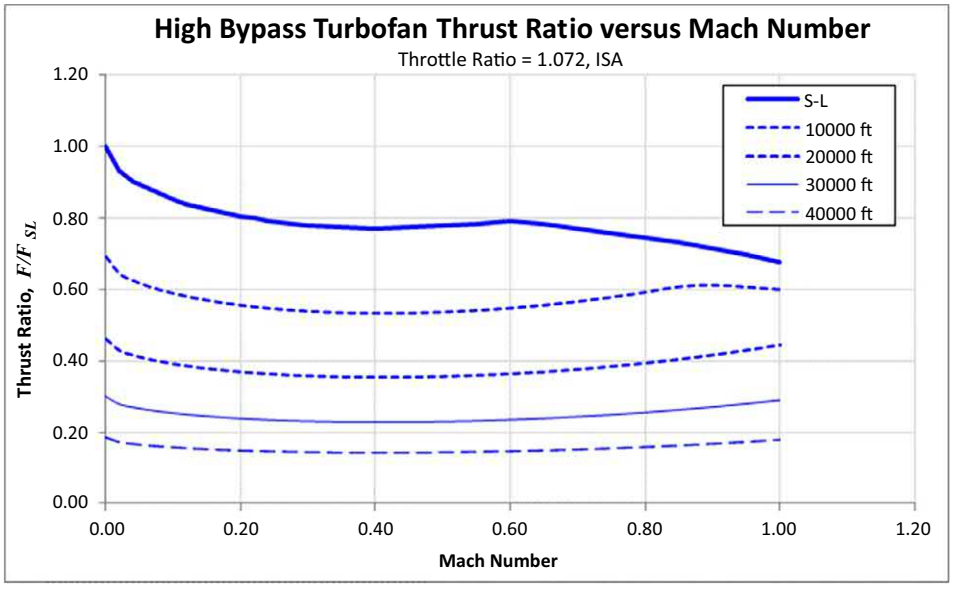


FIGURE 14-17 Thrust Ratio of a high bypass ratio turbofan as a function of Mach number and altitude.

```
Function Engine_Thrust(F_SL As Single, TR As Single, H As Single, M As Single, deltaOAT_C As Single,
Mode As Byte) As Single
'This routine can be used to estimate the change in thrust depending on
'flight conditions for the following engines:
'
'   1. Piston engines (Mode = 0)
'   2. Turboprops (Mode = 1)
'   3. Turbojets, maximum power (Mode = 2)
'   4. Turbojets, military power (Mode = 3)
'   5. Low Bypass Ratio Turbofans, maximum power (Mode = 4)
'   6. Low Bypass Ratio Turbofans, military power (Mode = 5)
'   7. High Bypass Ratio Turbofans (Mode = 6)
'
'Variables: F_SL        = Engine thrust, in lbf
'           TR          = Throttle ratio
'           H           = Altitude at condition, in ft
'           M           = Mach Number
'           deltaOAT    = Deviation from ISA in °C
'
'NOTE1: For piston engines, the function only treats the power, so F_SL is
'       the rated engine power at S-L and ISA.
'NOTE2: The function calls the AtmosProperty function, so it must be present.
'
'Initialize
    'Atmospheric properties
    Dim P As Single, OAT As Single, rho As Single, kappa as single
    'Property ratios
    Dim sigma As Single, delta As Single, theta As Single

'Presets
    kappa = -0.0000068756             'Temperature lapse in 1/ft
    P = 2116*(1 + kappa * H)^5.2561   'Pressure at H in lbf/ft²
    OAT = 518.67*(1 + kappa * H)      'Standard OAT at H in °R
    OAT = OAT + deltaOAT_C * 1.8      'Include temperature deviation. Note T °R = 1.8T K
    rho = P / (1716 * OAT)              'Density in slugs/ft3
    'Pressure ratio
    delta = P / 2116 * (1 + 0.2 * M ^ 2) ^ 3.5
    'Temperature ratio
    theta = OAT / 518.67 * (1 + 0.2 * M ^ 2)
    'Density ratio
    sigma = rho / 0.002377427

'Process
    Select Case Mode
    Case 0 'Piston per Gagg and Ferrar
        Engine_Thrust = F_SL * (1.132 * sigma - 0.132)
    Case 1 'Turboprop per Mattingly, et al.
        If M <= 0.1 Then
            Engine_Thrust = F_SL * delta
        Else
            If theta <= TR Then
                Engine_Thrust = F_SL * delta * (1 - 0.96 * (M - 0.1) ^ 0.25)
            Else
                Engine_Thrust = F_SL * delta * (1 - 0.96 * (M - 0.1) ^ 0.25 - 3 * (theta - TR) /
(8.13 * (M - 0.1)))
            End If
        End If
    Case 2, 3 'Turbojet per Mattingly, et al.
        If Mode = 2 Then    'Max thrust
            If theta <= TR Then
                Engine_Thrust = F_SL * delta * (1 - 0.3 * (theta - 1) - 0.1 * Sqr(M))
            Else
                Engine_Thrust = F_SL * delta * (1 - 0.3 * (theta - 1) - 0.1 * Sqr(M) - 1.5 * (theta
- TR) / theta)
            End If
        ElseIf Mode = 3 Then    'Military thrust (afterburner)
            If theta <= TR Then
                Engine_Thrust = 0.8 * F_SL * delta * (1 - 0.16 * Sqr(M))
            Else
                Engine_Thrust = 0.8 * F_SL * delta * (1 - 0.16 * Sqr(M) - 24 * (theta - TR) / ((9
+ M) * theta))
            End If
        End If
```

```
        Case 4, 5 'LBR Turbofan per Mattingly, et al.
            If Mode = 4 Then    'Max thrust
                If theta <= TR Then
                    Engine_Thrust = F_SL * delta
                Else
                    Engine_Thrust = F_SL * delta * (1 - 3.5 * (theta - TR) / theta)
                End If
            ElseIf Mode = 5 Then 'Military thrust
                If theta <= TR Then
                    Engine_Thrust = 0.6 * F_SL * delta
                Else
                     Engine_Thrust = 0.6 * F_SL * delta * (1 - 3.8 * (theta - TR) / theta)
                End If
            End If
        Case 6 'HBR Turbofan per Mattingly, et al.
            If theta <= TR Then
                Engine_Thrust = F_SL * delta * (1 - 0.49 * Sqr(M))
            Else
                Engine_Thrust = F_SL * delta * (1 - 0.49 * Sqr(M) - 3 * (theta - TR) / (1.5 + M))
            End If
        End Select
    End Function
```

EXERCISES

(1) Determine the SFC in the UK- and SI-systems for a jet engine consuming 660 lb_f of fuel per hour while generating 990 lb_f of thrust.

(2) Using the Mattingly method Estimate the maximum power of a Garrett TPE331–10 at 30,000 ft and Mach 0.45, using the basic T-O data of Table 7-9 and assuming a Throttle Ratio of 1.072. Estimate the fuel consumption in gallons of Jet-A per hour. Assuming a cruise segment at that altitude, how far can the airplane fly on 500 gal if equipped with two TPE331s?

(3) Using the Mattingly method to estimate the thrust of a Microturbo TRS 18–056 at 10,000 ft and Mach 0.39, using the basic T-O data of Table 7-10 and assuming a Throttle Ratio of 1.000. Estimate the fuel consumption in gallons of Jet-A per hour. How much fuel must this airplane carry to cover a 300 nm cruise segment at that altitude if equipped with only one TRS 18–056?

(4) Compare the thrust and fuel consumption of the two CFM56 engines in Table 7-11, at 35,000 ft and Mach 0.8 in terms of lb_f of Jet-A per hour, assuming it can be based on the T-O data.

References

[1] J.D. Anderson, *Fundamentals of Aerodynamics*, 6th ed., McGraw-Hill, 2011.

[2] J.D. Anderson, *Modern Compressible Flow with Historical Perspective*, 3rd ed., McGraw-Hill, 2003.

[3] J.J. Bertin, R.M. Cummings, *Aerodynamics for Engineers*, 6th ed., Pearson, 2013 April 4.

[4] Y.A. Cengel, J.M. Cimbala, *Fluid Mechanics: Fundamentals and Applications*, 4th ed., McGraw-Hill, 2017 February 27.

[5] R.W. Fox, A.T. McDonald, *Introduction to Fluid Mechanics*, 8th ed., John Wiley and Sons, 2011 October 10.

[6] E. Clapeyron, *Mémoire sur la Puissance Motrice de la Chaleur*, Journal de l'ÉcolePolytechnique XIV (1834) 153–190.

[7] J.W.R. Taylor, *Jane's All the World's Aircraft 1974–75*, Jane's Yearbooks, 1975.

[8] Source: http://aviation-safety.net/index.php. [Accessed on 07/20/2020]

[9] P.G. Hill, C.R. Peterson, *Mechanics and Thermodynamics of Propulsion*, Addison-Wesley Publishing Company, 1970.

[10] J.D. Mattingly, W.H. Heiser, D.T. Pratt, *Aircraft Engine Design*, 2nd ed., AIAA Education Series, 2002.

[11] J.D. Mattingly, *Elements of Gas Turbine Propulsion*, McGraw-Hill, 1996.

This page intentionally left blank

CHAPTER

15

Thrust Modeling for Propellers

OUTLINE

15.1 **Introduction** 597
- *15.1.1 The Content of This Chapter* 598
- *15.1.2 Propeller Configurations* 599
- *15.1.3 Important Nomenclature* 601
- *15.1.4 Propeller Geometry* 602
- *15.1.5 Fixed Versus Constant-Speed Propellers* 606

15.2 **Propeller Effects** 608
- *15.2.1 Angular Momentum and Gyroscopic Effects* 608
- *15.2.2 Slipstream Effects* 609
- *15.2.3 Propeller Normal and Side Force* 609
- *15.2.4 Asymmetric Yaw Effects—Single-Engine Aircraft* 611
- *15.2.5 Asymmetric Yaw Effects—Multiengine Aircraft* 611
- *15.2.6 Blockage Effects* 614
- *15.2.7 Hub and Tip Effects* 615
- *15.2.8 Effects of High Tip Speed* 616
- *15.2.9 Skewed Wake Effects—A·q Loads* 616
- *15.2.10 Propeller Noise* 617

15.3 **Properties and Selection of the Propeller** 620
- *15.3.1 Tips for Selecting a Suitable Propeller* 620
- *15.3.2 Rapid Estimation of Required Prop Diameter* 620
- *15.3.3 Rapid Estimation of Expected Geometric Propeller Pitch* 621
- *15.3.4 Estimation of Required Propeller Efficiency* 623
- *15.3.5 Advance Ratio* 624
- *15.3.6 Definition of Activity Factor* 624
- *15.3.7 Definition of Power and Thrust-Related Coefficients* 625
- *15.3.8 Propeller Efficiency* 626
- *15.3.9 Effect of Number of Blades on Efficiency, Thrust, and Power* 627
- *15.3.10 Moment of Inertia of the Propeller* 629

15.4 **Determination of Propeller Thrust** 630
- *15.4.1 Converting Engine Power to Thrust* 630
- *15.4.2 Determination of Static Thrust* 630
- *15.4.3 Initial Thrust Model for a Fixed-Pitch Propeller* 631
- *15.4.4 Initial Thrust Model for a Constant-Speed Propeller* 633
- *15.4.5 Step-by-Step: Determining Thrust Using a Propeller Efficiency Table* 636
- *15.4.6 Estimating Thrust From Manufacturer's Data* 637
- *15.4.7 Other Analytical Methods* 637

15.5 **Rankine-Froude Momentum Theory** 638
- *15.5.1 Formulation for a Free Propeller* 638
- *15.5.2 Formulation for Shrouded Propellers and Ducted Fans* 643

15.6 **Blade Element Theory** 646
- *15.6.1 Formulation* 646
- *15.6.2 Determination of w and α_i Using the Momentum Theory* 648
- *15.6.3 Compressibility Corrections* 649
- *15.6.4 Prandtl's Tip and Hub Loss Corrections* 649
- *15.6.5 Computer Code: Determination of the Propeller Induced Velocity* 655

References 656

15.1 INTRODUCTION

A propeller is a device that converts mechanical energy into a force (*thrust*) that is used to propel the vehicle to which it is attached. This is accomplished by rapidly rotating one or more lifting surfaces called *propeller blades*[1] using an engine. The blades develop an aerodynamic lift by the same principles as wing lift. Propellers

[1]Note that one bladed propeller usually features a single helical coil shaped like a wood screw. An example of this is David Bushnell's Turtle submarine from 1776.

https://doi.org/10.1016/B978-0-12-818465-3.00015-X

Copyright © 2022 Elsevier Inc. All rights reserved.

are, by far, the most common means of generating thrust for General Aviation aircraft (14 CFR Part 23) and the only option for Light Sport Aircraft (LSA). Propellers also power commercial aircraft (14 CFR Part 25) and military aircraft; primarily trainers and transport aircraft. In airplanes, propellers are driven by piston engines (*pistonprops*), electric motors (*electroprops*), or gas turbine engines (*turboprops*).

Propellers give a large mass of matter a modest acceleration (see Section 14.2.2). In comparison, rockets give a small mass of matter a large acceleration. The larger the acceleration, the larger the amount of chemical energy (fuel) required. Thrust generation by a propeller requires far less energy, making it the most energy efficient propulsive option available for airplanes [1]. Furthermore, manufacturing and maintaining a propeller is far less expensive than, say, a jet engine. Therefore, propellers are really the only option for low-cost aircraft. It is a drawback that propellers are usually limited to low subsonic applications. However, several propeller aircraft are capable of high subsonic airspeeds, although the cost is considerable engine power and propeller sophistication.

The McDonnell XF-88B is often cited as the fastest aircraft ever equipped with a propeller. Designed in the early 1950s, the airplane was a modified prototype of the XF-88 Voodoo fighter, powered by two Westinghouse J-34 turbojets. It also featured an 1800 SHP Allison T38 turboprop engine in the nose, installed for research purposes. The engine rotated a three-bladed, wide-chord propeller and was capable of just exceeding Mach 1 (thanks to its turbojets). The XF-88 (without the prop) later saw service with the USAF in the 1960s as the F-101 Voodoo fighter. Another aircraft, the Republic XF-84H Thunderscreech [2] is often called the true world's fastest propeller aircraft. Designed in the early 1950s, it was equipped with a 5850 SHP Allison XT40 turboprop engine. It is claimed it achieved a speed of Mach 0.83, although other sources say it only achieved Mach 0.70. The aircraft is considered by many as the loudest aircraft ever built, as the outer half of the propeller blades traveled at airspeed greater than Mach 1. It is said the noise could be heard 25 miles (40 km) away, explaining the airplane's nickname.

The above aircraft were experimental projects that never made it to production. The fastest mass-produced propeller powered aircraft is the four-engine Tupolev Tu-114, which carried over 220 passengers in a pressurized cabin at altitudes up to 39,000 ft (see Figure 15-1). Its maximum speed was about 470 KTAS ($M \approx 0.82$), although its cruising speed was closer to 415 KTAS ($M \approx 0.72$). It featured four of the world's most powerful turboprop engines, the Kuznetsov NK-12, each which developed 14,800 SHP, swinging contra-rotating propellers. Although obsolete by the late 60s, it was arguably way ahead of its time when designed in the mid-1950s, with its characteristic swept back wings and lower deck galleys and deck crew rest areas. The airplane was in operation by Aeroflot from 1961 until 1976.

The propeller often poses some analytical challenges for the aircraft designer. Ideally, the designer wants to determine propeller thrust using simple variables; for instance, using the engine's power setting. Unfortunately, the thrust involves a complex interaction between the forward motion of the propeller, its rotational speed, and geometry. This calls for an understanding of fundamentals not always covered in standard undergraduate engineering university coursework. This chapter presents two important theories for calculating propeller thrust: the *Froude–Rankine momentum theory* and the *blade-element theory*. There is a third theory of propulsive thrust generation that will not be covered here: The *propeller vortex theory*, which is a version of Prandtl's lifting-line theory applied to propellers. Additionally, many authors (including the author of this book) have used the Vortex-Lattice Method (VLM) for the same purpose, but both methods are highly mathematical and require computational proficiency well in excess of what is practical for conceptual aircraft design. These are tools best left for propeller manufacturers to wield.

The propeller can be thought of as a bridge between design requirements and available engines. A case in point is the 310 BHP Continental IO-550 engine. It powers aircraft like the amphibious Seawind 300C (145 KTAS cruising speed) and the high-performance Cirrus SR22 (185 KTAS). The dissimilarity in cruising speed shows the interplay of mission requirements and the available power plant is spanned only by the propeller. It highlights that the propeller must be considered early and not as an afterthought. Propeller design is a field of specialization requiring much more space than can be allotted here. The designer of new aircraft is well advised to establish a good working relationship with propeller manufacturers by committing to using their products early in the design process, preferably as soon as the engine has been selected. Not only will this lead to more accurate performance predictions, it will also reduce several problematic design issues that are likely to arise and lie outside the field of expertise of the aircraft designer.

15.1.1 The Content of This Chapter

- Section 15.2 discusses several effects the propeller has on an aircraft and the aircraft designer must be aware of.
- Section 15.3 presents tips to help the designer select the right propeller, ranging from initial estimation of diameter and pitch.



FIGURE 15-1 Tupolev Tu-114 passenger aircraft. Arguably the fastest propeller aircraft ever produced, with a cruising speed in excess of Mach 0.72. *Photo by Dmitry Avdeev—from Wikipedia Commons.*

- Section 15.4 presents methods to estimate propeller thrust.
- Section 15.5 presents the Rankine–Froude momentum theory, which can be used to estimate thrust, induced airspeed in the streamtube going through the propeller, and ideal propeller efficiency.
- Section 15.6 presents the blade element theory, which can be used to estimate thrust, propeller efficiency, and power required to rotate the propeller.

15.1.2 Propeller Configurations

Propellers can be mounted in a few ways to an airplane. Three common methods are shown in Figure 15-2; a *Tractor* (A), *Pusher* (B), and a configuration featuring the engine and propeller mounted on the wing in *Nacelles* (C). Configuration (C) is a variation of each (A) or (B). The advantages and disadvantages of these installation methods are listed in Table 15-1. Note that so-called "inline" configurations, which consist of a tractor and

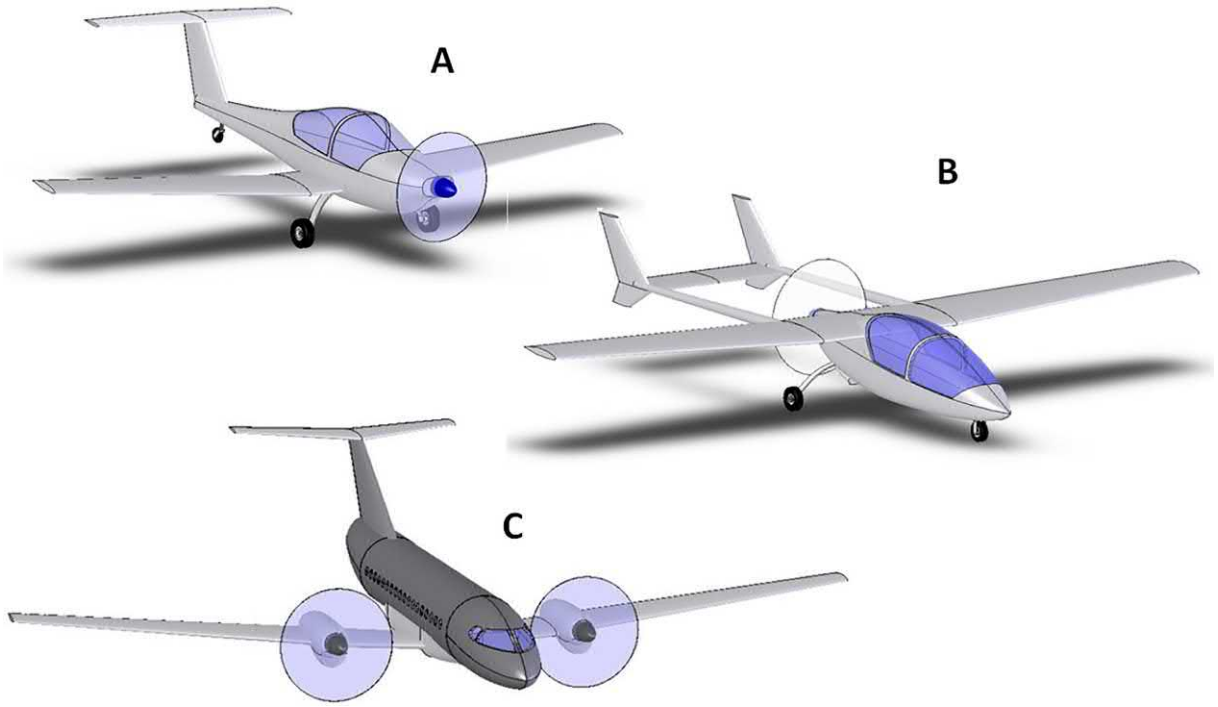
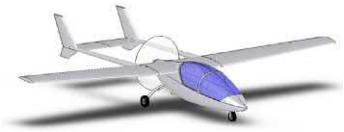


FIGURE 15-2 Three common methods to mount propellers (and engines). A is a *Tractor* configuration, B is a *Pusher* configuration, and C is a *Tractor mounted on a nacelle* configuration.

TABLE 15-1 Pros and cons of tractor, pusher, and nacelle configurations.

Configuration	Pros	Cons
(A) Tractor 	The incoming air is undisturbed. Ground clearance is not an issue during rotation at T-O, or flare before touch-down.[a] Placing the fuselage behind the propeller allows for a reduced streamtube inflow distortion and less asymmetric disc loading that would increase blade stresses. There is less chance that the propeller suffers damage due to *foreign object damage* (FOD), specifically when the aircraft is moving. Propeller is not subject to excessive heat from the exhaust. Propwash can help with T-O rotation during soft- or short-field take-offs, by increasing the dynamic pressure at the horizontal tail.	Obstructed forward view, which usually requires the back side of the prop to be painted black. Increased cabin noise. Normal force forward of CG decreases stability. The turbulent high-speed wake flows over a fuselage or a nacelle and (at least theoretically) increases drag. When placed in the front with nose landing gear, there is a risk of ground-strike in a hard landing. Frequency of propwash pressure pulses may excite structural frequencies at some specific RPMs, resulting is structural vibrations.
(B) Pusher 	Unobstructed forward view. Reduced cabin noise. Normal force aft of the CG increases stability. Turbulent high-speed wake does not flow over a fuselage or a nacelle, and, at least theoretically, results in less drag. The streamtube will energize the flow in front of propeller and suppress flow separation on the body, even at high AOA. Ideal for foldable propellers common on electric aircraft.	Ground clearance may be an issue during rotation at T-O, or flare before landing. Fuselage ahead of the propeller may distort flow inside the streamtube, causing asymmetric disc loading and increased blade stresses. This distortion may affect the propeller's performance. Propeller may suffer FOD, both in terms of pebbles shot by tires and ingestion by ice shedding off a fuselage. Propeller may be subject to excessive heat from the exhaust. Special regulatory requirements for pushers are stipulated in 14 CFR §23.905. Results in a higher fly-over noise and possible propeller corrosion issues (explained below).
(C) Nacelle 	The forward facing nacelle has many of the same advantages as the tractor configuration but is more efficient since the blockage of the nacelle is less than that of a fuselage. Similarly, aft facing nacelles for pusher propellers are also subject to many of the pros and cons of the pusher configuration.	The nacelle has many of the same disadvantages as the tractor configuration, however, since the nacelle usually extends far forward from the wing's structural support, the airframe may be subject to structural oscillations that, if ignored, may cause premature structural failure, and even whirl flutter phenomena.

[a] *Per 14 CFR §23.925 (Propeller clearance), there must be a minimum 7" ground clearance for a tricycle landing gear and 9" for taildraggers, at the most adverse combination of CG, weight, the most adverse pitch position of the propeller, and at static ground deflection of the landing gear. Aircraft with leaf spring struts as landing gear must comply with 1.5 times its most adverse weight.*

pusher, can simply be treated as a combination of configurations (A) and (B):

A few additional explanations are needed for the pusher propeller. As stated in Table 15-1 special regulatory requirements affect the certification of pusher aircraft and are stipulated in 14 CFR §23.905(e) through (f). Paragraph 23.905(e) states that[2]:

> All areas of the airplane forward of the pusher propeller that are likely to accumulate and shed ice into the propeller disc during any operating condition must be suitably protected to prevent ice formation, or it must be shown that any ice shed into the propeller disc will not create a hazardous condition.

Paragraph 23.905(f) states that:

> Each pusher propeller must be marked so that the disc is conspicuous under normal daylight ground conditions.

Paragraph 23.905(g) states that:

> If the engine exhaust gases are discharged into the pusher propeller disc, it must be shown by tests, or analysis supported by tests, that the propeller is capable of continuous safe operation.

And, finally, §23.905(h) states that:

> All engine cowling, access doors, and other removable items must be designed to ensure that they will not separate from the airplane and contact the pusher propeller.

There are further requirements made in §23.925(b) Propeller clearance that state that:

> (b) Aft-mounted propellers. In addition to the clearances specified in paragraph (a) of this section, an airplane with an aft mounted propeller must be designed such that the propeller

[2] Note that even though this cites the "old" Part 23 regulations, they are fully relevant in this context.

will not contact the runway surface when the airplane is in the maximum pitch attitude attainable during normal takeoffs and landings.

Excluding the last paragraph, these are extra requirements not demanded by the certification of tractor aircraft. Other drawbacks of the pusher propeller that need further explanation is a greater flyover noise and propeller corrosion. Experience has demonstrated that the ingestion of fuselage wake produces additional broadband noise,[3] often adding several dB(A) to the airplane's noise. Consequently, all other things being equal, pushers tend to be noisier than tractor configurations. Propeller blades behind the engine exhaust collects soot that is laden with acids that attack the propeller structure. Maintenance protocols for many pushers require the operator to wash the propeller after the last flight of the day as a preventative maintenance. The competent aircraft designer keeps such drawbacks in mind when choosing a pusher over a tractor. As stated in Chapter 4, there are important consequences to a configuration selection, some of which have environmental, operational, and maintenance impacts. It is not wise to base the choice on looks only—operational practicality should lead such decisions.

15.1.3 Important Nomenclature

Discussions about propellers involve jargon with which the designer must be familiar. For instance, if one overhears a propeller being described as "an advanced composite five-blade, constant-speed, reversible, and fully featherable." What does it mean? The following definitions help clarify these terms and must be kept in mind for the discussion that follows:

(1) Fixed-Pitch Propeller

A propeller whose pitch angle (the incidence of the blades with respect to the plane of rotation) cannot be changed. Such propellers are comparatively inexpensive, light, and require very little maintenance. The lack of a mechanical system renders them fail-safe; however, they will windmill in case of an engine failure and, thus, increase drag when a high glide ratio is sorely needed. Such propellers are typically designed for best efficiency at either climb ("climb prop") or cruise ("cruise prop").

(2) Ground-Adjustable Propeller

A propeller whose pitch angle can be adjusted using simple tools on the ground only. The operator can change the pitch from, say, a "climb" to a "cruise" style propeller (see Section 15.1.5) between flights. Such propellers have become popular among homebuilders and LSA aircraft.

(3) Two-Position Propeller

A propeller that allows the pilot to change the pitch of the blades mechanically in flight, but only allows two settings (versus multiple ones for the ground adjustable propeller). Thus, the pilot can select a climb setting for the take-off and subsequent climb, and then adjust it to a coarser cruise setting once cruise altitude is reached.

(4) Controllable-Pitch Propeller

A propeller that allows the pilot to change the pitch over a range of pitch angles during flight. This is usually accomplished using hydraulic boost built into the hub of the propeller. Such a system allows the pilot to adjust the propeller pitch for the most efficient thrust output possible.

(5) Constant-Speed Propeller

A propeller whose pitch is automatically adjusted to maintain a preset RPM, which otherwise is highly affected by airspeed. This is accomplished by a control mechanism, called a *governor*, which is mounted to the engine and balances centripetal and hydraulic forces.

(6) Feathering Propeller

A controllable pitch or a constant-speed propeller that allows the pilot to align the blade chordlines with the forward speed of the aircraft in case of an emergency, such as an engine failure. This prevents the propeller from wind milling and, thus, reduces the drag impact of the inoperative engine.

(7) Reversing Propeller

A controllable or a constant-speed propeller that allows the pilot to align the blades to angles beyond that possible with a feathering propeller. It allows the thrust force to be pointed in a direction opposite of the forward motion of the aircraft. This feature is used during landing to decelerate the airplane and even to allow the aircraft to "reverse" out from an air terminal using its own power. It is commonly found on turboprop engine installations.

An idealized *power lever quadrant* console is shown in Figure 15-3. Common reverse operation of propellers involves settings called *ground fine*, *reverse*, and *beta*. **Ground fine** is a low pitch setting used when taxiing the airplane with the engine running at a "reasonably high" rotation rate. Maintaining such RPMs on some turboprops is recommended to prevent damaging oscillation that may occur at lower RPMs. The ground fine setting prevents too high thrust from being generated at those rotation rates and this is most helpful for low-speed ground operations.

[3] Broadband noise refers to sound that extends over a wide range of frequencies, perhaps even the entire range of audible frequencies.

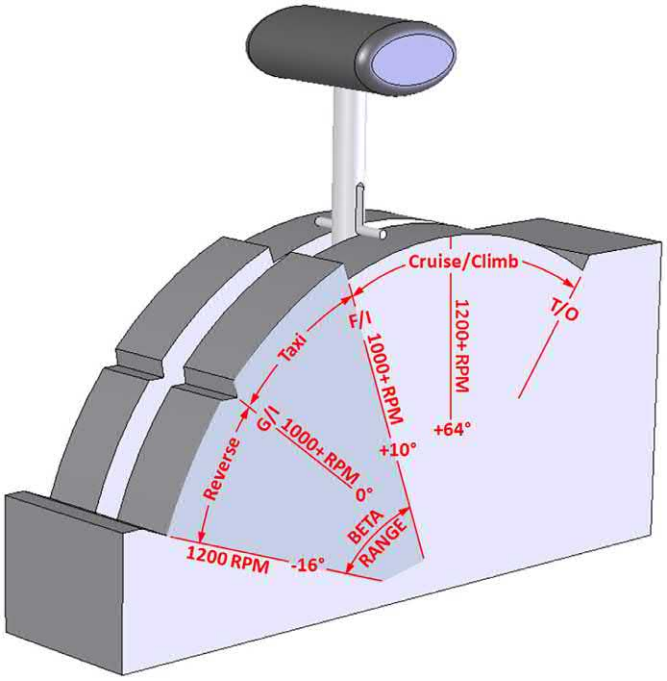


FIGURE 15-3 Idealized power lever quadrant for a typical turboprop. G/I is Ground Idle, F/I is Flight Idle, T/O is Take-Off.

The **reverse** setting, as stated earlier, generates thrust in the opposite direction and is helpful immediately after landing. The setting labeled "Taxi" in the figure is where the pilot would operate the power lever while taxing. In this range, the RPM is constant, but the blade pitch angles are adjusted. **Beta** refers to the range of power level positions that are used on the ground that include the reverse and taxi power settings.

(8) Beta Control Prop

A propeller specifically designed to allow operation of the propeller as described above.

(9) Material for Propellers

The modern propeller is made from three different materials: wood, forged aluminum, or composites. All have their pros and cons, but only aluminum and composites should be used for high-performance aircraft. Wooden propellers offer light weight that may come in handy as a solution for small airplanes with potential CG problems: e.g. if the CG too close to a forward limit (tractor) or aft limit (pusher).

(10) Propeller Extension

Consist of a separate spacer piece (most commonly for fixed pitch propellers) or an integral extension of the propeller hub (most common with constant-speed propellers). The purpose of the spacer or hub extension is to increase the spacing between the engine and propeller so that the geometry of the engine cover (cowling) may be made more aerodynamically efficient and, thus, reduce the drag penalty of the engine installation. This often improves cooling. While heavier, the overall reduction in drag may easily surpass the penalty of the weight addition. Propeller extensions must be carefully installed because if the propeller becomes misaligned, a severe vibration may result. Ideally, it should have a centering boss to make the installation easier.

15.1.4 Propeller Geometry

Figure 15-4 shows a three-bladed propeller rotating about an *axis of rotation*. The *spinner* is an aerodynamically shaped cover that (1) reduces the drag of the hub of the propeller and (2) protects it from the elements. The pressure differential between the front and aft face of the propeller blade results in a vortex that is shed from the tip of the blade and is carried back by the airflow going through the propeller. This forms the helical shape shown in the image. Note that for clarity, only one vortex is shown. Figure 15-5 shows a typical blade planform and its cross-sectional airfoils [3]. The planform geometry, including twist and airfoil camber, dictates thrust generation, strength, natural frequencies, and noise. Additional helpful information is provided in ref. [4].

(1) Basic Dimensions

Figure 15-6 shows a three-bladed propeller of diameter D_P, radius R_P, and disc area A_P. r is the radius to an arbitrary *blade station*, Ω is the rotation rate (in rad/s), and dr is the width of an infinitesimal blade segment.

(2) Geometric Pitch, P_G

If a propeller rotates one full circle, its tip rotates through an arc length (circumference) of $\pi D_p = 2\pi\ R_P$. For each full rotation, it "screws" itself some distance P forward (see Figure 15-7). Imagine the propeller rotating slowly through some highly viscous fluid. If this were possible, the propeller would move like a metal screw into a piece of wood. The distance it would cover in one full revolution is the *geometric pitch* or *pitch distance*, P_G. It is theoretical only and never achieved in practice. A propeller of a 42-in pitch would move 42 inches forward in one revolution (using the metal screw in wood analogy). Propeller manufacturers specify P_G at propeller radius ¾R.

(3) Geometric Pitch Angle, β

Imagine the propeller making one full rotation using the metal screw in wood analogy. An observer at the blade tip would rotate distance $2\pi\, R_P$, while (theoretically) helically advancing distance amounting to the geometric pitch, P_G. This engenders the term *geometric pitch angle* (β). It changes along the blade, from a maximum

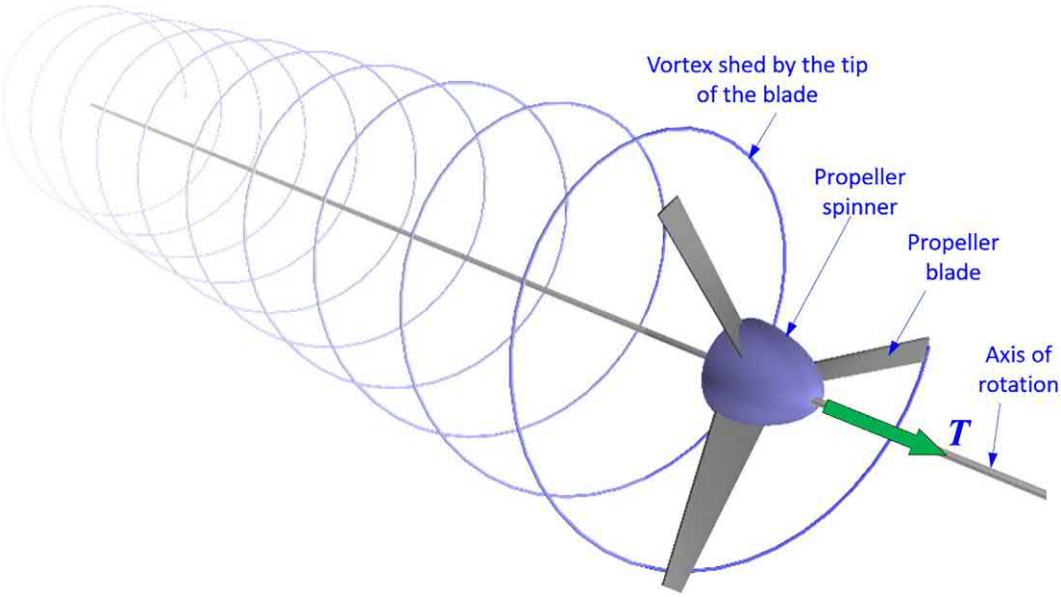


FIGURE 15-4 Propeller helix.

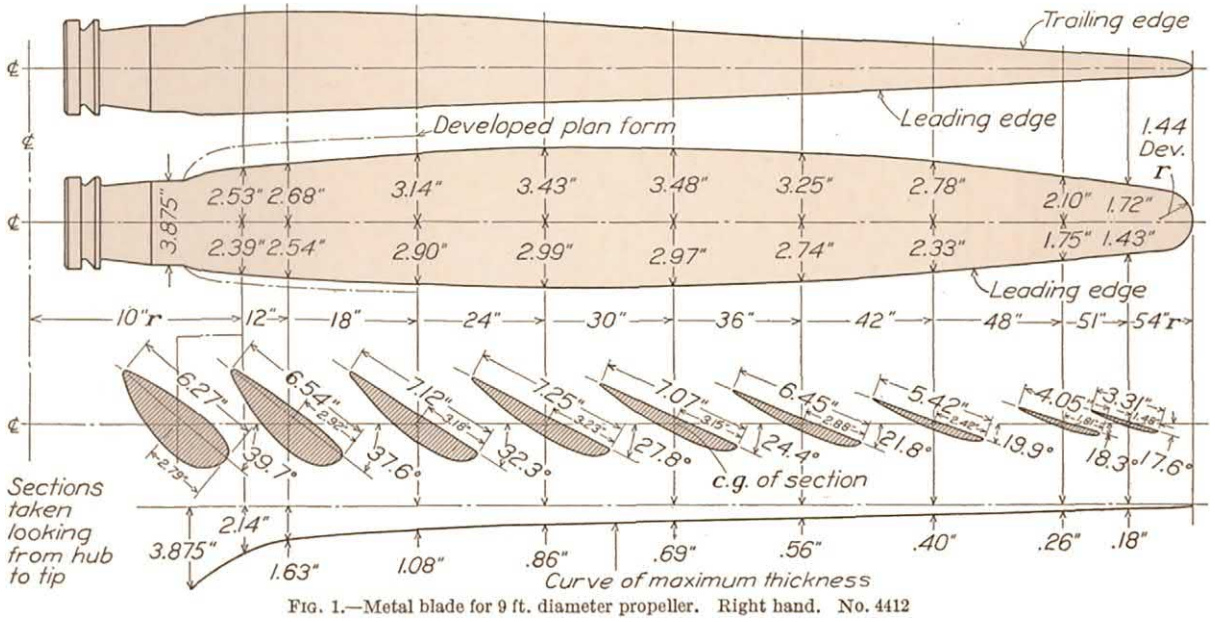


FIGURE 15-5 Geometry of a typical metal propeller blade. *From Weick, F.E., Full-Scale Wind Tunnel Tests of a Series of Metal Propellers on a VE-7 Aircraft, NACA TR-306, 1928.*

at the hub to a minimum at the tip. Using the geometry in Figure 15-7 (and here referencing the chordline) we define β as follows:

$$P_G = 2\pi r \tan\beta \quad \Rightarrow \quad \beta = \tan^{-1}\left(\frac{P_G}{2\pi r}\right) \tag{15-1}$$

At blade station $r = \frac{3}{4} R_P$, this becomes

$$\beta_G = \tan^{-1}\left(\frac{2P_G}{3\pi R_P}\right) = \tan^{-1}\left(\frac{4P_G}{3\pi D_p}\right) \tag{15-2}$$

Typical values of P_G range from 60% to 85% of the propeller diameter. An example of this is the Sensenich 69CK propeller used for the Cessna 152 two-seat, single-engine trainer. Its diameter is 69 in (1.753 m) and pitch ranges from 42 to 58 in (1.067–1.473 m), based on model. Its β_G ranges from $14.4° < \beta_G < 19.6°$. Note that if each rotation pulled the prop forward by distance P_G, its maximum theoretical forward speed would be

$$V_G = P_G\, n \tag{15-3}$$

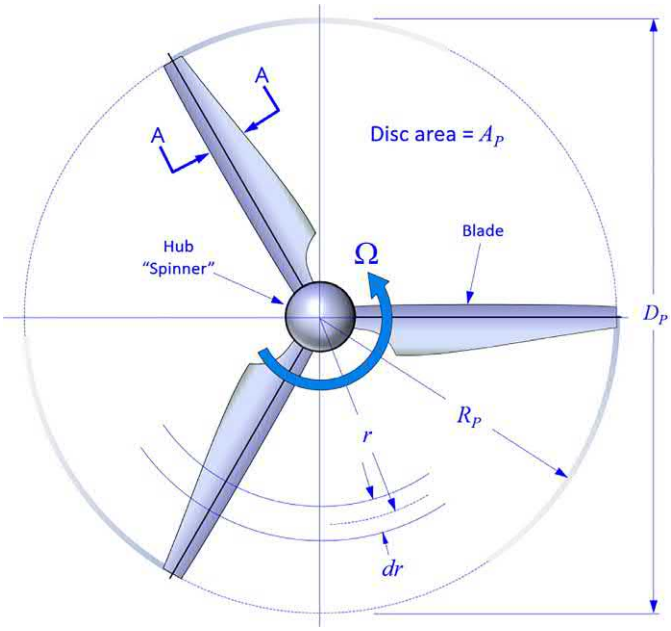


FIGURE 15-6 Propeller geometry.

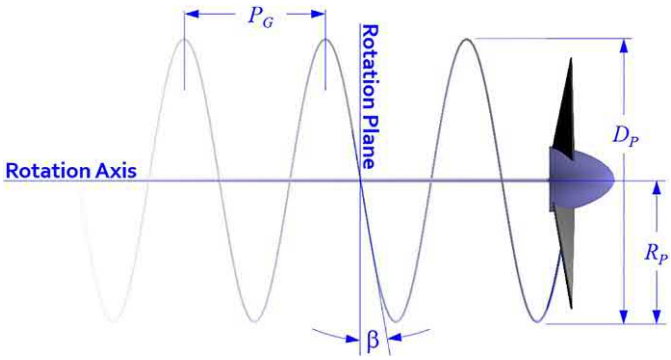


FIGURE 15-7 Schematic showing geometric properties.

(4) Pitch-Diameter Ratio

Is also used to identify propellers. Using the aforementioned propeller, we get $0.609 < P_G/D_p < 0.840$. Typical values range between 0.3 and 1.6. It is related to the geometric pitch through Equation (15-2) as follows:

$$\frac{P_G}{D_p} = \frac{3}{4}\pi \tan\beta_G \tag{15-4}$$

(5) Helix Angle, ϕ

A propeller moving through air covers less distance per revolution than indicated by the geometric pitch (see Figure 15-8). Therefore, the angle between the rotation plane and circumference $2\pi r$ at each blade station is less than the geometric pitch angle. This angle is called the *helix angle* and is denoted by ϕ. If $n = RPM/60$ (revolutions per second), V_∞ is the forward speed (see Section 15.5), ϕ at blade station r can be estimated using the following expression:

$$\tan\phi = \frac{V_\infty}{\Omega\, r} = \frac{V_\infty}{2\pi\, r\, n} = \frac{30 \cdot V_\infty}{\pi\, r\, RPM} \tag{15-5}$$

(6) Relationship between Pitch Angle and Angle-of-Attack

Consider the cross-section A-A of the propeller blade in Figure 15-6 at some arbitrary blade station at radius, r. This is shown in Figure 15-9. Since propeller blades usually feature cambered airfoils, their associated zero-lift AOA, α_{ZL}, is a negative number (negative AOA). The literature presents two types of datum for propeller airfoils: (1) Chordline or (2) the α_{ZL}-line. Both are a valid approach. Using the chordline is more in sync with how airfoils of lifting surfaces are referenced. Using the α_{ZL}-line is convenient for *blade element theory* because it allows lift coefficient to be determined using $C_l = C_{l\alpha}\alpha$. Here, we define the reference datum as the chordline of the airfoil. To generate thrust in a forward direction, the α_{ZL}-line must form a positive angle-of-attack to the relative wind as it moves about its rotation axis. This requires $\beta > \phi + \alpha_{ZL}$. At rest, $\alpha = \beta$. However, once moving at forward speed V_∞ with induced speed w in the streamtube the α becomes

$$\alpha = \beta - \phi = \beta - \tan^{-1}\left(\frac{V_\infty + w}{\Omega\, r}\right) \tag{15-6}$$

(7) Propeller Design—Spanwise Pitch Distribution

Refers to how change pitch changes along the blade span. Two examples are *constant pitch* and *variable pitch*. Do not confuse this with the *fixed* or *variable pitch* propellers discussed in Section 15.1.5. In general, the pitch angle near the hub must be larger than near the tip because the contribution from Ωr is smaller. Thus, ϕ is larger inboard. This is solved by twisting the propeller along the span. But there is more than one way to twist a prop.

Constant Pitch Distribution

The most common propeller blade twist is accomplished such that all radial stations have the same pitch distance, P_G. A graphical representation is show in Figure 15-10A. This permits a simple mathematical representation of the pitch angle $\beta = \beta(r)$ using Equation (15-1).

Variable Pitch Distribution

Refers to any blade twisting method other than the constant pitch distribution (see Figure 15-10B). The purpose is to load the propeller disc in some favorable way. For instance, to prevent the inboard propeller blades from stalling or keep pressure coefficients near the tip below some value to reduce noise. Or the purpose may be to shape the

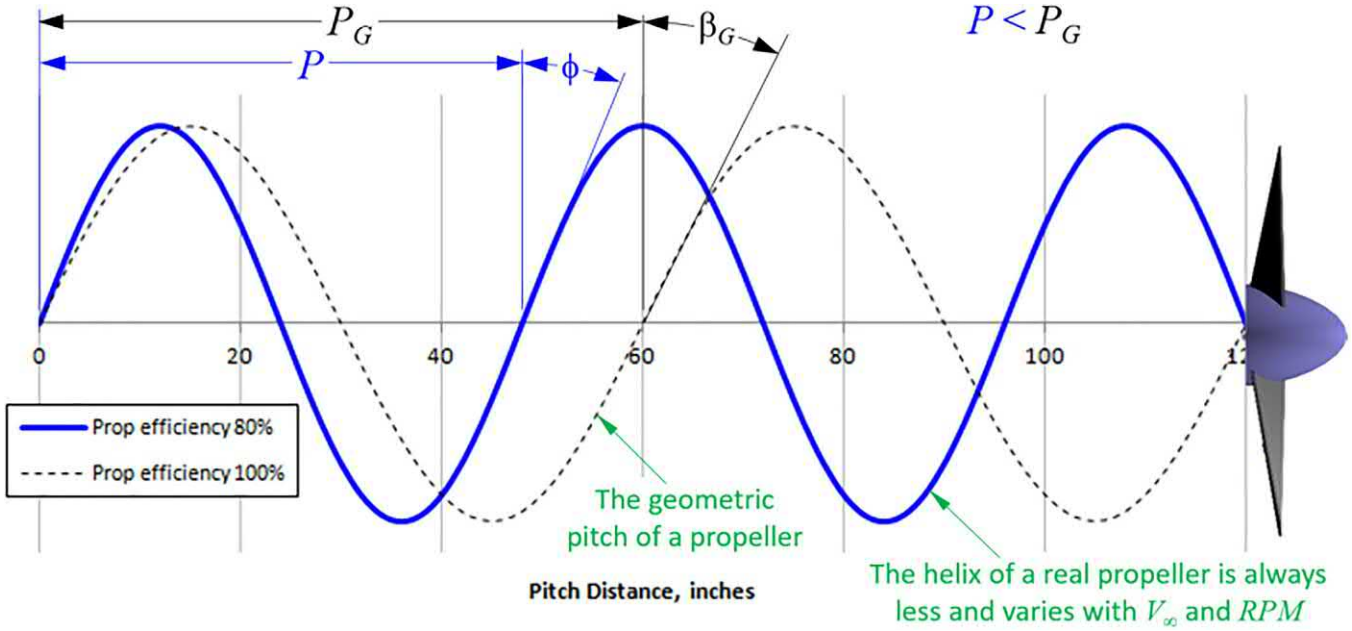


FIGURE 15-8 A real propeller advances shorter pitch distance than the geometric pitch indicates.

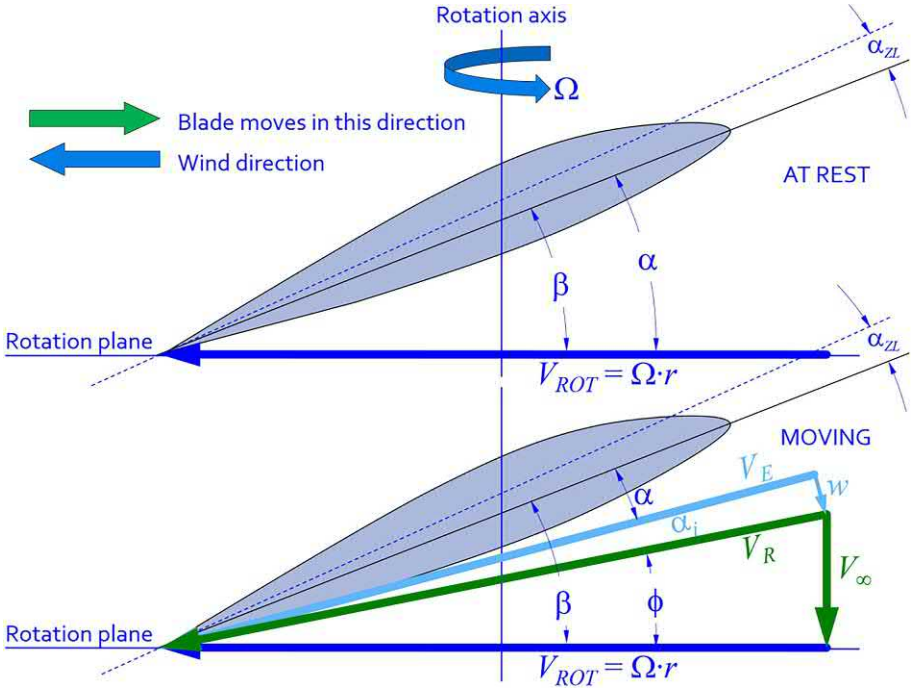


FIGURE 15-9 The upper propeller blade is rotating at rest ($V_\infty = 0$) and the lower one at some airspeed $V_\infty > 0$.

distribution of section lift coefficients to improve thrust along span.

(8) Propeller Rotation

The propeller *RPM* can be converted to *angular velocity* (Ω) as follows:

$$\Omega = 2\pi\, n = \pi\, RPM/30 \qquad [\text{rad/s}] \qquad (15\text{-}7)$$

Since the Ω is measured in rad/s the period (P_Ω) and frequency of the rotation (f_Ω) are given by

$$\Omega = \frac{2\pi}{P_\Omega} \;\Leftrightarrow\; P_\Omega = \frac{2\pi}{\Omega} = \frac{60}{RPM} \qquad [\text{seconds}] \qquad (15\text{-}8)$$

$$\Omega = 2\pi f_\Omega \;\Leftrightarrow\; f_\Omega = \frac{\Omega}{2\pi} = \frac{RPM}{60} \qquad [\text{Hertz}] \qquad (15\text{-}9)$$

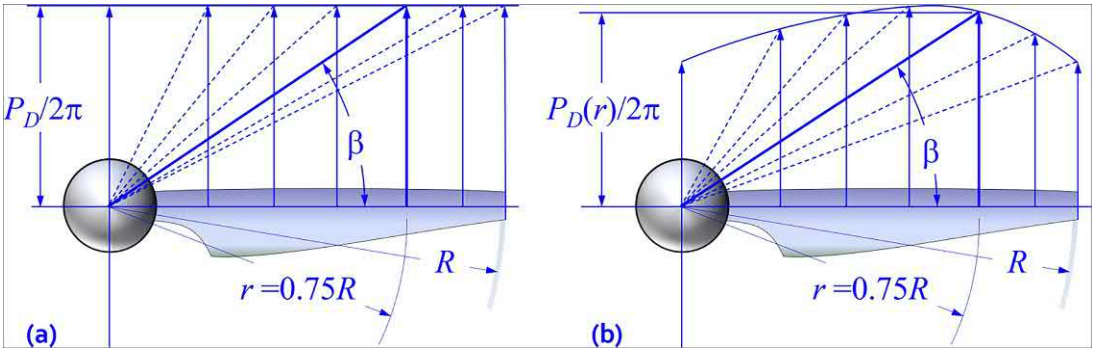


FIGURE 15-10 Constant pitch (a) and variable pitch (b) distribution.

(9) Propeller Speed

Figure 15-9 shows a propeller blade section at rest and moving a speed V_∞. The airspeed component in the rotation plane is denoted as V_{ROT}, given by

$$V_{ROT} = \Omega \cdot r \tag{15-10}$$

As stated in bullet (5), the forward motion of the propeller introduces the component $V_\infty + w$. Thus, the resultant speed "seen" by the airfoil can be obtained from the Pythagorean relation:

$$V_R = \sqrt{V_\infty^2 + V_{ROT}^2} = \sqrt{V_\infty^2 + (\Omega \cdot r)^2} \tag{15-11}$$

It follows that the propeller tip speed (V_{tip}) and Mach number (M_{tip}) are

$$V_{tip} = \sqrt{V_\infty^2 + (\Omega R_P)^2} = \sqrt{V_\infty^2 + (\pi n D_p)^2}$$
$$= \sqrt{V_\infty^2 + \left(\frac{\pi \cdot RPM \cdot D_p}{60}\right)^2} \tag{15-12}$$

$$M_{tip} = \frac{V_{tip}}{a} = \frac{V_{tip}}{\sqrt{\gamma RT}} \approx \frac{V_{tip}}{1116\sqrt{1 - 0.0000068753H}} \tag{15-13}$$

where a is the speed of sound at condition, γ is the ratio of specific heats (=1.4), R is the specific gas constant, H is altitude in ft, and T is the ambient temperature.

(10) Windmilling Propellers

Bullet (6) states that forward thrust requires $\beta > \phi + \alpha_{ZL}$. When this condition is not met (i.e., $\beta < \phi + \alpha_{ZL}$) a phenomenon called *windmilling* occurs. A generalized schematic is shown in Figure 15-11. Figure 15-11(a) shows the propeller blade under normal operation when it complies with $\beta > \phi + \alpha_{ZL}$. Figure 15-11(b) shows the propeller blade when $\beta < \phi + \alpha_{ZL}$. This means it operates at a negative AOA. Two consequences are evident from Figure 15-11(b): (1) The thrust generation is opposite of that in Figure 15-11(a). This has serious implications for a pilot of an aircraft suffering engine failure. The windmilling increases the airplane drag substantially and reduces its glide range. (2) The lift-force points toward the blade's leading edge. This drives the *autorotation* of the propeller such it maintains the RPM associated with this condition.

Recovery procedures in airplanes following a noncatastrophic engine failure (assuming engine components still rotate), in part, depend on whether it is a single- or multiengine and, in part, whether it is a fixed- or variable-pitch propeller. Modern variable-pitch props can be feathered, which stops the windmilling and reduces drag. If at all possible, the windmilling of the fixed-pitch propeller should be stopped. This requires the airplane to be slowed down to airspeeds close to stall. Thus, it is risky, requires practice, and it may be unsuccessful. A stopped propeller is less draggy than a windmilling one. A method to estimate the drag of windmilling (and stopped) propellers is presented in Section 16.4.13.

15.1.5 Fixed Versus Constant-Speed Propellers

Propeller efficiency is discussed in greater length in Section 15.3.8. It is a measure of how much engine power is converted into propulsive power (Thrust $\times$Airspeed). A propeller that is "0.80" efficient at a specific condition converts 80% of the engine power into propulsive power. Propeller efficiency is a function of airspeed, rotation rate, and propeller geometry.

Aircraft propellers are designed for a specific range of airspeeds specified by the airframe manufacturer. In this case, the following rules of thumb apply:

For low-speed operations use a low pitch.
For high-speed operations use a large (coarse) pitch.[4]

[4] If it helps, remember low pitch for low speed and high pitch for high speed.

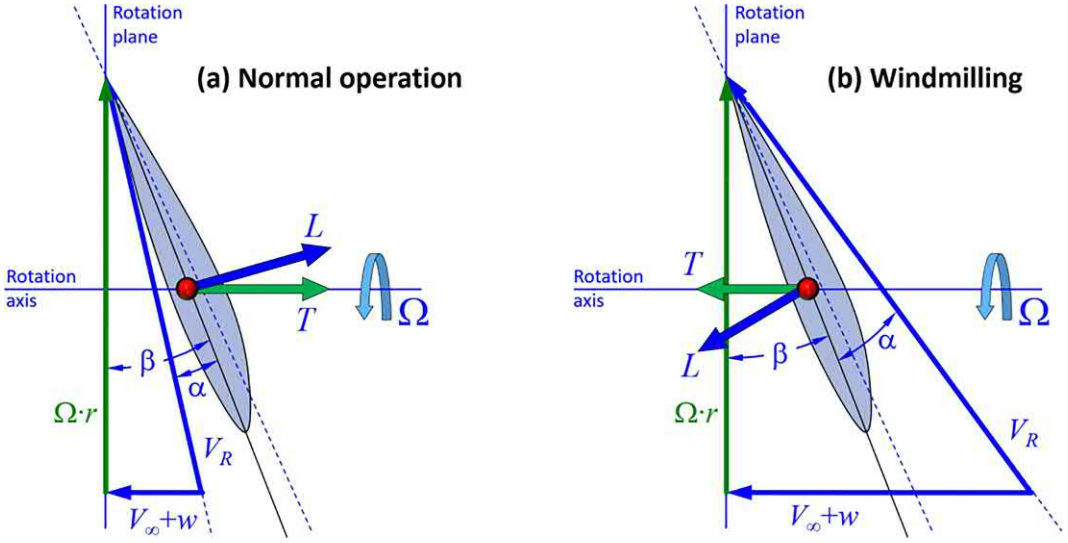


FIGURE 15-11 Normal operation of a propeller compared to windmilling.

A fixed-pitch propeller is one for which the blade pitch angles are permanently fixed. Such propellers are simple, light, and inexpensive. It is a drawback that their best efficiency is achieved at one airspeed only. This requires the designer to decide whether to emphasize climb or cruise performance and select an appropriate prop. Usually, two types of fixed-pitch propellers are available: The *fixed-pitch "climb"* propeller is designed to achieve its maximum propeller efficiency at a relatively low airspeed. This makes it suitable for airplanes for which climb performance is important, e.g., trainers and bush-planes. The *fixed-pitch "cruise"* propeller achieves its maximum efficiency at a higher airspeed, making it suitable for airplanes where higher cruising speed is of greater importance.

Pilots of aircraft with fixed-pitch propellers notice that, if initially at cruise, the engine *RPM* is reduced if climb is initiated and increased if descent is initiated. In the former case, climb inevitably reduces the speed the airplane and the propeller blades begin to experience a higher AOA. This generates more blade-drag, which increases the blade-torque, which reduces the *RPM*. In the latter case the opposite happens. The blades experience lower AOA as the aircraft speeds up. This reduces blade-drag and, thus, blade-torque. The reduced load on the engine increases the *RPM*. If equipped with a cruise prop, the change, in either case, reduces propeller efficiency, assuming it was operating at the airspeed of maximum efficiency. If a climb prop, slowing down makes the prop more efficient, but less if the airspeed is increased.

Airplanes designed as *cruisers* always feature cruise-propellers. Airspeed variations detrimentally affect their performance. This begs the question, is it possible to design a prop that is insensitive to airspeed changes and maintains the *RPM* set by the pilot? Such a propeller would surely offer high efficiency over a range of airspeeds. The answer is yes. Such propellers are called *constant-speed propellers*. They date to the 1920s, when Pierre Levasseur introduced manual control to adjust the blade pitch in flight [5] and, thus, "convert" a T-O prop into a climb prop, and a climb prop into a cruise one.

Despite improvements, the invention did not stop variations in *RPM* with airspeed. This led to the development of an automatic controller, called a *propeller governor*, or simply a governor. It accurately detects changes in the *RPM* set by the pilot and adjust pitch accordingly to maintain peak efficiency. Figure 15-12 shows how the propeller efficiency typically varies with airspeed for the three propeller types discussed above.

A detailed description of how the governor works is beyond the scope of this section. So, only a brief introduction will be given: Once the desired *RPM* has been set (using the cockpit *RPM* control), the governor automatically adjusts the propeller pitch as needed to maintain that *RPM*. This is accomplished by means of throttle setting and flyweights. The governor mechanically detects

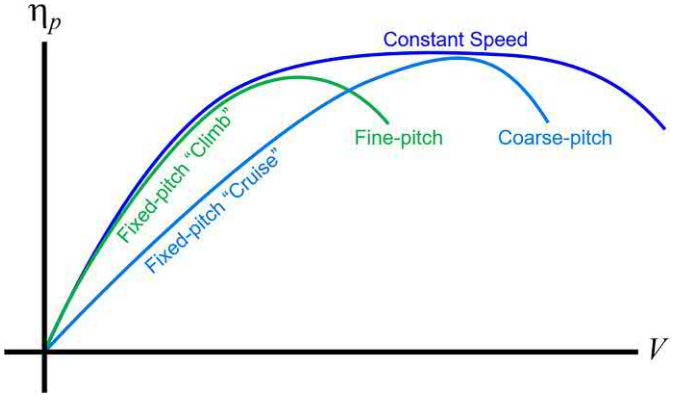


FIGURE 15-12 Comparing propeller efficiencies of three propeller.

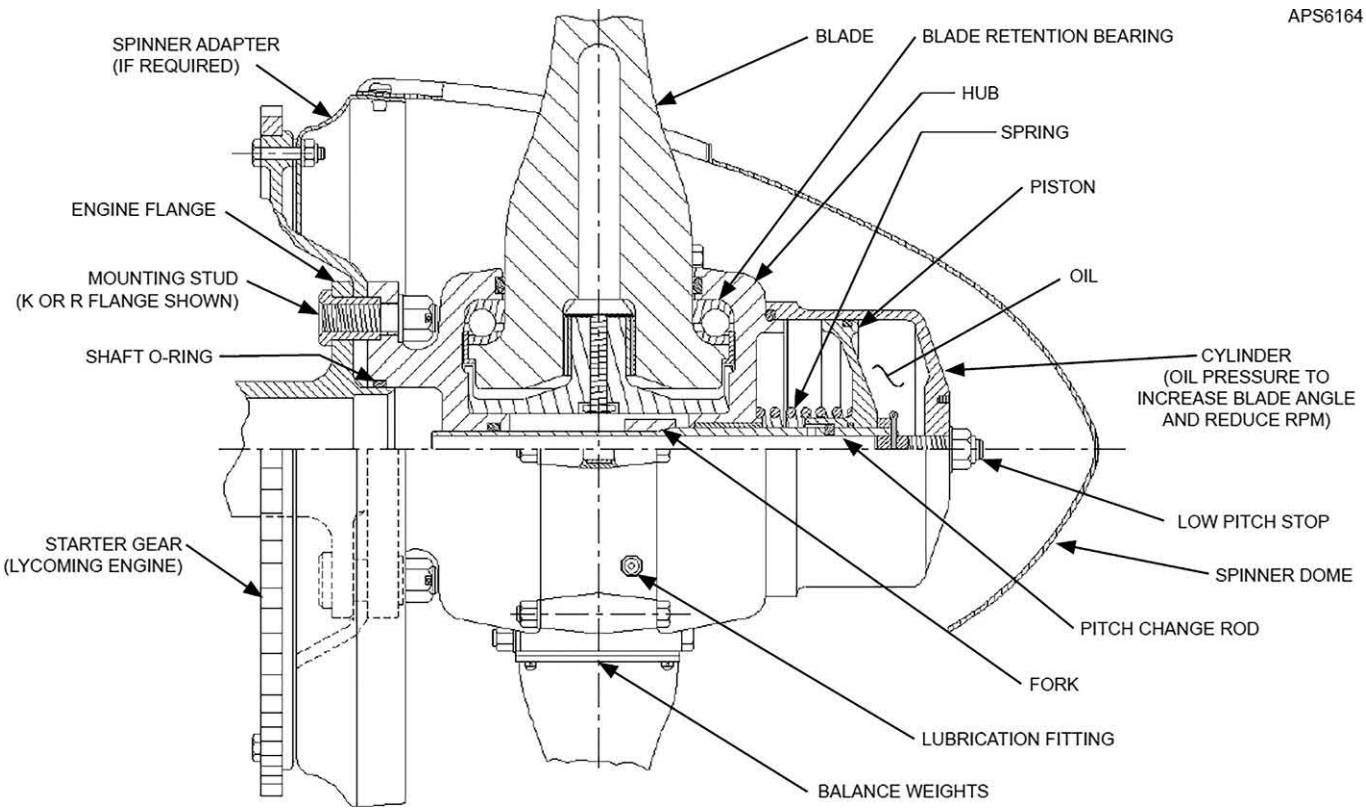


FIGURE 15-13 A section view of the inside of a constant-speed propeller. *Courtesy of Hartzell Propeller Inc.*

RPM via flyweights and uses it in conjunction with the throttle setting to maintain required oil pressure inside a pressurized oil reservoir. Consider an airplane whose pitch angle deviates from that at level flight such the *RPM* increases (e.g., nose pitches down). This implies an increase in airspeed. The governor will increase the propeller pitch to reduce until the original *RPM* is re-established. By the same token, a decrease in *RPM* indicates reduced airspeed (e.g., nose pitches up). The governor will reduce the propeller pitch until the original *RPM* is re-established. A section view of a hub of a constant-speed propeller is shown in Figure 15-13.

15.2 PROPELLER EFFECTS

This section considers important side effects caused by the presence of a propeller. These effects are significant and must be considered in the development of the airplane. Pilots of propeller aircraft are familiar with these effects call them *P-factor* (for Prop-factor). While some sources specifically call out the asymmetric yaw as the P-factor (see Section 15.2.4), others, such as Stinton [6], define P-factor as the combination of the angular momentum effects (Section 15.2.1), slipstream effects (Section 15.2.2), the normal force (Section 15.2.3), and the asymmetric yaw effect (Section 15.2.4). This author agrees with this classification for it is impossible for the pilot to distinguish between any of these effects. Pilots only feel that running the propeller at high *RPM* introduces effects not present when idle. In this text, the P-factor encompasses all the cited effects.

However, there are other effects to bring up that are of importance in the development of the aircraft. For instance, asymmetric yaw effect for multiengine aircraft (Section 15.2.5) that dictate which engine is critical in case of an engine failure, blockage effects (Section 15.2.6) which reduce the thrust, hub and tip effects (Section 15.2.7), the effects of high tip speed (Section 15.2.8), and skewed wake effects (Section 15.2.9) and the resulting $A \cdot q$ loads that are important for turboprops and electrically powered aircraft.

15.2.1 Angular Momentum and Gyroscopic Effects

Angular momentum and gyroscopic effects play an important role in *stability and control theory* and, thus, must be considered in the design process. Consider the propeller to the left in Figure 15-14, which rotates at a constant angular rate Ω_x (computed per Equation (15-7)). As it rotates about the x-axis (the axis of rotation), it generates an angular momentum, h_{SRx} (*SR* stands for spinning rotor). This momentum must be reacted by the airplane,

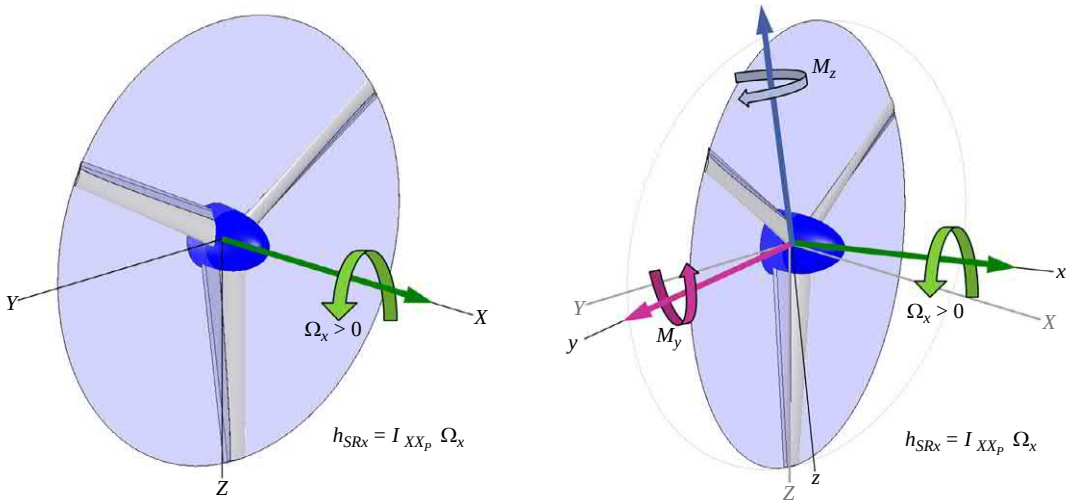


FIGURE 15-14 The left propeller rotates only along the x-axis. In the right image, it is in the process of changing orientation, which induces the restoring moments M_y and M_z.

otherwise it would spin in the opposite direction. This is easily suppressed by a slight, opposite aileron deflection. The angular momentum is given by:

$$h_{SRx} = I_{XX_P} \cdot \Omega_x \tag{15-14}$$

where

I_{XXP} = Moment of inertia of the propeller about its axis of rotation.
Ω_x = Angular velocity of the propeller. The subscript x denotes rotation about the x-axis.

Some multiengine aircraft feature an even number of engines (two, four, six, etc.) and propellers that rotate in opposite directions about the plane-of-symmetry. If all engines rotate at the same RPM, this cancels the angular moments.

Now consider the same propeller to the right in Figure 15-14. It shows the propeller to the left as it rotates to a new orientation (e.g. due to pilot control inputs). This change in orientation is called *gyroscopic precession*. As the motion takes place, additional gyroscopic couples, M_y and M_z, are generated. These moments are restoring since their action is to keep the propeller in the original orientation. As soon as the rotation ceases, so will those moments. If the angular velocity of the precession is given by $\boldsymbol{\omega}_P = p\mathbf{i} + q\mathbf{j} + r\mathbf{k}$, then the gyroscopic moments can be found from:

$$\mathbf{M}_P = \begin{bmatrix} M_x \\ M_y \\ M_z \end{bmatrix} = \boldsymbol{\omega}_P \times \mathbf{h}_{SR} = \begin{bmatrix} \mathbf{i} & \mathbf{j} & \mathbf{k} \\ \hat{p} & \hat{q} & \hat{r} \\ h_{SRx} & h_{SRy} & h_{SRz} \end{bmatrix} \tag{15-15}$$

where $\hat{p}$ is airplane rotation rate about the x-axis (roll), $\hat{q}$ about the y-axis (pitch), and $\hat{r}$ about the z-axis (yaw). Note that for the propeller in Figure 15-14, the gyroscopic moments would be given by:

$$\begin{bmatrix} M_x \\ M_y \\ M_z \end{bmatrix} = \begin{bmatrix} \mathbf{i} & \mathbf{j} & \mathbf{k} \\ \hat{p} & \hat{q} & \hat{r} \\ h_{SRx} & 0 & 0 \end{bmatrix} = (0)\mathbf{i} - (0 - \hat{r}h_{SRx})\mathbf{j} + (0 - \hat{q}h_{SRx})\mathbf{k}$$
$$= \hat{r}h_{SRx}\mathbf{j} - \hat{q}h_{SRx}\mathbf{k} \tag{15-16}$$

15.2.2 Slipstream Effects

A typical single-engine aircraft is shown in Figure 15-15. It features a standard propeller whose rotation is clockwise (seen by the pilot). Clockwise motion is common among American propeller manufacturers, whereas counterclockwise is common in Europe. The corkscrew-shaped blade tip vortex is sketched as it encloses the fuselage of the airplane. The tip vortex is caused by the pressure differential between the forward (low pressure) and rearward (high pressure) sides of the propeller, just as it is on a wing. The lower image of Figure 15-15 shows the vertical tail subjected to this vortex. It shows how the downwash component, which is perpendicular to the wake left by the propeller blade, changes its angle of attack, generating additional lift on it. For this aircraft, this causes a yawing moment that tends to move the nose to the left. It can be suppressed by a right deflected rudder (step on the right rudder), or by using a cambered airfoil for the VT (camber on the left side), or by a small *angle-of-incidence* adjustment (leading-edge left). All of these can suppress the yaw. The magnitude of the yawing moment depends on engine power, *RPM*, and the airspeed of the aircraft.

15.2.3 Propeller Normal and Side Force

(1) Normal Force

When the aircraft is operating such the incoming flow is not perpendicular to the propeller disc plane, its blades

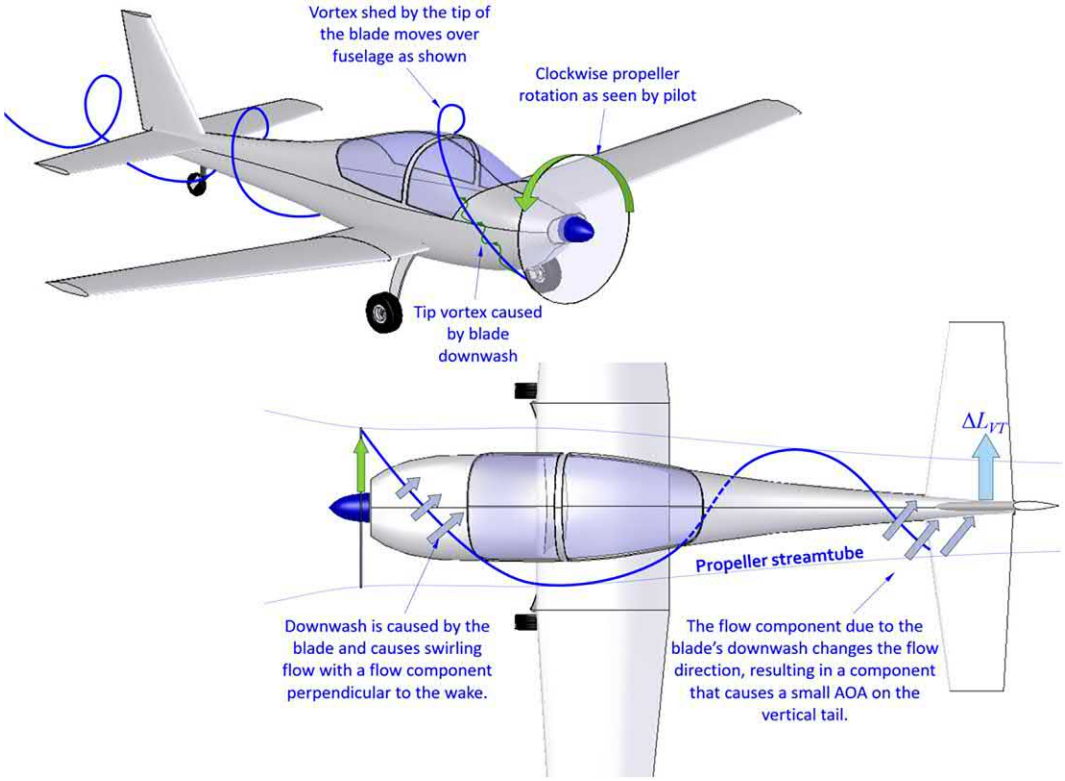
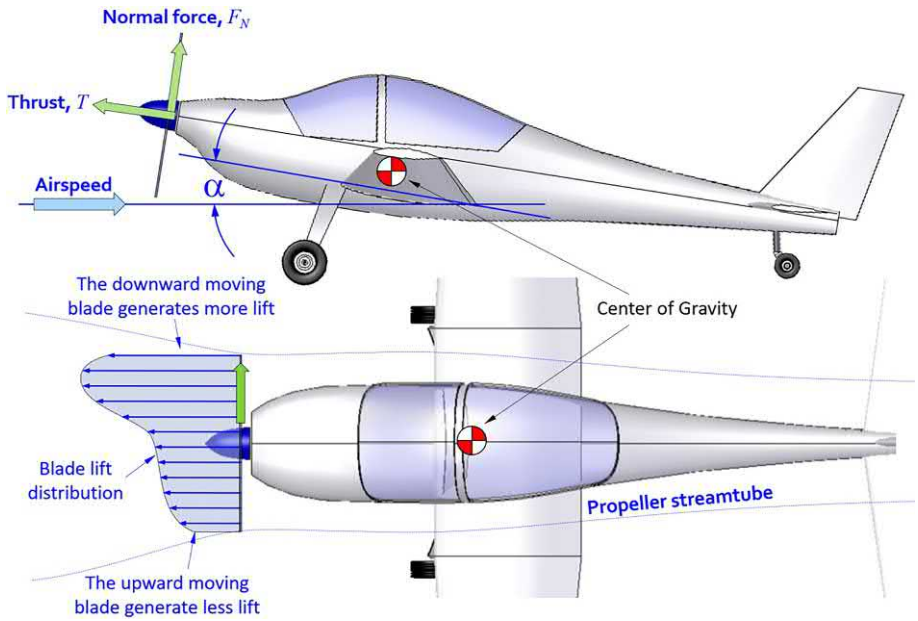


FIGURE 15-15 The swirling motion of air inside the propeller streamtube changes the AOA of the vertical tail. For a propeller rotating clockwise, this introduces a left yaw tendency.

are loaded asymmetrically (see Figure 15-16). This is caused by the downward rotation of the right propeller blade (assuming a clockwise rotation) and upward rotation of the left one. The rotation develops an upward airspeed component for the right blade, increasing its AOA and lift. The opposite happens for the left one. While most of the blade-lift points forward, there is a vertical component to it as well. The net result is a vertical force-component that acts upward. A method to estimate this force is given in Section 24.2.11.

FIGURE 15-16 The generation of asymmetric disc loading.



The CG of the tractor configuration in Figure 15-16 is aft of the propeller. Consequently, the normal force destabilizes the aircraft (nose pitch-up moment). However, if the propeller is aft of the CG, as is the case for most pushers, the effect is opposite or stabilizing (nose pitch-down moment). The moment about the vertical axis (*z*-axis) generated by the asymmetric disc loading also causes another effect; side force, something that some pilots erroneously consider the "P-factor" (see below).

(2) Side Force

An identical force is generated when the airplane is yawed; except it points sideways. The moment it develops depends on the position of the propeller with respect to the CG, just like the normal force. For a tractor configuration at high power, the moment is destabilizing and tends to increase the yaw angle (see Figure 15-17). This requires a rudder input to correct and makes it easier to exacerbate the yawed condition if care is not exercised. The designer should keep this effect in mind and ensure the directional stability ($C_{N\beta}$) is large enough to prevent this from becoming a problem.

15.2.4 Asymmetric Yaw Effects—Single-Engine Aircraft

The lower image of Figure 15-16 shows the asymmetric lift distribution over the propeller disc. The right halve of the disc generates more thrust than the left one. This effect generates a couple that tends to turn the nose to the left (again assuming a clockwise propeller). The pilot must step on the right rudder to suppress it. The magnitude of this couple depends on the engine power, *RPM*, and forward airspeed. In contrast, the suppressing moment generated by a rudder deflection depends on the airspeed of the aircraft. At low airspeed, it is low. However, the asymmetric moment may be high due to a high power and high AOA, which is typical for an initial climb after take-off or during a balked landing maneuver.

15.2.5 Asymmetric Yaw Effects—Multiengine Aircraft

The asymmetric yaw effect has serious implications for multiengine propeller aircraft. Consider the twin-engine aircraft in Figure 15-18. The left image shows the aircraft with two engines operating normally and both propellers rotating clockwise as seen from behind (reversed for propellers that rotate counterclockwise).[5] Both propellers are subject to asymmetric thrust that places their center of thrust (T) to the right of the rotation axis. The thrust of the left engine acts over a distance d_L and distance d_R for the right engine. Also note that d_R is larger than d_L. Thus, a small moment M is generated about the CG. It is reacted by introducing a small rudder deflection, δ_{rtrim} (with a minor adjustment in aileron trim, δ_{atrim}). For the clockwise propeller rotation shown, the moment M causes a nose-left tendency. While small, the pilot detects it by observing the "ball" on the Turn-and-Bank

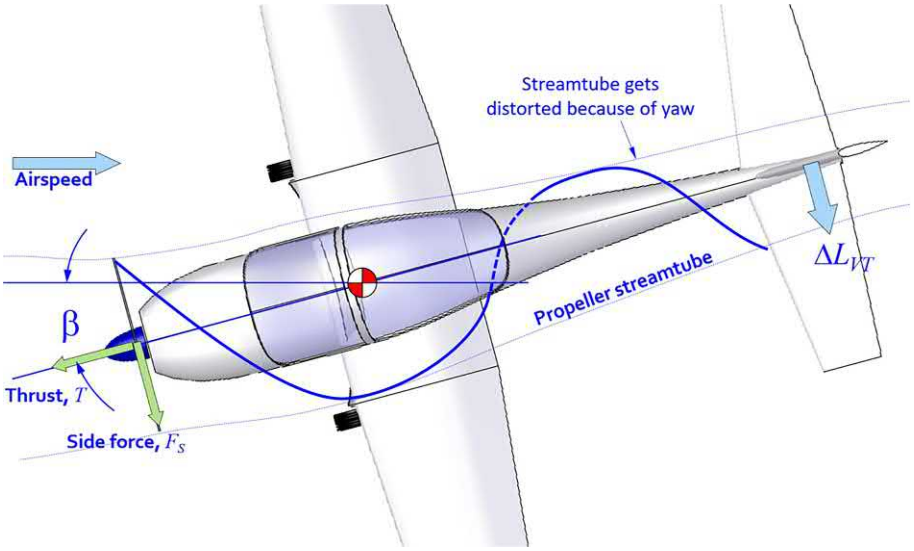


FIGURE 15-17 The generation of destabilizing side force for a tractor configuration.

[5] The De Havilland DASH 8 exemplifies a commuter with both propellers rotating clockwise as seen from behind. The Fokker F-27 Friendship exemplifies a commuter with both propellers rotating counterclockwise.

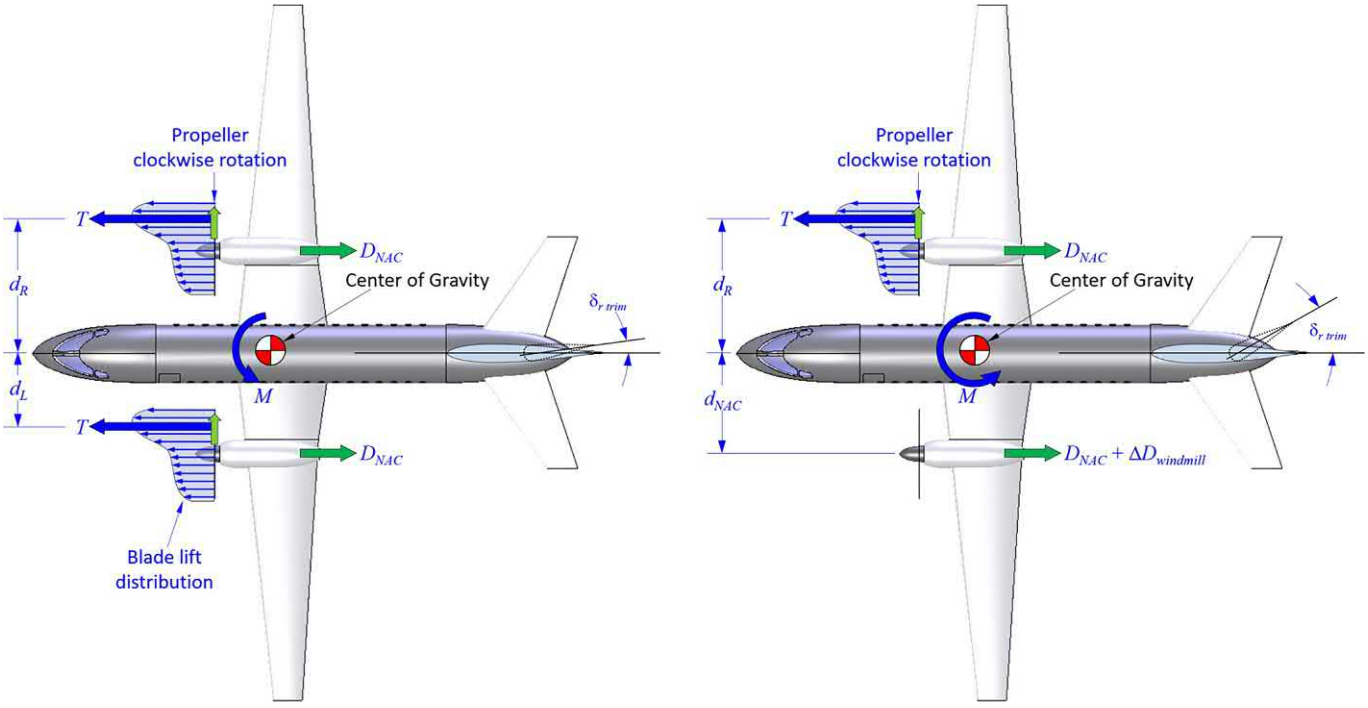


FIGURE 15-18 Asymmetric disc loading on a twin-engine aircraft in cruise (left) and in case of an engine failure (right). The rudder must be trimmed at a significantly higher deflection than for the normal operation, in addition to the recommended practice of "banking into the good engine" (see Figure 15-19 and text).

indicator swinging to the right of center. By pressing the right rudder pedal[6] or, more appropriately, by trimming the airplane nose-right using the rudder trim, the Turn-and-Bank indicator ball is centered. It is common in sailplanes to attach a yaw-string in the middle of the windscreen to provide similar help.

Now consider the right image in Figure 15-18, which shows a scenario in which the left (critical) engine has failed. This situation is referred to as flying with *one engine inoperative* (OEI) and constitutes a serious predicament for the pilot. Figure 15-18 shows that a failure of the left engine results in a substantially larger moment than if the right engine fails. Therefore, the left engine is called the *critical engine*. It presents a greater recovery problem than a failed right engine. In either case, the asymmetric thrust generates a powerful moment, M, which forces the aircraft to yaw toward the dead engine. This is compounded if the propeller is windmilling as this increases the drag ($\Delta D_{windmill}$) of the dead engine. The nacelle drag is denoted by D_{NAC}, and both act over a distance d_{NAC}. The drag is reduced by feathering the propeller (see Section 15.1.3), which is a mechanical feature offered on most twin-engine aircraft.

Standard procedures dictate that the pilot eliminates the yaw by stepping on the rudder pedal on the same side as the functional engine.[7] This is followed by banking the airplane between 2° and 5° toward the functional engine (see Figure 15-19). Then, the pilot will "feather" the dead engine.

Banking toward the functional engine establishes a turning tendency that reduces the need for rudder deflection. Increasing banking may even eliminate the need for rudder input, but usually at the cost of an already impaired performance. There is a limit to how much banking is practical. Too large and the rate-of-climb suffer. It may prevent the aircraft from maintaining altitude. As a rule of thumb, to achieve the maximum rate-of-climb in the OEI configuration (V_{YSE}) a bank angle of 2° is recommended if the noncritical engine fails, and 3° if the critical engine fails. A bank angle in the excess of 5° results in rate-of-descent (loss of altitude) for underpowered twins.

Another situation may confront the pilot operating a twin in an OEI configuration. First, high-power setting is required to maintain altitude. If the airplane slows below a certain airspeed, control authority is lost and the rudder will be incapable of opposing the yaw. This airspeed is called *minimum control airspeed*, denoted by V_{MC}. Per 14 CFR §23.149 in the "old" regulations, this airspeed must not exceed $1.2V_{S1}$ (stall speed in T-O

[6] Pilots use the mnemonic: "step on the rudder that's on the same side as the ball."

[7] Pilots use the mnemonic: "dead foot, dead engine."

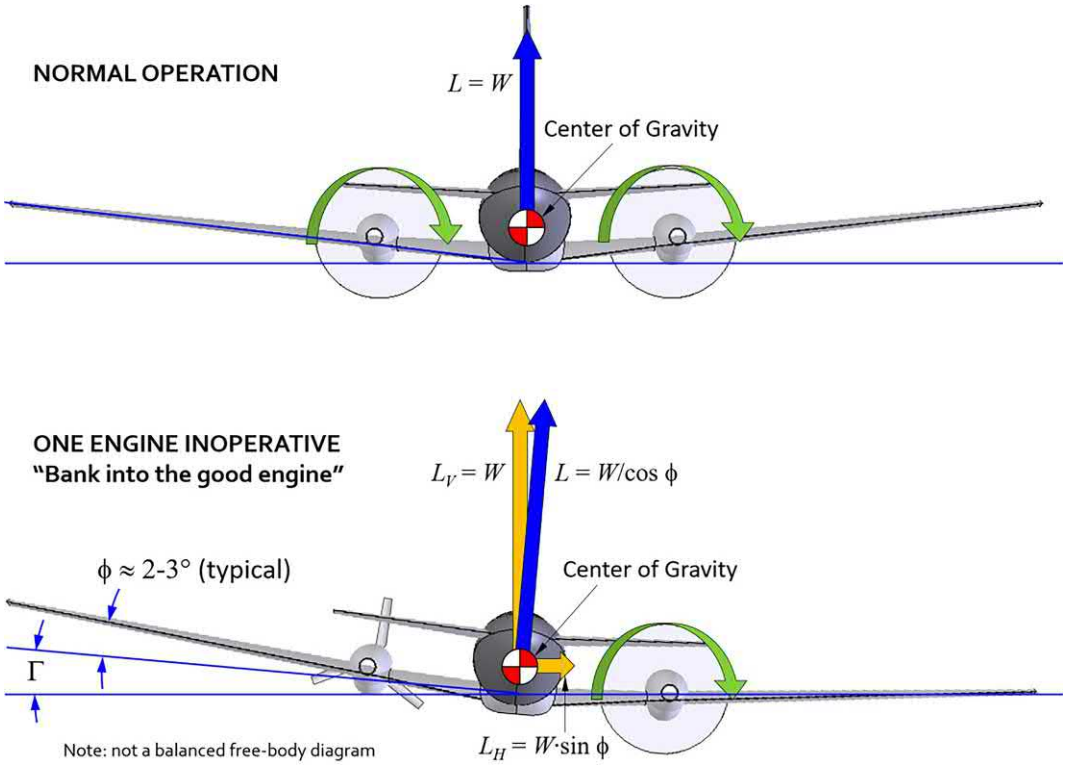


FIGURE 15-19 The standard practice of "banking into the good engine" reduces required rudder deflection when flying OEI.

configuration). If this happens, the aircraft is at risk of rolling upside down, possibly causing an inverted spin, if not impacting the ground first. The likelihood for fatalities is high. Thus, the pilot must maintain airspeed above V_{MC} and only slow down only after reducing power and pointing the nose down (e.g., during descent for landing).

(1) Remedies

This scenario is remedied by installing a *counter-rotating*[8] engine/propeller combination (see Figure 15-20). "*This provides balanced thrust during T-O and climb and eliminates the 'critical engine' factor in single-engine flight*." [7] The primary drawback is that it is more expensive to produce, as logistically it must feature two engines and propellers that are dissimilar because they rotate in the opposite direction. An operation of such an aircraft results in greater expenses as engine parts are not interchangeable. This can pose a peculiar situation to an operator, which might have parts for the left engine on hand, while none are in stock for a failed right engine. Such scenarios should not be overlooked when selecting an engine configuration as this could severely impact the finances of an operator. Instead, the designer should size the control system and surfaces to handle the critical engine.

It is of interest to note that the Wright Flyer featured two counter-rotating propellers, although this was due to the nature of the single-engine drive train. Asymmetric thrust would not have been an issue—engine failure stopped both propellers. Among other aircraft that feature this option are the De Havilland DH-103 Hornet (a derivative of the DH-98 Mosquito). The Lockheed P-38 Lightning featured counter-rotating propellers, although, surprisingly, both propellers rotated inversely of what is shown in Figure 15-20. This supports that a cancellation of propeller torque was driving that design decision and not asymmetric yaw. An identical arrangement is found on the Heinkel He-177 Greif. Aircraft featuring the arrangement of Figure 15-20 includes a series of Piper aircraft: the PA-31 Navajo Chieftain, PA-34 Seneca, PA-39 Twin Commanche, the canceled PA-40 Arapaho, and the PA-44 Seminole. Other aircraft include the Cessna T303 Crusader, Beech Model 76 Duchess, and Diamond DA-42 Twinstar, all which feature proper counter-rotating propeller rotation shown in Figure 15-20.

Large airplanes typically do not feature counter-rotating propellers. Aircraft, like the four-engine Lockheed P—3C Orion and C-130 Hercules, feature propellers that all rotate in a clockwise direction. This is driven by reduced operational costs in lieu of safety. An easy

[8] Note that it differs from *contra-rotating propellers*, which consist of two propellers mounted to the same engine and rotate in opposite directions. Such propellers are beyond the scope of this book.

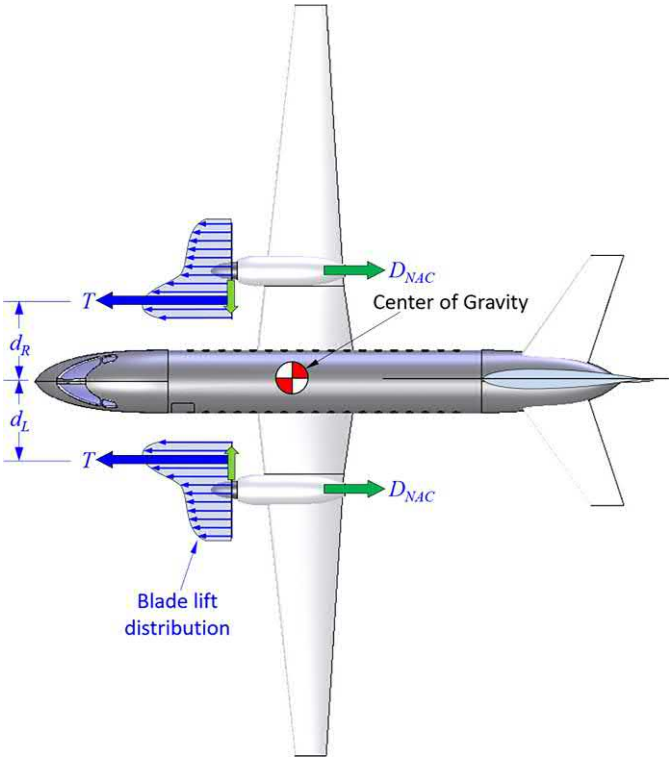


FIGURE 15-20 An aircraft with counter-rotating propellers as shown here does not have a critical engine and is a safer design, albeit, operationally more expensive.

counterargument is to state that safety is not compromised, but maintained by requiring rigorous pilot training, as well as providing hydraulically actuated control surfaces, and powerful engines—an argument that is hard to dispute. Many larger aircraft provide a *rudder boost system*; a pneumatically powered actuators that force the rudder to the proper deflection angle to counter the asymmetry (e.g., see ref. [8]). Such systems detect which engine has failed and react accordingly—improving safety. In addition, the operational history of these aircraft supports this notion—there are not many accidents in current times that can be attributed to asymmetric thrust on larger propeller powered aircraft. A notable exception is the Airbus A400, which features counter-rotating configuration. However, for small twins, this is not the case, as will now be demonstrated.

(2) Impact of Loss of Power

It is important to understand the implications of selecting a twin-engine configuration, specifically if the engine power is low. In addition to increased acquisition and maintenance cost, the selection has important safety and performance implications associated with it. From a development standpoint, such configurations (assuming a conventional on-wing engine layout) are draggier than single-engine aircraft of same power. This is a direct consequence of two nacelles on the wing in addition to the fuselage. This impact can be mitigated by a twin-engine configuration such as that of the Cessna 337 Skymaster and Adam A500 aircraft. However, performance degradation due to OEI is more serious. If spacious cabin and high cruising speed is desired, a solution as such offered by recent small GA aircraft should be considered. Aircraft such as the French DAHER TBM-700, TBM-850, and the Swiss Pilatus PC-12 are powered by a single Pratt & Whitney PT-6 turbine engine and cruise near 300 KTAS at 30,000 ft. This beats any of the previously mentioned twin-engine piston aircraft (excluding military twins).

The effect of loss of engine power on the performance of a small generic twin is illustrated in Figure 15-21. The figure shows that in normal operation, the aircraft climbs 1396 fpm at S-L and offers a maximum speed of 170 KCAS. Losing an engine drops this to 232 fpm and 118 KCAS, respectively. The analysis assumes a drag increase associated with maintaining a straight heading with OEI by adding 50 drag-counts ($\Delta C_{D\ OEI}$) to the original $C_{D_{\min}}$. This assumes the airplane being flown cross-controlled in a yawed configuration. It is disconcerting that the low rate-of-climb limits room for mistakes. An inexperienced or frantic pilot may easily maneuver the airplane off the peak conditions, causing it to lose altitude.

15.2.6 Blockage Effects

There are two sources of *blockage effects*: (1) A body placed in the streamtube ahead of the propeller disc (pusher configuration). (2) A body placed in the streamtube behind the disc (tractor configuration). An idealized streamtube going through a propeller disc is shown in Figure 15-41. The presence of the obstruction (e.g., fuselage or nacelle) inside the streamtube distorts it and deforms the *vena contracta*. This impedes the flow in the streamtube and reduces thrust through momentum loss. Figure 15-22 shows an ideal ("unblocked") streamtube superimposed on what the "blocked" streamtube might look like.

To estimate the impact of blockage on thrust requires the flow around the obstruction to be incorporated into the wake model (for instance, see the wake of Section 15.5). A reliable approach (excluding empirical methods or CFD) is to use the method of superposition, depicted in Figure 15-23. A version of this approach was investigated as early as 1928 in ref. [9]. More recent investigation is presented in ref. [10]. The mathematics of these methods are beyond the scope of this book. Propeller manufacturers consider blockage effects, although the methods used are usually proprietary. The aircraft designer can help mitigate blockage problems by considering a hub extension for piston-engine aircraft and select the largest spinner practical to cover the inboard and least efficient portion of the blade. This allows the cowling or nacelle to be sculpted in a manner less obstructive to the flow. Ideally, the cowling or nacelle design should be as

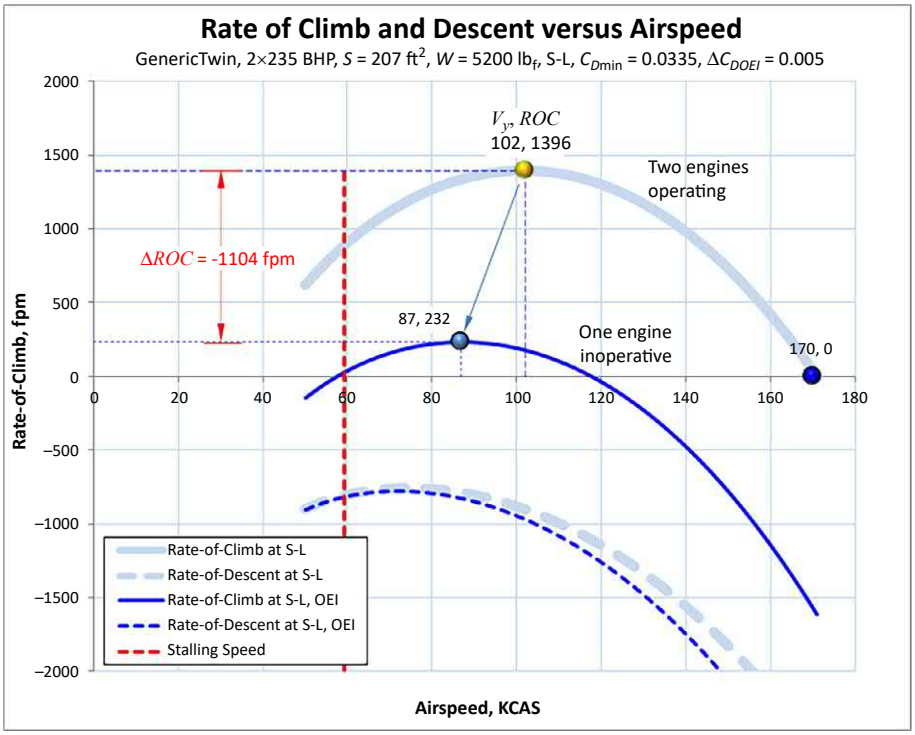


FIGURE 15-21 A performance degradation resulting from an engine out scenario for a small twin.

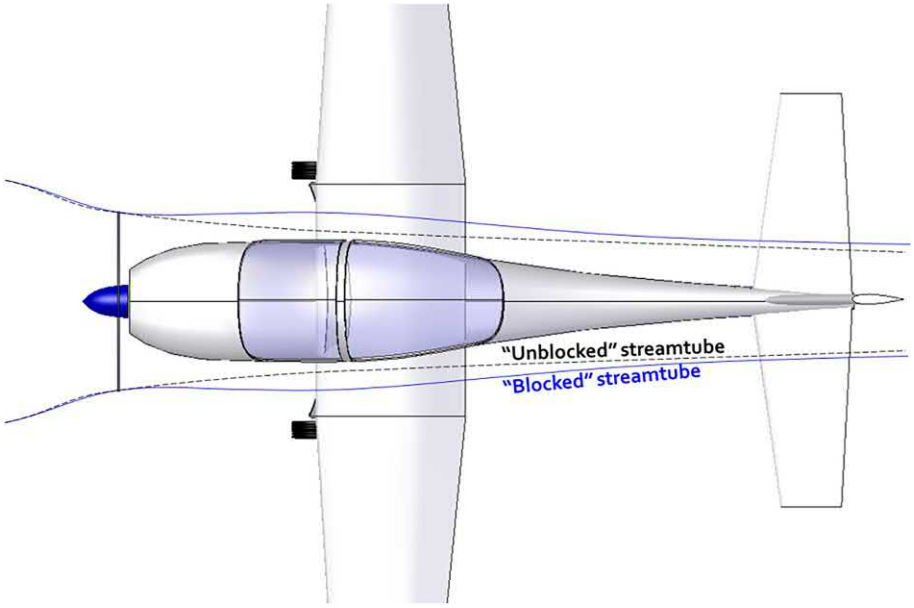


FIGURE 15-22 The difference between "blocked" and "unblocked" propwash.

axisymmetric as possible, as this yields higher installed propeller efficiency.

15.2.7 Hub and Tip Effects

The presence of the hub (root) and the blade-tip affects the distribution of section lift coefficients, as it does for the wing. An extreme example is the wind-turbine blade in Figure 15-24 (hub is omitted from the view). It shows how the lift diminishes near the root (left) and tip (right). The effect is less noticeable near the root because of less radial speed. The blade twist and camber of the airfoil influences this as well. This highlights that hub and tip effects must account for when analyzing propeller thrust.

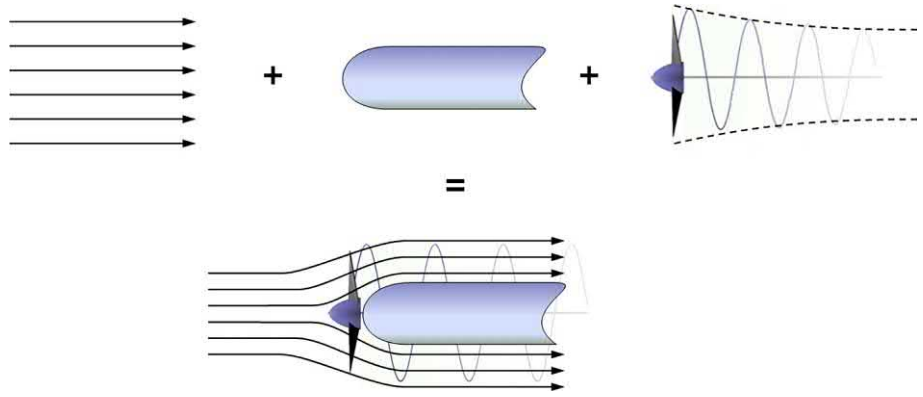


FIGURE 15-23 The philosophy of modeling blockage effects. *Based on Egolf, T. A., Anderson, O.L., Edwards, D.E., Landgre, A.J., An Analysis for High Speed Propeller-Nacelle Aerodynamic Performance Prediction, NASA CR-4199, 1988.*

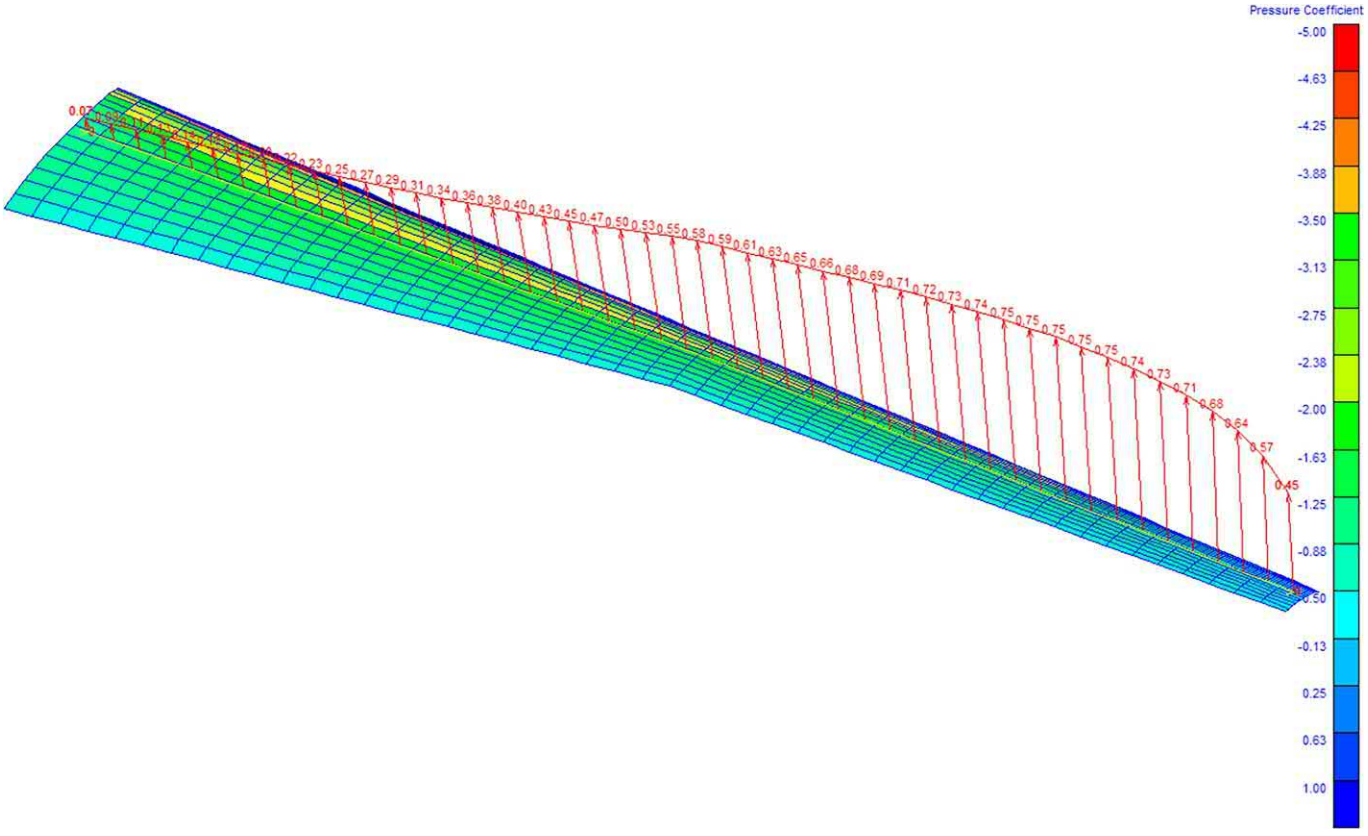


FIGURE 15-24 Section lift coefficients for a propeller blade of a small wind turbine, showing reduction in lift coefficient near the root (left) and the tip (right).

The so-called *Prandtl's Tip and Hub Loss Correction* is presented in Section 15.6.4, where it is used to correct analysis made by the *Blade Element Method*.

15.2.8 Effects of High Tip Speed

The primary effect of a high tip speed is the formation of shock waves. It reduces propeller efficiency, increases torque (requires more power to turn it), and increases the noise emitted by the propeller. The pitch, thickness, and curvature of the blade airfoil are important contributors. These effects are usually avoided by rotational speed in the $M \approx 0.6$ range for wooden propellers and in the $M \approx 0.75$–0.8 range for metal and composite propellers.

15.2.9 Skewed Wake Effects—$A \cdot q$ Loads

The term *skewed wake* refers to the streamtube through the propeller disc is at an angle to its plane (see Figure 15-25). This happens during climbs or when the

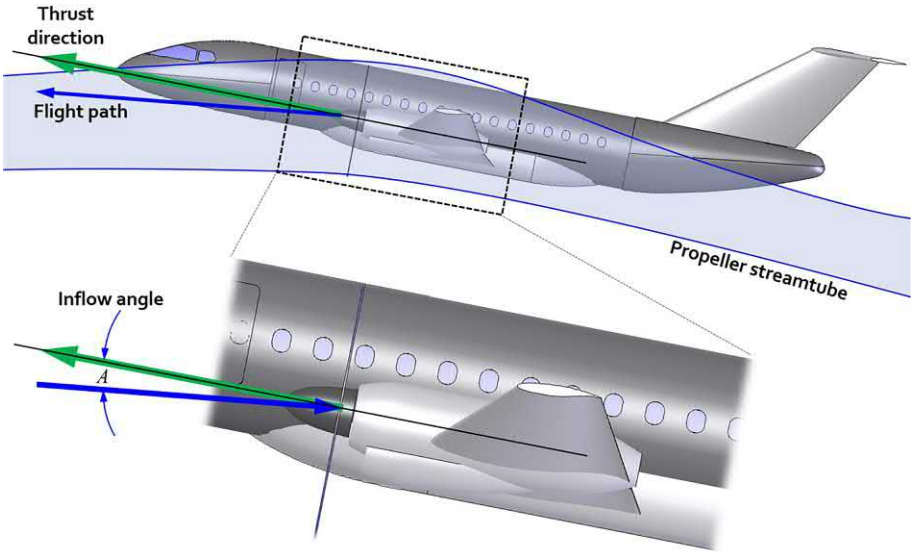


FIGURE 15-25 A flight condition (climb) that generates a skewed wake (upper image) and the definition of the inflow angle A (lower image).

aircraft yaws. The skewed wake affects noise and propeller loads and is important for turboprops. Let us consider these effects in some detail.

Figure 15-25 shows a turboprop with the propeller thrustline at an angle to the flight path. Using terminology familiar to propeller manufacturers, the streamtube is at an angle A to the thrustline. As the propeller rotates with angular speed Ω, each down-rotating blade encounters an increase in AOA and each up-rotating blade decrease, as explained earlier. This subjects each blade to cyclic loading at the frequency described by Equation (15-9). This is commonly referred to as *1P cyclic loading*, where 1P stands for *once per revolution*. A byproduct of this is increased noise. This is a main source of loads for a turboprop. These loads are directly proportional to the product of the angle A and the dynamic pressure of the free-stream, q. Thus, they are commonly called "$A \cdot q$" loads. For pistonprops, a comparable propeller load is the sudden acceleration caused by the shock of the cylinders firing and the subsequent torsional deformation of the crankshaft. These loads are much greater than the $A \cdot q$ loads.

The $A \cdot q$ loads are critical for turboprops and electric aircraft. The designer of turboprop and electric aircraft should evaluate the AOA of the vehicle at a representative cruise condition and, then, consider if aligning the thrustline so it is mostly parallel to the flight path is viable. This cannot be achieved over the entire airspeed range, so propeller manufacturers recommend a "balanced" approach. Thus, the product $A \cdot q$ is determined at the maximum and minimum operating weights (see Figure 15-26). Then, the thrustline is aligned for zero inflow angle using the average. Of course, low load is desirable: the less the load, the lighter the propeller. Failure to follow these guidelines may prevent compliance with 14 CFR §23.907 *Propeller vibration and fatigue*.

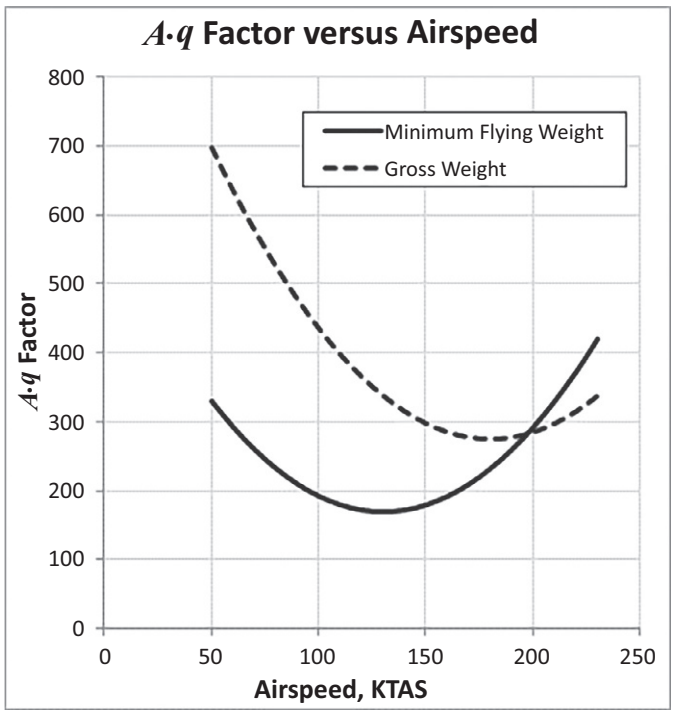


FIGURE 15-26 Skewed wakes at extreme weights reveal two distinct minimums—a compromise between the two should be made.

15.2.10 Propeller Noise

Noise associated with the operation of aircraft remains a topic of debate in society. Regardless of which side one takes, it is undeniable the debate has led to substantial reduction in aircraft noise over the decades, specifically for jet aircraft. Noise pollution due to propellers has also been lowered, although many high-performance piston aircraft still emit objectionable noise pollution. Propeller



FIGURE 15-27 A modern three-bladed scimitar shaped propeller. *Courtesy of Hartzell Propeller Inc.*

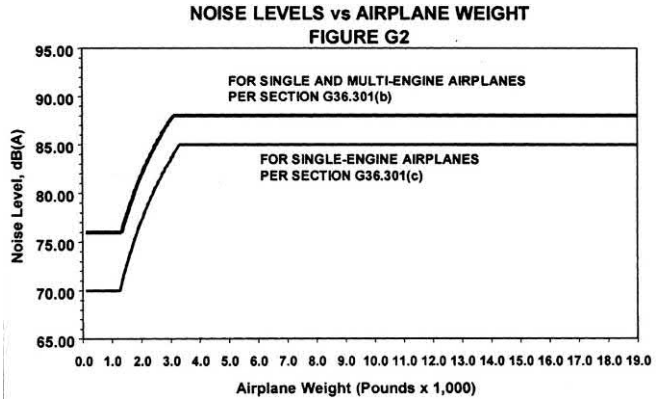


FIGURE 15-28 A graph from www.faa.gov showing the current noise level limitations for propeller aircraft (G36.301 Aircraft noise limits).

noise should be considered from the start of the design project. Once a propeller is selected, it is best to work with the manufacturer and use their expertise to design a quiet and efficient prop. Modern propeller blades feature airfoils of lower thickness-to-chord ratio and swept planform geometry near the tip. An example of such a design is the Scimitar-shaped propeller in Figure 15-27. Such blades are intended to reduce the magnitude of low-pressure peaks and delay the onset of normal shocks that increases the noise. Additionally, the trend has been toward an increased number of blades, as this allows the propeller diameter to be reduced, in turn, reducing the tip airspeed. Engine operating RPMs have also been reduced.

Propeller aircraft must comply with the requirements of 14 CFR Part 36 Appendix G [11]. Among several stipulations, this requires the aircraft to fly over a microphone placed some 8200 ft (2500 m) from brake release. The measured noise level must not exceed that shown in Figure 15-28.

The aircraft designer should not forget that two aircraft that use the exact same engine and propeller combination can have two different noise levels. All other things being equal, the aircraft with the larger wing area and wing span will lift off using a shorter ground run, it will climb faster at a lower airspeed (V_Y, see Chapter 19), resulting in a steeper climb gradient. In short, it will climb to a higher altitude in the given distance of 8200 ft, resulting in a lower measured noise level. If there is a concern the aircraft may not or marginally comply with 14 CFR Part 36, the designer should perform a sensitivity study of wing geometry and noise levels.

Estimation of Propeller Noise

Ref. [12] provides a simple method to theoretically predict the near-field and far-field noise of propellers. The method requires the designer to provide the tip Mach number, engine power, propeller diameter, number of blades, distance and angular position of the observer, and other related data. The reference has the designer estimate dependent parameters from numerous graphs, but the author has condensed most of them into convenient expressions to permit a rudimentary propeller noise evaluation using a spreadsheet. Note that when the equations and the graphs disagree, the graphs rule. Only the far-field estimation method is presented here.

STEP 1: Determine Tip Mach Number (M_{tip})

Use Equation (15-12) to calculate V_{tip} and (15-13) to calculate M_{tip}.

STEP 2: Determine Partial Level 1 (FL_1)

This is a partial level loudness emitted by the propeller. It depends on power input (P_{HP} in HP) and the Mach number of the tip. This is provided by several curves of Figure 3 in ref. [12]. These data have been compacted into the following equation:

$$FL_1 = 17.237 + 36.886 M_{tip} + 6.88 \ln(P_{HP}) \quad [\text{dB}] \qquad (15\text{-}17)$$

STEP 3: Determine Partial Level 2 (FL_2)

The loudness of Step 2 must be corrected for propeller diameter (D_p) and number of blades (N_B). This is provided by several curves of Figure 4 in ref. [12]. These have been condensed into the following equation:

$$FL_2 = 32.551 - 8.312 \ln(N_B) - 8.642 \ln(D_p) \qquad [\text{dB}] \qquad (15\text{-}18)$$

STEP 4: Determine Partial Level 3 (FL_3)

The loudness of Step 2 must also be corrected for atmospheric absorption and spherical spread of sound away from the source—the propeller. The following equation yields the curves of Figure 5 in ref. [12], where x_{ft} is distance from the source in ft. It is typically

$$FL_3 = \begin{cases} 16.29 - 0.5 \ln\left(x_{ft}\right) & \text{if } x_{ft} < 100 \text{ ft} \\ 56 - 9.1202 \ln\left(x_{ft}\right) & \text{if } x_{ft} \geq 100 \text{ ft} \end{cases} \quad [\text{dB}] \quad (15\text{-}19)$$

STEP 5: Determine Directivity Correction (DI)

The loudness must be corrected for directivity, i.e., on the angular position (θ) of the observer with respect to the propeller. The propeller axis in the forward direction, for which θ = 0°. The pattern is symmetric about the propeller axis, so *DI* for 100° is the same as for 260°. The following equation yields the curve of Figure 6 in ref. [12]:

$$DI = 4.4464 \times 10^{-11}\theta^6 - 2.1049 \times 10^{-8}\theta^5 + 3.56 \times 10^{-6}\theta^4 + \\ - 0.00025750\theta^3 + 0.006073\theta^2 + 0.15363\theta - 8.1226 \quad [\text{dB}] \quad (15\text{-}20)$$

STEP 6: Number of Propellers Correction (NC)

For single propeller $NC = 0$, for two $NC = 3$, for three $NC = 5$, and for four $NC = 6$.

STEP 7: Determine Overall Sound Pressure Level (SPL)

The *overall sound pressure level* (*SPL*) is the sum of the values obtained in Steps 2 through 6.

$$SPL = FL_1 + FL_2 + FL_3 + DI + NC \quad [\text{dB}] \quad (15\text{-}21)$$

STEP 8: Other Determinations

The method enables the determination of *perceived noise level* (*PNL*) for two- to eight-bladed propellers. This is done by adding corrections from Figures 7 through 10 in ref. [12]. The curves, too, have been digitized below. However, since the original curves are nonlinear, these equations will only give ballpark values. For greater accuracy, refer to ref. [12].

$$\begin{aligned} PNL_{2-blades} &= 5.574 - 3.123s - 4.649t - 3.473st \quad [\text{dB}] \\ PNL_{3-blades} &= 7.168 - 2.511s - 3.402t - 1.720st \quad [\text{dB}] \\ PNL_{4-blades} &= 8.114 - 2.009s - 3.125t - 1.928st \quad [\text{dB}] \\ PNL_{6/8-blades} &= 9.048 - 3.349s - 3.335t + 0.212st \quad [\text{dB}] \end{aligned} \quad (15\text{-}22)$$

where $s = 0.2D_P - 1$ and $t = 2.25 - 2.5M_{tip}$. Thus, *PNL* is given by

$$PNL = SPL + PNL_{N-blades} \quad [\text{dB}] \quad (15\text{-}23)$$

Once corrected, the *PNL* (in dB) can be converted to A-weighted *PNL* (dBA) by subtracting 14 dB from the *SPL*. That value must be compared to Figure 15-28. To convert to EPNdB, subtract 4 dB from the *PNL* for a T-O case and 2 dB for an approach case.

EXAMPLE 15-1

Determine if the noise emitted by a Cessna 172 meets the requirements of 14 CFR Part 36 in a 1000 ft flyover test. It is a single-engine aircraft powered by a 180 BHP Lycoming IO-360 that swings a two-bladed, 76-in diameter propeller. The airplane is operating at 120 KTAS on a standard day with the engine running at 2600 RPM. It weighs 2550 lb_f.

SOLUTION:

STEP 1: Tip speed is calculated from Equation (15-12), where $n = 2600/60 = 43.33$ rps and $D_P = 76/12 = 6.333$ ft

$$V_{tip} = \sqrt{V_\infty^2 + \left(\pi \cdot n \cdot D_p\right)^2} \\ = \sqrt{(120 \times 1.688)^2 + (\pi(43.33)(6.333))^2} = 885.7 \text{ ft/s}$$

The tip Mach number is calculated from Equation (15-13)

$$M_{tip} \approx \frac{V_{tip}}{1116\sqrt{1 - 0.0000068753H}} \\ = \frac{885.7}{1116\sqrt{1 - 0.0000068756(1000)}} = 0.7964$$

STEP 2: Calculate FL_1 using Equation (15-17) with $P_{HP} = 160$ BHP.

$$FL_1 = 17.237 + 36.886M_{tip} + 6.88 \ln(P_{HP}) \\ = 17.237 + 36.886(0.7964) + 6.88 \ln(160) = 81.5 \text{ [dB]}$$

STEP 3: Calculate FL_2 using Equation (15-18)

$$FL_2 = 32.551 - 8.312 \ln(N_B) - 8.642 \ln\left(D_p\right) \\ = 32.551 - 8.312 \ln(2) - 8.642 \ln(6.333) = 10.8 \text{ [dB]}$$

STEP 4: Calculate FL_3 using Equation (15-19)

$$FL_3 = 56 - 9.1202 \ln\left(x_{ft}\right) = 56 - 9.1202 \ln(1000) \\ = -7.0 \text{ [dB]}$$

STEP 5: Calculate *DI* using Equation (15-20) assuming θ = 90°.

$$DI = 4.4464 \times 10^{-11}\theta^6 - 2.1049 \times 10^{-8}\theta^5 + 3.56 \times 10^{-6}\theta^4 + \\ - 0.00025750\theta^3 + 0.006073\theta^2 + 0.15363\theta - 8.1226 \approx 0 \text{ [dB]}$$

STEP 6: One propeller ⇒ $NC = 0$.

STEP 7: Calculate *SPL* using Equation (15-21).

$$SPL = FL_1 + FL_2 + FL_3 + DI + NC = 81.5 + 10.8 - 7.0 + 0 + 0 \\ = 85.5 \text{ [dB]}$$

STEP 8: Calculate *PNL* using Equations (15-22) and (15-23):

$$s = 0.2D_p - 1 = 0.2(6.333) - 1 = 0.2667$$

$$t = 2.25 - 2.5M_{tip} = 2.25 - 2.5(0.7964) = 0.2591$$

$$PNL_{2-blades} = 5.574 - 3.123s - 4.649t - 3.473st = 3.3 \text{ [dB]}$$

$$PNL = SPL + PNL_{N-blades} = 85.5 + 3.3 = 88.8 \text{ [dB]}$$

Next, convert *PNL* (in dB) to A-weighted *PNL* (in dBA):

$$PNL_A = PNL - 14 = 88.8 - 14 = 74.8 \text{ [dBA]}$$

Using the weight of 2550 lb_f with Figure 15-28, the noise limit per G36.301(c) is near 81 dBA. Thus, we conclude that at this flight condition, the C-172 complies with G36.301(c).

15.3 PROPERTIES AND SELECTION OF THE PROPELLER

This section provides advice for those that are selecting a propeller for their aircraft. Managers of serious design projects (i.e., projects involving aircraft that will actually be built) should contact propeller manufacturers early to help with the selection. This requires the designer to provide the propeller manufacturer with detailed information about the new (or modified) aircraft. This information is used to select an existing design, or in some cases, support the design of a new propeller.

15.3.1 Tips for Selecting a Suitable Propeller

Although the aircraft designer should benefit from the experience of the propeller manufacturer, he should also be armed with several parameters. Among those are:

(1) An estimate of the propeller diameter (see Section 15.3.2).
(2) An estimate of the propeller pitch (see Section 15.3.3).
(3) An estimate of required propeller efficiency (see Section 15.3.4).
(4) The airplane's target performance. Requirements for take-off and climb performance, mission cruising speed and altitude strongly impacts the propeller selection. Do these call for a constant-speed propeller, or will a fixed-pitch design do? Constant-speed propellers are considered for engine power greater than 180 to 200 BHP and cruising speeds above 130 to 140 KTAS.
(5) Engine properties, such as BHP and operational RPM, are a must. The engine installation may cause detrimental interferences between components of the airplane and the propeller blades (e.g., torsional vibration). The nacelle shape influences the installation as well. It may require a hub extension to help with an aerodynamically "friendly" external geometry. Is it a single- or a multiengine aircraft? Shall it rotate clockwise or counterclockwise? It is a tractor or a pusher? Furthermore, several systems are required for some constant-speed propellers. For instance, a de-ice system for flight into known icing, a propeller pitch control, and a gear-reduction drive. Besides concerns for cost, weight, noise, and efficiency, also consider the following:

- Tip (refers to rotational and not helical) speed should be as high as possible, but there is an upper limit. Too high a tip speed increases noise and reduces efficiency (via shock formation).
- Rotational tip speeds for wooden propellers[9] are in the $M \approx 0.6$ range.
- Rotational tip speeds for metal propellers[10] are in the $M \approx 0.75$ to 0.8 range.
- Rotational tip speeds for advance composite[11] propellers are in the $M \approx 0.75$ to 0.8 range.
- If the engine RPM is too high a gear-reduction drive is required to slow it down.
- High rotational speed requires fewer blades or smaller blade area to generate thrust.
- High-powered engines, whose rotational rate limits the propeller radius, need more blades to help convert engine power into thrust.
- Too large a diameter may result in high tip speeds and noise. It can also cause ground proximity problems.
- Weight—a 3-bladed prop can be of a smaller diameter, but three blades weigh more than two blades.

15.3.2 Rapid Estimation of Required Prop Diameter

This section presents a couple of methods to rapid estimate propeller diameter. The diameter is needed to estimate thrust, propeller noise, and evaluating geometric constraints, such as the likelihood of ground-strike. Ref. [6] presents a method to calculate the diameter of wooden propellers in inches, based on the intended cruising speed in KTAS, engine power, and RPM.

Two-bladed wooden propeller:

$$D_p = 10000 \cdot \sqrt[4]{\frac{P_{BHP}}{53.5 \times RPM^2 \times V_{TAS}}} \tag{15-24}$$

Three-bladed wooden propeller:

$$D_p = 10000 \cdot \sqrt[4]{\frac{P_{BHP}}{75.8 \times RPM^2 \times V_{TAS}}} \tag{15-25}$$

Four-bladed wooden propeller:

$$D_p = 10000 \cdot \sqrt[4]{\frac{P_{BHP}}{111 \times RPM^2 \times V_{TAS}}} \tag{15-26}$$

[9] Refers to propellers whose structural core is wood. Propellers with a wooden structural core, covered by a thin, protective fiberglass coating and sheet metal leading edges (sometimes marketed as "composite") are is still wood and, thus, should not be misclassified as an advanced composite propeller. These wood-composite propellers have thicker tips and trailing edges just like the classic varnished wood blades.

[10] Refers to traditional forged-aluminum blades.

[11] Refers to typical carbon/epoxy blades with a metal leading edge erosion shield.

DERIVATION OF EQUATION (15-25)

The source document does not derive Equations (15-24) or (15-26), but states that a three-bladed propeller can be obtained by interpolating between the two expressions. This leads to the following closed form equation for a three-bladed propeller:

$$D_p = \frac{10000 \cdot \sqrt[4]{\frac{P_{BHP}}{53.5 \times RPM^2 \times V_{TAS}}} + 10000 \cdot \sqrt[4]{\frac{P_{BHP}}{111 \times RPM^2 \times V_{TAS}}}}{2}$$

Manipulating algebraically leads to:

$$\begin{aligned} D_p &= 10000 \cdot \left[\left(\frac{P_{BHP}}{53.5 \times RPM^2 \times V_{TAS} \times 16} \right)^{0.25} + \left(\frac{P_{BHP}}{111 \times RPM^2 \times V_{TAS} \times 16} \right)^{0.25} \right] \\ &= 10000 \cdot \frac{(P_{BHP})^{0.25}}{(RPM^2 \times V_{TAS})^{0.25}} \left[\frac{1}{75.8^{0.25}} \right] \\ &= 10000 \cdot \sqrt[4]{\frac{P_{BHP}}{75.8 \times RPM^2 \times V_{TAS}}} \end{aligned}$$

EXAMPLE 15-2

The Aerotrek A240 Light-Sport Aircraft is equipped with a 62.2-in diameter three-bladed composite propeller, driven by an 80 BHP Rotax 912UL engine. It can fly at 104 KTAS at 75% power. Calculate the recommended diameter of two, three, and four-bladed wooden propellers for this airplane, intended to rotate at 2300 RPM, and compare to the actual propeller diameter. What are the corresponding tip speeds?

SOLUTION:

Two-bladed propeller:

$$D_p = 10000 \cdot \sqrt[4]{\frac{P_{BHP}}{53.5 \times RPM^2 \times V_{TAS}}}$$

$$= 10000 \cdot \sqrt[4]{\frac{0.75 \times 80}{53.5 \times 2300^2 \times 104}} = 67.2 \text{ inches}$$

Rotation speed in terms of radians per second:

$$\Omega = 2\pi \left(\frac{RPM}{60} \right) = 2\pi \left(\frac{2300}{60} \right) = 240.9 \text{ rad/s}$$

Tip speed: $V_{tip} = \Omega \times R_P = 240.9 \times \frac{67.2/12}{2} = 675$ ft/s.

Three-bladed propeller:

$$D_p = 10000 \cdot \sqrt[4]{\frac{0.75 \times 80}{75.8 \times 2300^2 \times 104}} = 61.6 \text{ inches.}$$

Tip speed:

$$V_{tip} = \Omega \times R_P = 240.9 \times \frac{61.6/12}{2} = 618 \text{ ft/s.}$$

Four-bladed propeller:

$$D_p = 10000 \cdot \sqrt[4]{\frac{0.75 \times 80}{111 \times 2300^2 \times 104}} = 56.0 \text{ inches.}$$

Tip speed:

$$V_{tip} = \Omega \times R_P = 240.9 \times \frac{56.0/12}{2} = 562 \text{ ft/s.}$$

Note that the result for the three-bladed propeller can also be obtained from $(67.2 + 56.0)/2 = 61.6$ in.

Ref. [6] provides the following expressions to estimate a suitable diameter of metal propellers:

Two-bladed metal propellers:

$$D_p = 22 \sqrt[4]{P_{BHP}} \tag{15-27}$$

Three-bladed metal propellers:

$$D_p = 18 \sqrt[4]{P_{BHP}} \tag{15-28}$$

Ref. [13] presents the following expression, independent of propeller material. It states these are modified from those of Stinton [6]. The corresponding propeller diameter in ft or meters depending on K_P:

Propeller diameter:

$$D_p = K_p \sqrt[4]{P_{BHP}} \tag{15-29}$$

where the factor K_p is obtained from Table 15-2:

15.3.3 Rapid Estimation of Expected Geometric Propeller Pitch

The selection of a propeller requires its diameter and pitch to be specified. While the designer should consult with a propeller manufacturer, it never hurts to have a "ballpark value" in mind. The following expression can be used for this purpose. It only applies to fixed-pitch propellers rotating at RPM at some desired cruising speed, denoted by V_{KTAS}.

$$P_G \approx 1251 \left(\frac{V_{KTAS}}{RPM} \right) \tag{15-30}$$

For a fixed-pitched propeller, a reasonable estimate for pitch can be picked from Table 15-3. Table 15-4 shows a comparison of Equation (15-30) to a selection of GA aircraft with fixed propellers. Note that the low value of P_G

TABLE 15-2 Factor K_p for typical propeller types.

Type of propeller	K_p for P in BHP and D_p in inches	K_p for P in kW and D_p in m
2-bladed	20.4	0.56
3-bladed	19.2	0.52
4- or more blades	18.0	0.49

TABLE 15-3 Propeller pitch table.

RPM	INTENDED CRUISING AIRSPEED in KTAS														
	50	60	70	80	90	100	110	120	130	140	150	160	170	180	190
2000	31	38	44	50	56	63	69	75	81	88	94	100	106	113	119
2100	30	36	42	48	54	60	66	72	77	83	89	95	101	107	113
2200	28	34	40	46	51	57	63	68	74	80	85	91	97	102	108
2300	27	33	38	44	49	54	60	65	71	76	82	87	92	98	103
2400	26	31	36	42	47	52	57	63	68	73	78	83	89	94	99
2500	25	30	35	40	45	50	55	60	65	70	75	80	85	90	95
2600	24	29	34	39	43	48	53	58	63	67	72	77	82	87	91
2700	23	28	32	37	42	46	51	**56**	60	65	70	74	79	83	88
2800	22	27	31	36	40	45	49	54	58	63	67	72	76	80	85
2900	22	26	30	35	39	43	47	52	56	60	65	69	73	78	82
3000	21	25	29	33	38	42	46	50	54	58	63	67	71	75	79
3100	20	24	28	32	36	40	44	48	52	57	61	65	69	73	77
3200	20	23	27	31	35	39	43	47	51	55	59	63	66	70	74
3300	19	23	27	30	34	38	42	46	49	53	57	61	64	68	72
3400	18	22	26	29	33	37	40	44	48	52	55	59	63	66	70
3500	18	21	25	29	32	36	39	43	46	50	54	57	61	64	68

TABLE 15-4 Comparing predicted and actual pitch for selected aircraft.

PROPELLER PITCH FOR SELECTED AIRCRAFT					P_G true		Predicted
Make	Model	D_p inch	RPM	V_{KTAS}	Low	Top	P_G
Beech	77	72	2700	105	46	62	49
Cessna	150	69	2600	99	42	58	48
	152	69	2550	107	42	58	53
	172	76	2500	119	52	68	60
Piper	PA-18	74	2500	100	42	58	50
	PA-28	74	2700	117	58		54
		76	2700	117	53		54
	PA-38	72	2600	108	46	62	52

represents a "climb" propeller, the high value represents a "cruise" propeller. The predicted P_G tends to fall between those extremes.

DERIVATION OF EQUATION (15-30)

Consider a propeller rotating at rate RPM or $RPS = RPM/60$ with a pitch distance, P_G. The propeller will move forward at the rate shown below:

$$V = (RPM/60)P_G$$

We prefer to use P_G in inches and V in KTAS (and call it V_{KTAS}) because these are commonly used in aviation (in the United States). If P_G is in inches, then V must be in inches/second. Additionally, noting that 1 KTAS = 1.688 ft/s, we introduce the following conversions:

$$V_{KTAS} = V\left(\frac{1\text{ ft}}{12\text{ in}}\right)\left(\frac{1\text{ KTAS}}{1.688\text{ ft/s}}\right) = \frac{V}{20.256\text{ in/s}\cdot\text{KTAS}}$$

$$= \frac{(RPM/60)P_G}{20.256\text{ in/s}\cdot\text{KTAS}} = \frac{RPM\times P_G}{1251.36\text{ in/KTAS}}$$

Solving for P_G leads to:

$$V_{KTAS} = \frac{RPM\times P_G}{1251.36} \Rightarrow P_G = 1251.36\left(\frac{V_{KTAS}}{RPM}\right).$$

15.3.4 Estimation of Required Propeller Efficiency

Besides knowing the target propeller diameter and pitch, it is also helpful to determine the propeller efficiency required to meet performance goals. This section shows two ways to accomplished this.

(1) Graphical Method

The first step is a trustworthy drag model. It is used to prepare an *airspeed-thrust* or *airspeed-power* map, shown in Figure 15-29 and 15-30, respectively. The maps plot propeller efficiency isopleths using thrust or power and coplots target performance characteristics. The map reveals the propeller efficiency required to achieve those characteristics. It is easier explained using an example, here for the SR22. First consider Figure 15-29. The isopleths are plotted using Equation (15-52) for constant values of η_p. The static thrust was calculated using Equation (15-80). Then the drag force is plotted based on the available drag model. The $C_{D_{\min}}$ for the SR22 is extracted using POH data in Example 16-24. It is then used to plot the drag force curve shown in the graph. The *ROC* curve is based on solving Equation (19-19) for thrust required to achieve a given *ROC*:

$$ROC = 60\left(\frac{TV_\infty - DV_\infty}{W}\right) \quad \Rightarrow \quad T_{REQ} = D + \frac{ROC}{60V_\infty}W \tag{15-31}$$

Here 1300 fpm was selected, as this is close to the capability of the SR22 at gross weight at S-L at $V = 91$ KCAS (recall that at S-L KCAS and KTAS are equal). Thus, it is possible to explore that capability of its propeller. The graph of Figure 15-29 shows that a prop efficiency of around 0.85 is required to achieve a top speed of 186 KTAS at S-L. Similarly, to achieve the *ROC* at V_Y, the prop efficiency must be at least 0.64. The information can be very useful to the propeller manufacturer when helping to select or design a practical propeller.

Figure 15-30 is identical to Figure 15-29, except it uses power rather than force to relay the same information. Therefore, the propeller efficiency isopleths are horizontal lines, which may make it a tad easier to evaluate the propeller efficiencies. Other than that, it gives the same answers as the Airspeed-Thrust map.

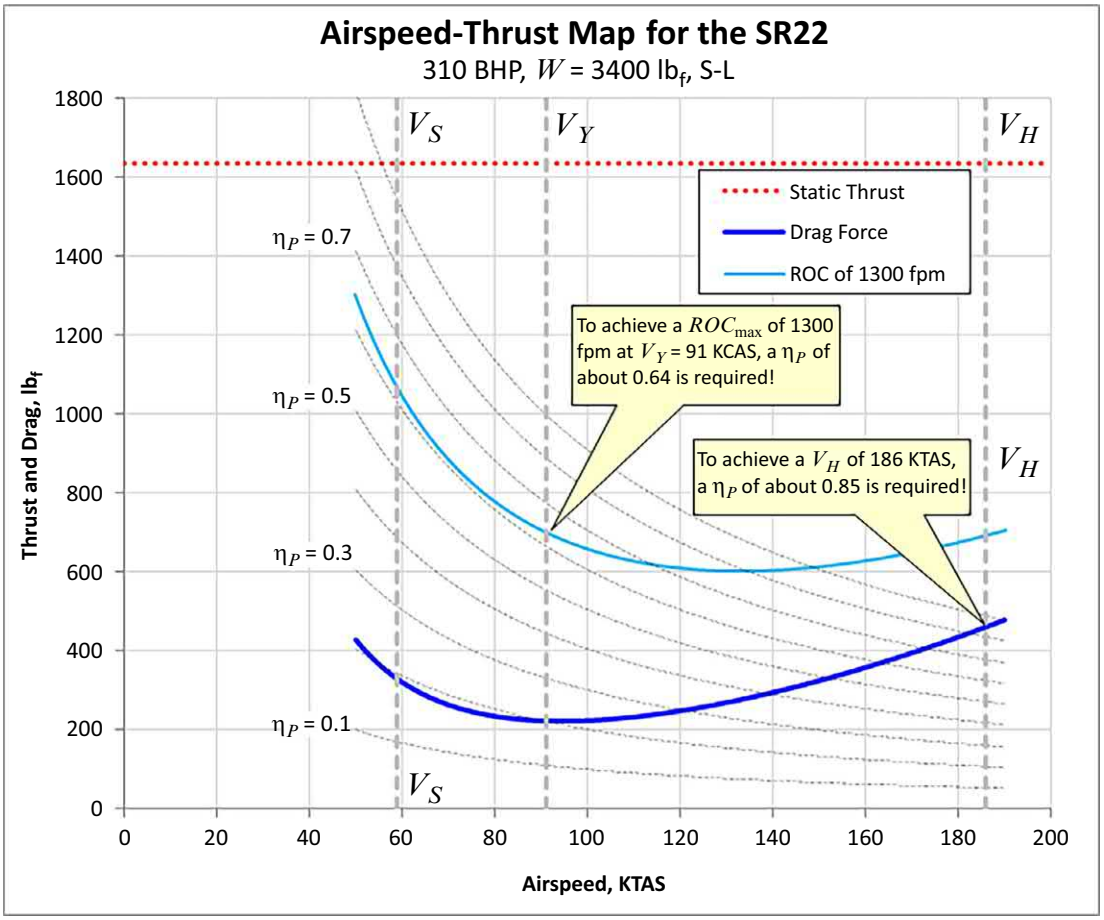


FIGURE 15-29 An Airspeed-Thrust map shows the propeller efficiency required to meet given performance goals in terms of thrust.

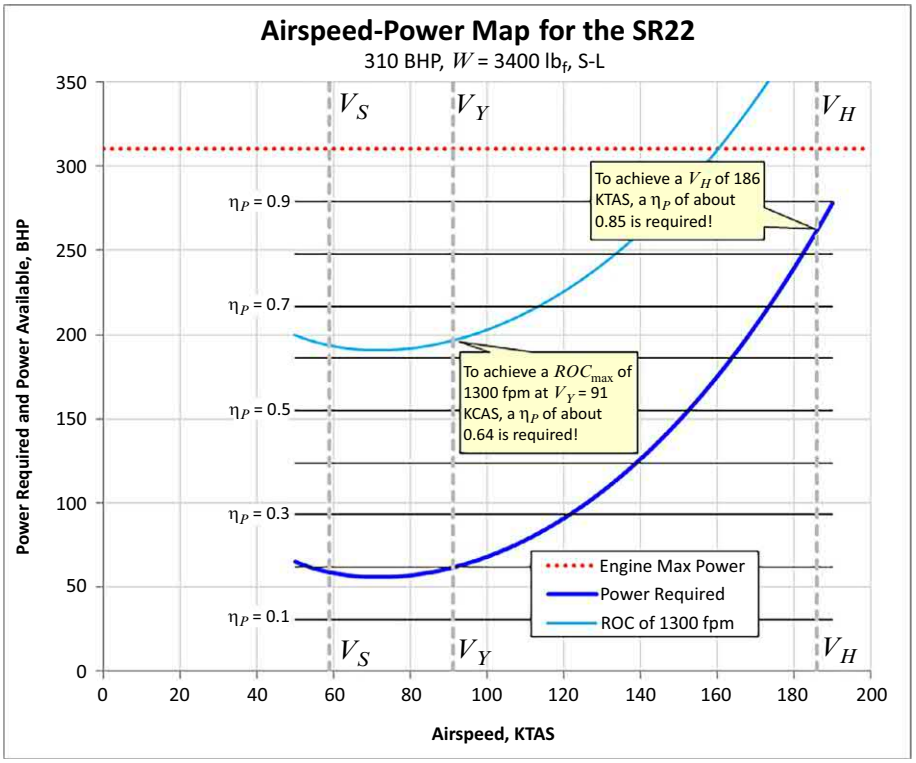


FIGURE 15-30 An Airspeed-Power map shows the propeller efficiency required to meet given performance goals in terms of power.

(2) Direct Estimation using Cruise Power and L/D

If we know the engine power and a target lift-to-drag ratio at a given cruise speed, we can extract a required propeller efficiency. This is done using the following expression:

$$T=\frac{P\cdot\eta_p}{V_\infty}\;\Leftrightarrow\;\frac{T}{W}=\frac{P\cdot\eta_p}{W\cdot V_\infty}\;\Rightarrow\;\eta_p=\left(\frac{T}{W}\right)\frac{W\cdot V_\infty}{P}=\frac{W\cdot V_\infty}{(L/D)P} \tag{15-32}$$

Consider a 1320 lb_f LSA operating at $V_C=110$ KTAS using 65 BHP engine power. If an expected cruise $L/D=10$ is achieved, the prop must have a propeller efficiency of at least 0.686.

15.3.5 Advance Ratio

The *Advance Ratio* is a measure of how far the propeller travels in unit time in terms of its diameter. The distance the prop travels per second is the vehicle's speed through the medium and is given by V_∞. For instance, if we measure an advance ratio of 0.5 for a 10 ft diameter propeller rotating at 600 RPM it means the propeller (i.e., the vehicle it is propelling) is moving at a forward speed of 50 ft/s.

$$J=\frac{V_\infty}{nD_p}=\frac{60\cdot V_\infty}{RPM\cdot D_p} \tag{15-33}$$

EXAMPLE 15-3

An aircraft equipped with a 76-in diameter propeller is operating at 185 KTAS with the propeller rotating at 2700 RPM. Determine the advance ratio.

SOLUTION:

Advance Ratio:

$$J=\frac{60\cdot V_\infty}{RPM\cdot D_p}=\frac{60\cdot(185\times1.688)}{2700\cdot(76/12)}=1.096.$$

15.3.6 Definition of Activity Factor

The *Activity Factor* (*AF*) is a measure of the power absorption of a propeller. It is a nuanced concept: two propeller blades of equal planform area but unequal *AF* have different characteristics. For instance, a propeller with a tip-chord wider than the hub-chord has higher *AF* than the opposite. It develops more thrust but rotating it requires more power. Small aircraft have an *AF* ranging from 80 to 115 per blade, while larger aircraft have an *AF* around 100 to 170. The *AF* is used as an identity for propeller efficiency maps prepared by propeller manufacturers. Such maps allow propeller efficiency to be read as a function of the advance ratio and power coefficient (see Section 15.3.7). The *AF* is defined as follows:

Blade Activity Factor:

$$AF = \frac{100\ 000}{16}\int_{0.15}^{1.0}\left(\frac{c}{D_P}\right)\left(\frac{r}{R_P}\right)^3 d\left(\frac{r}{R_P}\right) \tag{15-34}$$

Total Activity Factor:

$$AF_{TOT} = N_B \times AF \tag{15-35}$$

where R_P is blade radius, c is blade chord, and N_B is number of blades.

EXAMPLE 15-4

Estimate the AF of each blade of the airplane of Example 15-3, whose diameter is 76 in and chord is a constant 5 in.

SOLUTION:

Let $x = r/R_P$:

$$AF = \frac{100\ 000}{16}\int_{0.15}^{1.0}\left(\frac{c}{D_P}\right)\left(\frac{r}{R_P}\right)^3 d\left(\frac{r}{R_P}\right)$$

$$= \frac{100\ 000}{16}\left(\frac{5}{76}\right)\int_{0.15}^{1.0} x^3 dx = 411.2\left[\frac{x^4}{4}\right]_{0.15}^{1.0} = 102.7$$

EXAMPLE 15-5

Estimate the AF of a propeller blade whose chord is given by $c(r) = a_0 + a_1(r/R_P)$ and extends from $r = r_{hub}$ to R_P.

SOLUTION:

Let $x = r/R_P$:

$$AF = \frac{100\ 000}{16}\int_{0.15}^{1}\left(\frac{c}{D_P}\right)\left(\frac{r}{R_P}\right)^3 d\left(\frac{r}{R_P}\right)$$

$$= \frac{100\ 000}{16}\int_{0.15}^{1}\left(\frac{a_0 + a_1 x}{D_P}\right)(x)^3 dx$$

$$= \frac{100\ 000}{16D_P}\int_{0.15}^{1}\left(a_0 x^3 + a_1 x^4\right)dx$$

$$= \frac{100\ 000}{16D_P}\left[\frac{1}{4}a_0 x^4 + \frac{1}{5}a_1 x^5\right]_{0.15}^{1}$$

$$= \frac{100\ 000}{16D_P}\left[\frac{1}{4}a_0(1)^4 + \frac{1}{5}a_1(1)^5 - \left(\frac{1}{4}a_0(0.15)^4 + \frac{1}{5}a_1(0.15)^5\right)\right]$$

$$\cong \frac{100\ 000}{16D_P}\left[\frac{a_0}{4} + \frac{a_1}{5}\right]$$

15.3.7 Definition of Power and Thrust-Related Coefficients

The following coefficients describe the propeller thrust, torque, and required power.

Thrust coefficient:

$$C_T = \frac{T}{\rho n^2 D_P^4} = \frac{3600 \cdot T}{\rho\ RPM^2 D_P^4} \tag{15-36}$$

Torque coefficient:

$$C_Q = \frac{Q}{\rho n^2 D_P^5} = \frac{3600 \cdot Q}{\rho\ RPM^2\ D_P^5} = \frac{C_P}{2\pi} \tag{15-37}$$

Power coefficient:

$$C_P = \frac{P}{\rho n^3 D_P^5} = \frac{550 \times P_{BHP}}{\rho (RPM/60)^3 D_P^5} = \frac{118\ 800\ 000 \times P_{BHP}}{\rho\ RPM^3\ D_P^5} \tag{15-38}$$

Power and torque are related as shown below, obtained by combining Equations (15-38) and (15-37).

Power-Torque relation:

$$C_Q = \frac{Q}{\rho n^2 D_P^5} = \frac{C_P}{2\pi} = \frac{P/\rho n^3 D_P^5}{2\pi} \quad \Rightarrow \quad P = 2\pi n Q \tag{15-39}$$

where P is power, P_{BHP} is power in BHP, and Q is torque. Other variables have been defined in earlier sections. Note that the Greek letter τ is used for torque in Chapter 7, rather than Q. In Chapter 7, this was to avoid confusion with using Q for heat flow. Then, why not also use τ here? The answer: to adhere to convention in the literature.

Note there are two other kinds of thrust coefficients: (1) C_t, which is used in Seckel's normal force method presented in Section 24.2.11, and (2) T_C, which is used in Section 15.3.8.

Seckel's thrust coefficient [14]:

$$C_t = \frac{C_T}{J^2} = \frac{T}{\rho V_\infty^2 D_P^2} \tag{15-40}$$

Froude's thrust coefficient:

$$T_C = \frac{2T}{\rho V_\infty^2 A_2} = \frac{T}{qA_2} \tag{15-41}$$

EXAMPLE 15-6

Compute C_P and C_Q for the airplane in Example 15-3 for the same condition, if it is known its engine is generating 225 BHP.

SOLUTION:

Power coefficient:

$$C_P = \frac{118\ 800\ 000 \times P_{BHP}}{\rho \cdot RPM^3 \cdot D_P^5} = \frac{118\ 800\ 000 \times 225}{(0.002378)(2700)^3(76/12)^5} = 0.05604.$$

Torque coefficient:

$$C_Q = \frac{Q}{\rho n^2 D_P^5} = \frac{C_P}{2\pi} = \frac{0.05604}{2\pi} = 0.008919.$$

EXAMPLE 15-7

Estimate the required propeller diameter for a light airplane designed to operate around 120 KTAS, assuming:

EXAMPLE 15-7 (*cont'd*)

(a) A 2-bladed wooden prop, if the maximum expected engine power is 80 BHP and max engine *RPM* is 5800 RPM with a 2.27:1 gear reduction ratio.
(b) 3-bladed metal prop.
(c) Assume a max tip speed of $M=0.75$ at S-L.

SOLUTION:

(a) First determine *RPM* delivered to propeller:

$$RPM=\frac{RPM_{engine}}{GR}=\frac{5800}{2.27}=2555\text{ RPM}$$

Then, calculate the diameter of a two-bladed wooden propeller:

$$D_P=10000\cdot\sqrt[4]{\frac{P_{BHP}}{53.5\times RPM^2\times V_{TAS}}}$$

$$=10000\cdot\sqrt[4]{\frac{80}{53.5\times 2555^2\times 120}}=66\text{ inches}$$

(b) 3-bladed metal propeller:

$$D_P=18\sqrt[4]{P_{BHP}}=18\sqrt[4]{80}=54\text{ inches}$$

(c) Maintaining max tip speed of $M=0.75$:

$$M_{tip}=\frac{V_{tip}}{1116\sqrt{1-0.0000068753H}}<0.75\quad\Rightarrow\quad\frac{V_{tip}}{1116}<0.75$$

$$\Rightarrow\quad V_{tip}<0.75\times 1116=837\text{ ft/s}$$

Therefore, the maximum diameter can be determined as follows:

$$V_{tip}=\sqrt{V^2+\left(\frac{\pi\cdot RPM\cdot D_P}{60}\right)^2}<837\text{ ft/s}$$

$$\Rightarrow\quad D_P=\frac{60\sqrt{V_{tip}^2-V^2}}{\pi\cdot RPM}=\frac{60\sqrt{(837)^2-(120\times 1.688)^2}}{\pi\cdot 2555}$$

$$=6.07\text{ ft (73 inches)}$$

15.3.8 Propeller Efficiency

The power generated by an engine is not completely converted to a thrust force. Losses occur in the process due to an imperfect conversion process. This section treats the effectiveness of this process.

(1) Thrust-power

The product of thrust (T) and airspeed (V_∞) is called *thrust-power* (TV_∞). It facilitates an evaluation of how effectively mechanical power is converted to motion.

$$\text{Thrust Power}\equiv TV_\infty \tag{15-42}$$

(2) Propeller Efficiency

We define *propeller efficiency* as the ratio of thrust-power to engine power (P_{ENG}). It indicates how much of the engine power is converted into thrust-power.

$$\eta_p\equiv\frac{\text{Thrust Power}}{\text{Engine Power}}=\frac{TV_\infty}{P_{ENG}} \tag{15-43}$$

If an aircraft engine delivers 100 BHP (or 55,000 ft·lb$_f$/s) at some flight condition and its propeller is 80% efficient, then the thrust-power amounts to 80 BHP (or 44,000 ft·lb$_f$/s). The propeller efficiency is also presented as the product of *Froude efficiency* (η_i) and *viscous profile efficiency* (η_v), discussed later

$$\eta_p\equiv\eta_i\eta_v \tag{15-44}$$

Alternative forms of the propeller efficiency are given below:

$$\eta_p=\frac{TV_\infty}{P_{ENG}}=J\frac{C_T}{C_P}=\begin{cases}TV_\infty/1000P_{kW} & \text{SI}-\text{system}\\ TV_\infty/550P_{BHP} & \text{UK}-\text{system}\end{cases} \tag{15-45}$$

Realistic values of η_p range between $0<\eta_p<0.8$ for fixed-pitch propellers and $0<\eta_p<0.88$ for constant-speed propellers (e.g., see ref. [15]).

DERIVATION OF EQUATION (15-45)

Using the definitions of the power and thrust coefficients, we write:

$$P=\rho n^3D^5C_P\text{ and }T=\rho n^2D^4C_T$$

Inserting into Equation (15-22) and manipulating leads to Equation (15-23).

$$\eta_p=\frac{TV_\infty}{P}=\frac{\rho n^2D_p^4C_T\cdot V_\infty}{\rho n^3D_p^5C_P}=\frac{C_T\cdot V_\infty}{nD_pC_P}=\frac{V_\infty}{nD_p}\frac{C_T}{C_P}=J\frac{C_T}{C_P}$$

(3) Froude (or Ideal) Efficiency

Consider an aircraft flying at airspeed V_∞. The thrust, T, depends on the entry and exit speed of the flow through the propulsion device through *momentum flux*. The exit speed must be higher than the entry speed (otherwise thrust develops in the opposite direction—drag). Denote the entry and exit velocities as V_∞ and $V_\infty+w$, respectively. Their difference constitutes lost kinetic energy of the air flowing through the device. We write this as $\frac{1}{2}\,m[(V_\infty+w)-V_\infty]^2=\frac{1}{2}mw^2$ per unit time.[12] This change corresponds to the power of the force acting on the mass of air, times its speed, $T\cdot w$. The term $T\cdot w$ is the power consumed (or wasted) in driving the air

[12] Power is the rate of change of energy, i.e., $P=dE/dt$.

backwards. *Froude efficiency* (aka *ideal efficiency*) is defined as the ratio of the power required to propel a body (useful power) to the sum of this power and that which is lost in the conversion. It is expressed in the three common forms shown below:

$$\eta_i = \frac{\text{Thrust Power}}{\text{Thrust Power} + \text{Power lost}} = \frac{TV_\infty}{TV_\infty + Tw}$$

$$= \begin{cases} \dfrac{V_\infty}{V_\infty + w} \\ \dfrac{1}{(1 + w/V_\infty)} \\ \dfrac{2}{1 + \sqrt{1 + T_C}} \end{cases} \tag{15-46}$$

where T_C is *Froude's thrust coefficient* of Equation (15-41) and repeated below for convenience (where A_P is the propeller disc area):

$$T_C = \frac{2T}{\rho V_\infty^2 A_P} = \frac{T}{qA_P} \tag{15-41}$$

DERIVATION OF EQUATION (15-46)

Only the last expression warrants derivation. Introduce the fraction w/V_∞ into Equation (15-76) yields:

$$\frac{w}{V_\infty} = \frac{1}{2}\left[-1 + \sqrt{1 + \frac{2T}{\rho V_\infty^2 A_P}}\right] = \frac{1}{2}\left[-1 + \sqrt{1 + T_C}\right]$$

Substitute this into the center expression of Equation (15-56) and manipulate to get the bottom form.

(4) Viscous Efficiency

Comparing the propeller efficiency (η_p), for instance, obtained using the blade element theory of Section 15.6, to the Froude efficiency (η_i) reveals significant disparity. This is attributed to the inviscid nature of η_i. Real propellers are subject to viscous effects that result in nonlinear force coefficient. This effect is called *viscous profile efficiency* and is denoted by the term η_v. If we know η_p and η_i, it is obtained from

$$\eta_v = \frac{\eta_p}{\eta_i} \tag{15-47}$$

The range of value of η_v is typically $0 < \eta_v < 0.9$.

(5) Propeller Efficiency Map

Sometimes the propeller manufacturer presents the propeller efficiency in a map like that shown in Figure 15-31. In this format, the isopleths represent constant values of propeller efficiency. Such maps are defined in terms of a specific propeller blade activity factor and are read as follows. First, determine the advance ratio using Equation (15-33). Next, determine the power coefficient using Equation (15-38). Finally, use these to locate the propeller efficiency. The map needs to be digitized to be usable in a spreadsheet or other numerical methods. Ref. [16] presents a procedure for calculating propeller performance using maps of this nature for high-performance Hamilton-Standard propellers.

15.3.9 Effect of Number of Blades on Efficiency, Thrust, and Power

The number of blades is fundamental to how engine power is converted to thrust. Replacing propellers is a common occurrence in the aviation industry. Often, this involves a propeller with a different number of blades than the original one. An example is a four-bladed propeller replacing a two-bladed one. If the modification assumes identical blades, doubling the number of blades doubles the torque required to swing the new propeller at the same *RPM*. This is reflected in Figure 15-32,

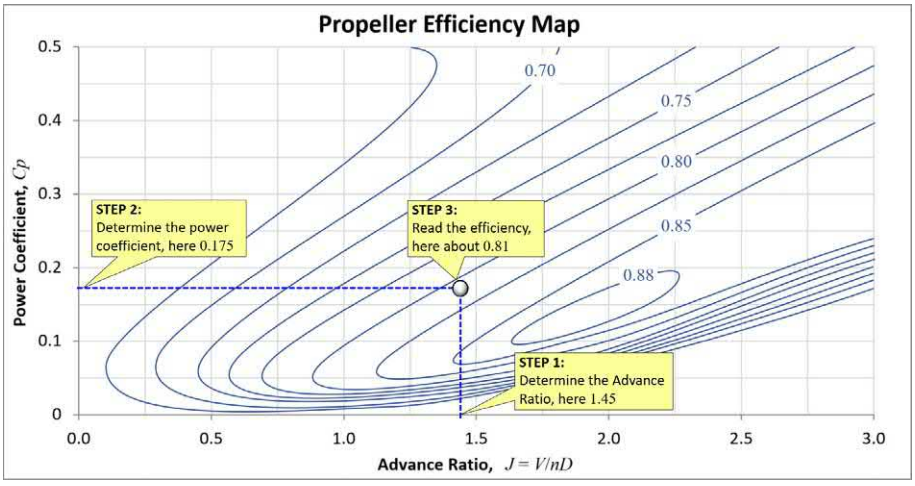


FIGURE 15-31 An idealized propeller efficiency map. Such maps are drawn for specific *AF*. Note the island where $\eta_p = 0.88$ is where the propeller should be sized to operate in cruise.

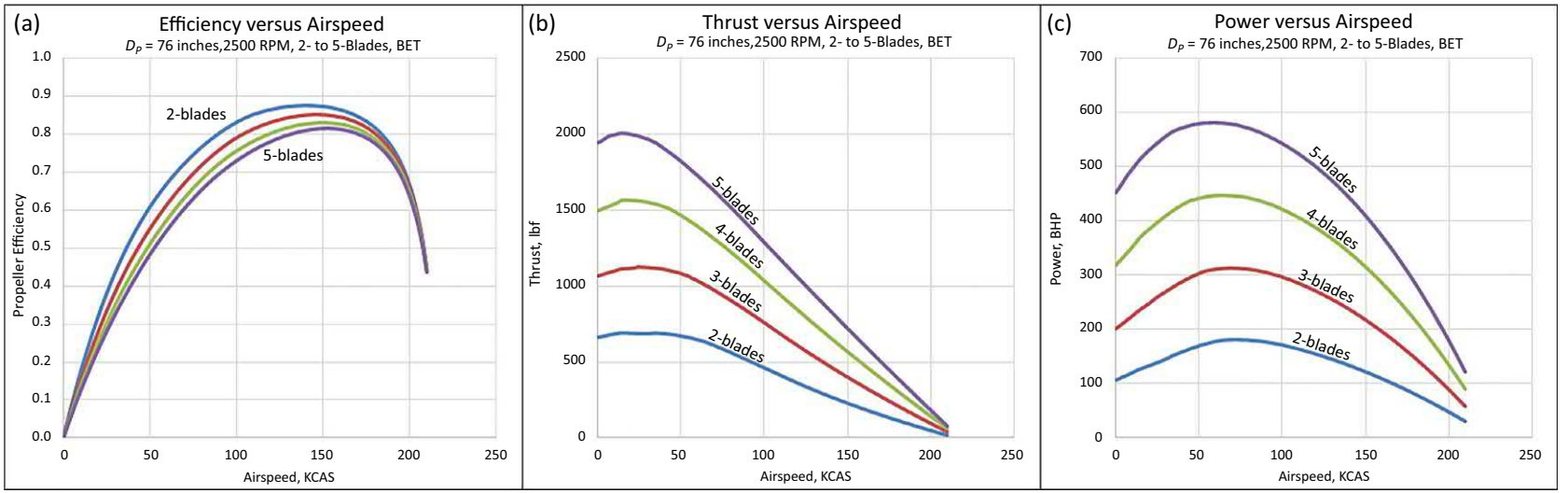


FIGURE 15-32 Effect of number of blades on a propeller's efficiency, thrust, and power.

developed using the formulation of Section 15.6. It assumes a Clark Y style airfoil for all blade stations. It shows how only changing the number of blades of a propeller affects efficiency, the thrust it delivers, and the power required to rotate it.

If the propeller is mounted on the same engine, the power available per blade reduces. The engine will no longer achieve the original maximum *RPM*. If it achieved, say, 2500 *RPM* with two blades, it may only achieve 2000 *RPM* with four at the same airspeed. Less thrust is generated, and the performance of the airplane suffers. If the same *RPM* is desired with the same engine, the torque per blade must be reduced. This can be achieved to a point by reducing the propeller diameter. Such a modification also reduces propeller noise, weight, and increases the ground clearance, an attractive option for a designer struggling with a potential prop strike scenario. Modifying the planform and airfoil may also be used. However, such changes are limited by physics and, eventually, call for an engine replacement. An example of a typical propeller replacement is revealed in the TCDS for the Cirrus SR22 [17]. It can feature a 78-in two-bladed or a 76-in three-bladed prop, a diameter ratio of 0.974. A comparison of the propeller blades reveals a dissimilar planform shape.

Figure 15-32(a) shows that increasing the number of blades reduces efficiency. This begs the question: Then why aren't all propellers two-bladed (or even one-bladed)? The answer is: Because their thrust is lower—much lower. The graph shows that efficiency drops by about 2% per blade—the maximum efficiency of the 5-bladed prop is about 93% of the 2-bladed one. However, its thrust is approximately 3× greater. It explains the use of multibladed propellers in many turboprops. Their power is converted to large thrust using multiple blades. These propellers can also be of smaller diameter, which reduces their noise.

15.3.10 Moment of Inertia of the Propeller

The propeller's moment of inertia is useful for stability and control. It can be estimated using the fundamental definition for moment of inertia of a body about a given axis:

$$I = \int_V \rho r^2 d\forall \tag{15-48}$$

where $\rho \cdot d\forall$ is the mass of an infinitesimal volume of the propeller blade, located a distance r from the reference axis (i.e., the axis of rotation of the propeller). While the propeller planform does not always yield an elegant closed form solution of Equation (15-48), a reasonably accurate estimate can be made by idealizing each blade as a thin rod of a uniform cross-sectional area A (see Figure 15-33). If the radius of the prop is R, its weight is W_{prop}, and the number of blades is N_B, then its moment of inertia can be estimated from:

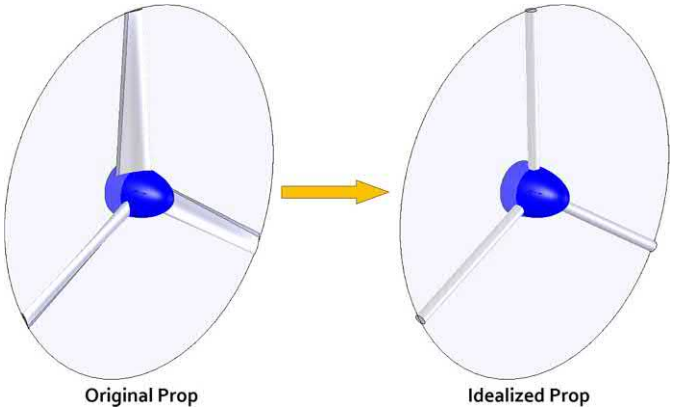


FIGURE 15-33 Idealizing the prop as constant diameter rods allows for a fast estimation of its moment of inertia.

$$I_{prop} = \frac{W_{prop} \cdot R_p^2}{3g} \tag{15-49}$$

where g is the acceleration due to gravity.

DERIVATION OF EQUATION (15-49)

The mass, m, of the propeller must be close to:

$$m = \rho_{prop} \cdot A \cdot R_P \cdot N_B \tag{i}$$

where ρ_{prop} is the density of the material used in the propeller blades. Its mass can also be computed if its weight, W_{prop}, is known, i.e., from $m = W_{prop}/g$. It follows the constant cross-sectional area is given by:

$$A = \frac{m}{\rho_{prop} \cdot R_P \cdot N_B} = \frac{W_{prop}}{\rho_{prop} \cdot g \cdot R_P \cdot N_B} \tag{ii}$$

Then, per Equation (15-48), we can compute the moment of inertia of a single rod extending from 0 to R_P:

$$I_{prop} = \int_V \rho r^2 dV = \int_0^{R_P} \rho_{prop} r^2 A dr$$

$$= \int_0^{R_P} \rho_{prop} r^2 \left(\frac{W_{prop}}{\rho_{prop} \cdot g \cdot R_P \cdot N_B} \right) dr = \int_0^R r^2 \left(\frac{W_{prop}}{g \cdot R_P \cdot N_B} \right) dr$$

$$= \left(\frac{W_B}{g \cdot R_P \cdot N_B} \right) \left[\frac{r^3}{3} \right]_0^R = \frac{W_{prop} R_P^3}{3g \cdot R_P \cdot N_B} = \frac{W_{prop} R_P^2}{3g \cdot N_B}$$

This result is for a single blade. If we have N_B blades, this simplifies to:

$$I_{prop} = N_B \times \frac{W_{prop} R_P^2}{3g \cdot N_B} = \frac{W_{prop} R_P^2}{3g}$$

EXAMPLE 15-8

To evaluate the result of Equation (15-49), let's compare it to the result using the standard expression for the moment of inertia of a thin rod. To do this, determine the moment of inertia of a thin rod of mass $m = 10\,\text{kg}$ and length (diameter) $D = 2R = 2\,\text{m}$ using each method.

SOLUTION:

Using the standard expression of moment of inertia, we find that:

$$I = ml^2/12 = (10)(2)^2/12 = 3.333\ \text{kg}\cdot\text{m}^2.$$

To prepare the method above, we note that the weight of the example rod is $10 \times 9.807 = 98.07\,\text{N}$ and its radius is 1 m. Therefore, using Equation (15-49), we get:

$$I_{prop} = W_{prop}\cdot R_P^2/3g = (98.07)\cdot(1)^2/3(9.807) = 3.333\ \text{kg}\cdot\text{m}^2$$

This is precisely what we would expect.

EXAMPLE 15-9

Compute the moment of inertia of a two-bladed aluminum propeller, whose weight is 40 lb_f and diameter is 80 in.

SOLUTION:

$$I_{prop} = \frac{W_{prop}\cdot R_P^2}{3g} = \frac{40\cdot(40/12)^2}{3(32.174)} = 4.605\ \text{slugs}\cdot\text{ft}^2$$

15.4 DETERMINATION OF PROPELLER THRUST

Analysis of performance, stability and control, and structures of propeller aircraft requires power to be converted into thrust. This section presents several methods for this purpose. Recall that power was defined in Table 7-1 as

$$\text{Power} = \text{Work}/\text{Time} \tag{15-50}$$

Since work is the application of a force over distance (*Force* × *Distance*), we get:

$$\text{Power} = \frac{\text{Work}}{\text{Time}} = \frac{\text{Force}\times\text{Distance}}{\text{Time}} = \text{Force}\times\frac{\text{Distance}}{\text{Time}} = \text{Force}\times\text{Speed}$$

For propellers, this corresponds to thrust and airspeed. The product is called *thrust-power*. This form relates the thrust required to produce a given airspeed to the power delivered to the propeller.

15.4.1 Converting Engine Power to Thrust

In the SI-system, if propeller efficiency (η_p), airspeed in m/s, and engine power in Watts (P_W) or kW (P_{kW}) are known at some condition, thrust can be determined using the following expression

$$T = \frac{\eta_p P}{V_\infty} = \frac{\eta_p \times P_W}{V_\infty} = \frac{\eta_p \times 1000 \times P_{kW}}{V_\infty} \tag{15-51}$$

In the UK-system, determining thrust requires airspeed in ft/s and engine power in horsepower (HP) (P_{HP}). This holds for brake- and shaft-horsepower:

$$T = \frac{\eta_p P}{V_\infty} = \frac{\eta_p \times 550 \times P_{HP}}{V_\infty} \tag{15-52}$$

The factor 550 converts the HP into $\text{ft}\cdot\text{lb}_\text{f}/\text{s}$. It is important to recognize that η_p is a function of airspeed, rotation rate, and propeller geometry (see Figure 15-12). This method cannot be applied to static thrust because $\eta_p = 0$. Static thrust of the propeller can be estimated using the methods of Section 15.4.2.

DERIVATION OF EQUATION (15-52)

Using propeller efficiency:

$$\eta_p = \frac{\text{Thrust Power}}{\text{Engine Power}} = \frac{TV_\infty}{P} = \frac{TV_\infty}{550\times P_{BHP}}.$$

Solving for T yields Equation (15-52).

EXAMPLE 15-10

An airplane is flying at 150 KTAS at a power setting that generates 150 BHP. If the propeller used on this airplane is known to be 80% effective, what is the thrust being generated?

SOLUTION:

$$T = \frac{\eta_p \times 550 \times P_{BHP}}{V_\infty} = \frac{(0.8)\times 550\times(150)}{(150\times 1.688)} = 260.7\ \text{lb}_\text{f}$$

15.4.2 Determination of Static Thrust

The following methods can be used to determine static thrust.

(1) Momentum Theory

See Equation (15-81).

(2) Diehl's Method

Ref. [18] gives the following expression to estimate static thrust in lb_f.

$$T_{STATIC} = 10000\left(11.22 - 5.7\frac{P_G}{D_P}\right)\frac{P_{BHP}}{RPM \times D_P} \quad (15\text{-}53)$$

All variables are defined elsewhere in this chapter. The ratio P_G/D_P is the *nominal pitch-diameter ratio* (also see Section 15.1.4). Typical values range between 0.3 and 1.6. The coefficient preceding $P_{BHP}/(RPM \times D_P)$ is a curve-fit to experimental data.

(3) NACA Method

Ref. [19] (authored by Diehl of ref. [18]) gives the following expression that returns static thrust in lb_f.

$$T_{STATIC} = \frac{K_{T_0} P_{BHP}}{RPM \times D_P} \quad (15\text{-}54)$$

where K_{T0} is the *static thrust coefficient*. The following expressions can be used to estimate it.

2-bladed wooden propellers [18]:

$$K_{T_0} = 10000\left(11.22 - 5.7\frac{P_G}{D_P}\right) \quad (15\text{-}55)$$

2-bladed metal propellers [18, 20]:

$$K_{T_0} = 145800 - 4220\beta_G \quad (15\text{-}56)$$

2-bladed metal propellers [18, 21]:

$$K_{T_0} = 42568 + 15006\beta_G - 1318.9\beta_G^2 + 37.212\beta_G^3 - 0.3485\beta_G^4 \quad (15\text{-}57)$$

3-bladed metal propellers [18, 21]:

$$K_{T_0} = 44093 + 11334\beta_G - 953.77\beta_G^2 + 25.052\beta_G^3 - 0.2146\beta_G^4 \quad (15\text{-}58)$$

4-bladed metal propellers [18, 21]:

$$K_{T_0} = 64139 + 3796.1\beta_G - 318.6\beta_G^2 + 5.0766\beta_G^3 \quad (15\text{-}59)$$

where D_P is in ft and β_G is the geometric pitch angle in degrees at the $0.75R_P$ station. Equation (15-56) is the author's curve-fit to Table II of ref. [18]. Equations (15-57) through (15-59) are the author's curve-fits to Figure 3 of ref. [18].

15.4.3 Initial Thrust Model for a Fixed-Pitch Propeller

During the conceptual design phase, the designer usually has limited details of the powerplant and none regarding the geometry of the propeller. This presents a challenge for performance analyses. The *quadratic interpolation method*, presented below, is one solution to this predicament. It assumes it is possible to approximate thrust over the propeller's operational range using a quadratic polynomial of the form $T = AV^2 + BV + C$.

The method is intended for fixed-pitch propellers only. It is based on the following premise: During the design process, the designer contacts a propeller manufacturer to order a propeller. The propeller manufacturer will request performance targets to allow a suitable propeller to be selected or designed. The performance targets include operational points such as expected best rate-of-climb airspeed (V_y) and cruising speed (V_c). The propeller manufacturer then delivers a propeller that is designed to hit optimum efficiency at these airspeeds. For a fixed-pitch propeller, this usually means propeller efficiency (η_p) near 0.60 to 0.65 for V_y and 0.75 to 0.80 for V_c. We will take advantage of this knowledge in the application of the method.

First, we need an estimate of (1) static thrust (T_{STATIC}), (2) airspeed of maximum propeller efficiency (V_{opt}), and (3) its expected maximum value (η_{opt}). Static thrust at a specific power setting can be estimated using the methods of Section 15.4.2 (e.g., using Equation (15-81)). The target airspeed for a climb-prop should be airspeed somewhere between the airspeed for best rate-of-climb and cruising speed. The target airspeed for a cruise-prop should be the intended cruising speed. The expected value for η_{opt} in both cases should be 0.75. With these parameters specified, the thrust as a function of airspeed is determined using the expression below:

$$T(V_\infty) = AV_\infty^2 + BV_\infty + T_{STATIC} \quad (15\text{-}60)$$

where

$$A = \left(T_{STATIC} - 2T_{opt}\right)/V_{opt}^2 \quad (15\text{-}61)$$

$$B = \left(3T_{opt} - 2T_{STATIC}\right)/V_{opt} \quad (15\text{-}62)$$

$$T_{opt} = \eta_{opt} 550 P_{HP}/V_{opt} \quad (15\text{-}63)$$

Effect of Power and Altitude

The propeller blade is largely a rotating wing that achieves its maximum efficiency (η_{opt}) at a specific combination of helix angle (ϕ) and induced speed (w). Consider an experiment in which we maintain a fixed RPM while varying airspeed (V_∞). Assume we measure engine power required to maintain that RPM and the resulting thrust (T). Eventually, we will find an airspeed that yields a maximum value of the ratio thrust-power (TV_∞) by engine power used (P_{ENG}). This is where maximum propeller efficiency (η_{opt}) occurs at that RPM (through Ω_{opt}). The airspeed is denoted as V_{opt}. If we know the values of V_{opt} and Ω_{opt}, we can calculate the helix angle (ϕ_{opt}) being developed. This is accomplished using Equation (15-64). Having computed ϕ_{opt} for one combination of V_∞ and Ω, we can determine V_{opt} associated with any Ω for other combinations using Equation (15-65). Thus, we can modify the thrust spline for flight conditions at other RPMs. Furthermore, since the spline depends on static thrust, it is possible to introduce altitude effects as well. This is accomplished in the step-by-step below:

***STEP* 1:** Calculate static thrust (T_{STATIC}), e.g., using Equation (15-81) at the given power setting and altitude.

***STEP* 2:** If we know that η_{opt} is achieved at a specific V_{opt} with the propeller operating at Ω_{opt}, we can estimate these at other RPMs as follows. First, estimate the helix angle at $r=0.75R$ using the known V_{opt} and Ω_{opt}:

$$\phi_{opt} = \tan^{-1}\left(\frac{V_{opt}}{\Omega_{opt} r_{0.75}}\right) \tag{15-64}$$

Then, the optimum airspeed at a different RPM is found from

$$V_{opt_{RPM}} = \Omega_{RPM}\ r_{0.75}\ \tan\phi_{opt} \tag{15-65}$$

***STEP* 3:** Calculate a new T_{opt} using the V_{optRPM} from Step 2.

***STEP* 4:** Substitute the T_{STATIC} from Step 1, V_{optRPM} from Step 2, and T_{opt} from Step 3 into Equations (15-61) through (15-63). This yields a new quadratic spline per Equation (15-60), applicable at that altitude and power setting.

For instance, if a propeller manufacturer discloses that $\eta_{opt}=0.8506$ for a 76-in diameter propeller ($0.75R=2.375$ ft) at 2500 RPM ($\Omega_{opt}=261.8$ rad/s) and 146 KTAS (246.4 ft/s) at S-L, then the ϕ_{opt} is found from:

$$\phi_{opt} = \tan^{-1}\left(\frac{V_{opt}}{\Omega_{opt}\ r_{0.75}}\right) = \tan^{-1}\left(\frac{246.4}{(261.8)(2.375)}\right)$$
$$= 21.62°$$

Thus, the optimum speed, V_{optRPM}, for 2300 RPM is

$$V_{opt_{RPM}} = \Omega_{RPM}\ r_{0.75}\ \tan\phi_{opt}$$
$$= \left(\frac{\pi \times 2300}{30}\right)(2.375)(\tan(21.62°))$$
$$= 226.7 \text{ ft/s} \quad (= 134 \text{ KTAS})$$

For 2700 RPM, it is 266.1 ft/s or 157.7 KTAS. These estimations compare well with analyses conducted using the blade element theory of Section 15.6. This is illustrated in Figure 15-34.

EXAMPLE 15-11

Determine the thrust model for an LSA powered by an engine rated at 100 BHP at S-L swinging a 69-in diameter cruise-propeller with an 18-in diameter spinner. The target cruising speed is 116 KTAS (195.8 ft/s) at 8000 ft ($\rho=0.001869$ slugs/ft^3) at 75% power (75 BHP). It is expected the propeller will be 83% efficient during cruise. Assume $K_P=0.7$.

SOLUTION:

Preliminaries:

$$A_P = \frac{\pi D_P^2}{4} = \frac{\pi(69/12)^2}{4} = 25.97 \text{ ft}^2$$
$$A_{spinner} = \frac{\pi D_{spinner}^2}{4} = \frac{\pi(18/12)^2}{4} = 1.767 \text{ ft}^2$$

Determine static thrust at the cruise condition per Equation (15-63),

$$T_{opt} = \frac{\eta_{opt} 550 P_{BHP}}{V_{opt}} = \frac{(0.83)550(75)}{195.8} = 174.9 \text{ lb}_f$$

Determine static thrust per Equation (15-81),

$$T_{STATIC} = K_P P^{2/3}(2\rho A_P)^{1/3}\left(1 - \frac{A_{spinner}}{A_P}\right)$$
$$= (0.7)(550 \times 75)^{2/3}(2(0.001869)(25.97))^{1/3}\left(1 - \frac{1.767}{25.97}\right)$$
$$= 357.9 \text{ lb}_f$$

Determine the coefficients A, B, and C, all using KTAS as base

$$A = (T_{STATIC} - 2T_{opt})/V_{opt}^2 = (357.6 - 2(183.3))/(116)^2$$
$$= 0.0006116 \text{ lb}_f/\text{KTAS}^2$$
$$B = (3T_{opt} - 2T_{STATIC})/V_{opt} = (3(183.3) - 2(357.6))/116$$
$$= -1.649 \text{ lb}_f/\text{KTAS}$$
$$C = T_{STATIC} = 357.9 \text{ lb}_f$$

Therefore, the quadratic spline is given by:

$$T(V_\infty) = 357.9 - 1.649 V_\infty + 0.0006116 V_\infty^2$$

Note that since the coefficients are based on airspeed in KTAS, V_∞ must be in KTAS as well.

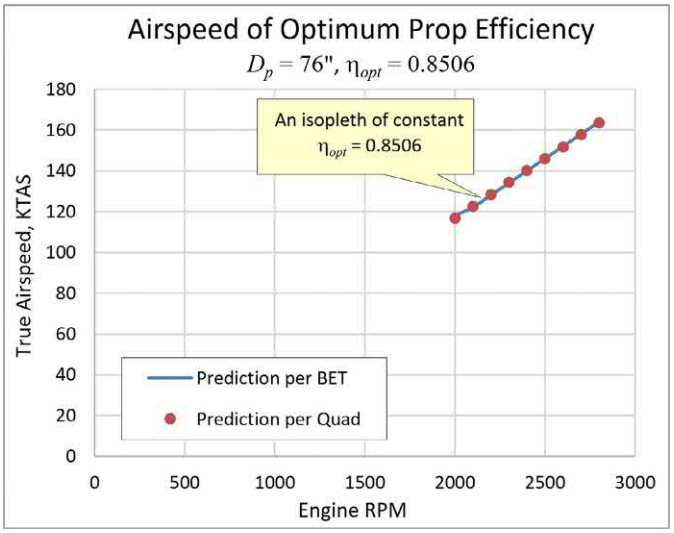


FIGURE 15-34 Variation of optimum airspeed with RPM.

DERIVATION OF EQUATION (15-60)

The goal is to develop a second-order polynomial that approximates the thrust of a propeller at constant RPM and varying airspeed. This requires three unknown constants: A, B, and C. This requires three independent equations:

At the first airspeed $(V_\infty = 0)$: $T_{STATIC} = AV_\infty^2 + BV_\infty + C = C$ (i)

At the second airspeed $(V_\infty = V_{opt})$:

$$T_{opt} = AV_{opt}^2 + BV_{opt} + C = AV_{opt}^2 + BV_{opt} + T_{STATIC} \quad \text{(ii)}$$

where T_{opt} refers to the thrust at V_{opt}. The slope of Equation (15-52) at V_{opt} can be used to get the third equation, where the slope is calculated from:

$$\frac{dT}{dV} = \frac{d}{dV}\left(\frac{\eta_p \times 550 \times P_{BHP}}{V_\infty}\right) = -\frac{\eta_p \times 550 \times P_{BHP}}{V_\infty^2}$$

Therefore, the third equation is:

$$\left.\frac{dT}{dV}\right|_{V_{opt}} = 2AV_{opt} + B = -\frac{\eta_{opt} \times 550 \times P_{BHP}}{V_{opt}^2} \quad \text{(iii)}$$

Equation (iii) gives:

$$B = -2AV_{opt} - \frac{\eta_{opt} \times 550 \times P_{BHP}}{V_{opt}^2} = -2AV_{opt} - \frac{T_{opt}}{V_{opt}}.$$

Inserting this into Equation (ii) yields:

$$\begin{aligned} T_{opt} &= AV_{opt}^2 + BV_{opt} + T_{STATIC} \\ &= AV_{opt}^2 - \left(2AV_{opt} + \frac{T_{opt}}{V_{opt}}\right)V_{opt} + T_{STATIC} \end{aligned}$$

Algebraic manipulations yield: $A = (T_{STATIC} - 2T_{opt})/V_{opt}^2$.

Thus, the coefficient B can be rewritten as follows:

$$B = \frac{3T_{opt} - 2T_{STATIC}}{V_{opt}}.$$

Which allows us to combine the coefficients as follows:

$$T(V) = \left(\frac{T_{STATIC} - 2T_{opt}}{V_{opt}^2}\right)V^2 + \left(\frac{3T_{opt} - 2T_{STATIC}}{V_{opt}}\right)V + T_{STATIC}$$

15.4.4 Initial Thrust Model for a Constant-Speed Propeller

The idea of the quadratic spline, presented in the previous section, will now be expanded to include constant-speed propellers. Such propellers increase the range of airspeeds over which airplanes can operate. This is accomplished by varying the pitch of the propeller blades as shown in Figure 15-35. The following method, which is justified using a similar premise as that of the fixed-pitch prop, can be used to help with conceptual studies. It can also be used for fixed-pitch propellers, although it involves more work than the previous method.

Figure 15-35 shows how the propeller efficiency of a variable-pitch propeller changes with advance ratio and pitch-angle. The graph is presented in ref. [22]. The wide-line curve is added to illustrate the shape of the propeller efficiency changes with pitch angle. This curve can be described using a fourth-order polynomial of the following form. It *is* the justification for this method. If nD_P is constant, then η_p is a function of V_∞ only. Thus, the curve can be described using

$$\eta_p = A_0 + A_1 V_\infty + A_2 V_\infty^2 + A_3 V_\infty^3 + A_4 V_\infty^4 \quad \text{(15-66)}$$

where A_1 through A_4 are the polynomial constants that must be determined and V_∞ is the true airspeed. Its implementation is presented in the following STEP-BY-STEP. Equation (15-66) can be represented in terms of the advance ratio ($J = V_\infty/(n\,D_P)$) rather than the airspeed. This is a hair more complicated, but permits RPM to be accounted for. Note that the geometry (e.g., propeller diameter and number of blades) is not needed because the method presumes that the propeller will hit the efficiencies specified. It also presumes the combination of the engine and propeller is appropriate. Of course, this subjects it to the wisdom of the designer, so garbage-in means garbage-out. Recommended airspeeds and efficiencies for constant-speed and fixed-pitch propellers are presented in Table 15-5.

***STEP* 1:** Specify expected best rate-of-climb airspeed (V_y), cruising speed (V_c), and choose an appropriate high speed (V_{hs}) and associated expected propeller efficiencies (η_p). For a constant-speed propeller, this will be near 0.75 to 0.80 for V_y and 0.85 to 0.88 for V_c and V_{hs}. For constant-speed propellers, choose a V_{hs} that is perhaps 100 KTAS higher than V_c. For fixed-pitch propellers, choose a V_{hs} that is perhaps 50 KTAS higher than V_c.

***STEP* 2:** Define and tabulate these targets as shown in Table 15-5, which presents recommended values.

***STEP* 3:** Substitute these values into the matrix of Equation (15-67). Solve. This will produce the

$$\begin{Bmatrix} A_1 \\ A_2 \\ A_3 \\ A_4 \end{Bmatrix} = \begin{bmatrix} V_y & V_y^2 & V_y^3 & V_y^4 \\ V_{opt} & V_{opt}^2 & V_{opt}^3 & V_{opt}^4 \\ 1 & 2V_{opt} & 3V_{opt}^2 & 4V_{opt}^3 \\ V_{hs} & V_{hs}^2 & V_{hs}^3 & V_{hs}^4 \end{bmatrix}^{-1} \begin{Bmatrix} \eta_{p_y} \\ \eta_{p_{opt}} \\ 0 \\ \eta_{p_{hs}} \end{Bmatrix} \quad \text{(15-67)}$$

***STEP* 4:** To calculate thrust using power in watts or horsepower, use Equations (15-51) or (15-52), repeated below in a slightly modified form.

$$T = \frac{\eta_p\, P}{aV_\infty} = \begin{cases} \dfrac{\eta_p\, P_W}{aV_\infty} = \dfrac{\eta_p\ 1000\ P_{kW}}{aV_\infty} \\ \dfrac{\eta_p\ 550\ P_{HP}}{aV_\infty} \end{cases} \quad \text{(15-68)}$$

where a is a conversion factor. Note that unit consistency is vital. Recall that when using these equations, V_∞ must be

FIGURE 15-35 Change in propeller efficiency with pitch change of a variable-pitch propeller [22].

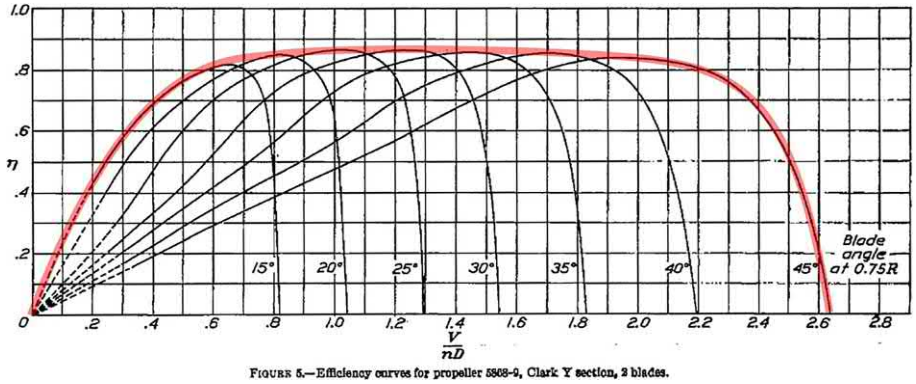


FIGURE 5.—Efficiency curves for propeller 5868-9, Clark Y section, 2 blades.

TABLE 15-5 Recommended operating points for common propellers.

Airspeed	V_∞	η_p	$d\eta_p/dV_\infty$	Recommended Values	
				η_p for fixed-pitch	η_p for const-speed
At rest	0	0	-	-	-
Best rate-of-climb airspeed	V_y	η_{py}	-	0.60-0.70	0.70-0.80
Target cruising speed	$V_{opt}=V_c$	η_{popt}	-	0.75-0.80	0.85-0.88
Target cruising speed is a stationary point	$V_{opt}=V_c$	0	0	-	-
High speed	$V_{hs}\approx V_c+100$	η_{phs}	-	0.60-0.70	0.70-0.80

in terms of m/s or ft/s. If V_∞ is in km/h, then $a=0.2778$. If V_∞ is in KTAS, then $a=1.688$. If V_∞ is in m/s or ft/s, then $a=1$. Thus, for the UK-system and expressing V_∞ in KTAS, Equation (15-68) can be written as:

$$T=\frac{\left(A_1V_\infty+A_2V_\infty^2+A_3V_\infty^3+A_4V_\infty^4\right)\ 550\ P_{HP}}{1.688V_\infty}$$
$$\cong 325.9\left(A_1+A_2V_\infty+A_3V_\infty^2+A_4V_\infty^3\right)P_{HP} \quad (15\text{-}69)$$

Setting $V_\infty=0$ yields static thrust $T_{STATIC}=325.9A_1P_{HP}$ (15-70)

where P is power in watts or ft·lb$_f$/s. Ensure unit consistency. For instance, if airspeed in KTAS is used to determine the coefficients A_1 through A_4, then A_1 must be divided by 1.688 to make it compatible with P. The static thrust per Equation (15-70) gives reasonable values, but compare to that of Section 15.4.2.

Altitude Corrections

The fact that propeller blade pitch can be modified in flight, gives constant-speed propellers a remarkable adaptability. This means that the propeller efficiency curve is largely independent of altitude. Thus, altitude corrections consist of accounting for altitude dependent power changes.

EXAMPLE 15-12

Create a thrust model for a Cessna 210 Centurion [23] powered by a normally aspirated, 285 BHP piston engine.[13] Use it to estimate thrust at cruising speed at 5000 ft. Its $V_y=89$ KTAS and cruising speed at 76% power (2500 RPM/25 MAP/216.6 BHP) is $V_c=160$ KTAS [24]. Also, estimate static thrust at max rated power at S-L.

SOLUTION:

Step 1 of the procedure is presented in the problem statement. Let us use the recommended numbers in Table 15-5 and substitute those into the matrix of Step 3 and solve.

$$\begin{Bmatrix}A_1\\A_2\\A_3\\A_4\end{Bmatrix}=\begin{bmatrix}89 & 89^2 & 89^3 & 89^4\\160 & 160^2 & 160^3 & 160^4\\1 & 2(160) & 3(160^2) & 4(160^3)\\260 & 260^2 & 260^3 & 260^4\end{bmatrix}^{-1}\begin{Bmatrix}0.75\\0.85\\0\\0.75\end{Bmatrix}$$
$$=\begin{Bmatrix}1.528\times10^{-2}\\-1.005\times10^{-4}\\2.959\times10^{-7}\\-3.563\times10^{-10}\end{Bmatrix}$$

Thus, using Equation (15-69), the thrust model for this condition is

[13] The standard Cessna 210 has a 300 BHP Continental engine, but the 300 BHP is only a 5-min maximum T-O power.

EXAMPLE 15-12 (*cont'd*)

$$T = 325.9\left(1.528 \times 10^{-2} - 1.005 \times 10^{-4} V_\infty + 2.959 \times 10^{-7} V_\infty^2 - 3.563 \times 10^{-10} V_\infty^3\right) P_{HP}$$

Then, we can estimate thrust at $V_{c=160\ \text{KTAS}}$. Note the curves for this power setting are plotted in Figure 15-36. Also note the common error shown in Figure 15-37. Make sure your η_p is realistic. The η_p-curve does not dip up or down, it flattens over a range of airspeeds (see Figure 15-35). In fact, the propeller efficiency curve in Figure 15-36 probably has insufficient flattening, compared to the real propeller.

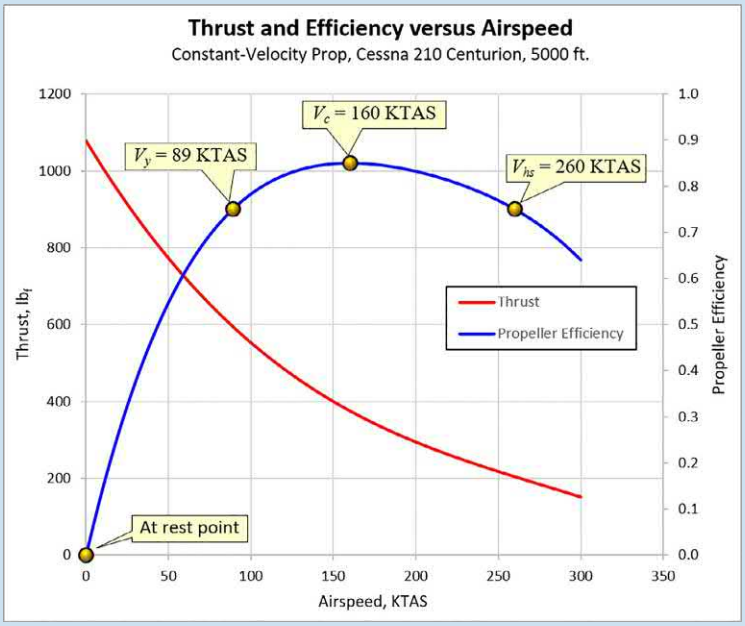


FIGURE 15-36 Thrust and propeller efficiency model for the Cessna 210.

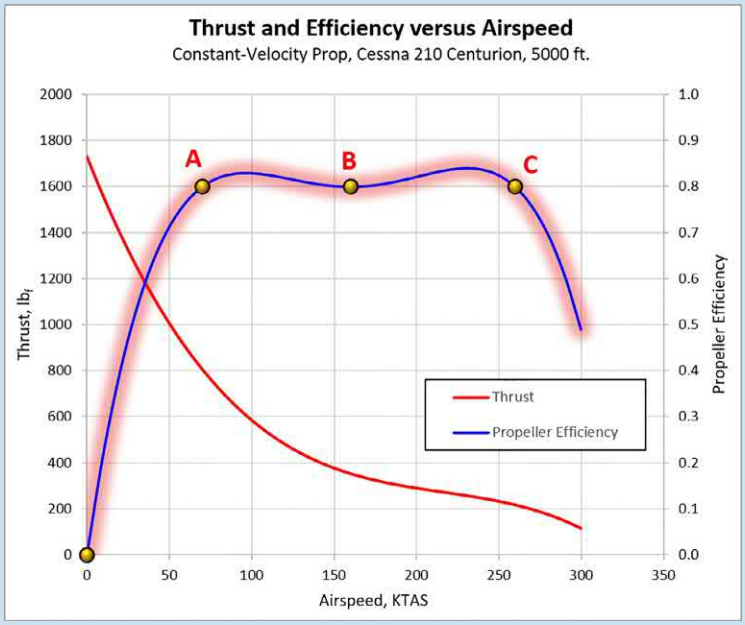


FIGURE 15-37 If your graph looks like this it is INCORRECT! The position of one or two of the points A, B, and C is wrong.

Continued

EXAMPLE 15-12 (*cont'd*)

$$T(160) = 325.9\left(1.528\times10^{-2} - 1.005\times10^{-4}(160) + 2.959 \times10^{-7}(160^2) - 3.563\times10^{-10}(160^3)\right)(216.6) = 309.5 \text{ lb}_\text{f}$$

Static thrust at max rated power is obtained using Equation (15-70) and simply changing the power.

$$T_{STATIC} = 325.9 A_1 P_{HP} = 325.9\left(1.528\times10^{-2}\right)300 = 1494 \text{ lb}_\text{f}$$

This compares to Equation (15-58) as follows (using the optimum K_{T0} obtained using $\beta_G = 8.5°$)

$$T_{STATIC} = \frac{K_{T_0} P_{BHP}}{RPM \times D_P} = \frac{(85786)(300)}{(2850)(80/12)} = 1355 \text{ lb}_\text{f}$$

DERIVATION OF EQUATION (15-67)

To form a spline to represent η_p, we need a fourth order polynomial of the form

$$\eta_p = A_0 + A_1 V_\infty + A_2 V_\infty^2 + A_3 V_\infty^3 + A_4 V_\infty^4 \qquad \text{(i)}$$

To force the spline through specific operational target points, we must select specific airspeeds and expected η_p at those airspeeds. These positions are plausible and it is possible to design a CSP propeller that approaches those target points. The airspeeds must be true airspeed (V_{TAS}). Ensure unit consistency when estimating the η_p.

For the "at rest" condition, the value of the polynomial is zero. Substituting $V_\infty = 0$ into Equation (i) results in $A_0 = 0$. Thus, we can simplify Equation (i) as follows:

$$\eta_p = A_1 V_\infty + A_2 V_\infty^2 + A_3 V_\infty^3 + A_4 V_\infty^4 \qquad \text{(ii)}$$

Note that in using this method, a zero-slope condition must be enforced at the cruise point. This is implemented by differentiating Equation (i) with respect to V_{TAS}

$$\frac{d\eta_p}{dV_{TAS}} = A_1 + 2A_2 V_\infty + 3A_3 V_\infty^2 + 4A_4 V_\infty^3 \qquad \text{(iii)}$$

We can now use Equations (ii) and (iii) with the target operational points to form the following set of linear equations:

$$\begin{Bmatrix} \eta_{p_y} \\ \eta_{p_{opt}} \\ 0 \\ \eta_{p_{hs}} \end{Bmatrix} = \begin{bmatrix} V_y & V_y^2 & V_y^3 & V_y^4 \\ V_{opt} & V_{opt}^2 & V_{opt}^3 & V_{opt}^4 \\ 1 & 2V_{opt} & 3V_{opt}^2 & 4V_{opt}^3 \\ V_{hs} & V_{hs}^2 & V_{hs}^3 & V_{hs}^4 \end{bmatrix} \begin{Bmatrix} A_1 \\ A_2 \\ A_3 \\ A_4 \end{Bmatrix} \qquad \text{(iv)}$$

15.4.5 Step-by-Step: Determining Thrust Using a Propeller Efficiency Table

Some propeller manufacturers provide propeller efficiency tables like the one shown in Figure 15-38. It presents propeller efficiency in terms of advance ratio (J—left most column) and power coefficient (C_P—top row). The table provides a convenient way to extract propeller efficiency for use with Equation (15-52). NOTE: The data only apply to a specific propeller—Do not use for other propellers!

Using such a table, the method of extracting thrust is as follows:

	C_p											
J	**0.02**	**0.03**	**0.04**	**0.05**	**0.06**	**0.07**	**0.08**	**0.09**	**0.1**	**0.11**	**0.12**	**0.13**
0.20	0.4960	0.4586	0.4126	0.3600	0.3059	0.2510	0.2019	0.1660	0.1410	0.1199	0.1021	0.0873
0.25	0.5664	0.5387	0.4959	0.4455	0.3888	0.3262	0.2633	0.2151	0.1820	0.1549	0.1325	0.1130
0.30	0.6227	0.6060	0.5683	0.5224	0.4672	0.4028	0.3296	0.2663	0.2246	0.1912	0.1637	0.1396
0.35	0.6664	0.6614	0.6300	0.5903	0.5400	0.4788	0.4003	0.3208	0.2689	0.2288	0.1958	0.1672
0.40	0.6976	0.7031	0.6775	0.6444	0.6028	0.5485	0.4756	0.3827	0.3165	0.2683	0.2295	0.1963
0.45	0.7196	0.7351	0.7147	0.6860	0.6515	0.6074	0.5461	0.4572	0.3686	0.3106	0.2655	0.2269
0.50	0.7370	0.7609	0.7451	0.7202	0.6913	0.6561	0.6077	0.5346	0.4294	0.3554	0.3034	0.2593
0.55	0.7510	0.7809	0.7691	0.7478	0.7230	0.6935	0.6574	0.6115	0.5016	0.4032	0.3436	0.2938
0.60	0.7600	0.7948	0.7868	0.7680	0.7458	0.7198	0.6879	0.6513	0.5869	0.4643	0.3885	0.3321
0.65	0.7673	0.8061	0.8011	0.7847	0.7648	0.7417	0.7134	0.6821	0.6419	0.5503	0.4372	0.3729
0.70	0.7730	0.8147	0.8124	0.7982	0.7802	0.7598	0.7345	0.7056	0.6740	0.6376	0.5001	0.4206
0.75	0.7770	0.8201	0.8208	0.8083	0.7918	0.7737	0.7510	0.7239	0.6950	0.6635	0.6096	0.4882
0.80	0.7787	0.8239	0.8264	0.8156	0.8007	0.7837	0.7636	0.7389	0.7113	0.6824	0.6494	0.5748
0.85	0.7793	0.8263	0.8305	0.8213	0.8077	0.7917	0.7735	0.7512	0.7251	0.6978	0.6687	0.6366
0.90	0.7790	0.8271	0.8333	0.8254	0.8129	0.7983	0.7810	0.7610	0.7369	0.7107	0.6833	0.6543
0.95	0.7773	0.8270	0.8347	0.8276	0.8161	0.8020	0.7857	0.7672	0.7446	0.7194	0.6932	0.6657
1.00	0.7743	0.8258	0.8351	0.8288	0.8180	0.8045	0.7891	0.7717	0.7507	0.7267	0.7015	0.6753
1.05	0.7701	0.8235	0.8346	0.8292	0.8190	0.8059	0.7913	0.7746	0.7551	0.7327	0.7083	0.6831
1.10	0.7649	0.8201	0.8324	0.8285	0.8193	0.8068	0.7923	0.7759	0.7579	0.7370	0.7132	0.6891
1.15	0.7584	0.8161	0.8298	0.8269	0.8184	0.8066	0.7925	0.7765	0.7587	0.7391	0.7164	0.6929
1.20	0.7503	0.8114	0.8266	0.8247	0.8167	0.8055	0.7919	0.7764	0.7587	0.7397	0.7184	0.6953

FIGURE 15-38 An example of a propeller efficiency table for a constant-speed propeller (no specific model).

STEP 1: Determine Advance Ratio

Calculate advance ratio from Equation (15-33):

$$J = \frac{V_\infty}{nD_P} = \frac{60 \cdot V_\infty}{RPM \cdot D_P}.$$

STEP 2: Determine Power Coefficient

Calculate power coefficient from Equation (15-38):

$$C_P = \frac{P}{\rho n^3 D_P^5}.$$

STEP 3: Extract Propeller Efficiency

Extract the propeller efficiency using the calculated J and C_P.

STEP 4: Calculate Thrust

Calculate thrust from Equation (15-52):

$$T = \frac{\eta_p \times 550 \times P_{BHP}}{V_\infty}.$$

EXAMPLE 15-13

An airplane is equipped with a 70″ diameter constant-speed propeller driven by a 150 BHP piston engine. If flying at sea-level at 130 KTAS with the prop swinging at 2700 RPM and max power and assuming the data in Figure 15-38 applies, what is the magnitude of the thrust?

SOLUTION:

STEP 1: Advance ratio

$$J = \frac{V_\infty}{nD_P} = \frac{60 \cdot (1.688 \times 130)}{2700 \cdot (70/12)} = 0.8360.$$

STEP 2: Power coefficient

$$C_P = \frac{P}{\rho n^3 D_P^5} = \frac{(550 \times 150)}{(0.002378)(2700/60)^3 (70/12)^5} = 0.05637.$$

STEP 3: Extract prop efficiency—here, by observation $\eta \approx 0.81$.

STEP 4: Thrust

$$T = \frac{\eta_p \times 550 \times P_{BHP}}{V_\infty} = \frac{0.81 \times 550 \times 150}{1.688 \times 130} = 304 \text{ lb}_\text{f}.$$

15.4.6 Estimating Thrust From Manufacturer's Data

As said earlier, it is wise for the aircraft designer to establish a good relationship with propeller manufacturers by committing to using their products. Such relationships may (1) encourage the propeller manufacturer to provide the designer with useful propeller performance information, and (2) if the business case is promising enough, even design a propeller to match the designer's desired characteristics.

J	C_T	C_P	η
0.3142	0.1250	0.0734	0.535
0.4398	0.1077	0.0710	0.667
0.5655	0.0898	0.0674	0.754
0.6912	0.0703	0.0596	0.815
0.8168	0.0497	0.0475	0.854
0.9425	0.0278	0.0306	0.856

Theoretical calculated performance

Includes inflow and spinner/hub drag

FIGURE 15-39 A typical propeller efficiency table.

An example of typical data provided by a propeller manufacturer is shown in Figure 15-39. The data are for an unspecified, two-bladed, 69-in diameter propeller for an LSA aircraft and are plotted in Figure 15-40, with the appropriate curve fits. So, now we have the properties of the propeller formulation as a function of Advance Ratio. NOTE: The data only apply to a specific propeller—Do not use for other propellers!

$$\begin{aligned} \eta_P &= 0.096574 + 1.703049J - 0.952281J^2 \\ C_T &= 0.162133 - 0.106480J - 0.038208J^2 \\ C_P &= 0.058005 + 0.084893J - 0.120439J^2 \end{aligned} \tag{15-71}$$

EXAMPLE 15-14

An airplane is equipped with a 69″ diameter fixed pitch propeller driven by a 100 BHP piston engine. If flying at sea level at 110 KCAS with the prop swinging at 2400 RPM and 75% power, using the above equations, what is the magnitude of the thrust?

SOLUTION:

STEP 1: Advance ratio

$$J = \frac{60 \cdot V}{RPM \cdot D} = \frac{60 \cdot (1.688 \times 110)}{2400 \cdot (69/12)} = 0.8073.$$

STEP 2: Propeller efficiency

$$\eta_P = 0.096574 + 1.703049J - 0.952281J^2 = 0.8508$$

STEP 3: Thrust

$$T = \frac{\eta_p \times 550 \times P_{BHP}}{V} = \frac{0.8508 \times 550 \times 75}{1.688 \times 110} = 189 \text{ lb}_\text{f}$$

15.4.7 Other Analytical Methods

Other analytical methods that allow one to extract thrust and other properties from propellers are extensive enough to be presented in their own *sec*tions. These are

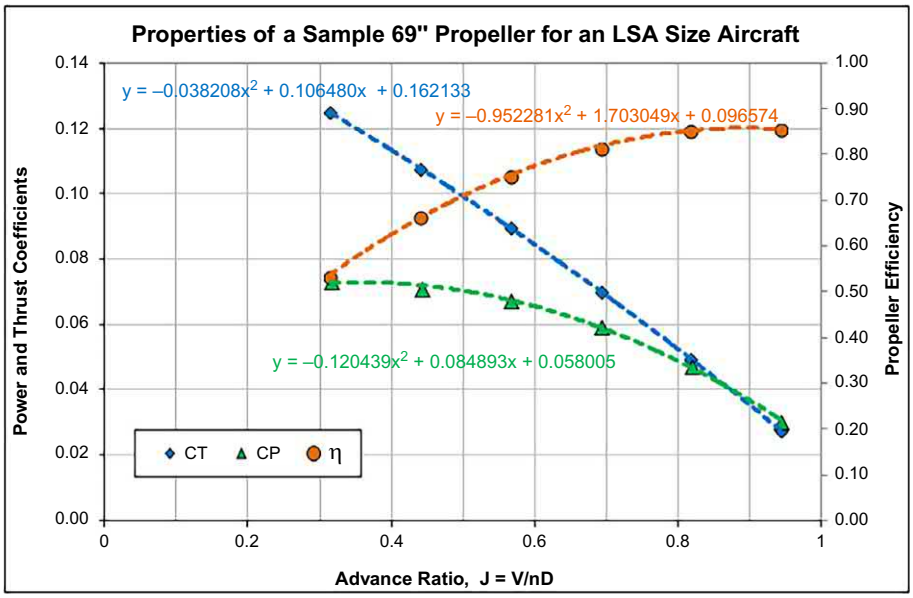


FIGURE 15-40 A typical propeller efficiency graph for a fix pitch propeller (no specific propeller type).

the *Rankine–Froude Momentum Theory* (Section 15.5) and *Blade Element Theory* (Section 15.6).

15.5 RANKINE-FROUDE MOMENTUM THEORY

Two of three big conservation laws that govern fluid flow are *conservation of mass* and *momentum* (see Section 14.2.1). These laws allow propeller thrust to be determined using the so-called *actuator disc theory* (ADT). It was originally developed in 1865 by the famed Scottish physicist William John Macquorn Rankine (1820–1872), who had a particularly prolific career as a scientist and to whom the Rankine temperature scale is credited. Important contributions were made by the English hydrodynamicist William Froude (1810–1879). Rankine's contribution dates to 1865, and that of Froude over the period from 1878 to 1889 [25].

One advantage of this theory is it provides means to estimate the airspeed inside the propeller streamtube, the *propeller-induced velocity*. It is used to supplement the *blade element theory* (BET), presented in Section 15.6. It also permits static thrust to be estimated. The ADT is based on the following assumptions:

(1) The propeller is replaced by an infinitesimally thin actuator disc that offers no resistance to air passing through it.
(2) The actuator disc is uniformly loaded and, therefore, the flow passing through it is uniform and is uniformly accelerated.
(3) A control volume surrounds the streamtube and sharply separates the flow going through it from the surrounding air.
(4) Flow outside the streamtube has constant stagnation pressure (which means no work is imparted on it).
(5) In the far-field, streamlines in front and behind the disc are parallel. Thus, the static pressure inside the streamtube far from the actuator disc equals the far-field pressure.
(6) The propeller does not impart rotation to the flow.
(7) The theory assumes steady, inviscid (no drag, no momentum diffusion), and incompressible flow.

15.5.1 Formulation for a Free Propeller

(1) Thrust, Power, and Propulsive Efficiency

Applying the ADT to a free propeller yields the following results:

Airspeed through propeller:

$$V_2 = V_\infty + w \tag{15-72}$$

Airspeed far behind propeller:

$$V_3 = V_\infty + 2w \tag{15-73}$$

Thrust:

$$T = \dot{m}w = 2\rho A_P (V_\infty + w)w \tag{15-74}$$

Power required for flight:

$$P_{req} = T(V_\infty + w) = TV_\infty + \frac{T^{1.5}}{\sqrt{2\rho A_P}} \tag{15-75}$$

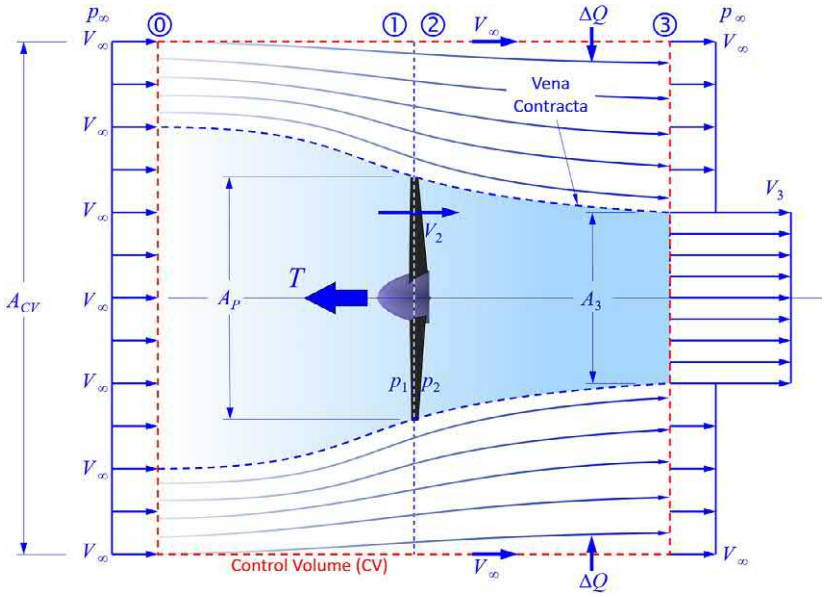


FIGURE 15-41 Idealized flow model for the Froude–Rankine momentum theory.

Induced airspeed:

$$w = \frac{1}{2}\left[-V_\infty + \sqrt{V_\infty^2 + 2T/(\rho A_P)}\right] \tag{15-76}$$

where A_P is the propeller disc area (see Figure 15-41). The propulsive efficiency of the free propeller can be written in terms of Equation (14-47)):

$$\eta_{prp} \equiv \frac{\text{Thrust Power}}{\text{Total Power for Flight}} = \frac{2}{(1 + V_3/V_\infty)} \tag{15-77}$$

(2) Determination of Static Thrust

Consider the special case when $V_\infty = 0$. In this case, the induced velocity per Equation (15-76) reduces to:

$$w = \sqrt{\frac{T}{2\rho A_P}} \tag{15-78}$$

Similarly, per Equation (15-75), since the propeller is at rest, only the induced power applies:

$$P_i = Tw = \frac{T^{1.5}}{\sqrt{2\rho A_P}} \tag{15-79}$$

This yields the following expression for static thrust, T_{STATIC}:

$$P_i = \frac{T^{1.5}}{\sqrt{2\rho A_P}} \quad \Rightarrow \quad T_{STATIC} = P_i^{2/3}(2\rho A_P)^{1/3} \tag{15-80}$$

Equation (15-80) overestimates T_{STATIC} for various reasons, such as absence of blockage effects, the presence of the hub, which reduces the disc area, reduction of lift distribution near the tip and hub, Reynolds number, and so on. Therefore, for design purposes, estimate T_{STATIC} by the following empirical correction:

$$T_{STATIC} = K_P P_{req}^{2/3}(2\rho A_P)^{1/3}\left(1 - \frac{A_{spinner}}{A_P}\right) \tag{15-81}$$

where K_P is a correction factor that depends on propeller geometry. Suitable values based on real airplanes are listed in Table 15-6.

TABLE 15-6 Scale-based correction factor.

Application	Range of K_P
RC aircraft	0.2–0.45
Small, fixed-pitch propellers (kitplanes)	0.5–0.65
Medium, fixed and constant speed propellers	0.7–0.75
Large turboprops, constant speed propellers	0.75–1.0

(3) Reflections on Power Required

The momentum formulation reveals that given fixed thrust, a large propeller diameter requires less w. To evaluate the implications, substitute Equation (15-74) into Equation (15-75). This leads to

$$T = \dot{m}w \quad \Rightarrow \quad P_{req} = T(V_\infty + w) = \dot{m}wV_\infty + \dot{m}w^2 \tag{15-82}$$

Consider P_{req} associated with fixed thrust for a specific cruising speed. We can use Equation (15-82) to investigate the effect of two possibilities: (1) reduced $\dot{m}$ and increased w and (2) increased $\dot{m}$ and reduced w. Assume we do this by a factor of two for each, as shown below.

(1) REDUCED $\dot{m}$ and INCREASED w	(2) INCREASED $\dot{m}$ and REDUCED w
$\dot{m}$ is ½ of baseline $\Rightarrow$ w must be doubled	$\dot{m}$ is 2× the baseline $\Rightarrow$ w must be halved
Thrust: $T = \left(\frac{\dot{m}}{2}\right)(2w) = \dot{m}w$	Thrust: $T = (2\dot{m})\left(\frac{w}{2}\right) = \dot{m}w$
Power: $P_{req} = \left(\frac{\dot{m}}{2}\right)(2w)V_\infty + \left(\frac{\dot{m}}{2}\right)(2w)^2 = \underbrace{\dot{m}wV_\infty}_{\text{unchanged per Eq.(15–82)}} + \underbrace{2\dot{m}w^2}_{\text{doubled over Eq.(15–82)}}$	Power: $P_{req} = (2\dot{m})\left(\frac{w}{2}\right)V_\infty + (2\dot{m})\left(\frac{w}{2}\right)^2 = \underbrace{\dot{m}wV_\infty}_{\text{unchanged per Eq.(15–82)}} + \underbrace{\frac{1}{2}\dot{m}w^2}_{\text{1/2 of baseline per Eq.(15–82)}}$

The same thrust is produced in either case, but approach (1) requires *more* power than the baseline, while approach (2) requires *less*.

(4) Basic Sizing Procedure

The momentum theorem operates under the premise we know how much thrust we need. We may know this from the expected drag at the target cruise speed. This allows the power required (and thus engine power) for a specific propeller diameter to be estimated. One way to estimate the expected aircraft drag in the conceptual phase is using the expression $D = W/(L/D)$, where W is the aircraft weight and L/D is the target lift-to-drag ratio in cruise (e.g., $L/D = 10 \Rightarrow D = W/10$).

STEP 1: Specify a target cruising speed (V_∞) for the vehicle and expected drag (D) at that airspeed.

STEP 2: Specify a desired propeller diameter (D_P) and calculate corresponding actuator disc area (A_P).

STEP 3: Calculate required induced velocity (w) per Equation (15-76), by setting $T = D$.

STEP 4: Calculate the required power for flight (P_{req}) using Equation (15-75). It will be in units of J/s (or watts) in the SI-system or ft·lb$_f$/s in the UK-system.

STEP 5: Calculate the required engine power (P_{ENG}) per Equation (15-92) with $K_{fan} = 1$ and some assumed η_p appropriate for aircraft class. It may be helpful to convert the power to kW or horsepower (see Table 7-1).

EXAMPLE 15-15

A two-bladed, 76-in diameter propeller generates 1500 lb$_f$ of thrust. What is the pressure rise (Δp) through the propeller disc according to the momentum theory?

SOLUTION:

The propeller disc area is:

$$A_P = \frac{\pi D^2}{4} = \frac{\pi(76)^2}{4} = 4536\ in^2 = 31.50\ ft^2.$$

Therefore, from Equation (15-86):

$$T = A_P(p_2 - p_1) = A_P\Delta p \quad \Rightarrow \quad \Delta p = \frac{T}{A_P} = \frac{1500}{31.50} = 47.6\ psf.$$

EXAMPLE 15-16

An airplane is powered by a two-bladed propeller whose diameter is 76″ is driven by a 310 BHP engine. What is the maximum static thrust one can expect from it at sea level? What is the static thrust if the spinner diameter is 18″? What is the speed of air through the propeller disc?

SOLUTION:

The propeller disc area is: $A_P = \frac{\pi D^2}{4} = 31.50\ ft^2$.

The spinner area is: $A_{spinner} = \frac{\pi(18/12)^2}{4} = 1.78\ ft^2$.

Power is: $P = 550 \times P_{BHP} = 170{,}500$ ft·lb$_f$/sec

Using Equation (15-80), we determine the maximum static thrust as follows:

$$T_{STATIC} = P^{2/3}(2\rho A_P)^{1/3} = (170500)^{2/3}(2(0.002378)(31.50))^{1/3} = 1633\ \text{lb}_f$$

Static thrust corrected for spinner:

$$T_{STATIC} = 0.85P^{2/3}(2\rho A_P)^{1/3}\left(1 - \frac{A_{spinner}}{A_P}\right) = 0.85(1633)\left(1 - \frac{1.78}{31.5}\right) = 1310\ \text{lb}_f$$

The speed of air through the propeller disc is found from Equation (15-78):

$$w = \sqrt{\frac{T}{2\rho A_P}} = \sqrt{\frac{1633}{2(0.002378)(31.50)}} = 104.4\ \text{ft/s}$$

The static thrust in the example is overestimated as it does not account for the fact that the distribution of lift along the blade of the propeller is not constant and necessarily becomes zero at the tip. This way the value represents a theoretical upper limit on the thrust.

EXAMPLE 15-17

The aircraft of the previous example is cruising at 185 KTAS (312.3 ft/s) at 8000 ft ($\rho = 0.001869$ slugs/ft^3), where its drag is estimated as 470 lb$_f$. Determine the average induced velocity and ideal efficiency at that condition.

EXAMPLE 15-17 *(cont'd)*

SOLUTION:

Area was determined to be $31.50\,\text{ft}^2$ in Example 15-15. Assuming $T=D$, the average induced velocity is found from Equation (15-76):

$$w=\frac{1}{2}\left[-V_\infty+\sqrt{V_\infty^2+\frac{2T}{\rho A_P}}\right]$$

$$=\frac{1}{2}\left[-312.3+\sqrt{312.3^2+\frac{2(470)}{(0.001869)(31.5)}}\right]=12.30\ \text{ft/s}$$

The ideal efficiency is calculated using Equation (15-46). One way is

$$T_C=\frac{2T}{\rho V_0^2 A_P}=\frac{2(470)}{(0.001869)(312.3)^2(31.50)}=0.1637$$

$$\Rightarrow\quad \eta_i=\frac{2}{1+\sqrt{1+T_C}}=\frac{2}{1+\sqrt{1+0.1637}}=0.9621$$

Another way is:

$$\eta_i=\frac{1}{(1+w/V_0)}=\frac{1}{(1+12.30/312.3)}=0.9621.$$

DERIVATION

To analyze the propeller, we need Equation (14-26) (mass conservation) and (14.28) (momentum conservation). These are repeated below, albeit adapted to assumption (7) stated earlier:

$$\oiint_A \rho\mathbf{V}\cdot d\mathbf{A}=0 \tag{15-83}$$

$$\mathbf{R}-\oiint_A p\,d\mathbf{A}=\oiint_A(\rho\mathbf{V}\cdot d\mathbf{A})\mathbf{V} \tag{15-84}$$

Refer to Chapter 14 for variable definitions. Figure 15-41 shows an idealized flow model for the actuator disc. It consists of four planes: ⓪, ①, ②, and ③. From Assumption (5), Plane ⓪ is far ahead of the actuator disc, where the streamlines are parallel. Plane ③ is far behind the disc, where the streamlines have become parallel again. Thus, the static pressure at either plane is constant and equal to the far-field pressure p_∞.

The surface area of the front face of the control volume (CV) is A_{CV}. The volumetric flow entering Plane ⓪ is $Q_0=V_\infty\cdot A_{CV}$. The volumetric flow exiting Plane ③ is $Q_3=V_\infty\cdot(A_{CV}-A_3)+V_3\cdot A_3$. The difference between the two is:

$$\Delta Q=Q_3-Q_0=V_\infty\cdot(A_{CV}-A_3)+V_3\cdot A_3-V_\infty\cdot A_{CV}$$
$$=(V_3-V_\infty)A_3 \tag{iii}$$

A nonzero ΔQ implies volumetric flow is entering the CV through the sides. The momentum flux of the fluid entering Plane ⓪ is $-\rho A_{CV}V_\infty^2$ (the negative sign indicates it is entering the volume). The momentum flux of the fluid exiting Plane ③ is $\rho[(A_{CV}-A_3)V_\infty^2+A_3V_3^2]$ (the positive sign indicates it is leaving the volume). The momentum flux entering through the sides is $-\rho\cdot\Delta Q\cdot V_\infty$. This allows the reaction force (**R**) to be estimated using Equation (15-84). Note that the pressure around the CV is equal, so the pressure term in Equation (15-84) drops out. Also, the flow is quasi-one-dimensional. Thus, the reaction force (here denoted as thrust, T) is found as follows:

$$T=\oiint_A(\rho\mathbf{V}\cdot d\mathbf{A})\mathbf{V}=\overbrace{\rho\left[(A_{CV}-A_3)V_\infty^2+A_3V_3^2\right]}^{\text{momentum flux OUT of (3)}}\ \underbrace{\overbrace{-\rho A_{CV}V_\infty^2}^{\text{momentum flux INTO (0)}}\ \overbrace{-\rho\cdot\Delta Q\cdot V_\infty}^{\text{momentum flux IN through sides}}}_{\text{Momentum drag}}=\rho A_3\left(V_3^2-V_\infty^2\right)-\rho\Delta QV_\infty \tag{15-85}$$

Gross thrust

Substituting $\Delta Q=(V_3-V_\infty)A_3$ from Equation (iii) into the above result and manipulating algebraically leads to:

$$T=\rho A_3\cdot V_3(V_3-V_\infty) \tag{iv}$$

Inspecting Figure 15-41 reveals that T can also be computed from:

$$T=A_P(p_2-p_1) \tag{15-86}$$

where p_1 and p_2 are pressure at planes ① and ② and A_P is propeller disc area. Note that since the actuator disc is infinitely thin, $A_P=A_1=A_2$. Figure 15-42 illustrates how pressure and airspeed vary far ahead of and behind the propeller.

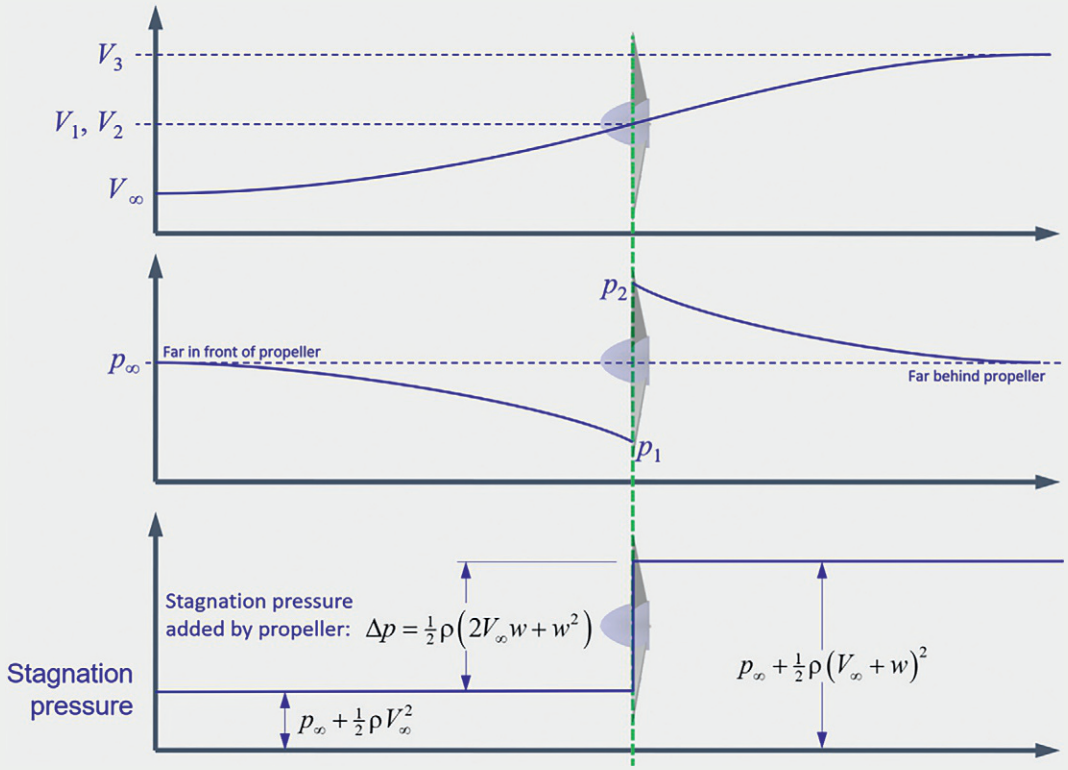


FIGURE 15-42 Flow properties inside control volume.

The propeller energy increases stagnation pressure. Its magnitude depends on the geometry of the propeller and the power delivered by the power plant.

We can calculate p_1 and p_2 using Bernoulli's principle by assuming streamlines originate far ahead of and extend to the actuator disc and immediately behind it, extending far behind it. This does not hold through the actuator disc, although it is reasonable to assume the velocity is continuous through the disc. This way, we can determine p_1 using the flow conditions at Plane ⓪, and p_2 using the flow conditions at Plane ③ as follows:

Pressure at Plane ①: $$p_\infty + \frac{1}{2}\rho V_\infty^2 = p_1 + \frac{1}{2}\rho V_1^2 \qquad \text{(v)}$$

Pressure at Plane ②: $$p_\infty + \frac{1}{2}\rho V_3^2 = p_2 + \frac{1}{2}\rho V_2^2 \qquad \text{(vi)}$$

Obtain the pressure difference by subtracting Equation (v) from (vi).

$$p_2 - p_1 + \frac{1}{2}\rho\left(V_2^2 - V_1^2\right) = \frac{1}{2}\rho\left(V_3^2 - V_\infty^2\right)$$

Since $V_1 = V_2$, this becomes: $$p_2 - p_1 = \frac{1}{2}\rho\left(V_3^2 - V_\infty^2\right) \qquad \text{(vii)}$$

Substitute Eq. (vii) into (iv) to get:

$$T = A_P(p_2 - p_1) = A_P \times \frac{1}{2}\rho\left(V_3^2 - V_\infty^2\right) \qquad \text{(viii)}$$

Equate this with Eq.(iv):

$$T = \rho A_3 \cdot V_3(V_3 - V_\infty) = \frac{1}{2}\rho\left(V_3^2 - V_\infty^2\right)A_P \qquad \text{(ix)}$$

Simplify to get: $$2A_3 \cdot V_3(V_3 - V_\infty) = A_P\left(V_3^2 - V_\infty^2\right)$$
$$= A_P(V_3 - V_\infty)(V_3 + V_\infty) \qquad \text{(x)}$$

Deleting like terms yields: $$2A_3 \cdot V_3 = A_P(V_3 + V_\infty) \qquad \text{(xi)}$$

Mass conservation of Equation (15-83) requires

$$A_P V_2 = A_3 V_3 \;\Rightarrow\; A_3 = \frac{A_P V_2}{V_3}$$

Substitute into (xi);

$$2A_3 \cdot V_3 = 2\frac{A_P V_2}{V_3} \cdot V_3 = A_P(V_3 + V_\infty) \qquad \text{(xii)}$$

And simplify to get:

$$V_2 = \frac{(V_3 + V_\infty)}{2} \qquad \text{(xiii)}$$

The above equation is recognized as *Froude's Theorem* [26]. It states that the airspeed through the propeller is the average of the far-field airspeed (V_∞) and the airspeed in the stream-tube far behind (V_3). Let us now define the following differences:

$$w = V_2 - V_\infty = V_3 - V_2 \qquad \text{(xiv)}$$

where w is called the *propeller-induced velocity*. It allows V_2 and V_3 to be rewritten as

$$V_2 = V_\infty + w \quad \text{(xv)}$$
$$V_3 = V_\infty + 2w \quad \text{(xvi)}$$

These are Equations (15-72) and (15-73). Substituting Equations (xv) and (xvi) into Equation (iv) results in:

$$T = \rho A_3 \cdot V_3(V_3 - V_\infty) = \rho \frac{A_P V_2}{V_3} \cdot V_3(V_3 - V_\infty)$$
$$= \rho A_P V_2 (V_3 - V_\infty) = \rho A_P (V_\infty + w)((V_\infty + 2w) - V_\infty)$$

Simplifying yields: $T = 2\rho A_P (V_\infty + w) w$ (xvii)

This is Equation (15-74). The power required for this system is the product force-times-speed, or

$$P_{req} = T(V_\infty + w) \quad \text{(xviii)}$$

This is Equation (15-75). It shows the power required by the propeller consist of *useful power* and *induced power*:

Useful power: $P_U = TV_\infty$ (xix)

Induced power: $P_i = Tw$ (xx)

We can determine the induced velocity, w, through the propeller disc form Equation (xvii):

$$T = 2\rho A_P (V_\infty + w) w \quad \Leftrightarrow \quad w^2 + V_\infty w - \frac{T}{2\rho A_P} = 0$$

This is a quadratic equation in terms of w and can be solved as such. Of the two solutions, only the plus-sign solution represents a physical condition. It yields Equation (15-76).

$$w = \frac{-V_\infty \pm \sqrt{V_\infty^2 + \frac{2T}{\rho A_P}}}{2} \quad \Leftrightarrow \quad w = \frac{1}{2}\left[-V_\infty + \sqrt{V_\infty^2 + \frac{2T}{\rho A_P}}\right]$$

15.5.2 Formulation for Shrouded Propellers and Ducted Fans

A ducted fan refers to a propeller enclosed by a cylindrical wing. The propeller is also called *rotor*. Some basic dimensions for a ducted fan are given in Figure 15-43. If the chord of the wing (c_{duct}) is less than the diameter of the enclosed rotor (D_R), it is called a *shrouded propeller*. If larger, it is called a *ducted fan*. This section attempts to provide basic information about such thrust devices.

Aviation history reveals only a handful of fixed-wing aircraft powered by ducted fans.[14] Among those are the Airbus *E*-Fan, Cessna XMC, Edgley Optica, MS State University's XAZ-1 and XV-11, Rhein-Flugzeugbau RF-1, Fantrainer 400, and 600, and the Stipa-Caproni.

(1) Pros of Ducted Fans

(A) The exit area of ducted fans may be larger than the prop's disc area. This reduces the exit velocity and increases

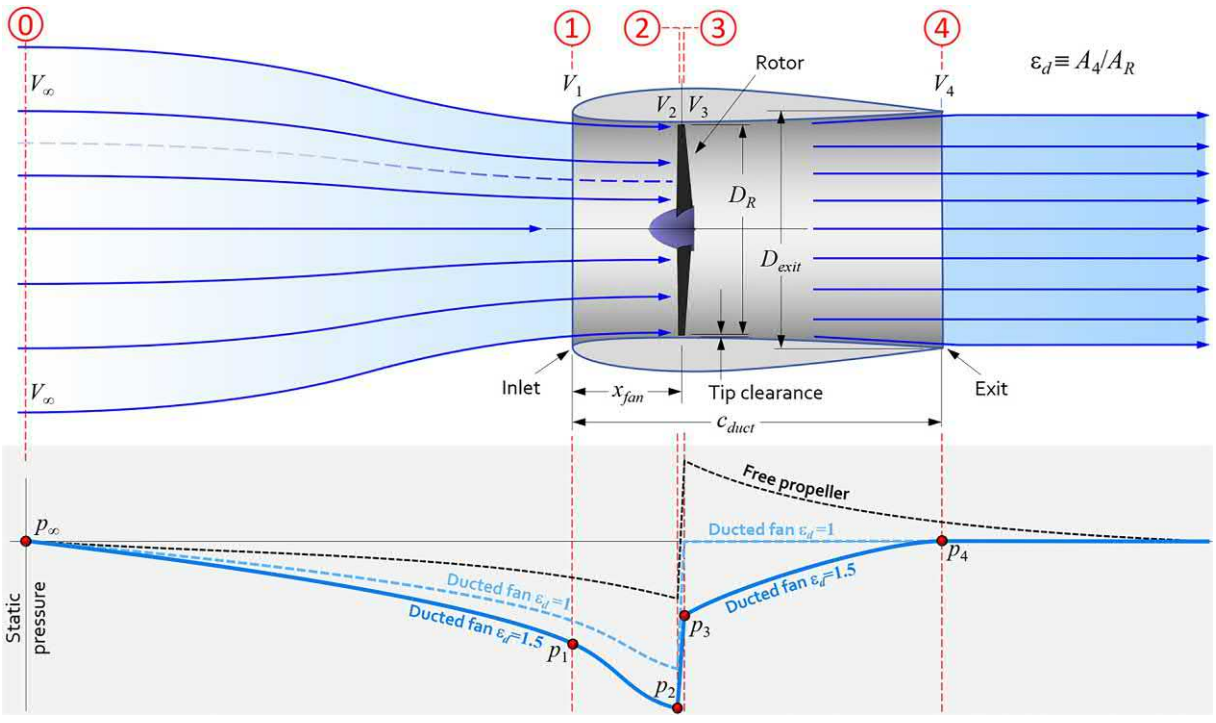


FIGURE 15-43 Idealized flow model for a ducted fan. Lower graph shows change in static pressure as a function of position (inspired by ref. [27]).

[14] This list only includes aircraft that have actually flown.

mass flow required to produce given thrust. Thus, its thrust generation uses less power compared to a free propeller (see Section 15.5.1(3)). Alternatively, it is possible to develop a given thrust using a smaller diameter rotor. (B) Smaller piston engines (intended for LSA or kitplanes) often run at much higher RPMs (e.g., Rotax 912 runs at about 5800 RPM), requiring a gear reduction unit to keep tip speed subsonic. It may be possible for a ducted fan to do away with the gear reduction unit by allowing a smaller diameter rotor. (C) Improved protection from FOD and for people walking around the aircraft with the rotor spinning. (D) A tight tolerance duct works like an endplate for a lifting surface (prop blade). This reduces blade-tip lift losses, increasing thrust for a given prop disc area. Thus, given the same disc area, the rotor blades of the ducted fan develop greater thrust than free propellers (assuming the same blade geometry and number for both). (E) The duct can serve as an effective noise suppressor. (F) If properly shaped, the duct develops supplemental thrust. (G) The ducted fan can provide vectored thrust using exit deflectors, something much harder to implement with free propellers. (H) Some people find the device attractive.

(2) Cons of Ducted Fans

(A) The wetted area and geometric interferences of the duct adds drag to the airplane. (B) The duct adds weight (although this may be offset by the removal of a gear reduction unit). (C) It is an additional component to be manufactured, adding acquisition and maintenance cost for the customer. (D) Duct must be designed for a specific cruise condition for improved system efficiency. (E) Duct requires tight tolerances between the blade tip and internal surface, which increases cost of manufacturing. (F) The duct contributes to stability of the aircraft. If flow is separated on one side, the consequence is undesirable asymmetric lift and moments (e.g., see [28, 29]). (G) Ducted fans are better suited for lower speeds than free propellers. Note that the fan of a turbofan engine is (a) most effective at high M, whereas at low speeds, the thrust is largely generated by the hot section and (b) a turbofan is a fan + engine that requires the thermal cycle to be considered in addition to the movement of mass of air. Of course, the efficiency can be improved at higher airspeed, but only with reduced low-speed performance (unless variable pitch is employed). See ref. [30] for more drawbacks.

(3) Thrust, Power, and Propulsive Efficiency

Investigation of the ducted fan dates to 1944 to work by Krueger [31]. This was followed by contributions by Kucheman and Weber [32]. Experimental work is presented by Mort in refs. [33, 34]. Additional information on ducted fan design is provided by Sheehy [35] and Yılmaz *et al.* [36], to name a few, with the latter reflecting a recent renewed interest by researchers. Ducted fans are analyzed using the momentum theorem, just like free propellers. The presence of the duct introduces important changes to the flow-field. For instance, the static pressure behind the fan increases to ambient static pressure at the exit of the duct. This prevents *vena contracta* from forming in the propwash and, thus, realigns streamlines to eliminate momentum flux through the sides of the control volume. Using the geometry of Figure 15-43, thrust is written using Equation (15-85). Assume that (1) static pressure at the inlet and exit are equal and (2) an absence of *vena contracta* behind the exit. This gives:

Airspeed through rotor:

$$V_3 = V_\infty + w = \frac{\varepsilon_d V_\infty}{2} + \sqrt{\left(\frac{\varepsilon_d V_\infty}{2}\right)^2 + \frac{\varepsilon_d T}{\rho A_R}} \tag{15-87}$$

Airspeed at the exit: $V_4 = V_\infty + \Delta V = V_3/\varepsilon_d$ (15-88)

Thrust: $T = \dot{m}\Delta V = \rho A_R V_3 \left(\frac{V_3}{\varepsilon_d} - V_\infty\right)$ (15-89)

Power: $P_{req} = \frac{3}{4} T V_\infty + \sqrt{\frac{T^2 V_\infty^2}{4^2} + \frac{T^3}{4\rho A_R \varepsilon_d}}$ (15-90)

Induced airspeed: $w = \left(\frac{1}{2}\varepsilon_d - 1\right) V_\infty + \sqrt{\left(\frac{\varepsilon_d V_\infty}{2}\right)^2 + \frac{\varepsilon_d T}{\rho A_R}}$ (15-91)

where A_R is the rotor disc area and $\varepsilon_d \equiv A_4/A_R$ is the *diffuser expansion ratio* (see Figure 15-41). An $\varepsilon_d = 1$ means the exit diameter (A_4) equals the rotor diameter (A_R). An $\varepsilon_d > 1$ means the exit diameter is larger. The expansion ratio is the most effective design variable for the ducted fan [37].

Of course, the designer is interested in what engine power this calls for. In real applications, the duct and fan may be located on the airframe and be subject to flow contamination. To improve fidelity, it is necessary to incorporate an empirical constant, call it *fan effectiveness*, K_{fan}. Thus, we write

$$P_{ENG} = K_{fan} P_{req}/\eta_p \tag{15-92}$$

where η_p is the propeller efficiency of the fan (rotor). For an ideal fan installation $K_{fan} = 1$. For typical aviation applications, expect the following range $1 < K_{fan} < 1.15$ (or even higher for poor installations).

(4) Determination of Static Thrust

Consider the special case when $V_\infty = 0$. In this case, the induced velocity per Equation (15-91) reduces to:

$$w = \sqrt{\frac{\varepsilon_d T}{\rho A_R}} \tag{15-93}$$

Similarly, per Equation (15-90), since the rotor is at rest, only the induced power applies:

$$P_i = \frac{T^{1.5}}{\sqrt{4\rho A_R \varepsilon_d}} \tag{15-94}$$

This yields the following expression for static thrust, T_{STATIC}:

$$P_i = \frac{T^{1.5}}{\sqrt{\rho A_R/\varepsilon_d}} \quad \Rightarrow \quad T_{STATIC} = P_i^{2/3}(\rho A_R/\varepsilon_d)^{1/3} \qquad (15\text{-}95)$$

Equation (15-95) overestimates T_{STATIC} for various reasons, such as absence of blockage effects, the presence of the hub, which reduces the disc area, reduction of lift distribution near the hub, and so on. Therefore, for design purposes, estimate T_{STATIC} by the following empirical correction:

$$T_{STATIC} = K_P P_i^{2/3}(\rho A_R/\varepsilon_d)^{1/3} \qquad (15\text{-}96)$$

where K_P is a correction factor that depends on propeller geometry. Suitable values based on real airplanes are listed in Table 15-6.

(5) Reflections on Power Required

Note an interesting insight is gleaned by comparing the static power relations of the free propeller and ducted fan, Equations (15-79) and (15-94), respectively:

$$\frac{(P_i)_{duct}}{(P_i)_{prop}} = \frac{\dfrac{T_{duct}^{1.5}}{\sqrt{4\rho A_R \varepsilon_d}}}{\dfrac{T_{prop}^{1.5}}{\sqrt{2\rho A_P}}} = \frac{1}{\sqrt{2}}\left(\frac{T_{duct}}{T_{prop}}\right)^{1.5}\sqrt{\frac{A_P}{A_R\varepsilon_d}} \qquad (15\text{-}97)$$

Considering $\varepsilon_d = 1$ and $A_R = A_P$, the expression shows that to generate equal static thrust, the ducted fan requires only 71% of the power of the free propeller. Alternatively, given the same power, the ducted fan will develop 26% greater static thrust.

(6) Basic Sizing Procedure

Refer to the basic sizing procedure in Section 15.5.1 for additional information. To improve fidelity, the drag should incorporate changes associated with the size of the duct. The larger the duct, the more drag it develops. This requires drag to be written as $D = D_{basic} + D_{duct}$, where D_{basic} is the drag of the airplane minus the duct and D_{duct} is the drag of the duct. D_{basic} can be assumed that which was determined in Section 15.5.1(4).[15] D_{duct} can be estimated as $D_{duct} = qS_{wetduct}C_f$, where q is the dynamic pressure at cruise, $S_{wetduct}$ is the wetted area of the duct, and C_f is the skin friction coefficient (see Table 16-4). The $S_{wetduct}$ can be approximated as the total surface area of a cylinder of diameter $d_4 = (4A_4/\pi)^{1/2}$ and depth of c_{duct}.

STEP 1: Specify a target cruising speed (V_∞) for the vehicle and expected drag (D) at that airspeed. This drag must account for the presence of the duct. The designer should expect the drag for the ducted fan aircraft to be larger than that for an identical un-ducted aircraft.

STEP 2: Specify a desired rotor diameter (D_R) and calculate corresponding actuator disc area (A_R).

STEP 3: Calculate required induced velocity (w) per Equation (15-91).

STEP 4: Calculate the required power for flight (P_{req}) using Equation (15-90). It will be in units of J/s (or watts) in the SI-system or ft·lb$_f$/s in the UK-system.

STEP 5: Calculate the required engine power (P_{ENG}) per Equation (15-92) with an appropriate K_{fan} and η_p appropriate for the fan. It may be helpful to convert the power to kW or horsepower (see Table 7-1).

DERIVATION

Refer to Figure 15-43 for geometric definitions and stations. Define *expansion ratio* as $\varepsilon_d = A_4/A_R$, airspeed through fan as $V_3 = V_\infty + w$, and exit airspeed as $V_4 = V_\infty + \Delta V = V_3/\varepsilon_d$. Thus, we can write the mass flow through the device as

$$\dot{m} = \rho A_R V_3 = \rho A_4 V_4 = \rho A_R(V_\infty + w) = \rho A_4(V_\infty + \Delta V) \qquad \text{(i)}$$

Note that ΔV can be written as

$$\Delta V = V_4 - V_\infty = \frac{V_3}{\varepsilon_d} - V_\infty = \frac{V_\infty + w}{\varepsilon_d} - V_\infty \qquad \text{(ii)}$$

Thus, thrust can be written as

$$T = \dot{m}\Delta V = \rho A_R V_3\left(\frac{V_3}{\varepsilon_d} - V_\infty\right) \qquad \text{(iii)}$$

Solving for the airspeed through the fan, V_3, leads to the following quadratic equation and solution:

$$V_3^2 + (-\varepsilon_d V_\infty)V_3 - \frac{\varepsilon_d T}{\rho A_R} = 0$$

$$\Leftrightarrow \quad V_3 = \frac{\varepsilon_d V_\infty}{2} + \sqrt{\left(\frac{\varepsilon_d V_\infty}{2}\right)^2 + \frac{\varepsilon_d T}{\rho A_R}} \qquad \text{(iv)}$$

Thus, the induced speed at the fan is

$$V_3 = V_\infty + w \quad \Leftrightarrow \quad w = \left(\frac{1}{2}\varepsilon_d - 1\right)V_\infty + \sqrt{\left(\frac{\varepsilon_d V_\infty}{2}\right)^2 + \frac{\varepsilon_d T}{\rho A_R}} \qquad \text{(v)}$$

The power required can be evaluated as follows

$$P_{req} = \frac{1}{2}\dot{m}_4(V_4^2 - V_\infty^2) \qquad \text{(vi)}$$

Substitute Eqs (i), (ii), followed by Equation (iii) to get

$$P_{req} = \frac{1}{2}(\rho A_R V_3)\left(\left(\frac{V_3}{\varepsilon_d}\right)^2 - V_\infty^2\right)$$

$$= \frac{1}{2}\overbrace{(\rho A_R V_3)\left(\frac{V_3}{\varepsilon_d} - V_\infty\right)}^{T_{NET}}\left(\frac{V_3}{\varepsilon_d} + V_\infty\right) = \frac{T}{2}\left(\frac{V_3}{\varepsilon_d} + V_\infty\right) \qquad \text{(vii)}$$

Then, substitute Equation (iv) for V_3 into (vii) and after algebraic manipulations, we get

$$P_{req} = \frac{3}{4}TV_\infty + \sqrt{\frac{T^2V_\infty^2}{4^2} + \frac{T^3}{4\rho A_R\varepsilon_d}} \qquad \text{(viii)}$$

[15] Recall that this is an approximation method for conceptual sizing.

15.6 BLADE ELEMENT THEORY

The *Blade Element Theory* (BET) attempts to estimate the thrust of a propeller by dividing each blade into several segments, called *blade elements*. It treats each element as an independent 2-dimensional airfoil. This allows aerodynamic forces to be calculated based on local conditions at the element. Once these have been determined, they are summed to represent the properties of the complete propeller. The application of the method can account for airfoil geometry, chord, and pitch changes along the blade.

The BET was first devised by the Polish scientist Stefan Drzewiecki (1844–1938). It was developed between 1892 and 1920 as the *primitive blade element theory*. It was published in 1920 in his book *Théorie Générale de L'Hélice* (General Theory of Helixes) [38]. This simplified theory ignored the induced flow inside the propeller streamtube [39]. The speed of air inside the streamtube is higher than the far-field airspeed. This changes the AOA of the blade, skewing thrust predictions. It was improved by contributions by Albert Betz (1885–1968) and Hermann Glauert (1892–1934). In part, by the incorporation of induced flow using the Rankine–Froude momentum theorem. For this reason, BET is more appropriately called the *blade element momentum theory* (BEM).

The BET offers several advantages over the momentum theory. It allows variation in the blade chord, angle-of-pitch, and aerodynamic characteristics. It allows torque to be estimated, which allows the designer to determine the power required to swing it. It also allows the inclusion of nonlinear aerodynamic effects, such as that of lift and drag. It permits propeller efficiency to be determined. These are the primary reasons for the method's popularity in propeller design.

The BET is not perfect. It assumes unobstructed flow inside the streamtube, which is invalid for distorted streamtubes (e.g., due to blockage effects). The aerodynamic forces are treated as 2-dimensional, which neglects spanwise flow. Spanwise flow is important if large pressure gradients exist along the propeller blade. The theory assumes steady flow and does not model thrust lag caused by change in operating conditions (e.g., change in RPM). The basic theory also assumes rigid blades, ignoring aeroelastic effects. Also, a special correction must be made at the hub and tip to account for diminished lift and for a skewed inflow, such as a propeller at a high AOA (e.g., see Figure 15-16).

15.6.1 Formulation

Figure 15-44 shows a propeller of radius R rotating with an angular velocity of Ω radians/s. A representative blade element is shown whose chord is denoted with $c(r)$ and width with dr. Its centerline is located at a distance r.

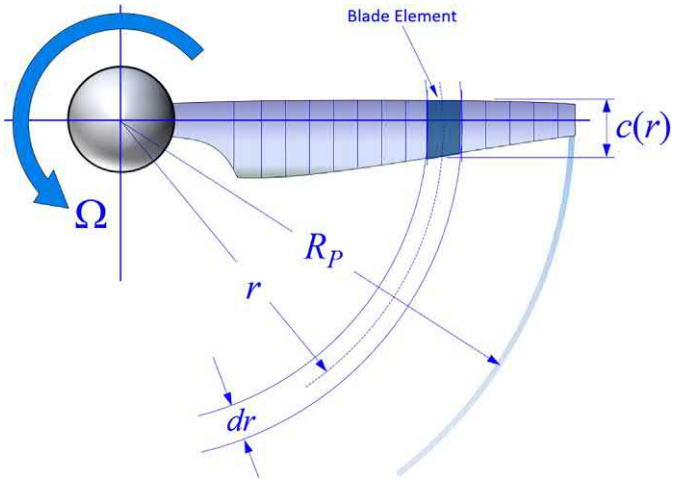


FIGURE 15-44 Definition of terms.

A cross-sectional view of this blade element, detailing airspeed components and angles, is shown in Figure 15-45.

The following parameters are identified in Figure 15-45:

r = Arbitrary distance from hub to blade element
V_∞ = Forward airspeed of the airplane
V_E = Effective resultant velocity
V_R = Resultant velocity
w = Elemental induced velocity due to streamtube flow being faster than the V_∞
Ω = Angular velocity of the propeller
α = Elemental angle-of-attack
α_i = Induced AOA that results from the induced velocity of air
α_{ZL} = Airfoil's zero lift angle
β = Pitch angle, which is defined as the angle between the rotation plane and the chordline of the blade element airfoil
ϕ = Helix angle

The differential lift and drag forces of the element, dL and dD, can now be written as follows:

$$dL = \frac{1}{2}\rho V_E^2 \cdot c(r) \cdot C_l \cdot dr = \frac{1}{2}\rho V_E^2 \cdot \Delta S \cdot C_l \qquad (15\text{-}98)$$

$$dD = \frac{1}{2}\rho V_E^2 \cdot c(r) \cdot C_d \cdot dr = \frac{1}{2}\rho V_E^2 \cdot \Delta S \cdot C_d \qquad (15\text{-}99)$$

where C_l and C_d are the section lift and drag coefficient of the element airfoil, respectively. The C_l of the element airfoil can also be written as follows:

$$C_l = f(\alpha) = \begin{cases} C_{l_\alpha}\alpha = C_{l_\alpha}(\beta - \phi - \alpha_i + \alpha_{ZL}) & \text{Form 1} \\ C_{l_o} + C_{l_\alpha}\alpha = C_{l_o} + C_{l_\alpha}(\beta - \phi - \alpha_i) & \text{Form 2} \\ C_l \ \ \text{look} - \text{up table} & \text{Form 3} \end{cases} \qquad (15\text{-}100)$$

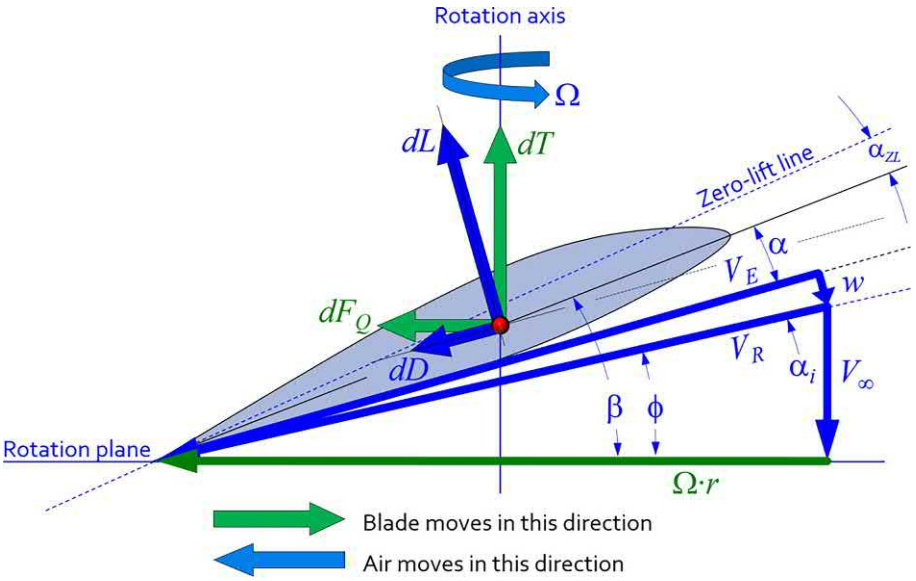


FIGURE 15-45 Definition of forces, angles, and velocity for the propeller blade.

Form 1 uses the airfoil's zero-lift line as a reference. Form 2 uses the chordline as a reference (presented here). Form 3 refers to the use of look-up tables. These typically reference the chordline. Similar approach can be used for C_d. The helix angle is calculated from the relation:

$$\phi = \tan^{-1}\left(\frac{V_\infty}{\Omega\, r}\right) \tag{15-101}$$

The term α_i is the angle-of-attack induced by w (see Section 15.6.2). If w is known, then α_i can be estimated from

$$\alpha_i = \sin^{-1}\left(\frac{w}{V_R}\right) = \sin^{-1}\left(\frac{w}{\sqrt{V_\infty^2 + (\Omega r)^2}}\right) \tag{15-102}$$

Knowing w also permits the effective resultant velocity, V_E, to be estimated as follows

$$V_E = \sqrt{(V_\infty + w)^2 + (\Omega r)^2} \tag{15-103}$$

As shown earlier, V_E must be used to calculate the aerodynamic forces acting on the element.

Figure 15-45 shows that dL is perpendicular to the vector V_E and dD is normal to it. Therefore, the differential thrust, torque, and power can be calculated as follows. Recall that power is Force × Speed. The power applied to each blade element equals the amount required to move it through air with force dF_Q at a speed $\Omega \cdot r$:

Elemental thrust:

$$dT = dL\cos(\phi + \alpha_i) - dD\sin(\phi + \alpha_i) \tag{15-104}$$

Elemental torque:

$$dQ = r \cdot dF_Q = r[dL\sin(\phi + \alpha_i) + dD\cos(\phi + \alpha_i)] \tag{15-105}$$

Elemental power:

$$dP = \Omega r \cdot dF_Q = \Omega r[dL\sin(\phi + \alpha_i) + dD\cos(\phi + \alpha_i)] \tag{15-106}$$

This allows us to calculate thrust and torque as follows:

Thrust:

$$T = N_B \int_{R_{hub}}^{R} dT = N_B \left[\int_{R_{hub}}^{R} dL\cos(\varphi + \alpha_i) - \int_{R_{hub}}^{R} dD\sin(\varphi + \alpha_i)\right] \tag{15-107}$$

Torque:

$$Q = N_B \int_{R_{hub}}^{R} r \cdot dF_Q = N_B \left[\int_{R_{hub}}^{R} r \cdot dL\sin(\varphi + \alpha_i) + \int_{R_{hub}}^{R} r \cdot dD\cos(\varphi + \alpha_i)\right] \tag{15-108}$$

Power:

$$P = N_B \int_{R_{hub}}^{R} \Omega r \cdot dF_Q = N_B \left[\int_{R_{hub}}^{R} \Omega r \cdot dL\sin(\varphi + \alpha_i) + \int_{R_{hub}}^{R} \Omega r \cdot dD\cos(\varphi + \alpha_i)\right] \tag{15-109}$$

where N_B is the number of propeller blades, R is the tip radius, and R_{hub} is the hub radius. Note that in the UK-system, the unit for torque is ft·lb$_f$ and ft·lb$_f$/s for

power. In the SI-system, the units are N·m (or J) and N·m/s (or W), respectively.

The remaining problem is to determine the induced AOA and its effect on the thrust and torque. It can be seen in Figure 15-45 that the presence of w reduces AOA and thus modifies the thrust and torque.

The BET does not directly evaluate the integrals of Equations (15-107)–(15-109). Rather, these are solved using numerical integration. This work is made easier using a spreadsheet or computer program. This increases flexibility and improves accuracy. This approach is used in this text. The following example displays how such a spreadsheet is constructed and incorporates real complexities such as a tapered blade chord, variable pitch angle, and lift and drag coefficients that are a function of the element's AOA.

15.6.2 Determination of w and α_i Using the Momentum Theory

We will now develop a method to determine the induced velocity, w and induced AOA, α_i. This is accomplished using the momentum theory of Section 15.5. It is best implemented in a spreadsheet or a computer program. Figure 15-45 shows how α_i depends on w, which, in turn, depends on the blade loading.

Consider the propeller of Figure 15-46. A circular area (or annulus) of width dr, located at blade station r is shown. The total area of the annulus is $dA = 2\pi r \cdot dr$. The total thrust of the propeller using the momentum theory of Section 15.5 is given by Equation 15.76), repeated here for convenience:

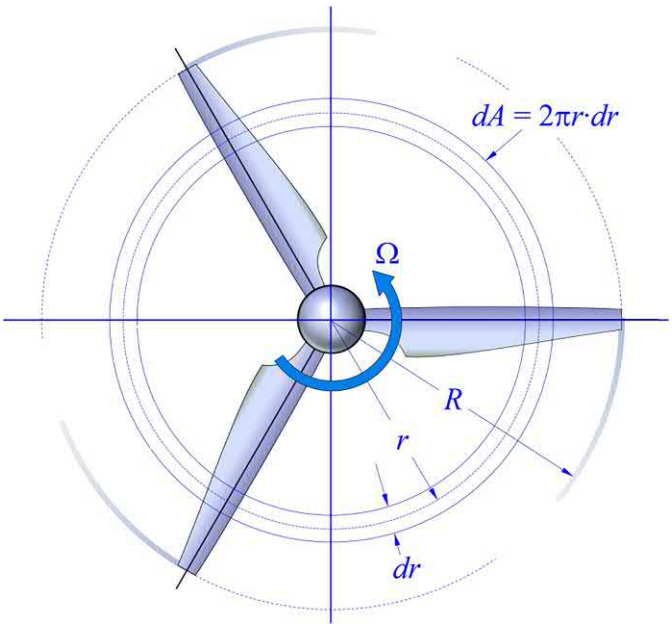


FIGURE 15-46 Annulus of an actuator disc.

$$T = 2\rho A_2 (V_\infty + w) w \tag{15-74}$$

where $A_P = \pi R^2$ is the area of the actuator disc, V_∞ is the far-field airspeed, ρ is density, and w is the velocity induced propeller at blade station r.

Therefore, the thrust generated by the annulus according to the momentum theory is:

$$dT = 2\rho(2\pi r \cdot dr)(V_\infty + w) w \tag{15-110}$$

In contrast, the thrust of the annulus per the BET is given by:

$$dT = \frac{N_B}{2}\rho \cdot c(r) \cdot \sqrt{(V_\infty + w)^2 + \Omega^2 r^2} \cdot [C_l \cdot (\Omega r) - C_d \cdot (V_\infty + w)] \cdot dr \tag{15-111}$$

Equating the two results and manipulating algebraically, leads to the following expression:

$$f(w) = \frac{8\pi r}{N_B \cdot c(r)} w - \sqrt{1 + \frac{\Omega^2 r^2}{(V_\infty + w)}}[C_l \cdot (\Omega r) - C_d \cdot (V_\infty + w)] \tag{15-112}$$

where $f(w)$ is a function whose root (w) we want to determine, i.e., the value of w that results in $f(w) = 0$. This condition is required for a proper inclusion of the propeller-induced velocity, w. One way, using the derivative of Equation (15-112), was presented in the first edition of this book. Another, more practical way is to implement a Newton–Raphson iterative scheme, like the one presented below.

STEP 1: Initial Value

Start with an initial value of w, call it w_0.

STEP 2: Determine $f'(w)$

Let h be a small value, e.g., $h = 0.01$. Calculate the slope of $f(w)$ using the following expression:

$$f'(w_0) = \frac{f(w_0 + h) - f(w_0 - h)}{2h}$$

STEP 3: Determine the Next w

Calculate the next value of w, call it w_1, using the following expression:

$$w_1 = w_0 - \frac{f(w_0)}{f'(w_0)}$$

where $f(w)$ is calculated from Equation (15-112).

STEP 4: Determine the Difference

Calculate the difference w_1–w_0. If this value is larger than, say, 0.01 then let $w_0 = w_1$ and go back to STEP 1. Otherwise, the value of w is the current value of w_1, completing the solution.

15.6.3 Compressibility Corrections

The local velocity of the blade elements near the tip of the propeller operate at high subsonic speeds. Consequently, these elements should be corrected for compressibility effects. These effects call for corrections of the drag that differ from that of lift. The corrections are applied to the drag and lift coefficients.

(1) Correction of Lift

The lift can be corrected using Prandtl–Glauert, Kármán–Tsien, or Laitone methods (see Section 8.3.8). The latter two must be applied to the pressure coefficients and, thus, require a knowledge of the chordwise distribution of pressure. The first one, Prandtl–Glauert, while simple to apply, becomes gradually inaccurate for airspeeds in the excess of Mach 0.70 to 0.75.

$$\text{Prandtl} - \text{Glauert: } C_{l_\alpha} = \frac{C_{l_{\alpha_0}}}{\sqrt{1-M^2}} \tag{15-113}$$

where

M = Helical Mach number (dependent on rotation and forward airspeed per Equation (15-11))
$C_{l\alpha}$ = Airfoil lift curve slope at the specific Mach number
$C_{l\alpha 0}$ = Incompressible airfoil lift curve slope.

(2) Correction of Drag

The propeller drag at high subsonic speeds must be corrected for skin-friction and wave-drag. Skin friction can be corrected using Equation (16-42) or (16-43), where the Mach number at each blade element is evaluated using Equation (15-11). Then, if the Mach number is greater than M_{crit} (see Section 8.3.7(3), *Airfoil Critical Mach Number*) the drag rise at the corresponding Mach number must be determined and applied.

15.6.4 Prandtl's Tip and Hub Loss Corrections

The section lift coefficients at the tip of any lifting surface vanish. Unmodified BET ignores this effect. This error was recognized by early scientists. The best known of those was Ludwig Prandtl (1875–1953) who developed a correction that is easily and conveniently incorporated into the BET [40]. This correction method has been expanded to include corrections at the hub as well (which is another radial where the lift goes to zero). Applying the corrections is a three-step process. Note that ϕ is the helix angle, N_B is the number of blades, and R_P is the propeller radius.

STEP 1: Tip Correction Parameter
Calculate a Tip Correction Parameter, P_{tip}:

$$P_{tip} = \frac{N_B}{2}\frac{R_P - r}{r\sin\phi} \tag{15-114}$$

STEP 2: Tip Correction
Calculate the Tip Correction factor, F_{tip}:

$$F_{tip} = \frac{2}{\pi}\cos^{-1}\left(e^{-P_{tip}}\right) \tag{15-115}$$

STEP 3: Hub Correction Parameter
Calculate a Hub Correction Parameter, P_{hub}:

$$P_{hub} = \frac{N_B}{2}\frac{r - R_{hub}}{r\sin\phi} \tag{15-116}$$

STEP 4: Hub Correction
Calculate a Hub Correction factor, F_{hub}:

$$F_{hub} = \frac{2}{\pi}\cos^{-1}\left(e^{-P_{hub}}\right) \tag{15-117}$$

STEP 5: Prandtl Correction
Calculate a common correction factor, F_P, for Prandtl correction:

$$F_P = F_{hub} \cdot F_{tip} \tag{15-118}$$

The factor F_P should vary from 0 at the hub, to a value close to 1 over the mid span of the blade, and back to 0 at the tip. This factor is then used by modifying Equations (15-107)–(15-109) as follows:

$$\text{Thrust: } T = N_B \cdot F_P \left[\int_{R_{hub}}^{R_P} dL\cos(\phi+\alpha_i) - \int_{R_{hub}}^{R_P} dD\sin(\phi+\alpha_i)\right] \tag{15-119}$$

$$\text{Torque: } Q = N_B \cdot F_P \left[\int_{R_{hub}}^{R_P} r\cdot dL\sin(\phi+\alpha_i) + \int_{R_{hub}}^{R_P} r\cdot dD\cos(\phi+\alpha_i)\right] \tag{15-120}$$

$$\text{Power: } P = N_B \cdot F_P \left[\int_{R_{hub}}^{R_P} \Omega r\cdot dL\sin(\phi+\alpha_i) + \int_{R_{hub}}^{R_P} \Omega r\cdot dD\cos(\phi+\alpha_i)\right] \tag{15-121}$$

EXAMPLE 15-18

Determine the thrust, torque, and power of a 69-in diameter, two-bladed propeller with an 18-in diameter hub. The blades are constant chord of $c(r) = 3.7$ in. The pitch varies linearly from 40° at the hub to 16° at the tip. The propeller rotates at 2500 RPM at a forward speed of 116 KTAS at S-L. The propeller's representative airfoil at $r = 0.75R_p$ is a Clark Y, whose lift and drag coefficients are given in ref. [41]. Use 20 elements.

SOLUTION:

This problem applies the blade-element theory using a spreadsheet. Blade dimensions are shown in Figure 15-47. Expect minor numerical differences if calculating along. The arithmetic was conducted using single floating-point accuracy and the arguments do not show the complete values. The solution is prepared as shown in the table in Figure 15-48. In interest of space, the table is broken into 3 subtables, consisting of Columns 2–11, 12–19, and 19–27 and each will be given more space so their content will be legible. Parameters associated the element in Row 10 (blue shading) are calculated below.

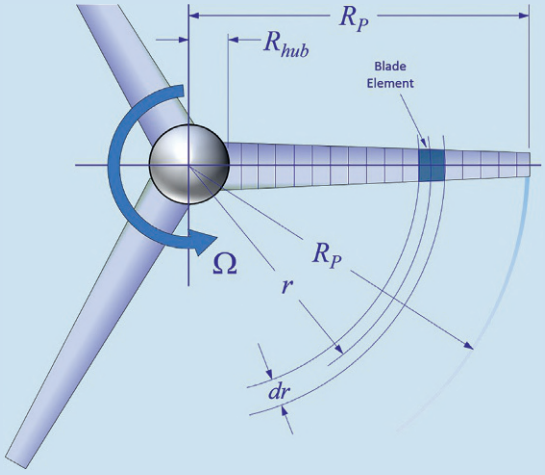


FIGURE 15-47 Arbitrary propeller blade geometry.

First, several preliminary values must be calculated: Revolutions per second:

$$n = \frac{RPM}{60} = \frac{2500}{60} = 41.67 \text{ rad/s}.$$

Angular velocity:

$$\Omega = 2\pi\left(\frac{RPM}{60}\right) = 2\pi\left(\frac{2500}{60}\right) = 261.8 \text{ rad/s}.$$

Hub radius: $R_{hub} = \left(\frac{18''}{2}\right)\left(\frac{1 \text{ ft}}{12''}\right) = 0.7500 \text{ ft}$

Tip radius: $R_P = \left(\frac{69''}{2}\right)\left(\frac{1 \text{ ft}}{12''}\right) = 2.875 \text{ ft}$

Element width:

$$\Delta r = \left(\frac{69'' - 18''}{2}\right)\left(\frac{1 \text{ ft}}{12''}\right)\frac{1}{20 \text{ elements}} = 0.1063 \frac{\text{ft}}{\text{element}}.$$

Speed of sound at S-L: $a = 1116$ ft/s.

Thus, the first blade station in Figure 15-49 (see Row 1) is the hub radius plus one half of the element width because the radials are positioned at the center of the elements (see Figure 15-47). Note that numerical subscripts refer to the row number, we get:

$$r_1 = R_{hub} + \frac{\Delta r}{2} = 0.7500 + \frac{0.1063}{2} = 0.8032 \text{ ft}$$

Subsequent blade stations can be calculated by simply adding Δr to the previous blade station.

STEP 1: Table Columns 2–11

Refer to Figure 15-49. Column 2 is calculated for each row by adding the element width Δr to the radial in the previous row. Thus, the radial in Row 10 equals the one in Row 9 (1.653) plus Δr, or:

$$r_{10} = r_9 + \Delta r = 1.653 + 0.1063 = 1.759 \text{ ft}$$

Column 3 is the fraction of the blade span (see for instance Figure 15-50), calculated as follows:

$$x_{10} = \frac{r_{10}}{R_P} = \frac{1.759}{2.875} = 0.6118$$

1	2	3	4	5	6	7	8	9	10	11	12	13	14	15	16	17	18	19	20	21	22	23	24	25	26	27
	Blade Geometry				Airspeed Components, ft/s						Flow Angles								Lift and Drag Coefficient			Blade Element Differentials				
	r	$x = r/R$	$c(r)$	ΔS	V_∞	Ωr	V_R	w	V_E	M	β		ϕ		α_i		$\alpha = \beta - \phi - \alpha_i$		Re	C_l	C_d	dL	dD	dT	dQ	dP
ID	ft		ft	ft²	ft/s	ft/s	ft/s	ft/s	ft/s		radians	degrees	radians	degrees	radians	degrees	radians	degrees				lb_f	lb_f	lb_f	ft-lb_f	ft-lb_f/s
1	0.803	0.279	0.3083	0.0328	195.8	210.3	287.3	1.476	288.3	0.258	0.688	39.40	0.7498	42.96	0.005	0.294	-0.067	-3.856	564542	0.1678	0.01123	0.54	0.04	0.4	0.3	84
2	0.909	0.316	0.3083	0.0328	195.8	238.1	308.3	3.017	310.2	0.278	0.667	38.20	0.688	39.44	0.010	0.561	-0.031	-1.797	607338	0.3134	0.01476	1.17	0.06	0.9	0.7	190
3	1.016	0.353	0.3083	0.0328	195.8	265.9	330.2	4.459	332.9	0.298	0.646	37.00	0.635	36.37	0.014	0.774	-0.002	-0.143	651774	0.4323	0.01947	1.87	0.08	1.4	1.2	317
4	1.122	0.390	0.3083	0.0328	195.8	293.7	353.0	5.796	356.2	0.319	0.625	35.80	0.588	33.69	0.016	0.941	0.020	1.169	697529	0.5275	0.02452	2.61	0.12	2.1	1.8	465
5	1.228	0.427	0.3083	0.0328	195.8	321.5	376.5	7.023	380.2	0.341	0.604	34.60	0.547	31.34	0.019	1.069	0.038	2.189	744352	0.6019	0.02932	3.39	0.17	2.8	2.4	629
6	1.334	0.464	0.3083	0.0328	195.8	349.3	400.5	8.138	404.5	0.362	0.583	33.40	0.511	29.27	0.020	1.164	0.052	2.965	792049	0.6583	0.03350	4.20	0.21	3.5	3.1	807
7	1.441	0.501	0.3083	0.0328	195.8	377.2	425.0	9.139	429.2	0.385	0.562	32.20	0.479	27.44	0.022	1.232	0.062	3.531	840468	0.6993	0.03686	5.02	0.26	4.3	3.8	996
8	1.547	0.538	0.3083	0.0328	195.8	405.0	449.8	10.027	454.3	0.407	0.541	31.00	0.450	25.80	0.022	1.277	0.068	3.918	889490	0.7272	0.03932	5.85	0.32	5.1	4.6	1192
9	1.653	0.575	0.3083	0.0328	195.8	432.8	475.0	10.803	479.6	0.430	0.520	29.80	0.425	24.34	0.023	1.303	0.072	4.153	939022	0.7441	0.04087	6.67	0.37	5.9	5.3	1392
10	1.759	0.612	0.3083	0.0328	195.8	460.6	500.5	11.470	505.1	0.453	0.499	28.60	0.402	23.03	0.023	1.313	0.074	4.256	988987	0.7514	0.04156	7.47	0.41	6.6	6.1	1591
11	1.866	0.649	0.3083	0.0328	195.8	488.4	526.2	12.025	530.8	0.476	0.478	27.40	0.381	21.85	0.023	1.309	0.074	4.245	1039320	0.7506	0.04148	8.24	0.46	7.4	6.8	1787
12	1.972	0.686	0.3083	0.0328	195.8	516.2	552.1	12.469	556.7	0.499	0.457	26.20	0.363	20.77	0.023	1.294	0.072	4.134	1089970	0.7427	0.04074	8.97	0.49	8.1	7.5	1974
13	2.078	0.723	0.3083	0.0328	195.8	544.1	578.2	12.801	582.7	0.522	0.436	25.00	0.345	19.79	0.022	1.269	0.069	3.937	1140893	0.7286	0.03944	9.64	0.52	8.8	8.2	2149
14	2.184	0.760	0.3083	0.0328	195.8	571.9	604.5	13.019	608.8	0.546	0.415	23.80	0.330	18.90	0.022	1.234	0.064	3.665	1192054	0.7090	0.03770	10.24	0.54	9.4	8.8	2307
15	2.291	0.797	0.3083	0.0328	195.8	599.7	630.8	13.121	635.0	0.569	0.394	22.60	0.316	18.08	0.021	1.192	0.058	3.325	1243420	0.6844	0.03561	10.75	0.56	10.0	9.3	2445
16	2.397	0.834	0.3083	0.0328	195.8	627.5	657.3	13.106	661.4	0.593	0.374	21.40	0.302	17.33	0.020	1.142	0.051	2.927	1294968	0.6556	0.03329	11.17	0.57	10.4	9.8	2558
17	2.503	0.871	0.3083	0.0328	195.8	655.3	683.9	12.972	687.8	0.616	0.353	20.20	0.290	16.64	0.019	1.087	0.043	2.477	1346674	0.6228	0.03081	11.48	0.57	10.8	10.1	2644
18	2.609	0.908	0.3083	0.0328	195.8	683.1	710.6	12.718	714.3	0.640	0.332	19.00	0.279	15.99	0.018	1.025	0.035	1.981	1398521	0.5867	0.02827	11.66	0.56	11.0	10.3	2698
19	2.716	0.945	0.3083	0.0328	195.8	710.9	737.4	12.343	740.8	0.664	0.311	17.80	0.269	15.40	0.017	0.959	0.025	1.442	1450494	0.5474	0.02573	11.70	0.55	11.1	10.4	2718
20	2.822	0.982	0.3083	0.0328	195.8	738.8	764.3	11.846	767.4	0.688	0.290	16.60	0.259	14.84	0.015	0.888	0.015	0.867	1502579	0.5055	0.02325	11.60	0.53	11.0	10.3	2702
																					SUMS =			130.8	120.9	31643

FIGURE 15-48 Completed spreadsheet analysis.

EXAMPLE 15-18 (*cont'd*)

Column 4 is the elemental chord. In this example, the chord is a constant 0.3083 ft. For trapezoidal elements, use the average chord. Column 5 is the area of the blade element and is calculated as follows:

$$\Delta S_{10} = c(r) \cdot \Delta r = 0.3083 \times 0.1063 = 0.03277 \text{ ft}^2$$

Column 6 is the far-field airspeed (i.e., the airplane's airspeed) converted to ft/s, i.e., 116 KTAS × 1.688 = 195.8 ft/s. It is equal for all the rows. Column 7 is the blade's angular velocity and is calculated as follows for Row 10:

$$\Omega \cdot r_{10} = 261.8 \times 1.759 = 460.6 \text{ ft/s}$$

V_R is calculated in Column 8 per Equation (15-11):

$$V_{R_{10}} = \sqrt{V_\infty^2 + \Omega^2 r_{10}^2} = \sqrt{195.8^2 + 460.6^2} = 500.5 \text{ ft/s}$$

The induced velocity is shown in Column 9. It is calculated later using a special iterative procedure detailed in a Step-by-Step below. It is presented like this because it helps to first introduce the required parameters in the other columns. If we know w, then the effective velocity, V_E, is calculated per Equation (15-103):

$$V_{E_{10}} = \sqrt{(V_\infty + w)^2 + (\Omega r)^2}$$
$$= \sqrt{(195.8 + 11.47)^2 + (261.8 \times 1.759)^2} = 505.1 \text{ ft/s}$$

Finally, the Mach number is calculated in Column 11. It is not used in this example, but may be needed for compressibility corrections.

$$M_{10} = V_{E_{10}}/a = 505.1/1116 = 0.453$$

STEP 2: Table Columns 12–19

The next subtable contains the flow angles (see Figure 15-51). Columns 12 and 13 contain the geometric pitch angle β in radians and degrees for each radial station. These were specified as 40° at the hub ($r = 0.75$ ft) and 16° at the tip ($r = 2.875$ ft). We can calculate β at

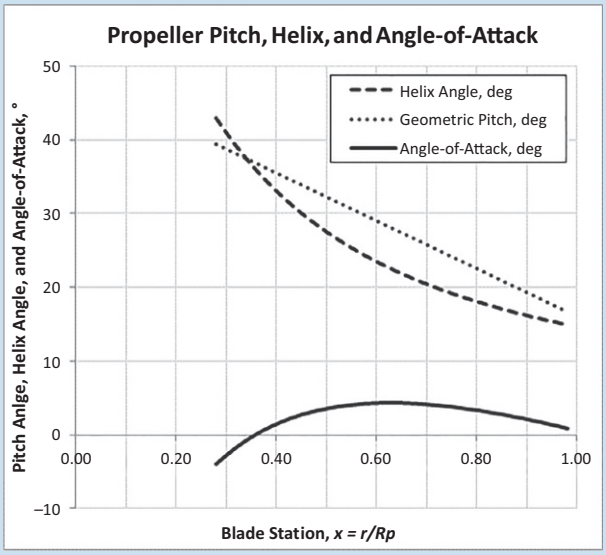


FIGURE 15-50 Results from angular analysis for the condition.

1	2	3	4	5	6	7	8	9	10	11
	Blade Geometry				Airspeed Components, ft/s					
	r	$x = r/R$	$c(r)$	ΔS	V_∞	Ωr	V_R	w	V_E	M
ID	ft		ft	ft²	ft/s	ft/s	ft/s	ft/s	ft/s	
1	0.803	0.279	0.3083	0.0328	195.8	210.3	287.3	1.476	288.3	0.258
2	0.909	0.316	0.3083	0.0328	195.8	238.1	308.3	3.017	310.2	0.278
3	1.016	0.353	0.3083	0.0328	195.8	265.9	330.2	4.459	332.9	0.298
4	1.122	0.390	0.3083	0.0328	195.8	293.7	353.0	5.796	356.2	0.319
5	1.228	0.427	0.3083	0.0328	195.8	321.5	376.5	7.023	380.2	0.341
6	1.334	0.464	0.3083	0.0328	195.8	349.3	400.5	8.138	404.5	0.362
7	1.441	0.501	0.3083	0.0328	195.8	377.2	425.0	9.139	429.2	0.385
8	1.547	0.538	0.3083	0.0328	195.8	405.0	449.8	10.027	454.3	0.407
9	1.653	0.575	0.3083	0.0328	195.8	432.8	475.0	10.803	479.6	0.430
10	1.759	0.612	0.3083	0.0328	195.8	460.6	500.5	11.470	505.1	0.453
11	1.866	0.649	0.3083	0.0328	195.8	488.4	526.2	12.025	530.8	0.476
12	1.972	0.686	0.3083	0.0328	195.8	516.2	552.1	12.469	556.7	0.499
13	2.078	0.723	0.3083	0.0328	195.8	544.1	578.2	12.801	582.7	0.522
14	2.184	0.760	0.3083	0.0328	195.8	571.9	604.5	13.019	608.8	0.546
15	2.291	0.797	0.3083	0.0328	195.8	599.7	630.8	13.121	635.0	0.569
16	2.397	0.834	0.3083	0.0328	195.8	627.5	657.3	13.106	661.4	0.593
17	2.503	0.871	0.3083	0.0328	195.8	655.3	683.9	12.972	687.8	0.616
18	2.609	0.908	0.3083	0.0328	195.8	683.1	710.6	12.718	714.3	0.640
19	2.716	0.945	0.3083	0.0328	195.8	710.9	737.4	12.343	740.8	0.664
20	2.822	0.982	0.3083	0.0328	195.8	738.8	764.3	11.846	767.4	0.688

FIGURE 15-49 Results for Columns 1 through 11.

EXAMPLE 15-18 (*cont'd*)

11	12	13	14	15	16	17	18	19
	Flow Angles							
M	β		ϕ		α_i		$\alpha = \beta - \phi - \alpha_i$	
	radians	degrees	radians	degrees	radians	degrees	radians	degrees
0.258	0.688	39.40	0.7498	42.96	0.005	0.294	-0.067	-3.856
0.278	0.667	38.20	0.688	39.44	0.010	0.561	-0.031	-1.797
0.298	0.646	37.00	0.635	36.37	0.014	0.774	-0.002	-0.143
0.319	0.625	35.80	0.588	33.69	0.016	0.941	0.020	1.169
0.341	0.604	34.60	0.547	31.34	0.019	1.069	0.038	2.189
0.362	0.583	33.40	0.511	29.27	0.020	1.164	0.052	2.965
0.385	0.562	32.20	0.479	27.44	0.022	1.232	0.062	3.531
0.407	0.541	31.00	0.450	25.80	0.022	1.277	0.068	3.918
0.430	0.520	29.80	0.425	24.34	0.023	1.303	0.072	4.153
0.453	0.499	28.60	0.402	23.03	0.023	1.313	0.074	4.256
0.476	0.478	27.40	0.381	21.85	0.023	1.309	0.074	4.245
0.499	0.457	26.20	0.363	20.77	0.023	1.294	0.072	4.134
0.522	0.436	25.00	0.345	19.79	0.022	1.269	0.069	3.937
0.546	0.415	23.80	0.330	18.90	0.022	1.234	0.064	3.665
0.569	0.394	22.60	0.316	18.08	0.021	1.192	0.058	3.325
0.593	0.374	21.40	0.302	17.33	0.020	1.142	0.051	2.927
0.616	0.353	20.20	0.290	16.64	0.019	1.087	0.043	2.477
0.640	0.332	19.00	0.279	15.99	0.018	1.025	0.035	1.981
0.664	0.311	17.80	0.269	15.40	0.017	0.959	0.025	1.442
0.688	0.290	16.60	0.259	14.84	0.015	0.888	0.015	0.867

FIGURE 15-51 Results for Columns 12 through 19.

any radial station using the parametric formulation below:

$$\beta_j = 40\left(1 - \frac{j-0.5}{20}\right) + 16\left(\frac{j-0.5}{20}\right)$$

$$\Rightarrow \quad \beta_{10} = 40\left(1 - \frac{10-0.5}{20}\right) + 16\left(\frac{10-0.5}{20}\right) = 28.6°$$

Note that 0.5 (rather than 1) is subtracted from the row index because we specify the angle at the middle of the elements. Columns 14 and 15 contain the helix angle in radians and degrees. For Row 10, this is calculated as follows:

$$\phi_{10} = \tan^{-1}\left(\frac{V_\infty}{\Omega \cdot r_{10}}\right) = \tan^{-1}\left(\frac{195.8}{460.6}\right) = 0.402 \text{ rad} = 23.0°$$

Columns 16 and 17 contain the induced flow angle, α_i, calculated using Equation (15-102).

$$\alpha_{i_{10}} = \sin^{-1}\left(\frac{w_{10}}{V_{R_{10}}}\right) = \sin^{-1}\left(\frac{11.47}{500.5}\right) = 0.0229 \text{ rad} \quad (= 1.31°)$$

Columns 18 and 19 contain the AOA of the airfoil element. Referring to Figure 15-51, we see that α is determined per Equation (15-100) as follows:

$$\alpha_{10} = \beta_{10} - \phi_{10} - \alpha_{i_{10}} = 28.60° - 23.03° - 1.313° = 4.256°$$

STEP 3: Table Columns 20–27

The next subtable contains the forces (see Figure 15-52). Column 20 contains the Reynolds number for the blade elements, calculated using Equation (16-25):

$$R_{e_{10}} \approx \frac{\rho V_{R_{10}} \cdot c(r_{10})}{\mu} = \frac{(0.002378)(505.1)(0.3083)}{3.7447 \times 10^{-7} \text{ lb}_\text{f} \cdot \text{s/ft}^2} = 988987$$

The R_e for the propeller elements ranges from approximately 560,000 to 1,500,000. Thus, Table III of ref. [41] was selected as a source of the C_l and C_d. These data are plotted in Figure 15-53 and curve-fitted using a best fit polynomial. It is valid only for $-9° < \alpha < 21°$. Note that Column 19 shows that all the elemental α are within this range. These curve-fits are presented below and calculated for Row 10 using the previously calculated $\alpha = 4.26°$ for that station:

$$C_{l_{10}} = -0.000004582 \cdot \alpha^4 - 0.00002926 \cdot \alpha^3 + 0.000249 \cdot \alpha^2 + 0.07239 \cdot \alpha + 0.4426 = 0.7514$$

$$C_{d_{10}} = 0.000006844 \cdot \alpha^3 + 0.0003439 \cdot \alpha^2 + 0.003488 \cdot \alpha + 0.01996 = 0.04156$$

Columns 23 and 24 contain the differential lift and drag acting on the element and is calculated using Equations (15-98) and (15-99). For Row 10 this becomes:

EXAMPLE 15-18 (*cont'd*)

18	19	20	21	22	23	24	25	26	27
		Lift and Drag Coefficient			Blade Element Differentials				
$\alpha = \beta - \phi - \alpha_i$		Re	C_l	C_d	dL	dD	dT	dQ	dP
radians	degrees				lb_f	lb_f	lb_f	ft·lb_f	ft·lb_f/s
-0.067	-3.856	564542	0.1678	0.01123	0.54	0.04	0.4	0.3	84
-0.031	-1.797	607338	0.3134	0.01476	1.17	0.06	0.9	0.7	190
-0.002	-0.143	651774	0.4323	0.01947	1.87	0.08	1.4	1.2	317
0.020	1.169	697529	0.5275	0.02452	2.61	0.12	2.1	1.8	465
0.038	2.189	744352	0.6019	0.02932	3.39	0.17	2.8	2.4	629
0.052	2.965	792049	0.6583	0.03350	4.20	0.21	3.5	3.1	807
0.062	3.531	840468	0.6993	0.03686	5.02	0.26	4.3	3.8	996
0.068	3.918	889490	0.7272	0.03932	5.85	0.32	5.1	4.6	1192
0.072	4.153	939022	0.7441	0.04087	6.67	0.37	5.9	5.3	1392
0.074	4.256	988987	0.7514	0.04156	7.47	0.41	6.6	6.1	1591
0.074	4.245	1039320	0.7506	0.04148	8.24	0.46	7.4	6.8	1787
0.072	4.134	1089970	0.7427	0.04074	8.97	0.49	8.1	7.5	1974
0.069	3.937	1140893	0.7286	0.03944	9.64	0.52	8.8	8.2	2149
0.064	3.665	1192054	0.7090	0.03770	10.24	0.54	9.4	8.8	2307
0.058	3.325	1243420	0.6844	0.03561	10.75	0.56	10.0	9.3	2445
0.051	2.927	1294968	0.6556	0.03329	11.17	0.57	10.4	9.8	2558
0.043	2.477	1346674	0.6228	0.03081	11.48	0.57	10.8	10.1	2644
0.035	1.981	1398521	0.5867	0.02827	11.66	0.56	11.0	10.3	2698
0.025	1.442	1450494	0.5474	0.02573	11.70	0.55	11.1	10.4	2718
0.015	0.867	1502579	0.5055	0.02325	11.60	0.53	11.0	10.3	2702
						SUMS =	**130.8**	**120.9**	**31643**

FIGURE 15-52 Results for Columns 18 through 25.

$$dL = \frac{1}{2}\rho V_E^2 \cdot \Delta S \cdot C_l$$
$$= \frac{1}{2}(0.002378)(505.1)^2 \cdot (0.03277) \cdot (0.7514) = 7.47\ lb_f$$
$$dD = \frac{1}{2}\rho V_E^2 \cdot \Delta S \cdot C_d$$
$$= \frac{1}{2}(0.002378)(505.1)^2 \cdot (0.03277) \cdot (0.04156) = 0.413\ lb_f$$

Column 25 contains the differential thrust calculated using Equation (15-104):

$$dT = dL\cos(\phi + \alpha_i) - dD\sin(\phi + \alpha_i)$$
$$= 7.47\ \cos(23.03 + 1.313) - 0.413\ \sin(23.03 + 1.313) = 6.63\ \text{lb}_\text{f}$$

Column 26 contains the differential torque calculated using Equation (15-105):

$$dQ = r[dL\sin(\phi + \alpha_i) + dD\cos(\phi + \alpha_i)]$$
$$= 1.759 \times [7.47\ \sin(23.03 + 1.313) + 0.413\ \cos(23.03 + 1.313)]$$
$$= 6.08\ \text{ft} \cdot \text{lb}_\text{f}$$

Column 27 contains the differential power calculated using Equation (15-106):

$$dP = \Omega r[dL\sin(\phi + \alpha_i) + dD\cos(\phi + \alpha_i)]$$
$$= 460.6 \times [7.47\ \sin(23.03 + 1.313)$$
$$+ 0.413\ \cos(23.03 + 1.313)] = 1591\ \text{ft} \cdot \text{lb}_\text{f}/\text{s}$$

Procedure to Obtain the Induced Velocity, w

The induced velocity requires an iterative scheme. Note that all columns formulas except Column 9. It contains a number. When starting the solution for a specific flight condition, we enter zero for w in all the cells of Column 9. Then, we calculate what the w should be according to Ω and the current values in columns 2 (r), 4 ($c(r)$), 6 (V_∞), 21 (C_l), and 22 (C_d). This is accomplished using the Newton–Raphson iterative scheme of Section 15.6.2. One way is using the VBA code of Section 15.6.5. In this example, the author placed the VBA function (called `Vinduced(Vinf, Omega, r, NB, CofR, Cd, Cl)`) in a dedicated column, to the right of the main table. Then, its content is repeatedly copied and pasted into Column 9, until both columns show the same results. Here, the results for Row 10 is shown. It usually takes 5 to 7 iterations to reach acceptable accuracy.

STEP 1: Start the iterative process to compute w_{10}. Note that in this first iteration (for which $w_{10} = 0$), $\alpha_{10} = 5.569°$. Thus, $C_{l10} = 0.8440$ and $C_{d10} = 0.05123$ are obtained from their above curve-fit expressions. These will change in subsequent iterations. Substitute the current values above into the `Vinduced` routine. This first call has the following arguments: `Vinduced(195.8,261.8,1.759,2,0.3083, 0.05123,0.8440)`. This call populates Equation (15-112) as follows

EXAMPLE 15-18 (*cont'd*)

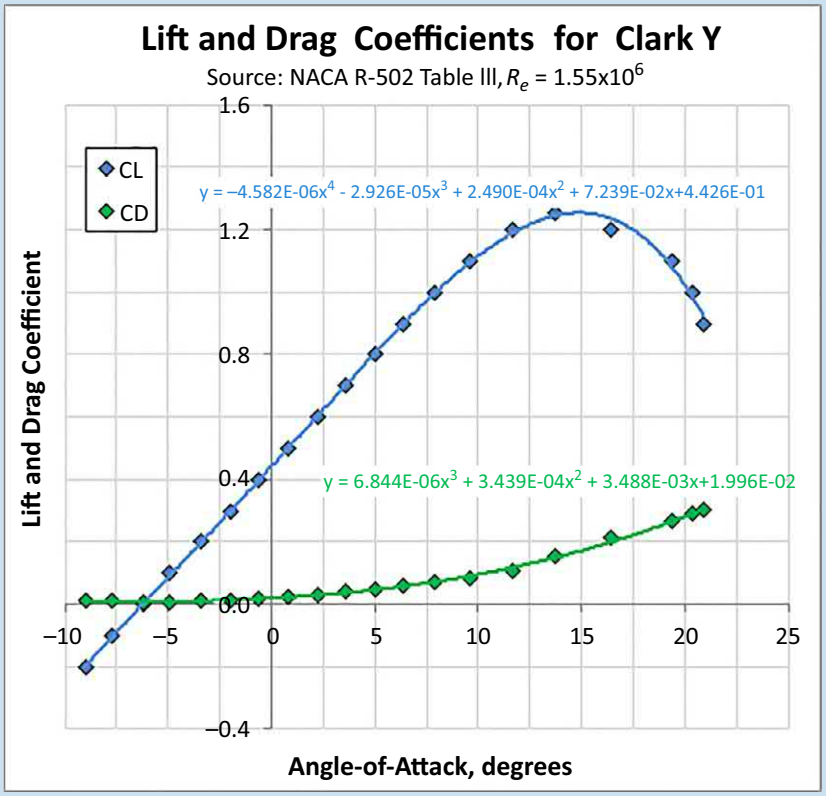


FIGURE 15-53 Original data from ref. [41] plotted and curve fitted.

$$f(w)=\frac{8\pi r}{N_B\cdot c(r)}w-\sqrt{1+\frac{(\Omega r)^2}{(V_\infty+w)}}[C_l\cdot(\Omega r)-C_d\cdot(V_\infty+w)]$$

$$=\frac{8\pi(1.759)}{(2)(0.3083)}w-\sqrt{1+\frac{(460.6)^2}{(195.8+w)}}[(0.8440)(460.6)-(0.05123)(195.8+w)]$$

$$=71.697w-\sqrt{1+\frac{212152}{(195.8+w)}}[378.72-0.05123w]$$

It then proceeds to solve the equation using the Newton–Raphson scheme. The first time, it returns $w_{10}=12.74$ ft/s.

STEP 2: Copy the column of induced velocities and paste as numbers into Column 9. This mirrors Step 1. The nonzero w will change the numbers in the other cells. Iteration 2 returned $w_{10}=11.32$ ft/s. Iteration 3 returned $w_{10}=11.49$ ft/s, and iteration 6 and 7 return the same number to the fifth significant number, $w_{10}=11.469$ ft/s.

Remaining Calculations

Once all the rows have been calculated in this fashion the next step is to sum up the dT, dQ, and dP, but the sum is the thrust, torque, and power generated by a single blade. These values must be multiplied by 2 to account for the two propeller blades. The resulting values are:

Thrust: $T=2\times130.8=261.6$ lb$_f$

Torque: $Q=2\times120.9=241.8$ ft · lb$_f$

Power: $P=2\times31643=63286$ ft · lb$_f$/s

$$=\frac{63286}{550}=115.1\text{ BHP}$$

Note that Prandtl's tip and hub correction of Section 15.6.4 is not used here. The reader can incorporate it easily by multiplying dT, dQ, and dP by the value of F_P, as shown in Equations (15-119)–(15-121).

We can calculate additional information as shown below:

Thrust coefficient:

$$C_T=\frac{T}{\rho n^2D_P^4}=\frac{261.6}{(0.002378)(41.67)^2(69/12)^4}=0.05797.$$

Torque coefficient:

$$C_Q=\frac{Q}{\rho n^2D_P^5}=\frac{782}{(0.002378)(41.67)^2(69/12)^5}=0.009316.$$

Power coefficient:

$$C_P=\frac{P}{\rho n^3D_P^5}=\frac{63286}{(0.002378)(41.67)^3(69/12)^5}=0.05853.$$

EXAMPLE 15-18 (*cont'd*)

Advance ratio: $J = \dfrac{V_\infty}{nD_P} = \dfrac{195.8}{(41.67)(69/12)} = 0.8173.$

Propeller efficiency:

$$\eta_p = J\frac{C_T}{C_P} = 0.8173\frac{0.05797}{0.05853} = 0.8094.$$

Finally, note that the power can also be calculated using the torque coefficient as follows:

$$C_P = 2\pi C_Q = 2\pi(0.009316) = 0.05853$$
$$\Rightarrow \quad P = \rho n^3 D^5 C_P = (0.002378)(41.67)^3(69/12)^5(0.05853)$$
$$= 63286 \text{ ft} \cdot \text{lb}_\text{f}/\text{s}$$

15.6.5 Computer Code: Determination of the Propeller Induced Velocity

The solution procedure shown in Example 15-18 was implemented in Microsoft Excel. The program allows the iterative determination of w using the Newton–Raphson algorithm to be written in Visual Basic for Applications (VBA) and is shown below. The function `F_of_w` calculates the value of $f(w)$ using a number of input variables V_∞, Ω, r, N_B, $c(r)$, C_d, C_l, and w, per Equation (15-112).

```
Function F_of_w(Vinf As Single, Omega As Single, r As Single, NB As Single, CofR As
Single,Cd As Single, Cl As Single, w As Single) As Single
'NOTE: 8 * 3.14159265358979 = 25.1327412287183
    F_of_w = 25.1327412287183 * w * r / (NB * CofR) - Sqr(1 + (Omega * r / (Vinf + w))
^ 2) * (Cl * Omega * r - Cd * (Vinf + w))
End Function
```

The function `Vinduced` below returns the final iterated w. It calculates $f'(w)$ using the Newton–Raphson iterative scheme in Section 15.6.2. It generally converges in fewer than 10 iterations. This function can be accessed from within Excel by a simple cell reference such as '`=Vinduced` (*list of input cells*)'.

```
Function Vinduced (Vinf As Single, Omega As Single, r As Single, NB As Single, CofR As
Single, Cd As Single, Cl As Single) As Single
'Initialize
    Dim W0 As Single, W1 As Single, h As Single, Count As Integer
    Dim F1 As Single, F2 As Single, FofW0 As Single, FprimeofW0 As Single

'Presets
    W0 = 1
    h = 0.01

'Iterate
    Do
        'Advance counter
        Count = Count + 1

        'Calculating the left-hand side, at a distance of h
        F1 = F_of_w(Vinf, Omega, R, Nb, CofR, CD, CL, W0 - h)
        'Calculating the right-hand side, at a distance of h
        F2 = F_of_w(Vinf, Omega, R, Nb, CofR, CD, CL, W0 + h)

        'Calculate slope, f'(W0)
        FprimeofW0 = 0.5 * (F2 - F1) / h

        'Calculate the function itself, f(W0)
        FofW0 = F_of_w(Vinf, Omega, R, Nb, CofR, CD, CL, W0)

        'Calculate the next value of the root, using Newton-Raphson
        If FprimeofW0 = 0 Then
            Count = 10
        Else
            W1 = W0 - FofW0 / FprimeofW0
            If Abs(W1 - W0) < 0.0001 Then Count = 10
            W0 = W1
        End If
    Loop Until Count = 10

'Return the current value of the induced velocity, w
    Vinduced = W0
End Function
```

References

[1] M.E. Kirchner, *Turboprop Airplane Control Problems Associated with Engine Failure Considerations, SAE International, SAE Paper 550193, October 11–15*. 1955, https://doi.org/10.4271/550193.

[2] W.C. Sleeman Jr., W.D. Morrison Jr., *Low-Speed Investigation of the Static Lateral Stability and Control Characteristics of a 1/6-Scale Model of the Republic XF-84H Airplane with the Propeller Operating, NACA RM-SL53G10*, 1953.

[3] F.E. Weick, *Full-Scale Wind-Tunnel Tests With a Series of Propellers of Different Diameters on a Single Fuselage, NACA R-339*, 1931.

[4] W.C. Nelson, *Airplane Propeller Principles*, John Wiley & Sons, New York, 1944.

[5] Flight International, *Last paragraph pp. 761, November 17th*, 1921.

[6] D. Stinton, *The Design of the Aeroplane*, Collins Professional and Technical Books, 1983, 304.

[7] Anonymous, *The Seneca Pilot's Operating Manual, Piper Aircraft, March 29*, 1977.

[8] Anonymous, *Beechcraft C90 King Air - Pilot Training Manual*, Flight-Safety International, 2002.

[9] T. Troller, *Influence of Fuselage on Propeller Design, NACA TM-492*, 1928.

[10] T.A. Egolf, O.L. Anderson, D.E. Edwards, A.J. Landgre, *An Analysis for High Speed Propeller-Nacelle Aerodynamic Performance Prediction, NASA CR-4199*, 1988.

[11] See, http://www.faa.gov/regulations_policies/faa_regulations/.

[12] Anonymous, *Prediction Procedure for Near-Field and Far-Field Propeller Noise, SAE-AIR-1407*, SAE, 1977.

[13] D.P. Raymer, *Aircraft Design: A Conceptual Approach*, 4th ed., AIAA Eduation Series, 2006.

[14] E. Seckel, *Stability and Control of Airplanes and Helicopters*, Academic Press, 1964.

[15] K.D. Wood, W.R. Woodward, *Propeller Efficiency of a Light Airplane, SAE International, SAE Paper 440036, April 5–7*. 1944, https://doi.org/10.4271/440036.

[16] Anonymous, *Generalized Method of Propeller Performance Estimation 1961–1963*, Hamilton Standard, Windsor Locks, CT, 1963.

[17] TCDS A00009CH, *Cirrus Design Corporation, Revision 18, 12/29/*, FAA, 2011.

[18] W.S. Diehl, *Engineering Aerodynamics*, The Ronald Press, 1928.

[19] W.S. Diehl, *Static Thrust of Airplane Propellers, NACA TR-447*, 1932.

[20] F.E. Weick, *Full-Scale Wind Tunnel Tests of a Series of Metal Propellers on a VE-7 Aircraft, NACA TR-306*, 1928.

[21] A. Fage, C.N.H. Lock, R.G. Howard, H. Bateman, *Experiments with a Family of Airscrews Including the Effect of Tractor and Pusher Bodies, Part I. Experiments with the Family of Airscrews Mounted in Front of a Small Body, ARC R.& M. No. 829*, British A.R.C., 1922.

[22] E.P. Hartman, D. Biermann, *The Aerodynamic Characteristics of Full-Scale Propellers Having 2, 3, and 4 Blades of Clark Y and R.A.F. 6 Airfoil Sections, NACA-TR-640, January 1*, 1938.

[23] J.W.R. Taylor, *Jane's All the World's Aircraft 1984–85*, Jane's Yearbooks, 1984.

[24] Anonymous, *Cessna 210 Operator's Manual*, Cessna Aircraft, 1980.

[25] W.Z. Stepniewski, C.N. Keys, *Rotary-Wing Aerodynamics*, Dover Publications, 1984, 46.

[26] B.S. Massey, J. Ward-Smith, *Mechanics of Fluids, Volume 1*, 7th ed., Nelson Thornes Ltd, 2001.

[27] M. Speck, J. Buchholz, M. Sellier, *A Mathematical Model of a Twin Ducted-Fan VTOL Jetpack (March 2013), Proceedings of the Institution of Mechanical Engineers Part G Journal of Aerospace Engineering*. January 2015, https://doi.org/10.1177/0954410013503060.

[28] A.R. Kriebel, *Theoretical Stability Derivatives for a Ducted Propeller, AIAA Paper 64-170*. 1964, https://doi.org/10.2514/6.1964-170.

[29] O.J. Ohanian III, *Ducted fan Aerodynamics and Modeling, with Applications of Steady and Synthetic Jet Flow Control*, Ph.D. DissertationVirgina Polytechnic Institute and State University, 2011.

[30] P.F. de Marc, G.E. Wright Jr., *Ducted Fan Design: Volume 1 - Propulsion Physics and Design of Fans and Long-Chord Ducts*, CreateSpace Independent Publishing, 2015 October 30.

[31] W. Krueger, *On Wind Tunnel Tests and Computations Concerning the Problem of Shrouded Propellers, NACA TM-1202*, 1949.

[32] D. Kucheman, J. Weber, *Aerodynamics of Propulsion*, McGraw Hill Book Company, Inc, New York, 1953.

[33] K.W. Mort, *Performance Characteristics of a 4-foot-diameter Ducted Fan at Zero Angle of Attack for Several Fan Blade Angles, NASA TN-D-3122*, 1965.

[34] K.W. Mort, B. Gamse, *A Wind-Tunnel Investigation of a 7-foot-Diameter Ducted Propeller, NASA TN-D-4142*, 1967.

[35] T.W. Sheehy, *Computer Aided Shrouded Propeller Design, AIAA Paper 73-54*. 1973, https://doi.org/10.2514/6.1973-54.

[36] S. Yılmaz, D. Erdem, M.Ş. Kavsaoğlu, *Effects of Duct Shape on a Ducted Propeller Performance, AIAA Paper 2013-0803*. 2013, https://doi.org/10.2514/6.2013-803.

[37] D.M. Black, H.S. Wainauski, C. Rohrbach, *Shrouded Propellers – A Comprehensive Performance Study, AIAA Paper 68-669*. 1968, https://doi.org/10.2514/6.1968-994.

[38] S. Drzewiecki, *Théorie Générale de L'Hélice*, Gauthiers-Villars et Cie Éditeurs, 1920.

[39] W.Z. Stepniewski, C.N. Keys, *Rotary-Wing Aerodynamics*, Dover Publications, 1984, 94.

[40] H. Glauert, W.F. Durand (Ed.), "Airplane Propellers." Aerodynamic Theory, Springer Verlag, Berlin, 1935 Div. L, Chapter XI.

[41] A. Silverstein, *Scale Effect on Clark Y Airfoil Characteristics from NACA Full-Scale Wind-Tunnel Tests, NACA TR-502*, 1935.

CHAPTER

16

Aircraft Drag Analysis

OUTLINE

16.1 **Introduction** 658
- 16.1.1 *The Content of This Chapter* 658
- 16.1.2 *Quick-Guide: How Do I Estimate the Drag of My Airplane?* 659

16.2 **The Basics of Drag Modeling** 659
- 16.2.1 *Fundamental Definitions* 659
- 16.2.2 *Quadratic Drag Modeling* 662
- 16.2.3 *Correcting the Drag Coefficient at High AOA* 668
- 16.2.4 *Drag Modeling using Higher Order Polynomials* 670
- 16.2.5 *Drag of a 2D Body in a Wind-Tunnel* 670
- 16.2.6 *Additional Topics on Drag* 672
- 16.2.7 *Various Means to Reduce Drag* 677

16.3 **Estimating the Drag of a Complete Aircraft** 678
- 16.3.1 *Estimating Skin Friction Drag: C_{Df}* 680
- 16.3.2 *Estimating Lift-Induced Drag: C_{D_i}* 691
- 16.3.3 *Estimating Wave Drag: C_{D_w}* 695
- 16.3.4 *Calculate $C_{D_{min}}$ Using the Rapid Drag Estimation Method* 701
- 16.3.5 *Calculate $C_{D_{min}}$ Using the Component Drag Buildup Method* 701
- 16.3.6 *Form Factors* 704
- 16.3.7 *Interference Factors* 711
- 16.3.8 *Cumulative Result of Undesirable Drag (CRUD)* 712
- 16.3.9 *Total Drag Coefficient: C_D* 712

16.4 **Miscellaneous or Additive Drag** 712
- 16.4.1 *Trim Drag* 713
- 16.4.2 *Cooling Drag* 714
- 16.4.3 *Drag of Simple Wing-like Surfaces* 716
- 16.4.4 *Drag of Streamlined Struts and Landing Gear Pant Fairings* 716
- 16.4.5 *Drag of Landing Gear* 717
- 16.4.6 *Drag of Floats* 722
- 16.4.7 *Drag of Deployed Flaps* 724
- 16.4.8 *Drag of Deployed Spoilers* 725
- 16.4.9 *Drag Correction for Cockpit Windows* 725
- 16.4.10 *Drag of Canopies* 727
- 16.4.11 *Drag of Blisters* 728
- 16.4.12 *Drag of Antennas* 729
- 16.4.13 *Drag of Windmilling and Stopped Propellers* 729
- 16.4.14 *Drag of Parachutes* 730
- 16.4.15 *Drag of Various Sources* 731

16.5 **Special Topics Involving Drag** 736
- 16.5.1 *Step-by-Step: Extracting Drag from LD_{max}* 736
- 16.5.2 *Step-by-Step: Extracting Drag From a Flight Polar Using the Quadratic Spline Method* 737
- 16.5.3 *Step-by-Step: Extracting Drag Coefficient for a Piston Powered Propeller Aircraft* 740
- 16.5.4 *Extracting Drag Coefficient From Published Data for Piston Aircraft* 742
- 16.5.5 *Determining Drag Characteristics From Wind Tunnel Data* 743

16.6 **Additional Information—Drag of Selected Aircraft** 744
- 16.6.1 *General Range of Subsonic Minimum Drag Coefficients* 745
- 16.6.2 *Drag of Various Aircraft by Class* 745

Exercises 745

References 750

https://doi.org/10.1016/B978-0-12-818465-3.00016-1

Copyright © 2022 Elsevier Inc. All rights reserved.

16.1 INTRODUCTION

Few tasks in aircraft design are as daunting as the estimation of drag. It puts a lid on creativity and, sometimes, transforms inspiration into disappointment. In aircraft design, the primary objective is usually to minimize drag. However, there is more to drag than meets the eyes. Ideally, we want to control it. During climb and cruise, we want low drag. During approach to landing, we want higher drag. This makes it easier to land. Sailplane pilots can attest to how challenging it would be to land without means to increase drag. Some aircraft, including many sailplanes, allow the drag polar to be shifted around using a cruise flap. This de-cambers the airfoil, moving the maximum glide ratio to a higher airspeed. Or increase camber to reduce drag during climb. This chapter provides the aircraft designer with methods to estimate drag and details of its causes and prevention.

Many areas of the aircraft design process rely on accurate drag estimation. This includes performance analysis, engine selection, and requirements for fuel capacity, to name a few. The subject must be approached with respect and caution. Drag is hard to predict accurately: it is easy to over- and underestimate. In part, this is because it is hard to identify and quantify its sources. An underestimation results in an airplane that performs far worse than predicted, risking a costly "drag-cleanup" effort, if not a program cancellation. In contrast, an overestimation by overly conservative approach may render the design so bad on paper the project it might be canceled before it even begins.

Recall Figure 1-14, which shows how the design project can be broken into manageable tasks. Among tasks are the *lift model* (see Sections 9.5.2 and 24.2.5) and *weight model* (see Section 6.4, *Statistical Weight Estimation Methods*). This chapter focuses on the *drag model*. The goal of drag analysis is clear: create a realistic drag model. This is accomplished per the flow chart of Figure 16-21. This chapter presents classical methods for this purpose.

The aspiring designer should not think that drag estimation is simple. "We'll just model it using CFD," is an idea often expressed by students of aerospace engineering who have yet to be humbled by Mother Nature by comparing predictions to wind tunnel or flight test data. While *Navier-Stokes Computational Fluid Dynamics* (NS-CFD) is a promising and exciting scientific advancement, it is not yet robust enough to allow novice users to estimate drag reliably.[1] In 2001, researchers from several aviation and science organizations, including the *American Institute of Aeronautics and Astronautics* (AIAA), conducted the first of several workshops on drag estimation using CFD methods [1, 2]. An Airbus-style passenger transport aircraft, consisting of a fuselage and wing only [3], was modeled by 18 participants using 14 different NS solvers. The analysis results were compared to wind tunnel data that were made available to the participants *after* they had submitted their estimates. In short, the lift and drag predictions left a lot to be desired. Some predictions were close to the wind tunnel data, while others (drag) were off by 50%–200% of the wind tunnel value [1, 2]. These predictions were performed by experts. If they have a hard time performing such predictions, the novice analyst should take note. The drag analyst is between a rock and a hard place—a dreaded place shared by the weights engineer.

Today, the state of the art in low drag aircraft is the modern sailplane (see Figure 16-1). *Natural laminar flow* (NLF) airfoils, segmented tapered wing planform, tadpole fuselage, sealed control surfaces, carefully tailored wing root fairings, T-tail, and disciplined attention to any detail that reduces drag, combine to make some sailplanes achieve glide ratio in excess of 50. No other aircraft are capable of this feat. The aircraft designer interested in developing low drag aircraft should pay special attention to sailplanes. There is a lot that can be learned.

16.1.1 The Content of This Chapter

- Section 16.2 discusses the nature of drag, what contributes to it, how it is modeled, and how it can be estimated. The section also discusses limitations of various estimation methods.
- Section 16.3 discusses the drag characteristics of the airplane as a whole and presents methods to estimate the total drag of aircraft. It is a go-to section for the reader interested in starting a drag estimation of a new aircraft.
- Section 16.4 presents methods to estimate the drag caused by the addition of necessary imperfections to aircraft, such as antennas, fairings, landing gear, and so on. Additionally, methods to estimate trim drag and cooling drag are presented.
- Section 16.5 presents methods to estimate the drag of existing aircraft using published performance data. These are intended to obtain drag characteristics for rival aircraft and are used to compare own drag coefficients to reduce chances of poor estimation.
- Section 16.6 tabulates the drag coefficients and maximum lift-to-drag ratios for selected aircraft, accumulated from various sources. These help the designer assessing the drag of comparable aircraft.

[1] Then again, many would argue that novices shouldn't be estimating drag in the first place.



FIGURE 16-1 No aircraft generate as little drag as the modern sailplane. A Rolladen-Schneider LS4 sailplane, moments before touchdown with wing spoilers deployed. *Photo by Phil Rademacher.*

16.1.2 Quick-Guide: How Do I Estimate the Drag of My Airplane?

Chances are you are reading this chapter to seek help in estimating the drag for your airplane. For immediate help, head to Section 16.3, *Estimating the Drag of a Complete Aircraft*.

16.2 THE BASICS OF DRAG MODELING

This section introduces various means to model the drag of an airplane. A *drag model* is a mathematical expression of the drag coefficient for a body. It primarily describes how the drag of the body changes with orientation in the flow field, but also includes effects of flow properties (R_e, M_∞). Unsurprisingly, higher fidelity modeling calls for mathematical complexity. A good drag model accounts for contributions from the deflection of control surfaces, deployment of landing gear, and growth of flow separation at high AOA and AOY. This is challenging to do analytically. Wind tunnel and flight testing remain the most reliable methods for this purpose.

16.2.1 Fundamental Definitions

(1) Definition of the Drag Model

A drag model is a mathematical representation of the drag coefficient of a body. It is denoted by C_d for 2D bodies and C_D for 3D bodies. For aircraft, the drag model is an expression of the form

$$C_D = f\left(geometry,\ R_e,\ M_\infty,\ \alpha,\ \beta,\ \delta_e,\ \delta_f,\ \delta_s,\ \delta_{LDG},\ \ldots\right) \tag{16-1}$$

Where: R_e = Reynolds number,

M_∞ = Mach number,
α = Angle-of-attack,
β = Angle-of-yaw,
δ_e = Elevator deflection,
δ_f = Deflection of high-lift devices,
δ_s = Deflection of spoilers, δ_f,
δ_{LDG} = Deployment of landing gear.

A good drag model accounts for (A) regions of laminar and turbulent boundary layer, as well as the location of laminar-to-turbulent transition, (B) flow separation regions, (C) compressibility, and (D) deployment of flight control and landing systems. A good drag model shows good agreement with experiment.

(2) Classification of Drag Analysis Methods

There are two basic classes of drag analysis methods: *Prediction* and *postdiction*. The former attempts to estimate the drag of a new aircraft before it flies. The latter does so for an existing aircraft. Prediction methods estimate an aircraft's drag based on its geometry. Postdiction methods evaluate drag using wind tunnel, or performance data derived from flight testing. This chapter primarily presents prediction methods, but a few basic postdiction methods are presented in Section 16.5, *Special Topics Involving Drag*.

(3) Sources of Drag

The total drag of a body stems from (A) pressure difference (*pressure drag*) and (B) skin friction (*skin friction drag*). Major contributors to each are

(1) **Pressure drag** is the component of the resultant aerodynamic force that is parallel to the tangent to the flight path. It is generated by the pressure differential formed by the body (see Equation 8-20).
(2) **Skin friction drag** is caused by molecules "rubbing" against the body's surface. The resulting friction primarily acts tangent to the flight path.
(3) **Lift-induced drag** is a pressure drag caused by the formation of wingtip vortices, which tilts the lift vector backward and creates a force component that adds to the total drag.
(4) **Wave drag** is caused by the localized rise in pressure around a body due to the formation of normal and oblique shocks on the airplane. This effect begins at high subsonic Mach numbers.
(5) **Miscellaneous drag** is caused by a number of "small," often overlooked, contributions such as small inlets and outlets, access panels, fuel caps, and antennas, to name a few.

In addition to the discussion presented in this chapter, the reader should also refer to Sections 8.1.7, *Forces and Moment per Unit Span* and 8.1.10, *Boundary Layer Basics*.

(4) Drag Model Fidelity

Drag models come in many shapes and forms. Their fidelity can be split into three classes:

Class 3—Simplified Drag Model

This is a *quadratic drag model* (see Section 16.2.2, *Quadratic Drag Modeling*) that assumes drag increases with the lift coefficient squared. It is the simplest and least accurate model at our disposal. It is acceptable for missiles and other axisymmetric vehicles, and a handful of fixed-wing aircraft. It is a poor predictor of drag for aircraft whose geometry features mean-line curvature (camber). It is useful for explaining important concepts in performance theory, where its simplicity permits closed-form solutions of complex performance concepts. However, this does not mean those solutions are accurate, just closed-form. The simplified drag model is typically presented in the following form

$$C_D = C_{D_{\min}} + kC_L^2 \tag{16-2}$$

Where $C_{D_{\min}}$ is the minimum drag coefficient, C_L is the lift coefficient, and k is the *lift-induced drag constant*.

Class 2—Adjusted Drag Model

This is a correction of the simplified model. It requires the position of the minimum drag coefficient ($C_{L_{\min D}}$) to be specified. Its inclusion shifts the quadratic drag polar to the left or right. This significantly improves the shortcomings of the simplified model. However, it too becomes gradually inaccurate a higher AOA. The adjusted drag model is typically presented in the following form

$$C_D = C_{D_{\min}} + k(C_L - C_{L_{\min D}})^2 \tag{16-3}$$

Class 1—Advanced Drag Model

Refers to any drag model that (A) corrects for the effect of flow separation at high AOA and AOY and (B) introduces contributions of configuration changes, such as the deflection of control surfaces, flaps, slats, spoilers, and deployed landing gear. A Class 1 drag model is in excellent agreement with experiment over the entire normal operating range of the aircraft and is sometimes defined between $-180\,\text{degrees} < \alpha \leq 180\,\text{degrees}$. Such drag models are created in serious development programs, where they are used for performance as well as stability and control (e.g., for use in flight simulators). An example of such a model is presented below (also see Section 24.2.6, *The Drag Model*).

$$C_D = C_{D_{\min}} + C_{D_\alpha}\alpha + C_{D_\beta}\beta + C_{D_{\delta_e}}\delta_e + C_{D_{\delta_f}}\delta_f + C_{D_{\delta_s}}\delta_s + C_{D_{\delta_{LDG}}}\delta_{LDG} + C_{D_w} + \ldots \tag{16-4}$$

Where: C_{D_α} = Drag curve slope,

C_{D_β} = Change in drag due to yaw,
C_{D_w} = Wave drag contribution,
$C_{D_{\delta e}}$ = Change in drag with elevator deflection, δ_e,
$C_{D_{\delta f}}$ = Change in drag with deployment of high-lift devices, δ_f,
$C_{D_{\delta s}}$ = Change in drag with deployment of spoilers, δ_f.
$C_{D_{\delta LDG}}$ = Change in drag with deployment of landing gear, δ_{LDG}.

Look-up Tables

Exemplifies another version of an advanced drag model. These are developed using wind tunnel testing or, analytically, using specialized analyses. They incorporate flow separation and other nonlinearities captured by experiment. Their primary use is in flight simulation and advanced performance theory.

(5) Drag Polar

wA *drag polar* is a graph that plots the drag coefficient, C_D, as a function of the lift coefficient, C_L (see Figure 16-2).

(6) Total Drag Force, C_D

Once the drag model is known, the drag force is calculated using the expression below.

$$D = \frac{1}{2}\rho V_\infty^2 S C_D \tag{16-5}$$

Where ρ is air density, V_∞ is far-field airspeed, and S is reference area (typically wing area).

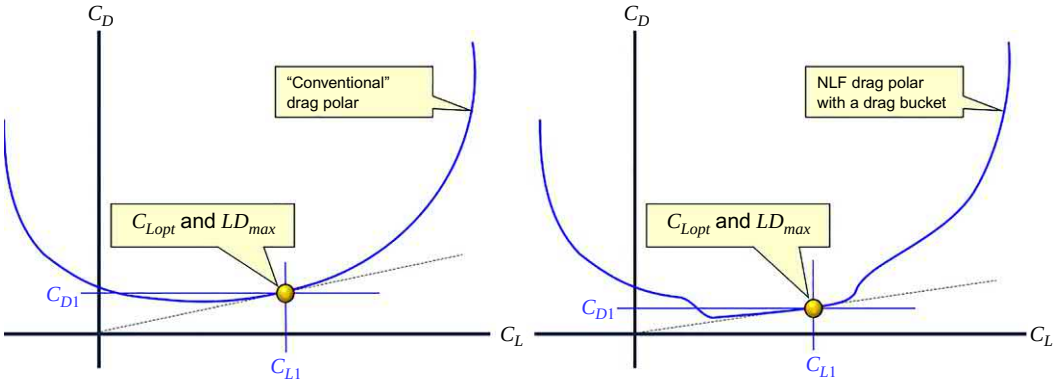


FIGURE 16-2 Graphical determination of $LD_{\max}$ and $C_{L_{opt}}$ for conventional (left) and NLF polars (right).

(7) Dragcounts

A *dragcount* is the drag coefficient multiplied by a factor of 10,000. For instance, 250 dragcounts is equivalent to a $C_D = 0.0250$; 363 dragcounts is equivalent to a $C_D = 0.0363$, and so on.

(8) Wetted Area, S_{wet}

Refers to the surface area of the airplane that is directly exposed to the outside air. As a rule of thumb, if the airplane was dipped in water, everything that gets wet externally belongs to the wetted area.

(9) Minimum Drag, $C_{D_{min}}$

Minimum drag is the lowest value of the drag coefficient. It combines contributions from pressure (pressure drag) and shear stresses (friction). It is easily identifiable in the drag polar. If the body to which it applies features *curvature*, its value occurs at a nonzero lift coefficient. *Parasitic drag* is another name for $C_{D_{min}}$. Methods to estimate its value are presented in Section 16.3, *Estimating the Drag of a Complete Aircraft*.

(10) Lift-Induced Drag, C_{D_i}

Lift-induced drag is defined in Bullet (3). It is denoted as C_{D_i}. Methods to estimate its value are presented in Section 16.3, *Estimating the Drag of a Complete Aircraft*.

(11) Wave Drag, C_{D_w}

As an aircraft approaches the speed of sound, its lift, drag, and moment characteristics change. This is called the *compressibility effect*. It greatly increases the drag of an airplane approaching and exceeding the speed of sound. The drag is called *wave drag* and is denoted by C_{D_w}. It is discussed for airfoils in Section 8.3.8, *The Effect of Compressibility*, for wings in Section 9.3.3, *Wing Sweep Angle*, and for drag in Section 16.3.3, *Estimating Wave Drag*.

(12) Effective Aspect Ratio, AR_e

The product AR_e, where AR is the wing's aspect ratio and is e is the *Oswald's span efficiency* (see Section 9.5.12, *Determination of Span Efficiency*), is often referred to as the *effective aspect ratio*, denoted by AR_e. In this respect, the Oswald efficiency can be considered a factor that renders the AR less effective than the geometric value indicates. The designer can consider planform and other geometric modifications, such as endplates or winglets, to increase the effective AR, but should be aware that such modifications increase the skin friction drag (and weight).

(13) Lift-Induced Drag Constant, k

It is the constant whose product with the lift coefficient squared yields the lift-induced drag (see Equations (16-2) and (16-3)). It is given by:

$$k = \frac{1}{\pi \cdot AR \cdot e} = \frac{1}{\pi \cdot AR_e} \tag{16-6}$$

Note that for a clean wing, if $AR_e \to \infty$ then $k \to 0$ and therefore $C_D \to C_d$, i.e., the drag coefficient becomes that of the airfoil.

(14) Lift-to-Drag Ratio, LD_{max}, and Optimum Lift Coefficient, $C_{L_{opt}}$

The ratio of lift-to-drag is hugely important in aircraft design. It plays a vital role in performance analysis, where it is a primary indicator of an airplane's efficiency. In this text, the lift-to-drag ratio is denoted by LD (rather than L/D) and is defined as follows:

$$LD \equiv \frac{L}{D} = \frac{C_L}{C_D} \tag{16-7}$$

The LD is primarily a function angle-of-attack and, thus, airspeed. It has secondary dependency on angle-of-yaw. The maximum value of LD is of particular interest to the

designer (and the pilot). It is denoted by $LD_{\max}$. The lift coefficient at which $LD_{\max}$ occurs is called the *optimum lift coefficient*, denoted by $C_{L_{opt}}$. If we know $C_{L_{opt}}$, we can calculate the airspeed at which it occurs using the expression

$$V_{opt} \cong \sqrt{\frac{2W}{\rho S C_{L_{opt}}}} \tag{16-8}$$

Where W is weight, ρ is density, and S is the reference area. This airspeed is also called the *best glide speed*.

(15) Graphical Determination of $LD_{\max}$

In the absence of knowing the exact numbers of a particular drag polar, it is possible to estimate the $LD_{\max}$ and $C_{L_{opt}}$ graphically. This is shown in Figure 16-2 for a conventional drag polar and one for a NLF aircraft (airfoil) featuring a drag bucket (see Bullet (19)). This is done by fairing a line from the origin such it becomes a tangent to the polar. The reason for why this yields $LD_{\max}$ can be visualized by recognizing that the tangent aligns with the smallest value of C_D at the greatest value of C_L.

(16) Equivalent Flat Plate Area (EFPA)

The *equivalent flat plate area* (denoted by f) is a value that is helpful when comparing the relative drag of different aircraft. It is simply the product of the minimum drag coefficient and the reference area, as shown below. Alternatively, it is the minimum drag force at the given airspeed, $D_{\min}$, divided by the dynamic pressure, q_∞:

$$f = SC_{D_{\min}} = \frac{D_{\min}}{q_\infty} \tag{16-9}$$

The concept assumes the drag of the airplane is equivalent to that of a fictitious plate that has a drag coefficient $C_D = 1.0$. Thus, if the flat plate area of an airplane is $10\,\text{ft}^2$, it means its drag amounts to that of a flat plate of the same area moving normal to the flight path. The concept is bogus in many respects. It disregards the effect of Reynolds and Mach numbers, the C_D of a flat plate at R_e around 10^5 is actually closer to 1.17 (e.g., see Figure 16-76), and no notion is given as to the true geometry of this "plate" (i.e., is it rectangular or circular or any other shape?). In spite of these shortcomings, like stated earlier, it is helpful mostly for comparison purposes. Table 16-22 lists the EFPA for a number of different aircraft.

(17) Profile Drag

For wing-only drag, refers to the difference between the total and lift-induced (and wave) drag, i.e., $C_{D_p} = C_D - C_{D_i} - C_{D_w}$. Sometimes refers to the drag of an aircraft due to friction only (e.g., see Ref. [4]). For airfoils, see Bullet (10) in Section 8.1.4, *Properties of Typical Airfoils*.

(18) Zero-Lift Drag

Zero-lift drag is the value of the drag coefficient where $C_L = 0$. It is equal to $C_{D_{\min}}$ only for the simplified drag model.

(19) Drag "Bucket"

Refers to a sharp drop in the profile drag of an airfoil. It is a consequence of sustained *natural laminar boundary layer* forming over the airfoil. An example of such a drag bucket is shown in center graph of Figure 8-39.

(20) Dependency of *CD* on α and β

When a body's orientation (denoted by α and β) changes with respect to the oncoming flow, its resultant force, R (see Figure 8-1), changes as well. Thus, so will lift and drag. See additional discussion in Section 16.2.6.

16.2.2 Quadratic Drag Modeling

First, let us establish the difference in how the drag of an airfoil and a wing changes with lift. For an airfoil, this is solely caused by changes in the distribution of pressure and shear stress over the airfoil's surface (see Figure 16-3). Note that the data to the left terminate just before a large vertical jump occurs. Regardless, it is evident that describing the drag using a quadratic model at large C_l leaves a lot to be desired.

The same changes happen for a wing, but are compounded by the aft-tilting of the lift-force. This introduces an additional contribution, called *lift-induced* or *vortex drag*. At low angles-of-attack, lift-induced drag is explained by theoretical predictions as a function of C_L^2. This theory agrees well with experiment at low angles-of-attack. However, as for the airfoil, extreme values of C_L cause a flow separation too significant for the C_L^2 contribution to capture. This is not a surprise; the contribution of C_L^2 originates in Prandtl's inviscid *lifting line theory* (see Section 9.7, *Prandtl's Lifting-Line Theory*)—whereas the flow separation is a viscous phenomenon.

This highlights the limitations of the quadratic modeling. Neglecting to correct for the sharp rise in drag at high C_L leads to very poor low-speed and high-g performance predictions.

(1) Simplified Drag Model

As discussed in Section 16.2.1, the simplified drag model is given by Equation (16-2), repeated below for convenience. The variables are defined there.

$$C_D = C_{D_{\min}} + kC_L^2 \tag{16-2}$$

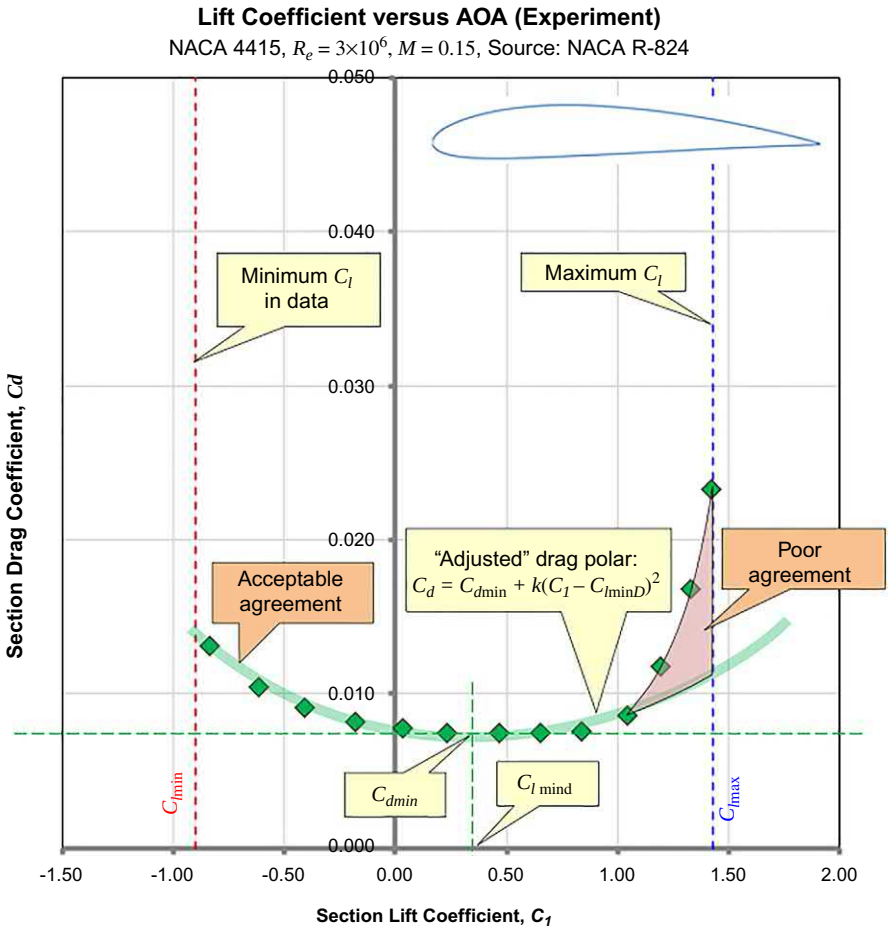


FIGURE 16-3 Quadratic assumption is in poor agreement with experiment for airfoils.

Where the lift-induced drag constant, k, is given by Equation (16-6). The optimum lift coefficient and maximum lift-to-drag ratio obtained using this model is

$$C_{L_{opt}} = \sqrt{\frac{C_{D_{\min}}}{k}} \text{ and } LD_{\max} = \frac{1}{\sqrt{4kC_{D_{\min}}}} \qquad (16\text{-}10)$$

DERIVATION OF EQUATION (16-10)

First, determine the C_L of the optimum lift-to-drag ratio, $C_{L_{opt}}$:

$$\frac{C_L}{C_D} = \frac{C_L}{C_{D_{\min}} + kC_L^2} \overset{\text{Quotient Rule}}{\Rightarrow}$$

$$\frac{d}{dC_L}\left(\frac{C_L}{C_D}\right) = \frac{\left(C_{D_{\min}} + kC_L^2\right)(1) - (2kC_L)(C_L)}{\left(C_{D_{\min}} + kC_L^2\right)^2} = 0$$

$$\Leftrightarrow \quad \left(C_{D_{\min}} + kC_L^2\right) - \left(2kC_L^2\right) = 0$$

$$\Rightarrow \quad C_{L_{opt}} = \sqrt{\frac{C_{D_{\min}}}{k}}$$

Substituting this into the expression for the lift-to-drag ratio and manipulating algebraically yields:

$$LD_{\max} = 1/\sqrt{4kC_{D_{\min}}}$$

(2) Adjusted Drag Model

As stated in Section 16.2.1, the adjusted drag model corrects the simplified model. The correction is very effective, despite its simplicity. It is far more realistic than the simplified one (see Figure 16-4). However, both models must be corrected for high lift coefficients.

$$C_D = C_{D_{\min}} + k(C_L - C_{L_{\min D}})^2 \qquad (16\text{-}11)$$

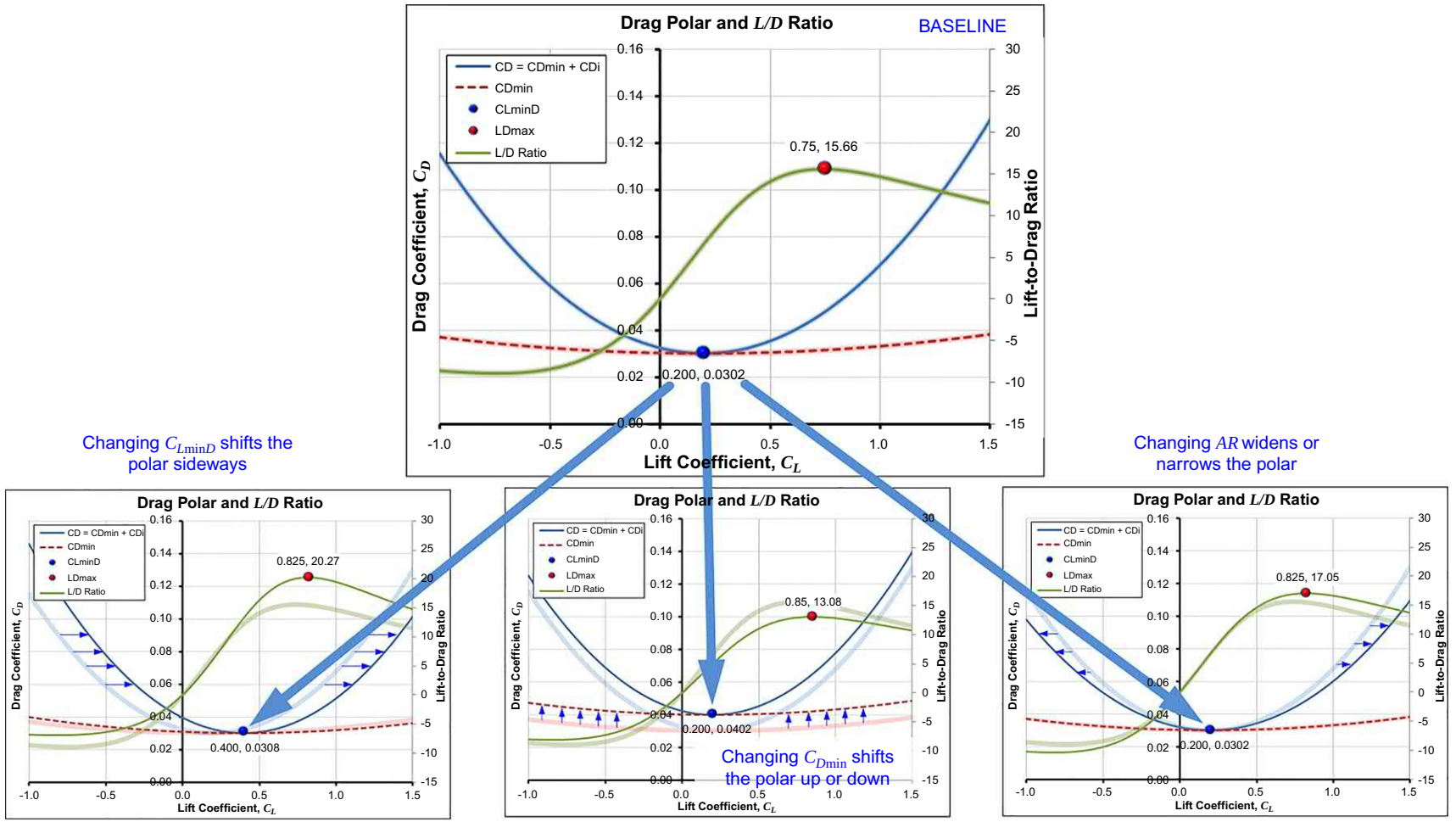


FIGURE 16-4 A schematic showing the effect of changing $C_{L_{minD}}$, $C_{D_{min}}$, and AR on the drag polar.

Where $C_{L_{minD}}$ is the lift coefficient where drag becomes a minimum. The maximum lift-to-drag ratio obtained using this model is (here using form that resembles that of Equation (16-10))

$$C_{L_{opt}} = \sqrt{\frac{C_{D_{min}}}{k} + C_{L_{minD}}^2} \quad \text{and}$$
$$LD_{max} = \frac{1}{\sqrt{4kC_{D_{min}} + (2kC_{L_{minD}})^2} - 2kC_{L_{minD}}} \tag{16-12}$$

DERIVATION OF EQUATION (16-12)

First, determine the C_L of the optimum lift-to-drag ratio, $C_{L_{opt}}$. To do this, we follow a parallel approach as that used for the derivation of Equation (16-10). The quotient rule of differentiation yields the following expression for the numerator:

$$\left(C_{D_{min}} + k(C_L - C_{L_{minD}})^2\right)(1) - 2k(C_L - C_{L_{minD}})(C_L) = 0$$

To obtain $C_{L_{opt}}$, we solve this expression for C_L. This gives $C_{L_{opt}} = \sqrt{C_{D_{min}}/k + C_{L_{minD}}^2}$. Substituting this into the expression for the lift-to-drag ratio and manipulating algebraically yields Equation (16-12).

(3) Impact of Geometry on the Drag Polar

The designer can shape the drag polar using the aircraft's geometry. Three effective means are through $C_{L_{minD}}$, $C_{D_{min}}$, and AR. This makes these parameters *design variables* as illustrated in Figure 16-4. The curvature of $C_{D_{min}}$ (red) represents the contribution of $m(C_L - C_{l_{mind}})^2$ in Equation (16-14).

AR as a Design Variable

Increasing aspect ratio reduces lift-induced drag, but in a similar fashion as $C_{L_{minD}}$: Increased LD_{max} and $C_{L_{opt}}$.

$C_{L_{minD}}$ as a Design Variable

The general effect of $C_{L_{minD}}$ is to shift the polar sideways using curvature. For instance, increasing airfoil camber increases $C_{L_{minD}}$. If $C_{L_{minD}} < 0$ then the curve is shifted left and right if $C_{L_{minD}} > 0$. As evident in Figure 16-4, shifting $C_{L_{minD}}$ right increases LD_{max}, but pushes it to a higher $C_{L_{opt}}$. This means the airplane will achieve its maximum range at a *lower* airspeed. Generally, our goal is to increase LD_{max} and push it to a *higher* airspeed (low $C_{L_{opt}}$). Note that high Mach numbers increase $C_{L_{minD}}$ slightly, albeit much less than $C_{D_{min}}$ (e.g., see Ref. [5]).

$C_{D_{min}}$ as a Design Variable

It is easy to relate to $C_{D_{min}}$. Changing $C_{D_{min}}$ shifts the drag polar up or down (see Figure 16-4). Decrease it to increase LD_{max} and reduce $C_{L_{opt}}$. Thus, reducing $C_{D_{min}}$ is an effective means to improve LD_{max} and $C_{L_{opt}}$. This reduction implies aerodynamic clean-up.

(4) Transformation of $C_D = A \cdot C_L^2 + B \cdot C_L + C$ to $C_D = C_{D_{min}} + k(C_L - C_{L_{minD}})^2$

A drag polar in the form $C_D = A \cdot C_L^2 + B \cdot C_L + C$ can be transformed to the more familiar form as follows:

$$\left.\begin{aligned} k &= A \\ C_{L_{minD}} &= -B/(2A) \\ C_{D_{min}} &= AC_{L_{minD}}^2 + BC_{L_{minD}} + D \end{aligned}\right\} \Rightarrow C_D = C_{D_{min}} + k\left(C_L - C_{L_{minD}}\right)^2 \tag{16-13}$$

The derivation of these expressions is provided in Section 16.5.5, *Determining Drag Characteristics From Wind Tunnel Data*.

(5) Application of the Adjusted Drag Model to Airfoils and Wings

The total drag coefficient of a "clean" wing can be approximated using the drag polars of its constituent airfoils. Figure 16-5 shows a symmetric, single-airfoil wing. Assume we know the distribution of section lift coefficients at some specific flight condition. The airfoil drag polar inserted in the figure shows how this leads to a spanwise distribution of drag along the wing (see the three span stations presented).

To estimate the C_D for the wing, the variation in spanwise drag must be properly accounted for. Using the adjusted drag model, the airfoil's drag coefficient (C_d) can be expressed in terms of the spanwise section lift coefficients (C_l) as follows

$$C_d = C_{d_{min}} + m(C_L - C_{L_{minD}})^2 \tag{16-14}$$

Where m is a constant that accounts for the increase in the airfoil's profile drag. Assume the distribution of section lift coefficients is given by the function f of spanwise position, y:

$$C_l = f(y) \tag{16-15}$$

Thus, we can determine the wing's *effective profile drag coefficient* at condition as

$$\begin{aligned} C_{D_p} &= \frac{2}{b}\int_0^{b/2} \left[C_{d_{min}} + m(C_l - C_{l_{minD}})^2\right] dy \\ &= C_{d_{min}} + \frac{2m}{b}\int_0^{b/2} (f(y) - C_{l_{minD}})^2 dy \end{aligned} \tag{16-16}$$

Therefore, we can express the total drag of the wing by including its lift-induced drag as shown below:

$$C_D = \overbrace{C_{d_{min}} + \underbrace{\frac{2m}{b}\int_0^{b/2} (f(y) - C_{l_{minD}})^2 dy}_{\text{change in airfoil } C_d \text{ due to spanwise } C_l}}^{=C_{D_p}} + \overbrace{k(C_L - C_{L_{minD}})^2}^{\text{wing lift induced drag}} \tag{16-17}$$

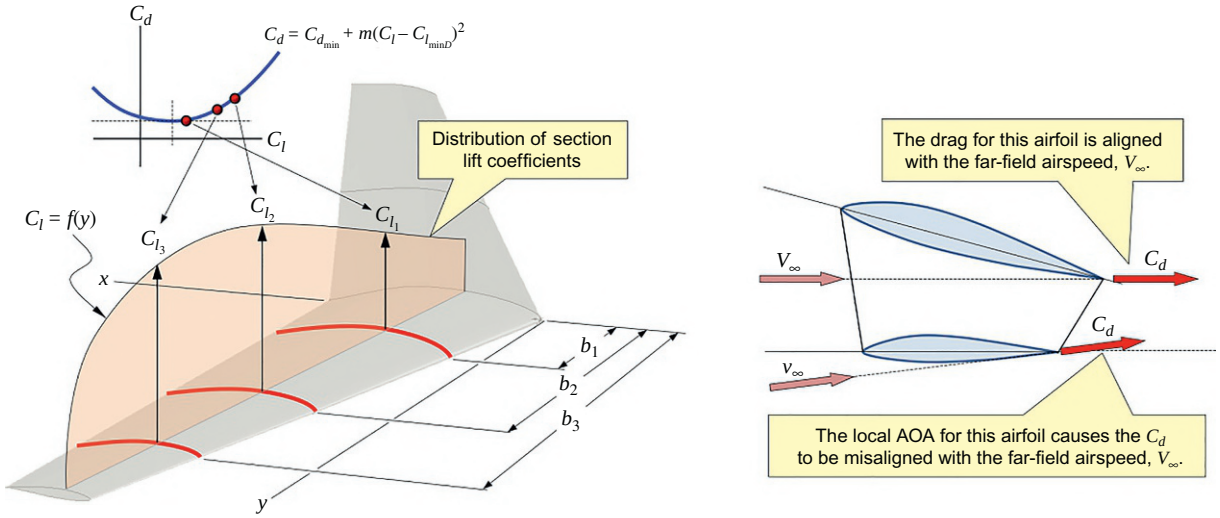


FIGURE 16-5 The distribution of section lift coefficients dictates the wing's total drag.

The expression reveals that changes in C_D with C_L are far more complex than standard models show. Such models "average" the drag. Equation (16-17) shows what it takes to estimate it more accurately. Note that at high α, the flow-field may introduce local misalignments in the lift and drag vectors that are significant enough to violate the small angle approximation (see Figure 16-5). The aerodynamicist can estimate this by comparing the local AOA to the chord-line orientation of the airfoil on the wing and correct if needed.

(6) Limitations of the Quadratic Drag Model

(A) Predictions at very low (negative) and high (positive) angles-of-attack are poor (see Figure 16-6). See Section 16.2.3, *Correcting the Drag Coefficient at High AOA* for a remedy. (B) Predictions for aircraft with unmasked drag buckets is poor (see Figure 16-6). It is not guaranteed that the drag bucket in the drag polar of aircraft with NLF-lifting surfaces will be "visible." For many such aircraft, the drag associated with the

EXAMPLE 16-1

Estimate the lift coefficient and effective profile drag coefficient for a Hershey bar wing, whose $S = 130\,\text{ft}^2$, $b = 32.5\,\text{ft}$, $c = 4\,\text{ft}$, and for which the distribution of section lift coefficients at some angle-of-attack is given by $C_l = 0.5 \cdot \cos(\pi y/b)$. The airfoil's profile drag is given by $C_d = 0.007166 + 0.003646(C_l - 0.3922)^2$.

SOLUTION:

Determine the lift coefficient per Equation (9-58). Note this lift distribution is only for demonstration.

$$C_L = \frac{2}{S}\int_0^{b/2} C_l(y)c(y)dy = \frac{4}{130}\int_0^{32.5/2} \cos\left(\frac{\pi y}{32.5}\right)dy$$

$$= \frac{4}{130}\frac{32.5}{\pi} = 0.3183$$

Determine the effective profile drag coefficient per Equation (16-16):

$$C_{D_p} = C_{d_{min}} + \frac{2m}{b}\int_0^{b/2} (f(y) - C_{l_{minD}})^2 dy$$

$$= C_{d_{min}} + \frac{2m}{b}\int_0^{b/2} \left(0.5\cos\left(\frac{\pi y}{b}\right) - C_{l_{minD}}\right)^2 dy$$

$$= C_{d_{min}} + \frac{2m}{b}\int_0^{b/2} \left(0.25\cos^2\left(\frac{\pi y}{b}\right) - \cos\left(\frac{\pi y}{b}\right)C_{l_{minD}} + C_{l_{minD}}^2\right)dy$$

$$= C_{d_{min}} + \frac{2m}{b}\left[\frac{2\pi y + b\sin(2\pi y/b)}{16\pi} - \frac{bC_{l_{minD}}}{\pi}\sin\left(\frac{\pi}{b}y\right) + C_{l_{minD}}^2 y\right]_0^{b/2}$$

$$= C_{d_{min}} + 2m\left[\frac{1}{16} - \frac{C_{l_{minD}}}{\pi} + \frac{C_{l_{minD}}^2}{2}\right]$$

$$= 0.007166 + 2(0.003646)\left[\frac{1}{16} - \frac{0.3922}{\pi} + \frac{0.3922^2}{2}\right] = 0.007272$$

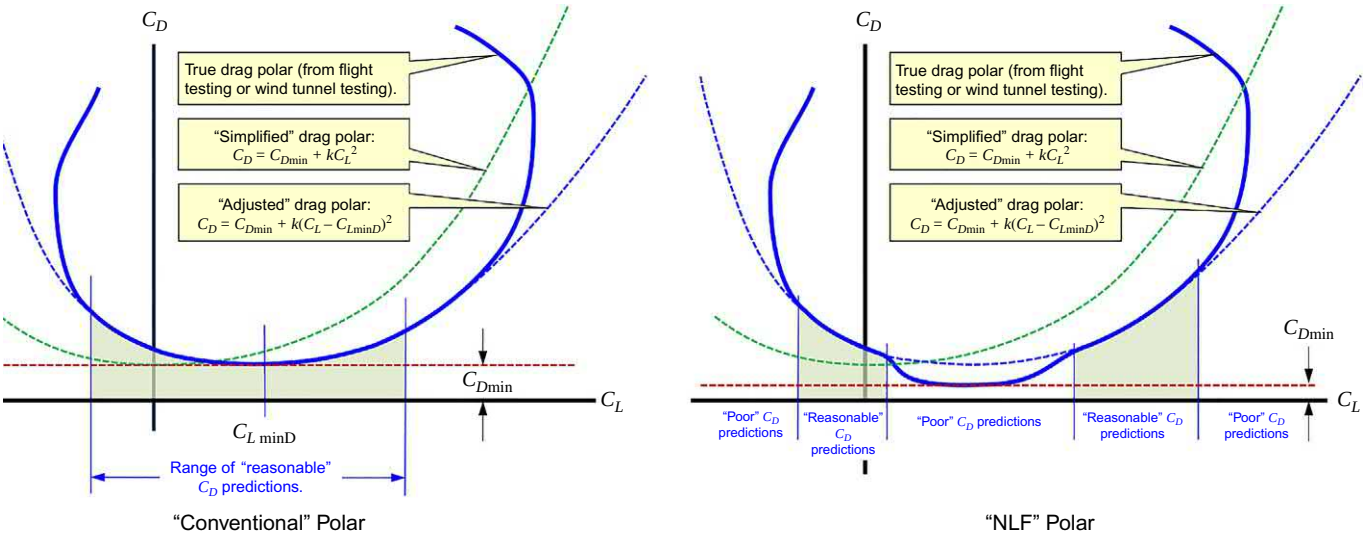


FIGURE 16-6 Approximating the *true* drag polar illustrates primary sources of error for both the simplified and adjusted drag models. The simplified one is like a stopped clock—it is correct in two places.

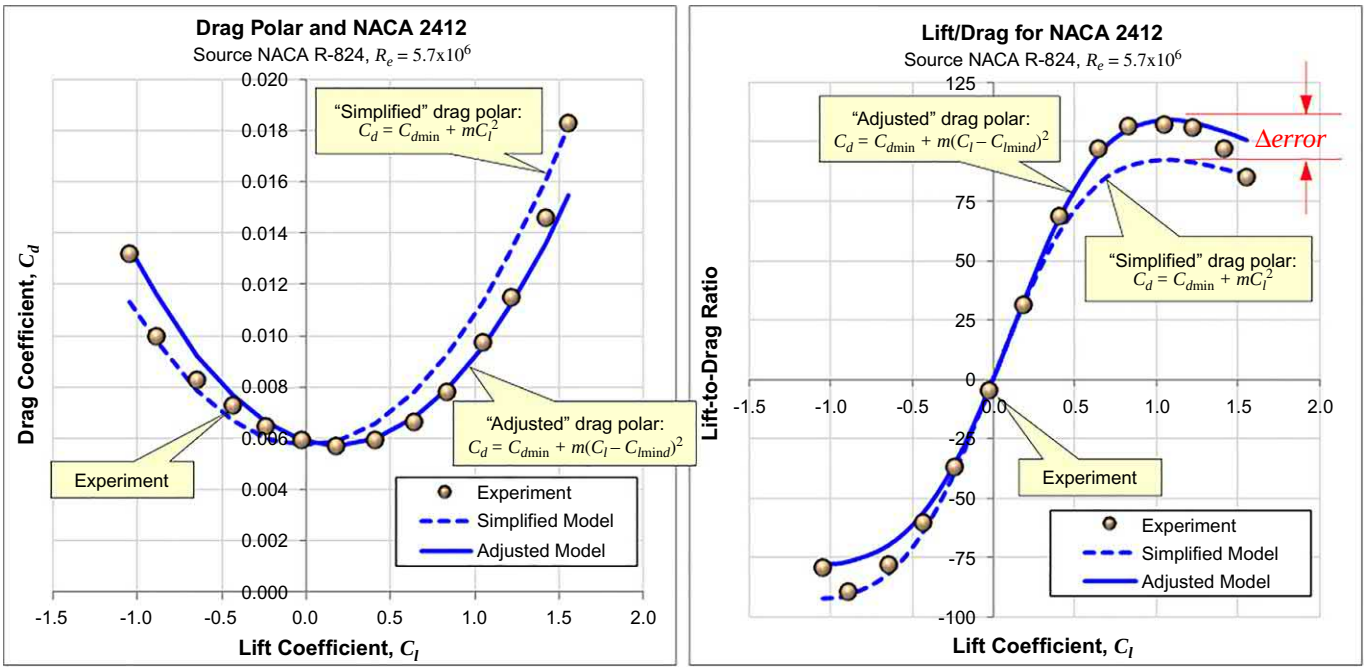


FIGURE 16-7 A comparison of the simplified and adjusted drag models to experimental data.

fuselage, powerplant, fixed landing gear, and so on, is large enough mask it. Quadratic drag models can treat those aircraft, because the resulting drag polar looks more like a "conventional" one. Otherwise, it is unwise to select this model for aircraft-like sailplanes.

(7) Comparing the Accuracy of the Simplified and Adjusted Drag Models

Differences between the simplified and adjusted drag models are best illustrated by a direct comparison to wind tunnel data (see Figure 16-7). It compares wind tunnel data for the NACA 2412 airfoil from Ref. [6]. This airfoil is used on a number of Cessna aircraft, for instance, the Model 150, 152, 172, and 182, to name a few. To do this, the drag polar was digitized and the smallest experimental value of the C_d selected as $C_{d_{min}}$ for each drag model. The value of $C_{l_{mind}}$ for the adjusted model was determined by trial-and-error before being used in the term $m(C_l - C_{l_{mind}})^2$. The term m was varied to get the best fit of each model (both models use the same k). A value of

$k \approx 62$ was found to best fit the experiment. Larger values (e.g., 200 or 400) only flatten the polar. The graphs show the adjusted drag model provides a substantially better fit to experiment. Another lesson to be learned is the dire consequences of estimating range for an aircraft using the simplified model. Since range depends explicitly on C_L/C_D (see Section 21.3, *Range Analysis*), any prediction based on the simplified drag model yields a range well below that indicated by the experiment. The opposite conclusion can also happen. The important lesson is that the adjusted model better matches experiment; the simplified does not and should be avoided.

16.2.3 Correcting the Drag Coefficient at High AOA

The problem of inaccurate drag modeling at high (and low) lift coefficients has already been discussed. This section develops a method to approximate the drag coefficient at higher lift coefficients.

Consider the hypothetical wind tunnel test data in Figure 16-8. The quadratic polar (blue curve) only approximates the data satisfactorily at lower lift coefficients for a handful of data points. This model is given by Equation (16-11), reproduced below for convenience:

$$C_D = C_{D_{\min}} + k(C_L - C_{L_{\min D}})^2 \qquad (16\text{-}11)$$

The test data in Figure 16-8 deviate sharply from the curve starting at $C_L = 1.15$ (and $C_L = -0.45$). Here, we are primarily interested in the positive lift coefficient, which is needed for low-speed performance predictions. To work around this predicament, the author has used the following methodology in the past with satisfactory results. In this method, once the C_L exceeds a certain value, from hereon called C_{Lm}, a quadratic spline is used to replace the values of the adjusted drag model. Other splines are possible; however, the advantage of the quadratic spline is simplicity and acceptable accuracy. The method blends the spline smoothly with the underlying adjusted drag model. First, define a *modified* drag coefficient ($C_{D\text{mod}}$) to be used when $C_L > C_{Lm}$. It can be represented with:

$$C_{D\text{mod}} = AC_L^2 + BC_L + C \qquad \text{if } C_L > C_{Lm} \qquad (16\text{-}18)$$

To determine the constants A, B, and C requires two conditions to be satisfied at C_{Lm}:

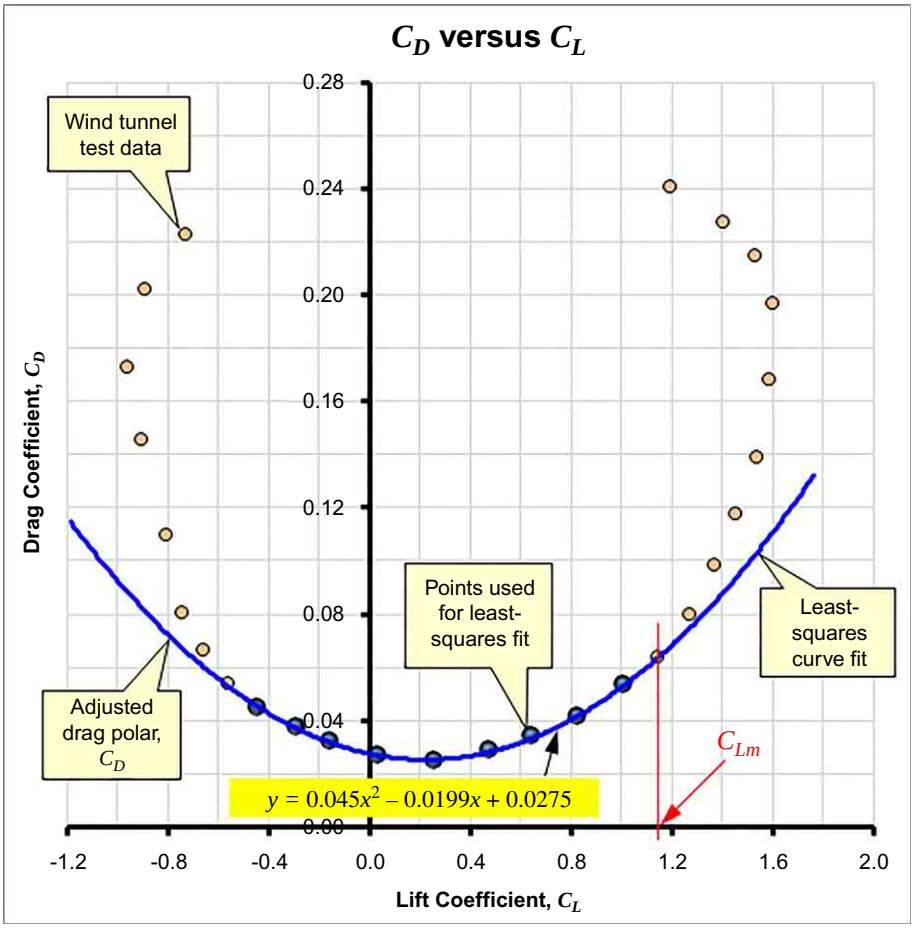


FIGURE 16-8 A hypothetical drag polar for an aircraft, showing the inaccuracy of the quadratic drag model at higher (or lower) lift coefficient.

Condition (1)—Equal drag at C_{Lm}:

$$C_{D\text{mod}}(C_{Lm}) = C_D(C_{Lm})$$

Condition (2)—Equal slope at C_{Lm}:

$$\left.\frac{\partial C_{D\text{mod}}}{\partial C_L}\right|_{at\ C_{Lm}} = \left.\frac{\partial C_D}{\partial C_L}\right|_{at\ C_{Lm}}$$

A third condition is needed to finalize the determination of A, B, and C: The value of $C_{D\text{mod}}$ at $C_{L_{max}}$ must match that of the wind tunnel data.

Since the function for $C_{D\text{mod}}$ has three constants (A, B, and C), we need three equations to determine them. One of those requires the derivatives of C_D and $C_{D\text{mod}}$ to be determined. These are presented below. Slope of C_D:

$$\frac{\partial C_D}{\partial C_L} = \frac{\partial}{\partial C_L}\left[C_{D_{\min}} + k(C_L - C_{L_{\min D}})^2\right]$$
$$= 2k(C_L - C_{L_{\min D}})$$

Slope of $C_{D\text{mod}}$: $\dfrac{\partial C_{D\text{mod}}}{\partial C_L} = \dfrac{\partial}{\partial C_L}\left[AC_L^2 + BC_L + C\right] = 2AC_L + B$

We now have three equations with three unknowns (A, B, and C):

Equation (1): $AC_{Lm}^2 + BC_{Lm} + C = C_{D_{\min}} + k(C_{Lm} - C_{L_{\min D}})^2$

Equation (2): $2AC_{Lm} + B = 2k(C_{Lm} - C_{L_{\min D}})$

Equation (3): $AC_{L_{\max}}^2 + BC_{L_{\max}} + C = C_{Dstall}$

Rearranging this in a matrix form yields the following expression that allows A, B, and C to be determined using matrix methods like Cramer's rule or matrix inversion:

$$\begin{bmatrix} C_{Lm}^2 & C_{Lm} & 1 \\ 2C_{Lm} & 1 & 0 \\ C_{L_{\max}}^2 & C_{L_{\max}} & 1 \end{bmatrix} \begin{Bmatrix} A \\ B \\ C \end{Bmatrix} = \begin{Bmatrix} C_{D_{\min}} + k(C_{Lm} - C_{L_{\min D}})^2 \\ 2k(C_{Lm} - C_{L_{\min D}}) \\ C_{Dstall} \end{Bmatrix} \tag{16-19}$$

Then, once A, B, and C have been determined, the drag model is further refined as follows:

$$C_D = \begin{cases} C_{D_{\min}} + k(C_L - C_{L_{\min D}})^2 & \text{if } C_L \le C_{Lm} \\ AC_L^2 + BC_L + C & \text{if } C_L > C_{Lm} \end{cases} \tag{16-20}$$

This model is implemented in Figure 16-9. Note that while the wind tunnel data are used here to pick C_{Lm}, it is reasonable to select C_{Lm} as the value $\frac{1}{2}(C_{L_{\min D}} + C_{L_{\max}})$ as a first guess.

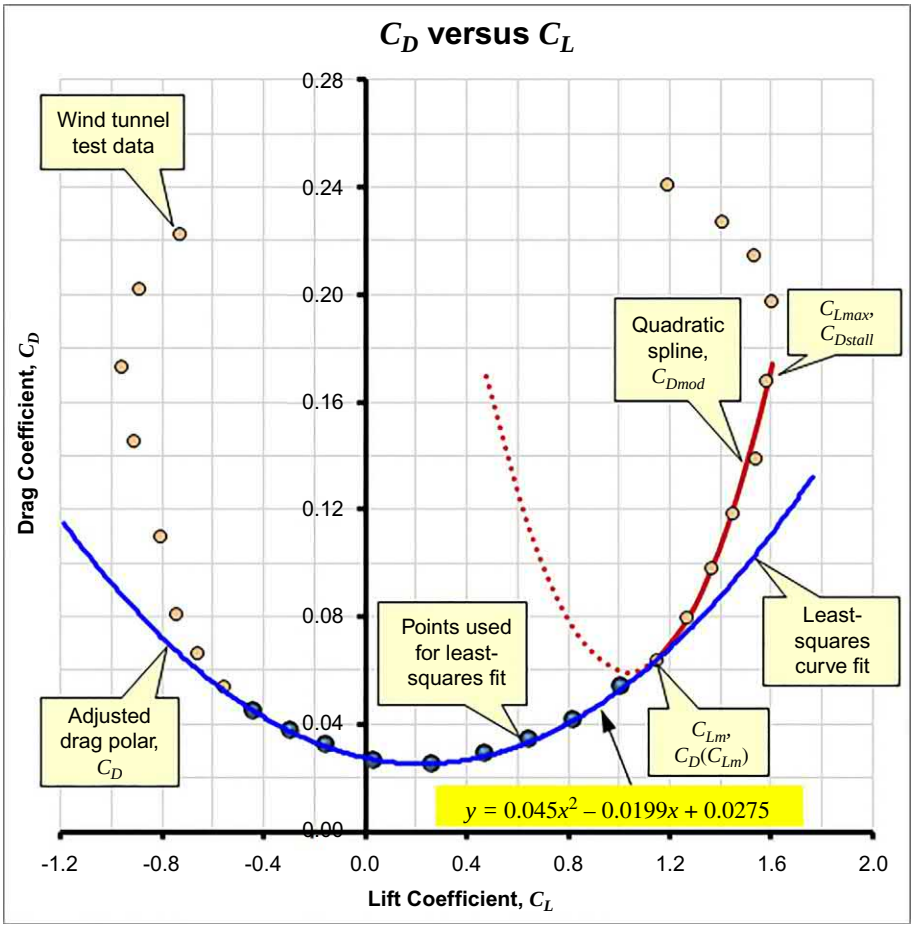


FIGURE 16-9 Prediction is improved at higher lift coefficients by the quadratic spline, C_{Dmod}.

EXAMPLE 16-2

The hypothetical wind tunnel data in Figure 16-10 represent an airplane whose $AR=9$. The least-squares quadratic curvefit for the data points is given by $C_D=0.045C_L^2-0.0199C_L+0.0275$. Determine the quadratic spline, assuming a $C_{Lm}=1.15$, and write the complete drag coefficient.

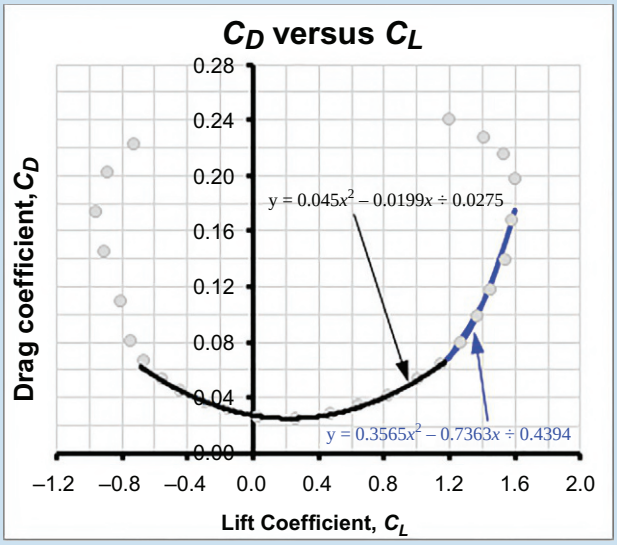


FIGURE 16-10 The modified drag model better fits experiment than the regular quadratic model.

SOLUTION:

Using the previously mentioned drag polar, extract $C_{D_{min}}$, $C_{L_{minD}}$, and the Oswald span efficiency (e) using the conversion method of Section 16.5.5. In particular, see Equations (16-194)–(16-196). The section presents an example as well, so only the results based on the previously mentioned polynomial will be presented.

$$C_{D_{min}}=0.02530,\quad C_{L_{minD}}=0.2211,\quad e=0.78595$$

Using e, we find the $k=1/(\pi\cdot AR\cdot e)=0.045$. Using this data, the matrix of Equation (16-19) becomes:

$$\begin{bmatrix}1.3225 & 1.15 & 1\\ 2.3 & 1 & 0\\ 2.5113 & 1.5847 & 1\end{bmatrix}\begin{Bmatrix}A\\B\\C\end{Bmatrix}=\begin{Bmatrix}0.06413\\0.08360\\0.16783\end{Bmatrix}$$

From which we find that $A=0.3565$, $B=-0.7363$, and $C=0.4394$. The resulting C_D can thus be represented by:

$$C_D=\begin{cases}0.0253+0.045\cdot(C_L-0.2211)^2 & \text{if } C_L\le 1.15\\ 0.3565\cdot C_L^2-0.7363\cdot C_L+0.4394 & \text{if } C_L>1.15\end{cases}$$

Note the resulting graph is shown in Figure 16-10.

16.2.4 Drag Modeling using Higher Order Polynomials

It is also possible to better approximate the drag polar using higher order polynomials or parametric splines. However, there are limits. Figure 16-11 shows a fourth-order polynomial in good agreement at higher lift coefficients, although it does not approach the minimum drag value as closely as the quadratic one. It is somewhat unwieldy compared to the quadratic form, although this is not an issue in spreadsheets or coding.

Generally, the presence of the drag bucket prevents the use of polynomials, as these do not follow the sharp change in curvature of the drag polar. Even polynomials of order as high as 16+ will not suffice, as they tend to oscillate inside the prediction region. Methods that can be used to represent such drag polars include a spline (e.g., B-spline) or a lookup table. These are outside the scope of this edition of the book.

16.2.5 Drag of a 2D Body in a Wind-Tunnel

Drag force of a 2D body (e.g., an airfoil) is estimated in wind tunnel testing by two means: (1) Using a force balance and (2) based on velocity profile in front and aft of model using the momentum theorem (see Section 14.2.1, *Conservation Laws*). The former is outside the scope of this book. The latter warrants a short introduction.

The momentum equation of Equation (14-26) can be simplified to allow the extraction of drag of a body in a wind tunnel, by assuming steady flow, absence of body forces, and uniformity of pressure in front and aft. Thus, only the momentum flux term remains. For instance, as shown in references such as Refs. [7–9], this leads to the following expression for drag force *per unit length*:

$$D'=\int_{-h/2}^{h/2}\rho u_e(u_i-u_e)dy \tag{16-21}$$

Where h is the height of the test section, u_i and u_e are the velocity profiles at the inlet and exit of the test section, respectively. It is assumed the body is placed near the vertical center of the test section (where $y=0$). See Example 16-3 for details of its use.

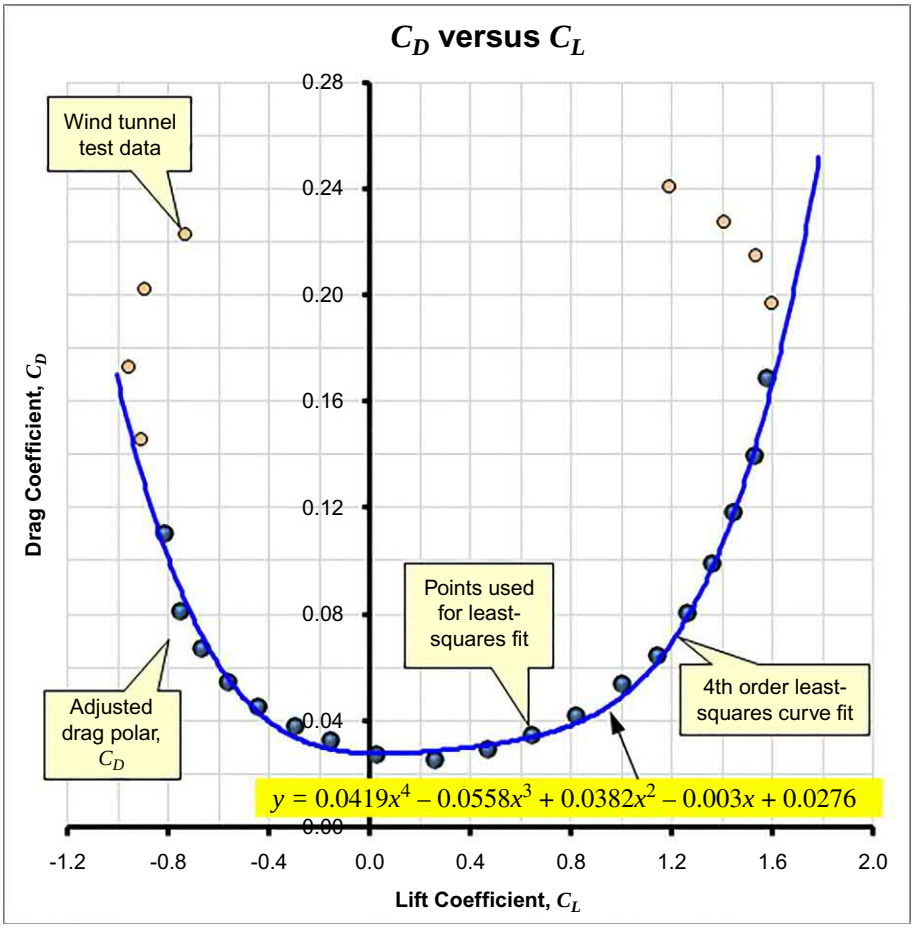


FIGURE 16-11 A quartic polynomial drag polar.

EXAMPLE 16-3

The wind tunnel setup shown in Figure 16-12 is used to measure drag of an airfoil. The distribution of velocity is measured at the inlet and exit of the test section. The airspeed profile at the inlet is uniform, but at the exit is $u_e(y) = \frac{1}{2}u_i\left(1 + 4y\,\mathrm{sgn}(y)/h\right)$ between $-h/4 \le y \le h/4$ and sgn() is the sign function. Elsewhere, $u_e = u_i$. Assume equal and uniform static pressures at entry and exit. Determine the *drag force per unit length* (D') acting on the airfoil.

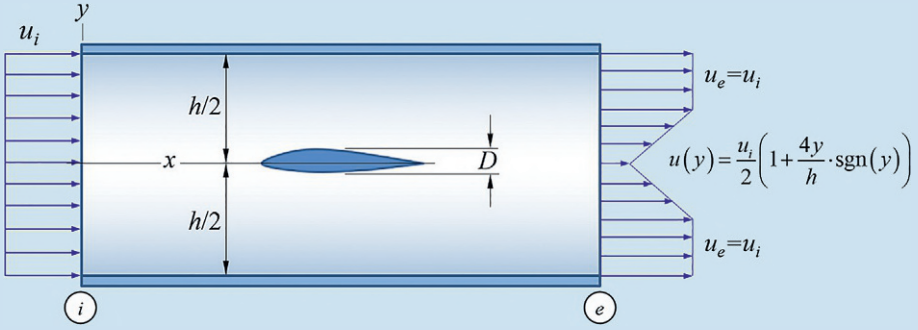


FIGURE 16-12 A 2D body in a wind tunnel.

EXAMPLE 16-3 (*cont'd*)

SOLUTION:

Let us break the integral of Equation (16-21) into four smaller integrals

$$D' = \int_{-h/2}^{h/2} \rho u_e (u_i - u_e) dy$$

$$= \overbrace{\int_{-h/2}^{-h/4} \rho u_i (u_i - u_i) dy}^{=0} + \int_{-h/4}^{0} \rho u_e (u_i - u_e) dy$$

$$+ \int_{0}^{h/4} \rho u_e (u_i - u_e) dy + \overbrace{\int_{h/4}^{h/2} \rho u_i (u_i - u_i) dy}^{=0}$$

As shown, the upper and lower fourths of the region return zero (because $u_e = u_i$). Due to the symmetry of this problem, the center two integrals are equal. Therefore, we can drop the sign function and integrate from 0 to h/4 and multiply the result by two, which reduces this to

$$D' = 2\rho \int_0^{h/4} \left(\frac{u_i}{2}\left(1 + \frac{4y}{h}\right)\right)\left(u_i - \frac{u_i}{2}\left(1 + \frac{4y}{h}\right)\right) dy$$

Substitute the given velocity profiles into Equation (16-21) and evaluate the integrals to give

$$D' = \rho u_i^2 \int_0^{h/4} \left(1 + \frac{4y}{h}\right)\left(2 - \left(1 + \frac{4y}{h}\right)\right) dy$$

$$= \rho u_i^2 \left[y - \frac{16y^3}{3h^2}\right]_0^{h/4} = \frac{\rho u_i^2 h}{6}$$

16.2.6 Additional Topics on Drag

This section discusses additional topics of interest.

(1) Effect of Aspect Ratio on Drag

In 1923, Prandtl [10] presented the results of an experiment that revealed the effect aspect ratio has on lift and drag of a wing. A copy of his results is shown in Figure 16-13. The left graph shows the impact of *AR* on drag, while the right graph shows its effect on lift.

(2) Effect of Yaw Angle β on Drag

As discussed in Section 16.3.2, *Estimating Lift-Induced Drag*, drag varies greatly with AOA. It also varies with yaw as shown in Figure 16-14. The yaw always increases drag. This fact is frequently used by pilots when landing. Pilots "coming in too high" yaw the airplane to decrease its *L*/*D* ratio, increasing its rate of descent. How much, depends on geometry. For analysis, the flow may be assumed unseparated for β up to ±10 degrees. Beyond that, flow separation is certain, as is the associated drag increase.

(3) Effect of Control Surface Deflection on Drag

Deflecting control surfaces beyond neutral deflection increases the drag of the aircraft. Deflecting the elevator shifts the drag polar vertically, increasing the $C_{D_{min}}$. This increases *trim drag* and calls for tail sizing that results in neutral elevator deflection in cruise (called an elevator "in trail").

Trim drag is most accurately estimated using wind tunnel tests. A graph similar to the one in Figure 16-15 is usually obtained, with several curves showing the drag polar for various elevator deflection angles. This allows the performance engineer to better estimate the capability of the airplane at different loading and flight conditions. In the absence of wind tunnel testing, this drag can be estimated by various means that include various airfoil codes.

A method to estimate trim drag based on CG location and thrust setting is presented in Section 16.4.1, *Trim Drag*.

(4) Effect of Flap Deflection on Drag

Deflecting flaps significantly shifts the drag polar to the right and up as shown in Figure 16-16. It increases the $C_{D_{min}}$ and $C_{L_{minD}}$, in addition to $C_{L_{max}}$. It affects the drag at stall, C_{Dstall}, less significantly.

(5) Effect of Waviness on Drag of NLF Surfaces

The British aerodynamicist Melvill Jones (1887–1975) rose to fame in 1929 for introducing aircraft manufacturers to the importance of streamlining [11]. In 1938, he pointed out the importance of smooth, waveless surfaces for sustaining extensive laminar boundary layer [12].

Surface waviness expedites (trips) laminar-to-turbulent transition. By quantifying the waviness of a surface, it is possible to implement quality control of NLF surfaces. In this capacity, Carmichael [13] summarizes research on NLF surfaces, listing experimental evidence and lessons learned. He presents methods, based on the work presented in Refs. [14–16], that can help the

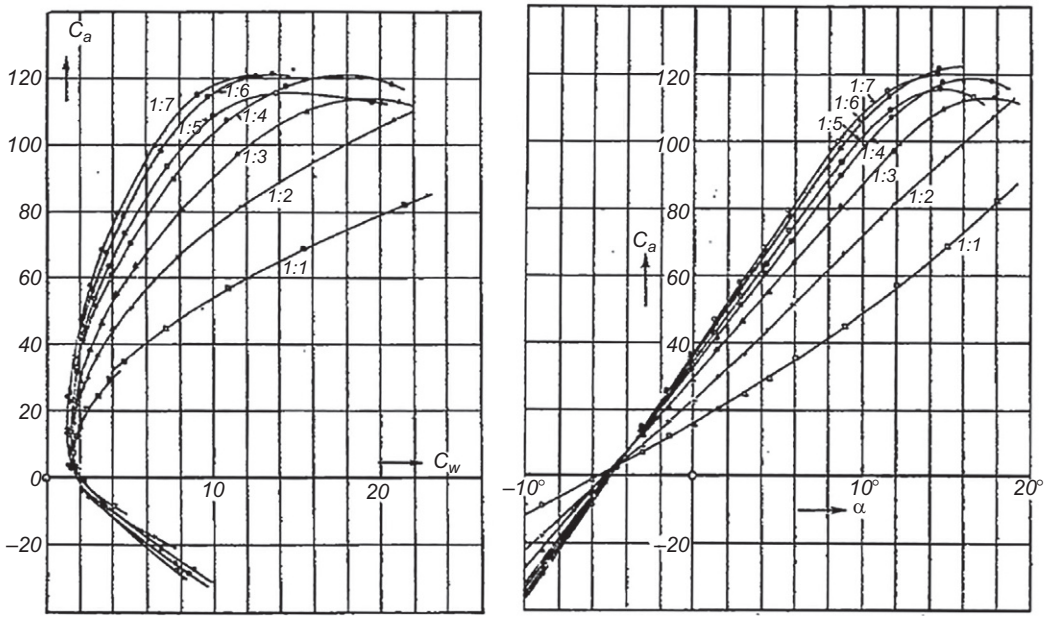


FIG. 16.—Polar diagrams for seven wings, aspect ratios 1:7, 1th, etc., 1:1.

FIG. 47.—Lift coefficients plotted as function of angle of attack for aspect ratios 1:7 to 1:1.

FIGURE 16-13 Ludwig Prandtl's original research reveals how lift and drag of a wing changes with *AR*. *From L. Prandtl, Applications of Modern Hydrodynamics to Aeronautics, NACA R-116, 1923.*

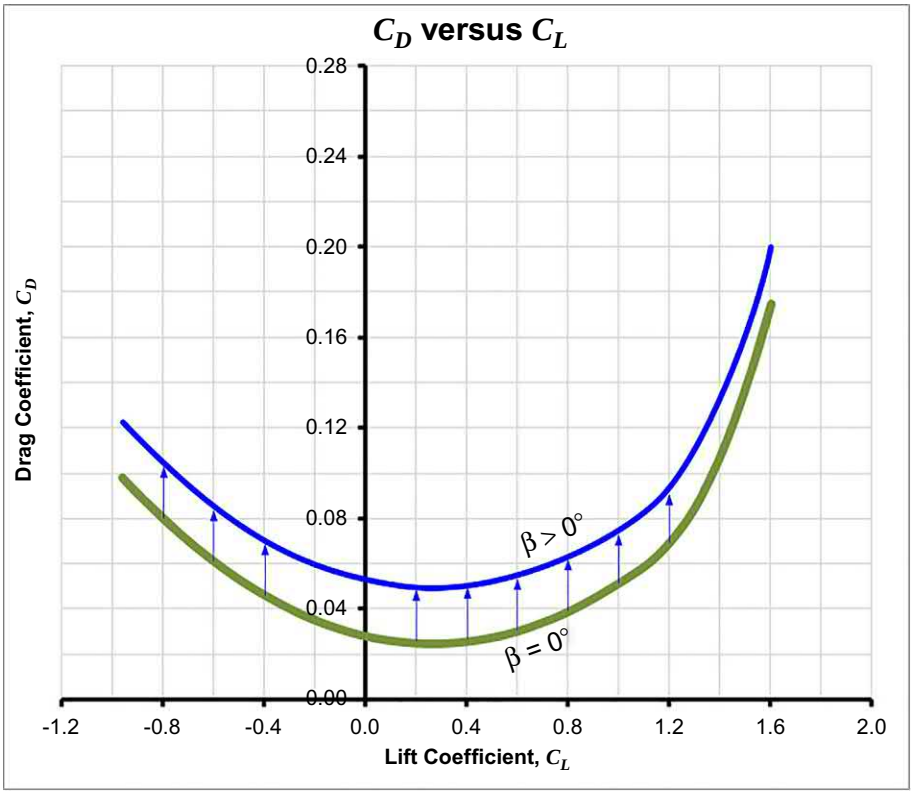


FIGURE 16-14 The effect of yawing the airplane to some yaw angle β.

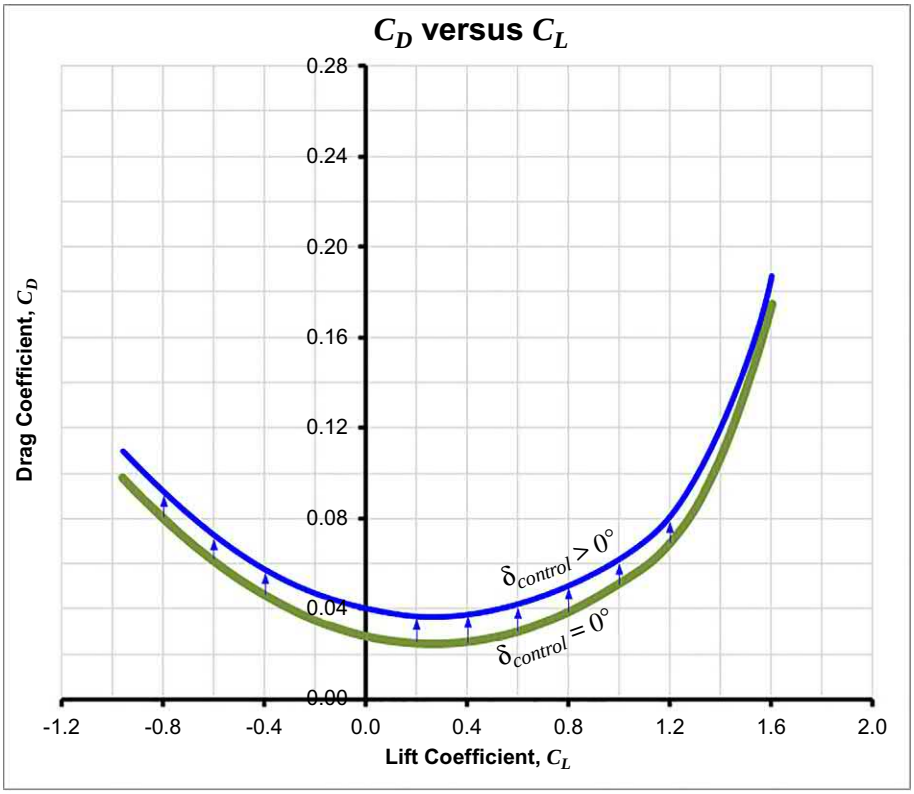


FIGURE 16-15 The effect of deflecting a control surface.

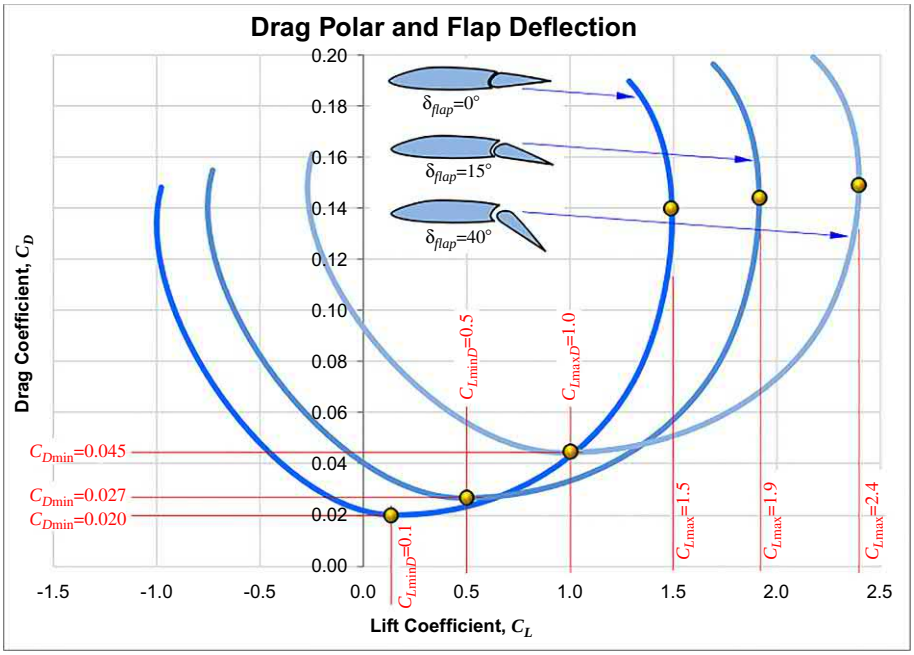


FIGURE 16-16 Deflecting flaps has significant impact on the drag polar. Typical numbers are shown.

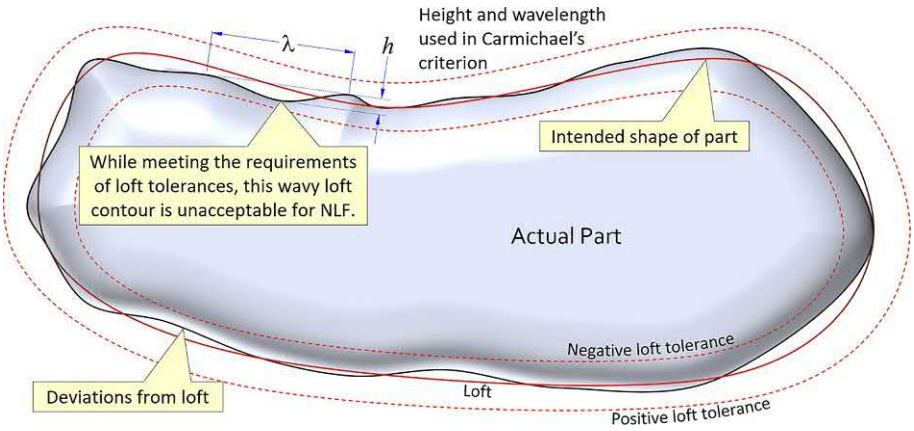


FIGURE 16-17 Definition of local contour deviations.

manufacturer evaluate the quality of the NLF surface. The expression is widely used and is often referred to as *Carmichael's criterion*. Presented below, it shows the maximum wave height-to-length (see Figure 16-17) below which early transition is avoided.

$$\frac{h}{\lambda} \leq \sqrt{\frac{59{,}000c\cos^2\Lambda_{LE}}{\lambda R_e^{1.5}}} \tag{16-22}$$

Where h is the double-amplitude wave height in inches, λ is wavelength in inches, c is streamwise chord in inches, Λ_{LE} is the wing leading edge sweep, and R_e is the Reynold's number based on chord.

(6) Musings on Prediction Accuracy

In 1940, NACA released the wartime report WR-L-489 [17] in which 11 military aircraft were investigated to determine why they failed to meet their predicted performance. The aircraft were wind tunnel tested in the NACA *Full-Scale Wind Tunnel* (FSWT) in Langley, Virginia.[2] The aircraft were stripped to a clean configuration by gradually removing components. The drag coefficient was measured after each removal step. The results give a timeless insight into the cumulative impact of small and easily ignored design details on the total drag.

One of the aircraft investigated was the Seversky P-35 that had been designed for the US Army Air Corps in the early 1930s (see Figure 16-18). At the time, it was an innovative single-engine fighter that offered a number of firsts. It was the Air Corps first all metal fighter, the first to feature retractable landing gear, and the first with an enclosed cockpit. Its promised maximum airspeed was 280 KTAS [18], but its actual speed was some 28 KTAS lower. While its engine could not develop the advertised power, which contributed to the problem, it did not fully explain the difference between practice and prediction. This simply implied its drag was higher than predicted—something common to the other 10 aircraft also studied in the report. This highlights a scenario to which anyone estimating the drag of a new airplane may be subject—to analyze Airplane 1 in Ref. [17], when in reality it will be closer to Airplane 18.

Such underpredictions are not limited to aircraft of the yesteryear. They still happen. A recently developed small twin-engine business jet was unable to meet the predicted performance advertised on the company website. This led to a costly redevelopment effort [19, 20]. A small single-engine propeller aircraft developed by a prominent car manufacturer also didn't meet the predicted performance due to higher than predicted drag [21]. Both aircraft were designed by very capable people. It shows that drag prediction must be treated with utmost respect.

Going back to Ref. [17], the source presents a detailed listing of the changes made to the airplane presented in a graphic and tabulates their effect on the total drag. The graphic is reproduced as Ref. [17] and the table is recreated as Table 16-1. It is of great value to review the table to see how contributions of seemingly insignificant modifications, such as a sanded walkway or an opened cowl flap affect the overall drag of the airplane. The problem is not the individual contribution, but their collective effect. To make the numbers easier to relate to, the impact of the change on maximum level airspeed (at 12,000 ft) is calculated. It shows that the airspeed change between the actual (ID18) and ideal airplane (ID1) is 44 KTAS.

[2] It was demolished between 2010 and 2014.

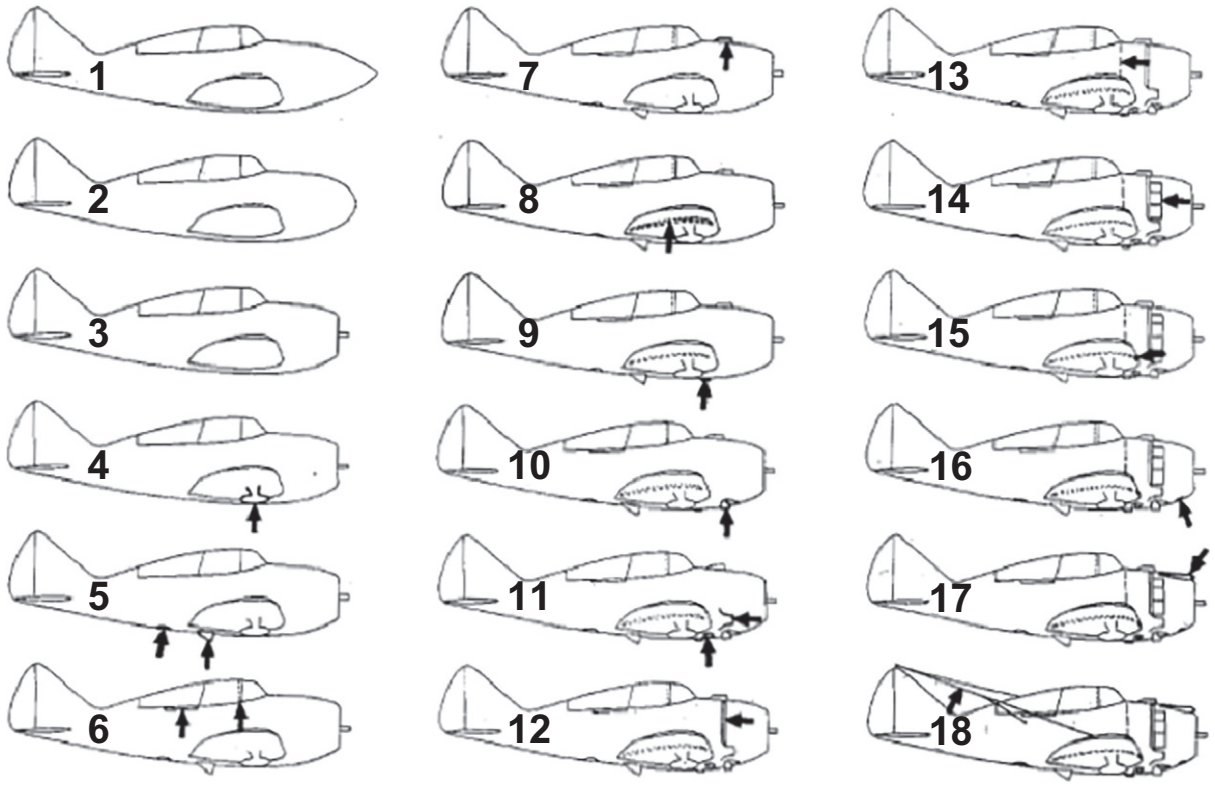


FIGURE 16-18 Order of modifications made to the Seversky P-35 aircraft during wind tunnel testing. *Figure from C.H. Dearborn, and A. Silverstein, Drag Analysis of Single-Engine Military Airplanes Tested in the NACA Full-Scale Wind Tunnel, NACA WR-L-489, 1940.*

TABLE 16-1 Component contribution to drag for the Seversky P-35 [17].

ID	Airplane Conditions	C_D	ΔC_D	ΔC_D %	V_{max}, KTAS
1	Completely faired condition with long nose fairing	0.0166	0	0	296
2	Completely faired condition with blunt nose fairing	0.0169	0.0003	1.8%	296
3	Completely faired condition with original NACA cowling (no air flowing through cowling)	0.0186	0.0020	12.0%	288
4	Same as 3 except landing gear seals and fairing removed	0.0188	0.0002	1.2%	287
5	Same as 4 except original oil cooler installed	0.0205	0.0017	10.2%	279
6	Same as 5 except canopy fairing removed	0.0203	-0.0002	-1.2%	280
7	Same as 6 except carburator scoop added	0.0209	0.0006	3.6%	277
8	Same as 7 except sanded walkway added	0.0216	0.0007	4.2%	274
9	Same as 8 except ejector chute added	0.0219	0.0003	1.8%	272
10	Same as 9 except exhaust stacks added	0.0225	0.0006	3.6%	270
11	Same as 10 except intercoolers added	0.0236	0.0011	6.6%	266
12	Same as 11 except cowling exit opened	0.0247	0.0011	6.6%	261
13	Same as 12 except accessory exit opened	0.0252	0.0005	3.0%	260
14	Same as 13 except cowling fairing and seals removed	0.0261	0.0009	5.4%	257
15	Same as 14 except cockpit ventilator opened	0.0262	0.0001	0.6%	256
16	Same as 15 except cowling venturis installed	0.0264	0.0002	1.2%	256
17	Same as 16 except blast tubes added	0.0267	0.0003	1.8%	255
18	Same as 17 except radio aerial installed	0.0275	0.0008	4.8%	252
	TOTAL DRAG CHANGE		**0.0109**	**65.7%**	

Percentages are based on ID 1

16.2.7 Various Means to Reduce Drag

It has already been stated that, generally, drag is a detrimental force in aircraft design, in particular, for fuel efficiency. In addition to "obvious" means to reduce drag, such as retractable landing gear and smooth NLF surfaces, people have been creative in the pursuit of reduced drag. This section introduces a few fruits of this labor.

(1) Reduction of Wing Drag via Laminar Flow Control (LFC)

The history of LFC dates back to 1930s and is well documented by Chambers [22] and in particular Braslow [23]. LFC is also referred to as *artificial laminar flow* (ALF) to contrast *natural laminar flow* (NLF). LFC attempts to maintain laminar boundary layer over a large surface area by "sucking" the turbulent boundary layer through tiny perforations in the wing skin. A variation of LFC, called *hybrid LFC* (HLFC), relies on NLF for a larger portion of the wing to reduce the power required for the ALF. The primary drawback of these methods is that they are *active* rather than *passive*. Thus, additional energy is required to draw in the external boundary layer. Furthermore, the perforations are detrimental to the structural integrity of the wing and require the operator to deal with nuisances such as insect removal that can clog the perforations, reducing system performance.

Figure 16-19 shows the difference in airflow over an airfoil with and without LFC. The left photo shows the airfoil at an AOA of 20 degrees with a fully separated wake behind it. The right photo shows the same airfoil with the LFC turned on. The change in the nature of the flow is clearly evident, with the separation being eliminated as far aft as 70% of the chord. This "unstalls" the airfoil, giving it a higher $C_{l_{max}}$ and reduced drag. It demonstrates the promising potential of LFC technology, although being severely hampered by a number of factors discussed in Ref. [22].

Early experiments involve the Northrop X-21A, a heavily modified Douglas WB-66D aircraft. Its two original Allison J71 engines, originally on the wing, were replaced with two GE XJ79s that were mounted to the rear fuselage. The bleed air from these engines was used to drive a compressor that, effectively, sucked the wing boundary layer through slots in the wing. While the system demonstrated the effectiveness of LFC, it turned out to be a manufacturing and maintenance nightmare and too costly to be practical.

In 1999, Marshall [24] investigated the effectiveness of a variable-porosity suction glove on the F-16XL-2 aircraft to demonstrate the feasibility of ALF for supersonic operation. It showed that at Mach 2 at 53,000 ft (R_e of the order of 22.7×10^6) laminar boundary layer was sustained as far aft as 46% of the chord. In 2010, van de Wal [25] showed merely 3.2% reduction in total drag of a small GA aircraft (ENAER Namcu), citing that installing a boundary layer suction system was not beneficial to its operation.

(2) Reduction of Lift-Induced Drag using Winglets

Winglets and the potential for a reduction in lift-induced drag is discussed in Section 10.5.9, *The Winglet*.

(3) Reduction of Wing Profile Drag using NLF Airfoils

Natural laminar flow airfoils are an obvious choice when trying to reduce drag. Of course, they have to be selected before the airplane is built. NLF airfoils are discussed in great detail earlier in this section and Chapter 8, *The Anatomy of the Airfoil*.

(4) Reduction of Fuselage Drag

Wortman [26] suggests that installing relatively large fixed pitch vortex generators on the bottom, near the beginning of the upsweep of the lower fuselage of transport aircraft can reduce the total drag by 1%–2%. The idea

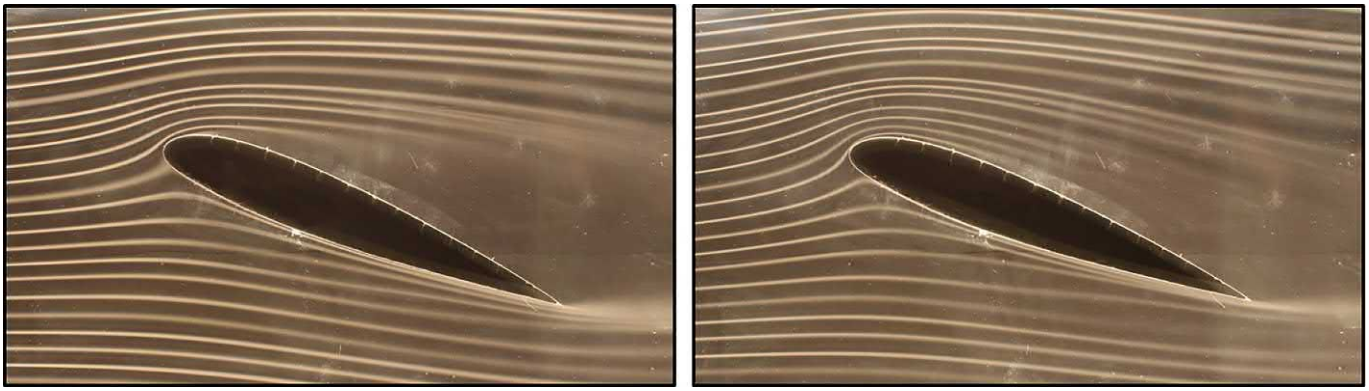


FIGURE 16-19 The effect of Laminar Flow Control. The AOA is approximately 20 degrees. *Photos by Phil Rademacher.*



FIGURE 16-20 Vortex generators on the aft fuselage of a B-52 Stratofortress. *Photo by Phil Rademacher.*

was validated in extensive wind tunnel tests using fuselage models of the Boeing 747 and Lockheed C-5 Galaxy transport aircraft. The author suggests the vortex generators can be installed on such aircraft for a fraction of the cost of their monthly operational cost. Such vortex generators are shown mounted to the aft lower fuselage of the B-52 Stratofortress in Figure 16-20.

Kentfield [27] suggests that using a stepped after-body can significantly reduce the drag of an axis-symmetric fuselage style bodies. The unorthodox idea forms entrapped vortices at each step of the conical after-body, which allows the airflow to better follow its geometry, ultimately reducing its drag. The method is untraditional and results in an unusual after-body geometry that would be hard to justify from an aesthetics standpoint, not to mention there could be some structural challenges.

A clear way to reduce fuselage drag is to employ tadpole fuselages, like those used for sailplanes. Naturally, such fuselages are not always practical considering the mission of the airplane. Tadpole fuselages are discussed in Section 12.2.3, *The Tadpole Fuselage*.

In evaluating the importance of smooth surfaces in maintaining NLF on lifting surfaces (wing, HT, and VT), Quast and Horstmann [28] demonstrate the magnitude of fuselage drag. Using the Airbus 300 as an example, they estimate the drag of the fuselage alone amounts to about 49% of the minimum drag. Such studies remind us it is easy to spend a tremendous effort eliminating a few dragcounts from the lifting surfaces, while overlooking the largest source of drag—the fuselage.

(5) Reduction of Fuselage/Wing Juncture Drag

The juncture of the fuselage and wing can be particularly bothersome as it is not always easy to estimate tendency for flow separation. The steep adverse pressure gradients that frequently form in the region promote flow separation, even at low AOAs. This increases drag during climb and even cruise, reducing performance.

Modern methodologies are being developed that use state-of-the-art *Navier-Stokes computational fluid dynamics* (NS CFD) tools to shape the wing fairing using genetic algorithms. Using such a tool, Peigin and Epstein [29] demonstrated a 43 dragcount drag reduction in a before-and-after investigation of a business jet.

16.3 ESTIMATING THE DRAG OF A COMPLETE AIRCRAFT

The focus of this section is the development of a drag model for an entire aircraft. This is a complex task that must be broken down into several subtasks. For typical aircraft, it is compounded by configuration changes. There is a *clean configuration* intended for cruise. There is a *T-O configuration*, which is the clean configuration with the addition of landing gear (if not fixed) and a high-lift system deployed for T-O. Then, there is a *landing configuration*, which comprises the clean configuration with landing gear and a high-lift system deployed for landing. Hence, the analyst must develop at least three drag models. The task is made simpler by starting with the clean aircraft configuration and then add contributions by the landing gear and high-lift devices.

Figure 16-21 shows a rudimentary plan of attack that applies to all configurations. The section numbers for the required analyses are shown right of each task. The product of this work is shown at the bottom of the figure: It is the *drag model*. Figure 16-22 further highlights important contributors to the drag. If you are new to this process you must first learn the ropes. You must learn how to calculate skin friction. This is required for wings, HT, VT, fuselage, and all components that resemble a wing or an axisymmetric body. You must learn how to boost the resulting coefficients to include pressure drag. Then, how to account for contributions made by small components that "dirty up" the airplane. You must also learn how to calculate lift-induced drag and, if your airplane

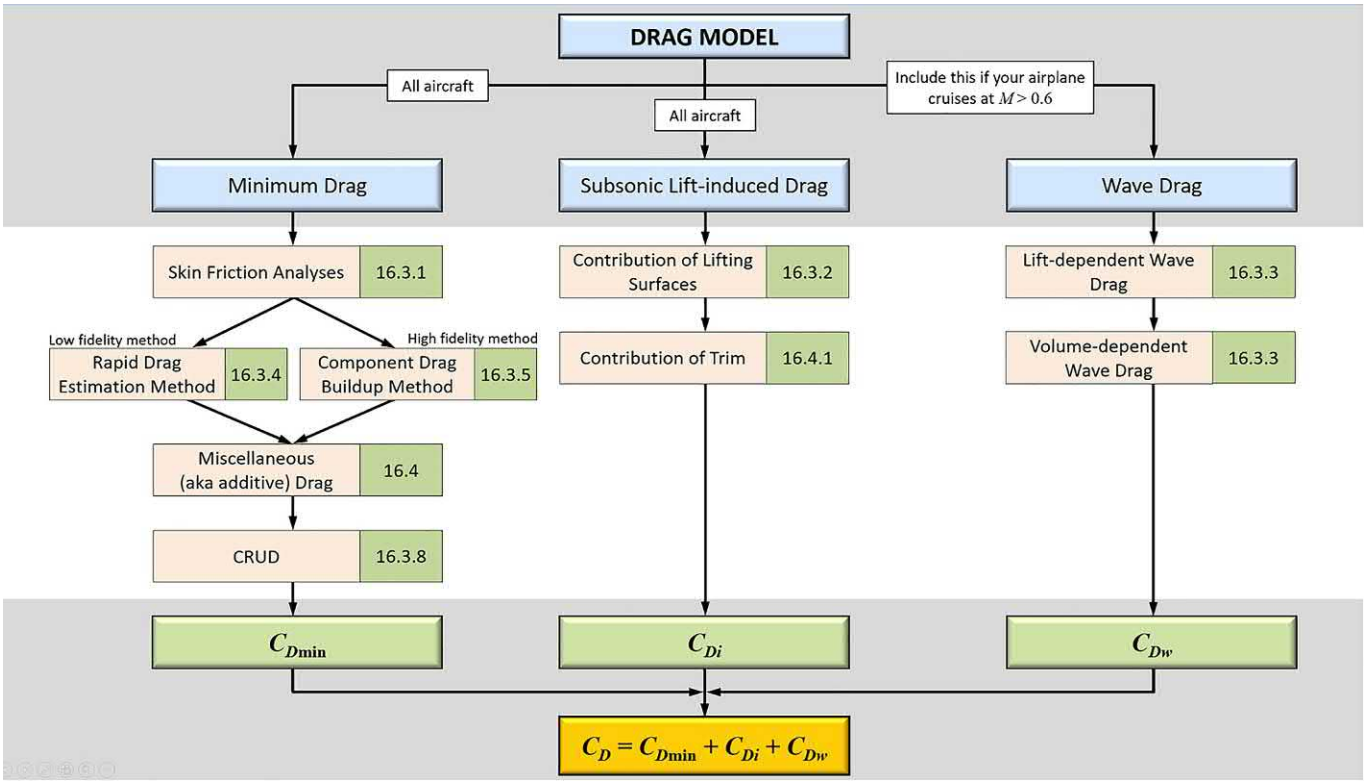


FIGURE 16-21 A flow chart depicting the development of the *drag model*.

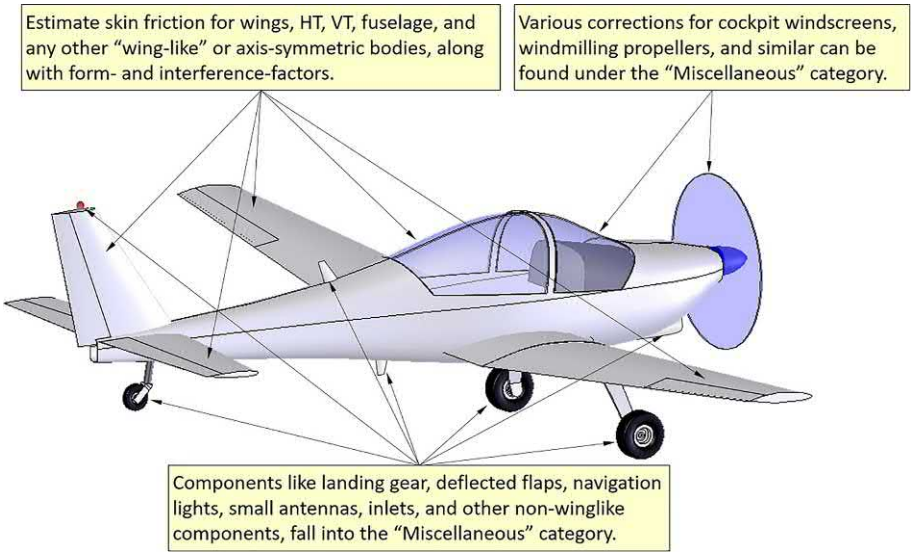


FIGURE 16-22 Contributions to the *drag model*.

operates in the transonic range, wave drag. This section is written for this purpose.

The tasks listed in Figure 16-22 are best tackled in the following (logical) order:

- Calculate skin friction per Section 16.3.1.
- Calculate aircraft profile drag per Section 16.3.4 or 16.3.5 (preferred).
- Calculate miscellaneous drag contributions per Section 16.4.
- Apply crud per Section 16.3.8.
- Calculate minimum drag coefficient per Section 16.3.9.
- Calculate lift-induced drag per Section 16.3.2.
- Calculate trim drag per Section 16.4.1.
- Calculate wave drag per Section 16.3.3.

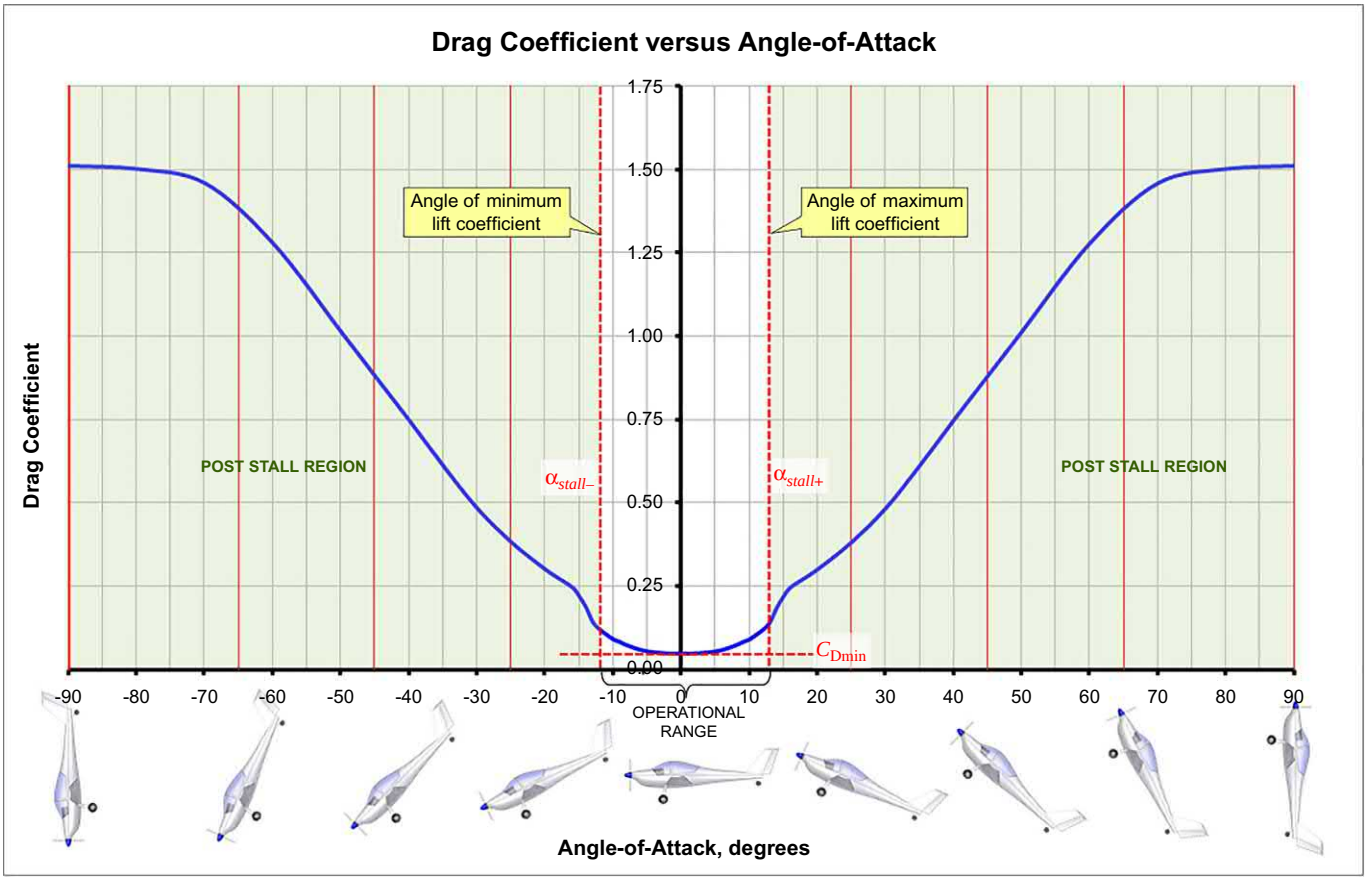


FIGURE 16-23 Typical variation of the drag coefficient for angle-of-attack between −90 degrees and +90 degrees.

Figure 16-23 shows a typical variation of the 3-dimensional drag coefficient for a complete aircraft (wings, fuselage, tail, etc.) with angle-of-attack for an AOA range of $-90 \text{ degrees} \leq \alpha \leq +90$ degrees. It is based on actual wind tunnel test data. The drag coefficient at the extreme AOAs typically ranges from 1.5 to 1.7. That beats the drag of the parachute in Section 16.4.14, *Drag of Parachutes*. Standard drag modeling is usually limited to the unshaded region in the center of the graph (the operational range).

16.3.1 Estimating Skin Friction Drag: C_{Df}

Recall that the drag of a body is caused by surface friction and pressure difference. This section focuses on the former—surface friction. Familiarity with Sections 8.1.6 (*Chordwise Pressure Distribution*), 8.1.7 (*Forces and Moment per Unit Span*), and 8.1.10 (*Boundary Layer Basics*) is an essential preparation for this section.

The formulation presented in subsequent subsections are the product of the *boundary layer theory*. The formulae are extracted from numerous sources, including Schlichting [30], Schetz and Bowersox [31], and Young [32]. Derivations of the formulae is provided in these texts. Only results important to aircraft drag analysis are presented here. The resulting relationships are plotted in Figure 16-26.

(1) Introduction

Figure 16-24 shows an airfoil immersed in airflow and illustrates several regions of interest. For skin friction, we are interested in the extent of *laminar* and *turbulent boundary layer* (BL) and *flow separation region*. The thick blue line that wraps around the leading edge represents a region of laminar BL. It terminates on both surfaces at the *transition point* (denoted by x_{tr_u} and x_{tr_l}) where it transforms into turbulent BL. Its extent depends on the geometry of the airfoil. The extent is shorter than shown for non-NLF airfoils. Eventually, this develops into separated flow. Figure 16-24 shows how angle-of-attack causes the two transition points move forward or aft. Other parameters affecting its extent are detailed in Section 8.1.10.

The extent of the laminar and turbulent BL impacts the airfoil's skin friction and, thus, its drag polar. Airfoils featuring geometries such as that shown in Figure 8-11, develop pressure distribution with extensive favorable pressure gradient (dp/dx). They sustain laminar BL over a large part of their surface. Such airfoils are called *natural laminar flow* (NLF) airfoils (see Sections 8.1.6 and 8.1.10).

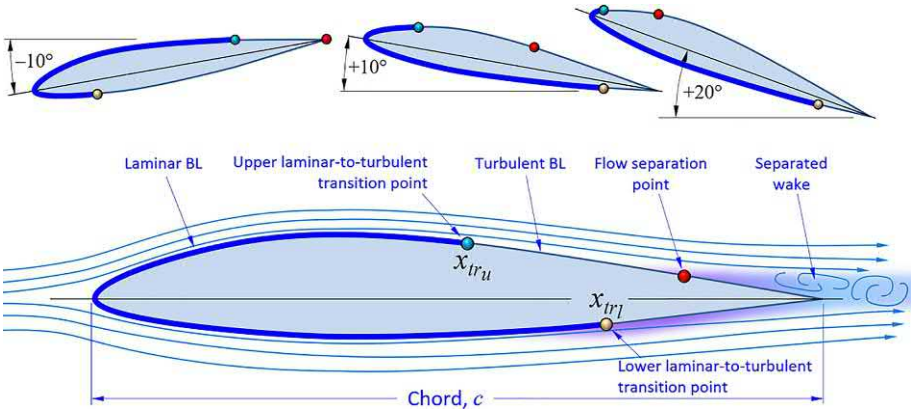


FIGURE 16-24 Flow regions over an airfoil. Inset shows extent of laminar BL at various angles-of-attack.

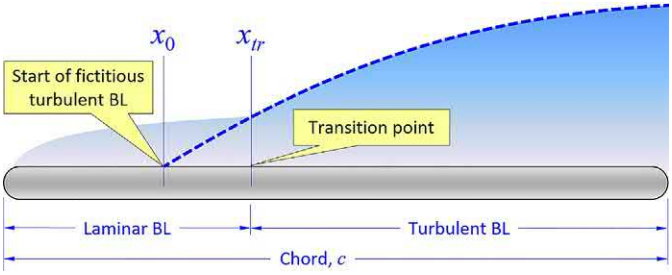


FIGURE 16-25 Transition from laminar to turbulent flow inside a mixed boundary layer.

Their primary advantage is considerably lower drag at low angles-of-attack, during cruise. The effect of such geometry differences is depicted in Figure 8-21.

The boundary layer develops on a curved surface similar to what it does on a flat plate. It is affected by all the same shortcomings. Figure 16-25 illustrates the transformation that takes place as the laminar BL transitions into turbulent one. The transition can be thought to take place forward of the transition point, at the so-called *fictitious transition point*. It causes the thickness of the BL to grow. This tends to occur once the R_{ex} (see Equation (16-26)) approaches and exceeds 10^6 [33, pp. 2–8], when dynamic flow forces become larger than the viscous forces (see Figure 16-25). As the flow speed increases (increasing R_{ex}) the transition points move farther forward, although never quite to the LE.

The laminar BL is sensitive to surface contamination. The presence of rivet-heads, uneven plate joints, insects, and even paint chips can destabilize it and initiate an early transition (see Section 8.3.7, *The Effect of Leading-Edge Roughness and Surface Smoothness*). The laminar BL is even sensitive to uncontrollable factors like the quality of the airflow. Figure 16-26 shows how the flat plate drag coefficient for laminar and turbulent BL changes with Reynolds number. Figure 16-26 shows how susceptible to transitioning the laminar

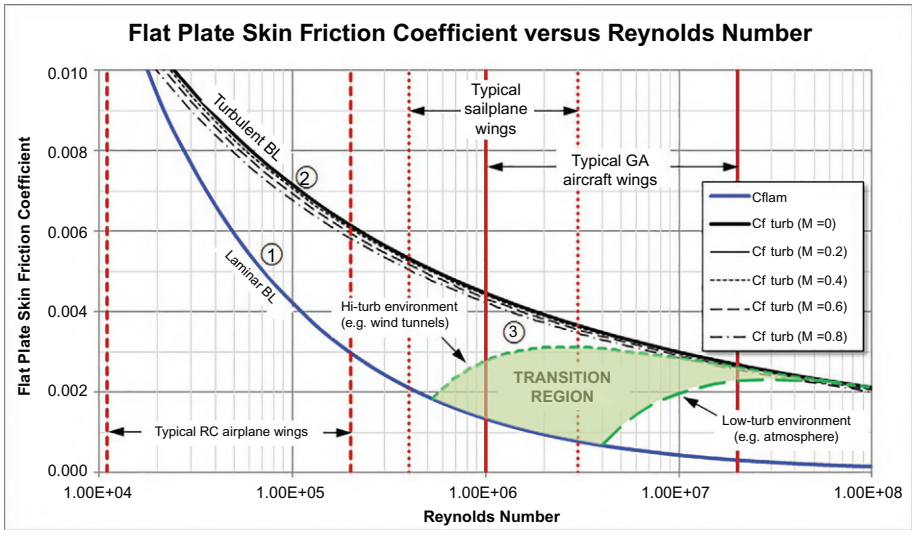


FIGURE 16-26 Change in skin friction with Reynolds number. ① is Equation (16-40), ② is Equation (16-43), ③ is Equation (16-46).

boundary layer is as it flows over a flat plate, operating within $4\times10^5 < R_e < 1\times10^7$.

(2) Basic Analysis Procedure

(A) List all components that can be classified as "winglike." This includes the wings, HT, VT, pylons, fuselage, engine nacelles, wingtip tanks, and so forth. Smaller components like small, wing-shaped antennas can be omitted, as these are treated as "miscellaneous" drag. (B) List geometric properties of each component, primarily chord-lengths and wetted areas. (C) Calculate the skin friction coefficients for each component using any of the applicable methods that follow. A similar approach is also used in the *component drag buildup method*, presented in Section 16.3.5.

(3) Skin Friction Drag Coefficient, C_{Df}

The skin friction drag coefficient applies to the entire aircraft. It is defined as

$$C_{Df} = \frac{2D_f}{\rho V_\infty^2 S} = C_f\left(\frac{S_{wet}}{S}\right) \tag{16-23}$$

Where D_f is skin friction drag force, S is the reference wing area, S_{wet} is wetted area, C_{Df} is *skin friction drag coefficient*, and C_f is *skin friction coefficient*. Note the difference between the two coefficients; C_f and C_{Df}.

(4) Viscosity

See introduction in Section 8.1.10, *Boundary Layer Basics*. The viscosity of air is given by the empirical Sutherland's formula [34]:

SI-system:

$$\mu = 1.458\times10^{-6}\left(\frac{T^{1.5}}{110.4+T}\right) \quad \left[\frac{\text{Ns}}{\text{m}^2}\right] \tag{16-24}$$

UK-system

$$\mu = 3.170\times10^{-11}\left(\frac{734.7T^{1.5}}{216+T}\right) \quad \left[\frac{\text{lb}_\text{f}\text{s}}{\text{ft}^2}\right] \tag{16-25}$$

Equation (16-25) is presented in Ref. [35] and cited by [36]. There are two kinds of viscosities of interest to the aircraft designer. (1) *Dynamic viscosity* (μ) is simply known as *viscosity* or viscosity coefficient. Common units are kg/ms, Ns/m^2, or slugs/fts. (2) *Kinematic viscosity* (ν) is the ratio of viscous to inertia forces in a fluid. Common units are m^2/s or ft^2/s. It is defined below:

$$\nu = \frac{\mu}{\rho} = \frac{\text{viscous force}}{\text{inertia force}} \tag{16-26}$$

(5) Reynolds Number

The Reynolds number is a measure of the ratio of inertial forces to viscous forces in fluid flow. It is derived using dimensional analysis. It is of great importance in the analysis of the boundary layer. It is defined as follows:

$$\text{Reynolds number:} \quad R_e \equiv \frac{\rho V_\infty c}{\mu} = \frac{V_\infty c}{\nu} \tag{16-27}$$

Where: c = Reference length, in ft or m,

V_∞ = Reference airspeed, in ft/s or m/s,
ρ = Air density, in slugs/ft^3 or kg/m^3,
μ = Air viscosity, in lb$_\text{f}$ s/ft^2 or Ns/m^2,
ν = Kinematic viscosity, in ft^2/s or m^2/s.

Note that *local* R_e is represented as a function of the distance from the leading edge of a body to a point of interest. It is written as follows:

$$R_{e_x} \equiv \frac{\rho V_\infty x}{\mu} = \frac{V_\infty x}{\nu} \tag{16-28}$$

The expression is used to estimate friction on a surface using integration (see later). The Reynolds number for a standard day, sea-level conditions only, is found from:

$$\text{UK-system } (V_\infty \text{ in ft/s}, c \text{ in ft}): \quad R_e \approx 6400 V_\infty c \tag{16-29}$$

$$\text{SI-system } (V_\infty \text{ in m/s}, c \text{ in m}): \quad R_e \approx 68{,}500 V_\infty c \tag{16-30}$$

(6) Cutoff Reynolds Number

Ref. [37] contends that poor surface qualities result in skin friction higher than that predicted by equations such as Equation (16-40) or (16-43). To remedy this discrepancy a special R_e, called a *cutoff* R_e, is calculated. When the actual R_e exceeds the cutoff R_e, the latter is used. It is calculated using the following expressions

$$\text{Subsonic:} \quad R_{e_{cutoff}} = 38.21\left(\frac{c}{\kappa}\right)^{1.053} \tag{16-31}$$

$$\text{Trans \& supersonic:} \quad R_{e_{cutoff}} = 44.62\left(\frac{c}{\kappa}\right)^{1.053} M^{1.16} \tag{16-32}$$

Where M_∞ is the far-field Mach number and κ is the skin roughness value specified in Table 16-2.

TABLE 16-2 Skin roughness values.

Surface type	κ (C in ft)
Camouflage paint on aluminum	3.33×10^{-5}
Smooth paint	2.08×10^{-5}
Production sheet metal	1.33×10^{-5}
Polished sheet metal	0.50×10^{-5}
Smooth molded composite	0.17×10^{-5}

Based on D.E. Hoak, USAF Stability and Control DATCOM, Flight Control Division, Air Force Flight Dynamics Laboratory, 1978, Section 4.1.5.1.

(7) Viscous Shear Stress

Two concepts of interest regarding viscous shear in the BL are *shear stress* (aka wall stress) and *shear force* (aka friction). The shear stress is determined as follows

$$\tau_w = \mu\left(\frac{du}{dy}\right)_{y=0} \tag{16-33}$$

Where u is the flow speed in the boundary layer and y is the axis normal to the surface. Units are N/m^2 (Pa) or lb_f/ft^2. The subscript $y=0$ indicates the shear stress should be evaluated at the surface (because the stress of interest takes place between the fluid and the surface). Note that Equation (16-33) is only valid for so-called *Newtonian fluids* (air, water, avgas). Non-Newtonian fluids are beyond the scope of this introduction.

(8) Skin Friction Coefficient, C_f

We prefer to relate skin friction to the dynamic pressure (q_∞) in the flow. This is defined as follows

$$\tau_w \equiv q_\infty C_f \quad \Rightarrow \quad C_f = \frac{\tau_w}{q_\infty} \tag{16-34}$$

(9) Average Skin Friction Coefficient

The friction coefficients come in two forms: (A) As a *local* function of R_{ex} or (B) *averaged* based on the R_e of the body's length (see Bullet (5)). Figure 16-27 plots the C_f for laminar, turbulent, and mixed boundary layers assuming $x_{tr}/c = 0.5$. It also illustrates the resulting average values. Figure 16-27 shows how three skin friction coefficients, $C_{f_{lam}}$, $C_{f_{turb}}$, and $C_{f_{mixed}}$, vary along the surface of the airfoil as functions of x (implicit functions of R_{ex}).

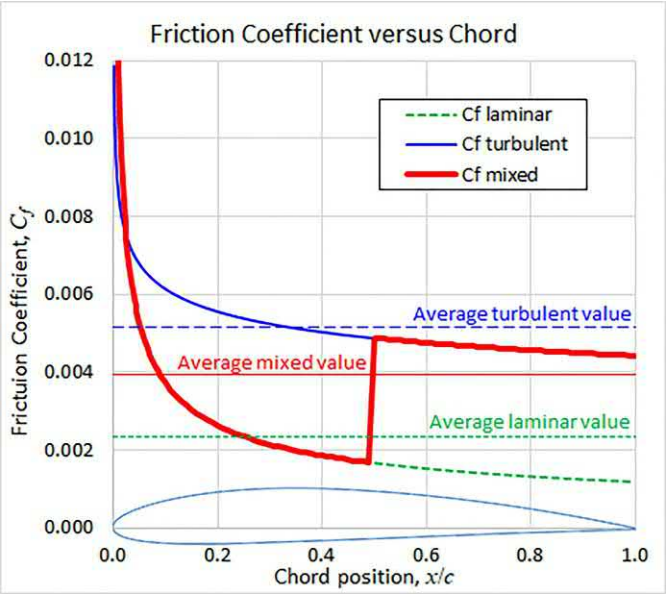


FIGURE 16-27 Distribution of C_f over an airfoil.

Their average value between the leading and trailing edges can be calculated using the following expression:

$$\underbrace{\overline{C}_f}_{\text{Averaged}} = \frac{1}{c}\int_0^c \underbrace{C_f}_{\text{Local}}\, dx \tag{16-35}$$

(10) *Friction Force, f*

Knowing the viscous shear stress, we can calculate the friction (f) (aka *skin friction* and *shear force*) acting on surface area A. There are two ways to do this; using *average shear stress* and *integration*. The former is convenient for rapid estimation and is determined as follows:

$$f = A\tau_w = A\mu\left(\frac{du}{dy}\right)_{y=0} \tag{16-36}$$

EXAMPLE 16-4

The "average" boundary layer velocity profile of air flowing over the surface of a flat plate with total surface area 50 m^2 is described by

$$u(y) = u_{max}\sin\left(\frac{\pi y}{2\delta}\right)$$

Where $u_{max} = 100\,m/s$ and $\delta = 0.0012\,m$. Estimate the total skin friction developed by the plate if $\mu = 1.73\times10^{-5}\,Ns/m^2$.

SOLUTION:

First, let us evaluate the derivative:

$$u = u_{max}\sin\left(\frac{\pi y}{2\delta}\right) \;\Leftrightarrow\; \left(\frac{du}{dy}\right)_{y=0} = \frac{\pi}{2}\frac{u_{max}}{\delta}\underbrace{\cos\left(\frac{\pi 0}{2\delta}\right)}_{=1} = \frac{\pi}{2}\frac{u_{max}}{\delta}$$

Thus, the shear force is determined as shown:

$$f = A\mu\left(\frac{du}{dy}\right)_{y=0} \;\Rightarrow\; f = A\mu\left(\frac{\pi}{2}\frac{u_{max}}{\delta}\right)$$

$$f = (50)\left(1.73\times10^{-5}\right)\left(\frac{\pi}{2}\frac{100}{0.0012}\right) = 113.2\ N$$

A more precise method is to integrate the *skin friction coefficient* (see Table 16-3) over the surface using Equation (16-65). Omitting the contribution of the pressure, the second equation becomes:

$$f = \int_{LE}^{TE}\tau_u\cos\theta_u ds_u + \int_{LE}^{TE}\tau_l\cos\theta_l ds_l = \int_0^c(\tau_u+\tau_l)dx$$

$$= q_\infty\int_0^c\left(C_{f_u}+C_{f_l}\right)dx \tag{16-37}$$

Where the subscripts u and l refer to the upper and lower surfaces, respectively.

TABLE 16-3 Properties of the boundary layer.

Property	Laminar	Turbulent	Turbulent (for pipe flow)
Boundary layer thickness	$\delta_{lam} = \frac{4.91x}{\sqrt{R_{e_x}}}$	$\delta_{turb} \cong \frac{0.16x}{R_{e_x}^{1/7}}$	$\delta_{turb} \cong \frac{0.38x}{R_{e_x}^{1/5}}$
Displacement thickness	$\delta^*_{lam} = \frac{1.72x}{\sqrt{R_{e_x}}}$	$\delta^*_{turb} \cong \frac{0.020x}{R_{e_x}^{1/7}}$	$\delta^*_{turb} \cong \frac{0.048x}{R_{e_x}^{1/5}}$
Momentum thickness	$\theta_{lam} = \frac{0.664x}{\sqrt{R_{e_x}}}$	$\theta_{turb} \cong \frac{0.016x}{R_{e_x}^{1/7}}$	$\theta_{turb} \cong \frac{0.037x}{R_{e_x}^{1/5}}$
Skin friction coefficient	$C_{f_{lam}} = \frac{0.664}{\sqrt{R_{e_x}}}$	$C_{f_{turb}} \cong \frac{0.027}{R_{e_x}^{1/7}}$	$C_{f_{turb}} \cong \frac{0.059}{R_{e_x}^{1/5}}$
Skin friction per unit width	$\frac{F}{w} = \rho V^2 \theta$	w = width normal to page	

Based on Y.A. Cengel, J.M. Cimbala, Fluid Mechanics—Fundamentals and Applications, McGraw-Hill, 2006.

(11) Laminar, Turbulent, and Mixed Boundary Layer

In this book, $C_{f_{lam}}$ represents the skin friction coefficient associated with *laminar* BL, $C_{f_{turb}}$ is associated with *turbulent* BL, and $C_{f_{mixed}}$ refers to *mixed* BL. A mixed boundary layer combines laminar and turbulent BL, such that $C_{f_{lam}}$ extends from the leading edge to the specified transition point, x_{tr}, after which $C_{f_{turb}}$ takes over (see Figure 16-27). The mixed skin friction coefficient can be defined as follows

$$C_{f_{mixed}} \equiv \begin{cases} C_{f_{lam}} & \text{if } x < x_{tr} \\ C_{f_{turb}} & \text{if } x \geq x_{tr} \end{cases} \tag{16-38}$$

(12) Estimation of Boundary Layer Properties

The derivation of the formulae in Table 16-3 is presented in Refs. [7, 38]. These assume flow over a smooth, flat plate. The *boundary layer thickness* (δ) is the height above the plate surface where the horizontal velocity component is 99% of the flow speed outside the BL. *Displacement thickness* (δ^*) refers to the distance that a streamline just outside the BL is deflected due to mass conservation. Its effect is analogous to an increase in the thickness of the plate. *Momentum thickness* (θ) is like the displacement thickness, except it accounts for loss of momentum flow inside the BL. These are illustrated in Figure 16-28. Finally, *skin friction coefficient* (C_f) is used to estimate friction force developed by the plate.

(13) Skin Friction Coefficient for Laminar Boundary Layer

The classical Blasius[3] solution for a laminar boundary layer yields the following *local skin friction coefficient*

$$C_{f_{lam}} = \frac{0.664}{\sqrt{R_{e_x}}} = \frac{0.664}{\sqrt{\rho V_\infty x/\mu}} = \frac{0.664}{\sqrt{x}}\sqrt{\frac{\mu}{\rho V_\infty}} \tag{16-39}$$

Where x is the distance from the leading edge. Consider the theoretical possibility that laminar flow is fully sustained over a flat plate surface. This permits the *averaged skin friction coefficient* to be determined. It is presented below.

$$\overline{C}_{f_{lam}} = \frac{1.328}{\sqrt{R_e}} \tag{16-40}$$

Where R_e is the Reynolds number based on the airfoil chord, c.

DERIVATION OF EQUATION (16-40)

Substitute Equation (16-39) into Equation (16-35) and solve.

$$\overline{C}_{f_{lam}} = \frac{1}{c}\int_0^c C_{f_{lam}}\,dx = \frac{1}{c}\int_0^c \left(\frac{0.664}{\sqrt{R_{e_x}}}\right)dx$$

$$= \frac{0.664}{c}\sqrt{\frac{\mu}{\rho V_\infty}}\int_0^c x^{-1/2}\,dx = \frac{0.664}{c}\sqrt{\frac{\mu}{\rho V_\infty}}\left[2\sqrt{c}\right] = \frac{1.328}{\sqrt{R_e}}$$

(14) Skin Friction Coefficient for Turbulent Boundary Layer

The following local skin friction coefficient for turbulent boundary layer is commonly referred to as *Prandtl's one-seventh power law coefficient* [8]:

$$C_{f_{turb}} \cong \frac{0.027}{R_{e_x}^{1/7}} = \frac{0.027}{(\rho V_\infty x/\mu)^{1/7}} = \frac{0.027}{x^{1/7}}\left(\frac{\mu}{\rho V_\infty}\right)^{1/7} \tag{16-41}$$

If it is assumed that turbulent flow is fully sustained over a flat plate surface, Equation (16-41) yields the following averaged skin friction coefficient

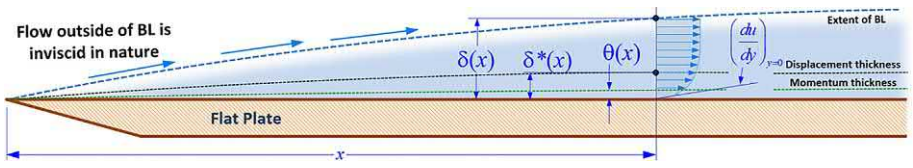


FIGURE 16-28 The thickness of the boundary layer depends on whether it is laminar and turbulent.

[3] Named after the German scientist Paul Blasius (1883–1970), one of Ludwig Prandtl's first doctoral students.

$$\overline{C}_{f_{turb}} = \frac{0.0315}{R_e^{1/7}} \tag{16-42}$$

DERIVATION OF EQUATION (16-42)

Substitute Equation (16-41) into Equation (16-35) and solve.

$$\begin{aligned}\overline{C}_{f_{turb}} &= \frac{1}{c}\int_0^c C_{f_{turb}}dx = \frac{1}{c}\int_0^c \left(\frac{0.027}{R_{e_x}^{1/7}}\right)dx \\ &= \frac{0.027}{c}\left(\frac{\mu}{\rho V_\infty}\right)^{1/7}\int_0^c x^{-1/7}dx \\ &= \frac{0.027}{c}\left(\frac{\mu}{\rho V_\infty}\right)^{1/7}\left[\frac{7}{6}c^{6/7}\right] = \frac{0.0315}{R_e^{1/7}}\end{aligned}$$

There are other averaged turbulent skin friction coefficients used. In fact, comparing those to experiment reveals Equation (16-42) underpredicts the drag. Thus, it should be avoided unless its use is supported by experiment. The so-called *Prandtl-Schlichting relation* [30, p. 438] is a commonly used model that agrees well with experiment.

$$\overline{C}_{f_{turb}} = \frac{0.455}{\left(\log_{10}R_e\right)^{2.58}} \tag{16-43}$$

The equation has roots in the so-called Schoenherr's friction equation [39]; $1/\sqrt{\overline{C}_{f_{turb}}} = 4.13\log_{10}\left(R_e\overline{C}_{f_{turb}}\right)$. Schlichting attributes that formula to the work of Theodore von Kárman [30, p. 439] from 1930. It shows up in Figure 4 of Ref. [40] as a translation of von Kárman's work from 1930, 2 years prior that of Schoenherr. Regardless, its transcendental nature makes it unwieldy for use. Prandtl evaluated its solution for Reynolds numbers between $10^5 < R_e < 1.5\times10^9$ [41]. Equation (16-43) is Schlichting's curvefit to Prandtl's data [30, 32].

Lazauskas [42] presents a collection of turbulent local and averaged skin friction coefficients, largely compiled using the work of Gadd [43] and Granville [44]. Some of these are listed in Table 16-4.

(15) Compressibility Corrections for Drag

As the far-field Mach number, M_∞, increases, the aerodynamic heating increases viscosity and decreases density. This increases BL thickness and reduces du/dy at the wall. This effect calls for a special compressibility correction, employed when $M_\infty > 0.3$ [45].

$$C_{f_c} = C_{f_{inc}}\left(1 + 0.144M_\infty^2\right)^{-0.65} \tag{16-44}$$

Where C_{f_c} is the compressible value of the incompressible skin friction $C_{f_{inc}}$. Another correction method is that of Frankl-Voishel [46, 47]:

$$\begin{aligned}C_{f_c} = C_{f_{inc}}\big(&0.000162M_\infty^5 - 0.00383M_\infty^4 + 0.0332M_\infty^3 \\ &-0.118M_\infty^2 + 0.0204M_\infty + 0.996\big)\end{aligned} \tag{16-45}$$

(16) Laminar-to-Turbulent Transition Model

The transition of laminar to turbulent boundary layer can be estimated using the so-called *Prandtl–Schlichting skin friction formula for a smooth flat plate at zero incidence* [30, p. 439], presented below.

$$C_{f_{turb}} = \frac{0.455}{\left(\log_{10}R_e\right)^{2.58}} - \frac{A}{R_e} \tag{16-46}$$

TABLE 16-4 Local and averaged turbulent skin friction coefficients.

Author	Formula	
Local Coefficients		
Prandtl-Schlichting (1932)	$C_{f_{turb}} = (2\log_{10}R_{e_x} - 0.65)^{-2.3}$	(16.47)
Th. Von Kárman (1935)	$\frac{1}{\sqrt{C_{f_{turb}}}} = 4.15\log_{10}\left(R_{e_x}C_{f_{turb}}\right) + 1.7$	(16.48)
Schultz-Grunow (1940)	$C_{f_{turb}} = 0.37(\log_{10}R_{e_x})^{-2.584}$	(16.49)
Dhawan (1953)	$\frac{1}{\sqrt{C_{f_{turb}}}} = 5.06\log_{10}\left(R_{e_x}C_{f_{turb}}\right) - 0.91$	(16.50)
ITTC (1957)	$C_{f_{turb}} = 0.075\left(1 - \frac{0.869}{\log_{10}R_{e_x}-2}\right)\left(\log_{10}R_{e_x} - 2\right)^{-2}$	(16.51)
Averaged Coefficients		
Prandtl (1927)	$\overline{C}_{f_{turb}} = 0.074R_e^{-1/5}$	(16.52)
Telfer (1927)	$\overline{C}_{f_{turb}} = 0.34R_e^{-1/3} + 0.0012$	(16.53)
Schoenherr (1932)	$\overline{C}_{f_{turb}} = 0.0586\left(\log_{10}\left(R_e\overline{C}_{f_{turb}}\right)\right)^{-2}$	(16.54)
Schultz-Grunow (1940)	$\overline{C}_{f_{turb}} = 0.427\left(\log_{10}R_e - 0.407\right)^{-2.64}$	(16.55)
Kempf-Karman (1951)	$\overline{C}_{f_{turb}} = 0.055R_e^{-0.182}$	(16.56)
Lap-Troost (1952)	$\overline{C}_{f_{turb}} = 0.0648\left(\log_{10}\left(R_e\sqrt{\overline{C}_{f_{turb}}}\right) - 0.9526\right)^{-2}$	(16.57)
Landweber (1953)	$\overline{C}_{f_{turb}} = 0.0816\left(\log_{10}R_e - 1.703\right)^{-2}$	(16.58)
Hughes (1954)	$\overline{C}_{f_{turb}} = 0.067\left(\log_{10}R_e - 2\right)^{-2}$	(16.59)
Wieghardt (1955)	$\overline{C}_{f_{turb}} = 0.52\left(\log_{10}R_e\right)^{-2.685}$	(16.60)
ITTC (1957)	$\overline{C}_{f_{turb}} = 0.075\left(\log_{10}R_e - 2\right)^{-2}$	(16.61)
Gadd (1967)	$\overline{C}_{f_{turb}} = 0.0113\left(\log_{10}R_e - 3.7\right)^{-1.15}$	(16.62)
Granville (1977)	$\overline{C}_{f_{turb}} = 0.0776\left(\log_{10}R_e - 1.88\right)^{-2} + 60/R_e$	(16.63)
Date-Turnock (1999)	$\overline{C}_{f_{turb}} = \left(4.06\log_{10}\left(R_e\overline{C}_{f_{turb}}\right) - 0.729\right)^{-2}$	(16.64)

Based on L.V. Lazauskas, Hydrodynamics of Advanced High-Speed Sealift Vessels, (Master's thesis), University of Adelaide, 2005; G.E. Gadd, A new turbulent friction formulation based on a re-appraisal of Hughes' results, Trans. RINA 109 (1967) 511–539; P.S. Granville, The viscous resistance of surfaces vessels and the skin friction of flat plates, Trans. SNAME 64 (1956) 209–240.

TABLE 16-5 Transition parameters.

Condition	High turbulence (e.g., wind tunnels)		Low-turbulence (e.g., atmosphere)	
Critical R_e	0.3×10^6	0.6×10^6	1.0×10^6	3.0×10^6
Constant A	1050	1700	3300	8700

Where A is read from Table 16-5 and is selected based on the R_e at which transition is expected (critical R_e).

(17) Method 1: Mixed Laminar-Turbulent Flow Skin Friction by Surface Integration

If the distribution of pressure and shear stress over the surface of a body (e.g., an airfoil), is known, we can estimate the *normal and chordwise force per unit length* (f_n and f_c) using the first two equations of Equation (8-20) (shown below for convenience)

$$f_n = -\int_{LE}^{TE}(p_u\cos\theta_u+\tau_u\sin\theta_u)ds_u+\int_{LE}^{TE}(p_l\cos\theta_l-\tau_l\sin\theta_l)ds_l$$
$$f_c = -\int_{LE}^{TE}(p_u\sin\theta_u-\tau_u\cos\theta_u)ds_u+\int_{LE}^{TE}(p_l\sin\theta_l+\tau_l\cos\theta_l)ds_l \tag{16-65}$$

Where p_u, τ_u and p_l, τ_l are the pressure and viscous shear stress along the upper and lower surfaces, respectively. θ_u and θ_l are the angles between the tangent and the coordinate system on the upper and lower surfaces, respectively (see Figure 8-13). To obtain the lift and drag per unit length, f_n and f_c must be transformed using Equation (8-19).

In order to only extract the skin friction, we set all pressure terms to zero. For airfoil geometry, this largely sets the upper equation of Equation (16-65) to zero. Using Equation (16-34), the lower equation becomes

$$f_c = q_\infty\int_0^c\left(C_{f_u}+C_{f_l}\right)dx \tag{16-66}$$

Where C_{f_u} and C_{f_l} are the skin friction coefficients along the upper and lower surfaces. The estimate of f_c is per unit span (so area is $c(1)=c$), the averaged skin friction coefficient becomes

$$\overline{C}_f = \frac{f_c}{qc}=\frac{1}{c}\int_0^c\left(C_{f_u}+C_{f_l}\right)dx \tag{16-67}$$

When applying Equation (16-66) to NLF airfoils, where the transition point is known to occur at x_{tr_u} on the upper surface and at x_{tr_l} on the lower one, the integrals are split up as follows

$$f_c = q_\infty\left[\int_0^{x_{tr_u}}C_{f_{lam}}dx+\int_{x_{tr_u}}^{c}C_{f_{turb}}dx+\int_0^{x_{tr_l}}C_{f_{lam}}dx+\int_{x_{tr_l}}^{c}C_{f_{turb}}dx\right] \tag{16-68}$$

Then substitute this value into Equation (16-67).

EXAMPLE 16-5

The flat plate airfoil of chord 1 m is operated at S-L at airspeed of 100 m/s. It develops laminar boundary layer over the first 25% of the chord and turbulent boundary layer over the remaining 75% of the chord, on both upper and lower surface. Estimate the airfoil's skin friction coefficient C_f. Assume the slope of both surfaces to be small enough to be considered parallel to the chordline. $\mu=1.8\times10^{-5}\,\text{N s/m}^2$ and $\rho=1.225\,\text{kg/m}^3$.

SOLUTION:

Taking advantage of the symmetry of the problem, we get

$$\overline{C}_f=\frac{1}{c}\left[\int_0^{c_{xtr_u}}C_{f_{lam}}dx+\int_{c_{xtr_u}}^{c}C_{f_{turb}}dx+\int_0^{c_{xtr_l}}C_{f_{lam}}dx+\int_{c_{xtr_l}}^{c}C_{f_{turb}}dx\right]$$
$$=\frac{2}{c}\left[\int_0^{c_{xtr_u}}C_{f_{lam}}dx+\int_{c_{xtr_u}}^{c}C_{f_{turb}}dx\right]$$
$$=\frac{2}{(1)}\left[\int_0^{0.25}C_{f_{lam}}dx+\int_{0.25}^{c}C_{f_{turb}}dx\right]$$
$$=2\left[0.664\sqrt{\frac{\mu}{\rho V_\infty}}\int_0^{0.25}x^{-1/2}dx+0.027\left(\frac{\mu}{\rho V_\infty}\right)^{1/7}\int_{0.25}^{c}x^{-1/7}dx\right]$$
$$\cong 0.0005091\left[2x^{1/2}\right]_0^{0.25}+0.005705\left[\frac{7}{6}x^{6/7}\right]_{0.25}^{1}=0.005137$$

(18) Method 2: Mixed Laminar-Turbulent Flow Skin Friction—Young's Method

Young [32, pp. 162–164] presents a two-step method to calculate the skin friction coefficient when the extent of the laminar flow is known. The first step requires the location of the *fictitious transition point*, x_0 (see Figure 16-25) to be calculated:

$$\left(\frac{x_0}{c}\right)=36.9\times\left(\frac{x_{tr}}{c}\right)^{0.625}\left(\frac{1}{R_e}\right)^{0.375} \tag{16-69}$$

Then, the skin friction coefficient is determined as follows:

$$\overline{C}_{f_{mixed}}=\frac{0.074}{R_e^{0.2}}\left(1-\left(\frac{x_{tr}-x_0}{c}\right)\right)^{0.8} \tag{16-70}$$

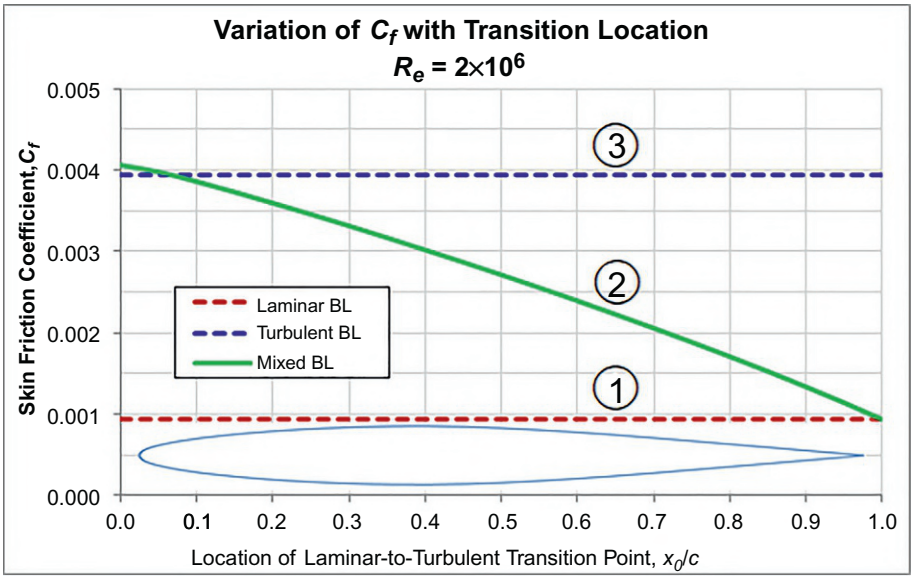


FIGURE 16-29 Skin friction coefficient as a function of transition point calculated using fully laminar, turbulent, and mixed theory. ① is Equation (16-40), ② is Equation (16-70), and ③ is Equation (16-43).

It is evident its origin lies in Prandtl's expression of Equation (16-52). It is of interest to compare Equations (16-40), (16-43), and (16-70) as done in Figure 16-29. The first two are independent of transition location, whereas the mixed boundary layer methodology depends on x_{tr}. It is seen to deviate from Equation (16-43) when $x_{tr}/c < 0.06$. This is to be expected since the model is based on Prandtl's expression.

(19) Skin Friction Coefficient for Multisurface Components

The skin friction of any component consisting of several subcomponents can be estimated as follows:

Skin friction coefficient:

$$C_f = \frac{1}{S_{wet}} \sum_{i=1}^{N} C_{f_i} \times S_{wet_i} \tag{16-71}$$

Skin friction drag coefficient:

$$C_{Df} = \left(\frac{S_{wet}}{S}\right) C_f = \left(\frac{1}{S}\right) \sum_{i=1}^{N} C_{f_i} \times S_{wet_i} \tag{16-72}$$

Where C_{f_i} is the skin friction coefficient of subcomponent i, S_{wet_i} is wetted area of subcomponent i, S_{wet} is the total wetted area, and N is the number of subcomponents.

(20) Compute the Skin Friction Drag Force

The skin friction drag force acting on each subcomponent can be calculated by two means: (A) Based on their wetted area or (B) on the reference area, S:

Using the skin friction coefficient:

$$D_f = \frac{1}{2}\rho V^2 C_f S_{wet} \tag{16-73}$$

Using the skin friction drag coefficient:

$$D_f = \frac{1}{2}\rho V^2 C_f S \tag{16-74}$$

(21) Step-by-Step: Procedure to Calculate Skin Friction for a Specific Component

This Step-by-Step presents how to calculate skin friction drag force for a specific component (e.g., a wing, HT, VT, etc.). It does not require form factors because these are used to account for the component's pressure drag.

Step 1: Determine the Viscosity of Air

Calculate μ using Equations (16-24) or (16-25).

Step 2: Determine Reynolds Number

Calculate R_e using Equation (16-27).

Step 3: Determine Cutoff Reynolds Number

Calculate the $R_{e_{cutoff}}$ for the surface. If smaller than R_e from Step 2, use it to determine the appropriate C_f.

Step 4: Determine the Skin Friction Coefficient

Select one of the previously discussed methodologies for calculating C_f. The most realistic options are (A) mixed boundary layer (bullets (17) and (18)) or (B) fully developed turbulent boundary layer (Bullet (14)). A fully developed laminar boundary layer is the aerodynamicist's folly. Calculate C_f per Equation (16-71).

Step 5: Compute Skin Friction Drag Coefficient

Calculate the skin friction *drag* coefficient, C_{Df}, per Equation (16-72).

Step 6: Compute the Total Skin Friction Drag Force

Calculate the total skin friction drag force for the component using Equation (16-73) or (16-74).

EXAMPLE 16-6
SKIN FRICTION DRAG OF A WING

In this example, the skin friction drag of the SR22 wing will be estimated. The wing's pertinent dimensions are shown in Figure 16-30, but these were obtained by scaling by the reported wing span of 38.3 ft. Assume a single NACA 65_2-415 class airfoil, capable of sustaining a laminar boundary layer on the upper and lower surfaces as indicated in the figure. Assume the wing's wetted area is 7% greater than that of the shaded planform area shown.

Determine C_{Df} and D_f acting on the wing due to the mixed laminar and turbulent BL regions when the airplane is cruising at 185 KTAS at S-L ISA. Compare to a wing with fully laminar or fully turbulent BL.

SOLUTION:

Note that the solution below was calculated using the spreadsheet software Microsoft Excel. A reader repeating the calculations should expect slight difference from the numbers shown.

Step 1: Determine the viscosity of air.

Use Sutherland's formula to compute the viscosity assuming an OAT of 518.67°R:

$$\mu = 3.170\times10^{-11}T^{1.5}\left(\frac{734.7}{T+216}\right)$$
$$= 3.170\times10^{-11}(518.67)^{1.5}\left(\frac{734.7}{518.67+216}\right)$$
$$= 3.745\times10^{-7}\ \text{lb}_\text{f}\text{s/ft}^2$$

Step 2: Determine the Reynold's Number for Root Airfoil.

Compute R_e for the root airfoil, using ISA density of 0.002378 slugs/ft^3 and an airspeed of 185 KTAS.

$$R_{e_1} = \frac{\rho V_\infty C_r}{\mu} = \frac{(0.002378)(185\times1.688)(4.88)}{3.745\times10^{-7}} = 9{,}667{,}562$$

Step 3: Determine the Reynold's Number for Tip Airfoil.

Compute R_e for the tip airfoil:

$$R_{e_2} = \frac{\rho V_\infty C_t}{\mu} = \frac{(0.002378)(185\times1.688)(2.59)}{3.745\times10^{-7}} = 5{,}126{,}287$$

Step 4: Fictitious Turbulent BL on Root Airfoil—Upper surface

For the upper surface of the root airfoil (45% coverage), we get:

$$\left(\frac{x_0}{c_r}\right) = 36.9\times\left(\frac{x_{tr}}{c_r}\right)^{0.625}\left(\frac{1}{R_{e_1}}\right)^{0.375}$$
$$= 36.9\times(0.45)^{0.625}\left(\frac{1}{9{,}667{,}562}\right)^{0.375} = 0.05380$$

Step 5: Fictitious Turbulent BL on Root Airfoil—Lower surface

For the lower surface of the root airfoil (45% coverage), we get the same value as on the upper surface:

$$(x_0/c_r) = 0.05380$$

Step 6: Fictitious Turbulent BL on Tip Airfoil—Upper surface

For the upper surface of the tip airfoil (60% coverage), we get the same value as on the lower surface:

$$\left(\frac{x_0}{c_t}\right) = 36.9\times(0.60)^{0.625}\left(\frac{1}{5{,}126{,}287}\right)^{0.375} = 0.08169$$

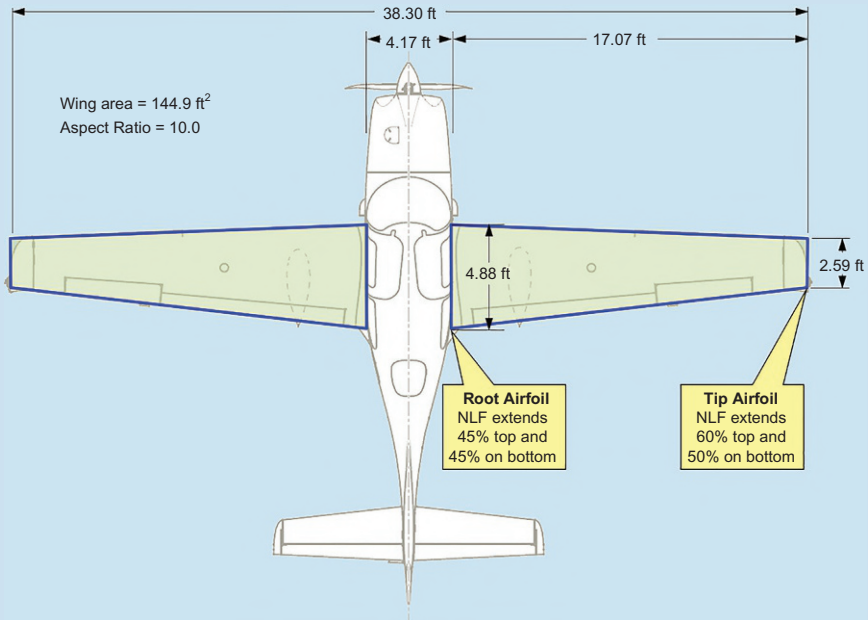


FIGURE 16-30 Dimension resulting from scaling the top-view based on the wing span. *Courtesy of Cirrus Aircraft. Copyright 2021 Cirrus Aircraft or its Affiliates. All Rights Reserved. Image reproduced with the permission of Cirrus.*

EXAMPLE 16-6
SKIN FRICTION DRAG OF A WING (*cont'd*)

Step 7: Fictitious Turbulent BL on Tip Airfoil—Lower surface

For the lower surface of the tip airfoil (50% coverage), we get:

$$\left(\frac{x_0}{c_t}\right) = 36.9 \times (0.50)^{0.625}\left(\frac{1}{5{,}126{,}287}\right)^{0.375} = 0.07290$$

Step 8: Skin Friction for Root Airfoil—Upper surface

For the upper surface of the root airfoil (45% coverage), we get:

$$\overline{C}_{f_{upper\ 1}} = \frac{0.074}{R_{e_1}^{0.2}}\left(1 - \left(\frac{x_{tr} - x_0}{c_r}\right)\right)^{0.8}$$
$$= \frac{0.074}{9{,}667{,}562^{0.2}}(1 - (0.45 - 0.05380))^{0.8} = 0.001981$$

Step 9: Skin Friction for Root Airfoil—Lower surface

For the lower surface of the root airfoil (45% coverage), we get:

$$\overline{C}_{f_{lower\ 1}} = 0.001981$$

Step 10: Average Skin Friction for Root Airfoil

The average of the upper and lower surfaces of the root airfoil yields:

$$\overline{C}_{f_1} = \frac{1}{2}(0.001981 + 0.001981) = 0.001981$$

Step 11: Skin Friction for Tip Airfoil—Upper surface

For the upper surface of the tip airfoil (60% coverage), we get:

$$\overline{C}_{f_{upper\ 2}} = \frac{0.074}{R_{e_2}^{0.2}}\left(1 - \left(\frac{x_{tr} - x_0}{c_t}\right)\right)^{0.8}$$
$$= \frac{0.074}{5{,}126{,}287^{0.2}}(1 - (0.60 - 0.08169))^{0.8} = 0.001877$$

Step 12: Skin Friction for Tip Airfoil—Lower surface

For the lower surface of the tip airfoil (50% coverage), we get:

$$\overline{C}_{f_{lower\ 2}} = \frac{0.074}{R_{e_2}^{0.2}}\left(1 - \left(\frac{x_{tr} - x_0}{c_t}\right)\right)^{0.8}$$
$$= \frac{0.074}{5{,}126{,}287^{0.2}}(1 - (0.50 - 0.07290))^{0.8} = 0.002156$$

Step 13: Average Skin Friction for Tip Airfoil

The average of the upper and lower surfaces of the tip airfoil yields:

$$\overline{C}_{f_2} = \frac{1}{2}(0.001877 + 0.002156) = 0.002017$$

Step 14: Average Skin Friction for Complete Wing

The skin friction coefficient for the total wetted surface is simply the average of the average coefficients for both airfoils, i.e.:

$$\overline{C}_f = \frac{1}{2}(0.001981 + 0.002017) = 0.001999$$

Step 15: Wing's Wetted Area

The wing's total wetted area is:

$$S_{wet} = 2 \times 1.07 \times \left[\frac{1}{2}(4.88 + 2.59) \times (38.3 - 4.17)\right] = 272.8\ \text{ft}^2$$

Step 16: Skin Friction Drag Coefficient for Complete Wing

The wing's skin friction drag coefficient is:

$$C_{Df} = \left(\frac{S_{wet}}{S_{ref}}\right)\overline{C}_f = \left(\frac{272.8}{144.9}\right)(0.001999) = 0.003758$$

Step 17: Skin Friction Drag Force for Complete Wing

Estimate skin friction drag due to the mixed boundary layer.

$$D_f = \frac{1}{2}\rho V^2 \times S_{wet} \times \overline{C}_f$$
$$= \frac{1}{2}(0.002378)(185 \times 1.688)^2(272.4)(0.001999) = 63.1\ \text{lb}_\text{f}$$

This means that the total flat plate skin friction drag for the wing only of the SR22 at cruising speed amounts to 63 lb_f. The contributions of interference with the fuselage and airfoil shape are not accounted for. It also omits drag due to the presence of control surfaces.

Step 18: Skin friction coefficient for 100% Laminar Flow.

Laminar flow coefficient for the root:

$$\overline{C}_{f_{lam}} = \frac{1.328}{\sqrt{R_{e1}}} = \frac{1.328}{\sqrt{9{,}667{,}562}} = 0.0004271$$

Laminar flow coefficient for the tip:

$$\overline{C}_{f_{lam}} = \frac{1.328}{\sqrt{R_{e2}}} = \frac{1.328}{\sqrt{5{,}126{,}287}} = 0.0005865$$

Average for the wing:

$$\overline{C}_f = \frac{0.0004271 + 0.0005865}{2} = 0.0005068$$

Step 19: Skin friction coefficient for 100% Turbulent Flow.

Turbulent flow coefficient for the root:

$$\overline{C}_{f_{turb}} = \frac{0.455}{(\log_{10}(R_{e1}))^{2.58}} = \frac{0.455}{(\log_{10}(9,667,562))^{2.58}} = 0.003020$$

Turbulent flow coefficient for the tip:

$$\overline{C}_{f_{turb}} = \frac{0.455}{(\log_{10}(R_{e2}))^{2.58}} = \frac{0.455}{(\log_{10}(5,126,287))^{2.58}} = 0.003350$$

Average for the wing:

$$\overline{C}_f = \tfrac{1}{2}(0.003020 + 0.003350) = 0.003185$$

Step 20: Comparison.

See Table 16-6 for a comparison of the analysis techniques.

EXAMPLE 16-6
SKIN FRICTION DRAG OF A WING (*cont'd*)

The comparison shows that were it possible to maintain laminar flow over the entire wing, its drag would be 25% of that predicted by the mixed boundary layer theory. Alternatively, if the wing sustained turbulent BL only, it would be almost 60% draggier than the NLF airfoils. It demonstrates the value of employing such airfoils.

TABLE 16-6 Comparing skin friction analysis methods.

Method	C_f	Comparison
Fully Laminar BL	0.0005068	25%
Fully Turbulent BL	0.003185	159%
Mixed BL	0.001999	100%

EXAMPLE 16-7
TOTAL SKIN FRICTION OF A MULTIPANEL WING

Figure 16-31 shows a half-span of a three section Schuemann wing. The skin friction coefficient for each section has been determined and is tabulated with the corresponding planform areas. If operating at 100 KCAS, estimate the following: (a) Total skin friction coefficient, (b) total skin friction drag coefficient, (c) skin friction drag force for individual surfaces, and (d) skin friction drag. Use the wing area as the reference area (S) and assume its wetted area amounts to $2S$ times a wetted area booster factor, K_b, of 1.1.

SOLUTION:

(a) Assemble Table 16-7 as shown (where $S_{wet_i} = 2K_bS_i$). Thus, the wetted area for panel ① is given by $S_{wet_①} = 2K_bS_① = 2(1.1)(35.0) = 77.0\,\text{ft}^2$. Multiplying this by $C_{f_①} = 0.0050$ and $q = \frac{1}{2}\rho V_\infty^2 = \frac{1}{2}(0.002378)(100 \times 1.688)^2 = 33.88\ \text{lb}_f/\text{ft}^2$ yields the other two columns. Complete similar calculations for the other two rows. Next, the three rightmost columns summed. Note that these apply to only one of the two wing halves.

The total skin friction coefficient can be found by the weighted contribution from each panel:

$$\overline{C}_f = \frac{\sum_{i=1}^{N} C_{f_i} \times S_{wet_i}}{S_{wet}} = \frac{77.0 \times 0.0050 + 69.3 \times 0.0055 + 46.2 \times 0.0065}{77.0 + 69.3 + 46.2} = \frac{1.100}{192.5} = 0.00554$$

TABLE 16-7 Comparing skin friction analysis methods.

	S_i	$C_{f\,i}$	$S_{wet\,i}$	$S_{wet\,i} \cdot C_{f\,i}$	$q \cdot S_{wet\,i} \cdot C_{f\,i}$
Part ①	35.0	0.0050	77.0	0.3850	13.04
Part ②	31.5	0.0055	69.3	0.3812	12.91
Part ③	21.0	0.0065	46.2	0.3003	10.17
		TOTALS:	192.5	1.1	36.1

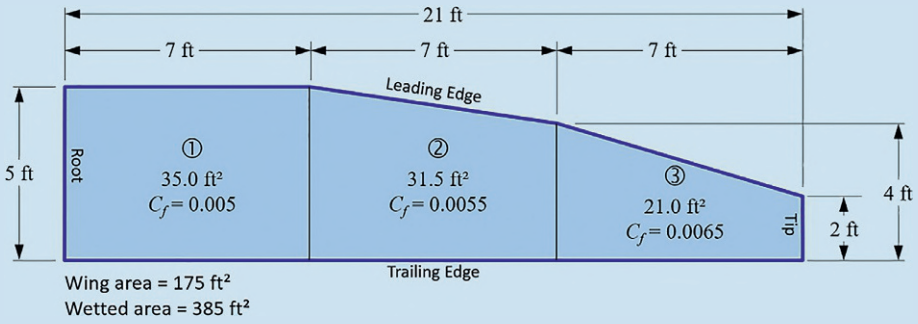


FIGURE 16-31 The multipanel wing used in this example.

EXAMPLE 16-7
TOTAL SKIN FRICTION OF A MULTIPANEL WING (*cont'd*)

This is the averaged skin friction coefficient for the wing.

(b) The total skin friction drag coefficient is always based on the reference area, which here is $S = 175\,\text{ft}^2$:

$$C_{Df} = \frac{S_{wet}}{S} C_f = \frac{385}{175} \times 0.00554 = 0.01219$$

This amounts to 121.9 dragcounts.

(c) And (d) since the skin friction coefficient differs from one panel to the next, the drag force on each surface must be determined using the wetted area of the individual surface per Equation (16-73):

$$D_{f_i} = \frac{1}{2}\rho V^2 C_{f_i} S_{wet_i} = q C_{f_i} S_{wet_i}$$

The total skin friction drag generated by both wing halves is the sum of the individual contributions:

$$D_f = 2 \times q \sum_{i=1}^{3} C_{fi} S_{wet\,i} = 2 \times (33.88)[(0.0050)(77.0) + (0.0055)(69.3) + (0.0065)(46.2)]$$

$$= 2 \times (33.88)[0.3850 + 0.3812 + 0.3003] = 72.3 \text{ lb}_\text{f}$$

or: $D_f = \frac{1}{2}\rho V^2 C_f S_{wet} = (33.88)(0.00554)(385) = 72.3 \text{ lb}_\text{f}$

or: $D_f = \frac{1}{2}\rho V^2 C_{Df} S_{ref} = (33.88)(0.01219)(175) = 72.3 \text{ lb}_\text{f}$

We can also calculate the skin friction drag coefficient, C_{Df_i}, for each panel for each wing half (assuming only half of the reference wing area) as shown below. Note the results are presented in Table 16-8:

$$C_{Df_1} = \frac{C_{f1} \cdot S_{wet\ 1}}{S_{ref}} = \frac{0.0050 \cdot 77.0}{(175/2)} = 0.004400$$

$$C_{Df_2} = \frac{C_{f2} \cdot S_{wet\ 2}}{S_{ref}} = \frac{0.0055 \cdot 69.3}{(175/2)} = 0.004356$$

$$C_{Df_3} = \frac{C_{f3} \cdot S_{wet\ 3}}{S_{ref}} = \frac{0.0065 \cdot 46.2}{(175/2)} = 0.003432$$

TABLE 16-8 Total skin friction of the multipanel wing.

	S_i	C_{fi}	$S_{wet\,i}$	$S_{wet\,i} \cdot C_{f\,i}$	$q \cdot S_{wet\,i} \cdot C_{f\,i}$	$C_{Df\,i}$
Part ①	35.0	0.0050	77.0	0.3850	13.04	0.004400
Part ②	31.5	0.0055	69.3	0.3812	12.91	0.004356
Part ③	21.0	0.0065	46.2	0.3003	10.17	0.003432
		TOTALS:	192.5	1.1	36.1	0.01219

16.3.2 Estimating Lift-Induced Drag: C_{D_i}

Consider a finite wing featuring a single airfoil at some specific AOA and airspeed. Contrast that with a straight wing segment featuring exactly the same airfoil, extending from wall-to-wall in a wind tunnel, at the same AOA and airspeed. The finite wing generates less lift per unit span than the one in the wind tunnel. It does so because the air must flow around its wingtips, which it does through the formation of *wingtip vortices*. Their presence absorbs a fraction of the energy present in the airflow, leaving less available for lift generation. Thus, the finite wing must be placed at a higher AOA to generate the same amount of lift as the wing in the wind tunnel. This process increases the drag of the finite wing beyond that attributed to the airfoil only. This additional drag is called a *lift-induced*, or *induced*, or *vortex* drag and is denoted by D_i. As usual the standard formulation of this drag involves the determination of a *lift-induced drag coefficient*. A number of methods to determine this drag coefficient are presented below. The lift induced drag is a pressure drag force.

(1) Method 1: Lift-Induced Drag from the Momentum Theorem

Familiarity with Section 8.1.9, *The Generation of Lift* is an essential preparation for this section. Consider Equation (8-27), repeated below for convenience. It expresses the average downwash (w) behind the wing in terms of lift coefficient (C_L), aspect ratio (AR), and airspeed (V_∞):

$$w = \frac{2C_L}{\pi AR} V_\infty \tag{16-75}$$

This is shown in Figure 16-32. The circulation introduces an upwash and downwash into the flow around the airfoil. The downwash is compounded by the contribution from the wingtip vortices. This reduces the *geometric* AOA (α) by an amount called the *induced* AOA (α_i). It amounts to half the theoretical downwash angle, given by w/V. The difference between the two is the *effective* AOA (α_e). Mathematically, the relation between w/V and α_i is given by

$$\frac{w}{V_\infty} = \frac{2C_L}{\pi AR} = 2\alpha_i \tag{16-76}$$

Using small angle relations, the induced AOA is found from

$$\alpha_i \approx \tan\ \alpha_i = \frac{1}{2}\frac{w}{V_\infty} = \frac{C_L}{\pi AR} \tag{16-77}$$

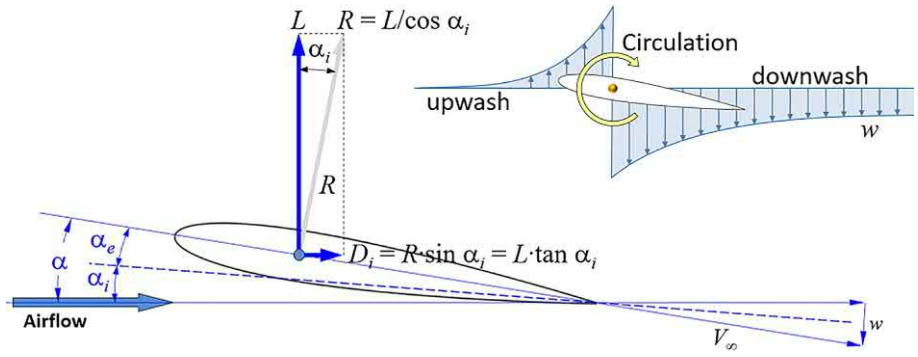


FIGURE 16-32 A schematic showing how the induced drag is a component of the lift force.

Referring to Figure 16-32, we see that the presence of the induced AOA effectively tilts the lift force back by the amount α_i. In the process, an additional force component, D_i, is developed. This is the *lift-induced drag*. It is calculated as shown in the figure.

$$D_i = R\sin\alpha_i = \frac{L}{\cos\alpha_i}\sin\alpha_i = L\tan\alpha_i \tag{16-78}$$

In coefficient form, this becomes:

$$C_{D_i} = C_L\tan\alpha_i = C_L\left(\frac{C_L}{\pi AR}\right) = \frac{C_L^2}{\pi AR} \tag{16-79}$$

The above derivation assumes an elliptical lift distribution or, alternatively, the distribution of constant spanwise section lift coefficients[4] (C_l). As shown in Chapter 9, *The Anatomy of the Wing*, this requires an elliptical planform. However, most wing planforms are not elliptical and, consequently, the distribution of section lift coefficients is not constant. This is corrected through *span efficiency*, discussed in Section 9.5.12, *Determination of Span Efficiency*.

The following representation of the lift-induced drag is of importance from an aircraft design standpoint. Using Equation (16-79) to determine induced drag leads to

$$D_i = qS\left(\frac{C_L^2}{\pi AR}\right) = qS\left(\frac{(W/qS)^2}{\pi(b^2/S)}\right) = qS\left(\frac{W^2S}{\pi b^2q^2S^2}\right) = \frac{W^2}{\pi b^2q} \tag{16-80}$$

Where b is wing span, S is wing area, q is dynamic pressure, and W is weight. The result shows that the lift-induced drag force depends on the wing span rather than wing area. Thus, only a span increase reduces the drag. Reducing chord to increase AR will not help.

(2) Method 2: Generic Formulation of the Lift-Induced Drag Coefficient

A generic formulation of wing characteristics is presented in Ref. [48], based on the work of Glauert [49] and Hueber [50]. It allows several wing characteristics associated with tapered wings to be evaluated, with and without rounded wingtips (popular when it was written). It presents the following formulation for C_{D_i}

$$C_{D_i} = \frac{2}{S}\int_0^{b/2}\alpha_i\cdot C_l\cdot c\cdot dy = \frac{2}{S}\int_0^{b/2}\left(\alpha - \frac{C_l}{C_{l_\alpha}}\right)\cdot C_l\cdot c\cdot dy \tag{16-81}$$

Where c is wing chord and y is spanwise location along the half-span. A more general version of this expression, which treats asymmetric wing loading, is presented below:

$$C_{D_i} = \frac{1}{S}\int_{-b/2}^{b/2}\alpha_i\cdot C_l\cdot c\cdot dy \tag{16-82}$$

DERIVATION OF EQUATION (16-81)

The effective lift coefficient can be calculated as $C_l = C_{l_\alpha}C_{l\alpha}\alpha_e = C_{l_\alpha}(\alpha - \alpha_i)$. Thus, α_i at any section along the wing can be computed based on section lift coefficients, C_l, and section lift curve slopes, C_{l_α}:

$$\alpha_i = \alpha - C_l/C_{l_\alpha} \tag{16-83}$$

Using small angle relations, the induced drag of the airfoil section can be computed from:

$$C_{d_i} = \alpha_i C_l = (\alpha - C_l/C_{l_\alpha})C_l = (\alpha C_l - C_l^2/C_{l_\alpha}) \tag{16-84}$$

The total lift-induced drag for the wing is the sum of the weighted contribution of all the sections, extending from tip-to-tip, or:

$$C_{D_i} = \frac{2}{S}\int_0^{b/2}C_{d_i}\cdot c\cdot dy \tag{16-85}$$

The weighted form is necessary as the planform shape is may be changing or affected by washout. Thus, multiplying it with the chord, c, inserting the result from Equation (16-84) and manipulate will yield Equation (16-81).

[4] Also refer to the derivation of Equation (9-162) using the lifting-line theory.

EXAMPLE 16-8

Estimate the induced drag coefficient for a Hershey bar wing for which wing area, span, and chord are given by, $S=145\,\text{ft}^2$, $b=38\,\text{ft}$, and $c=4\,\text{ft}$, respectively. The wing is operating at $\alpha=5°=0.08727\,\text{rad}$. The spanwise distribution of section lift coefficients is approximated by $C_l=0.5\cdot\cos(\pi y/b)$ (yes, it is just an approximation), as shown in Figure 16-33. The wing features an airfoil whose $C_{l_\alpha}=5.730$ per radian and is untwisted.

SOLUTION:

Solution is obtained by evaluating the integral of the distribution of the section lift coefficients along the half-span of the aircraft per Equation (16-81):

$$C_{D_i}=\frac{2}{S}\int_0^{b/2}\left(\alpha-\frac{C_l}{C_{l_\alpha}}\right)\cdot C_l\cdot c\cdot dy$$

$$\cong\frac{2}{145}\int_0^{38/2}\left(0.08727-\frac{0.5\cos\left(\frac{\pi y}{38}\right)}{5.730}\right)\left(0.5\cos\left(\frac{\pi y}{38}\right)\right)(4)dy$$

$$\cong\frac{4}{145}\int_0^{38/2}\left(0.08727-0.08726\cos\left(\frac{\pi y}{38}\right)\right)\cos\left(\frac{\pi y}{38}\right)dy$$

$$\cong 0.006251$$

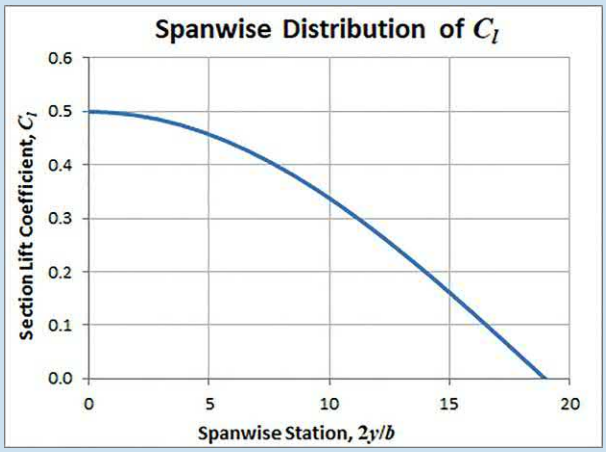


FIGURE 16-33 Spanwise distribution of section lift coefficients.

(3) Method 3: Simplified $k\cdot C_L^2$ Method

This is the simplest representation of lift-induced drag. As has already been demonstrated, is derived directly from the momentum theorem, or by using the lifting-line theory presented in Section 9.7, *Prandtl's Lifting-Line Theory*.

$$C_{D_i}=\frac{C_L^2}{\pi\cdot AR\cdot e}=k\cdot C_L^2 \qquad (16\text{-}86)$$

Where e is Oswald's efficiency and k is the lift-induced drag constant. Methods to estimate e are presented in Section 9.5.12, *Determination of Span Efficiency*. Also see Method 5 below. Note an important dependency of the induced drag coefficient on wing area, S, and wing span, b:

$$C_{D_i}=\frac{C_L^2}{\pi\cdot AR\cdot e}=\left(\frac{S}{b^2}\right)\frac{C_L^2}{\pi\cdot e} \qquad (16\text{-}87)$$

Like Equation (16-80), this reinforces the importance of wing span on induced drag.

(4) Method 4: Adjusted $k\cdot(C_L-C_{L_{\text{min}D}})^2$ Method

As already discussed, the adjusted drag model provides far superior estimate of lift-induced drag than the simplified model. This model is presented below:

$$C_{D_i}=\frac{(C_L-C_{L_{\text{min}D}})^2}{\pi\cdot AR\cdot e}=k\cdot(C_L-C_{L_{\text{min}D}})^2 \qquad (16\text{-}88)$$

Where $C_{L_{\text{min}D}}$ is the lift coefficient of minimum drag.

(5) Method 5: Lift-Induced Drag Using the Lifting-Line Theory

To determine the lift-induced drag constant, k, numerical methods such as the lifting-line or vortex-lattice methods may be used. Of the two, the former, presented in Section 9.7, *Prandtl's Lifting-Line Theory*, is relatively easy to apply, although it requires a matrix solver to calculate the constants of simultaneous linear equations. These are used to evaluate a special constant, called the *lift-induced drag factor*, denoted by the Greek letter δ. Once known, the lift-induced drag coefficient is calculated from:

Simplified drag model: $$C_{D_i}=\frac{C_L^2}{\pi\cdot AR}(1+\delta) \qquad (16\text{-}89)$$

Adjusted drag model: $$C_{D_i}=\frac{(C_L-C_{L_{\text{min}D}})^2}{\pi\cdot AR}(1+\delta) \qquad (16\text{-}90)$$

Note that these underestimate C_{D_i} and must be corrected per Section 9.5.12, *Determination of Span Efficiency*. Figure 9-75 shows the variation of the lift-induced drag factor, δ, for a range of taper ratios, λ, and aspect ratios, AR, as calculated by the lifting-line method. A code snippet, using Visual Basic for Applications, is also presented in Section 9.7.4, *Computer Code: Prandtl's Lifting-Line Method*, allowing the reader to determine the factor using Microsoft Excel. Note that the Oswald's span efficiency, e, is related to the lift-induced drag factor per Equations (9-127) and (9-128), repeated below for convenience.

$$e=e_{theo}\cdot k_{corr_1}\cdot k_{corr_2}\cdot\ldots=\left(\frac{1}{1+\delta}\right)\cdot k_{corr_1}\cdot k_{corr_2}\cdot\ldots \qquad (9\text{-}127)$$

EXAMPLE 16-9

An aircraft featuring an $AR=10$ and a $\lambda=0.5$ is flying at a condition that generates a $C_L=0.5$. Determine the lift-induced drag coefficient using Figure 9-75. For this example, assume $C_{L_{minD}}=0$.

SOLUTION:

Figure 9-75 shows that $\delta\approx 0.022$. This means that the lift-induced drag coefficient can be determined as follows:

$$C_{D_i}=\frac{C_L^2}{\pi\cdot AR}(1+\delta)=\frac{0.5^2}{\pi\cdot(10)}(1+0.022)=0.008133$$

This value is 2.2% higher than that for an elliptical wing of the same AR.

(6) Method 6: Prandtl-Betz integration in the Trefftz[5] plane

This method was developed by Ludwig Prandtl (1875–1953) and Albert Betz (1885–1968) around the year 1918. The method computes the induced drag of a wing based on disturbance it inflicts on the fluid flow in the far-field. By evaluating the disturbances in a plane, placed infinitely behind the wing (the *Trefftz plane*), the velocity component in the x-direction (denoted by u) can be eliminated from the integration. This way, a volumetric integration can be reduced to a surface integration.

$$D_i=\frac{\rho}{2}\iint_{\substack{\text{Trefftz}\\ \text{Plane}}}(v^2+w^2)dS \qquad (16\text{-}91)$$

The method is in computational fluid dynamics (CFD) methods, such as the vortex-lattice method and is primarily presented here for completeness. It requires v and w to be obtained using the concept of *velocity potential*.

(7) Correcting the Lift-Induced Drag

There may be reasons to consider several of the following corrections to the lift-induced drag estimate.

Wingtip Correction

In addition to the effect of AR and λ, the lift-induced drag is also affected by the wingtip geometry (see Section 10.5, *Wingtip Design*). It is usually assumed that the distance between the core of the two wingtip vortices equals that of the wingspan. However, the wingtip affects the roll-up of the vortices (see Figure 16-34). The wingtip geometry modifies the 3-dimensional flow field, shifting the wingtip vortices inboard or outboard. The separation changes the effective AR of the wing (see Equation 10-4).

Hoerner [33, pp. 7–5] presents this effect due to several wingtips (see Figure 16-35). The terms ΔAR are values that should be added to correct the geometric AR. The resulting value, denoted by AR_{corr}, is then used when calculating lift-induced drag, C_{D_i}. For instance, consider a wing whose $AR=7$. The selection of a round frontal view and round top view shows a $\Delta AR=-0.20$. Therefore, the AR to use with Equations (16-86) and (16-88) would be 6.8 and not 7. Generally, the figure shows that rounded tips reduce the effectiveness of the wing—it is simply better to feature a square rectangular tip. It is cheaper too. Other wingtips are presented in Section 10.5, *Wingtip Design*.

The effect of how the wingtip shape influences the lift-induced drag is based on how air flows around the wingtip. Three examples are shown in Figure 16-36. The top wingtip shape is round. It allows air to flow to the upper surfaces such the vortex core resides inside and on top of

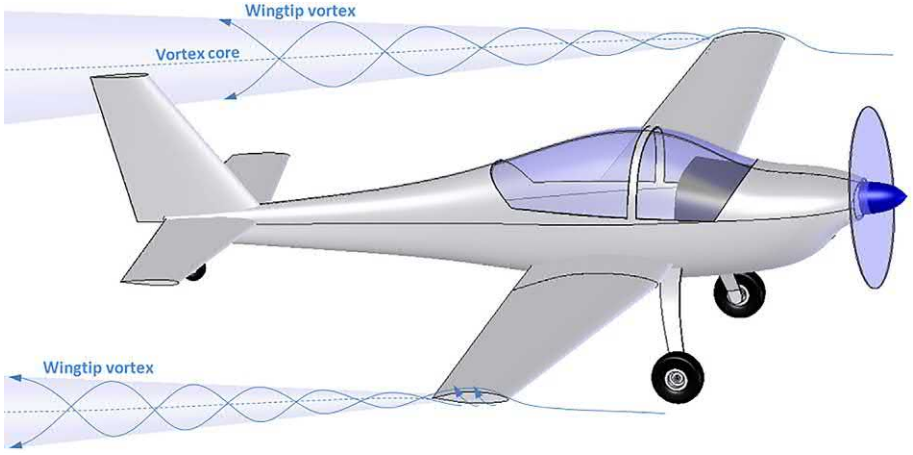


FIGURE 16-34 Pressure difference between the upper and lower surfaces forms the wingtip vortex.

[5] Named after the German mathematician Erich Trefftz (1888–1937).

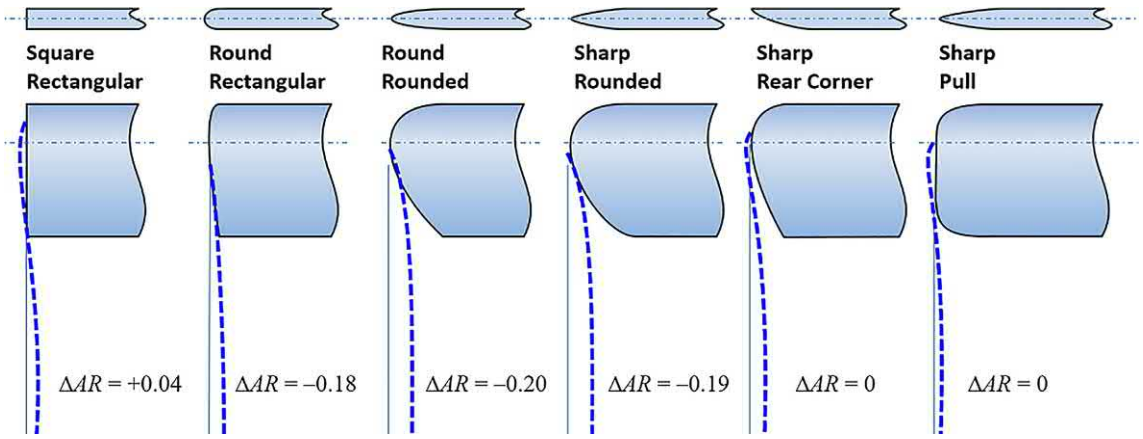


FIGURE 16-35 Effect of several types of wingtips on the separation of the cores of the wingtip vortices. Tested at $R_e = 10^6$ and $AR = 3$. *Reproduced from S.F. Hoerner, Fluid-Dynamic Drag, L. Hoerner, 1965.*

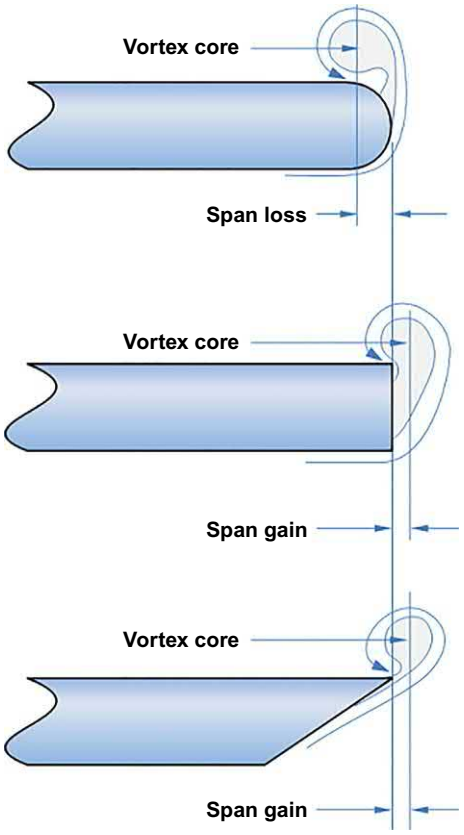


FIGURE 16-36 Location of vortex core for three different wingtip shapes.

the wingtip. This results in a wingtip vortex that is closer to the plane of symmetry than the physical wingtip, effectively reducing the wingspan. The center wingtip is square. It forces the spanwise flow component of the lower surface to make the turn around a very sharp corner. This forces the vortex core to reside farther away from the plane-of-symmetry than the actual wing span—it increases the effective wingspan, albeit by a fraction. The bottom wingtip is representative of the so-called Hoerner wingtip. It promotes spanwise flow outboard and upward that is forced to make a turn around a sharp corner.

This forces the vortex core to reside even farther outboard than the square wingtip in the middle. This idea is extended to the so-called upturned or downturned booster wingtip that helps placing the vortex such that a small effective wingspan increase is achieved, although this is not always realized in practice.

Correction of Lift-Induced Drag in Ground Effect

As shown in Section 9.5.11, *Ground Effect*, the lift-induced drag is reduced when the aircraft is operated close to the ground. This fact should be taken into account during T-O and landing analysis. The effect is favorable during the T-O ground run as the total drag of the airplane is reduced. It is unfavorable during the landing ground roll, for the same reason. Use any of the methods in the section to correct the lift-induced drag based on the height if the MGC above the ground.

Correcting Lift-Induced Drag due to Wing Washout

Horner suggest the following correction for lift-induced drag of a wing due to wing washout. It was shown in Chapter 9, *The Anatomy of the Wing* how the lift distribution is altered as wing twist is introduced. This can lead to an appreciable lift-induced drag, even when the wing is at an AOA for which no lift is generated.

$$\Delta C_{D_{i\phi}} = 0.00004\left(\phi_{tip} - \phi_{MGC}\right) = 0.00004 \cdot \Delta\phi \qquad (16\text{-}92)$$

Where ϕ_{tip} is the angle of the tip and ϕ_{MGC} is the angle of the MGC, both with respect to the root of the wing and both in degrees.

16.3.3 Estimating Wave Drag: C_{D_w}

Familiarity with Section 8.3.8, *The Effect of Compressibility* is an essential preparation for this section. The lift, drag, and moment of a body operating at a fixed α changes rapidly as it approaches the speed of sound. This

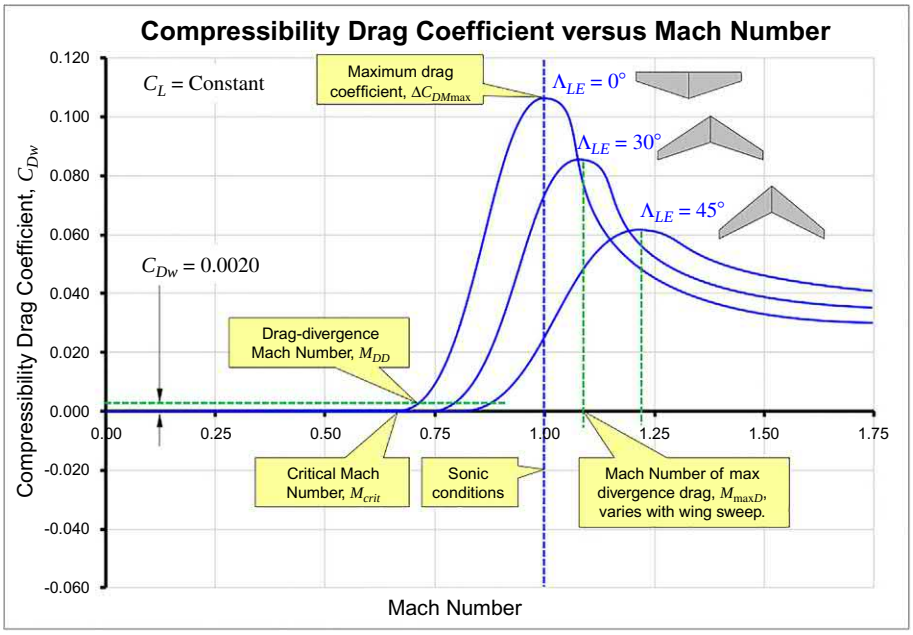


FIGURE 16-37 The effect of compressibility on drag. *Based on R. Whitford, Design for Air Combat, Jane's Publishing Company Limited, 1987; E. Torenbeek, Synthesis of Subsonic Aircraft Design, Delft University Press, 1986.*

change is called *compressibility effect*. Its onset begins at a specific airspeed called the *critical Mach number*, M_{crit}, defined in Bullet (3) of Section 8.3.8. It is driven by the formation of a normal shock that separates the flow on the aft part of an airfoil (e.g., see Figure 8-47). It can form in more than one place on an aircraft. The drag increase, called *wave drag*, is denoted by C_{dw} for 2D bodies and C_{D_w} for 3D bodies. An airplane with thick airfoils will experience it perhaps as early as $M = 0.6$, whereas a sleek high-performance jetliner begins to experience it at $M \approx 0.80$. The Mach number at which this happens is the *drag-divergence Mach number*. Figure 16-37 shows a hypothetical scenario in which an airplane flying at a constant C_L experiences a sharp rise in the compressible drag coefficient near $M = 0.7$. It further illustrates how M_{crit}, M_{DD}, and $M_{\text{max}D}$ are affected by wing sweep.

(1) Wing Drag Divergence Mach Number, M_{DD}

An introduction to *drag divergence* and *drag divergence Mach number* of airfoils is provided in Section 8.3.8. Thus, this section focuses only on wings. For wings, M_{DD} ranges from 1.02 to $1.04M_{crit}$, depending on wing sweep [51]. Drag divergence refers to the sudden rise of drag soon after M_{crit} is reached (see Figure 16-37). There are two common definitions used to establish when this happens: one is attributed to Boeing, the other to Douglas (see Figure 8-67 for graphical representation) [52]:

Boeing definition: $M_{DD} = M_\infty$ when $C_{D_w} = +0.002$ (16-93)

Douglas definition: $M_{DD} = M_\infty$ when $dC_{D_w}/dM = 0.10$ (16-94)

(2) Simple Sweep Theory

Consider the swept wing in Figure 16-38. The *simple sweep theory* contends that, at transonic speeds, the component of the airspeed normal to the line-of-sweep (V_N) dictates when shock begins to form. The far-field airspeed (V_∞) is broken into two components: V_P and V_N (see Figure 16-38); the acute angle is denoted by Λ_{eff}. The literature is surprisingly lax in what constitutes sweep angle. Authors tend to use one of the following: (1) Leading-edge sweep [53, 54] (2) quarter-chord sweep (e.g., Refs. [53, 55–58]), (3) mid-chord sweep (e.g., Refs. [53, 59, 60]), and (4) the angle of the normal-shock front along the span—which may be close to the mid-chord sweep (e.g., Refs. [61, 62]). In this text, Λ_{eff} is the sweep of the mid-chord, unless the weighted average of the shock-front is known (see Figure 16-38). If so, it is used based on [62]. The basic results of simple sweep theory follow:

$$V_N = V_\infty \cos \Lambda_{eff} \tag{16-95}$$

$$C_{L_N} = C_{L_\infty} / \cos^2 \Lambda_{eff} \tag{16-96}$$

$$V_P = V_\infty \sin \Lambda_{eff} \tag{16-97}$$

$$C_{D_N} = C_{D_\infty} / \cos^3 \Lambda_{eff} \tag{16-98}$$

$$M_N = M_\infty \cos \Lambda_{eff} \tag{16-99}$$

$$(t/c)_N = (t/c)_\infty / \cos \Lambda_{eff} \tag{16-100}$$

$$(M_N)_{crit} = (M_\infty)_{crit} \cos \Lambda_{eff} \tag{16-101}$$

$$C_{p_N} = C_{p_\infty} / \cos^2 \Lambda_{eff} \tag{16-102}$$

$$q_N = q_\infty \cos^2 \Lambda_{eff} \tag{16-103}$$

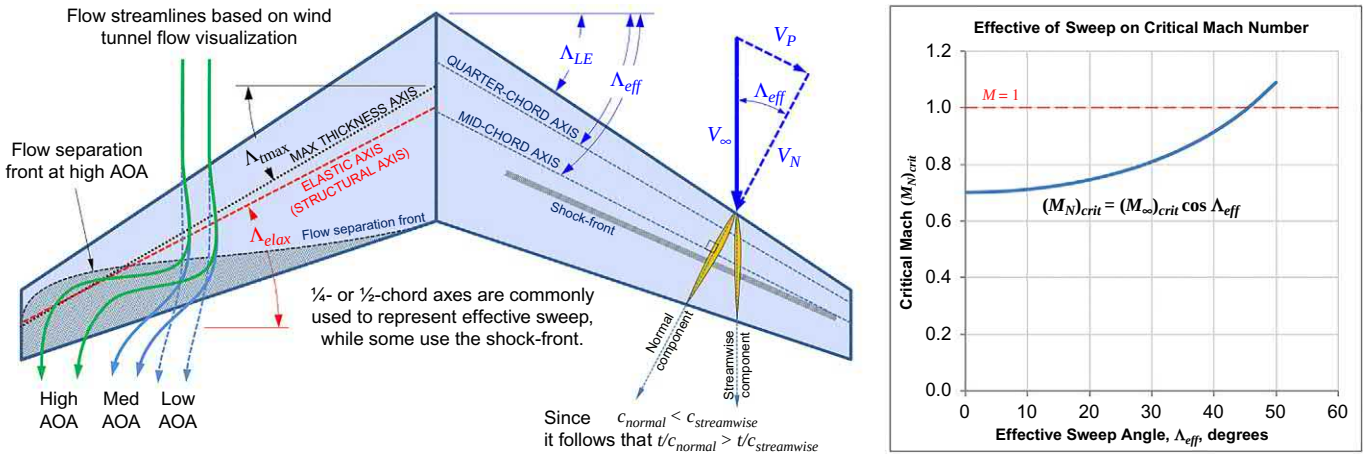


FIGURE 16-38 The deconstruction of the far-field airspeed into a normal (N) and parallel (P) components (left). Note the flow-separation front (left). The effect of sweeping the effective critical Mach number (right).

(3) The Korn Relation for Swept Wings

The *Korn relation*[6] was introduced in Section 8.3.8 as $M_{dd} = \kappa - t/c - 0.1C_{ld}$, where M_{dd} is the drag-divergence Mach number for an airfoil with thickness ratio t/c at a specific lift coefficient (C_{ld}). This simple empirical expression permits Mach-versus-lift trades to be conducted for airfoils [62]. Using the simple sweep theory, it can be adapted to swept wings as follows [59, 62, 63]:

$$M_{DD}\cos\Lambda_{eff} = \kappa - \frac{t/c}{\cos\Lambda_{eff}} - \frac{C_{L_C}}{10\cos^2\Lambda_{eff}} \qquad (16\text{-}104)$$

Where C_{LC} = design lift coefficient and κ = airfoil class constant, obtained using airfoil specific CFD analyses. Refer to the above references for details. In the absence of such work, use $\kappa = 0.87$ for conventional airfoils and 0.95 for NASA-style supercritical airfoils. The C_{L_C} for typical commercial jetliners ranges between $0.4 < C_{L_C} < 0.7$, depending on weight and altitude. M_{DD} is obtained from Equation (16-104) as follows:

$$M_{DD} = \frac{\kappa}{\cos\Lambda_{eff}} - \frac{t/c}{\cos^2\Lambda_{eff}} - \frac{C_{L_C}}{10\cos^3\Lambda_{eff}} \qquad (16\text{-}105)$$

In short, too little wing sweep and M_{DD} will be low. Too much and structural weight increases and exceeds the benefits of the higher M_{DD} [60]. Thus, a compromise in the sweep angle selection is necessary. It is also possible to apply the *Korn relation* to identify limits on M_{crit} for selected airfoils as follows:

$$M_{crit} = \frac{\kappa}{\cos\Lambda_{eff}} - \frac{t/c}{\cos^2\Lambda_{eff}} - \frac{C_{L_C}}{10\cos^3\Lambda_{eff}} - 0.1077 \qquad (16\text{-}106)$$

The coefficient -0.1077 is derived in Ref. [60]. These expressions allow wave drag to be estimated.

(4) Mason's Optimum Sweep Angle

By solving for C_{L_C} in Equation (16-105), Mason [59] showed that, in terms of M_{DD}, the optimum (mid-chord) sweep angle for a long-range transonic transport is given by:

$$\Lambda_{opt} = \cos^{-1}\left\{\frac{\kappa}{3M_{DD}} + \sqrt{\left(\frac{\kappa}{3M_{DD}}\right)^2 - \left(\frac{t/c}{3M_{DD}}\right)}\right\} \qquad (16\text{-}107)$$

This expression yields $\Lambda_{opt} \approx 44$ degrees, for an Airbus 320/Boeing 737 class aircraft, for which $t/c = 0.12$, $\kappa = 0.95$, and assuming $M_{DD} = 0.80$. Both aircraft have a quarter-chord sweep of 25 degrees [64]. Wing design for commercial jets considers other factors too.

DERIVATION OF EQUATION (16-107)

Differentiate the C_{L_C} obtained from Equation (16-105) with respect to sweep angle and set to zero

$$\frac{dC_{L_C}}{d\Lambda} = \frac{d}{d\Lambda}\left[10\kappa\cos^2(\Lambda) - 10(t/c)\cos\Lambda - 10M_{DD}\cos^3\Lambda\right]$$
$$= 10\sin\Lambda\left[(t/c) - 2\kappa\cos\Lambda + 3M_{DD}\cos^2\Lambda\right] = 0$$

The nontrivial solution is inside the brackets. It is a second-order polynomial in terms of cos Λ. It is solved in the standard form. Then, solving for Λ yields Equation (16-107).

(5) Method to Approximate Drag Divergence at Subsonic Airspeed

The following method uses a spline to approximate the typical shape of the drag divergence at high subsonic Mach numbers. It requires three following parameters to be known: (1) the critical Mach number, M_{crit}, (2) the

[6] Attributed to Dr. David Korn formerly of New York University's Courant Institute.

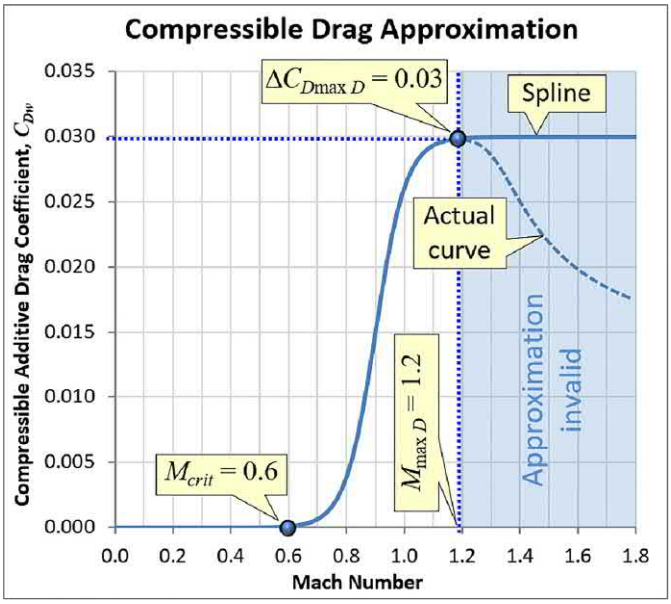


FIGURE 16-39 Method shown in action using $M_{crit}=0.6$, $M_{\max D}=1.2$, and $\Delta C_{D_{\max D}}=0.03$.

maximum Mach divergence drag, $\Delta C_{D_{\max D}}$, and (3) the Mach number at which it occurs, $M_{\max D}$ (see Figure 16-39). If these are known, the additional drag for Mach numbers ranging from 0 to $M_{\max D}$ can be estimated using the following expression:

$$C_{D_w} = \frac{\Delta C_{D_{\max D}}}{2}(1 + \tanh(AM_\infty + B)) \tag{16-108}$$

Where M_∞ is the Mach number and the constants A and B are determined using the following expressions:

$$A = \frac{\tanh^{-1}\left(\frac{2\Delta C_{D_{\max D}} - 0.0002}{\Delta C_{D_{\max D}}} - 1\right) - \tanh^{-1}\left(\frac{0.0002}{\Delta C_{D_{\max D}}} - 1\right)}{M_{\max D} - M_{crit}} \tag{16-109}$$

$$B = \tanh^{-1}\left(\frac{0.0002}{\Delta C_{D_{\max D}}} - 1\right) - AM_{crit} \tag{16-110}$$

It is unlikely that $\Delta C_{D_{\max D}}$ and $M_{\max D}$ are known early during conceptual design. In this case, Table 16-9 can provide some guidance. Note that performance analysis for subsonic aircraft does not wander into the supersonic regime. Therefore, we only need to approximate trends on the subsonic side of the drag rise in Figure 16-39.

TABLE 16-9 Token values of $M_{\max D}$ and $\Delta C_{D_{\max D}}$.

Description	M_{crit}	$M_{\max D}$	$\Delta C_{D_{\max D}}$	Reference
Straight wing "clean"	Eq. (16-105) or (8-62)	≈1.10	0.055	[33]
Swept wing $\Lambda_{c/4}$=34° "clean"		≈1.25	0.030	
Swept wing $\Lambda_{c/4}$=45° "clean"		≈1.65	0.020	
Swept wing $\Lambda_{c/4}$=60° "clean"		≈1.90	0.013	
Axisymmetric body (l/d=10)		≈1.03	0.004-0.012	[65]
Axisymmetric body (l/d=10) + wing ($\Lambda_{c/4}$=45°)		≈1.03	0.0145	
Axisymmetric body (l/d=10) (C in ref) (Λ_{LE}=23°)		≈1.05	0.019	[66]
Axisymmetric body (l/d=10) with waist (B in ref)		≈1.05	0.0165	

DERIVATION OF EQUATIONS (16-108)–(16-110)

Assume a spline function of the type:

$$C_{D_w} = \frac{\Delta C_{D_{\max D}}}{2}(1 + \tanh(AM_\infty + B))$$

Since the hyperbolic tangent has asymptotes at $y=-1$ and $y=1$, it is necessary to divide $\Delta C_{\max D}$ by 2 (because the asymptotes are separated by a value of 2). The value "1" is added to shift tanh upward, so the lower asymptote will be at $y=0$, rather than $y=-1$. The resulting function is a spline that can be used to approximate the drag divergence. This requires the constants A and B to be determined to fit the function through specific points on the drag versus Mach curve (see Figure 16-37). These points are: (1) M_{crit}, where the drag begins to rise and (2) $M_{\max D}$, where it reaches its maximum value, $\Delta C_{\max D}$. To work around the lower asymptote, we assume a very small increase in C_{D_w} at M_{crit}; Here assume 1 dragcount or 0.0001. To work around the upper asymptote, where C_{D_w} reaches its maximum value ($\Delta C_{\max D}$) we assume its value is $C_{D_w} = \Delta C_{\max D} - 0.0001$. Thus, we write:

At $M_\infty = M_{crit}$:

$$\Delta C_{D_M} = \frac{\Delta C_{D_{\max D}}}{2}(1 + \tanh(AM_{crit} + B)) = 0.0001$$

At $M_\infty = M_{\max D}$:

$$\Delta C_{D_M} = \frac{\Delta C_{D_{\max D}}}{2}(1 + \tanh(AM_{\max D} + B)) = \Delta C_{D_{\max D}} - 0.0001$$

We readily see that we can solve for the argument of the hyperbolic tangent as follows:

$$AM + B = \tanh^{-1}\left(\frac{2\Delta C_{D_M}}{\Delta C_{D_{\max D}}} - 1\right)$$

This allows us to write:

At $M_\infty = M_{crit}$:

$$AM_{crit} + B = \tanh^{-1}\left(\frac{2\Delta C_{D_M}}{\Delta C_{D_{maxD}}} - 1\right) = \tanh^{-1}\left(\frac{0.0002}{\Delta C_{D_{maxD}}} - 1\right)$$

At $M_\infty = M_{maxD}$:

$$AM_{maxD} + B = \tanh^{-1}\left(\frac{2\Delta C_{D_M}}{\Delta C_{D_{maxD}}} - 1\right) = \tanh^{-1}\left(\frac{2\Delta C_{D_{maxD}} - 0.0002}{\Delta C_{D_{maxD}}} - 1\right)$$

Solving for A and B yields Equations (16-109) and (16-110).

EXAMPLE 16-10

Determine drag divergence spline for the Learjet 45 (see Section 17.5.2, *Learjet 45*) assuming the following parameters: $M_{crit} = 0.80$, $\Delta C_{D_{maxD}} = 0.03$, and $M_{maxD} = 1.05$. Plot the drag coefficient as a function of calibrated airspeed between 0 and 500 KCAS for the aircraft at S-L, 25,000 ft, 35,000 ft, and 45,000 ft, if $C_{D_{min}} = 0.0200$, $k = 0.05236$, $C_{L_{minD}} = 0.20$, and physical data provided in Table 17.8.

SOLUTION:

This is largely a "plug-and-chug" problem. Use Equation (16-109) to get constant A:

$$A = \frac{\tanh^{-1}\left(\frac{2(0.03) - 0.0002}{0.03} - 1\right) - \tanh^{-1}\left(\frac{0.0002}{0.03} - 1\right)}{1.05 - 0.80} = 22.80$$

Use Equation (16-110) to get constant B:

$$B = \tanh^{-1}\left(\frac{0.0002}{0.03} - 1\right) - (22.80)(0.80) = -21.09$$

The wave drag spline is given by:

$$C_{D_w} = \frac{0.03}{2}(1 + \tanh(22.80M_\infty - 21.09)) = 0.015(1 + \tanh(22.80M_\infty - 21.09))$$

In interest of space, only the requested graph is shown in Figure 16-40. It plots $C_D = C_{D_{min}} + k(C_L - C_{L_{minD}})^2 + C_{D_w}$. It shows clearly how the drag divergence moves to a lower calibrated airspeed with altitude, a consequence of the reduced sonic speed and effect of density on the calibrated airspeed. Note that this model is also corrected using the high AOA correction of Equation (16-20). Also see Figure (20-4), which breaks down the total drag into minimum, lift-induced, and wave drag contributions.

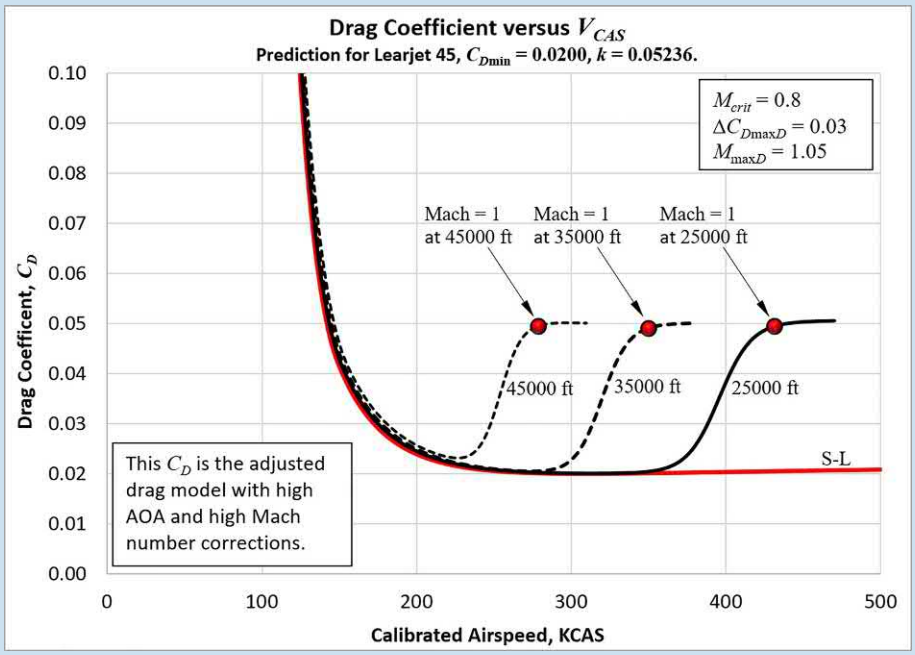


FIGURE 16-40 The incorporation of the wave drag spline to the drag coefficient.

(6) Transonic Area Rule

Refers to a method of estimating transonic and supersonic wave drag for aircraft. It was first conceived and formulated by the German scientist Otto Frenzl (1909–96) [67]. Frenzl theorized that the steepness of the drag rise of a body approaching the speed of sound was related to its distribution of cross-sectional area. As an employee of Junkers Aircraft, it should not surprise anyone that his invention shows up in a Junkers-owned patent number 932410 from 1944. The idea was further developed by Wallace D. Hayes (1918–2001) in his 1947 Ph.D. dissertation, where it was called the "supersonic area rule." [68] It is also called the "Hayes drag formula" in Ref. [69]. Its application to aircraft design was shown by the American aerodynamicist Richard T. Whitcomb (1921–2009). In 1951, Whitcomb attended a symposium on transonic flow presented by the renowned German aerodynamicist Dr. Adolf Busemann (1901–86) [70]. Afterward, Whitcomb hypothesized that narrowing the fuselage at the wing-juncture (called "waisting") should reduce the supersonic drag. He published an experimental confirmation of this approach in 1952 in Ref. [71], later superseded by Ref. [65].

A theoretical treatment of the method is provided by Jones [72] and Ashley and Landahl [69]. The theory presumes flow disturbances are independent of the body's arrangement. This is justified on the basis that no information about its shape is carried upstream because of its high speed. Thus, the cross section of a body at any fuselage station (x) can be regarded circular in shape. To calculate the wave drag requires a complicated numerical analysis of the geometry. The procedure passes multiple cutting planes along the length (along the x-axis) of the body. Each is rotated in steps through 180 degrees about the x-axis and the wave drag for each step is determined. The complete wave drag is then calculated per the procedure in Refs. [73, 74]. If $M_\infty = 1$, then the cross sections are *normal* to the x-axis. If $M_\infty > 1$, then the cross-sections are parallel to the Mach angle, μ, given by

$$\mu = \sin^{-1}(1/M_\infty) \tag{16-111}$$

This is illustrated in Figure 16-41. Moreover, the area distribution, $S(x)$, is done for several roll angles (ϕ) (each resulting in a different $S(x)$), which are then averaged. The wave drag is then calculated using the expression

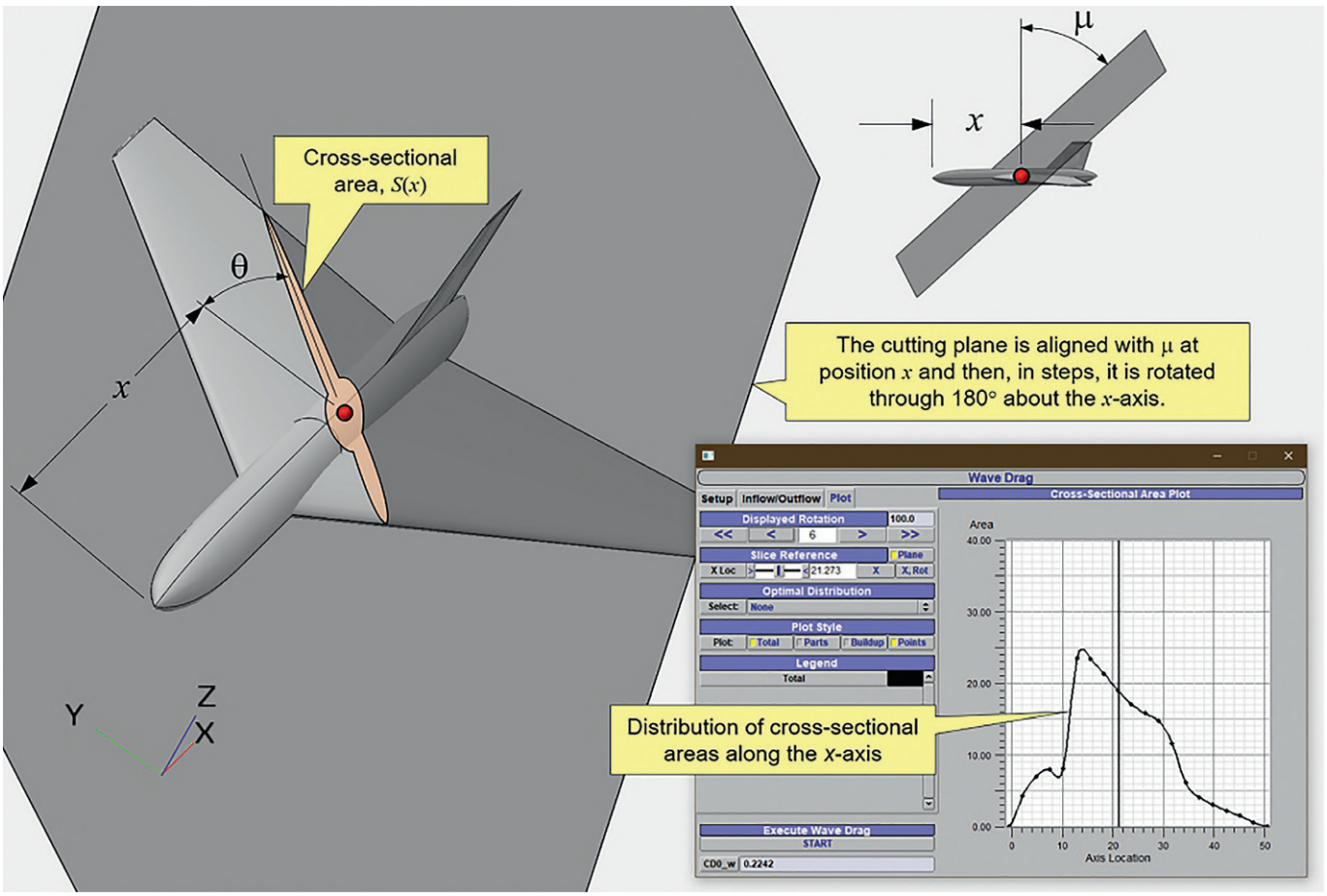


FIGURE 16-41 Implementation of the transonic area rule in the software OpenVSP [75].

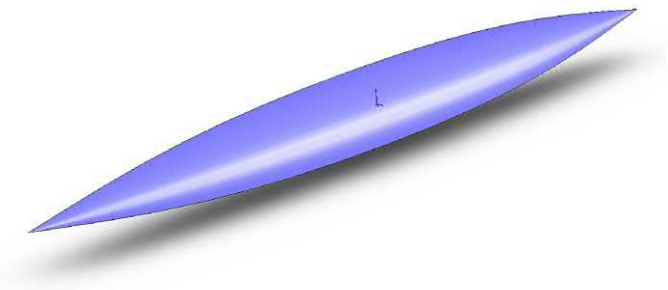


FIGURE 16-42 A Sears-Haack body.

$$C_{D_w} = \frac{-1}{2\pi S}\int_0^l \int_0^l S''(x)S''(\xi)\,\ln(x-\xi)dxd\xi \qquad (16\text{-}112)$$

Where l is the length of the body, S is the cross-sectional area, x refers to the longitudinal axis, ξ is an integration variable. The expression is derived in Ref. [69]. The configuration will develop its minimum wave drag coefficient at its operational Mach number when its distribution of $S(x)$ resembles the area distribution of a Sears-Haack body (see Figure 16-42). The Sears-Haack distribution develops the least wave drag. Therefore, the designer of supersonic vehicles tries to reshape the aircraft to match the Sears-Haack distribution.

Radius ($R_{\max}$ is maximum body radius):

$$r(x) = R_{\max}[4x(1-x)]^{3/4}$$

Cross-sectional area:

$$S(x) = \pi R_{\max}^2[4x(1-x)]^{3/2}$$

First derivative of $S(x)$:

$$S'(x) = 12\pi R_{\max}^2(1-2x)\sqrt{(x-x^2)}$$

Second derivative of $S(x)$:

$$S''(x) = 12\pi R_{\max}^2\left[\frac{(1-2x)^2}{2\sqrt{x-x^2}} - 2\sqrt{x-x^2}\right]$$

Volume (body only): $\forall = \frac{3\pi^2}{16}R_{\max}^2 l$

Wave drag (body only): $D_w = \frac{9\pi^3 R_{\max}^4}{4l^2}\rho V_\infty^2 = q_\infty \frac{9\pi^3 R_{\max}^4}{2l^2}$

Wave drag coefficient (body only): $C_{D_w} = \frac{D_{wave}}{q_\infty S} = \frac{9\pi^3 R_{\max}^4}{2l^2 S}$

The minimum supersonic drag of an aircraft is given by R.T. Jones' approximation [76, 77]:

$$D_{\min} = q_\infty S C_{D_{\min}} + \overbrace{\frac{W^2}{q_\infty \pi b^2}}^{\text{Wing's lift-induced drag}} + \overbrace{\frac{(M_\infty^2-1)W^2}{q_\infty \pi l^2}}^{\text{Fuselage's lift-induced drag}} + \overbrace{q_\infty \frac{128}{\pi}\frac{\forall^2}{l^4}}^{\text{Fuselage's volume dependent drag (for Sears-Haack)}} \qquad (16\text{-}113)$$

Where q_∞ is dynamic pressure, W is weight (which equals lift), b is wingspan, l is the overall (fuselage) length, and $\forall$ is volume. It shows how wave drag depends on lift, length, and volume. The approximation applies only at low supersonic speeds for wings whose leading-edge sweep is greater than the sweep of the Mach shock-lines.

16.3.4 Calculate $C_{D_{min}}$ Using the Rapid Drag Estimation Method

The *rapid drag estimation method* (RDEM) is the fastest way to estimate the drag of an airplane. However, it is a low-fidelity method. It presumes a relationship between the airplane's averaged skin friction coefficient ($\overline{C}_f$), total wetted area (S_{wet}), and $C_{D_{min}}$. Due to its low-fidelity nature, the method should only be used to check drag estimates by the *component drag buildup method* (CDBM). It allows for contributions by flaps and landing gear. The method calculates $C_{D_{min}}$ using the concept of EFPA (see Section 16.2.1, *Fundamental Definitions*) and Equation (16-9):

$$C_{D_{\min}} = (f/S + \Delta C_{D_{\min}})k_{crud} \qquad (16\text{-}114)$$

Where f is the equivalent flat plate (parasite) area, $\Delta C_{D_{min}}$ is the additive (miscellaneous) drag, and k_{crud} is the crud factor (see Section 16.3.9). The method involves using $\overline{C}_f$ and S_{wet} to extract the value of f for a "clean" aircraft from Figure 16-43, using the approach outlined in the figure. An accurate estimate of the aircraft's wetted area is essential. An example of the application of the method is shown in Figure 16-43.

The drag increments due to flaps, landing gear, speed brakes, etc., are accounted for using the following relation and then added to $C_{D_{min}}$:

$$\Delta C_{D_{\min}} = \frac{1}{S}\sum C_{D_\pi}A_\pi \qquad (16\text{-}115)$$

Where $\Delta C_{D_{min}}$ is the drag increment, C_{D_π} is the component's equivalent drag coefficient, and A_π is the equivalent parasite area. The equivalent parasite areas and coefficients are obtained from the Table 16-10, where A_C stands for maximum cross-sectional area, S is the wing reference area and S_{HT} is the HT planform area.

16.3.5 Calculate $C_{D_{min}}$ Using the Component Drag Buildup Method

The *component drag buildup method* (CDBM) estimates total drag by summing the skin friction of all external components comprising the airplane. Since pressure drag depends on viscous effects (e.g., through flow separation), the skin friction coefficient is corrected using a special factor called the *form factor* (*FF*). It accounts for the difference in drag generated by dissimilar geometries

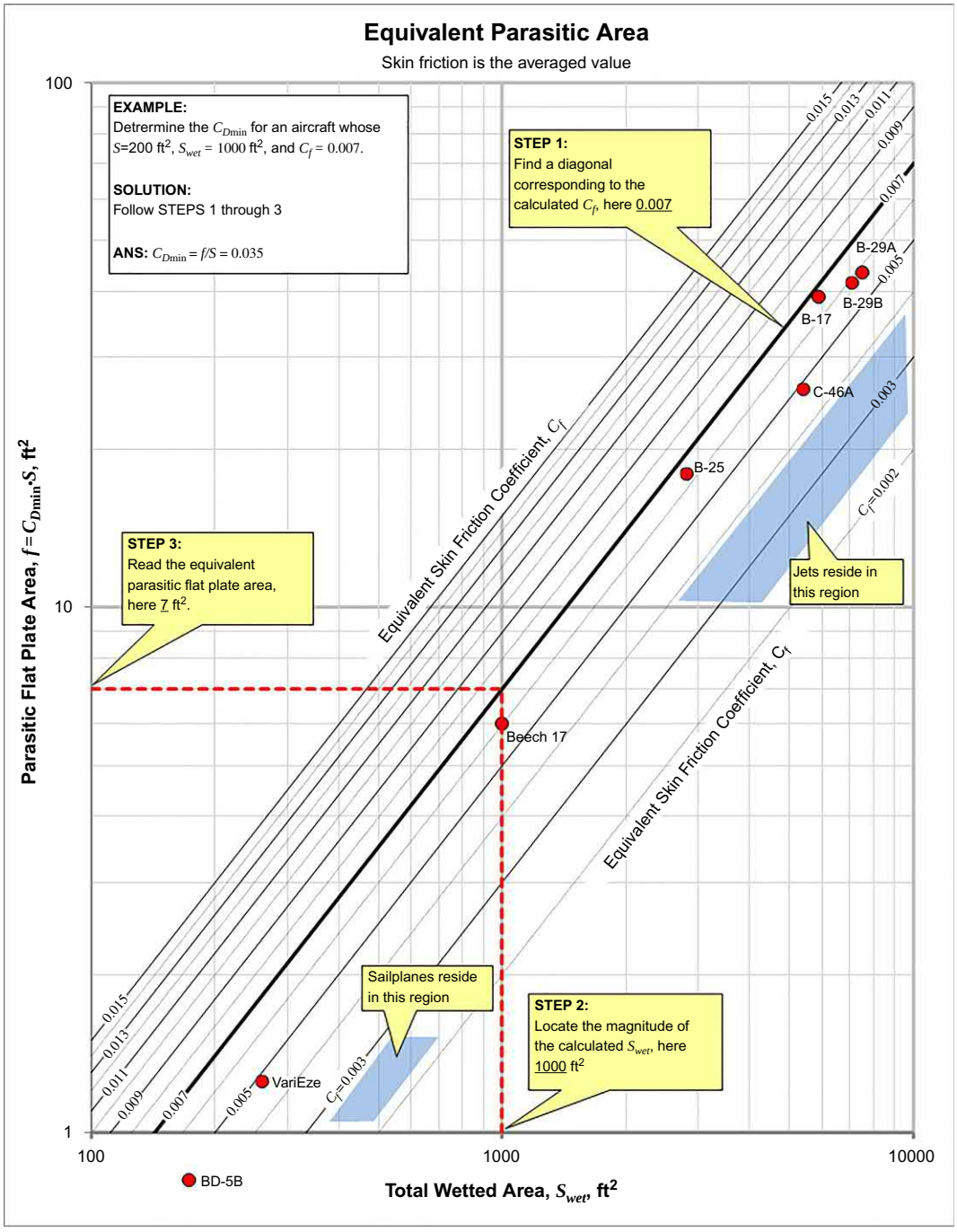


FIGURE 16-43 Determination of equivalent parasite area. *Based on C.D. Perkins, R.E. Hage, Airplane Performance, Stability, and Control, John Wiley & Sons, 1949; J. Roskam, Methods for Estimating Drag Polars of Subsonic Airplanes, 4th printing, 1984.*

that happen to have equal wetted area or skin friction coefficients. The CDBM also incorporates effects caused by the proximity of components to each other (interferences), using a so-called *interference factor* (*IF*). The procedure is illustrated in Figure 16-44 and implemented in Example 16-10. In the flow chart, the "+" sign means that contributions are added, whereas the "×" sign means multiplication. The following Step-by-Step describes how to implement the procedure.

Step 1: Identify and List Components

Tabulate all "winglike" components that constitute the external (wetted) geometry of the airplane. Identify each component using an index $j = 1,2,\ldots,N$ (= number of components) and specify their wetted areas, S_{wet_j}. This typically includes the wing, winglets, HT, VT, fuselage, pylons, nacelles, external fuel tanks, dorsal and ventral fins, and so forth. While it is easily argued that some of

TABLE 16-10 Equivalent parasite areas and coefficients.

Item	Comment	C_{D_π}	Area on which C_{D_π} is based
Wing	Standard operational roughness, airfoil $t/c = 10\%–20\%$.	0.005–0.009	S
HT and VT	Standard operational roughness, airfoil $t/c = 8\%–12\%$.	0.006–0.008	S_{HT}
Wing flaps	Plain, 60% span at 30-degree deflection	0.02–0.03	S
Fuselage	Streamlined and very smooth body	0.05	A_C
Fuselage	Small aircraft with engine in nose	0.09–0.13	A_C
Fuselage	Large transport aircraft (DC-4, DC-5)	0.07–0.10	A_C
Fuselage	Bomber (B-17)	0.08–0.12	A_C
Landing gear	Typical light twin, wheel wells closed	0.014	S
Landing gear	Typical light twin, wheel wells open	0.017	S
Nacelle, propeller	Above wing on a small aircraft (e.g., Cessna 310 type)	0.25	A_C
Nacelle, propeller	Relatively small leading-edge nacelle on a large aircraft	0.05–0.09	A_C
Nacelle, turbojet	Mounted on wing (e.g., Me-262)	0.05–0.07	A_C
Wingtip tank	Suspended below wingtip	0.10	A_C
Wingtip tank	Centrally mounted at wingtip	0.06	A_C
Wing tank	Suspended below wing, incl. support	0.19–0.21	A_C
Bomb	Suspended below wing, incl. support	0.22–0.25	A_C
Cooling flaps Speed brakes	Depends strongly on size, no realistic representative data can be given		

Based on C.D. Perkins, R.E. Hage, Airplane Performance, Stability, and Control, John Wiley & Sons, 1949; J. Roskam, Methods for Estimating Drag Polars of Subsonic Airplanes, 4th printing, 1984.

these are not quite winglike, these are included and the method is applied identically to all. However, components like a fuselage are analyzed using length in lieu of a chord. Exclude smaller wing-like components such as antennas. These are treated using the methods of Section 16.4, *Miscellaneous or Additive Drag*. The total wetted area, S_{wet}, of the aircraft is given by

$$S_{wet} = \sum_{j=1}^{N} S_{wet_j} \tag{16-116}$$

Step 2: Estimate Skin Friction of All Listed Components

Calculate the averaged skin friction, $\overline{C}_f$, of all listed components using the methods of Section 16.3.1, *Estimating Skin Friction Drag*. This is shown in Figure 16-44 as ①.

Step 3: Estimate the FF and IF of All Listed Components

Calculate the form- and interference-factors for all listed components. For *FF* use the methods of Section 16.3.6, *Form Factors*. For *IF* use the methods of Section 16.3.7, *Interference Factors*. This is shown in Figure 16-44 as ② and ③.

Step 4: Estimate the $C_{D_{misc}}$ of Remaining Components

This includes drag contributions of components like landing gear, inlets, outlets, antennas, fuel caps, flaps, canopies, control system components (bellcranks, hinges, etc.) and other nonwing–like parts. This is accomplished using the methods of Section 16.4, *Miscellaneous or Additive Drag*. This is shown in Figure 16-44 as ④.

Step 5: Estimate the $C_{D_{min}}$

The minimum drag is estimated using the following expression

$$C_{D_{\min}} = \left(C_{D_1} + C_{D_2} + C_{D_p} + C_{D_{misc}}\right) k_{crud} \tag{16-117}$$

Where the coefficients C_{D_1}, C_{D_2}, and C_{D_p} are given by the expressions below. $C_{D_{misc}}$ is the miscellaneous drag per Section 16.4, and k_{crud} is the crud factor ⑤ (see Section 16.3.8). The coefficient C_{D_1}, is estimated per the above Step-by-Step, where the tabulated component contributions are added as follows

$$C_{D_1} = \frac{1}{S}\left(\sum_{j=1}^{N} \overline{C}_{f_j} \times FF_j \times S_{wet_j} \times IF_j\right) \tag{16-118}$$

Where FF_j, S_{wet_j}, and IF_j are the form factor, wetted area, and interference factor of component j, respectively.

The coefficient C_{D_2} is optional. It accounts for drag of a wing-like component (e.g., wing, HT, VT) when a 2D drag polar of its airfoil is available. In this case, C_{d_j} represents the average airfoil profile drag obtained from the drag polar and S_j is the planform area. Of course, if using this scheme, the component must be excluded from the C_{D_1}. C_{D_2} is calculated using the expression

$$C_{D_2} = \frac{1}{S}\left(\sum_{j=1}^{M} C_{d_j} \times S_j \times IF_j\right) \tag{16-119}$$

Where M is the number of components. Note that the airfoil's C_{d_j} already includes the wetted area and contributions from pressure drag. Its use can be easily extended to account for drag rise with section lift coefficients. Additionally, it is scaled based on the component's planform area S_j. Therefore, C_{d_j} can be related to $\overline{C}_{f_j}$ as follows

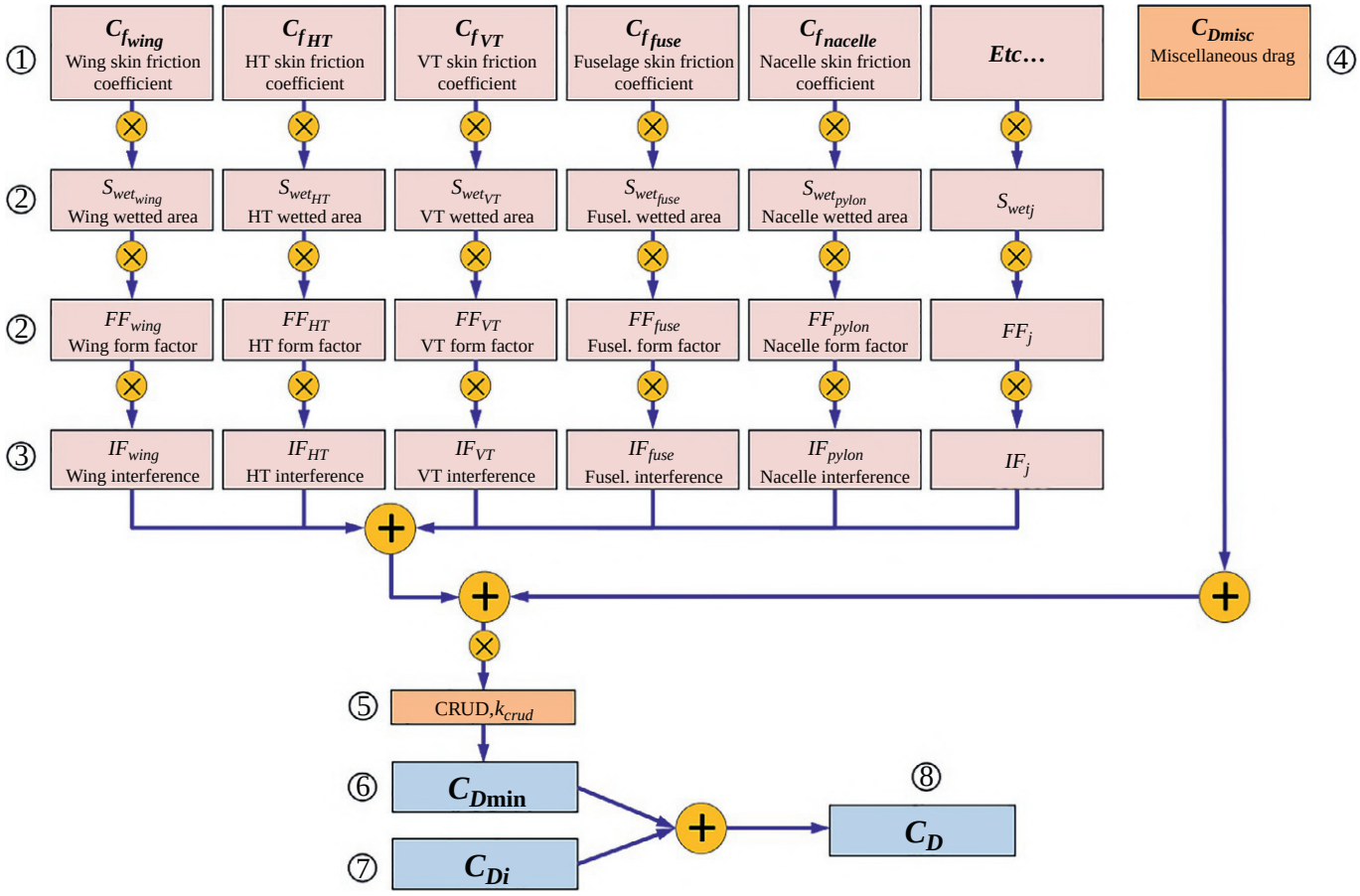


FIGURE 16-44 Flow chart describing the component drag buildup method.

$$C_{d_j} = \left(\frac{S_{wet_j}}{S_j}\right)\overline{C}_{f_j} \times FF_j \tag{16-120}$$

It can be seen that if substituted into Equation (16-119) it acquires the form of Equation (16-118). Thus, $\overline{C}_{f_j}$ can be written in terms of C_{d_j} as shown below

$$\overline{C}_{f_j} = \frac{1}{FF_j}\left(\frac{S_j}{S_{wet_j}}\right)C_{d_j} \tag{16-121}$$

The coefficient C_{D_p}, is also optional. It provides an alternative to C_{D_2} to account for the profile drag of the wing and incorporate AOA dependency in the drag estimate. This is accomplished through Equation (16-16), repeated below for convenience.

$$C_{D_p} = C_{d_{\min}} + \frac{2m}{b}\int_0^{b/2}(f(y) - C_{l_{\min D}})^2 dy \tag{16-16}$$

If C_{D_2} and C_{D_p} are disregarded, the component drag buildup is expressed in the following simpler form:

$$C_{D_{\min}} = \left(C_{D_{misc}} + \frac{1}{S}\sum_{j=1}^{N}\overline{C}_{f_j} \times FF_j \times S_{wet_j} \times IF_j\right)k_{crud} \tag{16-122}$$

16.3.6 Form Factors

As stated earlier, the form factor (*FF*) accounts for a component's pressure drag by boosting its skin friction drag. There are numerous methods available for this purpose. Some are only intended for wing-like components, while others are intended for axisymmetric components like fuselages. These form factors are typically derived by semiempirical methods that emphasize the component's thickness-to-chord ratio. The following form factors are found in the literature.

(1) Form Factors for Wing-like Components

The following *FF* are used with lifting surfaces like wings, HT, VT, streamlined wing-struts, engine pylons, wing-shaped antennas, and landing gear pant fairings, to name a few. This forces the designer to ask "which one do I pick?" Unless specific applications are cited the answer is often: "Use engineering judgment." The unsure designer can also take the average of two or more methods.

Hoerner [33, pp. 6–6] suggests the following *FF* for lifting surfaces featuring airfoils whose $(x/c)_{\max} = 0.30$:

$$FF = 1 + 2(t/c) + 60(t/c)^4 \tag{16-123}$$

Hoerner [33] suggests the following *FF* for lifting surfaces featuring airfoils whose $(x/c)_{max} = 0.40–0.50$, such as NACA 64 and 65 series airfoils:

$$FF = 1 + 1.2(t/c) + 70(t/c)^4 \tag{16-124}$$

Torenbeek [54, p. 499] suggests the following *FF* for lifting surfaces featuring airfoils whose $t/c \leq 0.21$:

$$FF = 1 + 2.7(t/c) + 100(t/c)^4 \tag{16-125}$$

None of the above models account for wing sweep nor compressibility effects. Shevell [51] suggests the following *FF* for lifting surfaces and introduces compressibility and sweep effects:

$$FF = 1 + \frac{\left(2 - M_\infty^2\right)\cos\Lambda_{c/4}}{\sqrt{1 - M_\infty^2 \cos^2\Lambda_{c/4}}}(t/c) + 100(t/c)^4 \tag{16-126}$$

Nicolai [78] and Raymer [79] suggest the following *FF* for lifting surfaces that also corrects for compressibility and the sweep of the maximum thickness line. The equation is only valid for $M_\infty \geq 0.2$ because the compressibility correction (the bracket on the right-hand side) is less than 1 for $M_\infty < 0.2$. Thus, omit the compressibility correction when $M_\infty < 0.2$.

$$FF = \left[1 + \frac{0.6}{(x/c)_{max}}(t/c) + 100(t/c)^4\right] \cdot \left[1.34 M_\infty^{0.18} (\cos\Lambda_{t\,max})^{0.28}\right] \tag{16-127}$$

Jenkinson [80] suggests two kinds of *FF*; one for the wing, the other for tail surfaces. The *FF* for a wing is given by:

$$FF = \left[3.3(t/c) - 0.008(t/c)^2 + 27.0(t/c)^3\right]\cos^2\Lambda_{c/2} + 1 \tag{16-128}$$

Furthermore, the reference recommends *IF* to use with the expression: *IF* = 1.0 for well-filleted low or mid wings, and 1.1–1.4 for small or no fillet. It recommends an *IF* = 1.2 for tail surfaces. The *FF* for tail surfaces is given by:

$$FF = [3.52(t/c)]\cos^2\Lambda_{c/2} + 1 \tag{16-129}$$

In the previously mentioned equations:

M_∞ = Mach number,
$_{c/4}$ = Sweep angle of the quarter-chord line,
$\Lambda_{c/2}$ = Sweep angle of the mid-chord line,
$\Lambda_{t\ max}$ = Sweep angle of maximum thickness line,
$(x/c)_{max}$ = Location of maximum airfoil thickness,
(t/c) = Airfoil thickness ratio.

Note that Equations (16-126) and (16-127) approach Torenbeek's form of Equation (16-125) for wings whose quarter-chord (Shevell) or maximum thickness (Nicolai, Raymer) sweep angle is 0 degrees, when $M_\infty = 0$ (Shevell) or $M_\infty = 0.2$ (Nicolai, Raymer).

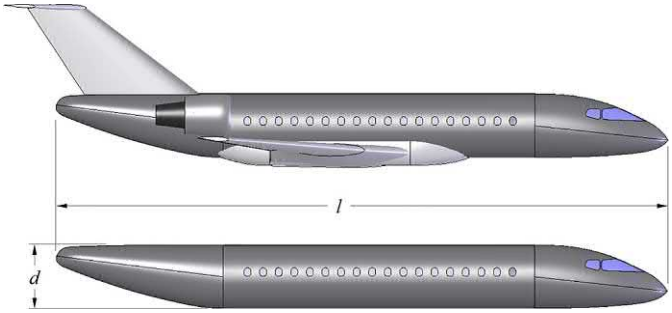


FIGURE 16-45 Definition of terms for use with the estimation of form factors for a fuselage.

(2) Form Factors for a Fuselage and a Smooth Canopy

The following *FF* are used with *streamlined bodies* (which typically represent fuselages) and *smooth canopies*. These can also be used for engine nacelles and external, streamlined fuel tanks. These typically use *fineness ratio*, defined as length (l) divided by the average diameter (d), as shown in Figs. 16.45 and 16.46. The former illustrates how to strip the fuselage of the wing, tail, and engines to extract the dimensions needed. Sometimes the distinction is not so clear, leaving no option besides engineering judgment.

A streamlined body usually refers to a body-of-revolution, whose cross section is similar to what is shown in Figure 16-46. A streamlined body is used to represent many types of fuselages, including airship hulls and engine nacelles. A canopy is sized geometrically as shown in Figure 16-46. For more realistic canopies, refer to Section 16.4.10, *Drag of Canopies*.

Fuselage as a Body of Revolution

In the following expressions, the *fineness ratio* (f) is a measure of the slenderness of a body-of-revolution. It is defined as follows:

$$f = l/d \tag{16-130}$$

Although devised for bodies-of-revolution, the expressions for the *FF* below are also applicable to bodies that feature noncircular cross sections (see Figure 16-46). For instance, a cross section might be shaped like an egg, or be box-shaped. Such shapes are treated based on their maximum cross-sectional area, A_{max}, which is related to that of a circular cross section using a "representative" fineness ratio as shown below:

$$f = l/d = \frac{l}{2}\sqrt{\frac{\pi}{A_{max}}} \tag{16-131}$$

Form Factors at Subcritical Reynolds Numbers

Hoerner [33, pp. 6–16] derives and suggests the following *FF* for streamlined bodies at subcritical Reynolds numbers ($R_e < 10^5$). This R_e applies to small vehicles, such as RC aircraft, or small Unmanned Aerial Vehicles. Note that

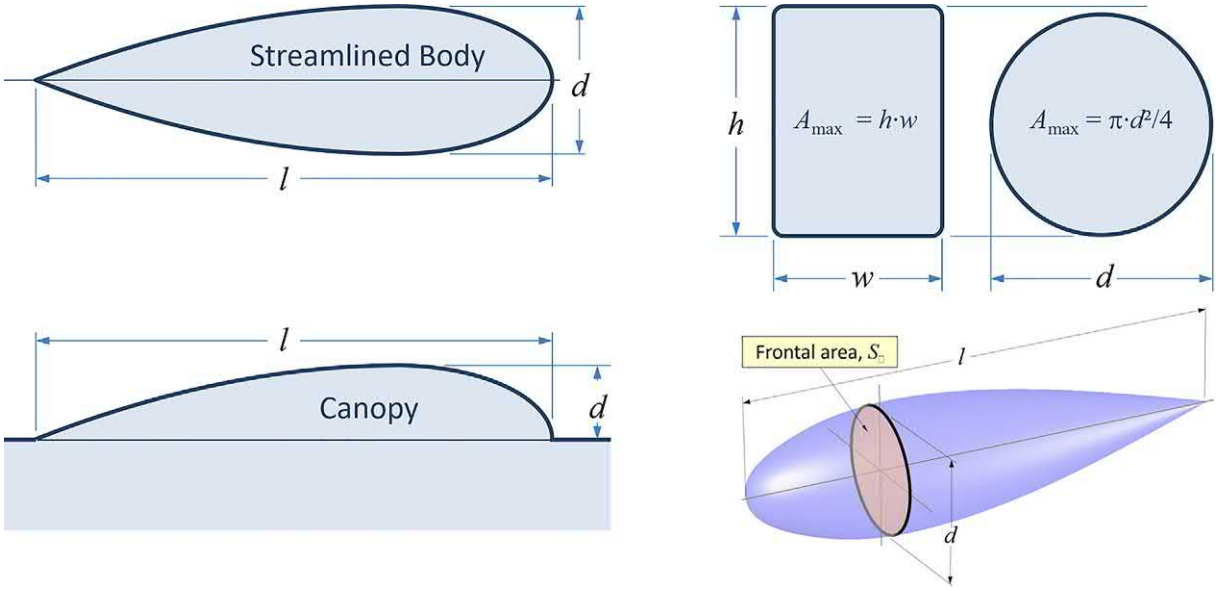


FIGURE 16-46 Definition of terms for use with streamlined bodies and canopies.

since the expression includes the pressure drag component, it is not represented as a standalone form factor, but rather what the product of the $\overline{C}_{fi} \times FF_i$ in Equation (16-122). It also requires the skin friction coefficient for laminar boundary layer of Equation (16-40) to be used:

$$\overline{C}_f \cdot FF = C_{f_{lam}}\left[1 + f^{-1.5}\right] + 0.11f^{-2}$$
$$= \frac{1.328}{\sqrt{R_e}}\left[1 + f^{-1.5}\right] + 0.11f^{-2} \qquad (16\text{-}132)$$

Form Factors at Supercritical Reynolds Numbers

Hoerner [33, pp. 6–17] suggests the following form factor for streamlined bodies in airflow whose $R_e > 10^5$:

$$FF = 1 + 1.5f^{-1.5} + 7f^{-3} \qquad (16\text{-}133)$$

Torenbeek [54] suggests the following form factor for a generic fuselage:

$$FF = 1 + 2.2f^{-1.5} + 3.8f^{-3} \qquad (16\text{-}134)$$

Likewise, Nicolai [78], Raymer [79], and Roskam [81] present the following form factor for a fuselage:

$$FF = 1 + 60f^{-3} + \frac{f}{400} \qquad (16\text{-}135)$$

Shevell [82] also provides a model for a fuselage given by:

$$FF = 2.939 - 0.7666f + 0.1328f^2 - 0.01074f^3 + 3.275 \times 10^{-4}f^4 \qquad (16\text{-}136)$$

Finally, Jenkinson's [80] model is given by:

$$FF = 1 + 2.2f^{-1.5} - 0.9f^{-3} \qquad (16\text{-}137)$$

Fuselage fineness ratios and wetted areas for selected GA aircraft are shown in Table 16-11.

TABLE 16-11 Fuselage fineness ratios and wetted areas for selected GA aircraft.

Aircraft	Fineness ratio, l/d	Wing area, S, ft^2	Fuselage S_{wetf}, ft^2	S_{wetf}/S
Beech Baron	5.69	199.2	362	1.82
Beech Bonanza (1958)	4.98	181	323	1.78
Beech Duke	5.59	212.9	586	2.75
Beech King Air	6.06	294	652	2.22
Beech Sierra	5.22	146	332	2.27
Cessna 185	5.15	176	292	1.66
Cessna 207	5.69	174	425	2.44
Cessna 210	5.02	175	319	1.82
Cessna 310	5.4	179	306	1.71
Cessna 414	5.52	195.7	488	2.49
Cirrus SR22	5.38	144.9	258	1.78
Gates Learjet 24	8.8	232	502	2.16
Piper Navajo	5.97	229	502	2.19
Piper Seneca	5.68	206.5	356	1.72

Mostly based on J. Roskam, Some comments about fuselage drag, in: Proceedings of the NASA-Industry-University GA Drag Reduction Workshop, Lawrence, KS, July 14-16, 1975.

Optimum Fineness Ratio, f_{opt}

The determination of the optimum fineness ratio involves the contribution of both the length (l) and diameter (d) of the body. Using the body's frontal (A_{max}) and wetted area (S_{wet}), this is accomplished through $FF \times S_{wet}/A_{max}$. The wetted area of a streamlined axisymmetric body ranges between 0.7 and 0.8

times its perimeter[7] (πd) times its length, l. For this discussion, assume this is $S_{wet} = 0.75\pi ld$ or $\frac{3}{4}\pi ld$. The frontal area is given by $A_{max} = \pi d^2/4$. Thus, the drag coefficient based on frontal area is given by

$$C_{D_A} = \overline{C}_f \times FF \times \frac{S_{wet}}{A_{max}} \tag{16-138}$$

Where the area ratio is given by: $\frac{S_{wet}}{A_{max}} = \frac{\frac{3}{4}\pi ld}{\frac{1}{4}\pi d^2} = 3\frac{l}{d} = 3f$

Substituting an FF of choice, e.g., per Equation (16-133), leads to

$$\begin{aligned} C_{D_A} &= \overline{C}_f \times FF \times \frac{S_{wet}}{A_{max}} \\ &= \overline{C}_f \left(1 + 1.5f^{-1.5} + 7f^{-3}\right)(3f) \\ &= \overline{C}_f \left(3f + 4.5f^{-1/2} + 21f^{-2}\right) \end{aligned} \tag{16-139}$$

Differentiating C_{D_A} with respect to f and setting equal to zero, yields the optimum fineness ratio

$$\begin{aligned} \frac{dC_{D_A}}{df} &= 3\overline{C}_f \left(1 - 0.75f^{-3/2} - 14f^{-3}\right) = 0 \\ &\Leftrightarrow \quad 0.75f^{-3/2} + 14f^{-3} = 1 \end{aligned}$$

From which we determine that $f_{opt} \approx 2.58$. A minimum fineness ratio of 2.6–3.5 for such bodies is well supported by experimental data and explains why fuselages of transport aircraft typically feature this fineness ratio for the aft end. A number of the previously mentioned form factors are plotted in Figure 16-47.

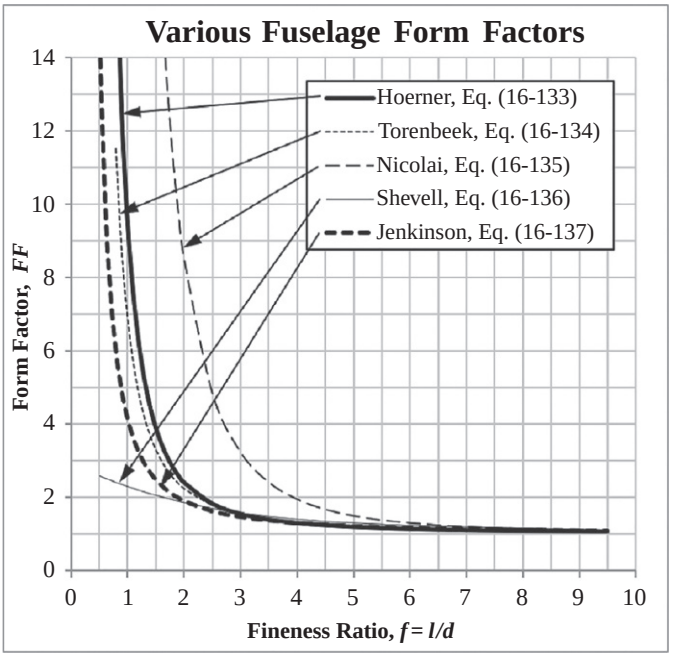


FIGURE 16-47 Comparison of various FFs.

Form Factor for Nacelle and Smooth External Store

Raymer [79] suggest the following form factors for nacelles:

$$FF = 1 + 0.35f^{-1} \tag{16-140}$$

Jenkinson [80] recommends simply using the constant $FF \cdot IF = 1.2$ for wing mounted nacelles and $FF \cdot IF = 1.44$

EXAMPLE 16-11

Use the *component drag buildup method* (CDBM) to determine the $C_{D_{min}}$ for the SR22 (see Figure 16-48). Note that this task begins here and is supported by multiple smaller examples to follow. The completed $C_{D_{min}}$ is presented in Example 16-22.

Assume:
(1) Flight condition at S-L and 185 KTAS.
(2) Wing sustains laminar flow as detailed in Example 16-6.
(3) HT sustains 50% laminar flow on lower and upper surfaces.
(4) VT sustains 50% laminar flow on left and right surfaces.
(5) Fuselage sustains 5% laminar flow, cut short due to engine cowling assembly.
(6) Wetted area booster coefficient of 1.07 for wing and 1.05 for HT and VT.
(7) Max thickness for wing, HT, and VT is at 50% of the chord for all.
(8) $t/c = 0.15$ for wing, 0.1 for HT and VT, and $4.17/22.42 = 0.186$ for the fuselage.
(9) Skin roughness value from Table 16-2.
(10) Assume the max thickness lines for the wing, HT, and VT is 0°, 5°, and 18°, respectively.
(11) $C_{D_{misc}}$ is 74.4 dragcounts (see Example 16-22).
(12) k_{crud} is 25% of the sum of the above (×1.25).

SOLUTION:

The solution to this problem is extensive due to the number of components involved. Luckily, many of the calculations are similar and, thus, conveniently implemented in a spreadsheet (see Figures 16-49 through 16-51). Each row is numbered for convenience and sample calculations provided below for selected rows. The spreadsheet allows geometry for other aircraft to be

[7] Depending on its "pudginess."

EXAMPLE 16-11 (*cont'd*)

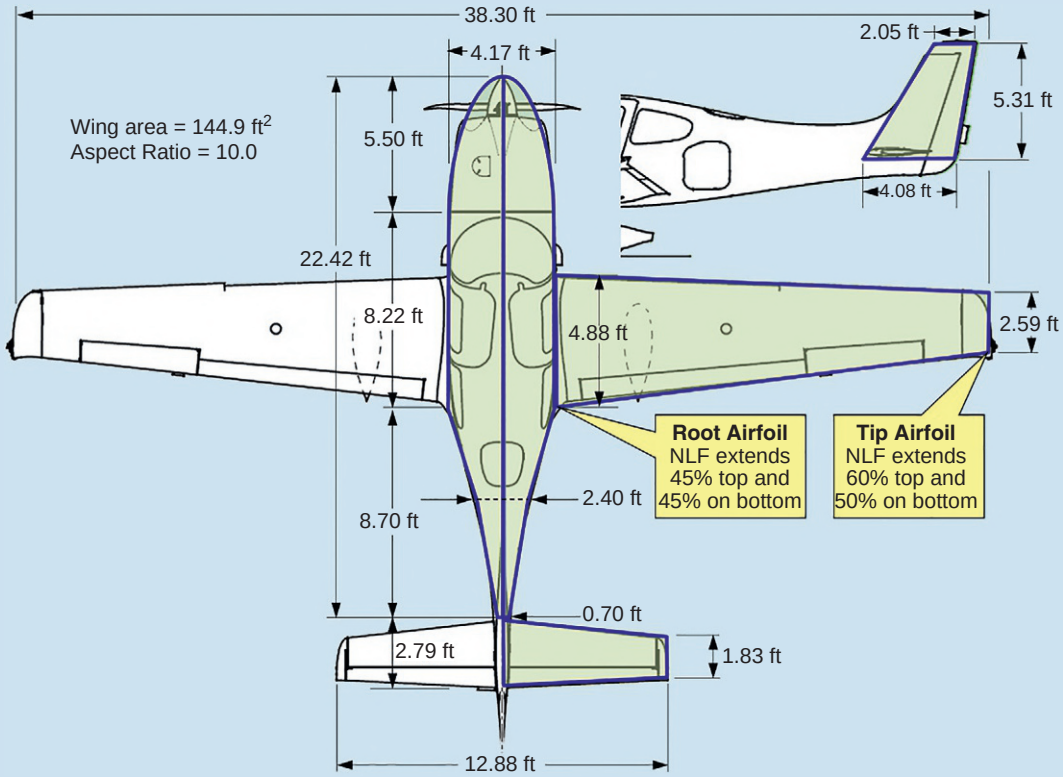


FIGURE 16-48 Geometry of the example aircraft showing the approximation of its wetted area. Note that for clarity some dimensions have been rounded off to two decimals. Copyright 2021 Cirrus Aircraft or its Affiliates. All Rights Reserved. Image reproduced with the permission of Cirrus.

FLIGHT CONDITION

1	Airspeed	V_∞ =	312.3	ft/s	User entry
2	Viscosity of air	μ =	3.745E-07	$lb_f \cdot s/ft^2$	Formula
3	Altitude	H =	0		
4	Density of air	ρ =	0.002378	$slugs/ft^3$	
5	Dynamic pressure	q =	115.95	lb_f/ft^2	

			WING	HT	VT	FUSELAGE	
6	Chord, root	c_r =	4.875	2.792	4.083	22.42	ft
7	Chord, tip	c_t =	2.585	1.834	2.050	22.42	ft
8	Exposed halfspan	$b/2$ =	17.07	6.442	5.313	2.083	ft
9	Exposed planform area	S_i =	127.30	29.79	16.29		ft^2
10	Reference area	S =	144.9				ft^2
11	Reference wing span	b =	38.30				ft
12	Aspect Ratio	$AR = b^2/S$ =	10.12				
13	Wetted area booster	k_b =	1.07	1.05	1.05		
14	Wetted area	$S_{wet\,j} = 2 \cdot S_i \cdot k_b$ =	272.4	62.6	34.2	257.6	ft^2
15	Location of max t	$(x/c)_{max}$ =	0.50	0.50	0.50	0.43	
16	Thickness-to-chord ratio	t/c =	0.150	0.100	0.100	0.186	
17	Skin roughness value	k =	1.7E-06	1.7E-06	1.7E-06	1.7E-06	

FIGURE 16-49 Geometric information of the example aircraft.

EXAMPLE 16-11 (*cont'd*)

	ROOT CHORD					
18	Upper surface transition	$x_{tr\ upper}$ =	0.45	0.50	0.30	0.05
19	Lower surface transition	$x_{tr\ lower}$ =	0.45	0.50	0.30	0.05
20	Reynolds Number based on c_r	Re_{Cr} =	9.668E+06	5.536E+06	8.098E+06	4.446E+07
21	Cutoff Reynolds Number	$Re_{cutoffroot}$ =	2.410E+08	1.340E+08	1.999E+08	1.202E+09
22	Analysis Reynolds Number	Re_{root} =	9.668E+06	5.536E+06	8.098E+06	4.446E+07
23	Upper surface fictitious trans	$x_{0\ upper}$ =	0.05380	0.07082	0.04463	0.00769
24	Upper surface skin friction	$C_{f\ upper}$ =	0.001981	0.002117	0.002427	0.002112
25	Lower surface fictitious trans	$x_{0\ lower}$ =	0.05380	0.07082	0.04463	0.00769
26	Lower surface skin friction	$C_{f\ lower}$ =	0.001981	0.002117	0.002427	0.002112
27	Average root skin friction	$C_{f\ avg}$ =	**0.001981**	**0.002117**	**0.002427**	**0.002112**

	TIP CHORD					
28	Upper surface transition	$x_{tr\ upper}$ =	0.60	0.50	0.30	0.05
29	Lower surface transition	$x_{tr\ lower}$ =	0.50	0.50	0.30	0.05
30	Reynolds Number based on c_t	Re_{Ct} =	5.126E+06	3.636E+06	4.065E+06	4.446E+07
31	Cutoff Reynolds Number	$Re_{cutoff\ tip}$ =	2.410E+08	1.340E+08	1.999E+08	1.202E+09
32	Analysis Reynolds Number	Re_{tip} =	5.126E+06	3.636E+06	4.065E+06	4.446E+07
33	Upper surface fictitious trans	$x_{0\ upper}$ =	0.08169	0.08292	0.05779	0.00769
34	Upper surface skin friction	$C_{f\ upper}$ =	0.001877	0.002342	0.002825	0.002112
35	Lower surface fictitious trans	$x_{0\ lower}$ =	0.07290	0.08292	0.05779	0.00769
36	Lower surface skin friction	$C_{f\ lower}$ =	0.002156	0.002342	0.002825	0.002112
37	Average tip skin friction	$C_{f\ avg}$ =	**0.002017**	**0.002342**	**0.002825**	**0.002112**
38	Average skin friction for panel	$C_{f\ avg\ panel}$ =	**0.001999**	**0.002230**	**0.002626**	**0.002112**

FIGURE 16-50 Calculated skin friction coefficients.

	DRAG ANALYSIS					
			Wing	HT	VT	Fuselage
39	**Sweep angle**	$\Lambda_{t\ max}$ =	**0.00**	**5.00**	**18.00**	°
40	**Form Factor**	FF_j =	**1.311**	**1.203**	**1.187**	**1.399**
41	**Intereference Factor, IF**	IF_j =	**1**	**1.05**	**1.05**	**1**
42	**Weighted drag factor**	$C_{fj} \cdot FF_j \cdot IF_j \cdot S_{wet\ j}$ =	**0.7140**	**0.1762**	**0.1120**	**0.7607**
43	**Skin friction drag**	$(1/S)\Sigma C_{fj} \cdot FF_j \cdot IF_j \cdot S_{wet\ j}$ =	**0.01217**			

FIGURE 16-51 Minimum drag analysis. See discussion about Line 43 in the text.

entered for analysis. Note that green colored cells are intended for user entry and blue cells contain formulas.

Begin by considering Figure 16-49, which shows cells with the given information (green cells) and five rows which show some calculation results (blue cells). Note the setup of the columns dedicated to the inboard and outboard wing elements, as well as the HT and VT.

Line 1: Airspeed is 185 KTAS × 1.688 ft/s = 312.3 ft/s.

Line 2: Viscosity of air:

$$\mu = 3.170 \times 10^{-11} T^{1.5} \left(\frac{734.7}{T + 216} \right)$$
$$= 3.170 \times 10^{-11} (518.67)^{1.5} \left(\frac{734.7}{518.67 + 216} \right)$$
$$= 3.745 \times 10^{-7}\ \text{lb}_\text{f}\text{s/ft}^2$$

Line 4: Density of air: $\rho = 0.002378 (1 - 0.0000068756h)^{4.2561} = 0.002378$ slugs/ft^3

Line 5: Dynamic pressure:

$$q = \tfrac{1}{2}\rho V^2 = \tfrac{1}{2}(0.002378)(312.3)^2 = 115.95\ \text{lb}_\text{f}/\text{ft}^3$$

EXAMPLE 16-11 (*cont'd*)

Lines 6–8, 10–13, and 16–17: Geometric data are obtained from Figure 16-48 and other data are entered based on the problem statement. Note that the exposed half-span (and planform area) excludes the area of the surface that is inside the fuselage. Here it will be assumed that, of the components shown, only a part of the wing is inside the fuselage and this is reflected as the exposed half-span and planform area.

Line 9: Exposed planform area.

Wing:	$S_W = (38.30 - 4.17)((4.875 + 2.585)/2) = 127.3\ \text{ft}^2$
HT:	$S_{HT} = \frac{1}{2}(2.792 + 1.834) \times 12.88 = 29.79\ \text{ft}^2$
VT:	$S_{VT} = \frac{1}{2}(4.083 + 2.050) \times 5.313 = 16.29\ \text{ft}^2$
Fuselage:	A different method is used to determine its wetted area.

Line 14: Total wetted area of all components (exposed wing, HT, VT, and fuselage):

Wing wetted area:	$S_{wet_W} = 1.07 \times 2 \times S_W = 272.4\ \text{ft}^2$
HT wetted area:	$S_{HT_{wet}} = 1.05 \times 2 \times S_{HT} = 62.6\ \text{ft}^2$
VT wetted area:	$S_{VT_{wet}} = 1.05 \times 2 \times S_{VT} = 34.2\ \text{ft}^2$

The total wetted area of the fuselage is estimated using the method of Section 12.4.3, *Surface Areas and Volumes of a Typical Tubular Fuselage*, and the fuselage geometry of Figure 16-48, using Equation (12-13), repeated here for convenience:

$$S_{fuse} = \pi D \left[\frac{(D^2 + 16L_1^2)^{3/2} - D^3}{96L_1^2} + L_2 + \frac{\sqrt{D^2 + 4L_3^2}}{4} \right]$$

Where: D = Maximum fuselage diameter = 4.17 ft

L_1 = Length of nose section = 5.50 ft
L_2 = Length of center section = 8.22 ft
L_3 = Length of tail section = 8.70 ft

Plugging and chugging those numbers into this equation yields 217 ft^2. However, the author's own approximation, which accounts for more details in the fuselage and spinner geometry, returned the following value:

$$\text{Fuselage wetted area}: \quad S_{FUSE} = 257.6\ \text{ft}^2$$

Note that it would be prudent to subtract the cross-sectional area of the wing on the left and right sides, where it enters the fuselage, but in the interest of simplicity it is left out of these calculations. To calculate this cross-sectional area, the reader can use the approximation of Section 9.2.6, *Wing Volume Approximation*. Now, let's consider Figure 16-50, which shows the skin friction analysis for the root and tip chords.

Lines 18–19 and 28–29: Data entered are based on the problem statement.

Line 20: Reynolds number for the root chord (using the wing column as an example).

$$\text{Re}_{root} = \frac{\rho V L}{\mu} = \frac{(0.002378)(312.3)(4.875)}{3.745 \times 10^{-7}} = 9{,}667{,}562$$

Lines 21–22 and 30–31: Here, the calculations for Lines 21–22 are used (see Figure 16-50). The cutoff Reynolds number for the root chord (again using the wing column as an example) using Equation (16-31).

$$R_{e_{cutoff}} = 38.21\left(\frac{c_r}{\kappa}\right)^{1.053} = 38.21\left(\frac{4.875}{1.7 \times 10^{-6}}\right)^{1.053} = 240{,}963{,}686$$

Since the R_e based on c_r is less than this value, it will be used throughout the remainder of these calculations. If the opposite had been the case, then the cutoff R_e would been used.

Line 23–27 and 33–38: Steps 4 through 14 of Example 16-6 detail how the values for the wing column were obtained. All the values in the other three columns are calculated in an identical fashion, yielding the table shown in Line 42. Finally, consider Figure 16-51 which shows how the minimum drag coefficient is calculated.

Line 39: Thickness sweep angles for the wing, HT, and VT are given in the problem statement as 0°, 5°, and 18°, respectively.

Line 40: The Form factor for the wing, HT, and VT is calculated using Equation (16-127) and Equation (16-135) for the fuselage. Note that 185 KTAS at sea level corresponds to $M_\infty \approx 0.28$.

Wing *FF*:

$$FF = \left[1 + \frac{0.6}{(x/c)_{\max}}\left(\frac{t}{c}\right) + 100\left(\frac{t}{c}\right)^4\right]\left[1.34M^{0.18}(\cos\Lambda_{t\max})^{0.28}\right]$$
$$= \left[1 + \frac{0.6}{0.50}(0.15) + 100(0.15)^4\right]\left[1.34(0.28)^{0.18}(\cos 0°)^{0.28}\right]$$
$$= 1.311$$

HT *FF*:

$$FF = \left[1 + \frac{0.6}{0.50}(0.10) + 100(0.10)^4\right]\left[1.34(0.28)^{0.18}(\cos 5°)^{0.28}\right]$$
$$= 1.203$$

VT *FF*:

$$FF = \left[1 + \frac{0.6}{0.50}(0.10) + 100(0.10)^4\right]\left[1.34(0.1513)^{0.18}(\cos 18°)^{0.28}\right]$$
$$= 1.187$$

Fuselage: $FF = \left[1 + \frac{60}{f^3} + \frac{f}{400}\right] = \left[1 + \frac{60}{5.376^3} + \frac{5.376}{400}\right] = 1.399$

EXAMPLE 16-11 (*cont'd*)

Where f is the fineness ratio, calculated from $f = l/d = 22.42/4.17 = 5.376$.

Line 41: Interference factors are selected from Table 16-12.

Line 42: Weighted drag factor calculated as shown in table. For instance, for the wing, we get

$$C_{f_j} \cdot FF_j \cdot IF_j \cdot S_{wet_j} = 0.001999 \times 1.311 \times 1 \times 272.4 = 0.7140$$

Line 43: Skin friction drag is calculated by summing up the cells in Line 42 and dividing by the reference area of 144.9 ft^2. The resulting total skin friction coefficient, which includes interference and form drag is:

$$\frac{1}{S}\sum_{j=1}^{N} C_{f_j} \times FF_j \times IF_j \times S_{wet_j}$$

$$= \frac{1}{144.9}(0.7140 + 0.1762 + 0.1120 + 0.7607) = 0.01217$$

This only partially completes the drag analysis—drag due to miscellaneous sources remains to be determined and added to the above value, in addition to other corrections that must be made. This will be done in the next section.

TABLE 16-12 Typical interference factors.

Component	*IF*
Nacelle or external store, directly under a fuselage.	1.5
Nacelle or external store, under a fuselage, less than about 1 diameter away.	1.3
Nacelle or external store, under a fuselage, more than about 1 diameter away.	1.0
Object, such as a fuel tank, mounted to a wingtip.	1.25
High wing or mid wing with carefully designed fairing	1.0
Unfilleted low wing	1.1–1.4
Whitcomb winglet	1.04
"Airbus" style winglet	1.04
Modern blended winglet	1.00–1.01
Aerodynamic or square leaf-spring main landing gear strut entering wing or fuselage	1.10
Aerodynamic wing strut entering wing on one end and fuselage on the other	1.10
Boundary layer diverter	~1.0
Conventional tail	1.04–1.05
Cruciform tail	1.06
V-tail	1.03
H-tail (B-25 Mitchell or A-10 Warthog style)	1.08
H-tail (Lockheed Model 10 Electra style)	1.13
H-tail (Beech D-18 style)	1.06
Triple-tail (Lockheed Constellation style)	1.10
T-tail	1.04

In part based on S.F. Hoerner, Fluid-Dynamic Drag, L. Hoerner, 1965; D. Raymer, Aircraft Design: A Conceptual Approach, fourth ed., AIAA Education Series, 2006.

for nacelles mounted on the rear of the airplane (a Sud-Est Caravelle configuration).

16.3.7 Interference Factors

As previously stated, *interference factors* (*IF*) account for the proximity of one component to another. For instance, consider the juncture between the wing and fuselage, which constrains the airflow compared to that of the individual components. This increases the local airspeeds, increasing the drag. However, the *IFs* do not account for additional drag that arises due to early separation in poorly designed wing/fuselage junctures.

Table 16-12 lists typical *IF*s, partially derived from Refs. [33, 79] and partially using factors that have worked well in drag analyses performed by the author. No claim is made about their accuracy beyond that. Note that when using the factors for multiple objects, e.g., the triple-tail of the L-1049 Constellation, the presented *IF* must be applied to all surfaces. Thus, when using the CDBM, each of the four surfaces constituting the tail (one HT and three VTs) must be multiplied by $IF = 1.10$. The following formulation illustrates how its contribution would be accounted for in the CDBM:

$$\sum_{i=1}^{N} \overline{C}_{f_i} \times FF_i \times S_{wet_i} \times IF_i = \ldots + \overbrace{\overline{C}_{f_{HT}} \times FF_{HT} \times S_{wet_{HT}} \times IF_{HT}}^{\text{HT}}$$

$$+ \overbrace{\overline{C}_{f_{VT_1}} \times FF_{VT_1} \times S_{wet_{VT_1}} \times IF_{VT_1}}^{\text{VT 1 of 3}} + \underbrace{\overline{C}_{f_{VT_2}} \times FF_{VT_2} \times S_{wet_{VT_2}} \times IF_{VT_2}}_{\text{VT 2 of 3}}$$

$$+ \underbrace{\overline{C}_{f_{VT_3}} \times FF_{VT_3} \times S_{wet_{VT_2}} \times IF_{VT_3}}_{\text{VT 3 of 3}} + \ldots$$

For this application, we would use

$$IF_{HT} = IF_{VT1} = IF_{VT2} = IF_{VT3} = 1.10.$$

16.3.8 Cumulative Result of Undesirable Drag (CRUD)

The above title is a play on words. The word crud means dirt, filth, or refuse. In aircraft design, it stands for the undesirable drag caused by exhaust stacks, misaligned sheet-metal panels, antennas, small inlets and outlets, sanded walkways, and so on. These contributions are easily overlooked when performing drag analysis, primarily because they appear small. But they add up. The aspiring designer should be aware of this additional drag and account for it appropriately. This section introduces how this is typically done. The crud factor is typically 25%, which means that Equations (16-117) and (16-122) are multiplied by $k_{crud} = 1.25$.

It is strongly recommended that the designer estimates the $C_{D_{\min}}$ of similar aircraft and compares to $C_{D_{\min}}$ extracted from published (or otherwise reliable) sources. This information should be used to evaluate an aircraft specific k_{crud}. This can be accomplished using some of the methods presented in Section 16.5, *Special Topics Involving Drag*.

16.3.9 Total Drag Coefficient: C_D

Once the drag contributions developed in this section have been estimated, the total drag coefficient at any flight condition is determined as follows:

$$C_D = C_{D_{\min}} + C_{D_i} + C_{D_w} \tag{16-141}$$

16.4 MISCELLANEOUS OR ADDITIVE DRAG

This section presents methods for evaluating drag caused by components that are not conveniently analyzed using the *component drag buildup method* (CDBM), discussed in Section 16.3.5. This includes methods to estimate the drag of landing gear, antennas, sharp corners, joints, fasteners, inlets, outlets, fairings, and various other protuberances generally found on aircraft. This drag, justifiably called *miscellaneous* or *additive drag*, can cause substantial increase in total drag. As shown in Equation (16-117) or (16-122), it is denoted by $C_{D_{misc}}$, and is given by

$$C_{D_{misc}} = \Delta C_{D_1} + \Delta C_{D_2} + \cdots + \Delta C_{D_N} \tag{16-142}$$

Where the terms ΔC_{D_1}, ΔC_{D_2}, … represent contributions by all known components (sources) that were not accounted for using the CDBM. These contributions comprise many disparate sources, many of which use reference areas other than the reference wing area, S. Thus, each ΔC_{D_i} has undergone adjustments to prepare its use with the reference wing area, S. How this is accomplished is shown in the derivation of Equation (16-144).

The geometric shape of protrusions common to aircraft is inherently irregular. For instance, consider the dissimilar geometry of antennas, blisters, or the main landing gear typical of ordinary aircraft. All lack consistent dimensions like those shared by lifting surfaces (e.g., span, root and tip chord). And most are geometrically complex enough to require drag estimation rooted in empirical formulation. Their drag is based on parameters like the thickness-to-length ratio (or fineness ratio), the location of the maximum thickness, frontal area, lengthwise distribution of thickness, leading-edge radius, trailing-edge angle, and camber, to name a few.

The first step in miscellaneous drag analysis is to evaluate each contribution independently. Each contribution is called a *source*. Descriptive subscripts add clarity when treating each source. It provides clarity to call the drag coefficient of an antenna $\Delta C_{D_{antenna}}$ than, say, ΔC_{D_7}. This naming convention is adopted here.

The next step is to establish a general method to handle reference areas for drag coefficients. Consider a source of interest whose drag force of magnitude D_S (where the subscript stands for *source*) was measured in a wind tunnel at dynamic pressure q. Furthermore, assume that D_S references some area, S_S, specific to the component (e.g., frontal area). This measurement can be converted into a drag coefficient, ΔC_{D_S}, based on S_S, as follows

$$D_S = qS_S\Delta C_{D_S} \quad \Rightarrow \quad \Delta C_{D_S} = \frac{D_S}{qS_S} \tag{16-143}$$

As stated above, we prefer to use this coefficient in terms of the reference wing area, S. This calls for a scaling procedure. To guarantee we get the same drag regardless of using ΔC_{D_S} or ΔC_D, the product $S \cdot \Delta C_{D_S}$ must equal $S \cdot \Delta C_D$. Assuming, the source is the above antenna, the drag coefficient based on S is

$$S\Delta C_{D_{antenna}} = S_S\Delta C_{D_S} \quad \Rightarrow \quad \Delta C_{D_{antenna}} = \Delta C_{D_S}\left(\frac{S_S}{S}\right) \tag{16-144}$$

Thus, ΔC_{D_S} refers to S_S, while $\Delta C_{D_{antenna}}$ (which is used with $C_{D_{misc}}$) refers to the reference wing area, S.

16.4.1 Trim Drag

Trim drag is the penalty paid for providing static stability. It is caused by (A) The difference in lift-induced drag of the airplane with and without balancing forces and (B) the increase in drag due to the deflection of the elevator (see Section 16.2.6, *Additional Topics on Drag*). Note that this drag is NOT added to $C_{D_{misc}}$. Rather, like $C_{D_{min}}$, it is added directly to the sum constituting total drag (see Figure 16-21).

(1) Drag Contribution of Elevator Deflection

It is denoted by $\Delta C_{D_{\delta_e}}$. Its value typically ranges from 0.0003 to 0.0007 per degree of elevator deflection (see Table 24-3). The total contribution depends on the elevator deflection to trim, δ_e. Note that this derivative *only* constitutes the change in drag of the surface and not the contribution of its lift to the trim drag. This is treated next.

(2) Drag Contribution of a Simple Wing-HT-Thrust Combination

If it were possible to sustain steady-level flight without a balancing force, there would be no trim drag. However, this is not an option. Instead, the balancing force of a conventional, statically stable tail-aft aircraft is added to the weight. This means the total lift generated exceeds the weight alone. Therefore, the aircraft must operate at a higher AOA and, thus, higher lift-induced drag than otherwise. Ordinarily, in cruise, trim drag constitutes a small fraction of the total drag of the airplane; it should range from 1% to 2%. It increases at higher AOAs. During conceptual design, it is practical to estimate the trim drag using the simple formulation presented below. This methodology can be revised for more complex situations.

Consider the simple wing–HT system operating at a low AOA, as shown in Figure 16-52. For this system, the trim drag is given by[8]:

$$\Delta C_{D_{trim}} = B\left(h_{HT_{CG}} A - \boldsymbol{C_{M_W}} + \boldsymbol{C_{M_{0_T}}}\right)^2 - kA^2 + \Delta C_{D_{\delta_e}} \cdot \delta_e \tag{16-145}$$

Where: $A = \dfrac{W}{qS}$ $\qquad B = \dfrac{k}{\left(h_{HT_{CG}} + h_{cg} - h_n\right)^2}$ (16-146)

and

W = Weight at condition,
$l_{HT_{CG}}$ = Tail arm (see Figure 16-52),
C_{LW} = Wing lift coefficient,
$\boldsymbol{C_{M_W}}$ = Wing pitching moment coefficient,
h_{cg} = Fractional distance between LE of c_{MGC} and the CG,
h_n = Fractional distance between LE of c_{MGC} and the AC,
$h_{HT_{CG}}$ = Fractional tail arm (see Figure 16-52),
$\boldsymbol{C_{M_{0T}}}$ = Pitching moment due to thrust.

Other variables have already been defined in multiple places. Also see relations in the derivation of the equations.

DERIVATION OF EQUATIONS (16-145) AND (16-146)

Referring to Figure 16-52, statics requires the following to hold in steady level flight (nose-up rotation is positive):

$$\sum F_z = 0; \qquad L_W + L_{HT} - W = 0$$

$$\sum M_{CG} = 0; \qquad (x_{cg} - x_n)L_W - l_{HT_{CG}} L_{HT} + M_W - z_T T = 0$$

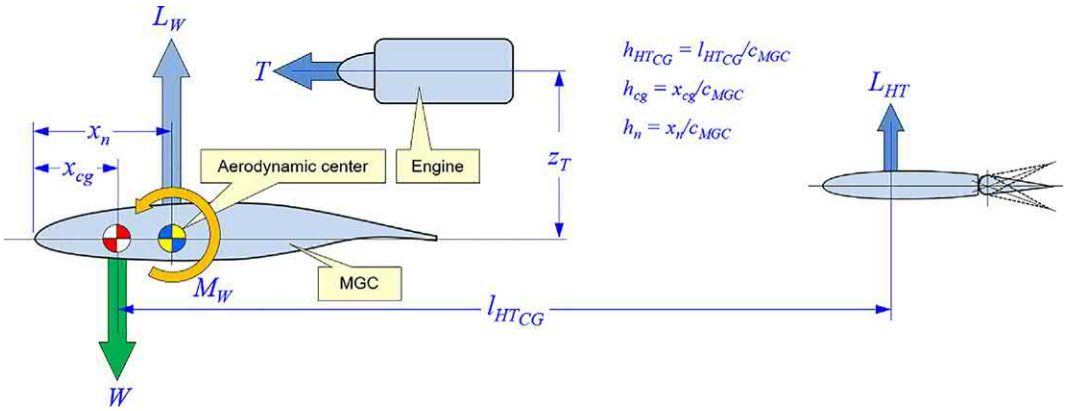


FIGURE 16-52 A simple free-body diagram used to derive the simplest formulation of trim drag.

[8] Note that this expression has been improved over that of the first edition of this book.

Note that M_W is a negative (nose-down) value. Next, divide through by qSc_{MGC} to convert the moment equation to coefficient form and noting the fractional distances of Chapter 24, $h_{cg}=x_{cg}/c_{MGC}$, $h_n=x_n/c_{MGC}$, and $h_{HT_{CG}}=l_{HT_{CG}}/c_{MGC}$, we get

$$(h_{cg}-h_n)C_{L_W}-h_{HT_{CG}}C_{L_{HT}}+\boldsymbol{C_{M_W}}-z_T\frac{T}{qSc_{MGC}}=0$$

Then, replace the thrust contribution by $\boldsymbol{C_{M_{0T}}}$, per Equation (24-109) and solve for the balancing force the HT must generate (in a coefficient form). Note that z_T is positive if the thrustline is above the CG and otherwise negative.

$$C_{L_{HT}}=\frac{(h_{cg}-h_n)C_{L_W}+\boldsymbol{C_{M_W}}-\boldsymbol{C_{M_{0_T}}}}{h_{HT_{CG}}} \qquad \text{(i)}$$

Convert the force equation into coefficient form by dividing through by qS and substitute Equation (i) into the force equation to get:

$$C_{L_W}+C_{L_{HT}}-\frac{W}{qS}=0 \;\Rightarrow\; C_{L_W}=\frac{h_{HT_{CG}}W/(qS)-\boldsymbol{C_{M_W}}+\boldsymbol{C_{M_{0_T}}}}{h_{HT_{CG}}+h_{cg}-h_n} \qquad \text{(ii)}$$

The trim drag is the difference between the lift coefficient with and without stabilizing moments. Thus, we write

$$\begin{aligned}\Delta C_{D_{trim}}&=(C_{D_i})_{\text{stab}}-(C_{D_i})_{\text{no stab}}+\Delta C_{D_{\delta_e}}\cdot\delta_e\\&=k\left(C_{L_W}^2-\left(\frac{W}{qS}\right)^2\right)+\Delta C_{D_{\delta_e}}\cdot\delta_e\end{aligned} \qquad \text{(iii)}$$

Substituting Equation (ii) into Equation (iii), followed by some algebraic manipulations, leads to

$$\Delta C_{D_{trim}}=k\left(\frac{1}{(h_{HT_{CG}}+h_{cg}-h_n)^2}\left(h_{HT_{CG}}\frac{W}{qS}-\boldsymbol{C_{M_W}}+\boldsymbol{C_{M_{0_T}}}\right)^2-\left(\frac{W}{qS}\right)^2\right)+\Delta C_{D_{\delta_e}}\cdot\delta_e \qquad \text{(iv)}$$

Next let $A=\dfrac{W}{qS}$ $\qquad B=\dfrac{k}{(h_{HT_{CG}}+h_{cg}-h_n)^2}$

These constitute Equation (16-146). Substitute Equation (ii) into Equation (iii), using A as defined above.

$$\Delta C_{D_{trim}}=B\left(h_{HT_{CG}}A-\boldsymbol{C_{M_W}}+\boldsymbol{C_{M_{0_T}}}\right)^2-kA^2+\Delta C_{D_{\delta_e}}\cdot\delta_e$$

This is Equation (16-145).

EXAMPLE 16-12

Estimate the trim drag coefficient and drag force for an SR22 cruising at 185 KTAS at S-L, assuming the following parameters:

EXAMPLE 16-12 (*cont'd*)

$W=3400$ lb$_f$	$S=144.9$ ft^2	$T=450$ lb$_f$
$k=0.04207$	$\boldsymbol{C_{M_W}}=-0.060$	$\Delta C_{D_{\delta_e}}\cdot\delta_e=0$
$l_{HT_{CG}}=14.06$ ft	$z_T=0.6$ ft	$c_{MGC}=3.783$ ft
$h_{cg}=0.25$	$h_n=0.40$	$h_{HT_{CG}}=3.717$

SOLUTION:

Dynamic pressure:

$$q=\tfrac{1}{2}\rho V^2=\tfrac{1}{2}(0.002378)(185\times1.688)^2=115.9\ \text{lb}_f/\text{ft}^2$$

Pitching moment due to thrust:

$$\boldsymbol{C_{M_{0_T}}}=z_T\frac{T}{qSc_{MGC}}=(0.6)\frac{450}{(115.9)(144.9)(3.783)}=0.004248$$

Constant A: $\quad A=\frac{W}{qS}=\frac{3400}{(115.9)(144.9)}=0.2024$

Constant B:

$$B=\frac{k}{\left(h_{HT_{CG}}+h_{cg}-h_n\right)^2}=\frac{0.04207}{(3.717+0.25-0.40)^2}=0.003307$$

Therefore, the trim drag amounts to

$$\begin{aligned}\Delta C_{D_{trim}}&=B\left(h_{HT_{CG}}A-\boldsymbol{C_{M_W}}+\boldsymbol{C_{M_{0_T}}}\right)^2-kA^2+\Delta C_{D_{\delta_e}}\cdot\delta_e\\&=(0.003307)((3.717)(0.2024)-0.06+0.004248)^2\\&\quad-(0.04207)(0.2024)^2+(0)\\&=0.0004812\end{aligned}$$

Thus, the trim drag force amounts to

$$D_{trim}=qS\Delta C_{D_{trim}}=(115.9)(144.9)(0.0004812)=8.1\ \text{lb}_f$$

16.4.2 Cooling Drag

The term *cooling drag* refers to drag associated with cooling the engine of a propeller driven aircraft. Its determination is not needed for jet engines; it is accounted for in their net thrust (which equals gross thrust minus engine drag). The aircraft designer must still account for nacelle/pylon drag (using the CDBM). See more about jet engine drag in Refs. [83, 84].

The overarching concern of cooling drag involves the design of the nacelle. It is a major contributor to wing drag (especially in climb) and cooling drag. The former is evaluated using the CDBM, the latter is treated here. The magnitude of cooling drag depends on external and internal contributions. The designer is urged to review the design guidelines of Section 7.2.7, *Piston Engine Inlet and Exit Sizing*, in particular of Refs. [85–90]. These provide excellent guidance for the inlet and exit design to help reduce cooling drag.

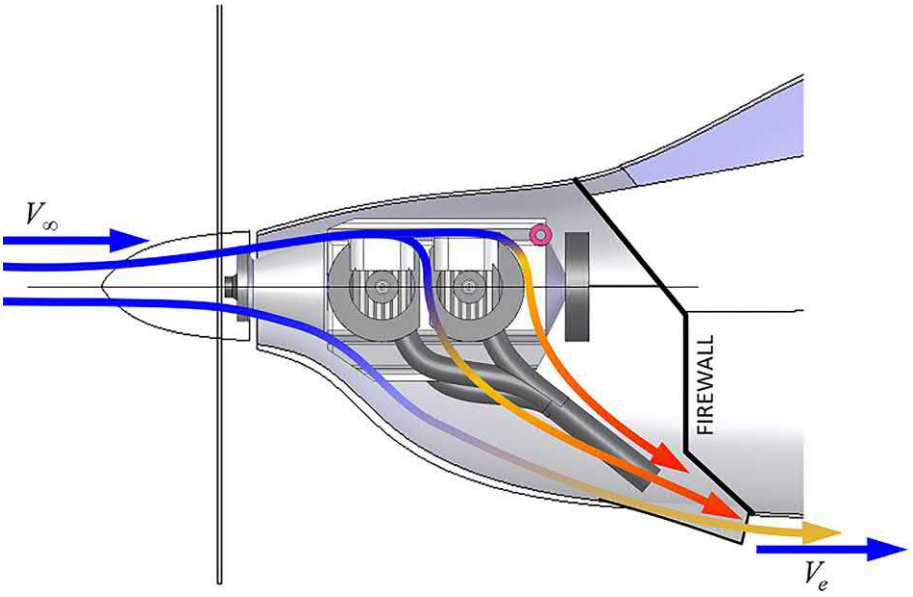


FIGURE 16-53 Idealization of a conventional engine installation.

The operation of powered aircraft affects drag through heat transfer. This exposes heat exchangers to the free stream airflow. The cylinder head fins of a piston engine and radiators for oil-cooling (and water-cooling if present) constitute a heat exchanger. The flow entering the heat exchanger has a total head of which some is lost as the air flows through it. This causes a drop in the total pressure of the flow and reduces its energy. Some of this energy loss is made up by adding heat to the flow. However, if the heat energy added is less than the energy lost due to the pressure drop, the flow's momentum flux is reduced. This reduction is manifested as a drag force and constitutes the *cooling drag*.

Cooling drag is hard to estimate due to the complexity of the flow field inside the engine compartment (see idealization in Figure 16-53). Typically, it is estimated using empirical methods based on testing performed by the engine manufacturer. The following method for estimating cooling drag is an example of such a methodology; here largely based on McCormick [91]. It yields the following expression for the cooling drag coefficient.

$$\Delta C_{D_{cool}} = \frac{\dot{m}(V_\infty - V_e)}{qS} \tag{16-147}$$

Where $\dot{m}$ is the mass flow rate through the engine compartment, V_∞ is the far-field airspeed (represents the inlet airspeed), and V_e is the average airspeed at the exit of the engine cowling.

DERIVATION OF EQUATION (16-147)

This derivation is based, in part, on Ref. [91]. The flow through the engine changes its kinetic energy from E_∞ in the far-field to E_e at the exit. This change in energy can be expressed as the rate of change of work

$$\Delta W = \frac{1}{2}\dot{m}\left(V_\infty^2 - V_e^2\right) \tag{i}$$

Algebraically, this can be rewritten as follows:

$$\Delta W = \frac{1}{2}\dot{m}\left(V_\infty^2 - V_e^2\right) = \dot{m}(V_\infty - V_e)\frac{(V_\infty + V_e)}{2} \tag{ii}$$

Where the term $\dot{m}(V_\infty - V_e)$ is the momentum flux (force) associated with the change in energy. Calling this force D_{cool}, we write

$$\Delta W = \overbrace{\dot{m}(V_\infty - V_e)}^{\equiv D_{cool}}\frac{(V_\infty + V_e)}{2} = D_{cool}\frac{(V_\infty + V_e)}{2} \tag{iii}$$

In order to convert D_{cool} to an additive drag coefficient, we write:

$$D_{cool} = qS\Delta C_{D_{cool}} = \dot{m}(V_\infty - V_e) \quad \Rightarrow \quad \Delta C_{D_{cool}} = \frac{\dot{m}(V_\infty - V_e)}{qS} \tag{iv}$$

EXAMPLE 16-13

Estimate the cooling drag and cooling drag coefficient of the airplane of Example 7-5, if its wing area is $S = 144.9\,\text{ft}^2$, far-field airspeed is $V_\infty = 185$ KTAS at 10,000 ft, engine compartment exit airspeed is $V_e = 199.3\,\text{ft/s}$, and flow of cooling air is 2.7 lb_f/s (i.e., $\dot{m} = 0.08392$ slugs/s).

SOLUTION:

The cooling drag is calculated per the momentum conservation. The momentum of air exiting the engine is less than that entering. Thus, per Equation (14-35), where the input values are taken from Example 7-5, we get

$$D_{cool} = -\dot{m}(V_e - V_\infty) = 0.08392((185)(1.688) - 199.3)$$
$$= 9.481\ \text{lb}_\text{f}$$

The cooling drag coefficient is estimated from Equation (16-147), where the dynamic pressure was given (in Example 7-5) as $q = 80.60\ \text{lb}_\text{f}/\text{ft}^2$:

EXAMPLE 16-13 (cont'd)

$$\Delta C_{D_{cool}} = \frac{\dot{m}(V_\infty - V_e)}{qS} = \frac{9.481}{(80.60)(144.9)} = 0.0008118$$

This amounts to about 8.12 dragcounts.

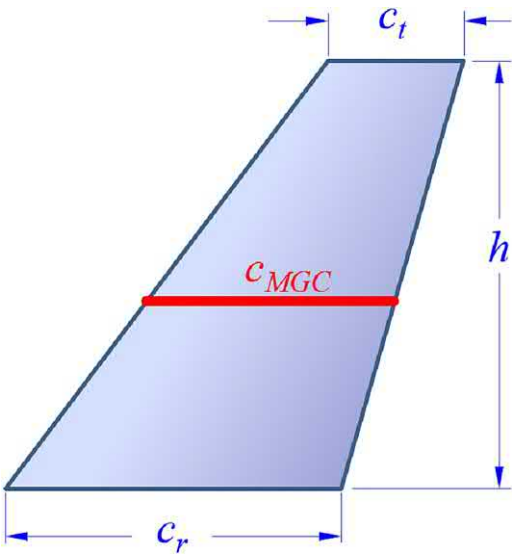


FIGURE 16-54 Geometric definition of a small wing-like surface.

16.4.3 Drag of Simple Wing-like Surfaces

Consider the wing-like surface in Figure 16-54. It represents an aerodynamically shaped antenna, or some other fin, and features a single airfoil. Its drag can be determined by estimating the averaged skin friction coefficient of the c_{MGC} or the average chord of the surface. The additive drag coefficient of this surface, here denoted by $\Delta C_{D_{fin}}$, can be estimated from:

$$\Delta C_{D_{fin}} = \overline{C}_f \left[1 + 2.7(t/c) + 100(t/c)^4\right] \frac{h(c_r + c_t)}{2S} \qquad (16\text{-}148)$$

This additive drag coefficient is based on the reference area, as can be seen in the equation. Here the form factor is based on Equation (16-125).

EXAMPLE 16-14

Determine the additive drag coefficient for a COM antenna for the SR22 airplane, if its root chord is 4.5 in., tip is 2 in., and height is 13.5 in. Assume an averaged skin friction coefficient of 0.0035 and a $t/c = 0.25$.

SOLUTION:

$$\Delta C_{D_{fin}} = \overline{C}_f \left[1 + 2.7(t/c) + 100(t/c)^4\right] \frac{h(c_r + c_t)}{2S}$$
$$= (0.0035)\left[1 + 2.7(0.25) + 100(0.25)^4\right] \cdot \frac{(13.5/12)((4.5+2)/12)}{2(144.9)} = 0.00001520$$

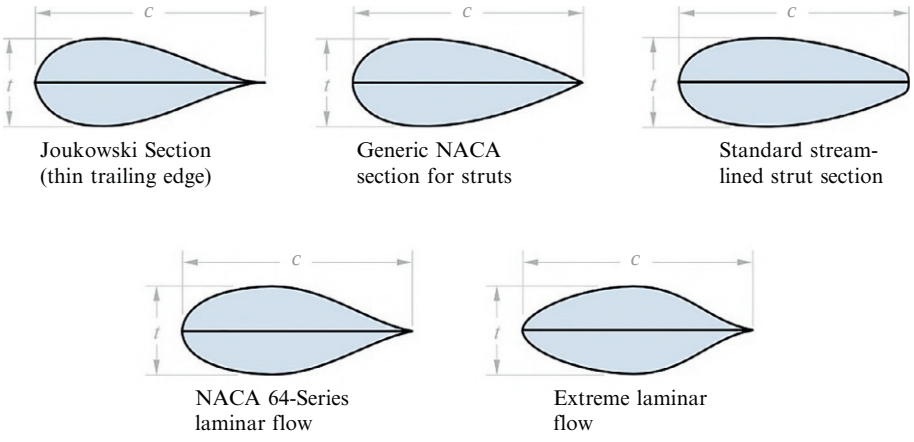
This amounts to about 0.152 dragcounts.

16.4.4 Drag of Streamlined Struts and Landing Gear Pant Fairings

The cross sections in Figure 16-55 are typical of those used for wing struts or to reduce the drag of leaf-spring landing gear legs. Such shapes typically operate in a low R_e region (based on chord, c). The drag of such sections is typically related to their thickness-to-chord ratios (t/c). The additive source drag coefficient for the strut, ΔC_{D_S}, is given by Ref. [33, pp. 6–5] and is based on empirical results:

$$\Delta C_{D_S} = \frac{D_S}{qS_S} = 2\overline{C}_f[1 + (t/c)] + (t/c)^2 \qquad (16\text{-}149)$$

FIGURE 16-55 Selected standard cross sections for wing- and landing gear struts. *Reproduced from S.F. Hoerner, Fluid-Dynamic Drag, L. Hoerner, 1965.*



Where S_S is the planform area of the strut (i.e., its length × chord) and the coefficient "2" accounts for the two sides of the planform. The additive drag coefficient for a strut, $\Delta C_{D_{strut}}$, of length l and chord c in terms of S is thus estimated from:

$$\Delta C_{D_{strut}} = \left[2\overline{C}_f(1 + t/c) + (t/c)^2\right]\left(\frac{l \times c}{S}\right) \qquad (16\text{-}150)$$

EXAMPLE 16-15

Determine the additive drag of a (Cessna-like) wing strut of 5-ft length, 4-in. chord, and $t/c = 0.2$ at 110 KTAS airspeed at S-L. The reference area is 160 ft^2. Assume no interference and $\overline{C}_f = 0.008$.

SOLUTION:

Using Equation (16-150), we get:

$$\Delta C_{D_{strut}} = \left[2\overline{C}_f(1 + t/c) + (t/c)^2\right]\left(\frac{l \times c}{S}\right)$$
$$= \left[2(0.008)(1 + 0.2) + (0.2)^2\right]\left(\frac{5 \times (4/12)}{160}\right)$$
$$= 0.0006167$$

This amounts to about 6.2 dragcounts. Therefore, the resulting drag amounts to:

$$D_{strut} = \frac{1}{2}\rho V^2 S \Delta C_{D_{strut}}$$
$$= \frac{1}{2}(0.002378)(100 \times 1.688)^2(160)(0.0006167)$$
$$= 3.34 \text{ lb}_f$$

This means that each strut (assuming there are two) adds 3.34 lb_f of drag to the total drag.

EXAMPLE 16-16

Determine the additive drag coefficient of a step onto the wing to help occupants enter the cabin of an SR22 aircraft. There are two such entry steps, whose cross section is the *standard streamlined strut section* that are approximately 12 in. long, 3-in. chord and 1-in. thickness. Assume no interference, ignore the break in the step where it changes from a step to a strut and $\overline{C}_f = 0.008$.

SOLUTION:

The t/c is 1/3 or about 0.333. Therefore, using Equation (16-150), we get for each step:

$$\Delta C_{D_{strut}} = \left[2(0.008)(1 + 0.333) + (0.333)^2\right]\left(\frac{(12/12) \times (3/12)}{144.9}\right)$$
$$= 0.0002281$$

This amounts to about 2.28 dragcounts and 4.56 dragcounts for two steps.

Thick Fairings

A fairing is a streamlined structure whose purpose is to reduce the drag that would be caused by the geometry it conceals. Hoerner [33, pp. 6–9] presents the following expression to determine the (2-dimensional) drag of a fairing whose chord is c, height is t, and length is l:

$$\Delta C_{d_{fairing}} = \overline{C}_f\left(4 + \frac{2}{(t/c)} + 120(t/c)^3\right) \qquad (16\text{-}151)$$

The term inside the parenthesis is the form factor. It accounts for pressure and friction (see Figure 16-56). This means that $\Delta C_{D_{strut}}$ for a strut of length l and thickness t (it is based on frontal area) in terms of S can be estimated from:

$$\Delta C_{D_{fairing}} = \overline{C}_f\left(4 + \frac{2}{(t/c)} + 120(t/c)^3\right)\left(\frac{l \times t}{S}\right) \qquad (16\text{-}152)$$

This allows the optimum thickness-to-chord ratio to be determined by determining the derivative, setting it equal to zero, and solve for the optimum t/c, as shown below:

$$FF = \left(4 + \frac{2}{(t/c)} + 120(t/c)^3\right)$$
$$\Rightarrow \quad \frac{dFF}{d(t/c)} = 360(t/c)^2 - \frac{2}{(t/c)^2} = 0$$
$$\Rightarrow \quad (t/c)_{opt} = \sqrt[4]{\frac{1}{180}} = 0.273$$

Therefore, the optimum thickness-to-chord ratio is 0.273. This corresponds to a fineness ratio of ≈3.7.

16.4.5 Drag of Landing Gear

(1) Drag of Tires Only

Figure 16-57 shows several types of aircraft tires, identified as A, B, C, and D. The drag generated by these styles is the focus of Ref. [92]. The drag coefficient of tires is usually based on their frontal area, defined as their diameter, d, times width, w. This is done in Figure 16-57 and Table 16-13. The additive drag coefficient of the tire can be estimated from:

$$\Delta C_{D_{tire}} = \frac{(d \times w)}{S}\Delta C_{D_S} \qquad (16\text{-}153)$$

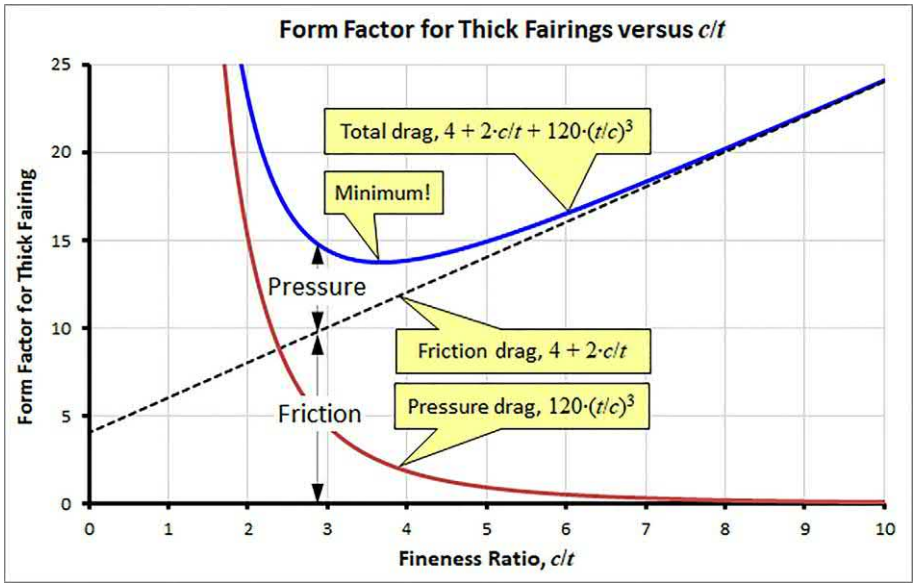


FIGURE 16-56 Form Factor plotted against the fineness ratio for wing- and landing gear struts.

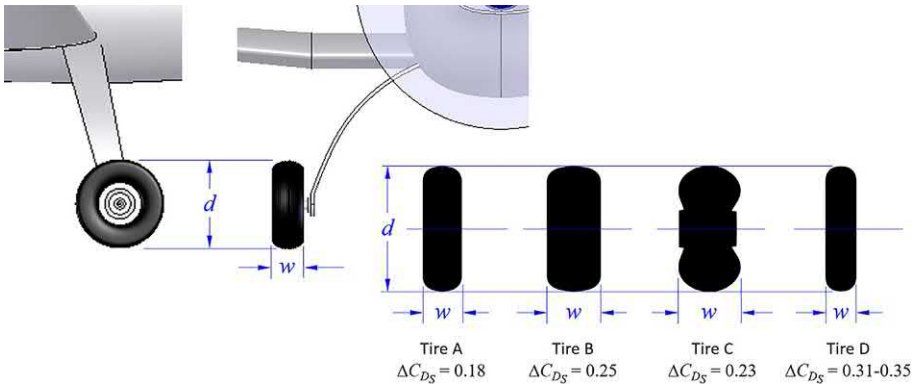


FIGURE 16-57 Most common types of modern tires for aircraft landing gear. *Based on W.H. Herrnstein, D. Biermann, The Drag of Airplane Wheels, Wheel Fairings, and Landing Gears—I, NACA R-485, 1935.*

TABLE 16-13 Drag of tires (d = diameter of tire, w = width of tire).

Tire Type	Corresponds to	Reference Area	ΔC_{D_S}	Reference
A	Three Part Type (GA)	$d \times w$	0.18	NACA R-485
B	Type III	$d \times w$	0.25	
C	Type III High Floatation (tundra)	$d \times w$	0.23	
D	Old fashioned disc wheel types	$d \times w$	0.31-0.35	

(2) Drag of Tires with Wheel Fairings

A wheel fairing reduces the aerodynamic drag of the tire. Figure 16-58 shows several fairing styles and Table 16-14 lists the applicable drag coefficients based on (1) the frontal area of the fairing and (2) the frontal area of the tire. It is left to the reader to select which one to use. While the data are based on a Type III tires, for preliminary design purposes it may be assumed the drag coefficients are independent of the type of tire. The additive drag coefficient of the tire with the fairing can be estimated from:

$$\Delta C_{D_{fairing}} = \frac{(H \times W)}{S} \Delta C_{D_S} \qquad (16\text{-}154)$$

Note that this coefficient is for a single tire with a fairing. This is emphasized because some texts present the drag coefficient for two wheels (e.g., assuming both main landing gear). However, some aircraft feature fairings on the main wheel only, while others have all three wheels (main and nose landing gear) with fairings.

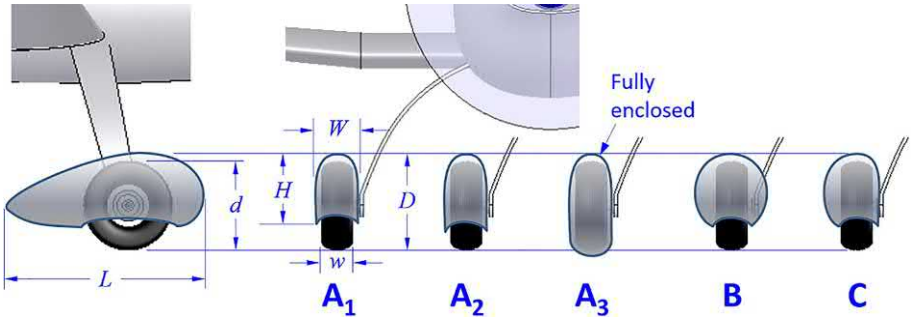


FIGURE 16-58 Selected types of landing gear wheel fairings. The drag of the landing gear wheel fairing styles denoted by "A" through "C" is presented in Table 16-13. *Based on W.H. Herrnstein, D. Biermann, The Drag of Airplane Wheels, Wheel Fairings, and Landing Gears—I, NACA R-485, 1935.*

TABLE 16-14 Drag of tires with fairings (H = fairing height, W = fairing width, d = tire diameter, w = tire width).

Fairing Type	Tire Type	ΔC_{D_S} Reference Area = $H \times W$	ΔC_{D_S} Reference Area = $d \times w$	Reference
A1	Type III (B)	0.130	0.143	NACA R-485
A2	Type III (B)	0.090	0.119	
A3 (tire fully covered)	Type III (B)	0.044	0.070	
B	Type III (B)	0.117	0.217	
C	Type III (B)	0.129	0.188	

(3) Drag of Fixed Landing Gear Struts with Tires

Drag coefficients for a number of typical fixed main landing gear with tires are presented in Table 16-15. All the drag coefficients are based on the dimensions of a single tire per side but apply to the entire installation (both wheels and support structure). The coefficients include interference drag, but exclude the nose landing gear, however. The additive drag coefficient of the fixed landing gear with the fairing can be estimated from:

$$\Delta C_{D_{fixed}} = \frac{(d \times w)}{S_{ref}} \Delta C_{D_S} \qquad (16\text{-}155)$$

Refer to Figure 16-59 for the shape of the landing gear configuration. Each configuration is identified with a letter ranging from A to Q. Ref. [92] presents results for these configurations, some of which feature more than one type of tire and even fairings. These differences are presented in Table 16-15 using numbers following the letter (note that only configurations A through N are featured in the table). For instance, configurations A and B both feature a Type III tire, whereas configuration C is presented with five different tires, of which one configuration is supported by a streamlined tension wire and the other with a tubular tension support. The remainder of the configurations utilizes that same tubular support.

TABLE 16-15 Drag of landing gear struts with and without fairings (h = height of tire, w = width of tire).

Strut Type	Tire Type		Reference Area	ΔC_{D_S}	Reference
A	8.5-10	B	$d \times w$	1.112	NACA R-485
B	8.5-10	B		1.204	
C1	8.5-10 + streamline wire	B		1.151	
C2	8.5-10 + tubular support	B		1.178	
C3	27-inch streamline + tube	A		1.082	
C4	25x11-4 X-low press + tube	C		0.940	
C5	30x5 disk wheel hi-press + tube	D1		1.779	
C6	32x6 disk wheel hi-press + tube	D2		1.373	
D1	8.5-10	B		1.230	
D2	8.5-10	B		1.191	
E	8.5-10	B		1.125	
F1	8.5-10	B		1.138	
F2	8.5-10 + Fairing C	B		0.877	
F3	27-inch streamline + tube	A		1.014	
F4	25x11-4 X-low press + tube	C		0.858	
F5	30x5 disk wheel hi-press + tube	D1		1.628	
G1	8.5-10	B		1.151	
G2	8.5-10+Fairing A2	B		0.733	
H	8.5-10	B		0.994	
I1	8.5-10 + Fairing B	B		0.536	
I2	8.5-10 + Fairing C	B		0.484	
I4	27-inch streamline + tube	A		0.564	
I5	27-inch streamline + tube	A		0.496	
J1	8.5-10	B		0.615	
J2	8.5-10 + Fairing A1	B		0.458	
J3	27-inch streamline	A		0.485	
K1	8.5-10	B		0.981	
K2	8.5-10 + Fairing C	B		0.641	
L	8.5-10	B		0.992	
M1	8.5-10 + Fairing A1	B		0.484	
M2	8.5-10+Fairing A1+Expanding fillet	B		0.315	
N	8.5-10	B		0.315	

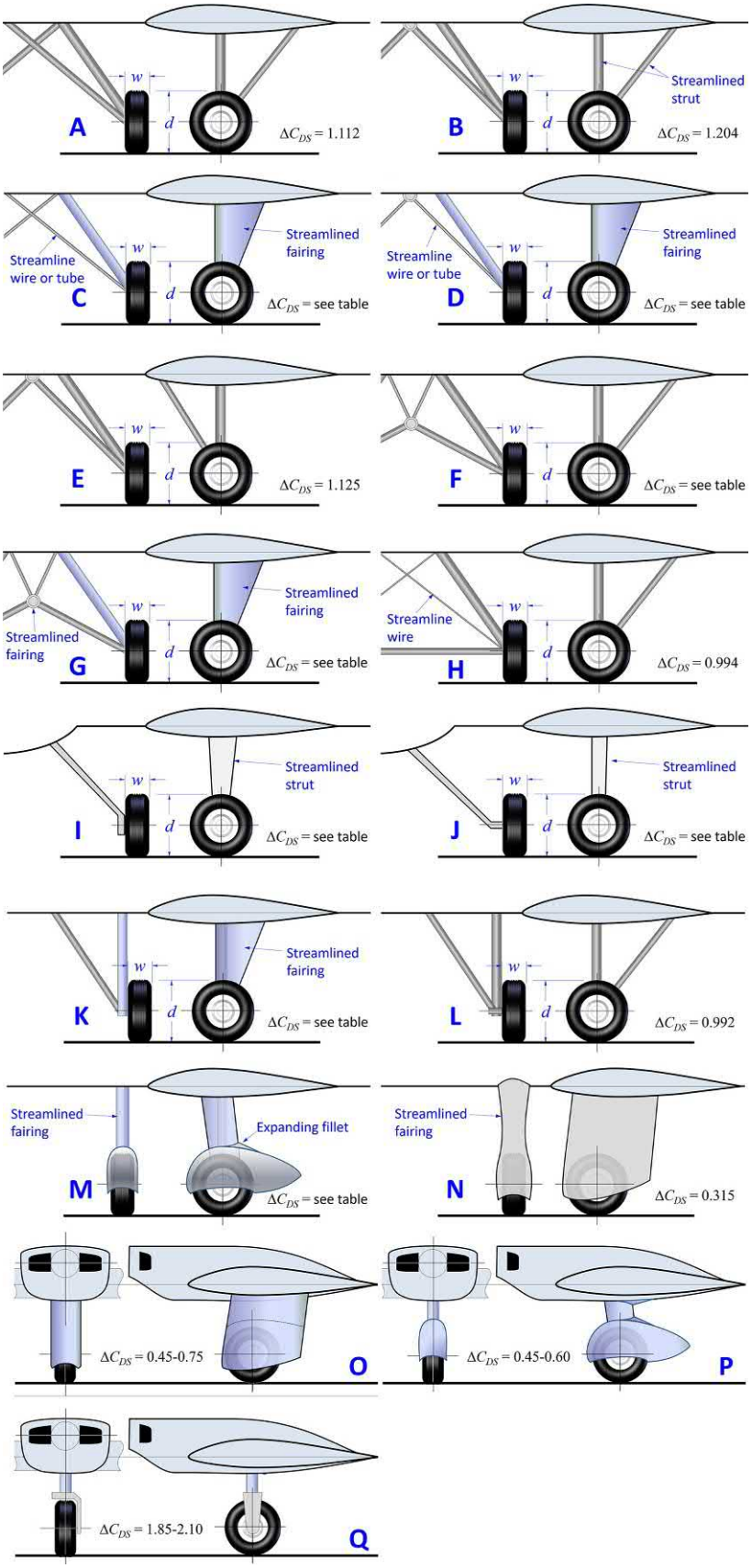


FIGURE 16-59 Drag of selected types of fixed landing gear installations. All struts are streamlined. All drag coefficients are based on the tire geometry and pertain to the entire installation (two main gear). See Table 16-15 for additional detail. *Based on W.H. Herrnstein, D. Biermann, The Drag of Airplane Wheels, Wheel Fairings, and Landing Gears—I, NACA R-485, 1935; J. Roskam, Methods for Estimating Drag Polars of Subsonic Airplanes, 4th printing, 1984.*

EXAMPLE 16-17

Determine the additive drag coefficient for the fixed landing gear of the SR22 airplane. Its wing area is 144.9 ft^2 and assumes the main landing gear tire dimensions are 15-in. diameter and 6-in. width and the nose gear tire is 14 by 5 in.

SOLUTION:

Approximate the main landing gear using Configuration I2 since the landing gear fairing (Style C) is similar in some ways to that of the SR22. The additive drag coefficient for I2 is $\Delta C_{D_s} = 0.484$. The nose landing gear can be represented using Configuration M1, for which $\Delta C_{D_s} = 0.484$ as well. Note that the drag refers to the entire installation, which consists of two wheels. Since the nose gear is a single wheel, we reduce this number by a factor of two, i.e., $\Delta C_{D_s} = 0.242$ for the nose gear. Thus, the drag contribution of the main and nose landing gear can be represented by (note that a factor of 144 is used to convert in.^{2} to ft^2):

$$\text{Main:}\quad \Delta C_{D_{main}} = \frac{(d \times w)}{S}\Delta C_{D_S} = \frac{(15 \times 6)/144}{144.9}(0.484) = 0.00209$$

$$\text{Nose:}\quad \Delta C_{D_{nose}} = \frac{(d \times w)}{S}\Delta C_{D_S} = \frac{(14 \times 5)/144}{144.9}(0.242) = 0.00081$$

This amounts to about 20.9 dragcounts due to the main gear and 8.1 counts due to the nose landing gear.

(4) Drag of Retractable Landing Gear

Mair and Birdsall [93] give the following empirical expressions for the additive drag of landing gear in the absence and presence of flaps. In other words, one expression applies to deployed landing gear and retracted flaps. The other applies to the both the landing gear and flaps extended. The equations are based on historical data and are presented in terms of weight, W (in lb$_f$) in the UK-system, or mass, m (in kg) in the SI-system. They are representative of commercial jetliners and business jet, and should not be used with lighter GA aircraft. The drag of landing gear with the flaps stowed is given as follows in the SI- and UK-systems, respectively, where subscripts indicate units required for terms:

Flaps retracted :

$$\Delta C_{D_{RG}} = \begin{cases} w_{N/m^2}\left(5.81 \times 10^{-5}\right) m_{kg}^{-0.215} = \dfrac{5.698 \times 10^{-4} m_{kg}^{0.785}}{S_{m^2}} & \text{SI} \\ \dfrac{0.003297 W_{lb_f}^{0.785}}{S_{ft^2}} & \text{UK} \end{cases} \tag{16-156}$$

If the flaps are fully deflected the expression becomes:

Flaps deployed :

$$\Delta C_{D_{RG}} = \begin{cases} w_{N/m^2}\left(3.16 \times 10^{-5}\right) m_{kg}^{-0.215} = \dfrac{3.099 \times 10^{-4} m_{kg}^{0.785}}{S_{m^2}} & \text{SI} \\ \dfrac{0.001793 W^{0.785}}{S_{ft^2}} & \text{UK} \end{cases} \tag{16-157}$$

EXAMPLE 16-18

Determine the additive drag coefficient of the retractable landing gear for an airplane that weighs 22,000 lb$_f$ and whose wing area is 300 ft^2, with and without flaps.

SOLUTION:

Using Equations (16-156) and (16-157), we get:

Without flaps:

$$\Delta C_{D_{wheel}} = \frac{0.003297 W^{0.785}}{S} = \frac{0.003297(22,000)^{0.785}}{300} = 0.02817$$

With flaps:

$$\Delta C_{D_{wheel}} = \frac{0.001793 W^{0.785}}{S} = \frac{0.001793(22,000)^{0.785}}{300} = 0.01532$$

This amounts to 282 and 153 dragcounts respectively.

Jenkinson [80] gives the following expression for the drag of the landing gear of commercial jetliners. Formulation for two classes of jetliners is given; for medium-to-large jetliners like the Boeing 747, 757, 767, DC-10, L-1011, etc. and for smaller jetliners, such as the F-100, DC-9, and B-737. The expressions are presented in terms of the flat plate area, $\Delta D/q$. However, these have been modified using the following relation, to adhere to the presentation in this book.

$$\Delta D/q \;\rightarrow\; \Delta C_D = \Delta D/(qS)$$

Medium to large jetliners:

$$\Delta C_{D_{RG}} = \begin{cases} \dfrac{0.00157(m_{NLG} + m_{MLG})^{0.73}}{S} & \text{SI} \\ \dfrac{0.0025(W_{NLG} + W_{MLG})^{0.73}}{S} & \text{UK} \end{cases} \tag{16-158}$$

Small jetliners:

$$\Delta C_{D_{RG}} = \begin{cases} \dfrac{0.00093(m_{NLG} + m_{MLG})^{0.73}}{S} & \text{SI} \\ \dfrac{0.006(W_{NLG} + W_{MLG})^{0.73}}{S} & \text{UK} \end{cases} \tag{16-159}$$

Where W_{NLG} and W_{MLG} is the weight (in lb_f) of the nose and main landing gear, respectively and m_{NLG} and m_{MLG} is the mass (in kg) of the nose and main landing gear, respectively. The result applies to the entire landing gear. It underpredicts smaller aircraft and should only be used for large aircraft.

Roskam [94] presents a simple method for determining the additive drag of retractable landing gear. To calculate the additive drag coefficient, it uses the ratio of the actual frontal area of the landing gear to the area of a rectangle enclosing the gear (see Figure 16-60). The method assumes an open wheel well, but suggests a 7% reduction to correct for closed wells. The formulation is presented below for open and closed wheel wells:

Open wheel wells: $$\Delta C_{D_{RG}} = 0.05328\left(\frac{d \times w}{S}\right)e^{5.615m} \tag{16-160}$$

Closed wheel wells: $$\Delta C_{D_{RG}} = 0.04955\left(\frac{d \times w}{S}\right)e^{5.615m} \tag{16-161}$$

Where $m = S_A/(d \times w)$. Note that even though the drag coefficient is based on the ratio m, the value of $\Delta C_{D_{RG}}$ applies to both legs of the main landing gear (the nose landing gear is not included). Also note a common error is to forget to convert d and w (which often are in inches) to ft, to ensure unit consistency with S in ft^2. If $m = 0.75$ and $S/(d \times w) = 130$, then the open wheel well $\Delta C_{D_{RG}} \approx 0.0272$.

(5) Drag of Nose Landing Gear

This method applies to both fixed and retractable *nose landing gear* (NLG). Essentials of the method are presented in Figure 16-61. It requires the distance of the NLG from the nose, a, its total length, e, and tire diameter, d, to be known. First, determine the ratio a/d. Use it to select the appropriate curve. Interpolate for values falling between curves. Next, calculate the wheel height ratio, e/d. Use it with the selected curve to read the source drag coefficient, ΔC_{D_s}, on the vertical axis. Finally, calculate the additive drag coefficient, $\Delta C_{D_{NLG}}$ (which is based on the reference wing area), as follows:

$$\Delta C_{D_{NLG}} = \frac{(d \times w)}{S}\Delta C_{D_s} \tag{16-160}$$

16.4.6 Drag of Floats

Floats are a popular option for many GA aircraft. Their primary drawbacks include a healthy dose of additive drag, inherent destabilizing moment, and weight. This section presents a method to estimate the drag. Ref.

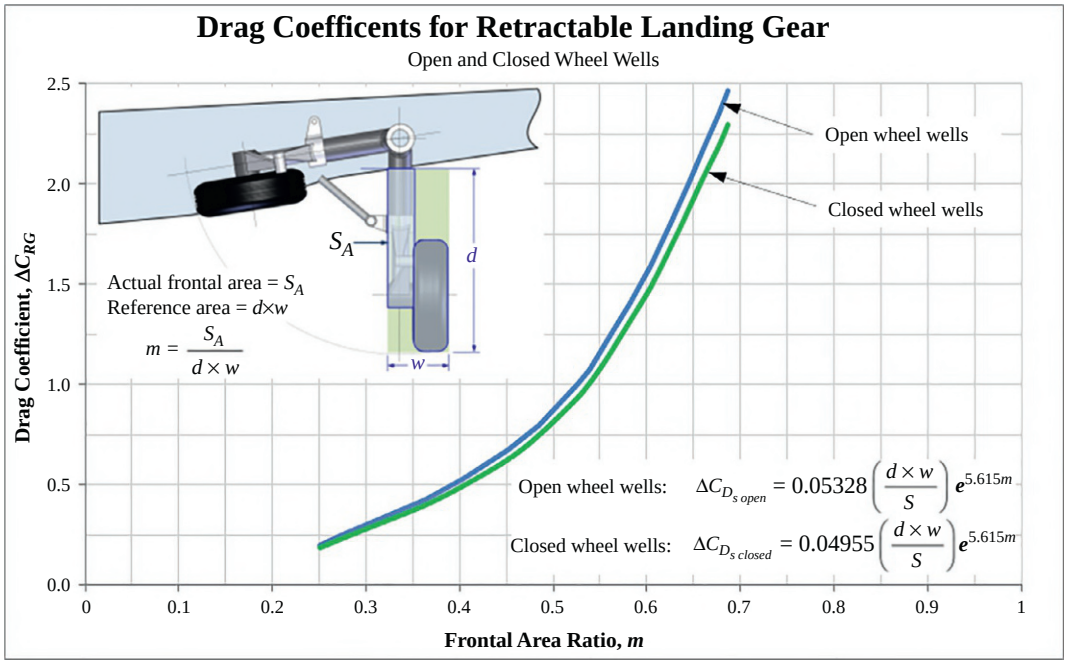


FIGURE 16-60 Estimating the drag contribution of a retractable landing gear. *Based on J. Roskam, Methods for Estimating Drag Polars of Subsonic Airplanes, 4th printing, 1984.*

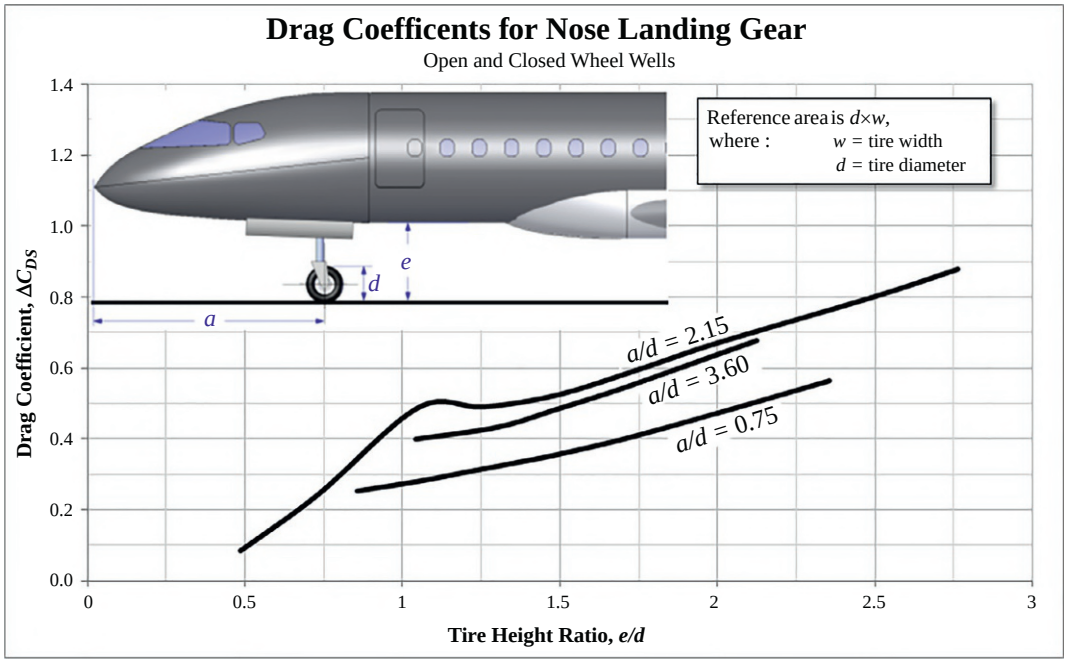


FIGURE 16-61 Estimating the drag contribution of a nose landing gear. *Based on J. Roskam, Methods for Estimating Drag Polars of Subsonic Airplanes, 4th printing, 1984.*

[95] investigated the drag of four full-scale floats used as a single float for large single-engine military aircraft, such as the Vought OS2U Kingfisher. The floats varied in length, ranging from about 24.8 to 26.6 ft (7.56 to 8.11 m), with maximum cross-sectional area ranging from 6.63 to 9.25 ft^2 (0.616 to 0.859 m^2). While larger than what is typically used for single-engine GA aircraft, the results permit the drag of smaller floats to be estimated. The reference concluded that the step constituted about 10% of the drag and adding a tail fairing reduced it by 8%. It found no benefit by counter-sunk rivets over normal universal head rivets aft of the step.

The following expressions refer to the configurations A, B, and C in Figure 16-62. The term A_{max} is the maximum cross-sectional area of the float and α is the AOA with respect to the horizontal upper surface. No provision was made to reduce the drag specifically, e.g., by removing hardware. The drag measurements included support fairings, except wire-bracings were not present. The $R_e = 25$ million, based on the length of the float. The drag was measure using an α-sweep from −6 degrees to +6 degrees at an airspeed of 87 KTAS. The drag applies to a single float only, so if using two floats, the additive drag coefficient must be doubled.

Ref. [96] investigated special NACA designed floats, referred to as the NACA 57 series. It was found that

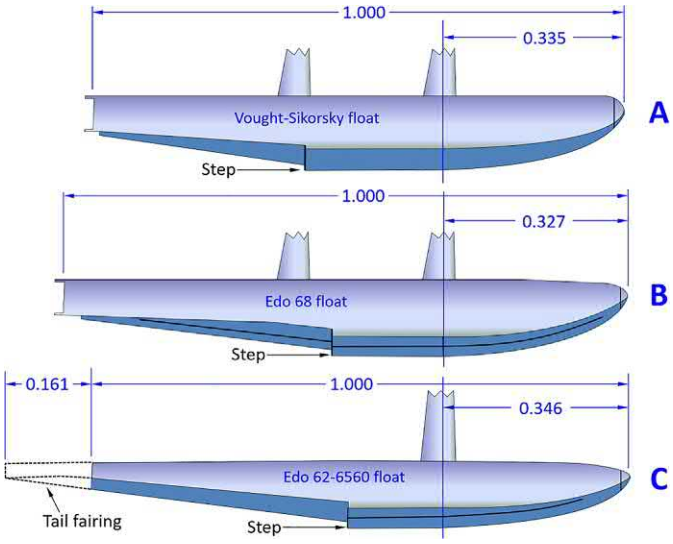


FIGURE 16-62 Float geometries. The drag of the float styles denoted by "A," "B," and "C" is presented in Equations (16-163), (16-164), and (16-165), respectively. *Based on R.N. Conway, J.D. Maynard, Wind-Tunnel Tests of Four Full-Scale Seaplane Floats, NACA WR-L-238, 1943.*

the dead-rise angle (the angle between the horizontal and the "v" of the float) had a small effect on the total drag: The greater the dead-rise angle the higher the drag. The drag coefficients increase with the AOA similar to that reflected by Equation (16-163); however, the minimum drag (ΔC_{D_s}) is less or about 0.13–0.155.

$$\text{Float A:}\quad \Delta C_{D_{float}} = \left(\frac{A_{max}}{S}\right)(0.00165\alpha^2 + 0.00413\alpha + 0.2142) \tag{16-163}$$

$$\text{Float B:}\quad \Delta C_{D_{float}} = \left(\frac{A_{max}}{S}\right)(0.00109\alpha^2 + 0.00052\alpha + 0.1771) \tag{16-164}$$

$$\text{Float C:}\quad \Delta C_{D_{float}} = \left(\frac{A_{max}}{S}\right)(0.00176\alpha^2 - 0.00105\alpha + 0.1981) \tag{16-165}$$

16.4.7 Drag of Deployed Flaps

Deflecting flaps modifies the drag model in two ways: (1) minimum drag and (2) lift-induced drag both increase (see Figure 16-16). This section introduces methods to account for this change.

Increase of $C_{D_{min}}$ due to Flaps

Young [97] presents an empirical method to estimate the drag of a number of types of flaps. The estimation depends on the flap type, flap chord (c_f), deflection angle (δ_f), and its span (b_f). The following expression is used for this estimation and it requires the two functions Δ_1 and Δ_2 to be determined. The former accounts for the contribution of the flap chord to the flap drag and the latter for the contribution of the flap deflection. These are detailed in the two graphs of Figure 16-63, and are discussed further below.

$$\Delta C_{D_{flap}} = \Delta_1 \Delta_2 \left(\frac{S_{flap}}{S}\right) \tag{16-166}$$

Flap Chord Contribution—The Function Δ_1

As stated earlier, the function Δ_1 represents the contribution of the flap chord to the flap drag. This contribution is shown in the left image of Figure 16-63, for plain, split, and slotted flaps, for airfoils of three thickness-to-chord ratios; 0.12, 0.21, and 0.30. The author has digitized these graphs and they be reconstructed using the polynomial curvefits shown in Table 16-16. Note that the parameter R_f is the flap chord ratio, i.e., R_f = flap chord/wing chord = c_f/c. This ratio typically ranges from 0.20 to 0.35.

Flap Deflection Contribution—The Function Δ_2

The Δ_2 function represents the contribution of the flap deflection angle to the flap drag, shown in the right image of Figure 16-63, for plain, split, and slotted flaps, for airfoils of three thickness-to-chord ratios; 0.12, 0.21, and 0.30. These are given by the polynomial curvefits shown in Table 16-17.

Corke [98] presents additive drag for several types of flaps at the 30- and 50-degree deflection. These are reproduced in Table 16-18. It is a limitation that these apply to the specific flap span and chord of 60% and 25%, respectively. Regardless, these can come in handy for initial estimation of flap drag.

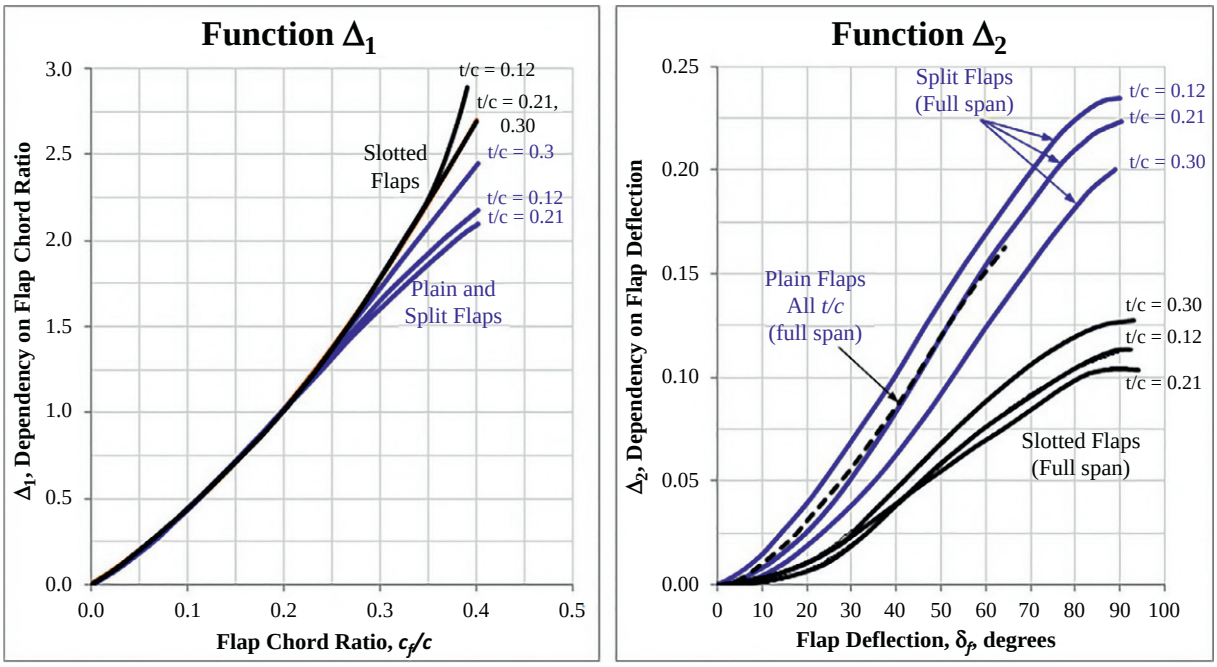


FIGURE 16-63 Estimation of the drag contribution of the flaps calls for the Δ_1 and Δ_2 functions to be determined. *Based on A.D. Young, The Aerodynamic Characteristics of Flaps, R.&M. No. 2622, British A. R. C., 1947.*

TABLE 16-16 Polynomial representations of the function Δ_1 for plain, split, and slotted flaps.

Plain and Split Flaps:	
t/c	**Function ($R_f = c_f/c$)**
0.12	$\Delta_1 = -21.090R_f^3 + 14.091R_f^2 + 3.165R_f - 0.00103$
0.21	$\Delta_1 = -19.988R_f^3 + 12.682R_f^2 + 3.363R_f - 0.0050$
0.30	$\Delta_1 = 4.6945R_f^2 + 4.3721R_f - 0.031$
Slotted Flaps:	
0.12	$\Delta_1 = 179.32R_f^4 - 111.6R_f^3 + 28.929R_f^2 + 2.3705R_f - 0.0089$
0.21, 0.30	$\Delta_1 = 8.2658R_f^2 + 3.4564R_f + 0.0054$

TABLE 16-18 Additive flap drag coefficients.

Flap type	Reference deflection, δ_f (degrees)	$\Delta C_{D_{flaps}}$
Split or plain flap	30	0.05
	50	0.10
Slotted flap	30	0.02
	50	0.05
Fowler flap	30	0.032
	50	0.083

Assumes 60% flap span and 25% chord.
Based on T.C. Corke, Design of Aircraft, Prentice-Hall, 2003.

16.4.8 Drag of Deployed Spoilers

Deflecting wing spoilers modifies the flow field in complex ways, depending on chord- and spanwise position and spanwise extent of the device (see Figure 16-64). The geometry of the device itself (height, deflection angle, and perforations) also play an important role. It is recommended the reader investigates the literature for experimental data, with which it is rich. For instance, refer to Refs. [33, 99–101], to name a few. Also, study some of their supporting references. In the absence of such data, the spoiler can be approximated as a 3-dimensional flat plate. In this capacity refer to Figure 16-76, which gives a $C_{D_s} = 1.17$ for a circular plate. The planform shape of plates has surprisingly small effect on the drag once the flow on the leeward side is fully separated. Thus, we can devise the following approximation:

$$\Delta C_{D_{sp}} \approx 1.17 \frac{b_{sp} h_{sp}}{S} \left(\frac{\delta_{sp}}{90} \right) \qquad (16\text{-}167)$$

Where b_{sp}, h_{sp}, and δ_{sp} are the span, height, and deflection angle (in degrees, where $0 \text{ degrees} \leq \delta_{sp} \leq 90 \text{ degrees}$) shown in Figure 16-64, respectively. The expression applies to one spoiler only. Thus, the additive drag coefficient of two (4 ft) × (0.5 ft) spoilers, deflected 45 degrees, on a wing of area 150 ft^2, is 156 dragcounts.

16.4.9 Drag Correction for Cockpit Windows

The form-factor estimation methods presented earlier assume a fuselage with a smooth round forward geometry that provides a smooth contour for air to flow across. Such smoothness is normally not present in airplanes; they often feature a sharp discontinuity around the cockpit windows. Cockpit windows are often flat, in particular in pressurized aircraft, with heated windscreens to improve bird-strike resistance and minimize optical distortion.

TABLE 16-17 Polynomial representations of the function Δ_2 for plain, split, and slotted flaps.

t/c	**Function**
Plain Flaps:	
0.12	$\Delta_2 = -3.795 \times 10^{-7}\delta_f^3 + 5.387 \times 10^{-5}\delta_f^2 + 6.843 \times 10^{-4}\delta_f - 1.4729 \times 10^{-3}$
Split Flaps:	
0.12	$\Delta_2 = -4.161 \times 10^{-7}\delta_f^3 + 5.5496 \times 10^{-5}\delta_f^2 + 1.0110 \times 10^{-3}\delta_f - 2.219 \times 10^{-5}$
0.21	$\Delta_2 = -5.1007 \times 10^{-7}\delta_f^3 + 7.4060 \times 10^{-5}\delta_f^2 - 4.8877 \times 10^{-5}\delta_f + 8.1775 \times 10^{-4}$
0.30	$\Delta_2 = -3.2740 \times 10^{-7}\delta_f^3 + 5.598 \times 10^{-5}\delta_f^2 - 1.2443 \times 10^{-4}\delta_f + 5.1647 \times 10^{-4}$
Slotted Flaps:	
0.12	$\Delta_2 = -2.4416 \times 10^{-12}\delta_f^6 + 6.3942 \times 10^{-10}\delta_f^5 - 6.2028 \times 10^{-8}\delta_f^4 + 2.4984 \times 10^{-6}\delta_f^3 + -1.8922 \times 10^{-5}\delta_f^2 + 3.1582 \times 10^{-4}\delta_f + 6.9698 \times 10^{-5}$
0.21	$\Delta_2 = 6.2317 \times 10^{-11}\delta_f^5 - 1.3354 \times 10^{-8}\delta_f^4 + 6.4833 \times 10^{-7}\delta_f^3 + 2.1134 \times 10^{-5}\delta_f^2 + -2.6425 \times 10^{-4}\delta_f + 5.2279 \times 10^{-4}$
0.30	$\Delta_2 = -3.7252 \times 10^{-7}\delta_f^3 + 5.4024 \times 10^{-5}\delta_f^2 - 4.4994 \times 10^{-4}\delta_f + 1.1175 \times 10^{-3}$

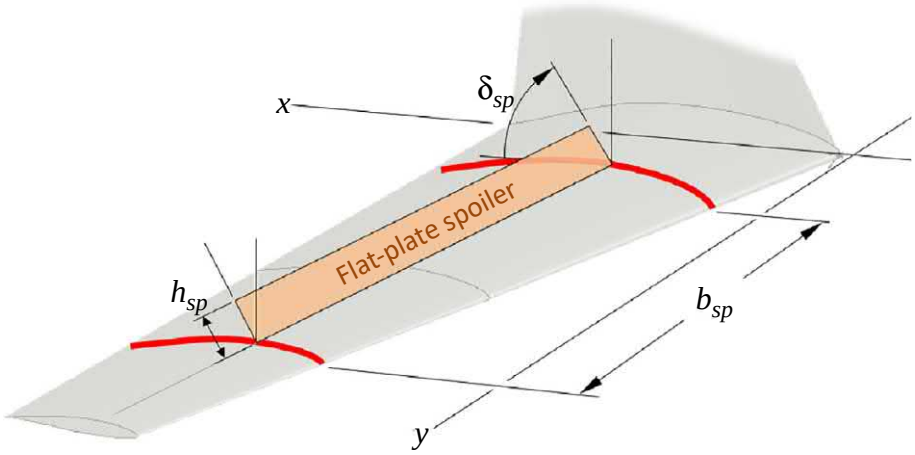


FIGURE 16-64 Idealized, unperforated, flat-plate spoiler.

(1) Drag of Conventional Cockpit Windows

A consequence of this discontinuity is a high-pressure region, caused by the reduction in airspeed over the geometry. This increases the drag of the airplane and must be accounted for using an additive drag contribution. Ref. [94], presents such a method, assuming the general geometry shown in Figure 16-65. The drag coefficients refer to the maximum frontal area of the fuselage (A_{max}) that can be estimated using a method such as the one shown in Figure 16-46. The source drag coefficients are given in Table 16-19:

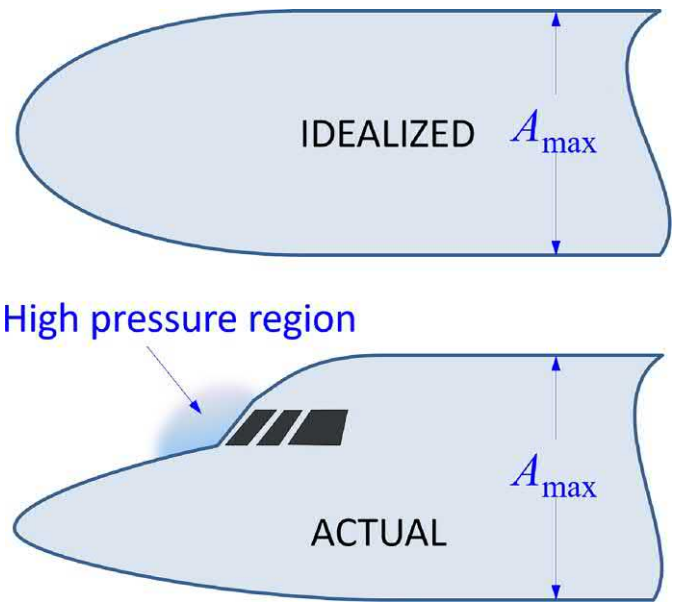


FIGURE 16-65 Idealized and actual forward geometry of typical aircraft.

TABLE 16-19 Additive drag coefficients for cockpit windows.

Description (drag references the fuselage frontal area)	ΔC_{D_s}
Flat windscreen with a protruding frame	0.016
Flat windscreen with a flush frame	0.011
Curved windscreen with a sharp upper edge	0.005
Curved windscreen with a round upper edge	0.002

$$\Delta C_{D_{window}} = \Delta C_{D_S} \frac{A_{max}}{S} \tag{16-168}$$

EXAMPLE 16-19

Estimate the additive drag of the SR22 due to the cockpit window, assuming a curved windscreen with a round upper edge. The fuselage cross-sectional area is approximately 14 ft^2.

SOLUTION:

$$\Delta C_{D_{window}} = \Delta C_{D_S} \frac{A_{max}}{S} = (0.002)\frac{14}{144.9} = 0.0001932$$

This amounts to about 1.93 dragcounts.

(2) Drag of Blunt Ordinary and Blunt Undercut Cockpit Windows

A cockpit windows installation is classified as *blunt* if the windscreen faces the oncoming airflow at angles ranging from normal to around 22 degrees in the horizontal plane and ±20 degrees from the vertical, respectively (see Figure 16-66). The vertical angle defines the *ordinary* and *undercut* configurations. The blunt installation leads to higher drag than curved geometry. The undercut installation

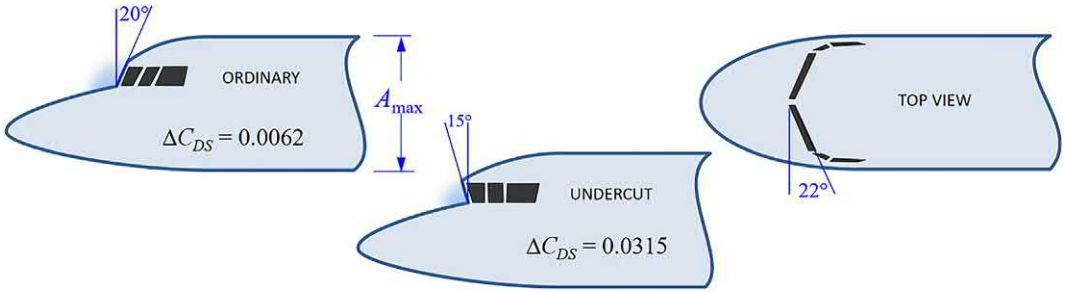


FIGURE 16-66 Drag of blunt and undercut cockpit windows. *Based on S.F. Hoerner, Fluid-Dynamic Drag, L. Hoerner, 1965; E.P. Hartman, The Aerodynamic Drag of Flying-Boat Hull Model as Measured in the NACA 20-foot Wind Tunnel I, NACA TN-525, 1935.*

was a popular approach in the 1930s to reduce the reflection of instrument lights at night (e.g., on the Boeing 247 [102] and the Vultee V-1). It is a very draggy configuration and should be avoided by all means. The source drag coefficients shown in the figure are used with Equation (16-168).

16.4.10 Drag of Canopies

Many single- to four-seat aircraft feature canopies rather than roofed cabins to improve the field-of-view. This section presents a simple method to estimate the drag caused by canopies. It is based on experimental data presented in Ref. [103], in which a number of dissimilar canopies were investigated at Mach numbers ranging from 0.19 to 0.71 and AOAs up to 6 degrees. The canopies are illustrated in Figure 16-67. The reference states the contribution of a well-designed canopy to the total drag of the airplane is approximately 2% of the total drag. However, a poorly designed canopy easily exceeds that 10-fold—it is 20% of the total drag. The drag is presented in terms of the maximum cross-sectional area of the window, A_{max}, using the following expression:

$$\Delta C_{D_{canopy}} = \Delta C_{D_S} \frac{A_{max}}{S} \tag{16-169}$$

The values of the ΔC_{D_S} for the various canopy geometries are shown in Figure 16-68, plotted for the cited range of Mach numbers. These data are only provided for a low AOA, although information for higher AOAs (up to

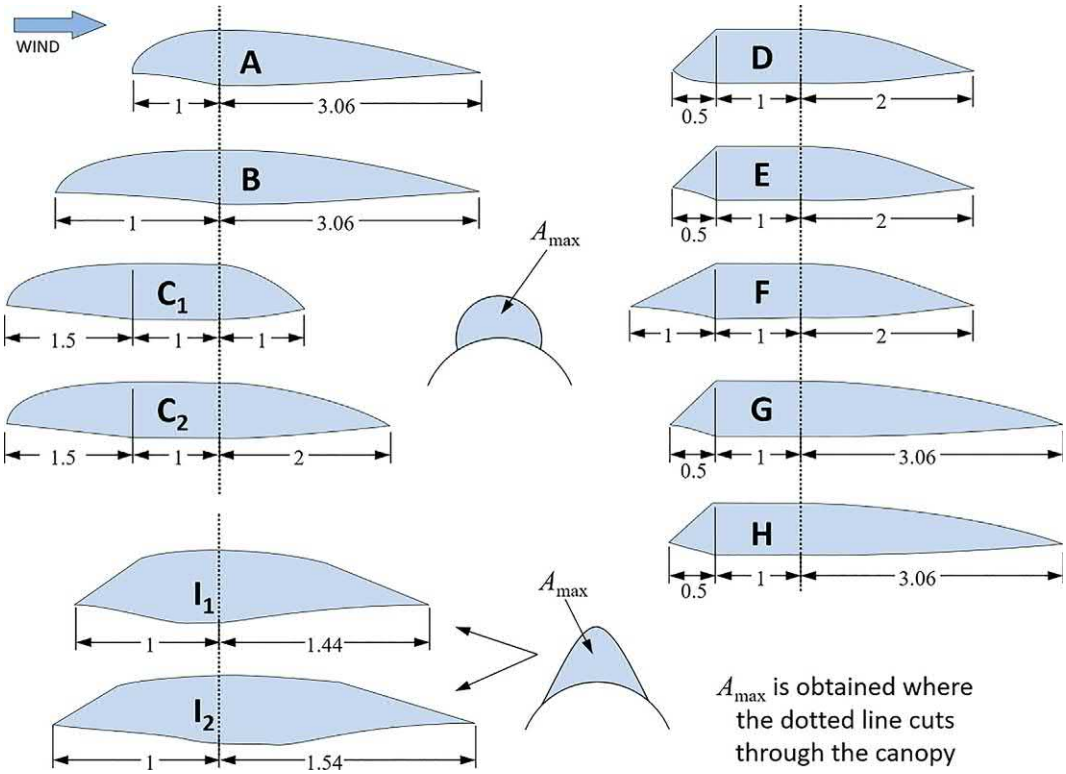


FIGURE 16-67 Canopy styles evaluated by Ref. 103. The drag of the canopy styles denoted by "A" through "I" is presented in the graph of Figure 16-68.

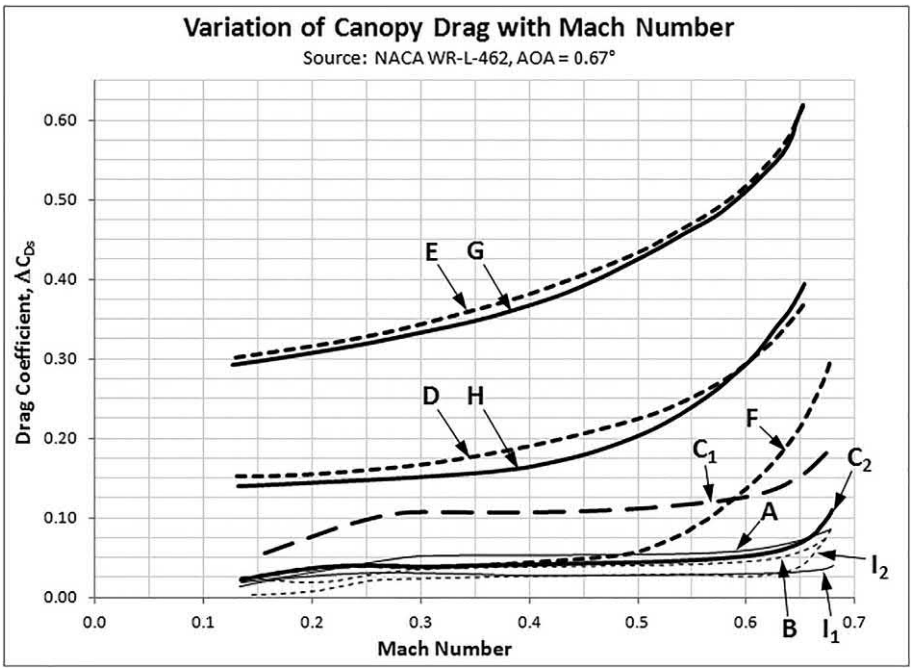


FIGURE 16-68 Drag coefficients for the canopy styles of Figure 16-67. *Reproduced from R.M. Wright, Investigation of Drag and Pressure Distribution of Windshields at High Speeds, NACA WR-L-462, 1942.*

6 degrees) is provided in Ref. [103]. The lower AOAs are important for efficient aircraft featuring canopies. The higher AOAs are important for design missions involving prolonged cruise near LD_{max} or high-speed maneuvers (where compressibility effect prevail). The reference presents the distribution of pressure coefficients, helpful when estimating critical Mach number (see Section 8.3.8, *The Effect of Compressibility*).

16.4.11 Drag of Blisters

Blisters are fairings that cover components that extend beyond the intended *outside mold line* (OML). GPS antennas are frequently shaped like blisters, as are covers for various mechanisms, such as flap actuation (e.g., Aero L-159 Alca) and landing gear (e.g., Supermarine Spitfire Mk XXI). Hoerner [33, pp. 8–5] provides source drag coefficients for several blister shapes. Thus, the additive drag coefficient for blisters can be calculated from

$$\Delta C_{D_{blister}} = \Delta C_{D_S}\left(\frac{A_{max}}{S_{ref}}\right) \tag{16-170}$$

Where: A_{max} = Cross-sectional area of shape as shown in Figure 16-69.

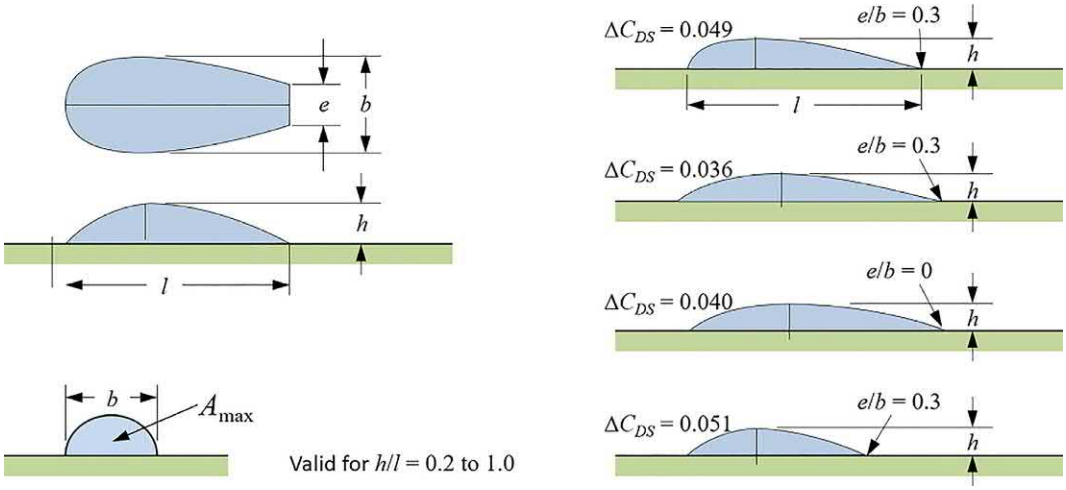


FIGURE 16-69 Drag contribution of typical blisters (bumps). *Based on S.F. Hoerner, Fluid-Dynamic Drag, L. Hoerner, 1965.*

EXAMPLE 16-20

Estimate the additive drag of a GPS blister antenna for the SR22, assuming a length × width × height of 4.7 × 3.0 × 0.78 in. Assume the base (e) is 30% of the width (b) and that its side view resembles that of the top blister in Figure 16-69. Furthermore, assume a maximum cross-sectional area of 14.1 in.^{2}.

SOLUTION:

The height ratio is about 0.78/4.7 = 0.17, a tad outside of the limits cited in Figure 16-69, but close enough to warrant using Equation (16-170).

$$\Delta C_{D_{blister}} = \Delta C_{D_S}\left(\frac{A_{max}}{S}\right) = 0.049\left(\left(\frac{14.1}{12\times 12}\right)/144.9\right) = 0.00003311$$

This amounts to approximately 0.33 dragcounts. Note that this antenna is about two times "draggier" than the wing-shaped antenna of Example 16-14.

16.4.12 Drag of Antennas

There are typically three kinds of antenna geometries planted on aircraft: (1) blister type, (2) wire type, and (3) wing type. Their drag can be estimated using the methods already presented in here. Typical placement and shapes of such antennas are shown in Figure 16-70. Their number can easily turn your nice, smooth airplane into something resembling a porcupine! If possible, try to mount as many antennas internally as practical, although this is often impossible due to reduced effectiveness of the antenna. Also, ask the manufacturer for an additive drag coefficient or drag force[9] associated with their antenna. Many have this readily available—it may save you analysis work. Others do not and for those you will have to estimate the drag based on the geometry using the approximations below.

- For wire antennas perpendicular to the airstream, use Equation (16-178).
- For wire antennas at an angle θ to the airstream, use Equation (16-181).
- For blister antennas, use Equation (16-170).
- For wing antennas, use Equation (16-148).

16.4.13 Drag of Windmilling and Stopped Propellers

Engine failure in propeller-driven aircraft leads to two possible scenarios: (1) Windmilling or (2) stopped propellers. In addition to loss of thrust, both increase the drag, but for different reasons. For single-engine aircraft, this dangerously cuts glide capability. For multiengine aircraft, it reduces range and climb performance, because of increased drag driven by the asymmetric thrust.

(1) Drag due to Windmilling Propellers

The rotating propeller acts as a wind turbine that drives the engine and must develop enough torque to overcome the internal friction of the engine. A thorough analysis of the phenomenon is beyond the scope of this book, but some experimental data are provided in Ref. [104]. The following methods are provided for initial estimation only.

Hoerner [33] proposes a method in which the power required to turn the engine is 10% of its rated power and the propeller efficiency expected through the

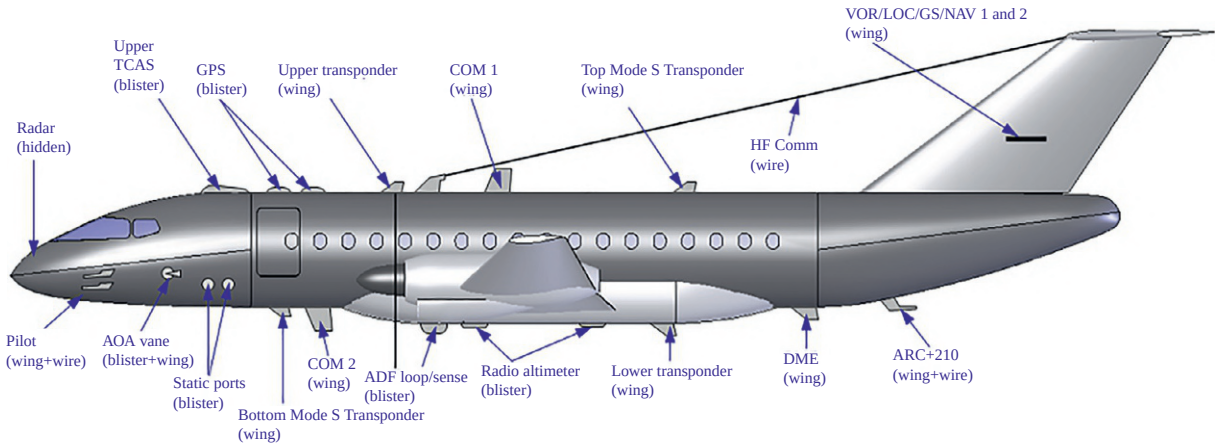


FIGURE 16-70 Typical placement and shape of various antennas and flight control components. Actual size is exaggerated for clarity.

[9] Convert to a drag coefficient per Equation (16-144).

windmilling is approximately 50%. In other words, 50% of the drag power is converted into the rotational power. This allows us to write:

$$0.1 \times 550 \times P_{HP_{\max}} = 0.5 \times D_{windmill} \times V_\infty \qquad (16\text{-}171)$$

Assuming the windmilling drag to depend on dynamic pressure and propeller disk area, A_P, we can write:

$$D_{windmill} = \frac{1}{2}\rho V^2 A_P C_{D_S} = \frac{1}{2}\rho V^2 S \Delta C_{Dwindmill}$$

Substitute this into Equation (16-169). Solving for the drag coefficient and referencing the reference area yields:

$$\Delta C_{Dwindmill} = \frac{220 P_{HP_{\max}}}{\rho V_\infty^3 S} \qquad (16\text{-}172)$$

Where V_∞ is the glide speed and ρ the density at condition. Comparison to existing aircraft reveals that Equation (16-172) over predicts the additive drag by a factor of 2–4. For this reason, for small engines with low internal friction, multiply the value by 0.25 and for larger engines with a high internal friction multiply by 0.33. The author's unpublished study of single-engine aircraft reveals that, on the average, windmilling propeller increased drag by approximately:

$$\Delta C_{Dwindmill} \approx 0.0150 \qquad (16\text{-}173)$$

With several excursions nearing and even exceeding 300 dragcounts! The above value will easily reduce the $LD_{\max}$ of a sleek airplane by a whopping one-third.

(2) Drag due to Stopped Propellers

When an engine malfunction causes the propeller to stop completely, the drag penalty is less than if it windmills. The resulting drag can be estimated using the blade planform area, assuming inclined flat-plate drag based on the blade angle at the 0.7R blade station (β). This angle is close to the airfoil's pitch angle (e.g., see Figure 15-9). When $\beta = 0$, the blade drag is high and when $\beta = 90$ degrees, the drag is at minimum. Hoerner [33], citing experiments from Ref. [104], provides the following expression to estimate the source drag coefficient of such a blade:

$$C_{D_S} = 0.1 + \cos^2\beta \qquad (16\text{-}174)$$

Where β may or may not be equal to the pitch angle referenced in Chapter 15, *Thrust Modeling for Propellers*. The blade drag coefficient varies between $0.1 < \Delta C_{D_S} < 1.1$. Thus, the drag of the stopped propeller (D_{sp}) can be written as follows:

$$D_{sp} = \frac{1}{2}\rho V^2 N_B S_B C_{DS} = \frac{1}{2}\rho V^2 S \Delta C_{Dsp}$$

Where N_B is the number of blades and S_B is the planform area of the blade. Solving for ΔC_{Dsp} (which is based on S) yields the following expression:

$$\Delta C_{Dsp} = \left(\frac{S_B}{S}\right) N_B C_{D_S} = \left(\frac{S_B}{S}\right) N_B \left(0.1 + \cos^2\beta\right) \qquad (16\text{-}175)$$

16.4.14 Drag of Parachutes

While the drag of parachutes may appear simple, it is surprisingly complicated. Accurate estimation of parachute drag and the time history of its development during deployment is a serious scientific discipline, applicable to a range of applications, including the deployment of re-entry parachutes or ejection seats.

Hoerner [33] provides a practical insight into the drag of parachutes. In general, the drag coefficient of inflated parachutes is based on simple geometric features, such as the height, diameter, and the projected frontal area of the inflated canopy. For initial sizing, the drag coefficient, $C_{D_{parachute}}$, can be estimated based on the aspect ratio (AR) of the parachute; defined as its inflated height, h, by the inflated diameter, d. This is shown in the graph of Figure 16-71, which shows the inflated drag coefficient as a function of h/d. An empirical expression based on the graph is given below. It is valid only for $h/d < 1.1$ and $10^5 < R_e < 10^6$, where R_e is based on the inflated diameter. The maximum drag coefficient is obtained for an $AR = 0.5$, which represents a hemispherical geometry. Further increase of the AR will make the parachute partially "fill in" the flow separation region, which will reduce the drag coefficient until it reaches a theoretical minimum of 1.0.

$$C_{D_{parachute}} = 2.239\left(\frac{h}{d}\right)^4 - 4.202\left(\frac{h}{d}\right)^3 + 1.227\left(\frac{h}{d}\right)^2 + 0.6167\left(\frac{h}{d}\right) + 1.174 \qquad (16\text{-}176)$$

The coefficient is then used to evaluate the total drag force of the parachute using the following expression, where S is the projected area of the chute and $S = \pi d^2/4$:

$$D = qSC_{D_{parachute}} = \frac{1}{2}\rho V^2 S C_{D_{parachute}} \qquad (16\text{-}177)$$

EXAMPLE 16-21

The Cirrus SR22 is equipped with the so-called Cirrus Airframe Parachute System (CAPS), to be deployed in case of an emergency. The POH for the SR22 states that the "the airplane will descend at less than 1700 feet-per-minute (or 28.3 ft/s) with a lateral speed equal to the velocity of the surface wind" (at a gross weight of 3400 lb_f) the airplane will not exceed 1700 fpm. The company website states the diameter of the canopy is 55 ft. Using this information, estimate the drag coefficient of the parachute.

SOLUTION:

Solve for $C_{D_{parachute}}$ using Equation (16-177):

$$C_{D_{parachute}} = \frac{2D_{parachute}}{\rho V^2 S} = \frac{2W}{\rho V^2 S} = \frac{2(3400)}{(0.002378)\left(\frac{1700}{60}\right)^2\left(\frac{\pi}{4}55^2\right)} = 1.499$$

Note that the R_e is close to 10^7.

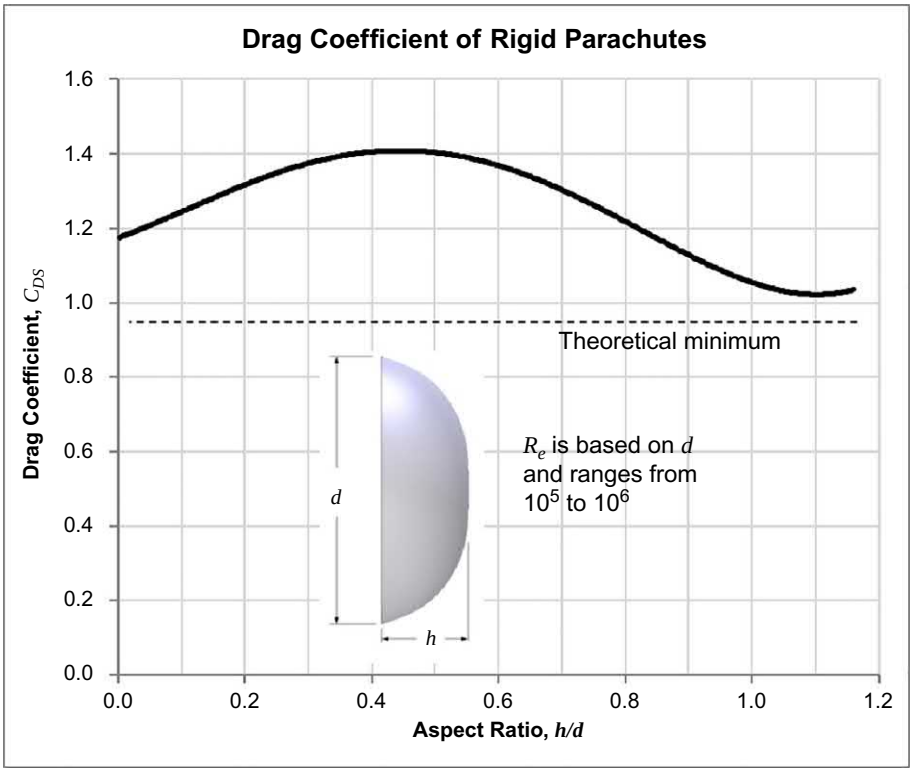


FIGURE 16-71 Drag coefficients of rigid objects shaped like parachutes. Valid only for $10^5 < R_e < 10^6$ and $h/d < 1.1$. *Reproduced from S.F. Hoerner, Fluid-Dynamic Drag, L. Hoerner, 1965.*

16.4.15 Drag of Various Sources

Figure 16-72 shows the 3-dimensional drag coefficient for a sphere and a circular cylinder, based on Schlichting [30]. The drag coefficient is defined using Equation (16-143), where S_S is the cross-sectional area ($\pi d^2/4$ for the sphere and $d \cdot l$, where l is the length of the cylinder). Schematics showing the nature of the separation have been superimposed to demonstrate how the drag coefficient depends on the nature of the flow separation that occurs. The dashed line indicates a specific region where the said flow takes place. Of importance is the sharp dip near a R_e of 300,000 (sphere) and 500,000 (cylinder), first discovered by Alexander Gustave Eiffel (1832–1923) [105]. This dip is indicative of the formation of a turbulent boundary layer that better follows the geometric shape of the solid, reducing the wake size and, thus, the pressure drag. The figure also shows the relatively constant drag coefficient of geometry over the range $10^3 < R_e < 10^5$. This is indicative of the formation of a laminar boundary layer (presuming smooth surface).

The range of R_e starting at 10^3 and higher includes most aircraft, even small RC aircraft, and is of great interest to the aircraft designer. This region is usually broken into four separate subregions called *subcritical*, *critical*, *supercritical*, and *transcritical* (see Figure 16-73).

In the subcritical region, laminar boundary layer is formed that separates once it flows to latitude of approximately 80 degrees (see the schematic to the right in Figure 16-73). In this range $10^3 < R_e < 10^5$ the C_D is largely independent of the R_e. In the critical region, the C_D drops sharply over a relatively narrow range of R_e, reaching a minimum value called the *critical Reynolds number*. This is caused by a sudden movement of the laminar boundary layer separation point to latitude of almost 95 degrees. At the critical R_e, a separation bubble is formed at this location that forces the laminar boundary layer to transition into a turbulent one. This, in turn, more easily follows the shape of the object, moving the separation point farther downstream to approximately 120 degrees. This reshapes the separation region, reducing its diameter and consequently the pressure drag. In the supercritical region, laminar-to-turbulent transition occurs in the attached boundary layer, causing the separation to begin to crawl upstream, gradually increasing the drag coefficient. In the transcritical region, the transition point has moved upstream closer to the stagnation point, eventually causing the drag to become independent of the R_e.

Figures. 16-74 and 16-76 show drag coefficients for selected geometry reproduced from Hoerner [33].

(1) 3D Drag of 2D Cross Sections of Given Length

Research shows that the drag coefficients for the 2-dimensional shapes shown in Figure 16-74 depends on their fineness ratio, here denoted by h/d (shown on

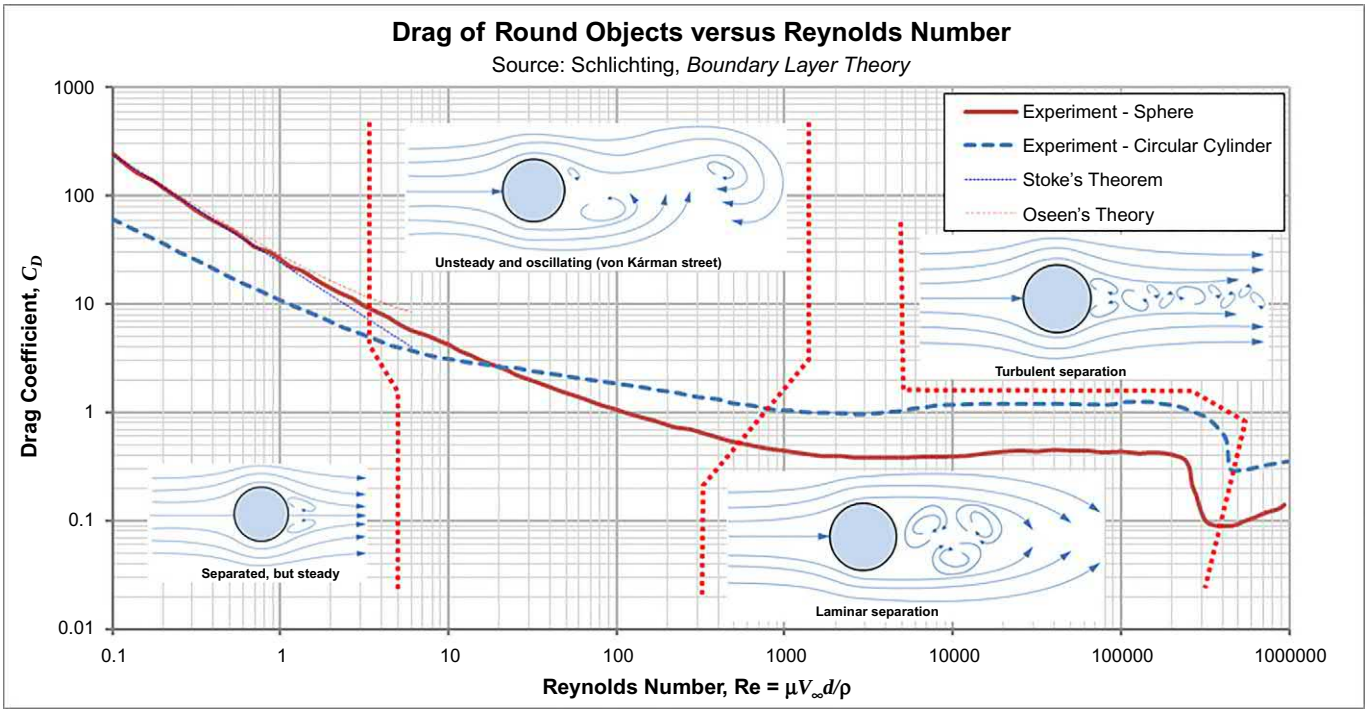
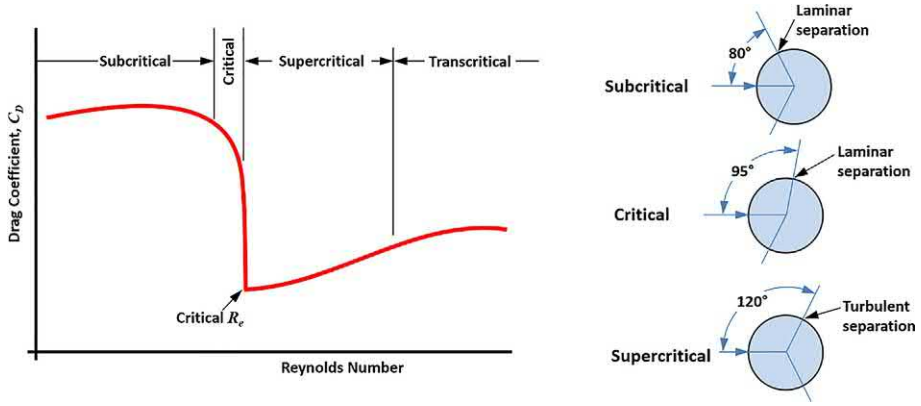


FIGURE 16-72 The drag coefficient of a sphere and a circular cylinder as a function of R_e. Insets are schematics showing the nature of the separation, whose consequence is the C_D shown in the graph.

FIGURE 16-73 The classification of flow regions on a sphere.



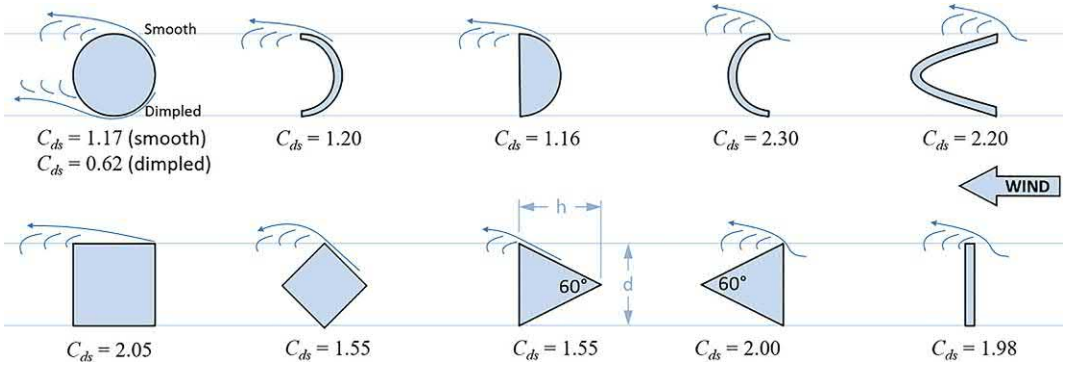


FIGURE 16-74 2-dimensional drag coefficients of several cross sections. Valid only for $10^4 < R_e < 10^5$.

the triangular shape in the center, lower row). However, their drag is determined using their frontal areas. Thus, the 3D drag of the shapes is calculated from:

$$\Delta C_{D_{2D-shape}} = \Delta C_{d_S}\left(\frac{d \times l}{S}\right) \tag{16-178}$$

Where d is the shape thickness, as shown in Figure 16-74, and l is the length of shape in the out-of-plane direction.

The *Cross-Flow Principle*

Hoerner [33] presents a practical method to calculate the drag of wires that are inclined with respect to the airflow (see Figure 16-75). This is referred to as the *cross-flow principle*. It can be used to estimate the drag and lift of a tube or cylinder of a given length, l, and a particular cross section whose 2-dimensional drag coefficient is known. The formulation below is used to calculate the coefficients in terms of the reference wing area so it (primarily the drag) can be added directly to the miscellaneous drag coefficient.

Note that the absolute sign in Equation (16-181) guarantees the drag is always greater than zero. Also note that the inclination angle of $\theta = 90$ degrees means the cylinder is perpendicular to airstream.

The cross-flow principle is very helpful in determining the drag of external aircraft components, such as HF radio wire antennas.

Resultant coefficient: $$\Delta C_{R_{cyl}} = \Delta C_{d_S}\left(\frac{d \times l}{S}\right)\sin^2\theta \tag{16-179}$$

Lift coefficient: $$\Delta C_{L_{cyl}} = \Delta C_{d_S}\left(\frac{d \times l}{S}\right)\sin^2\theta\cos\theta \tag{16-180}$$

Drag coefficient: $$\Delta C_{D_{cyl}} = \Delta C_{d_S}\left(\frac{d \times l}{S}\right)\cdot\left|\sin^3\theta\right| \tag{16-181}$$

Where θ is the angle of inclination (see Figure 16-75).

(2) Drag of 3-dimensional Objects

Figure 16-76 shows a number of 3-dimensional objects and the corresponding drag coefficients. The drag of these objects is also based on the cross-sectional area normal to the flow direction. Therefore, the cross-sectional area normal to the flow direction for the sphere is given

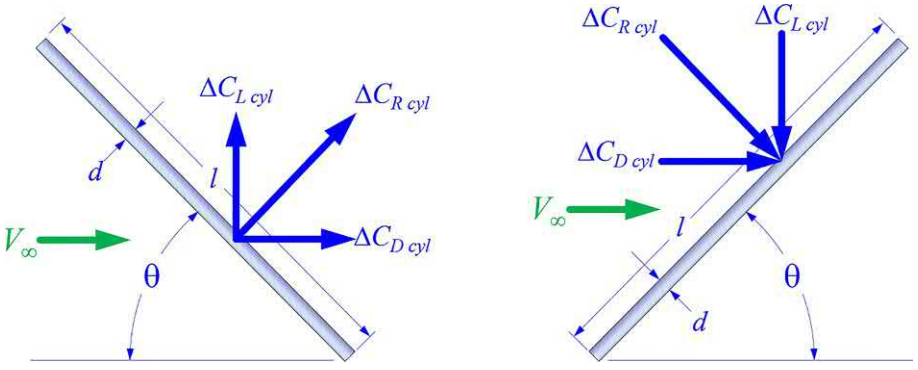


FIGURE 16-75 Dimensions for the applications of the cross-flow principle.

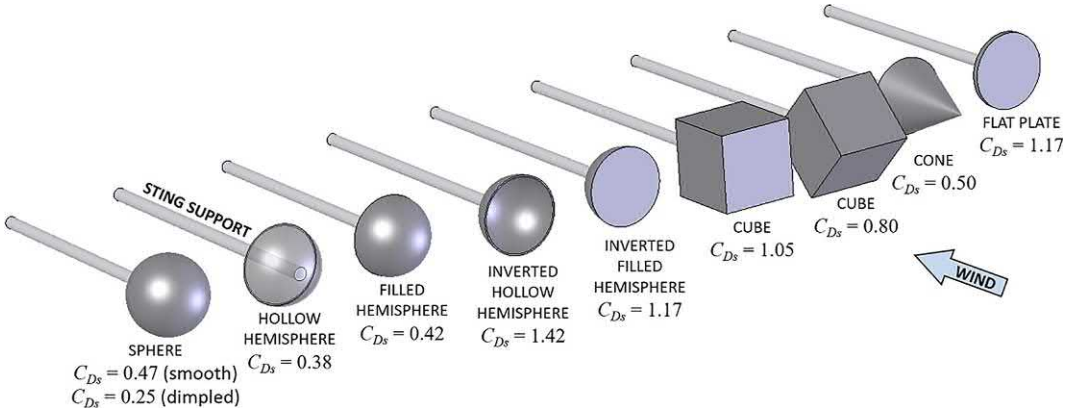


FIGURE 16-76 3-dimensional drag coefficients of various geometric shapes. Valid only for $10^4 < R_e < 10^5$.

by $\pi d^2/4$, where d is its diameter. In general, if S_N denotes this area (i.e., $S_N = \pi d^2/4$), the 3-dimensional drag coefficient is calculated from:

$$\Delta C_{D_{3D-shape}} = \Delta C_{D_S}(S_N/S) \tag{16-182}$$

(3) Drag of Sanded Walkway on Wing

As shown in Table 16-1, Ref. [17] indicates adding a sanded walkway (both sides of the fuselage) adds 7 dragcounts to the total drag. Thus, assume the following drag increase per side:

$$\Delta C_{D_{\text{walkway}}} = 0.00035 \tag{16-183}$$

(4) Drag of Gun Ports in the Nose of an Airplane

NACA WR-L-502 [106] presents the results from drag analysis of the introduction of openings for eight machine gun barrels in a P-38 Lightning style fuselage. It found the drag increase amounted to 5 dragcounts or 0.0005 total, based on the wing reference area. Based on this result, it is possible to estimate drag increase per opening as follows:

$$\Delta C_{D_{\text{gunport}}} = 0.0000625 \tag{16-184}$$

(5) Drag due to Ice Accretion

Drag due to ice accretion on the aircraft poses a serious challenge to safe flight. All aircraft can be classified as those that have been certified for *flight into known icing* (FIKI) and those that have not. Regardless of classification, all aircraft can accrete ice during operation. Ice formation was studied as early as 1938 by Gulick [107]. He concluded that airfoil C_d almost doubles and $C_{l_{\max}}$ reduced from 1.32 to 0.80, without changing the angle of stall. Further research took place in the early 1950s (e.g., see a paper by Gray and Glahn [108]). Since then, considerable research effort has been dedicated to the subject. The sheer volume of work cannot be adequately presented here. The interested reader is directed toward work published by NASA, SAE, and AIAA, to name a few.

(6) Drag of Streamlined External Fuel Tanks

External fuel tanks store additional fuel for military aircraft. However, they are also a plausible solution to a long-range operation of some GA aircraft. A similar shape is often used to house weather radars for GA aircraft. It is for this reason that their drag is presented here.

The drag of streamlined tanks depends on the interference between the tank and the wing. Careless installation can easily increase drag by a factor of four, as shown in Figure 16-77. The installation should always be improved using streamlined fairings. The drag coefficients shown in the figure are based on the frontal area of the tank, S_{tank}, and are related to the reference area as follows:

$$\Delta C_{D_{\text{tank}}} = \Delta C_{D_S}\left(\frac{S_{\text{tank}}}{S}\right) \tag{16-185}$$

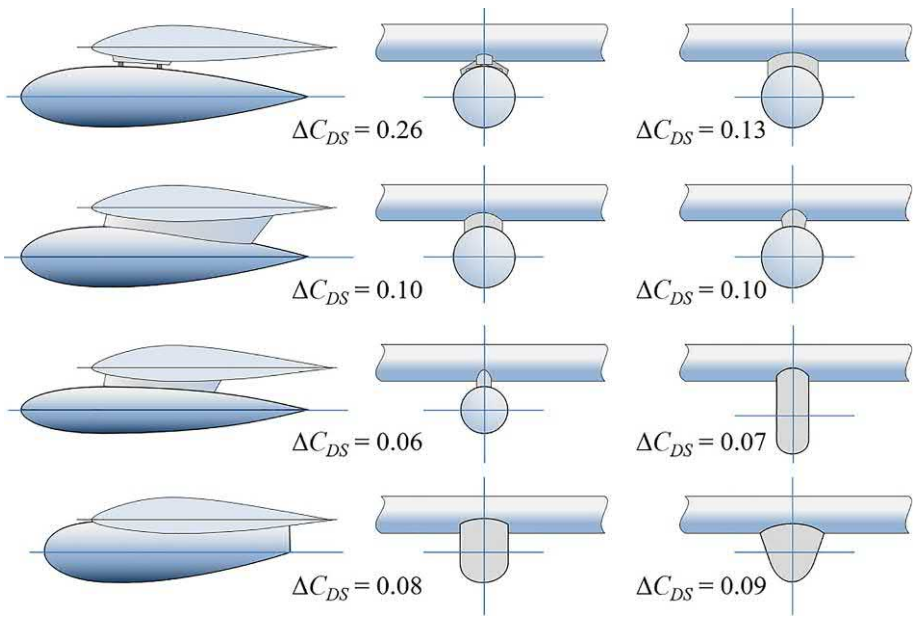


FIGURE 16-77 Drag of external fuel tanks. *Based on S.F. Hoerner, Fluid-Dynamic Drag, L. Hoerner, 1965.*

EXAMPLE 16-22

(a) Evaluate the complete minimum drag coefficient of the SR22 assuming the results from the component drag buildup method of Example 16-11, and the various additive drag contributions evaluated in this section. How does it compare to the $C_{D_{min}} = 0.02541$ calculated from published performance information?

(b) Perform this evaluation at other altitudes as well (only change will be in the skin friction). How will this affect the $C_{D_{min}}$?

SOLUTION:

(a) See Table 16-16 for the result and the discussion that follows:

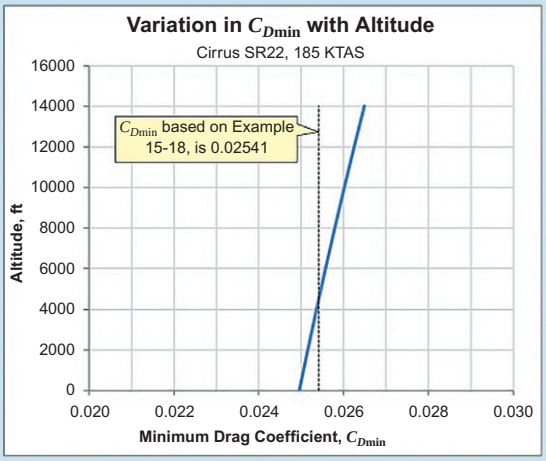
The table shows the estimated drag is in reasonable agreement with the one reverse-engineered from published performance data, or $100 \times 0.02495 / 0.02541 = 98.2\%$. There are many areas that can be refined; for instance, the airplane's tie-down rings and control surface gaps are not included. These would add to the total. On the other hand, it is debatable whether a 20 dragcounts penalty due to the presence of the engine cowling is justifiable (see row 44 in Table 16-20). This penalty is attributed to the fact the front part of the airplane features a cowling with an inlet and exit, which generates substantially higher drag than the smooth nose shape assumed by the fuselage skin friction estimation of Example 16-11. The 20 dragcounts in row 44 are based on an airplane (the P-35) that has a radial engine. It may be draggier than the horizontally opposed piston engine of the SR22. The important point is that while a careful prediction ought to put one in the neighborhood of the drag obtained by experiment, any contribution should be carefully reviewed and justified.

(b) Since the drag analysis was prepared in a spreadsheet, it is easy to change the altitude and get a new estimate. This has been done for altitudes ranging from S-L to 14,000 ft and this is shown in left graph of Figure 16-78. The flight test value of $C_{D_{min}} = 0.02541$ is shown as the vertical dashed line. Interestingly, this value was obtained using cruise data at 8000 ft (see Example 16-24). The right graph of Figure 16-78 shows the contribution of various sources of drag at two airspeeds. Note the large contribution of the lift-induced drag at the lower airspeed.

TABLE 16-20 Drag analysis.

	DRAG ANALYSIS						
			Wing	HT	VT	Fuselage	
39	Sweep angle	$\Lambda_{t\ max} =$	0.00	5.00	18.00		°
40	Form Factor	$FF_j =$	1.311	1.203	1.187	1.399	
41	Intereference Factor, IF	$IF_j =$	1	1.05	1.05	1	
42	Weighted drag factor	$C_{fj} \cdot FF_j \cdot IF_j \cdot S_{wet\,j} =$	0.7140	0.1762	0.1120	0.7607	
43	Skin friction drag	$(1/S)\Sigma C_{fj} \cdot FF_j \cdot IF_j \cdot S_{wet\,j} =$	0.01217				
44	Presence of engine cowling	$\Delta C_{Dcowl} =$	0.002000	Same penalty as that of the Severski P-35			
45	Cooling drag	$\Delta C_{Dcool} =$	0.000812	See Example 16-12			
46	Two COM antennas	$2 \times \Delta C_{Dfin} =$	0.000030	See Example 16-13			
47	Four half-sized "COM" antennas	$4 \times 0.5 \times \Delta C_{Dfin} =$	0.000030	See Example 16-13			
48	Two GPS antennas	$2 \times \Delta C_{Dblister} =$	0.000066	See Example 16-19			
49	Two wing entry steps	$\Delta C_{Dstrut} =$	0.000456	See Example 16-15			
50	6 Flap fairings (double "COM" drag)	$6 \times 2 \times \Delta C_{Dfin} =$	0.000182	Each fairing assumed 2x the COM geometry			
51	External wing tip nav lights	$2 \times \Delta C_{Dblister} =$	0.000066	Assumed to cause same drag as GPS antenna			
52	Main landing gear	$\Delta C_{Dmain} =$	0.002090	See Example 16-16			
53	Nose landing gear	$\Delta C_{Dnose} =$	0.000810	See Example 16-16			
54	Cockpit window drag correction	$\Delta C_{Dwindow} =$	0.000193	See Example 16-18			
55	Sanded walkway, both sides	$\Delta C_{Dwalkway} =$	0.000700	0.00035 per side			
56	Miscellaneous drag coeff.	$C_{D\,misc} =$	0.00744				
57	CRUD	$k_{crud} =$	1.25				
58	Minimum drag coefficient	$C_{D\,min} =$	0.02450	= (0.01217 + 0.00780)·1.25			
59							

EXAMPLE 16-22 (*cont'd*)



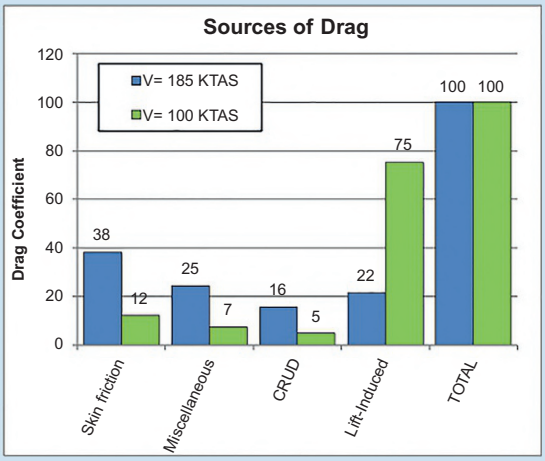


FIGURE 16-78 Variation in the $C_{D_{min}}$ of the SR22 with altitude.

16.5 SPECIAL TOPICS INVOLVING DRAG

Estimating drag for existing aircraft is common in aircraft design. This is helpful for validation or to evaluate the strength of a competitor. This section presents several methods for this purpose. Naturally, there are shortcomings to these methods and some extract less data than others. All assume the simplified or adjusted drag models of Section 16.2, *The Basics of Drag Modeling*.

First, a note of caution: The extraction of drag data for existing aircraft relies on published data. However, care must be exercised, for the source matters. The ideal source is manufacturer's *pilot's operating handbook* (POH) for said aircraft. This is followed by *Jane's All the World's Aircraft* (JAWA) [109]. A common shortcoming in other sources is ambiguity. Lack of clarity in airspeed units is frequent. It is frequently presented using unidentifiable knots. To laypeople a knot is "just a knot." However, to engineers (and pilots) this is far from the truth. An indicated knot (KIAS) is not equal to a calibrated knot (KCAS) and neither is equal to an equivalent knot, let alone a true knot (KTAS). When the only data available are vague, one must rely on sound judgment. A knot next to a stalling or climb speed is most likely KCAS. Yes, it could be KIAS, but this is less likely. A knot next to a cruising speed is most likely KTAS.

16.5.1 Step-by-Step: Extracting Drag from LD_{max}

The simplest method uses LD_{max} and the airspeed at which it is achieved. This information is commonly available from aircraft Pilot's Operating Handbooks (POH) and is almost always based on actual flight testing. The information this particular method extracts is the $C_{D_{min}}$, and assumes the UK-system of units. It is a limitation of the method that it uses the simplified drag model. However, since the $C_{L_{minD}}$ will primarily shift the drag polar sideways (see Section 16.2.2, *Quadratic Drag Modeling*) there really is no error introduced in the extraction of the $C_{D_{min}}$. Another issue is the extraction of drag for propeller powered aircraft. The LD_{max} reported in the POH will include drag from the wind milling propeller (since the purpose is to present the pilot with potentially life-saving information). This can easily double the minimum drag coefficient when compared to the other methods in this section and renders it much higher than required for accurate performance analyses. Therefore, care must be exercised when using these numbers.

Step 1: Gather Information from the Vehicle's POH

Assuming the reader has access to the aircraft's POH, gather the following information: Gross weight (W_0) in lb_f, best glide airspeed (V_{LDmax}), wing area (S) in ft^2, and wing Aspect Ratio (AR). If AR is not known, use wing span (b) in ft and compute it from b^2/S.

Step 2: Convert V_{LDmax} into Units of ft/s

Consistent units must be used. Therefore, if V is read in KTAS is must be converted to ft/s. Similarly, if V_V is given in fpm (ft/min) it must be converted to ft/s. Use the following conversion factors:

Convert KTAS or mph to ft/s:

$$V_{ft/s} = 1.688 \times V_{KTAS} = 1.688 \times 1.15 \times V_{mph}$$

Convert fpm to ft/s: $V_{ft/s} = V_{fpm}/60$

Often the POH will report the best glide airspeed in units of KIAS or KCAS. This must be converted to KTAS for this method is to be applied at altitude (see Section 17.3.2, *Airspeeds: Instrument, Calibrated, Equivalent, True, and Ground Airspeeds* for methods).

Step 3: Calculate the Optimum Glide Lift Coefficient

Calculate the lift coefficient at the best glide speed from:

$$C_{L_{opt}} = 2W_0/\left(\rho V_{LD\max}^2 S\right) \tag{16-186}$$

Step 4: Calculate Span Efficiency

Estimate the span efficiency, e, from any of the methods of Section 9.5.12, *Determination of Span Efficiency*.

Step 5: Compute Minimum Drag

Compute the minimum drag from the following expression:

$$C_{D_{\min}} = \frac{C_L}{LD_{\max}} - \frac{C_L^2}{\pi \cdot AR \cdot e} \tag{16-187}$$

DERIVATION OF EQUATION (16-187)

The simplified drag model is given by:

$$C_D = C_{D_{\min}} + \frac{C_L^2}{\pi \cdot AR \cdot e}$$

Knowledge of the lift-to-drag ratio at a specific condition (here conveniently selected to be the $LD_{\max}$, since many aircraft manufacturers graciously reports this for us), and the lift coefficient associated with it can then be used to extract the minimum drag coefficient.

$$LD_{\max} = \frac{C_L}{C_D} = \frac{C_L}{C_{D_{\min}} + \frac{C_L^2}{\pi \cdot AR \cdot e}}$$

$$\Leftrightarrow \quad C_{D_{\min}} = \frac{C_L}{LD_{\max}} - \frac{C_L^2}{\pi \cdot AR \cdot e}$$

16.5.2 Step-by-Step: Extracting Drag From a Flight Polar Using the Quadratic Spline Method

This method can be used if the Flight Polar (or Rate-of-Sink versus Airspeed or V_V versus V plot) is available, as it often is for sailplanes, gliders, and motor gliders. Usually, this polar is not available for powered airplanes. It can be used to extract $C_{D_{\min}}$, $C_{L_{\min D}}$, and e. This method will not retrieve a drag model that features a drag bucket, but a quadratic one.

Consider the sample Flight Polar in Figure 16-79. Follow the following the stepwise procedure to extract $C_{D_{\min}}$, $C_{L_{\min D}}$, and e.

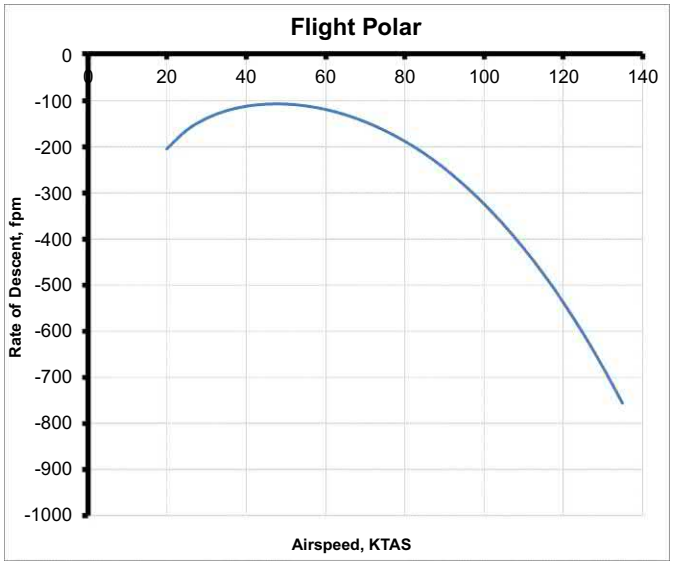


FIGURE 16-79 A typical Flight Polar.

Step 1: Select Data Points from the Flight Polar

Select three arbitrary points on the Flight Polar and record the corresponding V_V and V. For instance, select two points that enclose the minimum (near 50 KTAS in Figure 16-79) and one at a higher speed, for instance near 100 or 120 KTAS.

Step 2: Tabulate

Fill in the table below by entering the V_V and V selected in Step 1 in Columns 1 and 2 below. Calculate the values in Columns 3 through 5.

ID	1 V	2 V_V	3 $x = V^2$	4 $x^2 = V^4$	5 $y = V \cdot V_V$
1	V_1	V_{V1}	V_1^2	V_1^4	$V_1 \cdot V_{V1}$
2	V_2	V_{V2}	V_2^2	V_2^4	$V_2 \cdot V_{V2}$
3	V_3	V_{V3}	V_3^2	V_3^4	$V_3 \cdot V_{V3}$

Note 1: It is important that consistent units be used. Therefore, if V is read in KTAS is must be converted to ft/s. Similarly, if V_V is given in fpm (ft/min), it must be converted to ft/s. Use the conversion factors shown under the Note 1 of Step 2 of Section 16.6.1, *Step-by-Step: Extracting Drag from LDmax*:

Note 2: This formulation assumes the absolute value of the rate-of-sink. Thus, if the V_V is reported with a negative sign it must be converted to a positive number.

Step 3: Fill in the Conversion Matrix and Invert

Fill in the matrix below using the values in Column 4 for the first row in the matrix and Column 3 for the second row. This order is imperative. Then, invert the

matrix. This can be done by some software, for instance, any spreadsheet software offers means to invert matrices:

$$\begin{bmatrix} V_1^4 & V_1^2 & 1 \\ V_2^4 & V_2^2 & 1 \\ V_3^4 & V_3^2 & 1 \end{bmatrix} \rightarrow \begin{bmatrix} V_1^4 & V_1^2 & 1 \\ V_2^4 & V_2^2 & 1 \\ V_3^4 & V_3^2 & 1 \end{bmatrix}^{-1}$$

Step 4: Determine the Coefficients to the Quadratic Spline

Calculate the constants A, B, C by multiplying the inverted matrix in STEP 3 with the vector formed by Column 5 in the table above:

$$\begin{Bmatrix} A \\ B \\ C \end{Bmatrix} = \begin{bmatrix} V_1^4 & V_1^2 & 1 \\ V_2^4 & V_2^2 & 1 \\ V_3^4 & V_3^2 & 1 \end{bmatrix}^{-1} \begin{Bmatrix} V_1 \cdot V_{V1} \\ V_2 \cdot V_{V2} \\ V_3 \cdot V_{V3} \end{Bmatrix}$$

Step 5: Extract Aerodynamic Properties

Using the constants, A, B, C calculated in the previous step, extract the aerodynamic properties:

Induced drag constant: $$k = \left(\frac{\rho S}{2W}\right) C \tag{16-188}$$

Location of minimum drag: $$C_{L_{\min D}} = -\frac{B}{2k} \tag{16-189}$$

Minimum drag coefficient: $$C_{D_{\min}} = A\left(\frac{2W}{\rho S}\right) - kC_{L_{\min D}}^2 \tag{16-190}$$

Oswald efficiency: $$e = \frac{1}{\pi \cdot AR \cdot k} \tag{16-191}$$

DERIVATION OF EQUATIONS (16-188) THROUGH (16-191)

The adjusted drag model is given by:

$$C_D = C_{D_{\min}} + k(C_L - C_{L_{\min D}})^2 \tag{i}$$

This can be expanded as follows:

$$C_D = (C_{D_{\min}} + kC_{L_{\min D}}{}^2) - 2kC_{L_{\min D}} C_L + kC_L^2$$

Recall that the lift coefficient and the *rate-of-descent* (ROD) are given by:

$$C_L = \frac{2W}{\rho V^2 S} \tag{ii}$$

and

$$V_V = \frac{DV}{W} = \frac{\rho V^3 S C_D}{2W} \tag{iii}$$

Substitute Equation (i) into Equation (iii) and expand:

$$V_V = \frac{\rho V^3 S C_D}{2W}$$

$$= \frac{\rho V^3 S\left(\left(C_{D_{\min}} + kC_{L_{\min D}}^2\right) + \left(-2kC_{L_{\min D}}\right)C_L + (k)C_L^2\right)}{2W}$$

$$= \frac{\rho V^3 S\left(kC_L^2 + \left(-2kC_{L_{\min D}}\right)C_L + \left(C_{D_{\min}} + kC_{L_{\min D}}^2\right)\right)}{2W}$$

Substitute Equation (ii) into this and expand:

$$V_V = \frac{\rho V^3 S\left(k\left(\frac{2W}{\rho V^2 S}\right)^2 + \left(-2kC_{L_{\min D}}\right)\left(\frac{2W}{\rho V^2 S}\right) + \left(C_{D_{\min}} + kC_{L_{\min D}}^2\right)\right)}{2W}$$

$$= \frac{\rho V^3 S\left(k\frac{4W^2}{\rho^2 V^4 S^2} + \left(-2kC_{L_{\min D}}\right)\frac{2W}{\rho V^2 S} + \left(C_{D_{\min}} + kC_{L_{\min D}}^2\right)\right)}{2W}$$

Simplify:

$$V_V = \frac{k\frac{4W^2}{\rho V S} + \left(-2kC_{L_{\min D}}\right)2WV + \left(C_{D_{\min}} + kC_{L_{\min D}}^2\right)\rho V^3 S}{2W}$$

$$= k\frac{2W}{\rho V S} + \left(-2kC_{L_{\min D}}\right)V + \left(C_{D_{\min}} + kC_{L_{\min D}}^2\right)\frac{\rho V^3 S}{2W}$$

$$= k\left(\frac{2W}{\rho S}\right)\frac{1}{V} + \left(-2kC_{L_{\min D}}\right)V + \left(C_{D_{\min}} + kC_{L_{\min D}}^2\right)\left(\frac{\rho S}{2W}\right)V^3$$

Multiply through by V to get:

$$V \cdot V_V = \overbrace{k\left(\frac{2W}{\rho S}\right)}^{=C} + \overbrace{\left(-2kC_{L_{\min D}}\right)}^{=B}V^2 + \overbrace{\left(C_{D_{\min}} + kC_{L_{\min D}}^2\right)\left(\frac{\rho S}{2W}\right)}^{=A}V^4$$

$$= C + BV^2 + AV^4$$

Where:

$$A = \left(C_{D_{\min}} + kC_{L_{\min D}}^2\right)\left(\frac{\rho S}{2W}\right) \qquad B = -2kC_{L_{\min D}} \qquad C = k\left(\frac{2W}{\rho S}\right)$$

Therefore, we can rewrite:

$$V \cdot V_V = C + BV^2 + AV^4 = C + Bx + Ax^2$$

Where $x = V^2$. Also, let $y = V \cdot V_V$. We need 3 points (i.e., V_V corresponding to a V) to determine the constants A, B, C. Obtain by inverting the matrix.

$$\left.\begin{aligned} y_1 &= Ax_1^2 + Bx_1 + C \\ y_2 &= Ax_2^2 + Bx_2 + C \\ y_3 &= Ax_3^2 + Bx_3 + C \end{aligned}\right\} \Rightarrow \begin{bmatrix} x_1^2 & x_1 & 1 \\ x_2^2 & x_2 & 1 \\ x_3^2 & x_3 & 1 \end{bmatrix}\begin{Bmatrix} A \\ B \\ C \end{Bmatrix} = \begin{Bmatrix} y_1 \\ y_2 \\ y_3 \end{Bmatrix}$$

$$\Rightarrow \begin{Bmatrix} A \\ B \\ C \end{Bmatrix} = \begin{bmatrix} x_1^2 & x_1 & 1 \\ x_2^2 & x_2 & 1 \\ x_3^2 & x_3 & 1 \end{bmatrix}^{-1}\begin{Bmatrix} y_1 \\ y_2 \\ y_3 \end{Bmatrix}$$

Then, the coefficients can be found as follows:

$$C = k\left(\frac{2W}{\rho S}\right) \quad \Leftrightarrow \quad k = \left(\frac{\rho S}{2W}\right)C$$

$$B = -2kC_{L_{\min D}} \quad \Leftrightarrow \quad C_{L_{\min D}} = -\frac{B}{2k}$$

$$A = \left(C_{D_{\min}} + kC_{L_{\min D}}^2\right)\left(\frac{\rho S}{2W}\right)$$

$$\Leftrightarrow \quad C_{D_{\min}} = A\left(\frac{2W}{\rho S}\right) - kC_{L_{\min D}}^2$$

Also note that: $$k = \frac{1}{\pi \cdot AR \cdot e} \quad \Leftrightarrow \quad e = \frac{1}{\pi \cdot AR \cdot k}$$

EXAMPLE 16-23

Consider the Flight Polar for a powered sailplane shown in Figure 16-80. Extract its drag characteristics, ignoring the existence of a drag bucket and assuming it can be described using the adjusted drag model. Its gross weight is $W_0 = 1876\ \text{lb}_\text{f}$, wing area and aspect ratio are $S = 202\ \text{ft}^2$ and $AR = 29.29$, respectively.

SOLUTION:

Step 1 through 3: The three selected point are shown in Figure 16-80 and are tabulated below:

$$\begin{Bmatrix} A \\ B \\ C \end{Bmatrix} = \begin{bmatrix} x_1^2 & x_1 & 1 \\ x_2^2 & x_2 & 1 \\ x_3^2 & x_3 & 1 \end{bmatrix}^{-1} \begin{Bmatrix} y_1 \\ y_2 \\ y_3 \end{Bmatrix}$$

$$= \begin{bmatrix} 28{,}267{,}394 & 5317 & 1 \\ 368{,}383{,}509 & 19{,}193 & 1 \\ 1{,}104{,}195{,}089 & 33{,}229 & 1 \end{bmatrix}^{-1} \begin{Bmatrix} 133.7 \\ 461.8 \\ 1215.3 \end{Bmatrix}$$

Step 4: Calculate the constants A, B, C:

$$\begin{Bmatrix} A \\ B \\ C \end{Bmatrix} = \begin{Bmatrix} 1.07602 \times 10^{-6} \\ -0.00272772 \\ 117.7650518 \end{Bmatrix}$$

Step 5: Extract the aerodynamic properties using the constants A, B, C:

Induced drag constant:

$$k = \left(\frac{\rho S}{2W}\right) C = \left(\frac{(0.002378)(201.3)}{2(1876)}\right)(117.8)$$

$$= 0.015074$$

Location of minimum drag:

$$C_{L_{\text{min}D}} = -\frac{B}{2k} = -\frac{-0.00272772}{2 \times 0.015074} = 0.090478$$

Minimum drag coefficient:

$$C_{D_{\text{min}}} = A\left(\frac{2W}{\rho S}\right) - kC_{L_{\text{min}D}}^2 = 0.008283$$

Oswald efficiency:

$$e = \frac{1}{\pi \cdot AR \cdot k} = \frac{1}{\pi \cdot (29.29) \cdot (0.015074)}$$

$$= 0.72094$$

	Selected Data						
ID	V km/h	V_V, fpm	V KCAS	V ft/s	$x = V^2$	$x^2 = V^4$	$Y = V \cdot V_V$
1	80	110	43	73	5317	28267394	133.7
2	152	200	82	139	19193	368383509	461.8
3	200	400	108	182	33229	1104195089	1215.3

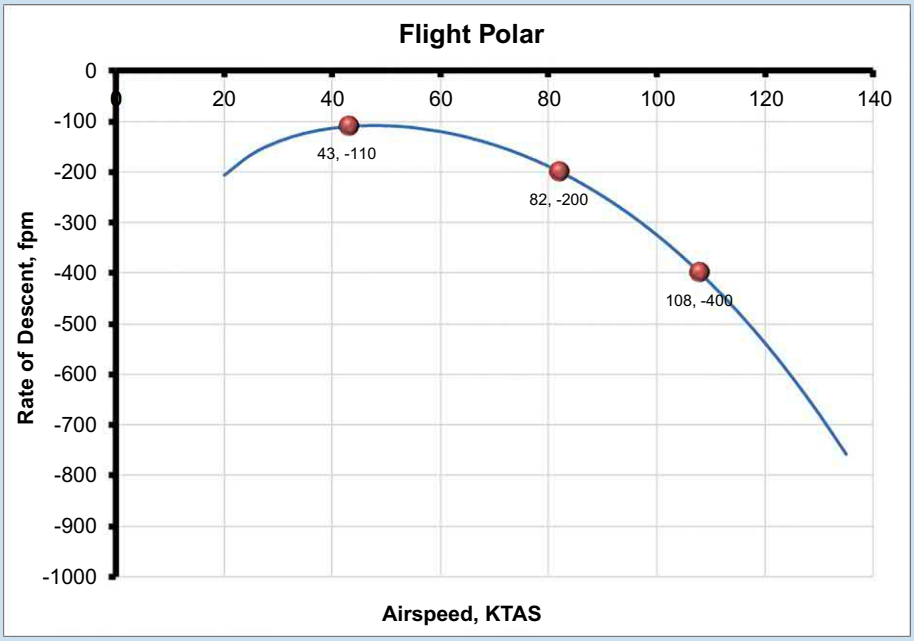


FIGURE 16-80 A Flight Polar for a powered sailplane.

16.5.3 Step-by-Step: Extracting Drag Coefficient for a Piston Powered Propeller Aircraft

The drag coefficient of piston-powered airplanes can be extracted from typical data provided in the POH. The accuracy is contingent on the quality of the data provided by the manufacturer. For propeller aircraft, the hardest parameter to obtain is the propeller efficiency. An "educated guess" is usually required. The methods of Chapter 15, *Thrust Modeling for Propellers* should help.

(1) Method 1: Extracting $C_{D_{min}}$ using Cruise Performance

The following procedure illustrates extraction of $C_{D_{min}}$ using cruise performance. The procedure may have to be modified for aircraft for which POH performance data of the kind shown here is not available. Here, we will illustrate the method using a data sheet for a Cirrus SR22.

Figure 16-81 shows a page from the POH for a Cirrus SR22. Similar information can also be obtained from the *Type Certificate Data Sheet* (TCDS) that can be downloaded from the FAA official website (www.faa.gov). The excerpt displays a format typically used for GA aircraft.

Step 1:

Determine the following parameters for the type: Reference area (S) in ft^2, aspect ratio (AR), rated engine power (P_A) in BHP, and gross weight (W_0) in lb$_f$.

Step 2:

Using the POH, extract the cruising speed and the associated altitude. Usually, these numbers are normalized to the gross weight. Manufacturers present the cruising speed in KTAS. The true airspeed in KTAS is required.

Step 3:

Determine the density of air, ρ, at the cruise altitude using Equation (17-7). Then, convert the airspeed in KTAS to ft/s by multiplying it by 1.688. This airspeed is V.

8000 Feet Pressure Altitude										
		ISA -30°C (-31°C)			ISA (-1°C)			ISA + 30°C (29°C)		
RPM	MAP	PWR	KTAS	GPH	PWR	KTAS	GPH	PWR	KTAS	GPH
2700	21.7	83%	183	19.7	78%	183	18.6	75%	178	17.7
2600	21.7	79%	180	18.8	75%	180	17.8	71%	175	17.0
2500	21.7	75%	176	17.7	71%	176	16.8	67%	171	16.0
2500	20.7	70%	172	16.7	66%	172	15.8	63%	167	15.0
2500	19.7	66%	168	15.6	62%	168	14.8	59%	163	14.0
2500	18.7	61%	163	14.5	58%	163	13.8	55%	158	13.1
2500	17.7	57%	159	13.5	54%	159	12.8	51%	153	12.1

FIGURE 16-81 Excerpt from a POH for Cirrus SR22. *Courtesy of Cirrus Aircraft. Copyright 2021 Cirrus Aircraft or its Affiliates. All Rights Reserved. Image reproduced with the permission of Cirrus.*

Step 4:

Determine the Oswald's efficiency and the lift-induced drag constant at the condition. For a medium AR aircraft, Equation (9-129) can be used, repeated below for convenience:

Oswald's efficiency: $e = 1.78(1 - 0.045AR^{0.68}) - 0.64$

Lift-induced drag constant: $k = 1/(\pi \cdot AR \cdot e)$

Step 5:

Calculate the minimum drag coefficient from:

$$C_{D_{min}} = \frac{\eta_p \times 1100 \times P_{BHP}}{\rho V^3 S} - k\left(\frac{2W}{\rho V^2 S}\right)^2 \qquad (16\text{-}192)$$

Note that the selection of η_p can be consequential. Be careful. If the propeller is a fixed pitch "climb" propeller use a value ranging from 0.68 to 0.72. If the propeller is a fixed pitch "cruise" propeller, use a value ranging from 0.75 to 0.80. If the airplane is equipped with a constant-speed propeller, use a value close to 0.85.

DERIVATION OF EQUATION (16-192)

The minimum drag can be estimated from:

$$C_D = C_{D_{min}} + C_{D_i} \quad \Leftrightarrow \quad C_{D_{min}} = C_D - C_{D_i}$$

Since thrust equals drag at this condition, we can determine the drag coefficient as follows:

$$T = D = \frac{1}{2}\rho V^2 S C_D \quad \Leftrightarrow$$

$$C_D = \frac{2T}{\rho V^2 S} = \frac{2\left(\eta_p \times 550 \times P_{BHP}/V\right)}{\rho V^2 S} = \frac{\eta_p \times 1100 \times P_{BHP}}{\rho V^3 S}$$

Furthermore, using the simplified drag model and the lift coefficient, the lift-induced drag is given by:

$$C_{D_i} = kC_L^2 = k\left(\frac{2W}{\rho V^2 S}\right)^2$$

Inserting this into the expression for $C_{D_{min}}$ yields:

$$C_{D_{min}} = C_D - C_{D_i} = \frac{\eta_p \times 1100 \times P_{BHP}}{\rho V^3 S} - k\left(\frac{2W}{\rho V^2 S}\right)^2$$

EXAMPLE 16-24

Estimate the total, induced, and minimum drag coefficient for the Cirrus SR22, using the data in Figure 16-81 using the published cruising speed of 183 KTAS (308.9 ft/s) at 8000 ft and 78% power at ISA condition.

EXAMPLE 16-24 (*cont'd*)

SOLUTION:
Steps 1–3:

Reference area: $S = 144.9\,\text{ft}^2$

Aspect ratio: $AR = 10.1$ (using $b = 38.3\,\text{ft}$).

Engine power at condition:
$P_A = 0.78 \times 310\,\text{BHP} = 241.8\,\text{BHP}$.

Gross weight: $W_0 = 3400\ \text{lb}_\text{f}$.

Density of air at 8000 ft:
$\rho = 0.002378(1 - 0.0000068756 \times 8000)^{4.2561}$
$= 0.001869\ \text{slugs/ft}^3$.

Step 4:
Both the Oswald's efficiency factor and lift-induced drag constant have been calculated multiple times throughout this book. We need the latter one for this problem. It is $k = 0.04207$.

Step 5:
Since we don't know the propeller efficiency, we must guess. The airplane features a constant-speed propeller, specifically designed for the aircraft. Thus, its propeller efficiency is as high as 0.85 at this condition. This is a guess, so regard the resulting drag coefficient with caution. The minimum drag coefficient is estimated as follows:

$$C_{D_{\min}} = \frac{\eta_p \times 1100 \times P_{BHP}}{\rho V^3 S} - k\left(\frac{2W}{\rho V^2 S}\right)^2$$
$$= \frac{0.85 \times 1100 \times 241.8}{(0.001869)(308.9)^3(144.9)}$$
$$-(0.04207)\left(\frac{2(3400)}{(0.001869)(308.9)^2(144.9)}\right)^2 = 0.02541$$

The total drag can be estimated using the thrust relation shown in the above derivation:
Total drag coefficient:

$$C_D = \frac{\eta_p \times 1100 \times P_A}{\rho V^3 S} = \frac{0.85 \times 1100 \times 241.8}{(0.001869)(308.9)^3(144.9)} = 0.02832$$

The lift-induced drag is the difference between the total and minimum drag:

$$C_{D_i} = C_D - C_{D_{\min}} = 0.02832 - 0.02541 = 0.00291$$

(2) Method 2: Extracting $C_{D_{\min}}$ using Climb Performance

The following procedure illustrates extraction of $C_{D_{\min}}$ using climb performance. This requires the *rate-of-climb* (ROC) and the associated airspeed and altitude to be established. Ideally, this should be the best ROC, obtained at V_y (the best ROC airspeed). Since V_y occurs at a relatively low AOA, with less flow separation than, say, V_x (the best *angle-of-climb* airspeed) and, thus, closer adherence to the quadratic drag model. It is also better to use data at S-L as this will require fewer corrections.

Step 1: Same as Step 1 of Method 1.

Step 2:
Using the POH, extract the ROC, the associated climb airspeed, and altitude (ideally V_y at S-L). Usually, these numbers are normalized using the gross weight. Correct climb speed presented in KIAS to KCAS before it is converted to KTAS, which is required for this procedure. This conversion should be implemented using the methods of Chapter 17, *Performance—Introduction*.

Step 3:
Determine the density of air (ρ) at the climb altitude using Equation (17-7). Ideally, this should be at S-L ($\rho = 0.002378\ \text{slugs/ft}^3$). Convert the ROC ($V_V$) in fpm to ft/s per $V_V = \text{ROC}/60$. Convert the airspeed in KTAS to ft/s by multiplying it by 1.688. This airspeed is denoted by V in the following formulas.

Step 4: Same as Step 4 of Method 1.

Step 5:
Calculate the minimum drag coefficient from:

$$C_{D_{\min}} = \frac{\eta_p 1100 P_{BHP} - 2WV_V}{\rho V^3 S} - k\left(\frac{2W}{\rho V^2 S}\right)^2 \qquad (16\text{-}191)$$

Again, note that if the propeller efficiency, η_p, is not known, one must rely on engineering judgment to assess its value, and this can be tricky. Assuming the flight condition to be at V_V, use a value ranging from 0.68 to 0.72 if the propeller is a fixed pitch "climb" propeller. If the propeller is a fixed pitch "cruise" propeller, use a value ranging from 0.6 to 0.7, and if equipped with a constant speed propeller, use a value ranging from 0.68–0.75. Also note that, just like for Method 1, correcting the power of normally aspirated engines to the altitude at which the aircraft is operating is crucial. For this, use the Gagg and Ferrar model of Equation (7-8).

DERIVATION

The vertical speed, V_V, is determined from:

$$V_V = \frac{ROC}{60} = \frac{TV - DV}{W}$$

Replacing the thrust (T) and drag (D) with the standard expressions yields:

$$V_V = \frac{\left(\frac{\eta_p 550 P_{BHP}}{V}\right)V - \left(\frac{1}{2}\rho V^2 S C_D\right)V}{W}$$
$$= \frac{\eta_p 550 P_{BHP} - \frac{1}{2}\rho V^3 S C_D}{W}$$

Multiplying through by W and substituting the simplified drag model and, then, the lift coefficient leads to:

$$WV_V = \eta_p 550 P_{BHP} - \frac{1}{2}\rho V^3 S\left(C_{D_{\min}} + kC_L^2\right)$$
$$= \eta_p 550 P_{BHP} - \frac{1}{2}\rho V^3 S\left(C_{D_{\min}} + k\left(\frac{2W}{\rho V^2 S}\right)^2\right)$$

Solving for the $C_{D_{\min}}$ returns:

$$C_{D_{\min}} = \frac{\eta_p 1100 P_{BHP} - 2WV_V}{\rho V^3 S} - k\left(\frac{2W}{\rho V^2 S}\right)^2$$

EXAMPLE 16-25

Estimate the minimum drag coefficient for the Cirrus SR22, using the climb performance extraction method at V_y and the following data in addition to S, k, and W from the previous example.

SOLUTION:
Step 1–5:

Engine power at condition, $P_A = 310\,\text{BHP}$

Best rate-of-climb

$ROC = 1398\,\text{fpm} \Rightarrow V_V = 1398/60 = 23.3\,\text{ft/s}$

Best rate-of-climb airspeed

$V_y = 101\,\text{KIAS} = 101\,\text{KCAS}$
$= 101\,\text{KTAS} = 170.5\,\text{ft/s}$ (at S-L)

Propeller efficiency at V_y $\eta_p = 0.7$ (guess)

EXAMPLE 16-25 *(cont'd)*

$$C_{D_{\min}} = \frac{\eta_p 1100 P_{BHP} - 2WV_V}{\rho V^3 S} - k\left(\frac{2W}{\rho V^2 S}\right)^2$$
$$= \frac{(0.7)1100(310) - 2(3400)(23.3)}{(0.002378)(170.5)^3(144.9)}$$
$$- (0.04207)\left(\frac{2(3400)}{(0.002378)(170.5)^2(144.9)}\right)^2$$
$$= 0.02761$$

Note that if the propeller efficiency is 0.689, rather than 0.7, then $C_{D_{\min}}$ will be 0.02541, which matches that of Method 1. This shows the importance of properly selecting the propeller efficiency. However, it is also possible the result reflects the presence of flow separation.

16.5.4 Extracting Drag Coefficient From Published Data for Piston Aircraft

The following Visual Basic for Applications routine can be used with Microsoft Excel to extract various drag-related parameters using the previously mentioned method. As shown, it estimates Oswald's efficiency assuming a straight wing. However, this is easy to modify. Also, note that the input power (`P_BHP`) is "at-condition." For instance, the rated power for the SR22 is 310 BHP, but the at-condition power used in Example 16-24, has dropped to 241.8 BHP.

```
Function Extract_CD(Sref As Single, AR As Single, W0 As Single, P_BHP As Single, eta
As Single, Vktas As Single, H As Single, Mode As Byte) As Single
'This function uses the method of Section 16.6.3 to extract CD, CDi, CDmin and others
'for a piston powered prop aircraft. Only valid for propeller aircraft with straight
'wings.
'
'Variables: Sref   = Reference wing area (ex. 145 ft²)
'           AR     = Aspect Ratio (ex. 10)
'           W0     = Weight at condition (e.g. altitude and airspeed) (ex. 3100 lbf)
'           P_BHP  = Horsepower at condition (e.g. 205 BHP)
'           eta    = Estimated propeller efficiency at condition (ex. 0.85)
'           Vktas  = Airspeed in KTAS at condition
'           H      = Altitude in ft at condition
'           Mode   = What to return: =0 for CD, =1 for CDi, =2 for CDmin,
'                                    =3 for CL, =10 for Thrust
'
'Initialize
    Dim rho As Single, V As Single
    Dim T As Single, e As Single
    Dim CL As Single, CD As Single, CDi As Single, CDmin As Single
```

```
'Presets                                                    'Airspeed in ft/s
    V = 1.688 * Vktas                                       'Illegitimate airspeed. Exit
    If V < 30 Then                                          'Indicate error
        Extract_CD = -1
        Exit Function
    End If
    rho = 0.002378 * (1 - 0.0000068756 * H) ^ 4.2561        'Density
    T = eta * 550 * P_BHP / V                               'Thrust
    CL = 2 * W0 / (rho * V ^ 2 * Sref)                      'Lift coefficient

'Calculate CD
    CD = eta * 1100 * P_BHP / (rho * V ^ 3 * Sref)

'Calculate CDi
    e = 1.78 * (1 - 0.045 * AR ^ 0.68) - 0.64
    CDi = CL ^ 2 / (3.14159265 * AR * e)

'Calculate CDmin
    CDmin = CD - CDi

'Return
    Select Case Mode
    Case 0 'CD
        Extract_CD = CD
    Case 1 'CDi
        Extract_CD = CDi
    Case 2 'CDmin
        Extract_CD = CDmin
    Case 3 'CL
        Extract_CD = CL
    Case 10 'T
        Extract_CD = T
    End Select
End Function
```

16.5.5 Determining Drag Characteristics From Wind Tunnel Data

Standard wind tunnel testing yields a number of static force and moment coefficients such as C_D, C_L, C_Y, $\boldsymbol{C_L}$, $\boldsymbol{C_M}$, and $\boldsymbol{C_N}$. This section focuses on the first two; C_L and C_D. A conventional alpha-sweep involves changing the AOA from some minimum value (e.g., −5 degrees) to some maximum value (e.g., +20 degrees). Thus, it returns a list of coefficients as a function of α. This permits a drag polar of the form $C_D = A \cdot C_L^2 + B \cdot C_L + C$ to be developed using a quadratic least-squares curvefit. The coefficients of this polynomial can be used to extract the coefficient $C_{D_{min}}$, $C_{L_{minD}}$, and the Oswald's span efficiency factor, e, provided the airplane's AR has be established. If so, it can then be shown that these parameters are related to the constants of the curvefit polynomial as follows:

$$e = \frac{1}{\pi \cdot AR \cdot A} \tag{16-194}$$

$$C_{L_{minD}} = -\frac{B}{2A} \tag{16-195}$$

$$C_{D_{min}} = C - \frac{B^2}{4A} \tag{16-196}$$

EXAMPLE 16-26

The following data from a wind tunnel test of a complete aircraft configuration are given in the following table:

C_L	-0.4649	-0.3240	-0.1917	-0.0767	0.0240	0.1217	0.2367	0.3518	0.4668	0.5617	0.6537	0.7169	0.7888	0.8492
C_D	0.0591	0.0488	0.0400	0.0334	0.0292	0.0280	0.0298	0.0334	0.0405	0.0478	0.0571	0.0669	0.0778	0.0891

Determine $C_{D_{min}}$, $C_{L_{minD}}$, and e using a quadratic, least-squares curvefit of the form $C_D = A \cdot C_L^2 + B \cdot C_L + C$, if the aspect ratio, $AR = 6$.

SOLUTION:

One way to obtain the curvefit is to use commercial spreadsheet software like Microsoft Excel, enter the data and plot using a scatter graph. Then, the user can select the curve and add a trendline with the associated equation and correlation coefficient displayed. This is shown in Figure 16-82. The resulting curvefit shows the polynomial constants are given by $A = 0.1056$, $B = -0.0226$, and $C = 0.0292$. Then the drag parameters can be determined as follows:

$$e = \frac{1}{\pi \cdot AR \cdot A} = \frac{1}{\pi \cdot 6 \cdot 0.1056} = 0.5024$$

$$C_{L_{minD}} = -\frac{B}{2A} = -\frac{-0.0229}{2 \cdot 0.1056} = 0.1070$$

$$C_{D_{min}} = C - \frac{B^2}{4A} = 0.0292 - \frac{(-0.0229)^2}{4 \cdot 0.1056} = 0.02799$$

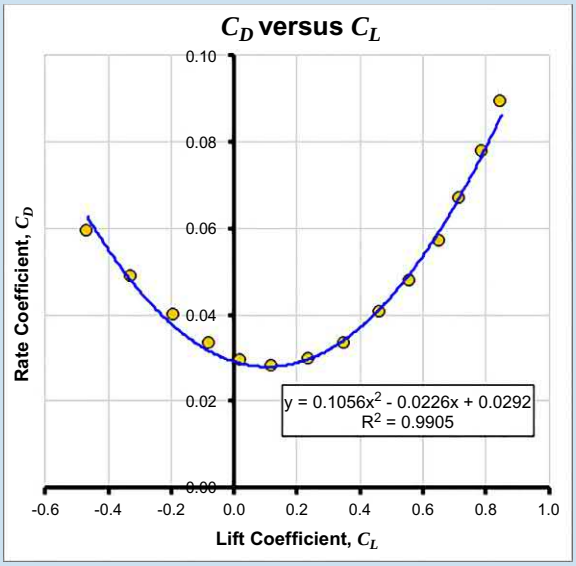


FIGURE 16-82 Hypothetical wind tunnel test data for some complete aircraft plotted with a trendline generated in Microsoft Excel.

DERIVATION OF EQUATIONS (16-194) THROUGH (16-196)

Begin by equating the two forms of the drag coefficients; the quadratic curvefit and the adjusted drag model of Equation (16-11):

$$C_D = AC_L^2 + BC_L + C = C_{D_{min}} + k(C_L - C_{L_{minD}})^2$$

Where $k = 1/(\pi \cdot AR \cdot e)$. Expand and sort coefficients based on their dependency on C_L^2 and C_L:

$$AC_L^2 + BC_L + C = \overbrace{k}^{=A} C_L^2 + \overbrace{(-2kC_{L_{minD}})}^{=B} C_L + \overbrace{C_{D_{min}} + kC_{L_{minD}}^2}^{=C}$$

Coefficient A yields the Oswald's efficiency:

$$k = A = \frac{1}{\pi \cdot AR \cdot e} \quad \Rightarrow \quad e = \frac{1}{\pi \cdot AR \cdot A}$$

Coefficient B yields the $C_{L_{minD}}$:

$$B = -2kC_{L_{minD}} = -2AC_{L_{minD}} \quad \Rightarrow \quad C_{L_{minD}} = -\frac{B}{2A}$$

Using the two previous results with Equation (iii), we get:

$$C = C_{D_{min}} + kC_{L_{minD}}^2 = C_{D_{min}} + A\left(-\frac{B}{2A}\right)^2 = C_{D_{min}} + \frac{B^2}{4A}$$

$$\Rightarrow \quad C_{D_{min}} = C - \frac{B^2}{4A}$$

16.6 ADDITIONAL INFORMATION—DRAG OF SELECTED AIRCRAFT

When estimating the drag of a new aircraft design, it is strongly recommended that the designer compares own results to that of the aircraft in the below tables that most similarly resembles the new aircraft. This can help flag a possible over- or underestimation. This section presents information for selected classes and models of aircraft that is helpful when validating the drag model for a new aircraft.

16.6.1 General Range of Subsonic Minimum Drag Coefficients

Table 16-21 shows the expected range of values of subsonic minimum drag coefficients for several classes of aircraft. These numbers do not bracket all possible aircraft configurations—there may be specific aircraft that are outside of the range shown. However, most aircraft reside between the lower and upper limits.

16.6.2 Drag of Various Aircraft by Class

Table 16-22 lists selected drag related figures for a number of aircraft of different classes. Some of these are displayed in Figure 16-43. The data were gathered from a number of sources. Note that some of the data were retrieved from graphs using "careful eyeballing" and should be regarded with care.

The numbers come from a variety of sources; Perkins and Hage [110], Stinton [111], Roskam [52], Nicolai [78], NASA SP-468 [112], NASA CR-114494 [113], and the author's own estimates. The author's estimations utilize Method 1 of Section 16.5.3, *Step-by-Step: Extracting Drag Coefficient for a Piston Powered Propeller Aircraft*, utilizing performance data from the corresponding aircraft's Pilots Operating Handbook (POH) or other reliable sources. The LD_{max} estimated by the author for propeller aircraft assumes no additional drag due to windmilling or stopped propellers. Refer to Section 16.4.13, *Drag of Windmilling and Stopped Propellers*, for methods on how to account for this drag. Windmilling propellers can easily increase the minimum drag coefficient by 150 dragcounts or more. Additionally, although expected, there is no guarantee the manufacturer has not bolstered performance values in the POH. For this reason, treat all drag data with caution.

EXERCISES

(1) Estimate the skin friction coefficient for an airfoil whose chord is 5.25 ft at 25,000 ft and 250 KTAS airspeed on a day at which the outside air temperature is 30°F warmer than a standard day. Do this using the following assumptions:
(a) fully laminar boundary layer,
(b) fully turbulent boundary layer assuming incompressible flow,
(c) fully turbulent boundary layer assuming compressible flow,
(d) mixed boundary layer for which the transition on the upper surface occurs at chord station 1.3 ft and at 65% chord on the lower surface.
Ans: (a) 0.0005037, (b) 0.003186, (c) 0.003139, (d) 0.002119.

(2) An aircraft has a drag polar given by $C_D = 0.035 + 0.052C_L^2$. Determine the C_L for LD_{max} and the magnitude of the LD_{max}. (Hint: $\frac{d}{dx}\left(\frac{u}{v}\right) = \frac{u' \cdot v - u \cdot v'}{v^2}$)
Ans: C_L where LD_{max} occurs is 0.8549, LD_{max} is 11.71.

(3) Consider the wing shown in Figure 16-83 and for which the representative skin friction coefficients for

TABLE 16-21 Range of subsonic minimum drag coefficients, $C_{D_{min}}$.

Class of Aircraft	Range of C_{Dmin}	
	Lower	Upper
World War I Era Aircraft 1914-1918	0.0317	0.0771
Interwar Era Aircraft 1918-1939	0.0182	0.0585
Multi-Engine WW-II Bombers (Piston)	0.0239	0.0406
Single and Multi-Engine WW-II Fighters (Piston)	0.0157	0.0314
Multi-Engine Commercial Transport Aircraft (Piston)	0.0191	0.0258
Kitplanes (Homebuilt) and LSA	0.0119	0.0447
Single Engine GA Aircraft (Piston and Turboprop)	0.0174	0.0680
GA ag-aircraft, single engine, propeller, clean	0.0550	0.0600
GA ag-aircraft, single engine, propeller, spray-system	0.0700	0.0800
Twin Engine GA Aircraft (Piston and Turboprop)	0.0230	0.0369
Flying Boats	0.0233	0.0899
Selected Jet Fighter/Trainer Aircraft	0.0083	0.0240
Selected Jet Bomber and Attack Aircraft	0.0068	0.0160
Commercial Jetliners and Business Jets	0.0160	0.0219
Various Subsonic Military Aircraft (Props and Jets)	0.0145	0.0250
High performance sailplane	0.0060	0.0100
Tailless aircraft, propeller	0.0150	0.0200
Tailless aircraft, jet	0.0080	0.0140
Low altitude subsonic cruise missile (high W/S)	0.0300	0.0400

TABLE 16-22 Drag characteristics of selected aircraft.

World War I Era Aircraft 1914-1918									
Make	Model	AR	S, ft²	S_{wet}, ft²	f, ft²	C_f	$C_{D\min}$	$LD_{\max}$	Reference
Albatross	D-III	4.65	231	-	10.74	-	0.0465	7.5	NASA SP-468
B.E.	2c	4.47	371	-	13.66	-	0.0368	8.2	NASA SP-468
Caproni	CA.42	5.43	2223	-	98.70	-	0.0444	8.2	NASA SP-468
De Havilland	DH-2	3.88	249	-	10.71	-	0.0430	7.0	NASA SP-468
	DH-4	4.97	440	-	21.82	-	0.0422	8.1	NASA SP-468
Fokker	D-VII	4.70	221	-	8.93	-	0.0404	8.1	NASA SP-468
	D-VIII	6.58	115	-	6.34	-	0.0552	8.1	NASA SP-468
	E-III	5.70	172	-	12.61	-	0.0771	6.4	NASA SP-468
	Dr.-1 Triplane	4.04	207	-	6.69	-	0.0323	8.0	NASA SP-468
Gotha	G.V	7.61	963	-	68.45	-	0.0711	7.7	NASA SP-468
Handley Page	0/400	7.31	1655	-	70.67	-	0.0427	9.7	NASA SP-468
Junkers	D-I	5.46	159	-	9.75	-	0.0612	7.0	NASA SP-468
	J-I	6.40	522	-	17.50	-	0.0335	10.3	NASA SP-468
Nieuport	Model 17	5.51	159	-	7.81	-	0.0491	7.9	NASA SP-468
Sopwith	5F.1 Dolphin	4.85	263	-	8.35	-	0.0317	9.2	NASA SP-468
	F.1 Camel	4.11	231	-	8.73	-	0.0378	7.7	NASA SP-468
SPAD	XIII C.1	3.69	227	-	8.33	-	0.0367	7.4	NASA SP-468

Interwar Era Aircraft 1918-1939									
Make	Model	AR	S, ft²	S_{wet}, ft²	f, ft²	C_f	$C_{D\min}$	$LD_{\max}$	Reference
Beechcraft	D17S	4.18	296	-	5.39	-	0.0182	11.7	NASA SP-468
Boeing	P-26A	5.24	149	-	6.68	-	0.0448	8.3	NASA SP-468
Curtiss	Hawk P-6E	4.76	252	-	9.35	-	0.0371	8.7	NASA SP-468
	JN-4H	7.76	352.6	-	17.64	-	0.0500	9.24	NASA SP-468
	R2C-1	4.18	140	-	2.88	-	0.0206	10.9	NASA SP-468
	Robin	7.54	223	-	13.10	-	0.0585	8.7	NASA SP-468
Dayton Wright RB	Hall Scott L-62	4.38	102	-	3.22	-	0.0316	9	NASA SP-468
Fokker	F-2	7.10	452	-	21.10	-	0.0466	9.4	NASA SP-468
Ford	5-AT	7.26	835	-	39.33	-	0.0471	9.5	NASA SP-468
Handley Page	W8F	4.67	1456	-	79.93	-	0.0549	7.1	NASA SP-468
Lockheed	Orion 9D	7.01	262	-	5.50	-	0.0210	14.1	NASA SP-468
	Vega 5C	6.11	275	-	7.65	-	0.0278	11.4	NASA SP-468
Northrop	Alpha	5.93	312	-	8.55	-	0.0274	11.3	NASA SP-468
Ryan	NYP	6.63	319	-	12.10	-	0.0379	10.1	NASA SP-468
Stinson	SR-8B	6.84	256	-	8.91	-	0.0348	10.8	NASA SP-468
Supermarine	S-4	6.84	136	-	3.73	-	0.0274	12.1	NASA SP-468

Multi-Engine WW-II Bombers (Piston)									
Make	Model	AR	S, ft²	S_{wet}, ft²	f, ft²	C_f	$C_{D\min}$	$LD_{\max}$	Reference
Boeing	B-17	7.58	1420	5900	39.00	0.0067	0.0275	-	Perkins & Hage
	B-17G	7.58	1420	-	42.83	-	0.0302	12.7	NASA SP-468
	B-29	11.50	1736	-	41.16	-	0.0241	16.8	NASA SP-468
	B-29A	11.49	1736	7500	43.50	0.0058	0.0251	-	Roskam
	B-29B	11.49	1736	7100	41.50	0.0058	0.0239	-	Roskam
Consolidated	B-24J	11.55	1048	-	42.54	-	0.0406	12.9	NASA SP-468
North American	B-25	7.49	610	2800	18.00	0.0064	0.0295	-	Perkins & Hage

Single and Multi-Engine WW-II Fighters (Piston)									
Make	Model	AR	S, ft²	S_{wet}, ft²	f, ft²	C_f	$C_{D\min}$	$LD_{\max}$	Reference
Curtiss	SB2C-1	5.88	422	-	9.52	-	0.0225	12.4	NASA SP-468
Grumman	F6F-3	5.34	334	-	7.05	-	0.0211	12.2	NASA SP-468
Lockheed	P-38	8.26	327.5	1500	8.20	0.0055	0.0250	-	Perkins & Hage
	P-38L	8.26	327.5	-	8.78	-	0.0268	13.5	NASA SP-468
Martin	B-26F	7.66	658	-	20.66	-	0.0314	12.0	NASA SP-468
North American	P-51B	5.83	235	880	3.70	0.0042	0.0157	-	Roskam
	P-51D	5.86	233	-	3.80	-	0.0163	14.6	NASA SP-468
Republic	P-47	5.54	300	1200	6.50	0.0054	0.0217	-	Perkins & Hage
Seversky	P-35	5.89	220	-	6.05	-	0.0275	11.3	NACA WR-L-489
					5.52		0.0251	11.8	NASA SP-468

TABLE 16-22 Drag characteristics of selected aircraft—cont'd

Selected Jet Fighter/Trainer Aircraft									
Make	**Model**	AR	S, ft²	S_{wet}, ft²	f, ft²	C_f	$C_{D\min}$	$LD_{\max}$	**Reference**
Cessna	T-37	6.20	183.9	770	3.15	0.0041	0.0171	-	Roskam
Convair	F-106A	2.10	697.8	-	5.80	-	0.0083	12.1	NASA SP-468
General Dynamics	F-111D	7.56	525	-	9.36	-	0.0186	15.8	NASA SP-468
	F-16 (clean)	3.56	300	-	-	-	0.0137	13.4	AGARD Vol. 242-19
Lockheed	F-104G	2.45	196.1	-	3.37	-	0.0172	9.2	NASA SP-468
	P-80A	6.37	237.6	-	3.20	-	0.0134	17.7	NASA SP-468
McDonnell-Douglas	F-4C	2.82	530	-	12.72	-	0.0240	8.7	Nicolai
	F-4E	2.77	530	-	11.87	-	0.0224	8.6	NASA SP-468
North American	F-100D	3.76	400.2	-	5.00	-	0.0130	13.9	NASA SP-468
	F-86E	4.78	287.9	-	3.80	-	0.0132	15.1	NASA SP-468
Northrop	F-5E	3.86	186	-	3.40	-	0.0200	10.0	NASA SP-468
Republic	F-105D	3.16	385	-	6.65	-	0.0173	10.4	NASA SP-468
Vought	F-8H	3.42	375	-	5.00	-	0.0133	12.8	NASA SP-468

Selected Jet Bomber and Attack Aircraft									
Make	**Model**	AR	S, ft²	S_{wet}, ft²	f, ft²	C_f	$C_{D\min}$	$LD_{\max}$	**Reference**
Boeing	B-47E	9.42	1428	-	21.13	-	0.0148	20	NASA SP-468
	B-52H	8.56	4000	-	47.60	-	0.0119	21.5	NASA SP-468
Convair	B-58A	2.09	1542	-	10.49	-	0.0068	11.3	NASA SP-468
Grumman	A-6E	5.31	529	-	7.64	-	0.0144	15.2	NASA SP-468
Martin	B-57B	4.27	960	-	11.45	-	0.0119	15	NASA SP-468
North American	B-45C	6.74	1175	-	18.80	-	0.0160	16.3	NASA SP-468

Various Subsonic Military Aircraft (Props and Jets)									
Make	**Model**	AR	S, ft²	S_{wet}, ft²	f, ft²	C_f	$C_{D\min}$	$LD_{\max}$	**Reference**
Grumman	S2F Tracker	6.89	485	-	15.25	-	0.0315	12.0	Author
Lockheed	U-2	10.61	1000	-	10.95	-	0.0110	23.0	Author
Lockheed	C-141	7.90	3228	-	46.81	-	0.0145	18.9	Nicolai

Flying Boats									
Make	**Model**	AR	S, ft²	S_{wet}, ft²	f, ft²	C_f	$C_{D\min}$	$LD_{\max}$	**Reference**
Boeing	314	8.06	2867	-	78.56	-	0.0274	13.00	NASA SP-468
Consolidated	Commodore	9.00	1110	-	62.38	-	0.0562	9.40	NASA SP-468
	PB2Y-3	7.43	1780	-	50.02	-	0.0281	12.30	NASA SP-468
	PBY-5A	7.73	1400	-	43.26	-	0.0309	11.90	NASA SP-468
Curtiss	Curtiss F-5L	9.33	1397	-	96.95	-	0.0694	8.60	NASA SP-468
	Curtiss H16	9.40	1164	-	85.92	-	0.0768	8.40	NASA SP-468
	Curtiss HS-2L	8.24	803	-	54.24	-	0.0676	8.20	NASA SP-468
Dornier	Do X	5.12	4844	-	228.64	-	0.0472	7.70	NASA SP-468
Douglas	Dolphin	6.08	592	-	25.46	-	0.0430	8.82	NASA SP-468
Fleetwings	F-5	7.25	235	-	8.11	-	0.0345	10.60	NASA SP-468
Grumman	G-21	6.40	375	-	12.19	-	0.0325	10.50	NASA SP-468
Hall	Hall XP2H-1	5.54	2742	-	79.76	-	0.0291	10.20	NASA SP-468
Loening	Loening OA-1C	4.86	504	-	23.08	-	0.0458	7.64	NASA SP-468
Martin	130	7.88	2170	-	65.75	-	0.0303	11.90	NASA SP-468
	JRM-1	10.86	3683	-	84.34	-	0.0233	16.40	NASA SP-468
	Martin PM-1	5.19	1236	-	59.08	-	0.0478	7.70	NASA SP-468
	P5M-2	9.92	1406	-	38.67	-	0.0275	14.40	NASA SP-468
	PBM-3D	9.89	1408	-	46.04	-	0.0327	13.20	NASA SP-468
Navy-Curtiss	Navy-Curtiss NC-4	8.07	2380	-	213.96	-	0.0899	7.00	NASA SP-468
Sikorsky	S-42	9.73	1340	-	47.51	-	0.0362	12.20	NASA SP-468
	Sikorsky S-38B	7.14	720	-	39.10	-	0.0543	8.50	NASA SP-468

Continued

TABLE 16-22 Drag characteristics of selected aircraft—cont'd

Kitplanes (Homebuilt) and LSA									
Make	Model	AR	S, ft²	S_{wet}, ft²	f, ft²	C_f	$C_{D\min}$	$LD_{\max}$	Reference
Bede	BD-5B	9.75	47.4	170	0.80	0.0048	0.0169	-	Stinton
Cozy	Mark IV	8.94	88.3	-	1.78	-	0.0201	16.5	Author
Falco	F.8L (160 & 180 BHP)	6.41	107.5	-	2.28	-	0.0212	14.2	Author
Flight Design	CTSW	7.29	107.4	-	3.64	-	0.0338	11.9	Author
Glassair	III (Standard Wing)	6.68	81.3	-	1.86	-	0.0229	14.0	Author
Icon	A5 (amphib)	9.03	128	-	5.72	-	0.0447	11.1	Author
Osprey	2 (amphib)	5.20	130	-	5.31	-	0.0408	9.5	Author
	GP-4	5.54	104	-	1.23	-	0.0119	18.0	Author
Progressive Aerodyne	Searey (amphib)	6.06	157	-	6.93	-	0.0441	9.7	Author
Pipistrel	Virus 912 LSA	14.10	118	-	1.50	-	0.0127	23.9	Author
Rutan	LongEz	8.31	82.0	-	1.88	-	0.0230	16.2	Author
	VariEze (wheelpants)	9.28	53.6	-	1.11	-	0.0207	16.5	Author
	VariEze (no whlpnts)	9.28	53.6	-	1.21	-	0.0226	15.8	Author
	VariEze	9.20	53.6	260	1.25	0.0047	0.0233	-	Stinton

Single Engine GA Aircraft (Piston and Turboprop)									
Make	Model	AR	S, ft²	S_{wet}, ft²	f, ft²	C_f	$C_{D\min}$	$LD_{\max}$	Reference
Beechcraft	Beech 17	6.91	296.5	1000	6.00	0.0059	0.0202	-	Stinton
	Bonanza V-35 (RG)	6.20	181	-	3.48	-	0.0192	13.8	NASA SP-468
Cessna	150	6.93	159.5	-	4.70	-	0.0295	12.5	Author
	152	6.93	159.5	-	5.52	-	0.0346	11.5	Author
	162 Skycatcher	7.67	120	-	3.95	-	0.0329	12.2	Author
	172 Skyhawk	7.45	174	-	5.06	-	0.0291	12.9	Author
	172 Skyhawk	7.32	175	-	5.58	-	0.0319	11.6	NASA SP-468
	177 (flaps dn)	7.40	175	-	8.23	-	0.047	8.3	Roskam
	177 (flaps up)	7.40	175	-	4.55	-	0.026	11.2	Roskam
	177 Cardinal	7.24	174	-	5.42	-	0.0312	12.3	Author
	177 Cardinal RG (RG)	7.24	174	-	3.79	-	0.0218	14.7	Author
	177 Cardinal RG II (RG)	7.66	174	-	3.88	-	0.0223	14.2	NASA SP-468
	180 Skywagon	7.45	174	700	4.30	0.0085	0.0247	-	Stinton
	180 Skywagon	7.45	174	-	5.16	-	0.0297	12.8	Author
	182 Skylane	7.45	174	-	4.69	-	0.0270	13.4	Author
	208 Caravan (FG-T)	9.71	279.4	-	9.92	-	0.0355	12.8	Author
Cirrus	SR20	9.16	135.2	-	3.45	-	0.0255	14.8	Author
	SR22	10.00	144.9	-	3.68	-	0.0254	15.3	Author
Commander	114B (RG)	7.06	152	-	4.37	-	0.0287	12.7	Author
De Havilland of Canada	DHC-2 Beaver (land)	9.22	250	-	12.19	-	0.0488	10.7	Author
	DHC-2 Beaver (floats)	9.22	250	-	17.00	-	0.0680	9.1	Author
Extra Aircraft	EA-500 (RG-T)	9.44	153.5	-	3.66		0.0239	15.5	Author
Mooney	M20F (RG)	7.45	174.8	-	3.46	-	0.0198	16.7	Author
	M20J (RG)	7.45	174.8	-	3.04	-	0.0174	16.7	Author
	231 (RG)	7.45	174.8	-	3.30	-	0.0189	16.0	AIAA-85-8038
Pacific Aerospace	PAC-750XL (FG-T)	5.78	305	-	9.77	-	0.0320	11.1	Author
Piper	J-3 Cub	5.81	178	-	6.64	-	0.0373	9.6	NASA SP-468
	PA-28 Cherokee	6.02	170	-	6.09	-	0.0258	10.0	NASA SP-468
	PA-38 Tomahawk	9.27	124.7	-	4.85	-	0.0389	12.1	Author
	PA-46 Malibu (RG)	10.57	174.9	-	4.14	-	0.0237	16.1	Author
	PA-46 Mirage (RG)	10.57	175	-	4.07	-	0.0232	16.3	Author
	PA-46 Meridian (RG-T)	10.10	183	-	4.37	-	0.0239	15.8	Author
SOCATA	TB10 (with WF)	8.22	128.04	-	5.70	-	0.0445	10.8	Author
	TB10 (without WF)	8.22	128.04	-	7.16	-	0.0559	9.6	Author
	TBM-700 (RG-T)	8.93	193.7	-	4.78	-	0.0247	14.9	Author
	TBM-850 (RG-T)	8.93	193.7	-	4.51	-	0.0233	15.4	Author

TABLE 16-22 Drag characteristics of selected aircraft—cont'd

Twin Engine GA Aircraft (Piston and Turboprop)									
Make	**Model**	AR	S, ft²	S_{wet}, ft²	f, ft²	C_f	$C_{D\min}$	LD_{max}	**Reference**
Aero	Ae-45	8.78	184	-	4.45	-	0.0242	15.0	Author
Beechcraft	D-18	6.51	349	1400	10.50	0.0080	0.0301	-	Stinton
	B55 Baron	7.19	199.2	-	4.59	-	0.0230	14.3	Author
	B8 Queen Air	8.59	293.9	-	6.82	-	0.0232	15.2	Author
Britten-Norman	BN-2	7.39	325	1350	12.00	0.0088	0.0369	-	Stinton
Cessna	310 II	7.61	179	-	4.78	-	0.0267	13.0	NASA SP-468
	310 (clean)	7.00	175.00	-	5.16	-	0.0295	12.3	Roskam
	310 (gear dn, flps 15°)	7.00	175.00	-	11.38	-	0.0650	8.6	Roskam
	310 (gear dn, flps 45°)	7.00	175.00	-	20.48	-	0.1170	6.5	Roskam
	337 Skymaster	7.18	201	-	6.08	-	0.0302	12.5	Author
Partenavia	P-68 Victor	7.74	200.2	-	5.89	-	0.0294	13.0	Author
Piper	PA-23-250 Aztec	6.67	207.6	-	6.74	-	0.0325	11.7	Author

Multi-Engine Commercial Transport Aircraft (Piston)									
Make	**Model**	AR	S, ft²	S_{wet}, ft²	f, ft²	C_f	$C_{D\min}$	LD_{max}	**Reference**
Boeing	247D	6.55	836	-	17.72	-	0.0212	13.5	NASA SP-468
Curtiss	C-46A	8.59	1358	5400	26.00	0.0047	0.0191	-	Roskam
Douglas	C-47B	9.24	987	3700	25.50	0.0069	0.0258	-	Roskam
	DC-3	9.14	987	-	24.58	-	0.0249	14.7	NASA SP-468
Lockheed	L-1049G	9.17	1650	-	34.82	-	0.0211	16.0	NASA SP-468

Commercial Jetliners and Business Jets									
Make	**Model**	AR	S, ft²	S_{wet}, ft²	f, ft²	C_f	$C_{D\min}$	LD_{max}	**Reference**
Boeing	B-747 (M = 0.7)	7.00	5500	-	88.00	-	0.0160	-	NASA-CR-114494
	B-747 (M = 0.8)	7.00	5500	-	96.80	-	0.0176	-	NASA-CR-114494
	B-747 (M = 0.9)	7.00	5500	-	120.45	-	0.0219	-	NASA-CR-114494
Gates	Learjet 24D	5.46	231.8	-	-	-	0.0234		NASA TN-D-6573

Sailplanes									
Make	**Model**	AR	S, ft²	S_{wet}, ft²	f, ft²	C_f	$C_{D\min}$	LD_{max}	**Reference**
DG Flugzeugbau	LS-8s	21.43	113	-	1.01	-	0.00892	43.0	Author
Stemme	S-10	29.29	202	-	1.75	-	0.00865	51.0	Author

RG = Retractable gear, FG = Fixed gear, T = Turboprop, WF = Wheel fairings, f = equivalent flat plate area = $C_{D_{min}} \times S$.

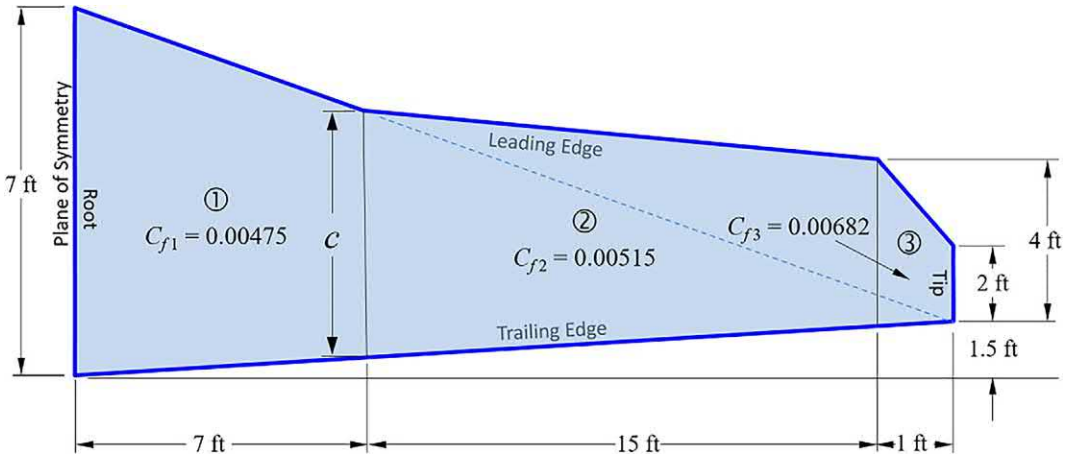


FIGURE 16-83 Wing used in Example (3).

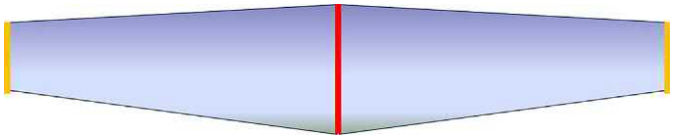


FIGURE 16-84 Wing used in Example (4).

C_L	C_D
-0.3149	0.0532
-0.1740	0.0439
-0.0417	0.0360
0.0733	0.0301
0.1740	0.0263
0.2717	0.0252
0.3867	0.0268
0.5018	0.0301
0.6168	0.0365
0.7117	0.0430
0.8037	0.0514
0.8669	0.0602
0.9388	0.0700
0.9992	0.0802

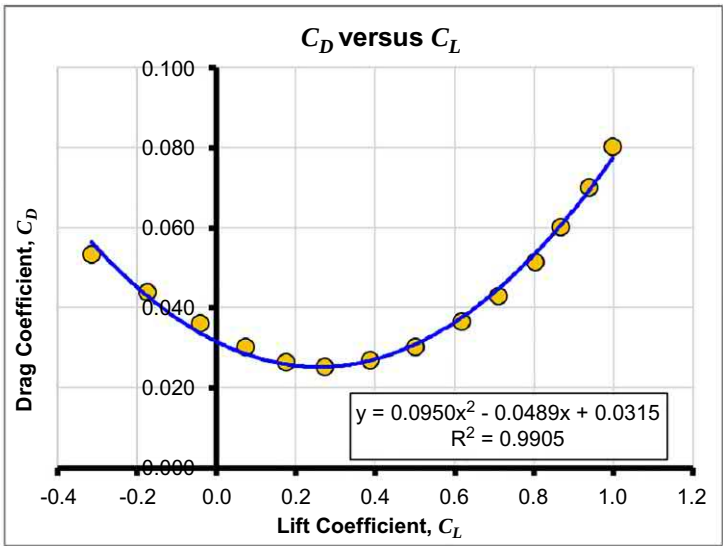


FIGURE 16-85 Information used in Example (6).

each of the three wing segments has already been calculated. Note that all data required for geometric evaluation are given in the figure. Assume wetted area booster factor of 1.07. Determine the total skin friction coefficient and total skin friction drag coefficient for the wing half. Estimate the total skin friction drag force of both wing halves at airspeed of 150 KTAS at S-L on a standard day.

Ans: $C_f = 0.005045$, $C_{Df} = 0.01080$, $D_f = 183\,\text{lb}_\text{f}$.

(4) An airplane has two dissimilar airfoils at the root and tip of the wing (see Figure 16-84). Important dimensions to use are:

$$b = 18\,\text{ft}, c_r = 3\,\text{ft}, c_t = 2\,\text{ft}, \text{and } S = 45\,\text{ft}^2.$$

The root airfoil is a NLF airfoil capable of sustaining 55% laminar flow on the upper surface and 35% on the lower. The tip airfoil is a turbulent flow airfoil that sustains laminar flow to 15% on the upper and lower surfaces.

If the airplane is cruising at 100 KTAS at S-L ISA, determine the skin friction drag coefficient and force acting on the wing due to the mixed laminar and turbulent BL regions. Compare to a wing with fully laminar or fully turbulent BL.

Ans: $C_f = 0.003115$, $C_{Df} = 0.006230$, $D_f = 9.5\,\text{lb}_\text{f}$.

(5) Extract the total, induced, and minimum drag coefficient for the single-piston engine propeller powered Cessna 172N Skyhawk II using the data below obtained from its POH. Hint: Use Equation (9-129) to estimate the Oswald's span efficiency and assume a propeller efficiency of 0.80.

Wing span is 36.08 ft, wing area is 174 ft^2, cruising speed at 8000 ft and 75% power is 122 KTAS. Engine is a Lycoming O-320 rated at 160 BHP at S-L. Gross weight is 2300 lb_f.

Ans: $C_D = 0.03714$, $C_{D_{\min}} = 0.03141$, $C_{D_i} = 0.005728$.

(6) Extract the $C_{L_{\min D}}$, $C_{D_{\min}}$, and e for the wind tunnel data (points) shown in the table and graph of Figure 16-85. The solid line is a least-squares curvefit whose constants and correlation coefficients are shown in the legend. The AR for the airplane being tested is 6.

Ans: $C_{L_{\min D}} = 0.2574$, $C_{D_{\min}} = 0.0252$, $e = 0.5584$.

References

[1] D. Levy, R. Wahls, T. Zickuhr, J. Vassberg, S. Agrawal, S. Pirzadeh, M. Hemsch, *AIAA CFD drag prediction workshop, data summary and comparison*, in: 40th AIAA Aerospace Sciences Meeting & Exhibit, June 9-10, 2001, https://doi-org.ezproxy.libproxy.db.erau.edu/10.2514/6.2002-841.

[2] Source: 1st AIAA CFD Drag Prediction Workshop, Anaheim, CA, June 2001, http://aiaa-dpw.larc.nasa.gov/Workshop1/workshop1.html (Accessed 06 September 2020).

[3] Anonymous, *A Selection of Experimental Test Cases for the Validation of CFD Codes*, AGARD-AR-303 vol. II, August 1994.

[4] D. Gyorgyfalvy, *Performance analysis of the Horten IV flying wing*, in: 8th Congress of the Organisation Scientifique et Technique Internationale du Vol a Voile (OSTIV), June 1960.

[5] P.W. Niewald, S.L. Parker, *Flight-test techniques employed to successfully verify F/A-18E in-flight lift and drag*, J. Aircr. 37 (2) 2000 194–200 AIAA.

[6] I.H. Abbott, A.E. von Doenhoff, L.S. Stivers Jr., *Summary of Airfoil Data*, NACA R-824 1945.

[7] J.D. Anderson, *Fundamentals of Aerodynamics*, sixth ed., McGraw-Hill, 2011.

[8] Y.A. Cengel, J.M. Cimbala, *Fluid Mechanics: Fundamentals and Applications*, fourth ed., McGraw-Hill, February 27, 2017.

[9] R.W. Fox, A.T. McDonald, *Introduction to Fluid Mechanics*, eighth ed., John Wiley and Sons, October 10, 2011.

[10] L. Prandtl, *Applications of Modern Hydrodynamics to Aeronautics*, NACA R-116 1923.

[11] B.M. Jones, *The streamline aeroplane*. J. R. Aeronaut. Soc. 33 (221) 1929 357–385, https://doi.org/10.1017/S0368393100136442.

[12] B.M. Jones, *Flight experiments on the boundary layer*, J. Aeronaut. Sci. 5 (3) 1938 81–94.

[13] B.H. Carmichael, *Summary of Past Experience in Natural Laminar Flow and Experimental Program for Resilient Leading Edge*, NASA CR-152276 May 1979.

[14] B.H. Carmichael, R.C. Whites, W. Pfenninger, *Low Drag Boundary Layer Suction Experiments in Flight on the Wing Glove of an F-94A Airplane*, Rep. No. NAI-57-1163 (BLC-101) Northrop Aircraft Inc., 1957.

[15] B.H. Carmichael, *Surface Waviness Criteria for Swept and Unswept Laminar Suction Wings*, Rep. No. NOR-59-438 (BLC-123) (Contract AF33 (616)-3168) Northrop Aircraft, Inc., 1959.

[16] B.H. Carmichael, W. Pfenninger, *Surface Imperfection Experiments on a Swept Laminar Suction Wing*, Rep. No. NOR-59-454 (BLC-124) Northrop Aircraft Inc., 1959.

[17] C.H. Dearborn, A. Silverstein, *Drag Analysis of Single-Engine Military Airplanes Tested in the NACA Full-Scale Wind Tunnel*, NACA WR-L-489 1940.

[18] L. Dwyer, *Seversky P-35*, *The Aviation History Online Museum*, Updated April 20 http://www.aviation-history.com/seversky/p35.htm, 2014 (Accessed 16 December 2020) .

[19] T. Haines, *Turbine Pilot: Eclipse 500: Typed and Tried Test Driving the Eclipse 500 and Its Training Program*, AOPA Online Article https://www.aopa.org/news-and-media/all-news/2008/august/01/turbine-pilot-eclipse-500-typed-and-tried, August 1, 2008 (Accessed 02 November 2020) .

[20] R. Goyer, *New Eclipse*, Flying Magazine Online February 16, 2011 https://www.flyingmag.com/aircraft/jets/new-eclipse/ (Accessed 02 November 2020) .

[21] P.J. Parmalee, *Kind of Drag, Aviation Week and Space Technology*, September 2, 2002 12–13.

[22] J.R. Chambers, *Innovation in Flight: Research of the NASA Langley Research Center on Revolutionary Advanced Concepts for Aeronautics*, NASA SP-2005-4539 2005 pp. 123–161.

[23] A.L. Braslow, *A History of Suction-Type Laminar-Flow Control With Emphasis on Flight Research*, Monographs in Aerospace History Number 13NASA, 1999.

[24] L.A. Marshall, *Boundary-Layer Transition Results From the F-16XL-2 Supersonic Laminar Flow Control Experiment*, NASA TM-1999-209013 1999.

[25] H.J.B. van de Wal, *Design of a Wing With Boundary Layer Suction*, (M.Sc. thesis) Delft University of Technology, 2010.

[26] A. Wortman, *Reduction of fuselage form drag by vortex flows*, J. Aircr. 36 (3) 1999 501–506.

[27] J.A.C. Kentfield, *Drag Reduction by Means of Controlled Separated Flows*, AIAA-1985-1800-493 1985.

[28] A. Quast, K.H. Horstmann, *Profile Design for Wings and Propellers*, NASA TM-77785 Nov. 1984.

[29] S. Peigin, B. Epstein, *Aerodynamic optimization of essentially three-dimensional shapes for wing-body fairing*, AIAA J. 46 (7) 2008 1814–1825.

[30] H. Schlichting, *Boundary Layer Theory*, English Edition Pergamon Press, 1955, 16.

[31] J.A. Schetz, R.D.W. Bowersox, *Boundary Layer Analysis*, American Institute of Aeronautics and Astronautics Education Series 2011.

[32] A.D. Young, *Boundary Layers*, American Institute of Aeronautics and Astronautics Education Series 1989.

[33] S.F. Hoerner, *Fluid-Dynamic Drag*, L. Hoerner, 1965.

[34] W. Sutherland, *LII. The viscosity of gases and molecular force*. Philosophical Magazine Series 5 36 (223) 1893 507–531, https://doi.org/10.1080/14786449308620508.

[35] V.L.E. Streeter, B. Wylie, *Fluid Mechanics*, McGraw-Hill, 1979.

[36] J. Roskam, C.-T.E. Lan, *Aircraft Aerodynamics and Performance*, DARcorporation, 1997.

[37] D.E. Hoak, *USAF Stability and Control DATCOM, Flight Control Division*, Air Force Flight Dynamics Laboratory, 1978 Section 4.1.5.1 .

[38] Y.A. Cengel, J.M. Cimbala, *Fluid Mechanics—Fundamentals and Applications*, McGraw-Hill, 2006.

[39] K.E. Schoenherr, *Resistance of flat surfaces moving through a fluid*, Trans. Soc. Nav. Arch. Mar. Eng. 40 1932 279.

[40] T. von Kárman, *Mechanical Similitude and Turbulence*, NACA TM-611 March 1931.

[41] L. Prandtl, *Über den Reibungswiderstand Strömender Luft*, Erg. AVA, Gottingen, 1932 III series; also IV series .

[42] L.V. Lazauskas, *Hydrodynamics of Advanced High-Speed Sealift Vessels*, (Master's thesis) University of Adelaide, 2005.

[43] G.E. Gadd, *A new turbulent friction formulation based on a re-appraisal of Hughes' results*, Trans. RINA 109 1967 511–539.

[44] P.S. Granville, *The viscous resistance of surfaces vessels and the skin friction of flat plates*, Trans. SNAME 64 1956 209–240.

[45] W.D. Hayes, R.F. Probstein, *Hypersonic Flow Theory*, Academic Press, New York, 1959.

[46] F. Frankl, V. Voishel, *Heat Transfer in the Turbulent Boundary Layer of a Compressible Gas at High Speeds*, NACA TM-1032 1942.

[47] F. Frankl, V. Voishel, *Turbulent Friction in the Boundary Layer of a Flat Plate in a Two-Dimensional Compressible Flow at High Speeds*, NACA TM-1053 1943.

[48] R.F. Anderson, *Determination of the Characteristics of Tapered Wings*, NACA-TR-572 1936.

[49] H. Glauert, S.B. Gates, *The Characteristics of a Tapered and Twisted Wing With Sweep-Back*, Aeronautical Research Council, 1929 R. &M. No. 1226 .

[50] J. Hueber, *Die Aerodynamischen Eigenschaften von Doppel-Trapezförmigen Tragflügeln*, Z.F.M., 13. Mai 1933, pp. 249–251, 29. May 1933, pp. 269–272.

[51] R.S. Shevell, *Fundamentals of Flight*, Prentice Hall, 1983, 178.

[52] J. Roskam, *Airplane Design*, Part VI DARcorporation, 2000.

[53] D. Cohen, R.T. Jones, *High Speed Wing Theory*, Princeton University Press, 1960.

[54] E. Torenbeek, *Synthesis of Subsonic Aircraft Design*, Delft University Press, 1986.

[55] R.M. Johnson, *An Empirical Method for the Prediction of Airplane Drag Divergence Mach Number*, RAND Research Memorandum RM-1188 1953.

[56] R.S. Shevell, F.P. Bayan, *Development of a Method for Predicting the Drag Divergence Mach Number and the Drag due to Compressibility for Conventional and Supercritical Wings*, SUDAAR 522 Department of Aeronautics and Astronautics, Stanford University, July 1980.

[57] L.W. Hunton, *Effects of Twist and Camber on the Low-Speed Characteristics of a Large-Scale 45 Degree Swept-back Wing*, NACA RM-A50A10 1950.

[58] W.C. Schneider, *A Comparison of the Spanwise Loading Calculated by Various Methods With Experimental Loadings Obtained on a 45 Degree Sweptback Wing of Aspect Ratio 8.02 at a Reynolds Number of 4.0x10 (6)*, NACA R-1208 1954.

[59] W. Mason, *Analytic Models for Technology Integration in Aircraft Design*. AIAA 90-3262-CP 1990https://doi.org/10.2514/6.1990-3262.

[60] B. Malone, W. Mason, *Multidisciplinary Optimization in Aircraft Design Using Analytic Technology Models*. AIAA 91-54093 1991, https://doi.org/10.2514/6.1991–3187.
[61] C.W. Boppe, *Computational Aerodynamic Design: X-29, the Gulfstream Series and a Tactical Fighter*, SAE Technical Paper Series, SAE-851789October 1985.
[62] C.W. Boppe, *CFD Drag Prediction for Aerodynamic Design, Technical Status Review on Drag Prediction and Analysis from Computational Fluid Dynamics: State of the Art*, AGARD AR 256 June 1989 pp. 8-1–8-27.
[63] S.S. Chauhan, J.R.R.A. Martins, *Low-Fidelity aerostructural optimization of aircraft wings with a simplified wingbox model using OpenAeroStruct*. in: Proceedings of the 6th International Conference on Engineering Optimization, EngOpt 2008, Springer, September 2018, https://doi.org/10.1007/978-3-319-97773-7_38.
[64] J.W.R. Taylor (Ed.), Jane's All the World's Aircraft 1987-88, Janes Yearbooks, 1988.
[65] R.T. Whitcomb, *A Study of the Zero-Lift Drag-Rise Characteristics of Wing-Body Combinations Near the Speed of Sound*, NACA TR-1273 1956.
[66] S. Hoffman, *Supersonic-Aera-Rule Design and Rocket-Propelled Flight Investigation of a Zero-Lift Straight-Wing-Body-Nacelle Configuration between Mach Numbers 0.8 and 1.53*, NACA RM-L56B27, April 26, 1956.
[67] H.-U. Meier, *German Development of the Swept Wing 1935-1945*, AIAA, 2010.
[68] Anonymous, *Wallace Hayes, Pioneer of Supersonic Flight, Dies*, Obituary from News from Princeton University, Office of Communications March 8, 2001.
[69] H. Ashley, M. Landahl, *Aerodynamics of Wings and Bodies*, Dover Publications, 1965.
[70] L.E. Wallace, *The whitcomb area rule: NACA aerodynamics research and innovation*, in: P.E. Mack (Ed.), From Engineering Science to Big Science: The NACA and NASA Collier Trophy Research Project Winners, NASA History Office, Washington, DC, 1998, , pp. 135–148.
[71] R.T. Whitcomb, *A Study of the Zero-Lift Drag-Rise Characteristics of Wing-Body Combinations Near the Speed of Sound*, NACA RM-L52H08, September 3, 1952.
[72] R.T. Jones, *Theory of Wing-Body Drag at Supersonic Speeds*, NACA TR-1284 1956.
[73] R.J. Harris, *An Analysis and Correlation of Aircraft Wave Drag*, NASA TM-X-947 March 1964.
[74] M.J. Waddington, *Development of an Interactive Wave Drag Capability for the OpenVSP Parametric Geometry Tool*, (Master's thesis) California Polytechnic State University, 2015.
[75] NASA Open Source Parametric Geometry Code. http://openvsp.org/ (Accessed 03 November 2020).
[76] R.T. Jones, *The minimum drag of thin wings in frictionless flow*, J. Aeronaut. Sci. 18 (2) 1951 75–81.
[77] R.T. Jones, *Theoretical determination of the minimum drag of airfoils at supersonic speeds*, J. Aeronaut. Sci. 1952 813–822.
[78] L. Nicolai, *Fundamentals of Aircraft Design*, second ed., 1984.
[79] D. Raymer, *Aircraft Design: A Conceptual Approach*, fourth ed., American Institute of Aeronautics and Astronautics Education Series 2006.
[80] L.R. Jenkinson, P. Simpkin, D. Rhodes, *Civil Jet Aircraft Design*, American Institute of Aeronautics and Astronautics Education Series 1999.
[81] J. Roskam, *Some comments about fuselage drag*, in: Proceedings of the NASA-Industry-University GA Drag Reduction Workshop, Lawrence, KS, July 14-16, 1975.
[82] R.S. Shevell, *Fundamentals of Flight*, Prentice Hall, 1983, 179 based on the digitization of Figure 11.4.
[83] G.C. Oates, *Aerothermodynamics of Gas Turbine and Rocket Propulsion*, American Institute of Aeronautics and Astronautics Education Series 1984.
[84] J.D. Mattingly, W.H. Heiser, D.T. Pratt, *Aircraft Engine Design*, second ed., American Institute of Aeronautics and Astronautics Education Series 2002.
[85] F. Monts, *The Development of Reciprocating Engine Installation Data for General Aviation Aircraft*, SAE Paper 730325, Business Aircraft Meeting, Wichita, Kansas, April 3-6 1973.
[86] V.R. Corsiglia, J. Katz, R.A. Kroeger, *Full-scale wind-tunnel study of the effect of nacelle shape on cooling drag*. J. Aircr. 18 (2) 1981 82–88, https://doi.org/10.2514/3.57469.
[87] J. Katz, V.R. Corsiglia, P.R. Barlow, *Cooling air inlet and exit geometries on aircraft engine installations*. J. Aircr. 19 (7) 1982 525–530, https://doi.org/10.2514/3.57425.
[88] J. Katz, V.R. Corsiglia, P.R. Barlow, *Effect of propeller on engine cooling system drag and performance*. J. Aircr. 19 (3) 1982 193–197, https://doi.org/10.2514/3.57375.
[89] S.J. Miley, E.J. Cross, J.K. Owens, *An Investigation of the Aerodynamics and Cooling of a Horizontally-Opposed Engine Installation*. SAE Technical Paper 770467 1977, https://doi.org/10.4271/770467.
[90] J.V. Becker, *Wind Tunnel Tests of Air Inlet and Outlet Openings on a Streamline Body*, NACA WR-L-300 November, 1940.
[91] B.W. McCormick, *Aerodynamics, Aeronautics, and Flight Mechanics*, John Wiley & Sons, 1979.
[92] W.H. Herrnstein, D. Biermann, *The Drag of Airplane Wheels, Wheel Fairings, and Landing Gears—I*, NACA R-485 1935.
[93] W. Austyn-Mair, D.L. Birdsall, *Aircraft Performance*, Cambridge University Press, Cambridge, 1992, 124 Method is based on ESDU 79015, Undercarriage Drag Prediction Methods .
[94] J. Roskam, *Methods for Estimating Drag Polars of Subsonic Airplanes*, Roskam Aviation and Engineering Corporation, 4th Printing 1984.
[95] R.N. Conway, J.D. Maynard, *Wind-Tunnel Tests of Four Full-Scale Seaplane Floats*, NACA WR-L-238 1943.
[96] J.B. Parkinson, R.E. Olson, R.O. House, *Hydrodynamic and Aerodynamic Tests of a Family of Models of Seaplane Floats With Varying Angles of Dead Rise*, NACA TN-716 1939.
[97] A.D. Young, *The Aerodynamic Characteristics of Flaps*, R.&M. No. 2622, British A. R. C. 1947
[98] T.C. Corke, *Design of Aircraft*, Prentice-Hall, 2003.
[99] P.E. Purser, T.R. Turner, *Wind-Tunnel Investigation of Perforated Split Flaps for Use as Dive Brakes on a Tapered NACA 23012 Airfoil*, NACA-WR-L-373 November 1, 1941.
[100] T.R. Turner, *Aerodynamic Characteristics and Flap Loads of Perforated Double Split Flaps on a Rectangular NACA 23012 Airfoil*, NACA-WR-L-415 January 1, 1943.
[101] J. Fischel, J.M. Wathon, *Investigation of Spoiler Ailerons for use as Speed Brakes or Glide-Path Controls on Two NACA 65-Series Wings Equipped With Full Span Slotted Flaps*, NACA-TR-1034 January 1, 1951.
[102] F. Linden, R. Van Der, *The Boeing 247: The First Modern Airliner*, University of Washington Press, 1991.
[103] R.M. Wright, *Investigation of Drag and Pressure Distribution of Windshields at High Speeds*, NACA WR-L-462 1942.
[104] E.P. Hartman, *Negative Thrust and Torque Characteristics of an Adjustable-Pitch Metal Propeller*, NACA R-464 1934.
[105] Eiffel is considered by many to be the father of Aerodynamics, while others place the honor on Cayley.
[106] H.A. Fedziuk, *High-Speed Wind-Tunnel Tests of Gun Openings in the Nose of the Fuselage of a 1/4-Scale Model*, NACA WR-L-502 1942.
[107] B.G. Gulick, *Effects of Simulated Ice Formation on the Aerodynamic Characteristics of an Airfoil*, NACA WR-L-292 1938.
[108] V.H. Gray, U.H. Von Glahn, *Effect of Ice and Frost Formations on Drag of NACA 65(sub 1)-212 Airfoil for Various Modes of Thermal Ice Protection*, NACA TN-2962 1953.
[109] Various editors, Jane's All the World's Aircraft, Janes Yearbooks, Various Years.
[110] C.D. Perkins, R.E. Hage, *Airplane Performance, Stability, and Control*, John Wiley & Sons, 1949.
[111] D. Stinton, *The Design of the Aeroplane*, Collins, 1983.
[112] L.K. Loftin Jr., *Quest for Performance; The Evolution of Modern Aircraft*, NASA SP-468 1985.
[113] C.R. Hanke, D.R. Nordwall, *The Simulation of a Jumbo Jet Transport Aircraft*, Modeling Datavol. 2, 1970NASA-CR-114494.

CHAPTER

17

Performance—Introduction

OUTLINE

17.1 **Introduction** 753
17.1.1 The Content of This Chapter 754
17.1.2 Equations-of-Motion for Performance Theory 754
17.1.3 Performance Padding Policy 756

17.2 **Atmospheric Modeling** 756
17.2.1 Classification of Atmospheric Layers 757
17.2.2 Atmospheric Model for Temperature, Pressure, and Density 757
17.2.3 Pressure and Density Altitudes Below 36,089 ft (11,000 m) 758
17.2.4 Corrections for Nonstandard Atmosphere 759

17.3 **Airspeed Theory** 760
17.3.1 Airspeed Indication Systems 761
17.3.2 Airspeeds: Instrument, Calibrated, Equivalent, True, and Ground 762
17.3.3 Important Airspeeds for Aircraft Design and Operation 767
17.3.4 Important Airspeeds for Propeller Aircraft 769
17.3.5 Important Airspeeds for Subsonic Jet Aircraft 769

17.4 **The Structural Envelope** 769
17.4.1 Step-by-Step: Create a V-n Diagram 772
17.4.2 Flight Envelopes for Various GA Aircraft 778

17.5 **Sample Aircraft** 778
17.5.1 Cirrus SR22 779
17.5.2 Learjet 45 779

Exercises 783

References 784

17.1 INTRODUCTION

Any flight can be split into phases (or segments) that are clearly distinct in nature. These are the *take-off*, *climb*, *cruise*, *descent*, and *landing*. Each phase consists of subphases called *maneuvers* (or movements). Maneuvers fall into three categories: *steady-state*, *quasi-steady*, and *accelerated*. A maneuver is initiated by a dedicated movement of primary flight controls to change (in contrast to maintain) the orientation of the aircraft. Then, it is maintained for some time until a new maneuver is initiated. For instance, the take-off phase consists of a ground run (a maneuver), followed by a rotation (another maneuver) that leads to a lift-off.

A steady-state maneuver is one that is void of acceleration—it is time-invariant. Examples include cruise and steady glide. This contrasts accelerated maneuvers. Such maneuvers include turning flight, rolls, loops, and others. A quasi-steady maneuver is one that involves acceleration so slight it can be treated as steady-state. The next six chapters present *aircraft performance theory* in a systematic manner intended to be helpful to you, the aircraft designer. The titles of these chapters are ordered based on the phase of flight:

18. Performance—Take-Off,
19. Performance—Climb,
20. Performance—Cruise,
21. Performance—Range and Endurance,
22. Performance—Descent, and
23. Performance—Landing.

This chapter serves as a prologue for the performance methods. It introduces the fundamentals of *performance theory*, *atmospheric modeling*, and *airspeed theory*. The chapter also introduces two aircraft to be used in subsequent chapters to demonstrate accuracy of the analysis methods.

The methods presented are standard in the industry. However, there are important limitations that must be

https://doi.org/10.1016/B978-0-12-818465-3.00017-3

Copyright © 2022 Elsevier Inc. All rights reserved.

brought up. The quality of the drag model weighs the most. This is discussed in length in Chapter 16. That chapter should be regarded a prologue to performance theory. The aspiring aircraft designer is advised to acquire experience by applying the methods to existing aircraft for which performance data have been published. This builds proficiency and understanding of their accuracy that serves well when assessing the performance of new designs.

17.1.1 The Content of This Chapter

- Section 17.2 presents a description of how to model the atmosphere.
- Section 17.3 presents methods to calculate true airspeed, equivalent airspeed, and other important airspeeds.
- Section 17.4 presents the so-called *V-n* diagram and shows how to create it.
- Section 17.5 presents two sample aircraft that will be used to demonstrate performance calculations; the Cirrus SR22 and the Learjet 45.

17.1.2 Equations-of-Motion for Performance Theory

The foundation of aircraft performance theory is immaculately captured in Miele's concise formulation of ref. [1]. It is presented below, adapted to this writing as the set of Equation (17-1). For the solution of general performance problems, this formulation considers the aircraft a point mass and evaluates its motion in a vertical and horizontal plane.

(1) Flight in the Vertical Plane

Consider an aircraft moving in the vertical plane along some trajectory (the *flight path*) as shown in Figure 17-1. The vertical plane is defined by the horizontal *x*-axis and vertical *h*-axis that are fixed to the ground. In contrast, the *normal* (*n*) and *tangential* (*t*) axes are fixed to the airplane's CG. We track the motion of the CG along the flight path, with respect to the *x*- and *h*-axes. The *t*-axis is tangent to the trajectory. The *n*-axis is normal to it. The airspeed, V_∞, is the norm of the velocity, which is tangent to the flight path. Also, a *datum* for reference has been drawn through the chord line of the *mean geometric chord* (MGC) of the wing. The angle between the datum and the tangent to the flight path is the *angle-of-attack* (α or AOA). The relationship between these angles during climb and descent are shown in Figure 17-3).

In Figure 17-1, the thrust, T, is shown oriented at an angle ε with respect to the *t*-axis. The angle between the *horizon* and the *t*-axis is the *climb angle* (γ). If $\gamma > 0$ the aircraft is *climbing*. If $\gamma = 0$ the aircraft is *flying straight and level* (cruising). If $\gamma < 0$ the aircraft is *descending*.

The unit vectors of the normal and tangential axes are denoted by **n** and **t**, respectively. They establish the *plane-of-symmetry*. Then, we define a third axis, the *binormal* axis, as $\mathbf{b} = \mathbf{t} \times \mathbf{n}$. This establishes a mutually orthogonal, right-handed coordinate system for which the binormal axis points out-of-page. The motion of the aircraft assumes no side-force and no yaw. It only involves translation along the *x*- and *h*-axis, and rotation about the binormal axis fixed to the aircraft's CG.

The equations-of-motion are listed as Equation (17-1). The top two equations describe horizontal and vertical translation, respectively. The next two represent the summation of forces along the **n-** and **t-**axes. The bottom equation describes the change in mass of the aircraft. The dot above some of the variables denotes time derivatives. These equations are subject to simplification depending on the phase of flight.

$$\begin{aligned} \dot{x} - V_\infty \cos\gamma &= 0 \\ \dot{h} - V_\infty \sin\gamma &= 0 \\ T\cos\varepsilon - D - m\left(g\sin\gamma + \dot{V}_\infty\right) &= 0 \\ T\sin\varepsilon + L - m(g\cos\gamma + V_\infty\dot{\gamma}) &= 0 \\ \dot{m}g + c_t T &= 0 \end{aligned} \tag{17-1}$$

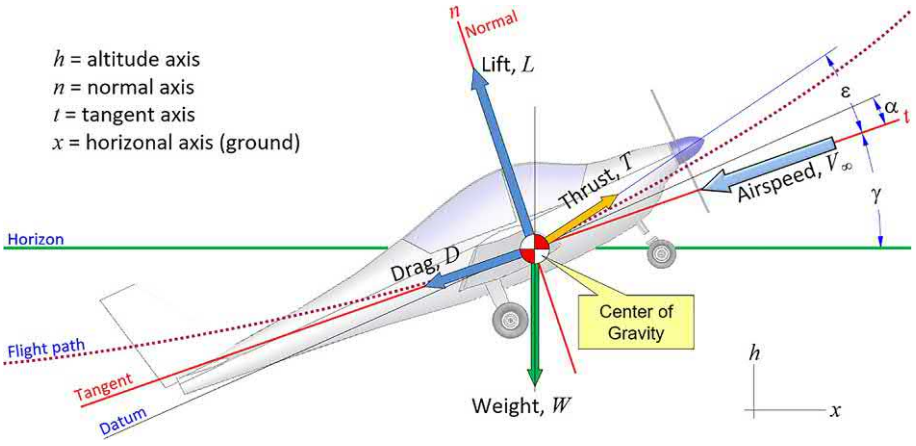


FIGURE 17-1 Force acting on an aircraft in the vertical plane.

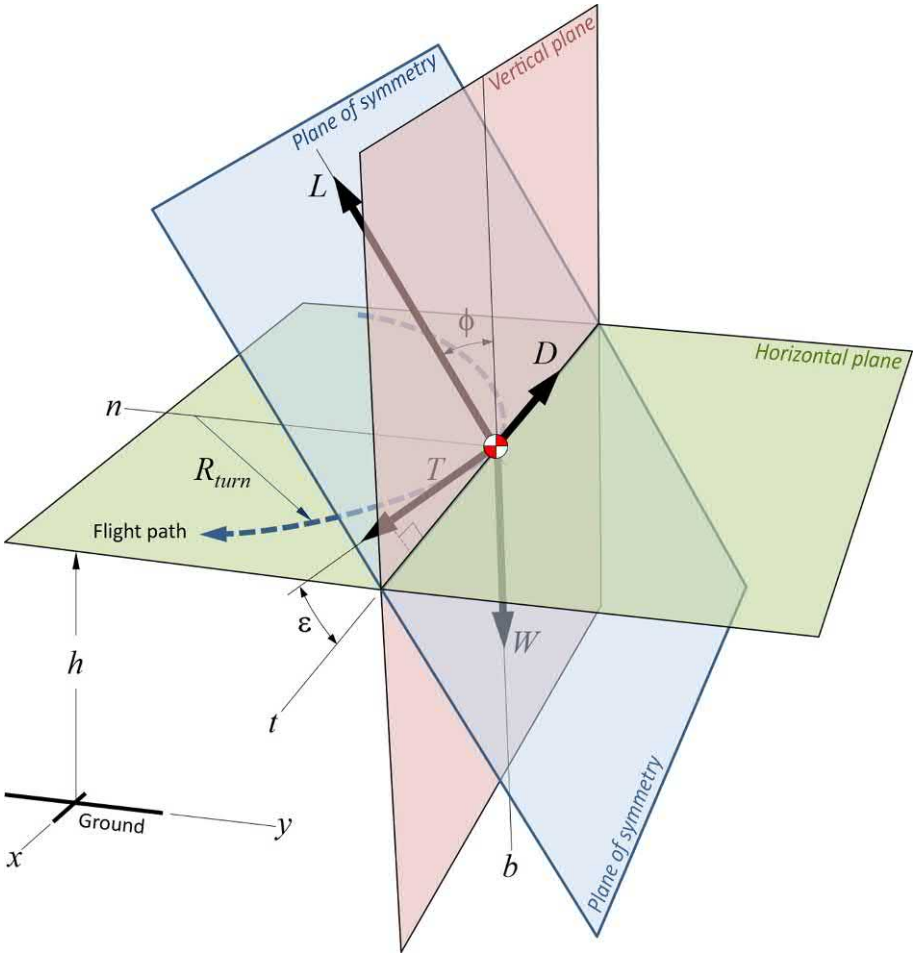


FIGURE 17-2 Force acting on an aircraft in the horizontal plane (inspired by ref. [1]).

(2) Flight in the Horizontal Plane

Consider the aircraft moving in the horizontal plane in Figure 17-2. Since this presentation is more complex than Figure 17-1, the aircraft is replaced by the CG symbol. The horizontal plane is fixed some distance h above the ground. The vertical plane is fixed to the tangent to the flight path, which is affixed to the horizontal plane. Figure 17-2 shows this at a specific instant; at a later time, the vertical plane has moved to a different position that may have different orientation.

The equations-of-motion for flight in the horizontal plane are listed as Equation (17-2). The top two equations describe horizontal translation along the x- and y-axis, respectively. They can be thought of as a set of fixed orthogonal axes parallel to the horizontal plane at a fixed reference point. The next three represent the summation of forces along the **t-**, **n-**, and **b-**axes. Note how the orientation of these axes differs from that of the vertical plane. The bottom equation describes the change in mass of the aircraft. The formulation assumes no side-force.

$$\begin{aligned} \dot{x} - V_\infty \cos\psi &= 0 \\ \dot{y} - V_\infty \sin\psi &= 0 \\ T\cos\varepsilon - D - m\dot{V}_\infty &= 0 \\ (T\sin\varepsilon + L)\sin\phi - mV\dot{\psi} &= 0 \\ (T\sin\varepsilon + L)\cos\phi - mg &= 0 \\ \dot{m}g + c_t T &= 0 \end{aligned} \tag{17-2}$$

where

x = horizontal distance,
y = horizontal distance,
V_∞ = true airspeed of the aircraft,
T = thrust,
D = drag,
L = lift,
m = aircraft mass,
g = gravitational acceleration,
ϕ = roll angle with respect to vertical plane,[1]

[1] May or may not equal the roll angle of the airplane with respect to its longitudinal body axis.

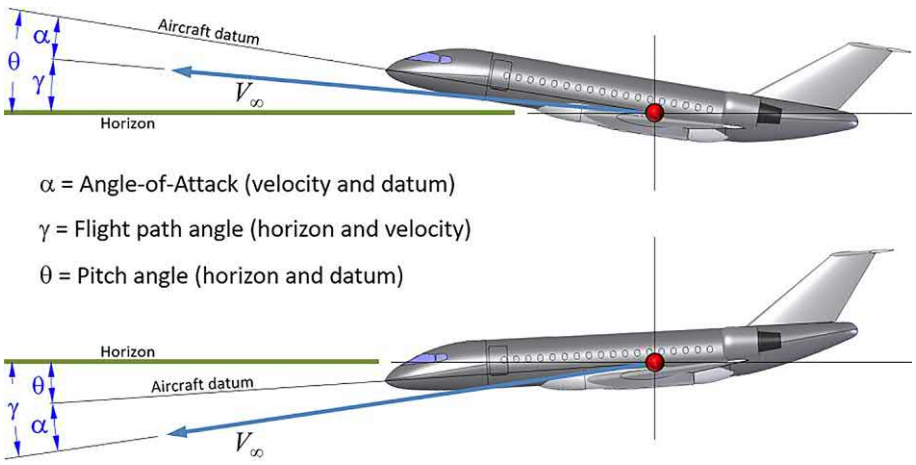


FIGURE 17-3 Definition of angles in the vertical plane.

γ = flight path angle,
ψ = yaw angle in the horizontal plane,[2]
ε = thrust angle,
c_t = thrust-specific fuel consumption.

17.1.3 Performance Padding Policy

Preliminary performance data are sensitive information. In part, because it comes without guarantees. The design team must disseminate performance predictions with great care. When the marketing department gets hold of the predictions, it will be used to sell airplanes. The problem is that the airplane may not yet exist. Yes, we like to sell airplanes. However, if you predict your airplane will cruise between 250 and 275 KTAS, marketing will latch on the 275 KTAS and use it to attract customers. All of this is fine, unless, of course, the airplane eventually "only delivers" 260 KTAS. Then, the manufacturer must spend effort, money, and loss of revenue pleasing unhappy customers who were "promised" 275 KTAS.

To avoid such annoyances, increase conservatism in prediction through padding factors. The cognizant design lead should establish a padding policy that enjoys a *need-to-know* only status (i.e., no one outside of the aero group knows the actual padding factors). Thus, if the predicted range of cruising speed is 250 to 275 KTAS, tell marketing it is 244 to 269 KTAS, or some other reasonable figures. This is not deceit but financial protection.

The disclosure of performance information can hurt the competitive edge of a company. This must be made clear to the labor force, ideally using examples. For instance, an ill-tempered test pilot in a moment of frustration shouting something along the lines of "the darn thing barely climbs" may be echoed elsewhere, perhaps by a careless technician who happened to overhear the pilot. The technician might not know the airplane was being tested with deployed landing gear, at gross weight, at a high-density altitude. Something as seemingly innocent as that can easily be spun by a rival company.

TABLE 17-1 Recommended padding factors.

		Multiply by	
Performance phase	**Parameter**	**Normal performance**	**High performance**
Taxi and take-off	Fuel quantity in lbf	1.25	1.50 to 1.75
Takeoff	T-O field length, ft	1.10	1.10
Climb	Rate-of-climb, fpm	0.95	0.97
Cruise	Cruising speed, KTAS	VTAS–4	VTAS–6
Descent	LDmax	0.90	0.95
Landing	Landing field length, ft	1.10	1.10
Range	Total range, nm	0.96	0.98

Table 17-1 shows suggested padding factors for normal and high-performance GA aircraft. An example of how it is used, consider an aircraft whose T-O field length has been predicted to be 1200 ft. The table suggests the performance team should report 1320 ft.

17.2 ATMOSPHERIC MODELING

Atmospheric modeling is the determination of the properties of air in which an airplane is operated. The properties of interest are *temperature*, *pressure*, *density*, and *viscosity*. The modeling considers the atmospheric strata. The most active layer is the *troposphere*. Most aircraft operate in this

[2] May or may not equal the yaw angle of the airplane with respect to its vertical body axis.

layer, although flying above it is common. Commercial and business jet aircraft operate routinely in the lower stratosphere. Current official altitude records for jets and propeller aircraft also reflect this: On August 31st, 1977 a modified Russian MiG-25 fighter aircraft climbed to an estimated altitude of 123,524 ft (37.65 km) [2]. In August 2001, an unmanned, solar-powered, experimental aircraft, aptly named Helios reached an altitude of 96,863 ft (31.78 km) [3]. In June 2003, it broke up in midair after an encounter with atmospheric turbulence [4].

One of the best known atmospheric models is the *U.S. Standard Atmosphere 1976*, developed by the National Oceanic and Atmospheric Administration (NOAA) [5]. A detailed atmospheric model, based on the *US Standard Atmosphere 1976*, and published by NOAA, NASA,[3] and the US Air Force is provided in Appendix A, *Atmospheric Modeling*. It extends to approximately 85 km (280,000 ft) The appendix also contains a *Visual Basic for Applications* (VBA) code intended for use with Microsoft's Excel spreadsheet program, to calculate the atmospheric properties. In interest of space, only fundamental equations for temperature, pressure, density, and viscosity in the troposphere are provided in this section. Derivations are provided in Appendix A.

17.2.1 Classification of Atmospheric Layers

The atmosphere is divided into several layers based on some specific characteristics (see Table 17-2). The *Troposphere* extends from the ground to some 11 to 16 km (6.8–10 miles). It is where most clouds form and winds and precipitation is most active. The next layer is a thin region called the *Tropopause*, where the Troposphere transitions to the third layer, the *Stratosphere*. Air temperature is constant in this layer. The bulk of the atmosphere is found within these three lowest layers. Above the Stratosphere is the *Mesosphere*, where temperature begins to decrease again with altitude. Layers above the Stratosphere are rarely used for aerodynamic flight. The *Ionosphere* follows the Mesosphere. It is also recognized as the *Thermosphere*, because of the relatively higher temperatures that prevail. The final layer is the *Exosphere*, which extends to some 9600 km (about 6000 miles) and is the outer limit of the atmosphere.

17.2.2 Atmospheric Model for Temperature, Pressure, and Density

The most elementary temperature model assumes linear change of temperature through altitude layers, i.e.,

$$T = T_0 + a(h - h_0) \tag{17-3}$$

[3] National Aeronautics and Space Administration.

TABLE 17-2 Layer classification of the atmosphere.

Name of layer	Altitude in km	Altitude in statute miles
Troposphere[a]	0–11 km	0–6.8 sm
Tropopause	11–11.5 km	6.8–7.1 sm
Stratosphere	11.5–46 km	11.5–29 sm
Stratopause	46–51 km	29–32 sm
Mesosphere	51–85 km	32–53 sm
Ionosphere (thermosphere)	85–640 km	53–400 sm
Exosphere	640–9600 km	400–6000 sm

[a] *In temperate latitudes this is approximately 0–9.7 km (6 miles). The troposphere can extend to 15 km in the tropics.*

In the world of aviation T is called the *outside air temperature* (OAT) or *ambient temperature*. For the troposphere $h_0 = 0$, so Equation (17-3) is rewritten as

$$T = T_0(1 + \kappa \cdot h) \tag{17-4}$$

where

a = lapse rate
h = altitude
h_0 = reference altitude
T = temperature at altitude h
T_0 = temperature at reference altitude h_0
κ = lapse rate constant = a/T_0

Using Equation (17-4), we define the *temperature ratio*, θ as follows:

$$\theta \equiv \frac{T}{T_0} = 1 + \kappa \cdot h \tag{17-5}$$

Substituting this temperature model into the hydrostatic equation of Equation (14-9) and evaluating the resulting integral leads to the following expression

$$p = p_0\ \theta^{5.2561} \tag{17-6}$$

where p_0 is the pressure at the reference altitude h_0. Substituting this into the ideal gas law of Equation (14-5) yields an expression for the density

$$\rho = \frac{p}{RT} = \frac{p_0\ \theta^{5.2561}}{RT_0\ \theta} = \rho_0\ \theta^{4.2561} \tag{17-7}$$

where ρ_0 is the density at the reference altitude h_0 and $\rho_0 = p_0/(RT_0)$. All aircraft must operate inside the troposphere, which ranges from S-L to 11,000 m (36,089 ft). The variables to be used with the above equations inside that range are summarized in Table 17-3. Fundamental constants at sea level are presented in Table 17-4.

TABLE 17-3 US standard atmosphere 1976 in the troposphere.

	UK-system	Units	SI-system	Units
Reference altitude	$h_0 = 0$	ft	$h_0 = 0$	m
Maximum altitude	$h_{max} = 36{,}089$	ft	$h_{max} = 11{,}000$	m
Reference temperature	$T_0 = 518.67$	°R	$T_0 = 288.15$	K
Reference pressure	$p_0 = 2116$	lb_f/ft^2	$p_0 = 101325$	N/m^2
Reference density	$\rho_0 = 0.002378$	$slugs/ft^3$	$\rho_0 = 1.225$	kg/m^3
Temperature ratio	$\theta = 1 - 0.0000068756h$	(17.8)	$\theta = 1 - 0.000022558h$	(17.9)
Pressure ratio	$\delta \equiv \frac{p}{p_0} = \theta^{5.2561} = \sigma^{1.235}$			(17.10)
Density ratio	$\sigma \equiv \frac{\rho}{\rho_0} = \theta^{4.2561} = \frac{\delta}{\theta} = \delta^{0.8097}$			(17.11)
Temperature	$T = 518.67\ \theta$	°R	$T = 288.15\ \theta$	K
Pressure	$p = 2116\ \theta^{5.2561}$	lb_f/ft^2	$p = 101325\ \theta^{5.2561}$	N/m^2
Density	$\rho = 0.002378\ \theta^{4.2561}$	$slugs/ft^3$	$\rho = 1.225\ \theta^{4.2561}$	kg/m^3
Lapse rate	$a = -0.00356616$	°R/ft	$a = -0.0065$	K/m
Lapse rate constant	$\kappa = \frac{a}{T_0} = \frac{-0.00356616}{518.67} = -0.0000068756$	/ft	$\kappa = \frac{a}{T_0} = \frac{-0.0065}{288.15} = -0.000022558$	/m
Viscosity	See Section 16.3.1: C_{Df}			

Note Equations (17-8)–(17-11).

TABLE 17-4 Standard properties of air at S-L.

Property	Symbol	UK-system	SI-system
Specific gas constant for air	R	$1716\,ft{\cdot}lb_f/(slug{\cdot}°R)$	$286.9\,m^2/(K{\cdot}s^2)$
Specific gas constant for water vapor	R_{H_2O}	$2760\,ft{\cdot}lb_f/(slug{\cdot}°R)$	$461.5\,m^2/(K{\cdot}s^2)$
Standard day pressure at S-L	p_0	$2116.2\ lb_f/ft^2$ $14.696\ lb_f/in^2$ 29.92 in Hg	$1.0132 \times 10^5\ N/m^2$ (or Pa) 760 mmHg
Standard day density at S-L	ρ_0	$0.002378\ slugs/ft^3$	$1.225\,kg/m^3$
Standard day temperature at S-L	T_0	518.69°R 59.0°F	288.16 K 15.0C
Absolute viscosity	μ	$3.737 \times 10^{-7}\ lb_f{\bullet}s/ft^2$	$1.789 \times 10^{-3}\,N{\cdot}s/m^2$
Kinematic viscosity	ν	$1.572 \times 10^{-4}\ 1/(ft^2{\cdot}s)$	$1.460 \times 10^{-3}\ 1/(m^2{\cdot}s)$
Speed of sound	a	1116.4 ft/s	340.3 m/s

EXAMPLE 17-1

Determine the state of the atmosphere at 8500 ft on a standard day, using the UK-System.

SOLUTION:

Temperature ratio:

$$\theta = (1 - 0.0000068756 \times 8500) = 0.9416$$

Pressure: $p = 2116\ \theta^{5.2561} = 1542$ psf

Density: $\rho = 0.002378\ \theta^{4.2561} = 0.001840$ slugs/ft^3

Temperature: $T = 518.67\ \theta = 488.4\ °R = 28.7\ °F$

Pressure ratio: $\delta = \theta^{5.2561} = 0.7287$

Density ratio: $\sigma = \theta^{4.2561} = 0.7739$

17.2.3 Pressure and Density Altitudes Below 36,089 ft (11,000 m)

When the pressure or density ratio is known, the altitude to which they correspond can be determined.

For instance, if the pressure ratio (δ) is known, the altitude to which it corresponds (called *pressure altitude*) can be calculated. It is calculated using the following expression, which is derived by solving for h embedded in θ in Equation (17-10).

$$h_p = 145442\left[1-\left(\frac{p}{p_0}\right)^{0.19026}\right] = 145442\left[1-\delta^{0.19026}\right] \tag{17-12}$$

The units are in ft. Similarly, using the density ratio (σ) we can determine the *density altitude*. It is calculated using the expression below (also in ft), which is derived by solving for h embedded in θ in Equation (17-11).

$$h_\rho = 145442\left[1-\left(\frac{\rho}{\rho_0}\right)^{0.234957}\right] = 145442\left[1-\sigma^{0.234957}\right] \tag{17-13}$$

17.2.4 Corrections for Nonstandard Atmosphere

Atmospheric conditions usually deviate from the atmospheric model of Section 17.2.2. This variability is driven by meteorological conditions, in which both pressure and temperature differ from that given by Equations (17-8)–(17-10). Figure 17-4 shows how altitudes are defined in aircraft operation. The *true altitude* is the actual height of the airplane above mean sea level. The *absolute altitude* is the height of the airplane above the ground below it. When dealing with the atmosphere, we always presume that the pressure altitude is the true altitude. This simplifies the modeling of nonstandard conditions, requiring only a correction of temperature.

(1) Temperature Deviation

If we know the ambient temperature, T_{amb}, at the airplane's operational altitude, we can calculate the *temperature deviation*, ΔT_{ISA}, as follows.

$$\Delta T_{ISA} = \overbrace{T_{amb}}^{\text{Measured temperature}} - \overbrace{T_0\,\theta}^{\text{Standard day temperature}} \tag{17-14}$$

On a cold day, the ambient temperature is lower than the standard day temperature given by $T_0\,\theta$. Thus, $\Delta T_{ISA} < 0$. This results in higher density at that altitude than experienced on a standard day. It is as if the airplane is operating at lower altitude using the standard atmosphere. Therefore, the airplane is said to be operating at a *low density-altitude* (see Figure 17-4). The performance of the airplane at the altitude is improved over that of a standard day. The opposite holds true for a hot day (*high-density altitude*).

(2) Density Corrections Based on Temperature Deviation

Density deviation due to nonstandard temperature is handled using the ideal gas law of Equation (14-5), the pressure per Equation (17-6), and by introducing the temperature deviation directly. This is reflected below, using the UK-system:

$$\rho = \frac{1.233\,\theta_{UK}^{5.2561}}{T_0\,\theta_{UK} + \Delta T_{ISA}} \tag{17-15}$$

where θ_{UK} is the temperature ratio per Equation (17-8). For the SI-system, the expression becomes

$$\rho = \frac{352.6\,\theta_{SI}^{5.2561}}{T_0\,\theta_{SI} + \Delta T_{ISA}} \tag{17-16}$$

where θ_{SI} is the temperature ratio per Equation (17-9).

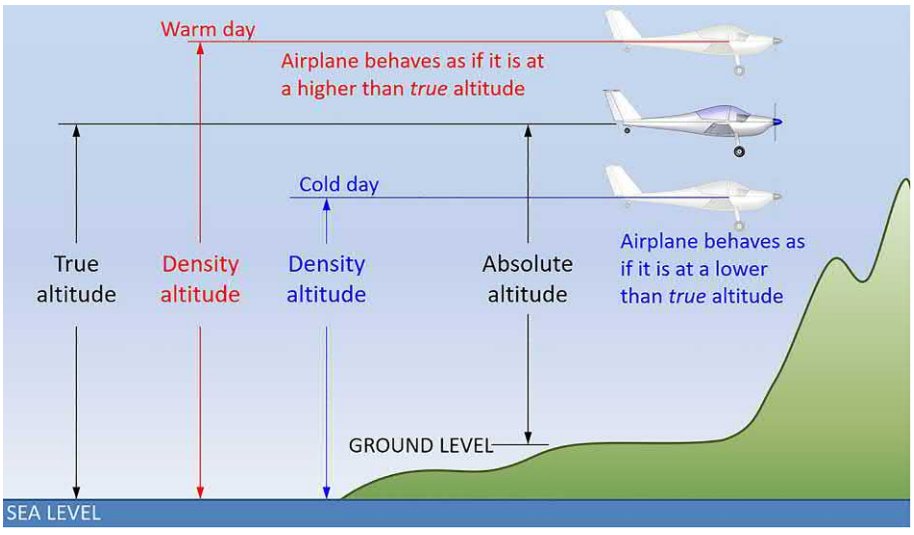


FIGURE 17-4 Definition of altitudes used in aviation.

EXAMPLE 17-2

Determine the density of air at 8500 ft on a day that is 30°F colder and hotter than standard day.

SOLUTION:

First, determine the ISA temperature ratio at 8500 ft:

$$\theta_{UK} = 1 - 0.0000068756 \times 8500 = 0.9416$$

Then, "plug and chug" Equation (17-15):

$$30°\text{F colder:}\quad \rho = \frac{1.233\ \theta_{UK}^{5.2561}}{T_0\ \theta_{UK} + \Delta T_{ISA}} = \frac{1.233\ (0.9416)^{5.2561}}{(518.67)(0.9416) - 30} = 0.001960\ \text{slugs/ft}^3$$

$$30°\text{F warmer:}\quad \rho = \frac{1.233\ \theta_{UK}^{5.2561}}{T_0\ \theta_{UK} + \Delta T_{ISA}} = \frac{1.233\ (0.9416)^{5.2561}}{(518.67)(0.9416) + 30} = 0.001733\text{slugs/ft}^3$$

These are 6.5% greater and 5.8% lower than standard day density (0.001840 slugs/ft^3), respectively.

(3) Density Correction due to Humidity

Density is also affected by humidity. Humidity is the amount of water vapor present in air. It reduces the lapse rate through a release of latent heat during condensation. The heat released is transferred to air molecules reducing the rate of cooling. For instance, the temperature changes −0.010 K/min dry air. It is called the *dry adiabatic rate* (DAR). In contrast, it is −0.006 K/min for saturated air. This is called the *saturated adiabatic rate* (SAR). These differ from *normal adiabatic rate* (NAR), which is −0.0065 K/min [6]. Humidity is typically stated in terms of:

- *Absolute Humidity* is the mass of water vapor per unit volume of air. Typical units are grams/m^3.
- *Relative Humidity* is the ratio of the water vapor pressure present in air to the vapor pressure that would saturate it [7]—if $RH = 1.00$ (or 100%), precipitation will occur. This is what is usually reported by weather forecasters on TV.
- *Specific Humidity* is the mass of water vapor per unit mass of air, including the water vapor—usually expressed as grams of H_2O per kilogram of air. Also referred to as *humidity ratio*.

As a rule of thumb; *the density of dry air is higher than that of humid air* [8]. The presence of water molecules in air displaces the Oxygen and Nitrogen atoms so their amount per unit volume decreases. Therefore, the mass of unit volume of the humid air decreases and the density is reduced. A general expression for the density of moist air is given below:

$$\rho = \rho_{std}\left(\frac{1+x}{1 + xR_{H_2O}/R}\right) = \rho_{std}\left(\frac{1+x}{1+1.609x}\right) \qquad (17\text{-}17)$$

where

ρ_{std} = Density at altitude, calculated by standard methods.
R = Specific gas constant for air, see Table 17-4.
R_{H_2O} = Specific gas constant for water vapor, see Table 17-4.
x = Humidity ratio in kg water vapor per kg of air.

Humidity is commonly represented using *relative humidity* (RH), presented as a percentage (e.g., 50% humidity). If the ambient temperature is known in °C, this can be converted into humidity ratio using the following relation:

$$x = \left(\frac{RH}{100}\right) 0.003878 \cdot e^{0.0656 \cdot (T\ °C)} \qquad (17\text{-}18)$$

EXAMPLE 17-3

If the outside temperature and relative humidity on a standard day at S-L is reported as 15°C and 50%, respectively, determine the density of air.

SOLUTION:

On a standard day, this yields a humidity ratio of $x = \frac{50}{100} 0.003878 \cdot e^{0.0656 \cdot (15)} = 0.00519$. The resulting density at sea level is thus:

$$\rho = \rho_{std}\left(\frac{1+x}{1+1.609x}\right) = 0.002378\left(\frac{1+0.00519}{1+1.609 \times 0.00519}\right) = 0.002371\ \text{slugs/ft}^3$$

17.3 AIRSPEED THEORY

Arguably, the *airspeed indicator* (ASI) is the most important instrument in any aircraft. This is so because the pilot operates the airplane based on airspeed. The decision to deflect the elevator to rotate for take-off is based on airspeed. To remain airborne requires airspeed to be above the stalling speed. To maintain the maximum rate-of-climb or angle-of-climb is based on airspeed. The maximization of range, endurance, or simply comply with air traffic controllers, is based on airspeed. Practically all maneuvering is based on airspeed. No other instrument is used quite like it.

This section focuses on the airspeed. It details how to determine the number of types of airspeed that are of importance to designers and pilots alike, such as true

airspeed, calibrated airspeed, and others. And it defines specific airspeeds that are important from a regulatory and operational angle—the so-called V-speeds.

17.3.1 Airspeed Indication Systems

Figure 17-5 shows the dial of a typical analog ASI. It displays the airspeed using units of *indicated knots* (KIAS). ASI that shows the airspeed in miles-per-hour or kilometers-per-hour are also available. However, the designer should be familiar with knot, for this remains the most common unit used for airspeed. This explains its extensive use in this book. A number of noticeable markings are shown in the ASI in Figure 17-5. These have specific meanings, as described in the figure. They are required by 14 CFR §23.1545, *Airspeed indicator* in the "old" regulations. Pilots are trained to operate the aircraft using these airspeeds. The airspeeds are discussed in Section 17.3.3.

Modern aircraft feature digital airspeed indicators that are displayed on monitors called the *primary flight display* (PFD). These improve the sophistication in messaging for the pilot and all but eliminate guess-work when operating the aircraft. The PFD shown in Figure 17-6 is an example of a typical such a screen in a modern passenger jet. The device directly relays the *calibrated airspeed* (V_{CAS}) (rather than *indicated airspeed*) [9], Mach number (M), and *ground speed* (GS). These are displayed in Figure 17-6 as 262 KCAS, 0.792, and 381 KGS, respectively. It also displays high- and low-speed limitations. For instance, the V_{MO}/M_{MO} limitations can be seen as the thick-dotted ribbon extending upward from 285 KCAS. The thin-lined ribbon extending from 275 to 285 KCAS indicates the maximum maneuvering speed, which typically provides a 1.3g margin for maneuvering. This means that the pilot can maintain a level 40 degrees bank angle at that altitude. The thin-lined ribbon extending

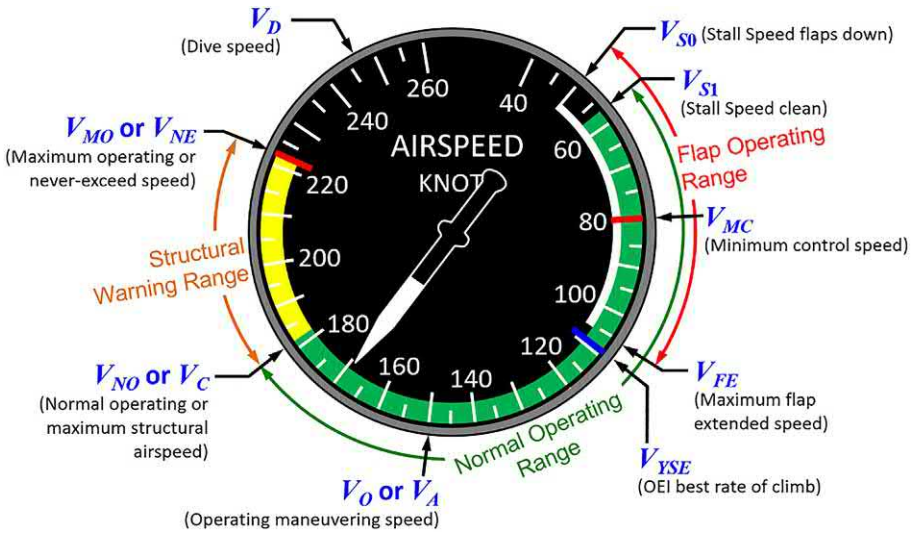


FIGURE 17-5 Markings of a typical analog airspeed indicator.

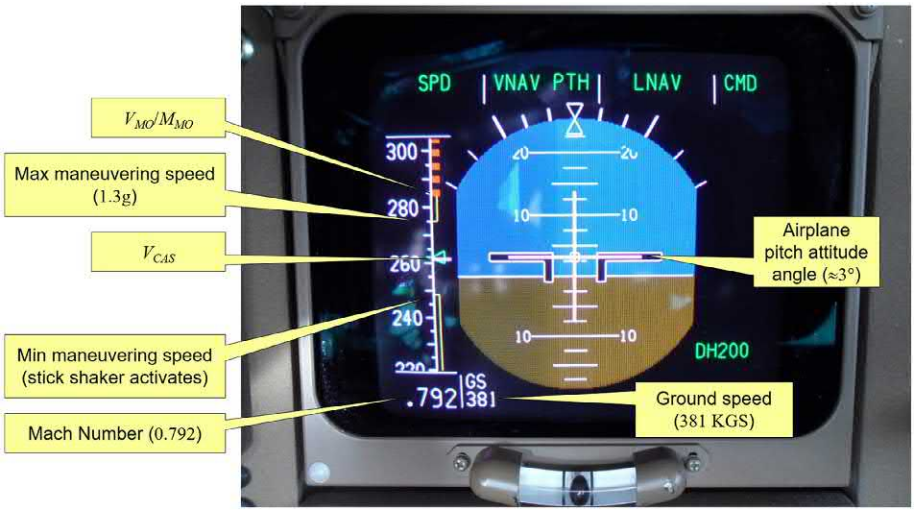


FIGURE 17-6 Markings of a modern ASI shown on a Primary Flight Display (PFD). *Photo by Gudbjartur Runarsson.*

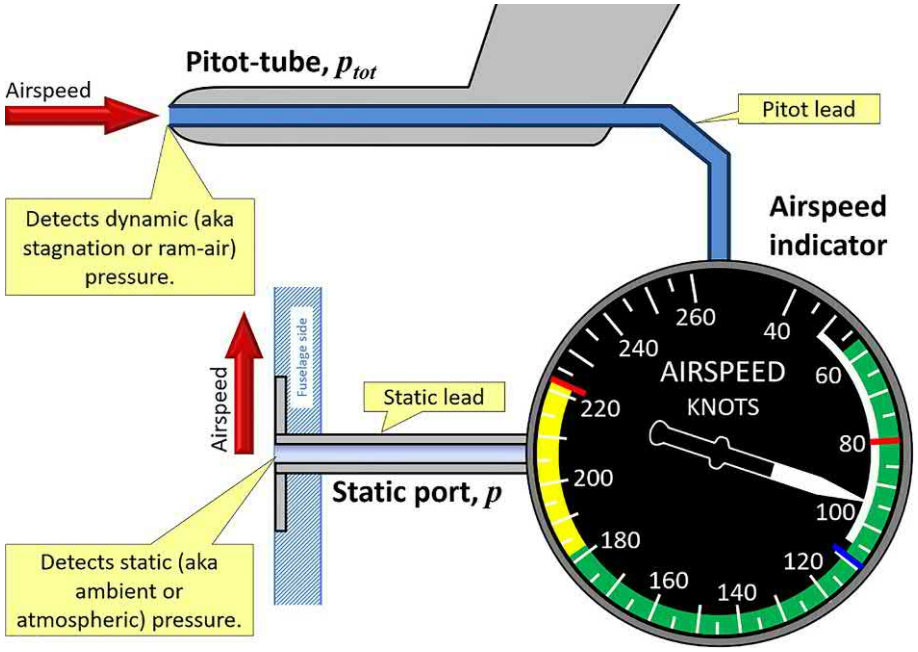


FIGURE 17-7 The basic ASI system.

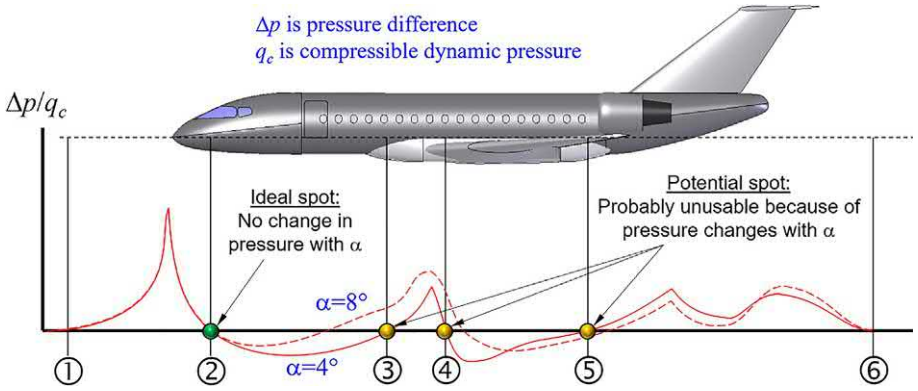


FIGURE 17-8 Pressure variation along a fuselage.

from the bottom to approximately 249 KCAS indicates where the airplane's stick shaker is activated. Some of these values are weight dependent and are determined in real time by the airplanes flight computer system.

An airspeed indicator requires two sources of pressure; a dynamic and an ambient. Dynamic pressure is obtained using a *Pitot*[4] *tube* (aka *Pitot*). Its opening faces the flow direction and senses stagnation pressure (see Figure 17-7). The ambient pressure probe, the *static port*, is oriented perpendicular to the flow direction. It senses static (ambient or atmospheric) pressure. The ASI displays the airspeed based on the pressure difference between the two sources. Of the two, measuring static pressure is far harder than the dynamic pressure. The static source is usually located on the fuselage. The ideal location is where the pressure equals the static pressure in the far-field at all AOAs and airspeeds. This is encumbered by localized distortion in the flow-field. The distortion depends on factors like airspeed, altitude, and AOA. This may render it next to impossible to find a suitable location. Figure 17-8 depicts typical pressure variation along a fuselage. It can be seen that four locations on the fuselage are potential spots for the static source. Only one is acceptable.

17.3.2 Airspeeds: Instrument, Calibrated, Equivalent, True, and Ground

The airspeed indicator is a pressure sensor that converts pressure difference into an airspeed. This is either done mechanically (analog) or digitally. Unfortunately, the discrepancy between the indicated airspeed and the

[4] It is named after the French engineer Henri Pitot (1695–1771). Pitot is pronounced similar to pea-toe.

actual speed at which one moves along the ground is bewildering at best. A proper interpretation requires understanding of the nature of its measurement.

Consider the calibration of an ASI for an aircraft flying at sea level on a standard, windless day. Say we measure its speed as 100 knots (185.2 km/h), perhaps, using a radar detector. This corresponds to a dynamic pressure of 33.9 lb_f/ft^2 (1621 Pa). Now, suppose we climb to an altitude to 30,000 ft and fly at some speed that develops precisely that dynamic pressure. At what airspeed is the airplane now moving? 100 knots? The answer is no—assuming a standard, windless day, we would measure something closer to 163 knots. Yes, the ASI, calibrated earlier to show 100 knots when detecting a dynamic pressure of 33.9 lb_f/ft^2, will show 100 knots. However, the airplane must move at 163 knots with respect to the ground to develop that dynamic pressure. This should convince the skeptical reader that means to distinguish between the displayed (or *indicated*) airspeed and the speed at which air approaches the airplane—the *true airspeed*, are warranted. We cannot ignore either speed. The pilot uses the indicated airspeed to operate the aircraft and the true airspeed to plan the amount of fuel required to get to the destination.

(1) Speed of Sound

Refers to the speed at which pressure propagates through fluid. For air, it can be estimated in terms of ft/s or m/s using the following expression, derived in ref. [10]:

$$a = \sqrt{\gamma RT} \tag{17-19}$$

For altitudes at which GA aircraft are most frequently operated, the ratio of specific heats is 1.4 and the specific gas constant is 1716 ft·lb_f/slug·°R in the UK-system and 286.9 $m^2/(K \cdot s^2)$ in the SI-system. Thus, Equation (17-19) can be rewritten as follows

$$a = \sqrt{\gamma RT} \approx \begin{cases} 49\sqrt{T_{\circ R}} \\ 20\sqrt{T_K} \end{cases} \tag{17-20}$$

(2) Instrument Airspeed (IAS), V_{IAS}

Refers to the airspeed the pilot reads off the airspeed indicator. The reading is affected by three kinds of error:

(1) *Indication error* (due to flaws in the instrument itself),
(2) *Position error* (due to incorrect location of static or Pitot sensors), and
(3) *Pressure lag error* (a transient error due to rapid change in pressure, such as when a fighter climbs so rapidly the indication system does not keep up with the change in pressure and "lags").

Instrument airspeed is denoted by the variable V_{IAS} and the error by ΔV_{IAS}. In the SI-system, the unit is typically km/h. In the UK-system, the units are mph or knots. It is useful to identify the units. Here this is done using KIAS, which stands for *Knots, Indicated Airspeed*.

14 CFR Part 23, §23.1323, *Airspeed indicating system* in the "old" regulations dictates "the calibration error may not exceed 3% of the calibrated airspeed or 5 knots, whichever is greater." This holds inside the flight envelope. Thus, an aircraft capable of 200 KCAS can have an error as great as 6 knots.

(3) Calibrated Airspeed (CAS), V_{CAS}

If the error in the airspeed indicator is known, denoted by ΔV_{IAS}, the calibrated airspeed is given by:

$$V_{CAS} = V_{IAS} + \Delta V_{IAS} \tag{17-21}$$

This can also be represented as a fraction of the indicated airspeed:

$$V_{CAS} = V_{IAS}(1 + r) \tag{17-22}$$

For General Aviation (GA) aircraft, compliance to 14 CFR Part 23, §23.1587(d)(10), *Performance Information*, requires a correlation between IAS and CAS to be determined and presented to the operator of the aircraft.

(4) Equivalent Airspeed (EAS), V_{EAS}

The equivalent airspeed is the airspeed the airplane would have to maintain at sea level in order to generate the dynamic pressure experienced at the specific flight condition (altitude and true airspeed). Figure 17-9 shows how the various airspeeds are related. It shows the determination of V_{EAS} depends on whether we are converting V_{CAS} to V_{EAS} or V_{TAS} to V_{EAS}.

Convert V_{CAS} to V_{EAS}

To convert V_{CAS} to V_{EAS} use the following expression:

$$V_{EAS} = V_{CAS}\sqrt{\frac{p}{p_0}}\sqrt{\frac{\left(\frac{q_c}{p}+1\right)^{0.2857}-1}{\left(\frac{q_c}{p_0}+1\right)^{0.2857}-1}} \tag{17-23}$$

Note that the power 0.286 is the ratio 1/3.5. It is also useful to convert V_{EAS} to V_{CAS}. This is accomplished by solving Equation (17-23) for V_{CAS} as shown below.

$$V_{CAS} = V_{EAS}\sqrt{\frac{p_0}{p}}\sqrt{\frac{\left(\frac{q_c}{p_0}+1\right)^{0.2857}-1}{\left(\frac{q_c}{p}+1\right)^{0.2857}-1}} \tag{17-24}$$

where the compressible dynamic pressure is given by:

$$q_c = p\left[\left(1 + 0.2M^2\right)^{3.5} - 1\right] \tag{17-25}$$

And Mach number is $M = V_{TAS}/a$ (17-26)

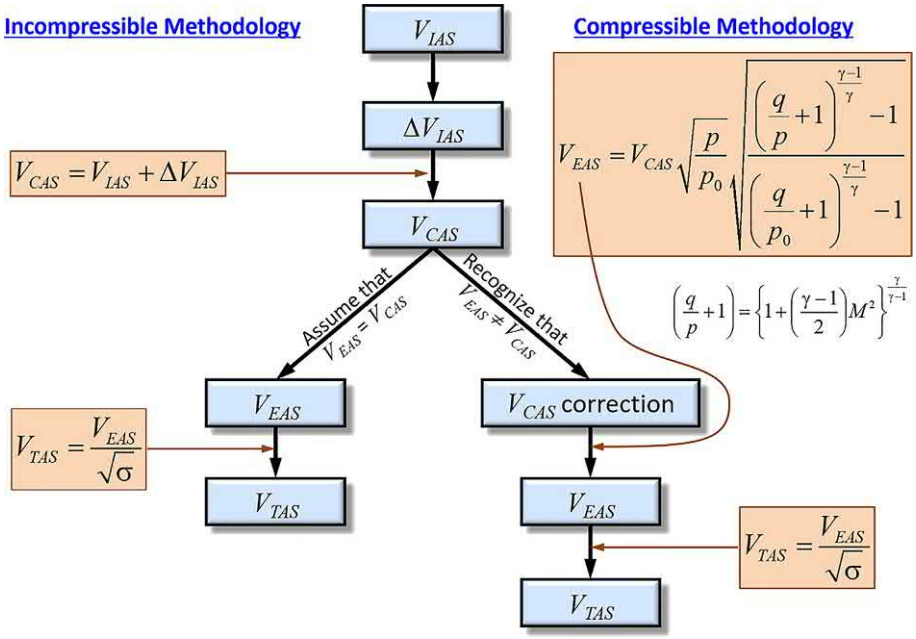


FIGURE 17-9 Flowchart showing relationships between different airspeeds.

An issue arises when we only know the calibrated airspeed: we need the Mach number, but it cannot be determined unless we know V_{TAS}, which requires V_{EAS} and which we are trying to determine. This hurdle can be overcome using the following expression:

$$M = \sqrt{\frac{2}{\gamma-1}\left(\left[\frac{1}{\delta}\left[\left\{1+\frac{\gamma-1}{2}\left(\frac{V_{CAS}}{a_0}\right)^2\right\}^{\frac{\gamma}{\gamma-1}}-1\right]+1\right]^{\frac{\gamma-1}{\gamma}}-1\right)} \tag{17-27}$$

where V_{CAS} is the calibrated airspeed, δ is the pressure ratio, and γ is the ratio of specific heats (1.4). The speed units must be consistent, i.e., if V_{CAS} is in KCAS, then so must the standard day sonic speed, a_0. Substituting $a_0 = 661.2$ KCAS for the UK-system and $a_0 = 1225$ km/h for the SI-system, and simplifying yields Equation (17-27), which is easier to enter when preparing spreadsheet solutions (the upper equation uses KCAS, the lower km/h):

$$M = \begin{cases} 2.236\sqrt{\left(\frac{\left(1+4.575\times10^{-7}V_{CAS_{KCAS}}^2\right)^{3.5}-1}{\delta}+1\right)^{0.2857}-1} \\ 2.236\sqrt{\left(\frac{\left(1+1.333\times10^{-7}V_{CAS_{kmh}}^2\right)^{3.5}-1}{\delta}+1\right)^{0.2857}-1} \end{cases} \tag{17-28}$$

Convert V_{TAS} to V_{EAS}

V_{EAS} is related to the true airspeed as follows:

$$V_{EAS} = V_{TAS}\sqrt{\rho/\rho_0} \tag{17-29}$$

(5) True Airspeed (TAS), V_{TAS}

True airspeed is the speed at which the air molecules in the far-field approach the aircraft. The following expression is used to convert equivalent airspeed to true airspeed, identified as the *compressible methodology* in Figure 17-9.

$$V_{TAS} = \frac{V_{EAS}}{\sqrt{\rho/\rho_0}} = \frac{V_{EAS}}{\sqrt{\sigma}} \tag{17-30}$$

If the airspeed is below $M0.3$, then V_{TAS} can be estimated without converting V_{CAS} to V_{EAS}. This is shown as the *incompressible methodology* in Figure 17-9. Figure 17-10 shows how V_{EAS}, V_{TAS}, and M change with altitude, assuming constant V_{EAS} of 265 KCAS.

$$V_{TAS} \approx \frac{V_{CAS}}{\sqrt{\rho/\rho_{SL}}} = \frac{V_{CAS}}{\sqrt{\sigma}} \tag{17-31}$$

(6) Ground Speed, V_{GS}

Ground speed is the speed at which the aircraft moves with respect to the ground. This speed equals the true airspeed if there is no wind aloft (perfectly calm). However, in windy conditions, the component of the wind parallel to the direction of the aircraft will either add (tailwind) or subtract (headwind) from the true airspeed. It also causes the airplane to drift, if not parallel to the plane of symmetry. This gives rise to *Navigation Theory*, which is outside the scope of this edition of the book. Thus, given the true airspeed vector, $\mathbf{V_{TAS}}$, and wind velocity, $\mathbf{V_w}$, the ground velocity, $\mathbf{V_{GS}}$, is given by

$$\mathbf{V_{GS}} = \mathbf{V_{TAS}} + \mathbf{V_w} \tag{17-32}$$

A comparison of the above airspeeds is provided in Figure 17-11.

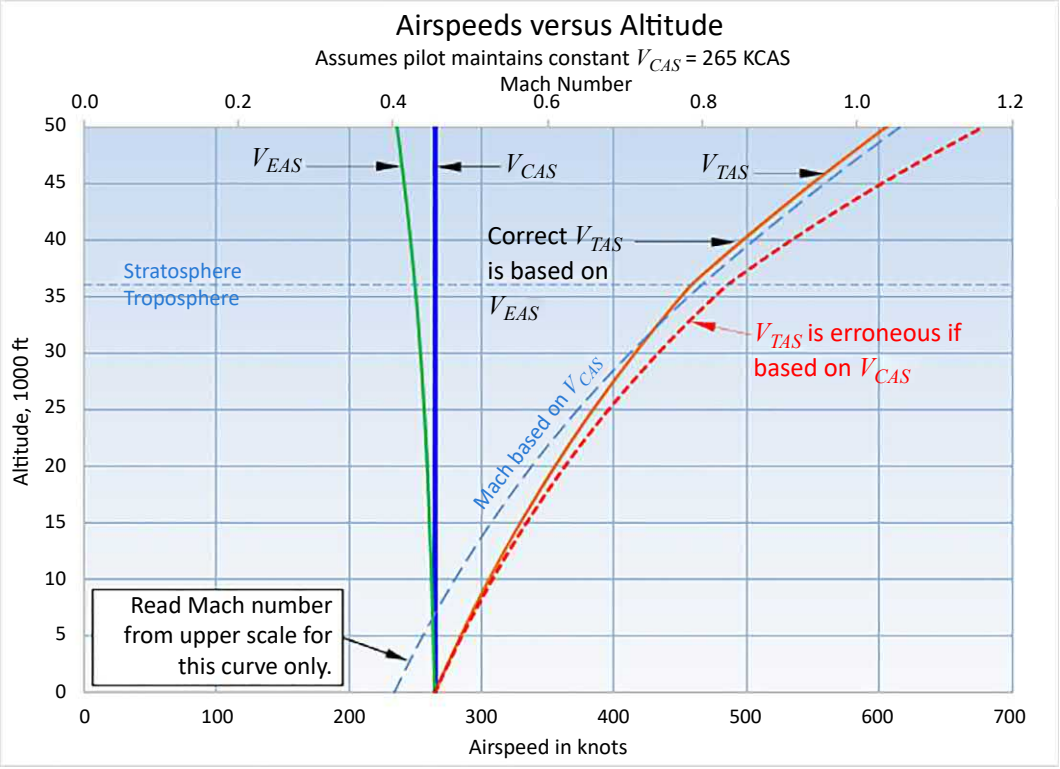


FIGURE 17-10 Variation in V_{EAS}, V_{TAS}, and M, assuming constant V_{CAS}.

EXAMPLE 17-4: AIRSPEED DETERMINATION

An aircraft is equipped with an ASI with an error of −3% and shows160 KCAS at 16,000 ft on a standard day. Determine V_{CAS}, V_{EAS}, and V_{TAS} at this condition.

SOLUTION:

First, determine the temperature, pressure, and density ratios using Equations (17-8), (17-10), and (17-11):

$$\theta = 1 - 0.0000068756 \cdot h = 1 - 0.0000068756 \times 16000 = 0.8900$$

$$\delta = \theta^{5.2561} = (0.8900)^{5.2561} = 0.5420$$

$$\sigma = \theta^{4.2561} = (0.8900)^{4.2561} = 0.6089$$

Determine static pressure at 16,000 ft using Equation (17-6):

$$p = p_0\,\theta^{5.2561} = (2116)(0.5420) = 1147 \text{ lb}_\text{f}/\text{ft}^2$$

Using Equation (17-22), calculate V_{CAS}:

$$V_{CAS} = V_{IAS}(1 + r) = (160)(1 - 0.03) = 155.2 \text{ KCAS}$$

Using Equation (17-22), calculate M:

$$M = 2.236\sqrt{\left(\frac{\left(1 + 4.575 \times 10^{-7} V_{CAS}^2\right)^{3.5} - 1}{\delta} + 1\right)^{0.2857} - 1}$$

$$= 2.236\sqrt{\left(\frac{\left(1 + 4.575 \times 10^{-7} (155.2)^2\right)^{3.5} - 1}{0.5420} + 1\right)^{0.2857} - 1 = 0.3170}$$

Using Equation (17-25), calculate q_c:

$$q_c = p\left[(1 + 0.2M^2)^{3.5} - 1\right]$$

$$= (1147)\left[\left(1 + 0.2(0.3170)^2\right)^{3.5} - 1\right] = 82.73 \text{ lb}_\text{f}/\text{ft}^2$$

Using Equation (17-23), calculate V_{EAS}:

$$V_{EAS} = V_{CAS}\sqrt{\frac{p}{p_0}}\sqrt{\frac{\left(\frac{q_c}{p} + 1\right)^{0.2857} - 1}{\left(\frac{q_c}{p_0} + 1\right)^{0.2857} - 1}}$$

$$= (155.2)\sqrt{\frac{1147}{2116}}\sqrt{\frac{\left(\frac{82.73}{1147} + 1\right)^{0.2857} - 1}{\left(\frac{82.73}{2116} + 1\right)^{0.2857} - 1}} = 154.3 \text{ KCAS}$$

Using Equation (17-30), calculate V_{TAS}:

$$V_{TAS} = \frac{V_{EAS}}{\sqrt{\sigma}} = \frac{154.3}{\sqrt{0.6089}} = 197.8 \text{ KTAS}$$

Calculate the Mach number using this speed to compare to the Mach number per Equation (17-22). This helps confirm if the arithmetic is proper.

$$M = \frac{V_{TAS}}{a} = \frac{V_{TAS}}{49\sqrt{T_0\,\theta}} = \frac{(197.8)(1.688)}{49\sqrt{(518.67)(0.8900)}} = 0.3170$$

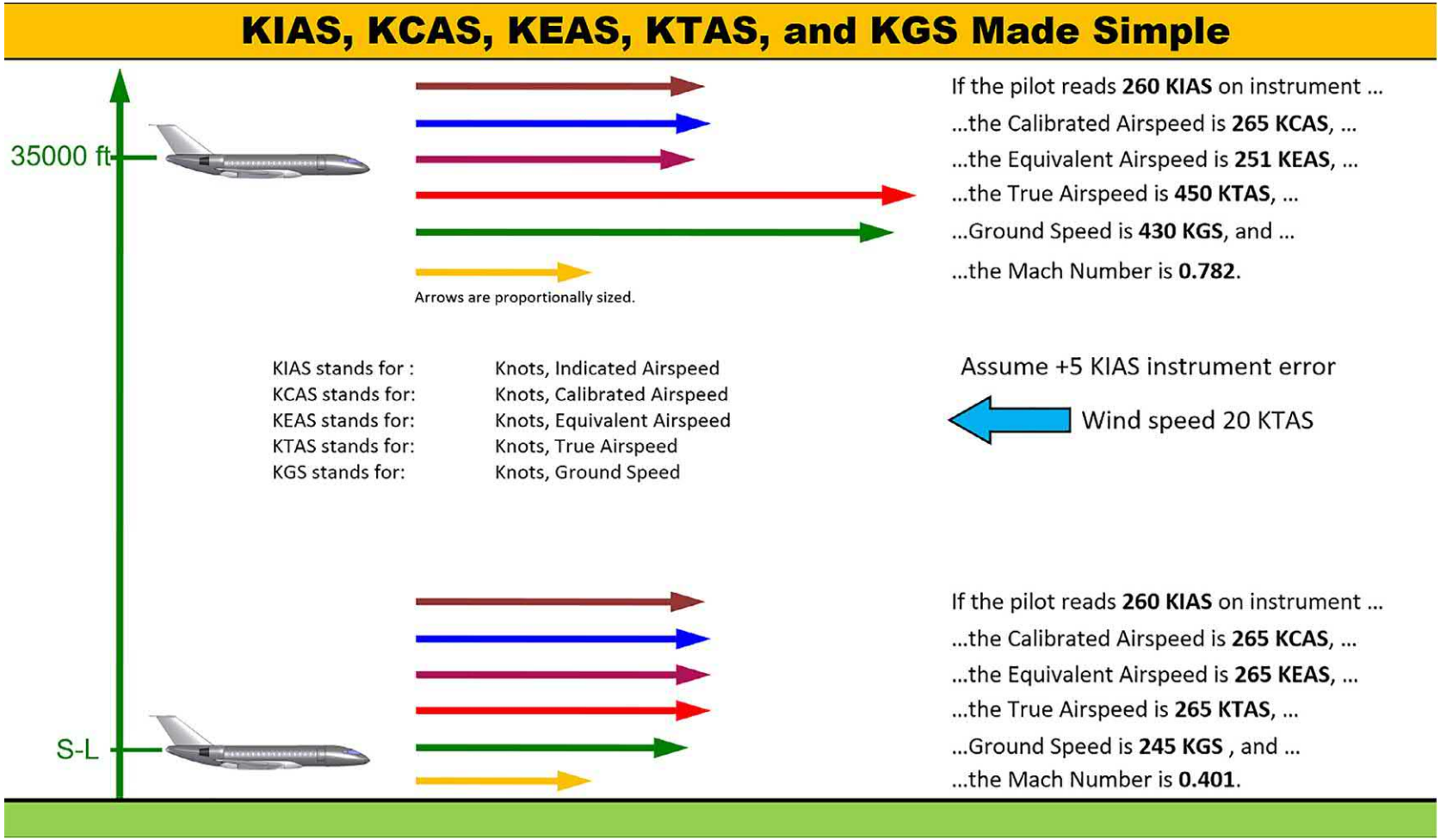


FIGURE 17-11 Graphical depiction of various airspeed types.

DERIVATION OF EQUATIONS (17-23), (17-24), (17-25), AND (17-29)

Compressible flows are analyzed using the so-called *isentropic relations* (see Section 14.1.3). Stagnation pressure is estimated using Equation (14-22), written here in a slightly different form

$$\frac{p_0}{p}=\frac{p+q_c}{p}=\left(1+\frac{\gamma-1}{2}M^2\right)^{\frac{\gamma-1}{\gamma}} \tag{i}$$

Solving this expression for the compressible dynamic pressure yields Equation (17-25). Airspeed indicators are calibrated by referencing S-L and ISA conditions. We denote temperature, pressure, and speed-of-sound at S-L by T_0, p_0, and a_0, respectively. This establishes the *calibrated airspeed*, V_{CAS}. Solving Equation (i) for M and substituting the reference pressure and speed-of-sound leads to

$$M_0=\frac{V_{CAS}}{a_0}=\sqrt{\left(\frac{2}{\gamma-1}\right)\left[(q_c/p_0+1)^{\frac{\gamma-1}{\gamma}}-1\right]} \tag{ii}$$

where the subscript "0" indicates the reference conditions. Therefore, the calibrated airspeed based on the stagnation pressure is simply:

$$V_{CAS}=a_0\sqrt{\left(\frac{2}{\gamma-1}\right)\left[(q_c/p_0+1)^{\frac{\gamma-1}{\gamma}}-1\right]} \tag{iii}$$

Since the ASI is a pressure sensor, an identical stagnation pressure measured at altitudes other than S-L should show an identical airspeed value on the ASI. Let us call it *equivalent airspeed*, V_{EAS}. Thus, if we know the *true airspeed*, V_{TAS}, at that instant, we can convert V_{TAS} to V_{EAS} using the dynamic pressure

$$\frac{1}{2}\rho V_{TAS}^2=\frac{1}{2}\rho_0 V_{EAS}^2 \Rightarrow V_{EAS}=V_{TAS}\sqrt{\frac{\rho}{\rho_0}}=V_{TAS}\sqrt{\sigma} \tag{iv}$$

This is Equation (17-29). This conversion exposes an important discrepancy when the true airspeed is high subsonic: The airspeed displayed by the ASI (V_{CAS} per Equation (iii)), is higher than the V_{EAS} returned by Equation (iv). This is not to say the discrepancy depends on high speed, rather, it is just more noticeable (see Figure 17-10). Writing the true airspeed in terms of *Mach number*, using the isentropic relationship of Equation (i), where it is based on T, p, and a, yields

$$V_{TAS}=aM=a\overbrace{\sqrt{\left(\frac{2}{\gamma-1}\right)\left[(q_c/p+1)^{\frac{\gamma-1}{\gamma}}-1\right]}}^{=M} \tag{v}$$

In terms of the equivalent airspeed, it becomes

$$V_{EAS}=a\sqrt{\frac{\rho}{\rho_0}}\sqrt{\left(\frac{2}{\gamma-1}\right)\left[(q_c/p+1)^{\frac{\gamma-1}{\gamma}}-1\right]} \tag{vi}$$

The ratio between V_{CAS} and V_{EAS} is thus

$$\frac{V_{CAS}}{V_{EAS}}=\frac{a_0\sqrt{\left(\frac{2}{\gamma-1}\right)\left[(q_c/p_0+1)^{\frac{\gamma-1}{\gamma}}-1\right]}}{a\sqrt{\frac{\rho}{\rho_0}}\sqrt{\left(\frac{2}{\gamma-1}\right)\left[(q_c/p+1)^{\frac{\gamma-1}{\gamma}}-1\right]}} \tag{vii}$$

Substituting Equation (17-20) for both sonic speeds and simplifying leads to

$$\frac{V_{CAS}}{V_{EAS}}=\frac{\sqrt{\gamma RT_0}\sqrt{\left(\frac{2}{\gamma-1}\right)\left[(q_c/p_0+1)^{\frac{\gamma-1}{\gamma}}-1\right]}}{\sqrt{\gamma RT}\sqrt{\frac{\rho}{\rho_0}}\sqrt{\left(\frac{2}{\gamma-1}\right)\left[(q_c/p+1)^{\frac{\gamma-1}{\gamma}}-1\right]}} \tag{viii}$$

$$=\sqrt{\frac{T_0}{T}}\sqrt{\frac{\rho_0}{\rho}}\sqrt{\frac{(q_c/p_0+1)^{\frac{\gamma-1}{\gamma}}-1}{(q_c/p+1)^{\frac{\gamma-1}{\gamma}}-1}}$$

Converting density per the ideal gas law of Equation (14-5) leads to

$$\frac{V_{CAS}}{V_{EAS}}=\sqrt{\frac{T_0}{T}}\sqrt{\frac{\frac{p_0}{RT_0}}{\frac{p}{RT}}}\sqrt{\frac{(q_c/p_0+1)^{\frac{\gamma-1}{\gamma}}-1}{(q_c/p+1)^{\frac{\gamma-1}{\gamma}}-1}} \tag{ix}$$

$$=\sqrt{\frac{p_0}{p}}\sqrt{\frac{(q_c/p_0+1)^{\frac{\gamma-1}{\gamma}}-1}{(q_c/p+1)^{\frac{\gamma-1}{\gamma}}-1}}$$

This expression yields both Equations (17-23) and (17-24). Knowing the dynamic pressure, we can calculate the Mach number using Equation (v), i.e.,

$$M=\sqrt{\left(\frac{2}{\gamma-1}\right)\left[(q_c/p+1)^{\frac{\gamma-1}{\gamma}}-1\right]} \tag{x}$$

Substitute Equation (17-25) for the compressible dynamic pressure, using S-L conditions (i.e., $M_0=V_{CAS}/a_0$) leads to

$$M=\sqrt{\left(\frac{2}{\gamma-1}\right)\left[\left(\frac{q_c}{p}+1\right)^{\frac{\gamma-1}{\gamma}}-1\right]}$$

$$=\sqrt{\left(\frac{2}{\gamma-1}\right)\left[\left(\frac{p_0}{p}\left[\left(1+\frac{\gamma-1}{2}M_0^2\right)^{\frac{\gamma}{\gamma-1}}-1\right]+1\right)^{\frac{\gamma-1}{\gamma}}-1\right]}$$

Replacing the pressures using the pressure ratio, δ, yields Equation (17-27).

17.3.3 Important Airspeeds for Aircraft Design and Operation

The term *V-speeds* is used for specific airspeeds that are important to the capabilities of an aircraft. It is imperative to be familiar with these terms. The "types" of airspeeds listed in Table 17-5 are of interest to the aircraft designer,

TABLE 17-5 Important airspeeds for aircraft design and operation.

V-speed	Description	Section or 14 CFR Part 23
M_C	Cruising speed in terms of Mach number.	§23.335
M_D	Dive Mach number.	§23.335
M_{MO}	Maximum operating Mach number.	§23.1505
V_1	T-O decision speed. Maximum speed during takeoff at which a pilot can either safely stop the aircraft without overrunning the runway or safely continue to V_2 takeoff even if a critical engine fails (between V_1 and V_2).	18.3.5
V_2	Takeoff safety speed. Airspeed the airplane must be capable of reaching 35 ft above the ground.	18.1.3 §23.57
V_{2min}	Minimum takeoff safety speed. Minimum value of the V_2 airspeed (see V_2). Defined for commercial aircraft per 14 CFR 25.	§25.107
V_3	Flap retraction speed.	–
V_A	Maneuvering speed. A certification airspeed below which the airplane must be capable of full deflection of aerodynamic controls.	17.4 §23.335
V_B	Design speed for maximum gust intensity. Most often used for commuter class aircraft. See Figure 17-22.	§23.335
V_{BA}	Minimum rate-of-descent airspeed, which yields the least altitude lost in a unit time.	22.3.5
V_{BG}	Best glide speed. Minimum or best angle-of-descent airspeed. This speed will result in the shallowest glide angle and will yield the longest range, should the airplane lose engine power.	20.3.4 22.3.7
V_{BR}	Airspeed when pilot begins to apply brakes after touch-down.	23.2.5
V_H	Maximum level airspeed.	20.3.2
V_{LOF}	Lift-off speed.	18.2.6
V_{max}	See V_H.	20.3.2
V_{MC}	Minimum control speed with the critical engine inoperative.	§23.149
V_{MCA}	Minimum control speed while airborne. See V_{MC}.	–
V_{MCG}	Minimum control speed on the ground. The minimum airspeed required to counteract an asymmetric yawing moment on the ground due to an engine failure on a multiengine aircraft.	§23.149
V_{MO}	Maximum operating speed.	§23.1505

TABLE 17-5 Important airspeeds for aircraft design and operation—cont'd

V-speed	Description	Section or 14 CFR Part 23
V_{MU}	Minimum unstick speed. The airspeed at which the airplane no longer "sticks" to the ground. It is a function of the ground attitude (or AOA) of the airplane. The minimum is achieved when the ground attitude is a $C_{L_{max}}$ or α_{stall}. Defined for commercial aircraft per 14 CFR 25.	§25.107
V_{NE}	Never-exceed speed or maximum structural airspeed.	§23.1505
V_{NO}	Normal operating speed; also called maximum structural cruising speed. It is the speed that should not be exceeded except in smooth air, and then only with caution.	§23.1505
V_O	The maximum operating maneuvering speed, V_O, is established by the manufacturer as an operating limitation and is not greater than $V_S\sqrt{n}$ established in §23.335(c).	§23.1507
V_R	Rotation speed. The speed at which the airplane's nose wheel leaves the ground. It is high enough to ensure the aircraft can reach V_2 at 50 ft (GA) or 35 ft (commercial) in case of an engine failure on a multiengine aircraft.	18.1.3 §23.51
V_{REF}	Landing reference speed or threshold crossing speed, typically $1.2V_{S_0}$ to $1.3V_{S_0}$. The factor 1.2 is typically used for military aircraft, but 1.3 for civilian aircraft per §23.73.[a]	23.2.5 §23.73
$V_{R_{max}}$	Best range speed. The airspeed that results in maximum distance flown.	20.3.9
V_S	Stalling speed or minimum steady flight speed for which the aircraft is still controllable.	20.3.3 §23.49, §23.335
V_{S_0}	Stalling speed or minimum steady flight speed for which the aircraft is still controllable in the landing configuration.	20.3.3 §23.49, §23.335
V_{SR}	Reference stalling speed. The stalling speed of the airplane at some condition other than gross weight. Important for heavy aircraft that consume a lot of fuel during a particular mission. The stalling speed at the start of the mission will be higher than at the end.	20.3.3 23.2.5
V_{SR0}	Reference stalling speed in landing configuration at some condition other than gross weight.	20.3.3 23.2.5
V_{SR1}	Reference stalling speed in a specific configuration at some condition other than gross weight.	20.3.3 23.2.5

TABLE 17-5 Important airspeeds for aircraft design and operation—cont'd

V_{SW}	Speed at which the stall warning will occur.	§23.207
V_{TD}	Touch-down airspeed.	23.2.5
V_{TR}	Transition airspeed; the average of V_{LOF} and V_2.	18.1.3
V_X	The best angle of climb airspeed (max altitude gain per unit distance).	19.3.4 (jet and prop)
V_Y	The best rate of climb airspeed (max altitude gain per unit time).	19.3.3 (jet and prop)
V_{YSE}	The best rate of climb airspeed in a multiengine aircraft with one engine inoperative.	19.3.3 (jet and prop)

[a] *Per 14 CFR §23.73* Reference Landing Approach Speed.

both from a performance and certification standpoint. Many can be determined by the analysis methods presented in this book. Others are requirements that must be complied with if the aircraft is to be certified.

Figure 17-12 and 17-13, depict how some of these airspeeds are obtained through an analysis the *available* and *required* power and thrust versus airspeed. Such analyses are presented in the subsequent chapters.

17.3.4 Important Airspeeds for Propeller Aircraft

See Figure 17-12.

17.3.5 Important Airspeeds for Subsonic Jet Aircraft

See Figure 17-13.

17.4 THE STRUCTURAL ENVELOPE

This section discusses the so-called *V-n diagram* or *structural envelope*. It plots specific load factors versus airspeed within which the airplane is designed to operate (see Figure 17-14). It is developed for the loads and structures groups, but also helps the pilot better understand the limitations of the airplane. The envelope depicts airspeed limitations such as maximum speeds for fully deflected control surfaces (V_A) and beyond which the airplane may not exceed (V_D). The *V-n* diagram is usually prepared in accordance with instructions found in aviation regulations such as 14 CFR Part 23, Part 25, or ASTM F2245, depending on aircraft class. In this section, the construction of a *V-n* diagram will be shown using 14 CFR Part 23.

Generally, several *V-n* diagrams are prepared to represent various conditions. Among those are:

- Configuration variations (e.g., T-O, cruise, and landing configuration)
- Altitudes (e.g., covering the altitudes from S-L to 20,000 ft and then from 20,000 ft to the design cruise altitude, necessitated by changes in gust load limitations).
- Weight (e.g., empty weight, gross weight, and perhaps some intermediary weights).

An airplane at rest on the ground is acted upon by the force of gravity alone: It is subject to a load factor of 1. If it accelerates, say upward, because of a force two times its weight, it is subject to a load factor of 2, and so on. The load factor is the ratio of the force acting on a body to its unaccelerated weight. A common way of expressing this is to say it is "reacts a 1-g load" or a "2-g load," and so on. This is defined in 14 CFR §23.321, *General* as follows:

> Flight load factors represent the ratio of the aerodynamic force component (acting normal to the assumed longitudinal axis of the airplane) to the weight of the airplane. A positive flight load factor is one in which the aerodynamic force acts upward, with respect to the airplane.

The *V-n* diagram consists of two separate diagrams; maneuvering and gust loading. These are coplotted to form the complete *V-n* diagram. Note that the "new" Part 23 is worthless for this purpose. To generate a *V-n* diagram in accordance with 14 CFR 23, follow paragraphs §23.321 through §23.341 of the "old" regulations. The reader not familiar with these is urged to have those handy when following the discussion below for the first time. This is helpful in understanding the legal language of those paragraphs.

Using the "old" 14 CFR Part 23, first specify the category to which the aircraft is certified (normal, utility, aerobatic, or commuter). The maneuvering loads depend on this classification. Next, gather information about the airplane of the kind shown in Table 17-6. All airspeeds used equivalent airspeed (e.g., KEAS) or Mach number. Then, prepare the maneuvering diagram, followed by the gust diagram. Finally, trace the outline of the diagram.

This process is best using an example using a hypothetical aircraft of very light wing loading. This introduces complexity to the generation of the diagram that may perplex even the seasoned aircraft designer—diagrams for other aircraft are destined to be simpler than the one shown. The characteristics of the aircraft for this exercise are shown in Table 17-6. It is assumed the aircraft has already been built and flown, as is indicated by the "maximum demonstrated level airspeed" in the table.

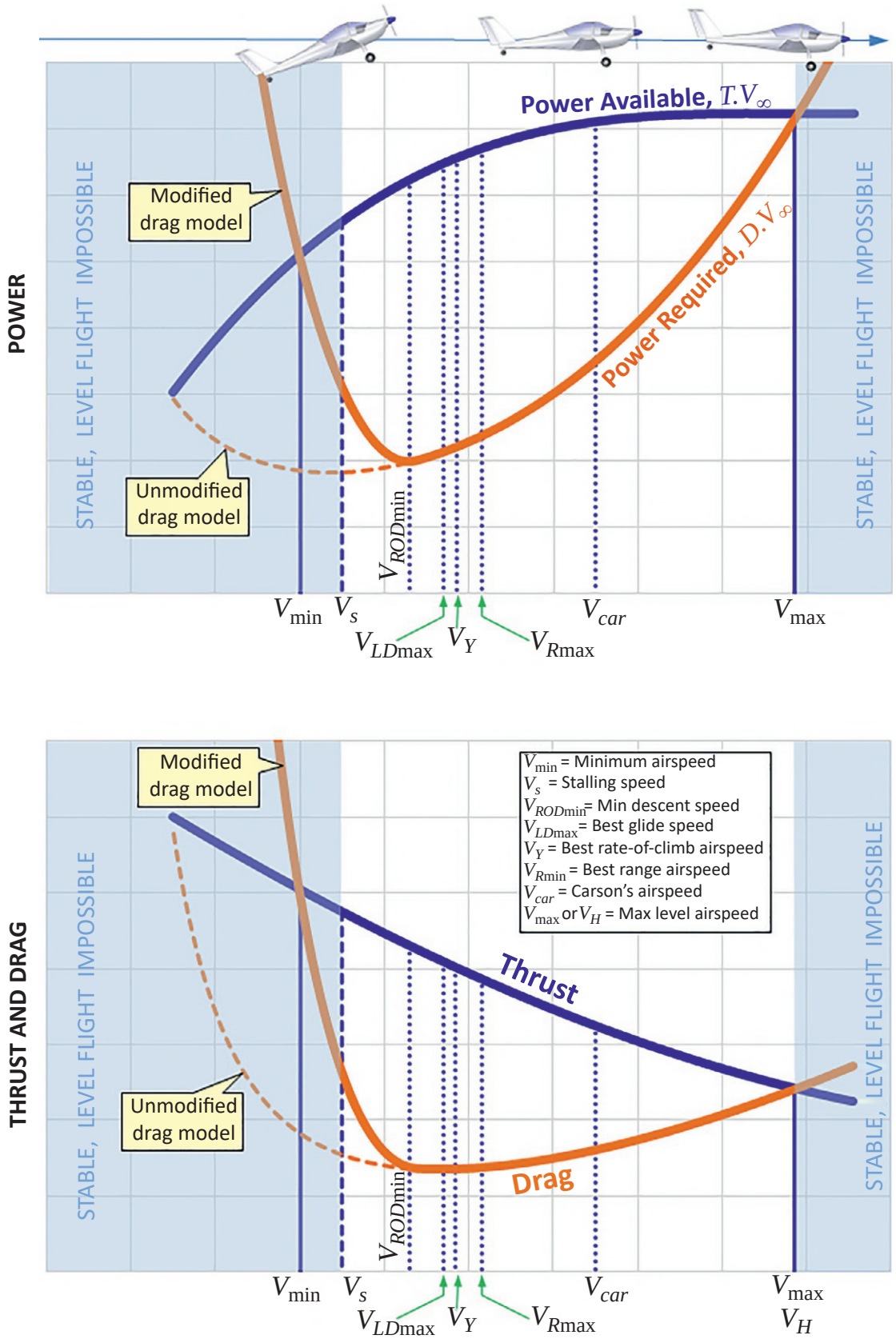


FIGURE 17-12 Important airspeeds for a propeller aircraft in cruising flight. Note that the modified drag model uses the method of Section 16.2.3.

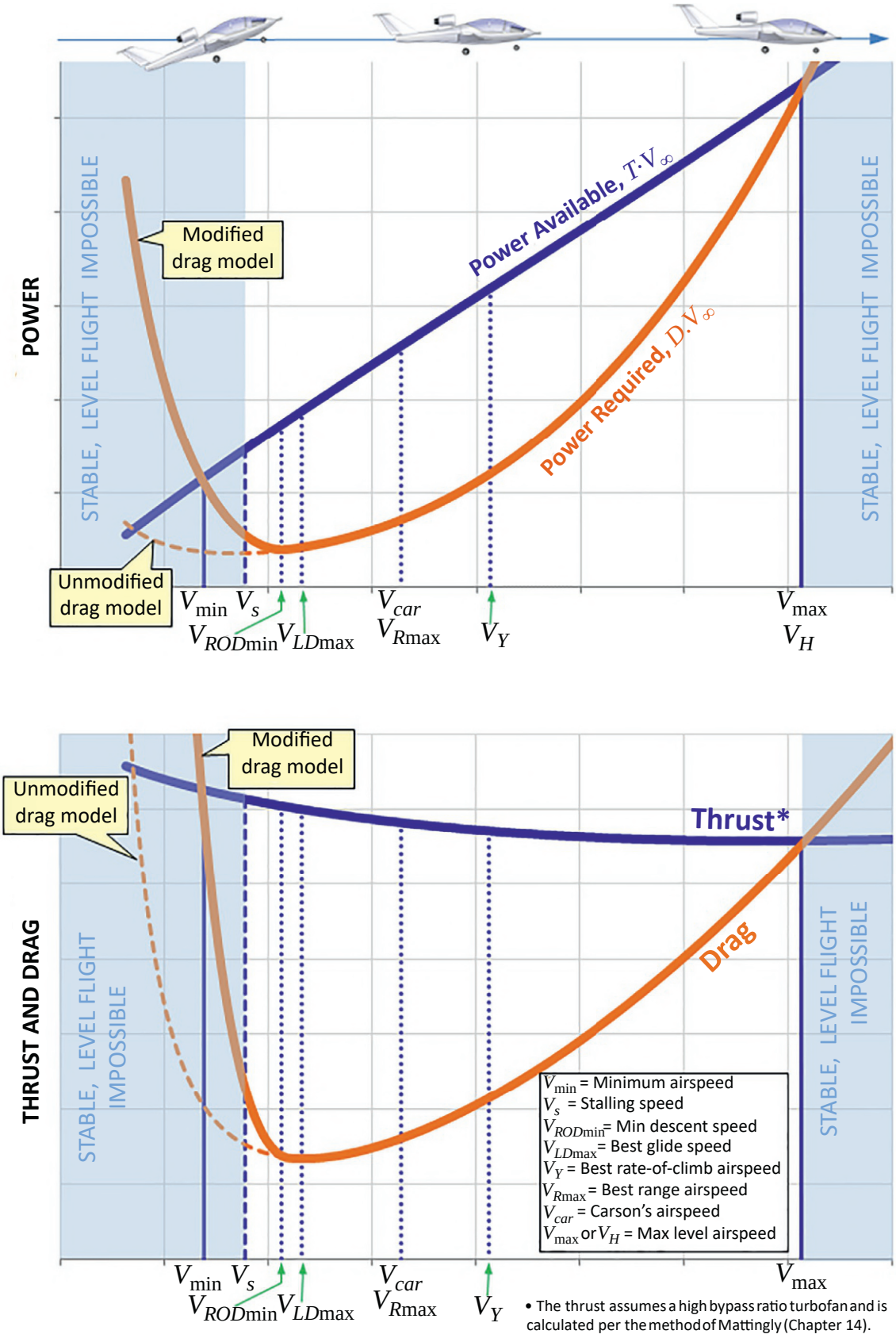


FIGURE 17-13 Important airspeeds for a jet aircraft in cruising flight. Note that the modified drag model uses the method of Section 16.2.3.

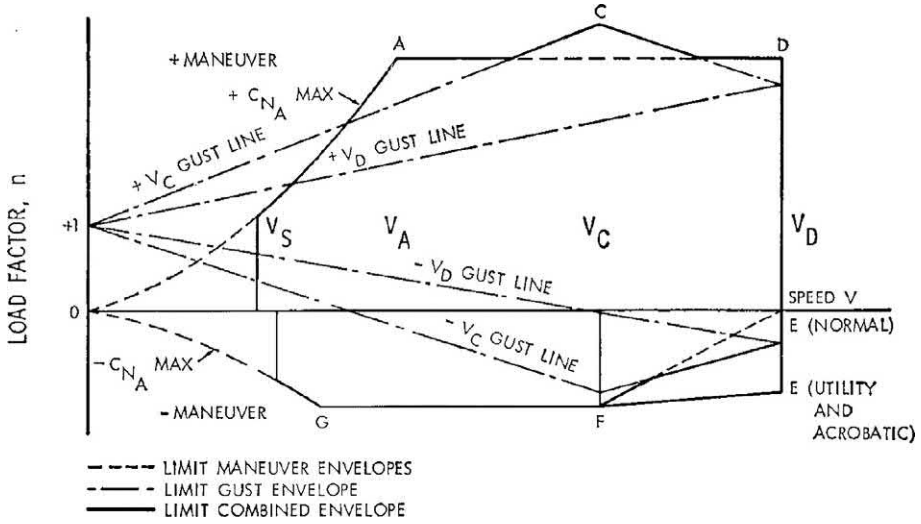


FIGURE 17-14 A generic *V-n* diagram presented in 14 CFR §23.333 for guidance.

TABLE 17-6 Applicable properties of the sample aircraft.

Item	Symbol	Value
Certification category	Normal	
Wing span	b	38 ft
Wing area	S	130 ft^2
Mean geometric chord	c_{MGC}	3.42 ft
Gross weight	W	1320 lb_f
Minimum flying weight	W_{min}	900 lb_f
Stalling speed (+ means normal)	$V_{S(+)}$	46.3 KEAS
Stalling speed (− means inverted)	$V_{S(-)}$	54.7 KEAS
Maximum demonstrated level airspeed	V_H	120 KEAS
3-dimensional lift curve slope	$C_{L\alpha}$	5.25 per radian
Maximum C_L (flaps up)	$C_{L_{max}}$	1.45
Minimum C_L (flaps up)	$C_{L_{min}}$	−1.00
Maximum C_L (flaps down)	$C_{L_{max}}$	2.10
Minimum C_L (flaps down)	$C_{L_{min}}$	−0.75

17.4.1 Step-by-Step: Create a *V-n* Diagram

This section shows how to step through the regulations to prepare the *V-n* diagram for the aircraft in Table 17-6.

STEP 1: Establish Load Factors n_+ and n_-

Per 14 CFR §23.337(a)(1) estimate the positive load factor that must be used for the aircraft (note that it does not have to be higher than 3.80):

Load factor §23.337(a)(1):

$$n_+ = 2.1 + \frac{24000}{W_0 + 10000} = 2.1 + \frac{24000}{1320 + 10000} = 4.22 \tag{17-33}$$

Since $n_+ > 3.80$, we can establish it as 3.80 if we so desire and this is what we will do. Then, §23.337(b)(1) stipulates that the negative load factor, n_-, "may not be less than" 0.4 times n_+. The sentence actually means the opposite: n_- may not be larger than $-0.4n_+$: However, it may be less. Of course, a lower value presents limited benefits, as this will almost certainly lead to heavier airframe. Therefore, $n_- = -0.4n_+ = -1.52$. We can now calculate the following design airspeeds for the gross weight condition:

STEP 2: Design Cruising Speed, V_C

The airplane must be designed to react gust loads at V_C. The purpose is to design the airplane for operation in turbulent air while in cruising flight. The regulations stipulate this to be done assuming a certain minimum value of the cruising speed. Again, the designer can select any speed above (and including) this value, although one must realize the ramifications of selecting a higher cruising speed. The cruising speed should be carefully picked for the two following reasons:

(1) Selecting a "certified" cruising speed below a cruising speed the airplane is capable of (and at which it will usually be operated) will require the airplane to be slowed down to that speed in the presence of atmospheric turbulence. This will annoy even the most docile pilot and may negatively affect the "reputation" of the aircraft in the long run.

(2) Selecting a "certified" cruising speed above a cruising speed the airplane is capable of increases the dive speed (see STEP 3) and result in a heavier airframe that offers less useful load. Therefore, the proper value of V_C should be no higher than the expected cruising speed of the aircraft.

The selection process requires the minimum and maximum cruising speeds to be determined and, then,

a representative value between the two is selected. Per §23.335(a)(1) the *minimum design cruising speed* may not be less than:

$$V_{C\min} = 33\sqrt{\frac{W_0}{S}} = 33\sqrt{\frac{1320}{130}} = 105.2 \text{ KEAS} \qquad (17\text{-}34)$$

Since the wing loading is $1320/130 = 10.2$ lb_f/ft^2 §23.335(a)(2) does not apply, but we must check §23.335(a)(3), which says that the cruising speed "need not be more than $0.9V_H$." This is the maximum design cruising speed:

$$V_{C\max} = 0.9V_H = 0.9(120) = 108 \text{ KEAS} \qquad (17\text{-}35)$$

It is tempting to select $V_C = 108$ KEAS for this airplane. But first, let us consider the resulting dive speeds, assuming it will be 40% greater (per the regulations as will be shown shortly). A $V_C = 105.2$ KEAS leads to a $V_D = 147.3$ KEAS. A $V_C = 108$ KEAS requires at least $V_D = 151$ KEAS. However, why not just select a cruising speed that result in a 150 KEAS dive speed? Such a number is easy to remember. Of course, selecting this airspeed based on "convenience" is not always the right thing to do. But it makes sense here and the resulting cruising speed (107 KEAS) falls between 105.2 KEAS and 108 KEAS.

Also, since this is a "slow aircraft" the stipulations of §23.335(a)(4) does not apply either.

STEP 3: Design Dive Speed, V_D

This is the maximum airspeed to which the airplane is designed. The aircraft must be free of flutter at airspeed up to $1.2V_D$ (per §23.629). The dive speed is calculated per §23.335(b)(2) as follows:

$$V_D > 1.40V_{C\min} = 1.40 \times 105.2 = 147.3 \text{ KEAS} \qquad (17\text{-}36)$$

However, we decided earlier to design the airplane for $1.40 \times 107 = 150$ KEAS and this complies with the above minimum. This also complies with the previous requirement of §23.335(b)(1). Note that paragraph §23.335(b)(3) does not apply to this aircraft. Also, paragraph §23.335(b)(4) can be used to reduce the dive speed. However, compliance requires sophisticated analysis and confirmation by flight testing and, for now, we ignore it and accept the higher dive speed of 150 KEAS.

STEP 4: Design Maneuvering Speeds, V_A and V_G

This is the airspeed below which the aircraft must be capable of withstanding the full deflection of control surfaces. Positive maneuvering speed per §23.335(c)(1):

$$V_A = V_S\sqrt{n_+} = 46.3\sqrt{3.8} = 90.3 \text{ KEAS} \qquad (17\text{-}37)$$

This airspeed is less than V_C (107 KEAS) and, therefore, complies with §23.335(c)(2). Also, calculate the negative or inverted maneuvering speed, denoted as Point G in Figure 17-14. This can be done per Equation (20-30) of Section 20.3.3, using $n = |-1.52| = 1.52$, $C_{L_{\min}} = |-1.00| = 1.00$, and $\rho = 0.002378$ slugs/ft^3. Negative maneuvering speed:

$$V_G = \sqrt{\frac{2|n_-|W}{\rho S C_{L_{\min}}}} = 113.9 \text{ ft/s} = 67.5 \text{ KEAS} \qquad (17\text{-}38)$$

STEP 5: Design Speed for Maximum Gust Intensity, V_B

It is best to consider this airspeed after the gust load diagram has been explained. This airspeed is determined in Section 17.4.1.

STEP 6: Set up the Initial Diagram

Having determined the load factors and airspeeds, it is possible to begin drafting the *V-n* diagram. This helps clarify what these values actually mean. First consider Figure 17-15, which shows a graph with the velocity axis extending from 0 to 160 KEAS and the load factor axis extending from −3 to 5. A number of vertical and horizontal construction lines have been drawn on this graph, for guidance with the rest of the diagram. The steps taken to accomplish this are labeled as well.

Next perform the following actions illustrated in Figure 17-16. First plot the vertical lines representing the positive and negative stall speeds (see Steps 9 and 10). Next, plot the *positive* and *negative stall lines* given by the following expressions:

$$\text{Positive stall line:} \qquad n_+(V) = 0.003388\frac{V^2 S C_{L_{\max}}}{W} \qquad (17\text{-}39)$$

$$\text{Negative stall line:} \qquad n_-(V) = -0.003388\frac{V^2 S C_{L_{\min}}}{W} \qquad (17\text{-}40)$$

where V is the airspeed in KEAS. The constant 0.003388 is simply the product of the S-L density (0.002378 slugs/ft^3) and the knots-to-ft/s conversion factor (1.688—which is squared due to the term V^2), divided by the factor "2" (as in $W \approx L = \frac{1}{2}\rho V^2 S C_{L_{\max}}$). In other words: $0.002378 \times 1.688^2/2 = 0.003388$. With the two curves plotted, the *V-n* diagram now looks as shown in Figure 17-16. Next, create solid lines from the construction lines to represent the outlines of the maneuvering envelope, as is shown in Figure 17-17. Gust lines will be added in the next step and the diagram will be refined.

(1) Gust Loads

All airplanes are subjected to gusts in level flight. These can be caused by thermals, mountain waves, and other similar atmospheric phenomena. As the airplane

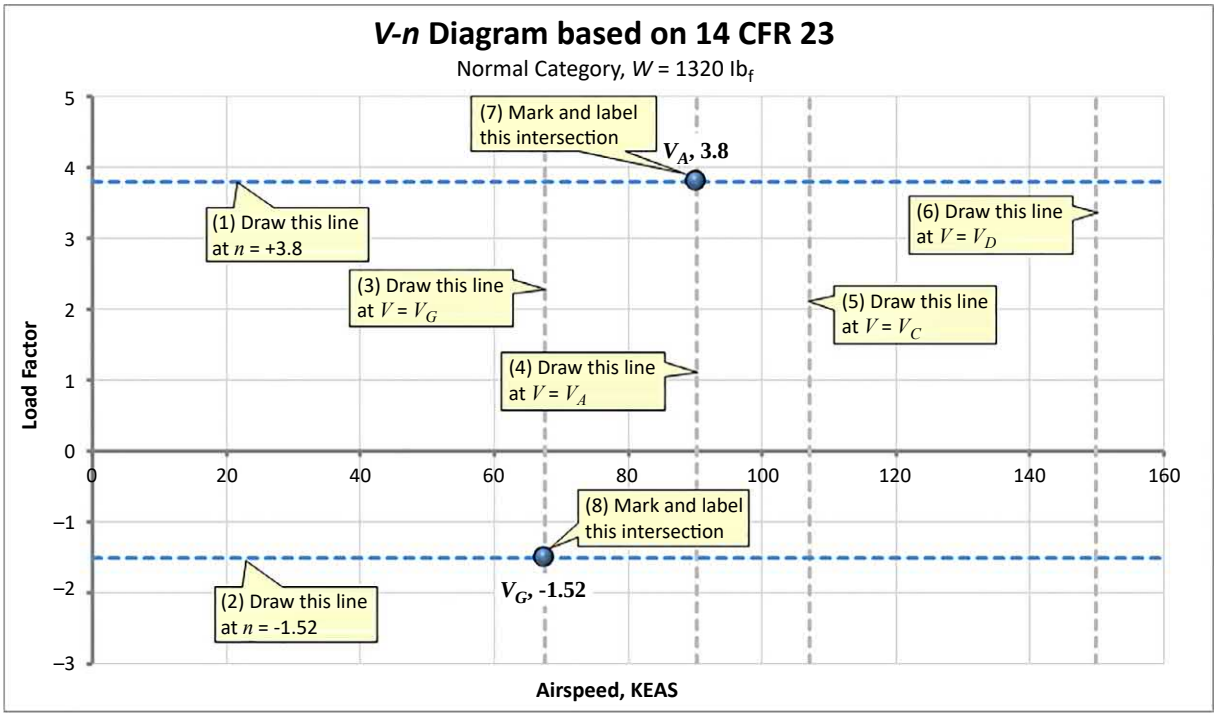


FIGURE 17-15 The first step taken to generate the *V-n* diagram. The dashed lines are "construction lines" that are removed once the diagram is completed.

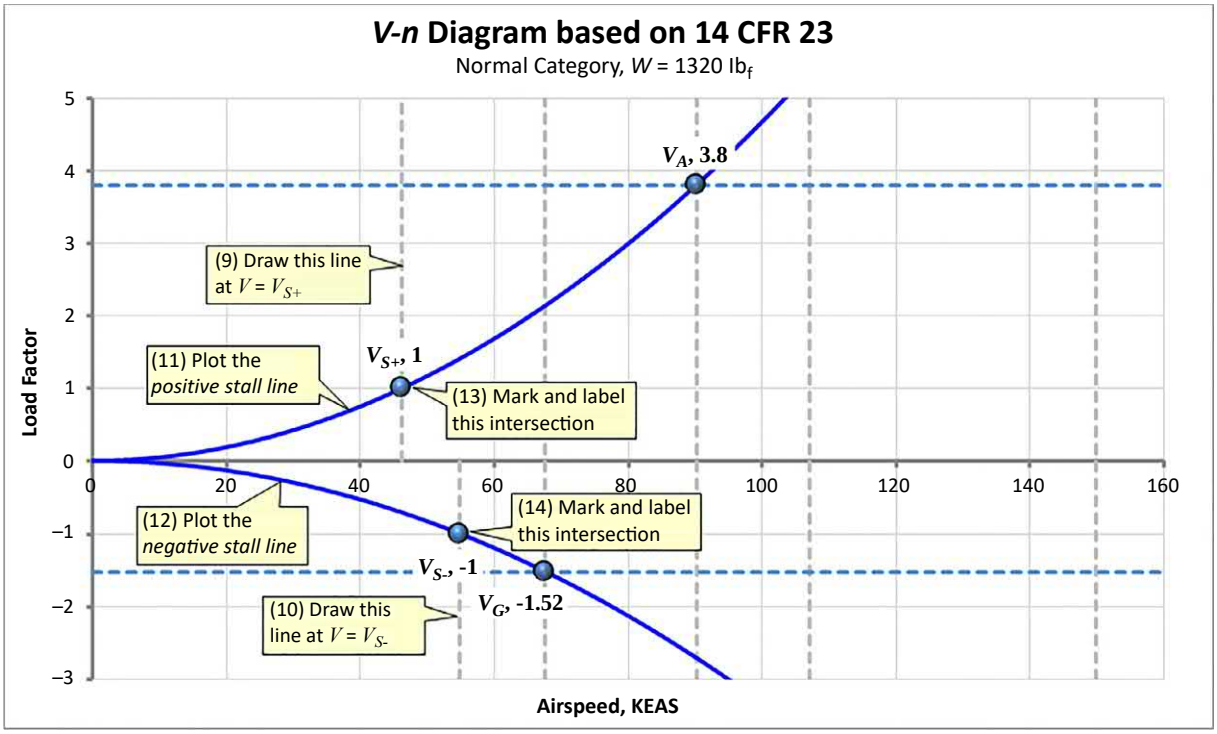


FIGURE 17-16 The second step taken to generate the *V-n* diagram.

penetrates a rising (or sinking) column of air this momentarily changes the angle of attack. This either increases (rising air) or decreases (sinking air) the lift of the wing, causing the "bumpiness" to be sensed by occupants and reacted by the airframe. This is the gust loading. It depends on the forward airspeed of the aircraft and the vertical speed of the rising (or sinking) air penetrated. The aviation authorities specify the gust load requirements in terms of the strength of the vertical speed of the gust.

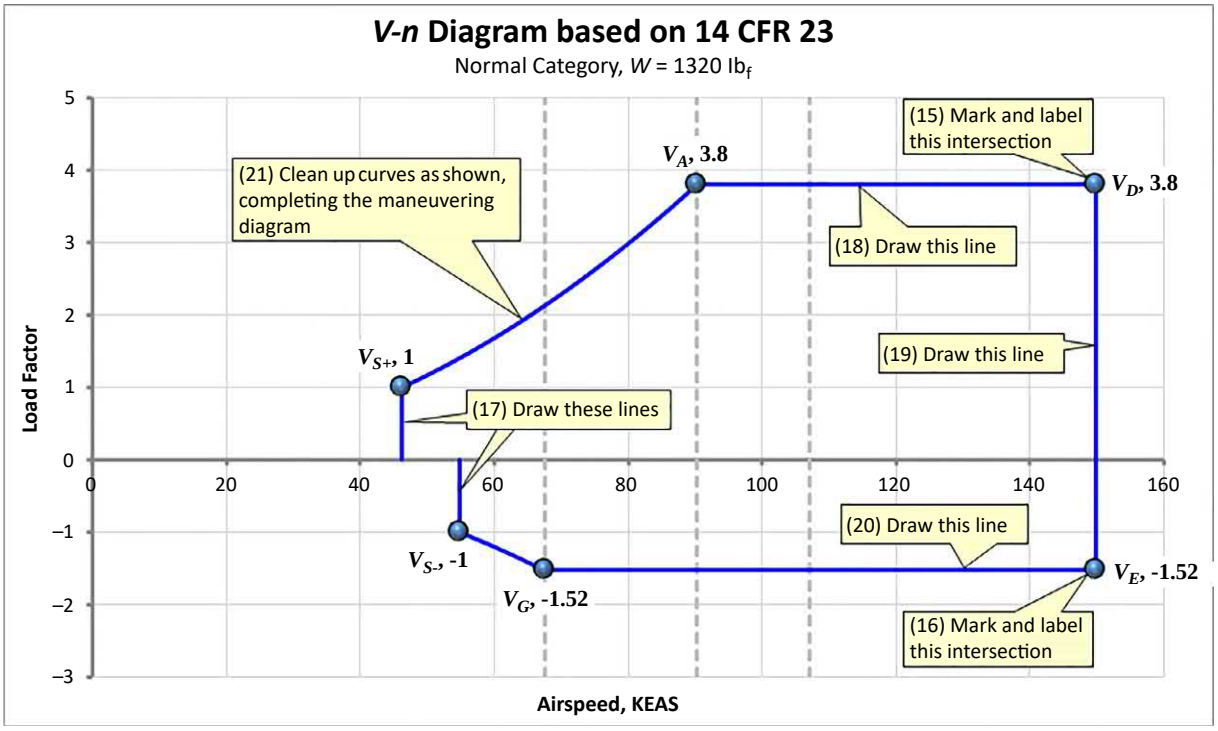


FIGURE 17-17 Completing the maneuvering portion of the *V-n* diagram.

In magnitude, the gust load ranges from being "annoying" to being so severe it may cause structural failure. Therefore, gust loads must be considered in the airframe design. The change in AOA is not instantaneous. Rather, it lasts a finite (albeit short) amount of time. Consequently, the resulting gust loads are lessened or "alleviated." The applicant can reduce the gust load factors by calculating a special gust alleviation factor (see STEP 8).

The gust load factors for GA aircraft are determined per 14 CFR §23.333(c) in accordance with the following rules (see Figure 17-18):

(1) Positive and negative gust velocity of 50 ft/s must be considered at V_C at altitudes from S-L to 20,000 ft. Above 20,000 ft, the gust velocity may be reduced linearly to 25 ft/s at 50,000 ft.

(2) Positive and negative gust velocity of 25 ft/s must be considered at V_D at altitudes from S-L to 20,000 ft. Above 20,000 ft, the gust velocity may be reduced linearly to 12.5 ft/s at 50,000 ft.

(3) Applicable to commuter category aircraft only, a positive and negative gust velocity of 66 ft/s must be considered at V_D at altitudes from S-L to 20,000 ft. Above 20,000 ft, the gust velocity may be reduced linearly to 38 ft/s at 50,000 ft. This gust must be applied at V_B.

As stated earlier, the gust load factor is alleviated per §23.341(c). This assumes the shape of the gust is sinusoidal as described by the following formula:

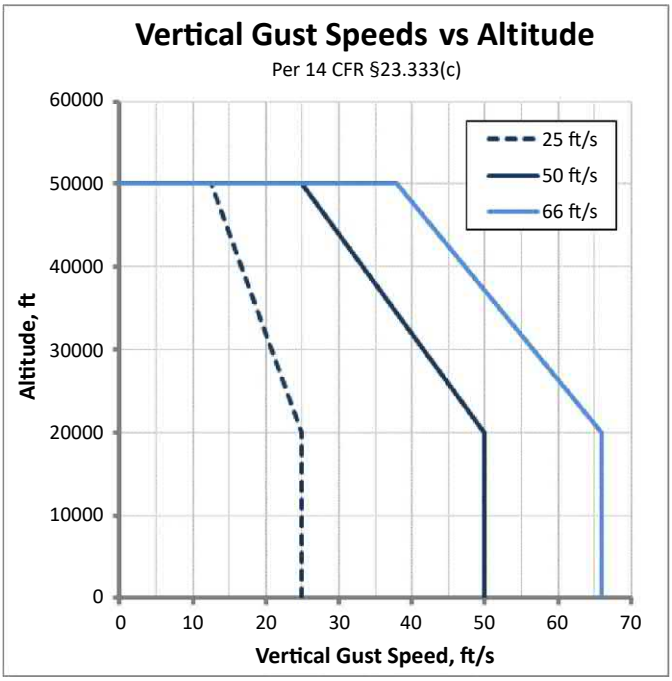


FIGURE 17-18 Regulation allow vertical gusts to be lessened at altitudes higher than 20,000 ft.

$$U = \frac{U_{de}}{2}\left(1 - \cos\frac{2\pi x}{25 \cdot c_{MGC}}\right) \qquad (17\text{-}41)$$

where U_{de} is the vertical gust velocity in ft/s per the above discussion and x is distance in ft penetrated into the gust.

Ordinarily, this formula is only used to demonstrate the nature of the gust. It is not needed for the actual gust load calculations shown below. The gust load portion of the diagram is created per §23.341(c). This process requires the gust response to be determined for the stated vertical gust velocities per §23.333(c). For this part, the designer should use the lift curve slope of the complete aircraft, although that of the wing usually suffices.

The *V-n* diagram must be constructed for all critical configurations, altitudes, and weights. Thus, separate *V-n* diagrams must be made for the airplane in the clean, take-off, and landing configurations. Making a diagram for the minimum flying weight is equally important to the one at gross weight. While air loads on primary structure like wing spars and skin are greater at gross weight, inertia loads of components that do not directly react aerodynamic loads (e.g., engines, avionics, etc.) are higher at minimum weight than at gross weight.

STEP 7: Calculated gust-related parameters

Start by computing the aircraft mass ratio per §23.341(c) as follows:

$$\mu_g = \frac{2(W/S)}{\rho c_{MGC} C_{L\alpha} g} = \frac{2(1320/130)}{(0.002378)(3.42)(5.25)(32.174)} = 14.77 \tag{17-42}$$

Then use this to compute the gust alleviation factor as shown below:

$$K_g = \frac{0.88\mu_g}{5.3+\mu_g} = \frac{0.88(14.77)}{5.3+14.77} = 0.6476 \tag{17-43}$$

STEP 8: Calculate gust load factor as a function of airspeed

With the data in STEP 7 available, the load factor for each of the four vertical gust velocities (±50 ft/s at V_C and ±25 ft/s at V_D) can be determined from:

$$n_g = 1 + \frac{K_g \cdot U_{de} \cdot V \cdot C_{L\alpha}}{498(W/S)} \tag{17-44}$$

where V is airspeed in KEAS. Equation (17-44) is used to plot the four gust lines in Figure 17-19. Next, combine the two diagrams and form a single one. Note that a potential issue has surfaced, in which the positive 50 ft/s gust line goes above V_A and not below as shown in Figure 17-14. This will be treated in the next step.

STEP 9: Calculate gust load factor as a function of airspeed

At this point it is of interest to determine directly the positive and negative gust load factors. This is accomplished using Equation (17-44):

$$n_g = 1 + \frac{(0.6476)(50)(107)(5.25)}{498(1320/130)} = 4.60$$

Similarly, the negative gust load factor can be found from:

$$n_g = 1 + \frac{(0.6476)(-50)(107)(5.25)}{498(1320/130)} = -2.60$$

STEP 10: Finalize gust diagram

Now, the final presentation of the diagram can be prepared. This is done by identifying all intersections

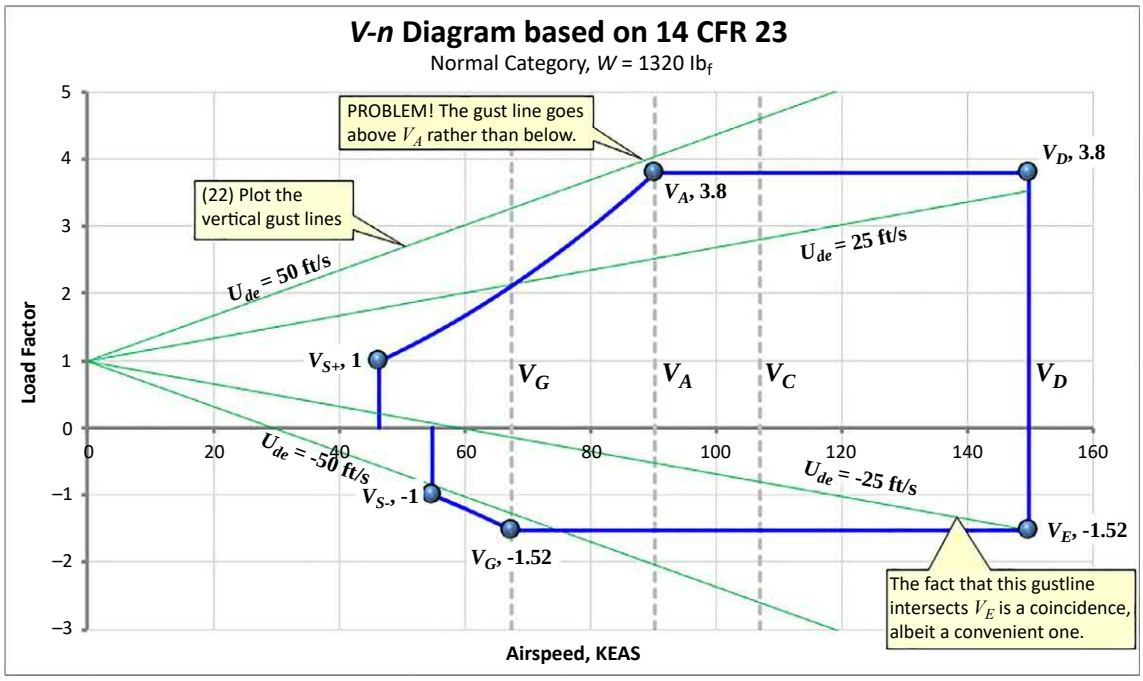


FIGURE 17-19 Initial plotting of the gust lines.

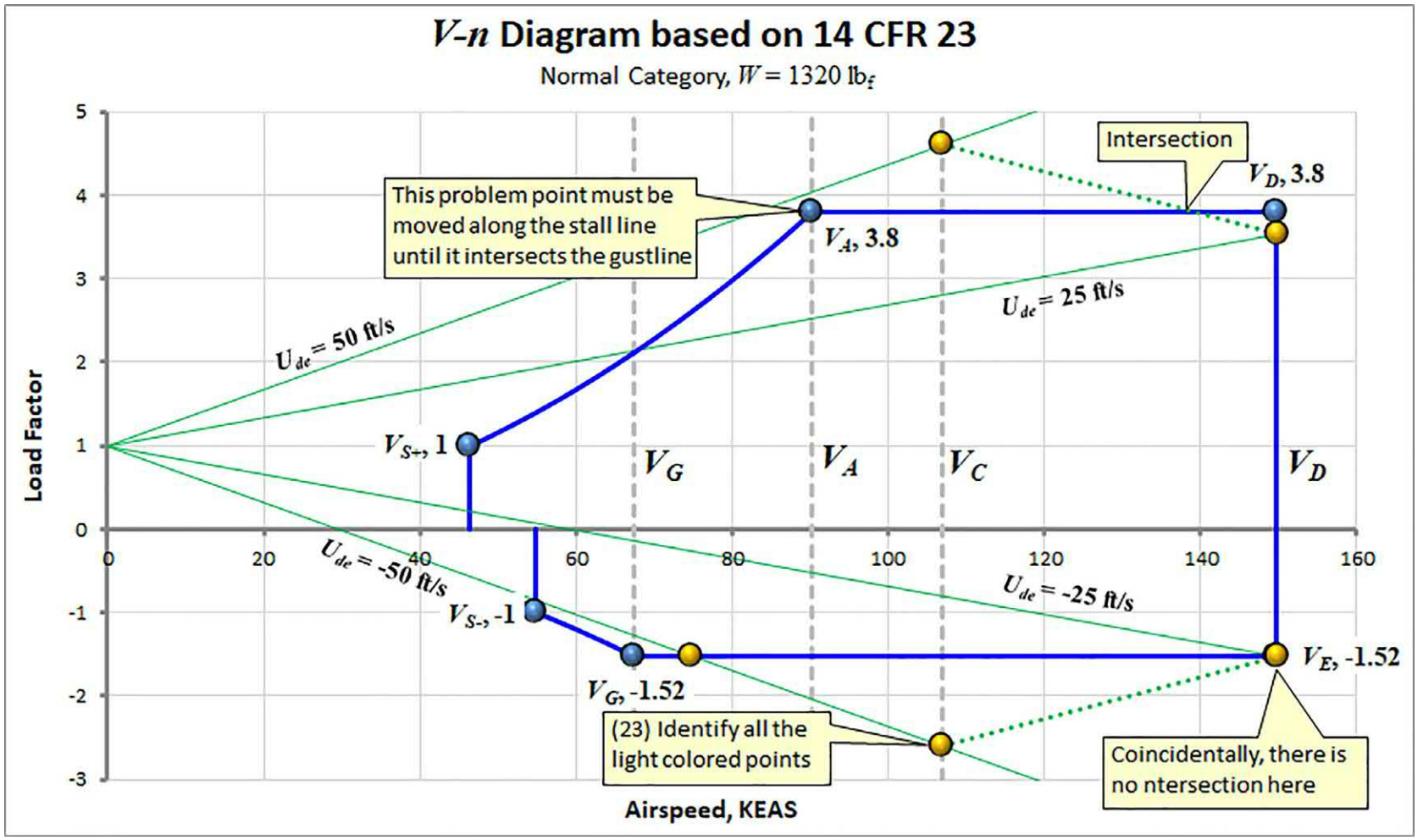


FIGURE 17-20 Refining the influence of the gust lines on the overall *V-n* diagram.

between the two diagrams, connect as needed with lines, and resolve any possible trouble areas (see Figure 17-20). It is here that the reason for selecting this particular airplane becomes apparent. In the view of this author, the diagram of Figure 17-14 is benign in nature. The one being created here poses a problem that appears daunting at first, but we must be able to handle it with confidence. The problem is primarily limited to aircraft with low wing loading and is caused by gust lines that are too steep.

(2) Convenient Relations to Determine Location of Intersections

When plotting the gust load factors it is often necessary to determine the airspeed at which a specific load factor occurs. This is useful when determining the intersection of maneuvering and gust lines. The following expressions can be used for this:

If $n_g > 0$ use this form: $$V = \frac{498(W/S)(n_g - 1)}{K_g \cdot U_{de} \cdot C_{L\alpha}} \quad (17\text{-}45)$$

If $n_g < 0$ use this form: $$V = \frac{498(W/S)(1 - n_g)}{K_g \cdot U_{de} \cdot C_{L\alpha}} \quad (17\text{-}46)$$

To determine how to extend the positive stall line to the positive 50 ft/s or 66 ft/s gust lines, the load factor calculated per Equation (17-39) must equal that of Equation (17-44). Unfortunately, the expression is more complicated, but the intersection depends on the solution to the following quadratic equation:

$$n_g = n_+(V) \Rightarrow (709.5 \cdot \rho \cdot C_{L_{max}}) \cdot V^2 - (K_g \cdot U_{de} \cdot C_{L\alpha}) \cdot V - 498(W/S) = 0 \quad (17\text{-}47)$$

Thus, the new V_A becomes (ignoring the negative solution):

$$(709.5(0.002378)(1.4)) \cdot V_A^2 - ((0.6476)(50)(5.25)) \cdot V_A - 498(1320/130) = 0$$

$$\Rightarrow \quad 2.362 \cdot V_A^2 - 170.0 \cdot V_A - 5057 = 0$$

$$\Rightarrow \quad V_A = 94.6 \text{ KEAS}$$

Equation (17-47) also conveniently allows the gust penetration speed, V_B to be determined (noting that the vertical gust velocity for the condition is given by $U_{de} = 66$ ft/s):

$$(709.5 \cdot \rho \cdot C_{L_{max}}) \cdot V_B^2 - 66(K_g \cdot C_{L\alpha}) \cdot V_B - 498(W/S) = 0 \quad \Leftrightarrow$$

$$V_B = \frac{33 \cdot (K_g \cdot C_{L\alpha}) + \sqrt{1089(K_g \cdot C_{L\alpha})^2 + 498 \cdot 709.5 \cdot (\rho \cdot C_{L_{max}})(W/S)}}{709.5 \cdot \rho \cdot C_{L_{max}}} \quad (17\text{-}48)$$

(3) Completing the Flight Envelope

The final step in the preparation of the diagram is to combine the maneuvering and gust envelopes. This is shown in Figure 17-21. The shaded region is where the airplane must be demonstrated to operate safely during certification. All the load factors represent *limit loads* and must be multiplied by a factor of safety of 1.5 to get ultimate loads.

(4) *V-n* Diagrams with Deployed High-Lift Devices

Note that deploying high-lift devices effectively requires a separate envelope to be prepared. This envelope will have its own V_A, V_D (which is called *flap extension speed*, denoted by V_{FE}), maneuvering load factor, and so on. The regulatory requirements to establish these values are presented in the appropriate regulations.

The flap is often superimposed on the *V-n* diagram for the clean configuration.

17.4.2 Flight Envelopes for Various GA Aircraft

Although the details of creating a *V-n* diagram are spelled out in the applicable regulations, not all aspects of this guidance are clear. For this reason, it is easy to become uncertain about the shape of the final diagram. The images of Figure 17-22 provide some guidance as to what shape to expect based on certification category.

NOTE: The *V-n* diagrams of Figure 17-22 do not reflect the use of high-lift devices.

17.5 SAMPLE AIRCRAFT

As aircraft designers, we must remain concerned about the accuracy of calculations and recognize the importance of comparing results from calculation methods to actual aircraft. A method unable to reasonably predict the performance of actual aircraft is limited at best and suspect at worst. This helps with the selection

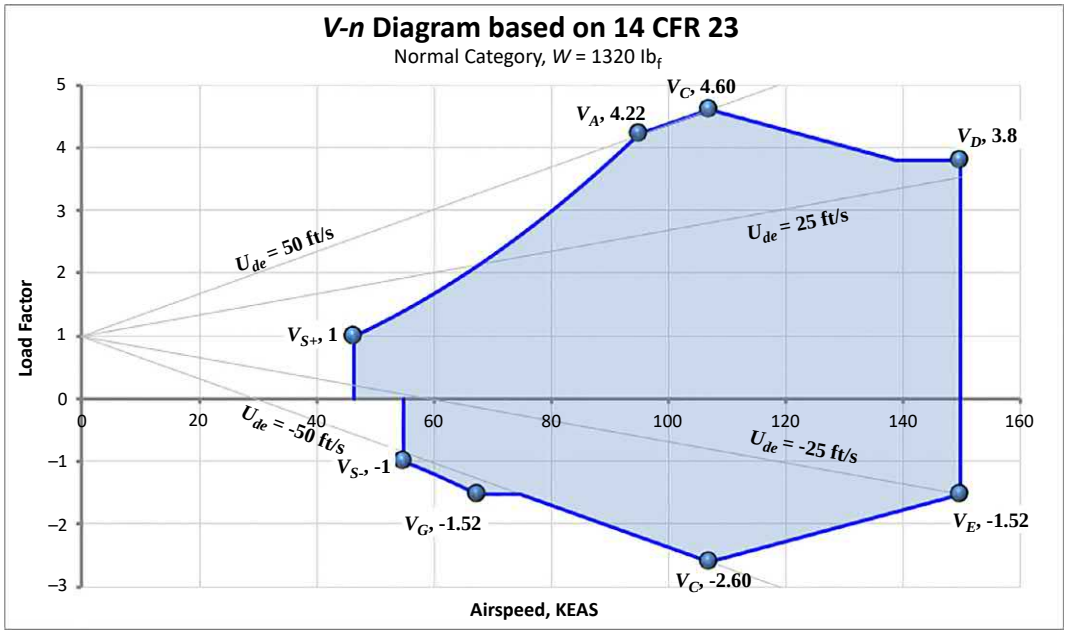


FIGURE 17-21 The completed *V-n* diagram.

of the right method. This section introduces two aircraft that are used to demonstrate performance concepts—the Cirrus SR22 and the Learjet 45. The former is a piston powered propeller aircraft and the latter is a twin-engine business jet. Using these aircraft, calculated values will be compared to published data, giving a valuable insight into the accuracy of the methods.

17.5.1 Cirrus SR22

The SR22 (see Figure 17-23) is designed and manufactured by Cirrus Aircraft, of Duluth, Minnesota. The aircraft was conceived as a more powerful derivative of the all-composite SR20, designed in the mid-1990s. The SR22 is a four-seat, single-engine, high-performance touring aircraft, and, since 2003, has remained the best-selling aircraft in its class. Powered by a 310 BHP Continental IO-550, six cylinder horizontally opposed piston engine, it cruises at 185 KTAS at 75% power at 8000 ft. While boasting high performance, it is designed with safety of operation in mind. The SR20 was the first aircraft in the history of aviation to be certified with an emergency parachute capable of lowering the entire airframe in case of an emergency. At the time of this writing (November 2020), the parachute system, called Cirrus Airframe Parachute System (CAPS) had saved the lives of some 207 people with 115 intentional deployments [11]. Table 17-7 shows properties of this airplane commonly used in examples in this text. All the data are obtained from the manufacturer's website (www.cirrusaircraft.com), using published performance data and the analysis methods provided in this book. All geometric data were obtained by scaling the three-view in Figure 17-24. Assumed values are marked by "*."

The reader should be mindful that the data extraction to be implemented for the SR22 can just as well be accomplished for any other aircraft. One only needs published geometric, inertia, and performance data, and a proportionally correct three-view drawing. Such data can be obtained from both Type Certificate Data Sheet (TCDS [12]) and Pilots Operation Handbook (POH), both of which are readily available; the former from the FAA website (www.faa.gov) and the latter from pilots. Be careful, however: POH data are copyrighted and cannot be made public in the manner shown here. Cirrus Aircraft has graciously given permission to the presentation of the data extracted in this text and this is fortunate, because the SR22 has far more exciting performance and handling characteristics than most aircraft in its class and, thus, offers a great learning potential on how to design fast and efficient single engine aircraft.

17.5.2 Learjet 45

Jet performance concepts will be demonstrated assuming a business jet in the class of the Learjet 45 (see Figure 17-25). Learjet was founded by an American inventor and an influential business man, William P. Lear (1902–1978). Learjet produced a number of well-

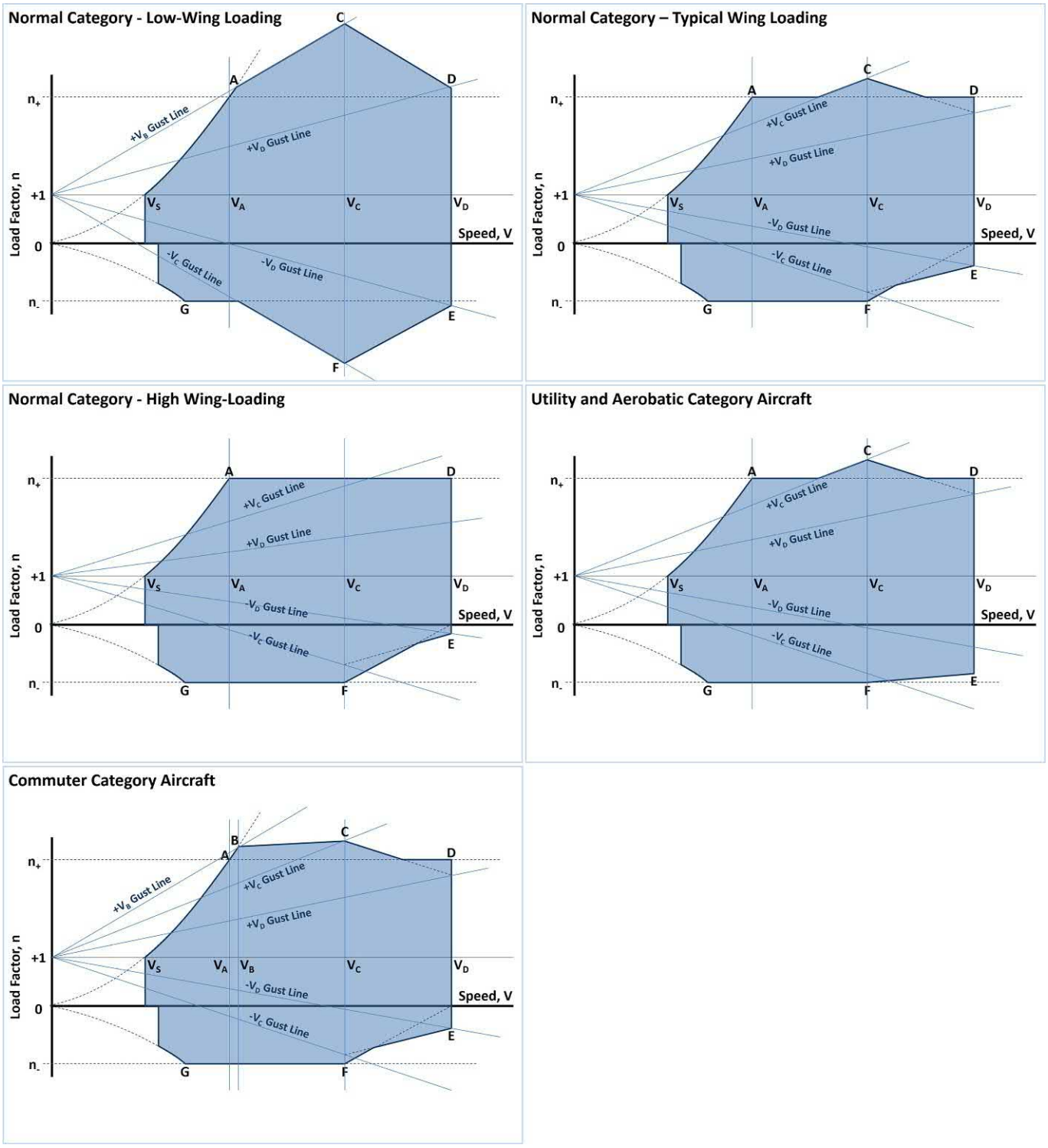


FIGURE 17-22 Typical *V-n* diagrams for selected certification categories.

known business jets, starting with the Learjet 23. In 1969, Learjet merged with Gates Aviation forming Gates Learjet Corporation. In 1990, the company was acquired by Bombardier Aerospace. The development of the 45 was announced by Bombardier in September 1992, and the first flight of the prototype aircraft took place on October 7, 1995. FAA certification was granted in September 1997. The aircraft is powered by two FADEC-controlled Honeywell TFE731–20 engines and is equipped with an internal *Auxiliary Power Unit* (APU) for ground power. The

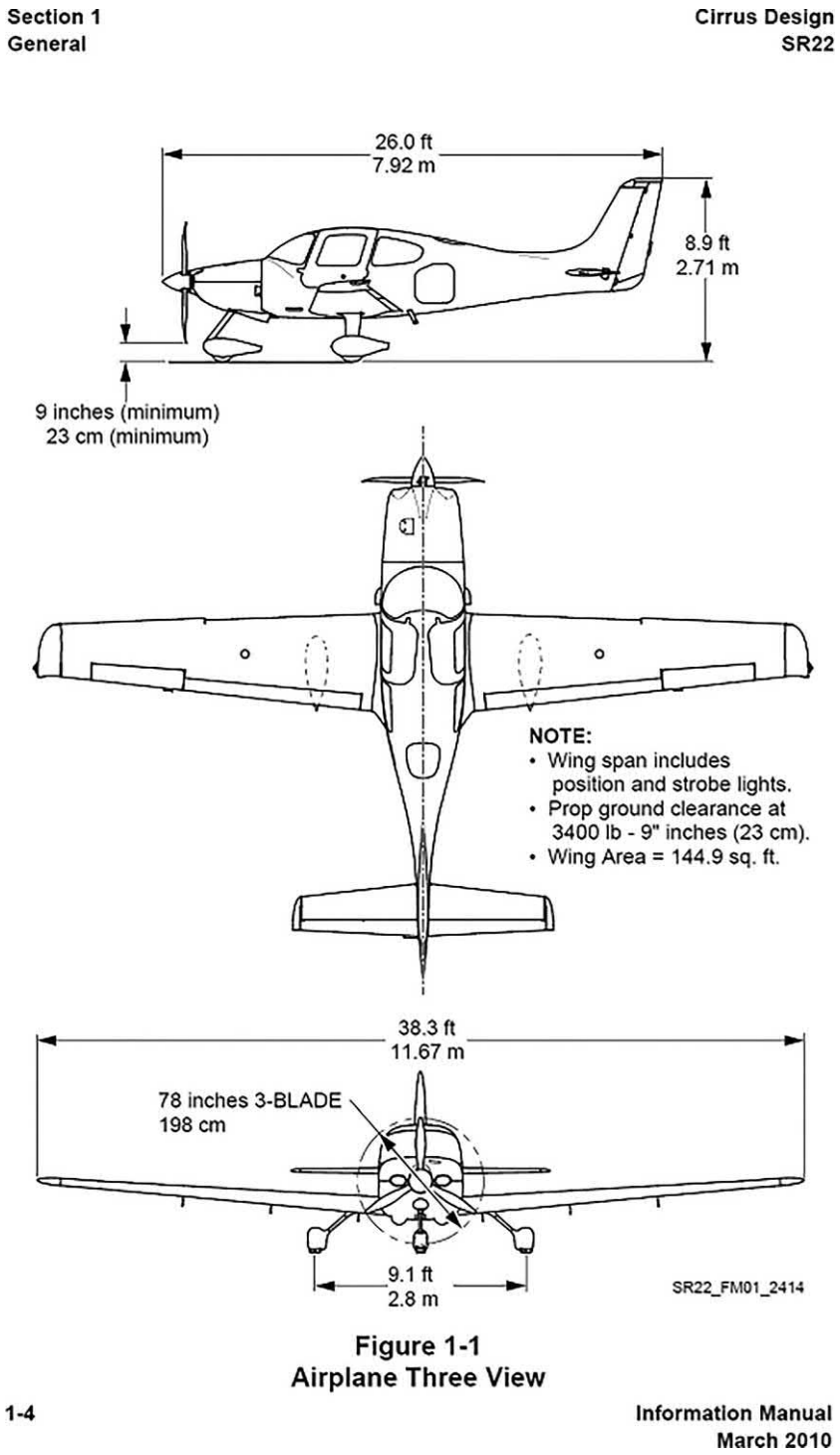


FIGURE 17-23 A three-view of the Cirrus SR22. *Copyright 2021 Cirrus Aircraft or its Affiliates. All Rights Reserved. Image reproduced with the permission of Cirrus.*

Learjet 45 was introduced in October 1995. Published and "assumed" parameters for the 45 are presented in Table 17-8. It is collected from refs. [13, 14].

Note that some of the below specifications is inaccurate. By comparing calculated and published performance, the $C_{D_{min}}$ appears too large (it is obtained from ref. [15] for the Learjet 24D in lieu of the actual aircraft). Regardless, this does not reduce its usefulness in performance examples. Assumed values are marked by "*."

TABLE 17-7 General properties of the Cirrus SR22.

Item	Symbol	Value
Wing span	b	38.3 ft
Wing area	S	144.9 ft^2
Wing chord equation	$c(y)$	5.18–0.1342·y (ft)
Wing mean geometric chord	c_{MGC}	4.03 ft
Span wise location of c_{MGC}	y_{MGC}	8.51 ft
Wing aspect ratio	AR	10.12
Gross weight	W	3400 lb_f
Engine	1 × Continental IO-550	
Max power at S-L	P	310 BHP
Lift-induced drag constant	k	0.04207*
Minimum drag coefficient	$C_{D_{min}}$	0.02541*
C_L of minimum drag	$C_{L_{minD}}$	0.20*
Maximum C_L(flaps up)	$C_{L_{max}}$	1.41
Maximum C_L(flaps for T-O)	$C_{L_{min}}$	1.99
Basic ($\alpha = 0$) C_L	C_{L0}	0.2*

* *Assumed values.*

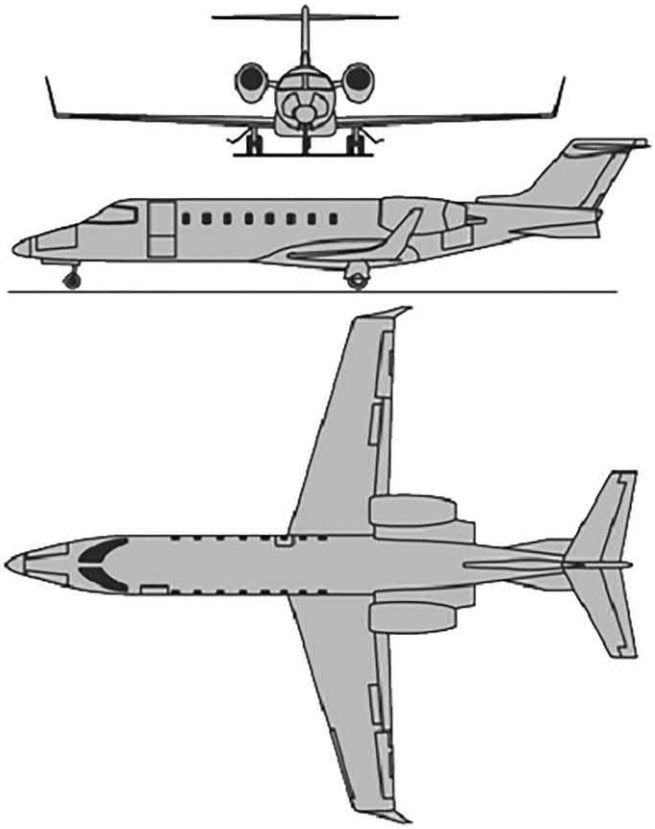


FIGURE 17-25 A 3-view of the Learjet 45.

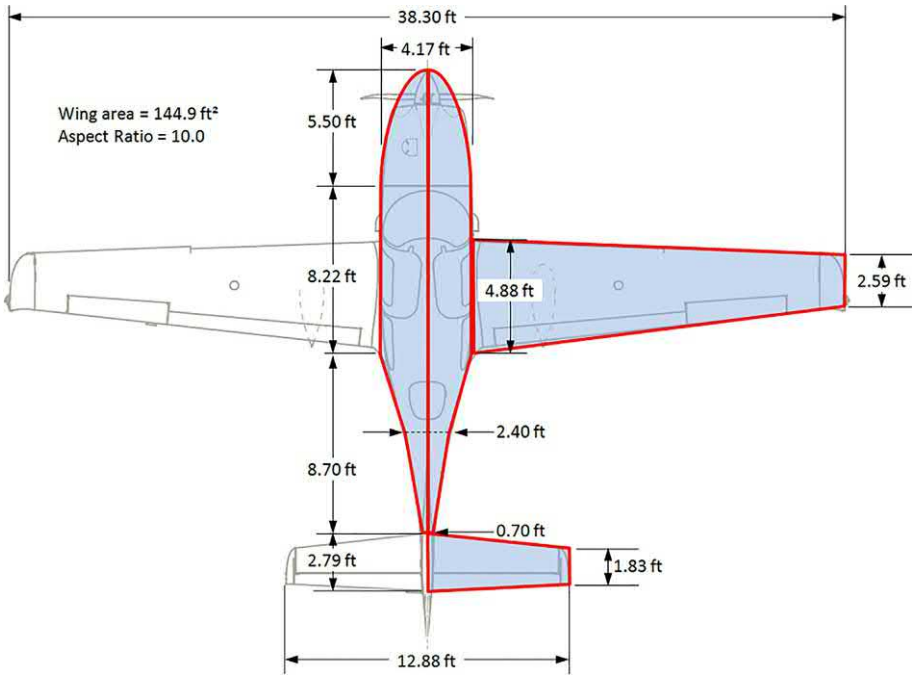


FIGURE 17-24 Scaling the top-view based on the wing span in the three-view of Figure 17-23 yields the following dimensions. *Copyright 2021 Cirrus Aircraft or its Affiliates. All Rights Reserved. Image reproduced with the permission of Cirrus.*

TABLE 17-8 General properties of the Learjet 45.

Item	Symbol	Value
Wing span	b	47.78 ft
Wing area	S	311.6 ft^2
Wing aspect ratio	AR	7.33
Wing taper ratio	λ	0.391
Gross weight	W	21,500 lb_f
Engines (low bypass ratio turbofan)	2 × Honeywell TFE731–20	
Max thrust at S-L	T	2 × 3500 lb_f
Bypass ratio	BPR	2.8
Lift-induced drag constant*	k	0.05236*
Minimum drag coefficient (clean)*	$C_{D_{min}}$	0.0200*
Minimum drag coefficient (T-O)*	$C_{D_{min}}$	0.045*
C_L of minimum drag*	$C_{L_{minD}}$	0.2*
Maximum C_L (flaps up)	$C_{L_{max}}$	1.527
Maximum C_L (flaps 8 degrees)	$C_{L_{max}}$	1.600
Maximum C_L (flaps 20 degrees)	$C_{L_{max}}$	1.718
Maximum C_L (flaps 40 degrees)	$C_{L_{min}}$	1.857
Basic ($\alpha = 0$ degree) C_L*	C_{L0}	0*
Throttle ratio*	TR	1.072*

* *Assumed values.*

EXERCISES

(1) Determine the pressure, temperature, and density and the corresponding ratios for the following conditions:
- **(a)** Altitude of 10,000 ft for Outside Air Temperature (OAT) differing some −30°F, 0°F, and 30°F from the ISA temperature. (ISA is the 0°F condition).
- **(b)** Altitude of 8.4 km for OAT differing some −30°C, 0°C, and 30°C from the ISA temperature.

Ans: (a) $p = 1455$ psf for all conditions, $T_{-30°F} = 453°F$, $T_{0°F} = 483°F$, $T_{30°F} = 513°F$, $\rho_{-30°F} = 0.001872$ slugs/ft^3, $\rho_{0°F} = 0.001756$ slugs/ft^3, $\rho_{30°F} = 0.001653$ slugs/ft^3.

(2) Convert the following airspeeds into ft/s:
- **(a)** 189 kmh
- **(b)** 16.6 in/h
- **(c)** 795 mph
- **(d)** 321 knots
- **(e)** 56.1 m/s
- **(f)** 23 furlongs/fortnight
- **(g)** The average of 121 mph, 65 knots, and 110 kmh
- **(h)** 19,510 nm/week

Ans: (a) 172.2 ft/s, (b) 0.0003843 ft/s, (c) 1166 ft/s, (d) 541.8 ft/s, (e) 184.1 ft/s, (f) 0.01255 ft/s, (g) 90.13 ft/s, (h) 0.05445 ft/s.

(3) Convert the following airspeeds into knots:
- **(a)** 125 kmh
- **(b)** 65,800 in/h
- **(c)** 698 mph
- **(d)** 452 km/day
- **(e)** 195.3 m/s
- **(f)** 22.5 furlongs/fortnight
- **(g)** The average of 32 mph, 48 m/s, and 62 kmh
- **(h)** 582 km/week

Ans: (a) 67.49 knots, (b) 0.9025 knots, (c) 606.6 knots, (d) 10.17 knots, (e) 379.6 knots, (f) 0.007274 knots, (g) 51.53 knots, (h) 1.871 knots.

(4) Determine the KTAS for the following airspeeds and altitudes (all airspeeds are calibrated airspeeds. Ignore compressibility):
- **(a)** 150 m/s at an altitude of 10,550 m
- **(b)** 276 kmh at an altitude of 3.3 statute miles
- **(c)** 432 ft/s at an altitude of 7.6 km
- **(d)** 299 mph at an altitude of 5.6 nm

Ans: (a) 519.9 KTAS, (b) 195.5 KTAS, (c) 381.9 KTAS, (d) 458.1 KTAS.

(5) Determine the KTAS for the following airspeeds and altitudes and OATs (ignore compressibility):
- **(a)** 225 KCAS at an altitude of 6000 ft at ISA.
- **(b)** 145 KIAS at an altitude of 15,000 ft at ISA + 20°C. Instrument error is −3 KIAS.
- **(c)** 270 KIAS at an altitude of 35,000 ft at ISA-20°C. Instrument error is +1.2%.

Ans: (a) 246.1 KTAS, (b) 185.8 KTAS, (c) 468.0 KTAS.

(6) Determine the KIAS for the following airspeeds and altitudes and OATs (ignore compressibility):
- **(a)** 225 KTAS at an altitude of 6000 ft at ISA.
- **(b)** 145 KTAS at an altitude of 15,000 ft at ISA + 20°C. Instrument error is −3 KIAS.
- **(c)** 270 KTAS at an altitude of 35,000 ft at ISA-20°C. Instrument error is +1.2%.

Ans: (a) 205.7 KIAS, (b) 107.8 KIAS, (c) 159.5 KIAS.

(7) Determine the KGS for the following airspeeds and altitudes and OATs and wind speeds (ignore compressibility):
- **(a)** 225 KTAS at an altitude of 6000 ft at ISA. Headwind is 35 knots.
- **(b)** 227 KIAS at an altitude of 15,000 ft at ISA + 15°C. Instrument error is +2.5 KIAS. Headwind is −18 knots.

(c) 270 KIAS at an altitude of 35,000 ft at ISA-30°C. Instrument error is +2.8%. Headwind is −95 knots.

Ans: (a) 190 KGS, (b) 315.6 KGS, (c) 558.3 KGS.

(8) Determine KTAS, KEAS, and KCAS for an airplane flying at M = 0.8 at 36,000 ft on a standard day. If the instrument error is −3.5 KIAS, determine the indicated airspeed as well.

(9) Create a V-n diagram for the aircraft presented in the below table.

Item	Symbol	Value
Certification category	Normal	
Wing span	b	39 ft
Wing area	S	220 ft^2
Wing mean geometric chord	c_{MGC}	4.5 ft
Gross weight	W	6000 lb_f
Minimum flying weight	W_{min}	4000 lb_f
Stalling speed (gross weight, flaps down)	$V_{S(+)}$	59 KEAS
Stalling speed (gross weight, flaps down)	$V_{S(-)}$	68 KEAS
Maximum level airspeed	V_H	350 KEAS
3-dimensional lift curve slope	$C_{L\alpha}$	4.6 per radian
Maximum C_L(flaps up)	$C_{L_{max}}$	1.50
Minimum C_L(flaps up)	$C_{L_{min}}$	−1.10
Maximum C_L(flaps down)	$C_{L_{max}}$	2.31
Minimum C_L(flaps down)	$C_{L_{min}}$	−1.74

References

[1] A. Miele, *Flight Mechanics – Theory of Flight Paths*, Dover Publications, 1990.

[2] http://www.fai.org/records/powered-aeroplanes-records. (Accessed 21 November 2020).

[3] http://www.nasa.gov/centers/dryden/history/pastprojects/Helios/index.html. (Accessed 21 November 2020).

[4] T.E. Noll, J.M. Brown, M.E. Perez-Davis, S.D. Ishmael, G.C. Tiffany, M. Gaier, *Investigation of the Helios Prototype Aircraft Mishap, Volume I Mishap Report*, NASA, January 2004. Available from http://www.nasa.gov/pdf/64317main_helios.pdf. (Accessed 21 November 2020).

[5] Anonymous, *U.S. Standard Atmosphere 1976*, National Oceanic and Atmospheric Administration, 1976.

[6] M. Ritter, *The Physical Environment*, Online ebook. https://www.earthonlinemedia.com/ebooks/tpe_3e/atmospheric_moisture/lapse_rates_1.html. (Accessed 21 November 2020).

[7] http://www.vaisala.com/humiditycalculator/help/index.html#calculating-humidity. (Accessed 21 November 2020).

[8] R. Stull, *Practical Meterology – An Algebra-Based Survey of Atmospheric Science*, University of British Columbia, Canada, 2016.

[9] Anonymous, *Boeing 757 FCOM, Boeing 757-27B/-208/-256/-308, Flight Crew Operations Manual*, Boeing Aircraft, 2011.

[10] J.D. Anderson, *Fundamentals of Aerodynamics*, sixth ed., McGraw-Hill, 2011.

[11] Source. http://www.cirruspilots.org/Content/CAPSHistory.aspx.

[12] TCDS A00009CH, Cirrus Design Corporation, Revision 18, 12/29/2011, FAA, 2011.

[13] P. Jackson (Ed.), *Jane's All the World's Aircraft 1998–99*, Jane's Yearbooks, 1999.

[14] Anonymous, *Learjet 45 – FAA Approved Airplane Flight Manual*, Bombardier Aerospace, 2004.

[15] P.T. Soderman, T.N. Aiken, *Full-Scale Wind-Tunnel Tests of a Small Unpowered Jet Aircraft with a T-Tail*, NASA TN-D-6573, November 1971.

CHAPTER

18

Performance—Take-Off

OUTLINE

18.1 **Introduction** 785
- *18.1.1 The Content of This Chapter* 786
- *18.1.2 What Analyses Must I Do?* 786
- *18.1.3 Important Segments of the T-O Phase* 786

18.2 **Fundamental Relations for the Take-Off Run** 790
- *18.2.1 General Free-Body Diagram for the T-O Ground Run* 790
- *18.2.2 Basic Kinematic Relations* 791
- *18.2.3 The Equation-of-Motion for the T-O Ground Run* 791
- *18.2.4 Formulation of Required Aerodynamic Forces* 792
- *18.2.5 Solution of Kinematic Problems Using Numerical Integration* 792
- *18.2.6 Determination of the Lift-Off Speed* 794
- *18.2.7 Ground Roll Friction Coefficients* 794
- *18.2.8 Determination of Time to Lift-Off* 794

18.3 **Conducting the Take-Off Analysis** 795
- *18.3.1 Calculating the Ground Run Distance, S_G* 795
- *18.3.2 Calculating the Rotation Distance, S_{ROT}* 802
- *18.3.3 Calculating the Transition Distance, S_{TR}* 802
- *18.3.4 Calculating the Climb Distance Over an Obstacle, S_C* 804
- *18.3.5 Calculating the Balanced Field Length, S_{BFL}* 805
- *18.3.6 Take-Off Sensitivity Studies* 807

18.4 **Database—T-O Performance of Selected Aircraft** 808

Exercises 809

References 810

18.1 INTRODUCTION

It is appropriate to begin the performance analysis with one of the most important maneuvers performed by any aircraft; the *take-off* (T-O). Figure 18-1 shows an organizational map displaying the T-O among other subjects of *performance theory*. The designer must understand not only the capability of the new aircraft during T-O but also its limitations and sensitivity. This chapter presents the formulation of the equation-of-motion for the T-O maneuver and presents practical solution methodologies for both propeller and jet-powered aircraft.

T-O performance typically refers to the distance required for an aircraft to accelerate from rest to lift-off and the distance required to attain a safe, initial climb. Aircraft are usually designed to meet specific runway length requirements. This dictates powerplant requirements, as most aircraft need far more power for T-O and climb than during cruise. A case in point are commercial aircraft. A new design must operate from runways used by the competition, and preferably require shorter runways, as this might give it a competitive edge.

T-O distance requirements specified in a typical *request-for-proposal* (RFP) warrants serious considerations. Not only must the T-O distance at ISA and S-L be determined, but also sensitivity to an uphill runway slope and hot-day, high-altitude conditions. There may even be a combination of high atmospheric temperature at high elevation. All detrimentally tax the capability of the aircraft. As an example, the Mariscal Sucre International airport in Quito, Ecuador, is at an altitude of 9228 ft. It presents an operational challenge to commercial aircraft. The largest type of aircraft to regularly operate from it is Airbus A-340. Various tools for T-O sensitivity studies are presented in Section 18.3.6.

A realistic T-O performance analysis also accounts for the type of landing gear featured on the aircraft. The analysis in this text assumes a conventional tri-cycle or taildragger configurations. Accounting for landing gear is particularly important for taildraggers. A taildragger lifts

https://doi.org/10.1016/B978-0-12-818465-3.00018-5

Copyright © 2022 Elsevier Inc. All rights reserved.

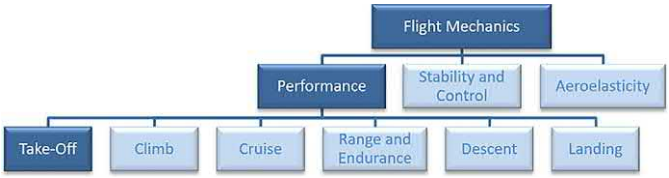


FIGURE 18-1 An organizational map placing performance theory among other the disciplines of *Flight Mechanics*, and highlighting the focus of this chapter; take-off performance.

the tailwheel off the runway as soon as certain airspeed is achieved. The airspeed at which this takes place may range from standstill to one-half of the airplane's lift-off speed. The T-O formulation must be modified to account for two rather than three landing gear contact points and the associated reduction in drag of the more horizontal configuration. This is discussed further in Bullet (4) in Section 18.3.1.

In general, the methods presented in here are "industry standard" and mirror that presented by a variety of authors, e.g., Perkins and Hage [1], Torenbeek [2], Nicolai [3], Roskam [4], Hale [5], Anderson [6], and many others.

18.1.1 The Content of This Chapter

- Section 18.2 presents the fundamental relations of the T-O ground run, including the equation-of-motion for a T-O ground run and the kinematics of the T-O run.
- Section 18.3 presents several methods to solve the equation-of-motion.
- Section 18.4 presents the T-O properties of selected aircraft types.

18.1.2 What Analyses Must I Do?

For the newcomer to T-O analysis, the burning question is: "What am I supposed to estimate and how do I conduct those estimations?" In short, the purpose of T-O analysis is to estimate the total T-O distance, its constituent segments, and the associated airspeeds. The results are then compared to the pertinent requirements, answering if the aircraft will meet them. This chapter can be split into three sections: Introduction, tools of the trade, and analyses. Tables 18-1 and 18-2 list the necessary tasks you should complete.

18.1.3 Important Segments of the T-O Phase

The T-O maneuver is split into the segments shown in Figure 18-2. The *ground run* is the distance from brake-release to the initiation of the rotation, when the pilot pulls the control wheel (or stick or yoke) backward to raise the nose of the aircraft. This action is required to increase the airplane's AOA to expedite it becoming airborne. The aircraft typically remains in this attitude for some 1 to 3 s, before the tires lose contact with the ground, depending on aircraft size and weight. This segment is called the *rotation*. The rotation phase concludes as the aircraft lifts off the ground and begins the *transition* and subsequent *climb phase*. Note that h_{obst} (see Figure 18-2) is the height of an imaginary obstacle the airplane clears some distance from the initial position. The sum of these contributions constitutes the total T-O distance.

TABLE 18-1 Task list based on 14 CFR part 23.

Paragraphs	Content	Section
14 CFR §23.2115[a]	Determination of take-off performance	18.2 and 18.3
14 CFR §23.51	Take-off speeds	18.2 and 18.3
14 CFR §23.53	Take-off performance	18.2 and 18.3
14 CFR §23.55	Accelerate-stop distance (multiengine jets and commuters)	18.2 and 18.3
14 CFR §23.57	Take-off path (multiengine jets and commuters)	18.2 and 18.3
14 CFR §23.59	Take-off distance and take-off run (multiengine jets and commuters)	18.2 and 18.3
14 CFR §23.61	Take-off flight path (multiengine jets and commuters)	18.2 and 18.3

[a] *"New" Part 23.*

TABLE 18.2 Task list for T-O analysis.

Task name	Terms	Weight	CG position	Altitude	Section
Ground roll	S_G	Gross	Forward CG is usually the critical one	0 ft 5000 ft 10,000 ft + highest elevation airport expected	18.3.1
Rotation	V_R, V_1, S_R				18.3.2
Transition	V_R, S_{TR}				18.3.3
Climb	V_2, S_C				18.3.4
Total T-O distance	S_{TOT}				The sum of the above.
Balanced Field Length	S_{BFL}	Gross	Forward	Same as above	18.3.5
Sensitivity analyses	Various	Various	Various	Various	18.3.6

(1) Impact of Landing Gear Configuration on T-O

The formulation of the T-O segments, in part, depends on the airplane's landing gear configuration. To better understand why, consider Figure 18-3, which shows the T-O maneuver for two of the most common landing gear configurations; a tricycle and taildragger landing gear.

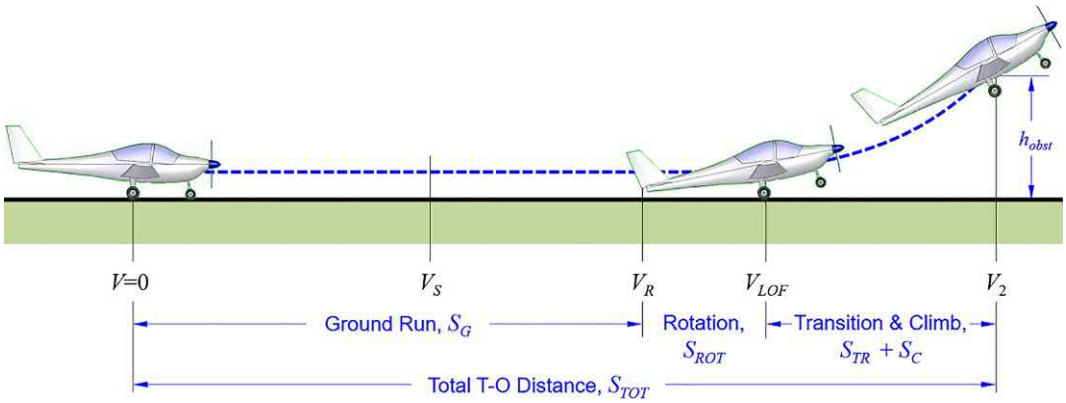


FIGURE 18-2 Important segments of the T-O phase.

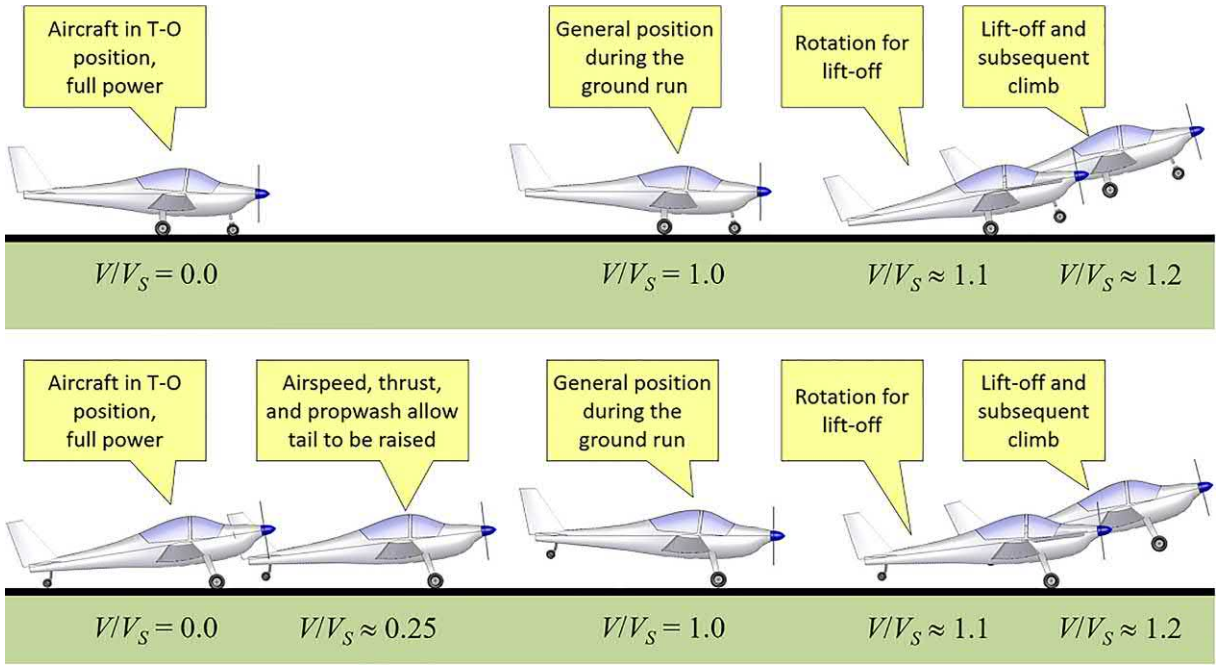


FIGURE 18-3 A sequence of images showing T-O ground run for a tricycle and taildragger aircraft.

In Figure 18-3, V is the instantaneous airspeed of the aircraft and V_S is its stalling speed in the T-O configuration (i.e., if the airplane features high-lift devices, V_S is the stalling speed with flaps deployed). The airplane must accelerate from rest to the lift-off speed (V_{LOF}). The tricycle configuration accelerates with the main and nose landing gears in contact with the ground. However, the taildragger, initially, has the main landing gear and tailwheel in contact with the ground. Eventually, the combination of forward airspeed, thrust, and propwash over the horizontal tail allows it to lift the tailwheel off the ground. For light taildraggers, this happens soon after brake-release. For others, primarily larger aircraft, some forward airspeed must be acquired before the tail can be raised off the ground. Sections 13.3.4 and 13.3.5 provide methods to estimate the airspeed at which a tricycle configuration can lift the nose gear off the ground and at which a taildragger can lift the tailwheel off the ground.

The T-O analysis of a tricycle and taildragger aircraft differs primarily in having to account for the tail of the latter being raised off the ground. From the standpoint of drag, the taildragger configuration with tailwheel on ground is different from that with the tailwheel off the ground. Initially, the taildragger is an airplane at a high AOA, whereas once the tailwheel is off the ground, it transforms into one at a low AOA. *A proper representation of this transformation is required for accurate estimation of the T-O of taildraggers.*

(2) Important Airspeeds for T-O Analysis

The airspeeds required for the T-O analysis are formally established per 14 CFR §23.51 *Take-off Speeds*. The

TABLE 18-3 Definition of important airspeeds for the take-off.[a]

Name	Airspeed	GA aircraft (FAR 23)
Stalling speed in T-O configuration	V_{S1}	Significant analysis required.
Ground run	V_R	$1.1V_{S1}$
T-O decision speed*	V_1	Significant analysis required.
Rotation	V_{LOF}	$1.1V_{S1}$
Transition	V_{TR}	$1.15V_{S1}$
Climb	V_2	$1.2V_{S1}$
Minimum control speed*	V_{MC}	Significant analysis required.
Engine failure speed*	V_{EF}	Assumed airspeed.

*Required for multi-engine aircraft only.

[a] *Airspeeds are formally established per 14 CFR Part 23, §23.51 Takeoff Speeds.*

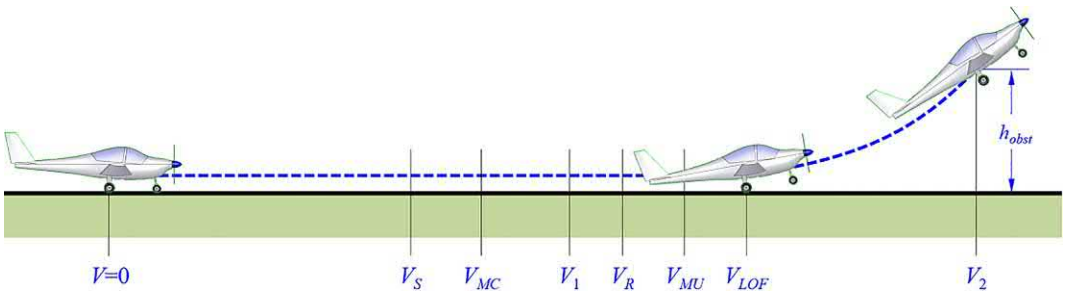


FIGURE 18-4 Important airspeeds during the T-O phase.

airspeeds referenced in the paragraph (and Figure 18-2) are shown in Table 18-3. The level of analysis required for some of them is significant. For others, not so much.

Figure 18-4 depicts the T-O run and shows important airspeeds. See Table 17-5 for the definition of the various airspeeds. The stalling speed (V_S) must be exceeded before the airplane can become airborne. It is always based on the aircraft configuration during the T-O run. Thus, if the airplane taking off with deflected flaps (typical deflection is somewhere between 10 and 20 degrees) its stalling speed will be less than in the clean configuration.

Note that the *minimum control speed with one engine inoperative* (V_{MC}) and the *take-off decision speed* (V_1) only apply to multiengine aircraft. The *unstick speed* is the airspeed at which the airplane no longer "sticks" to the runway and lifts off regardless of intent. It depends on the attitude (or AOA) of the airplane during the ground run. If the ground attitude is low, the unstick speed is high: The airplane needs a long distance before "unsticking." It reduces with increased AOA and its minimum value, the *minimum unstick speed* (V_{MU}), is achieved when the airplane is in a tail-strike position (at its maximum rotation angle). It depends on engine power whether this yields the minimum T-O distance, but the airplane must be able to lift-off in this configuration.

(3) Requirements for T-O speeds per 14 CFR Part 23 for GA aircraft

Note that determining V_{LOF} and other airspeeds for use in more detailed analysis must comply with regulations. Excerpts that deal with T-O analysis per 14 CFR Part 23 and 25 are provided below.

§ 23.51 Take-off speeds

(a) For normal, utility, and acrobatic category airplanes, rotation speed, V_R, is the speed at which the pilot makes a control input, with the intention of lifting the airplane out of contact with the runway or water surface.
- **(1)** For multiengine landplanes, V_R, must not be less than the greater of 1.05 V_{MC}; or 1.10 V_{S1};
- **(2)** For single-engine landplanes, V_R, must not be less than V_{S1}; and
- **(3)** For seaplanes and amphibians taking off from water, V_R, may be any speed that is shown to be safe under all reasonably expected conditions, including turbulence and complete failure of the critical engine.

(b) For normal, utility, and acrobatic category airplanes, the speed at 50 ft above the take-off surface level must not be less than:
- **(1)** or multiengine airplanes, the highest of—

(i) A speed that is shown to be safe for continued flight (or emergency landing, if applicable) under all reasonably expected conditions, including turbulence and complete failure of the critical engine;
(ii) 1.10 V_{MC}; or
(iii) 1.20 V_{S1}.

(2) For single-engine airplanes, the higher of—
(i) A speed that is shown to be safe under all reasonably expected conditions, including turbulence and complete engine failure; or
(ii) 1.20 V_{S1}.

(c) For commuter category airplanes, the following apply:

(1) V_1 must be established in relation to V_{EF} as follows:
(i) V_{EF} is the calibrated airspeed at which the critical engine is assumed to fail. V_{EF} must be selected by the applicant but must not be less than 1.05 V_{MC} determined under §23.149(b) or, at the option of the applicant, not less than V_{MC} determined under §23.149(f).
(ii) The take-off decision speed, V_1, is the calibrated airspeed on the ground at which, as a result of engine failure or other reasons, the pilot is assumed to have made a decision to continue or discontinue the take-off. The take-off decision speed, V_1, must be selected by the applicant but must not be less than V_{EF} plus the speed gained with the critical engine inoperative during the time interval between the instant at which the critical engine is failed and the instant at which the pilot recognizes and reacts to the engine failure, as indicated by the pilot's application of the first retarding means during the accelerate-stop determination of §23.55.

(2) The rotation speed, V_R, in terms of calibrated airspeed, must be selected by the applicant and must not be less than the greatest of the following:
(i) V_1;
(ii) 1.05 V_{MC} determined under §23.149(b);
(iii) 1.10 V_{S1}; or
(iv) The speed that allows attaining the initial climb-out speed, V_2, before reaching a height of 35 ft above the take-off surface in accordance with §23.57(c)(2).

(3) For any given set of conditions, such as weight, altitude, temperature, and configuration, a single value of V_R must be used to show compliance with both the one-engine-inoperative take-off and all-engines-operating take-off requirements.

(4) The take-off safety speed, V_2, in terms of calibrated airspeed, must be selected by the applicant so as to allow the gradient of climb required in §23.67 (c)(1) and (c)(2) but must not be less than 1.10 V_{MC} or less than 1.20 V_{S1}.

(5) The one-engine-inoperative take-off distance, using a normal rotation rate at a speed 5 knots less than V_R, established in accordance with paragraph (c)(2) of this section, must be shown not to exceed the corresponding one-engine-inoperative take-off distance, determined in accordance with §23.57 and §23.59(a)(1), using the established V_R. The take-off, otherwise performed in accordance with §23.57, must be continued safely from the point at which the airplane is 35 ft above the take-off surface and at a speed not less than the established V_2 minus 5 knots.

(6) The applicant must show, with all engines operating, that marked increases in the scheduled take-off distances, determined in accordance with §23.59(a)(2), do not result from overrotation of the airplane or out-of-trim conditions.

(4) Requirements for T-O speeds per 14 CFR Part 25 for Commercial Aviation aircraft

It is of interest to compare corresponding requirements for commercial aircraft.

§ 25.107 Take-off speeds

(a) V_1 must be established in relation to V_{EF} as follows:
(1) V_{EF} is the calibrated airspeed at which the critical engine is assumed to fail. V_{EF} must be selected by the applicant, but may not be less than V_{MC} determined under Sec. 25.149(e).
(2) V_1, in terms of calibrated airspeed, is the take-off decision speed selected by the applicant; however, V_1 may not be less than V_{EF} plus the speed gained with the critical engine inoperative during the time interval between the instant at which the critical engine is failed, and the instant at which the pilot recognizes and reacts to the engine failure, as indicated by the pilot's application of the first retarding means during accelerate stop tests.

(b) V_{2MIN}, in terms of calibrated airspeed, may not be less than—
(1) 1.2 V_S for–
(i) Two-engine and three-engine turbopropeller and reciprocating engine-powered airplanes; and
(ii) Turbojet-powered airplanes without provisions for obtaining a significant reduction in the one-engine-inoperative power-on stalling speed;
(2) 1.15 V_S for–

(i) Turbopropeller and reciprocating engine-powered airplanes with more than three engines; and

(ii) Turbojet-powered airplanes with provisions for obtaining a significant reduction in the one-engine-inoperative power-on stalling speed; and

(3) 1.10 times V_{MC} established under Sec. 25.149.

(c) V_2, in terms of calibrated airspeed, must be selected by the applicant to provide at least the gradient of climb required by Sec. 25.121(b) but may not be less than—

(1) V_{2MIN}, and

(2) V_R plus the speed increment attained (in accordance with Sec. 25.111 (c)(2) before reaching a height of 35 ft above the take-off surface.

(d) V_{MU} is the calibrated airspeed at and above which the airplane can safely lift off the ground, and continue the take-off. V_{MU} speeds must be selected by the applicant throughout the range of thrust-to-weight ratios to be certificated. These speeds may be established from free air data if these data are verified by ground take-off tests.

(e) V_R, in terms of calibrated airspeed, must be selected in accordance with the conditions of paragraphs (e) (1) through (4) of this section:

(1) V_R may not be less than–

(i) V_1;

(ii) 105% of V_{MC};

(iii) The speed (determined in accordance with Sec. 25.111(c)(2)) that allows reaching V_2 before reaching a height of 35 ft above the take-off surface; or

(iv) A speed that, if the airplane is rotated at its maximum practicable rate, will result in a V_{LOF} of not less than 110% of V_{MU} in the all-engines-operating condition and not less than 105% of V_{MU} determined at the thrust-to-weight ratio corresponding to the one-engine-inoperative condition.

(2) For any given set of conditions (such as weight, configuration, and temperature), a single value of V_R, obtained in accordance with this paragraph, must be used to show compliance with both the one-engine-inoperative and the all-engines-operating take-off provisions.

(3) It must be shown that the one-engine-inoperative take-off distance, using a rotation speed of 5 knots less than V_R established in accordance with paragraphs (e)(1) and (2) of this section, does not exceed the corresponding one-engine-inoperative take-off distance using the established V_R. The take-off distances must be determined in accordance with Sec. 25.113(a)(1).

(4) Reasonably expected variations in service from the established take-off procedures for the operation of the airplane (such as overrotation of the airplane and out-of-trim conditions) may not result in unsafe flight characteristics or in marked increases in the scheduled take-off distances established in accordance with Sec. 25.113(a).

(f) V_{LOF} is the calibrated airspeed at which the airplane first becomes airborne.

18.2 FUNDAMENTAL RELATIONS FOR THE TAKE-OFF RUN

This section focuses on the development of various tools of the trade. The equation-of-motion for the T-O will be derived, as well as some elementary relationships that can be used to evaluate the ground run segment of the T-O maneuver. Both conventional and taildragger configurations will be considered.

18.2.1 General Free-Body Diagram for the T-O Ground Run

Figures 18-5 and 18-6 show the free-body diagrams of a tricycle and taildragger configurations during a

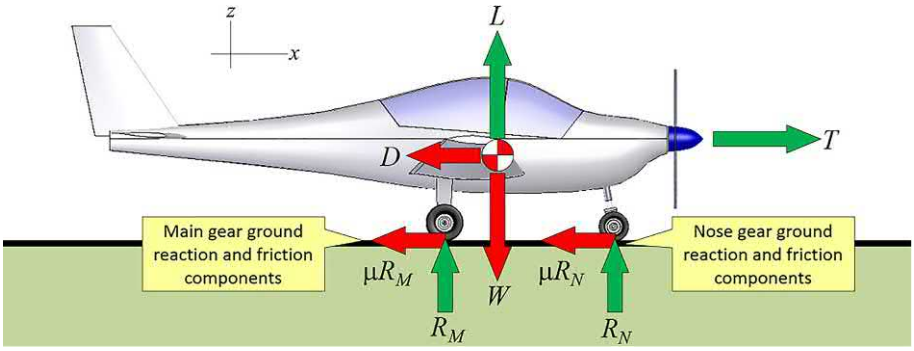


FIGURE 18-5 A balanced 2D free-body (forces only) for an aircraft with a tricycle landing gear.

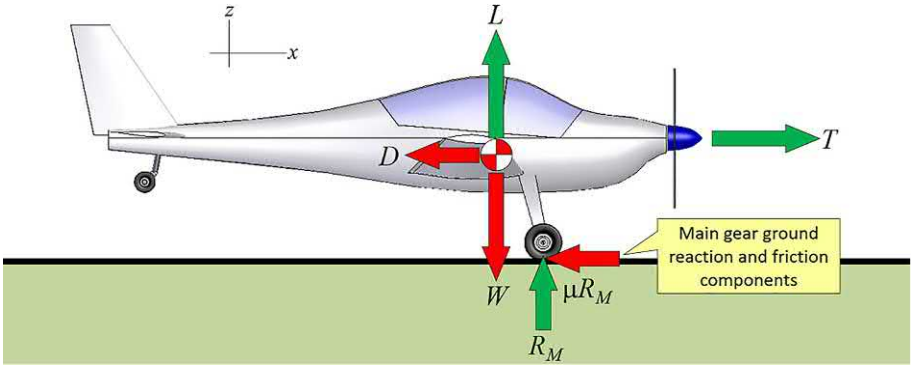


FIGURE 18-6 A balanced 2D free-body (forces only) for a taildragger aircraft.

developed T-O ground run. Moments are assumed to be balanced.

18.2.2 Basic Kinematic Relations

Kinematics is the study of the motion of objects that only involves the motion itself (e.g., acceleration, speed, and distance) and not what causes it (forces and moments). The kinematic formulation is essential for the study of the take-off run. The most basic formulation is presented below:

Velocity:

$$V = \int_0^t a\, dt = V_0 + at \tag{18-1}$$

Distance:

$$S = \int_0^t V\, dt = \int_0^t (V_0 + at)\, dt = S_0 + V_0 t + \frac{1}{2}at^2 \tag{18-2}$$

Alternative expression for distance:

$$S - S_0 = \frac{V^2 - V_0^2}{2a} \tag{18-3}$$

Note that these equations assume an average acceleration (a). The subscript 0 indicates initial values.

EXAMPLE 18-1

The Pilot's Operating Handbook (POH) for the single-engine, 4-seat, SR22 gives a lift-off speed of 73 KCAS and ground run distance ($=S_G+S_{ROT}$) of 1020 ft (ISA at S-L). Estimate the average acceleration and time in seconds from brake-release to lift-off.

SOLUTION:

Average acceleration:

$$S_G + S_{ROT} = \frac{V^2 - V_0^2}{2a}$$

$$\Rightarrow \quad a = \frac{V^2 - V_0^2}{2(S_G + S_{ROT})} = \frac{(73 \times 1.688)^2 - 0}{2 \times 1020} = 7.44 \text{ ft/s}^2$$

Time from brake-release to lift-off:

$$V = V_0 + at \quad \Rightarrow \quad t = \frac{V - V_0}{a} = \frac{73 \times 1.688 - 0}{7.44} = 16.6 \text{ s}$$

18.2.3 The Equation-of-Motion for the T-O Ground Run

The equation-of-motion for an aircraft during the ground run on a perfectly flat, horizontal runway is given by:

$$\frac{dV}{dt} = \frac{g}{W}[T - D - \mu(W - L)] \tag{18-4}$$

If the runway features an uphill or downhill slope γ (see Figure 18-7) the aircraft acceleration becomes

$$\frac{dV}{dt} = \frac{g}{W}[T - D - \mu(W\cos\gamma - L) - W\sin\gamma] \tag{18-5}$$

where

D = Drag as a function of V,
g = Acceleration due to gravity,
L = Lift as a function of V,
T = Thrust,
W = Weight,
μ = Ground friction coefficient (see Table 18-4),
γ = Runway slope (positive if uphill and negative if downhill)

Note that Equation (18-5) assumes the reference frame to be aligned with the runway. This is a reasonable assumption because the runway length reported will be

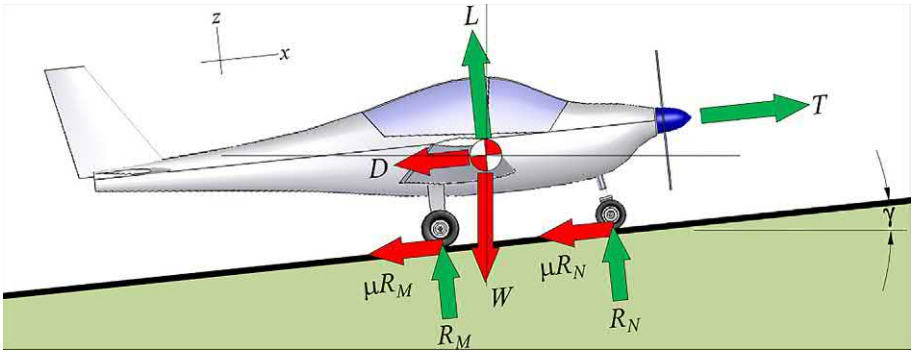


FIGURE 18-7 A balanced 2-dimensional free-body (forces only) of the T-O ground run for a tricycle gear aircraft on an uphill slope runway.

along the slope. We can also bring W into the bracket to express the acceleration in terms of thrust-to-weight ratio:

$$\frac{dV}{dt} = g\left[\frac{T}{W} - \frac{D}{W} - \mu\left(\cos\gamma - \frac{L}{W}\right) - \sin\gamma\right] \tag{18-6}$$

DERIVATION OF EQUATIONS (18-4) AND (18-5)

Consider the aircraft in Figures 18-5 and 18-6. Its motion can be described using classical kinematic formulation. Assume the aircraft is accelerating along an uphill or downhill runway with slope γ. Summing forces in the z-direction must yield no net vertical acceleration

$$\sum F_z = ma_z = 0 \quad \Rightarrow \quad R + L - W\cos\gamma = 0$$
$$\Rightarrow \quad R = W\cos\gamma - L \tag{i}$$

Summing forces in the x-direction yields:

$$\sum F_x = ma_x = \frac{W}{g}\frac{dV}{dt}$$
$$\Rightarrow \quad T - D - \mu(W\cos\gamma - L) - W\sin\gamma = \frac{W}{g}\frac{dV}{dt} \tag{ii}$$

Thus, the general acceleration on a sloped runway is given by

$$\frac{dV}{dt} = \frac{g}{W}[T - D - \mu(W\cos\gamma - L) - W\sin\gamma] \tag{iii}$$

This is Equation (18-5). For an uphill runway, the sign for γ should be positive, as this reduces the resulting acceleration. The opposite holds true for a downhill runway. To obtain Equation (18-4), simple set $\gamma = 0$.

$$\Rightarrow \quad \frac{dV}{dt} = \frac{g}{W}[T - D - \mu(W - L)] \tag{iv}$$

where μ is the ground friction coefficient. Its value depends on the runway surface.

18.2.4 Formulation of Required Aerodynamic Forces

The following formulation of aerodynamic forces is assumed during the T-O. Note that it includes ground effect.

C_L during T – O: $$C_{L_{TO}} = (C_{L_0} + C_{L_\alpha}\,\alpha_{TO})\Phi_L \tag{18-7}$$

Lift: $$L = \frac{1}{2}\rho V^2 S C_{L_{TO}} \tag{18-8}$$

Adjusted induced drag coefficient: $$C_{D_i} = k\left(C_{L_0} + C_{L_\alpha}\,\alpha_{TO} - C_{L_{\min_D}}\right)^2 \Phi_D \tag{18-9}$$

C_D during T – O: $$C_{D_{TO}} = C_{D_{\min}} + C_{D_i} \tag{18-10}$$

General drag: $$D = \frac{1}{2}\rho V^2 S C_{D_{TO}} \tag{18-11}$$

where C_{D_i} is the induced drag coefficient of aircraft during the T-O run, α_{TO} is the angle-of-attack during the T-O run (note it is close to horizontal), Φ_L and Φ_D are the ground influence coefficients for lift and drag, respectively. Refer to Section 9.5.11 for appropriate methods.

18.2.5 Solution of Kinematic Problems Using Numerical Integration

A closed form solution of Equation (18-4) that accurately accounts for various speed dependencies (e.g., D, L, and T, all which depend on speed) is prohibitive. Therefore, it is solved using a numerical integration scheme. This provides the designer with a very powerful technique. Properly applied, it allows discontinuous time dependent events to be accounted for during integration. For instance, consider a specialized T-O technique being modeled, in which the flaps remain retracted until a moment before lift-off, when they are instantly deflected. Or the ground run of many radial piston-powered airplanes of the past. To permit throttles for directional control on the ground,

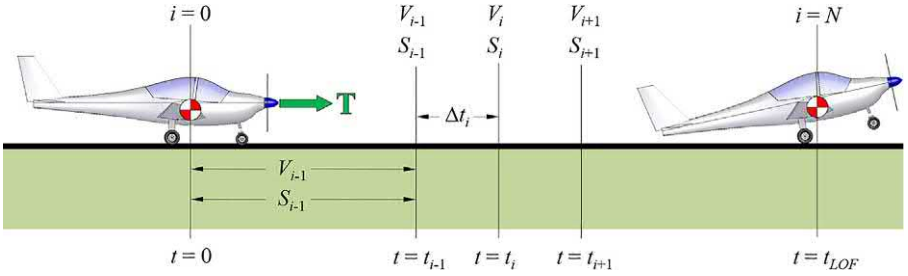


FIGURE 18-8 Nomenclature used for the numerical integration of the T-O ground run.

the throttles were "walked forward" slowly until rudder control was gained near 60 knots. Then, the throttles would be pushed forward steadily [7]. Or a taildragger rotating from a three-point (tail on ground) to a two-point attitude (tail off ground). Such complexities are relatively easy to account for using this method. It can even model the braking distance to simulate an engine failure. It is the recommended method for serious analysis work.

The first step in the scheme is to transform Equations (18-1) and (18-2) into the following discrete form:

$$V_i = \int_0^t a\, dt = \sum_{i=0}^{N} (V_{i-1} + a_i(t_i - t_{i-1})) \tag{18-12}$$

$$S_i = \int_0^t (V_0 + at)\, dt = \sum_{i=0}^{N} \left(S_{i-1} + V_{i-1} \cdot \Delta t_i + \frac{1}{2} a_i \cdot \Delta t_i^2 \right) \tag{18-13}$$

The variables are depicted in Figure 18-8. The method is implemented as follows, assuming we are solving Equation (18-4).

STEP 1: Calculate forces

Calculate thrust using any applicable methods of Chapters 7, 14, or 15. Calculate drag and lift per Section 18.2.4. Denote these as T_i (thrust), D_i (drag), and L_i (lift), where i is a timestep index. If implementing this in Microsoft Excel, calculate the dynamic pressure for Equations (18-8) and (18-11), using the speed from the previous timestep to prevent a circular error, i.e.,

$$q_i = \frac{1}{2}\rho(V_{i-1})^2 \tag{18-14}$$

STEP 2: Calculate acceleration

Calculate acceleration per Equation (18-4).

$$a_i = \frac{g}{W}[T_i - D_i - \mu(W - L_i)] \tag{18-15}$$

STEP 3: Calculate airspeed and distance

Calculate airspeed and distance per Equations (18-12) and (18-13).

$$V_i = V_{i-1} + a_i(t_i - t_{i-1}) = V_{i-1} + a_i\ \Delta t_i \tag{18-16}$$

$$S_i = S_{i-1} + V_{i-1} \cdot \Delta t_i + \frac{1}{2} a_i \cdot \Delta t_i^2 \tag{18-17}$$

Note that the formulation $\Delta t_i = t_i - t_{i-1}$ implies the method also handles uneven timesteps. $\Delta t_i = 0.25$ s works well.

STEP 4: March onward

Go to Step 1 and repeat until $V_i = V_{LOF}$. Note the distance, S_i, at this timestep. This is the ground run distance, S_G.

EXAMPLE 18-2

A vehicle accelerates with a constant $a = 10\,\text{m/s}^2$. Determine (a) its speed and (b) distance after 5 s using numerical integration and compare to the exact solution.

SOLUTION:

(a) Numerical integration of the speed (see Figure 18-9):

EXAMPLE 18-2 (*cont'd*)

Index	t sec	Δt sec	$V_i = V_{i-1} + a \cdot \Delta t$ m/s	$V_{i-1} \cdot \Delta t$ m	$\frac{1}{2} a \cdot \Delta t^2$ m	$\Delta S_i = V_{i-1} \cdot \Delta t + \frac{1}{2} a \cdot \Delta t^2$ m	$S_i = S_{i-1} + \Delta S_i$ m
0	0	0	0				
1	1	1-0 = 1	0 + 10 x 1 = 10				
2	2	2-1 = 1	10 + 10 x 1 = 20				
3	3	3-2 = 1	20 + 10 x 1 = 30				
4	4	4-3 = 1	30 + 10 x 1 = 40				
5	5	5-4 = 1	40 + 10 x 1 = 50				

FIGURE 18-9 Determination of speed using a numerical integration scheme.

(b) Numerical integration of the distance (see Figure 18-10):

Exact solutions: $V = at = 10 \times 5 = 50$ ft/s

$$S = \frac{1}{2}at^2 = \frac{1}{2} \times 10 \times 5^2 = 125 \text{ ft}$$

Index	t sec	Δt sec	$V_i = V_{i-1} + a \cdot \Delta t$ m/s	$V_{i-1} \cdot \Delta t$ m	$\frac{1}{2} a \cdot \Delta t^2$ m	$\Delta S_i = V_{i-1} \cdot \Delta t + \frac{1}{2} a \cdot \Delta t^2$ m	$S_i = S_{i-1} + \Delta S_i$ m
0	0	0	0	0	0	0	0
1	1	1	10	0	5	5	0+5 = 5
2	2	1	20	10	5	15	5+15 = 20
3	3	1	30	20	5	25	20+25 = 45
4	4	1	40	30	5	35	45+35 = 80
5	5	1	50	40	5	45	80+45 = 125

FIGURE 18-10 Determination of distance using a numerical integration scheme.

18.2.6 Determination of the Lift-Off Speed

Unless otherwise specified, the lift-off speed, V_{LOF}, is assumed to be 1.1 × the stalling speed in that particular configuration, V_{S1} (e.g., with flaps deployed, landing gear extended, etc.). Also, V_R is assumed to be $1.1 \times V_{S1}$. Using this assumption, V_{LOF} can be calculated directly using the maximum lift coefficient ($C_{L_{max}}$) for the T-O configuration, S for the reference area, and ρ for density:

$$V_{LOF} = 1.1 \times V_{S1} = 1.1\sqrt{\frac{2W}{\rho S C_{L_{max}}}} \approx 1.556\sqrt{\frac{W}{\rho S C_{L_{max}}}} \tag{18-18}$$

Most small airplanes lift off as soon as the pilot rotates the airplane at that speed, while larger ones lift off some 3 s after rotation initiates because of their higher inertia. *Unless otherwise specified, it is assumed that V_R and V_{LOF} are equal.*

18.2.7 Ground Roll Friction Coefficients

In addition to aerodynamic drag, the airplane must overcome ground friction during the ground run. The ground friction depends on the weight-on-wheels and the properties of the ground, which are assessed using the ground roll friction coefficients in Table 18-4.

18.2.8 Determination of Time to Lift-Off

The time from brake-release to lift-off can be approximated by solving Equation (18-2) for time, which assumes the average acceleration, a, is known:

$$S_G + S_{ROT} = \frac{1}{2}at^2 \quad \Rightarrow \quad t = \sqrt{\frac{2(S_G + S_{ROT})}{a}} \tag{18-19}$$

TABLE 18-4 Ground roll friction coefficients.

	Ground friction coefficient, μ	
Surface type	**Brakes off**	**Braking**
Dry asphalt or concrete	0.03–0.05	0.3–0.5
Wet asphalt or concrete	0.05	0.15–0.3
Icy asphalt or concrete	0.02	0.06–0.10
Hard turf	0.05	0.4
Firm dirt	0.04	0.3
Soft turf	0.07	0.2
Wet grass	0.08	0.2

18.3 CONDUCTING THE TAKE-OFF ANALYSIS

Now, using the tools of Section 18.2, we can start working on the tasks listed in Table 18.2.

18.3.1 Calculating the Ground Run Distance, S_G

Solving the equation-of-motion of the T-O run yields information such as acceleration—average or instantaneous, ground run distance, and duration of the ground run. With respect to the ground run, three methods are introduced. The first one is general in nature and applies to all aircraft as long as proper values of thrust, drag and lift can be quantified. The second method is intended for propeller-powered aircraft only. The third method uses numerical integration to solve the EOM and is, by far, the most powerful of the three.

(1) General Ground Run Estimation using Average Acceleration

This method is applicable to both propeller aircraft and jets; the only difference lies in how the thrust is calculated. The method uses Equations (18-4) or (18-5) to calculate the acceleration of the aircraft. With the acceleration in hands, Equation (18-3) is used to estimate the ground run distance. As can be seen, Equations (18-4) and (18-5) both require the estimation of thrust, T, drag, D, and lift, L. The only problem is that all are functions of the airspeed. This begs the question: What airspeed should be used to evaluate them? To answer the question, consider Figure 18-11. It shows how the airplane's airspeed typically changes during the ground run.

Initially, the acceleration is relatively large, but it gradually diminishes with airspeed (primarily due to aerodynamic drag). With this in mind, first consider the Point 1. It represents the aircraft at rest, when both $V=0$ and $S_G=0$. It is assumed the engines are allowed to develop full thrust before the airplane begins to accelerate. This helps it achieve large acceleration upon brake-release (large thrust, no drag). If we denote the rate-of-change of speed with distance by dV/dS, it is evident that Point 1 has the steepest slope during the ground run. Now consider Point 3. It marks the start of rotation and the end of the ground run. When compared to the start of the ground run, the value of dV/dS has reduced considerably. It has reached its lowest value over the entire ground run. It should be clear that if the acceleration at Point 1 is used with Equation (18-3), then the estimated ground run distance will be much less than the actual one, due to the high value of dV/dS. Likewise, if the

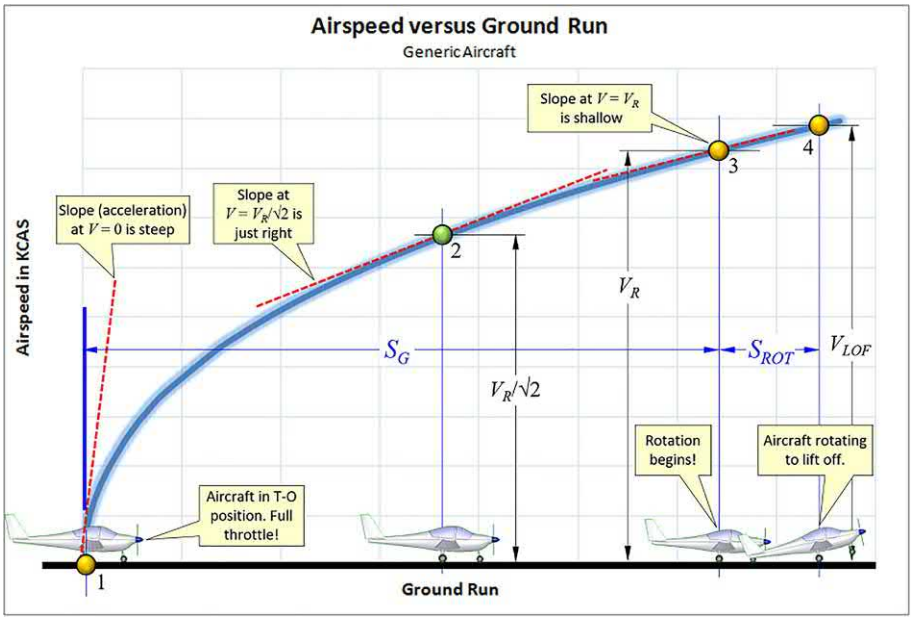


FIGURE 18-11 The reason for the term $V_R/\sqrt{2}$ explained.

acceleration at Point 3 is used, the ground run estimate will be much larger than experienced, due to the low value of dV/dS. This implies that somewhere between these two extremes exists an average airspeed for which the value of dV/dS gives the actual ground run distance. The plot of the acceleration as a function of airspeed squared between 0 and V_R^2 is close to a straight line [8]. Thus, we find this average airspeed is $V_R^2/2$, so $V_R/\sqrt{2}$, where V_R is the rotation speed.[a] Point 4 is the lift-off position.

STEP 1: Lift-Off Speed

Calculate a rotation speed (V_R) per Equation (18-18).

STEP 2: Ground Effect

Calculate C_{LIGE} and C_{DIGE} per Section 9.5.11.

STEP 3: Lift at the Reduced Rotation Speed

Calculate lift (L) per Equation (18-8) at $V_R/\sqrt{2}$.

STEP 4: Drag at the Reduced Rotation Speed

Calculate drag (D) per Equation (18-11) at $V_R/\sqrt{2}$.

STEP 5: Thrust at the Reduced Rotation Speed

Calculate thrust (T) at $V_R/\sqrt{2}$, depending on engine type as shown below.

Thrust for piston-powered aircraft:

$$T = \frac{\eta_P (550 \times P_{BHP})}{V_R/\sqrt{2}} \tag{18-20}$$

Thrust for jet-powered aircraft:

$$T = T\left(V_R/\sqrt{2}\right) \tag{18-21}$$

where

P_{BHP} = Piston engine horsepower
$T()$ = Jet engine thrust function using V as an argument
η_P = Propeller efficiency at $V_R/\sqrt{2}$.

STEP 6: Ground Run

Calculate the ground run, using Equation (18-4) or (18-5) with Equation (18-3) of Section 18.2.2, as shown below. Select an appropriate ground friction coefficient, μ, from Table 18-4.

$$S = \frac{V^2}{2a} \quad \Rightarrow \quad S_G = \frac{V_R^2\, W}{2g[T - D - \mu(W - L)]_{at\ (V_R/\sqrt{2})}} \tag{18-22}$$

EXAMPLE 18-3

During the T-O phase, the Continental IO-550 engine powering the SR22 generates 310 BHP with an assumed propeller efficiency of 0.65. What is the thrust generated at $V = 100$ ft/s? What about 120 ft/s (assuming the same propeller efficiency)? If this airplane weighs 3400 lb_f, what is the acceleration for both airspeeds (ignoring drag and ground friction)? Discuss results.

SOLUTION:

Thrust at $V = 100$ ft/s:

$$T = \eta_p \cdot 550 \cdot P_{BHP}/V_\infty$$
$$= (0.65 \cdot 550 \cdot 310)/100 = 1108\ lb_f$$

Acceleration at $V = 100$ ft/s:

$$a = T/m = Tg/W = (1108 \times 32.174)/3400 = 10.48\ ft/s^2$$

Thrust at $V = 120$ ft/s:

$$T = \eta_p \cdot 550 \cdot P_{BHP}/V_\infty$$
$$= (0.65 \cdot 550 \cdot 310)/120 = 924\ lb_f$$

Acceleration at $V = 120$ ft/s:

$$a = Tg/W = (924 \times 32.174)/3400 = 8.74\ ft/s^2$$

These represent the absolutely the largest acceleration the vehicle could possibly have at that condition (assuming the propeller efficiency is valid). The designer should be aware of the even though this kind of an analysis is simplistic, it serves superbly as a quick "sanity check" when performing a more sophisticated T-O analysis. In this case, it indicates that if using alternative analyses methods, an answer exceeding 10.48 ft/s^2 for an SR22 class aircraft is highly suspicious.

EXAMPLE 18-4

The airplane of previous example is observed to have an average acceleration of 8.74 ft/s^2 once it has acquired airspeed of 120 ft/s. If it assumed this is an "average" acceleration, what distance will the airplane have covered at that airspeed?

SOLUTION:

This problem can easily be solved using elementary kinematics:

$$S_G = \frac{V^2}{2a} = \frac{120^2}{2 \times 8.74} = 824\ ft$$

This problem is presented as another kind of "sanity check." The astute aircraft designer will perform such simple and fast checks to evaluate if errors may have crept into more sophisticated calculations.

[a] This was denoted as $V_{LOF}/\sqrt{2}$ in the first edition of the book. For all intents and purposes, V_R and V_{LOF} are close enough to be considered equal (see Table 18-3). This presentation is mathematically more rigorous.

EXAMPLE 18-5

Estimate the ground run distance for a Learjet 45 assuming the following properties (ignore ground effect):

$W = 21{,}500$ lb$_f$ $\quad C_{L_{max}} = 1.65$
$S = 311.6$ ft^2 $\quad T$ at $V_R/\sqrt{2} = 7000$ lb$_f$
$C_{LTO} = 0.90$ $\quad \mu = 0.02$
$C_{DTO} = 0.045$

SOLUTION:

Rotationspeed: $V_R \approx 1.556\sqrt{\dfrac{W}{\rho S C_{L_{max}}}}$

$$= 1.556\sqrt{\frac{21500}{(0.002378)(311.6)(1.65)}}$$

$$= 206.7 \text{ ft/s (122 KCAS)}$$

The value for the airspeed at $V_R/\sqrt{2}$ is thus:

$$\frac{V_R}{\sqrt{2}} = 146.2 \text{ ft/s (86.6 KCAS)}$$

Drag at that airspeed:

$$D = \frac{1}{2}(0.002378)(146.2)^2(311.6)(0.045) = 356.4 \text{ lb}_f$$

Lift at that airspeed:

$$L = \frac{1}{2}(0.002378)(146.2)^2(311.6)(0.90) = 7127 \text{ lb}_f$$

Average acceleration:

$$\frac{dV}{dt} = \frac{g}{W}[T - D - \mu(W - L)]$$

$$= \frac{32.174}{21500}[7000 - 356.4 - (0.02)(21500 - 7127)]$$

$$= 9.511 \text{ ft/s}^2$$

Ground run to lift – off is thus:

$$S_G = \frac{V_R^2}{2a} = \frac{206.7^2}{2 \times 9.511} = 2246 \text{ ft}$$

(2) Ground Run Estimation using Average Acceleration for Tricycle Propeller Aircraft Only

This is the previous method specifically adapted to the typical piston engine configuration. *It is NOT applicable to taildraggers* because the tail-on-ground/tail-off-ground transition is not accounted for.

$$S_G = \frac{V_R^3 W}{50051\ \eta_p\ P_{HP} + 16.09\rho S(\mu C_{L_{TO}} - C_{D_{TO}})V_R^3 - 64.35\mu W\ V_R} \tag{18-23}$$

NOTE: If the propeller efficiency, η_p, is not known, the following values can be used as expected approximations:

Fixed pitch climb propeller $\Rightarrow \eta_P = 0.45 - 0.50$
Fixed pitch cruise propeller $\Rightarrow \eta_P = 0.35 - 0.45$
Constant speed propeller $\Rightarrow \eta_P = 0.45 - 0.60$

DERIVATION OF EQUATION (18-23)

We begin with Equation (18-4) and rewrite the acceleration as follows:

$$a = \frac{g}{W}[T - D - \mu(W - L)] \tag{i}$$

Substitute Equations (18-8), (18-11), and (15-52) yields;

$$a = \frac{g}{W}\left[\frac{\eta_p(550\ P_{HP})}{V} - \frac{1}{2}\rho V^2 S C_{D_{TO}} - \mu\left(W - \frac{1}{2}\rho V^2 S C_{L_{TO}}\right)\right]$$

$$= \frac{g}{W}\left[\frac{\eta_p(550\ P_{HP})}{V} + \frac{1}{2}\rho V^2 S(\mu C_{L_{TO}} - C_{D_{TO}}) - \mu W\right] \tag{ii}$$

Substitute Equation (ii) into the expression for distance to lift-off to get:

$$S_G = \frac{V_{LOF}^2}{2a} = \frac{V_{LOF}^2 W}{2g\left[\dfrac{\eta_p(550\ P_{HP})}{V} + \dfrac{1}{2}\rho V^2 S(\mu C_{L_{TO}} - C_{D_{TO}}) - \mu W\right]} \tag{iii}$$

We evaluate the acceleration at $V_R/\sqrt{2}$, so substitute this as follows:

$$S_G = \frac{V_R^2 W}{2g\left[\dfrac{\eta_p(550\ P_{BHP})}{V_R/\sqrt{2}} + \dfrac{1}{2}\rho\left(V_R/\sqrt{2}\right)^2 S(\mu C_{L_{TO}} - C_{D_{TO}}) - \mu W\right]}$$

$$= \frac{V_R^2 W}{2g\left[\dfrac{\eta_p(550\ P_{BHP})\sqrt{2}}{V_R} + \dfrac{1}{4}\rho V_R^2 S(\mu C_{L_{TO}} - C_{D_{TO}}) - \mu W\right]}$$

Simplify further:

$$S_G = \frac{V_R^3 W}{\eta_p(550\ P_{HP})2\sqrt{2}g + \dfrac{1}{2}g\rho V_R^3 S(\mu C_{L_{TO}} - C_{D_{TO}}) - 2g\mu W V_R} \tag{iv}$$

Substitute $g = 32.174$ ft/s^2 and arithmetically evaluating the constants leads to:

$$S_G = \frac{V_R^3 W}{50051\ \eta_p\ P_{HP} + 16.09\rho V_R^3 S(\mu C_{L_{TO}} - C_{D_{TO}}) - 64.35\mu W V_R} \tag{v}$$

The advantage of this method is that it combines several steps in the general method of Bullet (1) and, thus, it lends itself better to parametric studies.

EXAMPLE 18-6

Determine the lift-off speed, T-O distance, and time from brake-release to lift-off at S-L for the Cirrus SR22 if it has the following characteristics:

EXAMPLE 18-6 *(cont'd)*

$W = 3400$ lb$_f$	$C_{LTO} = 0.500$ (assumed value)
$P_{BHP} = 310$ BHP	
$S = 144.9$ ft^2	$C_{DTO} = 0.0417$ (assumed value)
$C_{L_{max}} = 1.69$ (based on POH for T-O)	$\mu = 0.04$ (sample value)

Compare the results to published data from the airplane's Pilot's Operating Handbook (POH), which gives a lift-off speed of 73 KCAS, T-O distance of 1020 ft (ISA at S-L) and the calculated time to lift-off of 16.6 s from Example 18-1.

SOLUTION:

Rotation speed:

$$V_R \approx 1.556\sqrt{\frac{W}{\rho S C_{L_{max}}}} = 1.556\sqrt{\frac{1}{(0.002378)(1.69)}\left(\frac{3400}{144.9}\right)}$$
$$= 118.9 \text{ ft/s (70.4 KCAS)}$$

The value for the airspeed at $V_R/\sqrt{2}$ is thus:

$$V_R/\sqrt{2} = 84.1 \text{ ft/s (50 KCAS)}$$

Since the propeller efficiency is unknown, let's pick $\eta_p = 0.50$ and calculate lift-off distance:

Thrust at that airspeed:

$$T = \frac{0.5 \times 550 \times 310}{84.1} = 1014 \text{ lb}_f$$

Lift at that airspeed:

$$L = \frac{1}{2}(0.002378)(84.1)^2(144.9)(0.500) = 609 \text{ lb}_f$$

Drag at that airspeed:

$$D = \frac{1}{2}(0.002378)(84.1)^2(145)(0.0417) = 51 \text{ lb}_f$$

Average acceleration:

$$\frac{dV}{dt} = \frac{g}{W}[T - D - \mu(W - L)]$$
$$= \frac{32.174}{3400}[1014 - 51 - (0.04)(3400 - 609)]$$
$$= 8.06 \text{ ft/s}^2$$

Ground run to rotation is thus:

$$S_G = \frac{V_R^2}{2a} = \frac{118.9^2}{2 \times 8.06} = 877 \text{ ft}$$

Time from brake – release to rotation:

$$t = \sqrt{\frac{2S_G}{a}} = \sqrt{\frac{2 \times 877}{8.06}} = 14.8 \text{ s}$$

Since this does not account for the rotation segment, which would add 1 s to the time to lift-off and 118.9 ft to the total distance. This brings the true ground run $S_G + S_{ROT}$ to 996 ft, which compares favorably to the POH value of 1020 ft.

(3) Ground Run Estimation using Numerical Integration Method

This method was introduced in Section 18.2.5. It handles all take-off problems, but is more complex to use. Its application is best demonstrated in an example (see Example 18-7).

EXAMPLE 18-7

Determine the lift-off speed, T-O distance, and time from brake-release to lift-off at S-L for the Cirrus SR22 by solving the equation-of-motion using the *numerical integration method* with the following parameters (ignore ground effect):

$W = 3400$ lb$_f$	$C_{L_{max}} = 1.69$ (based on POH for T-O)
$P_{BHP} = 310$ BHP	
$S = 144.9$ ft^2	$\mu = 0.04$ (sample value)
$V_{LOF} = 73$ KCAS (per POH)	$C_{LTO} = 0.500$
	$C_{DTO} = 0.0417$

Use the method of Section 15.4.4 to approximate the thrust of the constant speed propeller. This method approximates the thrust as a function of airspeed using the following quartic spline:

$$T \cong 325.9\left(A_1 + A_2 V_\infty + A_3 V_\infty^2 + A_4 V_\infty^3\right) P_{HP} \qquad (15\text{-}69)$$

where V_∞ is the far-field airspeed and the constants A_1, A_2, A_3, and A_4 are determined using the matrix:

$$\begin{Bmatrix} A_1 \\ A_2 \\ A_3 \\ A_4 \end{Bmatrix} = \begin{bmatrix} V_y & V_y^2 & V_y^3 & V_y^4 \\ V_{opt} & V_{opt}^2 & V_{opt}^3 & V_{opt}^4 \\ 1 & 2V_{opt} & 3V_{opt}^2 & 4V_{opt}^3 \\ V_{hs} & V_{hs}^2 & V_{hs}^3 & V_{hs}^4 \end{bmatrix}^{-1} \begin{Bmatrix} \eta_{p_y} \\ \eta_{p_{opt}} \\ 0 \\ \eta_{p_{hs}} \end{Bmatrix} \qquad (15\text{-}67)$$

Instructions and variable identification for this method is given in Section 15.4.4. The values used in the solution are shown in Table 18-5. They are based on the airplane's Pilot's Operating Handbook (POH). Compare the results to published data from the POH, which give a lift-off speed of 73 KCAS, T-O distance of 1020 ft (ISA at S-L) and the calculated time to lift-off of 16.6 s from Example 18-1.

EXAMPLE 18-7 (*cont'd*)

TABLE 18-5 Ground run analysis using the numerical integration method.

GROUND RUN ANALYSIS

The calculations below are performed to determine the thrust function per Section 15.4.4, Initial Thrust Model for a Constant-Speed Propeller

INPUT VALUES

Max rated power P_{BHP} = 310.0 BHP

Static thrust (at condition) T_{STATIC} = 1169 lb_f

V_y =	101	KTAS	170.5	ft/s	⇨	η_p =	0.7200
V_{opt} =	185	KTAS	312.3	ft/s	⇨	η_p =	0.8500
V_{hz} =	285	KTAS	481.1	ft/s	⇨	η_p =	0.7500

$$\begin{Bmatrix} A_1 \\ A_2 \\ A_3 \\ A_4 \end{Bmatrix} = \begin{bmatrix} V_y & V_y^2 & V_y^3 & V_y^4 \\ V_{opt} & V_{opt}^2 & V_{opt}^3 & V_{opt}^4 \\ 1 & 2V_{opt} & 3V_{opt}^2 & 4V_{opt}^3 \\ V_{hz} & V_{hz}^2 & V_{hz}^3 & V_{hz}^4 \end{bmatrix}^{-1} \begin{Bmatrix} \eta_{P_y} \\ \eta_{P_{opt}} \\ 0 \\ \eta_{P_{hz}} \end{Bmatrix}$$

4×4 Matrix				4×1		Inverted 4×4 Matrix					Constants	
101	1.020E+04	1.030E+06	1.041E+08	A_1 =	0.72	⇨	7.4386E-02	-4.3574E-02	3.4268E+00	-6.5918E-03	⇨	A_1 = 1.158E-02
185	3.423E+04	6.332E+06	1.171E+09	A_2 =	0.85	⇨	-1.0652E-03	7.1972E-04	-6.4476E-02	1.3653E-04	⇨	A_2 = -5.277E-05
1	3.700E+02	1.027E+05	2.533E+07	A_3 =	0	⇨	4.9951E-06	-3.3295E-06	3.6744E-04	-8.9817E-07	⇨	A_3 = 9.273E-08
285	8.123E+04	2.315E+07	6.598E+09	A_4 =	0.75	⇨	-7.6261E-09	4.7041E-09	-6.4350E-07	1.9069E-09	⇨	A_4 = -6.210E-11

$$T = \frac{\left(A_1 V_\infty + A_2 V_\infty^2 + A_3 V_\infty^3 + A_4 V_\infty^4\right) 550\, P_{HP}}{1.688 V_\infty}$$

1	2	3	4	5	6	7	8	9	10	11	12	13	14
			Forces, lbf						Airspeed, V				
i	Time, s	Δt	q, lb_f/ft^2	$T(V)$	L	D	μ(W-L)	$a = dV/dt$	ft/s	KTAS	$V_{i-1} \cdot \Delta t$	$\frac{1}{2} a \cdot \Delta t^2$	$S_i = S_{i-1} + \Delta S_i$
0	0	-	0.00	1169	0	0	136	9.78	0.0	0.0	0	0	0
1	0.5	0.50	0.00	1169	0	0	136	9.78	4.9	2.9	0.0	1.22	1
2	1.0	0.50	0.03	1154	2	0	136	9.63	9.7	5.8	2.4	1.20	5
3	1.5	0.50	0.11	1139	8	1	136	9.49	14.4	8.6	4.9	1.19	11
4	2.0	0.50	0.25	1124	18	1	135	9.35	19.1	11.3	7.2	1.17	19
5	2.5	0.50	0.43	1110	31	3	135	9.21	23.7	14.1	9.6	1.15	30
6	3.0	0.50	0.67	1096	48	4	134	9.07	28.3	16.7	11.9	1.13	43
7	3.5	0.50	0.95	1083	69	6	133	8.93	32.7	19.4	14.1	1.12	58
8	4.0	0.50	1.27	1069	92	8	132	8.80	37.1	22.0	16.4	1.10	76
9	4.5	0.50	1.64	1057	119	10	131	8.66	41.5	24.6	18.6	1.08	95
10	5.0	0.50	2.04	1044	148	12	130	8.53	45.7	27.1	20.7	1.07	117
11	5.5	0.50	2.48	1032	180	15	129	8.40	49.9	29.6	22.9	1.05	141
12	6.0	0.50	2.96	1020	215	18	127	8.27	54.1	32.0	25.0	1.03	167
13	6.5	0.50	3.47	1008	252	21	126	8.15	58.1	34.4	27.0	1.02	195
14	7.0	0.50	4.02	997	291	24	124	8.02	62.1	36.8	29.1	1.00	225
15	7.5	0.50	4.59	985	333	28	123	7.90	66.1	39.2	31.1	0.99	257
16	8.0	0.50	5.19	975	376	31	121	7.78	70.0	41.5	33.0	0.97	291
17	8.5	0.50	5.82	964	422	35	119	7.66	73.8	43.7	35.0	0.96	327
18	9.0	0.50	6.48	954	469	39	117	7.54	77.6	46.0	36.9	0.94	365
19	9.5	0.50	7.16	943	519	43	115	7.43	81.3	48.2	38.8	0.93	405
20	10.0	0.50	7.86	934	569	47	113	7.31	85.0	50.3	40.7	0.91	446
21	10.5	0.50	8.58	924	622	52	111	7.20	88.6	52.5	42.5	0.90	490
22	11.0	0.50	9.32	915	676	56	109	7.09	92.1	54.6	44.3	0.89	535
23	11.5	0.50	10.09	905	731	61	107	6.98	95.6	56.6	46.1	0.87	582
24	12.0	0.50	10.86	896	787	66	105	6.87	99.0	58.7	47.8	0.86	630
25	12.5	0.50	11.66	888	845	70	102	6.77	102.4	60.7	49.5	0.85	681
26	13.0	0.50	12.47	879	903	75	100	6.66	105.7	62.6	51.2	0.83	733
27	13.5	0.50	13.29	871	963	80	97	6.56	109.0	64.6	52.9	0.82	787
28	14.0	0.50	14.13	862	1024	85	95	6.45	112.3	66.5	54.5	0.81	842
29	14.5	0.50	14.98	854	1085	90	93	6.35	115.4	68.4	56.1	0.79	899
30	15.0	0.50	15.84	847	1148	96	90	6.25	118.6	70.2	57.7	0.78	957
31	15.5	0.50	16.71	839	1211	101	88	6.16	121.6	72.1	59.3	0.77	1017
32	16.0	0.50	17.59	832	1274	106	85	6.06	124.7	73.9	60.8	0.76	1079
33	16.5	0.50	18.48	824	1339	112	82	5.96	127.6	75.6	62.3	0.75	1142
34	17.0	0.50	19.37	817	1403	117	80	5.87	130.6	77.4	63.8	0.73	1207

EXAMPLE 18-7 (*cont'd*)

SOLUTION:

The solution is implemented in Table 18-5 and was solved using Microsoft Excel. Note that the rotation speed (V_R), which depends on the above $C_{L_{max}}$, was already calculated in Example 18-6 and found to equal 118.9 ft/s or 70.4 KCAS. It serves as a flag in the below calculations—once the airspeed is greater than 118.9 ft/s, the ground run is assumed completed.

In order to help explain steps required to set up the spreadsheet, the columns have been numbered from 1 through 14. The first column (heading "*i*") lists the indexes used, here ranging from 1 through 35. All rows from 2 through 30 contain the same formulas, but Row 1 differs as it contains the initial conditions.

Column 1 is the index "*i*" shown in Equations (18-12) and (18-13). Row with the index 10 has been shaded to draw attention to it. It is used as an example of calculations.

Column 2 contains *time*. Here, the event starts at $t=0$ s and ends at $t=17$ s. The initial time (when $i=0$) is zero by definition. All subsequent times are obtained by simply adding 0.5 s to the value in the cell above. It is ultimately the user's decision how many rows to use to represent a time interval in which the event (T-O ground run) takes place.

Column 3 is the *time step*. Note that each row represents a specific time step, Δt. Here all the time steps are equal. Thus, the 10th time step (when $i=10$) takes place when $t=5.0$ s. It is recommended that time steps no larger than 0.25 s be used. A $\Delta t=0.5$ s is used here so the table will fit on the page. This is primarily to reduce error in the dynamic pressure, as it uses the velocity from the previous row in the spreadsheet. The time step is simply calculated by subtracting the previous time from the current time: The time step in Row 10 is obtained by $\Delta t=5.0-4.5=0.5$. The first row is the exception, as it does not have a preceding time. While constant time steps are used here, time steps can be of variable size. This allows higher definition around a specific event of interest.

Column 4 is the *propeller thrust*. It is calculated per earlier discussion, using a quartic polynomial of the argument V_∞. It is obtained from Column 11. As stated earlier, V_∞ (which is interchangeable with V) is taken from the previous row to prevent a circular error. Thus, the value of V_∞ used in Row 10 is that calculated in Row 9. The reader can set up the polynomial using either the airspeed in KTAS or ft/s. This example uses the former and calculates thrust using the formula shown above the column indices. Thus, the airspeed from Column 11 (and not Column 10) is used. To the reader repeating the following calculations: Remember that Excel uses double-floating point arithmetic. Thus, since the values shown are presented using 2 to 4 significant digits, expect to see discrepancies in your numbers. The resulting numbers presented below are edited to match Table 18-5.

Column 5 is the *dynamic pressure*, here calculated using density at S-L and the airspeed from Column 10 (in ft/s). Thus, the dynamic pressure in Row 10 is $q=\frac{1}{2}\rho V_\infty^2=\frac{1}{2}(0.002378)(41.5)^2=2.04$ lb$_f$/ft^2.

Column 6 is the *lift force*, here calculated using the dynamic pressure from Column 4 (=2.04 lb$_f$/ft^2) with S and the C_{LTO} given in the problem statement. The lift in Row 10 is $L=q\cdot S\cdot C_{LTO}=(2.04)(144.9)(0.500)=148$ lb$_f$.

Column 7 is the *drag force*, using the same parameters as for Column 6, exception the drag coefficient given by C_{DTO}. The drag in Row 10 is $D=q\cdot S\cdot C_{DTO}=(2.04)(144.9)(0.0417)=12$ lb$_f$.

Column 8 is the *ground friction*. It uses the value in Column 6, the weight W, and the ground friction constant μ, given in the problem statement. The ground friction in Row 10 is $\mu\cdot(W-L)=(0.04)(3400-148)=130$ lb$_f$.

Column 9 is the *acceleration*. Calculated by summing the forces and divide by the mass. The mass is the weight divided by the acceleration due to gravity, $g=32.174$ ft/s^2. Calculated from:

$$a=dV/dt=(T-D-\mu(W-L))/(W/g)$$

Thus, the acceleration in Row 10 is obtained as follows:

$$a_{10}=(T_{10}-D_{10}-\mu(W-L_{10}))/(W/g)$$
$$=(1044-12-130)/(3400/32.174)=8.53\text{ ft/s}^2$$

Columns 10 and **11** are the *airspeed*. Its value in Column 10 is calculated using the kinematic expression of Equation (18-12), $V_i=V_{i-1}+a_i\cdot\Delta t_i$. Using Row 10 as an example, $V_9=41.5$ ft/s, $a_{10}=8.53$ ft/s^2, and $\Delta t_{10}=0.5$ s. Therefore, $V_{10}=V_9+a_{10}\cdot\Delta t_{10}=41.5+8.53\cdot0.5=45.7$ ft/s. The value in Column 11 amounts to $V_i/1.688=27.1$ KTAS.

Columns 12 through **14** comprise the distance calculations shown in Equation (18-13). Column 12 is calculated from the expression $V_{i-1}\cdot\Delta t_i$. So, Row 10 becomes $V_9\cdot\Delta t_{10}=(41.5)(0.5)=20.7$ ft. Column 13 is calculated from the expression $\frac{1}{2}\cdot a_{i-1}\cdot(\Delta t_i)^2$. For Row 10, it becomes $\frac{1}{2}\cdot a_9\cdot(\Delta t_{10})^2=\frac{1}{2}(8.53)(0.5)^2=1.07$ ft. Column 14 is calculated per $S_i=S_{i-1}+V_{i-1}\cdot\Delta t_i+\frac{1}{2}\cdot a_{i-1}\cdot\Delta t_i^2$. For Row 10, it becomes: $S_{10}=S_9+V_9\cdot\Delta t_{10}+\frac{1}{2}\cdot a_9\cdot\Delta t_{10}^2=95+20.7+1.07=117$ ft. This represents the cumulative distance up to that point in time.

Let us evaluate the results. Table 18-5 shows that the airplane accelerates to V_R between rows 30 and 31

EXAMPLE 18-7 (*cont'd*)

TABLE 18-6 Analysis results.

	Parameter	POH value	Calculated value	Percent difference
Numerical Integration: Rotation at 15.1 s.	V_{LOF}	73 KCAS	70.4 KCAS	3.6%
	S_G	897 ft	963 ft	7.4%
	$S_G + S_{ROT}$	1020 ft	1082 ft	6.1%
	t_{LOF}	16.6 s	15.1 s	9.0%
	a_{avg}	8.46 ft/s^2	7.33 ft/s^2	13.4%
Numerical Integration: Lift-off at 73 KCAS.	V_{LOF}	73 KCAS	73 KCAS	–
	$S_G + S_{ROT}$	1020 ft	1050 ft	2.9%
	t_{LOF}	16.6 s	15.8 s	4.8%

(between 15.0 and 15.5 s). Interpolating between these two values yields $t = 15.1$ s and $S_G = 963$ ft. Adding the rotation segment, the distance increases by $S_{ROT} = |V_{LOF}| = 118.9$ ft, yields a total ground run of 1082 ft, and time to lift-off is 16.1 s. The distance is 62 ft longer than the POH figure. In contrast, if the airplane is allowed to accelerate to $V_{LOF} = 73$ knots, like the POH states, the lift-off occurs between rows 31 and 32, at $t = 15.8$ s and $S_G + S_{ROT} = 1050$ ft, 30 ft above the POH figure.

Other numbers are compared in Table 18-6. Note the KCAS units are used per the POH. Since the analysis is conducted at S-L, KCAS, and KTAS are equal.

Considering other results, Figure 18-12 shows the thrust and propeller efficiency models used for this analysis. The shaded region in the graph represents the focus of the above work and shows how the quartic spline method allows the thrust be determined over the entire airspeed range.

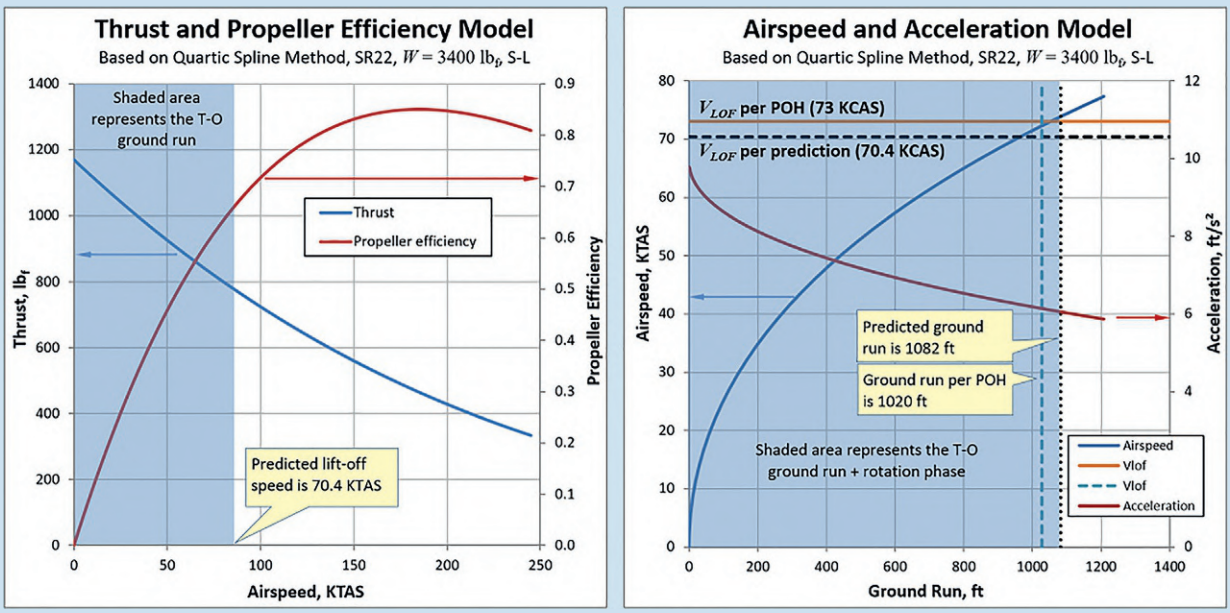


FIGURE 18-12 The thrust and propeller efficiency model for the SR22 used in the T-O ground run analysis.

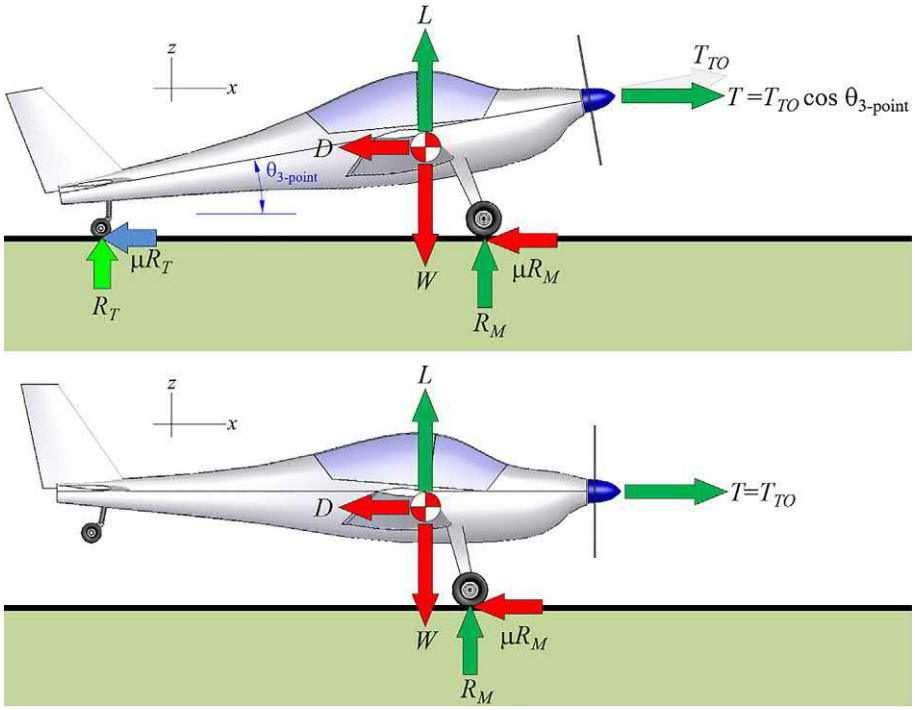


FIGURE 18-13 The taildragger adds complexity to the ground run analysis.

(4) Treatment of T-O Run for a Taildragger

The ground run analysis for a taildragger differs from that of a conventional tricycle aircraft, because the taildragger lifts its tailwheel off the ground during the ground run (see Figure 18-13). As far as drag, lift, and thrust are concerned, this transforms the taildragger from one configuration (with three ground contact-points) to another (with two ground contact-points). The 3-point configuration has larger C_D and C_L, and lower horizontal thrust, T, than the 2-point one. It is easiest to treat the T-O run using the numerical integration method. The transition can be handled using the parametric formulation shown below.

Let us distinguish the C_D, C_L, and take-off thrust, T_{TO}, for the two configurations using the subscripts *3-point* and *2-point*. Then, we can either estimate or guess the transition time, Δt_{tot}. It might last between 1 and 3 s. We also need a transition start time, call it t_{ini}. It is based on the airspeed at which this takes place, for instance estimated using the method of Section 13.3.5. Then, we can assess the parameters during transition as follows

$$\begin{aligned} C_D &= (1-p)C_{D_{3\text{-point}}} + p\ C_{D_{2\text{-point}}} \\ C_L &= (1-p)C_{L_{3\text{-point}}} + p\ C_{L_{2\text{-point}}} \\ T &= T_{TO}\cos\left((1-p)\theta_{3\text{-point}} + p\ \theta_{2\text{-point}}\right) \end{aligned} \qquad (18\text{-}24)$$

where θ is the angle the thrustline makes to the horizontal and $p = (t - t_{ini})/\Delta t_{tot}$ and $0 \le p \le 1$.

18.3.2 Calculating the Rotation Distance, S_{ROT}

Figure 18-14 shows an aircraft taking-off and clearing an obstruction of predetermined height shortly after lift-off. Rotation is a transient event during the T-O. Small airplanes lift off almost as soon as the pilot initiates the rotation at the *rotation point* (by deflecting the elevator to raise the nose). For large heavy aircraft, the rotation may last anywhere from 2 to 5 s. Accounting for the change in drag and lift during the rotation can be implemented using the numerical integration scheme of the previous section; however, it is far simpler to account for the distance traveled during rotation by assuming the distance a small aircraft travels in 1 s but 3 s for large ones. Mathematically:

Small aircraft: $S_{ROT} = |V_{LOF}|$ (18-25)

Large aircraft: $S_{ROT} = 3|V_{LOF}|$ (18-26)

The boundary between "small" and "large" aircraft is somewhat subjective. For this author, it is somewhere between a Beech 99 King Air and British Aerospace BAe 146, with Fokker F-27 or F-50 in that gray area.

18.3.3 Calculating the Transition Distance, S_{TR}

Again, refer to Figure 18-14. The transition segment begins with the lift-off and ends with the aircraft

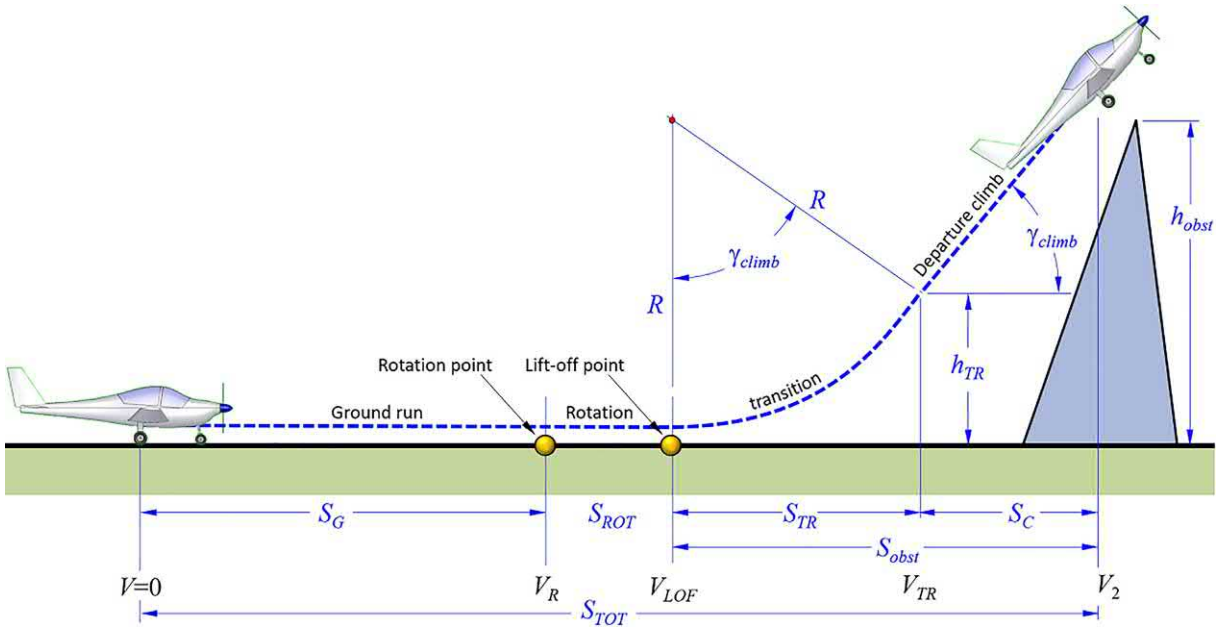


FIGURE 18-14 Determining the segments constituting the T-O run.

achieving a climb angle to be maintained until the obstacle height (h_{obst}) is achieved. Figure 18-15 shows a more detailed look at this scenario. We want to determine the total distance from the *lift-off point* to the location where the height of the airplane equals that of the obstacle, call it S_{obst}. To determine S_{obst} we must establish: Is the obstacle cleared *after* or *before* the transition segment is completed? A methodology to evaluate the S_{obst} will now be presented.

STEP 1: Climb angle

$$\sin\gamma_{\text{climb}} = \frac{T-D}{W} = \frac{T}{W} - \frac{1}{L/D} \qquad (19\text{-}27)$$

STEP 2: Transition radius

$$R \approx 0.2156\ V_{S1}^2 \qquad (18\text{-}27)$$

STEP 3: Transition distance

$$S_{TR} = R\sin\gamma_{\text{climb}} \qquad (18\text{-}28)$$

STEP 4: Transition height

$$h_{TR} = R(1-\cos\gamma_{\text{climb}}) \qquad (18\text{-}29)$$

STEP 5a: Aircraft Passes Obstacle AFTER Completing Transition ($h_{TR} < h_{obst}$)

Figure 18-15 left, shows the initial climb in which the aircraft passes the obstacle *after* transitioning, during a

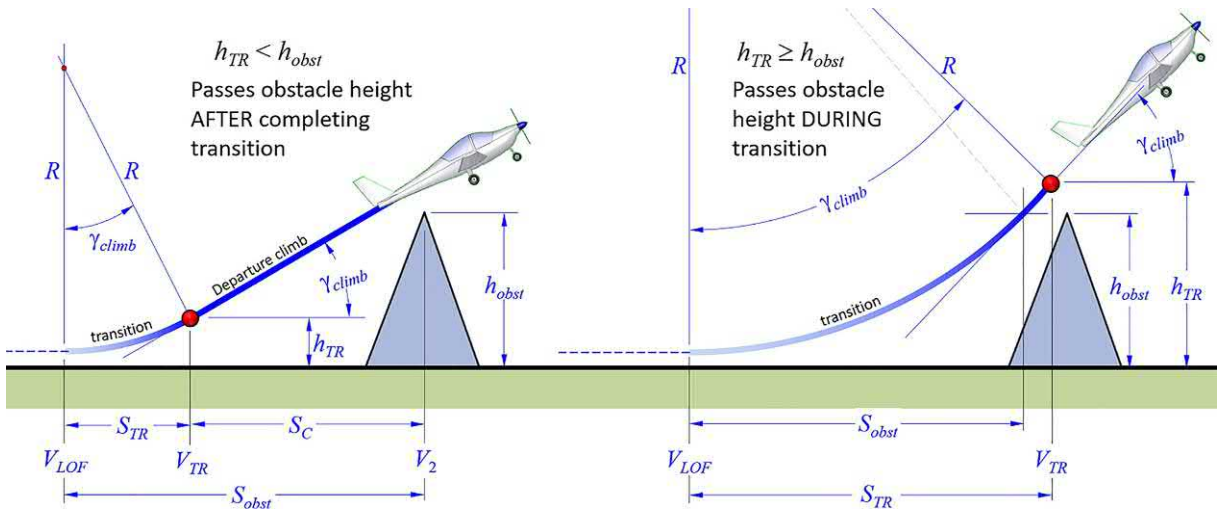


FIGURE 18-15 Evaluation of the T-O over an obstacle.

straight-climb. Thus, *add* $S_{obst} = S_{TR} + S_C$ *to the total T-O distance*. The trick is to determine $S_{obst} = S_{TR} + S_C$. By inspection, the horizontal distance (S_{TR}) equals $R \cdot \sin \gamma_{climb}$. Thus, the altitude gained during the transition amounts to $h_{TR} = R(1\text{-}\cos \gamma_{climb})$. These are expressed as Equations (18-28) and (18-29). S_C is expressed as Equation (18-32).

STEP 5b: Aircraft Passes Obstacle During Transition ($h_{TR} \geq h_{obst}$)

Figure 18-15 right, shows the aircraft passing the obstacle before completing the transition. Consequently, we only need to determine the distance to where it cleared the obstacle (i.e., reached height h_{obst}). *No climb calculation is needed*. This distance, again, is denoted by S_{obst}. The transition distance (S_{TR}) is given by the Pythagorean rule:

$$R^2 = S_{TR}^2 + (R - h_{TR})^2 \quad \Leftrightarrow \quad S_{TR} = \sqrt{R^2 - (R - h_{TR})^2} \tag{18-30}$$

Therefore, the horizontal distance required to clear the obstacle is approximated similarly

$$R^2 = S_{obst}^2 + (R - h_{obst})^2 \quad \Leftrightarrow \quad S_{obst} = \sqrt{R^2 - (R - h_{obst})^2} \tag{18-31}$$

DERIVATION OF EQUATION (18-27)

Transition generally implies acceleration from $1.1V_{S1}$ to a climb speed of $1.2V_{S1}$. Note that the climb speed is not necessarily the *best rate-of-* or *best angle-of-climb* for the airplane. The average speed for the two limits is $V_{TR} = 1.15V_{S1}$ and this is used in addition to an assumed lift coefficient of about $0.9C_{L_{max}}$ to determine distance traveled.

The average vertical acceleration in terms of load factor:

$$n = \frac{L}{W} = \frac{\frac{1}{2}\rho(1.15V_{S1})^2 \cdot S \cdot (0.9C_{L_{max}})}{\frac{1}{2}\rho V_{S1}{}^2 \cdot S \cdot C_{L_{max}}} = 1.1903 \tag{i}$$

Use the load factor to determine the radius of curved segment, by using the expression for the centripetal acceleration required. Load factor in terms of centripetal force:

$$n = \frac{L}{W} = \frac{W + m\frac{V^2}{R}}{W} = \frac{W + \frac{W}{g}\frac{V^2}{R}}{W} = 1 + \frac{V^2}{Rg}$$

Solving for the radius yields:

$$n = 1 + \frac{V^2}{Rg} \quad \Leftrightarrow \quad R = \frac{V^2}{g(n-1)} \tag{ii}$$

Therefore, using the transition airspeed, we get:

$$R = \frac{V_{TR}^2}{g(n-1)} = \frac{(1.15V_{S1})^2}{g(1.1903-1)} \approx 0.2156 \times V_{S1}^2 \tag{iii}$$

18.3.4 Calculating the Climb Distance Over an Obstacle, S_C

As stated above, if the value of h_{TR} is less than h_{obst}, the airplane reaches it while climbing. The distance it covers in climb is denoted as S_C. The required obstacle clearing height is 50 ft for Military and GA aircraft and 35 ft for Commercial Aircraft. This distance can be derived by observing the geometry of the left diagram of Figure 18-15:

$$\tan \gamma_{\text{climb}} = \frac{(h_{obst} - h_{TR})}{S_C} \quad \Rightarrow \quad S_C = \frac{(h_{obst} - h_{TR})}{\tan \gamma_{\text{climb}}} \tag{18-32}$$

EXAMPLE 18-8

Determine the transition distance and, if found necessary, the climb distance for the Cirrus SR22. Use data from Example 18-6 as needed. Assume the simplified drag model and the following characteristics:

$W = 3400$ lb$_f$	$C_{D_{min}} = 0.0350$ (T-O configuration, assumed)
$S = 144.9$ ft^2	$k = 0.04207$
$C_{L_{max}} = 1.69$ (based on POH for T-O)	

Compare the results to published data from the airplane's Pilot's Operating Handbook (POH), which give a lift-off speed of 73 KCAS, T-O distance of 1020 ft (ISA at S-L) and the calculated time to lift-off of 16.6 s from Example 18-1.

SOLUTION:

Stalling speed: $V_{S1} = 108.0$ ft/s (64 KCAS) (from POH)

Transition speed:

$V_{TR} = 1.15V_{S1} = 1.15(108.0) = 124.2$ ft/s (73.6 KCAS)

Lift coefficient at V_{TR}:

$$C_L = \frac{2W}{\rho V^2 S} = \frac{2(3400)}{(0.002378)(124.2)^2(144.9)} = 1.279$$

Drag coefficient at V_{TR}:

$C_D = C_{D_{min}} + kC_L^2 = 0.0350 + 0.04207 \times 1.279^2 = 0.1038$

Lift-to-drag ratio: $L/D = 1.279/0.1038 = 12.3$

Thrust at V_{TR}:

$T(73.6) = 825$ lb$_f$ (using thrust function of Example 18 – 7)

Climb angle at V_{TR}:

$$\gamma_{\text{climb}} = \sin^{-1}\left(\frac{T}{W} - \frac{1}{L/D}\right) = \sin^{-1}\left(\frac{825}{3400} - \frac{1}{12.3}\right) = 9.285°$$

Transition radius:

$$R \approx 0.2156 \times V_{S1}^2 = 0.2156 \times (108)^2 = 2515 \text{ ft}$$

EXAMPLE 18-8 *(cont'd)*

Transition distance: $S_{TR} \approx 0.2156\, V_{S1}^2 \left(\frac{T}{W} - \frac{1}{L/D}\right)$

$$= 0.2156 \times (108)^2 \times \left(\frac{825}{3400} - \frac{1}{12.3}\right) = 406 \text{ ft}$$

Transition height:

$$h_{TR} = R(1 - \cos\gamma_{climb}) = 2515(1 - \cos(9.285°)) = 32.9 \text{ ft}$$

Since the h_{TR} is less than the obstacle height of 50 ft, the climb segment must be included as well.

Climb distance: $S_C = \frac{h_{obst} - h_{TR}}{\tan\gamma_{climb}} = \frac{50 - 32.9}{\tan(9.285°)} = 104 \text{ ft}$

Therefore, the total T-O distance over 50 ft is 1082 + 406 + 104 = 1592 ft, if the estimated V_R of 70.4 KCAS is used and 1050 + 406 + 104 = 1560 ft, if the POH V_{LOF} of 73 KCAS is used. Both numbers compare favorably to published value of 1594 ft in the POH.

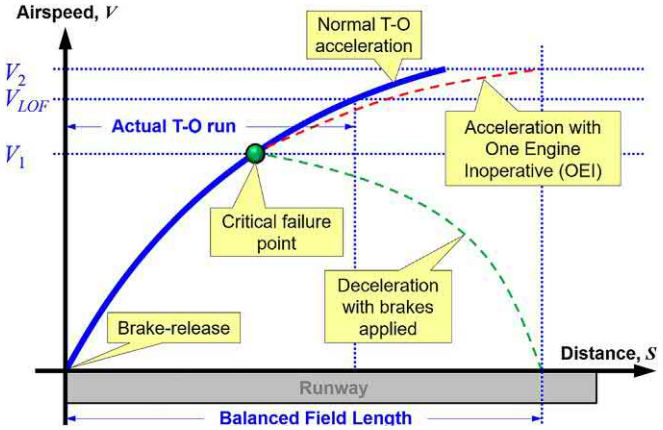


FIGURE 18-16 Definition of a balanced field length.

18.3.5 Calculating the Balanced Field Length, S_{BFL}

Figure 18-16 shows how the airspeed of a typical aircraft changes with distance from brake-release during a T-O run. Assume this graph reflects the relationship between airspeed and runway distance of a multiengine aircraft. Initially, while at rest, the airspeed and runway distance are both zero. However, as soon as the pilot increases thrust and releases the brakes, the aircraft begins to accelerate and the distance from this point increases.

Now, assume that some distance from the brake-release point one engine becomes inoperative. The airplane will continue to accelerate, only much slower than before. Now, two things can happen:

(1) If the airspeed is low (and the distance covered is short), the pilot can simply step on the brakes and bring the aircraft to a complete stop before running out of runway. Problem solved. This is shown as the left graph in Figure 18-17.

(2) On the other hand, if the airspeed is high (assuming the airplane is still on the ground) there may not be enough runway ahead of the plane to fully stop it in time, so braking is not an option. In this case, two new things can happen: (a) There is insufficient thrust remaining to accelerate to lift-off before running out of runway. Disaster strikes. (The pilot should never have attempted the T-O run.) (b) There is indeed enough thrust remaining to accelerate to lift off before running out of runway. Disaster is avoided. This is shown as the right graph in Figure 18-17.

While this logic is sound, it requires analysis effort which is not possible in a time of crisis. Also note that the following can be deduced from the graphs in Figure 18-17: If there is an airspeed at which the airplane

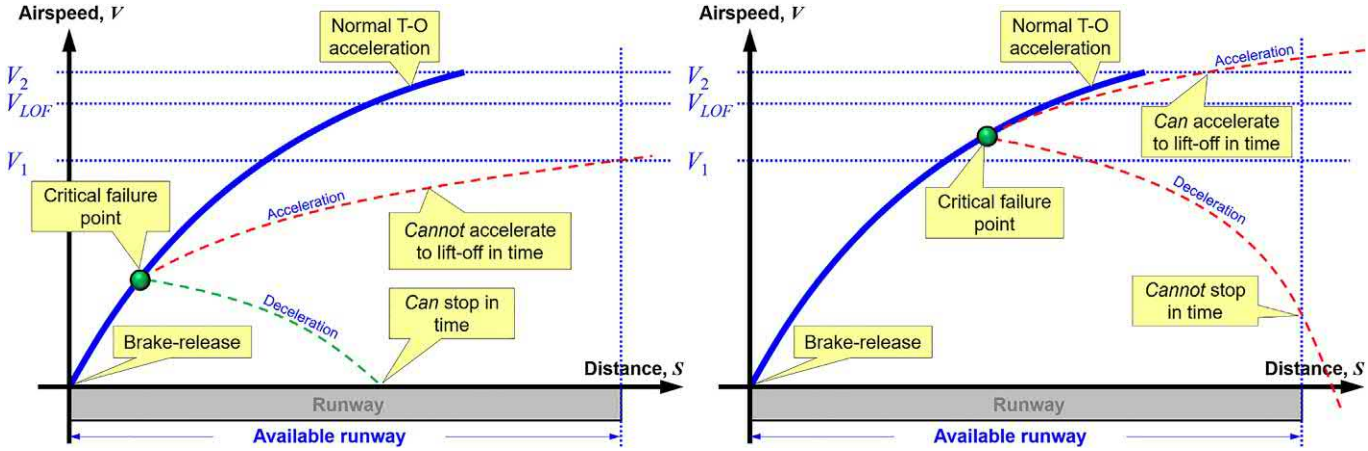


FIGURE 18-17 If the failure occurs early enough it is possible to stop the airplane (left). However, if moving too fast, it may not be able to stop, but may still be able to lift-off before runway runs out (right).

can be stopped in time (as shown in the left graph) and there is an airspeed at which it cannot be stopped in time, but accelerated to lift-off (as shown in the right graph), then there must be an airspeed between the two at which it can both be stopped and accelerated to lift-off in time (if not, then the runway is too short for a safe operation of the airplane). There is indeed such airspeed and it is called V_1, the T-O safety speed.

In an emergency, pilots are trained to react. If below, V_1 step on the brakes. If above, V_1 continue the take-off. The distance required to accelerate the aircraft to V_1 and then decelerate it to a complete stop by applying hard braking, is called; *Balanced Field Length* (BFL, sometimes called *accelerate-stop* distance). It is only applicable to multiengine airplanes and is not needed for single-engine aircraft. The only option is to brake. The importance of the BFL is that it gives the pilot two safe options.

Torenbeek [2, pp. 168–169] presents the following empirical expression to estimate the balanced field length for a multiengine aircraft:

$$S_{BFL} = \frac{0.863}{1+2.3\Delta\gamma_2}\left(\frac{W_{TO}/S}{\rho g C_{L_2}} + h_{obst}\right)\left(2.7 + \frac{1}{\overline{T}/W_{TO} - \mu'}\right) + \left(\frac{\Delta S_{to}}{\sqrt{\sigma}}\right) \tag{18-33}$$

where

C_{L2} = Lift coefficient at V_2. If $V_2 = 1.2V_S$, then it can be shown that $C_{L2} = 0.694C_{L_{max}}$,
g = Acceleration due to gravity,
ρ = Air density,
D_2 = Drag at V_2,
S = Reference wing area,
W_{TO} = Take-Off weight,
h_{obst} = Obstacle height = 35 ft (10.7 m) for commercial jetliners and 50 ft (15.2 m) for GA aircraft,
$\overline{T}$ = Average thrust during the T-O run, given by Equations (18-34) and (18-35),
$\mu' = 0.01C_{L_{max}} + 0.02$, where $C_{L_{max}}$ is that of the T-O configuration,
ΔS_{to} = Inertia distance = 655 ft (200 m),
$\Delta\gamma_2 = \gamma_2 - \gamma_{2min}$.

$$\gamma_2 = \sin^{-1}\left(\frac{T_{OEI} - D_2}{W_{TO}}\right) \text{ and } \gamma_{2\min} = \begin{cases} 0.024 & \text{for 2 engines} \\ 0.027 & \text{for 3 engines} \\ 0.030 & \text{for 4 engines} \end{cases}$$

Torenbeek's method requires the average thrust during the T-O run to be estimated for jets and propeller-powered aircraft using the following expressions:

$$\text{For jet aircraft:} \quad \overline{T} = 0.75T_{\max}\left(\frac{5+BPR}{4+BPR}\right) \tag{18-34}$$

where T_{max} is the maximum static thrust and BPR is the turbofan bypass ratio.

For an aircraft with a constant speed propeller:

$$\overline{T} = K_p P_{\max}\left(\frac{\sigma N_e D_P^2}{P_{\max}}\right)^{1/3} \tag{18-35}$$

where

D_P = Propeller diameter,
P_{max} = Maximum engine power, in BHP or kg·m/s (which is power in Watts divided by g),
σ = Density ratio,

$$K_p = \begin{cases} 5.75 & \text{for } P_{\max} \text{ in BHP} \\ 0.321 & \text{for } P_{\max} \text{ in kg}\cdot\text{m/s} \end{cases}$$

Note that the average thrust for a fixed-pitch propeller will be approximately 15% to 20% lower than that for a constant-speed propeller.

EXAMPLE 18-9

Estimate the Balanced Field Length for the Learjet 45 assuming its $C_{L_{max}}$ in the T-O configuration to be 1.60 and $V_2 = 1.2V_S$. Also, assume an obstacle height of 50 ft and gross weight of 21,500 lb_f. Note that other properties of the airplane are given in Table 17-8. Assume the simplified drag model and that the Oswald's span efficiency factor amounts to 0.8294 and $C_{D_{min}} = 0.045$ in the T-O configuration. Furthermore, assume the maximum thrust with One Engine Inoperable (OEI) to equal one half of the average thrust calculated in STEP 4 below.

SOLUTION:

***STEP 1*:** Determine the constant "k":

$$k = \frac{1}{\pi \cdot AR \cdot e} = \frac{1}{\pi \cdot (7.33) \cdot (0.8294)} = 0.05236$$

***STEP 2*:** Calculate the stalling speed in the T-O configuration using the given $C_{L_{max}}$ and Equation (20-29):

$$V_S = \sqrt{\frac{2W}{\rho S C_{L_{max}}}} = \sqrt{\frac{2(21500)}{(0.002378)(311.6)(1.60)}} = 190.4 \text{ ft/s} \quad (\approx 113 \text{ KCAS})$$

***STEP 3*:** Therefore, V_2 amounts to:

$$V_2 = 1.2V_S = 1.2 \times 190.4 = 228.5 \text{ ft/s} \quad (\approx 135 \text{ KCAS}).$$

EXAMPLE 18-9 (*cont'd*)

***STEP 4*:** Calculate the average thrust during the T-O run, $\overline{T}$, using Equation (18-34):

$$\overline{T} = 0.75T_{to}\left(\frac{5+BPR}{4+BPR}\right) = 0.75\times 7000\times\left(\frac{5+3.9}{4+3.9}\right) = 5915 \text{ lb}_\text{f}$$

***STEP 5*:** Determine the factor μ':

$$\mu' = 0.01C_{L_{\max}} + 0.02 = 0.036$$

***STEP 6*:** Estimate the drag at the airspeed V_2, but this requires the drag polar for the aircraft to be known. Here, assume the following drag polar for the aircraft in the T-O configuration: $C_D = C_{D_{\min}} + kC_L^2 = 0.045 + 0.05236C_L^2$.

Lift coefficient at V_2:

$$C_{L2} = 0.694C_{L_{\max}} = 0.694\times 1.60 = 1.11$$

Drag coefficient at V_2:

$$C_D = 0.045 + 0.05236(1.11)^2 = 0.1095$$

Drag force at V_2:

$$D_2 = \frac{1}{2}\rho V_2^2 S C_D = \frac{1}{2}(0.002378)(228.5)^2(311.6)(0.1095) = 2118 \text{ lb}_\text{f}.$$

***STEP 7*:** Estimate climb angle at V_2 and the difference $\Delta\gamma_2$. As stated in the introduction to this example, it will be assumed that the thrust with OEI amounts to one half that of $\overline{T}$ calculated in STEP 4, or 2955 lb_f. This yields the following climb angle:

$$\gamma_2 = \sin^{-1}\left(\frac{T_{OEI} - D_2}{W_{TO}}\right) = \sin^{-1}\left(\frac{2955-2118}{21500}\right) = 0.04080 \text{ rad}$$

Therefore: $\Delta\gamma_2 = \gamma_2 - \gamma_{2\min} = 0.04080 - 0.024 = 0.01680$ rad

***STEP 8*:** Finally calculate S_{BFL} using Equation (18-33):

$$S_{BFL} = \frac{0.863}{1+2.3\Delta\gamma_2}\left(\frac{W_{TO}/S}{\rho g C_{L_2}} + h_{obst}\right)\left(2.7 + \frac{1}{\overline{T}/W_{TO} - \mu'}\right) + \left(\frac{\Delta S_{to}}{\sqrt{\sigma}}\right)$$

$$= \frac{0.863}{1+2.3(0.01680)}\left(\frac{21500/311.6}{(0.002378)(32.174)(1.11)} + 50\right)\left(2.7 + \frac{1}{5915/21500 - 0.036}\right) + \left(\frac{655}{\sqrt{1}}\right)$$

$$= (0.8309)(862.5)(6.882) + 655 = 5587 \text{ ft}$$

This compares to 5500 ft published by ref. [9] for the type.

18.3.6 Take-Off Sensitivity Studies

It is helpful to study the impact of variation in atmospheric conditions, weight, runway slope, and other deviations on the operation of the airplane. Three sensitivity studies for the SR22 are shown in Figures 18-18–18-20. The first one evaluates the sensitivity of the T-O distance to changes in temperature and altitude. It shows that a T-O from an airfield at a 10,000 ft elevation on a standard

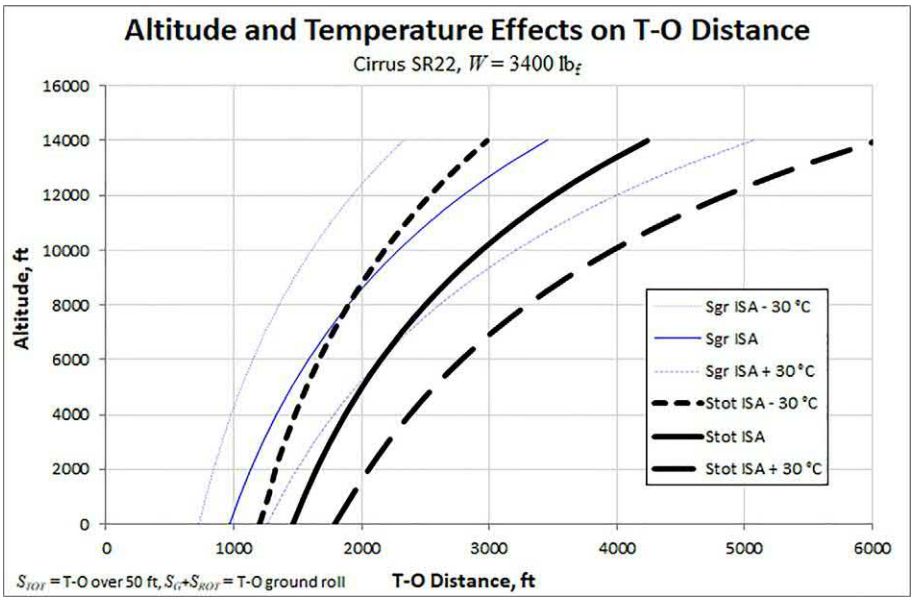


FIGURE 18-18 Sensitivity study showing the effect of altitude and temperature on the T-O distance of the SR22. The study was performed using the analysis method presented in this section.

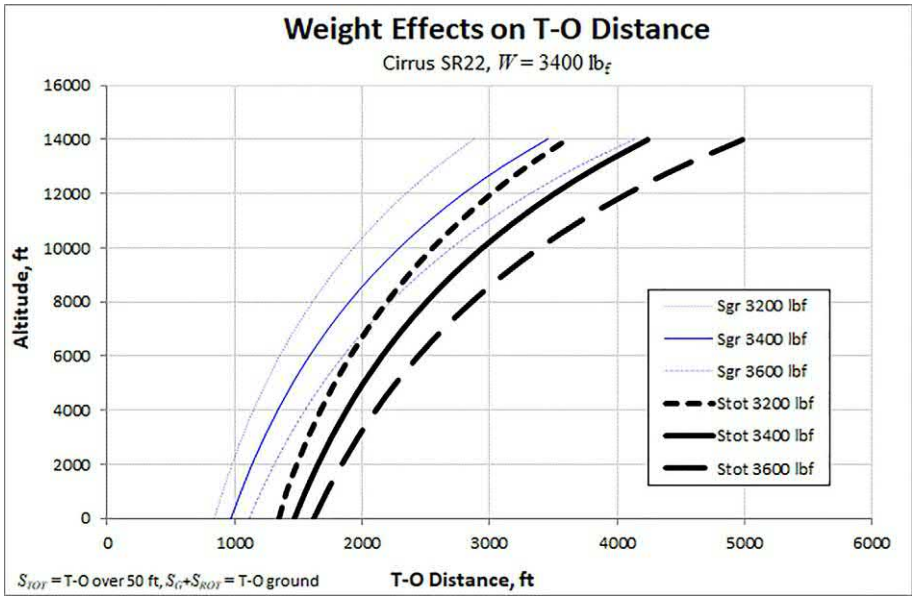


FIGURE 18-19 Sensitivity study showing the effect of weight change on the T-O distance of the SR22.

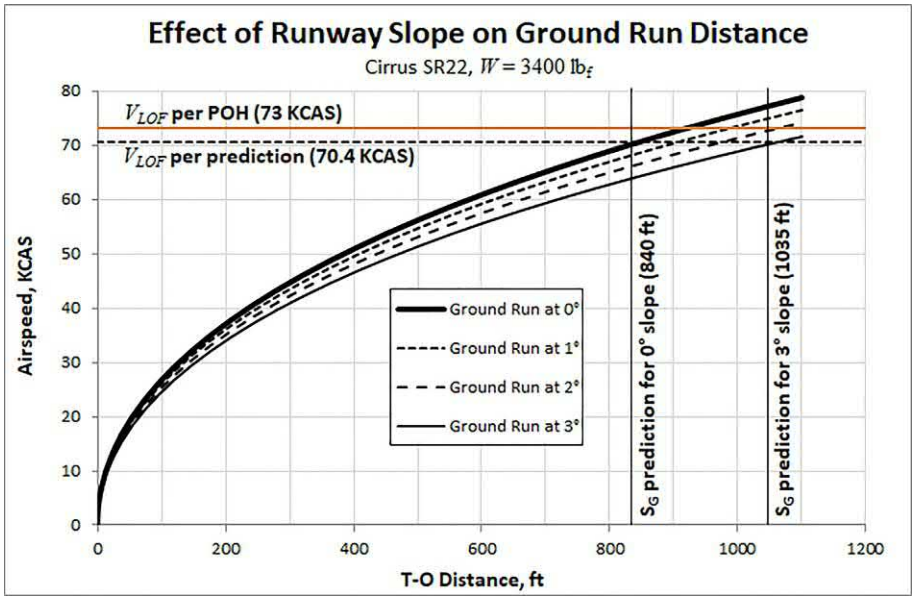


FIGURE 18-20 Sensitivity study showing the effect of runway slope change on the T-O distance of the SR22.

day doubles the T-O distance over 50 ft. On a day that is 30°C warmer than standard, the distance increases by a factor of 2.7.

The sensitivity evaluated in Figure 18-19 shows how weight and altitude affects the T-O distance. A study of this nature is helpful when evaluating the impact of a target gross weight not being met. Generally, increasing the gross weight by 200 lb_f will increase the ground run distance by 150 to 675 ft and T-O over 50 ft by 155 to 750 ft, depending on altitude.

The impact of a steep runway slope is presented in Figure 18-20 and is based on Equation (18-5). The figure shows that an uphill runway slope of some 3 degrees will increase the ground run distance by almost 200 ft, from 840 ft to 1035 ft. While this information is helpful for some preliminary design studies, it is vital for pilots once the aircraft is operational. Most runways feature some degree of uphill or downhill slopes; understanding the detrimental effect of uphill slopes, in particular, helps the pilot in the decision-making process.

18.4 DATABASE—T-O PERFORMANCE OF SELECTED AIRCRAFT

Table 18-7 shows the ground run and T-O distance for selected aircraft. These data are helpful when evaluating the accuracy of own calculations.

TABLE 18-7 T-O performance of selected aircraft.

Single Engine GA Aircraft				
Aircraft	**Gross Wgt, lb_f**	**Ground Run, ft**	**T-O to 50 ft, ft**	**Reference**
Aero Boero 115	1697	380	500	Jane's 1976-77
Beech A36 Bonanza	3600	1140	2040	Jane's 1978-79
Beech Sundowner	2030	1130	1955	
Beech V35 Bonanza	3400	1002	1769	
Cessna 152	1670	725	1340	
Cessna 172 Skyhawk	2300	805	1440	
Cessna 177 Cardinal	2800	890	1585	
Cessna 185 Skylane	2950	705	1350	
Cessna 210 Centurion	3800	1250	2030	
Cirrus SR20	3050	1478	2221	POH
Cirrus SR22	3400	1028	1594	
Piper PA-18 Super Cub	1750	200	500	Jane's 1978-79
Piper PA-28 Warrior II	2325	963	1490	
Piper PA-32 Lance II	3600	960	1690	
Piper PA-38 Tomahawk	1670	820	1460	
SIAI-Marchetti SF-260	2425	1837	2543	Jane's 1976-77

Multi Engine GA Aircraft					
Aircraft	**Gross Wgt, lb_f**	**Ground Run, ft**	**T-O to 50 ft, ft**	**S_{BFL}*, ft**	**Reference**
Beech Duchess 76	3900	1017	2119	-	Jane's 1978-79
Beech Duke B60	6775	2075	2626	-	
Beech King Air C90	9650	-	2261	3498	
Cessna 310	5500	1335	1700	-	
Cessna 337 Skymaster	4630	1000	1675	-	
Cessna 340	5990	1615	2175	-	
DHC-6 Twin Otter	12500	700-860	1200-1500	-	Jane's 1976-77
Partenavia P-68B Victor	4321	912	1539	-	
Piper PA-23 Aztec	5200	945	1695	1985	Jane's 1978-79
Piper PA-31 Cheyenne	9000	-	1980	3140	
Piper PA-31 Chieftain	7000	1360	2490	2100	
Piper PA-34 Seneca II	4570	900	1240	2520	

Commuter Aircraft				
Aircraft	**Gross Wgt, lb_f**	**Ground Run, ft**	**T-O to 50 ft, ft**	**Reference**
Let L-410 Turbolet	12566	1627	1850	Jane's 1976-77
GAF N22B Nomad	8500	600-970	1260-1350	
Embraer EMB-110 Bandeirante	13010	1245	1770	
DHC-5 Buffalo	49200	950-2300	1250-2875	Jane's 1978-79
Fokker F-27 Friendship	43952	3240-3970	-	Jane's 1976-77

* S_{BFL} = Balanced Field Length

EXERCISES

(1) The six-seat Beech B58 Baron has two 260 BHP Continental IO-470 engines that swing 78-in. diameter propellers. Its gross weight is 5100 lb_f and it as a 199.2 ft^2 wing area and a 37.83 ft wing span. Estimate its Balanced Field Length at S-L on a standard day, assuming the maximum lift coefficient in the T-O configuration to is 1.60, minimum drag coefficient is 0.035, lift-induced drag constant is 0.05906, and $V_2 = 1.2V_S$ for an obstacle height of 50 ft. Assume the simplified drag model. Assume the

maximum thrust with One Engine Inoperable (OEI) to equal one half of the average T-O thrust. Compare your number to the published value of about 2300 ft.

Ans: 2386 ft.

(2) Estimate the average acceleration and time from break release to lift-off for the following aircraft types, based on the ground run and lift-off speed specified in their Pilots Operating Handbooks (assume S-L conditions).

(a) Beechcraft B58 Baron, $S_G = 2000$ ft, $V_{LOF} = 84$ KCAS.
(b) SOCATA TBM-850, $S_G = 1017$ ft, $V_{LOF} = 77$ KCAS.
(c) Cessna C-208 Grand Caravan, $S_G = 1405$ ft, $V_{LOF} = 86$ KCAS.
(d) Piper PA-46 Malibu Mirage, $S_G = 1100$ ft, $V_{LOF} = 69$ KCAS.

Ans (a): 5.03 ft/s^2, 28.2 s.

(3) Estimate the ground run for the three engine Dassault Falcon 7× business jet, using the following properties:

$W = 70{,}000$ lb$_f$
$S = 761$ ft^2
$C_{LTO} = 0.85$
$C_{DTO} = 0.045$
$C_{L_{max}} = 1.5$
T at $V_R/\sqrt{2} = 3 \times 6000$ lb$_f$
$\mu = 0.03$
Ans: 4425 ft.

(4) Determine the lift-off speed (V_{LOF}), V_2, and total T-O distance to an obstacle height of 50 ft (includes ground roll, rotation, transition, and climb distances) for the turboprop-powered SOCATA TBM-850, assuming the following characteristics:

$W = 7394$ lb$_f$
$P = 850$ SHP (PT6A)
$S = 193.7$ ft^2
$C_{L_{max}} = 1.90$ (based on POH for T-O)
$C_{LTO} = 0.750$ (assumed value)
$C_{DTO} = 0.045$ (assumed value)
$\mu = 0.03$ (sample value)
$\eta_p = 0.65$

Compare the results to published data from the airplane's Pilot's Operating Handbook (POH). It gives a $V_{LOF} = 90$ KCAS, $V_2 = 99$ KCAS, ground roll distance of 2035 ft (ISA at S-L) and total T-O distance (to 50 ft) is 2840 ft.

References

[1] C.D. Perkins, R.E. Hage, *Airplane Performance, Stability, and Control*, John Wiley & Sons, 1949.
[2] E. Torenbeek, *Synthesis of Subsonic Aircraft Design*, 3rd ed., Delft University Press, 1986.
[3] L. Nicolai, *Fundamentals of Aircraft Design*, 2nd ed., (1984).
[4] J. Roskam, C.-T.E. Lan, *Airplane Aerodynamics and Performance*, DARcorporation, 1997.
[5] F.J. Hale, *Aircraft Performance, Selection, and Design*, John Wiley & Sons, 1984, pp. 137–138.
[6] J.D. Anderson Jr., *Aircraft Performance & Design*, 1st ed., McGraw-Hill, 1998.
[7] Anonymous, *The B-29 – Airplane Commander Training Manual for the Superfortress, AAF Manual No. 50-9*, Office of Flying Safety, Army Air Forces, February 1945.
[8] Anonymous, *Boeing Jet Transport Performance Methods – 737/747/757/767*, 7th ed., Being Flight Operations Engineering, May 1989.
[9] Anonymous, *Learjet 45 – Airplane Flight Manual*, Bombardier Learjet, 2004.

CHAPTER

19

Performance—Climb

OUTLINE

19.1 **Introduction** 811
19.1.1 The Content of This Chapter 811
19.1.2 What Analyses Must I Do? 811

19.2 **Fundamental Relations for the Climb Maneuver** 812
19.2.1 General Equations-of-Motion for Climb 813
19.2.2 Power Available, Power Required, and Excess Power 814
19.2.3 Vertical Air speed in Terms of Thrust or Power 814
19.2.4 Rate-of-Climb 815

19.3 **General Climb Analysis Methods** 815
19.3.1 General Expression for Rate-of-Climb 815
19.3.2 General Expression for Angle-of-Climb 817
19.3.3 Formulation of Best (Maximum) Rate-of-Climb 817
19.3.4 Formulation of Best (Maximum) Angle-of-Climb 822
19.3.5 Formulation of Specific Optimal Climb Problems 824
19.3.6 Time to Altitude 826
19.3.7 Absolute/Service Ceiling Altitude 827
19.3.8 Numerical Analysis of the Climb Maneuver—Sensitivity Studies 828

19.4 **Aircraft Database—Rate-of-Climb of Selected Aircraft** 830

References 832

19.1 INTRODUCTION

The study of the climb primarily involves the determination of the rate at which an airplane increases its altitude (called the *rate-of-climb* or ROC) and the angle its flight path makes to the ground (called the *angle-of-climb* or AOC). Understanding how rapidly an aircraft climbs is of major importance to the designer and operators alike. Great climb performance sells aircraft. Not only does it impact time to reach cruise altitude but also the perception of its noise footprint. Figure 19-1 shows an organizational map displaying the climb among other subjects of *performance theory*.

This chapter presents the formulation and solution of the equations-of-motion for the climb and presents practical solutions for both for propeller and jet-powered aircraft. For the designer, the primary information of interest includes the maximum ROC, best (highest) AOC, the corresponding airspeeds, the ROC and AOC for a given power setting, and climb range, to name a few. In general, the methods presented in here are "industry standard" and mirror that presented by a variety of authors, e.g., Perkins and Hage [1], Torenbeek [2], Nicolai [3], Roskam [4], Hale [5], Anderson [6], and Miele [7], to name a few.

19.1.1 The Content of This Chapter

- Section 19.2 develops fundamental relationships necessary to evaluate climb characteristics, most importantly the equation-of-motion for climbing flight.
- Section 19.3 presents an assortment of methods to predict the specific climb characteristics of an airplane. This includes some optimal climb methods.
- Section 19.4 presents the climb performance of selected aircraft types.

19.1.2 What Analyses Must I Do?

For the newcomer to climb analysis, the burning question is: "What am I supposed to estimate and how do I conduct those estimations?" In short, the purpose of climb analysis is to evaluate if the airplane possesses enough power to permit safe operation. This applies to

https://doi.org/10.1016/B978-0-12-818465-3.00019-7

Copyright © 2022 Elsevier Inc. All rights reserved.

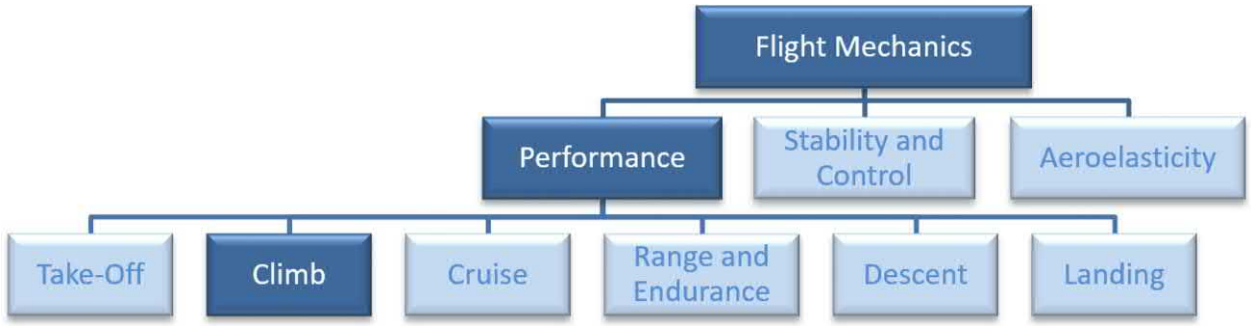


FIGURE 19-1 An organizational map placing performance theory among the disciplines of *Flight Mechanics*, and highlighting the focus of this chapter; climb performance analysis.

single engine and multiengine aircraft with all engines operating and one engine inoperative. A review of historical and current 14 CFR Part 23 reveals an assortment of requirements. Regardless of claims to the contrary, the current regulations (§23.2120 and §23.2125) are prescriptive in nature, like the historical ones. Tables 19-1 and 19-2 list the necessary tasks you should complete.

An important byproduct of climb analysis is the determination of optimal airspeeds that lead to the steepest *angle-of-climb* and fastest *rate-of-climb*. This is illustrated in Figure 19-2, which shows the trajectory of the same aircraft at its *best angle-of-climb airspeed* (V_X, denoted as **A**) and *best rate-of-climb airspeed* (V_Y, denoted as **B**). After some unit time, e.g., 1-min, aircraft **A** is behind and below aircraft **B**, but its path angle (γ_X) is steeper. This means its altitude gained (z_X) per unit horizontal distance (x_X) is greater than that of aircraft **B**.

TABLE 19-1 Task list based on 14 CFR Part 23.

Paragraphs	Content	Section
14 CFR §23.2120[a]	Compliance with various climb gradients	19.2 and 19.3
14 CFR §23.2125[a]	Climb data that must be collected	19.3.1 and 19.3.2
14 CFR §23.63	General stipulations regarding the below paragraphs	19.2 and 19.3.1
14 CFR §23.65	Climb requirements with all engines operating	19.2 and 19.3.1
14 CFR §23.66	Take-off climb with one engine inoperative	19.2 and 19.3.1
14 CFR §23.67	Climb with one engine inoperative	19.2 and 19.3.1
14 CFR §23.69	En-route climb and descent	19.2 and 19.3.1
14 CFR §23.77	Balked landing	19.2 and 19.3.1
14 CFR 36	Noise Standards: Aircraft Type and Airworthiness Certification	19.3.2

[a] *"New" Part 23.*

TABLE 19-2 Task list for climb analysis.

Task name	Terms	Section
General rate-of-climb (ROC)	V_∞ and V_V	19.3.1
Best ROC for a jet	V_Y and V_{Vopt}	19.3.1(2)
Best ROC for a propeller	V_Y and V_{Vopt}	19.3.1(3)
General angle-of-climb (AOC)	V_∞ and γ	19.3.2
Best AOC for a jet	V_X and γ_{opt}	19.3.2(2)
Best AOC for a propeller	V_X and γ_{opt}	19.3.2(3)
Time to altitude	t	19.3.6
Service ceiling	h_{sc}	19.3.7
Absolute ceiling	h_{abs}	19.3.7
Optimum climb methods	Various	19.3.1, 19.3.2, 19.3.5

19.2 FUNDAMENTAL RELATIONS FOR THE CLIMB MANEUVER

This section presents basic mathematical relationships required to analyze the climb maneuver. A review of Section 7.1.3, *The Basics of Energy, Work, and Power* may be helpful before covering the following topics. Climb is the change in potential energy per unit time. Consider an airplane at altitude h_1 at time t_1 and h_2 at time t_2. The time rate-of-change in its potential energy can be written as

$$\frac{\Delta(PE)}{\Delta t}=\frac{mgh_2-mgh_1}{t_2-t_1}=W\frac{\Delta h}{\Delta t}$$
$$\Rightarrow \quad \frac{d(PE)}{dt}=P\dot{E}=W\left(\lim_{\Delta t\to 0}\frac{\Delta h}{\Delta t}\right)=WV_V \tag{19-1}$$

Where PE is potential energy, m is mass, g is gravitational acceleration, V_V is the vertical speed (climb speed), and $W=mg$. The expression shows the time rate-of-change of potential energy is the product WV_V: It *is* force × speed = power. The importance of this relationship becomes evident in Section 19.2.3.

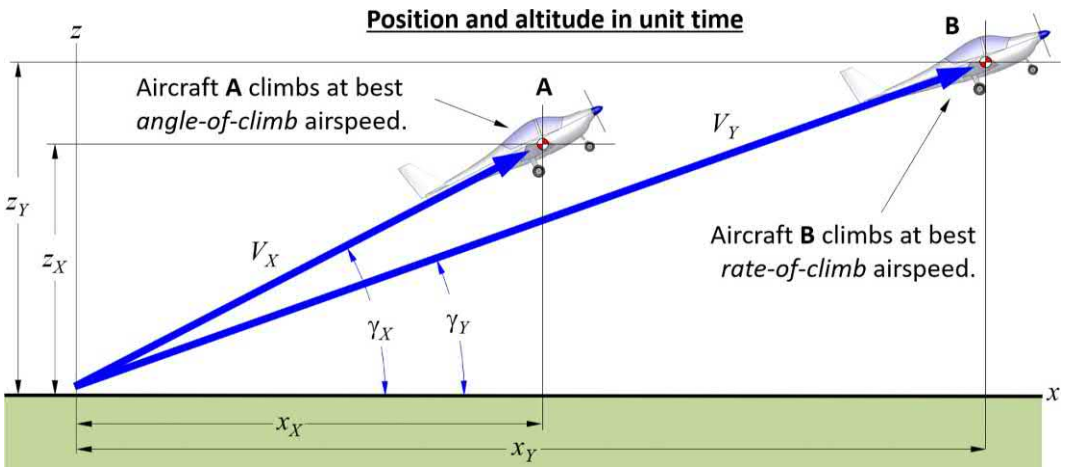


FIGURE 19-2 The consequence of climbing at V_X or V_Y for a unit time.

19.2.1 General Equations-of-Motion for Climb

The equations-of-motion for an aircraft in the horizontal and vertical planes were developed in Section 17.1.2, *Equations-of-Motion for Performance Theory*. These are presented as Miele's set of Equation (17-1). It is recommended the reader reviews these. Also review Figure 17-1. This set of equations is adapted to climb as Equation (19-2). The transformation assumes (1) the thrust angle $\varepsilon = 0$, (2) climb is conducted at constant airspeed, V_∞, so the time derivative terms are zero, and (3) constant flight path angle, $\gamma > 0$. Furthermore, let $W = mg$. This reduces Equation (17-1) as shown below

$$\begin{aligned} \dot{x} - V_\infty \cos\gamma &= 0 \\ \dot{h} - V_\infty \sin\gamma &= 0 \\ T\cos\varepsilon - D - m\left(g\sin\gamma + \dot{V}_\infty\right) &= 0 \\ T\sin\varepsilon + L - m(g\cos\gamma + V_\infty\dot{\gamma}) &= 0 \\ \dot{m}g + c_t T &= 0 \end{aligned} \quad \Rightarrow \quad \begin{aligned} \dot{x} - V_\infty \cos\gamma &= 0 \\ \dot{h} - V_\infty \sin\gamma &= 0 \\ T - D - W\sin\gamma &= 0 \\ L - W\cos\gamma &= 0 \\ \dot{W} + c_t T &= 0 \end{aligned} \tag{19-2}$$

(1) General Planar Equations-of-Motion of an Airplane

The top two equations of Equation (19-2) are translation relations. The next two equations are referred to as the *general planar equations-of-motion*. They are obtained by summing forces along the *t*- and *n*-axes. They assume no rotation about the binomial axis (see Figure 17-1).

$$T\cos\varepsilon - D - mg\sin\gamma = m\dot{V}_\infty \tag{19-3}$$

$$T\sin\varepsilon + L - mg\cos\gamma = mV_\infty\dot{\gamma} = m\dot{V}_V \tag{19-4}$$

(2) Equations-of-Motion for Climbing Flight

As shown above, Equation (19-2) is developed by adapting the planar equations-of-motion to a steady climb based on the stated assumptions. Thus, for a steady climb we get

$$T - D - W\sin\gamma = 0 \quad \Rightarrow \quad T - D = W\sin\gamma \tag{19-5}$$

$$L - W\cos\gamma = 0 \quad \Rightarrow \quad L = W\cos\gamma \tag{19-6}$$

Equation (19-6) shows that, in climb, lift is less than the weight. The difference is balanced by the vertical component of the thrust. The lift coefficient at this condition is thus:

$$C_L = \frac{2W\cos\gamma}{\rho V^2 S} = \frac{W}{qS}\cos\gamma \tag{19-7}$$

(3) Drag during Climb

Using the adjusted drag model,[1] the drag force is given by:

$$D = qS\left(C_{D_{\min}} + k(C_L - C_{L_{\min D}})^2\right) \tag{19-8}$$

Substitute Equation (19-7) into Equation (19-8) to get

$$D = qS\left(C_{D_{\min}} + k\left(\frac{W}{qS}\cos\gamma - C_{L_{\min D}}\right)^2\right) \tag{19-9}$$

Expanding leads to

$$D = qSC_{D_{\min}} + k\left(\left(\frac{W^2}{qS}\right)\cos^2\gamma - 2W\cos\gamma C_{L_{\min D}} + qSC_{L_{\min D}}^2\right) \tag{19-10}$$

Note that if $C_{L_{\min D}} = 0$ this becomes the simplified drag model

$$D = qSC_{D_{\min}} + k\left(\frac{W^2}{qS}\right)\cos^2\gamma \tag{19-11}$$

Note that drag, D, as calculated by Equation (19-10) or (19-11) should be used with Equations (19-17) and (19-19). This, however, requires an iterative scheme to

[1] See Section 16.2, *The Basics of Drag Modeling* for details, including definition of variables.

solve for ROC and γ. However, as demonstrated by Mair and Birdsall [8], assuming that $\cos\gamma \approx 1$ offers acceptable accuracy for modest climb angles. In particular, the error for GA aircraft is small, as their angle-of-climb is usually less than 15 degrees. According to Figure 4.1 of Ref. [8], at the best rate-of-climb airspeed, even an angle-of-climb of 20°, omitting the cosine will cause the result to deviate about 0.2° off the exact value. At $\gamma = 40°$ the deviation remains short of 1.0°. Assuming that $\cos\gamma \approx 1$ holds, results in considerable time savings in analysis work, with low difference from the exact method.

(4) Horizontal and Vertical Airspeed

Before developing the analysis methods of Section 19.3, first define the *Horizontal Airspeed*. It is important when estimating the horizontal distance covered during a long climb to altitude:

$$\dot{x} \equiv V_H = V_\infty \cos\gamma \tag{19-12}$$

Then it is possible to define the *Vertical Airspeed*, also called the *rate-of-climb* (ROC):

$$\dot{h} \equiv V_V = V_\infty \sin\gamma \tag{19-13}$$

Both can be derived by observation from Figure 19-3. Note that in terms of calibrated airspeed, V_∞ is the airspeed indicated on the airspeed indicator, V_V is observed on the *vertical speed indicator* (VSI), and V_H is the ground speed. Note that this V_H should not be confused with the maximum level airspeed to be discussed in this chapter.

19.2.2 Power Available, Power Required, and Excess Power

The *power available*, *power required*, and *excess power* are instrumental in defining the climb capability of the aircraft. The term *thrust-power* was defined in Section 15.3.8, *Propeller Efficiency*, as the product of thrust and speed. Thrust is *the* source of thrust-power in aircraft. It is also referred to as *power available* in performance theory. This contrasts the retarding power produced by the product of drag and velocity; the *required power*. We define *excess power* as the difference between these two, as shown below.

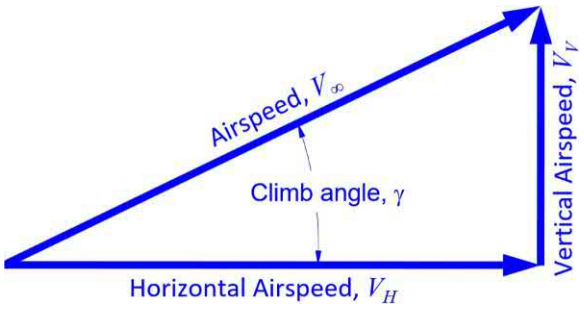


FIGURE 19-3 Airspeed components during climb.

Power available:

$$P_{AV} \equiv Force \times Speed = TV_\infty = \eta_p \cdot P_{ENG} \tag{19-14}$$

Power required:

$$P_{REQ} \equiv Force \times Speed = DV_\infty \tag{19-15}$$

Excess power:

$$P_{EX} \equiv P_{AV} - P_{REQ} \tag{19-16}$$

19.2.3 Vertical Air speed in Terms of Thrust or Power

Equation (19-1) shows that the product WV_V is the power associated with bringing the aircraft from altitude h_1 to h_2. This amounts to the difference between the power available (P_{AV}) and power required (P_{REQ}) for level flight at condition. Thus, the vertical airspeed can be estimated if the thrust and drag of the aircraft is known.

For jets:

$$V_V \equiv \frac{TV_\infty - DV_\infty}{W} = V_\infty \sin\gamma \tag{19-17}$$

For propellers:

$$V_V \equiv \frac{P_{AV} - P_{REQ}}{W} = \frac{\eta_p P_{ENG} - P_{REQ}}{W} = V_\infty \sin\gamma \tag{19-18}$$

Where η_p is propeller efficiency and P_{ENG} is engine power (in J/s or $ft\,lb_f/s$). The above expressions are some of the most important equations in the entire climb analysis methodology. Ultimately, we want to determine specific values of V_V, for instance the maximum value, or the one that results in the steepest climb possible, and so on. Knowing these are of great importance to the pilot and, as it turns out, also for the certifiability of the aircraft. Additionally, the formulation shows that in order for an airplane to increase its altitude, its thrust power (TV_∞) or available power (P_{AV}) must be larger than the drag power (DV_∞) or required power (P_{REQ}) for level flight.

DERIVATION OF EQUATION (19-17)

Multiply Equation (19-5) by V_∞/W to get:

$$\frac{V_\infty}{W}(T - D = W\sin\gamma) \;\Rightarrow\; T\frac{V_\infty}{W} - D\frac{V_\infty}{W} = \frac{V_\infty}{W}W\sin\gamma$$

$$\Rightarrow\; \frac{TV_\infty - DV_\infty}{W} = V_\infty \sin\gamma$$

DERIVATION OF EQUATION (19-18)

From Equation (19-17), we identify the product TV_∞ as the power available and DV_∞ as the power required. It follows that

$$\frac{TV_\infty - DV_\infty}{W} = \frac{P_{AV} - P_{REQ}}{W} = \frac{\eta_p P_{ENG} - P_{REQ}}{W} = V_\infty \sin\gamma$$

19.2.4 Rate-of-Climb

The rate-of-climb (ROC) is of great importance to the pilot as well as a superb indicator of the airplane's capability as it is directly dependent on its thrust and drag characteristics. If the thrust and drag can be quantified at a flight condition, the instantaneous ROC in units of ft/min (or fpm) can be calculated as follows:

$$V_V \equiv 60\left(\frac{TV_\infty - DV_\infty}{W}\right) = 60\left(\frac{P_{AV} - P_{REQ}}{W}\right) \qquad (19\text{-}19)$$

NOTE 1

The units for ROC in Equation (19-17) are commonly ft/min or fpm. This is why we multiply it by 60 to convert the ROC in ft/s into fpm.

NOTE 2

In the SI system ROC is usually in terms of m/s, rendering the factor 60 unnecessary. The reader must be aware of the difference in the representation of time between the UK and SI systems.

NOTE 3

Unless otherwise specified the ROC is in fpm. It is also possible that the ROC is given in ft/s.

(1) Important Climb Parameters

The following parameters are of primary importance in climb analysis:

Best rate-of-climb	Is the maximum rate at which an aircraft can increase its altitude assuming constant airspeed V_∞.
Best angle-of-climb	Is the steepest gradient (see Figure 19-4) an aircraft can achieve assuming constant airspeed V_∞.
Best rate-of-climb airspeed	The airspeed, V_∞, at which the best rate-of-climb is achieved. It is usually denoted as V_Y. For pilot operation it is typically identified as calibrated airspeed (CAS), e.g., KCAS.
Best angle-of-climb airspeed	The airspeed, V_∞, at which the best angle-of-climb is achieved. It is usually denoted as V_X. For pilot operation it is typically identified as calibrated airspeed (CAS), e.g., KCAS.

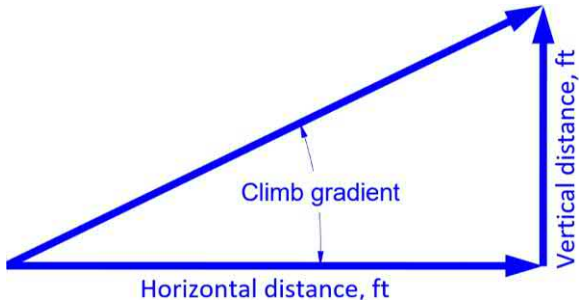


FIGURE 19-4 Distance components during climb.

(2) Climb Gradient

Climb is sometimes expressed in terms of % climb gradient. For instance, 14 CFR Part 23 refers to climb gradients in lieu of fpm or m/s. This places the regulatory requirements in a form applicable to all aircraft. The concept assumes no wind and is defined as follows (see Figure 19-4):

$$\text{Climb Gradient} = \frac{\text{Rise}}{\text{Run}} = \frac{\text{Rise}/\Delta t}{\text{Run}/\Delta t} = \frac{\dot{h}}{\dot{x}} = \tan\gamma \qquad (19\text{-}20)$$

From which we get that

$$V_V = V_\infty \sin\left(\tan^{-1}(\gamma)\right) \qquad (19\text{-}21)$$

Consider an airplane whose climb gradient is 0.1 at ground speed $V_{GS} = 100$ KTAS (nm/h) in no wind conditions. Its rate-of-climb in fpm is

$$V_V \approx 0.1 \times \frac{100 \text{ nm/h}}{60 \text{ min/h}} \times 6076 \text{ ft/nm} = 1013 \text{ ft/min}$$

Consider an airplane whose climb gradient is 0.1 at airspeed $V_\infty = 100$ KTAS (nm/h) in no wind conditions. Its rate-of-climb in fpm is

$$V_V = \left[\frac{100 \text{ nm/h}}{60 \text{ min/h}} \times 6076 \text{ ft/nm}\right] \times \sin\left(\tan^{-1}(0.1)\right) = 1008 \text{ ft/min}$$

19.3 GENERAL CLIMB ANALYSIS METHODS

Armed with the equation-of-motion, we can evaluate the climb characteristics of a new aircraft design. In this section, a number of methods to estimate the most important climb properties of the aircraft are introduced. These methods primarily include the simplified and adjusted drag models ($C_{L_{minD}} \neq 0$). For an insight into the quality of analysis these models provide, see Section 20.2.2(11), *Fundamental Concepts*.

19.3.1 General Expression for Rate-of-Climb

A general expression for estimating the ROC based on thrust-to-weight ratio and wing loading is presented in

this section. It is handy for evaluating general climb performance. It is presented for the simplified and adjusted drag models and assumes a small flight path angle, γ. This justifies cos γ≈1, although γ is carried through in the derivation below. The expression returns the vertical airspeed in terms of ft/s or m/s. Using the simplified drag model, it is computed from:

$$V_V = V_\infty \sin\gamma = V_\infty \left(\frac{T}{W} - \frac{qC_{D_{\min}}}{(W/S)} - \frac{k}{q}\left(\frac{W}{S}\right) \right) \tag{19-22}$$

Using the adjusted drag model, it is computed using:

$$V_V = V_\infty \sin\gamma = V_\infty \left(\frac{T}{W} - \frac{q}{(W/S)}\left(C_{D_{\min}} + kC_{L_{\min D}}^2\right) - \left(\frac{W}{S}\right)\frac{k}{q} + 2kC_{L_{\min D}}) \right) \tag{19-23}$$

DERIVATION OF EQUATIONS (19-22) AND (19-23)

Substitute Equations (19-10) and (19-11) into (19-17) and manipulate algebraically, as shown:

$$V_\infty \sin\gamma = \frac{TV_\infty - DV_\infty}{W} = \frac{T}{W}V_\infty - \frac{1}{W}V_\infty$$

$$\left(qSC_{D_{\min}} + k\left(\left(\frac{W^2}{qS}\right)\cos^2\gamma - 2W\cos\gamma C_{L_{\min D}} + qSC_{L_{\min D}}^2 \right) \right)$$

$$= V_\infty \left[\frac{T}{W} - \left(qS\frac{1}{W}C_{D_{\min}} + k\left(\frac{1}{W}\left(\frac{W^2}{qS}\right)\cos^2\gamma - 2W\frac{1}{W}\cos\gamma C_{L_{\min D}} + qS\frac{1}{W}C_{L_{\min D}}^2 \right) \right) \right]$$

$$= V_\infty \left[\frac{T}{W} - \left(\frac{qC_{D_{\min}}}{W/S} + k\left(\left(\frac{W}{S}\right)\frac{\cos^2\gamma}{q} - 2\cos\gamma C_{L_{\min D}} + \frac{qC_{L_{\min D}}^2}{W/S} \right) \right) \right]$$

Thus, we get

$$V_\infty \sin\gamma = V_\infty \left(\frac{T}{W} - \frac{q}{(W/S)}\left(C_{D_{\min}} + kC_{L_{\min D}}^2\right) - \left(\frac{W}{S}\right)\frac{k\cos^2\gamma}{q} + 2k\cos\gamma C_{L_{\min D}}) \right) \tag{19-24}$$

This expression is generally simplified as follows: (1) Substituting cos γ≈1 and simplifying leads to Equation (19-23). (2) Substituting $C_{L_{\min D}}=0$ into Equation (19-23) yields Equation (19-22).

EXAMPLE 19-1

Determine the vertical airspeed for the sample aircraft (Learjet 45) flying at 250 KCAS at S-L at thrust of 4635 lb_f (per Section 14.3.4, *Mattingly Model for a Turbofan Engine* for a low bypass ratio turbofan) and at a weight of 21,500 lb_f. For simplicity, assume the simplified drag model and use the parameters of Table 17-8. Compare to Figure 19-5, which plots rate-of-climb versus airspeed for three altitudes, using the adjusted drag model, modified using high- and low-speed splines (see Chapter 16).

SOLUTION:

Dynamic pressure:

$$q = \frac{1}{2}\rho V_\infty^2 = \frac{1}{2}(0.002378)(250\times 1.688)^2 = 211.7\ lb_f/ft^2$$

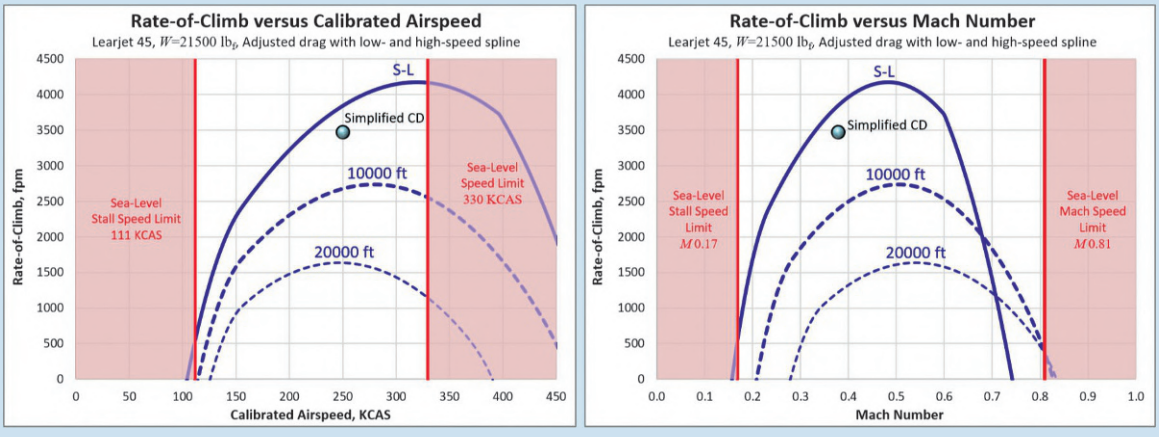


FIGURE 19-5 Excess power and rate-of-climb at three altitudes.

EXAMPLE 19-1 (*cont'd*)

Insert and evaluate the rate-of-climb at the condition:

$$V_\infty \sin\gamma = V_\infty\left(\frac{T}{W}-\frac{qC_{D_{\min}}}{(W/S)}-\frac{k}{q}\left(\frac{W}{S}\right)\right)$$
$$=(250\times 1.688)\left(\frac{4635}{21500}-\frac{(211.7)}{(21,500/311.6)}(0.0200)\right.$$
$$\left.-\left(\frac{21,500}{311.6}\right)\frac{0.05236}{(211.7)}\right)=57.9\,\text{ft/s}$$

This amounts to 3472 fpm. This value (using the label "Simplified CD") is plotted in Figure 19-5 against the adjusted drag model. It returns a dissimilar result.

19.3.2 General Expression for Angle-of-Climb

The climb angle is of great importance when comes to obstruction clearance, or when showing compliance to noise regulations per 14 CFR Part 36, as well as evaluation of deck angle during climb. Using the simplified drag model, an expression for the climb angle is obtained from Equation (19-22) by dropping V_∞ on either side of the equal sign.

$$\sin\gamma=\frac{T}{W}-\frac{qC_{D_{\min}}}{(W/S)}-\frac{k}{q}\left(\frac{W}{S}\right) \tag{19-5}$$

Using the adjusted drag model, such an expression is obtained using Equation (19-23)

$$\sin\gamma=\frac{T}{W}-\frac{q}{(W/S)}\left(C_{D_{\min}}+kC_{L_{\min D}}^2\right)-\left(\frac{W}{S}\right)\frac{k}{q}+2kC_{L_{\min D}} \tag{19-26}$$

The angle-of-climb can also be related to the thrust-to-weight and lift-to-drag ratio as follows:

$$\sin\gamma=\frac{T}{W}-\frac{1}{L/D} \tag{19-27}$$

DERIVATION OF EQUATION (19-27)

Divide with V_∞ on either side of Equation (19-17):

$$V_\infty\sin\gamma=\frac{TV_\infty-DV_\infty}{W}$$
$$\Rightarrow\quad \sin\gamma=\frac{T-D}{W}\approx\frac{T}{W}-\frac{D}{L}=\frac{T}{W}-\frac{1}{L/D}$$

EXAMPLE 19-2

Determine the angle of climb for the sample aircraft flying at 250 KCAS at S-L at thrust of 5045 lb_f and at a weight of 20,000 lb_f.

SOLUTION:

Using the same dynamic pressure as in Example 19-1.

$$\sin\gamma=\frac{T}{W}-q\left(\frac{S}{W}\right)C_{D_{\min}}-\frac{k}{q}\left(\frac{W}{S}\right)$$
$$=\frac{5045}{20,000}-(211.7)\left(\frac{311.6}{20,000}\right)(0.0234)-\frac{(0.05236)}{(211.7)}\left(\frac{20,000}{311.6}\right)$$
$$=0.1592\,\text{rad}\quad(=9.12^\circ)$$

19.3.3 Formulation of Best (Maximum) Rate-of-Climb

This section presents formulation to estimate the maximum rate at which an aircraft ascends. Figure 19-5 shows how the ROC for aircraft trends with airspeed. Its maximum value is called the *best rate-of-climb*, denoted by V_{Vopt}. It is realized at one and only one airspeed called the *best rate-of-climb airspeed* (denoted by V_Y). This airspeed is important for it allows aircraft to reach cruise altitude with the least amount of fuel consumed (see Section 19.3.5, *Formulation of Specific Optimal Climb Problems*).

(1) General Treatment of the Best Rate-of-Climb Problem

Estimating V_Y and the associated V_{Vopt} is not as straight forward as one might think. The problem is compounded by aircraft-specific expressions for thrust and drag. Classical analytical solutions, such as those presented in this section, rely on substantial simplifications. They assume constant power or thrust and use the simplified drag model. This limits their usefulness to initial estimates only. Improved accuracy in output requires improved accuracy in input. The designer interested in greater accuracy can follow the two procedures given below.

Procedure 1: Analytical Approach

First, consider the methods of Chapters 14–16 for a more detailed modeling of thrust and drag in terms of airspeed, V_∞. Note that most engines allow thrust to be modeled using piecewise polynomials. Substitute the resulting functions, $T(V_\infty)$ and $D(V_\infty)$, into Equation (19-17). Next, differentiate and set the derivative equal to zero. Solve

the resulting expression for the optimum airspeed. Finally, substitute the optimum speed into Equation (19-23) (or Equation 19-22) to estimate the rate-of-climb. This approach is summarized below.

$$V_V = \frac{TV_\infty - DV_\infty}{W} \Rightarrow \frac{\partial(TV_\infty - DV_\infty)}{\partial V_\infty} = 0 \quad (19\text{-}28)$$
$$\Rightarrow V_Y \Rightarrow V_{Vopt}$$

A simple example of this process that uses a quadratic polynomial for thrust (T) and the simplified drag model (D) is presented below. Let T and D be defined as

$$T \equiv AV_\infty^2 + BV_\infty + C \quad \text{and}$$
$$D \equiv \frac{1}{2}\rho V_\infty^2 S C_D = \frac{1}{2}\rho V_\infty^2 S\left(C_{D_{\min}} + kC_L^2\right) \quad (19\text{-}29)$$

Substitute the lift coefficient into the expression for drag and expand

$$D = \frac{1}{2}\rho V_\infty^2 S C_{D_{\min}} + \frac{2kW^2}{\rho V_\infty^2 S} \quad (19\text{-}30)$$

Substitute these into Equation (19-17). This leads to

$$V_V = \frac{TV_\infty - DV_\infty}{W} = \frac{1}{W}\left(AV_\infty^3 + BV_\infty^2 + CV_\infty - \frac{1}{2}\rho V_\infty^3 S C_{D_{\min}} - \frac{2kW^2}{\rho V_\infty^2 S}\right)$$

Differentiate with respect to V_∞ and set equal to zero

$$\frac{\partial V_V}{\partial V_\infty} = \left(3AV_\infty^2 + 2BV_\infty + C - \frac{3}{2}\rho V_\infty^2 S C_{D_{\min}} + \frac{2kW^2}{\rho S V_\infty^2}\right) = 0 \quad (19\text{-}31)$$

This leads to the following quartic equation, whose solution gives the best rate-of-climb airspeed, V_Y:

$$\Rightarrow \left(3A - \frac{3}{2}\rho S C_{D_{\min}}\right)V_Y^4 + 2BV_Y^3 + CV_Y^2 + \frac{2kW^2}{\rho S} = 0 \quad (19\text{-}32)$$

Procedure 2: Numerical Approach

Refers to the method detailed in Section 19.3.7, *Numerical Analysis of the Climb Maneuver*. It is this author's favorite. It is ideal for spreadsheets or computer codes. It permits Class 1 drag models, consisting of higher order polynomials, cubic- or B-splines, and look-up tables. Similar refinement of thrust models is also possible.

EXAMPLE 19-3

Estimate the V_Y and V_{Vopt} for the Cessna C-162 Skycatcher of Example 3-1 at 8000 ft, using the quadratic thrust model of Section 15.4.3, *Initial Thrust Model for a Fixed-Pitch Propeller*. Assume $T_{STATIC} = 360.4\,\text{lb}_\text{f}$, $T_{opt} = 159.6\,\text{lb}_\text{f}$, and $V_{opt} = 195.8\,\text{ft/s}$.

SOLUTION:

From Example 3-1, $C_{D_{\min}} = 0.0333$, $k = 0.04909$, $S = 120\,\text{ft}^2$, and $W = 1320\,\text{lb}_\text{f}$. Also, $\rho = 0.001869\,\text{slugs/ft}^3$. The thrust model is of the form $T(V_\infty) = AV_\infty^2 + BV_\infty + C$, per Equation (15-60) where the coefficients are calculated as follows, using Equations (15-61) through (15-63)

$$A = \left(T_{STATIC} - 2T_{opt}\right)/V_{opt}^2 = (360.4 - 2(159.6))/(195.8)^2$$
$$= 0.0001073\ \text{lb}_\text{f}\text{s}^2/\text{ft}^2$$
$$B = \left(3T_{opt} - 2T_{STATIC}\right)/V_{opt}$$
$$= (3(159.6) - 2(360.4))/(195.8) = -1.2354\ \text{lb}_\text{f}\text{s/ft}$$
$$C = T_{STATIC} = 360.4\ \text{lb}_\text{f}$$

Note that unit consistency is vital in this method and, here, using airspeed in ft/s rather than KTAS is more practical. Therefore, we do not use the thrust model in Example 15-11, whose coefficients are based on KTAS. Next, substitute all the applicable parameters into Equation (19-32), which becomes

$$\left(3A - \frac{3}{2}\rho S C_{D_{\min}}\right)V_Y^4 + 2BV_Y^3 + CV_Y^2 + \frac{2kW^2}{\rho S} = 0$$
$$\Rightarrow -0.007985V_Y^4 - 2.4707V_Y^3 + 360.4V_Y^2 + 762{,}697 = 0$$

The quartic equation can be solved by various method, for instance, Regula Falsi or the bi-section method. It is also easy to solve in Microsoft Excel, using its "Goal Seek" feature. Note that it returns V_Y as true airspeed. For this problem $V_Y = 120.4\,\text{ft/s}$ ($\approx 71.3\,\text{KTAS}$), which is 63.2 KCAS. Even using the simplified drag model, it is in good agreement with the published value of 63 KCAS, per Ref. [9]. Then, estimate ROC using Equation (19-22) and the following parameters, calculated at V_Y: $T = 227.3\,\text{lb}_\text{f}$ and $q = 13.54\,\text{lb}_\text{f}/\text{ft}^2$.

$$V_{Vopt} = V_Y\left(\frac{T}{W} - \frac{qC_{D_{\min}}}{(W/S)} - \frac{k}{q}\left(\frac{W}{S}\right)\right)$$
$$= (120.4)\left(\frac{227.3}{1320} - \frac{(13.54)(0.0333)}{(1320/120)} - \frac{0.04909}{13.54}\left(\frac{1320}{120}\right)\right)$$
$$= 10.99\ \text{fpm}$$

This amounts to 659 fpm and compares less favorably to the published value of 450 fpm, per Ref. [9].

(2) Best Rate-of-Climb for a Jet Aircraft

For jets, the value of V_{Vopt} can be computed from the following expression. It assumes the simplified drag model and constant thrust.

$$V_{Vopt} = \sqrt{\frac{(W/S)Z}{3\rho C_{D_{\min}}}}\left(\frac{T}{W}\right)^{3/2}\left(1 - \frac{Z}{6} - \frac{3}{2(T/W)^2 L D_{\max}^2 Z}\right) \quad (19\text{-}33)$$

Again, we must determine the airspeed of best rate-of-climb, V_Y. For a jet, it can be computed from the expression below that assumes the simplified drag model and constant thrust:

$$V_Y = \sqrt{\frac{(T/W)(W/S)}{3\rho C_{D_{\min}}}\left[1+\sqrt{1+\frac{3}{LD_{\max}^2(T/W)^2}}\right]} \quad (19\text{-}34)$$

This formulation can also be used to estimate the best rate-of-climb airspeed for a multiengine aircraft suffering a *one engine inoperative* (OEI) condition. That airspeed is denoted by V_{YSE}. Of course, the thrust must be reduced by the contribution of the failed engine and the minimum drag $C_{D_{\min}}$ must reflect the attitude of the airplane necessary to fly straight and level. Also, $LD_{\max}$ must be recalculated as it is reduced at this condition.

EXAMPLE 19-4

Determine the airspeed for maximum rate-of-climb for the Learjet 45 at S-L at a weight of 20,000 lb_f. Assume the thrust is that which is given in Example 19-1 (4635 lb_f).

SOLUTION:

Step 1: Determine $LD_{\max}$

$$LD_{\max} = \frac{1}{\sqrt{4(0.0200)(0.05236)}} = 15.45 \;\Rightarrow\; LD_{\max}^2 = 238.7$$

Step 2: Determine T/W and W/S

$$\frac{T}{W} = \frac{4635}{20{,}000} = 0.2318 \text{ and } \frac{W}{S} = \frac{20{,}000}{311.6} = 64.2\ \text{lbf/ft}^2$$

Step 3: Best rate-of-climb speed is therefore:

$$V_Y = \sqrt{\frac{(T/W)(W/S)}{3\rho C_{D_{\min}}}\left[1+\sqrt{1+\frac{3}{LD_{\max}^2(T/W)^2}}\right]}$$

$$= \sqrt{\frac{(0.2523)(64.2)}{3(0.002378)(0.0200)}\left[1+\sqrt{1+\frac{3}{(238.7)(0.2523)^2}}\right]}$$

$$= 469.1\ \text{ft/s} \quad (\approx 278\ \text{KCAS})$$

Note that since our thrust varies with airspeed (see Example 19-1), we must verify thrust is indeed 4635 lb_f (that value is associated with 250 KCAS). It is not so. Rather, at $V_Y = 278$ KCAS it is $T = 4743\ lb_f$. This implies that V_Y is a hair higher. Thus, we must iteratively recalculate Step 2 and 3, until the resulting V_Y no longer yields T different from the one we use to calculate T/W. Performing such an iteration led to $V_Y = 281$ KCAS. Note that these values are well above the 250 KCAS airspeed limit at altitudes below 10,000 ft (per 4 CFR §91.117).

(3) Best Rate-of-Climb for a Propeller-Powered Aircraft

For propeller-powered aircraft, V_{Vopt} can be computed from the following expression. It assumes the simplified drag model and constant engine power, P_{ENG}.

$$V_{Vopt} = \frac{\eta_p P_{ENG}}{W} - \sqrt{\frac{2}{\rho}\left(\frac{W}{S}\right)\sqrt{\frac{k}{3\cdot C_{D_{\min}}}}\frac{1.1547}{LD_{\max}}} \quad (19\text{-}35)$$

This method also assumes the *best rate-of-climb airspeed*, V_Y, equals that of *minimum power required* when using the simplified drag model.

$$V_Y = V_{TR_{\min}} = \sqrt{\frac{2}{\rho}\left(\frac{W}{S}\right)\sqrt{\frac{k}{3C_{D_{\min}}}}} \quad (19\text{-}36)$$

If using the adjusted drag model, it is given by

$$V_Y = \sqrt{\frac{2}{\rho}\left(\frac{W}{S}\right)\frac{\sqrt{k}}{\sqrt{3C_{D_{\min}} + 4kC_{L_{\min D}}^2} - \sqrt{k}C_{L_{\min D}}}} \quad (19\text{-}37)$$

These equations are derived in Sections 20.3.6 and 20.3.8. As shown in Figure 19-6, the assumptions have their limitations, so use the method with caution.

Figure 19-6 plots the available and required power versus calibrated airspeed for a typical small LSA. A realistic power curve is coplotted for comparison. The above assumptions land the V_Y at 45 KCAS, versus 63 KCAS for the realistic thrust (per Section 15.4.3, *Initial Thrust Model for a Fixed-Pitch Propeller*). The "realistic V_Y" is far closer to published values for aircraft in this class (around 62 ± 5 KCAS. Also see Eq- 3.3).

If V_Y is known and its value is desired in fpm, it can be calculated from:

$$V_{Vopt} = 60\left(\frac{\eta_p P_{ENG}}{W} - V_Y\frac{1.1547}{LD_{\max}}\right) \quad (19\text{-}38)$$

Note that P_{ENG} must be in terms of ft·lb_f/s in the UK-system and watts in the SI-system. If power is given in horsepower, it must be multiplied by the factor 550 to be converted to the proper units.

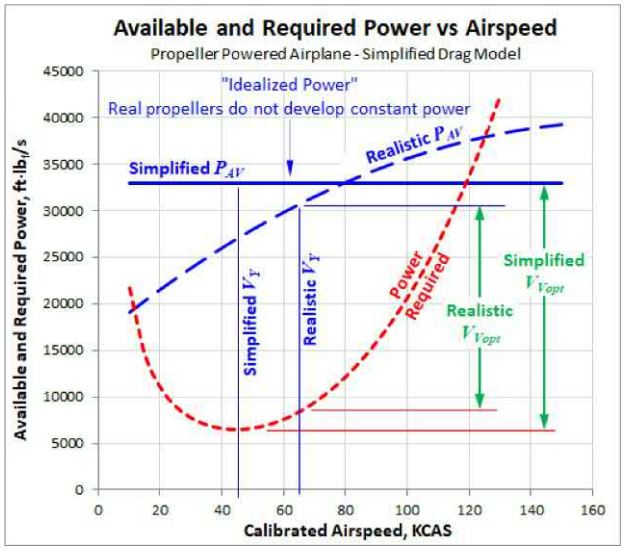


FIGURE 19-6 Power-available and power-required for a propeller powered airplane.

EXAMPLE 19-5

Since Equation (19-36) is based on the simplified drag model, it is of interest to evaluate its accuracy for a real airplane. Here, estimate V_Y for the SR22 at a weight of 3400 lb_f at S-L and 10,000 ft. Compare to the POH value (V_Y = 101 KCAS at S-L and 96 KCAS at 10,000 ft). Use the minimum drag coefficient extracted for the airplane in Example 16-18 ($C_{D_{min}} = 0.02541$), $S = 144.9\ ft^2$, $AR = 10$, and $e = 0.7566$.

SOLUTION:

The density of air at S-L is 0.002378 slugs/ft^3 and at 10,000 ft it is 0.001756 slugs/ft^3. Also, the lift-induced drag constant $k = 1/(\pi \cdot AR \cdot e) = 0.04207$. Next, calculate the V_Y by substituting these values into Equation (19-36), first at S-L as follows:

$$V_Y = \sqrt{\frac{2}{\rho}\left(\frac{W}{S}\right)\sqrt{\frac{k}{3 \cdot C_{D_{min}}}}}$$

$$= \sqrt{\frac{2}{0.002378}\left(\frac{3400}{144.9}\right)\sqrt{\frac{0.04207}{3(0.02541)}}} = 121.1 \text{ ft/s}$$

$$= 71.7 \text{ KCAS}$$

And then at 10,000 ft:

$$V_Y = \sqrt{\frac{2}{0.001756}\left(\frac{3400}{144.9}\right)\sqrt{\frac{0.04207}{3 \times 0.02541}}} = 140.9 \text{ ft/s}$$

$$= 83.5 \text{ KTAS}$$

This also amounts to 71.7 KCAS, which contrasts 101 KCAS at S-L and 96 KCAS at 10,000 ft for the real aircraft. It can be seen that the underlying assumptions render a poor agreement with experiment and the reader must recognize this shortcoming.

EXAMPLE 19-6

It is also of interest to evaluate the accuracy of Equation (19-38), similar to that done in Example 19-5. Here, determine the V_{Vopt} for the SR22 at a weight of 3400 lb_f at S-L and compare to the POH value (V_{Vopt} = 1398 fpm at S-L). Use the same parameters used in Example 19-5, but calculate and compare for three propeller efficiencies, $\eta_p = 0.6$, 0.7, and 0.8, to bracket the true (but unknown) η_p. The maximum engine power at S-L is 310 BHP. Here, use the value of V_Y determined in Example 19-5, even though it has been shown to be incorrect.

SOLUTION:

The rate-of-climb will only be calculated using the first propeller efficiency, but the results for the other two will be shown. First, calculate the ROC at S-L assuming $\eta_p = 0.6$:

$$V_{Vopt} = 60\left(\frac{\eta_p P_{ENG}}{W} - V_Y \frac{1.1547}{LD_{max}}\right)$$

$$= 60\left(\frac{0.6 \times 550 \times 310}{3400} - 121.1\frac{1.1547}{15.6}\right) = 1267 \text{ fpm}$$

Results for the other values of the propeller efficiency over a range of "hypothetical" best rate-of-climb airspeeds are plotted in Figure 19-7. It indicates the propeller is a little over 70% efficient during climb. It also shows considerable discrepancy between the predicted and experimental V_Y for the airplane. This is the risk of using the simplified drag model—it is convenience versus precision.

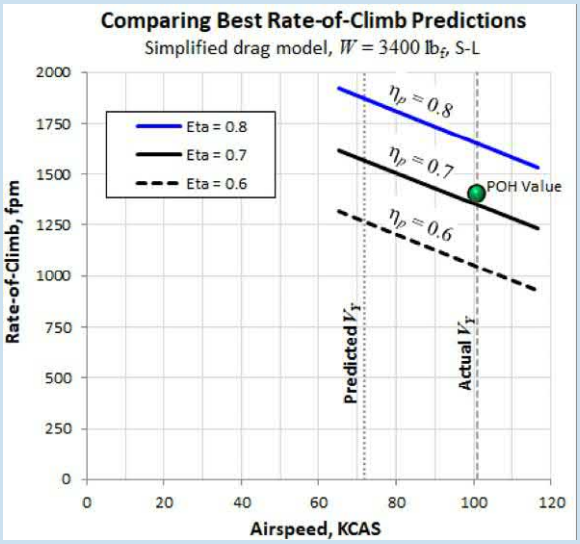


FIGURE 19-7 Best ROC (fpm) as a function of airspeed (KCAS) and propeller efficiency.

DERIVATION OF EQUATION (19-33)

The equation for the best ROC is obtained by substituting V_Y from Equation (19-34) into Equation (19-22). To simplify the resulting expression, let us first define the variable Z such that:

$$Z = 1 + \sqrt{1 + \frac{3}{LD_{max}^2 (T/W)^2}} \quad \text{(i)}$$

Then, Eq. (19.34) becomes: $$V_Y = \sqrt{\frac{(T/W)(W/S)Z}{3\rho C_{D_{min}}}} \quad \text{(ii)}$$

Then, substitute Equation (ii) into Equation (19-22) in a form that includes cos γ:

$$V_Y \sin\gamma = V_Y\left(\frac{T}{W} - \frac{qC_{D_{\min}}}{(W/S)} - \frac{k}{q}\left(\frac{W}{S}\right)\cos^2\gamma\right)$$

This results in:

$$V_{Vopt} = \sqrt{\frac{(T/W)(W/S)Z}{3\rho C_{D_{\min}}}}\left(\frac{T}{W} - \frac{1}{2}\rho\left(\frac{(T/W)(W/S)Z}{3\rho C_{D_{\min}}}\right)\left(\frac{S}{W}\right)C_{D_{\min}} - 2k\left(\frac{W}{S}\right)\frac{\cos^2\gamma}{\rho\dfrac{(T/W)(W/S)Z}{3\rho C_{D_{\min}}}}\right)$$

Simplifying yields:

$$V_{Vopt} = \sqrt{\frac{(T/W)(W/S)Z}{3\rho C_{D_{\min}}}}\left(\frac{T}{W} - \frac{Z}{6}\frac{T}{W} - \frac{6kC_{D_{\min}}\cos^2\gamma}{(T/W)Z}\right) \quad \text{(iii)}$$

Recall Equation (20-33) for $LD_{\max}$: $4C_{D_{\min}}k = 1/LD^2_{\max}$

Use this to modify the last term of Equation (iii), noting the following arithmetic scheme: $6 = 12/2 = 4\cdot 3/2 = (3/2)\cdot 4$:

$$\frac{6kC_{D_{\min}}\cos^2\gamma}{(T/W)Z} = \frac{(T/W)}{(T/W)^2}\frac{(3/2)(4kC_{D_{\min}})\cos^2\gamma}{Z} = \frac{3T/W}{2(T/W)^2}\frac{\cos^2\gamma}{LD^2_{\max}Z} \quad \text{(iv)}$$

Substitute this into Equation (iii) and rewrite:

$$V_{Vopt} = \sqrt{\frac{(T/W)(W/S)Z}{3\rho C_{D_{\min}}}}\left(\frac{T}{W} - \frac{Z}{6}\frac{T}{W} - \frac{3T/W}{2(T/W)^2}\frac{\cos^2\gamma}{LD^2_{\max}Z}\right)$$

Rearranging:

$$V_{Vopt} = \sqrt{\frac{(W/S)Z}{3\rho C_{D_{\min}}}}\sqrt{\frac{T}{W}}\left(\frac{T}{W} - \frac{Z}{6}\frac{T}{W} - \frac{3T/W}{2(T/W)^2}\frac{\cos^2\gamma}{LD^2_{\max}Z}\right)$$

Bringing T/W out of the parenthesis and assuming small angles of climb (so $\cos\gamma \approx 1$) yields Equation (19-33).

DERIVATION OF EQUATION (19-34)

The general rate-of-climb (V_V) is given by Equation (19-22). Write the dynamic pressure explicitly ($q = \frac{1}{2}\rho V^2_\infty$) and differentiate (using the product rule of Calculus) with respect to V_∞, as follows:

$$\frac{d(V_V)}{dV_\infty} = \frac{d(V_\infty)}{dV_\infty}\left(\frac{T}{W} - \frac{1}{2}\rho V^2_\infty\frac{C_{D_{\min}}}{(W/S)} - \left(\frac{W}{S}\right)\frac{2k}{\rho V^2_\infty}\right) + V_\infty\frac{d}{dV_\infty}\left(\frac{T}{W} - \frac{1}{2}\rho V^2_\infty\frac{C_{D_{\min}}}{(W/S)} - \left(\frac{W}{S}\right)\frac{2k}{\rho V^2_\infty}\right)$$

Manipulating algebraically;

$$\frac{d(V_V)}{dV_\infty} = \left(\frac{T}{W} - \frac{1}{2}\rho V^2_\infty\frac{C_{D_{\min}}}{(W/S)} - \left(\frac{W}{S}\right)\frac{2k}{\rho V^2_\infty}\right) + V_\infty\left(-\rho V_\infty\frac{C_{D_{\min}}}{(W/S)} + 2\left(\frac{W}{S}\right)\frac{2k}{\rho V^3_\infty}\right)$$

$$= \frac{T}{W} - \frac{1}{2}\rho V^2_\infty\frac{C_{D_{\min}}}{(W/S)} - \left(\frac{W}{S}\right)\frac{2k}{\rho V^2_\infty} - \rho V^2_\infty\frac{C_{D_{\min}}}{(W/S)} + 2\left(\frac{W}{S}\right)\frac{2k}{\rho V^2_\infty} \quad \text{(i)}$$

$$\Rightarrow \frac{d(V_V)}{dV_\infty} = \frac{T}{W} - \frac{3}{2}\rho V^2_\infty\frac{C_{D_{\min}}}{(W/S)} + \left(\frac{W}{S}\right)\frac{2k}{\rho V^2_\infty}$$

The optimum is found when the derivative is zero. Set the result to zero and multiply Equation (i) by V^2_∞ to get

$$\frac{3}{2}\rho\frac{C_{D_{\min}}}{(W/S)}V^4_\infty - \frac{T}{W}V^2_\infty - \left(\frac{W}{S}\right)\frac{2k}{\rho} = 0 \quad \text{(ii)}$$

Then, divide through by the constant multiplied to V^4_∞:

$$V^4_\infty - \frac{2}{3}\frac{T}{\rho SC_{D_{\min}}}V^2_\infty - \frac{4}{3}\left(\frac{W}{S}\right)^2\frac{k}{\rho^2 C_{D_{\min}}} = 0 \quad \text{(iii)}$$

Note that the last term resembles the expression for $LD_{\max}$ (see Equation 20-33):

$$LD_{\max} = \frac{1}{\sqrt{4C_{D_{\min}}k}} \quad \Leftrightarrow \quad 4C_{D_{\min}}k = \frac{1}{LD^2_{\max}}$$

Substitute into Equation (iii):

$$V^4_\infty - \frac{2}{3}\frac{T}{\rho SC_{D_{\min}}}V^2_\infty - \left(\frac{W}{S}\right)^2\frac{1}{3\rho^2 C^2_{D_{\min}}LD^2_{\max}} = 0 \quad \text{(iv)}$$

Rewrite Equation (iv), noting that $T/S = (T/W)(W/S)$:

$$V^4_\infty - \frac{2}{3}\frac{(T/W)(W/S)}{\rho C_{D_{\min}}}V^2_\infty - \left(\frac{W}{S}\right)^2\frac{1}{3\rho^2 C^2_{D_{\min}}LD^2_{\max}} = 0 \quad \text{(v)}$$

For convenience define the variables Q and x as follows:

$$Q \equiv \frac{W/S}{3\rho C_{D_{\min}}} \quad \text{and} \quad x \equiv V^2_\infty$$

Substitute into Equation (v)

$$x^2 - 2\frac{T}{W}Qx - \frac{3Q^2}{LD^2_{\max}} = 0 \quad \text{(vi)}$$

This is a quadratic equation in terms of x (or V^2_∞) whose solution is given by:

$$x = \frac{2(T/W)Q \pm \sqrt{4(T/W)^2Q^2 + 12Q^2/LD^2_{\max}}}{2} \quad \text{(vii)}$$

Factor out $(T/W)Q$ out of the radical to get:

$$x=\frac{T}{W}Q\pm\frac{T}{W}Q\sqrt{1+3/\left(LD^2_{\max}(T/W)^2\right)} \quad \text{(viii)}$$

$$\text{or:}\quad x=\frac{T}{W}Q\left[1\pm\sqrt{1+3/\left(LD^2_{\max}(T/W)^2\right)}\right] \quad \text{(ix)}$$

Only the positive sign in front of the radical makes physical sense. Writing this in terms of the original definitions of Q and x leads to:

$$V_Y=\sqrt{\frac{(T/W)(W/S)}{3\rho C_{D_{\min}}}\left[1+\sqrt{1+\frac{3}{LD^2_{\max}(T/W)^2}}\right]} \quad \text{(x)}$$

DERIVATION OF EQUATIONS (19-35) AND (19-38)

For a propeller powered airplane, the power available is given by:

$$P_{AV}=TV_\infty=\eta_p P_{ENG} \quad \text{(i)}$$

Begin by substituting the dynamic pressure into Equation (19-22) and then by expanding it:

$$V_\infty\sin\gamma=\frac{TV_\infty}{W}-V_\infty\left[\frac{1}{2}\rho V^2_\infty\left(\frac{S}{W}\right)C_{D_{\min}}+k\left(\frac{W}{S}\right)\frac{\cos^2\gamma}{\frac{1}{2}\rho V^2_\infty}\right] \quad \text{(ii)}$$

Modify the term TV_∞ in Equation (ii) by substituting Equation (i):

$$V_\infty\sin\gamma=\frac{\eta_p P_{ENG}}{W}-V_\infty\left[\frac{1}{2}\rho V^2_\infty\left(\frac{S}{W}\right)C_{D_{\min}}+k\left(\frac{W}{S}\right)\frac{2\cos^2\gamma}{\rho V^2_\infty}\right] \quad \text{(iii)}$$

Now, substitute Equation (19-36) into Equation (iii) and rename $V_\infty=V_Y$ for the best ROC airspeed:

$$\overbrace{V_Y\sin\gamma}^{=V_{Vopt}}=\frac{\eta_p P_{ENG}}{W}-V_Y\left[\frac{1}{2}\rho\left(\frac{2}{\rho}\left(\frac{W}{S}\right)\sqrt{\frac{k}{3\cdot C_{D_{\min}}}}\right)\left(\frac{S}{W}\right)C_{D_{\min}}+k\left(\frac{W}{S}\right)\frac{2\cos^2\gamma}{\rho\left(\frac{2}{\rho}\left(\frac{W}{S}\right)\sqrt{\frac{k}{3\cdot C_{D_{\min}}}}\right)}\right]$$

Assuming $\cos^2\gamma\approx 1$, further manipulation leads to:

$$V_{Vopt}=\frac{\eta_p P_{ENG}}{W}-V_Y\left[\sqrt{\frac{kC_{D_{\min}}}{3}}+\sqrt{3k\cdot C_{D_{\min}}}\right]$$

$$=\frac{\eta_p P_{ENG}}{W}-V_Y\sqrt{kC_{D_{\min}}}\left[\frac{1}{\sqrt{3}}+\sqrt{3}\right]$$

Substitute Equation (20-33) for $LD_{\max}$ leads to

$$V_{Vopt}=\frac{\eta_p P_{ENG}}{W}-V_Y\frac{\sqrt{4kC_{D_{\min}}}}{2}\left[\frac{1}{\sqrt{3}}+\sqrt{3}\right]$$

$$\approx\frac{\eta P_{ENG}}{W}-V_Y\frac{1.1547}{LD_{\max}}$$

19.3.4 Formulation of Best (Maximum) Angle-of-Climb

This section presents formulation to estimate the maximum angle at which an aircraft ascends. It is called the *best rate-of-climb*, denoted by γ_{opt}. It is realized at one and only one airspeed, called the *best angle-of-climb airspeed* (denoted by V_X). The maximum climb angle is of great importance in evaluating the capability of the aircraft to clear terrain during departure in mountainous regions. Another important reason is noise certification (14 CFR Part 36). The steeper this angle, the higher above the sound-level meter will the airplane be when its right above it (a regulatory requirement).

(1) General Treatment of the Best Angle-of-Climb Problem

Like the best rate-of-climb problem, estimating V_X and the associated γ_{opt} is challenging for all the same reasons. It is also subject to the same limitations. The designer interested in greater accuracy can follow the two procedures given below.

Procedure 1: Analytical Approach

First, consider the methods of Chapters 14–16 for a more detailed modeling of thrust and drag in terms of airspeed, V_∞. Note that most engines allow thrust to be modeled using piecewise polynomials. Substitute the resulting functions, $T(V_\infty)$ and $D(V_\infty)$, into Equation (19-17). Next, differentiate and set the derivative equal to zero. Solve to obtain the optimum airspeed. Finally, substitute the optimum speed into Equation (19-25) to estimate the angle-of-climb. This approach is summarized below.

$$\sin\gamma=\frac{T-D}{W}\ \Rightarrow\ \frac{\partial(T-D)}{\partial V_\infty}=0\ \Rightarrow\ V_X\ \Rightarrow\ \gamma_{opt} \quad (19\text{-}39)$$

Consider a simple example of this process that uses the simplified drag model and polynomial thrust from

Section 19.3.3. Substitute these into Equation (19-17). Differentiate with respect to V_∞ and set equal to zero leads to

$$\sin\gamma = \frac{T-D}{W} \quad \Rightarrow$$

$$\frac{\partial}{\partial V_\infty}\left(AV_\infty^2 + BV_\infty + C - \frac{1}{2}\rho V_\infty^2 S C_{D_{\min}} - \frac{2kW^2}{\rho V_\infty^2 S}\right) = 0 \tag{19-40}$$

This leads to the following quartic polynomial, whose solution gives the best angle-of-climb airspeed, V_X:

$$\Rightarrow \quad (2A - \rho S C_{D_{\min}})V_X^4 + BV_X^3 + \frac{4kW^2}{\rho S} = 0 \tag{19-41}$$

It can be solved in a fashion similar to that shown in Example 19-3.

Procedure 2: Numerical Approach

The method is that detailed in Section 19.3.8, *Numerical Analysis of the Climb Maneuver*, introduced in Section 19.3.3.

(2) Best Angle-of-Climb for a Jet

For jets, the value of γ_{opt} can be computed from the following expression. It assumes the simplified drag model and relatively constant thrust.

$$\gamma_{opt} \approx \sin^{-1}\left(\frac{T}{W} - \sqrt{4C_{D_{\min}}k}\right) \tag{19-42}$$

The airspeed the pilot must maintain to realize the best angle-of-climb is denoted by V_X. For a jet, V_X can be computed from the expression below that assumes the simplified drag model and relatively constant thrust:

$$V_X = \sqrt{\frac{2}{\rho}\left(\frac{W}{S}\right)\sqrt{\frac{k}{C_{D_{\min}}}}\cos\gamma_{opt}} \tag{19-43}$$

It is also of interest to calculate the ROC associated with V_X. This is less than the ROC associated with V_Y. For a jet, the ROC at V_X can be calculated from:

$$V_{V_X} = 60 \cdot V_X \cdot \sin\gamma_{opt} \tag{19-44}$$

EXAMPLE 19-7

Determine the γ_{opt}, V_X, and V_{VX} for the Learjet 45 at S-L at a weight of 20,000 lb_f. Assume the thrust is that given in Example 19-1.

SOLUTION:

$$\gamma_{opt} \approx \sin^{-1}\left(\frac{T_{\max}}{W} - \sqrt{4C_{D_{\min}}k}\right)$$

EXAMPLE 19-7 (*cont'd*)

$$= \sin^{-1}\left(\frac{4635}{20{,}000} - \sqrt{4(0.0200)(0.05236)}\right) = 9.62°$$

$$V_X = \sqrt{\frac{2}{\rho}\left(\frac{W}{S}\right)\sqrt{\frac{k}{C_{D_{\min}}}}\cos\gamma_{opt}}$$

$$= \sqrt{\frac{2}{0.002378}\left(\frac{20{,}000}{311.6}\right)\sqrt{\frac{0.05236}{0.0200}}\cos(9.62°)}$$

$$= 293.5\ \text{ft/s} \quad (\approx 174\ \text{KCAS})$$

$$V_{V_X} = 60 \cdot V_X \cdot \sin\gamma_{opt} = 60(293.5)\sin(9.62°) = 2941\ \text{fpm}$$

(3) Best Angle-of-Climb for a Propeller-Powered Aircraft

The best angle-of-climb for a propeller-powered airplane is found by solving for V_X using the following expression. It assumes the simplified drag model and constant engine power, P_{ENG}.

$$V_X^4 + \frac{\eta_p P_{ENG}}{\rho S C_{D_{\min}}}V_X - \left(\frac{W}{S}\right)^2 \frac{4k}{\rho^2 C_{D_{\min}}} = 0 \tag{19-45}$$

Note that P_{ENG} must be in terms of ft·lb_f/s in the UK-system and watts in the SI-system. The solution requires an iterative numerical scheme. Then, obtain γ_{opt} using Equation (19-25) with V_X.

DERIVATION OF EQUATION (19-45)

The thrust of a propeller driven airplane is given by Equation (15-52):

$$T = \frac{\eta_p P_{ENG}}{V_\infty} \tag{15-52}$$

Using the simplified drag model, the climb angle is given by Equation (19-25):

$$\sin\gamma = \frac{T}{W} - q\left(\frac{S}{W}\right)C_{D_{\min}} - \frac{k}{q}\left(\frac{W}{S}\right)$$

Substitute Equation (15-52) into Equation (19-25) and write it explicitly in terms of V_∞:

$$\sin\gamma = \frac{\eta_p P_{ENG}}{WV_\infty} - \frac{1}{2}\rho V_\infty^2\left(\frac{S}{W}\right)C_{D_{\min}} - \left(\frac{W}{S}\right)\frac{2k}{\rho V_\infty^2}$$

Then, differentiate with respect to V_∞ and set to zero to get the maximum:

$$\frac{\partial(\sin\gamma)}{\partial V_\infty} = -\frac{\eta_p P_{ENG}}{WV_\infty^2} - \rho V_\infty\left(\frac{S}{W}\right)C_{D_{\min}} + \left(\frac{W}{S}\right)\frac{4k}{\rho V_\infty^3} = 0$$

Multiply by V_∞^3 for convenience and manipulate algebraically:

$$V_\infty^4 + \frac{\eta_p P_{ENG}}{\rho S C_{D_{\min}}} V_\infty - \left(\frac{W}{S}\right)^2 \frac{4k}{\rho^2 C_{D_{\min}}} = 0$$

Replace V_∞ with V_X to get Equation (19-45).

DERIVATION OF EQUATION (19-42)

Rewrite Equation (19-17):

$$V_\infty \sin\gamma = \frac{TV_\infty - DV_\infty}{W} \quad \Leftrightarrow \quad \sin\gamma = \frac{T}{W} - \frac{D}{W}$$

Substitute Equation (19-6):

$$W = \frac{L}{\cos\gamma} \quad \Rightarrow \quad \sin\gamma = \frac{T}{W} - \frac{D}{W} = \frac{T}{W} - \frac{\cos\gamma}{L/D}$$

Assuming $\cos\gamma \approx 1$: $\quad \sin\gamma \approx \frac{T}{W} - \frac{1}{L/D}$

The climb angle will reach an upper limit when the L/D is maximum, $LD_{\max}$. In other words:

$$\sin\gamma_{opt} \approx \frac{T}{W} - \frac{1}{LD_{\max}}$$

Recalling Equation (20-33), $LD_{\max}$ can be rewritten as:

$$\sin\gamma_{opt} \approx \tfrac{T}{W} - \sqrt{4C_{D_{\min}} k}$$

DERIVATION OF EQUATION (19-43)

Rewrite Equation (19-6): $\quad L = W\cos\gamma = \frac{1}{2}\rho V^2 S C_L$

Lift coefficient for $LD_{\max}$: $\quad C_L = \sqrt{C_{D_{\min}}/k}$

Substitute this into Equation (19-6), where γ and V_∞ become γ_{opt} and V_X:

$$W\cos\gamma_{\max} = \frac{1}{2}\rho V_X^2 S C_L = \frac{1}{2}\rho V_X^2 S \sqrt{\frac{C_{D_{\min}}}{k}} \quad \Rightarrow$$

$$V_X = \sqrt{\frac{2}{\rho}\left(\frac{W\cos\gamma_{\max}}{S}\right)\sqrt{\frac{C_{D_{\min}}}{k}}}$$

$$= \sqrt{\frac{2}{\rho}\left(\frac{W}{S}\right)\sqrt{\frac{C_{D_{\min}}}{k}}\cos\gamma_{\max}}$$

DERIVATION OF EQUATION (19-44)

Use γ_{opt} and V_X with Equation (19-13):

$$V_V = V\sin\gamma \quad \Rightarrow V_{V_X} = 60 \cdot V_X \cdot \sin\gamma_{opt}$$

19.3.5 Formulation of Specific Optimal Climb Problems

This section presents introduction to two optimal climb problems involving steady flight: (1) the *maximum economic climb* and (2) the *minimum flight time climb*.

(1) Maximum Economic Climb

The thrust of turbojet and turbofan engines depends directly on altitude and airspeed. Thus, so does their fuel consumption. This contrasts propeller aircraft, whose fuel consumption is related to engine power. Theoretically, at a fixed throttle and altitude, piston engines develop constant power regardless of airspeed. Yes, how much of this power is converted to thrust power depends on airspeed. But the engine power is constant. Therefore, their fuel consumption is constant with speed. What changes is their thrust and resulting climb rate. Thus, the maximum economic climb for piston engines is the best rate-of-climb airspeed, V_Y. The following method applies to jet engines.

The *maximum economic climb*, denoted by V_{Vecon}, stipulates that climbing at airspeed slightly below V_Y improves fuel economy [7]. It is realized at one and only one airspeed, the *maximum economic climb airspeed* (denoted here as V_{econ}). Consider an airplane that weighs W_1 at altitude h_1 and W_2 at altitude h_2, such that $W_1 > W_2$ and $h_1 < h_2$. Thus, its weight changes with altitude as follows

$$-\frac{W_2 - W_1}{h_2 - h_1} = -\frac{\Delta W}{\Delta h} = -\frac{\Delta W/\Delta t}{\Delta h/\Delta t} = \frac{c_t T}{V_V} \tag{19-46}$$

The minus accounts for the fact the weight reduces as the aircraft climbs and ensures a positive ratio. In the limit as $\Delta h \to 0$ we get the derivative form

$$\lim_{\Delta h \to 0}\left(-\frac{\Delta W}{\Delta h}\right) = -\frac{dW}{dh} = \frac{c_t T}{V_V} \tag{19-47}$$

Substituting Equation (19-17) for V_V yields

$$-\frac{dW}{dh} = \frac{c_t T}{V_V} = \frac{c_t T}{(TV_\infty - DV_\infty)/W} = \frac{(c_t T)W}{TV_\infty - DV_\infty} \tag{19-48}$$

The goal is to maximize altitude gained per unit reduction in weight. Therefore, differentiate the reciprocal of Equation (19-48), dh/dW, and set the derivative equal to zero. Solve to obtain the optimum airspeed. Finally, substitute the optimum speed into Equation (19-23) to estimate the rate-of-climb. This approach is summarized below.

$$\frac{\partial}{\partial V_\infty}\left(-\frac{dh}{dW}\right) = \frac{\partial}{\partial V_\infty}\left(\frac{TV_\infty - DV_\infty}{\dot{c}T}\right) = 0$$

$$\Rightarrow \quad V_{econ} \quad \Rightarrow \quad V_{Vecon} \tag{19-49}$$

(2) Climb for Minimum Flight-Time

Let us introduce the following problem using simple numbers in context of Figure 19-8. Consider a mission of range $R = 100$ nm consisting of an initial climb at constant calibrated airspeed, V_1, to some cruise altitude h and a subsequent cruise at $V_2 = 100$ KCAS. Assume a calm,

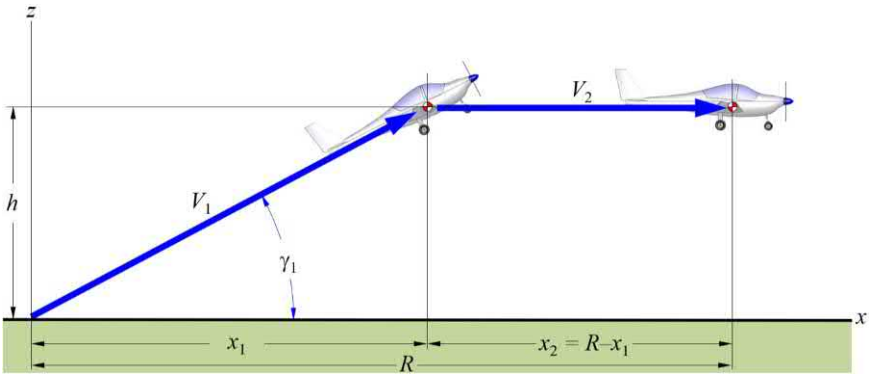


FIGURE 19-8 Parameters for minimum flight-time climb.

standard day. If $h=0$, there is no climb segment and the flight consists of a 60-min cruise only.[2] If $h>0$, a climb segment is required during which the airplane operates at air speed $V_1 \le V_2$. The climb lengthens the flight time and we must make up for it in cruise through increased true airspeed. The larger the h the greater the true airspeed needed. However, larger h calls for more time for climb. This begs the question: Is there a combination of cruise altitude and climb speed that leads to a minimum total flight time?

Consider the 100-nm mission conducted at $h=15{,}000$ ft. Say, we climb while maintaining constant V_{CAS} and it takes 30 min to complete the climb, during which we cover 30 nm. This implies an average ground speed of 60 KGS (knots, ground speed) and rate-of-climb of 500 fpm. At top-of-climb, the remaining distance is $100-30=70$ nm. At 15,000 ft, the airplane covers it at $V_2=126$ KTAS (or 100 KCAS). Therefore, this mission lasts $30+60\times(70/126)=63$ min. In contrast, if we complete climbing in 15 min and 20 nm distance (80 KGS, 1000 fpm, and 80 nm remaining), this drops to $15+60\times 80/126=53$ min. In short, such a climb airspeed is indeed possible, although there are situations in which a global minimum does not exist.

While the problem is not complex, its analytical solution is mathematically challenging. For one, performance changes due to altitude, airspeed, and weight must be accounted for. This requires an altitude- and airspeed-dependent thrust model and weight reduction during climb. Numerical optimization is more practical to implement. Figure 19-9 shows results from such an optimization for a 200-nm mission by an LSA. At $V_2=100$ KCAS (100 KTAS) and $h=0$, the mission takes 120 min. At altitudes between 0 and 12,000 ft, a global minimum is absent. Above, it is present. Significant reduction in mission duration ($\approx$18 min) is possible when maintaining $V_1=83$ KCAS from 0 to 15,000 ft. Note that these results only apply to the hypothetical aircraft modeled. This evaluation assumes a normally aspirated 100 BHP piston

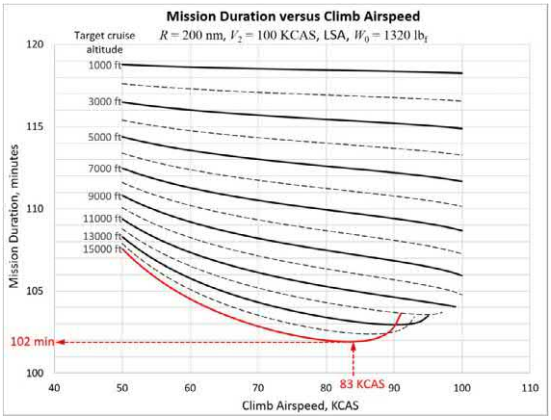


FIGURE 19-9 Optimal climb airspeed at various altitudes.

engine and accounts for power reduction of with altitude. Regardless, it assumes that $V_2=100$ KCAS is achievable at all altitudes. This may not always hold. It estimates the engine power required for cruise using Equation (20-14) and a propeller efficiency of 0.75. A mathematical formulation of this problem, based on Figure 19-8, is presented below.

$$R=\overbrace{x_1}^{\text{climb}}+\overbrace{x_2}^{\text{cruise}}=\overline{V}_1\cos\overline{\gamma}_1 t_1+\overline{V}_2 t_2$$
$$\Rightarrow\quad t_{tot}=t_1+t_2=\int\frac{dh}{\overline{V}_V}+\frac{(R-x_1)}{\overline{V}_2} \tag{19-50}$$
$$\Rightarrow\quad \frac{\partial t_{tot}}{\partial \overline{V}_1}=0$$

Where all airspeeds are true airspeeds and parameters with bars represent averaged values. The graph in Figure 19-8 is read as follows: If targeting a 15,000 ft cruise altitude, maintaining an 83 KCAS climb speed from the ground to top-of-climb (followed by a 100 KCAS level cruising speed to destination) would yield an approximate flight time of some 102 min.

[2] Recall that 1 knot = 1 nautical mile/h (i.e., nm/h). Therefore, at 100 knots, we cover 100 nm in 1 h.

19.3.6 Time to Altitude

The time required to climb through the altitude band h_0 (initial altitude) to h_1 (target altitude) can be determined from the following expression. If the rate-of-climb (ROC) is in terms of fpm, it returns time in minutes. If in terms of ft/s or m/s then the time will be in seconds.

$$t = \int_{h_0}^{h_1} \frac{dh}{V_V} \tag{19-51}$$

Where V_V is the ROC. For subsonic aircraft, the minimum time to altitude is achieved by maintaining the best rate-of-climb airspeed (V_Y) through the entire climb maneuver.

Rapid Approximation

For a rapid assessment of time-to-climb, V_V may be assumed constant. Thus, it can be moved outside the integral sign. For more accurate estimation, the ROC should be a representative value between the initial and final altitude, here denoted by $\overline{V}_V$ and called the *representative ROC*. If the initial and final altitudes are close, it can be approximated as the average of the ROC at the initial and final altitudes. Otherwise, it should be biased toward the ROC at higher altitude as the aircraft spends more time completing the last half of the climb than the first one. Since this approach treats the representative ROC as a constant, it can be taken out of the integral of Equation (19-51) yielding the following expression:

$$t = \int_{h_0}^{h_1} \frac{dh}{V_V} \cong \frac{1}{\overline{V}_V} \int_{h_0}^{h_1} dh = \frac{(h_1 - h_0)}{\overline{V}_V} \tag{19-52}$$

If airspeed such as V_Y is maintained through the climb, the decrease in ROC with altitude is close to being linear and can be approximated as $V_V(h) = Ah + B$. Then, the resulting $\overline{V}_V$ can be estimated as follows:

$$\overline{V}_V = \frac{A(h_1 - h_0)}{\ln(Ah_1 + B) - \ln(Ah_0 + B)} \tag{19-53}$$

In this case the time to altitude is given by:

$$t = \int_{h_0}^{h_1} \frac{dh}{Ah + B} = \frac{\ln(Ah_1 + B) - \ln(Ah_0 + B)}{A} \tag{19-54}$$

DERIVATION OF EQUATION (19-51)

The ROC is the rate-of-change of altitude, given by dh/dt. Therefore,

$$\frac{dh}{dt} = V_V \;\Rightarrow\; dt = \frac{dh}{V_V} \;\Rightarrow\; t = \int \frac{dh}{V_V}$$

DERIVATION OF EQUATION (19-53)

If ROC is approximated as a linear function of altitude, $V_V(h) = Ah + B$, the representative ROC can be determined from using Equation (19-54)

$$t = \frac{\ln(Ah_1 + B) - \ln(Ah_0 + B)}{A} = \frac{h_1 - h_0}{\overline{V}_V}$$

$$\Rightarrow\; \overline{V}_V = \frac{A(h_1 - h_0)}{\ln(Ah_1 + B) - \ln(Ah_0 + B)}$$

DERIVATION OF EQUATION (19-54)

If ROC is approximated as a linear function of altitude, $V_V(h) = Ah + B$, then the time to altitude can be found from:

$$t = \int_{h_0}^{h_1} \frac{dh}{V_V} = \int_{h_0}^{h_1} \frac{dh}{Ah + B} = \frac{\ln(Ah + B)}{A}\Big]_{h_0}^{h_1}$$
$$= \frac{\ln(Ah_1 + B) - \ln(Ah_0 + B)}{A}$$

EXAMPLE 19-8

Consider the ROC versus Altitude graph for the Cirrus SR22 in Figure 19-10. Consider the aircraft at 4000 ft, weighing 2900 lb_f, when a climb at V_Y is initiated. How long will it take to get to 20,000 ft? Determine this

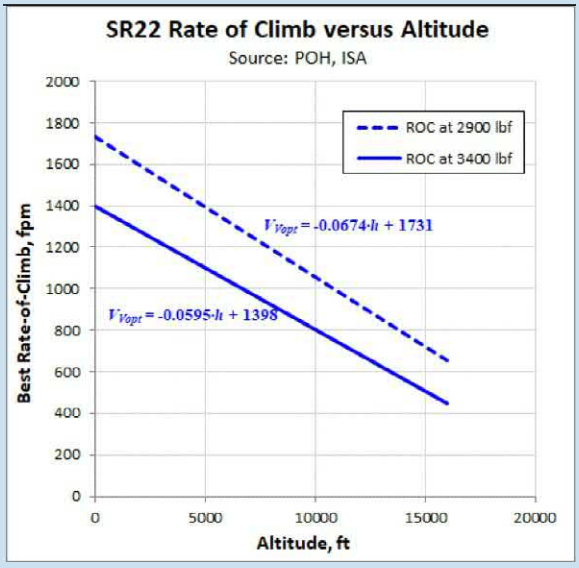


FIGURE 19-10 ROC (fpm) as a function of altitude (ft) for the Cirrus SR22 for two weights [10].

EXAMPLE 19-8 (*cont'd*)

using the three following approaches: (a) $\overline{V}_V$ is average of the ROC at the initial and final altitude. (b) Calculate $\overline{V}_V$ using Equation (19-53). (c) Use Equation (19-54) directly.

SOLUTION: (a) Calculate ROC at the initial and final altitudes using the trend line for 2900 lb_f shown in Figure 19-10:

At 4000 ft: $V_V = 1731 - 0.0674 \times 4000 = 1461$ fpm

At 20,000 ft: $V_V = 1731 - 0.0674 \times 20,000 = 383$ fpm

Representative ROC: $\overline{V}_V = \dfrac{1461 + 383}{2} = 922$ fpm.

From Equation (19-52):

$$t = \frac{(h_1 - h_0)}{\overline{V}_V} = \frac{(20,000 - 4000)}{922} = 17.4 \text{ min}$$

(b) Calculate $\overline{V}_V$ using Equation (19-53), where $A = -0.0674$ and $B = 1731$:

$$\overline{V}_V = \frac{A(h_1 - h_0)}{\ln(Ah_1 + B) - \ln(Ah_0 + B)}$$

$$= \frac{-0.0674 \cdot (20,000 - 4000)}{\ln(-0.0674 \cdot 20,000 + 1731) - \ln(-0.0674 \cdot 4000 + 1731)}$$

$$= 805.3 \text{ fpm}$$

From Equation (19-52):

$$t = \frac{(h_1 - h_0)}{ROC_a} = \frac{(20,000 - 4000)}{805.3} = 19.9 \text{ min}$$

(c) Use Equation (19.54) directly:

$$t = \frac{\ln(Ah_1 + B) - \ln(Ah_0 + B)}{A} = \frac{\ln(383) - \ln(1461)}{-0.0674} = 19.9 \text{ min}$$

19.3.7 Absolute/Service Ceiling Altitude

Two frequently referenced performance parameters are: (1) The *absolute ceiling* is the maximum altitude at which the airplane can maintain level flight. (2) The *service ceiling* is the altitude at which the aircraft is capable of some 100-fpm rate-of-climb. Note the shortcoming of these altitudes: (1) Each ceiling depends on the aircraft weight and atmospheric conditions. They can deviate thousands of feet (or meters) from the calculated values. (2) Modern day aviation regulations often limit these altitudes. For instance, 14 CFR Part 23 stipulates requirements for high-altitude operation of aircraft. These requirements have everything to do with equipment onboard, and not capability to reach those altitudes. Some business jets have theoretical service ceilings in excess of 50,000 ft, but are certified to fly only as high as 41,000 ft. Such limitations are referred to as *max operational altitude*.

The theoretical absolute and service ceilings can be computed by the following method:

STEP 1: Compute V_{Vopt} at several altitudes.

STEP 2: Create a trend line in the form of a line or a polynomial.

STEP 3: Solve the trend line for $V_V = 100$ fpm. This is the *Service Ceiling*, h_{sc}.

STEP 4: Solve the trend line for $V_V = 0$ fpm. This is the *Absolute Ceiling*, h_{abs}.

EXAMPLE 19-9

Determine the absolute and service ceilings for the Cirrus SR22 at 2900 and 3400 lb_f weights using the data from its POH, shown in Figure 19-11.

SOLUTION:

Using the published data of an existing aircraft renders it relatively easy to determine a trend line. If working with a new design, such a document is not available, so the max ROC must be calculated for a number of altitudes, e.g., S-L, 7000 ft, and 14,000 ft or similar.

With respect to the SR22, using information from its POH we find that the resulting linear fit is given by:

At 2900 lb_f: $H = 25,666 - 14.828 V_{Vopt}$

At 3400 lb_f: $H = 23,496 - 16.807 V_{Vopt}$

From which we see that at the lighter weight (2900 lb_f) the absolute Ceiling is 25,666 ft and 23,496 ft at maximum gross weight (3400 lb_f). Of course, the airplane would always weigh less than its maximum gross weight, as it would have to burn considerable amount of fuel to get there in the first place. By the same token, it is easy to evaluate the Service Ceiling based on a 100-fpm climb rate:

At 2900 lb_f: $H = 25,666 - 14.828 \times 100 = 24,183$ ft

At 3400 lb_f: $H = 23,496 - 16.807 \times 100 = 21,815$ ft

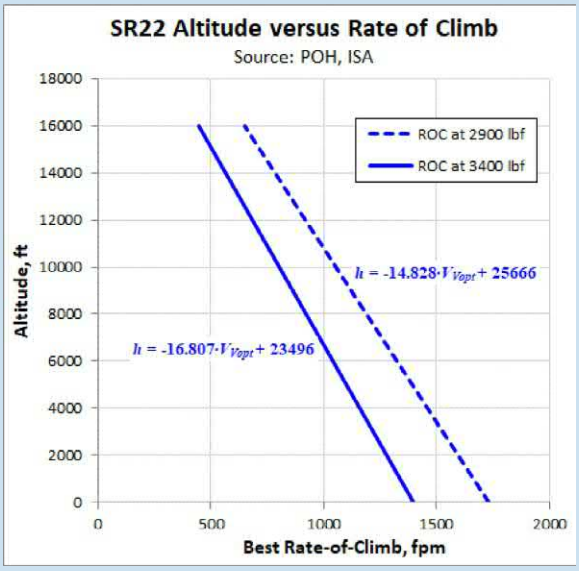


FIGURE 19-11 Determining of service and absolute ceilings.

19.3.8 Numerical Analysis of the Climb Maneuver—Sensitivity Studies

This section presents a method to analyze the climb characteristic of a new aircraft using numerical analysis. It is illustrated using the spreadsheet below, prepared for a propeller aircraft. It applies equally to any form of properly prepared thrust model. This approach brings power to the analysis effort because it handles nonlinearities that many of the preceding analytical methods do not. The approach is indifferent to detail like $C_{L_{minD}} > 0$, drag buckets, or nonlinearities due to early flow separation. A screen capture of the spreadsheet is shown in Figure 19-12.

The general input values are self-explanatory in light of the preceding discussion and will not be elaborated on. The columns in the main table have been labeled from 1 through 12, in contrast, require some explanation.

Column 1 contains a range of calibrated airspeeds (30 KCAS increasing by 5 to 130 KCAS). This is used to calculate the true airspeed in **Column 2** using Equation (17-31) as follows (using 100 KCAS as an example):

$$V_{KTAS} = \frac{V_{KCAS}}{\sqrt{\sigma}} = \frac{100}{\sqrt{0.7860}} = 112.8\,\text{KTAS}$$

Note that this step bypasses converting *VCAS* to *VEAS*, which is acceptable provided $M < 0.3$. This is converted to ft/s in **Column 3** by multiplying by 1.688. This gives 190.4 ft/s.

Column 4 contains dynamic pressure, calculated from:

$$q = \frac{1}{2}\rho V_\infty^2 = \frac{1}{2}(0.001869)(190.4)^2 = 33.88\,\text{slugs/ft}^3$$

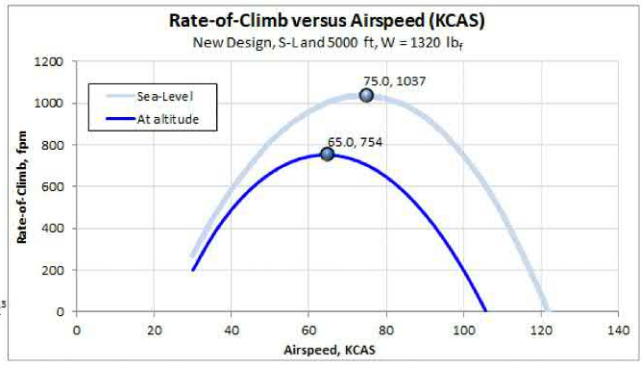
Column 5 contains the lift coefficient, calculated as follows:

$$C_L = \frac{W}{qS} = \frac{1320}{(33.88)(130)} = 0.2997$$

RATE OF CLIMB ANALYSIS FOR A PROPELLER POWERED AIRCRAFT

Adjusted Drag Model

		User entry	Formula	
AIRCRAFT SPECIFIC DATA				
Weight	W =	1320		lb$_f$
Wing area	S =	130		ft^2
Aspect Ratio	AR =	8		
Oswald's span efficiency	e =	0.8106		
Max lift coefficient	$C_{L\,max}$ =	1.450		
C_L of minimum drag	$C_{L\,minD}$ =	0.1000		
Mi drag coefficient	$C_{D\,min}$ =	0.03000		
ATMOSPHERICS				
Altitude	h =	8000		ft
Air density	ρ =	0.001869		slugs/ft^3
Density ratio	σ =	0.7860		



ENGINE/PROPELLER SPECIFIC DATA

Rated engine power at S-L	P_{HP} =	100	BHP	Scale-based correction	K_p =	0.7		A =	0.0010387
Engine power at altitude	P_{HPa} =	75.8	BHP	Altitude of optimal airspeed	h_{opt} =	5000	ft	B =	-1.2220
Engine speed	RPM =	2500		Optimal airspeed	V_{opt} =	116	KTAS	C =	359.1
Propeller diameter	D_P =	69	inches	Optimal prop efficiency	η_{opt} =	0.75			
Spinner diameter	$D_{spinner}$ =	15	inches	Momentum theorem	T_{STATIC} =	359.1	lb$_f$		

1	2	3	4	5	6	7	8	9	10	11	12
Airspeed			q	C_L	C_{Di}	C_D	D	η_P	T	TV-DV	V_V
KCAS	KTAS	ft/s	lb$_f$/ft^2				lb$_f$		lb$_f$	ft-lb$_f$/s	fpm
30	33.8	57.1	3.05	3.3301	0.51215	0.54215	215	0.4010	293	4443	202
35	39.5	66.6	4.15	2.4466	0.27030	0.30030	162	0.4512	282	8014	364
40	45.1	76.2	5.42	1.8732	0.15434	0.18434	130	0.4970	272	10826	492
45	50.8	85.7	6.86	1.4801	0.09349	0.12349	110	0.5385	262	13013	592
50	56.4	95.2	8.47	1.1988	0.05927	0.08927	98	0.5758	252	14649	666
55	62.0	104.7	10.25	0.9908	0.03895	0.06895	92	0.6092	243	15776	717
60	67.7	114.2	12.20	0.8325	0.02634	0.05634	89	0.6386	233	16418	746
65	73.3	123.8	14.31	0.7094	0.01823	0.04823	90	0.6643	224	16587	754
70	79.0	133.3	16.60	0.6117	0.01285	0.04285	92	0.6863	215	16286	740
75	84.6	142.8	19.06	0.5328	0.00920	0.03920	97	0.7048	206	15517	705
80	90.2	152.3	21.68	0.4683	0.00666	0.03666	103	0.7200	197	14276	649
85	95.9	161.8	24.48	0.4148	0.00487	0.03487	111	0.7318	189	12556	571
90	101.5	171.4	27.44	0.3700	0.00358	0.03358	120	0.7406	180	10350	470
95	107.2	180.9	30.58	0.3321	0.00264	0.03264	130	0.7464	172	7648	348
100	112.8	190.4	33.88	0.2997	0.00196	0.03196	141	0.7493	164	4441	202
105	118.4	199.9	37.35	0.2718	0.00145	0.03145	153	0.7495	156	718	33
110	124.1	209.4	40.99	0.2477	0.00107	0.03107	166	0.7471	149	-3532	-161
115	129.7	219.0	44.80	0.2266	0.00079	0.03079	179	0.7422	141	-8321	-378
120	135.4	228.5	48.79	0.2081	0.00057	0.03057	194	0.7350	134	-13661	-621
125	141.0	238.0	52.94	0.1918	0.00041	0.03041	209	0.7255	127	-19565	-889
130	146.6	247.5	57.26	0.1773	0.00029	0.03029	225	0.7140	120	-26045	-1184

FIGURE 19-12 Spreadsheet designed to estimate climb performance.

Column 6 contains lift-induced drag coefficient, calculated as follows:

$$C_{D_i} = \frac{(C_L - C_{L_{\min D}})^2}{\pi \cdot AR \cdot e} = \frac{(0.2997 - 0.1000)^2}{\pi \cdot (10)(0.7566)} = 0.00196$$

Column 7 contains the total drag coefficient, calculated as follows:

$$C_D = C_{D_{\min}} + C_{D_i} = 0.03000 + 0.00196 = 0.03196$$

Column 8 contains the total drag, calculated as follows:

$$D = qSC_D = (33.88)(130)(0.03196) = 141 \text{ lb}_\text{f}$$

Fundamentally, the method "does not care" how the drag is determined. For instance, while the adjusted drag model is used here, Columns 6 through 8 could also contain a nonquadratic drag coefficient. For instance, a lookup table containing a drag model with a drag bucket could simply replace the existing C_D.

Column 9 is an optional column that contains the propeller efficiency, η_p, calculated here using Equation (15-45), the power at altitude (P_{HPa}), and the thrust (T) in **Column 10**.

$$\eta_p = TV_\infty / (550 P_{HP_a})$$

Column 10 contains the propeller thrust (in lb_f), here calculated using the thrust spline method of Section 15.4.3, *Initial Thrust Model for a Fixed-Pitch Propeller*. The value of the coefficients A, B, and C, depends on the altitude, propeller geometry, and other parameters discussed in the section. Once determined, thrust at that altitude is calculated using the quadratic polynomial below

$$T(V_\infty, h) = AV_\infty^2 + BV_\infty + C$$

Column 11 contains the excess power, calculated using Equation (19-16):

$$P_{EX} = TV_\infty - DV_\infty = (164)(190.4) - (141)(190.4) = 4441 \text{ ftlb}_\text{f}/\text{s}$$

Column 12 (finally) contains the rate-of-climb, calculated using Equation (19-19):

$$V_V = 60\left(\frac{TV_\infty - DV_\infty}{W}\right) = 60\left(\frac{4441}{1320}\right) = 202 \text{ ft/min}$$

By performing the same calculations for other rows, it is trivial to extract the maximum ROC using Microsoft Excel's MAX() function. It returns an ROC of 754 fpm at 65 KCAS (at 8000 ft). The airspeed can be extracted using the MATCH() and the INDEX() functions. Better yet, nest the former inside the latter (i.e., INDEX(MATCH())). The details are left to the reader to figure out.

More accurate calculations should account for weight reduction with altitude. For instance, the airplane will burn several gallons of fuel climbing to 10,000 ft and this improves the ROC at that altitude. The graph accompanying the spreadsheet contains a reference curve showing the climb performance at S-L. This is conveniently presented to help the designer realize performance degradation with altitude. It is left as an exercise for the reader to figure out how to do this (hint—it is simpler than you might think). Once completed, it can be used to perform various sensitivity studies, of which three are shown below.

(1) Altitude Sensitivity

Altitude sensitivity reveals how the design is affected by high-altitude operation or at high-altitude/hot-day (high density altitude). This is important when considering departure from high-elevation airports in mountainous regions. Such departures can pose serious challenges, in particular if the aircraft is fully loaded. For instance, the graph in Figure 19-13 shows that at 10,000 ft, the new design climbs near 670 fpm, close to ½ of its S-L capability.

(2) Weight Sensitivity

Weight sensitivity reveals how the design is affected by deviations from the target design weight. This is important when demonstrating the importance of meeting target design weights. For instance, assume that the baseline gross weight of the airplane shown in Figure 19-14 is 1320 lb_f. If this target is not met and the manufacturer is forced to increase it to, say, 1400 lb_f, then the airplane's best ROC likely drops from about 1123 fpm to 1038 fpm. This could impact its competitive edge.

(3) Propeller Efficiency Sensitivity

Propeller efficiency sensitivity reveals how the design is affected by a substandard propeller or by a more efficient (and perhaps more expensive) propeller. If the selected propeller in Figure 19-15 is 85% efficient, the best ROC may increase from about 1123 fpm to 1286 fpm.

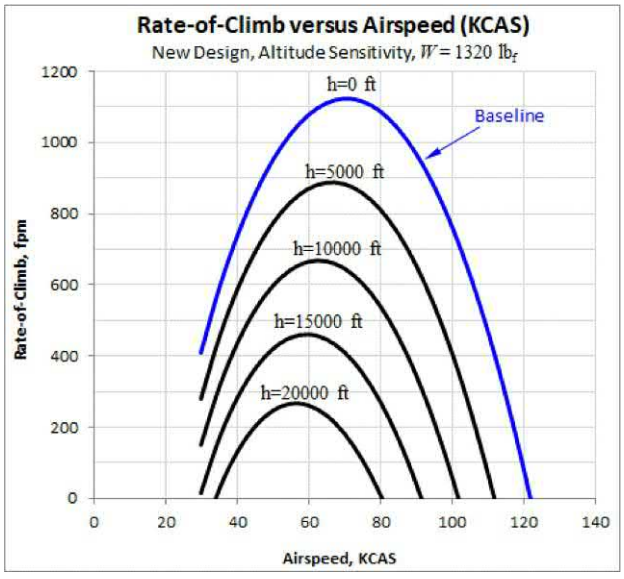


FIGURE 19-13 Altitude sensitivity plot.

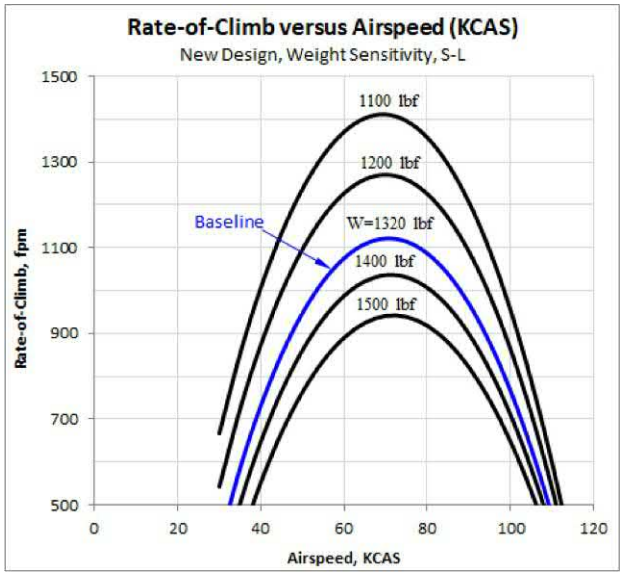


FIGURE 19-14 Weight sensitivity plot.

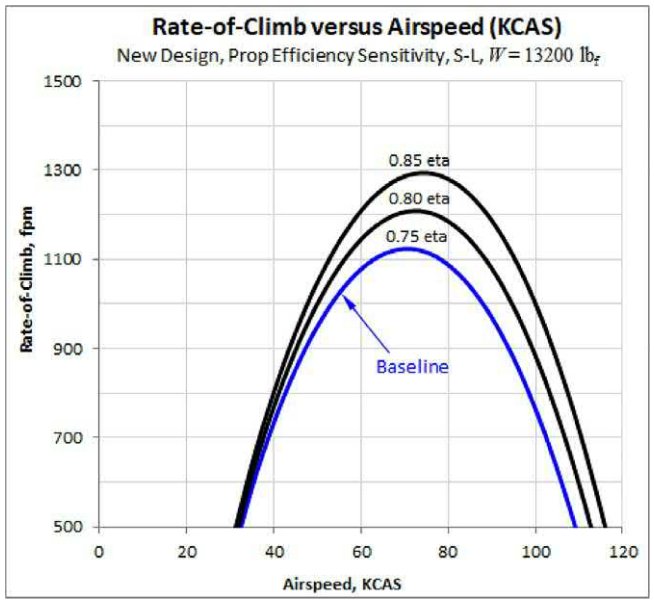


FIGURE 19-15 Propeller efficiency sensitivity plot.

It can also be helpful to extend the sensitivity evaluation to one that considers sensitivities associated with wing geometry.

19.4 AIRCRAFT DATABASE—RATE-OF-CLIMB OF SELECTED AIRCRAFT

Table 19-3 shows the rate-of-climb and best angle-of- and best rate-of-climb airspeeds for selected classes of aircraft. These data are very helpful when evaluating the accuracy of own calculations. Note that for heavier aircraft, it is practically impossible to specify a single V_X or V_Y as these vary greatly with weight and are usually determined for the pilot on a trip-to-trip basis.

TABLE 19-3 Climb performance of selected aircraft.

Name	Gross Weight lb_f	Wing Area ft^2	ROC at S-L & W_o fpm	V_X KCAS	V_Y KCAS	Service Ceiling ft	Source
Single Engine							
Aerotec A-122A	1825	145	787	-	-	14760	JAWA
Bede BD-5B Micro	660	47	2145	-	-	18000	JAWA
Cessna 150 Commuter	1600	160	670	-	64	12650	POH
Cessna 162 Skycatcher	1320	120	880	57	62	14625	POH
Cessna 172N Skyhawk	2450	174	770	59	73	14200	POH
Cessna 182 Skylane	2950	174	1010	54	78	16500	POH
Cessna 208B Grand Caravan	8750	279	1240	89	105	25000	POH
Cirrus SR20	3050	145	828	89	96	17500	POH
Cirrus SR22	3400	145	1400	91	101	17500	POH
DAHER TBM-850	7394	194	2005	-	126	31000	POH/AOPA Article
Embraer EMB-201	3417	194	1050	-	-	11380	JAWA
ExtremeAir XA42 Sbach	2205	121	2720	78	90	15000	POH
Let Z-37A Cmelak (Bumble-Bee)	3855	256	925	-	-	-	JAWA
Neiva N621A	3748	185	1380	-	-	19700	JAWA
Piper PA-46-350 Malibu	4340	175	1220	81	110	25000	POH
Rockwell Commander 112A	2650	152	900	72	100	20000	POH/TCDS
Taylor J.T.1 Monoplane	610	76	1000	-	-	-	JAWA
Transavia PL-12 Airtruk (400)	4000	288	550	-	-	12500	JAWA
Twin Engine, Propeller							
Beechcraft Baron 55	5100	199	1577	91	100	19700	POH
Beechcraft Duke B60	6775	213	1601	99	120	30800	Unconf
Beechcraft Queenair B80	8800	294	1275	-	-	26800	JAWA
Cessna 337 Skymaster	3800	201	1520	-	94	20500	POH
	4630	201	1100	79	96	18000	POH
Cessna 421 Golden Eagle	7450	215	1940	-	117	30200	POH
Partenavia P.68	4387	200	1500	76	90	19200	POH/JAWA
Pilatus Britten-Norman BN-2B Islander	6600	325	1130	-	-	18000	JAWA
Piper PA-44-180 Seminole	3800	184	1350	82	88	17100	POH/JAWA
Commuter Turboprops							
ATR-42-300	36807	586	1320	-	-	25000	ATR Brochure
ATR-42-600	41005	586	1851	-	-	25000	ATR Brochure
Beechcraft Kingair A100	10600	298	2200	-	-		JAWA
Beechcraft Kingair C90	9650	294	2000	101	112		POH
Casa C.212 Aviocar	13889	431	1800	-	-		JAWA
Frakes Turbo-Mallard	14000	444	1350	-	-		JAWA
Let L-140 Turbolet (L-140)	11905	354	1615	-	-		JAWA
Lockheed Model 85 Orion P-3	135000	1300	1950	-	-		Unconf
Nomad N22	8000	324	1410	-	-		JAWA
Piper PA-31P Pressurized Navajo	7800	229	1740	-	-		JAWA
Rockwell Commander 690A	10250	266	2849	-	-		JAWA
Shorts SD3-30	22000	453	1210	-	-		JAWA

Continued

TABLE 19-3 Climb performance of selected aircraft—cont'd

Name	Gross Weight lb_f	Wing Area ft^2	ROC at S-L & W_o fpm	V_X KCAS	V_Y KCAS	Service Ceiling ft	Source
Business jets							
Beechjet 400a	16100	241	3770	-	-		Unconf
Beechjet 850XP	18000	374	-	138	145		POH
Beechjet 850XP	24000	374	-	161	172.5		POH
Beechjet 850XP	28000	374	-	170	187		POH
Cessna Citation CJ1	10700	240	3200	-	-		Unconf
Cessna Citation Mustang	8645	210	3010	-	-		Unconf
Cirrus Vision Prototype	6000	195.7			120		Unconf
Dasault Falcon 900	45500	527	3700	-	-		Unconf
Dassault-Breguet Mystere-Falcon 900	20640	528	2000	-	-		Unconf
Embraer Phenom 100	10472	202		-	-		Unconf
Falcon 2000X	41000	527	3730	-	-		Unconf
Gates Learjet 24D	13500	232	6800	-	-		JAWA
Gulfstream 450	40000	950.39	-	-	128		Unconf
	50000		-	-	143		Unconf
	60000		-	-	157		Unconf
	70000		-	-	169		Unconf
	80000		-	-	181		Unconf
Gulfstream Aerospace IV	71700	950	4219	-	-		Unconf
Safire S-26	5130	143	2900	-	-		JAWA
Commercial Jetliners							
A300-B4	360000	2800	-	-	-		Unconf
A320-200	170000	1320	2400	-	-		Unconf
A330	520000	3892	4000	-	-		FCOM
A340-200	610000	3892	4000	-	-		FCOM
B737-400	150000	1135	3760	-	-		JAWA
B757-200	255000	1994	3000	-	-		Unconf
B777-200A	247200	4605	3800	-	-		Unconf
Boeing 727-200	172000	1700	1800	-	-		FCOM
Fokker 100	95000	1006	-	-	-		Unconf
Lockheed L-1011-1 Tristar	430000	2800	2800	-	-		JAWA

Unconf = Unconfirmed. A reliable source has not been located for the specified value. Treat values with caution. JAWA = Jane's All the World's Aircraft. POH = Pilot's Operating Handbook. FCOM = Flight Crew Operational Manual.

References

[1] C.D. Perkins, R.E. Hage, *Airplane Performance, Stability, and Control*, John Wiley & Sons, 1949.

[2] E. Torenbeek, *Synthesis of Subsonic Aircraft Design*, third ed., Delft University Press, 1986.

[3] L. Nicolai, *Fundamentals of Aircraft Design*, second ed., (1984).

[4] J. Roskam, C.-T.E. Lan, *Airplane Aerodynamics and Performance*, DARcorporation, 1997.

[5] F.J. Hale, *Aircraft Performance, Selection, and Design*, John Wiley & Sons, 1984, pp. 137–138.

[6] J.D. Anderson Jr., *Aircraft Performance & Design*, first ed., McGraw-Hill, 1998.

[7] A. Miele, *Flight Mechanics—Theory of Flight Paths*, Dover Publications, 1990.

[8] W. Austyn-Mair, D.L. Birdsall, *Aircraft Performance*, Cambridge University Press, Cambridge, 1992, pp. 47–49.

[9] Anonymous, *Cessna 162 Skycatcher Pilot's Operating Handbook and Flight Training Supplement, Rev.2*, Cessna Aircraft Company, April 26, 2010.

[10] Anonymous, *Cirrus SR22 Pilot's Operating Handbook*, Cirrus Design Corporation, October 10, 2003.

CHAPTER

20

Performance—Cruise

OUTLINE

20.1 **Introduction** 833
20.1.1 The Content of This Chapter 833
20.1.2 What Analyses Must I Do? 834

20.2 **Fundamental Relations for the Cruise Maneuver** 834
20.2.1 General Equations-of-Motion for Cruise 834
20.2.2 Fundamental Concepts 835

20.3 **General Cruise Analysis Methods for Steady Flight** 839
20.3.1 Airspeed in Terms of Thrust 839
20.3.2 Estimation of Minimum and Maximum Airspeed 840
20.3.3 Estimation of Stalling Speed 843
20.3.4 Airspeed of Maximum Lift-to-Drag Ratio 845
20.3.5 Airspeed of Minimum Thrust Required 848
20.3.6 Airspeed of Minimum Power Required 850
20.3.7 Airspeeds of Maximum ROC and AOC 851
20.3.8 Airspeed of Maximum Endurance 851
20.3.9 Airspeed of Maximum Range 853
20.3.10 Flight Envelope 854
20.3.11 Computer Code: Determining Maximum Level Airspeed, V_{max}, for a Propeller Aircraft 856
20.3.12 Computer Code: Determining Maximum Level Airspeed, V_{max}, for a Jet 858

20.4 **General Analysis Methods for Accelerated Flight** 859
20.4.1 Analysis of a General Level Constant Velocity Turn 859
20.4.2 Extremes of Constant Velocity Turns 862
20.4.3 Analysis of the Loop Maneuver 863
20.4.4 Energy State 863

References 866

20.1 INTRODUCTION

This chapter presents an assortment of methods to predict the properties of the cruise maneuver. The maneuver comprises straight and level, steady flight and encompasses the slowest to the highest airspeed the airplane can maintain. There are several airspeeds of interest that occur in between those, such as the airspeed for best range, endurance, and glide, to name a few. In addition, topics like the development of flight envelope and accelerated maneuvers are presented. Figure 20-1 shows an organizational map displaying the cruise among other topics within performance theory.

Common adjectives used to describe cruise are *straight*, *level*, and *steady*. *Straight* means the absence of a roll, which would result in a heading change. *Level* means no change in altitude. *Steady* means absence of acceleration. There are modes of cruise that involve *quasi-steady* changes in altitude, airspeed, and heading. These changes are so slow and gradual that they can be treated as if they were constant. Cruise methods involving quasi-steady changes in altitude and airspeed are presented in Chapter 21, Performance—Range Analysis. Quasi-steady heading changes are presented in Section 20.4, *General Analysis Methods for Accelerated Flight*.

The methods presented in here are "industry standard" and mirror that presented by a variety of authors, e.g., Perkins and Hage [1], Torenbeek [2], Nicolai [3], Roskam [4], Hale [5], Anderson [6], and Miele [7], to name a few.

20.1.1 The Content of This Chapter

- Section 20.2 presents the equation-of-motion for steady, level, and accelerated performance analysis.
- Section 20.3 presents classical analysis methods to determine a number of important steady-level cruise performance characteristics. Among those are the most

https://doi.org/10.1016/B978-0-12-818465-3.00020-3

Copyright © 2022 Elsevier Inc. All rights reserved.

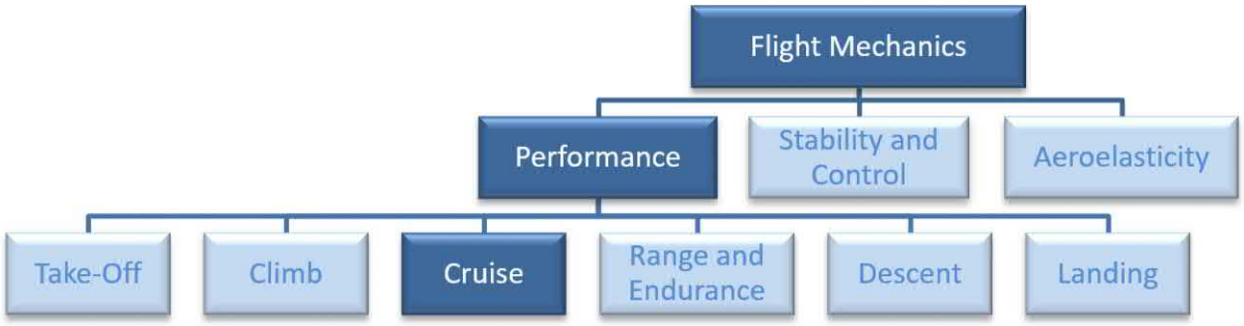


FIGURE 20-1 An organizational map placing performance theory among other the disciplines of *Flight Mechanics*, and highlighting the focus of this chapter; cruise performance.

important types of cruising speeds encountered in the operation of aircraft.

- Section 20.4 presents classical analysis methods to determine a number of important performance parameters for accelerated flight.

20.1.2 What Analyses Must I Do?

For the newcomer to cruise analysis, the burning question is: "What am I supposed to estimate and how do I conduct those estimations?" The cruise analysis has multiple purposes. (1) An evaluation of the airplane's performance in straight and level steady flight. This includes the estimation of optimal airspeeds, such as best glide speed, max range and associated airspeed, and minimum power required airspeed, which gives maximum endurance for propeller aircraft. (2) For 14 CFR Part 23, level performance analysis supports certification through the identification of specific operational airspeeds (e.g., design cruise speed) and airspeed limits (e.g., never exceed or maximum operating airspeeds) of importance for both Subpart B and G. This includes glide airspeed. (3) The performance analysis is used by sales and marketing people to help sell the airplane. That said, the designer should, at minimum, provide estimates of the following airspeeds (Table 20-1).

TABLE 20-1 Task list for cruise analysis.

Task name	Terms	Section
Minimum level airspeed	$V_{\min}$	20.3.2
Stalling speed	V_S, V_{S_n}, V_{S_ϕ}	20.3.3
Best glide airspeed $(C_L/C_D)_{\max}$	V_{BG}, $V_{LD_{\max}}$, $LD_{\max}$	20.3.4
Airspeed of maximum $(C_L^{0.5}/C_D)_{\max}$	See airspeeds below	20.3.4
Airspeed of maximum $(C_L^{1.5}/C_D)_{\max}$	See airspeeds below	20.3.4
Minimum thrust required airspeed	$V_{TR_{\min}}$	20.3.5
Minimum power required airspeed	$V_{PR_{\min}}$	20.3.6
Maximum endurance airspeed for a propeller	$V_{E_{\max}}$	20.3.8
Maximum endurance airspeed for a jet	$V_{E_{\max}}$	20.3.8
Maximum range airspeed for a propeller	$V_{R_{\max}}$	20.3.9
Maximum range airspeed for a jet	$V_{R_{\max}}$	20.3.9
Carson's airspeed	V_{CAR}	20.3.9
Minimum rate of descent airspeed	$V_{ROD_{\min}}$	22.3.5
Maximum level airspeed	$V_{\max}$	20.2.2
Flight envelope		20.3.10

20.2 FUNDAMENTAL RELATIONS FOR THE CRUISE MANEUVER

This section presents basic mathematical relationships and aerodynamic concepts required to analyze the cruise maneuver. It is helpful to first review Sections 7.1.3, *The Basics of Energy, Work, and Power* and 19.2, *Fundamental Relations for the Climb Maneuver*.

20.2.1 General Equations-of-Motion for Cruise

A general free-body diagram for steady, level flight is presented in Figure 20-2. It is based on Figure 17-1, but modified to represent level flight. This yields a form familiar to many, in which $L=W$ and $T=D$. The free-body assumes all forces are applied at the center-of-gravity (CG) and all moments are balanced.

(1) Flight in the Vertical Plane

The equations-of-motion for an aircraft in the horizontal and vertical planes were developed in Section 17.1.2, *Equations-of-Motion for Performance Theory*. These are presented as Miele's set of Equation (17-1) and illustrated in Figure 17-1. It is recommended the reader reviews these. This set of equations is adapted to the cruise maneuver as Equations (20-1). The transformation assumes (1) the

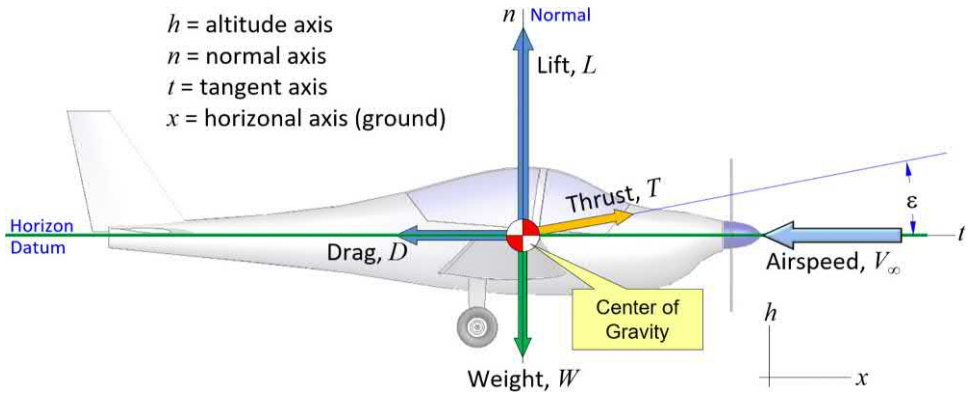


FIGURE 20-2 A 2-dimensional free-body of the airplane in level flight.

thrust angle $\varepsilon = 0$, (2) constant airspeed, V_∞, and altitude, h, so the corresponding time derivatives are zero, (3) angle-of-attack, α, is small, and (4) constant flight path angle, $\gamma = 0$. Furthermore, let $W = mg$. This reduces Equation (17-1) as shown below

$$\begin{aligned} \dot{x} - V_\infty \cos\gamma &= 0 \\ \dot{h} - V_\infty \sin\gamma &= 0 \\ T\cos\varepsilon - D - m\left(g\sin\gamma + \dot{V}_\infty\right) &= 0 \\ T\sin\varepsilon + L - m(g\cos\gamma + V_\infty\dot{\gamma}) &= 0 \\ \dot{m}g + c_t T &= 0 \end{aligned} \quad \Rightarrow \quad \begin{aligned} \dot{x} - V_\infty &= 0 \\ \dot{h} &= 0 \\ T - D &= 0 \\ L - W &= 0 \\ \dot{W} + c_t T &= 0 \end{aligned} \tag{20-1}$$

The third and fourth equations of Equations (20-1) are the *planar equations-of-motion for steady, level flight*. They assume no rotation about the binomial axis (normal to page).

$$D = T \tag{20-2}$$

$$L = W \tag{20-3}$$

(2) Flight in the Horizontal Plane

For accelerated flight, we must also include forces in the horizontal plane. For this set of equations, review Equation (17-2) and Figure 17-2. The equations-of-motion are adapted to this chapter as Equations (20-4). Variables are defined in Section 17.1.2. The top two equations describe horizontal translation along the x- and y-axis, respectively. The next three represent the summation of forces along the **t-**, **n-**, and **b-**axes. Note how these axes differ from that of the vertical plane. The bottom equation describes the change in the weight of the aircraft. The formulation assumes no side force.

$$\begin{aligned} \dot{x} - V_\infty \cos\psi &= 0 \\ \dot{y} - V_\infty \sin\psi &= 0 \\ T\cos\varepsilon - D - m\dot{V}_\infty &= 0 \\ (T\sin\varepsilon + L)\sin\phi - mV\dot{\psi} &= 0 \\ (T\sin\varepsilon + L)\cos\phi - mg &= 0 \\ \dot{m}g + c_t T &= 0 \end{aligned} \quad \Rightarrow \quad \begin{aligned} \dot{x} - V_\infty \cos\psi &= 0 \\ \dot{y} - V_\infty \sin\psi &= 0 \\ T - D &= 0 \\ L\sin\phi - mV\dot{\psi} &= 0 \\ L\cos\phi - mg &= 0 \\ \dot{m}g + c_t T &= 0 \end{aligned} \tag{20-4}$$

The third, fourth, and fifth equations of Equations (20-4) are called the *governing equations-of-motion for flight in the horizontal plane*. Note that $V_\infty = R_{turn}\dot{\psi} \;\Leftrightarrow\; \dot{\psi} = V_\infty / R_{turn}$, where R_{turn} is the turn radius (see Figure 17-2).

$$\text{Fore-aft forces:} \qquad D = T \tag{20-5}$$

$$\text{Lateral forces:} \qquad L\sin\phi - \frac{W}{g}\frac{V_\infty^2}{R_{turn}} = 0 \tag{20-6}$$

$$\text{Vertical forces:} \qquad L\cos\phi - W = 0 \tag{20-7}$$

20.2.2 Fundamental Concepts

This section presents and restates several important concepts for analysis of steady, level cruising speed.

(1) Weight Model

Is a mathematical description of the weight of the aircraft. It should account for weight due to changes in fuel, number of occupants, and baggage. A detailed weight model also provides the resulting center-of-gravity and inertia parameters (moments and products of inertia). For steady-state flight, we primarily need weight and CG-position (to account for trim drag). See Sections 6.4, *Statistical Weight Estimation Methods* and 6.6, *Inertia Properties* for more information. This model could resemble something as shown below

$$W = W_e + W_c + W_p + \left[W_f - \int_0^{\Delta t} (c_t T)dt\right] \tag{20-8}$$

Where W_e is empty weight, W_c is crew weight, W_p is payload, W_f is initial fuel weight, the product inside the integral is the fuel consumption in units of weight per unit time, and Δt is duration of flight (see Section 21.1.4, *Specific Fuel Consumption*). It permits time history of the fuel consumption to be accounted for. Frequently, the integration is unnecessary as we know the fuel weight at specific stages of the mission. For instance, this can be assessed using the mission analysis of Section 6.2.3, *Method 3: Initial Gross Weight Estimation using Mission Analysis*.

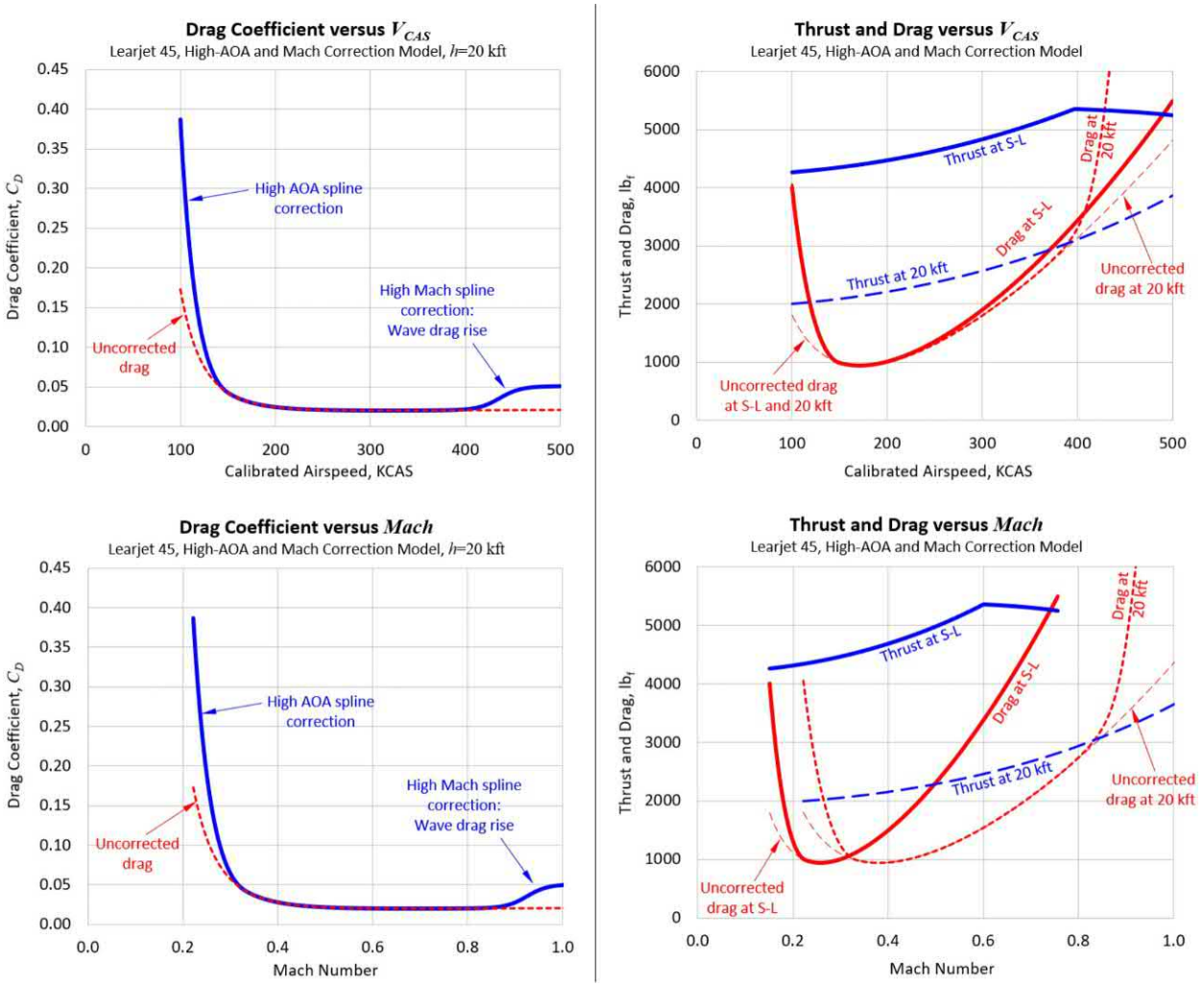


FIGURE 20-3 Estimated drag and thrust for the Learjet 45 at S-L and 20,000 ft.

(2) Thrust Model

Is a mathematical description of the thrust and/or thrust coefficient. See Section 24.2.4, *The Thrust Model*. Various methods to develop a thrust model are provided in Chapters 7, 14, and 15. An example thrust model is shown in Figure 20-3. It uses the Mattingly model of Section 14.3.4, *Mattingly Model for a Turbofan Engine*.

$$T = T(h, V_\infty, \delta_T) \tag{20-9}$$

Where δ_T is the power lever variable.

(3) Lift Model

Is a mathematical description of the lift coefficient, C_L. It is necessary to prepare a specific lift model for each configuration of the aircraft, i.e., the *clean*, *T-O*, and *landing configurations* will each have their own lift model. See Sections 9.5.2, *The Lift Model* and 24.2.5, The Lift Model for more information.

(4) Drag Model

Is a mathematical description of the drag coefficient. Like the lift model, a specific drag model must be prepared for each configuration of the aircraft. See Sections 16.2.1, *Fundamental Definitions* and 24.2.6, *The Drag Model* for more information. An estimation of the drag and thrust for a small business jet is shown in Figure 20-3. The drag coefficient versus V_{CAS} (upper image) and Mach (lower image) are shown in the left column. The corresponding thrust and drag forces are shown in the right column. Figure 20-4 shows the total drag force broken into its three constituent contributors; minimum, lift induced, and wave drag.

(5) Drag Polar

Is a graph of C_D versus C_L (see Section 16.2.1(5)). It is a product of the drag model. Figure 20-5 shows a drag polar example for the Learjet 45. It shows how drag changes with lift and how higher Mach numbers affect

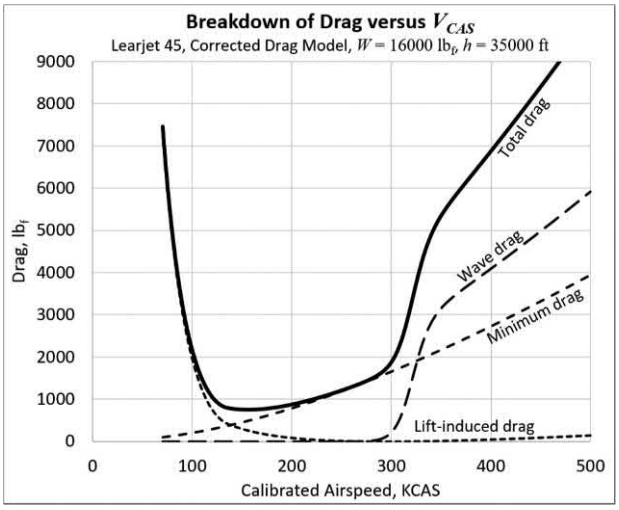


FIGURE 20-4 A break-down of contributors to the total drag of the Learjet 45.

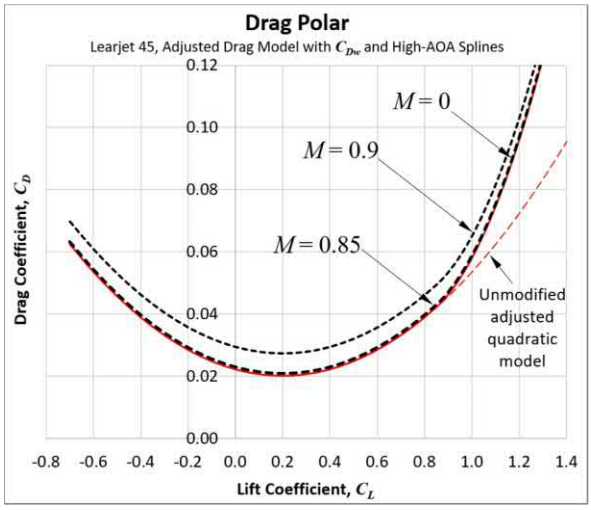


FIGURE 20-5 The drag polar for the Learjet 45.

this relationship. These changes are modeled using Equation (16-106) of Section 16.3.3, *Estimating Wave Drag*. The $M = 0$ curve also includes the high-AOA correction spline Equation (16-20) of Section 16.2.3, *Correcting the Drag Coefficient at High AOA*.

(6) Airspeed Associated with a Specific Lift Coefficient

The airspeed that must be maintained given a specific C_L is obtained by solving the lift equation for V_∞ (see derivation for Equation 20-29)

$$V_\infty = \sqrt{\frac{2W}{\rho S C_L}} \tag{20-10}$$

(7) Thrust Required and Thrust Available

Thrust required, T_{REQ}, is the thrust the power plant must develop to maintain altitude at the specified airspeed. As we have shown, this means

$$T_{REQ} = D \tag{20-11}$$

Thrust available, T_{AV}, is the thrust delivered by the power plant at a given instant. This depends on the position of the engine's power lever. Per Equation (24-31), thrust can be expressed as

$$T_{AV} = T(h, V_\infty, \delta_T) \tag{20-12}$$

(8) Power Required

Power required, P_{REQ}, is the power required to maintain level flight at a specific airspeed and altitude ("at condition"). It is the product of drag and true airspeed.

$$P_{REQ} = DV_\infty \tag{20-13}$$

Where D is the drag at airspeed V_∞. If we know the lift and drag coefficient at the specific flight condition, we can also calculate P_{REQ} for level flight at that condition using the expression below:

$$P_{REQ} = \sqrt{\frac{2W^3 C_D^2}{\rho S C_L^3}} \tag{20-14}$$

If using the UK-system, P_{REQ} will be in terms of ft lb$_f$/s and can be converted to BHP by a division by 550. In the SI-system the units are in Watts or Joules/second. By inspection, the power required to propel the aircraft at a given flight condition (specified through C_L and C_D) depends on:

$$P_{REQ} \propto \frac{C_D}{C_L^{3/2}} \tag{20-15}$$

The smaller this ratio, the less is the power required to maintain level flight. The minimum of this ratio corresponds to the airspeed of minimum power required and the maximum of the ratio $C_L^{3/2}/C_D$. It can be calculated from Equation (20-48).

(9) Power Available

Power available, P_{AV}, is the available thrust-power at the specified airspeed. This depends on the position of the engine's power lever. Per Equation (24-31), thrust can be expressed as

$$P_{AV} = T(h, V_\infty, \delta_T) V_\infty = TV_\infty \tag{20-16}$$

If the power generated by a piston engine and propeller efficiency is known, the power available for propulsion is defined using the expression below:

$$P_{AV} = T_{AV} \cdot V_\infty = \eta_p \cdot 550 \cdot P_{BHP} \tag{20-17}$$

Note that η_p is the propeller efficiency and it is a function of the airspeed, RPM, and propeller geometry. Refer to Chapter 15, *Thrust Modeling for Propellers*, for more information. An equilibrium flight is achieved when $P_{AV} = P_{REQ}$ and coincides with $T_{AV} = T_{REQ}$.

(10) Region of Speed Stability

An important point can be made regarding T_{AV} and T_{REQ}. Figure 20-6 shows two regions of importance, referred to as the regions of *speed stability* and *instability*.

Region of Speed Stability

Assume the airplane in Figure 20-6 is flying at, say, 270 KCAS when a sudden gust or change in attitude reduces its airspeed. This reduces its drag, which, in turn, gives rise to tendency for the airspeed to increase (assuming fixed thrust setting), eventually bringing it back to 270 KCAS (at least theoretically). By the same token, should the gust increase the airspeed of the airplane, its drag increases, reducing the airspeed, again, bringing it back to 270 KCAS. This phenomenon is recognized by pilots as *speed stability*.

Region of Speed Instability

Again consider Figure 20-6. Assume we are flying at 150 KCAS when the airplane experiences a speed reduction. This increases the drag, reducing the airspeed further. Should the airplane experience a speed increase, its drag is reduced, increasing the airspeed further. This phenomenon is called *speed instability* and is recognized by pilots as flying "on the back side of the power curve." Speed instability can be helpful during landing, as it helps the pilot slow down the airplane during flare. It can also be detrimental if the aircraft slows rapidly and stalls.

DERIVATION OF EQUATION (20-14)

Preliminary definitions:

$$P_{REQ} = T_{REQ} \cdot V_\infty \quad \text{and} \quad \frac{C_L}{C_D} = \frac{L}{D} = \frac{W}{T} \quad \text{and} \quad V_\infty = \sqrt{\frac{2W}{\rho S C_L}}$$

Therefore: $P_{REQ} = T_{REQ} \cdot V_\infty$

$$= \left(\frac{W}{C_L/C_D}\right)_{REQ} \cdot \sqrt{\frac{2W}{\rho S C_L}} = \frac{W}{C_L/C_D} \cdot \sqrt{\frac{2W}{\rho S C_L}} = \sqrt{\frac{2W^3 C_D^2}{\rho S C_L^3}}$$

(11) A Few Words about Analysis Quality

The quality of the performance analysis should be of great concern to anyone involved in aircraft design. This author finds it helpful to score the analysis based on the quality of the drag and propulsion models. It also helps students understand that both models contribute to the overall accuracy. This gives rise to the following classes (Class A = most accurate, Class D = least accurate):

	Constant Thrust or Power	Non-constant Thrust or Power
(1) Advanced drag models	Class B	Class A
(2) Adjusted drag model	Class C	Class B
(3) Simplified drag model	Class D	Class C

Class D methods are primarily helpful in introducing performance concepts to students. They can also help establish initial values for iteration schemes. However, they should not be used for serious analysis work. Class B and C methods are an improvement, but their limitations should be stated in serious analysis work. Class C is a practical approach in university classes. Class A methods are time consuming to implement, but return

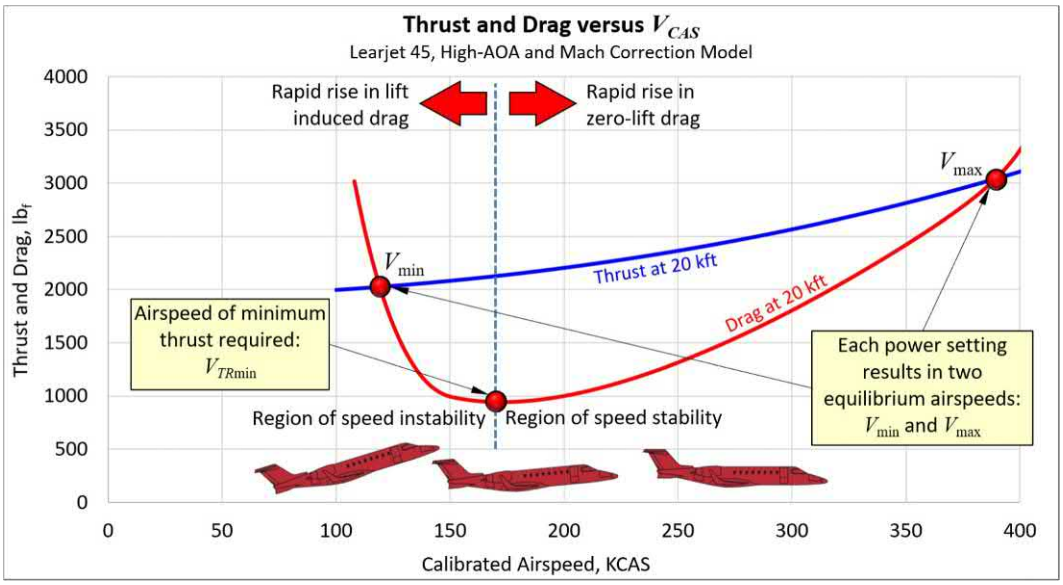


FIGURE 20-6 Regions of speed stability and instability.

the most realistic results. Such methods are usually implemented in spreadsheets and computer codes, as well as in flight simulators. They incorporate sophisticated drag analyses, ideally based on wind-tunnel testing and the use of engine deck developed by an engine manufacturer.

20.3 GENERAL CRUISE ANALYSIS METHODS FOR STEADY FLIGHT

This section introduces classical analysis methods for steady, level cruise performance. The methods are presented in two forms, as closed-form solutions and, for improved accuracy, as formulae requiring iterative solution schemes.

20.3.1 Airspeed in Terms of Thrust

This section presents a method to estimate airspeed as a function of thrust.

(1) A General Expression of Airspeed in Terms of Thrust:

Consider thrust and drag given by the quadratic polynomial and adjusted drag model below

$$T \equiv AV_\infty^2 + BV_\infty + C \quad \text{and}$$
$$D = \frac{1}{2}\rho V_\infty^2 S\left(C_{D_{\min}} + k(C_L - C_{L_{\min D}})^2\right) \tag{20-18}$$

Then, the minimum and maximum airspeeds can be estimated by solving the quartic equation

$$\left(A - \frac{1}{2}\rho S\left(C_{D_{\min}} + kC_{L_{\min D}}^2\right)\right)V_\infty^4 + BV_\infty^3 + (C + 2kWC_{L_{\min D}})V_\infty^2 - \frac{2kW^2}{\rho S} = 0 \tag{20-19}$$

This expression is best solved using an iterative scheme, for instance the *bisection method* or *Regula Falsi*. It applies to propeller-powered and jet aircraft with airspeed-dependent thrust. Generally, there are two solutions. One is associated with low speed, the other with high speed. It has closed-form solutions for the specific cases presented below.

(2) Special Solution for Constant Thrust and Simplified Drag Model

In this case, $C_{L_{\min D}} = 0$, $A = B = 0$, and $C = T =$ constant. Thus, Equation (20-19) becomes

$$\frac{1}{2}\rho S C_{D_{\min}} V_\infty^4 - TV_\infty^2 + \frac{2kW^2}{\rho S} = 0 \tag{20-20}$$

To solve for V_∞, set $u = V_\infty^2$ and solve the resulting quadratic form for u and, then, take the square-root of u. This gives the following expression

$$V_\infty = \sqrt{\frac{T \pm \sqrt{T^2 - 4kW^2 C_{D_{\min}}}}{\rho S C_{D_{\min}}}} \tag{20-21}$$

The plus-sign under the outside radical returns $V_{\max}$, while the minus returns $V_{\min}$ at the specific thrust T. As usual, the units for the airspeed are ft/s in the UK-system and m/s in the SI-system.

(3) Special Solution for Constant Thrust and Adjusted Drag Model

In this case, $C_{L_{\min D}} \neq 0$, $A = B = 0$, and $C = T =$ constant. Thus, Equation (20-19) becomes

$$\frac{1}{2}\rho S\left(C_{D_{\min}} + kC_{L_{\min D}}^2\right)V_\infty^4 - (T + 2kWC_{L_{\min D}})V_\infty^2 + \frac{2kW^2}{\rho S} = 0 \tag{20-22}$$

To solve for V_∞, set $u = V_\infty^2$ and solve the resulting quadratic form for u and, then, take the square-root of u. This gives the following expression

$$V_\infty = \sqrt{\frac{(T + 2kWC_{L_{\min D}}) \pm \sqrt{(T + 2kWC_{L_{\min D}})^2 - 4kW^2\left(C_{D_{\min}} + kC_{L_{\min D}}^2\right)}}{\rho S\left(C_{D_{\min}} + kC_{L_{\min D}}^2\right)}} \tag{20-23}$$

DERIVATION OF EQUATION (20-19)

Equilibrium requires $T = D$. Therefore, we get

$$AV_\infty^2 + BV_\infty + C = \frac{1}{2}\rho V_\infty^2 S\left(C_{D_{\min}} + k\left(\frac{W}{\frac{1}{2}\rho V_\infty^2 S} - C_{L_{\min D}}\right)^2\right)$$

Expand the drag coefficient to get

$$AV_\infty^2 + BV_\infty + C = \frac{1}{2}\rho V_\infty^2 S C_{D_{\min}} + \frac{1}{2}\rho V_\infty^2 Sk\left(\frac{4W^2}{\rho^2 V_\infty^4 S^2} - \frac{4W}{\rho V_\infty^2 S}C_{L_{\min D}} + C_{L_{\min D}}^2\right)$$

Expand the expression right of the equal sign and collect terms.

DERIVATION OF EQUATION (20-19) (*cont'd*)

$$AV_\infty^2 - \frac{1}{2}\rho V_\infty^2 S C_{D_{\min}} - \frac{1}{2}\rho V_\infty^2 S k C_{L_{minD}}^2 + BV_\infty - \frac{2kW^2}{\rho V_\infty^2 S} + (C - 2kWC_{L_{minD}}) = 0$$

Simplifying leads to Equation (20-19).

20.3.2 Estimation of Minimum and Maximum Airspeed

Figure 20-6 shows an important consequence of available and required thrust; two possible equilibrium airspeeds, one low ($V_{\min}$) and one high ($V_{\max}$). At those points, $T_{AV} = T_{REQ}$. One and only one airspeed will result in a condition at which the two are equal; this is the *airspeed of minimum thrust required* ($V_{TR_{\min}}$).

Note that while these airspeeds are associated with specific thrust settings, their lowest $V_{\min}$ and largest $V_{\max}$ values occur at the maximum available thrust at the specific altitude. Unless otherwise specified, the variables $V_{\min}$ and $V_{\max}$ denote those extremes at the maximum thrust. These methods apply propeller-powered and jet aircraft.

(1) Minimum Level Airspeed, $V_{\min}$

To estimate $V_{\min}$ using Equation (20-19), apply an iterative solution. Select a low value of V_∞ as an initial value. If estimating $V_{\min}$ using Equation (20-21) or (20-23), substitute the maximum thrust available ($T_{AV_{\max}}$) at the specific altitude. Using the simplified drag model and constant thrust, $V_{\min}$ is given by

$$V_{\min} = \sqrt{\frac{T_{AV_{\max}} - \sqrt{T_{AV_{\max}}^2 - 4kW^2 C_{D_{\min}}}}{\rho S C_{D_{\min}}}} \tag{20-24}$$

Using the adjusted model, $V_{\min}$ is given by

$$V_{\min} = \sqrt{\frac{(T_{AV_{\max}} + 2kWC_{L_{minD}}) - \sqrt{(T_{AV_{\max}} + 2kWC_{L_{minD}})^2 - 4kW^2\left(C_{D_{\min}} + kC_{L_{minD}}^2\right)}}{\rho S\left(C_{D_{\min}} + kC_{L_{minD}}^2\right)}} \tag{20-25}$$

It is common in *theoretical analyses* that $V_{\min}$ is less than the stalling speed, V_S (see Figures 17-12 and 17-13). In this case, set $V_{\min} = V_S$. In *practice*, chances are that $V_{\min}$ is greater than V_S. This is a consequence of forward CG position or high altitude. This is undesirable, because in the eyes of the authorities, $V_{\min}$ impacts various regulatory paragraphs, making compliance harder. The lower the available thrust, the closer will these speeds be to each other.

(2) Maximum Level Airspeed, $V_{\max}$

$V_{\max}$ is of great interest in the marketing, certification, and operation of the aircraft. High maximum airspeed has a great marketing appeal, especially when compared to slower rival aircraft. This airspeed is denoted by the variable V_H in 14 CFR Part 23.

To estimate $V_{\max}$ using Equation (20-19), apply an iterative solution. Select a high value of V_∞ as an initial value. For instance, estimate $V_{\max}$ using Equation (20-21) or (20-23) for use as an initial value. Use the maximum thrust available ($T_{AV_{\max}}$) at the specific altitude. Using the simplified drag model and constant thrust, $V_{\max}$ is given by

$$V_{\max} = \sqrt{\frac{T_{AV_{\max}} + \sqrt{T_{AV_{\max}}^2 - 4kW^2 C_{D_{\min}}}}{\rho S C_{D_{\min}}}} \tag{20-26}$$

For the adjusted drag model use:

$$V_{\max} = \sqrt{\frac{(T_{AV_{\max}} + 2kWC_{L_{minD}}) + \sqrt{(T_{AV_{\max}} + 2kWC_{L_{minD}})^2 - 4kW^2\left(C_{D_{\min}} + kC_{L_{minD}}^2\right)}}{\rho S\left(C_{D_{\min}} + kC_{L_{minD}}^2\right)}} \tag{20-27}$$

It is common in *theoretical analyses* that $V_{\max}$ exceeds the regulatory constraints such as 14 CFR §91.117 *Aircraft Speed*[1] and aerodynamic constraints such as V_{MO} and M_{MO} (maximum operating airspeed/Mach number). Equations (20-26) and (20-27) are implemented in the computer code in Section 20.3.12.

[1] §91.117 stipulates 250 KIAS maximum airspeed at 2500 ft < h < 10,000 ft and 250 KIAS maximum airspeed at h < 2500 ft, depending on airspace Class.

EXAMPLE 20-1

Determine V_{min} and V_{max} for the Learjet 45 using the simplified and adjusted drag models. Assume a constant thrust of 2000 lb_f, altitude of 30,000 ft, and weight of 20,000 lb_f.

$$V = \sqrt{\frac{2000 \pm \sqrt{2000^2 - 4(0.05236)(20,000)^2(0.0234)}}{(0.0008897)(311.6)(0.0234)}} = \begin{cases} 727.0\,\text{ft/s} = 430.7\,\text{KTAS} \\ 296.9\,\text{ft/s} = 175.9\,\text{KTAS} \end{cases}$$

SOLUTION:

Simplified drag model: $V = \sqrt{\dfrac{T \pm \sqrt{T^2 - 4kW^2 C_{D_{min}}}}{\rho S C_{D_{min}}}}$

Adjusted drag model: $V = \sqrt{\dfrac{(T + 2kWC_{L_{minD}}) \pm \sqrt{(T + 2kWC_{L_{minD}})^2 - 4kW^2\left(C_{D_{min}} + kC_{L_{minD}}^2\right)}}{\rho S\left(C_{D_{min}} + kC_{L_{minD}}^2\right)}}$

$$V = \begin{cases} 849.4\,\text{ft/s} = 503.2\,\text{KTAS} \\ 261.5\,\text{ft/s} = 154.9\,\text{KTAS} \end{cases}$$

The following observations can be made:

(1) V_{max} increases with $T_{AV_{max}}$
(2) V_{max} increases with W/S
(3) V_{max} increases if $C_{D_{min}}$ and/or k decreases (AR increases).

(3) Special Case: V_{max} for Propeller Aircraft

If the thrust model of Section 15.4.3, *Initial Thrust Model for a Fixed-Pitch Propeller* is used with a propeller aircraft, its coefficients A, B, and C can be substituted directly into Equation (20-19), provided they are based on m/s or ft/s true airspeed. Alternatively, if such a model has not been developed, it is possible to estimate V_{max} by assuming a likely propeller efficiency (η_p) and solving the following expression iteratively. Note that it assumes the simplified drag model.

$$\rho S C_{D_{min}} V_{max}^3 - 550\eta_p P_{HP} - \sqrt{\left(550\eta_p P_{HP}\right)^2 - 4kW^2 V_{max}^2 C_{D_{min}}} = 0 \tag{20-28}$$

The terms under the radical must satisfy $550\eta_p P_{HP} > 2WV_{max}\sqrt{kC_{D_{min}}}$. This method is implemented in the computer code in Section 20.3.11.

DERIVATION OF EQUATION (20-28)

Formulation is obtained by substituting Equation (15-52) into Equation (20-26):

$$V_{max} = \sqrt{\frac{T_{AV_{max}} + \sqrt{T_{AV_{max}}^2 - 4kW^2 C_{D_{min}}}}{\rho S C_{D_{min}}}} = \sqrt{\frac{\dfrac{550\eta_p P_{HP}}{V_{max}} + \sqrt{\left(\dfrac{550\eta_p P_{HP}}{V_{max}}\right)^2 - 4kW^2 C_{D_{min}}}}{\rho S C_{D_{min}}}}$$

tWhere P_{HP} is the engine power rating in HP. Manipulate algebraically:

$$V_{max} = \sqrt{\frac{550\eta_p P_{HP} + \sqrt{\left(550\eta_p P_{HP}\right)^2 - 4kW^2 V_{max}^2 C_{D_{min}}}}{V_{max}\rho S C_{D_{min}}}}$$

From which we get:

$$V_{max}^2 = \frac{550\eta_p P_{BHP} + \sqrt{\left(550\eta_p P_{BHP}\right)^2 - 4kW^2 V_{max}^2 C_{D_{min}}}}{V_{max}\rho S C_{D_{min}}}$$

$$\Rightarrow \quad \rho S C_{D_{min}} V_{max}^3 = 550\eta_p P_{BHP} + \sqrt{\left(550\eta_p P_{BHP}\right)^2 - 4kW^2 V_{max}^2 C_{D_{min}}}$$

EXAMPLE 20-2

The POH for the SR22 gives a cruising speed of 169 KTAS at 55% power at 14,000 ft. Using the minimum drag coefficient extracted for the airplane in Example 16-24 ($C_{D_{min}} = 0.02541$), solve Equation (20-28) iteratively to estimate V_{max} (which here is the cruising speed at 55% power). The Oswald's efficiency was calculated in Example 16-24 and amounts to 0.7566. Wing area is 144.9 ft^2 and density at 14,000 ft is 0.001546 slugs/ft^3. Assume a propeller efficiency of 0.85 and max rated S-L power of 310 BHP.

SOLUTION:

Begin by calculating all coefficient products in Equation (20-28) (ignoring to show units):

$$\rho S C_{D_{min}} = (0.001546)(144.9)(0.02541) = 0.005691$$

$$550\eta_p P_{BHP} = (550)(0.85)(0.55 \times 310) = 79{,}708.75$$

$$4kW^2 C_{D_{min}} = 4W^2 C_{D_{min}} \left(\frac{1}{\pi \cdot AR \cdot e}\right) = 48{,}274.421$$

Substituting these into Equation (20-28) leads to:

$$\rho S C_{D_{min}} V_{max}^3 - 550\eta_p P_{HP} - \sqrt{\left(550\eta_p P_{HP}\right)^2 - 4kW^2 V_{max}^2 C_{D_{min}}} = 0$$

$$\Rightarrow \quad 0.005691 V_{max}^3 - 79{,}709 - \sqrt{79{,}709^2 - 48{,}274 V_{max}^2} = 0$$

Let us begin the iteration by picking a token initial value for V_{max}, say 270 ft/s:

Iteration 1—V_{max} = 270 ft/s:

$$\Delta_1 = 0.005691(270)^3 - \left(79{,}709 + \sqrt{79{,}709^2 - 48{,}274(270)^2}\right) = -20{,}926.53226$$

The value is negative so increase V_{max}.

Iteration 2—V_{max} = 280 ft/s:

$$\Delta_2 = 0.005691(280)^3 - \left(79{,}709 + \sqrt{79{,}709^2 - 48{,}274(280)^2}\right) = -5458.251944$$

Since the difference is smaller than before, we are getting closer to a solution. It is still negative so let's increase V_{max} a tad, say 283.5 ft/s.

Iteration 3—V_{max} = 283.5 ft/s:

$$\Delta_3 = 0.005691(283.5)^3 - \left(79{,}709 + \sqrt{79{,}709^2 - 48{,}274(283.5)^2}\right) = 233.6918365$$

Continuing in this manner, we can show the solution converges to $V_{max} = 283.4$ ft/s. This amounts to 167.9 KTAS, which compares favorably with the POH value.

EXAMPLE 20-3

The POH for the SR22 gives maximum cruising speed for altitudes ranging from 2000 to 17,000 ft. Using the subroutine of Section 20.3.11 with Microsoft Excel, estimate the maximum level airspeed up to 25,000 ft and compare to the POH values. Use the same properties used in the previous examples, but account for the fact that the weight of the aircraft reduces with altitude. That is, while it takes off at 3400 lb$_f$, it will certainly weigh less at top-of-climb. The amount of fuel consumed is also given in the POH and by interpolating this data, the following expression was derived to calculate weight as a function of altitude:

$$W(h) = W_0 - 0.000000062809h^2 - 0.0013875h - 0.90965$$

Where the gross weight is $W_0 = 3400$ lb$_f$.

SOLUTION:

The solution was implemented in Microsoft Excel and the results presented in Figure 20-7 were obtained. Note that the method assumes the simplified drag model.

EXAMPLE 20-3 (*cont'd*)

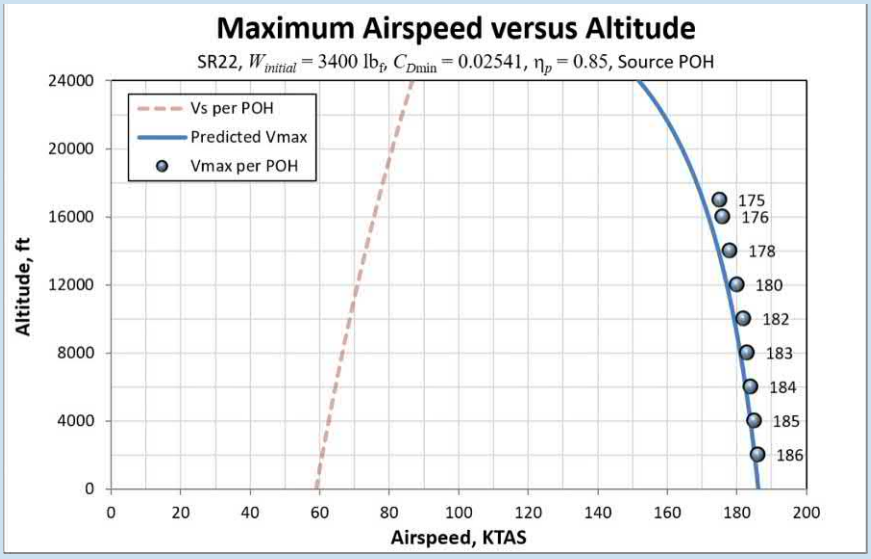


FIGURE 20-7 Comparing maximum airspeed predictions generated using the computer code presented in this section to actual flight data from the Pilot's Operating Handbook (POH).

20.3.3 Estimation of Stalling Speed

The stalling speed, V_S, is the minimum speed at which an airplane can maintain altitude. Theoretically, if the airspeed is slowed a hair below the stalling speed, a well-designed airplane drops its nose uncontrollably, while maintaining wings level. This nose drop is followed by a dive during which the airplane again becomes airborne. This is illustrated in Figure 9-92. During conceptual design, the maximum lift coefficient, $C_{L_{max}}$, is estimated, allowing the 1-*g stalling speed* to be estimated:

$$V_S = \sqrt{\frac{2W}{\rho S C_{L_{max}}}} \tag{20-29}$$

Figure 20-8 shows how the stalling speed changes with altitude in terms of specific airspeed types. Consider a stalling speed of 120 KEAS (which is constant with altitude). The pilot would see the V_S increase slightly in terms of indicated and/or calibrated airspeed. In contrast, the true airspeed increases significantly with altitude. It affects impact loads in emergency landings and durability of brakes for airplanes consistently operated from high altitude airports.

(1) Level Stalling Speed with a Load Factor *n*

If the airplane is performing some specific wings level maneuver, e.g., a *loop*, it is subjected to an increase in load factor. If the total load factor is denoted by n ($n = 1$ for level flight), the stalling speed will change and can be calculated by making the following modification to Equation (20-29):

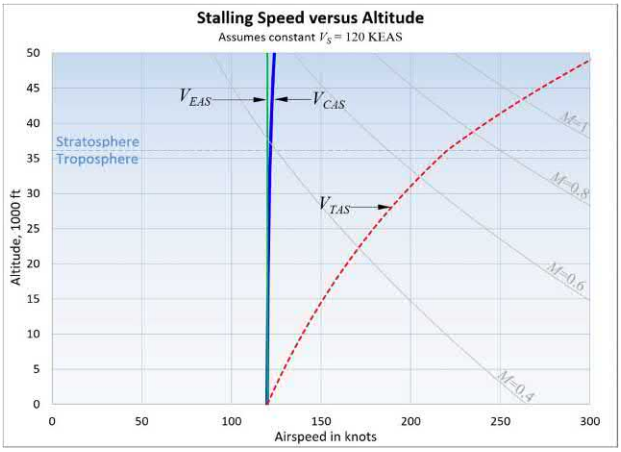


FIGURE 20-8 V_S in KEAS, KCAS, and KTAS as a function of altitude.

$$V_{S_n} = \sqrt{\frac{2nW}{\rho S C_{L_{max}}}} = V_S\sqrt{n} \tag{20-30}$$

(2) Stalling Speed during Banking

If the airplane's bank-angle is ϕ in level flight (level constant speed turn) the load factor acting on it increases. Thus, its stalling speed increases. Using Equation (20-30), the stalling speed at a specific bank-angle ϕ is given by

$$V_{S_\phi} = \sqrt{\frac{2W}{\rho S C_{L_{max}} \cos\phi}} = \frac{V_S}{\sqrt{\cos\phi}} \tag{20-31}$$

(3) Level Stalling Speed with Thrust, Flap, and CG Effects

In practice, the stalling speed is affected by engine thrust, flap deflection, and the CG location. Thrust and deployed flaps reduce the stalling speed, while a forward location of the CG increases it. The forward CG requires higher download to be generated by the HT for trim. This load is added to the weight of the aircraft, which means the wing must generate lift greater than the weight of the airplane. This increases the stalling speed. The same stabilizing effect due to flaps will also render the stall speed reduction smaller than in its absence. To approximate these effects, the stalling speed must be calculated as shown below:

$$V_S = \sqrt{\frac{2}{\rho S C_{L_{max}}}\left(1-\frac{x_{CG}-x_n}{l_{HT}}\right)\left[W-\frac{M_W}{l_{HT}-x_{CG}+x_n}-\left(\frac{x_T\cdot\sin\alpha - z_T\cdot\cos\alpha}{l_{HT}-x_{CG}+x_n}+\sin\alpha\right)T\right]} \tag{20-32}$$

Where M_W is the wing pitching moment about the wing's aerodynamic center. Refer to Figure 20-9 for the dimensions x_{CG}, x_n, x_T, z_T, and l_{HT}. This expression is suitable for conventional tail-aft configurations only. It requires an iterative scheme to solve, because both M_W and T depend on airspeed. If the expected stalling speed is known, it can be used to calculate both M_W and T, which can then be used as constants in the formulation with acceptable accuracy. However, implementing the calculations in a spreadsheet will make it easy to solve iteratively. Note that the effect of flaps must be accounted for in the variable M_W. Example 20-4 demonstrates the use of this equation and evaluates its accuracy.

DERIVATION OF EQUATIONS (20-29)–(20-31)

Formulation is obtained from Equation (8-7), by solving the lift equation for V_∞. It applies to all three equations:

$$L=\frac{1}{2}\rho V_\infty^2 S C_L \quad\Leftrightarrow\quad V_\infty=\sqrt{\frac{2W}{\rho S C_L}}$$

DERIVATION OF EQUATION (20-32)

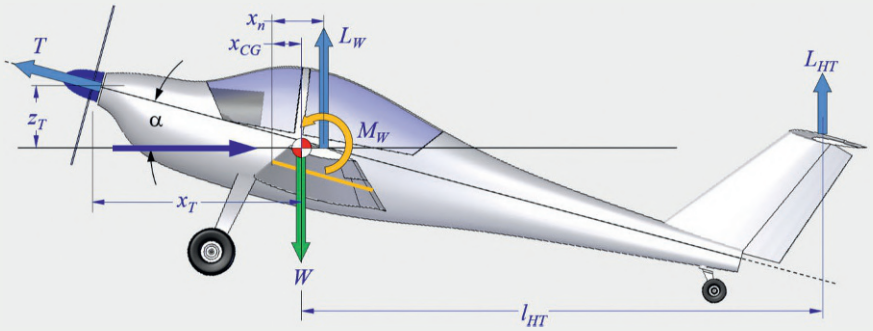


FIGURE 20-9 A simple system used to derive the simplest formulation of trim drag.

Referring to Figure 20-9, statics requires the following to hold in steady-level flight, where at the point of stall, the lift of the wing, L_W, will depend on the maximum lift coefficient of the wing.

Referring to Figure 20-9, statics requires the following to hold in steady-level flight (positive moments are clockwise):

$$\sum F_z = 0; \qquad L_W + L_{HT} + T\sin\alpha - W = 0$$

$$\sum M_{CG} = 0; \qquad M_W + (x_{CG}-x_n)L_W - (l_{HT}-x_{CG}+x_n)L_{HT} + x_T\cdot T\sin\alpha - z_T\cdot T\cos\alpha = 0$$

Note that M_W is a negative (nose-down) value. Following a similar process as for the derivation of Equation (16-142), the moment equation can be solved for the balancing force the HT must generate:

$$L_{HT}=\frac{M_W+(x_{CG}-x_n)L_W+x_T\cdot T\sin\alpha - z_T\cdot T\cos\alpha}{(l_{HT}-x_{CG}+x_n)}$$

This includes any tail efficiency, η_{HT}, the HT is subjected to. Substituting this result into the force equation and simplifying leads to

$$\left(\frac{l_{HT}}{l_{HT}-x_{CG}+x_n}\right)L_W = W-\frac{M_W}{l_{HT}-x_{CG}+x_n} - \left(\frac{x_T\cdot\sin\alpha - z_T\cdot\cos\alpha}{l_{HT}-x_{CG}+x_n}+\sin\alpha\right)T$$

DERIVATION OF EQUATION (20-32) (*cont'd*)

Solving for L_W leads to

$$L_W = \left(1 - \frac{x_{CG} - x_n}{l_{HT}}\right)\left[W - \frac{M_W}{l_{HT} - x_{CG} + x_n} - \left(\frac{x_T \cdot \sin\alpha - z_T \cdot \cos\alpha}{l_{HT} - x_{CG} + x_n} + \sin\alpha\right)T\right]$$

At stall, $L_W = \frac{1}{2}\rho V_S^2 S C_{L_{max}}$, so solving for V_S yields:

$$V_S = \sqrt{\frac{2}{\rho S C_{L_{max}}}\left(1 - \frac{x_{CG} - x_n}{l_{HT}}\right)\left[W - \frac{M_W}{l_{HT} - x_{CG} + x_n} - \left(\frac{x_T \cdot \sin\alpha - z_T \cdot \cos\alpha}{l_{HT} - x_{CG} + x_n} + \sin\alpha\right)T\right]}$$

EXAMPLE 20-4

Determine the S-L stalling speed (i.e., in KCAS) of the SR22 at its forward and aft CG limits at gross weight, with and without full power, using Equation (20-32). Assume the stall AOA is 16 degrees, maximum lift coefficient of 1.45, and the following parameters:

S = Wing area = 144.9 ft^2	c_{MGC} = 3.783 ft	W = Gross weight = 3400 lb$_f$
$C_{m_W} = -0.06$	l_{HT} = 14.06 ft	
$x_{CG_{fwd}} = 0.192 c_{MGC}$	$x_{CGaft} = 0.315 c_{MGC}$	$x_n = 0.40 c_{MGC}$ (assumed)
x_T = 5 ft	$z_T = 1$	η_p = Propeller efficiency = 0.65

The forward CG limit is at $0.192c_{MGC}$, and the aft at $0.315c_{MGC}$, according to the POH. Compare the power off values to the POH (V_S at forward CG is 70 KCAS and at aft CG is 69 KCAS). Therefore, use 70 KCAS to calculate the value of M_W.

SOLUTION:

Solution will be demonstrated for only one case of the four being requested; the forward CG power off case. Only the results for the others will be presented. Wing pitching moment at 70 KCAS is:

$$M_W = \frac{1}{2}\rho V_S^2 S c_{MGC} C_{m_W}$$
$$= \frac{1}{2}(0.002378)(70 \times 1.688)^2(144.9)(3.783)(-0.06)$$
$$= -546 \text{ ft lb}_f$$

For the power-on cases use the following thrust at 70 KCAS, given by Equation (15-52):

$$T = \frac{\eta_p 550 P_{BHP}}{V_\infty} = \frac{(0.65)(550)(310)}{(70)(1.688)} = 938 \text{ lb}_f$$

Simplify Equation (20-32) by rewriting it as follows:

$$V_S = \sqrt{A \cdot B \cdot C}$$

Here, the power off, forward CG case is being solved (assume $T = 0$). This yields the following values of A, B, and C:

$$A = \frac{2}{\rho S C_{L_{max}}} = \frac{2}{(0.002378)(144.9)(1.45)} = 4.003$$

$$B = 1 - \frac{x_{CG} - x_n}{l_{HT}} = 1 - \frac{(0.192 - 0.40)(3.783)}{14.06} = 1.056$$

$$C = W - \frac{M_W}{l_{HT} - x_{CG} + x_n} - \left(\frac{x_T \cdot \sin\alpha - z_T \cdot \cos\alpha}{l_{HT} - x_{CG} + x_n} + \sin\alpha\right)T = 3437 \text{ lb}_f$$

Therefore, the power-off stalling speed at the forward CG-limit is:

$$V_S = \sqrt{A \cdot B \cdot C} = \sqrt{(4.003)(1.056)(3437)} = 120.5 \text{ ft/s} = 71.4 \text{ KCAS}$$

Similarly, the power-off stalling speed at the aft CG-limit is:	V_S = 70.3 KCAS
Power-on stall at the forward CG-limit is:	V_S = 68.4 KCAS
And power-on stall at the aft CG-limit is:	V_S = 67.3 KCAS

The analysis shows the power-off results compare favorably with the published numbers.

20.3.4 Airspeed of Maximum Lift-to-Drag Ratio

One of the most important performance parameters of an aircraft is its maximum lift-to-drag ratio, LD_{max}. In addition to the properties stated in Bullet (3) of this section, this ratio indicates how far an airplane will glide from a given altitude (see Section 22.3.8, *Glide Distance*). Table 16-22 shows typical values for LD_{max} for several classes of aircraft.

The ratio is commonly known as the *best glide ratio* and, less commonly, as the *minimum-thrust-required-to-weight-ratio*. Here, two methods to calculate LD_{max} are presented; one using the simplified and the other the adjusted drag model. If using the simplified drag model, the LD_{max} is given by

$$LD_{max} = \left(\frac{C_L}{C_D}\right)_{max} = \frac{1}{\sqrt{4kC_{D_{min}}}} \qquad (20\text{-}33)$$

Figures 20-11 and 20-12 show that the airspeed of LD_{max} changes with altitude in terms of KTAS, but not KCAS. This is helpful to the pilot who only has to remember one number; the KCAS value. If using the adjusted drag model, the LD_{max} is determined using the following expression:

$$LD_{\max} = \left(\frac{C_L}{C_D}\right)_{\max} = \frac{1}{\sqrt{4kC_{D_{\min}} + (2kC_{L_{\min D}})^2} - 2kC_{L_{\min D}}} \tag{20-34}$$

The expressions show that the magnitude of the $LD_{\max}$ is independent of altitude. The C_L of $LD_{\max}$ called $C_{L_{opt}}$, can be determined using the relations below:

Simplified drag model: $C_{L_{opt}} = \sqrt{\frac{C_{D_{\min}}}{k}}$ (20-35)

Adjusted drag model: $C_{L_{opt}} = \sqrt{\frac{C_{D_{\min}}}{k} + C_{L_{\min D}}^2}$ (20-36)

(1) Airspeed for LD_{max}

The airspeed at which the $LD_{\max}$ is achieved is imperative from a standpoint of safety. Pilots of single engine aircraft are trained to establish this airspeed as soon as possible in case of engine failure. This provides maximum glide distance, thus, improving survivability. It is also known as the *airspeed for minimum thrust required*. Using the simplified drag model, the airspeed for $LD_{\max}$ is given by Equation (20-39), repeated here for convenience.

$$V_{LD_{\max}} = V_{BG} = V_{TR_{\min}} = \sqrt{\frac{2}{\rho}\left(\frac{W}{S}\right)\sqrt{\frac{k}{C_{D_{\min}}}}} \tag{20-37}$$

If using the adjusted drag model, the airspeed is given by Equation (20-40):

$$V_{LD_{\max}} = V_{BG} = V_{TR_{\min}} = \sqrt{\frac{2}{\rho}\left(\frac{W}{S}\right)\sqrt{\frac{k}{C_{D_{\min}} + kC_{L_{\min D}}^2}}} \tag{20-38}$$

(2) Various Lift-to-Drag Ratios

As evident by many of the methodologies in this chapter, many important optimum performance properties can be extracted once the drag polar has been defined. In particular, if the simplified and adjusted drag models are used either with constant thrust (jet) or constant power (propeller) with airspeed, many optimal airspeeds are associated with three specific ratios of C_L and C_D: $(C_L/C_D)_{\max}$, $(C_L^{1.5}/C_D)_{\max}$, and $(C_L^{0.5}/C_D)_{\max}$.

These ratios are co-plotted in Figure 20-10 for the Learjet 45, showing their relative positions and magnitude of their optimums. Specific relationships are listed in Table 20-2. **Note: In practice, thrust and power are rarely constant with airspeed. The airspeeds in the table must be considered from that perspective.**

FIGURE 20-10 Various specific lift-to-drag ratios.

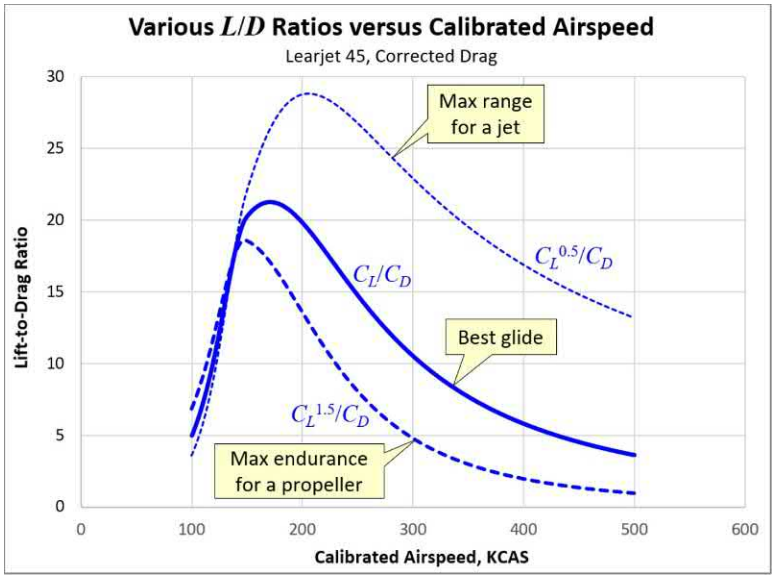


TABLE 20-2 Optimal airspeeds assuming simplified/adjusted drag models.

	CONSTANT THRUST - JET	CONSTANT POWER - PROPELLER
$(C_L/C_D)_{max}$	Maximum glide distance ($V_{LD\max}$)	Maximum glide distance ($V_{LD\max}$)
	Minimum drag or thrust required ($V_{TR\min}$)	Minimum drag or thrust required ($V_{TR\min}$)
	Maximum endurance ($V_{E\max}$)	Maximum range ($V_{R\max}$)
	Maximum V_{CAR}=1.32$V_{LD\max}$	Maximum V_{CAR}=1.32$V_{LD\max}$
$(C_L^{1.5}/C_D)_{max}$	Minimum power required ($V_{PR\min}$)	Minimum power required ($V_{PR\min}$)
	Maximum AOC (V_X)	Maximum ROC (V_Y)
	-	Maximum endurance ($V_{E\max}$)
$(C_L^{0.5}/C_D)_{max}$	Maximum range ($V_{R\max}$)	Max performance efficiency $(D/V_\infty)_{\min}$
	Max performance efficiency $(D/V_\infty)_{\min}$	-

EXAMPLE 20-5

Compare the maximum lift-to-drag ratio for the Learjet 45 using the simplified, adjusted, and "corrected" drag models, where the last one is the adjusted model corrected for low speed drag rise. What is the C_L at which LD_{max} occurs for the first two? Plot the three forms of L/D as a function of calibrated airspeed and the corrected one at S-L, 15,000 ft, and 30,000 ft.

SOLUTION:

Using the simplified drag model, we get:

$$LD_{max} = \frac{1}{\sqrt{4kC_{D_{min}}}} = \frac{1}{\sqrt{4(0.05236)(0.0200)}} = 15.5$$

$$C_L = \sqrt{\frac{C_{D_{min}}}{k}} = \sqrt{\frac{0.0200}{0.05236}} = 0.6180$$

Using the adjusted drag model, we start by calculating the lift coefficient of LD_{max} as follows:

$$LD_{max} = \frac{1}{\sqrt{4kC_{D_{min}} + (2kC_{L_{minD}})^2} - 2kC_{L_{minD}}} = 21.2$$

$$C_L = \sqrt{\frac{C_{D_{min}}}{k} + C_{L_{minD}}^2} = \sqrt{\frac{0.020}{0.05236} + 0.20^2} = 0.6496$$

The L/D as a function of requested airspeeds are plotted in Figures 20-11 and 20-12. Figure 20-11 shows how the simplified model leads to lower LD_{max} than the adjusted and corrected ones. This is a potential trap for the new aircraft designer. For one, it results in shorter range than the actual air will likely turn out to have. Figure 20-12 shows that the magnitude of LD_{max} is invariant with altitude. In fact, it occurs at the same KEAS at all altitudes. Note that the formulation does not account for the change in the minimum drag coefficient, $C_{D_{min}}$, due to change in Reynolds number with altitude, nor the presence of wave drag at higher airspeeds.

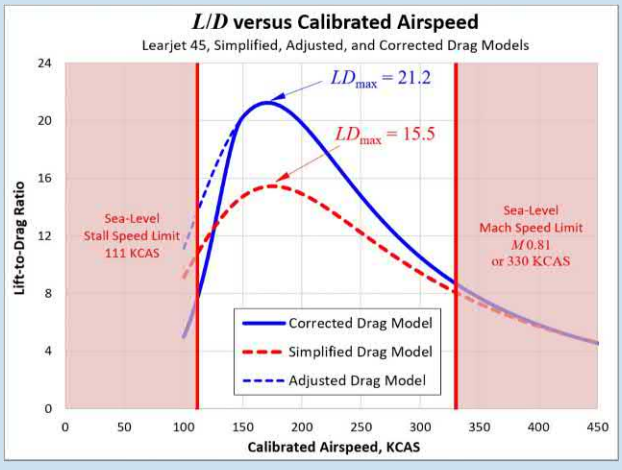


FIGURE 20-11 Maximum lift-to-drag ratio (*LD*) for the Learjet 45 using each drag model.

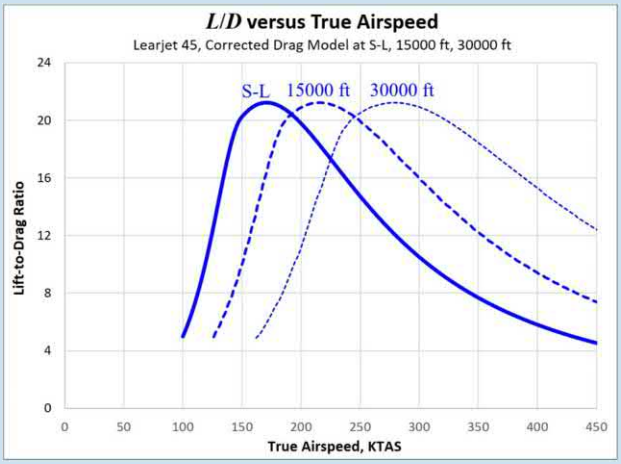


FIGURE 20-12 Change in *LD* with true airspeed, using the simplified drag model.

DERIVATION OF EQUATIONS (20-33) THROUGH (20-36)

Start by writing the expression for L/D:

$$\frac{L}{D} = \frac{C_L}{C_D} = \frac{C_L}{C_{D_{min}} + k(C_L - C_{L_{minD}})^2} = \frac{C_L}{kC_L^2 - 2kC_{L_{minD}}C_L + \left(C_{D_{min}} + kC_{L_{minD}}^2\right)} \quad \text{(i)}$$

Differentiate with respect to C_L, using the product rule

$$\frac{d}{dC_L}\left(\frac{C_L}{C_D}\right) = \frac{d(C_L)}{dC_L}\left(\frac{1}{kC_L^2 - 2kC_{L_{minD}}C_L + \left(C_{D_{min}} + kC_{L_{minD}}^2\right)}\right) + (C_L)\frac{d}{dC_L}\left(\frac{1}{kC_L^2 - 2kC_{L_{minD}}C_L + \left(C_{D_{min}} + kC_{L_{minD}}^2\right)}\right)$$

Complete differentiation and manipulate algebraically to get:

$$\frac{d}{dC_L}\left(\frac{C_L}{C_D}\right) = \frac{1}{C_{D_{min}} + k(C_L - C_{L_{minD}})^2} - \frac{2kC_L^2 - 2kC_{L_{minD}}C_L}{\left(C_{D_{min}} + k(C_L - C_{L_{minD}})^2\right)^2}$$

Cross-multiply and manipulate further to get

$$\frac{d}{dC_L}\left(\frac{C_L}{C_D}\right) = \frac{-kC_L^2 + C_{D_{min}} + kC_{L_{minD}}^2}{\left(C_{D_{min}} + k(C_L - C_{L_{minD}})^2\right)^2}$$

DERIVATION OF EQUATIONS (20-33) THROUGH (20-36) (cont'd)

Therefore, the maximum can be found for C_L when the numerator equals zero, or:

$$-kC_L^2 + C_{D_{\min}} + kC_{L_{minD}}^2 = 0$$

Using this expression, the value of C_L reduces to

$$C_L = \sqrt{\frac{C_{D_{\min}} + kC_{L_{minD}}^2}{k}} = \sqrt{\frac{C_{D_{\min}}}{k} + C_{L_{minD}}^2} \qquad \text{(ii)}$$

This is Equation (20-36) and is the C_L of $LD_{\max}$. Substitute this into Equation (i) to get:

$$\left(\frac{C_L}{C_D}\right)_{\max} = \left(\frac{C_L}{C_{D_{\min}} + k(C_L - C_{L_{minD}})^2}\right)_{\max} = \frac{\sqrt{C_{D_{\min}}/k + C_{L_{minD}}^2}}{C_{D_{\min}} + k(C_L - C_{L_{minD}})^2}$$

For clarity let's treat the denominator separately:

$$\begin{aligned} &kC_L^2 - 2kC_{L_{minD}}C_L + \left(C_{D_{\min}} + kC_{L_{minD}}^2\right) \\ &= k\left(\frac{C_{D_{\min}}}{k} + C_{L_{minD}}^2\right) \\ &\quad - 2kC_{L_{minD}}\sqrt{\frac{C_{D_{\min}}}{k} + C_{L_{minD}}^2} \\ &\quad + \left(C_{D_{\min}} + kC_{L_{minD}}^2\right) = 2\left(C_{D_{\min}} + kC_{L_{minD}}^2\right) \\ &\quad - 2kC_{L_{minD}}\sqrt{\frac{C_{D_{\min}}}{k} + C_{L_{minD}}^2} \end{aligned}$$

Noting that $(C_L/C_D)_{\max} = (C_D/C_L)_{\min}$ we get:

$$\begin{aligned} \left(\frac{C_D}{C_L}\right)_{\min} &= \frac{2\left(C_{D_{\min}} + kC_{L_{minD}}^2\right) - 2kC_{L_{minD}}\sqrt{\frac{C_{D_{\min}}}{k} + C_{L_{minD}}^2}}{\sqrt{\frac{C_{D_{\min}}}{k} + C_{L_{minD}}^2}} \\ \left(\frac{C_D}{C_L}\right)_{\min} &= \frac{2k\left(\frac{C_{D_{\min}}}{k} + C_{L_{minD}}^2\right)}{\sqrt{\frac{C_{D_{\min}}}{k} + C_{L_{minD}}^2}} - 2kC_{L_{minD}} \\ &= \sqrt{4kC_{D_{\min}} + (2kC_{L_{minD}})^2} - 2kC_{L_{minD}} \\ \Leftrightarrow \quad \left(\frac{C_L}{C_D}\right)_{\max} &= \frac{1}{\sqrt{4kC_{D_{\min}} + (2kC_{L_{minD}})^2} - 2kC_{L_{minD}}} \end{aligned}$$

To get Equation (20-33), substitute $C_{L_{minD}} = 0$ into the above result. To get Equation (20-35), substitute $C_{L_{minD}} = 0$ into Equation (20-36).

DERIVATION OF EQUATIONS (20-37) AND (20-38)

The C_L for $LD_{\max}$ using the adjusted drag model is:

$$C_L = \sqrt{\frac{C_{D_{\min}}}{k} + C_{L_{minD}}^2}$$

Substitute this into the lift equation and solve for V_∞, which is $V_{LD_{\max}}$:

$$V_{LD_{\max}} = \sqrt{\frac{2W}{\rho S C_L}} = \sqrt{\frac{2W}{\rho S\sqrt{\frac{C_{D_{\min}}}{k} + C_{L_{minD}}^2}}} = \sqrt{\frac{2}{\rho}\left(\frac{W}{S}\right)\sqrt{\frac{k}{C_{D_{\min}} + kC_{L_{minD}}^2}}}$$

To get Equation (20-37), substitute $C_{L_{minD}} = 0$ into the above result.

20.3.5 Airspeed of Minimum Thrust Required

The lower graph in Figure 17-13 shows a distinct minimum in the thrust-required curve. The airspeed at which it occurs is called the *airspeed of minimum thrust required* and is denoted by $V_{TR_{\min}}$. If using the simplified drag model, $V_{TR_{\min}}$ is calculated from:

$$V_{TR_{\min}} = \sqrt{\frac{2}{\rho}\left(\frac{W}{S}\right)\sqrt{\frac{k}{C_{D_{\min}}}}} \qquad \text{(20-39)}$$

If using the adjusted drag model, it is given by

$$V_{TR_{\min}} = \sqrt{\frac{2}{\rho}\left(\frac{W}{S}\right)\sqrt{\frac{k}{C_{D_{\min}} + kC_{L_{minD}}^2}}} \qquad \text{(20-40)}$$

By substituting Equation (20-40) into the lift equation, it is possible to show the lift coefficients associated with the above airspeeds are given by Equations (20-35) and (20-36), respectively. Substituting Equation (20-36) into the drag equation leads to the following expressions for the minimum required thrust:

Simplified drag model:

$$T_{TR\min} = W\sqrt{\frac{k}{C_{D_{\min}}}}\left(C_{D_{\min}} + kC_L^2\right) \qquad \text{(20-41)}$$

Adjusted drag model:

$$T_{TR\min} = W\sqrt{\frac{k}{C_{D_{\min}} + kC_{L_{minD}}^2}}\left(C_{D_{\min}} + k(C_L - C_{L_{minD}})^2\right) \qquad \text{(20-42)}$$

Where C_L is that obtained by Equation (20-35) or (20-36). An alternative expression that gives the same results is obtained using Equation (20-22):

Simplified drag model: $T_{TR\min} = 2W\sqrt{kC_{D_{\min}}}$ (20-43)

Adjusted drag model:

$$T_{TR\min} = 2W\sqrt{k\left(C_{D_{\min}} + kC_{L_{\min D}}^2\right)} - 2WkC_{L_{\min D}} \tag{20-44}$$

EXAMPLE 20-6

The Learjet 45 is cruising at 30,000 ft and at a weight of 20,000 lb_f. Determine minimum thrust and the corresponding calibrated airspeed the pilot should maintain (ignore compressibility effect):

SOLUTION:

Simplified drag:

$$\begin{aligned} T_{TR\min} &= 2W\sqrt{kC_{D_{\min}}} \\ &= 2(20,000)\sqrt{(0.05236)(0.0200)} = 1294\,\text{lb}_\text{f} \\ V_{TR_{\min}} &= \sqrt{\frac{2(20,000)}{(0.0008897)(311.6)}}\sqrt{\frac{0.05236}{0.0200}} \\ &= 483.2\,\text{ft/s} = 286.2\,\text{KTAS} \\ \Rightarrow\quad V_{TR_{\min}} &= 286.2\sqrt{\frac{0.0008897}{0.002378}} = 175.1\,\text{KCAS} \end{aligned}$$

To conserve fuel, the pilot must maintain an airspeed of 175 KCAS. It is also of interest to solve the problem using the adjusted drag model. This yields the following thrust required:

$$\begin{aligned} T_{TR\min} &= 2W\sqrt{k\left(C_{D_{\min}} + kC_{L_{\min D}}^2\right)} - 2WkC_{L_{\min D}} \\ &= 2(20,000)\sqrt{(0.05236)\left(0.0200 + (0.05236)(0.2)^2\right)} \\ &\quad - 2(20,000)(0.05236)(0.2) = 941.6\,\text{lb}_\text{f} \end{aligned}$$

The adjusted drag model indicates that the required thrust will be even less, or 941.6 lb_f. Equation (20-40) yields the airspeed the pilot must maintain:

$$\begin{aligned} V_{TR_{\min}} &= \sqrt{\frac{2}{\rho}\left(\frac{W}{S}\right)}\sqrt{\frac{k}{C_{D_{\min}} + kC_{L_{\min D}}^2}} = 471.3\,\text{ft/s} \\ &= 279.2\,\text{KTAS} \\ \Rightarrow\quad V_{TR_{\min}} &= 279.2\sqrt{0.0008897/0.002378} = 171\,\text{KCAS} \end{aligned}$$

DERIVATION OF EQUATIONS (20-39) THROUGH (20-42)

By expanding the adjusted drag model and substituting $2W/(\rho V_\infty^2 S)$ for C_L, we can write the drag as follows

$$D = \frac{1}{2}\rho V_\infty^2 S C_{D_{\min}} + \frac{2kW^2}{\rho V_\infty^2 S} - 2kWC_{L_{\min D}} + \frac{1}{2}\rho V_\infty^2 S k C_{L_{\min D}}^2$$

Differentiate this with respect to V_∞ and simplify to get

$$\frac{\partial D}{\partial V_\infty} = \rho V_\infty S\left(C_{D_{\min}} + kC_{L_{\min D}}^2\right) - \frac{4kW^2}{\rho V_\infty^3 S}$$

Set equal to zero and solve for V_∞^4 and then for V_∞, gives

$$V_\infty^4 = \left(\frac{2W}{\rho S}\right)^2 \frac{k}{\left(C_{D_{\min}} + kC_{L_{\min D}}^2\right)}$$

$$\Rightarrow\quad V_{TR_{\min}} = \sqrt{\frac{2W}{\rho S}}\sqrt{\frac{k}{\left(C_{D_{\min}} + kC_{L_{\min D}}^2\right)}}$$

This is Equation (20-40). Substitute $C_{L_{\min D}} = 0$ into this expression to get Equation (20-39). To determine $T_{TR_{\min}}$, substitute Equation (20-36) into the expression for adjusted drag coefficient

$$\begin{aligned} C_L &= \sqrt{\frac{C_{D_{\min}}}{k} + C_{L_{\min D}}^2} \\ \Rightarrow\quad C_D &= C_{D_{\min}} + k(C_L - C_{L_{\min D}})^2 \\ \Rightarrow\quad T_{TR_{\min}} &= \frac{1}{2}\rho V_{TR\min}^2 S C_{D_{TR\min}} \\ &= \frac{1}{2}\rho V_{TR\min}^2 S\left(C_{D_{\min}} + k(C_L - C_{L_{\min D}})^2\right) \\ &= W\sqrt{\frac{k}{\left(C_{D_{\min}} + kC_{L_{\min D}}^2\right)}}\left(C_{D_{\min}} + k(C_L - C_{L_{\min D}})^2\right) \end{aligned}$$

Where, C_L implies $C_{LTR_{\min}}$, which is that obtained by Equation (20-35) or (20-36). This is Equation (20-42). Substitute $C_{L_{\min D}} = 0$ into this expression to get Equation (20-41).

DERIVATION OF EQUATIONS (20-43) AND (20-44)

Airspeed as a function of thrust was found from Equation (20-22):

$$V_\infty = \sqrt{\frac{(T + 2kWC_{L_{\min D}}) \pm \sqrt{(T + 2kWC_{L_{\min D}})^2 - 4kW^2\left(C_{D_{\min}} + kC_{L_{\min D}}^2\right)}}{\rho S\left(C_{D_{\min}} + kC_{L_{\min D}}^2\right)}}$$

DERIVATION OF EQUATIONS (20-43) AND (20-44) (cont'd)

When the inside radical is zero, the solution is $V_{TR_{min}}$. Thus, the associated thrust is $T_{TR_{min}}$ and can be determined as follows:

$$(T_{TR_{min}} + 2WkC_{L_{minD}})^2 - 4W^2k\left(C_{D_{min}} + kC_{L_{minD}}^2\right) = 0$$

$$\Leftrightarrow \quad T_{TR_{min}}^2 + 4WkC_{L_{minD}}T_{TR_{min}} - 4W^2kC_{D_{min}} = 0$$

The solution to the quadratic formulation is:

$$T_{TR_{min}} = \frac{-4WkC_{L_{minD}} \pm \sqrt{(4WkC_{L_{minD}})^2 + 16W^2kC_{D_{min}}}}{2}$$

$$\Leftrightarrow \quad T_{TR_{min}} = \frac{-4WkC_{L_{minD}} \pm \sqrt{16W^2k^2C_{L_{minD}}^2 + 16W^2kC_{D_{min}}}}{2}$$

$$\Leftrightarrow \quad T_{TR_{min}} = -2WkC_{L_{minD}} \pm 2W\sqrt{k\left(C_{D_{min}} + kC_{L_{minD}}^2\right)}$$

Only the positive solution makes physical sense. This is Equation (20-44). Substitute $C_{L_{minD}} = 0$ into this expression to get Equation (20-43).

20.3.6 Airspeed of Minimum Power Required

The upper graph in Figure 17-12 shows a distinct minimum in the power-required curve. The airspeed at which it occurs is called the *airspeed of minimum power required* and is denoted by $V_{PR_{min}}$. If using the simplified drag model, it is given by

$$V_{PR_{min}} = \sqrt{\frac{2}{\rho}\left(\frac{W}{S}\right)\sqrt{\frac{k}{3C_{D_{min}}}}} \qquad (20\text{-}45)$$

If using the adjusted drag model, this is given by

$$V_{PR_{min}} = \sqrt{\left(\frac{2}{\rho}\right)\left(\frac{W}{S}\right)\left[AC_{L_{minD}} + \sqrt{(AC_{L_{minD}})^2 + A}\right]} \qquad (20\text{-}46)$$

Where

$$A = \frac{k}{3\left(C_{D_{min}} + kC_{L_{minD}}^2\right)} \qquad (20\text{-}47)$$

DERIVATION OF EQUATIONS (20-45) AND (20-46)

By expanding the adjusted drag model and substituting $2W/(\rho V_\infty^2 S)$ for C_L, we can write the power required as follows

$$DV_\infty = \frac{1}{2}\rho V_\infty^3 SC_{D_{min}} + \frac{2kW^2}{\rho V_\infty S} - 2kWC_{L_{minD}}V_\infty + \frac{1}{2}\rho V_\infty^3 SkC_{L_{minD}}^2$$

Differentiate this with respect to V_∞ and simplify to get

$$\frac{\partial(DV_\infty)}{\partial V_\infty} = \frac{3}{2}\rho V_\infty^2 S\left(C_{D_{min}} + kC_{L_{minD}}^2\right) - \frac{2kW^2}{\rho V_\infty^2 S} - 2kWC_{L_{minD}}$$

Set equal to zero, rearrange, and let $u = V_\infty^2$:

$$u^2 - \frac{2}{3}\left(\frac{2W}{\rho S}\right)\frac{kC_{L_{minD}}}{\left(C_{D_{min}} + kC_{L_{minD}}^2\right)}u - \left(\frac{2W}{\rho S}\right)^2\frac{k}{3\left(C_{D_{min}} + kC_{L_{minD}}^2\right)} = 0$$

Solve the quadratic form for u and then for V_∞, gives

$$V_\infty = \sqrt{\left(\frac{2}{\rho}\right)\left(\frac{W}{S}\right)\left[\frac{kC_{L_{minD}}}{3\left(C_{D_{min}} + kC_{L_{minD}}^2\right)} \pm \sqrt{\left(\frac{kC_{L_{minD}}}{3\left(C_{D_{min}} + kC_{L_{minD}}^2\right)}\right)^2 + \frac{k}{3\left(C_{D_{min}} + kC_{L_{minD}}^2\right)}}\right]}$$

This is Equation (20-46). Substitute $C_{L_{minD}} = 0$ into this expression to get Equation (20-45).

20.3.7 Airspeeds of Maximum ROC and AOC

(1) Propeller Aircraft

For airspeed of maximum rate-of-climb (V_Y) see Equations (19-36) and (19-37) of Section 19.3.3, *Formulation of Best (Maximum) Rate-of-Climb*. For airspeed of maximum angle-of-climb (V_X) see Equation (19-45) of Section 19.3.4, *Formulation of Best (Maximum) Angle-of-Climb*.

(2) Jet Aircraft

For airspeed of maximum rate-of-climb (V_Y) see Equation (19-34) of Section 19.3.3, *Formulation of Best (Maximum) Rate-of-Climb*. For airspeed of maximum angle-of-climb (V_X) see Equation (19-43) of Section 19.3.4, *Formulation of Best (Maximum) Angle-of-Climb*.

20.3.8 Airspeed of Maximum Endurance

This section presents various methods to assess the airspeed for maximum endurance. It occurs at different airspeeds for propeller and jet aircraft. In either case, it is denoted by $V_{E_{max}}$.

(1) *Maximum Endurance of a Propeller-Powered Airplane*

Equation (21-13) shows how the fuel consumption of a propeller-powered aircraft depends on engine power developed. As shown in Section 20.3.6, the minimum engine power required to maintain altitude occurs at $V_{TR_{min}}$. This is where the aircraft can stay airborne the longest: It is the *maximum endurance speed*, $V_{E_{max}}$.

Equation (21-66) of Section 21.4.2, *Endurance Profile 2: Constant Attitude/Altitude Cruise* shows that the maximum endurance of a propeller-powered airplane occurs with the maximum of the ratio $C_L^{1.5}/C_D$. If using the simplified drag model, this maximum, called *endurance ratio*, can be calculated directly using the expression below.

$$\left(\frac{C_L^{1.5}}{C_D}\right)_{max} = \frac{1}{4}\left(\frac{3}{k(C_{D_{min}})^{1/3}}\right)^{3/4} \tag{20-48}$$

The lift coefficient at this condition is given by

$$\text{Simplified drag model:} \quad C_L = \sqrt{\frac{3C_{D_{min}}}{k}} \tag{20-49}$$

The airspeed at which this occurs is given by Equation (20-45), repeated below for convenience.

$$V_{E_{max}} = V_{PR_{min}} = \sqrt{\frac{2}{\rho}\left(\frac{W}{S}\right)\sqrt{\frac{k}{3C_{D_{min}}}}} \tag{20-50}$$

If using the adjusted drag model, the lift coefficient at this condition is given by

Adjusted drag model:

$$C_L = \sqrt{\frac{3C_{D_{min}}}{k} + 4C_{L_{minD}}^2} - C_{L_{minD}} \tag{20-51}$$

The airspeed at which this occurs is given by Equation (20-46). However, the same equation (in a different form) can be derived using the lift coefficient of Equation (20-51) and is given below

$$V_{E_{max}} = V_{PR_{min}} = \sqrt{\frac{2}{\rho}\left(\frac{W}{S}\right)\frac{\sqrt{k}}{\sqrt{3C_{D_{min}} + 4kC_{L_{minD}}^2} - \sqrt{k}C_{L_{minD}}}} \tag{20-52}$$

Comparison to the Best Glide Speed

Using the specific results based on the simplified drag model, it is of interest to compare Equation (20-50) to Equation (20-37), repeated below for convenience. These expressions are only valid for the simplified drag model.

$$V_{E_{max}} = \sqrt{\frac{2}{\rho}\left(\frac{W}{S}\right)\sqrt{\frac{k}{3C_{D_{min}}}}} \quad \text{and}$$

$$V_{LD_{max}} = \sqrt{\frac{2}{\rho}\left(\frac{W}{S}\right)\sqrt{\frac{k}{C_{D_{min}}}}}.$$

Dividing the former by the latter reveals the following difference between the two:

$$\frac{V_{E_{max}}}{V_{LD_{max}}} = \frac{\sqrt{\frac{2}{\rho}\left(\frac{W}{S}\right)\sqrt{\frac{k}{3C_{D_{min}}}}}}{\sqrt{\frac{2}{\rho}\left(\frac{W}{S}\right)\sqrt{\frac{k}{C_{D_{min}}}}}} = \left(\frac{1}{3}\right)^{1/4} \approx 0.76$$

In short, the best endurance speed is about 76% of the speed for best LD_{max}.

EXAMPLE 20-7

Determine the maximum endurance ratio for the SR22 using the simplified drag model:

SOLUTION:

$$\left(\frac{C_L^{3/2}}{C_D}\right)_{max} = \frac{1}{4C_{D_{min}}}\left(\frac{3C_{D_{min}}}{k}\right)^{3/4} = \frac{1}{(4)(0.02541)}\left(\frac{(3)(0.02541)}{0.04207}\right)^{3/4} = 15.37$$

(2) Maximum Endurance of a Jet Aircraft

Equation (21-68) of Section 21.4.3, *Endurance Profile 3: Constant Airspeed/Attitude Cruise* shows that the maximum endurance of a jet occurs at LD_{max}. The corresponding airspeed is $V_{TR_{min}}$, the airspeed of minimum thrust required. It is the *maximum endurance airspeed* for a jet. The airspeed is important for airplanes whose mission demands prolonged periods of loitering, for instance, reconnaissance and fighter aircraft, whose mission often requires prolonged time in a specific geographic location. The corresponding airspeeds using the simplified and adjusted drag models are given by Equations (20-39) and (20-40), repeated below for convenience.

Simplified drag model:

$$V_{E_{max}} = V_{TR_{min}} = \sqrt{\frac{2}{\rho}\left(\frac{W}{S}\right)\sqrt{\frac{k}{C_{D_{min}}}}} \tag{20-53}$$

Adjusted drag model:

$$V_{E_{max}} = V_{TR_{min}} = \sqrt{\frac{2W}{\rho S}\sqrt{\frac{k}{\left(C_{D_{min}} + kC_{L_{minD}}^2\right)}}} \tag{20-54}$$

DERIVATION OF EQUATIONS (20-48)–(20-51)

Start by writing the ratio:

$$\frac{C_L^{3/2}}{C_D} = \frac{C_L^{3/2}}{C_{D_{min}} + k\cdot\left(C_L - C_{L_{minD}}\right)^2} = \frac{C_L^{3/2}}{AC_L^2 + BC_L + C} \tag{i}$$

Where; $A = k \qquad B = -2kC_{L_{minD}} \qquad C = C_{D_{min}} + kC_{L_{minD}}^2$

Differentiate with respect to C_L, using the product rule

$$\begin{aligned}\frac{d}{dC_L}\left(\frac{C_L^{3/2}}{C_D}\right) &= \frac{d\left(C_L^{3/2}\right)}{dC_L}\left(\frac{1}{AC_L^2 + BC_L + C}\right) \\ &\quad + \left(C_L^{3/2}\right)\frac{d}{dC_L}\left(\frac{1}{AC_L^2 + BC_L + C}\right) \\ &= \frac{3}{2}\frac{\sqrt{C_L}}{AC_L^2 + BC_L + C} \\ &\quad - \left(C_L^{3/2}\right)\left(AC_L^2 + BC_L + C\right)^{-2}\left(2AC_L + B\right)\end{aligned}$$

Manipulate algebraically to get

$$\frac{d}{dC_L}\left(\frac{C_L^{3/2}}{C_D}\right) = \frac{\frac{3}{2}\sqrt{C_L}\left(AC_L^2 + BC_L + C\right) - \left(2AC_L^{5/2} + BC_L^{3/2}\right)}{\left(AC_L^2 + BC_L + C\right)^2} = 0$$

The maximum can be found when the numerator equals zero, or;

$$\begin{aligned}&\Leftrightarrow \quad \frac{3}{2}\sqrt{C_L}\left(AC_L^2 + BC_L + C\right) - \left(2AC_L^{5/2} + BC_L^{3/2}\right) = 0 \\ &\Rightarrow \quad 3C_L^{1/2}\left(AC_L^2 + BC_L + C\right) = C_L^{1/2}\left(4AC_L^{4/2} + 2BC_L^{2/2}\right) \\ &\Rightarrow \quad 3AC_L^2 + 3BC_L + 3C = 4AC_L^2 + 2BC_L \\ &\Rightarrow \quad AC_L^2 - BC_L - 3C = 0\end{aligned}$$

Solve the classical quadratic formulation is solved as follows

$$\begin{aligned}C_L &= \frac{-B \pm \sqrt{B^2 + 12AC}}{2A} \\ &= \frac{-2kC_{L_{minD}} \pm \sqrt{4k^2C_{L_{minD}}^2 + 12k\left(C_{D_{min}} + kC_{L_{minD}}^2\right)}}{2k} \\ &= \frac{-2kC_{L_{minD}}}{2k} \pm \sqrt{\frac{4k^2C_{L_{minD}}^2 + 12k\left(C_{D_{min}} + kC_{L_{minD}}^2\right)}{4k^2}} \\ &= -C_{L_{minD}} \pm \sqrt{4C_{L_{minD}}^2 + \frac{3C_{D_{min}}}{k}}\end{aligned}$$

By observation we note that $C_L > 0$ is required for the solution to make physical sense (because the airplane needs a positive C_L to maintain altitude). Therefore, we must select the plus sign in front of the radical.

$$C_L = \sqrt{4C_{L_{minD}}^2 + \frac{3C_{D_{min}}}{k}} - C_{L_{minD}} \tag{ii}$$

This is Equation (20-51). Substitute $C_{L_{minD}} = 0$ into Equation (ii) to get Equation (20-49). Then, substitute Equation (20-49) into Equation (i) and manipulate to get Equation (20-48).

DERIVATION OF EQUATIONS (20-50) AND (20-52)

We demonstrated that C_L for minimum power required was given by Equation (20-51). Substitute it into Equation (20-10) and manipulate algebraically

$$\begin{aligned}V_\infty &= \sqrt{\frac{2W}{\rho S C_L}} \\ &= \sqrt{\frac{2W}{\rho S\left(\sqrt{\frac{3C_{D_{min}}}{k} + 4C_{L_{minD}}^2} - C_{L_{minD}}\right)}} \\ &= \sqrt{\frac{2}{\rho}\left(\frac{W}{S}\right)\frac{\sqrt{k}}{\sqrt{3C_{D_{min}} + 4kC_{L_{minD}}^2} - \sqrt{k}C_{L_{minD}}}}\end{aligned}$$

This is Equation (20-52). Substitute $C_{L_{minD}} = 0$ into this expression to get Equation (20-50). Note the limitation of this expression: It assumes constant thrust with airspeed.

20.3.9 Airspeed of Maximum Range

This section presents various methods to assess the airspeed for maximum range. It occurs at different airspeeds for propeller and jet aircraft. In either case, it is called the *maximum range speed* and is denoted by $V_{R_{max}}$.

(1) Best Range Airspeed for a Propeller Aircraft

Equation (21-38) of Section 21.3.4, *Range Profile 3: Constant Airspeed/Attitude Cruise* shows that the maximum range of a propeller-powered airplane occurs at LD_{max}. This has already been discussed in detail in Section 20.3.4. The corresponding airspeed is $V_{TR_{min}}$—the airspeed of minimum thrust. Using the simplified and adjusted drag models, the corresponding airspeeds are given by Equations (20-39) and (20-40), respectively, repeated below for convenience.

Simplified drag model:

$$V_{R_{max}} = V_{TR_{min}} = \sqrt{\frac{2}{\rho}\left(\frac{W}{S}\right)\sqrt{\frac{k}{C_{D_{min}}}}} \tag{20-55}$$

Adjusted drag model:

$$V_{R_{max}} = V_{TR_{min}} = \sqrt{\frac{2W}{\rho S}\sqrt{\frac{k}{\left(C_{D_{min}} + kC_{L_{minD}}^2\right)}}} \tag{20-56}$$

(2) Best Range Airspeed for a Jet

Equation (21-32) of Section 21.3.3, *Range Profile 2: Constant Attitude/Altitude Cruise* shows that the maximum range of jet-powered airplane depends on the maximum of the ratio $C_L^{0.5}/C_D$. This maximum can be determined from the following expression, which is only valid for the simplified drag model:

$$\left(\frac{C_L^{1/2}}{C_D}\right)_{max} = \frac{3}{4}\left(\frac{1}{3kC_{D_{min}}^3}\right)^{1/4} \tag{20-57}$$

If using the simplified or adjusted drag models, $V_{R_{max}}$ for a jet can be calculated per the following expressions. This airspeed is usually too low to be practical for passenger transportation. However, the trick to increase it is to increase the wing loading.

Simplified drag model:

$$V_{R_{max}} = V_{TR_{min}} = \sqrt{\frac{2}{\rho}\left(\frac{W}{S}\right)\sqrt{\frac{3k}{C_{D_{min}}}}} \tag{20-58}$$

Adjusted drag model: $V_{R_{max}} = V_{TR_{min}}$

$$= \sqrt{\frac{2}{\rho}\left(\frac{W}{S}\right)\left(\frac{C_{L_{minD}}}{3} \pm \sqrt{\left(\frac{C_{L_{minD}}}{3}\right)^2 + \frac{C_{D_{min}} + kC_{L_{minD}}^2}{3k}}\right)^{-1}} \tag{20-59}$$

Comparison to the Best Glide Speed

Similar to an earlier comparison that used the specific results based on the simplified drag model, it is of interest to compare Equation (20-58) to Equation (20-37), repeated below for convenience:

$$V_{R_{max}} = \sqrt{\frac{2}{\rho}\left(\frac{W}{S}\right)\sqrt{\frac{3k}{C_{D_{min}}}}} \quad \text{and}$$

$$V_{LD_{max}} = \sqrt{\frac{2}{\rho}\left(\frac{W}{S}\right)\sqrt{\frac{k}{C_{D_{min}}}}}.$$

We observe the following difference between the two:

$$\frac{V_{R_{max}}}{V_{LD_{max}}} = \frac{\sqrt{\frac{2}{\rho}\left(\frac{W}{S}\right)\sqrt{\frac{3k}{C_{D_{min}}}}}}{\sqrt{\frac{2}{\rho}\left(\frac{W}{S}\right)\sqrt{\frac{k}{C_{D_{min}}}}}} = (3)^{1/4} \approx 1.32$$

In other words, the best range speed is about 32% greater than the speed for best L/D.

EXAMPLE 20-8

Determine the maximum range ratio for the Learjet 45, assuming the simplified drag model:

SOLUTION:

$$\left(C_L^{1/2}/C_D\right)_{max} = \frac{3}{4}\left(1/\left(3kC_{D_{min}}^3\right)\right)^{1/4}$$
$$= \frac{3}{4}\left(1/\left(3(0.05236)(0.0200)^3\right)\right)^{1/4} = 22.40$$

DERIVATION OF EQUATIONS (20-58) AND (20-59)

Start by writing the ratio:

$$\frac{C_L^{1/2}}{C_D} = \frac{C_L^{1/2}}{C_{D_{min}} + k\cdot(C_L - C_{L_{minD}})^2} = \frac{C_L^{1/2}}{AC_L^2 + BC_L + C} \tag{i}$$

Where; $A = k \quad B = -2kC_{L_{minD}} \quad C = C_{D_{min}} + kC_{L_{minD}}^2$

Differentiate with respect to C_L, using the product rule, a simplify algebraically

DERIVATION OF EQUATIONS (20-58) AND (20-59) (cont'd)

$$\frac{d}{dC_L}\left(\frac{C_L^{1/2}}{C_D}\right)=\frac{d\left(C_L^{1/2}\right)}{dC_L}\left(\frac{1}{AC_L^2+BC_L+C}\right)$$
$$+\left(C_L^{1/2}\right)\frac{d}{dC_L}\left(\frac{1}{AC_L^2+BC_L+C}\right)=\frac{1}{2\sqrt{C_L}}\frac{1}{AC_L^2+BC_L+C}$$
$$-\sqrt{C_L}\left(AC_L^2+BC_L+C\right)^{-2}(2AC_L+B)$$
$$=\frac{1}{2\sqrt{C_L}}\left[\frac{-3AC_L^2-BC_L+C}{\left(AC_L^2+BC_L+C\right)^2}\right]$$

Set the numerator equal to zero to get the optimum value

$$-3AC_L^2-BC_L+C=0 \;\Rightarrow\; 3AC_L^2+BC_L-C=0$$

Use the classical solution of the quadratic equation to solve for C_L and substitute the parameters for A, B, and C

$$C_L=\frac{-(-2kC_{L_{minD}})\pm\sqrt{(-2kC_{L_{minD}})^2+4(3k)\left(C_{D_{min}}+kC_{L_{minD}}^2\right)}}{2(3k)}$$
$$=\frac{C_{L_{minD}}}{3}\pm\sqrt{\left(\frac{C_{L_{minD}}}{3}\right)^2+\frac{C_{D_{min}}+kC_{L_{minD}}^2}{3k}}$$

Substitute this into the lift equation to calculate $V_{R_{max}}$

$$V_{R_{max}}=\sqrt{\frac{2W}{\rho SC_L}}$$
$$=\sqrt{\frac{2}{\rho}\left(\frac{W}{S}\right)\left(\frac{C_{L_{minD}}}{3}\pm\sqrt{\left(\frac{C_{L_{minD}}}{3}\right)^2+\frac{C_{D_{min}}+kC_{L_{minD}}^2}{3k}}\right)^{-1}}$$

This is Equation (20-59). Substitute $C_{L_{minD}}=0$ into this expression to get Equation (20-58).

(3) Carson's Airspeed

In a paper titled *Fuel Efficiency of Small Aircraft* [8], B.H. Carson discusses the mismatch between the amount of power required for climb and cruise in small propeller-driven aircraft. In the paper, Carson demonstrates that this excess power can be used more efficiently by bringing it closer to the so-called Gabrielli-Von Kárman limit for vehicle performance [9]. Carson states that (1) aircraft fuel economy is directly proportional to L/D and the optimum is usually realized only at unacceptably low airspeeds. (2) Power required for climb results in aircraft airspeeds well beyond this optimum. (3) This results in greater fuel penalties than otherwise. Carson suggests that flying at a speed faster than the airspeed for LD_{max} is more advantageous, as the flying public generally values time en-route more than fuel efficiency. From a certain point of view, Carson's airspeed can be considered the "fastest efficient airspeed" to fly.

The most frequently cited measure of efficiency is the so-called *transport efficiency*, defined as WV_∞/P, where W is the vehicle weight, V_∞ its speed of travel, and P is the installed power. Expanding on this idea, Carson derives a relation for a specific airspeed that is about 32% larger than the best glide airspeed (see Equation (20-37)). This speed is now recognized as *Carson's airspeed*.

Carson's airspeed:

$$V_{CAR}=3^{0.25}V_{LDmax}\approx 1.32V_{LDmax}$$
$$=1.32\sqrt{\frac{2}{\rho}\left(\frac{W}{S}\right)\sqrt{\frac{k}{C_{D_{min}}}}} \qquad (20\text{-}60)$$

DERIVATION OF EQUATION (20-60)

Reader is directed to Ref. [8] for derivation and a paper by Smith [10] for additional discussion.

20.3.10 Flight Envelope

This section presents several concepts associated with the construction of the *flight envelope*. The flight envelope demonstrates the capability of the aircraft in terms of its minimum and maximum airspeed with altitude. Such a diagram co-plots the stalling, minimum and maximum airspeed as function of altitude. It is created using the thrust/drag-versus-airspeed (e.g., see the right-hand side plots of Figure 20-3) at multiple altitudes. It shows how altitude affects the drag and thrust of the airplane. It depicts how the intersection of the drag and thrust curves changes with altitude, to name a few. A different presentation of this information is shown in Figure 20-13. It plots the predicted maximum and minimum airspeed using the Learjet 45 as an example. It was compiled using 46 thrust/drag-versus airspeed graphs for each of the two weights. Also, Mach isopleths are coplotted for additional insight.

(1) Basic Flight Envelope

The flight envelope shows the capability of the aircraft over its entire altitude range. It usually omits any regulatory or structural considerations. For these refer to Bullets (3) and (4) of this section. The graph is fundamentally simple and helpful to management and customers in addition to the designer. It also helps to superimpose various optimal airspeeds on the graph, such as V_X, V_Y, and V_{BG}. This further illustrates the airplane's performance relative to its low and high-speed limitations. It is also

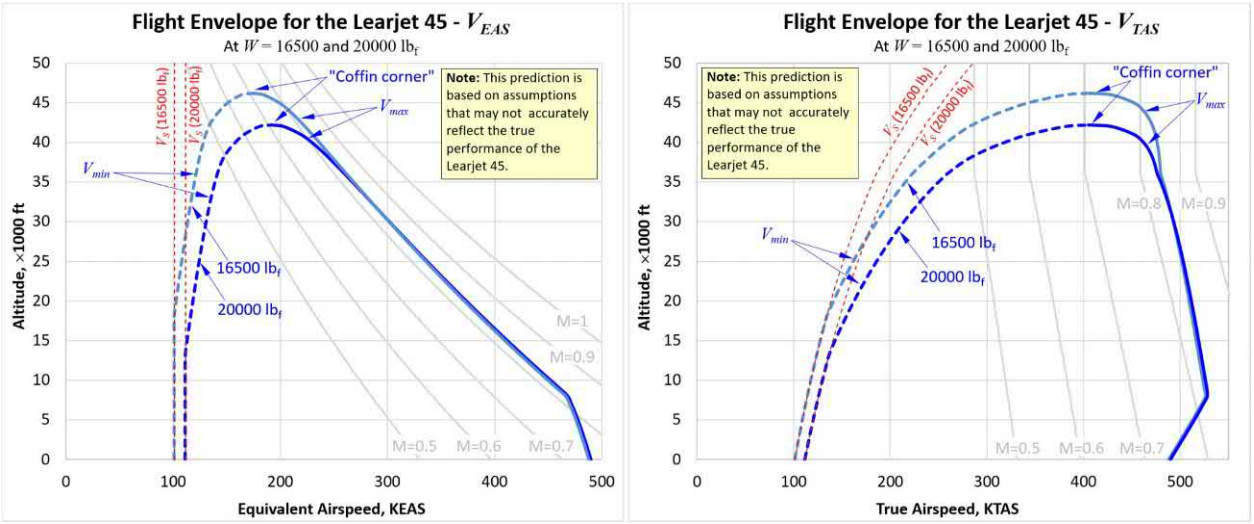


FIGURE 20-13 Flight envelope for the Learjet 45 at two weights, using two types of airspeed.

used to create a set of airspeeds and altitudes at which the dynamic stability characteristics and aeroelastic test matrix for the aircraft can be evaluated. For instance, the designer should map a matrix of points (e.g., minimum, maximum, and the average of the two) at selected altitudes (e.g., 0, 5000, 10,000 ft, etc.) and evaluate phugoid and Dutch roll damping at those points. A similar matrix should be prepared for aero-elastic evaluation of the structure. This allows the flight test team to plan where structural shakers should be activated during flutter testing.

(2) "Coffin Corner"

The maximum airspeed of a high-flying jet aircraft is called the M_{MO} (*maximum operating Mach number*). When the airplane hits this speed, local airspeeds over the airplane have already begun to exceed Mach 1 and forming weak shocks. Exceeding this speed is accompanied by a sharp rise in drag and changes in pitching moment. This results from the center-of-lift on the lifting surfaces beginning to move to a different location, perhaps as far aft as 50% of the MGC. This increases the distance between the CG and the center of lift, leading to the phenomenon called *Mach tuck*. It is a powerful nose pitch-down moment that renders the aircraft uncontrollable if not designed to handle it. The nose pitch-down tendency increases its speed further. This may lead to structural failure during recovery, and certain demise if recovery is not possible. The shock formation may also lead to abnormal shaking and wing rocking. Compounding the problem is the formation of shockwaves on the lifting surfaces leads to a *shock-stall* (see Figure 8-47). It results in control surfaces operating inside the separated wake, rendering them far less effective.

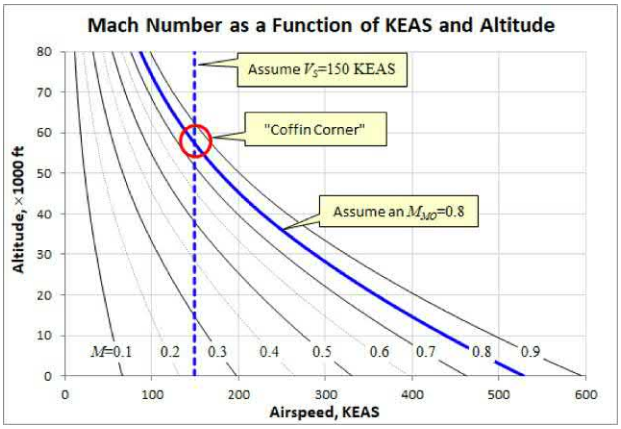


FIGURE 20-14 Determination of the Coffin Corner.

As shown in Figure 20-13, as the airplane increases its altitude, the stalling speed in terms of true airspeed increases, while its equivalent airspeed is constant. In this context, consider Figure 20-14, which shows Mach isopleths extending from S-L to 80,000 ft plotted against the airspeed in KEAS. The graph allows the altitude at which a given airspeed reaches a set Mach number to be determined. For instance, 300 KEAS corresponds to Mach 0.8 at approximately 28,000 ft. Now consider a high-flying aircraft whose M_{MO} is 0.80 and stalling speed, V_S, is 150 KEAS. These are represented as the thick solid and dotted curves in the figure.

Assume the pilot maintains constant equivalent airspeed during climb, say 200 KEAS. The Mach number keeps increasing with altitude. At 25,000 ft the Mach number is 0.5 and 0.7 at 40,000 ft. Eventually, the aircraft approaches its M_{MO} and the equivalent airspeed must be reduced with further increase in altitude. For instance,

if maintaining 200 KEAS during climb, once the airplane approaches 45,000 ft, the pilot must reduce the airspeed to avoid exceeding M_{MO}. If the climb continues, a new dilemma confronts the pilot at approximately at 57,000 ft; the M_{MO} and stalling *intersect* each other. Slowing down further will cause the airplane to stall and this may easily result in a dive that takes the airplane beyond M_{MO}. If the airplane accelerates, the plane will hit M_{MO}. This peculiar situation is called the "*Coffin Corner*" (or *Q-corner* by the FAA [11]) because any change in airspeed can, potentially lead to a very dangerous situation. Flying near the coffin corner requires the use of an autopilot.

The graph also shows two solutions for increasing the altitude further. (1) Reducing wing loading reduces the stalling speed and moves the coffin corner to a lower equivalent airspeed and higher altitude. This is the solution picked for the Lockheed U-2 reconnaissance aircraft. Its wing loading at gross weight was 40 lb_f/ft^2, which dropped to 11.6 lb_f/ft^2 at landing weight [12, 13]. (2) Fly faster than Mach 1. This is the solution picked for the famous Lockheed SR-71 (gross weight wing loading near 95 lb_f/ft^2).

To create the graph of Figure 20-14, the equivalent airspeed is determined for a given Mach number and altitude. For instance, the true airspeed in knots corresponding to $M = 0.1$ at S-L is $0.1 \times (1116\,ft/s)/(1.688\,ft/s$ per knot) or 66.1 KTAS. To convert this to KEAS use Equation (17-29). Do this for a range of altitudes and Mach numbers ranging from 0.1 to 0.9 as shown.

(3) Standard Altitude-*versus*-Mach Flight Envelope

Refers to a standard flight envelope that accounts for regulatory and compressibility constraints. For instance, 14 CFR §91.117(a), *Aircraft speed* specifies that no aircraft shall operate at indicated airspeed greater than 250 knots at 10,000 ft or below (unless otherwise authorized). At higher altitudes, the aircraft is subject to a maximum operating Mach number, M_{MO}. Figure 20-15 left shows an example of such a diagram. The diagram shows the maximum airspeed expansion at 10,000 ft, followed by Mach speed restrictions starting at 39,000 ft for this aircraft.

(4) Standard Altitude-*versus*-V_{CAS} Flight Envelope

The same as the Altitude-versus-Mach flight envelope, except displays calibrated airspeed, rather than Mach number on the horizontal scale. Figure 20-15 right shows an example of this diagram. The higher dive-speed at low altitude results from its definition in the left diagram, in which M_D was simply specified as $M_{MO} + 0.05$. This is only done for demonstration purposes (ignoring regulations).

20.3.11 Computer Code: Determining Maximum Level Airspeed, V_{max}, for a Propeller Aircraft

The following Visual Basic for Applications functions are used to determine V_{max} for a propeller-powered aircraft by solving Equation (20-28) using and iterative scheme such as the bisection method. Note that the function `PERF_Vmax_Prop()` calls `PERF_f_of_V()`. Note that as long as the value under the radical of Equation (20-28) is greater than zero, a solution is possible. The arguments are explained in the comment section of the code.

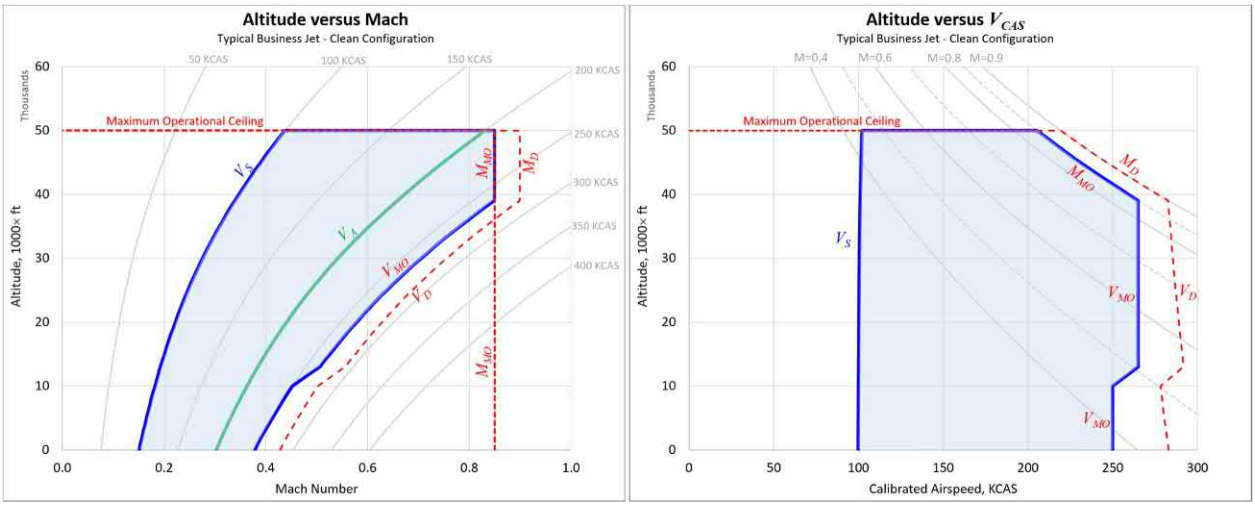


FIGURE 20-15 Typical Alt-versus-Mach flight envelope (left) and Alt-versus-VCAS flight envelope (right).

```
Function PERF_Vmax_Prop(S As Single, k As Single, CDmin As Single, W As Single, H As
Single, BHP As Single, eta As Single) As Single
'This routine determines the maximum speed of a propeller powered aircraft by solving
'Equation(20-28)using the Bisection Method. It returns the airspeed in ft/s.
'
'Input values:   S     = Wing area in ft^2
'                k     = Lift-induced drag constant
'                CDmin = Minimum drag coefficient
'                W     = Weight in lbf
'                H     = Altitude in ft
'                BHP   = Piston engine power in BHP
'                eta   = Propeller efficiency
'
'Initialize
    Dim Counter As Single, flag As Byte
    'Variables for the Bisection Method
    Dim V0 As Single, V1 As Single, Vmid As Single
    Dim F0 As Single, Fmid As Single
    Dim rho As Single

'Presets
    rho = 0.002378 * (1 - 0.0000068756 * H)^4.2561
    Counter = 0
    V0 = 0
    V1 = 500
    F0 = -1100 * eta * BHP

'Process
    Do
        'Set flag
        flag = 1

        'Advance counter
        Counter = Counter + 1

        'Compute midpoint values
        Vmid = 0.5 * (V0 + V1)
        Fmid = PERF_f_of_V(rho, S, CDmin, k, W, BHP, eta, Vmid)

        'Use logic
        If F0 * Fmid < 0 Then
            V1 = Vmid
        Else
            V0 = Vmid
            F0 = Fmid
        End If

        'Evaluate difference and adjust Vini for next iteration
        If Abs(V1 - V0) < 0.0001 Then flag = 0
    Loop Until flag = 0 Or Counter = 100
'Return results (return -1 if solution was not found)
    PERF_Vmax_Prop = 0.5 * (V0 + V1)
    If Counter = 100 Then PERF_Vmax_Prop = -1
End Function

Function PERF_f_of_V(rho As Single, S As Single, CDmin As Single, k As Single, W As
Single, BHP As Single, eta As Single, V As Single) As Single
```

```
        'This routine calculates the value of Equation(20-28).
        '
        'Initialize
            Dim K1 As Single

        'Presets
            K1 = (550 * eta * BHP) ^ 2 - (2 * W * V) ^ 2 * CDmin * k

        'This is a trick to ensure the routine can solve to higher altitudes
            If K1 < 0 Then K1 = 0

        'Calculate the value of Equation (20-28)
            PERF_f_of_V = rho * S * CDmin * V ^ 3 - 550 * eta * BHP
            PERF_f_of_V = PERF_f_of_V - Sqr(K1)
        End Function
```

20.3.12 Computer Code: Determining Maximum Level Airspeed, V_{max}, for a Jet

The following Visual Basic for Applications routine can be used to determine V_{max} based on Equation (20-26).

```
Function PERF_Vmax_Jet(H As Single, Tmax As Single, S As Single, W As Single, CDmin As u0325
Single, CLminD As Single, k As Single, Mode As Byte) As Single
'This routine calculate the maximum airspeed for an aircraft whose maximum thrust
'is specified. The routine returns the airspeed in ft/s.
'
'Input values:   H      = Altitude in ft
'                Tmax   = Maximum thrust in lbf
'                S      = Wing area in ft^2
'                W      = Weight in lbf
'                CDmin  = Minimum drag coefficient
'                CLminD = Lift coefficient where drag is minimum
'                k      = Lift-induced drag constant
'                Mode   = 0 to use the simplified drag model, = 1 to use adj. model
'
'Initialize
    Dim Radical As Single

'Process
    If Mode = 0 Then 'Simplified drag model
        Radical = Tmax ^ 2 - 4 * k * CDmin * W ^ 2
        If Radical >= 0 Then
            PERF_Vmax_Jet = Sqr((Tmax + Sqr(Radical)) / (AtmosProperty(H, 12) * S *
CDmin))
        Else
            PERF_Vmax_Jet = 0
        End If
    ElseIf Mode = 1 Then 'Adjusted dragmodel
        Radical = (Tmax + 2 * W * k * CLminD) ^ 2 - 4 * k * (CDmin + k * CLminD ^ 2) *
W ^ 2
        If Radical >= 0 Then
            PERF_Vmax_Jet = Sqr((Tmax + 2 * W * k * CLminD + Sqr(Radical)) /
(AtmosProperty(H, 12) * S * (CDmin + k * CLminD ^ 2)))
        Else
            PERF_Vmax_Jet = 0
        End If
    End If
End Function
```

20.4 GENERAL ANALYSIS METHODS FOR ACCELERATED FLIGHT

The previous section developed analysis methods for aircraft in steady, level flight. This section introduces a number of common analysis methods intended to evaluate maneuvers involving accelerated flight. Such maneuvers include turning flight, pull-up (loop), and accelerated rate-of-climb. All utilize the simplified drag model.

20.4.1 Analysis of a General Level Constant Velocity Turn

The aircraft in Figure 20-16 is banking at an angle ϕ. To maintain altitude (no slipping or skidding), its lift must balance the weight while generating a centripetal force component that balances the centrifugal force component. The resulting motion results in a steady heading change. This feat requires the magnitude of the lift to be larger than the weight of the aircraft (otherwise the airplane will lose altitude). Consequently, the airframe is loaded up beyond that of wings-level flight. The resulting loading is represented in the load factor, defined as $n = L/W$. The set of equations describing the motion of the airplane in this condition are Equations (20-5)–(20-7), introduced in Section 20.2.1, *General Equations-of-Motion for Cruise*. They are repeated below for convenience:

Fore-aft forces: $$D = T \tag{20-5}$$

Lateral forces: $$L\sin\phi - \frac{W}{g}\frac{V_\infty^2}{R_{turn}} = 0 \tag{20-6}$$

Vertical forces: $$L\cos\phi - W = 0 \tag{20-7}$$

The level constant velocity turn can be analyzed using the following set of equations:

Bank angle: $$\phi = \cos^{-1}\left(\frac{1}{n}\right) \tag{20-61}$$

Load factor: $$n = \frac{1}{\cos\phi} = \left(\frac{T}{W}\right)\left(\frac{L}{D}\right) \tag{20-62}$$

Turn radius: $$R_{turn} = \frac{V_\infty^2}{ng\sin\phi} = \frac{V_\infty^2}{g\sqrt{n^2-1}} \tag{20-63}$$

Time to turn ψ degrees: $$t_\psi = \frac{R_{turn}}{V_\infty}\left(\psi\frac{\pi}{180}\right) \tag{20-64}$$

Turn rate in radians/s: $$\dot{\psi} = \frac{g\sqrt{n^2-1}}{V_\infty} = \frac{V_\infty}{R_{turn}} \tag{20-65}$$

Thrust required at a load factor n:

$$T_{REQ} = qS\left[C_{D_{\min}} + k\left(\frac{nW}{qS}\right)^2\right] + D_{trim} \tag{20-66}$$

Where D_{trim} is the trim drag. The load factor that can be sustained given thrust, T, and airspeed, V_∞, can be estimated using the expression below. Substituting the maximum thrust yields the maximum load factor attainable at a given airspeed:

$$n = \frac{qS}{W}\sqrt{\frac{1}{k}\left(\frac{T}{qS} - C_{D_{\min}}\right)} \tag{20-67}$$

This expression is used to plot a part of the banking constraint diagram of Figure 20-17.

Airspeed for a given C_L: $$V = \sqrt{\frac{2W}{\rho S C_L}\left(\frac{1}{\cos\phi}\right)} \tag{20-68}$$

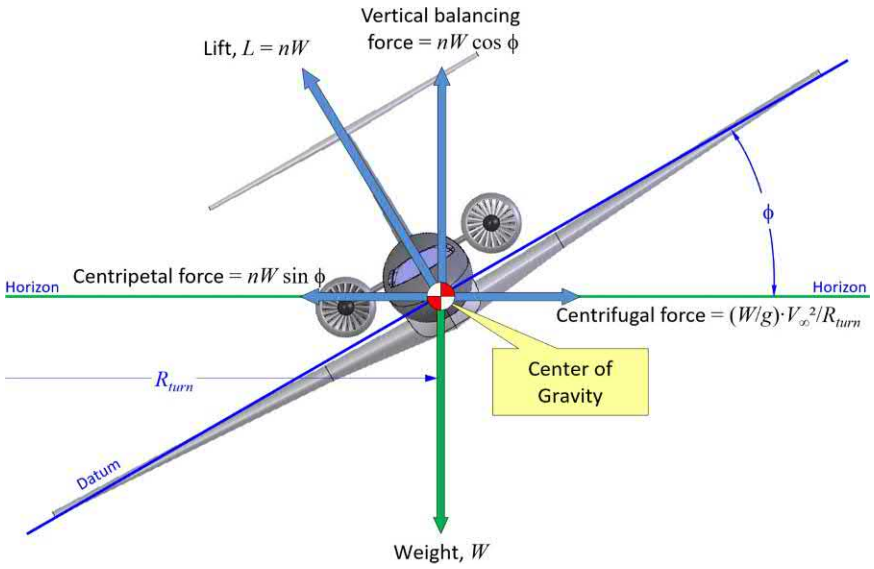


FIGURE 20-16 Forces on an aircraft in a level constant velocity turn.

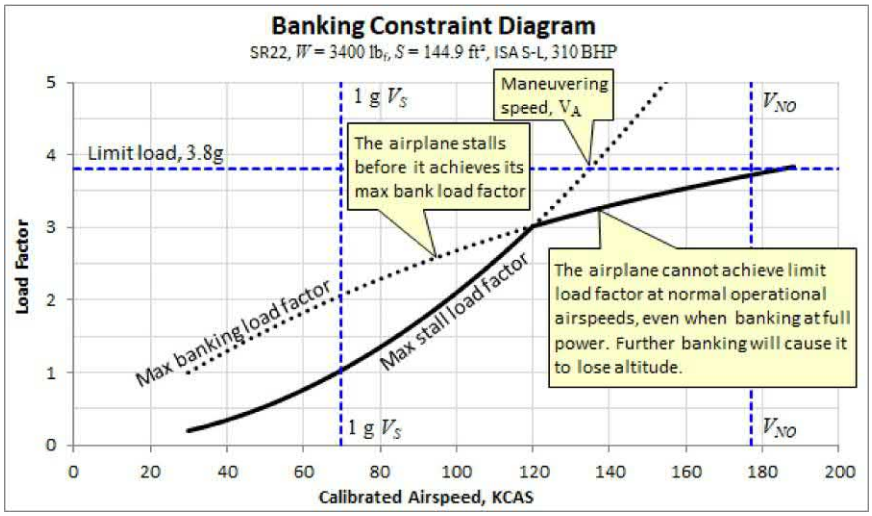


FIGURE 20-17 A Banking constraint diagram for the SR22. The maximum stall load factor is calculated by solving Equation (20-30) for the load factor. The maximum banking load factor is calculated using Equation (20-67).

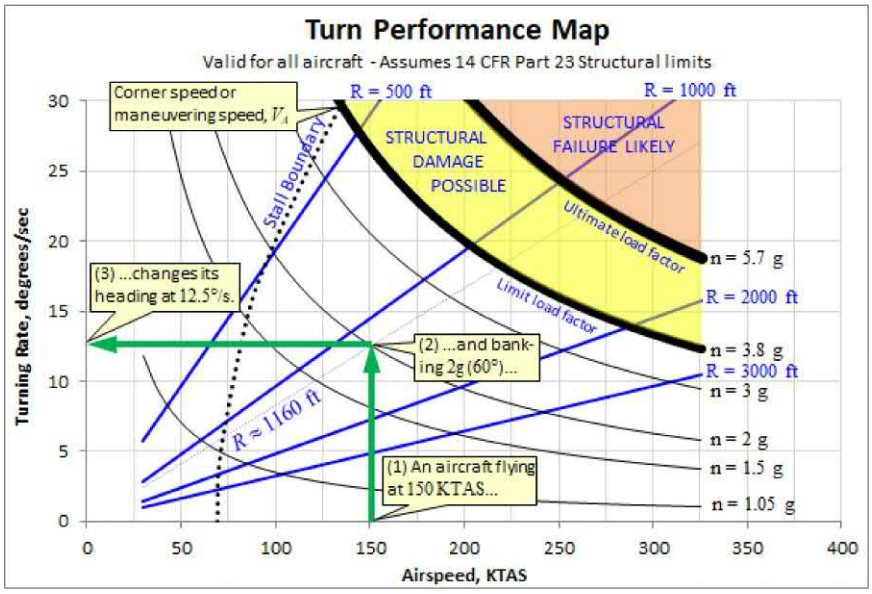


FIGURE 20-18 A turn performance map is constructed using Equation (20-65).

A common way to present the turn performance of an aircraft can be seen in the *Banking Constraint Diagram* of Figure 20-17 and the *Turn Performance Map* of Figure 20-18. First, consider the banking constraint diagram of Figure 20-17, here based on the SR22 sample aircraft. The straight dashed horizontal line shows the limit load factor of 3.8 g. The two vertical dashed lines show the clean stalling speed at normal 1 g loading (V_S, to the left) and the normal operating speed (V_{NO}, to the right). These two lines enclose the normal speed range of the aircraft. The solid curve, labeled "Max stall load factor," shows the stalling speed of the aircraft at various load factors. It plots n obtained from Equation (20-30). It shows the airplane stalls near 120 KCAS at a load factor of 3 g. This curve is a part of the standard *V-n* diagram. The dotted curve, labeled "Max banking load factor," shows the maximum "g" at which the aircraft can bank at while maintaining altitude. It plots n per Equation (20-67). It shows that, between V_S and 120 KCAS, the airplane simply stalls before achieving its maximum "theoretical" banking load factor. Thus, at 100 KCAS, if the airplane didn't stall first (at $n \approx 2.1g$) it could achieve $n = 2.7g$ before it would begin to lose altitude. At airspeeds beyond 120 KCAS, the airplane cannot achieve 3.8g (its limit load factor) and maintain altitude while banking. This means that when flight testing the aircraft for structural flight tests (e.g., per 14 CFR §23.307, *Proof of structure*), means other than constant altitude banking may have to be considered. Conversely, for some other aircraft, it might reveal the aircraft can indeed exceed the limit load factor in some airspeed range.

Next, consider the turn performance map of Figure 20-18. It coplots the center and right terms of Equation (20-65). The straight lines indicate turn-rate with airspeed, given fixed turn radius. The curves indicate turn-rate with airspeed, given fixed load factor. Since the equation does not contain parameters dependent on aircraft geometry, it is valid for all aircraft. However, Figure 20-18 is drawn for aircraft that comply with the "old" 14 CFR Part 23. Also, the "Stall boundary" indicates theoretical turn-rate at stall speed at increasing bank angle. Flying on the left-hand side of the boundary is impossible. This boundary varies from airplane to airplane. The map shows how rapidly an aircraft can maneuver at specific airspeeds. The maneuvering speed is where the stall boundary intersects the curve for the limit load factor. It is also called the *corner speed* and is the lowest airspeed where the airplane achieves its maximum bank angle, most rapid heading change, and minimum turning radius.

EXAMPLE 20-9

Consider some arbitrary aircraft. (a) What bank angle requires a 2*g* load to be reacted by the aircraft? (b) If it is flying at 200 KTAS at 10,000 ft, what is the resulting turn radius? (c) How much time will it take to complete a full circle?

SOLUTION:

(a) Angle of bank: $\phi = \cos^{-1}\left(\frac{1}{n}\right) = \cos^{-1}\left(\frac{1}{2}\right)$
$= 60$ degrees

(b) Turn radius: $R_{turn} = \frac{V^2}{g\sqrt{n^2-1}} = \frac{(200\times 1.688)^2}{(32.174)\sqrt{(2)^2-1}}$
$= 2045$ ft

(c) Time to turn 360 degrees: $t_\psi = \frac{R_{turn}}{V}\left(\psi\frac{\pi}{180}\right) = t_\psi$
$= \frac{2045}{(200\times 1.688)}(2\pi) = 38$ s

DERIVATION OF EQUATION (20-61)

Load factor n is defined as $n = L/W$. From Figure 20-16 we readily see that:

$$W = L\cos\phi = nW\cos\phi \quad \Leftrightarrow \quad \cos\phi = 1/n$$

DERIVATION OF EQUATION (20-62)

Divide Equation (20-7) by Equation (20-5):

$$\frac{L\cos\phi - W = 0}{T - D = 0} \quad \Rightarrow \quad \frac{L\cos\phi}{D} = \frac{W}{T} \quad \Rightarrow \quad \frac{L}{D}\frac{1}{n} = \frac{W}{T}$$
$$\Leftrightarrow \quad n = \left(\frac{T}{W}\right)\left(\frac{L}{D}\right)$$

DERIVATION OF EQUATION (20-63)

Centrifugal force corresponding to the force diagram in Figure 20-16 can be found from the standard curvilinear relation mV^2/R:

$$m\frac{V_\infty^2}{R_{turn}} = \left(\frac{W}{g}\right)\frac{V_\infty^2}{R_{turn}} = nW\sin\phi$$

Manipulating algebraically leads to:

$$\left(\frac{W}{g}\right)\frac{V_\infty^2}{R_{turn}} = nW\sin\phi \quad \Rightarrow \quad \frac{V_\infty^2}{R_{turn}} = ng\sin\phi \quad \Rightarrow \quad R_{turn} = \frac{V_\infty^2}{ng\sin\phi}$$

DERIVATION OF EQUATION (20-64)

The distance the airplane covers in the turn at an airspeed V_∞ in time t_ψ equals the arc length of a circle of radius R_{turn} through the angle ψ. In other words:

$$\text{arclength} = R_{turn}\times\psi = V\times t_\psi$$

By solving for t_ψ in the above expression and noting the angle to be used must be in radians (note the conversion factor $\pi/180$) we get the expression for the time to turn.

DERIVATION OF EQUATION (20-65)

Turn rate is the change in heading with respect to time and can be written as follows:

$$\dot\psi = \frac{d\psi}{dt} \cong \frac{\psi}{t_{turn}} = \frac{\psi}{\frac{R_{turn}\times\psi}{V}} = \frac{V}{R_{turn}} = \frac{V}{\frac{V^2}{g\sqrt{n^2-1}}} = \frac{g\sqrt{n^2-1}}{V}$$

DERIVATION OF EQUATION (20-66)

The level constant velocity turn requires thrust to equal the drag of the airplane in the turn, in other words (assuming the simplified drag model):

$$T_{REQ} = D = qSC_D \quad \Rightarrow$$
$$T_{REQ} = qS\left[C_{D_{\min}} + kC_L^2\right] = qS\left[C_{D_{\min}} + k\left(\frac{nW}{qS}\right)^2\right]$$

Since the elevator is used to trim the airplane in the turn, the increase in trim drag should be considered if it is significant. This term, D_{trim}, is shown in Equation (20-66).

DERIVATION OF EQUATION (20-67)

First note that, typically, D_{trim} is around 1%–4% of the total drag of the airplane and, thus, ignoring it is acceptable. Use Equation (20-66), assuming $D_{trim} = 0$ and solve for the load factor, n.

DERIVATION OF EQUATION (20-67) (cont'd)

$$T_{REQ} = qS\left[C_{D_{\min}} + k\left(\frac{nW}{qS}\right)^2\right]$$

$$\Rightarrow \quad \frac{T_{REQ}}{qS} - C_{D_{\min}} = k\left(\frac{nW}{qS}\right)^2$$

$$\Rightarrow \quad n = \frac{qS}{W}\sqrt{\frac{1}{k}\left(\frac{T_{REQ}}{qS} - C_{D_{\min}}\right)}$$

Then, if we know the required thrust, the maximum load factor can be determined.

20.4.2 Extremes of Constant Velocity Turns

(1) Maximum Sustainable Load Factor, n_{max}

The maximum load factor that the aircraft can sustain without stalling is obtained from Equation (20-62) when the thrust-to-weight and lift-to-drag ratios are at their maximum values:

Max Sustainable Load Factor:

$$n_{\max} = \left(\frac{T_{\max}}{W}\right) LD_{\max} \tag{20-69}$$

(2) Maximum Sustainable Turn Rate, $\dot{\psi}_{max}$

The maximum turn rate is a strong indicator of an airplane's maneuver ability. A large T/W and $AR \cdot e$ combined with a low W/S and altitude yield the smallest turning radius. This is the fastest heading change the airplane can achieve and is given by the following relation:

Turn rate in radians/s:
$$\dot{\psi}_{\max} = \frac{g\sqrt{n_{\max}^2 - 1}}{V_{\max\dot{\psi}}} \tag{20-70}$$

Where: $V_{\max\dot{\psi}}$ = Fastest turn velocity, given by Equation (20-39), repeated below for convenience.

$$V_{\max\dot{\psi}} = V_{TR_{\min}} = \sqrt{\frac{2}{\rho}\left(\frac{W}{S}\right)\sqrt{\frac{k}{C_{D_{\min}}}}} \tag{20-39}$$

A derivation of this result is given by Asselin [14].

(3) Minimum Sustainable Turning Radius

The minimum sustainable turning radius is another important indicator of an airplane's maneuverability. A large T/W and $AR \cdot e$ combined with a low W/S and altitude yield the smallest turning radius. It can be calculated from the following relation:

Turn radius:
$$R_{turn_{\min}} = \frac{V_{turn_{\min}}^2}{g\sqrt{n_{R_{\min}}^2 - 1}} \tag{20-71}$$

Where: $n_{turn_{\min}} = \sqrt{2 - 1/n_{\max}^2}$ = Load factor for minimum turning radius

$V_{turn_{\min}} = 2\sqrt{\frac{(W/S)}{(T/W)}\frac{k}{\rho}}$ = Airspeed for minimum turning radius

A derivation of this result is given by Asselin [14].

(4) Maximum Bank Angle

This is the maximum angle the aircraft can bank while maintaining altitude (provided it has enough power or thrust) and sustain the limit load factor to which it has been designed. It can simply be determined using Equation (20-61) with $n_{\lim}$ being the limit load factor:

Maximum Level Bank angle:

$$\phi_{\max} = \cos^{-1}\left(\frac{1}{n_{\max}}\right) \tag{20-72}$$

(5) Airspeed for Maximum Bank Angle

Using the simplified drag model, the airspeed required to reach the limit load factor for a given thrust setting is given by the following expression:

$$V_{\lim} = \sqrt{\frac{\left(T \pm \sqrt{T^2 - 4kC_{D_{\min}}(n_{\lim}W)^2}\right)}{\rho S C_{D_{\min}}}} \tag{20-73}$$

The expression will return two airspeeds, one for each sign. These represent a low and high-speed conditions.

DERIVATION OF EQUATION (20-73)

Consider Equation (20-67) for turning load factor:

$$n = \frac{qS}{W}\sqrt{\frac{1}{k}\left(\frac{T}{qS} - C_{D_{\min}}\right)}$$

Begin by solving for the dynamic pressure when banking at the limit load, $n_{\lim}$:

$$n_{\lim}^2 = \left(\frac{q_{\lim}S}{W}\right)^2\left(\frac{1}{k}\left(\frac{T}{q_{\lim}S} - C_{D_{\min}}\right)\right)$$

$$\Leftrightarrow \quad \frac{kn_{\lim}^2W^2}{S^2} = (q_{\lim}^2)\left(\frac{T}{q_{\lim}S} - C_{D_{\min}}\right)$$

$$\Rightarrow \quad k\left(\frac{n_{\lim}W}{S}\right)^2 = \frac{T}{S}q_{\lim} - C_{D_{\min}}q_{\lim}^2$$

$$\Rightarrow \quad C_{D_{\min}}q_{\lim}^2 - \frac{T}{S}q_{\lim} + k\left(\frac{n_{\lim}W}{S}\right)^2 = 0$$

This can be solved as a quadratic equation as shown below:

$$q_{\lim} = \frac{1}{2}\rho V_{\lim}^2 = \frac{\frac{T}{S} \pm \sqrt{\left(\frac{T}{S}\right)^2 - 4(C_{D_{\min}})k\left(\frac{n_{\lim}W}{S}\right)^2}}{2C_{D_{\min}}}$$

DERIVATION OF EQUATION (20-73) (cont'd)

Further manipulations lead to:

$$V_{\lim}=\sqrt{\frac{\frac{T}{S}\pm\sqrt{\left(\frac{T}{S}\right)^2-4(C_{D_{\min}})k\left(\frac{n_{\lim}W}{S}\right)^2}}{\rho C_{D_{\min}}}}$$

$$=\sqrt{\frac{\left(T\pm\sqrt{T^2-4kC_{D_{\min}}(n_{\lim}W)^2}\right)}{\rho SC_{D_{\min}}}}$$

EXAMPLE 20-10

Calculate the maximum bank angle for the Learjet 45 that corresponds to a limit load factor of 3.5*g*? What airspeeds at S-L allow it to be achieved at S-L, when it weighs of 20,000 lb_f with 7000 lb_f of thrust?

SOLUTION:

Maximum bank angle:

$$\phi_{\max}=\cos^{-1}\left(\frac{1}{n_{\lim}}\right)=\cos^{-1}\left(\frac{1}{3.5}\right)=73.4^\circ$$

Airspeed required to achieve the limit load factor:

$$V_{\lim}=\sqrt{\frac{\left(T\pm\sqrt{T^2-4kC_{D_{\min}}(n_{\lim}W)^2}\right)}{\rho SC_{D_{\min}}}}$$

$$V_{\lim}=\sqrt{\frac{\left(7000\pm\sqrt{7000^2-4(0.05236)(0.0200)(3.5\times20,000)^2}\right)}{(0.002378)(311.6)(0.0200)}}$$

$$=\begin{cases}335.1\text{ ft/s (198.5 KTAS)}\\912.4\text{ ft/s (540 KTAS)}\end{cases}$$

20.4.3 Analysis of the Loop Maneuver

The loop is a common maneuver performed by aerobatic pilots. Figure 20-19 shows an idealized version of this maneuver (real loop usually tends to be more elliptic in shape than what is shown). It can be seen that the *load factor*, *n*, depends on the angular position of the airplane in the loop: It is maximum at Point A and minimum at Point C. It is given by

$$n=\frac{V_\infty^2}{gR}+\cos\theta \tag{20-74}$$

If we know the load factor at a specific angular position, we can calculate the radius of the loop by solving for *R* in Equation (20-74).

$$R=\frac{V_\infty^2}{g(n-\cos\theta)} \tag{20-75}$$

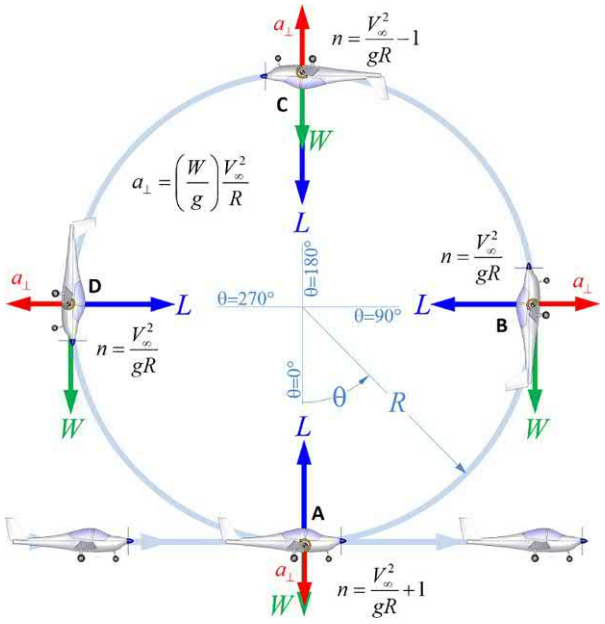


FIGURE 20-19 A diagram of the loop maneuver.

The force diagram applies equally to inverted loop, except the airplane is rotated 180 degrees. Thus, the generation of lift requires a negative angle-of-attack.

DERIVATION OF EQUATION (20.74)

Consider the airplane at the bottom of the loop. By summing the forces along its vertical axis, we get

$$\sum F=ma\ \Rightarrow\ L-W\cos\theta-\left(\frac{W}{g}\right)\frac{V_\infty^2}{R}=0$$

$$\Rightarrow\ L=\left(\frac{W}{g}\right)\frac{V_\infty^2}{R}+W\cos\theta=\overbrace{\left(\frac{V_\infty^2}{gR}+\cos\theta\right)}^{n}W=nW$$

20.4.4 Energy State

(1) Energy Height

The total energy of an airplane of mass *m* and weight *W* flying at altitude *h* and airspeed V_∞ is a linear combination of its potential and kinetic energy and can be computed from:

$$E_{total}=mgh+\frac{1}{2}mV_\infty^2=Wh+\frac{1}{2}\frac{W}{g}V_\infty^2 \tag{20-76}$$

(2) Specific Energy and Energy Height

The *specific energy* is defined as the total energy per unit weight and can be computed as follows:

$$H_E\equiv\frac{E_{total}}{W}=h+\frac{V_\infty^2}{2g} \tag{20-77}$$

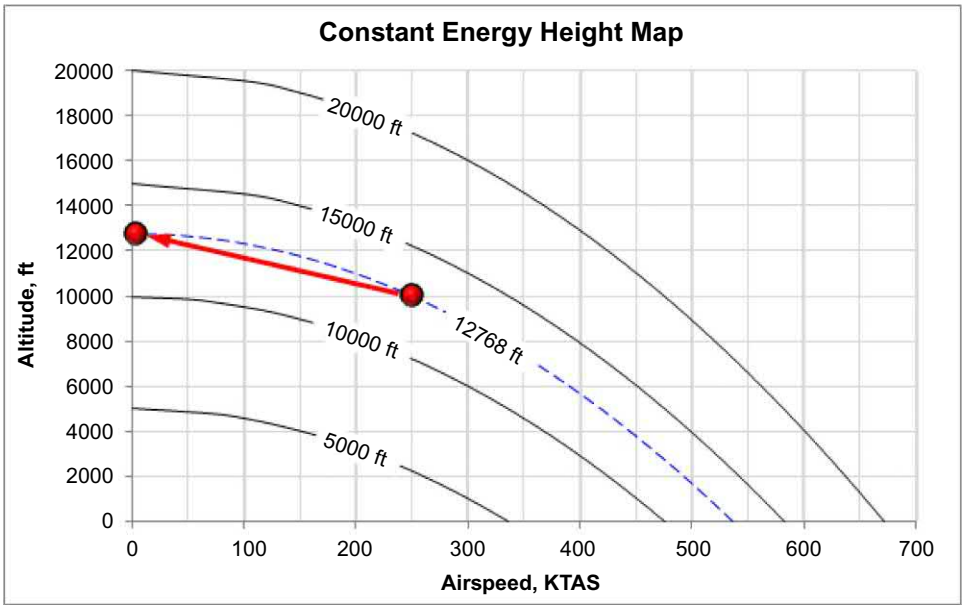


FIGURE 20-20 Constant energy height isopleths.

Since the units of specific energy is that of height (ft or m) it is also called *energy height*. It highlights that the maneuvering of an airplane can be considered an exchange of potential and kinetic energy. To explain what this means, consider an airplane cruising at an altitude of 10,000 ft at airspeed of 250 KTAS (422 ft/s), as shown in Figure 20-20. Its specific energy is then $10{,}000+400^2/(2\cdot 32.174)=12{,}768$ ft. This means that if the pilot exchanged all the kinetic energy into potential energy, by raising the nose of the aircraft and allowing it to climb until the airspeed drains to zero (this maneuver is called *zooming*), the airplane would reach an altitude of 12,768 ft.

The graph of Figure 20-20 is called a *Constant Energy Height Map*. It consists of isopleths of constant energy height that extend from the vertical to the horizontal axis. The airspeed at any altitude can be calculated for a given energy height by solving for the airspeed in Equation (20-77) as follows:

$$V_\infty=\sqrt{2g(H_E-h)} \tag{20-78}$$

Equation (20-78) was used to create the constant energy height map of Figure 20-20. The figure shows isopleths for energy heights (H_E) of 5000, 10,000, 15,000, and 20,000 ft, with the one of 12,768 ft shown as a dashed line. Furthermore, the exchange from the initial altitude of 10,000 ft and 250 KTAS to 12,768 ft and 0 KTAS is shown as well. The plot applies to all aircraft, regardless of weight. A more type-dependent representation is obtained by determining and plotting the *Specific Excess Power* contour plots (see below).

(3) Specific Excess Power

Just like the specific energy was defined as the total energy per unit weight, we also define *specific excess power* as the excess power (per Equation 19-16):

$$P_S\equiv\frac{P_{EX}}{W}=\frac{TV_\infty-DV_\infty}{W} \tag{20-79}$$

The specific excess power can also be written as follows:

$$P_S=\frac{dh}{dt}+\frac{V_\infty}{g}\frac{dV}{dt} \tag{20-80}$$

The expression shows that the specific excess power of an airplane is the combination of its rate-of-climb (dh/dt) and forward acceleration ($V_\infty/g\cdot dV_\infty/dt$). Thus, if $dV_\infty/dt=0$ (steady state), the specific excess power is simply the ROC of the airplane. Likewise, if $dh/dt=0$, the specific excess power is simply its acceleration. An inspection of Equation (20-77) reveals its time derivative equals the specific excess power, that is:

$$\frac{d}{dt}\left(h+\frac{V_\infty^2}{2g}\right)=\frac{dH_E}{dt}=\frac{dh}{dt}+\frac{V_\infty}{g}\frac{dV_\infty}{dt} \tag{20-81}$$

In short, the specific excess power is the time rate of change of the Energy Height.

$$P_S=\frac{dH_E}{dt} \tag{20-82}$$

DERIVATION OF EQUATION (20-80)

Begin with the dynamic version of the equations-of-motion, i.e., Equation (19-3), repeated here for convenience (assuming the thrust angle $\varepsilon=0$):

$$T-D-W\sin\gamma=\frac{W}{g}\frac{dV}{dt} \tag{19.3}$$

DERIVATION OF EQUATION (20-80) (*cont'd*)

This can be rewritten as follows:

$$T - D = W\sin\theta + \frac{W}{g}\frac{dV}{dt} = W\left(\sin\theta + \frac{1}{g}\frac{dV}{dt}\right) \quad \text{(i)}$$

Multiply by V_∞/W:

$$\frac{TV - DV}{W} = \frac{P_{EX}}{W} = P_S = V\sin\theta + \frac{V}{g}\frac{dV}{dt} \quad \text{(ii)}$$

Noticing that $V_\infty\sin\theta$ = rate-of-climb = dh/dt we can rewrite Equation (ii) as follows:

$$P_S = \frac{dh}{dt} + \frac{V}{g}\frac{dV}{dt} \quad \text{(20-80)}$$

(4) Constructing a Specific Excess Power Contour Plot

A specific excess power contour plot is used to demonstrate the maneuvering capability of the aircraft throughout its operational airspeed and altitude range. An example of such a contour plot is shown as the lower graph of Figure 20-21. It is typically constructed by plotting rate-of-climb for a range of altitudes, as shown in the upper graph of Figure 20-21. Thus, the P_S contour for zero ROC ($P_S = 0$ ft/s, which represents the minimum and maximum airspeed) is constructed by transferring the points labeled *a* through *i* to the lower graph. The P_S contour for the $P_S = 10$ ft/s (an ROC of 600 fpm) is constructed in a similar manner, by transferring the points along the line A-A to the lower graph. The P_S contour for the $P_S = 20$ ft/s (an ROC of

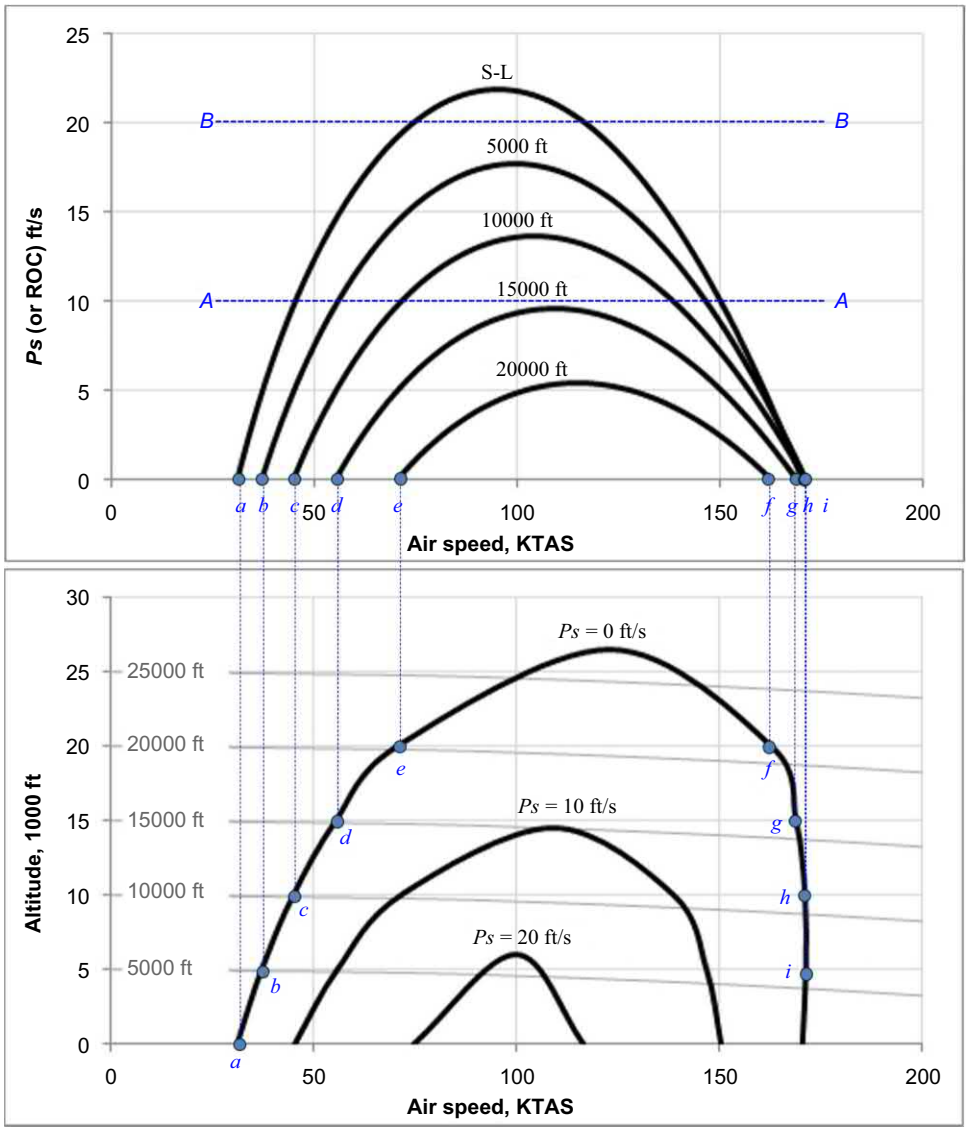


FIGURE 20-21 Constructing a specific excess power contour plot for an SR22-class aircraft. The light-colored curves (labeled 5000 ft through 25,000 ft) are the constant energy height isopleths plotted in Figure 20-20.

1200 fpm) is constructed by transferring the points along the line B-B to the lower graph.

References

[1] C.D. Perkins, R.E. Hage, *Airplane Performance, Stability, and Control*, John Wiley & Sons, 1949.

[2] E. Torenbeek, *Synthesis of Subsonic Aircraft Design*, third ed., Delft University Press, 1986.

[3] L. Nicolai, *Fundamentals of Aircraft Design*, second ed., 1984.

[4] J. Roskam, C.-T.E. Lan, *Airplane Aerodynamics and Performance*, DARcorporation, 1997.

[5] F.J. Hale, *Aircraft Performance, Selection, and Design*, John Wiley & Sons, 1984, pp. 137–138.

[6] J.D. Anderson Jr., *Aircraft Performance & Design*, first ed., McGraw-Hill, 1998.

[7] A. Miele, *Flight Mechanics—Theory of Flight Paths*, Dover Publications, 1990.

[8] B.H. Carson, *Fuel Efficiency of Small Aircraft, Flight*. AIAA-80-1847, 1980, https://doi.org/10.2514/6.1980-1847.

[9] G. Gabrielli, T. von Kármán, *What price speed? Specific power required for propulsion of vehicles*, Mech. Eng. 72 (10) 1950 775–781.

[10] H.C. Smith, *An Application of the Carson Cruise Optimum Airspeed—A Compromise Between Speed and Efficiency*, SAE SP-621, Paper 850867, 1985.

[11] Anonymous, *Aircraft Operations at Altitudes Above 25,000 Feet Mean Sea Level or Mach Numbers Greater Than .75*, AC 61-107B, Federal Aviation Administration, March 29, 2013.

[12] J.W.R. Taylor (Ed.), *Jane's All the World's Aircraft 1984-85*, In: Jane's Yearbooks, Jane's Information Group, Ltd., 1985.

[13] Anonymous, *Lockheed U-2C and U-2F Flight Manual*, AF(C)-1-1, May 10, 1967.

[14] M. Asselin, *An Introduction to Aircraft Performance*, AIAA Education Series, American Institute of Aeronautics and Astronautics, 1997.

CHAPTER

21

Performance—Range and Endurance

OUTLINE

21.1 **Introduction** 867
21.1.1 The Content of This Chapter 868
21.1.2 What Analyses Must I Do? 868

21.2 **Fundamental Relations for Range and Endurance** 868
21.2.1 General Equations-of-Motion for Range and Endurance 869
21.2.2 Fundamentals of Range and Endurance of Fossil-Fueled Aircraft 869
21.2.3 Fundamentals of Range and Endurance for Electric Aircraft 871
21.2.4 Specific Fuel Consumption 871

21.3 **Range Analysis** 873
21.3.1 Mission Profiles 873
21.3.2 Range Profile 1: Constant Airspeed/Altitude Cruise 873
21.3.3 Range Profile 2: Constant Attitude/Altitude Cruise 875
21.3.4 Range Profile 3: Constant Airspeed/Attitude Cruise 877
21.3.5 Range Profile 4: Cruise Range of Electric Aircraft 880
21.3.6 Specific Range 881
21.3.7 Determining Fuel Required for a Mission 882
21.3.8 Range Sensitivity Studies 883

21.4 **Endurance Analysis** 884
21.4.1 Endurance Profile 1: Constant Airspeed/Altitude Cruise 884
21.4.2 Endurance Profile 2: Constant Attitude/Altitude Cruise 885
21.4.3 Endurance Profile 3: Constant Airspeed/Attitude Cruise 885
21.4.4 Endurance Profile 4: Cruise Range of Electric Aircraft 886

21.5 **Analysis of Mission Profile** 886
21.5.1 Basics of Mission Profile Analysis 886
21.5.2 Special Range Mission 1: IFR Cruise Mission 887
21.5.3 Special Range Mission 2: NBAA Cruise Mission 888
21.5.4 Payload-Range Sensitivity Study 889

Exercises 890

References 890

21.1 INTRODUCTION

An aircraft is first and foremost a transportation device. It should not come as a surprise that range and endurance at high-altitude are the primary impetus for the development of many aircraft. The importance of long-range, high-altitude cruise was popularized in the media in the early to mid-20th century. A case in point is this paragraph in the May 1946 edition of the Boeing Magazine:

> High-altitude flight attracted Boeing designers and airline operators for several reasons. Clear skies are found in 95 per cent of the flights above 20,000 feet. Flight cancellations due to bad weather fall to a minimum for high-flying planes capable of long-range operation. Operating costs are greatly reduced. Air speed increases with altitude. At 20,000 feet an airplane flies 20 to 25 per cent faster than it does at sea level, on the same power. By choosing one of several levels, pilots often can take advantage of high-velocity winds prevailing in the sub-stratosphere [1].

While aircraft are certainly designed to satisfy other requirements, range and endurance are almost always included as some of the most important ones. Even the fastest and most maneuverable aircraft would not pass the muster without offering acceptable range or endurance. The focus of this chapter are methods for estimating

https://doi.org/10.1016/B978-0-12-818465-3.00021-5

Copyright © 2022 Elsevier Inc. All rights reserved.

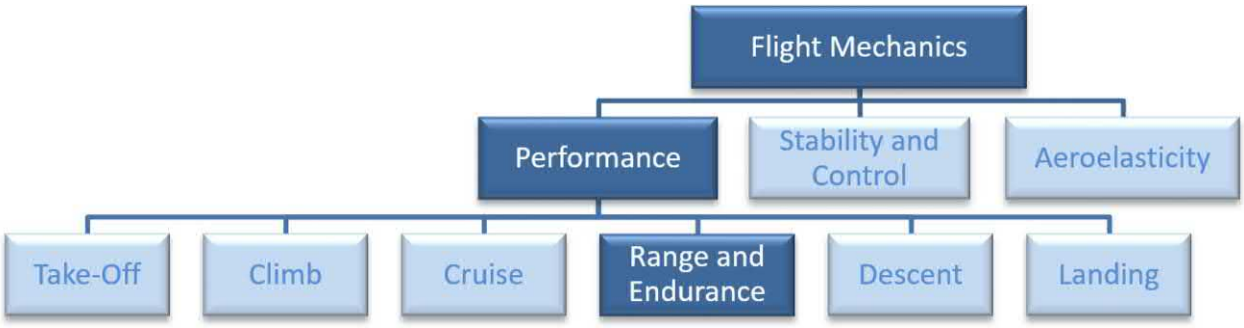


FIGURE 21-1 An organizational map placing range and endurance theory among the disciplines of *Flight Mechanics*, and highlighting the focus of this chapter; range and endurance.

the range and endurance performance of aircraft. Figure 21-1 shows how range and endurance fit among the other branches of performance theory.

In general, the methods presented in here are "industry standard" and mirror that presented by a variety of authors, e.g., Perkins and Hage [2], Torenbeek [3], Nicolai [4], Roskam [5], Hale [6], Anderson [7], and Miele [8], to name a few. Also note that Torenbeek presents various range optimization methods in reference [9].

21.1.1 The Content of This Chapter

- Section 21.1 presents fundamental theory of range analysis, as well as information required to complete such analysis.
- Section 21.2 presents classical range analysis methods using three different cruise profiles for aircraft powered by fossil fuels, and one aimed at aircraft that use electric power. These profiles are referred to as a *Constant Airspeed/Altitude*, *Constant Attitude/Altitude*, *Constant Airspeed/Attitude*, and *Constant Weight* profiles, respectively. The end of the section presents methods to evaluate range sensitivity.
- Section 21.3 presents the concept of specific range.
- Section 21.4 presents classical endurance analysis methods in a manner similar to that of the range analysis.
- Section 21.5 presents methods to analyze the mission profile of the aircraft, but these are needed to determine realistic fuel requirements for the new aircraft. The section also introduces two important and common mission profiles to which many GA aircraft are designed; the standard *IFR Cruise Mission* and *NBAA Cruise Mission*. The section also presents the important *Payload-Range* analysis.

21.1.2 What Analyses Must I Do?

For the newcomer to range/endurance analysis, the burning question is: "What am I supposed to estimate and how do I conduct those estimations?" Range analysis is conducted to evaluate how far the airplane can fly and how much fuel it takes. Endurance evaluates how long it can stay airborne given specific amount of fuel. Additionally, both are affected by how the cruise segment of the mission is conducted and if the aircraft is powered using fossil fuel or electricity. For 14 CFR Part 23, level performance analysis supports certification through the identification of specific operational airspeeds and airspeed limits of importance for both Subpart B and G. That said, the designer should, at minimum, provide estimates of the following performance characteristics (Table 21-1).

TABLE 21-1 Task list for cruise analysis.

Task name	Terms	Section
Constant airspeed/altitude cruise range	R_1	21.3.2
Constant attitude/altitude cruise range	R_2	21.3.3
Constant airspeed/attitude cruise range	R_3	21.3.4
Cruise range for electric aircraft	R_3	21.3.5
Specific range	SR	21.3.6
Constant airspeed/altitude cruise endurance	E_1	21.4.1
Constant attitude/altitude cruise endurance	E_2	21.4.2
Constant airspeed/attitude cruise endurance	E_3	21.4.3
Cruise endurance for electric aircraft	E_3	21.4.4
Range and endurance sensitivity studies		21.3.8
IFR cruise mission		21.5.2
NBAA cruise mission		21.5.3
Payload-range sensitivity		21.5.4

21.2 FUNDAMENTAL RELATIONS FOR RANGE AND ENDURANCE

This section presents basic mathematical relationships and aerodynamic concepts required to analyze range and endurance. It is helpful to first review Sections 7.1.3

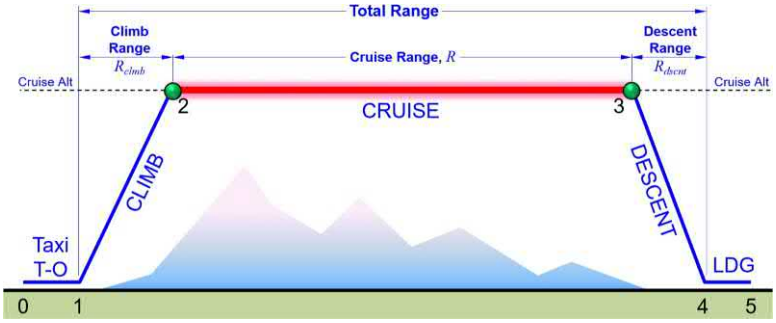


FIGURE 21-2 The breakdown of a mission into climb, cruise, and descent segments.

and 20.2. Range and endurance are analyzed in two ways: (1) for fossil-fueled aircraft it is based on the weight of fuel consumed with time or (2) for electric aircraft it is based on the quantity of battery energy consumed with time. This explains the organization of this chapter.

Range is the distance an airplane can fly in a given amount of time or fuel. *Endurance* is the time it can stay aloft in a given amount of fuel. As already stated, the mission of an aircraft is broken into basic segments: climb, cruise, and descent (see Figure 21-2). In this book, the climb segment is treated in Chapter 19 and the descent segment in Chapter 22. This chapter (with the support of Chapter 20) solely focuses on the cruise segment. This arrangement allows specific initial conditions to be established that help with problem solving. Note that some consider total range consisting only of the climb and cruise segments. This is arguably safer for mission planning.

21.2.1 General Equations-of-Motion for Range and Endurance

Refer to Section 20.2.1.

21.2.2 Fundamentals of Range and Endurance of Fossil-Fueled Aircraft

The basic cruise segment for aircraft using fossil fuels is shown in Figure 21-3. The aircraft begins the cruise at some initial weight, W_{ini}, and after covering some distance, R, its final weight is W_{fin}, such that $W_{fin} < W_{ini}$.

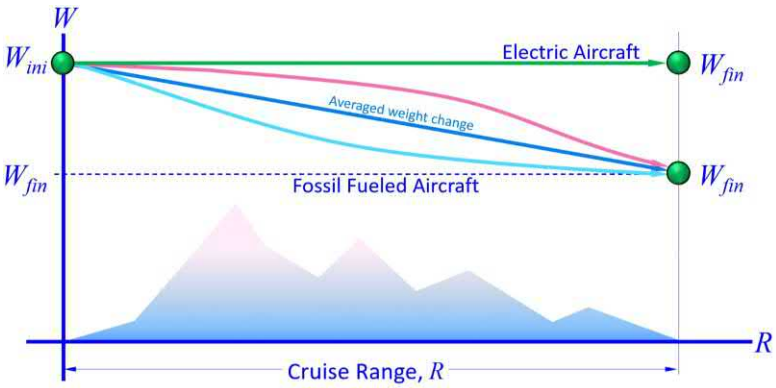


FIGURE 21-3 Impact of travel on weight for fossil-fueled versus electric aircraft.

This shows the distance can be related to the change in weight (electric aircraft require a different method). The two nonlinear curves in Figure 21-3 indicate the aircraft may initially burn more (lower curve) or less fuel (upper curve) than later in the segment. However, for simplicity, we assume (1) a linear fuel burn (straight line) and (2) constant specific fuel consumption. The latter one is an important simplification (see Equations (14-60)–(14-65)). Mixed-rate fuel burn can be broken into smaller linear segments to simplify analysis.

(1) Basic Range

In its simplest form, range is the product of speed, V_∞, and time, Δt.

$$R \equiv V_\infty \Delta t \tag{21-1}$$

(2) Range versus Change in Weight

For mathematical convenience, it helps to transpose the axes in Figure 21-3, to that shown in Figure 21-4. In this figure, the horizontal axis represents weight and the vertical one range. Then, the range changes from 0 at W_{ini} to the final range, R_{fin}, at W_{fin}.

From this, we can define the *change in range* as follows:

$$\frac{dR}{dW} = \frac{\text{Rate of change of distance}}{\text{Rate of change of weight}} = \frac{V_\infty}{-c_t T} \tag{21-2}$$

where c_t is the thrust specific fuel consumption, discussed in Section 21.2.4, (in 1/s or 1/h), V_∞ is airspeed, and T is thrust.

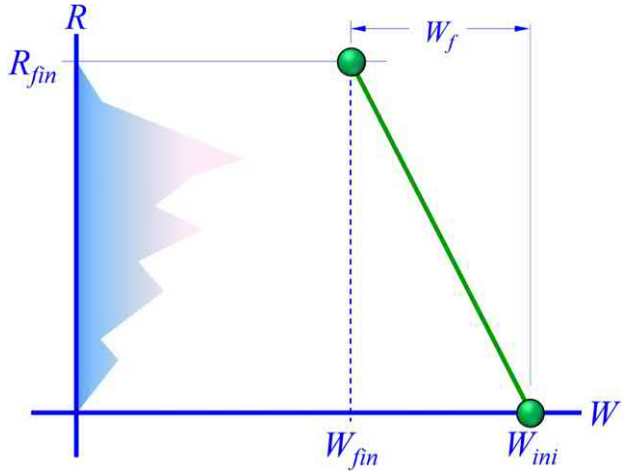


FIGURE 21-4 The basic cruise segment with transposed axes.

During cruise $T=D$ and $D=W/(L/D)$. Therefore, we can rewrite the change in range as follows:

$$dR=\frac{V_\infty}{-c_tT}dW=\frac{V_\infty}{-c_tD}dW=\frac{V_\infty(L/D)}{-c_tW}dW \qquad (21\text{-}3)$$

(3) Endurance versus Change in Weight

Endurance is the time an airplane can stay airborne while consuming a specific amount of fuel. Like range, endurance is analyzed as a *cruise segment*. Such a segment is shown in Figure 21-5 and is identical to Figure 21-4, except the vertical axis represents time.

Recall the definition of c_t in Section 21.2.4:

$$c_t\equiv\frac{\dot{w}_{fuel}}{T}=\frac{dW/dt}{T}\Rightarrow dW/dt=-c_tT \qquad (21\text{-}4)$$

The inverse of the derivative dW/dt is simply the rate-of-change of time with respect to weight. This allows us to write the change in time aloft as follows:

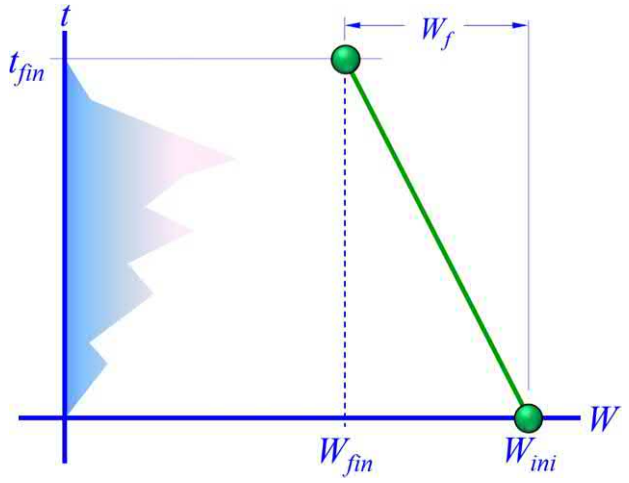


FIGURE 21-5 The basic cruise segment in terms of time of flight.

$$\frac{dW}{dt}=-c_tT\Leftrightarrow dt=\frac{dW}{-c_tT} \qquad (21\text{-}5)$$

Using the assumption used for Equation (21-3), i.e., $T=D=W/(L/D)$, expand this expression to get

$$dt=\frac{1}{-c_tT}dW=\frac{1}{-c_tD}dW=\frac{(L/D)}{-c_tW}dW \qquad (21\text{-}6)$$

The solution of Equations (21-3) and (21-6) requires the incorporation of the dependency of V_∞, LD, and c_t on W. Equations (21-3) and (21-6) form a basis for estimating range and endurance of fossil-fueled aircraft. This is implemented using the so-called "*Breguet*" *range and endurance equations*. It is attributed to the French aircraft designer Louis Charles Breguet (1880–1955), an early pioneer of aviation.

(4) Breguet Range Equation

The range is estimated by integrating Equation (21-3), where the limits are the initial and final weight during the cruise segment.

$$R=\int_{W_{ini}}^{W_{ini}-W_f}\frac{V_\infty(L/D)}{-c_tW}dW=\int_{W_{fin}}^{W_{ini}}\frac{V_\infty}{c_t}\frac{C_L}{C_D}\frac{1}{W}dW \qquad (21\text{-}7)$$

Note the inversion of the integration limits because of the minus sign. Clearly, this is not a finished solution. As stated earlier, this requires the incorporation of the dependency of V_∞, L/D, and c_t on W. A unit inspection of the integrand of Equation (21-7) reveals the following:

$$\frac{V_\infty}{c_t}\frac{C_L}{C_D}\frac{1}{W}\rightarrow\frac{[\mathrm{m/s}]}{\left[\frac{\mathrm{kg/s}}{\mathrm{N}}\right]}[1]\frac{1}{[\mathrm{N}]}=\frac{\mathrm{m}}{\mathrm{kg}}$$

While Equation (21-7) is easily integrated numerically, closed-form solutions exist using some simplifying assumptions. One such assumption is constant specific fuel consumption. Other assumptions involve the simplified drag model and the "kind" of cruise flown. Several well-known closed-form solutions of the Breguet equation are provided in Section 21.3.

(5) Breguet Endurance Equation

As for the range, Equation (21-6) is solved for the endurance by integration, in which the limits are the initial and final weight during that segment.

$$E=\int_{W_{ini}}^{W_{ini}-W_f}\frac{(L/D)}{-c_tW}dW=\int_{W_{fin}}^{W_{ini}}\frac{1}{c_t}\frac{C_L}{C_D}\frac{1}{W}dW \qquad (21\text{-}8)$$

The solution of Equation (21-8) is subject to identical ramifications as Equation (21-7), regarding dependency of V_∞, L/D, and c_t on W. Closed-form solutions exist for all the same cases as for the range. Several well-known closed-form solutions are given in Section 21.4. A unit inspection of the integrand of Equation (21-8) reveals the following:

$$\frac{1}{c_t}\frac{C_L}{C_D}\frac{1}{W} \rightarrow \frac{1}{\left[\frac{\text{kg/s}}{\text{N}}\right]}[1]\frac{1}{[\text{N}]} = \frac{\text{s}}{\text{kg}}$$

21.2.3 Fundamentals of Range and Endurance for Electric Aircraft

The range and endurance for electric aircraft can be approximated using the approach of reference [10]. Note additional discussion in Sections 6.2.1 and 7.4. First, let us define fundamental variables.

Battery and Power Train

The following is a regurgitation of topics covered in Section 7.4, presented for convenience.

Mass-specific energy:

$$E^* \equiv \frac{UI\Delta t}{m_{batt}}\ [\text{Wh/kg}] \tag{7.47}$$

Energy capacity:

$$E_{batt} \equiv E^* m_{batt}\ [\text{Wh}] \tag{7.50}$$

Available motor power:

$$P_{AV_{mot}} = \eta_{system}\ UI\ [\text{W}] \tag{7.67}$$

Battery power extracted:

$$P_{batt} = UI\ [\text{W}] \tag{21-9}$$

where U is voltage (volts), I is current (amps), and m_{batt} is the mass of the battery driving the motor. Refer to Figure 7-56 for total system efficiency, η_{system}. The *available motor power* (P_{AVmot}) corresponds to the power delivered to the shaft of a piston engine. It is delivered on the *motor side* (see Figure 7-56) and remains to be modified by the propeller efficiency, η_p. *Battery power extracted* is the power extracted from the battery. It is generated by the chemical reaction on the *battery side*. A shown in Figure 7-56, how much of this energy is converted to thrust-power depends on the overall system efficiency.

21.2.4 Specific Fuel Consumption

Predictions involving range and endurance require the change in weight due to fuel consumption to be tracked. This is accomplished using *specific fuel consumption*, *SFC*, which comes in two versions:

(1) *Thrust specific fuel consumption* is used for jet aircraft and has units of 1/h in both the UK- and SI-systems. It is denoted by *TSFC*, *SFC*, or c_t.

(2) *Power specific fuel consumption* is used for propeller aircraft. In the UK-system, it has units of $\text{lb}_\text{f}/(\text{HP}\cdot\text{h})$ and is denoted by SFC_{hp} or c_{hp} for engine power in *horsepower* (hp). In the SI-system, it has units of kg/(kW·h) and is denoted by SFC_{kW} or c_{kW}.

(1) Specific Fuel Consumption based on Thrust

The fuel consumption of jet engines is usually measured in terms of weight or mass of fuel-flow per unit time per unit thrust force. Consider a jet engine that develops constant thrust T over time Δt, while consuming weight ΔW_f (or mass Δm_f) units of fuel. Thus, the *thrust specific fuel consumption* is defined as follows:

$$\bar{c}_t \equiv \left(\frac{1}{T}\right)\frac{\Delta W_f}{\Delta t} \Rightarrow c_t \equiv \left(\frac{1}{T}\right)\frac{dW_f}{dt} = \frac{\dot{w}_f}{T} \tag{21-10}$$

The bar represents the averaged value (otherwise it is the instantaneous value). In the UK-system, the most common units are in terms of "*lb_f-of-fuel per lb_f-of-thrust each hour*." This is written as $\text{lb}_\text{f}/(\text{lb}_\text{f}\cdot\text{h})$, or simply as 1/h. In the SI-system, the most common units are in terms of "*kg-of-fuel per N-of-thrust each hour*" or kg/(N·h). It must be multiplied by g to convert it into 1/h. While the *SFC* is sometimes presented in seconds, presenting it in terms of hours is more practical for GA aircraft and this is the approach taken in this edition of the book.

If working in the UK system, the thrust and *fuel-flow* are given in lb_f and lb_f/h, respectively. Therefore, the *SFC* is computed as shown below. When estimating range or endurance, use airspeed in KTAS and *SFC* in 1/h.

$$SFC = c_t \equiv \frac{\text{weight of fuel in lbs/hour}}{\text{thrust in pounds force}} = \frac{\dot{w}_f}{T}\ \left[\frac{\text{lb}_\text{f}/\text{hr}}{\text{lb}_\text{f}}\right] = \left[\frac{1}{\text{hr}}\right] \tag{21-11}$$

If working in the SI-system, the thrust and fuel-flow are given in N and kg/h, respectively. The *SFC* is computed as shown below. The kg/h must be converted into N/h. When estimating range or endurance, use airspeed in km/h and *SFC* in 1/h.

$$SFC = c_t \equiv \frac{9.807 \times (\text{mass of fuel in kg/hr})}{\text{thrust in Newtons}} = \frac{\dot{w}_f}{T}\ \left[\frac{\text{N/hr}}{\text{N}}\right] = \left[\frac{1}{\text{hr}}\right] \tag{21-12}$$

EXAMPLE 21-1

At a specific airspeed, a small turbofan is found to consume 1000 lb_f of fuel per hour while generating 1500 lb_f of thrust. Determine c_t in the UK-system and SI-system in terms of hour and seconds as reference time.

SOLUTION:

$$c_t = \frac{1000\ \text{lb}_\text{f}/\text{hr}}{1500\ \text{lb}_\text{f}} = 0.667\ \frac{1}{\text{hr}} \quad \text{and}$$

$$c_t = \frac{(453\ \text{kg/hr})}{6664\ \text{N}} = 0.0680\frac{\text{kg}}{\text{N}\cdot\text{s}}$$

(2) Specific Fuel Consumption based on Power

The fuel consumption of propeller/engine installations is measured in terms of weight or mass of fuel-flow per unit time per unit power. Consider a piston engine that develops constant engine power P_{ENG} during a time period Δt, while consuming weight ΔW_f (or mass Δm_f) units of fuel. Thus, the *power specific fuel consumption* is defined as follows:

$$\bar{c}_p \equiv \left(\frac{1}{P_{ENG}}\right)\frac{\Delta W_f}{\Delta t} \Rightarrow c_p \equiv \left(\frac{1}{P_{ENG}}\right)\frac{dW_f}{dt} = \frac{\dot{w}_f}{P_{ENG}} \quad (21\text{-}13)$$

The power is typically specified in BHP, SHP, or Watts (or kilo-Watts). It is convenient to use subscripts to distinguish between different engine types. Thus, we will write c_{bhp} for a piston engine whose power is rated as BHP, c_{shp} for a turboprop whose power is rated as SHP, c_{kW} for engines whose power is rated as kW (e.g., electric motors), and c_{hp} for a nonspecific horsepower. In the UK-system, the most common units are in terms of "*lb_f-of-fuel per horsepower each hour*." This is written as $\text{lb}_\text{f}/(\text{HP}\cdot\text{h})$. Using the different units of power, this is also written as $\text{lb}_\text{f}/(\text{BHP}\cdot\text{h})$ or $\text{lb}_\text{f}/(\text{SHP}\cdot\text{h})$. In the SI-system, the most common units are in terms of "*kg-of-fuel per kW-power each hour*" or $\text{kg}/(\text{kW}\cdot\text{h})$.

If working in the UK-system, the power and *fuel-flow* are given in HP and $\text{lb}_\text{f}/\text{h}$, respectively. The SFC_{hp} is computed as shown below. When estimating range or endurance, use airspeed in KTAS and *SFC* in 1/h.

$$SFC_{hp} = c_{hp} \equiv \frac{\text{weight of fuel in lbs/hour}}{\text{power in horsepower}} = \frac{\dot{w}_f}{P_{HP}} \quad \left[\frac{\text{lb}_\text{f}}{\text{HP}\cdot\text{hr}}\right] \quad (21\text{-}14)$$

The literature frequently states power and *fuel-flow* for piston engines in the SI system in kW and kg/h, respectively. In this case, we write

$$SFC_{kW} = c_{kW} \equiv \frac{\text{mass of fuel in kg/hr}}{\text{Power in kiloWatts}} = \frac{\dot{w}_f}{P_{kW}} \quad \left[\frac{\text{kg}}{\text{kW}\cdot\text{hr}}\right] \quad (21\text{-}15)$$

It is also common that the only available *SFC* is in the UK-system (as SFC_{hp}). However, to use the formulation in this chapter dedicated for the SI-system, this must be converted to $\text{kg}/(\text{kW}\cdot\text{h})$. It is done as shown below:

$$SFC_{kW} = c_{kW} = 0.6083\ SFC_{hp} = 0.6083\ c_{hp} \quad \left[\frac{\text{kg}}{\text{kW}\cdot\text{hr}}\right] \quad (21\text{-}16)$$

where the constant 0.6083 is the ratio $(0.4536\,\text{kg}/\text{lb}_\text{f})/(0.7457\,\text{kW}/\text{HP})$.

EXAMPLE 21-2

A piston engine consumes 12.5 gal per hour of Avgas while generating 150 BHP. Determine c_{bhp} and c_{kW} (in the UK- and SI-systems, respectively). Avgas weighs 6 lb_f/gal. Its mass is 2.72 kg/gal.

SOLUTION:

$$c_{bhp} = \frac{12.5\,\text{gallons/hr}}{150\,\text{BHP}} = \frac{75\,\text{lb}_\text{f}/\text{hr}}{150\,\text{BHP}} = 0.500\,\frac{\text{lb}_\text{f}}{\text{BHP}\cdot\text{hr}}$$

$$c_{kW} = \frac{12.5\times 2.72\,\text{kg/hr}}{150\,\text{BHP}} = \frac{34\,\text{kg/hr}}{111.9\,\text{kW}} = 0.304\,\frac{\text{kg}}{\text{kW}\cdot\text{hr}}$$

(3) Relating Power and Thrust Specific Fuel Consumptions

For jet aircraft, Equations (21-11) and (21-12) can be used directly. This is not possible for propeller aircraft because their power must be converted to thrust. As shown in earlier chapters, the propeller converts the engine power, P_{ENG}, into thrust-power (or power available), P_{AV}, through propeller efficiency, η_p. The fuel consumption depends on P_{ENG} and not P_{AV}. The relationship between the two can be presented as follows

$$P_{AV} = \eta_p\ P_{ENG} = TV_\infty \Leftrightarrow \begin{cases} T = P_{AV}/V_\infty \\ P_{ENG} = P_{AV}/\eta_p \end{cases} \quad (21\text{-}17)$$

where V_∞ is true airspeed. Since $\dot{w}_f = c_t T$ and $\dot{w}_f = c_p P_{ENG}$, we can combine these to yield

$$c_t = c_p P_{ENG}/T \quad (21\text{-}18)$$

Replacing T and P_{AV} in Equation (21-18) by their counterparts in Equation (21-17), gives us means to convert the power specific fuel consumption into thrust specific fuel consumption.

$$c_t = c_p \frac{P_{AV}/\eta_p}{P_{AV}/V_\infty} = \frac{c_p V_\infty}{\eta_p} \quad (21\text{-}19)$$

If working with airspeed in KTAS when estimating range, the c_{hp} is related to c_t as follows:

$$c_t = \frac{c_{hp} V_{KTAS}}{325.9\ \eta_p} \quad \left[\frac{1}{\text{hr}}\right] \quad (21\text{-}20)$$

where the constant 325.9 is the ratio $(550\,\text{ft}\cdot\text{lb}_\text{f}/\text{s})/(1.688\,\text{ft}\cdot\text{h}/(\text{s}\cdot\text{nm}))$, as shown in the derivation of the equation. If working with airspeed in kmh, then c_{kW} is related to c_t as follows:

$$c_t = \frac{c_{kW} V_{\text{kmh}}}{367.1\ \eta_p} \quad \left[\frac{1}{\text{hr}}\right] \quad (21\text{-}21)$$

where the constant 367.1 is the ratio $(3600\,\text{s/h})/(9.807\,\text{m/s}^2)$, as shown in the derivation of the equation.

(4) Fuel-flow, $\dot{w}_f$

The instantaneous fuel consumption, also called *fuel-flow*, is given by.

Turbojets and turbofans:

$$\dot{w}_f = SFC\ T = c_t\ T \tag{21-22}$$

Piston and turboprops:

$$\dot{w}_f = SFC_{hp}\ P_{hp} = c_{hp}\ P_{hp} \tag{21-23}$$

$$\dot{m}_f = SFC_{kW}\ P_{kW} = c_{kW}\ P_{kW} \tag{21-24}$$

where $\dot{w}_f$ is the fuel consumption in lb_f/h and $\dot{m}_f$ is in kg/h.

DERIVATION OF EQUATION (21-20)

Substitute units of horsepower and V_∞ in ft/s into Equation (21-19) to get.

$$c_t = \frac{c_{hp} V_{ft/s}}{\eta_p} \rightarrow \frac{\left[\frac{lb_f/hr}{bhp}\right]\left[\frac{ft}{s}\right]}{\langle 1\rangle} \rightarrow \left[\frac{lb_f/hr}{bhp}\right]\left[\frac{ft}{s}\right]$$

$$\rightarrow \left[\frac{lb_f/hr}{bhp}\right]\left[\frac{ft}{s}\right]\left[\frac{1\,bhp\cdot s}{550\,ft\cdot lb_f}\right] \rightarrow \frac{c_{hp} V_{ft/s}}{550\eta_p}\left[\frac{1}{hr}\right]$$

Unit consistency in the Breguet equation requires units of 1/h. Thus, substitute airspeed in KTAS into the above

$$c_t = \frac{c_{hp} V_{ft/s}}{550\eta_p}\left[\frac{1}{hr}\right] = \frac{c_{hp}(1.688 V_{KTAS})}{550\eta_p}\left[\frac{1}{hr}\right] = \frac{c_{hp} V_{KTAS}}{325.9\eta_p}\left[\frac{1}{hr}\right]$$

DERIVATION OF EQUATION (21-21)

Substituting kW and V_∞ in kmh into Equation (21-19) results in the following unit conundrum. Note that we need to turn the mass/h unit into weight/h, which we do by multiplying it by $g = 9.807\,m/s^2$. Also, unit consistency in the Breguet equation requires units of 1/h. To convert, we must replace $N = kg\cdot m/s^2$ and $W = N\cdot m/s = kg\cdot m^2/s^3$.

$$c_t = \frac{c_{kW} V_\infty}{\eta_p} \rightarrow \frac{\left[9.807\frac{m}{s^2}\right]\left[\frac{kg/hr}{1000\,W}\right] \times \left[\frac{1000\,m}{3600\,s}\right]}{\langle 1\rangle}$$

$$\rightarrow \frac{c_{kW} V_\infty}{367.1\eta_p}\left[\frac{1}{hr}\right]$$

21.3 RANGE ANALYSIS

This section presents methods to conduct range analyses. Range analysis investigates how far an aircraft can fly given specific quantity of fuel or battery energy. The analysis permits the determination of airspeeds that must be maintained to achieve optimum range and how to evaluate the cost of operating at off-optimum airspeeds. It also allows various sensitivities to be evaluated, such as the effect of fuel weight and altitude.

21.3.1 Mission Profiles

The Breguet range equation is identified as Equation (21-7). A closed-form solution of this equation of requires simplifications of the cruise profile. A *range profile* refers to which flight parameters the pilot attempts to maintain during cruise. Generally, airplanes adhere to three distinct cruise profiles. These are based on a combination of the physical and mathematical interpretations shown in Table 21-2.

Closed-form solutions are provided for the combinations of parameters in Table 21-3. It is helpful to keep the first formula of Equation (8-7) in mind when considering these combinations, repeated here for convenience:

$$L = \frac{1}{2}\rho V_\infty^2 S C_L \tag{8-7}$$

21.3.2 Range Profile 1: Constant Airspeed/ Altitude Cruise

This range profile assumes constant airspeed and altitude between Nodes 2 and 3 (the cruise segment) in Figure 21-6. The profile corresponds to common operation of aircraft, as directed by air traffic controllers. Since the weight of

TABLE 21-2 Physical and mathematical interpretation of parameters for mission analysis.

Physical interpretation	Mathematical interpretation
Constant airspeed implies…	… V_∞ = Constant
Constant altitude implies…	… ρ = Constant
Constant attitude (i.e., AOA) implies…	… C_L/C_D = Constant

TABLE 21-3 Definition of several range profiles.

Section	Type of range profile	V_∞	ρ	C_L/C_D
21.3.2	Constant airspeed/ altitude	Constant	Constant	–
21.3.3	Constant attitude/ altitude	–	Constant	Constant
21.3.4	Constant airspeed/ attitude	Constant	–	Constant
21.3.5	Constant weight	Constant	Constant	Constant

the airplane reduces with time (as fuel is consumed), the AOA (the attitude) of the aircraft is reduced as well. This, in turn, reduces the lift coefficient, which, as can be seen from Equation (8-7), is the only way to reduce the lift if V_∞ and ρ are constant.

(1) Requirements

Airspeed—constant during cruise (V_∞ = Constant)
Altitude—constant during cruise (ρ = Constant)
Attitude—AOA must be reduced during cruise (C_L/C_D = Variable)

(2) Range Equation 1 for Jet Aircraft

The resulting range equation can be presented in two forms. The first form uses the weight at the initial and final nodes.

$$R = \frac{V_\infty}{c_t\sqrt{kC_{D_{\min}}}}\left[\tan^{-1}(AW_{ini}) - \tan^{-1}(AW_{fin})\right] \quad (21\text{-}25)$$

where

$$A = \frac{2}{\rho V_\infty^2 S}\sqrt{\frac{k}{C_{D_{\min}}}} \quad (21\text{-}26)$$

Note the resemblance of $AW = (2/\rho)(W/S)(k/C_{D_{\min}})^{1/2}$ to $V_{R_{\max}}$ of Equation (20-55). The second form allows Equation (21-25) to be written in terms of the lift coefficient at the initial and final nodes. This is the second form.

$$R = \frac{V_\infty}{c_t\sqrt{kC_{D_{\min}}}} \times \left[\tan^{-1}\left(C_{L_{ini}}\sqrt{\frac{k}{C_{D_{\min}}}}\right) - \tan^{-1}\left(C_{L_{fin}}\sqrt{\frac{k}{C_{D_{\min}}}}\right)\right] \quad (21\text{-}27)$$

NOTE 1:
The constant A requires V_∞ in ft/s (or m/s), because of unit consistency. This renders it a potential error source if the intent is to use V_∞ in knots or kmh in the numerator of Equation (21-25).

NOTE 2:
The expression is largely $R = V_\infty \Delta t$, where Δt is the ratio of the dimensionless value inside the bracket and the denominator. The unit of time for this ratio is dictated by c_t. Thus, if V_∞ in the numerator is in KTAS (or kmh) and c_t is in 1/h, the equation will return range in nm (or km).

NOTE 3:
For range R in nautical miles (nm), Equation (21-26) can be modified as follows if it is preferred to use V_{KTAS} rather than in ft/s. This also assumes ρ in slugs/ft^3, S in ft^2, W in lb$_f$, and c_t in 1/h:

$$A = \frac{0.7021}{\rho V_{KTAS}^2 S}\sqrt{\frac{k}{C_{D_{\min}}}} \quad (21\text{-}28)$$

Since $V_\infty = 1.688\, V_{KTAS}$, we simplify the expression using $2/1.688^2 = 0.7021$. For range in km, use the following form of Equation (21-26). It assumes ρ in kg/m^3, S in m^2, W in N, V_∞ in kmh, and c_t in 1/h:

$$A = \frac{25.908}{\rho V_{kmh}^2 S}\sqrt{\frac{k}{C_{D_{\min}}}} \quad (21\text{-}29)$$

The coefficient 25.908 is obtained by substituting appropriate scaling factors between parameters in the SI- and UK-systems into Equation (21-26).

(3) Range Equation 1 for Propeller Aircraft

The same expressions are used for propeller aircraft. We must make an important modification to c_{hp}. It must be converted to c_t, through $c_t = c_{hp}V_\infty/\eta_p$. Since the airspeed is constant, there is no impact of $c_t = c_{hp}V_\infty/\eta_p$ on the integration. If using power in horsepower and airspeed in KTAS this is accomplished using Equation (21-20). Thus, if ρ is in slugs/ft^3, S in ft^2, W in lb$_f$, V_∞ in KTAS, c_{hp} in lb$_f$/(HP·h), and R in nm, then Equation (21-25) becomes

$$R = \frac{325.9\eta_p}{c_{hp}\sqrt{kC_{D_{\min}}}}\left[\tan^{-1}(AW_{ini}) - \tan^{-1}(AW_{fin})\right] \quad (21\text{-}30)$$

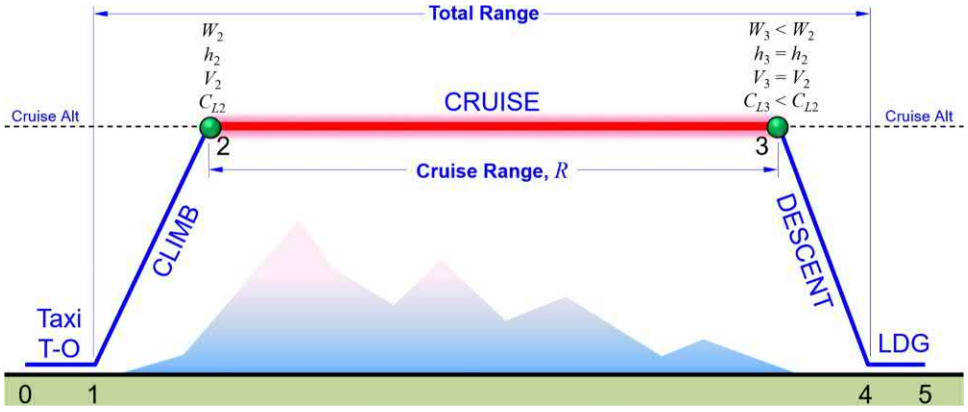


FIGURE 21-6 Constant airspeed/constant altitude cruise mission.

where A is calculated per Equation (21-28). Notes 1 and 2 above, apply here as well. Similarly, Equation (21-25) is transformed to the SI-system using Equation (21-21). If ρ is in kg/m^3, S in m^2, W in N, V_∞ in kmh, c_{kW} in kg/(kW·h), and R in km, then Equation (21-25) becomes

$$R = \frac{367.1\ \eta_p}{c_{kW}\sqrt{kC_{D_{\min}}}}\left[\tan^{-1}(AW_{ini}) - \tan^{-1}(AW_{fin})\right] \quad (21\text{-}31)$$

where A is calculated per Equation (21-29). If necessary, convert c_{hp} to c_{kW} per Equation (21-16).

EXAMPLE 21-3

Note that this exercise forms a part of solving Example 21-6. A light airplane starts its cruise segment at 150 KTAS at 10,000 ft when it weighs 3200 lb$_f$. After cruising for a period of time at that altitude it is noticed it weighs 2800 lb$_f$. Using a wing area of S = 145 ft^2 compute the initial and final lift coefficients if the pilot maintains constant airspeed. Density at 10,000 ft is 0.001756 slugs/ft^3.

SOLUTION:

Initial lift coefficient:

$$C_{L_{ini}} = \frac{2W}{\rho V^2 S} = \frac{2(3200)}{(0.001756)(1.688\times 150)^2(145)} = 0.3921.$$

Final lift coefficient:

$$C_{L_{fin}} = \frac{2W}{\rho V^2 S} = \frac{2(2800)}{(0.001756)(1.688\times 150)^2(145)} = 0.3431.$$

DERIVATION OF EQUATION (21-25)

In this case, V_∞ = constant and ρ = constant. However, since the ratio C_L/C_D depends on the weight, it must remain inside the integral. Therefore, we write Equation (21-7) as follows:

$$R = \int_{W_{fin}}^{W_{ini}} \frac{V_\infty}{c_t}\frac{C_L}{C_D}\frac{1}{W}dW = \frac{V_\infty}{c_t}\int_{W_{fin}}^{W_{ini}} \frac{C_L}{C_D}\frac{1}{W}dW$$

Substitute the expression for drag (here using the simplified drag model of Equation (16-2) to get:

$$R = \frac{V_\infty}{c_t}\int_{W_{fin}}^{W_{ini}} \frac{C_L}{\left(C_{D_{\min}} + kC_L^2\right)}\frac{1}{W}dW$$

$$= \frac{V_\infty}{c_t}\int_{W_{fin}}^{W_{ini}} \frac{(2W/\rho V_\infty^2 S)}{\left(C_{D_{\min}} + k(2W/\rho V_\infty^2 S)^2\right)}\frac{1}{W}dW$$

$$= \frac{V_\infty}{c_t}\frac{2}{\rho V_\infty^2 S}\int_{W_{fin}}^{W_{ini}} \frac{1}{\left(C_{D_{\min}} + 4kW^2/\rho^2 V_\infty^4 S^2\right)}dW$$

Expanding further and manipulating algebraically leads to:

$$R = \frac{V_\infty}{c_t}\frac{2}{\rho V_\infty^2 S}\frac{\rho^2 V_\infty^4 S^2}{4k}\int_{W_{fin}}^{W_{ini}} \frac{1}{\left(C_{D_{\min}}\rho^2 V_\infty^4 S^2/4k + W^2\right)}dW$$

$$= \frac{\rho V_\infty^3 S}{2kc_t}\int_{W_{fin}}^{W_{ini}} \frac{1}{\left(C_{D_{\min}}\rho^2 V_\infty^4 S^2/4k + W^2\right)}dW$$

Define a such that: $$a = \sqrt{\frac{C_{D_{\min}}}{k}}\frac{\rho V_\infty^2 S}{2}$$

$$\Leftrightarrow\quad a^2 = \frac{C_{D_{\min}}}{k}\frac{\rho^2 V_\infty^4 S^2}{4}.$$

Also note that: $$\frac{1}{a} = \frac{2}{\rho V_\infty^2 S}\sqrt{\frac{k}{C_{D_{\min}}}}.$$

And that: $$\int \frac{dx}{a^2 + x^2} = \frac{1}{a}\tan^{-1}\frac{x}{a}$$

Therefore; $$R = \frac{\rho V_\infty^3 S}{2kc_t}\int_{W_{fin}}^{W_{ini}} \frac{1}{(a^2 + W^2)}dW$$

$$= \frac{\rho V_\infty^3 S}{4kc_t}\frac{1}{a}\left[\tan^{-1}\frac{W}{a}\right]_{W_{fin}}^{W_{ini}}$$

$$= \frac{\rho V_\infty^3 S}{2kc_t}\frac{1}{a}\left[\tan^{-1}\frac{W_{ini}}{a} - \tan^{-1}\frac{W_{fin}}{a}\right]$$

Substitute the parameters that constitute a and manipulate to get

$$R = \frac{V_\infty}{c_t\sqrt{kC_{D_{\min}}}}\left[\tan^{-1}\left(\frac{2}{\rho V^2 S}\sqrt{\frac{k}{C_{D_{\min}}}}W_{ini}\right) - \tan^{-1}\left(\frac{2}{\rho V^2 S}\sqrt{\frac{k}{C_{D_{\min}}}}W_{fin}\right)\right]$$

21.3.3 Range Profile 2: Constant Attitude/Altitude Cruise

This range profile requires constant attitude and altitude between Nodes 2 and 3 (the cruise segment) in Figure 21-7. Since the weight of the airplane reduces with time (as fuel is consumed), its airspeed must be reduced to maintain constant lift coefficient.

(1) Requirements

Airspeed—must be reduced during cruise (V_∞ = Variable)
Altitude—constant during cruise (ρ = Constant)
Attitude—constant during cruise (C_L/C_D = Constant)

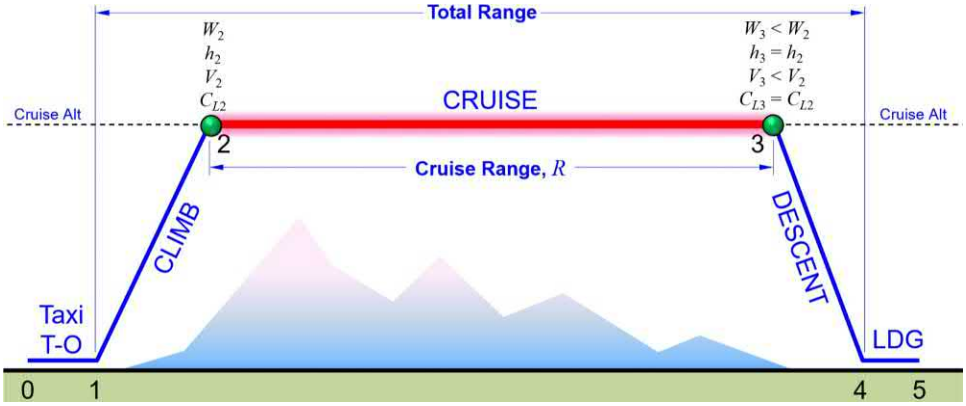


FIGURE 21-7 Constant altitude/constant attitude cruise mission.

(2) Range Equation 2 for Jet Aircraft

The resulting range equation for a jet is presented below. It assumes ρ in slugs/ft^3, S in ft^2, W in lb$_f$, V_∞ in ft/s, and c_t in 1/s. The effect of velocity is incorporated implicitly through the lift- and drag-coefficients. However, as can be seen in the derivation, unit consistency requires c_t in 1/s and ρS is in slugs/ft for the equation below. Thus, a proper use requires $c_t = SFC/3600$ and the resulting R will be in ft.

$$R = \frac{2\sqrt{2}}{c_t\sqrt{\rho S}}\frac{\sqrt{C_L}}{C_D}\left(\sqrt{W_{ini}} - \sqrt{W_{fin}}\right) \qquad (21\text{-}32)$$

NOTE 1:
For range in nautical miles (nm), use the following form of Equation (21-32). It assumes ρ in slugs/ft^3, S in ft^2, W in lb$_f$, V_∞ in KTAS, and c_t in 1/h. The coefficient 0.5925 is the ratio (3600 s/h)/(6076 ft/nm) converts the result into nautical miles.

$$R_{nm} = 0.5925\frac{2\sqrt{2}}{c_t\sqrt{\rho S}}\frac{\sqrt{C_L}}{C_D}\left(\sqrt{W_{ini}} - \sqrt{W_{fin}}\right) \qquad (21\text{-}33)$$

NOTE 2:
For range in km, use the following form of Equation (21-32) for ρ in kg/m^3, S in m^2, W in N, and c_t in 1/h. The coefficient 24.9 is obtained by substituting the appropriate scaling factors between parameters in the SI- and UK-systems.

$$R_{km} = 24.9\frac{2\sqrt{2}}{c_t\sqrt{\rho S}}\frac{\sqrt{C_L}}{C_D}\left(\sqrt{W_{ini}} - \sqrt{W_{fin}}\right) \qquad (21\text{-}34)$$

(3) Range Equation 2 for Propeller Aircraft

The same expressions are used for propeller aircraft, but, as before, we must convert c_p to c_t. If using power in horsepower and airspeed in KTAS this is accomplished using Equation (21-20). Thus, if ρ is in slugs/ft^3, S in ft^2, W in lb$_f$, V_∞ in KTAS, c_{hp} in lb$_f$/(HP·h), and R in nm, then Equation (21-33) becomes

$$R = \frac{193.1\ \eta_p}{c_{hp}V_{KTAS}}\frac{2\sqrt{2}}{\sqrt{\rho S}}\frac{\sqrt{C_L}}{C_D}\left(\sqrt{W_{ini}} - \sqrt{W_{fin}}\right) \qquad (21\text{-}35)$$

where the coefficient 193.1 is 0.5925×325.9. Equation (21-32) is transformed to the SI-system by substituting Equation (21-21) for c_t. Thus, if ρ is in kg/m^3, S in m^2, W in N, V_∞ in kmh, c_{kW} in kg/(kW·h), and R in km, then Equation (21-34) becomes

$$R_{km} = \frac{1321.6\ \eta_p}{c_{kW}\ V_{\text{kmh}}\sqrt{\rho S}}\frac{\sqrt{C_L}}{C_D}\left(\sqrt{W_{ini}} - \sqrt{W_{fin}}\right) \qquad (21\text{-}36)$$

The coefficient 1321.6 is obtained by substituting the appropriate scaling factors between parameters in the SI- and UK-systems.

EXAMPLE 21-4

Note that this exercise forms a part of solving Example 21-6. The light airplane of Example 21-3 again starts its cruise segment at 150 KTAS at 10,000 ft when it weighs 3200 lb$_f$. After cruising for a period of time at that altitude it is noticed it now weighs 2800 lb$_f$. Using a wing area of S = 145 ft^2 compute the final airspeed if the pilot maintains a constant lift coefficient. Density at 10,000 ft is 0.001756 slugs/ft^3.

SOLUTION:

Initial and final lift coefficient:

$$C_L = \frac{2W}{\rho V_\infty^2 S} = \frac{2(3200)}{(0.001756)(1.688\times 150)^2(145)} = 0.3921.$$

Final airspeed:

$$V_\infty = \sqrt{\frac{2W}{\rho S C_L}} = \sqrt{\frac{2(2800)}{(0.001756)(145)(0.3921)}} = 237\ \text{ft/s}$$
$$= 140.3\ \text{KTAS}.$$

DERIVATION OF EQUATION (21-32)

In this case, V_∞ = variable, ρ = constant, and C_L/C_D = constant. Thus, V_∞ and the weight must remain inside the integral. Therefore, we write Equation (21-7) as follows:

$$R=\int_{W_{fin}}^{W_{ini}}\frac{V_\infty}{c_t}\frac{C_L}{C_D}\frac{1}{W}dW=\frac{1}{c_t}\frac{C_L}{C_D}\int_{W_{fin}}^{W_{ini}}\frac{V_\infty}{W}dW$$

$$=\frac{1}{c_t}\frac{C_L}{C_D}\int_{W_{fin}}^{W_{ini}}\frac{\sqrt{2W/(\rho SC_L)}}{W}dW$$

$$=\frac{1}{c_t}\frac{C_L}{C_D}\frac{\sqrt{2}}{\sqrt{\rho SC_L}}\int_{W_{fin}}^{W_{ini}}\frac{\sqrt{W}}{W}dW$$

$$=\frac{1}{c_t}\frac{C_L}{C_D}\frac{\sqrt{2}}{\sqrt{\rho SC_L}}\int_{W_{fin}}^{W_{ini}}(W)^{-1/2}dW$$

$$=\frac{1}{c_t}\frac{C_L}{C_D}\frac{\sqrt{2}}{\sqrt{\rho SC_L}}\left[\frac{\sqrt{W}}{1/2}\right]_{W_{fin}}^{W_{ini}}$$

Therefore:

$$R=\frac{1}{c_t}\frac{\sqrt{C_L}}{C_D}\frac{2\sqrt{2}}{\sqrt{\rho S}}\left(\sqrt{W_{ini}}-\sqrt{W_{fin}}\right)$$

$$=\frac{1}{c_tC_D}\sqrt{\frac{8C_L}{\rho S}}\left(\sqrt{W_{ini}}-\sqrt{W_{fin}}\right)$$

This is Equation (21-32).

21.3.4 Range Profile 3: Constant Airspeed/Attitude Cruise

This range profile requires constant airspeed and attitude between Nodes 2 and 3 (the cruise segment) in Figure 21-8. Since the weight of the airplane reduces with time (as fuel is consumed), its airspeed must be reduced to maintain constant lift coefficient.

(1) Requirements

Airspeed—constant during cruise (V_∞ = Constant)
Altitude—must be increased during cruise (ρ = Variable)
Attitude—constant during cruise (C_L/C_D = Constant)

(2) Range Equation 3 for Jet Aircraft

The range equation for a jet is presented below. Note that all the same stipulations regarding unit consistency that were discussed in Section 21.3.2, apply here as well.

$$R=\frac{V_\infty}{c_t}\frac{C_L}{C_D}\ln\left(\frac{W_{ini}}{W_{fin}}\right) \tag{21-37}$$

No special forms are required for this expression.

(3) Range Equation 3 for Propeller Aircraft

The same expressions are used for propeller aircraft, but, as before, we must convert c_p to c_t. If using power in horsepower and airspeed in KTAS this is accomplished using Equation (21-20). Thus, if ρ is in slugs/ft^3, S in ft^2, W in lb$_f$, V_∞ in KTAS, c_{hp} in lb$_f$/(HP·h), and R in nm, then Equation (21-37) becomes

$$R=\frac{325.9\eta_p}{c_{hp}}\frac{C_L}{C_D}\ln\left(\frac{W_{ini}}{W_{fin}}\right) \tag{21-38}$$

Equation (21-37) is transformed to the SI-system by substituting Equation (21-21) for c_t. Thus, if ρ is in kg/m^3, S in m^2, W in N, V_∞ in kmh, c_{kW} in kg/(kW·h), and R in km, then Equation (21-34) becomes

$$R=\frac{367.1\ \eta_p}{c_{kW}}\frac{C_L}{C_D}\ln\left(\frac{W_{ini}}{W_{fin}}\right) \tag{21-39}$$

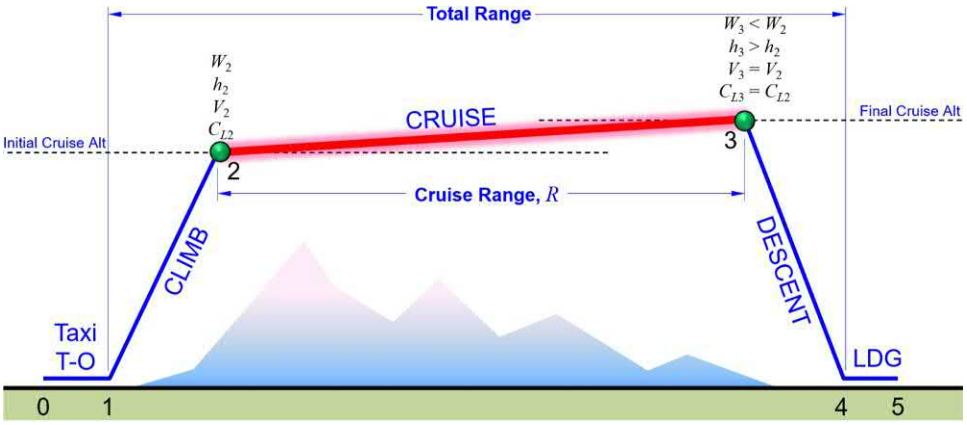


FIGURE 21-8 Constant airspeed/attitude cruise mission.

EXAMPLE 21-5

Note that this exercise forms a part of solving Example 21-6. The light airplane of Example 21-3 again starts its cruise segment at 150 KTAS at 10,000 ft when it weighs 3200 lb_f. After cruising for a period of time at that altitude it is noticed it now weighs 2800 lb_f. Using a wing area of $S = 145\,ft^2$ compute the final density altitude if the pilot maintains a constant airspeed and AOA. Compute dynamic pressure at the beginning and end of the cruise. Density at 10,000 ft is 0.001756 slugs/ft^3.

SOLUTION:

Initial lift coefficient:

$$C_L = \frac{2W}{\rho V_\infty^2 S} = \frac{2(3200)}{(0.001756)(1.688\times 150)^2(145)} = 0.3921.$$

Density at end of cruise:

$$\rho = \frac{2W}{V_\infty^2 S C_L} = \frac{2(2800)}{(1.688\times 150)^2(145)(0.3921)} = 0.001536\,\text{slugs/ft}^3.$$

Initial dynamic pressure:

$$q = \frac{1}{2}\rho V_\infty^2 = \frac{1}{2}(0.001756)(1.688\times 150)^2 = 56.3\,lb_f/ft^2.$$

Final dynamic pressure:

$$q = \frac{1}{2}\rho V_\infty^2 = \frac{1}{2}(0.001536)(1.688\times 150)^2 = 49.2\,lb_f/ft^2.$$

Density altitude per Equation (17-13):

$$H_\rho = 145448\left(1-\left(\frac{\rho}{\rho_0}\right)^{0.234957}\right) = 145448\left(1-\left(\frac{0.001536}{0.002378}\right)^{0.234957}\right) = 14195\,ft$$

DERIVATION OF EQUATION (21-37)

In this case, V_∞ = constant, ρ = variable, and C_L/C_D = constant. Thus, V_∞ and C_L/C_D can be outside the integral. Therefore, we write Equation (21-7) as follows:

$$R = \int_{W_{fin}}^{W_{ini}} \frac{V_\infty}{c_t}\frac{C_L}{C_D}\frac{1}{W}dW = \frac{V_\infty}{c_t}\frac{C_L}{C_D}\int_{W_{fin}}^{W_{ini}}\frac{1}{W}dW = \frac{V_\infty}{c_t}\frac{C_L}{C_D}[\ln(W)]_{W_{fin}}^{W_{ini}} = \frac{V_\infty}{c_t}\frac{C_L}{C_D}\ln\left(\frac{W_{ini}}{W_{fin}}\right)$$

EXAMPLE 21-6: RANGE PROFILE COMPARISON

Compare the range calculated for the light airplane of Examples 21-3 through 21-5. Do this using (a) Equation (21-1), (b) Profile 1, (c) Profile 2, (d) Profile 3, and (e) optimum range per Section 20.3.9. In all cases, it starts its cruise segment at 150 KTAS at 10,000 ft when it weighs 3200 lb_f. After cruising for a period of time at that altitude it is noticed it now weighs 2800 lb_f. The following additional data is given: Wing area, $S = 145\,ft^2$, lift-induced drag constant, $k = 0.04207$, minimum drag coefficient, $C_{D_{min}} = 0.025$, power specific fuel consumption, $SFC = c_{bhp} = 0.60$ $lb_f/(BHP\cdot h)$, engine power, $P_{ENG} = 150$ BHP, propeller efficiency, $\eta_p = 0.85$, density at 10,000 ft, and $\rho = 0.001756$ slugs/ft^3. Assume the simplified drag model. Note the node numbers (2 and 3) as subscripts for selected variables. Refer to Figures 21-6–21-8 for mission profiles.

SOLUTION:

All profiles at Node 2:
Air density:

$$\rho_2 = 0.001756\,\text{slugs/ft}^3$$

Airspeed:

$$V_2 = 1.688 V_{TAS} = 1.688\times(150) = 253.2\,ft/s$$

Lift coefficient:

$$C_{L_2} = 0.3921 \text{ (see Example 21-3).}$$

Drag coefficient:

$$C_D = C_{D_{min}} + kC_L^2 = (0.025) + (0.04207)(0.3921)^2 = 0.03147.$$

Glide ratio:

$$C_{L_2}/C_{D_2} = 0.3921/0.03147 = 12.46.$$

(a) Range Profile per Equation (21-1)

Total fuel consumed:

$$W_f = 3200 - 2800 = 400\,lb_f$$

Time to burn W_f:

$$\Delta t = \frac{W_f}{150\,BHP\times 0.60\,lb_f/(BHP\cdot hr)} = \frac{400\,lb_f}{90\,lb_f/hr} = 4.444\,hrs.$$

Distance covered:

$$R = V_2\Delta t = (150\,nm/hr)(4.444\,hrs) = 667\,nm.$$

EXAMPLE 21-6: RANGE PROFILE COMPARISON (cont'd)

(b) Range Profile 1: Constant Airspeed/Altitude Cruise

$$A=\frac{2}{\rho V_2^2 S}\sqrt{\frac{k}{C_{D_{\min}}}}=\frac{2}{(0.001756)(253.2)^2(145)}\sqrt{\frac{0.04207}{0.025}}$$
$$=0.0001589$$
$$R=\frac{325.9\eta_p}{c_{hp}\sqrt{kC_{D_{\min}}}}\left[\tan^{-1}(AW_2)-\tan^{-1}(AW_3)\right]$$
$$=\frac{325.9(0.85)}{(0.60)\sqrt{(0.04207)(0.025)}}$$
$$\left[\tan^{-1}(\mathrm{A}(3200))-\tan^{-1}(\mathrm{A}(2800))\right]=737\,\text{nm}$$

Note that per Example 21-3, the lift coefficient at Node 3 is $C_{L3}=0.3431$.

(c) Range Profile 2: Constant Attitude/Altitude Cruise

$$R=\frac{325.9\eta_p}{c_{hp}V_2}\frac{\sqrt{C_{L_2}}}{C_{D_2}}\frac{2\sqrt{2}}{\sqrt{\rho_2 S}}\left(\sqrt{W_2}-\sqrt{W_3}\right)$$
$$=\frac{325.9(0.85)}{(0.60)(253.2)}\frac{\sqrt{0.3921}}{(0.03147)}$$
$$\frac{2\sqrt{2}}{\sqrt{(0.001756)(145)}}\left(\sqrt{3200}-\sqrt{2800}\right)=743\,\text{nm}$$

Note that per Example 21-4, the airspeed at Node 3 is $V_3=140.3$ KTAS.

(d) Range Profile 3: Constant Airspeed/Attitude Cruise

$$R=\frac{325.9\eta_p}{c_{hp}}\frac{C_{L_2}}{C_{D_2}}\ln\left(\frac{W_2}{W_3}\right)$$
$$=\frac{325.9(0.85)}{(0.60)}\frac{(0.3921)}{(0.03147)}\ln\left(\frac{3200}{2800}\right)=768\,\text{nm}$$

Note that per Example 21-5, the altitude at Node 3 is $h_3=14{,}195$ ft.

(e) Optimum Range (Achieved while flying at LD_{max})

$$LD_{\max}=\frac{1}{\sqrt{4kC_{D_{\min}}}}=\frac{1}{\sqrt{4(0.03455)(0.020)}}=19.0$$
$$V_{LD_{\max}}=\sqrt{\frac{2}{\rho}\left(\frac{W}{S}\right)}\sqrt{\frac{k}{C_{D_{\min}}}}$$
$$=\frac{1}{1.688}\sqrt{\frac{2}{(0.001756)}\left(\frac{3200}{145}\right)}\sqrt{\frac{0.04207}{0.025}}=82.5\ \text{KTAS}$$
$$R=\frac{325.9\eta_p LD_{\max}}{c_{hp}}\ln\left(\frac{W_2}{W_3}\right)$$
$$=\frac{325.9(0.85)(19.0)}{(0.60)}\ln\left(\frac{3200}{2800}\right)=950\,\text{nm}$$

EXAMPLE 21-6: RANGE PROFILE COMPARISON (cont'd)

Repeating these calculations for 157 KTAS yields the following summary:

	150 KTAS	157 KTAS
Range Profile per Equation (21-1):	667 nm	698 nm
Range Profile 1:	737 nm	694 nm
Range Profile 2:	743 nm	702 nm
Range Profile 3:	768 nm	725 nm
Optimum Range (at 82.5 KTAS)	950 nm	

Equation (21-1) really serves as a "sanity check." It underpredicts the range at lower airspeeds because it operates at "Node 2" conditions during the entire mission.

EXAMPLE 21-7

Recalculate the range of item (e) in Example 21-6, using the SI-System. Also, compare the c_t using the UK- and SI-systems.

SOLUTION:

We only need to recalculate R. Note that the weight ratio inside the parenthesis is $W_2/W_3=3200/2800=1.143$ remains unchanged for the SI-system. However, we must convert $c_{bhp}=0.60$ lb$_f$/(BHP·h) to c_{kW}. We do this using Equation (21-16):

$$c_{kW}=0.6083\ c_{hp}=0.6083\ (0.60)=0.3650\ \text{kg/(kW}\cdot\text{hr)}$$

Therefore, the range using the SI-system is

$$R=\frac{367.1\ \eta_p LD_{\max}}{c_{kW}}\ln\left(\frac{W_2}{W_3}\right)=\frac{367.1(0.85)(19.0)}{(0.3650)}\ln(1.143)$$
$$=1760\,\text{km}$$

Convert this to nautical miles to compare to Example 21-6(e): $1760/1.852=950$ nm. Next, let us calculate c_t using both unit systems. First, calculate it per Equation (21-20):

$$c_t=\frac{c_{hp}V_{KTAS}}{325.9\ \eta_p}=\frac{(0.60)(82.5)}{325.9\ (0.85)}=0.1787\ \frac{1}{\text{hr}}$$

Then, calculate c_t per Equation (21-21):

$$c_t=\frac{c_{kW}V_{\text{kmh}}}{367.1\ \eta_p}=\frac{(0.3650)(82.5\times1.852)}{367.1\ (0.85)}=0.1787\ \frac{1}{\text{hr}}$$

21.3.5 Range Profile 4: Cruise Range of Electric Aircraft

Electric airplanes were introduced in Section 7.4. Conceptual design guidance is provided in Section 6.2.1.

As stated earlier, running an electric motor will not change the weight of the aircraft. Thus, we must develop an approach different from the three preceding range profiles for fossil fuel aircraft. The following approach is developed by Hepperle [10]. We specify *mass specific energy* E^*, per Equation (7-47), *energy capacity* E_{batt}, per Equation (7-50), and *available motor power* P_{AVmot}, per Equation (7-67). Thus, under ideal conditions, during which the voltage U and current I are relatively constant, the time (in hours) it takes to drain the battery is given by

$$\Delta t = \frac{m_{batt}E^*}{U \cdot I} = \frac{E_{batt}}{P_{batt}} \tag{21-40}$$

Note that for all intents and purposes, this is the endurance. For real applications, the current draw changes the voltage and is subject to Peukert's law (see Section 7.4.2). Such processes reduce Δt. However, if I is below the maximum continuous current, $I_{\max}$, Equation (21-40) is an acceptable approximation. Here, we will ignore these effects and assume the above expression is applicable to the range/endurance problem.

The power available for flight can be related to the power that must be developed by the battery as follows:

$$P_{AV} = \eta_p P_{AV_{mot}} = \eta_p \eta_{system} P_{batt} \Rightarrow P_{batt} = \frac{P_{AV}}{\eta_p \eta_{system}} \tag{21-41}$$

Following reference [10], let $\eta_{tot} = \eta_p \eta_{system}$ as the total power-efficiency of the drivetrain. η_p is the propeller efficiency and η_{system} is the system efficiency (see Figure 7-56). We now have means to estimate the depletion time of the battery (Δt) in terms of aircraft performance. Thus, if we know the true airspeed (V_∞) the no-wind range can be estimated using Equation (21-1).

$$R = V_\infty \Delta t = V_\infty \left(\frac{E_{batt}}{P_{batt}}\right) = V_\infty \left(\frac{\eta_{tot} E_{batt}}{P_{AV}}\right) \tag{21-42}$$

This expression reflects a steady, level cruise, during which $P_{AV} = P_{REQ} = DV_\infty$. Drag ($D$) can be written in terms of weight and lift-to-drag ratio as $D = W/(L/D)$, allowing us to rewrite P_{AV} as follows.

$$P_{AV} = DV_\infty = \frac{W}{C_L/C_D} V_\infty \tag{21-43}$$

Substitute this into Equation (21-42) to get

$$R = V_\infty \left(\frac{\eta_{tot} E_{batt}}{P_{AV}}\right) = \frac{\eta_{tot} E_{batt}}{W} \left(\frac{C_L}{C_D}\right) \tag{21-44}$$

Note that the effect of velocity is implicitly involved through the lift- and drag-coefficients, and propeller efficiency. Next, write this in terms of battery properties ($E_{batt} = m_{batt}E^*$) and vehicle mass ($W = mg$), we get

$$R = \frac{\eta_{tot} m_{batt} E^*}{mg} \left(\frac{C_L}{C_D}\right) = \frac{E^* \cdot \eta_{tot}}{g} \left(\frac{C_L}{C_D}\right) \left(\frac{m_{batt}}{m}\right) \tag{21-45}$$

If using standard SI-units with Equation (21-45), there is a unit discrepancy in the units for E^* (W**h**/kg) and g (m/**s**^{2}). Conducting a unit analysis leads to:

$$[\text{m}] = \frac{[\text{W} \cdot \text{h/kg}] \cdot [1] \cdot [1]}{[\text{m/s}^2]} \left[\frac{\text{kg}}{\text{kg}}\right] = \frac{[\text{N} \cdot \text{m} \cdot \text{h/s}]}{[\text{kg} \cdot \text{m/s}^2]} = \left[\text{m}\frac{\text{h}}{\text{s}}\right] = 3600[\text{m}]$$

Furthermore, since we desire the range in km and noting that 1 km = 1000 m, we rewrite the final version of Equation (21-45):

$$R = \frac{3.6E^* \cdot \eta_{tot}}{g} \left(\frac{C_L}{C_D}\right) \left(\frac{m_{batt}}{m}\right) \tag{21-46}$$

The above expression exposes which parameter to consider for maximum range. These are.

- L/D (or C_L/C_D) should be as large as possible.
- The battery mass ratio, m_{batt}/m, must be large.
- The product of system and propeller efficiencies, $\eta_p \eta_{system}$, must be large.
- Mass-specific energy, E^*, must be large.

Additional guidance for the design of electric airplanes is given in Sections 6.2.1 and 7.4. Get further guidance from refs. [10, 11].

EXAMPLE 21-8

An LSA-class electric airplane is being designed. The maximum gross mass is 600 kg and includes a 200 kg Lithium-Ion battery. Its electric motor is rated at 76 kW at full power (76,000 W). Its wing area is 12 m^2, $AR = 14$, and $C_{D_{\min}} = 0.020$. Determine its best range at altitude of 600 m ($\rho = 1.156$ kg/m^3), assuming the simplified drag model, a total system efficiency of 0.72, and energy density of 150 Wh/kg. Ignore energy needed to climb to the cruise altitude. Also, estimate the endurance in hours.

SOLUTION:

Per Equations (9-129), (16-2), and (16-6), the drag polar is

$$C_D = C_{D_{\min}} + kC_L^2 = 0.020 + 0.03455C_L^2$$

Using Equations (20-33) and (20-37), the $LD_{\max}$ and $V_{LD\max}$ equals

$$LD_{\max} = \frac{1}{\sqrt{4kC_{D_{\min}}}} = \frac{1}{\sqrt{4(0.03455)(0.020)}} = 19.0$$

$$V_{LD_{\max}} = \sqrt{\frac{2}{\rho}\left(\frac{W}{S}\right)\sqrt{\frac{k}{C_{D_{\min}}}}} = \sqrt{\frac{2}{(1.156)}\left(\frac{(600)(9.807)}{(12)}\right)\sqrt{\frac{0.03455}{0.020}}} = 33.3 \text{ m/s}$$

EXAMPLE 21-8 (*cont'd*)

The airspeed corresponds to approximately 65 KTAS. The maximum range is thus

$$R = \frac{3.6E^* \cdot \eta_{tot}}{g}\left(\frac{C_L}{C_D}\right)\left(\frac{m_{batt}}{m}\right) = \frac{3.6(150)(0.72)}{9.807}(19.0)\left(\frac{200}{600}\right)$$
$$= 251 \text{ km} \quad (\approx 135 \text{ nm})$$

The endurance is obtained per Equation (21-1) (where 3.6 converts m/s to kmh).

$$E = \Delta t = \frac{R}{V_\infty} = \frac{251}{(33.3 \times 3.6)} = 2.10 \text{ hr}$$

EXAMPLE 21-9

A light airplane is cruising at a true airspeed of 150 KTAS, burning 15 gals/h. What is its *instantaneous specific range*? If it travels 768 nm using 400 lb_f of fuel, what is its *average specific range*?

SOLUTION:

Instantaneous *SR*:

$$SR = \frac{V_{KTAS}}{\dot{w}_f} = \frac{150 \text{ nm/hr}}{(15 \text{ gals/hr})(6 \text{ lb}_f/\text{gal})} = 1.667 \text{ nm/lb}_f.$$

Average *SR*:

$$SR = \frac{R}{W_f} = \frac{765 \text{ nm}}{400 \text{ lb}_f} = 1.913 \text{ nm/lb}_f.$$

21.3.6 Specific Range

Specific range (*SR*) is the distance an airplane can fly per unit mass or weight of fuel. This quantity is important when comparing the efficiency of different aircraft or when determining the optimum range airspeed for a specific aircraft. It is defined as follows:

$$SR \equiv \frac{\text{Distance covered}}{\text{Quantity of fuel used}} \tag{21-47}$$

Specific range is analogous to *gas mileage* for cars. The primary difference is that it is frequently stated in terms of lb_f rather than gallons, i.e., 3 nm/lb_f rather than 24 nm/gal (assuming 6 lb_f/gal). If we know the weight of fuel (W_f) consumed over given distance (R), we can calculate the *average SR* from the following expression:

$$SR = \frac{R}{W_f} \tag{21-48}$$

We can also compute the *instantaneous SR* as follows:

$$SR = \frac{\Delta R/\Delta t}{W_f/\Delta t} = \frac{V_{TAS}}{\dot{w}_f} = \frac{\text{True airspeed}}{\text{Fuel weight per unit time}} = \frac{\text{True airspeed}}{\text{Fuel flow}} \tag{21-49}$$

This can also be represented in terms of thrust specific fuel consumption (c_t or *SFC*), weight (W), and lift-to-drag ratio (LD) as shown below:

$$SR = \frac{V_{TAS}}{\dot{w}_f} = \frac{V_{TAS}}{c_t \cdot T} = \frac{V_{TAS} \cdot LD}{c_t \cdot W} \tag{21-50}$$

Ensure unit consistency when using these expressions.

Other Range-Related Parameters for Assessing Efficiency

Besides specific range, other parameters are also used to evaluate the effectiveness of aircraft. A selection is presented below (in multiple forms).

Passenger-Specific-Productivity (PXSP):

$$PXSP = \frac{N_{pax}R}{W_f} = \frac{N_{pax}\Delta R}{\dot{w}_f \Delta t} = \frac{N_{pax} \cdot V_{TAS}}{c_t \cdot T} = \frac{N_{pax} \cdot V_{TAS} \cdot LD}{c_t \cdot W}$$
$$= N_{pax} \cdot SR \tag{21-51}$$

Example units are pax·nm/lb_f or pax·km/kg (assuming W_p is converted to kg).

Payload-Specific-Productivity (PLSP):

$$PLSP = \frac{W_p R}{W_f} = \frac{W_p \cdot V_{TAS} \cdot LD}{c_t \cdot W} = W_p \cdot SR \tag{21-52}$$

Example units are lb_f·nm/lb_f (or simply nm) or kg·km/kg (or simply km).

Payload-Productivity (PLP):

$$PLSP = W_p \cdot R \tag{21-53}$$

Example units are lb_f·nm or kg·km (assuming W_p is converted to kg).

Range-Cost (RC):

$$RC = \frac{\text{Distance}}{\text{Fuel cost}} = \frac{R}{FP \times W_f} = \frac{R}{FP \times (\dot{w}_f \Delta t)} = \frac{V_{TAS}}{FP \times (c_t \cdot T)}$$
$$= \frac{V_{TAS} \cdot LD}{FP \times (c_t \cdot W)} \tag{21-54}$$

where FP is fuel price (e.g., \$/lb_f of fuel). Example units are nm/\$ or km/\$. Also, consider cost-of-available-seat-mile (CASM) and revenue-of-available-seat-mile (RASM) introduced in Section 2.1.4.

21.3.7 Determining Fuel Required for a Mission

This section presents methods to predict fuel required for a specific cruise range. Of the three range profiles presented in Sections 21.3.2-4, only profiles 2 and 3 results in closed-form solutions. These are shown below.

(1) Mission Fuel based on Range Profile 2

Jet aircraft:

$$W_f = A\sqrt{W_{ini}} - \frac{1}{4}A^2 \tag{21-55}$$

where:

$$A = Rc_t\sqrt{\frac{\rho S}{2}}\frac{C_D}{\sqrt{C_L}} \qquad \text{for jet aircraft} \tag{21-56}$$

$$A = \frac{Rc_{bhp}V_\infty}{325.9\eta_p}\sqrt{\frac{\rho S}{2}}\frac{C_D}{\sqrt{C_L}} \qquad \text{for propeller aircraft} \tag{21-57}$$

(2) Mission Fuel based on Range Profile 3

Jet aircraft:

$$W_f = W_{ini}\left(1 - \exp\left(-\frac{Rc_t}{V_\infty(C_L/C_D)}\right)\right) \tag{21-58}$$

Propeller aircraft:

$$W_f = W_f = W_{ini}\left(1 - \exp\left(-\frac{Rc_{hp}}{325.9\eta_p}\right)\right) \tag{21-59}$$

Range profile 3 is also helpful for determining weight ratios when determining initial gross weight through mission analysis that involves range or endurance (e.g., see Section 6.2.3). The following set of equations is derived using the same derivations as the above equations.

Jet aircraft:

$$\begin{aligned} R &= \frac{V_\infty}{SFC}\left(\frac{L}{D}\right)\ln\left(\frac{W_{ini}}{W_{fin}}\right) \Leftrightarrow \frac{W_{fin}}{W_{ini}} = e^{-\frac{R\times SFC}{V_\infty\times(L/D)}} \\ E &= \frac{1}{SFC}\left(\frac{L}{D}\right)\ln\left(\frac{W_{ini}}{W_{fin}}\right) \Leftrightarrow \frac{W_{fin}}{W_{ini}} = e^{-\frac{E\times SFC}{(L/D)}} \end{aligned} \tag{21-60}$$

Propeller aircraft:

$$\begin{aligned} R &= \frac{325.9\eta_p}{SFC_{hp}}\frac{L}{D}\ln\left(\frac{W_{ini}}{W_{fin}}\right) \Leftrightarrow \frac{W_{fin}}{W_{ini}} = e^{\frac{R\times SFC_{hp}}{325.9\eta_p\times(L/D)}} \\ E &= \frac{325.9\eta_p}{SFC_{hp}V_\infty}\frac{L}{D}\ln\left(\frac{W_{ini}}{W_{fin}}\right) \Leftrightarrow \frac{W_{fin}}{W_{ini}} = e^{-\frac{E\times SFC_{hp}V_\infty}{325.9\eta_p(L/D)}} \end{aligned} \tag{21-61}$$

DERIVATION OF EQUATIONS (21-55)–(21-57)

Noting that $W_f = W_{ini} - W_{fin}$, we solve Equation (21-32) for the jet aircraft as shown below:

$$\begin{aligned} R &= \frac{1}{c_t}\frac{\sqrt{C_L}}{C_D}\frac{2\sqrt{2}}{\sqrt{\rho S}}\left(\sqrt{W_{ini}} - \sqrt{W_{ini} - W_f}\right) \\ \Rightarrow W_{ini} - W_f &= \left(\sqrt{W_{ini}} - \frac{Rc_t\sqrt{\rho S}}{2\sqrt{2}}\frac{C_D}{\sqrt{C_L}}\right)^2 \\ \Rightarrow W_{ini} - W_f &= W_{ini} - 2\sqrt{W_{ini}}\frac{Rc_t\sqrt{\rho S}}{2\sqrt{2}}\frac{C_D}{\sqrt{C_L}} \\ &\quad + \left(\frac{R^2c_t^2\rho S}{8}\frac{C_D^2}{C_L}\right) \\ \Rightarrow W_f &= Rc_t\sqrt{\frac{W_{ini}\rho S}{2}}\frac{C_D}{\sqrt{C_L}} - \frac{R^2c_t^2\rho S}{8}\frac{C_D^2}{C_L} \end{aligned}$$

This is Equation (21-55) before simplification using the constant A. The constant A for jet becomes Equation (21-56). For the propeller aircraft, we solve Equation (21-35) in a similar fashion:

$$\begin{aligned} R &= \frac{325.9\eta_p}{c_{bhp}V_\infty}\frac{\sqrt{C_L}}{C_D}\frac{2\sqrt{2}}{\sqrt{\rho S}}\left(\sqrt{W_{ini}} - \sqrt{W_{ini} - W_f}\right) \\ \Rightarrow W_{ini} - W_f &= \left(\sqrt{W_{ini}} - \frac{Rc_{bhp}V_\infty}{325.9\eta_p}\frac{C_D}{\sqrt{C_L}}\frac{\sqrt{\rho S}}{2\sqrt{2}}\right)^2 \\ \Rightarrow W_{ini} - W_f &= W_{ini} - 2\sqrt{W_{ini}}\frac{Rc_{bhp}V_\infty}{325.9\eta_p}\frac{C_D}{\sqrt{C_L}}\frac{\sqrt{\rho S}}{2\sqrt{2}} \\ &\quad + \left(\frac{R^2{c_{bhp}}^2{V_\infty}^2{C_D}^2}{325.9^2{\eta_p}^2}\frac{\rho S}{C_L\,2^2 2}\right) \\ \Rightarrow W_f &= \sqrt{W_{ini}}\frac{Rc_{bhp}V_\infty}{325.9\eta_p}\frac{C_D}{\sqrt{C_L}}\sqrt{\frac{\rho S}{2}} \\ &\quad - \left(\frac{Rc_{bhp}V_\infty}{325.9\eta_p}\right)^2\frac{{C_D}^2}{C_L}\frac{\rho S}{8} \end{aligned}$$

This is Equation (21-55) for propeller aircraft. The constant A for such aircraft becomes Equation (21-57).

DERIVATION OF EQUATIONS (21-58) AND (21-59)

For jet aircraft, solve Equation (21-37) for W_f:

$$\begin{aligned} R &= \frac{V_\infty}{c_t}\frac{C_L}{C_D}\ln\left(\frac{W_{ini}}{W_{fin}}\right) \Rightarrow \frac{W_{ini}}{W_{fin}} = e^{\left(\frac{Rc_t}{V_\infty(C_L/C_D)}\right)} \\ \Rightarrow \frac{W_{fin}}{W_{ini}} &= e^{\left(-\frac{Rc_t}{V_\infty(C_L/C_D)}\right)} \\ \Rightarrow W_f &= W_{ini}\left(1 - \exp\left(-\frac{Rc_t}{V_\infty(C_L/C_D)}\right)\right) \end{aligned}$$

This is Equation (21-58). For propeller aircraft, solve Equation (21-38) for W_f:

DERIVATION OF EQUATIONS (21-58) AND (21-59) *(cont'd)*

$$R = \frac{325.9\eta_p}{c_{hp}} \ln\left(\frac{W_{ini}}{W_{fin}}\right) \Rightarrow \frac{W_{ini}}{W_{fin}} = e^{\left(\frac{Rc_{hp}}{325.9\eta_p}\right)}$$

$$\Rightarrow \frac{W_{fin}}{W_{ini}} = e^{\left(-\frac{Rc_{hp}}{325.9\eta_p}\right)}$$

$$\Rightarrow W_f = W_{ini}\left(1 - \exp\left(-\frac{Rc_{hp}}{325.9\eta_p}\right)\right)$$

This is Equation (21-59).

21.3.8 Range Sensitivity Studies

As stated in the introduction to this section, range and endurance are of paramount importance in most aircraft design projects. Many models of aircraft sell only because of their range or endurance. If the predicted range is not met, the entire development project may be compromised. Therefore, it is imperative to assess the sensitivity of the design to deviations from standard operational parameters. For instance, consider a project in which the empty weight is higher than planned. This, cuts into the fuel quantity that can be carried for the design mission. A sensitivity study can help expose a possible weakness in the design early enough to justify modifications that may remedy the situation.

The following examples use the methods presented in this section. A sensitivity study focuses on varying a specific variable, while all others are fixed.

(1) Empty Weight Sensitivity

The empty weight sensitivity shows the effect of deviations in empty weight on the range of the airplane (see Figure 21-9). Here, let us assume the target empty weight to amount to 2200 lb_f. If the production aircraft ends up being 300 lb_f heavier than anticipated, the maximum range drops from about 1315 nm to about 771 nm for the particular loading (which here consists of two 200 lb_f individuals and 50 lb_f of baggage).

It is helpful to plot the capability of the competition on the weight sensitivity graph. This exposes the competitive capability of the new design.

(2) Drag Sensitivity

The drag sensitivity shows the effect of deviations in drag coefficient on the range of the airplane (see Figure 21-10). Here, the target empty weight is assumed 2200 lb_f. If the production aircraft generates 20 drag counts above expected value, the baseline range of 1315 nm drops to 1240 nm and 1180 nm if it generates 40 additional drag counts. The additional drag can stem from a number of sources. For instance, larger than expected flow separation regions during cruise (poor wing fairing design, poor geometric quality), nonmaterialization of NLF (turbulent boundary layer in regions where NLF is expected), protrusions such as antennas and entry steps, cooling drag, CRUD, and so on.

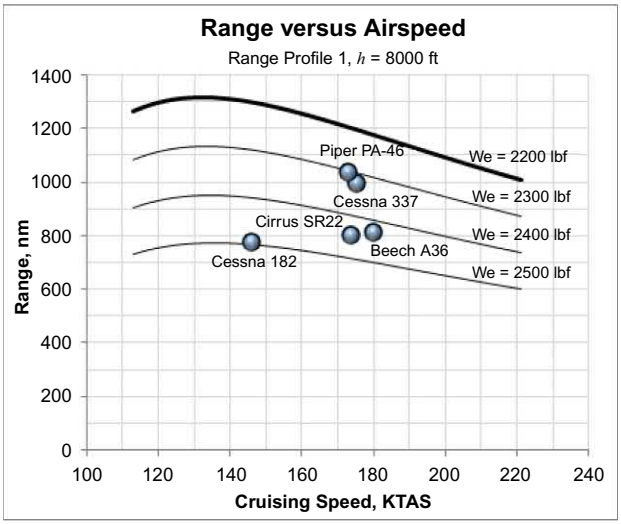


FIGURE 21-9 The impact of W_e on the range of a small piston-powered aircraft.

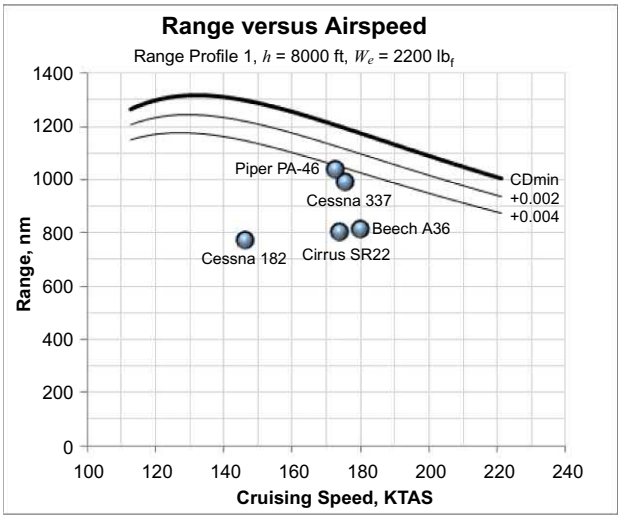


FIGURE 21-10 The impact of $C_{D_{min}}$ on range.

(3) Aspect Ratio Sensitivity

The Aspect Ratio sensitivity reveals the effect of the wing AR on the range of the airplane (see Figure 21-11). Here, the target AR of 10 yields a baseline range of 1315 nm. Reducing this to, say, 6 results in a drop of 115 nm to 1200 nm.

The primary advantage of AR is reduction in lift induced drag. Most of this is realized at lower dynamic pressures, when the airplane must fly at higher AOAs. Also, remember that given fixed wing area, reducing AR will reduce internal volume of the wing. This means: less

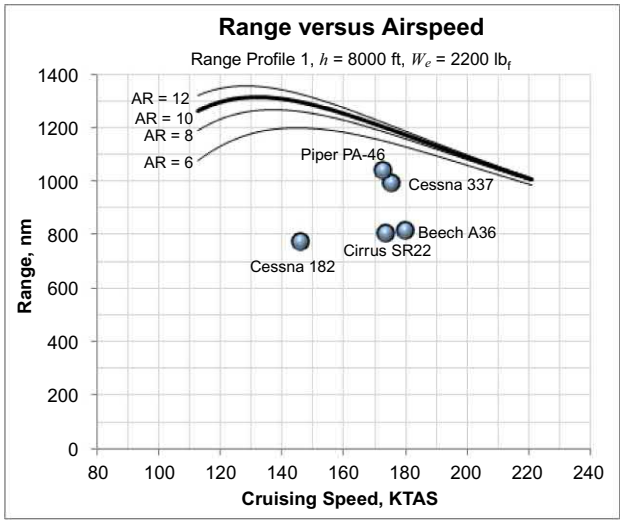


FIGURE 21-11 The impact of *AR* on range.

fuel in the wing and, thus, reduced range. Chances are that the increase in range due to increased AR is far less than the decrease in range due to reduced fuel volume.

21.4 ENDURANCE ANALYSIS

This section presents methods to conduct endurance analyses. Endurance analysis investigates for how long an aircraft can remain airborne given specific quantity of fuel or battery energy. The analysis helps determining airspeeds that must be maintained to maximize endurance. Like range analysis, it also allows various sensitivities to be evaluated, such as the effect of fuel weight and altitude.

An inspection of the resulting equations exposes a commonality between all. To achieve a long endurance capability, the airplane must be designed with the following features in mind:

1. It must have a high operational L/D ratio. It must be as sleek as possible.
2. It must have a low Specific Fuel Consumption.
3. If driven by a propeller it must feature the highest possible propeller efficiency and operate at a low altitude (high ρ).
4. It must carry as much fuel as possible.

Formulation for the estimation of endurance will now be developed assuming the same profiles used for the development of the range equations.

21.4.1 Endurance Profile 1: Constant Airspeed/ Altitude Cruise

Refer to Section 21.3.2 and Figure 21-6 for more details on this cruise profile. *This result is valid only for the simplified drag model.*

(1) Endurance Equation 1 for Jet Aircraft

Review stipulations for range profile 1. The unit of time for E (1/h or 1/s) is dictated by c_t.

$$E=\frac{1}{c_t\sqrt{kC_{D_{\min}}}}\left[\tan^{-1}(AW_{ini})-\tan^{-1}(AW_{fin})\right] \quad (21\text{-}62)$$

where

$$A=\frac{2}{\rho V_\infty^2 S}\sqrt{\frac{k}{C_{D_{\min}}}} \quad (21\text{-}26)$$

Calculate A per Equation (21-28) for the UK-system and (21-29) for the SI-system, with all the same stipulations. Note that since the airspeed is constant in this profile, the endurance can also be calculated from $E=R/V_\infty$, where R is the range calculated using range profile 1.

(2) Endurance Equation 1 for Propeller Aircraft

As with the range equations, endurance is adapted to propeller aircraft by changing c_t per Equations (21-20) and (21-21). If ρ is in slugs/ft^3, S in ft^2, W in lb$_f$, V_∞ in KTAS, and c_{hp} in kg/(HP·h), then E in hours is given by:

$$E=\frac{325.9\eta_p}{c_{hp}V_{KTAS}\sqrt{kC_{D_{\min}}}}\left[\tan^{-1}(AW_{ini})-\tan^{-1}(AW_{fin})\right] \quad (21\text{-}63)$$

If ρ is in kg/m^3, S in m^2, W in N, V_∞ in kmh, c_{kW} in kg/(kW·h), then E in hours is given by:

$$E=\frac{367.1\ \eta_p}{c_{kW}\sqrt{kC_{D_{\min}}}}\left[\tan^{-1}(AW_{ini})-\tan^{-1}(AW_{fin})\right] \quad (21\text{-}64)$$

DERIVATION OF EQUATION (21-62)

In this case, V_∞ = constant and ρ = constant. However, since C_L/C_D depends on the weight it must remain inside the integral. Therefore, we write Equation (21-8) as follows, introducing the simplified drag model:

$$E=\int_{W_{fin}}^{W_{ini}}\frac{1}{c_t}\frac{C_L}{C_D}\frac{1}{W}dW=\frac{1}{c_t}\int_{W_{fin}}^{W_{ini}}\frac{C_L}{C_D}\frac{1}{W}dW$$
$$=\frac{1}{c_t}\int_{W_{fin}}^{W_{ini}}\frac{C_L}{\left(C_{D_{\min}}+kC_L^2\right)}\frac{1}{W}dW$$

Next, we expand by substituting the expression for the lift coefficient, followed by algebraic manipulations, similar to the derivation of Equation (21-25). This leads to

$$E=\frac{1}{c_t}\frac{\rho V_\infty^2}{2k}S\int_{W_{fin}}^{W_{ini}}\frac{1}{(a^2+W^2)}dW=\frac{1}{c_t}\frac{\rho V_\infty^2}{2k}S\frac{1}{a}\left[\tan^{-1}\frac{W}{a}\right]_{W_{fin}}^{W_{ini}}$$
$$=\frac{1}{c_t\sqrt{kC_{D_{\min}}}}\left[\tan^{-1}\left(\frac{2\sqrt{k}}{\rho V^2 S\sqrt{C_{D_{\min}}}}W_{ini}\right)\right.$$
$$\left.-\tan^{-1}\left(\frac{2\sqrt{k}}{\rho V^2 S\sqrt{C_{D_{\min}}}}W_{fin}\right)\right]$$

21.4.2 Endurance Profile 2: Constant Attitude/Altitude Cruise

Refer to Section 21.3.3 and Figure 21-7 for more details on this cruise profile. Both following results are valid regardless of drag model choice.

(1) Endurance Equation 2 for Jet Aircraft

Review stipulations for range profile 2. The unit of time for E (h or s) is dictated by c_t. Note that while c_t is treated here (and in the range equations) as a constant, it may be a function of airspeed. This would require c_t to be included in the integration. However, if the initial and final airspeeds are relatively close to each other, treating the average c_t as a constant is justified.

$$E = \frac{1}{c_t}\frac{C_L}{C_D}\ln\left(\frac{W_{ini}}{W_{fin}}\right) \tag{21-65}$$

(2) Endurance Equation 2 for Propeller Aircraft

As with the range equations, endurance is adapted to propeller aircraft by changing c_t using Equations (21-20) and (21-21). For ρ in slugs/ft^3, S in ft^2, W in lb$_f$, and c_{hp} in kg/(HP·h), then E in hours is given by:

$$E = \frac{550\eta_p}{c_{hp}}\sqrt{2\rho S}\frac{C_L^{3/2}}{C_D}\left(\frac{1}{\sqrt{W_{fin}}}-\frac{1}{\sqrt{W_{ini}}}\right) \tag{21-66}$$

If ρ is in kg/m^3, S in m^2, W in N, c_{kW} in kg/(kW·h), then E in hours is found by the converting c_{hp} to c_{kW} using Equation (21-16):

$$E = \frac{102\eta_p}{c_{kW}}\sqrt{2\rho S}\frac{C_L^{3/2}}{C_D}\left(\frac{1}{\sqrt{W_{fin}}}-\frac{1}{\sqrt{W_{ini}}}\right) \tag{21-67}$$

DERIVATION OF EQUATION (21-65)

In this case, V_∞ = variable, ρ = constant, and C_L/C_D = constant. Since the attitude is constant, move C_L/C_D outside of the integral and integrate Equation (21-8) as follows:

$$E = \frac{1}{c_t}\int_{W_{fin}}^{W_{ini}}\frac{C_L}{C_D}\frac{1}{W}dW = \frac{1}{c_t}\frac{C_L}{C_D}\int_{W_{fin}}^{W_{ini}}\frac{1}{W}dW$$
$$= \frac{1}{c_t}\frac{C_L}{C_D}\left[\ln W\right]_{W_{fin}}^{W_{ini}} = \frac{1}{c_t}\frac{C_L}{C_D}\ln\left(\frac{W_{ini}}{W_{fin}}\right)$$

DERIVATION OF EQUATIONS (21-66) AND (21-67)

In this case, $V_\infty = \sqrt{2W/(\rho S C_L)}$, ρ = constant, C_L/C_D = constant, and $c_t = c_{hp}V_\infty/\eta_p$. Since the attitude is constant, move C_L/C_D outside of the integral and integrate Equation (21-8) as follows:

$$E = \int_{W_{fin}}^{W_{ini}}\frac{1}{c_t}\frac{C_L}{C_D}\frac{1}{W}dW = \int_{W_{fin}}^{W_{ini}}\frac{\eta_p}{c_{hp}V_\infty}\frac{C_L}{C_D}\frac{1}{W}dW$$
$$= \frac{\eta_p}{c_{hp}}\frac{C_L}{C_D}\int_{W_{fin}}^{W_{ini}}\frac{1}{V_\infty}\frac{1}{W}dW = \frac{\eta_p}{c_{hp}}\frac{C_L}{C_D}\int_{W_{fin}}^{W_{ini}}\sqrt{\frac{\rho S C_L}{2W}}\frac{1}{W}dW$$
$$= \frac{\eta_p}{c_{hp}}\frac{C_L^{3/2}}{C_D}\sqrt{\frac{\rho S}{2}}\int_{W_{fin}}^{W_{ini}}\frac{dW}{W^{3/2}}$$
$$= \frac{\eta_p}{c_{hp}}\sqrt{2\rho S}\frac{C_L^{3/2}}{C_D}\left(\frac{1}{\sqrt{W_{fin}}}-\frac{1}{\sqrt{W_{ini}}}\right)$$

Note that since c_p is in terms of HP^{-1}, it must be multiplied by 550 ft·lb$_f$/s. The product c_pV_∞ leads to

$$c_{hp}V_\infty \rightarrow \left[\frac{\text{lb}_f}{\text{HP}\cdot\text{hr}}\right]\left[\frac{\text{ft}}{\text{s}}\right] \rightarrow \left[\frac{\text{lb}_f}{\text{HP}\cdot\text{hr}}\times\frac{\text{HP}}{550\ \text{ft}\cdot\text{lb}_f/\text{s}}\right]\left[\frac{\text{ft}}{\text{s}}\right]$$
$$\rightarrow \left[\frac{1}{\text{hr}}\times\frac{1}{550}\right]$$

The resulting equation is Equation (21-66). Equation (21-67) is obtained by substituting $c_{hp} = c_{kW}/0.6083$.

21.4.3 Endurance Profile 3: Constant Airspeed/Attitude Cruise

Refer to Section 21.3.4 and Figure 21-8 for more details on this cruise profile. Both following results are valid regardless of drag model choice.

(1) Endurance Equation 3 for Jet Aircraft

Review stipulations for range profile 3. The unit of time for E (h or s) is dictated by c_t.

$$E = \frac{1}{c_t}\frac{C_L}{C_D}\ln\left(\frac{W_{ini}}{W_{fin}}\right) \tag{21-68}$$

(2) Endurance Equation 3 for Propeller Aircraft

As with the range equations, endurance is adapted to propeller aircraft by changing c_t using Equations (21-20) and (21-21). This is easy for this profile because V_∞ and C_L/C_D are constants. Thus, Equation (21-68) can be used unmodified. For ρ in slugs/ft^3, S in ft^2, W in lb$_f$, V_∞ in KTAS, and c_{hp} in kg/(HP·h), then E in hours is given by:

$$E = \frac{325.9\ \eta_p}{c_{hp}V_{KTAS}}\frac{C_L}{C_D}\ln\left(\frac{W_{ini}}{W_{fin}}\right) \tag{21-69}$$

If ρ is in kg/m^3, S in m^2, W in N, V_∞ in kmh, c_{kW} in kg/(kW·h), then E in hours is found by substituting $c_{hp} = c_{kW}/0.6083$ and $V_{KTAS} = V_{kmh}/1.852$ into Equation (21-69), which changes the coefficient

$$E = \frac{367.1\ \eta_p}{c_{kW}V_{kmh}}\frac{C_L}{C_D}\ln\left(\frac{W_{ini}}{W_{fin}}\right) \tag{21-70}$$

DERIVATION OF EQUATION (21-68)

Here, V_∞ = constant, ρ = variable, and C_L/C_D = constant. Thus, V_∞ and C_L/C_D can be outside the integral. Therefore, we write Equation (21-7) as follows:

$$E = \frac{1}{c_t}\int_{W_{fin}}^{W_{ini}} \frac{C_L}{C_D}\frac{1}{W}dW = \frac{1}{c_t}\frac{C_L}{C_D}\int_{W_{fin}}^{W_{ini}} \frac{1}{W}dW = \frac{1}{c_t}\frac{C_L}{C_D}[\ln W]_{W_{fin}}^{W_{ini}}$$
$$= \frac{1}{c_t}\frac{C_L}{C_D}\ln\left(\frac{W_{ini}}{W_{fin}}\right)$$

EXAMPLE 21-10

Calculate the endurance for the light airplane of Example 21-6 for range profiles 1 and 2. The lift and drag coefficients at condition are $C_L = 0.3921$ and $C_D = 0.03147$, respectively.

SOLUTION:

Endurance Profile 1: Constant Airspeed/Altitude Cruise

$$A = \frac{2}{\rho V_2^2 S}\sqrt{\frac{k}{C_{D_{\min}}}}$$
$$= \frac{2}{(0.001756)(253.2)^2(145)}\sqrt{\frac{0.04207}{0.025}}$$
$$= 0.0001589$$
$$E = \frac{325.9\eta_p}{c_{hp}V_{KTAS}\sqrt{kC_{D_{\min}}}}\left[\tan^{-1}(AW_{ini}) - \tan^{-1}(AW_{fin})\right]$$
$$= \frac{325.9(0.85)}{(0.60)(150)\sqrt{(0.04207)(0.025)}}\left[\tan^{-1}(\mathrm{A}(3200)) - \tan^{-1}(\mathrm{A}(2800))\right] = 4.92\,\text{hrs}$$

Endurance Profile 2: Constant Attitude/Altitude Cruise

$$E = \frac{550\eta_p}{c_{hp}}\sqrt{2\rho S}\frac{C_L^{3/2}}{C_D}\left(\frac{1}{\sqrt{W_{fin}}} - \frac{1}{\sqrt{W_{ini}}}\right)$$
$$= \frac{550(0.85)}{0.60}\sqrt{2(0.001756)(145)}\frac{(0.3921)^{3/2}}{0.03147}$$
$$\left(\frac{1}{\sqrt{2800}} - \frac{1}{\sqrt{3200}}\right) = 5.29\,\text{hrs}$$

21.4.4 Endurance Profile 4: Cruise Range of Electric Aircraft

See discussion about electric airplanes in Section 21.3.5. In short, the endurance of electric aircraft can be calculated per Equation (21-44),

$$R = V_\infty\left(\frac{\eta_{tot}E_{batt}}{P_{AV}}\right) \Rightarrow E = \frac{\eta_{tot}E_{batt}}{P_{AV}} = \frac{\eta_{tot}E_{batt}}{DV_\infty} \quad (21\text{-}71)$$

Since drag (D) can be written as $D = W/(L/D)$, we can rewrite this as follows.

$$E = \frac{\eta_{tot}E_{batt}}{W}\left(\frac{C_L}{C_D}\right) \quad (21\text{-}72)$$

All variables are defined in Section 21.3.5.

21.5 ANALYSIS OF MISSION PROFILE

Now that formulation for estimating range and endurance has been developed, it is time to introduce the fundamentals of mission analysis. *Mission analysis* investigates the entire flight of an airplane, from engine start-up to shut-down. It breaks the mission into multiple distinct segments, simplifying the analysis of properties such as weight, airspeed, and others.

Serious mission planning accounts for (a) fuel required to complete the mission and (b) *reserve fuel* to allow the airplane to divert to an alternative airport in case inclement weather at the original destination compromises a safe landing. The preceding sections have ignored this fuel and treated it as a part of the empty weight (which it is not). Any range or endurance analysis should account for reserve fuel in the final weight (W_{fin})—reducing the total fuel available for the design mission. The reserve fuel must be sufficient to climb to a new cruise altitude after an attempted and missed approach for landing, and continue flying to an alternate airport that may be as far as 100 or 200 nm from the original destination. There are generally two operational cruise missions that designers of GA aircraft should be aware of; IFR and NBAA missions. These will be discussed later in this section. First, fundamentals of *mission analysis* will be presented.

21.5.1 Basics of Mission Profile Analysis

Consider a scenario in which the mission, from engine start-up to engine shut-down, consists of the segments shown in Figure 21-12. Each segment is denoted as a line drawn between two points, called *nodes*. Each node is numbered from 0 to 7 (8 nodes and 7 segments). The mission may be more or less complicated than shown here. It is important to recognize that as the airplane covers each segment, assuming it consumes fossil fuel, its weight is reduced. Thus, its weight at Node 1 is less than at Node 0. Similarly, after climbing to its cruise altitude, denoted by Node 2, its weight is less than after T-O at Node 1, and so on. Usually, the weight change from node to node is the amount of fuel consumed during the segment. However, it may also constitute the weight of parachutists,

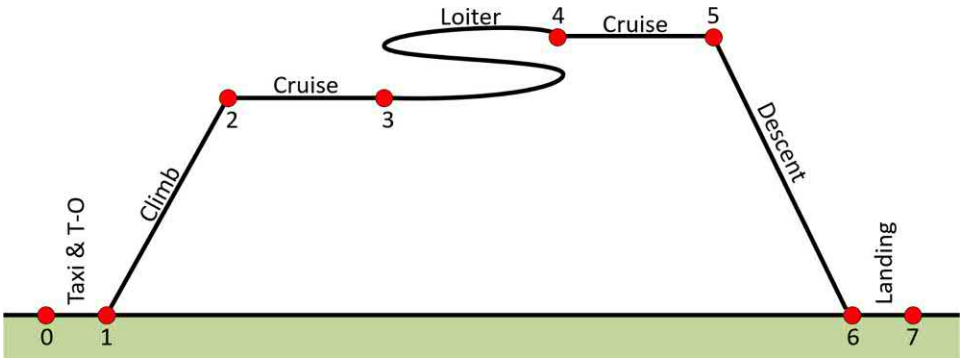


FIGURE 21-12 Aircraft mission analysis.

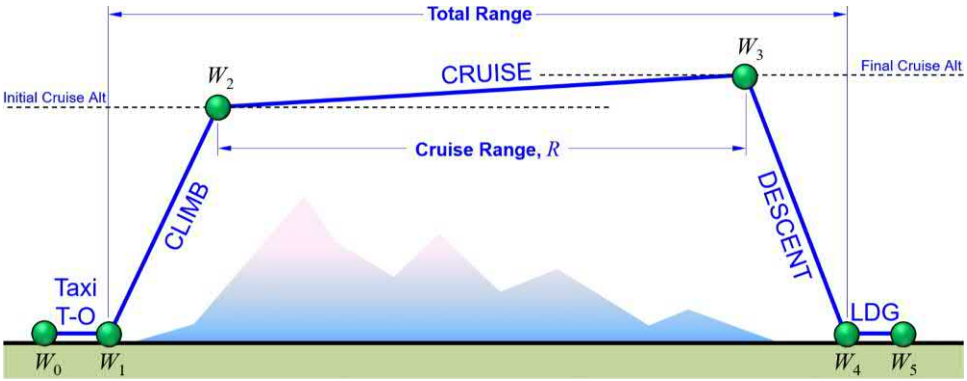


FIGURE 21-13 The break-down of a mission into a number of segments.

fertilizer, or external stores. Detailed mission analysis is presented in Section 6.2.3.

An example of a simple mission is shown in Figure 21-13. It consists of segments that entail engine start, warm-up, run-up, taxi into T-O position, the T-O, climb to cruise altitude, cruise, descent, landing, and finally taxi and parking. In interest of clarity, the segments are identified at each intersection by nodes. Each node has a weight associated with it, denoted by W_0, W_1, …, W_5. Then, the mission is analyzed by determining the weight (and therefore fuel consumed) at each node.

As an example, consider a scenario in which we have to determine the fuel available for cruise (cruise range); this is the fraction W_3/W_2 in Figure 21-13. In some cases, the engine start-up weight, W_0, and mission fuel weight, W_{fm}, are known. Assume it has been estimated (for instance, using historical data or knowledge of engine fuel consumption) that the engine start-up, warm-up, and taxi to T-O position consumes fuel so at Node 1 the airplane weighs 99% of W_0. In this case, it is possible to write the weight at Node 1 as follows:

$$W_1 = \left(\frac{W_1}{W_0}\right) W_0 = 0.99 W_0$$

Similarly, assume that during the climb to the cruise altitude the airplane consumes fuel and weighs 93% of the weight at Node 1. This can be expressed as follows:

$$W_2 = \left(\frac{W_2}{W_1}\right) W_1 = 0.93 W_1$$

In effect, this would allow the weight at Node 2 to be determined based on the initial weight, W_0, as shown below:

$$W_2 = \left(\frac{W_2}{W_1}\right) \times W_1 = \left(\frac{W_2}{W_1}\right) \times \left(\frac{W_1}{W_0}\right) W_0$$
$$= (0.93) \times (0.99) W_0 = 0.9207 W_0$$

This means that at top-of-climb, the airplane weighs 92.07% of its engine start-up weight. In fact, the entire mission can be represented as the product of the segment weight ratios:

$$\left(\frac{W_1}{W_0}\right)\left(\frac{W_2}{W_1}\right)\left(\frac{W_3}{W_2}\right)\left(\frac{W_4}{W_3}\right)\left(\frac{W_5}{W_4}\right) = \frac{W_5}{W_0}$$

This representation boils the problem of determining the amount of fuel required for cruise (represented by W_3/W_2) down to determining the other weight ratios and use them to estimate other weights of interest. See a thorough application of this methodology in Section 6.2.3.

21.5.2 Special Range Mission 1: IFR Cruise Mission

GA aircraft intended for operation under *instrument flight rules* (IFR), must carry fuel in compliance with 14

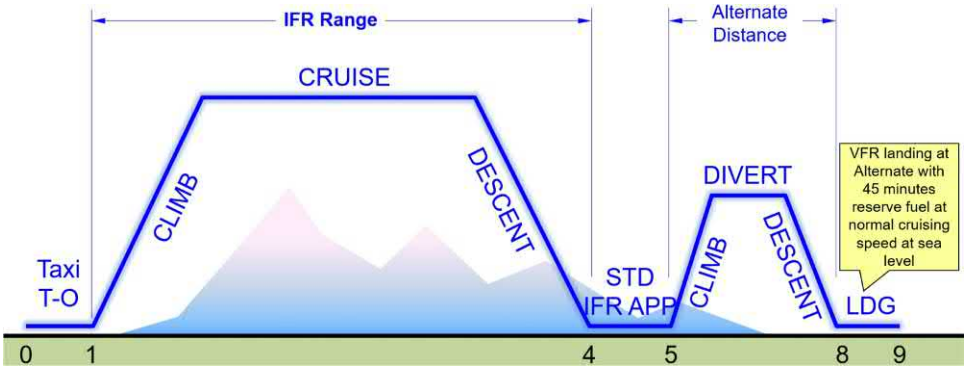


FIGURE 21-14 A schematic for an *Instrument Flight Regulation* mission for a GA aircraft.

CFR Part 91, §91.167, Fuel Requirements for Flight in IFR Conditions. The regulation is intended to prevent accidents due to fuel starvation or fuel mismanagement, but such accidents, in spite of the regulation, remain fairly common, with 75 such accidents in 2008 and 74 in 2009 in the United States alone.[1] GA aircraft operated in IFR conditions must carry fuel as stipulated below:

§91.167 Fuel Requirements for Flight in IFR Conditions

(a) No person may operate a civil aircraft in IFR conditions unless it carries enough fuel (considering weather reports and forecasts and weather conditions) to—
- **(1)** Complete the flight to the first airport of intended landing;
- **(2)** Except as provided in paragraph (b) of this section, fly from that airport to the alternate airport; and
- **(3)** Fly after that for 45 min at normal cruising speed or, for helicopters, fly after that for 30 min at normal cruising speed.

(b) Paragraph (a)(2) of this section does not apply if:
- **(1)** Part 97 of this chapter prescribes a standard instrument approach procedure to, or a special instrument approach procedure has been issued by the Administrator to the operator for, the first airport of intended landing; and
- **(2)** Appropriate weather reports or weather forecasts, or a combination of them, indicate the following:
  - (i) For aircraft other than helicopters. For at least 1 h before and for 1 h after the estimated time of arrival, the ceiling will be at least 2000 ft above the airport elevation and the visibility will be at least 3 statute miles.
  - (ii) For helicopters. At the estimated time of arrival and for 1 h after the estimated time of arrival, the ceiling will be at least 1000 ft above the airport elevation, or at least 400 ft above the lowest applicable approach minima, whichever is higher, and the visibility will be at least 2 statute miles.

The paragraph requires the operator of the aircraft to carry enough fuel to complete the flight to the initial airport, then fly from that airport to the alternate airport (if one is required) and, then fly for 45 min (30 min for helicopters) at normal cruising speed.[2] In short, this includes fuel to the destination plus fuel to the alternate plus fuel for 45 min of additional flying. It is important to be mindful of such regulatory "curveballs" so that the range (or size of fuel tanks) will not be underestimated. The author can attest to students of engineering completely overlooking this step.

A schematic of an IFR flight profile is shown in Figure 21-14. The term "STD IFR APP" stands for Standard IFR Approach. Even though such flight planning is the responsibility of the operator, the designer should prepare range estimation for comparison with other aircraft by assuming a 100 or 200 nm diverted flight to an alternative, depending on the size of the aircraft. This will shed brighter light on the utility of the new design.

21.5.3 Special Range Mission 2: NBAA Cruise Mission

The *National Business Aviation Association* (NBAA) is an organization of people who try to promote and expand the use of General Aviation aircraft for business purposes globally.[3] It was founded in 1947 and has its headquarters in Washington, DC. According to its Statement of Purpose, the organization represents more than 8000 companies and organizes the world's largest aviation trades show; the NBAA Annual Meeting & Convention. When comes to the concept of range, NBAA has promoted a special range profile that carries its name. A schematic of this profile is provided in

[1] The Nall Report 2010, Air Safety Foundation, p. 17.

[2] For instance, see: InFO 08004, Federal Aviation Administration, 02/07/2008.

[3] See http://www.nbaa.org/about/

Figure 21-15. This profile is typically used in the marketing of business aircraft.

21.5.4 Payload-Range Sensitivity Study

It is helpful, when not necessary, to conduct a *payload-range sensitivity* study to help evaluate how payload affects the range of the aircraft. Most aircraft have issues with the combination of fuel and occupant loading. This is manifested in full-fuel-tanks and all-seats-occupied busting the max gross weight limit. This requires reduced fuel weight when flying with full occupancy and this reduces range significantly.

Figure 21-16 illustrates the problem using a hypothetical, single-pilot operated, ten-seat turboprop commuter of a maximum gross weight of 7500 lb_f. Assume the airplane is designed to carry 2000 lb_f of Jet A-1, giving it a

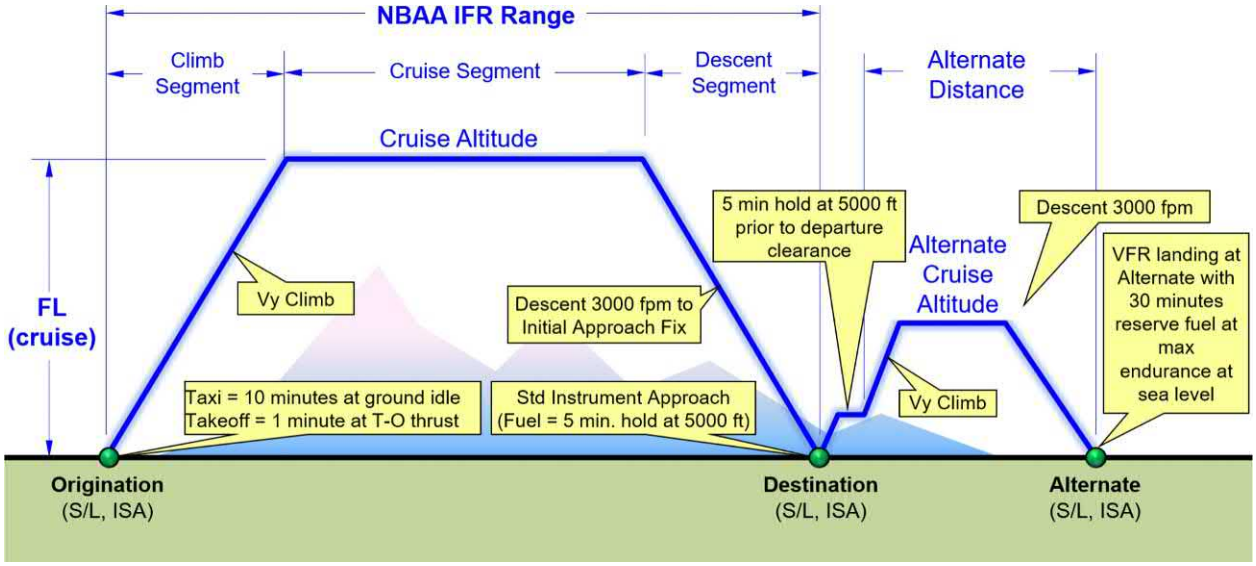


FIGURE 21-15 A schematic for an NBAA mission for a Part 23 Business aircraft.

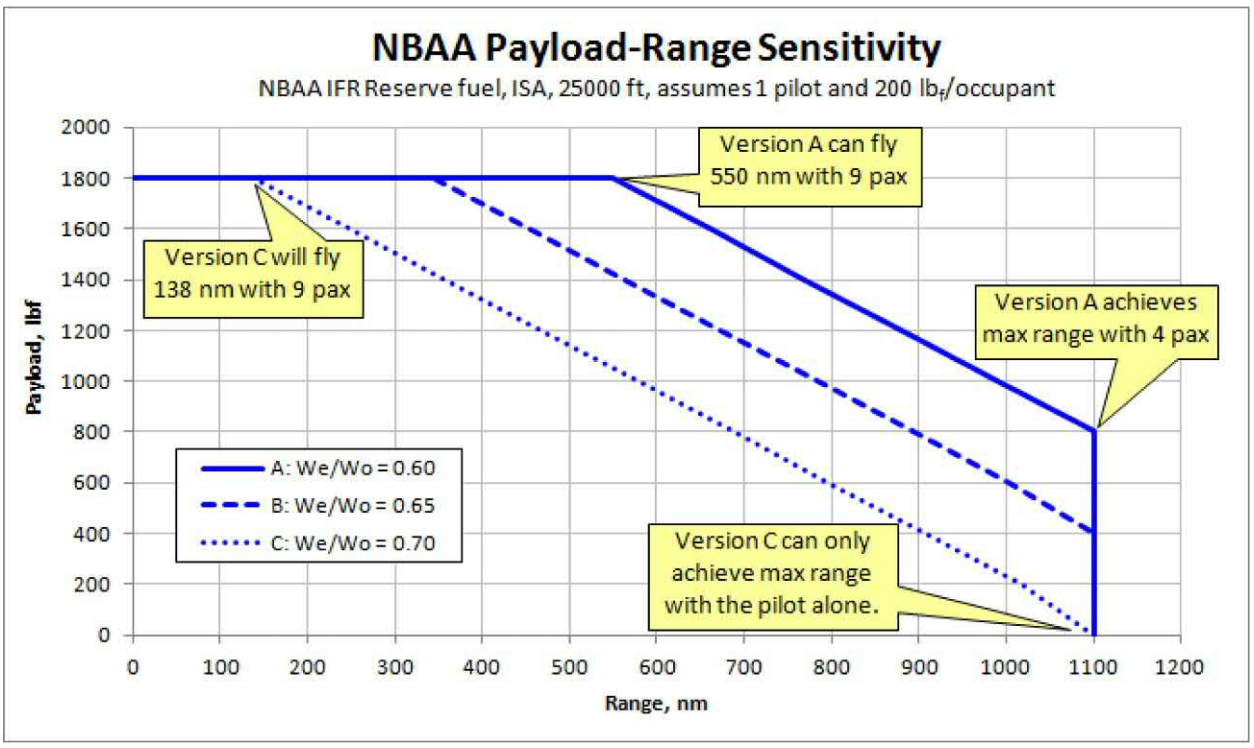


FIGURE 21-16 An NBAA payload-range sensitivity plot for a hypothetical 10-seat commuter design.

TABLE 21-4 Example of payload-range analysis.

Gross weight, lb_f	$W_0 =$	7500
Max fuel weight, lb_f	$W_f =$	2000
Weight of occupant, lb_f	$W_{occupant} =$	200

			VERSION A			VERSION B			VERSION C		
Empty weight ratio		$W_e/W_0 =$	0.6			0.65			0.7		
Empty weight, lb_f		$W_e =$	4500			4875			5250		
Passengers	Pilot	Payload, lb_f	Fuel, lb_f	Gross, lb_f	Range, nm	Fuel, lb_f	Gross, lb_f	Range, nm	Fuel, lb_f	Gross, lb_f	Range, nm
0	1	0	2000	6700	1100	2000	7075	1100	2000	7450	1100
1	1	200	2000	6900	1100	2000	7275	1100	1850	7500	1018
2	1	400	2000	7100	1100	2000	7475	1100	1650	7500	908
3	1	600	2000	7300	1100	1825	7500	1004	1450	7500	798
4	1	800	2000	7500	1100	1625	7500	894	1250	7500	688
5	1	1000	1800	7500	990	1425	7500	784	1050	7500	578
6	1	1200	1600	7500	880	1225	7500	674	850	7500	468
7	1	1400	1400	7500	770	1025	7500	564	650	7500	358
8	1	1600	1200	7500	660	825	7500	454	450	7500	248
9	1	1800	1000	7500	550	625	7500	344	250	7500	138

range of 1100 nm. This means that given any combination of fuel, passengers, and baggage, the airplane shall not exceed 7500 lb_f at the start of the T-O run. Furthermore, assume that based on historical data, it is expected an empty weight ratio of 0.6 can be achieved. This corresponds to an empty weight of 4500 lb_f and useful load of 7500–4500 = 3000 lb_f. Assuming each occupant weighs 200 lb_f, including baggage, it is easy to see that, with 10 people onboard, the airplane weighs $4500 + 10 \times 200 = 6500$ lb_f; this corresponds to a payload of 9 people (the pilot is not a part of the payload) or 1800 lb_f. Therefore, the pilot can only add 1000 lb_f of fuel. Thus, the full tank range of 1100 nm is not possible. For simplicity, assume the aircraft can achieve a range of 0.55 nm/lb_f of fuel.

Results for other payloads are presented in Table 21-4 (and graphically in Figure 21-16). It is intended to help with the preparation of such sensitivity graphs. It not only displays how range is affected by payload, but also how detrimental it may be if the desired empty weight ratio is not met. Payload-range sensitivity studies are very helpful when evaluating new aircraft designs and clearly highlights the importance of achieving the design empty-weight ratio.

Table 21-4 presents the payload-range sensitivity for three empty weight ratios; 0.60, 0.65, and 0.70, designated as Versions A, B, and C, respectively. Version A can carry four passengers and pilot 1100 nm, but only 550 nm with nine passengers onboard. However, if the $W_e/W_0 = 0.60$ is not met and, say, it ends up being 0.65 (Version B), the airplane will be much less competitive as it can only fly 1100 nm with two passengers onboard. If $W_e/W_0 = 0.70$ (Version C), the market prospects of the resulting aircraft may be catastrophic. This highlights its sensitivity to deviations from the target empty weight ratio.

EXERCISES

(1) You have been asked to design a single-engine, turbofan-powered research aircraft that, on a no-wind standard day, is capable of an 800 nm loiter range. The loitering segment will begin at an initial altitude of 20,000 ft and requires a constant airspeed of 250 KTAS to be maintained. The research equipment on board must be calibrated at the beginning of the segment, after which the autopilot is programmed to maintain constant attitude of the aircraft with respect to the ground. The SFC of the turbofan is 0.6 $lb_f/h/lb_f$, wing area is 350 ft^2, and the weight at the start of cruise is 15,000 lb_f. The average fuel consumption of the engine during the loitering segment is 115 gal/h of Jet-A. If you are considering a configuration featuring a straight tapered wing with an AR of 10, estimate (a) the highest value the minimum drag coefficient, $C_{D_{min}}$, can take and still meet the range requirement. (b) Also, estimate thrust required at the start of cruise. Assume the simplified drag model applies.

Ans: (a) $C_{D_{min}} = 0.0295$, (b) $T = 1403$ lb_f.

References

[1] L.R. Huber, *Super Highways*, Boeing Magazine, May 1946.
[2] C.D. Perkins, R.E. Hage, *Airplane Performance, Stability, and Control*, John Wiley & Sons, 1949.
[3] E. Torenbeek, *Synthesis of Subsonic Aircraft Design*, 3rd ed., Delft University Press, 1986.
[4] L. Nicolai, *Fundamentals of Aircraft Design*, 2nd ed., (1984).
[5] J. Roskam, C.-T.E. Lan, *Airplane Aerodynamics and Performance*, DARcorporation, 1997.

[6] F.J. Hale, *Aircraft Performance, Selection, and Design*, John Wiley & Sons, 1984, pp. 137–138.
[7] J.D. Anderson Jr., *Aircraft Performance & Design*, 1st ed., McGraw-Hill, 1998.
[8] A. Miele, *Flight Mechanics – Theory of Flight Paths*, Dover Publications, 1990.
[9] E. Torenbeek, *Optimum Cruise Performance of Subsonic Transport Aircraft*, 3rd ed., Delft University Press, 1998.
[10] M. Hepperle, *Electric Flight – Potential and Limitations, NATO Technical Paper STO-MP-AVT-209*, Energy Efficient Technologies and Concepts Operation, Lisbon, 2012. October 22–24.
[11] D.F. Finger, *Methodology for Multidisciplinary Aircraft Design under Consideration of Hybrid-Electric Propulsion Technology*, Ph.D. Dissertation, RMIT University, September 2020.

This page intentionally left blank

CHAPTER

22

Performance—Descent

OUTLINE

22.1 **Introduction** 893
22.1.1 The Content of This Chapter 893
22.1.2 What Analyses Must I Do? 894

22.2 **Fundamental Relations for the Descent Maneuver** 894
22.2.1 General Equations-of-Motion for Descent 894

22.3 **General Descent Analysis Methods** 895
22.3.1 General Angle-of-Descent 895
22.3.2 General Rate-of-Descent 896
22.3.3 Equilibrium Glide Speed 897
22.3.4 Sink Rate 898
22.3.5 Airspeed of Minimum Sink Rate, V_{BA} 898
22.3.6 Minimum Angle of Descent 898
22.3.7 Best Glide Speed, V_{BG} 899
22.3.8 Glide Distance 899

22.4 **Sailplane Glide Performance** 900
22.4.1 Sailplane Fundamentals 900
22.4.2 Sailplane Glide Performance 902
22.4.3 The Speed Polar 904
22.4.4 Speeds-to-Fly 907
22.4.5 Circling Flight 911

References 914

22.1 INTRODUCTION

For powered flight, the analysis of gliding flight is essential from the standpoint of safety and efficiency. For unpowered flight, glide performance sets one sailplane apart from another. But there are oddities too. While we prefer large glide ratio (L/D ratio) for improved range, surprisingly, this may cause a problem—during landing. For instance, a powered airplane with a high glide ratio is very favorable if it experiences engine failure and must rely on this characteristic to reach the nearest emergency landing site. However, the high L/D ratio will actually make it harder to land as it would have to fly at a very shallow approach path angle to keep the airspeed low. The shallow angle not only makes it challenging to assess the point of touch-down, it promotes the airplane floating in ground effect, compounding the difficulty. Figure 22-1 shows an organizational map displaying the descent among other topics of performance theory.

This chapter presents the formulation of and the solution of the equation-of-motion for the descent and present practical as well as numerical solution methodologies that can be used both for propeller and jet-powered aircraft. When appropriate, each method will be accompanied by a derivation and an illustrative example using the sample aircraft. The primary information we want to extract from this analysis is characteristics like minimum rate-of-descent (*ROD*), best (lowest) angle-of-descent (*AOD*), the corresponding airspeeds, the *AOD* for a given power setting, and unpowered glide distance.

In general, the methods presented in here are "industry standard" and mirror that presented by a variety of authors, e.g., Perkins and Hage [1], Torenbeek [2], Nicolai [3], Roskam [4], Hale [5], Anderson [6], and Miele [7], to name a few.

22.1.1 The Content of This Chapter

- Section 22.2 develops fundamental relationships necessary to evaluate the characteristics of gliding flight, most importantly the equations-of-motion for descending flight.
- Section 22.3 presents an assortment of methods to predict the various descent characteristics of an airplane.
- Section 22.3 presents sailplane glide performance, including optimal glide speeds in head- and tailwind, and up- and downdrafts. It also discusses performance of circling flight inside thermals.

https://doi.org/10.1016/B978-0-12-818465-3.00022-7

Copyright © 2022 Elsevier Inc. All rights reserved.

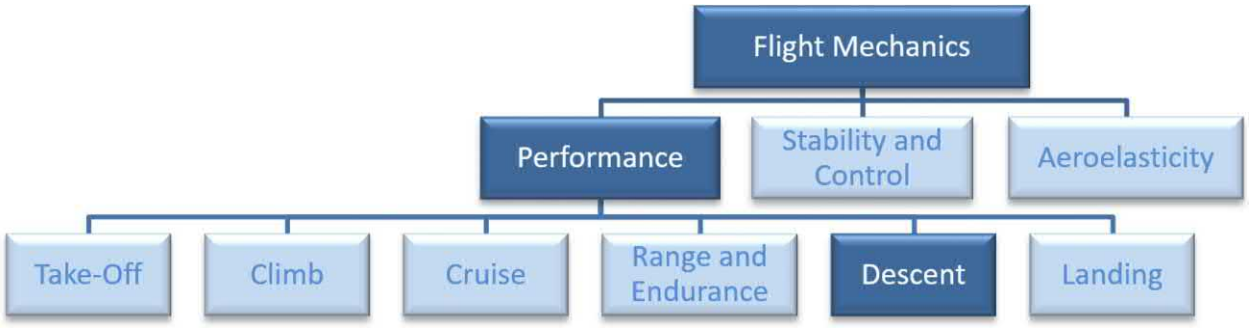


FIGURE 22-1 An organizational map placing performance theory among the disciplines of *Flight Mechanics*, and highlighting the focus of this chapter; descent performance analysis.

TABLE 22-1 Task list based on 14 CFR Part 23.

Paragraphs	Content	Section
14 CFR §23.2620[a]	Information for airplane flight manual	22.3
14 CFR §23.33(b)(1)	Throttle-closed glide at V_{NE}	22.3
14 CFR §23.71	Glide: Single-engine airplanes	22.3
14 CFR §23.145(d)	Glide in landing configuration landing	22.3
14 CFR §23.1001(b)(1)	Glide and fuel jettisoning systems	22.3
14 CFR §23.1585(b)	Glide following engine failure	22.3
14 CFR §23.1587(c)(6)	Performance information regarding glide	22.3

[a] *"New" Part 23.*

TABLE 22-2 Task list for descent analysis.

Task name	Terms	Section
Minimum sink rate	$V_{V\min}$	22.3.2
Airspeed of minimum sink rate	V_{BA}	22.3.5
Airspeed of minimum angle-of-descent	V_{BG}	22.3.7
Minimum angle-of-descent	$\gamma_{\min}$	22.3.6
Glide range for various altitudes	R_{glide}	22.3.8
Glide performance sensitivities		22.3
Sailplane glide performance		22.4
Speed (Flight) Polar		22.4.3

22.1.2 What Analyses Must I Do?

For the newcomer to descent analysis, the burning question is: "What am I supposed to estimate and how do I conduct those estimations?" In short, such analyses evaluate the descent characteristics of the airplane. This includes optimal characteristics, such as the lowest rate- and angle-of-descent, and their corresponding airspeeds. The results are then compared to the pertinent requirements, answering if the aircraft will meet them. This chapter can be split into three sections: Introduction, tools of the trade, and analyses. Tables 22-1 and 22-2 list the necessary tasks you should complete.

22.2 FUNDAMENTAL RELATIONS FOR THE DESCENT MANEUVER

This section presents a derivation of the equation-of-motion for the descent maneuver, as well as all fundamental relationships used to evaluate its most important characteristics. First, a general 2-dimensional free body diagram will be presented to allow the formulation to be developed. Only the 2-dimensional version of the equation will be developed as this is sufficient for all aspects of aircraft design.

22.2.1 General Equations-of-Motion for Descent

The equations-of-motion for an aircraft in the horizontal and vertical planes were developed in Section 17.1.2, *Equations-of-Motion for Performance Theory*. These are presented as Miele's set of Equation (17-1). It is recommended the reader reviews these. Also review Figure 17-1. This set of equations is adapted to descent as Equation (22-1). The transformation assumes (1) the thrust angle $\varepsilon = 0$, (2) the descent is conducted at constant airspeed, V_∞, so the time derivative terms are zero, and (3) constant flight path angle, $\gamma < 0$. Furthermore, let $W = mg$. This reduces Equation (17-1) as shown below

$$\begin{aligned} \dot{x} - V_\infty \cos\gamma &= 0 \\ \dot{h} - V_\infty \sin\gamma &= 0 \\ T\cos\varepsilon - D - m\left(g\sin\gamma + \dot{V}_\infty\right) &= 0 \\ T\sin\varepsilon + L - m(g\cos\gamma + V_\infty\dot{\gamma}) &= 0 \\ \dot{m}g + c_t T &= 0 \end{aligned} \quad \Rightarrow \quad \begin{aligned} \dot{x} - V_\infty \cos\gamma &= 0 \\ \dot{h} - V_\infty \sin\gamma &= 0 \\ T - D + W\sin\gamma &= 0 \\ L - W\cos\gamma &= 0 \\ \dot{W} + c_t T &= 0 \end{aligned} \tag{22-1}$$

(1) Equations-of-Motion for Powered Descent

Equation (22-1) for steady-powered descent is obtained by summing forces along the *t*- and *n*-axes (see Figure 17-1).

$$T - D + W\sin\gamma = 0 \Rightarrow D = T + W\sin\gamma \tag{22-2}$$

$$L - W\cos\gamma = 0 \Rightarrow L = W\cos\gamma \tag{22-3}$$

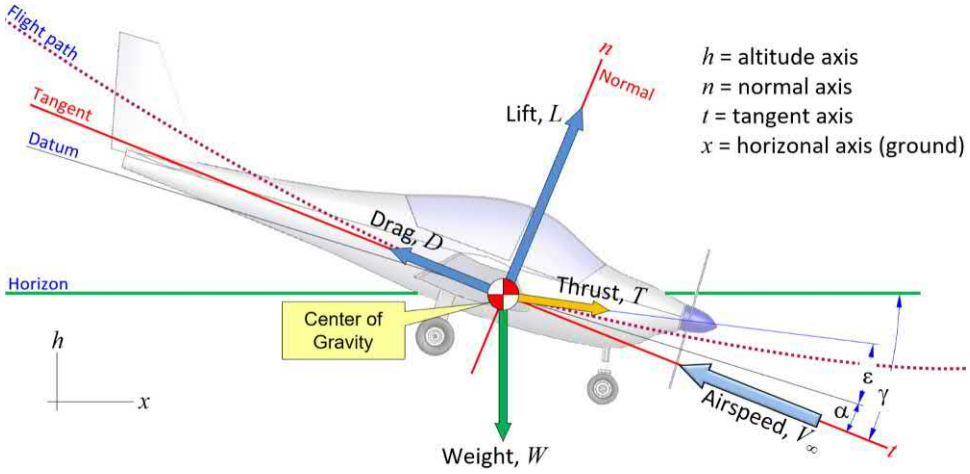


FIGURE 22-2 Free body for the airplane during descent (moments omitted, but add up to zero).

Note that the angle-of-descent (AOD), γ, is a negative value for descent (positive for climb). AOD is also known as a*ngle-of-glide* (AOG) or *glide angle*.

(2) Equations-of-Motion for Unpowered Descent

For steady, unpowered descent (glide), Equation (22-1) becomes

$$D = W\sin\gamma \tag{22-4}$$

$$L = W\cos\gamma \tag{22-5}$$

Since $\gamma < 0$ for descent the minus indicates the drag force is in an opposite direction to W sin γ (see Figure 22-2). Equation (22-5) shows that, as for the climb maneuver, in descent, lift is less than the weight. The lift coefficient at this condition is

$$C_L = \frac{2W\cos\gamma}{\rho V^2 S} = \frac{W}{qS}\cos\gamma \tag{22-6}$$

(3) Drag During Descent

Drag during descent is obtained identically as that for climb. It was shown in Section 19.2.1(3) as Equations (19-10) for the adjusted drag model and (19-11) for the simplified drag model.

(4) Horizontal and Vertical Airspeed

As done for the climb maneuver, we specify the *Horizontal Airspeed*. It is important when estimating the horizontal distance covered during a long glide:

$$\dot{x} \equiv V_H = V_\infty \cos\gamma \tag{22-7}$$

We also define the *Vertical Airspeed*, also called the *rate-of-descent* (ROD) as follows:

$$\dot{h} \equiv V_V = V_\infty \sin\gamma \tag{22-8}$$

Both velocity components can be derived by observation using Figure 22-3. Note that while the airspeeds in Figure 22-3 are true airspeeds, in terms of calibrated airspeed, V_∞ is the airspeed indicated on the airspeed indicator, V_V

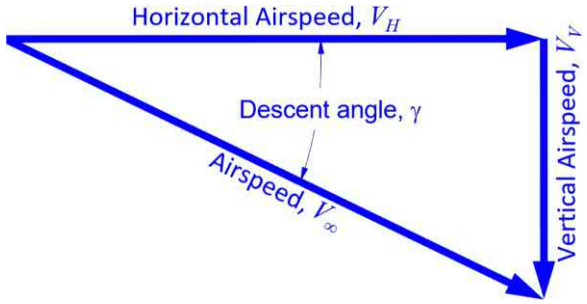


FIGURE 22-3 Airspeed components during descent.

is observed on the *vertical speed indicator* (VSI, it is a true airspeed), and V_H is the ground speed. Note that this V_H should not be confused with the maximum level airspeed discussed in Chapter 20.

22.3 GENERAL DESCENT ANALYSIS METHODS

This section utilizes the equation-of-motion for descent to evaluate the descent characteristics of a new aircraft design. Several methods to estimate the most important descent properties are introduced. These methods primarily include the simplified and adjusted drag models ($C_{L_{minD}} \neq 0$). For an insight into the quality of analysis these models provide, see Bullet (11) of Section 20.2.2, *Fundamental Concepts*.

22.3.1 General Angle-of-Descent

The angle-of-descent is the flight path angle to the horizontal and is computed from:

$$\text{Powered descent:}\quad \sin\gamma = \frac{D}{W} - \frac{T}{W} \approx \frac{1}{L/D} - \frac{T}{W} \tag{22-9}$$

$$\text{Unpowered descent:}\quad \tan\gamma = \frac{D}{L} = \frac{1}{L/D} \approx \frac{D}{W} \tag{22-10}$$

The right approximations (≈) are valid for low AOD, γ, provided the CG is not too far forward. Forward CG loads up the stabilizing surface and invalidates the approximation $L \approx W$. Many airplanes, in particular sailplanes, have high glide ratios that makes the landing challenging. Such aircraft are equipped with speed-brakes or spoilers, which are panels that deflect from the wing surface (see Figure 16-64) and cause flow separation, increasing drag and reducing lift. The same holds for high-speed jets.

DERIVATION OF EQUATION (22-10) AND (22-9)

We get Equation (22-9) From Equation (22-2):

$$D = T + W\sin\gamma \Leftrightarrow \sin\gamma = \frac{D-T}{W} = \frac{D}{W} - \frac{T}{W}$$

We get Equation (22-10) by dividing Equation (22-4) by Equation (22-5):

$$\frac{D}{L} = \frac{W\sin\gamma}{W\cos\gamma} = \tan\gamma$$

22.3.2 General Rate-of-Descent

The rate at which an aircraft reduces altitude is given below:

$$V_V = \frac{DV_\infty}{W} = \frac{V_\infty}{(C_L/C_D)} \tag{22-11}$$

The above expression returns vertical speed in units of ft/s or m/s. Generally, the units preferred by pilots are in terms of feet per minute or fpm for General Aviation, Commercial Aviation, and Military, but m/s for sailplanes and many nations that use the metric system. To convert Equation (22-11) into units of fpm multiply by 60. This expression is often presented with a minus-sign to indicate descent.

DERIVATION OF EQUATION (22-11)

Begin by multiplying Equation (22-4) by V_∞. Then rewrite $V_\infty \sin\gamma$ using Equation (22-8):

$$D = W\sin\gamma \quad \text{and} \quad V_V = V_\infty \sin\gamma$$
$$\Rightarrow DV_\infty = WV_\infty \sin\gamma = WV_V \Leftrightarrow V_V = \frac{DV_\infty}{W}$$

EXAMPLE 22-1

Plot the rate of descent for the Learjet 45 at S-L, 15,000 ft, and 30,000 ft at a weight of 20,000 lb_f assuming no thrust and the simplified drag model. Plot the descent rate as a function of true airspeed in knots (KTAS).

SOLUTION:

Sample calculation for the sample aircraft gliding at 175 KCAS (LD_{max}) at S-L and at 20,000 lb_f (no thrust).

$$LD_{max} = 1/\sqrt{4kC_{D_{min}}} = 1/\sqrt{4(0.05236)(0.0200)} = 15.45$$
$$D = W/LD_{max} = 20{,}000/15.45 = 1294\,lb_f$$

At S-L the density is 0.002378 slugs/ft^3. Therefore:

$$V_V = DV_\infty/W = (1294)(175 \times 1.688)/20{,}000 = 19.1\,ft/s$$

This amounts to 1147 fpm. The Rate-of-Descent for other airspeeds is plotted in the *flight polar* of Figure 22-4. Figure 22-5 shows the corresponding glide angle and L/D for the aircraft at S-L. Figure 22-6 shows how important performance characteristics, such as the airspeed for minimum power required and best glide ratio can be extracted from the rate-of-descent plot.

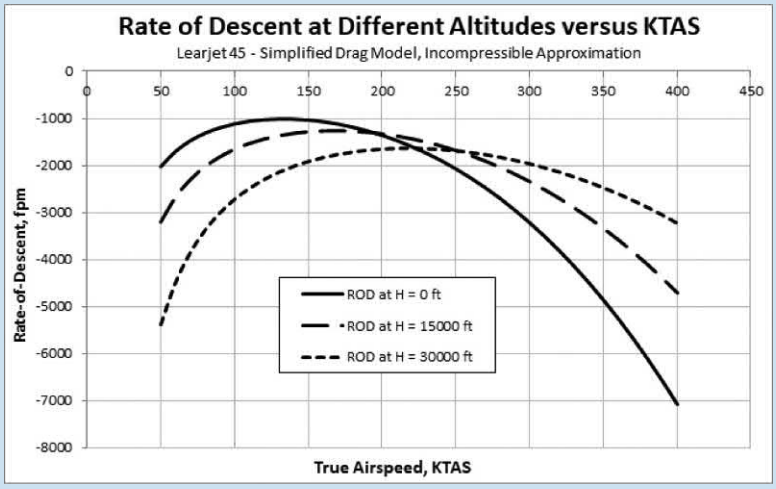


FIGURE 22-4 A *flight polar*, also known as *ROD* vs Airspeed graph.

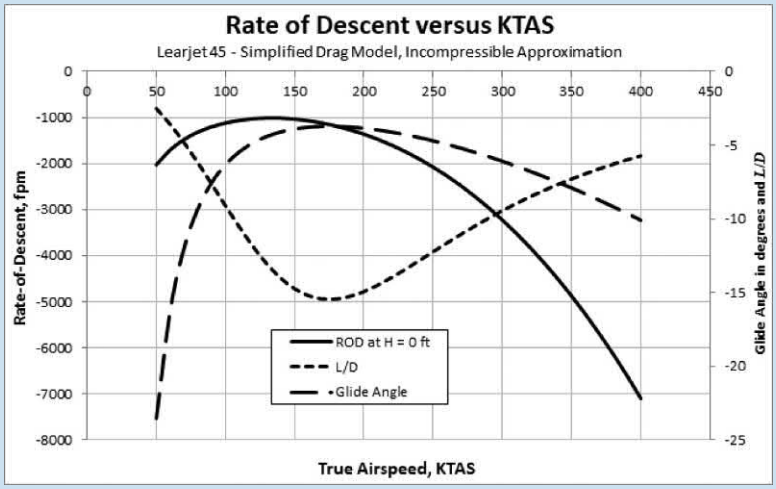


FIGURE 22-5 *ROD*, *L/D*, and glide angle superimposed on the same graph (at S-L).

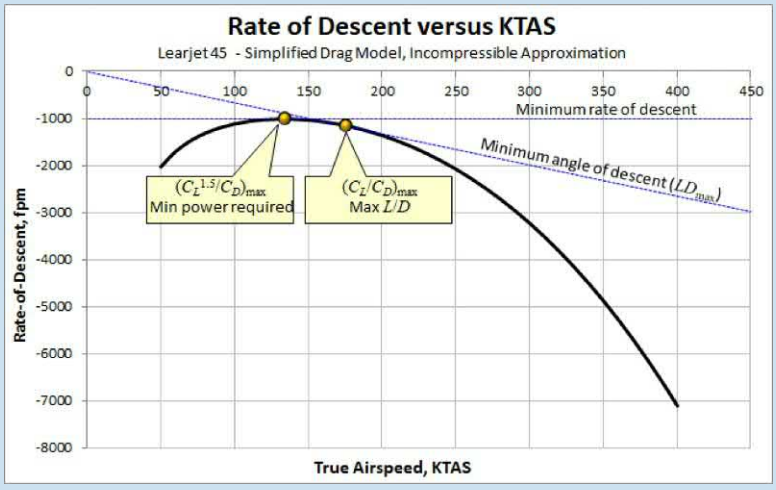


FIGURE 22-6 Important characteristics extracted from the flight polar (at S-L).

22.3.3 Equilibrium Glide Speed

Equilibrium glide speed is the airspeed that must be maintained to achieve a specific glide angle given some specific AOA. A common use is to determine the airspeed required to maintain a specific flight path angle, γ.

$$V_\infty = \sqrt{\frac{2\cos\gamma}{\rho C_L}\left(\frac{W}{S}\right)} \tag{22-12}$$

The lift coefficient can be determined based on the AOA required for the airspeed using $C_L = C_{L0} + C_{L\alpha}\cdot\alpha$.

EXAMPLE 22-2

During flight testing, the pilot of a test aircraft wants to maintain a 3-degree glide path angle at $\alpha = 5°$. What airspeed must be maintained? Assume a test wing loading of 22.4 lb_f/ft^2, ISA at S-L conditions, $C_{L0} = 0.4$ and $C_{L\alpha} = 5.5/\text{rad}$.

SOLUTION:

Lift coefficient: $C_L = C_{L_0} + C_{L_\alpha}\cdot\alpha$

$$= 0.4 + 5.5 \times \left(\frac{5\times\pi}{180°}\right) = 0.8800$$

EXAMPLE 22-2 *(cont'd)*

We can now compute the airspeed necessary to maintain the said glide path angle:

$$V_\infty = \sqrt{\frac{2\cos\gamma}{\rho C_L}\left(\frac{W}{S}\right)} = \sqrt{\frac{2\cos(5°)}{(0.002378)(0.8800)}} \quad (22.4)$$

$$= 146 \text{ ft/s} = 86.6 \text{ KTAS}$$

DERIVATION OF EQUATION (22-12)

From Equation (22-5) we get:

$$L = W\cos\gamma \Leftrightarrow \frac{1}{2}\rho V_\infty^2 S C_L = W\cos\gamma$$

$$\Leftrightarrow V_\infty = \sqrt{\frac{2\cos\gamma}{\rho C_L}\left(\frac{W}{S}\right)}$$

22.3.4 Sink Rate

Sink rate is the rate at which an aircraft descends. This is most commonly expressed in terms of ft/min or m/s. If the lift and drag coefficients can be determined for a specific glide condition (e.g., from knowing the AOA), the sink rate can be computed from:

Straight and level sink:

$$V_V = \sqrt{\frac{2}{\rho}\left(\frac{W}{S}\right)\frac{1}{(C_L^3/C_D^2)}} = \frac{C_D}{C_L^{3/2}}\sqrt{\frac{2}{\rho}\left(\frac{W}{S}\right)} \quad (22\text{-}13)$$

The above expression will return the sink rate in terms of ft/s or m/s. To convert to fpm multiply by 60. If the airplane is turning while banking at angle ϕ, then the sink rate increases and amounts to:

Sink rate at bank angle ϕ:

$$V_V = \sqrt{\frac{2}{\rho\left((C_L\cos\phi)^3/C_D^2\right)}\left(\frac{W}{S}\right)} = \frac{C_D}{C_L^{3/2}\cos^{3/2}\phi}\sqrt{\frac{2}{\rho}\left(\frac{W}{S}\right)} \quad (22\text{-}14)$$

DERIVATION OF EQUATIONS (22-13) AND (22-14)

Substitute Equation (22-12) into Equation (22-8) to get:

$$V_V = V_\infty \sin\gamma = \sqrt{\frac{2\cos\gamma}{\rho C_L}\left(\frac{W}{S}\right)}\sin\gamma \quad \text{(i)}$$

Divide Equation (22-4) by Equation (22-5) to get:

$$\frac{W\sin\gamma}{W\cos\gamma} = \frac{D}{L} \Leftrightarrow \sin\gamma = \frac{D}{L}\cos\gamma = \frac{C_D}{C_L}\cos\gamma \quad \text{(ii)}$$

Substitute Equation (ii) into Equation (i) to get:

$$V_V = \sqrt{\frac{2\cos\gamma}{\rho C_L}\left(\frac{W}{S}\right)}\sin\gamma = \sqrt{\frac{2\cos\gamma}{\rho C_L}\left(\frac{W}{S}\right)}\left(\frac{C_D}{C_L}\cos\gamma\right)$$

$$= \sqrt{\frac{2}{\rho}\left(\frac{W}{S}\right)\frac{\cos^3\gamma}{(C_L^3/C_D^2)}}$$

If we assume $\cos\gamma \approx 1$ we get Equation (22-13).

To get Equation (22-14) we refer to Figure 20-16 and see that $W = L\cdot\cos\phi = qS\cdot C_L\cdot\cos\phi$. When level ($\phi = 0°$) the same relationship is $W = L = qS\cdot C_L$. This shows that lift depends on the product $C_L\cdot\cos\phi$. Therefore, it is more accurate to replace the lift coefficient in the above formulation with the product.

22.3.5 Airspeed of Minimum Sink Rate, V_{BA}

Just like rate-of-climb, the sink rate varies with airspeed. It too has a minimum value that is of interest to the operator of the vehicle. This is because the kinetic energy of the vertical speed also has a minimum that may affect survivability in an unpowered glide (as impact energy is a function of the square of the speed). If the simplified drag model applies, the minimum sink speed is given by

$$V_{BA} = V_{E_{max}} = \sqrt{\frac{2}{\rho}\left(\frac{W}{S}\right)\sqrt{\frac{k}{3C_{D_{min}}}}} \quad (22\text{-}15)$$

Note that this only holds in air mass that is neither rising nor sinking.

DERIVATION OF EQUATION (22-15)

Inspection of Equation (22-13) reveals that when $C_L^{1.5}/C_D$ is maximum, V_V is minimum. The airspeed at which this takes place has already been derived as Equation (20-45).

22.3.6 Minimum Angle of Descent

This angle results in a maximum glide distance from a given altitude and is of great importance to both glider pilots as well as pilots of powered aircraft.

$$\tan\gamma_{min} = \frac{1}{LD_{max}} = \sqrt{4kC_{D_{min}}} \quad (22\text{-}16)$$

Note that the drag model yields a γ_{min} that is independent of altitude.

EXAMPLE 22-3

Determine the minimum angle of descent for the Learjet 45 flying at S-L at a weight of 20,000 lb_f.

SOLUTION:

$$\tan\gamma_{min} = \frac{1}{LD_{max}} = \sqrt{4kC_{D_{min}}} = \sqrt{4(0.05236)(0.0200)}$$
$$= 0.06472 \text{ rad}$$

This amounts to 3.7°.

DERIVATION OF EQUATION (22-16)

Equation (20-33) gives the maximum lift to drag ratio for the simplified drag model (repeated below for convenience) and is substituted into Equation (22-10):

$$LD_{max} = \frac{1}{\sqrt{4kC_{D_{min}}}}$$

22.3.7 Best Glide Speed, V_{BG}

The best glide speed is the airspeed at which the airplane will achieve maximum range in glide. It is considered a matter of survival for the occupants of an aircraft, as evident from its inclusion in 14 CFR§23.1587(c)(6), *Performance information*. A part of pilot training requires this airspeed to be remembered in case of an engine failure. It can be calculated using Equation (22-17) below:

$$V_{BG} = V_{LD\max} = \sqrt{\frac{2}{\rho}\left(\frac{W}{S}\right)\sqrt{\frac{k}{C_{D_{min}}}}} \qquad (22\text{-}17)$$

Note that this expression only holds in air mass that is neither rising nor sinking.

DERIVATION OF EQUATION (22-17)

Using Equation (22-12) and the assumption that at the best glide angle $\cos\gamma \approx 1$, we get:

$$V_\infty = \sqrt{\frac{2\cos\gamma}{\rho C_L}\left(\frac{W}{S}\right)} \Rightarrow V_\infty = \sqrt{\frac{2}{\rho C_L}\left(\frac{W}{S}\right)}$$

It was demonstrated in the derivation for Equation (20-35) that at LD_{max} the lift coefficient:$C_L = \sqrt{C_{D_{min}}/k}$. Substituting it into the above expression and manipulating leads to:

$$V_\infty = \sqrt{\frac{2}{\rho C_L}\left(\frac{W}{S}\right)} = \sqrt{\frac{2}{\rho\sqrt{\frac{C_{D_{min}}}{k}}}\left(\frac{W}{S}\right)} = \sqrt{\frac{2}{\rho}\left(\frac{W}{S}\right)\sqrt{\frac{k}{C_{D_{min}}}}}$$

EXAMPLE 22-4

Determine the airspeed of minimum angle-of-descent for the Learjet 45 flying at 30,000 ft and S-L at a weight of 20,000 lb_f.

SOLUTION:

At 30,000 ft the density is 0.0008897 slugs/ft^3. Therefore:

$$V_{LD\max} = \sqrt{\frac{2}{\rho}\left(\frac{W}{S}\right)\sqrt{\frac{k}{C_{D_{min}}}}}$$
$$= \sqrt{\frac{2}{0.0008897}\left(\frac{20{,}000}{311.6}\right)\sqrt{\frac{0.05236}{0.0200}}}$$
$$= 483.2 \text{ ft/s} \quad (\approx 286 \text{ KTAS})$$

At S-L the density is 0.002378 slugs/ft^3. Therefore:

$$V_{LD\max} = \sqrt{\frac{2}{\rho}\left(\frac{W}{S}\right)\sqrt{\frac{k}{C_{D_{min}}}}}$$
$$= \sqrt{\frac{2}{0.002378}\left(\frac{20{,}000}{311.6}\right)\sqrt{\frac{0.05236}{0.0200}}}$$
$$= 295.5 \text{ ft/s} \quad (\approx 175 \text{ KTAS})$$

This amounts to 175 KCAS in both cases (ignoring compressibility). Ref. [8] states best glide speed for the Learjet 45 is 160 KCAS.

22.3.8 Glide Distance

For a powered airplane, knowing how far one can glide in case of an emergency is a matter of survivability. Such information is required information for the operation of GA aircraft per 14 CFR §23.1587(d)(10), *Performance Information*, and must be determined per §23.71, *Glide: Single-Engine Airplanes* (see below) and presented to the operator of the aircraft. This is typically done in the form of a glide chart, which shows clearly how far the airplane will glide for every 1000 ft lost in altitude.

> §23.71 Glide: Single-Engine Airplanes.
>
> The maximum horizontal distance traveled in still air, in nautical miles, per 1000 ft of altitude lost in a glide, and the speed necessary to achieve this must be determined with the engine inoperative, its propeller in the minimum drag position, and landing gear and wing flaps in the most favorable available position.

During the design phase, this distance can be calculated from the following expression (which is shown

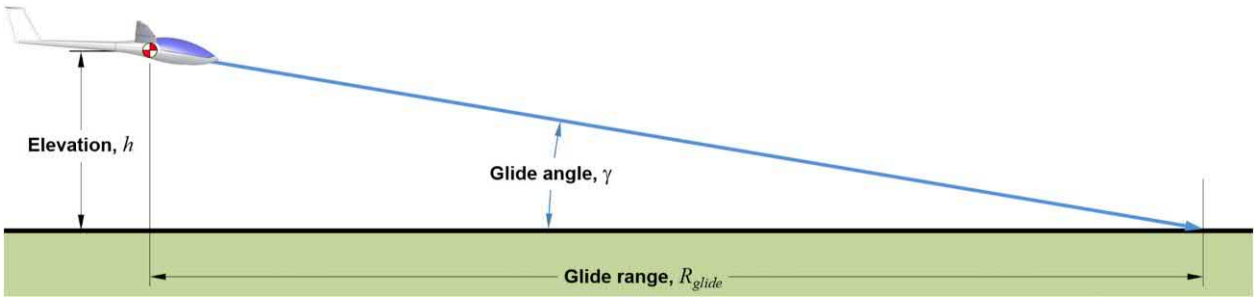


FIGURE 22-7 Distance covered during glide can be estimated using the L/D ratio.

schematically in Figure 22-7). Note that this expression only holds in air mass that is neither rising nor sinking:

$$R_{glide} = h \cdot \left(\frac{L}{D}\right) = h \cdot \left(\frac{C_L}{C_D}\right) \tag{22-18}$$

DERIVATION OF EQUATION (22-18)

First, note the following relation between the speed and distance:

$$\frac{V_V}{V_H} = \frac{h/\Delta t}{R_{glide}/\Delta t} = \frac{h}{R_{glide}}$$

Assuming that γ is small, we can say that $V_H \approx V_\infty$. Therefore, using Equation (22-11) we get:

$$V_V = \frac{DV_\infty}{W} \Rightarrow \frac{V_V}{V_\infty} = \frac{h}{R_{glide}} = \frac{D}{W}$$

Using Equation (22-3) and the assumption that for small angles $\cos\gamma \approx 1$, we get:

$$L = W\cos\theta \Rightarrow \frac{h}{R_{glide}} = \frac{D}{W} = \frac{D}{L/\cos\theta}$$
$$\Rightarrow \frac{h}{R_{glide}} = \left(\frac{D}{L}\right)\cos\theta \approx \left(\frac{D}{L}\right)$$

EXAMPLE 22-5

Determine the maximum glide distance for the Learjet 45 flying at 30,000 ft.

SOLUTION:

Using the maximum LD calculated in Example 22-1 we get ($LD_{max} = 15.45$):

$$R_{glide} = h \cdot \left(\frac{L}{D}\right)_{max} = 30{,}000 \times (15.45)$$
$$= 463{,}500\,\text{ft} \quad (\approx 76.3\,\text{nm})$$

The Learjet flight manual of Ref. [8] states that in an emergency in which both engines become inoperative, the still-air gliding distance (in cruise configuration) is approximately 2 nm per 1000 ft. This corresponds to 60 nm from 30,000 ft. Part of the discrepancy between the book values and the above analysis is caused by the increased drag due to the inoperative engines, which in this situation produce drag rather than net thrust. The value from Ref. [8] implies a $LD_{max} = 12.15$. Using Equation (16-185), this means $C_{D_{min}} = 0.0322$. If correct, the engines likely add 122 drag counts to the total, give or take.

22.4 SAILPLANE GLIDE PERFORMANCE

Flying sailplanes and gliders remains a popular past time for many people. Gliding is the oldest form of heavier-than-air flight, dating back to the days of Otto Lilienthal (1848–96) who pioneered the craft. For many, the absence of power offers unmatched simplicity and purity that allows the aviator to experience what it is to fly like the birds. However, the apparent simplicity is a veil that covers aerodynamic sophistication far superior to most GA aircraft. Any aircraft designer pondering efficient aircraft design must study sailplanes. This section presents a few important elements of glide performance. It is largely based on references such as Reichmann [9], Welch and Irving [10], Thomas [11], Stewart [12], Pajno [13], and Scull [14].

22.4.1 Sailplane Fundamentals

Figure 22-8 shows a typical modern sailplane during touch-down. No aircraft generate less drag than sailplanes; their efficiency is a marvel of modern engineering. The typical sailplane carries one to two people, with gross weight $800 < W_0 < 1800\,\text{lb}_\text{f}$ ($360 < m_0 < 815\,\text{kg}$), wingspan $35 < b < 101$ ft ($10 < b < 31$ m), wing aspect ratio $10 < AR < 51$, and wing loading from 5 to 12 $\text{lb}_\text{f}/\text{ft}^2$ (24–59 kg/m^2). Today, serious sailplanes are only fabricated using composite materials that yield the smoothest aerodynamic surfaces possible.



FIGURE 22-8 A Rolladen-Schneider LS-4 sailplane touching down using standard tail-first technique. Note the deployed spoilers on the upper surface of the wing. The sleekness of sailplanes would make them very hard to land were it not for spoilers that allow the drag to be increased temporarily during approach to landing, enabling standard approach angles to be used. *Photo by Phil Rademacher.*

The modern sailplane features a tadpole fuselage, whose forward section is shaped to sustain natural laminar boundary layer (NLF) and contracted tail-boom to minimize the wetted area subject to turbulent boundary layer [15]. The fuselage is shaped to minimize the frontal area, requiring the pilot to sit in an inclined position. More efficient sailplanes use a single piece canopy to help sustain NLF far back as possible. Many sailplanes feature a Schumann style wing and polyhedral dihedral to reduce lift-induced drag (see Sections 9.4.8, *Cranked Planforms* and 10.5.10, *The Polyhedral Wing(tip)*). The NLF wing and tail surfaces, all which feature NLF airfoils, cement its low-drag properties.

(1) Classes of Sailplanes

The mission definition of sailplanes depends on factors such as how and where it is going to be used. Is it intended for training, competition, aerobatics, and so on? Is it designed to operate in thermals or mountain waves? Sailplane design is also contingent upon the "class" for which it is intended, as defined by the Fédération Aéronautique Internationale (FAI—The World Air Sports Federation) and listed in Table 22-3.

TABLE 22-3 Classes of competition sailplanes per FAI definition.

Class name	Description
Open Class	No restrictions. Max mass is 850 kg (1875 lb_f)
Standard Class	Max wingspan 15 m (49.2 ft), no camber-changing devices, max mass is 525 kg (1159 lb_f)
15-m Class	Max wingspan 15 m (49.2 ft), camber-changing devices allowed, max mass is 525 kg (1159 lb_f)
18-m Class	Max wingspan 18 m (59.1 ft), max mass is 600 kg (1325 lb_f)
20-m Two-Seater Class	Max wingspan 20 m (65.6 ft), max mass is 750 kg (1656 lb_f)
World class	Limited class for an inexpensive class of sailplanes (see the PW-5 sailplane)
Club Class	For older and smaller gliders. Handicap system is used to level the playing field.

(2) Operation of Sailplanes

Sailplanes require proper flying techniques. Pilots must know how to position the sailplane "on tow," how to develop "feel" when searching for lift, how to get the most out of thermals, and how best to manage approach and landing, which leaves no room for error [10]. The sailplane designer must be mindful of cockpit ergonomics, in addition to other factors (performance, stability, transportation, maintenance, etc.).

Good sailplanes offer a large LD_{max}, ideally, attainable at a relatively high airspeed. A remarkably low rate-of-descent allows them to stay airborne for long periods, because even anemic atmospheric convection rises faster than their rate of descent. Sailplane pilots take advantage of four kinds of convection (or *lift*); *thermals*, *ridge lift*, *standing mountain waves*, and *convergence lift*. A thermal is a column of rising air created by ground heating. Thermals can reach altitudes as high as 18,000 ft, although 5000–6000 ft is more common. Thermals can often be identified by the cumulus clouds that reside on top of them. Ridge lift results from wind being forced over ground features, such as cliffs, mountains, and ridges. Wave lift is the consequence of oscillatory motion of air (*atmospheric gravity waves*). Convergence lift occurs when two masses of air collide, such as sea-breeze and inland air mass. Additionally, *dynamic soaring* can be employed provided certain atmospheric conditions prevail (wind shear). It is commonly performed using specialized RC sailplanes. It is utilized by many species of sea birds to travel great distances; of which the best known is the Albatross.

The current altitude record in a sailplane is 76,000 ft (23,165 m), set on September 3rd, 2018, in a specifically designed Airbus Perlan Mission II sailplane [16]. The current long-range record stands at about

1214 nm (2248 km), set by Klaus Ohlman on 2nd of December 2003, in a Schempp-Hirth Nimbus Open Class sailplane [17].

(3) Sailplane Airfoils

The modern sailplane uses NLF airfoils that sustain laminar boundary layer up to 75% chord on the upper surface and 95% chord on the lower one. Many sailplanes feature "cruise" flaps, a mechanism that allows normal flaps to be raised a few degrees, Trailing Edge Up (TEU), above neutral deflection. This shifts the drag polar toward a lower C_l. Thus, the ld_{max} is achievable at a higher airspeed, something helpful in long distance competition. A typical, single-wall NLF drag polar and l/d graph for a modern sailplane airfoil is shown in Figure 22-9. The unconventional shape of the l/d curve is evident.

(4) The Importance of Minimizing Drag

Figure 22-10 illustrates the importance of NLF on a hypothetical sailplane. The shape of the drag polar and L/D curve is classic for all NLF airfoils that feature a distinct two-wall drag bucket, including the double peak shape of the L/D curve (e.g., most NACA 65- and 66-series airfoils). The figure shows that reducing $C_{D_{min}}$ by 30 drag counts (from 0.013 to 0.010) increases LD_{max} by 4.2 and shifts its location to a lower C_L. Thus, LD_{max} is realized at higher airspeed; something very beneficial to a sailplane (and powered aircraft). Note that the presence of a wing drag bucket (and, thus, a double-peak L/D curve) of real sailplanes is often masked by the drag formed by the rest of the airplane.

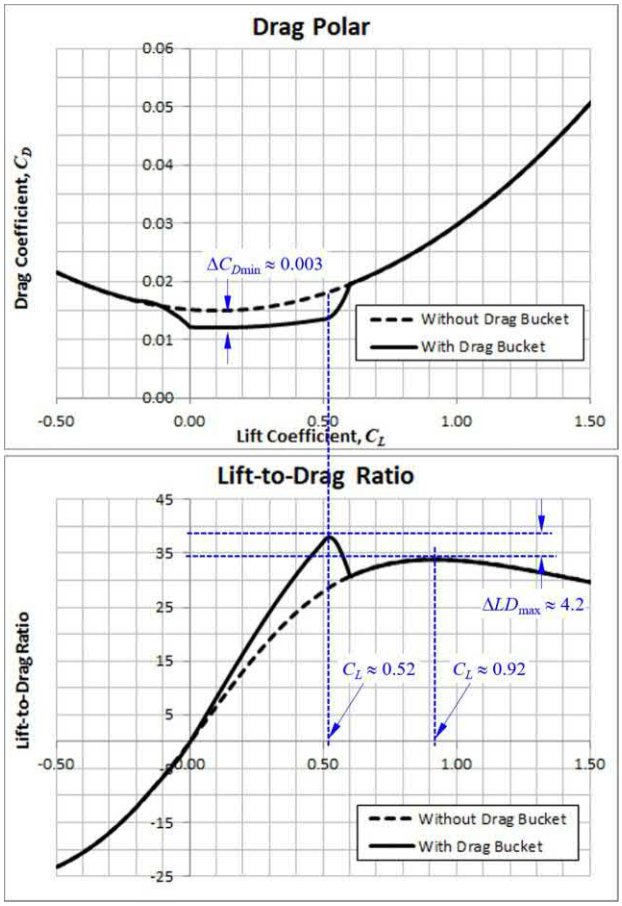


FIGURE 22-10 Example of the benefit of achieving NLF on a hypothetical sailplane.

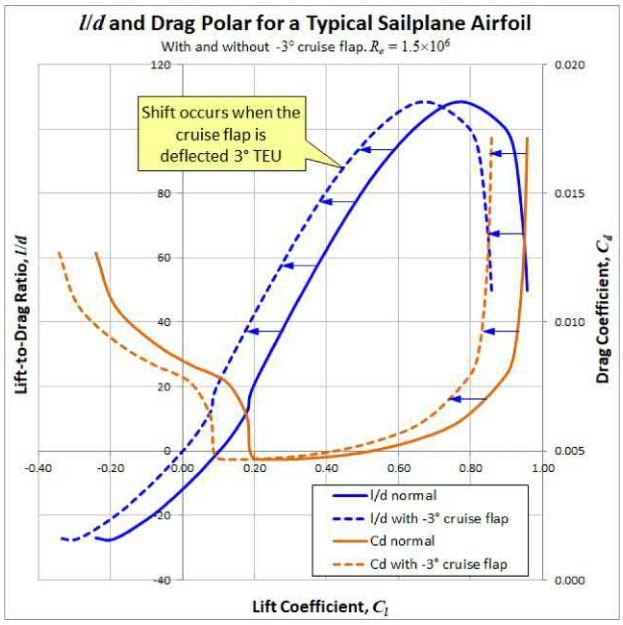


FIGURE 22-9 Lift and drag characteristics of a typical modern sailplane airfoil. *The graph is based on experimental data from L.M.M. Boermans, Research on Sailplane Aerodynamics at Delft University of Technology—Recent and Present Developments, presented to Netherlands Association of Aeronautical Engineers (NVvL), 2006.*

Consider sailplanes A and B, which are identical except A does not develop a laminar drag bucket, while B does. Assume a wing loading of 10 lb_f/ft^2 and the glide characteristics presented in Figure 22-10. Consider a scenario in which the sailplanes are towed to 1500 ft AGL on a calm, sunny day and set out to reach a thermal some 4 nm away. What is the altitude and time of their arrival? Using the performance methods of Section 20.3 and noting that maintaining V_{LDmax} minimizes altitude loss, we can show that Sailplane A achieves its LD_{max} at 58 KTAS and B at 77 KTAS. It will take Sailplane A about 4m09s to fly 4-nm during which it loses 719 ft in altitude. Sailplane B covers this in 3m07s and loses 640 ft (see Figure 22-11). Yes, this is simplistic, but helps explaining the importance of minimizing drag in sailplane design.

22.4.2 Sailplane Glide Performance

The standard operation of sailplanes is highly influenced by the presence of rising and sinking air, as well

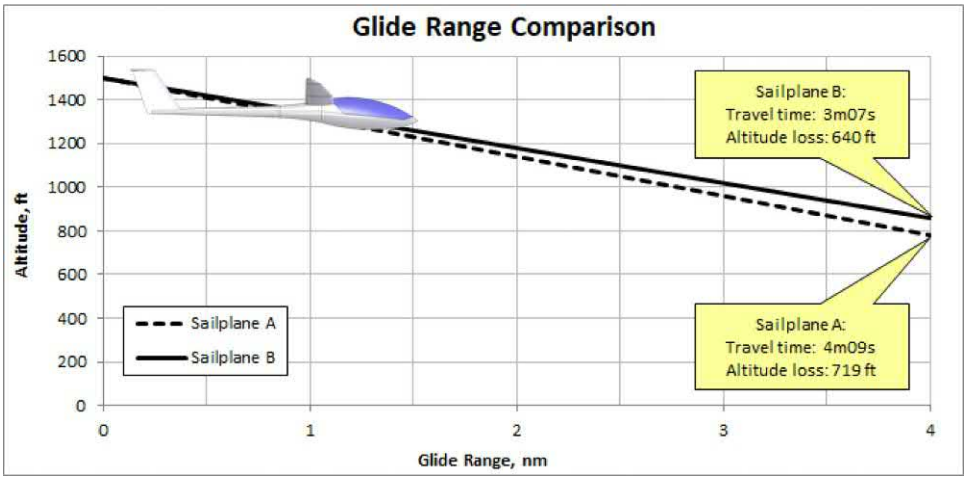


FIGURE 22-11 Glide range for two identical sailplanes. Sailplane A does not develop NLF, but B does.

as head- and tailwinds. Thus, these convection effects must be accounted for in their performance. To help explain the fundamentals of glide performance, let us use a hypothetical sailplane, called *Lava-Gull*, to further the discussion that follows for the remainder of the chapter. To keep things manageable, a simplified quadratic drag model is used, given by $C_D = 0.010 + 0.01498 \cdot C_L^2$. Also, note the time format in which 6.25 min is written as 6m15s.

(1) Glide Range and Glide Endurance

The *glide range* is the horizontal distance a gliding aircraft covers between two specific altitudes. The maximum range in still air is obtained by maintaining the *best-glide airspeed*, denoted by $V_{BG} = V_{LD\max}$. The *glide endurance* is the time that takes a gliding aircraft to descend between the two altitudes. The maximum endurance in still air is obtained while maintaining the airspeed for minimum rate-of-descent, denoted by V_{BA}. This is shown schematically in Figure 22-12 (and Figure 22-7).

(2) Summary of Mathematical Relations for Still-Air Glide Performance

The following expressions are derived in derived in Section 22.3, *General Descent Analysis Methods* and are repeated here for convenience. All assume pure unpowered glide in still air and the simplified drag model.

$$\text{Angle of descent:}\quad \tan\gamma = \frac{D}{L} = \frac{1}{L/D} \approx \frac{D}{W} \tag{22-10}$$

$$\text{Rate-of-descent:}\quad V_V = \frac{DV_\infty}{W} = \frac{V_\infty}{(C_L/C_D)} \tag{22-11}$$

$$\text{Rate-of-descent:}\quad V_V = \frac{C_D}{C_L^{3/2}}\sqrt{\frac{2}{\rho}\left(\frac{W}{S}\right)} \tag{22-13}$$

$$\text{Sink rate while banking at } \phi:\quad V_V = \frac{C_D}{C_L^{3/2}\cos^{3/2}\phi}\sqrt{\frac{2}{\rho}\left(\frac{W}{S}\right)} \tag{22-14}$$

$$\text{Equilibrium glide speed}\quad V_\infty = \sqrt{\frac{2\cos\gamma}{\rho C_L}\left(\frac{W}{S}\right)} \tag{22-12}$$

Airspeed of minimum sink rate:

$$V_{BA} = \sqrt{\frac{2}{\rho}\left(\frac{W}{S}\right)}\sqrt{\frac{k}{3 \cdot C_{D_{\min}}}} \tag{22-15}$$

Minimum angle-of-descent:

$$\tan\gamma_{\min} = \frac{1}{LD_{\max}} = \sqrt{4kC_{D_{\min}}} \tag{22-16}$$

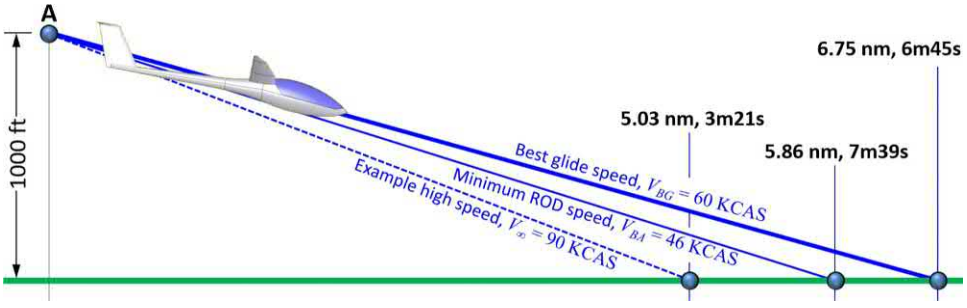


FIGURE 22-12 Illustrating the impact of airspeed on *still-air* glide range and endurance for the Lava-Gull, from an altitude of 1000 ft. In still air, V_{BG} always yields the longest range and V_{BA} the longest time aloft.

Best glide speed (still air):

$$V_{BG} = V_{LD\max} = \sqrt{\frac{2}{\rho}\left(\frac{W}{S}\right)\sqrt{\frac{k}{C_{D_{\min}}}}} \qquad (22\text{-}17)$$

Glide range: $R_{glide} = h \cdot \left(\frac{L}{D}\right) = h \cdot \left(\frac{C_L}{C_D}\right)$ (22-18)

Refer to appropriate equation number for explanation of variables.

22.4.3 The Speed Polar

(1) The Basic Speed Polar—Optimum Glide in Still Air

Sailplane glide performance is determined using the *speed polar* (also called a *flight polar*); a diagram that shows the *rate-of-descent* (ROD) as a function of airspeed. This is obtained by plotting Equation (22-11) (with a minus-sign) versus airspeed. Note that the presentation that follows should only be considered basic and introductory.

The basic speed polar of Figure 22-13 shows the glide characteristics in still air, in the absence of lift or sink. Negative ROD means the sailplane loses altitude. Positive ROD means the sailplane gains altitude (climbs). Three important parameters are indicated; the stalling speed, V_S, the airspeeds of minimum ROD, V_{BA}, and minimum glide angle, V_{BG}. It shows that the Lava-Gull achieves a minimum *ROD* of 131 fpm at $V_{BA} = 46$ KCAS (V_{BA}) and $LD_{\max} = 40.9$ at $V_{BG} = 60$ KCAS. The *ROD* at V_{BG} is 149 fpm. Maintaining V_{BA} yields the longest time aloft (endurance) and V_{BG} yields the greatest distance flown (range). These are optimum values in no-wind, no-thermal conditions only.

In the world of sailplane piloting, the stalling speed (V_S) is always indicated where the speed polar is terminated on the left-hand side (see Figure 22-13). Note that the stalling speed shown leads to an unrealistically high $C_{L_{max}}$, a fact we will conveniently ignore, as the Lava-Gull is purely intended for explaining concepts.

(2) The Speed Polar with Variable Wing Loading

The speed polar for the sailplane is often prepared with one or two specific and frequently used weights in mind. If the sailplane is loaded to higher weight, for instance, due to the addition of a second occupant or water ballast, the speed polar is shifted to a higher airspeed compared to the lighter weight (see Figure 22-14). The general rule-of-thumb is that there is no change in the $LD_{\max}$, only the airspeed at which it occurs. As is to be expected, the magnitude of $ROD_{\min}$ increases, as does the airspeed at which it occurs. The figure shows this is akin to sliding the polar along the sloped line, although it also "expands" as shown.

There is no change in the magnitude of the $LD_{\max}$ with weight, but For the Lava-Gull, the airspeed where it is achieved increases from 60 to 69 KCAS with 30% increase in weight. However, $ROD_{\min}$ increases from 131 to 149 fpm and its airspeed from 46 to 52 KCAS.

(3) Optimum Glide in Sinking Air

If the sailplane enters a column of air sinking at some average rate, say 200 fpm, this is akin to shifting the speed polar downward as shown in the left graph of Figure 22-15. This does not affect V_{BA}. However, V_{BG} is shifted to a higher airspeed, here, from 60 to 77 KCAS. As stated

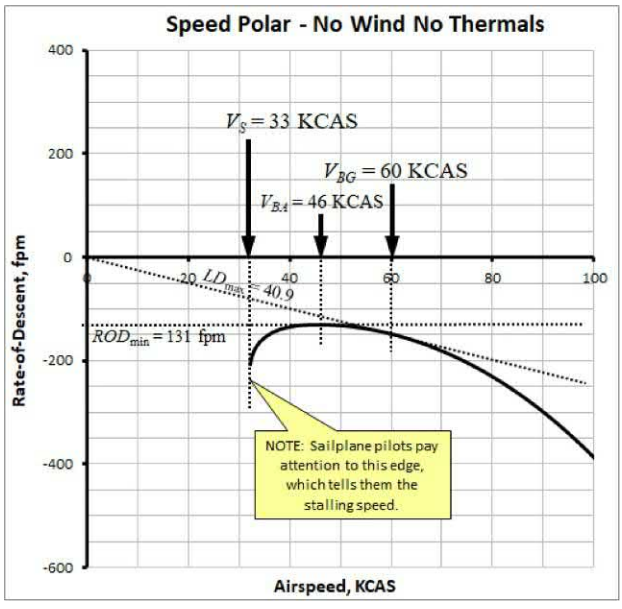


FIGURE 22-13 Basic speed polar for the Lava-Gull at S-L.

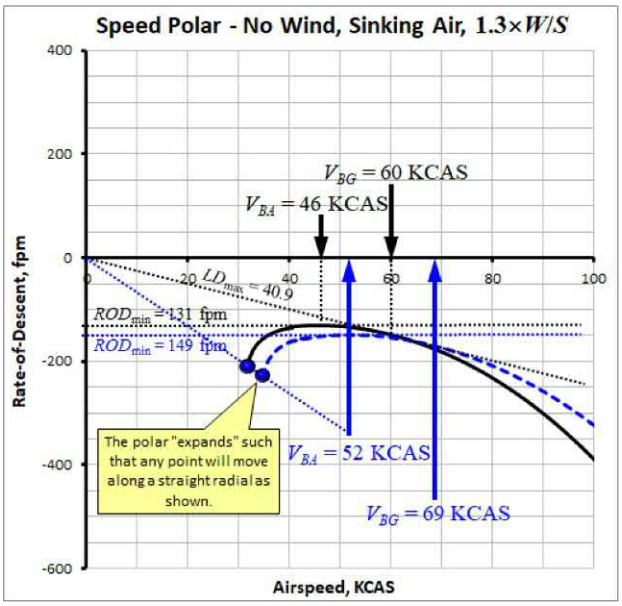


FIGURE 22-14 The solid curve shows the basic speed polar for the Lava-Gull at S-L. The dashed one shows it at 30% over gross weight.

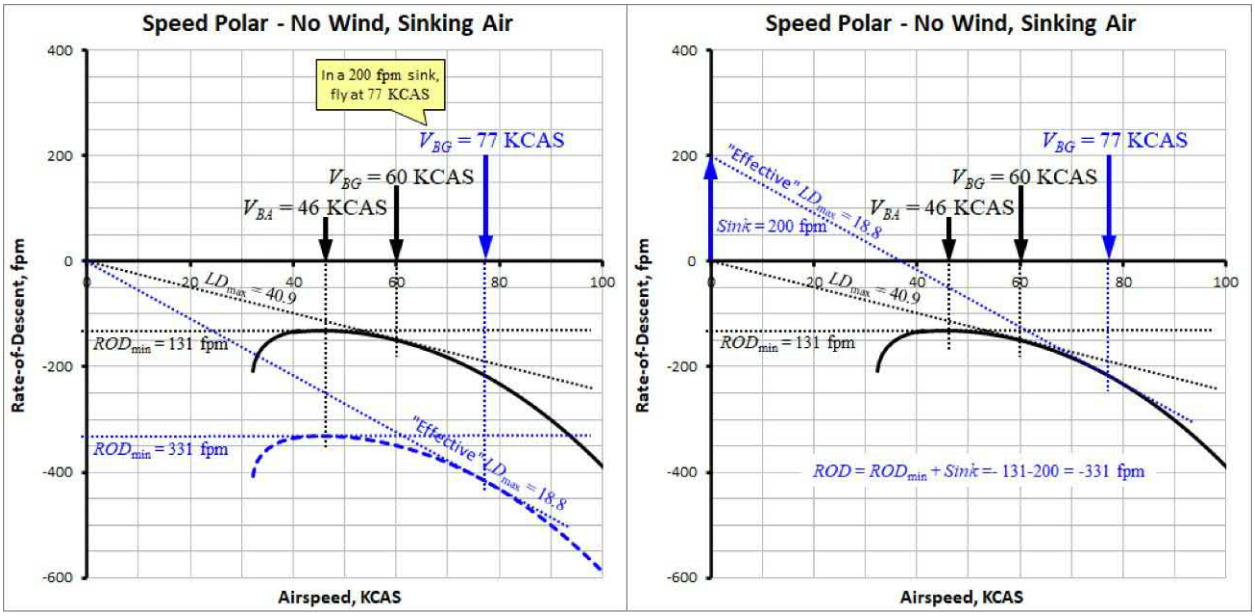


FIGURE 22-15 The speed polar for the Lava-Gull, assuming it enters a column of air sinking at 200 fpm (≈1 m/s). Both graphs display the same information. By shifting the origin of the vertical axis in the right graph up by 200 fpm, the same answer is obtained as in the left graph.

before, in the absence of lift or sink, the normal *ROD* at these two airspeeds is 131 fpm (at V_{BA}) and 148 fpm (at V_{BG}), respectively. The *effective* LD_{max} (defined here as V_H/V_V) reduces from 40.9 to 18.8. It is not important whether the polar is shifted downward or the origin is shifted upward, as shown in the right graph of Figure 22-15. The right graph, thus, presents a clever method to determine the best airspeed-to-fly using a polar made for standard conditions only. This is discussed in more detail later.

To help understand why an airspeed increase is beneficial, assume the sailplane (at S-L conditions, so we can refer to KCAS rather than KTAS) glides through the center of a column of uniformly sinking air, whose diameter is 1 nm, and average rate is 200 fpm. At 60 KCAS, it takes the sailplane 1-min flat to fly through the column, during which it descends at 131 + 200 = 331 fpm and, thus, loses 331 ft of altitude. At 77 KCAS, the sailplane descends at 148 + 200 = 348 fpm and takes 47 s to fly through it. Thus, it loses (47/60) × 348 = 273 ft: Less altitude is lost by flying at the higher airspeed.

Figure 22-16 shows how the downdraft affects the glide from a different perspective; presenting it as L/D versus airspeed. The peak L/D is reduced and shifted to a higher airspeed.

(4) Optimum Glide in Rising Air

If the sailplane enters a column of air rising at, say, 200 fpm, this corresponds to shifting the speed polar upward by that amount, as shown in Figure 22-17. Again, this has no effect on V_{BA}, which now is analogous to V_Y

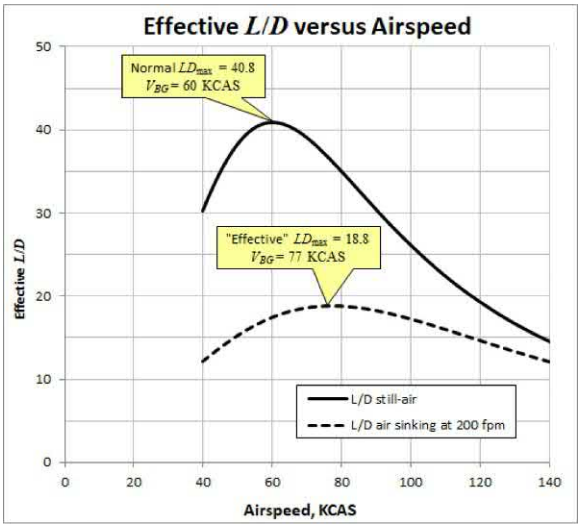


FIGURE 22-16 Standard and "effective" L/D curves for the Lava-Gull at S-L.

(best rate-of-climb airspeed) for powered aircraft. Similarly, V_{BG} becomes the *best-angle-of-climb* airspeed (denoted by V_X for powered aircraft).

(5) Optimum Glide in Headwind or Tailwind

Consider the Lava-Gull gliding in a 10-knot headwind (or tailwind) at constant calibrated airspeed of 60 KCAS. With respect to the ground, the glide speeds will be 10 knots slower (or faster). Thus, the best glide speed of 60 KCAS (V_{BG}) actually corresponds to 50 (or 70) KGS (Knots Ground Speed). At 60 KCAS, while the *ROD* is constant at 148 fpm, the glide range will vary greatly

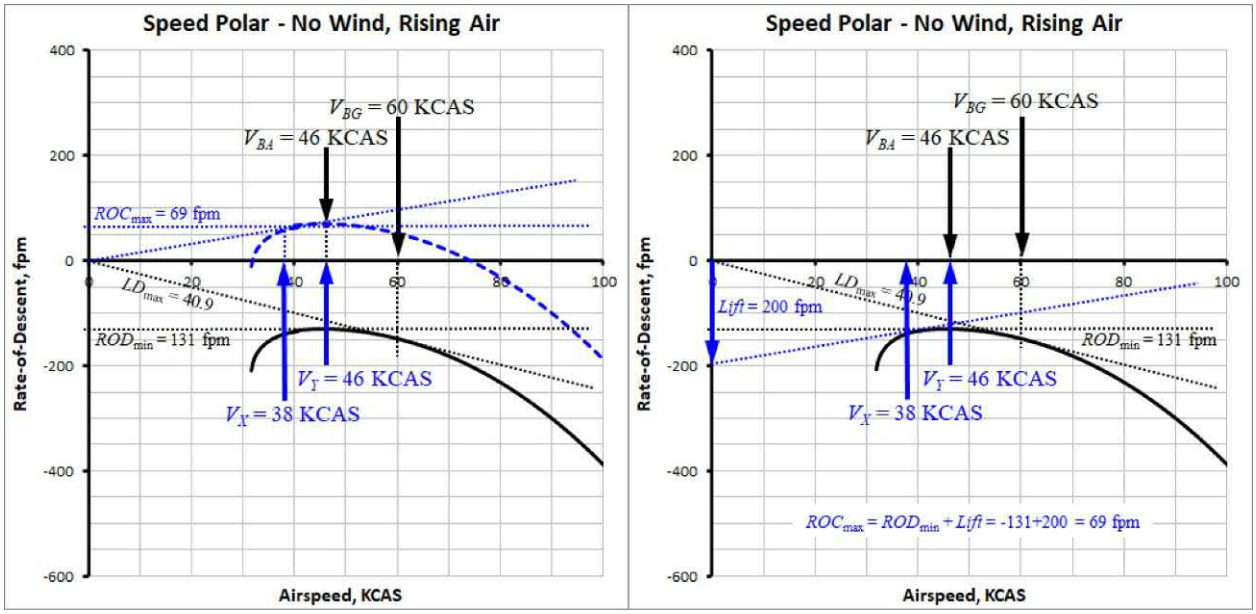


FIGURE 22-17 The speed polar for the Lava-Gull, assuming it enters a lift of 200 fpm (≈2 knots or 1 m/s). Both graphs display the same information. By shifting the origin of the vertical axis in the right graph down by 200 fpm, the same answer is obtained as that in the left graph.

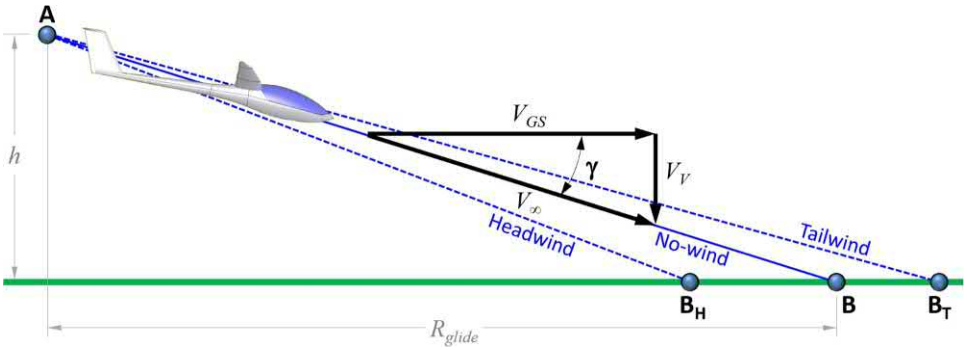


FIGURE 22-18 A simple schematic showing the impact of head- or tailwind on the glide range assuming the pilot maintains the same indicated (or calibrated) airspeed in all three cases.

(see Figure 22-18). The same holds for the glide angle, γ, with respect to the ground, which can be determined as follows:

In a 10-knot tailwind:

$$\gamma = \tan^{-1}[(148/60)/(70 \times 1.688)] = 1.20°$$
$$\Delta\gamma = -0.20°$$

In no-wind conditions:

$$\gamma = \tan^{-1}[(148/60)/(60 \times 1.688)] = 1.40°$$

In a 10-knot headwind:

$$\gamma = \tan^{-1}[(148/60)/(50 \times 1.688)] = 1.67°$$
$$\Delta\gamma = +0.27°$$

Where Δγ is the difference between the still-air and windy glide-angle. If the sailplane begins its glide 1000 ft above the ground, it touches down in 1000/148 = 6m45s in all three cases. However, the range in headwind will be approximately (50 nm/60 min) × (6.75 min) = 5.63 nm (B_H), 6.76 nm (B) in still air, and 7.88 nm (B_T) in tailwind.

This begs the question: In headwind, is there a specific airspeed that yields range greater than 5.63 nm? To answer this question, suppose the Lava-Gull is being flown in a 10-knot headwind at 63 KCAS (rather than 60 KCAS). The *ROD* at this airspeed is 156 fpm, the ground speed is 53 KGS and the glide lasts for 1000/156 = 6m24s (≈6.40 min). In that time, it covers (53 nm/60 min) × (6.40 min) = 5.65 nm, which is greater than 5.63 nm at 60 KCAS. This shows that increasing the airspeed (up to a certain point) in headwind, yields greater range. The inverse is true for tailwind.

A sailplane gliding in headwind equal to its forward speed will not make any headway with respect to the ground. Rather, it descends vertically—its γ = 90°. Horizontal distance can only be achieved by a forward glide speed faster than the headwind. The airspeed that yields the greatest range can be determined by shifting the origin of the speed polar horizontally by a distance that

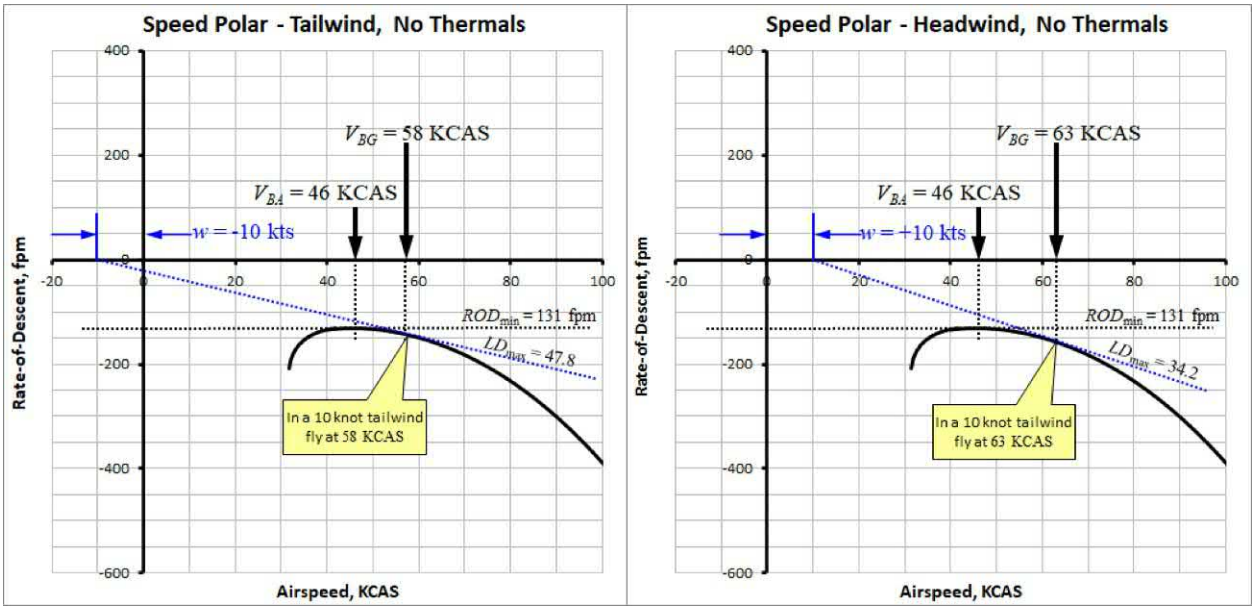


FIGURE 22-19 The speed polar for the Lava-Gull, for a glide in a 10-knot tail- and headwind. By shifting the origin of the horizontal axis to the left or right by 10 knots, an ideal airspeed for glide is obtained.

equals the wind speed, and then draw a tangent to the speed polar. Like the previous discussion demonstrates, in headwind, the origin of the coordinate system is shifted to the right, while for tailwind it is shifted to the left, as shown in Figure 22-19.

22.4.4 Speeds-to-Fly

The preceding discussion shows how the speed polar for no-wind, no-thermal conditions can be used to determine the proper airspeed to fly in nonstandard conditions. The particular airspeed obtained this way is called *Speed-to-Fly* by sailplane pilots. It is determined by shifting the origin around as shown in Figure 22-20. For headwind, the origin is shifted to the right. For headwind and sink, it is shifted to the right and up, and so on. Let us investigate this further, using the aerodynamics of the Lava-Gull.

(1) Average Cross-Country Speed

Physics dictates that while cruising toward a thermal a sailplane exchanges altitude for distance. Ideally, once inside the thermal the altitude will eventually be recovered. The total time consumed while traveling to the thermal and "get back" to the original altitude is a figure-of-merit for sailplanes and pilot skills in long distance competitions. Consider the sailplane in Figure 22-21, where the segment A-B is the glide segment and B-C the climb segment. The *average cross-country speed*, denoted by V_{avg} (also shown in Figure 22-20) can be defined as the distance traveled to the thermal, divided by the total time it takes to reach it and recover the lost altitude. Mathematically, this can be represented as follows:

$$V_{avg} = \frac{R_{glide}}{t} = \frac{R_{glide}}{t_{glide} + t_{climb}} \tag{22-19}$$

Where t_{glide} and t_{climb} is the time spent in glide and climb, respectively, and R_{glide} is the total distance covered. These variables (R_{glide}, t_{glide}, and t_{climb}) are further defined as follows:

$$R_{glide} = \left(\frac{V_{GS}}{V_V}\right)h \quad t_{glide} = \frac{h}{V_V} \quad t_{climb} = \frac{h}{V_C} \tag{22-20}$$

Where V_V is the vertical speed, V_{GS} is an arbitrary horizontal glide speed (see Figure 22-21), and V_C is vertical speed in climb.

Substitute these into Equation (22-19) and manipulate algebraically to yield:

$$V_{avg} = \frac{V_{GS}V_C}{V_C + V_V} \Rightarrow \frac{V_{avg}}{V_{GS}} = \frac{V_C}{V_C + V_V} \tag{22-21}$$

The speed of climb, V_C, is the difference between the *thermal strength* (the rate at which air is rising), denoted by V_T, and the rate of sink of the sailplane as it circles inside the thermal, V_{SC}:

$$V_C = V_T - V_{SC} \Rightarrow \frac{V_{avg}}{V_{GS}} = \frac{V_T - V_{SC}}{V_T - V_{SC} + V_V} \tag{22-22}$$

(2) Optimum Speed-to-Fly Between Thermals in Still Air

Now, let us address what optimum airspeed to maintain when flying between thermals in still-air. Consider the Lava-Gull in Figure 22-22, at Point A, some 2000-ft above the ground, as it begins its 4-nm journey toward

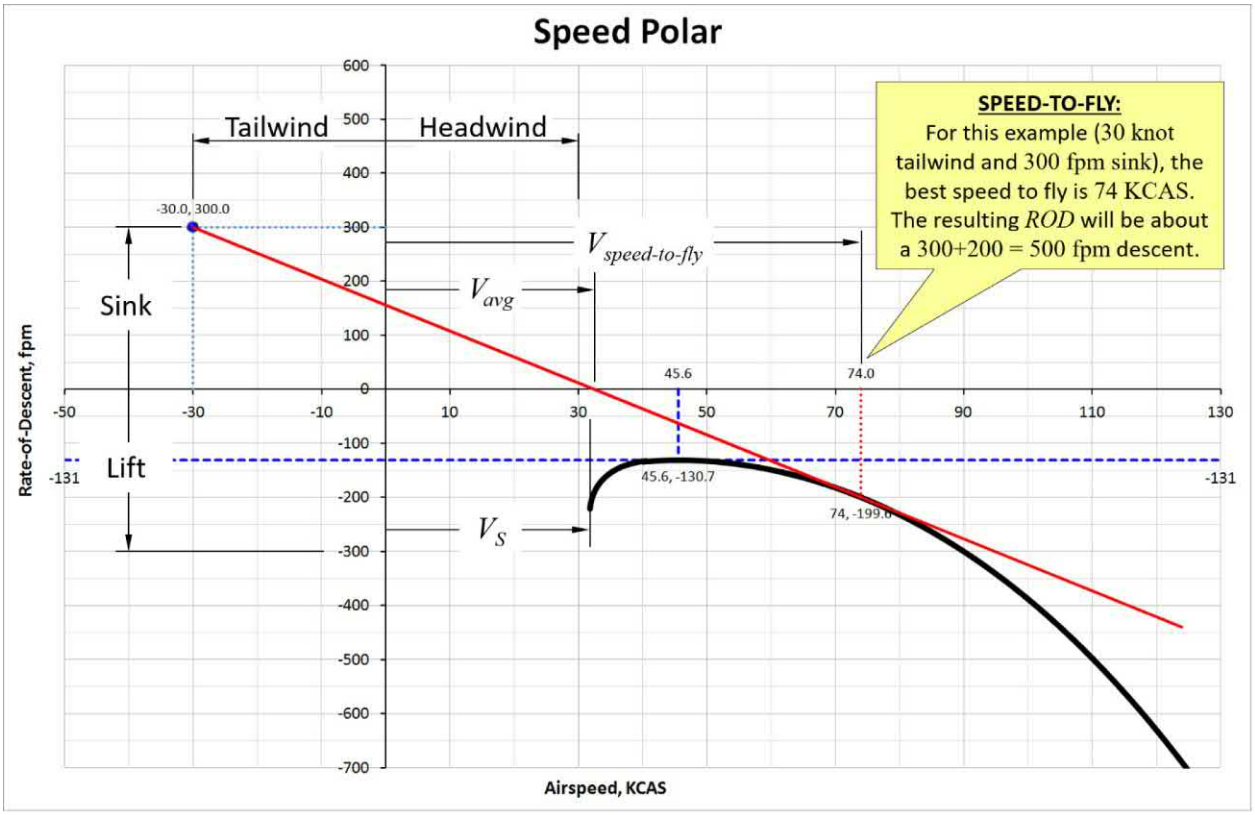


FIGURE 22-20 Putting it all together—here for the Lava-Gull. The appropriate directions in which to move the origin of the polar based on wind and thermal properties are shown. Then, a tangent from the offset origin to the polar is drawn to reveal the *Speed-to-Fly* and *average cross-country speed*.

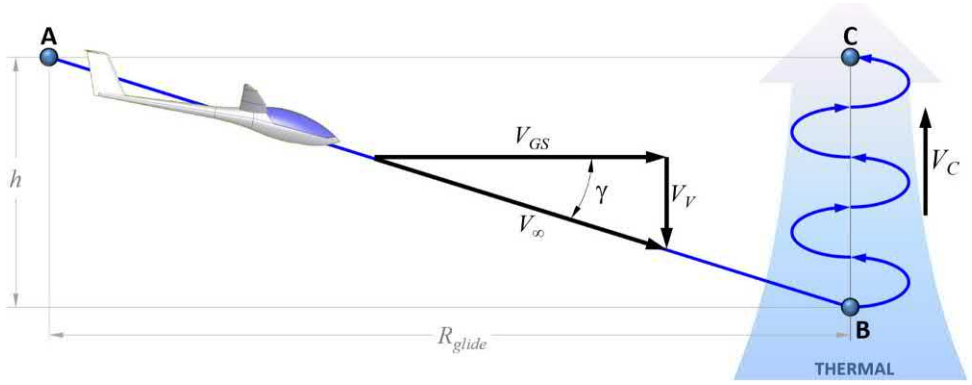


FIGURE 22-21 Definition of a *cross-country model. Based on F. Thomas, Fundamentals of Sailplane Design, College Park Press, 1999.*

a thermal. Assume the thermal strength is 400 fpm. Let us consider three airspeeds to fly; $V_1 = V_{BG} = 60$ KCAS, $V_2 = 80$ KCAS, and $V_3 = 100$ KCAS. Clearly, maintaining V_{BG} will lead to the longest travel time, however, it also leads to the least amount of altitude lost. Conversely, maintaining V_3 leads to the earliest arrival time, but the greatest altitude to be made up. Details of this speed selection is shown in Table 22-4, which assumes uniform S-L atmospheric properties and that V_{BA} is maintained inside the thermal in all three cases (in straight and level flight). Table 22-4 shows that the second airspeed, $V_2 = 80$ KCAS, is superior to the other two, as it leads to the least amount of total time required to reach the original altitude of 2000 ft. Consequently, its V_{avg} is the fastest.

Table 22-4 shows the lift-to-drag ratio, vertical speed, V_V, in fpm, altitude lost en-route, Δh_{cruise}, in ft, time in cruise, Δt_{cruise}, time to climb back to 2000 ft, Δt_{climb}, and total time, Δt_{total}, all in minutes. The last column is an indication of progress made during the glide and subsequent climb. It is the average cross-country speed, here 4 nm divided by the total time, Δt_{total}.

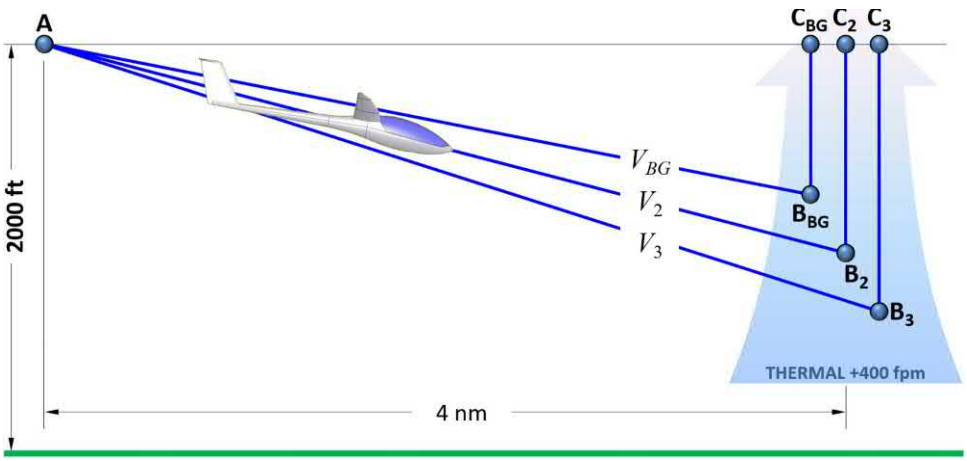


FIGURE 22-22 The Lava-Gull headed to a thermal whose strength is known to be 400 fpm.

TABLE 22-4 Summary of trip parameters for a 4-nm cruise to a thermal and subsequent climb to 2000 ft.

Route	V	L/D	V_Y, fpm		Δh_{cruise}	Δt_{cruise}	Δt_{climb}	Δt_{total}	V_{avg}
	KCAS		in cruise	in thermal	ft	min	min	min	KCAS
A-B_{BG}-C_{BG}	60	40.9	-148	269	595	4.00	2.21	6.21	38.7
A-B_2-C_2	80	35.1	-230	269	693	3.00	2.57	5.57	43.1
A-B_3-C_3	100	26.2	-386	269	928	2.40	3.45	5.85	41.1

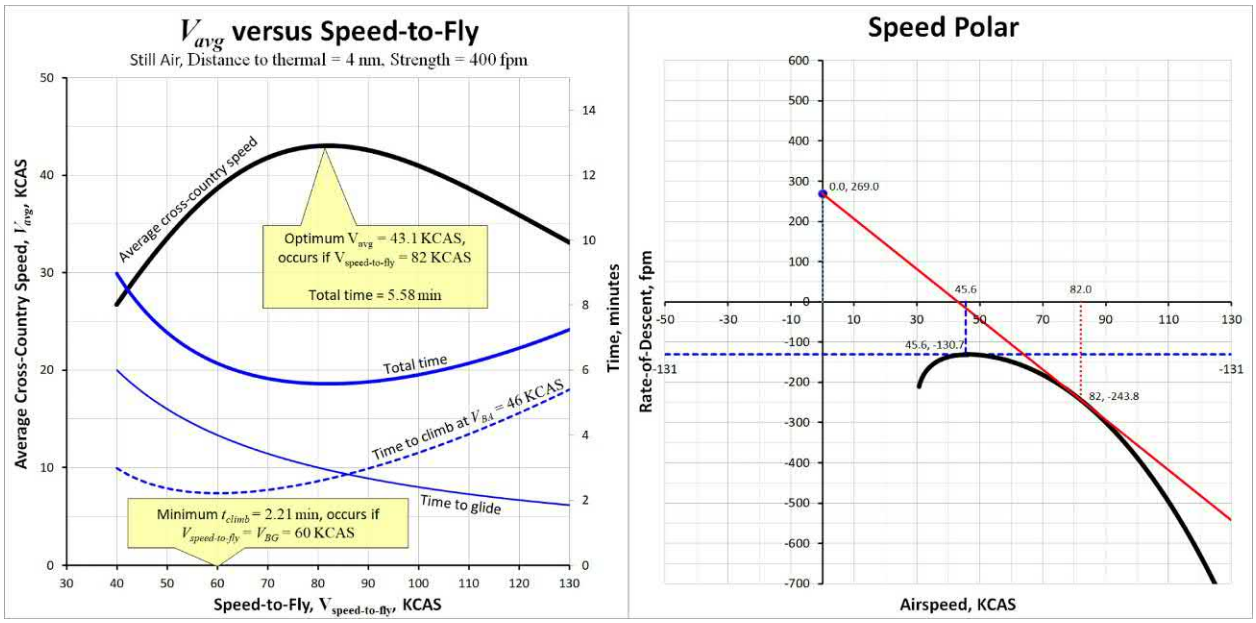


FIGURE 22-23 Left graph shows how V_{avg} varies with the Speed-to-Fly for the Lava-Gull under specific conditions. The right graph shows how the speed polar can be used to extract $V_{speed\text{-}to\text{-}fly}$ and V_{avg}.

Figure 22-23 shows how V_{avg} varies with $V_{speed\text{-}to\text{-}fly}$ for the Lava-Gull on an idealized no-wind day with a thermal of strength 400 fpm. It is assumed the pilot maintains V_{BA} (=46 KCAS with a 131-fpm rate-of-sink) inside the thermal, which is large enough to allow circling flight at shallow bank angle. The right graph shows how the speed polar can be used to extract $V_{speed\text{-}to\text{-}fly}$ (82 KCAS), while allowing V_{avg} (43 KCAS) to be extracted at the same time. The mathematical derivation of why this leads to the correct result is provided by Ref. [9].

(3) Optimum Speed-to-Fly Between Thermals in Moving Air

Now, let us address what optimum airspeed to maintain in moving-air. If the sailplane is subject to lift or sink, as well as head- or tailwind, the V_{avg} and $V_{speed\text{-}to\text{-}fly}$ can be determined by moving the origin of the flight polar to a new position dictated by horizontal wind and expected climb rate in the thermal as shown Figure 22-23. This airspeed can also be determined analytically using Equation (22-21), which leads to the following solution that requires an iterative scheme to solve for the optimum lift coefficient, C_{Lopt}, given some expected rate-of-climb, V_C:

Optimum lift coefficient:

$$C_{D_{\min}} - kC_{Lopt}^2 - V_C\sqrt{\frac{\rho}{8}\left(\frac{S}{W}\right)}C_{Lopt}^{3/2} = 0 \tag{22-23}$$

With C_{Lopt} known, the average cross-country speed can be calculated from Equation (22-24). Since the expression applies to any lift coefficient, C_L, this is used rather than limit it to C_{Lopt} only.

Average cross – country speed:

$$V_{avg} = \frac{V_C C_L^{-1/2}}{V_C\sqrt{\frac{\rho}{2}\left(\frac{S}{W}\right)} + \frac{C_{D_{\min}} + kC_L^2}{C_L^{3/2}}} \tag{22-24}$$

DERIVATION OF EQUATIONS (22-23) AND (22-24)

The glide speed for a glide angle close to zero is given by Equation (22-12). Using small angle relations this is:

$$V_{GS} = \sqrt{\frac{2\cos\gamma}{\rho C_L}\left(\frac{W}{S}\right)} \approx \sqrt{\frac{2}{\rho C_L}\left(\frac{W}{S}\right)}$$

The rate-of-descent is given by Equation (22-13):

$$V_V = \frac{C_D}{C_L^{3/2}}\sqrt{\frac{2}{\rho}\left(\frac{W}{S}\right)}$$

Replace V_{GS} and V_V in Equation (22-21) leads to:

$$V_{avg} = \frac{V_{GS}V_C}{V_C + V_V} = \frac{V_C\sqrt{\frac{2}{\rho C_L}\left(\frac{W}{S}\right)}}{V_C + \frac{C_D}{C_L^{3/2}}\sqrt{\frac{2}{\rho}\left(\frac{W}{S}\right)}}$$

$$V_{avg} = \frac{V_C C_L^{3/2} C_L^{-1/2}\sqrt{\frac{2W}{\rho S}}}{C_L^{3/2}V_C + C_D\sqrt{\frac{2W}{\rho S}}} = \frac{V_C C_L^{-1/2}}{V_C\sqrt{\frac{\rho S}{2W}} + \frac{C_D}{C_L^{3/2}}}$$

Using the simplified drag polar, $C_D = C_{D_{\min}} + k\cdot C_L^2$, this becomes:

$$V_{avg} = \frac{V_C C_L^{-1/2}}{V_C\sqrt{\frac{\rho}{2}\left(\frac{S}{W}\right)} + \frac{C_{D_{\min}} + kC_L^2}{C_L^{3/2}}} = \frac{V_C C_L^{-1/2}}{V_C\sqrt{\frac{\rho}{2}\left(\frac{S}{W}\right)} + \frac{C_{D_{\min}}}{C_L^{3/2}} + kC_L^{1/2}} \tag{i}$$

This is Equation (22-24). C_{Lopt} is obtained by differentiating Equation (i) with respect to C_L and setting the derivative to zero. Using the quotient rule of calculus, we get:

$$\frac{dV_{avg}}{dC_L} = \frac{\left(-\frac{V_C C_L^{-3/2}}{2}\right)\left(V_C\sqrt{\frac{\rho S}{2W}} + \frac{C_{D_{\min}}}{C_L^{3/2}} + kC_L^{1/2}\right) - \left(V_C C_L^{-1/2}\right)\left(-\frac{3}{2}C_{D_{\min}}C_L^{-5/2} + \frac{1}{2}kC_L^{-1/2}\right)}{\left(V_C\sqrt{\frac{\rho S}{2W}} + \frac{C_{D_{\min}}}{C_L^{3/2}} + kC_L^{1/2}\right)^2} = 0$$

Of which we only need the numerator:

$$\left(-\frac{V_C C_L^{-3/2}}{2}\right)\left(V_C\sqrt{\frac{\rho S}{2W}} + \frac{C_{D_{\min}}}{C_L^{3/2}} + kC_L^{1/2}\right) - \left(V_C C_L^{-1/2}\right)\left(-\frac{3}{2}C_{D_{\min}}C_L^{-5/2} + \frac{1}{2}kC_L^{-1/2}\right) = 0$$

Some algebraic acrobatics of this equation leads to Equation (22-23).

(4) The MacCready Speed Ring

It is evident that it is not easy to figure out the best speed-to-fly "on-the-fly." This problem is solved by a device called the *MacCready ring* that is mounted to the variometer (the Rate-of-Climb indicator) in sailplanes. The device is a dial on which airspeeds for various sink or lift conditions are marked. The ring is rotated such that its index arrow indicates the lift expected in the next thermal. This rotates the airspeed markings such the needle of the variometer points at $V_{speed\text{-}to\text{-}fly}$, allowing the pilot to quickly read this airspeed directly. The name of the device is attributed to the late Dr. Paul MacCready (1925–2007) who developed it. More details on its operation are beyond the scope of this text. Today, sailplanes use electronic variometers and flight computers that provide this information in real time.

22.4.5 Circling Flight

Once in a thermal, the sailplane is often maneuvered in circles to take advantage of the rising air. Unfortunately, banking increases its sink rate (V_{SC}) over that in straight and level flight (V_V). The steeper the bank, the greater the sink rate and less potential energy is gained per unit time. The advantage of a steep bank angle is smaller turning radius, which allows the pilot stay closer to the region of maximum updraft. This implies that an optimum bank angle exists that maximizes the rate of climb, given a specific turning radius and strength of lift.

Before determining this optimum bank angle, we must develop formulation that allows the sink rate to be assessed based on bank angle and turning radius. For this, consider Figure 22-24, which shows the forces acting on the sailplane banking at an angle ϕ, while flying at airspeed V_∞. If the lift (L), weight (W), mass (m), and turn radius (R_{turn}) are known, the sinking speed in circling flight can be determined from:

$$V_{SC} = \frac{C_D}{C_L^{3/2}}\sqrt{\frac{2}{\rho}\left(\frac{W}{S}\right)}\frac{1}{\left[1-\left(\frac{2}{\rho}\left(\frac{W}{S}\right)\frac{1}{R_{turn}gC_L}\right)^2\right]^{3/4}} \tag{22-25}$$

Equation (22-25) can be used to construct the map in Figure 22-25. Both styles of curves are plotted using Equation (22-25). It allows us to evaluate the turning performance of the sailplane, while circling inside a thermal. The diagram shows that given fixed bank angle, the turn radius reduces only if the sailplane slows down. Similarly, for a fixed airspeed, the turn radius can only be reduced by banking steeper—which increases the sink rate further. It shows that at $\phi = 60°$, the minimum sink rate occurs around 67 KCAS, resulting in a turning radius of about 225 ft.

The solid curves are generated by first calculating C_L for a range of airspeeds using Equation (20-68) assuming a fixed ϕ. The C_Ls are then used to calculate C_D using the drag polar. The turning radius is also computed using Eq. (ii) in the following derivation. Finally, these are inserted into Equation (22-25). The dashed curves are calculated for a range of turning radii and fixed airspeeds. First, the bank angle is calculated using Equation (i) in the derivation below. Then, this is used to calculate C_L and C_D as before. Again, these are substituted into Equation (22-25).

Note that Equation (22-25) can be used during the design stage to help shape parameters, such as wing area, AR, and drag characteristics, in an attempt to bias the turn performance curves toward a desirable turn radius and bank angle inside a thermal of specific characteristics. Of course, this must take into account the net rate of climb, $V_T + V_{SC}$, assuming V_{SC} has a negative value. Recall that V_T is the thermal strength (e.g., in ft/s or m/s) and V_{SC} is the rate of sink of the sailplane as it circles inside the thermal. A proper determination requires thermals to be modeled mathematically, as presented below.

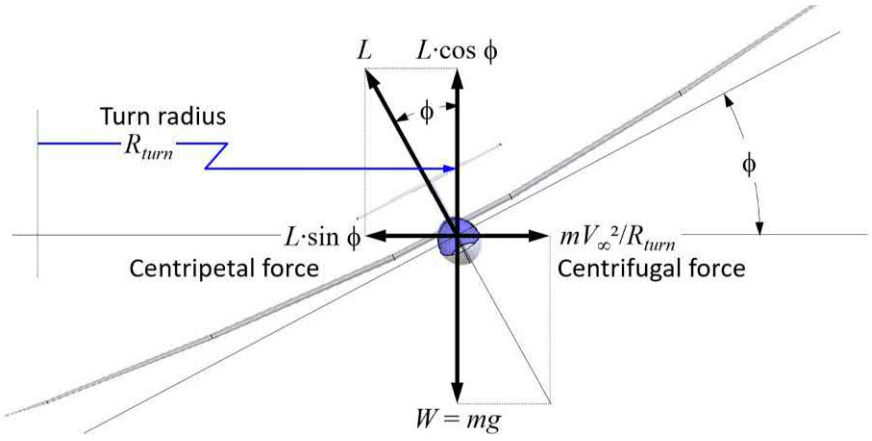


FIGURE 22-24 Forces acting on the Lava-Gull as it is banked in a circling flight.

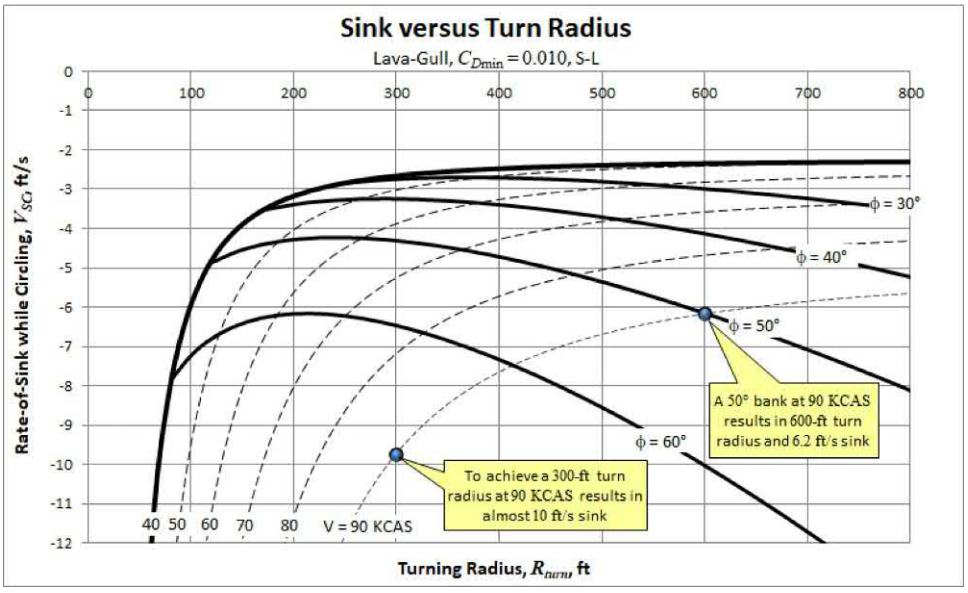


FIGURE 22-25 Turn performance map for the Lava-Gull, shows its rate-of-descent while banking at the specific angles and airspeeds.

DERIVATION OF EQUATION (22-25)

The free-body diagram of Figure 22-24 shows that:

$$\tan\phi = \frac{mV_\infty^2/R_{turn}}{mg} = \frac{V_\infty^2}{R_{turn}g} \qquad \text{(i)}$$

Therefore,

$$V_\infty = \sqrt{R_{turn}g\tan\phi} \quad \text{or} \quad R_{turn} = V_\infty^2/(g\tan\phi) \qquad \text{(ii)}$$

Using these equations, any of the variables V_∞, ϕ, and R_{turn}, can be estimated if two of the others are known. Then, Equation (20-68), repeated below for convenience, can be used to estimate the speed of the airplane as a function of the lift coefficient, C_L, and bank angle, ϕ:

$$V_\infty = \sqrt{\frac{2W}{\rho S C_L}\left(\frac{1}{\cos\phi}\right)} \qquad \text{(20-68)}$$

The equation can be used to extract the lift coefficient, C_L, required during bank at a given airspeed, from which the drag coefficient, C_D, can be determined. Using Equation (ii) a relationship between the airspeed, bank angle, and turning radius can be established:

$$V_\infty^2 = \frac{2W}{\rho S C_L}\left(\frac{1}{\cos\phi}\right) = R_{turn}g\tan\phi = R_{turn}g\frac{\sin\phi}{\cos\phi}$$

Which leads to: $$\sin\phi = \frac{2W}{\rho S C_L R_{turn}g}$$

Using the trigonometric identity $\cos^2 x + \sin^2 x = 1$, it is now possible to write:

$$\cos\phi = \sqrt{1 - \left(\frac{2W}{\rho S C_L R_{turn}g}\right)^2}$$

This relates the turning radius to the bank angle. Substituting this into Equation (22-14) yields Equation (22-25).

EXAMPLE 22-6

Estimate the sink rate for the Lava-Gull as it banks 45° at an airspeed of 90 KCAS. Its wing loading is $W/S = 10\,\text{lb}_f/\text{ft}^2$. Use the drag model given earlier, $C_D = 0.010 + 0.01498 \cdot C_L^2$ and assume S-L conditions.

SOLUTION:

First estimate the lift coefficient at the condition using Equation (20-68):

$$C_L = \frac{2}{\rho V^2}\left(\frac{W}{S}\right)\left(\frac{1}{\cos\phi}\right) = \frac{2}{(0.002378)(90\times 1.688)^2}(10)\left(\frac{1}{\cos 45°}\right) = 0.5154$$

This contrasts 0.3644 for the straight and level condition at the same airspeed. Next calculate the drag coefficient:

$$C_D = 0.010 + 0.01498C_L^2 = 0.010 + 0.01498(0.5154)^2 = 0.01398$$

Calculate the turn radius:

$$R_{turn} = \frac{V_\infty^2}{g\tan\phi} = \frac{(90\times 1.688)^2}{(32.174)\tan 45°} = 711 \text{ ft}$$

Then insert values into Equation (22-25) to get the *ROD* in ft/s:

$$V_{SC} = \frac{C_D}{C_L^{3/2}}\sqrt{\frac{2}{\rho}\left(\frac{W}{S}\right)}\frac{1}{\left[1-\left(\frac{2}{\rho}\left(\frac{W}{S}\right)\frac{1}{R_{turn}gC_L}\right)^2\right]^{3/4}}$$

$$= \frac{0.01398}{(0.5154)^{3/2}}\sqrt{\frac{2}{0.002378}(10)} \cdot \frac{1}{\left[1-\left(\frac{2}{0.002378}(10)\frac{1}{711\times 32.174\times 0.5154}\right)^2\right]^{3/4}} = 5.906 \text{ ft/s}$$

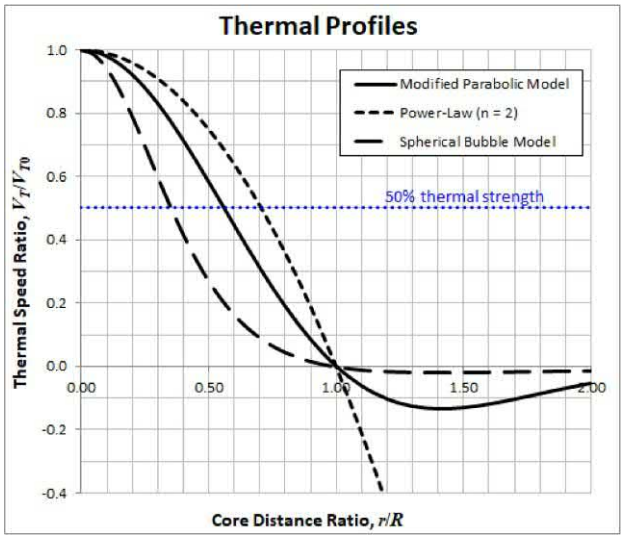


FIGURE 22-26 Common models used to approximate the vertical speed profile inside a thermal.

Thermal Velocity Profiles

The 3-dimensional shape of thermals is an important consideration in the design and operation of sailplanes. Since thermals are of finite dimension, the sailplane pilot must assertively bank inside it and ideally circle around its core while gaining as much altitude as possible. A small turning radius allows the maximum lift to be extracted out of the thermal. However, the smaller the turning radius, the steeper is the bank required. This inevitably comes at the cost of reduced climb rate. Too shallow a bank will fly the sailplane out of the thermal. Too steep a bank will reduce the altitude gain and may even result in altitude being lost. A mathematical description of the vertical velocity inside the thermal gives a helpful insight into determining the optimum bank angle, based on the distance of the sailplane from the core.

Ref. [10] presents a number of idealized thermal profiles, of which three are shown in Figure 22-26. Generally, the vertical speed, V_T, in a thermal will be greatest at its core. This maximum speed is denoted by V_{T0}. Even though the following mathematical models indicate the thermal is symmetrical, this is not necessarily so in real thermals. After all, these are idealized for mathematical convenience and clarity. The three thermal profiles are defined mathematically below. The ratio r/R denotes the fractional distance from the center of a thermal whose diameter is $2R$. Of the three presented, the *power-law* using $n=2$, is sometimes used for competition handicapping purposes, assuming a thermal radius of $R=1000$ ft and with a core strength $V_{T0}=4.2$ knots [10].

$$\text{Power}-\text{Law Velocity Profile:}\quad \frac{V_T}{V_{T0}}=1-(r/R)^n \qquad (22\text{-}26)$$

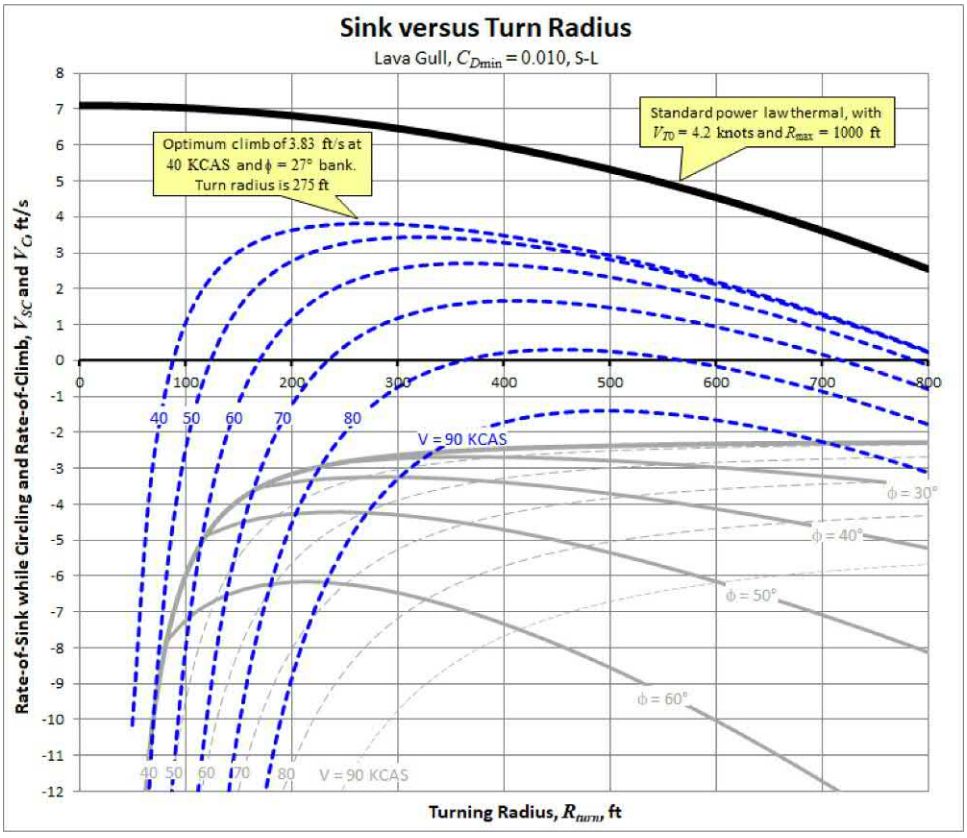


FIGURE 22-27 Turn performance map for the Lava-Gull assuming a maximum thermal radius of 1000 ft and core strength of 4.2 knots used to evaluate best ROC and the corresponding speed and bank angle.

$$\text{Spherical Bubble Model:}\quad \frac{V_T}{V_{T0}} = \frac{1-(r/R)^2}{\left[1-2(r/R)^2\right]^{2.5}} \tag{22-27}$$

$$\text{Modified Parabolic Model:}\quad \frac{V_T}{V_{T0}} = \left[1-(r/R)^2\right]\cdot e^{-(r/R)^2} \tag{22-28}$$

The second element of thermal velocity profiles is their strength. Carmichael [18] defines thermal strength as follows:

(1) *Strong thermal* has a maximum vertical speed of 20 ft/s (≈12 knots) that falls to 10 ft/s when $r = 200$ ft.

(2) *Weak thermal* has a maximum vertical speed of 10 ft/s (≈6 knots) that falls to 5 ft/s when $r = 200$ ft.

(3) *Wide thermal* has a maximum vertical speed of 15 ft/s (≈9 knots) that falls to 7.5 ft/s when $r = 400$ ft.

This information can be combined with the turn performance map to create a representation displaying the optimum bank angle given specific airspeed. This is shown for the Lava-Gull in Figure 22-27. The optimum climb for the selected airspeeds is easily identifiable. The map also shows that only airspeeds below 80 KCAS result in climb in this condition and that exceeding 30° of bank is detrimental to the climb performance.

The thick dashed, blue-colored curves in Figure 22-27 are obtained by adding V_T and V_{SC}, which is calculated using Equation (22-25). The value of V_T is calculated using any of the Equations (22-26) through (22-28). This shifts the fixed V_{SC}-isopleths (the thin dashed gray-colored curves) upward into the new position, with the associated maximums.

References

[1] C.D. Perkins, R.E. Hage, *Airplane Performance, Stability, and Control*, John Wiley & Sons, 1949.

[2] E. Torenbeek, *Synthesis of Subsonic Aircraft Design*, third ed., Delft University Press, 1986.

[3] L. Nicolai, *Fundamentals of Aircraft Design*, second ed., 1984.

[4] J. Roskam, C.-T.E. Lan, *Airplane Aerodynamics and Performance*, DARcorporation, 1997.

[5] F.J. Hale, *Aircraft Performance, Selection, and Design*, John Wiley & Sons, 1984, pp. 137–138.

[6] J.D. Anderson Jr., *Aircraft Performance & Design*, first ed., McGraw-Hill, 1998.

[7] A. Miele, *Flight Mechanics—Theory of Flight Paths*, Dover Publications, 1990.

[8] Anonymous, *Learjet 45—FAA Approved Airplane Flight Manual*, Bombardier Aerospace, 2004.

[9] H. Reichmann, *Cross-Country Soaring*, second ed., Soaring Society of America, 1993.

[10] A. Welch, L. Welch, F. Irving, *The Complete Soaring Pilot's Handbook*, David McKay Company, 1977.

[11] F. Thomas, *Fundamentals of Sailplane Design*, College Park Press, 1999.

[12] K. Stewart, *The Soaring Pilot's Manual*, second ed., Airlife Publishing, 2008.

[13] V. Pajno, S. Design, *A Guide for Students and Designers*, IBN Editore, 2010.

[14] B. Scull, *Soaring Across Country*, Pelham Books, 1979.

[15] NASA CR-2315, *Motorless Flight Research*, Althaus, Dieter, 1972.

[16] https://www.airbus.com/newsroom/press-releases/en/2018/09/airbus-perlan-mission-ii-glider-soars-to-76-000-feet-to-break-ow.html. (Accessed 31 December 2020).

[17] FédérationAéronautiqueInternationale, Record ID 8198.

[18] B.H. Carmichael, *What Price Performance*, Soaring Magazine, May-June, 1954.

CHAPTER

23

Performance—Landing

OUTLINE

23.1 **Introduction** 915
- *23.1.1 The Content of This Chapter* 915
- *23.1.2 What Analyses Must I Do?* 916
- *23.1.3 Important Segments of the Landing Phase* 916

23.2 **Fundamental Relations for the Landing Phase** 917
- *23.2.1 General Free-Body Diagram of the Landing Ground Run* 918
- *23.2.2 The Equation-of-Motion for the Landing Ground Run* 918
- *23.2.3 Formulation of Required Aerodynamic Forces* 918
- *23.2.4 Ground Roll Friction Coefficients* 918
- *23.2.5 Determination of the Approach Distance, S_A* 919
- *23.2.6 Determination of the Flare Distance, S_F* 920
- *23.2.7 Determination of the Free-Roll Distance, S_{FR}* 920
- *23.2.8 Determination of the Braking Distance, S_{BR}* 920
- *23.2.9 Landing Distance Sensitivity Studies* 922
- *23.2.10 COMPUTER CODE: Estimation of Landing Performance* 922

23.3 **Database—Landing Performance of Selected Aircraft** 923

References 924

23.1 INTRODUCTION

Just like the set of chapters about performance began with the T-O, it is appropriate to end with the landing phase. Figure 23-1 shows an organizational map displaying the landing phase among other topics of performance theory. It is equally important to understand the limitations and sensitivity of this important phase as that of the T-O. This chapter presents the formulation of and the solution of the equation-of-motion for the landing and present practical as well as numerical solution methodologies that can be used both for propeller- and jet-powered aircraft.

The landing phase is in many ways the inverse of the T-O phase. It begins with an approach to landing in the form of a steady descent. This is followed by a flare maneuver, in which the pilot raises the nose of the aircraft to reduce its sink rate to permit a soft touch-down on the runway. The phase terminates with a deceleration from the touch-down airspeed to rest.

The landing phase can inflict a serious challenge to aircraft, in particular if its approach speed is high. As the airplane nears the runway it succumbs to ground effect, decreasing lift-induced drag and increasing lift. This may cause the airplane to "float" before eventually settling down on the runway. If its airspeed is high, a significant portion of the runway may be consumed before the airplane even begins to decelerate. Understanding the types and length of runways the airplane is likely to operate from will help size wing area, select landing gear system, select a high-lift and speed-control systems to make it possible to meet the prescribed requirements.

In general, the methods presented in here are "industry standard" and mirror that presented by a variety of authors, e.g., Perkins and Hage [1], Torenbeek [2], Nicolai [3], Roskam and Lan [4], Hale [5], Anderson [6], and Miele [7], to name a few.

23.1.1 The Content of This Chapter

- Section 23.2 presents the fundamental relations of the landing phase, including the equation-of-motion for a landing ground run and its kinematics.

https://doi.org/10.1016/B978-0-12-818465-3.00002-1

Copyright © 2022 Elsevier Inc. All rights reserved.

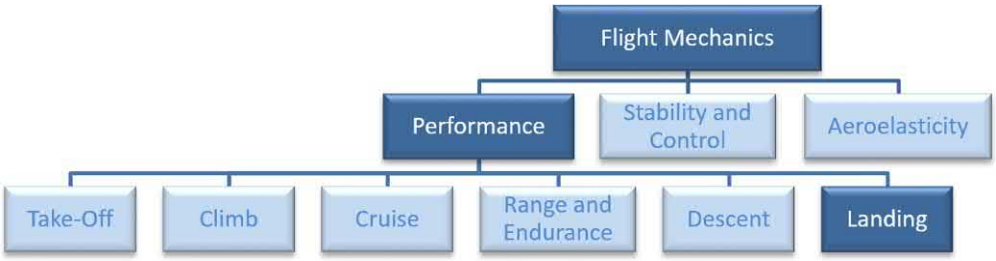


FIGURE 23-1 An organizational map placing Performance Theory among the disciplines of Dynamics of Flight, and highlighting the focus of this chapter; Landing Performance Analysis.

- Section 23.3 presents the landing characteristics of selected aircraft types.

23.1.2 What Analyses Must I Do?

For the newcomer to landing analysis, the burning question is: "What am I supposed to estimate and how do I conduct those estimations?" In short, the purpose of landing analysis is to estimate the total landing distance, its constituent segments, and the associated airspeeds. The results are then compared to the pertinent requirements, answering if the aircraft will meet them. Tables 23-1 and 23-2 list the necessary tasks you should complete.

TABLE 23-1 Task list based on 14 CFR Part 23.

Paragraphs	Content	Section
14 CFR §23.2130[a]	Determination of landing performance	23.2
14 CFR §23.73	Reference landing approach speed	23.2
14 CFR §23.75	Landing distance	23.2
14 CFR §23.77	Balked landing	See Chapter 18

[a] *"New" Part 23.*

23.1.3 Important Segments of the Landing Phase

Generally, the landing phase is split into the segments shown in Figure 23-2. The *Approach Distance* is measured from the point at which the airplane is 50 ft above ground; the point where the pilot initiates the next maneuver—the *flare*—by pulling the control wheel (or stick or yoke) in order to raise the nose of the aircraft. This maneuver is required to slow the descent of the airplane in an attempt to help it gently touch-down on the runway. The next distance is the *Flare Distance*, which extends to the point where the airplane touches-down. Then, the airplane typically rolls briefly before the pilot applies the brakes. This distance is referred to as the *Free-Roll Distance*. Finally, the *Braking Distance* accounts for the length of runway required to apply brakes (thrust reversers, drag chute, wheel brakes, etc.) and bring the aircraft to a complete stop.

In short, the purpose of the landing analysis is to estimate the total landing distance by breaking it up into the aforementioned segments and analyze each of those using simplified physics that pertain primarily to those specific segments. For analysis the segments are denoted by the nomenclature indicated in Figure 23-2 and listed Table 23-2.

The designer shall be particularly concerned with paragraph 14 CFR §23.77, *Balked Landing*, which can be seriously challenging for some aircraft.

Certification requirements for General Aviation (GA) aircraft are largely stipulated in 14 CFR Part 23,

TABLE 23-2 Task list for landing analysis.

Task name	Terms	Weight	CG position	Altitude	Section
Approach distance	V_{REF}, S_A	Gross	Forward CG is usually the critical one	0 ft 5000 ft 10,000 ft +highest elevation airport expected	23.2.5
Flare distance	V_{FLR}, V_{TD}, S_F				23.2.6
Free-roll distance	V_{BR}, S_{FR}				23.2.7
Braking distance	V_{BR}, S_{BR}				23.2.8
Total landing distance	S_{LDG}				The sum of the above
Sensitivity analyses	Various	Various	Various	Various	23.2.9

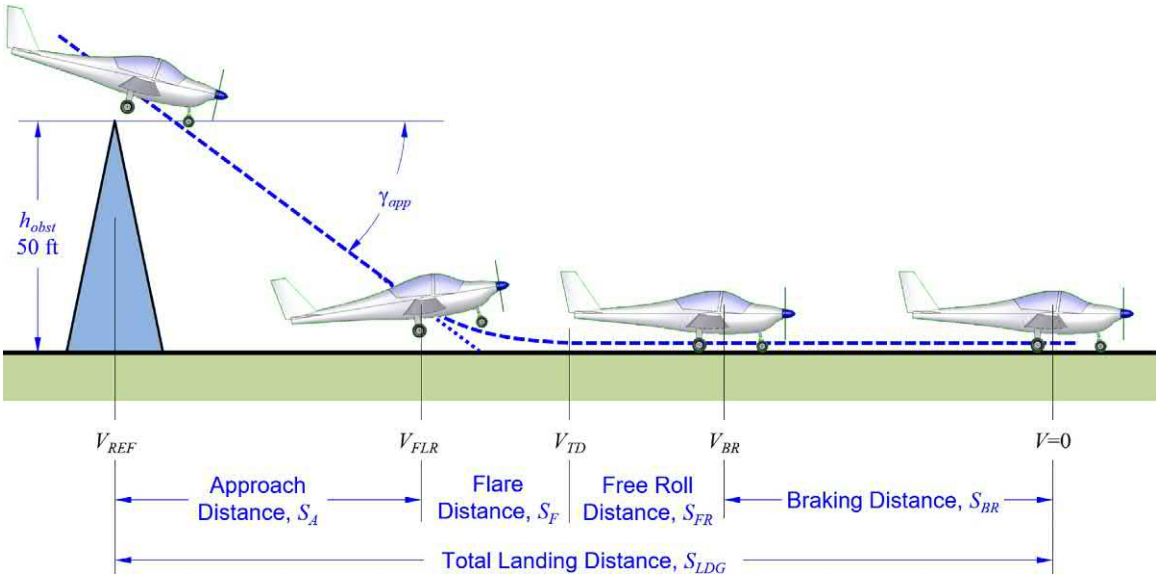


FIGURE 23-2 Important segments of the landing phase.

paragraphs 23.73 through 23.77. Paragraph 23.75 details requirements for the landing distance, shown below:

§23.75 Landing Distance.

The horizontal distance necessary to land and come to a complete stop from a point 50 ft above the landing surface must be determined, for standard temperatures at each weight and altitude within the operational limits established for landing, as follows:

(a) A steady approach at not less than V_{REF}, determined in accordance with §23.73 (a), (b), or (c), as appropriate, must be maintained down to the 50-ft height and—
- **(1)** The steady approach must be at a gradient of descent not greater than 5.2% (3 degrees) down to the 50-ft height.
- **(2)** In addition, an applicant may demonstrate by tests that a maximum steady approach gradient steeper than 5.2%, down to the 50-ft height, is safe. The gradient must be established as an operating limitation and the information necessary to display the gradient must be available to the pilot by an appropriate instrument.

(b) A constant configuration must be maintained throughout the maneuver.

(c) The landing must be made without excessive vertical acceleration or tendency to bounce, nose over, ground loop, porpoise, or water loop.

(d) It must be shown that a safe transition to the balked landing conditions of §23.77 can be made from the conditions that exist at the 50-ft height, at maximum landing weight, or at the maximum landing weight for altitude and temperature of §23.63 (c)(2) or (d)(2), as appropriate.

(e) The brakes must be used so as to not cause excessive wear of brakes or tires.

(f) Retardation means other than wheel brakes may be used if that means—
- **(1)** Is safe and reliable; and
- **(2)** Is used so that consistent results can be expected in service.

(g) If any device is used that depends on the operation of any engine, and the landing distance would be increased when a landing is made with that engine inoperative, the landing distance must be determined with that engine inoperative unless the use of other compensating means will result in a landing distance not more than that with each engine operating.

[Amdt. 23–21, 43 FR 2318, Jan. 16, 1978, as amended by Amdt. 23–34, 52 FR 1828, Jan. 15, 1987; Amdt. 23–42, 56 FR 351, Jan. 3, 1991; Amdt. 23–50, 61 FR 5187, Feb. 9, 1996]

23.2 FUNDAMENTAL RELATIONS FOR THE LANDING PHASE

In this section, we will derive the equation-of-motion for the landing, as well as all fundamental relationships used to evaluate the ground run segment of the T-O maneuver. We will consider both conventional and tail-dragger configurations.

23.2.1 General Free-Body Diagram of the Landing Ground Run

Figure 22-2 shows a free-body diagram of the aircraft during descent. Figures 18-5 and 18-6 show a free-body diagram of the aircraft for take-off for tricycle and tail-dragger configurations, respectively. These also apply to the landing after touch-down. Note that the drag, D, should be modified to reflect the aircraft in its landing configuration and the application of braking devices.

23.2.2 The Equation-of-Motion for the Landing Ground Run

The equation-of-motion for an aircraft during ground roll, after touch-down, on a perfectly horizontal and flat runway can be estimated from Equation (18-1) with slight modifications. If the landing sequence includes the deployment of multiple braking devices at different points during the ground run, it is advisable to adapt the numerical integration scheme of Section 18.2.5, *Solution of Kinematic Problems Using Numerical Integration* to the ground run. The application of mechanical brakes is treated using the ground friction coefficient, μ. The application of thrust reversers is treated using the thrust variable, T. The deployment of drag chutes, spoilers, or speed brakes is treated using the drag variable, D_{ldg}, where they are added to the $C_{D_{\min}}$ of the aircraft in the landing configuration. Deployed landing gear, flaps, and slats greatly increase the drag of the aircraft. Additionally, for landing, the term $dV_\infty/dt < 0$.

Deceleration on a flat runway:

$$\frac{dV}{dt} = \frac{g}{W}\left[T - D_{ldg} - \mu(W - L)\right] \tag{23-1}$$

where

D_{ldg} = Drag in the landing configuration as a function of V_∞,
g = Acceleration due to gravity,
L = Lift of the airplane in the landing configuration as a function of V_∞,
T = Thrust (small and even negative during landing),
W = Weight, assumed constant,
μ = Ground roll friction coefficient (see Table 23-3)

We can also formulate the deceleration of the airplane on a downhill slope, which will increase the total landing distance. This formulation is based on Equation (18-5) with slight modifications.

Deceleration on a downhill slope γ:

$$\frac{dV}{dt} = \frac{g}{W}\left[T - D_{ldg} - \mu(W - L) + W\sin\gamma\right] \tag{23-2}$$

TABLE 23-3 Ground roll friction coefficients.

	Ground friction coefficient (μ)	
Surface type	**Brakes off**	**Braking**
Dry asphalt or concrete	0.03–0.05	0.3–0.5
Wet asphalt or concrete	0.05	0.15–0.3
Icy asphalt or concrete	0.02	0.06–0.10
Hard turf	0.05	0.4
Firm dirt	0.04	0.3
Soft turf	0.07	0.2
Wet grass	0.08	0.2

23.2.3 Formulation of Required Aerodynamic Forces

The following formulation of aerodynamic forces is assumed during the landing. It includes ground effect.

C_L after touchdown:

$$C_{L_{LDG}} = (C_{L_0} + C_{L_\alpha}\alpha_{LDG})\Phi_L \tag{23-3}$$

Lift:
$$L = \frac{1}{2}\rho V^2 S C_{L_{LDG}} \tag{23-4}$$

Adjusted induced drag coefficient:

$$C_{D_i} = k\left(C_{L_0} + C_{L_\alpha}\alpha_{LDG} - C_{L_{\min_D}}\right)^2 \Phi_D \tag{23-5}$$

C_D during T-O:

$$C_{D_{LDG}} = C_{D_{\min}} + \Delta C_{D_{flaps}} + C_{D_i} \tag{23-6}$$

General-drag:
$$D = \frac{1}{2}\rho V^2 S C_{D_{LDG}} \tag{23-7}$$

where C_{D_i} is the induced drag coefficient of aircraft during the landing ground run, α_{LDG} is the angle-of-attack during the T-O run, and Φ_L and Φ_D are the ground influence coefficients for lift and drag, respectively. Refer to Section 9.5.11, *Ground Effect* for appropriate methods. $\Delta C_{D_{flaps}}$ is added drag due to flaps. Use the methods of Section 16.4.7, *Drag of Deployed Flaps*, to estimate $\Delta C_{D_{flaps}}$. Also note that the induced drag must be corrected for ground effect, in particular if the airplane uses flaps or if its attitude is such its ground run AOA is high.

23.2.4 Ground Roll Friction Coefficients

The airplane has to overcome aerodynamic drag and ground friction during the ground roll. The ground friction depends on the weight-on-wheels and the properties of the ground. These are assessed using the ground roll friction coefficients in Table 23-3. This is the same table as Table 18-4, and is merely repeated here for convenience.

23.2.5 Determination of the Approach Distance, S_A

The geometry of the approach for landing is shown in Figure 23-3. In order to determine the distance from the obstacle to the point where the pilot initiates flare the approach angle, γ_{app}, and flare height, h_F, must be computed. The target approach angle for most airplanes is 3 degrees. For instance, airport approach lights (VASIS for *visual approach slope indicator system*) give the correct light signal when the airplane is approaching at that descent angle. For other applications, the approach angle can also be calculated using Equation (22-9) or (22-10) for unpowered or powered descents, repeated here for convenience:

Powered descent:

$$\sin\gamma = \frac{D}{W} - \frac{T}{W} \approx \frac{1}{L/D} - \frac{T}{W} \tag{22-9}$$

Unpowered descent:

$$\tan\gamma = \frac{D}{L} = \frac{1}{L/D} \approx \frac{D}{W} \tag{22-10}$$

However, as stated above. Simply assuming $\gamma_{app} = 3°$ is a good initial assumption. Knowing γ_{app} allows the approach distance, S_A, to be estimated by first calculating the flare height, h_F, from the following expression:

$$h_F = R\left(1 - \cos\gamma_{app}\right) \approx 0.1512 \times V_{S_0}^2 \times \left(1 - \cos\gamma_{app}\right) \tag{23-8}$$

Then, the approach distance, S_A, can be determined from:

$$S_A = \frac{(h_{obst} - h_F)}{\tan\gamma_{app}} \tag{23-9}$$

The airspeeds used in the analysis are listed in Table 23-4.

TABLE 23-4 Definition of important airspeeds for the landing run.

Name	Airspeed	GA aircraft (FAR 23)[a]	Commercial (FAR 25)[b]	Military
Reference	V_{REF}	$1.3V_{S_0}$	$<1.23V_{S_0}$	$1.2V_{S_0}$
Flare	V_{FLR}	$1.3V_{S_0}$	$<1.23V_{S_0}$	$1.2V_{S_0}$
Touch-down	V_{TD}	$1.1V_{S_0}$	$1.1V_{S_0}$	$1.1V_{S_0}$
Braking	V_{BR}	$1.1V_{S_0}$	$1.1V_{S_0}$	$1.1V_{S_0}$

[a] *Per 14 CFR Part 23, §23.73 Reference Landing Approach Speed.*
[b] *Actual* V_{REF} *is established per 14 CFR Part 25, § 25.125 Landing.*

DERIVATION OF EQUATIONS (23-8) AND (23-9)

Assume the flare involves slowing down from V_{REF} ($= 1.3V_{S_0}$) to airspeed just above stall, where V_{S_0} is the stalling speed in the landing configuration. Many pilots of light aircraft slow down enough to initiate the audible stall warning of the airplane, reminding us that pilot technique can have great influence on the total landing distance. The aural warning often begins to sound some 5 knots above the stalling speed. This may be less than 10% of the stalling speed. This is further influenced by the "floating" of the airplane in ground effect. For analysis purposes, we must rigorously define the characteristics of the landing maneuver, while simultaneously be mindful of the importance of pilot technique. Larger GA aircraft slow down to perhaps 10%–15% above stall. Here the airspeed immediately before touchdown will be assumed to be 10% of the stalling speed or $V_{TD} = 1.1V_{S_0}$. This implies an average airspeed of $1.2V_{S_0}$

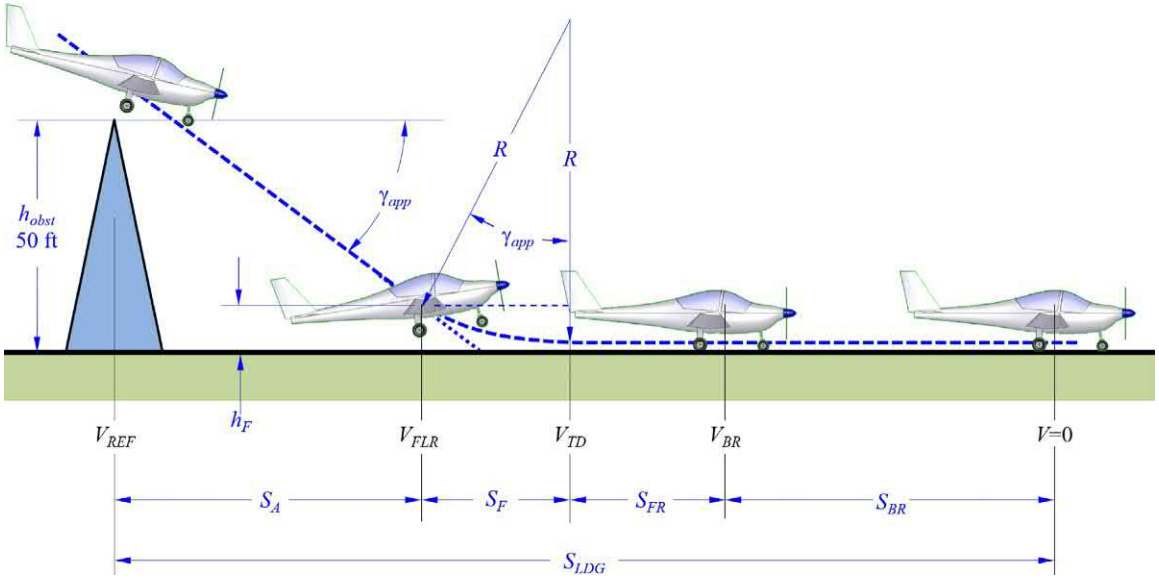


FIGURE 23-3 Evaluation of the landing over an obstacle.

during the maneuver and this is used in addition to an assumed lift coefficient of about $0.9C_{L_{max}}$ to determine distance traveled as follows:

Average vertical acceleration in terms of load factor.

$$n=\frac{L}{W}=\frac{\frac{1}{2}\rho(1.2V_{S_0})^2S(0.9C_{L_{max}})}{\frac{1}{2}\rho V_{S_0}{}^2\,SC_{L_{max}}}=1.296 \qquad (23\text{-}10)$$

Using Equation (18-27) (derived in Chapter 18), we calculate the transition radius, R, where we replace the transition speed, V_{TR}, by $1.2V_{S_0}$.

$$R=\frac{V_{TR}^2}{g(n-1)}=\frac{(1.2V_{S_0})^2}{g(1.296-1)}\approx 0.1512\;V_{S_0}^2 \qquad (23\text{-}11)$$

Where $g=32.174\,\text{ft/s}^2$. The resulting constant of 0.1512 is applicable to GA aircraft only in the UK-system. It amounts to 0.4961 in the SI-system.

Determine the flare height:

$$h_F=R\left(1-\cos\gamma_{app}\right)\approx 0.1512\times V_{S_0}^2\times\left(1-\cos\gamma_{app}\right) \qquad (23\text{-}12)$$

23.2.6 Determination of the Flare Distance, S_F

By observation using Figure 23-3 the flare distance, S_F, can be determined from:

$$S_F=R\sin\gamma_{app}\approx 0.1512\times V_{S_0}^2\times\sin\gamma_{app} \qquad (23\text{-}13)$$

23.2.7 Determination of the Free-Roll Distance, S_{FR}

The free-roll distance is determined similarly as the rotation distance in the T-O analysis. The airplane is assumed to roll freely for a few seconds only. The airspeed is assumed constant at V_{TD} (see Figure 23-3), which implies $V_{TD}=V_{BR}$. It is appropriate to assume that small aircraft travel freely for 1 and 3 s for large ones. This results in similar equations as that of Section 18.3.2, *Calculating the Rotation Distance*, or:

Small aircraft: $$S_{FR}=|V_{TD}| \qquad (23\text{-}14)$$

Large aircraft: $$S_{FR}=3|V_{TD}| \qquad (23\text{-}15)$$

23.2.8 Determination of the Braking Distance, S_{BR}

The final segment involves the determination of the distance when the pilot begins to apply any braking device until the airplane comes to a complete stop. Braking devices were introduced in Section 23.2.2. As stated in Section 23.2.2, nonsimultaneous application of braking devices calls for numerical integration. Otherwise, a simpler approach can be based on method presented in Section 18.3.1, *Calculating the Ground Run Distance*. In this approach, the deceleration can be assumed to consist of the simultaneous application of all braking devices. The approach is applicable to both piston engine airplanes and jets, the only difference lies in how the thrust is calculated. The ratios inside the brackets are evaluated when $V=V_{BR}/\sqrt{2}$, where V_{BR} is the airspeed where the braking is first applied:

$$S=\frac{V^2}{2a}\;\Rightarrow\;S_{BR}=-\frac{V_{BR}^2W}{2g\left[T-D_{ldg}-\mu(W-L)\right]_{at\;\left(V_{BR}/\sqrt{2}\right)}} \qquad (23\text{-}16)$$

The thrust, T, can be positive or negative (see Table 23-5). It is positive for fixed pitch or constant speed propellers, but is negative if reverse thrust is applied. Also note that the negative sign in front of the expression ensures that the distance will be a positive value, since the denominator (the deceleration) will have a negative sign.

The term D_{lgd} is the drag of the airplane in the landing configuration with braking. This usually implies deployed high lift devices (flaps and slats), but also spoilers or speed brakes. Typically, speed brakes are deployed (often automatically) as soon as the aircraft touches down and then later are retracted before the airplane comes to a complete stop. A similar scenario holds for the thrust reversers. Equation (23-16) is not applicable to such intermittent use of braking devices. These

TABLE 23-5 Suggested thrust values for braking distance.

Type of engine	Sign of thrust	Comment
Fixed pitch propeller	$T>0$	Assume $T\approx$5%–7% of static thrust. Five percent for cruise propellers and 7% for climb propellers
Constant speed propeller	$T>0$	Assume $T\approx$7% of static thrust
Reverse thrust props—piston	$T<0$	Assume $T\approx-40\%$ of static thrust
Reverse thrust props—turboprop	$T<0$	Assume $T\approx-60\%$ of static thrust
Jet—no thrust reverser	$T>0$	Assume $T=T_{idle}$
Jet—thrust reverser	$T<0$	Assume $T\approx-40\%$ to -60% of static thrust. Can typically only be operated at airspeeds higher than 40–50 KCAS

must be solved using numerical integration as mentioned earlier.

If the propeller efficiency and engine power at $V = V_{BR}/\sqrt{2}$ is known, Equation (23-16) can be rewritten as follows:

$$S = \frac{V^2}{2a} \Rightarrow$$

$$S_{BR} = -\frac{V_{BR}^2 W}{2g\left[\frac{\sqrt{2}\cdot\eta_p\cdot 550\cdot P_{BHP}}{V_{BR}} - D_{ldg} - \mu(W-L)\right]_{at\ (V_{BR}/\sqrt{2})}} \tag{23-17}$$

EXAMPLE 23-1

Determine the landing distance over 50 ft obstacle and landing run for the SR22 on a standard day at S-L. Consider a runway whose braking conditions are estimated using the ground friction coefficient of $\mu = 0.3$. Assume a 3 degrees glide path (γ_{app}), a landing weight of 3400 lb_f, propeller efficiency of 0.45 and idle engine power of 50 BHP at the airspeed $V = V_{BR}/\sqrt{2}$. Furthermore, assume a $C_{DLDG} = 0.040$ and $C_{LLDG} = 0.9$. Compare to the POH values of 1141 ft ground roll and 2344 ft over 50 ft.

SOLUTION:

Begin by determining the four airspeeds of interest, V_{REF}, V_{FLR}, V_{TD}, and V_{BR}, based on GA aircraft and noting that the stalling speed in the landing configuration is $V_{S_0} = 59$ KCAS.

$$V_{REF} = 1.3\ V_{S_0} = 76.7\ \text{KCAS} = 129.5\,\text{ft/s}$$
$$V_{FLR} = 1.3\ V_{S_0} = 76.7\ \text{KCAS} = 129.5\,\text{ft/s}$$
$$V_{TD} = 1.1\ V_{S_0} = 64.9\ \text{KCAS} = 109.6\,\text{ft/s}$$
$$V_{BR} = 1.1\ V_{S_0} = 64.9\ \text{KCAS} = 109.6\,\text{ft/s}$$

Then, the approach distance must be determined. The flare height, h_F, is estimated using Equation (23-8):

$$h_F \approx 0.1512\cdot V_{S_0}^2\cdot\left(1-\cos\gamma_{app}\right)$$
$$= 0.1512\cdot(59\times 1.688)^2\cdot(1-\cos 3^\circ) = 2.1\,\text{ft}$$

The obstacle height, h_{obst}, for GA aircraft is 50 ft. The distance covered from an altitude of 50 ft to the beginning of the flare is determined using Equation (23-9):

$$S_A = (h_{obst} - h_F)/\tan\gamma_{app} = (50-2.1)/\tan 3^\circ = 914\,\text{ft}$$

The distance covered during the flare is given by Equation (23-13):

$$S_F \approx 0.1512\times V_{S_0}^2\times\sin\gamma_{app} = 0.1512(59\times 1.688)^2\sin 3^\circ$$
$$= 78.5\,\text{ft}$$

The airplane will roll for a brief moment after touchdown before the pilot applies brakes. The distance covered during this time, which for a GA aircraft is considered 1 s, is the free-roll distance, S_{FR}. It is obtained using Equation (23-14):

$$S_{FR} = V_{TD} = 109.6\,\text{ft}$$

Finally, the braking distance is calculated using Equation (23-17):

$$S_{BR} = -\frac{V_{BR}^2 W}{2g\left[\sqrt{2}\cdot\eta_p\cdot 550\cdot P_{BHP}/V_{BR} - D_{ldg} - \mu(W-L)\right]_{at\ (V_{BR}/\sqrt{2})}}$$

To solve this, it is easiest to calculate the lift and drag separately. Note that the value of $C_{LLDG} = 0.9$, is simply the value at $\alpha_{LDG} = 0^\circ$ (or whatever landing attitude is considered realistic), with the flaps deflected in the landing setting (for the SR22 this is 32°).

Lift: $$L = \frac{1}{2}\rho\left(\frac{V_{BR}}{\sqrt{2}}\right)^2 S C_{L_{LDG}}$$
$$= \frac{1}{2}(0.002378)\left(\frac{109.6}{\sqrt{2}}\right)^2(144.9)(1.0) = 1035\ \text{lb}_\text{f}$$

Drag: $$D = \frac{1}{2}\rho\left(\frac{V_{BR}}{\sqrt{2}}\right)^2 S C_{D_{LDG}}$$
$$= \frac{1}{2}(0.002378)\left(\frac{109.6}{\sqrt{2}}\right)^2(144.9)(0.04) = 41.4\ \text{lb}_\text{f}$$

Substituting these numbers into Equation (23-17), yields:

$$S_{BR} = -\frac{(109.6)^2(3400)}{2(32.174)\left[\frac{\sqrt{2}\cdot(0.45)\cdot 550\cdot(50)}{109.6} - 41.4 - (0.3)(3400-1035)\right]}$$
$$= 1074\ \text{ft}$$

The total landing distance from 50 ft is thus:

$$S_{LDG} = S_A + S_F + S_{FR} + S_{BR} = 914 + 78.5 + 109.6 + 1074$$
$$= 2176\,\text{ft}$$

The landing ground roll is:

$$S_{FR} + S_{BR} = 109.6 + 1074 = 1184\,\text{ft}$$

These number deviate as follows from the POH values:

Total landing distance: $100\left(\frac{2176-2344}{2344}\right) = -7.2\%$

Ground roll distance: $100\left(\frac{1184-1141}{1141}\right) = +3.8\%$

This method is in good agreement with the book values.

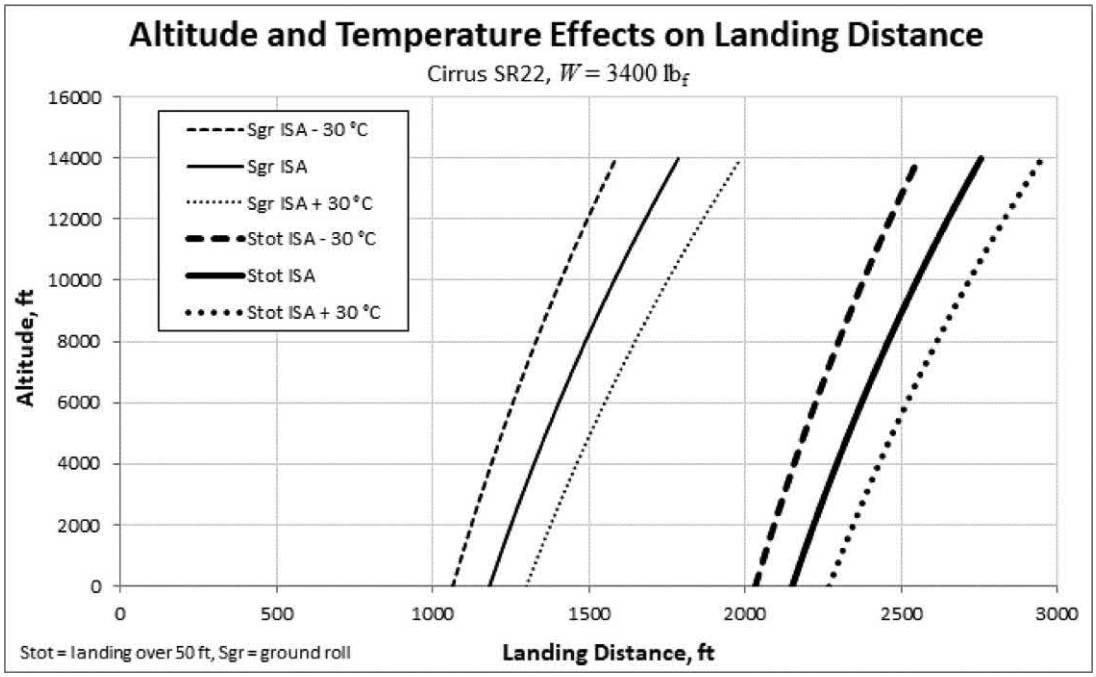


FIGURE 23-4 Sensitivity study showing the effect of altitude and temperature on the landing distance of the SR22. The study was performed using the analysis method presented in this section.

23.2.9 Landing Distance Sensitivity Studies

Landing at high elevation and on hot days, when density is much lower than on standard day at S-L, poses serious challenges to airplane operations. Since the airplane moves faster with respect to the ground than at lower altitudes, the landing distance increases and the brake energy required to slow down is much higher (it depends on the kinetic energy). These effects are studied using density altitude and true airspeed. These are called *landing distance sensitivity analysis*.

The results of an analysis of the change in landing distance due to altitude and ambient temperate is presented in Figure 23-4. The graph plots the estimated landing distance for the SR22 from S-L to 14,000 ft for ±30°C deviations from ISA. It can be seen that at S-L the temperature deviation results in about ±120 ft change in landing over 50 ft obstacle, when compared to standard day conditions.

23.2.10 COMPUTER CODE: Estimation of Landing Performance

The following Visual Basic for Applications routine can be used to determine the landing distance for an aircraft. If the obstacle height is larger than zero, the routine calculates the entire landing distance. Set the obstacle height to zero to extract only the landing ground run. The routine makes calls to the routine `AtmosProperty` (see Section A.2.10, *COMPUTER CODE A-1: Atmospheric Modeling*) to allow the user to evaluate landing distances at hot and high airports. The affected instructions can be replaced with the atmospheric formulas of Chapter 17. This is done using the arguments `H` and `deltaISA`, where the temperature deviation is that from the standard temperature at that altitude. This code was used with Microsoft Excel to generate the graph of Figure 23-4.

```
Function PERF_Landing(W As Single, S As Single, CL_ldg As Single, CD_ldg As Single, T
As Single, theta_app As Single, mu As Single, Vso As Single, H As Single, deltaISA As
Single, Hobst As Byte) As Single
'This routine will calculate the landing distance for an aircraft using the method of
'Chapter 22, Performance - Landing.
'
'Variables:     W          = Weight in lbf
'               S          = Reference wing area in ft²
'               CL_ldg     = Lift coefficient during ground run
'               CD_ldg     = Drag coefficient during ground run
'               T          = Thrust at VBR/sqr(2)
'               theta_app  = Approach angle in degrees (typ. 3°)
'               mu         = Ground friction coefficient
'               Vso        = Stalling speed in the landing configuration in ft/s
```

```
'               H         = Airport elevation in ft
'               deltaISA  = Deviation from ISA in °R
'               Hobst     = Obstacle height in ft. Set Hobst=0 for ground roll only.
'
'Note that this routine calls the function AtmosProperty, so it must be present.
'
'Initialize
    Dim Vref As Single, Vflr As Single, Vtd As Single, Vbr As Single
    Dim SA As Single, SF As Single, SFR As Single, SBR As Single
    Dim Hf As Single, theta As Single
    Dim OAT As Single, P As Single, rho As Single, sigma As Single
    Dim L As Single, Dldg As Single

'Presets

    theta = theta_app * 3.14159265 / 180    'Convert approach angle to radians
    OAT = AtmosProperty(H, 10) + deltaISA   'Corrected temperature at altitude
    P = AtmosProperty(H, 11)                'Pressure at altitude
    rho = P / (1716 * OAT)                  'Corrected density at altitude
    sigma = rho / 0.002378                  'Density ratio at altitude
    Vref = 1.3 * Vso * 1.688 / Sqr(sigma)   'Reference airspeed
    Vflr = 1.3 * Vso * 1.688 / Sqr(sigma)   'Flare airspeed
    Vtd = 1.1 * Vso * 1.688 / Sqr(sigma)    'Touchdown airspeed
    Vbr = 1.1 * Vso * 1.688 / Sqr(sigma)    'Braking airspeed

'Determine approach distance, SA
    Hf = 0.1512 * Vso ^ 2 * (1 - Cos(theta))
    SA = (Hobst - Hf) / Tan(theta)

'Determine flare distance, SF
    SF = 0.1512 * Vso ^ 2 * Sin(theta)

'Determine free roll distance, SFR
    SFR = Vtd

'Determine braking distance, SBR (note that 0.5*rho*(Vbr/Sqr(2))^2 = 0.25*rho*Vbr^2
    Dldg = 0.25 * rho * Vbr ^ 2 * S * CD_ldg
    L = 0.25 * rho * Vbr ^ 2 * S * CL_ldg
    SBR = -Vbr ^ 2 * W / (2 * 32.174 * (T - Dldg - mu * (W - L)))

'Determine distance
    If Hobst = 0 Then 'Ground run only is being requested
        PERF_Landing = SFR + SBR
    Else
        PERF_Landing = SA + SF + SFR + SBR
    End If
End Function
```

23.3 DATABASE—LANDING PERFORMANCE OF SELECTED AIRCRAFT

Table 23-6 shows the landing run and distance from a 50-ft altitude above ground level. These data are a helpful reference when evaluating the accuracy of own calculations.

TABLE 23-6 Landing performance of selected aircraft.

Aircraft	Gross Wgt (lb_f)	Ldg from 50 ft (ft)	Landing run (ft)	References
Single-engine GA aircraft				
Aero Boero 115	1697	500	150	Jane's 1976–77

Continued

TABLE 23-6 Landing performance of selected aircraft—cont'd

Aircraft	Gross Wgt (lb_f)	Ldg from 50 ft (ft)	Landing run (ft)	References
Beech A36 Bonanza	3600	1450	840	Jane's 1978–79
Beech Sundowner	2030	1484	703	
Beech V35 Bonanza	3400	1324	763	
Cessna 152	1670	1200	475	
Cessna 172 Skyhawk	2300	1250	520	
Cessna 177 Cardinal	2800	1350	730	

Continued

TABLE 23-6 Landing performance of selected aircraft—cont'd

Aircraft	Gross Wgt (lb_f)	Ldg from 50 ft (ft)	Landing run (ft)	References
Cessna 185 Skylane	2950	1350	590	
Cessna 210 Centurion	3800	1500	765	
Cirrus SR20	3050	2636	853	POH
Cirrus SR22	3400	2344	1141	
Piper PA-18 Super Cub	1750	885	350	Jane's 1978–79
Piper PA-28 Warrior II	2325	1115	595	
Piper PA-32 Lance II	3600	1710	880	
Piper PA-38 Tomahawk	1670	1465	625	
SIAI-Marchetti SF-260	2425	2264	1132	Jane's 1976–77
Multiengine GA aircraft				
Beech Duchess 76	3900	1881	1000	Jane's 1978–79

TABLE 23-6 Landing performance of selected aircraft—cont'd

Aircraft	Gross Wgt (lb_f)	Ldg from 50 ft (ft)	Landing run (ft)	References
Beech Duke B60	6775	3065	1318	
Beech King Air C90	9650	2010	1075	
Cessna 310	5500	1790	640	
Cessna 337 Skymaster	4630	1650	700	
Cessna 340	5990	1615	2175	
DHC-6 Twin Otter	12,500	1050–1940	515–950	Jane's 1976–77
Partenavia P-68B Victor	4321	1295	820	
Piper PA-23 Aztec	5200	1310	–	Jane's 1978–79
Piper PA-31 Cheyenne	9000	1860	–	
Piper PA-31 Chieftain	7000	1880	1045	
Piper PA-34 Seneca II	4570	2090	1380	

References

[1] C.D. Perkins, R.E. Hage, *Airplane Performance, Stability, and Control*, John Wiley & Sons, 1949.

[2] E. Torenbeek, *Synthesis of Subsonic Aircraft Design*, third ed., Delft University Press, 1986.

[3] L. Nicolai, *Fundamentals of Aircraft Design*, second ed., 1984.

[4] J. Roskam, C.-T.E. Lan, *Airplane Aerodynamics and Performance*, DAR-corporation, 1997.

[5] F.J. Hale, *Aircraft Performance, Selection, and Design*, John Wiley & Sons, 1984, pp. 137–138.

[6] J.D. Anderson Jr., *Aircraft Performance & Design*, first ed., McGraw-Hill, 1998.

[7] A. Miele, *Flight Mechanics—Theory of Flight Paths*, Dover Publications, 1990.

CHAPTER

24

Longitudinal Stability and Control

OUTLINE

24.1 **Introduction** 925
- *24.1.1 The Content of This Chapter* 926
- *24.1.2 Coordinate Systems for Stability and Control* 926
- *24.1.3 Coordinate Transformation Matrices* 927
- *24.1.4 The Rigid Body Equations-of-Motion* 929
- *24.1.5 Formulation of Forces and Moments* 929
- *24.1.6 Basics of Aircraft Control* 930
- *24.1.7 Basic Aircraft Geometry for Longitudinal Stability and Control* 931
- *24.1.8 Important Note to the Reader* 931

24.2 **Static Longitudinal Stability and Control** 931
- *24.2.1 Equations-of-Motion for Static Longitudinal Stability* 932
- *24.2.2 Requirements for Static Longitudinal Stability* 932
- *24.2.3 Historical Values of $C_{M\alpha}$* 935
- *24.2.4 The Thrust Model, C_T* 937
- *24.2.5 The Lift Model, C_L* 937
- *24.2.6 The Drag Model, C_D* 940
- *24.2.7 The Pitching Moment Model, C_M* 941
- *24.2.8 Horizontal Tail Downwash Angle and Angle-of-Attack* 944
- *24.2.9 Tail Efficiency Factor, η_{HT}* 945
- *24.2.10 Forces and Moments due to Fuselage and Nacelles* 945
- *24.2.11 Contribution of Thrust—Moment due to Offset Thrustline and Normal Force* 951
- *24.2.12 Contribution of the Landing Gear* 955
- *24.2.13 Compressibility Effect on Pitching Moment* 957

24.3 **Refined Horizontal Tail Sizing** 957
- *24.3.1 Fundamentals of Pitch Control* 957
- *24.3.2 Roadmap to Sizing the Horizontal Tail and Elevator* 958
- *24.3.3 Longitudinal Stability of a Simple Wing–HT–Engine System* 960
- *24.3.4 The Stick-Fixed Neutral Point (Aerodynamic Center)* 961
- *24.3.5 Trimming for Steady Level Flight* 964
- *24.3.6 A Simplified Theory of V-Tails* 966

24.4 **Introduction to Hinge Moments** 966
- *24.4.1 Fundamental Definitions* 967
- *24.4.2 Introduction to Control System Loads and Gain* 970
- *24.4.3 Trim Tabs* 971
- *24.4.4 Control Horns* 972

References 973

24.1 INTRODUCTION

Heavier-than-air flight requires specific ingredients: *lift*, *stability*, and *control*. The generation of lift has already been expounded on. *Stability* refers to the tendency of an airplane to maintain its attitude in flight. For instance, we want the airplane to maintain a specific angle-of-attack (AOA or α) and angle-of-yaw (AOY or β). *Control* refers to the ability to change the airplane's attitude. An airplane has *static longitudinal stability* if it maintains a desired α. Otherwise, it is longitudinally unstable.[1] This is stability about the *y*-axis in Figure 24-2. The airplane must also possess stability about the *x*- and *z*-axes. These are referred to as *rolling* (or *lateral*) and *directional stability*. This chapter focuses primarily on longitudinal stability, while Chapter 25 treats lateral and directional stability.

The longitudinal stability of an aircraft is achieved by placing its center-of-gravity (CG) ahead of the

[1] Dynamic stability is another aspect of stability theory not presented in this version of the book. An airplane can be simultaneously statically stable and dynamically unstable.

https://doi.org/10.1016/B978-0-12-818465-3.00024-0

Copyright © 2022 Elsevier Inc. All rights reserved.

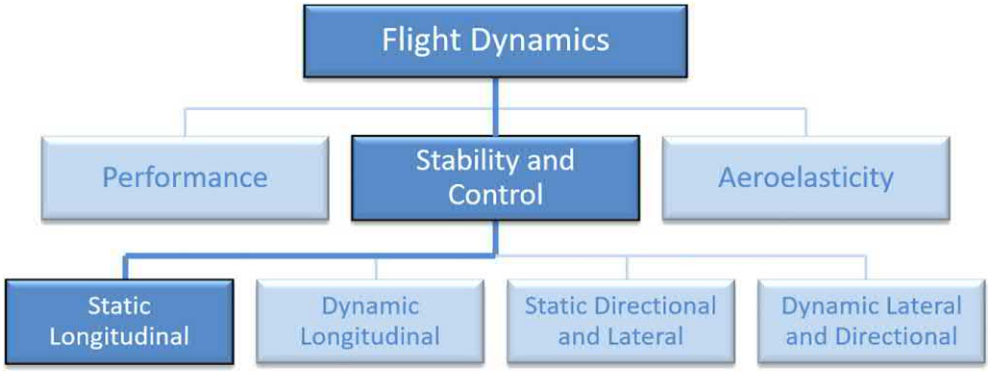


FIGURE 24-1 Static longitudinal stability.

aerodynamic center (AC, aka *stick-fixed neutral point*). This was illustrated in Figures 9-20 and 9-56. Deviations in the motion of the aircraft requires *control* to be exerted. The aircraft designer must be able to predict the positions of the CG and AC, and, accordingly, size control surfaces to provide adequate control, while providing pleasant control feel (handling). These problems demand a scientific investigation supported by mathematics. This is the essence of *stability and control theory*. It is a subfield inside *flight dynamics*, a branch of *mechanics*. Flight dynamics is often broken into *performance*, *stability-and-control*, and *aeroelasticity* (see Figure 24-1). Stability and control comprise two sub-fields: *statics* and *dynamics*. Statics considers the equilibrium of matter for which linear and angular acceleration is zero. Dynamics studies the equilibrium of matter undergoing linear and angular accelerations.

The presentation in this chapter is in a *review format*. The literature offers multiple texts on the topic in a *derivation format*. This is helpful to students. Review format is common in design texts. It is important to professionals already familiar with the field. Advantage: faster read due to absence of explanatory material with which professionals are already familiar. Drawback: the reader must recognize the mathematics and concepts presented.

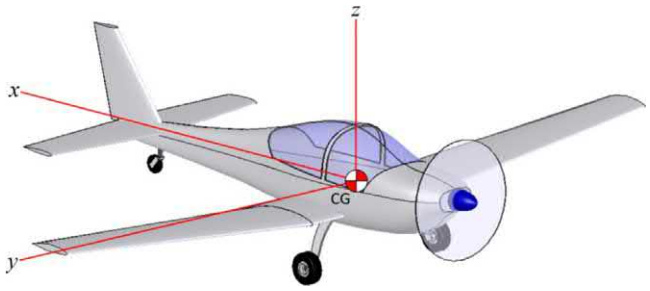


FIGURE 24-2 Vehicle coordinate system (VCS).

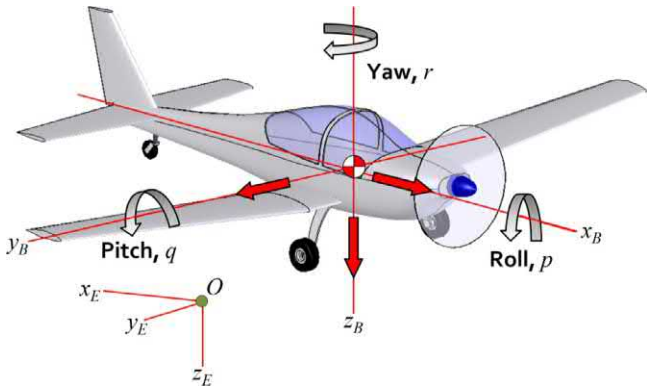


FIGURE 24-3 Body (BC) and fixed earth (FES) coordinate systems.

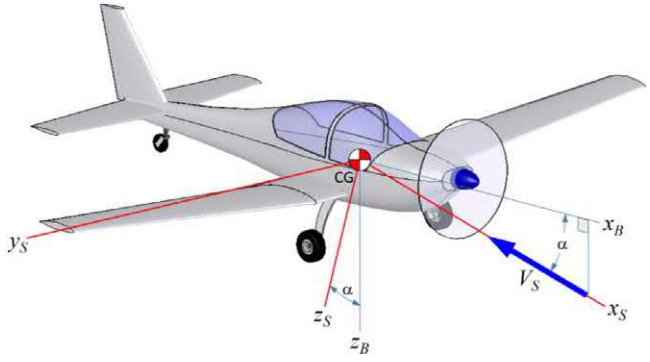


FIGURE 24-4 Stability coordinate system (SCS).

24.1.1 The Content of This Chapter

- Section 24.2 presents the essence of static longitudinal stability theory.
- Section 24.3 presents the essence of static lateral–directional stability theory.
- Section 24.4 Introduces hinge moments and associated analyses.

24.1.2 Coordinate Systems for Stability and Control

Stability and control theory uses several coordinate systems. Four are shown in Figures 24-2–24-5. All are

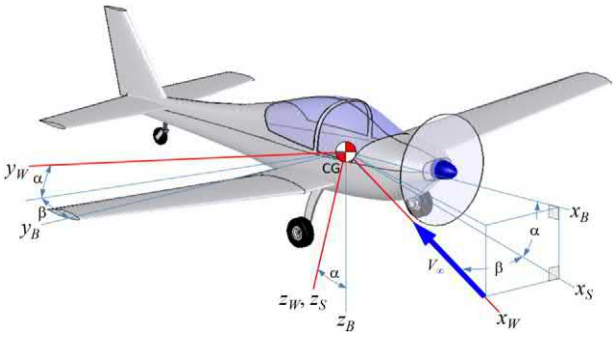


FIGURE 24-5 Wind axis coordinate system (WAS).

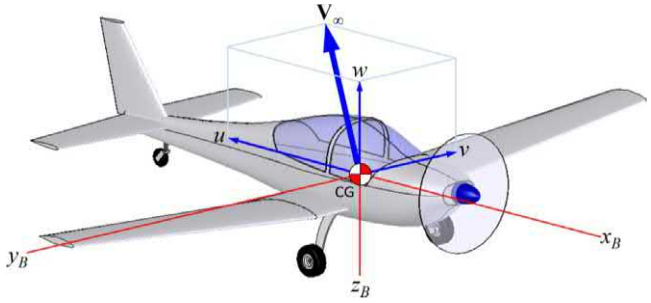


FIGURE 24-6 Velocity components.

orthogonal Cartesian coordinate systems that usually place the origin at the center-of-gravity (CG).

(1) Vehicle Coordinate System (VCS)

Basic problems involving aerodynamics and solid mechanics (structures) use the VCS. In this system, the x-axis points toward the tail, the y-axis points at the right wingtip, and the z-axis points upward (Figure 24-2). The origin may be placed at the CG, as shown, or any other fixed reference point. It is a right-handed coordinate system for which lift and drag have positive signs, while thrust and weight have negative signs.

(2) Body Coordinate System (BCS)

The origin of the BCS is always at the airplane's CG. Its axes are denoted using the subscript "B." It is oriented such the positive x_B-axis points forward, y_B-axis points at the right wingtip, and the z_B-axis points downwards. The x_B- and z_B-axes *form* the plane-of-symmetry (see Figure 24-3). It is used to specify aerodynamic forces with respect to the aircraft. In this system, lift and drag have negative signs, while thrust and weight have positive signs. The rotation about the x-axis is called *roll*, about the y-axis is *pitch*, and about the z-axis is *yaw*. Using the right-hand rule of rotation, positive roll rotates the right wing down, positive pitch rotates the nose up, and positive yaw rotates the nose to the right. These positive rotations are indicated in Figure 24-3.

(3) Fixed Earth Coordinate System (FES)

This coordinate system is required for flight simulation. It is shown as O-x_E-y_E-z_E in Figure 24-3. This system is sometimes called NED for North-East-Down.

The far-field velocity is a vector $\mathbf{V}_\infty = u\mathbf{i} + v\mathbf{j} + w\mathbf{k}$, as illustrated in Figure 24-6. Where u is the component of the airspeed along the x_B-axis, v along the y_B-axis, and w along the z_B-axis (see Figure 24-6). Thus, we can define α, β, and airspeed as follows:

$$\tan\alpha = w/u \tag{24-1}$$

$$\sin\beta = v/V_\infty \tag{24-2}$$

$$V_{uw} = \sqrt{u^2 + w^2} \tag{24-3}$$

$$V_\infty = |\mathbf{V}_\infty| = \sqrt{u^2 + v^2 + w^2} \tag{24-4}$$

(4) Stability Coordinate System (SCS)

The origin of the SCS is always the airplane's CG and is denoted using the subscript "S." The positive x_S-axis points forward, y_S-axis points at the right wingtip, and the z_S-axis points downwards (see Figure 24-4). The x_S and z_S axes *form* the plane-of-symmetry but are rotated so the x_S-axis is aligned with the projection of the far-field velocity on the plane-of-symmetry. The angle between the x_B-axis and the x_S-axis is the *angle-of-attack*, α (see Figure 24-4).

(5) Wind Axis Coordinate System (WAS)

The origin of the WAS is always at the airplane's CG and is denoted using the subscript "W." The positive x_W-axis is aligned with the far-field velocity, while the z_W-axis lies in the plane-of-symmetry (like the z_S-axis). Thus, the y_W-axis is rotated about the z_W/z_S-axis through angle β, called the *angle-of-yaw* (see Figure 24-5). The wind axis is important because it defines the orientation of the airplane with respect to the wind. *NOTE: Figure 24-5 shows a positive* α *and positive* β.

The angular accelerations can play a role in the total moment of the aircraft through the stability derivatives $\boldsymbol{C}_{\boldsymbol{M}_{\dot\alpha}}$ and $\boldsymbol{C}_{\boldsymbol{M}_{\dot\beta}}$. As shown by Stevens and Lewis [1] and Allerton [2], these are calculated in following fashion.

Rate-of-change of α:
$$\dot\alpha = \frac{u\cdot\dot w - w\cdot\dot u}{V_{uw}} \tag{24-5}$$

Rate-of-change of β:
$$\dot\beta = \frac{\dot v\cdot V_{uw} - v\,(u\cdot\dot u + w\cdot\dot w)}{V_{uw}\cdot V_\infty^2} \tag{24-6}$$

where $\dot u, \dot v, \dot w$ are the translational accelerations.

24.1.3 Coordinate Transformation Matrices

Our goal is to establish the *equations-of-motion* (EOM) for the aircraft along its body axis. Since V_∞ defines the

TABLE 24-1 Nomenclature for stability and control terms.

Description	Symbol	Remarks
Position	x,y,z	
Airspeed components (BCS)	$\mathbf{V}_\infty = (u,v,w)$	(V_x,V_y,V_z) is also used. Positive u is in the direction of flight. Positive v is to the right. Positive w is down.
Linear acceleration	$\dot{\mathbf{V}}_\infty = (\dot{u},\dot{v},\dot{w})$	Where $\dot{*} \equiv \frac{d*}{dt}$, where * is some argument.
Angular velocity (BCS)	$\Omega = (\hat{p},\hat{q},\hat{r})$	$\hat{p}$ is rotation about the x-axis (roll), $\hat{q}$ about the y-axis (pitch), and $\hat{r}$ about the z-axis (yaw).
Angular acceleration (BCS)	$\dot{\Omega} = \left(\dot{\hat{p}},\dot{\hat{q}},\dot{\hat{r}}\right)$	$\dot{\hat{p}}$is roll acceleration, $\dot{\hat{q}}$ is pitch acceleration, and $\dot{\hat{r}}$ is yaw acceleration.
Euler Angles (NED)	ϕ, θ, ψ	ϕ is rotation about the NED x-axis (roll), θ about the NED y-axis (pitch), and ψ about the NED z-axis (yaw).
Forces along Body Axes (BCS)	X,Y,Z	(F_x,F_y,F_z) is also used.
Moments about Body Axes (BCS)	$\boldsymbol{L,M,N}$	$T=(T_x,T_y,T_z)$ or $M=(M_x,M_y,M_z)$ is also used.

wind axis, we seek transformations that allow us to switch from one coordinate system to the next. We do this using rotation matrices based on the *Euler angles* $\{\phi, \theta, \psi\}$, where ϕ is roll, θ is pitch, and ψ is yaw. See Table 24-1 for common nomenclature.

(1) Transforming Body Axes to Stability Axes

Comparing Figures 24-3 and 24-4 shows the following relationship holds:

$$\begin{bmatrix} x_S \\ y_S \\ z_S \end{bmatrix} = \begin{bmatrix} \cos\alpha & 0 & \sin\alpha \\ 0 & 1 & 0 \\ -\sin\alpha & 0 & \cos\alpha \end{bmatrix} \begin{bmatrix} x_B \\ y_B \\ z_B \end{bmatrix} \tag{24-7}$$

(2) Transforming Stability Axes to Body Axes

By inspection, comparing Figures 24-3 and 24-4 reveals the following relationship holds:

$$\begin{bmatrix} x_B \\ y_B \\ z_B \end{bmatrix} = \begin{bmatrix} \sin\alpha & 0 & -\cos\alpha \\ 0 & 1 & 0 \\ -\cos\alpha & 0 & -\sin\alpha \end{bmatrix} \begin{bmatrix} x_S \\ y_S \\ z_S \end{bmatrix} \tag{24-8}$$

(3) Transforming Stability Axes to Wind Axes

Inspection and familiarity with rotation matrices shows that by comparing Figures 24-4 and 24-5 the following relationship (called *Euler angle rotation*) holds:

$$\begin{bmatrix} x_W \\ y_W \\ z_W \end{bmatrix} = \begin{bmatrix} \cos\beta & \sin\beta & 0 \\ -\sin\beta & \cos\beta & 0 \\ 0 & 0 & 1 \end{bmatrix} \begin{bmatrix} x_S \\ y_S \\ z_S \end{bmatrix} \tag{24-9}$$

(4) Transforming Body Axes to Wind Axes

Converting body axes to wind axes requires transformations (1) and (3) to be multiplied:

$$\begin{bmatrix} x_W \\ y_W \\ z_W \end{bmatrix} = \begin{bmatrix} \cos\alpha\cos\beta & \sin\beta & \sin\alpha\cos\beta \\ -\cos\alpha\sin\beta & \cos\beta & -\sin\alpha\sin\beta \\ -\sin\alpha & 0 & \cos\alpha \end{bmatrix} \begin{bmatrix} x_B \\ y_B \\ z_B \end{bmatrix} \tag{24-10}$$

(5) Transforming the Wind Axes to Body Axes

Transforming the velocity or force of gravity to the body axes system is accomplished using Euler rotations. The reader is directed to refs. [3–7] for better insight. What we do here is to use what is called the 3-2-1 sequence Euler rotation to compile the rotation matrix below

$$\begin{Bmatrix} x \\ y \\ z \end{Bmatrix} = \begin{bmatrix} C\psi\ C\theta & S\psi\ C\theta & -S\theta \\ -S\psi\ C\phi + C\psi\ S\theta\ S\phi & C\psi\ C\phi + S\psi\ S\theta\ S\phi & C\theta\ S\phi \\ S\psi\ S\phi + C\psi\ S\theta\ C\phi & -C\psi\ S\phi + S\psi\ S\theta\ C\phi & C\theta\ C\phi \end{bmatrix} \cdot \begin{Bmatrix} x_{old} \\ y_{old} \\ z_{old} \end{Bmatrix} \tag{24-11}$$

where $C(\cdot) = \cos(\cdot)$ and $S(\cdot) = \sin(\cdot)$. Note the following limits of the Euler angles $\{\phi, \theta, \psi\}$.

$$-\pi \le \psi \le +\pi, \quad -\pi \le \phi \le +\pi, \quad -\pi/2 \le \theta \le +\pi/2$$

(6) Transforming the Velocity to Body Axes Components

The velocity vector in the WAS is given by $\{V_\infty,0,0\}^T$. It is transformed to the velocity components u, v, w by noting that the Euler angles $\{\phi, \theta, \psi\}$ correspond to the angles of attack and yaw as $\{0, \alpha, -\beta\}$, where the minus sign "–" denotes that a positive side-slip angle is negative yaw angle. Substituting these into Equation (24-11) and simplifying leads to

$$\begin{Bmatrix} u \\ v \\ w \end{Bmatrix} = \begin{bmatrix} \cos\alpha\ \cos\beta & -\cos\alpha\ \sin\beta & -\sin\alpha \\ \sin\beta & \cos\beta & 0 \\ \sin\alpha\ \cos\beta & -\sin\alpha\ \sin\beta & \cos\alpha \end{bmatrix} \begin{Bmatrix} V_\infty \\ 0 \\ 0 \end{Bmatrix} = \begin{bmatrix} V_\infty\cos\alpha\cos\beta \\ V_\infty\sin\beta \\ V_\infty\sin\alpha\cos\beta \end{bmatrix} \tag{24-12}$$

24.1.4 The Rigid Body Equations-of-Motion

(1) Comments about Notation

(A) The similarity of variables used in stability and control theory and general aerodynamics requires means of separating the two. In this book, moments are presented in bold, e.g., rolling moment is $\boldsymbol{L}$ and its corresponding coefficient is $\boldsymbol{C_L}$, while forces are not. Thus, lift is denoted by L and lift coefficient by C_L. Bold typeface is only used for 3D moments.

(B) The literature uses the letter q to denote pitch rate and dynamic pressure. This is confusing. In this book, the rotation rates (in radians/s) are denoted with a hat; $\hat{p},\hat{q},\hat{r}$ while angular accelerations (in radians/s^2) are denoted by $\dot{\hat{p}},\dot{\hat{q}},\dot{\hat{r}}$, where the dot denotes a time derivative. However, this does not extend to associated derivates (e.g., $\boldsymbol{C_{Lq}}$ is used without a hat).

(2) The Rigid Body Equations-of-Motion

The motion of aircraft is subject to six degrees-of-freedom (DOF): three translational (along the x-, y-, and z-axes) and three rotational (about those axes). This motion is separated into longitudinal (*pitch*) and lateral–directional (*roll* and *yaw*). The former is treated in this chapter, the latter in Chapter 25. To describe the aircraft's motion, the six-DOFs require the set of 12 *equations-of-motion* (EOM) shown below. They describe the translation and rotation of the aircraft's CG.

Force Equations:

$$\begin{aligned} X - mg\sin\theta &= m(\dot{u} + \hat{q}w - \hat{r}v) \\ Y + mg\cos\theta\sin\phi &= m(\dot{v} + \hat{r}u - \hat{p}w) \\ Z + mg\cos\theta\cos\phi &= m(\dot{w} + \hat{p}v - \hat{q}u) \end{aligned} \tag{24-13}$$

Moment Equations:

$$\begin{aligned} \boldsymbol{L} &= I_{xx}\dot{\hat{p}} - I_{xz}\dot{\hat{r}} + (I_{zz} - I_{yy})\hat{q}\hat{r} - I_{xz}\hat{p}\hat{q} + (\hat{q}h_{SRz} - \hat{r}h_{SRy}) \\ \boldsymbol{M} &= I_{yy}\dot{\hat{q}} + (I_{xx} - I_{zz})\hat{p}\hat{r} + I_{xz}\left(\hat{p}^2 - \hat{r}^2\right) + (\hat{r}h_{SRx} - \hat{p}h_{SRz}) \\ \boldsymbol{N} &= I_{zz}\dot{\hat{r}} - I_{xz}\dot{\hat{p}} + (I_{yy} - I_{xx})\hat{p}\hat{q} + I_{xz}\hat{q}\hat{r} + (\hat{p}h_{SRy} - \hat{q}h_{SRx}) \end{aligned} \tag{24-14}$$

Rotation Rate Equations:

$$\begin{aligned} \hat{p} &= \dot{\phi} - \dot{\psi}\sin\theta \\ \hat{q} &= \dot{\theta}\cos\phi + \dot{\psi}\cos\theta\sin\phi \\ \hat{r} &= \dot{\psi}\cos\theta\cos\phi - \dot{\theta}\sin\phi \end{aligned} \tag{24-15}$$

Euler Rate Equations:

$$\begin{aligned} \dot{\phi} &= \hat{p} + \hat{q}\sin\phi\tan\theta + \hat{r}\cos\phi\tan\theta \\ \dot{\theta} &= \hat{q}\cos\phi - \hat{r}\sin\phi \\ \dot{\psi} &= \hat{q}\sin\phi\sec\theta + \hat{r}\cos\phi\sec\theta \end{aligned} \tag{24-16}$$

where

g = Gravitational acceleration,
h_x, h_y, h_z = Angular momentums about the x, y, and z axes, respectively,
h_{SRx}, h_{SRy}, h_{SRz} = Angular momentum of spinning rotors about the x, y, and z axes, respectively,
I_{xx}, I_{yy}, I_{zz}, I_{yz} = Moments and product of inertia about the x, y, and z axes, respectively,
m = Mass of the vehicle,
$\boldsymbol{L}$, $\boldsymbol{M}$, $\boldsymbol{N}$ = Aerodynamic (including propulsive) moments about x, y, and z axes, respectively,
$\hat{p},\hat{q},\hat{r}$ = Rotation rates about x, y, and z axes, respectively (radians/s),
$\dot{\hat{p}},\dot{\hat{q}},\dot{\hat{r}}$ = Angular accelerations about x, y, and z axes, respectively (radians/s^2),
u, v, w = Speeds along x, y, and z axes, respectively,
X, Y, Z = Aerodynamic and mechanical forces along x, y, and z axes, respectively,
ϕ, θ, ψ = Roll, pitch, and yaw components of the Euler angles, respectively (see Figure 24-7).

The equations are derived using Newton's second law of motion. Their derivation is provided in several references, for instance, by Stevens and Lewis [1], Allerton [2], Nelson [3], Etkin [4], Napolitano [5], Perkins and Hage [6], and Roskam [7]. Additional insights are provided by Abzug and Larrabee [8]. The equations feature translation and rotation-rate parameters, which permit a complete flight simulation when time-integrated. While flexible structures can be accounted for in these equations, the form presented here assumes rigid bodies. This simplification is acceptable if the airplane does not deform too much while loaded. Assuming this applies to sailplanes and some modern commercial jetliners is questionable.

24.1.5 Formulation of Forces and Moments

The terms X, Y, Z and $\boldsymbol{L}$, $\boldsymbol{M}$, $\boldsymbol{N}$ represent forces and moments acting on the vehicle. These are generated in two ways: (1) Aerodynamic and (2) mechanical (thrust). Additionally, there is a gravitational force, *weight*.

(1) Formulating Forces

First, we represent the mechanical force (thrust), F, in a coefficient format as follows.

Thrust force:

$$F = qSC_F \tag{24-17}$$

where q is dynamic pressure ($=\frac{1}{2}\rho V_\infty^2$), V_∞ is the far-field airspeed, S is wing area, and C_F is the force coefficient. When the force is thrust, it is assumed to act parallel to the x-axis. The forces X, Y, Z are obtained in the BCS of Figure 24-3 in the follow form.

Force along x-axis:

$$X = qS \cdot C_x \tag{24-18}$$

Force along y-axis:

$$Y = qS \cdot C_y \tag{24-19}$$

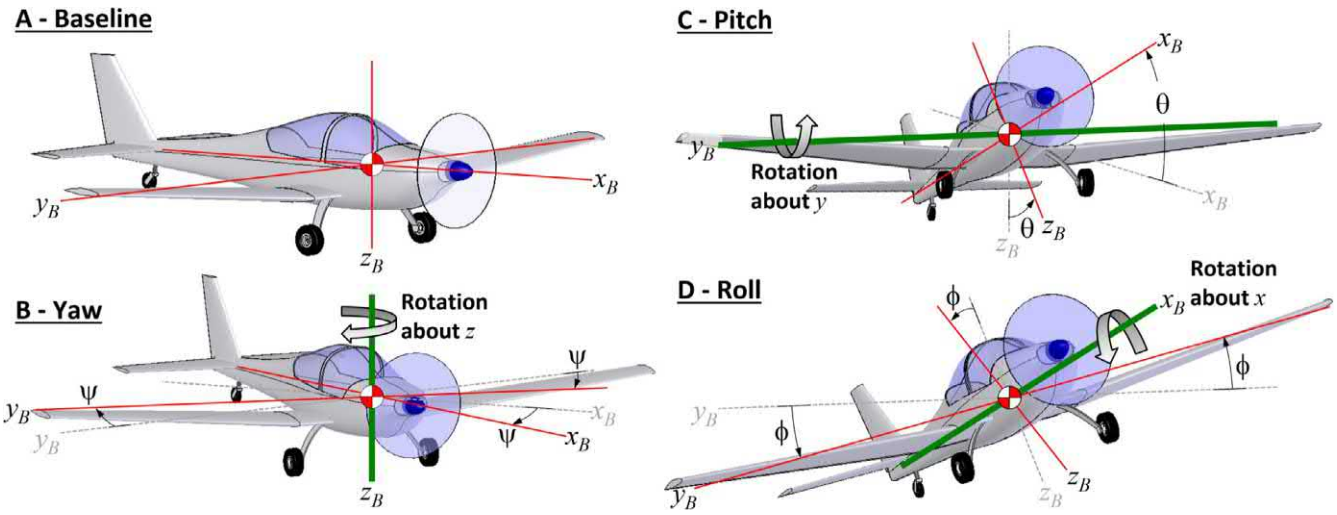


FIGURE 24-7 Implementing Euler-angle rotation (order of rotation is imperative). All rotations are positive.

Force along z-axis:

$$Z = qS \cdot C_z \tag{24-20}$$

where C_x, C_y, C_z are nondimensional force coefficients in the BCS. They are obtained by transforming the aerodynamic forces obtained in the SCS of Figure 24-4 to the BCS using Equation (24-8) (note that only the x- and z-axes are rotated). Then, we add the thrust coefficient and side force generated in yaw.

$$\begin{aligned} C_x &= C_{F_x} + C_L \sin\alpha - C_D \cos\alpha \\ C_y &= C_{y_\beta}\beta \\ C_z &= C_{F_z} - C_L \cos\alpha - C_D \sin\alpha \end{aligned} \tag{24-21}$$

where C_L is given by Equation (24-37) and C_D by Equation (24-60). C_{Fx} and C_{Fz} are components of the thrust in the x- and z-directions. Equation (24-21) is sometimes represented using small angle relations (i.e., $\sin\alpha \approx \alpha$ and $\cos\alpha \approx 1$). Such simplifications are not used in flight simulation but are handy for other situations.

$$\begin{aligned} C_x &= C_{F_x} + C_L\alpha - C_D \\ C_y &= C_{y_\beta}\beta \\ C_z &= C_{F_z} - C_L - C_D\alpha \end{aligned} \tag{24-22}$$

The gravitational force contribution is obtained using Equation (24-11), where the gravity vector is given by $\{0,0,mg\}^T$, where m is the mass of the aircraft ($m = W/g$). Thus, using the symbology of Equation (24-11), we get

$$\begin{Bmatrix} F_x \\ F_y \\ F_z \end{Bmatrix} = \begin{bmatrix} C\psi\ C\theta & S\psi\ C\theta & -S\theta \\ -S\psi\ C\phi + C\psi\ S\theta\ S\phi & C\psi\ C\phi + S\psi\ S\theta\ S\phi & C\theta\ S\phi \\ S\psi\ S\phi + C\psi\ S\theta\ C\phi & -C\psi\ S\phi + S\psi\ S\theta\ C\phi & C\theta\ C\phi \end{bmatrix}$$
$$\begin{Bmatrix} 0 \\ 0 \\ mg \end{Bmatrix} = \begin{Bmatrix} -mg\sin\theta \\ mg\cos\theta\sin\phi \\ mg\cos\theta\cos\phi \end{Bmatrix} \tag{24-23}$$

(2) Formulating Moments

A stable and trimmed aircraft requires the summation of the moments about a given axis to equal zero. The aerodynamic moments are defined as follows:

Rolling moment (about x-axis):

$$\boldsymbol{L} = M_x = qSb \cdot \boldsymbol{C_L} \tag{24-24}$$

Pitching moment (about y-axis):

$$\boldsymbol{M} = M_y = qSc_{MGC} \cdot \boldsymbol{C_M} \tag{24-25}$$

Yawing moment (about z-axis):

$$\boldsymbol{N} = M_z = qSb \cdot \boldsymbol{C_N} \tag{24-26}$$

where

c_{MGC} = Mean geometric chord
$\boldsymbol{C_L}$ = Rolling moment coefficient
$\boldsymbol{C_M}$ = Pitching moment coefficient
$\boldsymbol{C_N}$ = Yawing moment coefficient

Note that $\boldsymbol{C_L}$ is given by Equation (25-52), $\boldsymbol{C_M}$ is given by Equation (24-64), and $\boldsymbol{C_N}$ is given by Equation (25-24).

24.1.6 Basics of Aircraft Control

Figure 24-8 shows typical control surface layout for a small aircraft. The roll is controlled using *ailerons*, pitch is controlled using an *elevator*, and yaw is controlled using a *rudder*. This chapter only focuses on longitudinal control (*elevator*). Lateral–directional control (*aileron* and *rudder*) are dealt with in Chapter 25.

A positive aileron deflection is right aileron trailing-edge down (TED). It develops a negative rolling moment in the BCS and SCS. A positive elevator deflection (TED) pitches the nose down (negative pitching moment). A positive

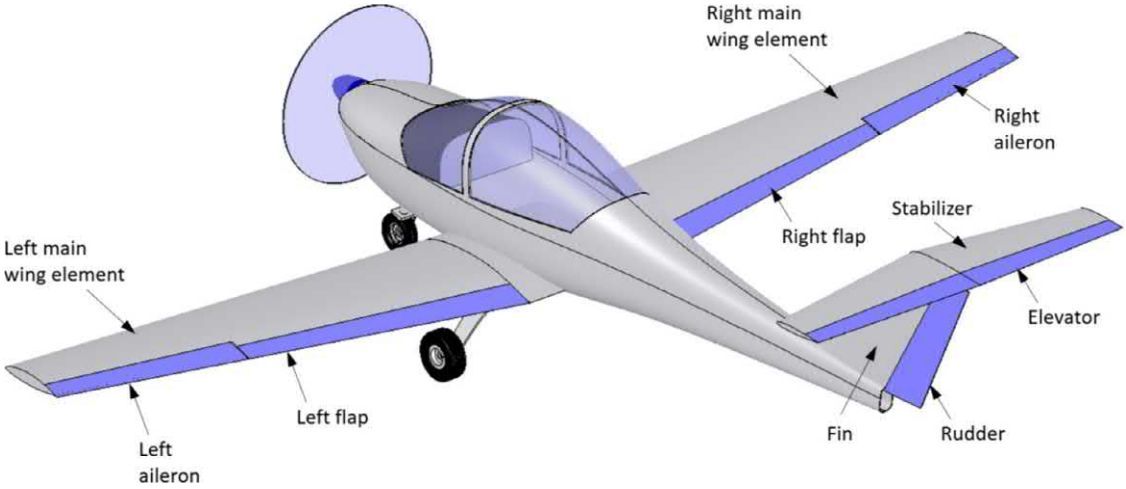


FIGURE 24-8 Typical layout of aircraft control surfaces.

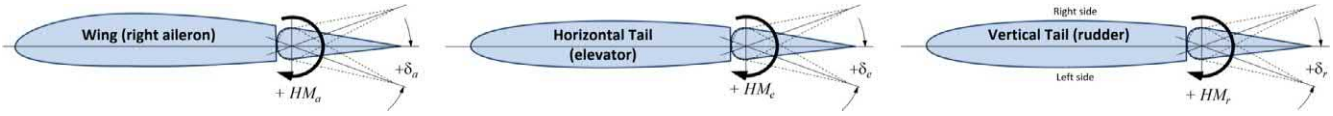


FIGURE 24-9 Conventions associated with control surface deflections.

rudder deflection is trailing edge left (TEL) and generates a positive side force (in the direction of positive y) and negative (nose left) yawing moment. These conventions are important for the discussion that follows (see Figure 24-9).

These rotations can be achieved by other means. Many military fighters combine ailerons and elevator in an all-movable control surface called *elevons*. Flying wings use elevons and often combine it with rudder functionality in a clamshell like control surface on the outboard wing. During flight, the upper clamshell is deflected a few degrees *trailing edge up* (TEU) and the lower one TED. This generates directional stability through wingtip drag (see pictures of the B-2 Spirit bomber). Such devices are beyond the current discussion. Here, we will only consider conventional configurations.

24.1.7 Basic Aircraft Geometry for Longitudinal Stability and Control

Figure 24-10 shows dimensions referenced in this chapter. Note that general dimensions of lifting surfaces are detailed in Section 9.2. The term *fractional dimensions* (in Figure 24-10) refers to physical dimensions divided by the mean geometric chord, c_{MGC}. Thus, if x_{CG} is the position of the CG with respect to the leading edge of the c_{MGC}, then $h_{cg} = x_{CG}/c_{MGC}$.

24.1.8 Important Note to the Reader

The author has meticulously digitized a large number of graphs for the convenience of the reader. This chapter and Chapter 25 feature more such expressions than elsewhere in the book. The resulting formulae allow the original graphs to be bypassed in lieu of direct calculations. All such formulas have a sentence stating this explicitly in interest of transparency. That said, before using any such expression, the reader is responsible for comparing its output to the original graph to evaluate accuracy.

24.2 STATIC LONGITUDINAL STABILITY AND CONTROL

This section reviews formulation associated with longitudinal stability and control. Static and dynamic stability analyses revolve around (1) developing the equations-of-motion, (2) evaluating component contributions to stability, and (3) use these to evaluate various static and dynamic stability characteristics. The analysis evaluates force and moment contributions of components like wings, HT, VT, fuselage, landing gear, powerplant, and so forth. There can be a further breakdown based on subcomponents—for instance, the contribution of the wing is broken down into that of the main wing element, high-lift devices, and so on. The magnitude of the forces and moments is then summed along and about the three axes, respectively. An airplane can maintain steady unaccelerated flight only when the sum of all forces and moments about its CG is zero.

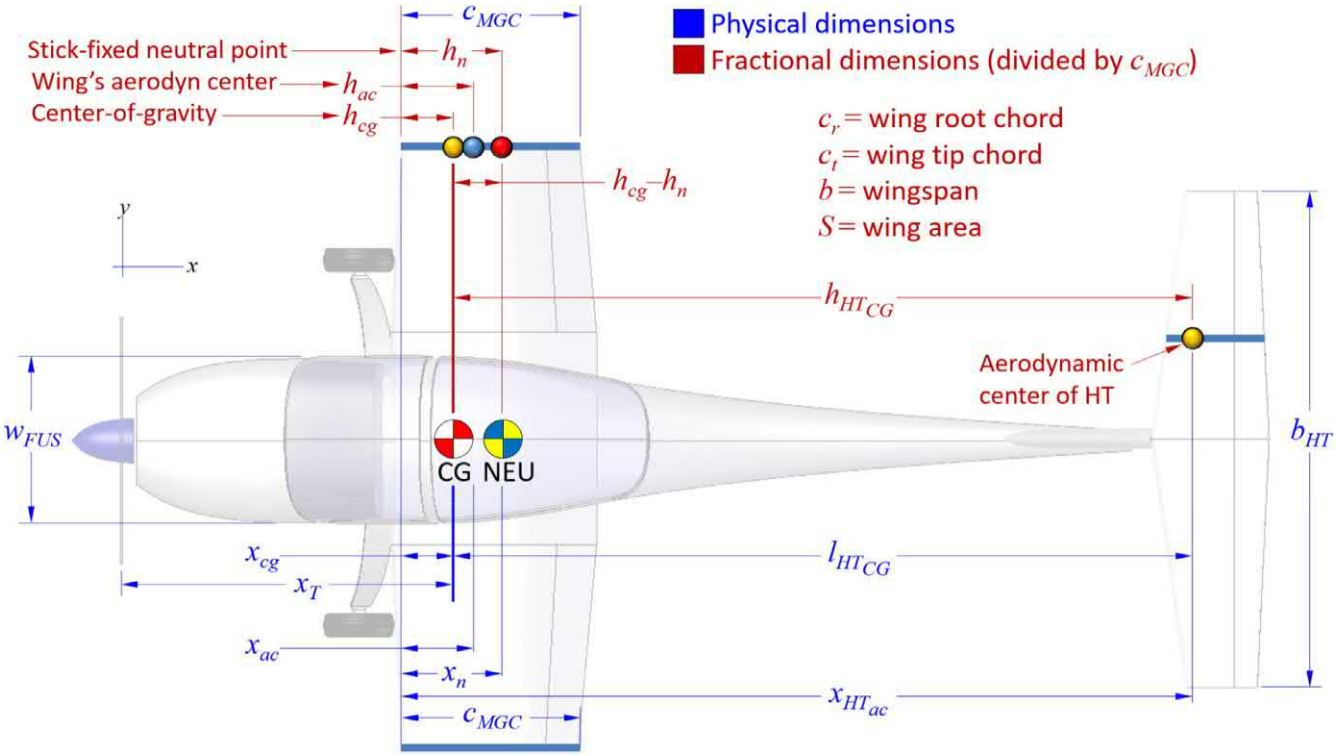


FIGURE 24-10 Establishing dimensions for wing and HT. CG is center-of-gravity. NEU = Stick-fixed neutral point..

24.2.1 Equations-of-Motion for Static Longitudinal Stability

The *equations-of-motion* (EOM) for longitudinal motion are extracted from Equations (24-13) through (24-16) and summarized below:

$$\begin{aligned}
&X - mg\sin\theta = m(\dot{u} + \hat{q}w - \hat{r}v)\\
&Z + mg\cos\theta\cos\phi = m(\dot{w} + \hat{p}v - \hat{q}u)\\
&\boldsymbol{M} = I_{yy}\dot{\hat{q}} + (I_{xx} - I_{zz})\hat{p}\hat{r} + I_{xz}\left(\hat{p}^2 - \hat{r}^2\right) + (\hat{r}h_{SRx} - \hat{p}h_{SRz})\\
&\hat{q} = \dot{\theta}\cos\phi + \dot{\psi}\cos\theta\sin\phi\\
&\theta = \hat{q}\cos\phi - \hat{r}\sin\phi
\end{aligned} \tag{24-27}$$

The term *static* means all rotations and accelerations are zero. Thus, Equation set (24-27) becomes

$$\begin{aligned}
&X - mg\sin\theta = 0\\
&Z + mg\cos\theta\cos\phi = 0\\
&\boldsymbol{M} = 0\\
&\hat{q} = 0\\
&\theta = 0
\end{aligned} \tag{24-28}$$

For this discussion, we are only interested in the top three equations, where X is given by Equation (24-18), Z by Equation (24-20), and $\boldsymbol{M}$ by Equation (24-25). These three constitute the EOM for static longitudinal equilibrium:

$$\begin{aligned}
&qS \cdot C_x - mg\sin\theta = 0\\
&qS \cdot C_z + mg\cos\theta\cos\phi = 0\\
&qSc_{MGC} \cdot \boldsymbol{C_M} = 0
\end{aligned} \tag{24-29}$$

Substituting Equation (24-22) into Equation (24-29) and rearranging yields:

$$\begin{aligned}
&C_{F_x} + C_L\sin\alpha - C_D\cos\alpha = (mg/qS)\sin\theta\\
&C_L\cos\alpha + C_D\sin\alpha - C_{F_z} = (mg/qS)\cos\theta\cos\phi\\
&\boldsymbol{C_M} = 0
\end{aligned} \tag{24-30}$$

Thus, our task is to formulate the coefficients C_F (thrust), C_L (lift), C_D (drag), and $\boldsymbol{C_M}$ (moment). This is accomplished using the various models discussed below. Note that unless otherwise specified, α is taken to be that of the MGC, α_W.

24.2.2 Requirements for Static Longitudinal Stability

For an aircraft to fly, it must be *stable and trimmable*. Consider the airplane in Figure 24-11. The left image shows it at high AOA and the right one at low AOA. The figure explains what *longitudinal stability* means. In the left image, the HT generates lift force, L_{HT}, which points upward and, thus, tends to reduce the AOA by rotating the nose down.

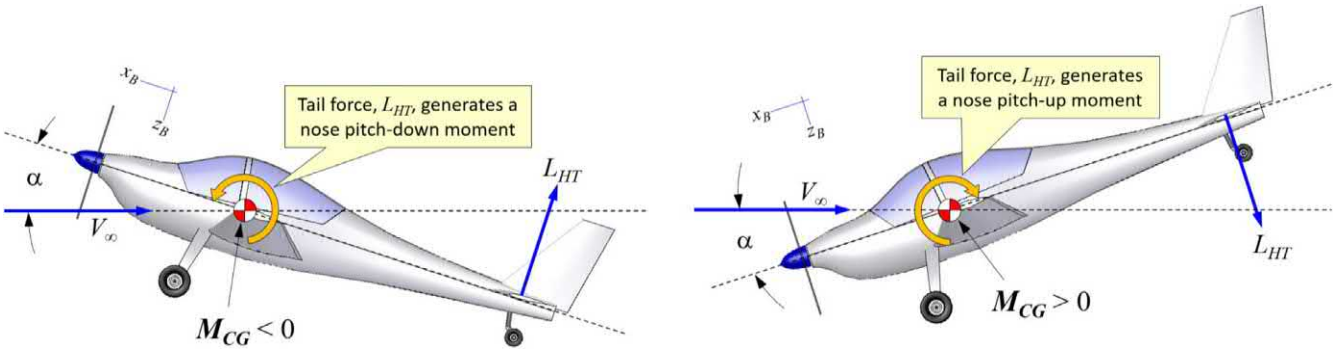


FIGURE 24-11 The generation of longitudinal stability.

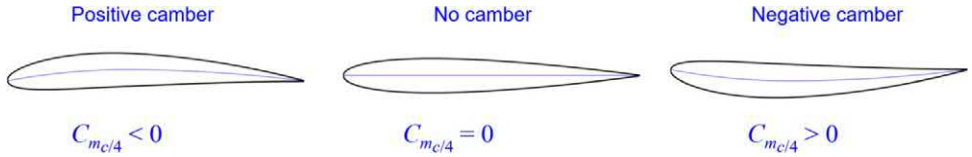


FIGURE 24-12 Stability requires a pitching moment curve with a negative slope ($C_{M\alpha}$). It must intersect the C_M-axis at a positive value (C_{M0}) to be trimmable at a positive AOA (required to generate lift that opposes weight).

Based on the SCS in Figure 24-3, the resulting moment has a negative magnitude: If we grab around the *y*-axis (sticking *into-page*) with our right hand, the fingers will indicate direction of rotation while the thumb points in the direction of the moment vector. To generate this nose-down rotation, the thumb must point in the negative *y*-direction (*out-of-page*). To pitch the nose up requires the thumb to point in the positive *y*-direction.

The right image of Figure 24-11 shows the opposite. The low AOA causes the HT to generate a downward L_{HT} that will increase the AOA. This means that somewhere between the two extremes is an AOA for which there is no tendency for the HT to increase or decrease the AOA. *The resulting moment is zero*. This is the *trim AOA*. An airplane whose stabilizing surface (here the HT) generates enough lift force to force the aircraft to a specific trim AOA is called a *stable aircraft*.

It is not enough for the aircraft to just be stable, it must also be *trimmable*—it must develop zero moment while generating lift that equals the weight. To see this, the two conditions in Figure 24-11 have been plotted in Figure 24-13. The conditions consist of $\alpha > 0$ and $\boldsymbol{M} < 0$ in the left image and $\alpha < 0$ and $\boldsymbol{M} > 0$ in the right image. The line drawn through the two points is the *pitching moment curve*. The graph shows that for the aircraft to be stable it must have a negative slope. Its $\boldsymbol{C_{M\alpha}}$ (longitudinal stability derivative) must be negative. Additionally, it must develop upward lift that opposes the weight. This requires the intersection to the *y*-axis ($\boldsymbol{C_M}$-axis), denoted by $\boldsymbol{C_{M0}}$, to be larger than zero. Mathematically, this is written as follows:

Requirement for static stability:

$$\boldsymbol{C_{M_\alpha}} = \frac{\partial C_M}{\partial \alpha} < 0 \qquad (24\text{-}31)$$

Requirement for trimmability:

$$\boldsymbol{C_{M_0}} > 0 \quad \text{such that} \quad C_L > 0 \qquad (24\text{-}32)$$

For airplanes, a positive $\boldsymbol{C_{M0}}$ is created by a stabilizing surface like a HT. Control is created by equipping it with an *elevator*. It is a "tool" that allows $\boldsymbol{C_{M0}}$ to be moved up or down at will (e.g., see Example 24-6). The longitudinal stability derivative can be written as follows:

$$\boldsymbol{C_{M_\alpha}} = \frac{\partial C_M}{\partial \alpha} = \frac{\partial C_M}{\partial C_L}\frac{\partial C_L}{\partial \alpha} = \frac{\partial C_M}{\partial C_L} C_{L_\alpha} \qquad (24\text{-}33)$$

The solid and dashed stability curves in Figure 24-13 intersect the horizontal axis at $\alpha_{trim} = 7.5°$. Considering the solid curve, imagine the aircraft is perturbed from α_{trim} to, say, 5°. This lowers the nose, generating a nose-up tendency that brings the airplane back to α_{trim}. Should the perturbation result in a slightly higher AOA, say 10°, the opposite happens, bringing the nose back down to α_{trim}. Alternatively, if statically unstable (dashed line), a perturbation that lowers the nose will be accompanied by a tendency to reduce the AOA further. If the tendency is strong, the airplane will become impossible for a human pilot to control—we do not want that in civilian aircraft.

Simplest Case of Static Longitudinal Stability

Trimmability for an airfoil can be achieved by selecting the proper camber (see Figure 24-12). Positive camber has a negative $C_{mc/4}$, while the opposite holds for negative camber. This is illustrated in Example 24-1.

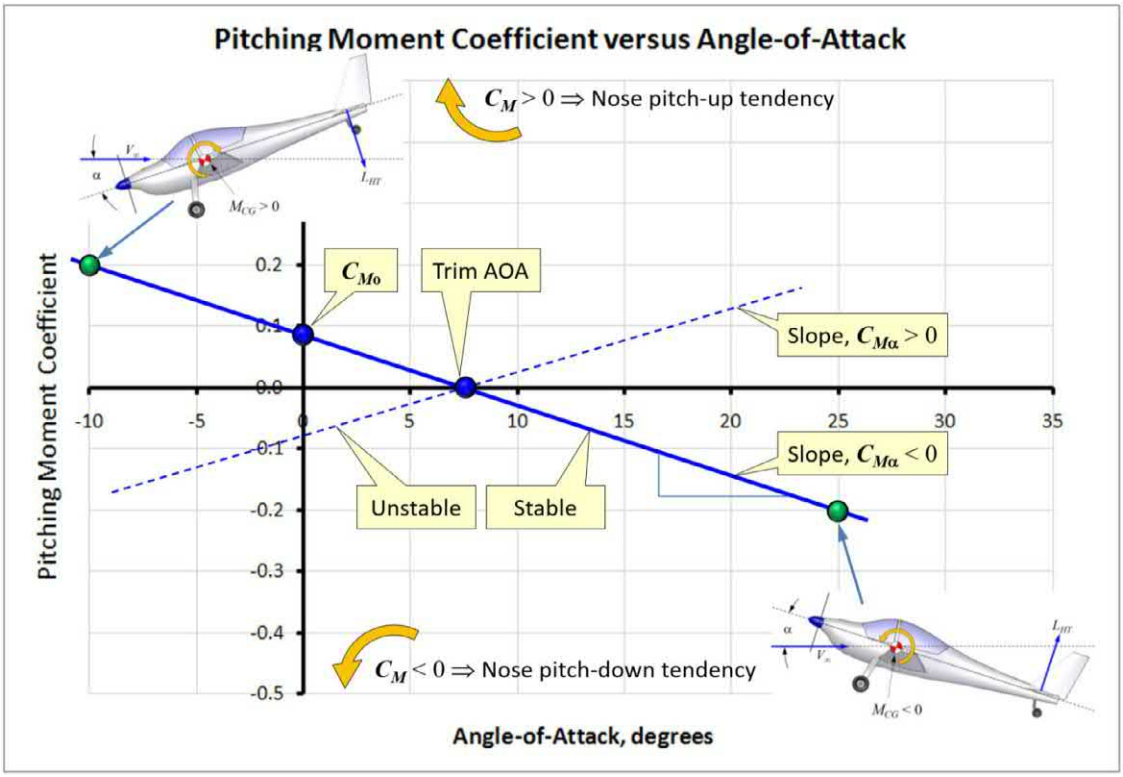


FIGURE 24-13 The requirement for trimmability requires an airfoil to feature a negative camber.

EXAMPLE 24-1

Determine the pitching moment curve for the NACA 4412 airfoil in Figure 24-14, about its CG. Its lift and pitching moment coefficients about the quarter-chord are given by the following cubic approximations:

$$C_l(\alpha) = 0.40575 + 0.11885 \cdot \alpha + 0.00028215 \cdot \alpha^2 - 0.00017205 \cdot \alpha^3$$

$$C_{m_{c/4}}(\alpha) = -0.10076 + 0.001121 \cdot \alpha + 0.00025507 \cdot \alpha^2 - 0.000012469 \cdot \alpha^3$$

The weight, W, is placed distance h_{cg} from the leading edge. These approximations are plotted in the left graph of Figure 24-15. Plot the resulting C_m curve of the airfoil for the following CG locations; $h_{cg} = 0$, 0.1, 0.25, and 0.3.

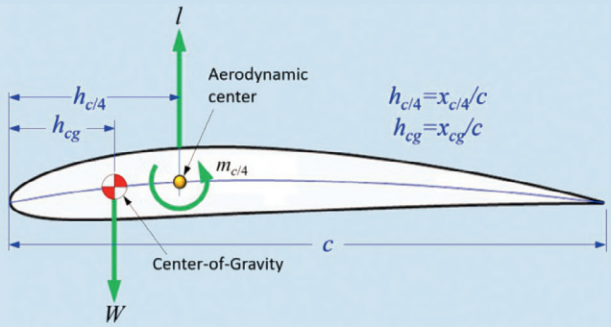


FIGURE 24-14 NACA 4412 airfoil.

SOLUTION:

First, note the lift of the airfoil is given by: $l = qc \cdot C_l$.

Similarly, the moment about $c/4$ is given by:

$$m_{c/4} = qc^2 \cdot C_{m_{c/4}}.$$

where q is the dynamic pressure and c is the chord length. Summing the moments about the CG (assuming clockwise rotation is positive) gives:

$$\sum m_{CG} = m = m_{c/4} - l \cdot (c/4 - h_{cg})$$

Expanding leads to:

$$m = m_{c/4} - l \cdot (c/4 - h_{cg}) = qc^2 \cdot C_{m_{c/4}}(\alpha) - qc \cdot C_l(\alpha) \cdot (c/4 - h_{cg})$$

Convert to coefficient form by dividing through by qc:

$$C_m = c \cdot C_{m_{c/4}}(\alpha) - C_l(\alpha) \cdot (c/4 - h_{cg})$$

Substitute the cubic splines:

$$C_m = c \cdot [-0.10076 + 0.001121 \cdot \alpha + 0.00025507 \cdot \alpha^2 - 0.000012469 \cdot \alpha^3] + \hookleftarrow - [0.40575 + 0.11885 \cdot \alpha + 0.00028215 \cdot \alpha^2 - 0.00017205 \cdot \alpha^3] \cdot (c/4 - h_{cg})$$

EXAMPLE 24-1 (*cont'd*)

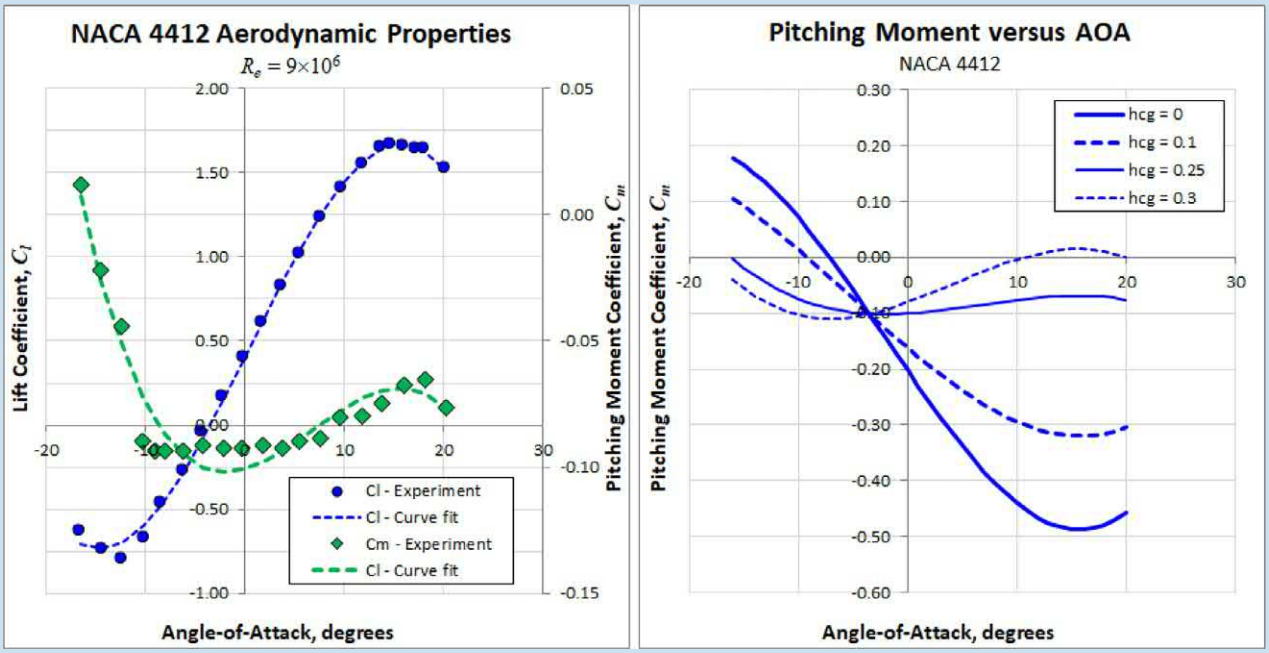


FIGURE 24-15 Experimental and curve-fit lift and pitching moment coefficients for the NACA 4412 airfoil (left). Resulting pitching moment curves for the four positions of the CG (right).

The resulting plot is shown in the right graph of Figure 24-15. When the weight is at the leading edge ($h_{cg}=0$) the airfoil has the greatest stability of the positions plotted (steepest negative slope). When the weight is at or behind the quarter-chord ($h_{cg}=0.25$ and 0.3), the airfoil is neutrally stable and unstable, respectively.

24.2.3 Historical Values of $C_{M\alpha}$

It is important that the designer knows what longitudinal stability derivatives to aim for. The history of aviation presents us with many candidate values. Table 24-2 lists several longitudinal stability derivatives, gathered from refs. [3, 9–11], and the author's personal notes. A selection of the airplanes is coplotted in Figure 24-16. Transport aircraft usually have "high" pitch stability, which is reflected in a low value of $\boldsymbol{C_{M\alpha}}$, often in the −1.2 to −1.7 per radian range. GA aircraft are typically in the −0.6 to −1.0 per radian range. On the other hand, the modern fighter aircraft is purposely unstable ($\boldsymbol{C_{M\alpha}}>0$) at subsonic airspeeds (become stable at $M_\infty>1$).

It is also important the designer recognizes the HT volume as a "tool" to design desired static longitudinal stability into the airplane (see Equation (24-74)). By solving Equation (24-130) for V_{HT} we obtain four parameters (S_{HT}, l_{HTCG}, S, and c_{MGC}) that we can adjust to develop the desired $\boldsymbol{C_{M\alpha}}$.

$$V_{HT}=\frac{S_{HT}l_{HT_{CG}}}{Sc_{MGC}}=\frac{\boldsymbol{C_{M_\alpha}}-C_{L_{\alpha_W}}(h_{cg}-h_{ac})}{\eta_{HT}C_{L_{\alpha_{HT}}}(1-\partial\varepsilon/\partial\alpha)} \qquad (24\text{-}34)$$

As an example, the equation can be rearranged to determine the required HT area, S_{HT}, given fixed values of l_{HTCG}, S, and c_{MGC}.

It is of interest to see how the derivatives are affected by high Mach numbers (see Figure 24-16). It is important to realize that the $\boldsymbol{C_{M\alpha}}$ is not constant. It is a function of Mach number, CG, and configuration changes because of retracting landing gear and flaps. Compressibility effects are shown for the F-104 Starfighter, a third-generation fighter as the solid line in Figure 24-16. Marginal instability was not used for that generation. Thus, its stability derivative, $\boldsymbol{C_{M\alpha}}<0$ over its Mach range (marginally stable and unstable fighters emerged first with fourth-generation fighter aircraft). Also, note the range of stability of the F-4 Phantom fighter (also third-generation) is marginal at $M=0.2$ (landing configuration), but becomes noticeably stable at $M=2$. It is also of interest to see how the Mach number changes the longitudinal stability of commercial jetliners, like the Boeing 727, 747, and Convair CV-880.

TABLE 24-2 Pitch stability derivatives for selected aircraft.

Longitudinal Stability for Selected Aircraft								
Make	**Model**	M	AR	c_{MGC}, ft	b, ft	S, ft²	$C_{M\alpha}$	**Reference**
Bede	BD-5A*	0.27	6.76	2.60	17	42.78	-0.830	Author
Beech	D-18*	0.23	6.51	8.89	47.7	349	-1.748	Author
	V-35 Bonanza*	0.23	6.10	5.49	33.5	184	-0.455	Author
Boeing	727-100*	0.76	7.07	15.28	108	1650	-1.500	[9]
		0.60	7.07	15.28	108	1650	-1.672	Author
	747 (Pwr Appr)	0.25	6.96	27.31	195.7	5500	-1.450	[10]
	747	0.30	6.96	27.31	195.7	5500	-1.216	[10]
		0.60	6.96	27.31	195.7	5500	-0.685	[10]
		0.80	6.96	27.31	195.7	5500	-0.630	[10]
Cessna	182 Skylane	0.14	7.45	4.83	36	174	-0.900	[9]
Convair	CV-880	0.60	7.20	18.94	120.0	2000	-0.522	[10]
		0.80	7.20	18.94	120.0	2000	-0.650	[10]
Convair	CV-880 (Pwr Appr)	0.25	7.20	18.94	120.0	2000	-0.903	[10]
De Havilland Canada	DHC-6	0.22	10.00	6.5	65.0	423	-1.200	[11]
Lockheed	A-4 Skyhawk	0.40	2.71	-	26.5	259	-0.380	[3]
		0.80	2.71	-	26.5	259	-0.410	[3]
	C-5 (Pwr Appr)	0.22	7.75	30.1	219.2	6200	-0.827	[10]
	F-104 Starfighter	0.80	2.45	9.55	21.9	196	-0.901	[10]
		2.00	2.45	9.55	21.9	196	-0.736	[10]
	Jetstar	0.60	5.33	10.93	53.8	543	-0.663	[10]
		0.80	5.33	10.93	53.8	543	-0.717	[10]
	Jetstar (Pwr Appr)	0.20	5.33	10.93	53.8	543	-0.800	[10]
	NT-34 (Pwr Appr)	0.20	6.00	6.72	37.5	235	-0.401	[10]
McDonnell Douglas	F-4	0.60	2.82	16.04	38.7	530	-0.279	[10]
		2.00	2.82	16.04	38.7	530	-0.606	[10]
	F-4 (Pwr Appr)	0.21	2.82	16.04	38.7	530	-0.098	[10]
Ryan	Navion	0.16	6.06	5.7	33.4	184	-0.683	[3]
Start & Flug	H-101 Salto*	0.06	21.51	2.07	44.6	92.4	-1.206	Author

*CG at quarter-chord of the MGC

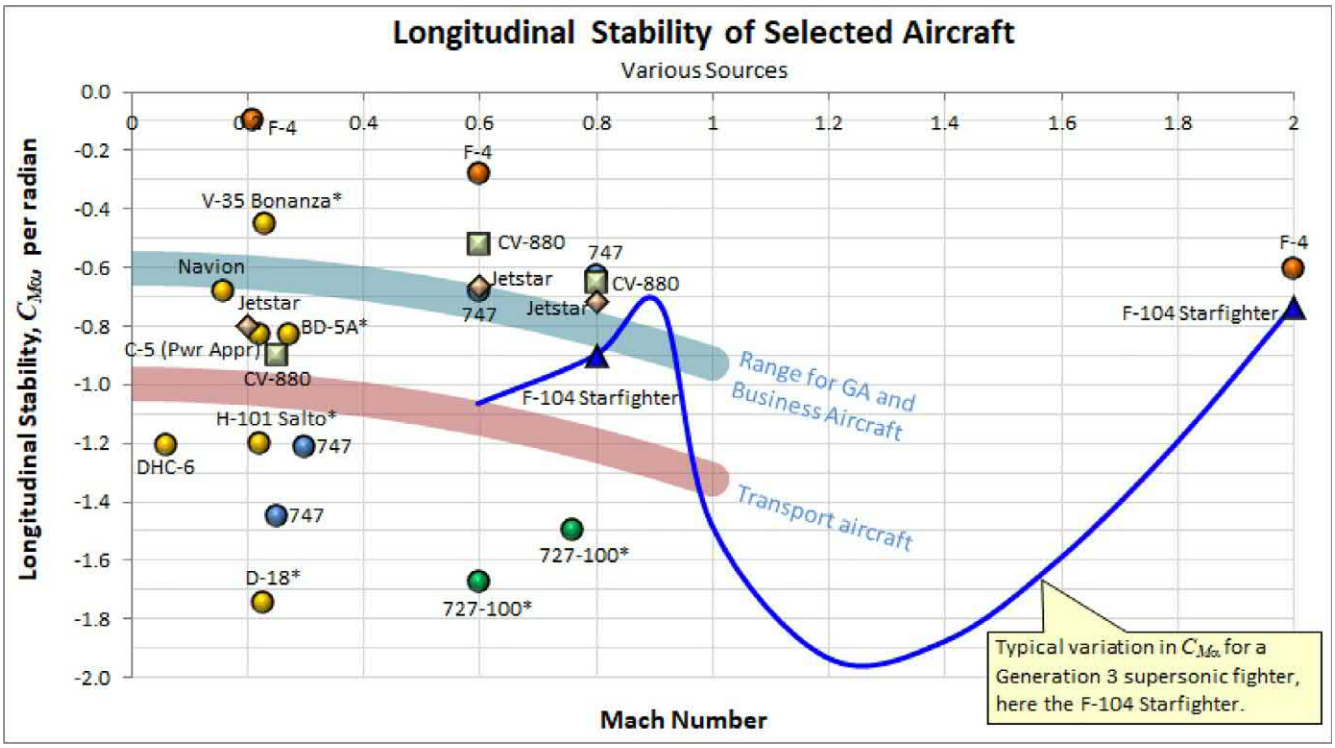


FIGURE 24-16 Trends of longitudinal stability derivatives for selected aircraft.

24.2.4 The Thrust Model, C_T

The thrust coefficient is given by Equation (24-17). To model a controllable propulsion device, we account for a power lever, δ_T, such that $T = T(\delta_T)$. Thus, we define the thrust coefficient as a function of δ_T

$$C_F(\delta_T) = \frac{2T(\delta_T)}{\rho V^2 S} = \frac{T(\delta_T)}{qS} \tag{24-35}$$

Various techniques to develop a thrust model are provided in Chapters 7, 14, and 15. Also, see Section 24.2.11. It is possible the thrust is at some angle ε_F with respect to the BCS. Thus, we define thrust components as follows:

$$\begin{aligned} C_{F_x} &= C_F(\delta_T)\cos\varepsilon_F \\ C_{F_z} &= C_F(\delta_T)\sin\varepsilon_F \end{aligned} \tag{24-36}$$

Also note two other thrust coefficients. First, $C_t = T/(\rho V^2 D_P^2)$. It is related to another thrust coefficient, $C_T = T/(\rho n^2 D_P^4)$, through the relation $C_t = C_T/J^2$. D_P = propeller diameter, n = revolutions per seconds.

24.2.5 The Lift Model, C_L

A typical aircraft consists of a wing, stabilizing surfaces, fuselage, and, sometimes, engine nacelles and external stores. The total lift generated includes contributions from these sources. While the largest one is that of the wing, accurate prediction requires the others to be included. The *lift model* can be expressed as follows:

$$C_L = C_{L_0} + C_{L_\alpha}\alpha + C_{L_{\dot\alpha}}\left(\frac{\dot\alpha c_{MGC}}{2V_\infty}\right) + C_{L_\beta}\beta + C_{L_q}\left(\frac{\hat q c_{MGC}}{2V_\infty}\right) + \hookleftarrow$$
$$C_{L_{i_{HT}}} i_{HT} + C_{L_{\delta_e}}\delta_e + C_{L_{\delta_f}}\delta_f + C_{L_{\delta_s}}\delta_s + C_{L_u}u + \cdots \tag{24-37}$$

where

C_{L0} = Zero-α lift coefficient,
$C_{L\alpha}$ = *Lift curve slope*,
$C_{L_{\dot\alpha}}$ = Change in lift with downwash lag,
$C_{L\beta}$ = Change in lift due to yaw,
C_{Lq} = *Lift damping derivative*,
$C_{Li_{HT}}$ = Change in lift with stabilizer incidence, i_{HT},
$C_{L_{\delta_e}}$ = Change in lift with elevator deflection, δ_e,
$C_{L_{\delta_f}}$ = Change in lift due to high-lift devices, δ_f,
$C_{L\delta s}$ = Change in lift with deployment of spoilers, δ_s,
C_{Lu} = Change in lift with airspeed, u,

The dots imply add further terms if needed. *NOTE: It is the responsibility of the expert to ensure angular consistency. A derivative multiplied by an angle in degrees (or radians) must be represented in terms of per degrees (or per radian).* As stated in Section 9.5.2, in steady flight the C_L obtained using Equation (9-64) and Equation (24-37) must be equal. For straight, steady-state flight, Equation (24-37) reduces to

$$C_L = C_{L_0} + C_{L_\alpha}\alpha + C_{L_{i_{HT}}} i_{HT} + C_{L_{\delta_e}}\delta_e + C_{L_{\delta_f}}\delta_f + C_{L_{\delta_s}}\delta_s \tag{24-38}$$

(1) The Zero-α Lift Coefficient, C_{L0}

Primary contributors are wing (C_{L0W}) and HT (C_{L0HT}). The HT can be aft or forward mounted (canard). The coefficient is given by

Zero AOA lift:

$$C_{L_0} = C_{L_{0_W}} + \eta_{HT}\frac{S_{HT}}{S}C_{L_{0_{HT}}} \tag{24-39}$$

where S is wing reference area and S_{HT} is HT planform area. $C_{L_{0_{HT}}}$ is the horizontal tail lift at $\alpha_{HT} = i_{HT} = \delta_e = 0$. If the HT features a symmetric airfoil $C_{L_{0_{HT}}} = 0$. Obtain $C_{L_{0_W}}$ and $C_{L_{0_{HT}}}$ from Section 9.5.3.

(2) The Lift Curve Slope, $C_{L\alpha}$

Primary contributors are the lift curve slope of the wing ($C_{L\alpha_W}$) and HT ($C_{L\alpha_{HT}}$). It is given by.

Lift curve slope:

$$C_{L_\alpha} = K_{WB}C_{L_{\alpha_W}} + \eta_{HT}\frac{S_{HT}}{S}C_{L_{\alpha_{HT}}}\left(1 - \frac{\partial\varepsilon}{\partial\alpha}\right) \tag{24-40}$$

where

$C_{L\alpha_W}$ = Wing lift curve slope, see Section 9.5.4
η_{HT} = HT effectiveness, see Section 24.2.9,
$\partial\varepsilon/\partial\alpha$ = Wing downwash, see Section 24.2.8,
$C_{L\alpha_{HT}}$ = HT lift curve slope, see Section 9.5.4,
K_{WB} = Wing-body correction, see below.

Correction Factor K_{WB}

The coefficient K_{WB} corrects for the wing-body combination. The wing causes upwash in front of the leading edge that affects the lift contribution of the fuselage. The effect depends on *body-width* and how much of the wing is *outside* (or *exposed*) of the fuselage (see Figure 24-17). It requires the wing to be "redefined." This is manifested as a change in the wing's $C_{L\alpha W}$. Ref. [5] suggest the following expression, which leads to values of K_{WB} close to 1 for common GA aircraft fuselages.

$$K_{WB} = 1 + 0.025(d_{FUS}/b) - 0.25(d_{FUS}/b)^2 \tag{24-41}$$

where d_{FUS} is the maximum external width of the fuselage. Ref. [12] suggests a more laborious method that returns a larger value of K_{WB} than Equation (24-41).

$$K_{WB}C_{L_{\alpha_W}} = [k_{WB_1} + k_{WB_2} + K_N]C_{L_{\alpha_e}}\frac{S_e}{S} \tag{24-42}$$

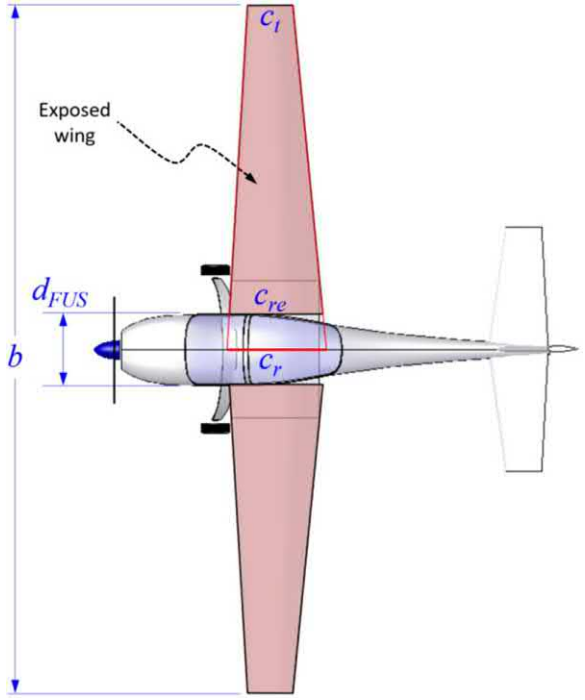


FIGURE 24-17 Exposed wing.

where

c_{re} = Exposed wing root chord = $(1–d_{FUS}/b)$
$c_r + (d_{FUS}/b)c_t$,
S_e = Exposed wing area = ½$(c_{re}+c_t)(b–d_{FUS})$,
AR_e = Exposed wing aspect ratio = $2(b–d_{FUS})/(c_{re}+c_t)$,

$$k_{WB_1} + k_{WB_2} = 1 + 2.1(d_{FUS}/b) + 0.9(d_{FUS}/b)^2 \qquad (24\text{-}43)$$

If using Equation (9-82) to calculate $C_{L\alpha W}$, it can be shown that

$$K_N = \frac{d_{FUS}^2}{2(b-d_{FUS})^2}\left(1+\sqrt{1+\left(\frac{b-d_{FUS}}{c_{re}+c_t}\right)^2}\right) \qquad (24\text{-}44)$$

If the $C_{L\alpha W}$ is calculated using other methods, then

$$K_N = \frac{\pi d_{FUS}^2}{2C_{L_{\alpha_e}} S_e} \qquad (24\text{-}45)$$

where $C_{L\alpha e}$ is the aspect ratio of the exposed wing. Equation (24-43) is a combined curve fit of the two curves of Figure 4.3.1.2-10 in ref. [12]. Equation (24-44) is derived using Equation (9-71).[2]

(3) Change in Lift due to Downwash Lag, $C_{L_{\dot\alpha}}$

The derivative $C_{L_{\dot\alpha}}$ represents the change in lift due to the time rate-of-change of α (*downwash lag*) that follows a sudden change in α. It lasts for a short time during which airflow "adapts" to a new orientation of the aircraft. For conventional configurations, the effect comprises contributions from the wing, fuselage (body), and HT, of which the wing-body contribution can be neglected:

$$C_{L_{\dot\alpha}} = \overbrace{C_{L_{\dot\alpha_{WB}}}}^{\text{wing-body contribution}} + \overbrace{C_{L_{\dot\alpha_{HT}}}}^{\text{HT contribution}} \approx C_{L_{\dot\alpha_{HT}}} \qquad (24\text{-}46)$$

The effect involves unsteady aerodynamics. The estimation of the wing-body contribution uses *Theodorsen's complex function* $C(k) = F(k) + i\,G(k)$ per Theordorsen [13] and Tobak [14], where $F(k)$ and $G(k)$ are Bessel functions of the first and second kind, $i = -1$, and k is the *reduced frequency*, given by $k = c_{MGC}\omega/2V_\infty$, where ω is the frequency of oscillation. That said, it is usually negligible. The contribution of the HT is easier to estimate. The following two forms are given in [4, 5, 12], to name a few.

$$C_{L_{\dot\alpha_{HT}}} \approx 2C_{L_{\alpha_{HT}}}\eta_{HT}V_{HT}\frac{\partial\varepsilon}{\partial\alpha} = 2C_{L_{\alpha_{HT}}}\eta_{HT}\frac{S_{HT}\cdot l_{HT_{CG}}}{S\cdot c_{MGC}}\frac{\partial\varepsilon}{\partial\alpha} \qquad (24\text{-}47)$$

where $\partial\varepsilon/\partial\alpha$ is the downwash angle (see Section 24.2.8). Ref. [15] states a typical range of values for this derivative is 1.5 to 3.0.

(4) Change in Lift with Yaw, $C_{L\beta}$

The derivative $C_{L\beta}$ is the rate-of-change of lift coefficient with yaw angle, β. A yawing aircraft is subject to change in the lift coefficient. For low values of β, its magnitude is usually low and can be neglected. Typical range is ±0.012 per radian (±0.000209 per degree).

(5) Lift Damping Derivative, C_{Lq}

This derivative captures the transient effect when the airplane pitches up or down, momentarily changing the AOA. The stabilizing surface (tail or canard) is usually the largest contributor, with minor one by the wing. C_{Lq} is defined as follows.

$$C_{L_q} \equiv \frac{dC_L}{d\left(\frac{\hat{q}c_{MGC}}{2V_\infty}\right)} \qquad (24\text{-}48)$$

Per ref. [12], it is calculated as the following combination

$$C_{L_q} = \overbrace{C_{L_{q_{WB}}}}^{\text{wing-body contribution}} + \overbrace{C_{L_{q_{HT}}}}^{\text{HT contribution}} \approx \overbrace{C_{L_{q_W}}}^{\text{wing contribution}} + C_{L_{q_{HT}}} \qquad (24\text{-}49)$$

[2] Derivation omitted for space.

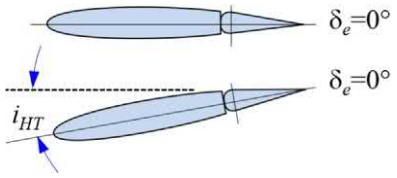


FIGURE 24-18 Changing i_{HT} does not change δ_e.

The wing-body contribution often only includes that of the wing. It is estimated using the expression below, which is derived in ref. [16]:

$$C_{L_{q_W}} = \left(\frac{1}{2} + 2\left(h_n - h_{cg}\right)\right) K_{WB} C_{L_{\alpha_W}} \tag{24-50}$$

where $h_{cg} = x_{cg}/c_{MGC}$ is fractional position of the CG and $h_n = x_n/c_{MGC}$ is fractional position of the stick-fixed neutral point (aerodynamic center for complete aircraft). For this equation, compute $C_{L\alpha W}$ using Equation (9-72) to include the effect of compressibility and wing sweep. The contribution of the HT is given by

$$C_{L_{q_{HT}}} \approx 2C_{L_{\alpha_{HT}}} \eta_{HT} V_{HT} = 2C_{L_{\alpha_{HT}}} \eta_{HT} \frac{S_{HT} \cdot l_{HT_{CG}}}{S \cdot c_{MGC}} \tag{24-51}$$

(6) Change in Lift with Elevator Deflection, $C_{Li_{HT}}$

The derivative $C_{Li_{HT}}$ is the change of the lift coefficient of the complete aircraft due to the deflection of the stabilizer surface i_{HT} (the HT consists of a stabilizer and an elevator):

$$C_{L_{i_{HT}}} \equiv \frac{\partial C_L}{\partial i_{HT}} = \eta_{HT} \frac{S_{HT}}{S} \frac{\partial C_{L_{HT}}}{\partial i_{HT}} = \eta_{HT} \frac{S_{HT}}{S} C_{L_{\alpha_{HT}}} \tag{24-52}$$

Figure 24-18 shows that when i_{HT} is changed, the 0° of δ_e remains aligned with the chordline. Note that as shown, i_{HT} should be negative and $C_{Li_{HT}}$ positive. This generates lift opposite that of the wing. The expression for $C_{Li_{HT}}$ is valid for both an aft- and forward-mounted stabilizing surface. It can be approximated as shown below:

$$C_{L_{i_{HT}}} \approx \frac{\Delta C_{L_{HT}}}{\Delta i_{HT}} \tag{24-53}$$

Example 24-2 shows *one* way to obtain this derivative from wind tunnel testing. Another way is to use data such as that provided in Tables 10-3 and 10-5, for *plain flap* elevators. Typical range is 0.57 to 3.44 per radian (0.01–0.06 per degree).

(7) Change in Lift with Elevator Deflection, $C_{L_{\delta_e}}$

The derivative $C_{L_{\delta_e}}$ is the rate of change of the lift coefficient of the *complete aircraft* due to deflection of the elevator δ_e.

$$C_{L_{\delta_e}} \equiv \frac{\partial C_L}{\partial \delta_e} = \begin{cases} \dfrac{\partial C_{L_{WB}}}{\partial \delta_e} & \text{For tailless aircraft} \\ \eta_{HT} \dfrac{S_{HT}}{S} \dfrac{\partial C_{L_{HT}}}{\partial \delta_e} & \text{For conventional aircraft} \end{cases} \tag{24-54}$$

where C_{LWB} is the lift coefficient of the wing-body combination and only applies to tailless aircraft (flying wings). The expression for $C_{L_{\delta_e}}$ is valid for both an aft- and forward-mounted stabilizing surface. It is derived below and shown to be

$$C_{L_{\delta_e}} = \eta_{HT} \frac{S_{HT}}{S} C_{L_{\delta_{e_{HT}}}} \tag{24-55}$$

The derivative $C_{L\delta eHT}$ represents change in the lift of the stabilizing surface with elevator deflection. It can be approximated as shown below:

$$C_{L_{\delta_{eHT}}} \equiv \frac{\partial C_{L_{HT}}}{\partial \delta_e} \approx \frac{\Delta C_{L_{HT}}}{\Delta \delta_e} \tag{24-56}$$

As for previously mentioned bullet (6), Example 24-2 shows one way to obtain this derivative from wind tunnel testing. Another way is data such as that of Tables 10-3 and 10-5, for *plain flap* elevators. Typical range is also 0.57 to 3.44 per radian (0.01–0.06 per degree).

(8) Change in Lift with Deployment of High-Lift Devices, $C_{L_{\delta_f}}$

The derivative $C_{L_{\delta_f}}$ is the rate of change in the lift coefficient due to deflection of flaps, δ_f, or other high-lift devices (e.g., slats) if present. Again, Example 24-2 shows *one* way to obtain this derivative. Also consider Tables 10-3 and 10-5.

$$C_{L_{\delta_f}} \equiv \frac{\partial C_L}{\partial \delta_f} \tag{24-57}$$

(9) Change in Lift with Deployment of spoilers, $C_{L\delta s}$

$C_{L\delta s}$ is the rate of change in the lift coefficient due to deflection of spoilers or other drag increasing controls, δ_s, if present. There are two common kinds of spoilers: wing-mounted, and fuselage-mounted. The former changes lift and drag significantly, the latter changes drag only. A spoiler will decrease lift over the portion of the wing from which it deploys. This must be made up by increasing AOA or airspeed or a combination of both. The derivative is defined as follows

$$C_{L_{\delta_s}} \equiv \frac{\partial C_L}{\partial \delta_s} \tag{24-58}$$

(10) Change in Lift with High Subsonic Airspeed, C_{Lu}

The deployment of high-lift devices can be accounted for using Equation (10-3) with appropriate airfoil data.

$$C_{L_u} \equiv \frac{\partial C_L}{\partial u} = \left(\frac{M_\infty^2}{1 - M_\infty^2}\right) C_L \tag{24-59}$$

DERIVATION OF EQUATIONS (24-39), (24-40), AND (24-55)

The lift coefficient of the HT (C_{LHT}) is expressed as follows:

$$C_{L_{HT}} = C_{L_{0_{HT}}} + C_{L_{\alpha_{HT}}}\alpha_{HT} + C_{L_{\delta_{e_{HT}}}}\delta_e$$

where α_{HT} is the angle-of-attack of the horizontal tail, $C_{L\alpha HT}$ is the lift curve slope of the HT, and $C_{L\delta eHT}$ is the change in lift of the HT with elevator deflection, δ_e. Thus, we can write the total lift of the wing and HT as

$$\begin{aligned} qSC_L &= qSC_{L_W} + \eta_{HT}qS_{HT}C_{L_{HT}} \\ &= qSC_{L_W} + \eta_{HT}qS_{HT}\left(C_{L_{0_{HT}}} + C_{L_{\alpha_{HT}}}\alpha + C_{L_{\delta_{e_{HT}}}}\delta_e\right) \end{aligned}$$

Divide through by qS to get the lift coefficient form:

$$C_L = \overbrace{\left(C_{L_0} + k_{WB}C_{L_{\alpha_W}}\alpha\right)}^{\text{wing contribution}} + \overbrace{\eta_{HT}\frac{S_{HT}}{S}\left(C_{L_{0_{HT}}} + C_{L_{\alpha_{HT}}}\alpha_{HT} + C_{L_{\delta_{e_{HT}}}}\delta_e\right)}^{\text{contribution from HT}}$$

Substitute wing downwash, $\partial\varepsilon/\partial\alpha$, as estimated per Equation (24-91):

$$\begin{aligned} C_L &= (C_{L_0} + k_{WB}C_{L_{\alpha W}}\alpha) \\ &\quad + \eta_{HT}\frac{S_{HT}}{S}\left(C_{L_{0_{HT}}} + C_{L_{\alpha_{HT}}}\alpha\left(1 - \frac{\partial\varepsilon}{\partial\alpha}\right) + C_{L_{\delta_{e_{HT}}}}\delta_e\right) \end{aligned}$$

Gather like terms, yielding Equations (24-39), (24-40), and (24-55):

$$C_L = \overbrace{\left(C_{L_0} + \eta_{HT}\frac{S_{HT}}{S}C_{L_{0_{HT}}}\right)}^{\equiv C_{L_0}} + \overbrace{\left[k_{WB}C_{L_{\alpha W}} + \eta_{HT}\frac{S_{HT}}{S}C_{L_{\alpha_{HT}}}\left(1 - \frac{\partial\varepsilon}{\partial\alpha}\right)\right]}^{\equiv C_{L_\alpha}}\alpha + \overbrace{\eta_{HT}\frac{S_{HT}}{S}C_{L_{\delta_{e_{HT}}}}}^{\equiv C_{L_{\delta_e}}}\delta_e$$

where M_∞ is Mach number and C_L is the steady-state lift coefficient. Can be ignored up to $M_\infty < 0.7$.

24.2.6 The Drag Model, C_D

As the airplane is operated in flight, it is subject to changes in drag. For instance, AOA and AOY change, control surfaces are deflected, landing gear and flaps may be deployed or retracted, and so on. An accurate prediction must account for these contributions and this is done using a *drag model* such as that shown below:

$$\begin{aligned} C_D &= C_{D_{\min}} + C_{D_\alpha}\alpha + C_{D_\beta}\beta + C_{D_{\delta_e}}\delta_e + C_{D_{\delta_f}}\delta_f \\ &\quad + C_{D_{\delta_s}}\delta_s + C_{D_{\delta_{LDG}}}\delta_{LDG} + \cdots \end{aligned} \tag{24-60}$$

where

$C_{D_{\min}}$ = Minimum drag coefficient,
C_{D_α} = Drag curve slope,
C_{D_β} = Change in drag due to yaw,
$C_{D_{\delta_e}}$ = Change in drag with elevator deflection, δ_e,
$C_{D_{\delta_f}}$ = Change in drag with deployment of high-lift devices, δ_f,
$C_{D\delta s}$ = Change in drag with deployment of spoilers, δ_f.
$C_{D\delta_{LDG}}$ = Change in drag with deployment of landing gear, δ_{LDG}.

(1) The Minimum Drag Coefficient, $C_{D_{\min}}$

See Section 16.3.

(2) The Drag Curve Slope, C_{D_α}

The drag coefficient is usually represented in terms of C_L using the familiar expression of Equation (16-3), provided the C_L is in the linear range:

$$C_D = C_{D_{\min}} + k(C_L - C_{L_{\min D}})^2 \tag{24-61}$$

In the linear range, $C_L = C_{L0} + C_{L\alpha}\alpha$. Thus, the derivate C_{D_α} is obtained by substituting it into Equation (24-61) and differentiate with respect to α, yielding

$$\begin{aligned} & C_D = C_{D_{\min}} + k(C_{L_0} + C_{L_\alpha}\alpha - C_{L_{\min D}})^2 \\ \Rightarrow\quad & C_{D_\alpha} = \frac{\partial C_D}{\partial\alpha} = 2kC_{L_\alpha}(C_{L_0} + C_{L_\alpha}\alpha - C_{L_{\min D}}) \end{aligned} \tag{24-62}$$

(3) The Drag Curve Slope, C_{D_β}

When the airplane yaws, its geometry with respect to the airflow changes, such that greater drag is generated. This derivative depends on the shape of the aircraft and methods to predict it are scarce.

(4) Drag Derivatives due to Control Surface Deflections, $C_{D_{\delta_e}}$, $C_{D_{\delta_f}}$, $C_{D\delta s}$, and $C_{D\delta_{LDG}}$

These derivatives can be obtained in a similar fashion as that of flaps. If presented with wind tunnel data, refer to Example 24-2 or Tables 10-3, 10-5, and Section 16.4.7. Typical ranges are shown in Table 24-3 and depends on factors like installation "cleanliness" and flap type. The term δ_{LDG} is not an angle, but a *Boolean* with a value 0 (retracted) or 1 (deployed). Landing gear drag and moment is presented in Section 24.2.12.

TABLE 24-3 Typical range of drag derivatives.

Description	Symbol	Range (per unit span)
Change in drag with elevator deflection	$C_{D_{\delta_e}}$	0.017–0.040 per radian 0.0003–0.0007 per degree
Change in drag with deployment of high-lift devices	$C_{D_{\delta_f}}$	Tables 10-3, 10-5, Section 16.4.7
Change in drag with deployment of spoilers	$C_{D\delta s}$	Section 16.4.8
Change in drag with deployment of landing gear	$C_{D\delta_{LDG}}$	Section 16.4.5

EXAMPLE 24-2

Estimate the change in lift with flap deflection for the NACA 65_3–618 airfoil with a 0.20*c* plain flap. The red curve represents the airfoil with the flap at neutral deflection ($\delta_f = 0°$). Its lift curve has been approximated using a cubic spline, given by

$$C_{L_{0°}}(\alpha) = -0.000037115\alpha^3 - 0.0017479\alpha^2 + 0.098365\alpha + 0.53428$$

The blue lift curve is a cubic spline for the airfoil with the flap deflected $\delta_f = 5°$ TED.

$$C_{L_{5°}}(\alpha) = -0.000018839\alpha^3 - 0.0020116\alpha^2 + 0.089079\alpha + 0.7519$$

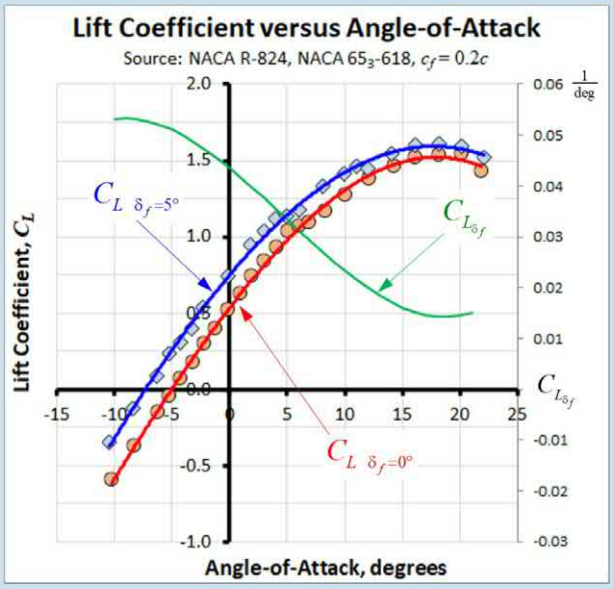


FIGURE 24-19 The pitching moment curve.

SOLUTION:

Note that even though this derivative is specified for a flap, this method can be used for all flapped control surfaces, ailerons, elevator, rudder, and even spoilers. To estimate the derivative, we subtract $C_{L0°}$ from $C_{L5°}$ and divide by the difference in flap deflection angle (5°).

$$C_{L_{\delta_f}} \approx \frac{\Delta C_L}{\Delta \delta_f} = \frac{C_{L_{5°}} - C_{L_{0°}}}{\Delta \delta_f}$$

$$= \frac{0.000018276\alpha^3 - 0.002637\alpha^2 - 0.009286\alpha + 0.21762}{5°}$$

$$= 0.000003654\alpha^3 - 0.0005274\alpha^2 - 0.0018572\alpha + 0.043524$$

The derivative is coplotted in Figure 24-19, where it uses the right vertical scale. It can be seen the value depends on flap chord and span, deflection angle, and AOA.

24.2.7 The Pitching Moment Model, C_M

The longitudinal equilibrium is the second expression of Equations (24-14) and (24-25). It becomes

$$\boldsymbol{M} = 0 \quad \Leftrightarrow \quad \sum M_{CG} = qSc_{MGC} \cdot \boldsymbol{C_M} = 0 \tag{24-63}$$

where $\boldsymbol{M_{CG}}$ means the moments are summed about the CG. This gives rise to the *pitching moment coefficient*:

$$\boldsymbol{C_M} = \boldsymbol{C_{M_0}} + \boldsymbol{C_{M_\alpha}}\alpha + \boldsymbol{C_{M_\beta}}\beta + \boldsymbol{C_{M_{\dot\alpha}}}\left(\frac{\dot\alpha c_{MGC}}{2V_\infty}\right) + \boldsymbol{C_{M_q}}\left(\frac{\hat q c_{MGC}}{2V_\infty}\right) + \hookleftarrow$$

$$\boldsymbol{C_{M_{i_{HT}}}} i_{HT} + \boldsymbol{C_{M_{\delta_e}}}\delta_e + \boldsymbol{C_{M_{\delta_f}}}\delta_f + \boldsymbol{C_{M_{LDG}}}\delta_{LDG} + \boldsymbol{C_{M_u}} + \ldots \tag{24-64}$$

where

$\boldsymbol{C_{M0}}$ = Residual pitching moment,
$\boldsymbol{C_{M\alpha}}$ = *Longitudinal stability derivative*,
$\boldsymbol{C_{M\beta}}$ = Change in $\boldsymbol{C_M}$ with β,
$\boldsymbol{C_{Mq}}$ = *Pitch damping coefficient*,
$\boldsymbol{C_{M_{\dot\alpha}}}$ = Change in C_M with $\dot\alpha$,
$\boldsymbol{C_{M_{i_{HT}}}}$ = Change in moment with stabilizer incidence, i_{HT},
$\boldsymbol{C_{M\delta_e}}$ = *Elevator authority derivative*, δ_e,
$\boldsymbol{C_{M\delta_f}}$ = Change in $\boldsymbol{C_M}$ with δ_f,
$\boldsymbol{C_{M\delta_{LDG}}}$ = Change in $\boldsymbol{C_M}$ with δ_{LDG},
$\boldsymbol{C_{M_u}}$ = Change in CM with airspeed.

For straight, steady-state flight, Equation (24-64) reduces to

$$\boldsymbol{C_M} = \boldsymbol{C_{M_0}} + \boldsymbol{C_{M_\alpha}}\alpha + \boldsymbol{C_{M_{i_{HT}}}} i_{HT} + \boldsymbol{C_{M_{\delta_e}}}\delta_e + \boldsymbol{C_{M_{\delta_f}}}\delta_f + \boldsymbol{C_{M_{LDG}}}\delta_{LDG} = 0 \tag{24-65}$$

(1) Residual Pitching Moment Coefficient, C_{M0}

This derivative represents the pitching moment coefficient, C_M, with all other contributions zero (e.g., $\alpha=0$, $\beta=0$, …). It consists of multiple contributions, wing, fuselage, and so on. Some are involved enough to warrant their own sections.

$$C_{M_0} = C_{M_{0_W}} + C_{M_{0_{HT}}} + C_{M_{0_{FUS}}} + C_{M_{0_{NAC}}} + C_{M_{0_T}} + \ldots \quad (24\text{-}66)$$

where

$C_{M_{0_W}}$ = Residual pitching moment due to the wing, see Equation (24-67),
$C_{M_{0_{HT}}}$ = Residual pitching moment due to the HT, see Equation (24-68),
$C_{M_{0_{FUS}}}$ = Residual pitching moment due to the fuselage, see Equation (24-107),
$C_{M_{0_{NAC}}}$ = Residual pitching moment due to nacelles, see Equation (24-107),
$C_{M_{0_T}}$ = Pitching moment due to thrustline, see Equation (24-109).

Contribution by the Wing

The residual pitching moment due to the wing is the sum of its moment about the *aerodynamic center* (AC) of the complete aircraft and the zero-lift acting at the CG (see Figure 24-10 for the fractional dimensions h_{cg} and h_{ac}):

$$C_{M_{0_W}} = C_{M_{ac_W}} + C_{L_{0_W}}\left(h_{cg} - h_{ac}\right) \quad (24\text{-}67)$$

where $C_{M_{ac_W}}$ is the pitching moment about the aerodynamic center of the wing. The fractional distance h_{cg}–h_{ac} is of great importance in stability and control theory. It specifies the *static margin*, $SM \equiv -100(h_{cg}-h_{ac})$.

Contribution by the HT

The residual pitching moment due to the HT only applies to unsymmetrical airfoils (see Figure 24-10 for dimensions h_{cg} and h_{ac}):

$$C_{M_{0_{HT}}} = C_{M_{ac_{HT}}} + C_{L_{0_{HT}}}\left(\frac{l_{HT_{CG}}}{c_{MGC}}\right) \quad (24\text{-}68)$$

Where C_{MacHT} is the pitching moment about the aerodynamic center of the HT.

(2) Longitudinal Stability Derivative, $C_{M\alpha}$

This derivative represents how pitching moment changes with angle-of-attack, α. The derivative can be treated as the linear combination of contributions due to the wing, fuselage, HT, nacelles, normal force (for propeller aircraft), and so forth. Mathematically, we write

$$C_{M_\alpha} = C_{M_{\alpha_W}} + C_{M_{\alpha_{HT}}} + C_{M_{\alpha_{FUS}}} + C_{M_{\alpha_{NAC}}} + C_{M_{\alpha_{T_N}}} + \ldots \quad (24\text{-}69)$$

where

$C_{M\alpha_W}$ = Longitudinal derivative due to the wing, see Equation (24-70),

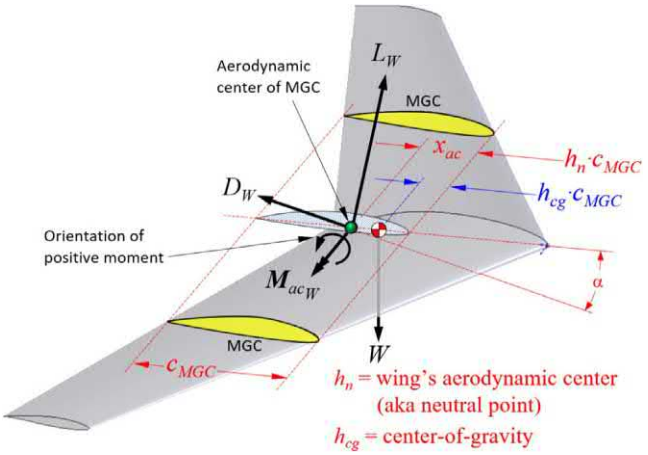


FIGURE 24-20 Lift, drag, moment, and weight acting on a wing.

$C_{M\alpha_{HT}}$ = Longitudinal derivative due to the HT, see Equation (24-72),
$C_{M\alpha_{FUS}}$ = Longitudinal derivative due to the fuselage, see Equation (24-108),
$C_{M\alpha_{NAC}}$ = Longitudinal derivative due to the nacelle, see Equation (24-108),
$C_{M\alpha_{T_N}}$ = Longitudinal derivative due to propeller normal force, see Equation (24-111).

Wing Contribution

Figure 24-20 shows inertia and aerodynamic forces and moment acting on a wing. The longitudinal stability derivative for the wing can be written as follows

$$C_{M_{\alpha_W}} = C_{L_{\alpha_W}}\left(\frac{x_{cg}}{c_{MGC}} - \frac{x_{ac}}{c_{MGC}}\right) \quad (24\text{-}70)$$

The wing-body correction, K_{WB}, is ignored because it is accounted for in the evaluation of $C_{M\alpha_{FUS}}$. Rewrite this by substituting the fractional dimensions of Figure 24-20 (and Figure 24-10):

$$C_{M_{\alpha_W}} = C_{L_{\alpha_W}}\left(h_{cg} - h_{ac}\right) \quad (24\text{-}71)$$

HT Contribution

The lift curve slope of the HT ($C_{L\alpha_{HT}}$) acts over the arm $l_{HT_{CG}} = x_{HTac} - x_{cg}$ (see Figure 24-10). This contribution increases stability (after all that is why we bother to add the HT), so it has a negative sign. It is given by:

$$C_{M_{\alpha_{HT}}} = -\eta_{HT}\frac{S_{HT}}{S}C_{L_{\alpha_{HT}}}\left(1 - \frac{\partial\varepsilon}{\partial\alpha}\right)\frac{l_{HT_{CG}}}{c_{MGC}} \quad (24\text{-}72)$$

This is commonly rearranged as follows

$$C_{M_{\alpha_{HT}}} = -\eta_{HT}\frac{S_{HT}}{S}\frac{l_{HT_{CG}}}{c_{MGC}}C_{L_{\alpha_{HT}}}\left(1 - \frac{\partial\varepsilon}{\partial\alpha}\right) \quad (24\text{-}73)$$

where the ratio of geometric terms is combined into a new dimensionless parameter called *horizontal tail volume* (V_{HT}). It is defined as

$$V_{HT} \equiv \frac{S_{HT} \cdot l_{HT_{CG}}}{S \cdot c_{MGC}} \quad (24\text{-}74)$$

(3) Change in Pitching Moment with Angle-of-Yaw, $C_{M\beta}$

The derivative $C_{M\beta}$ is the rate-of-change of pitching coefficient with yaw angle, β. Its magnitude is usually low and can be neglected. Typical range is ±0.006 per radian (±0.0001 per degree). May assume 0 for conceptual work.

(4) Pitch Damping Coefficient, C_{Mq}

Related to the lift-damping derivative, C_{Lq}. It is caused by the change in lift due to pitch rate that acts on components positioned forward and aft of the CG. The largest contribution is that of the stabilizing surface, with minor one by the wing. Thus, it is expressed in a form like that of C_{Lq}:

$$C_{M_q} = \overbrace{C_{M_{q_{WB}}}}^{\text{wing-body contribution}} + \overbrace{C_{M_{q_{HT}}}}^{\text{HT contribution}} \approx \overbrace{C_{M_{q_W}}}^{\text{wing contribution}} + C_{M_{q_{HT}}} \quad (24\text{-}75)$$

Wing Contribution

Per ref. [12], the contribution of the wing is given by the following method. If $M_\infty \le 0.2$ then

$$\left(C_{M_{q_W}}\right)_{M_\infty \le 0.2} = -0.7 C_{l_\alpha} \cos\Lambda_{c/4} \times \left[\frac{AR\left(\frac{1}{2}\left(h_{ac}-h_{cg}\right)+2\left(h_{ac}-h_{cg}\right)^2\right)}{AR+2\cos\Lambda_{c/4}} + \frac{1}{24}\left(\frac{AR^3\tan^2\Lambda_{c/4}}{AR+6\cos\Lambda_{c/4}}\right)+\frac{1}{8}\right] \quad (24\text{-}76)$$

where $K_q = \frac{1}{10}(8+\tanh(AR-8))$. If $M_\infty > 0.2$ then, Equation (24-76) is corrected as shown below

$$\left(C_{M_{q_W}}\right)_{M>0.2} = \left[\frac{A_1}{A_2}\right]\left(C_{M_{q_W}}\right)_{M\le 0.2} \quad (24\text{-}77)$$

where A_1 and A_2 are given by

$$A_1 = \frac{AR^3\tan^2\Lambda_{c/4}}{AR\sqrt{1-\left(M_\infty\cos\Lambda_{c/4}\right)^2}+6\cos\Lambda_{c/4}} + \frac{3}{\sqrt{1-\left(M_\infty\cos\Lambda_{c/4}\right)^2}} \quad (24\text{-}78)$$

$$A_2 = \frac{AR^3\tan^2\Lambda_{c/4}}{AR+6\cos\Lambda_{c/4}} + 3 \quad (24\text{-}79)$$

Note that despite this complexity, the wing contribution is small.

HT Contribution

The contribution of the HT is given by

$$C_{M_{q_{HT}}} \approx C_{L_{q_{HT}}} l_{HT_{CG}} = -2C_{L_{\alpha_{HT}}}\eta_{HT}\frac{S_{HT}}{S}l_{HT_{CG}}^2 \quad (24\text{-}80)$$

Ref. [6] suggests that $C_{Mq} \approx 1.1 C_{Mq_{HT}}$.

(5) Change in Pitching Moment due to Downwash Lag, $C_{M_{\dot\alpha}}$

The derivative $C_{M_{\dot\alpha}}$ is related to $C_{L_{\dot\alpha}}$. It represents the change in pitching moment due to the rate-of-change of α (downwash lag) that follows a sudden change in α. The effect comprises contributions from the wing, fuselage (body), and HT, of which the wing-body contribution can generally be neglected:

$$C_{M_{\dot\alpha}} = \overbrace{C_{M_{\dot\alpha_{WB}}}}^{\text{wing-body contribution}} + \overbrace{C_{M_{\dot\alpha_{HT}}}}^{\text{HT contribution}} \approx C_{M_{\dot\alpha_{HT}}} \quad (24\text{-}81)$$

The contribution of the HT is given by [12].

$$C_{M_{\dot\alpha_{HT}}} \approx -2C_{L_{\alpha_{HT}}}\eta_{HT}\left(\frac{S_{HT}}{S}\right)\left(\frac{l_{HT_{CG}}}{c_{MGC}}\right)^2\frac{\partial\varepsilon}{\partial\alpha} = -2C_{L_{\alpha_{HT}}}\eta_{HT}V_{HT}\left(\frac{l_{HT_{CG}}}{c_{MGC}}\right)\frac{\partial\varepsilon}{\partial\alpha} \quad (24\text{-}82)$$

(6) Pitching Authority Derivative, $C_{Mi_{HT}}$

The elevator authority derivative, $C_{Mi_{HT}}$, is defined as

$$C_{M_{i_{HT}}} \equiv \frac{\partial C_M}{\partial i_{HT}} = -\eta_{HT}\frac{S_{HT}}{S}C_{L_{\alpha_{HT}}}l_{HT_{CG}} \quad (24\text{-}83)$$

Rotating the leading-edge of the HT down (negative tail incidence angle) destabilizes the airplane (nose pitches up = positive moment). Thus, the angle-of-incidence must be negative for such a rotation.

(7) Pitching (Elevator) Authority Derivative, $C_{M\delta e}$

The elevator authority derivative, $C_{M\delta e}$, is defined and approximated as follows:

$$C_{M_{\delta_e}} \equiv \frac{\partial C_M}{\partial\delta_e} \approx C_{L_{\delta_e}}\left(h_{cg}-h_{ac}\right) - V_{HT}\frac{\partial C_{L_{HT}}}{\partial\delta_e} \approx \left(\eta_{HT}\left(\frac{S_{HT}}{S}\right)\left(h_{cg}-h_{ac}\right) - V_{HT}\right)\frac{\partial C_{L_{HT}}}{\partial\delta_e} \quad (24\text{-}84)$$

where the derivative $\partial C_{LHT}/\partial\delta_e$ is represented using the relation

$$\frac{\partial C_{L_{HT}}}{\partial\delta_e} = \underbrace{\frac{\partial C_{L_{HT}}}{\partial\alpha_{HT}}}_{C_{L_{\alpha_{HT}}}}\underbrace{\frac{\partial\alpha_{HT}}{\partial\delta_e}}_{\tau} = C_{L_{\alpha_{HT}}}\tau_e \quad (24\text{-}85)$$

The value of the *elevator effectiveness factor*, τ_e, is given in refs. [6], where it is graphed in terms of the ratio of the elevator area *behind* the hingeline (see S_e in Figure 24-21) to the total area of the HT, S_{HT}. The author has digitized this curve, allowing τ to be estimated (for *elevator ratios* of $0.025 < r_e < 0.5$, where $r_e \equiv S_e/S_{HT} = c_e/c_{HT}$) per the expression

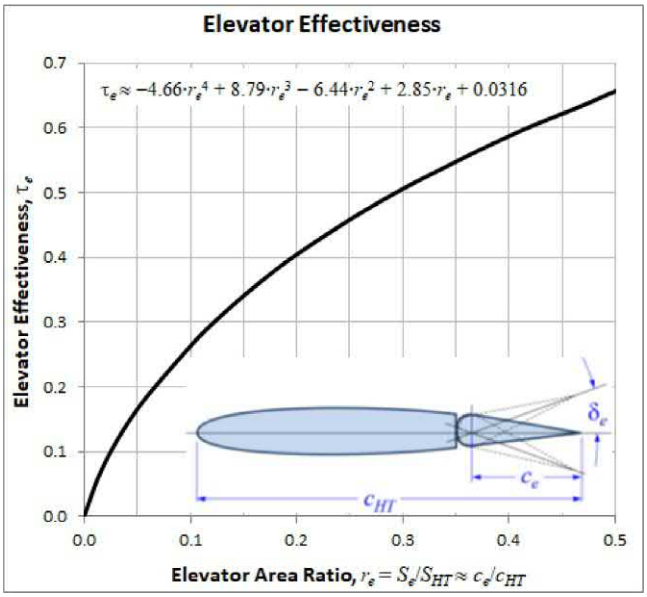


FIGURE 24-21 Elevator effectiveness can be approximated using the polynomial shown.

$$\tau_e \approx -4.66r_e^4 + 8.79r_e^3 - 6.44r_e^2 + 2.85r_e + 0.0316 \qquad (24\text{-}86)$$

Note that ref. [17] presents two other methods to approximate τ_e, but we will let this suffice here. Note that deflecting the elevator trailing edge up destabilizes the airplane (nose pitches up = positive moment). Thus, the angle-of-incidence of the HT must be negative (LE down and TE up) for such a rotation (just like elevator deflection TEU is negative).

(8) Change in Pitching Moment with Deployment of High-Lift Device, $C_{M\delta f}$

The deployment of high-lift devices can be accounted for using Equation (10-3) with appropriate airfoil data.

(9) Change in Pitching Moment with Deployment of Landing Gear, $C_{M\delta_{LDG}}$

The deployment of the landing-gear (LDG) primarily adds to the drag, however, since center of drag is below the CG, it stabilizes the airplane. This contribution can be estimated as

$$C_{M_{\delta_{LDG}}} \equiv \frac{\partial C_M}{\partial \delta_{LDG}} = -\frac{S_{LDG}}{S} C_{D_{\delta_{LDG}}} z_{LDG_{CG}} \qquad (24\text{-}87)$$

where $z_{LDG_{CG}}$ is the distance between the CG and center of LDG drag, S_{LDG} is a reference area used to calculate the drag acting on the LDG, and $C_{D\delta_{LDG}}$ is the LDG drag coefficient. See more details in Section 24.2.12.

(10) Change in Pitching Moment with High Subsonic Airspeed, C_{Mu}

The derivative C_{Mu} accounts for transonic changes. It can be ignored for $M_\infty < 0.7$. It is defined as follows

$$C_{M_u} \equiv \frac{\partial C_M}{\partial M_\infty} = -C_L \frac{\partial h_{ac_W}}{\partial M_\infty} \qquad (24\text{-}88)$$

24.2.8 Horizontal Tail Downwash Angle and Angle-of-Attack

If the horizontal tail (HT) is placed behind the wing (as is common for most airplanes) it is subject to a downward flow-component (*downwash*) that changes the AOA on the tail. For instance, consider the main wing at $\alpha = 10°$. One might assume the AOA of the HT is also 10°, but this is not the case. The downwash from the main wing reduces it, so it might only be 5°. This affects the stability of the airplane and, thus, must be accounted for.

Downwash per the Momentum Theory

The momentum theory of Section 8.1.9 provides a simple method to predict downwash. Its shortcoming is that it returns an average value for an elliptical planform, whereas in real flow the magnitude varies with spanwise position. Its advantage is ease of estimation. Its results are acceptable for conceptual design; however, it is not reliable for predicting effects associated with the vertical position of the HT. The downwash angle (ε) is expressed using the following linear relation:

$$\varepsilon = \varepsilon_0 + \frac{\partial \varepsilon}{\partial \alpha}\alpha \qquad (24\text{-}89)$$

where ε_0 is the residual downwash (when $\alpha = 0$) which is only present if the wing features cambered airfoils and when flaps are deflected. The derivative $\partial\varepsilon/\partial\alpha$ indicates the change in downwash with α. Once ε is known, we can determine the AOA on the horizontal tail, using the schematic of Figure 24-22. The momentum theorem allows ε to be presented in terms of the $C_{L\alpha_W}$ of the wing per Equation (8-28) repeated below for convenience:

$$\varepsilon \approx 2C_{L_W}/(\pi AR) \qquad (8\text{-}28)$$

where C_{L_W} is the lift coefficient of the wing only. The units for the angle are radians. Substituting $C_{LW} = C_{L0W} + C_{L\alpha_W}\alpha$ into Equation (8-27) leads to

$$\varepsilon = \varepsilon_0 + \frac{\partial \varepsilon}{\partial \alpha}\alpha = \frac{2}{\pi AR}\left(C_{L_{0_W}} + C_{L_{\alpha_W}}\alpha\right) \qquad (24\text{-}90)$$

Thus, we can define the *residual* and α-*dependent* downwash as follows:

$$\varepsilon_0 = \frac{2C_{L_{0_W}}}{\pi AR} \quad \text{and} \quad \frac{\partial \varepsilon}{\partial \alpha} = \frac{2C_{L_{\alpha_W}}}{\pi AR} \qquad (24\text{-}91)$$

The AOA at the HT can be calculated by substituting Equation (24-91) into (24-90):

$$\alpha_{HT} = \alpha_W - \varepsilon + i_{HT} = \alpha_W\left(1 - \frac{2C_{L_{\alpha_W}}}{\pi AR}\right) - \frac{2C_{L_{0_W}}}{\pi AR} + i_{HT} \qquad (24\text{-}92)$$

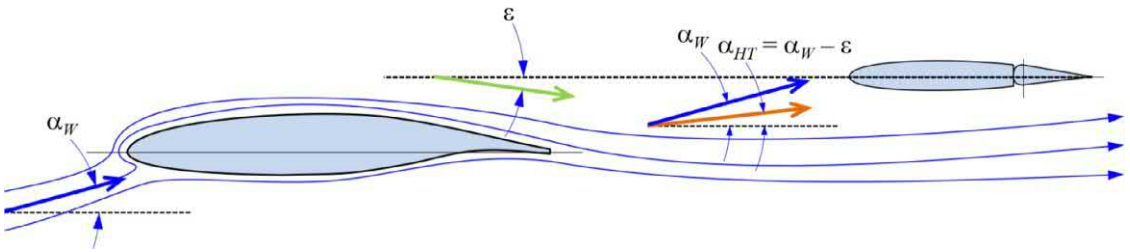


FIGURE 24-22 A schematic showing how the downwash angle, ε, affects the AOA of the horizontal tail.

where i_{HT} is the HT *angle-of-incidence* (the plus sign in front of it is needed because $i_{HT}<0$ when the LE is down). However, once an *angle-of-incidence* (i_W or AOI) is introduced to the wing and HT, things get a bit more complicated (see Figure 24-23). Note that a positive i_W and negative i_{HT} are depicted as most aircraft feature that geometry. Given a fixed α, increasing i_W reduces the fuselage α_{FUS}. Adding i_{HT} as shown, further reduces the α_{HT}. Therefore, the α_{HT} can be summarized as follows:

$$\alpha_{HT} = \alpha_W - \varepsilon + i_{HT} \approx \alpha_W \left(1 - \frac{2C_{L_{\alpha_W}}}{\pi AR}\right) - \frac{2C_{L_{0_W}}}{\pi AR} + i_{HT} \tag{24-93}$$

As an example, if $\alpha = 10°$, α_{HT} might be ≈5°. If $i_{HT}=-3°$ (LE of HT is down) then α_{HT} might be around 2°. It is convenient to define the AOA of the *wing-body* combination as shown in Figure 24-23 and write Equation (24-93) as follows:

$$\alpha_{HT} = \alpha_{WB} - \varepsilon + i_{HT} \tag{24-94}$$

24.2.9 Tail Efficiency Factor, η_{HT}

The propwash of the aircraft in Figure 24-24 is deformed by the fuselage. The airspeed inside the streamtube is higher than outside, which drops the static pressure below that of the outside air. This reduces its diameter, forming a *vena-contracta*. In the absence of a better estimate, it will be assumed that, for a conventional tail-aft configuration, the diameter of the propwash streamtube is 85% of the propeller diameter (D_P). Therefore, the lift generated by the HT is a combination of the lift generated by the planform inside and outside the streamtube. The associated dynamic pressures are denoted by q_P and q, respectively. This allows the *tail efficiency factor*, η_{HT} to be estimated using the following expression:

$$\eta_{HT} = 1 + \left(\frac{q_P}{q} - 1\right)\frac{0.85D_P}{b_{HT}} \tag{24-95}$$

Since $q = \frac{1}{2}\rho V_\infty^2$, this can also be written as:

$$\eta_{HT} = 1 + \left(\frac{V_P^2}{V_\infty^2} - 1\right)\frac{0.85D_P}{b_{HT}} \tag{24-96}$$

where V_P is the airspeed inside the streamtube at the HT. Using the methods of Section 15.5 with mass conservation, it is found as shown below

$$\dot{m}_{prop} = \dot{m}_{HT} \;\Rightarrow\; (V_2 + w)\frac{\pi D_P^2}{4} = V_P \frac{\pi (0.85D_P)^2}{4}$$
$$\Rightarrow\; V_P \approx 1.384(V_2 + w)$$

24.2.10 Forces and Moments due to Fuselage and Nacelles

The forces and moments due to the fuselage are shown schematically in Figure 24-25. The contribution of the fuselage and nacelles to the static longitudinal stability is usually destabilizing. To estimate its magnitude, the fuselage and nacelle are assumed to be bodies-of-revolution. In flight, the geometry forms high- and low-pressure regions at their front and aft ends (see Figure 24-26). This pressure difference generates the destabilizing pitching moment. In fact, the neutral point of such bodies is far

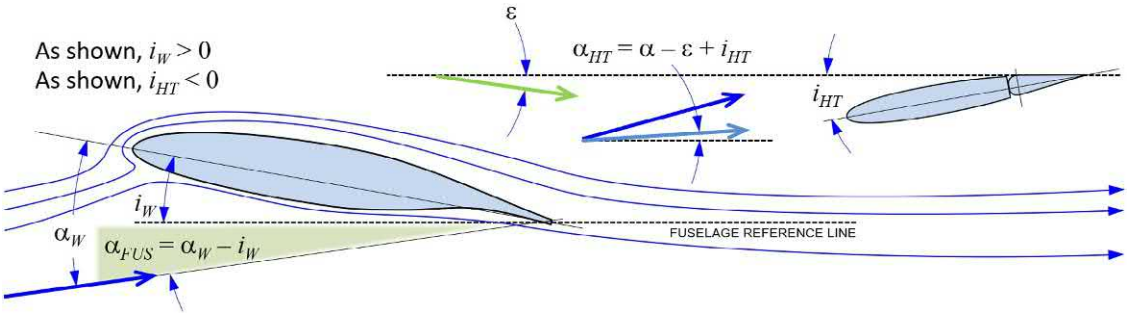


FIGURE 24-23 A schematic showing how i_{HT}, and ε, affect α_{HT}.

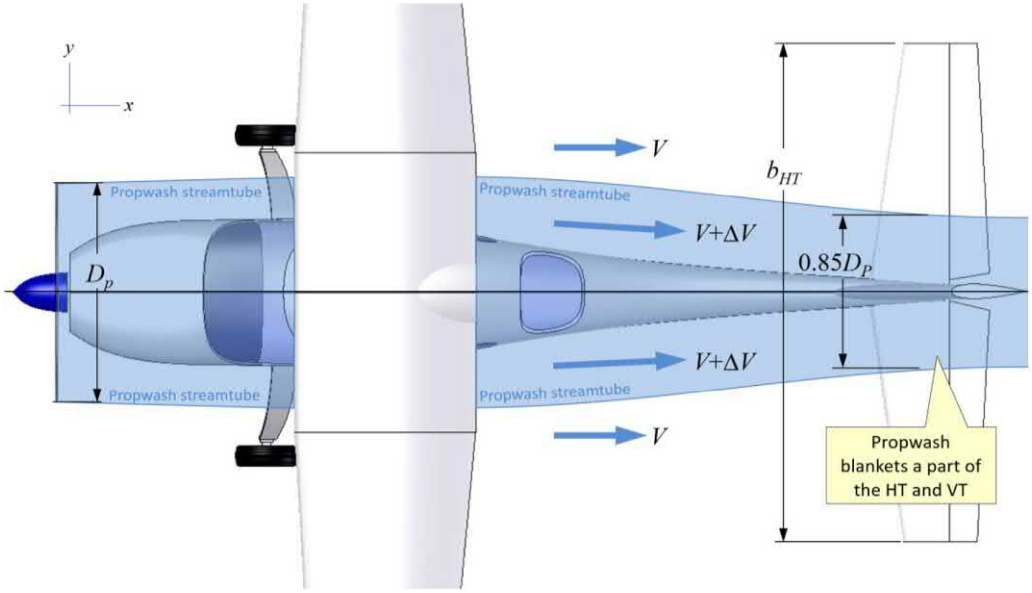


FIGURE 24-24 The propwash increases the dynamic pressure on the tail, improving its effectiveness.

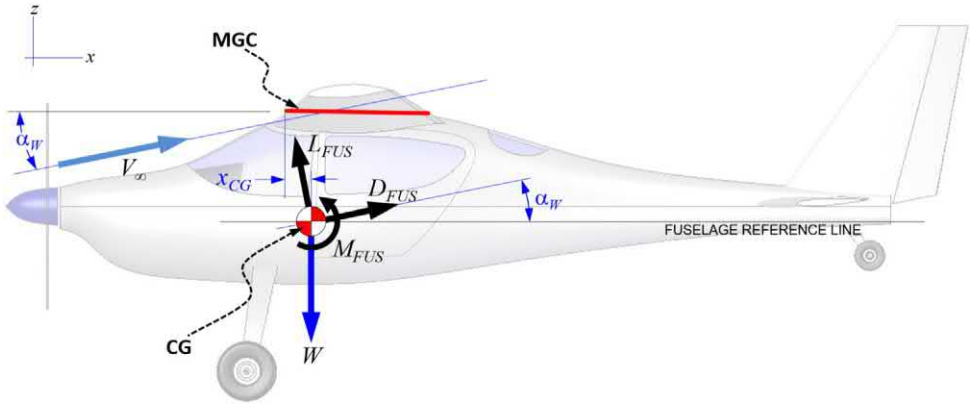


FIGURE 24-25 The contribution of the fuselage.

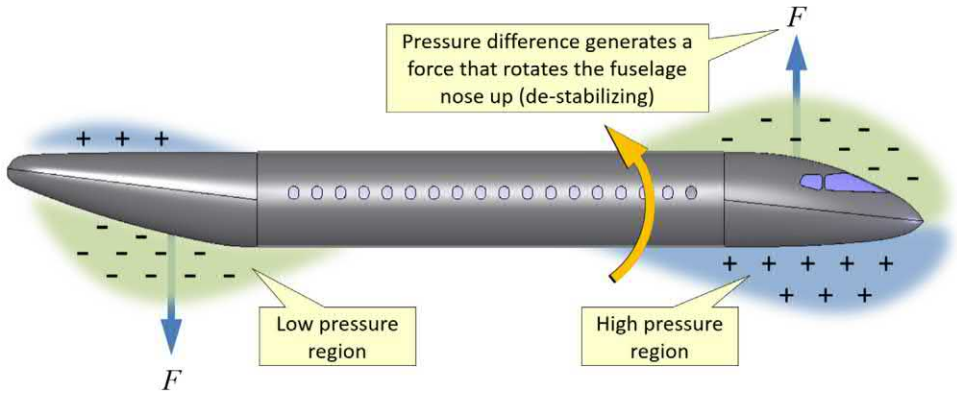


FIGURE 24-26 The cause of the destabilizing fuselage moment.

ahead of the nose. In the absence of wind tunnel testing (or reliable CFD software), the magnitude of this moment is estimated using the so-called *Munk–Multhopp method*. The magnitude of the lift and drag generated by the body is also important. Methods to estimate each are presented below.

(1) Fuselage Lift and Drag

For most applications, it is acceptable to assume these to act at the CG. Here, three methods can be used to calculate fuselage drag:

(A) The method of Section 16.3.4. This is a low fidelity method.

(B) The method of Section 16.4.6. In this method, the drag of a body-of-revolution is estimated by first calculating its skin friction coefficient using the method of Section 16.3.1. Then, an appropriate *form factor* (*FF*) per Section 16.3.6 is applied. Once, completed, the resulting drag coefficient is already in terms of the reference area, *S*, in accordance with:

$$C_{D_{FUS}} = \frac{C_{f_{FUS}} \cdot FF_{FUS} \cdot S_{WET_{FUS}}}{S} \tag{24-97}$$

(C) The following method uses empirical approximations to estimate both lift and drag.

The lift of a typical fuselage is modest compared to that of the wing, ranging from 2% to 12% of total lift. Ref. [18] investigated 209 wing-fuselage combinations, using fuselages of round and rectangular cross sections. These data are used to generate Figure 24-27. Note that the data in ref. [18] have been normalized to the fuselage geometry, rather than the wing dimensions as done in the reference. This makes it more useful for other fuselage geometries. The adjustment for the force was done by multiplying the experimental values (Table II in the reference) by $S/A_{\max}$, where S is the test wing area and $A_{\max}$ is the maximum cross-sectional area of the fuselage. Similarly, the pitching moment was adjusted by multiplying the experimental data by $c/l_{FUS} \times S/A_{\max}$, where c is the average chord of the wing and l_{FUS} is the fuselage length used in the reference. The lift and drag can be estimated using the following polynomials (digitized by the author). These are applicable to fuselages whose fineness ratio (l_{FUS}/d_{FUS}) is between 5 and 6.67.

$$\begin{aligned} C_{L_{FUS-ROUND}} &= 0.0009223 \cdot \alpha + 0.001153 \cdot \alpha^2 \\ C_{D_{FUS-ROUND}} &= 0.06672 - 0.001406 \cdot \alpha + 0.0003603 \cdot \alpha^2 \\ C_{L_{FUS-RECT}} &= 0.01654 \cdot \alpha + 0.001513 \cdot \alpha^2 \\ C_{D_{FUS-RECT}} &= 0.08157 - 0.003061 \cdot \alpha + 0.0008142 \cdot \alpha^2 \end{aligned} \tag{24-98}$$

The reference area is the maximum cross-sectional area of the fuselage. To adjust these coefficients for use with the reference area, S_{ref}, use Equation (16-141), where $S_S = A_{\max}$.

(2) Pitching Moment about the CG due to the Fuselage

The pitching moment can be obtained using two methods: (1) the data from the right graph of Figure 24-27 and (2) the Munk–Multhopp method. As stated earlier,

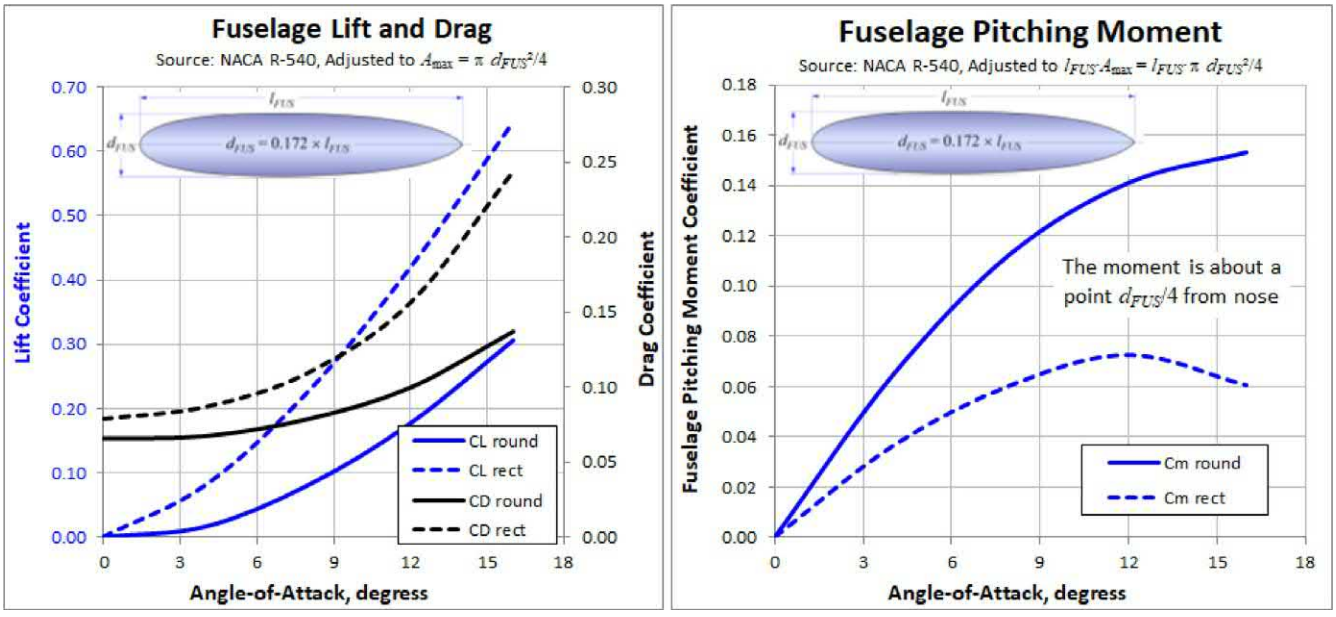


FIGURE 24-27 Experimental lift, drag, and pitching moment for a generic round and rectangular fuselage. *From E.N. Jacobs, K.E. Ward, Interference of Wing and Fuselage from Tests of 209 Combinations in the NACA Variable-Density Tunnel, NACA R-540, 1935.*

Figure 24-27 is applicable fuselages whose l_{FUS}/d_{FUS} is between 5 and 6.67. The moment is obtained using the following polynomials, digitized by the author.

$$C_{M_{FUS-ROUND}} = \left(-0.1153 + 18.52 \cdot \alpha - 0.5584 \cdot \alpha^2\right)/1000$$
$$C_{M_{FUS-RECT}} = \left(0.1729 + 9.547 \cdot \alpha - 0.1081 \cdot \alpha^2 - 0.01576 \cdot \alpha^3\right)/1000 \quad (24\text{-}99)$$

The limitation of the previously mentioned method is the range of fuselage fineness ratios. The Munk–Multhopp method is not subject to such limitations. It is attributed to Max Munk (1890–1986) and Hans Multhopp (1913–1972). Munk's method was originally developed for airships [19]. Using potential flow theory, he demonstrated that the pitching moment of a body-of-revolution depended on its volume and dynamic pressure. The effect of the slenderness of the body was accounted for using a special correction factor. Since this work involved airships there was no need to account for the upwash and downwash that occurs in front of and behind a wing. Multhopp improved Munk's method to account for this [20]. The pitching moment of a fuselage is given by the following expression:

$$C_{M_{FUS}} = C_{M_{0_{FUS}}} + C_{M_{\alpha_{FUS}}} \cdot \alpha \quad (24\text{-}100)$$

where the zero-alpha moment is calculated using the following expression, where the constant 36.5 converts radians to degrees (allowing the use of degrees rather than radians)

$$C_{M_{0_{FUS}}} = \frac{k_2 - k_1}{36.5 \cdot S \cdot c_{MGC}} \int_0^{l_{FUS}} w_f^2 \left(\alpha_{ZL_W} + i_f\right) dx \quad (24\text{-}101)$$

The dependency on α is given by:

$$C_{M_{\alpha_{FUS}}} = \frac{1}{36.5 \cdot S \cdot c_{MGC}} \int_0^{l_{FUS}} w_f^2 \frac{\partial \beta}{\partial \alpha} dx \quad (24\text{-}102)$$

where

k_2–k_1 = Correction factor to account for the fuselage slenderness ratio (see Figure 24-29 and Equation (24-103)).
w_f = Average width of a fuselage section
α_{ZL_w} = Wing zero-lift angle relative to the fuselage reference line (see Figure 24-25). Considering Figure 24-28, if the zero lift AOA is −2° and the AOI of the wing is +1°, then this angle is +3°.
i_f = Fuselage camber incidence angle. See Figure 24-28 for more details.
$\partial\beta/\partial\alpha$ = Upwash gradient (see Figure 24-29)

The correction factor, k_2–k_1, can be determined from Figure 24-29 (left) or through the following approximation to the data (digitized by the author):

$$k_2 - k_1 = 1 - \frac{1}{f} + \left(\frac{0.24f^3 - 5.6f^2 + 44f - 72}{1000}\right) \quad (24\text{-}103)$$

where

$f = l_{FUS}/d_{FUS}$ = Fuselage fineness ratio
l_{FUS} = Fuselage length
d_{FUS} = Fuselage width or depth

The upwash curves in Figure 24-29 (right) have also been digitized by the author and are presented below.

Upwash Curve 1:

$$\left(\frac{\partial \beta}{\partial \alpha}\right)_1 = 1.4758 - 0.40485\left(\frac{x}{c_{MGC}}\right) + 0.09107\left(\frac{x}{c_{MGC}}\right)^2 \quad (24\text{-}104)$$

Upwash Curve 2:

$$\left(\frac{\partial \beta}{\partial \alpha}\right)_2 = 1.74611\left(\frac{x}{c_{MGC}}\right)^{-0.4254} \quad (24\text{-}105)$$

Use the following formulation for the downwash region behind the wing:

$$\left(\frac{\partial \beta}{\partial \alpha}\right) = \frac{x_i}{l_h}\left[1 - \frac{\partial \varepsilon}{\partial \alpha}\right] \quad (24\text{-}106)$$

The computation of the two pitching moment coefficients is implemented through numerical integration. This is done by segmenting the fuselage as shown in Figure 24-30. Note that the number of segments should be based on the complexity of the fuselage geometry.

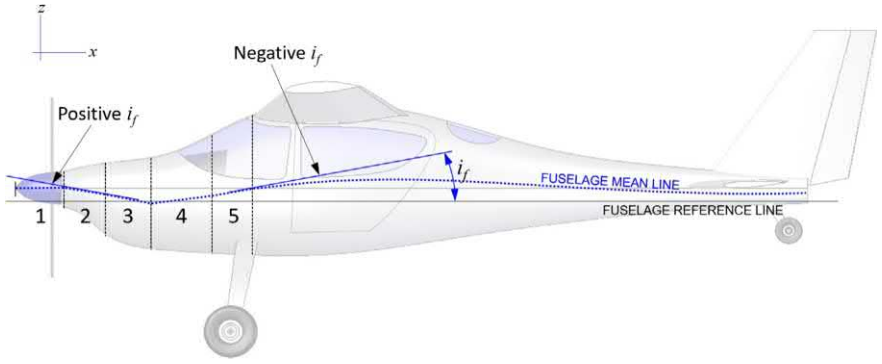


FIGURE 24-28 Definition of a positive and negative fuselage camber incidence.

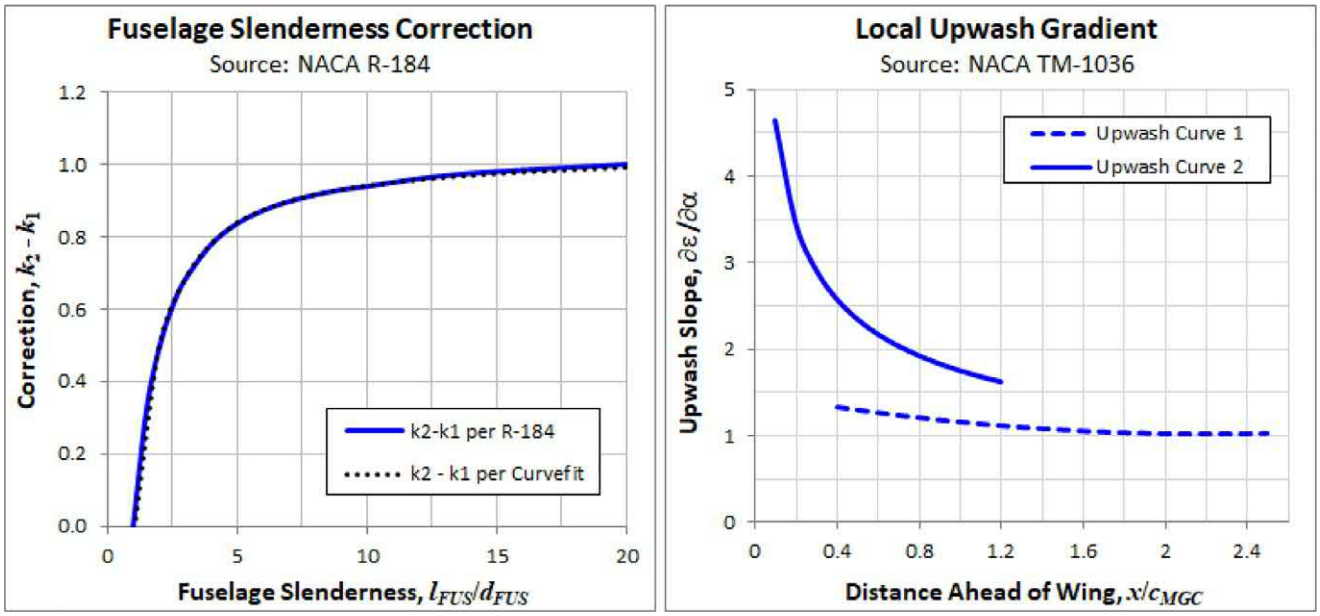


FIGURE 24-29 Fuselage slenderness correction and a handy approximation. The following curve fits will generate the curves in the right graph of Figure 24-29. See Figure 24-30 for instructions on where to apply them.

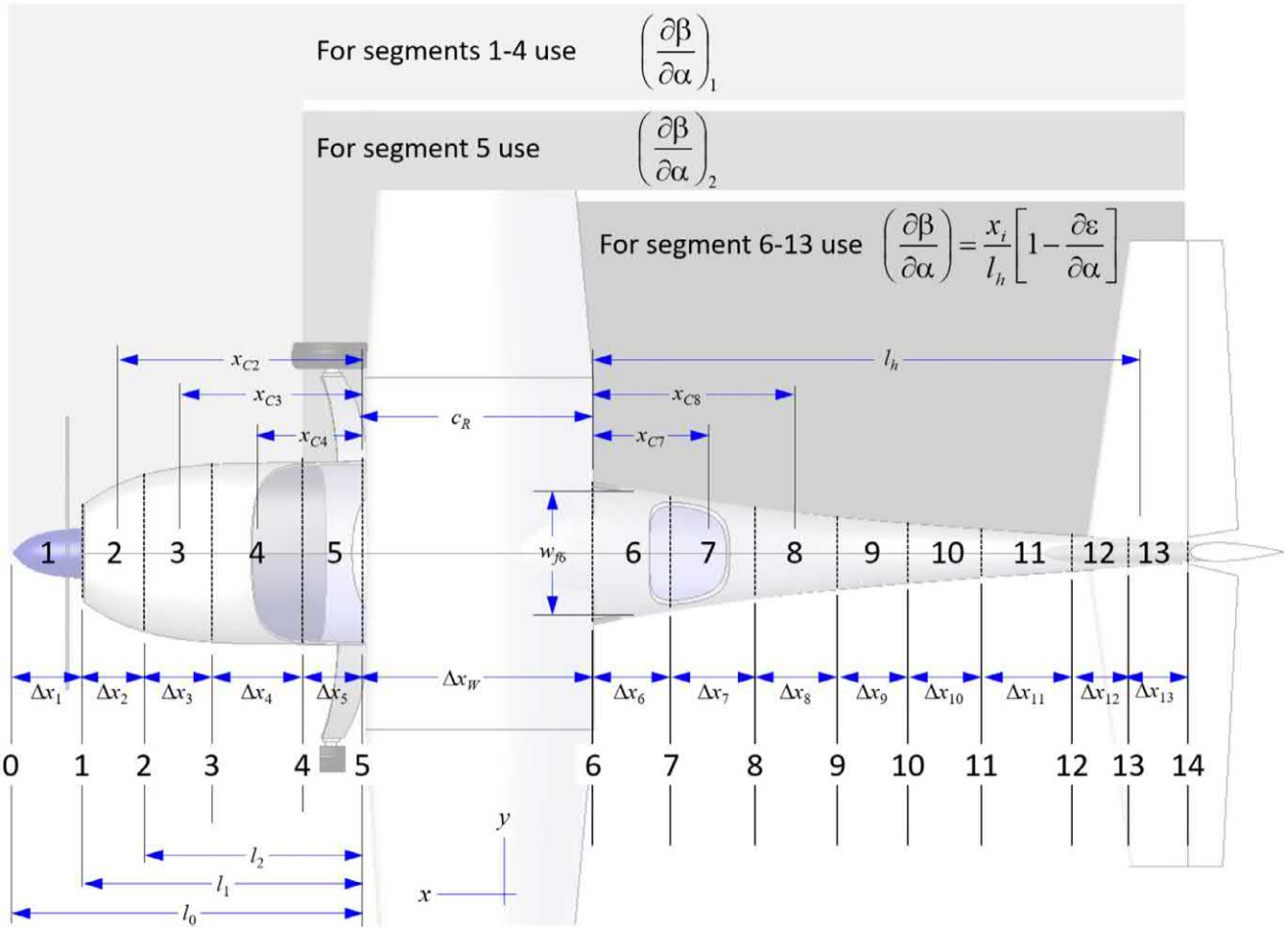


FIGURE 24-30 The implementation of the *Munk–Multhopp method* for a fuselage or nacelle.

For most applications 10 to 20 segments suffices. The coefficients of Equation (24-100) are calculated using the following discrete representations:

$$C_{M_{0_{FUS}}} = \frac{k_2 - k_1}{36.5\ S\ c_{MGC}} \sum_{x=0}^{x=l_{FUS}} w_f^2 \left(\alpha_{ZL_W} + i_f\right) \Delta x \qquad (24\text{-}107)$$

$$C_{M_{\alpha_{FUS}}} = \frac{1}{36.5\ S\ c_{MGC}} \sum_{x=0}^{x=l_{FUS}} w_f^2 \frac{\partial \beta}{\partial \alpha} \Delta x \qquad (24\text{-}108)$$

The solution process is demonstrated in Example 24-3. The method is applied precisely the same way for nacelles, despite limited aft "fuselage." The nacelles of many twin-engine aircraft featuring wing-mounted engines only consist of a forward "fuselage." The nacelles of aircraft such as the Fokker F-27 Friendship, on the other hand, would be represented using both a forward and aft "fuselage" segments. The nacelles of the Rockwell OV-10 Bronco, which also serve as tailbooms, would consist mostly of an aft section and small forward section.

EXAMPLE 24-3

Determine the pitching moment coefficients for the fuselage of the SR22.

SOLUTION:

The process is implemented in Table 24-4. In it, Column ① contains the distance to each segment, as shown in Figure 24-30. Column ② is the width of each segment, calculated by subtracting subsequent sections. Thus, if the segment belongs to the forward fuselage (see Figure 24-31), it is calculated using the expression $\Delta x_i = l_{i-1} - l_i$. This means that the segment distance in Row 3 is $\Delta x_3 = l_2 - l_3$. The value of Δx for the wing row is simply the wing chord at root. For the aft fuselage, the process is reversed, i.e., $\Delta x_i = l_i - l_{i+1}$. Therefore, in Row 7, we would get: $\Delta x_7 = l_7 - l_8$.

Column ③ is the distance to the center of the segment. The center of a segment in the forward fuselage is $x_{Ci} = l_i + \frac{1}{2}\Delta x_{i-1}$, while for the aft fuselage it is $x_{Ci} = l_i - \frac{1}{2}\Delta x_{i+1}$.

Column ④ is the width of the segment at the station identified by ID (first column), while Column ⑤ is the average width of the segment. The average of a segment belonging to the forward fuselage is calculated by $w_{fi} = \frac{1}{2}(w_i + w_{i-1})$, while for the aft fuselage is determined from: $w_{fi} = \frac{1}{2}(w_i + w_{i+1})$.

TABLE 24-4 Determination of fuselage stability derivatives.

l_{FUS} =	22.73 ft	S =	144.9 ft²	l_{HT} =	14.37 ft		
d_{FUS} =	4.17 ft	c_{MGC} =	3.783 ft	$\partial\varepsilon/\partial\alpha$ =	0.333		
l_{FUS}/d_{FUS} =	5.46	AR =	10	$C_{M0\,FUS}$ =	-0.003381		
$k_2 - k_1$ =	0.857	$C_{L\alpha W}$ =	5.24	$C_{M\alpha\,FUS}$ =	0.008671	per degree	

	ID	① l_i, ft	② Δx_i, ft	③ x_{ci}, ft	④ w_i, ft	⑤ w_{fi}, ft	⑥ $(\alpha_{ZLW} + i_f)_i$	⑦ $w_{fi}^2[\alpha_{ZLW} + i_f]\Delta x_i$	⑧ $(\partial\beta/\partial\alpha)_i$	⑨ $w_{fi}^2[\partial\beta/\partial\alpha]\Delta x_i$
FWD FUSELAGE	0	7.57			0.00					
	1	5.66	1.90	6.62	3.24	1.62	5.9	29.4	0.943	4.70
	2	3.76	1.90	4.71	3.72	3.48	0.9	19.7	1.061	24.45
	3	1.90	1.86	2.83	3.95	3.83	-1.5	-42.1	1.205	32.90
	4	0.00	1.90	0.95	4.08	4.01	-2.0	-61.4	3.141	96.21
WING	W	0.00	5.20	2.60	4.08	4.08	-2.0	-173.3		
AFT FUSELAGE	5	-5.20	1.49	-5.94	3.77	3.48	2.3	41.4	0.276	4.96
	6	-6.69	1.60	-7.49	3.19	2.84	3.8	49.2	0.347	4.48
	7	-8.29	1.60	-9.09	2.48	2.06	5.0	34.1	0.422	2.87
	8	-9.89	1.32	-10.55	1.64	1.42	5.4	14.4	0.489	1.30
	9	-11.21	1.37	-11.90	1.20	1.02	4.9	6.9	0.552	0.79
	10	-12.58	1.49	-13.32	0.84	0.75	3.3	2.8	0.618	0.52
	11	-14.07	1.23	-14.68	0.66	0.62	0.1	0.0	0.681	0.32
	12	-15.30			0.58					
							Sum =	-78.9		173.49

EXAMPLE 24-3 (*cont'd*)

Column ⑥ is the sum of the wing's zero-lift line angle (α_{ZLW}) with respect to the *fuselage reference line* and the fuselage mean-line angle at the center of each segment with respect to the fuselage reference line (i_f) (see Figure 24-28). The α_{ZLW} is 2.9° and the slope of the fuselage mean-line was approximated using a fourth-order polynomial, which was differentiated to get the slope. Finally, the slope was converted to an angle by evaluating the inverse tangent.

Column ⑦ is the product of columns ②, ⑤, and ⑥. Column ⑧ is the upwash and downwash around the fuselage, calculated depending on region as shown in Figure 24-30. Column ⑨ is the product of columns ②, ⑤, and ⑧.

Then, the numbers in columns ⑦ and ⑨ are summed up. They are used with Equations (24-107) and (24-108) to determine the two pitching moment coefficients.

The resulting zero AOA and AOA dependent pitching moment coefficients are shown in the shaded box above the main table. These can be presented using Equation (24-100) as shown below:

$$C_{M_{FUS}} = C_{M_{0_{FUS}}} + C_{M_{\alpha_{FUS}}} \cdot \alpha = -0.00338 + 0.008671 \cdot \alpha$$

where α is in degrees. This result tells us the fuselage is strongly destabilizing, something the designer should anticipate for wide forward fuselages.

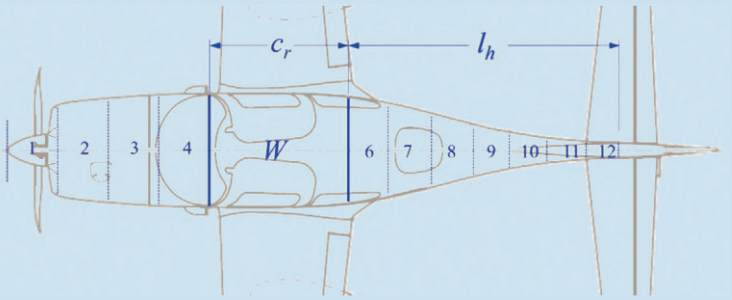


FIGURE 24-31 The implementation of the Munk–Multhopp method for the SR22. *Copyright 2021 Cirrus Aircraft or its Affiliates. All Rights Reserved. Image reproduced with the permission of Cirrus.*

24.2.11 Contribution of Thrust—Moment due to Offset Thrustline and Normal Force

The generation of thrust (T) usually affects longitudinal stability in the following ways:

(1) Pitching moment is generated if the thrustline is either above or below the CG (z_T in Figure 24-32). This contribution primarily changes the trim of the aircraft and, as such, only depends on thrust and not AOA. While there are subtle changes in thrust with AOA, these must be evaluated on a project basis. For conceptual design work these may usually be ignored.

(2) Normal force (T_N) acts on propellers or nacelles (see Figure 24-32). It depends on thrust and AOA (or AOY) and affects the pitching and yawing moments. The propeller normal force is recognized as *fin effect* in some literature.

(3) The presence of jet exhaust near a stabilizing surface affects the local flow field as shown in Figure 11-17, although this effect is not considered here. The same

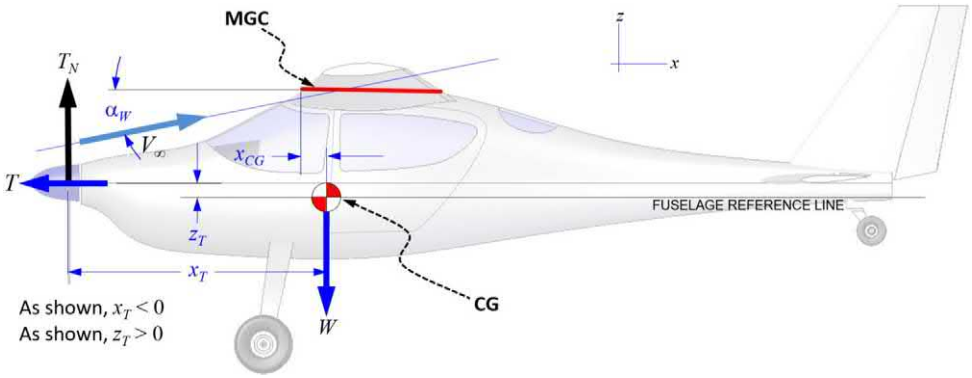


FIGURE 24-32 The contribution of thrust only.

holds for propeller downwash, which is generated by the normal force. A method to account for this effect for a propeller is presented by Seckel [21] and is omitted from further discussion as it is small in magnitude for most applications.

The thrustline and normal force effects can be very noticeable to pilots. Some of these extend to lateral–directional stability as well.

(1) Pitching Moment about the CG due to an Offset Thrustline

First, consider the moment due to the vertical location of the thrustline with respect to the CG. The following expression converts it into a coefficient form that is independent of the AOA. Thus, it is added to the C_{M0} in Equation (24-66). The expression applies to all propulsive devices, provided the thrust force is known:

$$C_{M_{0_T}} = \frac{T(\delta_T) \cdot z_T}{qSc_{MGC}} \tag{24-109}$$

where δ_T is power lever angle (pilot controlled) and the dimensional variable z_T is shown in Figure 24-32. The variables in the denominator are defined in multiple places in the book. This moment is negative (stabilizing) if the thrustline is above the CG and positive (destabilizing) if below. This coefficient affects the trimmed AOA and elevator deflection. The effect of thrust can be estimated using the methods provided in the text:

- Chapter 7, 14, and 15 present methods to estimate thrust of various types of power plants.
- Section 24.3.3 presents methods to estimate the contribution of thrust to longitudinal static stability.
- Section 16.4.1 presents methods to estimate the effect of offset thrustline on trim drag.

(2) Pitching Moment about the CG due to Normal Force

Next, consider the normal force effects. The contribution depends on engine type (propeller or jet). For jet engines, it depends on the nacelle geometry, which may be unknown early in the conceptual design. In the absence of experimental methods, it is possible to resort to CFD methods. This discussion focuses on normal force generated by the propeller. It depends on thrust and α, so it is added to the $C_{M\alpha}$ in Equation (24-69). If the normal force, T_N, is known it can be converted to the coefficient form below:

$$C_{M_{T_N}} = C_{M_{\alpha_{T_N}}} \cdot \alpha = \left(\frac{x_T \cdot T_N}{qSc_{MGC}}\right) \cdot \alpha \tag{24-110}$$

where x_T is the horizontal distance (moment arm) from the CG to the thrust generator (see Figure 24-32). The variables in the denominator are defined in multiple places in the book.

If the propeller disc is perpendicular to the oncoming airflow the normal force is zero. However, if it is askew with respect to the flow, the α of the up- and down moving blades will be asymmetric. This means the aerodynamic load on the blades is asymmetric too. The difference generates the normal force. The following empirical method is based on the work of Ribner [22] and is presented in a simplified form by Seckel [21]. The ensuing stability derivative due to a propeller normal force is given by:

$$C_{M_{\alpha_{T_N}}} = N_{ENG}\left(\frac{x_T}{c_{MGC}}\right)\left(\frac{A_P}{S}\right)\frac{dC_{N_B}}{\partial\alpha}\frac{\partial\beta}{\partial\alpha}f(T) \tag{24-111}$$

where

A_P = Propeller disc area = $\pi D_P^2/4$,
D_P = Propeller diameter,
N_{ENG} = Number of engines (or propellers).

The derivatives $dC_{NB}/d\alpha$ and $d\beta/d\alpha$, and the function $f(T)$ will be explained shortly as part of the following STEP-BY-STEP for determining $C_{M\alpha TN}$.

STEP 1: Determine the Side-Force Factor, SFF

The propeller normal force derivative depends on the blade geometry and *advance ratio* (see Section 15.3.5). To account for the blade geometry, a special parameter, called the *side-force factor* (*SFF*) is defined and must be calculated using the expression below:

$$SFF = 525\left[\left(\frac{c_b}{D_P}\right)_{0.3R} + \left(\frac{c_b}{D_P}\right)_{0.6R}\right] + 270\left(\frac{c_b}{D_P}\right)_{0.9R} \tag{24-112}$$

where

c_b = Blade chord at stations $0.3R$, $0.6R$, and $0.9R$ (R = propeller radius = $D_P/2$).

A propeller blade with an $SFF = 81$ exemplifies a narrow-chord blade (e.g., Cessna 172 prop). A propeller blade with an $SFF = 132$ exemplifies a wide-chord blade (e.g., Lockheed P-3C props). The ratio c_b/D_P is analogous to the inverse aspect ratio of a wing. Thus, for constant chord blades, $SFF = 81$ corresponds to an AR of about 16.3, while $SFF = 132$ corresponds to $AR = 10$. Wide-bladed propellers are commonly found on turboprop aircraft. Narrow-bladed propellers are typically found on piston powered GA aircraft, although several recent such aircraft feature wide-bladed high-performance composite propellers.

STEP 2: Determine the Propeller Advance Ratio, J

Next, estimate the propeller *advance ratio*, using Equation (15-33), repeated below for convenience:

$$J = V_\infty/(nD_P) \tag{24-113}$$

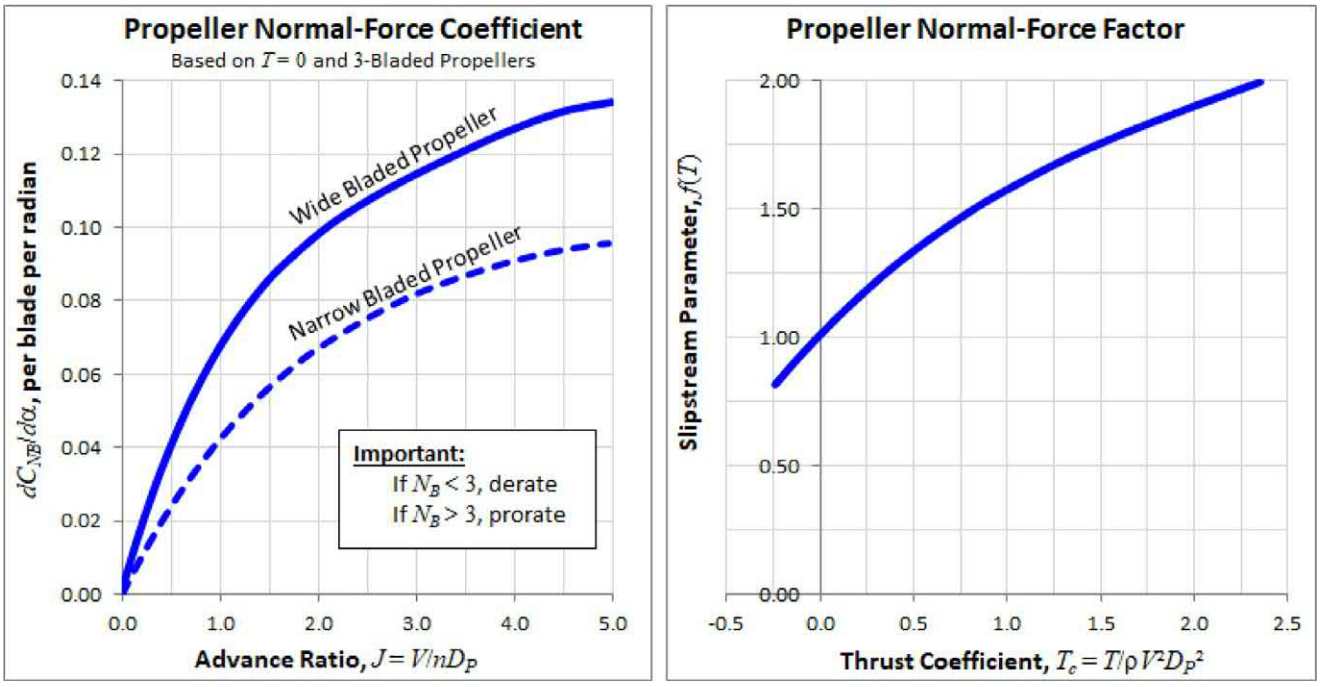


FIGURE 24-33 Graphs used to determine propeller normal force. *Based on E. Seckel, Stability and Control of Airplanes and Helicopters, Academic Press, 1964.*

where V_∞ is the far-field airspeed, n is propeller revolutions per second = $RPM/60$, and D_P is propeller diameter.

STEP 3: Determine the Propeller Normal Force Derivative, $dC_{NB}/d\alpha$

Once the Side-Force-Factor, *SFF*, and Advance Ratio, *J*, have been calculated, the *propeller normal force derivative* ($dC_{NB}/d\alpha$) can be determined. Seckel [21] presents the two graphs in Figure 24-33 to help in this capacity. The left graph is used to estimate $dC_{NB}/d\alpha$, while the right one is used in STEP 4. Note that the left graph is based on a three-bladed prop. Therefore, it is necessary to *de-rate* its values for two-bladed props and *pro-rate* it for props with more than three blades. This is taken care of in the formulation below using the variable N_B (number of blades). Additionally, the graph shows the derivative varies with *J* for the two-blade types: narrow ($SFF = 81$) and wide blade ($SFF = 132$).

In short, read the proper value of $dC_{NB}/d\alpha$ using *J* and by positioning *SFF* between the narrow and wide-bladed props. Since the resulting *SFF* is likely to fall somewhere between 81 and 132, an appropriate normal force coefficient can be interpolated between those values. Avoid extrapolating outside of these limits. Alternatively, the spreadsheet-savvy analyst can estimate the derivative for the two extreme values of *SFF* (81 and 132) using the following expressions, and then interpolate linearly between them. Theses expressions are polynomial curve fits, digitized by the author, to the left graph of Figure 24-33:

Narrow bladed prop:

$$\frac{dC_{N_B}}{d\alpha} = \frac{-0.7053 + 545.7J - 140.6J^2 + 20.47J^3 - 1.302J^4}{10000}\left(\frac{N_B}{3}\right) \quad (24\text{-}114)$$

Wide-bladed prop:

$$\frac{dC_{N_B}}{d\alpha} = \frac{1.773 + 93.83J - 33.69J^2 + 6.392J^3 - 0.4696J^4}{1000}\left(\frac{N_B}{3}\right) \quad (24\text{-}115)$$

This derivative is in terms of per radian and is based on the propeller disc area (in addition to the advance ratio). Note that while it applies to one propeller only, multiengine aircraft are prorated in Equation (24-111). Also, note that the left graph of Figure 24-33 is based on propellers whose thrust is zero. The next step determines a factor to correct $dC_{NB}/d\alpha$ for nonzero thrust.

STEP 4: Determine the Propeller Normal Force Factor, f(T)

Next, the propeller normal force factor, $f(T)$ is determined using the right graph of Figure 24-33. It is used to correct the normal force derivative, determined in the previous step, which is based on zero-thrust. This correction factor can be approximated using the following expression, digitized by the author:

$$f(T) = 0.03392C_t^3 - 0.2228C_t^2 + 0.7546C_t + 1.012 \quad (24\text{-}116)$$

where

C_t = Thrust coefficient = $T/(\rho V^2 D_P^2)$

Note that C_t is related to another thrust coefficient, $C_T = T/(\rho n^2 D_P^4)$, through the relation $C_t = C_T/J^2$. At some equilibrium condition, e.g., cruise, it is convenient to substitute drag for thrust. During climb, even steady climb, the actual thrust must be used.

STEP 5: Determine the Upwash or Downwash Gradient, dβ/dα

It is important to account for flow-field changes induced by the wing. If the propeller is placed in front of the wing, it is subject to the upwash generated by the wing. Conversely, if behind the wing (i.e., pusher configuration) it is subject to downwash. These effects can be accounted for using the same formulas developed for the fuselage/nacelle effects presented in Section 24.2.10. These equations are repeated below for convenience:

Propeller in front of the wing:

$$\text{If } x_T/c_{MGC} < 1: \quad \left(\frac{\partial\beta}{\partial\alpha}\right)_2 = 1.74611\left(\frac{x_T}{c_{MGC}}\right)^{-0.4254} \tag{24-105}$$

If $x_T/c_{MGC} \geq 1$:

$$\left(\frac{\partial\beta}{\partial\alpha}\right)_1 = 1.4758 - 0.40485\left(\frac{x_T}{c_{MGC}}\right) + 0.09107\left(\frac{x_T}{c_{MGC}}\right)^2 \tag{24-104}$$

Propeller behind the wing:

$$\left(\frac{\partial\beta}{\partial\alpha}\right) = \frac{x_T}{l_h}\left[1 - \frac{\partial\varepsilon}{\partial\alpha}\right] \tag{24-106}$$

STEP 6: Determine the Propeller Normal Force Derivative, $C_{M\alpha TN}$

The contribution of the propeller normal force to the pitching moment of the airplane can be evaluated by direct substitution of the parameters determined to this point into Equation (24-111).

STEP 7 (Optional): Determine the Propeller Normal Force, T_N

You may have noticed that the propeller normal force, *per se*, has yet to be directly determined. However, it is possible to "reverse engineer" the contribution and figure out the actual normal force to which it corresponds, using the following expression:

$$T_N = q \cdot \left[N_{ENG} A_P \frac{dC_{N_B}}{d\alpha}\frac{d\beta}{d\alpha} f(T)\right] \cdot \alpha \tag{24-117}$$

EXAMPLE 24-4

A single-engine turboprop aircraft is equipped with a 91-in diameter, five-bladed propeller, placed some 10.5 ft ahead of the wing. The propeller blades have a planform shape that can be considered a constant chord of an average chord of $c_b = 8$ in. Determine the propeller normal force derivative and normal force at S-L while climbing at airspeed of 130 KCAS and $\alpha = 5°$, when the engine power is 901 ESHP and the prop rotates at 2080 RPM ($n = 34.7$ RPS). Assume jet thrust contribution to the ESHP amounts to 6% and that the total thrust is 1000 lb_f. The airplane's $c_{MGC} = 4.65$ ft and $S = 194\,ft^2$.

SOLUTION:

This can be solved using the preceding STEP-BY-STEP.

STEP 1: Determine the Side-Force Factor, SFF

Take advantage of the propeller diameter (D_P) and blade chords (c_b) being given in units of inches:

$$SFF = 525\left[\left(\frac{c_b}{D_P}\right)_{0.3R} + \left(\frac{c_b}{D_P}\right)_{0.6R}\right] + 270\left(\frac{c_b}{D_P}\right)_{0.9R}$$

$$= 525\left[\left(\frac{8}{91}\right)_{0.3R} + \left(\frac{8}{91}\right)_{0.6R}\right] + 270\left(\frac{8}{91}\right)_{0.9R} = 116$$

STEP 2: Determine the Propeller Advance Ratio

Here we need the airspeed (V) in ft/s, rotational frequency (n) in per seconds, and propeller diameter (D_P) in ft:

$$J = \frac{V}{nD_P} = \frac{130 \times 1.688}{(2080/60)(91/12)} = 0.8347$$

STEP 3: Determine the Propeller Normal Force Derivative

Use the advance ratio and number of blades ($N_B = 5$) with Equations (24-114) and (24-115):

For $SFF = 81$:

$$\frac{dC_{N_B}}{d\alpha} = \frac{-0.7053 + 545.7J - 140.6J^2 + 20.47J^3 - 1.302J^4}{10000}\left(\frac{N_B}{3}\right)$$

$$= 0.06135$$

For $SFF = 132$:

$$\frac{dC_{N_B}}{d\alpha} = \frac{1.773 + 93.83J - 33.69J^2 + 6.392J^3 - 0.4696J^4}{1000}\left(\frac{N_B}{3}\right)$$

$$= 0.1002$$

EXAMPLE 24-4 (*cont'd*)

Next, we must interpolate between these extremes to get the derivative for our *SFF* of 116. Here, this is done using parametric formulation:

$$\frac{dC_{N_B}}{d\alpha} = 0.06135\left(1-\frac{116-81}{132-81}\right)+0.1002\left(\frac{116-81}{132-81}\right) = 0.08804$$

STEP 4: Determine the Propeller Normal Force Factor

First, we must determine the thrust coefficient. Since jet thrust accounts for 6% of the ESHP, the propeller is absorbing 901/1.06 = 850 SHP. Since the ESHP is the sum of the shaft power and the power exerted by the jet thrust, we may write:

$$P_{ESHP} = P_{SHP} + \frac{T_{jet}V_\infty}{550} \Rightarrow$$

$$T_{jet} = \frac{550(P_{ESHP}-P_{SHP})}{V} = \frac{550(901-850)}{(130\times 1.688)} = 128 \text{ lb}_\text{f}$$

Therefore, the total thrust attributed to the propeller is $T = 1000–128 = 872$ lb_f, yielding the following thrust coefficient:

$$C_t = \frac{T}{\rho V_\infty^2 D_P^2} = \frac{872}{(0.002378)(130\times 1.688)^2(91/12)^2} = 0.1324$$

Consequently, the propeller normal force factor is found to equal

$$f(T) = 0.03392C_t^3 - 0.2228C_t^2 + 0.7546C_t + 1.012 = 1.108$$

STEP 5: Determine the Upwash or Downwash Gradient

The propeller is in front of the wing and $x_T/c_{MGC} = 10.5/4.65 = 2.258 \geq 1$, so use Equation (24-104) to determine the upwash:

$$\left(\frac{\partial\beta}{\partial\alpha}\right)_1 = 1.4758 - 0.40485(2.258) + 0.09107(2.258)^2 = 1.026$$

STEP 6: Determine the Propeller Normal Force Derivative

Plug and chug the above data into Equation (24-111) to get the contribution of the propeller to the pitching moment. Note that the propeller disc area is $\pi D_P^2/4 = 45.17\ \text{ft}^2$:

$$\boldsymbol{C}_{\boldsymbol{M}_{\alpha_{T_N}}} = N_{ENG}\left(\frac{x_T}{c_{MGC}}\right)\left(\frac{A_P}{S}\right)\frac{dC_{N_B}}{d\alpha}\frac{d\beta}{d\alpha}f(T)$$

$$= (1)(2.258)\left(\frac{45.17}{194}\right)(0.08804)(1.026)(1.108)$$

$$= 0.05262 \text{ per radian}$$

EXAMPLE 24-4 (*cont'd*)

STEP 7: Determine the Propeller Normal Force

The dynamic pressure is $\frac{1}{2}\rho V^2 = 57.26\ \text{lb}_\text{f}/\text{ft}^2$.

$$T_N = q\cdot\left[N_{ENG}A_P\frac{dC_{N_B}}{d\alpha}\frac{d\beta}{d\alpha}f(T)\right]\cdot\alpha$$

$$= (57.26)\cdot[(1)(45.17)(0.08804)(1.026)(1.108)]\cdot\left(5^\circ\frac{\pi}{180}\right) = 22.6\ \text{lb}_\text{f}$$

DERIVATION OF EQUATION (24-109)

The moment about the CG due to the vertical separation of the CG and thrustline can be written as follows:

$$qSc_{MGC}\boldsymbol{C}_{\boldsymbol{M}_{0_T}} = T\cdot z_T \Rightarrow \boldsymbol{C}_{\boldsymbol{M}_{0_T}} = \frac{T\cdot z_T}{qSc_{MGC}}$$

DERIVATION OF EQUATION (24-117)

The total moment due to the propeller normal force can be written as follows:

$$M_{T_N} = x_T\cdot T_N = qSc_{MGC}\cdot\boldsymbol{C}_{\boldsymbol{M}_{T_N}} \Leftrightarrow T_N = qS\left(\frac{c_{MGC}}{x_T}\right)\cdot\boldsymbol{C}_{\boldsymbol{M}_{T_N}}$$

Since $\boldsymbol{C}_{\boldsymbol{M}TN} = \boldsymbol{C}_{\boldsymbol{M}\alpha TN}\,\alpha$ from Equation (24-110), this becomes:

$$T_N = qS\left(\frac{c_{MGC}}{x_T}\right)\cdot\boldsymbol{C}_{\boldsymbol{M}_{T_N}} = qS\left(\frac{c_{MGC}}{x_T}\right)\cdot\boldsymbol{C}_{\boldsymbol{M}_{\alpha_{T_N}}}\cdot\alpha$$

Substituting the derivative of Equation (24-111) we get:

$$T_N = qS\left(\frac{c_{MGC}}{x_T}\right)\cdot\boldsymbol{C}_{\boldsymbol{M}_{\alpha_{T_N}}}\cdot\alpha$$

$$= qS\left(\frac{c_{MGC}}{x_T}\right)\cdot\left[N_{ENG}\left(\frac{x_T}{c_{MGC}}\right)\left(\frac{A_P}{S}\right)\frac{dC_{N_B}}{d\alpha}\frac{d\beta}{d\alpha}f(T)\right]\cdot\alpha$$

which reduces to $T_N = q\cdot\left[N_{ENG}A_P\frac{dC_{N_B}}{d\alpha}\frac{d\beta}{d\alpha}f(T)\right]\cdot\alpha$.

24.2.12 Contribution of the Landing Gear

The landing gear contributes to drag and moment (see Figure 24-34). The moment contribution results from the position of its center-of-drag, which is well below the CG. Use the methods of Section 16.4.5 to estimate the drag coefficient for the landing gear. For tires, the drag coefficient ranges from 0.18 to 0.35, based on type and references the frontal area of the tire; the product of its diameter and width ($d\times w$). For more information on tire sizes and landing gear, refer to Chapter 13.

(1) Landing Gear Drag Force

Figure 24-34 shows the resulting force consists of horizontal and vertical components in the BCS. This is included in the formulation for the moments. The total drag of the

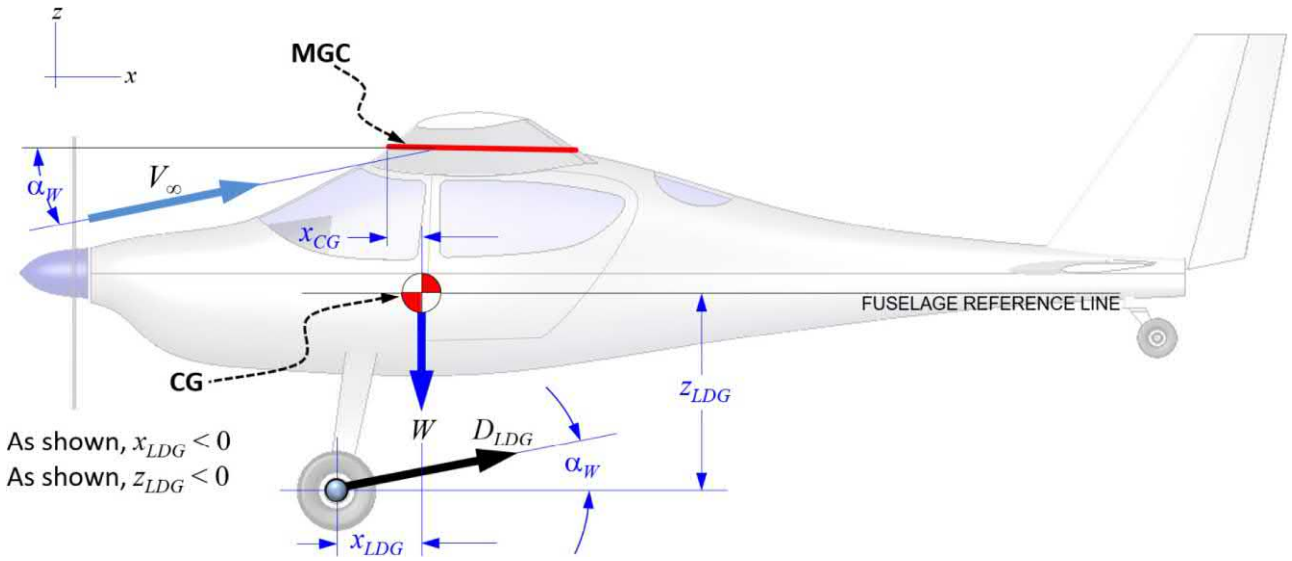


FIGURE 24-34 The contribution of the landing gear only.

landing gear can be estimated using the expression below, where the drag coefficient C_{DT} can refer to a single tire, a tire and landing gear strut, or a complete gear bogie.

$$C_{D_{LDG}} = \frac{1}{S}\sum_{i=1}^{N_{tires}} C_{D_{T_i}} \cdot (d_i \times w_i) \tag{24-118}$$

where

C_{DT} = Drag coefficient based on tire type,
d = Tire diameter,
w = Tire width,
i = Index to separate individual tires.

(2) Pitching Moment about the CG due to the Landing Gear

The contribution of a single landing gear with index i about the CG can be accounted for as shown below:

$$(\boldsymbol{C}_{\boldsymbol{M}_{LDG}})_i = \frac{C_{D_{T_i}}}{S \cdot c_{MGC}} \cdot (d_i \times w_i)\{z_{LDG_i}\cos\alpha_W - x_{LDG_i}\sin\alpha_W\} \tag{24-119}$$

Note that the value of z_{LDG} is negative since the landing gear is below the CG. This leads to a stabilizing (negative) contribution to the total pitching moment. The value of x_{LDG} is negative if the tire is in front of the CG, as shown in Figure 24-34. This yields a de-stabilizing (positive) moment contribution. Thus, the negative sign in front of it. The tail wheel, in contrast, is far aft of the CG ($x_{LDG} > 0$) and generates a stabilizing moment. The total contribution of the complete landing gear is

$$\boldsymbol{C}_{\boldsymbol{M}_{LDG}} = \frac{1}{S \cdot c_{MGC}}\sum_{i=1}^{N_{tires}} C_{D_{T_i}} \cdot (d_i \times w_i) \{z_{LDG_i}\cos\alpha_W - x_{LDG_i}\sin\alpha_W\} \tag{24-120}$$

Since this moment depends on the AOA, it could be included with the $\boldsymbol{C}_{\boldsymbol{M}\alpha}$-terms in Equation (24-69), although is shown separately in Equation (24-64). The contribution of the vertical component of the landing gear drag is generally small and may be ignored.

(3) Simplified Pitching Moment about the CG due to the Landing Gear

Equation (24-120) can be simplified while yielding acceptable accuracy for most geometry. If the AOA is small, then sin α_W is small as well so the vertical contribution is negligible. Additionally, since cos $\alpha_W \approx 1$, the contribution is independent of the AOA and can be considered a member of Equation (24-66):

$$\boldsymbol{C}_{\boldsymbol{M}_{LDG}} = \frac{1}{S \cdot c_{MGC}}\sum_{i=1}^{N_{tires}} C_{D_{T_i}} \cdot (d_i \times w_i) z_{LDG_i} \tag{24-121}$$

DERIVATION OF EQUATION (24-119)

The moment about the CG due to the landing gear can be written as follows:

$$qSc_{MGC}\boldsymbol{C}_{\boldsymbol{M}_{LDG}} = qS(x_{cg} - x_{LDG})C_{D_{LDG}}\sin\alpha + qSz_{LDG}C_{D_{LDG}}\cos\alpha$$

Solving for $\boldsymbol{C}_{\boldsymbol{M}_{LDG}}$ leads to:

$$\boldsymbol{C}_{\boldsymbol{M}_{LDG}} = \frac{(x_{cg} - x_{LDG})}{c_{MGC}}C_{D_{LDG}}\sin\alpha + \frac{z_{LDG}}{c_{MGC}}C_{D_{LDG}}\cos\alpha.$$

DERIVATION OF EQUATION (24-120)

The moment about the CG due to the landing gear can be written as follows:

$$\frac{d\boldsymbol{C}_{\boldsymbol{M}_{LDG}}}{d\alpha} = C_{D_{LDG}}\left(\frac{(x_{cg} - x_{LDG})}{c_{MGC}}\cos\alpha - \frac{z_{LDG}}{c_{MGC}}\sin\alpha\right)$$

EXAMPLE 24-5

Determine the pitching moment contribution of the SR22 main gear using the simplified formulation. The main wheels are 15 × 6.00–6 (Three Part Type) and the nose wheel is 5.00–5 (Type III). Assume the wheel fairings cut the drag in half. All the wheels are 2.5 ft below the CG.

SOLUTION:

Per Chapter 13, the diameter, and width of the main wheel is 15″ and 6″, respectively, and 14″ and 5″ for the nose wheel. These must be converted into ft to ensure unit consistency. The diameter and width of the main wheel is 1.25′ by 0.5′, respectively, and 1.17′ and 0.42′ of the nose gear. Per Section 15.4.5, the drag coefficient for the main and nose wheels is 0.18 and 0.25, respectively, based on the tire diameter and width. Therefore, we get:

$$C_{M_{LDG}} = \frac{1}{S \cdot c_{MGC}} \sum_{i=1}^{N_{tires}} C_{D_{T_i}} \cdot (d_i \times w_i) z_{LDG_i} = \frac{1}{144.9 \times 3.783}$$

$$\{2 \times (0.18 \times 1.25 \times 0.5) + 0.25 \times 1.17 \times 0.42\}$$

$$(-2.5) = -0.001586$$

24.2.13 Compressibility Effect on Pitching Moment

Refs. [23, 24] present experimental data that demonstrate how the pitching moment of an airfoil diverges at transonic speeds. Its impact on the longitudinal stability of aircraft is of great interest. Consider the general effect of compressibility on pitch stability ($C_{M\alpha}$) and stick force, which is the force the pilot must exert for longitudinal control. This is illustrated in Figure 24-35 for a hypothetical aircraft trimmed at $M_\infty = 0.5$. The graph differs for other aircraft, CG-locations, control system, airfoil types, trim points, and so on. Static stability of aircraft requires $C_{M\alpha}$ to be negative. The aircraft in this example is near $C_{M\alpha} = -1.0$ at low Mach numbers. This means that at low airspeeds, the pilot must pull on the yoke (or stick or column) to slow down further. Alternatively, the pilot must push to fly at Mach numbers higher than 0.5.

As the aircraft enters the transonic regime, shocks begin to form over the aircraft. This is followed by a sharp rise in pitch stability and stick force. The center of pressure moves from the quarter-chord to the mid-chord. The effect is akin to the CG being moved forward by that amount at subsonic speeds. If the airplane is not designed for this, the magnitude of the stick force may render it uncontrollable—it will enter a dive, which increases the airspeed further and from which it may not recover.

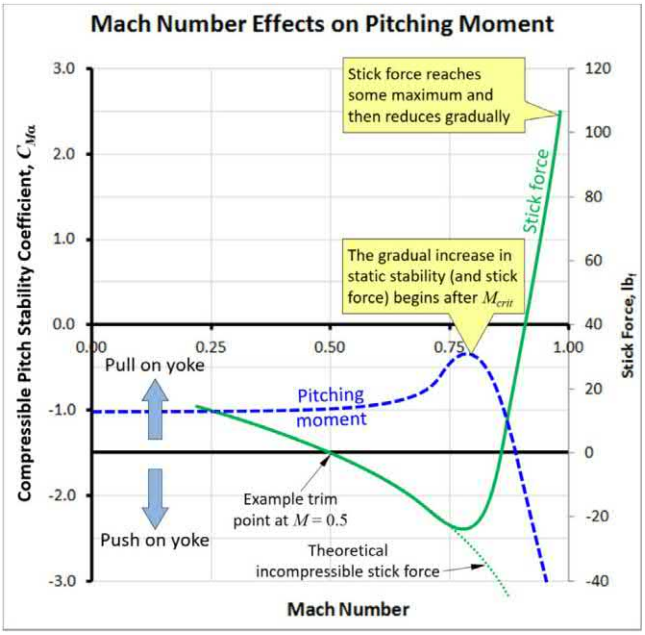


FIGURE 24-35 The effect of Mach number on pitching moment.

24.3 REFINED HORIZONTAL TAIL SIZING

The sizing of stabilizing surfaces constitutes some of the most important tasks in the development of a new aircraft. Aircraft handling refers to its response to control inputs and the effort exerted. Handling is often described using two adjectives: *sluggish* or *responsive*. The former is to be avoided. The latter is the goal—albeit with limitations. The aircraft should be *sufficiently* responsive for its mission. For instance, the practicality of demanding cargo transport aircraft to offer a steady-state roll rate of 360°/s is debatable—such a maneuver is certainly not needed to complete its mission. Instead, it must be responsive enough to provide good handling during landing in turbulent crosswind conditions (or similar criterion). Insufficient responsiveness is unacceptable, but too much is detrimental too. It results in greater structural loads and requires heavier airframe. It can also lead to *pilot induced oscillation* (PIO).

There are two aspects to control surface sizing: (1) *Effectiveness* (responsiveness) and (2) *control forces* (hinge moments). The former should be treated during the conceptual design and the latter during preliminary one (see Section 24.4). In this section, simple methods to size the elevator are presented. Due to space constraints, only a rudimentary introduction can be given for hinge moments.

24.3.1 Fundamentals of Pitch Control

The elevator provides control about the pitch axis by modifying the pitching moment coefficient, C_M.

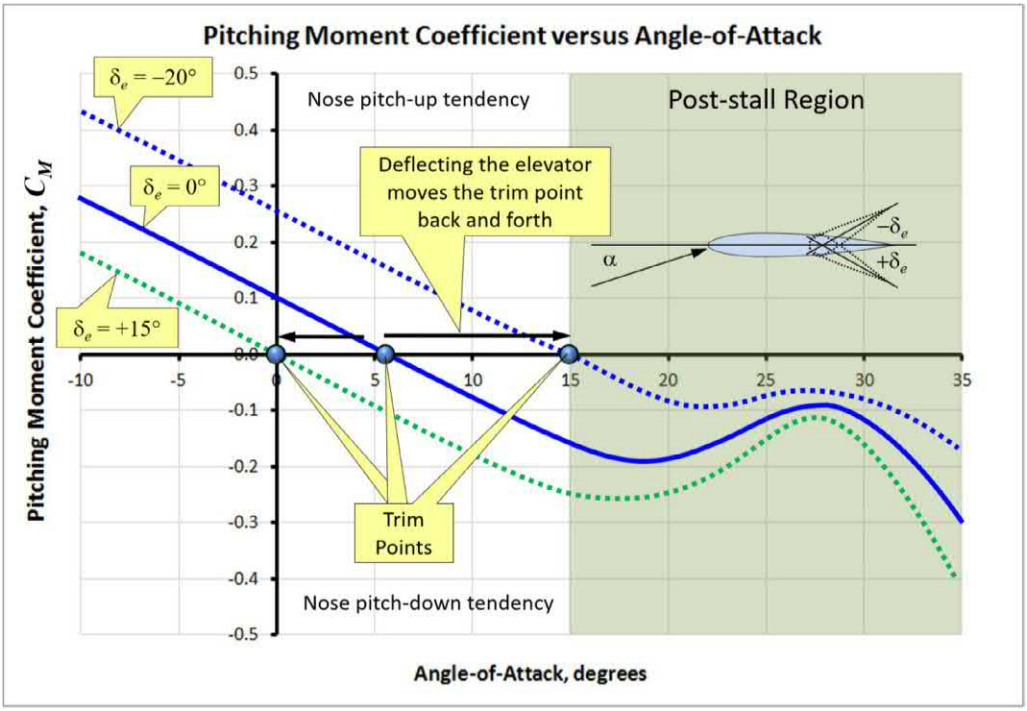


FIGURE 24-36 Pitch control explained.

Figure 24-36 shows a general graph of C_M versus angle-of-attack (α) for a complete aircraft. The curves depict the C_M for three different elevator deflections (δ_e): $\delta_e = 0°$ (blue solid), $\delta_e = +15°$ (green dotted), and $\delta_e = -20°$ (blue dotted). The elevator can be considered a means to change the intersection of the C_M–curve to the vertical axis (C_{M0}). This, in turn, changes its intersection to the α-axis (*x*-axis). This is the angle-of-attack at which $C_M = 0$ (or equilibrium α) and is called a *trim point*. It means the orientation of the airplane develops a specific C_L for equilibrium at the given airspeed. While the stability analyst considers pitch control in terms of equilibrium C_M and C_L, the pilot considers it in terms of airspeed.

The vertical separation of the three curves in Figure 24-36 indicates the controllability or *control authority* of the aircraft. For the elevator, it is also called *elevator authority*. It is represented with Equation (24-84). While it is not directly classified with C_{M0}, its effect is precisely as if it were. In the neutral position ($\delta_e = 0°$), the aircraft trims out near $\alpha \approx 5.5°$ as stated earlier. At $\delta_e = -20°$, it trims out at $\alpha \approx 15°$ and so on. The elevator should provide enough authority to allow the airplane to achieve airspeed greater than cruising speed and low enough to be stalled.

24.3.2 Roadmap to Sizing the Horizontal Tail and Elevator

Two methods to assess if the HT and elevator provide adequate authority are discussed below. Ideally, both should be used. Note that it is recommended the tail is designed only as large as it needs to be, considering all constraints to which it is subject. While there certainly is a lower limit to the size of the HT, the upper limit is not constrained in the same way: If an aft-mounted HT is sized such it is larger than the wing, it is no longer the HT, but the wing of a canard configuration. A large HT moves the stick-fixed neutral point aft. So, if a large CG-range is desired, one solution is a large HT with a large elevator to provide authority for forward loading. That said, the cost of an excessively large HT is airframe weight, drag, large hinge moments, and so forth.

(1) Assessing Control Authority using a Graphic Scheme

This method is presented by Roskam [7, 25]. It coplots Figure 24-36 and the lift curve. Using the trim points discussed above, the shift in C_M– and C_L–versus–α, due to δ_e is shown in Figure 24-37. In the upper graph, the points A, B, C, and D represent trim points for the given δ_e. Consider Point A on the C_M–α curve that represents the minimum elevator deflection (TED $\delta_e = +10°$). Transferring it to the appropriate C_L–α curve below lands it on a C_L–value too high to trim the airplane at cruising speed. In contrast, Point D on the C_M–α curve represents the maximum elevator deflection (TEU $\delta_e = -20°$). Transferring it to the appropriate C_L–α curve shows its α-value is too low to permit stalling speed to be achieved. The limited range of trim points between A and D renders the aircraft unacceptable. The designer can resort to geometric (and CG) fixes to modify C_{M0}, $C_{M\alpha}$, $C_{M i_{HT}}$, $\delta_{i_{HT}}$, $C_{L_{\delta_e}}$, and $C_{M\delta e}$.

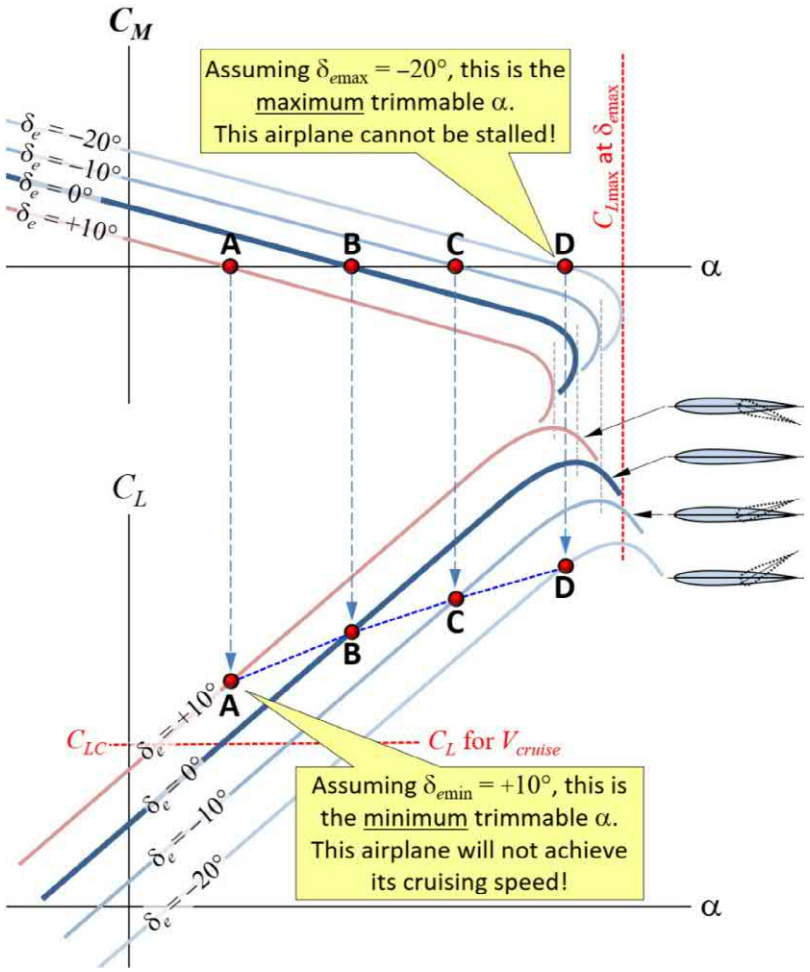


FIGURE 24-37 Roskam's graphic scheme for assessing the trimming ability of the aircraft at some specific CG position.

(2) Assessing Control Authority through Evaluation

This is a trial-and-error method that directly evaluates various critical flight conditions to pinpoint which critical condition is flawed. It uses the initial tail dimensions obtained using the methods of Chapter 11 as a baseline value to be expanded. It also assumes that a target CG-range has already been established.

STEP 1: Initial HT Sizing

Use the methods of Chapter 11 to devise an initial HT geometry (baseline).

STEP 2: Compile a List of Flight Critical Conditions

Compile a list of flight critical conditions based on regulatory or design specific constraints. Include items and constraints per Section 26.2 and Figure 6-26. A sample of what such a list could look like is presented as Table 24-5. The list shows suggested values, but reader should modify and adapt to own design.

STEP 3: Estimate Stability Parameters

Use methods such as those presented below to estimate as many parameters as possible.

STEP 4: Conduct Elevator Authority Evaluation

Evaluation approach (assumes conceptual design phase):

- ID1 and ID2: Use the lifting-line method at minimum, vortex-lattice or doublet-lattice is better. ID2 is required for stall speed estimation. Use Method 2 of Section 9.5.5. If the resulting stall speed is greater than the target, consider increasing wing area or improved airfoils.
- ID3 establishes the initial aft-most CG-limit per the methods of Chapter 6.
- ID4 establishes if cruise can be achieved per ID4.
- ID5 through ID9 establishes the maximum forward CG position. The aftmost of these is the forwardmost CG limit. Keep in mind the recommended control surface deflection limits per Section 26.2.

TABLE 24-5 Example checklist for control authority assessment.

Check ID	Condition	W lb_f	x_{CG} %MGC	V_∞ KCAS	h ft	T lb_f	α deg	δ_e deg	δ_f deg	Comment
1	C_{Lmax} for basic stall	W_0	Fwd	-	0	0				Determine α_{stall}
2	C_{Lmax} for controlled stall	W_0	Fwd	V_{S0}	0	0				Determine α_{stall}, use it to get V_{S0}
3	Stick-fixed neutral point	-	-	-	-	0	0	0	0	Purely an aerodynamic entity
4	Trim for cruise at $0.25c_{MGC}$	W_0	Aft	V_c	h_{cruise}	T_{cruise}				Is $\delta_e < \delta_{efwd}$?
5	Trim for stall at $0.25c_{MGC}$	W_0	25%	V_{S0}	0	0				Use these to extrapolate to predict $x_{cg\ fwd}$ per Equation (24-122)
6	Trim for stall at $0.15c_{MGC}$	W_0	15%	V_{S0}	0	0				
7	Trim for balked landing	W_0	15-25%	$1.2V_{S0}$	0	$T_{required}$				Predict x_{cgfwd} similar to 5 and 6
8	Trim for flare	W_0	15-25%		0	0				Predict x_{cgfwd} similar to 5 and 6
9	Trim for $0.9V_{S1}$ for T-O	W_0	15-25%		0	T_{max}				Predict x_{cgfwd} similar to 5 and 6
10	Dyn Stab: Short period		Fwd-Aft	V_c	h_{cruise}	T_{cruise}				Confirm convergence & cycles
11	Dyn Stab: Phugoid		Fwd-Aft	V_c	h_{cruise}	T_{cruise}				Confirm convergence & cycles
12	Dyn Stab: Spiral		Fwd-Aft	V_c	h_{cruise}	T_{cruise}				Confirm convergence
13	Dyn Stab: Roll convergence		Fwd-Aft	V_c	h_{cruise}	T_{cruise}				Confirm convergence
14	Dyn Stab: Dutch roll		Fwd-Aft	V_c	h_{cruise}	T_{cruise}				Confirm convergence & cycles

- IDs 10 through 14 are optional but recommended. An airplane can be statically stable, but dynamically unstable. The goal is to ensure the cited stability modes are converging.

To estimate the allowable maximum forward CG-location, x_{CGfwd}, based on an established maximum elevator deflection, δ_{efwd}, substitute two CG-locations (x_{CG1} and x_{CG2}) and their corresponding elevator deflections to trim (δ_{e1} and δ_{e2}) into the following expression.

$$x_{CG_{FWD}} = x_{CG_1} + \left(\frac{\delta_{e_{fwd}} - \delta_{e_1}}{\delta_{e_2} - \delta_{e_1}}\right)(x_{CG_2} - x_{CG_1}) \qquad (24\text{-}122)$$

As an example, if $\delta_{efwd} = -15°$, $x_{CG1} = 0.15c_{MGC}$, $\delta_{e1} = -20°$, $x_{CG2} = 0.25c_{MGC}$, and $\delta_{e2} = -8°$, then $x_{CGfwd} = 0.192c_{MGC}$. The expression assumes a relatively linear relation between the required elevator deflection to trim and CG-position.

STEP 5: Fixes

Depending on results, modify geometry that affects C_{M0}, $C_{M\alpha}$, $C_{Mi_{HT}}$, $\delta_{i_{HT}}$, $C_{L_{\delta_e}}$, and $C_{M\delta e}$. Return to Step 3 and repeat until the HT geometry meets all critical conditions.

24.3.3 Longitudinal Stability of a Simple Wing–HT–Engine System

It is to be expected that the flood of equations in the previous section may leave some readers disheartened. Do not fret, these will now be put to work using a simple aircraft configuration. It consists of a wing, HT, and engine (see Figure 24-38). We will derive a few longitudinal static stability methods that are helpful when sizing conventional aircraft. First, write the static longitudinal stability equations for straight, steady-state flight. For this specific configuration, ignore the fuselage and transients

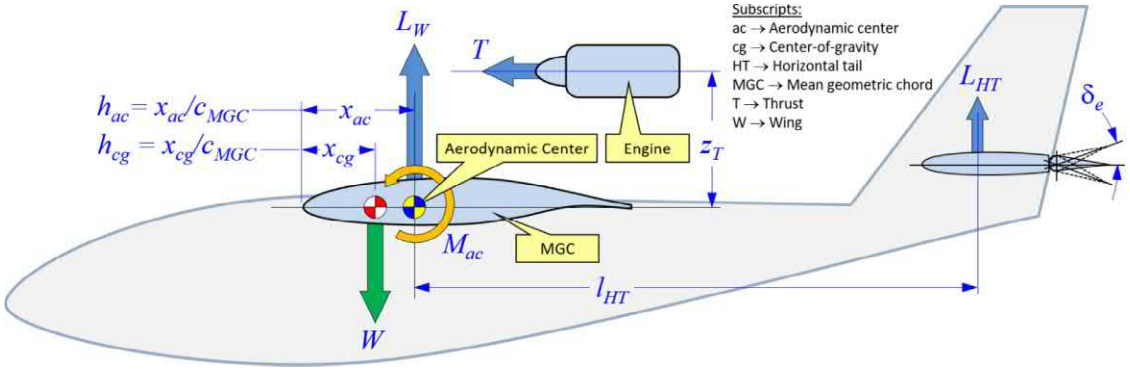


FIGURE 24-38 A simple wing–HT–engine system used for longitudinal stability analysis.

($\dot{\hat{q}}$ and $\dot{\alpha}$) and set $i_{HT} = \delta_f = \delta_{LDG} = 0$. Also note that since all variables have already been defined in various places in this chapter they will not be repeated here.

The lift model is a shortened version of Equation (24-37):

$$C_L = C_{L_0} + C_{L_\alpha}\alpha + C_{L_{\delta_e}}\delta_e \tag{24-123}$$

The drag model is a shortened version of Equation (24-60):

$$C_D = C_{D_{\min}} + C_{D_\alpha}\alpha + C_{D_{\delta_e}}\delta_e \tag{24-124}$$

The pitching moment model is a shortened version of Equation (24-64):

$$\boldsymbol{C_M} = \boldsymbol{C_{M_0}} + \boldsymbol{C_{M_\alpha}}\alpha + \boldsymbol{C_{M_{\delta_e}}}\delta_e = 0 \tag{24-125}$$

This equation, with $\boldsymbol{C_{M_{\delta_e}}} = 0$, is plotted in Figure 24-39 and shows how it is affected by CG. The *residual pitching moment coefficient* is compiled using Equation (24-66), reduced here for this application.

$$\boldsymbol{C_{M_0}} = \boldsymbol{C_{M_{0_W}}} + \boldsymbol{C_{M_{0_{HT}}}} + \boldsymbol{C_{M_{0_T}}} \tag{24-126}$$

By substituting Equations (24-67), (24-68), and (24-109), we get:

$$\boldsymbol{C_{M_0}} = \overbrace{\boldsymbol{C_{M_{ac_W}}} + C_{L_{0_W}}\left(h_{cg} - h_{ac}\right)}^{\boldsymbol{C_{M_{0_W}}}} + \overbrace{\boldsymbol{C_{M_{ac_{HT}}}} + C_{L_{0_{HT}}}\left(\frac{l_{HT_{CG}}}{c_{MGC}}\right)}^{\boldsymbol{C_{M_{0_{HT}}}}} + \overbrace{\frac{T(\delta_T)\cdot z_T}{qSc_{MGC}}}^{\boldsymbol{C_{M_{0_T}}}} \tag{24-127}$$

The *longitudinal stability derivative* is given by Equation (24-69), also reduced for this configuration.

$$\boldsymbol{C_{M_\alpha}} = \boldsymbol{C_{M_{\alpha_W}}} + \boldsymbol{C_{M_{\alpha_{HT}}}} + \boldsymbol{C_{M_{\alpha_{T_N}}}} \tag{24-128}$$

By substituting Equations (24-70), (24-72), and (24-111), we get:

$$\boldsymbol{C_{M_\alpha}} = \overbrace{C_{L_{\alpha_W}}\left(h_{cg} - h_{ac}\right)}^{\boldsymbol{C_{M_{\alpha_W}}}} - \overbrace{\eta_{HT}V_{HT}C_{L_{\alpha_{HT}}}\left(1 - \frac{\partial\varepsilon}{\partial\alpha}\right)}^{\boldsymbol{C_{M_{\alpha_{HT}}}}} + \overbrace{N_e\left(\frac{x_T}{c_{MGC}}\right)\left(\frac{A_P}{S}\right)\frac{dC_{N_B}}{d\alpha}\frac{d\beta}{d\alpha}f(T)}^{\boldsymbol{C_{M_{\alpha_{T_N}}}}} \tag{24-129}$$

where V_{HT} is the horizontal tail volume of Equation (24-74). If the sum of these moments acts to rotate the nose down, then $\boldsymbol{M_{CG}} < 0$ (negative sign means it is stabilizing). If $\boldsymbol{M_{CG}} > 0$ the opposite holds.

24.3.4 The Stick-Fixed Neutral Point (Aerodynamic Center)

In the view of this author, the single most important concept in all of stability and control theory is the *stick-fixed neutral point* (aka *aerodynamic center* of the complete aircraft). Equation (24-129) reveals how longitudinal stability depends on the position of the CG. Let us rewrite it for gliding flight (so $\boldsymbol{C_{M\alpha TN}} = 0$):

$$\boldsymbol{C_{M_\alpha}} = C_{L_{\alpha_W}}\left(h_{cg} - h_{ac}\right) - \eta_{HT}V_{HT}C_{L_{\alpha_{HT}}}\left(1 - \frac{\partial\varepsilon}{\partial\alpha}\right) \tag{24-130}$$

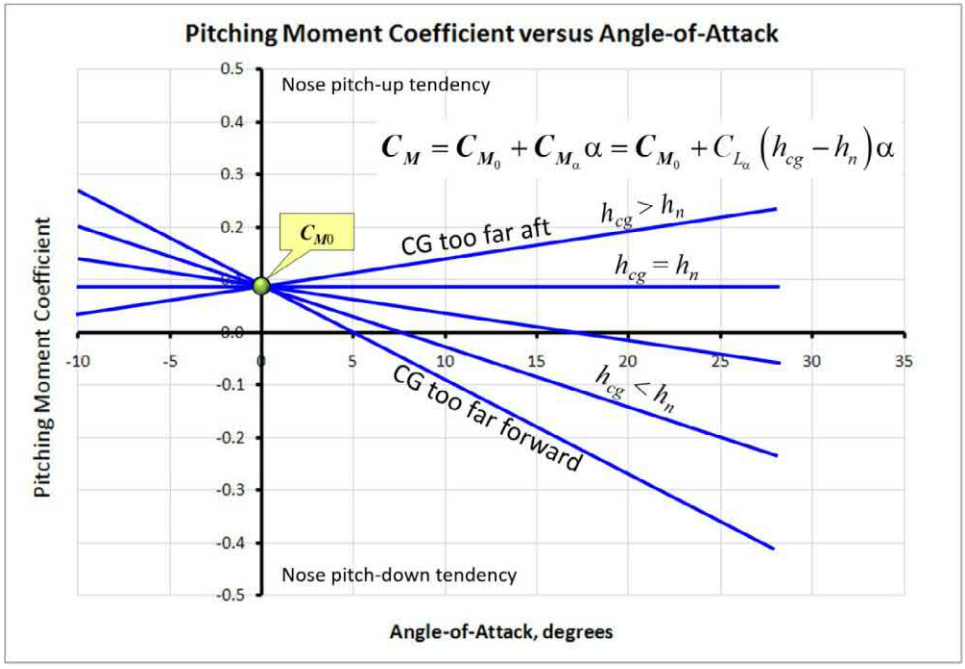


FIGURE 24-39 Impact of CG-position on longitudinal stability analysis.

From Section 24.2.2, for the airplane to be statically stable $\boldsymbol{M_{CG}} < 0$. This requires $\boldsymbol{C_{M\alpha}} < 0$. If $\boldsymbol{C_{M\alpha}} = 0$, then the airplane becomes *neutrally stable*. This means

$$\boldsymbol{C_{M_\alpha}} = 0 \;\Leftrightarrow\; C_{L_{\alpha_W}}(h_{cg} - h_{ac}) - \eta_{HT} V_{HT} C_{L_{\alpha_{HT}}}\left(1 - \frac{\partial \varepsilon}{\partial \alpha}\right) = 0 \tag{24-131}$$

The value of h_{cg} obtained represents the aftmost *CG* position for static stability. Therefore, it is of great importance to the designer. It is the *stick-fixed neutral point*. We denote this position as h_n $(= x_n / c_{MGC})$ and solve for it using Equation (24-130)

$$h_n = h_{ac} + \eta_{HT} V_{HT} \frac{C_{L_{\alpha_{HT}}}}{C_{L_{\alpha_W}}}\left(1 - \frac{\partial \varepsilon}{\partial \alpha}\right) \tag{24-132}$$

The result only holds for a system of wing + HT. It shows that the HT shifts the h_n aft. Thrust affects this position as well. If $\boldsymbol{C_{M\alpha TN}} \neq 0$ we get the *stick-fixed neutral point with power on*, h_{np}:

$$h_{np} = h_{ac} + \eta_{HT} V_{HT} \frac{C_{L_{\alpha_{HT}}}}{C_{L_{\alpha_W}}}\left(1 - \frac{\partial \varepsilon}{\partial \alpha}\right) - \frac{N_e}{C_{L_{\alpha_W}}}\left(\frac{x_T}{c_{MGC}}\right)\left(\frac{A_P}{S}\right)\frac{dC_{N_B}}{d\alpha}\frac{d\beta}{d\alpha} f(T) \tag{24-133}$$

A propeller positioned *ahead* of the CG or external jet engine nacelles ahead of the CG *destabilize* the aircraft. This moves the h_n forward. If these thrust devices are aft of the CG, the opposite happens: h_n moves aft. Typical values of h_n for aircraft range between 0.4 and 0.6 for GA aircraft, 0.35 to 0.45 for commercial transports, and 0.3 to 0.35 for fighter aircraft [5]. The minimum SM (see Section 24.2.7) should be 8% to 10%. The maximum SM is typically 28% to 30%. The CG-range is the difference between the two. Table 6-6 lists the CG-range for an assortment of aircraft.

EXAMPLE 24-6

Consider the wing–HT configuration in Figure 24-40, defined by the specifications below. Assuming a glider without a fuselage, estimate the following:

(a) Stick-fixed neutral point and.
(b) Calculate $\boldsymbol{C_{M0}}$ and $\boldsymbol{C_{M\alpha}}$ and plot for $-5° \leq \alpha \leq 20°$.
(c) Determine the value of $\boldsymbol{C_{M0}}$ required to trim the airplane $\alpha = 10°$.
(d) Determine $\boldsymbol{C_{M\delta e}}$ if $r_e = c_e / c_{HT} = 0.3$ and write the complete longitudinal moment equation.

Assume the wing airfoil is NACA 4412 and that the HT has a symmetrical airfoil. The following specifications are given below for the system.

Specifications for Main Wing:

CG position, $x_{cg} = 1.039$ ft (aft of wing LE),
wing MGC, $c_{MGC} = 2.0$ ft,
wingspan, $b = 20.0$ ft,
wing area, $S = 40\,\text{ft}^2$,
wing aspect ratio, $AR = 10$,
wing zero-alpha lift, $C_{L0W} = 0.35$,
wing moment about AC, $\boldsymbol{C_{Mac_W}} = -0.1$,
wing angle-of-incidence, $i_W = 0°$,
wing's aerodynamic center, $h_{ac} = 0.25$.

Specifications for Horizontal Tail:

HT average chord, $c_{HT} = 1.0$ ft,
HT span, $b_{HT} = 6.0$ ft,

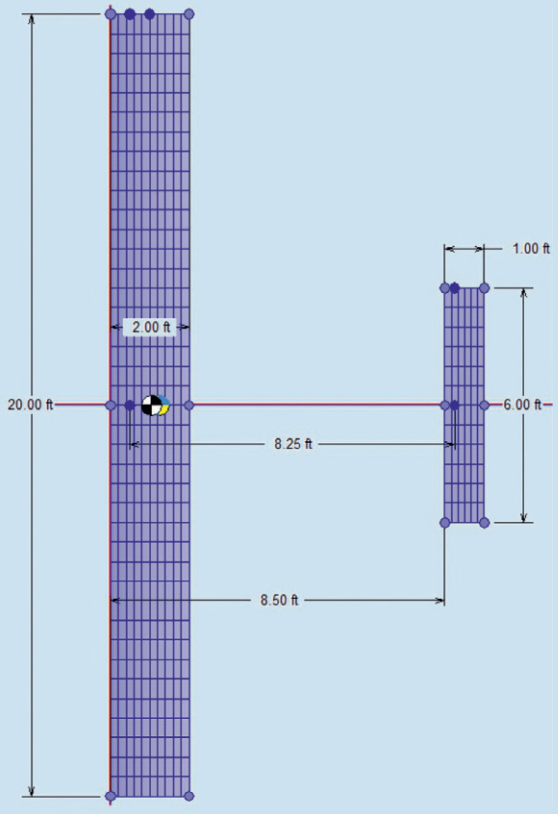


FIGURE 24-40 The example configuration.

EXAMPLE 24-6 (*cont'd*)

HT area, $S_{HT}=6.0\,\text{ft}^2$,
HT zero-alpha lift, $C_{L0HT}=0.0$ (symmetric airfoil),
HT moment about AC, $C_{MacHT}=0$ (symmetric airfoil),
HT angle-of-incidence, $i_{HT}=0°$,
HT arm, $l_{HTCG}=8.50+0.25-1.039=7.711\,\text{ft}$,
HT effectiveness, $\eta_{HT}=1$.

SOLUTION:

(a) Stick-fixed neutral point is calculated using Equation (24-132), as shown below. Calculate HT volume using Equation (24-74):

$$V_{HT}=\frac{S_{HT}\cdot l_{HT}}{S\cdot c_{MGC}}=\frac{6.0\times 7.711}{40\times 2.0}=0.5783$$

Calculate the wing and HT lift curve slopes using Equation (9-72):

$$C_{L_{\alpha_W}}=\frac{2\pi\cdot AR_W}{2+\sqrt{AR_W^2+4}}=\frac{2\pi\cdot(10)}{2+\sqrt{(10)^2+4}}=5.151\ \text{per rad}$$
$$C_{L_{\alpha_{HT}}}=\frac{2\pi\cdot AR_{HT}}{2+\sqrt{AR_{HT}^2+4}}=\frac{2\pi\cdot(6)}{2+\sqrt{(6)^2+4}}=4.529\ \text{per rad}$$

Calculate the downwash angle using Equation (24-91) and the stick-fixed neutral point using Equation (24-132):

$$h_n=h_{ac}+\eta_{HT}V_{HT}\frac{C_{L_{\alpha_{HT}}}}{C_{L_{\alpha_W}}}\left(1-\frac{2C_{L_{\alpha_W}}}{\pi\cdot AR}\right)$$
$$=0.25+(1)(0.5783)\frac{4.529}{5.151}\cdot\left(1-\frac{2\times 5.151}{\pi\times 10}\right)=0.5917$$

(b) Calculate C_{M0} using Equation (24-127) and $C_{M\alpha}$ using Equation (24-130). Plot for $-5°\le\alpha\le 20°$ is shown in Figure 24-41.

$$C_{M_0}=\overbrace{C_{M_{ac_W}}+C_{L_{0_W}}(h_{cg}-h_{ac})}^{C_{M_{0_W}}}+\overbrace{C_{M_{ac_{HT}}}+C_{L_{0_{HT}}}\left(\frac{l_{HT_{CG}}}{c_{MGC}}\right)}^{C_{M_{0_{HT}}}}$$
$$=-0.1+(0.35)\left(\frac{1.039}{2}-0.25\right)+0+0\left(\frac{7.711}{2}\right)=-0.005675$$
$$C_{M_\alpha}=C_{L_{\alpha_W}}(h_{cg}-h_{ac})-\eta_{HT}V_{HT}C_{L_{\alpha_{HT}}}\left(1-\frac{\partial\varepsilon}{\partial\alpha}\right)$$
$$=5.151\left(\frac{1.039}{2}-0.25\right)-(1)(0.5783)(4.529)\left(1-\frac{2(5.151)}{\pi(10)}\right)$$
$$=-0.3721\ \ 1/\text{rad}$$
$$=-0.006493\ \ 1/\text{deg}$$

(c) Determine the value of C_{M0} required to trim the airplane $\alpha=10°$. The longitudinal equation is (note the use of $C_{M\alpha}$ in terms of "per degree"):

$$C_M=C_{M_0}+C_{M_\alpha}\alpha=-0.005675-0.006493\alpha$$

Thus, to trim at $\alpha=10°$ the residual pitching moment, C_{M0}, must be

$$C_M=C_{M_0}-0.006493\alpha=C_{M_0}-0.006493(10°)=0$$
$$\Leftrightarrow\quad C_{M_0}=0.006493(10°)=0.06494$$

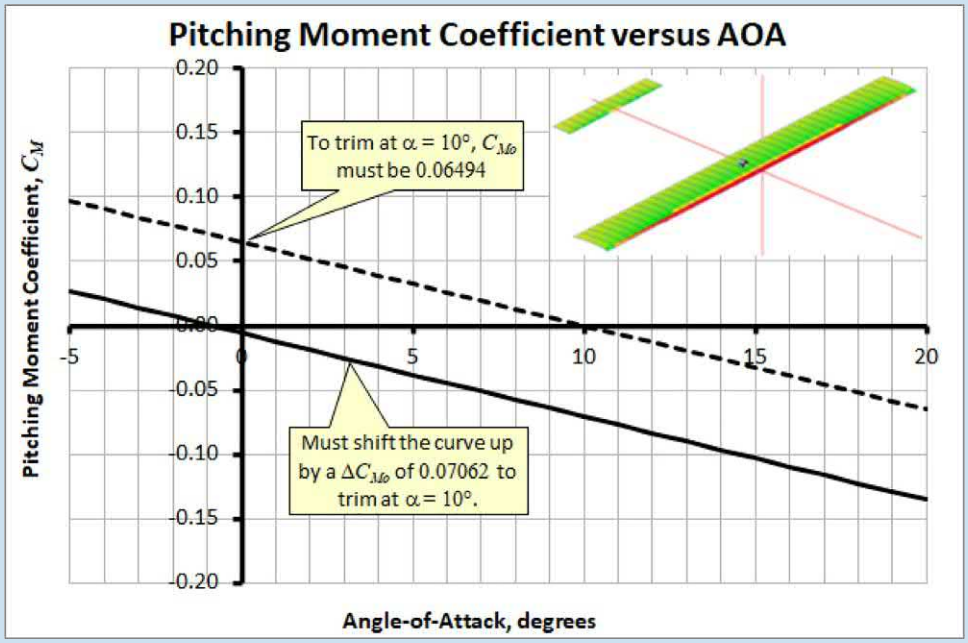


FIGURE 24-41 The pitching moment coefficient curve for the wing–HT system.

EXAMPLE 24-6 (*cont'd*)

(d) Determine $C_{M\delta e}$ if $r_e = c_e/c_{HT} = 0.3$ and δ_e to trim at $\alpha = 10°$. First, determine τ_e from Equation (24-86) for $r_e = c_e/c_{HT} = 0.3$:

$$\tau_e \approx -4.66r_e^4 + 8.79r_e^3 - 6.44r_e^2 + 2.85r_e + 0.0316 = 0.5066$$

$$\text{Therefore, } \frac{\partial C_{L_{HT}}}{\partial \delta_e} = C_{L_{\alpha_{HT}}}\tau_e = (4.529)(0.5066)$$
$$= 2.294 \text{ per rad} \quad (= 0.04004 \text{ per deg})$$

Calculate $C_{M\delta e}$ using Equation (24-84) (note how it is transformed to allow δ_e in degrees)

$$C_{M_{\delta_e}} \approx \left(\eta_{HT}\left(\frac{S_{HT}}{S}\right)(h_{cg} - h_{ac}) - V_{HT}\right)\frac{\partial C_{L_{HT}}}{\partial \delta_e}$$
$$= \left((1)\left(\frac{6}{40}\right)\left(\frac{1.039}{2} - 0.25\right) - 0.5783\right)(0.04004)$$
$$= -0.02154 \text{ per deg}$$

Complete longitudinal equation for this system is (angles are in degrees).

$$C_M = C_{M_0} + C_{M_\alpha}\alpha + C_{M_{\delta_e}}\delta_e = 0.06494 - 0.006493\alpha - 0.02154\delta_e$$

24.3.5 Trimming for Steady Level Flight

To size the elevator, the designer must start with a *baseline* geometry and evaluate its control authority. This must include deflection of high-lift devices and propulsive forces. The following formulation is used to determine the AOA (α), elevator deflection (δ_e), and thrust (T) required for steady level flight. To accomplish this, we look again to Equation (24-30) and substitute $\theta = \phi = 0°$. This leads to

$$C_{F_x} + C_L \sin\alpha - C_D \cos\alpha = 0$$
$$C_L \cos\alpha + C_D \sin\alpha - C_{F_z} = (mg/qS)$$
$$C_M = 0$$

It is applicable to any fixed-wing configuration, provided the stability derivatives are determined correctly. Assuming α is small, we convert these equations to a coefficient form as follows:

Along x-axis:

$$\left(C_{D_{\min}} + C_{D_\alpha}\alpha + C_{D_{\delta_e}}\delta_e + C_{D_{\delta_f}}\delta_f\right) - \frac{T}{qS}\cos\varepsilon_T = 0 \quad (24\text{-}134)$$

Along z-axis:

$$\left(C_{L_0} + C_{L_\alpha}\alpha + C_{L_{\delta_e}}\delta_e + C_{L_{\delta_f}}\delta_f\right) + \frac{T}{qS}\sin\varepsilon_T = \frac{W}{qS} \quad (24\text{-}135)$$

Pitching moment:

$$\left(C_{M_0} + C_{M_{0_T}}\right) + \left(C_{M_\alpha} + C_{M_{\alpha_{T_N}}}\right)\alpha + C_{M_{\delta_e}}\delta_e + C_{M_{\delta_f}}\delta_f = 0 \quad (24\text{-}136)$$

Where ε_T is the thrust force angle. Next, rearrange the above equations for α, δ_e, and T:

Along x-axis:

$$C_{D_\alpha}\alpha + C_{D_{\delta_e}}\delta_e - \frac{\cos\varepsilon_T}{qS}T = -C_{D_{\min}} - C_{D_{\delta_f}}\delta_f \quad (24\text{-}137)$$

Along z-axis:

$$C_{L_\alpha}\alpha + C_{L_{\delta_e}}\delta_e + \frac{\sin\varepsilon_T}{qS}T = \frac{W}{qS} - C_{L_0} - C_{L_{\delta_f}}\delta_f \quad (24\text{-}138)$$

The moment equation poses a challenge when dealing with propeller normal force, reflected in the coefficient $C_{M\alpha TN}$. The propeller normal force depends on thrust and AOA, but it is one of the unknowns. Therefore, the moment portion would have to be solved iteratively, which is not always convenient. The workaround is to treat it as a constant based on an expected thrust value.

$$C_{M_\alpha}\alpha + C_{M_{\delta_e}}\delta_e + C_{M_{0_T}} = -\left\{C_{M_{\alpha_{T_N}}}\alpha\right\} - C_{M_0} - C_{M_{\delta_f}}\delta_f \quad (24\text{-}139)$$

where the product inside {} is treated as a constant. Substituting parameters into Equation (24-139) results in

$$C_{M_\alpha}\alpha + C_{M_{\delta_e}}\delta_e + \frac{z_T}{qSc_{MGC}}T = -\frac{T_N \cdot x_T}{qSc_{MGC}} - C_{M_0} - C_{M_{\delta_f}}\delta_f \quad (24\text{-}140)$$

The equations can now be rearranged in the following matrix form:

$$\begin{bmatrix} C_{D_\alpha} & C_{D_{\delta_e}} & -\dfrac{\cos\varepsilon_T}{qS} \\ C_{L_\alpha} & C_{L_{\delta_e}} & \dfrac{\sin\varepsilon_T}{qS} \\ C_{M_\alpha} & C_{M_{\delta_e}} & \dfrac{z_T}{qSc_{MGC}} \end{bmatrix} \begin{Bmatrix} \alpha \\ \delta_e \\ T \end{Bmatrix} = \begin{Bmatrix} -C_{D_{\min}} - C_{D_{\delta_f}}\delta_f \\ \dfrac{W}{qS} - C_{L_0} - C_{L_{\delta_f}}\delta_f \\ -\dfrac{T_N \cdot x_T}{qSc_{MGC}} - C_{M_0} - C_{M_{\delta_f}}\delta_f \end{Bmatrix} \quad (24\text{-}141)$$

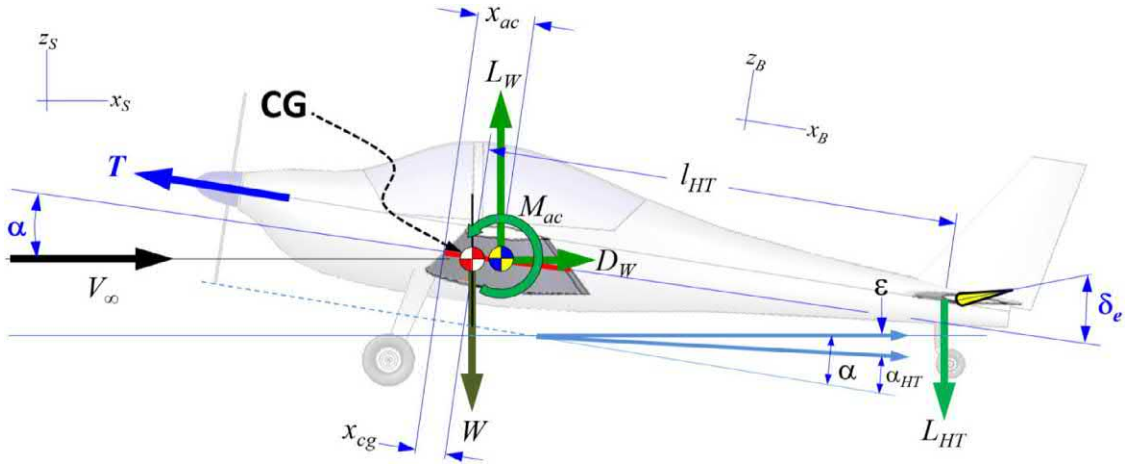


FIGURE 24-42 A simple wing–HT–engine system used for trim analysis.

See Figures 24-10 and 25-2 for dimensions. When solved, Equation (24-141) yields the angle-of-attack, elevator deflection, and thrust required for a longitudinally stable flight at a given airspeed and atmospheric conditions (see Figure 24-42). The solution can be implemented using a simple method such as the 3×3 Cramer's Rule. Once implemented, the formulation can be used to estimate suitable elevator deflection range (by varying the CG location) and power requirements at various conditions, including high altitudes and with flaps (or landing gear) deployed.

Recall the elevator authority derivative, $\boldsymbol{C_{M\delta e}}$. Using the derivative $\partial C_{LHT}/\partial\delta_e$, it can be rewritten as follows:

$$\boldsymbol{C_{M_{\delta_e}}} \approx \left(\eta_{HT}\left(\frac{S_{HT}}{S}\right)(h_{cg}-h_{ac}) - V_{HT}\right) C_{L_{\alpha_{HT}}}\tau_e \quad (24\text{-}142)$$

where τ_e is the elevator effectiveness, given by Equation (24-86). It depends on the elevator ratio, r_e, which gives the designer a valuable tool to study its impact on trimmed, steady flight at critical flight conditions.

Note that typical values of the derivatives for small GA aircraft fall within the following limits (all the derivatives are in terms of radians and all angles, α, δ_e, and δ_f are in radians). Typical δ_{emax} is 20 to 25° (0.349–0.436 rad) and δ_{fmax} is 25 to 45° (0.524–0.785 rad). These are only intended to give "ballpark" numbers and are not a substitute for analysis. The derivatives of your airplane may deviate significantly from these.

$$0.010 < C_{D_{\min}} < 0.06 \qquad 0 < C_{L_0} < 0.6$$

$$C_{D_\alpha} = 2kC_{L_\alpha}(C_{L_0} + C_{L_\alpha}\alpha - C_{L_{\min D}}) \qquad 3.0 < C_{L_\alpha} < 6.0 \qquad -0.2 < \boldsymbol{C_{M_0}} < 0.2$$

$$C_{D_{\delta_e}} \approx \frac{0.001}{\delta_{e_{\max}(in\ radians)}} \qquad C_{L_{\delta_e}} \approx \frac{0.2}{\delta_{e_{\max}(in\ radians)}} \qquad \boldsymbol{C_{M_\alpha}} = C_{L_\alpha}(h_{cg}-h_{ac})$$

$$C_{D_{\delta_f}} \approx \frac{0.01}{\delta_{f_{\max}(in\ radians)}} \qquad C_{L_{\delta_f}} \approx \frac{0.9}{\delta_{f_{\max}(in\ radians)}} \qquad -0.5 < \boldsymbol{C_{M_{\delta_e}}} < -1.0$$

$$-0.7 < \boldsymbol{C_{M_{\delta_f}}} < -0.2$$

EXAMPLE 24-7

Determine the α, δ_e, and T required for a steady level flight with flaps retracted at S-L and (a) 180 KCAS ($q=109.8$ lb$_f$/ft^2) and (b) 75 KCAS ($q=19.06$ lb$_f$/ft^2). The aircraft weighs 3400 lb$_f$, $S=144.9$ ft^2, $c_{MGC}=3.78$ ft, $x_T=13.06$ ft, $z_T=-0.5$ ft, $\varepsilon=0°$, $k=0.04207$ and the pertinent coefficients are given by:

EXAMPLE 24-7 (*cont'd*)

$$C_{D_\alpha} = \begin{cases} 0.0863 & \text{for (a)} \\ 0.4973 & \text{for (b)} \end{cases} \quad C_{D_{\delta_e}} = 0.000175 \quad C_{D_{\min}} = 0.02541$$

$$C_{L_\alpha} = 4.8 \qquad C_{L_{\delta_e}} = 0.355 \qquad C_{L_0} = 0.2$$

$$\boldsymbol{C_{M_\alpha}} = -0.72 \qquad \boldsymbol{C_{M_{\delta_e}}} = -0.923 \qquad \boldsymbol{C_{M_0}} = 0 \qquad T_N = 50 \text{ lb}_f$$

Note that all the stability derivatives are in terms of radians. If we assume propeller efficiency, η_p, of 0.85 for the high-speed case and 0.60 for the low-speed

EXAMPLE 24-7 (*cont'd*)

one, how much engine power is required to achieve this? Use Equation (15-52) to convert thrust to power.

SOLUTION:

(a) Begin by populating the matrices of Equation (24-141):

$$\begin{bmatrix} 0.0863 & 0.000175 & -\dfrac{1}{(109.8)(144.9)} \\ 4.8 & 0.355 & 0 \\ -0.72 & -0.923 & \dfrac{-0.5}{(109.8)(144.9)(3.78)} \end{bmatrix} \begin{Bmatrix} \alpha \\ \delta_e \\ T \end{Bmatrix}$$

$$= \begin{Bmatrix} -0.02541 \\ \dfrac{3400}{(109.8)(144.9)} - 0.2 \\ -\dfrac{(50)(13.06)}{(109.8)(144.9)(3.78)} \end{Bmatrix} = \begin{Bmatrix} -0.02541 \\ 0.01370 \\ -0.01086 \end{Bmatrix}$$

Then, solve for the three arguments α, δ_e, and T, using any matrix method. Here the solution yields:

$$\begin{Bmatrix} \alpha \\ \delta_e \\ T \end{Bmatrix} = \begin{Bmatrix} 0.002409 \text{ rad} \\ 0.006217 \text{ rad} \\ 407.5 \text{ lb}_\text{f} \end{Bmatrix} = \begin{Bmatrix} 0.138 \text{ deg} \\ 0.356 \text{ deg} \\ 407.5 \text{ lb}_\text{f} \end{Bmatrix}$$

The power requirements are thus:

$$P = \frac{TV}{\eta_p \times 550} = \frac{407.5 \times (180 \times 1.688)}{0.85 \times 550}$$
$$= 265 \text{ BHP} \quad (\text{or about } 85\% \text{Power})$$

(b) The results are: $\begin{Bmatrix} \alpha \\ \delta_e \\ T \end{Bmatrix} = \begin{Bmatrix} 12.9 \text{ deg} \\ -7.26 \text{ deg} \\ 378 \text{ lb}_\text{f} \end{Bmatrix}$.

The power requirements are thus 145 BHP or about 47% power. This power is underestimated as it is based on the simplified drag model (see Chapter 16), which underpredicts the drag at high-lift coefficients.

24.3.6 A Simplified Theory of V-Tails

Ref. [26] lists several expressions that are handy in the design of V-tails. It also presents a step-by-step for design. The reference presents the following set of experimentally supported formulation to help with the design of the configuration (derivation is provided in the reference document)

Lift curve slope of the V-tail:

$$C_{L_{\alpha_{HT}}} = C_{L_{\alpha_N}} \cos^2\Gamma \tag{24-143}$$

Elevator authority of the V-tail:

$$C_{L_{\delta_e}} = C_{L_{\alpha_N}} \tau \cos\Gamma \tag{24-144}$$

Side force slope of the V-tail:

$$C_{Y_{\beta_r}} = -KC_{L_{\alpha_N}} \sin^2\Gamma \tag{24-145}$$

Rudder authority of the V-tail:

$$C_{Y_{\delta_r}} = KC_{L_{\alpha_N}} \tau \sin\Gamma \tag{24-146}$$

where

Γ = Dihedral of the V-tail,
$C_{L_{\alpha N}}$ = Lift curve slope of the planform at a zero dihedral,
τ = Control effectiveness parameter,
K = The ratio of sum of lifts obtained by equal and opposite changes in angle-of-attack of two semispans of tail to lift obtained by an equal change in angle-of-attack for complete tail.

Two formulas for the *required* control effectiveness parameter, τ, are given in the reference document. This helps establish a minimum value of τ. One of the two equations is shown below (with some variable notation changes to align with the presentation in here).

$$\tau = \frac{C_{M_{\delta_e}}}{\eta_{HT}\left(\dfrac{l_{HT}}{c_{MGC}}\right) C_{L_{\alpha_N}} \left(\dfrac{S_V}{S_W}\right) \cos\Gamma} \tag{24-147}$$

24.4 INTRODUCTION TO HINGE MOMENTS

Deflecting a control surface flap (e.g., aileron, elevator, rudder, flap, spoiler, etc.) requires an effort. This is caused by the pressure difference across its surface, which develops a moment about the point of rotation: the *hinge point*. The moment is the *hinge moment*. The pilot effort must overcome the hinge moment.

Consider the symmetric airfoil and flap at $\alpha = 0°$ and $\delta_f = 0°$ in Figure 24-43(a). The pressure-field over the upper and lower surface is symmetric: No moment is developed about the hinge point. In Figure 24-43(b), the flap is deflected, modifying the pressure-field. The pressure on the upper surface is higher than on the lower one. This develops hinge moment that "wants" to rotate the flap back to neutral. In Figure 24-43(c), the flap is neutral, but at an angle-of-attack. This, too, changes the pressure-field, generating hinge moment that "wants" to rotate the flap away from neutral, as shown by the dotted outline. To bring the flap back to neutral in this situation, requires a pilot effort. Figure 24-43(d) illustrates how the hinge moment developed by the aerodynamic force (and must be overcome by pilot force) is the product of the force and the distance of the center of force from the hinge point. In short, the hinge moment depends on airfoil and flap geometry, flap deflection (δ_f), and surface AOA (α).

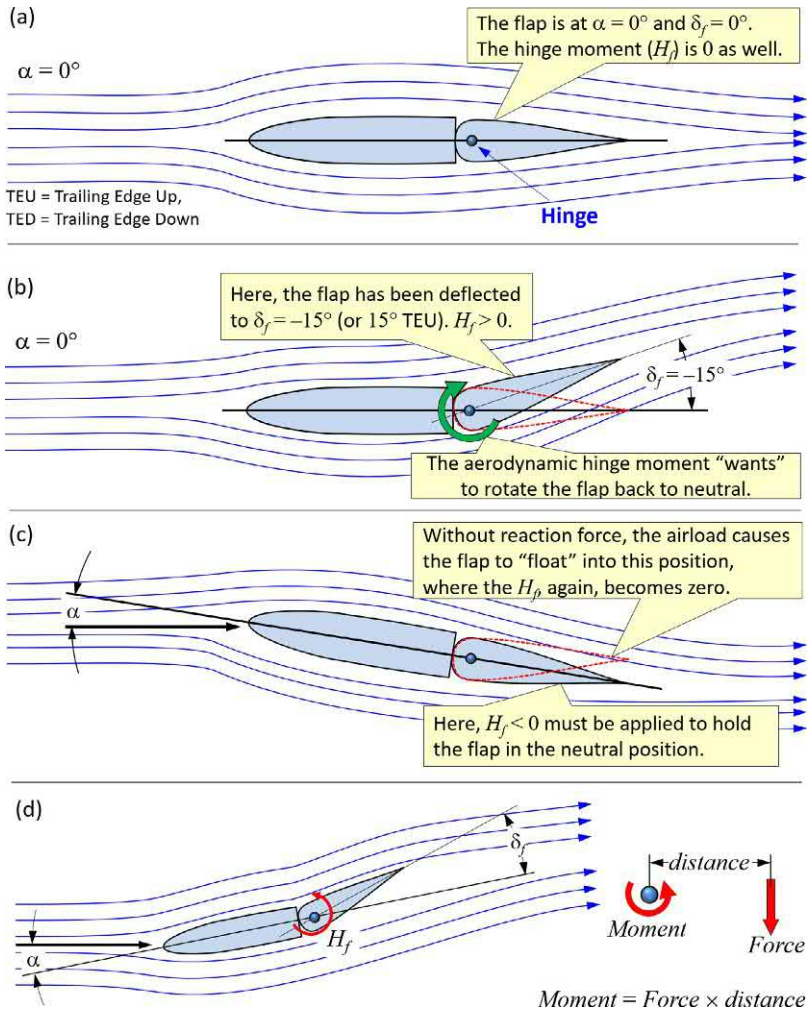


FIGURE 24-43 The generation of the hinge moment.

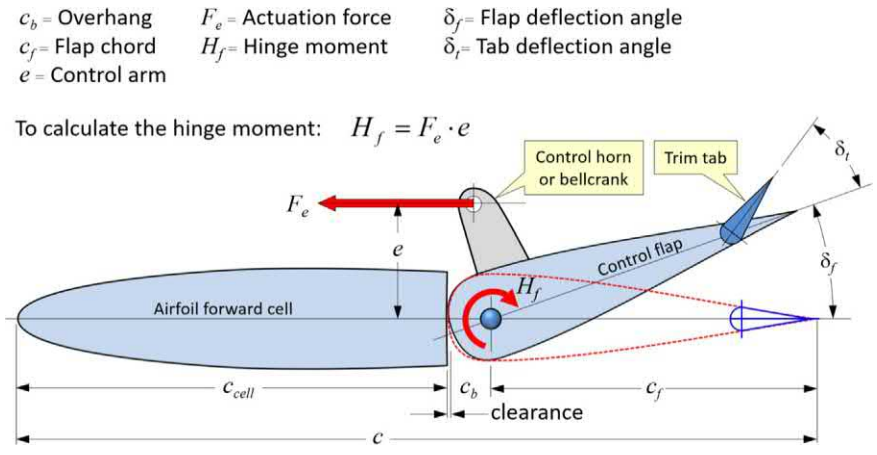


FIGURE 24-44 The hinge moment (*HM*) is reacted as a force, either directly by the pilot or by a control system (typically hydraulic or electric).

24.4.1 Fundamental Definitions

Hinge moment analysis revolves around estimating the magnitude of the moment and the required reaction force. Consider the control surface flap in Figure 24-44. To deflect the flap, the *mechanical moment* developed by the actuation force F_e, acting over the arm e equals the *aerodynamic hinge moment* developed at deflection angle δ_f. The hinge moment depends on the airfoil and flap geometry, flap deflection angle (δ_f), and the α of the combination. The force is applied using a stick, a yoke, a "steering wheel," foot pedals, and, sometimes, hydraulic, or electrical actuation system.

(1) Hinge Moments

The hinge moments generated by the ailerons, elevator, and rudder are denoted by H_a, H_e, and H_r,

respectively. Other hinge moments (e.g., by flaps, spoilers, etc.) are denoted using suitable subscripts. A general expression for the hinge moment of a flapped control surface (using subscript *f*) is given by

$$H_f = \frac{1}{2}\rho V_\infty^2 c_f S_f C_{H_f} \tag{24-148}$$

where

c_f = Flap chord (aft of hingeline)
S_f = Flap area (aft of hingeline)
C_{Hf} = Hinge moment coefficient

(2) Hinge Moment and Stick-Force

The pilot effort is called *stick-force*. The stick-force required to deflect a control surface through a specific angle is related to its hinge moment through the expression

$$F_f = -GH_f \tag{24-149}$$

where G is the *gearing constant* and the subscript f refers to a flapped control surface (e.g., aileron, elevator, etc.). See more detail in Section 24.4.2.

(3) The Hinge Moment Coefficient

The hinge moment coefficient is denoted by C_H, and is typically presented using an appropriate subscript to denote the control surface to which it belongs. A general form of the hinge moment coefficient is given by:

$$C_{H_f} = \overbrace{C_{H_{0_f}}}^{\substack{=0 \text{ for} \\ \text{symmetrical} \\ \text{airfoils}}} + \overbrace{C_{H_{\alpha_f}}}^{\substack{\text{change} \\ \text{in } HM \text{ with} \\ \text{change in } \alpha}} \cdot \overbrace{\alpha_f}^{\substack{\alpha \text{ of the surface} \\ \text{to which the} \\ \text{flap is mounted}}} + \overbrace{C_{H_{\delta_f}}}^{\substack{\text{change} \\ \text{in } HM \text{ with} \\ \text{change in } \delta_f}} \cdot \overbrace{\delta_f}^{\substack{\text{flap} \\ \text{deflection}}} + \overbrace{C_{H_{\delta_t}}}^{\substack{\text{change in } HM \\ \text{with change in} \\ \text{trim tab} \\ \text{deflection}}} \cdot \overbrace{\delta_t}^{\substack{\text{trim tab} \\ \text{deflection}}} \tag{24-150}$$

For symmetrical control surfaces without a trim tab, this reduces to

$$C_{H_f} = \overbrace{C_{H_{\alpha_f}}}^{\substack{\text{Floating} \\ \text{tendency}}} \cdot \alpha_f + \overbrace{C_{H_{\delta_f}}}^{\substack{\text{Restoring} \\ \text{tendency}}} \cdot \delta_f \tag{24-151}$$

As a rule of thumb, we want (1) $C_{H\alpha f} = 0$ to suppress deflection due to α, and (2) a small, negative value of $C_{H\delta f}$ for reduced stick forces at high airspeed. But we do not want it so small it leads to *pilot-induced oscillation*. Recall the conventions assigned to the deflection angle discussed in Section 24.1.6 and Figure 24-9.

(4) The Hinge Moment Coefficients for Aileron, Elevator, and Rudder

Hinge moments for primary controls (ailerons, elevator, and rudder) are usually presented as follows:

Aileron hinge moment:

$$C_{H_a} = C_{H_{0_a}} + C_{H_{\alpha_a}}\alpha + C_{H_{\delta_a}}\delta_a + C_{H_{\delta_{ta}}}\delta_{ta} \tag{24-152}$$

Elevator hinge moment:

$$C_{H_e} = C_{H_{0_e}} + C_{H_{\alpha_e}}\alpha_{HT} + C_{H_{\delta_e}}\delta_e + C_{H_{\delta_{te}}}\delta_{te} \tag{24-153}$$

Rudder hinge moment:

$$C_{H_r} = C_{H_{0_r}} + C_{H_{\beta_r}}\beta + C_{H_{\delta_r}}\delta_r + C_{H_{\delta_{tr}}}\delta_{tr} \tag{24-154}$$

(5) Predicting and Tailoring the Hinge Moment

Predicting the hinge moments is challenging because of the complex interaction of geometry, surface deflection and angle-of-attack, viscous effects, and many others. Analysis method is provided in refs. [6, 12, 27] to name a few. The magnitude of the aerodynamic hinge moment can be modified for any given geometry as listed below:

(1) An effective means to modify C_H is by changing the *overhang*. This involves shifting the hingeline (see B and C in Figure 24-45). Shifting it aft toward the trailing edge reduces the hinge moment ($C_{H\delta f}$). Shifting it forward increases it. Be aware of the changes this makes to the travel of the flap's leading edge. Also be aware of a hinge moment reversal that can occur if the hingeline is shifted too far aft. It can create a very dangerous condition for the pilot.

(2) The leading-edge geometry can be shaped to modify the hinge moment. However, this requires an aft-shifted hingeline to ensure the LE is exposed to the airflow (see C in Figure 24-43). For instance, a "square" shaped leading edge (see F) decreases the hinge moment because of the low-pressure peak on the flap ahead of the hinge.

(3) The geometry of the trailing edge can also be modified (see G and H). For instance, a rounded TE (G) generates a low-pressure region that is located far aft of the hinge—reducing the hinge moment. In contrast, the wedge (H) induces a high-pressure region and increases it. A similar effect is obtained by installing a Gurney flap (see Chapter 10).

Tailoring of hinge moments is used to fine-tune the hinge moments of control surfaces to achieve desirable stick forces. This is usually done during development flight testing. This is important for GA aircraft with manual control system. It is also important for the development of boosted control actuation and autopilot integration.

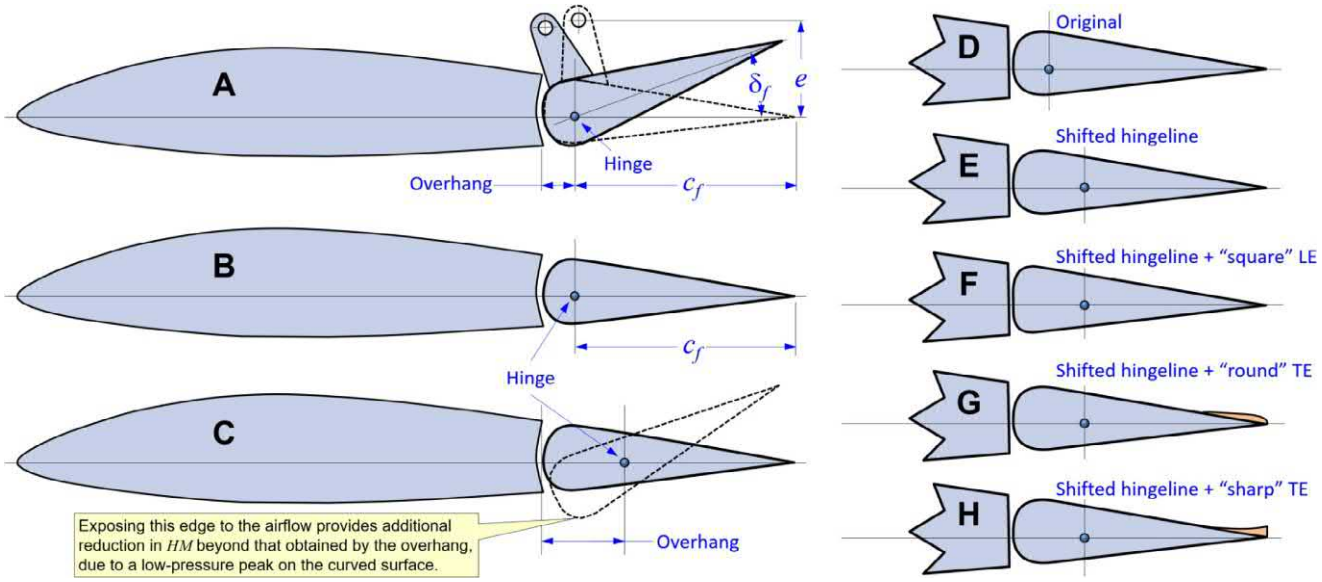


FIGURE 24-45 Means to modify the hinge moment.

(6) Typical Control Surface Flap Chords and Deflection Angles

Table 24-6 shows typical flap chord sizes by control surface type and their usual deflection limits.

(7) Control Surface Floating for the Elevator

Figure 24-46 illustrates trends of $C_{H\delta e}$ and $C_{H\alpha e}$ for a typical elevator control system. Equation (24-151) reflects what transpires if control forces are relinquished and the surface is allowed to "float" freely. Depending on airspeed and angle-of-attack, the surface will "float" to a deflection angle given by the following expression

$$\delta_e = -\frac{C_{H_{\alpha_e}}}{C_{H_{\delta_e}}} \cdot \alpha_{HT} \tag{24-155}$$

If this happens to the elevator, it changes the lift curve slope of the HT, changing the longitudinal stability derivative, $C_{M\alpha}$ [21]. This is illustrated in Figure 24-47. The

TABLE 24-6 Typical ranges of control surface flap chords and deflection angles.

Control surface	Chord size, c_f	Deflection angles, δ_f
Aileron	0.20–0.35	15–25° TEU 15–20° TED
Elevator	0.20–0.35	20–27° TEU 15–20° TED
Rudder	0.20–0.40	20–25° TEL 20–25° TER
Flaps	0.25–0.40	0–10° TEU (cruise flaps) 25–50° TED

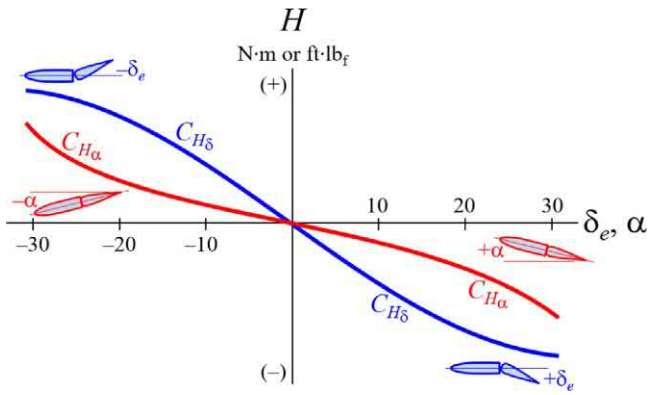


FIGURE 24-46 Dependency of hinge moment on AOA and control deflection. *Based on C.D. Perkins, R.E. Hage, Airplane Performance, Stability, and Control, John Wiley & Sons, 1949.*

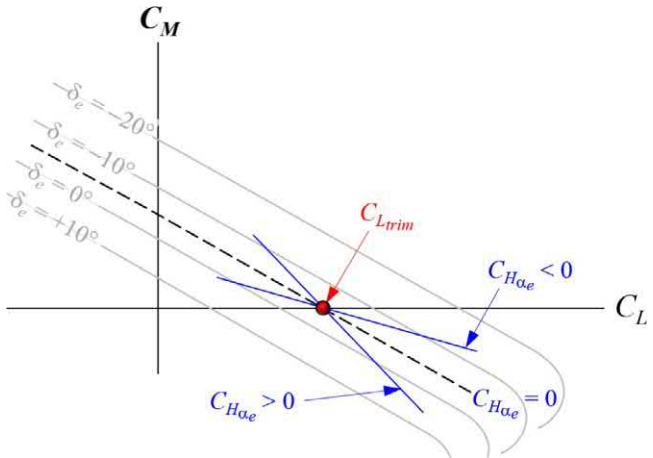


FIGURE 24-47 Impact of $C_{H\alpha e}$ on $C_{M\alpha}$. *Based on E. Seckel, Stability and Control of Airplanes and Helicopters, Academic Press, 1964.*

elevator floats depending on the sign of the derivative $C_{H\alpha e}$, as specified below

$$\delta_e = -\frac{C_{H_{\alpha_e}}}{C_{H_{\delta_e}}} \cdot \alpha_{HT} \quad \Rightarrow \quad \begin{cases} C_{H_{\alpha_e}} > 0 \;\Rightarrow\; \boldsymbol{C_{M_\alpha}} \text{ increases} \\ C_{H_{\alpha_e}} < 0 \;\Rightarrow\; \boldsymbol{C_{M_\alpha}} \text{ decreases} \end{cases} \tag{24-156}$$

The lift curve slope of the HT is changed by the factor

$$1 - \tau_e \frac{C_{H_{\alpha_e}}}{C_{H_{\delta_e}}} \tag{24-157}$$

where τ_e is the elevator effectiveness factor of Equation (24-86). Thus, Equation (24-85) is rewritten as

$$\frac{\partial C_{L_{HT}}}{\partial \delta_e} = C_{L_{\alpha_{HT}}} \tau_e \left(1 - \tau_e \frac{C_{H_{\alpha_e}}}{C_{H_{\delta_e}}}\right) = C_{L_{\alpha_{HT}}} \left(\tau_e - \tau_e^2 \frac{C_{H_{\alpha_e}}}{C_{H_{\delta_e}}}\right) \tag{24-158}$$

The $C_{H\alpha e}$ affects the elevator in the following ways:

(1) If $C_{H\alpha e} < 0$ then the elevator is *underbalanced*. It tends to float and *align with the wind*, i.e., TEU increases with AOA. This destabilizes the airplane. It is the most common situation and occurs when control horns (see Section 24.2.4) are small or absent.

(2) If $C_{H\alpha e} = 0$ then the elevator is *unbalanced*. It is unaffected by the AOA. This is desirable, so our goal is to neutralize $C_{H\alpha e}$ using aerodynamic balancing.

(3) If $C_{H\alpha e} > 0$ then the elevator is *overbalanced*. It tends to float and *align normal to the wind*, i.e., TED increases with AOA. This stabilizes the airplane. It is detrimental in that it leads to an elevator response that tends oppose pilot intention. It is a consequence of excessively large control horns.

24.4.2 Introduction to Control System Loads and Gain

The determination of hinge moments is of great importance because of *stick-free stability and control* and when designing the control system. The general process of control system analysis is to (1) estimate the aerodynamic loads and (2) pilot generated loads. Their impact must be evaluated in a *control system load analysis*. For instance, per the "old" 14 CFR §23.143(c) specifies pilot applied stick-force limits that shall not be exceeded. Chances are that these, rather than the aerodynamic hinge moments, may be the largest loads reacted by the control system.

Figure 24-48 shows a simple manual control system for the elevator. The pilot applies stick force F_S which rotates the stick through angle δ_S. This results in the following:

Pushrod shift:

$$\Delta x = l_2 \sin \delta_S \tag{24-159}$$

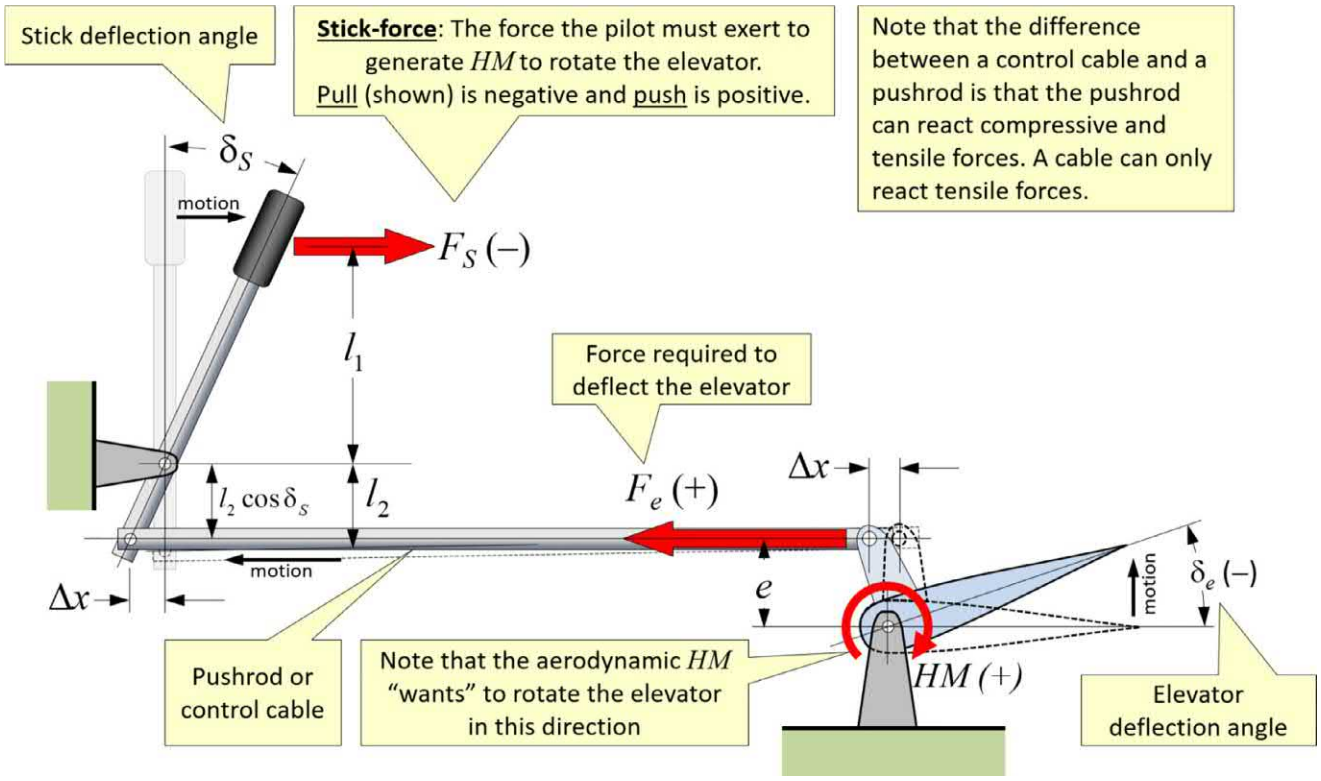


FIGURE 24-48 A simple manual elevator control system. Note how actuation changes the geometry.

Force generated in pushrod:

$$F_e = F_S \frac{l_1}{l_2 \cos\delta_S} \approx F_S \frac{l_1}{l_2} \tag{24-160}$$

Elevator rotation angle:

$$\delta_e = \sin^{-1}(\Delta x/e) = \sin^{-1}(l_2 \sin\delta_S/e) \tag{24-161}$$

Mechanical hinge moment:

$$HM = F_e e = F_S \frac{l_1}{l_2 \cos\delta_S} e \approx F_S \frac{l_1}{l_2} e \tag{24-162}$$

We can now define the control system gain as: (1) The ratio of F_S to F_e and (2) the ratio δ_S to δ_e. These are denoted by G_S and G_δ, respectively.

Stick-force gain:

$$F_e \approx F_S \frac{l_1}{l_2} = F_S G_S \quad \Rightarrow \quad G_S = \frac{l_1}{l_2} \tag{24-163}$$

Rotation gain:

$$\delta_e = \sin^{-1}(\Delta x/e) = \sin^{-1}(l_2 \sin\delta_S/e) = \delta_S G_\delta \quad \Rightarrow \quad G_\delta \approx \frac{\delta_e}{\delta_S} \tag{24-164}$$

Equations (24-163) and (24-164) reveal a limitation of the manual control system. To reduce the stick-force, a large G_S is favored. For instance, if $G_S = 5$ then a 10 lb_f stick-force results in $F_e = 50$ lb_f. However, because l_1 is limited by flight-deck and human dimensions, Δx will be small. Thus, G_δ may end up being small as well. This highlights that G_S and G_δ are limited inside a given range. Methods specifically aimed at movable trim tabs are provided in ref. [28].

24.4.3 Trim Tabs

We have seen how the hinge moment changes with airspeed, deflection, and angle-of-attack. Equations (24-148) through (24-154) show the details of this interaction. For effective control, it must be possible to bring the stick forces to zero. This is called to *trim the airplane*. Having to continuously apply muscle force to control the airplane will quickly wear out even the strongest of us. The trim tab is the remedy—it brings stick forces to zero. *For the stability and control analyst, trimmed airplane implies values of* α, δ_e, *and T that results in equilibrium flight (see Section 24.3.5). For the pilot, trimmed airplane implies zero stick forces in straight and level flight.*

(1) The Fixed Trim Tab

Simple airplanes usually feature fixed tabs for ailerons and rudder and adjustable trim tab for the elevator only. The tab can be as simple as a thin sheet of aluminum, manually bent to ensure the control surface "floats" to a neutral deflection or to bias the float to up- or down-deflection. Figure 24-49(a) shows a *fixed trim tab*, while

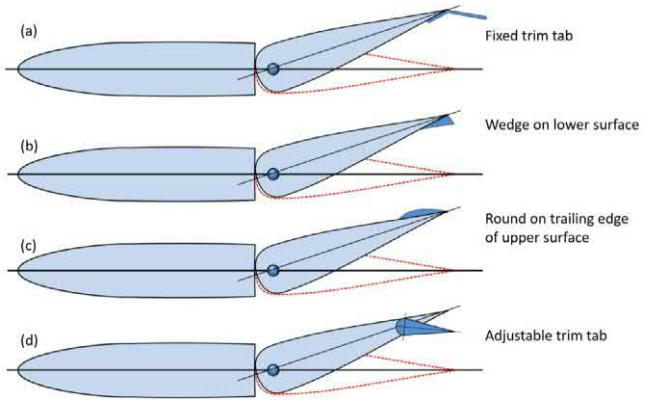


FIGURE 24-49 Simple trim Tables.

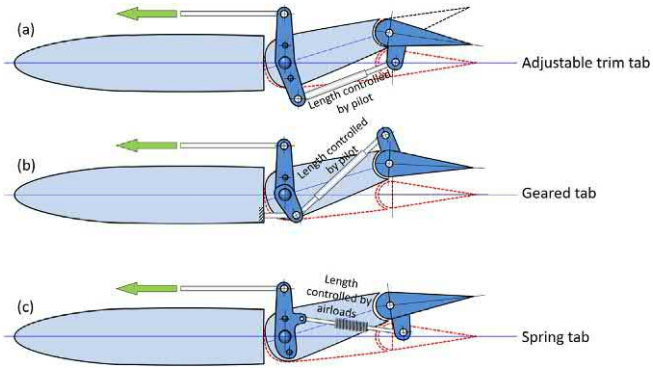


FIGURE 24-50 Movable Tables.

(b) and (c) are alternative means to do the same thing. (b) and (c) are common modifications to the trailing edge. Compare these to an adjustable trim tab Figure 24-49(d). As shown, all the configurations deflect the flap TEU. Also, see additional "tricks" in Figure 24-45.

(2) The Movable Trim Tab

Figure 24-50(a) shows the *adjustable trim tab* is shown in more detail. High-performance aircraft usually feature such trim tabs for ailerons, elevator, and rudder. The pilot adjusts its deflection by changing the length of an actuation arm using a wheel inside the cabin or using an electric motor.

(3) The Geared Tab

Figure 24-50(b) shows a *geared trim tab*. It resembles the adjustable trim tab, except the gearing changes the tab's deflection during the motion of the control surface. Thus, it can provide increased tab deflection at higher surface deflection angles to reduce the otherwise higher hinge moments.

(4) The Spring Tab

Figure 24-50(c) shows a *spring trim tab* is designed to reduce the tab deflection at high dynamic pressure.

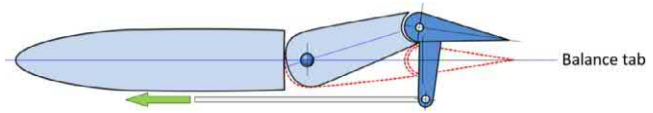


FIGURE 24-51 A balance tab.

The dynamic pressure at high airspeed pushes is to a larger deflection (with respect to the flap) than at low airspeed. This makes it more effective in reducing the hinge moment at high airspeed, when it is needed. At lower airspeeds, the tab deflection is substantially less, maintaining adequate hinge moments.

(5) The Balance Tab (aka Control Tab)

Figure 24-51 shows a *balance tab* (also called *control tab*—e.g., DC-9). Its purpose is to deflect a larger control surface using the much smaller balance tab. It is used on some large aircraft (e.g., Canadair CL-44, Boeing 707, and Douglas DC-9). In this function, the pilot force suffices to deflect the balance tab. It develops a moment large enough to deflect the larger surface. Sluggish control is an adjective used by pilots of some of these aircraft.

(6) The Servo Tab

Figure 24-52(a) shows a *servo tab*, also known as *Flettner tab*. It lowers too large hinge moments. As the flap deflects upward, the servo tab deflects downward through a mechanical action. Pilot adjustment of the tab allows for further fine-tuning.

(7) The Antiservo Tabs

Figure 24-52(b) shows an *antiservo tab*. It is used to remedy too high (servo tab) or too low (antiservo tab) hinge moments. Antiservo tabs are used in the Piper Pa-28 series aircraft.

(8) The Movable Stabilizer

Figure 24-53 shows *movable stabilizer*. It is used to trim large commercial aircraft with wide physical CG-ranges. It is a very effective means to trim an aircraft, although mechanically quite complex. A strong jackscrew, driven by an electric motor, is usually used to move the stabilizer

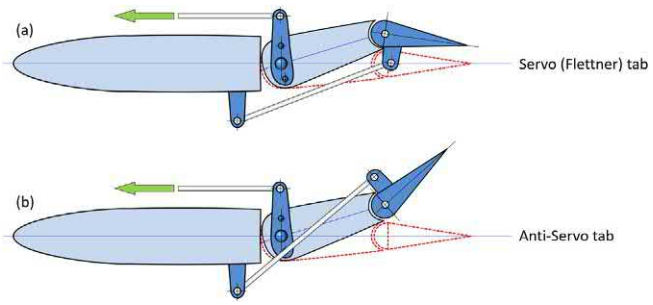


FIGURE 24-52 Servo and antiservo Tables.

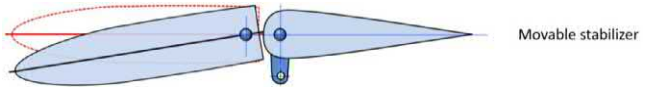


FIGURE 24-53 Movable stabilizer.

up and down. Most modern commercial jetliners and business jets use movable stabilizers.

24.4.4 Control Horns

The control horn is another way to modify the hinge moment. It consists of extending a portion of the control surface ahead of the hinge line. This affects both $C_{H\alpha}$ and $C_{H\delta}$. There are typically two kinds of horns: exposed and shielded.

(1) The Exposed Control Horn

Figure 24-54A shows an *exposed control horn*. The advantage of the exposed horn is simpler (horizontal or vertical) stabilizer structure. A drawback is that, when flying in icing conditions, ice accretes on its leading edge and may form a bridge between it and the stabilizer, preventing the flap from rotating. For this reason, it is

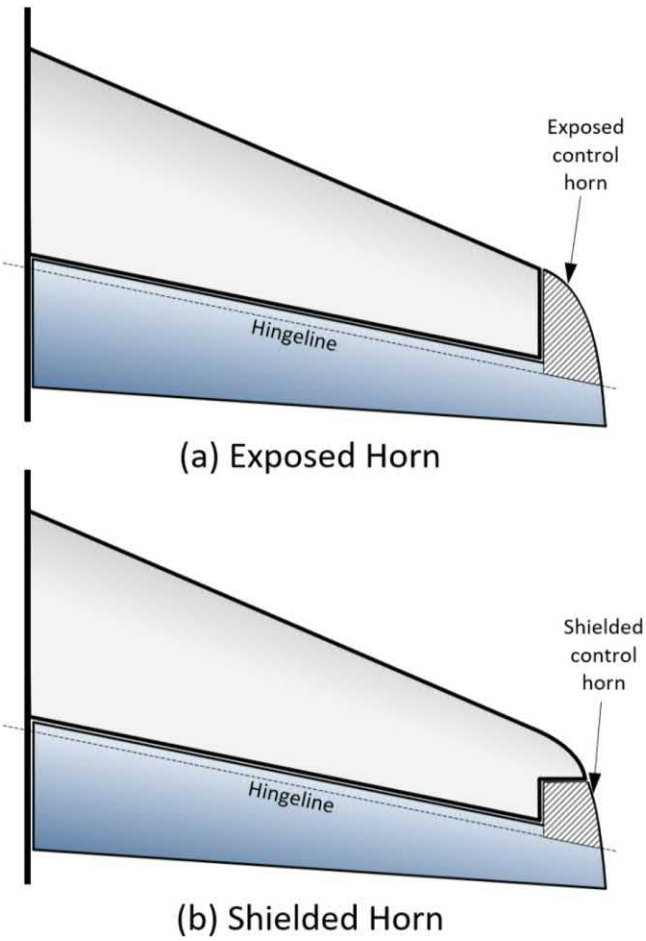


FIGURE 24-54 Typical control horns.



FIGURE 24-55 Elevator and control horn on an ATR72-600. *Photo by Phil Rademacher.*

generally avoided in aircraft certified for *flight into known icing* (FIKI). A notable exception from that rule is the ATR42 and ATR72 turboprop commuters, which feature electrically heated anti-icing device for the control surfaces [29] (see the chrome leading edge on an ATR72-600 in Figure 24-55)).

(2) The Shielded Control Horn

Figure 24-54B shows an *exposed control horn*. The advantage of the control horn is it is shielded from ice accretion. It is a drawback that the manufacturing complexity is increased because of the extension of the stabilizer surface.

The control horns frequently serve in a secondary role as an aerodynamic fairing for a bob weight required for control surface mass-balancing (required to prevent flap-flutter).

References

[1] B.L. Stevens, F.L. Lewis, *Aircraft Control and Simulation*, 1st ed., John Wiley and Sons, Inc, 1992.

[2] D. Allerton, *Principles of Flight Simulation*, AIAA Education Series, 2009.

[3] R.C. Nelson, *Flight Stability and Automatic Control*, 2nd ed., McGraw-Hill, 1998.

[4] B. Etkin, *Dynamics of Flight – Stability and Control*, 2nd ed., John Wiley and Sons, 1982.

[5] M.R. Napolitano, *Aircraft Dynamics – From Modeling to Simulation*, John Wiley and Sons, 2012.

[6] C.D. Perkins, R.E. Hage, *Airplane Performance, Stability, and Control*, John Wiley & Sons, 1949.

[7] J. Roskam, *Airplane Flight Dynamics and Automatic Flight Controls, Part 1*, DAR Corporation, 2001.

[8] M.J. Abzug, E.E. Larrabee, *Airplane Stability and Control: A History of the Technologies that Made Aviation Possible*, 2nd ed., Cambridge Aerospace Series, 2002.

[9] D. Raymer, *Aircraft Design: A Conceptual Approach*, 4th ed., AIAA Education Series, 2006.

[10] K. Robert, W.F. Jewell, *Aircraft Handling Quality Data*, NASA CR-2144, Heffley, December 1972.

[11] T.P. Ratvasky, R.J. Ranaudo, *Icing Effects on Aircraft Stability and Control Determined From Flight Data - Preliminary Results*, NASA TM-105977, 1993.

[12] D.E. Hoak, *USAF Stability and Control DATCOM*, Flight Control Division, Air Force Flight Dynamics Laboratory, 1978.

[13] T. Theodorsen, *General Theory of Aerodynamic Instability and the Mechanism of Flutter, NACA TR-496*, 1935.

[14] M. Tobak, *On the Use of the Indicial-Function Concept in the Analysis of Unsteady Motions of Wings and Wing-Tail Combinations, NACA TR-1188*, 1954.

[15] F.O. Smetana, *Computer Assisted Analysis of Aircraft Performance, Stability, and Control*, McGraw-Hill Book Company, 1984.

[16] T.A. Toll, M.J. Queijo, *Approximate Relations and Charts for Low-Speed Stability Derivatives of Swept Wings, NACA-TN-1581*, 1948.

[17] B.W. McCormick, *Aerodynamics, Aeronautics, and Flight Mechanics*, John Wiley & Sons, 1979.

[18] E.N. Jacobs, K.E. Ward, *Interference of Wing and Fuselage from Tests of 209 Combinations in the NACA Variable-Density Tunnel, NACA R-540*, 1935.

[19] M.M. Munk, *The Aerodynamic Forces on Airship Hulls, NACA R-184*, 1924.

[20] H. Multhopp, *Aerodynamics of the Fuselage, NACA TM-1036*, 1942.

[21] E. Seckel, *Stability and Control of Airplanes and Helicopters*, Academic Press, 1964.

[22] H.S. Ribner, *Formulas for Propellers in Yaw and Charts of the Side-Force Derivative, NACA R-819*, 1945.

[23] A. Ferri, *Completed Tabulation in the United States of Tests of 24 Airfoils at High Mach Numbers, NACA WR L-143*, 1945.

[24] D.J. Graham, *High-Speed Tests of an Airfoil Section Cambered to Have Critical Mach Numbers Higher Than Those Attainable with a Uniform-Load Mean Line, NACA TN-1396*, August 1947.

[25] J. Roskam, *Airplane Design – Part VI: Preliminary Calculation of Aerodynamic, Thrust and Power Characteristics*, DAR Corporation, 2001.

[26] P.E. Purser, J.P. Campell, *Experimental Verification of a Simplified Vee-Tail Theory and Analysis for Available Data on Complete Model with Vee Tails, NACA R-823*, 1944.

[27] R.M. Crane, *Computation of Hinge-Moment Characteristics of Horizontal Tails from Section Data, NACA-WR-A-11 (CB No. 5B05)*, April 1945.

[28] R.J. Woodcock, D.E. Drake, *Estimation of Flying Qualities of Piloted Airplanes, AFFDL-TR-65-218*, Air Force Flight Dynamics Laboratory, Wright-Patterson AFB, April 1966.

[29] Anonymous, Cold Weather Operations - Be Prepared for Icing, ATR Customer Services, March 2011.

This page intentionally left blank

CHAPTER

25

LAT-DIR Stability and Control

OUTLINE

25.1 **Introduction** 975
- *25.1.1 The Content of This Chapter* 975
- *25.1.2 Basic Aircraft Geometry for Lateral and Directional Stability* 975

25.2 **Lateral-Directional Stability and Control** 975
- *25.2.1 Basic Definitions* 976
- *25.2.2 Equations-of-Motion for Static Lateral-Directional Stability* 977
- *25.2.3 Requirements for Directional Stability* 977
- *25.2.4 Requirements for Lateral Stability* 978
- *25.2.5 Historical Values of C_{L_β} and C_{N_β}* 979

25.3 **Directional Stability and Control** 979
- *25.3.1 The Side-Force Model, C_{Y_β}* 979
- *25.3.2 The Yawing Moment Model, C_N* 983

25.4 **Lateral Stability and Control** 988
- *25.4.1 Important Contributions to Rolling Moment* 988
- *25.4.2 The Rolling Moment Model, C_L* 988

25.5 **Basics of Roll and Yaw Control** 999
- *25.5.1 Fundamentals of Roll Control* 999
- *25.5.2 Aileron Sizing* 1001
- *25.5.3 Fundamentals of Yaw Control* 1003

References 1005

25.1 INTRODUCTION

This chapter introduces lateral and directional stability. It rests on the foundation established by Chapter 24, through its presentation of coordinate systems, equations-of-motion, and formulation of forces and moments. Readers that are new to stability and control are advised to review Section 24.1, *Introduction* before attempting this chapter. Figure 25-1 shows how lateral-directional stability fits inside the subfield *flight dynamics* (also see Figure 24-1).

25.1.1 The Content of This Chapter

- Section 25.2 presents the basics of lateral and directional stability. It introduces important concepts and requirements as well as historical values of the primary static lateral and directional stability derivatives.
- Section 25.3 presents multiple methods to estimate directional stability derivatives, allowing the designer to evaluate if the new aircraft is directionally stable.
- Section 25.4 focuses on lateral stability. It presents multiple methods to estimate lateral stability derivatives, allowing the designer to evaluate if the new aircraft is laterally stable.
- Section 25.5 introduces the basics of roll and yaw control.

25.1.2 Basic Aircraft Geometry for Lateral and Directional Stability

Figure 25-2 shows dimensions referenced in this chapter. Note that general dimensions of lifting surfaces are detailed in Section 9.2, *The Trapezoidal Wing Planform*. The term *fractional dimensions* (in Figure 25-2) refers to physical dimensions divided by the mean geometric chord, c_{MGC}. Thus, if x_{CG} is the position of the CG with respect to the leading edge of the c_{MGC}, then $h_{cg} = x_{CG}/c_{MGC}$.

25.2 LATERAL-DIRECTIONAL STABILITY AND CONTROL

There are many similarities between longitudinal and lateral-directional stability analyses. There are big differences too. For one, lateral and directional motion is

https://doi.org/10.1016/B978-0-12-818465-3.00025-2

Copyright © 2022 Elsevier Inc. All rights reserved.

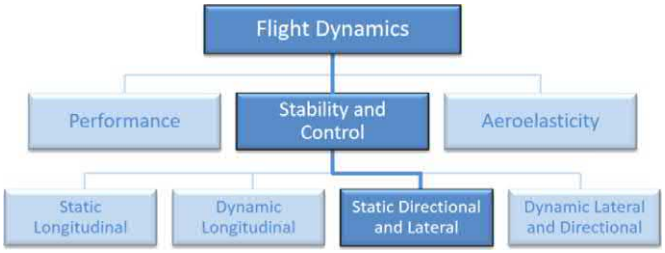


FIGURE 25-1 Static lateral-directional stability.

coupled: roll induces yaw and yaw induces roll. However, an important difference is that straight and level flight requires the residual longitudinal moment $C_{M0} > 0$, whereas the corresponding residuals for lateral and directional motion are $C_{L_0} = C_{N_0} = 0$. This difference results from gravity affecting the mass of the aircraft from one direction only. Additionally, for flight, we must generate lift to counteract weight. However, the symmetry of straight flight requires no net lateral or directional forces acting on the aircraft. Thankfully, this leads to mathematical convenience in the resulting formulation.

25.2.1 Basic Definitions

Before embarking on the analysis of lateral and directional stability, a few terms must be defined.

(1) Roll or Bank

An airplane is said to be rolling (or banking) if rotated about the x-axis such that one wingtip is higher than the other (see Figure 24-7D). Roll is a primary method for changing the direction of flight (heading). It is primarily controlled using the ailerons, although this is supplemented by spoilers in some aircraft. The rudder is merely used to "fine tune" the heading change through coordination,

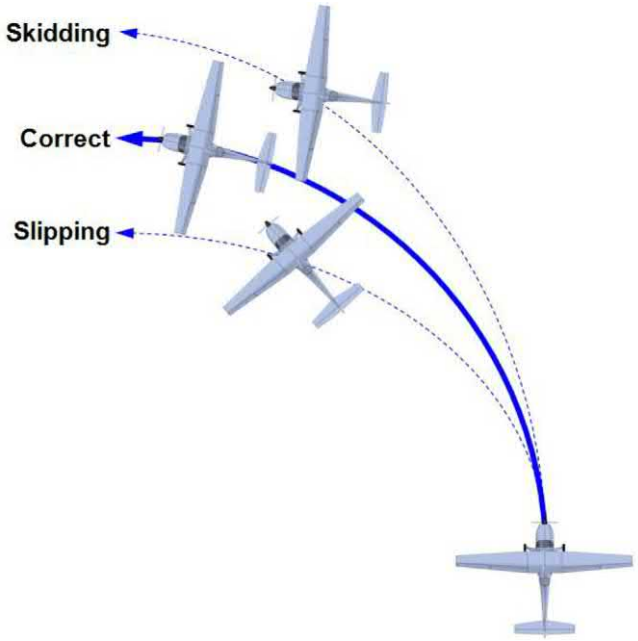


FIGURE 25-3 The definition of slipping (sideslip) and skidding.

by preventing *skidding* or *slipping* (see Figure 25-3). The reason why banking is more effective for changing heading than using the rudder can be explained using mechanics. A heading change results from acceleration in the horizontal plane that changes the original flight direction. The side-force generated by the VT through rudder deflection is much smaller than that generated by the wing. Thus, turn rate using only the VT is significantly slower compared to banking.

(2) Yaw

An airplane is said to be *yawed* if its centerline is not parallel to the x_W-z_W plane (see Figure 24-5). This implies

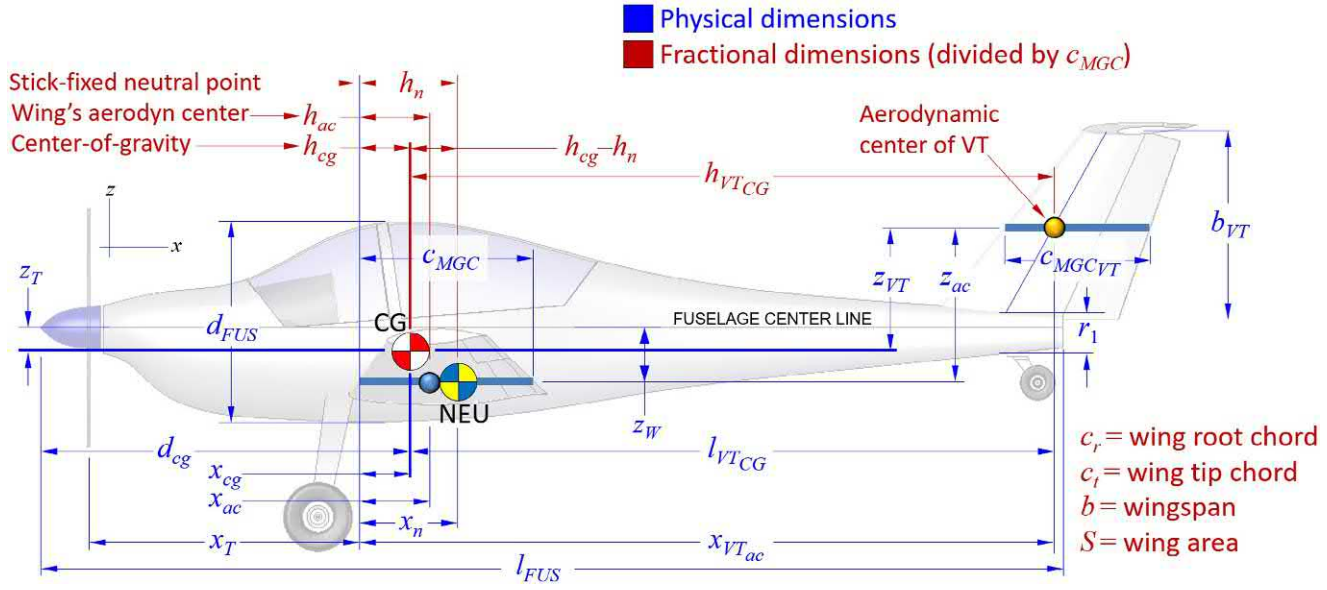


FIGURE 25-2 Establishing dimensions for wing and VT.

a rotation about its vertical axis—the z-axis (the yaw-axis). Based on the assumption that most airplanes are symmetrical about the x_B-z_B plane (see Figure 24-5). this rotation makes it unsymmetrical with respect to the airflow, which inevitably generates a side-force and moment about the yaw axis.

(3) Slipping (Sideslip)

If the airplane is "yawed out of a turn" (i.e., the nose points outside of the trajectory of the turn) it is said to be *slipping* (see Figure 25-3). If banking left, this means the nose points to the right. The bank angle of the airplane is steeper than the rate-of-heading change would indicate. Slips primarily happen two ways: (1) as a consequence of uncoordinated deflection of ailerons and rudder or (2) the consequence of the intentional application of opposite rudder during a bank to increase drag or align the ground track while landing in a crosswind. Slip is also used by pilots for altitude or airspeed control because the resulting yaw increases the drag of the airplane.

(4) Skidding

If the airplane is "yawed into a turn," i.e., if the nose points inside of the trajectory of the turn, it is said to be *skidding* (see Figure 25-3). If banking left, this means the nose points further left than indicated by the rate-of-turn; the airplane's bank angle is smaller than indicated by the rate-of-turn. Skids primarily happen two ways: (1) because of uncoordinated deflection of ailerons and rudder or (2) the consequence of the intentional and excessive application of pro-bank rudder.

All aircraft certified to 14 CFR Part 23 must be demonstrably laterally and directionally stable per 14 CFR §23.177 *Static Directional and Lateral Stability*. Thus, slipping and skidding are pilot induced maneuvers—once the pilot discontinues the required control input, the airplane must attain its original symmetric attitude naturally. Even an airplane operating with asymmetric thrust, such as a multiengine aircraft with *one engine inoperable* (OEI), must acquire a "symmetric attitude" for straight and level flight. Only it does so by coordinated deflection of control surfaces—yes, its geometry is no longer symmetric with respect to flight direction, but it is aerodynamically symmetric as all moments are 0 due to control surface deflection. Thus, we differentiate between *geometric symmetry* and *aerodynamic symmetry*.

25.2.2 Equations-of-Motion for Static Lateral-Directional Stability

The *equations-of-motion* (EOM) for lateral-directional motion are extracted from Equations (24-13) through (24-16) and summarized below:

$$
\begin{aligned}
&Y + mg\cos\theta\sin\phi = m(\dot{v} + \hat{r}u - \hat{p}w)\\
&\boldsymbol{L} = I_{xx}\dot{\hat{p}} - I_{xz}\dot{\hat{r}} + \left(I_{zz} - I_{yy}\right)\hat{q}\hat{r} - I_{xz}\hat{p}\hat{q} + \left(\hat{q}h_{SRz} - \hat{r}h_{SRy}\right)\\
&\boldsymbol{N} = I_{zz}\dot{\hat{r}} - I_{xz}\dot{\hat{p}} + \left(I_{yy} - I_{xx}\right)\hat{p}\hat{q} + I_{xz}\hat{q}\hat{r} + \left(\hat{p}h_{SRy} - \hat{q}h_{SRx}\right)\\
&\hat{p} = \dot{\phi} - \dot{\psi}\sin\theta\\
&\hat{r} = \dot{\psi}\cos\theta\cos\phi - \dot{\theta}\sin\phi\\
&\dot{\phi} = \hat{p} + \hat{q}\sin\phi\tan\theta + \hat{r}\cos\phi\tan\theta\\
&\dot{\psi} = \hat{q}\sin\phi\sec\theta + \hat{r}\cos\phi\sec\theta
\end{aligned}
\qquad (25\text{-}1)
$$

Again, the bold typeface is used to separate moments from forces. The term *static* means all rotational rates and accelerations are zero. Additionally, as done for the longitudinal set, we are only interested in the first three equations. Thus, Equation (25-1) becomes

$$
\begin{aligned}
&Y + mg\cos\theta\sin\phi = 0\\
&\boldsymbol{L} = 0,\\
&\boldsymbol{N} = 0
\end{aligned}
\qquad (25\text{-}2)
$$

Where Y is given by Equation (24-19), $\boldsymbol{L}$ by Equation (24-24), and $\boldsymbol{N}$ by Equation (24-26). These three constitute the EOM for static lateral-directional stability:

$$
\begin{aligned}
&qS \cdot C_Y + mg\cos\theta\sin\phi = 0\\
&qSc_{MGC} \cdot \boldsymbol{C_L} = 0\\
&qSc_{MGC} \cdot \boldsymbol{C_N} = 0
\end{aligned}
\qquad (25\text{-}3)
$$

Substituting the second expression of Equation (24-21) and rearranging yields:

$$
\begin{aligned}
&C_{Y_\beta}\beta + (mg/qS)\cos\theta\sin\phi = 0\\
&\boldsymbol{C_L} = 0\\
&\boldsymbol{C_N} = 0
\end{aligned}
\qquad (25\text{-}4)
$$

Thus, our task is to formulate the coefficients C_{Y_β} (side-force), $\boldsymbol{C_L}$ (rolling moment), and $\boldsymbol{C_N}$ (yawing moment). This is accomplished in Sections 25.3 and 25.4 using the various models discussed below.

25.2.3 Requirements for Directional Stability

Directional stability is the capability of the vehicle to weathervane. Imagine standing behind a weathervane with the wind directly in the face. If the vane is rotated such its nose points, say, right (and the tail points left) intuition tells us its tail generates lift that points right, in the positive y-direction (see depiction in Figure 25-4). This, in turn, generates a moment whose tendency is to rotate the nose left and align it (and the tail) with the wind. Since the moment corrects the alignment, it is said to be *restoring*.

If the weathervane is yawed nose right, then, using the Stability Coordinate System (SCS—see Chapter 24) the angle $\beta < 0$. This means that if looking along the centerline of the vane, the wind would strike the left cheek. The restoring moment is negative because per the right-hand rule, the resulting rotation is analogous to grabbing the z-axis with the right hand to rotate it with the right thumb

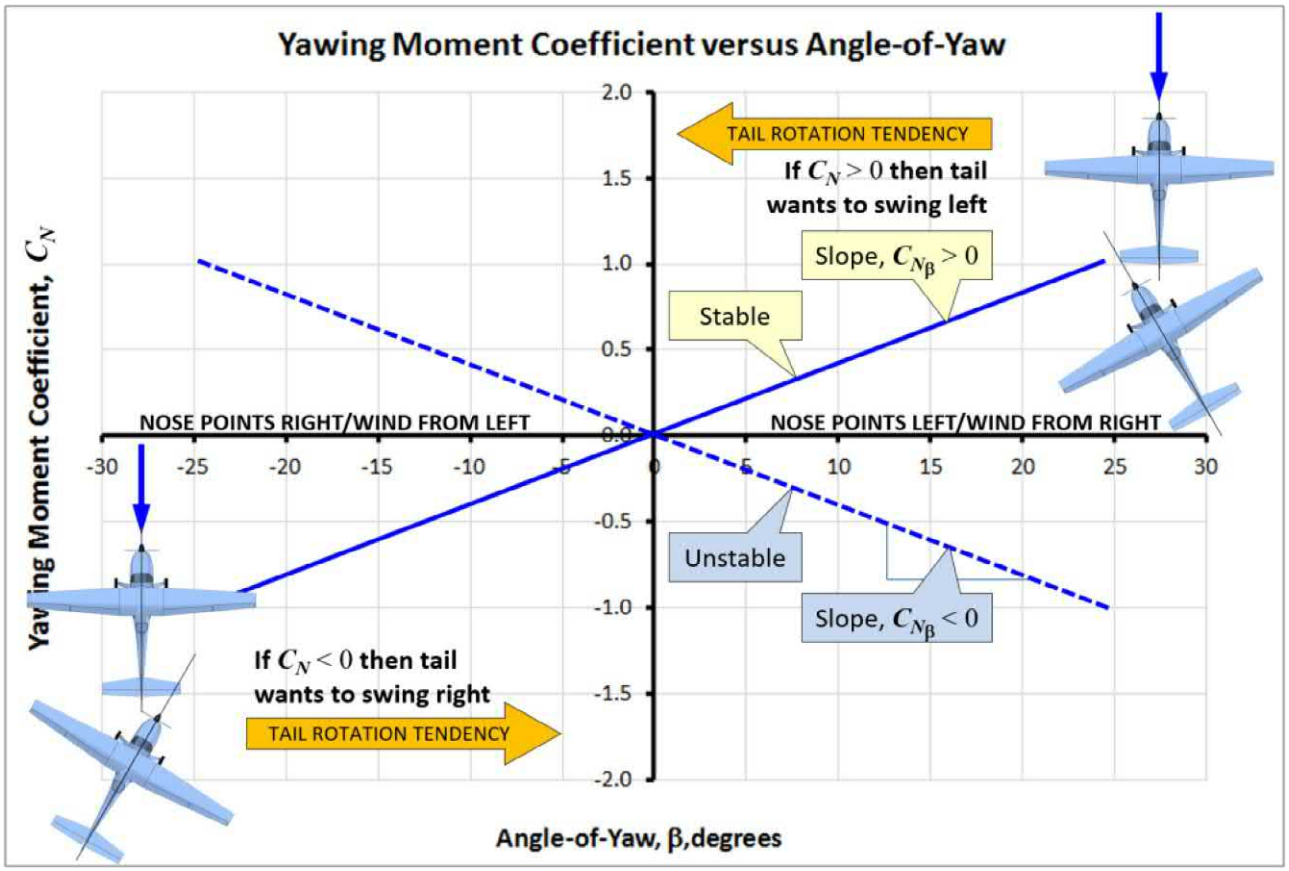


FIGURE 25-4 The requirement for directional stability.

pointing upward—in the negative *z*-direction. The opposite holds true if the weathervane is rotated nose left: a positive moment (thumb pointing down) is required to rotate the nose right to the initial position.

Figure 25-4 shows how this establishes requirements for static directional stability: The slope of the yawing moment curve must have a positive slope. Mathematically, this is written as follows:

Requirements for static directional stability:

$$C_{N_\beta} = \frac{\partial C_N}{\partial \beta} > 0 \quad \text{and} \quad C_N = 0 \quad \text{if} \quad \beta = 0 \tag{25-5}$$

A target range for directional stability is $+0.05 < C_{N_\beta} < +0.15$ per radian. To narrow the range, the designer should estimate the C_{N_β} for airplanes in the same class as the one being designed and for which handling is considered favorable.

25.2.4 Requirements for Lateral Stability

Lateral stability refers to the tendency of an airplane to level its wing during yaw. It differs from both longitudinal and directional stability in that it requires sideslip (or yaw) to be corrected (see Figure 25-5). An airplane is *laterally stable* if it generates negative rolling moment (left wing down) when subjected to a positive yaw angle (β from the right). This is accomplished using the *dihedral effect*.

Consider the airplane in the upper left part of Figure 25-5, whose nose points to the right of the wind direction. It is also shown from above in the lower left corner. The left wing leads the right one. This causes asymmetric loading on the wing that generates more lift on the left wing than the right one. The difference creates a rolling moment that rotates the wing back to level. At this (negative) yaw angle (β), the rolling moment is positive because, according to the right-hand rule, the resulting moment vector points forward (the thumb would point forward) along the positive *x*-axis. The opposite holds if the nose is yawed to the left (positive β), so the right-wing leads; a negative moment is created. This tells us that when $\beta < 0$ a restoring moment must be positive. When $\beta > 0$ the moment must be negative. By plotting a line between those two conditions, as done in Figure 25-5, we can see that restoring rolling moment must have a negative slope in order to be stable. Mathematically:

Requirements for lateral stability:

$$C_{L_\beta} = \frac{\partial C_L}{\partial \beta} < 0 \quad \text{and} \quad C_L = 0 \quad \text{if} \quad \beta = 0 \tag{25-6}$$

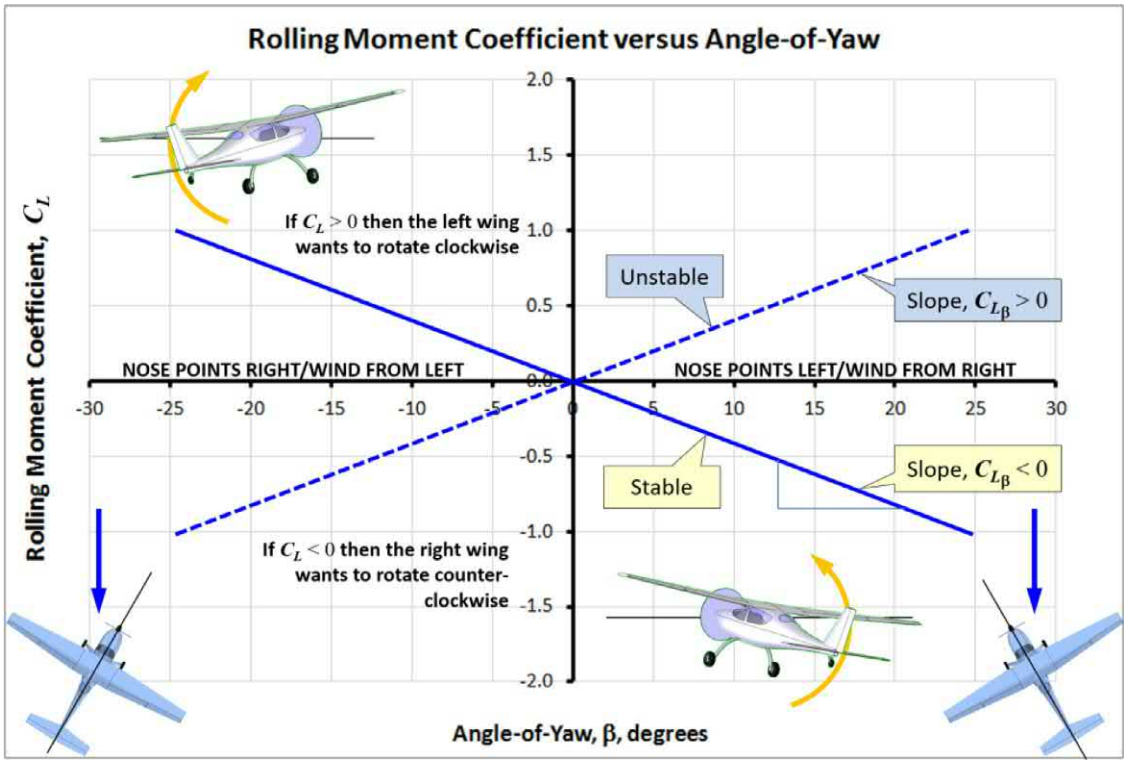


FIGURE 25-5 The requirement for lateral stability.

A target range for lateral stability is $-0.15 < C_{L_\beta} < -0.05$ per radian. To narrow the range, the designer should estimate the C_{L_β} for airplanes in the same class as the one being designed and for which handling is considered favorable.

25.2.5 Historical Values of C_{L_β} and C_{N_β}

During the design of the aircraft, it is important to know what directional and roll stability derivatives to aim for. As usual, the History of Aviation presents us with many candidate values. C_{N_β} and C_{L_β} for several aircraft are shown in Figure. 25-6 and 25-7, respectively. Also, Table 25-1 lists several directional and lateral stability derivatives gathered from Refs. [1–4], and the author's personal notes. These derivatives are in terms of per radian. To convert to per degree, divide by 57.3.

25.3 DIRECTIONAL STABILITY AND CONTROL

An introduction to directional stability is given in Section 25.2.3, *Requirements for Directional Stability*. This section considers aircraft directional stability per the first and third expressions of Equation (25-4). These equations involve multiple contributions that are presented in this section. The reader is directed toward Section 24.1.8, *Important Note to the Reader* regarding digitization of the various graphs presented in this chapter.

25.3.1 The Side-Force Model, C_{Y_β}

A typical aircraft consists of a wing, stabilizing surfaces, fuselage, and, sometimes, engine nacelles and external stores. When subject to flow from the left or right side, the components develop a side-force. These contributions are *stabilizing* and *destabilizing*, depending on their spatial position. The primary duty of the designer is to size the geometry such the sum of the contributions leads to an aircraft that has adequate directional stability that permits safe pilot control. While the largest one is that of the vertical tail (VT), accurate prediction requires the others to be included. The *side-force model* can be expressed as follows:

$$C_Y = C_{Y_0} + C_{Y_\beta}\beta + C_{Y_{\dot\beta}}\left(\frac{\dot\beta b}{2V_\infty}\right) + C_{Y_p}\left(\frac{\hat p b}{2V_\infty}\right) + C_{Y_r}\left(\frac{\hat r b}{2V_\infty}\right) + C_{Y_{\delta_a}}\delta_a + C_{Y_{\delta_r}}\delta_r \qquad (25\text{-}7)$$

Where: C_{Y_0} = Residual side-force, =0 if symmetric,

C_{Y_β} = *Side-force derivative*,
$C_{Y_{\dot\beta}}$ = Change in side-force with $\dot\beta$, ≈0,
C_{Y_p} = Side-force due to roll,

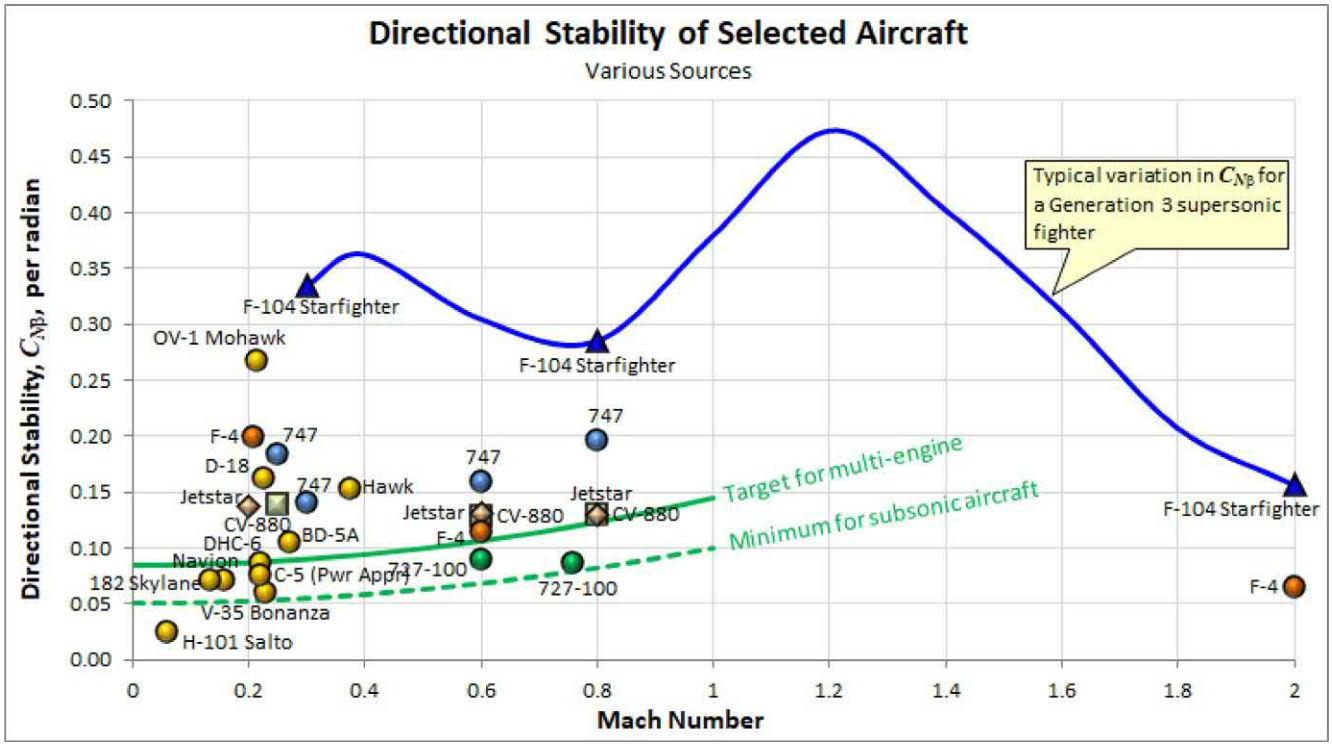


FIGURE 25-6 Trends of directional stability derivatives, C_{N_β} among selected aircraft.

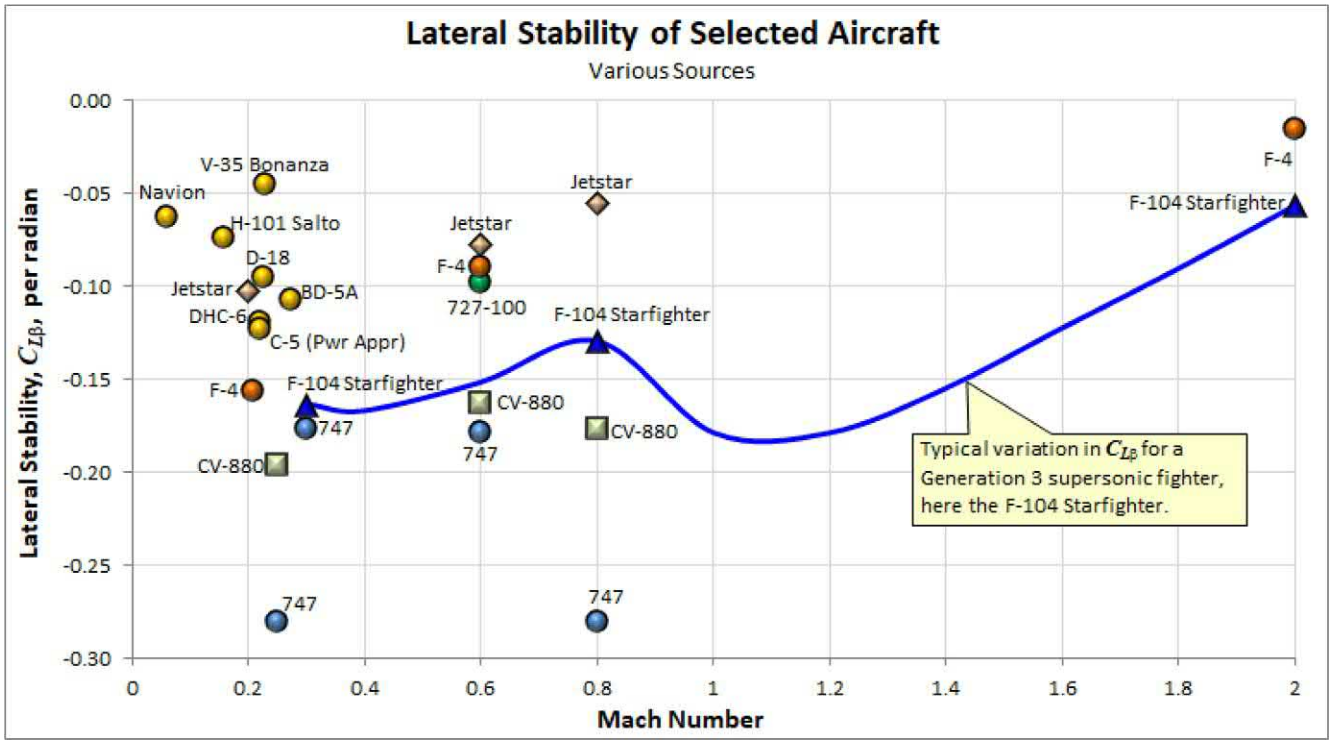


FIGURE 25-7 Trends of lateral stability derivatives, C_{L_β} among selected aircraft.

TABLE 25-1 Directional and roll stability derivatives for selected aircraft.

Directional and Lateral Stability for Selected Aircraft										
Make	Model	M	AR	c_{MGC} ft	b ft	S ft²	C_{y_β} 1/rad	C_{n_β} 1/rad	C_{l_β} 1/rad	Reference
Bede	BD-5A	0.27	6.76	2.60	17	42.78	-1.428	0.105	-0.107	Author
Beech	D-18	0.23	6.51	8.89	47.7	349	-0.927	0.162	-0.095	Author
	V-35 Bonanza	0.23	6.10	5.49	33.5	184	-0.331	0.060	-0.045	Author
Boeing	727-100	0.76	7.07	15.28	108	1650	-	0.086	-	[1]
		0.60	7.07	15.28	108	1650	-0.898	0.090	-0.098	Author
	747 (Pwr Appr)	0.25	6.96	27.31	195.7	5500	-1.080	0.184	-0.281	[2]
	747	0.30	6.96	27.31	195.7	5500	-0.866	0.140	-0.177	[2]
		0.60	6.96	27.31	195.7	5500	-0.893	0.159	-0.179	[2]
		0.80	6.96	27.31	195.7	5500	-0.889	0.196	-0.280	[2]
British Aerospace	Hawk	0.37	5.92	5.51	32.6	179.64	-	0.153	-	[1]
Cessna	182 Skylane	0.14	7.45	4.83	36	174	-	0.07	-	[1]
Convair	CV-880	0.60	7.20	18.94	120.0	2000	-0.788	0.128	-0.163	[2]
		0.80	7.20	18.94	120.0	2000	-0.813	0.129	-0.177	[2]
Convair	CV-880 (Pwr Appr)	0.25	7.20	18.94	120.0	2000	-0.877	0.139	-0.196	[2]
De Havilland Canada	DHC-6	0.22	10.00	6.5	65.0	423	-0.866	0.087	-0.119	[4]
Grumman	OV-1 Mohawk	0.22	6.40	7.5	48	360	-	0.267	-	[1]
Lockheed	A-4 Skyhawk	0.40	2.71	-	26.5	259	-	0.25	-0.12	[3]
		0.80	2.71	-	26.5	259	-	0.27	-0.14	[3]
	C-5 (Pwr Appr)	0.22	7.75	30.1	219.2	6200	-0.770	0.075	-0.123	[2]
	F-104 Starfighter	0.30	2.45	9.55	21.9	196	-1.170	0.335	-0.164	[2]
		0.80	2.45	9.55	21.9	196	-	0.285	-0.130	[2]
		2.00	2.45	9.55	21.9	196	-	0.158	-0.056	[2]
	Jetstar	0.60	5.33	10.93	53.8	543	-0.718	0.1307	-0.077	[2]
		0.80	5.33	10.93	53.8	543	-0.742	0.12948	-0.055	[2]
	Jetstar (Pwr Appr)	0.20	5.33	10.93	53.8	543	-0.720	0.137	-0.103	[2]
	NT-34 (Pwr Appr)	0.20	6.00	6.72	37.5	235	-0.720	0.049	-0.127	[2]
McDonnell Douglas	F-4	0.60	2.82	16.04	38.7	530	-0.642	0.114	-0.0895	[2]
		2.00	2.82	16.04	38.7	530	-0.647	0.065	-0.0156	[2]
	F-4 (Pwr Appr)	0.21	2.82	16.04	38.7	530	-0.655	0.199	-0.156	[2]
Northrop	T-38	0.79	3.77	6.72	25.3	170	-	0.279	-	[1]
Ryan	Navion	0.16	6.06	5.7	33.4	184	-0.564	0.071	-0.074	[3]
Start & Flug	H-101 Salto	0.06	21.51	2.07	44.6	92.4	-0.216	0.024	-0.063	Author

C_{Y_r} = Side-force due to yaw,
$C_{Y_{\delta a}}$ = Side-force with aileron deflection, δ_a,
$C_{Y_{\delta r}}$ = Side-force with rudder deflection, δ_r.

Note: It is the responsibility of the expert to ensure angular consistency. A derivative multiplied by an angle in degrees (or radians) must be represented in terms of *per degrees* (or *per radian*). Also, refer to Figure 25-2 for aircraft dimensions.

(1) Side-Force Derivative, C_{Y_β}

This derivative is to side-force what C_{L_α} is to lift. It allows aerobatic aircraft to maintain altitude while rolled on the side ($\phi = 90°$). The side-force is the linear combination of contributions by the following sources:

$$C_{Y_\beta} = C_{Y_{\beta_W}} + C_{Y_{\beta_{HT}}} + C_{Y_{\beta_{VT}}} + C_{Y_{\beta_{FUS}}} + C_{Y_{\beta_{NAC}}} + C_{Y_{\beta_{T_Y}}} \quad (25\text{-}8)$$

Where: $C_{Y_{\beta W}}$ = Directional derivative due to the wing, see Equation (25-9),

$C_{Y_{\beta HT}}$ = Directional derivative due to the HT, see Equation (25-10),
$C_{Y_{\beta VT}}$ = Directional derivative due to the VT, see Equation (25-12),
$C_{Y_{\beta FUS}}$ = Directional derivative due to the fuselage, see Equation (25-15),

$C_{Y_{\beta NAC}}$ = Directional derivative due to nacelles, see Equation (25-15),
$C_{Y_{\beta TY}}$ = Directional derivative due to the propeller side-force, see Equation (25-33) or (25-34).

Recall that positive β corresponds to the wind striking the right side of the aircraft. This means the side-force points in the negative y-direction. Therefore, $C_{Y_\beta} < 0$. Typical range of values is $-0.2 < C_{Y_\beta} < -1.4$ per radian [5]. Too high a value may be troublesome in cross-wind landings.

Wing Contribution (Sweep and Dihedral)

Refs. [6, 7] give the following expression for wings in subsonic conditions. Note that the contribution by sweep is small and can be ignored for small sweep angles. Units are 1/rad. Note that it is in 1/degree in the two references and the following form has been modified (by multiplying it by 57.3 to convert to radians).

$$C_{Y_{\beta_W}} \approx -0.00573\left|\Gamma_{W_{\text{deg}}}\right| + \text{sgn}(\beta)\frac{C_L^2}{30}\frac{\tan\Lambda_{c/4}\sin\Lambda_{c/4}}{AR\left(AR + 4\cos\Lambda_{c/4}\right)} \tag{25-9}$$

Where $\Gamma_{W_{\text{deg}}}$ is the wing dihedral angle in degrees and sgn() is the *sign* function, i.e., sgn(−5.3) = −1, while sgn(5.3) = +1.

HT Contribution

If the HT has a dihedral (or anhedral), like the wing, it contributes to the side-force. The SAAB 340 exemplifies an aircraft with a large HT-dihedral, while the F-4 Phantom exemplifies one with a large anhedral. This term is affected by sidewash caused by the wingtip vortex as shown in Figure 25-10. Units are 1/rad.

$$C_{Y_{\beta_{HT}}} \approx -0.00573\left|\Gamma_{HT_{\text{deg}}}\right|\eta_{HT}\left(1 + \frac{\partial\sigma}{\partial\beta}\right)\frac{S_{HT}}{S} \tag{25-10}$$

Where σ is sidewash angle and $\Gamma_{HT_{\text{deg}}}$ is the HT dihedral angle in degrees. The sidewash contribution is given by:

$$\eta_{HT}\left(1 + \frac{\partial\sigma}{\partial\beta}\right) = 0.724 + 3.06\frac{S_{HT}/S}{1 + \cos\Lambda_{c/4}} + 0.4\frac{z_W}{d_{FUS}} + 0.009AR_W \tag{25-11}$$

VT Contribution

The contribution by the vertical tail to the side-force is given by the following expression (where units are 1/rad).

$$C_{Y_{\beta_{VT}}} \approx -K_{Y_{VT}}\left|C_{L_{\alpha_{VT}}}\right|\eta_{VT}\left(1 + \frac{\partial\sigma}{\partial\beta}\right)\frac{S_{VT}}{S} \tag{25-12}$$

Where $K_{Y_{VT}}$ is given by the following formulation, digitized by the author, that replicates the graph of Figure 5.3.1.1-22 of Ref. [6]:

$$K_{Y_{VT}} = \begin{cases} 0.76 & \text{if } b_{VT}/2r_1 < 2 \\ 0.4 + 0.16(b_{VT}/2r_1) & \text{if } 2 \le b_{VT}/2r_1 \le 3.5 \\ 1 & \text{if } b_{VT}/2r_1 > 3.5 \end{cases} \tag{25-13}$$

The sidewash contribution by the VT is given by:

$$\eta_{VT}\left(1 + \frac{\partial\sigma}{\partial\beta}\right) = 0.724 + 3.06\frac{S_{VT}/S}{1 + \cos\Lambda_{c/4}} + 0.4\frac{z_W}{d_{FUS}} + 0.009AR_W \tag{25-14}$$

Fuselage and Nacelle Contributions

The contribution by the fuselage is given by the following equation (where units are 1/rad) [5].

$$C_{Y_{\beta_{FUS}}} \approx -K_i C_{L_{\alpha_{FUS}}}\frac{\forall_{FUS}^{2/3}}{S} \tag{25-15}$$

$$K_i = \begin{cases} 3z_W/d_{FUS} & \text{Low-wing} \\ 3.75z_W/d_{FUS} & \text{High-wing} \end{cases} \tag{25-16}$$

Where $\forall_{FUS}$ is the fuselage volume and S is wing area. Refer to Figure 25-2 for dimensions. Nacelles are analyzed as "mini-fuselages."

Propeller Side-Force Contribution

Ref. [8] expresses $C_{Y_{\beta TY}}$ in the following form, which has been adapted to the format in this book.

$$C_{Y_{\beta_{T_Y}}} = N_{ENG}\frac{T_Y}{qA_P} \tag{25-17}$$

Where N_{ENG} is the number of propellers, Ap is the propeller disc area, and q is dynamic pressure. Also see Equation (25-34).

(2) Side-Force due to Roll Rate, C_{Y_p}

When the aircraft rolls, the AOA on its side-silhouette is subject to transient side-flow of air. This changes the side-force on the aircraft, most of which is attributed to the VT. Neglecting other contributions, the side-force due to roll rate is given by (see Figure 25-2 for dimensions). Units are in 1/rad:

$$C_{Y_p} \approx C_{Y_{p_{VT}}} \approx 2C_{Y_{\beta_{VT}}}\frac{(z_{VT}\cos\alpha - l_{VT_{CG}}\sin\alpha)}{b} \tag{25-18}$$

Where $C_{Y_{\beta VT}}$ is the sidewash contribution by the VT, given by Equation (25-12). See Figure 25-2 for dimensions. Expected range of values is $-0.3 < C_{Y_p} < +0.3$ per radian [9].

(3) Side-Force due to Yaw Rate, C_{Y_r}

When the aircraft yaws, the AOA on its side-silhouette goes through transient variation. This changes the side-force, although most of this is attributed to the VT.

Neglecting other contributions, the side-force due to yaw rate is given by (see Figure 25-2 for dimensions). Units are in 1/rad:

$$C_{Y_r} \approx C_{Y_{r_{VT}}} \approx -2C_{Y_{\beta_{VT}}} \frac{(l_{VT_{CG}} \cos\alpha - z_{VT} \sin\alpha)}{b} \qquad (25\text{-}19)$$

Where $C_{Y_{\beta VT}}$ is the sidewash contribution by the VT, given by Equation (25-12). See Figure 25-2 for dimensions. Expected range of values is $-0.3 < C_{Y_r} < +0.3$ per radian [9].

(4) Side-Force with Aileron Deflection, $C_{Y_{\delta a}}$

The deflection of ailerons may induce pressure difference across the plane-of-symmetry that is manifested as a small increase in side-force. However, it is usually negligible, although it may be nonzero for low *AR*, highly swept wings (e.g., delta wings). Thus

$$C_{Y_{\delta_a}} \approx 0 \qquad (25\text{-}20)$$

(5) Rudder Authority Derivative, $C_{Y_{\delta r}}$

Represents change in side-force with rudder deflection. As such, it is analogous to $C_{L_{\delta_f}}$. Units depend on the lift-curve slope of the VT ($C_{L_{\beta VT}}$ in 1/rad or 1/degree):

$$\begin{aligned} C_{Y_{\delta_r}} &= C_{L_{\beta_{VT}}} \eta_{VT} \frac{S_{VT}}{S} \Delta K_R \tau_R \\ &= C_{L_{\beta_{VT}}} \eta_{VT} \frac{S_{VT}}{S} [K_b(z_2) - K_b(z_1)] \tau_R \end{aligned} \qquad (25\text{-}21)$$

Where τ_R is the *rudder effectiveness factor*. It corresponds to the elevator effectiveness factor [8], and thus can be estimated per Figure 24-21 or Equation (24-86). ΔK_R accounts for the possibility the rudder span is shorter than that of the VT. It depends on the taper of the VT and is calculated using the following set of functions for the parameter K_b (called *span factor*). This applies to all control surfaces, not just the rudder (even though the following expression would imply otherwise). It is given by the following polynomials, digitized by the author, that replicate the graph of Figure 6.1.4.1-15 of Ref. [6]. Dimensions z_1, z_2, and b_{VT} are shown in Figure 25-8:

$$\begin{aligned} K_b(z) &= -0.6766(z/b_{VT})^2 + 1.6984(z/b_{VT}) - 0.0075 \quad \text{for } \lambda_{VT} = 0 \\ K_b(z) &= -0.5199(z/b_{VT})^2 + 1.5511(z/b_{VT}) - 0.012 \quad \text{for } \lambda_{VT} = 0.5 \\ K_b(z) &= -0.396(z/b_{VT})^2 + 1.4216(z/b_{VT}) - 0.0103 \quad \text{for } \lambda_{VT} = 1 \end{aligned} \qquad (25\text{-}22)$$

Typical range of values is $+0.12 < C_{Y_{\delta r}} < +0.24$ per radian [5].

25.3.2 The Yawing Moment Model, C_N

The yawing moment is the third equation of Equations (24-14) and (24-25). It becomes

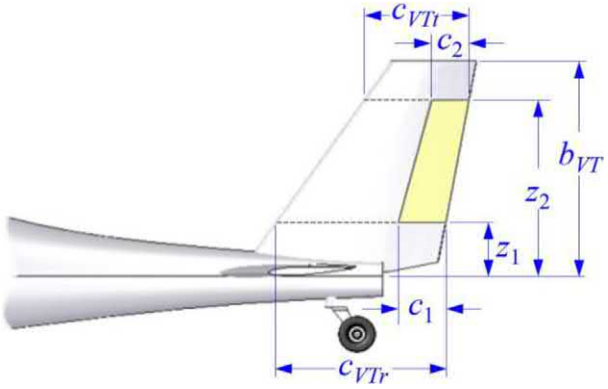


FIGURE 25-8 The definition of VT dimensions.

$$N = 0 \;\Leftrightarrow\; \sum \boldsymbol{N}_{CG} = qSb \cdot \boldsymbol{C}_N = 0 \qquad (25\text{-}23)$$

Where $\boldsymbol{N}_{CG}$ means the moments are summed about the CG. This gives rise to the yawing moment coefficient:

$$\boldsymbol{C}_N = \boldsymbol{C}_{N_0} + \boldsymbol{C}_{N_\beta}\beta + \boldsymbol{C}_{N_p}\left(\frac{\hat{p}b}{2V_\infty}\right) + \boldsymbol{C}_{N_r}\left(\frac{\hat{r}b}{2V_\infty}\right) + \boldsymbol{C}_{N_{\delta_a}}\delta_a + \boldsymbol{C}_{N_{\delta_r}}\delta_r \qquad (25\text{-}24)$$

Where: $\boldsymbol{C}_{N_0}$ = Residual yawing moment coefficient, =0 for symmetric aircraft,

$\boldsymbol{C}_{N_\beta}$ = *Directional stability*,
$\boldsymbol{C}_{N_p}$ = *Yaw-due-to-roll* derivative,
$\boldsymbol{C}_{N_r}$ = *Yaw damping* derivative,
$\boldsymbol{C}_{N_{\delta a}}$ = Yawing moment with aileron deflection, δ_a,
$\boldsymbol{C}_{N_{\delta r}}$ = Yawing moment with rudder deflection, δ_r.

Note: It is the responsibility of the expert to ensure angular consistency. A derivative multiplied by an angle in degrees (or radians) must be represented in terms of *per degrees* (or *per radian*).

(1) Directional Stability, C_{N_β}

The meaning of the term *directional stability* is discussed in Section 25.2.3, *Requirements for Directional Stability*. The three largest contributors to directional stability are the vertical tail, fuselage, and wing. Other contributions are usually minor.

$$\boldsymbol{C}_{N_\beta} = \boldsymbol{C}_{N_{\beta_W}} + \boldsymbol{C}_{N_{\beta_{VT}}} + \boldsymbol{C}_{N_{\beta_{FUS}}} + \boldsymbol{C}_{N_{\beta_{NAC}}} + \boldsymbol{C}_{N_{\beta_{T_Y}}} \qquad (25\text{-}25)$$

Where: $\boldsymbol{C}_{N_{\beta W}}$ = Directional derivative due to the wing, see Equation (25-26),

$\boldsymbol{C}_{N_{\beta VT}}$ = Directional derivative due to the VT, see Equation (25-28),
$\boldsymbol{C}_{N_{\beta FUS}}$ = Directional derivative due to the fuselage, see Equation (25-29) or (25-30),
$\boldsymbol{C}_{N_{\beta NAC}}$ = Directional derivative due to nacelles, see Equation (25-29),

$C_{N_{\beta TY}}$ = Directional derivative due to the propeller side-force, see Equation (25-33) or (25-34).

Typical range of values is $+0.03 < C_{N_\beta} < +0.2$ per radian, where multiengine aircraft are biased toward the higher values.

Yawing Moment due to Wing

The contribution by the wing to the directional stability is usually small. Here, two contributions are combined into one: (1) Yawing moment due to wing sweep and (2) yawing moment due to the vertical position of the wing.

Yawing moment due to wing sweep is only important for forward- or aft-swept wings. Ref. [8] presents the following formula for estimating the contribution by the wing to the directional stability. It has been modified to account for the vertical position of the wing as well.

$$C_{N_{\beta_W}} = \begin{cases} 0.00006k\sqrt{\Lambda_{c/4}} + \Delta_{pos} & \text{per degree} \\ 0.00344k\sqrt{\Lambda_{c/4}} + \Delta_{pos} & \text{per radian} \end{cases} \quad (25\text{-}26)$$

Where $k = -1$ for a forward swept wing (destabilizing) and $k = +1$ for an aft swept one (stabilizing). The term Δ_{pos} accounts for the vertical wing position. As a first estimate, $\Delta_{pos} = 0\,\text{rad}^{-1}$ for low-wing configurations, $\Delta_{pos} = 0.0057\,\text{rad}^{-1}$ for mid-wings, and $\Delta_{pos} = 0.0115\,\text{rad}^{-1}$ for high wings. Divide by 57.3 to convert into degree^{-1} for use with the upper ("per degree") equation.

Vertical Tail Contribution

Yawing moment due to the Vertical Tail (VT) is identical to the restoring moment generated by the tail of a weathervane. This means $C_{N_{\beta VT}} > 0$. The yawing moment coefficient for aircraft involves two reference dimensions associated with the geometry of the airplane: the *wing area* and *span*.

A simple weathervane consists only of the VT itself (see Figure 25-9). The tail arm, l_{VT}, extends from the hinge to the quarter-chord of the MGC of the fin is given by and the lift generated at a yaw angle β, then the yawing moment derivative due to the VT is given by:

$$C_{N_{\beta_{VT}}} \equiv \frac{\partial C_N}{\partial \beta} = l_{VT} C_{L_{\beta_{VT}}} \quad (25\text{-}27)$$

Where $C_{L_{\beta VT}}$ is the lift curve slope of the VT (or fin). It is determined like it is for a wing (using its aspect ratio). The value of $C_{N_{\beta VT}}$ is positive for the setup shown in Figure 25-9. This basic introduction serves as a helpful sanity check for the stability analyst.

An airplane differs from the weathervane in that it also has a wing and fuselage (see Figure 25-10). These, too, contribute to the directional stability. For instance, the fuselage reduces directional stability (it is destabilizing). The wing is stabilizing if swept aft and destabilizing if swept forward (see later). The directional stability derivative due to the VT only is given by:

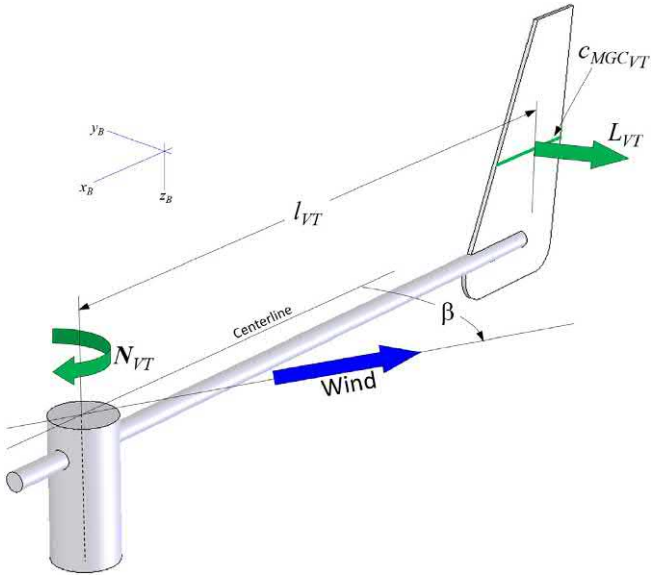


FIGURE 25-9 Aerodynamic force and moment on a weathervane.

$$C_{N_{\beta_{VT}}} \equiv \frac{\partial C_N}{\partial \beta} = \frac{S_{VT} l_{VT_{CG}}}{Sb} C_{L_{\beta_{VT}}} (\beta + \sigma)\eta_{VT} = V_{VT} C_{L_{\beta_{VT}}} (\beta + \sigma)\eta_{VT} \quad (25\text{-}28)$$

Where σ is the sidewash angle. The sidewash is caused when the windward side of the VT approaches the core of the wingtip vortex (see Figure 25-10). That side is subject to increased side-flow, while there is less side-flow on the leeward side. The net result is an increase in the effective yaw angle at the VT. The net result is an increase in the effective yaw angle at the VT. Also, note the ratio of geometric terms in Equation (25-28). It is analogous to the horizontal tail volume (V_{HT}) of Equation (24-74). It is called vertical tail volume and defined as follows:

$$V_{VT} \equiv \frac{S_{VT} \cdot l_{VT_{CG}}}{S \cdot b}$$

Fuselage and Nacelle Contribution

The contribution by the fuselage and nacelles to directional stability is almost always destabilizing. This means $C_{N_{\beta FUS}} < 0$. It is a major contributor to the total directional stability and cannot be neglected. Large and voluminous fuselages require large vertical tail volume. Ref. [8] presents two methods to estimate this destabilizing influence: (a) *Munk's method* and (b) The *North American Aviation method*. The reader may recall Munk's method from Chapter 24, where it is used to estimate the contribution by the fuselage to longitudinal stability. Its use there is more complicated than it is for yaw because of the corrections required by the up- and downwash near the wing. This is absent for yaw. Also, the contribution by nacelles that only extend forward must be analyzed using Munk's method.

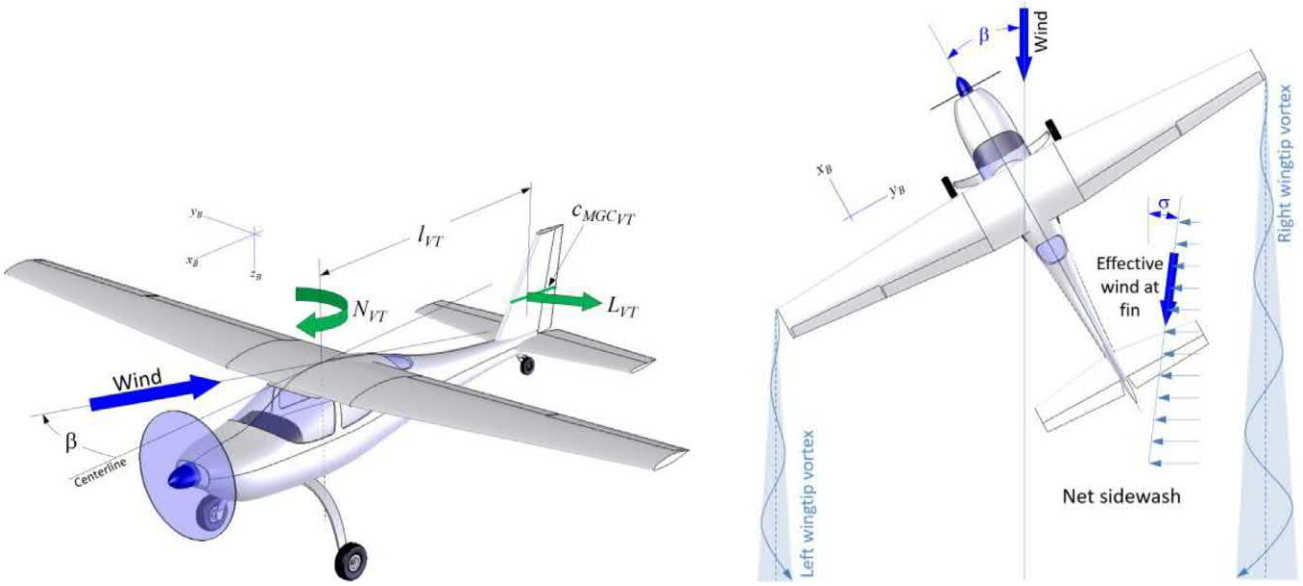


FIGURE 25-10 Parameters affecting the yawing moment on an aircraft due to the VT (left). The origin of the sidewash angle (right).

(a) Fuselage Yawing Moment per Munk's Method

The contribution by the fuselage to the directional stability is presented in the yawing moment coefficient below.

$$C_{N_{\beta_{FUS}}} = \begin{cases} -\dfrac{\pi(k_2-k_1)}{2(57.3)Sb}\displaystyle\int_0^{l_{FUS}} w_f^2 dx & \text{per degree} \\ -\dfrac{\pi(k_2-k_1)}{2Sb}\displaystyle\int_0^{l_{FUS}} w_f^2 dx & \text{per radian} \end{cases} \tag{25-29}$$

Where: k_2-k_1 = Correction factor to account for the fuselage slenderness ratio (see Figure 24-29 and Equation (24-103), repeated below),

w_f = Average width of a fuselage section.

S and b are wing area and span, respectively. The correction factor, k_2-k_1, can be determined from Figure 24-29 or using the following approximation (digitized by the author) to the data. Also, see Example 24.3 for other details.

$$k_2-k_1 = 1-\frac{1}{f}+\left(\frac{0.24f^3-5.6f^2+44f-72}{1000}\right) \tag{24-103}$$

Where: $f = l_{FUS}/d_{FUS}$ = Fuselage fineness ratio

l_{FUS} = Fuselage length
d_{FUS} = Fuselage depth

(b) Fuselage Yawing Moment per the North American Aviation Method

The following formula for estimating the contribution by the fuselage or a nacelle to the directional stability. It is obtained from Ref. [8], where variables are explained in Figure 25-11.

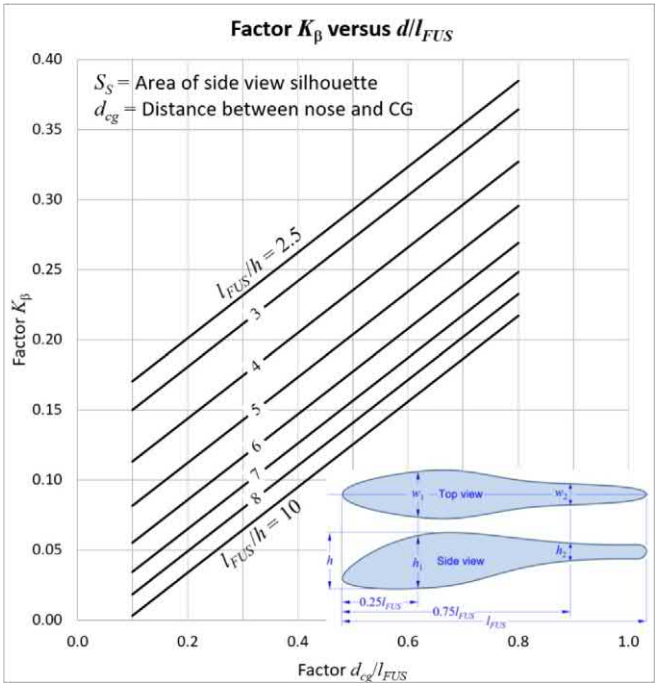


FIGURE 25-11 Fuselage directional stability derivative. *Based on C.H. Zimmerman, An Analysis of Lateral Stability in Power-Off Flight With Charts for Use in Design, NACA-TR-589, November 17, 1936.*

$$C_{N_{\beta_{FUS}}} = \begin{cases} -0.01676K_\beta\left(\dfrac{S_S}{S}\right)\left(\dfrac{l_{FUS}}{b}\right)\left(\dfrac{h_1}{h_2}\right)^{1/2}\left(\dfrac{w_1}{w_2}\right)^{1/3} & \text{per degree} \\ -0.96K_\beta\left(\dfrac{S_S}{S}\right)\left(\dfrac{l_{FUS}}{b}\right)\left(\dfrac{h_1}{h_2}\right)^{1/2}\left(\dfrac{w_1}{w_2}\right)^{1/3} & \text{per radian} \end{cases} \tag{25-30}$$

Where:

$$K_\beta = 0.2927 - 0.05553\left(\frac{l_{FUS}}{h}\right) + 0.002655\left(\frac{l_{FUS}}{h}\right)^2 + 0.3051\left(\frac{d_{cg}}{l_{FUS}} - 0.1\right) \tag{25-31}$$

The function is derived numerically by the author using the curves in Figure 8-4 of Ref. [10]. Figure 25-11 is based on that figure.

Yawing Moment due to Propeller Effects

Section 24.2.11, *Contribution of Thrust—Moment due to Offset Thrustline and Normal Force* introduces the effect of a rotating propeller on longitudinal stability through the *normal force*, T_N. The normal force changes with angle-of-attack and is presented in Equations (24-110) and (24-111). The same phenomenon arises in yaw, where it is called a *propeller side-force* (see Figure 25-12). Let us denote it by T_Y. It *is* the normal force applied sideways. Thus, we estimate it using a similar approach as the normal force. If we know T_Y, its contribution to directional stability can be rewritten as

$$C_{N_{T_Y}} = \left(\frac{x_T \cdot T_Y}{qSb}\right) = C_{N_{\beta_{T_Y}}} \cdot \beta \tag{25-32}$$

Where $C_{N_{\beta TY}}$ is given by a modification to Equation (24-111), whereby $d\beta/d\alpha = 1$, and all variables associated with α are now associated with β. The effect is destabilizing for a tractor propeller ($C_{N_{\beta TY}} < 0$) and stabilizing for a pusher ($C_{N_{\beta TY}} > 0$). Thus, we rewrite Equation (24-111) as follows

$$C_{N_{\beta_{T_Y}}} = N_{ENG}\left(\frac{x_T}{b}\right)\left(\frac{A_P}{S}\right)\frac{dC_{N_B}}{d\beta}f(T) \tag{25-33}$$

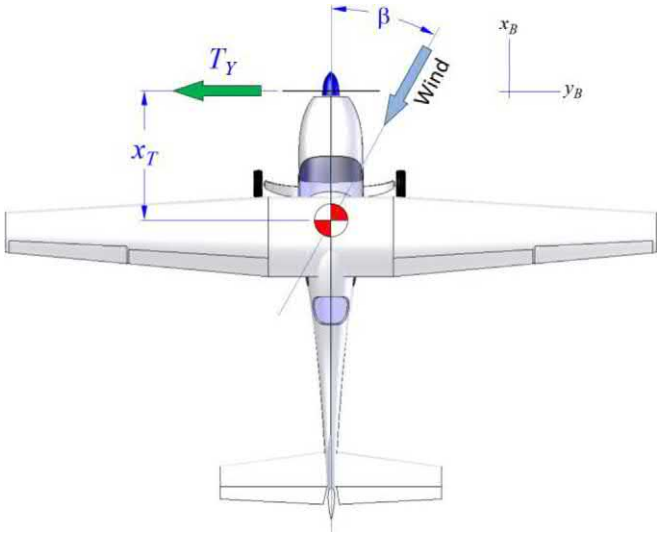


FIGURE 25-12 Generation of propeller side-force.

TABLE 25-2 Typical values for the coefficient K_{T_Y}.

Propeller type	Propeller windmilling		Propeller at full power	
	Per radian	Per degree	Per radian	Per degree
Two-bladed	0.0945	0.00165	0.1418	0.00248
Three-bladed	0.1347	0.00235	0.3034	0.00353
Four-bladed	0.1696	0.00296	0.3816	0.00444
Six-bladed counter-rotating	0.2922	0.00510	0.4383	0.00765

Where $dC_{N_B}/d\beta$ is given by Equation (24-114) or (24-115) (as $dC_{N_B}/d\alpha$) and $f(T)$ by Equation (24-116). N_{ENG} is the number of engines and A_P is the propeller disc area. Ref. [8] expresses $C_{N_{\beta TY}}$ in the following form, which has been adapted to the format in this book.

$$C_{N_{\beta_{T_Y}}} = N_{ENG}\frac{\pi D_P^2}{4S}\frac{x_T}{b}K_{T_Y} \tag{25-34}$$

Where D_P is the propeller diameter and K_{T_Y} is a constant that depends on the number of propeller blades. It is given in Table 25-2.

DERIVATION OF EQUATION (25-27)

$$C_{N_{VT}} = \frac{N_{VT}}{qSb} = \frac{L_{VT}l_{VT_{CG}}}{qSb} = \frac{\left(qSC_{L_{\beta_{VT}}} \cdot \beta\right)l_{VT_{CG}}}{qSb} = \frac{l_{VT_{CG}}}{b}\left(C_{L_{\beta_{VT}}} \cdot \beta\right)$$

$$\Rightarrow \quad C_{N_{\beta_{VT}}} \equiv \frac{\partial C_{N_{VT}}}{\partial \beta} = \frac{l_{VT_{CG}}}{b}C_{L_{\beta_{VT}}}$$

DERIVATION OF EQUATION (25-28)

$$C_{N_{VT}} = \frac{N_{VT}}{qSb} = \frac{L_{VT}l_{VT_{CG}}}{qSb} = \frac{\left(qSC_{L_{\beta_{VT}}}(\beta+\sigma)\eta_{VT}\right)l_{VT_{CG}}}{qSb}$$

$$= \frac{l_{VT_{CG}}}{b}\left(C_{L_{\beta_{VT}}}(\beta+\sigma)\eta_{VT}\right) \Rightarrow \quad C_{N_{\beta_{VT}}} \equiv \frac{\partial C_{N_{VT}}}{\partial \beta}$$

$$= \frac{l_{VT_{CG}}}{b}C_{L_{\beta_{VT}}}(\beta+\sigma)\eta_{VT}$$

(2) Yaw-due-to-Roll Derivative, C_{N_p}

This derivative is one of several that couples yaw with roll. It is primarily attributed to the wing and vertical tail.

$$C_{N_p} \cong C_{N_{p_W}} + C_{N_{p_{VT}}} \tag{25-35}$$

Typical range of values is $-0.01 < C_{N_p} < -0.10$ per radian [5].

Wing Contribution

Ref. [8] gives the following expression for the contribution by the wing

$$C_{N_{p_W}} = -C_L/8 \quad \text{Per radian} \tag{25-36}$$

Ref. [11] presents a graph whose results were fit by the following line in Ref. [5]. It is based on a wing of $AR = 5.16$, $\lambda = 1$, and $\Lambda_{LE} = 0°$ over the range $0 < C_L < 1.05$.

$$C_{N_{p_W}} = -0.043C_L - 0.0044 \quad \text{Per radian} \tag{25-37}$$

The two above relations do not reflect that the sign tends to reverse at high AOA and low AOA for highly aft swept wings [5]. The following expression that accounts for wing sweep is presented in Ref. [7]:

$$C_{N_{p_W}} = C_L \frac{AR+4}{AR+4\cos\Lambda_{LE}}\left[1+6\left(1+\frac{\cos\Lambda_{LE}}{AR}\right)\right.$$
$$\left.\times\left(\frac{\bar{x}}{c_{MGC}}\frac{\tan\Lambda_{LE}}{AR}+\frac{\tan^2\Lambda_{LE}}{12}\right)\right]\left(\frac{C_{N_p}}{C_L}\right)_{\Lambda_{LE}=0} \tag{25-38}$$

Where $\bar{x}$ is the longitudinal distance from the airplane's CG to the wing's aerodynamic center [11]. It can be approximated as the quarter-chord of the MGC. The term $(C_{N_p}/C_L)_{\Lambda_{LE}=0}$ is obtained by the curve in Figure 25 in Ref. [7], which was digitized by the author.

$$\left(\frac{C_{N_p}}{C_L}\right)_{\Lambda_{LE}=0} = 0.0002595AR^2 - 0.009192AR - 0.004912 \tag{25-39}$$

Contribution by the Vertical Tail

Ref. [12] presents the following approximation for the contribution by the VT.

$$C_{N_{p_{VT}}} \cong -2C_{Y_{\beta_{VT}}}\frac{1}{b^2}(l_{VT_{CG}}\cos\alpha + z_{VT}\sin\alpha)$$
$$\times(z_{VT}\cos\alpha - l_{VT_{CG}}\sin\alpha - z_{VT}) \tag{25-40}$$

Where b is the wing span and $C_{Y_{\beta_{VT}}}$ is the sidewash contribution by the VT, given by Equation (25-12). See Figure 25-2 for dimensions.

(3) Yaw Damping Derivative, C_{N_r}

When the airplane yaws, a restoring moment is generated. This is *yaw damping*. It is analogous to pitch damping, discussed in Section 24.2.5(4). It is primarily attributed to the wing and vertical tail.

$$C_{N_r} \cong C_{N_{r_W}} + C_{N_{r_{VT}}} \tag{25-41}$$

Typical range of values is $-0.05 < C_{N_r} < -0.14$ per radian [5].

Contribution by the Wing

Ref. [12] gives the following expression for the contribution by the wing

$$C_{N_{r_W}} = \left(\frac{C_{N_r}}{C_L^2}\right)C_L^2 \tag{25-42}$$

Where the ratio (C_{N_r}/C_L^2) is given by Figure 13 in Ref. [7]. Ref. [5] gives the following expression, which is based on work in Ref. [13]:

$$C_{N_{r_W}} = -0.33\left(\frac{1+3\lambda}{2+2\lambda}\right)C_{D_{\min}} - 0.024\left(1-\frac{AR-6}{13}-\frac{1-\lambda}{2.5}\right)C_L^2 \tag{25-43}$$

Contribution by the Vertical Tail

Ref. [14] gives the following expression for the contribution by the VT.

$$C_{N_{r_{VT}}} = 2\left(\frac{l_{VT_{CG}}}{b}\right)^2 C_{Y_{\beta_{VT}}} \tag{25-44}$$

Where $C_{Y_{\beta_{VT}}}$ is the sidewash contribution by the VT, given by Equation (25-12). See Figure 25-2 for dimensions. Ref. [15] gives the following expression.

$$C_{N_{r_{VT}}} = -2\frac{S_{VT}}{S}\left(\frac{l_{VT_{CG}}}{b}\right)^2 \eta_{VT} C_{L_{\beta_{VT}}} \tag{25-45}$$

Where S and S_{VT} are the wing and VT areas, respectively and η_{VT} is the VT effectiveness, which is analogous to η_{HT} for the HT. Note that $C_{L_{\beta_{VT}}}$ is to the vertical tail what C_{L_α} is to the wing. Finally, Ref. [13] gives

$$C_{N_{r_{VT}}} = -2\left(\frac{l_{VT_{CG}}}{b}\right)C_{L_{\beta_{VT}}} \tag{25-46}$$

(4) Yawing Moment with Aileron Deflection, $C_{N_{\delta a}}$

Deflecting ailerons distorts the flow field around the airplane, introducing asymmetry. This, in turn, changes the pressure distribution over the aircraft, generating a yawing moment (in addition to rolling moment). Ref. [6] presents the following expression to account for this effect.

$$C_{N_{\delta_a}} = 2KC_L C_{L_{\delta_a}} \tag{25-47}$$

Where C_L is the lift coefficient at zero aileron deflection and $C_{L_{\delta_a}}$ is the *rolling moment coefficient due to aileron deflection* (see Section 25.5). It is in units of per radian for Equation (25-47). The constant K is a correlation coefficient given by Figure 6.2.2.1-9 in Ref. [6]. The method assumes the ailerons extends from the wingtip to a spanwise station denoted by η. The author has digitized the curves of the figure in the following expression

$$K = A_1\eta^3 + A_2\eta^2 + A_3\eta + A_4 \tag{25-48}$$

TABLE 25-3 Coefficients for Equation (25-48).

	λ = 0.25				λ = 0.50				λ = 0.75				λ = 1.00			
	A_1	A_2	A_3	A_4	A_1	A_2	A_3	A_4	A_1	A_2	A_3	A_4	A_1	A_2	A_3	A_4
AR = 3	-0.081435	-0.017512	0.048749	-0.285211	-0.05611	0.004418	0.012606	-0.338655	-0.32955	0.20571	-0.03425	-0.32616	0	0	0	-0.3572
AR = 4	0.010063	-0.086097	0.072400	-0.232663	-0.02645	-0.02499	0.010231	-0.24925	-0.02272	-0.09021	0.02881	-0.26101	0.040875	-0.115908	-0.001942	-0.261436
AR = 6	-0.14396	0.08157	0.02679	-0.15937	-0.09994	0.02209	0.005763	-0.17012	-0.04837	-0.04577	0.01179	-0.17973	-0.11112	0.044045	-0.04867	-0.18136
AR = 8	-0.22975	0.18915	-0.00832	-0.12004	-0.15677	0.10194	-0.01469	-0.13018	-0.02047	-0.08124	0.02315	-0.13834	-0.10085	0.02521	-0.0298	-0.14398

Where η is the inboard spanwise station of the aileron, given by $\eta = 2y/b$. The coefficients A_1 through A_4 depend on taper ratio (λ) and aspect ratio (AR) and are given in Table 25-3. The moment coefficient due to this contribution is thus

$$C_N = 2KC_L C_{L_{\delta_a}} \frac{\delta_{a_{LFT}} - \delta_{a_{RGT}}}{2} \tag{25-49}$$

Where $\delta_{a_{LFT}}$ and $\delta_{a_{RGT}}$ are the left and right aileron deflections (in radians). Their value is positive when the aileron is deflected TED.

Typical range of values is $-0.004 < C_{N_{\delta a}} < -0.09$ per radian [5].

(5) Yawing Moment with Rudder Deflection, $C_{N_{\delta r}}$

A large yawing moment is generated by deflecting the rudder. This contribution is given by the following expression

$$\begin{aligned} C_{N_{\delta_r}} &= -\eta_{VT} C_{L_{\beta_{VT}}} \frac{S_{VT}}{S} \frac{l_{VT_{CG}}}{b} \Delta K_R \tau_R \\ &= -\eta_{VT} C_{L_{\beta_{VT}}} \frac{S_{VT}}{S} \frac{l_{VT_{CG}}}{b} [K_b(z_2) - K_b(z_1)] \tau_R \end{aligned} \tag{25-50}$$

See Figure 25-2 and Figure 25-8 for dimensions. Note that $C_{L_{\beta VT}}$ is to the vertical tail what C_{L_α} is to the wing. ΔK_R accounts for the possibility the rudder span is shorter than that of the VT. It depends on the taper of the VT and is calculated using the function set K_b (span factor) of Equation (25-22). The term τ_R is the *rudder effectiveness factor*, which corresponds to the elevator effectiveness factor [8]. Thus, it can be calculated using Figure 24-21 or Equation (24-86). See more details associated with Equation (25-21) and Figure 25-8. Typical value of $C_{N_{\delta r}} \approx -0.06$ per radian, but varies markedly between aircraft configurations [5].

25.4 LATERAL STABILITY AND CONTROL

This section focuses on aircraft lateral stability per the second expression of Equation (25-4). An introduction to lateral stability is given in Section 25.2.4, *Requirements for Lateral Stability*. Also, be advised of the difference between *lift* and *lift coefficient* (denoted by L and C_L, respectively) and *rolling moment* and *rolling moment coefficient* (denoted by $\boldsymbol{L}$ and $\boldsymbol{C_L}$, respectively).



FIGURE 25-13 Definition of dihedral angle.

25.4.1 Important Contributions to Rolling Moment

Wing dihedral is one of the most important contributors to rolling moment (see Figure 25-13). The contribution is called *dihedral effect*. The dihedral angle, denoted by Γ, is positive when the vertical position of the wingtip is above the root. Otherwise, it is called *anhedral* angle.

Figure 25-14 shows an airplane banking with associated yaw (sideslip). As stated in Section 25.2.4, the leading wing generates higher lift than the trailing one. The difference in loading creates a rolling moment that tends to level the wing. Simultaneously, directional stability tends to neutralize the yaw angle, as illustrated in segments ① through ④ in Figure 25-14. These tendencies comprise our design goal.

Wing sweep is another important contributor to dihedral effect. Figure 25-15 shows an aircraft with an aft swept wing at $\beta = 0$ (left) and $\beta \neq 0$ (right). It shows that the yaw (here with nose pointing left) increases the effective span of the right wing by amount Δb_R and reduces its sweep angle by amount β. Simultaneously, the span of the left wing is reduced by amount Δb_L, while its sweep angle increases. This improves the lift generation of the right wing and reduces that of the left wing. The asymmetric lift generates the rolling moment. The greater the sweep, the greater the moment. These and other contributions to the rolling moment will now be presented.

25.4.2 The Rolling Moment Model, C_L

The rolling moment is the first equation of Equations (24-14) and (24-24). It becomes

$$\boldsymbol{L} = 0 \;\Leftrightarrow\; \sum \boldsymbol{L}_{CG} = qSb \cdot \boldsymbol{C_L} = 0 \tag{25-51}$$

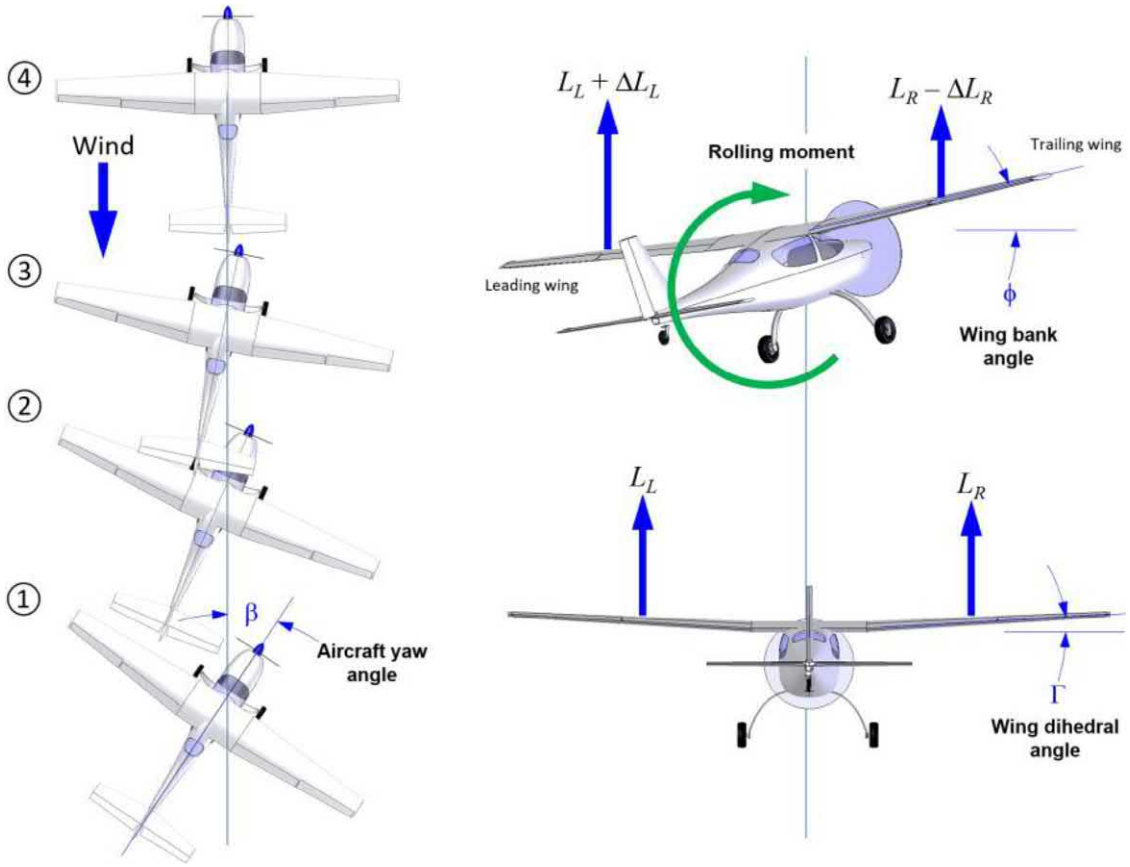


FIGURE 25-14 Rolling moment due to wing dihedral angle explained.

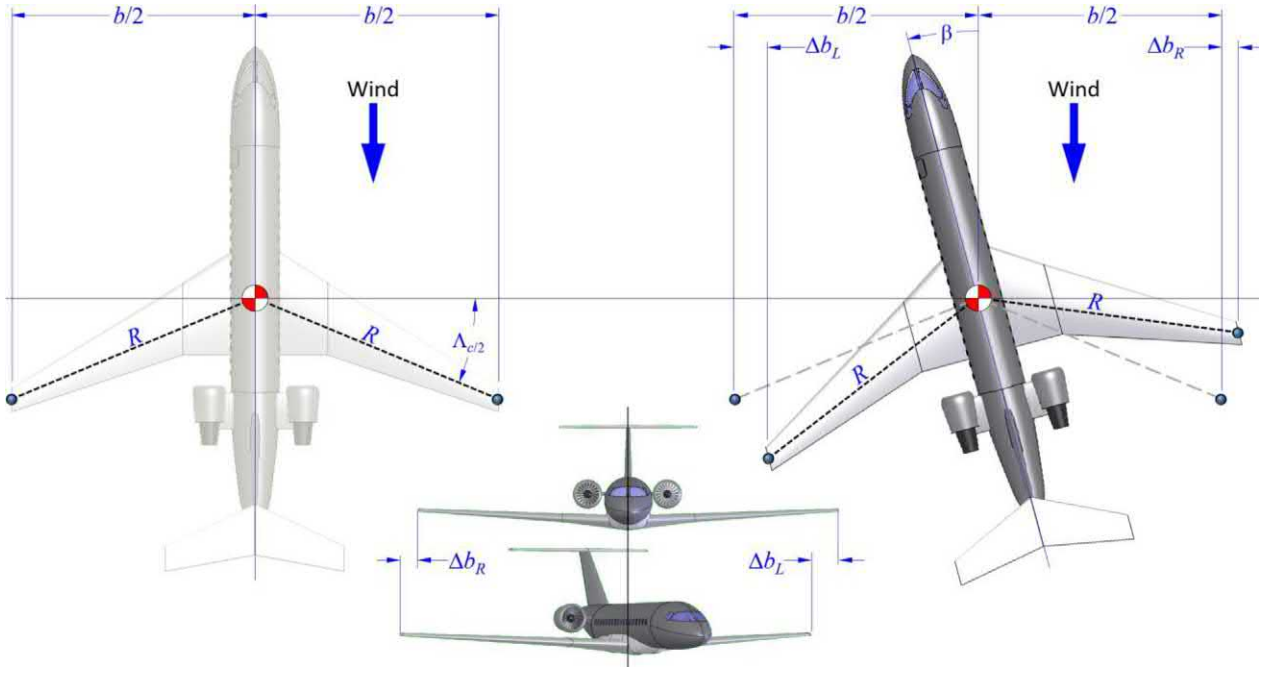


FIGURE 25-15 Rolling moment due to wing sweep explained.

Where $\boldsymbol{L_{CG}}$ means the moments are summed about the CG. This gives rise to the rolling moment coefficient:

$$C_L = C_{L_0} + C_{L_\beta}\beta + C_{L_p}\left(\frac{\hat{p}b}{2V_\infty}\right) + C_{L_r}\left(\frac{\hat{r}b}{2V_\infty}\right) + C_{L_{\delta_a}}\delta_a + C_{L_{\delta_r}}\delta_r \tag{25-52}$$

Where: C_{L_0} = Residual rolling moment coefficient, = 0 for symmetric aircraft,

C_{L_β} = *Dihedral effect*,
C_{L_p} = *Roll damping derivative*,
C_{L_r} = *Roll-due-to-yaw* derivative,
$C_{L_{\delta_a}}$ = *Aileron authority* derivative (rolling moment with aileron deflection, δ_a),
$C_{L_{\delta r}}$ = Rolling moment with rudder deflection, δ_r.

Note: It is the responsibility of the expert to ensure angular consistency. A derivative multiplied by an angle in degrees (or radians) must be represented in terms of *per degrees* (or *per radian*).

(1) Dihedral Effect, C_{L_β}

Like directional stability, C_{L_β} is a very important derivative. It provides roll stability and strongly affects two dynamic lateral-directional modes: *Spiral convergence* and *Dutch roll*. Unfortunately, their ideal value conflicts. To improve spiral convergence, a large negative value is desirable. However, a small negative value improves Dutch roll damping. Ref. [16] presents experimental evaluation of effect of dihedral on lateral stability. It states that the best flight characteristics are obtained for low effective dihedral angle of approximately 2°. In the opinion of this author, this would be ill-advisable as it would make it hard to also raise the wing using rudder control per the "old" 14 CFR §23.177 *Static directional and lateral stability*. Ref. [16] also states that in order to provide good lateral control using the rudder alone, a dihedral in excess of 10° is needed. This implies that to meet both, a dihedral angle between 2 and 10° is a compromise. This notion is supported by historical data (e.g., see Table 9-6). Low-wing aircraft typically feature dihedral between 5 and 7°. Even many high-wing aircraft feature a small dihedral.

The dihedral effect is the linear combination of contributions by wing sweep, aspect- and taper-ratio, dihedral, and other geometric features of the aircraft [8]. It can be represented as shown below:

$$C_{L_\beta} = \overbrace{\left[C_{L_{\beta_{\Lambda_{c/2}}}} + C_{L_{\beta_{AR}}} + C_{L_{\beta_{\Gamma_W}}} + C_{L_{\beta_{z_W}}} + C_{L_{\beta_{TIP}}}\right]}^{C_{L_{\beta_W}} \equiv \text{Contribution by the wing}} + C_{L_{\beta_{HT}}} + C_{L_{\beta_{VT}}} \tag{25-53}$$

Where: $C_{L_{\beta\Lambda c/2}}$ = Dihedral effect by wing sweep,
$C_{L_{\beta_{AR}}}$ = Dihedral effect by AR and λ,
$C_{L_{\beta_{\Gamma W}}}$ = Dihedral effect by wing dihedral,
$C_{L_{\beta_{zW}}}$ = Dihedral effect by wing height on fuselage,
$C_{L_{\beta_{TIP}}}$ = Dihedral effect by wing tip,
$C_{L_{\beta_W}}$ = Dihedral effect by the complete wing,
$C_{L_{\beta_{HT}}}$ = Dihedral effect by HT,
$C_{L_{\beta_{VT}}}$ = Dihedral effect by VT.

Contribution by the Wing

The contribution by the wing can be estimated by more than one method. Here, two methods are presented: Per Refs. [6, 8].

(a) Method per Ref. [6]

Ref. [6] presents the following expression to estimate the contribution of the wing to the lateral stability.

$$C_{L_{\beta_W}} = C_L\left[\left(\frac{C_{L_\beta}}{C_L}\right)_{\Lambda_{c/2}} K_{M_\Lambda} + \left(\frac{C_{L_\beta}}{C_L}\right)_{AR}\right] + \Gamma\left(\frac{C_{L_\beta}}{\Gamma}K_{M_\Gamma}\right) + \phi\tan\Lambda_{\Lambda_{c/4}}\left(\frac{\Delta C_{L_\beta}}{\phi\tan\Lambda_{\Lambda_{c/4}}}\right) \tag{25-54}$$

Where C_L is the lift coefficient at condition and Γ is the dihedral angle. Other terms are explained below. The units for C_{L_β} in the above expression are in per degree. To convert to per radian, multiply by 57.3. Typical range of values is $-0.03 < C_{L_\beta} < -0.12$ per radian [5].

The first term inside the bracket is the wing-sweep contribution. It is a gradient for C_L. It is estimated using Figure 5.1.2.1-27 in Ref. [6]. The author has derived the following polynomial curve fits to most of those curves. The curves are presented based on the mid-chord sweep angle, $\Lambda_{c/2}$, and are valid for $0 \le \lambda \le 1$. The following polynomial is valid for $\lambda = 0$ between $4 \le AR \le 8$. It serves to permit interpolations for $0 \le \lambda \le 0.5$. Units are 1/degree.

$$\left(\frac{C_{L_\beta}}{C_L}\right)_{\Lambda_{c/2}} = -2.3473\times10^{-8}\Lambda_{c/2}^3 + 5.9269\times10^{-7}\Lambda_{c/2}^2 - 6.975\times10^{-5}\Lambda_{c/2} - 1.0468\times10^{-4} \tag{25-55}$$

Where C_L is the lift coefficient at condition and $\Lambda_{c/2}$ is the mid-chord sweep angle. The following polynomials are valid for $\lambda = 0.5$ and $AR = 4$ and $AR = 8$.

$$\left(\frac{C_{L_\beta}}{C_L}\right)_{\Lambda_{c/2}} = -2.1573\times10^{-8}\Lambda_{c/2}^3 + 4.0183\times10^{-7}\Lambda_{c/2}^2 - 6.6738\times10^{-5}\Lambda_{c/2} - 7.7413\times10^{-5} \quad \text{for } AR = 4$$

$$\left(\frac{C_{L_\beta}}{C_L}\right)_{\Lambda_{c/2}} = -2.8639\times10^{-8}\Lambda_{c/2}^3 + 5.7675\times10^{-7}\Lambda_{c/2}^2 - 7.4987\times10^{-5}\Lambda_{c/2} - 8.2421\times10^{-5} \quad \text{for } AR = 8 \tag{25-56}$$

The following polynomials are valid for $\lambda = 1$ and $AR = 4$ and $AR = 8$.

$$\left(\frac{C_{L_\beta}}{C_L}\right)_{\Lambda_{c/2}} = -2.1884\times10^{-8}\Lambda_{c/2}^3 + 3.7973\times10^{-7}\Lambda_{c/2}^2 - 6.7664\times10^{-5}\Lambda_{c/2} - 7.6132\times10^{-4} \quad \text{for } AR=4$$
$$\left(\frac{C_{L_\beta}}{C_L}\right)_{\Lambda_{c/2}} = -3.5863\times10^{-8}\Lambda_{c/2}^3 + 7.2655\times10^{-7}\Lambda_{c/2}^2 - 7.6262\times10^{-5}\Lambda_{c/2} - 1.4569\times10^{-4} \quad \text{for } AR=8 \tag{25-57}$$

The previously mentioned contributions are corrected for compressibility using the following polynomial curve fits that were digitized by the author for Figure 5.1.2.1-28a in Ref. [6]. The parameter K_{M_Λ} is dimensionless and $x \equiv M_\infty \cos\Lambda_{c/2}$.

$$K_{M_\Lambda} = 1.0573 - 0.4241x + 1.0453x^2 - 0.5680x^3 \quad \text{for } \frac{AR}{\cos\Lambda_{c/2}} = 4$$
$$K_{M_\Lambda} = 1.0013 - 0.1204x + 0.5429x^2 \quad \text{for } \frac{AR}{\cos\Lambda_{c/2}} = 6$$
$$K_{M_\Lambda} = 0.7766 + 1.3372x - 2.3077x^2 + 2.0271x^3 \quad \text{for } \frac{AR}{\cos\Lambda_{c/2}} = 8$$
$$K_{M_\Lambda} = 1.0407 - 0.7448x + 4.3662x^2 - 7.3356x^3 + 5.0454x^4 \quad \text{for } \frac{AR}{\cos\Lambda_{c/2}} = 10 \tag{25-58}$$

Contributions by aspect and taper ratios can be obtained using the curves of Figure 5.1.2.1-28b in Ref. [6]. These curves, too, have been digitized by the author and are given below. Units are 1/degree.

$$\left(\frac{C_{L_\beta}}{C_L}\right)_{AR} = -\frac{0.01}{AR} + \frac{0.0039}{AR^{0.45}} \quad \text{if } \lambda = 0$$
$$\left(\frac{C_{L_\beta}}{C_L}\right)_{AR} = -\frac{0.009804}{AR} + \frac{0.001}{AR^{0.005}} \quad \text{if } \lambda = 0.5$$
$$\left(\frac{C_{L_\beta}}{C_L}\right)_{AR} = -\frac{0.01299}{AR^{1.24}} - \frac{0.0014}{AR^2} \quad \text{if } \lambda = 1 \tag{25-59}$$

Contributions by the wing dihedral can be obtained using the curves of Figure 5.1.2.1-29 in Ref. [6]. These curves have been digitized by the author and are given below. The following polynomial is valid for $\lambda = 0$ for $AR \le 8$. Units are 1/degree^2.

$$\frac{C_{L_\beta}}{\Gamma} = \left(-7.422 - 42.50AR + 2.539AR^2\right)\times10^{-6} \quad \text{if } \Lambda_{c/2} = 0°$$
$$\frac{C_{L_\beta}}{\Gamma} = \left(-8.366 - 40.96AR + 2.643AR^2\right)\times10^{-6} \quad \text{if } \Lambda_{c/2} = \pm40° \tag{25-60}$$

The following polynomial is valid for $\lambda = 0.5$ for $AR \le 8$.

$$\frac{C_{L_\beta}}{\Gamma} = \left(-2.786 - 50.46AR + 2.653AR^2\right)\times10^{-6} \quad \text{if } \Lambda_{c/2} = 0°$$
$$\frac{C_{L_\beta}}{\Gamma} = \left(-2.706 - 47.47AR + 4.618AR^2\right)\times10^{-6} \quad \text{if } \Lambda_{c/2} = \pm40° \tag{25-61}$$

The following polynomial is valid for $\lambda = 1.0$ for $AR \le 8$.

$$\frac{C_{L_\beta}}{\Gamma} = \left(-2.012 - 51.41AR + 2.569AR^2\right)\times10^{-6} \quad \text{if } \Lambda_{c/2} = 0°$$
$$\frac{C_{L_\beta}}{\Gamma} = \left(-2.682 - 49.82AR + 2.793AR^2\right)\times10^{-6} \quad \text{if } \Lambda_{c/2} = \pm40° \tag{25-62}$$

The previously mentioned contributions must be corrected for compressibility. This is accomplished using Figure 5.1.2.1-30a in Ref. [6]. The author has digitized the curves in the figure, yielding the following expression. The parameter K_{M_Γ} is dimensionless and $x \equiv M_\infty \cos\Lambda_{c/2}$.

$$K_{M_\Gamma} = 1 + \left(-0.1969x + 1.6231x^2 - 2.8513x^3 + 2.1992x^4\right) \times (0.1193\ AR - 0.1961) \tag{25-63}$$

The last term in Equation (25-54) corrects for wing washout. Wing twist is denoted by θ in Ref. [6], but ϕ in this book. It is negative for washout and positive for washin (see Section 9.3.5, *Wing Twist—Washout and Washin*). In interest of clarity, define the parameter A as follows

$$A \equiv \frac{\Delta C_{L_\beta}}{\phi \tan\Lambda_{\Lambda_{c/4}}}$$

The value of this parameter is is obtained based on AR using Figure 5.1.2.1-30b in Ref. [6]. Those curves have been digitized by the author and are presented below. They are valid for $M_\infty \ge 0.1$:

$$A_{\lambda=0} = (-0.00221865AR^6 + 0.0923573AR^5 - 1.53349AR^4 + 12.8264AR^3 - 56.0907AR^2 + 118.452AR - 112.262) \times 10^{-6}$$
$$A_{\lambda=0.4} = (0.00220558AR^4 - 0.213208AR^3 + 3.93453AR^2 - 26.7907AR + 28.6223) \times 10^{-6}$$
$$A_{0.6\le\lambda\le1} = (-0.00405554AR^4 - 0.0382416AR^3 + 2.16404AR^2 - 19.4860AR + 17.0698) \times 10^{-6} \quad (25\text{-}64)$$

(b) Method per Ref. [8]

Ref. [8] presents the following expression to determine the dihedral effect due to the wing. The method assumes the wing contribution is relatively linear with Γ. Note that Ref. [8] reverses the signs for both C_{N_β} and C_{L_β}. This is accounted for in the following expressions.

$$C_{L_{\beta_W}} = C_{L_{\beta_{W_{\Gamma=0}}}} + C_{L_{\beta_{z_W}}} + C_{L_{\beta_{TIP}}} + \frac{C_{L_\beta}}{\Gamma}\Gamma \quad (25\text{-}65)$$

To estimate $C_{L_{\beta W}}$ for cranked wings, such as that of the Vought F4U Corsair and FMA IA-58 Pucará, use the method of Ref. [17]. The contribution of the vertical wing position on fuselage, $C_{L_{\beta z W}}$, is shown in Figure 25-16. The contribution of the wingtip shape, $C_{L_{\beta TIP}}$, is shown in Figure 25-17. Ref. [18] presents the following expressions for the *inherent dihedral effect*, e.g., for a zero-dihedral angle, $C_{L_{\beta WT=0}}$. For an elliptical wing with an unswept mid-chord, this effect is given by

$$C_{L_{\beta_{W_{\Gamma=0^\circ}}}} = C_L\left[-\frac{16}{3\pi^2 AR} + 0.05\right] \quad \text{per radian} \quad (25\text{-}66)$$

Ref. [18] also gives the following equation for straight wings of specific taper ratio (λ).

$$C_{L_{\beta_{W_{\Gamma=0^\circ}}}} = C_L\left[-\left(\frac{\kappa}{AR}\right)\frac{0.71\lambda + 0.29}{1+\lambda} + 0.05\right] \quad \text{per radian} \quad (25\text{-}67)$$

Where κ = 1 for straight wingtips and κ = 1.5 for rounded wingtips. Ref. [8] uses $C_{L_\beta}/C_L = -0.0002$ per degree, but this value is independent of *AR* and λ. The reader can use Equations (25-60) through (25-62), and Equation (25-63) to calculate C_{L_β}/C_L in lieu of this constant value.

Contribution by HT, $C_{L_{\beta HT}}$

The contribution of the HT is estimated the same way as that of the wing.

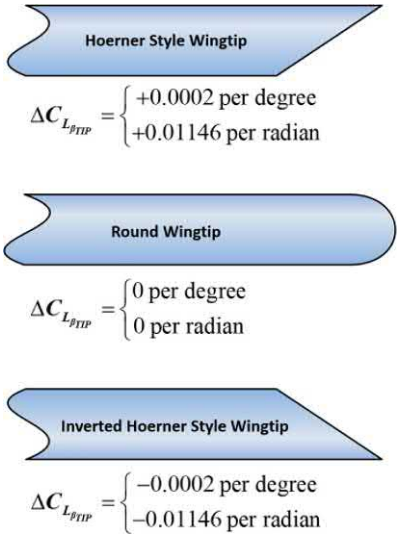
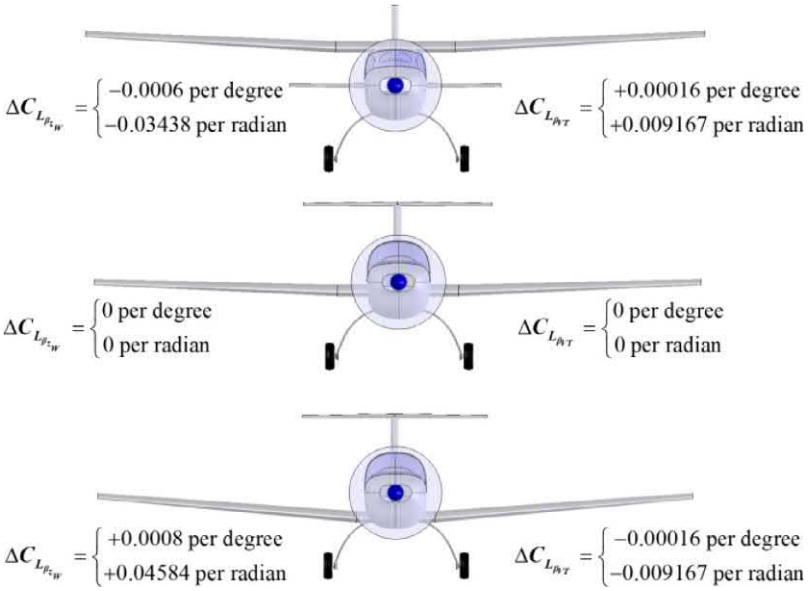


FIGURE 25-17 Rolling moment due to wingtip style. *Based on C.D. Perkins, R.E. Hage, Airplane Performance, Stability, and Control, John Wiley & Sons, 1949.*

FIGURE 25-16 Rolling moment due to wing position on the fuselage and vertical tail. *Based on C.D. Perkins, R. E. Hage, Airplane Performance, Stability, and Control, John Wiley & Sons, 1949.*



Contribution by HT, $C_{L_{\beta VT}}$

The contribution of the vertical tail is estimated per the following expression

$$\begin{aligned} C_{L_{\beta_{VT}}} &= -\eta_{VT} C_{L_{\beta_{VT}}} \frac{S_{VT}}{S}\frac{z_{VT}}{b} + \Delta C_{L_{\beta_{VT}}} \\ &= -C_{N_{\beta_{VT}}} \frac{z_{VT}}{l_{VT_{CG}}} + \Delta C_{L_{\beta_{VT}}} \end{aligned} \tag{25-68}$$

See Figure 25-2 for dimensions. $\Delta C_{L_{\beta VT}}$ represents interference effects by wing on VT. It is obtained from Figure 25-16. Note that $C_{L_{\beta VT}}$ is to the vertical tail what C_{L_α} is to the wing.

(2) Roll Damping Derivative, C_{L_p}

When an aircraft rolls, its wing is subject to linear change in local AOA along the span (see Figure 25-18). This loads the wing asymmetrically and generates a moment that resists the roll. This moment is called *roll damping*. It depends on roll rate, $\hat{p}$ (in degrees/s or rad/s). The derivative is evaluated with respect to the ratio ($\hat{p}b/2V_\infty$), where b is wingspan, and V_∞ is far-field airspeed. The product $\hat{p}b/2$ is the rotation speed of the wingtip; divided by V_∞ it represents the helix angle (in radians) formed by the motion.

If S and b are the reference wing area and span, $c(y)$ is the wing chord as a function of the spanwise station y, and q is the dynamic pressure, the rolling moment is given by:

$$L_{\hat{p}} = \frac{2q\hat{p}(C_{l_\alpha} + C_{d_{\min}})}{V_\infty}\int_0^{b/2} y^2 c(y)dy \tag{25-69}$$

Where C_{l_α} and $C_{d_{\min}}$ are the representative airfoil lift-curve slope and minimum drag coefficient (e.g., obtained using the law-of-effectiveness) and q is the dynamic pressure. Divide by qSb to get the rolling moment coefficient due to roll damping in terms of $\hat{p}b/2V_\infty$ is calculated as shown below:

$$C_L = \frac{L_{\hat{p}}}{qSb} = -\left(\frac{\hat{p}b}{2V_\infty}\right)\frac{4(C_{l_\alpha} + C_{d_{\min}})}{Sb^2}\int_0^{b/2} y^2 c(y)dy \tag{25-70}$$

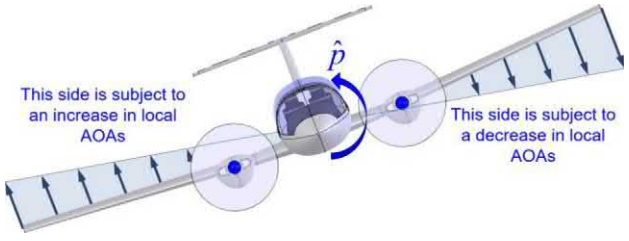


FIGURE 25-18 Arrows show change in airspeed due to roll to the right. This increases the AOA on the right wing (which is to the left in the figure) and decreases it on the left one.

The change in rolling moment coefficient due to roll rate $\hat{p}$ is called the *roll damping coefficient* and can be found from:

$$C_{L_p} = -\frac{4(C_{l_\alpha} + C_{d_{\min}})}{Sb^2}\int_0^{b/2} y^2 c(y)dy \tag{25-71}$$

Units are per radian (since C_{l_α} must be in per radian). Typical range of values is $-0.25 < C_{L_p} < -0.80$ per radian. The closed form solution for two common wing planforms is given below.

Let us simplify the solution of Equation (25-71) for two special but common wing planform shapes.

Case 1: Straight Tapered Wing with Taper Ratio λ:

$$C_{L_p} = -\frac{(C_{l_\alpha} + C_{d_{\min}})\cdot c_r b}{24S}[1 + 3\lambda] \tag{25-72}$$

Case 2: Rectangular Wing ($\lambda = 1$):

$$C_{L_p} = -\frac{C_{l_\alpha} + C_{d_{\min}}}{6} \tag{25-73}$$

Note that the airfoil's lift curve slope is the predominant factor in Equation (25-73) as its magnitude is generally much larger than that of the drag coefficient. Consider Figure 9-57, which shows how the lift curve changes as a function of AOA. Although the figure is for an entire airplane, airfoils behave in a similar manner. Below stall, at low AOA, C_{l_α} is positive, so the value of $C_{L_p} < 0$ and this will slow down rotation. However, in the immediate poststall region, C_{l_α} is negative and the value of $C_{L_p} > 0$, which is a pro-rotation effect. Consequently, the roll damping derivative plays an imperative role in autorotation during spinning.

EXAMPLE 25-1

A UAV is being designed with a Hershey-bar wing whose dimensions are shown in Figure 25-19. Determine its roll damping. Assume $C_{l_\alpha} = 6.283$ per radian and $C_{d_{\min}} = 0.010$.

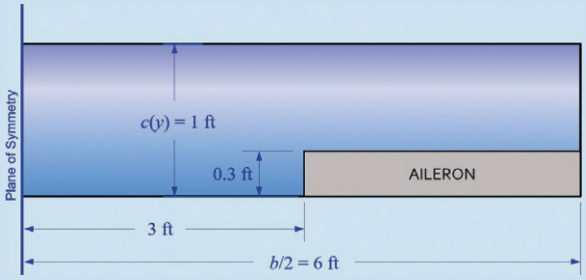


FIGURE 25-19 Example geometry.

SOLUTION:

Per Equation (25-73), the roll damping is:

$$C_{L_p} = -\frac{C_{l_\alpha} + C_{d_{\min}}}{6}$$

$$= -\frac{6.283 + 0.010}{6} = -1.049 \text{ rad}$$

In comparison, the roll damping of the *potential flow model* (PLM) in Figure 25-24 was found to equal −0.6366/rad with ailerons deflected 15° and −0.6388/rad with neutral ailerons. The model analysis accounts for tip effects, which is not the case for the analytical method of Equation (25-73). The accuracy is improved by using the wing's C_{L_α} rather than C_{l_α}.

DERIVATION OF EQUATIONS (25-69) THROUGH (25-71)

Per Figure 25-18, $\hat{p}$ changes the local angle of attack by an amount $\Delta\alpha(y)$ along the wing. It is given by $\Delta\alpha = \hat{p}y/V_\infty$. Figure 25-20 shows the airfoil at an arbitrary wing station y on the up- and downgoing wings. The first row shows the original α. The second row shows the change in α due to $\hat{p}$. The bottom row shows the combination of the two. Figure 25-21 shows pertinent wing dimensions for this derivation.

The change in the section lift coefficient due to the roll rate, ΔC_{l_y}, can be expressed as shown below:

$$\Delta C_{l_y} = C_{l_\alpha}(y) \cdot \Delta\alpha = C_{l_\alpha}(y) \cdot \frac{\hat{p}y}{V_\infty}$$

The lift coefficient is thus:

$$C_{l_y} = C_{l_y}(\alpha) + C_{l_\alpha}(y) \cdot \Delta\alpha = C_{l_y}(\alpha) + C_{l_\alpha}(y) \cdot \frac{\hat{p}y}{V_\infty}$$

Where $C_{l_\alpha}(y)$ and $C_{d_{\min}}$ are the airfoil's lift curve slope and drag coefficient at wing station y. Now, consider the drag coefficient of the airfoil at that station:

$$C_{d_y} = C_{d_{\min}} + C_{d_\alpha} \cdot \Delta\alpha = C_{d_{\min}} + C_{d_\alpha}(\alpha) \cdot \frac{\hat{p}y}{V_\infty}$$

We can now write the infinitesimal lift and drag as follows:

$$\text{Lift:} \quad dL = q \cdot dS \cdot C_{l_y} = q \cdot C_{l_y}(y) \cdot c(y) \cdot dy$$

$$\text{Drag:} \quad dD = q \cdot dS \cdot C_{d_y} = q \cdot C_{d_y}(y) \cdot c(y) \cdot dy$$

Where q is the dynamic pressure and $c(y)$ is the chord at station y.

Next, estimate the projections of the lift and drag onto the z-axis, which is normal to the axis of rotation (the x-axis). Refer to Figure 25-22, which shows the alignment of the

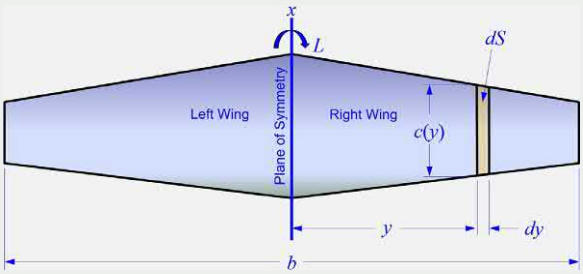


FIGURE 25-21 Wing geometry.

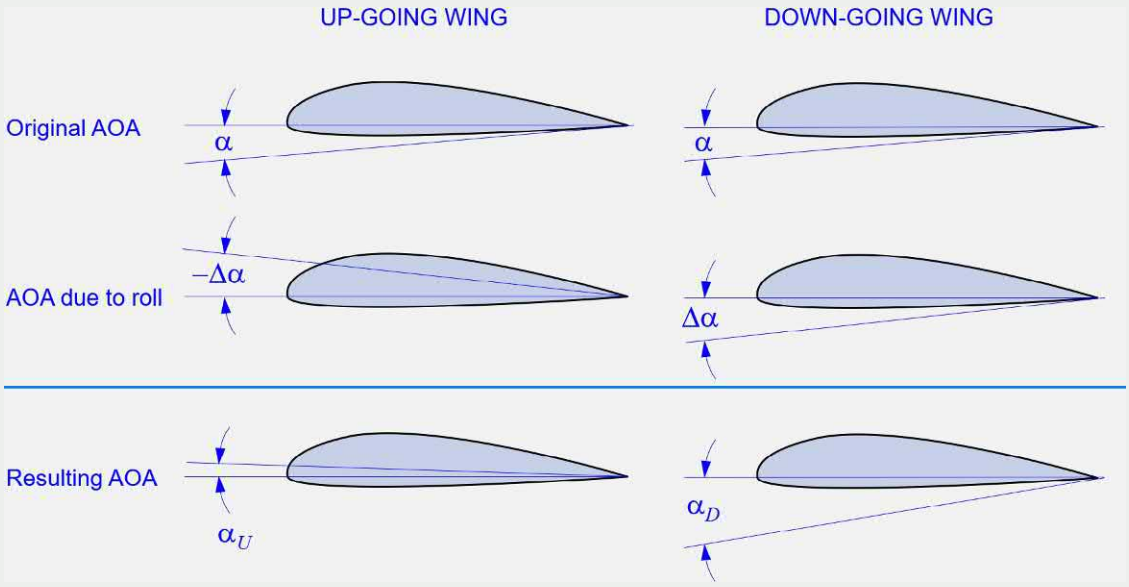


FIGURE 25-20 Changes in local AOA due to roll.

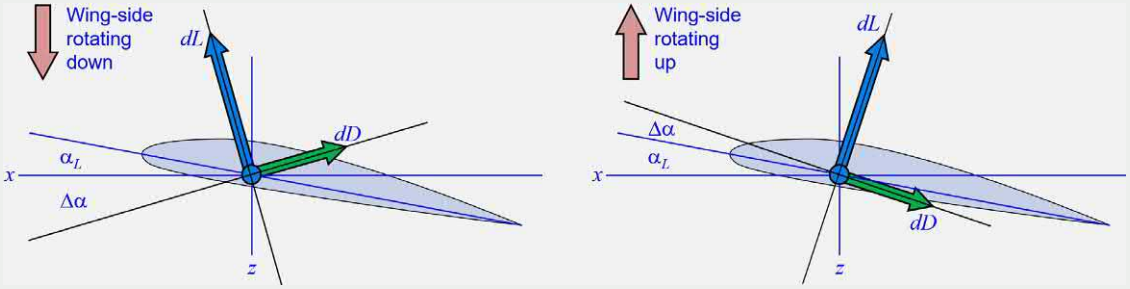


FIGURE 25-22 Changes in AOA due to roll on either side of the plane-of-symmetry.

x-z axes with respect to the lift and drag. The rotation takes place about the x-axis and the retarding moment (roll damping) is generated through the force that acts perpendicular to it, the z-axis. Therefore, we can determine the roll damping force:

$$dZ = -dL \cdot \cos(\Delta\alpha) - dD \cdot \sin(\Delta\alpha)$$

The moment due to roll is caused by the asymmetric loading on the wing, or more precisely, its projection onto the z-axis. The image shows we can define the projections of the lift and drag coefficient on the z-axis as follows (note that positive z is down):

Wing moving up:

$$C_{LU} = \left[C_{l_y}(\alpha) - C_{l_\alpha}(y) \cdot \frac{\hat{p}y}{V_\infty}\right] \cdot \cos\left(\frac{\hat{p}y}{V_\infty}\right)$$

$$C_{DU} = \left[C_{d_{\min}} - c_{d_\alpha}(\alpha) \cdot \frac{\hat{p}y}{V_\infty}\right] \cdot \sin\left(\frac{\hat{p}y}{V_\infty}\right)$$

The elemental force:

$$\begin{aligned} dZ_U &= -q \cdot [C_{LU} - C_{DU}] \cdot c(y)dy \\ &= q \cdot C_{DU} \cdot c(y)dy - q \cdot C_{LU} \cdot c(y)dy \end{aligned}$$

Wing moving down:

$$C_{LD} = \left[C_{l_y}(\alpha) + C_{l_\alpha}(y) \cdot \frac{\hat{p}y}{V_\infty}\right] \cdot \cos\left(\frac{\hat{p}y}{V_\infty}\right)$$

$$C_{DD} = \left[C_{d_{\min}} + C_{d_\alpha}(\alpha) \cdot \frac{\hat{p}y}{V_\infty}\right] \cdot \sin\left(\frac{\hat{p}y}{V_\infty}\right)$$

The elemental force:

$$\begin{aligned} dZ_D &= -q \cdot [C_{LD} + C_{DD}] \cdot c(y)dy \\ &= -q \cdot C_{LD} \cdot c(y)dy - q \cdot C_{DD} \cdot c(y)dy \end{aligned}$$

The roll damping is caused by the difference between dZ_U and dZ_D, integrated across the wing (note that the limits of integration are 0 to $b/2$). The difference between the two is given by:

$$\begin{aligned} dZ_U - dZ_D &= q \cdot C_{LD} \cdot c(y)dy - q \cdot C_{LU} \cdot c(y)dy \\ &\quad + q \cdot C_{DD} \cdot c(y)dy + q \cdot C_{DU} \cdot c(y)dy \\ &= q \cdot (C_{LD} - C_{LU} + C_{DD} + C_{DU}) \cdot c(y)dy \end{aligned}$$

Consider the summation of the lift and drag coefficients. Substituting the coefficients as defined above results in:

$$\begin{aligned} C_{LD} - C_{LU} + C_{DD} + C_{DU} &= \left[C_{l_y}(\alpha) + C_{l_\alpha}(y) \cdot \frac{\hat{p}y}{V_\infty}\right] \\ &\cdot \cos\left(\frac{\hat{p}y}{V_\infty}\right) - \left[C_{l_y}(\alpha) - C_{l_\alpha}(y) \cdot \frac{\hat{p}y}{V_\infty}\right] \\ &\cdot \cos\left(\frac{\hat{p}y}{V_\infty}\right) + \left[C_{d_{\min}} + C_{d_\alpha}(\alpha) \cdot \frac{\hat{p}y}{V_\infty}\right] \\ &\cdot \sin\left(\frac{\hat{p}y}{V_\infty}\right) + \left[C_{d_{\min}} - C_{d_\alpha}(\alpha) \cdot \frac{\hat{p}y}{V_\infty}\right] \cdot \sin\left(\frac{\hat{p}y}{V_\infty}\right) \end{aligned}$$

Simplifying and assuming constant C_{l_α} along the span:

$$\begin{aligned} &C_{LD} - C_{LU} + C_{DD} + C_{DU} \\ &= \left[C_{l_y}(\alpha) + C_{l_\alpha} \cdot \frac{\hat{p}y}{V_\infty} - C_{l_y}(\alpha) + C_{l_\alpha} \cdot \frac{\hat{p}y}{V_\infty}\right] \\ &\cdot \cos\left(\frac{\hat{p}y}{V_\infty}\right) + \left[C_{d_{\min}} + C_{d_\alpha}(\alpha) \cdot \frac{\hat{p}y}{V_\infty} + C_{d_{\min}} - C_{d_\alpha}(\alpha) \cdot \frac{\hat{p}y}{V_\infty}\right] \\ &\cdot \sin\left(\frac{\hat{p}y}{V_\infty}\right) \end{aligned}$$

Therefore, the summation is:

$$\begin{aligned} &C_{LD} - C_{LU} + C_{DD} + C_{DU} = \\ &2C_{l_\alpha} \cdot \frac{\hat{p}y}{V_\infty} \cdot \cos\left(\frac{\hat{p}y}{V_\infty}\right) + 2C_{d_{\min}} \cdot \sin\left(\frac{\hat{p}y}{V_\infty}\right) \end{aligned} \quad \text{(i)}$$

If the roll rate is low enough to assume small angle relations ($\cos\Delta\alpha \approx 1$ and $\sin\Delta\alpha \approx \Delta\alpha$), we can rewrite Equation (i) as follows:

$$\begin{aligned} C_{LD} - C_{LU} + C_{DD} + C_{DU} &= 2C_{l_\alpha} \cdot \frac{\hat{p}y}{V_\infty} + 2C_{d_{\min}} \cdot \frac{\hat{p}y}{V_\infty} \\ &= 2(C_{l_\alpha} + C_{d_{\min}}) \cdot \frac{\hat{p}y}{V_\infty} \end{aligned}$$

The total restoring moment due to roll, $\boldsymbol{L}_{\hat{p}}$, is thus:

$$\begin{aligned} \boldsymbol{L}_{\hat{p}} &= \int_0^{b/2} y \cdot (dZ_U - dZ_D) \\ &= \int_0^{b/2} y \cdot q \cdot (c_{LD} - c_{LU} + c_{DD} + c_{DU}) \cdot c(y)dy \end{aligned}$$

Or:

$$L_{\hat{p}} = \int_0^{b/2} y \cdot q \cdot \left(2(C_{l_\alpha} + C_{d_{\min}}) \cdot \frac{\hat{p}y}{V_\infty}\right) \cdot c(y)dy$$
$$= \frac{2q\hat{p}(C_{l_\alpha} + C_{d_{\min}})}{V_\infty} \int_0^{b/2} y^2 \cdot c(y)dy$$

From the definition of the rolling moment coefficient, we get:

$$C_{L_p} = \frac{L_{\hat{p}}}{qSb} = \frac{2q\hat{p}(C_{l_\alpha} + C_{d_{\min}})}{qSbV_\infty} \int_0^{b/2} y^2 \cdot c(y)dy$$
$$= \frac{2\hat{p}(C_{l_\alpha} + C_{d_{\min}})}{SbV_\infty} \int_0^{b/2} y^2 \cdot c(y)dy$$

Preparing this in terms of $(\hat{p}b/2V_\infty)$ leads to:

$$C_{L_p} = \frac{2\hat{p}(C_{l_\alpha} + C_{d_{\min}})}{SbV_\infty} \int_0^{b/2} y^2 \cdot c(y)dy$$
$$= \left(\frac{\hat{p}b}{2V_\infty}\right) \frac{4(C_{l_\alpha} + C_{d_{\min}})}{Sb^2} \int_0^{b/2} y^2 \cdot c(y)dy$$

Finally, we can determine the roll damping derivative by differentiating with respect to $(\hat{p}b/2V_\infty)$ and then evaluate the geometric integral. Note that since the effect retards the motion it is always negative:

$$C_{L_p} = \frac{\partial C_L}{\partial\left(\frac{\hat{p}y}{2V_\infty}\right)}$$
$$= \frac{\partial}{\partial\left(\frac{\hat{p}y}{2V_\infty}\right)} \left[\left(\frac{\hat{p}y}{2V_\infty}\right) \frac{4(C_{l_\alpha} + C_{d_{\min}})}{Sb^2} \int_0^{b/2} y^2 \cdot c(y)dy\right]$$
$$= -\frac{4(C_{l_\alpha} + C_{d_{\min}})}{Sb^2} \int_0^{b/2} y^2 \cdot c(y)dy$$

DERIVATION OF EQUATIONS (25-72) AND (25-73)

Assume a straight tapered wing whose taper ratio is λ, root chord c_r, and span is b. A parametric representation of the chord as a function of y is given by Equation (9-34):

$$c(y) = c_R\left(1 + \frac{2(\lambda - 1)}{b}y\right) \tag{9-34}$$

Substitute it into Equation (25-71) and expand to get Equation (25-72);

$$C_{L_p} = -\frac{4(C_{l_\alpha} + C_{d_{\min}})}{Sb^2} \int_0^{b/2} y^2 \cdot c(y)dy$$
$$= -\frac{4(C_{l_\alpha} + C_{d_{\min}})}{Sb^2} \int_0^{b/2} y^2 \cdot c_r\left(1 + \frac{2(\lambda - 1)}{b}y\right)dy$$
$$= -\frac{4(C_{l_\alpha} + C_{d_{\min}}) \cdot c_r}{Sb^2} \int_0^{b/2} \left(y^2 + \frac{2(\lambda - 1)}{b}y^3\right)dy$$
$$= -\frac{4(C_{l_\alpha} + C_{d_{\min}}) \cdot c_r}{Sb^2} \left[\frac{y^3}{3} + \frac{2(\lambda - 1)}{b}\frac{y^4}{4}\right]_0^{b/2}$$
$$= -\frac{(C_{l_\alpha} + C_{d_{\min}}) \cdot c_r b}{24S}[1 + 3\lambda]$$

We get Equation (25-73) for a rectangular wing, when $\lambda = 1$, for which $S = c_r b$:

$$C_{L_p} = -\frac{(C_{l_\alpha} + C_{d_{\min}}) \cdot c_r b}{24S}[1 + 3\lambda]$$
$$= -\frac{(C_{l_\alpha} + C_{d_{\min}}) \cdot c_r b}{24(c_r b)}[1 + 3] = -\frac{C_{l_\alpha} + C_{d_{\min}}}{6}$$

(3) Roll-due-to-Yaw Derivative, C_{L_r}

This derivative, like C_{N_p} (see Section 25.3.2(2)), is indicative of the coupling between yaw and roll. It accounts for rolling moment generated by yaw rate. This is largely due to the wing, but the VT contributes as well. Positive yaw rate rotates the left wing forward and the right wing backward. This increases the lift on the left wing and reduces it on the right one. This interaction develops a positive rolling moment. This derivative is significant for spiral stability, but less so for Dutch roll. It can be estimated using

$$C_{L_r} \cong C_{L_{r_W}} + C_{L_{r_{VT}}} \tag{25-74}$$

Typical range of values is $+0.04 < C_{L_r} < +0.12$ per radian [5].

Wing Contribution

Ref. [10] uses data from Refs. [19, 20] to estimate C_{L_r} for a rectangular and elliptical (or moderately tapered) wing. Also see discussion in Ref. [5].

Rectangular wing: $C_{L_{r_W}} = C_L/3$ (25-75)

Elliptical or tapered wing: $C_{L_{r_W}} = C_L/4$ (25-76)

VT Contribution

Per Ref. [21], the contribution by the vertical tails is given by

$$C_{L_{r_{VT}}} = -2\frac{l_{VT_{CG}}}{b}\frac{z_{VT}}{b}C_{Y_{\beta_{VT}}} = -2\frac{l_{VT_{CG}}}{b}C_{L_{\beta_{VT}}} \tag{25-77}$$

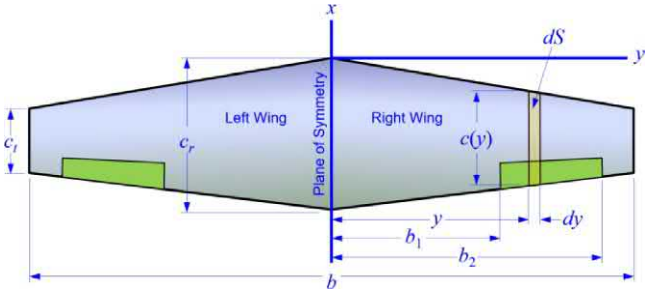


FIGURE 25-23 Definition of the aileron geometry.

Where $C_{L_{\beta VT}}$ is calculated using Equation (25-68). Using it is recommended because it includes interference effects.

(4) Aileron Authority Derivative, $C_{L_{\delta_a}}$

The aileron authority indicates the capability of an airplane to roll. The larger the ailerons, the larger the derivative. It is estimated using the *strip integration method*. However, it requires change in the airfoil's lift coefficient with aileron deflection (denoted by $C_{l_{\delta_a}}$) to be known. $C_{l_{\delta_a}}$ represents the change in the lift coefficient of the airfoil with control surface deflection (see Section 24.2.5(8) and Example 24.2). Typical range of values is $+0.03 < C_{l_{\delta_a}} < +0.08$ per degree. The aileron authority derivative is given by

$$C_{L_{\delta_a}} = \frac{dC_L}{d\delta_a} = \frac{2C_{l_{\delta_a}}}{Sb}\int_{b_1}^{b_2} cy\,dy \qquad (25\text{-}78)$$

Units are per radian or per degree. The dimensions b_1 and b_2 are shown in Figure 25-23. The expression overestimates the roll authority by not accounting for end effects on either side of each aileron. Example 25-2 compares the analytical $C_{L_{\delta_a}}$ to potential flow theory, which does account for the tip effects.

Let us simplify the solution of Equation (25-78) for two common wing planform shapes.

Case 1: Straight Tapered Wing with Taper Ratio λ:

$$C_{L_{\delta_a}} = \frac{C_{l_{\delta_a}} c_r}{Sb}\left[\left(b_2^2 - b_1^2\right) + \frac{4(\lambda-1)}{3b}\left(b_2^3 - b_1^3\right)\right] \qquad (25\text{-}79)$$

Case 2: Rectangular Wing (λ = 1):

$$C_{L_{\delta_a}} = \frac{C_{l_{\delta_a}}\left(b_2^2 - b_1^2\right)}{b^2} \qquad (25\text{-}80)$$

DERIVATION OF EQUATION (25-78)

Consider Figure 25-23 which shows the top view of a wing planform. When one aileron is deflected trailing edge down (TED), the section lift coefficient (C_l) in the area of the ailerons increases by $C_{l_{\delta_a}} \cdot \delta_a$ and decreases by the same amount on the opposite wing (assuming no *aileron differential*). Thus, the C_l at spanwise station y becomes:

Upgoing wing: $C_{l_{up}} = C_{l_y} + C_{l_{\delta_a}} \cdot \delta_a$

Downgoing wing: $C_{l_{down}} = C_{l_y} - C_{l_{\delta_a}} \cdot \delta_a$

Where C_{l_y} is the value of the C_l at station y with the aileron in the neutral position. The general definition of the rolling moment coefficient is:

$$C_L = \frac{L}{qSb} = \frac{L_a + L_{\hat{p}}}{qSb}$$

Where L is rolling moment in ft·lb$_f$ or N·m, and is typically a combination of moment due to the aileron deflection, L_a, and roll damping, $L_{\hat{p}}$. Here, we are only concerned with the former. We start by writing the section lift for the up- and down moving sides at spanwise station y as follows:

$$dF_{up} = q \cdot C_{l_{up}} \cdot dS = q \cdot \left(C_{l_y} + C_{l_{\delta_a}} \cdot \delta_a\right) \cdot c \cdot dy$$
$$dF_{down} = q \cdot C_{l_{down}} \cdot dS = q \cdot \left(C_{l_y} - C_{l_{\delta_a}} \cdot \delta_a\right) \cdot c \cdot dy$$

The infinitesimal moment attributed to the area at spanwise station y is the difference between the two forces acting over distance y from the plane of symmetry:

$$\begin{aligned} dL_a &= y \cdot dF_{up} - y \cdot dF_{down} \\ &= y \cdot q \cdot \left(C_{l_y} + C_{l_{\delta_a}} \cdot \delta_a\right) \cdot c \cdot dy - y \cdot q \cdot \left(C_{l_y} - C_{l_{\delta_a}} \cdot \delta_a\right) \cdot c \cdot dy \\ &= y \cdot q \cdot \left[2C_{l_{\delta_a}} \cdot \delta_a\right] \cdot c \cdot dy \end{aligned}$$

This allows us to write the infinitesimal rolling moment due to δ_a as follows:

$$dC_L = \frac{dL_a}{qSb} = \frac{y \cdot q \cdot \left[2C_{l_{\delta_a}} \cdot \delta_a\right] \cdot c \cdot dy}{qSb} = \frac{2C_{l_{\delta_a}} \cdot \delta_a \cdot c}{Sb} y \cdot dy$$

The total rolling moment over the entire span of the ailerons is thus

$$C_L = \int_{b_1}^{b_2} dC_L = \int_{b_1}^{b_2} \frac{2C_{l_{\delta_a}} \cdot \delta_a \cdot c}{Sb} y \cdot dy = \frac{2C_{l_{\delta_a}} \cdot \delta_a}{Sb}\int_{b_1}^{b_2} c \cdot y \cdot dy$$

From which we get the following dependency on the aileron deflection (recall that C_L = rolling moment coefficient and C_l = section lift coefficient):

$$C_{L_{\delta_a}} = \frac{dC_L}{d\delta_a} = \frac{2C_{l_{\delta_a}}}{Sb}\int_{b_1}^{b_2} c \cdot y \cdot dy$$

DERIVATION OF EQUATIONS (25-79) AND (25-80)

Assume a straight tapered wing whose taper ratio is λ, root chord c_r, and span is b. A parametric representation of the chord as a function of y is given by Equation (9-34):

$$c(y) = c_R\left(1 + \frac{2(\lambda-1)}{b} y\right) \qquad (9\text{-}34)$$

If the wing features a single airfoil, the lift curve slope may be assumed constant. Therefore, we can write the aileron authority as follows:

$$C_{L_{\delta_a}} = \frac{2C_{l_{\delta_a}}}{Sb}\int_{b_1}^{b_2} c\cdot y\cdot dy$$
$$= \frac{2C_{l_{\delta_a}}}{Sb}\int_{b_1}^{b_2} c_r\left(1+\frac{2(\lambda-1)}{b}y\right)\cdot y\cdot dy$$
$$= \frac{2C_{l_{\delta_a}}c_r}{Sb}\int_{b_1}^{b_2}\left(y+\frac{2(\lambda-1)}{b}y^2\right)\cdot dy$$
$$= \frac{2C_{l_{\delta_a}}c_r}{Sb}\left[\frac{y^2}{2}+\frac{2(\lambda-1)}{3b}y^3\right]_{b_1}^{b_2}$$

Substituting the limits and manipulating algebraically yields:

$$C_{L_{\delta_a}} = \frac{2C_{l_{\delta_a}}c_r}{Sb}\left[\frac{1}{2}(b_2^2-b_1^2)+\frac{2(\lambda-1)}{3b}(b_2^3-b_1^3)\right]$$
$$= \frac{C_{l_{\delta_a}}c_r}{Sb}\left[(b_2^2-b_1^2)+\frac{4(\lambda-1)}{3b}(b_2^3-b_1^3)\right]$$

Consider the special case for a rectangular wing, when $\lambda=1$, for which $S=c_r b$:

$$C_{L_{\delta_a}} = \frac{C_{l_{\delta_a}}(b_2^2-b_1^2)c_r}{(c_r b)b} = \frac{C_{l_{\delta_a}}(b_2^2-b_1^2)}{b^2}$$

EXAMPLE 25-2

Determine the aileron authority of the UAV in Example 25-1, if change in lift with aileron deflection, $C_{l_{\delta_a}}$, is 0.057 per degree (i.e., 10° deflection increases C_l by 0.57). Refer to Figure 25-19 for dimensions.

SOLUTION:

From Figure 25-19, we see that $b_1=3$ ft, $b_2=6$ ft, $S=12$ ft^2, $b=12$ ft, and $c(y)=1$ ft. Therefore, per Equation (25-78) and noting that the chord is constant:

$$C_{L_{\delta_a}} = \frac{dC_L}{d\delta_a} = \frac{2C_{l_{\delta_a}}}{Sb}c\cdot\int_{b_1}^{b_2} y\cdot dy = \frac{2(0.057)}{12\times12}(1)\left[\frac{y^2}{2}\right]_3^6$$
$$= 0.01069/\text{degree} = 0.6123/\text{rad}$$

Note that Equation (25-80) gives the same value

$$C_{L_{\delta_a}} = \frac{C_{l_{\delta_a}}(b_2^2-b_1^2)}{b^2} = \frac{0.057(6^2-3^2)}{12^2} = 0.01069/\text{degree}$$

Additional Information: A *potential flow model* (PLM) of this wing is shown Figure 25-24, and assumes a symmetrical airfoil. The PLM solution accounts for end effects. The value of $C_{l_{\delta_a}}=0.057$/degree was obtained by deflecting its entire trailing edge at $\alpha=2°$ with flap neutral and deflected 1°. The former gave $C_L=0.17682$, the latter $C_L=0.23382$. Therefore, $C_{l_{\delta_a}}=(0.23382-0.17682)/(1°-0°)=0.05700$/degree. The distribution of section lift coefficients (C_l) is shown in the figure and reveals how C_l rise gradually rather than instantly, as assumed by the strip integration method.

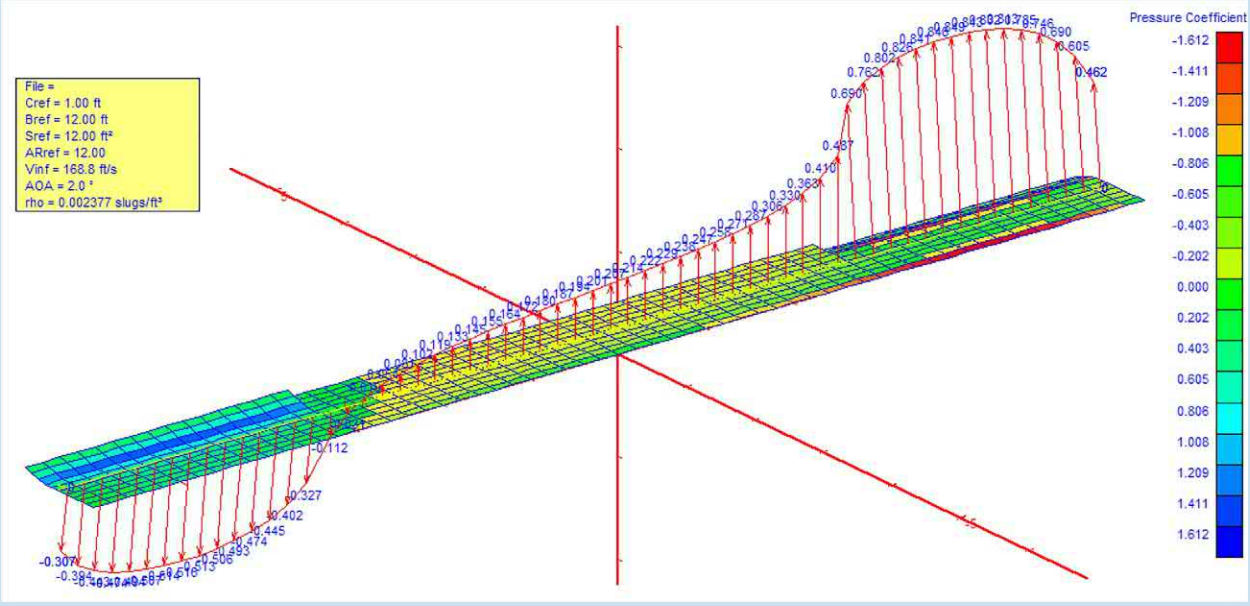


FIGURE 25-24 Distribution of C_l with aileron deflected.

(5) Rolling Moment with Rudder Deflection, $C_{L_{\delta r}}$

Since the center-of-lift acting on the vertical tail is generally above the CG, deflecting the rudder introduces a rolling moment. Etkin [22] presents the following expression to estimate this effect

$$C_{L_{\delta_r}} = \eta_{VT} C_{L_{\beta_{VT}}} \frac{S_{VT}}{S} \frac{z_{VT}}{b} \Delta K_R \tau_R$$
$$= \eta_{VT} C_{L_{\beta_{VT}}} \frac{S_{VT}}{S} \frac{z_{VT}}{b} [K_b(z_2) - K_b(z_1)] \tau_R \qquad (25\text{-}81)$$

See Figure 25-2 for dimensions. Note that $C_{L_{\beta VT}}$ is to the vertical tail what C_{L_α} is to the wing. ΔK_R accounts for the possibility the rudder span is shorter than that of the VT. It depends on the taper of the VT and is calculated using the function K_b (span factor) of Equation (25-22). The term τ_R is the *rudder effectiveness factor*, which corresponds to the elevator effectiveness factor [8]. Thus, it can be calculated using Figure 24-21 or Equation (24-86). See more details associated with Equation (25-21) and Figure 25-8.

25.5 BASICS OF ROLL AND YAW CONTROL

This section discusses issues to consider in the sizing of aileron and rudder control systems. Design goals for the control system are discussed in the introductory paragraph of Section 24.3. This section introduces basic considerations for the design of the aileron and rudder control systems.

25.5.1 Fundamentals of Roll Control

Ailerons provide control about the airplane's roll axis. This is accomplished by deflecting the aileron on one side trailing edge up (TEU) and the other side trailing edge down (TED). The same effect is also achieved by deflecting a spoiler on one side and aileron on the other. This introduces asymmetry into the lift distribution along each wing, generating a rolling moment.

The effect of deflecting aileron on the distribution of section lift-coefficients predicted by potential flow theory is shown in Figure 25-25. The ailerons are deflected 15° and the wing's AOA amounts to 8° at 100 KCAS. Figure 25-26 shows the resulting impact on the flow field behind the wing. It highlights how the wing that travels up generates higher lift-induced drag than the opposite wing, causing a phenomenon called *adverse yaw*. It is also important for the designer to remember that ailerons compete with flaps for real estate. Large span ailerons reduce flap span, affecting runway performance. This impact must be evaluated during the design process.

There are three common types of ailerons used in modern airplanes; *plain-flap ailerons*, *Frise ailerons*, and *spoiler-flap ailerons*, also called *spoileron* (a combination of spoilers and ailerons). These are illustrated in Figure 25-27. Other styles include the *flaperon* (a combination of flaps and ailerons) and *elevon* (a combination of elevators and ailerons). There are also highly specialized types of ailerons such as the *slot-lip aileron* and *microjet ailerons*.

(1) Plain Flap Ailerons

The plain flap is the most common aileron style. They are effective and inexpensive to manufacture. They can be found on aircraft ranging from primary trainers to commercial aircraft. As shown in Figure 25-27, the aileron on the upgoing wing is deflected Trailing Edge Down (TED) and the downgoing wing is deflected Trailing Edge Up (TEU).

(2) Frise Ailerons

The Frise aileron (see Figure 25-27) was invented by the famed designer Leslie George Frise (1897–1979).[1] Frise ailerons were developed during the 1930s [23]. Their purpose is to (A) reduce stick-forces at high airspeeds and (B) to eliminate adverse yaw. This is accomplished by offsetting the hingeline below the wing surface. This causes it to have a large radius motion that exposes the LE of the aileron deflected TEU to the airstream. This, in turn, generates a suction peak that reduces the hinge moment.

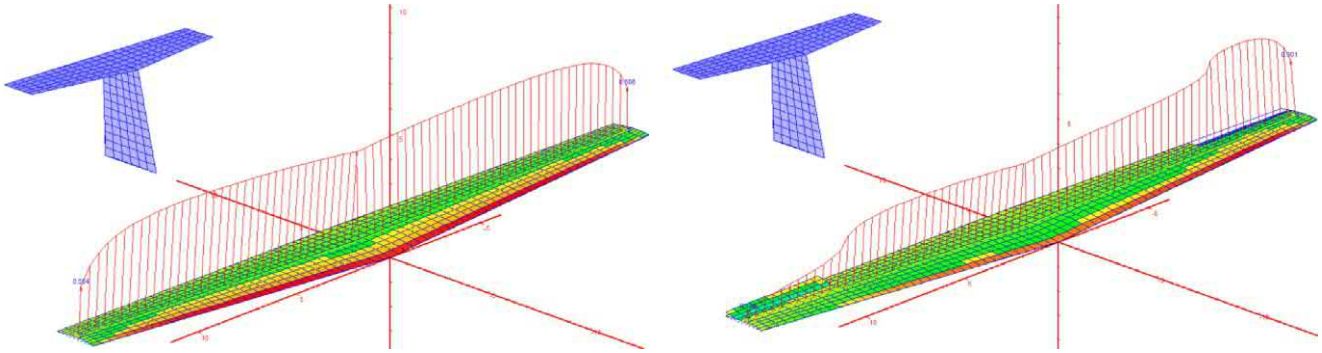


FIGURE 25-25 Typical impact of deflecting ailerons on the section lift coefficients.

[1] Contributed include the Bristol Fighter (1916), Bristol Bulldog (1927), Bristol Beaufighter (1941), and the Hunting Percival Jet Provost (1954).

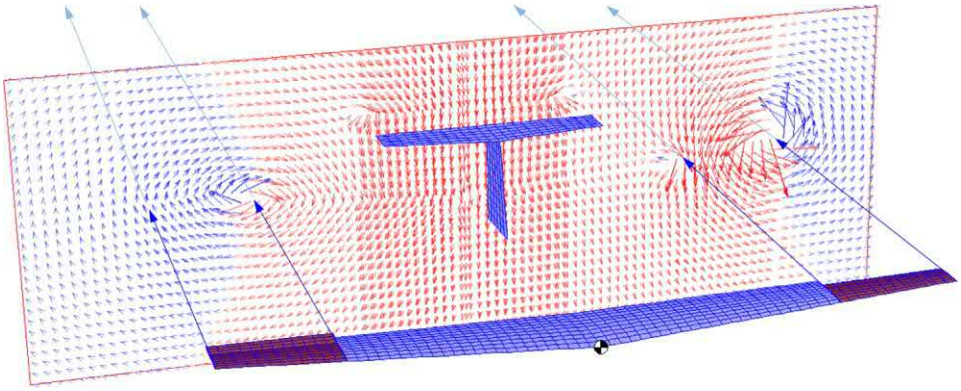


FIGURE 25-26 Impact of aileron deflection on the flow field behind the aircraft predicted by the potential flow theory. Note the difference in the size and source of the various wing tip vortices.

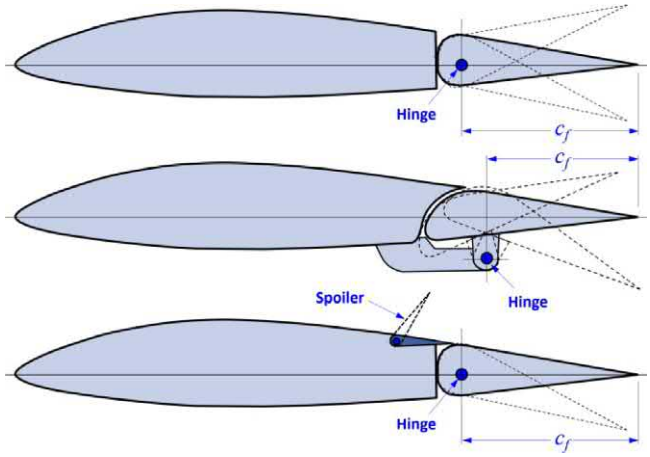


FIGURE 25-27 Three common types of ailerons; Plain Flap (top), Frise (middle), and Spoiler-Flap (bottom).

It also increases the drag of that wing side, reducing adverse yaw. The aileron deflected TED has its aerodynamic center offset from the hingeline, also helping to reduce the hinge moment. This explains its use in both fast and large aircraft before the advent of hydraulically boosted control systems. If the nose is too sharp the lower surface may stall, which can cause severe buffeting [23]. Frise ailerons have seen use on many different aircraft types; among them the B-17, Bell P-39, Grumman F6F-3 and TBF, the Spitfire, Hurricane, Focke-Wulf 190, Curtiss Wright C-46, and DC-4, and many Cessna models.

(3) Spoiler-Flap Ailerons

Several airplanes feature this type of ailerons (e.g., Mitsubishi MU-2, Boeing B-52, and others). This aileron style features a flap that is deflected TED on the upgoing wing and a small spoiler on the downgoing side. Deploying the spoiler reduces lift on the downgoing side and increases its drag. This counteracts adverse yaw. The aileron on that side may or may not deflect TEU at the same time. A common complaint holds that the system tends to be sluggish at low airspeeds, as separated flow creeps forward toward the leading edge of the wing and reduces the effectiveness of the spoiler. Regardless, this does not affect the popularity of this aileron style. The control system may display peculiar side effects on swept wings. It is well known that B-52 pilots complain about a significant nose pitch-up moment associated with aileron deflection. As its spoilers are deployed, the center-of-lift moves forward causing the nose-up pitch. An assertive nose pitch-down correction is required by the pilot.

(4) Slot-Lip Ailerons

The slot-lip aileron [24, 25] is a lateral control device that regulates the flow of air through a slot made into the wing using a small flap (see Figure 25-28). The flap conforms to the shape of the upper surface of the wing when not in use and is designed reduce the flow of air through the slot. The slot must not be completely closed in the neutral deflection. However, when deployed, air will flow freely through the slot and modify the wing flow field such that the aircraft can be rolled.

Slot-lip ailerons date to the 1930s. Investigation by Refs. [24, 25] revealed excessive lag in control response. This was found to depend on the distance of the device from leading edge (denoted by c_s in Figure 25-28). This lag was found to be excessive unless the device is placed 80% of the chord from the leading edge. In general, the aileron was found to result in sluggish response.

It was also found that the slot must be open, albeit less open when not in use for roll control. The device delays

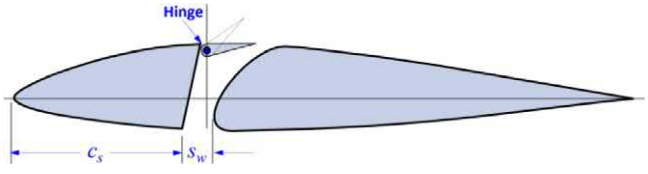


FIGURE 25-28 A schematic of the slot-lip aileron.

the stall of the wing tip, while maintaining roll damping, although this is only true if the device is located farther aft than 50% of chord from LE (which is where the resulting lag is high). The aileron was found to increase drag of the wing by about 10% in cruise and 35% in climb. If simplicity and safety is of higher importance than cruise and climb performance the slot-lip aileron might be useful. It is featured on the Fairchild F-22 test airplane and the controversial GAF N-22 Nomad. In interest of fairness, there are some that speak favorably of the device as used in the Nomad, e.g., Ref. [26].

(5) Flaperon

A flaperon is a control surface that serves the role of a flap and aileron. It is typically used with full span flaps. Flaperons are presented in Section 10.4.1, *Lift Distribution on Wings with Flaps Deflected*.

(6) Elevon

An elevon is a control surface for which the elevator serves as an aileron in addition to its normal function. It is used for flying wings and tailless delta wing aircraft. It can also be found on some variable sweep winged supersonic fighters.

(7) Differential Ailerons

Figure 8-60 of Section 8.3.4, *The Effect of a Trailing Edge Flap* shows that as a flap is deflected the drag of the airfoil increases. As stated earlier, using conventional aileron configuration, the airplane is banked by deflecting one aileron TEU and the other TED. The down deflected aileron largely causes the adverse yaw. The phenomenon is more pronounced for aircraft with large Aspect Ratios ($AR > 8$). To help remedy this tendency, *differential ailerons* are employed. For such ailerons, the deflection angle for the down deflected aileron is a smaller than that of the up deflected one (see Figure 25-29). The result is less aileron induced drag and, thus, less adverse yaw. A typical ratio between the up and down traveling ailerons is 1:0.75. This means that if one aileron is rotated 10° TEU, the opposite one will rotate 7.5° TED.

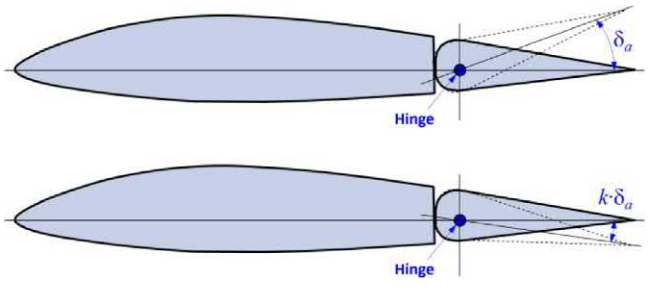


FIGURE 25-29 Differential ailerons.

(8) Aileron Design Requirements

Among critical design points for ailerons are the following:

- Responsiveness at low airspeed.
- Responsiveness at high speeds with low deflections.
- Comfortable stick forces throughout flight envelope.

Another term for responsiveness is *roll authority*. Although responsiveness at slow speeds is imperative (low dynamic pressure requires greater deflection or control surface area, or a combination of the two), high-speed functionality is of great importance as well. It has been known for a long time that a pilot's conception of adequate roll control is tied to the helix angle made by the wing as the airplane rolls at a given airspeed [8]; denoted by $\hat{p}b/2V_\infty$ (variables are defined elsewhere in this chapter). Ref. [8] recommends that for specific types of aircraft the ratios in Table 25-4 are met or exceeded.

For the aircraft designer this means that the physical dimensions of the ailerons can be determined based on the desired roll rate. A step-by-step design approach is presented below. However, first we must define two important stability derivatives: The *aileron authority derivative* and *roll damping*.

25.5.2 Aileron Sizing

With the preliminaries out of the way in the preceding section, it is now possible to present the following method to help with the sizing of the ailerons. The procedure involves estimating the steady-state roll rate using the aileron authority and roll damping derivatives.

(1) Estimating Steady-State Roll Rate

When the ailerons are deflected the airplane begins to roll (see Figure 25-30). The motion consists of a transient rotational acceleration that gradually subsides and vanishes once the airplane achieves its steady state roll rate. Theoretically, the rotation makes the wingtips travel along a helical path that parallels a rotating propeller (see Figure 15-4).

The steady-state roll helix angle is determined from:

$$\frac{\hat{p}b}{2V_\infty} = -\frac{C_{l_{\delta_a}}}{C_{l_p}}\delta_a \tag{25-82}$$

TABLE 25-4 Typical roll helix angles (radians).

Cargo or heavy-lift aircraft:	Fighter aircraft:
$\frac{\hat{p}b}{2V_\infty} > 0.07$	$\frac{\hat{p}b}{2V_\infty} > 0.09$

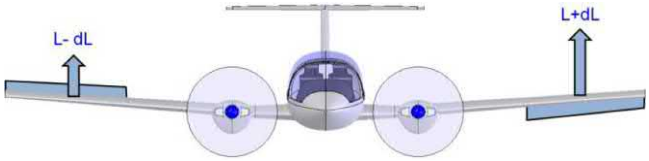


FIGURE 25-30 Change in lift due to aileron deflection.

Therefore, the steady-state roll rate (in rad/s) can be determined from:

$$\hat{p} = -\frac{C_{l_{\delta_a}}}{C_{l_p}}\delta_a\left(\frac{2V_\infty}{b}\right) \tag{25-83}$$

Step 1: Initial Dimensions

Establish initial dimensions based on Figure 25-23. Also determine the aileron deflection angle, δ_a. Note that the control system will stretch in flight reducing the maximum ground deflection. This means that a control system designed for a maximum deflection of, say, 15° on the ground, may only deflect as much as 75% of that in flight. Some control systems are so poorly designed[2] that they may only achieve 25% of the maximum deflection. At any rate, 75% is a reasonable "first stab" estimate for an average control system. This would mean that, in flight, a maximum deflection of 15° might be closer to 11.3°.

Step 2: Estimate Roll Damping

Using the geometry from Step 1, estimate roll damping, C_{L_p}. Use Equation (25-71) for an arbitrary wing planform shape, Equation (25-72) for a straight tapered wing, and Equation (25-73) for a "Hershey bar" wing.

Step 3: Estimate Roll Authority

Using the geometry from Step 1, estimate the roll authority, $C_{l_{\delta_a}}$. Use Equation (25-78) for an arbitrary wing planform shape. Use Equation (25-79) for a straight tapered wing, and Equation (25-80) for a "Hershey bar" wing.

Step 4: Estimate Roll Helix Angle

Determine a desired "target" roll helix angle per Section 25.5.2 using Equation (25-82). If the calculated value is less than the selected target, enlarge b_1 or b_2, or both. Note that b_2 can never be larger than $b/2$ and $0 < b_1 < b_2$.

(2) Special Case Aileron Sizing: Constant Chord Wing

The following expression can be used to determine the spanwise location of the inboard edge of the aileron, for a given outboard edge. It only applies to constant chord ("Hershey bar") wings.

Physical dimension:
$$b_1 = \sqrt{\left(\frac{\hat{p}b}{2V_\infty}\right)\frac{C_{L_p}}{C_{l_{\delta_a}}\cdot\delta_a}b^2 + b_2^2} \tag{25-84}$$

Fractional dimension:
$$\frac{b_1}{b} = \sqrt{\left(\frac{\hat{p}b}{2V_\infty}\right)\frac{C_{L_p}}{C_{l_{\delta_a}}\cdot\delta_a} + \left(\frac{b_1}{b}\right)^2} \tag{25-85}$$

Where:

b_1 = Spanwise station for the inboard edge of the aileron, in ft or m,

b_2 = Spanwise station for the outboard edge of the aileron, in ft or m.

DERIVATION OF EQUATION (25-82)

Assume the wing is rigid and the rolling motion is caused by deflecting the ailerons to an angle δ_a. Further assume the roll rate $\hat{p}$ is impeded by the roll damping due to a local change in AOA along the wing (with a minor contribution from the vertical tail). Therefore, we can write the equation of rolling motion for the aircraft as follows:

$$I_{xx}\dot{\hat{p}} = \frac{\partial L}{\partial \hat{p}}\left(\frac{\hat{p}b}{2V_\infty}\right) + \frac{\partial L}{\partial \delta_a}\delta_a \tag{i}$$

Where I_{xx} is the aircraft's moment of inertia (in slugs·ft^2 or kg·m^2) $\dot{\hat{p}}$ is the roll acceleration in rad/s^2, L is the rolling moment in ft·lb$_f$ or N·m, and δ_a is the aileron deflection in degrees. At steady state Equation (i) becomes.

$$0 = \frac{\partial L}{\partial \hat{p}}\left(\frac{\hat{p}b}{2V_\infty}\right) + \frac{\partial L}{\partial \delta_a}\delta_a$$

$$\Leftrightarrow \quad \frac{\partial L}{\partial \hat{p}}\left(\frac{\hat{p}b}{2V_\infty}\right) = -\frac{\partial L}{\partial \delta_a}\delta_a \quad \Rightarrow \quad \left(\frac{\hat{p}b}{2V_\infty}\right) = -\frac{\partial L/\partial \delta_a}{\partial L/\partial \hat{p}}\delta_a$$

In terms of stability derivatives, we can write:

$$\left(\frac{\hat{p}b}{2V_\infty}\right) = -\frac{C_{l_{\delta_a}}}{C_{L_p}}\delta_a \tag{ii}$$

DERIVATION OF EQUATION (25-84)

Begin with Equation (25-82) and solve for $C_{l_{\delta a}}$:

$$\left(\frac{\hat{p}b}{2V_\infty}\right) = -\frac{C_{l_{\delta_a}}}{C_{L_p}}\delta_a \quad \Rightarrow \quad C_{l_{\delta_a}} = -\left(\frac{\hat{p}b}{2V_\infty}\right)\frac{C_{L_p}}{\delta_a} \tag{i}$$

Insert Eq. (25-80): $$C_{l_{\delta_a}} = -\left(\frac{\hat{p}b}{2V_\infty}\right)\frac{C_{L_p}}{\delta_a} = \frac{C_{l_{\delta_a}}\left(b_2^2 - b_1^2\right)}{b^2} \tag{ii}$$

Since our target is to determine the inboard station, b_1, for the aileron we solve for it:

$$b_1 = \sqrt{\left(\frac{\hat{p}b}{2V_\infty}\right)\frac{C_{L_p}}{\delta_a}\frac{b^2}{C_{l_{\delta_a}}} + b_2^2} \tag{iii}$$

[2] Here, "poorly designed" means it results in excessive stretching.

EXAMPLE 25-3

A UAV is being designed with a Hershey bar wing whose dimensions are shown in Figure 25-31. The maximum aileron ground deflection is 20°. Determine the roll rate for an aileron deflection of 10° at $V_\infty = 100$ KTAS if change in lift with aileron deflection is given by $C_{l_{\delta_a}} = 0.05524$ per degree. Note that this geometry is also analyzed in Examples 25-1 and 25-2. Compare the results to that obtained using the potential flow model presented in the same examples.

SOLUTION:

Step 1: Determine the derivative $C_{L_{\delta_a}}$

This was done in Example 25-1 and was shown to amount to;

$$C_{L_{\delta_a}} = \frac{dC_L}{d\delta_a} = \frac{2C_{l_{\delta_a}}}{Sb} c \int_{b_1}^{b_2} y \cdot dy = \frac{2(0.057)}{12 \times 12}(1)\left[\frac{y^2}{2}\right]_3^6$$
$$= 0.01069/\text{degree} = 0.6123/\text{rad}$$

Step 2: Determine the derivative C_{L_p}

This was done in Example 25-2 and was shown to equal;

$$C_{L_p} = -\frac{C_{l_\alpha} + C_{d_{\min}}}{6} = -\frac{6.283 + 0.010}{6} = -1.049/\text{rad}$$

Step 3: Determine the roll helix angle

Based on this, the roll rate using $\delta_a = 10°$ at 100 KTAS can be found from Equation (25-82):

$$\frac{\hat{p}b}{2V_\infty} = -\frac{C_{L_{\delta_a}}}{C_{L_p}}\delta_a = -\frac{0.6123}{-1.049}(10°) = 5.837°$$

Step 4: Determine the roll rate $\hat{p}$

$$\hat{p} = -\frac{C_{L_{\delta_a}}}{C_{L_p}}\delta_a\left(\frac{2V_\infty}{b}\right) = -\frac{0.6123}{-1.049}(10°)\left(\frac{2 \times 168.8}{12}\right) = 164.2°/\text{s}$$

Determining the roll rate using the potential flow analysis (see Examples 25-1 and 25-2):

$$\hat{p} = -\frac{C_{L_{\delta_a}}}{C_{L_p}}\delta_a\left(\frac{2V_\infty}{b}\right) = -\frac{0.6123}{-0.6388}(10°)\left(\frac{2 \times 168.8}{12}\right)$$
$$= 269.7°/\text{s}$$

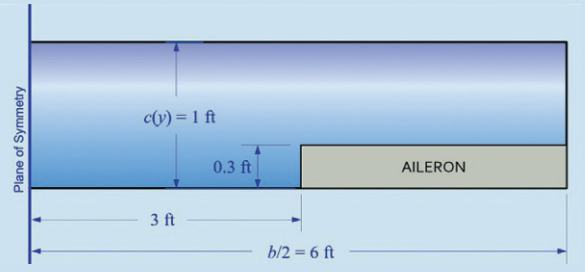


FIGURE 25-31 Example geometry.

(3) Maximizing Responsiveness

Some airplanes require flap span to be maximized to meet requirements for stall speed. This means that the aileron span is less than ideal. The designer can attempt to improve the effectiveness of the remaining ailerons by positioning the centroid of the aileron planform as close as possible to the location where their spanwise section moment reaches maximum.

Consider the tapered wing planform (halfspan) in Figure 25-32, which shows the spanwise section moment (analogous to section lift or section lift coefficient) can be defined as follows:

$$\Delta C_m = y \cdot C_l \quad \Leftrightarrow \quad \Delta M_x = y \cdot (q \cdot C_l \cdot \Delta S)$$

Where;

ΔC_m = Elemental moment coefficient
C_l = Section lift coefficient
ΔM_x = Elemental rolling moment
y = Spanwise station
q = Dynamic pressure
ΔS = Area of elemental strip

Figure 25-33 shows the variation of the section rolling moment coefficient along the span of the wing shown in Figure 25-25. It shows that the peak of the section moment coefficients along the wing with the ailerons neutral occurs near the 85% spanwise station. This is where one should try and place the centroid of small ailerons to maximize their effectiveness. The location of this peak is highly dependent on the wing geometry.

25.5.3 Fundamentals of Yaw Control

The rudder sizing largely considers three conditions: (A) Crosswind requirements. (B) Asymmetric thrust due to *one-engine-inoperable* (OEI) for multiengine aircraft. (C) Spin recovery. Unfortunately, the last condition is challenging to analyze during conceptual design because of the separated flow field in which the VT operates. Thus, the rudder is generally sized to conditions (A) and (B). Chances are it will be adequately sized for spin

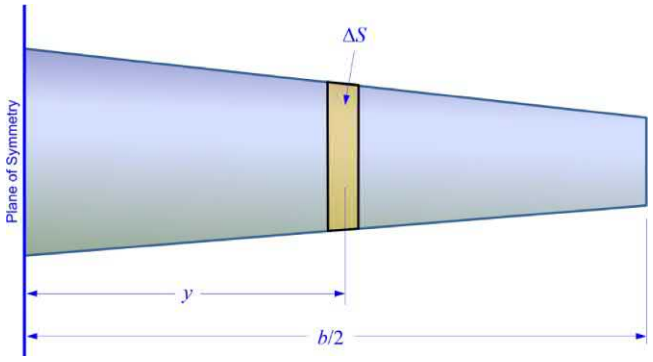


FIGURE 25-32 Definition of an infinitesimal segment ΔS on the wing.

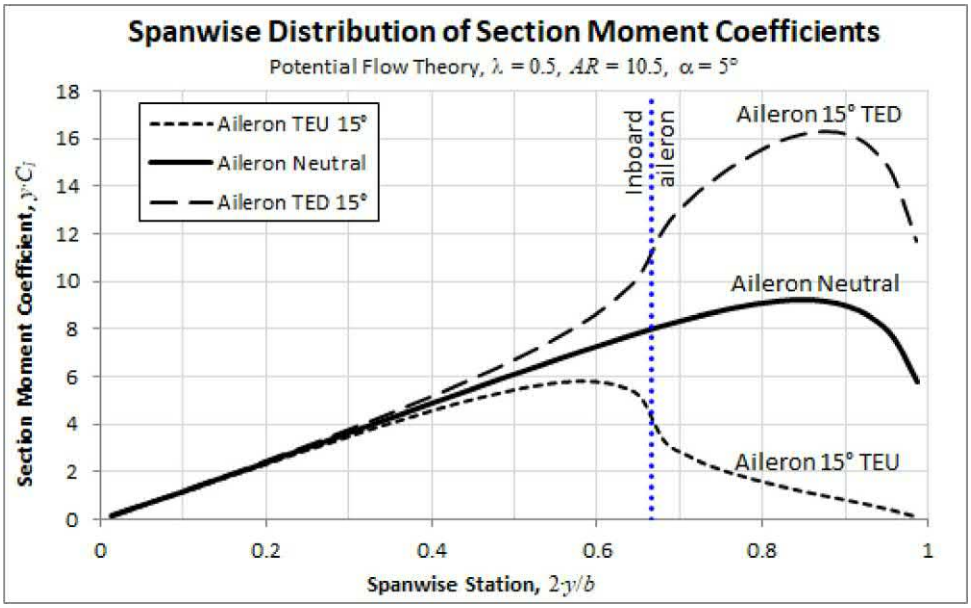


FIGURE 25-33 Distribution of section moments along the wing (in Figure 25-25).

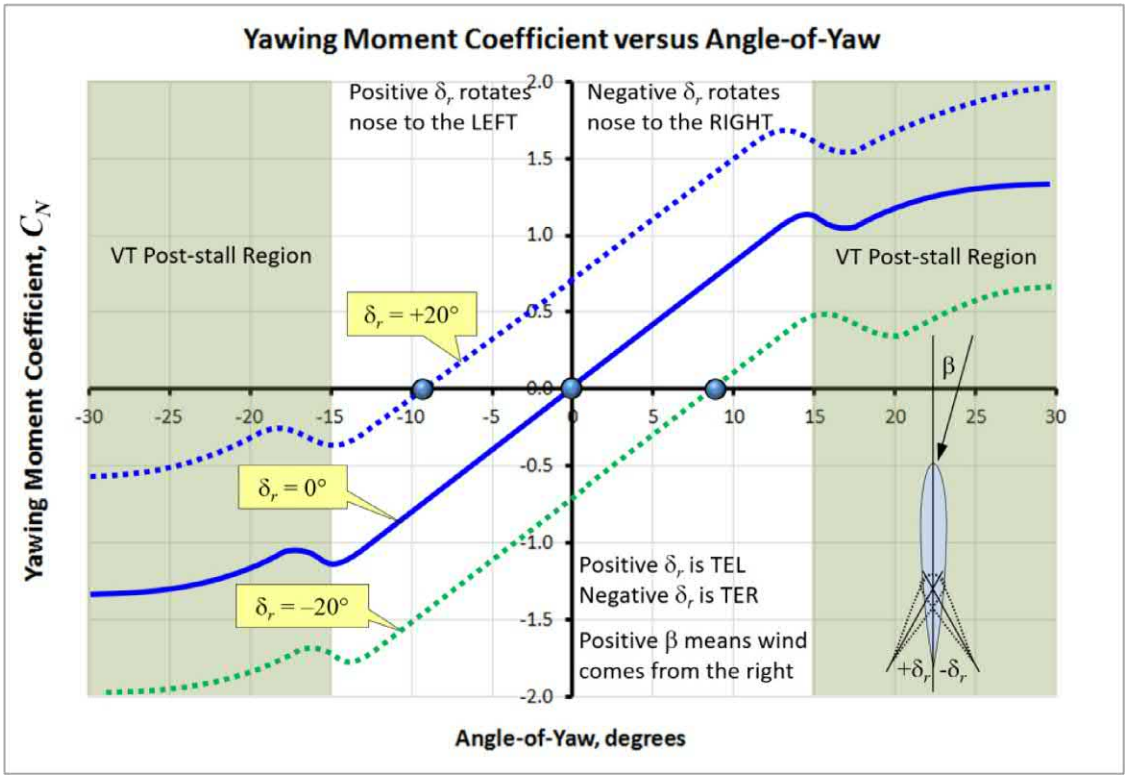


FIGURE 25-34 Yaw control explained. (VT = Vertical Tail, TEL = Trailing Edge Left, and TER = Trailing Edge Right.)

recovery, provided the designer follows the guidelines of Section 11.2.4. If this approach is not acceptable, the airplane configuration must be tested in a rotary balance wind tunnel or a spin tunnel. If unacceptable spin recovery is discovered after the prototype flies, there are several aerodynamic fixes to consider, some of which are presented in Section 11.2.4 and Chapter 26. Success is not guaranteed.

Figure 25-34 shows the yawing moment coefficient, C_N, versus angle-of-yaw (AOY) for an airplane with a conventional tail. This graph does not belong to any specific aircraft type, but rather shows what results one would expect from a wind tunnel test. The three curves represent the C_N for a complete aircraft with the rudder deflected left, neutral, and right. As with the elevator, it shows how deflecting of the rudder will shift the yawing

moment curve up or down, such the airplane is trimmed with the nose pointed to the left or right. The left most curve shows the C_N with the rudder deflected 20° Trailing Edge Left (TEL) ($\delta_r = +20°$) as would happen for a nose left slip. The center curve depicts the C_N with the rudder in a neutral position ($\delta_r = 0°$), and the bottom one depicts the rudder deflected 20° Trailing Edge Right (TER) ($\delta_r = -20°$), as would happen for a nose right slip. The separation between the curves represents the effective *rudder authority* for the aircraft. The curves show the classic linear upward slope required for a naturally statically and directionally stable aircraft. It also shows that below a certain AOY (typically around 12–15°) the C_N is linear, but beyond that becomes nonlinear.

As discussed in Section 25.2.3, *Requirements for Directional Stability*, the slope of the C_N curve must be positive as shown in Figure 25-34 for the aircraft to be directionally stable. This is indicated by the magnitude of the stability derivative C_{N_β}, simply referred to as *directional stability*. The required size of the rudder should be based on the investigation of the capability of the tail at the extreme yaw conditions stipulated in Section 26.2, *General Aviation Aircraft Design Checklist*. Such an investigation should evaluate the AOY at which the airplane can be trimmed with a given rudder deflection over the aircraft's entire airspeed- and CG-range. The sizing should ensure the required rudder deflection is less than what is available, per Section 26.2.

References

[1] D. Raymer, *Aircraft Design: A Conceptual Approach*, fourth Ed., AIAA Education Series. American Institute of Aeronautics and Astronautics, 2006.

[2] K. Robert, W.F. Jewell, *Aircraft Handling Quality Data*, Heffley, NASA CR-2144, Dec. 1972.

[3] R.C. Nelson, *Flight Stability and Automatic Control*, second Ed., McGraw-Hill, 1998.

[4] T.P. Ratvasky, R.J. Ranaudo, *Icing Effects on Aircraft Stability and Control Determined From Flight Data—Preliminary Results*, NASA TM-105977, 1993.

[5] F.O. Smetana, *Computer Assisted Analysis of Aircraft Performance, Stability, and Control*, McGraw-Hill Book Company, 1984.

[6] D.E. Hoak, *USAF Stability and Control DATCOM*, Flight Control Division, Air Force Flight Dynamics Laboratory, 1978.

[7] T.A. Toll, M.J. Queijo, *Approximate Relations and Charts for Low-Speed Stability Derivatives of Swept Wings*, NACA TN-1581, May 1948.

[8] C.D. Perkins, R.E. Hage, *Airplane Performance, Stability, and Control*, John Wiley & Sons, 1949.

[9] B.B. Klawans, J.A. White, *A Method Utilizing Data on the Spiral, Roll-Subsidence, and Dutch Roll Modes for Determining Lateral Stability Derivatives From Flight Measurements*, NACA-TN-4066, August, 1957.

[10] C.H. Zimmerman, *An Analysis of Lateral Stability in Power-Off Flight With Charts for Use in Design*, NACA-TR-589, November 17, 1936.

[11] A. Goodman, L.R. Fisher, *Investigation at Low Speeds of the Effect of Aspect Ratio and Sweep on Rolling Stability Derivatives of Untapered Wings*, NACA-TR-968, 1950.

[12] M.R. Napolitano, *Aircraft Dynamics—From Modeling to Simulation*, John Wiley and Sons, 2012.

[13] J.P. Campell, W.O. Mathews, *Experimental Determination of the Yawing Moment Due to Yawing Contributed by the Wing, Fuselage, and Vertical Tail of a Midwing Airplane Model*, NACA-WR-L-387, June 1, 1943.

[14] J.P. Campell, M.O. McKinney, *Summary of Methods for Calculating Dynamic Lateral Stability and Response and for Estimating Lateral Stability Derivatives*, NACA-TR-1098, January 1, 1952.

[15] J.H. Blakelock, *Automatic Control of Aircraft and Missiles*, John Wiley and Sons, 1965.

[16] M. McKinney Jr., *Experimental Determination of the Effects of Dihedral, Vertical-Tail Area, and Lift Coefficient on Lateral Stability and Control Characteristics*, NACA-TN-1094, July 1946.

[17] H.A. Pearson, R.T. Jones, *Theoretical Stability and Control Characteristics of Wings with Various Amounts of Taper and Twist*, NACA-TR-635, April 19, 1938.

[18] M.J. Queijo, *Theoretical Span Load Distributions and Rolling Moments for Sideslipping Wings of Arbitrary Plan Form in Incompressible Flow*, NACA-TR-1269, 1956.

[19] H. Glauert, *Calculation of the Rotary Derivatives Due to Yawing for a Monoplane Wing*, ARC R&M No. 866, 1923.

[20] A.S. Halliday, *Stability Derivatives of the Bristol Fighter*, ARC R&M No. 1277, 1930.

[21] J.P. Campell, A. Goodman, *A Semiempirical Method for Estimating the Rolling Moment due to Yawing of Airplanes*, NACA-TN-1984, December 1949.

[22] B. Etkin, *Dynamics of Flight—Stability and Control*, second ed., John Wiley and Sons, 1982.

[23] M.J. Abzug, E.E. Larrabee, *Airplane Stability and Control: A History of the Technologies that Made Aviation Possible*, second ed., Cambridge Aerospace Series, Cambridge University Press, 2002.

[24] F.E. Weick, J.A. Shortal, *Development of the N.A.C.A. Slot-Lip Aileron*, NACA TN-547, 1935.

[25] J.A. Shortal, *Wind Tunnel and Flight Test of Slot-Lip Ailerons*, NACA R-602, 1937.

[26] G. Duus, *The Nomad Story*, Online history of the GAF N-22 Nomadhttp://www.fourays.org/features_2005/nomad/nomad_1.htm, 2005 (Accessed 29 October 2011).

This page intentionally left blank

CHAPTER

26

Miscellaneous Design Notes

OUTLINE

26.1 **Introduction** 1007
26.1.1 The Content of This Chapter 1007
26.2 **General Aviation Aircraft Design Checklist** 1007
26.2.1 Control System Stretching 1007
26.2.2 Crosswind Capability at Touch-Down 1008
26.2.3 Balked Landing Capability 1008
26.2.4 Take-Off Rotation Capability 1009
26.2.5 Stall Characteristics 1009
26.2.6 Trim at Stall and Flare at Landing 1010
26.2.7 Horizontal Tail Stall 1010
26.2.8 Roll Authority 1012
26.2.9 Control System Harmony 1013
26.2.10 Climb Capability 1013
26.2.11 One-Engine-Inoperative Trim and Climb Capability 1013
26.2.12 Natural Damping Capability 1014
26.2.13 Miscellaneous Topics 1014
26.3 **Faults and Fixes** 1017
26.3.1 Stability and Control 1017
26.3.2 Stall Handling 1019
26.3.3 Flow Improvements 1024
References 1029

26.1 INTRODUCTION

The purpose of this final chapter is to gather in one place information considered important by the author, but hard to place in any other specific chapters.

26.1.1 The Content of This Chapter

- Section 26.2 presents a design checklist intended to help the project engineer identify potential shortcomings or important capabilities and how to design them out of or into the airplane. There are many areas where one can go wrong in the design of a new aircraft. The checklist helps to steer away from some of them.
- Section 26.3 presents examples of fixes to faulty aerodynamic characteristics. Since the airplane is a compromise of many focus areas, it is always possible it will suffer in one or more areas. Aircraft designers have been imaginative in the past and have come up with solutions to improve this, that, or the other thing. It is helpful to the aspiring designer to know there are possible solutions to an imperfect design.

26.2 GENERAL AVIATION AIRCRAFT DESIGN CHECKLIST

The following checklist is partially based on aviation regulations and partially on the author's own design and development experience. Its purpose is to help the aircraft designer steer away from common pitfalls during the design process. The designer should try and meet all applicable capabilities listed below, most of which are intended to increase the safety of the airplane. Any airplane that meets the below requirements should provide ample controllability and good handling. Note that many of the concepts are introduced in various sections of the book but are collected here for convenience.

26.2.1 Control System Stretching

When a pilot deflects a primary flight control (ailerons, elevator, or rudder) the aerodynamic hinge moment generated by the surface is carried through the entire control system. This stretches cables and loads up pulleys and other parts of the control system.

https://doi.org/10.1016/B978-0-12-818465-3.00026-4

Copyright © 2022 Elsevier Inc. All rights reserved.

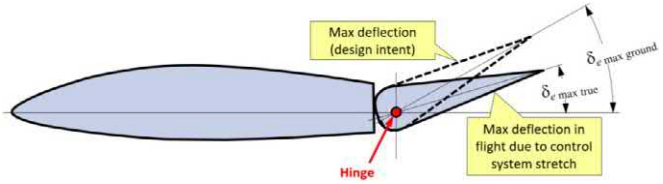


FIGURE 26-1 The consequence of a control system stretching.

If care is not exercised in its structural design, pulleys may be anchored to flexible foundations. This can substantially reduce the actual in-flight control surface deflection, compared to that measured on the ground (see Figure 26-1). The consequence is a serious reduction in control responsiveness.

The design team must thoroughly check the control system for flex during the construction of the first prototype. This must be accomplished by simulating the expected hinge moments. Some control systems are so poorly designed that some 25% of the ground deflection is available in flight. The result is sluggish responsiveness and dangerous handling characteristics. Consider an airplane, at a forward CG, initiating a flare maneuver just before landing. The maneuver may require, say 10 degrees of elevator deflection. In flight, a flexible control system may muster only 5 degrees, with the stick fully aft. An unsuspecting pilot might discover this when flaring and the result may be a broken nose landing gear if not worse. If certified, this would be discovered in the flying prototype and be rejected, requiring a redesign.

Figure 26-2 illustrates a common source of control system flexibility. The pulleys, A and B, have been mounted to brackets (or intercostals) that are attached to a bulkhead. The bracket for pulley A is longer than for pulley B. Additionally, pulley B is braced using a support bracket. Its deformation under load is insignificant compared to that of pulley A. Therefore, when the control system is loaded up, pulley A will be considerably displaced, causing cable slack that reduces the actual control surface deflection.

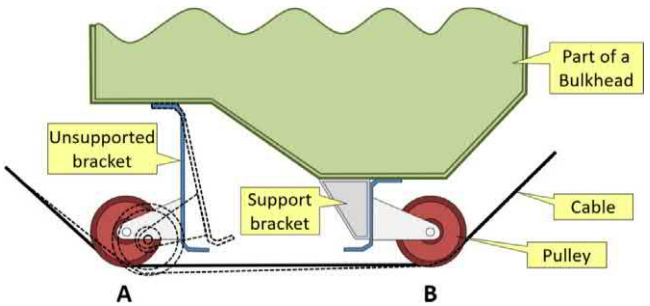


FIGURE 26-2 Control system loads cause the cable-pulley system to flex excessively rendering it ineffective.

Action Items

This is evaluated during the detail design phase. Always perform a thorough load analysis of the control system. Evaluate reaction forces at all hardpoints, where pulleys are mounted to the airframe. Knowing the reaction forces at each hardpoint, determine the deflection of the structure to which pulleys are attached. Use this to estimate the total deformation of the control system. For instance, consider an elevator control system designed to deflect to a maximum deflection of 25 degrees on the ground. The pilot should be capable of deflecting it to at least 19 degrees with maximum aerodynamic loads applied. If unable to, the control system flex points should be redesigned.

26.2.2 Crosswind Capability at Touch-Down

The airplane should be capable of maintaining *straight and level* (i.e., constant airspeed, heading, and altitude) flight while yawed 12–15 degrees (β) at an airspeed of $1.2V_{S_0}$, where V_{S_0} is the stalling speed in the landing configuration. This corresponds to a crosswind component of approximately:

$$V_W \approx 1.2V_{S_0} \cdot \tan(15°) = 0.322 \cdot V_{S_0} \tag{26-1}$$

Action Items

Evaluate this capability by a trim analysis at $\beta = 15°$ and $V = 1.2V_{S_0}$, with the CG in the most adverse location and with power required for level flight (at minimum a 3-degree approach angle). The control surface deflection required to trim the airplane should comply with the following:

(1) Aileron deflection, $\delta_a < 0.25\delta_{a\ max}$.
(2) Elevator deflection, $\delta_e < 0.50\delta_{e\ max}$.
(3) Rudder deflection, $\delta_r < 0.75\delta_{r\ max}$.

A factor like 0.75 is intended to leave 25% deflection capability remaining to allow the pilot to respond to gusts. If met, this requirement prevents the control surfaces from being undersized. Note that the maximums refer to deflections under airload and not ground deflections.

26.2.3 Balked Landing Capability

Balked landing occurs when a pilot aborts a landing, for instance, due to a vehicle driving across the runway. At this moment, the aircraft is in the landing configuration on final, maintaining its *landing reference airspeed* (V_{REF}) with landing gear and high-lift systems deployed. This is compounded by a sudden application of full power. At this condition, the dynamic pressure is low, which will require large control surface deflection. This

requirement is one of a few intended to prevent the HT from being undersized. Paragraph 14 CFR §23.73 defines V_{REF} as follows:

Normal, utility, and aerobatic piston powered aircraft with $W_0 \leq 6000\,\text{lb}_\text{f}$:

$$V_{REF} = \text{the larger of} \begin{cases} 1.3 \cdot V_{S1} \\ V_{MC} \end{cases} \tag{26-2}$$

Normal, utility, and aerobatic pistons and turbine powered aircraft with $W_0 > 6000\,\text{lb}_\text{f}$:

$$V_{REF} = \text{the larger of} \begin{cases} 1.3 \cdot V_{S_0} \\ V_{MC} \end{cases} \tag{26-3}$$

Commuter category aircraft with $W_0 > 6000\,\text{lb}_\text{f}$:

$$V_{REF} = \text{the larger of} \begin{cases} 1.3 \cdot V_{S_0} \\ 1.05 \cdot V_{MC} \end{cases} \tag{26-4}$$

Where: V_{S_0} = Stalling speed in the landing configuration.

V_{S1} = Stalling speed in the take-off configuration (max T-O flap setting).
V_{MC} = Minimum control speed (per 14 CFR §23.149(b)).

Action Items

Evaluate this capability by a trim analysis. It must be possible to trim the aircraft at V_{REF}, and it must be capable of a 3% climb gradient while at:

(1) Maximum power or thrust.
(2) At the forward edge of the proposed CG envelope.
(3) In the most adverse configuration (typically the landing configuration).

Control system stretch must be considered (see Section 26.2.1, *Control System Stretching*).

26.2.4 Take-Off Rotation Capability

The elevator authority must be sufficient to rotate the airplane at airspeeds below the liftoff speed, V_{LOF} with the CG in the most adverse location (forward for conventional aircraft). If met, this requirement (also see Section 26.2.3, *Balked Landing Capability*) helps prevent the HT from being undersized for elevator authority.

Action Items

Evaluate this capability using the formulation required to comply with Section 13.3.4, *Tricycle Landing Gear Reaction Loads*. Also, see Example 13-2. Strictly speaking, the analysis should demonstrate that the nose landing gear can be raised at airspeed below $0.9V_{S1}$.

26.2.5 Stall Characteristics

The aircraft should be designed with forgiving (docile) stall characteristics. There should be no wing roll at stall, no deep stall tendency, and, ideally, spin resistance should be considered. While stall characteristics cannot be guaranteed during the conceptual design phase, the designer can do much to improve the odds of docile stalls. Stalls must comply with 14 CFR §23.2110 and §23.2150 (14 CFR §23.49, and §23.201-207 in the "old" regulations).

(1) Normal Stalls—Terminology

"Stall-break"—It refers to the sudden, unstoppable nose-down pitch that occurs at stall.

Power-off Stall—The basic stall procedure as practiced by pilots: Power is idle, 1 knot/s deceleration while attempting to maintain altitude. This is done straight and level in the clean, T-O, and landing configurations. Target characteristics result in an aircraft that repeatedly recovers without rolling on one wing or the other.

Power-on Stall—It is also called *departure stall*. It can occur during climb after T-O and differs from the power-off stall in that it occurs at high power settings. Pilots practice this climbing straight and slightly banked (15–20 degrees). Target characteristics result in an aircraft that repeatedly recovers without rolling on one wing or the other.

Accelerated Stall—It occurs when performing steep turns, pull-ups, and similar maneuvers, such the load factor exceeds 1. This can happen when banking steeply, while maintaining altitude but, inadvertently, slowing down. The accelerated stall speed, V_{S_ϕ}, associated with bank angle ϕ, can be calculated from the expression below:

$$V_{S_\phi} = V_{S_{\phi=0^\circ}} \sqrt{n} = \frac{V_{S_{\phi=0^\circ}}}{\sqrt{\cos\phi}} \tag{26-5}$$

Where $V_{S_{\phi=0^\circ}}$ is the stalling speed with level wings.

Secondary Stall—It is caused when a pilot uses abrupt elevator input to recover from a previous stall. Depending on power setting and abruptness of control input, this stall could be a mixture of a power-on and accelerated stall. While this is a pilot error, the airplane should be expected to recover without rolling.

Action Items

Roll-off at Stall—Improve chances of docile stall characteristics using design tools such as wing washout, high-lift airfoils for the tip, and leading-edge extension per the design guidelines of Section 9.6.3, *Tailoring the Stall Progression*. Also note the wing planform shape has a significant

impact on stall characteristics. Selection of a planform that leads to poor stall characteristics demands strong arguments for justification. See Section 9.6, *Wing Stall Characteristics* for more information. Stall tailoring should be the norm for GA aircraft. The designer should also be familiar with the design topics discussed in Chapter 11, *The Anatomy of the Tail*.

(2) Abused Stalls—Terminology

Cross-Control Stall—It refers to an uncoordinated stall performed with ailerons deflected one way (e.g., left bank) and the rudder deflected left or right. Such a stall sometimes results when a pilot attempts to overcorrect a poorly executed approach and can lead to a crash at low altitudes (see Section 11.2.4, *Basics of Spin and Spin-Recovery*). Recovering from a cross-controlled stall is a required training for flight instructors, but not regular pilots [1].

Whip Stall—It occurs when an airplane is pitched to a near vertical attitude, after which it falls on its nose such the wing is subjected to AOA close to 90 degrees. This can demand a dangerous recovery procedure [2]. This maneuver should not be performed by regular pilots.

Deep Stall—It occurs when an airplane has a trim point in the poststall region. Related to the selection of T-tails.

Action Items

Cross-Control Stall—Improve chances of spin-recoverable characteristics per the discussion of Section 11.2.4, *Basics of Spin and Spin-Recovery*.

Whip Stall—Just don't do them.

Deep-stall—For deep-stall prone tail selection, confirm that no trim points exist in the poststall region in a wind tunnel (or by other reliable and acceptable means). Review the discussion of Sections 11.2.3, 11.3.3, and 11.3.13. Consider the installation of ventral fins.

26.2.6 Trim at Stall and Flare at Landing

There must be sufficient elevator authority to stall the airplane in its most adverse configuration. The stalling speed is the lowest airspeed at which the airplane can maintain level flight. An airplane has insufficient elevator authority if it does not experience a normal "stall-break." Instead, it descends rapidly at airspeed higher than the stalling speed. This can happen for specific forward CG-positions and even the entire CG-range. As far as aviation authorities are concerned, this becomes the airplane's minimum airspeed. This requires higher T-O and landing speed, with the associated demand for runway length. This can also cause a serious predicament if the aircraft cannot comply with the emergency landing requirements of 14 CFR Part 23, or the 45 KCAS stall speed limit of the LSA regulations.

Another easily overlooked characteristic is the ability to flare the aircraft in the most adverse configuration during touch-down. There are aircraft that have been certified with insufficient elevator authority. Such airplanes pose a serious risk to unsuspecting pilots. Any certified aircraft that is discovered to suffer from insufficient elevator authority should have a forward CG limitation imposed on it. Ideally, this is designed out of the airplane during the conceptual design phase.

Action Items

It must be possible to trim the aircraft at V_{S_0} while at:

(1) Minimum power.
(2) At the forward end of the proposed CG envelope.
(3) In the most adverse configuration (typically the landing configuration).

Control system stretch must be considered (see Section 26.2.1, *Control System Stretching*).

26.2.7 Horizontal Tail Stall

Tail aft configurations are subject horizontal tail stall under specific conditions, some of which include:

(1) Extreme wing downwash, such as that associated with the deployment of high lift devices. This increases the angle-of-attack on the stabilizing surface and may cause it to stall, fully or partially (see Figure 26-3). This is particularly serious if the HT has ice contamination.
(2) If flow separation develops in the HT/fuselage juncture (like that which occurs on the wing).
(3) Rapid nose-down pitch rate associated with the so-called *pushover maneuver* required per the "old" 14 CFR §23.145(a) (see Figure 26-4). It can be encountered when a pilot abruptly levels the airplane following a steep climb. This requires an elevator TED to initiate and a subsequent elevator TEU to terminate. If flaps are deployed, even in T-O setting, the HT angle-of-attack can reach its α_{stall}. Ref. [3] presents an in-flight investigation of an ice contaminated tailplane of a DHC-6 Twin Otter aircraft that gives insight into this problem.

A combination of these may suffice to push the HT over the line. The consequences range from a nuisance such as a broken nose gear and ground-struck propeller

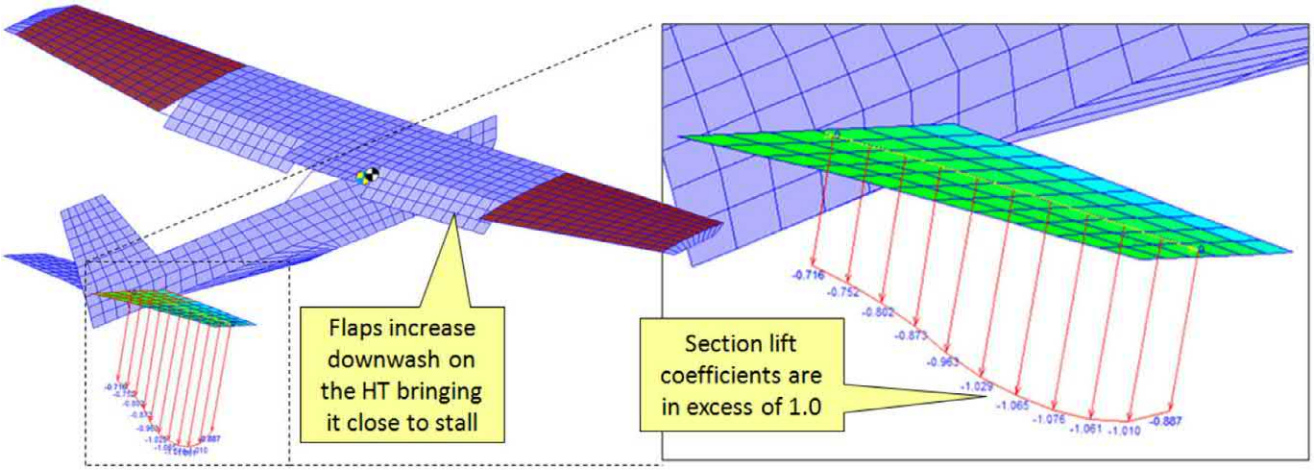


FIGURE 26-3 A VLM of a high wing aircraft with an all-movable stabilator reveals the stabilator section lift coefficients are close to their $C_{l_{max}}$ at 55 KCAS, $\alpha = 10$ degrees, flaps are deflected $\delta_f = 30$ degrees and stabilator $\delta_e = 15$ degrees.

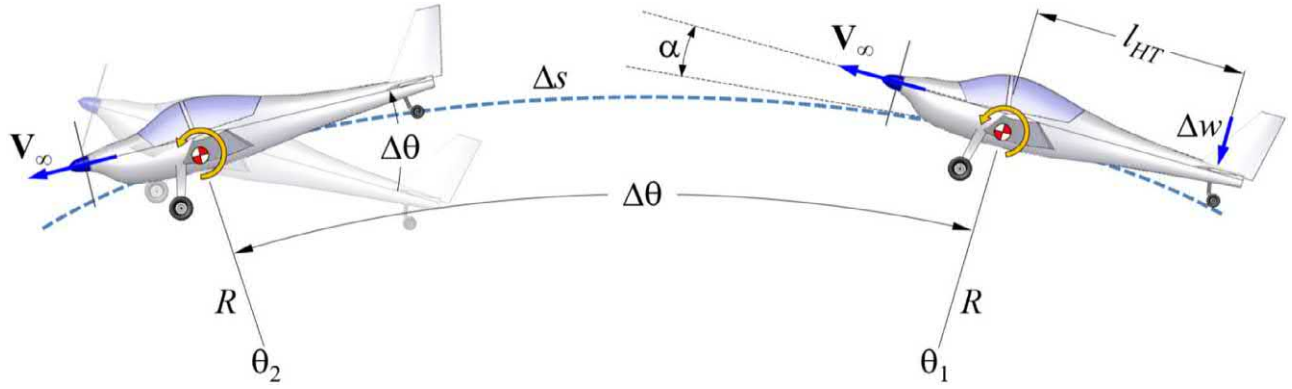


FIGURE 26-4 An aircraft undergoing push-over maneuver, changes its α_{HT}.

to dangerous in-flight handling problems that may cause the airplane to pitch over, nose-first.

The diagram of Figure 26-4 illustrates the pushover maneuver. As displayed, it represents what a flight test evaluation might look like. The angle-of-attack of the HT during the maneuver can be estimated per

$$\alpha_{HT} = \alpha\left(1 - \frac{2C_{L_\alpha}}{\pi AR}\right) - \frac{2C_{L_{0_W}}}{\pi AR} + i_{HT} - \frac{g(1-n)l_{HT}}{V_\infty^2} \qquad (26\text{-}6)$$

Action Items

Perform an analytical stability check on the airplane in its most adverse condition, with full flaps and most adverse forward CG and estimate the spanwise distribution of section lift coefficients (C_l) along the HT. This check can be accomplished using Vortex-Lattice or Doublet-Lattice solvers at minimum and, ideally, a Navier-Stokes solver or a wind tunnel test. Just calculating the total lift coefficient (C_{LHT}) generated by the HT is not enough. This does not indicate the spanwise distribution of C_l. For instance, the total lift coefficient generated by the HT in Figure 26-3 amounts to about $C_{LHT} = 0.95$, while the C_l peaks near 1.1. The maximum section lift coefficient ($C_{l_{max}}$) should be at least 0.2 above the largest C_l in the worst-case scenario. When the tail is contaminated with ice, the $C_{l_{max}}$ is significantly reduced. Thus, for the airplane in Figure 26-3, ice contamination could be a serious threat.

DERIVATION OF EQUATION (26-6)

Figure 26-4 shows the arclength is $\Delta s = V_\infty \Delta t$ and angular segment is $\Delta\theta = \theta_1 - \theta_2 = \Delta s / R$. The pitch rate is estimated from $\hat{q} = d\theta/dt \approx \Delta\theta/\Delta t = V_\infty / R$. The pitch-rate induces a vertical speed component (Δw) at the HT. This allows the corresponding change in AOA at the HT to be estimated:

$$\Delta w = \hat{q} l_{HT} = \frac{V_\infty}{R} l_{HT} \quad \Rightarrow \quad \Delta\alpha_{HT} = \frac{\Delta w}{V_\infty} = \frac{l_{HT}}{R}$$

At the top of the trajectory, its radius can be calculated as follows (note the different aircraft orientation compared to Figure (20-19)):

$$R = \frac{V_\infty^2}{g(1-n)} \quad \Rightarrow \quad \Delta\alpha_{HT} = \frac{l_{HT}}{R} = \frac{g(1-n)l_{HT}}{V_\infty^2}$$

Thus, the actual AOA at the HT depends on the true AOA (α), downwash (ε), HT angle-of-incidence (i_{HT}), and $\Delta\alpha_{HT}$. Assuming the downwash angle is given by Equation (24-89) as $\varepsilon = \varepsilon_0 + \alpha \cdot \partial\varepsilon/\partial\alpha$ and implemented per Equation (24-91), and further noting the direction of the pitch-down induced velocity component at the HT, we get

$$\alpha_{HT} = \alpha - \varepsilon - i_{HT} + \Delta\alpha_{HT}$$

$$= \alpha\left(1 - \frac{\partial\alpha}{\partial\varepsilon}\right) - \frac{2C_{L_{0_W}}}{\pi AR} + i_{HT} - \overbrace{\frac{g(1-n)l_{HT}}{V_\infty^2}}^{=\Delta\alpha_{HT}}$$

Furthermore, substituting $\partial\varepsilon/\partial\alpha = 2C_{L_\alpha}/(\pi AR)$, this becomes

$$\alpha_{HT} = \alpha\left(1 - \frac{2C_{L_\alpha}}{\pi AR}\right) - \frac{2C_{L_{0_W}}}{\pi AR} + i_{HT} - \frac{g(1-n)l_{HT}}{V_\infty^2}$$

EXAMPLE 26-1

An aircraft has tail arm $l_{HT} = 25.7$ ft, aspect ratio $AR = 10$, zero-alpha lift $C_{L_{0W}} = 0.45$ (no flaps) and 2.0 (35-degree flaps), lift curve slope $C_{L_\alpha} = 5.15$ per radian. Estimate α_{HT} for a pushover maneuver developing a load factor of $n = 0.5$ for the two flap settings as the airplane operates at 90 KCAS and wing loading of $W/S = 30\,\text{lb}_\text{f}/\text{ft}^2$. Assume the HT incidence angle (i_{HT}) is 0 degrees.

SOLUTION:

First, determine the lift coefficient:

$$C_L = \frac{2}{\rho V_\infty^2}\left(\frac{W}{S}\right) = \frac{2}{(0.002378)(90 \times 1.688)^2}(30) = 1.093$$

AOA for no – flaps condition:

$$\alpha = \frac{C_L - C_{L_0}}{C_{L_\alpha}} = \frac{1.093 - 0.45}{5.15(\pi/180)} = 0.1249 \text{ rad} \quad (= 7.156°)$$

AOA for HT at condition (no-flaps):

$$\alpha_{HT} = \alpha\left(1 - \frac{2C_{L_\alpha}}{\pi AR}\right) - \frac{2C_{L_{0_W}}}{\pi AR} - i_{HT} - \frac{g(1-n)l_{HT}}{V_\infty^2}$$

$$\alpha_{HT} = (0.1249)\left(1 - \frac{2(5.15)}{\pi(10)}\right) - \frac{2(0.45)}{\pi(10)} - (0) - \frac{(32.174)(1-0.5)(25.7)}{(90 \times 1.688)^2}$$

$$= 0.03739 \text{ rad} \quad (= 2.142°)$$

AOA for 35° flap condition: $\alpha = \dfrac{C_L - C_{L_0}}{C_{L_\alpha}}$

$$= \frac{1.093 - 2.0}{5.15(\pi/180)} = -0.1761 \text{ rad} \quad (= -10.09°)$$

AOA for HT at condition (35° flaps):

$$\alpha_{HT} = \alpha\left(1 - \frac{2C_{L_\alpha}}{\pi AR}\right) - \frac{2C_{L_{0_W}}}{\pi AR} - i_{HT} - \frac{g(1-n)l_{HT}}{V_\infty^2}$$

$$= (-0.1761)\left(1 - \frac{2(5.15)}{\pi(10)}\right) - \frac{2(2.0)}{\pi(10)} - (0) - \frac{(32.174)(1-0.5)(25.7)}{(90 \times 1.688)^2}$$

$$= -0.2636 \text{ rad} \quad (= -15.10°)$$

Two observations: (1) This example assumes a Twin-Otter "class" aircraft, presented in Ref. [3]. It assumes a NACA 63A516 airfoil, like that of the Twin-Otter. These results seem reasonable when compared to Figure 4 in the reference. (2) It is not hard to imagine that an ice contaminated HT at an AOA of −15° would stall.

26.2.8 Roll Authority

The airplane must provide roll capability appropriate to the class in which it falls. This affects ailerons sizing. Aerobatic airplanes offer *steady state roll rate* ranging from 130°/s to greater than 360°/s. A responsive GA aircraft roll as fast as 90°/s and sluggish ones as slowly as 30°/s. Roll requirements are stipulated in 14 CFR §23.157, *Rate of Roll*. The paragraph is split into two parts; take-off and approach for landing, as listed below.

(1) Take-Off Requirement

The airplane must have flaps in the T-O position and retractable landing gear should be in the stowed position. Single engine aircraft must be at maximum T-O power. Multiengine aircraft must have the critical engine inoperative (see Chapter 15, *Thrust Modeling for Propellers*) and the others at the maximum T-O power. The airplane shall be trimmed at airspeed equal to the greater of $1.2V_{S1}$ or $1.1V_{MC}$ or as close as possible in trim for straight flight. In this condition, the airplane must be capable of rolling from −30 to +30 degrees (or the other way around) within the following time constraints:

$$t = \begin{cases} 5\,\text{s} & \text{if } W \le 6000 \text{ lb}_\text{f} \\ \left(\dfrac{W + 500}{1300}\right) \text{ up to } 10\,\text{s} & \text{if } W > 6000 \text{ lb}_\text{f} \end{cases} \qquad (26\text{-}7)$$

(2) Approach Requirement

The airplane must have flaps in the landing position and retractable landing gear must be extended. All engines must be operating at a power setting for a 3°

approach angle. The airplane shall be trimmed at V_{REF}. In this condition, the airplane must be capable of rolling from −30 to +30 degrees within the following time constraints:

$$t = \begin{cases} 4\,\text{s} & \text{if } W \le 6000\ \text{lb}_\text{f} \\ (W + 2800)/2200 \text{ up to } 7\,\text{s} & \text{if } W > 6000\ \text{lb}_\text{f} \end{cases} \quad (26\text{-}8)$$

Action Items

During the conceptual or preliminary design phase, the designer should evaluate the aileron authority derivative (see Section 25.5.1, *Fundamentals of Roll Control*) and calculate the steady-state roll rate at the high and low speed ends of the flight envelope (see Section 20.3.10, *Flight Envelope*). This should then be compared to the requirements of 14 CFR §23.157 to evaluate if the design will comply. It is imperative not to overlook that the aileron span cuts into the span of the flaps. Therefore, if the solution to a potentially sluggish design is to add aileron span, the impact on the stalling speed of the vehicle should be evaluated as well. However, the evaluation should not stop there. The designer should calculate the aileron authority derivative for other aircraft as well for comparison; in particular, aircraft that are known to be considered sluggish by its pilots. Sluggishness should be designed out of the aircraft during the conceptual design phase—failing to do so may require difficult design fixes once the Proof-of-Concept aircraft demonstrates lack of responsiveness.

26.2.9 Control System Harmony

Design the control system such the harmony in control forces will be aileron:elevator:rudder = 1:2:4. This means that the effort required to actuate the elevator will be about 2 times that of the aileron and the rudder about 4 times that of the aileron. This calls for awareness of how to estimate hinge moments of control surfaces and control system gains. See Section 24.4, *Introduction to Hinge Moments* for more detail.

26.2.10 Climb Capability

With all engines operating, the airplane must have enough power to maintain the following steady climb gradients (also see Section 19.3, *General Climb Analysis Methods* on how to calculate V_Y) at sea-level:

Normal, Utility, and Aerobatic piston powered aircraft with $W_0 \le 6000\,\text{lb}_\text{f}$:

$$\text{Landplanes:} \quad ROC > 0.083\frac{V_Y}{60} \times 6076 = 8.405 V_Y \quad (26\text{-}9)$$

Seaplanes and amphibians:

$$ROC > 0.067\frac{V_Y}{60} \times 6076 = 6.785 V_Y \quad (26\text{-}10)$$

Where V_Y is the best rate of climb airspeed in KTAS.

These are minimums (per the "old" 14 CFR Part 23) at *maximum continuous power* (MCP) conditions at Sea-Level. The airplane may have landing gear retracted and flaps in the take-off position. The value of V_Y for multiengine airplanes shall be greater or equal to the greater of $1.1V_{MC}$ and $1.2V_{S1}$. For single engine aircraft V_Y shall be greater or equal to $1.2V_{S1}$.

Normal, Utility, and Aerobatic pistons and turbine powered aircraft (landplanes) with $W_0 > 6000\,\text{lb}_\text{f}$:

$$ROC > 0.040\frac{V_Y}{60} \times 6076 = 4.051 V_Y \quad (26\text{-}11)$$

These are minimums at *take-off power* at Sea-Level. The airplane shall have landing gear extracted unless it can be retracted in fewer than 7 s. Flaps shall be in the take-off position.

Action Items

Demonstrate through analysis, assuming conservative conditions, by evaluating the climb capability on a hot day (ISA + 20°C) at S-L and diminished propeller efficiency or jet engine thrust. Although not a direct requirement, multiengine aircraft should be evaluated in the take-off condition. Consider redesign if the condition is marginally met, including more powerful engines.

26.2.11 One-Engine-Inoperative Trim and Climb Capability

Multiengine aircraft must offer safe trim capability and enough power to climb with *one-engine-inoperative* (Section 15.2.5, *Asymmetric Yaw Effects—Multi–Engine Aircraft* details the origin of the asymmetric yaw). Such aircraft must be capable of straight and level flight (albeit with control surfaces deflected and $\beta \neq 0$ and $\phi \neq 0$). This can be done in "countless" ways [4]. Three such cases are shown in Figure 26-5.

Case 1: The rudder balances the asymmetric moment. However, its side force must be balanced out. This is accomplished by slightly banking the airplane in the opposite direction (on the good engine). This is the standard procedure because it results in low drag and stick forces.

Case 2: This is an extreme version of Case 1 in which the airplane is yawed to a large sideslip angle. This

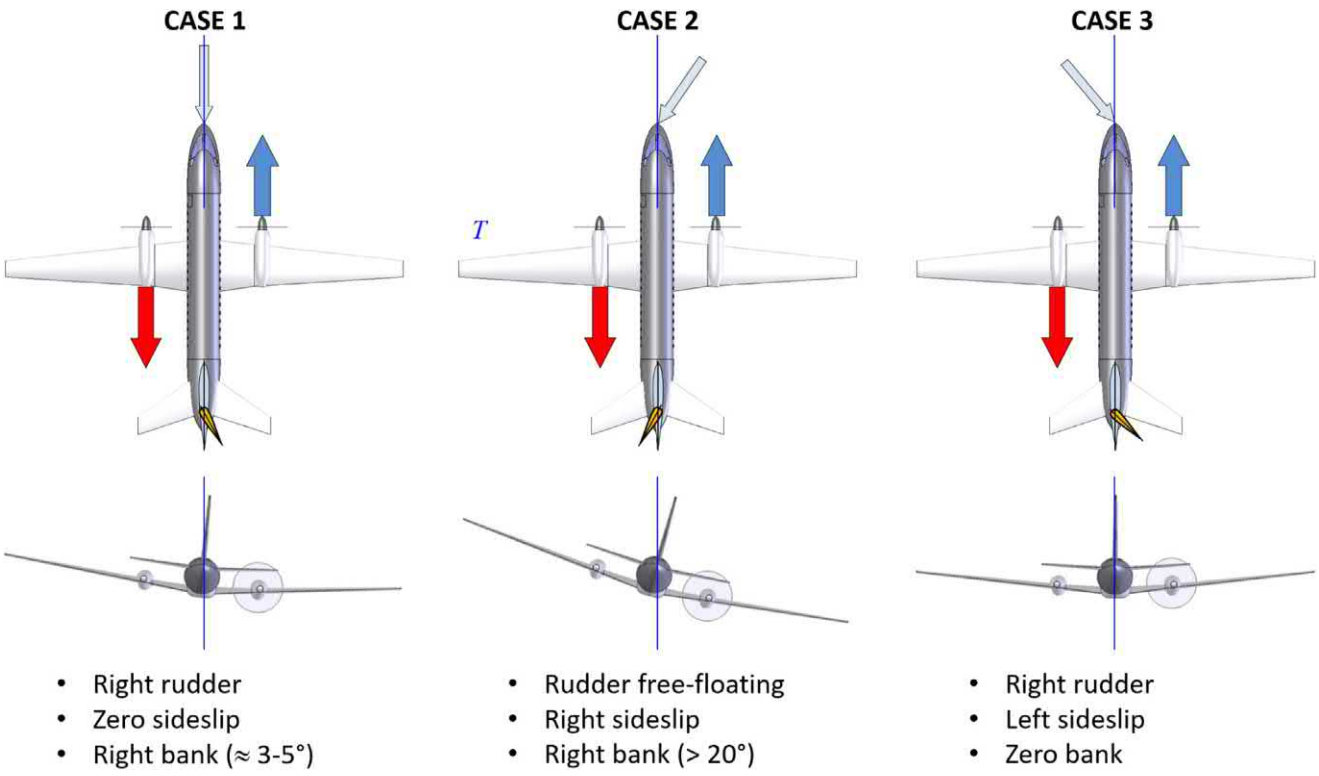


FIGURE 26-5 Three combinations of sideslip and banking that result in straight flight path with asymmetric power. *Based on F.D. Nelson, AFFTC Stability and Control Techniques, AFFTC-TN-59-21, Air Force Flight Test Center, 1959.*

induces a large side force angle that is balanced using a large bank angle on the good engine. This leaves the rudder with low to none hinge moment in the opposite direction as shown in the figure.

Case 3: A powerful enough rudder can balance the asymmetric thrust, while producing sideslip opposite the rudder side force. This permits a straight and level (zero bank angle).

Action Items

During the development phase of the aircraft, this capa bility can be demonstrated through analysis using the analysis methods presented in this book; for instance, those of Chapter 19, *Performance—Climb*, using reduced engine power, increased drag coefficient (due to asymmetry), at gross weight, and on a hot day (ISA+20°C). Consider redesign if the condition is marginally met, including more powerful engines.

26.2.12 Natural Damping Capability

The airplane should be designed such its dynamic stability modes are naturally damped. Albeit undesirable, diverging nonoscillatory modes may be acceptable, provided the time to double amplitude is long enough to allow the pilot an effortless correction. However, oscillatory modes should always be convergent. This is required per ASTM F2245 for LSA.

Action Items

Perform a detailed dynamic stability analysis of the airplane in all operational configurations (take-off, cruise, and landing) over the operational flight envelope of aircraft. All oscillatory modes should be convergent, as required by applicable airworthiness regulations. Identify regions of divergent dynamic modes, if these exist, and consider the introduction of aerodynamic fixes or limitations of the flight envelope. These can be lifted if findings are rejected by flight test work.

26.2.13 Miscellaneous Topics

The remaining items do not require specific action items other than recognition when they occur within your organization. If they do, ensure the awareness is shared.

(1) Reliance on Analysis Technology

Despite convenience and computational prowess, computer analysis methods pose a pitfall for the aircraft designer. Extremely compelling images generated by such software make it easy for even the most seasoned

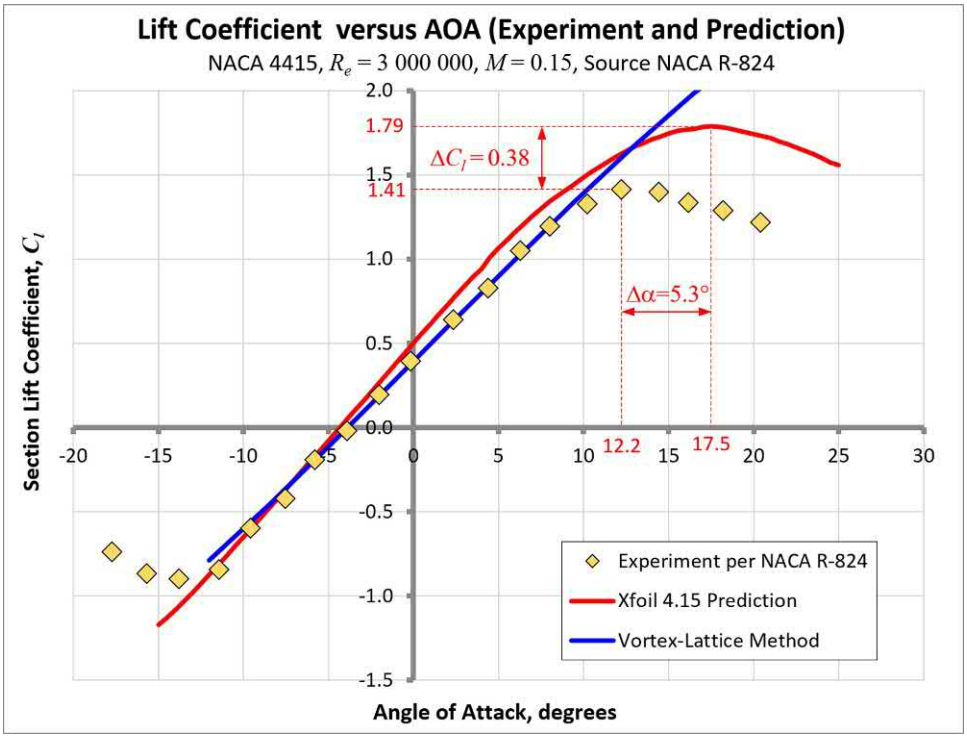


FIGURE 26-6 Experimental lift curve compared to two computational techniques.

designer to forget to second-guess the results. The results may be way off. Figure 26-6 shows an example of two computational methods as compared to an experiment for the NACA 4415 airfoil as reported in Ref. [5]. One uses the widely used code Xfoil and the other is the Vortex-Lattice code Surfaces. Two important observations can be made by studying the figure.

First, inviscid computational methods such as the Vortex-Lattice Method (VLM) do not predict flow separation. While the VLM results are in good agreement with the experiment, this is only true in the linear range. The speed and flexibility of VLM renders it a great tool for the aircraft designer, but results are valid only if the airflow is mostly attached. For instance, in this example, the VLM results are acceptable over the AOA range of $-12\,^\circ < \alpha < 10\,^\circ$.

Second, while Xfoil predicts a docile stall behavior as shown in the experiment, its predictions are off in slope, and both $C_{l_{max}}$ and α_{stall} are too large, just to name a few. The important to recognize that the unaware aircraft designer is likely take such predictions at face value and, in this case, underestimate wing area. The best advice is to check results for similar airfoils first and fully understand the limitations of the computational method. Just because a computational method offers viscous approximation does not mean it is accurate. An operator error is always a possible explanation too. For the record, in the experience of this author, Xfoil gives good predictions for some airfoils.



FIGURE 26-7 Two dissimilar predictions of stall progression on a wing design. The left side uses a structured mesh, the right one an unstructured mesh. The left and right sides are geometric mirror images. The left side ended up better resembling experiment and had favorable stall characteristics.

Figure 26-7 shows stall progression predictions by two Navier-Stokes solvers. The left-wing half was meshed using a structured grid, and the right one using an unstructured grid. The image shows flow separation patterns at $\alpha = 18\,^\circ$. The disparity in the stall pattern is evident. Which prediction better resembles reality? Neither? Obviously, it is impossible to answer without experiment. However, an aerodynamicist armed with only one solver has no choice but to rely on it—often erroneously. Be careful—your development program may be at stake.

Always check the results of any computer analysis software by conducting validation tests. When dealing with aerodynamics design, validation is only acceptable when it consists of comparison to actual wind tunnel tests. *"Validation" using two computational methods is not a validation, but a comparison*. When possible, select wind tunnel test results for geometry that most closely resembles the one being analyzed. If such wind tunnel test results cannot be found, select a different, trustworthy

geometry. When dealing with structural tests, validation is only acceptable when compared to actual load tests. Such comparison will build trust in software and expose the limitations of the methods. Only an understanding of the limitations of a computational method will lead to a proper use.

(2) Weight Estimation Pitfalls

The most common pitfall in the estimation of weight is underestimation. This usually stems from the omission of systems whose weight is poorly defined, but sometimes simply a human trait—optimism. If left to its own devices, it can bring about serious trouble. Inevitably, an inexperienced designer asked to guess the weight of a component inside some weight range, is likely to pick the lower end of the range if the component is destined for use in his own design. Of course, this is less of a problem among experienced designers, but a pitfall it remains nonetheless. The remedy? Realism enforced by thorough regular checks and reporting using a weights range based on low and high component weights, rather than a single value.

(3) Drag Estimation Pitfalls

There are two common pitfalls when estimating drag: over- and underestimation. Drag is notoriously hard to estimate correctly. Overestimation may make an otherwise promising idea appear as a slug on paper and lead to project termination before it even begins. Underestimation is devastatingly disappointing once the airplane flies. It can also be a financial catastrophe. It is often caused when significant protrusions being "left out" of the calculations during the conceptual design phase (for instance see Section 15.5.1, *Cumulative Result of Undesirable Drag (CRUD)*). The remedy? Ensure the drag estimation is thoroughly checked by experienced people, although this does not always suffice. Estimate the drag of several airplanes that appear like the one being designed. If the drag estimate of the new design deviates from those this should raise a flag. While this discussion pertains to the state of the project before a wind tunnel model is even considered, it is possible the right answer will not emerge until it has been conducted.

(4) Center of Gravity Travel during Flight

Most airplanes experience a movement of the center-of-gravity (CG) during flight. This is caused by fuel consumption and, sometimes, by mass being ejected; for instance, military aircraft dropping ordnance, aerial firefighter dropping water, or parachutists jumping. The designer should plot the CG travel as a function of such weight reduction and ensure it remains inside the prescribed CG limits. This is discussed in more detail in Section 6.7.4, *In-Flight Movement of the CG*.

(5) Flow Separation in Wing/Fuselage Juncture

The juncture where the wing joins the fuselage can increase drag. It is often left to flight testing to evaluate, but by then, it might require expensive design changes. Established companies spend resources on developing proper wing root fairings; however, recent ones often wait for flight testing to assess the severity of the flow separation. Before flight-testing, the initial fairing geometry can be designed using some straightforward rules of thumb. Ultimately, a Navier-Stokes solver or wind-tunnel testing is required to complete the shape as the flow field in this region is simply too complicated to assess by other means.

(6) Fuel Tank Selector

Airplanes with multiple fuel tanks and a fuel tank selector should always place it inside the cockpit in the field of view of the pilot. Never place it such the pilot must look away or "feel" to figure out the currently selected fuel tank. Many aircraft crash every year because of fuel starvation attributed to pilot "thinking" the correct tank had been selected [6]. Also, when flying by Instrument Flight Rules (IFR), vertigo can result if the pilot is forced to turn away from the instrument panel to view the fuel selector. The convenience of the pilot takes precedence over the convenience of the engineer or the technician routing or installing the fuel selector valve.

When designing the cockpit ensure the fuel tank selector is inside the pilot's field of view and range of reach. This important control should be treated as if it was between the primary (ailerons, elevator, rudder, throttles, etc.) and secondary controls (flaps, trim controls, speed brakes, etc.) in importance. The detail may have to be developed using a cockpit mockup.

(7) Control System Jamming

Control system jamming is a serious threat in brand new airplanes. It is easy to overlook how control surfaces can get stuck (or jam) as they flex due to air loads, or how the deformation of the control system might get cables and pushrods into positions that might get things stuck. Conduct a design review with cognizant engineers and critically evaluate possible control-system jamming scenarios. Do not dismiss scenarios that seem "outlandish." Unlikely scenarios are the ones that tend show up in practice. Get fresh eyes to look at the design as well. Be critical.

(8) Ground Impact Resistance

Airplanes with forward facing firewalls should feature a canted firewall (see Figure 26-8). This can prevent the aircraft from "digging in" during a nose-down crash attitude. The reduced deceleration improves the chances of survival, making the difference between life and death.

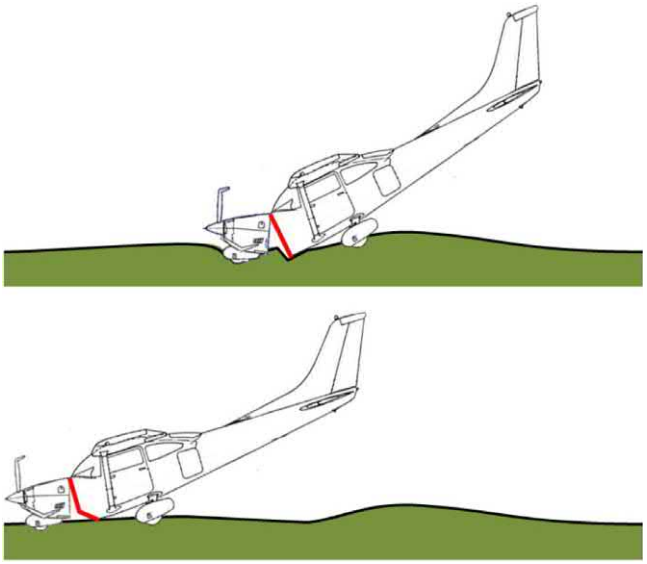


FIGURE 26-8 The difference between canted and uncanted firewalls is improved survivability.

Design a forward-facing firewall such its lower edge is canted aft as shown in Figure 26-8. Awareness is key and renders the topic a nonissue if this is introduced during the conceptual/preliminary design phase.

26.3 FAULTS AND FIXES

While aircraft design is more science than art, the combination of the two plays a profound role in the final product. Many design decisions are biased by a sense of aesthetics and ergonomics of operation. Often, during flight testing, the resulting aircraft displays unexpected and undesirable characteristics. These range from a nuisance to being a threat to the viability of the project. Many require aerodynamic fixes. This section addresses common faults and fixes of this nature. It is intended to provide possible solutions to challenges for the practicing engineer.

26.3.1 Stability and Control

(1) Dorsal Fin and Rudder Locking

The primary reason for the installation of a dorsal fin is to prevent *rudder locking*, a phenomenon that may occur if the yaw angle of the aircraft becomes too large. The phenomenon is discussed in detail in Section 11.2.3, *Various Tail Fixes*.

(2) Ventral Fin and Deep Stall

As stated in Section 11.2.3, *Various Tail Fixes*, there are two kinds of ventral fins: (A) to prevent deep stall or (B) to fix Dutch roll. Let us deal with the former here. While it is well-known that T-tail may cause deep stall (in particular



FIGURE 26-9 The ventral fin on this Learjet 60 improves longitudinal stability that prevents it from entering deep stall. *Photo by Phil Rademacher.*

swept wing aircraft), it remains a common choice in aircraft design. The justification varies: The T-tail configuration of the Lockheed F-104 Starfighter was intended to increase its effectiveness through an endplate effect [7]. Other justifications range from improvements in spin recovery to reduced pitch-changes and aesthetics (see Section 11.3.3, *T-Tail*). If deep stall tendency is discovered in wind tunnel or flight testing, a ventral fin is a proven fix. Reynolds [8] present a good discussion of the development of ventral fins on the Learjet 55. Figure 26-9 shows the ventral fins on a Learjet 60.

(3) Ventral Fin and Dutch Roll

A ventral fin is also used to increase the vertical or side silhouette of an airplane to improve its Dutch roll damping or increase directional stability of a multiengine aircraft when operating with One Engine Inoperative (OEI). Ventral fins for this purpose are installed in a far more vertical position than those intended to fix deep stall.

(4) Forebody Strakes

As discussed in Section 26.2, *General Aviation Aircraft Design Checklist*, the sizing of the vertical tail considers critical asymmetric flight conditions: crosswind landings, balked landing, one-engine-inoperative trim capability, and many others. The resulting fin size can be large and increases both drag and airframe weight. It is common in the commercial aviation industry to "stretch" or lengthen jetliners to accommodate more payload. The modification is frequently accomplished without resizing the VT. This destabilizes the aircraft, longitudinally and directionally, and may result in unacceptable handling. Alternatives that neither increase drag nor require an expensive redesign are attractive and of great interest to the aircraft designer. The forebody strake is one such alternative.

One of the best-known research programs on forebody strakes was run by NASA's Dryden Flight Research Center, Edwards, CA. A retired F-18 Hornet fighter was restored and equipped as a *High Angle-of-Attack Research Vehicle* (HARV). The flight research program lasting from

April 1987 until September 1996 [9]. The program focused on flight at $\alpha > 30°$ and identified the nose geometry as a key player in the lateral stability of the aircraft at high AOAs [10]. The resulting crossflow on the forebody is considerable and the resulting asymmetry in pressure on the nose generates significant side force. This force acts across a large distance between the forebody and the CG, creating a large yawing moment. The research successfully demonstrated that directional control could be exerted using deployable strakes installed in the nose. This research lead to a cooperation between NASA Langley Research Center and McDonnell-Douglas Corporation (now Boeing) to develop strake technology for use with transport aircraft. Of course, such aircraft operate at much lower AOAs, something closer to 8° during approach for landing, so different kind of strakes had to be developed.

Shah and Granda [11] studied the use of forebody strakes to improve directional stability of a wind tunnel model of a generic commercial jetliner. This was done as part of a cooperative research between NASA and Boeing referred to as Strake Technology Research Application to Transport Aircraft (STRATA). The strake is a flat plate that is mounted on the forward part of the fuselage, of which an example can be seen in Figures 26-10 and 26-11. These were mounted to the 50-series of the McDonnell-Douglas DC-9 when it was stretched from the 30-series aircraft. These were also installed on the DC-9-80, also known as the MD-80. Their findings are summarized below. The MD90, another derivative of the DC-9, features *engine strakes* to enhance longitudinal control for poststall recovery [12] (see Figure 26-12).

1. A set of baseline strakes similar in planform and location to those on the MD-80 aircraft improved the model's static directional stability. As AOA increased, the AOY at which the strakes became effective decreased. This indicates that a critical level of fuselage crossflow is required for the strakes to become effective.
2. It was found that it is the leeward strake that alters the flow-field and improves stability; the windward strake has negligible effect.
3. The improvement in directional stability is proportional to the span of the strake.
4. The effect of strake chord on stability is nonlinear; most of the effectiveness above stall a can be achieved with a strake with a small chord.
5. A nose-up incidence of the strake has minimal effect on longitudinal stability; negative incidence has a nonlinear and degrading effect.
6. The effectiveness of single or differentially deflected strakes as a directional control device was small and very nonlinear; however, only a limited investigation was conducted in this area.

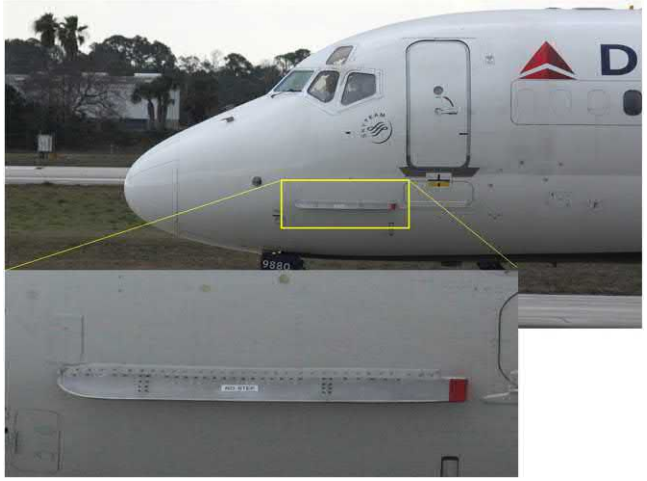


FIGURE 26-10 A forebody strake is mounted to the nose section of this DC-9 commercial jetliner. *Photo by Phil Rademacher.*

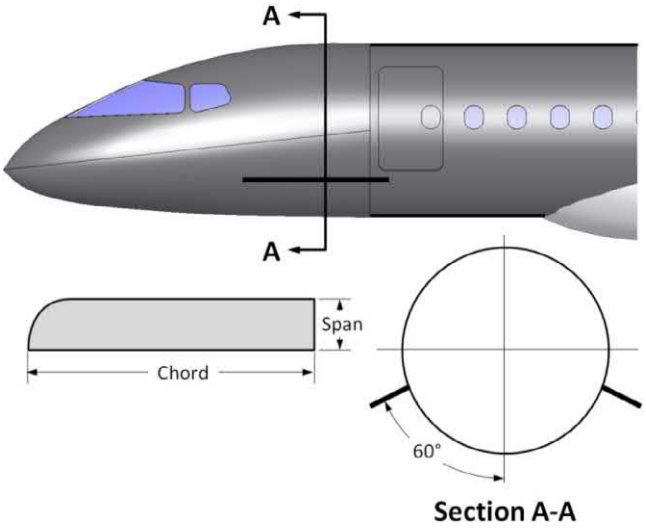


FIGURE 26-11 Forebody strake geometry and positioning.



FIGURE 26-12 An engine strake on a MD90 commercial jetliner. *Photo by Phil Rademacher.*

7. The forebody strakes are de-coupled control effectors—very little impact on static longitudinal and lateral characteristics was seen.

(5) Taillets and Stabilons

Taillets and *stabilons* are terms coined for modifications made to the twin-engine Beech 1900 commuter aircraft (see Figure 26-13). The design dates to the late 1970s and early 1980s, developed from the Beech Super King Air to compete with the Swearingen Metro and the British Aerospace Jetstream. It accommodates 19 passengers in a pressurized cabin and is powered by two 1100 SHP Pratt & Whitney PT6 turboprops, driving 4-blade propellers, capable of 235 KTAS at 25,000 ft. The Beech 1900D is a variant of the 1900 with an enlarged fuselage that offers a stand-up cabin. This was accomplished without changing the dimensions of the original tail. This increased drag, requiring more powerful engines. This, combined with reduced directional stability due to a larger fuselage, called for the addition of ventral fins and taillets. Each taillet adds about 1.67 ft^2 of area to the total vertical stabilizing area and improves Dutch roll damping. This prevents the airplane's yaw damper from being a nondispatch critical component [13].

The term stabilon refers to a couple of 7.75 ft^2 horizontal ventral fins that are mounted to the lower aft part of the fuselage (again see Figure 26-13). These increase longitudinal stability and allow the Center of Gravity to be farther aft than otherwise, making the airplane less sensitive to passenger and baggage loading. According to Ref. [13] (which cites Beech sources) the stabilons increase the aft CG limit from 32% MGC to 40%. They also improve "deep" stall recovery characteristics.

(6) Stability and Control–Control Horns

Control horns are extensions that are placed on control surfaces, such as ailerons, elevators, and rudders for reducing aerodynamic hinge moments. This is accomplished by adding area of the surface ahead of the hingeline. Control horns come in many sizes and shapes. There are two common types: *unshielded* and *shielded*. Shielded control horns are recommended for airplanes that are certified to fly into known icing (FIKI—Flying Into Known Icing) as they do not accrete ice like control horns that are more directly exposed to the elements (see Section 24.4.4).

26.3.2 Stall Handling

(1) Stall Handling—Stall Strips

A stall strip is a small triangular strip made out of metal or rubber that is bonded to the leading edge of a wing to suppress roll tendency during stall (see Figure 26-14). Such a strip can be seen on the leading edges of most manufactured aircraft, as they must comply with regulations such as 14 CFR Part §23.201, Wings level stall.

Production tolerances render all serial numbers of a given aircraft model similar, but not precisely the same.

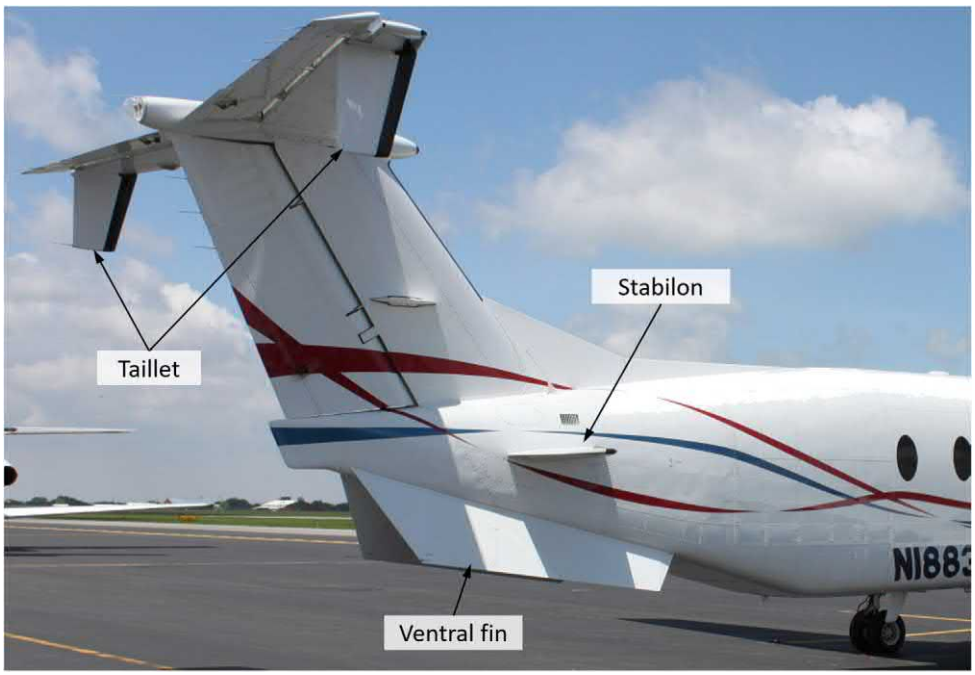


FIGURE 26-13 This is what happens when an existing airframe is adapted to modified requirements. A Beech 1900 commuter boasts an assortment of aerodynamic fixes: taillets (small vertical surfaces on each stabilizer), ventral fins (bottom of fuselage), and stabilons (above the lower ventral fins). *Photo by Phil Rademacher.*



FIGURE 26-14 Stall strips on a Cessna Citation X and Diamond DA-42 Twinstar aircraft. *Photo by Phil Rademacher.*

Yes, all Cessna 172 aircraft look alike to the untrained eye. However, when compared to the intended Outside Mold Line (OML) they are all dissimilar in small way. This holds for all mass-produced aircraft. When airplanes come off the production line, they are test flown by the production flight test team and stalled to confirm stall characteristics. Then, based on the observation of the test pilot, stall strips are bonded in a specific location on the leading edge.

Stall strips are detrimental in that they may cause an early separation even at climb AOA. This is manifested as a reduction in climb performance. They can also be detrimental on NLF wings as they may trip the boundary layer aft of their location, causing an earlier transition than otherwise.

The stall strip is located at a specific *spanwise station* and *clocked* using a process of trial and error (see Figure 26-15). It is common that one wing has a stall strip and the other does not. During production flight testing, the experienced aerodynamicist creates a test matrix with potential locations and clocking positions. Then, the test pilot stalls the aircraft and describes change using terms like "good," "bad," "improved," and so forth. It is essential to use information from each stall to its utmost, as each flight is costly. Using CFD may help, provided there is evidence to support it correctly predicts flow

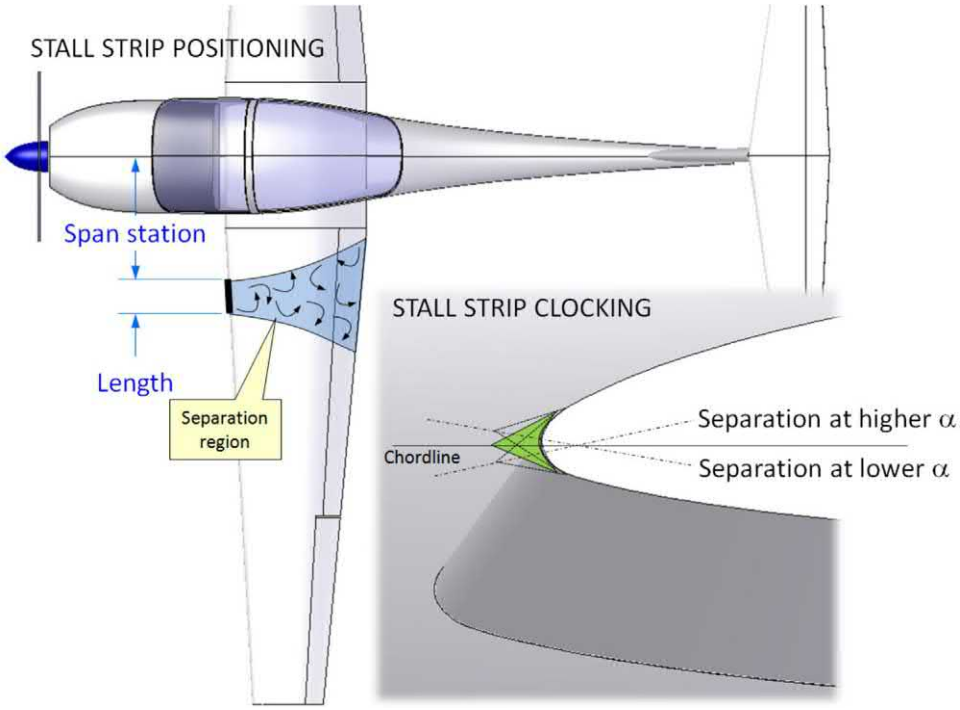


FIGURE 26-15 Placing a stall strip on the wing is a trial-and-error endeavor. Proper positioning is essential.

separation. Such evidence should comprise pictures of the flow field and separation area as seen using a tufted wing and subsequent comparison to CFD predictions. In the absence of such evidence, CFD should not be relied upon—incorrect predictions simply muddy the waters.

(2) Wing Fence

A *fence* (aka *boundary-layer fences*) is a vertical panel mounted on the upper surface of sweptback wings (see Figure 26-16). The invention is attributed to research from 1937 by the German aerodynamicist Wolfgang Liebe at the Deutsche Versuchsanstalt für Luftfahrt [14, p. 224] (or the DVL—The German Aeronautical Test Establishment). This work was carried out to remedy dangerous wing roll-offs during stall of aircraft such as the Heinkel He70 and Messerschmitt Me 109.

Early versions of the fence extended from the leading to trailing edge, while the more modern configuration extends a short distance back. The wing fence is a less common today and is mostly found on some business jets (e.g., Cessna Citation III, Beechcraft 400 Beechjet, Learjet 35, and Gulfstream II). Earlier commercial aircraft featuring wing fences include the Boeing 727 (see Figure 26-16), Comet 1, Sud-Est Caravelle, and Tupolev Tu-154, to name a few. Wing fences can also be found on many fighter aircraft, such as the MiG-15, North American F-86 Sabre, and even relatively recent aircraft such as the Hawker Hawk (US designation T-45 Goshawk), Fiat G91 and SIAI-Marchetti S211. It can even be found on GA aircraft such as the De Havilland Canada DHC-6 Twin Otter, German Akaflieg Braunschweig SB-13 sailplane, and the Australian Eagle 150 tandem wing aircraft.



FIGURE 26-16 The wing fence of a Boeing 727 commercial jetliner. *Photo by Phil Rademacher.*

Fences affect the wing in the following ways:

(A) It modifies the distribution of section lift coefficients, delaying wingtip stall. This is shown in Figure 26-17 as the drop in the distribution of C_l.

(B) The fence blocks the outboard spanwise flow of the low-energy boundary layer and reduces the possibility of wing tip stall on swept wings.

(C) The spanwise flow places the fence at a small AOA, forming a vortex on its outboard side. When the AOA of the wing is low, a single vortex is formed on the outboard side. However, at higher AOAs this develops into a complex two core vortex with opposite rotation [14, p. 107]. The fence is thus a type of leading-edge discontinuity that segments the wing into two smaller AR parts whose stall AOA is higher.

(3) Wing Pylons

Jet engine pylons on the wing have been shown to improve the stall characteristics of jet aircraft. Larrabee and Abzug [15, p. 174] explain it by pointing out that the bound vortex on the wing induces side-wash on the engine pylon as shown in Figure 26-18. This generates

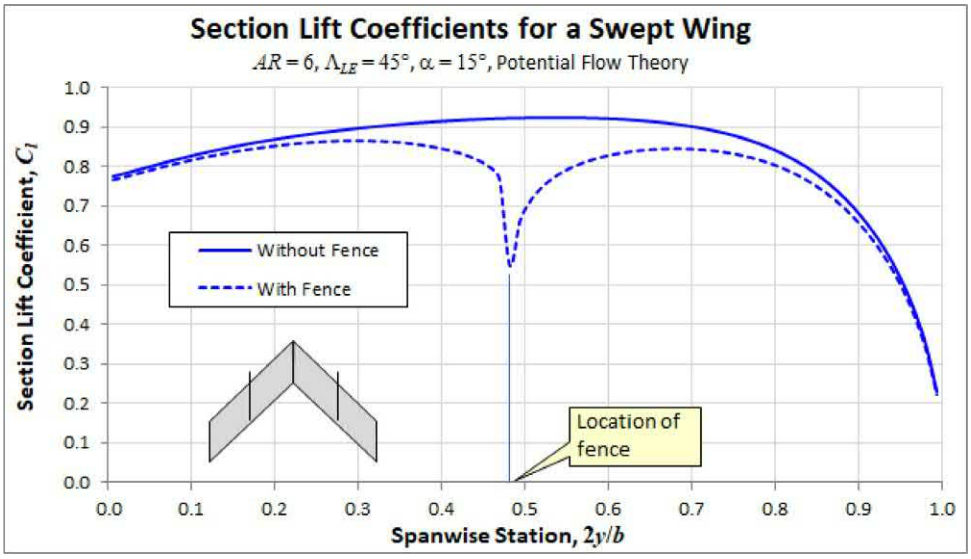


FIGURE 26-17 While the effect of the wing fence is highly viscous, it also changes the flow field in a manner that can be approximated using potential flow theory. Here, the reduction in section lift coefficients mid-span and outboard is clearly visible, helping to delay tip stall.

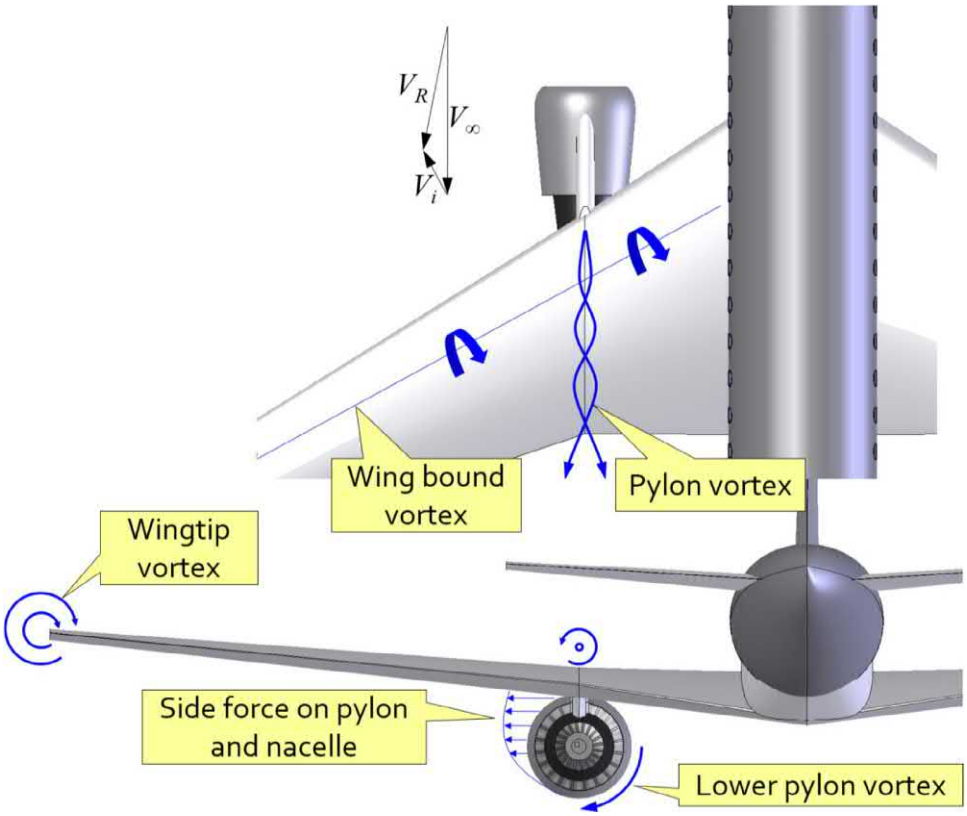


FIGURE 26-18 The bound vortex on the wing induces side-wash on the engine pylon. This forms a vortex on the upper surface of the wing that opposes the wingtip vortex and, thus, causes the normal outflow of air in the spanwise direction. This, in turn creates a vortex on the upper surface whose effect suppresses early wingtip flow separation. *Based on M.J. Abzug, E.E. Larrabee, Airplane Stability and Control—A History of the Technologies that Made Aviation Possible, second ed., Cambridge Aerospace Series, 2002.*

an outboard side force on the nacelle and pylon. The pylon generates a vortex on the upper surface of the wing, whose flow direction is opposite of the outboard spanwise flow. This suppresses early wingtip flow separation.

It is alleged in Ref. [15] that the effect was discovered by Boeing, most likely when developing the B-47 Stratojet in the late 1940s. Both the Boeing 707 and B-52 Stratofortress feature two pylons per wing, and neither has wing fences, common on swept wing aircraft of the era. This spurred the development of another aerodynamic fix—a small "pylon" without the nacelle. The device was conceived by Douglas Aircraft aerodynamicists and was mounted to the DC-9, whose engines are mounted at the back of the fuselage. The devices were patented under the name *vortilons*. It was developed as an element of a three-part solution to a possible deep-stall scenario on the DC-9 [16]. It was mounted inboard, where the vortex it generated at high AOAs favorably improved flow over the horizontal tail. The other two elements were an enlarged horizontal tail and hydraulically boosted nose pitch down control.

(4) Vortilons

As explained above, a vortilon is a small pylon-shaped fence mounted to the lower surface of a swept back wing. It can be mounted alone, as it is under the wing of DC-9/MD80/MD90 commercial jetliners (see Figure 26-19), or in a row (as it is on the outboard wing of the ERJ-145 shown in Figure 26-20). Its purpose is to shed a vortex at high AOAs that aerodynamically partitions the wing into several low AR segments, reducing section lift coefficients and delaying stall (see Figure 26-21). In case of the DC-9/MD80/MD90, the vortex also induces an inboard upwash that contributes to the ability of the HT to produce a pitch-down force beyond stall [12]. It is not as



FIGURE 26-19 A vortilon under the wing of an MD83 commercial jetliner. *Photo by Phil Rademacher.*

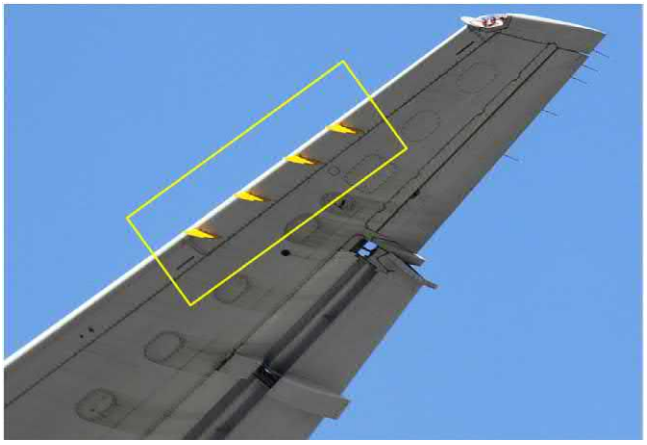


FIGURE 26-20 Vortilons on the outboard wing of an Embraer ERJ 145. *Photo by Phil Rademacher.*

effective as the fence, but adds less drag to the airplane [8].

(5) Wing Droop (Cuffs, Leading-Edge Droop)

The term *wing droop* (also called a *cuff* or *leading-edge droop* or *leading-edge extension*) is used to describe a wing whose outboard region has enlarged airfoil chord (see Figure 26-22). The droop introduces a discontinuity in the wing's leading edge. As the AOA increases, a vortex forms at the discontinuity, partitioning the wing into three regions: two small-*AR* outboard wing regions (I and III in Figure 26-22), and a larger *AR* center region (II in Figure 26-22). Reduced *AR* means a shallower C_{L_α} and delays the stall to a higher AOA. Thus, the outboard regions stall at higher AOA than the center one, which provides roll stability.

In 1982, NASA investigated the effectiveness of leading-edge devices for stall departure and spin resistance using a Piper PA-32 Lance with a T-tail [17]. The investigation revealed that the partial span leading edges eliminated the abrupt stall tendency of the 1/6th scale wind tunnel model and a tendency for autorotation, improving spin resistance. While some of the results depend on airplane geometry and Reynolds number, they are still important indicators of the potential benefits of wing droop. Among results were:

(1) The inboard wing of the model stalled at an $\alpha_{stall} = 12°$, whereas the tip with the wing droop stalled at $\alpha_{stall} = 32°$, improving roll stability and providing spin resistance.
(2) A wing droop starting at span station 0.55–0.60 was found to provide the most favorable outboard aerodynamics.
(3) Partitioning of the wing into a lower *AR* wing segments, per bullet (1), lowers the section lift coefficients as the lift curve slope of the region is lowered, increasing its α_{stall}.
(4) The wing chord extension permits lift to be generated along a longer chord. This brings down the peak C_p and delays flow separation.
(5) The airfoil of the LEX is modified as well and the combination of a larger LE radius and camber, $C_{l_{max}}$ is pushed up as well.

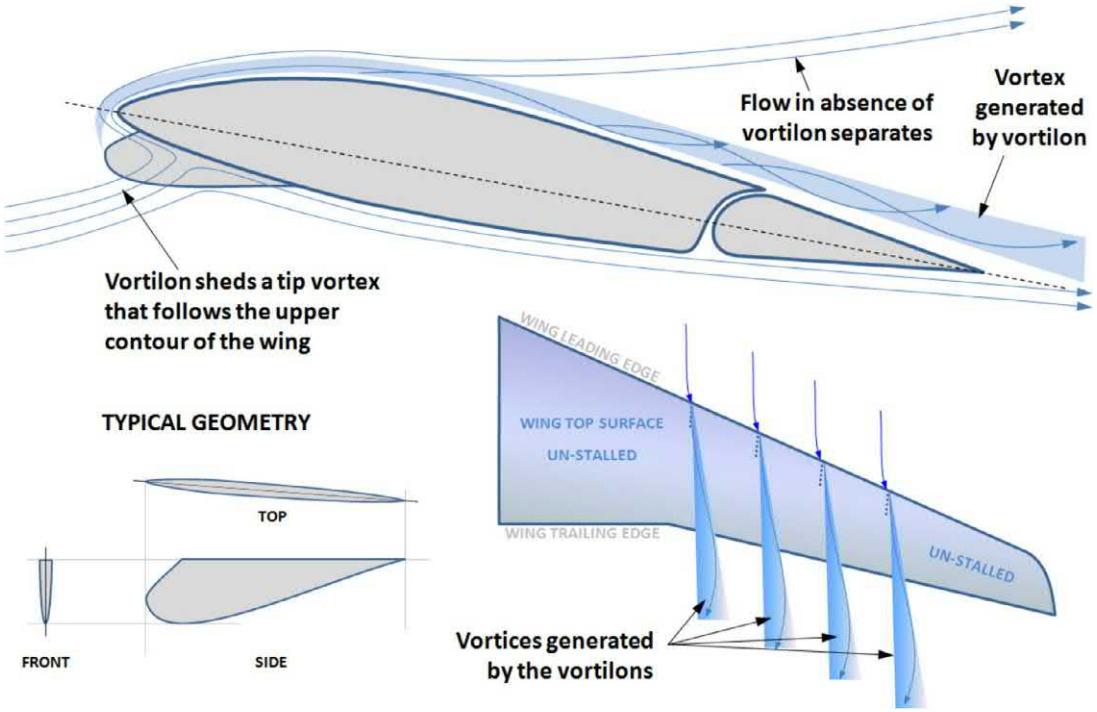


FIGURE 26-21 The vortilon in action. *Based on P. Reynolds, Ten Years of Stall Testing, AIAA-1990-1268, 1990.*

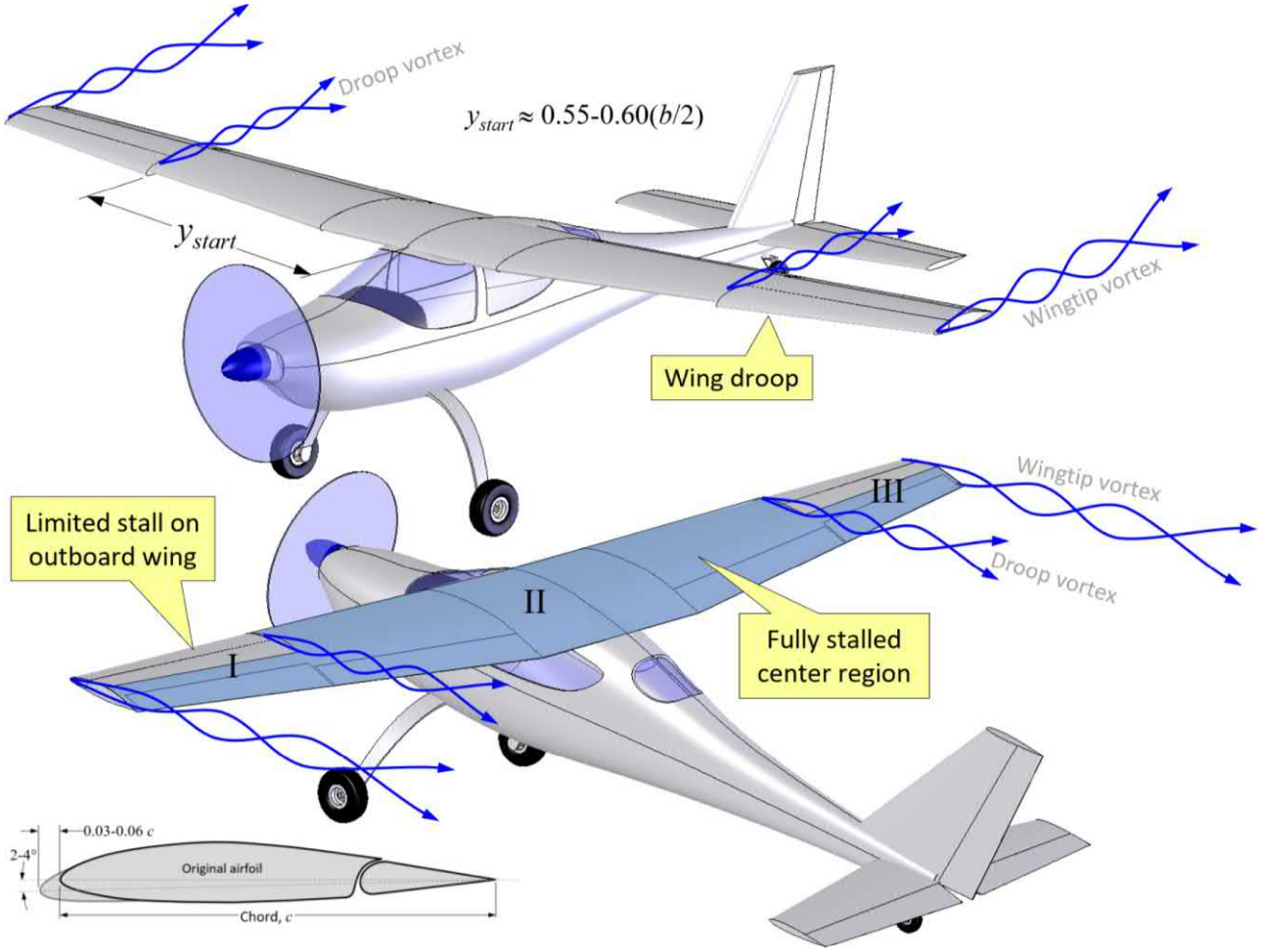


FIGURE 26-22 The workings of the wing droop. It partitions the original wing into three regions. The outboard regions are "small *AR* wings" that stall at a higher AOA. This helps the aircraft retain roll stability.

The most serious drawback of wing droop is that it may make spin recovery harder. The feature that improves roll stability at stall is often detrimental in spin, requiring greater moment for recovery. Other drawbacks include higher drag and added manufacturing complexity. Leading-edge droop for composite aircraft are typically manufactured by two means: as an integrated structure (LE droop) or an add-on (cuff). The former is desirable, as it reduces part count, weight, and labor. However, the quality of the laminate layup may suffer due to fiber dryness often associated with sharp corners.

26.3.3 Flow Improvements

(1) Vortex Generators

A vortex generator (also called VG) is a device that initiates and maintains vortex motion in fluid flow. However, the term usually applies to devices that generate localized vortices on a lifting surface to improve the airflow over them. There are typically two reasons for their installation: to alleviate buffeting and loss of control effectiveness due to shock interaction at transonic airspeeds [18] or to suppress flow separation at high AOAs at low subsonic airspeeds. The latter is the focus here. Figure 26-23 shows a common application of VGs; on the lower surface of the HT where it maintains the effectiveness of the elevator by delaying separation at high deflection angles and low-dynamic pressures.

Much information on VGs is available in technical journals, like NACA, NASA, AIAA, ESDU, and others, so only basic information will be given here. A good insight is given by Wentz and Seetharam [19], who investigated the effect of VGs on a GA(W)-1 airfoil. They found the VGs to be very effective in suppressing flow separation. The VGs increased the C_{l_α} and $C_{l_{max}}$ but lowered the α_{stall}. There was substantial increase in the section drag coefficient, about 25 drag-counts. However, the drag at higher AOAs was lower due to the delay in separation, although the cross-over point was at a $C_L \approx 1.1$. Guidelines for the sizing of VGs are given below and are obtained from various sources, including Refs. [18–20].



FIGURE 26-23 A row of Vortex Generators on the lower HT surface of the Aero L-39 Albatros trainer aircraft delays flow separation on the elevator at low speeds and large deflection (i.e., during flare) improving elevator authority. *Photo by Phil Rademacher.*



FIGURE 26-24 A dual vortex generator on a B36TC (left) and G36 Bonanzas. *Photos by Phil Rademacher.*

Height:	1–2 times the boundary layer thickness at their position
Aspect Ratio:	0.25–1.00 (AR = height/chord)
Taper Ratio:	0.6–0.8 (recommended to help "load up" the VG and make it more effective)
Angle-of-Incidence:	10–20 degrees
Spacing:	5–10 × the height
Chordwise location:	Approximately 20 boundary layer thicknesses ahead of the separation point
Orientation:	For unswept wing use counter rotating VGs (possibly even in pairs). For swept wings use co-rotating VGs.



FIGURE 26-25 A row of micro vortex generators on a flap. *Photo by author.*

Very small VGs, called micro-VGs are used in applications where small size is of importance; for instance, to improve flow over control surfaces and flaps. An example is shown in Figure 26-25. Their purpose is to delay flow separation over specific control surface. In the case of flaps, they have the potential of increasing $C_{L_{max}}$ while having no impact on cruise drag, as they are only exposed to the airflow when the flap is deployed. It is a drawback that they may cause an interference with the free motion and stowage of the flap. Refer to Lin [21] for recommendations regarding sizing, spacing, and location.

(2) Beechcraft Dual Vortex-Generator (Spin Recovery Wedge)

In 1982, Beech Aircraft certified the B36TC Bonanza, which was derived from the A36TC. The primary aerodynamic difference was an extended wingspan (increased from 33.50 to 37.83 ft [22]). It was discovered during certification that the aircraft no longer met the regulatory requirement for a 1-turn recovery in a 1-turn spin at aft CG [23]. As detailed in Ref. [23], an assortment of fixes was tested with the *dual vortex generator* emerging as the ideal solution (see Figure 26-24). The device develops two strong vortices on each side that are required to provide the roll damping needed to comply with 14 CFR §23.221.

(3) Trailing Edge Tabs for Multielement Airfoils

Ross et al. [24, 25] investigated the installation of a special lift-enhancing tab (or a *cove-tab*), similar to a Gurney flap on the pressure side of a two-element airfoil (NACA 63_2-215) with 30% chord single-slotted flap and on a multielement airfoil. The idea is patented as US Patent 5,249,080.

A cove-tab with typical dimensions is shown in Figure 26-26. The tab's size and location depend on the geometry of the flap and cove. Thus, the dimensions shown do not necessarily hold for all applications. The tab also presents an issue during flap retraction and deployment and, therefore, must be mechanically actuated, adding complexity to the installation. It is an advantage that the cove-tab is passive—it does not require a separate power source to function, like for instance a jet-flap.

The installation and wind-tunnel testing of the cove-tab on the two-element airfoil was the focus of Ref. [24]. It increased the $C_{l_{max}}$ by 10.3% with the flap deflected at 42°, attributed to a reduction in flow separation on the upper surface of the flap. The tab was found to be less effective (even detrimental) for lower deflections. However, a combination of a cove-tab with a Gurney flap and vortex generators on the flap increased the maximum lift at a high flap deflection by 17% over the optimum flap position of the baseline.

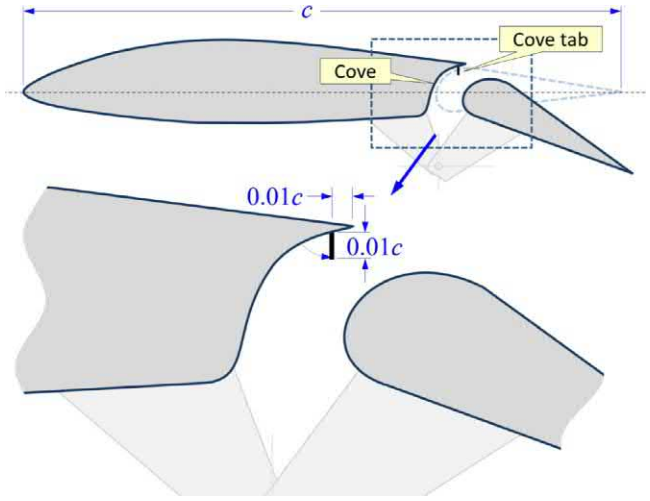


FIGURE 26-26 Typical positioning of a cove-tab.

Ref. [25] investigated various flow mechanics of the cove-tab installation using a Navier-Stokes solver. Among notable conclusions is that, as the flap element is moved away from its optimum position, the flow separation increases, reducing lift. Such a movement can result from tolerance stack-up or incorrect positioning during design. Adding the cove-tap reduced the separation and restored the flap lift to within 1% of its optimum. Thus, it may serve as "fix" for incorrectly positioned flaps.

The investigation revealed the tab is detrimental to the lift at low flap deflection (T-O configuration), where it reduces the suction peak on the leading edge of the flap. However, it delayed flow separation at large flap deflection (landing), improving its capability.

(4) Fuselage Strakes and Nacelle Strakes

Fuselage strakes refer to means to suppress flow separation occurring in the region between the wing and fuselage at high AOAs. The term strake may refer to (1) a sharp leading-edge, wing extension near the root or (2) a vortex generators installed on the fuselage, a short distance in front of the wing. The former is common in military fighters (e.g., F-16). The latter is common in GA aircraft. Such strakes can be found on aircraft such as the Cirrus SR20, SR22, and SF50. They are highly effective and not only suppress this flow separation, but also eliminate the violent oscillation of stabilizing surfaces inside the wing wake at stall. The author was involved in a development program where a fuselage strake increased the $C_{L_{max}}$ by 0.25 by suppressing such flow separation.

Nacelle strakes are vortex generators commonly found on the engines of modern jet transport aircraft, civilian and military. At high AOAs the strake generates a vortex that makes up for the flow separation and loss of lift due to the presence of the nacelle. The strake typically has a LE sweep of approximately 70 degrees and it is aligned with the airstream at cruise to minimize its interference drag. A CFD study by Keller et al. [26] indicates an increase of $C_{L_{max}}$ by 0.17 for a commuter style turboprop. An example of a nacelle strake on an Airbus A319 commercial jetliner is shown in Figure 26-27.

(5) Kárman Fairing

It refers to a fairing that typically covers the wing/fuselage juncture on high-wing commuter aircraft (e.g., ATR48, ATR72, and DASH8). Such fairings are installed to reduce the drag of a high-set wing by



FIGURE 26-27 Nacelle strakes on an Airbus A319 commercial jetliner. *Photo by Phil Rademacher.*

eliminating the high-pressure region in front of the wing and preventing flow-separation behind it. Regardless, there usually is room for improvements. Nicolosi and Della Vecchia [27] present a method for optimizing Kárman fairings using *nonuniform rational B-splines* (NURBS). Figure 26-28 shows the baseline aircraft, an ATR-style commuter, to which the method is applied. It shows the flow separation emanating from the aft fairing, wetting the entire aft upper fuselage. While the optimized fairing had larger wetted area than the original one, it removed geometric discontinuities in the front and aft regions. The resulting reshaping eliminated the separation front, reducing cruise drag by 3.1 dragcounts and climb by 5.6 dragcounts. That is a reduction well worth the redesign effort.

(6) Bubble-Drag, Turbulators, and Transition Ramps

The wings of small radio-controlled aircraft and sailplanes that operate at low Reynolds Numbers ($60{,}000 < R_e < 500{,}000$) are often subject to the formation of a laminar boundary layer separation bubble along the leading edge. An example of such a separation bubble is shown in Figure 8-25. Such bubbles can be very detrimental to the flight characteristics of the corresponding aircraft; detrimentally affecting the lift and drag (forming so-called *bubble-drag*). They can even lead to unpredictable and sudden changes in the magnitude of these forces. Two methods can be used to reduce the bubble-drag: (1) *turbulators* and (2) tailoring of the *transition curve*.

Turbulators (also called *trip strips* or *boundary layer trips*) are often installed near the leading edge of such aircraft. It is intended to force the laminar boundary layer to transition immediately to a turbulent one to prevent the formation of or reduce the size of the more detrimental separation bubble. The presence of a turbulator affects lift and drag of the airfoil. It is difficult to accurately predict its influence, calling for trial-and-error approaches in

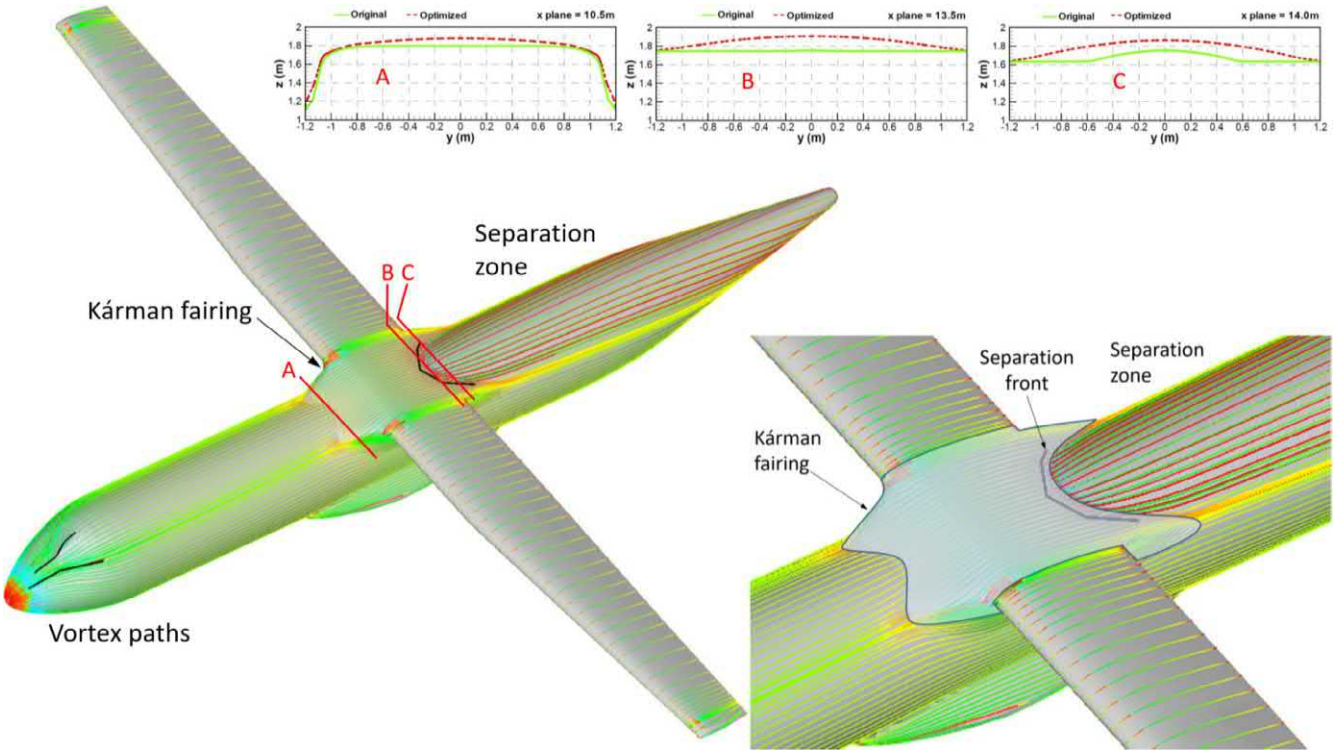


FIGURE 26-28 A Kárman fairing at the juncture of the wing and fuselage. *Images from F. Nicolosi, D.V. Pierluigi, Aerodynamic guidelines in the design and optimization of new regional turboprop aircraft, in: 3rd CEAS Air & Space Conference, 21st AIDAA Congress, 2011.*

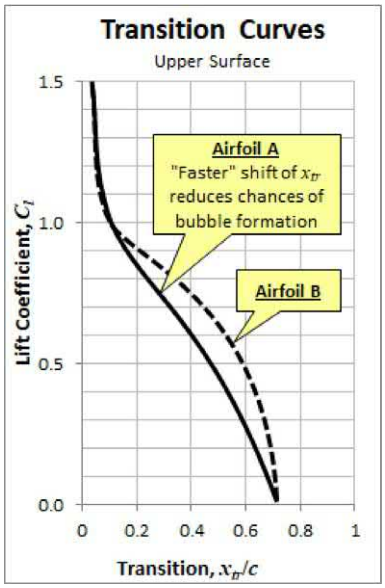


FIGURE 26-29 The shape of the transition curve on the upper surface indicates a tendency for bubble-drag formation. *Based on A. Gopalarathnam, et al. Design of low Reynolds number airfoils with trips, J. Aircr. 40(4) (2003).*

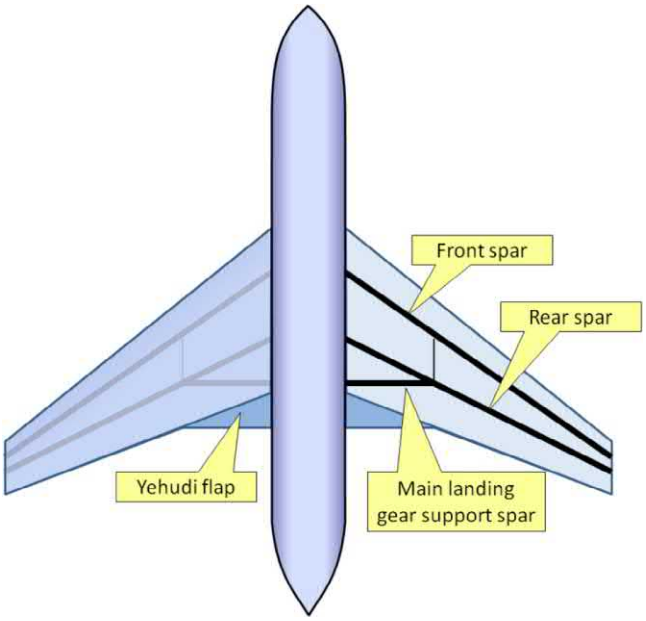


FIGURE 26-30 The Yehudi flap.

wind tunnel or flight tests. This is further compounded by the fact that a trip strip configuration found suitable for a specific airfoil at a given AOA, may be detrimental to it at another operating condition [28].

Tailoring the *transition curve* refers to the proactive design of airfoils to encourage a more rapid movement of the laminar-to-turbulent BL transition point on the upper surface toward the leading edge. This is shown in Figure 26-29. It depicts how the derivative $\partial C_l/\partial(x_{tr}/c)$ is steeper for Airfoil A than B. This is referred to as the shape of the *transition ramp*. In other words, in the lift coefficient range $0 < C_l < 1.0$, the transition point, x_{tr}/c for Airfoil A "moves faster" toward the LE than Airfoil B. Gopalarathnam et al. [28] show that this results in a lower bubble-drag for airfoil A. This observation makes it possible to design airfoils for operation in low Reynolds number flow that area less likely to suffer this undesirable type of pressure drag.

(7) Yehudi "Flap"

The *Yehudi flap* is not a flap in the traditional sense. Rather, it is a modification to an existing wing planform achieved by increasing the root chord, while breaking the straight line of the trailing edge (see the dark area in Figure 26-30). Generally, the following reasons justify this extra area: (1) Increasing the chord "thickens" the airfoil, allowing the main landing gear to be completely enclosed inside the wing. (2) It permits structure to be installed to react main landing gear loads. (3) It lowers the section lift coefficients in the area adjacent to the fuselage, helping to preventing flow separation along the wing root. (4) It also prevents or weakens normal shock that may form in the wing/fuselage region at high Mach numbers (see Bullet (8)—Flattop Airfoils). The effect on the section lift coefficient is depicted in Figure 26-31. Note that the example wing planform does not feature a washout, which explains the highly tip loaded distribution of section lift coefficients.

Cook [29, p. 83] explains the Yehudi flap was first introduced on the Boeing B-29 Superfortress bomber, as the small chord extension behind the inboard engine nacelle. This was done to make up for the loss of lift of the unmodified nacelle. More details on its aerodynamic benefits are given by Snyder [30]. Later it was introduced on the Boeing 707-320 and DC-8 jetliners. Mason [31] explains in his online writing that the name Yehudi came from when the modification was being wind tunnel tested by Boeing. Each component being tested required a specific name, but the flap didn't have one. At the time popular radio show starring the late Bob Hope featured the late violinist Yehudi Menuhin as a frequent guest. In the show, Bob Hope's sidekick Jerry Colonna, who apparently was entertained by the name, would repeatedly ask "Who's Yehudi?" According to the reference, a Boeing engineer working on the wind tunnel testing thought that Yehudi was as good a name as any other, and decided to call the part a Yehudi flap.

(8) Flattop Airfoils

Refers to airfoils adjacent to the fuselage of aircraft that operate at high subsonic airspeeds, such as commercial jetliners and business aircraft (see Figure 26-32). Their purpose is to reduce the low-pressure peaks in this region and, thus, suppress the formation of drag-increasing

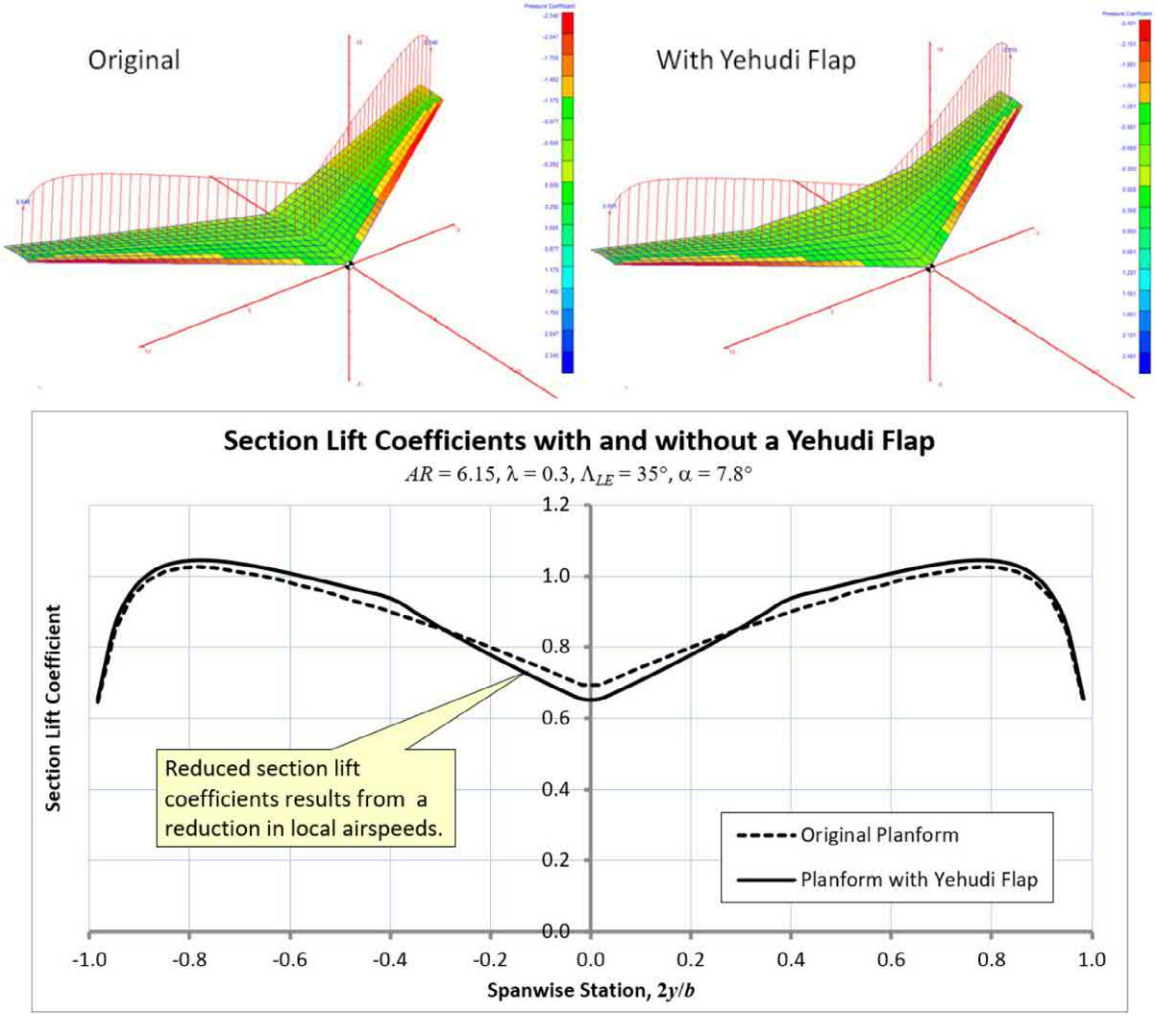


FIGURE 26-31 The effect of the Yehudi flap on section lift coefficients for a typical sweptback wing. Note that the wing area of the modified wing is larger than that of the original wing.



FIGURE 26-32 Flattop airfoil on a Boeing 757-300 commercial jetliner. *Photo by Phil Rademacher.*

normal shock at high airspeeds. This also reduces chances of flow separation at lower airspeeds (high AOA), such as during climb.

The airfoil at the fuselage juncture has negative camber that transitions into a regular high-speed airfoil near the first break in the wing. The inboard wing has larger angle-of-incidence in this region to increase the section lift coefficients in this region.

References

[1] Anonymous, *Airplane Flying Handbook*, FAA-H-8083-3BFAA, 2016.
[2] Anonymous, *Weight-Shift Control Aircraft Flying Handbook*, FAA-H-8083-5FAA, 2008.
[3] T.P. Ratvasky, J.F. Van Zante, A. Sim, *NASA/FAA Tailplane Icing Program: Flight Test Report*, DOT/FAA/AR-99/85, NASA/TP—2000-209908(March 2000).
[4] F.D. Nelson, *AFFTC Stability and Control Techniques*, AFFTC-TN-59-21Air Force Flight Test Center, 1959.

[5] I.H. Abbott, A.E. von Doenhoff, L.S. Stivers Jr., *Summary of Airfoil Data*, NACA-TR-824, 1945.
[6] Anonymous, *Special Study U.S. General Aviation Accidents Involving Fuel Starvation 1970-1972*, NTSB-AAS-74-1, NTSB, 1974.
[7] R. Whitford, *Design for Air Combat*, Jane's Publishing Company Limited, 1987.
[8] P. Reynolds, *Ten Years of Stall Testing*, AIAA-1990-1268, 1990.
[9] Source: http://www.nasa.gov/centers/dryden/news/FactSheets/FS-002-DFRC.html (Accessed 01 August 2020).
[10] R.M. Hall, et al., *Overview of HATP Experimental Aerodynamics Data for the Baseline F/A-18 Configuration*, NASA-TM-112360, 1996.
[11] G.H. Shah, J.N. Granda, *Application of Forebody Strakes for Directional Stability and Control of Transport Aircraft*, AIAA-98-4448, 1998.
[12] Anonymous, *Delta Airlines MD-88/90 Flight Crew Training Manual*, Rev. 5, Delta Airlines, 2008.
[13] Anonymous, *Beechcraft 1900*, Flight International, November 20, 1982.
[14] H.-U. Meier, *German Development of the Swept Wing 1935-1945*, AIAA, 2006.
[15] M.J. Abzug, E.E. Larrabee, *Airplane Stability and Control—A History of the Technologies that Made Aviation Possible*, second ed., Cambridge Aerospace Series, Cambridge University Press, 2002.
[16] Anonymous, *The DC-9 and the Deep Stall*, Flight International, March 25, 1965.
[17] E.R. White, *Wind-Tunnel Investigation of Effects of Wing-Leading-Edge Modifications on the High Angle-of-Attack Characteristics of a T-Tail Low-Wing General-Aviation Aircraft*, NASA CR-3636, 1982.
[18] J.B.W. Edwards, *Free-Flight Tests of Vortex Generator Configurations at Transonic Speeds*, C.P. No. 729British A. R. C., 1966.
[19] W.H. Wentz Jr., H.C. Seetharam, *Development of a Fowler Flap System for a High Performance General Aviation Airfoil*, NASA CR-2443, 1974.
[20] L.H. Tanner, H.H. Pearcey, C.M. Tracy, *Vortex Generators, Their Design and Their Effects on Turbulent Boundary-Layers*, A.R.C. 16.487, January, 1954.
[21] J.C. Lin, *Control of Turbulent Boundary-Layer Separation Using Micro-Vortex Generators*, AIAA 99-3404AIAA, 1999.
[22] E. Phillips, *The Best Bonanza Ever?*, online articlewww.kingairmagazine.com (web archive link, 02 August 2020), October 6, 2017. http://www.kingairmagazine.com/article/2725/ (Accessed 02 August 2020).
[23] D. Crider, *Development of Wing Leading Edge Vortex Generators for a Single Engine General Aviation Airplane*. SAE Technical Paper 830770, February 1983. https://doi.org/10.4271/830770.
[24] J.C. Ross, B.L. Storms, *An Experimental Study of Lift-Enhancing Tabs on a Two-Element Airfoil*, AIAA-1994-1868, 1994.
[25] J.C. Ross, P.G. Carrannanto, B.L. Stroms, R.M. Cummings, *Navier-Stokes Analysis of Lift-Enhancing Tabs on Multi-Element Airfoils*, AIAA-1994-50, 1994.
[26] K. Dennis, H.Y. Julian, R. Ralf, *Nacelle Strake design for short takeoff and landing configuration with turboprop engines*. J. Aircr. 55 (6) 2018 https://doi.org/10.2514/1.C035065.
[27] F. Nicolosi, D.V. Pierluigi, *Aerodynamic guidelines in the design and optimization of new regional turboprop aircraft*, in: 3rd CEAS Air & Space Conference, 21st AIDAA Congress, 2011.
[28] A. Gopalarathnam, et al., *Design of low Reynolds number airfoils with trips*, J. Aircr. 40 (4) (2003) 768–775.
[29] W.C. Cook, *The Road to the 707*, TYC Publishing, Bellevue, 1991.
[30] G. Snyder, *Structural design problems in the B-29 airplane*, Aeronaut. Eng. Rev. (1946) 9–12.
[31] W.H. Mason, *6. Subsonic Aerodynamics of Airfoils and Wings*, http://www.dept.aoe.vt.edu/~mason/Mason_f/ConfigAeroSubFoilWing.pdf.

APPENDIX

A

Atmospheric Modeling

A.1 INTRODUCTION

Multiple organizations have developed sophisticated models of the atmosphere. These models allow atmospheric properties to be determined at different altitudes. A case in point is the National Oceanic and Atmospheric Administration's (NOAA) development of the well-known *US Standard Atmosphere 1976* [1]. More sophisticated models include the NRLMSISE-00 (*Naval Research Laboratory Mass Spectrometer and Incoherent Scatter*, where E means from surface of the Earth to the Exosphere). The user specifies input data in terms of year, day, time of day, altitude, geodetic latitude and longitude, and many others. The model returns temperature, mass density, and molecular densities of Oxygen (O_2), Nitrogen (N_2), mono-atomic Oxygen (O) and Nitrogen (N), Argon (Ar), and Hydrogen (H). These can be used to estimate other properties, such as the *specific gas constant* (R), pressure, and the *ratio of specific heats* (γ). The model is used when predicting the orbital decay of satellites due to atmospheric drag and to study the effect of atmospheric gravity waves. The temperature and density from this atmospheric model are shown in Figure A-1. The figure shows the two gas states up to an altitude of 500 km, well beyond the so-called *von Kárman Line*, a limit above which the density is too low for atmospheric flight.

In this text, all atmospheric data are based on the US Standard Atmosphere 1976, unless otherwise specified. Additionally, examples in this book take place in the troposphere, below 36,089 ft (see Figure A-2), unless otherwise specified.

A.1.1 General Information About the Atmosphere

An atmosphere is the mixture of gases surrounding a celestial object (i.e., planet) whose gravitational field is strong enough to prevent its molecules from escaping. In particular, the atmosphere refers to the gaseous envelope of the Earth.

Formation of

The current mixture of gases in the air is thought to have taken some 4.5 billion years to evolve. The early atmosphere is believed to have consisted of volcanic gases alone. Since gases from erupting volcanoes today are mostly a mixture of water vapor (H_2O), carbon dioxide (CO_2), sulfur dioxide (SO_2), and nitrogen (N), it is postulated that this likely was the composition of the early atmosphere as well. Numerous chemical processes are thought to have preceded the current atmosphere.

One such process is *condensation*. It was a natural consequence of the cooling of the earth's crust and early atmosphere. This condensation is thought to have slowly but surely filled valleys in the barren landscape forming the earliest oceans. Some CO_2 would have reacted with the rocks of the earth's crust to form carbonate minerals, while others dissolved in the new rising oceans. Later, as primitive life capable of photosynthesis evolved in the oceans, new marine organisms began producing oxygen. Almost all the free oxygen in the air today is attributed to this process; by photosynthetic combination of CO_2 with water.

About 570 million years ago, the oxygen content of the atmosphere and oceans became high enough to permit marine life capable of respiration. 170 million years later, the atmosphere would have contained enough oxygen for air-breathing animals to emerge from the seas.

A.1.2 Chemical Composition of Standard Air

Research shows the chemical composition of the atmosphere is practically independent of altitude from ground level to at least 88 km (55 mi). The continuous stirring produced by atmospheric currents counteracts the tendency of the heavier gases to settle below the lighter ones. In the lower atmosphere, ozone is present in extremely low concentrations. The layer of atmosphere from 19 to 48 km (12 to 30 mi) up contains more ozone, produced by the action of ultraviolet radiation from the sun. Even in this layer the percentage of ozone is only 0.001 by volume. Atmospheric disturbances and downdrafts carry varying amounts of this ozone to the surface of the earth. Human activity adds to ozone in the lower atmosphere, where it becomes a pollutant that can cause extensive crop damage. Table A-1 lists the chemical composition of the atmosphere.

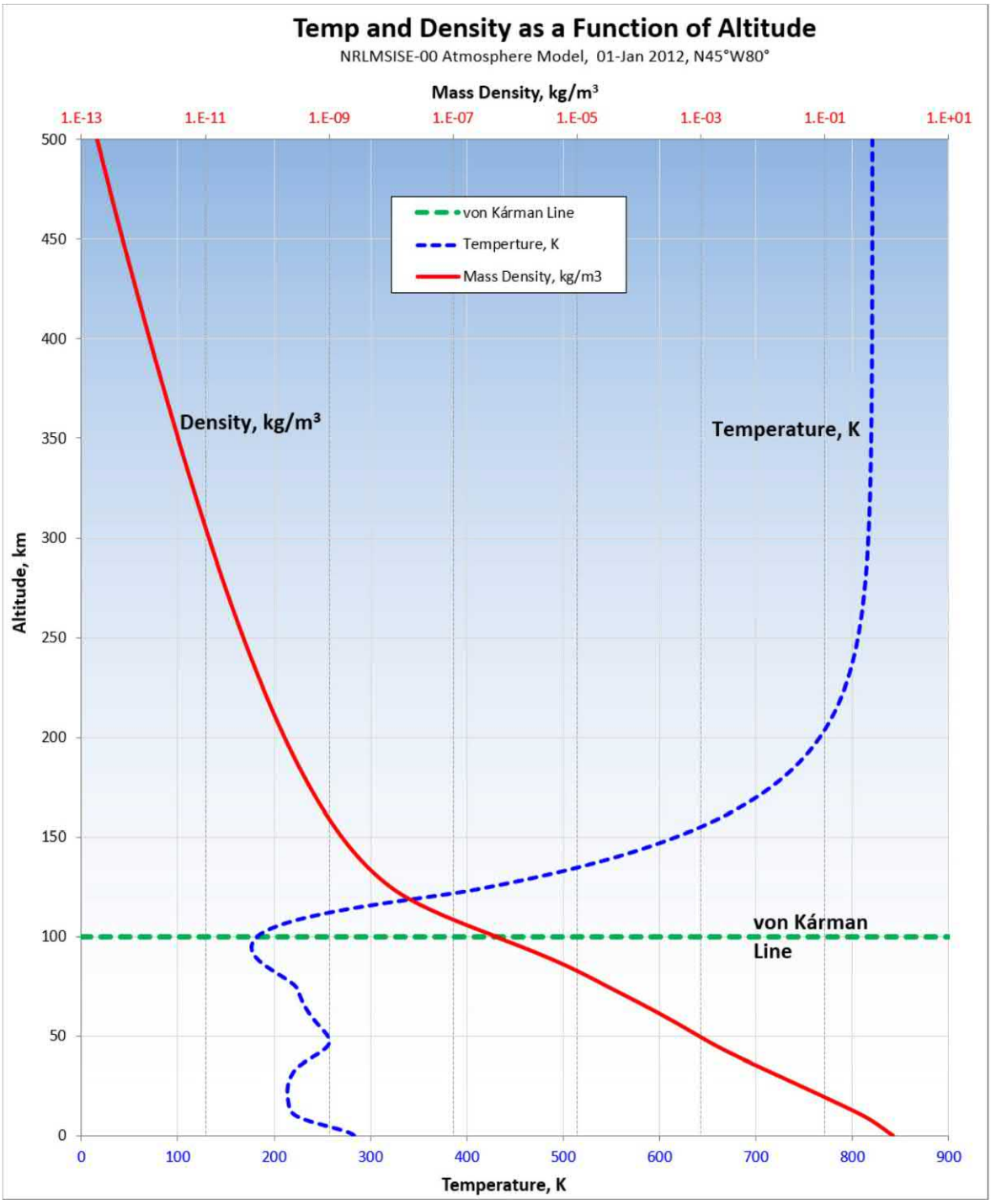


FIGURE A-1 An output from the NRLMSISE-00 atmospheric model showing temperature and mass density as a function of altitude ranging from S-L to 500 km on January 1st, 2012.

A.1.3 Layer Classification of the Atmosphere

The atmosphere is divided into several layers based on specific characteristics (see Table A-2). The *Troposphere* extends from the ground to some 11–16 km (6.8–10 mi). It is where most clouds occur and weather (winds and precipitation) is most active. It transitions into the next layer; the *Stratosphere*, through a thin region called the *Tropopause*. Most of the atmosphere is found within these two lowest layers. Above the Stratosphere is the *Mesosphere*, which is characterized by a decrease in temperature with altitude. Research of propagation and reflection of radio waves starting at an altitude of

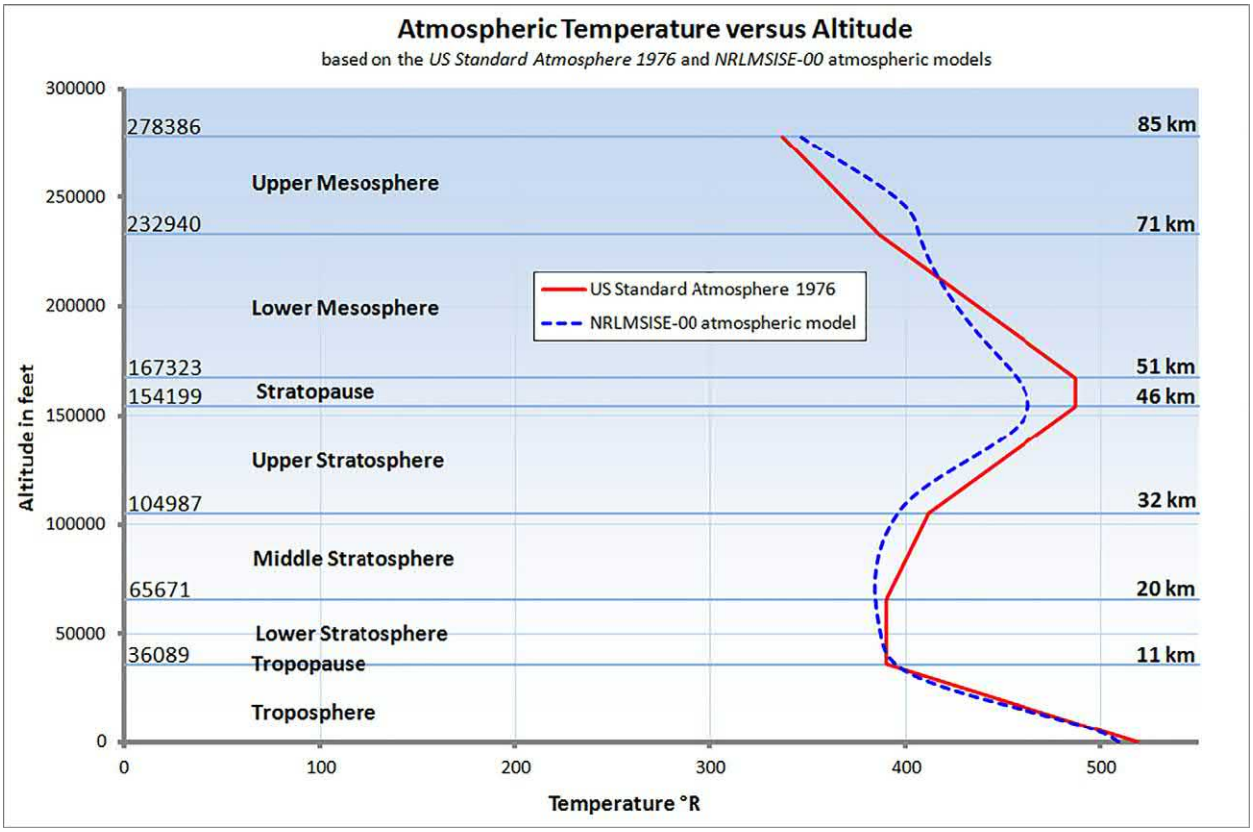


FIGURE A-2 A comparison of temperature changes with altitude up to 85 km, using the US Standard Atmosphere 1976 and NRLMSISE-00 atmospheric models. The former represents standard conditions, whereas the latter is at a geodesic location N45° W80° on January 1st, 2012.

TABLE A-1 Chemical composition of standard air per Ref. [1].

Name of chemical	Chemical formula	Molecular weight (kg/kmol)	Fractional volume (dimensionless) [1]
Nitrogen	N_2	28.0134	0.78084
Oxygen	O_2	31.9988	0.209476
Argon	Ar	39.948	0.00934
Carbon dioxide	CO_2	44.00995	0.000314
Neon	Ne	20.183	0.00001818
Helium	He	4.0026	0.00000524
Krypton	Kr	83.80	0.00000114
Xenon	Xe	131.30	0.000000087
Methane	CH_4	16.04303	0.000002
Hydrogen	H_2	2.01594	0.0000005
Water vapor (varying)	H_2O	Varying	Varying
Ozone	O_3	–	–
Carbon monoxide	CO	–	–

80 km (50 mi) to some 640 km (400 mi) indicates that ultraviolet radiation, X-rays, and showers of electrons from the sun ionize this layer of the atmosphere, causing it to conduct electricity and reflect radio waves of certain frequencies back to earth. Thus, it is called the *Ionosphere*. It is also termed the *Thermosphere*, because of the relatively higher temperatures in this layer. Above it is the *Exosphere*, which extends to the outer limit of the

TABLE A-2 Layer classification of the atmosphere.

Name of layer	Altitude in km	Altitude in statute miles
Troposphere[a]	0–11	0–6.8
Tropopause	11–11.5	6.8–7.1
Stratosphere	11.5–46	11.5–29
Stratopause	46–51	29–32
Mesosphere	51–85	32–53
Ionosphere (Thermosphere)	85–640	53–400
Exosphere	640–9600	400–6000

[a] *In temperate latitudes, this is approximately 0–9.7 km (6 mi). The troposphere can extend to 15 km in the tropics.*

atmosphere, at about 9600 km (about 6000 mi). Figure A-2 shows how temperature changes through the lowest layers of the atmosphere. The classification of the atmosphere based on an average height of the layers.

A.2 MODELING ATMOSPHERIC PROPERTIES

A.2.1 Atmospheric Ambient Temperature

Change in air temperature with altitude can be approximated using a linear function:

$$T = T_0 + a(h - h_0) \tag{A-1}$$

In the troposphere, where $h_0 = 0$, this becomes

$$T = T_0 + ah = T_0 \cdot \left(1 + \frac{a}{T_0} \cdot h\right) = T_0 \cdot (1 + \kappa \cdot h) \tag{A-2}$$

Where: a = Lapse rate,
h = altitude of interest,
h_0 = reference altitude,
T = temperature at altitude h,
T_0 = temperature at reference altitude h_0,
κ = lapse rate constant = a/T_0.

A.2.2 Atmospheric Pressure and Density for Altitudes Below 36,089 ft (11,000 m)

The hydrostatic equilibrium equations allow the pressure, p, and density, ρ, to be calculated as functions of altitude, h, as follows:

$$\text{Pressure:}\quad p = p_0(1 + \kappa h)^{5.2561} = p_0\theta^{5.2561} \tag{A-3}$$

$$\text{Density:}\quad \rho = \frac{p}{RT} = \frac{p_0(1 + \kappa h)^{5.2561}}{RT_0(1 + \kappa h)} = \rho_0(1 + \kappa h)^{4.2561} = \rho_0\theta^{4.2561} \tag{A-4}$$

Where θ = temperature ratio = $T/T_0 = 1 + \kappa h$.

DERIVATION

Begin with the hydrostatic Equation (14-8). For gases at rest, it becomes $dp = -\rho g dh$. Substitute the ideal gas law, $\rho = p/(RT) = p/(RT_0(1 + \kappa h))$ for ρ to get

$$\Rightarrow\quad dp = -\rho g dh = -\frac{p}{RT_0(1 + \kappa h)} g dh \quad\Rightarrow\quad \frac{dp}{p} = -\frac{g}{RT_0(1 + \kappa h)} dh$$

$$\Rightarrow\quad \int_{p_1}^{p_2} \frac{dp}{p} = -\frac{g}{RT_0} \int_{z_1}^{z_2} \frac{1}{(1 + \kappa h)} dh \quad\Rightarrow\quad \ln(p_2) - \ln(p_1) = -\frac{g}{RT_0}\left[\frac{\ln(1 + \kappa h)}{\kappa}\right]_{h_1}^{h_2}$$

$$\Rightarrow\quad \ln\left(\frac{p_2}{p_1}\right) = -\frac{g}{RT_0\kappa}(\ln(1 + \kappa h_2) - \ln(1 + \kappa h_1))$$

$$\overset{\substack{h_1=0\\ h_2=h}}{\Rightarrow}\quad \ln\left(\frac{p}{p_o}\right) = -\frac{g}{RT_0\kappa}\ln(1 + \kappa h) \qquad \overset{\substack{\ln y = C \ln x\\ \Leftrightarrow\ y = x^C}}{\Rightarrow}\quad \frac{p}{p_0} = (1 + \kappa h)^{-\frac{g}{RT_0\kappa}}$$

A.2.3 Density due to Temperature Deviations From the Standard Atmosphere

Atmospheric conditions often deviate from models shown above. Such deviations are handled using the ideal gas law. Thus, using the definitions of Table 17-3, we get

$$\rho = \frac{p}{RT} = \frac{p_0\theta^{5.2561}}{R(T_0\theta + \Delta T_{ISA})} = \begin{cases} \dfrac{1.2330\theta^{5.2561}}{(T + \Delta T_{ISA})} & \text{UK-system} \\ \dfrac{352.6\theta^{5.2561}}{(T_0\theta + \Delta T_{ISA})} & \text{SI-system} \end{cases} \tag{A-5}$$

Where; θ = Temperature ratio = $T/T_0 = 1 + \kappa h$,

h = Altitude of interest, in ft or m. Only valid for $h < 36{,}068$ ft or $h < 11{,}000$ m.

T = standard day temperature at altitude per ISA, in °R or K. At S-L it is 518.67 °R (288.15 K), at 10,000 ft (3,048 m) it is 483 °R (268 K), and so on.
ΔT_{ISA} = Deviation from International Standard Atmosphere in °F or °R (°C or K).

A.2.4 Pressure and Density Altitudes Below 36,089 ft (11,000 m)

Sometimes the pressure or density ratios are known for one reason or another. It is then possible to determine the altitudes to which they correspond. For instance, if the pressure ratio is known, we can calculate the altitude to which it corresponds. The altitude is then called *pressure altitude*. Similarly, from the density ratio, we can determine the *density altitude*.

Pressure altitude in ft:

$$h_P = 145,442\left[1-\left(\frac{p}{p_0}\right)^{0.19026}\right] \quad \text{(A-6)}$$

Density altitude in ft:

$$h_\rho = 145,442\left[1-\left(\frac{\rho}{\rho_0}\right)^{0.234957}\right] \quad \text{(A-7)}$$

DERIVATION

Begin with Equation (A-3) and solve for the altitude h, through the following algebraic maneuvers:

$$\frac{p}{p_0} = (1+\kappa h)^{5.2561} \Rightarrow \left(\frac{p}{p_0}\right)^{1/5.2561} = 1+\kappa h \Rightarrow$$

$$h = -\frac{1}{\kappa}\left[1-\left(\frac{p}{p_0}\right)^{0.19026}\right]$$

Substituting the coefficient $\kappa = -0.0000068756/\text{ft}$ (from Table 17-3) and carrying out the arithmetic yield Equation (A-6). The derivation of Equation (A-7) follows identical steps.

A.2.5 The US Standard Atmosphere 1976

As stated earlier, the properties of the atmosphere above the Troposphere are detailed in the document *US Standard Atmosphere 1976*, published by NOAA (National Oceanic and Atmospheric Administration), NASA (National Aeronautics and Space Administration), and the US Air Force. The formulation in Table A-3 is based on a summary from http://www.atmosculator.com/, which is based on the US Standard Atmosphere 1976. The temperature (in °R), pressure (in $\text{lb}_\text{f}/\text{ft}^2$), and density (in slugs/ft^3) are plotted in Figure A-3 from S-L to 278,386 ft. Let θ be the temperature ratio, δ be the pressure ratio, and σ be the density ratio.

TABLE A-3 Formulation for the US Standard Atmosphere 1976.

$0 \le h \le 36,089$ ft	**$0 \le h \le 5.94$ nm**	**Troposphere**
Temperature ratio:	$\theta = 1 - 0.0000068756h$	
Pressure ratio:	$\delta = \theta^{5.2561}$	
Density ratio:	$\sigma = \theta^{4.2561}$	
$36,068 < h \le 65,617$ ft	**$5.94 < h \le 10.8$ nm**	**Lower stratosphere Isothermal segment**
Temperature ratio:	$\theta = 0.751865$	
Pressure ratio:	$\delta = 0.223361 \cdot e^{-(h-36,089)/20,\,806}$	
Density ratio:	$\sigma = 0.297076 \cdot e^{-(h-36,089)/20,\,806}$	
$65,617 < h \le 104,987$ ft	**$10.8 < h \le 17.3$ nm**	**Middle stratosphere Temperature inversion segment**
Temperature ratio:	$\theta = 0.682457 + h/945,374$	
Pressure ratio:	$\delta = (0.988626 + h/652,600)^{-34.16320}$	
Density ratio:	$\sigma = (0.978261 + h/659,515)^{-35.16320}$	
$104,987 < h \le 154,199$ ft	**$17.3 < h \le 25.4$ nm**	**Upper stratosphere**
Temperature ratio:	$\theta = 0.482561 + h/337,634$	
Pressure ratio:	$\delta = (0.898309 + h/181,373)^{-12.20114}$	
Density ratio:	$\sigma = (0.857003 + h/190,115)^{-13.20114}$	
$154,199 < h \le 167,323$ ft	**$25.4 < h \le 27.5$ nm**	**Isothermal**
Temperature ratio:	$\theta = 0.939268$	
Pressure ratio:	$\delta = 0.00109456 \cdot e^{-(h-154,199)/25,\,992}$	
Density ratio:	$\sigma = 0.00116533 \cdot e^{-(h-154,199)/25,\,992}$	

TABLE A-3 Formulation for the US Standard Atmosphere 1976—cont'd

167,323 < h ≤ 232,940 ft	**27.5 < h ≤ 38.3 nm**	**Lower mesosphere**
Temperature ratio:	$\theta = 1.434843 - h/337,634$	
Pressure ratio:	$\delta = (0.838263 - h/577,922)^{12.20114}$	
Density ratio:	$\sigma = (0.798990 - h/606,330)^{11.20114}$	
232,940 < h ≤ 278,386 ft	**38.3 < h ≤ 45.8 nm**	**Upper mesosphere**
Temperature ratio:	$\theta = 1.237723 - h/472,687$	
Pressure ratio:	$\delta = (0.917131 - h/637,919)^{17.08160}$	
Density ratio:	$\sigma = (0.900194 - h/649,922)^{16.08160}$	

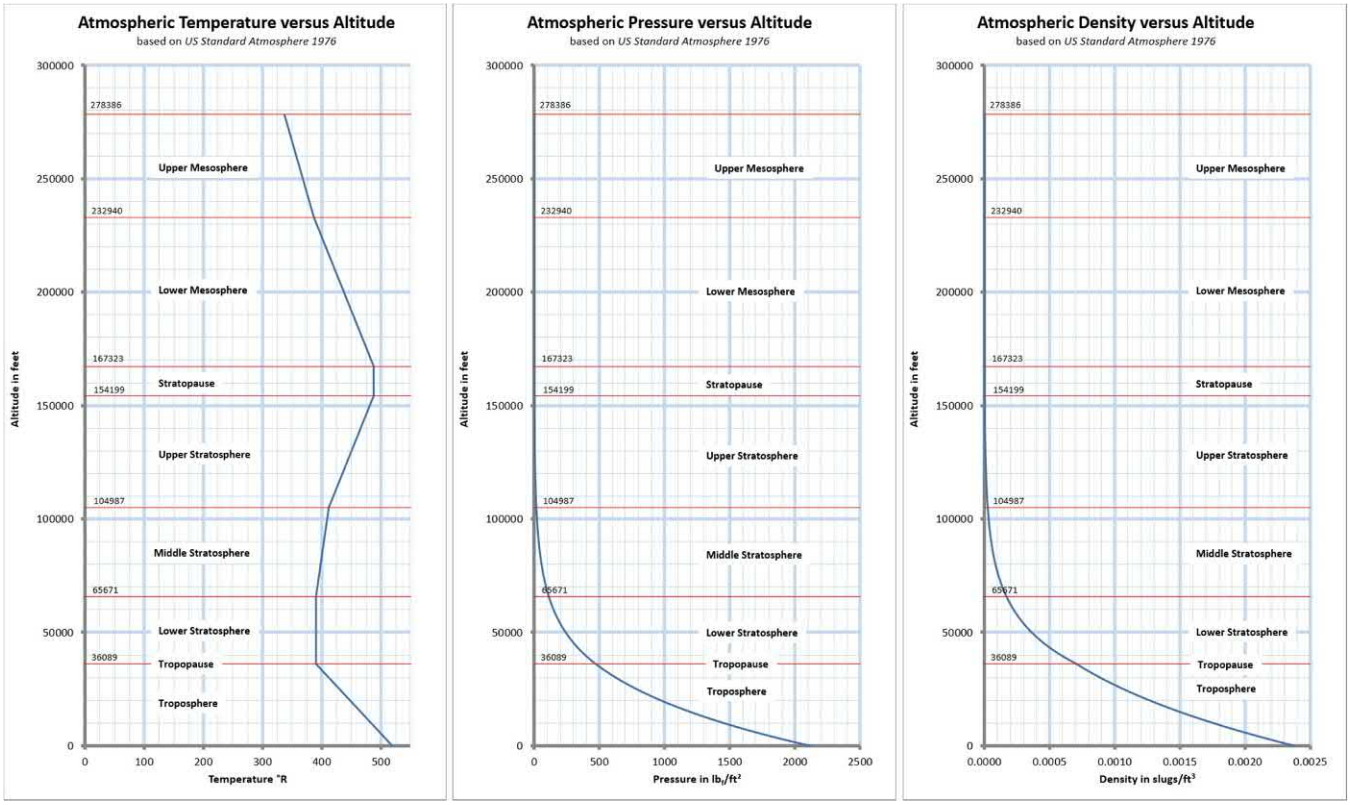


FIGURE A-3 The US Standard Atmosphere 1976 plotted from S-L to 278,386 ft, using the formulation in Section A.2.5, *The US Standard Atmosphere 1976*.

A.2.6 Computer Code: Atmospheric Modeling

The following function, written in Visual Basic for Applications, can be used in Microsoft Excel to determine temperature, pressure, or density at any altitude up to 278,386 ft. To use, insert a VBA module into the spreadsheet and enter the function. Assume we have entered an altitude in cell A1. Then calls are made to it from any other cell by entering a statement like " `=AtmosProperty(A1,0)`." The rightmost argument (i.e., the ", 0"), called the `PropertyID`, would cause the function to return the Temperature ratio. If the `PropertyID` were 10 (i.e., the ", 10"), it would return the temperature and so on. The allowable values for `PropertyID` are shown in the comment lines below.

```
Function AtmosProperty(H As Single, PropertyID As Byte) As Single
'This function calculates an atmospheric property based on the variable
'PropertyID at the given altitude H in ft, where:
'
'   If PropertyID = 0 then return Temperature ratio
'   If PropertyID = 1 then return Pressure ratio
'   If PropertyID = 2 then return Density ratio
'   If PropertyID = 10 then return Temperature
'   If PropertyID = 11 then return Pressure
'   If PropertyID = 12 then return Density
'
'Initialize
    Dim TempRatio As Single, R As Single
    Dim PressRatio As Single
    Dim DensRatio As Single
'Select altitude
    If H < 36089 Then
        R = 1 - 0.0000068756 * H
        TempRatio = R
        PressRatio = R ^ 5.2561
        DensRatio = R ^ 4.2561
    ElseIf H >= 36089 And H < 65617 Then
        R = -(H - 36089) / 20806
        TempRatio = 0.751865
        PressRatio = 0.223361 * Exp(R)
        DensRatio = 0.297176 * Exp(R)
    ElseIf H >= 65617 And H < 104987 Then
        TempRatio = 0.682457 + H / 945374
        PressRatio = (0.988626 + H / 652600) ^ -34.1632
        DensRatio = (0.978261 + H / 659515) ^ -35.1632
    ElseIf H >= 104987 And H < 154199 Then
        TempRatio = 0.482561 + H / 337634
        PressRatio = (0.898309 + H / 181373) ^ -12.20114
        DensRatio = (0.857003 + H / 190115) ^ -13.20114
    ElseIf H >= 154199 And H < 167323 Then
        R = -(H - 154199) / 25992
        TempRatio = 0.939268
        PressRatio = 0.00109456 * Exp(R)
        DensRatio = 0.00116533 * Exp(R)
    ElseIf H >= 167323 And H < 232940 Then
        TempRatio = 1.434843 - H / 337634
        PressRatio = (0.838263 - H / 577922) ^ 12.20114
        DensRatio = (0.79899 - H / 606330) ^ 11.20114
    ElseIf H >= 232940 And H < 278386 Then
        TempRatio = 1.237723 - H / 472687
        PressRatio = (0.917131 - H / 637919) ^ 17.0816
        DensRatio = (0.900194 - H / 649922) ^ 16.0816
    End If
```

```
'Output
    Select Case PropertyID
    Case 0
        AtmosProperty = TempRatio
    Case 1
        AtmosProperty = PressRatio
    Case 2
        AtmosProperty = DensRatio
    Case 10
        AtmosProperty = TempRatio * 518.67
    Case 11
        AtmosProperty = PressRatio * 2116
    Case 12
        AtmosProperty = DensRatio * 0.002378
    End Select
End Function
```

Reference

[1] *U.S. Standard Atmosphere 1976*, National Oceanic and Atmospheric Administration, 1976.

APPENDIX

B

The Aerospace Engineer's Formula Sheet

B.1 COST ANALYSIS

Fixed and variable cost:	$C(N) = C_{fix} + C_{var} \times N$
Break-Even Analysis:	$N_{BE} = C_{fix}/(P_{unit} - C_{var})$
Quantity discount factor:	$QDF = (F_{EXP})^{1.4427 \cdot \ln N}$
Engineering workhours:	$H_{ENG} = 0.0396 \cdot W_{airframe}^{0.791} \cdot V_H^{1.526} \cdot N^{0.183} \cdot F_{CERT} \cdot F_{CF} \cdot F_{COMP} \cdot F_{PRESS}$
Tooling workhours:	$H_{TOOL} = 1.0032 \cdot W_{airframe}^{0.764} \cdot V_H^{0.899} \cdot N^{0.178} \cdot Q_m^{0.066} \cdot F_{TAPER} \cdot F_{CF} \cdot F_{COMP} \cdot F_{PRESS}$
Mfg labor workhours:	$H_{MFG} = 9.6613 \cdot W_{airframe}^{0.74} \cdot V_H^{0.543} \cdot N^{0.524} \cdot F_{CERT} \cdot F_{CF} \cdot F_{COMP}$

B.2 CONSTRAINT ANALYSIS

T/W for a desired T-O Distance:	$\frac{T}{W} = \frac{1.21}{g\rho C_{L_{max}} \cdot S_G}\left(\frac{W}{S}\right) + \frac{0.605}{C_{L_{max}}}(C_{D\ TO} - \mu C_{L\ TO}) + \mu$
T/W for a desired Rate-of-Climb:	$\frac{T}{W} = \frac{V_V}{V} + \frac{q}{(W/S)}C_{D_{min}} + \frac{k}{q} \cdot \left(\frac{W}{S}\right)$
T/W for a desired Angle-of-Climb:	$\frac{T}{W} = \sin\gamma + \sqrt{4kC_{D_{min}}}$
T/W for a level constant velocity turn (CVT):	$\frac{T}{W} = q\left[\frac{C_{D_{min}}}{(W/S)} + k\left(\frac{n}{q}\right)^2\left(\frac{W}{S}\right)\right]$
T/W for a climbing CVT:	$\frac{T}{W} = q\left[\frac{C_{D_{min}}}{(W/S)} + k\left(\frac{n}{q}\right)^2\left(\frac{W}{S}\right)^2\right] + \frac{P_S}{V}$
T/W for a desired cruise airspeed:	$\frac{T}{W} = qC_{D_{min}}\left(\frac{1}{W/S}\right) + k\left(\frac{1}{q}\right)\left(\frac{W}{S}\right)$
T/W for a Service Ceiling:	$\frac{T}{W} = \frac{1.667}{V_Y} + \frac{q}{(W/S)}C_{D_{min}} + \frac{k}{q} \cdot \left(\frac{W}{S}\right)$
T/W for a desired cruise L/D:	$\frac{T}{W} = \frac{1}{L/D}$
$C_{L_{max}}$ for a Desired Stalling Speed:	$C_{L_{max}} = \frac{1}{q_{stall}}\left(\frac{W}{S}\right)$

B.3 WEIGHT ANALYSIS

Design gross weight:	$W_0 = W_e + W_u$
Useful load:	$W_u = W_c + W_f + W_p$
W_0 consists of:	$W_0 = W_e + W_c + W_f + W_p$
Fuel weight ratio:	$W_f = \left(\frac{W_f}{W_0}\right) W_0$
Empty weight ratio:	$W_e = \left(\frac{W_e}{W_0}\right) W_0$
This can be solved for W_0:	$W_0 = \frac{W_c + W_p}{\left[1 - \left(\frac{W_e}{W_0}\right) - \left(\frac{W_f}{W_0}\right)\right]}$
Analogous expression for electric aircraft:	$m_0 = \frac{m_c + m_p}{1 - \left(\frac{m_e}{m_0}\right) - \left(\frac{g \cdot R}{3.6E^* \cdot \eta_{tot} \cdot LD_C}\right)}$
Mission analysis:	$\frac{W_N}{W_0} = \prod_{i=1}^{N} \frac{W_i}{W_{i-1}}$ solved through $\frac{W_N}{W_0} - \frac{W_c + W_p}{W_0} = \left(\frac{W_e}{W_0}\right)_{hist}$

Where the historical weight ratios, $\left(\frac{W_e}{W_0}\right)_{hist}$, for classes of aircraft are given by

Sailplanes:	$\frac{W_e}{W_0} = \begin{cases} 0.2950 + 0.0386 \cdot \ln W_0 & \text{if } W_0 \text{ is in lb}_f \\ 0.3255 + 0.0386 \cdot \ln W_0 & \text{if } W_0 \text{ is in kg} \end{cases}$
Powered sailplanes:	$\frac{W_e}{W_0} = \begin{cases} 0.3068 + 0.0510 \cdot \ln W_0 & \text{if } W_0 \text{ is in lb}_f \\ 0.3471 + 0.0510 \cdot \ln W_0 & \text{if } W_0 \text{ is in kg} \end{cases}$
Light Sport Aircraft (land):	$\frac{W_e}{W_0} = \begin{cases} 1.5451 - 0.1402 \cdot \ln W_0 & \text{if } W_0 \text{ is in lb}_f \\ 1.4343 - 0.1402 \cdot \ln W_0 & \text{if } W_0 \text{ is in kg} \end{cases}$
Light Sport Aircraft (amphib):	$\frac{W_e}{W_0} = \begin{cases} 1.6351 - 0.1402 \cdot \ln W_0 & \text{if } W_0 \text{ is in lb}_f \\ 1.5243 - 0.1402 \cdot \ln W_0 & \text{if } W_0 \text{ is in kg} \end{cases}$
GA Single Engine:	$\frac{W_e}{W_0} = \begin{cases} 0.8841 - 0.0333 \cdot \ln W_0 & \text{if } W_0 \text{ is in lb}_f \\ 0.8578 - 0.0333 \cdot \ln W_0 & \text{if } W_0 \text{ is in kg} \end{cases}$
GA Twin Piston:	$\frac{W_e}{W_0} = \begin{cases} 0.4074 + 0.0253 \cdot \ln W_0 & \text{if } W_0 \text{ is in lb}_f \\ 0.4274 + 0.0253 \cdot \ln W_0 & \text{if } W_0 \text{ is in kg} \end{cases}$
GA Twin Turboprop:	$\frac{W_e}{W_0} = \begin{cases} 0.5319 + 0.0066 \cdot \ln W_0 & \text{if } W_0 \text{ is in lb}_f \\ 0.5371 + 0.0066 \cdot \ln W_0 & \text{if } W_0 \text{ is in kg} \end{cases}$
Agricultural:	$\frac{W_e}{W_0} = \begin{cases} 1.4029 - 0.0995 \cdot \ln W_0 & \text{if } W_0 \text{ is in lb}_f \\ 1.3242 - 0.0995 \cdot \ln W_0 & \text{if } W_0 \text{ is in kg} \end{cases}$
Business jets:	$\frac{W_e}{W_0} = \begin{cases} 0.9038 - 0.03163 \cdot \ln W_0 & \text{if } W_0 \text{ is in lb}_f \\ 0.8788 - 0.03163 \cdot \ln W_0 & \text{if } W_0 \text{ is in kg} \end{cases}$

In interest of space, the statistical weight estimation methods have been omitted. See Section 6.4.

Center of Gravity:	$X_{CG} = \frac{M_X}{W_{tot}} = \frac{\sum_{i=1}^{N} W_i \times x_i}{W_{tot}}$ $Y_{CG} = \frac{M_Y}{W_{tot}} = \frac{\sum_{i=1}^{N} W_i \times y_i}{W_{tot}}$ $Z_{CG} = \frac{M_Z}{W_{tot}} = \frac{\sum_{i=1}^{N} W_i \times z_i}{W_{tot}}$
CG in terms of %MGC:	$X_{CG_{MGC}} = 100 \times \left(\frac{X_{CG} - X_{MGC}}{MGC} \right)$

Moments and products of inertia of a discrete system of point masses:

$$I_{xx} = \frac{1}{g}\sum_{i=1}^{N}\left(W_i\left[(y_i - Y_{CG})^2 + (z_i - Z_{CG})^2\right] + I_{xx_i}\right) \quad I_{xy} = \frac{1}{g}\sum_{i=1}^{N}\left(W_i(x_i - X_{CG})(y_i - Y_{CG}) + I_{xy_i}\right)$$
$$I_{yy} = \frac{1}{g}\sum_{i=1}^{N}\left(W_i\left[(x_i - X_{CG})^2 + (z_i - Z_{CG})^2\right] + I_{yy_i}\right) \quad I_{xz} = \frac{1}{g}\sum_{i=1}^{N}\left(W_i(x_i - X_{CG})(z_i - Z_{CG}) + I_{xz_i}\right)$$
$$I_{zz} = \frac{1}{g}\sum_{i=1}^{N}\left(W_i\left[(x_i - X_{CG})^2 + (y_i - Y_{CG})^2\right] + I_{zz_i}\right) \quad I_{yz} = \frac{1}{g}\sum_{i=1}^{N}\left(W_i(y_i - Y_{CG})(z_i - Z_{CG}) + I_{yz_i}\right)$$

B.4 POWER PLANT

The Basics of Energy, Work, and Power:

		Units	
Concept	**Formulation**	**SI system**	**UK system**
Energy The conservation of energy is one of the fundamental conservation laws of physics. It states that energy can neither be created nor destroyed, but it changes form. The form of energy refers to potential, kinetic, electrical, nuclear, chemical, and other forms of energy.	Kinetic energy: $KE = \frac{1}{2} mV^2$ Potential energy: $PE = mgh$ Pressure energy: $E_{press} = pV$ Electric energy: $E_{el} = UI \cdot \Delta t$	Joules (J) ($J = N\,m = kg\,m^2/s^2$) Wh or kWh 1 Wh = 3600 J	BTU (heat required to raise the temperature of 1 lb of H_2O by 1°F) 1 BTU = 1055.06 J 1 BTU = 778.169 ft lb_f
Work Work is defined as the product of force and distance. Work is also the same as *torque*.	Work ≡ Force × Distance	Joules N m	ft lb_f
Power Power is defined as the amount of work done in given time. It is also possible to define it as shown.	$\text{Power} \equiv \frac{\text{Work}}{\text{Time}} \equiv \frac{\text{Force} \times \text{Distance}}{\text{Time}} \equiv \text{Force} \times \text{Speed} \equiv \frac{\text{Torque}}{\text{Time}} \equiv \frac{dW}{dt} = \dot{W}$	W J/s N m/s	hp ft lb_f /s

Continued

The Basics of Energy, Work, and Power—cont'd

Concept	Formulation	Units: SI system	Units: UK system
One "Horsepower"		746 W 0.746 kW	33,000 ft lb_f/min 550 ft lb_f/s
UK system (T in lb_f, V in ft/s): $THP = \frac{TV}{550}$		SI system (T in N, V in m/s): $THP = \frac{TV}{746}$	
To convert torque and RPM to SHP:		$SHP = \frac{torque \times 2\pi \times RPM}{33{,}000} = \frac{torque \times RPM}{5252}$	
Gagg and Ferrar model:		$P = P_{SL}\left(\sigma - \frac{(1-\sigma)}{7.55}\right) = P_{SL}(1.132\sigma - 0.132) = P_{SL}\frac{(\sigma - 0.117)}{0.883}$	

Use the Mattingly Method in Chapter 14 to estimate the effect of airspeed and altitude on the thrust of gas turbine engines.

Electric Power:

Voltage (Volts):	$U = \begin{cases} I \times R \\ P/I \\ \sqrt{P \times R} \end{cases}$	**Current (Amps):**	$I = \begin{cases} \sqrt{P/R} \\ P/U \\ U/R \end{cases}$
Resistance (Ohms):	$R = \begin{cases} U/I \\ U^2/P \\ P/I^2 \end{cases}$	**Power (Watts or Volt-Amps):**	$P = \begin{cases} U^2/R \\ I^2 \times R \\ U \times I \end{cases}$

Electric energy (Watt-hours or Joules): $E_{el} = \int_0^T P dt = U \times I \times T$

Mass-Specific Energy (Wh/kg):	$E^* \equiv \frac{UI\Delta t}{m_{batt}}$
Volume-Specific Energy (Wh/liter):	$\cancel{V}^* \equiv \frac{UI\Delta t}{\cancel{V}_{batt}}$
Mass-Specific Power (W/kg):	$P^* \equiv \frac{UI}{m_{batt}}$
Battery capacity (Wh, kWh, AVh):	$E_{batt} = \begin{cases} C_{batt} U_{nom} \\ E^* m_{batt} \end{cases}$

Cyclic function: $y = A\sin(\omega t + \phi) = A\sin(2\pi f t + \phi)$

Where A = amplitude, ω = angular speed in rad/s, ϕ = phase angle, t = time in s, and f = frequency in Hertz.

Frequency (f) and period (T):	$f = 1/T$	[cycles/s or Hertz]
Angular speed (ω):	$\omega = \frac{2\pi}{T} = 2\pi f$	[radians/s]
Convert RPM to ω:	$\omega = \frac{2\pi RPM}{60}$	[radians/s]
Convert RPS to ω:	$\omega = 2\pi RPS$	[radians/s]

Relationship between power (P), torque (τ), and rotation:

$$P = \overbrace{\overbrace{F2\pi r}^{\text{work=}\atop\text{force}\cdot\text{dist}}\frac{RPM}{60}}^{\text{work done each second}} = \overbrace{Fr}^{\tau=\text{torque}} \overbrace{\frac{2\pi RPM}{60}}^{\omega=\text{angular speed}\atop\text{in radians/s}} = \tau\omega = \tau\frac{2\pi}{T} = \tau(2\pi f)$$

Relationship between power (P), torque (τ), and RPM:

Power in Watts:	$P_W \approx 745.7P_{HP} \approx \overbrace{0.1047}^{=2\pi/60}\tau_{[\text{Nm}]}RPM \approx \overbrace{0.07734}^{=2\pi/(60\cdot 1.354)}\tau_{[\text{ft lb}_\text{f}]}RPM$
Torque in Nm:	$\tau_{[\text{Nm}]} \approx \frac{9.549P_W}{RPM} \approx \frac{9549P_{kW}}{RPM} \approx \frac{7121P_{HP}}{RPM}$
Torque in ft lb$_\text{f}$:	$\tau_{[\text{ft lb}_\text{f}]} \approx \frac{7.053P_W}{RPM} \approx \frac{7053P_{kW}}{RPM} \approx \frac{5259P_{HP}}{RPM}$

B.5 WING PLANFORM

Aspect Ratio—general: $AR = b^2/S$	Wing span from AR: $b = \sqrt{AR \cdot S}$
Aspect ratio—constant chord: $AR = b/\bar{c}$	Average chord: $c_{avg} = \left(\frac{c_r + c_t}{2}\right) = \frac{b}{AR}$
Taper ratio: $\lambda = c_t/c_r$	Root chord: $c_r = \frac{2S}{b(1+\lambda)}$
Wing loading: $w = W/S$	Mean Geometric Chord: $c_{MGC} = \left(\frac{2}{3}\right)c_r\left(\frac{1+\lambda+\lambda^2}{1+\lambda}\right)$
Y-location of MGC$_\text{LE}$: $y_{MGC} = \left(\frac{b}{6}\right)\left(\frac{1+2\lambda}{1+\lambda}\right)$	Mean Aerodynamic Chord: $MAC \approx MGC$
X-location of MGC$_\text{LE}$: $x_{MGC} = y_{MGC}\tan\Lambda_{LE}$	Wing area: $S = b\left(\frac{c_r + c_t}{2}\right)$
Angle of quarter-chord line: $\tan\Lambda_{c/4} = \tan\Lambda_{LE} + \frac{c_r}{2b}(\lambda - 1)$	Average chord: $c_{avg} = \frac{c_r + c_t}{2} = \frac{c_r}{2}(1+\lambda)$

General lift curve slope:	$C_{L_\alpha} = \frac{2\pi \cdot AR}{2 + \sqrt{\left(\frac{AR\cdot\beta}{\kappa}\right)^2\left(1 + \frac{\tan^2\Lambda_{c/2}}{\beta^2}\right) + 4}}$
The Law of Effectiveness:	$P_{MGC} = P_{root} + \frac{2y_{MGC}}{b}(P_{tip} - P_{root})$
Method 1: Empirical Estimation for Straight Wings:	$e = 1.78(1 - 0.045AR^{0.68}) - 0.64$
Method 2: Empirical Estimation for Swept Wings:	$e = 4.61(1 - 0.045AR^{0.68})(\cos\Lambda_{LE})^{0.15} - 3.1$
Method 3: Brandt's Method:	$e = \frac{2}{2 - AR + \sqrt{4 + AR^2(1 + \tan^2\Lambda_{t_{\max}})}}$
Method 4: Douglas Method:	$e = \frac{1}{\pi \cdot AR \cdot r \cdot C_{D_{\min}} + 1/((1 + 0.03t - 2t^2)u)}$
Method 5: Howe's Method for Subsonic to Transonic Range	$e = \frac{1}{(1 + 0.12M_\infty^6)\left\{1 + \frac{0.142 + f(\lambda)AR_{corr}(10t/c)^{0.33}}{\cos^2\Lambda_{c/4}} + \frac{0.1(3N_{PP}+1)}{(4 + AR_{corr})^{0.8}}\right\}}$

B.6 TAIL SIZING

Horizontal tail volume: $V_{HT} = \dfrac{l_{HT} \cdot S_{HT}}{c_{MGC} \cdot S}$

Vertical tail volume: $V_{VT} = \dfrac{l_{VT} \cdot S_{VT}}{b \cdot S}$

HT-dependent tail arm: $l_{HT} = \sqrt{\dfrac{2 \cdot V_{HT} \cdot S \cdot c_{MGC}}{\pi(R_1 + R_2)}}$

VT-dependent tail arm: $l_{VT} = \sqrt{\dfrac{2 \cdot V_{VT} \cdot S \cdot b}{\pi(R_1 + R_2)}}$

HT- and VT-dependent tail arm: $l_T = \sqrt{\dfrac{2 \cdot S(V_{HT} \cdot c_{MGC} + V_{VT} \cdot b)}{\pi(R_1 + R_2)}}$

B.7 LIFT AND DRAG

Dynamic pressure: $q = \dfrac{1}{2}\rho V^2$

Induced drag constant k: $k = \dfrac{1}{\pi \cdot AR \cdot e}$

Drag: $D = \dfrac{1}{2}\rho V^2 S C_D = D_{\min} + D_i$

Lift: $L = \dfrac{1}{2}\rho V^2 S C_L$

Lift coefficient: $C_L = \dfrac{2L}{\rho V^2 S} \approx \dfrac{2W}{\rho V^2 S}$

Span efficiency:

$e = 1.78\left(1 - 0.045AR^{0.68}\right) - 0.64$ Straight wing

$e = 4.61\left(1 - 0.045AR^{0.68}\right)(\cos\Lambda_{LE})^{0.15} - 3.1$ Swept back

Simplified drag model: $C_D = \dfrac{2D}{\rho V^2 S} = \dfrac{2T}{\rho V^2 S} = C_{D_{\min}} + kC_L^2$

Adjusted drag model: $C_D = C_{D_{\min}} + k(C_L - C_{L_{\min D}})^2$

B.8 THE PROPELLER

Power coefficient: $C_P = \dfrac{P}{\rho n^3 D^5} = \dfrac{550 \times P_{BHP}}{\rho\left(\dfrac{RPM}{60}\right)^3 D^5} = \dfrac{118{,}800{,}000 \times P_{BHP}}{\rho \cdot RPM^3 \cdot D^5}$

Thrust coefficient: $C_T = \dfrac{T}{\rho n^2 D^4} = \dfrac{3600 \cdot T}{\rho \cdot RPM^2 D^4}$

Torque coefficient: $C_Q = \dfrac{Q}{\rho n^2 D^5} = \dfrac{3600 \cdot Q}{\rho \cdot RPM^2 \cdot D^5} = \dfrac{C_P}{2\pi}$

Power-Torque relation: $C_Q = \dfrac{Q}{\rho n^2 D^5} = \dfrac{C_P}{2\pi} = \dfrac{P/\rho n^3 D^5}{2\pi} \Rightarrow P = 2\pi n Q$

Propeller efficiency: $\eta_p = \dfrac{\mathrm{TV}}{\mathrm{P}} = \dfrac{TV}{550BHP} = J\dfrac{C_T}{C_P}$

Propeller thrust: $T = \dfrac{\eta_p P}{V} = \dfrac{\eta_p \times 550 \times P_{BHP}}{V}$

Thrust quadratic spline: $T(V) = \left(\dfrac{T_{STATIC} - 2T_{\max}}{V_{\max}^2}\right)V^2 + \left(\dfrac{3T_{\max} - 2T_{STATIC}}{V_{\max}}\right)V + T_{STATIC}$

Ideal efficiency:	$\eta_i = \dfrac{1}{(1+w/V_0)} = \dfrac{2}{1+\sqrt{1+C_T}}$
Static thrust, T_{STATIC}:	$T_{STATIC} = P^{2/3}(2\rho A_2)^{1/3} T_{STATIC} = P^{2/3}(2\rho A_2)^{1/3}$
Corrected static thrust:	$T_{STATIC} = 0.85P^{2/3}(2\rho A_2)^{1/3}\left(1 - \dfrac{A_{spinner}}{A_2}\right)$

B.9 THE ATMOSPHERE

Pressure: $p = p_0\theta^{5.2561}$	Pressure ratio: $\delta = p/p_0 = \theta^{5.2561}$
Density: $\rho = \rho_0\theta^{4.2561}$	Density ratio: $\sigma = \rho/\rho_0 = \theta^{4.2561} = \delta/\theta$
Temperature: $T = T_0\theta$	Temperature ratio: $\theta = 1 + \kappa h = \begin{cases} 1 - 0.0000068756h & \text{UK} - \text{system} \\ 1 - 0.000022558h & \text{SI} - \text{system} \end{cases}$
Pressure altitude: $h_P = 145{,}442\left(1 - \left(\dfrac{p}{p_0}\right)^{0.19026}\right)$	Density altitude: $h_\rho = 145{,}442\left(1 - \left(\dfrac{\rho}{\rho_0}\right)^{0.234957}\right)$

B.10 AIRSPEEDS

Calibrated Airspeed:	$KCAS = KIAS + \Delta error$
Equivalent Airspeed	$KEAS = KCAS\sqrt{\dfrac{p}{p_0}}\sqrt{\dfrac{\left(\frac{q_c}{p}+1\right)^{0.286} - 1}{\left(\frac{q_c}{p_0}+1\right)^{0.286} - 1}}$
True Airspeed:	$KTAS = \dfrac{KEAS}{\sqrt{\rho/\rho_{SL}}} \approx \dfrac{KCAS}{\sqrt{\rho/\rho_{SL}}} = \dfrac{KCAS}{\sqrt{\sigma}}$
Mach Number:	$M = \dfrac{V}{a_0} = \dfrac{V}{\sqrt{\gamma RT}}$
Speed of sound:	$a_0 = \sqrt{\gamma RT} \approx 49.01\sqrt{OAT_{\circ R}}$

B.11 TAKE-OFF

Torenbeek's Balanced Field Length:
$$BFL = \frac{0.863}{1+2.3\Delta\gamma_2}\left(\frac{W_{to}/S}{\rho g C_{L2}} + h_{to}\right)\left(2.7 + \frac{1}{\overline{T}/W_{to} - \mu'}\right) + \left(\frac{\Delta S_{to}}{\sqrt{\sigma}}\right)$$

Acceleration on a flat runway:
$$\frac{dV}{dt} = \frac{g}{W}[T - D - \mu(W - L)]$$

Acceleration on an uphill slope γ:
$$\frac{dV}{dt} = \frac{g}{W}[T - D - \mu(W\cos\gamma - L) - W\sin\gamma]$$

Liftoff speed:
$$V_{LOF} = 1.1 \times V_{S1} = 1.1\sqrt{\frac{2W}{\rho S C_{L_{max}}}} \approx 1.556\sqrt{\frac{W}{\rho S C_{L_{max}}}}$$

Time to lift-off:
$$t = \sqrt{\frac{2S_G}{a}} + \begin{cases} 1 & \text{for small aircraft} \\ 3 & \text{for large aircraft} \end{cases}$$

Ground run:
$$S_G = \frac{V_{LOF}^2 W}{2g[T - D - \mu(W - L)]_{at\ (V_{LOF}/\sqrt{2})}}$$

Ground run for piston props:
$$S_G = \frac{V_{LOF}^2 W}{\frac{50{,}051 \times \eta_P \times P_{BHP}}{V_{LOF}} + 16.09\rho V_{LOF}^2 S(\mu C_{L\ TO} - C_{D\ TO}) - 64.35\mu W}$$

Rotation distance:
$$S_{ROT} = \begin{cases} |V_{LOF}| & \text{for small aircraft} \\ 3|V_{LOF}| & \text{for large aircraft} \end{cases}$$

Climb angle:
$$\sin\theta_{climb} = \frac{T - D}{W} = \frac{T}{W} - \frac{1}{L/D}$$

Transition distance:
$$S_{TR} = R\sin\theta_{climb} \approx 0.2156 \times V_{S1}^2 \times \left(\frac{T}{W} - \frac{1}{L/D}\right)$$

Transition height:
$$h_{TR} = R(1 - \cos\theta_{climb})$$

B.12 CLIMB, CRUISE, AND MANEUVERING FLIGHT

Jets in climb:
$$V_V \equiv \frac{TV - DV}{W} = V\sin\theta$$

Propellers in climb:
$$V_V \equiv \frac{P_{AV} - P_{REQ}}{W} = \frac{\eta_p \cdot P_{ENG} - P_{REQ}}{W} = V\sin\theta$$

Rate-of-Climb:
$$ROC \equiv 60\left(\frac{TV - DV}{W}\right) = 60\left(\frac{P_{AV} - P_{REQ}}{W}\right)$$

General Angle-of-climb (AOC):
$$\sin\theta = \frac{T}{W} - \frac{1}{L/D}$$

Min/max airspeed:
$$V = \sqrt{\frac{T \pm \sqrt{T^2 - 4C_{D_{min}} kW^2}}{\rho S C_{D_{min}}}}$$

Stalling speed:
$$V_S = \sqrt{\frac{2W}{\rho S C_{L_{max}}}}$$

Level stalling speed at load factor n:
$$V_S = \sqrt{\frac{2nW}{\rho S C_{L_{max}}}}$$

Stalling speed at angle of bank ϕ:

$$V_S = \sqrt{\frac{2W}{\rho S C_{L_{\max}} \cos\phi}} = \frac{V_{S_{level}}}{\sqrt{\cos\phi}}$$

Minimum Thrust Required, $V_{TR_{min}}$, or Best Glide Speed, V_{BG}, $V_{LD_{max}}$:

$$V_{TR_{\min}} = \sqrt{\frac{2}{\rho}\left(\frac{W}{S}\right)\sqrt{\frac{k}{C_{D_{\min}}}}}$$

Max L/D:

$$LD_{\max} = \left(\frac{C_L}{C_D}\right)_{\max} = \frac{1}{\sqrt{4 \cdot C_{D_{\min}} \cdot k}}$$

Carson's airspeed:

$$V_{CAR} = 3^{0.25} V_{LD_{\max}} \approx 1.32 V_{LD_{\max}}$$

Power required:

$$P_{REQ} = \sqrt{\frac{2W^3 C_D^2}{\rho S C_L^3}}$$

Bank angle:

$$\phi = \cos^{-1}\left(\frac{1}{n}\right)$$

Load factor:

$$n = \frac{1}{\cos\phi} = \left(\frac{T}{W}\right)\left(\frac{L}{D}\right)$$

Turn radius:

$$R_{turn} = \frac{V^2}{n \cdot g \cdot \sin\phi} = \frac{V^2}{g\sqrt{n^2 - 1}}$$

Time to turn ψ *degrees*:

$$t_\psi = \frac{R_{turn}}{V}\left(\psi\frac{\pi}{180}\right)$$

Turn rate in radians/s:

$$\dot{\psi} = \frac{g\sqrt{n^2 - 1}}{V} = \frac{V}{R_{turn}}$$

Thrust required at a load factor n:

$$T_R = qS\left[C_{D_{\min}} + k\left(\frac{nW}{qS}\right)^2\right] + D_{trim}$$

Load factor that can be sustained at a given thrust, T, and airspeed, V:

$$n = \frac{qS}{W}\sqrt{\frac{1}{k}\left(\frac{T}{qS} - C_{D_{\min}}\right)}$$

Airspeed for a given C_L:

$$V = \sqrt{\frac{2W}{\rho S C_L}\left(\frac{1}{\cos\phi}\right)}$$

Max Sustainable Load Factor:

$$n_{\max} = \left(\frac{T_{\max}}{W}\right) LD_{\max}$$

Maximum Sustainable Turn Rate, $\dot{\psi}_{max}$:

$$\dot{\psi}_{\max} = \frac{g\sqrt{n_{\max}^2 - 1}}{V_{\max\dot{\psi}}}$$

Minimum Sustainable Turning Radius:

$$R_{\min} = \frac{V_{R_{\min}}^2}{g\sqrt{n_{R_{\min}}^2 - 1}}$$

Where: $n_{R_{\min}} = \sqrt{2 - 1/n_{\max}^2}$ = Load factor and $V_{R_{\min}} = 2\sqrt{\frac{(W/S)k}{(T/W)\rho}}$ = Airspeed for minimum turning radius

Maximum Level Bank angle:

$$\phi_{\max} = \cos^{-1}\left(\frac{1}{n_{\max}}\right)$$

Specific Excess Power:

$$P_S \equiv \frac{P_{EX}}{W} = \frac{TV - DV}{W} = \frac{dh}{dt} + \frac{V}{g}\frac{dV}{dt}$$

Specific energy and height:

$$E_{total} = mgh + \tfrac{1}{2}mV^2 = Wh + \tfrac{1}{2}\tfrac{W}{g}V^2 \quad \text{and} \quad H_E \equiv \tfrac{E_{total}}{W} = h + \tfrac{V^2}{2g}$$

B.13 RANGE AND ENDURANCE

Range profile 1:
$$R = \frac{V}{c_t\sqrt{kC_{D0}}}\left[\tan^{-1}\left(\frac{2\sqrt{k}}{\rho V^2 S\sqrt{C_{D0}}}W_{ini}\right) - \tan^{-1}\left(\frac{2\sqrt{k}}{\rho V^2 S\sqrt{C_{D0}}}W_{fin}\right)\right]$$

Range profile 2:
$$R = \frac{1}{c_t}\frac{\sqrt{C_L}}{C_D}\frac{2\sqrt{2}}{\sqrt{\rho S}}\left(\sqrt{W_{ini}} - \sqrt{W_{fin}}\right) = \frac{1}{c_t C_D}\sqrt{\frac{8C_L}{\rho S}}\left(\sqrt{W_{ini}} - \sqrt{W_{fin}}\right)$$

Range profile 3:
$$R = \frac{V}{c_t}\frac{C_L}{C_D}\ln\left(\frac{W_{ini}}{W_{fin}}\right)$$

Endurance profile 1:
$$E = \frac{1}{c_t\sqrt{kC_{D0}}}\left[\tan^{-1}\left(\frac{2\sqrt{k}}{\rho V^2 S\sqrt{C_{D0}}}W_{ini}\right) - \tan^{-1}\left(\frac{2\sqrt{k}}{\rho V^2 S\sqrt{C_{D0}}}W_{fin}\right)\right]$$

Endurance profile 2:
$$E = \frac{1}{c_t}\frac{C_L}{C_D}\ln\left(\frac{W_{ini}}{W_{fin}}\right)$$

Endurance profile 3:
$$E = \frac{1}{c_t}\frac{C_L}{C_D}\ln\left(\frac{W_{ini}}{W_{fin}}\right)$$

TSFC for a Jet:
$$c_t = \left(\frac{c_{jet}}{3600}\right)\left\langle\frac{\text{lb}_\text{f}/\text{s}}{\text{lb}_\text{f}}\right\rangle \quad \text{where } c_{jet} = SFC \text{ for a jet}$$

TSFC for a Piston:
$$c_t = \frac{c_{bhp}V}{1{,}980{,}000\eta_p}\left\langle\frac{1}{\text{s}}\right\rangle \quad \text{where } c_{bhp} = SFC \text{ for a piston}$$

Specific Range:
$$SR \equiv \frac{\text{Distance}}{\text{Quantity of Fuel}} = \frac{\text{R}}{W_f} = \frac{V_{TAS}}{\dot{w}_{fuel}} = \frac{\text{True Airspeed}}{\text{Fuel Weight Flow}}$$

APPENDIX

C

Design of Biplanes and Seaplanes

This section gives a brief insight into the design of two classes of common aircraft—biplanes and seaplanes. The presentation in this appendix is largely a consequence of the challenge involved in finding a suitable place in the main body of the book.

C.1 CONCEPTUAL DESIGN OF BIPLANES

The golden age of the biplane lasted from 1903 to 1940 [1]. Although the monoplane surpassed the biplane in acceptance, it is still a viable option for many missions; e.g., as an aerobatic or agricultural aircraft. Both missions require responsive roll characteristics permitted by the compact size of its wings. Figure C-1 shows examples of five single-engine biplanes with different tail configurations, all taildraggers.

(1) The Biplane as an Agricultural Aircraft

The biplane configuration is well suited as an agricultural aircraft (aka ag-plane). Examples include the Antonov An-2, Grumman Ag-Cat, Transavia PL-12 Airtruk, and the PZL M-15 Belphegor. Good ag-planes are strong, reliable, and durable. They provide years of hard service with minimum maintenance. The ideal ag-plane is efficient and safe. In this context, efficiency refers to quickly spraying a large acreage of farmland. This is helped by the four wingtip vortices. The safety of the ideal ag-plane, in part, is increased by a reinforced cockpit that can survive in one piece in case of an accident. The cockpit should be carefully designed with pilot ergonomics and safety as priorities. Thus, pilot egress should be easy and fast. It should offer amenities like air-conditioning for added comfort; after all, it is the pilot's office for up to 15 h a day. The aircraft should offer a large fuel tank to minimize fuel stops during operation and a large fertilizer tank (*hopper*). It should be fast so it can quickly fly from one farm field to the next. The biplane offers an ideal solution to many of these considerations.

(2) Pros

A shorter wing span is achieved by splitting the required wing area into two wing panels. This is beneficial in several ways. (A) Roll damping is reduced compared to a monoplane of equal wing area. This offers greater steady-state roll rate (see Equation 25-83). (B) The shorter wing span reduces the moment of inertia about the roll axis. The increased roll acceleration gives the biplane a great roll response. (C) The shorter wingspan reduces wing bending moments, so the wing can be made lighter and stiffer. Ref. [2] states biplanes wings weigh 80%–90% of comparable monoplane wings. (D) Biplanes pack a large wing area inside a small span, reducing take-off and landing distances while eliminating the need for a complex high-lift system. This also permits operation from unimproved landing strips. (E) Biplanes can be designed to offer great stall characteristics by ensuring the upper wing (forward stagger) or lower wing (aft stagger) stalls first. The sudden drop in lift of one of the two wings generates a gentle nose-down pitching moment, facilitating good stall recovery.

(3) Cons

The following constitute drawbacks: (A) The high drag of external struts and bracing associated with typical biplanes is unsuitable for long range/endurance missions. A possible exception is the Griffon Aerospace Lionheart, a six-seat modernized replica of Beech's famed 1930s Staggerwing. It was designed and built in the early 2000s. It featured NLF airfoils, retractable landing gear, and was void of external struts and bracing. It was clean and fast for a biplane, although its 450 BHP Pratt & Whitney R-945 radial engine gave it a cruising speed similar to the 300 BHP Cirrus SR22 and Cessna TTx (both which enjoy the safety and reduced maintenance cost of a fixed landing gear). The original Beech Staggerwing had the upper wing aft of the lower wing, a relatively rare configuration in the history of aviation. As discussed later, this configuration leads to a less "destructive" interference between the two wings compared to a conventional

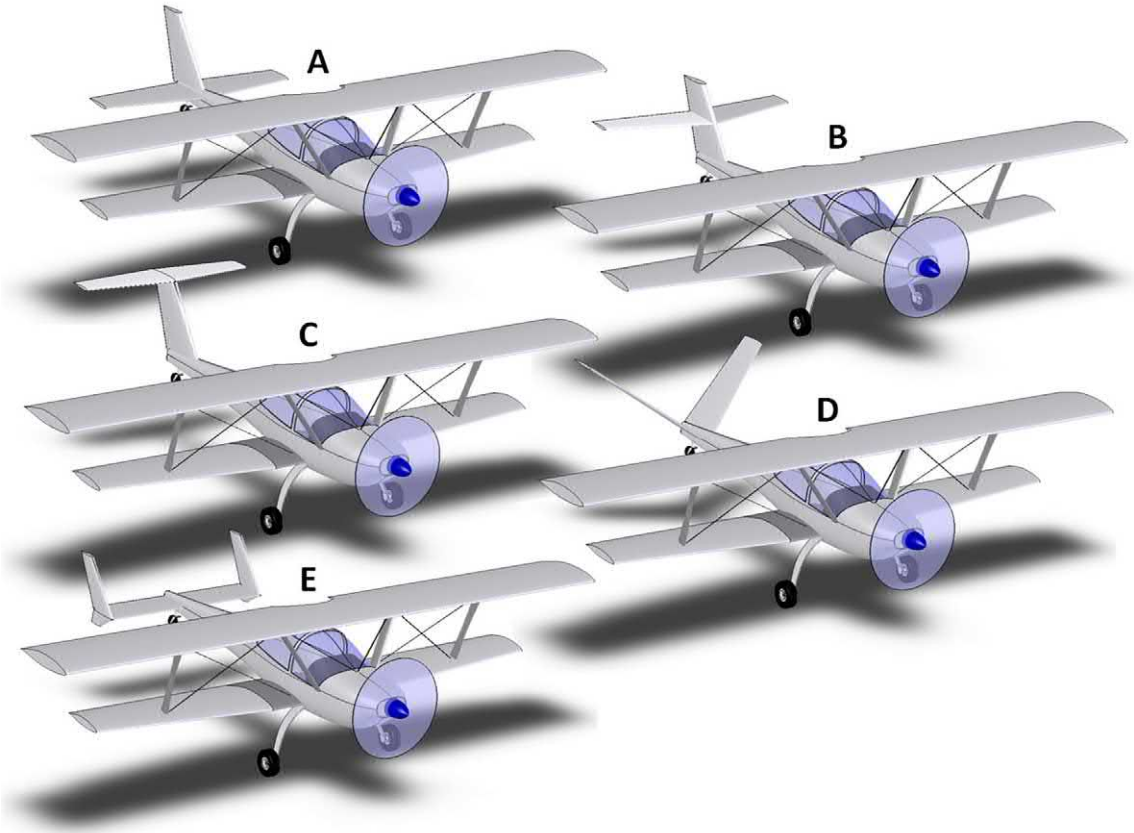


FIGURE C-1 Five single-engine, taildragger biplane configurations with tractor propellers.

arrangement, although only marginally so. Ref. [3] investigated specialized biplane configurations with improved L/Ds that are comparable with some monoplanes.

(B) The high-pressure region of the upper wing affects the low-pressure region of the lower wing. This effect can also be explained in terms of lumped spanwise vortices: The lower wing increases the circulation around the upper wing, while suffering from the vorticity of the upper one. This is shown in Figure C-2. The severity of this effect depends on the relative geometry of the two wings, in particular, decalage angle and stagger (see Figure C-4). The influence is low for zero decalage, but otherwise can be quite significant. Using potential flow analysis, an average AR biplane with a 4-degree decalage can easily load the upper wing to generate $2\times$ more lift than the lower one. A 2-to-1 ratio renders it very inefficient—ideally, both wings should contribute equally to the total lift. This means the lower wing is largely there for the ride. Such a configuration develops higher lift-induced drag, also evident by four wingtip vortices versus two for a monoplane.

(C) Biplanes have a very shallow lift curve slope (see Figure C-5). This requires a higher AOA (or deck angle) to produce a given C_L. While this makes the airplane less susceptible to gust loading, this is offset by its generally low wing loading.

C.1.1 Nomenclature for Biplanes

Figure C-3 shows the front view of a typical biplane and the nomenclature applied to the structural arrangement between the two wings. The aspect ratio for biplanes is obtained by dividing the square of the span of the larger wing (the upper one in Figure C-3) by the total planform area of both wings.

C.1.2 Various Effects That Apply to Biplanes Only

(1) Gap

The *gap* is the separation between the upper and lower wings. The high-pressure region on the lower surface of the upper wing detrimentally affects the low-pressure region on the upper surface of the lower wing. The greater the separation, the less is the interference. A large gap increases the weight of the airframe as support struts and bracing wires get longer.

(2) Decalage Angle

For biplanes, the *decalage angle* is the difference between the incidence angles of the top and bottom wing (see Figure C-4). It is *positive* when the AOI of the lower

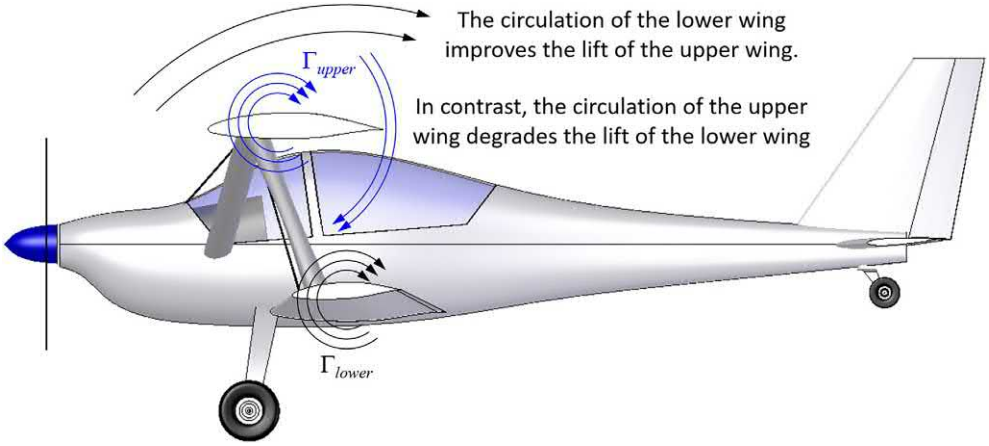


FIGURE C-2 The interference of the upper and lower wing circulations leads to asymmetry in lift generation.

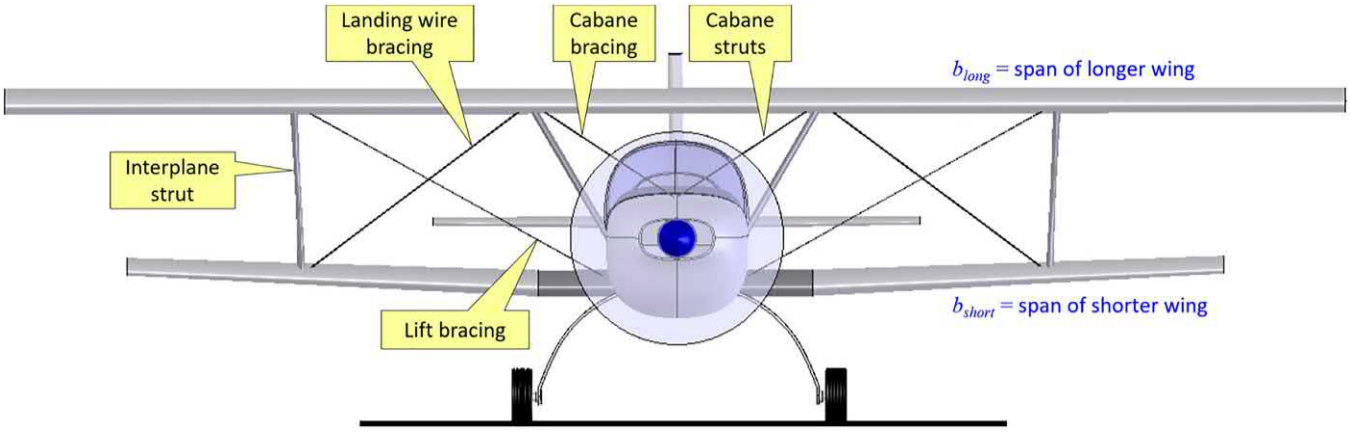


FIGURE C-3 Nomenclature for the wing layout of a biplane.

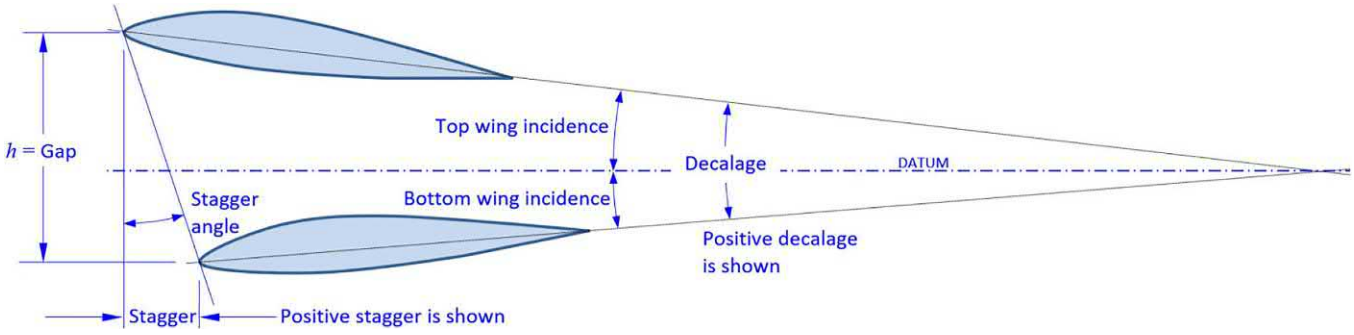


FIGURE C-4 Definition of a decalage angle for a biplane.

wing is less than that of the upper wing. Decalage allows one to control whether the upper or lower wing stalls first. If the biplane has a *positive stagger*, it is desirable to ensure the upper wing stalls first. At stall, this shifts the center-of-lift aft and ensures the airplane drops the nose gently. However, as discussed in Ref. [4], the effect is more complex. The decalage also controls the relative circulation strength around the two wings. The stagger angle and gap dictate the pressure distribution between the two wings and affect the maximum lift capability (see discussion on combined effect momentarily).

Ref. [2] details that the average wing incidence for early biplanes (those that had thin undercambered[1] airfoils) ranges from +2 to +5 degrees. For post-World

[1] An undercambered airfoil is one for which the lower surface is above the chordline. These were early airfoils emulated by bird wings. See the low-Re airfoil in Table 8-2.

War I biplanes, this value ranges from +2 to +3 degrees. It also states that the decalage varies from 0 to +1 degrees for both classes [2].

(3) Positive and Negative Stagger

Stagger is the relative position of the leading edges of the upper and lower wings. A positive stagger means the upper wing is forward of the lower wing. A negative stagger is the opposite. Most biplanes feature a positive stagger. The effect of stagger is investigated in Ref. [5], where it was concluded that a positive stagger yields a higher $C_{L_{max}}$ than a negative one. The greater the positive stagger, the greater is $C_{L_{max}}$. However, cruise drag was marginally higher for positive stagger. Stagger can be selected based on pilot visibility, as long as the designer is aware of the implications.

Figure C-5 shows that stagger affects the lift curve slope and the stick-fixed neutral point. Note that the *x*-axis is inverted to match the inserted image. A positive stagger of *chord-length one* means the trailing-edge of the upper wing is directly above the leading-edge of the lower one (assuming both wings have equal chords). First, consider the lift curve slope (the solid curve). The highest values of C_{L_α} are realized at the extremes of the range evaluated. The minimum occurs when the upper wing is "on-top" of the lower one. This is caused by the destructive interference illustrated in Figure C-6: The high-pressure region generated by the lower surface of the upper wing conflicts with the low-pressure region on top of the lower one. The minimum C_{L_α} is approximately 93% of the extreme positive stagger.

Next, consider the change in the stick-fixed neutral point (dashed curve), here referenced with respect to the LE of the lower wing. For a positive stagger of one chord-length, the neutral point is approximately at −32% MGC (ahead of the LE). For zero-stagger, the neutral point has moved to approximately 27% MGC. At negative one chord-length stagger, the neutral point is at 68% MGC. Stagger allows the longitudinal stability of the biplane to be controlled.

(4) Combined Effect of Stagger and Decalage

The combination of stagger and decalage gives rise to what is called *constructive* and *destructive interference*. Figure C-6 illustrates this concept in terms of the lumped vortex analogy introduced in Figure C-2. Figure C-6 shows how positive decalage causes *destructive interference* between the wings, regardless of stagger, while negative decalage induces *constructive interference*. The only drawback is that constructive interference requires the two wings to develop opposite lift forces. It is important to remember that, in the scheme of things, this interference is small. It will not turn a bad design into a good one, or the other way around. The combined effect is too complicated to easily explain in words. A graphical explanation, using typical biplane dimensions, is presented in Figure C-7 (read caption). It shows that while specific combinations of stagger and decalage yield a larger lift-to-drag ratio than others, the range is limited. All combinations are substantially inferior to monoplanes of equal wing area and aspect ratio.

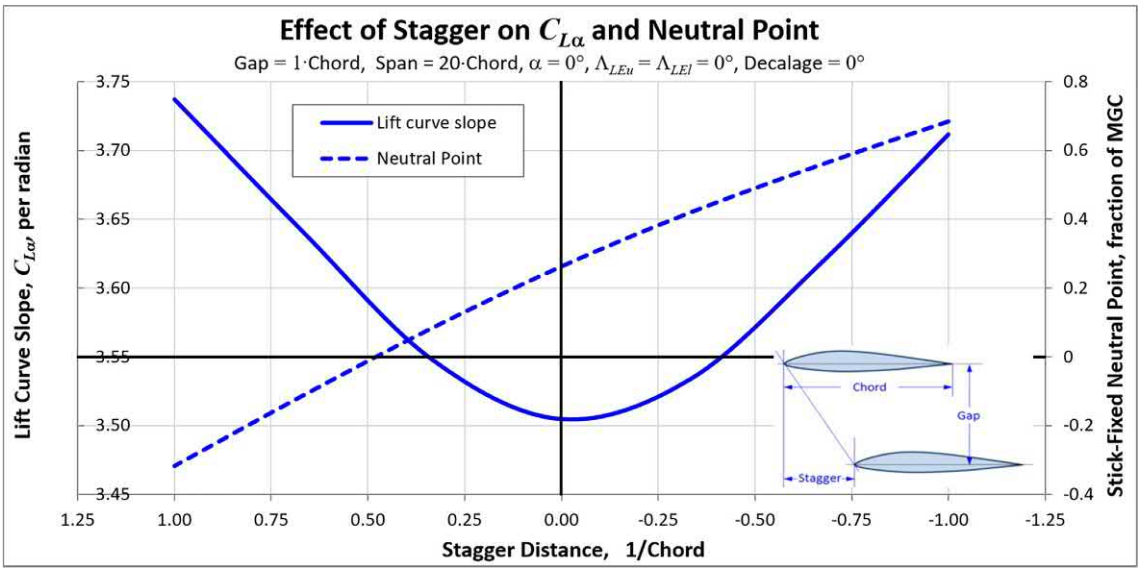


FIGURE C-5 The impact of stagger on lift curve slope and stick fixed neutral point of a typical biplane wing configuration. Negative stagger means the LE of the upper wing is ahead of the lower wing LE.

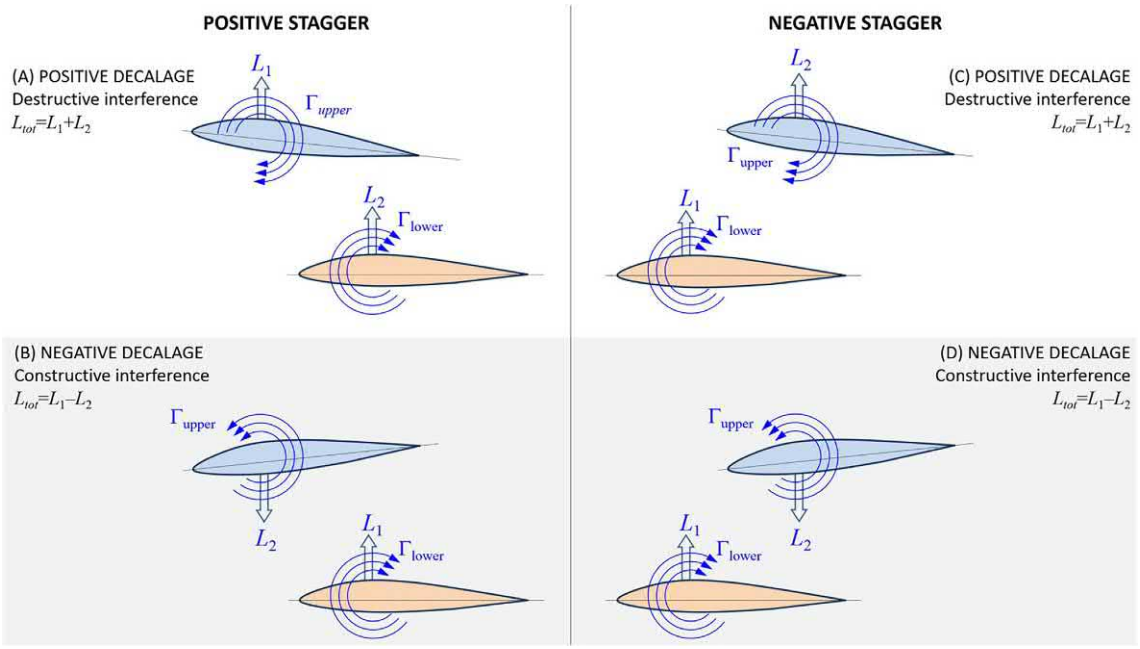


FIGURE C-6 The impact of stagger on the lift-curve slope and stick-fixed neutral point of a typical biplane wing configuration. Positive stagger means the LE of the upper wing is ahead of the lower wing LE.

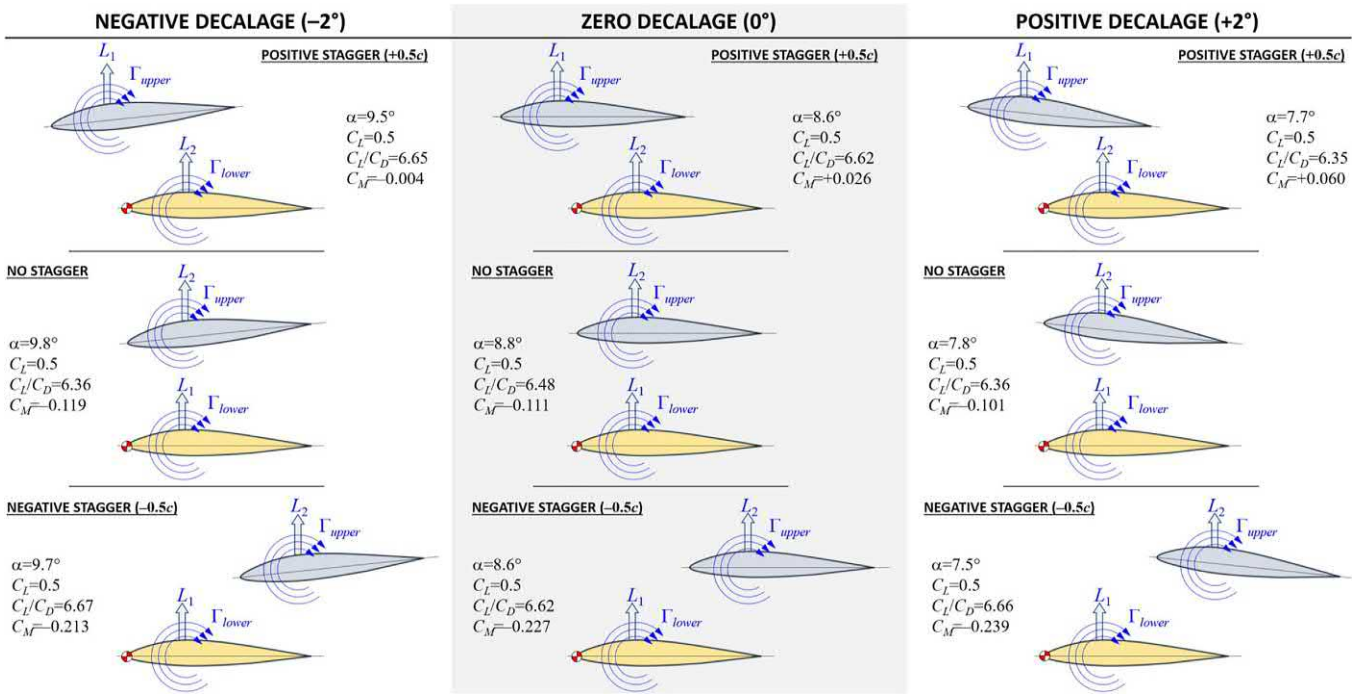


FIGURE C-7 The combined effect of stagger and decalage on C_L/C_D. The numbers refer to a biplane of $AR=5.33$, $\lambda=1$, decalage $=\pm 2$ degrees, gap = chord, and stagger $=\pm$½chord. All cases show α required to achieve $C_L=0.5$ (using symmetric airfoils). The pitching moment (C_M) references the LE of the lower wing. A monoplane of equal W/S with $AR=5.33$ achieves a $C_L/C_D=11.93$. A monoplane of equal W/S with $2\times b$ achieves a $C_L/C_D=16.39$. Hands down, the monoplane wins in efficiency.

C.1.3 Aerodynamic Properties of the Biplane Configuration

(1) Biplane Aspect Ratio

The aspect ratio of biplanes is assessed in two different ways. First, as shown by the following expression, it is estimated using the larger wing and one-half of the total wing area. However, this approximates the AR of the larger wing only.

$$AR_{biplane}=\frac{2b^2_{\text{larger wing}}}{S} \tag{C-1}$$

A second method is offered by Jones [6]. It uses the *equivalent monoplane aspect ratio* (EMAR), calculated from

$$EMAR = \frac{S}{c_u^2 + 2\sigma c_u c_l + c_l^2} \tag{C-2}$$

where c_u and c_l are the average chords of the upper and lower wings, respectively, and σ is the biplane interference factor (see Bullet (4)). It is also possible to evaluate EMAR based on the equivalent monoplane wingspan as $k \cdot b$ (see Bullet (3)). Thus, EMAR is written as

$$EMAR = \frac{(kb)^2}{S} \tag{C-3}$$

(2) Equivalent Monoplane Theorem

The concept of the *equivalent monoplane* was proposed by Munk [7] in the early 1900s to help simplify analyses of biplanes. It presumes the biplane configuration can be replaced by a monoplane wing of equal wing area and lift-induced drag. This difference can be represented as follows:

$$\frac{\varepsilon_{biplane}}{\varepsilon_{monoplane}} = 1 + \frac{\Delta\varepsilon}{\varepsilon} = 1 + \sigma \tag{C-4}$$

Where: $\varepsilon_{monoplane}$ = Monoplane downwash = $C_L/(\pi \cdot AR \cdot e)$

$\varepsilon_{biplane}$ = Downwash by a biplane of equal weight and wing area = $(1+\sigma)C_L/(\pi \cdot AR \cdot e)$
σ = Biplane interference factor (to be discussed momentarily)

(3) Munk's Span Factor, *k*

As stated above, Munk's *Equivalent Monoplane Theorem* replaces the biplane wings with a monoplane wing of equal area and lift-induced drag. Thus, if the biplane's maximum wing span is b, the corresponding equivalent monoplane wingspan is $k \cdot b$, where k is *Munk's Span Factor* [8], where $k = 1$ for monoplanes and $k > 1$ for biplanes. It is a function of the following ratios:

(1) Gap ratio is gap/(average wingspan) = (h/b_{avg}),
(2) span ratio is (shorter wingspan)/(longer wingspan), $\mu = b_{short}/b_{long}$, and
(3) area ratio, $r = S_{long}/S = (S - S_{short})/S$.

Where:

h = Gap height (see Figure C-4),
$b_{avg} = \frac{1}{2}(b_{long} + b_{short})$ (see Figure C-3),
S = total area of both wings,
S_{long} and S_{short} = planform areas of the two wings.

Munk's span factor is given by the following expression:

$$k = \sqrt{\frac{2}{1+\sigma}} \tag{C-5}$$

(4) Biplane Interference Factor, σ

The biplane interference factor, σ, accounts for the effect of bringing two lifting surfaces close to one another. A method developed by Prandtl [9] can be used to estimate σ if both wings are of an equal span. It is valid for $0.05 \le (h/b_{avg}) \le 0.5$:

$$\sigma = \frac{1 - 0.66(h/b_{avg})}{1.055 + 3.7(h/b_{avg})} \tag{C-6}$$

Diehl [8] presents a graph of Prandtl's biplane interference factors for other span ratios, μ. It is plotted in Figure C-8. The following expression was derived by the author to calculate σ for other span ratios based on this graph. It is valid for $0.4 \le \mu \le 1.0$ and $0.05 \le (h/b_{avg}) \le 0.5$. It provides an acceptable fit for the curves in Diehl's graph.

$$\sigma = \left(\frac{6}{75}\right)\frac{75\mu - (28 + 20\mu)(h/b_{avg})}{6 + (29\mu - 5)(h/b_{avg})} \tag{C-7}$$

(5) Lift-Induced Drag of a Biplane

Once the biplane interference factor has been determined, the lift-induced drag can be determined using the expression:

Biplane lift-induced drag:

$$C_{D_i} = \frac{C_L^2}{\pi \cdot AR \cdot e}(1+\sigma) = \frac{SC_L^2}{\pi \cdot (2b^2) \cdot e}(1+\sigma) \tag{C-8}$$

Prandtl also showed that the drag of one wing in the presence of the other is given by:

$$D_{12} = \left(\frac{\sigma}{\pi q}\right)\frac{L_{long}L_{short}}{b_{long}b_{short}} \tag{C-9}$$

Where q is dynamic pressure, L_{long}, b_{long} and L_{short}, b_{short} are the lift and span of the longer and shorter wings, respectively. Furthermore, Prandtl determined the total lift-induced drag to be:

$$D_i = \left(\frac{1}{\pi q}\right)\left[\frac{L_{long}^2}{b_{long}^2} + 2\sigma\frac{L_{long}L_{short}}{b_{long}b_{short}} + \frac{L_{short}^2}{b_{short}^2}\right] \tag{C-10}$$

The expression allows the geometry for minimum lift-induced drag to be determined. This happens when:

$$\frac{L_{long}}{L_{short}} = \frac{\mu - \sigma}{1/\mu - \sigma}$$

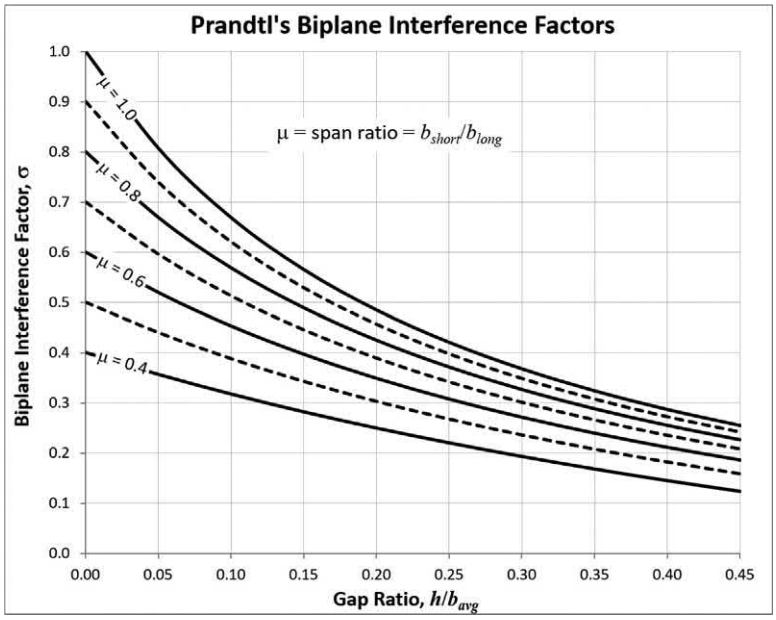


FIGURE C-8 A map of Prandtl's biplane interference factors as functions of the gap and span ratios. *Based on W.S. Diehl, Engineering Aerodynamics, Ronald Press Company, 1936.*

Thus, the minimum lift-induced drag is:

$$D_i = \left(\frac{L^2}{\pi q b_{long}^2}\right)\left[\frac{1-\sigma^2}{1-2\sigma\mu+\mu^2}\right] \qquad \text{(C-11)}$$

Where $L = L_{long} + L_{short}$ is the lift (or weight of the aircraft). If the two wings are of different geometry, then we assume the lift is proportional to the area ratio, r (defined earlier). Thus, the following rules hold:

Wing areas: $$r = \frac{S_{long}}{S} = \frac{S - S_{short}}{S}$$
$$\Leftrightarrow \quad S_{long} = rS \quad \text{and} \quad S_{short} = (1-r)S$$

Wing lift: $$L_{long} = rL = rW \quad \text{and}$$
$$L_{short} = (1-r)L = (1-r)W$$

Substituting this into Equation (C-11) leads to another helpful expression of the minimum lift-induced drag in terms of weight at condition W, and the area ratio r:

$$D_i = \left(\frac{W^2}{\pi q b_{long}^2}\right)\left[r^2 + \frac{2\sigma}{\mu}r(1-r) + \left(\frac{1-r}{\mu}\right)^2\right] \qquad \text{(C-12)}$$

Finally, as presented by Diehl [8], Munk's span factor for this optimized configuration is given by:

$$k = \sqrt{\frac{\mu^2}{r^2(\mu^2 - 2\mu\sigma + 1) + 2r(\mu\sigma - 1) + 1}} \qquad \text{(C-13)}$$

Diehl [8] presents additional graphs, that give further insight into the design of efficient biplanes.

With these tools in hand, we can implement a reasonable performance analysis for the biplane. The biplane interference factor, σ, reveals that even a very clean biplane generates more drag than a comparable monoplane. This is further compounded by a larger interference drag due to two rather than one wing, which increases $C_{D_{\min}}$ as well. In short, L/D efficiency is not a compelling argument for a biplane. The favorable properties discussed at the beginning of this section are.

DERIVATION OF EQUATION (C-5)

Lift-induced drag of the equivalent monoplane of wing span $k \cdot b$ is given by:

$$C_{D_i} = \frac{C_L^2}{\pi \cdot AR \cdot e} = \frac{C_L^2}{\pi \cdot (k^2 b^2/S) \cdot e} = \frac{SC_L^2}{\pi \cdot (k^2 b^2) \cdot e} \qquad \text{(i)}$$

Lift-induced drag of the biplane:

$$C_{D_i} = \frac{C_L^2}{\pi \cdot AR \cdot e}(1+\sigma) = \frac{C_L^2}{\pi \cdot (2b^2/S) \cdot e}(1+\sigma) = \frac{SC_L^2}{\pi \cdot (2b^2) \cdot e}(1+\sigma) \qquad \text{(ii)}$$

Per Munk, the lift-induced drag for the biplane and its equivalent monoplane configuration must be equal, which enables the factor k to be determined, yielding Equation (C-5).

C.2 CONCEPTUAL DESIGN OF SEAPLANES

Seaplanes are specialized aircraft that operate off water and, thus, do not rely on regular land-based airfields. Seaplanes appeal to many people who associate them with the ultimate freedom offered only by aviation: being able to fly into the wilderness and land on an obscure lake, far from the hustle and bustle of modernity.



FIGURE C-9 The Lake LA-250 Renegade, shown here during climb after T-O, is a popular amphibious aircraft. The large deflected flap on the horizontal tail is a hydraulically actuated trim tab used for slow speed operations only. It trims out the thrust effect of the highly mounted piston-propeller, improving its handling. *Photo by Phil Rademacher.*

Besides appealing to adventurers, such aircraft also offer other practicalities. They are ideal for law enforcement or reconnaissance operations near coastal areas (see Figure C-9). It is a drawback that operating such aircraft requires a special pilot training to help avert a number of possible dangerous scenarios to which landplanes are ordinarily not subjected. See Refs. [10,11] for more details.

Multiple operational issues accompanying seaplanes include the maintenance of a rigorous corrosion protection necessary to ensure the longevity of the airframe. This is compounded by the susceptibility to dings and damage to the hull as it slams into waves or floating debris, or when sliding up on a sandy beach, or banging against a dock. This demands a sturdy hull, which explains why seaplanes are heavier than conventional aircraft. As discussed later, the hull must also feature specific geometry to facilitate water operations (e.g., take-off, landing, and maneuvering). Unfortunately, this shape is not aerodynamically efficient. Therefore, seaplanes also generate more drag than conventional aircraft and, thus, given same power, offer lower rate-of-climb and cruising speed.

The term *seaplane* is used for an airplane designed to operate from water. There are three kinds of seaplanes; *floatplanes*, *flying boats*, and *amphibians*. A *floatplane* is a landplane that has had its landing gear removed and replaced with pontoons that are partially submerged floats (see Figure C-10). Such floats place the fuselage well above the water surface. A *flying boat* is a seaplane in which the occupants and freight is carried inside a fuselage specifically designed to function as a hull for operation on the water. They are also called *hull seaplanes*. An *amphibian* is an aircraft that features a hull-type fuselage for water operations and retractable landing gear to also permit landings on land (see Figure C-10). Generally, floatplanes are thought to be easier to dock than hull-type seaplanes [11], as their wings sit higher and they don't have sponsons that interfere with docking operations.

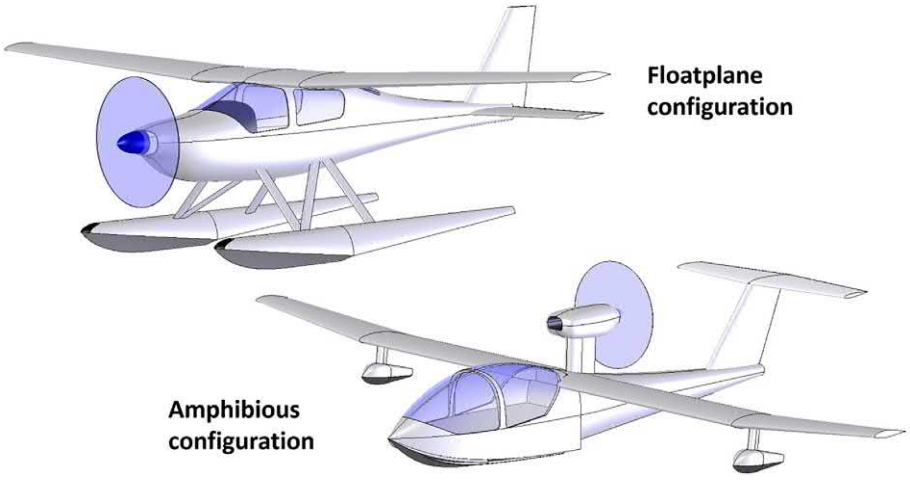


FIGURE C-10 A floatplane and amphibious configuration.

TABLE C-1 A summary of important capabilities for seaplane design.

Low-speed operations on water	• The vehicle must be watertight. This is particularly important for doors, windows, and access panels that cover dry components. • The vehicle must possess transverse and longitudinal hydrostatic stability at all speeds. • The vehicle must be controllable when aerodynamic forces are small or absent (e.g., water rudders). • If equipped with propellers, the rudder(s) should be placed in the propwash to aid with control on water. • The hull should allow the airplane to be "beached."
High-speed operations on water	• The hull must be capable of withstanding impact with various floating debris. • There must be provisions to protect the propulsive unit and the airframe from the spray of water. • The vehicle must be controllable in the water at all airspeeds from rest to lift-off speed.
T-O performance	• The vehicle should be capable of taking off in less than 60 s. • Maximum T-O distance should be no greater than 10,000 ft for a large seaplane, and preferably less than 5000 ft.
Cruise	• The vehicle should have as low drag as possible to improve its utility capability.
Landing	• It should be possible to land the vehicle without excessive impact forces to the airframe. • It should not generate excessive water spray upon touch-down and while "on the step." • The vehicle must be controllable in the water at all airspeeds from touch-down speed to rest. • The cockpit should offer good visibility to the water to help with the judging of altitude.

Basic Requirements for Seaplanes

Table C-1 summarizes a number of characteristics of importance in seaplanes design. These are gathered from various sources.

A number of GA and homebuilt seaplanes that the aspiring designer should be aware of and inspect for good and bad ideas are presented in Table C-2.

TABLE C-2 Selected seaplanes and amphibians.

Configuration	Example aircraft
Amphibian	Anderson Kingfisher, Osprey 2, Spencer S-12-E Air Car, Taylor Coot Amphibian, Thurston TA16 Trojan, Volmer VJ-22 Sportsman, Airmax Seamax M22, Mermaid M6, Icon A5, Colyaer S100 Freedom, AeroVolga LA-8, SeaRey, Piaggio P136, LISA Akoya.
Flying boat	Short Sunderland, Consolidated PBY-5 Catalina, Dornier Do J Wa, Dornier Libelle, Do-18, Do-24, Dornier Seastar, Dornier S-Ray 007, Spratt Control Wing.
Floatplane	A large number of options, including various Cessna and De Havilland of Canada built aircraft.

C.2.1 Basics of Seaplane Hydrodynamics

(1) The Archimedes Principle

The principle is attributed to Archimedes of Syracuse (287–212 BCE). The law states that any object, entirely or partially immersed in a fluid, experiences a force of buoyancy equal to the weight of the fluid it displaces. The law ignores surface tension (capillarity) acting on the body.

Apparent Weight

The Archimedes principle leads to several mathematical results of interest. The first is the *apparent weight of objects* submerged in a liquid. Mathematically, it is written as follows:

$$W_a = W - F_{df} \tag{C-14}$$

Where W_a is the apparent weight of the object as measured in the liquid, W is the true weight of the object in reference fluid (e.g., air) or vacuum, and F_{df} is the weight of the displaced fluid (liquid or gas).

Buoyancy Force

The second result of interest is the *buoyancy force*, F_{buoy} also denoted by Δ. It is estimated from:

$$F_{buoy} = \Delta = \rho_W g \forbidden{V} \tag{C-15}$$

Where g is acceleration due to gravity, $\forbidden{V}$ is the volume of the object that displaces the fluid, and ρ_W is the mass density of the displaced fluid (liquid or gas). If the object is floating, then $\forbidden{V}$ is the submerged volume only. If fully submerged, then $\forbidden{V}$ is its entire volume. Weight density of pure water is $62.5\,\text{lb}_\text{f}/\text{ft}^3$ or $9807\,\text{N}/\text{m}^3$ ($1000\,\text{kg}/\text{m}^3$). Weight density of seawater is $63.8–64.7\,\text{lb}_\text{f}/\text{ft}^3$ or $10{,}003–10{,}150\,\text{N}/\text{m}^3$ ($1020–1035\,\text{kg}/\text{m}^3$), depending on the source.

Floating Tendency

The third result of interest; *floating tendency* as shown below:

$$F_{net} = mg - \rho_W g \forbidden{V} \tag{C-16}$$

Where m is the mass of the object. If $F_{net} > 0$, the object will sink (weight is greater than buoyancy). If $F_{net} < 0$, the object will float (weight is less than buoyancy). The expression can be used to estimate volume for any watercraft (including seaplanes), as well as balloons and airships. When the volume is filled with a different type

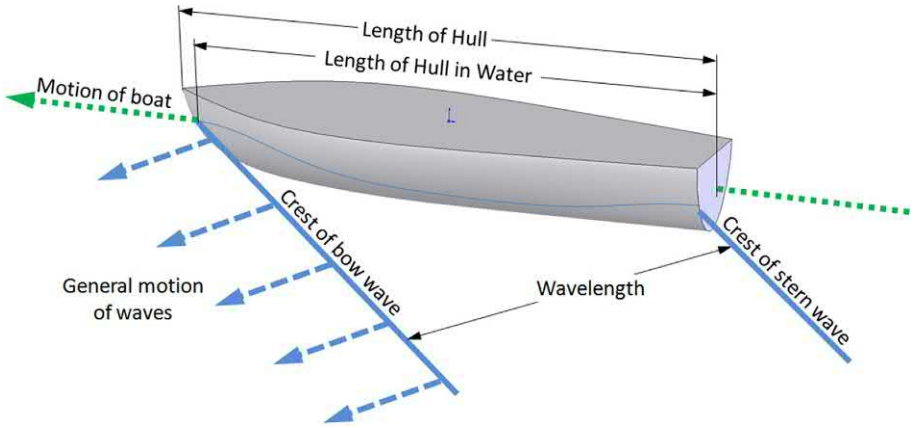


FIGURE C-11 A schematic showing a hull moving in water with the bow and stern waves coinciding, constituting *hull speed*.

of gas, such as hydrogen or helium, the expression must include the effect of the gas, i.e.:

$$F_{net} = mg + (\rho_1 - \rho_2)g\forall \qquad \text{(C-17)}$$

Where ρ_1 is mass density of the fluid used to displace the heavier fluid (e.g., Helium) and ρ_2 is mass density of the displaced fluid (e.g., air). Note that the density of the fluid used to displace the heavier fluid depends on its pressure inside the volume. The greater the pressure, the greater will be the density. This can be estimated using the *ideal gas law* (see Equation 14-5).

Hydrostatic Weighing

The fourth result of interest is *hydrostatic weighing*. It allows the density of an object (or a liquid) to be determined by measuring its weight in and out of the liquid. This can be done without a prior knowledge of its volume. This is achieved using the following expression.

$$\frac{\rho_{object}}{\rho_{liquid}} = \frac{W_{in\ air}}{W_{in\ air} - W_{in\ liquid}} \qquad \text{(C-18)}$$

Where $W_{in\ air}$ and $W_{in\ liquid}$ is the object's weight in air and in liquid, respectively, ρ_{object} is mass density of the object, and ρ_{liquid} is mass density of the liquid.

(2) Hull Speed

Bodies moving in water generate substantially greater hydrodynamic drag than in less viscous fluids such as air. Per the *Archimedes Principle*, a body entirely or partially immersed in fluid experiences a force of buoyancy equal to the weight of the fluid it displaces. In order to move, this fluid must be forced out of the way. This creates water waves that emanate from its bow and stern and are, appropriately, called *bow* and *stern waves*.

As evident by observing actual boats, the length of these waves is initially only a fraction of the length of the hull. However, as the speed increases, they grow in length. At a specific speed, called the *hull speed*, the wavelength equals the length of the hull [12]. This is accompanied by a considerable increase in the hydrodynamic drag because the hull pitches up as it attempts to ride on top of the bow wave. If not correctly shaped, this inflicts a serious hurdle for further acceleration of the hull, often making the hull speed the maximum speed that can be achieved (see a schematic of the condition in Figure C-11).

Speedboats circumvent the hull speed problem by shaping the hull with a flat plane that generates hydrodynamic lift that supplements the buoyancy lift. This additional lift is called *hydroplaning*. It partially lifts the boat out of the water, reducing the magnitude of the wave system and, thus, its drag. Hydroplaning allows speedboats to accelerate to speeds well above their hull speed. Seaplanes and the floats of floatplanes feature similar hull geometries, allowing them to accelerate to liftoff speed. In interest of completeness, a formula to calculate the hull speed of a vessel is presented below. Its derivation is beyond the scope of this text.

Hull speed in knots:

$$V_{hull} \approx K_{hull}\sqrt{\text{Hull Water Length}} \qquad \text{(C-19)}$$

Where $K_{hull} \approx 1.3\text{–}1.5\,\text{knots}/\text{ft}^{1/2}$ or $4.4\text{–}5.0\,\text{kmh}/\text{m}^{1/2}$ with the hull water length in ft or m, respectively. Seaplane hulls are shaped like that of speedboats to deliberately generate a large hydrodynamic lift, even while moving relatively slowly in water. The lift is created as the hull deflects water downward. At a certain speed, the hull lifts out of the water and, thereafter, the weight of the seaplane is mostly supported by hydroplaning (and wing lift). Pilots call it to get "on the step." This dramatically reduces the hydrodynamic drag of the seaplane and allows it to accelerate to lift-off speed.

Seaplane hulls feature a discontinuity in the bottom hull that is not present in speedboats. It is called a *step* (see Figure C-18). It serves a dual purpose: (1) Once the aircraft begins to hydroplane, the surface area in contact with the water reduces substantially, further reducing the hydrodynamic drag. (2) Once near liftoff speed, the step allows the airplane to rotate to lift off. Selected details

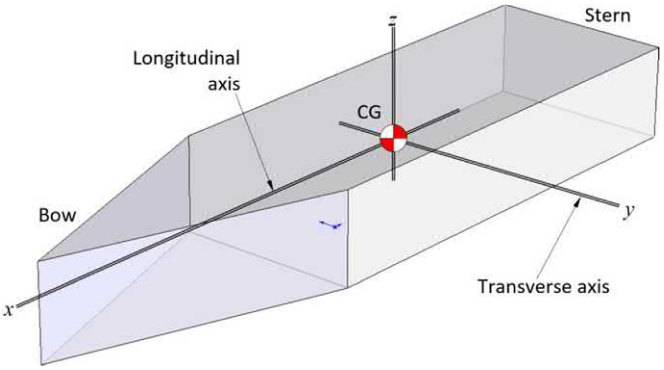


FIGURE C-12 A basic floating vessel configuration.

from the lower surface of a seaplane are shown in Figure C-18 and discussed below.

(3) Hydrostatic Stability

Hydrostatic stability refers to the tendency of a floating vessel to return to its *at-rest* attitude, once forcibly tilted one way or the other. Any such vessel must have hydrostatic stability about two axes; the *longitudinal* and *transverse* (see Figure C-12). The former refers to the axis along its length (from stern to bow) and the latter to an axis normal to the former, as shown in the figure. Both are normal to a vertical axis that goes through the *Center of Gravity* (CG) of the vessel. The CG has already been discussed at length and it is assumed here that the reader is familiar with methods to determine it.

(4) Center of Buoyancy

Before proceeding further, a couple of concepts must be introduced. The first is the *Center of Buoyancy* (CB). It is the centroid of the hydrostatic pressure force acting on the submerged part of a vessel. The location of the CB must be determined before the vessel can be declared hydrostatically stable or unstable. The CB of any planar cross-section can be found using the expression below, where the terms are defined in Figure C-13. The location of the CB is denoted by (y_{CB}, z_{CB}) and is found from:

$$y_{CB} = \frac{\int y \cdot h(y)dy}{\int h(y)dy} \tag{C-20}$$

$$z_{CB} = \frac{\int z \cdot w(z)dz}{\int w(z)dz} \tag{C-21}$$

Where $h(y)$ is the height of a strip at position y and $w(z)$ is the width of a strip at depth z. Note that the 3-dimensional location of the CB for ships, boats, floats, and seaplanes is generally determined by estimating it in two planes; the x-z and y-z planes in Figure C-12. This

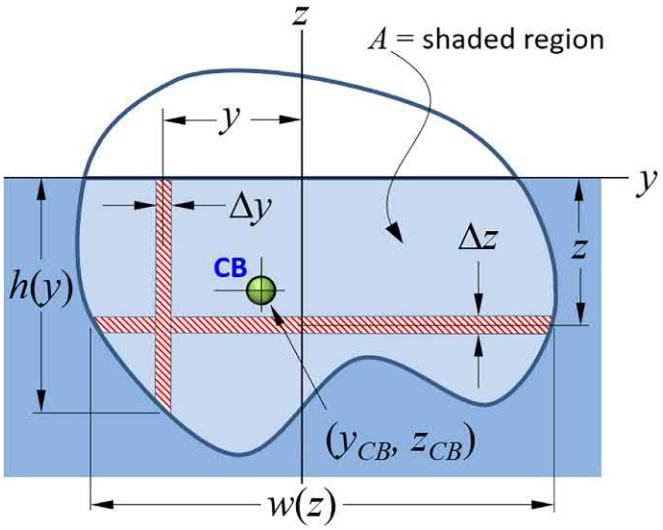


FIGURE C-13 A 2-dimensional submerged body.

is only permissible as long as the body has a definable plane of symmetry, such as the x-z plane.

(5) Metacenter and Metacentric Height

The *Metacenter* (MC) is the second concept of importance. It is an imaginary point that is determined to evaluate if the vessel is *stable* or *unstable*. Consider Figure C-14, which shows the cross-section of a vessel, initially at rest (left), and then disturbed so it is tilted through an angle θ (heel angle). The rotation moves the *Center of Buoyancy* (CB) sideways, a distance Δy away from its at-rest position. If hydrostatically stable, this generates a restoring moment (see Figure C-14). The magnitude of this restoring moment is given by:

$$M_R = W \cdot \Delta y = \rho_W \theta \int_A y^2 dA = \rho \theta I_{zz} \tag{C-22}$$

Where A is cross-sectional area of the section-cut, I_{zz} is the second area moment (aka second moment of area) of the submerged cross-section, and ρ_W is the mass density of the liquid in which the body is submerged. A derivation of Equation (C-22) is provided in Ref. [13]. Note that the relation holds as long as θ has a sufficiently small value. The second area moment, I_{zz}, is taken about the z-axis and only includes the part of the body that is submerged.

The intersection of a vertical line drawn through the CB and the rotated line that goes through the CG is the *metacenter* (see Figure C-14). If the metacenter is above the CG, its value is *positive*. This means the vessel has a tendency to right itself and return to its at-rest attitude. Conversely, a *negative metacenter* implies the vessel is unstable and will rotate until it finds another stable orientation. For the operators of unstable ships and seaplanes, this pretty much means upside down. Figure C-14 should help the reader visualize that if the tilt angle increases further, the arm denoted by Δy may begin to shorten again.

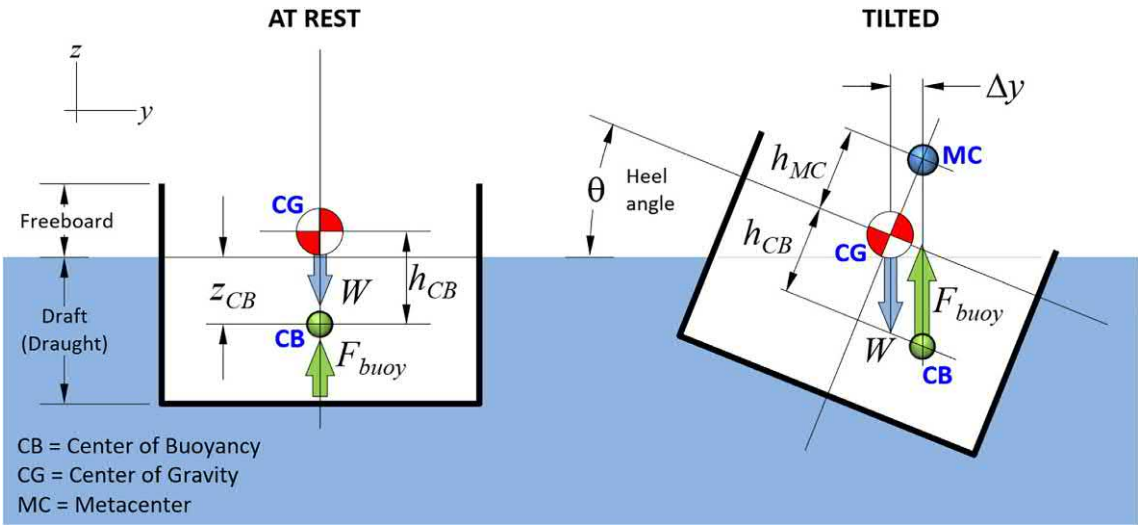


FIGURE C-14 Fundamentals of hydrostatic stability. As the body is tilted, the center of buoyancy shifts sideways due to the change in the submerged geometry. The off-set force F_{buoy} generates a restoring (or righting) moment.

This means the metacenter will end up below the CG; the vessel has become unstable. Floating vessels have a maximum heel angle beyond which this occurs. This angle is called the *angle of loll*.

EXAMPLE C-1

Find the CB of the cross-sectional area in Figure C-15.

SOLUTION:

We can see that we only need to apply Equation (C-20) to one half of the geometry, thanks to its symmetry. We can also see that when $z=0$, then $y=5$ and when $z=-10$, then $y=0$. This means that the equation for the half-width strip is simply $w(z)=z/2+5$. Substituting these into Equation (C-20) yields:

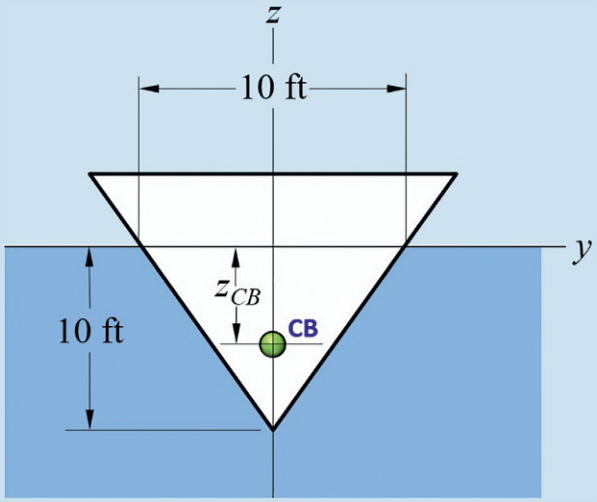


FIGURE C-15 A triangular cross-sectional area used to demonstrate how CB can be calculated.

$$z_{CB}=\frac{\int z\cdot w(z)dz}{\int w(z)dz}=\frac{\int_{-10}^{0} z\cdot(z/2+5)dz}{\int_{-10}^{0}(z/2+5)dz}=\frac{\left.\frac{z^3}{6}+\frac{5z^2}{2}\right|_{-10}^{0}}{\left.\frac{z^2}{4}+5z\right|_{-10}^{0}}$$

$$=\frac{83\frac{1}{3}}{-25}=-3\frac{1}{3}\text{ ft}$$

Ref. [13] also derives the following handy expressions. The distance over which CB is shifted is given by

$$\Delta y=\rho_W\theta\frac{I_{zz}}{W}=\theta I_{zz}\cancel{V}\approx(h_{CB}+h_{MC})\theta \qquad \text{(C-23)}$$

Where h_{CB} is the distance between CB and CG, h_{MC} is the distance between MC and CG along the rotated z-axis, and $\cancel{V}$ is the displaced volume of the liquid ($=W/\rho$). The metacentric height is given by:

$$h_{MC}=\frac{\Delta y}{\theta}-h_{CB}=\frac{I_{zz}}{V}-h_{CB}=\rho_W\frac{I_{zz}}{W}-h_{CB} \qquad \text{(C-24)}$$

(6) Metacentric Heights for Seaplanes

Per Diehl [8] it has been established empirically that seaplanes have good hydrostatic stability as long as the transverse and longitudinal metacentric heights are similar (see Figure C-12 for the transverse and longitudinal axes). However, the transverse metacenter should not be larger than the longitudinal one. Satisfactory stability is achieved if the metacentric height is given by:

$$h_{MC}=K\sqrt[3]{W_0} \qquad \text{(C-25)}$$

Where K is a constant that depends on the type of seaplane and W_0 is the gross weight of the seaplane in lb_f. Values for the constant K are given in Table C-3. The metacentric height for a flying boat with wingtip floats, such as the 35,000 lb_f Consolidated PBY-5 Catalina should be around 32.7 ft. The value for a 2690 lb_f Lake LA-4-200 Buccaneer should be around 13.9 ft.

Diehl is also the author of Ref. [14], in which a number of results of interest to designers of seaplanes are presented. The reference suggests that for single or twin float seaplanes, the transverse and longitudinal metacentric heights should be designed to match the following values:

Transverse metacentric height (twin floats only):

$$h_{MC_T} = \frac{19.5BLs^2}{W_0} \tag{C-26}$$

Longitudinal metacentric height (for single and twin floats):

$$h_{MC_L} = \frac{2.10nBL^3}{W_0} \tag{C-27}$$

Where: $B = Beam$ is the width of a float in ft,

L = float length in ft,
n = number of floats,
s = spacing between floats (center-to-center) in ft,
W_0 = gross weight in lb_f.

(7) Estimating Float Geometry

Note that the metacentric height obtained using Equation (C-25) with Equation (C-26) can be used to estimate a suitable spacing (s) between the floats of twin-float seaplanes, given known length (L) and beam (B). This leads to the following expression:

Recommended spacing for twin floats:

$$s = \frac{0.2679W_0^{2/3}}{\sqrt{BL}} \tag{C-28}$$

The units are in ft and the value for K from Table C-3 is 1.4. Similarly, a recommended float length (L) which results in satisfactory static stability can be estimated using Equation (C-25) with Equation (C-27), given the beam (B). The resulting expression is shown below:

TABLE C-3 Constant K for class of seaplanes.

Type of seaplane	Constant K
Flying boats with side-floats	0.75
Flying boats with wingtip floats	1.0
Floatplanes with one main float	1.2
Floatplanes with two main floats	1.4

Recommended float length:

$$L = 0.7809W_0^{4/9}\left[\frac{K}{nB}\right]^{1/3} \tag{C-29}$$

EXAMPLE C-2

Consider the vessel of Figure C-16. Determine the following parameters if it is placed in pure water:

(a) Maximum buoyancy force.
(b) Center of buoyancy when completely submerged.
(c) Find the draft (see Figure C-14) if the vessel weighs 300 lb_f (applied at the CG).
(d) Determine the transverse metacenter. Is it stable?
(e) Determine the longitudinal metacenter. Is it stable?

SOLUTION:

(a) The maximum buoyancy force is the weight of the water the vessel can displace—in other words; the density of water (62.5 $\text{lb}_\text{f}/\text{ft}^3$) times the volume, denoted by $\forall$, of the vessel. This is calculated as follows:

$$\forall = \overbrace{4\cdot 2\cdot 1}^{\text{rectangle}} + \overbrace{\frac{1}{2}\cdot 3\cdot 2\cdot 1}^{\text{triangle}} = 11 \text{ ft}^3$$

$$\Rightarrow \quad F_{\max} = \rho_W \forall = 62.5 \times 11 = 687.5 \text{ lb}_\text{f}$$

(b) By inspection, the transverse CB is at the plane of symmetry, at $(y_{CB}, z_{CB}) = (1, 0.5)$ ft. The x-coordinate of the longitudinal CB, on the other hand, has the same coordinates as the centroid of the combined rectangular and triangular regions in the x-y plane.

Taking advantage of the simplicity of the geometry, this can be calculated as follows (where the subscript 1 refers to the rectangular area and 2 to the triangular one). Note that the centroid of the rectangular region is located at $x_{C1} = 2$ ft and the triangular region at $x_{C2} = 4 + 3/3 = 5$ ft. Therefore, x_{CB} of the combined region is

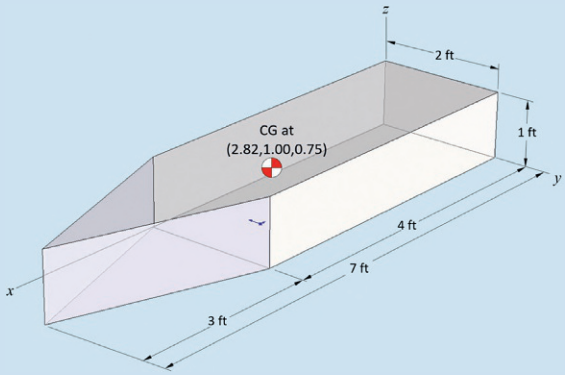


FIGURE C-16 A hypothetical vessel used for Example C-2.

EXAMPLE C-2 (cont'd)

$$x_{CB} = \frac{x_{C_1} \cdot A_1 + x_{C_2} \cdot A_2}{A_1 + A_2} = \frac{(2) \cdot (2 \times 4) + (5) \cdot \left(\frac{1}{2} 2 \times 3\right)}{8 + 3}$$

$$= \frac{31}{11} \approx 2.82 \text{ ft}$$

Therefore, when fully submerged, the CB is located at $(x_{CB}, y_{CB}, z_{CB}) = (2.82, 1, 0.5)$ ft.

(c) Due to the simplicity of the geometry, it is easy to see in Figure C-17 that the draft is $W/F_{max} = 300/687.5 = 0.436$ ft (i.e., the bottom 0.436 ft will be submerged). Note that this means that the CB has a different location in space (here it is ½ of 0.436 ft).

(d) Since the CG is conveniently placed above the CB (see Figure C-16), the orientation of the vessel is without any tilting (listing). Therefore, the longitudinal metacenter can be found using Equation (C-24), where the second area moment of the submerged cross-section is in the plane of symmetry. Noting that the cross-section is rectangular, the I_{zz} can be found from the expression:

$$I_{zz} = \frac{bh^3}{12} = \frac{0.436 \times 2^3}{12} = 0.2907 \text{ ft}^4$$

The distance between the CG and the CB, h_{CB}, can be obtained by inspection and is given by:

$$h_{CB} = 0.75 - \frac{0.436}{2} = 0.532 \text{ ft}$$

Therefore, the metacentric height of the transverse metacenter can be found using Equation (C-24) as follows:

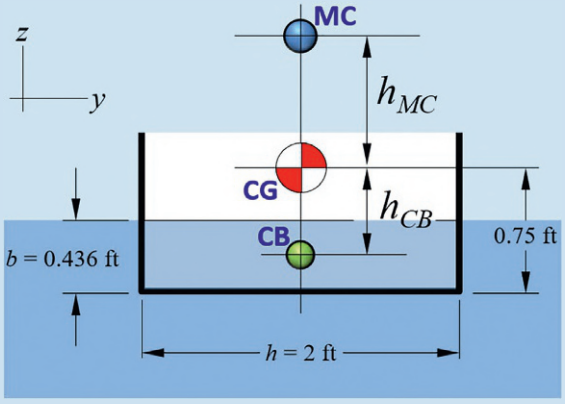


FIGURE C-17 The vessel cross-sectional view, showing the draft of 0.436 ft at a weight of 300 lb_f.

$$h_{MC} = \rho \frac{I_{zz}}{W} - h_{CB} = (62.5) \frac{0.2907}{300} - 0.532 = -0.471 \text{ ft}$$

The vessel is transversely unstable—the CG is too high above the CB.

(e) Finally, determine the longitudinal metacenter. First, calculate the second area moment again, this time using the length of the vessel (along the x-axis) as the value of h. Again, the cross-section in the plane-of-symmetry is rectangular, so I_{zz} is easily determined as it was in part (d):

$$I_{zz} = \frac{bh^3}{12} = \frac{0.436 \times 7^3}{12} = 12.46 \text{ ft}^4$$

Next, determine the metacentric height of the longitudinal metacenter as follows, again using Equation (C-24):

$$h_{MC} = \rho \frac{I_{zz}}{W} - h_{CB} = (62.5) \frac{12.46}{300} - 0.532 = +2.064 \text{ ft}$$

As one would expect, the longitudinal metacenter is well above the CG, so the vessel is longitudinally stable.

(8) Frictional Resistance of Submerged Surfaces

The most basic expression used to calculate the frictional resistance of a plank in tow, is that of William Froude (1810–79). Froude experimentation led to the discovery that speed and surface properties are fundamental to the magnitude of the resistance, formulated below [15]:

Froude's liquid resistance formula:

$$R_{Froude} = f \cdot S_{wet} \cdot V^n \qquad \text{(C-30)}$$

Where f is the coefficient of frictional resistance, S_{wet} is wetted area in ft^2, V is speed in knots, and n is a constant that depends on surface quality. The term f depends on surface quality. For surfaces ranging from 2 to 20 ft in length, it can be taken to be 0.012 to 0.010 for smooth surfaces, 0.0231 to 0.0137 for surface quality resembling fine grit sandpaper, 0.0257 to 0.0152 for medium grit sandpaper, and 0.0314 to 0.168 for coarse type sandpaper. It is acceptable to interpolate linearly for most applications. The term n is usually close to 2, so assuming $n = 2$ is accurate enough for most applications. Thus, the coefficient of frictional resistance for a smooth 10 ft long surface can be estimated using a parametric representation as shown below:

$$f = \left(\frac{20 - L}{20 - 2}\right) 0.012 + \left(1 - \frac{20 - L}{20 - 2}\right) 0.010 = 0.011$$

Therefore, a 10 ft long surface of 20 ft^2 wetted area, moving at 30 knots generates $0.011 \times 20 \times 30^2 = 198$ lb_f of resistance.

C.2.2 Seaplane Design Tips

Stinton [2] and Thurston [11] list a number of helpful design tips for seaplanes. Faure [18] discusses floatplanes from the standpoint of the experienced pilot and offers a great insight into how such airplanes are operated. While aimed at pilots, it is highly recommended that novice seaplane designers read such text for increased awareness. Nelson [16] and Wood [17] also offer great many tips for seaplane design, although these references may be hard to find nowadays. Tips from many of these have been collected and are presented below for convenience.

(1) Operational Considerations

Pilot operation of seaplanes is beyond the scope of this text. Common techniques are described in Refs. [10,18]. Both reveal multiple important, albeit, easily overlooked features that must be kept in mind when designing seaplanes. Some have to do with the low and high-speed operation of the vehicle on water, others with the structural and hydrodynamic properties of the hull or floats. The designer must be aware of other important topics regarding a proper design of controls and structure for such airplanes. One such topic is regulations. Seaplane operations requires compliance with special rules, most of which are stipulated in 14 CFR Part 1, 61, and 91. Generally, nautical terms are used when considering seaplanes, so the designer may want to become familiar with some of them. For instance, *port* and *starboard* are used for left and right, *windward* and *leeward* for upwind and downwind sides of a body, and so on. The nose of the airplane is called a *bow* and the bottom of the empennage is the *stern*.

Figure C-18 shows multiple features present on seaplane hulls. The hull features a *keel* to help guide the vehicle in a straight line by resisting side-motion. The *step* is the discontinuity in the bottom of the hull that reduces hydrodynamic drag and allows the airplane to rotate. It does so by introducing a layer of air between the wake and the *rearstep*. Sometimes the keel features a short but robust plate, called a *skeg*, which extends a few inches beyond the step. It prevents the plane from tipping back onto the tail when sitting on floats on land. It is more common on floatplanes. A *chine* refers to the seam where the side of the hull joins the bottom. It directs the water spray away from the hull and contributes to hydrodynamic lift. Between the keel and chine are structural members called *sister keelson*. They add strength to the hull and provide additional straight-line guidance like the keel. Sister keelsons can often be found on floats, where they allow the airplane to sit on the floats on land. The *spray rails* are mounted along the chines to reduce the amount of water spray that can hit the propeller. Water spray can be destructive to a propeller—in particular at high RPMs.

Figure C-19 shows a floatplane and identifies typical components of the floats. The *forward* and *aft spreader bars* prevent the floats from separating during water operations. They usually react the separation force in tension. The system of *struts* transfer water loads into the fuselage hard points. The floats must feature *retractable water*

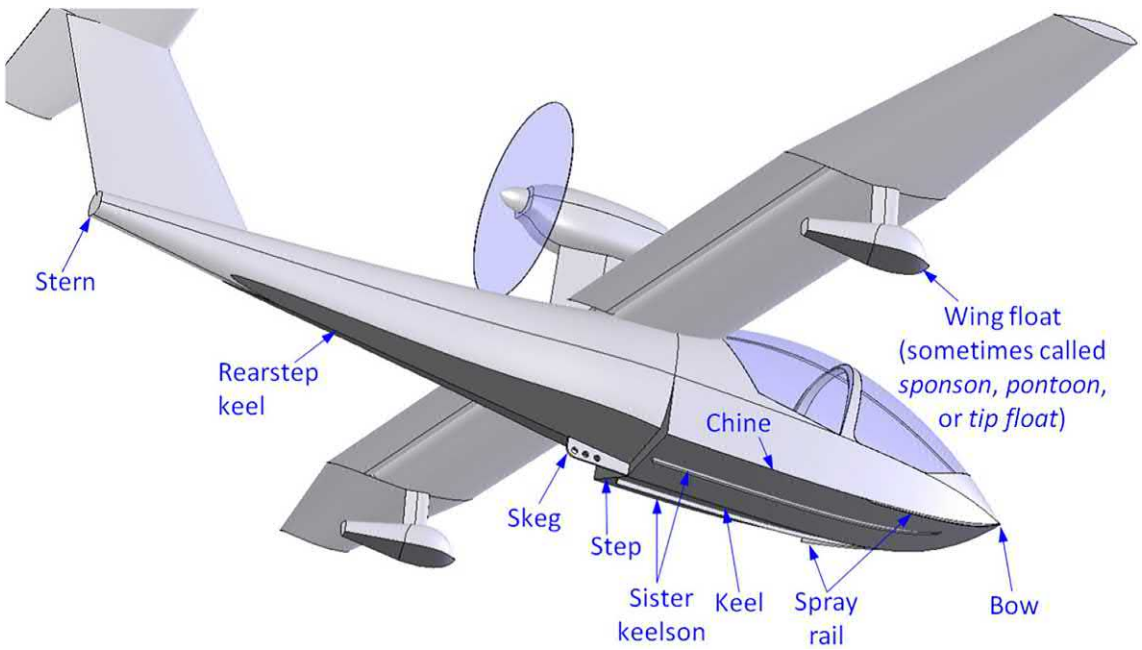


FIGURE C-18 A schematic showing important details on the lower surface of a seaplane.

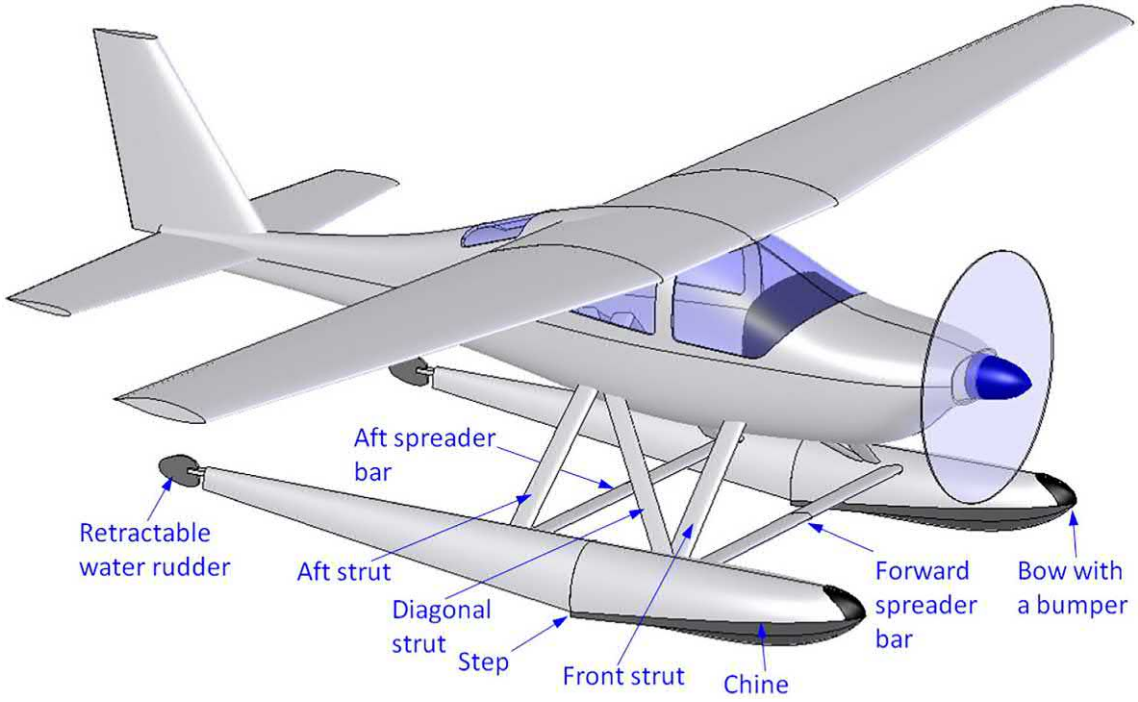


FIGURE C-19 A schematic showing important details on the lower surface of a seaplane.

rudders to allow the pilot to control the airplane in water. They must be retractable because they get in the way of advanced docking operations, such as approaching a dock by reversing in strong wind [18].

Landing a seaplane can be tricky and the technique depends on the condition of the surface of the water. Generally, pilots have to contend with three types of water conditions: a *normal rippled water*, *glassy or mirror-like water*, and *rough water*. Each requires a dissimilar landing technique, again, highlighting the need for specialized pilot training. For instance, and contrary to intuition, the glassy landing is challenging because the pilot cannot use wave height of the water for visual clues as to how high above water the airplane is. Thus, it is essential to provide good visibility in a new seaplane design.

The operation of seaplanes on water, in particular saltwater, requires a rigorous adherence to corrosion protection. This is necessary for all aluminum seaplanes, as saltwater will quickly corrode the material if left unprotected. Aluminum surfaces should be protected using materials such as polychromate primer or zinc chromate. Regular inspections should be mandated, particularly in hard to see areas that are subject to standing water. Also, the hull and sponsons should feature holes with removable plugs to allow water that may collect during normal water operation to leak out.

(2) Hull Styles

Figure C-20 shows a number of cross-sections along the length of a *conventional* and *planing-tail* seaplane hulls. It reveals complexity not present in ordinary fuselages. Ref. [19] recommends the planning-tail style for improved water operation. There are other styles to consider, for instance the approach of the LISA Akoya amphibious aircraft that uses hydrofoils. Stinton [2] and Thurston [11] present helpful design tips for hull design.

(3) Buoyancy and Hydrostatic Stability

As stated earlier, buoyancy requires the hull to displace enough water to support the weight of the aircraft. The designer must ensure the interaction between the CG and the metacentric height of the hull provides a restoring moment. This is accomplished on floatplanes by separating the floats (see Figure C-21). The ideal angle θ ranges from 45 to 55 degrees. Thus, the resulting ratio s/h is approximately 1.4–1.7. Alternatively, the separation can also be determined using Equation (C-28). On amphibians, this is usually done by mounting floats near the wingtip (called tip floats, pontoons, sponsons, or auxiliary floats). However, the same effect is also achieved by widening the lower part of the airplane in order to raise the metacentric height. The Icon A5 is an example of such an aircraft.

(4) Low Water-drag and High Hydrodynamic Lift

The hull must be shaped to generate enough vertical force at low speed to bring the airplane "on the step" and allowing it to accelerate to liftoff airspeed. This requires a flat or curved deadrise (see Figure C-22). Hydrodynamic drag must also be reduced, requiring a step to be designed into the hull at the proper location.

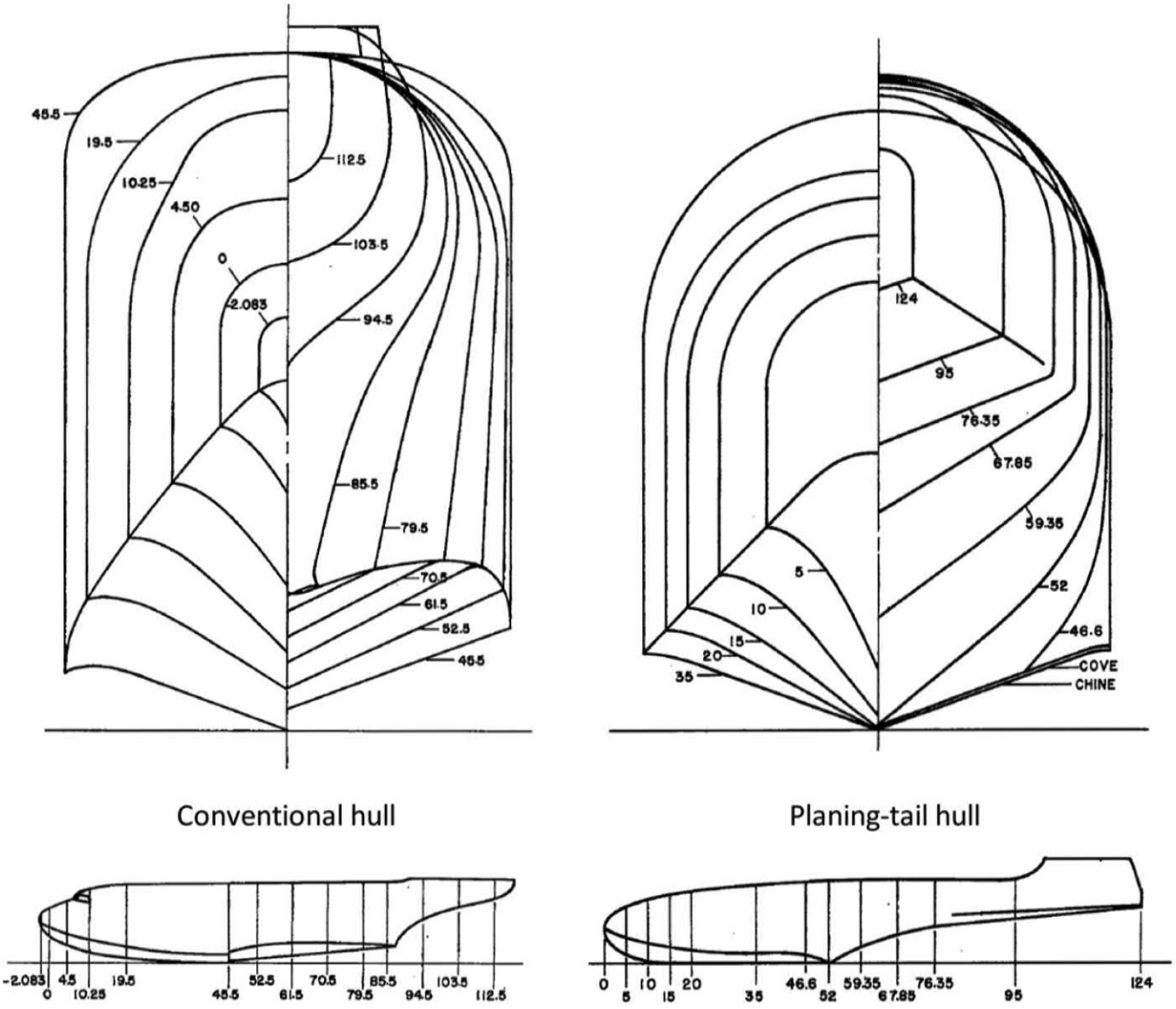


FIGURE C-20 Cross-sectional geometries for the forward and aft hull of a conventional flying boat. *From H.B. Suydam, Hydrodynamic Characteristics of a Low-Drag Planing-Tail Flying-Boat Hull, NACA TN-2481, 1952.*

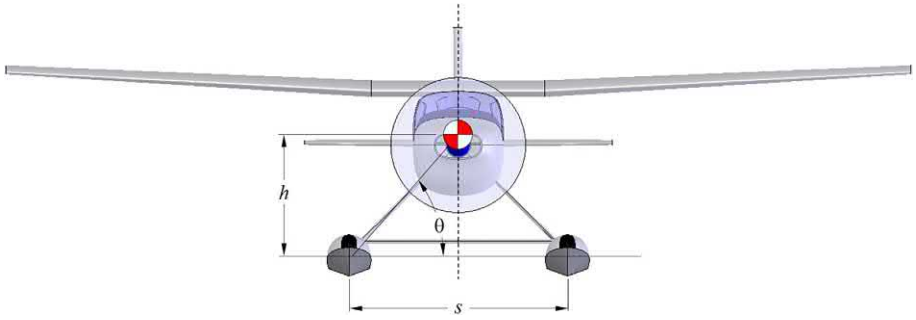


FIGURE C-21 Placement of floats.

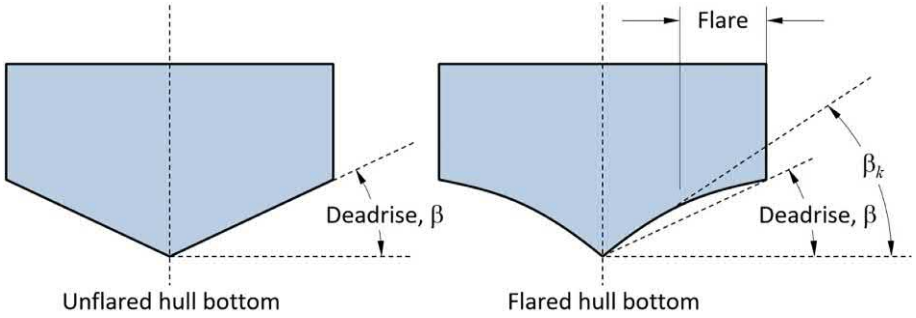


FIGURE C-22 Two common shapes of hull bottoms; an unflared and flared one.

(5) Suppression of Water Spray

The hull must be shaped to force water spray sideways and away from sensitive areas, such as propellers, engine and cabin air inlets. The use of spray rails may be required to reduce the amount of water. Spray can be suppressed by increasing the curvature of the hull between the keel and chines ("flaring" see Figure C-22). It is advantageous to incline the keel 1–2 degrees up as demonstrated in Ref. [20].

Per Ref. [20], refined hulls with flared bottoms and increased fore- and afterbody deadrise warping, improves the hull's hydrodynamic characteristics, even though the gains may not warrant the added complexity and cost of manufacturing. This mostly pertains to aluminum aircraft—composite hulls offer a promising potential, as compound surfaces are far easier to manufacture. Composite materials also have an outstanding service history in and around water, as evident by countless speedboats and jet-skis with composite hulls. Ref. [20] concludes that narrow hulls offer less resistance (a fact well known to athletic rowers), however, their draft is greater and this increases water spray.

(6) Dynamic stability on the Step

Once "on the step," seaplanes are afflicted by three types of dynamic instability: *porpoising*, *skipping*, and *pattering*. Porpoising is a rhythmic pitching motion of a seaplane, caused by the dynamic instability in forces acting on the bottom of the floats [10]. The sensation is often likened to that when rocking back and forth. The phenomenon may occur if the airplane exceeds a relatively narrow range of pitch attitudes and begins as a cyclic pitch oscillation that may increase and terminate with the aircraft nosing into the water and possibly capsizing. It can also occur if the longitudinal attitude of the airplane is too high while "on the step." This can cause the airplane to stall and drop the nose into the water. Porpoising can also be caused by the step being placed too far forward of or behind the CG [2]. It can be reduced by flattening the aft part of the fore body to about 1.5 times the beam. This results in more uniform pressure along the bottom, whereas a curved shape causes pressure to vary, which promotes a more dynamic response.

Skipping is an instability that may occur when landing at excessive speed with the nose pointed too high or when crossing the wake of a boat [10]. The sensation is likened to an up and down bounce. Hulls featuring a shallow step suffer from a poor ventilation behind it and are more prone to skipping. Pattering is a short period pitch oscillation. Ref. [21] presents methods to estimate the dynamic response of ships that extend to seaplanes as well.

(7) Maneuverability and Controllability

The airplane should feature means for control while in the water at low airspeeds, when aerodynamic control is minimal. This is done by installing a rudder at the stern. Once "on the step," the hull should feature a straight keel to help the airplane move along a straight line. Adding sister keelsons may be called for to improve the directional stability. Excessively long forebody reduces directional stability in the water and may cause it to ground loop (i.e., "water-loop") [2]. Reducing such a tendency requires an enlarged vertical tail, ideally placed in the propwash for increased control authority.

(8) Step Geometry

The edge of the step is placed slightly aft of the CG, approximately as shown in Figure C-23. The angle made to the vertical will then range approximately between 10 and 15 degrees. The intent is to allow the airplane to rotate effortlessly. The height of the step is typically approximately 0.05–0.08 × Beam [20]. Unfortunately, this surface discontinuity increases the airplane's aerodynamic drag and constitutes a portion of the "cost" of designing a seaplane. The drag problem is a hard one to remedy, as discussed in Ref. [22], which explores a number of step designs intended to reduce drag.

(9) Sternpost Angle

The sternpost angle typically ranges from about 7 to 9 degrees. It allows the seaplane to rotate to a higher AOA once "on the step" without the rearstep keel entering the water. If the rearstep enters the water the hydrodynamic drag increases, reducing the acceleration and lengthening the T-O run.

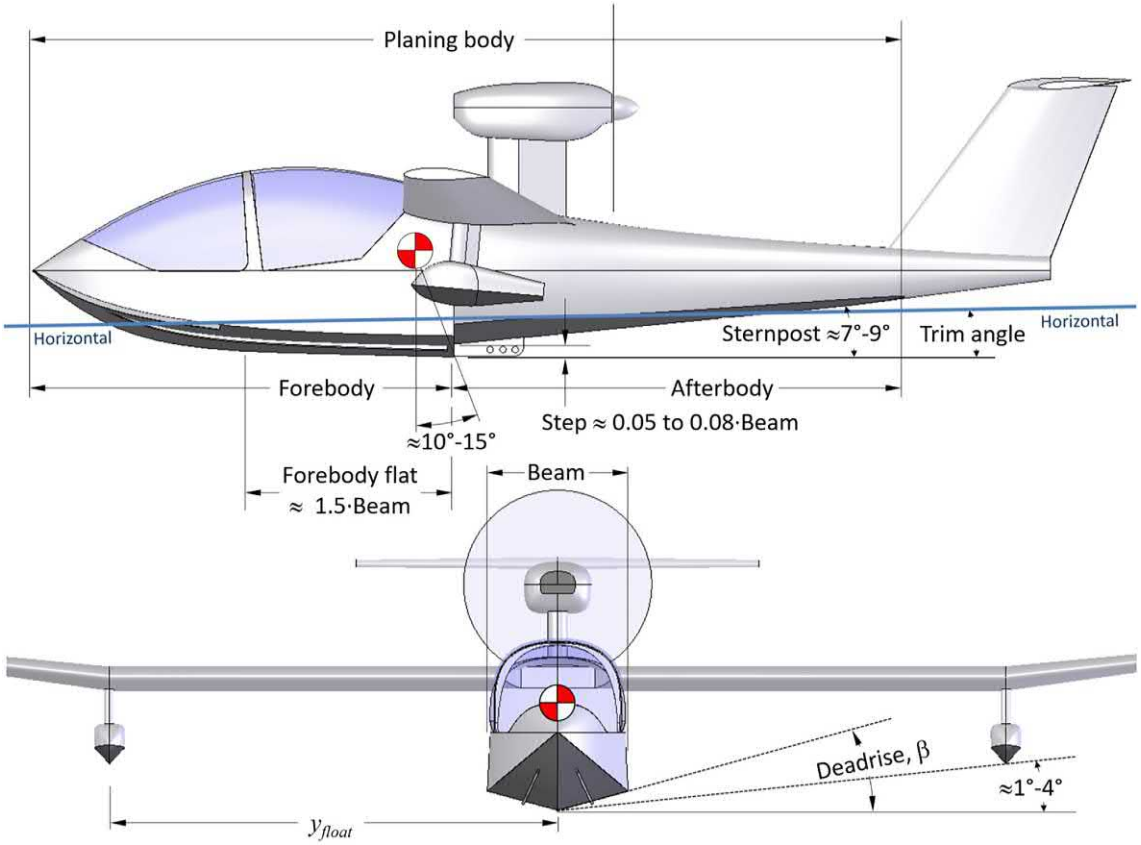


FIGURE C-23 A schematic showing important details that must be considered when designing a seaplane.

(10) Forebody Flat

The length of the forebody float should be approximately 1.5 × Beam. This reduces porpoising tendency.

(11) Deadrise Angle

Deadrise angle typically ranges from 15 to 40 degrees. The greater this angle, the less is the water impact load (hull load) and this directly affects the weight of the airframe. It will also make water landings feel smoother. The hull load factor is usually estimated using 14 CFR §23.527. However, the larger angle causes the hull to sit deeper in the water. If the intention is to allow the aircraft to be beached, the larger deadrise angle could make this impossible—the airplane will run aground far from dry land (relatively speaking). There is a golden medium between lower hull loads and being able to beach the airplane. Ref. [20] states that warping the deadrise of the afterbody is an effective means to reduce the height of the step by about 50% (page 20).

(12) Tip Floats, Auxiliary Floats, Sponsons, and Pontoons.

Per 14 CFR Part §23.757, auxiliary floats must be arranged such they provide a restoring moment of at least 1.5 times the upsetting moment of the tilted seaplane, when fully submerged. This moment is determined as the product of the tip float displacement and its spanwise location along the wing, denoted by y_{float} (see Figure C-23). The larger the distance y_{float}, the smaller the volume of the tip float. A smaller tip float reduces aerodynamic drag, but the impact loads per 14 CFR §23.535, increase the magnitude of the reaction forces.

(13) Wave Height Limitations

There is a limit to the wave height of water a seaplane of a given hull displacement can safely handle. Ref. [11] presents the following empirical expression to estimate the wave height as a function of gross weight:

$$h_{wave} \approx 1.25 \ln(W_0) - 8.6414 \qquad \text{(C-31)}$$

(14) Aerodynamic Drag

Seaplanes, whether amphibious or floatplanes are generally very draggy. This is evident in Table 16-22 and Section 16.4.6, *Drag of Floats*. The shape of the hull, or the floats and their associated support structure, generates a lot of drag. The seaplane should feature a powerful engine to reduce its take-off distance on water and to

make up for the increased drag and gross weight. Since the geometry of the seaplane is required by the hydrodynamic operation, it is hard to reduce its drag. Drag must be minimized by other means, such as using streamlined cleats (used to tie the seaplane when mooring) or the use of flush rivets (or composite materials). Struts should feature thick symmetrical airfoil, such as generic NACA strut airfoils or standard streamlined strut sections (see Section 16.4.4, *Drag of Streamlined Struts and Landing Gear Pant Fairings*). Also, the LISA Akoya represents a new design philosophy to consider as well.

C.2.3 Seaplane Take-Off Estimation

Estimating the T-O distance for seaplanes is more complicated than for conventional land aircraft. This is due to the disparate sources of drag the seaplane must overcome. In addition to aerodynamic drag, it is subject to water resistance, which depends on the airplane's speed and attitude in the water. Ref. [17] presents the following method for this purpose. First, the following concepts must be defined:

Buoyancy force (or load) coefficient:

$$C_{\Delta} = \frac{F_{buoy}}{\rho_W B^3} = \frac{\Delta}{\rho_W B^3} \tag{C-32}$$

A desirable range of C_{Δ} at gross weight is generally between 1 and 2 (per Ref. [17]). As the airplane generates aerodynamic lift during the T-O run, its value gradually reduces to 0 at lift-off. This means that the resistance will vary as well: It too depends on the displacement of the hull in the water and, thus, C_{Δ}. The resistance coefficient is presented as follows. Its value is unique for each geometry and, thus, it must be obtained using towing tests in a water tank.

Resistance coefficient:

$$C_R = \frac{R}{\rho_W B^3} \quad \text{and} \quad C_R = C_R(C_{\Delta}) \tag{C-33}$$

The speed coefficient is defined as follows:

Speed coefficient:

$$C_V = \frac{V}{\sqrt{gB}} \tag{C-34}$$

Where B is the beam of the seaplane (its largest submerged width of the hull), R is the water resistance force, and V is speed with respect to the water. To evaluate hulls of different length-to-beam ratios (L/B), the following coefficients must also be introduced, as they are typically used in the literature to document the variation of load and resistance:

Buoyancy force coefficient:

$$C_{\Delta_2} = \frac{F_{buoy}}{\rho_W L^2 B} = C_{\Delta}\left(\frac{B}{L}\right)^2 \tag{C-35}$$

Resistance coefficient:

$$C_{R_2} = \frac{R}{\rho_W L^2 B} = C_R\left(\frac{B}{L}\right)^2 \tag{C-36}$$

Speed coefficient:

$$C_{V_2} = \frac{V}{g^{1/2} L^{1/3} B^{1/6}} = C_V\left(\frac{B}{L}\right)^{1/3} \tag{C-37}$$

Moment coefficient:

$$C_{M_2} = \frac{M}{\rho_W (L^2 B)^{4/3}} \tag{C-38}$$

Draft coefficient:

$$C_{DR} = \frac{d}{(L^2 B)^{1/3}} \tag{C-39}$$

Rolling moment coefficient:

$$C_{M_R} = \frac{M_R}{\rho_W (L^2 B)^{4/3}} \tag{C-40}$$

Where d is draft in ft or m, g is acceleration due to gravity, M is trimming moment (which affects the trim angle), and M_R is rolling moment in ft lb$_f$ or N m.

The evaluation of the trim angle (see Figure C-23) is also important because the trimming moment, M, must be close to zero at low speed when the elevator is ineffective. Then, as the airspeed increases, the pilot can adjust the trim moment using the elevator to change the airplane trim angle for minimum water resistance, R, if not the minimum of the sum of R and aerodynamic drag.

The length-to-beam ratio, L/B, is typically around 5–9, but can be as large as 15 (such as the Martin P6M jet powered seaplane designed in the 1950s). High L/B, while less draggy in the water, will result in a slender body that is usually not be suitable for small seaplanes.

Typical shape of water resistance and trim angle variation versus speed coefficient are presented in Figures C-24 and C-25. The data is based on towing tests for two distinct hulls shapes; conventional and planing-tail, presented in Ref. [19]. The investigation concluded the planing-tail offers superior hydrodynamic and aerodynamic characteristics. The shape of the resistance curves in Figure C-24 show this. The water resistance increases until the aircraft gets on the "step." The ratio F_{buoy}/R is analogous to lift-to-drag ratio. If $F_{buoy} = W_0$, the maximum resistance amounts to about 22% of W_0 for the conventional hull and 15% for the planing-tail hull. The former represents a formidable difficulty for conventional flying boats. However, this resistance is not solely due to the hull geometry. The "hump" or the peak of the curves (especially noticeable for the conventional hull) results from the aircraft approaching its hull speed. When this happens, standard seaplane operations dictate that the pilot should rotate the airplane sharply to try to help it get "on the step."

The trim angle indicates the orientation of the seaplane in the water during the T-O run. This characteristic is of great importance to the T-O analysis, as it directly affects the AOA. The AOA is determined by adding the trim angle to the AOI of the wing with respect to the tangent

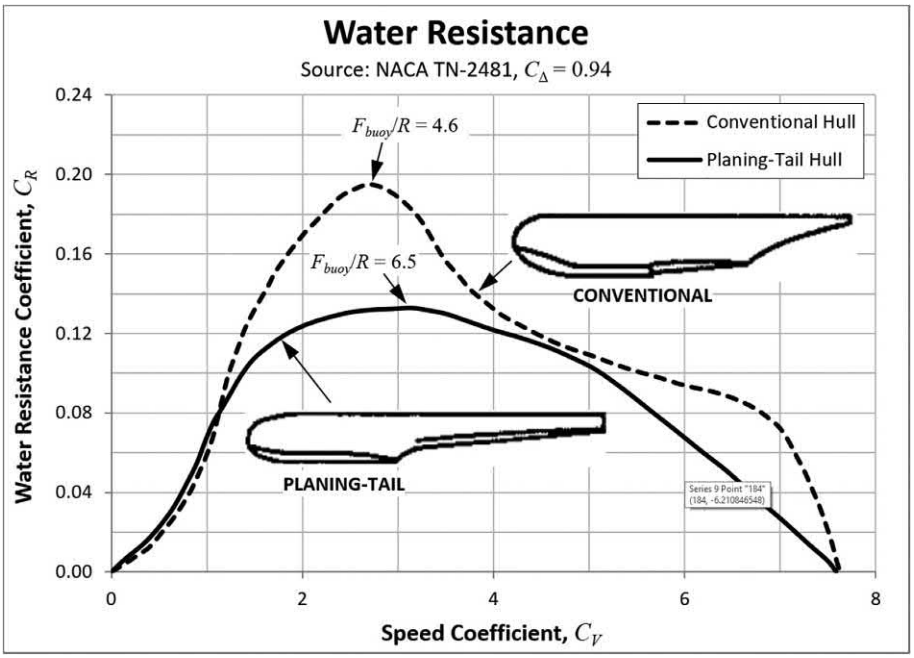


FIGURE C-24 Water resistance versus speed coefficient for two hull styles; a conventional and planing-tail shows the latter generates substantially less resistance and has smaller hump than the former. *Reproduced from H.B. Suydam, Hydrodynamic Characteristics of a Low-Drag Planing-Tail Flying-Boat Hull, NACA TN-2481, 1952.*

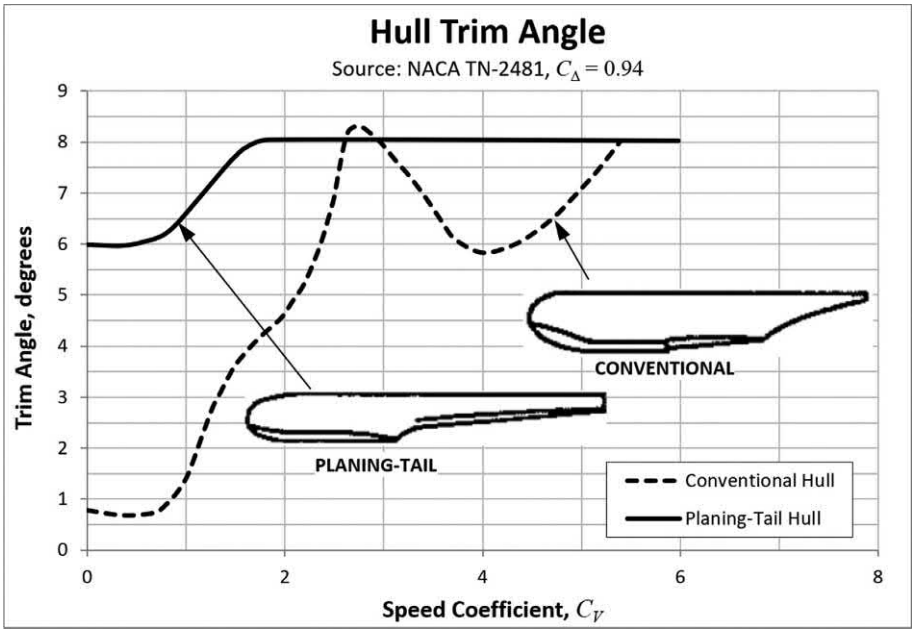


FIGURE C-25 Trim angle versus speed coefficient for the two hull styles shows the planing-tail requires simpler trimming than the conventional. *Reproduced from H.B. Suydam, Hydrodynamic Characteristics of a Low-Drag Planing-Tail Flying-Boat Hull, NACA TN-2481, 1952.*

to the keel (to which the trim angle refers). Figure C-25 shows how the trim angle varies with the speed coefficient for the two hull styles. The planing-tail hull merely requires a 2-degree increase in trim angle over the duration of the T-O, requiring simpler pilot correction. Also note how this is taken into account in the T-O analysis of Example C-3.

The trim angle curve for the planing-tail hull allows for the following approximation, derived by the author based on the shape of the curve. It cannot be used for the conventional hull:

$$\alpha_{trim} = \alpha_1 + \frac{(\alpha_2 - \alpha_1)}{2}(1 + \tanh(AC_V + B)) \qquad \text{(C-41)}$$

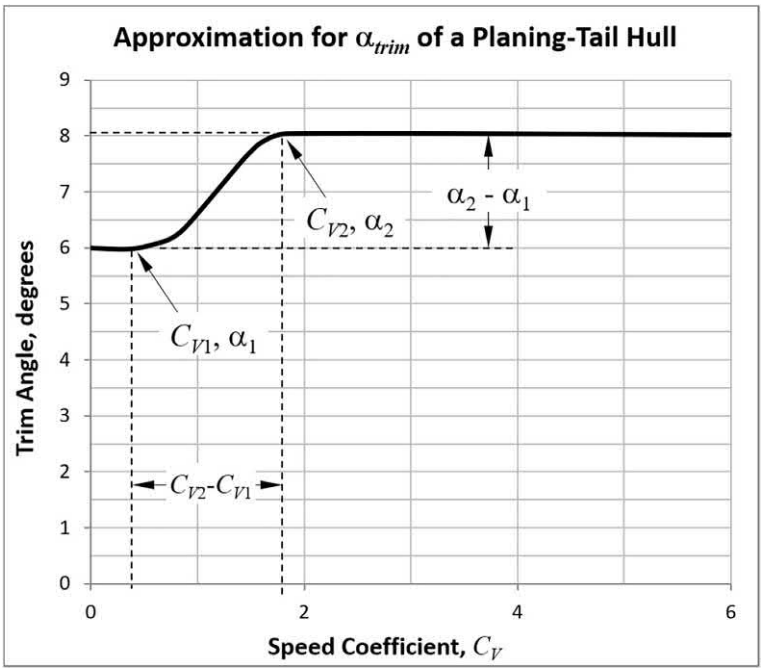


FIGURE C-26 The trim angle of the planing-tail hull behaves similar to the curve above.

Where: A and B = Constants, calculated as shown below

α_1 = Trim angle at the start of the T-O run (beginning of rise = C_{V_1}, see Figure C-26)
α_2 = Trim angle at the end of the T-O run (rise completes = C_{V_2})

Constant A: $$A = 5.294/(C_{V2} - C_{V1}) \qquad \text{(C-42)}$$

Constant B: $$B = -(2.647 + AC_{V1}) \qquad \text{(C-43)}$$

A reliable T-O analysis for seaplanes calls for its physics to be simulated and integrated over the duration of the take-off, similar to what we do for landplanes. Thus, the resistance and trim angle must be simulated as shown in Example C-3.

DERIVATION OF EQUATIONS (C-41), (C-42), AND (C-43):

We proceed similar to the derivation of Equation (16-106). Consider the curve of Figure C-26. Then, we observe that the argument of the hyperbolic tangent can be determined by solving for it, as shown below:

$$AC_V + B = \tanh^{-1}\left[\frac{2(\alpha_{trim} - \alpha_1)}{(\alpha_2 - \alpha_1)} - 1\right]$$

Noting that $-1 \le \tanh(x) \le 1$, this allows the two following expressions to be written:

When $C_V = C_{V_1}$, then $\alpha_{trim} = \alpha_1$:

$$AC_{V_1} + B = \tanh^{-1}(-1)$$

When $C_V = C_{V_2}$, then $\alpha_{trim} = \alpha_2$:

$$AC_{V_2} + B = \tanh^{-1}(+1)$$

Since the inverse arguments lead to infinite results, we have to reduce them to values that will allow the constants A and B to be evaluated with reasonable accuracy. For instance, if we replace the arguments -1 and $+1$ with -0.99 and $+0.99$, respectively, we get the following useful result:

$$\left.\begin{aligned} AC_{V_1} + B &= \tanh^{-1}(-0.99) = -2.647 \\ AC_{V_2} + B &= \tanh^{-1}(+0.99) = +2.647 \end{aligned}\right\} \Rightarrow \begin{cases} A = 5.294/(C_{V_2} - C_{V_1}) \\ B = -(2.647 + AC_{V_1}) \end{cases}$$

EXAMPLE C-3

A flying boat of the planning-tail configuration is being designed to carry eight occupants. Estimate the T-O distance, given the following information:

Fuselage beam	$B = 5.0\,\text{ft}$
Fuselage water length	$L = 27.8\,\text{ft}$
Wing span	$b = 49.0\,\text{ft}$
Wing area	$S = 375\,\text{ft}^2$
Wing Aspect Ratio	$AR = 6.41\,\text{ft}^2$
Wing AOI with respect to keel	$i_W = 4.5$ degrees
Gross weight	$W_0 = 8000\,\text{lb}_\text{f}$
Engines	$N_e = 2$
Engine power	$P_{BHP} = 450\,\text{BHP}$ each
Propeller diameter	$D_P = 8.5\,\text{ft}$
Spinner frontal area	$A_{\text{spinner}} = 7.0\,\text{ft}^2$
Maximum speed at 5000 ft	$V_{\max} = 175\,\text{KTAS}$, when $\eta_p = 0.82$
Thrust function at max power	$T = 0.01040\,V^2 - 10.065\,V + 3225$, in lb_f; V is in ft/s
Drag coefficient	$C_D = 0.06 + 0.058 \cdot C_L^2$
Water resistance coefficient	$C_R = 0.0011C_V^3 - 0.0221C_V^2 + 0.1062C_V - 0.0149$
Trim angle	$\alpha_{trim} = 7 + \tanh(3.553C_V - 3.891)$
Density of sea water	$\rho_W = 63.5\,\text{lb}_\text{f}/\text{ft}^3$

Note that the modeling for the trim angle and water resistance coefficient is shown in Figure C-27. The graph shows that the curve fitting formulation offers a good fit to the original test data. The trim angle formulation uses $(C_{V_1}, \alpha_1) = (0.35, 6\text{ degrees})$ and $(C_{V_2}, \alpha_2) = (2, 8\text{ degrees})$ with Equation (C-41).

Assumption 1:

In this example, we account for the reduction in resistance with loading using the following expression:

$$C_{R\Delta} = C_R \cdot (C_\Delta / C_{\Delta_0})$$

Where: C_{Δ_0} = Load coefficient at the T-O weight and at rest.

This expression is only used here to model the reduction in the water resistance with displacement of the hull. It is based on the observation that as wing lift increases, the draft of the hull decreases and, thus, the resistance. For real applications, the relationship between draft and resistance must be determined by experiment.

Assumption 2:

Once the speed coefficient exceeds 7.5, the value of R is zero, because the fuselage is out of the water and, thus, there is no hull displacement of water. There is no guarantee that the airplane is airborne at this moment, but rather it is hydroplaning. This implies the bottom of the airplane is still in contact with water and is generating hydrodynamic resistance. Account for this hydroplaning friction using the Froude frictional resistance of Equation (C-30), assuming a wetted area of $1\,\text{ft} \times B\,(=5\,\text{ft}^2)$ and smooth surface, whose frictional coefficient f amounts to 0.012.

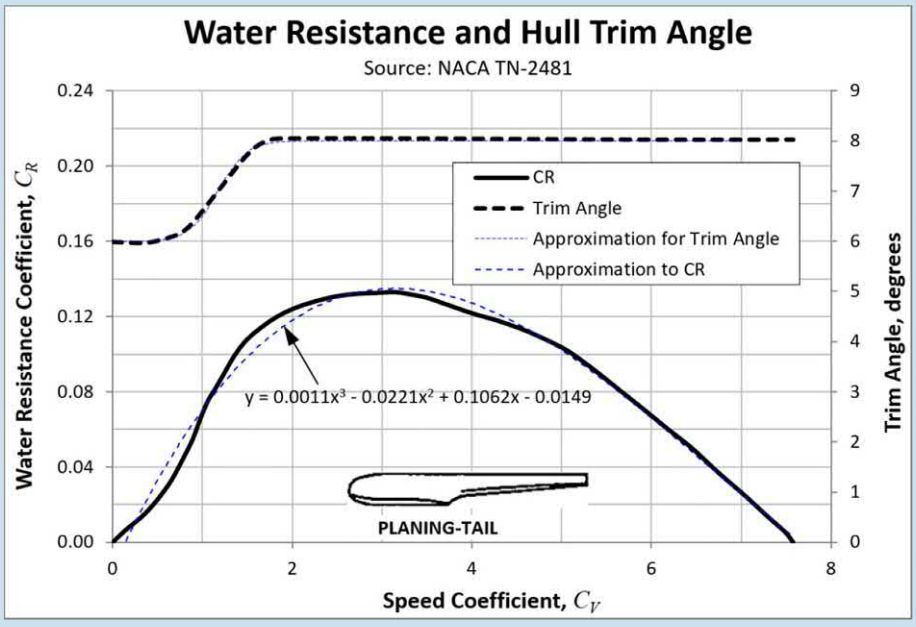


FIGURE C-27 Trim angle and resistance coefficient modeling for this example.

EXAMPLE C-3 (*cont'd*)

Assumption 3:

As the seaplane begins its T-O run, the engine is already generating some thrust. Pilot technique often dictates that the thrust is increased slowly rather than quickly—observation shows over 6–10 s before the throttle is fully open. Account for this technique by assuming a 10 s throttle up time, using the following model:

$$r = \begin{cases} 0.25 + 0.75(t/10) & \text{if } t < 10\,\text{s} \\ 1 & \text{if } t \geq 10\,\text{s} \end{cases}$$

Then, multiply the thrust by this factor to account for the ramp-up. This model ensures that initially, 25% of the maximum thrust is applied and once $t > 10$ s, the full thrust available at the given airspeed is used.

SOLUTION:

Using the data given above, the thrust function was created using Equation (15-60), where T_{STATIC} is calculated using Equation (15-81) and propeller efficiency, η_p, of 0.82 was assumed at a maximum airspeed of 175 KTAS at 5000 ft.

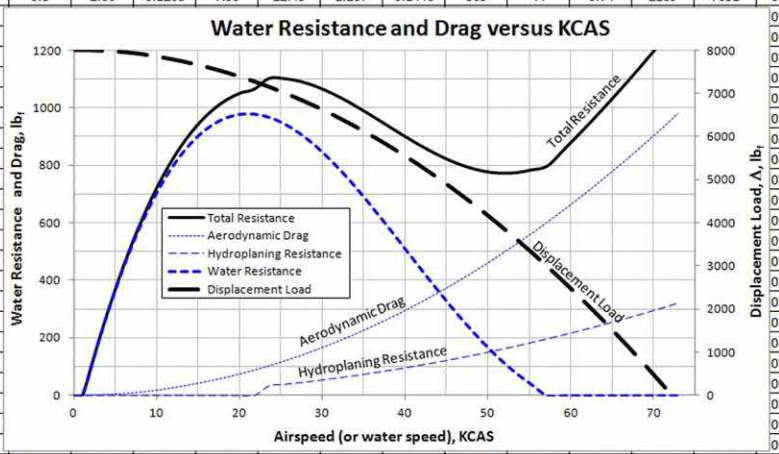
The resulting analysis is shown in Table C-4. The columns are calculated as follows, using the row with ID 10 as a numerical example (note that additional significant digits are shown in row 10 for this reason):

Column	Content
1	Contains the elapsed time, here obtained by adding 0.5 s to the previous value: 4.0 + 0.5 = 4.5 s.
2	Difference between time steps. $\Delta t = 4.5 - 4.0 = 0.5$. Note that dissimilar time steps are allowed.
3	Water or airspeed (no wind condition) in knots. Calculated by dividing the speed in ft/s by 1.688.
4	Speed in ft/s, obtained using numerical integration scheme of Section 18.2.5, *Solution of Kinematic Problems using Numerical Integration*, here using Equation (18-16). Example: $V_{10} = V_9 + a_9 \cdot \Delta t_{10} = 15.09 + 4.149 \times 0.5 = 17.16$ ft/s
5	Dynamic pressure: $q = \frac{1}{2}\rho V^2$. Example: $q_{10} = \frac{1}{2} \times 0.002378 \times (17.16)^2 = 0.3502$ lb$_f$/ft^2
6	Speed coefficient, calculated using Equation (C-34). Example: $C_{V_{10}} = V_{10}/\sqrt{gB} = 17.16/\sqrt{32.174 \times 5} = 1.353$
7	Resistance coefficient, calculated using the polynomial for C_R given in the problem statement. Example: $C_{R_{10}} = 0.0011 \times {C_{V_{10}}}^3 - 0.0221 {C_{V_{10}}}^2 + 0.1062 \times C_{V_{10}} - 0.0149 = 0.09174$
8	Angle of trim, calculated using the polynomial for α_{trim} given in the problem statement. Example: $\alpha_{trim10} = 7 + \tanh(3.553 \times C_{V_{10}} - 3.891) = 7.516$ degrees
9	Angle of attack, α, is the sum of the angle-of-trim and wing incidence angle (given as 4.5 degrees in the problem statement). Thus, $\alpha_{10} = 7.516$ degrees + 4.5 degrees = 12.02 degrees
10	Lift coefficient, calculated using the expression for C_L given in the problem statement. Example: $C_{L10} = 0.2 + 4.62 \times \alpha_{10} \bullet \pi/180 = 1.169$
11	Drag coefficient, calculated using the expression for C_D given in the problem statement. Example: $C_{D10} = 0.06 + 0.058 \times C_{L10}^2 = 0.1393$
12	Lift force, calculated using $L = qSC_L$. Example: $L_{10} = q_{10} S C_{L10} = 0.349 \times 375 \times 1.169 = 153.5$ lb$_f$
13	Drag force, calculated using $D = qSC_D$. Example: $D_{10} = q_{10} S C_{D10} = 0.349 \times 375 \times 0.1393 = 18.29$ lb$_f$
14	Ramp-up factor, calculated as described in Assumption 3. The time elapsed for the 10th row is 4.5 s, which is less than 10 s. Therefore, $r_{10} = 0.25 + 0.75 \times 4.5/10 = 0.5875$
15	Thrust force, calculated using the expression for T given in the problem statement. Example: $T_{10} = 0.01040 V_{10}^2 - 10.065 V_{10} + 3225 = 1795$ lb$_f$
16	Load or displacement or F_{buoy}, calculated by subtracting the lift from the weight of the aircraft. Example: $D_{10} = W - L_{10} = 8000 - 153.5 = 7846$ lb$_f$
17	Buoyancy or load coefficient, calculated using Equation (C-32) and the load from Column 16. Example: $C_{\Delta_{10}} = \Delta_{10}/(\rho_W B^3) = 7846/(63.5 \times 5^3) = 0.9885$
18	Resistance coefficient, reduced to account for reduced draft. Calculated in accordance with Assumption 1, where $C_{\Delta_0} = C_{\Delta_1} = 1.008$. Example: $C_{R_{\Delta 10}} = C_{R_{10}}(C_{\Delta_{10}}/C_{\Delta_0}) = 0.09174 \times (0.9885/1.008) = 0.08998$
19	Water resistance, calculated using Equation (C-33). Note that the author uses an `IF()` statement in this column in Microsoft Excel to ensure that if $C_R < 0$, then $C_R = 0$. This is a possible scenario when $C_V \approx 0$ and $C_V \approx 7.5$ because of the cubic polynomial used to approximate C_R. which is only valid for $0 < C_R \leq 7.5$. The `IF()` statement also forces the resistance to $C_R = 0$ for any $C_V > 7.5$. Once C_V exceeds 7.5, the only resistance caused by the water is the Froude resistance treated in the next column. This is justified based on the observation that the airplane is out of the water and "on the step"; its only contact with water is through hydroplaning. Example: $R_{10} = C_{R_{\Delta 10}}(\rho_W B^3) = 0.08998(63.5 \times 5^5) = 714.2$ lb$_f$
20	Hydroplaning resistance, calculated using Froude's formula of Equation (C-30). Note that it is not taken into account until around $t = 8.5$ s, as this is when the plane gets "on the step." However, since the time is 4.5 s, its value is set to zero using an `IF()` statement in Microsoft Excel. The 6.202 lb$_f$ calculated below represents a value that would be used if the airplane was already "on the step." Note that this formulation assumes speed is given in knots. Example: $R_{Froude10} = f S_{wet} V_{10}^2 = 0.012 \times 5 \times 17.16^2 = 6.202$ lb$_f$
21	Net force acting on the airplane: $T_{net10} = T_{10} - D_{10} - R_{10} - R_{froude10} = 1063$ lb$_f$
22	Acceleration of the airplane: $a_{10} = T_{net10}/(W/g) = 1056/(8000/32.174) = 4.273$ ft/s^2
23	Distance in ft, obtained using numerical integration scheme of Section 18.2.5, here using Equation (18-17). Example: $S_{10} = S_9 + V_9 \cdot \Delta t_{10} + \frac{1}{2} \cdot a_9 \cdot \Delta t_{10}^2 = 29.39 + 15.09 \times 0.5 + \frac{1}{2} \times 4.149 \times 0.5^2 = 37.47$ ft

EXAMPLE C-3 *(cont'd)*

TABLE C-4 T-O performance prediction.

	1	2	3	4	5	6	7	8	9	10	11	12	13	14	15	16	17	18	19	20	21	22	23
	Time		Water/Airspeed		q	C_V	C_R	α_{trim}	α	C_L	C_D	Lift	Drag	r	Thrust·r	$\Delta = W - L$	C_Δ	$C_{R\Delta}$	R	R_{Froude}	T_{net}	a	S
ID	t, sec	Δt, sec	KTAS	ft/s	lb_f/ft^2			deg	deg			lb_f	lb_f		lb_f	lb_f			lb_f	lb_f	lb_f	ft/s^2	ft
1	0.0		0	0.0	0.0	0.00	-0.0149	6.00	10.50	1.047	0.1235	0	0	0.25	806	8000	1.008	-0.0149	0	0	806	3.24	0
2	0.5	0.5	1	1.6	0.0	0.13	-0.0016	6.00	10.50	1.047	0.1236	1	0	0.29	923	7999	1.008	-0.0016	0	0	922	3.71	0
3	1.0	0.5	2	3.5	0.0	0.27	0.0127	6.01	10.51	1.047	0.1236	6	1	0.33	1037	7994	1.007	0.0127	101	0	935	3.76	2
4	1.5	0.5	3	5.4	0.0	0.42	0.0263	6.02	10.52	1.048	0.1237	13	2	0.36	1150	7987	1.006	0.0263	208	0	940	3.78	4
5	2.0	0.5	4	7.2	0.1	0.57	0.0391	6.04	10.54	1.050	0.1239	25	3	0.40	1261	7975	1.005	0.0389	309	0	949	3.82	7
6	2.5	0.5	5	9.2	0.1	0.72	0.0510	6.10	10.60	1.055	0.1246	39	5	0.44	1371	7961	1.003	0.0508	403	0	963	3.87	11
7	3.0	0.5	7	11.1	0.1	0.87	0.0622	6.25	10.75	1.067	0.1260	59	7	0.48	1479	7941	1.000	0.0618	490	0	982	3.95	16
8	3.5	0.5	8	13.1	0.2	1.03	0.0728	6.57	11.07	1.092	0.1292	83	10	0.51	1586	7917	0.997	0.0720	572	0	1005	4.04	22
9	4.0	0.5	9	15.09	0.3	1.19	0.0826	7.05	11.55	1.131	0.1342	115	14	0.55	1692	7885	0.993	0.0814	646	0	1032	4.149	29.39
10	4.5	0.5	10	17.16	0.3502	1.353	0.09174	7.516	12.02	1.169	0.1393	153.5	18.29	0.5875	1795	7846	0.9885	0.08998	714.2	0.000	1063	4.273	37.47
11	5.0	0.5	11	19.3	0.4	1.52	0.1002	7.80	12.30	1.192	0.1424	198	24	0.63	1897	7802	0.983	0.0977	775	0	1098	4.41	47
12	5.5	0.5	13	21.5	0.5	1.70	0.1078	7.93	12.43	1.202	0.1439	248	30	0.66	1996	7752	0.977	0.1045	829	0	1137	4.57	57
13	6.0	0.5	14	23.8	0.7	1.88	0.1147	7.98	12.48	1.206	0.1444	304	36	0.70	2094	7696	0.970	0.1104	876	0	1181	4.75	68
14	6.5	0.5	16	26.2	0.8	2.06	0.1208	7.99	12.49	1.207	0.1446	369	44	0.74	2189	7631	0.961	0.1153	915	0	1230	4.95	81
15	7.0	0.5	17	28.6													0.952	0.1191	945	0	1285	5.17	94
16	7.5	0.5	18	31.2													0.942	0.1217	966	0	1344	5.41	109
17	8.0	0.5	20	33.9													0.930	0.1231	977	0	1410	5.67	126
18	8.5	0.5	22	36.8													0.916	0.1232	978	0	1482	5.96	143
19	9.0	0.5	24	39.7													0.901	0.1218	967	33	1526	6.14	163
20	9.5	0.5	25	42.8													0.884	0.1190	945	39	1606	6.46	183
21	10.0	0.5	27	46.0													0.864	0.1147	911	45	1692	6.80	206
22	10.5	0.5	29	49.4													0.842	0.1089	864	51	1679	6.75	229
23	11.0	0.5	31	52.8													0.819	0.1020	810	59	1674	6.73	255
24	11.5	0.5	33	56.2													0.794	0.0943	748	66	1674	6.73	282
25	12.0	0.5	35	59.6													0.767	0.0858	681	75	1678	6.75	311
26	12.5	0.5	37	62.9													0.739	0.0769	610	83	1684	6.77	342
27	13.0	0.5	39	66.3													0.709	0.0676	537	93	1690	6.80	374
28	13.5	0.5	41	69.7													0.678	0.0582	462	102	1696	6.82	408
29	14.0	0.5	43	73.1													0.645	0.0490	389	113	1699	6.83	444
30	14.5	0.5	45	76.5													0.610	0.0399	317	123	1698	6.83	481
31	15.0	0.5	47	80.0													0.574	0.0314	249	135	1691	6.80	520
32	15.5	0.5	49	83.4													0.536	0.0234	186	146	1678	6.75	561
33	16.0	0.5	51	86.7													0.498	0.0163	130	158	1657	6.67	604
34	16.5	0.5	53	90.1													0.458	0.0101	80	171	1629	6.55	648
35	17.0	0.5	55	93.3													0.417	0.0049	39	183	1592	6.40	694
36	17.5	0.5	57	96.5													0.376	0.0007	0	196	1553	6.25	741
37	18.0	0.5	59	99.7	11.8	7.86	-0.0073	8.00	12.50	1.208	0.1446	5349	640	1.00	2325	2651	0.334	-0.0024	0	209	1476	5.93	790
38	18.5	0.5	61	102.6	12.5	8.09	-0.0157	8.00	12.50	1.208	0.1446	5672	679	1.00	2302	2328	0.293	-0.0046	0	222	1401	5.63	841
39	19.0	0.5	62	105.4	13.2	8.31	-0.0232	8.00	12.50	1.208	0.1446	5988	717	1.00	2279	2012	0.253	-0.0058	0	234	1328	5.34	893
40	19.5	0.5	64	108.1	13.9	8.52	-0.0299	8.00	12.50	1.208	0.1446	6295	754	1.00	2258	1705	0.215	-0.0064	0	246	1259	5.06	946
41	20.0	0.5	66	110.6	14.6	8.72	-0.0357	8.00	12.50	1.208	0.1446	6593	789	1.00	2239	1407	0.177	-0.0063	0	258	1191	4.79	1001
42	20.5	0.5	67	113.0	15.2	8.91	-0.0407	8.00	12.50	1.208	0.1446	6882	824	1.00	2220	1118	0.141	-0.0057	0	269	1127	4.53	1057
43	21.0	0.5	68	115.3	15.8	9.09	-0.0449	8.00	12.50	1.208	0.1446	7161	857	1.00	2203	839	0.106	-0.0047	0	280	1065	4.28	1114
44	21.5	0.5	70	117.4	16.4	9.26	-0.0485	8.00	12.50	1.208	0.1446	7429	890	1.00	2186	571	0.072	-0.0035	0	290	1006	4.05	1172
45	22.0	0.5	71	119.5	17.0	9.42	-0.0514	8.00	12.50	1.208	0.1446	7688	920	1.00	2171	312	0.039	-0.0020	0	301	950	3.82	1231
46	22.5	0.5	72	121.4	17.5	9.57	-0.0537	8.00	12.50	1.208	0.1446	7935	950	1.00	2157	65	0.008	-0.0004	0	310	896	3.60	1291
47	23.0	0.5	73	123.2	18.0	9.71	-0.0555	8.00	12.50	1.208	0.1446	8173	979	1.00	2143	-173	-0.022	0.0012	0	320	845	3.40	1352



C.2.4 14 CFR Part 23 Regulations for Seaplanes

In addition to paragraphs in 14 CFR Part 23 that apply to conventional aircraft, a specific selection applies only to seaplanes. These are listed below. They are from the "old" Part 23, but remain helpful. The aspiring seaplane designer should be familiar with these regulations as they provide a great insight into issues that pertain to seaplanes only.

§ 23.237 Operation on water.
§ 23.239 Spray characteristics.
§ 23.521 Water load conditions.
§ 23.523 Design weights and center of gravity positions.
§ 23.525 Application of loads.
§ 23.527 Hull and main float load factors.
§ 23.529 Hull and main float landing conditions.
§ 23.531 Hull and main float takeoff condition.
§ 23.533 Hull and main float bottom pressures.
§ 23.535 Auxiliary float loads.
§ 23.537 Seawing loads.
§ 23.751 Main float buoyancy.
§ 23.753 Main float design.
§ 23.755 Hulls.
§ 23.757 Auxiliary floats.

References

[1] C. Bowyer, *The Age of the Biplane*, The Hamlyn Publishing Group, 1981.
[2] D. Stinton, *The Design of the Aeroplane*, Collins Professional and Technical Books, 1983.
[3] E.C. Olson, B.P. Selberg, *Experimental determination of improved aerodynamic characteristics using biplane wing configurations*. J. Aircr. 13 (4) 1976. https://doi.org/10.2514/3.44523 AIAA.
[4] R.M. Mock, *The Distribution of Loads Between the Wings of a Biplane Having Decalage*, NACA TN-2691927.
[5] F.H. Norton, *The Effect of Stagger*, NACA R-701921.
[6] B. Jones, *Elements of Practical Aerodynamics*, second ed., John Wiley & Sons, 1939
[7] M.M. Munk, *Fundamentals of Fluid Dynamics for Aircraft Designers*, Ronald Press Company, 1923.
[8] W.S. Diehl, *Engineering Aerodynamics*, Ronald Press Company, 1936.
[9] L. Prandtl, *Applications of Modern Hydrodynamics to Aeronautics*, NACA R-116, 1923.
[10] FAA-H-8083-23, *Seaplane, Skiplane, and Float/Ski Equipped Helicopter Operations Handbook*, U.S. Department of Transportation, Federal Aviation Administration, Flight Standards Service, 2004.
[11] D. Thurston, *Design for Flying*, TAB Books, 1995.
[12] D. Savitsky, *On the Subject of High-Speed Monohulls*, Presented to the Greek Section Of the Society Of Naval Architects and Marine Engineers Athens, Greece, October 2, 2003.
[13] L. Prandtl, O.G. Tietjens, *Fundamentals of Hydro- and Aeromechanics*, Dover Publications, 1957.
[14] W.S. Diehl, *Static Stability of Seaplane Floats and Hulls*, NACA TN-183, 1924.
[15] Anon, *Marine Fouling and Its Prevention*, Contribution No. 580 from the Woods Hole Oceanographic InstituteGeorge Banta Publishing, 1952.
[16] W. Nelson, *Seaplane Design*, McGraw-Hill, 1934.
[17] K.D. Wood, *Aircraft Design—Aerospace Vehicle Design*, vol. I, Johnson Publishing Company, 1968.
[18] M. Faure, *Flying a Floatplane*, TAB Books, 1985.
[19] H.B. Suydam, *Hydrodynamic Characteristics of a Low-Drag Planing-Tail Flying-Boat Hull*, NACA TN-2481, 1952.
[20] W.C. Hugli Jr., W.C. Axt, *Hydrodynamic Investigation of a Series of Hull Models Suitable for Small Flying Boats and Amphibians*, NACA TN-2503, 1951.
[21] A. Biran, *Ship Hydrostatics and Stability*, Butterworth-Heinemann, 2003.
[22] R.F. Havens, *Tank Tests of a Flying-Boat Model Equipped With Several Types of Fairing Designed to Reduce the Air Drag of the Main Step*, NACA-WR-L-150, 1945.

APPENDIX

D

Derivation of Landing Side-Constraint

First write a common version of the four equations that apply to the complete landing distance for the aircraft.

Step 1: Determine Approach Distance in Terms of Wing Loading

Start with Equation (23-8) for flare height, h_F, Equation (23-9) for approach distance, S_A, and assume an approach angle, θ_{app}, of 3 degrees:

$$S_A = \frac{h_{obst} - h_F}{\tan\theta_{app}} \approx \frac{h_{obst} - 0.1512 \times V_{S_0}^2 \times \overbrace{(1-\cos\theta_{app})}^{=1-\cos 3^\circ \approx 1/729.7}}{\underbrace{\tan\theta_{app}}_{=\tan 3^\circ \approx 1/19.08}}$$

$$= 19.08\left[h_{obst} - 0.1512 \times V_{S_0}^2 \times \frac{1}{729.7}\right]$$

$$= 19.08 h_{obst} - 19.08 \times 0.1512 \times V_{S_0}^2 \times \frac{1}{729.7}$$

$$= 19.08 h_{obst} - 0.003954 \times V_{S_0}^2$$

Since $V_{S_0} = \sqrt{\dfrac{2W}{\rho S C_{L_{max_0}}}}$, this becomes:

$$S_A = 19.08 h_{obst} - 0.003954 \times \frac{2W}{\rho S C_{L_{max_0}}}$$

$$= 19.08 h_{obst} - \frac{0.007907}{\rho C_{L_{max_0}}} \times \left(\frac{W}{S}\right)$$

Step 2: Determine Flare Distance in Terms of Wing Loading

Start with Equation (23-13) for flare distance, S_F, and substitute into it the expression for V_{S_0}:

$$S_F = 0.1512 \times V_{S_0}^2 \times \sin\theta_{app} = 0.007913 \times V_{S_0}^2$$

$$= \frac{0.01583}{\rho C_{L_{max_0}}} \times \left(\frac{W}{S}\right)$$

$$S_A = 19.08 h_{obst} - 0.003954 \times \frac{2W}{\rho S C_{L_{max_0}}}$$

$$= 19.08 h_{obst} - \frac{0.007907}{\rho C_{L_{max_0}}} \times \left(\frac{W}{S}\right)$$

Step 3: Determine Free Rolling Distance in Terms of Wing Loading

Start with Equation (23-14) or (23-15) for free rolling distance, S_{FR}, and substitute into it the expression for V_{S_0}, noting that $V_{TD} = 1.1\ V_{S_0}$ and τ is the time for free roll, typically between 1 and 3 s.

$$S_{FR} = 1.1\tau V_{S_0} = 1.556\tau\sqrt{\frac{1}{\rho C_{L_{max_0}}} \times \left(\frac{W}{S}\right)}$$

Step 4: Determine Braking Distance in Terms of Wing Loading

Start with Equation (23-16) for braking distance, S_{BR}, and substitute into it the expression for V_{S_0}, noting that $V_{BR} = 1.1\ V_{S_0}$ and that values of the lift, L, drag, D, and (idle) thrust, T, are estimated at $V_{BR}/\sqrt{2}$:

$$S_{BR} = -\frac{V_{BR}^2 W}{2g[T - D - \mu(W - L)]}$$

$$= -\frac{\overbrace{V_{BR}^2}^{=(1.1V_{S_0})^2} W}{2g\left[T - qSC_{D\ LDG} - \mu\left(W - qSC_{D\ LDG}\right)\right]}$$

$$= \frac{1.21}{g\rho C_{L_{max_0}}\left[\dfrac{qC_{D\ LDG}}{W/S} - \dfrac{\mu q C_{L\ LDG}}{W/S} + \mu - \dfrac{T}{W}\right]}\left(\frac{W}{S}\right)$$

The dynamic pressure is given by

$$q=\frac{1}{2}\rho\left(\frac{V_{BR}}{\sqrt{2}}\right)^2=\frac{1}{2}\rho\left(\frac{1.1V_{S_0}}{\sqrt{2}}\right)^2=\frac{1}{2}\rho\left(\frac{1.21}{2}\frac{2W}{\rho SC_{L_{\max_0}}}\right)=\left(\frac{1.21}{2C_{L_{\max_0}}}\right)\left(\frac{W}{S}\right)$$
$$=\frac{1.21}{g\rho C_{L_{\max_0}}\left[\left(\frac{1.21}{2C_{L_{\max_0}}}\right)\left(\frac{W}{S}\right)C_{D\ LDG}/(W/S)-\mu\left(\frac{1.21}{2C_{L_{\max_0}}}\right)\left(\frac{W}{S}\right)C_{L\ LDG}/(W/S)+\mu-\frac{T}{W}\right]}\left(\frac{W}{S}\right)$$
$$=\frac{1.21}{g\rho C_{L_{\max_0}}\left[\frac{0.605}{C_{L_{\max_0}}}(C_{D\ LDG}-\mu C_{L\ LDG})+\mu-\frac{T}{W}\right]}\left(\frac{W}{S}\right)$$

Step 5: Determine Total Landing Distance in Terms of Wing Loading

The total landing distance is given by: $S_{LDG}=S_A+S_F+S_{FR}+S_{BR}$

$$S_{LDG}=\overbrace{19.08h_{obst}-\frac{0.007907}{\rho C_{L_{\max_0}}}\times\left(\frac{W}{S}\right)}^{S_A}+\overbrace{\frac{0.01583}{\rho C_{L_{\max_0}}}\times\left(\frac{W}{S}\right)}^{S_F}+\overbrace{1.556\tau\sqrt{\frac{1}{\rho C_{L_{\max_0}}}\times\left(\frac{W}{S}\right)}}^{S_{FR}}$$
$$+\overbrace{\frac{1.21}{g\rho C_{L_{\max_0}}\left[\frac{0.605}{C_{L_{\max_0}}}(C_{D\ LDG}-\mu C_{L\ LDG})+\mu-\frac{T}{W}\right]}\left(\frac{W}{S}\right)}^{S_{BR}}$$
$$=19.08h_{obst}+\frac{1}{\rho C_{L_{\max_0}}}\left[0.01583\left(\frac{W}{S}\right)-0.007907\left(\frac{W}{S}\right)+1.556\tau\sqrt{\rho C_{L_{\max_0}}}\frac{(W/S)^{0.5}}{(W/S)^{0.5}}\left(\frac{W}{S}\right)^{0.5}\right]$$
$$+\frac{1.21}{g\rho C_{L_{\max_0}}\left[\frac{0.605}{C_{L_{\max_0}}}(C_{D\ LDG}-\mu C_{L\ LDG})+\mu-\frac{T}{W}\right]}\left(\frac{W}{S}\right)$$
$$=19.08h_{obst}+\left[0.007923+1.556\tau\sqrt{\frac{\rho C_{L_{\max_0}}}{W/S}}+\frac{1.21}{g\left[\frac{0.605}{C_{L_{\max_0}}}(C_{D\ LDG}-\mu C_{L\ LDG})+\mu-\frac{T}{W}\right]}\right]\frac{(W/S)}{\rho C_{L_{\max_0}}}$$

Substituting the above results leads to

This is a transcendental equation in W/S and must be solved iteratively.

Step 6: Determine Ground Roll Distance in Terms of Wing Loading

The ground roll distance is given by: $S_{LGR}=S_F+S_{FR}+S_{BR}$. Note that in this form, the flare distance is included.

$$S_{LGR}=\overbrace{\frac{0.01583}{\rho C_{L_{\max_0}}}\times\left(\frac{W}{S}\right)}^{S_F}+\overbrace{1.556\tau\sqrt{\frac{1}{\rho C_{L_{\max_0}}}\times\left(\frac{W}{S}\right)}}^{S_{BR}}+\overbrace{\frac{1.21}{g\rho C_{L_{\max_0}}\left[\frac{0.605}{C_{L_{\max_0}}}(C_{D\ LDG}-\mu C_{L\ LDG})+\mu-\frac{T}{W}\right]}\left(\frac{W}{S}\right)}^{S_{BR}}$$

The reader can easily omit it from consideration by following the derivation below.

$$= \frac{0.01583}{\rho C_{L_{\max_0}}} \times \left(\frac{W}{S}\right) + 1.556\tau \sqrt{\frac{1}{\rho C_{L_{\max_0}}}} \times \left(\frac{W}{S}\right)^{0.5} + \frac{1.21}{g\rho C_{L_{\max_0}} \left[\frac{0.605}{C_{L_{\max_0}}}(C_{D\ LDG} - \mu C_{L\ LDG}) + \mu - \frac{T}{W}\right]} \left(\frac{W}{S}\right)$$

$$= 1.556\tau \sqrt{\frac{1}{\rho C_{L_{\max_0}}}} \times \frac{(W/S)^{0.5}}{(W/S)^{0.5}} \left(\frac{W}{S}\right)^{0.5} + \left\{ \frac{0.01583}{\rho C_{L_{\max_0}}} + \frac{1.21}{g\rho C_{L_{\max_0}} \left[\frac{0.605}{C_{L_{\max_0}}}(C_{D\ LDG} - \mu C_{L\ LDG}) + \mu - \frac{T}{W}\right]} \right\} \left(\frac{W}{S}\right)$$

$$= \left\{ \frac{0.01583}{\rho C_{L_{\max_0}}} + 1.556\tau \sqrt{\frac{1}{\rho C_{L_{\max_0}}(W/S)}} + \frac{1.21}{g\rho C_{L_{\max_0}} \left[\frac{0.605}{C_{L_{\max_0}}}(C_{D\ LDG} - \mu C_{L\ LDG}) + \mu - \frac{T}{W}\right]} \right\} \left(\frac{W}{S}\right)$$

$$= \left\{ 0.01583 + 1.556\tau \sqrt{\frac{\rho C_{L_{\max_0}}}{(W/S)}} + \frac{1.21}{g \left[\frac{0.605}{C_{L_{\max_0}}}(C_{D\ LDG} - \mu C_{L\ LDG}) + \mu - \frac{T}{W}\right]} \right\} \frac{(W/S)}{\rho C_{L_{\max_0}}}$$

This page intentionally left blank

Index

Note: Page numbers followed by *f* indicate figures, *t* indicate tables, and *b* indicate boxes.

A

Absolute ceiling, 827
Accelerated stall, 1009
Acceleration, 791–793, 795–796
  graph for SR22, 801*f*
  ground run distance estimation with, 795
  thrust-to-weight ratios, 791–792
  on uphill slope, 791
Accessibility, 7
Accommodation, 527
Acrylics, 528
Active high-lift devices, 416
Activity factor (AF), 624–625, 625*b*
Actuation binding, 446
Actuator disc, annulus, 648, 648*f*
Actuator disc theory (ADT), 638
AD. *See* Airworthiness Directive (AD)
Additive drag
  of antennas, 729
    placement and shape, 729, 729*f*
  of blisters, 728–729
    drag contribution, 728*f*
    example, 729*b*
  of canopies, 727–728
    canopy styles, 727*f*
    drag coefficients for canopy styles, 727–728, 727*f*
  cooling drag, 714–716
    cooling drag coefficient, 715
    idealization of engine installation, 715*f*
  CRUD, 712
    component contribution, 676*t*
    Seversky P-35, 675, 676*f*
    twin-engine business jet, 675
    WR-L-489, 675
  of deployed flaps, 724
    Δ1 function, 724
    Δ2 function, 724, 725*t*
    increase of $C_{D_{min}}$ due to flaps, 723–724
  drag correction for cockpit windows, 725–727
    drag of blunt ordinary and undercut, 726, 727*f*
    drag of conventional cockpit windows, 726
  drag of various geometry
    critical Reynolds number, 731
    cross-flow principle, 733
    2D cross-section, 3D drag of, 733
    2D drag coefficient, 732*f*
    3D drag coefficient, 733–734, 733*f*
    drag of 3D objects, 733
    flow regions on sphere, 731, 732*f*
  due to compressibility effects, 727–728
  due to ice accretion, 734
  of floats, 722–724
    float geometries, 723*f*
    special NACA-designed floats, 723–724
  geometric shape of protrusions, 712
  of gun ports in airplane nose, 734
  landing gear drag
    of fixed landing gear struts with tires, 719
    of nose landing gear, 722
    of retractable landing gear, 721
    of tires only, 717
    of tires with wheel fairings, 718
  landing gear pant fairings, 716–717
    thick fairings, 717
  lift-induced drag corrections
    example, 694*b*
    in ground effect, 695
    pressure difference, 694*f*
    vortex core location, 695*f*
    wingtip correction, 694
    wingtips effect, 695*f*
  of parachutes, 730
    drag coefficient, 730, 731*f*
    example, 730*b*
    total drag force evaluation, 730–731
  of sanded walkway on wing, 734
  scaling, 712
  stopped propellers, 729–730
  of streamlined external fuel tanks, 734, 734*f*
  streamlined struts drag, 716–717
  trim drag, 713–714
    balancing force, 713
    due to wing washout, 695
    windmilling propellers, 729
    wing-horizontal tail combination, 713
    wing-horizontal tail-thrustline combination, 713
    wing-like surface drag, 716
Adiabatic process, 581*t*
Adjustable trim tab, 971, 971*f*
Adjusted drag model, 663
Advance ratio (AR), 624, 952–953, 954–955*b*
Adverse roll, 497–498
Adverse yaw, 999
Advisory circular (AC), 14
Aerobatic aircraft, 492
Aerobatic category, 490
Aerodynamic center, 270, 364
Aerodynamic forces, 918
Aerodynamic hinge moment, 967
Aerodynamic influence matrix, 405
Aerodynamic loads, 565
Aerodynamics, 574
Aerodynamic washout, 344, 345*f*
AeroFoil, 281
Aesthetics, 7, 93, 95–96*t*, 503
Aft spar, 136–137
Aft sweep, 339, 358
Aileron, 930
  design requirements, 1001, 1001*f*
  differential, 1001, 1001*f*
  frise, 999, 1000*f*
  hinge moment coefficient, 968
  hinges, 138
  plain-flap, 999, 1000*f*
  sizing, 1001–1003
  slot-lip, 1000, 1000*f*
  spoiler-flap, 1000, 1000*f*
Aileron authority, rolling moment, 997, 997*f*
Air-breathing mechanical engines, 573
Air conditioning, 164
Aircraft, aerodynamic characteristics of, 62*t*
Aircraft conceptual design algorithm, 15–18
  for general aviation (GA) aircraft, 16–18, 16–17*t*, 17*f*
  implementation, 18
    organizational hierarchy of spreadsheet, 18–19*f*
    3-dimensional spreadsheet software, 18
    VBA function, 18
  modern spreadsheet, 15–16
Aircraft control, 930–931, 931*f*
Aircraft design
  certainty, 94
  cost, 94
  drag, 94
  efficiency, 94
  integration, 95
  maintenance, 94
  newness, 95

Aircraft design *(Continued)*
progressiveness, 95
reliability, 94
requirements, 94
scheduling, 95
simplicity, 94
weight, 94
Aircraft design process, 2–10
certification, 10–15, 10*f*, 11*t*, 13*t*
concepts of importance
accessibility, 7
aesthetics, 7
certifiability, 7
ease of manufacturing, 6, 6*f*
features and upgradability, 7
handling requirements, 6
integrated product teams (IPT), 9
lean engineering and manufacturing, 8
maintainability, 7
mission, 6
performance requirements and sensitivity, 6
elementary outline, 2, 3*f*
for general aviation (GA) aircraft, 3, 4*f*
conceptual design algorithm, 16–18, 16–17*t*, 17*f*
development timeline, 9–10, 9*f*
regulations, 10–14
per Torenbeek, 3, 3*f*
phases
conceptual design, 4
detail design, 5
development program, 5
postdevelopment programs, 5
preliminary design, 4
proof-of-concept aircraft and testing, 5
requirements, 4
project management, 18–27
document standards, 22–23
Fishbone diagram, 20–21, 23*f*
Gantt diagrams, 20
house of quality (HQ), 23–27, 24–27*f*
practical drawing numbering system, 23, 24*f*
Program Evaluation and Review Task (PERT) chart, 20, 22*f*
project plan, 18–19
quality function deployment (QFD), 23–27
task management, 20
task matrix, 20, 21*f*
team leadership, 19
project presentation, 27–32
computational fluid dynamics (CFD), 29, 30*f*
cutaway drawings, 29, 31*f*
engineering drawings, 30
engineering reports, 30
finite element modelers, 28, 29*f*
solid modelers, 28, 28*f*
three-view drawings, 28
regulations, 10–15, 11*f*
regulatory concepts
advisory circular (AC), 14
airworthiness, 14
Airworthiness Directives (AD), 14
maintenance requirements, 14
parts manufacturer approval (PMA), 14
service bulletin (SB), 14
special airworthiness certificate (S-AC), 14
standard airworthiness certificate (AC), 15
supplemental type certificate (STC), 15
technical standard order (TSO), 15
technical standard order authorization (TSOA), 15
type certificate (TC), 15
stall speed, 12
Aircraft development cost
of business aircraft, 47–48
development support, total cost of, 48
engineering, total cost of, 48
engineering workhours, 47
fixed cost, 48
flight test operations, total cost of, 48
manufacturing labor workhours, 48
manufacturing, total cost of, 48
materials, total cost of, 48
quality control, total cost of, 48
tooling, total cost of, 48
tooling workhours, 48
variable cost, 48
of GA aircraft, 38–46, 38*f*
cost analysis, 41
development support, total cost of, 41
engineering, total cost of, 41
engineering workhours, 39
fixed cost, 43, 43*b*
flight test operations, total cost of, 42
manufacturing labor workhours, 40
manufacturing, total cost of, 42
materials, total cost of, 42
product liability costs, 39
quality control, total cost of, 42
quantity discount factor (QDF), 39
tooling, total cost of, 42
tooling workhours, 40
variable cost, 43, 44–47*b*
Aircraft operational map, 197, 198*f*
Aircraft prices, predicted *vs*.actual, 49–50, 49*t*
Aircraft sizing
at condition, 57
constraint analysis, 58–68
design of experiments (DOE), 58, 72–73, 73*f*
effectiveness, 58
mathematical optimization, 58
operational efficiency, 58
parametric analysis, 58
performance efficiency, 58
trade study, 58, 69–73
Aircraft weighing, 180
Aircraft weight
design gross weight, 149
empty weight, 149
empty weight ratio, 149
fuel weight, 149
fuel weight ratio, 149
gross weight, 149
useful load, 149
Airfoil Critical Mach Number, 308
Airfoil Drag Divergence Mach Number, 310
Airfoil efficiency ratio, 315
Airfoils, 257–282
aerodynamic center, 270
alternative analogy, 273
boundary layer theory (BLT), 273–277
center of pressure (CP), 270
chordwise pressure distribution, 266–269
Clark Y airfoil, 290, 293*f*, 304*f*
classes of, 260, 261–262*t*
Davis Wing airfoil, 296, 296*f*
design, 280–282
dimensional analysis, Buckingham's π–theorem, 258–259
Fauvel Flying Wing airfoils, 299, 299*f*
force and moment
characteristics of, 299–317
per unit span, 269–270, 269*f*
representation of, 259–260
GA(W)-1, 295, 295*f*
generation of lift, 271–273
geometry of
camber, 282
chordline, 282
cusp, 283
leading edge (LE), 282
LE radius, 282
mean-line, 282
NACA five-digit airfoils, 285–286, 286*t*
NACA four-digit airfoils, 284–285
NACA 1-series airfoils, 286, 286*f*
NACA 6-series airfoils, 286–287, 287*f*
NACA 7-series airfoils, 287–288, 288*f*
NACA 8-series airfoils, 288
plotting NACA 4- and 5-digit airfoils, 288–290
properties, 282
representation of, 282
square trailing edges, 283
thickness-to-chord ratio, 282
trailing edge (TE), 282
Horten, 299, 299*f*
ice accretion analysis, 279
Joukowski airfoils, 298, 298*f*
Liebeck airfoils, 298, 298*f*
LS(1)-0417, 295
NACA 23012, 291, 294*f*
Peaky, 296, 297*f*
pressure coefficient, 264–266
properties of
angle-of-attack, at zero lift, 260
C_l at Zero AOA, 263
lift coefficient of minimum drag, 264
lift curve slope, 260
lift-to-drag and airfoil efficiency ratios, 264
linear range, 263
maximum theoretical lift coefficient, 260
minimum drag coefficient, 264
pitching moment coefficient, 264
profile drag, 264
section lift coefficient, 260
stall and maximum and minimum lift coefficients, 260
zero-Lift AOA, for selected NACA airfoils, 263
quarter-chord moment, 270
stall characteristics

leading-edge (LE) stall, 278
trailing-edge (TE) stall, 277
supercritical airfoils, 297
USA-35B, 291, 294*f*
Airships, 705
Airspeed indicator (ASI), 760
markings of analog, 761*f*
markings of modern, 761*f*
pressure sources, 762
Airspeed-power map, 624*f*
Airspeeds
propeller aircraft, 769
subsonic jet aircraft, 769
Airspeed theory, 760–769
Airspeed-thrust map, 623*f*
Air transport economics
business capital, 37
cash flow, 36, 36*f*
cost of available seat-mile (CASM), 37
depreciation, 36
direct operating cost (DOC), 37
equity, 37
indirect operating cost (IOC), 37
life-cycle cost (LCC), 37
return of investment (ROI), 37
revenue per available seat-mile (RASM), 37
Airworthiness, 14
Airworthiness Directive (AD), 14
Altitude dependency models, 207
Altitude performance, 212–213
Altitude sensitivity, 829, 829*f*
Aluminum alloy, 119–121
applications in general aviation (GA) aircraft, 121*t*
designation of, 120
extrusion for, 116
flaws, 119
endurance limit, 120
galvanic corrosion, 121
stress corrosion, 120
identification, 120
precure, 129
properties of, 119, 122*t*
sheet metal thicknesses for, 122*t*
Aluminum constant speed propellers, 44
Aluminum wheels, 551
Amphibian, 104
Analysis technology, 1014
Angle-of-attack (AOA), 259–260
horizontal tail, 944–945
movement of transition points with, 680, 680*f*
pitch angle and, 604
at zero lift, 260
Angle-of-climb (AOC), 812, 812*t*, 817
Angle-of-descent (AOD), 895–896
Angle-of-glide (AOG), 895
Angle-of-incidence (AOI), 263, 339–340, 348–350, 503
horizontal tail, 944–945
symmetrical airfoil at, 141
Angle-of-yaw (AOY), 927, 1004–1005
Angular momentum, 608–609
Annealing, 122
Antennas, 729
Antiicing, 164
Antiservo tabs, 972, 972*f*
Antispin fillets, 489
AOA. *See* Angle-of-attack (AOA)
AOC. *See* Angle-of-climb (AOC)
AOD. *See* Angle-of-descent (AOD)
AOG. *See* Angle-of-glide (AOG)
AOI. *See* Angle-of-incidence (AOI)
AOY. *See* Angle-of-yaw (AOY)
Approach distance, 916, 916*t*, 919–920
Approach for landing, 919
Arbitrary fuselage, 513–515, 513*f*
Arbitrary planform, geometric formulation of, 323–324
Arload actuated slat (Automated Handley-Page Slat), 428, 429*f*
Arrhenius equation, 246
Articulating-vane double-slotted flap, 448
ASI. *See* Airspeed indicator (ASI)
Aspect ratio (AR), 258, 324
for HT and VT, 325
multiwing configurations, 325
of wing, 331–337
winglets, correction for, 387
Aspect ratio sensitivity, 883, 884*f*
Asphalt, 795*t*, 918*t*
ASTM standards, 11–14
Asymmetric wing, 324
Asymmetric yaw effects
multiengine aircraft, 611–614, 612*f*
single-engine aircraft, 611
A-tail, 500
Atmospheric model, 757–758
Atmospheric modeling, 756–760
air deviation density, 759, 760*b*
change due to humidity, 760, 760*b*
formulas for standard atmosphere, 759
standard properties, 758*t*
atmospheric ambient temperature, 759
density altitude, 759
example, 758*b*
pressure altitude, 758–759
temperature constants in troposphere, 758*t*
Auto-ignition temperature, 205–206
Autorotation, 486
Average chord
for HT, 510
for VT, 510
Average cross-country speed, 907
Average mass flow, 579
Average mass flux, 579
Avionics systems, weight, 164
Avogadro's law, 575–576
Axis of rotation, 602

B

Baffles, 217
Balanced field length, 805–806, 805*f*
analysis effort, 805–806
empirical expression, 806
example, 806–807*b*
Torenbeek's method, 806
Balance tab, 972, 972*f*
Balked landing, 916, 916*t*
capability, 1008–1009
Baseline parametric analysis, 69, 70*f*
Basic drag, 659–678
Battery
capacity and energy capacity, 241
cells and modules, 241
cold-cranking amps (CCA), 243
C-rating, 243
cycle life, 243
depth-of-discharge (DOD), 243
energy and power density of, 241
energy efficiency, 243
historical perspective, 241
impedance, 243
memory effect, 244
nominal voltage, 244
self-discharge, 244
serial and parallel battery circuits, 242
state-of-discharge (SOC), 243
thermal runaway, 244
Battery eliminator circuit (BEC), 251
Battery power extracted, 871
Bearing housing, 551
Bed mounts, 216
Beechcraft dual vortex-generator, 1026
Bending moments, 167, 171, 171*f*, 173
Bernoulli's equation, 222, 224, 266, 583
Bernoulli theorem, 271–272
Best angle-of-climb, 815*t*
formulation of, 822–824
for jet, 823
for propeller-powered aircraft, 823
Best angle-of-climb airspeed, 741, 817
for jet aircraft, 851
for propeller-powered aircraft, 851
Best endurance airspeed, 834*t*, 851–852
Best glide
lift coefficient, 737
ratio, 845
Best glide speed, 851, 899
comparison to, 851, 853
Best range airspeed, 853–854
vs. best glide speed, 853
Carson's airspeed, 854
for jet, 853
for propeller aircraft, 853
Best rate-of-climb, 59, 60*t*, 61, 741, 812*t*, 815*t*
formulation of, 817–822
for jet aircraft, 818
for propeller-powered aircraft, 819
Best rate-of-climb airspeed, 741, 817
example, 820*b*, 820*f*
for jet aircraft, 851
for propeller-powered aircraft, 851
of selected aircraft, 830–832, 831–832*t*
BET. *See* Blade element theory (BET)
Beta control prop, 602
Beta range, 602
BHP. *See* Brake horsepower (BHP)
Bifurcated inlet, 235–236
Biot-Savart law, 400
Biplane, 102–103
Blade activity factor, 625
Blade element, local velocity of, 649
Blade element momentum (BEM) theory, 646
Blade element theory (BET), 458, 646

Blade element theory (BET) *(Continued)*
advantages, 646
compressibility corrections, 649
drag correction, 649
lift correction, 649
example, 650–655*b*
formulation, 646–648
differential lift and drag forces, 646
parameters, 646
propeller, 646, 646*f*
hub loss corrections, 649–654
induced AOA, 648
Prandtl's tip, 649–654
propeller induced velocity, 655–656
spreadsheet analysis, 650*f*
Blended winglet, 473, 474*f*
Blind-rivet, 118
Blisters, 728–729
Blockage effects, propeller, 614–615, 616*f*
Body coordinate system (BCS), 486–488, 926*f*, 927
Booster pump, 216
Booster wingtips, 465–466
Boundary layer
fences, 1021, 1021*f*
mixed, 681*f*, 683–684, 687
turbulent, local airspeeds, 521
Boundary layer theory (BLT), 273–277
flow separation, 276–277
fluid flow inside, 274
laminar boundary layer, 275
viscosity, 274
Brake caliper, 555
Brake horsepower (BHP), 204
Brake-release, 786, 794–796, 805
Brakes, 551, 552*f*
Braking, 544
airspeed, 919*t*
devices, 920–921
Braking distance, 916, 916*t*, 920–921
Brandt's method, 385
Brayton cycle, 202
Break-even analysis, 36, 47*f*, 55
Breguet endurance equation, 870
Breguet range equation, 870
Breguet's range, 88
Bubble-drag, 277, 1027, 1028*f*
Bulkhead, 130
pressure, 144
Bungee landing gear, 554, 554*f*
Business capital, 37
Business jet aircraft
operational costs for, 54*t*
variable and fixed cost analysis for, 53*t*
Butterfly-tail. *See* V-tail

C

Cabin dimensions, 527, 528*f*, 537–538*t*
Cabin pressurization, 198
Calibrated airspeed, 761–763, 856
Camber, 282
effect of, 299
Canard, 481, 501–503, 501*f*
Canonical pressure coefficient, 266
Canopy, 104–105, 727–728
acrylic, 105–106
smooth, 705
styles evaluation, 727*f*
Carbon, 117, 122
Carbon reinforced plastics (CRP), 124
Carpet plot, 69, 71*f*
cruise speed, 71–72, 71*t*
stall speed, 71–72, 71*t*
Carson's airspeed, 834*t*, 854
Cash flow, 36, 36*f*
Cast alloy, 120
Castering, 546, 546*f*
Casting, 115
Center-chord line, 324
Center of gravity (CG), 101, 176, 178–180, 183–194, 483–484, 490
travel during flight, 1016
Center-of-gravity (CG) envelope, 183–194, 183–184*f*, 186–188*t*, 191*t*
Center-of-mass (CM), 178–180
Center of pressure (CP), 270
Centroid-of-volume (CV), 179
Certifiability, 7
Certification
basis for classes of aircraft, 11*t*
in Light Sport Aircraft, 13–14
requirements for GA aircraft, 916–917
Certification Standard (CS), 7, 10
Cessna 172F, 465, 465*f*
CFD. *See* Computational fluid dynamics (CFD)
CG. *See* Center of gravity (CG)
CG envelope, 183–194
Chordline, 282
Chordwise pressure distribution, airfoils, 266–269
Chromoly, 122
Circling flight, 911–914, 911*f*
thermal velocity profiles, 913, 913*f*
Circular Advisory. *See* Advisory circular (AC)
Cirrus SR22, 465–466, 465*f*, 779
maximum lift coefficient, 375–376*b*
Civil Aviation Regulations (CAR), 10
Clark Y airfoil, 290, 293*f*, 304*f*
Classical laminate theory (CLT), 126
Climb
angle, 802–803, 807
capability, 1013
equations-of-motion, 813–814
gradient, 815
minimum flight-time, 824, 825*f*
numerical analysis, 828–830
parameters in, 815*t*
problems, 824–825
T/W for desired rate of, 59
Climb airspeed, 741
Climb angle, 60, 817
Climb flaps, 303
Climb gradient, 789–790
Climb performance, 811, 812*f*
extracting $C_{D_{min}}$ using, 741
of selected aircraft, 830–832, 831–832*t*
spreadsheet for estimation, 828*f*
Climb propeller, 621–623
CM. *See* Center-of-mass (CM)
Cockpit layout, 527–529
galley design, 529
in large business jet, 528, 531*f*
lavatory design, 529, 532*f*
passenger cabin, 528, 531*f*
pilot visibility, 527, 529*f*
transparencies, 528
typical seating for, 530*f*
Cockpit windows, 725–727
Code of Federal Regulations (CFR), 10
Coefficient of drag
2D, 732*f*
3D, 733–734, 733*f*
Coefficient of lift. *See* Lift coefficient
Coffin corner, 855, 855*f*
Cold working, 122
Combustor inlet air temperature (CET), 199–200
Commercial aircraft
passenger door in, 144
pitch of seats in, 528–529, 531*f*
Commercial aviation regulations, 93–94, 184
Commuter aircraft, 139
Commuter category, 775
Component drag buildup method (CDBM), 701–704, 712, 714
Composite images, 2
Composite material, 124–130
aircraft construction methodologies, 129
fabrication methods, 129
fibers, 126
gelcoat, 129
glass transition temperature, 129
precure, 129
pros and cons of, 124
resin, 127
thermoplastics, 128
thermosets, 127
sandwich core materials, 128
structural analysis of, 125
types of, 125
Composite propellers
for LSA, 44
for ultralight aircraft, 44
Composites, 6–7, 114, 124–125
Compound delta. *See* Double-delta planform shape
Compound surface flex, 116, 116*f*
Compound-tapered planforms, 357
Compressibility corrections, 309, 387, 649
of drag, 649
for lift, 306
of lift, 649
for pressure coefficient, 306
Compressibility effect, 306–310, 661
drag due to, 727–728
on pitching moment, 957
Compression ignition (CI), 205–206
Compressor exit temperature (CET), 588–589
Computational fluid dynamics (CFD), 29, 30*f*, 272, 433, 491–492
Prandtl-Betz integration, 694
Concave function, 76
Conceptual design, 2, 4, 15
algorithm for GA aircraft, 16–18, 16–17*t*, 17*f*
implementation of, 18

Configuration layout
cabin configurations, 104–106, 105*f*
common targets, 95
configuration decision matrix, 109–111
engine placement, 106–108
fundamentals, 100–111
landing gear configurations, 108–109
propeller configuration, 106
tail configurations, 109
vertical wing location, 100–102
Boeing 737-800 in landing configuration, 99*f*
Consolidated PBY-5 Catalina, 102*f*
field-of-view (FOV), 101
impact on airframe design, 101
impact on flight, 102
nomenclature, 101*f*
operational characteristics, 102
parasol wings, 102
properties of aircraft, 100*t*
wing configuration, 102–103, 103*f*
wing dihedral, 103–104
effect, 103*f*
nomenclature, 104*f*
wing structural configuration, 104
cantilever/braced with struts, 104*f*
shear and moment diagrams, 105*f*
Conical mounts, 216
Conservation laws, 581–583
Conservation of energy, 582–583
Conservation of mass, 582
Conservation of momentum, 582
Constant airspeed/altitude cruise
endurance analysis, 884
range analysis, 873–875, 874*f*
Constant airspeed/attitude cruise
endurance analysis, 885–886
range analysis, 877–879, 877*f*
Constant attitude/altitude cruise
endurance analysis, 885
range analysis, 875–877, 876*f*
Constant chord ("Hershey bar") planform, 354–355
Constant energy height map, 864, 864*f*
Constant pitch propeller, 604, 606*f*
Constant-speed propeller, 44, 601
vs. fixed-pitch, 606–608, 607*f*
initial thrust model, 633–636, 634*f*
operating points for, 634*t*
propeller efficiency table for, 636*f*
section view of inside, 608*f*
Constant velocity turns, 862–863
Constraint analysis, 58–68
$C_{L_{max}}$ for desired stalling speed, 67, 67*f*
effectiveness of, 64–66*b*
general methodology, 59–63
climbing constant velocity turn, T/W for, 60
cruise airspeed, T/W for desired, 60
cruise lift-to-drag ratio, T/W for desired, 61
level constant velocity turn, T/W for, 60
maximum angle of climb, T/W for desired, 60
rate of climb, T/W for desired, 59, 60*t*
service ceiling, T/W for desired, 61
target total landing distance, W/S for, 61
T-O ground run distance, T/W for desired, 59
optimum design points, 59
piston engines, normally aspirated, 64–66
typical design space, 58–59, 58*f*
Constraint diagram, 66*f*
banking, 859, 860*f*
$C_{L_{max}}$ for desired stalling speed, 67
stall speed limits, 67, 67*f*
Constraints
equality, 76
inequality, 76
Consumer Price Index (CPI), 38–39, 41, 55
Continuity laws, 581–582
Control, 925
Control authority assessment
checklist, 960*t*
graphic scheme, 958–959, 959*f*
through evaluation, 959
Control horn, 972, 1019
on ATR72-600 turboprop commuter, 973, 973*f*
exposed, 972
shielded, 973
Controllable-pitch propeller, 601
Control surface flap chords, 969, 969*t*
Control surfaces/control volumes, 580, 580*f*
deflection effect, 125*f*
fabrication and installation of, 141
Control system
loads and gain, 970–971
mixer, 497
Control system harmony, 1013
Control system jamming, 1016
Control system stretching, 1007–1008, 1008*f*
Conventional-tail, 109, 491–493, 491*f*
Converging–diverging nozzle, 228
Convex function, 76
Cooling
drag, 714–716
quenching, 122
Corner speed, 861–862
Cost analysis, 35–36
development
break-even analysis, 36
cost-per-unit, 36
fixed and variable cost, 35
price-per-unit, 36
revenue function, 36
methods, 7
project, 45*t*
variable and fixed, for typical business jet aircraft, 53*t*
Cost estimating relationships (CER), 33
Cost function, 75–76, 90
Cost of available seat-mile (CASM), 37
Cost-of-available-seat-mile (CASM), 881
Cost-per-unit, 36
Cost-volume-profit-analysis, 36
Counter-rotating propellers, 613, 614*f*
Cove-tab, 1026, 1026*f*
positioning of, 1026, 1026*f*
Cowl-flap, 218–219
Cowling, 614–615
CPI. *See* Consumer Price Index (CPI)
Cranked dihedral, 104
Cranked planform, geometric formulation of, 326–328, 359–361
Crazing, 528
Crescent planform, 360
Crew weight, 149
Critical Mach number, 296–297
Critical path method (CPM), 20
Cross-control stall, 1010
Cross-country model, 907, 908*f*
Crosswind, capability at touch-down, 1008
Cruciform-tail, 109, 493–494, 493–494*f*
CRUD. *See* Cumulative result of undesirable drag (CRUD)
Cruise
analysis methods
for accelerated flight, 859–866
for steady flight, 839–858
equations-of-motion, 834–835
organizational map, 833, 834*f*
Cruise airspeed, 60
Cruise flaps, 303, 303*f*
Cruise performance, 740
Cruise propeller, 621–623, 740–742
Cruise speed carpet plot, 71–72
Cruise thrust, 67
Cruising speed, 134
design, 772
CS. *See* Certification Standard (CS)
Cuffs, 1023
Culver twist formula, 347
Culver wing twist formula, 346
Cumulative result of undesirable drag (CRUD), 712
Cusp, 283
Cutaway drawings, 29, 31*f*

D

DAPCA-IV, 7, 33, 45
Data basis, 115
Datum, 322
Davis Wing airfoil, 296, 296*f*
Dead rise angle, 723–724
Decalage angle, 350
Decision matrix, 315
for airfoil selection
airfoil drag, 310
airfoil efficiency ratio, 315
airfoil maximum lift and stall characteristics, 310
airfoil thickness, 314
boundary layer transition and flow separation, 313
Critical Mach Number, 314
designing decision matrix, 315
lift-to-drag ratio, 315
NACA recommended criteria, 316
pitching moment, 313
wing-fuselage juncture, 314
Decks, engine, 573
Deep stall, 495, 496*f*, 1010
Deflection angles, 969, 969*t*
Delta planforms, 361–363

Delta planforms *(Continued)*
double-delta planform shape, 363
lift curve for, 376–378
Density
of air deviations, 759
atmospheric model for, 757–758
change due to humidity, 760
fluid, 575
Density altitude, 759
Departure stall. *See* Power-on stall
Deployed flaps, 724
Deployed spoilers, 725
Depreciation, 36
Descent
with altitude change, 155
equations-of-motion, 894–895, 895*f*
Descent performance
analysis methods
airspeed of minimum sink rate, 898
angle-of-descent, 895–896
equilibrium glide speed, 897–898
glide distance, 899, 900*f*
minimum angle-of-descent, 898–899, 899*b*
rate-of-descent, 896, 896–897*b*
sink rate, 898
descent maneuver, fundamental relations, 894–895
organizational map, 893, 894*f*
Design airspeed for maximum gust intensity, 773
Design algorithm
for GA aircraft, 758*t*, 778
implementation, 779
Design gross weight, 148–149
Design lift coefficient, 365
angle-of-attack for, 366
Design of experiments (DOE), 58, 72–73, 73*f*
Design optimization, 73–89
classification, 73, 73–74*t*
constrained, nonlinear surfaces, 83, 83*f*, 85*f*
constraints, 76
convex and concave functions, 76
convex and nonconvex sets, 76
design variables, 75
feasible and infeasible region, 76
general problems, 75
gradient methods, 74
grid search, 74
Lagrange multipliers, 83, 84*f*
linear programming (LP), 80–81, 80*f*
local *vs.* global optimum, 77, 77*f*
multidisciplinary optimization (MDO), 74
objective function, 75, 76*f*, 78–79, 78*f*, 78–79*b*
optimum, 77
pattern search, 74
random search, 74
unconstrained and constrained problems, 76
unconstrained, nonlinear surfaces, 82, 82–83*f*
wing sizing optimization, 86–89
Design space, 58–59, 58*f*, 74, 76
Design variables, 75
Detail design, 5
Development cost analysis
break-even analysis, 36
cost-per-unit, 36
fixed and variable cost, 35
price-per-unit, 36
revenue function, 36
Development program phase, 5
Diehl's method, 630
Differential ailerons, 1001, 1001*f*
Diffuser expansion ratio, 644
Dihedral
configurations, 104
correction for, 387
wing dihedral, 103–104
effect, 103*f*
nomenclature, 104*f*
Dihedral angle, 103, 988*f*
Dihedral effect, 102, 103*f*, 490, 497–498, 988, 990
Direct analysis method, 282
Directional stability, 72, 485, 502–503, 925, 977, 978*f*
derivation of, 484
improvement to, 499
Directional stability and control
side-force model, 979–983
yawing moment model, 983–988
Direct operational cost (DOC), 37
of business aircraft, 52–54
of GA Aircraft, 50–52
Direct weight estimation methods, 167–175
variation of weight with *AR*, 170–175, 170*f*
for wing, 151*t*, 167–169, 167–168*f*
Disc brake, 551
Dive airspeed, 773
Document standards, 22–23
DOE. *See* Design of experiments (DOE)
Dorsal fin, 485, 485*f*, 489, 1017
on Dornier Do 228, 485*f*
rudder locking, 485, 485*f*
surface extension between the VT and fuselage, 485, 485*f*
Double-delta planform shape, 363
Double-ellipse, 355
Double-slotted flaps, 446–449, 450*f*
Double-slotted fowler flap, 449
Douglas Aircraft, 453–454
Douglas method, 385
Downdraft, 905
Downturned booster wingtip, 466
Downwash lag
lift due to, 938
pitching moment due to, 943
Drag
of aircraft by class, 745
of airfoils and wings, 665
analysis, 735*t*
antennas, 729
basic drag modeling, 659–678
blisters, 728–729
canopies, 727–728
CDBM, 701–704, 712, 714
during climb, 813
cockpit windows, 725–727
compressibility effect on, 695–696
cooling, 714–716
correction for cockpit windows, 725–727
CRUD, 712
deployed flaps, 724
deployed spoilers, 725
estimation pitfalls, 1016
of external sources, 734
floats, 722–724
landing gear, 717–722
of landing gear pant fairings, 716–717
lift-induced drag coefficient, 692
means to reducing, 677–678
nacelle, 612
parachutes, 730
quadratic drag modeling, 660, 662–668
sensitivity, 883, 883*f*
simple wing-like surfaces, 716
skin friction drag coefficient, 682
static longitudinal stability, 940–941, 941*t*
stopped propellers, 729–730
of streamlined struts, 716–717
total drag coefficient, 712
trim, 713–714
of various geometry, 731–735
windmilling, 729–730
windmilling propeller, 606
Drag curve slope, 940
Drag-divergence Mach number, 339
Drag model, 836
definition, 659
higher order polynomials, 670
Drag polar, 836
for Learjet 45, 837*f*
Drum brake, 551
Dual vortex generator, 1026
Ducted fan, 643
idealized flow model, 643*f*
pros and cons, 643–644
static thrust determination, 644
thrust, power, and propulsive efficiency, 644
Dynafocal mounts, 216
Dynamic pressure, 762
Dynamics, 925–926
Dynamic stability, 142, 483

E

Early flow separation, effect of, 301–302, 301*f*
EASA. *See* European Aviation Safety Agency (EASA)
EASA regulations, 10
Eastlake model, 33
of business aircraft, 47–48
development support, total cost of, 48
engineering, total cost of, 48
engineering workhours, 47
fixed cost, 48
flight test operations, total cost of, 48
manufacturing labor workhours, 48
manufacturing, total cost of, 48
materials, total cost of, 48
quality control, total cost of, 48
tooling, total cost of, 48
tooling workhours, 48
variable cost, 48
of GA aircraft, 38–46, 38*f*, 40–41*b*
cost analysis, 41
development support, total cost of, 41
engineering, total cost of, 41
engineering workhours, 39

fixed cost, 43, 43*b*
flight test operations, total cost of, 42
manufacturing labor workhours, 40
manufacturing, total cost of, 42
materials, total cost of, 42
product liability costs, 39
quality control, total cost of, 42
quantity discount factor (QDF), 39
tooling, total cost of, 42
tooling workhours, 40
variable cost, 43, 44–47*b*
Effectiveness, 58
Efficiency, 586
EHP. *See* Equivalent horsepower (EHP)
Electric aircraft
endurance profile, 886
fossil-fueled *vs.*, 869*f*
gross weight for, 151
range and endurance, 871
range profile, 880–881
Electrical system, 164
Electronic speed controller (ESC), 239
Electroprops, 597–598
Elevator, 493, 501
control force, 483
control mixer, 497, 498*f*
control surface floating for, 969
control system, 970, 970*f*
hinge moment, 968
stall limit, 186–187*t*
Elevator authority, 482, 486, 492–493, 495–497, 958
Elevator deflection, 492–493, 495
Elevator effectiveness, 943–944, 944*f*
Elevon, 1001
Elliptical wing planform, 355–356
Empennage, 483
Empty weight, 147–148, 171*f*
fractions, 152–153
ratio, 149
sensitivity, 883, 883*f*
End-of-mission landing, 155
Endplate wingtip, 469–470
Endurance, 869
Breguet equation, 870
vs. change in weight, 870
constant airspeed/altitude cruise, 884
constant airspeed/attitude cruise, 885–886
constant attitude/altitude cruise, 885
Endurance ratio, 851
Energy, 580, 580*t*
conservation of, 582–583
Energy height, 864
Engine decks, 573
Engineering
drawings, 30
lean, 8
workhours, 39, 47
Engineering cost, 41, 48
Engineering reports, 30
EOM. *See* Equation-of-motion (EOM)
Epoxy, 124, 128*t*
Equation-of-motion (EOM), 791–792
for climb maneuver, 813–814
for cruise, 834–835
for descent maneuver, 894–895, 895*f*
for landing ground run, 918
lateral-directional stability and control, 977
for performance theory, 754–756
rigid body, 929
static longitudinal stability, 932
for T-O ground run, 791–792
Equilibrium glide speed, 897–898
Equity, 37
Equivalent airspeed, 763
Equivalent horsepower (EHP), 226
Eulerian approach, 578, 578*f*
European Aviation Safety Agency (EASA), 10
Evolutionary algorithms, 74–75
Excess power, 814, 816*f*
Exotic planform shapes, 363
Expansion ratio, 645
Experience effectiveness, 39, 39*f*
Exposed control horn, 972, 972*f*
Exposed wing, 937–938, 938*f*

F

FAA. *See* Federal Aviation Administration (FAA)
FAA regulations, 50, 128–129*t*
FAR. *See* Federal Aviation Regulations (FAR)
FAR 14 CFR Part 23, 815, 840
business aircraft certification, 47–48
fire extinguishing systems, 518
GA aircraft certification, 7
requirements for T-O speeds, 788
restrictions for aircraft classes certification, 13*t*
Fasteners, 118–119
Fauvel Flying Wing airfoils, 299, 299*f*
FEA. *See* Finite element analysis (FEA)
Feathering propeller, 601
Features and upgradability, 7
Federal Aviation Administration (FAA), 1, 10–13
Federal Aviation Regulations (FAR), 10
Fence, wing, 1021, 1021*f*
Fiberglass, 124
boat glass, 124, 127*t*
R-glass, 127*t*
Fiber-reinforced plastics (FRP), 124
Fibers, 126
aramid, 127*t*
boron, 127*t*
carbon, 127*t*
graphite, 127*t*
Field-of-view (FOV), 101, 527–528, 529*f*
Finite element analysis (FEA), 28, 29*f*
Firewall, 518
canted *vs.* uncanted, 1017*f*
First law of thermodynamics, 580
Fishbone diagram, 20–21
for preliminary airplane design, 20–21
typical, 23*f*
Fixed cost, 35
Fixed earth coordinate system (FES), 926*f*, 927
Fixed landing gear, 16–17*t*
Fixed pitch aluminum propellers, 44
Fixed-pitch climb propeller, 607
Fixed-pitch cruise propeller, 607
Fixed-pitch propeller, 44, 55, 601
vs. constant-speed, 606–608, 607*f*
initial thrust model, 631–633, 632*f*
operating points for, 634*t*
propeller efficiency graph for, 638*f*
Fixed slot, 422–424
Fixed trim tab, 971, 971*f*
Fixed-vane double-slotted flap, 448
Flap chords, control surface, 969, 969*t*
Flaperons, 457, 1001
Flap extension airspeed, 778
Flare distance, 916, 916*t*, 920
Flare maneuver, 915
Flattop airfoils, 1028, 1029*f*
Flettner tab. *See* Servo tab
Flight control system, weight, 164
Flight envelope, 778, 854–856, 855*f*
altitude-*vs.*-Mach, 856, 856*f*
altitude-*vs.*-V_{CAS}, 856, 856*f*
completion, 778
for GA aircraft, 778
gust loads, 773
maneuvering loads, 769
Flight into known icing (FIKI), 233, 235–236, 279
Flight polar, 896–897, 896–897*f*
Floats, 722–724
Float-type sensors, 216
Fluid
dynamics, 574
properties of, 574, 575*t*
statics, 574, 576
Fluid flow, 578
steady *vs.* unsteady, 578, 579*f*
Fluid mechanics, 574
control surfaces/control volumes, 580, 580*f*
isentropic flow relations, 580
mass flow, 579
mass flux, 579
momentum flux, 580
Newton's laws of motion, 578
normal velocity, 579
volumetric flow rate, 579
Flying boat, 132
Flying wing, twist of, 139
Forces, formulation of, 929
Forebody strakes, 1017, 1018*f*
Forging, 115–116
Form factor (FF), 704–711
Forward sweep, 339–340
Forward swept planform, 359
Fossil-fueled aircraft, 869–871
Four-bladed wooden propeller, 620–621
Fourier coefficients, 368
Fowler flaps, 449–452
Fowler motion, 445
Fractional dimensions, 931
Fractions, 174
Free-body
airplane during descent, 895, 895*f*
reaction forces on, 557*f*
for steady level flight, 834, 835*f*
T-O ground run, 790–791
Free expansion, 581*t*
Free-roll distance, 916, 916*t*, 920

Frise ailerons, 999, 1000*f*
Froude efficiency, 626
Froude–Rankine momentum theory, 231, 598
Froude's theorem, 642–643
Froude's thrust coefficient, 625–626
Frustum dimensions, 514*f*
Frustum fuselage, 519
  Piper PA-28 Cherokee, 519*f*
  vs. tadpole fuselage, 520*f*
Fuel, 101
  estimation, 67
  for mission, 882–883
  operational cost, 55
  system weight, 163
Fuel consumption
  comparable turbofan aircraft, 501
  power specific, 871
  thrust specific, 871
Fuel control system, 200
Fuel-flow, 873
Fuel system
  gravity-fed, 101
  weight, 163
Fuel tank
  definition, 86*f*
  external, 489
Fuel tank selector, 1016
Fuel weight
  maximum zero, 149
  ratio, 149–150, 194
Full span flaps, 457
Furnishings, 164
Fuselage
  camber incidence, 948, 948*f*
  correction for, 387
  design, 517, 521–525
  frustum-shaped, 519, 519*f*
  function, 517–518
  internal dimensions, 526–527, 527*f*
  lift and drag, 947, 947*f*
  pitching moment, 947*f*
  pressure tube, 519, 519*f*
  side-force and, 982
  slenderness correction, 949*f*
  tubular, 519, 533–534
  yawing moment
    Munk's method, 985
    North American Aviation method, 985
Fuselage geometry
  large aircraft, 528, 531*f*
  surface areas and volumes, 535
  tadpole fuselage, 519–521, 519*f*
Fuselage sizing, 521
  cockpit layout, 527–529
  external shape
    initial design, 521–525, 522–524*f*
    refining, 525–526, 525–526*f*
  internal dimensions, 526–527, 527*f*
Fuselage strakes, 1026
Fuselage volume, 25
Fuselage weight, 161

G

GA(W)-1, 295, 295*f*
Gagg-Ferrar model, 64, 68, 207–209
Galley, 529
Galvanic corrosion, 121–122, 139
GAMA. *See* General Aviation Manufacturers Association (GAMA)
Gantt diagram, 20
Gas laws, 575, 575*f*
Gas turbine engines
  engine torque and turboprop engines, 228
  equivalent horsepower, 226
  installation of, 233
    turbo machinery and rotor-burst, 234
    turboprop installations, 233
  shaft horsepower, 226
  subsonic inlet design
    diffuser inlet, design guidance for, 236
    diffuser length, 238
    external inlet types, for jet engines, 234
    inlet lip radius, 238
    internal inlet types, for jet engines, 234
    pressure recovery ratio, 237
    stagger/rake angle, 239
  thrust horsepower, 226
  turboprop engines
    cons of, 225
    inertial separators, 228
    power, airspeed and altitude effect on, 227
    pros of, 225
    thrust modeling for, 226
  typical specific fuel consumption, 226
Gas turbines, thrust model, 588
  computer code, 592–595
  specific thrust, 588
  theta break and throttle ratio, 588
  thrust-specific fuel consumption, 589
Geared trim tab, 971, 971*f*
General Aviation aircraft
  CG envelope for light, 183*f*
  design checklist
    balked landing capability, 1008–1009
    center of gravity travel during flight, 1016
    climb capability, 1013
    control system harmony, 1013
    control system jamming, 1016
    control system stretching, 1007–1008, 1008*f*
    crosswind capability at touch-down, 1008
    drag estimation pitfalls, 1016
    fuel tank selector, 1016
    ground impact resistance, 1016, 1017*f*
    horizontal tail stall, 1010–1012, 1011*f*
    natural damping capability, 1014
    one-engine-inoperative trim and climb capability, 1013–1014, 1014*f*
    reliance on analysis technology, 1014
    roll authority, 1012–1013
    stall characteristics, 1009–1010
    take-off rotation capability, 1009
    trim at stall and flare at landing, 1010
    weight estimation pitfalls, 1016
    wing/fuselage juncture flow separation, 1016
General Aviation Manufacturers Association (GAMA), 34, 119
General Aviation Revitalization Act, 35
General process of aircraft design
  design process
    elementary outline, 2, 3*f*
    for general aviation (GA) aircraft, 3, 4*f*
      conceptual design algorithm, 16–18, 16–17*t*, 17*f*
      development timeline, 9–10, 9*f*
      regulations, 10–14
    per Torenbeek, 3, 3*f*
    regulatory concepts
      advisory circular (AC), 14
      airworthiness, 14
      Airworthiness Directives (AD), 14
      maintenance requirements, 14
      parts manufacturer approval (PMA), 14
      service bulletin (SB), 14
      special airworthiness certificate (S-AC), 14
      standard airworthiness certificate (AC), 15
      supplemental type certificate (STC), 15
      technical standard order (TSO), 15
      technical standard order authorization (TSOA), 15
      type certificate (TC), 15
General thrust equation, 573, 583–586, 584*b*
  propellers, 585
  rockets, 585
  thrust-to-weight ratio, 585, 586*t*
  turbofans, 585, 585*f*
  turbojets, 584, 585*f*
Genetic algorithms (GA), 74–75
Geometric dimensioning and tolerancing (GDT), 27–28
Geometric pitch angle, 602
Geometric pitch, propeller, 602
Geometric washout, 344, 345*f*
Glass-transition temperature, 129
Glide
  comparison, 853
  distance, 899, 900*f*
  equilibrium glide speed, 897–898
  lift coefficient, 737
  POH, 737
Glide distance, 845
Glide endurance, 903
Glide range, 903
Governor, propeller, 601, 607
Graphite, 127*t*, 129
Gross weight
  for electric aircraft, 151
  properties, 100*t*
  using historical relations, 150–152
Ground-adjustable propeller, 601
Ground effect, 381
  high-wing aircraft, 102
  lift-induced drag correction in, 695
Ground fine, propeller, 601
Ground friction
  main gear tire, 559
  weight on wheels, 794
Ground impact resistance, 1016, 1017*f*
Ground influence coefficient, 380
Ground-loop, 559
Ground roll friction coefficients, 794, 918, 918*t*
Ground roll, take-off, 794

Ground run distance, 795–802
Ground speed (GS), 764
Growth
  features and upgradability, 7
  intermittent periods, 35*f*
Grumman American AA-1, 466, 466*f*
GS. *See* Ground speed (GS)
Gull-wing dihedral, 104
Gurney flap, 452–454, 452*f*
Gust load, 171
  design cruising speed, 772
  step-by-step, 775
Gyroscopic effects, 608–609

H

Handley Page slat, 429
Handling requirements, 6
Heat treating, 122
Helix
  angle, 604
  propeller, 603*f*
Helmholz's vortex theorems, 401
"Hershey bar", 322–323
High-Altitude Long Endurance (HALE) aircraft, 298–299
High Angleof-Attack Research Vehicle (HARV), 1017–1018
High bypass ratio turbofan, thrust ratio, 592, 593*f*
High-lift system (HLS), 416, 417*t*
High-speed flight, 339
High tip speed effect, 616
High-wing
  airplanes, 100–101
  configuration, 101
  ground effect, 102
  location, 109–110
  wing-struts, 101
Himmelblau's function, 77*f*, 82–83
Hinged leading edge (droop nose), 420–421, 421*f*
Hinge moment (HM), 966–967, 967*f*
  coefficient, 968
  generation of, 967*f*
  high pressure, 142
  mechanical, 971
  predicting and tailoring, 968, 969*f*
  and stick-force, 968
Hirth Engines, 204, 204*f*
HM. *See* Hinge moment (HM)
Hoerner wingtip, 466
Hoop frame, 101–102
  aluminum semi-monocoque fuselage, 142
  landing gear loads, 518
  underlying fuselage structure, 143*f*
Horizontal airspeed, 814, 895
Horizontal tail (HT), 96, 107, 325, 481, 944
  angle-of-attack, 944–945
  angle-of-incidence, 944–945
  design requirements for, 482–483
  downwash, 491–492, 503
  downwash angle, 944–945, 945*f*
  endplate-effect of, 494–495
  initial tail sizing optimization, 510–511
  mean geometric chord, 484
  reference geometry, 484, 484*f*
  side-force and, 982
  sizing, 957–966
  stall, 1010–1012, 1011*f*
  trim drag, 713–714
  weight, 161
  weight budgeting, 191, 193*t*
Horizontal tail volume, 484, 942–943
  initial tail sizing optimization, 510–511
  on location of stick-fixed neutral point, 508, 509*f*
Horten airfoils, 299, 299*f*
House of quality (HQ), 23–27, 24–27*f*
Howe's method, 385
HT. *See* Horizontal tail (HT)
H-tail, 142, 499–500, 500*f*
Hub, 18
  effect, 615–616
  loss corrections, 649–654
Hub loss corrections, 615–616, 649–654
Humidity, 760
Hydraulic system, 164
Hydrodynamics, 574
Hydrostatic equation, 576
  application of, 577–578*b*
Hydrostatic stability, 757–758
Hyperplane, 80

I

Ice accretion analysis, 279
Ideal gas law, 575
Impingement limits, 279
Indicated airspeed, 762–763
Indirect operating cost (IOC), 37
Induced angle-of-attack, 406
Induced drag coefficient, 918
Induced velocity, propeller, 655–656
Inertia matrix, 183
Infinitesimal mass, 579
Infinitesimal mass flow, 579
Infinitesimal mass flux, 579
Infinitesimal vector area, 579
Infinitesimal volume, 579
Inflation pressure, 548
  for typical aircraft, 550*t*
In-flight movement, of CG, 191
Inherent dihedral effect, 992
Initial tail sizing methods
  arbitrary fuselage, 513–515
  horizontal and vertical tail, 511–513
  horizontal tail (HT), 510–511
  HT for stick-fixed neutral point, 508, 509*f*
  vertical tail (VT), 511
  V_{HT} and V_{VT}
    formulation of initial estimation of, 508–510, 509*f*
    initial values for, 505–507, 505–508*t*
Initial thrust model
  constant-speed propeller, 633–636, 634*f*
  fixed-pitch propeller, 631–633, 632*f*
Initial weight analysis, 149–158
Inlet, STC, 15
Installation
  cockpit window, 726–727
  ventral fin, 486
Instrument flight rules (IFR), 887–888, 888*b*, 888*f*
Insurance
  annual insurance cost, 54
  cost, 51
  form of liability, 35
Integrated product teams (IPT), 9
Intermolecular momentum, 274
Inverse airfoil design method, 282
Inverted gull-wing dihedral, 104
Inverted V-tail, 499, 499*f*
Inverted Y-tail, 499, 499*f*
IPT. *See* Integrated product teams (IPT)
Isentropic flow, 580, 581*t*
Isentropic flow relations, 221
Isentropic relations, 767
Ishikawa diagram. *See* Fishbone diagram
Isobaric process, 581*t*
Isopleth, 58–59
Isothermal process, 581*t*
Isotropy, 119
Isovolumetric process, 581*t*

J

JavaFoil, 281
Jet, range and endurance for, 155
Jodel wing, 104, 132
Joining
  by riveting, 117
  by threaded fasteners, 118
  by welding, 117
Joint Aviation Authorities (JAA), 10
Joint Aviation Regulations (JAR), 10
Joukowski airfoils, 298, 298*f*
Junkers flap/external flap, 444–445

K

Karman fairing, 1026, 1027*f*
KCAS. *See* Knots calibrated airspeed (KCAS)
KEAS. *See* Knots equivalent airspeed (KEAS)
Kerr's criterion, 488
KGS. *See* Knots ground speed (KGS)
KIAS. *See* Knots indicated airspeed (KIAS)
Kinematic viscosity, 758*t*
Kinetic energy (KE), 552
  derivation of equation, 552
  energy height, 864
  rate-of-climb, 898
Klegecell, 128–129*t*
Knots calibrated airspeed (KCAS), 736
Knots equivalent airspeed (KEAS), 773
  design maneuvering speed, 773
  properties, 782*t*
Knots ground speed (KGS), 549*t*, 783
Knots indicated airspeed (KIAS), 761
Knots true airspeed (KTAS), 736
Knots, using airspeeds, 736
Krüger flap, 424–427
KTAS. *See* Knots true airspeed (KTAS)
Küchemann wingtip, 466–467, 467–468*f*
Kutta–Joukowski circulation theorem, 271–272

L

Labor cost, 40
Lagrange multipliers, 83, 84*f*

Lagrangian approach, 578, 578*f*
Laminar boundary layer, 275
Laminar turbulent, 274
Landing distance, 916*t*, 917
  sensitivity analysis, 922
Landing gear, 490, 717–722
  arrangements, 542, 542*f*, 542–543*t*
  components, vendors of, 543, 544*t*
  design, 541–542
  design checklist, 543–544
  drag force, 955, 956*f*
  functions, 541
  geometric layout, 559–570
  impact response, 557, 558*f*
  legs, 554–556
  retractable, 547–548, 547*f*
Landing gear forces, 556–558
Landing ground run, 918
Landing over 50 ft, 922
Landing performance
  estimation of, 922
  of selected aircraft, 923, 923–924*t*
Landing phase
  fundamental relations, 917–922
  organizational map, 915, 916*f*
  segments of, 916–917, 917*f*
Landing wire bracing, 723
Laplace's equation, 400
Lapse rate, 760
  atmospheric ambient temperature, 759
  temperature constants, 758*t*
Lateral directional stability, 481
Lateral-directional stability and control, 975, 976*f*
  $C_{L\beta}$ and $C_{N\beta}$ historical values, 979, 980*f*
  equations-of-motion, 977
  requirement for, 977–978, 978*f*
  roll/bank, 976
  yaw, 976
Lateral stability, 978, 979*f*
  overturn angle, 562
  rolling moment, 988, 989*f*
Laurent equation, 63
Lavatory design, 529, 532*f*
Law of effectiveness, 379
Leading edge (LE), 276, 282, 323–324
  roughness and surface smoothness, 305–306
Leading-edge droop, 1023
Leading-edge (LE) high-lift device, 432
  aerodynamic properties, 417–419, 419*t*, 431
  airload actuated slat (Automated Handley-Page Slat), 428, 429*f*
  fixed slot, 422–424
  general design guidelines, 420
  hinged leading edge (droop nose), 420–421
  Krüger flap, 424–427
  leading-edge slat, 427–432
  Maxwell slot, 429, 430*f*
  quick-guide, 417–419, 418*t*
  three-position slat, 428, 430*f*
  two-position slat, 428, 428*f*
  variable camber leading edge, 422, 422*f*
Leading-edge parameter (LEP), 373
Leading-edge suction parameter, 385
Leaf spring landing gear, 554–555, 554*f*
  landing gear legs, 716–717
  for small aircraft, 555*f*
Lean engineering, 8
Lean manufacturing, 8
Learjet 45XR, 779–783
  drag and thrust, 836, 837*f*
  example, 841*b*
  flight envelope for, 854, 855*f*
  properties, 783*t*
  three-view, 782*f*
Level constant-velocity turn, 859–862, 859*f*
LEWICE, 279
Liability cost, 39
Liebeck airfoils, 298, 298*f*
Life-cycle cost (LCC), 37
Lift
  and drag, 25
  engine placement, 106–108
  fuselage, 100
  maximum lift coefficient, 67
  and moment characteristics of wings
    3-dimensional lift curve, properties of, 364–366
    lift curve slope, 367–370
    maximum lift coefficient, 370–376
    model, 366–367
    zero-α lift, 367
  performance efficiency, 58
  positive relation, 25
  SAS, 6
  spanwise location, 171–172, 174–175
Lift coefficient
  AOA, 102–103
  maximum and minimum, 364
  maximum, for desired stalling speed, 67
  section, 102–103
Lift coefficient of minimum drag, 264
Lift curve slope, 260, 364, 937
  arbitrary wings, 368
  elliptical wing, 367
Lift damping derivative, 938
Lift distribution, 343
  drag due to wing washout, 695
Lift enhancement
  deploying high-lift devices on wings, effect of
  lift distribution on wings, with flaps deflected, 456–458
  wing partition method, 458–460
  high-lift system (HLS), 416, 417*t*
  leading-edge (LE) high-lift device, 432
    aerodynamic properties, 417–419, 419*t*, 431
    airload actuated slat (Automated Handley-Page Slat), 428, 429*f*
    fixed slot, 422–424
    general design guidelines, 430
    hinged leading edge (droop nose), 420–421
    Krüger flap, 424–427
    leading-edge slat, 427–432
    Maxwell slot, 429, 430*f*
    quick-guide, 417–419, 418*t*
    three-position slat, 429, 430*f*
    two-position slat, 428, 428*f*
    variable camber leading edge, 422, 422*f*
  passive high-lift devices, 416
  trailing-edge (TE) high-lift devices, 454–456
    double-slotted flaps, 446–449, 450*f*
    flaps, 432–433
    Gurney flap, 452–454, 452*f*
    junkers flap/external flap, 444–445
    plain flap, 433–442, 435–440*t*
    quick-guide, 433, 433–434*t*
    single-slotted flap, 445–446
    split flap, 442–444, 443*f*
  wingtip design
    aerodynamic effectiveness of, 462
    booster wingtips, 465–466
    endplate wingtip, 469–470
    Hoerner wingtip, 466
    Küchemann wingtip, 466–467, 467–468*f*
    lift-induced drag, 461–462
    polyhedral wingtip, 474–476, 475*f*
    potential flow theory, 476–477
    raked wingtip, 467–469, 468–469*f*
    round wingtip, 462–463, 463*f*
    spherical wingtip, 463–464, 463*f*
    square wingtip, 464, 464*f*
    winglet, 470–474, 471*f*
Lift-induced drag, 691–695
  correction factors, 694
    Oswald efficiency, 693
    span efficiency, 692
  corrections
    in ground effect, 695
    wingtip correction, 694
  Prandtl-Betz integration, 694
  using lifting-line method, 693–694
Lift-induced drag coefficient
  AOA and airspeed, 691
  generic formulation, 692
  from momentum theorem, 691
  Prandtl-Betz integration, 694
  using lifting-line method, 693
Lifting-line formulation, 401
Lifting line theory, 88
Lifting surface, 322
Lift model, 836, 937–940
Lift-to-drag ratio, 315, 846*f*
  maximum, 845–848, 847*f*
    graphical determination, 661*f*, 662
  performance efficiency, 58
Lightening holes and slots, 138
Light sport aircraft (LSA), 9–10, 13–14, 59, 597–598
  aircraft classes, 11*t*
  establishing weight ratios for, 162*t*
  KCAS for, 59
Limit load, 114
Linear momentum, 180–181
Linear programming (LP), 80–81, 80*f*
Linear range, 263, 365
Lithium-Cobalt oxide ($LiCoO_2$), 239
Lithium-ion (Li-Ion) battery, 239
Lithium-Manganese oxide ($LiMn_2O_4$), 239
Lithium-polymer batteries (LiPos), 239
Loading cloud, 189–191, 189*f*, 192*t*, 522, 524*f*
Lockheed Aircraft, 452
Long-bubble leading-edge stall, 278

Longeron, 116, 130, 132
Longitudinal stability, 925–926
  generation of, 933*f*
  for selected aircraft, 936*t*, 936*f*
  static
    $C_{M\alpha}$ historical values, 935–936
    drag model, 940–941, 941*t*
    equations-of-motion, 932
    lift model, 937–940
    pitching moment model, 941–944
    requirements for, 932–934
    thrust model, 937
  thrust and, 951–955
  wing–HT–engine system, 960–961, 960*f*
Loop maneuver, 863, 863*f*
Loss function, 75–76
Low bypass ratio turbofan, thrust ratio, 592, 593*f*
Low-wing, 100–101
  aircraft, 102
  configuration, 101–102
Low wing location, 100–102
LS(1)-0417, 295

M

MacCready speed ring, 911
Machining, 117, 139–140
Mach number, 228, 229*f*, 230, 239, 275
  vs. thrust ratio, 590*f*, 593*f*
  tip, 619*b*
Mach number correction factor (MNCF), 374
Main landing gear (MLG)
  CG-envelope, 188–189
  comparison, 193*t*
  main wheel tires, 550
  structural limits, 187–188*t*, 188–189
Main spar, 136
  cross sections, 136, 137*f*
  leading edge rib, 138
  main ribs, 137
Maintainability, 7
Maintenance, 14
  cost, 50, 52
  to flight hour ratio, 50, 52
  laminar boundary layer, 677
  repair stations, 495
  requirements, 14
Maneuvering airspeed, 773
Maneuvering load, 769
Manifold pressure (MAP), 205
Mannequin, 535–537, 535*f*
  dimensions of, 536–537*t*
Manufacturing labor
  cost analysis, 41
  total cost of, 42, 48
  workhours, 40, 48
Mass flow, 579
Mass flux, 579
Mass moment of inertia, 180–182, 180–181*f*
Mass product of inertia, 182–183
Mass-springdamper system, 557–558
Materials
  aircraft fabrication and, 114–130
  basic properties, 114–115
  composite materials, 124–130
  aircraft construction methodologies, 129
  fabrication methods, 129
  fibers, 126
  gelcoat, 129
  glass transition temperature, 129
  precure, 129
  pros and cons of, 124
  resin, 127
  sandwich core materials, 128
  structural analysis of, 125
  types of, 125
  technical standard order (TSO), 15
  total cost of, 42, 48
Mathematical optimization, 58
Mattingly model
  for turbofan engine, 592
  for turbojet, 591
  for turboprop engine, 590–591
Maximum bank angle, 862
  airspeed for, 862
Maximum economic climb, 824
Maximum endurance speed
  vs. best glide speed, 851
  jet aircraft, 852
  propeller-powered airplane, 851
Maximum landing weight, 149
Maximum level airspeed, 840
  computer code
    for jet, 858
    for propeller aircraft, 856–857
Maximum lift coefficient, 339, 364, 459
  angle-of-attack for, 365
  for desired stalling speed, 67
  general model for, 370
  selected aircraft, 376, 377*t*
  stalling speed, wing loading on, 370
  wing sweep correction, 371
Maximum lift-to-drag ratio, 845–848, 847*f*
Maximum operating Mach number, 855
Maximum sustainable load factor, 862
Maximum sustainable turn rate, 862
Maximum theoretical lift coefficient, 260
Maximum zero fuel weight, 149
Max operational altitude, 827
Maxwell slot, 429, 430*f*
McDonnell XF-88B, 598
MDO. *See* Multidisciplinary optimization (MDO)
Mean aerodynamic chord (MAC), 324
Mean chord, 324
Mean effective pressure, 204–205
Mean geometric chord (MGC), 259, 324, 328, 484
  CG-location, 179
  Cirrus SR22 properties, 782*t*
  comparison, 176*t*
  spanwise location, 171
  trapezoidal wing, 171
Means-of-compliance (MOC), 13
Metallurgy, 122
Metal propeller blade, 602, 603*f*
Metric tire, 549–550*t*
MGC. *See* Mean geometric chord (MGC)
Micro-mechanics, 125–126
Micro vortex generators (micro-VGs), 1025–1026, 1025*f*
Mid-wing
  aircraft design, 101–102
  configurations, 101–102
Miele's set of equations of motion, 754
Minimum angle-of-descent, 898–899, 899*b*
Minimum control airspeed, 612–613
Minimum descent airspeed, 834*t*
Minimum drag coefficient, 68, 264, 940
Minimum flight-time climb, 824, 825*f*
Minimum level airspeed, 840
Minimum lift coefficient, 364
Minimum power required airspeed, 850
Minimum pressure coefficient, 308
Minimum sink rate, 898
Minimum sustainable turning radius, 862
Minimum thrust required airspeed, 840, 848–849
Minimum wetted area, 482, 508, 514, 516
Miscellaneous drag. *See* Additive drag
Mission
  definition, 6, 93–94
  fuel, 882–883
  weight ratios, 154
Mission analysis, gross weight estimation using, 153–158
Mission profile analysis, 886–887, 887*f*
  instrument flight rules (IFR), 887–888, 888*b*, 888*f*
  National Business Aviation Association (NBAA), 888–889, 889*f*
  payload-range sensitivity, 889–890, 889*f*, 890*t*
  segments, 887, 887*f*
Mogas (motor gasoline), 201
Molding, 115
Moment of inertia
  comparison, 176*t*
  inertia properties, 179*t*
  parallel-axis theorem, 181
  propeller, 629–630, 629*f*
  system of discrete point loads, 181
  trapezoidal wing, 171
Moments, formulation of, 930
Momentum equation, 582
Momentum flux, 580
Momentum theorem, 271
Momentum theory, 648
Monocoque, 132
Monoplane equation, 102–103, 405–406
Mono-wheel
  advantages and disadvantages, 542–543*t*
  landing gear with outriggers, 564, 564–565*f*
  with outriggers, 108
  structural weight, 109
Monte Carlo approach, 74
Mountain peaks function, 82–83, 83*f*
Movable stabilizer, 972, 972*f*
Movable trim tab, 971, 971*f*
Multidisciplinary optimization (MDO), 74
Multiengine aircraft, asymmetric yaw effects, 611–614, 612*f*
Multiexit thrust device, propulsive efficiency, 587

Multiwing aircraft, 325
Munk–Multhopp method, 948, 949*f*
  for SR22, 951*f*

N
NACA, 316
NACA 23012, 291, 294*f*
NACA five-digit airfoils, 285–286, 286*t*
NACA four-digit airfoils, 284–285
NACA inlet, 234–235, 235*f*
NACA method, 631
NACA 1-series airfoils, 286, 286*f*
NACA 6-series airfoils, 286–287, 287*f*
NACA 7-series airfoils, 287–288, 288*f*
NACA 8-series airfoils, 288
Nacelle, 100
  configurations, 599–600, 599*f*, 600*t*
  drag, 612
  forces and moments due to, 945–950
  side-force and, 982
  strake on Airbus A319 commercial jetliner, 1027*f*
Nacelle/cowling weight, 163
Nacelle strakes, 1026
National Business Aviation Association (NBAA) mission, 888–889, 889*f*
National Oceanic and Atmospheric Administration (NOAA), 757
Natural damping capability, 1014
Natural laminar flow (NLF), 658
  airfoil, 268, 677, 680–681, 686, 750
  LFC, 677
Navier-Stokes equations (NSE), 273–274, 399
Navigation theory, 764–767
Neihouse–Lichtenstein–Pepoon's (NLP) criterion, 488
Never-exceed airspeed, 768–769*t*
Newton's laws of motion, 578
Nine-point parametric analysis, 69–70, 70*b*, 70*f*
95th percentile human, 527, 528*f*
NLF. *See* Natural laminar flow (NLF)
NLF airfoil
  composite sandwich construction, 134
  pressure-recovery region, 521
  for stabilizing surfaces, 141
NOAA. *See* National Oceanic and Atmospheric Administration (NOAA)
Noise
  advisory circular (AC), 14
  climb angle, 817
  propeller, 617–619
Nominal pitch-diameter ratio, 631
Nonconventional aircraft, 11*t*
Normal category
  aluminum alloys, 122*t*
  applicable properties, 772*t*
  40ft wingspan, 140
Normal force, 951–955
  propeller, 609, 953*f*
Normal velocity, 579
Nose landing gear (NLG)
  CG-envelope, 188–189
  CG location, 178
  comparison, 193*t*
  drag of, 722
  geometric definitions, 544–545, 545*f*
  nosewheel tires, 551
  weight, 162
Numerical integration method, 798, 799*t*
  equation of take-off motion
    closed-form integration, 792–793
    nomenclature, 793*f*
    using spreadsheet, 800
  ground run analysis, 799*t*
  propeller thrust at low airspeeds, 800

O
Objective function, 75, 76*f*, 78–79, 78*f*, 78–79*b*
Occupant weights, 537, 537*t*
Offset thrustline, 951–955
Oleo-pneumatic landing gear, 555, 556*f*
Oleo-pneumatic trailing link landing gear, 556
Oleo-strut landing gear, 555*f*
One engine inoperative (OEI), 499–500
Operational cost
  aircraft estimation
    cost-of-ownership, 50
    marketing airplanes, 50
  business aircraft, 52–54, 54*t*
    annual fuel cost, 52
    annual inspection cost, 54
    annual insurance cost, 54
    annual loan payment, 54
    crew cost, 54
    engine overhaul, 54
    maintenance cost, 52
    storage cost, 52
  GA aircraft, 40–41*b*, 50–52
    annual inspection cost, 51
    assumptions, 50
    engine overhaul, 51
    fuel cost, 50
    insurance cost, 51
    loan payments, cost of, 51
    maintenance cost, 50
    storage cost, 50
    total annual operational cost, 51
Operational efficiency, 58
Optimal climb airspeed, 825, 825*f*
Optimal climb problems, 824–825
Optimum fineness ratio, 706
Optimum glide
  in headwind/tailwind, 764–767, 905, 906–907*f*
  in rising air, 773–774, 905, 905*f*
  in sinking air, 773–774, 904, 905*f*
  in still air, 904
Optimum lift distribution, 352–354
Oswald's span efficiency, 335–336, 383–388
  correction methods, 387
  Learjet 45, 386*b*
  minimum drag coefficient, estimation of, 68–69
Otto cycle, 201–202
Outrigger
  design guidelines, 565*f*
  monowheel landing gear with, 564, 564–565*f*
  monowheel with, 108
Outside mold-line (OML), 3, 75, 394–395, 398, 424
Overall efficiency, 588
Overall pressure ratio (OPR), 588–589
Overhaul
  engine, 51, 54
  engine overhaul fund, 51–52, 54
  time-between-overhaul (TBO), 51, 55

P
Panknin twist formula, 346–347
Panknin wing twist formula, 346
Parachutes, 730
Parametric analysis, 58, 69–70, 69*f*
Parasol wing, 102
  configurations, 101–102
  consolidated PBY-5 Catalina, 102*f*
  dihedral effect, 102
  location, 101–102
  lower lift-induced drag, 102
  wing configurations, 103*f*
Parthian batteries, 241
Parts manufacturer approval (PMA), 14
Passenger-specific-productivity, 881
Passive high-lift devices, 416
Payload, 149
  fuselage, 521
Payload-productivity (PLP), 881
Payload-range sensitivity, 889–890, 889*f*, 890*t*
Payload-specific-productivity (PLSP), 881
Peaky airfoils, 296, 297*f*
Perceived noise level (PNL), 619
Performance efficiency, 58
Performance padding policy, 756
Personal jet, 592
P-factor, 608, 611
Phases, aircraft design process
  conceptual design, 4
  detail design, 5
  development program, 5
  postdevelopment programs, 5
  preliminary design, 4
  proof-of-concept aircraft and testing, 5
  requirements, 4
Pilot visibility, 527, 529*f*
Piston Aircraft, 742
Piston engines, 44
  aero-diesel engines, 205
  air-to-fuel ratio (AF), 205
  brake horsepower, 204
  common configurations, 202, 202*f*
  compression ratio, 205
  cons of, 202
  displacement volume, 205
  extracting piston power from engine performance charts, 210–211
    Petty equation, 211
  friction horsepower, 204
  gearboxes, use of, 209–210
  indicated horsepower, 204
  inertia loads, 114
  inlet and exit sizing, 218*f*
    basics of operation, 217, 218*f*
    cooling drag, 216–217
    design guidelines, 218
    inlet-exit dependent heat transfer, 220
    inlet-radiator-exit method, 220

updraft and downdraft cooling, 218
installation
cowling, 212
danger zones around propeller aircraft, 214
engine mounts, types of, 216
fire proofing, 213
firewall, 212–213
fuel system, 216, 217*f*
Hobbs indicator, 216
requirements, 214
systems integration, 215
internal combustion engines, basic theory of
airspeed on engine power, effect of, 207
altitude on engine power, effect of, 207
manifold pressure (MAP) and RPM on engine power, effect of, 209
supercharging, 207–208
temperature on engine power, effect of, 208
turbocharger, 208
turbo-normalization, 208
manufacturers, 203, 203*t*
normally aspirated, 64–66
P normalization, power at altitude, 64
T conversion, power at altitude, 64
thrust, T/W conversion, 64
operating square, 205
over square, 205
pressure ratio, 205
propellers, thrust modeling for, 202
pros of, 202
two-stroke *vs.* four-stroke engines, 204
typical specific fuel consumption for, 205
weight of, 165, 166*f*
Piston propeller, supplemental type certificate, 15
Pistonprops, 597–598
Pitch angle, geometric, 602
Pitch control, 957–958, 958*f*
Pitch damping coefficient, 943
Pitch-diameter ratio, 604
Pitching authority derivative, 943
Pitching moment, 486, 492, 501, 941–944
aft-swept and straight wing configuration, 503, 504*f*
airfoil's pitching moments, 136
center of gravity
due to fuselage, 947
due to landing gear, 956
compressibility effect on, 957
Mach number, effect of, 957*f*
nonlinearity, 503
stall effect types on, 138*f*
swept back wing, 503, 504*f*
Pitching moment coefficient, 264, 376, 459, 941
residual, 942, 961
wing-HT-engine system, 963*f*
Pitching moment curve, 941*f*
Pitch table, propeller, 622*t*
Plain flap, 433–442, 435–440*t*
polynomial representations, 725*t*
Plain-flap ailerons, 999, 1000*f*
Planar motion equations, airplane, 813
Plane-of-symmetry, 323–324
PMA. *See* Parts manufacturer approval (PMA)
Pod-style fuselage, 535, 535*f*
Polycarbonate, 528
Polhamus equation, 368
Polhamus' theory, 376
Polyhedral wingtip, 474–476, 475*f*
Positive aileron deflection, 930–931
Postdevelopment programs, 5
Potential flow model (PLM), 998*b*
Potential flow theory (PFT), 260, 476–477
Power
in BHP, 68
correlation, 166*f*
ducted fan, 644
free propeller, 638
for F-104 Starfighter, 490
noticeable power effects, 102
number of blades effect on, 627–629, 628*f*
optimum design points, 59
plant expert, 9
propeller aircraft, 68
specific excess power, 864
three halves power law, 520
thrust-power, 626
Power available, 814, 837
Power coefficient, 625
Powered descent, equations-of-motion for, 894
Power factor (PF), 240–241
Power-off stall, 1009
Power-on stall, 1009
Powerplant
electric motors and battery technology
alternating current, 239–240
battery discharge curves, 244
brushed *vs.* brushless motors, 249
cons of, 248
current and voltage of solar cell, 247
direct current, 239–240
discharge effects-Peukert's law, 244
electric aircraft, 248
electronic speed controller (ESC), 250
formulae, 249
fuel cells, 247
inrunner *vs.* outrunner motors, 249
modeling energy consumption of, 251
pros of, 248
small electric motors, 250
solar energy basics, 246
temperature effects—The Arrhenius Equation, 246
Tremblay's method for creating a discharge curve, 244
energy, work and power, basics of, 199, 199*t*
factors, 197–199
fuel basics
density of aviation gasoline (Avgas), 200
energy content of fuel, piston engines, 201
fuel octane rating, 201
jet fuel, fuel grades for, 201
piston engines, fuel grades for, 201
specific fuel consumption (SFC), 201
fundamental definitions
de-rating, 200
dry, take-off, 200
flat rating, 200
maximum continuous power/thrust, 200
maximum cruise power/thrust, 200
wet, take-off, 199
gas turbine engines (*see* Gas turbine engines)
piston engines (*see* Piston engines)
thermodynamics of
gas turbines, 202
piston engines, 201
turbofans (*see* Turbofan engines)
turbojets (*see* Turbojets)
Power required, 814, 837
Power specific fuel consumption, 871
Power-torque relation, 625
Prandtl's lifting-line theory, 367–368, 379–381
arbitrary wings, 405–409
Biot-Savart law, 400
computer code, 410
elliptical wing, 403–404
Navier-Stokes equations (NSE), 399
vortex filament, 400
Prandtl's tip, 615–616, 649–654
Pratt & Whitney JT3D (turbofan), 199–200
Preliminary design, 4
selection of tire sizes, 550
weight tolerancing, 191–193
Prepressurization, 207
Pressure
aerodynamic loads, 114
atmospheric model for, 757–758
dynamic
example, 816–817*b*
pitot tube or pitot, 762
stalling speed expression, 67
fluid, 574–575
inflation, 548
lag error, 763
molding, 115
slipstream effects, 609
static port, 96
static source, 762
tires and tire inflation, 543
tube fuselage, 519, 519*f*
vessels, 129, 144
Pressure altitude
hydrostatic equilibrium equations, 757–758
pressure or density ratios, 758–759
Pressure coefficient, 264–266
compressibility corrections, 306
Pressure distribution, 680–681
conventional airfoils, 266
NLF airfoils, 268
Pressure drag
CDBM, 701–702
drag modeling, 731
form factor, 704
generated by object, 731
Reynolds number, 1028
Pressure recovery
efficiency, 586
at front face of compressor, 108
Pressure-tube, fuselage, 519, 519*f*
Pressurization, 164
for an aircraft, 9
cabin, 144, 145*f*
characteristics, 4

Pressurization *(Continued)*
correction factors, 38
special considerations, 144
Pressurized fuselage, 113
Price-per-unit, 36
Primary (disposable) cells, 241
Principal moments of inertia, 183
Product of inertia
inertia properties, 179*t*
parallel-axis theorem, 182
system of discrete point loads, 182
PROFILE ("The Eppler Code"), 281
Profile drag, 264
Program Evaluation and Review Task (PERT) chart, 20, 22*f*
Project cost
analysis, 45*t*
comparison, 46*t*
Project management, 18–27
document standards, 22–23
Fishbone diagram, 20–21, 23*f*
Gantt diagrams, 20
house of quality (HQ), 23–27, 24–27*f*
practical drawing numbering system, 23, 24*f*
Program Evaluation and Review Task (PERT) chart, 20, 22*f*
project plan, 18–19
quality function deployment (QFD), 23–27
task management, 20
task matrix, 20, 21*f*
team leadership, 19
Proof-of-concept aircraft, 5
Propeller, 15, 597–598
asymmetric yaw effects
multiengine aircraft, 611–614, 612*f*
single-engine aircraft, 611
blade element theory, 646
compressibility corrections, 649
computer code, 655–656
determination, 648
formulation, 646–648
Prandtl's tip and hub loss corrections, 649–654
configurations, 599–601, 599*f*
constant pitch, 604, 606*f*
constant-speed, 44, 601
controllable-pitch, 601
cost of, 44
effects, 608
angular momentum and gyroscopic effects, 608–609
blockage, 614–615, 616*f*
of high tip speed, 616
hub and tip, 615–616
noise, 617–619
skewed wake, 616–617, 617*f*
slipstream, 609
extension, 602
feathering, 601
fixed-pitch, 601
fixed *vs.* constant-speed propellers, 606–608, 607*f*
geometric pitch, 602
geometry, 602–606, 604*f*
ground-adjustable, 601
ground clearance, 543
material for, 602
moment of inertia, 629–630, 629*f*
normal force, 609
normal force derivative, 953
normal force factor, 953–954
operating points for, 634*t*
properties and selection, 620
activity factor, 624–625
advance ratio, 624
number of blades, 627–629, 628*f*
pitch estimation, 621–622
power-and thrust-related coefficients, 625–626
prop diameter estimation, 620–621
propeller efficiency estimation, 623–624
tips for selecting suitable propeller, 620
pros and cons of, 600*t*
range and endurance for, 155
Rankine-Froude momentum theory, 638
formulation, 638–642
idealized flow model for, 639*f*
reversing, 601
rotating/rotation, 107, 605
side force, 611, 611*f*
single-engine piston-engine propeller airplane, 89
speed, 606
thrust equations, 585
thrust for, 565, 573–574
tractor configuration, 106–107
Tupolev Tu-114 passenger aircraft, 599*f*
two-position, 601
variable pitch, 604–605, 606*f*
windmilling, 606, 607*f*
Propeller asymmetric thrust effect, 485
Propeller blade, 597–598
forces, angles and velocity for, 647*f*
metal, geometry of, 602, 603*f*
section lift coefficients for, 616*f*
spanwise flow, 646
Propeller diameter, 620
Propeller efficiency, 64*t*, 626
airspeed-power map, 624*f*
airspeed-thrust map, 623*f*
estimation, 623–624
function, 90
graph for fixed-pitch propeller, 638*f*
map, 627, 627*f*
number of blades effect on, 627–629, 628*f*
sensitivity plot, 829, 830*f*
table, 636–637, 636*f*
Propeller helix, 603*f*
Propeller-induced velocity, 642–643
Propeller Speed Reduction Unit (PSRU), 226
Propeller thrust
determination, 630
analytical methods, 637–638
converting engine power to thrust, 630
initial thrust model, 631–636
from manufacturer's data, 637
static thrust, 630–631
step-by-step, 636–637
tractor propeller configuration, 106–107
Propeller tip effect, 543
Propeller vortex theory, 598
Propulsive efficiency, 586–588
ducted fan, 644
free propeller, 638
for multiexit thrust device, 587
overall efficiency, 588
pressure recovery efficiency, 586
for single-exit thrust device, 586
thermal efficiency, 588
Propwash, 945, 946*f*
advantage, 491–492
blocked and unblocked, 615*f*
HT, 492, 494–495, 500
tractor configuration, 106
VT, 499–500
Proton exchange membrane (PEM), 247–248
Pulse-width modulation (PWM) technology, 239
Pusher propeller, 106
configuration, 599–600, 599*f*
pros and cons, 600*t*
Pushover maneuver, 1010, 1011*f*
Pylons, wing, 1021, 1022*f*

Q

Quadratic drag modeling, 662–668
Quadratic spline, 513, 514*f*
Quality control
flight test operations, 42
total cost of, 42–43, 48
Quality function deployment (QFD), 23–27
comparison matrix, 26
customer requirements, 24–25
GA airplane, 23–24
HQ preparation, 23
interrelationship matrix, 25–26
roof, 25, 25*f*
survey responses, 23
targets, 26, 26*f*
technical requirements, 25, 25*f*
Quantity discount factor (QDF), 38–39
depends on experience effectiveness, 39, 39*f*
vendor supplied components (VSC), 39
Quarter-chord line, 324
Quarter-chord moment, 270
Quenching, 122

R

Radial tire, 549–550*t*
Radio controlled (RC) aircraft, 239
Radio controlled (RC) flying wings, 346–347
Raked wingtip, 467–469, 468–469*f*
Rakelet, 469
Ramp weight, 149
Range, 869
airspeed of maximum, 853–854
Breguet equation, 870
vs. change in weight, 869, 870*f*
constant airspeed/altitude cruise, 873–875, 874*f*
constant airspeed/attitude cruise, 877–879, 877*f*
constant attitude/altitude cruise, 875–877, 876*f*
inflation pressures for aircraft, 550*t*

mission analysis, 873, 873*t*
profile comparison, 878–879*b*
sensitivity, 883–884
aspect ratio sensitivity, 883, 884*f*
drag sensitivity, 883, 883*f*
empty weight sensitivity, 883, 883*f*
specific range, 881
subsonic minimum drag coefficients, 745
Range-cost (RC), 881
Rankine–Froude momentum theory, 226, 638
flow properties inside control volume, 642*f*
formulation
free propeller, 638–642
shrouded propellers and ducted fans, 643–645
idealized flow model for, 639*f*
Rapid drag estimation method (RDEM), 701
Rate-of-climb (ROC), 812*t*, 814–815
airplane, 61
airspeeds, 768–769*t*
climb gradient, 815
expression for, 815–816
performance handbooks, 741
representative, 826
of selected aircraft, 830–832, 831–832*t*
Rate-of-descent (ROD), 895–896
aircraft reduces altitude, 896
in airplanes, 555
derivation of equation, 896–897*b*
Reaction loads
taildragger landing gear, 568–570, 568*f*
tailwheel, 571*f*
tricycle landing gear, 559–562
Reactive thrust, 581
conservation laws, 581–583
general thrust equation, 583–586, 584*b*
Reference altitude
atmospheric conditions, 757–758
temperature constants, 758*t*
Reference area
definition of, 322
drag of tires, 718*t*
reference geometry, 484
T-O configuration, 794
Reference locations, 177, 177*f*
Reference speed, 768–769*t*
Reference temperature, 758*t*
Regulations, 10–15, 11*f*
aircraft classes certification, 11*t*
center of gravity envelope, 184
GA aircraft, 10–14
Klegecell, 128–129*t*
spin, 490
standards, 10
vertical gusts, 775*f*
V-n diagram, 769
Regulatory concepts
advisory circular (AC), 14
airworthiness, 14
Airworthiness Directives (AD), 14
maintenance requirements, 14
parts manufacturer approval (PMA), 14
service bulletin (SB), 14
special airworthiness certificate (S-AC), 14
standard airworthiness certificate (AC), 15
supplemental type certificate (STC), 15
technical standard order (TSO), 15
technical standard order authorization (TSOA), 15
type certificate (TC), 15
Representative ROC, 826
Request for Proposal (RFP), 2
Requirement phase, 4
Reserve fuel weight, 149
Residual pitching moment coefficient, 942, 961
Resin
fibers, 126–127
fibrous composites, 125
pre-preg, 129
properties, 131*t*
purpose, 127
RTM, 129–130*t*
thermoplastics, 128*t*
thermosets, 127
Responsiveness, control systems, 1007–1008
Retractable landing gear, 547–548, 547*f*, 67
advent of, 547
benefit of, 548
drag of, 720*f*, 721
fads in aircraft design, 96*t*
fixed *vs.*, 67
internal volume, 548
kinematics, 548
Mooney M20R Ovation, 134
retraction and extension, 548
stick diagrams, 548, 549*f*
take-off requirement, 1012
Retractable nacelles, 108
Return of investment (ROI), 37
Revenue function, 36
Revenue per available seat-mile (RASM), 37, 881
Reverse setting, propeller, 602
Reversing propeller, 601
Reynolds number, 88, 277, 420, 433, 446, 455–456
change in skin friction coefficient with, 681*f*
critical, 731
determination, 687
effect of, 299–300, 300*f*
form factors at subcritical, 705
form factors at supercritical, 706
Rib flange, 137
Ribs
leading edge rib, 138
parallel, 138
plywood, 132–133
structural member, 137
stub ribs, 138
swept back wings, 138
weight of, 151*t*
Rigid body equations-of-motion, 929
Rivet
blind-riveting, 118
bucking-bar, 117
head types, 118
standard procedure, 117
Robertson Aircraft, 452
ROC. *See* Rate-of-climb (ROC)
Rockets, thrust equations, 585
Roll authority, 1012–1013
Roll/bank, 976
Roll control, 999–1001
aileron
design requirements, 1001, 1001*f*
differential, 1001, 1001*f*
frise, 999, 1000*f*
plain-flap, 999, 1000*f*
slot-lip, 1000, 1000*f*
spoiler-flap, 1000, 1000*f*
elevon, 1001
flaperon, 1001
Roll damping, 993
Dutch, 486, 497–499
Rolling, 925
cold, 119
Rolling moment, 103, 486–488, 495, 988
aileron authority, 997, 997*f*
dihedral effect, 990
due to wing sweep, 988, 989*f*
due to wingtip style, 992, 992*f*
due-to-yaw, 996
with rudder deflection, 999
Roll-off at stall, 1009–1010
Roll-reversal, 339
Rolls-Royce Dart, 199–200
Roofed-cabin, 104–105
Roskam's graphic scheme, 958–959, 959*f*
Rotation, 802
double-subscripts, 181
mass moment of inertia, 181
propeller, 605
take-off, 483
inverted V-tail configuration, 499
Rotation airspeed, 567, 568*f*
Rotor, 643
Round wingtip, 462–463, 463*f*
Rubber doughnut landing gear, 554, 554*f*
Rudder, 485
boost system, 613–614
control mixer, 497, 498*f*
functionality, 142
gravity of, 485
rudder lock, 482, 485–486, 485*f*, 496–497
rudder-lock, 1017
standard practice, 613*f*
vertical ventral fin, 499
Rudder authority
side-force, 983
V-tail, 966
Y-tail, 499
Rudder effectiveness factor, 988
Rudder hinge moment, 968
Rudder pedal
control system interaction, 497–498
sideslip airplane on, 497
steering, 546
Rutan VariEze, 129
canard configuration, 501–502

S

Sailplane
airfoils, 902
certification, 11*t*
classes, 336, 901, 901*t*

Sailplane *(Continued)*
dihedral configurations, 104
drag, minimizing, 902, 902*f*
glide performance, 902–904, 903*f*
monowheel with outriggers, 108
operation, 901
properties, 100*t*
regulations using quadratic spline method, 737–739
speed polar, 904–907, 904*f*
speed-to-fly, 907–911, 908*f*
touch-down, 900, 901*f*
Sailplane class aircraft, 336
Sailplane operation
GA aircraft, 534
V-tails, 496, 505*t*
Sandwich construction, 134
Sandwich laminates, stiffness of, 125
SB. *See* Service bulletin (SB)
Schrenk flap, 443
Schuemann planform, 360
Scimitar-shaped propeller, 617–618, 618*f*
Sea-level performance, 212
Seaplane
hull, 544
noticeable power effects, 102
Seckel's thrust coefficient, 625
Secondary (rechargeable) cells, 241
Secondary stall, 1009
Section lift coefficient, 260
distribution, 693*f*
hub and tip effects, 615–616
for propeller blade, 616*f*
Semitapered planform, 360
Sensitivity, 807–808
climb maneuver, 828–830
altitude sensitivity, 829, 829*f*
calibrated airspeeds, 828
propeller efficiency, 829
spreadsheet, 828*f*
landing distance sensitivity studies, 922, 922*f*
payload-range, 889–890, 889*f*, 890*t*
range, 883–884
aspect ratio sensitivity, 883, 884*f*
drag sensitivity, 883, 883*f*
empty weight sensitivity, 883, 883*f*
take-off sensitivity studies, 807–808
weight, 829, 830*f*
Service bulletin (SB), 14
Service ceiling, 827
T/W for, 61
Servo tab, 972, 972*f*
Sesquiplane, 8, 103
SFC. *See* Specific fuel consumption (SFC)
Shaft horsepower (SHP), 226
Shear web, 101
aft, 136
main spar, 136
stub rib, 138
Sheet metal forming, 115
Shielded control horn, 972*f*, 973, 1019
Shimmy, 546, 556
Shimmy damper, 546, 547*t*
Shock absorption, landing gear, 554, 555*f*
Shock-stall, 296–297
Short-bubble leading-edge stall, 278
Short Take-Off and Landing (STOL), 357, 422, 466
SHP. *See* Shaft horsepower (SHP)
Shrouded propeller, 643
Side-force
with aileron deflection, 983
due to roll rate, 982
due to yaw rate, 982
fuselage and nacelle contributions, 982
horizontal tail contributions, 982
inflation pressure, 548
jet engine pylons, 1021–1022
propeller, 611, 611*f*, 982
rudder authority, 983
vertical tail contributions, 982
V-tail, 966
wing contribution, 982
Side-force-factor (SFF), 952–953, 954–955*b*
Simple surface flex, 116
Simple-tapered planform, 328–329, 328*f*
Simplified drag model, 60, 337, 662
Single duct, 235
Single-engine aircraft, asymmetric yaw effects, 611
Single-exit thrust device, propulsive efficiency, 586
Single-slotted flap, 445–446
special lift-enhancing tab, 1026
Single-slotted fowler flap, 449, 450*f*
Sink rate, 898
Skewed wake, 616–617, 617*f*
Skidding, 976–977, 976*f*
Skin
analysis methods, 690*t*
friction, 649
fuselage, 132–133, 142
multi-panel wing, 691*t*
plywood, 132–133
stringers, 139
weight, 138
Skin friction drag, 680–690
force for complete wing, 689
using surface wetted area, 687
Skin friction drag coefficient, 682
calculation, 687
Slat-effect, 423
Slipping, 976–977, 976*f*
Slipstream effects, 609
Slot-lip aileron, 1000, 1000*f*
Slot/slats, effect of, 303, 304*f*
Slotted flap, 725*t*
Smeaton lift equation (Obsolete), 259
Solid modeling, 28, 28*f*
components, 167
Solids, properties of, 531–533, 532*f*
Span efficiency, determination of, 383–388
Spanwise lift distribution, 351–352
Spar
cross sections for GA aircraft, 137*f*
low-wing aircraft, 518
low wing structure, 101–102
main, 136
Spar cap
extrusion, 116
main spar cross sections, 136
weight, 174, 176*t*
Spark ignition (SI), 205–206
Spar-rib-stringers-skin, 322
Special airworthiness certificate (S-AC), 14
Specific energy, 863
Specific excess power, 864
contour plot, 865, 865*f*
Specific fuel consumption (SFC), 149, 871–873
power, 872
thrust, 871
Specific range (SR), 881
instantaneous, 881
Specific thrust, 588
Speed of sound, 763
airplanes, 700
drag coefficient, 661
Speed polar, 904–907, 904*f*
with variable wing loading, 904, 904*f*
Speed, propeller, 606
Speed stability, 838, 838*f*
Speed-to-fly, 904, 904*f*, 907–911, 908*f*
Spherical wingtip, 463–464, 463*f*
Spin
regulations, 490
resistance, 490
and spin recovery, 486–491
airplane relative-density coefficient, 488
antispin fillets, 489
autorotation, 486
center-of-gravity, 490
design guidance, 490
design tools, 488
external fuel tanks, 489
factors affecting spin, 488
Kerr's criterion, 488
mass distribution, 488
Neihouse–Lichtenstein–Pepoon's (NLP) criterion, 488
power, 490
recovery control inputs for spinning aircraft, 488*t*
spinning motion
degree-of-freedom (DOF), 486–488
equations-of-motion for, 486
spin regulations, 490
spin resistance, 490
tail configuration, 488
tail-damping power factor (TDPF), 488
tail length, 490
ventral and dorsal fins, 489
wing flaps and landing gear, 490
wing position, 490
wingtips, 489
Spin entry, inadvertent, 490–491
Spinner, 602
Spinning motion
degree-of-freedom (DOF), 486–488
equations-of-motion for, 486
Spin recovery, 486–491
T-tail aircraft poststall at, 494–495, 495*f*
wing droops, 1024
Spin resistance, 490
Split flap, 442–444, 443*f*
polynomial representations, 725*t*

Split winglet, 473, 474*f*
Spoiler, effect of, 303–305
Spoiler-flap ailerons, 1000, 1000*f*
Spring trim tab, 971, 971*f*
Square trailing edges, 283
Square wingtip, 464, 464*f*
SR. *See* Specific range (SR)
SR22
  banking constraint diagram, 860, 860*f*
  Cirrus, 598, 779
  composite sandwich construction, 134
  flat plate skin friction, 689
  landing performance, 923–924*t*
  Munk-Multhopp method, 951*f*
  sensitivity studies, 807–808
  variation, 736*f*
Stability and control, 925–926
  control horn, 1019
  coordinate systems, 926–927
  coordinate transformation matrices, 927–928
  dorsal fin and rudder locking, 1017
  forebody strakes, 1017, 1018*f*
  geometry for, 931
  landing gear, 955–957
  lateral-directional, 975, 976*f*
    $C_{L\beta}$ *and* $C_{N\beta}$ historical values, 979, 980*f*
    equations-of-motion, 977
    requirement for, 977–978, 978*f*
    roll/bank, 976
    yaw, 976
  nomenclature for, 927–928, 928*t*
  static
    $C_{M\alpha}$ historical values, 935–936
    drag model, 940–941, 941*t*
    equations-of-motion, 932
    lift model, 937–940
    pitching moment model, 941–944
    requirements for, 932–934
    thrust model, 937
  taillets and stabilons, 1019
  ventral fin
    and deep stall, 1017
    and Dutch roll, 1017
Stability augmentation system (SAS), 6
Stability coordinate system (SCS), 926*f*, 927
Stabilon, 1019
Stable aircraft, 933
Stall
  angle-of-attack
    correction for, 375
    of wing, 375
  horizontal tail, 1010–1012, 1011*f*
  speed limits, 67, 67*f*
  strips, 1019, 1020*f*
Stall-break, 1009
Stall characteristics, 1009–1010
  jet aircraft, 1021–1022
  stall strips, 1019, 1020*f*
Stall handling
  stall strips, 1019
  vortilons, 1022, 1022–1023*f*
  wing droop, 1023, 1024*f*
  wing fence, 1021, 1021*f*
  wing pylons, 1021, 1022*f*
Stalling airspeed
  $C_{L_{max}}$ for desired, 67
  level stalling speed with load factor, 60
  stalling speed during banking, 60
  wing area function, 71*t*
Stalling speed, 843, 843*f*
  during banking, 843
  with load factor, 843
  with thrust, flap, and CG effects, 844
Stall progression
  design guidelines, 391
  with multiple airfoils, 393
  wing design, 1015*f*
Stall-proofing, 502–503
Stall speed
  $C_{L_{max}}$ for desired, 67
  constraint diagram with, 67*f*
  cruise speed carpet plot, 71–72
  limits, 67, 67*f*
Stall strips, 1019
Standard airworthiness certificate (AC), 15
Standard atmosphere, 757, 759
Standard IFR Approach, 888
Standard NACA-notation, 282
Standing mountain wave, 773–774
Statement of Compliance (SOC), 13–14
State of industry, 34–35
Static lateral-directional stability, 975, 976*f*
Static loads, 565, 568
Static longitudinal stability, 925, 926*f*
Statics, 925–926
Static thrust coefficient, 631
Static thrust, determination
  ducted fan, 644
  free propeller, 630–631, 639
Statistical weight analysis, 160–167
  aircraft, 160
  engine weight estimation, 165–167
    piston engines, 165, 166*f*
    turbofan engines, 165, 166*f*
    turboprop engines, 165, 166*f*
  GA aircraft components
    air conditioning, 164
    antiicing, 164
    avionics systems weight, 164
    electrical system, 164
    flight control system weight, 164
    fuel system weight, 163
    furnishings, 164
    fuselage weight, 161
    horizontal tail (HT) weight, 161
    hydraulic system weight, 164
    installed engine weight, 163
    main landing gear weight, 162
    nacelle/cowling weight, 163
    nose landing gear weight, 162
    pressurization, 164
    uninstalled (dry) engine weight, 163
    vertical tail (VT) weight, 161
    wing weight, 160
STC. *See* Supplemental type certificate (STC)
Steady climb, motion equations, 813
Steady fluid flow, 578, 579*f*
Steady-state roll rate, 1001
Steel
  alloy, 121–122
  endurance limit, 120
  low-carbon grade, 117
  properties, 123*t*
  truss, 134
  types, 555*f*
Steel alloy, 121–122
Steel truss, 134
Step
  fuselage external shape initial design, 521–525, 522–524*f*
  geometric layout
    taildragger landing gear, 562–564, 563–564*f*
    tricycle landing gear layout, 559–562, 560–562*f*
  propeller efficiency table, 636–637
Stick-fixed neutral point, 187–188*t*, 961–963
  design guidance, 508
  impact of horizontal tail volume, 509*f*
Stick-force, 968
Still-air glide performance, 903, 903*f*
Stopped propellers, 729–730
Straight leading edges, 356
Straight-tapered planforms, 356–357
Straight-tapered wing planform, 338, 338*f*
Strake Technology Research Application to Transport Aircraft (STRATA), 1018–1019
Stress corrosion, 120
Stressed-skin construction, 132, 134
Stretched acrylics, 528
Strict liability, 35
Structural envelope, 769–778
Structural layout, 113
  airframe, 130–145
    fuselage structure layout, 141
    horizontal vertical tail structure layout, 140–142
  structural concepts, 130–134
  wing structure layout, 134–140
Strut-braced wing
  cantilever configuration, 104
  maximum shear and bending loads, 104
Supercritical airfoils, 297
Supplemental type certificate (STC), 15
Surface area
  body of revolution, 530–531
  cone, 532
  elliptic cylinder, 532
  frustum, 514–515
  paraboloid, 532
  pod-style fuselage, 535
  tubular fuselage, 533–534
  uniform cylinder, 532
Sweep angle, 338–340
Swept back wings, 137–138
  aircraft inspection with, 138
  pitch-up boundary for, 396–398, 503, 504*f*
rib layouts for, 137*f*
  spanwise flow for, 395–396
Swept planforms, 357–359
  USAF DATCOM method, 385
Symmetric wing, 324

T

Tadpole fuselage, 519–521
  advantages, 520
  approximation, 534*f*
  vs. frustum fuselages, 520*f*
  modern sailplane, 658
  properties, 520
  reduction, 521, 521*f*
  Rolladen-Schneider LS4 sailplane boasts, 519*f*
  surface areas and volumes, 534–535
  transition and total fuselage drag, 520*f*
Tail
  conventional, 491–493, 491*f*
  cruciform, 493–494, 493–494*f*
  HT weight, 161
  inverted U-tail, 500, 501*f*
  types, 547*t*
  VT weight, 161
  weight data for, 195*t*
Tail-Aft stabilizing surfaces, 503
Tail arm, 72
  determination, 510
  directional moment coefficient, 72
  horizontal, 161
  weight data for, 195*t*
Tail configuration, 109
  A-tail, 500, 500*f*
  conventional, 491, 491*f*
  cruciform tail, 493, 493–494*f*
    aft podded engine configuration, 493–494
    drawbacks, 494
  design guidelines, 503–505
  H-tail, 499–500, 500*f*
  inverted V-tail configuration, 499, 499*f*
  rudder during spin on, 488–489, 489*f*
  T-tail, 494–495, 494–495*f*
  U-tail, 500, 500*f*
  V-tail/butterfly tail, 495, 496*f*
  Y-tail, 499, 499*f*
Tail-damping power factor (TDPF), 488
Taildragger, 542, 542*f*, 787, 790–791, 802
  advantages, 108–109
  castering-wheel configurations, 546*f*
  configurations, 108–109
  free-body diagram, 918
  geometric layout, 562–564
  ground characteristics, 559
  pros and cons, 542–543*t*
  reaction loads, 568–570, 568*f*
  T-O analysis, 785–786
  treatment of T-O run for, 800
Tail efficiency factor, 945
Tail, geometry of, 483–491
  horizontal and vertical tail volumes, 484–485
  reference geometry, 484, 484*f*
  spin and spin recovery, 486–491
  tail fixes, 485–486
Tailless aircraft, 745*t*
Taillet, 1019, 1019*f*
Tail sizing process, 482–483, 482*t*
Tail upsweep, 525, 525*f*
Tailwheel
  castering nose and, 546, 547*t*
  positioning, 543
  reaction, 568
Take-off, 785
  padding factors, 756*t*
  rotation capability, 1009
Take-off over
  sensitivity, 807–808
  steep runway slope impact, 808
Take-off performance, 786*f*
Take-off (T-O) rotation
  inverted V-tail configuration, 499
  limit, 186–187*t*
Takeoff safety airspeed, 768–769*t*
Take-off (T-O) weight
  mission airplane design, 148–149
  restrictions, 13*t*
Take-off weight ratios, 155
Tandem
  configuration, 108
  fixed landing gear, 108
  monowheel with outriggers, 108
Tandem wheel
  advantages and disadvantages, 542–543*t*
  configuration, 108
  fixed landing gear, 108
Tandem wing, 1021
Taper ratio (TR), 324, 332*t*, 337
Taper ratio correction factor (TRCF), 373
TC. *See* Type certificate (TC)
Technical standard order (TSO), 15
Technical standard order authorization (TSOA), 15
Temperature
  atmospheric ambient, 759
  equations for, 757
  fluid, 575
  glass-transition, 129
  high cabin, 105
Tetraethyl lead (TEL), 201
Theodorsen's airfoil theory, 286–287
Thermal efficiency, 588
Thermodynamics
  equations of, 580–581
  processes, 581*t*
Theta break, 588
Thickness-to-chord ratio, 282
THP. *See* Thrust horsepower (THP)
Three-bladed wooden propeller, 620
Three halves power law, 520
Three Part Type tire, 549*t*, 550*f*
Three-surface configuration, 501, 501*f*
Three-view drawings, 28
Throttle ratio (TR), 200, 588
Thrust, 43–44
  airspeed in, 839–840
  analytical methods, 637–638
  asymmetric, 485, 490
  for braking distance, 920, 920*t*
  constraint analysis, 58–59
  ducted fan, 644
  efficiency model for, 635*f*, 801*f*
  free propeller, 638
  generation of, 583*f*
  for jet-powered aircraft, 796
  for Learjet 45, 836*f*
  level stalling speed with, 844
  number of blades effect on, 627–629, 628*f*
  optimum design points, 59
  Prandtl correction, 649
  for propeller, 565
  reactive, 581
  static, 630–631
  static longitudinal stability, 937
Thrust available, 837
Thrust coefficient, 625
  Froude's, 625–627
  Seckel's, 625
Thrust effects, 107
Thrust horsepower (THP), 226
Thrustline
  effect of high or low, 106*f*
  free-body diagram, 713*f*
  trim drag, 713
Thrust model, 573, 836
  for gas turbines, 588
    computer code, 592–595
    specific thrust, 588
    theta break and throttle ratio, 588
    thrust-specific fuel consumption, 589
  for jet engines, 573
  propeller, 573–574
  turbofan engine, 574*f*
Thrust-power, 626, 630
Thrust required, 837
Thrust specific fuel consumption (TSFC), 589, 871
Thrust-to-weight ratio, 154, 585, 586*t*
Time-between-overhaul (TBO), 51, 54, 202
Time to altitude, 826–827
Tire
  for business jet aircraft, 553*t*
  drag of tires, 718*t*
  footprint, 545, 546*f*
  geometry, 548, 550*f*, 720*f*
  inflation pressure, 543–544
  for single engine propeller aircraft, 553*t*
  sizes, 548
    selection of, 550
  for twin engine propeller aircraft, 554*t*
  types, 548, 549*t*, 550*f*
Titanium, 123
  properties, 123, 123*t*
Titanium alloy, 123, 123*t*
Tooling, 4–5
  cost analysis, 41
  total cost of, 42–43, 48
  work hours, 7
  workhours, 40, 48
Torque
  calculation, 647
  coefficient, 625
Tort reform, 35
Total activity factor, 625
Total distance
  determination, 802–803
  landing phase, 916, 916*t*
Touch-down
  airspeeds, 919*t*
  landing phase, 916
  motion equation, 918
  sailplane, 900, 901*f*

Touch-down airspeed, 915
Touchdown sink rate, 557
Toyotism, 9
Tractor propeller
  configuration, 107, 599–600, 599*f*
  designing team, 525
Trade study, 58
  design of experiments (DOE), 72–73, 73*f*
  parametric analysis, 69–70, 69*f*
    baseline, 69, 70*f*
    carpet plots, 69
  stall speed–cruise speed carpet plot, 71–72, 71*t*
Trailing edge (TE), 282, 323–324, 356
Trailing edge down (TED), 302–303, 501
Trailing-edge flap, effect of, 302–303
Trailing-edge (TE) high-lift devices, 454–456
  double-slotted flaps, 446–449, 450*f*
  flaps, 432–433
  Gurney flap, 452–454, 452*f*
  junkers flap/external flap, 444–445
  plain flap, 433–442, 435–440*t*
  quick-guide, 433, 433–434*t*
  single-slotted flap, 445–446
  split flap, 442–444, 443*f*
Trailing edges, 356
Trailing edge tab, 1026
Trailing edge up (TEU), 302–303
Trailing link landing gear, 555–556
Transferability, 299
Transition
  distance determination, 802–804
  FRPs and GRPs, 129
  laminar-to-turbulent, 731
  from laminar to turbulent flow, 681*f*
  parameters, 686*t*
  T-O run segments, 786*t*
Transition ramp, 277
  transition curve, 1028
Transition Reynolds number, 274
Transport efficiency, 854
Trapezoidal wing planform
  arbitrary planform, geometric formulation of, 323–324
  cranked planform, geometric formulation of, 326–328
  geometric formulation of, 324–325
  MGC, Poor Man's determination of, 328
  wing volume approximation, 329–330
Tricycle, 542, 542*f*, 787, 790–791, 802
  configuration, 108
  fixed landing gear, 108–109
  geometric layout, 559–562
  ground stability, 560*f*
  landing gear, 559
  landing gear reaction loads, 559–562
    aerodynamic loads, 565
    Balanced Force Diagram, 565*f*
    static loads, 565
  location, 560*f*
  pros and cons, 542–543*t*
  stable on, 108–109
  taildragger configuration, 108–109
Trim drag, 713–714
Trimmability, 933, 934*f*
Trimming, 964–966
Trim point, 957–958
Trim tabs, 971
  antiservo tabs, 972, 972*f*
  balance tab, 972, 972*f*
  fixed, 971, 971*f*
  geared, 971, 971*f*
  movable, 971, 971*f*
  movable stabilizer, 972, 972*f*
  servo tab, 972, 972*f*
  spring, 971, 971*f*
Triplane
  drag characteristics, 746–749*t*
  primary advantage, 102–103
Triple-slotted fowler flap, 450, 451*f*
True airspeed, 763–764, 767
  equivalent airspeed, 763
  ground speed, 764
  landing distance, 922
  using simplified drag mode, 847*f*
TSO. *See* Technical standard order (TSO)
TSOA. *See* Technical standard order authorization (TSOA)
T-tail, 494–495, 494–495*f*
Tubular
  fuselage, 519, 533–534
  landing gear struts drag, 719*t*
  streamlined tension wire, 719–721
Tupolev Tu-114 passenger aircraft, 599*f*
Turbine entry temperature (TET), 199–200, 588–589
Turbofan engines, 44
  bypass ratio (BPR), 230
  flow characteristics, 230
  Mattingly model, 592
  mounted pylons, 6
  specific fuel consumption, 231
  thrust ratio, 593*f*
  *vs.*turbojets, 230
  weight of, 165, 166*f*
Turbofans, 199, 585*f*
  thrust equations, 585
Turbojet engine, 44
Turbojets, 199
  bleed air, 230
  characteristics of flow, 228
  cons of turbojet engines, 228
  engine pressure ratio (EPR), 228
  Mattingly model, 591
  overall pressure ratio (OPR), 230
  pros of, 228
  specific fuel consumption, 228
  throttle ratio (TR), 589
  thrust equations, 584, 585*f*
  thrust modeling for, 228
  thrust ratio, 591*f*
Turboprop engines, 43–44
  reversing propeller, 601
  weight of, 165, 166*f*
Turboprops, 199, 597–598
  Mattingly model, 590–591
  thrust ratio *vs.* Mach number, 590*f*
Turbulators, 1027–1028
Turbulent boundary layer
  laminar-to-turbulent transition, 685
  skin friction coefficient for, 684
Turbulent flow
  skin friction coefficient, 686
  tip airfoil, 688
Turf, 795*t*, 918*t*
Turning radius
  aircraft, 544
  distance to turning center, 544–545
  geometric definitions for, 545*f*
  minimum sustainable, 862
Turn performance map, 860*f*, 861–862
Twin-engine aircraft, asymmetric disc loading, 611–612, 612*f*
Twin tail boom, 500, 500*f*, 512. *See also* U-tail
Two-bladed wooden propeller, 620
Two-position propeller, 601
Two-surface configurations, 501
Type certificate (TC), 15
  STC, 15
  TCDS, 740
Type Certificate Data Sheet (TCDS), 457
Type III tire, 543, 721
Type VII tire, 543

U

Ultimate load, 114
Unit normal vector area, 579
Universal gas constant, 575
Unpowered descent, equations-of-motion for, 895
Unshielded control horn, 1019
Unsteady fluid flow, 578, 579*f*
Upturned booster wingtip, 465, 465*f*
Upwash/downwash gradient, 954
USA-35B, 291, 294*f*
USAF DATCOM
  method 1, 371
  method 2, 372
US Air Force Wright Aeronautical Laboratories (AFWAL), 211
Useful load, 149
US standard atmosphere 1976, 757, 758*t*
U-tail
  inverted U-tail, 500, 501*f*
  propeller configurations, 500
  twin tail-boom configuration, 500, 500*f*

V

Variable camber Krüger flap (VCK), 424
Variable camber leading edge, 422, 422*f*
Variable cost, 35
Variable Density Tunnel (VDT), 282–283
Variable pitch propeller, 604–605, 606*f*
Variable sweep planform, 359
VBA code, 514
Vehicle coordinate system (VCS), 926*f*, 927
Vendor supplied components (VSC), 39, 43
  avionics, 44*t*, 68
  cost of engines, 68
  cost of propellers, 44
  fixed *vs.* retractable landing gear, 67
Ventral fin, 486, 489
  AOA, 486
  impact for hypothetical airplane, 486
  installation, 486, 486*f*

Ventral fin *(Continued)*
on Learjet 60, 1017*f*
stability and control, 1017
Vertex, 80
Vertical airspeed, 814, 895
in thrust/power, 814–815
Vertical speed indicator (VSI), 895
Vertical tail (VT), 72, 140, 325, 481
aircraft components, 96
control surfaces, 141
design requirements for, 482–483
empennage, 100
heavy aircraft, 141
larger airplanes feature, 141
mean geometric chord, 484
side-force and, 982
sidewash, 982
unconventional tails, 142
volumes, 484–485, 505*t*
yawing moment and, 984, 985*f*
Viscosity, 575
Viscous profile efficiency, 627
Visual Basic for Applications (VBA), 410
V-n diagram. *See* Structural envelope
Volume
absolute humidity, 760
break-even analysis, 36
infinitesimal, 579, 629–630
passenger, 101–102
structural standpoint, 144
Volumetric flow rate, 579
Vortex
filament, 400
flow improvement, 1024, 1025*f*
generators on aft fuselage, 678*f*
pylon, 1021–1022
wingtip correction, 694
Vortex generator
on aft fuselage, 678*f*
application, 1024, 1025*f*
dual, 1026
large fixed-pitch, 677–678
on lower HT surface, 1025*f*
micro, 1025–1026, 1025*f*
nacelle strakes, 1026
Vortex-lattice method (VLM), 88, 310, 354, 368–370, 368–369*t*, 1015
Vortex-lattice theory, 379
Vortex-lift, 362–363
Vortilons, 1022, 1022–1023*f*
V-speeds, 767–769
V-tail
advantages, 496–497
configurations, 109, 495, 496*f*
difference in yaw response, 498*f*
inverted, 498–499*f*, 499
pitch-up moment, 496–497
Rudlicki, 495
simplified theory, 495, 966
unconventional tails, 142

W

Washin, 340–348
Washout, drag due to wing, 695
Washout, wing twist, 340–348
Water spray, 102, 106
Wave drag, 695–701
Weathervane, 984, 984*f*
Weight analysis methods, 149–158
gross weight estimation
using historical relations, 150–152
using mission analysis, 153–158
historical empty weight fractions, 152–153
secondary, 159–160
Weight budget, 191
acceptable for test vehicle, 191
actual weights, 193*t*
aircraft into categories, 191
Weight estimation, 147–148
Weight model, 835
Weight sensitivity, 829, 830*f*
Weight tolerances, 191–194
Weight, units of, 148
Welding, 117
Wet grass, 795*t*, 918*t*
Wheel
castering-wheel configurations, 546*f*
configurations, 108
fairings, 718
modern and aluminum wheels, 551
open and closed, 722
positioning, 543
Wheel track, 544
ground instability, 560*f*
overturn angle, 562
Whip stall, 1010
Whistling, 556
Whitcomb winglet, 471, 473*f*
Wieselberger's coefficient, 381
Wind axis coordinate system (WAS), 927, 927*f*
Windmilling propeller, 606, 607*f*, 729–730, 736
Wing
angle-of-incidence (AOI), 348–350
aspect ratio, 100*t*
geometric layout of
angle-of-incidence (AOI), 348–350
aspect ratio (AR), 331–337
dihedral and anhedral, 340
selected aircraft, properties of, 350
sweep angle, 338–340
taper ratio (TR), 337
washout and washin, 340–348
lift and moment characteristics of
delta wing, lift curve for, 376–378
3-dimensional lift curve, properties of, 364–366
flexible wings, 379
ground effect, 379–382, 380*f*
lift curve slope, 367–370
lift model, 366–367
maximum lift coefficient, 370–376
nonlinearity, to lift curve, 378–379
span efficiency, determination of, 383–388
zero-α lift, 367
planform selection
compound-tapered planforms, 357
constant chord ("Hershey Bar") planform, 354–355
cranked planforms, 359–361
delta planforms, 361–363
elliptical planforms, 355–356
exotic planform shapes, 363
optimum lift distribution, 352–354
spanwise lift distribution, 351–352
straight-tapered planforms, 356–357
swept planforms, 357–359
stall characteristics
flow separation growth, on aircraft, 389, 390*f*
generic stall pattern, 389–391
manufacturing tolerances, 398–399
pitch-up stall boundary, swept back wing planform, 396–398
progression, 391–395
spanwise flow, swept back wing planform, 395–396
Wing area
constraint analysis, 58
stall speeds, 71, 71*t*
Wing attachment, 28–29
aft, 140
extrusions, 116
fastener orientation, 139
transfer wing torsion, 137
Wing chord, 87
Wing droop, 1023, 1024*f*
Wing fence, 1021, 1021*f*
Wing flaps, 490
Wing-fuselage juncture, 314
Wing–HT–engine system
longitudinal stability, 960–961, 960*f*
pitching moment coefficient, 963*f*
Winglet, 470–474, 471*f*
interference factors, 711*t*
Wing-like surfaces, 716
Wing pylons, 1021, 1022*f*
Wing shear web, weight of, 151*t*
Wing sizing, 322
Wing sizing optimization, 86–89
aerodynamic analysis, 88
estimate range, 88
maximum fuel volume, 87
maximum fuel weight, 87
penalty function range, 88, 89*f*
wing fuel tanks, 87
wing geometry, 87
wing weight, 87
Wing skin, 132–133, 137
turbulent boundary layer, 677
weight of, 151*t*
Wing span, 323–324
scaling top view based on, 688*f*
Wing spar caps, weight of, 151*t*
Wingtip, 103, 489
correction, 694
parasite areas and coefficients, 703*t*
Wingtip design
aerodynamic effectiveness of, 462
booster wingtips, 465–466
endplate wingtip, 469–470
Hoerner wingtip, 466
Küchemann wingtip, 466–467, 467–468*f*
lift-induced drag, 461–462

polyhedral wingtip, 474–476, 475*f*
potential flow theory, 476–477
raked wingtip, 467–469, 468–469*f*
round wingtip, 462–463, 463*f*
spherical wingtip, 463–464, 463*f*
square wingtip, 464, 464*f*
winglet, 470–474, 471*f*
Wing volume approximation, 329–330
Wing weight, 160
Wood construction, 132
Work
hardening, 116–117
integrated product teams (IPT), 9
wing fence, 1021
Workhours
engineering, 39, 47
manufacturing labor, 40, 48
tooling, 40, 48
Wragg compound wing, 444
Wrought alloy, 119*t*, 120

X
XFLR5, 281, 281*f*
Xfoil, 281, 281*f*
vortex-lattice code, 1015

Y
Yaw, 481, 976
adverse, 497–498, 999
angle, 72
dorsal fin, 485*f*
due-to-roll, 986
Yaw control, 1003–1005, 1004*f*
Yaw damping, 987
Yawing, 497
airplane effect, 673*f*
stabilizing moment, 559
Yawing moment, 72, 983
with aileron deflection, 987
due to wing, 984
fuselage and nacelle contribution, 984
H-tail, 499–500
nacelles, 108
propeller effects, 986
with rudder deflection, 988
vertical tail contribution, 984, 985*f*
Yawing moment coefficient, 72
Yehudi flap, 96*t*, 1028, 1028–1029*f*
Y-tail, 109
configuration, 499, 499*f*
inverted, 499, 499*f*
shorter-span V-tail, 499
V-tail variation, 499

Z
Zap flap, 443
Zero-α lift coefficient, 367, 937
Zero lift angle-of-attack
and lift curve slope, 374
for selected NACA airfoils, 263

This page intentionally left blank

SECOND EDITION

GENERAL AVIATION AIRCRAFT DESIGN

APPLIED METHODS AND PROCEDURES

SNORRI GUDMUNDSSON

General Aviation Aircraft Design, 2nd Edition, continues to be the engineer's best source for answers to realistic aircraft design questions. The book has been expanded to provide design guidance for additional classes of aircraft, including seaplanes, biplanes, UAS, high-speed business jets, and electric airplanes. In addition to conventional powerplants, design guidance for battery systems, electric motors, and complete electric powertrains is offered. The second edition features three new chapters - two of which focus on stability and control:

- Thrust Modeling for Gas Turbines
- Longitudinal Stability and Control
- Lateral and Directional Stability and Control

These new chapters offer multiple practical methods to simplify the estimation of stability derivatives and introduce hinge moments and basic control system design. Furthermore, all chapters have been reorganized and feature updated material with additional analysis methods. This edition also provides an introduction to design optimization using a wing optimization as an example for the beginner. Written by an engineer with more than 25 years of design experience, professional engineers, aircraft designers, aerodynamicists, structural analysts, performance analysts, researchers, and aerospace engineering students will value this book as the classic go-to for aircraft design.

Key Features

- Presents the most common methods for conceptual aircraft design
- Features design topics that range from the "new" 14 CFR Part 23 to analysis of ducted fans
- Contains real-world examples using aircraft such as the Cirrus SR-22 and Learjet 45
- New and clear presentation splits text into shaded regions, separating engineering topics from mathematical derivations and examples

About the Author

Dr. Snorri Gudmundsson served from 1995 to 2009 at Cirrus Aircraft. He held various engineering roles in the development of several aircraft, including the Cirrus SR20 and SR22 aircraft. From 2005 to 2009 he served as Chief Aerodynamicist, where he was responsible for the aerodynamics of the SF50 Vision jet (recipient of the 2017 Collier Trophy). He had two appointments as Designated Engineering Representative (DER) for the for the FAA, as a Structural and Flight Analyst. He has contributed to the certification of several aircraft which includes development and certification flight and structural testing. He has conducted load analysis, stability and control evaluation, and performance analysis on various single and multi-engine aircraft. In 2010 Dr. Gudmundsson joined the faculty at Embry-Riddle Aeronautical University, where he is currently Associate Professor of Aerospace Engineering, teaching aircraft design and aerodynamics.

ISBN 978-0-12-818465-3

9 780128 184653

Butterworth-Heinemann
An imprint of Elsevier
elsevier.com/books-and-journals